N-I/28091--080

Phase I Flow and Transport Model Document for Corrective Action Unit 97: Yucca Flat/Climax Mine, Nevada National Security Site, Nye County, Nevada

Navarro-Intera

Revision No.: 1

September 2013

UNCLASSIFIED

/s/ Joseph P. Johnston, N-I CO 09/13/2013

Prepared for U.S. Department of Energy under Contract No. DE-AC52-09NA28091.

Approved for public release; further dissemination unlimited.

Available for sale to the public from:

U.S. Department of Commerce
National Technical Information Service
5301 Shawnee Road
Alexandria, VA 22312
Telephone: 800.553.6847
Fax: 703.605.6900
E-mail: *orders@ntis.gov*
Online Ordering: *http://www.ntis.gov/help/ordermethods.aspx*

Available electronically at *http://www.osti.gov/bridge*

Available for a processing fee to U.S. Department of Energy and its contractors, in paper, from:

U.S. Department of Energy
Office of Scientific and Technical Information
P.O. Box 62
Oak Ridge, TN 37831-0062
Phone: 865.576.8401
Fax: 865.576.5728
Email: *reports@adonis.osti.gov*

Reference herein to any specific commercial product, process, or service by trade name, trademark, manufacturer, or otherwise, does not necessarily constitute or imply its endorsement, recommendation, or favoring by the United States Government or any agency thereof or its contractors or subcontractors.

Printed on recycled paper

N-I/28091--080

PHASE I FLOW AND TRANSPORT MODEL DOCUMENT FOR CORRECTIVE ACTION UNIT 97: YUCCA FLAT/CLIMAX MINE, NEVADA NATIONAL SECURITY SITE, NYE COUNTY, NEVADA

Revision No.: 1
September 2013
Navarro-Intera, LLC
c/o U.S. DOE
P.O. Box 98952
Las Vegas, NV 89193-8952

Prepared for U.S. Department of Energy under Contract No. DE-AC52-09NA28091.

Approved for public release; further dissemination unlimited.

PHASE I FLOW AND TRANSPORT MODEL DOCUMENT FOR CORRECTIVE ACTION UNIT 97: YUCCA FLAT/CLIMAX MINE, NEVADA NATIONAL SECURITY SITE, NYE COUNTY, NEVADA

Approved by; /s/ Sam Marutzky Date: 9-25-13

Sam Marutzky, UGTA Project Manager
Navarro-Intera, LLC

TABLE OF CONTENTS

List of Figures xvi
List of Tables lix
List of Acronyms and Abbreviations lxviii
Acknowledgement lxxvi
Executive Summary ES-1

1.0 Introduction 1-1

1.1 Purpose and Scope 1-4
1.2 Regulatory Background 1-6
1.3 Yucca Flat Background Information—Physiography and Geology 1-10
1.4 Yucca Flat Background Information—Hydrostratigraphy and Groundwater Flow 1-16
1.5 Yucca Flat Background Information—Underground Nuclear Testing 1-33
1.6 Flow and Transport Modeling Approach 1-40
1.7 Flow and Transport Modeling Strategy 1-47
1.8 Yucca Flat Supporting Documents 1-51
1.9 Report Organization 1-52

2.0 Yucca Flat Unclassified Hydrologic Source Term 2-1

2.1 Underground Nuclear Detonation Categories at Yucca Flat 2-2
2.1.1 Unsaturated-Zone Detonations 2-5
2.1.2 Saturated-Zone Detonations 2-5
2.1.3 Detonations with Exchange Volumes Intersecting the Saturated LCA 2-6
2.2 Source-Term Conceptual Model 2-7
2.2.1 Source-Area Altered Zones 2-10
2.2.2 HST Processes 2-12
2.2.2.1 HST Processes for the Unsaturated-Zone Model 2-12
2.2.2.2 HST Processes for the Saturated Alluvial/Volcanic Aquifer System Model 2-14
2.2.2.3 HST Processes for the Saturated LCA Model 2-16
2.2.2.4 Implementation of HST Processes 2-16
2.3 Unclassified Yucca Flat Radionuclide Inventory 2-19
2.3.1 Radionuclide Screening 2-29
2.3.2 Radionuclide Distribution in the Subsurface 2-29
2.3.3 Allocation of Radionuclides between Models 2-32
2.4 HST Uncertainties 2-38
2.4.1 HST Conceptual Model Uncertainty 2-39
2.4.2 HST Parametric Uncertainty 2-41
2.5 Summary and Conclusions 2-47

TABLE OF CONTENTS (CONTINUED)

3.0 Yucca Flat Unsaturated-Zone Flow and Transport Model 3-1

3.1 Introduction 3-1

3.1.1 Summary of Unsaturated-Zone Nuclear Detonations at Yucca Flat 3-5

3.1.2 Hydrogeologic Setting 3-6

3.1.3 Previous Studies 3-9

3.1.3.1 Past and Present Background Infiltration 3-9

3.1.3.2 Infiltration Maps 3-13

3.1.3.3 Surface Effects Maps 3-14

3.1.3.4 Crater Infiltration Studies 3-18

3.1.3.5 Underground Nuclear Detonation Categorization 3-19

3.1.3.6 Faults and Fractures 3-20

3.1.3.7 Unsaturated-Zone HST Modeling 3-22

3.1.3.7.1 One- and Two-Dimensional Radially Symmetric Models 3-22

3.1.3.7.2 Three-Dimensional Models of ^{14}C and ^{3}H Transport from Representative Shallow and Deep Detonations 3-24

3.2 Unsaturated-Zone Data 3-26

3.3 Surface Water Runoff and Infiltration into Nuclear Subsidence Craters 3-35

3.4 Model Design and Setup 3-37

3.4.1 Numerical Grids 3-37

3.4.2 Boundary Conditions 3-44

3.4.2.1 Land Surface 3-44

3.4.2.2 Lateral Boundaries 3-46

3.4.2.3 Water-Table Boundary 3-47

3.4.3 Rock and Sediment Hydraulic and Transport Properties 3-47

3.4.3.1 Background 3-48

3.4.3.2 Application of Soil Methods to Intact and Fractured Rock 3-49

3.4.3.3 Alluvium Properties 3-51

3.4.3.4 Rock Properties 3-55

3.4.3.4.1 Data Summaries in the Hydrologic Data Document 3-55

3.4.3.4.2 Data from Unsaturated-Zone Studies at Rainier Mesa 3-58

3.4.3.4.3 Data on Pre-Tertiary Rocks from Winograd and Thordarson (1975) 3-58

3.4.3.4.4 Tuff Matrix Hydraulic Properties from Yucca Mountain 3-62

TABLE OF CONTENTS (CONTINUED)

3.4.3.4.5 Hydraulic and Transport Properties Used in the Unsaturated-Zone Models for Yucca Flat 3-63
3.5 Uncertainty and Sensitivity Approach 3-68
3.5.1 Sensitivity Matrix 3-68
3.5.2 Source-Term Simplification and the Rationale for Radionuclide Selection 3-70
3.5.2.1 Selection of Radionuclide Species 3-72
3.5.2.2 Assumptions and Simplifications 3-72
3.6 Flow and Transport Model Results. 3-73
3.6.1 Steady-State Flow Model 3-73
3.6.1.1 Recharge at the Water Table 3-74
3.6.2 Transient Flow and Transport Model Results: Examples from Runs 2.1.1.2.1.2 and 2.1.3.2.1.2. 3-77
3.6.3 ^{14}C Breakthrough at the Water Table. 3-81
3.6.3.1 All Results 3-81
3.6.3.2 Effect of Background Infiltration 3-83
3.6.3.3 Effect of Exchange Volume Radius 3-84
3.6.3.4 Effect of Crater Infiltration Rates 3-84
3.6.3.5 Effect of Sediment Anisotropy 3-85
3.6.3.6 Effect of Tuff Confining Unit Anisotropy 3-85
3.6.3.7 Effect of Tuff Confining Unit Porosity 3-87
3.6.3.8 Effect of Collapse Chimneys 3-88
3.6.4 Estimation of Mass Arrival at the Water Table for Other Radionuclides 3-89
3.6.5 Maps Showing Breakthrough of Selected Radionuclides at the Water Table. 3-90
3.6.5.1 Model Run 2.1.1.2.1.2 3-92
3.6.5.2 Model Run 2.1.3.2.1.2 3-100
3.6.6 Water and Radionuclide Fluxes to the Saturated-Zone Models 3-100
3.6.7 Model Limitations 3-110
3.7 Evaluation of the Impact of Liquid-Gas Partitioning of ^{14}C and Sediment Heterogeneity on Radionuclide Transport 3-111
3.7.1 Effect of Liquid-Gas Partitioning on ^{14}C Transport to the Water Table 3-112
3.7.2 Effect of Alluvial Heterogeneity on Radionuclide Transport 3-117
3.7.2.1 Sediment Hydrologic Properties 3-119
3.7.2.2 Steady-State Recharge at the Water Table 3-119
3.7.2.3 Transport Model Results for Heterogeneous Alluvium Model 3-119

TABLE OF CONTENTS (CONTINUED)

3.8 Unsaturated-Zone Models with Alternative HST Conceptualization 3-124
3.8.1 Alternative Model Run 1.2.1.2.1.2' 3-125
3.8.2 Model Run 5.4.2.1.2.1 3-129
3.9 Summary and Conclusions 3-134

4.0 Yucca Flat Saturated Alluvial/Volcanic Aquifer System Flow and Transport Model 4-1

4.1 Introduction 4-1
4.2 Hydrogeologic Conceptual Model 4-4
4.2.1 Flow Directions 4-4
4.2.2 Predevelopment and Detonation-Induced Fluxes through the Saturated Volcanics 4-6
4.2.3 Hydrostratigraphy 4-9
4.2.4 Hydraulic Properties 4-14
4.2.5 Hydrologic Connection to the LCA 4-14
4.2.6 Testing Effects 4-17
4.3 Numerical Model Development 4-19
4.3.1 Numerical Mesh 4-21
4.3.2 Testing Effects 4-29
4.3.3 The Coupled Model 4-32
4.4 Model Calibration 4-33
4.4.1 Water-Level Data Selection 4-33
4.4.2 Calibration and Model Uncertainty Assessment Process 4-38
4.5 Flow and Advective Transport 4-42
4.5.1 Representative Flow Field with Advective Transport 4-44
4.5.2 Sensitivity Analysis 4-51
4.5.3 Post-audit: InSAR 4-58
4.5.4 Flow Model Limitations 4-61
4.6 Radionuclide Transport 4-61
4.6.1 Methodology 4-61
4.6.2 Implementation 4-63
4.6.2.1 Particle Trajectories 4-63
4.6.2.2 Assigning Mass Flux to Each Particle 4-64
4.6.2.3 Transport Properties of Rocks and Fault Zones 4-68
4.6.3 Three Representative Results 4-77
4.6.4 Impact of Numerical Approximations on Saturated Alluvial/Volcanic Aquifer System Flow and Transport Model 4-92
4.6.4.1 Position of Particles at the Water Table 4-92
4.6.4.2 Increasing the Number of Time-Varying Segments 4-93
4.6.4.3 Uniform Distribution versus Three Shells of Particles 4-95

TABLE OF CONTENTS (CONTINUED)

4.6.5 Sensitivity Analysis 4-97
4.6.6 Breaching the Lower Model Boundary 4-105
4.6.7 Transport Parameter Sensitivity Analysis 4-108
4.6.8 Transport Parameter Uncertainty Analysis 4-113
4.6.8.1 Effects of Source-Term Uncertainties 4-113
4.6.8.2 Source-Term Inventory Uncertainty 4-113
4.6.8.3 Uncertainty in Melt-Glass Partitioning Factor 4-116
4.6.8.4 Uncertainty in Source Term and Melt-Glass Partitioning Factor 4-122
4.6.8.5 Uncertainty due to Source-Term Inventory, Partitioning Factor, and Transport Parameters 4-122
4.6.9 Comparison of Model Results to Measurement Data. 4-126
4.7 Summary and Conclusions 4-133

5.0 Yucca Flat Saturated Lower Carbonate Aquifer Flow Model 5-1

5.1 Introduction. 5-2
5.2 Background Hydrogeologic Data 5-7
5.2.1 Introduction 5-7
5.2.2 Yucca Flat Hydrostratigraphic Framework 5-7
5.2.3 Groundwater Discharge 5-12
5.2.4 Hydraulic Heads 5-15
5.2.5 Hydraulic Properties of Saturated Media 5-22
5.2.5.1 Hydraulic Conductivity Data 5-22
5.2.5.2 Aquifer Storage Data 5-22
5.2.5.3 Horizontal Anisotropy 5-24
5.2.5.4 Vertical Anisotropy 5-24
5.2.6 Groundwater Chemistry 5-25
5.2.6.1 Geochemical Modeling 5-25
5.2.6.2 Carbon-Dating Analysis 5-30
5.2.6.3 Geochemical Analysis 5-32
5.2.7 Groundwater Temperatures 5-34
5.2.8 LCA Flow Model Conceptualization 5-36
5.3 Previous Modeling Studies 5-38
5.3.1 USGS 2004 DVRFS Model 5-39
5.3.2 SNJV 2006 Yucca Flat/Climax Mine CAU Groundwater Flow Model. 5-43
5.3.3 DRI 2007 Climax Mine Flow Model 5-47
5.3.4 DRI 2012 Climax Mine Flow Model 5-53
5.3.5 USGS 2012 DVRFS Model 5-56
5.3.6 Summary. 5-57
5.4 LCA Groundwater Flow Model Construction 5-61
5.4.1 Model Area. 5-62
5.4.2 Model Mesh 5-63

TABLE OF CONTENTS (CONTINUED)

5.4.3 Material Assignment and Parameter Distribution 5-65
5.4.4 Boundary Conditions 5-69
5.5 Flow Model Calibration 5-74
5.5.1 Calibration Background 5-78
5.5.1.1 Calibration Metrics 5-78
5.5.1.2 Model Parameterization 5-81
5.5.1.3 Calibration Data 5-87
5.5.1.4 Calibration Approach 5-88
5.5.2 Calibration Results 5-95
5.5.3 Model Limitations 5-106
5.6 Flow Model Uncertainty Analyses 5-111
5.6.1 Introduction 5-111
5.6.2 Global Uncertainty Analysis 5-112
5.6.3 Northern Boundary Flux Uncertainty. 5-127
5.6.4 HFM Uncertainty 5-134
5.6.5 Fault-Zone Parametric Uncertainty 5-138
5.6.6 Narrower Fault Zone Alternative Model (Level 3 Mesh) 5-142
5.7 Parameter Sensitivity Analysis 5-144
5.7.1 Background. 5-144
5.7.2 Parameter Sensitivity Analysis. 5-147
5.7.3 Parameter Perturbation Analysis 5-150
5.7.4 Global Velocity Sensitivity 5-154
5.7.5 Sensitivity Summary 5-165
5.8 Summary and Conclusions 5-166
5.8.1 Summary of Hydrogeology and Conceptual Model. 5-166
5.8.2 Summary of LCA Flow Model Calibration 5-168
5.8.3 Conclusions 5-172
5.8.4 Model Limitations 5-175

6.0 Yucca Flat Saturated Lower Carbonate Aquifer Transport Model. 6-1

6.1 Transport Conceptual Model and Parameters. 6-3
6.1.1 Advective and Dispersive Transport 6-4
6.1.2 Matrix Diffusion. 6-5
6.1.3 Matrix and Fracture Sorption 6-6
6.1.4 Colloid-Facilitated Transport 6-7
6.1.5 Radioactive Decay Chains 6-7
6.2 Numerical Model Approach 6-8
6.2.1 Introduction 6-9
6.2.2 FEHM Particle Tracking 6-11
6.2.3 PLUMECALC 6-11

TABLE OF CONTENTS (CONTINUED)

6.3 Parameters 6-13
6.3.1 Fracture Parameters 6-16
6.3.1.1 Fracture Porosity 6-22
6.3.1.2 Fracture Aperture 6-26
6.3.1.3 Fracture Spacing 6-37
6.3.1.4 Summary Discussion of Fracture Parameters 6-41
6.3.2 Matrix Porosity 6-42
6.3.3 Matrix Diffusion Coefficient Parameters 6-42
6.3.3.1 Matrix Tortuosity 6-43
6.3.3.2 Free-Water Diffusion Coefficients 6-45
6.3.4 Dispersivity 6-46
6.3.5 Fracture Retardation and Matrix Sorption 6-47
6.3.5.1 Fracture Retardation 6-47
6.3.5.2 Matrix Sorption 6-48
6.3.6 Input Parameters for the Alternative LCA Parametrization Simulation 6-50
6.3.6.1 Alternative Fracture Parameter Values 6-52
6.3.6.2 Alternative Matrix Porosity Values 6-55
6.3.6.3 Alternative Matrix Diffusion Coefficient Values 6-59
6.4 Integration of the LCA Flow Model and HST Inputs to the LCA Transport Model 6-59
6.4.1 LCA Flow Model Particle-Tracking Results 6-60
6.4.2 Unsaturated-Zone Source Inputs to the LCA Transport Model 6-74
6.4.3 Saturated-Zone Source Inputs to the LCA Transport Model 6-85
6.4.4 LCA Source Inputs to the LCA Transport Model 6-94
6.4.5 Comparison of Source Inputs to the LCA Transport Model 6-94
6.4.6 LCA Transport Model Contaminant Concentrations 6-104
6.5 LCA Transport Model Results 6-105
6.5.1 Introduction 6-106
6.5.2 Base Case 6-109
6.5.3 Alternative LCA HSTs 6-131
6.5.4 Alternative Infiltration Rates 6-135
6.5.5 Alternative Saturated Alluvial/Volcanics Aquifer System Flow and Transport Models 6-144
6.5.6 Alternative LCA Flow Fields 6-150
6.5.7 Alternative LCA Transport Parameters 6-155
6.5.8 Combined Transport Model Runs 6-162
6.5.9 Sensitivity Importance Analyses 6-163
6.5.9.1 Approach 6-168
6.5.9.2 Stepwise Regression Analysis Results 6-168

TABLE OF CONTENTS (CONTINUED)

6.5.9.3 Entropy Analysis Results 6-171
6.5.9.4 Classification Tree Analysis Results 6-173
6.5.9.5 Results of Uncertainty Importance/Sensitivity Analyses for Alternative Modeling Scenarios 6-180
6.5.10 Composite Contaminant Boundaries and Conclusions 6-182
6.6 Summary and Conclusions 6-192

7.0 Summary and Conclusions 7-1

8.0 References 8-1

Appendix A - Quality Assurance Project Plan Implementation

A.1.0 Implementation of QAPP Requirements in Yucca Flat/Climax Mine CAU Flow and Transport Model A-1

A.2.0 References A-22

Appendix B - Yucca Flat/Climax Mine CAU Detonation Characteristics

B.1.0 Yucca Flat/Climax Mine CAU Detonation Characteristics B-1

B.2.0 References B-26

Appendix C - Yucca Flat/Climax Mine CAU Hydrologic Source Term Allocation and Screening

C.1.0 Introduction C-1

C.2.0 Objectives C-2

C.3.0 Hydrologic Source Term Conceptual Model C-3

C.3.1 Phenomenology C-4
C.3.2 Altered Zones C-6
C.3.3 Radiologic Source Term C-7
C.3.4 Physical Partitioning and Spatial Distribution of the RST C-13

C.4.0 Hydrologic Source Term Screening C-19

C.4.1 Purpose C-19
C.4.2 Conceptual Model and Basis C-19
C.4.3 Approach C-19
C.4.4 Simplifications C-20
C.4.5 Parameter Distributions and Basis Used in HST Screening C-21
C.4.6 Results C-24
C.4.7 Conclusions C-26

C.5.0 Hydrologic Source Term Allocation between Models C-28

C.6.0 References C-63

TABLE OF CONTENTS (CONTINUED)

Appendix D - Contamination Observations in Yucca Flat Wells

D.1.0 Introduction D-1

D.1.1 Background D-1
D.1.2 Purpose/objectives D-1
D.1.3 Observation wells in Yucca Flat D-2
D.1.4 Sampling of observation wells in Yucca Flat D-4
D.1.5 Contents of Appendix D-4

D.2.0 Observation Wells Completed in Saturated Alluvial-Volcanic Aquifer System Near Underground Nuclear Detonations D-12

D.2.1 ALEMAN and SANDREEF D-12
D.2.2 BASEBALL D-13
D.2.3 DALHART D-15
D.2.4 GASCON D-17
D.2.5 INGOT D-18

D.3.0 Observation Wells Completed in Saturated Lower Carbonate Aquifer Near Underground Nuclear Detonations D-20

D.3.1 BILBY D-20
D.3.2 BOURBON D-23
D.3.3 NASH D-24
D.3.4 MICKEY and TORRIDO D-27

D.4.0 Summary and Conclusions D-28

D.5.0 References D-29

Appendix E - Enhanced Crater Recharge Model and Analyses

E.1.0 Introduction E-1

E.2.0 Methods and Parameters E-3

E.2.1 Crater Catchment Delineation E-3
E.2.2 Precipitation Data E-3
E.2.3 Potential Evapotranspiration E-3
E.2.4 Calibration of HYDRUS-1D to Lysimeter Data E-5
E.2.5 Soil Conservation Service Curve Number (SCS-CN) Method E-5

E.3.0 GIS Analyses E-9

E.3.1 GIS Analysis Files E-9
E.3.2 GIS Analysis Results E-24
E.3.2.1 Crater Dimensions E-24
E.3.2.2 Watershed Areas E-24
E.3.2.3 Crater Characteristics E-26

TABLE OF CONTENTS (CONTINUED)

E.4.0 Coupled Runoff and Infiltration Model Calibration for Enhanced Crater Recharge E-30

E.4.1 Crater U-10i (BYE) E-31
E.4.2 Crater U-3fd (LAGUNA) E-32
E.4.3 Crater U-3bh (HYRAX) E-34
E.4.4 Crater U-5a (WISHBONE). E-38

E.5.0 Results. E-40

E.6.0 References. E-66

Appendix F - Saturated Zone Pluvial Drainage Model

F.1.0 Alternative Conceptual Models and Parameters of Saturated Volcanic Rock Units at Yucca Flat F-1

F.1.1 Evaluating the 'Slow Drainage' Hypothesis. F-1
F.1.2 Numerical Models and Supporting Data F-4
F.1.3 Transient Simulations F-5
F.1.3.1 Sensitivity Analysis Results F-7
F.1.3.2 Implications for Flow and Transport Modeling F-12

F.2.0 References. F-15

Appendix G - Saturated Volcanic Aquifer System Test-Induced Overpressure Conceptual Model and Characteristics

G.1.0 Simulating Underground Nuclear Testing Effects within the CAU-Scale Model G-1

G.1.1 Rationale G-1
G.1.2 Approach G-3
G.1.3 Numerical Model Details G-5
G.1.3.1 Pressurization G-5
G.1.3.2 Rock Property Changes due to Testing G-7
G.1.4 Comparison of Model Results to Measured Heads at TW-7 . . . . . G-16
G.1.4.1 Previous Studies of TW-7 Response G-18
G.1.4.2 Radial Flow Model. G-20
G.1.4.3 Three-Dimensional Flow Models. G-22

G.2.0 Hydrologic Analysis of Core from Yucca Flat. G-26

G.3.0 References. G-31

TABLE OF CONTENTS (CONTINUED)

Appendix H - Thermohydrologic Flow Model and Analyses

H.1.0 Introduction H-1

H.2.0 Simplified Geothermal Models H-8

H.2.1 Central Box Model H-9
H.2.2 Northern Thermal Model H-20

H.3.0 References H-33

Appendix I - Transient Flow Model for the Lower Carbonate Aquifer in Yucca Flat

I.1.0 Introduction I-1

I.2.0 Effect of Alternative Boundary Conditions on the Simulated LCA Flow Model during the MWAT I-2

I.2.1 Background and Objectives I-2
I.2.2 Technical Approach I-2
I.2.3 Simulation Results and Conclusions I-3

I.3.0 Effect of Long-term Groundwater Discharge on the LCA Flow Field I-10

I.3.1 Background and Objectives I-10
I.3.2 Technical Approach I-10
I.3.3 Simulation Results and Conclusions I-10

I.4.0 Effect of Post-Detonation Transient Recharge to the LCA from the Overlying Unsaturated Zone and Saturated Alluvial/Volcanic Aquifer System I-16

I.4.1 Effect of Transient Recharge from the Unsaturated Zone I-16
I.4.2 Effect of Transient Recharge from the Saturated Alluvial/Volcanic Aquifer System I-20

I.5.0 Conclusions I-32

I.6.0 References I-33

Appendix J - LCA Fault Zone Conceptual Model and Characteristics

J.1.0 Introduction J-1

J.1.1 Objectives J-1
J.1.2 General Description of LCA Fault Zones J-2
J.1.3 Summary of Geologic Information/Interpretations of LCA Fault Zones J-2
J.1.4 Summary of Hydrogeologic Information/Interpretations of LCA Fault Zones J-6

TABLE OF CONTENTS (CONTINUED)

J.1.5 Geologic and Hydrogeologic Information/Interpretations of Analog Fault Zones J-7

J.2.0 Lower Carbonate Aquifer Flowing Feature Analysis J-10

J.2.1 Introduction J-10
J.2.2 LCA Fracture Database – Yucca Flat J-10
J.2.3 Approach to Flowing Feature Analysis J-13
J.2.4 LCA Flowing Feature Analysis J-15
J.2.4.1 Synthesis of Available LCA Fracture Data J-15
J.2.4.2 Detailed Analysis of SFM and Fracture Data J-23
J.2.4.3 Detailed Analysis of SFM Data to Discriminate Large- versus Smaller-Scale Flowing Features J-25
J.2.4.4 Analysis of Smaller-Scale Features and the Correlation Between Measured Properties and Flow Rate J-27
J.2.5 Study Conclusions and Potential for Application J-30

J.3.0 Summary J-35

J.4.0 References J-36

Appendix K - Technical Basis for Transport Model Software Selection

K.1.0 Introduction K-1

K.1.1 FFACO and QAPP Software Requirements K-2
K.1.2 Software Selection Criteria and Approach K-3
K.1.3 UGTA Software Selection Background K-5
K.1.4 Contents of Appendix K K-6

K.2.0 Particle-Tracking Software Selection Basis K-7

K.2.1 Introduction to FEHM_sptr and Walkabout K-7
K.2.2 Comparisons to Analytical Solutions and Alternative Software K-8

K.3.0 Transport Model Software Selection Basis K-19

K.3.1 Introduction to PLUMECALC K-19
K.3.2 One-Dimensional Comparisons to Analytical Solutions K-19
K.3.3 Three-Dimensional Comparisons to Alternative Corroborative Software K-20

K.4.0 Conclusions K-30

K.5.0 References K-31

TABLE OF CONTENTS (CONTINUED)

Appendix L - Groundwater ^{14}C Ages and Velocity Estimates for the Lower Carbonate Aquifer in Yucca Flat

L.1.0 Introduction L-1

L.1.1 Previous Geochemical Analyses L-1
L.1.2 Factors Affecting Estimates of Groundwater Velocity Derived from ^{14}C Observations L-3

L.2.0 Analyses of Groundwater ^{14}C Ages L-5

L.2.1 Maps of Groundwater ^{14}C Ages L-13
L.2.2 Comparison of ^{14}C Ages with LCA Groundwater Flow Regime L-15
L.2.3 Laboratory ^{14}C Sorption and Diffusion Studies L-16
L.2.4 Inferences from Devils Hole L-18

L.3.0 Assessment of Groundwater ^{14}C Ages in Yucca Flat Using Terrestrial and Groundwater ^{36}Cl /Cl Ratios L-20

L.4.0 Evaluation of Groundwater ^{14}C Velocities with a One-Dimensional Flow and Transport Model L-25

L.5.0 Summary and Conclusions L-31

L.6.0 References L-33

Appendix M - Evaluation of the Importance of Colloid Transport in the Lower Carbonate Aquifer in Yucca Flat

M.1.0 Introduction M-1

M.2.0 Effective Flow and Transport Parameters M-4

M.2.1 Fracture Parameters, Flow Rate, and Matrix Porosity M-4
M.2.2 Conductivity and Inflow Rate M-5
M.2.3 Matrix Diffusion Coefficient and Fracture Dispersivity M-5
M.2.4 Sorption Distribution Coefficients M-6
M.2.5 Colloid Load M-8
M.2.6 Rate Constants for Colloid-Facilitated Plutonium Transport M-10
M.2.7 Initial Concentrations of Radionuclides in the BOURBON Source Area M-13

M.3.0 Radionuclide Reactive Transport along a Streamtube in the LCA M-16

M.3.1 Generalized Dual-Porosity Model M-16
M.3.2 One-Dimensional Streamtube M-16
M.3.3 Radionuclide Reaction Processes M-17

TABLE OF CONTENTS (CONTINUED)

M.4.0 Parameter Sampling and Monte Carlo Simulations M-19

M.4.1 Framework of Monte Carlo Simulation M-19
M.4.2 Parameters Sampled with Latin Hypercube Sampling M-20

M.5.0 Radionuclide Reactive Transport Simulation Results M-31

M.5.1 Contaminant Lengths for Radionuclide Transport in the LCA M-31
M.5.2 Concentration Profiles for Each Radionuclide at 1,000 Years M-39
M.5.3 Plutonium Reduction Factor M-44

M.6.0 Global Sensitivity Analysis M-51

M.6.1 Methods for Global Sensitivity Analysis M-51
M.6.2 Normalization of Input Parameters M-52

M.7.0 Summary M-63

M.8.0 References M-66

Appendix N - Corroborative Software Analyses

N.1.0 Introduction N-1

N.1.1 Purpose/Objectives Approach N-1
N.1.2 Corroborative Software N-1
N.1.2.1 MODFLOW/MT3DMS N-2
N.1.2.2 FEFLOW N-3
N.1.2.3 FracMan/MAFIC N-5
N.1.3 Description of Model used for Corroborative Software Analyses N-7
N.1.3.1 Model Domain N-7
N.1.3.2 Model Description and Inputs N-11
N.1.3.2.1 Flow Model Parameters N-11
N.1.3.2.2 Flow Model Boundary Conditions N-11
N.1.3.2.3 Transport Model Parameters N-13
N.1.3.2.4 Transport Model Source Inputs N-13
N.1.3.3 FEHM Flow Model Results N-16
N.1.3.4 PLUMECALC Transport Model Results N-16
N.1.4 Outline of Appendix N-20

N.2.0 MODFLOW/MT3DMS N-21

N.2.1 Model Description N-21
N.2.2 Flow Model Results N-23
N.2.3 Transport Model Results N-26
N.2.4 Summary N-35

TABLE OF CONTENTS (CONTINUED)

N.3.0 Feflow N-36

N.3.1 Model Description N-36
N.3.2 Flow Model Results N-48
N.3.3 Transport Model Results. N-48
N.3.4 Discussion N-48

N.4.0 FracMan/MAFIC N-55

N.4.1 Model Description N-55
N.4.1.1 FracMan Model Domain N-59
N.4.1.2 EPM (Volumetric Element Mesh) Implementation N-59
N.4.1.3 Discrete Fracture Network (DFN) Implementation N-61
N.4.1.4 Boundary Conditions – Flow and Transport N-63
N.4.1.5 Flow Field Solution N-68
N.4.1.6 Solute Transport Solution. N-68
N.4.2 FracMan Flow Simulation Results N-72
N.4.2.1 FracMan Transport Simulation Results – Advection/Dispersion N-76
N.4.2.2 FracMan Transport Simulation Results – Decay/Matrix Diffusion N-79

N.5.0 Summary N-87

N.6.0 References. N-88

Appendix O - Nevada Division of Environmental Protection Comment Responses

LIST OF FIGURES

NUMBER	TITLE	PAGE
ES-1	Physiographic Features and Nuclear Detonations of the Yucca Flat/Climax Mine CAU	E-2
ES-2	Three-Dimensional Perspective of Yucca Flat/Climax Mine CAU Model Domains	E-7
ES-3	Composite Time-Cumulative Contaminant Boundaries for the Yucca Flat/Climax Mine CAU	E-17
ES-4	Composite Contaminant Boundary at (a) 100 Years, (b) 300 Years, and (c) 1,000 Years	E-18
1-1	Location of the Yucca Flat/Climax Mine CAU and Other UGTA CAUs	1-7
1-2	Process Flow Diagram for the UGTA CAUs	1-8
1-3	Satellite Image and Physiographic Features of the Yucca Flat/Climax Mine CAU	1-11
1-4	Generalized Geologic Map of the Yucca Flat/Climax Mine Region and Associated Physiographic Features	1-12
1-5	Surface Topography Showing the Effects of Underground Nuclear Tests in Shafts and Tunnels at the Yucca Flat/Climax Mine CAU	1-14
1-6	Aerial Photograph of Surface Craters in the Yucca Flat/Climax Mine CAU Viewed to the Northeast	1-15
1-7	Perspective Plot of the Yucca Flat/Climax Mine CAU HFM Viewed to the Northwest	1-17
1-8	Fence Diagram of the Yucca Flat/Climax Mine CAU HFM Viewed to the Northwest	1-18
1-9	Distribution of HSUs at the Water Table for the Yucca Flat/Climax Mine CAU Model Area	1-24
1-10a	West–East Profile of HSUs for the Yucca Flat/Climax Mine CAU Model Area	1-25
1-10b	North–South Profile of HSUs for the Yucca Flat/Climax Mine CAU Model Area	1-26

LIST OF FIGURES (CONTINUED)

NUMBER	TITLE	PAGE
1-11	General Groundwater Flow Paths in the Alluvial/Volcanic Aquifer System in Yucca Flat	1-27
1-12	Potentiometric Surface in the LCA in Yucca Flat and Surrounding Areas, Including Ash Meadows	1-29
1-13	Interpreted LCA Flow Directions in the Yucca Flat/Climax Mine CAU and Vicinity	1-30
1-14	Yucca Flat/Climax Mine CAU Underground Nuclear Detonations Ranked by Size of Maximum Yield-Weighted Cavity Size	1-36
1-15	Yucca Flat/Climax Mine CAU Underground Nuclear Detonations Ranked by Fraction of Maximum Yield-Weighted Total Initial Inventory	1-37
1-16	Relationships between the Yucca Flat/Climax Mine CAU Model Domains in Three-Dimensional Perspective	1-45
1-17	Lateral Boundaries of the Yucca Flat/Climax Mine CAU Model Domains	1-46
2-1	Perspective View of Underground Nuclear Detonations at Yucca Flat	2-3
2-2	Underground Nuclear Detonations at Yucca Flat with Exchange Volumes That Intersect the Saturated LCA When an Exchange Volume Radius of 3 R_c Is Assumed	2-8
2-3	Underground Nuclear Detonations at Yucca Flat with Exchange Volumes That Intersect the Saturated LCA When an Exchange Volume Radius of 2 R_c Is Assumed	2-9
2-4	Schematic Diagram of the Source-Area Altered Zones	2-11
2-5	Total Radionuclide Activity versus Time	2-23
2-6	MCL-Normalized Cavity Concentration versus Time	2-25
2-7	MCL-Normalized Cavity Concentration versus Time Less Melt-Glass Inventory	2-26
2-8	MCL-Normalized Cavity Concentration versus Time Less Melt-Glass Inventory Considering Sorption	2-27

LIST OF FIGURES (CONTINUED)

NUMBER	TITLE	PAGE
2-9	Block-Diagram Perspective of the CORDUROY Detonation within the HFM	2-35
2-10	Inventory Allocation Fraction Uncertainty for the Unsaturated-Zone Model	2-44
2-11	Inventory Allocation Fraction Uncertainty for the Saturated Alluvial/Volcanic Aquifer System Model	2-45
2-12	Inventory Allocation Fraction Uncertainty for the Saturated LCA Model	2-46
2-13	Uncertainty in Radionuclide Inventory from the BOURBON Detonation for the Saturated LCA Model	2-48
3-1	Relationship between Different Supporting Studies and the Overall Unsaturated-Zone Model for Yucca Flat	3-3
3-2a	Elevations of Unsaturated-Zone Detonations Relative to the Water Table: All Unsaturated-Zone Detonations	3-7
3-2b	Elevations of Unsaturated-Zone Detonations Relative to the Water Table: Detonations within 100 m of the Water Table	3-8
3-3	UGTA Revised Infiltration Map for the Yucca Flat Area	3-15
3-4	USGS Model 1 (with Runoff) Infiltration Map for the Yucca Flat Area	3-15
3-5	DRI-CMB (Alluvial and Elevation Mask) Infiltration Map for the Yucca Flat Area	3-16
3-6	Composite Surface Effects Map in the Vicinity of U-2dg (CARPETBAG)	3-17
3-7	Data from Area 3 Boreholes in Uncratered Areas: (a) Volumetric Moisture Content, and (b) Saturation	3-27
3-8	Volumetric Moisture Contents in the Area 5 Pilot Wells	3-27
3-9	Saturation, Porosity, and Moisture Content Profiles for Boreholes: (a) UE- 2aa (2317 ft), (b) UE-2co, (c) UE-2eh, (d) UE-2en, (e) UE-2fa, and (f) UE-2fb	3-30
3-10	Saturation, Porosity, and Moisture Content Profiles for Boreholes: (a) UE-4g 2,(b) UE-4p, (c) UE- 4ab (2650 ft), (d) UE-4ad/Inst., (e) UE- 4ae (2457 ft), and (f) UE-4ah	3-31

LIST OF FIGURES (CONTINUED)

NUMBER	TITLE	PAGE
3-11	Saturation, Porosity, and Moisture Content Profiles for Boreholes: (a) UE-7ax, (b) UE-7be, (c) UE-8e, and (d) UE-8n	3-32
3-12	Saturation, Porosity, and Moisture Content Profiles for Boreholes: (a) U-3ht, (b) U-3ji, (c) U-3kq, (d) U-3ks, (e) U-3kt, and (f) U-3kv	3-33
3-13	Saturation, Porosity, and Moisture Content Profiles for Boreholes: (a) U-2ar, (b) U-2dz, (c) U-4ad/Inst., (d) U-4ah, (e) U-4f, and (f) U-7ab	3-34
3-14	Saturation, Porosity, and Moisture Content Profiles for Boreholes: (a) U-7an, and (b) U-9cv	3-35
3-15	Preliminary and Final Infiltration Results	3-36
3-16	Map Showing Crater Catchment Areas and Infiltration Flux for Each Crater	3-38
3-17	Figure Showing Grid Refinement near Crater, Cavity, and Chimney Regions	3-42
3-18	HSUs in the 12 Model Grids for the Unsaturated Zone after Removal of Alluvial Aquifers	3-43
3-19	Example of Fault Discretization in the Unsaturated-Zone Model	3-44
3-20	Elevations of Water-Table Nodes in the 12 Grids	3-45
3-21	Examples of (a) Effective Permeability versus Matric Potential and (b) Saturation versus Matric Potential Relationships for Fractures and for Vitric and Zeolitic Tuffs	3-50
3-22	Example of a Composite Permeability Curve for Fractured Zeolitic Rocks	3-51
3-23	Comparison of Characteristic Curves for Alluvium from beneath and Adjacent to Subsidence Craters at the Area 3 RWMS: (a) Saturation versus Matric Potential, and (b) Effective Permeability versus Matrix Potential	3-54
3-24	Saturated Permeability versus Depth Based on Sediment Samples from Four Boreholes at the Area 3 RWMS	3-56
3-25	HSU Matrix and Fracture Continuum Permeabilities Used in the Unsaturated-Zone Models for Yucca Flat	3-64

LIST OF FIGURES (CONTINUED)

NUMBER	TITLE	PAGE
3-26	HSU Porosities Used in the Unsaturated-Zone Flow and Transport Models for Yucca Flat	3-68
3-27	Effect of Sediment Anisotropy on Recharge at the Water Table Assuming a Uniform 5-mm/yr Background Infiltration Rate	3-75
3-28	Effect of Anisotropy in the LTCU, OSBCU, and ATCU on Recharge at the Water Table Assuming a Uniform 5-mm/yr Background Infiltration Rate	3-76
3-29	Water Saturations and ^{14}C Concentrations in Grid 2 at 1,000 Years for Run 2.1.1.2.1.2	3-78
3-30	Water Saturations and ^{14}C Concentrations in Grid 4 at 1,000 Years for Run 2.1.1.2.1.2	3-79
3-31	Water Saturations and ^{14}C Concentrations in Grid 8 at 1,000 Years for Run 2.1.1.2.1.2	3-80
3-32	Results from Run 2.1.1.2.1.2 for Grid 8 at 1,000 Years	3-82
3-33	Cumulative Mass Arrival of ^{14}C at the Water Table—All Results	3-83
3-34	Cumulative Mass Arrival of ^{14}C at the Water Table—Effect of Background Infiltration Rates	3-84
3-35	Cumulative Mass Arrival of ^{14}C at the Water Table—Effect of Exchange Volume Radius and Crater Infiltration Rates	3-85
3-36	Cumulative Mass Arrival of ^{14}C at the Water Table—Effect of Crater Infiltration Rates	3-86
3-37	Cumulative Mass Arrival of ^{14}C at the Water Table—Effect of Sediment Anisotropy (k_v/k_h)	3-87
3-38	Cumulative Mass Arrival of ^{14}C at the Water Table—Effect of Tuff Confining Unit Anisotropy (k_v/k_h)	3-89
3-39	Cumulative Mass Arrival of ^{14}C at the Water Table—Effect of Tuff Confining Unit Transport Porosity	3-89
3-40	Cumulative Mass Arrival of ^{14}C at the Water Table—Effect of Collapse Chimneys	3-90

LIST OF FIGURES (CONTINUED)

NUMBER	TITLE	PAGE
3-41	Cumulative Mass Arrival at the Water Table for Run 2.1.1.2.1.2 (a) to Volcanic Rocks and (b) to the LCA	3-91
3-42	Cumulative Mass Arrival at the Water Table for Run 2.1.3.2.1.2 (a) to Volcanic Rocks and (b) to the LCA	3-91
3-43	^{14}C Concentrations at the Water Table at Different Times for Case 2.1.1.2.1.2(a) 0, (b) 500, and (c) 1,000 Years	3-93
3-44	^{36}Cl Concentrations at the Water Table at Different Times for Case 2.1.1.2.1.2(a) 0, (b) 500, and (c) 1,000 Years	3-94
3-45	^{129}I Concentrations at the Water Table at Different Times for Case 2.1.1.2.1.2(a) 0, (b) 500, and (c) 1,000 Years	3-95
3-46	^{3}H Concentrations at the Water Table at Different Times for Case 2.1.1.2.1.2(a) 0, (b) 100, and (c) 250 Years	3-96
3-47	^{99}Tc Concentrations at the Water Table at Different Times for Case 2.1.1.2.1.2(a) 0, (b) 500, and (c) 1,000 Years	3-97
3-48	^{237}Np Concentrations at the Water Table at Different Times for Case 2.1.1.2.1.2(a) 0, (b) 500, and (c) 1,000 Years	3-98
3-49	Total U Concentrations at the Water Table at Different Times for Case 2.1.1.2.1.2(a) 0, (b) 500, and (c) 1,000 Years	3-99
3-50	^{14}C Concentrations at the Water Table at Different Times for Case 2.1.3.2.1.2(a) 0, (b) 500, and (c) 1,000 Years	3-101
3-51	^{36}Cl Concentrations at the Water Table at Different Times for Case 2.1.3.2.1.2(a) 0, (b) 500, and (c) 1,000 Years	3-102
3-52	^{129}I Concentrations at the Water Table at Different Times for Case 2.1.3.2.1.2(a) 0, (b) 500, and (c) 1,000 Years	3-103
3-53	^{3}H Concentrations at the Water Table at Different Times for Case 2.1.3.2.1.2(a) 0, (b) 100, and (c) 250 Years	3-104
3-54	^{99}Tc Concentrations at the Water Table at Different Times for Case 2.1.3.2.1.2(a) 0, (b) 500, and (c) 1,000 Years	3-105

LIST OF FIGURES (CONTINUED)

NUMBER	TITLE	PAGE
3-55	^{237}Np Concentrations at the Water Table at Different Times for Case 2.1.3.2.1.2(a) 0, (b) 500, and (c) 1,000 Years	3-106
3-56	Total U Concentrations at the Water Table at Different Times for Case 2.1.3.2.1.2(a) 0, (b) 500, and (c) 1,000 Years	3-107
3-57	Schematic Diagram Showing How Multiple Nodes in the More Refined Unsaturated-Zone Grid Map onto a Single Node in the Coarser Saturated-Zone Model Grid	3-108
3-58	Effect of Henry's Law Partitioning of ^{14}C on Mass Transport to the Water Table in Grids 1, 2, 3, 5, 6, and 9 for Run 2.2.1.2.1.1	3-114
3-59	Effects of Henry's Law Partitioning of ^{14}C on Transport and Peak Concentrations in Grid 2 for Run 2.2.1.2.1.1	3-115
3-60	Effects of Henry's Law Partitioning of ^{14}C on Transport and Peak Concentrations in Grid 9 for Run 2.2.1.2.1.1	3-116
3-61	Figure Showing the Distribution of Alluvial Facies Based On Driller's Logs	3-118
3-62	A Comparison between the Recharge Rates at the Water Table Simulated with a Uniform 5-mm/yr Infiltration Rate and Either (a) Uniform Alluvial Properties or (b) Spatially Variable Alluvial Properties.	3-122
3-63	Cumulative Moles of ^{14}C Leaving the Unsaturated Zone over Time in Run 2.1.3.2.1.2 with Either Uniform or Heterogeneous Alluvium	3-123
3-64	Cumulative Moles of ^{14}C Leaving the Unsaturated Zone over Time in Run 2.1.3.2.1.2 by Grid with Either (a) Uniform Alluvium or (b) Heterogeneous Alluvium	3-124
3-65	Comparison of Radionuclide Mass Flux to the Saturated Alluvial/Volcanic Aquifer System Model for Old and New Source-Term Conceptualizations for Runs 1.2.1.2.1.2 and 1.2.1.2.1.2': (a) ^{3}H, (b) ^{14}C, (c) ^{36}Cl, (d) ^{129}I, (e) ^{99}Tc, (f) ^{237}Np, and (g) Total U	3-127
3-66	Comparison of Radionuclide Mass Flux to the Saturated Zone LCA Model for Old and New Source-Term Conceptualizations for Runs 1.2.1.2.1.2 and 1.2.1.2.1.2': (a) ^{3}H, (b) ^{14}C, (c) ^{36}Cl, (d) ^{129}I, (e) ^{99}Tc, (f) ^{237}Np, and (g) Total U	3-128

LIST OF FIGURES (CONTINUED)

NUMBER	TITLE	PAGE
3-67	Cumulative Mass Flux from the 1.2.1.2.1.2' Model to the Saturated Alluvial/Volcanic Aquifer System Model: (a) ^{90}Sr, and (b) ^{137}Cs	3-130
3-68	Infiltration Rates from USGS DVRFS Model 1 (with Redistribution), along with Outlines for the 12 Unsaturated-Zone Model Grids and the Saturated Alluvial/Volcanic Aquifer System Model	3-131
3-69	Cumulative Radionuclide Mass Reaching the Water Table during Unsaturated-Zone Model Run 5.4.2.1.2.1: (a) Saturated Alluvial/Volcanic Aquifer System Model, and (b) LCA Model	3-133
3-70	Water Flux Reaching the Saturated Alluvial/Volcanic Aquifer System and LCA Models in Unsaturated-Zone Model Run 5.4.2.1.2.1	3-134
4-1	Saturated Alluvial/Volcanic Aquifer System Model Domain with Selected Wells and Previously Modeled Areas	4-2
4-2	Water-Table Water Levels (SNJV, 2006b) and Interpreted Contours (This Study)	4-5
4-3	Measured Ground Surface Displacement for Three Time Periods Using InSAR Data	4-10
4-4	Thickness of the Tuff Confining Units	4-12
4-5	Distribution of Rock Types at the Water Table	4-13
4-6	Groundwater ^{36}Cl/Cl Ratios (× 1E+15) of (a) Alluvial/Volcanic Aquifers and Clastic Confining Rocks and (b) the LCA	4-16
4-7	Wells with Completions in the Saturated Volcanics and Selected Hydrographs Showing Long-Term Effects of Testing	4-18
4-8	Conceptual Model of Flow from the Unsaturated Zone and Downward into the LCA along Faults	4-20
4-9	Locations of Increased Grid Resolution near Cavities	4-21
4-10	Numerical Mesh, Colored by HSUs and Faults (Pink Dots)	4-22
4-11	Constant Head Nodes at the Intersection of Faults and the Top of the LCA	4-24

LIST OF FIGURES (CONTINUED)

NUMBER	TITLE	PAGE
4-12	Results of Hydrologic Testing, Compared to Calibrated Values	4-25
4-13	Distributions of Modeled Levels of Pressurization	4-30
4-14	Spatial Distributions of Overpressurization Datasets for Sets A through E Shown in Figure 4-13	4-31
4-15	Locations of Wells Used for Calibration	4-37
4-16	Water Levels Used for Evaluating Model Performance	4-38
4-17	Sensitivity Coefficient for Model Parameters	4-41
4-18	Example Comparisons of Simulated and Measured Hydrographs	4-43
4-19	Measured versus Simulated Heads	4-45
4-20	Simulated Heads in Years 1967, 1971, 1992, and 2978	4-46
4-21	Total Flux of Water Leaving Model	4-47
4-22	Spatial and Temporal Distributions of Outflow Fluxes (kg/s) (Case 211212.1.14.5.1.2.N3.B2.s/)	4-48
4-23	Particle Breakthrough at Lower Model Boundary	4-56
4-24	Detonations That Contribute to Significant Particle Outflow to the LCA	4-59
4-25	Comparison of Measured Subsidence and the Range of Predicted Subsidence for an Ensemble of Flow Models along an East–West Cross Section	4-61
4-26	Distribution of Particles at the Water Table	4-64
4-27	Distribution of Particles Representing Saturated-Zone Source Mass	4-65
4-28	Comparison of Mass Release according to Uniform Mass-Based Allocation Method and Approximate Method	4-67
4-29a	Concentration of ^{14}C (mol/L) within Saturated Alluvial/Volcanic Aquifer System Model Domain at 20, 50, 100, and 1,000 Years (Case 211212.1.14.5.1.2.N3.B2.s)	4-78

LIST OF FIGURES (CONTINUED)

NUMBER	TITLE	PAGE
4-29b	Mass Flux of ^{14}C (mol/day) Transported to LCA from Saturated Alluvial/Volcanic Aquifer System Model Domain at 20, 50, 100, and 1,000 Years (Case 211212.1.14.5.1.2.N3.B2.s)	4-79
4-29c	Concentration of ^{14}C (mol/L) within Saturated Alluvial/Volcanic Aquifer System Model Domain at 20, 50, 100, and 1,000 Years (Case 211212.1.14.5.1.2.N3.B2.v.1)	4-80
4-29d	Mass Flux of ^{14}C (mol/day) Transported to LCA from Saturated Alluvial/Volcanic Aquifer System Model Domain at 20, 50, 100, and 1,000 Years (Case 211212.1.14.5.1.2.N3.B2.v.1)	4-81
4-29e	Concentration of ^{14}C (mol/L) within Saturated Alluvial/Volcanic Aquifer System Model Domain at 20, 50, 100, and 1,000 Years (Case 542121.12.2.8.1.11.2012_HST.N3.B2.s)	4-82
4-29f	Mass Flux of ^{14}C (mol/day) Transported to LCA from Saturated Alluvial/Volcanic Aquifer System Model Domain at 20, 50, 100, and 1,000 Years (Case 542121.12.2.8.1.11.2012_HST.N3.B2.s)	4-83
4-30	Three-Dimensional View of the ^{14}C Plume (in mol/L) within Saturated Alluvial/Volcanic Aquifer System Model Domain at Day 18,250 (50 Years) for Case 211212.1.14.5.1.2.N3.B2.s	4-84
4-31	Exceedance Volume Calculations for Case 211212.1.14.5.1.2.N3.B2.s	4-86
4-32	Cumulative Mass (Decay-Corrected) That Has Left the Model (in Moles)	4-87
4-33	Inflow Mass from Internal (In (SZ)) and Unsaturated-Zone (In (UZ)) Sources, and Outflow Mass Calculated with Testing-Effects Conceptual Models 1 (Out (1)) and 2 (Out (2))	4-88
4-34	Exceedance Volume Calculations for Case 211212.1.14.5.1.2.N3.B2.v.1	4-89
4-35	Cumulative Mass That Leaves the Model (in Moles)	4-90
4-36	Particles Mean Positions for Two Cases	4-95
4-37	Distribution of Particles as Random and Uniform versus Within Three Concentric Shells	4-96

LIST OF FIGURES (CONTINUED)

NUMBER	TITLE	PAGE
4-38	Cumulative breakthrough of ^{14}C to the LCA for Various Combinations of Simulations Comparisons: (a) Effects of Exchange Volume and Background Recharge, (b) Testing Effects of Conceptual Models, and (c) Effects of Overpressurization and HST Configuration	4-102
4-39	Cumulative Moles of ^{14}C Leaving the Model	4-104
4-40	Locations of Boundary Nodes Affected by Lower Boundary Breaching Cases	4-107
4-41	Cumulative Breakthrough of ^{14}C Flux to the LCA for Four Hydrofracturing Cases	4-108
4-42	Histograms of Predictions of Mass Leaving the Model for Each Radionuclide	4-112
4-43	Histograms of Masses to LCA Model	4-115
4-44	Histograms of Mass into LCA Model Using Distributions of Melt-Glass Partitioning Factors Given in Table 4-40 with a Constant Melt-Glass Partitioning Factor Applied to All 179 Detonations in Each Realization (Based on 100 Model Runs)	4-118
4-45	Histograms of Mass into LCA Model Using Distributions of Melt-Glass Partitioning Factors Given in Table 4-40 with a Constant Melt-Glass Partitioning Factor Applied to All 179 Detonations in Each Realization (from Calculation with Equation (4-18) Based on 10,000 Samples)	4-120
4-46	Histograms of Mass into LCA Model due to Uncertainty in Both Source Inventory and Melt-Glass Partitioning Factor	4-123
4-47	Histograms of Mass into LCA Model due to Uncertainty in Source Inventory, the Melt-Glass Partitioning Factor, and Transport Parameters for Case 121212.5.14.5.1.2.2012_HST.N3.B2.s (SAE_13)	4-125
4-48	Locations of Wells with Tritium Measurements in Saturated Alluvial/Volcanic Aquifer System Model	4-127
4-49	Northern Portion of Saturated Alluvial/Volcanic Aquifer System Model Showing Grid Size and Locations of Far-Field and Near-Field Wells	4-132

LIST OF FIGURES (CONTINUED)

NUMBER	TITLE	PAGE
4-50	Fraction of Source That Breaks Through to the LCA in 1,000 Years	4-134
4-51	Contribution of Mass to the LCA Model from 44 Individual Detonations for Case 211212.1.14.5.1.2.N3.B2.s	4-136
5-1	Mass of the LCA in the Yucca Flat Groundwater Flow Model	5-9
5-2	Faults in the Yucca Flat LCA Flow Model Area	5-10
5-3	Three-Dimensional Representation of Faults in the Yucca Flat HFM and Groundwater Flow Model	5-11
5-4	Locations of Groundwater Pumping Wells in the Yucca Flat/Climax Mine CAU	5-13
5-5	Production History for Yucca Flat Groundwater Pumping Wells	5-14
5-6	Annual Groundwater Production and Water Levels in LCA Wells HTH-2 (WW-2) and WW-C-1	5-15
5-7	Historical Water Levels in LCA Observation Wells in Yucca Flat	5-17
5-8	Hydraulic Heads at LCA Observation Wells in Yucca Flat	5-18
5-9	Historical Hydraulic Head at UE-1h and Precipitation Indices at Rainier Mesa and Pahranagat Valley	5-19
5-10	Water-Level Drawdowns Recorded at Observation Wells Monitored during ER-6-1-2 MWAT	5-21
5-11	LCA Pumping-Scale Hydraulic Conductivity Probability Distribution for the Yucca Flat/Climax Mine CAU Dataset	5-23
5-12	Specific Storage Data for the Yucca Flat/Climax Mine CAU Dataset	5-24
5-13	Conceptual LCA Flow Paths Evaluated in the Yucca Flat/Climax Mine CAU Geochemical Study	5-26
5-14	Estimated LCA Retarded Groundwater Ages Using ^{14}C Data	5-31
5-15	Groundwater Chemistry and Geochemical Facies at Yucca Flat	5-33
5-16	Temperature Distribution at the Water Table in Yucca Flat	5-35

LIST OF FIGURES (CONTINUED)

NUMBER	TITLE	PAGE
5-17	Temperature Distribution in Yucca Flat at Various Elevations	5-37
5-18	Delineations of Regional Groundwater Flow Models of the DVRFS Region	5-40
5-19	Simulated Steady-State Groundwater Flux in the LCA through the North–South Cell Face of the USGS 2004 DVRFS Model	5-41
5-20	Simulated Steady-State Groundwater Flux in the LCA through the East–West Cell Face of the USGS 2004 DVRFS Model	5-42
5-21	Map of the Major Rock Types Outcropping in the Region of Yucca Flat Showing the Climax Mine Granite Intrusion Being Exposed in the Extreme Northern End of Yucca Flat	5-48
5-22	West–East Hydrogeologic Cross Section through the Climax Stock and the Adjacent Clastic Confining Units at the Northern End of Yucca Flat	5-49
5-23	Plan View of the Climax Mine Flow Model Domain Showing Areas of Mesh Refinement	5-51
5-24	Total Flow Rate into Yucca Flat from the North (near Climax Mine)	5-54
5-25	Hydraulic Head and Flux along Southern Boundary of Climax Mine Model for UGTA Base/USGS Run-On and Runoff Alternative	5-55
5-26	Simulated Steady-State Groundwater Flux in the LCA through the North–South Cell Face of the USGS 2012 DVRFS Model	5-58
5-27	Simulated Steady-State Groundwater Flux in the LCA through the East–West Cell Face of the USGS 2012 DVRFS Model	5-59
5-28	Mesh Discretization Highlighting Fault Core and Damage Zones	5-64
5-29	Modeled LCA Permeability Zones in the Yucca Flat Flow Model	5-66
5-30	Faults Included in the Yucca Flat LCA Flow and Transport Model	5-67
5-31	Geologic Map Showing French Peak Accommodation Zone	5-68
5-32	Boundary Types along the Lateral Edges and Top of the Yucca Flat LCA Model	5-71

LIST OF FIGURES (CONTINUED)

NUMBER	TITLE	PAGE
5-33	USGS Recharge Distribution in the Calibrated Steady-State Version of the DVRFS Model	5-72
5-34	Recharge Distribution in USGS Alternative Regional Models	5-73
5-35	Cumulative Infiltration (kg/s) Corresponding to the DVRFS Calibrated Steady-State Model in Yucca Flat Recharge Zones	5-75
5-36	Cumulative Infiltration and Recharge in Individual Zones in the USGS Base and Alternative Models	5-76
5-37	Spatial Distribution of Top Boundary Flux Corresponding to Recharge Rate of 5 mm/yr	5-77
5-38	Singular Value of Jacobian Matrix for All Adjustable Parameters	5-89
5-39	Identifiability Index for Adjustable Parameters: (a) All Parameters, and (b) Parameters with Identifiability Index Greater than or Equal to 0.16	5-90
5-40	Modeled Region of MWAT Drawdown Influence	5-92
5-41	Identifiability Index of Longitudinal Permeability for Yucca Flat Modeled Faults	5-93
5-42	Matrix Condition Number as a Function of Steady-State Head and MWAT Drawdown Weights	5-94
5-43	Calibrated LCA Potentiometric Surface at -1,000 m amsl and Associated Head Residuals at Steady-State Observation Wells	5-97
5-44	Steady-State Head Residuals in the LCA	5-98
5-45	Observed and Simulated LCA Heads	5-99
5-46	Simulated and Observed Drawdowns at the MWAT Sites	5-101
5-47	Velocity Vectors between -500 and +500 m amsl	5-105
5-48	Key Locations Receiving Contamination from Sources in the Unsaturated Zone, Saturated Alluvial/Volcanic Aquifer System, and LCA	5-107

LIST OF FIGURES (CONTINUED)

NUMBER	TITLE	PAGE
5-49	Particle Travel Paths and Times for Radionuclide Transport from 12 Key Locations for the Base-Case Calibration	5-108
5-50	Particle Travel Paths and Times for Contamination Released at Each of the 12 Key Locations for the Base-Case Calibration	5-109
5-51	Breakthrough Curves at Model Northing Location 4,090,000 m for Particles Released at 12 Key Locations in the LCA	5-110
5-52	Calibration Convergence of Northern Boundary Model Influx	5-114
5-53	Calibration Objective Function as a Function of Lateral Western and Eastern Boundary Fluxes	5-115
5-54	Initial and Final Objective Functions for the Alternative NSMC Models	5-116
5-55	Calibrated Objective Functions (Sorted) for the Alternative NSMC Models	5-116
5-56	Variation in Northern Boundary Inflow for the NSMC Simulations	5-118
5-57	Variation of Recharge in the Center of the Basin for the NSMC Simulations	5-119
5-58	Variation in Cumulative Boundary Inflows for the Alternative NSMC Simulations	5-120
5-59	Histogram and Cumulative Distribution Curve for Total Boundary Influx	5-120
5-60	Variation in Geometric Mean of Major Faults for the NSMC Simulations	5-121
5-61	Variation in Permeability of Western Splay of Topgallant Fault for the NSMC Simulations	5-121
5-62	Variation in Permeability of Fault 210 in Alternative NSMC Simulations	5-122
5-63	Variation in Storage Coefficient for Alternative NSMC Simulations	5-123
5-64	Variation in Permeability of LCA East and LCA West in Alternative NSMC Simulations	5-124

LIST OF FIGURES (CONTINUED)

NUMBER	TITLE	PAGE
5-65	Distribution and Histogram for Total Number of Particles Reaching the Model Northing Location of 4,090,000 m from 12 Key Locations in the LCA	5-126
5-66	Distribution and Histogram for Total Number of Particles Reaching the Model Northing Location of 4,090,000 m from 7 Key Locations in the LCA	5-128
5-67	Advective Particle Travel Paths and Times for Representative Slow, Medium, and Fast Flow Fields at Location 1 (BILBY)	5-129
5-68	Advective Particle Travel Paths and Times for Representative Slow, Medium, and Fast Flow Fields at Location 8 (TORRIDO)	5-130
5-69	Advective Particle Travel Paths and Times for Representative Slow, Medium, and Fast Flow Fields at Location 11 (TORTUGAS)	5-131
5-70	Breakthrough Curves for Particles Released at Three Representative Locations for Slow, Medium, and Fast Flow Fields	5-132
5-71	Advective Particle Travel Paths and Times from 12 Key Locations for the Alternative Northern Boundary Flux Model.	5-135
5-72	Advective Particle Travel Paths and Times at Locations 1, 8, and 11 (BILBY, TORRIDO, and TORTUGAS) for the Alternative Northern Boundary Flux Model.	5-136
5-73	Breakthrough Curves for Particles Released at Locations 1, 8, and 11 (BILBY, TORRIDO, and TORTUGAS) for the Alternative Northern Boundary Flux Model.	5-137
5-74	Modeled LCA Permeability Zones Showing Narrow Yucca Flat Accommodation Zone	5-140
5-75	Breakthrough Curves at Model Northing Location 4,090,000 m for Alternative Fault Models	5-141
5-76	Particle Travel Paths and Times for Base Case and Alternative Area3n9 Fault Models for Contamination Released near BILBY	5-143
5-77	Particle Breakthrough Curves at Northing Location of 4,090,000 m for the Level 3 Mesh, and the Fast, Medium, and Slow Level 2 Mesh Cases	5-145

LIST OF FIGURES (CONTINUED)

NUMBER	TITLE	PAGE
5-78	Particle Travel Paths and Times for the Level 3 Mesh, and Representative Slow, Medium, and Fast Level 2 Mesh Alternative Models	5-146
5-79	Sensitivity Coefficients of Model Adjustable Parameters	5-149
5-80	Sensitivity Coefficients of 20 Highest Sensitive Parameters	5-150
5-81	Sensitivity Analysis for Northern Boundary Flux	5-151
5-82	Sensitivity Analysis for (a) Carpetbag Fault (Faults 176 and 177) and (b) Topgallant Fault (Faults 178 and 190)	5-152
5-83	Sensitivity Analysis for Yucca Fault: (a) Fault 145, and (b) Fault 148	5-153
5-84	Sensitivity Analysis of LCA Rock Permeabilities for (a) LCA Central and (b) LCA East	5-155
5-85	Sensitivity Analysis of LCA Rock and Fault Anisotropies	5-156
5-86	Sensitivity Analysis for Storativity of Fault and Rock: (a) Rock Matrix, and (b) Faults	5-157
5-87	Detonation Locations Where Sensitivity to Darcy Velocity Was Estimated	5-159
5-88	Velocity Sensitivity Analysis: (a) North Flux, (b) Yucca Fault Horizontal Anisotropy, and (c) LCA Horizontal Anisotropy	5-160
5-89	Velocity Sensitivity Analysis: (a) Permeability of the Western Splay of Yucca Fault, (b) Permeability of LCA Central, and (c) Horizontal Anisotropy of Minor Faults	5-161
5-90	Velocity Sensitivity Analysis: (a) Permeability of LCA East, (b) Vertical Anisotropy of Minor Faults, and (c) Permeability of Fault 114	5-162
5-91	Velocity Sensitivity Analysis for Lateral Barrier: (a) All Minor East Faults, (b) Top Flux, and (c) Permeability of Eastern Splay of Yucca Fault	5-163
6-1	Fracture Porosity: (a) Distribution Sampled, and (b) Distribution of the Model Values for the Country Rock and Fault Zones	6-25

LIST OF FIGURES (CONTINUED)

NUMBER	TITLE	PAGE
6-2	Hydraulic Conductivity: (a) Distribution Sampled, and (b) Distribution of the Sampled Values Used to Calculate Hydraulic Fracture Aperture for the Country Rock and Fault Zones	6-27
6-3	Cumulative Probability and Frequency for Fracture Spacing Data in the LCA from Analyses of Borehole Image Logs Conducted in Wells ER-6-1-2 and ER-7-1	6-28
6-4	Fracture Aperture: (a) Distribution of Model Values for the Country Rock and Fault Zones, and (b) Scatterplot of Paired Model Values in the Country Rock and Fault Zones for the 400 Realizations	6-34
6-5	Scatterplot of Model Fracture Aperture and Model Fracture Porosity for the Country Rock and Fault Zones for the 400 Realizations	6-35
6-6	Fracture Spacing: (a) Distribution of Model Values for the Country Rock and Fault Zones, and (b) Scatterplot of Model Values in the Country Rock and Fault Zones for the 400 Realizations	6-38
6-7	Scatterplot of Model Fracture Aperture and Calculated Fracture Spacing for the Country Rock and Fault Zones for the 400 Realizations	6-39
6-8	Scatterplot of Model Fracture Porosity and Calculated Fracture Spacing for the Country Rock and Fault Zones for the 400 Realizations	6-39
6-9	Distribution of Model Values of Matrix Porosity	6-43
6-10	Log Tortuosity versus Porosity from Laboratory Tracer Diffusion Experiments in Carbonate Rock	6-45
6-11	Distribution of Model Values of Matrix Tortuosity	6-46
6-12	Strontium Fracture Retardation Distribution of the LCA	6-49
6-13	Uranium Matrix Sorption (K_d) Distribution of the LCA	6-51
6-14	Distributions of Model Values of Fracture Porosity in the Country Rock and Fault Zones for the Base-Case and Alternative Models	6-53
6-15	Distributions of Model Values of Fracture Aperture in the Country Rock and Fault Zones for the Base-Case and Alternative Models	6-54

LIST OF FIGURES (CONTINUED)

NUMBER	TITLE	PAGE
6-16	Distributions of Calculated Values of Fracture Spacing in the Country Rock and Fault Zones for the Base-Case and Alternative Models	6-54
6-17	Scatterplot of Model Fracture Aperture and Model Fracture Porosity for the Country Rock and Fault Zones for the 400 Alternative Model Realizations	6-55
6-18	Scatterplot of Model Fracture Aperture and Calculated Fracture Spacing for the Country Rock and Fault Zones for the 400 Alternative Model Realizations	6-56
6-19	Scatterplot of Model Fracture Porosity and Calculated Fracture Spacing for the Country Rock and Fault Zones for the 400 Alternative Model Realizations	6-56
6-20	Distribution of Matrix Porosity Reduction Factor for the Country Rock	6-58
6-21	Distributions of Model Values of Matrix Porosity for the Country Rock and Fault Zones for the Base-Case and Alternative Models	6-58
6-22	Perspective View of Particle Starting Locations for the Portion of the CORDUROY Detonation Intersecting the Saturated LCA	6-62
6-23	Perspective View of Particle Starting Locations for the Portion of the BOURBON Detonation Intersecting the Saturated LCA	6-63
6-24	Locations of LCA Source Nodes Associated with Contaminant Influx from the Unsaturated Zone and Saturated Alluvial/Volcanic Aquifer System Models for Infiltration Rate of 0.1 mm/yr	6-66
6-25	Locations of LCA Source Nodes Associated with Contaminant Influx from the Unsaturated Zone and Saturated Alluvial/Volcanic Aquifer System Models for Infiltration Rate of 1 mm/yr	6-67
6-26	Perspective View of Particle Starting Locations for a Typical Node Receiving Mass Input from the Overlying Saturated Alluvial/Volcanic Aquifer System Model	6-68
6-27	Perspective Plot of LCA Particle Trajectories from the CORDUROY Detonation	6-70
6-28	Perspective Plot of LCA Particle Trajectories from the BOURBON Detonation	6-71

LIST OF FIGURES (CONTINUED)

NUMBER	TITLE	PAGE
6-29	Perspective Plot of LCA Particle Trajectories near Representative Nodes Receiving Contaminant Influx from the Saturated Alluvial/Volcanic Aquifer System Model	6-72
6-30	Perspective Plot of LCA Particle Trajectories from Representative Source Nodes	6-73
6-31	Map of Total ^{3}H Flux to the LCA from Unsaturated-Zone Sources for Infiltration Rate of 0.1 mm/yr	6-76
6-32	Map of Total ^{3}H Flux to the LCA from Unsaturated-Zone Sources for Infiltration Rate of 1 mm/yr	6-77
6-33	Map of Total 129I Flux to the LCA from the Unsaturated-Zone Sources for Infiltration Rate of 0.1 mm/yr	6-78
6-34	Map of Total 129I Flux to the LCA from the Unsaturated-Zone Sources for Infiltration Rate of 1 mm/yr	6-79
6-35	Time History of ^{3}H Flux to the LCA from Unsaturated-Zone Sources for Recharge Rate of 1 mm/yr	6-80
6-36	Time History of 129I Flux to the LCA from Unsaturated-Zone Sources for Recharge Rate of 1 mm/yr	6-80
6-37	Time History of ^{3}H Flux to the LCA from Unsaturated-Zone Sources for Recharge Rate of 0.1 mm/yr	6-81
6-38	Time History of 129I Flux to the LCA from Unsaturated-Zone Sources for Recharge Rate of 0.1 mm/yr	6-81
6-39	Temporal Variation in ^{3}H Flux to the LCA from Key Unsaturated-Zone Working-Point Detonations for Recharge Rate of 1 mm/yr	6-83
6-40	Temporal Variation in ^{129}I Flux to the LCA from Key Unsaturated-Zone Working-Point Detonations for Recharge Rate of 1 mm/yr	6-84
6-41	Map of 1,000-Year Cumulative ^{3}H Mass Flux from the Saturated Alluvial/Volcanic Aquifer System to the LCA for Infiltration Rate of 0.1 mm/yr	6-86

LIST OF FIGURES (CONTINUED)

NUMBER	TITLE	PAGE
6-42	Map of 1,000-Year Cumulative ^{3}H Mass Flux from the Saturated Alluvial/Volcanic Aquifer System to the LCA for Infiltration Rate of 1 mm/yr	6-87
6-43	Map of 1,000-Year Cumulative 129I Mass Flux from the Saturated Alluvial/Volcanic Aquifer System to the LCA for Infiltration Rate of 0.1 mm/yr	6-88
6-44	Map of 1,000-Year Cumulative ^{129}I Mass Flux from the Saturated Alluvial/Volcanic Aquifer System to the LCA for Infiltration Rate of 1 mm/yr	6-89
6-45	Time History of Total ^{3}H Mass Flux from the Saturated Alluvial/Volcanic Aquifer System to the LCA for Recharge Rate of 1 mm/yr	6-90
6-46	Time History of Total 129I Mass Flux from the Saturated Alluvial/Volcanic Aquifer System to the LCA for Recharge Rate of 1 mm/yr	6-91
6-47	Time History of Total ^{3}H Mass Flux from the Saturated Alluvial/Volcanic Aquifer System to the LCA for Recharge Rate of 0.1 mm/yr	6-91
6-48	Time History of Total 129I Mass Flux from the Saturated Alluvial/Volcanic Aquifer System to the LCA for Recharge Rate of 0.1 mm/yr	6-92
6-49	Time History of ^{3}H Mass Flux from the Top 20 Saturated Alluvial/Volcanic Aquifer System Source Nodes to the LCA for Recharge Rate of 1 mm/yr	6-93
6-50	Time History of ^{129}I Mass Flux from the Top 20 Saturated Alluvial/Volcanic Aquifer System Source Nodes to the LCA for Recharge Rate of 1 mm/yr	6-93
6-51	Temporal Variation in ^{3}H Flux to the LCA from Key Saturated-Zone Working-Point Detonations for Recharge Rate of 1 mm/yr	6-95
6-52	Temporal Variation in ^{129}I Flux to the LCA from Key Saturated-Zone Working-Point Detonations for Infiltration Rate of 1 mm/yr (Case SAE_2)	6-96
6-53	Base-Case Representative ^{3}H Concentrations for Saturated-Zone Sources: (a) 50 Years, and (b) 100 Years	6-115
6-54	Base-Case Representative ^{129}I Concentrations for Saturated-Zone Sources: (a) 300 Years, and (b) 1,000 Years	6-116

LIST OF FIGURES (CONTINUED)

NUMBER	TITLE	PAGE
6-55	Base-Case Probability of Exceedance of MCL for Saturated-Zone Sources: (a) 50 Years, and (b) 100 Years	6-117
6-56	Base-Case Probability of Exceedance of MCL for Saturated-Zone Sources: (a) 300 Years, and (b) 1,000 Years	6-118
6-57	Base-Case Time-Cumulative Probability of Exceedance of MCLs for Saturated-Zone Sources: (a) Alpha-Emitter MCLs, and (b) Beta- and Photon-Emitter MCLs	6-119
6-58	Base-Case Fractional Exceedance Volume for Saturated-Zone Sources	6-120
6-59	Base-Case Representative ^{3}H Concentrations for LCA Sources: (a) 50 Years, and (b) 100 Years	6-122
6-60	Base-Case Representative ^{129}I Concentrations for LCA Sources: (a) 300 Years, and (b) 1,000 Years	6-123
6-61	Base-Case Representative ^{90}Sr Concentrations for LCA Sources: (a) 50 Years, and (b) 300 Years	6-124
6-62	Base-Case Probability of Exceedance of MCL for LCA Sources: (a) 50 Years, and (b) 100 Years	6-125
6-63	Base-Case Probability of Exceedance of MCL for LCA Sources: (a) 300 Years, and (b) 1,000 Years	6-126
6-64	Base-Case Time-Cumulative Probability of Exceedance of MCLs for LCA Sources: (a) Alpha-Emitter MCLs, and (b) Beta- and Photon-Emitter MCLs	6-127
6-65	Base-Case Fractional Exceedance Volume for LCA Sources	6-128
6-66	Base-Case CDFs for Saturated Zone and LCA Sources: (a) Cumulative MCL Exceedance Volume, and (b) Maximum Southern Extent of MCL Exceedance	6-129
6-67	Time-Cumulative Probability of Exceedance of MCLs for Alternative LCA Sources: (a) Preliminary 2 R_c, and (b) Alternative Bounding HST	6-133
6-68	CDFs for LCA Sources with Alternative HSTs: (a) Cumulative MCL Exceedance Volume, and (b) Maximum Southern Extent of MCL Exceedance	6-134

LIST OF FIGURES (CONTINUED)

NUMBER	TITLE	PAGE
6-69	Time-Cumulative Probability of Exceedance of MCLs for Unsaturated-Zone Sources with Alternative Infiltration Rates: (a) 1 mm/yr, and (b) 5 mm/yr	6-137
6-70	Time-Cumulative Probability of Exceedance of MCLs for Saturated-Zone Sources with Alternative Infiltration Rates: (a) 1 mm/yr, and (b) 5 mm/yr	6-138
6-71	Probability of Exceeding MCL for Saturated-Zone Sources with Infiltration Rate of 1 mm/yr: (a) 50 Years, and (b) 100 Years	6-139
6-72	Probability of Exceeding MCL for Saturated-Zone Sources with Infiltration Rate of 1 mm/yr: (a) 300 Years, and (b) 1,000 Years	6-140
6-73	Fractional Exceedance Volume for Unsaturated-Zone Sources with Infiltration Rate of 1 mm/yr	6-141
6-74	Fractional Exceedance Volume for Saturated-Zone Sources with Infiltration Rate of 1 mm/yr	6-142
6-75	CDFs for Unsaturated-Zone and Saturated-Zone Sources with Alternative Infiltration Rates: (a) Cumulative MCL Exceedance Volume, and (b) Maximum Southern Extent of MCL Exceedance	6-143
6-76	Time-Cumulative Probability of Exceedance of MCLs for Saturated-Zone Sources with (a) Alternative Overpressurization Model (SAE_5), and (b) Alternative Hydraulic Communication Model (SAE_7)	6-145
6-77	Time-Cumulative Probability of Exceedance of MCLs for Saturated-Zone Sources with Alternative Hydraulic Communication Models: (a) SAE_10, and (b) SAE_11	6-146
6-78	Time-Cumulative Probability of Exceedance of MCLs for Saturated-Zone Sources, 400 Realizations	6-147
6-79	CDFs for Saturated-Zone Sources with Alternative Hydraulic Communication and Overpressure Effects: (a) Cumulative MCL Exceedance Volume, and (b) Maximum Southern Extent of MCL Exceedance	6-148
6-80	CDFs for Saturated-Zone Sources, 400 Realizations: (a) Cumulative MCL Exceedance Volume, and (b) Maximum Southern Extent of MCL Exceedance	6-149

LIST OF FIGURES (CONTINUED)

NUMBER	TITLE	PAGE
6-81	Time-Cumulative Probability of Exceedance of MCLs for LCA Sources with Alternative NSMC LCA Flow Fields: (a) NSMC Slow, and (b) NSMC Fast	6-152
6-82	Time-Cumulative Probability of Exceedance of MCLs for LCA Sources with Alternative LCA Flow Fields: (a) Base Case, and (b) Alternative Northern Boundary Flux Model	6-153
6-83	CDFs for LCA Sources with Alternative NSMC LCA Flow Fields: (a) Cumulative MCL Exceedance Volume, and (b) Maximum Southern Extent of MCL Exceedance	6-154
6-84	Time-Cumulative Probability of Exceedance of MCLs for LCA Sources with Alternative LCA Transport Parameters: (a) Alternative Matrix Sorption for Sr, Cs, C, and Ni, and (b) Scale-Dependent Matrix Diffusion	6-157
6-85	Time-Cumulative Probability of Exceedance of MCLs for LCA Sources with Alternative LCA Transport Parameters: (a) Alternative Fault Fracture Porosity, and (b) Walkabout	6-158
6-86	Time-Cumulative Probability of Exceedance of MCLs for LCA Sources: (a) Base Case, and (b) Alternative Northern Boundary Flux Model with Alternative LCA Transport Parameters	6-159
6-87	Fractional Exceedance Volume for LCA Sources with Alternative Matrix Sorption for Sr, Cs, C, and Ni	6-160
6-88	CDFs for LCA Sources with Alternative LCA Transport Parameters: (a) Cumulative MCL Exceedance Volume, and (b) Maximum Southern Extent of MCL Exceedance	6-161
6-89	Time-Cumulative Probability of Exceedance of MCLs for Infiltration Rate of 0.1 mm/yr: (a) Base-Case LCA Sources, and (b) Combined Unsaturated-Zone, Saturated-Zone, and LCA Sources	6-164
6-90	Time-Cumulative Probability of Exceedance of MCLs for Infiltration Rate of 1 mm/yr: (a) Base-Case LCA Sources, and (b) Combined Unsaturated-Zone, Saturated-Zone, and LCA Sources	6-165
6-91	Time-Cumulative Probability of Exceedance of MCLs for Infiltration Rate of 5 mm/yr: (a) Base-Case LCA Sources, and (b) Combined Unsaturated-Zone, Saturated-Zone, and LCA Sources	6-166

LIST OF FIGURES (CONTINUED)

NUMBER	TITLE	PAGE
6-92	CDFs of Cumulative MCL Exceedance Volume for Combined Unsaturated-Zone, Saturated-Zone, and LCA Sources	6-167
6-93	Scatterplots for Time-Cumulative MCL Exceedance Metric for the Base-Case LCA HST	6-169
6-94	Contingency Tables for Time-Cumulative Probability of MCL Exceedance Volume Sensitivity to Transport Parameter Uncertainty for the Base-Case LCA HST	6-174
6-95	Contingency Tables of Southern Extent of Maximum Concentration Sensitivity to Transport Parameter Uncertainty for the Base-Case LCA HST	6-175
6-96	Classification Tree for Time-Cumulative Exceedance Volume for the Base-Case LCA HST	6-176
6-97	Partition Plots for Base-Case LCA Sources Transport Model: (a) Time-Cumulative MCL Exceedance Volume, and (b) Maximum Southern Extent of MCL Exceedance	6-178
6-98	Boxplot of Transport Parameters for Top 10 Percent of Cumulative Exceedance Volume Distribution for the Base-Case LCA HST Model	6-179
6-99	Time-Cumulative Composite Contaminant Boundaries	6-183
6-100	Temporal Variation of the Composite Contaminant Boundaries: (a) 100 Years, and (b) 300 Years	6-184
6-101	Temporal Variation of the Composite Contaminant Boundaries: (a) 500 Years, and (b) 1,000 Years	6-185
6-102	Extent of Contamination for Varying Probabilities: (a) 5 Percent, and (b) 25 Percent	6-186
6-103	Extent of Contamination for Varying Probabilities: (a) 50 Percent, and (b) 75 Percent	6-187
6-104	Summary of 95th Percentile Results for Unsaturated-Zone and Saturated-Zone Sources: (a) Cumulative MCL Exceedance Volume, and (b) Maximum Southern Extent of MCL Exceedance	6-190

LIST OF FIGURES (CONTINUED)

NUMBER	TITLE	PAGE
6-105	Summary of 95th Percentile Results for LCA Sources: (a) Cumulative MCL Exceedance Volume, and (b) Maximum Southern Extent of MCL Exceedance	6-191
B-1	Identification of Yucca Flat/Climax Mine CAU Detonations within 5 R_c of the LCA and Faults	B-25
C-1	Phenomenology of an Underground Nuclear Explosion Showing Accretion of Melt Glass, Redistribution of More Volatile Radionuclides, Initially as Gases, Later as Condensates, and Collapse of the Chimney	C-5
C-2	Schematic Diagram for Geometry of Detonation-Altered Zones	C-8
C-3	Comparison of (a) ^{3}H and (b) ^{90}Sr RSTs at t_0 for All Yucca Flat Detonations Using the New versus Traditional Yield-Weighting Methods	C-21
C-4	Probability Distributions of Initial Radionuclide Concentrations (Relative to MCLs) in All Detonations within the Yucca Flat/Climax Mine CAU	C-25
D-1	Location of Observation Wells in Yucca Flat	D-3
D-2	Perspective View of ALEMAN and SANDREEF (2 R_c) and Well UE-3e 4	D-13
D-3	Radionuclide Activity Relative to MCL for Well UE-3e 4	D-14
D-4	Perspective View of BASEBALL and DALHART Detonations (2 R_c) and Wells U-4u PS 2A and U-7ba PS 1AS	D-15
D-5	Radionuclide Activity Relative to MCL for U-4u PS 2A	D-16
D-6	Perspective View of GASCON Detonation (2 R_c) and Wells U-4t PS 3A and UE-4t	D-17
D-7	Perspective View of INGOT Detonation (2 R_c) and Well U-2gg PSE 3A	D-18
D-8	Perspective View of BILBY Detonation (2 R_c) and Wells U-3cn 5 and U-3cn PS2	D-21
D-9	Radionuclide Activity Relative to MCL for U-3cn PS 2	D-21
D-10	Tritium Activity Relative to MCL for U-3cn 5	D-23

LIST OF FIGURES (CONTINUED)

NUMBER	TITLE	PAGE
D-11	Perspective View of BOURBON Detonation (2 R_c) and Nearby Observations Wells	D-24
D-12	Radionuclide Activity Relative to MCL for UE-7ns	D-25
D-13	Perspective View of NASH Detonation (2 R_c) and Well UE-2ce	D-26
D-14	Radionuclide Activity Relative to MCL for UE-2ce	D-26
D-15	Perspective View of TORRIDO and MICKEY Detonations (2 R_c) and Well ER-7-1	D-27
E-1	43-Year Precipitation Record from BJY, PHS, and W5B (Left) and CDFs of Annual Precipitation from 1,000-Year Synthetic Precipitation Record (Right)	E-4
E-2	Calculated and Sine Curve Fitted PET	E-4
E-3	Schematic Diagram of Weighing Lysimeter (Left) and Photo of Area 5 Non-vegetated Weighing Lysimeter (Right)	E-5
E-4	Calibration of H1D to Weighing Lysimeter Soil Water Storage Data	E-6
E-5	Surface Soil Water Potential, Calibrated Water Potential Thresholds, and Daily Precipitation for First 2,000 Days of 43-Year Record	E-7
E-6	Yucca Flat Hydrologic Basin Overlaid on Shaded Relief Map Derived from the Combined USGS and SRTM DEMs	E-14
E-7	3D High Oblique View Illustrates how Drainage Lines (Blue) Either Flow through Craters (Yellow) Not Acting as Hydrologic Sinks (U9IT28) and Craters that Act as Hydrologic Sinks (U9BX)	E-15
E-8	QuickBird Satellite Image 132 Band Combination Used to Help Analyze Drainage Patterns in and Around Craters	E-17
E-9	QuickBird Satellite Image 432 Band Combination Highlighting Vegetation Health in Proximity To Crater Rims	E-18
E-10	Concentric Nature and Size of Crater Bottoms (Blue) Relative to the Extent of Each Crater (Tan)	E-22

LIST OF FIGURES (CONTINUED)

NUMBER	TITLE	PAGE
E-11	Sorted Crater Depths and Sorted Top and Bottom Diameters	E-25
E-12	CDF of Crater Volumes Calculated using Frustum Geometry	E-25
E-13	CDF of Catchment Areas of Yucca Flat Craters	E-27
E-14	Crater Attributes versus Catchment Area for All Craters	E-28
E-15	Photo of U-10i Crater after the February 23–24, 1998, Ponding Event	E-31
E-16	Calculated Pond Height for U-10i for 43-Year Record	E-32
E-17	Photo of U-3fd Crater Taken in March 1995	E-33
E-18	Calculated Pond Height for U-3fd in March (Top) and August (Bottom) 1983 and Measured Values from Pohll, Warwick, and Tyler (1996)	E-35
E-19	Calculated and Measured Soil Water Content (Left) and Potential (Right) at U-3fd	E-36
E-20	Photo of U-3bh Taken in 1998 (Left) and Calculated Pond Height for U-3bh Crater for 33-Year Simulation Period (Right)	E-36
E-21	Calculated and Measured Soil Water Content (Left) and Potential (Right) at U-3bh	E-37
E-22	Calculated Pond Heights for U-5a Crater (Left), and Photo of U-5a (Right)	E-38
E-23	Final and Preliminary Infiltration Results	E-41
E-24	Map Showing Crater Catchment Areas and Infiltration Flux for Each Crater	E-42
F-1	Simplified Models (a) Computational Grid, (b) Features	F-5
F-2	Sensitivity of Simulated Water Table Elevations to Uncertainty in (a) Initial Height of Water Table and (b) Aquifer Porosity	F-8
F-3	Relationship between Aquifer Permeability and (a) Height of Present Water Table after 8,000 Years of Drainage, and (b) Time to Reach Equilibrium with Lower Recharge Rate	F-9

LIST OF FIGURES (CONTINUED)

NUMBER	TITLE	PAGE
F-4	Results of 500 Transient Simulations, Showing which Parameter Combinations were Incompatible and Compatible with the Draining Conceptual Model	F-11
F-5	Matrix Permeabilities versus Porosities for Tuff Confining Units (TCUs), Vitric Tuff Aquifers (VTAs) and Welded Tuff Aquifers (WTAs)	F-12
F-6	Matrix Permeability versus Elevation Profiles from Boreholes (a) UE-7f (b) UE-7bc (c) UE-7ax (d) UE-7az (e) UE-6d #2 and (f) UE-3e #2	F-13
G-1	Illustration of Mechanical and Hydrologic Effects from an Underground Nuclear Detonation	G-2
G-2	Definition of Crushed and Compressed Zones	G-4
G-3	Overpressure (dH) as a Function of Radial Distance from the Working Point (r), according to Two Conceptual Models: (a) Model 1, and (b) Model 2	G-5
G-4	Definition of Chimney, Cavity, and Overpressurized Zones	G-6
G-5	Example Initial Permeability and Head Assumed for Model 2 (dH = 300 m; Mild Permeability Reduction)	G-11
G-6	Example Initial Permeability and Head Assumed for Model 2 (dH = 1,000 m; Mild Permeability Reduction)	G-12
G-7	Example Initial Permeability and Head Assumed for Model 2 (dH = 300 m; Enhanced Permeability)	G-12
G-8	Example Initial Permeability and Head Assumed for Model 2 (dH = 300 m; Strong Permeability Reduction)	G-13
G-9	Example Initial Permeability and Head Assumed for Model 1 (H_o = 300 m; Permeability Enhanced 50 ×, Low Head Criteria)	G-13
G-10	Example Initial Permeability and Head Assumed for Model 1 (H_o = 300 m; Permeability Enhanced 50 ×, High Head Criteria)	G-14
G-11	Example Initial Permeability and Head Assumed for Model 1 (H_o = 300 m; No Permeability Change, Low Head Criteria)	G-14

LIST OF FIGURES (CONTINUED)

NUMBER	TITLE	PAGE
G-12	Example Initial Permeability and Head Assumed for Model 1 (H_o = 600 m; Permeability Reduction × 0.02, Low Head Criteria)	G-15
G-13	Water Levels at TW-7 for the Entire Period of Record	G-17
G-14	Water Levels at TW-7, Emphasizing the Pre-1965 Record	G-17
G-15	Water Levels at TW-7 Immediately After the BILBY Detonation	G-19
G-16	Simulated and Measured Water Levels at TW-7 Immediately After the BILBY Detonation, Using Radial Model and Parameters Listed in Table G-5	G-21
G-17a	High-Resolution Three-Dimensional Model of the BILBY Detonation	G-22
G-17b	High-Resolution Three-Dimensional Model of the BILBY Detonation (Inset)	G-23
G-18	Simulated and Measured Water Levels at TW-7 Immediately After the BILBY Detonation, Using Three-Dimensional Model	G-25
H-1	Temperature Measurement Sites in Reiner (2007)	H-2
H-2	Temperature Distribution at the Water Table in Yucca Flat	H-3
H-3	Conceptual Model of Geothermal Transport in Central Yucca Flat	H-4
H-4	Locations of NNES Temperature Measurement Sites and Temperature Log at Observation Well ER-8-1	H-6
H-5	Interpreted Groundwater Age in the LCA Using ^{14}C Data	H-10
H-6a	Schematic Representation of Central Box Model Showing Groundwater Pathways	H-11
H-6b	Near-Surface Temperature Variation as a Function of Depth	H-13
H-7	Simulated Temperatures at 500 m bls with Basal Heat Flux of 55 mW/m^2 and Base-Case Thermal Conductivities	H-14
H-8	Temperatures at the Water Table along Three East–West Cross Sections	H-15
H-9	Simulated and Observed Geothermal Gradients for the Central Box Model	H-16

LIST OF FIGURES (CONTINUED)

NUMBER	TITLE	PAGE
H-10	Sensitivity Simulations Involving Variations in Modeled Thermal Conductivity	H-17
H-11	Variation in Laboratory-Derived Values of Thermal Conductivity in Tuff Material at the NNSS	H-17
H-12	Sensitivity Simulations Involving Variations in Modeled Base Heat Flux	H-19
H-13a	Groundwater Flow Rates within the Regional Model Domain	H-20
H-13b	Thermal Profile in a One-Dimensional Vertical Volcanic Column Subjected to Recharge Rates of 0 and 5 mm/yr	H-22
H-14	Areal Extent of the Contiguous Portion of the LCA in Yucca Flat and the Locations of Wells ER-8-1 and UE-10j near Climax Mine	H-23
H-15	Areal Extent of the Entire Yucca Flat Northern Thermal Model	H-24
H-16	Typical Simulated Groundwater Velocities between 0 and +500 m amsl in the Northern Thermal Model	H-27
H-17a	Simulated and Observed Temperatures at Well ER-8-1—Base Case	H-28
H-17b	Simulated and Observed Temperatures at Well ER-8-1—High Basal Heat Flux Case	H-28
H-17c	Simulated and Observed Temperatures at Well ER-8-1—Low Thermal Conductivity Case	H-29
H-17d	Simulated and Observed Temperatures at Well ER-8-1—High Thermal Conductivity Case	H-29
H-18a	Simulated and Observed Temperatures at Well UE-10j—Base Case	H-30
H-18b	Simulated and Observed Temperatures at Well UE-10j—High Basal Heat Flux Case	H-30
H-18c	Simulated and Observed Temperatures at Well UE-10j—Low Thermal Conductivity Case	H-31
H-18d	Simulated and Observed Temperatures at Well UE-10j—High Thermal Conductivity Case	H-31

LIST OF FIGURES (CONTINUED)

NUMBER	TITLE	PAGE
I-1	Observed and Simulated Drawdowns at Observation Wells ER-3-1 and ER-7-1	I-3
I-2	Observed and Simulated Drawdowns at Observation Wells UE-1h, UE-7nS, and U-3cn-5	I-4
I-3	Transient Simulated and Observed Water Levels at Well Sites (a) WW-C-1 and (b) TW-D	I-11
I-4	Transient Simulated and Observed Water Levels at Well Sites (a) UE-1q and (b) ER-7-1	I-12
I-5	Transient Simulated and Observed Water Levels at Well Sites (a) UE-7nS and (b) ER-6-1-1	I-13
I-6	Transient Simulated and Observed Water Levels at Well Sites (a) WW-2 and (b) UE-7aa	I-14
I-7	Map of Pre-detonation Steady-State Water Flux to the LCA from the Unsaturated-Zone Model Domain with an Assumed Net Infiltration Rate of 5 mm/yr	I-18
I-8	Map of 1,000-Year Water Flux to the LCA from the Unsaturated-Zone Model Domain with an Assumed Net Infiltration Rate of 5 mm/yr	I-19
I-9	Time History of Total Water Flux to the LCA from the Unsaturated-Zone Model Domain with an Assumed Net Infiltration Rate of 5 mm/yr	I-20
I-10	Map of Pre-detonation Steady-State Water Flux to the LCA from the Saturated Alluvial/Volcanic Aquifer System with an Assumed Infiltration Rate of 5 mm/yr	I-22
I-11	Time History of Total Water Flux to the LCA from the Saturated Alluvial/Volcanic Aquifer System with an Assumed Infiltration Rate of 5 mm/yr	I-23
I-12	Map of Modeled Water Flux to the LCA from the Saturated Alluvial/Volcanic Aquifer System at Day 3,000 (October 12, 1965) with an Assumed Infiltration Rate of 5 mm/yr	I-24
I-13	Map of Modeled Water Flux to the LCA from the Saturated Alluvial/Volcanic Aquifer System at Day 7,800 (December 3, 1978) with an Assumed Infiltration Rate of 5 mm/yr	I-25

LIST OF FIGURES (CONTINUED)

NUMBER	TITLE	PAGE
I-14	Map of Modeled Water Flux to the LCA from the Saturated Alluvial/Volcanic Aquifer System from Day 18,250 (July 26, 2007) to Day 365,250 (July 26, 2957) with an Assumed Infiltration Rate of 5 mm/yr	I-26
I-15	Calculated Increase in LCA Potentiometric Surface due to Underground Nuclear Testing: (a) 8.5 Years, and (b) 12.5 Years (with an Assumed Recharge Rate of 5 mm/yr)	I-28
I-16	Calculated Increase in LCA Potentiometric Surface due to Underground Nuclear Testing: (a) 18 Years, and (b) 31 Years (with an Assumed Recharge Rate of 5 mm/yr)	I-29
I-17	Calculated Particle Travel Times from Representative Contaminant Source Nodes: (a) Transient Flow Field due to Underground Nuclear Testing, and (b) Steady-State Flow Field (with an Assumed Recharge Rate of 5 mm/yr and Fracture Effective Porosity of 0.0045)	I-30
J-1	Schematic Cross-Sectional View Across a Fault Zone Showing Architectural Components and Associated Structural Features	J-3
J-2	Relationship Between Fault Displacement and Damage Zone Width for the Nevada National Security Site	J-5
J-3	Estimated Hydraulic Conductivity of Faults in Yucca Flat Derived from Analyses of ER-6-1 MWAT	J-8
J-4	Location of Environmental Characterization Boreholes Completed into the LCA in Yucca Flat	J-12
J-5	Flow Percentage Data from Analysis of SFM Logs	J-16
J-6	Accumulation of Flow from SFM Logs	J-17
J-7	Flow Percentage and Fracture Data for ER-6-1#2	J-19
J-8	Flow Percentage and Fracture Data for ER-7-1	J-20
J-9	Flow Percentage and Fracture Data for ER-6-1	J-21
J-10	Flow Percentage and Fracture Data for ER-6-2	J-22
J-11	Comparison of Flow Percentages from SFM Logs and Analyses of Pumping TFM Logs and Tracer Test Observations	J-24

LIST OF FIGURES (CONTINUED)

NUMBER	TITLE	PAGE
J-12	Raw and Smoothed SFM Log Data for ER-6-1#2	J-26
J-13	Derivative of Smoothed SFM Data and Flowing Feature Identification for ER-6-1#2	J-27
J-14	Spacing between Smaller-scale Flowing Features for Boreholes ER-6-1, ER-6-1#2, and ER-6-2 (a) Distribution (b) Fit	J-28
J-15	Cumulative Distribution Function (a) EMI Fracture Spacing for ER-6-1 and ER-7-1, (b) Spacing between Smaller-scale Flowing Features for ER-6-1, ER-6-1#2, and ER-6-2	J-29
J-16	Correlation Cross Plot, West Dipping Fractures for ER-6-1#2	J-31
J-17	Correlation Cross Plot, East Dipping Fractures for ER-6-1#2	J-32
J-18	Conceptual Composite Distribution of LCA Flowing Features	J-33
J-19	Application to CAU Transport - LCA Hydrostructural Domains	J-34
K-1	Comparison of Walkabout Particle-Tracking Results at Discrete Times with Theoretical Curves	K-9
K-2	Walkabout Particle-Tracking Results for Verification Test 1a of Painter (2011)	K-9
K-3	Comparison of Potentiometric Surfaces of FEHM and MODFLOW for Walkabout Verification Test	K-10
K-4	Walkabout Particle Transport Times for Verification Test (1.0 m Longitudinal Dispersivity)	K-12
K-5	Comparison of Particle-Tracking Results for Walkabout and RWHet for Verification Test (1.0 m Longitudinal Dispersivity)	K-13
K-6	Comparison of Particle-Tracking Results for FEHM/Walkabout and MODFLOW/RWHet for Dispersivities of 1.0, 0.1, and 0.0 m	K-14
K-7	Comparison of Particle-Tracking Results at Discrete Times for FEHM/Walkabout and MODFLOW/RWHet for Dispersivities of 1.0, 0.1, and 0.0 m	K-15

LIST OF FIGURES (CONTINUED)

NUMBER	TITLE	PAGE
K-8	Comparison of Particle-Tracking Breakthrough Times for FEHM/Walkabout and MODFLOW/RWHet for Dispersivities of 1.0, 0.1, and 0.0 m	K-16
K-9	Comparison of FEHM_sptr and Walkabout Particle Transport Times	K-17
K-10	Comparison of FEHM_sptr and Walkabout Normalized Steady-State Concentrations	K-18
K-11	Single-Porosity Verification of PLUMECALC Comparison to Analytical Solution	K-21
K-12	Dual-Porosity Verification of PLUMECALC Comparison to Analytical Solution	K-22
K-13	Dual-Porosity Verification of PLUMECALC Comparison to Analytical Solution for a Range of Transport Parameters	K-23
K-14	Comparison of FEHM_sptr/PLUMECALC and MODFLOW/MT3D for Heterogeneous Permeability Field	K-24
K-15	Comparison of Walkabout/PLUMECALC and MODFLOW/MT3D for Heterogeneous Permeability Field	K-25
K-16	Comparison of Walkabout/PLUMECALC and MODFLOW/RWHet for Heterogeneous Flow Field at 20 and 100 Days	K-27
K-17	Comparison of Walkabout/PLUMECALC and MODFLOW/RWHet for Heterogeneous Flow Field at 500 and 1,000 Days	K-28
K-18	Comparison of Walkabout/PLUMECALC, MODFLOW/RWHet, MODFLOW/MT3D, and FEHM/Walkabout for Heterogeneous Flow Field	K-29
L-1	Relation between the Groundwater $^{36}Cl/Cl$ Ratios and Inverse Cl Concentrations	L-2
L-2	Distribution of Sampling Locations (a) within and Adjacent to the Yucca Flat Study Area of SNJV (2006a) and (b) within the Yucca Flat Study Area	L-6
L-3	Relationship between ^{14}C and $\delta^{13}C$: (a) All Data, and (b) Isotopically Heavy Data with Low ^{14}C	L-7

LIST OF FIGURES (CONTINUED)

NUMBER	TITLE	PAGE
L-4	$\delta^{13}C$ and Inverse Alkalinity in Yucca Flat Area Groundwater	L-10
L-5	Comparison of $\delta^{13}C$-Corrected versus DIC-Corrected Groundwater Ages for the Alluvial/Volcanic Aquifer System	L-11
L-6	Comparison of $\delta^{13}C$-Corrected versus DIC-Corrected Groundwater Ages for the LCA	L-12
L-7	Comparison of $\delta^{13}C$-Corrected versus DIC-Corrected Groundwater Ages for the LCCU and UCCU	L-12
L-8	Groundwater ^{14}C Ages for (a) Pre-Tertiary Rocks and (b) Alluvial/Volcanic Aquifer System in Yucca Flat	L-14
L-9	δD versus $\delta^{18}O$ for Yucca Flat Area Groundwater and Perched Springs	L-22
L-10	Comparison of Groundwater and Terrestrial $^{36}Cl/Cl$ versus ^{14}C Age: (a) LCA Groundwater, (b) Alluvial/Volcanic Aquifer System Groundwater, and (c) LCA Groundwater and Alluvial/Volcanic Aquifer System Groundwater	L-23
L-11	Effect of Matrix Diffusivity on Tracer Breakthrough	L-27
L-12	Effect of Saturated Hydraulic Conductivity on Tracer Breakthrough	L-28
L-13	Effect of Fracture Porosity (and Fracture Spacing) on Tracer Breakthrough	L-29
L-14	Effect of Matrix K_d on Tracer Breakthrough	L-30
M-1	The One-Dimensional Streamtube Model Extending Southward from the BOURBON Detonation	M-2
M-2	Conceptual Model of Colloid-Facilitated Plutonium Reactive Transport in Fractured Rock	M-10
M-3	Calculation of Initial Concentrations of Radionuclides in the BOURBON Source Area	M-14
M-4	Sampled Flow and Transport Parameters: Fracture Porosity (porF), Matrix Porosity (porM), Fracture Aperture (fb, m), Fracture Spacing (S_f, m), Hydraulic Conductivity (Conductivity, m/day), and Inflow Rate (flowr, kg/s)	M-21

LIST OF FIGURES (CONTINUED)

NUMBER	TITLE	PAGE
M-5a	Sampled Matrix Diffusion Coefficients (D_m, m^2/s) for Different Radionuclides	M-22
M-5b	Sampled Matrix Diffusion Coefficients (D_m, m^2/s) for Different Radionuclides and Longitudinal Dispersivity (Disp, m)	M-23
M-6	Sampled Fracture Sorption Coefficients (K_{df}, mL/cm^2) for ^{14}C, ^{90}Sr, ^{137}Cs, ^{237}Np, U, and Pu	M-24
M-7	Sampled Matrix Sorption Coefficients (K_{dm}, mL/g) for ^{14}C, ^{90}Sr, ^{137}Cs, ^{237}Np, U, Pu, and Eu	M-25
M-8	Sampled Colloid Load Concentration (C_{col}, mol sites/mL), Colloid Sorption Coefficient in Fracture (K_{df}-Col, mL/cm^2), Forward Rate Constant in Fracture for Pu-Col (k_f-PuCol, 1/hr), Forward and Reverse Rate Constants of Plutonium Sorption onto Colloids (k_f-Col and k_r-Col, 1/hr), and Forward Rate Constants for Plutonium and Europium Sorption onto Immobile Minerals in Matrix (k_f-Pu and k_f-Eu, 1/hr)	M-26
M-9	Sampled Inventory Uncertainty Factors (f_{RSTH3} for ^3H; f_{RST1} for Activation Products ^{14}C, ^{36}Cl, ^{59}Ni, ^{63}Ni, ^{152}Eu, and ^{154}Eu; f_{RST2} for Fission Products ^{99}Tc, ^{129}I, ^{90}Sr, and ^{137}Cs; and f_{RST3} for Residual Fuel/Tracers ^{237}Np, U_{all}, and $^{238–242}Pu$) and the Exchange Volume Radius Factor (f_{ev}) (Tompson et al., 2011)	M-27
M-10a	Sampled Initial Concentrations (in multiples of MCL) for ^3H, ^{14}C, ^{36}Cl, ^{99}Tc, ^{129}I, ^{90}Sr, ^{59}Ni, and ^{63}Ni in the Fractures of the Exchange Volume	M-28
M-10b	Sampled Initial Concentrations (in multiples of MCL) for ^{137}Cs, ^{152}Eu, ^{154}Eu, ^{237}Np, and U_{all} in the Fractures of the Exchange Volume	M-29
M-10c	Sampled Initial Concentrations (in multiples of MCL) for Plutonium Isotopes ($^{238–242}Pu$) in the Fractures of the Exchange Volume	M-30
M-11	Computed Plutonium Contaminant Lengths at the 5th, 50th, and 95th Percentiles from the Colloid-Facilitated Plutonium Transport Modeling	M-34
M-12	Computed Contaminant Lengths at the 5th, 50th, and 95th Percentiles for Decaying Species ^3H, ^{90}Sr, ^{137}Cs, ^{152}Eu, and ^{154}Eu	M-35

LIST OF FIGURES (CONTINUED)

NUMBER	TITLE	PAGE
M-13	Computed Contaminant Lengths at the 5th, 50th, and 95th Percentiles for the Radionuclides ^{237}Np, U_{all}, ^{59}Ni, and ^{63}Ni Sorbed onto Both Fracture Surfaces and Matrix	M-36
M-14	Computed Contaminant Lengths at the 5th, 50th, and 95th Percentiles for the Radionuclides ^{14}C, ^{36}Cl, ^{99}Tc, and ^{129}I	M-37
M-15	Computed Concentration Profiles at the 5th, 50th, and 95th Percentiles for Plutonium Isotopes at 1,000 Years	M-40
M-16	Computed Concentration Profiles at the 5th, 50th, and 95th Percentiles for ^{3}H, ^{90}Sr, ^{137}Cs, ^{152}Eu, and ^{154}Eu at 1,000 Years	M-41
M-17	Computed Concentration Profiles at the 5th, 50th, and 95th Percentiles for ^{237}Np, U_{all}, ^{59}Ni, and ^{63}Ni at 1,000 Years	M-42
M-18	Computed Concentration Profiles at the 5th, 50th, and 95th Percentiles for ^{14}C, ^{36}Cl, ^{99}Tc, and ^{129}I at 1,000 Years	M-43
M-19	^{238}Pu Concentration Distributions at Different Times	M-45
M-20	^{239}Pu Concentration Distributions at Different Times	M-45
M-21	^{240}Pu Concentration Distributions at Different Times	M-46
M-22	^{241}Pu Concentration Distributions at Different Times	M-46
M-23	^{242}Pu Concentration Distributions at Different Times	M-47
M-24	The Concentration Distributions of Plutonium Isotopes and Total Plutonium at 1,000 Years	M-47
M-25	The Mean ^{239}Pu Concentration Profiles at 1,000 Years Computed from (a) Monte Carlo Simulations and (b) ^{239}Pu Reduction Factors	M-49
M-26	The Fit Results of the Simplified Pu-Col Model against the Process Model That Includes All of Competitive Transport Processes of the Colloid-Facilitated Plutonium Transport	M-50
M-27	Global Sensitivity Analysis of ^{238}Pu Contaminant Lengths to 58 Sampled Parameters of the Monte Carlo Simulations	M-53

LIST OF FIGURES (CONTINUED)

NUMBER	TITLE	PAGE
M-28	Global Sensitivity Analysis of ^{239}Pu Contaminant Lengths to 58 Sampled Parameters of the Monte Carlo Simulations	M-53
M-29	Global Sensitivity Analysis of ^{240}Pu Contaminant Lengths to 58 Sampled Parameters of the Monte Carlo Simulations	M-54
M-30	Global Sensitivity Analysis of ^{241}Pu Contaminant Lengths to 58 Sampled Parameters of the Monte Carlo Simulations	M-54
M-31	Global Sensitivity Analysis of ^{242}Pu Contaminant Lengths to 58 Sampled Parameters of the Monte Carlo Simulations	M-55
M-32	Global Sensitivity Analysis of ^{3}H Contaminant Lengths to 58 Sampled Parameters of the Monte Carlo Simulations	M-55
M-33	Global Sensitivity Analysis of ^{14}C Contaminant Lengths to 58 Sampled Parameters of the Monte Carlo Simulations	M-56
M-34	Global Sensitivity Analysis of ^{36}Cl Contaminant Lengths to 58 Sampled Parameters of the Monte Carlo Simulations	M-56
M-35	Global Sensitivity Analysis of ^{99}Tc Contaminant Lengths to 58 Sampled Parameters of the Monte Carlo Simulations	M-57
M-36	Global Sensitivity Analysis of ^{129}I Contaminant Lengths to 58 Sampled Parameters of the Monte Carlo Simulations	M-57
M-37	Global Sensitivity Analysis of ^{237}Np Contaminant Lengths to 58 Sampled Parameters of the Monte Carlo Simulations	M-58
M-38	Global Sensitivity Analysis of Uranium Contaminant Lengths to 58 Sampled Parameters of the Monte Carlo Simulations	M-58
M-39	Global Sensitivity Analysis of ^{90}Sr Contaminant Lengths to 58 Sampled Parameters of the Monte Carlo Simulations	M-59
M-40	Global Sensitivity Analysis of ^{137}Cs Contaminant Lengths to 58 Sampled Parameters of the Monte Carlo Simulations	M-59
M-41	Global Sensitivity Analysis of ^{152}Eu Contaminant Lengths to 58 Sampled Parameters of the Monte Carlo Simulations	M-60

LIST OF FIGURES (CONTINUED)

NUMBER	TITLE	PAGE
M-42	Global Sensitivity Analysis of ^{154}Eu Contaminant Lengths to 58 Sampled Parameters of the Monte Carlo Simulations	M-60
M-43	Global Sensitivity Analysis of ^{59}Ni Contaminant Lengths to 58 Sampled Parameters of the Monte Carlo Simulations	M-61
M-44	Global Sensitivity Analysis of ^{63}Ni Contaminant Lengths to 58 Sampled Parameters of the Monte Carlo Simulations	M-61
N-1	FracMan Hybrid DFN/EPM Discrete Fracture Network/Equivalent Porous Media Model	N-6
N-2	FracMan Laplace Transform Galerkin Solute Transport Model – Pipe Network Pathways through Fractured Rock	N-8
N-3	Perspective Plot of Yucca Flat LCA Subarea Model Domain	N-9
N-4	Map View of Yucca Flat LCA Subarea Model Domain with Significant HST Detonations Included in Corroborative Analysis	N-10
N-5	LCA Permeability Zones within the Subarea Model Domain	N-12
N-6	Mass Flux to the Saturated LCA from the BOURBON, MICKEY/TORRIDO and BILBY Detonations	N-15
N-7	Modeled LCA Groundwater Flow Paths from Sources in the Subarea Model	N-17
N-8	^{3}H Concentrations in Subarea Model Calculated by FEHM_sptr and PLUMECALC	N-18
N-9	^{129}I Concentrations in Subarea Model Calculated by FEHM_sptr and PLUMECALC	N-19
N-10	MODFLOW/MT3DMS Grid: (a) XZ Cross Section and (b) XY Cross Section	N-22
N-11	Comparison of Particle Tracks for MODPATH and FEHM sptr	N-24
N-12	CDF of Ratio of MODFLOW Travel Time to FEHM Travel Time	N-25
N-13	Comparison of ^{3}H Concentrations (mol/L) at 10 Years (^{3}H MCL = 6.88E-13 mol/L)	N-27

LIST OF FIGURES (CONTINUED)

NUMBER	TITLE	PAGE
N-14	Comparison of ^{3}H Concentrations (mol/L) at 50 Years (^{3}H MCL = 6.88E-13 mol/L)	N-28
N-15	Comparison of ^{3}H Concentrations (mol/L) at 100 Years (^{3}H MCL = 6.88E-13 mol/L)	N-29
N-16	Comparison of ^{129}I Concentrations (mol/L) at 100 Years (^{129}I MCL = 4.39E-11 mol/L)	N-31
N-17	Comparison of ^{129}I Concentrations (mol/L) at 300 Years (^{129}I MCL = 4.39E-11 mol/L)	N-32
N-18	Comparison of ^{129}I Concentrations (mol/L) at 1,000 Years (^{129}I MCL = 4.39E-11 mol/L)	N-33
N-19	Comparison of Radionuclide Mass from MT3DMS and PLUMECALC Inside the Corroborative Model Domain	N-34
N-20	3D Perspective View of the LCA and Fault Surfaces Exported from the HFM Relative to an Arbitrary Lower Surface of -990 m Elevation Surface Framed by the Subdomain Model Boundaries	N-37
N-21	Comparison of the FEFLOW Mesh (a) and the FEHM Nodes (b) Relative to a Flattened Projection of the Fault Surfaces Within the Subdomain Exported from the HFM	N-39
N-22	3D Perspective View of the 30 Slices Used to Discretize the FEFLOW Subdomain Model	N-40
N-23	Material Assignments in FEFLOW Model (a) Anisotropy Angle and (b) Kyy Hydraulic Conductivity	N-42
N-24	Location of Fault-core and Fault-damage Zone Nodes from the FEHM Model after being Summed and Snapped to the Respective Fault Zones as Represented (a) in the FEFLOW Model and (b) Flux into the LCA Surface in the FEFLOW Model as Defined from Snapping the FEHM Nodes to the Nearest Node of the Corresponding Permeability Zone	N-46
N-25	Comparison of Heads at the LCA Surface Simulated by the FEFLOW (a) Subdomain Model and (b) the FEHM Model	N-49
N-26	Groundwater Velocities: (a) and Particle Tracks (b) Simulated by the FEFLOW Subdomain Model at Slice-1 of the Model	N-50

LIST OF FIGURES (CONTINUED)

NUMBER	TITLE	PAGE
N-27	Results of the FEFLOW Mass Transport Simulation at 10, 50, and 100 Years Showing the Simulated Distribution of $^{3}H > 2.1 \times 10\text{-}9$ mg/L	N-51
N-28	Results of the FEFLOW Mass Transport Simulation at 100, 300, and 1,000 Years Showing the Simulated Distribution of $^{129}I > 5.7 \times 10\text{-}6$ mg/L	N-52
N-29	Perspective View of the Results from the FEFLOW Simulation of ^{3}H and ^{129}I Mass Transport	N-53
N-30	FracMan DFN Model for Yucca Flat Fault Damage Zones	N-56
N-31	FracMan EFN Model for Background Rock Mass Hydraulic Conductivity	N-57
N-32	Workflow Diagram for FracMan Hybrid DFN/EPM Flow and Transport Simulation	N-58
N-33	Mapping from FEHM Voronoi Centers to FracMan Tetrahedral Volume Elements	N-60
N-34	Model for Fault Core and Damage Zones	N-62
N-35	Assignment of Heads to Faces of FracMan Model Region based on FEHM Voronoi Control Volume Center Points	N-64
N-36	Fixed Head Boundary Conditions on North and South Faces of FracMan Model Region, with Comparison to Interpolated Values from FEHM Control Volume Center Points	N-65
N-37	Transport Boundary Conditions	N-66
N-38	Laplace Transform Galerkin Transport through Hybrid DFN/EPM Flow Field – Pathways Defined by Particle Tracking	N-70
N-39	Variation of Pipe Width – Series Flow Pathway Conserving Flux	N-71
N-40	Comparison of FracMan and FEHM Head Fields	N-73
N-41	Comparison of FracMan and FEHM Head Fields – 2D Vertical Section	N-74
N-42	Comparison of FracMan and FEHM North-South Velocity Fields ($V_{n\text{-}s}$) – 2D Horizontal Section	N-75

LIST OF FIGURES (CONTINUED)

NUMBER	TITLE	PAGE
N-43	Locations of Anisotropic Voronoi Volumes in FEHM Model – (K_{max}/K_{min} >2), Showing Faults from FracMan Model	N-77
N-44	Model Particle Trajectories: (a) FracMan and (b) FEHM	N-78
N-45	Solute Transport from FracMan Simulation – ^{3}H – Concentrations based on Pipe Flow Volumes	N-81
N-46	Solute Transport from FracMan Simulation – ^{3}H – Concentrations based on Mobile Porosity in EPM Volumes	N-82
N-47	Solute Transport from FracMan Simulation – ^{3}H – Concentrations based on Pipe Flow Volumes with MCL Cut-off	N-83
N-48	Solute Transport from FracMan Simulation– ^{129}I – Concentrations based on Pipe Flow Volumes	N-84
N-49	Solute Transport from FracMan Simulation– ^{129}I – Concentrations based on Mobile Porosity in EPM Volumes	N-85
N-50	Solute Transport from FracMan Simulation – ^{129}I – Concentrations based on Pipe Flow Volumes with MCL Cut-off	N-86

LIST OF TABLES

NUMBER	TITLE	PAGE
1-1	Descriptions of Major HSUs in the Model Domain	1-20
1-2	Treatment of Water and Contaminant Boundary Fluxes for Yucca Flat/Climax Mine CAU Model Domains	1-42
1-3	Yucca Flat/Climax Mine CAU CAI Planning Documents	1-52
1-4	Major Supporting Documents	1-53
2-1	Treatment of HST Processes and Associated Transport Effect for the Unsaturated-Zone Model	2-17
2-2	Treatment of HST Processes and Associated Transport Effect for the Saturated Alluvial/Volcanic Aquifer System Model	2-18
2-3	Treatment of HST Processes and Associated Transport Effect for the Saturated LCA Model	2-19
2-4	The Bowen Radionuclide Inventory for Yucca Flat	2-20
2-5	Volcanic and Carbonate Rock Cavity Sorption (K_d) Values	2-28
2-6	Radionuclide Partitioning for Silicic-Rock Working-Point Detonations	2-31
2-7	Radionuclide Partitioning for Carbonate-Rock Working-Point Detonations	2-31
2-8	Initial HST Allocation Fractions in the Unsaturated Zone, Saturated Alluvial/Volcanic Aquifer System, and Saturated LCA Models for All Detonations	2-36
2-9	Initial HST ^{3}H and ^{14}C Inventory Fractions in the Unsaturated Zone, Saturated Alluvial/Volcanic Aquifer System, and Saturated LCA Models for All Detonations	2-37
2-10	Retained Radionuclide Categories and Radionuclide Groups	2-42
2-11	Distributions of Source-Term Parameters	2-42
3-1	Statistics for Preliminary and Final Infiltration Results	3-37
3-2	Grid Extent with Numbers of Nodes and Elements	3-39
3-3	Hydrologic Properties of Alluvium at the Area 3 RWMS	3-52

LIST OF TABLES (CONTINUED)

NUMBER	TITLE	PAGE
3-4	Summary of Selected HSU Permeabilities at the Pumping, Slug-Test, and Laboratory Scales within the Yucca Flat and NNSS Investigation Areas	3-57
3-5	Mean Parameter Values by HSU for Combined Samples Recovered from U-12b.07c (Rainier Mesa Exploratory #1) and UE-12t 1	3-59
3-6	Summary of Hydraulic Conductivity and Porosity Data from Winograd and Thordarson (1975)	3-60
3-7	Base-Case Hydrologic Parameters Used in the Yucca Flat Unsaturated-Zone Models	3-64
3-8	Matrix of Transport Model Sensitivity Cases	3-66
3-9	Radionuclides Considered in the Unsaturated-Zone Transport Models	3-71
3-10	Estimated Hydraulic Properties for the Sediment Textural Classifications in Sweetkind and Drake (2007b)	3-120
3-11	Sorption Coefficients (k_d) Used for ^{90}Sr and ^{137}Cs in Model Runs 1.2.1.2.1.2' and 5.4.2.1.2.1	3-129
3-12	Modifications to Unsaturated-Zone Model Parameters Based on Saturated Alluvial/Volcanic Aquifer System Model Calibration to the USGS Infiltration Map with Runoff	3-132
4-1	Compilation of 12 Single-Well Testing Results for the Tuff Confining Units	4-7
4-2	Calculated Volume of Aquifer Compression from InSAR Data	4-11
4-3	Summary of Node Count and Total Volume of Each HSU (and Faults) within the Active Model Domain	4-22
4-4	Intrinsic Permeability Values (Log, m^2)	4-26
4-5	Specific Storage Values (Log 1/m) Compared to Those Reported by SNJV (2006b)	4-27
4-6	Porosity Values	4-27
4-7	Permeability Anisotropy Values	4-28

LIST OF TABLES (CONTINUED)

NUMBER	TITLE	PAGE
4-8	Wells Used for Calibration Purposes	4-34
4-9	Parameters Used in Model Calibration	4-39
4-10	Parameters That Were Relatively Well Constrained by Model Calibration	4-42
4-11	Description of Case Names	4-44
4-12	Total Volume of Water Outflow in Excess of Steady-State Flow	4-49
4-13	Sensitivity Analysis Models and Results	4-52
4-14	Glass Retention Factors	4-67
4-15	Conceptual Model of Flow in Each HSU	4-68
4-16	Free-Water Diffusion Coefficients	4-69
4-17	Estimated Total Mass Decayed at 1,000 Years (in Moles) (for the Base Case 211212.1.14.5.1.2.N3.B2.s)	4-70
4-18	Statistics of Datasets Used to Derive Parameters for PLUMECALC Simulations	4-71
4-19	Matrix Porosity	4-74
4-20	Bulk Rock Density	4-74
4-21	Matrix Tortuosity	4-75
4-22	Fracture Porosity	4-75
4-23	Fracture Spacing	4-75
4-24	K_d of Neptunium	4-75
4-25	K_d of Uranium	4-76
4-26	Mean Fracture Aperture	4-76
4-27	Evaluation of Importance of Various Transport Processes, Using Case 211212.1.14.5.1.2.N3.B2.s	4-91

LIST OF TABLES (CONTINUED)

NUMBER	TITLE	PAGE
4-28	Sensitivity Analysis, Varying Starting Elevation of Particles Representing Unsaturated-Zone Sources	4-93
4-29	Mass Distribution at 1,000 Years Using 4 or 9 Time Divisions to Approximate Transient Flow	4-94
4-30	Comparison of Results Using Concentric Shells and Uniform Distribution of Particles for Case 211212.1.14.5.1.2.2.N3.B2.s	4-97
4-31	Transport Results for Variations in Flow Models	4-98
4-32	Impact of Testing-Effects Assumptions	4-104
4-33	Detonations with Particles Moved Upward to Approximate Thermal Buoyancy	4-105
4-34	Cases Considering Overpressurization in the Tuff Pile Area and Upward Buoyancy of the Source Term due to Thermal Effects	4-106
4-35	Criteria for Lower Boundary Breaching Scenarios	4-106
4-36	Five Most Important Transport Parameters for Each Radionuclide Based on Sensitivity Analysis of 3,000 Realizations	4-109
4-37	Contribution of Unsaturated-Zone and Saturated-Zone Sources to LCA Model for Case 211212.1.14.5.1.2.N3.B2.s at 1,000 years (Decay-Corrected)	4-114
4-38	RST Uncertainty Distributions	4-114
4-39	Statistics of Mass into LCA Model due to Variability of Source-Term Inventory	4-116
4-40	Distributions of the Melt-Glass Partitioning Factor (f)	4-116
4-41	Statistics of Mass Into LCA Model due to Variability of Melt-Glass Partitioning Factors	4-119
4-42	Statistics of Mass Into LCA Model due to Variability of Melt Glass Factors	4-121
4-43	Statistics of Mass into LCA Model due to Variability on Both Source Inventory and Melt-Glass Partitioning Factor	4-124

LIST OF TABLES (CONTINUED)

NUMBER	TITLE	PAGE
4-44	Statistics of Mass into LCA Model due to Variability in Source Inventory, Melt-Glass Partitioning Factor, and Transport Parameters	4-126
4-45	Wells in Saturated Alluvial/Volcanic Aquifer System Model with Tritium Measurements	4-128
4-46	Wells within Saturated Alluvial/Volcanic Aquifer System Model Domain with Tritium Measurements	4-130
4-47	Simulations Used for Comparison to Tritium Measurements	4-131
5-1	Naming Conventions for Alternative HFMs in the SNJV Yucca Flat/Climax Mine CAU Groundwater Flow Model	5-44
5-2	Naming Conventions for Alternative Recharge Models in the SNJV Yucca Flat/Climax Mine CAU Groundwater Flow Model	5-44
5-3	Total Water Balance for the Alternative Flow Models of the Yucca Flat/Climax Mine CAU	5-45
5-4	Summary of Net Boundary Flux Ranges for Yucca Flat/Climax Mine Model Boundaries	5-47
5-5	Naming Conventions for Alternative HFMs in the Climax Mine Flow Model	5-52
5-6	Naming Conventions for Alternative Recharge Models in the Climax Mine Flow Model	5-52
5-7	Estimated Fluxes (kg/s) along Northern and Southern Boundaries of Yucca Flat Flow Model	5-61
5-8	List of Adjustable Hydrogeologic Parameters and Boundary Conditions	5-81
5-9	Summary of Calibration Statistics	5-99
5-10	Mass Balance Summary	5-100
5-11	Calibrated Model Parameter Values	5-102
5-12	Detonation Locations of Interest for Velocity Sensitivity Analysis	5-158

LIST OF TABLES (CONTINUED)

NUMBER	TITLE	PAGE
6-1	Source Data Distributions and Methodology for Developing Fracture Parameters, Matrix Porosity, and Tortuosity Distributions	6-17
6-2	LCA Transport Model Fracture Retardation Distributions	6-20
6-3	LCA Transport Model Matrix Sorption (K_d) Distributions	6-20
6-4	Comparison Summary of Hydraulic and Tracer Fracture Apertures Determined from Field Investigations and a Laboratory Experiment	6-30
6-5	Mobile Initial Inventory in the Saturated LCA for ^{3}H, ^{14}C, ^{129}I, and ^{90}Sr	6-97
6-6	Summary of Mass Distribution of ^{3}H, ^{14}C, ^{129}I, and ^{90}Sr between Different Model Components of the Yucca Flat/Climax Mine CAU Assuming an Exchange Volume of 2 R_c and Base-Case Unsaturated- and Saturated-Zone Flow and Transport Properties	6-99
6-7	Initial ^{3}H Inventory for Selected LCA Significant Detonations	6-101
6-8	Initial Mobile ^{129}I Inventory for Selected LCA Significant Detonations	6-102
6-9	Summary of LCA Transport Model Analyses	6-107
6-10	Significant LCA Contaminant Transport Parameter Abbreviations and Descriptions	6-170
6-11	Ranked Stepwise Regression Analysis for Contaminant Boundary Performance Metrics for the Base-Case LCA HST Model	6-171
6-12	Ranked Entropy Analysis for Contaminant Boundary Performance Metrics for the Base-Case LCA HST Model	6-173
6-13	Summary of Ranked LCA Transport Parameter Significance Based on Regression, Entropy, and Classification Tree Sensitivity Analyses	6-181
7-1	Addressing FFACO UGTA Corrective Action Strategy Requirements for CAU Flow and Transport Models in the Yucca Flat/Climax Mine CAU Flow and Transport Model Document	7-23
A-1	Implementation of QAPP Modeling and Software Requirements in the Yucca Flat/Climax Mine CAU Flow and Transport Model	A-2

LIST OF TABLES (CONTINUED)

NUMBER	TITLE	PAGE
A-2	Implementation of QAPP Data Management Requirements in the Yucca Flat/Climax Mine CAU Flow and Transport Model	A-14
B-1	Yucca Flat/Climax Mine Detonation Characteristics	B-2
C-1	Long-Lived Radioactive Isotopes Deemed Pertinent to CAU Studies	C-9
C-2	Recommended Ranges of Exchange Volume Radius Multipliers for the Radionuclides Identified as Potentially Relevant to the Calculation of Contaminant Boundaries in Table C-1	C-17
C-3	Initial RST Fractions for Detonations in the Unsaturated Zone, Saturated Alluvial/Volcanic Aquifer System, and Saturated LCA Models	C-29
D-1	Sampling Dates and Radioisotopes for Sampled Observations Wells in Yucca Flat	D-5
D-2	Summary of Near Field Wells and Associated Underground Nuclear Detonations in Yucca Flat/Climax Mine CAU	D-10
E-1	List of GIS Files Used and Created for Completion of Project Tasks	E-9
E-2	Statistics of Yucca Flat Crater Dimensions and Catchment Sizes	E-26
E-3	Calibration Surface Soil Water Potential Thresholds and PET Multipliers for Preliminary and Final Results	E-30
E-4	Statistics for Final and Preliminary Infiltration Results	E-41
E-5	Yucca Flat/Climax Mine Surface Crater Characteristics	E-43
F-1	Measured Head Differences between the Volcanic Rocks and the Carbonate Aquifer	F-1
F-2	Aquifer Parameters and Recharge Estimates	F-6
F-3	Values used to Create 500 Unique Parameter Combinations for Uncertainty Analysis	F-10
G-1	Base-Case Model Parameters for Model 1 (8 Test Independent, 1 Test Dependent)	G-9

LIST OF TABLES (CONTINUED)

NUMBER	TITLE	PAGE
G-2	Base-Case Model Parameters for Model 2 (10 Test Independent, 1 Test Dependent)	G-10
G-3	Example Realizations of Conceptual Model 2	G-15
G-4	Representative Cases for Model 1	G-16
G-5	Parameters used in Radial Flow Model	G-20
G-6	Testing-Effects Parameters and Rock Properties Used for Three-Dimensional Model	G-24
G-7	Total and Effective Porosity	G-26
G-8	Saturated Hydraulic Conductivity	G-28
H-1	Ranges of Thermal Conductivities for Volcanic, Alluvial, Carbonate, Granite, and Clastic Units	H-32
H-2	Range of Thermal Conductivity for the Granitic Stock	H-32
I-1	Calibrated Parameters for Base and Alternative Cases of Southern Boundary Conditions	I-5
J-1	LCA Interval and Completion Interval for Boreholes in Yucca Flat	J-13
J-2	Availability of LCA Interval Fracture Data in Yucca Flat Boreholes	J-13
J-3	LCA, Completion, and SFM Log Intervals for Boreholes in Yucca Flat	J-15
L-1	$\delta^{13}C$ and Alkalinity Values Used in the Groundwater ^{14}C Age Corrections	L-10
L-2	Comparison of Model Parameters with Estimated Distributions	L-26
M-1	Statistics of the Flow and Transport Parameters for the LCA at Yucca Flat	M-5
M-2	Diffusion Coefficients and Dispersivity for the LCA at Yucca Flat	M-7
M-3	Statistics of the Sorption Parameters for the LCA at Yucca Flat	M-7
M-4	Statistics of the Parameters for Colloid-Facilitated Transport in the LCA at Yucca Flat	M-9

LIST OF TABLES (CONTINUED)

NUMBER	TITLE	PAGE
M-5	Initial Concentration Uncertainty Parameters for the 18 Radionuclides	M-15
M-6	Radionuclide Reactions in the LCA Fracture and Matrix	M-18
M-7	The Maximum Contaminant Levels of the Selected Radionuclides	M-32
M-8	The Statistics of the Computed Contaminant Lengths of the 18 Radionuclides	M-38
N-1	Source Term Used in Corroborative Software Analyses	N-14
N-2	Transport Parameters	N-23
N-3	Subdomain Model Boundaries	N-36
N-4	Hydraulic Conductivity Assignment by Permeability Zone	N-43
N-5	Storativity Assignments	N-44
N-6	Mass Transport Material Assignments	N-47
N-7	Mass Transport Initial Flux Assignments	N-47
N-8	Solute Transport Boundary Conditions	N-67
N-9	FracMan Solute Transport Parameters	N-72
N-10	Advective/Dispersive Solute Transport in FracMan Hybrid DFN/EPM Model	N-79

LIST OF ACRONYMS AND ABBREVIATIONS

General Acronyms and Abbreviations

ADRS	Amargosa Desert Research Site
amsl	Above mean sea level
bls	Below land surface
CADD	Corrective action decision document
CAI	Corrective action investigation
CAIP	Corrective action investigation plan
CAP	Corrective action plan
CAS	Corrective action site
CAU	Corrective action unit
CBPT	Convolution-based particle tracking
CDF	Cumulative distribution function
CMB	Chloride mass balance
CR	Closure report
DIC	Dissolved inorganic carbon
DOE	U.S. Department of Energy
DRI	Desert Research Institute
DVRFS	Death Valley Regional Flow System
ECDF	Empirical cumulative distribution function
EC/IT	Electron capture/isomeric transition
EPA	U.S. Environmental Protection Agency
ET	Evapotranspiration
FEHM	Finite element heat and mass
FFACO	*Federal Facility Agreement and Consent Order*
GAO	U.S. Government Accountability Office
GDPM	Generalized dual-porosity model
GIS	Geographic Information Systems
GMWL	Global Meteoric Water Line
HDD	Hydrologic data document
HDO	Hydrogen deuterium oxide
HFM	Hydrostratigraphic framework model
HGU	Hydrogeologic unit

LIST OF ACRONYMS AND ABBREVIATIONS (CONTINUED)

HST	Hydrologic source term
HSU	Hydrostratigraphic unit
HTO	Hydrogen tritium oxide
InSAR	Interferometric synthetic aperture radar
IAEA	International Atomic Energy Agency
ka	Thousand years before present
K-S	Kolmogorov-Smirnov
LaGriT	Los Alamos Grid Toolbox
LANL	Los Alamos National Laboratory
LLNL	Lawrence Livermore National Laboratory
Ma	Million years ago
MARS	Multivariate adaptive regression spline
MCL	Maximum contaminant level
MLBMA	Maximum Likelihood Bayesian Model Averaging
M&O	Management and operating
MT	Magnetotelluric
MWAT	Multiple-well aquifer test
NA	Not available
N/A	Not applicable
NAD	North American Datum
NDEP	Nevada Division of Environmental Protection
N-I	Navarro-Intera, LLC
NNES	Navarro Nevada Environmental Services, LLC
NNSA/NSO	U.S. Department of Energy, National Nuclear Security Administration Nevada Site Office
NNSS	Nevada National Security Site
NOAA	National Oceanic and Atmospheric Administration
NSMC	Null-space Monte Carlo
NSTec	National Security Technologies, LLC
NTS	Nevada Test Site
PDF	Probability density function
QAP	Quality assurance plan
QAPP	Quality assurance project plan
RST	Radiologic source term

LIST OF ACRONYMS AND ABBREVIATIONS (CONTINUED)

RWMS	Radioactive waste management site
SD	Standard deviation
SDWA	*Safe Drinking Water Act*
SNJV	Stoller-Navarro Joint Venture
sptr	Streamline particle tracking
SRC	Standard regression coefficient
SVD	Singular value decomposition
SZ	Saturated zone
TNT	Trinitrotoluene
TDD	Transport data document
UGTA	Underground test area
USGS	U.S. Geological Survey
UTM	Universal Transverse Mercator
UZ	Unsaturated zone
VOIA	Value of Information Analysis
WIPP	Waste Isolation Pilot Plant
YF	Yucca Flat
YMP	Yucca Mountain Project

Stratigraphic, Geologic, Hydrostratigraphic, and Hydrogeologic Unit Abbreviations and Symbols

AA	Alluvial aquifer
AA1	Alluvial aquifer 1
AA2	Alluvial aquifer 2
AA3	Alluvial aquifer 3
ATCU	Argillic tuff confining unit
BLFA	Basalt lava-flow aquifer
BRA	Belted Range aquifer
BRCU	Belted Range confining unit
CA	Carbonate aquifer
CCU	Clastic confining unit
CPT	CP thrust

LIST OF ACRONYMS AND ABBREVIATIONS (CONTINUED)

GCU	Granite confining unit
LCA	Lower carbonate aquifer
LCA3	Lower carbonate aquifer thrust plate
LCCU	Lower clastic confining unit
LCCU1	Lower clastic confining unit thrust plate 1
LCCU2	Lower clastic confining unit thrust plate 2
LFA	Lava-flow aquifer
LTCU	Lower tuff confining unit
LVTA	Lower vitric-tuff aquifer
LVTA1	Lower vitric-tuff aquifer 1
MGCU	Mesozoic granite confining unit
OSBCU	Oak Spring Butte confining unit
PBRCM	Pre-Belted Range composite unit
PCU	Playa confining unit
PCUT	Playa confining unit
PRETBG	Pre-Grouse Canyon Tuff lava-flow aquifer
PRETBG1	Pre-Grouse Canyon Tuff lava-flow aquifer 1
TCU	Tuff confining unit
TM-LVTA	Timber Mountain lower vitric-tuff aquifer
Tmr	Rainier Mesa Tuff
TM-UVTA	Timber Mountain upper vitric-tuff aquifer
TM-WTA	Timber Mountain welded-tuff aquifer
Tor	Redrock Valley Tuff
TSA	Topopah Spring aquifer
TUBA	Tub Spring aquifer
UCA	Upper carbonate aquifer
UCCU	Upper clastic confining unit
UTCU	Upper tuff confining unit
VA	Volcanic aquifer
VCU	Volcaniclastic confining unit
VTA	Vitric-tuff aquifer
WTA	Welded-tuff aquifer

LIST OF ACRONYMS AND ABBREVIATIONS (CONTINUED)

Symbols for Elements and Compounds

Al	Aluminum
Am	Americium
Ar	Argon
C	Carbon
Ca	Calcium
Cd	Cadmium
Cl	Chlorine
Cm	Curium
CO_2	Carbon dioxide
$^{14}CO_2$	Radiocarbon dioxide
Cs	Cesium
Eu	Europium
H	Hydrogen
^{3}H	Tritium
Ho	Holmium
I	Iodine
K	Potassium
Kr	Krypton
Nb	Niobium
Ni	Nickel
Np	Neptunium
Pd	Palladium
Pu	Plutonium
Sm	Samarium
Sn	Tin
Sr	Strontium
Tc	Technetium
Th	Thorium
U	Uranium
Zr	Zirconium

LIST OF ACRONYMS AND ABBREVIATIONS (CONTINUED)

Symbols for Variables

A	Area
b	Fracture aperture
D_m	Matrix diffusion coefficient
D_o	Free water diffusion coefficient
k	Permeability
K	Hydraulic conductivity
K_d	Distribution coefficient
$n(0)$	Initial number of moles
n_{eff}	Effective porosity
$n(t)$	Number of moles remaining after time t
Q	Flux
R_c	Cavity radius
s	Fracture spacing
S	Storage coefficient
S_s	Specific storage
t	Time
$t_{1/2}$	Half-life
T	Temperature
T_0	Reference temperature
v	Velocity
Y	Yield
ρ	Density
τ	Tortuosity
ϕ	Porosity
ϕ_f	Fracture porosity
ϕ_m	Matrix porosity
λ	Decay constant
Φ	Objective function

LIST OF ACRONYMS AND ABBREVIATIONS (CONTINUED)

Units of Measure

°C	Degree Celsius
°C/km	Degree Celsius per kilometer
Ci	Curie
Ci/mL	Curies per milliliter
cm/yr	Centimeters per year
ft	Foot
g/cm^3	Grams per cubic centimeter
g/g	Grams per gram
gpm	Gallons per minute
kg/s	Kilograms per second (1 kg/s = 86.4 m^3/day)
km	Kilometer
km^2	Square kilometer
kt	Kiloton
K	Kelvin
L/mg	Liters per milligram
m	Meter
m/day	Meters per day
m/s	Meters per second
m/yr	Meters per year
m^2	Square meter
m^2/s	Square meters per second
m^3	Cubic meter
m^3/day	Cubic meters per day (1.0 m^3/day = 0.0116 kg/s)
meq/L	Milliequivalents per liter
mg/L	Milligrams per liter
mL/cm^2	Milliliters per square centimeter
mL/g	Milliliters per gram
mm/yr	Millimeters per year
mol	Mole
mol/day	Moles per day
mol/kg	Moles per kilogram

LIST OF ACRONYMS AND ABBREVIATIONS (CONTINUED)

mol/L	Moles per liter
mol/yr	Moles per year
mrem/yr	Millirems per year
mW/m^2	Milliwatts per square meter
pCi/L	Picocuries per liter
pmc	Percent modern carbon
ppm	Parts per million
s	Second
W/(m·K)	Watts per meter kelvin
µg/L	Micrograms per liter
‰	Per mil

ACKNOWLEDGEMENT

This document is the result of the contributions of many individuals from several underground test area (UGTA) participant organizations. These individuals have either contributed to the technical/scientific content of the document or key supporting documents, the editorial and graphical display of the technical information or the technical and quality review of the contents of the document. In addition, the management of the activities and staff supporting the document are acknowledged.

The technical/scientific contributions to the document and key supporting documents have been provided by the following institutions and staff members:

Los Alamos National Laboratory (LANL)
Ed Kwicklis, Elizabeth Keating, Dan Levitt, Zhenxue Dai, Zhiming Lu , Andy Wolfsberg, and Zora Dash

Navarro-Intera, LLC (N-I)
Robert Andrews, Tiraz Birdie, Tim deBues, Tim Vogt, Pete Martian, Ian Nienhueser, and Irene Farnham

INTERA Inc.
Toya Jones, Clark Griffith, Dennis Fryar, Joan Blainey, Neil Deeds, and John Pickens

Lawrence Livermore National Laboratory (LLNL)
Andy Tompson, Steve Carle, Gayle Pawloski, Walt McNab, and Mavrik Zavarin

Golder Associates
Nicole DeNovio and Bill Dershowitz

Geohydros Inc.
Todd Kincaid and Brent Meyer

National Security Technologies, LLC (NSTec)
Sig Drellack and Lance Prothro

U.S. Geological Survey (USGS)
Joe Fenelon and Keith Halford

Desert Research Institute (DRI)
Karl Pohlmann

ACKNOWLEDGEMENT

The editorial and graphical display of information in this document has been greatly aided by the N-I Document Production and Geographic Information Systems departments (Christy Morris, Katsura Rast, Afief Fadil, John Flinn, Danae Cummings, John Hand, and Matthew Knop).

Technical reviews of drafts of this document significantly improved the quality and content of this report. These reviews were performed by Andy Tompson, Mavrik Zavarin and Gayle Pawloski (of LLNL), Matt Reeves and Chuck Russell (of DRI), Keith Halford (of the USGS), Britt Jacobson (of the Nevada Division of Environmental Protection) and Bruce Crowe (of N-I). Quality reviews of the document were performed by Janet Richardson, Susan Krenzien, and Joe Johnston (of N-I).

Management of the staff and activities supporting this document include Sam Marutzky (N-I) and Naomi Becker (LANL). This work was sponsored by the UGTA management team at the U.S. Department of Energy, National Nuclear Security Administration Nevada Field Office, notably Bill Wilborn and Bimal Mukhopadhyay.

EXECUTIVE SUMMARY

The Underground Test Area (UGTA) Corrective Action Unit (CAU) 97, Yucca Flat/Climax Mine, in the northeast part of the Nevada National Security Site (NNSS) requires environmental corrective action activities to assess contamination resulting from underground nuclear testing. These activities are necessary to comply with the UGTA corrective action strategy defined in Appendix VI, Revision No. 4, of the *Federal Facility Agreement and Consent Order* (FFACO) (1996, as amended) (hereinafter referred to as the UGTA strategy). The corrective action investigation phase of the UGTA strategy requires the development of groundwater flow and contaminant transport models whose purpose is to identify the lateral and vertical extent of contaminant migration over the next 1,000 years. In particular, the goal is to calculate the contaminant boundary, which is defined as a probabilistic model-forecast perimeter and a lower hydrostratigraphic unit (HSU) boundary that delineate the possible extent of radionuclide-contaminated groundwater from underground nuclear testing. Because of structural uncertainty in the contaminant boundary, a range of potential contaminant boundaries was forecast, resulting in an ensemble of contaminant boundaries. The contaminant boundary extent is determined by the volume of groundwater that has at least a 5 percent chance of exceeding the radiological standards of the *Safe Drinking Water Act* (SDWA) (CFR, 2012).

Objectives

This document addresses the UGTA strategy corrective action investigation phase requirements for the Yucca Flat/Climax Mine CAU. The Yucca Flat/Climax Mine CAU is located about 140 kilometers northwest of Las Vegas, Nevada, in a topographically closed basin. The CAU consists of the residual contamination from 747 detonations, 3 of which are at Climax Mine, and the remaining 744 are in Yucca Flat (Figure ES-1).

As noted in the UGTA strategy, the technical basis for achieving the UGTA strategy is through an evaluation of each CAU using a combination of approaches, including the following:

- Data collection consisting of, but not limited to, drilling exploration, hydrologic testing, and field and laboratory studies designed to characterize the hydrogeological setting
- Modeling of the hydrogeological setting, the radiological source term, and flow and contaminant transport to forecast areas of current and future contamination for 1,000 years

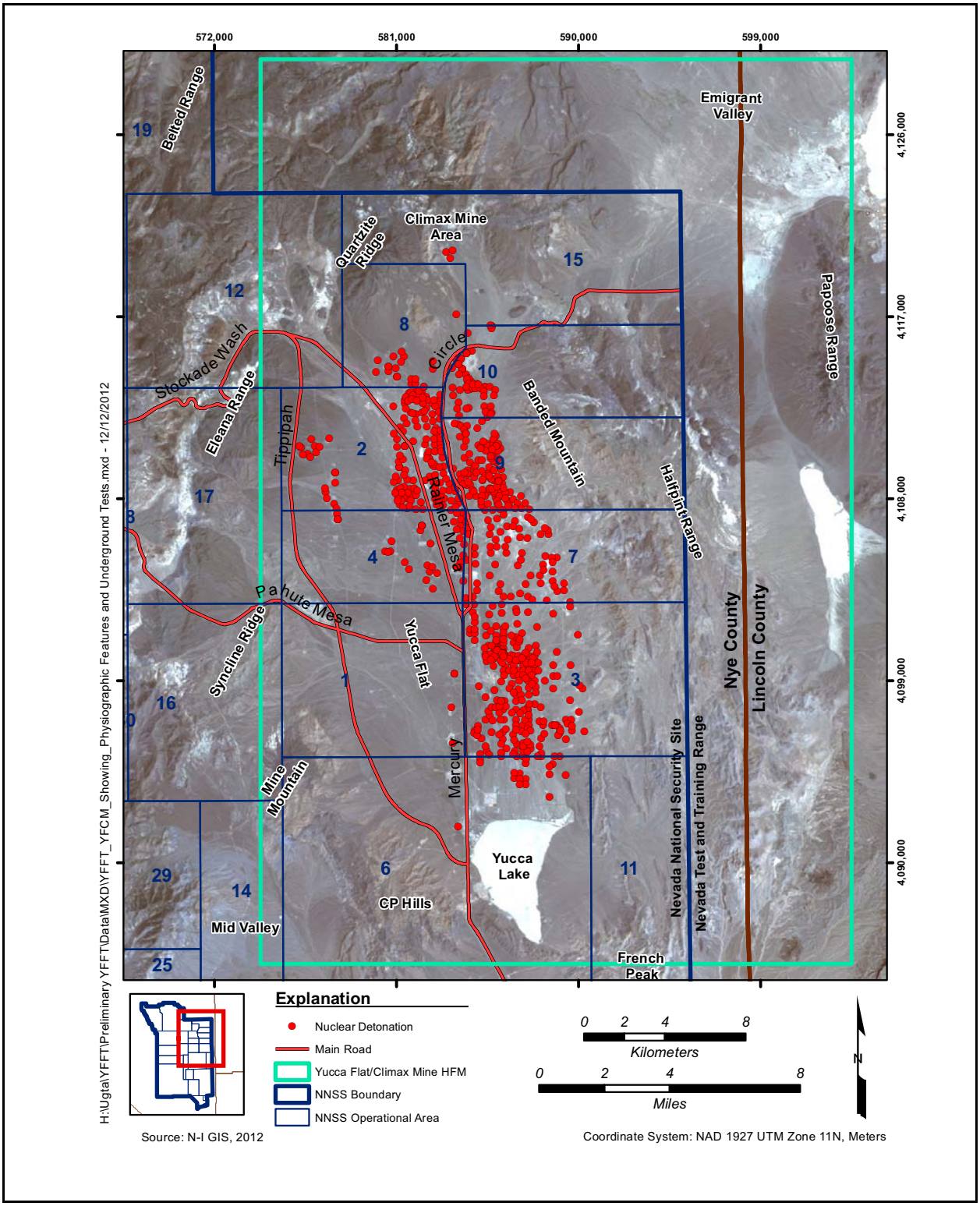

Figure ES-1
Physiographic Features and Nuclear Detonations of the Yucca Flat/Climax Mine CAU

- Iterative model evaluations and monitoring of groundwater near and downgradient of areas of past underground testing
- Identification and documentation of land-use policies (institutional controls) designed to restrict future public access to groundwater contaminated by underground testing

The data collection aspect related to the Yucca Flat/Climax Mine CAU is summarized in the *Phase I Hydrologic Data for the Groundwater Flow and Contaminant Transport Model of Corrective Action Unit 97: Yucca Flat/Climax Mine, Nevada Test Site, Nye County, Nevada* (SNJV, 2006b), and the *Phase I Contaminant Transport Parameters for the Groundwater Flow and Contaminant Transport Model of Corrective Action Unit 97: Yucca Flat/Climax Mine, Nevada Test Site, Nye County, Nevada* (SNJV, 2007); this document presents additional data and analyses that supplement the information provided in these documents. The hydrogeologic framework model (BN, 2006) that forms the basis for the Yucca Flat numerical flow and transport models incorporates surface-mapping, drill-hole, and geophysical data spanning more than 50 years of weapons testing and subsequent characterization activities. Modeling of the radiological source term is documented in Pawloski et al. (2008) and SNJV (2009); this document presents additional analyses that supplement these earlier studies. Modeling of the hydrogeologic setting, and groundwater flow and contaminant transport to forecast areas of current and future contamination for 1,000 years is presented in this document. The subsequent activities—namely, iterative model evaluations, monitoring of groundwater, and the identification of institutional controls to restrict future public access—are planned to commence in the corrective action decision document/corrective action plan phase of the UGTA strategy.

The specific requirements for the CAU flow and transport models as identified in the FFACO (1996, as amended) and the locations in this document where these requirements are addressed are identified below:

1. Alternative hydrological framework models of the CAU modeling domain—Sections 4.0 and 5.0
2. Uncertainty in the radiological and hydrological source terms—Section 2.0 and Appendix C
3. Alternative models of recharge—Sections 3.0, 4.0, and 5.0
4. Alternative boundary conditions and groundwater flows—Sections 4.0 and 5.0
5. Multiple permissive sets of calibrated flow models—Sections 3.0, 4.0, and 5.0

6. Probabilistic simulations of transport using plausible sets of alternative framework and recharge models, and boundary and groundwater flows from calibrated flow models—Sections 4.0 and 6.0

7. Ensembles of forecasts of contaminant boundaries for the CAU—Section 6.0

8. Sensitivity and uncertainty analysis of the model output—Sections 3.0, 4.0, 5.0, and 6.0

This document presents the groundwater flow and contaminant transport models used to develop the contaminant boundary for the Yucca Flat/Climax Mine CAU. The document also presents the forecast contaminant boundaries and evaluates the impact that conceptual model and model parameter uncertainties have on the forecast contaminant boundaries.

Background

The conceptual model of groundwater flow and contaminant transport in Yucca Flat suggests that the basin has several attributes that limit the extent of contamination resulting from the underground testing of nuclear weapons that took place there between 1957 and 1992. The overall hydrogeologic setting of Yucca Flat is discussed in Winograd and Thordarson (1975), Laczniak et al. (1996), SNJV (2006a, 2006b, 2007), and Fenelon et al. (2012). These studies indicate that (1) the lower carbonate aquifer (LCA) in Yucca Flat is the only groundwater pathway for radionuclides to leave the Yucca Flat basin; (2) the LCA in much of Yucca Flat may have limited hydraulic communication with the regional LCA upgradient from the basin because of the presence of structurally high, low-permeability clastic and igneous rocks on much of the basin perimeter; (3) present-day recharge may be effectively limited to the bedrock hills surrounding the basin, or the slow drainage of paleoinfiltration from the alluvium and tuffaceous rocks that overlie the LCA in central Yucca Flat; and (4) drainage from tuffaceous aquifers to the LCA may be restricted to where large-offset normal faults cut and significantly thin the intervening, sparsely fractured tuff confining units. Additionally, 668 of the 744 detonations in Yucca Flat proper were conducted in the unsaturated zone, and more than 90 percent of the unsaturated-zone detonations were emplaced above areas underlain by tuff aquifers and confining units, which provided an additional buffer against migration of radionuclides to the LCA. Therefore, despite the large number of detonations in Yucca Flat, only a few handful emerge as potential contributors to significant groundwater contamination.

Several auxiliary studies done as part of this report and documented in the appendices to this report tend to support the conceptual models of groundwater flow and contaminant transport. Appendix L

builds on the geochemical analyses documented in SNJV (2006a) and presents evidence based on naturally occurring groundwater carbon-14 (^{14}C) and chlorine-36 (^{36}Cl) data (which serve as natural analogs to the same test-generated radionuclides) that groundwater velocities are small enough to keep radionuclides within the basin over the next 1,000 years. The calculated groundwater ^{14}C ages from the alluvium and tuffs are consistent with the conclusion of published unsaturated-zone analyses that significant infiltration and recharge in the center of the basin stopped shortly after the end of the last pluvial (wet) period approximately 10,000 years ago. Based on patterns of ^{14}C and ^{36}Cl in LCA groundwater, late pluvial-age recharge appears to be draining from the overlying alluvial and volcanic aquifers to the LCA in the vicinity of major basin-forming faults. Relatively low water-table temperatures in the center of the basin near major faults also indicate the drainage of cooler, shallower groundwater from the volcanic rocks and alluvium near these faults (Appendix H).

The hydraulic head data estimated for the pretesting period in Yucca Flat (Fenelon et al., 2012) indicate a head difference of 6 to 30 meters (m) between the alluvial and volcanic aquifers and the underlying LCA, suggesting the potential for downward flow between these aquifers. The cause of this head difference has been hypothesized to be the incomplete drainage of paleorecharge to the LCA due to the presence of low-permeability tuff confining units separating the alluvial and tuff aquifers from the LCA (Winograd and Thordarson, 1975; Fenelon et al., 2012). Appendix F demonstrates the use of model sensitivity studies to identify combinations of model parameters that are consistent with that hypothesis. The sensitivity studies indicate that the paleodrainage hypothesis requires that the large-scale permeability of the tuff confining units be at the low end of the measurement range, despite some smaller-scale data indicating locally higher permeability values. The low estimated permeabilities of the tuff confining units are consistent with the sparse fracturing of these units as observed in rock cores, and suggest that rapid radionuclide transport through the tuff confining units may be restricted to faults and the altered zones created by weapons testing.

Modeling Approach

This report presents the flow and transport models that are developed to explore a wide range of possible hydrologic and transport conditions reflective of the significant uncertainty in the conceptual models and parameters and to account for possible alternative interpretations. The philosophy adopted is to be conservative in the modeling assumptions when they are likely to affect the forecast extent and magnitude of radionuclide transport, especially when data are sparse or may be subject to

alternative interpretations. This philosophy has led to the decision to use models or parameter values that tend to overestimate the potential contaminant transport. The forecast contaminant transport overestimation is demonstrated by comparing modeled contaminant transport with discrete contaminant concentration observations downgradient from test cavities. The impact of these conservative assumptions is evaluated in a range of sensitivity analyses.

The Yucca Flat/Climax Mine CAU flow and transport model development consists of four separate models, namely, the following:

- Climax Mine flow and transport model
- Yucca Flat unsaturated-zone flow and transport model
- Yucca Flat saturated alluvial/volcanic aquifer system flow and transport model
- Yucca Flat saturated LCA flow and transport model

These different models, which are illustrated in Figure ES-2, address the most significant hydrogeological features, and flow and transport processes at spatial and temporal scales relevant to the analyses. Models of groundwater flow and contaminant transport for the three detonations conducted in the Climax granitic stock north of Yucca Flat were documented by Pohlmann et al. (2007). The contaminant flux from the Climax stock to the saturated LCA is insignificant in comparison to the inventory that is initially in place in the LCA or that is forecast to be transported to the LCA from the overlying unsaturated zone and saturated alluvial/volcanic rock units. Therefore, because of their relatively small radionuclide inventory and northern location, the Climax Mine detonations are not explicitly included in the transport models for Yucca Flat proper.

The three coupled Yucca Flat flow and transport models are presented in this document. Each of these three models uses the Los Alamos National Laboratory Finite Element Heat and Mass (FEHM) computer code (Zyvoloski et al., 1997) to model flow and transport. The grid flexibility allowed by the FEHM finite-element meshing approach is essential to represent the complex hydrogeologic setting in Yucca Flat and near-field features associated with underground nuclear detonations. In addition, the common computational platform provided by FEHM facilitates the transfer of results from one model to another, which takes place primarily through the exchange of outputs and inputs along the common model boundaries.

Because the 744 underground nuclear detonations in Yucca Flat were conducted either above the water table (668 detonations) or in the local saturated alluvial/volcanic aquifer system

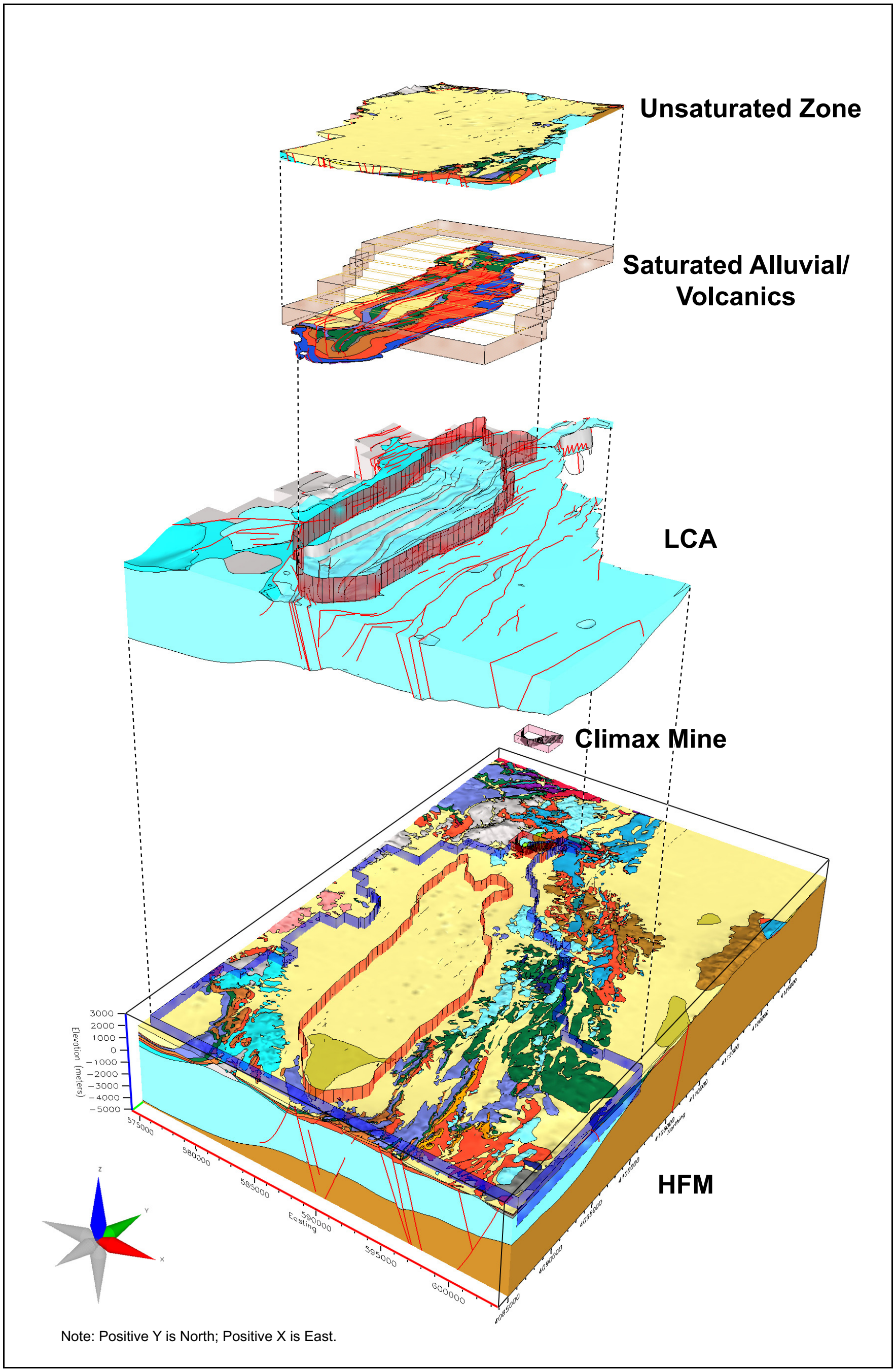

Figure ES-2
Three-Dimensional Perspective of Yucca Flat/Climax Mine CAU Model Domains

(76 detonations), a major role of the unsaturated-zone and saturated alluvial/volcanic aquifer system models is the calculation of radionuclide fluxes from the detonation locations (working points) in the unsaturated zone and the saturated alluvial/volcanic aquifer system to the regionally connected LCA. The Yucca Flat unsaturated-zone flow and transport model evaluates the effects of enhanced crater recharge, background net infiltration, and other factors in the Yucca Flat basin on contaminant transport to both the saturated alluvial/volcanic aquifer system and LCA. The Yucca Flat saturated alluvial/volcanic aquifer system flow and transport model evaluates the effects of transient, test-induced overpressurization on contaminant transport to the saturated LCA. The Yucca Flat saturated LCA flow and transport model evaluates groundwater flow and contaminant transport downgradient from detonations with exchange volumes that intersect the saturated LCA. Exchange volume refers to the spherical volume that encompasses the immediate extent of radioactive contamination resulting from an underground nuclear detonation, and is conceptualized as having its center at the detonation working point. This model also evaluates contaminant migration from detonations with working points in the overlying unsaturated zone or saturated alluvial/volcanic aquifer system to the saturated LCA.

The total inventory in the Yucca Flat/Climax Mine CAU comprises about 39 percent of the total radionuclide activity in 1992 of all detonations in the UGTA program. Radionuclides listed in the unclassified radionuclide inventory for Yucca Flat (Bowen et al., 2001) are screened to identify only those that are potentially relevant to the Yucca Flat contaminant boundary calculations. Initial radionuclide concentrations distributed around each detonation point in the exchange volume are calculated considering uncertainties in the radionuclide inventory, melt-glass partitioning factors, exchange volume size, glass dissolution amounts, and matrix sorption (Appendix C). If the initial concentration of a radionuclide has a 5 percent or greater probability of exceeding one-tenth of its maximum contaminant level (MCL) as listed in the SDWA (CFR, 2012), the radionuclide becomes a candidate for inclusion in the transport models. The radionuclides retained as a result of this screening are tritium (^{3}H), carbon-14 (^{14}C), chlorine-36 (^{36}Cl), calcium-41 (^{41}Ca), nickel-63 (^{63}Ni), strontium-90 (^{90}Sr), technetium-99 (^{99}Tc), iodine-129 (^{129}I), cesium (Cs) isotopes ^{135}Cs and ^{137}Cs, uranium (U) isotopes ^{235}U and ^{238}U, neptunium-237 (^{237}Np), and plutonium (Pu) isotopes ^{238}Pu, ^{239}Pu, and ^{240}Pu. However, because ^{41}Ca, ^{63}Ni, ^{90}Sr, ^{135}Cs, ^{137}Cs, ^{238}Pu, ^{239}Pu, and ^{240}Pu have high matrix sorption coefficients and limited mobility in volcanic rock and alluvium, only ^{3}H, ^{14}C, ^{36}Cl, ^{99}Tc, ^{129}I, ^{235}U, ^{238}U, and ^{237}Np are simulated in the unsaturated-zone and saturated alluvial/volcanic aquifer system transport models. These radionuclides, as well as ^{63}Ni, ^{90}Sr, and

^{137}Cs from the sources initially in the saturated LCA, are simulated in the LCA transport model because of their lower sorption coefficients in carbonate rock. Colloid-facilitated transport of ^{238}Pu, ^{239}Pu, and ^{240}Pu in the LCA is investigated with a one-dimensional model in Appendix M. These radionuclides are shown to be far less important than other non-sorbing or slightly sorbing radionuclides in defining the contaminant boundary in the LCA, so they are not considered in the three-dimensional transport model of the LCA.

The groundwater flow regime in the Yucca Flat/Climax Mine CAU is influenced by local recharge, and in the LCA, also by limited underflow from areas to the north, east, and west of Yucca Flat. Current understanding is that infiltration rates through the alluvium in the center of the basin are small (less than 0.1 millimeter per year [mm/yr]) and that recharge there may be primarily from the continued drainage of paleoinfiltration from the unsaturated zone. In contrast, present-day infiltration and recharge rates in the bedrock hills bordering the basin may be several millimeters per year. Unsaturated-zone model results indicate that percolation through the unsaturated zone is generally downward with some lateral flow along the dipping lower-permeability tuff confining units toward faults. Groundwater flow in the alluvial/volcanic aquifer system is confined to Yucca Flat because the aquifers and aquitards in this system thin or become unsaturated along the margins of the basin. The groundwater in the alluvial/volcanic aquifer system drains into the underlying, regionally extensive LCA by either diffuse leakage through the low-permeability tuff confining units or focused flow along the numerous north–south trending normal faults that cut the confining units in the center of the Yucca Flat basin. The contours of hydraulic heads presented in Fenelon et al. (2012) and model results presented in this report indicate that flow in the LCA is inward from the margins of the basin and generally southward. The absence of significant declines in hydraulic heads in the LCA across the accommodation zone that separates Yucca Flat and Frenchman Flat indicates that the LCA is hydraulically well connected between these basins, despite their different structural styles and the termination of major basin-forming Yucca Flat faults in this area.

Unsaturated-Zone Flow and Transport Model

The Yucca Flat unsaturated-zone flow and transport model is developed to calculate the migration of contaminants from the 668 detonations expended above the regional water table to the saturated zone. This model consists of 12 three-dimensional computational grids that each contain 0.5 to 1.5 million nodes. These grids capture the dips of the HSUs, and the numerous fault pathways through the

unsaturated tuffs and LCA. The grids use a sophisticated meshing technique that allows the grids to be locally refined in the vicinity of the craters, collapse chimneys, and detonation cavities in a series of concentric circles that grade outward into an orthogonal mesh. The mesh refinement near the detonation points allows the water-accessible radionuclides (i.e., the hydrologic source term [HST]) to be placed directly into the flow and transport model so that absolute consistency between the source release and transient flow rate can be maintained through time. This approach represents a significant advance in the coupling of radionuclide releases with model-specific hydraulic conditions, which proved to be difficult in past UGTA CAU-scale flow and transport modeling studies.

The percolation flux in this model includes both background, steady-state net infiltration, and the transient effects of enhanced recharge associated with the subsidence craters that formed above 459 of the 744 detonations in Yucca Flat. The enhanced recharge associated with the subsidence craters results from overland flow in the watersheds that feed individual craters following significant precipitation events. These watersheds are estimated from Geographic Information Systems (GIS) studies, and long-term (1,000-year average) infiltration rates are estimated by the use of these watersheds, daily stochastic rainfall/runoff models and one-dimensional infiltration models for each crater, and the specific geometry and watershed areas of each crater (Appendix E). Subsurface moisture data from beneath a small number of craters and observations of ponding depths in the craters following rainstorms are used, along with lysimeter data from Frenchman Flat, to calibrate relevant model parameters. The background net infiltration outside the craters is assumed to range from less than 0.1 mm/yr (based on regional infiltration maps) to 1, 5, and 10 mm/yr (based on alternative cases) to bound the possible effects of pluvial drainage.

The Yucca Flat unsaturated-zone transport model simulates radionuclide transport with the standard advection-dispersion equation incorporated in FEHM and represents the fractured porous rock as a single equivalent porous medium. In an HSU where flow is likely to be primarily through the matrix (e.g., the tuff confining unit), the HSU is assigned a transport porosity based on its matrix porosity, whereas in an HSU where matrix permeability is low and flow is dominantly through fractures (faults, collapse chimneys, welded tuffs, and the LCA), the HSU is assigned a transport porosity that reflects fracture porosity. Radionuclide releases to the saturated zone from detonations above the water table are significantly affected by the assumed steady-state percolation flux, which controls radionuclide movement before the enhanced crater infiltration arrives at the detonation's radionuclide

exchange volume. Because of the slow transport through the unsaturated zone, contaminants from the unsaturated-zone sources remain in the unsaturated zone except in the vicinity of detonations that underlie craters with significant crater recharge or that have exchange volumes near the water table.

Unsaturated-zone detonations with working points and exchange volumes near the water table are the only detonations that result in discharge concentrations to the saturated zone exceeding an MCL because of the low percolation fluxes and advective transport velocities in the unsaturated zone. The calculated contaminant flux from the unsaturated-zone sources to the water table is a small fraction of the mass initially in place in the unsaturated zone. Tritium can be used as an indicator of potential significance of contaminant flux originating from the unsaturated-zone sources because of its large initial inventory and concentration. Of the approximately 3,050 moles of ^{3}H initially in place in the unsaturated zone because of the 668 detonations, only about 1 to 8 moles reach the water table in 1,000 years assuming a background average infiltration rate of 1 to 5 mm/yr. Most ^{3}H transport to the water table occurs from detonations near the water table in the first few decades, after which transport is limited by a combination of radioactive decay and low water flux. Most (about 98 percent for the 5-mm/yr infiltration rate case) of the radionuclide mass that does arrive at the water table does so in the portion of the model domain underlain by the saturated alluvial/volcanic aquifer system, which provides an additional barrier to the migration of radionuclides to the LCA.

Saturated Alluvial/Volcanic Aquifer System Flow and Transport Model

The Yucca Flat saturated alluvial/volcanic aquifer system flow and transport model is developed to calculate the migration of contaminants from the 76 detonations that were expended below the water table, as well as the detonations that were expended above the water table but have exchange volumes that extend below the water table. Like the unsaturated-zone model, this model uses a sophisticated gridding process that allows the volume centered around each detonation point to be locally refined, thereby enabling the radionuclide mass to be emplaced directly into the model. With this approach, complex, near-field transient flow processes associated with the nuclear detonations can be simulated and their influence on radionuclide transport explicitly calculated. The model uses transient pressure responses measured at a number of wells in the tuff aquifers and confining units, as well as measured ground subsidence data, to calibrate some HSU and fault permeabilities, and some parameters related to conceptual models for different test effects. The model demonstrates that aquifer compaction caused by the shock waves from underground nuclear detonations resulted in elevated pore pressures

that, over the decades of active testing and for decades thereafter, caused drainage rates from the saturated tuffs to the LCA to be many times the long-term infiltration rates. Both the rock properties and ambient flow conditions in the saturated alluvial/volcanic aquifer system are thus conceptualized as being significantly changed as a result of nuclear testing. Different conceptual models of permeability and pore-pressure changes in the damage zones adjacent to detonations, and initial radionuclide distributions in the exchange volume are investigated with detailed sub-models (Appendix G) and the three-dimensional saturated alluvial/volcanic aquifer system model.

Simulation of contaminant transport in the saturated alluvial/volcanic aquifer system model is done with a particle-tracking subroutine in FEHM and a convolution-based post-processing algorithm (PLUMECALC) that allows superposition of radionuclide mass from multiple source locations. The technique allows for an efficient analysis of the effects of transport-parameter and source-term uncertainties on the transport results, consistent with the requirement of the FFACO (1996, as amended) that contaminant boundaries be calculated in a probabilistic framework. The source term associated with the 76 detonations conducted in the saturated zone is introduced into the model at 11 discrete times so that the impact of time-dependent, test-induced changes in the flow system on transport can be accurately represented. In most of the saturated alluvial/volcanic aquifer system model runs, the contaminant pathways from the saturated alluvial/volcanic rock units to the LCA are conceptualized as being restricted to the major faults in the central portion of Yucca Flat. This conceptualization is a result of the assumption that fracture networks are discontinuous in the thick tuff confining units between the working points and the LCA or sealed by clays and paleosols at the top of the LCA, thereby preventing contaminants from migrating directly downward from the exchange volumes to the LCA. However, alternative saturated alluvial/volcanic aquifer system model runs are made to allow for the possibility that test-induced fracturing creates permeable pathways through which radionuclides can migrate vertically downward from the detonation locations to the LCA. Results that represent some of the largest amounts of radionuclide transport to the LCA are produced by these alternative model runs.

Radionuclide contaminants that are initially emplaced within the saturated alluvial/volcanic aquifer system model or that enter the model by downward percolation from the overlying unsaturated-zone sources remain within the saturated alluvial/volcanic aquifer system. Again, ^{3}H can be used as an indicator of potential significance of contaminant flux from the overlying source zone to the LCA. Of the approximately 2,090 moles of ^{3}H initially in the saturated alluvial/volcanic aquifer system

because of the 76 detonations, only about 8 to 18 moles reach the LCA in 1,000 years assuming a background average recharge rate of 1 to 5 mm/yr. As in the case of contaminant flux from the unsaturated-zone sources, the contaminant flux from the saturated alluvial/volcanic aquifer system sources to the LCA is most significant in the first few decades after the detonations occurred and decrease with time to insignificant levels owing to the radioactive decay.

The contaminant flux to the LCA is controlled by releases from a small subset of the 76 detonations conducted in the saturated alluvial/volcanic aquifer system whose exchange volumes directly intersect the fault damage zones. This is because contaminants from those detonations can be transported directly down the fault to the LCA. For those detonations with exchange volumes that do not directly intersect faults, the contaminants can migrate laterally in the aquifer until the travel path intersects the nearest fault, at which point the transport occurs downward through the transmissive fault to the LCA; however, release rates from those detonations are small because of the low advective velocities in the alluvial/volcanic aquifer system. Mobile, longer-lived radionuclides such as ^{14}C, ^{36}Cl, ^{99}Tc, and ^{129}I may be transported downward to the underlying LCA along major faults that intersect the aquifers and confining units; however, less than 5 percent of the mass that is initially in place in the saturated alluvial/volcanic aquifer system or that enters the saturated zone from the unsaturated zone is transported to the LCA in 1,000 years, even with the larger average recharge rates of 5 and 10 mm/yr.

Saturated LCA Flow and Transport Model

The Yucca Flat saturated LCA flow model includes all of the major faults in the basin with offsets greater than 60 m. A total of 106 faults or fault segments are incorporated into the model grid of the LCA where they are discretized in a way that allows the low-permeability fault cores and high-permeability damage zones to be explicitly represented in the model. Calibration of the LCA flow model is accomplished by the use of both long-term steady-state hydraulic head data and drawdown data associated with an 87-day multi-well aquifer test (MWAT), during which drawdowns propagated more than 10 kilometers along north-striking faults. The use of the MWAT data in the model calibration provides important constraints on uncertain parameters, most importantly, groundwater inflow from the north, which strongly affects radionuclide transport rates and transport distances.

A calibration-constrained Monte Carlo approach known as null-space Monte Carlo (NSMC) is used to determine which model parameters can be changed and by how much, while still keeping the model in calibration. From this analysis, posterior distributions of inflow rates from north of Yucca Flat are generated that can be used as boundary conditions to the radionuclide transport models for the LCA. The inflows from the north are estimated from the NSMC analysis at a rate of 130 kilograms per second (kg/s), with a range of 60 to 400 kg/s. These values are far smaller than the value of 1,300 kg/s estimated by Pohlmann et al. (2007) for Climax Mine models, but still larger than the value of 55 kg/s estimated with the most recent USGS Death Valley Regional Flow System Model (Faunt et al., 2012) or the value of approximately 1 kg/s advocated by other USGS researchers (Winograd and Thordarson, 1975; Halford, 2012). An alternative numerical flow and transport model for the LCA is developed that investigates a conceptual model of limited hydraulic continuity of the LCA across northern Yucca Flat and a reduced inflow rate of 1 kg/s. This alternative model is calibrated to the observed steady-state and transient MWAT datasets, and results in less radionuclide contaminant transport than the conservative base-case flow model.

Like the transport model for the saturated alluvial/volcanic aquifer system, the LCA transport model uses a particle-tracking subroutine in FEHM and a convolution-based post-processing algorithm (PLUMECALC) that allows superposition of radionuclide mass from multiple source locations. This enables the LCA transport model to superimpose radionuclide inputs from the overlying unsaturated zone and saturated alluvial/volcanic aquifer system, as well as from contaminants initially in the LCA, to create an integrated contaminant boundary. The LCA portion of the radionuclide source term is assumed to be immediately available for transport within the saturated LCA, whereas radionuclide inputs from the overlying unsaturated zone and saturated alluvial/volcanic aquifer system are assumed to arrive significantly later after much of the inventory of short-lived radionuclides such as ^{3}H has decayed.

The ability of the LCA model to consider radionuclide inputs from the unsaturated zone, the saturated alluvial/volcanic aquifer system, and the saturated LCA separately allows the relative importance of these inputs to the overall LCA source term to be evaluated. The metrics used to evaluate the importance of these individual contributions to the overall LCA source term are the exceedance volume and the maximum southern extent of contamination. The exceedance volume is the volume of the saturated LCA where the probability of exceeding the MCL of even one radionuclide is 5 percent or greater. The maximum southern extent of contamination is selected because of the propensity of

radionuclides to migrate along the thin damage zones of major faults, which are represented as high-permeability zones in the LCA models.

The direct contributions to the LCA source term from the unsaturated zone arrive predominantly along the basin margins in the northern part of Yucca Flat where the water table is in the LCA. The exceedance volume and maximum southern extent for the radionuclide inputs from the unsaturated zone are not significant relative to these metrics for the source-term contributions from the saturated alluvial/volcanic aquifer system or from the sources initially in the LCA.

The sources originating from the saturated alluvial/volcanic aquifer system are more important than the unsaturated-zone sources but less important than the radionuclide sources initially in the LCA. The contaminant boundary associated with the saturated alluvial/volcanic aquifer system sources is controlled by the more mobile species such as the short-lived ^{3}H and long-lived ^{129}I, ^{99}Tc, and ^{36}Cl. The saturated alluvial/volcanic aquifer system model contributions to the LCA are nearly the same with or without the unsaturated-zone contributions, demonstrating the effectiveness of the saturated tuffs as a barrier that limits the radionuclide migration from the unsaturated zone to the LCA.

The radionuclide mass assumed to be initially in place in the LCA dominates the calculated exceedance volume and maximum southern extent of contamination in the LCA model. For assumed exchange volumes of 1, 2, and 3 cavity radii, and a cavity radius calculated from the maximum announced yield, there are 4, 12, and 39 detonations whose exchange volumes extend into the top of the saturated LCA. The contaminant boundary associated with these sources is controlled by the initial mass assumed to be emplaced in the saturated portion of the LCA and by the mobility of ^{3}H, ^{90}Sr, and ^{137}Cs. Using ^{3}H as an indicator of potential significance of the initial radionuclide mass in the saturated LCA to the determination of the contaminant boundary, approximately 7 moles of ^{3}H are initially assumed to be in the saturated LCA. In the LCA model, the mobility of ^{3}H, ^{90}Sr, and ^{137}Cs is determined by the groundwater flow rates through the basin, transport model parameters such as fracture porosity and spacing, and sorption coefficients for ^{90}Sr and ^{137}Cs.

Modeling Results and Forecast Contaminant Boundaries

Uncertainty exists in the groundwater flow and contaminant transport models and in the parameters used to forecast the possible extent of contaminant migration in the next 1,000 years. This uncertainty relates to both discrete structural uncertainty and epistemic parameter uncertainty. Examples of

structural uncertainty include the background steady-state infiltration rate; the conceptual model of the allocation of initial inventory between the unsaturated zone, saturated alluvial/volcanic aquifer system, and LCA transport models; the possibility of sorption of ^{90}Sr and ^{137}Cs in the LCA; and the hydraulic continuity of the LCA in northern Yucca Flat. Examples of epistemic parameter uncertainty include the fracture porosity in the saturated LCA and the size of the exchange volume for each detonation that intersects the saturated LCA. These uncertainties affect the calculated extent of contaminant migration, resulting in multiple flow and transport scenarios and hence multiple contaminant boundaries. A single contaminant boundary includes the effects of epistemic parameter uncertainty, whereas an ensemble of multiple contaminant boundaries represents the effects of both epistemic parameter uncertainty and discrete structural uncertainty. Therefore, this report documents, in compliance with the requirements of the FFACO (1996, as amended), a range of contaminant boundaries in the LCA that incorporate uncertainties in the LCA flow model, LCA source term, contaminant influx to the LCA from the overlying unsaturated zone and saturated alluvial/volcanic aquifer system, and LCA transport parameters.

The model-forecast contaminant boundary for the Yucca Flat/Climax Mine CAU is controlled by the extent of contamination calculated for the regionally extensive LCA. Because of uncertainty in the conceptual models, a range of alternative contaminant boundaries have been developed. The composite of these contaminant boundaries is illustrated in Figure ES-3. This figure is drawn with the 5th percentile of the time-cumulative concentrations exceeding the SDWA MCL. The figure is developed by layering the model forecasts with the bottom blue layer (Base Case [3 R_c]) having the most extensive contaminant forecast and each successive layer having a lesser contaminant forecast ending with the least contaminant forecast case in yellow. The time-cumulative forecast of contaminant migration implies that this is the maximum extent of the probability of exceeding the SDWA MCL within the 1,000-year simulation period. Because this probability varies with time, Figure ES-4 illustrates the time variation of the 5th percentile concentrations exceeding the SDWA MCLs. The significant decrease with time is indicative that the time-cumulative contaminant boundary is controlled by the short-lived radionuclides such as ^{3}H, ^{90}Sr, and ^{137}Cs. The different conceptual models included in these contaminant boundary figures are as follows:

- Base case
- Alternative HST model (e.g., initial HST)

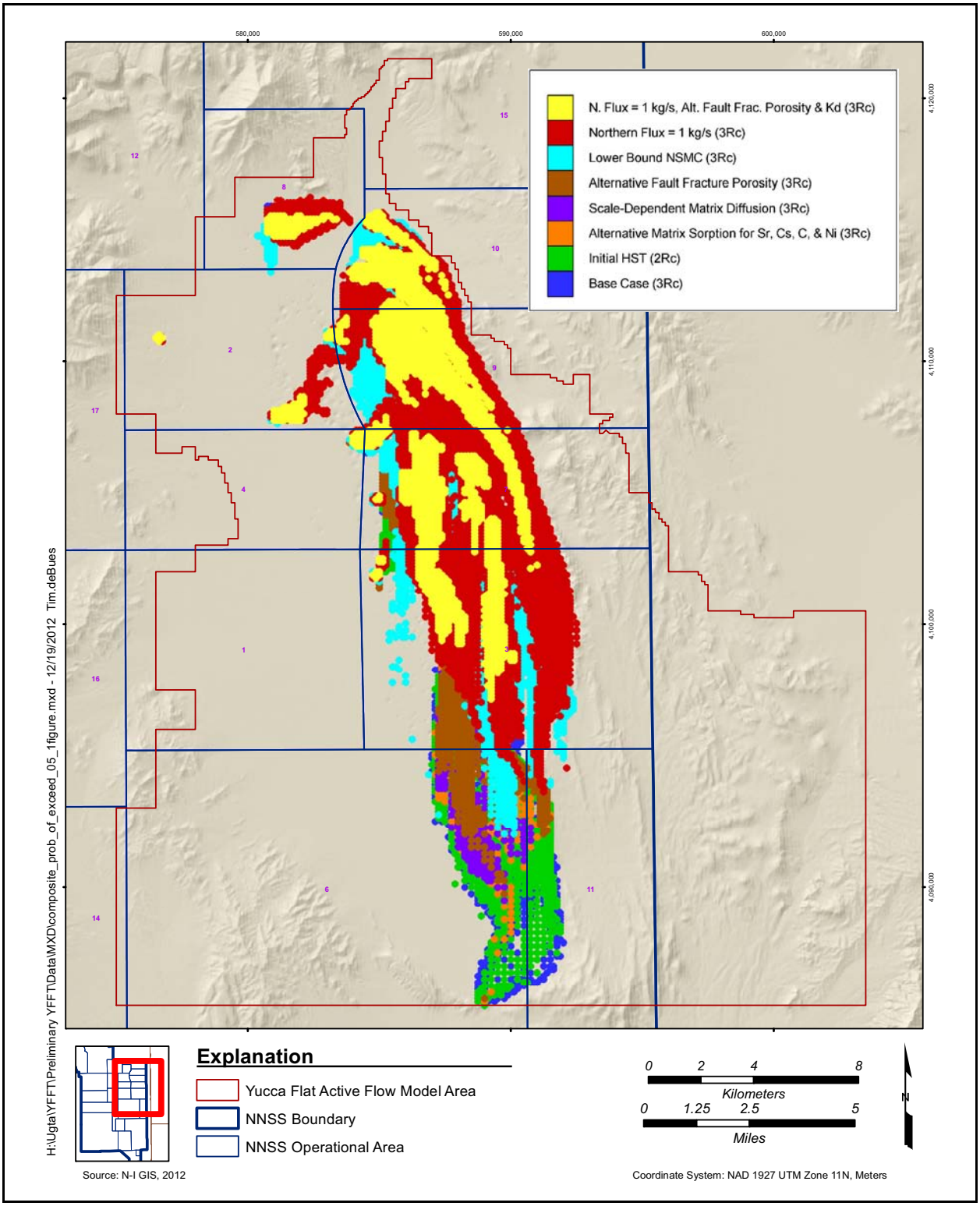

Figure ES-3
Composite Time-Cumulative Contaminant Boundaries for the Yucca Flat/Climax Mine CAU

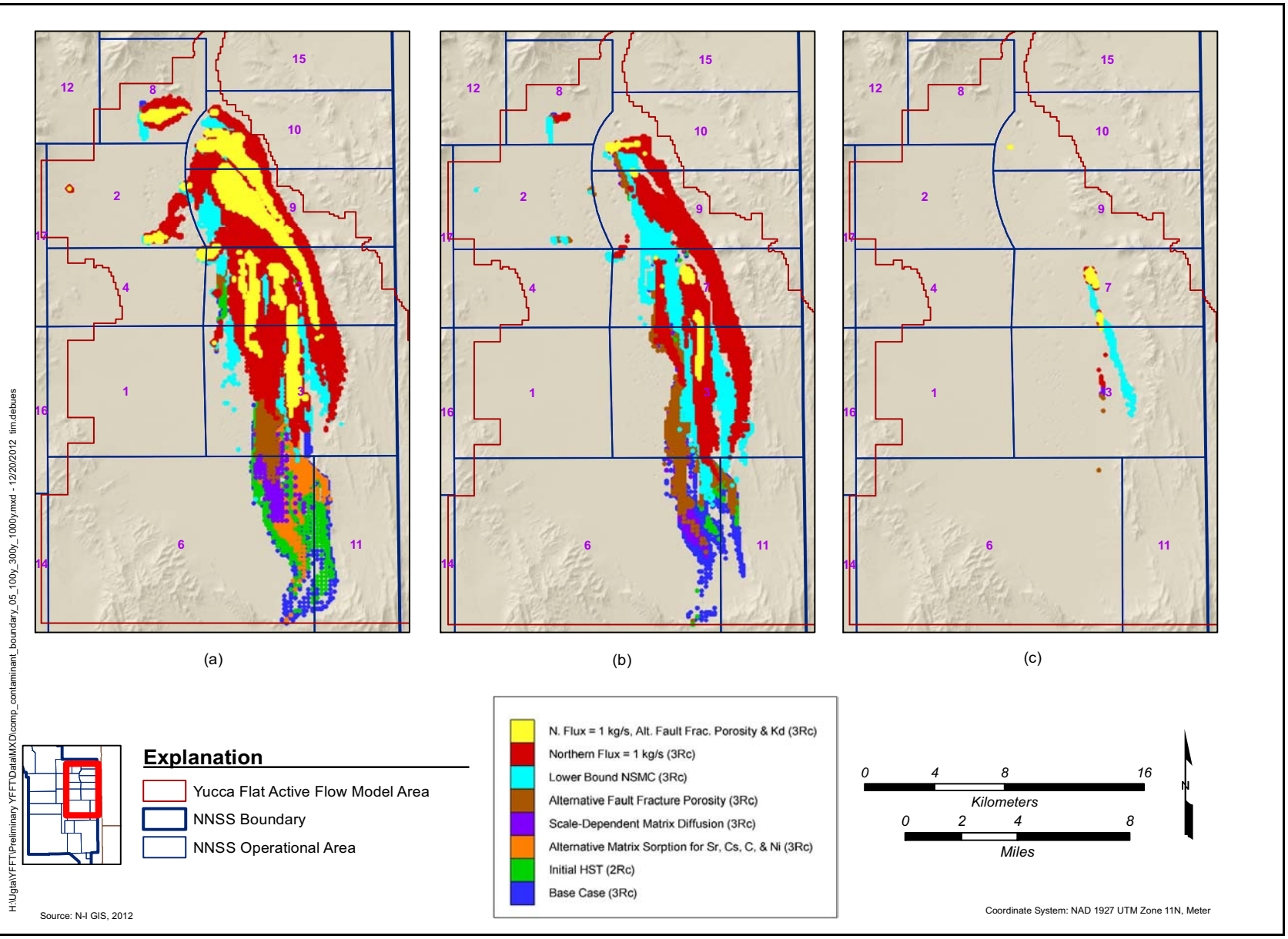

Figure ES-4
Composite Contaminant Boundary at (a) 100 Years, (b) 300 Years, and (c) 1,000 Years

- Alternative LCA transport model including alternative matrix sorption for ^{90}Sr, ^{137}Cs, ^{14}C, and ^{63}Ni
- Alternative LCA transport model including scale-dependent matrix diffusion
- Alternative LCA transport model including alternative fault fracture porosity
- Alternative LCA flow model including the lower bounds of NSMC flow parameters
- Alternative LCA flow model of northern boundary influx of 1 kg/s
- Alternative LCA flow model of northern boundary influx of 1 kg/s, combined with alternative LCA transport model including sorption of ^{90}Sr, ^{137}Cs, ^{14}C, and ^{63}Ni, and alternative LCA transport model including alternative fault fracture porosity.

The model results indicate a generally southerly migration of contaminants that enter the LCA from detonations with exchange volumes that are near or straddle the saturated LCA or that are near faults with assumed hydraulic connection to the LCA. Contaminant migration is generally aligned with and centered about major faults, which are assumed to have damage zones with higher permeability than the unfaulted country rock. The extent of contaminant migration is a function of the uncertainty in the fracture properties of the major faults and the conceptualization of the LCA flow field. These contaminant boundaries indicate that the contamination is generally contained within the Yucca Flat/Climax Mine CAU. Although some conceptual models indicate the potential for contamination in excess of the SDWA MCL to leave the southern boundary of the Yucca Flat/Climax Mine CAU and enter Frenchman Flat, these models represent the more conservative end members of the range of possible alternatives. However, even for these more conservative models, it is useful to note that the MCL exceedance is dominated by short-lived radionuclides—notably, ^{3}H, ^{90}Sr, and ^{137}Cs—that decay to levels below regulatory concern in a few hundred years.

Although contamination from underground nuclear detonations conducted in the Yucca Flat/Climax Mine CAU is forecast to extend into the LCA and then be transported in a generally southerly direction in the LCA, the vast majority of contamination initially in place in the CAU is modeled as being retained over the 1,000-year simulation period in the unsaturated zone and saturated alluvial/volcanic aquifer system above the LCA. This results from the immobility of a large fraction of the inventory in the melt glass as well as the slow release and transport of the mobile fraction of the inventory due to (1) the large distance between the exchange volumes and the water table in the LCA, (2) the low permeability and significant thickness of the tuff confining units between the exchange

volumes and the LCA, and (3) the small water flux through the unsaturated zone and the saturated alluvial/volcanic aquifer system.

Relatively few of the 744 detonations in Yucca Flat significantly affect the extent of contaminant migration and the forecast contaminant boundary in the LCA. Of greatest significance are a few detonations with exchange volumes that potentially extend below the top of the saturated LCA—notably, BOURBON, TORRIDO, SHUFFLE, and CORDUROY. Of lesser significance are detonations near faults or near the top of the saturated LCA, or detonations assumed to have a high initial overpressure in the saturated tuff confining units—notably, BILBY, CALABASH, LUBBOCK, and TORTUGAS . Of even lesser significance are detonations with working points in the unsaturated zone, except for those detonations in the unsaturated LCA—notably, BOURBON and KANKAKEE, which have relatively short transport distances to the water table in the LCA.

Comparison of Model Results to In Situ Observations

Observation wells have been placed in the saturated LCA downgradient from several of the important detonations noted above where contamination, if it existed, was likely to be detected. In particular, UE-7nS is 137 m from BOURBON, ER-7-1 is 200 m from TORRIDO and 500 m from MICKEY, U-3cn-5 is 129 m southeast of BILBY, and UE-2ce is 183 m from NASH. Each of these wells is completed in the upper portion of the LCA (or LCA3 in the case of UE-2ce) where contaminants would most likely be present, if at all. However, with the exception of Well UE-2ce, each of these wells has a limited extent of observation due to their low water production. Generally, cell volumes in the models (typically on the order of 100 m $\times$ 100 m $\times$ 50 m or 500,000 m^3 in the upper part of the LCA) are much larger than the aquifer volume interrogated by the sampling wells, so simulated concentrations are expected to be less than actual concentrations if a similar radionuclide mass was introduced to the aquifer. These relatively small aquifer volumes also mean that any nearby contamination, if it existed, may go undetected by the well, Both of these factors complicates direct comparison of measured and simulated concentration at most locations. However, at Well UE-2ce pumping conducted from 1977 to 1984 yielded about 42,000 m^3 of water and another pumping event in 2008 yielded about 150 m^3 of water. Assuming a typical fracture porosity of 0.001 for the LCA, this equates to an aquifer volume of roughly 42×10^6 m^3 being interrogated by the pumping well, or approximately equivalent to 80 LCA cell volumes. Therefore, Well UE-2ce provides a relatively unique opportunity to compare measured and simulated radionuclide concentrations at the top of the

LCA. Observed radionuclide concentrations in these boreholes tend to support the conclusion that the models of groundwater flow and contaminant transport presented in this report are conservative:

- Data from Well UE-7nS indicate slight contamination (several hundred to several thousand picocuries per liter [pCi/L] of ^{3}H), while the model results indicate contamination at this location of greater than the MCL of 20,000 pCi/L for ^{3}H. This difference could be because the modeling strategy adopted for this study is conservative, and because the actual exchange volume size is less than the modeled exchange volume size based on the maximum announced test yield or because conductive features in the LCA may have been missed by this borehole.

- Data from Well ER-7-1 indicate no contamination, while the model results indicate contamination at this location of greater than the MCL of 20,000 pCi/L for ^{3}H. This difference could be again because the modeling strategy adopted for this study is conservative, and because the actual exchange volume size is less than the modeled exchange volume size based on the maximum announced test yield or because conductive features in the LCA may have been missed by this borehole.

- Data from Well U-3cn-5 indicate no contamination, which is consistent with the model results when a recharge rate of 0.1 mm/yr is assumed or when the BILBY overpressures are assumed minimal. However, alternative modeling cases that assume high overpressures for the BILBY detonation and a high value for the recharge rate (i.e., 1, 5, or 10 mm/yr) yield significant contamination (above the MCL for ^{3}H) at U-3cn-5. This difference may be indicative that the recharge rate of 0.1 mm/yr is most reasonable; however, it cannot be ruled out that conductive features in the LCA may have been missed by this borehole.

- Data from Well UE-2ce indicate significant contamination (5 to 10 times the ^{3}H MCL), which is consistent with the model results when local recharge rates in the vicinity of the NASH detonation are assumed higher (1 mm/yr or greater) or when the effects of drill-back fluid losses and chimney drainage are included in the model. These results could indicate that the infiltration rate near NASH is at the higher end of the distribution (which may be due to the higher elevation and presence of arroyos near NASH) or that local drainage of perched zones down the NASH chimney or drill-back fluid losses are more likely at this location.

- Well ER-2-1 is located in the saturated tuff confining unit in close proximity to a number of detonations with working points in the tuff confining units, such as REBLOCHEN (about 250 m to the southwest of ER-2-1), CHIBERTA (about 260 m to the north of ER-2-1) and STARWORT (about 390 m to the southeast of ER-2-1). The lack of any significant contamination at this observation well supports the limited lateral contaminant transport from these detonations.

Conclusions

Based on the models and analyses of groundwater flow and contaminant transport presented in this document, it is likely that contaminants that originate from underground nuclear testing in the Yucca

Flat/Climax Mine CAU will be confined to the Yucca Flat basin over the next 1,000 years. This is especially true for greater than 99 percent of the radionuclide inventory that is initially in the unsaturated zone and the saturated alluvial/volcanic aquifer system, where releases to the LCA are delayed and peak concentrations decrease because of natural attenuation associated with decay, diffusion, and sorption. This delay is especially important for short-lived radionuclides such as ^{3}H, ^{90}Sr, and ^{137}Cs, which are considered mobile in the LCA. Observations of radionuclide concentrations at wells adjacent to underground nuclear detonations of potential importance for radionuclide migration in the LCA indicate that site conditions are conservatively represented by the conceptual and numerical flow and transport models presented in this report. For radionuclides that either reach or are initially in the LCA, most are likely to remain within the Yucca Flat basin or be removed by radioactive decay over the next several hundred years.

As a result of uncertainty in hydraulic and transport parameters, including the rate of groundwater inflow into the Yucca Flat basin, a sufficiently broad range of assumptions regarding these parameters are evaluated to ensure that the model outcomes do not underestimate the possible extent of contamination. Even with these conservative assumptions, the model outcomes indicate a limited potential for concentrations to exceed the SDWA MCL beyond the Yucca Flat basin. The most significant of these contaminants—notably, ^{3}H, ^{90}Sr, and ^{137}Cs—will be attenuated by decay in the next few hundred years. Based on model runs, other, long-lived contaminants are unlikely to be transported out of the Yucca Flat basin at concentrations above their MCLs because of a combination of limited groundwater inflow to the basin, matrix diffusion and dilution associated with dispersion, and matrix retardation. As noted earlier, the model results presented in this report are expected to be evaluated during the model evaluation studies in the corrective action decision document/corrective action plan phase of the UGTA strategy.

REFERENCES

BN, see Bechtel Nevada.

Bechtel Nevada. 2006. *A Hydrostratigraphic Model and Alternatives for the Groundwater Flow and Contaminant Transport Model of Corrective Action Unit 97: Yucca Flat-Climax Mine, Lincoln and Nye Counties, Nevada*, DOE/NV/11718--1119. Prepared for the U.S. Department of Energy, National Nuclear Security Administration Nevada Site Office. Las Vegas, NV.

Bowen, S.M., D.L. Finnegan, J.L. Thompson, C.M. Miller, P.L. Baca, L.F. Olivas, C.G. Geoffrion, D.K. Smith, W. Goishi, B.K. Esser, J.W. Meadows, N. Namboodiri, and J.F. Wild. 2001. *Nevada Test Site Radionuclide Inventory, 1951–1992*, LA-13859-MS. Los Alamos, NM: Los Alamos National Laboratory.

CFR, see *Code of Federal Regulations*.

Code of Federal Regulations. 2012. Title 40 CFR, Part 141, "National Primary Drinking Water Regulations." Washington, DC: U.S. Government Printing Office.

FFACO, see *Federal Facility Agreement and Consent Order.*

Faunt, C.C, D.S. Sweetkind, M.C. Hill, M.T. Pavelko, and W.R. Belcher. 2012. Written communication. Subject: *Update of the Death Valley Regional Groundwater Flow System Transient Model, Nevada and California*. U.S. Geological Survey.

Federal Facility Agreement and Consent Order. 1996 (as amended March 2010). Agreed to by the State of Nevada; U.S. Department of Energy, Environmental Management; U.S. Department of Defense; and U.S. Department of Energy, Legacy Management. Appendix VI, which contains the Underground Test Area Strategy, was last modified May 2011, Revision No. 4.

Fenelon, J.M., D.S. Sweetkind, P.E. Elliot, and R.J. Laczniak. 2012. *Conceptualization of the Predevelopment Groundwater Flow System and Transient Water-Level Responses in Yucca Flat, Nevada National Security Site, Nevada*, Scientific Investigations Report 2012-5196. Reston, VA: U.S. Geological Survey.

Halford, K., U.S. Geological Survey. 2012. Personal communication to A. Tompson (LLNL) regarding groundwater flow estimates for the Yucca Flat/Climax Mine CAU. 9 October.

Laczniak, R.L., J.C. Cole, D.A. Sawyer, and D.A. Trudeau. 1996. *Summary of Hydrogeologic Controls on Ground-Water Flow at the Nevada Test Site, Nye County, Nevada*, Water-Resources Investigations Report 96-4109. Carson City, NV: U.S. Geological Survey.

N-I GIS, see Navarro-Intera Geographic Information Systems.

Navarro-Intera Geographic Information Systems. 2012. ESRI ArcGIS Software.

Pawloski, G.A., A.F.B. Tompson, S.F. Carle, R.L. Detwiler, Q. Hu, S. Kollet, R.M. Maxwell, W.W. McNab, S.K. Roberts, D.E. Shumaker, Y. Sun, and M. Zavarin. 2008. *Evaluation of Hydrologic Source Term Processes for Underground Nuclear Tests in Yucca Flat, Nevada Test Site: Introduction and Executive Summary*, LLNL-TR-403428. Livermore, CA: Lawrence Livermore National Laboratory.

Pohlmann, K., M. Ye, D. Reeves, D. Decker, J. Chapman, and M. Zavarin. 2007. *Modeling of Groundwater Flow and Radionuclide Transport at the Climax Mine Sub-CAU, Nevada Test Site*, DOE/NV/26383-06; Publication No. 45226. Las Vegas, NV: Desert Research Institute.

SNJV, see Stoller-Navarro Joint Venture.

Stoller-Navarro Joint Venture. 2006a. *Geochemical and Isotopic Evaluation of Groundwater Movement in Corrective Action Unit 97: Yucca Flat/Climax Mine, Nevada Test Site, Nevada*, Rev. 0, S-N/99205--070. Las Vegas, NV.

Stoller-Navarro Joint Venture. 2006b. *Phase I Hydrologic Data for the Groundwater Flow and Contaminant Transport Model of Corrective Action Unit 97: Yucca Flat/Climax Mine, Nevada Test Site, Nye County, Nevada*, Rev. 0, S-N/99205--077. Las Vegas, NV.

Stoller-Navarro Joint Venture. 2007. *Phase I Contaminant Transport Parameters for the Groundwater Flow and Contaminant Transport Model of Corrective Action Unit 97: Yucca Flat/Climax Mine, Nevada Test Site, Nye County, Nevada*, Rev. 0, S-N/99205--096. Las Vegas, NV.

Stoller-Navarro Joint Venture. 2009. *Unclassified Source Term and Radionuclide Data for Corrective Action Unit 97: Yucca Flat/Climax Mine, Nevada Test Site, Nevada*, Rev. 2, S-N/99205--114. Las Vegas, NV.

Winograd, I.J., and W. Thordarson. 1975. *Hydrogeologic and Hydrochemical Framework, South-Central Great Basin, Nevada-California, with Special Reference to the Nevada Test Site*, Professional Paper 712-C. U.S. Geological Survey.

Zyvoloski, G.A., B.A. Robinson, Z.V. Dash, and L.L. Trease. 1997. *Summary of the Models and Methods for the FEHM Application—A Finite-Element Heat- and Mass-Transfer Code*, LA-13307-MS. Los Alamos, NM: Los Alamos National Laboratory.

1.0 INTRODUCTION

The U.S. Department of Energy, National Nuclear Security Administration Nevada Site Office (NNSA/NSO) initiated the Underground Test Area (UGTA) Project, now referred to as the UGTA Activity, to assess and evaluate the effects of the underground shaft and tunnel nuclear weapons tests on groundwater at the Nevada Test Site (NTS), now known as the Nevada National Security Site (NNSS), and vicinity. The framework for this assessment and evaluation is provided in Appendix VI, Revision No. 4, of the *Federal Facility Agreement and Consent Order* (FFACO) (1996, as amended), which describes the processes that will be used to complete corrective actions pursuant to the FFACO. The objective of the corrective action strategy described in Appendix VI, Revision No. 4, of the FFACO (1996, as amended) for the UGTA Activity is to analyze and evaluate each UGTA corrective action unit (CAU) through a combination of data and information collection and evaluation, and groundwater flow and contaminant transport simulation.

The FFACO corrective action process for the Yucca Flat/Climax Mine CAU was initiated with the *Corrective Action Investigation Plan* (CAIP) *for Corrective Action Unit 97: Yucca Flat/Climax Mine, Nevada Test Site, Nevada* (DOE/NV, 2000a). The Yucca Flat/Climax Mine CAU CAIP identified a three-step model development process to evaluate the impact of underground nuclear testing on the Yucca Flat/Climax Mine CAU groundwater flow system. The first step is the data analysis task to compile and evaluate existing and new data for use in the model. The second step is the development of the Yucca Flat/Climax Mine CAU groundwater flow model. The third step is the development of the Yucca Flat/Climax Mine CAU contaminant transport model.

The first step has been completed and is documented in a series of data compilation and analysis reports:

- *Phase I Hydrologic Data for the Groundwater Flow and Contaminant Transport Model of Corrective Action Unit 97: Yucca Flat/Climax Mine, Nevada Test Site, Nye County, Nevada* (hereinafter referred to as the Yucca Flat/Climax Mine hydrologic data document [HDD]) (SNJV, 2006b)

- *Phase I Contaminant Transport Parameters for the Groundwater Flow and Contaminant Transport Model of Corrective Action Unit 97: Yucca Flat/Climax Mine, Nevada Test Site, Nye County, Nevada* (hereinafter referred to as the Yucca Flat/Climax Mine transport data document [TDD]) (SNJV, 2007)

- *A Hydrostratigraphic Model and Alternatives for the Groundwater Flow and Contaminant Transport Model of Corrective Action Unit 97: Yucca Flat-Climax Mine, Lincoln and Nye Counties, Nevada* (BN, 2006)

- *Evaluation of Hydrologic Source Term Processes for Underground Nuclear Tests in Yucca Flat, Nevada Test Site: Introduction and Executive Summary* (Pawloski et al., 2008)

The present document addresses the second and third steps identified in the Yucca Flat/Climax Mine CAU CAIP, i.e., the development of flow and transport models, respectively. The scope of the modeling effort includes use of the transport model for the purpose of forecasting the extent of the contaminant transport within 1,000 years as required in the FFACO (1996, as amended). As such, the calculated three-dimensional contaminant transport concentrations are integrated into probabilistic forecasts of the likelihood of contaminants in groundwater exceeding or remaining below the radiological standards of the *Safe Drinking Water Act* (SDWA) (CFR, 2012). As identified in the FFACO, these forecasts provide planning tools to facilitate regulatory decisions designed to protect the health and safety of the public.

This document presents the analysis and evaluation of groundwater flow and contaminant transport for CAU 97: Yucca Flat/Climax Mine. Section 1.0 provides background information as a prelude to the specific topics discussed in this report. Section 1.1 discusses the purpose and scope of the Yucca Flat/Climax Mine CAU groundwater flow and contaminant transport modeling effort. Section 1.2 presents the regulatory background and framework in which this modeling effort takes place. Section 1.3 summarizes the geographic and geologic setting of the site. Section 1.4 presents background information related to the hydrogeologic setting of the site. Section 1.5 provides a background and summary of the Yucca Flat underground nuclear testing program. Section 1.6 presents a summary of the modeling approach adopted for the Yucca Flat/Climax Mine CAU and the basis for separating the modeling into discrete domains to appropriately address the significant processes, conceptual models, and parameters affecting groundwater flow and contaminant transport in the CAU. Section 1.7 summarizes the groundwater flow and contaminant transport modeling strategy for the Yucca Flat/Climax Mine CAU, including a summary discussion of the key assumptions used in the modeling. Section 1.8 identifies general supporting work that has contributed

to the evolution and development of the modeling described in this report. Finally, Section 1.9 outlines the structure and content of the report.

The Yucca Flat/Climax Mine CAU flow and transport model development consists of four separate groundwater flow and contaminant transport modeling efforts. As discussed in Section 1.6, the following four separate flow and transport models are developed to evaluate the significant processes and conceptual differences in the hydrogeologic environments for the different hydrologic source terms (HSTs) into which test-related radionuclides are released (as defined and identified in Pawloski et al., 2008, and Section 2.0):

- Climax Mine flow and transport model (Pohlmann et al., 2007)
- Yucca Flat unsaturated-zone flow and transport model
- Yucca Flat saturated alluvial/volcanic aquifer system flow and transport model
- Yucca Flat saturated lower carbonate aquifer (LCA) flow and transport model

(Note that the alluvial aquifers and volcanic aquifers are combined into a single aquifer system and referred to as the alluvial/volcanic aquifer system in this document. See Section 1.4.)

Models of flow and contaminant transport for the Climax Mine detonations have been documented in Pohlmann et al. (2007). These models have been used to calculate the possible contaminant flux from the three Climax Mine detonations to the edge of the Climax stock that enters the LCA. As discussed in more detail later in this report (see Section 6.0), the release of contaminants from the Climax stock to the LCA contributes no significant contaminant flux to the rest of the Yucca Flat/Climax Mine CAU. This document, therefore, focuses on groundwater flow and contaminant migration in the Yucca Flat area of CAU 97.

The three remaining flow and transport models listed above focus on groundwater flow and contaminant transport in the Yucca Flat area of CAU 97 and are described in detail in Sections 3.0 to 6.0. The Yucca Flat unsaturated-zone flow and transport model is addressed in Section 3.0. The Yucca Flat saturated alluvial/volcanic aquifer system flow and transport model is addressed in Section 4.0. The Yucca Flat saturated LCA flow model is addressed in Section 5.0. The Yucca Flat saturated LCA transport model is addressed in Section 6.0.

In the present set of models, as with the previous modeling performed for the Frenchman Flat and Pahute Mesa CAUs, flow and transport processes can be mathematically decoupled and are thus

treated separately. For each of the three model domains (unsaturated zone, saturated alluvial/volcanic aquifer system, and saturated LCA), the flow model is presented first, followed by the transport model and then the forecast of contaminant migration based on the developed flow and transport models. The flow model calibration uses an inverse approach that iteratively adjusts the hydraulic parameters to evolve a calculated solution that best matches observed water levels and hydraulic pressure measurements. Different observations appropriate for the individual model domains are used for each flow model. The calibrated flow fields within each model domain are then used as input to the Yucca Flat transport model runs.

Determination of the vertical and horizontal extent of contaminant migration is the ultimate objective of the corrective action investigation (CAI) phase of the UGTA corrective action strategy. To support this objective, the present study focuses on understanding the behavior of radionuclide migration in the Yucca Flat/Climax Mine CAU and defining, both qualitatively and quantitatively, the sensitivity of such behavior to uncertainty in the flow and transport model conceptualization and parameterization.

1.1 Purpose and Scope

The purpose of the Yucca Flat/Climax Mine CAU flow and transport modeling is to support the UGTA corrective action strategy objective of estimating the vertical and horizontal extent of contaminant migration for the CAU to forecast contaminant boundaries. A contaminant boundary is the projected lateral perimeter at the ground surface that defines the extent (over all operable depths) of groundwater contamination with radionuclides from underground nuclear testing that exceeds the drinking water standards set forth in the SDWA (CFR, 2012). The contaminant boundary specifically consists of both a lateral perimeter boundary and a lower hydrostratigraphic unit (HSU) boundary. At Yucca Flat, the lower HSU boundary is within the LCA; therefore, the focus of the present study is to define the lateral perimeter boundary of contaminant migration within the LCA.

The objectives of the Yucca Flat flow and transport modeling, as stated in the Yucca Flat/Climax Mine CAU CAIP (DOE/NV, 2000a) and the associated strategy and approach document (Shaw, 2003), are as follows:

- Develop models that integrate a wide variety of data into a mass conservative description of contaminant migration in groundwater from underground nuclear test locations in the CAU.

- Simulate, as output, the concentrations of individual contaminants downgradient of underground test locations over a time period of 1,000 years. These concentrations will be used to define a contaminant boundary based on a composite dose of 4 millirem per year (mrem/yr) for beta-emitting radionuclides and 15 mrem/yr for alpha-emitting radionuclides.

- Serve as a tool to evaluate impacts of future flow system changes on the migration of contaminants in the CAU.

The specific objectives of the Yucca Flat flow modeling are as follows:

- Develop a three-dimensional mathematical flow model that incorporates the important physical features of the flow system and honors CAU-specific data and information.

- Simulate the groundwater flow system to determine the direction and magnitude of groundwater fluxes based on calibration to Yucca Flat hydrogeologic data.

- Quantify the uncertainty in the direction and magnitude of groundwater flow due to uncertainty in parameter values and alternative component conceptual models (e.g., geology, boundary flux, and recharge).

The specific objectives of the Yucca Flat transport modeling are as follows:

- Superimpose three-dimensional transport model properties onto the Yucca Flat flow model domain.

- Develop contaminant concentrations for underground nuclear test sites using alternative conceptual models for the source term and input to the CAU-scale model.

- Simulate contaminant transport from the underground test sites using a stochastic approach that provides multiple realizations of plume migration and calculation of the exceedance volume, which is the quantification of the statistical distribution for the cumulative maximum contaminant level (MCL) from each realization projected out to 1,000 years.

- Quantify the radionuclide spread due to uncertainty in parametric values and alternative conceptual models of the source term, and flow and transport.

These objective are achieved in the remainder of this document. As noted in Section 1.6, these objectives are achieved by dividing the overall modeling domain into four subdomains to effectively capture the key processes and uncertainties that could affect contaminant migration from the underground nuclear test sites at the Yucca Flat/Climax Mine CAU.

1.2 Regulatory Background

Since 1996, the Nevada Division of Environmental Protection (NDEP) has regulated NNSA/NSO corrective actions through the FFACO (1996, as amended). The individual locations covered by the agreement are known as corrective action sites (CASs), and these are grouped into CAUs. The UGTA CAUs are Yucca Flat/Climax Mine, Frenchman Flat, Rainier Mesa/Shoshone Mountain, Central Pahute Mesa, and Western Pahute Mesa (Figure 1-1).

Appendix VI, Revision No. 4, of the FFACO (1996, as amended in May 2011) describes the processes that will be used to complete corrective actions at CAUs, including the UGTA CAUs. It provides the current regulatory guidance on the UGTA corrective action strategy and is incorporated into this document. All references in this document to the FFACO or its appendices refer to Appendix VI, Revision No. 4, of the FFACO. Figure 1-2 presents the decision process used to implement the strategy for the Yucca Flat/Climax Mine CAU. The major decision points in the process are numbered and highlighted in the figure.

The CAU-specific corrective action process comprises six major components: corrective action investigation plan (CAIP), corrective action investigation (CAI), corrective action decision document (CADD), corrective action plan (CAP), closure report (CR), and long-term monitoring. The purposes or contents of these components are summarized as follows:

- The CAIP is an FFACO-required document that documents the CAI planning and provides or references all specific information for planning CAI activities.
- The CAI includes the collection of new data, the evaluation of new and existing data, and the development and use of CAU-specific groundwater flow and transport models (to which this document applies).
- The CADD is an FFACO-required report that documents the CAI. It describes the results of the CAI, the corrective action alternatives considered, the results of their comparative evaluation, the selected corrective action, and the rationale for its selection.
- The CAP is an FFACO-required document that describes how the selected remedial alternative is to be implemented. The CAP contains all specifications, including engineering design specifications, that are necessary to implement the selected remedial alternative.

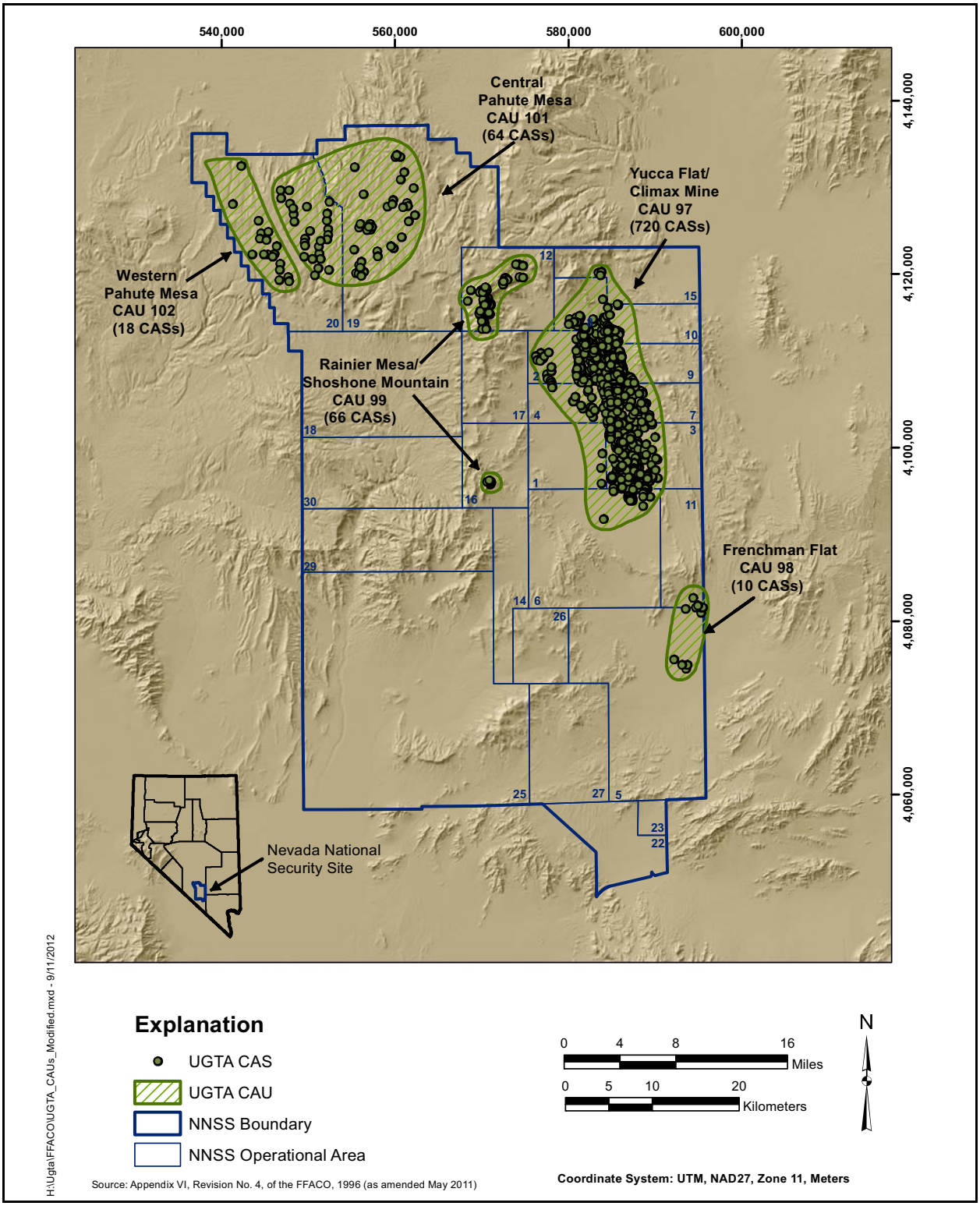

Figure 1-1
Location of the Yucca Flat/Climax Mine CAU and Other UGTA CAUs

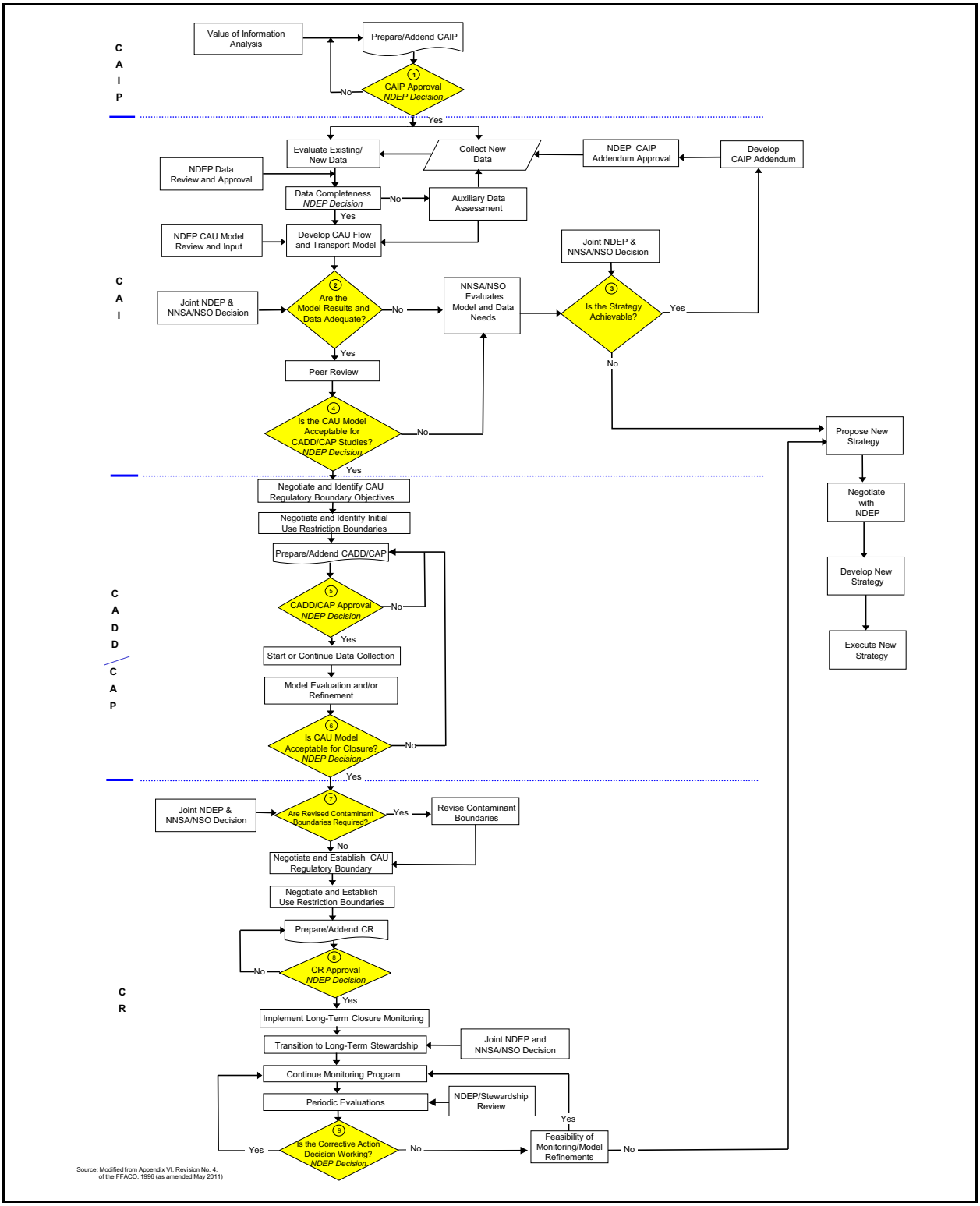

Figure 1-2
Process Flow Diagram for the UGTA CAUs

- The UGTA corrective action strategy has provisions for CAU closure that apply if the alternative that calls for long-term monitoring is selected. Closure activities include the preparation of a CR, a review of the CR by NDEP, and long-term closure monitoring by NNSA/NSO.

- The long-term, post-closure monitoring is designed to ensure that the regulatory boundary is not violated.

The CAIP has been completed for the Yucca Flat/Climax Mine CAU (DOE/NV, 2000a). The CAIP provides information necessary to plan subsequent CAI activities at the Yucca Flat/Climax Mine CAU, including the location of the potential model area.

The CAI phase of the corrective action process focuses on developing CAU-specific models that incorporate CAU- and NNSS-specific data. The CAU-specific modeling objective at this stage is to determine the range of possible contaminant boundaries that encompass the extent of contamination as defined in the FFACO (1996, as amended). The present study, therefore, focuses on developing models that are suitable for use in the analysis of groundwater flow and contaminant transport in the Yucca Flat/Climax Mine CAU. The flow and transport modeling for the Yucca Flat/Climax Mine CAU takes into consideration the following factors as specified in the FFACO:

1. Alternative hydrological framework models of the CAU modeling domain

2. Uncertainty in the radiological and hydrological source term

3. Alternative models of groundwater recharge

4. Alternative model boundary conditions and models of groundwater flow

5. Multiple permissive sets of calibrated flow models

6. Probabilistic simulations of transport using plausible sets of alternative framework and recharge models, model boundary conditions, and models of groundwater flow from calibrated flow models

7. Ensembles of forecasts of contaminant boundaries for the CAU

8. Sensitivity and uncertainty analysis of the model outputs

The saturated-zone models were used to perform probabilistic simulations of transport, considering the uncertainty in the transport characteristics and the source term. However, uncertainty in the transport characteristics were evaluated in the unsaturated-zone model by the use of discrete model

runs rather than probabilistic techniques because of the complexity of the models and the simulation approach chosen.

The technical suitability of the models used to evaluate groundwater flow and contaminant transport in the Yucca Flat/Climax Mine CAU is supported by the implementation of the quality assurance requirements identified in the *Underground Test Area Quality Assurance Project Plan, Nevada National Security Site, Nevada* (NNSA/NSO, 2011). The relevant requirements are the following:

- A.8 Data Management
- A.9 Computer Software and Codes
- B.4 Non-direct Data
- B.5 Groundwater Flow and Transport Modeling
- B.6 Model Evaluation
- B.7 Configuration Control
- C.4 Document Review and Issuance

Appendix A summarizes how each of the quality assurance requirements has been addressed in the activities supporting the development and application of the Yucca Flat/Climax Mine CAU flow and transport models.

1.3 Yucca Flat Background Information—Physiography and Geology

The Yucca Flat/Climax Mine CAU is located about 140 kilometers (km) northwest of Las Vegas, Nevada. The Yucca Flat/Climax Mine CAU is located in the northeastern part of the NNSS that includes Areas 1, 2, 3, 4, 6, 7, 8, 9, 10, 11, and 15 (Figure 1-1).

Yucca Flat is an intermontane valley in the northern portion of the Basin and Range physiographic province. Yucca Flat is a topographically closed basin with a playa at its southern end. The basin is bounded by the Halfpint Range on the east, by Rainier Mesa and the Belted Range on the north, by the Eleana Range and Mine Mountain on the west, and by the CP Hills and Massachusetts Mountain on the south (Figure 1-3).

The general topographic relief at Yucca Flat ranges from about 1,200 meters (m) above mean sea level (amsl) at the southern low point at Yucca Lake to more than 1,500 m amsl along the northwestern and northeastern margins of the basin, where the Tertiary alluvium intersects the underlying Paleozoic strata that outcrop in the Eleana Range, Quartzite Ridge, and Halfpint Range (Figure 1-4). Many of the underground nuclear tests conducted in the area have resulted in a number

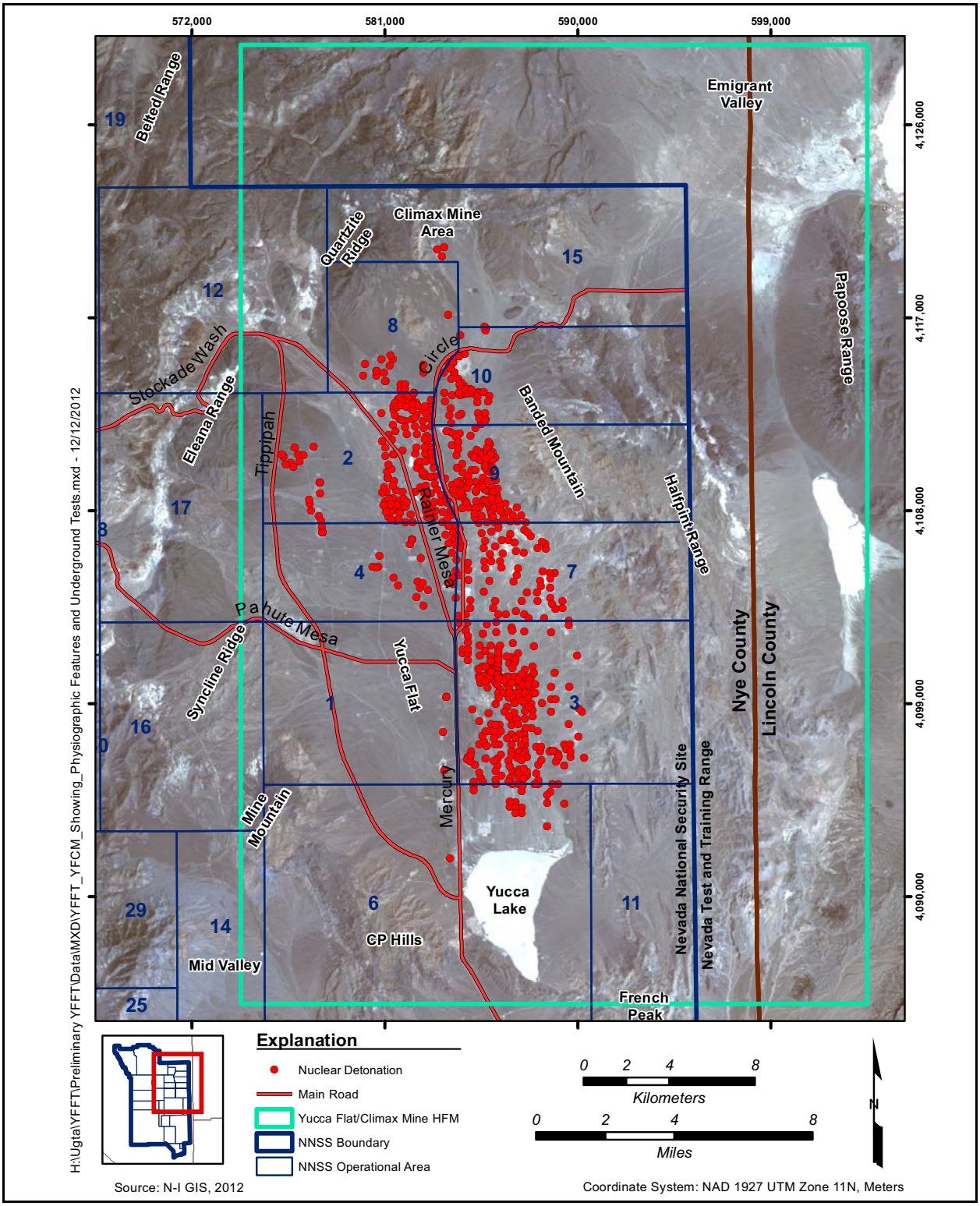

Figure 1-3
Satellite Image and Physiographic Features of the Yucca Flat/Climax Mine CAU

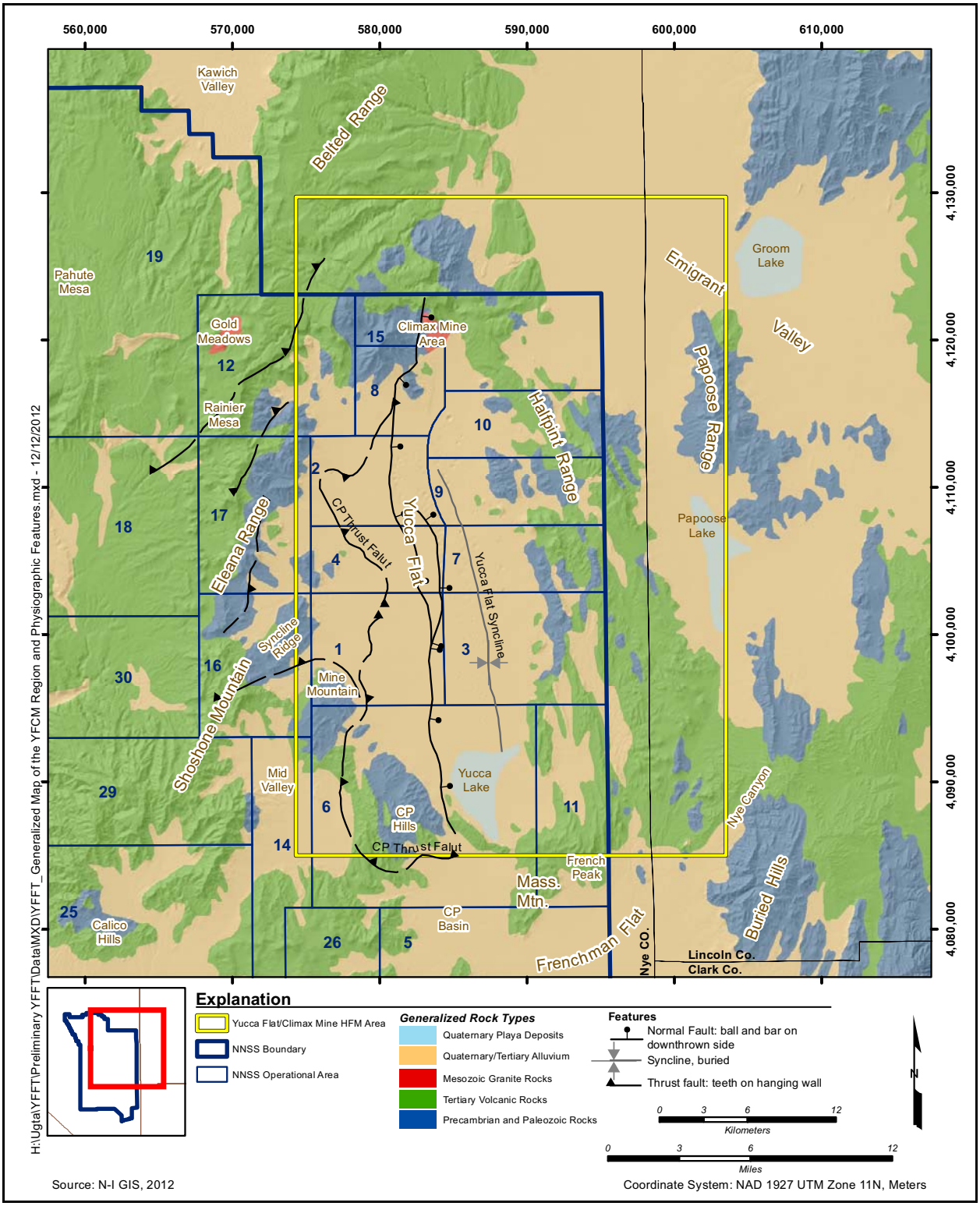

Figure 1-4
Generalized Geologic Map of the Yucca Flat/Climax Mine Region and Associated Physiographic Features

of surface craters of varying sizes that have significantly affected the area's topography (Figures 1-5 and 1-6).

The general geology of the Yucca Flat/Climax Mine CAU is described in *A Hydrostratigraphic Model and Alternatives for the Groundwater Flow and Contaminant Transport Model of Corrective Action Unit 97*: *Yucca Flat-Climax Mine, Lincoln and Nye Counties, Nevada* (BN, 2006). The geologic sequence in the Yucca Flat/Climax Mine area includes a thick Cenozoic volcanic and sedimentary section that unconformably overlies previously deformed rocks of Paleozoic age. Rocks within the basin include Precambrian and Paleozoic carbonate and clastic rocks that outcrop in the bedrock hills east of the basin in the Halfpint Range and west of the basin in the Eleana Range and Syncline Ridge. The Climax stock on the northern edge of the basin is composed of Cretaceous granitic intrusions dated at roughly 100 million years ago (Ma). Tertiary-age ash-flow, ash-fall, and reworked tuffs from volcanic centers to the west of the basin were deposited between about 15 and 11 Ma on the irregular erosional surface of the pre-Tertiary rocks.

The pre-Cenozoic section includes late Proterozoic and lower Cambrian siliceous and argillaceous metasediments; an approximately 4,500-m-thick sequence of middle Cambrian through middle Devonian carbonate-dominated rocks (dolomite and limestone); a 1,000- to 2,000-m-thick sequence of upper Devonian through Mississippian siliceous siltstone, sandstone, and conglomerate; and a thin Pennsylvanian limestone and local Mesozoic granitic intrusive bodies. Paleozoic sedimentary rocks are exposed along the margins of Yucca Flat and consist mostly of carbonate rocks ranging in age from Cambrian to Mississippian. The Paleozoic rocks show contractional deformation most likely related to both east- and west-directed thrusting during the Mesozoic (e.g., Belted Range and CP thrust faults). However, contractional deformation has been overprinted by significant extensional deformation related to basin-and-range extension during the late Cenozoic (BN, 2006). During the middle Late Cretaceous, granitic bodies (including the Climax stock in northern Yucca Flat) intruded these deformed rocks.

The Cenozoic section includes Miocene volcanic rhyolitic ash-flow sheets and local rhyolitic lava flows, and post-Miocene alluvial basin-fill deposits. The Miocene tuffs are generally rhyolitic composition erupted from large calderas and associated vents located 30 km west of Yucca Flat. These rocks dominate much of the highlands surrounding Yucca Flat. The volcanic rocks include ash-flow, ash-fall, and reworked tuffs. These units vary in thickness and extent because of the

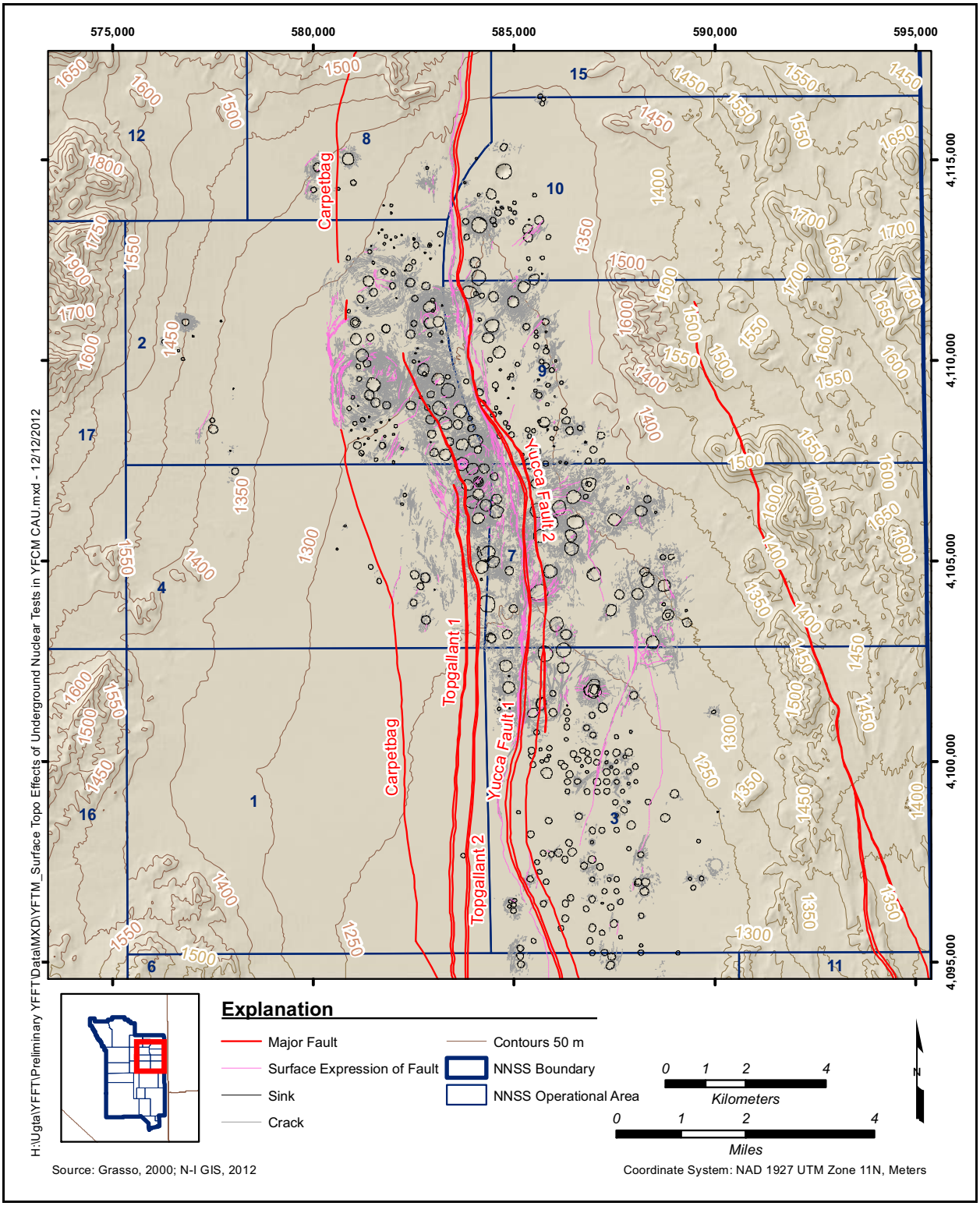

Figure 1-5
Surface Topography Showing the Effects of Underground Nuclear Tests in Shafts and Tunnels at the Yucca Flat/Climax Mine CAU

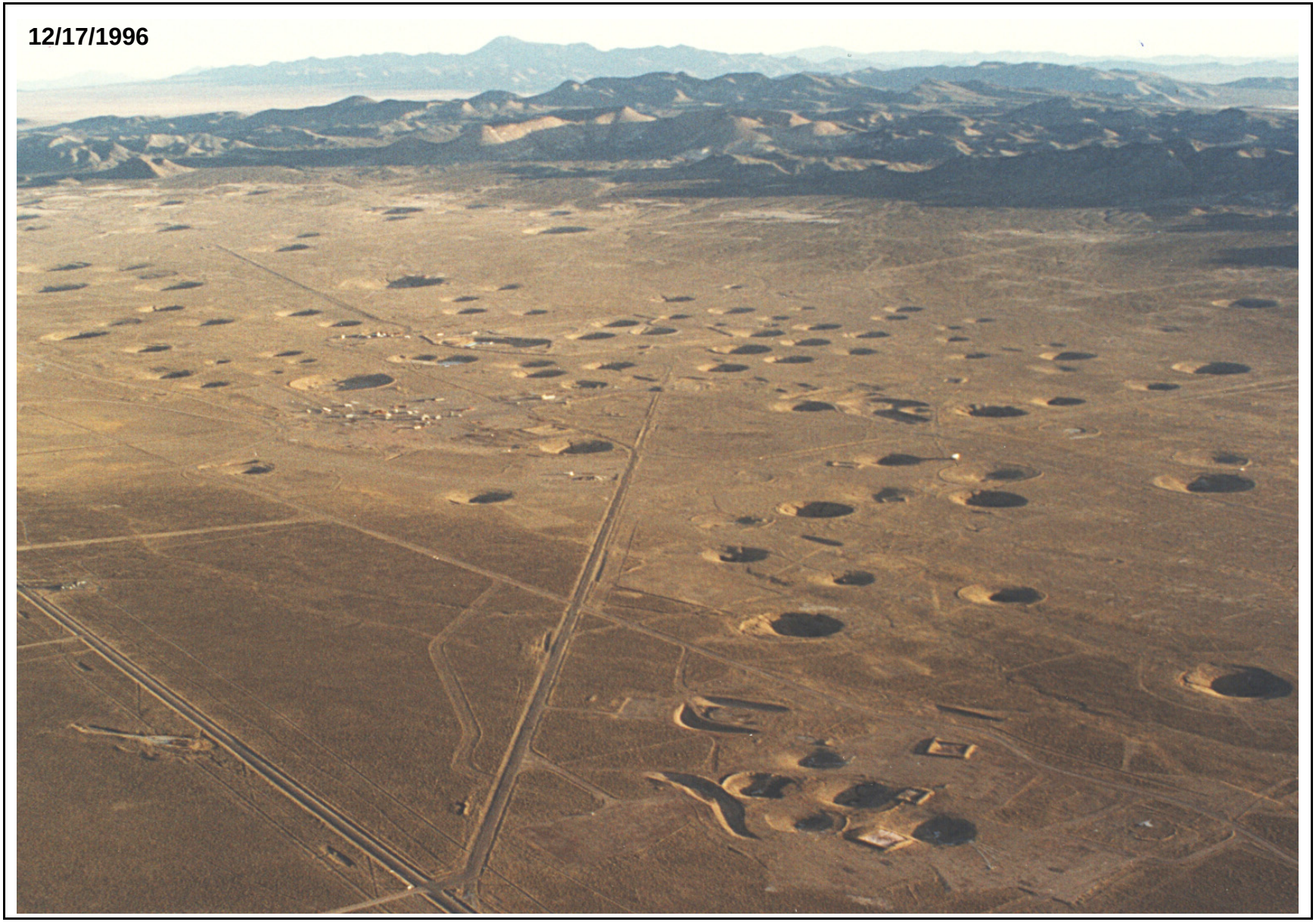

Figure 1-6
Aerial Photograph of Surface Craters in the Yucca Flat/Climax Mine CAU Viewed to the Northeast

irregularity of the underlying depositional surface and the paleotopography between Yucca Flat and the source areas to the west. The central portion of the Yucca Flat basin contains a thick sequence of these volcanic units deposited over the regionally extensive carbonate units. These volcanic units thin along all margins of the basin. Overlying the volcanic units is a thick sequence of alluvium that thickens in the center of the basin and thins along the basin margins. The volcanic and sedimentary rocks are covered in many areas by surficial deposits of late Tertiary and Quaternary ages. These deposits consist of alluvium, colluvium, eolian deposits, basalt lavas, and playa deposits.
A perspective view of the Yucca Flat hydrostratigraphic framework model (HFM) is illustrated in Figure 1-7, with the corresponding fence diagram illustrated in Figure 1-8.

The Yucca Flat/Climax Mine CAU and surrounding areas were affected by two opposing styles of tectonic deformation: mid-Mesozoic through Eocene compressive deformation, and a subsequent phase of mid-to-late Cenozoic extension. The early period of compressional deformation produced a series of anticlines, synclines, and thrust faults (Belted Range and CP thrust faults) sometime between 280 and 100 Ma. The structural folds include the Halfpint Range anticline, the Syncline Ridge syncline, the Yucca Flat syncline, and the Quartzite Ridge anticline. Yucca Flat is a Cenozoic basin formed in response to basin-and-range extension.

This early period of compressional deformation was followed by a later period of extension that resulted in a series of roughly north-striking normal faults. Basin extension commenced between about 11.5 and 8.1 Ma (BN, 2006). Much of the vertical displacement in the eastern portion of the basin is taken up along the eastward-dipping Carpetbag-Topgallant and Yucca fault systems, so the Tertiary volcanic rocks dip predominantly to the west despite the numerous small grabens created by occasional west-dipping faults. The HFM includes 178 normal faults with displacements greater than 60 m (200 feet [ft]) (BN, 2006). Most of these faults are within the lateral boundaries of the unsaturated- and saturated-zone flow and transport models. Although some of these faults extend through the alluvial material and have experienced recent offsets, including those induced during the underground nuclear testing program, the surficial geologic expression of these faults is limited. Several of the major faults are depicted in the fence diagram (Figure 1-8).

1.4 Yucca Flat Background Information—Hydrostratigraphy and Groundwater Flow

The mapped geologic units within the CAU and surrounding areas have been grouped as HSUs on the basis of similar geologic and hydraulic properties (BN, 2006). Three general groupings of the most

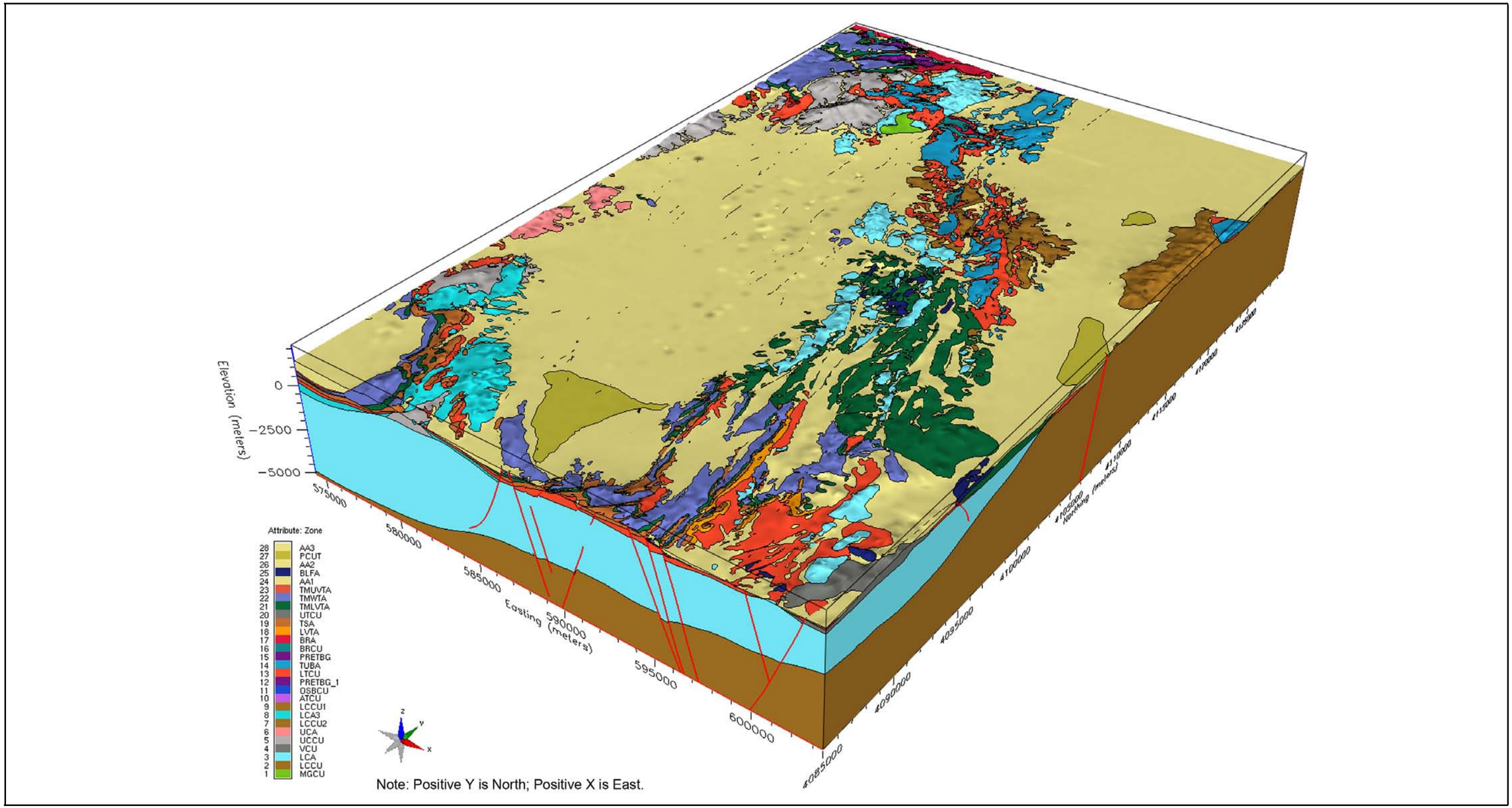

Figure 1-7
Perspective Plot of the Yucca Flat/Climax Mine CAU HFM Viewed to the Northwest

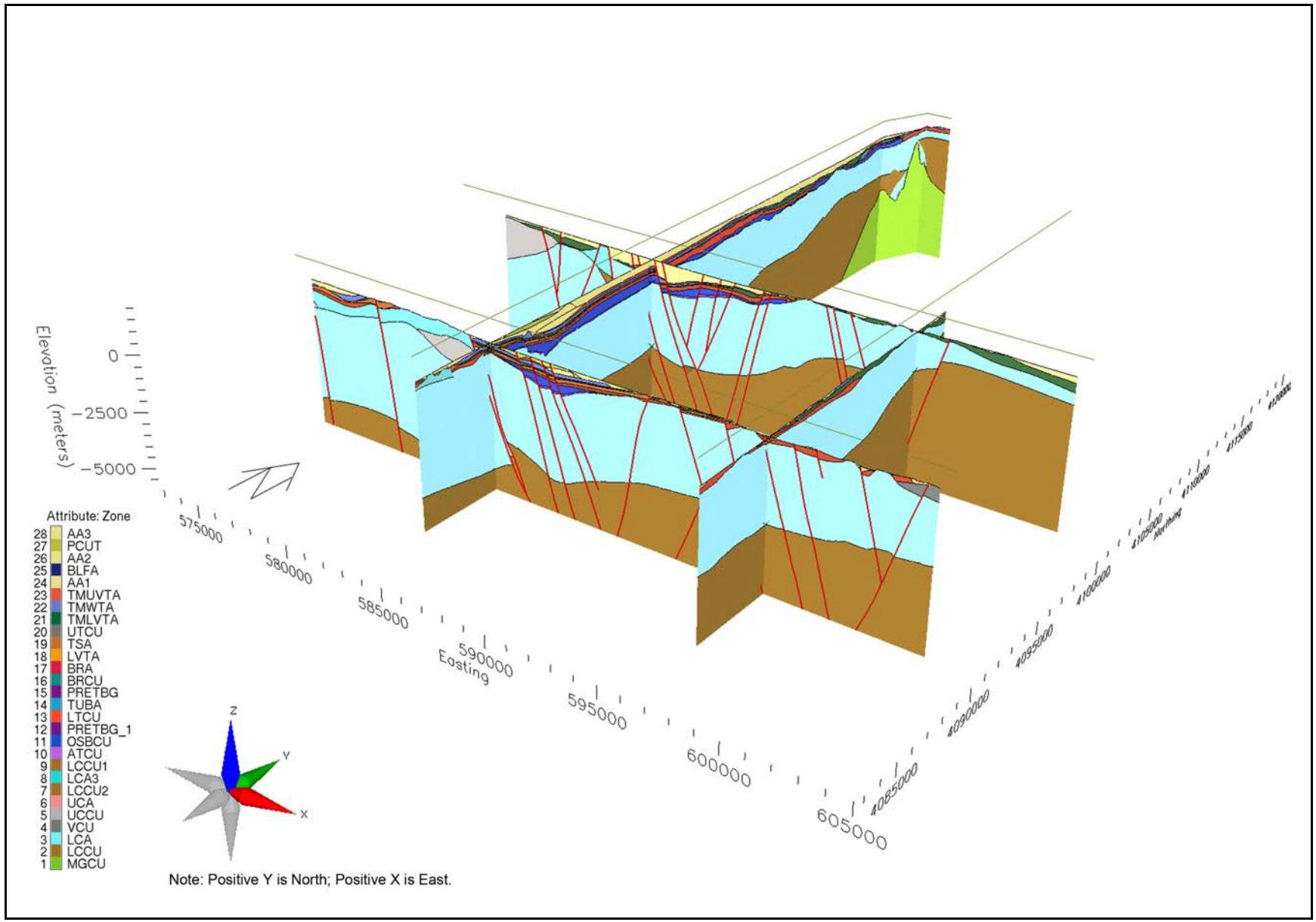

Figure 1-8
Fence Diagram of the Yucca Flat/Climax Mine CAU HFM Viewed to the Northwest

permeable HSUs have been classified as aquifers: basin-fill alluvial deposits, volcanic rocks consisting of welded tuffs and lava flows, and fractured carbonate rocks. The principal carbonate-rock aquifer consists of the thick sequence of Paleozoic carbonate rock that extends throughout much of the subsurface of central and southeastern Nevada. Although the fractured Cenozoic volcanic rock and permeable Cenozoic basin-fill alluvium can form important regional aquifers in other portions of the NNSS, in the Yucca Flat/Climax Mine CAU, these units only form local aquifers that contribute flow to the underlying Paleozoic carbonate-rock aquifer (Fenelon et al., 2010). Groundwater flow in the Yucca Flat/Climax Mine CAU is diverted by low-permeability rocks that form confining units. Proterozoic to early Cambrian metamorphic and siliciclastic rocks and Paleozoic siliciclastic rock form a basement confining unit, whereas the zeolitically altered and nonwelded tuffs within the Cenozoic volcanic section and fine-grained parts of the Cenozoic basin fill form local confining units (Blankennagel and Weir, 1973; Winograd and Thordarson, 1975; Fenelon et al., 2010; Fenelon et al., 2012).

The HFM used as a basis for the flow and transport models described in this report includes the Precambrian and Paleozoic clastic and carbonate rocks, the Tertiary volcanic rocks, and alluvium. These general lithologic units have been split into discrete hydrostratigraphic confining units and aquifers as delineated in Table 1-1. The pre-Tertiary rocks represented in the models include the lower clastic confining unit (LCCU) and upper clastic confining unit (UCCU) that outcrop along the perimeter of the basin, the older lower carbonate aquifer (LCA) that underlies most of the basin, and the younger upper carbonate aquifer (UCA) and lower carbonate aquifer thrust plate (LCA3) that were emplaced over the UCCU in the western part of the basin as part of the deformation associated with the CP thrust fault. The volcanic section includes clay-rich bedded tuffs, sediments, and paleocolluvium (argillic tuff confining unit [ATCU]); relatively thick and widespread zeolitized tuff confining units (e.g., Oak Spring Butte confining unit [OSBCU] and lower tuff confining unit [LTCU]) and local zeolitized tuff confining units (e.g., Belted Range confining unit [BRCU] and upper tuff confining unit [UTCU]); relatively thin and localized fractured, welded tuff (Tub Spring aquifer [TUBA], Belted Range aquifer [BRA], Topopah Spring aquifer [TSA], and Timber Mountain welded-tuff aquifer [TM-WTA]), and lava-flow aquifers (pre-Grouse Canyon Tuff lava-flow aquifer 1 [PRETBG1], pre-Grouse Canyon Tuff lava-flow aquifer [PRETBG], and basalt lava-flow aquifer [BLFA]); and porous vitric-tuff aquifers (lower vitric-tuff aquifer [LVTA], Timber Mountain lower vitric-tuff aquifer [TM-LVTA], and Timber Mountain upper vitric-tuff aquifer [TM-UVTA]). The ATCU, OSBCU, and LTCU generally separate the overlying aquifers from the LCA except

Table 1-1
Descriptions of Major HSUs in the Model Domain
(Page 1 of 3)

HSU	Dominant Hydrogeologic Unit(s)	Typical Lithologies	Hydrologic Significance
Alluvial aquifer (AA)	AA	Alluvium: gravelly sand; also includes one or more thin basalt flows, playa deposits (differentiated as separate HSUs), and eolian sands	Generally unsaturated except in deepest structural basins in central Yucca Flat.
Playa confining unit (PCUT)	Playa confining unit (PCU)	Clayey silt and sandy silt	Forms surface and near-surface playas at Yucca Lake. Low permeability could impede downward recharge or could concentrate local recharge through surface cracks.
Basalt lava-flow aquifer (BLFA)	Lava-flow aquifer (LFA)	Basalt lava flows	Isolated flows identified in the middle of the unsaturated alluvial section.
Timber Mountain upper vitric-tuff aquifer (TM-UVTA)	Vitric-tuff aquifer (VTA) minor (<15%) Welded-tuff aquifer (WTA)	Includes vitric nonwelded to partially welded ash-flow and bedded tuff	Typically saturated only in the deepest structural basins in central Yucca Flat. This HSU comprises only the Ammonia Tanks Tuff, which stratigraphically overlies the TM-WTA.
Timber Mountain welded-tuff aquifer (TM-WTA)	WTA minor (<20%) VTA	Partially to densely welded ash-flow tuff; vitric to devitrified	Typically saturated only in deep structural basins in central Yucca Flat. Strongly welded zones typically sandwiched between less welded zones.
Timber Mountain lower vitric-tuff aquifer (TM-LVTA)	VTA	Nonwelded ash-flow and bedded tuff; vitric	Typically includes the nonzeolitized, nonwelded lower portion of the Rainier Mesa Tuff. However, this HSU can encompass all nonzeolitized, nonwelded, and bedded units below the welded Rainier Mesa Tuff and above the level of pervasive zeolitization. Unaltered nonwelded and ash-fall tuffs generally not found at depths much below the static water level due to tendency to become zeolitized (which drastically reduces permeability) under saturated conditions.
Upper tuff confining unit (UTCU)	Tuff confining unit (TCU)	Zeolitized bedded tuff	Defined to encompass the zeolitized bedded tuffs that stratigraphically overlie the Topopah Spring aquifer (TSA). Although some geologic units of the UTCU are laterally continuous with those of the LTCU, the UTCU is limited areally to extreme southern Yucca Flat, where the welded Topopah Spring Tuff is an important aquifer present between the two tuff confining units (UTCU and LTCU).
Topopah Spring aquifer (TSA)	WTA minor (<15%) VTA	Welded ash-flow tuff	Distribution is limited to the extreme southern portion of Yucca Flat, south of the N 4,098,000 m NAD27 grid line. Hydrogeologic properties are similar to those of the TM-WTA.

Table 1-1
Descriptions of Major HSUs in the Model Domain
(Page 2 of 3)

HSU	Dominant Hydrogeologic Unit(s)	Typical Lithologies	Hydrologic Significance
Lower vitric-tuff aquifer (LVTA)	VTA	Nonwelded and bedded ash-flow tuff; vitric	Relatively thin VTA unit below the TSA. Grouped with the TM-LVTA where TSA is not present.
Belted Range aquifer (BRA)	WTA	Welded ash-flow tuff	Limited extent in the northern portion of Yucca Flat.
Belted Range confining unit (BRCU)	TCU	Zeolitized bedded tuff	Limited extent in the northern portion of Yucca Flat.
Pre-Grouse Canyon Tuff lava-flow aquifer (PRETBG)	LFA	Lava flow	Limited extent in the northern portion of Yucca Flat.
Tub Spring aquifer (TUBA)	WTA	Welded ash-flow tuff	Limited extent in the northern portion of Yucca Flat.
Pre-Grouse Canyon Tuff lava-flow aquifer 1 (PRETBG1)	LFA	Lava flow	Limited extent in the northern portion of Yucca Flat.
Lower tuff confining unit (LTCU)	TCU	Zeolitized bedded tuff with interbedded but less significant zeolitized, nonwelded to partially welded ash-flow tuff	Generally includes all zeolitized tuff in the Yucca Flat area. Stratigraphically, the LTCU may include all units from the base of the Rainier Mesa Tuff to the top of the Paleozoic rocks. The strongly argillized older tuffs and paleocolluvium that immediately overlie the pre-Tertiary rocks may also be included. The uppermost zeolitized bedded tuffs overlying the TSA in southern Yucca Flat form a separate HSU (the UTCU). Subdivided in the Yucca Flat basin (see below).
Oak Spring Butte confining unit (OSBCU)	TCU	Devitrified to zeolitic to partially welded tuffs and intervening bedded tuffs	Includes altered older ash-flow tuff units and Tunnel beds 1 and 2. Welding in the older ash flow units may increase overall hydraulic conductivity. Devitrification of the ash-flow units may have limited zeolitization. Differentiated in the Yucca Flat basin.
Argillic tuff confining unit (ATCU)	TCU	Argillic bedded tuff, minor paleocolluvium	Includes the argillic, lowermost Tertiary volcanic units and paleocolluvium that immediately overlie the pre-Tertiary rocks. Differentiated in the Yucca flat basin.
Volcaniclastic confining unit (VCU)	80% AA 20% TCU	Sandy gravel, siltstone, tuffaceous sandstone	Older Tertiary-age sedimentary rocks. Similar to the AA, but name retained to correlate with the Frenchman Flat model in the area of overlap in southeastern Yucca Flat.

Table 1-1
Descriptions of Major HSUs in the Model Domain
(Page 3 of 3)

HSU	Dominant Hydrogeologic Unit(s)	Typical Lithologies	Hydrologic Significance
Lower clastic confining unit thrust plate (LCCU1 and LCCU2)	Clastic confining unit (CCU)	Quartzite and siltstone	Includes Proterozoic through lower Cambrian units that have been thrust over younger units.
Lower carbonate aquifer thrust plate (LCA3)	Carbonate aquifer (CA)	Limestone and dolomite	Typically includes the Cambrian through Devonian units that have been thrust over the Eleana formation and the Chainman shale.
Upper carbonate aquifer (UCA)	CA	Limestone	Includes the Tippipah Limestone, which stratigraphically overlies the Chainman shale at Syncline Ridge, and thus may contain perched water.
Upper clastic confining unit (UCCU)	CCU	Argillite and quartzite	As much as 2,745 m (9,000 ft) thick. Typically forms foot walls of thrust faults in NNSS region. Limited areal extent in western Yucca Flat.
Lower carbonate aquifer (LCA)	CA	Dolomite and limestone	Important regional aquifer underlying most of southern Nevada. Composite thickness up to 4,430 m (14,500 ft). Transmissivity values are dependent on fracture and fault frequency.
Lower clastic confining unit (LCCU)	CCU	Quartzite and siltstone	Significant regional confining unit. Composite thickness about 2,870 m (9,400 ft). May present barrier to deep regional groundwater flow where structurally high (e.g., northeastern Yucca Flat).
Mesozoic granite confining unit (MGCU)	Granite confining unit (GCU)	Granodiorite and quartz monzonite	Climax and Gold Meadows stocks. A confining unit of very low permeability that contributes to a hydrologic barrier at the north end of Yucca Flat.

Source: Modified from BN, 2006

where they have been significantly thinned or removed altogether by faulting. Most of the unsaturated zone is composed of the sands and gravels of the alluvial aquifer (AA) that were deposited on coalescing alluvial fans by sheet-flow and debris-flow processes, and locally, as eolian sands. In the deeper southern part of the basin, fine-grained clay, silt, and carbonate sediments form the playa confining unit (PCUT).

A three-dimensional HFM for the Yucca Flat/Climax Mine CAU was completed in 2005 and is documented in BN (2006). A diverse set of geological and geophysical data collected over the past 50 years was used to develop a structural model and hydrostratigraphic system for the basin. The

primary objective of the hydrostratigraphic modeling effort was to produce a three-dimensional framework that depicts the geometric relationships of HSUs and structural features in the CAU model area. This also included development of alternative HFMs to account for some of the nonunique geophysical interpretations.

A map of the HSUs at the water table is shown in Figure 1-9. Corresponding west–east and north–south cross sections through the HFM are illustrated in Figures 1-10a and b, respectively. The map and cross sections show that the water table is in carbonate rocks (LCA, LCA3, or UCA) or clastic confining units (LCCU or UCCU) throughout much of Yucca Flat, with saturated volcanic rocks and alluvium occurring primarily in the deepest parts of the basin east of the Carpetbag-Topgallant fault system. Small additional areas with saturated volcanic rock and alluvium exist in the western part of the Yucca Flat basin and in the southwest corner of the model domain in the CP basin, but these are not hydraulically connected with the saturated tuffs and alluvium in the eastern part of the Yucca Flat basin. The profiles shown in Figures 1-10a and b illustrate the relationships between the HSUs and structures in various vertical planes.

As discussed in Fenelon et al. (2010), depending on their extent and degree of interconnection, the aquifers in the vicinity of the Yucca Flat/Climax Mine CAU can form either regional or local flow systems. Interconnected aquifer systems can make up regional flow systems in which groundwater moves almost freely over long distances. Poorly connected, less extensive aquifers make up semi-isolated local flow systems that can provide a source of diffuse leakage or local drainage to an underlying regional flow system. Diffuse leakage occurs at a low rate over a widespread area and is generally associated with leakage across an intervening confining unit. Local drainage occurs at a higher rate over a limited area and is generally associated with flow through permeable fault zones.

Within the Yucca Flat/Climax Mine CAU, the Cenozoic alluvial and volcanic aquifers have been grouped into a local groundwater flow system (termed the alluvial/volcanic aquifer system by Fenelon et al., 2010) whose flow is constrained to the Yucca Flat basin; the only regional groundwater flow system in the CAU is in the deeper LCA (Fenelon et al., 2010; Fenelon et al., 2012). Recharge to the alluvial/volcanic aquifer system is generally limited to local inflow from deep percolation through the unsaturated zone with little opportunity for lateral inflow or outflow due to the restricted nature of these saturated units in the basin. The general flow direction in the alluvial/volcanic aquifer system is illustrated in Figure 1-11. The complex flow patterns estimated from pre-development hydraulic

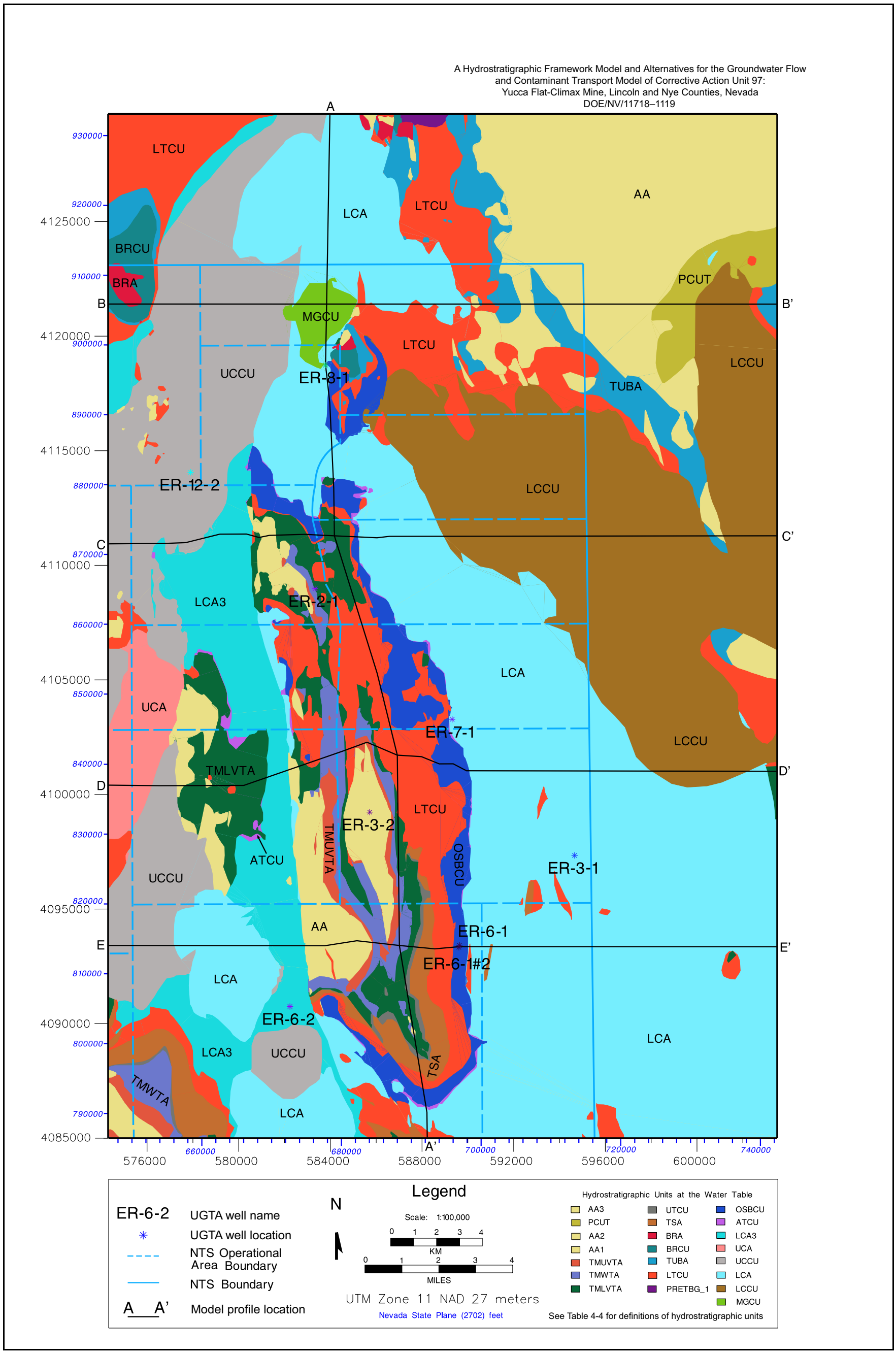

Figure 1-9
Distribution of HSUs at the Water Table for the Yucca Flat/Climax Mine CAU Model Area
Source: BN, 2006

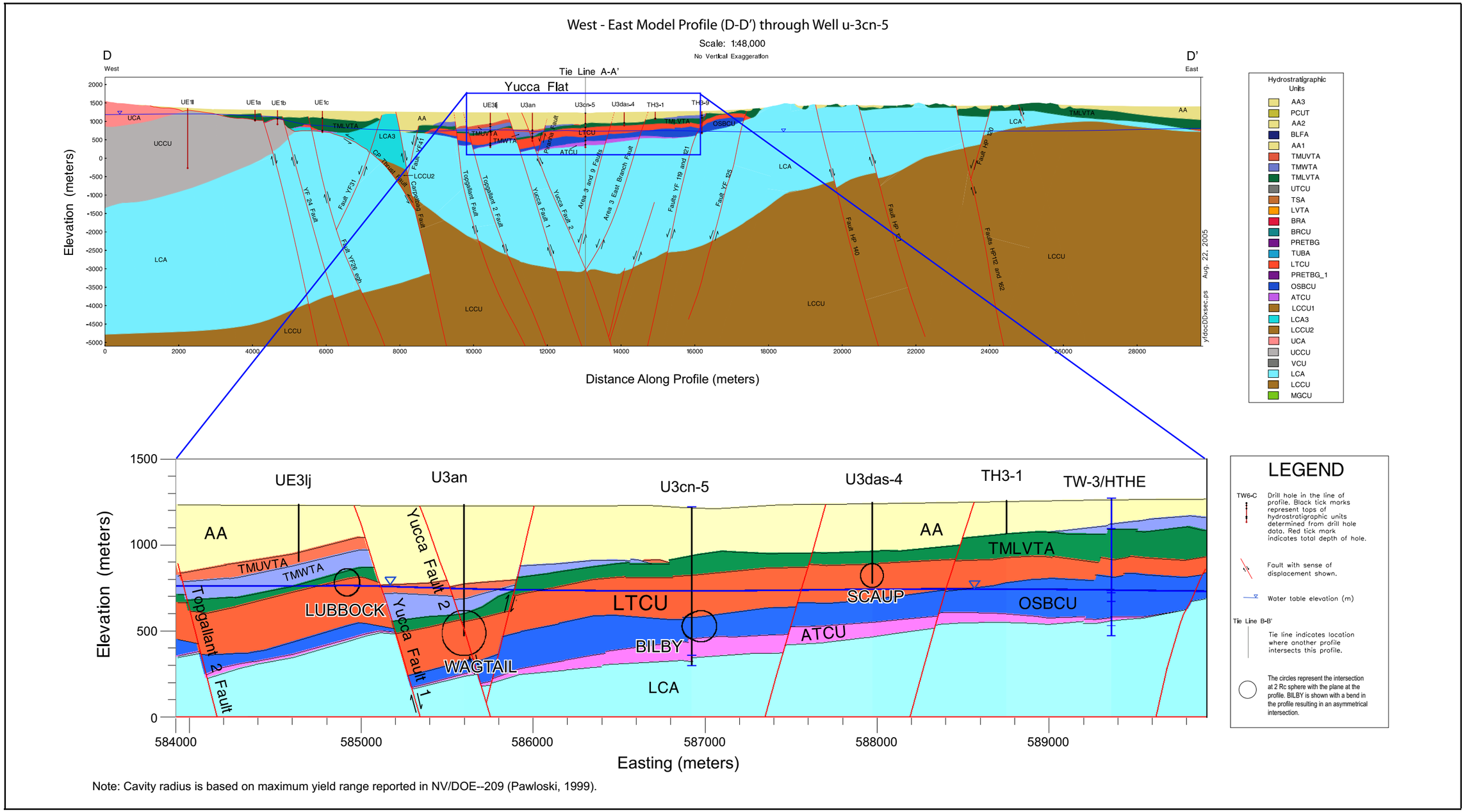

Note: Cavity radius is based on maximum yield range reported in NV/DOE--209 (Pawloski, 1999).

Figure 1-10a
West–East Profile of HSUs for the Yucca Flat/Climax Mine CAU Model Area
Source: Modified from BN, 2006, and SNJV, 2006b

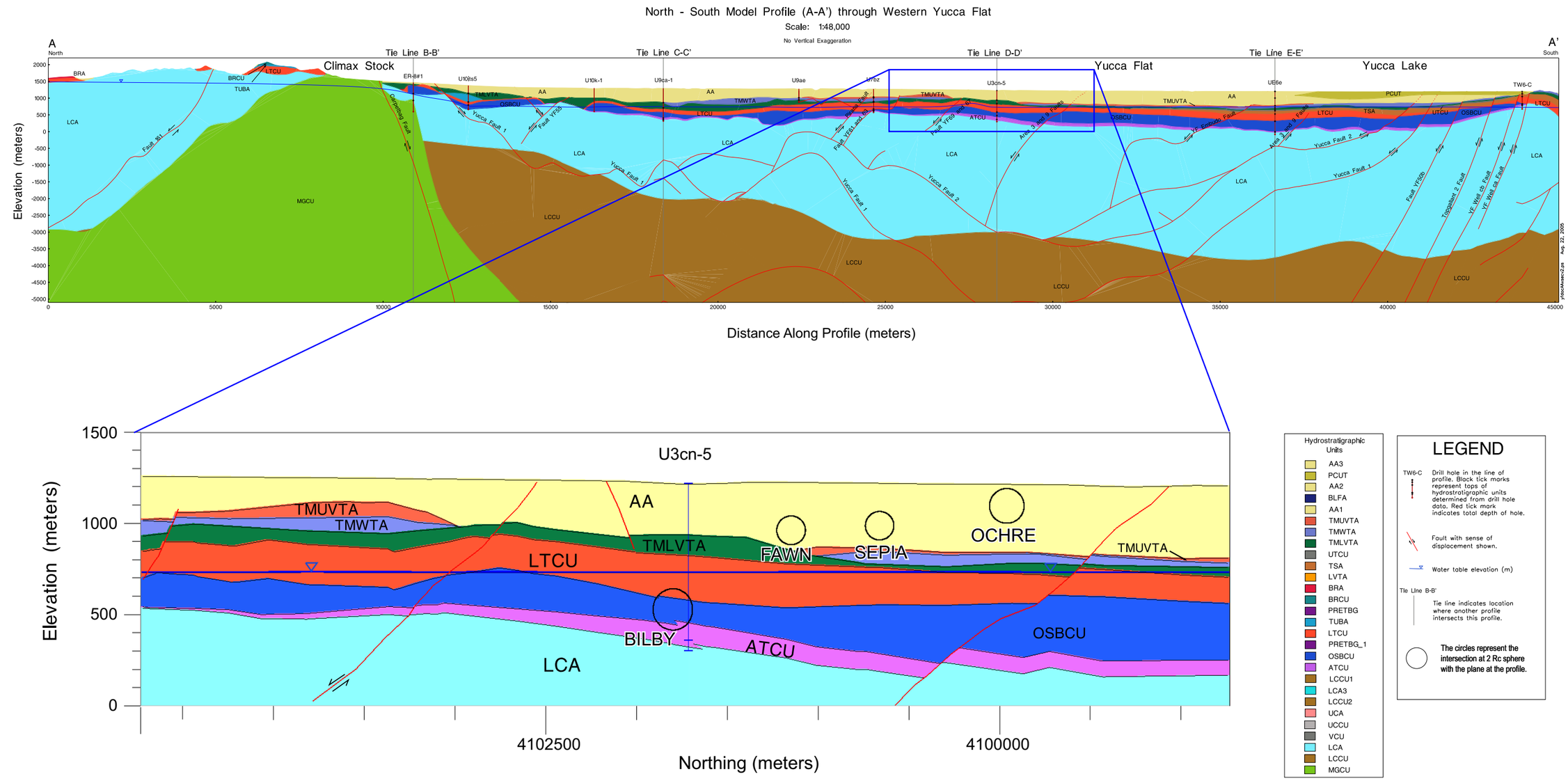

Note: Cavity radius is based on maximum yield range reported in NV/DOE--209 (Pawloski, 1999).

Figure 1-10b
North–South Profile of HSUs for the Yucca Flat/Climax Mine CAU Model Area
Source: Modified from BN, 2006, and SNJV, 2006b

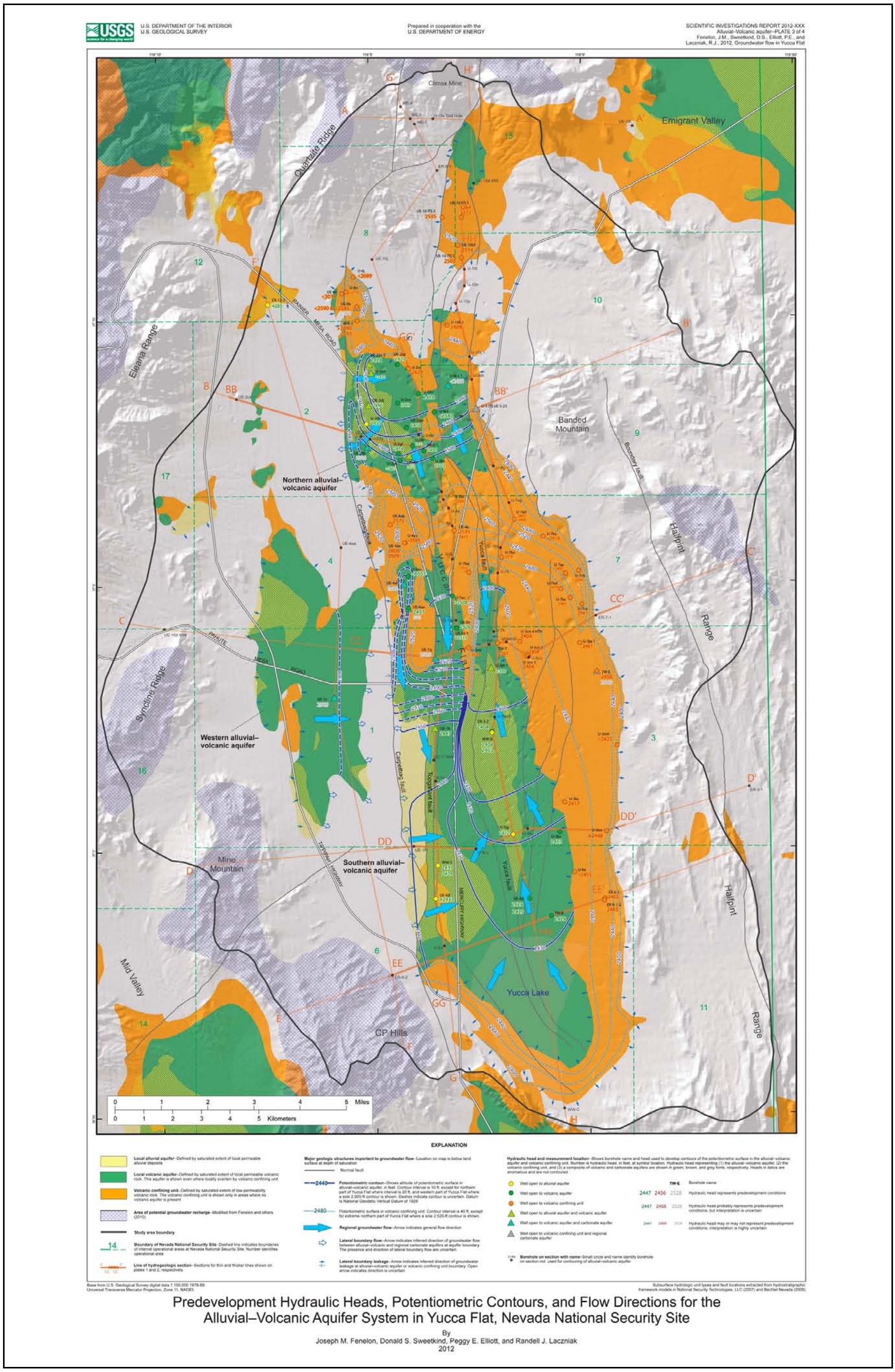

Figure 1-11
General Groundwater Flow Paths in the Alluvial/Volcanic Aquifer System in Yucca Flat
Source: Fenelon et al., 2012

heads by Fenelon et al. (2012) in Figure 1-11 are based on the compartmentalization of the tuff aquifers by the water table and by confining units juxtaposed along faults.

The LCA is a regionally extensive aquifer. In central Yucca Flat, the LCA is bound to the northeast by the LCCU, to the northwest by the UCCU, and to the north by the juxtaposition of the UCCU, MGCU, and LCCU (Figure 1-9). These confining units significantly restrict the possible inflow of groundwater into the LCA as illustrated in Figures 1-12 and 1-13, which present, respectively, interpretations of the potentiometric surface in the LCA from a regional perspective and general flow directions in the LCA from a Yucca Flat perspective. Although Figure 1-12 was developed almost 40 years ago by Winograd and Thordarson (1975), it still captures the regional potentiometric surface of the LCA and has not been significantly modified by information developed in the intervening decades.

As illustrated in Figure 1-12, the basin-scale groundwater flow system in the LCA in the vicinity of Yucca Flat is controlled to a large extent by the distribution of the clastic confining units to the east-northeast and west of the Yucca Flat basin proper. These units, in combination with the granitic confining unit to the north of Yucca Flat, restrict the lateral inflow of groundwater along these boundaries into Yucca Flat (Fenelon et al., 2010). Inflow into the basin is limited by the ridges of the low-permeability UCCU along the western and northwestern boundary, the MGCU along the northern boundary, and the LCCU along the northeastern boundary. The presence of these confining units has significantly disrupted the continuity between the LCA within Yucca Flat and LCA outside the basin. This is evident from the large hydraulic gradients that have been measured across at least some of these confining units. Winograd and Thordarson (1975) calculate gradients in the LCA across the LCCU between Emigrant Valley and northeast Yucca Flat of up to 246 m/km and across the UCCU in northwest Yucca Flat of 62 m/km. In contrast, based on data in Fenelon (2005), the average hydraulic gradient in the LCA within Yucca Flat over the 30-km distance between UE-10j and WW-C-1 is about 0.3 m/km. The UCCU and LCCU impede flow into the basin through these areas. Laczniak et al. (1996) and Winograd and Thordarson (1975) point out, however, the LCA proper beneath the UCCU and the LCA3 thrust plate in western Yucca Flat could allow more inflow into Yucca Flat from the west, although they also note that recharge into the LCA west of the basin may be limited by low-permeability confining units (the UCCU and TCU) that overlie it.

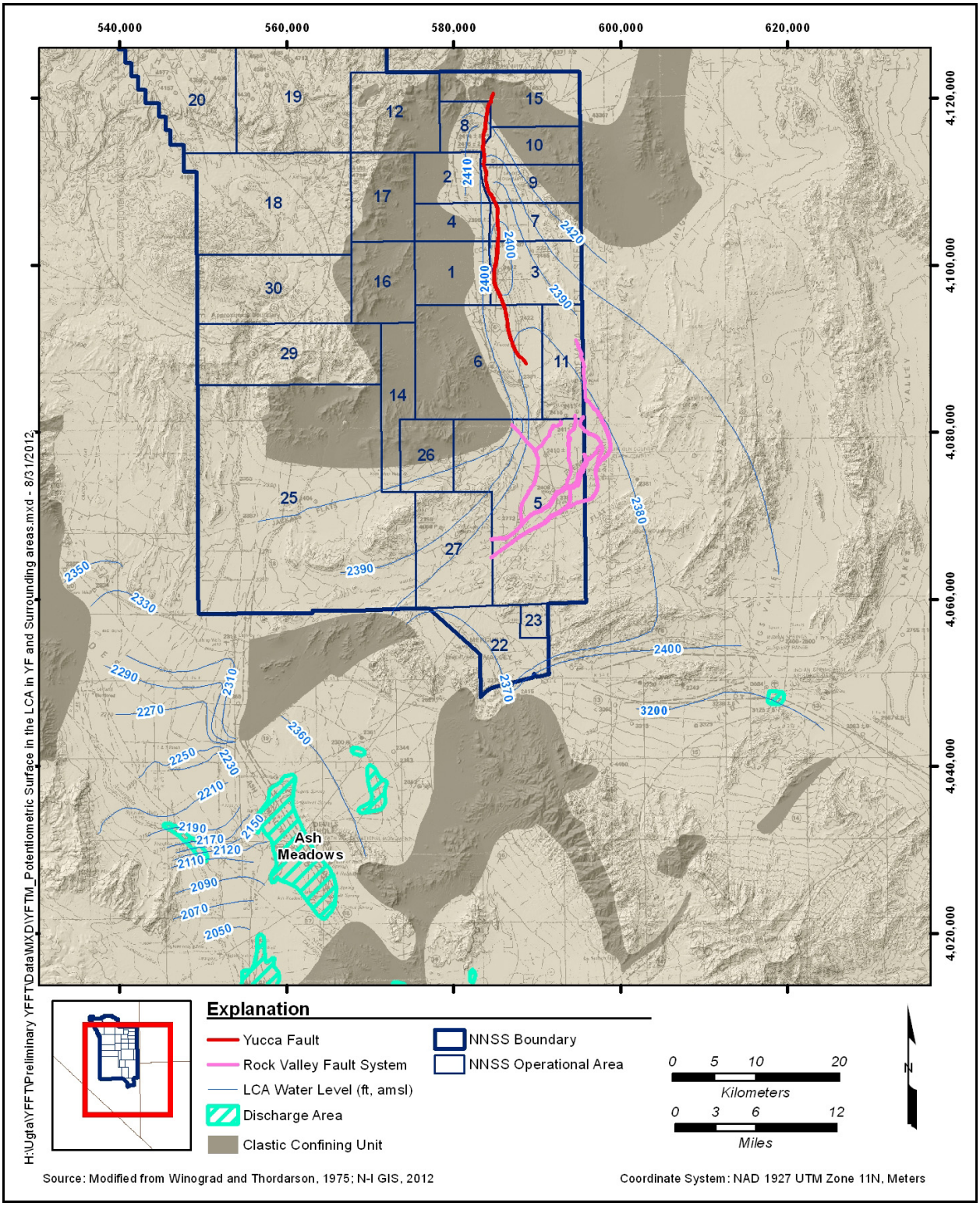

Figure 1-12
Potentiometric Surface in the LCA in Yucca Flat and Surrounding Areas, Including Ash Meadows

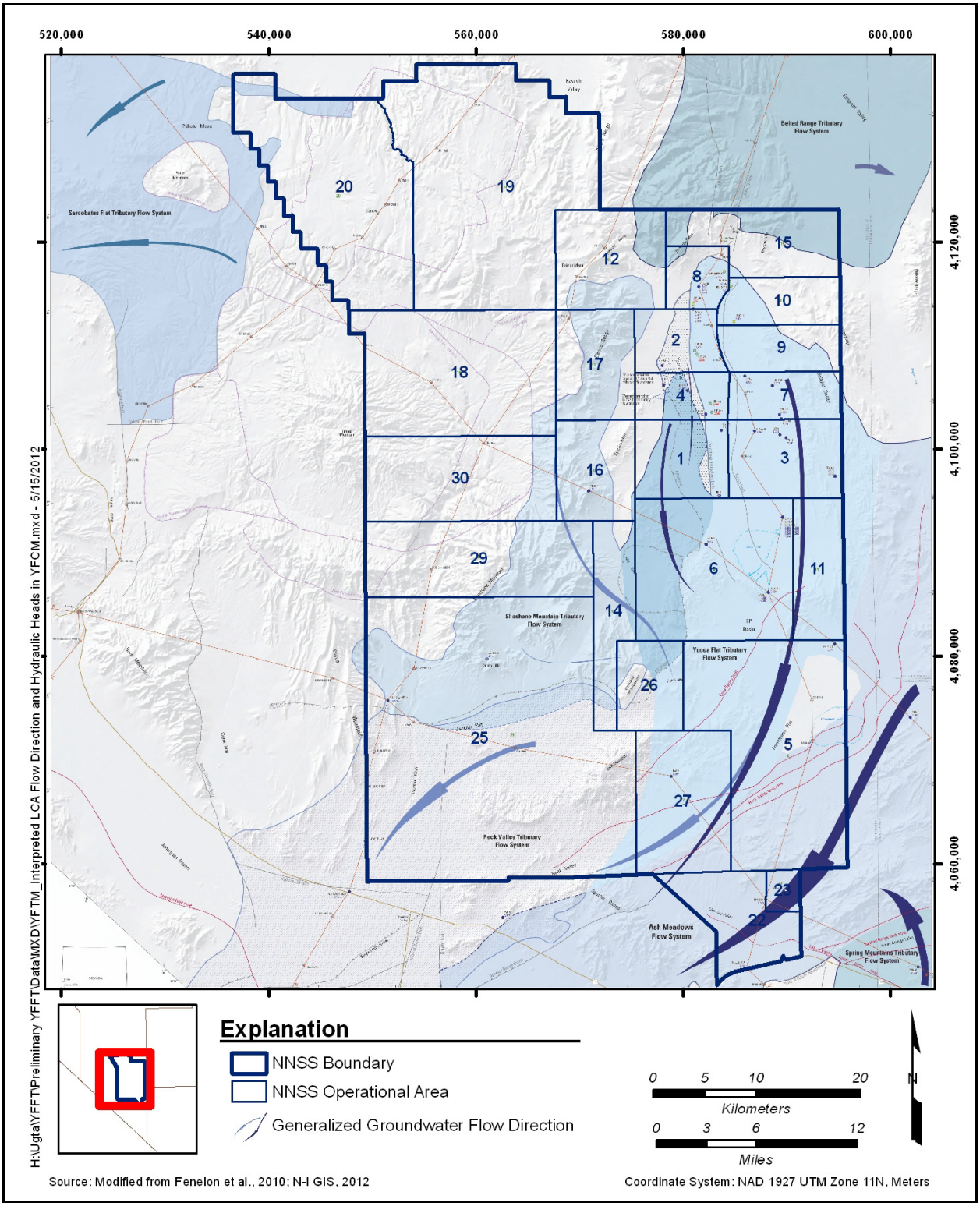

Figure 1-13
Interpreted LCA Flow Directions in the
Yucca Flat/Climax Mine CAU and Vicinity

Groundwater flowing beneath the NNSS in general and the Yucca Flat/Climax Mine CAU originates as precipitation falling in highland areas. In the vicinity of the Yucca Flat/Climax Mine CAU, water recharges the groundwater flow system locally in highland areas, such as Rainier Mesa and Shoshone Mountain, and along the Belted Range. The other major source of recharge is precipitation falling on upland and mountainous areas north and east of the study area in central Nevada. As noted by Fenelon et al. (2010), recharge occurs as some of the precipitation falling on these highland areas collects in surface fractures and openings, and infiltrates downward by way of interconnected fractures or through the rock matrix to depths beyond the influence of active evaporation and transpiration.

Recent studies of infiltration in thick alluvial basins such as Yucca Flat have concluded that present-day net infiltration past the root zone of desert vegetation may be zero or negative, although drainage of water that infiltrated during past pluvial periods that ended 10 thousand years before present (ka) continues to recharge the water table at several tenths of a millimeter per year (mm/yr) (Walvoord, Phillips, et al., 2002; Walvoord et al., 2004; Kwicklis et al., 2006). Infiltration maps presented in SNJV (2006a) generally reflect these conclusions, with more significant present-day infiltration restricted to the bordering bedrock hills and the margins of the basin. Therefore, there is a limited amount of flux moving downward to the water table beneath the testing areas in much of Yucca Flat.

Recharge to the groundwater domain in the Yucca Flat basin, whether due to local infiltration or infiltration in highland areas around the basin, flows into the underlying HSUs at the water table. Along the margins of the basin, the water table is in the LCA or LCA3. As one traverses toward the center of the basin, the water table transitions from being in the tuff confining units to the volcanic aquifer units to the alluvial aquifer. The LCA is a regionally extensive aquifer that extends from north of Yucca Flat to the discharge in Ash Meadows, whereas the alluvial/volcanic aquifer system is a local flow system that allows no lateral drainage out of the Yucca Flat basin proper.

The water levels in the deep, regionally extensive LCA are very flat with generally a southerly gradient, although there is a tendency for lateral flow toward the center of the basin. The water levels in the overlying saturated alluvial and volcanics aquifer units are higher than the potentiometric surface in the LCA; therefore, there is a downward gradient from the alluvial and tuff aquifer units across the tuff confining units to the LCA. The potentiometric difference between the saturated

volcanic aquifer units and the underlying LCA is even more pronounced in the central portion of the basin, where water levels in the confining units may be locally higher because of compaction, subsidence, or pressurization effects associated with underground nuclear testing. The potentiometric difference is maintained because of the low permeability of the thick, extensive zeolitic tuff confining units that are present between the tuff aquifer units and the LCA.

Researchers as far back as Winograd and Thordarson (1975) and continuing through Fenelon et al. (2012) have postulated that higher heads in the tuffs relative to the LCA could be due to the slow, continued drainage of water that infiltrated at the end of the last pluvial period 9,000 years ago through the low-permeability confining units (especially the ATCU) that separate the tuff aquifers from the LCA. Detailed fracture studies of over 1.8 km of core from four boreholes in Area 7 reported by Prothro (2005) have indicated sparse fracturing in the tuff confining units, with intervals spanning hundreds of feet over which no open fractures can be identified. Therefore, despite the local presence of fractures, the large-scale fracture permeability in the tuff confining units away from fault zones is low.

Percolation through the vadose zone, whether through the thick alluvium or the unsaturated tuffs, is downward and may be concentrated along major fault discontinuities in the center of the basin. That is, the downward migration of percolating groundwater may intersect tuff confining units, resulting in semiperched conditions and lateral flow downdip to major structural drains.

Because of the deep, relatively flat water table in the volcanic aquifer units and the general basin-like structural contours on the top of the tuff aquifer and confining units, the groundwater flow system within the tuff aquifer units is isolated in the Yucca Flat basin. That is, there is no lateral flow from the tuff aquifer units to outside the Yucca Flat basin, and all groundwater in the tuff aquifer units flows downward to the LCA. This conceptual model is depicted by the limited extent of the groundwater flow system illustrated in Figure 1-11. The LCA acts as the regional drain for all lateral inflow and vertical recharge in the Yucca Flat basin, as illustrated in Figure 1-12. Figure 1-13 shows that the discharge from the LCA occurs to the south-southwest along the trend of the Cane Spring and Rock Valley fault systems.

An analysis was done to estimate flow directions, mixing relationships, and groundwater velocities in Yucca Flat using naturally occurring geochemical and isotopic tracers (SNJV, 2006a). Although flow directions and mixing ratios were often nonunique, the study concluded that (1) inflow into the basin

could be limited because shallow LCA groundwater compositions even in northern Yucca Flat appeared to be dominated by local recharge, (2) a volcanic aquifer geochemical signature near major faults was indicative of possibly local leakage to the LCA along the faults, and (3) groundwater velocity estimated from carbon-14 (^{14}C) in the LCA is generally slow (on the order of 2 meters per year [m/yr]), except between Wells ER-3-1 and WW-C-1, where the greater depth of the LCCU allows hydraulic communication in the southeastern part of the HFM area.

In summary, the hydrostratigraphy and other structural features of Yucca Flat provide unique, separate, and distinct settings for groundwater flow and contaminant transport. The vast majority of the Yucca Flat area consists of Holocene alluvial material and associated playa deposits that are very thick (up to several hundred meters) in the center of the basin and thin along the basin margins. Underlying the alluvial materials is a thick sequence of Tertiary volcanic tuffs, both vitric- and welded-tuff aquifers that are underlain by an extensive zeolitic tuff confining units. Because the Yucca Flat basin is an extensional basin, these volcanic units have been down dropped in the center of the basin and eroded along the basin margins. Underlying the tuff confining units in the center of the basin is the regionally extensive Paleozoic LCA. Along the basin margins, the LCA (or the associated thrust plate, the LCA3, in the western portion of the basin) outcrops at the surface, especially in the Half Pint Range to the northeast of Yucca Flat, and Mine Mountain and CP Hills to the southwest. The extensional basin has resulted in numerous north–south trending normal faults, many with offsets of more than 60 m and several with north–south extensions of more than 10 km. These normal faults intersect the tuff aquifer and confining units and extend into the LCA.

1.5 Yucca Flat Background Information—Underground Nuclear Testing

Of the 878 CASs in the UGTA CAUs, 720 CASs are in the Yucca Flat/Climax Mine CAU. These 720 CASs consist of 747 underground nuclear detonations, inclusive of multiple detonations conducted in several holes. Of the total unclassified ^{3}H radionuclide activity (which dominates the total activity) decay corrected to September 23, 1992, presented in Bowen et al. (2001), about 39 percent is within the Yucca Flat/Climax Mine CAU. The history of nuclear testing in Yucca Flat and other areas of the NNSS is described in DOE/NV (2000b).

Subsurface testing in Yucca Flat began with the PASCAL-A detonation on July 26, 1957, and ended with the DIVIDER detonation on September 23, 1992. A total of 744 underground nuclear detonations were conducted in Yucca Flat proper. The explosive energy of each detonation, referred

to as the yield of the explosion, is often expressed in terms of the amount (mass, in metric tons) of trinitrotoluene (TNT) with an equivalent explosive yield. Unless a specific yield has been announced, most detonations have a reported range of yield values reported for national security reasons. As explained in Section 2.0, the estimated cavity size and the fraction of the total radionuclide inventory associated with each detonation is calculated using the maximum announced yield of the detonation and the equations in Pawloski (1999) or Boardman (1970). The underground detonations conducted in Yucca Flat range in yield from 0 to 500 kilotons (kt). The sum of the maximum announced yields for all subsurface detonations conducted at the Yucca Flat/Climax Mine CAU is 39,051 kt.

In addition to the 744 underground detonations in Yucca Flat proper, 3 detonations, with a total maximum announced yield of 87.7 kt, were conducted in tunnels in the Climax stock just north of Yucca Flat (PILE DRIVER, 62 kt; HARD HAT, 5.7 kt; and TINY TOT, less than 20 kt). These tunnel detonations are considered in the combined Yucca Flat/Climax Mine CAU flow and transport model. As discussed in Section 6.0, however, the contribution of the Climax Mine detonations to the overall contaminant flux into the Yucca Flat aquifers is minimal.

The underground nuclear detonations in Yucca Flat can be subdivided in terms of their working-point locations relative to the location of the regional water table. Bowen et al. (2001) subdivide the Yucca Flat detonations into those detonations whose working-point depths are more than 100 m above the water table and those detonations whose working-point depths are below that level. The 744 detonations in Yucca Flat range in depth of burial from 57.9 to 782.4 m below ground surface. Of these, 577 were detonated 100 m or more above the water table (as defined by Bowen et al., 2001), and 668 had working points above the water table (assuming the same water-table elevation as used in Bowen et al., 2001). Likewise, Pawloski et al. (2008) categorize detonations with working points greater than 100 m above the water table as “unsaturated” and detonations with working points below that level as “saturated.” The categorization of detonations presented in the unclassified source term report for the Yucca Flat/Climax Mine CAU (SNJV, 2009b) conforms to the assumptions used in the CAU modeling study, namely, that detonations with working points above the water table are categorized as unsaturated-zone detonations and that detonations with working points below the water table are categorized as saturated-zone detonations. Therefore, detonation categories from SNJV (2009b) are presented in this report, and the discussion of unsaturated-zone or saturated-zone detonations refers to the location of the detonation being above or below the water table.

Figure 1-14 shows the locations of underground nuclear detonations within the Yucca Flat/Climax Mine CAU and their relationship to the regional water-table surface. The red circles represent detonations with working points above the water table, and the blue circles represent detonations with working points below the water table. The diameters of the circles are drawn to equal two times the yield-dependent cavity diameters based on the relationship presented in Pawloski (1999). Figure 1-15 provides a similar perspective but with the diameter determined by the fraction of total inventory from Bowen et al. (2001) ascribed to each detonation based on the maximum yield of each detonation.

The 747 underground nuclear detonations conducted in the Yucca Flat/Climax Mine CAU have working points in the unsaturated alluvial or tuff units, the saturated alluvial or volcanic units (principally the tuff confining units), the unsaturated LCA, or the Climax Mine granitic stock. Most of the detonations (668 in Yucca Flat proper) have working points in the unsaturated zone (i.e., above the water table), and most of these (413) were expended in the unsaturated alluvium. The detonations with working points in the unsaturated zone include the four detonations with working points in unsaturated carbonate rocks (three in the LCA and one in the LCA3). The remainder of the detonations (76 in Yucca Flat proper) have working points in the saturated zone (i.e., below the water table). Most of these detonations (62) have working points in the tuff confining units, including the LTCU, the OSBCU and the ATCU. The three detonations conducted in the Climax stock have working points in the MGCU. The details of the detonation categorization are presented in Section 2.1.

Based on the unique hydrogeologic environments for the different detonation categories in the Yucca Flat/Climax Mine CAU, it is possible to identify the most significant processes that likely affect the release and transport of radionuclide contaminants. The most significant processes in the near field have been identified in the three HST reports organized by the working-point hydrogeologic conditions, namely, detonations with working points in the unsaturated zone (McNab, 2008), the saturated zone (Tompson, 2008), and carbonate rock (Carle et al., 2008); the Yucca Flat HST introduction and executive summary report (Pawloski et al., 2008); and the unclassified source term report (SNJV, 2009b). These documents provide a basis for determining the processes that potentially could affect the calculated contaminant release from the sources and the subsequent contaminant transport through the unsaturated and saturated zones. The determination of such processes is key to

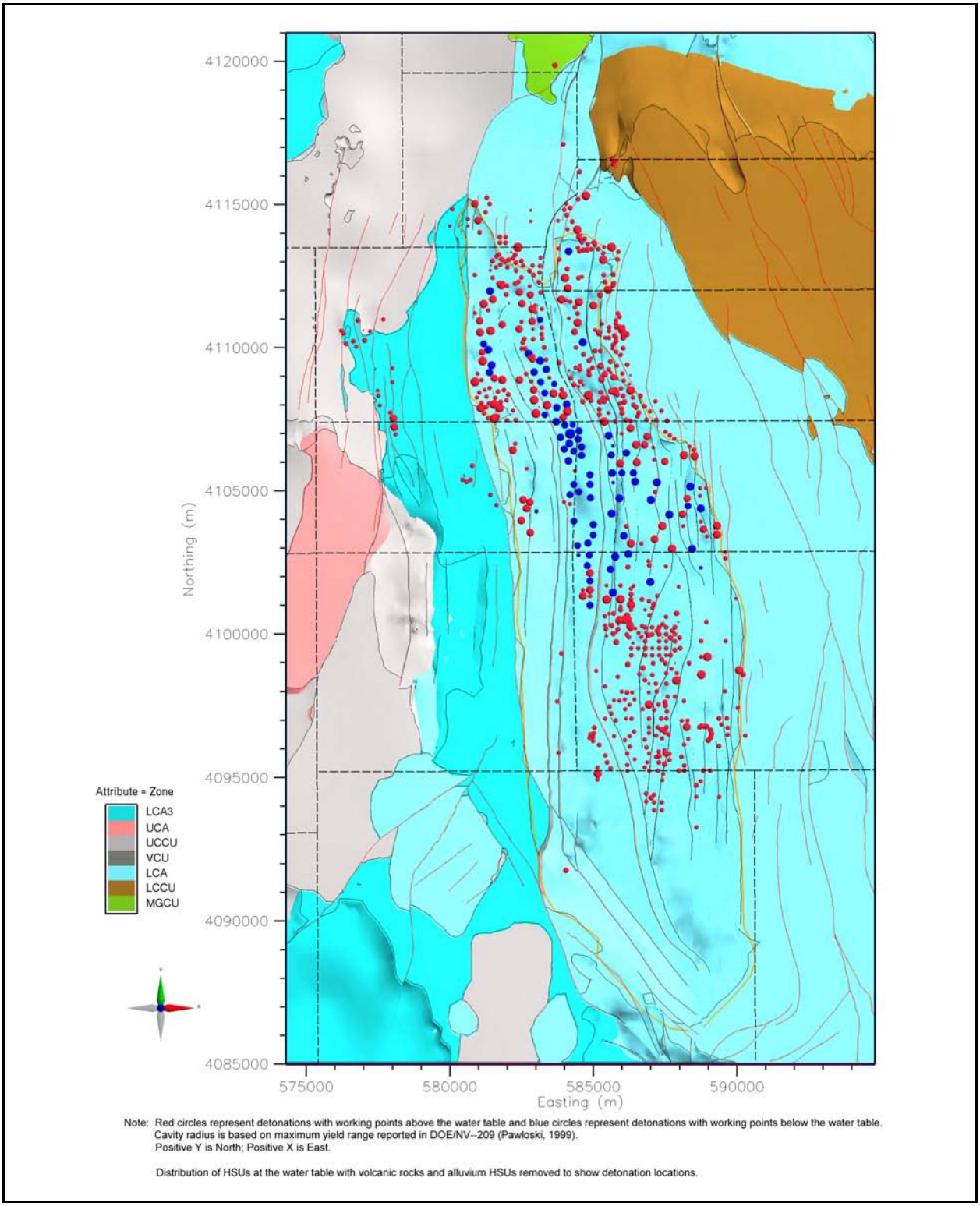

Figure 1-14
Yucca Flat/Climax Mine CAU Underground Nuclear Detonations Ranked by Size of Maximum Yield-Weighted Cavity Size

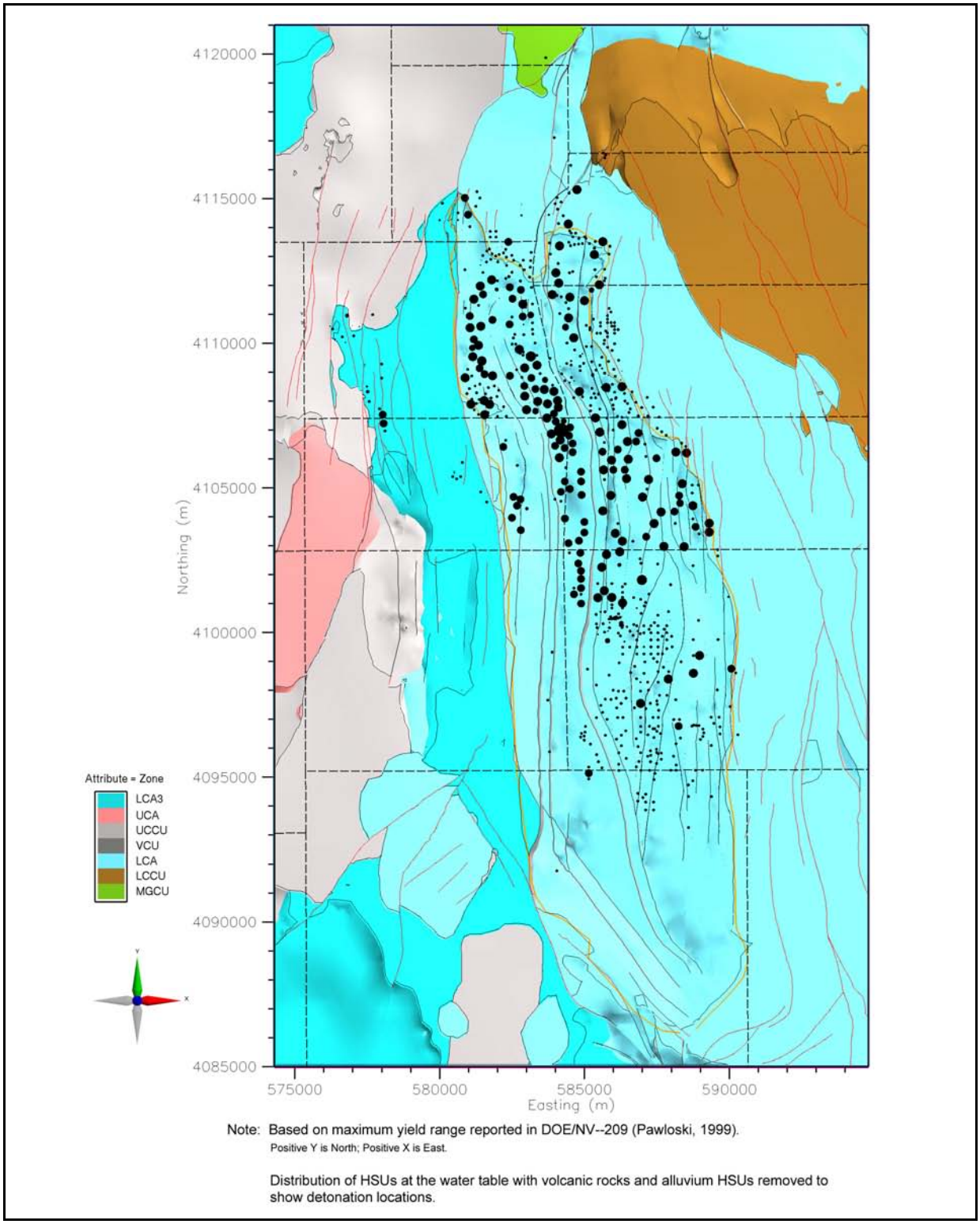

Figure 1-15
Yucca Flat/Climax Mine CAU Underground Nuclear Detonations Ranked by Fraction of Maximum Yield-Weighted Total Initial Inventory

developing contaminant boundaries as required in the UGTA corrective action strategy. The most significant processes are summarized in Section 2.2.2.

Given the groundwater flow conceptual model presented above, contamination that results from detonations expended in the unsaturated zone could be transported downward to the water table via gravity-driven percolation through the vadose zone. Once contaminants that are originally in place in the unsaturated zone enter the saturated alluvial/volcanic aquifer system, they can be transported laterally and downward to the LCA. Contamination that results from detonations expended below the water table can be transported laterally for some distance; however, given the prevalent vertical downward hydraulic gradient, the transport flow paths are oriented downward through the tuff confining units to the underlying LCA. The downward transport may be either by diffuse flow through the tuff confining units or concentrated in the subvertical normal faults that cut the tuff confining units. Ultimately, the contaminants released from detonations with working points in the unsaturated and saturated zones are transported to the regionally extensive LCA, where transport is generally laterally to the south. Because of the unique hydrogeologic conditions in the Yucca Flat basin, notably that groundwater flow and any associated contaminant transport in the saturated alluvial/volcanic aquifer system would either be confined to the Yucca Flat basin or migrate downward into the LCA, the most significant component of the contaminant boundary at Yucca Flat is associated with contaminant migration in the LCA.

An important characteristic of underground nuclear detonations is the exchange volume. The exchange volume is defined as the volume of rock that encompasses the immediate extent of non-melt-glass radioactive contamination following an underground nuclear detonation. The exchange volume is conceptualized as a spherical region centered around the detonation working point. The radius of this sphere is generally considered as a multiple of the radius of the detonation cavity (R_c), which in turn is a function of the yield of the detonation, the depth of burial (distance from the ground surface to the working point), and the bulk density of the geologic media above the working point. The basis for this conceptual model and the use of the exchange volume to assign the initial inventory following the detonation are described in Section 2.0 and Appendix C.

The key processes affecting contaminant migration from the unsaturated-zone working-point detonations to the water table include the percolation flux through the unsaturated zone, which in turn is affected by the ambient net infiltration rate and by the likelihood and magnitude of enhanced crater

recharge under those detonations with craters. Preliminary analyses indicate that the detonations with exchange volumes close to or intersecting the water table are most likely to have significant transport to the saturated zone during the next 1,000 years. This is as expected given the short transport distances and corresponding short transit times for those detonations near the water table. Of the 668 Yucca Flat detonations with working points in the unsaturated zone, 13 percent (90) are within 2 R_c of the water table. The above percentages are regardless of whether the water table is in the alluvial/volcanic aquifer system or the LCA. The detonations that are most likely to produce significant contaminant sources are those that are likely to breach the water table in the LCA. Because of the particular importance of the LCA groundwater flow and contaminant transport pathways, it is relevant to note that there are 2 unsaturated-zone working-point detonations within 1 R_c of the saturated LCA (BOURBON and TORRIDO), 7 unsaturated-zone working-point detonations within 2 R_c of the saturated LCA (BOURBON, COTTAGE, KLICKITAT, MICKEY, MUNDO, SHUFFLE, and TORRIDO), and 23 unsaturated-zone working-point detonations within 3 R_c of the saturated LCA.

Contaminant transport from the unsaturated-zone working-point detonations to the water table is also likely to be affected by the effective transport porosity and retardation of the radionuclides. More sorbing radionuclides are generally retained in the porous alluvial materials in the unsaturated zone.

The key processes affecting contaminant migration away from the saturated-zone working-point detonations include the advective flow and transport in the volcanic aquifers, which is generally laterally away from the cavities. Contaminants that are laterally transported within the volcanic aquifers generally intersect faults, which are assumed to provide the principal hydraulic communication with the underlying LCA given the confining nature of the zeolitic tuff units. For some detonations in the saturated tuff confining units, significant overpressures were developed that tend to enhance the gradients away from the detonation cavities, although the flow rates and velocities are generally low because of the low permeability of the confining units. Of the 76 detonations in Yucca Flat proper with working points in the saturated zone, 2 are within 1 R_c of the LCA (CORDUROY and LAMPBLACK), 5 are within 2 R_c of the LCA (CORDUROY, GRAPE A, LAMPBLACK, SHAPER, and STRAIT), and 16 are within 3 R_c of the LCA.

Contaminants enter the LCA because either the volume of initial contamination resulting from the detonation extends into the saturated LCA or contaminant transport occurs from the overlying

unsaturated- or saturated-zone detonations. The key processes affecting contaminants that enter the LCA are flow and transport in the dual-porosity domain of the LCA. The dual-porosity domain allows for advective-dispersive transport in the fracture porosity, and matrix diffusion and sorption in the matrix porosity. The flow and transport are significantly affected by the major north–south-trending normal faults that intersect the LCA.

Table B-1 presents the basic characteristics of the detonations relevant to the Yucca Flat/Climax Mine CAU arranged by the date of the detonation. Table B-1 presents the characteristics of the detonations with respect to the water table and significant HSUs relevant to the Yucca Flat/Climax Mine CAU. Table B-1 is arranged alphabetically by the name of the detonation.

1.6 Flow and Transport Modeling Approach

Radionuclide migration away from subsurface nuclear detonations is affected by multiple physical and chemical processes that depend on either the hydrogeologic system and its properties or the specific properties of the radionuclides. These processes include radioactive decay of the species, advection in both porous and fractured media, diffusion from fracture water into matrix water, sorption onto immobile minerals, sorption onto mobile colloidal minerals, and attachment and detachment of colloids from immobile surfaces. The processes may be modeled differently depending upon the spatial scale of interest and the significance of different processes to the transport of contaminants.

The conceptual model and physical processes of groundwater flow and transport are the framework upon which the numerical transport model is built. The numerical model is the simplified mathematical analog of the spatially distributed processes and properties translated into model space. The model conceptualization refers to the understanding of the processes that define system behavior and the geometric arrangement of these processes in a three-dimensional space. Conceptualization can be understood in the context of the physical processes that are derived from spatial and temporal laboratory and field tests of the physical domain, and the translation of the physical conceptualization to a numerical analog.

The aspects of the Yucca Flat hydrogeologic conceptual model presented in Section 1.4, in combination with the differences in the hydrogeologic conditions within the categories of underground nuclear detonations conducted at Yucca Flat presented in Section 1.5, provide a basis for

the approach to model groundwater flow and contaminant transport within the Yucca Flat/Climax Mine CAU. The different hydrogeologic settings and the resulting different HST environments make it necessary to evaluate different processes at different scales relevant to contaminant transport within the Yucca Flat/Climax Mine CAU. To meet this need, this study has adopted the modeling approach that breaks the CAU into four separate modeling domains, with linkages between the domains to provide water and contaminant flux to the downgradient domain. These four domains are as follows:

- Climax Mine (consisting of 3 detonations)
- Yucca Flat unsaturated zone (consisting of 668 unsaturated-zone working-point detonations, 90 and 7 of which have 2 R_c exchange volumes that extend below the water table in the alluvial/volcanic aquifer system and the LCA, respectively)
- Yucca Flat saturated alluvial/volcanic aquifer system (consisting of 76 saturated-zone working-point detonations, 5 of which have 2 R_c exchange volumes that extend into the saturated LCA)
- Yucca Flat saturated LCA (consisting of both the LCA and the LCA3) (consisting of no detonations within the saturated carbonate aquifers, but 12 detonations with 2 R_c exchange volumes that extend into the saturated LCA)

Breaking the modeling domain into these four separate domains allows the processes that are unique and relevant to the different model domains to be quantified separately, while ensuring that the entire contaminant source is accounted for in the different models. This method is appropriate because there is a one-way coupling of water and mass flux between the model domains as summarized in Table 1-2. For example, the gravitationally dominated flow system in the unsaturated zone results in only downward groundwater flow and contaminant transport to the saturated zone. The saturated zone is in the alluvial/volcanic aquifer system in the center of the basin and in the LCA along the eastern margin of the basin. The limited lateral extent of the saturated alluvial/volcanic aquifer system in the Yucca Flat basin results in generally downward groundwater flow and contaminant transport to the underlying LCA. By assigning the water and contaminant flux calculated from the upgradient model to the downgradient model, it is possible to maintain internally consistent water and contaminant fluxes across the interfaces between the models.

The Climax Mine model (Pohlmann et al., 2007) includes explicit evaluation of the three detonations performed in Climax Mine and calculates the groundwater flow through and around the Climax stock, which is dominated by the flow into the LCA along the southern extent of the Climax Mine model

Table 1-2
Treatment of Water and Contaminant Boundary Fluxes for Yucca Flat/Climax Mine CAU Model Domains

Model Domain	Water Influx Boundary	Water Efflux Boundary	Contaminant Sources (RST)	Contaminant Efflux Boundary
Climax Mine	Steady-state regional-model flux and infiltration	Water flux to LCA in northern Yucca Flat	3 detonations	Contaminant flux to LCA in northern Yucca Flat
Yucca Flat Unsaturated Zone	Steady-state regional-model infiltration rate and transient enhanced crater recharge	Transient percolation flux at bottom of unsaturated zone	668 detonations with working points in the unsaturated zone	Contaminant flux to saturated alluvial/volcanic aquifer system or LCA model (depending on location)
Yucca Flat Saturated Alluvial/Volcanic Aquifer System	Transient percolation flux from unsaturated-zone model	Transient discharge to LCA model, including transient discharge caused by underground detonations conducted in TCU	76 detonations with working points in saturated alluvial/volcanic aquifer system, 90 detonations with working points in the unsaturated zone with 2 R_c RST extending into saturated alluvial/volcanic aquifer system, contaminant flux from unsaturated-zone model	Contaminant flux to LCA model
Yucca Flat Saturated LCA	Steady-state regional-model infiltration rate in areas outside unsaturated-zone model domain, steady-state influx from north from Climax Mine model, transient recharge from unsaturated-zone model, transient recharge from saturated-zone model	Lateral efflux from Yucca Flat basin to south	12 detonations with 2 R_c exchange volume initially in LCA, transient contaminant flux of significant radionuclides from overlying unsaturated-zone and saturated-zone models	N/A. Although contaminants may be transported out of the CAU, the concentrations are below the SDWA MCLs.

N/A = Not applicable
RST = Radiologic source term

domain. The Climax Mine model also calculates the contaminant mass flux into the LCA at the southern boundary of the Climax Mine model domain, which is along the northern boundary of the LCA transport model.

The Yucca Flat unsaturated-zone model (discussed in detail in Section 3.0) includes a dozen three-dimensional flow and transport models that each have about one million nodes to capture the details of the unsaturated-zone portion of the HFM and the HSTs in the vicinity of the

668 unsaturated-zone working-point detonations, with particular focus on the 459 detonations that created surface craters, 100 of which have crater depths of 0 m (Appendix E). This model includes both steady-state infiltration representative of pretesting topography of Yucca Flat and the possibility for focused enhanced recharge that occurs because of the change in the surface water drainage associated with the post-testing craters. The radiologic source term (RST) is the total residual inventory of radionuclides associated with one or more detonations. The RST associated with the portion of the exchange volumes that extend below the water table (either into the saturated alluvial/volcanic aquifer system or the saturated LCA depending on the location of the detonation) is placed in the corresponding underlying saturated-zone model domain. The generally vertical downward flow and transport in the unsaturated-zone domain has a varied amount of lateral flow and transport because of the vertical heterogeneity associated with laterally continuous tuff confining units that are offset by major vertical faults.

The Yucca Flat saturated alluvial/volcanic aquifer system model (discussed in detail in Section 4.0) is a three-dimensional flow and transport model that has about 520,000 nodes to capture the details of the saturated alluvial/volcanic aquifer system portion of the HFM as well as the details of the exchange volumes and test-altered disturbed zones around the 76 detonations with working points below the water table. For simplicity, the RST associated with the portion of the exchange volumes that extend above the water table is placed in the domain of this model. This conservative assumption reduces the complexity of the unsaturated-zone transport model to ensure contaminant transport is not underestimated. The significant transient effects associated with underground nuclear detonations conducted in the tuff confining units, in particular the overpressures created in the Tuff Pile area in the center of Yucca Flat, are considered by the saturated alluvial/volcanic aquifer system model, and conceptual uncertainty is captured by applying different conceptualizations of the near-field disturbed zones in the vicinity of these detonations. Groundwater flow and contaminant transport in the saturated alluvial/volcanic aquifer system is generally lateral within the tuff aquifers and vertical through major faults that intersect the tuff confining units and provide for hydraulic communication with the underlying LCA.

The Yucca Flat saturated LCA flow and transport model (discussed in detail in Sections 5.0 and 6.0) is a three-dimensional flow and transport model that has about 540,000 nodes to capture the details of the spatial distribution of the water and contaminant influx as well as the three-dimensional geometry of the major faults that intersect the LCA. The RST of the 12 detonations that have exchange volumes

that intersect the saturated LCA (assuming a 2 R_c exchange volume radius) is placed in the fractures of the LCA as a semispherical source. Water and contaminant influxes from the Climax Mine area are provided from the Climax Mine model to support the calibration of the LCA flow model and evaluate the significance of contaminant transport from the sources in Climax Mine. Water and contaminant influxes from the overlying unsaturated zone and saturated alluvial/volcanic aquifer system are provided from the unsaturated-zone model and the saturated alluvial/volcanic aquifer system model. Groundwater flow and contaminant transport in the LCA is generally southerly and follows the strike of the major structural discontinuities.

The spatial relationships between the four model domains are illustrated in Figures 1-16 and 1-17. The outer domain of each of these figures depicts the spatial extent of the HFM that is used as a basis for the HSU characterizations in the different flow and transport models. From these figures, it can be observed that the LCA flow and transport model domain extends beyond the lateral boundaries of the unsaturated-zone and saturated alluvial/volcanic aquifer system model domains except in the northern parts of the basin where the unsaturated-zone model domain includes areas of lower-permeability confining units that outcrop at the higher elevations around the basin. These figures also indicate the portion of the saturated LCA flow model domain where the water table is in the LCA along the eastern and southeastern portions of the model domain.

As discussed in Sections 3.0 to 6.0, the three Yucca Flat model domains have developed numerical models to simulate groundwater flow and contaminant transport. These models use numerical meshes that allow greater resolution around areas of particular importance to the conceptual model and likely contaminant transport. For example, the unsaturated-zone model mesh has been refined in the vicinity of cavities and chimneys associated with detonations with working points in the unsaturated zone, the saturated alluvial/volcanic aquifer system model mesh has been refined near cavities and exchange volumes associated with detonations with working points below the water table, and the saturated LCA model mesh has been refined near fault zones for the major faults identified in the HFM.

The numerical models of groundwater flow in the three Yucca Flat model domains have been developed and calibrated to available data with additional information used to support the model results. In the unsaturated-zone groundwater flow model, the calibration has included comparing results to water saturations and potentials, as well as independent lines of evidence including crater recharge rates. In the saturated alluvial/volcanic aquifer system groundwater flow model, the

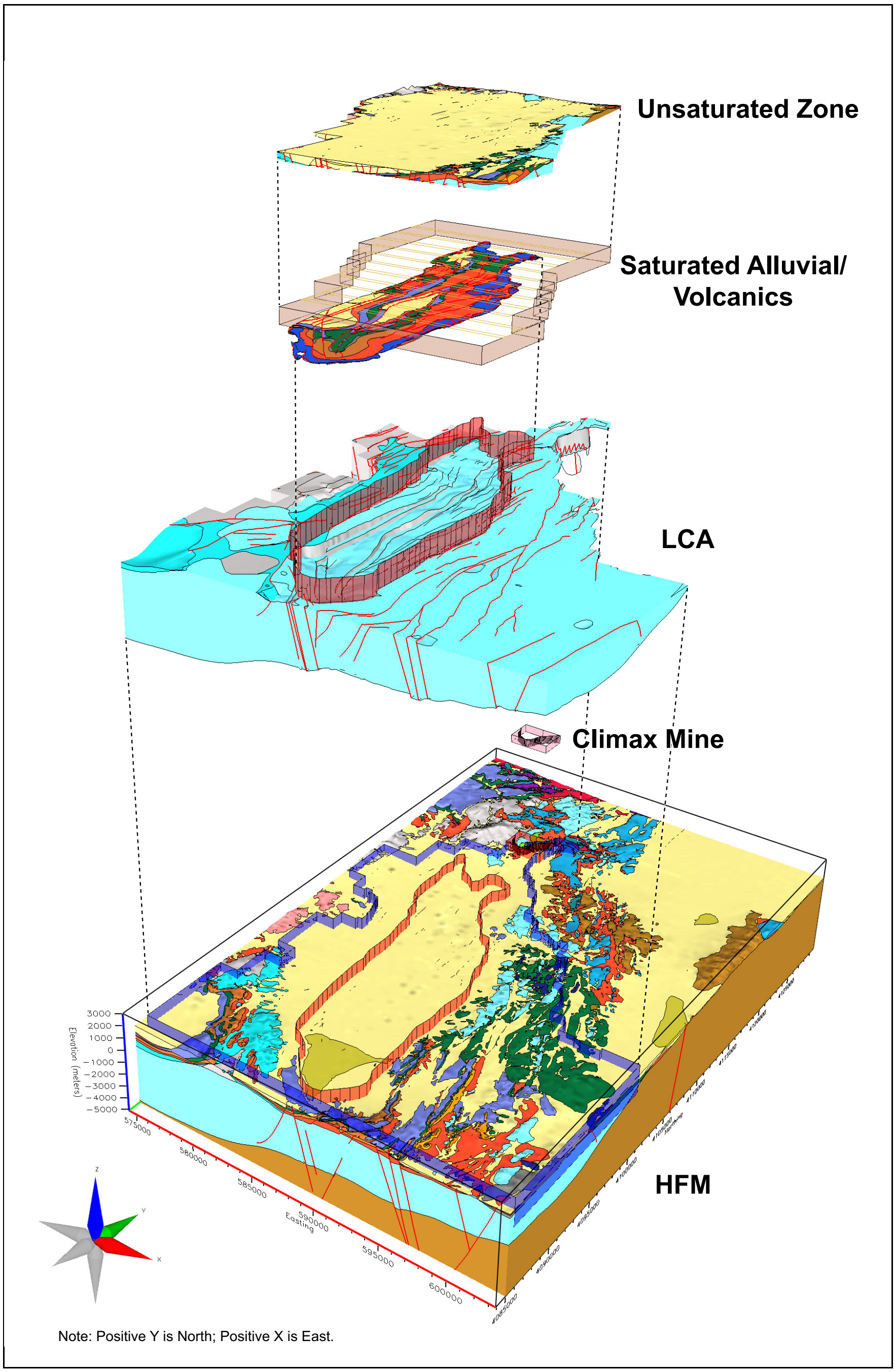

Note: Positive Y is North; Positive X is East.

Figure 1-16
Relationships between the Yucca Flat/Climax Mine CAU Model Domains in Three-Dimensional Perspective

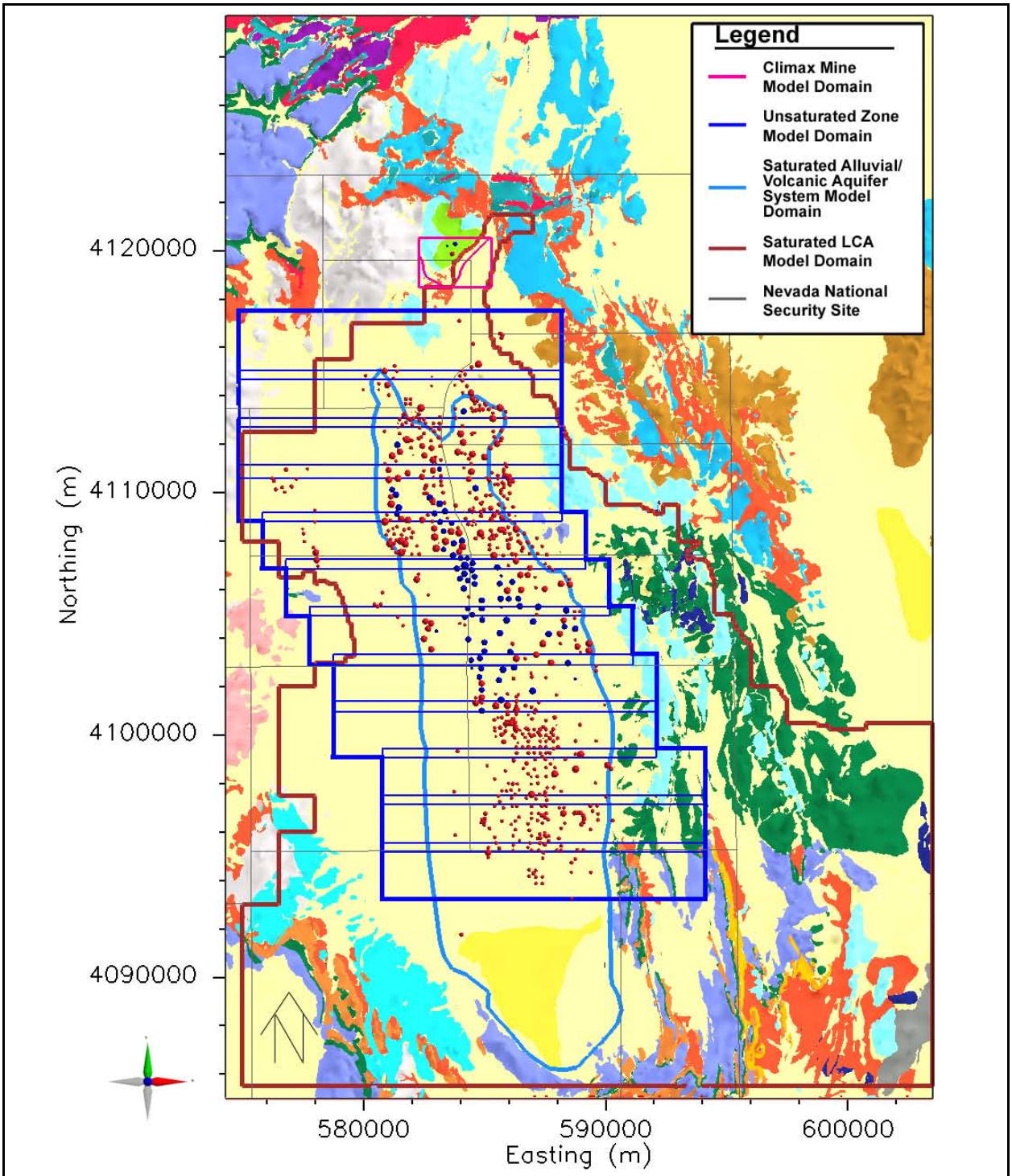

Note: Red circles represent detonations with working points above the water table and blue circles represent detonations with working points below the water table. Positive Y is North; Positive X is East.

Figure 1-17
Lateral Boundaries of the Yucca Flat/Climax Mine CAU Model Domains

calibration has been to steady-state and underground nuclear detonation-induced transient water levels, as well as independent lines of evidence from observed subsidence data. In the saturated LCA groundwater flow model, the calibration has been to steady-state water levels and transient water levels from a large-scale multiple-well aquifer test (MWAT), as well as independent lines of evidence including thermal and geochemical observations. Automated parameter estimation methods have been used to support the calibration of the saturated alluvial/volcanic aquifer system and LCA groundwater flow models.

The results of the numerical models of contaminant transport in the saturated zone have been compared to observed contaminant concentrations where applicable. However, these comparisons have not been used to calibrate the saturated alluvial/volcanic aquifer system and LCA contaminant transport models, given the large spatial domains of the models and the limited domain sampled in the observation wells.

The numerical models of Yucca Flat groundwater flow and contaminant transport have been evaluated using the Finite Element Heat and Mass (FEHM) computer code and related software (Zyvoloski et al., 1997; Painter, 2011; Robinson et al., 2011). The unsaturated-zone model used FEHM to evaluate the transient unsaturated flow, and the tracer data (trac) macro in FEHM that directly solves the advective-dispersive transport equation to evaluate the equivalent porosity transport. The saturated alluvial/volcanic aquifer system model used FEHM to evaluate the transient groundwater flow, and the streamline particle tracking (sptr) subroutine of FEHM to evaluate the advective particle transit times, in combination with the PLUMECALC dual-porosity transport software for matrix diffusion, fracture and matrix sorption, and radionuclide decay. The saturated LCA flow model used FEHM to evaluate steady-state flow, and the sptr subroutine of FEHM or Walkabout for advective-dispersive particle tracking, in combination with the PLUMECALC dual-porosity transport software for matrix diffusion, fracture and matrix sorption, and radionuclide decay.

1.7 Flow and Transport Modeling Strategy

An important aspect of the goals and objectives of the Yucca Flat/Climax Mine CAU flow and transport modeling identified in Sections 1.1 and 1.2 is the treatment of uncertainty in conceptual models and parameter values. The definition of the contaminant boundary explicitly recognizes that there is uncertainty in the calculated extent of contaminant migration and that this uncertainty should

be quantified to the extent practical to determine the probability that the calculated contaminant concentrations exceed the MCLs of the SDWA. However, that implies that all uncertainties can be quantified and that alternative models or parameters can be assigned a probability. While it is generally possible to develop probability density functions for transport model parameters based on information provided in the Yucca Flat/Climax Mine HDD (SNJV, 2006b) and TDD (SNJV, 2007), quantifying the probability of alternative flow models or other aspects of nonparametric structural uncertainty is subjective.

The strategy adopted in the development and implementation of the different models (i.e., source-term models, unsaturated-zone flow and transport models, saturated alluvial/volcanic aquifer system flow and transport models, and saturated LCA flow and transport models) used in the Yucca Flat/Climax Mine CAU flow and transport modeling is to discretely analyze the effect of the structural uncertainty associated with alternative conceptual models in a manner that does not underestimate the possible extent of contaminant migration. In this context, the models may be considered conservative with respect to the objective of forecasting the contaminant boundary. The strategy is also to directly explore the effect of the conservative assumptions when feasible, even if the assumed scenario has a low probability. In applying this strategy of using models that are not expected to underestimate the calculated extent of contaminant migration it is recognized that the effects of compounded conservative assumptions may yield a result that is increasingly skewed and divergent from reality. For example, two independent model assumptions with a 10 percent or less chance of occurring individually would have less than a 1 percent chance of occurring together in the same model, had the model run been done in a Monte Carlo framework. Although low-probability runs are done as part of broader sensitivity studies, and are presented and described in this report, they are not included in the summaries of contaminant boundaries because of their low probability of occurrence.

Although the details of the strategy used to address structural uncertainty in conceptual models are presented in the individual model sections in the remainder of this document, it is useful in this introductory section to summarize some of the major alternative representations that have been explored and to identify the nature of the conservative approximation.

Examples of conservative assumptions related to the development and implementation of the source-term models discussed in Section 2.0 include the following:

- For detonations where a yield range rather than a specific yield was announced, the maximum of the announced yield range is used to define the cavity size. Using the maximum of the announced yield range results in the development of the largest cavity radius for each detonation, which results in a greater likelihood that the extent of initial contamination at each detonation location could extend into the saturated LCA. Even though a larger cavity radius results in reduced concentrations for the same initial mass, the effect of increasing the probability that initial contamination extends into the LCA has a greater impact on the contaminant boundary.

- For detonations with working points below the water table, the portion of the initial contamination that may extend above the water table is placed below the water table. This is done for convenience to reduce the complexity of the unsaturated-zone model because the unsaturated-zone model does not have sufficient grid resolution at these locations. The impact of this conservation is not significant because these detonations do not significantly contribute to contaminant fluxes to the LCA.

Examples of conservative assumptions related to the development and implementation of the unsaturated-zone flow and transport models discussed in Section 3.0 include the following:

- A wide range of possible average net infiltration rates, from 0.1 to 10 mm/yr, are used. Values at the lower end of this range (0.1 mm/yr) are representative of present-day conditions. Values at the upper end of this range (i.e., 5 and 10 mm/yr) are used to explore the sensitivity of the contaminant transport to this assumption and conservatively estimate possible contaminant releases to the saturated alluvial/volcanic aquifer system and LCA.

- Henry's law partitioning effects on ^{14}C transport are excluded. The exclusion of this process tends to ignore the diluting effects of gaseous diffusion and overestimate ^{14}C transport at concentrations exceeding the MCL to the saturated zone.

Examples of conservative assumptions related to the development and implementation of the saturated alluvial/volcanic aquifer system flow and transport models discussed in Section 4.0 include the following:

- A wide range of possible average net recharge rates, from 0.1 to 10 mm/yr, are used. Values at the lower end of this range (0.1 mm/yr) are representative of present-day and pluvial recharge. Values at the upper end of this range (i.e., 5 and 10 mm/yr) are used to explore the sensitivity of the contaminant transport to this assumption and conservatively estimate possible contaminant releases to the saturated LCA.

- Faults are generally assumed to provide hydraulic communication through the tuff confining units to the saturated LCA, although the actual hydraulic properties are largely unmeasured. This communication conservatively increases the possibility of contaminant transport to the saturated LCA.

- Test-induced overpressures are simulated with different conceptual models to explore the significance of the test-induced pressures on contaminant transport. These conceptual models include alternatives that increase the possibility of contaminant transport to the saturated LCA.

Examples of conservative assumptions related to the development and implementation of the saturated LCA flow model discussed in Section 5.0 include the following:

- Hydraulic continuity of the LCA in northern Yucca Flat is assumed for the base-case flow model. This results in an influx on the order of a hundred kilograms per second (kg/s) into the LCA in northern Yucca Flat. An alternative conceptual model considers the possibility that there is minimal communication between the LCA north of Yucca Flat and Yucca Flat proper. This alternative assumes an influx of 1 kg/s in northern Yucca Flat. This significant difference in boundary flux has a significant effect on the groundwater velocity in the LCA considering that all other boundary fluxes and recharge rates are on the order of 150 kg/s.

- Groundwater velocities in the LCA inferred from ^{14}C age dating assume that these ages are representative of ^{14}C transport that includes the effects of retardation of ^{14}C. The groundwater velocities inferred from this assumption are similar to the modeled velocities of about 10 to 20 m/yr. If ^{14}C transport is unretarded, then the inferred velocities would be about a factor of 10 times smaller, yielding velocities of about 1 to 2 m/yr.

Examples of conservative assumptions related to the development and implementation of the saturated LCA transport model discussed in Section 6.0 include the following:

- The spacing of fractures in fault damage zones is based on a conservative relationship of fracture transport aperture to hydraulic aperture, as estimated from hydraulic conductivity and the cubic law. The base-case relationship has larger spacings, leading to less matrix diffusion and greater extent of transport. An alternative representation based on the distribution of flowing features yields less conservative (i.e., smaller) fracture spacing, and therefore greater matrix diffusion and a smaller extent of transport.

- Sorption of carbon-14 (^{14}C), strontium-90 (^{90}Sr), cesium-137 (^{137}Cs), and nickel-63 (^{63}Ni) is not considered. An alternative representation considers these radionuclides to be sorbed, which leads to significantly less transport for these radionuclides.

- The transport properties are assumed to be laterally homogeneous. Heterogeneity in transport properties would result in greater spatial averaging of these properties, which would reduce averaged property variance. As a result, extreme values in the tails of the parameter distributions would exert a smaller influence on the low-probability model outcomes that define the contaminant boundary. This would result in contaminant boundaries closer to the 50th percentile of MCL exceedance.

The significance of most of these conservative assumptions has been evaluated in the flow and transport modeling, with two exceptions: (1) the assumption that the yield of each detonation used in the analysis is always the maximum of the announced yield range specified in DOE/NV (2000b) was not evaluated for significance, and (2) no LCA transport models were run including the effects of heterogeneous transport parameters. In some cases, the significance of a conservative assumption is evaluated in the context of the impacted model to explore model sensitivity to that assumption, but the results are neither propagated to downstream models nor included in the composite contaminant boundary. This is the case for net infiltration rates of 10 mm/yr and an alternative bounding source-term model for the LCA. The net effect of the combined and individual conservative assumptions is presented in Section 6.0, because the ultimate effect of conservative assumptions in upstream models is on the calculated extent of contamination in the LCA, the regional aquifer in the eastern portion of the NNSS.

Because of the discrete unweighted alternative models, rather than a single contaminant boundary that directly includes the quantification of the different sources of uncertainty, the strategy is to forecast a composite contaminant boundary. The composite contaminant boundary includes the individual contaminant boundaries developed for the discrete alternatives in order to provide a more complete depiction of the range of possible outcomes, even though some of these alternatives may include the effects of multiple conservative assumptions.

1.8 Yucca Flat Supporting Documents

The Yucca Flat/Climax Mine CAU CAI planning documents and descriptions are listed in Table 1-3. The Value of Information Analysis (VOIA) report for the Yucca Flat/Climax Mine CAU (IT, 1999) assessed the value of different possible data collection activities with respect to reduction in uncertainty of the contaminant boundary and provided the basis for identifying the data collection activities specified in the Yucca Flat/Climax Mine CAU CAIP (DOE/NV, 2000a) before the initiation of modeling activities. The modeling strategy report for groundwater flow and contaminant transport in the Yucca Flat/Climax Mine CAU (Shaw, 2003) specifies the modeling data requirements.

The Yucca Flat/Climax Mine CAU flow and transport models are supported by a number of major reports that describe a series of data analysis and modeling tasks. Table 1-4 summarizes these reports and identifies their contributions to the development of the Yucca Flat/Climax Mine CAU flow and transport models.

Table 1-3
Yucca Flat/Climax Mine CAU CAI Planning Documents

Title	Description
Value of Information Analysis for Corrective Action Unit 97: Yucca Flat, Nevada Test Site, Nevada (IT, 1999)	This document describes the evaluation of the sufficiency of existing information to support the CAI and identifies the major problems anticipated in developing the geologic, flow, and transport models. Potential data collection activities to improve characterization data are evaluated for potential benefit and prioritization.
Corrective Action Investigation Plan for Corrective Action Unit 97: Yucca Flat/Climax Mine, Nevada Test Site, Nevada (DOE/NV, 2000a)	This document is required by the FFACO (1996, as amended) and summarizes the historical data for the Yucca Flat/Climax Mine CAU. It describes the characterization activities that will be implemented to evaluate the extent of contamination in groundwater due to underground nuclear testing and supports the development of groundwater flow and transport models to predict the contaminant boundary.
Modeling Approach/Strategy for Corrective Action Unit 97, Yucca Flat and Climax Mine (Shaw, 2003)	This document describes two approaches to modeling flow and transport through the hydrogeologic system over time. One approach is the development of numerical process models to represent the processes that control flow and transport. The other approach uses simplified representations of the process models to assess the interactions between model and parameter uncertainty.

1.9 Report Organization

Following this introductory section, the remainder of this report is organized as follows:

Section 2.0 presents information on the Yucca Flat/Climax Mine CAU RST and HST. This section summarizes the potentially important processes that influence radionuclide migration from the source area in each flow and transport model, categories of nuclear test hydrogeologic conditions, unclassified radionuclide inventory and screening, and radionuclide distribution in the subsurface. This section also presents the approach to allocating the total radionuclide source term to the three different transport models that are used to forecast contaminant transport in Yucca Flat and the uncertainty associated with the HST.

Section 3.0 presents information on the unsaturated-zone flow and transport model. This section includes a description of the key processes, conceptual models, numerical models, and parameter ranges used to evaluate contaminant migration from the radionuclide sources in the unsaturated alluvium, and volcanic and carbonate rocks. The key processes include natural infiltration, crater-induced recharge, advective-dispersive transport, retardation, and decay. The output of the unsaturated-zone flow and transport models provides water and contaminant flux input to the underlying saturated alluvial/volcanic aquifer system and LCA flow and transport models.

Table 1-4
Major Supporting Documents
(Page 1 of 6)

Report	Report Synopsis	Contribution to Flow and Transport Model
Hydrogeologic and Hydrochemical Framework, South-Central Great Basin, Nevada-California, with Special Reference to the Nevada Test Site (Winograd and Thordarson, 1975)	This document presents the basic groundwater flow conceptual model for the NNSS.	• Conceptual model of groundwater flow at the NNSS • Major structural and hydrogeologic controls on groundwater flow
Summary of Hydrogeologic Controls on Ground-Water Flow at the Nevada Test Site, Nye County, Nevada (Laczniak et al., 1996)	This report summarizes what is known and inferred about groundwater flow throughout the region. As such, major controls on groundwater flow are identified, some uncertainties about groundwater flow are highlighted, and technical needs are prioritized and identified relative to the NNSA/NSO Environmental Management Operations Activity.	• Conceptual model
Regional Groundwater Flow and Tritium Transport Modeling and Risk Assessment of the Underground Test Area, Nevada Test Site, Nevada (DOE/NV, 1997a)	This report provides the initial rationale for determining the magnitude of risk to the public and the environment posed by potential groundwater contamination from underground nuclear tests conducted on the site. The regional evaluation consisted of data analysis, model development, and model predictions. Results of the regional evaluation of groundwater flow, tritium migration, and risk assessment performed for the underground test areas are presented in this report. As such, the regional evaluation was used during the planning of the Yucca Flat/Climax Mine CAU CAI and is used to inform the general development of the CAU conceptual model.	• Conceptual model • Regional model framework • Boundary fluxes
Summary of the Models and Methods for the FEHM Application—A Finite-Element Heat- and Mass-Transfer Code (Zyvoloski et al., 1997)	This document presents the technical basis, assumptions, and testing of the FEHM transfer code.	• Numerical basis for the flow model used for unsaturated-zone flow and transport and saturated-zone flow and transport
Corrective Action Investigation Plan for Corrective Action Unit 97: Yucca Flat/Climax Mine, Nevada Test Site, Nevada (DOE/NV, 2000a)	This report is a requirement of the FFACO (1996, as amended) and summarizes the site-specific historical data for the Yucca Flat/Climax Mine CAU. It describes the characterization activities implemented to evaluate the extent of contamination in groundwater due to the underground nuclear testing and supports the development of a groundwater flow and contaminant transport model to predict the perimeter of the contaminant boundary.	• Summary of historical data • Background information • General CAU model approach

Table 1-4
Major Supporting Documents
(Page 2 of 6)

Report	Report Synopsis	Contribution to Flow and Transport Model
Nevada Test Site Radionuclide Inventory, 1951–1992 (Bowen et al., 2001)	This document summarizes the unclassified radionuclide inventory for the UGTA CAUs. Per the FFACO (1996, as amended), Appendix VI, Section 3.2.1, this report defines the radionuclide source term.	• Radionuclide source term and allocation of inventory 100 m above and below the water table
Reconnaissance Estimates of Recharge Based on an Elevation-Dependent Chloride Mass-Balance Approach (Russell and Minor, 2002)	This study describes the Desert Research Institute (DRI) evaluation of net infiltration and determination of recharge via the development of recharge models for data gathered from 17 springs located in the Sheep Range and Spring Mountains and on the NNSS. The objective was to improve an existing aquifer-response method based on the chloride mass-balance approach. Results of the recharge estimates are reported.	• Recharge models
TYBO/BENHAM: Model Analysis of Groundwater Flow and Radionuclide Migration from Underground Nuclear Tests in Southwestern Pahute Mesa, Nevada (Wolfsberg et al., 2002)	This report provides a description of an integrated modeling approach used to simulate groundwater flow, radionuclide release, and radionuclide transport near the TYBO and BENHAM underground nuclear test sites. The report includes an analysis and interpretation related to colloidally transported species.	• Test case for modeling groundwater flow and radionuclide migration from underground nuclear tests using the FEHM transfer code • Results that help parameterize the CAU model, including treatment of colloidally transported radionuclides
Simulation of Net Infiltration and Potential Recharge Using a Distributed-Parameter Watershed Model for the Death Valley Region, Nevada and California (Hevesi et al., 2003)	This study reports the development and application of a distributed-parameter watershed model to estimate the temporal and spatial distribution of net infiltration for the Death Valley region. As stated, because of uncertainty relative to the input parameters, "averaging results from multiple realizations is more likely to provide a more robust estimate of current climate potential recharge."	• Recharge models
Modeling Approach/Strategy for Corrective Action Unit 97, Yucca Flat/Climax Mine (Shaw, 2003)	This report summarizes the approach and methodology that provided overall guidance in the development of the Yucca Flat/Climax Mine CAU groundwater flow and contaminant transport models.	• Numerical code selection • Overall approach
Death Valley Regional Ground-Water Flow System, Nevada and California—Hydrogeologic Framework and Transient Ground-Water Flow Model (Belcher et al., 2004)	This report presents the current status of the regional steady-state and transient groundwater flow model in the vicinity of the NNSS.	• Boundary fluxes in the different HSUs of relevance to flow and transport in the Yucca Flat/Climax Mine CAU

Table 1-4
Major Supporting Documents
(Page 3 of 6)

Report	Report Synopsis	Contribution to Flow and Transport Model
Analysis of Ground-Water Levels and Associated Trends in Yucca Flat, Nevada Test Site, Nye County, Nevada, 1951–2003 (Fenelon, 2005)	This document presents the short-term, test-induced, and long-term, transient water-level responses in the vicinity of Yucca Flat.	• Steady-state heads for calibrating the LCA flow model • Long-term groundwater discharge estimates from wells in the Yucca Flat area
Radionuclide Transport in Tuff and Carbonate Fractures from Yucca Flat, Nevada Test Site (Zavarin et al., 2005)	This document presents the results of laboratory testing of tuff and carbonate core for fracture retardation and matrix sorption of radionuclides of potential interest to transport at Yucca Flat.	• Low retardation of some radionuclides on fracture surfaces • Low sorption of strontium and cesium on matrix minerals of the LCA
Mineralogic Zonation within the Tuff Confining Unit, Yucca Flat, Nevada Test Site (Prothro, 2005)	This document presents a three-dimensional model of the mineralogic zonation of the TCU beneath Yucca Flat.	• Information that supports HSUs used in the HFM • Type, quantity, and distribution of TCU alteration minerals that are significant to radionuclide sorption
A Hydrostratigraphic Model and Alternatives for the Groundwater Flow and Contaminant Transport Model of Corrective Action Unit 97: Yucca Flat-Climax Mine, Lincoln and Nye Counties, Nevada (BN, 2006)	This report presents the evaluation of geologic data and the resulting three-dimensional HFM for the Yucca Flat/Climax Mine CAU. The framework was built by the use of a collection of stratigraphic, lithologic, and alteration data; a structural model; and results of geophysical, geological, and hydrological studies to formulate the hydrostratigraphic system.	• HFM • Alternative HFMs • HSU definition and description
Tracer Transport Properties in the Lower Carbonate Aquifer of Yucca Flat (Reimus et al., 2006)	This report presents laboratory data related to matrix diffusion, fracture sorption, and microsphere attenuation in LCA core.	• Matrix diffusion coefficients • Weak sorption of ^{14}C • Attenuation of colloid particles
Geochemical and Isotopic Evaluation of Groundwater Movement in Corrective Action Unit 97: Yucca Flat/Climax Mine, Nevada Test Site, Nevada (SNJV, 2006a)	This report summarizes the findings of a geochemical investigation of the Yucca Flat groundwater flow system in support of the flow and contaminant transport modeling for the Yucca Flat/Climax Mine CAU.	• Flow paths derived from geochemical analysis used to qualitatively assess flow model
Phase I Hydrologic Data for the Groundwater Flow and Contaminant Transport Model of Corrective Action Unit 97: Yucca Flat/Climax Mine, Nevada Test Site, Nye County, Nevada (SNJV, 2006b)	This report describes an assessment of hydrologic data and information in support of the Yucca Flat/Climax Mine CAU LCA groundwater flow model. It analyzes relevant information, existing data, and newly acquired data for the hydrologic components of the groundwater flow system of Yucca Flat and vicinity.	• Hydraulic head data for calibration • Hydraulic property data • Discharge due to pumping • Boundary fluxes • Recharge models • Flow paths derived from geochemical analysis

Table 1-4
Major Supporting Documents
(Page 4 of 6)

Report	Report Synopsis	Contribution to Flow and Transport Model
Modeling of Groundwater Flow and Radionuclide Transport at the Climax Mine Sub-CAU, Nevada Test Site (Pohlmann et al., 2007)	This report presents results of groundwater flow modeling conducted in the Climax Mine area of the Yucca Flat/Climax Mine CAU. In addition, analyses of contaminant transport from the three detonations conducted in Climax Mine are presented.	• Evaluation of boundary water flux into the LCA to the north of Yucca Flat • Demonstration of the relative insignificance of contaminants released from the three Climax Mine detonations
Phase I Contaminant Transport Parameters for the Groundwater Flow and Contaminant Transport Model of Unit 97: Yucca Flat/Climax Mine, Nevada Test Site, Nye County, Nevada (SNJV, 2007)	This report is a compilation of transport parameters that will be used by the transport model. Parameter values and estimated variability in the parameters also are defined. The data quality is evaluated based on the number and source of data points available to define each parameter.	• Transport model parameters and distribution ranges
Summary of Radionuclide Reactive Transport Experiments in Fractured Tuff and Carbonate Rocks from Yucca Flat, Nevada Test Site (Zavarin et al., 2007)	This report presents a summary of transport experiments conducted on fractured tuff and carbonate cores to evaluate matrix diffusion and matrix sorption.	• Transport and sorption data
Evaluation of Hydrologic Source Term Processes for Underground Nuclear Tests in Yucca Flat, Nevada Test Site: Introduction and Executive Summary (Pawloski et al., 2008)	This report summarizes the unclassified analyses that allow for the characterization of the HST in the different hydrogeologic and geochemical environments of relevance to Yucca Flat.	• Background • Basis for development of the source-term scenarios
Evaluation of Hydrologic Source Term Processes for Underground Nuclear Tests in Yucca Flat, Nevada Test Site: Unsaturated Tests and the Impact of Recharge (McNab, 2008)	This report summarizes the unclassified analyses that allow for the characterization of the HST for those detonations in the unsaturated zone at Yucca Flat.	• Background source-term information • Basis for development of the source-term scenarios for detonations with working points 100 m above the water table • Calculations illustrating insignificance of detonations with no surface collapse crater
Evaluation of Hydrologic Source Term Processes for Underground Nuclear Tests in Yucca Flat, Nevada Test Site: Saturated Tests (Tompson, 2008)	This report summarizes the unclassified analyses that allow for the characterization of the HST for those detonations within 100 m of the water table and below the water table at Yucca Flat.	• Background source-term information • Basis for development of the source-term scenarios for detonations with working points within 100 m of the water table
Evaluation of Hydrologic Source Term Processes for Underground Nuclear Tests in Yucca Flat, Nevada Test Site: Carbonate Tests (Carle et al., 2008)	This report summarizes the unclassified analyses that allow for the characterization of the HST for those detonations with working points in the LCA at Yucca Flat.	• Background source-term information • Basis for development of the source-term scenarios for the detonations with working points in carbonate rock

Table 1-4
Major Supporting Documents
(Page 5 of 6)

Report	Report Synopsis	Contribution to Flow and Transport Model
Analysis of Fractures in Cores from the Tuff Confining Unit beneath Yucca Flat, Nevada Test Site (Prothro, 2008)	This report presents the results of analyses of the hydraulic and transport characteristics of cores from the tuff confining units with the goal of evaluating the role of these aquitards in affecting groundwater flow and transport in Yucca Flat.	• Results indicate the tuff confining unit is poorly fractured. • Fractures in tested cores do not significantly affect the permeability of these units. • This study relates to fractures from areas away from major faults and underground nuclear detonations.
Observations on Faults and Associated Permeability Structures in Hydrogeologic Units at the Nevada Test Site (Prothro et al., 2009)	This report summarizes borehole and direct field observations of fault and fracture characteristics of the HSUs in Yucca Flat.	• General information used to support the conceptual model of fracture- and fault-dominated flow in the aquifers (volcanic aquifer units and LCA) and the limited potential for vertical communication through the tuff confining units.
Unclassified Source Term and Radionuclide Data for Corrective Action Unit 97: Yucca Flat/Climax Mine, Nevada Test Site, Nevada (SNJV, 2009b)	This report identifies the radionuclide inventory and the mechanics of an underground nuclear test, which include changes that occur to the hydrologic properties of the rocks and distribution of the radionuclide source, and describes the approach used to build and simplify the HST process model.	• Source inventory at individual test sites • Phenomenology of underground test • Partitioning of radionuclides between water and melt glass • Source term used in the CAU-scale model
Groundwater Flow Systems at the Nevada Test Site, Nevada: A Synthesis of Potentiometric Contours, Hydrostratigraphy, and Geologic Structures (Fenelon et al., 2010)	This report summarizes interpretations of the general flow directions in the saturated volcanic and carbonate aquifers of the NNSS. It is based on interpreted contours of the potentiometric surfaces in these two aquifer units, which in turn are based on static water-level measurements in and around the NNSS.	• General information on flow paths and qualitative evaluation of flow rates in the Yucca Flat basin and surrounding area

Table 1-4
Major Supporting Documents
(Page 6 of 6)

Report	Report Synopsis	Contribution to Flow and Transport Model
Update of Death Valley Regional Groundwater Flow System Transient Model, Nevada and California (Faunt et al., 2012)	This draft report presents a revision of the Death Valley Regional Flow System (DVRFS) model to incorporate additional hydrostratigraphic information and related flow-model constraints to better represent groundwater flow into and through the LCA in Yucca Flat.	• Information that supports a revised estimate of inflow into the LCA in northern Yucca Flat
Conceptualization of the Predevelopment Groundwater Flow System and Transient Water-Level Responses in Yucca Flat, Nevada National Security Site, Nevada (Fenelon et al., 2012)	This report summarizes available potentiometric data in the vicinity of the Yucca Flat/Climax Mine CAU and analyzes the representativeness of these data with respect to the pretesting groundwater flow regime.	• General information that supports the conceptual model of groundwater flow in the local alluvial/volcanic aquifer system and the regional carbonate aquifer
Numerical Simulation of Inter-basin Groundwater Flow into Northern Yucca Flat, Nevada National Security Site, Using the Death Valley Regional Flow System Model (Pohlmann and Ye, 2012)	This report summarizes sensitivity analyses performed with the DVRFS model (Belcher et al., 2004) to evaluate the effect of the uncertainty in the model's boundary condition on modeled flow rates into northern Yucca Flat.	• Information that supports interpretation of limited flow rates into northern Yucca Flat

Section 4.0 presents information on the saturated alluvial/volcanic aquifer system flow and transport model. This section includes a description of the key processes, conceptual models, numerical models, and parameter ranges used to evaluate contaminant migration from the radionuclide sources in the saturated alluvial/volcanic aquifer system as well as contaminants that enter the saturated alluvial/volcanic aquifer system from the overlying unsaturated alluvium and volcanic rocks. The key processes include transient testing effects, advective transport, retardation, and decay. The output of the saturated alluvial/volcanic aquifer system flow and transport model defines the extent of the contaminant migration in the saturated units and provides water and contaminant flux input to the underlying LCA flow and transport models.

Section 5.0 presents information on the saturated LCA flow model. This section includes a description of the key background information and the approach used in the development and calibration of the LCA flow model, the results of the model calibration for the base-case LCA flow model, and uncertainty analyses performed to investigate a range of alternative LCA flow models. The results of the alternative LCA flow models are calibrated flow fields that describe the likely flow paths and flow rates within the LCA. The results are then used to define expected advective velocities for use in the LCA transport model.

Section 6.0 presents information on the saturated LCA transport model. This section includes a description of the key processes, alternative conceptual models, numerical models, and parameter ranges used to evaluate contaminant migration from the radionuclide sources in the saturated LCA as well as contaminants that enter the LCA from the overlying unsaturated and saturated alluvium and volcanic rocks. The key processes include advective-dispersive transport, matrix diffusion, retardation, and decay. The output of the LCA transport model defines the extent of lateral and vertical contaminant migration in the LCA as well as the uncertainty in the extent of contamination. This information is used to define the range of likely contaminant boundaries for the Yucca Flat/Climax Mine CAU.

Section 7.0 presents a summary and conclusions of the flow and transport models discussed in this document.

Section 8.0 presents the references cited in this document.

Appendix A presents information on the data, model, and software quality assurance requirements identified in the UGTA Quality Assurance Project Plan (NNSA/NSO, 2011) and how these requirements are addressed in the analyses presented in this document and supporting documents.

Appendix B presents information on the physical characteristics of the 747 underground nuclear detonations conducted in the Yucca Flat/Climax Mine CAU.

Appendix C presents information on the source-term characteristics of the 747 underground nuclear detonations conducted in the Yucca Flat/Climax Mine CAU.

Appendix D presents information on the observed unclassified radionuclide contaminant concentrations in observation wells drilled in the vicinity of the underground nuclear detonations in the Yucca Flat/Climax Mine CAU.

Appendix E presents information on the enhanced crater recharge model used in the unsaturated-zone flow and transport model.

Appendix F presents information on the transient pluvial drainage alternative model and its potential to affect recharge to the saturated zone.

Appendix G presents information on the hydrologic effects of underground nuclear testing in the saturated volcanic rocks in the Yucca Flat area. This information is used to support the conceptualization and parameterization of the hydrologic conditions in the crushed and compressed zones around cavities in the volcanic rocks of the saturated alluvial/volcanic aquifer system flow and transport model. This includes information on laboratory testing to characterize the hydrologic properties of the tuff confining units.

Appendix H presents information related to the thermal observations that may be used to estimate the lateral boundary flux and vertical recharge flux to the LCA. The thermal observations are used to support the range of estimated flux values used in the calibrated LCA groundwater flow model.

Appendix I presents an analysis of potential transient effects on groundwater flow in the LCA.

Appendix J presents information on conceptual models of fault zones as well as analyses of groundwater flow and transport characteristics of fault zones based on testing performed in Yucca Flat.

Appendix K presents the basis for selection of software used to forecast contaminant boundaries in the LCA.

Appendix L presents information related to the interpretation of ^{14}C observations in the LCA and how these observations may be used to evaluate groundwater velocities in the LCA.

Appendix M presents information on an alternative model used to evaluate the significance of colloid-facilitated radionuclide transport in the LCA.

Appendix N presents information on LCA transport analyses performed with corroborative software to evaluate the effect of alternative software assumptions on contaminant transport.

Appendix O presents NDEP comments on the draft version of this document and comment responses to NDEP.

2.0 YUCCA FLAT UNCLASSIFIED HYDROLOGIC SOURCE TERM

This section documents the unclassified HST for the underground nuclear detonations conducted in the Yucca Flat area of CAU 97. As defined in Section 1.6, the RST is the total residual radionuclide inventory in water, glass, other phases, or mineralogic forms resulting from one or more underground nuclear detonations. The HST of an underground nuclear detonation is the portion of the total RST that is released into the groundwater following the detonation. The HST presented in this section represents the radionuclide release some time after the explosion and does not include the rapidly evolving mechanical, thermal, and chemical processes during the explosion.

In groundwater transport modeling, the HST defines the boundary condition for the contaminant releases to the environment, and accurately knowing the HST is crucial for assessing the potential public exposure to groundwater contamination. Furthermore, because of the extremely high costs of remedial actions for groundwater contamination, overly conservative assessment of potential exposure should be avoided. The development of the Yucca Flat HST uses the “best-estimate” process treatment or parameter values whenever possible and identifies conservative assumptions or approximations when used.

The framework for the initial development of HST conceptual models for Yucca Flat is described in SNJV (2009b). The implementation of the HST conceptual models in the present analysis is somewhat different from that in SNJV (2009b). Only the most important HST processes that affect radionuclide release and transport were directly implemented in each model. The less important processes were either implemented using simplifications or excluded because preliminary analysis indicated that they would not significantly affect the contaminant migration forecast.

Nuclear detonations are not synonymous with nuclear tests. A nuclear “test” is defined as either a single underground nuclear explosion (detonation) conducted at a test site, or two or more underground nuclear explosions (detonations) conducted within an area delineated by a circle having a diameter of 2 km and within a total period of time not to exceed 0.1 second (DOE/NV, 2000b). In this section, the term “detonation” is generally used, because some of the Yucca Flat tests consisted of

multiple detonations, and the HST for each individual detonation is parameterized within the Yucca Flat flow and transport models.

The vast majority of the Yucca Flat/Climax Mine CAU detonations were conducted in the alluvial, volcanic, and carbonate rocks in Yucca Flat proper. However, three underground nuclear detonations were conducted for weapons effects testing in the granitic Climax stock between 1962 and 1966: HARD HAT, PILE DRIVER, and TINY TOT. The announced yields reported in DOE/NV (2000b) are 5.7 kt for HARD HAT, 62 kt for PILE DRIVER, and less than 20 kt for TINY TOT. Although there is uncertainty regarding the position of the water table in the stock, it is likely that all three detonations were conducted in the unsaturated zone. The HST associated with the Climax Mine detonations is discussed in detail in Pohlmann et al. (2007). The Climax Mine testing area is located north of Yucca Flat, and groundwater flows away from Climax Mine and into the lower carbonate aquifer in northern Yucca Flat. As discussed in Section 6.0, the Climax Mine radionuclide release rates to the saturated LCA model are insignificant to the determination of the extent of the Yucca Flat/Climax Mine CAU contaminant boundary, and the HST discussed in this section is limited to that associated with the detonations conducted in Yucca Flat.

2.1 Underground Nuclear Detonation Categories at Yucca Flat

A total of 744 underground nuclear detonations were conducted within the subsurface of Yucca Flat between 1957 and 1992. Each of these detonations is listed in DOE/NV (2000b) with the announced yield information. The yield information is given as either a specific value or a range of values. The total yield for all Yucca Flat detonations is 38,964 kt, when the maxima of the announced yield ranges are summed. The nuclear detonations within Yucca Flat were performed in a variety of hydrogeologic settings. The processes controlling radionuclide migration away from the source areas in these settings are sufficiently different that this study considers modeling the releases from these sources separately with different models. These different settings include (1) the unsaturated zone with enhanced subsidence crater recharge, (2) the saturated zone with detonation-induced transient high pressures occurring within the low-permeability tuff confining units, and (3) the fractured carbonate rock with highly conductive faults. Figure 2-1 illustrates the locations of the Yucca Flat detonations, the LCA HSU, and the boundary of the saturated LCA model. Each sphere is centered about the detonation location (working point) and is scaled by the announced yield or the maximum of the

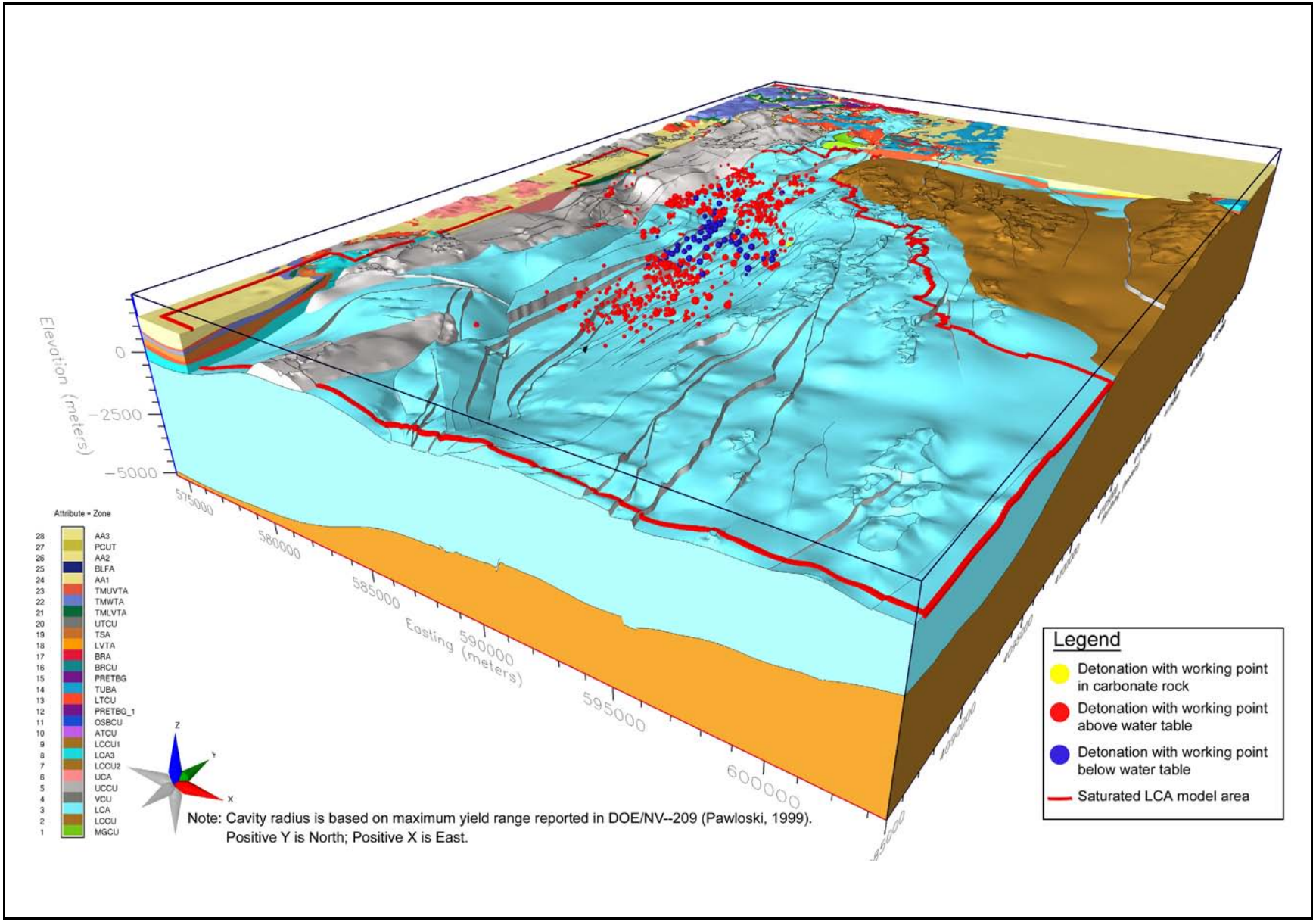

Figure 2-1
Perspective View of Underground Nuclear Detonations at Yucca Flat

announced yield range provided in DOE/NV (2000b). The sphere colors denote the locations of the detonations within the unsaturated zone (red), the saturated zone (blue), and carbonate rock (yellow), and the red line represents the boundary of the saturated LCA model.

Bowen et al. (2001) provided a comprehensive unclassified inventory of the RST for the NNSS, which was later amended by Smith et al. (2003). Bowen et al. (2001) subdivide the inventory into five areas that roughly correspond to the five UGTA CAUs. (The locations of the five UGTA CAUs are shown in Figure 1-1.) For the Yucca Flat region, the inventory is further subdivided according to the location of each detonation relative to the water table. As mentioned in Section 1.5, the criterion used in Bowen et al. (2001) in subdividing the Yucca Flat inventory is 100 m above the water table. Based on this criterion, Bowen et al. (2001) define detonations with working points located within 100 m of the water table as “saturated” because such detonations have the potential to interact with the regional water table. The majority of the Yucca Flat detonations and total yield are located above the water table, and the estimated location of the water table and the actual detonation location (i.e., working point) relative to the water table are used in the analyses presented herein.

To better understand the magnitude of the Yucca Flat source term within each hydrogeologic setting, Pawloski et al. (2008) and SNJV (2009b) categorized nuclear testing in Yucca Flat in terms of detonation date, depth, geology, and elevation relative to the water table. Pawloski et al. (2008) categorized detonations using the Bowen et al. (2001) definition of “saturated-zone” and “unsaturated-zone” detonations. The SNJV (2009b) categorization conforms to the assumptions used in the CAU modeling study, namely, that detonations with working points above the water table are considered unsaturated-zone detonations and that detonations with working points below the water table are considered saturated-zone detonations. Therefore, detonation categories from SNJV (2009b) are presented in this report, and the discussion of unsaturated-zone or saturated-zone detonations refers to the location of the detonation being above or below the water table.

The exchange volume is commonly defined as the volume of rock that encompasses the immediate extent of radioactive contamination following an underground nuclear detonation that may interact with groundwater. As discussed in this section and Appendix C, evolving HST work has improved the understanding of exchange volume. The extent of the exchange volume is dependent on conditions specific to the detonation location (e.g., pre-detonation rock saturation) and the nature of

the radionuclides (e.g., radionuclide condensation temperatures). The exchange volume is typically simplified as a spherical volume centered about the working point and is depicted as a multiple of the cavity radius. Many of the Yucca Flat detonations have exchange volumes that extend across the water table (i.e., either unsaturated-zone working-point detonations with exchange volumes that extend below the water table or saturated-zone working-point detonations with exchange volumes that extend above the water table). There is uncertainty in the extent of the exchange volume and distribution of radionuclides within the exchange volume. Therefore, two methods are used to allocate the initial inventory to the different model domains. The methods used and uncertainty are described in Sections 2.3.3 and 2.4, respectively.

2.1.1 Unsaturated-Zone Detonations

Excluding the 4 detonations conducted in unsaturated carbonate rock, there are 664 underground detonations with working points located above the water table at Yucca Flat. The total yield for the 664 detonations is 26,340 kt and is 68 percent of the total maximum announced yield reported by DOE/NV (2000b) for the detonations conducted at Yucca Flat proper. Of the 664 detonations, 98 have initial contamination partially below the water table when it is assumed that the initial contamination in the exchange volume extends 3 R_c. 3 R_c is likely the maximum extent of initial contamination for most radionuclides. The total maximum announced yield for the 98 detonations is 14,243 kt. Because the size of the exchange volume is uncertain, the fraction of the total yield and inventory initially within the unsaturated zone also is uncertain. These uncertainties are discussed in more detail in Section 2.4.

The four Yucca Flat detonations conducted in carbonate rock are HANDCAR, KANKAKEE, NASH, and BOURBON (Carle et al., 2008). All the carbonate detonations have working points located above the water table. The total maximum announced yield for the carbonate detonations is 451 kt (DOE/NV, 2000b).

2.1.2 Saturated-Zone Detonations

The Yucca Flat detonations include 76 detonations with working points located below the water table. The total maximum announced yield for these detonations is 12,173 kt and is 31 percent of the total maximum announced yield reported by DOE/NV (2000b) for the detonations conducted at Yucca Flat

proper. When the saturated-zone detonations are each assumed to have an exchange volume with a radius that equals 3 R_c, 65 of these detonations have exchange volumes extending above the water table. The total maximum announced yield is 10,504 kt for these detonations (DOE/NV, 2000b).

The zeolitic tuff contains 82 percent of the working points and 83 percent of the total maximum announced yield for the saturated-zone detonations conducted in Yucca Flat. There are 49 detonations with initial contamination and chimneys completely contained in tuff confining units (SNJV, 2009b). The total maximum announced yield is 7,839 kt for these detonations and is approximately 64 percent of the total maximum announced yield for the saturated-zone detonations in Yucca Flat. The Yucca Flat saturated-zone detonations are provided in Appendix B to SNJV (2009b).

2.1.3 Detonations with Exchange Volumes Intersecting the Saturated LCA

Detonations that directly impact the saturated LCA are of particular importance to the Yucca Flat HST because they represent a direct source to the LCA and will not be attenuated by slow unsaturated water movement or sorption within the volcanic tuffs. The number of detonations with exchange volumes that potentially intersect the saturated LCA varies depending on the size of the exchange volume. Detonations that intersect the saturated LCA3 are of less importance than those that intersect the saturated LCA because the LCA3 is generally isolated from the LCA by the low-permeability UCCU HSU. As discussed in Section 5.5, the LCA3 is less permeable than the LCA, resulting in slower groundwater velocity compared to the LCA. Furthermore, detonations with a volumetric fraction of exchange volume pore space less than 1E-4 within the saturated LCA also are excluded. This exclusion is supported by uncertainty in the extent and shape of the exchange volume (see Section 2.4), possible overestimation of the exchange volume size resulting from calculating the cavity size from the maximum announced yield (see Section 2.3.3), and a desire for parsimony in the source-term modeling approach. Therefore, the detonations discussed in this section are only those that have significant exchange volumes within the saturated LCA, with the exception of the NASH detonation, which was detonated within the LCA3 carbonate rock and has nearby radionuclide concentration observations in Well UE-2ce (see Appendix D). Appendix B identifies the distance between the working point and the saturated LCA or LCA3 for each detonation, and the total number of detonations identified in Appendix B as having exchange volumes intersecting the saturated carbonate rock is larger because of the additional consideration of proximity to the LCA3.

Assuming an exchange volume of 3 R_c, 39 Yucca Flat detonations intersect the saturated LCA, and the total maximum announced yield is 7,256 kt for these detonations. Figure 2-2 provides a perspective view of these 39 detonations and identifies the detonations by name. When the assumed exchange volume radius is reduced to 2 R_c, the number of detonations with exchange volumes that intersect the saturated LCA decreases to 12. Figure 2-3 provides a perspective view of these 12 detonations. When the assumed exchange volume radius is further reduced to 1 R_c (i.e., the exchange volume = the volume of the cavity), the number of detonations with exchange volumes (cavities) that partially intersect the saturated LCA decreases to four. Two of the four, the CORDUROY and LAMPBLACK detonations, have saturated working points. The remaining two, the TORRIDO and BOURBON detonations, have unsaturated working points. Each of these four detonations has a maximum announced yield of 200 kt (DOE/NV, 2000b).

2.2 Source-Term Conceptual Model

This section summarizes the potentially important processes that influence radionuclide migration away from the source areas in the three Yucca Flat flow and transport models and how these processes were conceptualized and implemented in the transport calculations. The phenomenology of underground nuclear detonations and Yucca Flat HST conceptual models are described in detail in SNJV (2009b) and Pawloski et al. (2008).

The large number of detonations conducted at Yucca Flat and possible HST interactions between the detonation sites preclude developing independent HST models for each detonation. Instead, the important processes controlling release of radionuclides from the Yucca Flat detonations are directly incorporated into the Yucca Flat flow and transport models, calculated externally to the models, or simply approximated. For example, enhanced infiltration in subsidence craters is directly simulated in the unsaturated model, the dissolution of melt glass for detonations in volcanic rock is calculated external to the models by the use of a temperature-dependent melt-glass dissolution model, and the process of thermal convection in chimneys is addressed by moving the initial source zone from the cavity area to the chimney aquifer in the saturated alluvial/volcanic aquifer system model.

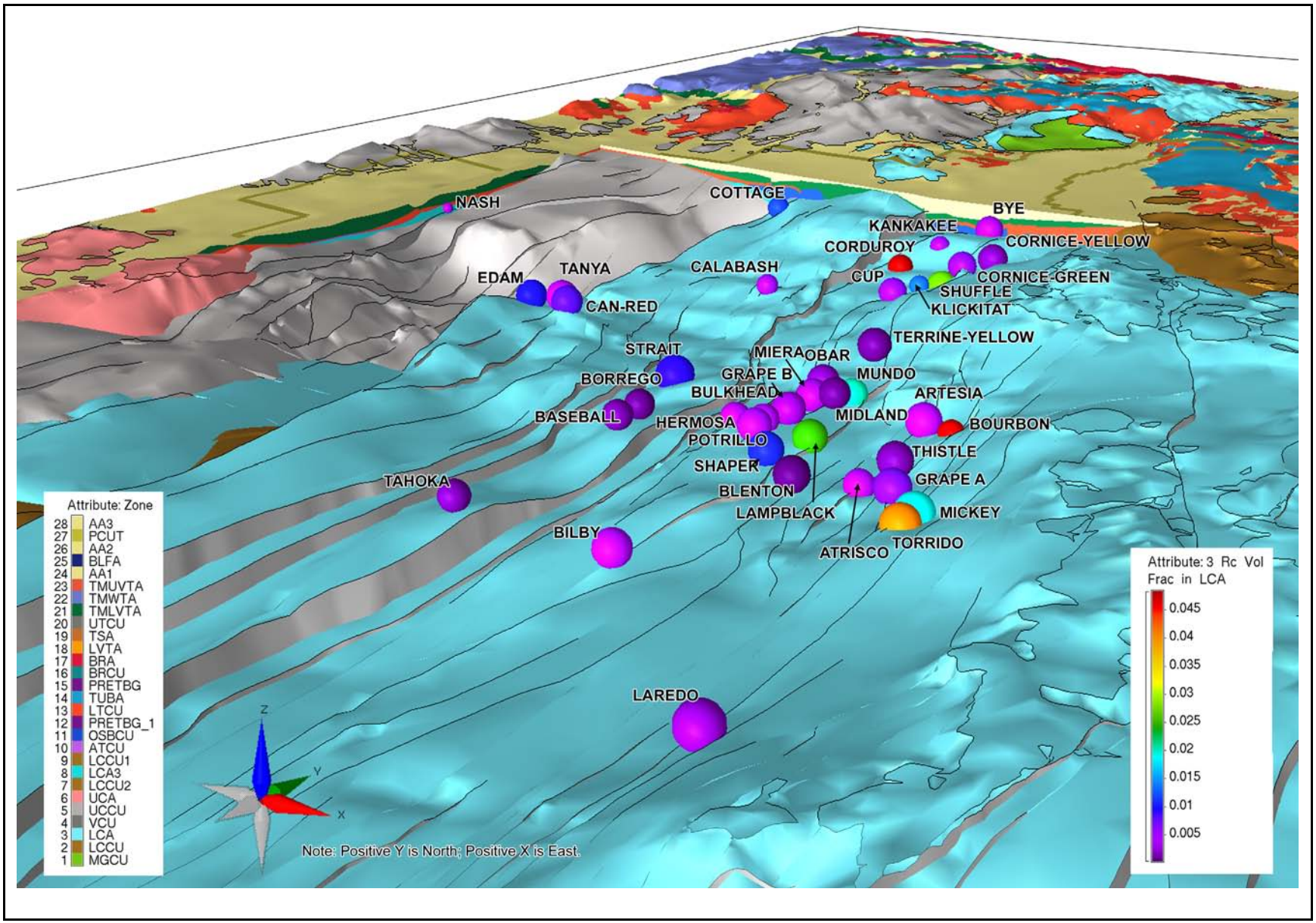

Figure 2-2
Underground Nuclear Detonations at Yucca Flat with Exchange Volumes That Intersect the Saturated LCA When an Exchange Volume Radius of 3 R_c Is Assumed

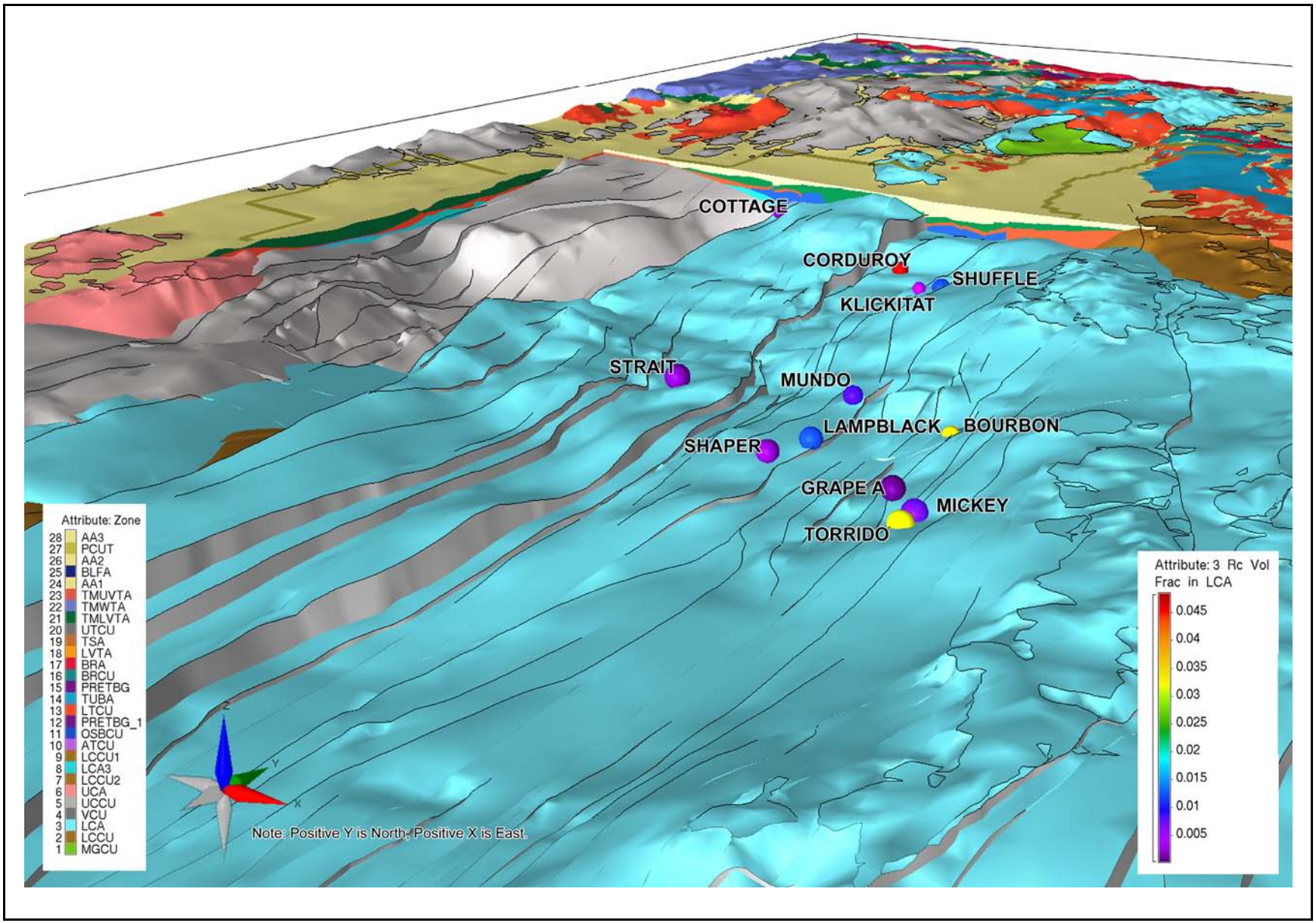

Figure 2-3
Underground Nuclear Detonations at Yucca Flat with Exchange Volumes That Intersect the Saturated LCA When an Exchange Volume Radius of 2 R_c Is Assumed

2.2.1 Source-Area Altered Zones

The volumes of geologic material physically altered by an underground nuclear detonation are referred to as the source-area altered zones. The source-area altered zones are parameterized within the Yucca Flat flow and transport models by approximating the volumes of the altered zones as spheres and sphere sections. A schematic diagram depicting the altered zones is presented in Figure 2-4. The altered zones include the cavity zone, melt-glass zone, crushed zone, and chimney zone. The exchange volume includes the volume surrounding the detonation point that contains radionuclides resulting from the nuclear detonation. The exchange volume depicted in Figure 2-4 encompasses the cavity, melt glass, and crushed zones. Radionuclides are initially distributed within the exchange volume. Short-term processes that cause this distribution to occur (i.e., extreme temperatures and pressures following the detonation) are not directly addressed in the Yucca Flat flow and transport models but are indirectly accounted for through the simulation of initial conditions and modified hydrogeologic properties for flow and transport. The modifications made include the following:

- ***Increased permeability within the cavity and upper crushed zone.*** The cavity is the void volume surrounding the working point created by the extreme heat and pressure of the detonation. The upper crushed zone is the volume above the cavity within the radius of the crushed zone. The cavity and upper crushed zone include the unconsolidated rubble from the collapsed chimney and cavity walls.

- ***Increased permeability in the volcanic rock chimney.*** The chimney zone is conceptualized to be a cylindrical volume with a radius set to the radius of the cavity. The chimney zone that extends from the cavity to the subsidence crater bottom in volcanic rock has increased permeability. Chimney zones located in alluvium are unlikely to have hydraulic properties that are significantly different from those outside the chimney zones (BN, 1998).

- ***Increased or decreased permeability within the crushed zone.*** The crushed zone consists of the rock surrounding the cavity that has mechanically failed, and permanently lost or gained permeability and porosity because of the compressional shock wave. The crushed zone occurring within ductile alluvium or vitric tuff may have reduced permeability. The crushed zone occurring within brittle hard rock (e.g., welded tuff, lava, or carbonate) may have increased permeability (SNJV, 2009b). The crushed zone permeability within zeolitized or argillitized tuff confining units may be increased due to pressurization in excess of lithostatic resulting in hydrofracturing (Wolfsberg, 2006) or decreased due to pulverization and compaction (Tompson, 2008).

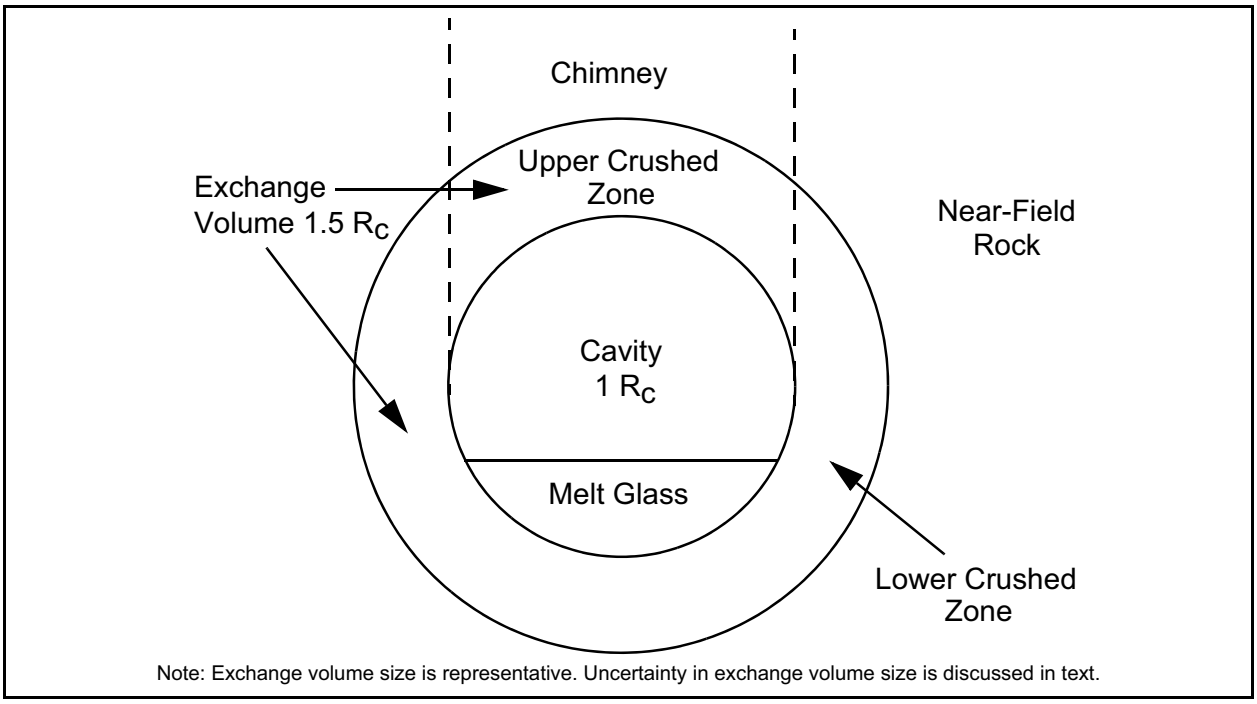

Figure 2-4
Schematic Diagram of the Source-Area Altered Zones
Source: Modified from SNJV, 2009b

- ***Exchange volume extending beyond the cavity.*** The exchange volume contains the initial radionuclide contamination immediately following the detonation. The exchange volume encompasses the cavity zone and melt-glass zone, and a spherical zone extending beyond the cavity zone. The exchange volume may extend into or beyond the crushed zone.

Radionuclide diffusion from the cavity rubble fracture porosity to the matrix porosity can become established over relatively short time periods (approximately 1 year) because of the small rubble block sizes and high fracture porosity. However, the radionuclides are expected to reside primarily within the more accessible exchange volume fractures beyond the cavity. The altered-zone conceptual model assumes the initial condition that radionuclide equilibrium is established between the fracture and matrix porosities within the cavity and that nonequilibrium exists between matrix and fracture porosities within the exchange volume outside the cavity (see Appendix C).

2.2.2 HST Processes

2.2.2.1 HST Processes for the Unsaturated-Zone Model

As described in previous UGTA reports (e.g., Carle et al., 2008; McNab, 2008; Tompson, 2008; SNJV, 2009b), complex processes can affect the initial distribution of radionuclides in the minutes, days, and weeks following a nuclear detonation. A comprehensive description of the phenomenology of an underground nuclear detonation is provided in Appendix C. Some of these processes pertinent to the unsaturated zone include (1) steam-bubble expansion of ambient pore water and injected fluids that were lost during drill-back operations following the detonation; (2) drainage of perched water (if present) down cavity collapse chimneys; and (3) carbon dioxide bubble generation and expansion from the thermal decomposition of limestone, dolomite, or alluvium calcite. Longer-term processes affecting radionuclide movement to the water table include (1) gas-phase diffusion of volatile radionuclides such as ^{14}C and ^{3}H; (2) advective transport in pore water due to precipitation-derived net infiltration or focused infiltration into craters resulting from surface runoff; and (3) dissolution of melt glass with associated release of high-melting-point radionuclides such as plutonium, strontium, and americium.

The subsidence craters above the detonations capture water from a larger area and focus the recharge in the crater playas. Several studies of infiltration occurring in Yucca Flat and Frenchman Flat subsidence craters have been conducted (Tyler et al., 1986; Tyler et al., 1992; Hokett and Gillespie, 1996; Pohll et al., 1996; Hokett and French, 1998; Wilson et al., 2000). All the studies concluded that enhanced subsidence crater recharge is occurring. The recharge estimates in these studies range from a few millimeters to approximately 1 m per year (m/yr). Individual craters have different recharge rates, and the recharge rate is dependent on the local catchment basin area of each crater.

The process of perched-water drainage due to detonation-induced high permeability in the chimney rubble may transport radionuclides to the aquifer. This process most likely occurs if the chimney extends into low-permeability tuffs and the recharge is high. Carle et al. (2008) performed near-field modeling of variably saturated flow and transport processes occurring at the NASH detonation source area. The modeling hypothesized that water-level transients observed in the UE-2ce satellite well resulted from chimney and vadose-zone drainage of perched water.

Reentry holes were drilled into the cavity soon after each detonation, and drilling fluids were injected into the boreholes for lubrication and cooling of the drilling bits and stems. The residual heat from the detonation and the need for radiologic control required more fluids to be injected compared to typical boreholes in the same setting (Carle et al., 2008). In general, drilling or sampling activities started within 24 hours of detonation. The Red Book (RSN, 1991) indicates that 628 of the 744 detonations conducted at Yucca Flat proper had post-detonation holes drilled and that most of these holes have an average of two to three sidetracks. Drilling mud is a thick, highly viscous fluid and was typically not lost in a large quantity until it intersected the cavity. The viscous nature of drilling mud will also limit its exit from the cavity compared to pure water. The drilling mud will also retard the movement of some radionuclides because of the sorptive properties of clay within the mud.

The carbonate detonations in the unsaturated zone are expected to release large amounts of carbon dioxide at detonation, because dolomite will decompose into calcite, magnesium oxide, and carbon dioxide, and calcite will decompose into calcium oxide and carbon dioxide. The net carbon dioxide production in the source areas of the carbonate detonations is approximately 4E+06 moles per kiloton yield (Carle et al., 2008). The large quantity of carbon dioxide gas released and high gas pressure may increase the distribution of radionuclides external to the cavity region initially by pressure-driven gas expansion and later by density-driven gas descension to the water table. This will result in larger exchange volumes for volatile radionuclides or radionuclides with volatile precursors at carbonate detonation sites than at detonation sites in volcanic rock. Carle et al. (2008) recommended using the following exchange volume radii for radionuclides at carbonate detonation locations: 1 to 3 R_c for nonvolatile radionuclide precursors, 3 to 6 R_c for volatile radionuclides, and 5 to 10 R_c for gaseous radionuclides. The alluvium can contain up to a few weight percent of carbonate rock. Therefore, a detonation in alluvium will also release carbon dioxide gas from thermal decomposition of the carbonate, which may affect the extent of initial contamination from volatile radionuclides. However, the effect will be much less than that from a detonation conducted in fully carbonate rock.

The transport of ^{14}C within the unsaturated zone is unique in that transport occurs in the aqueous and gaseous phases at ambient temperatures and pressures. The diffusion coefficients for the gaseous phase are generally four orders of magnitude greater than those for the aqueous phase, and at low aqueous-phase saturations, gaseous diffusion dominates. At very high aqueous-phase saturations, the gaseous-phase tortuosity increases and aqueous-phase transport dominates.

All detonations with working points in silicic rock will have a melt-glass zone consisting of vaporized, melted, and infallen rubble at the cavity bottom. The radionuclide flux to the near-field environment from melt-glass dissolution is controlled by the rate of glass dissolution, which in turn is controlled by the glass temperature and saturation of glass in solution. Tompson et al. (2011) calculated melt-glass dissolution using a range of working-point depths and glass-dissolution parameters for the Rainier Mesa/Shoshone Mountain HST. Only the very deep detonations (average depth of 534 m) were expected to have a maximum melt-glass dissolution of more than 1 percent over 1,000 years. The maximum unsaturated working-point detonation depth is 515 m, and the average depth is 191 m. The glass-dissolution rates calculated for very deep detonations by Tompson et al. (2011) likely apply to only the Yucca Flat saturated-zone detonations. The combination of small dissolution amount and slow solute transport through the unsaturated zone allows neglecting melt-glass radionuclide flux from the unsaturated-zone modeling.

The phenomenology of carbonate working-point detonations does not result in a silicate glass puddle but creates a highly radioactive rock decomposition product zone at the cavity bottom. The highly radioactive zone is stable compared to silicate melt glass and will not dissolve over time (Carle et al., 2008).

2.2.2.2 HST Processes for the Saturated Alluvial/Volcanic Aquifer System Model

The local hydraulic gradient, near-field permeability, and crushed-zone permeability determine the groundwater flow through the exchange volume and melt glass. Contrasts between the near-field and crushed-zone permeabilities can result in convergent or divergent flow through the exchange volume. If the crushed-zone permeability is lower than the near-field permeability, divergent flow will occur, and the groundwater flux through the cavity will be less than that through an equivalent cross-sectional area outside the cavity. If the crushed zone has a higher permeability than the near-field rock, convergent flow will occur, and the groundwater flux through the cavity will be greater than that through an equivalent cross-sectional area outside the cavity.

Anomalously high groundwater heads were recorded in emplacement holes and wells in some Yucca Flat locations after subsurface testing began. These high heads were observed only in the low-permeability and highly zeolitized tuff confining units. The high heads have persisted for decades in the saturated volcanic area known as the Tuff Pile (Wolfsberg et al., 2006), but have also

been observed for shorter periods at detonation locations outside the Tuff Pile (Tompson, 2008). The Tuff Pile is located between the Yucca and Topgallant faults in Areas 1, 3, 4, and 7. The timescale of pressure dissipation is likely influenced by specific geologic conditions, and detonations conducted in the rock with the lowest conductivity will likely experience the longest timescale. The high gradients resulting from these detonations may drive contaminants vertically down to the LCA or laterally toward the faults, but the low conductivity of the tuff confining units will greatly moderate water and radionuclide movement resulting from the high gradients.

The presence of a high-permeability chimney allows buoyancy effects from test-related heat to potentially drive groundwater upward and away from the cavity. Heat-induced convection can be important for detonations with saturated chimneys that intersect an aquifer. Detonations that have chimneys entirely contained in confining units or that have the water table below the high-permeability units are not expected to be affected by buoyancy-driven flow (Tompson, 2008).

The radionuclide flux to the near-field environment from melt-glass dissolution is controlled by the rate of glass dissolution, the concentration of the radionuclides within the melt glass, and the volume of the melt glass. The rate of glass dissolution is largely controlled by the glass temperature and saturation of glass in solution. High temperatures persist longer at locations of larger detonations and at locations entirely contained in confining units. The higher boiling-point temperatures associated with the high pressure at locations of deep saturated-zone detonations allow more glass dissolution to occur compared to shallow detonation locations. This is because glass dissolution begins only after water condenses and returns to the cavity, and this occurs at a higher temperature for deep detonation locations compared to shallow detonation locations. Detonations performed within high permeability rock will allow advective flow to cool the cavity and melt glass more quickly than detonations performed in low permeability rock, which must cool with conductive heat flow alone. However, the low permeability rock will greatly moderate radionuclide movement away from the cavity. Either prolonged elevated temperatures promote significant melt glass dissolution in a limited transport setting or shortened elevated temperatures inhibit melt glass dissolution in a expedited transport environment.

2.2.2.3 HST Processes for the Saturated LCA Model

As mentioned in Section 1.6, there are no detonations in Yucca Flat that have working points located within the saturated carbonate aquifers. Nonetheless, the HST for the saturated LCA flow and transport modeling takes into account radionuclides in cavities and exchange volumes that extend into the saturated LCA. As identified in Section 2.1.3, there are 4 detonations with cavities that intersect the saturated LCA, and 39 detonations with exchange volumes that potentially intersect the saturated LCA when an exchange volume radius of 3 R_c is assumed. Carle et al. (2008) do not explicitly address exchange volumes that extend into the saturated LCA but state that the altered zones surrounding the cavity in carbonate rock are more fractured than those in weaker rock types and that the test-induced fractures increase porosity and permeability in the carbonate rock surrounding the cavity. Although contrasts between the near-field and crushed-zone permeabilities may result in convergent flow through the exchange volumes extending into the saturated LCA, the permeability of the LCA is generally sufficiently large and the lateral extent of convergent flow sufficiently small that these potential effects are insignificant to lateral transport in the LCA away from the exchange volumes.

All four detonations with cavities breaching the saturated LCA are expected to have a silicate glass puddle, and glass dissolution will release radionuclides to the HST. Although the BOURBON detonation is a carbonate-rock working-point detonation, it is expected to have some silicate glass puddle characteristics because its cavity encompasses both volcanic and carbonate rocks.

2.2.2.4 Implementation of HST Processes

The HST processes that most significantly affect the release and transport of radionuclides were implemented directly in each model. The less important processes were either implemented using simplifications or excluded because preliminary analysis indicated that they would not significantly affect the contaminant migration forecast. The processes, approaches to treating the processes, and implications to the release of radionuclides to groundwater are summarized in Tables 2-1 to 2-3 for the unsaturated zone, saturated alluvial/volcanic aquifer system, and saturated LCA models, respectively.

Table 2-1
Treatment of HST Processes and Associated Transport Effect for the Unsaturated-Zone Model

Process	Treatment	Effect on Transport
Infiltration through the crater bottoms	Directly parameterized using rates from infiltration modeling (see Section 3.3).	The net infiltration through the crater bottom is one of the most important processes releasing radionuclides to groundwater from the unsaturated zone. The infiltration modeling predicted a large variability in rates for individual craters and considers high and low estimates.
^{14}C gas-phase transport and large initial gaseous radionuclide exchange volumes	Directly parameterized for a single sensitivity simulation (see Section 3.7).	The radionuclides transported in the gas phase have larger exchange volumes, resulting in lower initial concentrations (Carle et al., 2008). Gas-phase transport may result in more or less mass arriving at the water table. Diffusion spreads radionuclides away from the recharge footprint (SNJV, 2009b), but may also transport radionuclides to the water table. Initial cavity concentrations of ^{14}C are only slightly above the MCL, and concentrations are reduced by gas-phase transport.
Enhanced chimney permeability and possible drainage	Directly parameterized (see Section 3.0).	The increased chimney permeability will result in perched-water drainage, if present, and will enhance radionuclide transport to the aquifer.
Reentry borehole drilling fluid injection	Neglected except for the carbonate working-point detonations (see Section 2.4.1). Approximated by placing the HST for these detonations directly in the saturated LCA model.	No significant effect. For the vast majority of detonations performed in the alluvium or Tertiary volcanic rock, the effect of drill-back fluid injection is small compared to enhanced crater infiltration. Simulations of drill-back fluid injection by SNJV (2009b) found essentially no difference in the radionuclide breakthrough times to the aquifer or the peak aquifer concentrations when compared to the simulations without drill-back fluid injection. Drilling muds, being thick, highly viscous fluids, were typically not lost in large quantities until they intersected the cavity, and they would not exit the cavity as readily as pure water. However, the low primary and secondary porosity of the carbonate rock may result in drill-back fluid transport of mobile radionuclides such as ^{3}H to the saturated zone.
Melt-glass dissolution	Neglected.	No significant effect. The melt glass contains the more refractory radionuclides (i.e., actinides), which tend to have more retardation. The Climax Mine modeling by Pohlmann et al. (2007) concluded that radionuclides within the melt glass play a minor role in contaminant transport. Melt-glass dissolution is a slow, long-term process and allows more dilution with recharge and aquifer water compared to other processes.

Table 2-2
Treatment of HST Processes and Associated Transport Effect for the Saturated Alluvial/Volcanic Aquifer System Model

Process	Treatment	Effect on Transport
High-pressure gradients observed in the Tuff Pile	Directly parameterized.	The transport processes associated with anomalously high-pressure gradients observed in the Tuff Pile is potentially an important process releasing radionuclides to groundwater from the saturated volcanics, but the low hydraulic conductivity of the tuff confining units will greatly moderate water and radionuclide movement resulting from the high pressure gradients.
Test-induced hydraulic properties of the altered zones	Directly parameterized. The permeability of the crushed zone surrounding the cavity is an uncertain parameter. Uncertainty analyses consider a range of increased and decreased permeabilities.	In the absence of residual pressurization, increased crushed-zone permeability will result in convergent flow and increase the radionuclide flux exiting the exchange volume. Decreased crushed-zone permeability will result in divergent flow and decrease the radionuclide flux exiting the exchange volume.
Buoyancy-driven flow for detonations with working points in a low-permeability unit and chimneys that intersect an aquifer	Approximated. The process is included in a transport sensitivity simulation and is parameterized by raising the radionuclide source from the exchange volume to the chimney aquifer.	Conservative. Placing all the non-melt-glass inventory directly into the chimney aquifer overestimates radionuclide transport away from the altered zones.
Melt-glass dissolution	The process is included in a sensitivity analysis that assumes the immediate release of the melt-glass dissolution fraction.	Conservative. Melt-glass dissolution is a slow process that will gradually release radionuclides over time. Assuming the immediate release of the melt-glass fraction will overestimate groundwater concentrations.

Table 2-3
Treatment of HST Processes and Associated Transport Effect for the Saturated LCA Model

Process	Treatment	Effect on Transport
Hydraulic properties of the altered zones	Properties are unchanged from those of the surrounding rock. The fraction of the inventory contained in the exchange volume intersecting the saturated carbonate rock is initialized directly into the carbonate rock fractures.	Mostly conservative. The carbonate aquifer is conceptualized as fractured and faulted rock that is highly permeable. The increased altered-zone permeability will result in convergent flow and underestimate the radionuclide flux exiting the exchange volume. However, convergent flow will result in lower concentrations of solutes exiting the exchange volume. Neglecting the high cavity porosity will overestimate initial concentrations in the exchange volume and overestimate solute velocity within the cavity.
Melt-glass dissolution	Neglected.	No significant effect. The melt glass contains the more refractory radionuclides (i.e., actinides), which tend to have more retardation. The Climax Mine modeling by Pohlmann et al. (2007) concluded that radionuclides within the melt glass play a minor role in contaminant transport. Melt-glass dissolution is a slow, long-term process and allows more dilution with recharge and aquifer water compared to other processes.

2.3 Unclassified Yucca Flat Radionuclide Inventory

The unclassified inventory of the RST for the NNSS presented in Bowen et al. (2001) provides an estimate of radioactivity remaining underground after the nuclear testing. This inventory is referred to as the “Bowen inventory” in this section. The Bowen inventory is decay corrected to September 23, 1992, the date of the last underground nuclear test at the NNSS. The inventory includes radionuclides associated with (1) residual fissile and tracer materials, (2) fission products, (3) tritium, and (4) neutron activation of device parts and the surrounding geologic medium. Radionuclides with very short half-lives are screened from inclusion in the Bowen inventory. Also screened from inclusion in the Bowen inventory are radionuclides produced in low abundance that result in, by 2092 (100 years from the 1992 moratorium on nuclear testing), fully saturated cavity concentrations less than one-tenth the MCLs proposed for drinking water by the U.S. Environmental Protection Agency (EPA) (EPA, 1991). Radionuclides with no concentrations proposed by EPA were screened from inclusion in the Bowen inventory (Bowen et al., 2001) at a concentration of 1E-08 curies per milliliter (Ci/mL). The Bowen inventory includes 43 radionuclides that have half-lives greater than 10 years (with the exception of europium-154 [^{154}Eu]).

The Bowen inventory for Yucca Flat is provided in Table 2-4. The total inventory for detonations located 100 m or more above the water table is approximately half that for detonations located below or within 100 m of the water table. An individual detonation inventory is calculated from the Bowen inventory in four steps: (1) normalize the Yucca Flat above-the-water-table inventory by the total maximum announced yield for all Yucca Flat detonations located 100 m or more above the water table, (2) normalize the Yucca Flat below-the-water-table inventory by the total maximum announced yield for all Yucca Flat detonations located below or within 100 m of the water table, (3) multiply the normalized inventory by the individual detonation yield; and (4) decay correct the resultant individual detonation inventory from September 23, 1992, to the time of each detonation. The individual fractions of the Bowen inventory for all detonations conducted at Yucca Flat proper are presented in Appendix C.

Table 2-4
The Bowen Radionuclide Inventory for Yucca Flat
(Page 1 of 2)

Element	Radionuclide	Half-Life (Years)	Moles		Curies	
			Above Water Table [a]	Below Water Table [b]	Above Water Table [a]	Below Water Table [b]
Hydrogen	^{3}H	1.23E+01	5.073E+02	1.143E+03	1.472E+07	3.316E+07
Carbon	^{14}C	5.73E+03	1.817E+01	1.341E+01	1.137E+03	8.389E+02
Aluminum	^{26}Al	7.17E+05	1.107E-01	7.140E-02	5.573E-02	3.595E-02
Chlorine	^{36}Cl	3.01E+05	9.796E+01	1.944E+02	1.163E+02	2.309E+02
Argon	^{39}Ar	2.69E+02	2.411E-01	7.187E-01	3.204E+02	9.551E+02
Potassium	^{40}K	1.27E+09	2.919E+05	8.603E+05	8.219E+01	2.422E+02
Calcium	^{41}Ca	1.03E+05	2.463E+02	4.786E+02	8.545E+02	1.661E+03
Nickel	^{59}Ni	7.51E+04	4.547E+00	9.067E+00	2.139E+01	4.265E+01
	^{63}Ni	1.00E+02	6.529E-01	1.463E+00	2.334E+03	5.229E+03
Krypton	^{85}Kr	1.07E+01	3.421E-01	1.747E+00	1.137E+04	5.805E+04
Strontium	^{90}Sr	2.91E+01	1.206E+01	6.021E+01	1.499E+05	7.479E+05
Zirconium	^{93}Zr	1.53E+06	2.874E+01	1.094E+02	6.852E+00	2.607E+01
Niobium	^{93m}Nb	1.61E+01	2.813E-02	3.030E-01	6.246E+02	6.730E+03
	^{94}Nb	2.03E+04	1.284E+00	1.105E+01	2.296E+01	1.975E+02
Technetium	^{99}Tc	2.13E+05	3.666E+01	1.117E+02	6.153E+01	1.875E+02
Palladium	^{107}Pd	6.50E+06	1.388E+01	1.677E+01	7.634E-01	9.226E-01
Cadmium	^{113m}Cd	1.41E+01	6.176E-03	1.969E-02	1.566E+02	4.994E+02

Table 2-4
The Bowen Radionuclide Inventory for Yucca Flat
(Page 2 of 2)

Element	Radionuclide	Half-Life (Years)	Moles		Curies	
			Above Water Table [a]	Below Water Table [b]	Above Water Table [a]	Below Water Table [b]
Tin	^{121m}Sn	5.50E+01	1.037E-01	2.951E-01	6.738E+02	1.918E+03
	^{126}Sn	1.00E+05	2.380E+00	6.406E+00	3.402E+00	9.161E+00
Iodine	^{129}I	1.57E+07	9.130E+00	2.381E+01	2.079E-01	5.422E-01
Cesium	^{135}Cs	2.30E+06	4.455E+01	1.267E+02	6.926E+00	1.970E+01
	^{137}Cs	3.02E+01	2.454E+01	7.821E+01	2.919E+05	9.299E+05
Samarium	^{151}Sm	9.00E+01	3.495E+00	8.029E+00	1.388E+04	3.189E+04
Europium	^{150}Eu	3.60E+01	1.363E+00	1.107E-02	1.354E+04	1.099E+02
	^{152}Eu	1.35E+01	1.376E+00	2.682E+00	3.634E+04	7.083E+04
	^{154}Eu	8.59E+00	7.135E-01	1.317E+00	2.968E+04	5.480E+04
Holmium	^{166m}Ho	1.20E+03	8.945E-02	1.852E-01	2.665E+01	5.514E+01
Thorium	^{232}Th	1.40E+10	2.338E+05	6.863E+05	5.969E+00	1.752E+01
Uranium	^{232}U	6.89E+01	1.759E-02	7.203E-02	9.004E+01	3.690E+02
	^{233}U	1.59E+05	5.352E+01	6.792E+01	1.202E+02	1.525E+02
	^{234}U	2.46E+05	5.868E+01	1.029E+02	8.528E+01	1.495E+02
	^{235}U	7.04E+08	5.035E+03	6.342E+03	2.557E+00	3.220E+00
	^{236}U	2.34E+07	5.976E+01	2.265E+02	9.123E-01	3.458E+00
	^{238}U	4.47E+09	1.084E+05	1.963E+05	8.674E+00	1.570E+01
Neptunium	^{237}Np	2.14E+06	6.821E+00	6.415E+01	1.140E+00	1.072E+01
Plutonium	^{238}Pu	8.77E+01	4.352E+00	2.735E+00	1.774E+04	1.115E+04
	^{239}Pu	2.41E+04	6.738E+03	1.852E+03	9.997E+04	2.746E+04
	^{240}Pu	6.56E+03	4.646E+02	1.293E+02	2.523E+04	7.045E+03
	^{241}Pu	1.44E+01	1.376E+01	4.165E+00	3.415E+05	1.034E+05
	^{242}Pu	3.75E+05	7.851E+00	4.847E+00	7.485E+00	4.621E+00
Americium	^{241}Am	4.33E+02	2.795E+01	7.368E+00	2.309E+04	6.088E+03
	^{243}Am	7.37E+03	5.530E-02	7.042E-02	2.682E+00	3.416E+00
Curium	^{244}Cm	1.81E+01	8.030E-02	1.269E-01	1.586E+03	2.506E+03
Total			**6.477E+05**	**1.754E+06**	**1.578E+07**	**3.523E+07**

Source: Modified from Bowen et al., 2001

Note: Data are decay corrected to September 23, 1992 (the date of the last underground nuclear test at the NNSS).

[a] Total inventory for detonations conducted more than 100 m above the water table.
[b] Total inventory for detonations conducted below or within 100 m of the water table.

The decay correction for each radionuclide was accomplished with the following formula:

$$n(t) = n(0)e^{-\lambda t} \tag{2-1}$$

where

λ = decay constant = $\ln(2)/t_{1/2}$, where $t_{1/2}$ = half-life (years)
$n(0)$ = number of moles of radionuclide at the time of the detonation ($t = 0$)
t = time elapsed between the time of the detonation and September 23, 1992 (years)
$n(t)$ = number of moles of radionuclide reported in Bowen et al. (2001) (decay corrected to September 23, 1992)

Ingrowth from parent radionuclides in a decay chain can provide an additional source of inventory, and the decay correction of the Bowen inventory to the time of detonation should include ingrowth. The only radionuclide decay chain with parent radionuclide half-lives sufficiently short as to influence the inventory within 1,000 years is $^{241}Pu \rightarrow {}^{241}Am \rightarrow {}^{237}Np$. However, the correct amount of the parent radionuclide at the time of the detonation cannot be calculated from the Bowen inventory because the amount of daughter radionuclides is the total from many different detonations conducted at very different times. The Yucca Flat testing period spanned 35 years, and the ratio of parent to daughter radionuclides is incorrect for the elapsed time. The result is that erroneous amounts of parent radionuclides will be calculated. Instead, the individual detonation inventory uses a conservatively overestimated amount of longer-lived and more mobile ^{237}Np at the time of the detonation.

Carle et al. (2008) identified additional unclassified sources of information to estimate ^{14}C and ^{39}Ar inventories for the HANDCAR detonation and ^{3}H and ^{85}Kr inventories for the NASH detonation. The additional sources provided lower or comparable inventories for these radionuclides except for ^{14}C for the HANDCAR detonation. A total of 5.3 curies (Ci) (0.085 mole) of ^{14}C was reportedly loaded onto the HANDCAR device as a tracer and is approximately one order of magnitude greater than the yield-weighted estimate. This value was used in place of the yield-weighted ^{14}C inventory for the HANDCAR detonation provided in Bowen et al. (2001).

Figure 2-5 illustrates the Yucca Flat inventory and relative percentage of inventory that is remaining through time starting in 1992. The radionuclides illustrated in Figure 2-5 are only those identified as relevant in the screening process presented in Section 2.3.1. The radionuclides that initially dominate the inventory are ^{3}H, ^{137}Cs, and ^{90}Sr, but they are overtaken by ^{239}Pu and ^{240}Pu after approximately

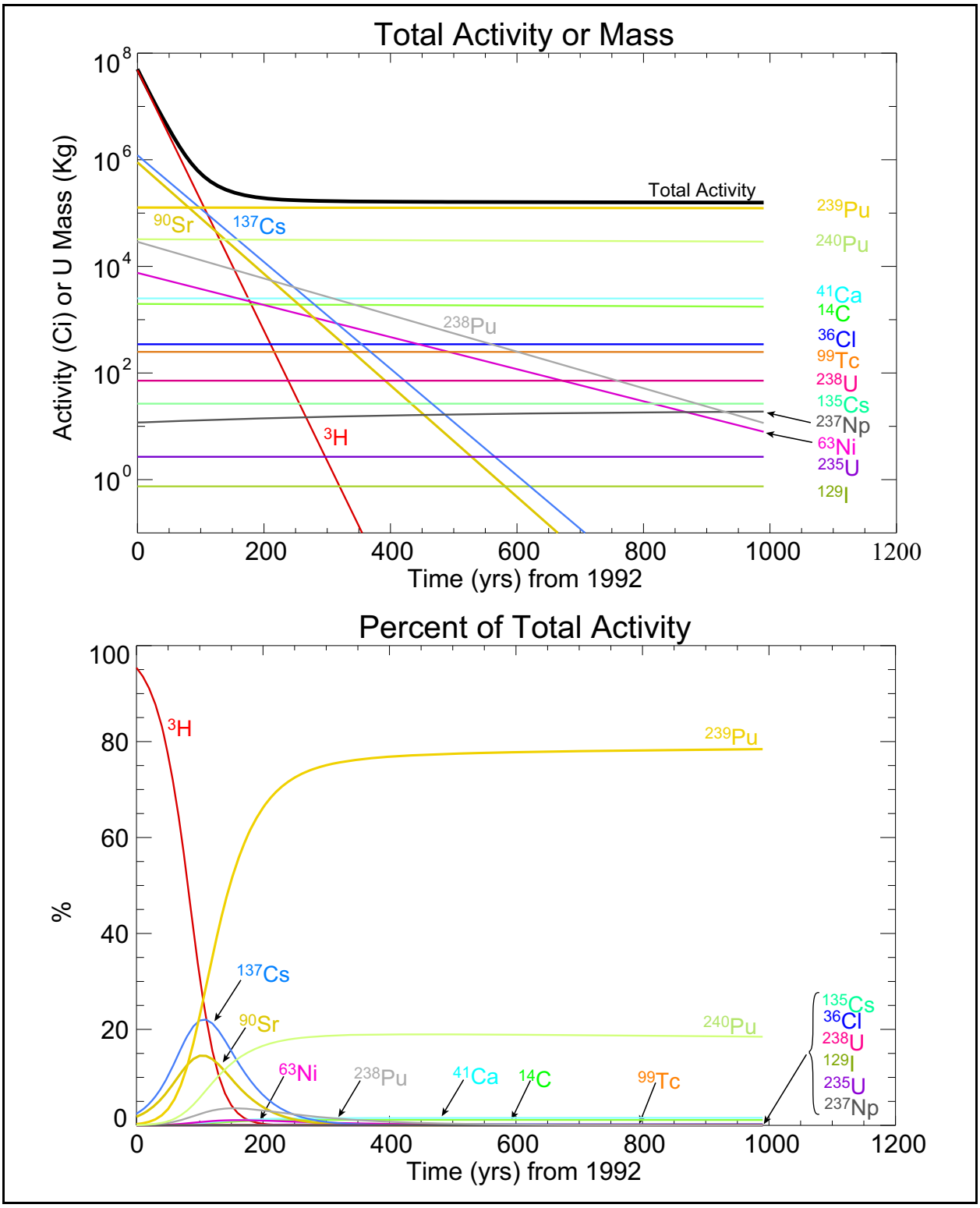

Figure 2-5
Total Radionuclide Activity versus Time

200 years. The influence of the decay chain $^{241}Pu \rightarrow {}^{241}Am \rightarrow {}^{237}Np$ is seen by the increase of ^{237}Np through time, which has increased by a factor of 1.6 within 1,000 years. Figure 2-6 illustrates the MCL-normalized cavity concentrations through time for representative silicic- and carbonate-rock working-point detonations assuming a burial depth of 400 m, an overburden bulk density of 2.0 grams per cubic centimeter (g/cm^3) and cavity porosity of 0.4. The R_c (in meters) for the silicic-rock representative detonation is calculated with the following equation (Pawloski, 1999):

$$R_c = \frac{70.2\,Y^{1/3}}{(\rho_b DOB)^{1/4}} \qquad (2\text{-}2)$$

where

Y	=	maximum yield (kt)
ρ_b	=	overburden density (g/cm^3)
70.2	=	constant developed for variably saturated silicic rocks at the NNSS
DOB	=	depth of burial (m)

The carbonate detonations have significantly smaller measured R_c (in meters) values than predicted with the empirical relationship expressed in Equation (2-2), and the cube-root energy-scaling equation developed by Boardman (1970) is used for the carbonate detonations:

$$R_c = CY^{1/3} \qquad (2\text{-}3)$$

where C is the constant developed for dense dolomite and limestone rock at the NNSS, and its value is 9.05. The maximum yield range reported in DOE/NV (2000b) is used for Y, regardless of the cavity radius equation used.

The smaller carbonate-rock cavity size results in a concentration that is approximately a factor of 3 higher than that for the silicic-rock cavity.

The fraction of radionuclides partitioned into the melt glass will be largely unavailable to groundwater. Figure 2-7 illustrates the MCL-normalized concentrations through time in the cavity excluding the inventory associated with melt glass. Removing the melt-glass inventory from the cavity reduces plutonium abundance by approximately a factor of 40 and strontium abundance by approximately a factor of 3.

The aqueous concentrations of many of the relevant radionuclides (including ^{90}Sr, ^{239}Pu, and ^{137}Cs) will be greatly reduced by sorption processes. Figure 2-8 illustrates the MCL-normalized

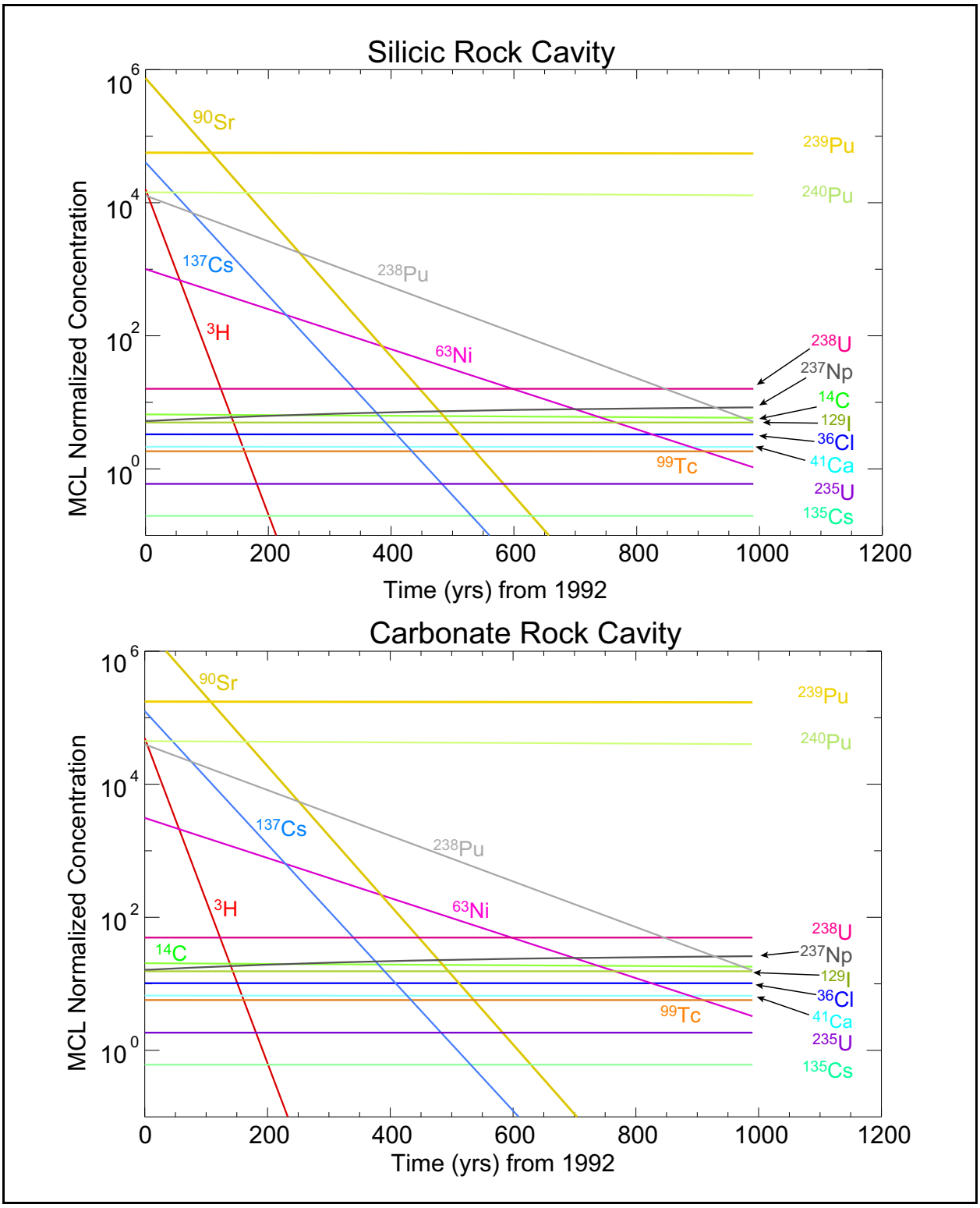

Figure 2-6
MCL-Normalized Cavity Concentration versus Time

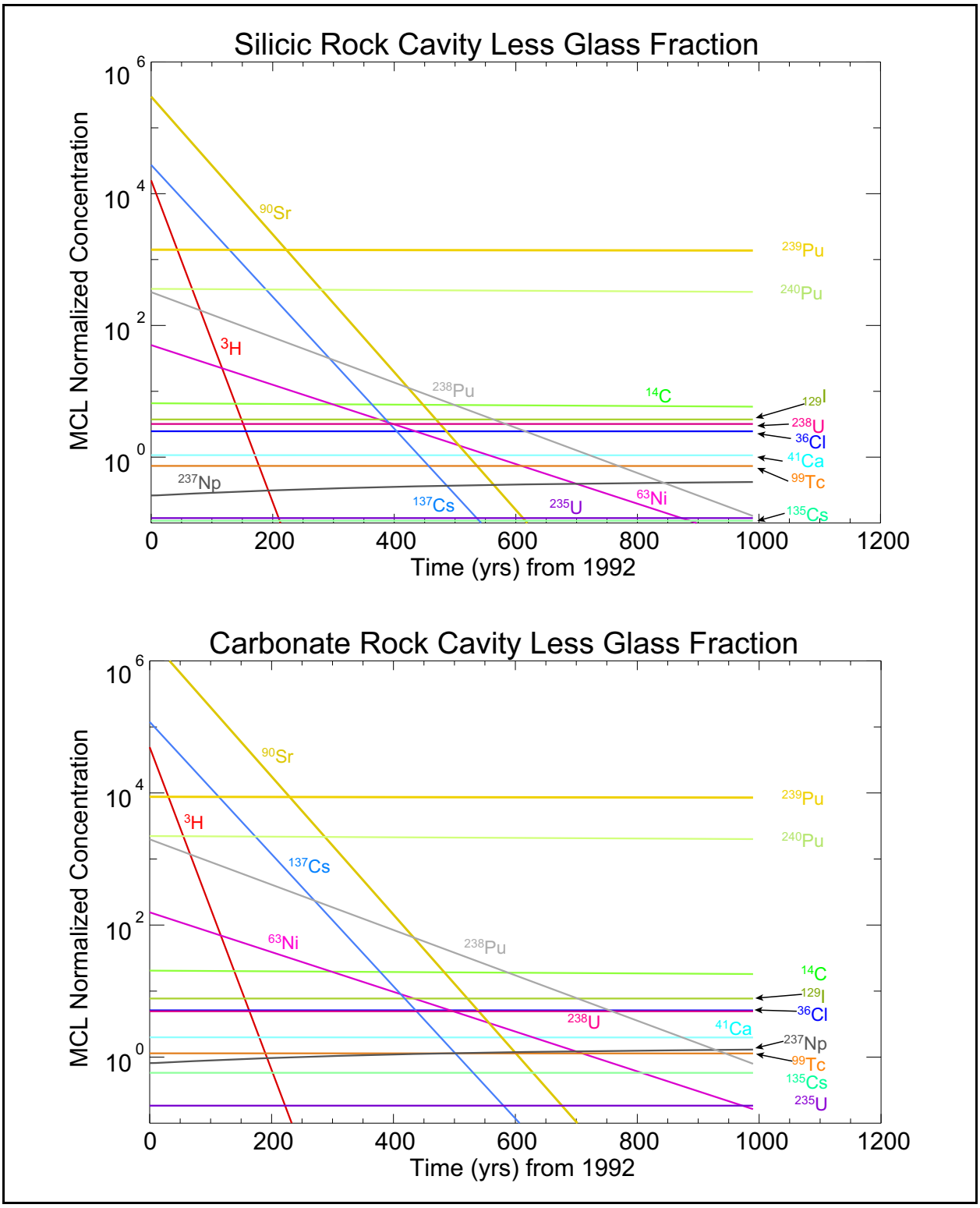

Figure 2-7
MCL-Normalized Cavity Concentration versus Time Less Melt-Glass Inventory

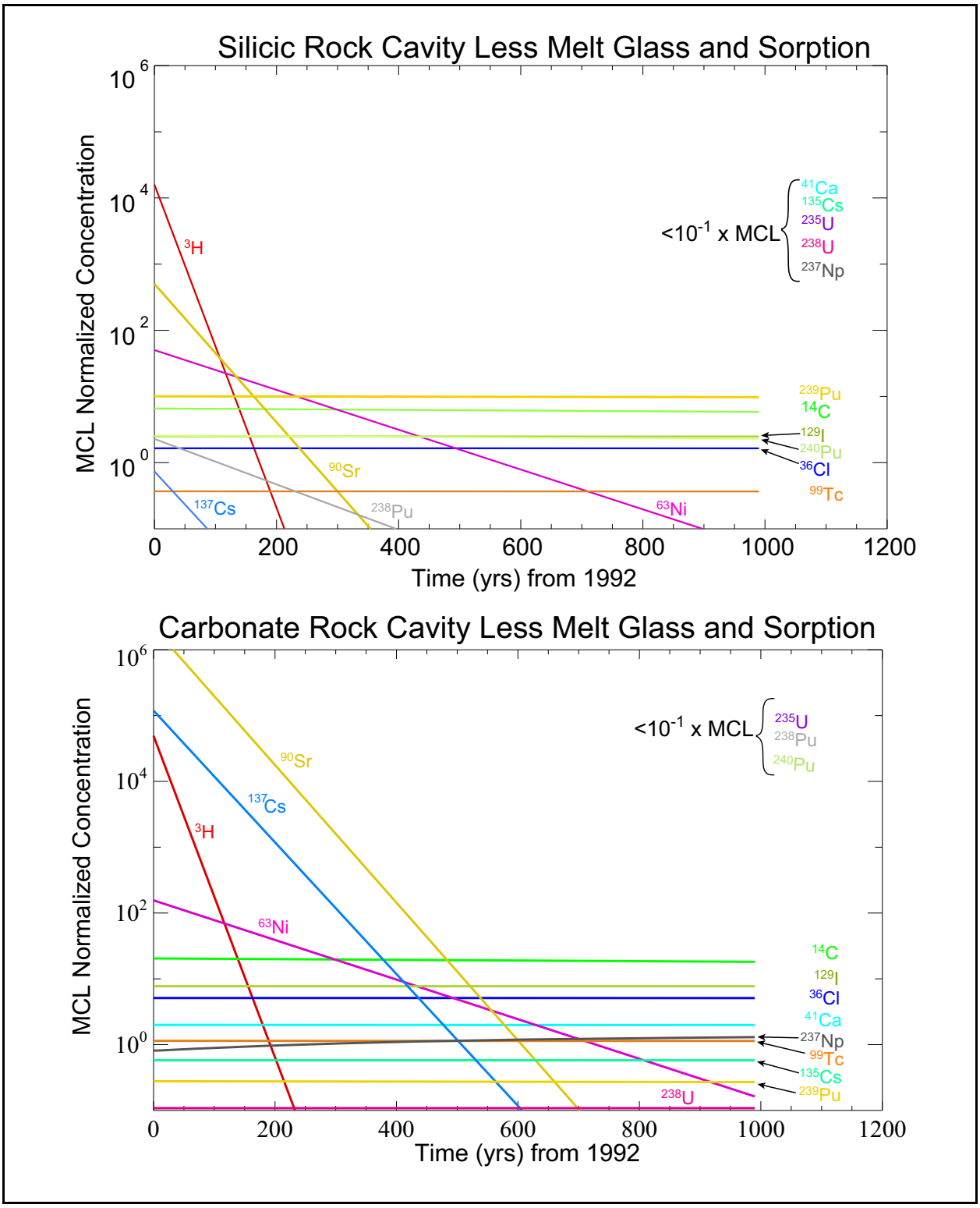

Figure 2-8
MCL-Normalized Cavity Concentration versus Time
Less Melt-Glass Inventory Considering Sorption

concentrations through time in the cavity. The normalized concentrations presented in the figure exclude the inventory associated with melt glass while taking into consideration the effect of sorption. The silicic rock K_d values used to generate Figure 2-8 are average values for the tuff confining units provided in the Yucca Flat/Climax Mine transport data document (TDD) (SNJV, 2007). The carbonate rock K_d values are the average used for the saturated LCA modeling presented in Section 6.3.5.2. Table 2-5 presents the volcanic and carbonate rock K_d values used to generate Figure 2-8. The strontium and plutonium concentrations are reduced several orders of magnitude for cavities located in tuff confining units. Only the plutonium and uranium concentrations are greatly reduced for cavities located in carbonate rock. The ^{90}Sr concentration within the LCA rock is initially very high, suggesting that ^{90}Sr is potentially significant to the Yucca Flat contaminant boundary for detonations with initial inventory residing in the LCA. This is an interesting result because past studies have demonstrated that ^{90}Sr contributes little to contaminant boundaries at the Pahute Mesa and Frenchman Flat CAUs. The larger influence is due to two reasons: first, sorption of ^{90}Sr in carbonate rock is much less than that in alluvium or volcanic rock; and second, ^{90}Sr is initially abundant (9.0E+06 Ci), similar to ^{3}H (4.8E+07 Ci), but the ^{90}Sr MCL is a factor of 2,500 less than the ^{3}H MCL.

Table 2-5
Volcanic and Carbonate Rock Cavity Sorption (K_d) Values

Radionuclide	Volcanic Rock K_d (mL/g)	Carbonate Rock K_d (mL/g)
^{41}Ca	871	0
^{90}Sr	468	0
$^{135/137}$Cs	17,400	0
U	23.4	15.0
^{237}Np	15.1	0
$^{239/240/242}$Pu	93.3	10,500

Source: Modified from SNJV, 2007

Note: All other radionuclides are considered to not be sorbed within the cavity.

If the melt-glass inventory is removed and sorption is considered, ^{3}H has the highest concentration in the tuff confining units, and ^{90}Sr has the highest concentration in the LCA. If radioactive decay also is

taken into consideration, ^{14}C, ^{129}I, and ^{36}Cl will have the highest concentrations over the long term within carbonate rock. The concentrations of ^{239}Pu and ^{240}Pu will also remain high within silicic rock.

2.3.1 Radionuclide Screening

As mentioned earlier, the Bowen inventory includes only those radionuclides with sufficient abundance to have concentrations above one-tenth of the MCLs for drinking water (EPA, 1991) in a fully saturated cavity 100 years from 1992. Bowen et al. (2001) did not consider radionuclide incorporation into melt glass or sorption processes, and an evaluation has shown that many of the radionuclides included in the Bowen inventory are unlikely to contribute to the contaminant boundary. Therefore, the radionuclides included in the Bowen inventory are further screened to identify only those that are relevant to forecasting the Yucca Flat contaminant boundary. Initial radionuclide concentrations in exchange volumes are calculated considering uncertainties in inventory, partitioning, exchange volume size, glass dissolution, and matrix sorption. The 95th percentile concentration at one-tenth of the MCL was used as the screening criteria to determine which radionuclides should be retained for analysis. The retained radionuclides are ^{3}H, ^{14}C, ^{36}Cl, ^{41}Ca, ^{63}Ni, ^{90}Sr, ^{99}Tc, ^{129}I, ^{135}Cs, ^{137}Cs, ^{235}U, ^{238}U, ^{237}Np, ^{238}Pu, ^{239}Pu, and ^{240}Pu. The screening analysis is presented Appendix C.

The only uranium isotopes considered in the Yucca Flat HST analysis are ^{235}U and ^{238}U. Neglecting the other uranium isotopes is appropriate because uranium is regulated based on its mass concentration rather than dose, and ^{238}U dominates the other uranium isotopes in mass. The Yucca Flat Bowen inventory contains 1.83E+29 atoms of ^{238}U. The uranium isotope ^{235}U is the second most abundant isotope, and the mass of ^{235}U is approximately 27 times less than the mass of ^{238}U. The masses of all other uranium isotopes are approximately 1,000 times less than the mass of ^{238}U.

2.3.2 Radionuclide Distribution in the Subsurface

At a very gross level, radionuclides associated with an underground nuclear detonation are partitioned into melt glass (or for carbonate detonations, carbonate-rock decomposition products), gas, rubble, and water phases. The melt glass or carbonate rock decomposition products are concentrated at the bottom of the cavity, and the remaining phases are usually grouped together and distributed within an exchange volume, which is conceptualized as a spherical region centered at the detonation

working point. Within the exchange volume, radionuclides are not distributed uniformly in the cavity or chimney region, but are partitioned based on physical and chemical characteristics.

Recent HST analysis and modeling by Tompson et al. (2011) reviewed radionuclide measurements and performed detailed modeling to provide the most current understanding of radionuclide distribution soon after a detonation. This recent HST work is summarized in Appendix C and provides the basis for a radionuclide-specific range of partitioning behavior. The uncertainty in the extent and shape of the exchange volume may be represented with one degree of freedom, which is a multiple of the cavity radius (the R_c multiplier). The exchange volumes for more volatile radionuclides will be larger than those for refractory radionuclides, and gas-phase redistribution in unsaturated settings will produce the largest exchange volumes for gaseous radionuclides such as $^{14}CO_2$. The following criteria for assigning exchange volume size to the radionuclides included in the Bowen inventory are used:

- If a radionuclide partitions into glass at greater than or equal to 90 percent, its exchange volume range is 1 to 1.5 R_c.
- If a radionuclide partitions into glass at less than 90 percent but greater than 0 percent, its exchange volume range is 1.5 to 3 R_c.
- If a radionuclide partitions into glass at 0 percent, its exchange volume range is 3 to 5 R_c.
- For ^{3}H, an exchange volume range is 1.5 to 3 R_c.
- For ^{14}C, the above-water-table exchange volume range is 3 to 5 R_c.
- For carbonate detonations, ^{90}Sr and ^{137}Cs have ranges that are higher than those shown in earlier Yucca Flat HST studies. The exchange volume range is 1.5 to 3 R_c in the saturated zone and 3 to 5 R_c in the unsaturated zone.

Table 2-6 presents the radionuclides and their partitioning for silicic-rock working-point detonations as described in Tompson et al. (2011) and Appendix C. Table 2-7 presents radionuclides and their partitioning for carbonate-rock working-point detonations as described by Carle et al. (2008). The radionuclides that were screened out based on the analyses in Appendix C are not included in Tables 2-6 and 2-7.

Table 2-6
Radionuclide Partitioning for Silicic-Rock Working-Point Detonations

Radionuclide	Partitioning Percent			
	Glass		Gas, Water, and Rubble	
	Minimum	Maximum	Minimum	Maximum
^{3}H, ^{14}C	0	0	0	100
^{63}Ni, ^{237}Np	90	100	0	10
^{36}Cl, ^{129}I	0	50	50	100
^{41}Ca	30	70	30	70
^{90}Sr, ^{99}Tc	40	80	20	60
^{135}Cs	20	70	30	80
^{137}Cs	25	40	60	75
^{235}U, ^{238}U	70	90	10	30
^{238}Pu, ^{239}Pu, ^{240}Pu	95	100	0	5

Source: Modified from Tompson et al., 2011

Table 2-7
Radionuclide Partitioning for Carbonate-Rock Working-Point Detonations

Radionuclide	Partitioning Percent			
	Glass [a]	Rubble	Gas	Water
^{3}H	0	0	2	98
^{14}C	0	10	80	10
^{36}Cl, ^{129}I	50	40	0	10
^{41}Ca	70	30	0	0
^{63}Ni, ^{237}Np, ^{238}Pu, ^{239}Pu, ^{240}Pu	95	5	0	0
^{90}Sr, ^{135}Cs, ^{137}Cs	5	95	0	0
^{99}Tc	80	20	0	0
^{235}U, ^{238}U	90	10	0	0

Source: Modified from SNJV, 2009b

[a] The “glass” consists of calcite, dolomite, and their decomposition products instead of silicate glass. Among the four carbonate detonations conducted at Yucca Flat, only the BOURBON detonation has a silicate glass puddle.

Radionuclides incorporated in the melt-glass matrix are accessible to groundwater only through the slow processes of melt-glass dissolution. The radionuclides associated with rubble, gas, and water are predominantly associated with surfaces, and are immediately accessible to groundwater dependent on the sorption characteristics of the radionuclides (Smith, 1995). The radionuclides associated with the highly radioactive zone at the cavity bottom of the carbonate detonation are considered insoluble (SNJV, 2009b).

2.3.3 Allocation of Radionuclides between Models

Many of the Yucca Flat detonations have exchange volumes that span across the models. There is considerable uncertainty in the extent of the exchange volume and initial distribution of radionuclides within the exchange volume. Therefore, two allocation methods are considered to capture the conceptual uncertainty of the post-detonation conceptual model (see Section 2.4.1). This section describes the two methods used to allocate the initial inventory between the three Yucca Flat transport models.

The first allocation method assumes that the exchange volume has a uniform radius of 1, 2, or 3 R_c and that radionuclides in the exchange volume are allocated by the fraction of total (fracture and matrix) pore space within each model domain. All radionuclides use the same exchange volume extent, and different exchange volume radii are used to capture conceptual uncertainty in the extent of the exchange volume for all radionuclides in unison. The HSU porosities used to calculate the total pore space are the mean values provided in SNJV (2007). The total porosity is used for HSUs with lithologic characteristics of a welded-tuff aquifer or a carbonate aquifer. The other HSUs are considered porous media and use the matrix porosity. The total porosity assumed for the detonation cavity is 0.4, which includes the rubble interstitial and matrix porosity. This value is representative of the average value used in HST modeling performed by Lawrence Livermore National Laboratory (LLNL) (Carle et al., 2003; Carle et al., 2007; Tompson, 2008; Tompson et al., 2011). Because this first allocation method is based on uniform mass within the pore space, it is referred to as the uniform-mass allocation method in this document.

The second allocation method implements the recent conceptual understanding of the radionuclide physical and chemical partitioning developed for the Rainier Mesa HST (Tompson et al., 2011). A summary of this conceptual understanding is provided in Appendix C. The conceptual model for

this allocation is that the radionuclide concentration in the water within the exchange volume is uniform and that the source for this water is the condensed steam generated from matrix saturation in the original rock that has been melted or vaporized by the detonation heat. The method uses the total pre-detonation volume of water located within the cavity zone to determine the post-detonation cavity saturation using a range of possible cavity porosity values. The pre-detonation HSU porosity and saturation values are from the CAU modeling values presented in Sections 3.0, 4.0, and 6.0. The total porosity assumed for the cavity after the detonation varies from 0.3 to 0.5 and is representative of the range of values used in HST modeling performed by LLNL (Carle et al., 2003; Carle et al., 2007; Tompson, 2008; Tompson et al., 2011). Beyond the cavity, all rock types, except the alluvium, which is considered a porous media, are considered fractured. The fracture porosity for the exchange volume is assumed to be 0.001 beyond the cavity, and the unsaturated-zone fracture saturation is zero. The actual post-detonation fracture saturation is unknown, but is likely greater than zero and is dependent on the geologic conditions and *in situ* saturation of the rock surrounding the detonation. Because the post-detonation saturation is highly uncertain, it is assumed to be zero. This is a conservative assumption that will overestimate the allocation of radionuclides in the downstream saturated models and their potential contributions to the contaminant boundary for detonations with exchange volumes that extend across the water table. This second allocation method also considers radionuclide-specific exchange volume radii. The extent of radionuclide distribution within the exchange volume is known to be heterogeneous and dependent on the type of device, detonation-specific phenomenology (e.g., collapse timing, chimney formation), geologic conditions, inherent saturation conditions in the rock surrounding the detonation location, and radionuclide-specific thermodynamic properties (Tompson et al., 2011). Because this second allocation method is based on the assumption of uniform concentration within the pore space, it is referred to as the uniform-concentration allocation method in this document.

The elevation of the water table used in both allocation methods is the actual estimated value from DOE/NV (1997b). One exception implemented in both allocation methods is to move the inventory of the saturated-zone working-point detonations that extends into the unsaturated-zone model domain down to the saturated alluvial/volcanic aquifer system model domain. This was done because the unsaturated-zone model does not have mesh refinement in the cavity/exchange volume region for the detonations with working points below the water table and cannot accurately simulate radionuclide

transport from the source areas of these detonations. This is a conservative assumption that will overestimate radionuclide concentrations and potential contributions to the contaminant boundary. The individual detonation RST and inventory distribution between the three models are provided in Appendix C.

Figure 2-9 illustrates the stratigraphy at the CORDUROY detonation site. If one assumes an exchange volume radius of 2 R_c, the CORDUROY detonation has an exchange volume that spans across all three models, but the cavity (1 R_c) spans only the saturated alluvial/volcanic aquifer system model and the saturated LCA model. The first allocation method assumes that the porosities are 0.4 for the tuff confining units, 0.4 for the cavity, and 0.03 for the LCA. The resulting inventory allocation is 6 percent to the unsaturated-zone model, 92 percent to the saturated alluvial/volcanic aquifer system model, and 2 percent to the saturated LCA model. The second allocation method assumes that the exchange volume extent and cavity porosity values are random variables (see Section 2.4.2). When a mean cavity porosity of 0.4 and an exchange volume extent of 2.25 R_c (^{90}Sr mean exchange volume radius from Table C-2) are used, the resulting allocation is 0 percent to the unsaturated-zone model, 85 percent to the saturated alluvial/volcanic aquifer system model, and 15 percent to the saturated LCA model.

Table 2-8 summarizes the total inventory fractions for each Yucca Flat model domain for the two allocation methods. The uniform-mass allocation fractions represent the fractions of total exchange volume pore space present in each model domain, and the uniform-concentration fractions represent the fractions of total exchange volume water present in each model domain. The allocation fractions are used to distribute the Bowen inventory between the three model domains, but are not directly proportional to the total inventory assigned to each model domain for two reasons:

- Bowen et al. (2001) subdivide the Yucca Flat inventory according to the location of each detonation relative to the water table. Totals are presented for those detonations located more than 100 m above the water table and those detonations located below the water table or within 100 m of the water table. The yield-normalized inventory is different for the two inventories. For example, the yield-normalized inventory ratio of more than 100 m above the water table to below the water table is 0.65 for ^{3}H and 2.0 for ^{14}C.

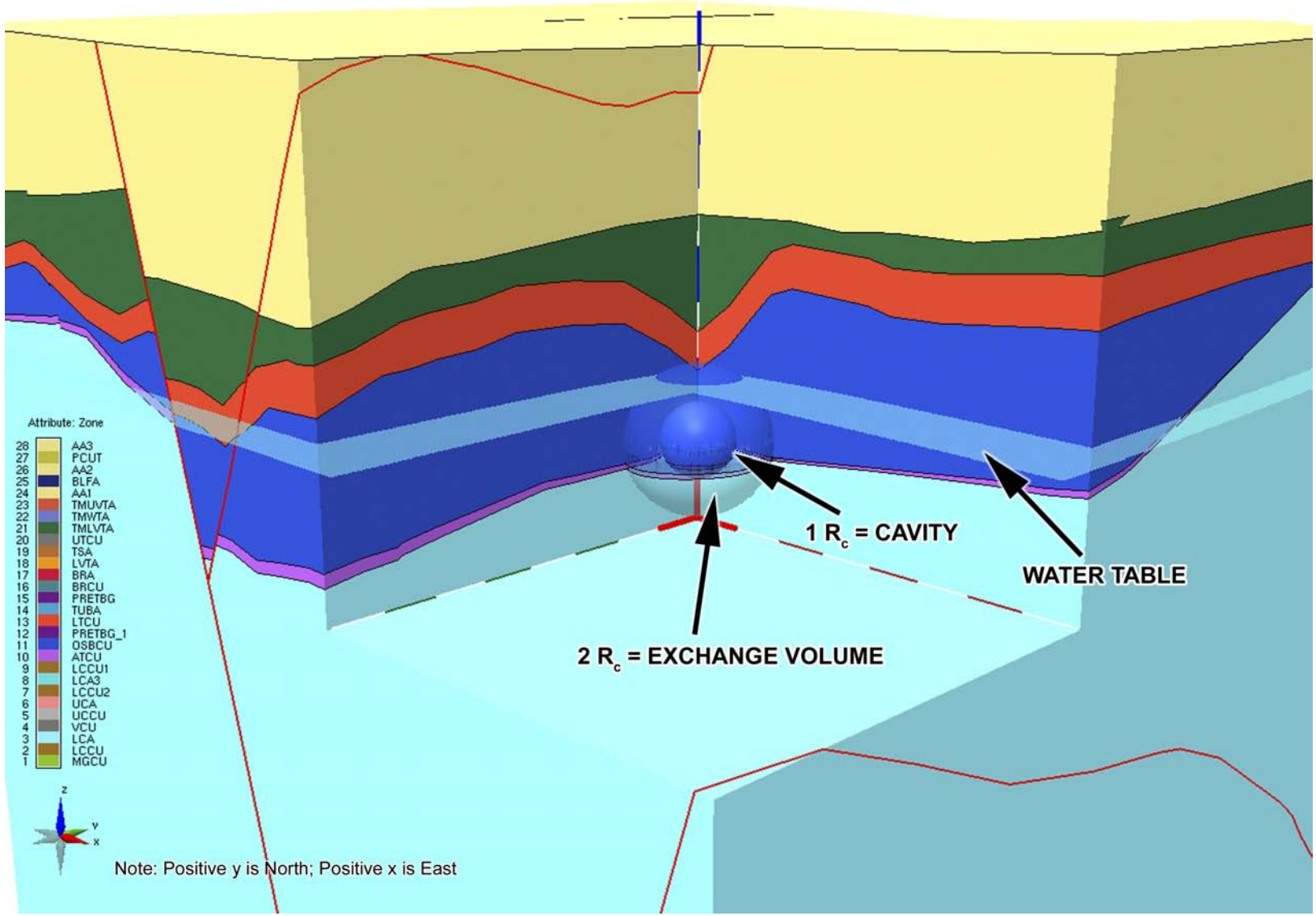

Figure 2-9
Block-Diagram Perspective of the CORDUROY Detonation within the HFM

Table 2-8
Initial HST Allocation Fractions in the Unsaturated Zone, Saturated Alluvial/Volcanic Aquifer System, and Saturated LCA Models for All Detonations

Allocation Method	Allocation Fractions		
	Unsaturated Zone	Saturated Alluvial/Volcanic Aquifer System	Saturated LCA
Uniform-Mass Allocation Method (2 R_c Exchange Volume)	0.75	0.25	0.00044
Uniform-Concentration Allocation Method			
Volatile Radionuclides (2.25 R_c Exchange Volume) [a]	0.75	0.24	0.00072
Gaseous Radionuclides (4 R_c Exchange Volume in Unsaturated Zone and 2.25 R_c Exchange Volume in Saturated Zone) [a]	0.92	0.075	0.00017
Refractory Radionuclides (1.25 R_c Exchange Volume) [a]	0.50	0.49	0.0017

[a] Exchange volume radius is the mean value from Table C-2, using the radionuclide exchange volume category from Table 2-10.

- Bowen inventory represents the amount of radionuclides as of September 23, 1992. The Bowen inventory associated with individual detonations is decay corrected back to the time of detonation before being assigned to each detonation within the models. The Yucca Flat testing period spanned 35 years, and the total amount of inventory assigned to each detonation can be very different for short-lived radionuclides. For example, a period of 35 years represents approximately three ^{3}H half-lives, and the amount of ^{3}H present may be a factor of 10 different over this time period.

The resulting fractions of total radionuclides assigned to each model can be very different from the allocation fractions and very different between individual radionuclides. Table 2-9 summarizes the ^{3}H and ^{14}C total inventory fractions for each Yucca Flat model domain for the two allocation methods using the Bowen et al. (2001) inventory as of 1992. The uniform mass inventory fractions for ^{3}H and ^{14}C illustrate the influence of the smaller and larger above-the-water-table-to-below-the-water-table yield-normalized inventory ratios for ^{3}H and ^{14}C. The ^{3}H unsaturated-zone model inventory fraction is decreased and the ^{14}C unsaturated-zone model inventory fraction slightly increased compared to the allocation fractions provided in Table 2-8.

As seen in Table 2-8, the uniform-concentration allocation method results in a larger unsaturated-zone allocation fraction for gaseous radionuclides (e.g., ^{14}C) compared to the uniform-mass allocation method. The larger unsaturated-zone model fraction is due to the influence

Table 2-9
Initial HST ^{3}H and ^{14}C Inventory Fractions in the Unsaturated Zone, Saturated Alluvial/Volcanic Aquifer System, and Saturated LCA Models for All Detonations

Allocation Method and Radionuclide	Inventory Fractions		
	Unsaturated Zone	Saturated Alluvial/Volcanic Aquifer System	Saturated LCA
Uniform-Mass Allocation Method			
^{3}H	0.61	0.39	0.0011
^{14}C	0.76	0.24	0.00066
Uniform-Concentration Allocation Method			
^{3}H	0.56	0.43	0.0061
^{14}C	0.74	0.25	0.0037

of the larger exchange volume within the unsaturated zone (4 R_c) compared to the exchange volume within the saturated zone (2.25 R_c) for those detonations that are near the water table and are located within the alluvium. The unsaturated-zone inventory fraction of ^{14}C in Table 2-9 is less than the gaseous radionuclide allocation fraction in Table 2-8, because the deep alluvial detonations are located below or within 100 m of the water table, and the ratio of 2.0 for above- to below-the-water-table yield-normalized inventories decreases the unsaturated-zone inventory fraction of ^{14}C compared to the allocation fraction.

Overall, the inventory fractions calculated using the uniform-mass and uniform-concentration allocation methods are similar when summed across all Yucca Flat detonations. However, the individual detonation allocations using the two methods can be very different. The CORDUROY detonation example discussed earlier in this section and the ^{14}C allocation discussed in the preceding paragraph illustrate these differences.

In general, the uniform-mass allocation method will result in higher concentrations within the unsaturated portion of the exchange volume compared to the uniform-concentration allocation method. However, the uniform-mass allocation method also considers the exchange volume extent to be radionuclide independent and distributes all non-melt-glass radionuclides homogeneously throughout the exchange volume. This assumption will overestimate the volatile radionuclide (e.g., ^{3}H) initial concentration within a 1 R_c exchange volume, but underestimate the refractory

radionuclide (e.g., ^{240}Pu) initial concentration within a 3 R_c exchange volume compared to the uniform-concentration allocation method. The uniform-mass allocation method will also place more mass within the unsaturated portion of the exchange volume compared to the uniform-concentration allocation method because it neglects saturation in the allocation. However, at specific detonation locations, the consideration that the extent of the exchange volume is radionuclide independent may place more or less mass in the unsaturated exchange volume compared to the uniform-concentration allocation method depending on the location of the exchange volume relative to the water table. For example, when an exchange volume of 3 R_c is assumed at a location with the cavity mostly located above the water table, the uniform-mass allocation method will place less ^{240}Pu in the unsaturated exchange volume compared to the uniform-concentration allocation method.

Both allocation methods use the cavity size estimated from the maximum announced yield, which is mandated by DOE guidance for all unclassified analyses. The the cavity radius is most strongly a function of yield, and lesser a function of working-point depth and overburden density (Pawloski, 1999), and using the maximum announced yield results in the maximum possible cavity and exchange volume size. The larger exchange volume sizes will conservatively place more of the RST directly within the saturated LCA because all detonations were performed above the saturated LCA, and increasing the size conservatively results in a larger fraction of the exchange volume residing within the saturated LCA.

2.4 HST Uncertainties

Uncertainty in model prediction results from two types of uncertainties: (1) conceptual model uncertainty, and (2) parameter uncertainty. Conceptual model uncertainty results from oversimplification or incomplete understanding of complex processes being modeled. Parametric uncertainty arises from a lack of knowledge about model parameter values. Conceptual model uncertainty is incorporated into the Yucca Flat flow and transport modeling by developing alternative conceptual models. Parametric uncertainty is incorporated into the Yucca Flat flow and transport modeling through statistical distributions of uncertain parameters and Monte Carlo methods.

The HST uncertainty discussed in this section is limited to the HST aspects that are generic to all three CAU models (e.g., Bowen inventory, exchange volume radii, and RST allocation between model domains). The treatment of HST uncertainties specific to each Yucca Flat flow and transport model (e.g., altered-zone properties) is described in detail in Sections 3.0 to 6.0.

2.4.1 HST Conceptual Model Uncertainty

There are several sites in Yucca Flat (e.g., BASEBALL, INGOT, HYRAX, HANDCAR, NASH, BOURBON, BILBY, ALEMAN, SANDREEF, DALHART, and GASCON) where information about the distance of radionuclide migration in the near field is available, but information about radionuclide concentrations in the near field is limited or absent for most of the other detonations conducted in Yucca Flat. The large number of Yucca Flat detonations and limited data preclude assessing uncertainties in the HST conceptual model or model calibration for each detonation. Therefore, the HST conceptual model uncertainty considers alternative HST allocations between the three CAU models, investigating the sensitivity of the contaminant boundary forecast to several HST processes that include the following:

- ***Altered-zone permeability enhancement and cavity/chimney drainage.*** The HST modeling of the NASH detonation (Carle et al., 2008) concluded that permeability enhancement resulting from cavity collapse, fracturing of *in situ* rocks surrounding the cavity, and chimney formation can induce rapid drainage of perched water and transport mobile radionuclides to the saturated zone.
- ***Drill-back fluid.*** The HST modeling of the HANDCAR detonation (Carle et al., 2008) concluded that 5,660 m^3 of drilling fluid associated with post-detonation drilling activities can transport mobile radionuclides such as ^3H to the saturated zone.
- ***Allocation derived from pre-detonation exchange volume water.*** According to the relatively recent conceptual understanding of the radionuclide physical and chemical partitioning described in Tompson et al. (2011) and summarized in Appendix C, the source for cavity water is the condensed steam generated from matrix saturation in the original rock that melted or vaporized after the detonation, and upon condensation, this water will redistribute in the cavity at saturations dictated by the post-detonation total porosity (Section 2.3.3).
- ***Allocation derived from radionuclide-specific exchange volume extent.*** This conceptual understanding of the radionuclide physical and chemical partitioning also takes into consideration exchange volume radii specific to radionuclides. According to this understanding, the exchange volumes for more volatile radionuclides will be larger than those for refractory radionuclides, and gas-phase redistribution in unsaturated settings will produce the largest exchange volumes for gaseous radionuclides such as $^{14}CO_2$ (Appendix C and Section 2.3.3).

Conceptual model uncertainties will have the most significant effect on the detonations within or very near the LCA because the low primary and secondary porosities of the carbonate rock will produce relatively fast water movement compared to the volcanic rock or alluvium. Uncertainties related to HST processes are addressed through an approach that places the RST for several detonations directly into the saturated LCA. This approach is applied to the following detonations because of the processes identified in parentheses following the detonation name(s): BOURBON, HANDCAR, KANKAKEE, and NASH (carbonate-rock working point, potential cavity/chimney drainage and drill-back fluid injection); CORDUROY, TORRIDO, and LAMPBLACK (altered-zone permeability enhancement and hydraulic communication, and drill-back fluid injection); and CALABASH (altered-zone permeability enhancement, drill-back fluid injection, and chimney drainage). This is an extremely conservative assumption that will overestimate allocation of radionuclides in the saturated LCA and their potential contributions to the contaminant boundary for these detonations.

Conceptual uncertainties associated with inventory allocation between the models is addressed by implementing the two allocation methods presented in Section 2.3.3. The unsaturated-zone model and the saturated alluvial/volcanic aquifer system model consider the uniform-mass allocation between the models as the base case and the uniform-concentration allocation calculated with mean values as a sensitivity case (Section 2.3.3). The saturated LCA model considers the uniform-concentration allocation as the base case and the uniform-mass allocation as a sensitivity case. Both allocation methods are generally consistent with the post-detonation conceptual model presented in Section 2.2, but the uniform-mass allocation method is more consistent with the most recent understanding of the post-detonation radionuclide partitioning within the exchange volume presented in Appendix C. The different treatment of base-case and sensitivity-case allocation methods is due to the timing of the Yucca Flat modeling work compared to the development of the post-detonation conceptual model presented in Appendix C. The Appendix C conceptual model was developed for the Rainier Mesa HST (Tompson et al., 2011), but is also considered applicable to the Yucca Flat HST. This Rainier Mesa work was performed after much of the Yucca Flat unsaturated-zone and saturated alluvial/volcanic aquifer modeling was completed, which precluded its full implementation in these modeling efforts.

In summary, the unsaturated-zone and saturated alluvial/volcanic aquifer system models consider the uniform-mass allocation with a 2 R_c exchange volume extent as the base-case HST and evaluate the

base case against the following sensitivity cases: (1) uniform-mass allocation with a 1 R_c exchange volume extent, (2) uniform-mass allocation with a 3 R_c exchange volume extent, and (3) uniform-concentration allocation with a radionuclide-specific, mean exchange volume extent. The saturated LCA model considers the uniform-concentration allocation as the base case. In this model, the exchange volume extent is considered a random variable that is radionuclide specific. Two sensitivity cases are considered. The first sensitivity case is the uniform-mass allocation with a 2 R_c exchange volume extent. The 2 R_c exchange volume extent represents the midpoint of the range of variability expected in exchange volume radii (between 1 and 3) associated with the Yucca Flat HST (Pawloski et al., 2008). The second sensitivity case is a uniform-concentration allocation with the HST of detonations associated with possible fast transport to the saturated LCA placed directly within the saturated LCA (BOURBON, HANDCAR, KANKAKEE, NASH, CORDUROY, TORRIDO, LAMPBLACK, and CALABASH).

2.4.2 HST Parametric Uncertainty

Tompson et al. (2011) estimated ranges of partitioning behavior for different radionuclide categories (Section 2.3.2), and Bowen et al. (2001) estimated the accuracies of the inventories reported for different groups of radionuclides. Parametric uncertainties associated with calculating allocation between the Yucca Flat models include uncertainties in the extent of exchange volume and cavity porosity. Parametric uncertainties associated with calculating the radionuclide release to the model domains include allocation fraction, melt-glass fraction, and inventory uncertainties. Table 2-10 presents the exchange volume category, radionuclide group, and inventory accuracy assigned to each of the retained radionuclides, and Table 2-11 presents the parameter distributions as defined in Appendix C. Uncertainties in the exchange volume extent, melt-glass partitioning, and inventory are represented as multiplicative factors for the cavity radius, melt-glass fraction, and Bowen inventory, respectively.

The saturated LCA sources are the most significant for the contaminant boundary calculation, which warrants propagation of parametric HST uncertainty to the saturated LCA model. In the unsaturated-zone model and the saturated alluvial/volcanic aquifer system model, HST parametric uncertainty is insignificant compared to other uncertainties (e.g., infiltration rate and overpressurization effects); therefore, HST parametric uncertainty in these models is investigated by

Table 2-10
Retained Radionuclide Categories and Radionuclide Groups

Radionuclide	Exchange Volume Category	Radionuclide Group [a]	Inventory Accuracy [a]
^{3}H	Volatile	Residual Tritium	~300% or better
^{14}C	Gaseous	Activation Products	~a factor of 10
^{36}Cl	Volatile	Activation Products	~a factor of 10
^{41}Ca	Volatile	Activation Products	~a factor of 10
^{63}Ni	Refractory	Activation Products	~a factor of 10
^{90}Sr	Volatile	Fission Products	~10–30%
^{99}Tc	Volatile	Fission Products	~10–30%
^{129}I	Volatile	Fission Products	~10–30%
^{135}Cs	Volatile	Fission Products	~10–30%
^{137}Cs	Volatile	Fission Products	~10–30%
^{235}U	Refractory	Unspent Fuel Materials	~20% or better
^{238}U	Refractory	Unspent Fuel Materials	~20% or better
^{237}Np	Refractory	Unspent Fuel Materials	~20% or better
^{238}Pu	Refractory	Unspent Fuel Materials	~20% or better
^{239}Pu	Refractory	Unspent Fuel Materials	~20% or better
^{240}Pu	Refractory	Unspent Fuel Materials	~20% or better

[a] Source: Bowen et al., 2001

Table 2-11
Distributions of Source-Term Parameters
(Page 1 of 2)

Parameter	Distribution Type	Low	High	Mode
Gaseous Radionuclide Exchange Volume Radius/R_c	Triangular	3	5	4
Volatile Radionuclide Exchange Volume Radius/R_c	Triangular	1.5	3	2.25
Refractory Radionuclide Exchange Volume Radius/R_c	Triangular	1	1.5	1.25
^{36}Cl Melt Glass Percentage	Triangular	0	50	25
^{90}Sr Melt Glass Percentage	Triangular	40	80	60
^{63}Ni Melt Glass Percentage	Triangular	90	100	95
^{129}I Melt Glass Percentage	Triangular	0	50	25
^{99}Tc Melt Glass Percentage	Triangular	40	80	60
^{237}Np Melt Glass Percentage	Triangular	90	100	95
^{238}U Melt Glass Percentage	Triangular	70	90	80

Table 2-11
Distributions of Source-Term Parameters
(Page 2 of 2)

Parameter	Distribution Type	Low	High	Mode
Pu Melt Glass Percentage	Triangular	95	100	97.5
^{241}Am Melt Glass Percentage	Triangular	95	100	97.5
Fission Products RST Multiplier	Log Triangular [a]	–0.114	0.114	0 [a]
Unspent Fuel Materials RST Multiplier	Log Triangular [a]	–0.079	0.079	0 [a]
Nuclear Fuel Activation Products Log RST Multiplier	Log Triangular [a]	–0.176	0.176	0 [a]
^{3}H Log RST Multiplier	Log Triangular [a]	–0.477	0.477	0 [a]
Activation Products Log RST Multiplier	Log Triangular [a]	–1	1	0

[a] The log distribution data are the log10 of the values.

the use of a few discrete sensitivity cases. However, the saturated alluvial/volcanic aquifer system model investigates HST uncertainty related to the Bowen inventory and melt-glass partitioning using probabilistic methods within each discrete case. The saturated LCA model implements parametric HST uncertainty with 100 source terms for each detonation with an exchange volume extending into the saturated LCA for both allocation methods. Uncertain parameters are assumed to be independent of one another, and sampling of the distributions is performed with the Latin hypercube method. Uncertainty is propagated through the three model domains by selecting outputs from the upstream models that are consistent in terms of flow boundary conditions, exchange volume radii, and HST allocation methods.

Figures 2-10 to 2-12 illustrate the cumulative distribution functions (CDFs) and probability density functions (PDFs) of inventory allocation fractions for each exchange volume category for each Yucca Flat model. The inventory allocation fractions presented in these figures are the composite of all Yucca Flat detonations and display little variability because the parameter distributions are independently sampled for each detonation and the large number of Yucca Flat detonations produces an averaging effect. The PDFs for the unsaturated-zone model and saturated alluvial/volcanic aquifer system model have positive and negative skewness because of the movement of inventory from the saturated working-point detonations that extends into the unsaturated-zone model down to the saturated alluvial/volcanic aquifer system model. The allocation fractions for refractory radionuclides have a mostly triangular PDF, because the exchange volume radii range from 1 to 1.5 R_c, and the uncertainty is primarily introduced from the triangular cavity porosity distribution.

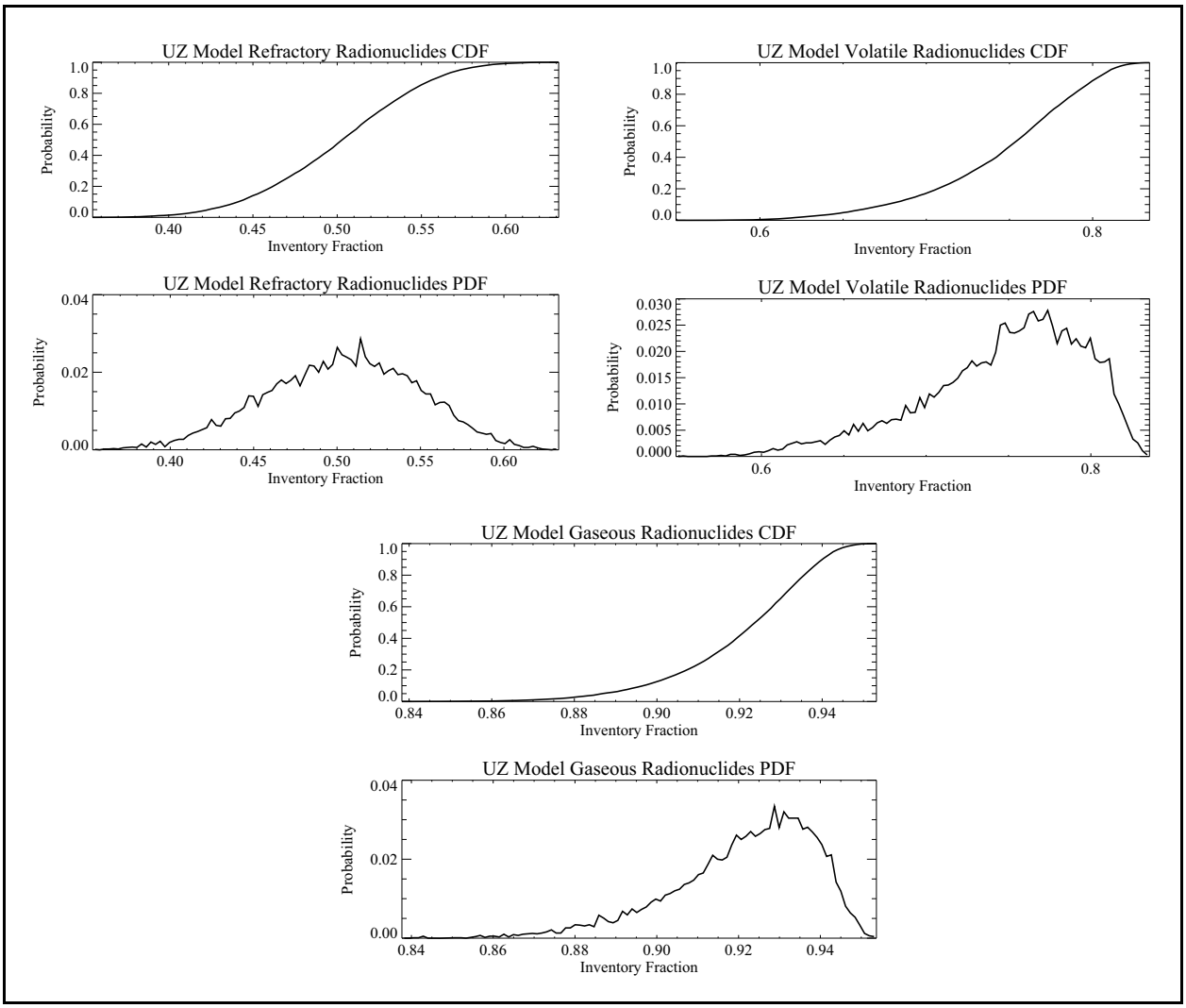

Figure 2-10
Inventory Allocation Fraction Uncertainty for the Unsaturated-Zone Model

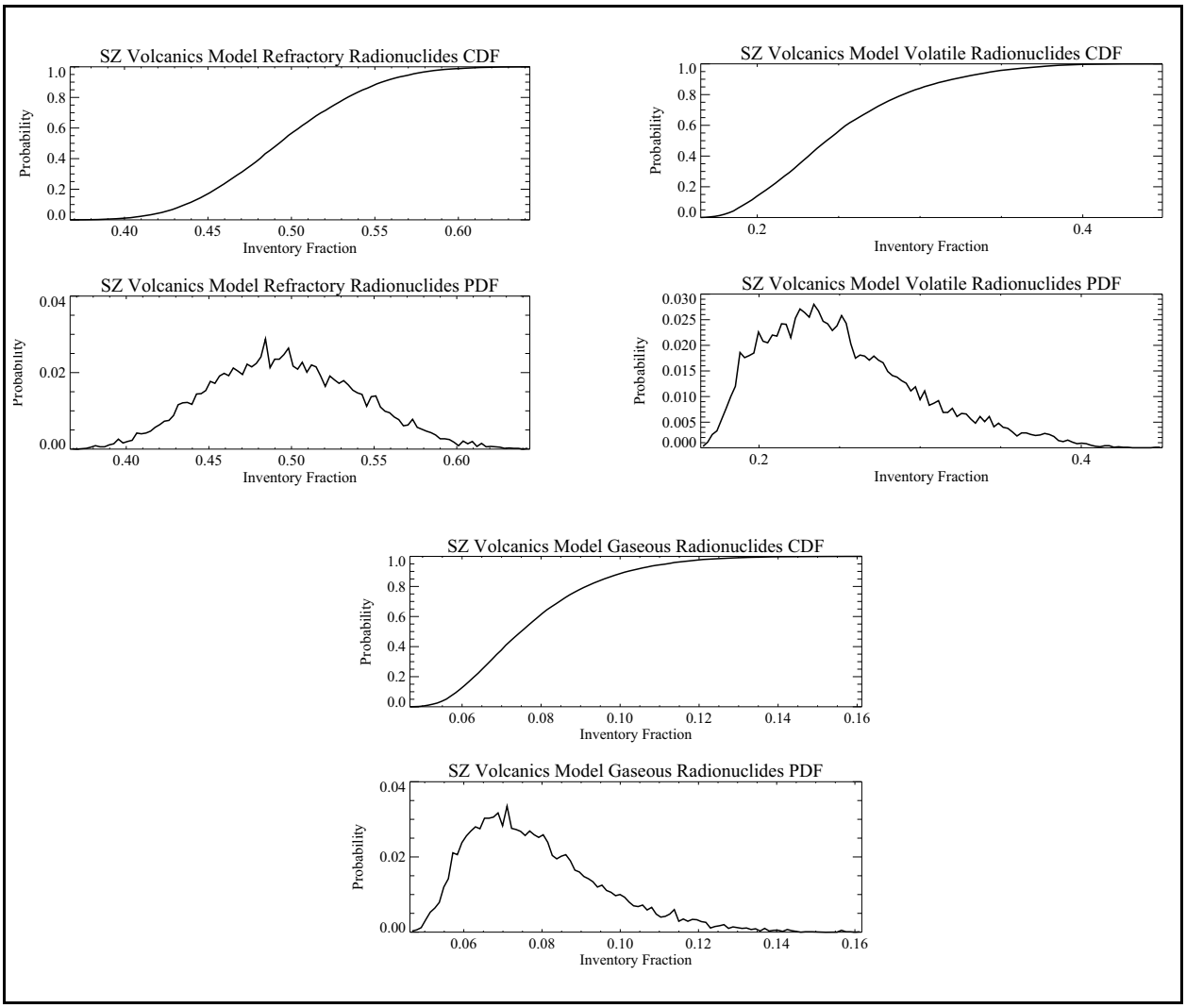

Figure 2-11
Inventory Allocation Fraction Uncertainty for the Saturated Alluvial/Volcanic Aquifer System Model

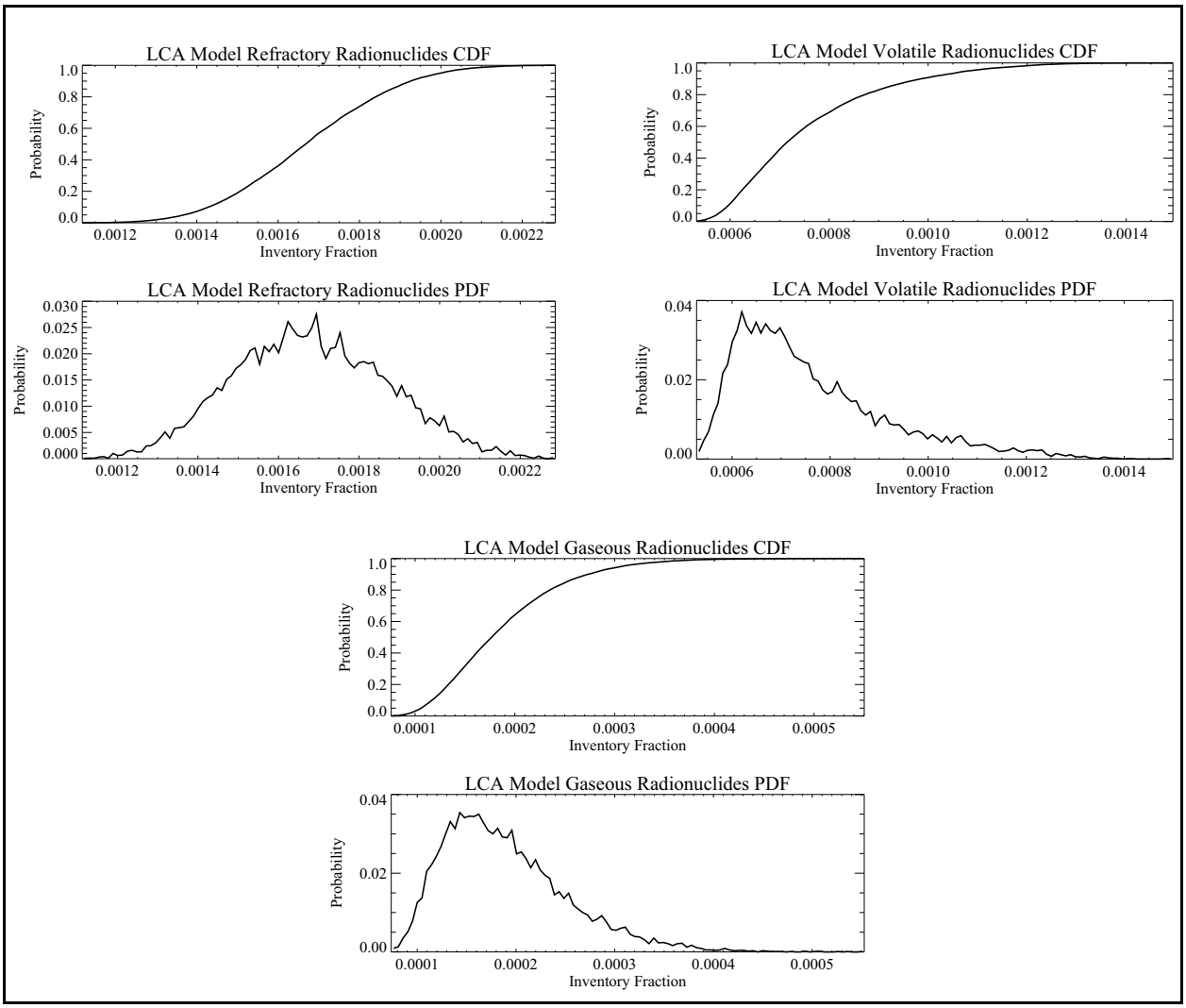

Figure 2-12
Inventory Allocation Fraction Uncertainty for the Saturated LCA Model

Figure 2-13 illustrates the CDFs and PDFs for three example radionuclides (^{3}H, ^{14}C, and ^{239}Pu) from the BOURBON detonation for the saturated LCA model. The CDFs and PDFs illustrated in Figure 2-13 are for a multiplicative factor operating on the fraction of the RST reported by Bowen et al. (2001) and assigned to the BOURBON detonation, and include the uncertainty associated with allocation fraction, melt-glass fraction, and RST inventory. The figure shows that ^{14}C has the largest uncertainty because the radionuclide belongs to the activation product group, which is the most uncertain (factor of 10). The ^{239}Pu RST multiplicative factor is least uncertain because inventory accuracy for unspent fuel materials is the highest among the radionuclide groups. The ^{239}Pu RST multiplicative factor is small because a large fraction of the ^{239}Pu inventory is incorporated into the melt glass and assumed inaccessible to groundwater. For example, the mean saturated LCA model allocation fraction is 0.388, and the mean ^{239}Pu inventory fraction partitioning within rubble is 0.025. The product of the allocation and rubble fraction is 0.0097, which is the 50 percent probability point for the LCA model ^{239}Pu CDF in Figure 2-13.

2.5 Summary and Conclusions

At Yucca Flat proper, a total of 744 underground nuclear detonations were conducted between 1957 and 1992. The total announced yield computed from the maximum yield provided in DOE/NV (2000b) is 38,964 kt. The HST described in this section is the portion of the RST that is released into the groundwater through time for each of the 744 detonations. The nuclear detonations within Yucca Flat were conducted in a variety of hydrogeologic settings. The processes controlling radionuclide migration away from the source areas in these settings are sufficiently different that modeling the releases from these sources is considered separately with different models. These different settings include (1) the unsaturated zone with enhanced subsidence crater recharge, (2) the saturated zone with detonation-induced transient high pressures occurring within the low-permeability tuff confining units, and (3) the fractured carbonate rock with highly conductive faults. The large number of Yucca Flat detonations and possible source-term interactions due to their close proximity to one another require implementing the relevant source-term processes directly within the Yucca Flat flow and transport models.

As shown in the modeling studies conducted for the Pahute Mesa CAU (SNJV, 2009a) and the Frenchman Flat CAU (NNES, 2010b), where contaminant boundaries were defined by a relatively

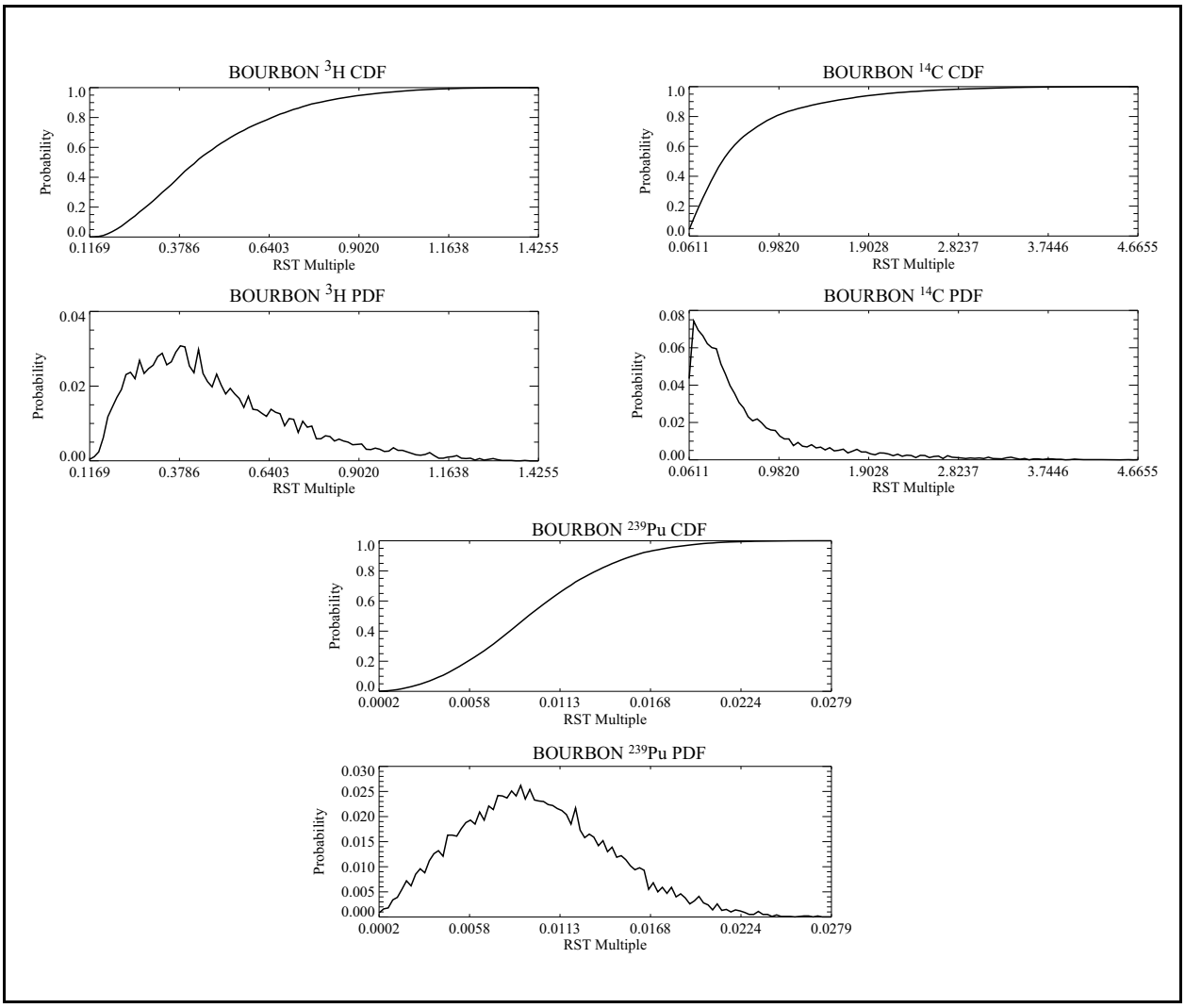

Figure 2-13
Uncertainty in Radionuclide Inventory from the BOURBON Detonation for the Saturated LCA Model

few radionuclides, all of the 43 radionuclides included in the Bowen inventory are unlikely to contribute to the contaminant boundary because of their incorporation into melt glass or sorption processes. Therefore, the radionuclides included in the Bowen inventory were further screened to identify those that are relevant to forecasting the Yucca Flat contaminant boundary. The screening process involved calculating radionuclide concentrations within the exchange volume considering uncertainties in inventory, partitioning, exchange volume size, glass dissolution, and matrix sorption. The 95th percentile concentration at one-tenth of the MCL was used as the screening criteria. All but 16 radionuclides were screened from further analysis. The retained radionuclides are ^{3}H, ^{14}C, ^{36}Cl, ^{41}Ca, ^{63}Ni, ^{90}Sr, ^{99}Tc, ^{129}I, ^{135}Cs, ^{137}Cs, ^{235}U, ^{238}U, ^{237}Np, ^{238}Pu, ^{239}Pu, and ^{240}Pu.

Among the retained radionuclides, ^{3}H, ^{137}Cs, and ^{90}Sr initially dominate the inventory, but they are overtaken by ^{239}Pu and ^{240}Pu after approximately 200 years of radioactive decay. Considering the sequestration of radionuclides in melt glass and reduced concentrations due to sorption, ^{3}H has the highest concentration within the tuff confining units, and ^{90}Sr has the highest concentration in the LCA. If radioactive decay also is considered, ^{14}C, ^{129}I, and ^{36}Cl will have the highest concentrations over the long term.

The development of the HST included assessing both conceptual and parametric uncertainties. The assessment of conceptual uncertainty included evaluating model sensitivity to the hydrology of the altered zones for detonations very near the saturated LCA and considering an alternative conceptual model for allocating inventory between the models. The conceptual model for alternative allocation implemented the relatively recent conceptual understanding of physical and chemical partitioning described in Tompson et al. (2011) and summarized in Appendix C. The assessment of parametric uncertainty included analyzing inventory, exchange volume extent, cavity porosity, and fraction of the RST partitioned within melt glass.

The HST conceptual models and parameter values define the boundary condition for the spatial and temporal release of contaminants to the groundwater. While the HST conceptual models and parameter values are based on available information, uncertainty remains. As a result, assumptions are necessary to address this uncertainty. Several potentially conservative assumptions in the Yucca Flat flow and transport analysis are made regarding the HST. The conservative assumptions are identified throughout this section and are summarized below with a qualitative assessment of their impact on the transport simulations.

- Decay correcting the Bowen inventory from 1992 to the time of detonation does not include the decay chain $^{241}Pu \rightarrow {}^{241}Am \rightarrow {}^{237}Np$ and uses the 1992 amount of longer-lived and more mobile ^{237}Np at the time of the detonation. This assumption has a negligible impact on the contaminant boundary because the ^{237}Np contribution is insignificant.

- Both allocation methods use cavity size estimates based on the maximum announced yield, which will conservatively place more of the RST directly within the saturated LCA because all detonations were performed above the saturated LCA, and increasing the size results in a larger fraction of the exchange volume residing within the saturated LCA.

- The uniform-concentration allocation method assumes that the unsaturated-zone fracture saturation is zero when calculating the model allocation fraction in each model domain. This assumption conservatively places more mass in the saturated exchange volume for exchange volumes spanning the water table. The impact of this assumption is small, because the vast majority of detonations that span the water table are located within the saturated alluvial/volcanic aquifer system model domain.

- The uniform-mass and uniform-concentration allocation methods move the inventory of the saturated-zone working-point detonations that extend into the unsaturated-zone model domain down to the saturated alluvial/volcanic aquifer system model domain. The effect of this assumption is similar to assuming a zero fracture saturation in the allocation and is small.

- Buoyancy-driven flow due to thermal effects within the saturated alluvial/volcanic aquifer system model is approximated by raising the radionuclide source from the cavity to the chimney aquifer. The effect of this assumption is evaluated in a sensitivity case presented in Section 4.6.5.

- Melt-glass dissolution within the saturated alluvial/volcanic aquifer system model is approximated by immediately releasing the fraction of radionuclides associated with 1,000 years of glass dissolution. The effect of this assumption is evaluated in a sensitivity case presented in Section 4.6.8.

- An alternative allocation is considered that places the inventory of detonations associated with possible fast transport to the saturated LCA directly within the saturated LCA (BOURBON, HANDCAR, KANKAKEE, NASH, CORDUROY, TORRIDO, LAMPBLACK, and CALABASH). This alternative inventory allocation scenario is extremely conservative and unlikely, and is intended to bound the potential effects of drill-back fluid losses on those detonations with exchange volumes near the saturated LCA. The potential impact of this conservative assumption is presented in Section 6.5.3.

3.0 YUCCA FLAT UNSATURATED-ZONE FLOW AND TRANSPORT MODEL

3.1 Introduction

This section describes the development of the unsaturated-zone flow and transport model for Yucca Flat. As described in the preceding sections, most (668 of 744) of the nuclear devices detonated in the subsurface of Yucca Flat between 1957 and 1992 were emplaced above the water table. Although the contamination of unsaturated-zone pore water in Yucca Flat does not directly affect the determination of the contaminant boundary, radionuclides initially in the unsaturated zone may potentially migrate into the saturated zone. As a result, the focus of the unsaturated-zone modeling effort is on the transport of radionuclides from their initial post-detonation distribution in the unsaturated zone to the water table.

The unsaturated-zone models presented in this section focus on the advective transport of radionuclides to the water table due to both background water movement in the unsaturated zone and focused infiltration through the crater bottoms due to surface runoff. In particular, the models consider the complex interplay between the geologic structures, hydrologic properties, surface watersheds, and detonation locations in estimating the potential for radionuclide transport to the water table. A subset of the models also allows for the drainage of any existing perched water into collapse chimneys that overlie the nuclear cavities in hard rocks, and a different subset of models examines the effects of gas–liquid partitioning of ^{14}C on transport to the water table.

As discussed in Section 2.2.2, other processes such as steam-bubble or carbon dioxide expansion and melt-glass dissolution are insignificant contributors to contaminant flux to the saturated zone. Melt-glass dissolution is not an important process in the unsaturated zone, because glass dissolution rates are low and both background and crater-enhanced infiltration rates are sufficiently low that releases to the water table from glass dissolution are insignificant. Steam-bubble and carbon dioxide generation and expansion were not considered directly in the unsaturated-zone model. These processes tend to spread volatile radionuclides such as ^{14}C over a large enough volume that these radionuclides would drop below concentrations of regulatory concern in the associated pore water.

Gas–liquid partitioning of ^{14}C is modeled in SNJV (2009b) and discussed later in this section (Section 3.7).

Modeling unsaturated-zone radionuclide transport to the water table involved several related modeling activities, including the following:

- Developed estimates of daily precipitation over the next 1,000 years based on an analysis of the existing precipitation records from Yucca Flat.
- Identified subsidence crater characteristics (size, depth, associated watershed areas, and vegetation status) in a Geographic Information Systems (GIS) study.
- Estimated parameters controlling evapotranspiration (ET) from a 10-year-long weighing-lysimeter study in Frenchman Flat.
- Compiled sediment and rock hydraulic properties for variably saturated conditions.
- Estimated surface runoff and crater infiltration rates for every nuclear detonation that produced a subsidence crater. Runoff parameters were calibrated by the use of historical observations of ponding and infiltration in craters.
- Develop computational grids with sufficient spatial resolution to accurately represent not only the complex hydrogeologic framework, but also the details of the craters, chimneys, and cavities associated with each detonation.
- Mapped the results from the detailed crater infiltration analysis onto the appropriate crater grid nodes in each of the 12 computational grids that were created to span the underground detonation sites at Yucca Flat.
- Applied the appropriate radionuclide source terms to each exchange volume surrounding a detonation in the numerical models.

Figure 3-1 shows the relationship between the many facets of the unsaturated-zone model for Yucca Flat. Because factors such as the detonation proximity to faults, crater infiltration rates, device emplacement depth, and geologic setting all interact to influence radionuclide movement to the water table, no *a priori* decisions were made regarding which individual detonations to include in or exclude from the unsaturated-zone models.

All detonations with working points in the unsaturated zone at Yucca Flat were explicitly included in the unsaturated-zone transport models, with the exception of two isolated, low-yield (announced yield less than 20 kt each) detonations located in southern Yucca Flat. These two detonations

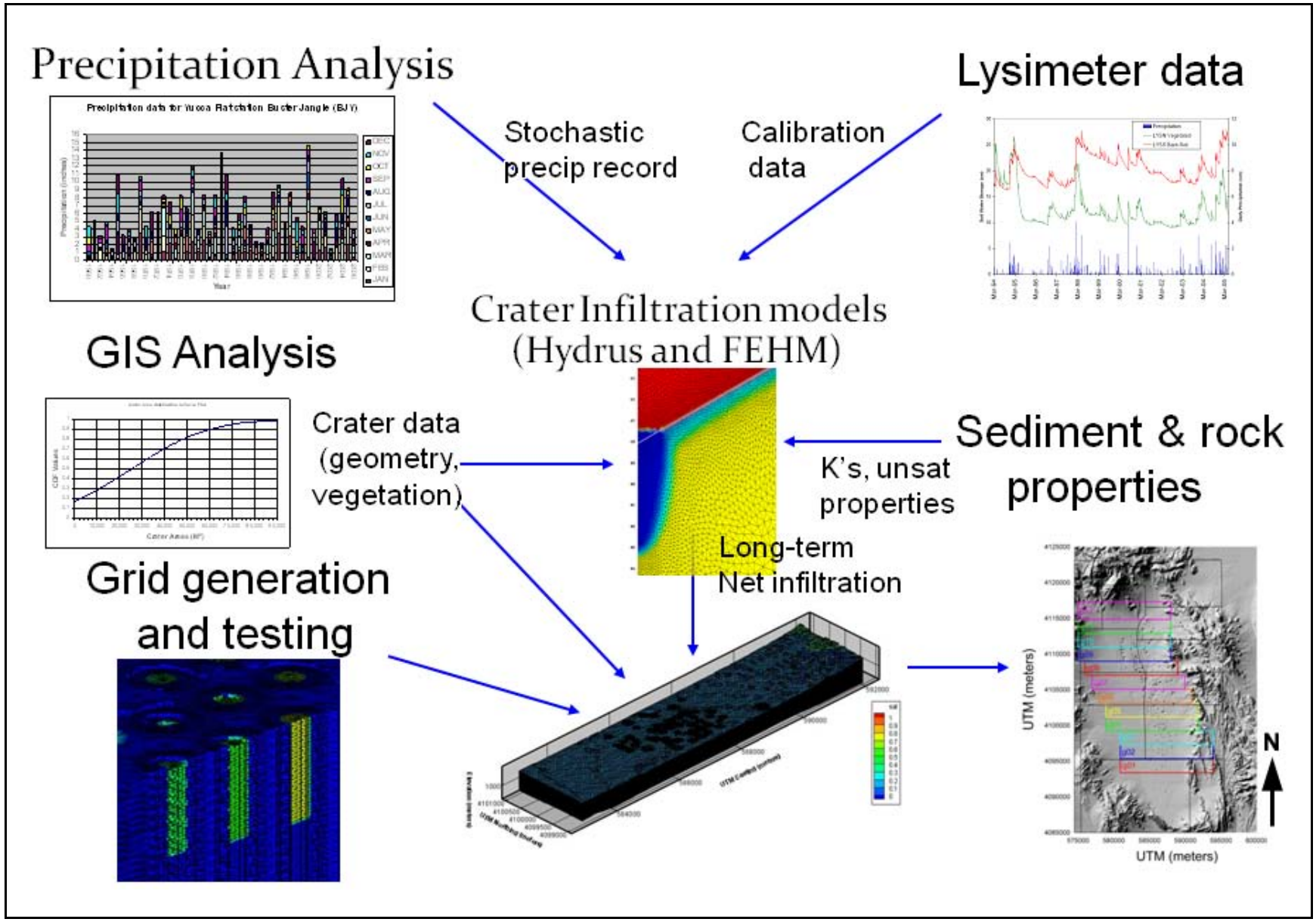

Figure 3-1
Relationship between Different Supporting Studies and the Overall Unsaturated-Zone Model for Yucca Flat

(RUSSET and PRESIDIO) were not explicitly modeled because of the operational expense in modeling these two isolated detonations. Because these two detonations have no surface craters to enhance the recharge (Table E-5), are located several cavity radii above the water table (Table B-1), and have been determined to be insignificant contributors to contaminant transport from the unsaturated zone (McNab, 2008), their exclusion from the unsaturated-zone models does not affect the contaminant flux to the water table.

The HSTs associated with each detonation for selected non-sorbing radionuclides (^{3}H, ^{14}C, ^{36}Cl, ^{99}Tc, ^{129}I, U, and ^{237}Np) were estimated from the unclassified radionuclide inventory for Yucca Flat calculated by Bowen et al. (2001) assuming the inventory scaled with the maximum announced yield of the detonation. The yield-weighted inventory for each detonation was then decay corrected to its detonation date to compensate for the effects of radioactive decay incorporated into the Bowen et al. (2001) inventory, which estimated the radionuclide masses as of September 23, 1992. However, in order to synchronize the unsaturated-zone models with the saturated-zone alluvial/volcanic aquifer system models presented in Section 4.0, the radionuclide masses estimated for each detonation were assumed to be available for transport as of December 3, 1961, the time of the FISHER detonation. The date is also the start time of the unsaturated-zone transport simulations. In making this simplification, it is recognized that the later (more recent) detonations have transport starting years or decades before the actual event. For individual detonations, this simplification can produce radionuclide arrival times at the water table that are as much as three decades earlier than would be calculated had the radionuclide mass been introduced on the actual detonation date. This is an acceptable approximation because the contaminant boundaries are calculated based on the maximum extent of contamination at any time within the 1,000-year regulatory period, and so the exact timing of the unsaturated zone inputs to the saturated-zone models are less important from that perspective.

The radionuclide mass available for immediate transport by water (i.e., the HST) was then represented directly in the model for each detonation. The highly sophisticated numerical grids that were used allowed the HST for each detonation to be inserted directly into the flow and transport model so that absolute consistency between radionuclide and water mass fluxes exiting each detonation's exchange volume was enforced for each model run.

As described in Section 2.0, conceptual understanding of the spatial distribution of different radionuclide groups has evolved over the course of the Yucca Flat modeling study (e.g., Rose et al.,

2011; Tompson et al., 2011). Most of the simulations of unsaturated-zone transport presented in this section assume that the radionuclide mass is uniformly distributed around the emplacement location of each detonation within an exchange volume having a radius of 1 to 3 R_c without regard to the volatility of the radionuclide or its precursor. This is the uniform mass-based allocation method described in Section 2.3.3. This is an acceptable approximation in the unsaturated-zone models given the scale of the models, the large number of detonations, and the fact that uncertainty in the exchange volume radius is explicitly investigated.

A subset of model runs presented in Section 3.8 examines the impact of an alternative conceptualization of the radionuclide source term that uses a uniform-concentration allocation with exchange volumes that are radionuclide dependent. As noted in Section 2.0 and Appendix C, this alternative source-term representation places a greater fraction of the initial inventory below the water table; therefore, the results presented with the uniform-mass allocation tend to overstate the expected mass flux to the water table from the unsaturated zone.

3.1.1 Summary of Unsaturated-Zone Nuclear Detonations at Yucca Flat

As described in Section 1.5 and in DOE/NV (2000b), subsurface testing in Yucca Flat began with the PASCAL-A detonation on July 26, 1957, and ended with the DIVIDER detonation on September 23, 1992. A total of 744 nuclear devices were detonated underground in Yucca Flat proper over this time period, with 3 additional detonations in the Climax granitic stock north of Yucca Flat.

As discussed in Section 1.5, the underground detonations conducted in Yucca Flat range in depth of burial from 114.5 m to 782.4 m below ground surface and range in yield from 0 to 500 kt. Of the 744 nuclear devices detonated in Yucca Flat proper, 577 were detonated more than 100 m above the water table, and 668 had working points above the water table.These 668 detonations had a maximum announced yield of 26,791 kt, whereas the 76 detonations with working points below the water table had a maximum announced yield of 12,173 kt. As described in Section 2.0, radionuclide distributions in the unsaturated-zone model, the saturated alluvial/volcanic aquifer system model, and the saturated LCA model were apportioned based on the fraction of the assumed exchange volume associated with each model and the porosities of the individual HSUs in the exchange volume. Therefore, the relative distribution of yield cited above is only an approximation of how radionuclides are apportioned among the three models. As discussed in Section 2.1.1, the total yield estimated for exchange volumes that are either completely or partially below the water table is 14,243 kt. Thus,

approximately 24,800 kt (64 percent) of the total maximum yield of 39,051 kt estimated for the Yucca Flat/Climax Mine CAU is assigned to the unsaturated-zone model.

The working-point elevations of all unsaturated-zone detonations relative to the water table are shown in Figure 3-2a, and the locations of unsaturated-zone detonations within 100 m of the water table are shown in Figure 3-2b. Large-yield detonations with working-point elevations within 100 m of the water table are more likely than low-yield detonations to have exchange volumes close to or intersecting the water table; therefore, all other factors being equal, radionuclide travel times from large-yield detonations close to the water table could be relatively short. Radionuclides from detonations near faults may also have a greater potential to reach the water table compared to those from detonations away from faults. From these figures, it is clear that most of the nuclear detonations in the unsaturated zone and all but five of the unsaturated-zone detonations within 100 m of the water table are located above saturated volcanic rocks or alluvium. Therefore, the saturated volcanic rocks and the saturated alluvium provide an additional buffer between most of the unsaturated-zone detonations and the LCA. The five unsaturated-zone detonations within 100 m of the water table and above the saturated LCA are in the northwest or northern part of the basin.

3.1.2 Hydrogeologic Setting

The general hydrogeologic setting and hydrostratigraphy of Yucca Flat discussed in Sections 1.3 and 1.4 highlight the diversity of rock types found in the basin. Precambrian metasedimentary confining units, fractured tuff and carbonate aquifers, argillic and zeolitic tuffaceous confining units, and coarse-grained alluvial sediments are found in the basin. Fine-grained playa sediments also are found at the southern end of the basin. Tectonic structures superimposed on these rocks include compressional folds and thrust faults that predate the tuffaceous rocks and sediments, and normal faults and fractures that affect the Tertiary volcanic rocks and are associated with the opening of the basin. As described in Section 1.3, most of the major faults, such as the Carpetbag-Topgallant and Yucca faults, are aligned roughly north to south, dip steeply eastward, and create stratigraphic offsets that are downdropped to the east, causing the tuffs to dip to the west. Smaller, associated faults dip steeply westward and create local grabens. The contrasts in primary permeability and porosity associated with different rock types, as well as the presence of hundreds of known faults and the variable propensity of different rocks to fracture (Table 1-1), necessitate the use of three-dimensional

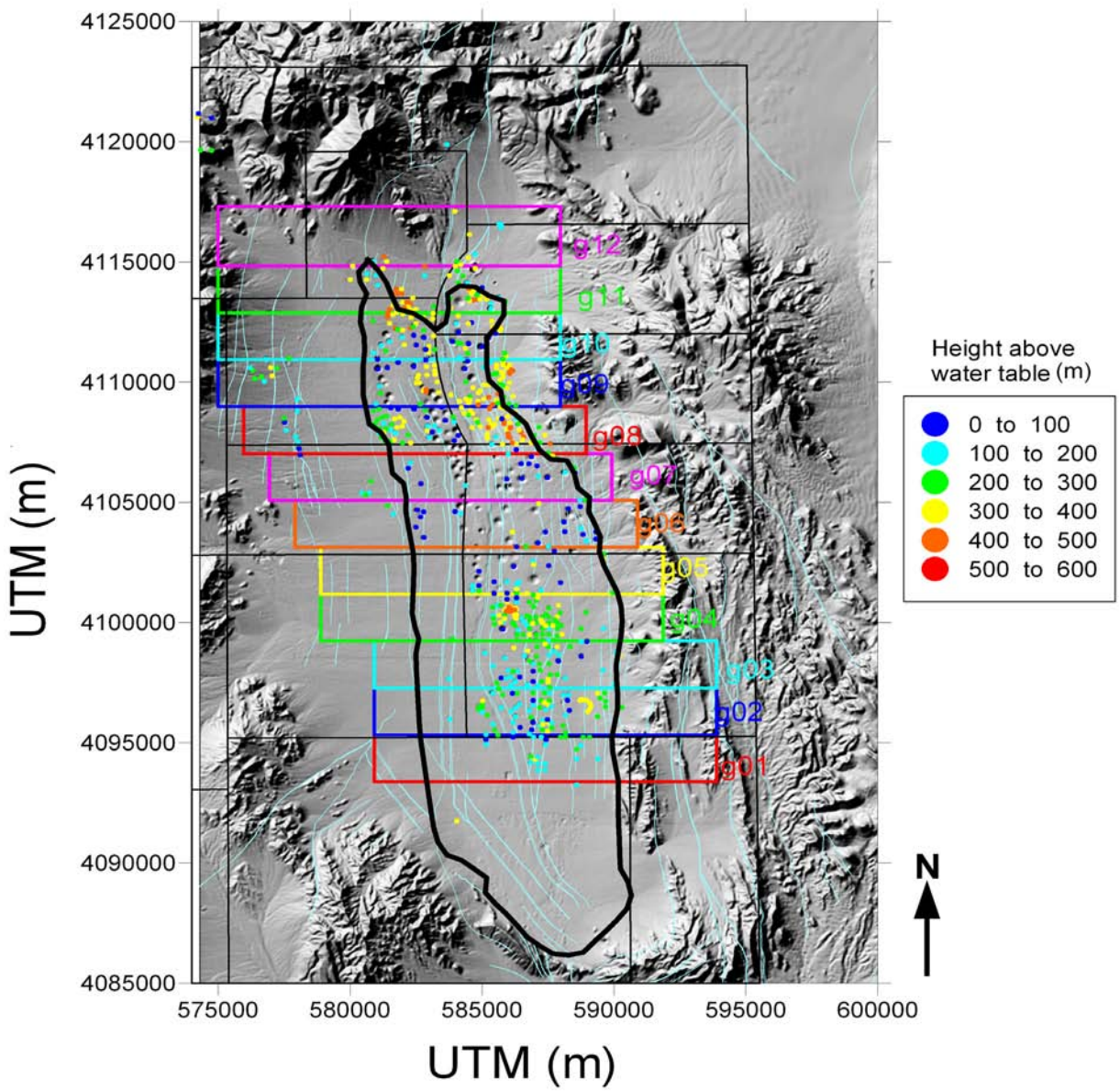

Note: Also shown are the extent of the 12 unsaturated-zone model grids and the outline of the saturated alluvial/volcanic aquifer system model. Cyan lines are fault locations at the water table.

Figure 3-2a
Elevations of Unsaturated-Zone Detonations Relative to the Water Table: All Unsaturated-Zone Detonations

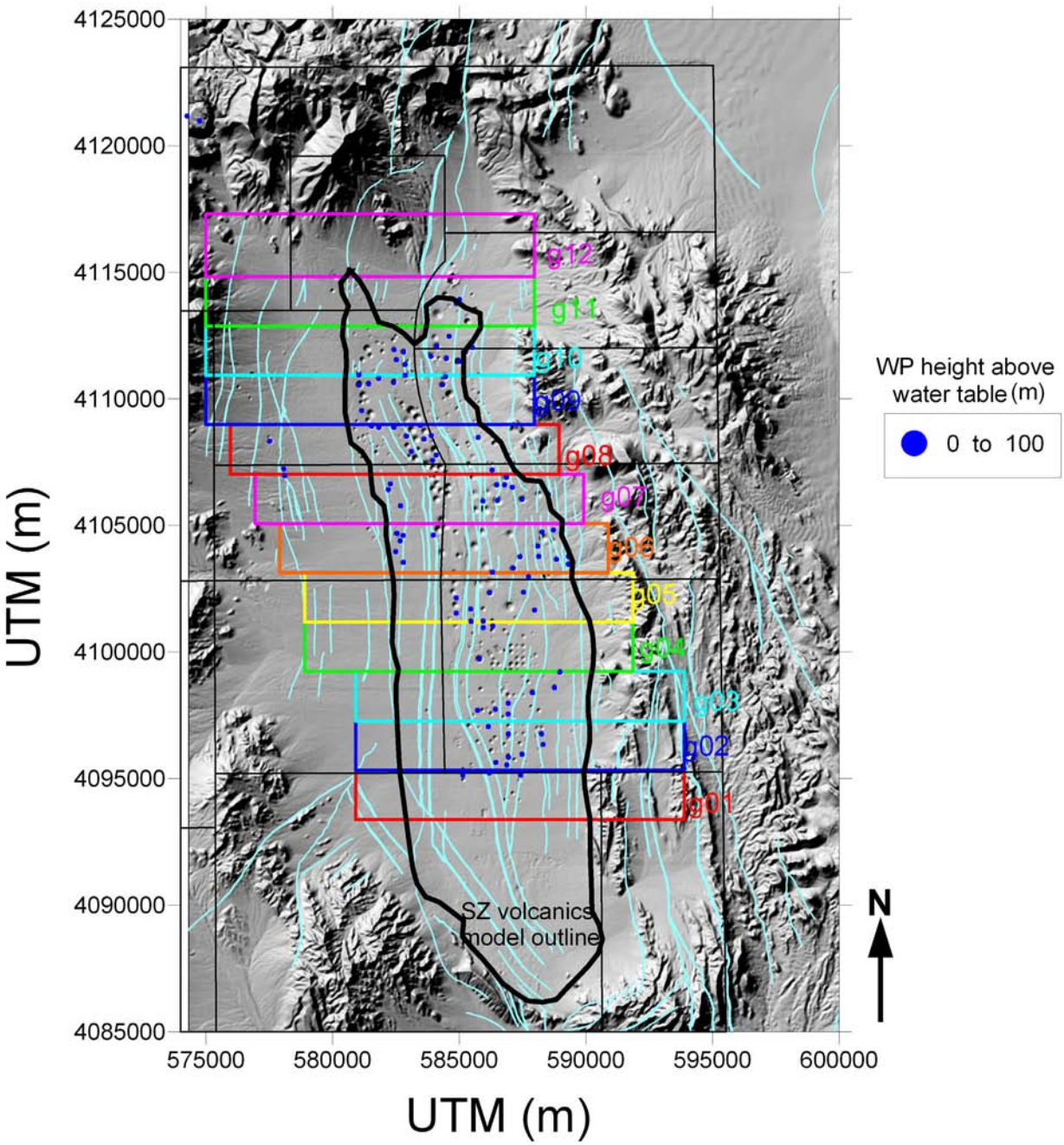

Note: Also shown are the extent of the 12 unsaturated-zone model grids and the outline of the saturated alluvial/volcanic aquifer system model. Cyan lines are fault locations at the water table.

Figure 3-2b
Elevations of Unsaturated-Zone Detonations Relative to the Water Table: Detonations within 100 m of the Water Table

numerical models to adequately investigate the potential for complex flow patterns in the unsaturated zone and focused recharge at the water table that could result.

3.1.3 Previous Studies

3.1.3.1 Past and Present Background Infiltration

Recent studies of the unsaturated zone in thick alluvial basins at the NNSS and vicinity have contributed significantly to the understanding of the roles of paleoclimate, vegetation, and gas-phase transport in water and solute movement in arid environments (Tyler et al., 1996; Walvoord, Phillips, et al., 2002; Walvoord, Plummer, et al., 2002; Scanlon et al., 2003; Walvoord et al., 2004; Walvoord et al., 2005; Kwicklis et al., 2006a). Unsaturated-zone numerical models have been applied to pore-water chloride and water potential profiles to convincingly demonstrate that thick unsaturated zones in arid settings contain water and solutes in their deeper intervals that infiltrated during pluvial periods at the end of the last ice age and have been undergoing long-term drying and drainage since the modern arid climate and desert vegetation were established roughly 10,000 years ago. These studies have highlighted the important role that climate-induced vegetation changes in the southern Great Basin have played in determining subroot-zone infiltration rates at the end of the last ice age. In particular, Walvoord, Phillips, et al. (2002), Walvoord, Plummer, et al. (2002), and Kwicklis et al. (2006a) evaluated the hydrologic evolution of the unsaturated zone in Yucca Flat when vegetation transitioned from a juniper-pinyon community to a creosote-saltbush community at the end of pluvial conditions roughly 10,000 years ago. This vegetation transition to desert plant communities, the nature and timing of which is established by studying and dating plant remains preserved in pack-rat middens (e.g., Spaulding and Graumlich, 1986; Spaulding, 1990), has prevented liquid water from penetrating significantly past the root zone in the alluvium since the end of the last pluvial period.

Soil-water potential gradients measured in boreholes indicate that total water gradients are upwards toward the root zone in the upper several tens of meters of the subsurface, whereas deeper parts of the profiles are consistent with small rates (less than 1 millimeter per year [mm/yr]) of continued downward drainage to the water table (Walvoord, Phillips, et al., 2002; Kwicklis et al., 2006a). This conceptual model, as well as the timing of the vegetation transition, is confirmed by pore-water chloride concentrations indicating that roughly 10,000 years' worth of atmospheric chloride deposition is accounted for in the soil-water chloride "bulge" centered on the root zone; more dilute chloride concentrations in the deeper parts of the soil-water chloride profile below the bulge can be

used to estimate paleoinfiltration rates before the vegetation transition (Tyler et al., 1996; Walvoord, Phillips, et al., 2002). Long-term hydraulic transients can last several tens of thousands of years, far longer than past interpluvial periods have lasted, depending on soil hydraulic parameters and thermal gradients, which influence the rapidity of the drainage and the rates of gas-phase transport of water vapor, respectively. Vapor transport is upward from the water table to the root zone and is affected by thermal gradients and vapor-pressure lowering associated with dry pore-water conditions near the root zone (Walvoord, Plummer, et al., 2002).

Walvoord, Phillips, et al. (2002) interpreted water potential and pore-water chloride concentration data from Frenchman Flat and Yucca Flat to estimate the paleoinfiltration and present-day recharge rates in these basins. Based on the combined deep pore-water chloride concentrations below the root zone at boreholes UE-6s and UE-6e (46 milligrams per liter [mg/L]), and assuming that the estimated present chloride deposition rate of 105 milligrams per square meter per year persisted throughout the pluvial period, an infiltration rate of 2.3 mm/yr was estimated near these boreholes for a period of several tens of thousands of years before the end of the last pluvial period. The chloride profiles from two of the three boreholes in Frenchman Flat (UE5PW-1 and UE5PW-3) differed from those from boreholes UE-6s and UE-6e in that both shallow and deep chloride bulges were present in the profiles. The deeper chloride bulge was interpreted to represent chloride accumulation from the penultimate interpluvial period that lasted from 110 to 95 thousand years before present (ka), whereas the shallow chloride bulge is associated with the present interpluvial. The deeper chloride bulges at boreholes UE5PW-1 and UE5PW-3 were estimated through modeling to have been displaced from their initial locations near the root zone by a short pluvial event that lasted roughly 1,000 years between 14 and 13 ka. The estimated infiltration rates during these brief pluvial periods were 2 mm/yr at UE5PW-1 and 5 mm/yr at UE5PW-3. A third borehole in Frenchman Flat (UE5PW-2), contained only a shallow chloride bulge centered on the root zone. Based on chloride concentrations below the chloride bulge, infiltration rates before 13 ka were about 4.4 mm/yr for some unknown length of time. Modeled present-day recharge fluxes due to the continued downward drainage of paleowater near the water table and condensate from vapor transport ranged from 0.05 to 0.2 mm/yr for the Frenchman Flat boreholes and 0.4 mm/yr for boreholes UE-6s and UE-6e. The Yucca Flat estimate was higher because the thicker column of alluvium for Yucca Flat (500 m) compared to Frenchman Flat (210 m) took longer to drain and the higher geothermal gradient assumed in the model for Yucca Flat generates more vapor condensate.

Walvoord et al. (2004) also used $\delta^{18}O$ and $\delta^{2}H$ data in addition to water potential and pore-water chloride data to constrain the paleohydrologic evolution of the unsaturated zone at the U.S. Geological Survey (USGS) Amargosa Desert Research Site (ADRS) near a former low-level radioactive waste site. They estimated that present-day recharge rates at the approximately 110-m-deep water table are on the order of 0.01 to 0.1 mm/yr and are relatively insensitive to assumed paleoinfiltration rates or root-zone water potentials over their range of likely values. They also found that the timing of the hydraulic transition resulting from the vegetation transition had the largest impact on present-day recharge rates, but different aspects of their dataset suggested different optimal transition times when time since the transition was the only variable considered.

Using data from a series of shallow boreholes at the Area 3 Radioactive Waste Management Site (RWMS) in Yucca Flat and the data from boreholes UE-6s and UE-6e used by Walvoord, Phillips, et al. (2002), as well as $\delta^{18}O$ and $\delta^{2}H$ data to help calibrate vapor transport parameters, Kwicklis et al. (2006b) generated 1,000 Monte Carlo realizations to estimate present-day water-table recharge rates of 0.13 ± 0.03 mm/yr (1 SD) near the Area 3 RWMS. They also estimated that the depth separating the shallow upward liquid flux regime from the deeper regime characterized by downward liquid drainage was presently between 63 and 70 m.

Despite convincing evidence that shallow unsaturated-zone flow is upward beneath the interfluvial areas of Yucca Flat and in similar deep alluvial basins throughout the arid southwest, the possibility remains that infiltration rates in Yucca Flat could be higher beneath arroyos and the normally dry playa at the southern end of Yucca Flat that periodically floods. Stonestrom et al. (2003) used temperature, chloride, moisture content, and water potential data from a series of shallow holes beneath native vegetation, the ephemeral Amargosa River channel, and irrigated fields to estimate recharge in the Amargosa Desert. In contrast to the native vegetation at which, as at the ADRS, the infiltration rates were zero or upward, infiltration rates beneath the channel sites and irrigated fields were downward. Water potentials immediately beneath the channel were close to zero (as opposed to strongly negative beneath the native vegetation), and chloride concentration profiles at two sites beneath the channel show that the chloride bulge either is absent or was originally present but has been flushed to a deeper location when the channel migrated to its present position. Estimated time-averaged infiltration rates at the two channel sites are 90 mm/yr at the upstream site and 40 mm/yr at the downstream site, which represent about 12 to 15 percent of the estimated channel losses.

Although studies such as Stonestrom et al. (2003) indicate the potential for infiltration and recharge beneath arroyos in Yucca Flat, the natural drainage patterns in Yucca Flat have been significantly altered by roads and subsidence craters associated with nuclear testing, so past natural drainage patterns have little bearing on radionuclide migration in the future. Additionally, the unsaturated-zone flow and transport models developed in this section consider the routing of overland flow to subsidence craters based on the current, crater-dominated topography (Appendix E), which is far more relevant to radionuclide transport. Nonetheless, based on the data from beneath the Amargosa River channel, pre-1950s infiltration beneath arroyos that ultimately would have drained to Yucca Lake playa could have been larger than the interfluvial infiltration rates summarized above, although a volumetrically minor contributor to basin-scale recharge because of the small area represented by the arroyos.

No systematic studies of infiltration have been done beneath Yucca Lake playa, which is normally dry most of the year but floods following spring runoff and thunderstorms. However, based on borehole water potential, and tritium and chloride profiles beneath and adjacent to playa lakes in Texas, Scanlon and Goldsmith (1997) demonstrated that playas are sites of focused groundwater recharge. Sediments beneath the playas tend to have larger water potentials, higher tritium concentrations, and lower chloride concentrations than those in the adjacent interplaya areas. Sediment in the annular regions between the playa and interplaya areas displayed hydrologic behavior that was intermediate between that of the playa and that of the interplaya area. Time-averaged recharge rates beneath the playas were estimated with a modified chloride mass-balance equation that accounted for run-on and from tritium profiles. The estimated recharge rates ranged from 60 to 120 mm/yr, whereas infiltration rates at sites adjacent to the playas have been less than 0.1 mm/yr over the last 2,000 to 5,000 years. Dye experiments showed that preferential flow along roots and desiccation cracks appeared to be the dominant factor allowing infiltration in the fine-grained, clay-rich playa sediments.

In Yucca Flat, Doty and Rush (1985) reported that 5 million cubic feet of surface runoff to Yucca Lake playa was drained between 1974 and 1976 (39 acre-feet per year) by fissures that have since sealed themselves. The 1.6-km-long fissure, which opened in 1969, was one of a series of four northeast-trending cracks that are known to have existed in the playa over the decades going back to the pre-1950s period. The fissures opened as thin (less than 1 inch) cracks that were subsequently widened to more than several feet by erosion and piping before they were filled with sediment. Collectively, the Scanlon and Goldsmith (1997) and Doty and Rush (1985) studies support

the notion that infiltration rates could be higher beneath the playa than in the interfluvial areas elsewhere in Yucca Flat. However, the self-sealing aspect of the fissures, along with the fact that no new fissures have developed since 1969, suggests that playa recharge has a relatively minor effect on the overall water balance of Yucca Flat. In particular, Doty and Rush (1985) estimated that inflow into the fissure constituted less than 1 percent of the recharge in the Yucca Flat basin on an annual basis. In any case, because no nuclear tests were conducted within or below the present-day Yucca Lake playa (Figure 1-3), uncertainty in infiltration rates beneath the playa has no effect on the calculated rates of radionuclide flux to the water table or on rates of groundwater movement beneath the testing areas of Yucca Flat.

3.1.3.2 Infiltration Maps

A total of seven alternative recharge models created for use with either the UGTA regional model (IT, 1996a) or the DVRFS model (Belcher et al., 2004) are presented in SNJV (2006b, Section 7.0). The seven alternative recharge models include two UGTA models (UGTA Original and UGTA Revised). These models are based on the empirical Maxey-Eakin recharge model, which relies on the concept that fixed percentages of precipitation become recharge in different elevation or precipitation zones: recharge is assumed to occur (1) only where precipitation is above 20 cm (Maxey and Eakin, 1949), or (2) because of the correlation between precipitation and elevation in southern Nevada, at elevations above 1,700 m (Eakin et al., 1951). The UGTA Revised model allows some fraction of the estimated recharge in upland areas to be redistributed along adjacent downstream washes. USGS created three alternative infiltration models in support of the DVRFS model based on a spatially distributed soil-water-budget model that considers physical processes affecting soil drainage, runoff, and ET (Hevesi et al., 2003). Sensitive model parameters include soil hydraulic conductivity and depth, bedrock permeability, rooting depth, and soil ET parameters. These three models (1) include surface runoff and re-infiltration (USGS Model 1), (2) ignore surface runoff and re-infiltration (USGS Model 2), or (3) include surface runoff and re-infiltration, but with infiltration values scaled during calibration of the DVRFS model (USGS Model 3). The remaining two infiltration models are based on an elevation-dependent chloride-mass-balance (CMB) method in which net infiltration (or equivalently, recharge) is estimated from the increase in the concentration of chloride in soil water or spring discharge relative to the chloride concentration in precipitation (Russell and Minor, 2002). These two models—DRI-CMB (alluvial mask) and DRI-CMB (alluvial and elevation mask)—were calibrated and verified against regional spring measurements, and superimpose additional limits on

infiltration based on observations that infiltration is negligible in thick alluvium (e.g., Walvoord, Phillips, et al., 2002; Walvoord, Plummer, et al., 2002) or below a certain elevation (1,237 m, the elevation of Cane Spring). All of the models preserve the general relationship that net infiltration and recharge increase with elevation and precipitation in southern Nevada.

For the Yucca Flat area, all seven of the infiltration models—except the UGTA Original model (later corrected and superceded by the UGTA Revised model)—show that infiltration is small or negligible in the thick alluvium on the basin floor but increases to several millimeters per year in the bedrock hills surrounding the basin. Figures 3-3 to 3-5 show the model results in the Yucca Flat area for the UGTA Revised model, USGS Model 1 (with runoff), and DRI-CMB (alluvial and elevation mask) model. The estimates of net infiltration over the vast majority of the unsaturated-zone model domain from regional estimates, regional modeling, and site-specific observations summarized above are very low—less than 0.1 mm/yr. These estimates have been used to define the expected flow regime and recharge. However, with the recognition of the potential significance of this parameter to radionuclide transport, a wide range of alternative assumptions have been used to maximize the potential release and extent of radionuclide transport. Average values of 1, 5, and 10 mm/yr have been used, even though the higher end of this range is considered highly improbable based on the estimated present-day recharge rates, and paleoinfiltration rates and durations discussed in Section 3.1.3.1.

3.1.3.3 Surface Effects Maps

Surface effects of underground nuclear detonations have been studied and mapped for more than 40 years in Yucca Flat, resulting in surface effects maps for 530 of the 747 underground detonations conducted at the Yucca Flat/Climax Mine CAU (some of these maps showed no surface effects) (Grasso, 2000, 2001). The surface effects maps were produced with field mapping, aerial photography, and photogrammetric techniques (Allen et al., 1997; Hawkins and Wohletz, 1997). The maps that were originally produced in the days or weeks following individual detonations were digitized and overlain by Grasso (2000, Plate 1) to produce a composite surface effects map for Yucca Flat that includes craters, collapse sinks, cracks, faults, and pressure ridges. The term “crater”—although used synonymously with “collapse sink” in this report—technically refers to a topographic depression caused by an explosion near the surface that throws out or vaporizes surface materials. In contrast, the term “collapse sink” technically refers to a topographic depression caused by surface subsidence that forms above an underground nuclear detonation. An underground

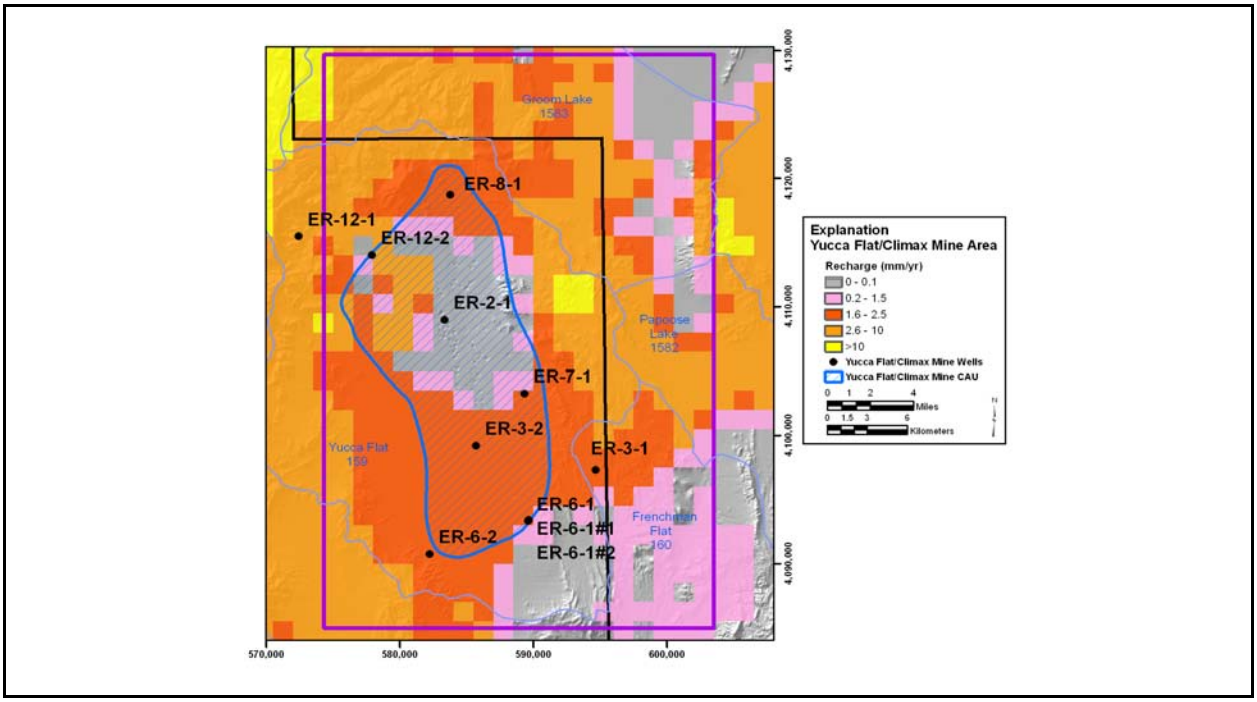

Figure 3-3
UGTA Revised Infiltration Map for the Yucca Flat Area

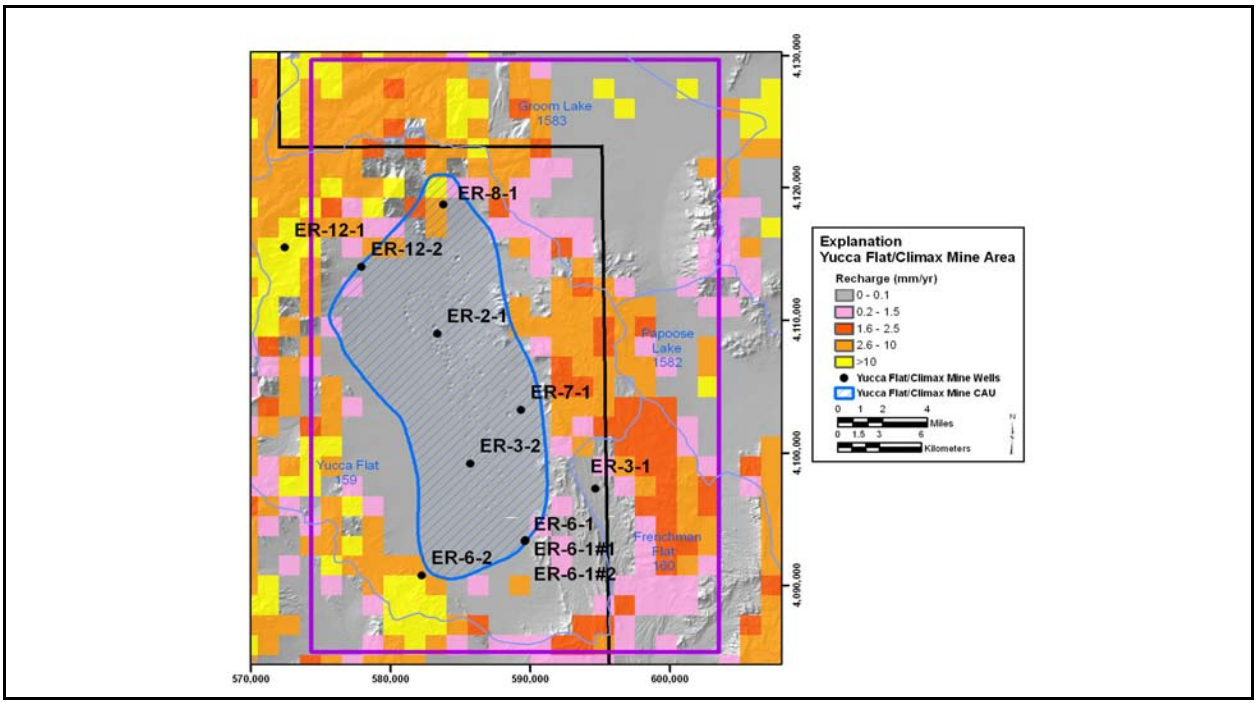

Figure 3-4
USGS Model 1 (with Runoff) Infiltration Map for the Yucca Flat Area

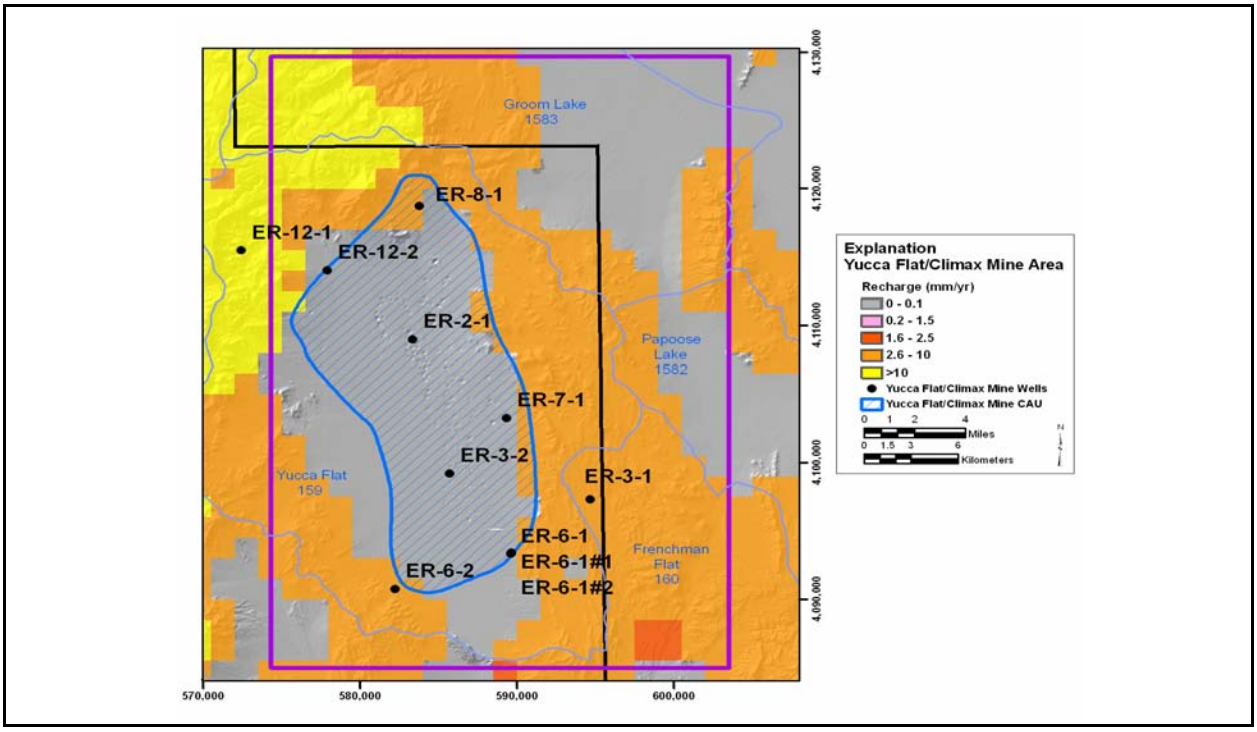

Figure 3-5
DRI-CMB (Alluvial and Elevation Mask) Infiltration Map for the Yucca Flat Area

detonation vaporizes surrounding material and creates a subsurface cavity; a collapse sink forms from the subsequent collapse of surface materials into this cavity. A surface depression created by either mechanism is referred to as a crater in this report.

In addition to the craters and collapse sinks, the surface effects map of Grasso (2000) shows the movement along the Yucca and Carpetbag fault systems that results from underground nuclear testing at Yucca Flat, and the typical radial, concentric, and tangential crack patterns formed around the surface ground zero. An example surface effects map is shown for the CARPETBAG detonation in Figure 3-6. According to Grasso (2001), radial and circumferential cracks result from the rising and falling of ground surface when the shock wave from the explosion intersects and rebounds from the surface. The complex crack patterns surrounding individual detonations, such as those shown in Figure 3-6, were not considered in this study when surface runoff patterns to and within a crater were analyzed. These cracks, mapped soon after the detonations, are assumed to be transient features that eventually become muted or disappear because of wind, rain, and runoff, and therefore, generally have small long-term effects on the surficial hydrology. A far more significant long-term effect is likely to be the disruption of the original long-term drainage pattern that existed in the basin by the addition of hundreds of craters, each of which can form a local hydrologic sink.

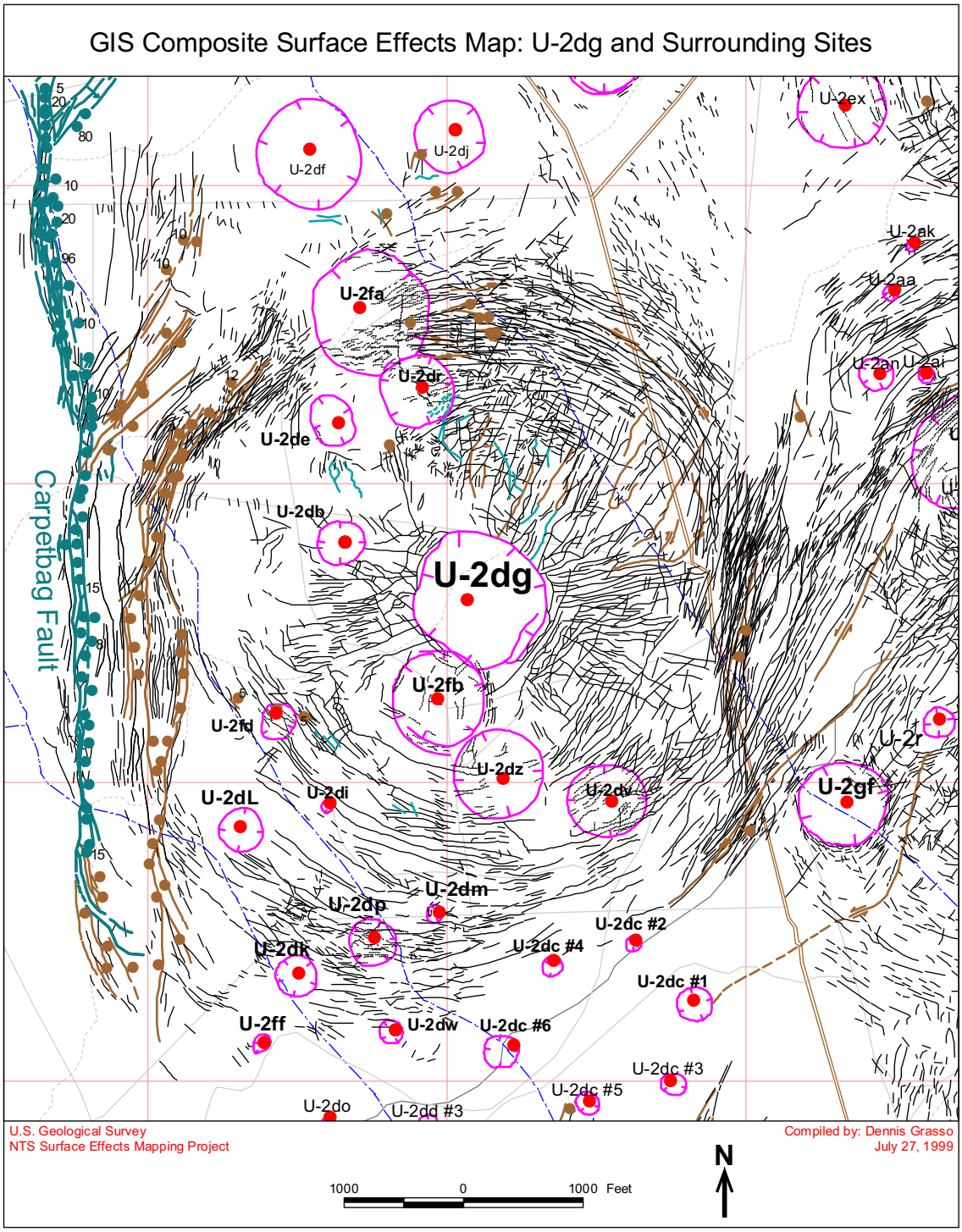

Note: Red dots indicate surface ground zero from underground detonations. Green and brown bars and balls indicate faults with vertical displacement (ball on downthrown side). Green symbols are associated with the Carpetbag Fault.

Figure 3-6
Composite Surface Effects Map in the Vicinity of U-2dg (CARPETBAG)
Source: Modified from Grasso, 2000

The crater outlines from the surface effects map of Grasso (2000) formed the starting point for the GIS analysis conducted as part of the present study, which mapped the locations and extent of the craters in Yucca Flat (see Appendix E). Additional craters not on the original map of Grasso (2000) were subsequently digitized and included in the Los Alamos National Laboratory (LANL) crater database.

3.1.3.4 Crater Infiltration Studies

It has long been recognized that surface craters in Yucca Flat and elsewhere at the NNSS form potential hydrologic sinks that could serve to capture surface runoff and focus infiltration at the crater bottoms (e.g., Teller et al., 1968). A small number of craters have been directly observed to pond water periodically, and infiltration beneath these craters has been studied through a combination of surface and subsurface measurements. These measurements have included measurements or estimates of ponding depth following specific precipitation events, and measurements of soil properties, soil moisture, and in some cases, water potential beneath and adjacent to the craters. The craters for which some estimates of crater infiltration rates exist include U-10i (BYE), U-3fd (LAGUNA), and U-3bh (HYRAX) in Yucca Flat, and U-5a in Frenchman Flat. The results of these studies are discussed in detail in Appendix E, where they are used to calibrate parameters that influence the generation of surface runoff and soil hydrologic parameters. In general, however, these studies indicate that infiltration beneath these craters, while highly episodic, can have long-term average rates of several hundred millimeters per year or more (Tyler et al., 1992; Pohll et al., 1996; Hokett and French, 1998; Hokett et al., 2000; Wilson et al., 2000). There is also some indication from these studies that craters may have a tendency to seal themselves over time because of the fine-grained layers that are deposited when sediment settles through standing water. These fining-upward sequences have been used to estimate the number of runoff events that have taken place since crater formation (Hokett et al., 2000; Wilson et al., 2000). Although entirely plausible, crater self-sealing was not considered during this study because of the difficulty in estimating the future evolution of the sediment properties at the crater bottom in a scientifically defensible way. Therefore, estimates of crater infiltration produced as part of the present study may overestimate future infiltration if craters seal themselves as proposed by the authors of the aforementioned studies.

3.1.3.5 Underground Nuclear Detonation Categorization

A number of possible underground nuclear detonation categorization strategies have been proposed by those who had the intent of providing a framework for structuring flow and transport modeling in Yucca Flat. Bowen et al. (2001) considered detonations anywhere on the NNSS with working points more than 100 m above the water table to be unsaturated-zone detonations and detonations either below or less than 100 m above the water table to be saturated-zone detonations, but otherwise did not attempt to further categorize the detonations. Pawloski et al. (2008) retained the same basic definitions of saturated- and unsaturated-zone detonations, but further categorized the detonations conducted at Yucca Flat based on the HSUs that hosted the detonation working points as interpreted from the HFM for Yucca Flat (BN, 2006). Pawloski et al. (2008) also estimated the HSUs that would be present at the water table if the detonations were projected vertically downward so that detonations conducted above saturated aquifers could be distinguished from those conducted above saturated confining units. McNab (2008) used one-dimensional analytical models to categorize detonations according to the minimum crater infiltration rates necessary to cause radionuclides to reach the water table within 1,000 years, and further estimated which detonations would be incapable of sustaining that percolation flux based on the presence of low-permeability confining layers between the working points and the water table. SNJV (2009b) used three-dimensional models to examine radionuclide migration from representative shallow (175 m deep) and deep (435 m deep) detonations in an idealized 526-m-deep unsaturated zone consisting entirely of alluvium. The study generally concluded that radionuclides from deeper detonations with higher crater recharge rates were likely to reach the water table sooner and at higher concentrations than radionuclides from shallow detonations with lower crater infiltration rates; in the absence of gas- or liquid-phase partitioning, even craters with an infiltration rate of 250 mm/yr failed to produce breakthrough of either ^{14}C or ^{3}H at the water table above regulatory limits for the shallow detonations.

The conclusions of McNab (2008) and SNJV (2009b) were still being developed after this study was well under way and while the crater-specific infiltration rates were being developed (see Section 3.3 and Appendix E). Therefore, it was unknown at the start of the present study whether the influence of detonation depths, crater infiltration rates, or other factors such as proximity of detonations to faults or the creation of collapse chimneys through the low-permeability confining units would dominate the overall transport of radionuclides to the water table. Consequently, because construction of the numerical grids required relatively early decisions as to which detonations to include or exclude,

a decision was made to include all of the unsaturated-zone detonations and let the models themselves calculate how these competing factors, such as crater infiltration rates, depths of the detonations, geology, proximity to faults, assumed exchange volume radii, and sediment and tuff anisotropy, affected the transport of radionuclides to the water table.

3.1.3.6 Faults and Fractures

Prothro et al. (2009) described the characteristics of faults in the NNSS area in the context of widely accepted concepts of fault-zone architecture to develop conceptual models of the likely impact of faults in different HSUs on groundwater flow. Their observations of faults were based on outcrops, fault interceptions in tunnels, cores, and borehole videos from large-diameter device-emplacement holes. They emphasized the impact that differences in the mechanical strengths of different rocks have on the development of each of the architectural elements. In hard rocks such as welded tuffs, carbonate rock, granite, and coarse-grained pre-Tertiary rocks, these fault-zone elements generally include (1) a fault core containing gouge, finely granulated material, or matrix-supported breccia; (2) a damage zone with more intense fracturing and minor faulting relative to the surrounding country rock, with enhanced fracturing or clast-supported breccias immediately adjacent to the core and lower fracture intensity outward from the core; and (3) country rock with little fault-related damage. Damage zone width and fracture intensity were observed by Prothro et al. (2009) to increase in higher strength rocks such as welded tuffs or carbonate rock when these rocks were juxtaposed along the same fault from vitric or zeolitic rocks. In porous, softer rocks such as vitric tuffs and some zeolitic tuffs, and in poorly consolidated sediments, the damage zone is also more likely to be expressed as deformation bands consisting of lower porosity granulated material rather than open fractures. In sediments, the core can include fine-grained sediment layers that have been smeared along the slip plane, and the damage zone can include mixed sediment layers.

Based on these observations, Prothro et al. (2009) proposed that in hard rocks, the presence of enhanced fracturing in the damage zone (where fractures are often oriented subparallel to the fault), combined with a low-permeability fault core, will promote fault-parallel flow and inhibit cross-fault flow. In softer rocks and sediments, the fault core and subparallel deformation bands in the damage zone will also inhibit cross-fault flow, but probably not enhance fault-parallel flow.

Prothro et al. (2009) noted that zeolitic rocks and, to a lesser degree, vitric rocks can exhibit fault characteristics that resemble either hard or soft rocks depending on their degree of induration.

Phenomena such as local silicification or argillization can increase rock strength. A series of photographs taken of faults in zeolitic rocks in the N-, T-, and E-Tunnel complexes at Rainier Mesa show that the relatively small displacement faults exposed in the tunnels generally have nonexistent or narrow (several meters thick) damage zones as well as nonexistent or narrow (several inches thick) cores. Sweetkind and Drake (2007a) present data from surface outcrops that indicate that damage zone width increases linearly with fault offset. At Rainier Mesa, fault offsets are typically in the range of meters to tens of meters. The much larger fault offsets in Yucca Flat (tens to hundreds of meters) suggest that damage zone widths could be much larger in Yucca Flat.

NSTec (2008) provided a summary of fracture characteristics for the combined tuff confining unit in Yucca Flat, which includes the upper and lower parts of the LTCU, the OSBCU, and the ATCU. NSTec (2008) examined 1,842 m of core from four boreholes (UE-7f, UE-7az, UE-7ba, and UE-7bc) and identified 502 natural fractures. Of these natural fractures, an average of 23 percent were classified as “open,” with the remainder completely sealed with secondary minerals. Zeolites were found in roughly 48 percent of the fractures, followed by iron and manganese oxides (37 percent), silica minerals (16 percent), and calcite (7 percent). However, even fractures classified as open contained an average of only 10 percent open void space (NSTec, 2008, Table 2-5). True spacing of open fractures (correcting for the average fracture dip of 69 degrees) was estimated to range between 2.4 m in UE-7f and 16.1 m in UE-7bc and average 5 m for the four boreholes (NSTec, 2008, Table 2-4a). Fracture logs showing the distribution of open fractures in each borehole showed many intervals of hundreds of feet containing no open fractures. In particular, the argillic tuffs of the ATCU almost uniformly contained no open fractures. The absence of open fractures was attributed by NSTec (2008) to the high clay content of the ATCU, although it was also acknowledged that fractures, if present, would have been difficult to identify given that cores from the ATCU were often highly fragmented. NSTec (2008) concluded that fractures contribute little to the overall permeability of the HSUs that compose the combined tuff confining unit in Yucca Flat. This conclusion is consistent with earlier assumptions made by Winograd and Thordarson (1975), who estimated leakage through the tuff confining unit to the LCA based solely on matrix flow. NSTec (2008) also noted that carbonate rocks near the top of the LCA tended to be filled with clays derived from the overlying paleocolluvium of the ATCU or possibly precipitated in place and that this would further tend to inhibit hydraulic communication between the tuff confining unit and LCA along fractures.

Collectively, these observations of fault and fracture characteristics suggest that most of whatever hydraulic communication exists between the tuff confining unit and LCA in Yucca Flat takes place through a combination of low rates of diffuse matrix flow (approximately 0.5 mm/yr, according to Winograd and Thordarson [1975]) and preferential flow along faults (Fenelon et al., 2012). Fracturing related to nuclear testing at Yucca Flat, which was not part of the NSTec (2008) study, may also be locally important.

3.1.3.7 Unsaturated-Zone HST Modeling

3.1.3.7.1 One- and Two-Dimensional Radially Symmetric Models

McNab (2008) developed a set of two-dimensional radially symmetric numerical models to examine factors affecting wetting front propagation beneath a subsidence crater subjected to episodic ponding events. Based on an analysis of the return period of rainfall events likely to produce surface runoff and observations from the U-10i crater (Hokett et al., 2000), McNab (2008) applied an infiltration rate of 0.1 m/yr for 20 days every 10 years for a time-averaged infiltration rate of 200 mm/yr to the bottom of the crater. For the hydrologic properties used in the simulations, he found that individual episodic infiltration events tended to merge with increasing depth below the crater bottom and that as a result, over time, the moisture distribution was not substantially different from the one generated with a constant time-averaged infiltration rate of 200 mm/yr. When wetting front movement was not impeded by low-permeability layers, McNab (2008) found that the wetting front could reach the water table at a depth of 500 m within 1,000 years. However, he also found that wetting front propagation was delayed and lateral spreading promoted when the vertical hydraulic conductivity was locally less than the time-averaged infiltration rate because of anisotropy, heterogeneity, or the presence of low-permeability HSUs. Other notable conclusions from these models were (1) lateral spreading in the alluvium due to capillary gradients was negligible because of the relatively coarse-grained nature of the sediments, (2) fine-grained playa sediments deposited at the crater bottoms during earlier ponding events could decrease infiltration resulting from future ponding events (by up to 50 percent for the conditions examined), and (3) collapse chimneys formed in low-permeability rocks above the working points could allow crater infiltration to reach the detonation locations sooner than would otherwise have been possible.

One-dimensional analytical models also were developed by McNab (2008) to estimate the minimum infiltration rates necessary to transport both non-sorbing and sorbing radionuclides to the water table

within 1,000 years. For a given constant infiltration rate, the analytical models first calculate the time required for the wetting front to reach the working point and then calculate the solute velocity and travel time between the working point and the water table. Besides infiltration rates, the travel time estimates also depend on the assumed alluvial and rock unsaturated hydrologic properties because of the inherent relation between effective hydraulic conductivity, matric potential, and moisture content. Initial moisture content and the moisture content behind the wetting front affect both wetting front propagation rates and solute velocity. McNab (2008) demonstrated this by making different assumptions regarding the ability of the tuff and sedimentary confining units to transmit water and radionuclides via fracture flow. Assuming that matrix of the tuff confining units have a sufficiently low permeability (saturated hydraulic conductivity K_s = 1.0E-04 meters per day [m/day], or saturated intrinsic permeability k_s = 1.2E-16 square meters [m^2]) and that these HSUs are unfractured, approximately half (164 of the 345) of the unsaturated-zone detonations had tuff confining unit permeabilities that were too low to transmit water at rates required for radionuclides to reach the water table within 1,000 years (assuming one-dimensional vertical flow). The remaining 181 unsaturated-zone detonations required time-averaged infiltration rates of between about 20 and 100 mm/yr for non-sorbing radionuclides. For partition coefficient (K_d) values of 1 and 10 milliliters per gram (mL/g), the estimated 145 detonations with sufficient vertical permeability to transmit the minimum necessary fluxes required time-averaged infiltration rates of between about 250 and 800 mm/yr and between about 900 and 7,000 mm/yr, respectively. These results demonstrate the decreasing likelihood that strongly sorbing radionuclides like Ni, Sr, Eu, Cs, Sm, Am, or Pu will reach the water table from unsaturated-zone detonations except where the detonations are sufficiently close to or directly intersect the water table. The variability in required crater infiltration rates for a given K_d results from differences in the working-point elevations, the depths to groundwater, and the HSUs present at individual detonation locations. Appendix A of McNab (2008) lists the minimum infiltration rates necessary for radionuclide breakthrough at the water table within 1,000 years for individual detonations and K_d classes both when recharge rates are assumed to be limited by the low matrix permeability of the tuff and clastic confining units and when flow through these units is augmented by fractures or faults.

3.1.3.7.2 Three-Dimensional Models of ^{14}C and ^{3}H Transport from Representative Shallow and Deep Detonations

SNJV (2009b) created three-dimensional models of representative shallow and deep detonations in the alluvium of Yucca Flat to investigate the sensitivity of ^{14}C and ^{3}H transport to crater infiltration rates, crater-bottom infiltration areas ("playas"), gas-phase partitioning and diffusion, solid-phase sorption, and the presence of low-permeability crush zones. In addition to a 526-m-thick section of unsaturated alluvium, the models included a saturated alluvial aquifer in the lower 224 m of the model so that maximum aquifer concentrations could be calculated as a function of time. Mass ^{14}C and ^{3}H fluxes to the water table also were tracked as a function of time over the 1,000-year regulatory period represented in the simulations. Crater infiltration rates of 5, 50, 250, and 5,000 mm/yr were considered, with 250 mm/yr treated as the base case for which gas-phase diffusion and solid-phase sorption were included or excluded in various combinations to test model sensitivity to these processes. While crater infiltration rates shown later in this section indicate that infiltration rates approaching 5,000 mm/yr are possible for a few craters with large contributing watersheds, these infiltration rates are unrealistically large for most craters in Yucca Flat.

For ^{14}C, gas-phase partitioning via Henry's law and diffusion in the gas-phase, combined with a solid-phase partition coefficient (K_d = 0.8 mL/g) to account for ^{14}C sorption onto calcite, were shown to be effective attenuation mechanisms that delayed and reduced the peak mass fluxes to and concentrations in the underlying aquifer. Gas-phase diffusion spread the initial ^{14}C mass within a larger volume of the unsaturated zone where ^{14}C equilibrated with the pore water; as a result, less ^{14}C was entrained by infiltration moving downward from the crater bottom. For the shallow detonation (175 m below land surface [bls]), dilution of ^{14}C through gas-phase diffusion reduced peak aquifer concentrations to less than 1 percent of the MCL for ^{14}C (2,000 picocuries per liter [pCi/L]) in scenarios with crater infiltration rates of 250 mm/yr or less, and to less than 10 percent of the MCL in scenarios with a crater infiltration rate of 5,000 mm/yr. For infiltration rates of 250 mm/yr or less, the fraction of the initial ^{14}C inventory reaching the water table was less than 1 percent when sorption was included and less than 3 percent when sorption was ignored. Ignoring both gas-diffusion and solid-phase sorption increased the peak concentrations in the underlying aquifer to only about 20 percent of the MCL, indicating that ^{14}C from shallow detonations posed little risk to the underlying aquifer. For the representative deep detonation (435 m bls, with an exchange volume extending to within 1 m of the water table), peak water-table concentrations were a much larger fraction of the

MCL for ^{14}C for all cases, but exceeded the MCL only when gas- and liquid-phase partitioning was ignored and the crater infiltration rate of 5,000 mm/yr was assumed. The relative unimportance of ^{14}C as a contaminant of regulatory concern was partly because solid-phase sorption and, to a lesser extent, gas-phase partitioning reduced peak pore-water concentrations in the exchange volume to or below the MCL (SNJV, 2009b, Table 5-5). Therefore, even a small amount of additional dilution from crater infiltration or mixing with groundwater in the underlying aquifer reduces peak aquifer concentrations to below the MCL.

Gas-phase diffusion of ^{3}H was much less important than that of ^{14}C because most of the ^{3}H (99.99 percent) resides in the liquid phase at temperatures near 20 degrees Celsius (°C). Consequently, gas-phase transport of ^{3}H from either the shallow or deep detonations was not nearly as significant as that of ^{14}C. However, for all but very high crater infiltration rates (e.g., 5,000 mm/yr), crater infiltration was not important for ^{3}H transport to the water table because ^{3}H decayed to less than its MCL of 20,000 pCi/L before the wetting front arrived. Most ^{3}H transport to the water table was from deep detonations where a background infiltration rate of 1 mm/yr and large initial concentration gradients were sufficient to drive transport to the underlying aquifer within a few hundred years. Ironically, although the short half-life of ^{3}H (12.3 years) led to a smaller fraction of the initial inventory reaching the water table within 1,000 years (generally, less than 0.01 percent), the much higher initial concentrations of ^{3}H in the exchange volume relative to its MCL made ^{3}H a much more significant problem than ^{14}C from a regulatory standpoint due to the absence of dilution from gas-phase processes.

The sensitivity analysis showed that the crater bottom area through which infiltration occurs is also a factor in mass transport to the water table. Wetting front arrivals are shorter when infiltration area increases, because the overall mass of infiltrating water is larger and a smaller fraction of it is lost because of lateral capillary gradients. The biggest impact was for ^{14}C in the deep detonations where the fraction of the initial ^{14}C mass arriving at the water table increased from 9.3 to 33 percent when the crater infiltration area increased from one-half to the entire crater radius (SNJV, 2009b, Table 5-5). However, because crater infiltration is conceptualized as taking place only at the bottom of the crater, the case in which crater infiltration takes place across the entire crater diameter has value primarily from a sensitivity standpoint, and not as a physically representative case.

SNJV (2009b) also examined the impact of water introduced during drill-back operations on ^{3}H and ^{14}C transport to the water table. As described in Section 2.2.2.1, drill-back operations typically took place in the days to weeks following a test to retrieve samples that would allow an evaluation of test performance, and these operations introduced drilling fluid into the near-field environment. Carle et al. (2008) estimated that drilling fluid injection would affect radionuclide transport in the unsaturated zone for carbonate detonations. Using estimates of water loss near the cavity from angled boreholes and typical drilling fluid loss rates, SNJV (2009b) found that peak concentrations in the aquifer and the fraction of the initial mass arriving at the water table did not change significantly when water from drill-back operations was added to the base case (SNJV, 2009b, Table 5-5). Part of the reason for the minimal effect is that, because drill-back boreholes are angled to avoid the collapse crater, only the part of the borehole that is in alignment with the cavity is likely to introduce water directly to the exchange volume. A second part of the explanation is that the alluvium has a large drained porosity under pre-detonation conditions and is capable of absorbing a large amount of drilling fluid. Therefore, although the permeability of the alluvium is high, the large transport porosity tends to reduce transport velocities to a fraction of what is believed to be typical of fractured rocks where effective porosities can be orders of magnitude smaller. A third factor that mitigates the impact of drilling fluid losses is that the high-viscosity drilling mud used in the drill-back operations was commonly recirculated until the drill-back hole reached the cavity rubble, at which point fluid losses then increased (Becker, 2012). Because of its high viscosity and high clay content, the lost drilling fluid had limited mobility beyond the open cavity and collapsed rubble.

3.2 Unsaturated-Zone Data

Wood (2007) compiled lithologic, rock property, and hydraulic data collected at the NNSS over more than five decades. That compilation included data on water saturation, porosity, and moisture content from the unsaturated zone in Yucca Flat. This section presents a portion of the compiled data from the unsaturated zone in Yucca Flat and discusses aspects of that dataset as well as potential limitations. These data were presented in a general way by McNab (2008) as possible evidence that conditions in the deep unsaturated zone of Yucca Flat are relatively wet, reflecting continued drainage from past wetter conditions. If the data prove reliable, they might also provide a basis for calibrating the large-scale percolation rates and hydraulic properties of the unsaturated-zone models presented in this section. Therefore, this section analyzes these data with these possible interpretations and applications in mind.

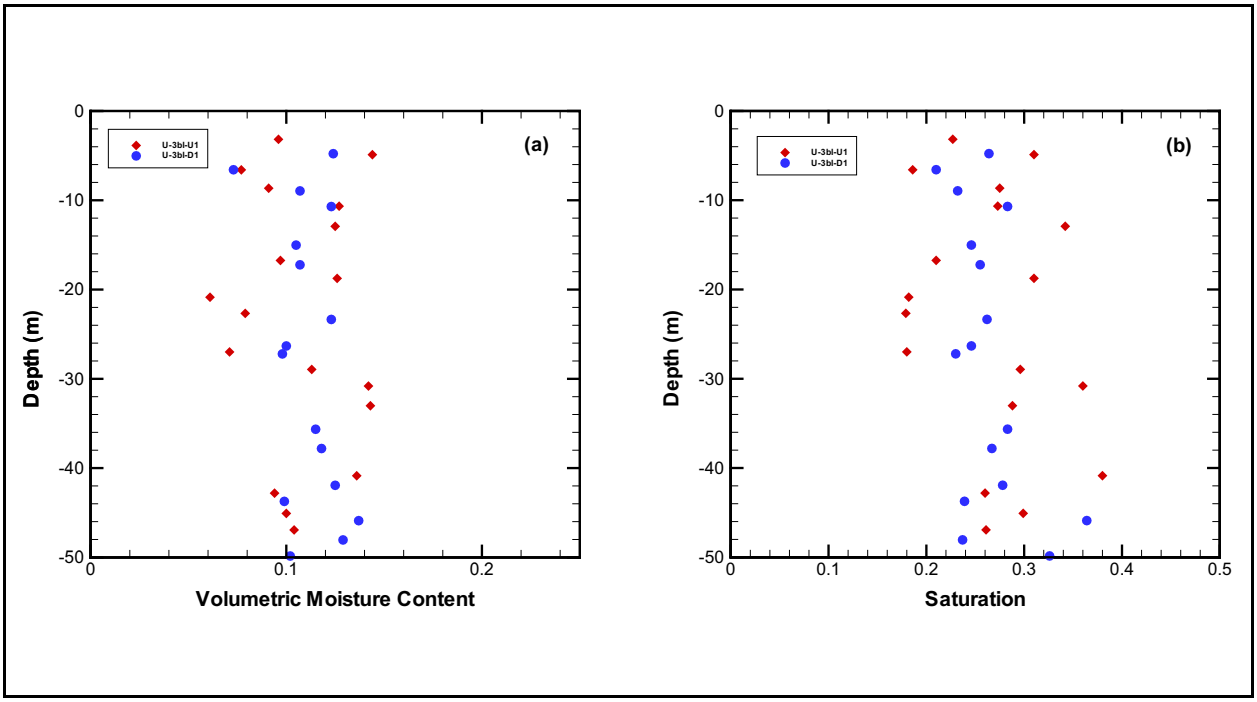

Figure 3-7
Data from Area 3 Boreholes in Uncratered Areas:
(a) Volumetric Moisture Content, and (b) Saturation
Source: Modified from Kwicklis et al., 2006b

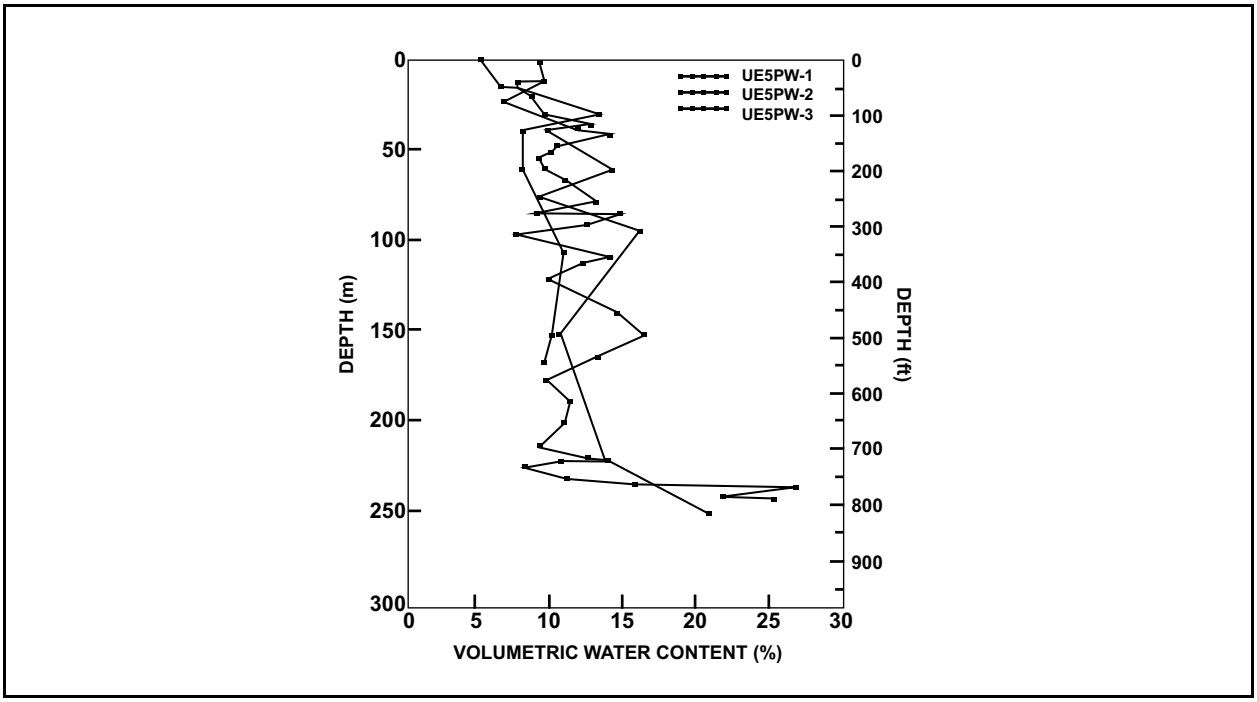

Figure 3-8
Volumetric Moisture Contents in the Area 5 Pilot Wells
Source: REECO, 1994

As described in Section 3.1.3.1, moisture content, porosity, and saturation data were collected from relatively shallow (approximately 50 m deep) boreholes at the Area 3 RWMS with dry-drilling techniques that involved air as a drilling fluid. These data show moisture contents from two boreholes drilled in relatively undisturbed areas adjacent to the subsidence craters. Volumetric moisture contents ranged from about 6 to 14 percent, and water saturations ranged from 18 to 38 percent (Figure 3-7). Although these data are from relatively shallow depths and cannot address questions about moisture content changes at greater depths in Yucca Flat, data from dry-drilled pilot wells at the Area 5 RWMS in northern Frenchman Flat extend from land surface to the water table at a depth of roughly 230 m. These data (Figure 3-8) show similar ranges in moisture contents above the water table (5 to 16 percent), and moisture contents do not systematically increase between depths of 30 and 230 m (REECO, 1994, Fig. 3.21). Between land surface and a depth of 30 m, volumetric moisture contents are generally between 5 and 10 percent.

The deepest characterization samples recovered from undisturbed alluvium at the Area 3 RWMS were from 50 m (164 ft). No characterization samples were taken below 148 m (486 ft). The Lyner Complex, located 4.8 km (3 miles) from the Area 3 RWMS, provides access for sampling at a depth of 296 m (971 ft). Seventeen gravimetric water contents measured in grams per gram (g/g) in these dry-drilled boreholes ranged from 0.0374 to 0.117 g/g. No bulk density measurements were taken with these gravimetric moisture contents that would facilitate their conversion to volumetric moisture contents. However, assuming a typical soil bulk density value of 1.65 g/cm^3 for these samples, volumetric water contents in cubic meters per cubic meter (m^3/m^3) can be calculated. The volumetric water contents range from 0.062 to 0.196 m^3/m^3, with a mean and standard deviation of 0.129 ± 0.04 m^3/m^3. This range is similar to that for the shallow samples from the boreholes at the Area 3 RWMS and the samples from the pilot wells at the Area 5 RWMS, suggesting that volumetric water contents do not increase systematically with depth in the alluvium above a depth of approximately 250 m.

Unlike data collected specifically to characterize moisture in the unsaturated zone at the Area 3 RWMS in Yucca Flat (BN, 1998) and the Area 5 RWMS in Frenchman Flat (REECO, 1994), the moisture data in Wood (2007) were collected from boreholes in which water was a component of the drilling fluid. Water/air/foam mixtures were used to drill the exploratory holes (UE-series boreholes), and traditional drilling mud mixtures were used to drill the large-diameter device emplacement holes (U-series boreholes). The moisture content and porosity data in Wood (2007) are mostly from

sidewall cores collected from the borehole walls soon after drilling. The sidewall cores in the exploratory holes were taken with a percussion gun that retrieved approximately 1-by-1-inch samples. The samples from the emplacement holes were sometimes no more than scrapings from the borehole walls taken by angling a 1-ft-long core barrel roughly 40 degrees from horizontal into the borehole walls (W. Hawkins, LANL, personal communication). Because of the shallow depth of the samples, the influence of borehole drilling fluids on the measured moisture contents is a concern, particularly in the emplacement holes where approximately 200 to 300 ft of drilling mud was maintained above the drill against the borehole wall. In the exploratory holes, the water/air/foam mixture moved down the drill stem and up the borehole. In both types of boreholes, sidewall samples were taken in the days following drilling after geophysical logs had been obtained.

Saturation, porosity, and volumetric moisture content profiles for selected UE-series boreholes are shown in Figures 3-9 to 3-11, along with the HSU boundaries identified from the FEHM models. For some boreholes with very thick alluvial sections spanning 400 m or more (e.g., UE-2eh, UE-2en, UE-2fa, UE-2fb, and UE-4ah/Inst.), the measured moisture contents, porosities, and saturations all tend to increase with depth. Moisture contents range from about 15 to 20 percent in the shallowest parts of the profile and increase to 30 or even 40 percent in the deepest parts of the alluvial section. The water table in Yucca Flat alluvium and volcanic rock is less than 750 m, so measurements above about 800 m should be well above the capillary fringe. Because the porosity increases rather than decreases with increasing depth in most cases, the moisture content and saturation increases with depth cannot be explained by a reduction in permeability due to compaction from increasing overburden pressure. The porosity profiles from the alluvial sections also show the variability in porosity due to fine-scale layering and heterogeneity within the alluvium. Where thick sections of the LTCU are present such as at boreholes UE-4g 2, UE-4p, and UE-7be/Inst., or a thick section of a vitric tuff is present as in boreholes UE-2aa, UE-2co, and UE- 8e/Inst. (UE- 8e (2470 ft)), the data also indicate heterogeneity in their porosity (and presumably, in their permeability). The LTCU (and OSBCU) intervals have much higher saturations (sometimes approaching 100 percent) than the TM-LVTA intervals, even when they are well above the water table (approximately 750 m elevation), presumably because of their much lower matrix permeability.

Figure 3-12 shows saturation, porosity, and moisture content profiles for six U-series boreholes located in Area 3. Data from these boreholes are useful because the shallow parts of the profiles can be compared directly with the shallow data from the boreholes at the Area 3 RWMS to evaluate the

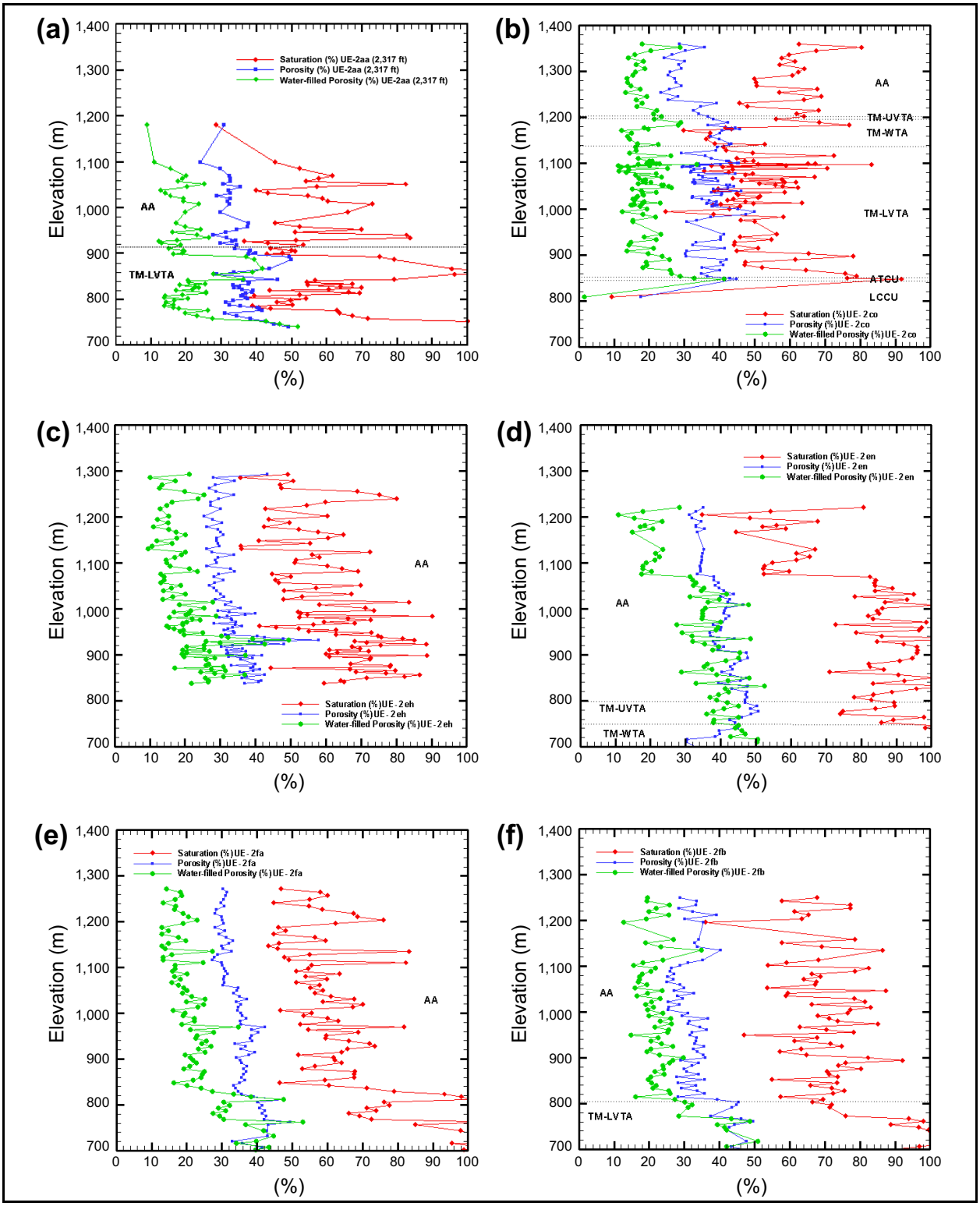

Figure 3-9
Saturation, Porosity, and Moisture Content Profiles for Boreholes: (a) UE- 2aa (2317 ft), (b) UE-2co, (c) UE-2eh, (d) UE-2en, (e) UE-2fa, and (f) UE-2fb

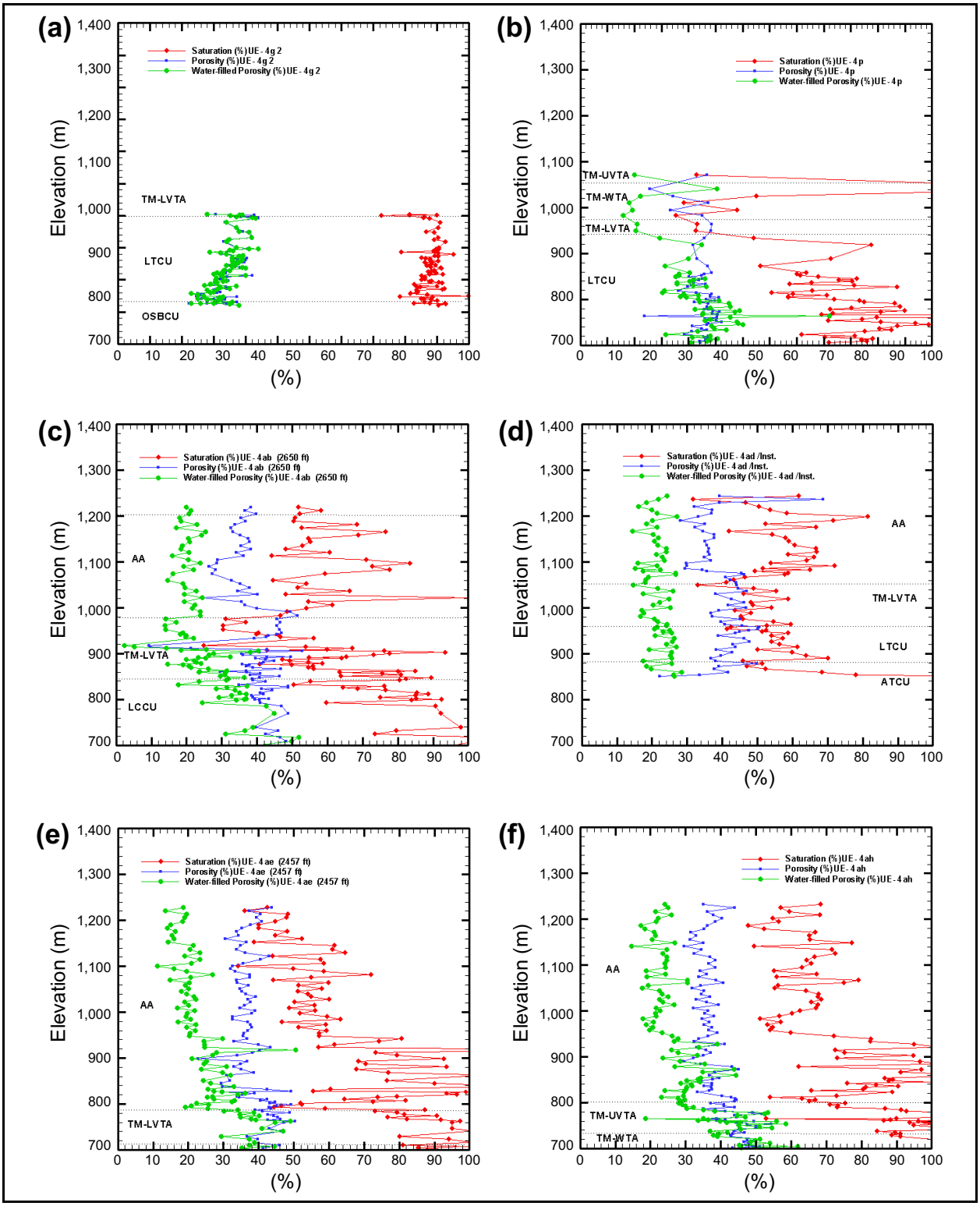

Figure 3-10
Saturation, Porosity, and Moisture Content Profiles for Boreholes: (a) UE-4g 2,(b) UE-4p, (c) UE- 4ab (2650 ft), (d) UE-4ad/Inst., (e) UE- 4ae (2457 ft), and (f) UE-4ah

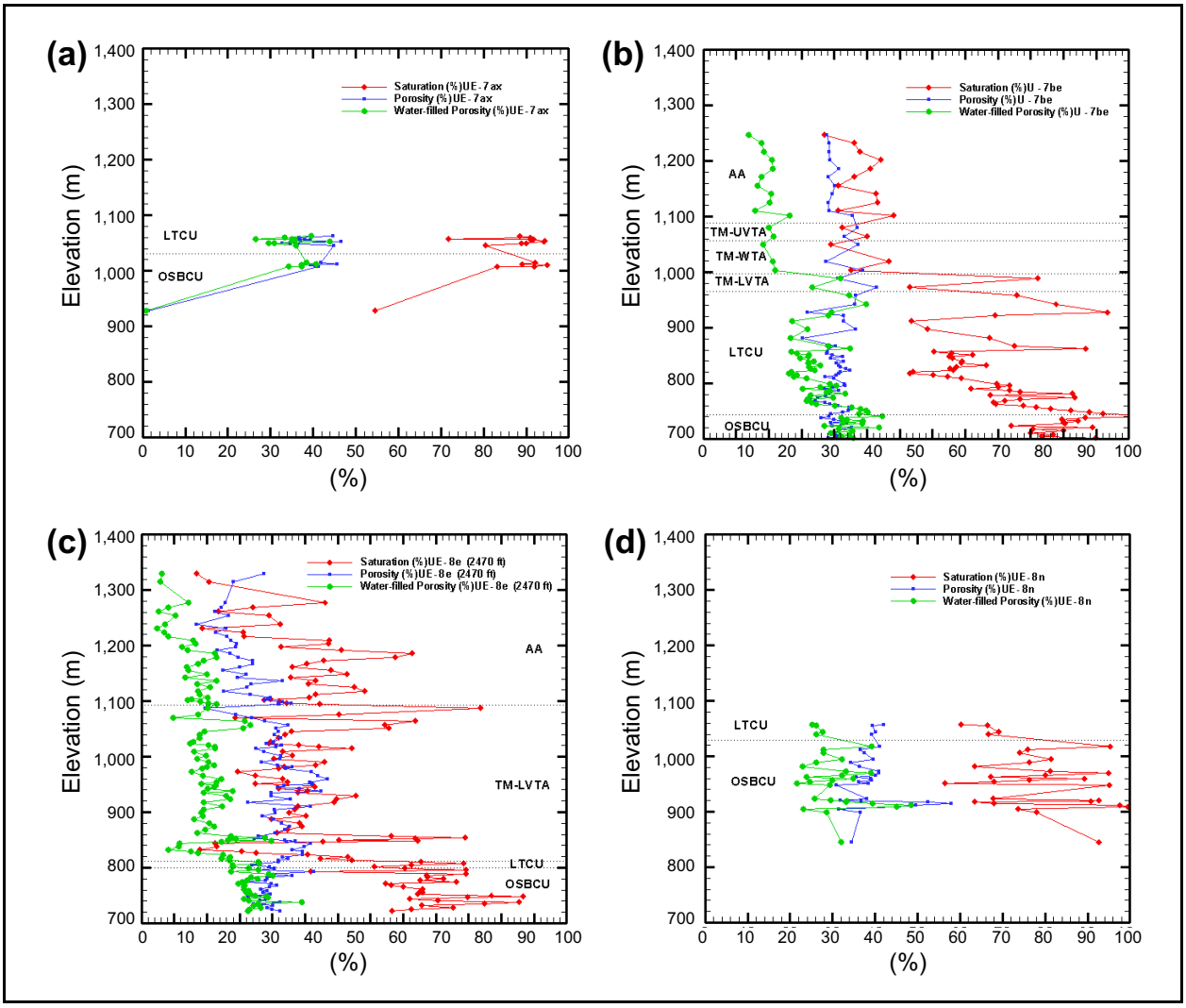

Figure 3-11
Saturation, Porosity, and Moisture Content Profiles for Boreholes: (a) UE-7ax, (b) UE-7be, (c) UE-8e, and (d) UE-8n

effects of drilling fluid losses on moisture contents. Moisture data from the UE-series holes in Area 3 were not available. Like the UE-series boreholes, moisture contents in the U-series boreholes from the shallow parts of the unsaturated zone are typically about 20 percent, or approximately twice the moisture contents measured as part of the Area 3 RWMS characterization program. Only borehole U-3kv has shallow water contents of about 10 percent. Water contents decrease with depth (U-3ht), increase with depth (U-3kv), or remain approximately constant with depth (U-3kq, U-3kt) in the U-series boreholes in Area 3. Elsewhere, emplacement boreholes with thick alluvial sections such as U-2ar and U-2dz (Figure 3-13) show increases in moisture content, saturation, and porosity similar to exploratory boreholes in Area 2 such as UE-2eh and UE-2fa (Figure 3-9). Shallow moisture contents

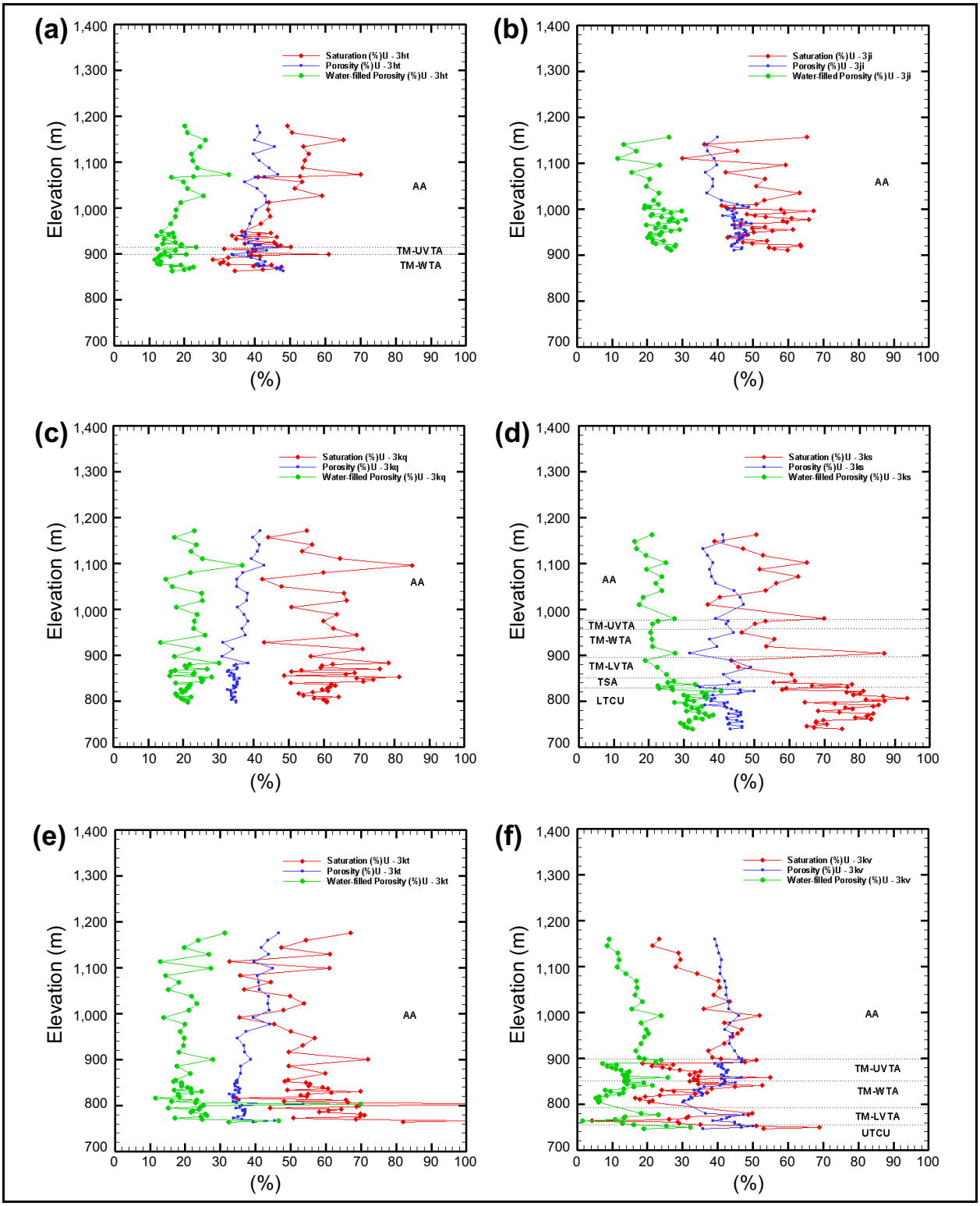

Figure 3-12
Saturation, Porosity, and Moisture Content Profiles for Boreholes: (a) U-3ht, (b) U-3ji, (c) U-3kq, (d) U-3ks, (e) U-3kt, and (f) U-3kv

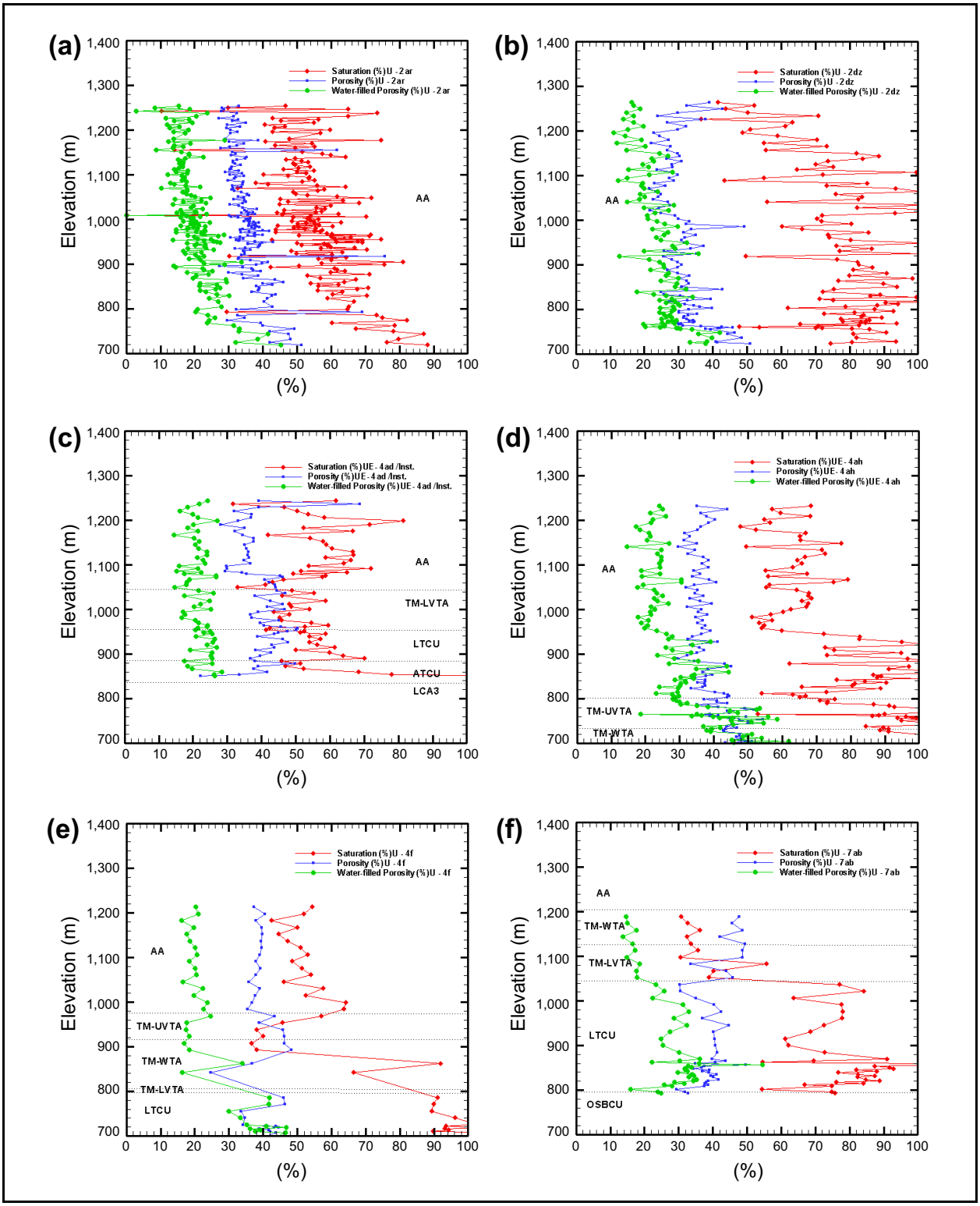

Figure 3-13
Saturation, Porosity, and Moisture Content Profiles for Boreholes: (a) U-2ar, (b) U-2dz, (c) U-4ad/Inst., (d) U-4ah, (e) U-4f, and (f) U-7ab

are in the range of 10 to 20 percent in both the exploratory (UE-series) and emplacement (U-series) boreholes, suggesting that difference in drilling fluids used in the exploratory and emplacement holes produced similar perturbations to the ambient moisture contents based on a comparison with data from the dry-drilled holes at the Area 3 RWMS and Area 5 RWMS.

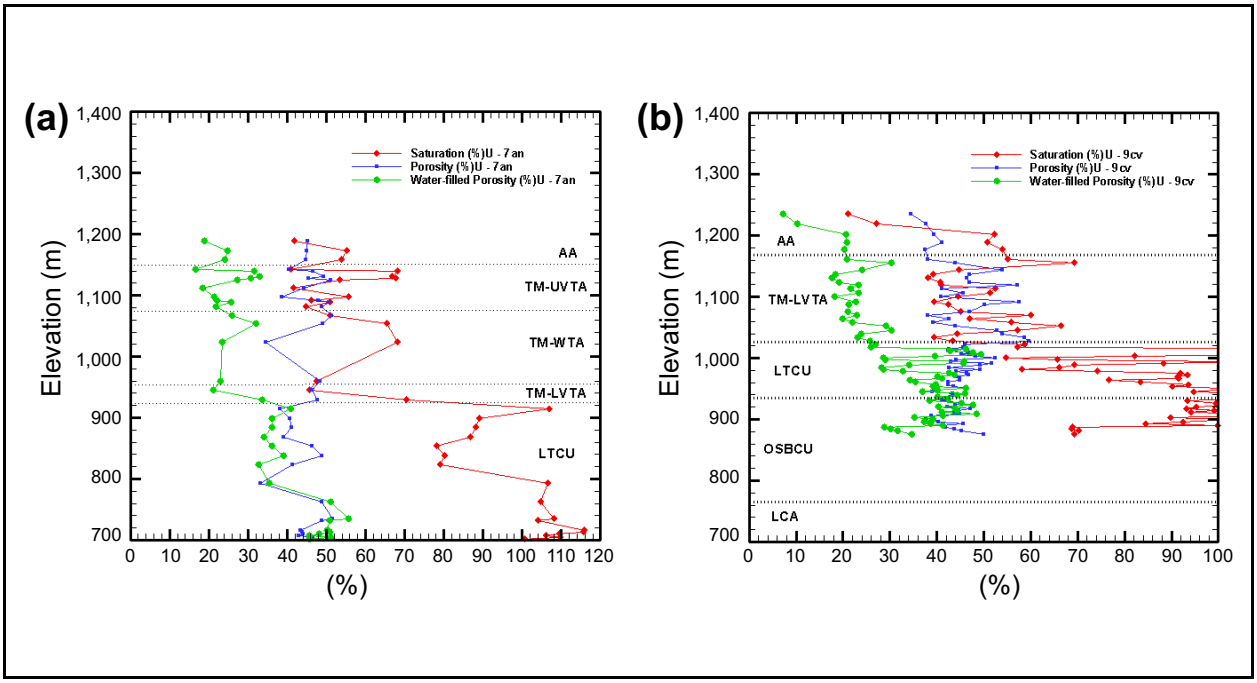

Figure 3-14
Saturation, Porosity, and Moisture Content Profiles for Boreholes: (a) U-7an, and (b) U-9cv

Although the absolute values of moisture content and saturation from the exploratory and emplacement boreholes may have been impacted by drilling fluids, the frequently observed increases in moisture content and saturation with depth, combined with increases in porosity with depth, suggest the possibility that wetter conditions prevail at depth in the alluvium in Yucca Flat. Like the exploratory boreholes, the emplacement wells also tend to show relatively high saturations in the LTCU (Figures 3-13 and 3-14) possibly reflecting the low permeability of the tuff confining units. As discussed earlier, higher water contents at depth would be compatible with the idea that infiltration from past pluvial periods is still draining from the unsaturated zone.

3.3 Surface Water Runoff and Infiltration into Nuclear Subsidence Craters

Crater infiltration was calculated for all 462 craters in Yucca Flat by the use of the 1,000-year synthetic precipitation record and HYDRUS-1D (H1D), where the average annual crater infiltration

rate over the 1,000-year simulation period is calculated as the sum of the total recharge from the base of the model plus the change in water storage, divided by 1,000. The runoff and infiltration models were calibrated using a variety of datasets as described in Appendix E.

Surface water runoff and infiltration into all Yucca Flat craters were calculated by the use of the Soil Conservation Service Curve Number (SCS-CN) method with H1D. The runoff model was calibrated by adjusting surface soil water potential thresholds that separate curve number antecedent runoff conditions until runoff and infiltration model results best matched ponding data and subsurface moisture conditions for three craters in Yucca Flat and one crater in Frenchman Flat. Long-term (1,000-year), one-dimensional simulations of infiltration were then conducted for all 462 craters, where infiltration was calculated as recharge plus change in soil water storage. Model results indicate that the median and mean infiltration for all craters were 62 and 206 mm/yr, respectively. Figure 3-15 shows the preliminary and final results of sorted infiltration for all craters. As discussed in Appendix E, the preliminary results included upper and lower bounds, while the final results include one set of results. Table 3-1 provides some statistics on the preliminary and final results.

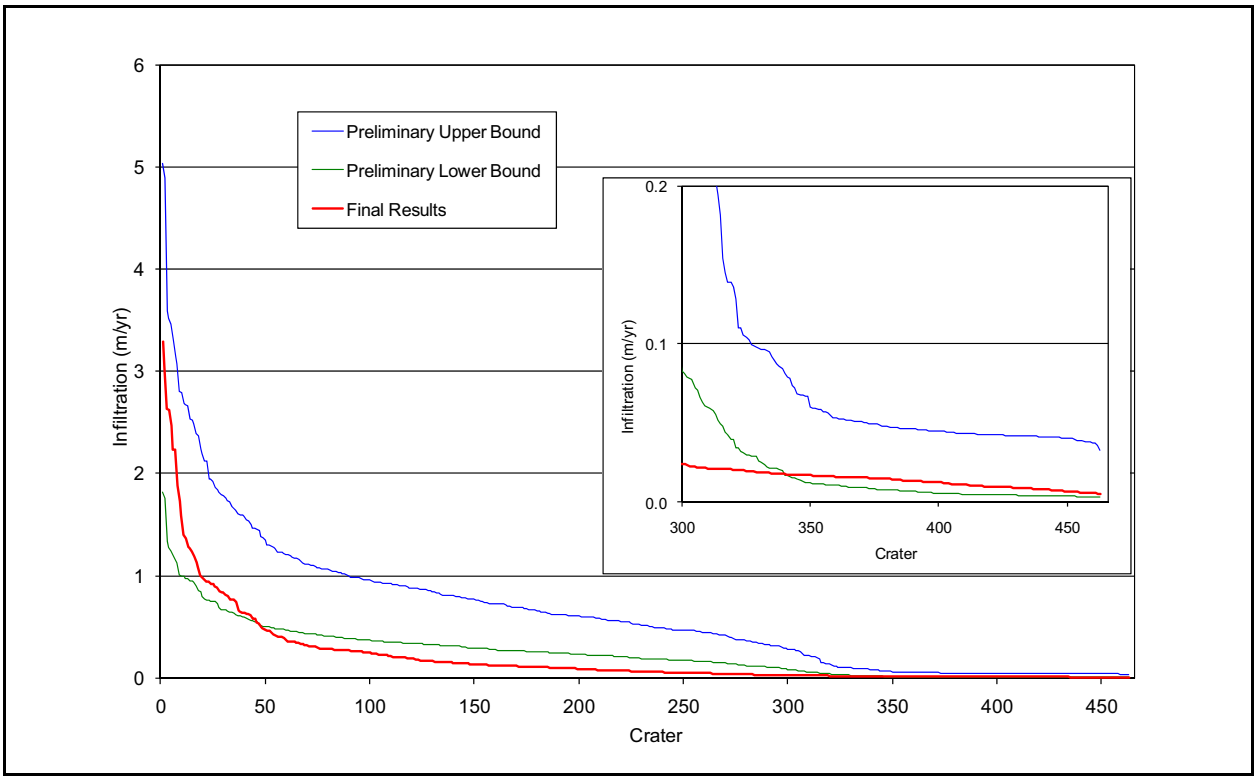

Figure 3-15
Preliminary and Final Infiltration Results

Table 3-1
Statistics for Preliminary and Final Infiltration Results

Statistic	Preliminary		Final
	Upper Bound	Lower Bound	
	(m/yr)		
Minimum	0.032	0.003	0.005
Median	0.512	0.189	0.062
Mean	0.648	0.240	0.206
Maximum	5.035	1.818	3.288

Figure 3-16 shows a map of Yucca Flat with crater catchment areas and infiltration flux for all 462 craters. Crater catchment areas and therefore infiltration rates tend to be largest on the north and west sides of Yucca Flat, rather than on the east side or in the center of Yucca Flat.

The methods used to make these calculations include many assumptions, the largest of which include uniform precipitation over large catchment areas, no transmission losses over large catchment areas, and frustum geometries of craters. However, model calibration to data collected at U-10i, U-3fd, U-3bh, and U-5a provides confidence in the model results, and model results are consistent with the conclusions of other researchers with regard to ponding volumes and infiltration fluxes (Tyler et al., 1992; Pohll et al., 1996; French et al., 1999; Hokett et al., 2000; Wilson et al., 2000). This work clearly shows that a nuclear subsidence crater is a potential groundwater recharge point if the crater catchment area is relatively large. Model results and observations made at the U-5a crater suggest that craters with large catchments areas will also fill with sediment, which eventually eliminates a groundwater pathway.

3.4 Model Design and Setup

3.4.1 Numerical Grids

The complex geology and large number of nuclear detonations in the unsaturated zone of Yucca Flat required that the overall model be divided into 12 separate numerical grids in order to keep the model computationally tractable. The grid locations were shown relative to the detonation locations and NNSS areas in Figure 3-2. Grids extend 2,325 to 2,850 m in the north–south direction, 13,350 m in the east–west direction, and 730 to 1,110 m in the vertical direction (Table 3-2). Grids overlapped by 370 to 530 m in the north–south direction in order to create buffer zones in the model adjacent to

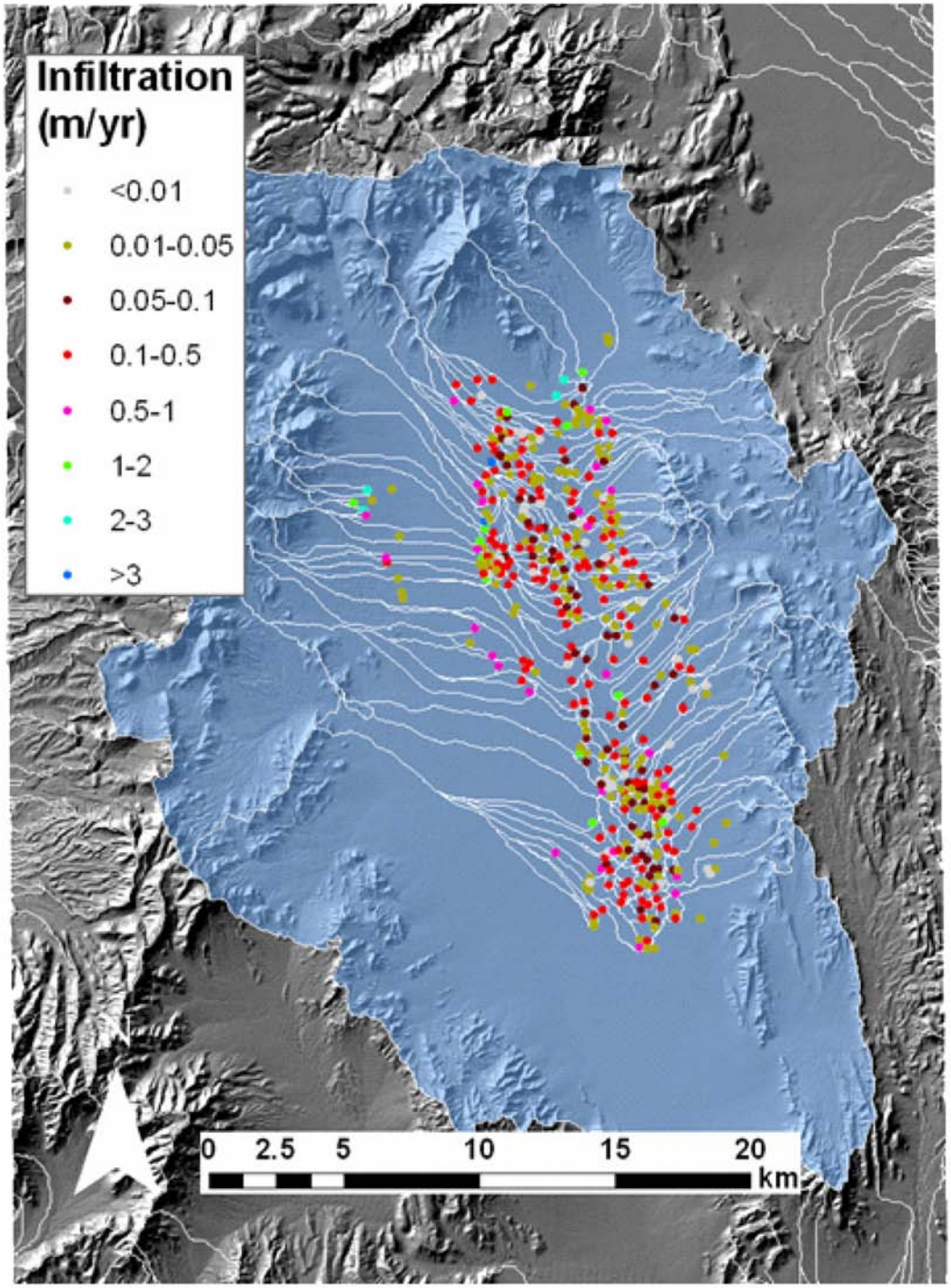

Note: The blue highlighted area is the watershed area of Yucca Flat, the white lines delineate the catchment areas contributing to individual craters, and the colored circles indicate the magnitude of the crater infiltration rates.

Figure 3-16
Map Showing Crater Catchment Areas and Infiltration Flux for Each Crater

Table 3-2
Grid Extent with Numbers of Nodes and Elements
(Page 1 of 2)

Grid Number and Extent	Minimum [a]	Maximum [a]	Distance	Number of Nodes	Number of Elements
Grid 1	--	--	--	530,507	3,038,999
x	580,775.0	594,125.0	13,350.0	--	--
y	4,093,230.0	4,095,550.0	2,325.0	--	--
z	700.0	1,430.0	730.0	--	--
Grid 2	--	--	--	963,920	5,419,728
x	580,775.0	594,125.0	13,350.0	--	--
y	4,095,180.0	4,097,500.0	2,325.0	--	--
z	700.0	1,440.0	740.0	--	--
Grid 3	--	--	--	815,799	4,600,203
x	580,775.0	594,125.0	13,350.0	--	--
y	4,097,130.0	4,099,450.0	2,325.0	--	--
z	680.0	1,510.0	830.0	--	--
Grid 4	--	--	--	1,040,163	5,940,608
x	578,750.0	592,100.0	13,350.0	--	--
y	4,099,080.0	4,101,400.0	2,325.0	--	--
z	680.0	1,490.0	810.0	--	--
Grid 5	--	--	--	585,942	3,347,906
x	578,750.0	592,100.0	13,350.0	--	--
y	4,100,950.0	4,103,350.0	2,400.0	--	--
z	680.0	1,590.0	910.0	--	--
Grid 6	--	--	--	616,831	3,471,126
x	577,775.0	591,125.0	13,350.0	--	--
y	4,102,900.0	4,105,300.0	2,400.0	--	--
z	670.0	1,490.0	820.0	--	--
Grid 7	--	--	--	615,156	3,489,184
x	576,800.0	590,150.0	13,350.0	--	--
y	4,104,920.0	4,107,250.0	2,325.0	--	--
z	680.0	1,480.0	800.0	--	--
Grid 8	--	--	--	1,403,468	8,262,077
x	575,825.0	589,175.0	13,350.0	--	--
y	4,106,875.0	4,109,200.0	2,325.0	--	--
z	700.0	1,500.0	800.0	--	--

Table 3-2
Grid Extent with Numbers of Nodes and Elements
(Page 2 of 2)

Grid Number and Extent	Minimum [a]	Maximum [a]	Distance	Number of Nodes	Number of Elements
Grid 9	--	--	--	1,121,974	6,403,444
x	574,850.0	588,200.0	13,350.0	--	--
y	4,108,830.0	4,111,150.0	2,325.0	--	--
z	680.0	1,660.0	980.0	--	--
Grid 10	--	--	--	1,025,816	5,793,974
x	574,850.0	588,200.0	13,350.0	--	--
y	4,110,620.0	4,113,100.0	2,475.0	--	--
z	700.0	1,810.0	1,110.0	--	--
Grid 11	--	--	--	871,843	4,944,100
x	574,850.0	588,200.0	13,350.0	--	--
y	4,112,730.0	4,115,050.0	2,325.0	--	--
z	690.0	1,860.0	1,170.0	--	--
Grid 12	--	--	--	480,432	2,667,456
x	574,850.0	588,200.0	13,350.0	--	--
y	4,114,680.0	4,117,520.0	2,850.0	--	--
z	690.0	1,760.0	1,070.0	--	--

[a] *x* and *y* are in UTM NAD 27 coordinates in meters; *z* is elevation amsl in meters.

-- = Not applicable

Note: Grids 1 through 12 of this table correspond to g01 through g12 in Figure 3-2.

detonations located near the north and south edges of the grids. Even though the grids overlapped, the detonations near the north or south edges were assigned to one grid or another (but not both). Grid sizes range from 480,432 nodes and 2,667,456 tetrahedral elements in the case of grid 12 to 1,403,468 nodes and 8,262,077 tetrahedral elements in the case of grid 8 (Table 3-2). The size of the grids was largely dependent on the number of detonations in the area encompassed by the grid.

Lateral capillary pressure and radionuclide concentration gradients are expected to result from relatively high infiltration through the crater bottoms and initially high radionuclide concentrations in the exchange volume following a detonation. To accurately simulate these gradients, the grids near each detonation extend radially outward from each detonation's working point in a series of gradually thickening concentric shells that eventually merge with the orthogonal background mesh

(Figure 3-17). The orthogonal background mesh has a node spacing of $\Delta x = \Delta y = 75$ m and $\Delta z = 10$ m. The concentric portion of the mesh extends outward from the working point until a radius of 1.5 times either the cavity or crater radius is reached, depending on whichever is larger. Generally, the crater radius was used when the detonation produced a crater, and the cavity radius was used when the detonation did not cause a crater to form. In areas where detonation density is high and areas of concentric mesh refinement overlap, the overlapping portion of the concentric mesh for the earlier detonation is overwritten by the concentric mesh for the later detonation. The concentric portion of the mesh is centered on the each detonation's working point and, depending on the size of the crater or cavity, has nodes at fixed radial distances from the working point of r = 0, 5, 15, 25, 35, 45, 55, 65, 75, 85, 95, 105, 125, 145, 165, 195, 225, 255, and 285 m. The concentric portions of the mesh ranged from 65 to 285 m in radial distance from the working point. The smallest concentric regions of the mesh were for a detonation with a maximum announced yield of 20 kt (cavity radius of approximately 40 m) and no crater.

The 12 model grids were constructed in a way that incorporates the 25 different HSUs and the 178 high-angle normal faults and 2 low-angle thrust faults in the HFM for Yucca Flat described in BN (2006). The geology is continuous across the grids (Figure 3-18), and each HSU or fault in the HFM is given the same material identifier in each of the grids to facilitate the assignment of hydraulic and transport properties in a consistent manner. As described previously, the grids become more refined in the vicinity of nuclear detonations to represent details of the crater, chimney, and cavity associated with each nuclear detonation. The fault thickness in each grid is determined by the background grid spacing in the orthogonal portions of the grid ($\Delta x = \Delta y = 75$ m and $\Delta z = 10$ m) where it is generally 2 nodes thick (Figure 3-19). This fault thickness is maintained through the more refined areas of the grid associated with nuclear detonations so that each fault has many more nodes across its width but the same overall thickness across these refined areas.

To facilitate grid construction for the unsaturated-zone model, each grid is initially built in order that it extends slightly above land surface and below the water table. These parts of each grid are effectively removed in FEHM at run time through use of an option that allows the user to inactivate nodes by assigning them a negative porosity. The nodes above land surface were identified by intersecting the grids with the Digital Elevation Model (DEM) for Yucca Flat (DOE/NV, 1997b). The nodes at and below the water table were identified by intersecting the water-table surface defined by the data provided in DOE/NV (1997b) with the model grids. The relatively complex water-table

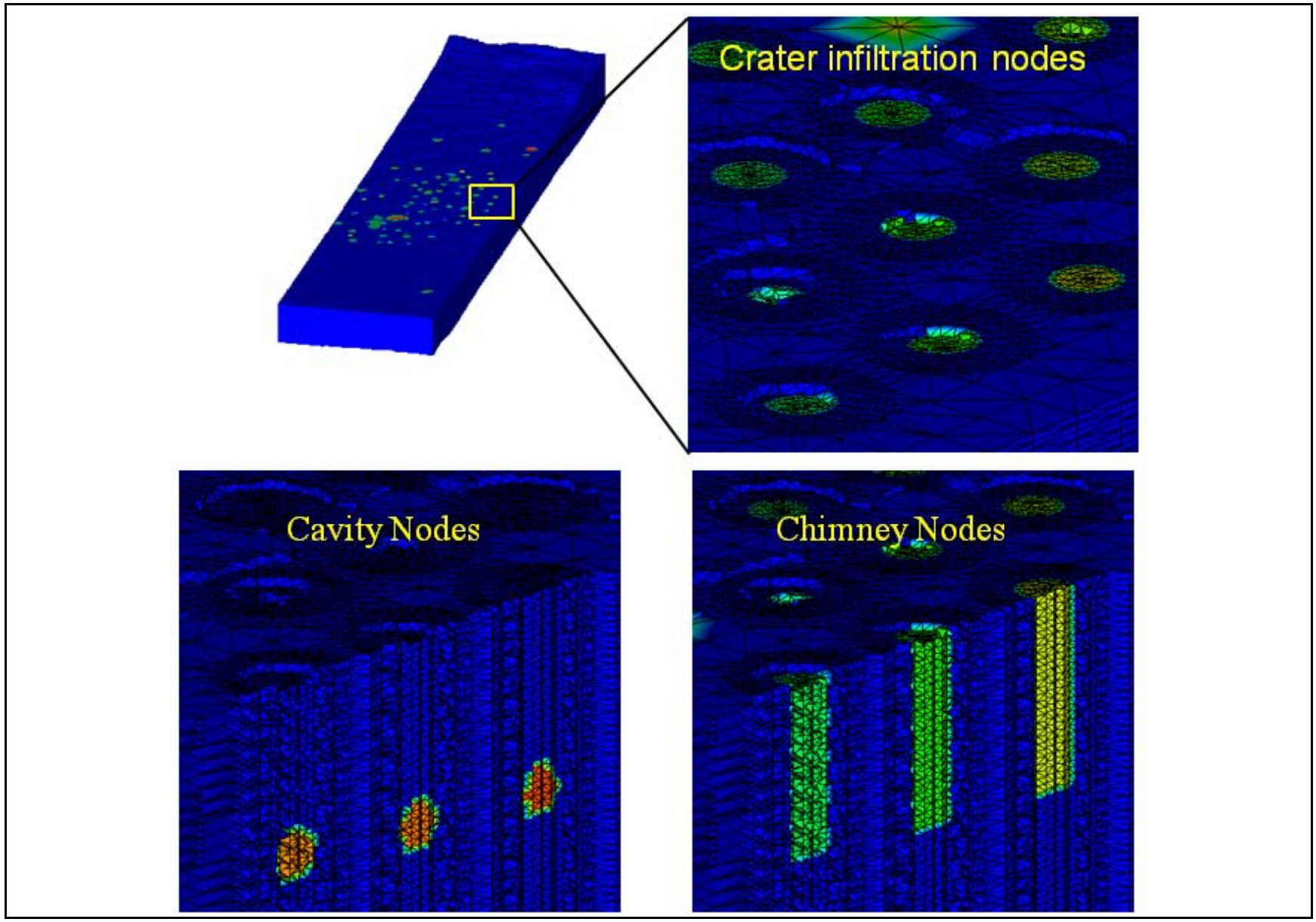

Figure 3-17
Figure Showing Grid Refinement near Crater, Cavity, and Chimney Regions

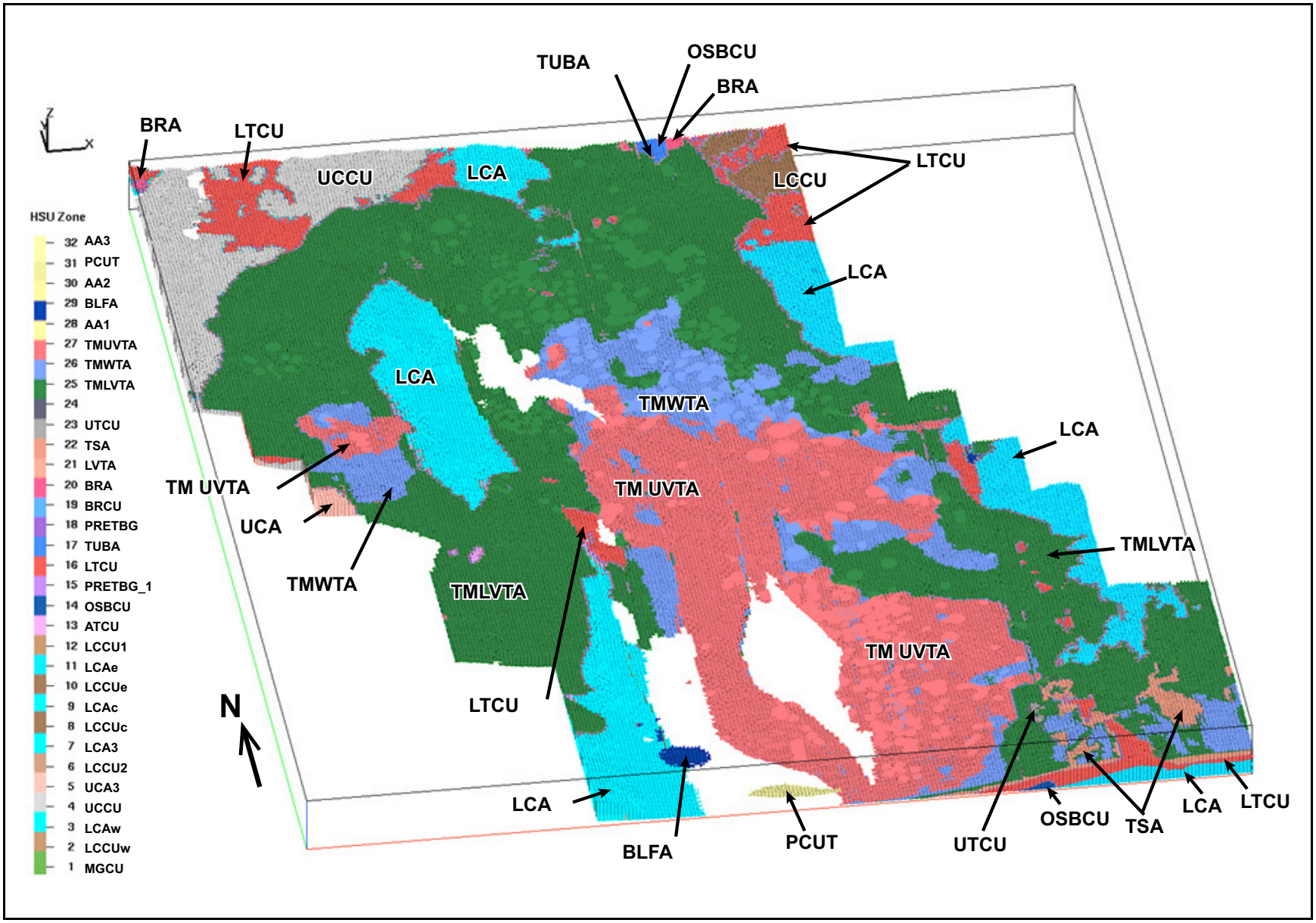

Figure 3-18
HSUs in the 12 Model Grids for the Unsaturated Zone after Removal of Alluvial Aquifers

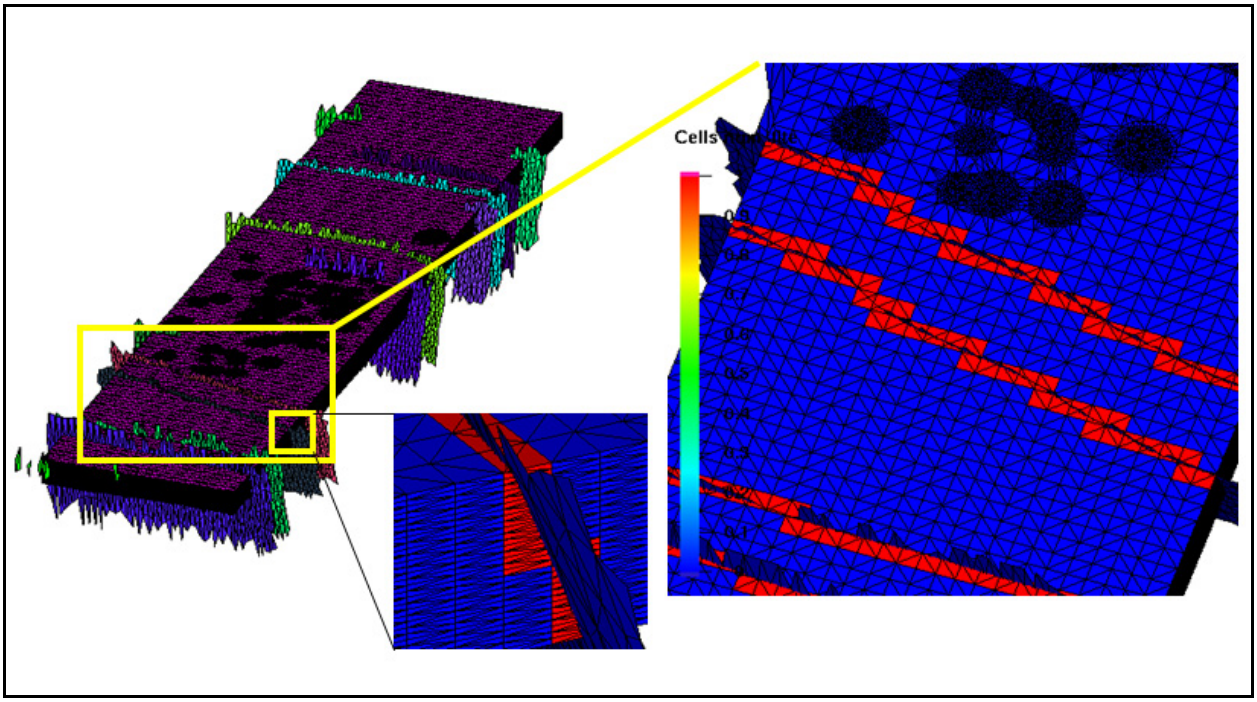

Figure 3-19
Example of Fault Discretization in the Unsaturated-Zone Model

surface used to define the lower boundary of the unsaturated zone is shown in Figure 3-20 for the combined alluvial, tuff, and carbonate, and clastic rock system. The water-table elevations exhibit an overall decrease from the highlands on the northern and western parts of the basin toward the east and south, where the water table is in the LCA. However, these large-scale trends are interrupted locally by areas with higher water-table elevations that are attributable, at least in part, to detonation-induced overpressures in low-permeability HSUs near the detonations (see Section 4.0).

3.4.2 Boundary Conditions

3.4.2.1 Land Surface

As discussed in Section 3.1, the unsaturated-zone models included both a pretesting, steady-state flow period to establish background moisture distributions and percolation fluxes at the start of the nuclear testing; and a transient flow and transport period that applies the same steady-state infiltration rates to non-cratered locations, and the long-term annual crater infiltration rates calculated in Appendix E to the crater bottoms. The start time for the transient flow and transport period begins on December 3, 1961, when the first nuclear detonation in the saturated zone (FISHER) was conducted. For the steady-state portion of the simulation, uniform infiltration rates of 1, 5, or 10 mm/yr were

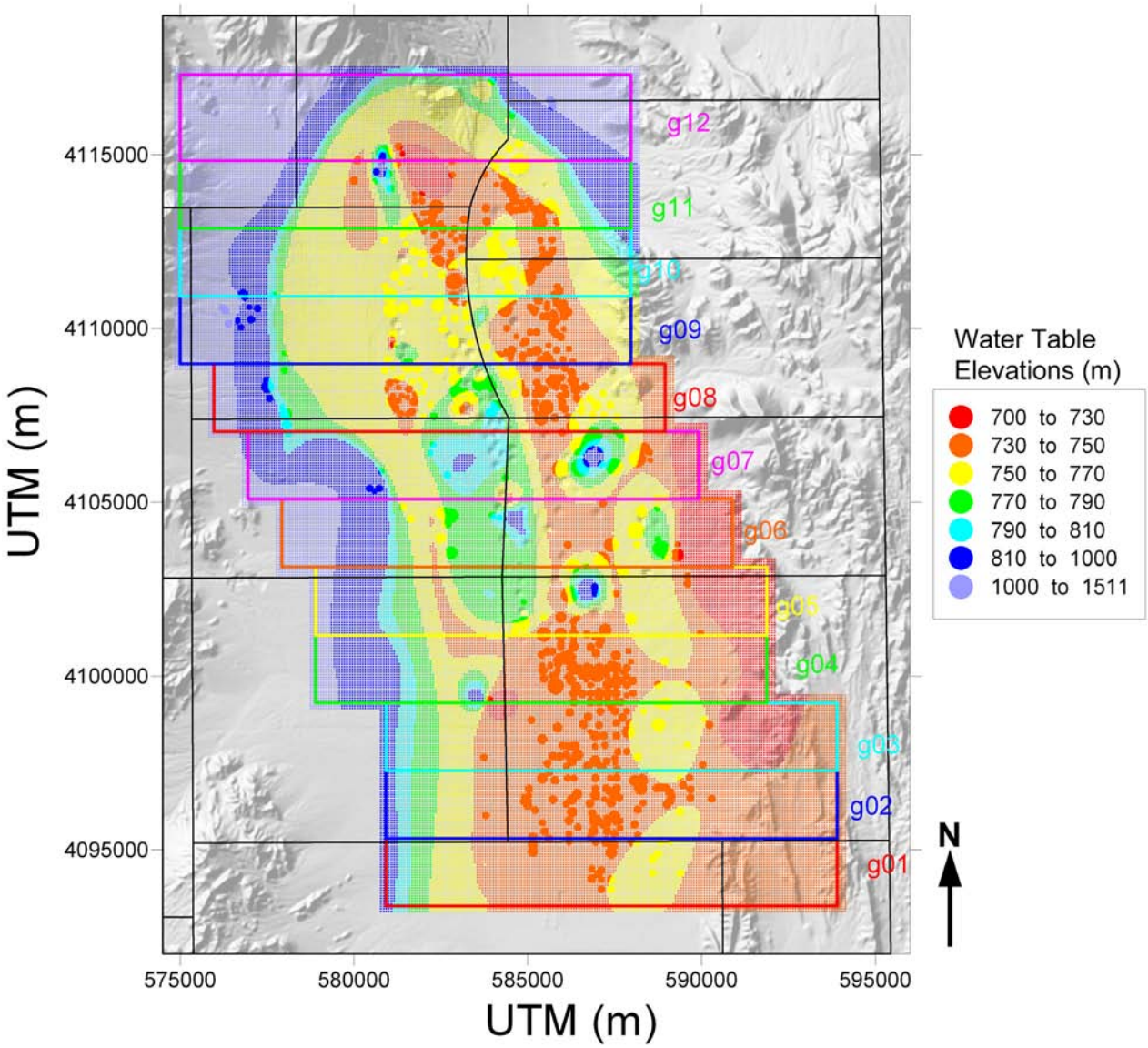

Note: Spotty appearance is a result of higher node densities near the detonations with working points above the water table. Water table elevations are based on DOE/NV (1997b). Water table mounding (locally prominent in grids g04, g05, g06, and g07) is probably related to pore compression caused by weapons tests.

Figure 3-20
Elevations of Water-Table Nodes in the 12 Grids

applied across the upper boundary. As discussed in Section 3.1.3.1, all of these infiltration rates may be too high throughout most of the alluvium, where experimental data and modeling studies in the interfluvial areas have convincingly demonstrated that no infiltration has occurred since the end of pluvial times roughly 10,000 years ago (Walvoord, Phillips, et al., 2002; Walvoord, Plummer, et al., 2002; Kwicklis et al., 2006a). The much higher values assumed in this study, while clearly not applicable in most parts of the basin, were adopted to account for the possibly higher (but as yet unmeasured) infiltration rates beneath arroyos and Yucca Lake playa, and on the margins of the basin due to runoff from the surrounding hills. The high background infiltration rates were also adopted to account for the continued drainage of paleoinfiltration at depth, although present-day rates of paleoinfiltration at the water table are also calculated to be much smaller than the assumed background infiltration rates (Walvoord, Phillips, et al., 2002; Kwicklis et al., 2006a). At the beginning of the transient simulation period, infiltration rates estimated for individual craters in Section 3.3 are applied to the crater bottom nodes and held constant throughout the 1,000-year-long transient simulation. The background infiltration rates assumed in the earlier steady-state simulation period are maintained at all other nodes throughout the transient simulation.

3.4.2.2 Lateral Boundaries

The lateral boundaries along each of the 12 model grids were not assigned any specific head or flux conditions and became no-flow boundaries by default. This implicitly assumes that lateral flow in the unsaturated zone is not a significant part of the overall water balance for any of the grids and that, in particular, north–south-directed flow or transport of radionuclides in the unsaturated zone would not occur across the grid boundaries. The rationale for this assumption is based on the following observations. First, there have been no reported occurrences of perched water in the unsaturated zone of Yucca Flat that would suggest that infiltration locally exceeds the vertical permeability of the rock and thus would likely be diverted laterally above the low-permeability layers. Second, the orientations of the HSUs in the unsaturated zone are controlled by the north–south-trending normal faults and tend to be predominantly east or west dipping with very little north–south component to their dip (BN, 2006). Thus, if perched water were to form in the future above low-permeability layers in response to high crater infiltration rates, it would more likely tend to flow downdip along the east- or west-dipping strata where it would drain down faults. Third, examination of the saturation results for the flow simulations generated for this report provides no evidence that saturations are higher

along the lateral edges of the models, which would indicate that some water is accumulating against the grid boundaries because of north or south lateral flow.

3.4.2.3 Water-Table Boundary

The bottom boundary node elevations correspond to the water table (Figure 3-20) and are assigned constant water pressures of 100,000 pascals (Pa) (atmospheric pressure) throughout the steady-state and transient simulation periods. This is in accordance with the standard definition of the water table as the location where water and atmospheric pressures are equal (zero capillary pressure).

3.4.3 Rock and Sediment Hydraulic and Transport Properties

The hydraulic property data used in the unsaturated-zone models for Yucca Flat come from a variety of sources. The hydraulic property data for alluvium come largely from reports that document the drilling, sampling, and testing results from the Area 3 RWMS (BN, 1998, 2005b). These data included measurements of sediment properties from areas adjacent to the collapse craters and areas within the chimney regions beneath the collapse craters. The hydraulic properties of the rock matrix are taken largely from testing results on approximately 60 rock cores taken from boreholes on Rainier Mesa that intersect the same HSUs as those currently found beneath Yucca Flat (Kwicklis et al., 2008) or, for the pre-Tertiary rocks, from matrix properties reported by Winograd and Thordarson (1975) as summarized in Kwicklis et al. (2008, Table 7). These were supplemented by a less extensive set of tuff samples taken from boreholes in Area 7 of Yucca Flat (see Appendix F). The use of matrix property data from Rainier Mesa to estimate the matrix properties of the same HSUs beneath Yucca Flat is appropriate because originally the HSUs formed one continuous volcanic plateau; the rocks beneath Yucca Flat have been downdropped more than 1 km relative to their initial elevations when the Yucca Flat basin opened sometime between 11.45 and 8.1 Ma along a series of normal faults and reactivated thrust faults (BN, 2006, p. 3-4).

Fracture hydraulic properties were not measured directly in most HSUs. Fracture permeability for most HSUs was assigned based on the propensity of individual HSUs to develop and maintain open fractures (e.g., NSTec, 2008; Winograd and Thordarson, 1975) or, for a subset of HSUs, based on calibration of the saturated alluvial/volcanic aquifer system model to detonation-generated changes in hydraulic heads (see Section 4.0). More discussion of the assignment of hydraulic properties is provided in the following sections.

3.4.3.1 Background

Under variably saturated conditions such as those that exist above the water table in Yucca Flat, the effective hydraulic conductivity (K_{eff}), water saturation (S), and water potential (ψ) of sediments, rocks, and fractures are interrelated. For unsaturated conditions, water potential (or, neglecting the osmotic component, matric potential) is negative relative to free water at the same elevation, because the water in the rock pores is held by capillary forces and adsorbed to grain surfaces. Typically, the relations between K_{eff}, S, and ψ measured at a few values of saturation or water potential are fit with functions developed from capillary theory in order to interpolate these relations to other, intermediate values. These functions can be characterized by a relatively few parameters and have the additional virtue that they are smooth and differentiable and thus readily incorporated into numerical models of unsaturated flow that rely on partial differential equations.

The functions that relate K_{eff}, S, and ψ in this study are those of van Genuchten (1980):

$$S_{eff}(\psi) = [1 + (\alpha|\psi|)^n]^{-m} \tag{3-1}$$

where α is a scaling parameter (m^{-1}), n is a parameter related to the pore-size distribution, m is related to n by $m = 1 - 1/n$, and effective saturation $S_{eff}(\psi)$ is given by

$$S_{eff}(\psi) = \frac{S(\psi) - S_r}{S_s - S_r} \tag{3-2}$$

where S_r and S_s are residual and satiated saturation, respectively. As in many studies, the parameters α, n, m, S_s, and S_r are determined in the present study by fitting the ψ versus S data that define the moisture retention curve. The $K_{eff}(S_{eff})$ and $K_{eff}(\psi)$ relations are predicted from measurements of saturated hydraulic conductivity (K_s) and capillary theory using the pore-size information contained in the α, n, and m parameters:

$$K_{eff}(S_{eff}) = K_s S_{eff}^{1/2}[1 - (1 - S_{eff}^{1/m})^m]^2 \tag{3-3a}$$

$$K_{eff}(\psi) = K_s \frac{(1 - (\alpha|\psi|)^{n-1}[1 + (\alpha|\psi|)^n]^{-m})^2}{(1 + (\alpha|\psi|)^n)^{m/2}} \tag{3-3b}$$

The satiated saturation is related to the satiated moisture content (θ_s) by $S_s = \theta_s/\varphi$, where φ is the porosity. In Kwicklis et al. (2008), φ is estimated from the grain (ρ_g) and dry bulk (ρ_b) densities of the

samples ($\varphi = 1 - \rho_b/\rho_g$), whereas θ_s is determined gravimetrically by first drying and then filling the sample under a vacuum. Because φ may include dead-end pore spaces, θ_s is considered more representative of the effective or fillable porosity of the sample and is used as the effective matrix porosity (φ_{eff}) throughout this report. Using this definition of effective porosity, S_s is unity for all samples in this report.

3.4.3.2 Application of Soil Methods to Intact and Fractured Rock

Although the van Genuchten (1980) functions were originally developed for soils and sediments, they have been routinely applied to rocks in many unsaturated-zone experimental and modeling studies (e.g., Flint, 1998; Bodvarrson et al., 2001). Furthermore, there have been some theoretical modeling studies of variable aperture fractures that suggest that fractures drain or fill over a range of matric potentials in a manner similar to coarse-textured sands or gravels and that the relations in fractures can also be represented by the van Genuchten (1980) equations (Pruess and Tsang, 1990; Kwicklis and Healy, 1993; Kwicklis et al., 1998).

Theoretical modeling studies of single fractures with variable apertures have been done to develop the relations between K_{eff}, S, and ψ for fractures with different mean apertures (Kwicklis et al., 1998). These relationships are shown in Figure 3-21 for fractures with mean physical apertures of 2.5, 25, 125, and 250 microns (or micrometers [µm]), along with typical relations for a zeolitic tuff and a vitric tuff. The theoretical relations for fractures are consistent with capillary theory that suggests that fine-grained materials retain moisture over a larger range of matric potentials than coarse-grained materials so that eventually the coarse-textured sediments become less permeable when matric potentials become large enough. In this case, however, fractures with larger apertures drain and become impermeable at smaller matric potentials than fractures with small apertures, and vitric tuffs drain and become impermeable more quickly than zeolitic tuffs.

The present modeling study also adopts the methods of Montazer and Wilson (1984) and Peters and Klavetter (1988), which proposed that the contributions from the fractures and matrix can be combined to create effective properties for a fractured matrix block (Figure 3-21). The basic concept is that, at steady-state or under slowly changing flow conditions, the fracture and matrix continua are in matric-potential equilibrium so that the effective hydraulic conductivities of the fracture and matrix continua are additive at a given matric potential. (Note that the single fracture permeability is weighted by assumed fracture porosity, in this case, $\varphi_f = 0.001$, to reflect its relative volume and

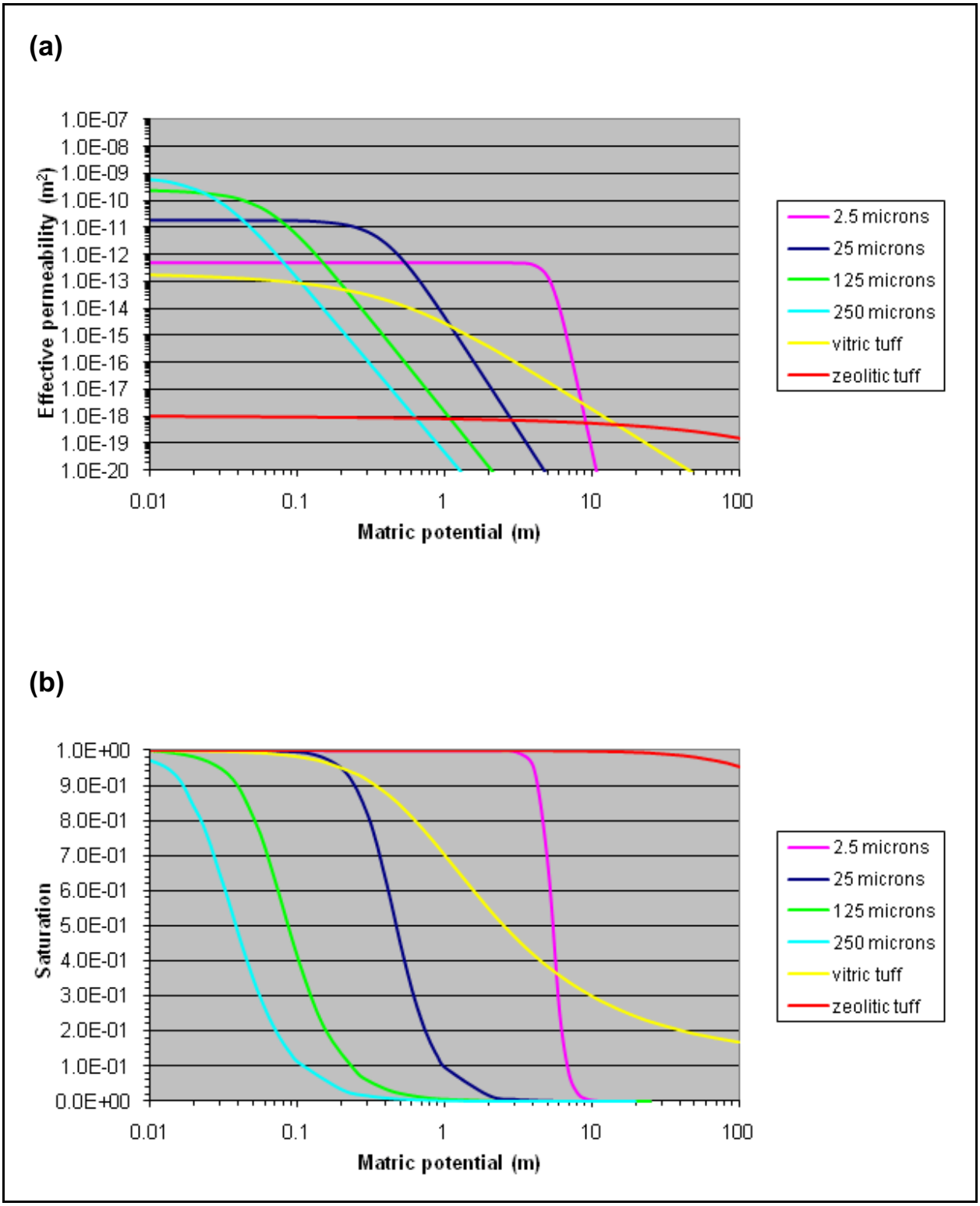

Figure 3-21
Examples of (a) Effective Permeability versus Matric Potential and (b) Saturation versus Matric Potential Relationships for Fractures and for Vitric and Zeolitic Tuffs

cross-sectional area in the overall rock mass.) As shown in Figure 3-22, the fractures do not contribute to the overall permeability of the rock when the rock is dry and the fractures are drained (i.e., at large matric potentials), but the fractures allow water to be transmitted at high fluxes when matric potentials are small and the fractures begin to fill with water. The use of consistent fracture and matric potential relationships such as those shown in Figures 3-21 and 3-22 is necessary to correctly apportion the flux between fractures and matrix in the fractured rock mass. The Yucca Flat study implicitly assumes that the fractured rocks are sufficiently buffered from near-surface flow transients by the overlying alluvium so that the conditions under which the effective continuum approach of Figure 3-21 is valid are maintained even under conditions of high crater infiltration.

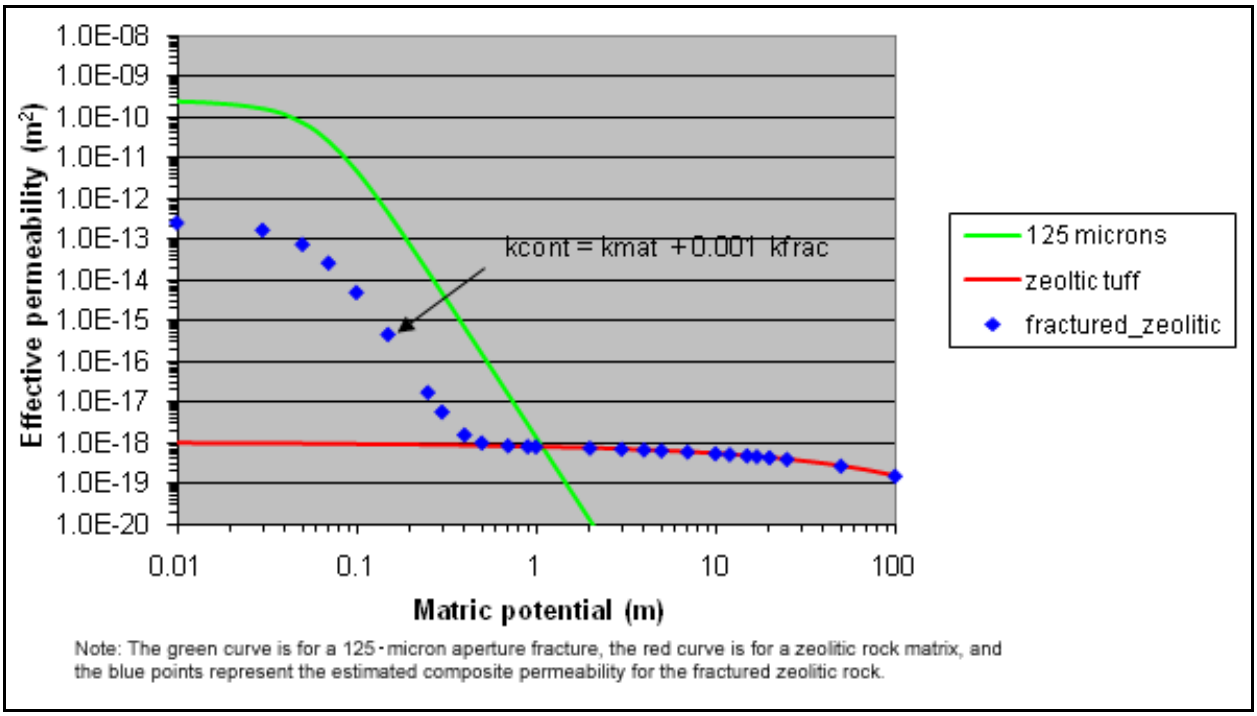

Figure 3-22
Example of a Composite Permeability Curve for Fractured Zeolitic Rocks

3.4.3.3 Alluvium Properties

The properties of alluvium used in most of the unsaturated-zone models for Yucca Flat are based on the mean properties of the undisturbed alluvial samples listed in Table 1-1 of BN (1998). These properties are reproduced in Table 3-3, along with the properties of alluvium from beneath the collapse zones.

Table 3-3
Hydrologic Properties of Alluvium at the Area 3 RWMS

Property	Undisturbed		U-3bh Collapse Zone		U-3at/U3-bL Collapse Zones		Combined	
	Mean	Standard Deviation	Mean	Standard Deviation	Mean	Standard Deviation	Mean	Standard Deviation
Particle density (mg/m^3)	2.49	0.0815	2.44	0.0646	2.41	0.0876	2.44	0.0863
Bulk density (mg/m^3)	1.5	0.154	1.49	0.114	1.55	0.15	1.52	0.137
Porosity (m^3/m^3)	0.382	0.0632	0.387	0.0466	0.364	0.0618	0.373	0.0581
Sand fraction (wt%)	83.8	8	81	7.6	80.1	8.9	80.6	8.5
Silt fraction (wt%)	7.3	4.2	10.2	7.3	10.3	6.8	10.1	6.8
Clay fraction (wt%)	8.9	4.3	8.5	2.6	9.7	4.4	9.3	4
ln saturated conductivity (m/s)	–11.4	1.45	–11.2	1.6	–12.1	1.74	–11.7	1.68
log saturated conductivity (m/s)	–4.95	0.63	–4.86	0.69	–5.25	0.76	–5.08	0.73
log saturated permeability (m^2)	–11.94	0.63	–11.85	0.69	–12.24	0.76	–12.07	0.73
Saturated permeability (m^2)	1.146E-12	--	1.399E-12	--	5.689E-13	--	8.488E-13	--
van Genuchten Parameters								
ln α (1/cm)	–3.34	1.37	–4.42	0.89	–4.42	1.06	–4.18	1.18
log α (1/cm)	–1.45	0.59	–1.92	0.39	–1.92	0.46	–1.82	0.51
log α (1/m)	0.55	0.59	0.08	0.39	0.08	0.46	0.18	0.51
α (1/m)	3.54	--	1.20	--	1.20	--	1.53	--
n	1.49	0.368	1.74	0.274	1.74	0.337	1.68	0.344
Residual moisture content	0.067	0.057	0.132	0.033	0.135	0.041	0.12	0.052
Residual saturation	0.175	--	0.341	--	0.371	--	0.322	--

Source: BN, 1998

-- = Not applicable

Figure 3-23 compares the saturation versus matric potential and effective permeability versus matric potential relationships for repacked alluvial samples from undisturbed areas adjacent to the subsidence craters and for samples from the collapse zones centered on detonations at U-3bh and U-3at/U-3bL (these craters intersect). The samples from the collapse zones appear to drain more slowly with increasing matric potential and are less completely drained at high matric potentials compared with samples from the undisturbed areas (Figure 3-23). This reflects the larger residual saturations and smaller van Genuchten α parameters estimated for the samples from the collapse zones (Table 3-3). Because the collapse-zone sediments have a higher saturation than the undisturbed samples at a given matric potential, the effective permeabilities estimated with Equation (3-3) also are higher at that matric potential (Figure 3-23b).

In the present modeling study, the hydraulic properties from the undisturbed areas were used to represent the alluvium in both the undisturbed areas and in the collapse zones. The hydraulic properties from the undisturbed areas were used for several reasons. First, most (greater than 99 percent) of the alluvium in the model is outside the collapse crater, so the properties of the undisturbed samples represent almost all of the alluvium in the model. Second, the mean residual moisture contents of 0.132 and 0.135 estimated for the samples from the collapse zones (Table 3-3) are larger than the moisture contents actually measured in the undisturbed areas (0.106), so they are clearly not compatible with *in situ* field measurements of moisture content either from within or outside the craters. Thirdly, although differences in the moisture retention curves would appear to suggest a fundamental difference in the texture and hydraulic properties of the undisturbed- and collapse-zone sediments, these differences may be due mostly to the use of different measurement techniques rather than fundamental differences in the hydraulic properties. Saturation versus matric potential data for the undisturbed-zone samples (from U-3bL-U1 borehole) and one set of collapse-zone samples (from U-3bL-D1 borehole) were collected by traditional methods (pressure chambers, hanging water columns, and oven drying), whereas data for the collapse-zone samples (from remaining Area 3 RWMS boreholes) were obtained by spinning the samples dry with a centrifuge (Conca et al., 1999). Data from U-3bL-U1 and U-3bL-D1 boreholes are described in BN (2005b), whereas data from all other Area 3 RWMS boreholes are described in BN (1998). All Area 3 RWMS borehole data are summarized in NSTec (2007).

Profiles of permeability versus depth were examined for the alluvium from the Area 3 boreholes in order to get an estimate of the vertical-to-horizontal anisotropy in permeability (k_v/k_h) of the alluvium

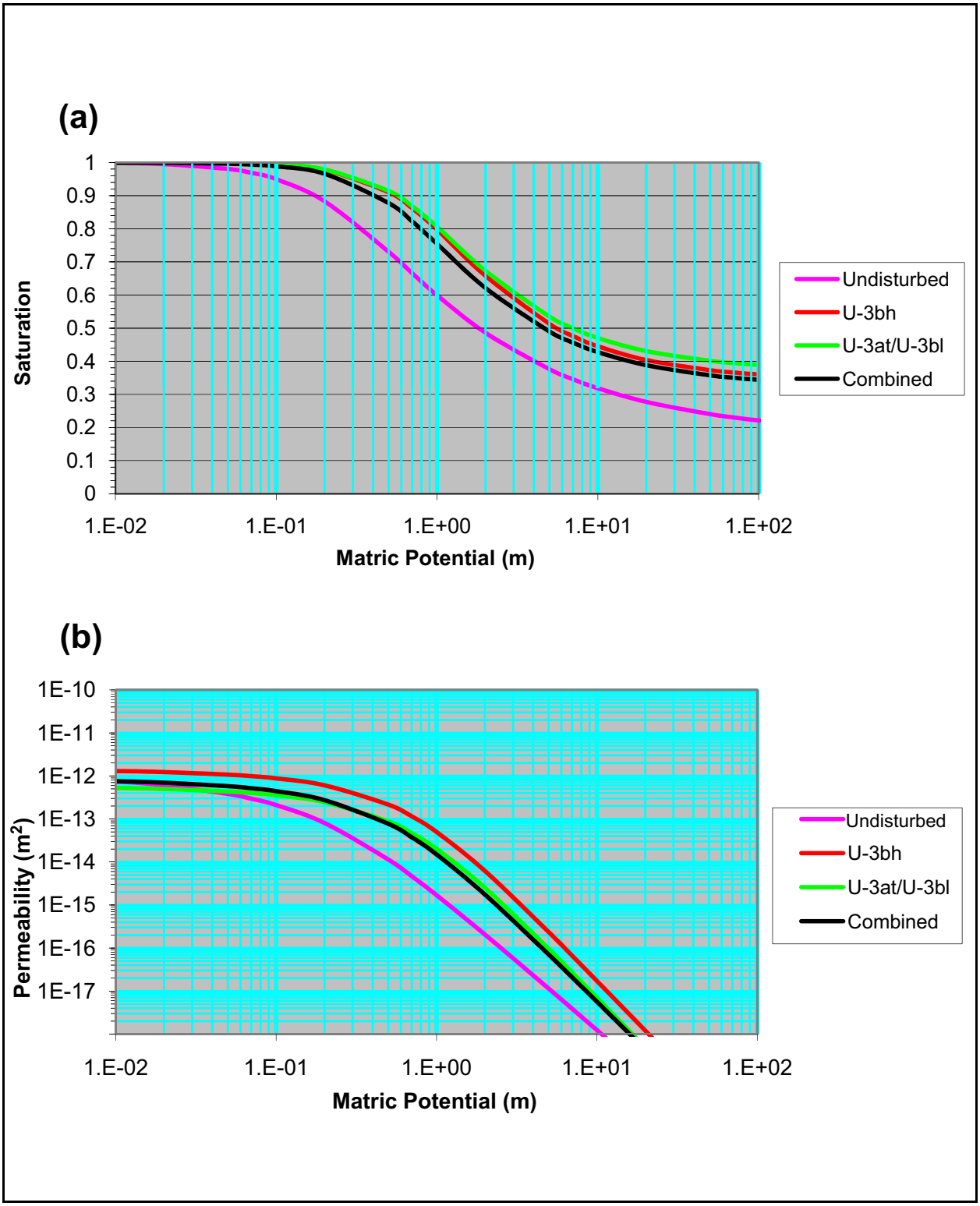

Figure 3-23
Comparison of Characteristic Curves for Alluvium from beneath and Adjacent to Subsidence Craters at the Area 3 RWMS: (a) Saturation versus Matric Potential, and (b) Effective Permeability versus Matrix Potential

(Figure 3-24). The estimated values of k_v/k_h for four boreholes range from 0.02 to 0.16. The borehole profiles in some cases show systematic trends that reflect the persistence of layering even in samples from the collapse zones.

3.4.3.4 Rock Properties

3.4.3.4.1 Data Summaries in the Hydrologic Data Document

Hydrologic data reported in the hydrologic data summary for Yucca Flat (SNJV, 2006b, Tables 6-1, 6-2, and 6-6) include core-, slug-, and pumping-scale tests, for both the Yucca Flat/Climax Mine area (which includes adjacent areas at Rainier Mesa, Frenchman Flat, and Emigrant Valley) and the much larger investigation area, which encompasses the entire NNSS, the Yucca Mountain and Thirsty Canyon areas west of the NNSS, and essentially the entire DVRFS model domain (SNJV, 2006b, Figure 6-1). Slug-scale tests are based on instantaneously adding or removing a volume of water from the well and observing the water-level recovery to the static condition. Pumping-scale tests are based on pumping a significant volume of water over an extended time period and observing the water-level drawdown and recovery. As summarized in SNJV (2006b, Section 6.4.1), the pumping-scale test results provide the most appropriate information for use in large-scale modeling, because they provide results representative of the greatest aquifer volume and are more likely to reflect high hydraulic conductivity structure in tested formations. As summarized in SNJV (2006b, Section 6.4.1), the pumping-scale test results are considered to provide the most appropriate information for use in large-scale modeling, because they provide results representative of the greatest aquifer volume and are more likely to reflect high hydraulic conductivity structure in tested formations.Summary statistics for permeability are given in Table 3-4 for each of these scales and investigation areas.

In general, the laboratory-scale measurements reflect the permeability of the rock matrix, whereas the larger-scale measurements reflect both the matrix permeability and any additional permeability that results from fracturing and faulting. The data for the LCA in Table 3-4 illustrates these effects, with matrix permeabilities from laboratory-scale tests on the order of 1E-16 to 1E-17 m^2 and from pumping-scale tests on the order of 1E-11 to 1E-12 m^2. The LCCU and TCU also seem to exhibit the effects of fractures and faults at increasingly larger scales, although for the LCCU, this conclusion is based on a far more limited dataset. At the other end of the spectrum, the mean permeability of the AA is similar across scales, partly because the AA does not maintain open fractures. The VA category

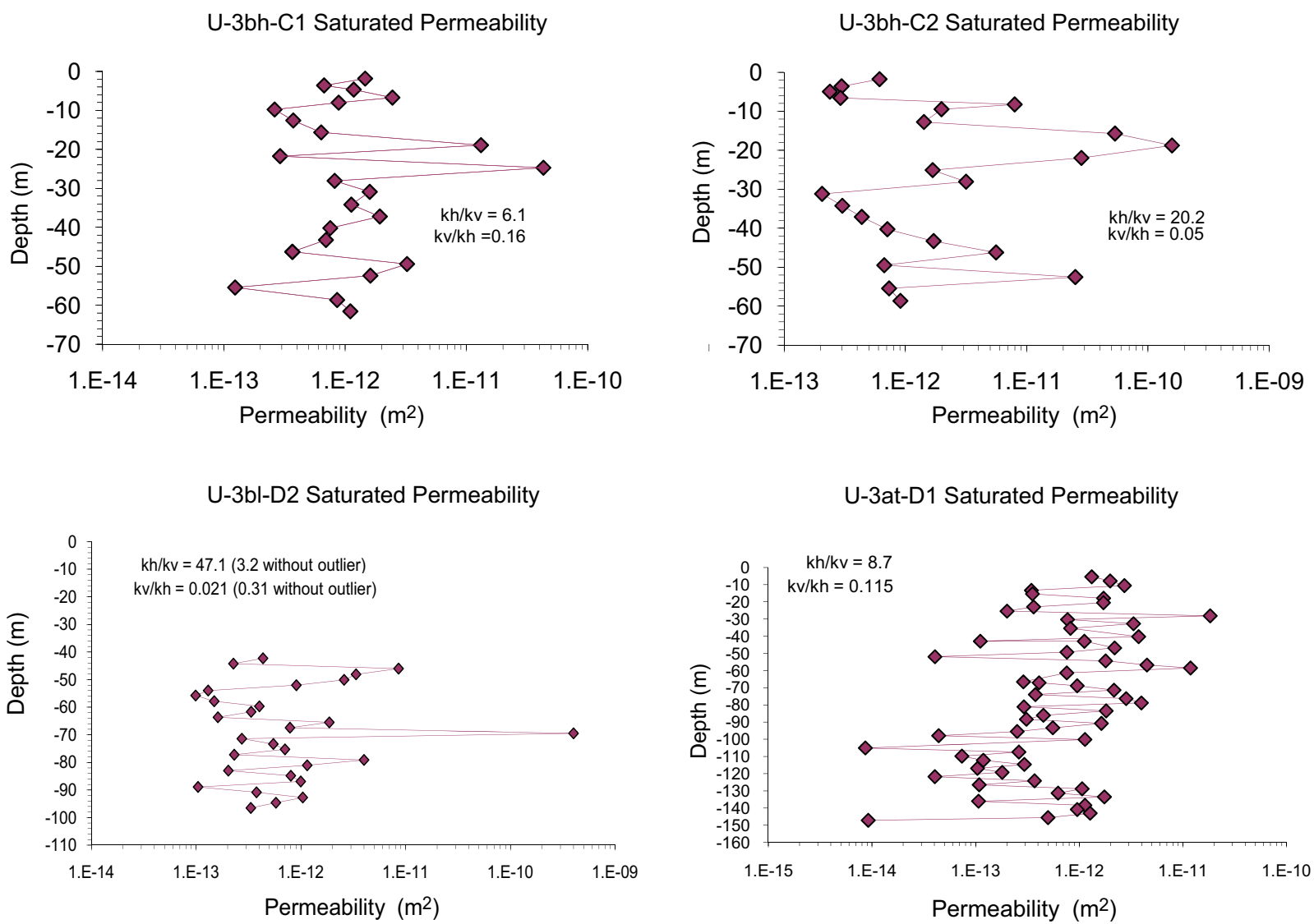

Note: Boreholes U-3bh-C1 and U-3bh-C2 are vertical holes drilled entirely within the U-3bh collapse crater. Boreholes U-3-bl-D2 and U-3at-D1 are angle holes that begin in undisturbed areas but penetrate the collapse zones beneath the U-3bl and U-3at craters at depth.

Figure 3-24
Saturated Permeability versus Depth Based on Sediment Samples from Four Boreholes at the Area 3 RWMS

Table 3-4
Summary of Selected HSU Permeabilities at the Pumping, Slug-Test, and Laboratory Scales within the Yucca Flat and NNSS Investigation Areas

HSU	Area	Pumping-Test Scale			Slug-Test Scale			Laboratory Scale		
		Mean	Standard Deviation	Count	Mean	Standard Deviation	Count	Mean	Standard Deviation	Count
AA	Yucca Flat	–12.06	0.93	22	–12.33	0.38	6	–12.27	0.71	60
	NNSS	–11.48	0.93	51	–12.63	1.17	14	–12.69	1.56	73
VA	Yucca Flat	–11.70	1.10	20	–13.91	0.84	16	–14.02	0.81	8
	NNSS	–12.05	1.29	142	–14.42	1.08	142	–15.70	2.23	403
LFA	Yucca Flat	NA	NA	NA	NA	NA	NA	NA	NA	NA
	NNSS	–12.19	0.95	29	NA	NA	NA	NA	NA	NA
TCU	Yucca Flat	–13.00	NA	1	–14.31	0.56	10	–15.50	1.14	34
	NNSS	–12.84	1.43	127	–14.27	1.12	258	–16.35	1.55	637
MGCU	Yucca Flat	–14.42	NA	1	–13.09	1.78	3	NA	NA	NA
	NNSS	–14.42	NA	1	–13.09	1.78	3	NA	NA	NA
UCCU	Yucca Flat	–14.57	1.15	3	–13.92	0.73	4	NA	NA	NA
	NNSS	–14.57	1.15	3	–14.28	0.79	7	NA	NA	NA
LCA	Yucca Flat	–11.90	1.31	36	–12.96	0.46	9	–17.14	0.40	4
	NNSS	–11.77	1.34	77	–13.09	1.09	24	–16.32	1.28	32
LCCU	Yucca Flat	–14.14	NA	1	NA	NA	NA	–18.49	0.66	30
	NNSS	–12.71	2.02	2	NA	NA	NA	–18.49	0.66	30

Source: SNJV, 2006b

Notes:
Permeabilities are in square meters.
When the count is 1, the mean is the single measurement and no standard deviation was calculated.

NA = Data not available

in Table 3-4 incorporates both porous vitric-tuff aquifers (VTAs), which have substantial matrix permeability but are generally thought to be incapable of maintaining open fractures (e.g., BN, 2006), and welded-tuff aquifers (WTAs), which have low porosity and matrix permeability but fracture easily. Therefore, the effect of scale is somewhat muted for the VA in Table 3-4 compared to some other HSUs like the LCA.

The current belief shared among the UGTA Activity participants is that the summary statistics at the slug-test and pumping-test scales presented in Table 3-4 are biased toward the high end, particularly in sparsely fractured HSUs like the TCU, because hydrologic testing typically relies on flow logs to

locate the most permeable intervals to set packers or a well screen to conduct a pumping test. An additional limitation is that summary statistics such as those presented in Table 3-4 provide no indication whether the permeability measurement was made over 1-m-depth intervals or depth intervals of hundreds of meters—all measurements are weighted equally. However, intuitively, measurements made over longer intervals should be more representative of average properties than those measured over short-length intervals. The net effect of these measurement and reporting biases would be to provide permeability distributions that tend to overestimate groundwater fluxes and velocities that form the basis of groundwater transport models, with the result that the extent of the calculated contaminant boundaries may also be overestimated.

3.4.3.4.2 Data from Unsaturated-Zone Studies at Rainier Mesa

Because the data in Table 3-4 had no corresponding measurements of unsaturated water retention characteristics or unsaturated relative permeability, and it is important to have internally consistent sets of saturated and unsaturated hydrologic properties, the data summarized in Table 3-4 were not used directly in the models. The alluvial properties, as described earlier, originated from soil property measurements made at the Area 3 RWMS at Yucca Flat. The hydrologic properties of the rock matrix for the HSUs in Yucca Flat are based on the results of laboratory measurements of approximately 60 rock cores taken from boreholes U-12b.07c (Rainier Mesa Exploratory #1) and UE-12t 1 at Rainier Mesa, as reported in Kwicklis et al. (2008). Table 3-5 shows the mean hydrologic properties of the rock matrix, including the parameters of the van Genuchten (1980) relationships, based on the results of laboratory testing. As the table indicates, some HSUs such as the BRCU (or equivalently, the LTCU), the OSBCU, and the TM-LVTA were sampled more heavily than the others. In particular, the matrix properties of welded-tuff aquifers, such as the TM-WTA, BRA, TUBA, and Redrock Valley welded-tuff aquifer (RVA), where fracture flow is expected to be more important than flow through the low-permeability matrix, received considerably less attention.

3.4.3.4.3 Data on Pre-Tertiary Rocks from Winograd and Thordarson (1975)

Very little core-scale data were available from the UE-12t 1 and U-12b.07c (Rainier Mesa Exploratory #1) boreholes for deeper HSUs such the MGCU, UCCU, LCA3, and LCCU. Core-scale K_s and φ data for the LCA and LCCU and for zeolitic and clayey tuffs were available from Winograd and Thordarson (1975) (Table 3-6). Unfortunately, comparable measurements for the MGCU and

Table 3-5
Mean Parameter Values by HSU for Combined Samples Recovered from U-12b.07c (Rainier Mesa Exploratory #1) and UE-12t 1

HSU	*N*	α (1/m) Geometric Mean [a]	*n* (-)	θ_s (%)	θ_r (%)	ρ_g (g/cm³)	ρ_b (g/cm³)	φ (%)	k_s (m²) Geometric Mean	K_s (mm/yr) Geometric Mean
TM-WTA [b]	2	2.155E-01	1.384	20.8	0.17	2.55	2.01	21.1	1.20E-14	3,700
TM-LVTA	9	4.706E-01	1.911	36.6	2.25	2.36	1.37	42.3	2.90E-14	8,960
BRA [c]	1	--	--	2.6	--	2.40	2.33	2.8	--	--
LVTA1	1	5.280E-01	2.019	48.1	6.14	2.36	1.11	53.1	3.53E-13	109,000
BRCU [d]	12	3.049E-02	1.308	32.4	0.00	2.46	1.61	34.4	6.32E-17	19.5
TUBA	1	9.000E-03	1.486	4.2	0.00	2.64	2.43	7.9	6.57E-17	20.3
OSBCU [e]	20	5.198E-02	1.368	29.2	0.47	2.56	1.80	30.0	2.14E-16	66.1
RVA [f]	3	9.524E-03	1.494	11.2	0.00	2.53	2.23	11.9	1.83E-18	0.6
ATCU	5	5.496E-02	1.194	26.4	0.00	2.73	2.14	21.5	6.86E-16	212
LCA3 [g]	1	4.311E+00	1.176	5.9	0.00	2.87	2.63	8.5	9.08E-17	28.0

[a] The geometric mean was used because these data, like hydraulic conductivity, tend to be lognormally distributed and span orders of magnitude.
[b] The sample from the 267-ft depth in UE-12t 1 was excluded from this summary based on the likelihood it contained microfractures.
[c] The bulk and grain densities, satiated moisture content, and porosity were included, but hydraulic conductivity and moisture-retention parameters were not, based on the likelihood that the sample from the 736-ft depth at UE-12t 1 was fractured.
[d] The BRCU samples from the 1,705- and 1,940-ft depths at U-12b.07c (Rainier Mesa Exploratory #1) were excluded from this summary based on the anomalous K_s versus α relation of these samples.
[e] The OSBCU samples from the 2,670- and 3,158-ft depths at U-12b.07c (Rainier Mesa Exploratory #1) were excluded from this summary based on the anomalous K_s versus α relation of these samples.
[f] The K_s value measured with the flexible-wall permeameter was used for the RVA sample from the 3,295-ft depth at U-12b.07c (Rainier Mesa Exploratory #1).
[g] The single LCA3 sample from the 2,251-ft depth at UE-12t 1 was retained because it represents the only measurements for this HSU, despite the anomalous K_s versus α relation of this sample.

Notes:
N is the number of measurements, α and n are van Genuchten fitting parameters, θ_s and θ_r are the satiated and residual water contents, ρ_g and ρ_b are grain and dry bulk densities, φ is porosity, and k_s and K_s are the saturated permeability and hydraulic conductivity.

When the count is 1, the mean is the single measurement and no standard deviation was calculated

UCCU do not exist, and no unsaturated-zone hydraulic data were measured as part of the early studies summarized in Winograd and Thordarson (1975).

The data for the LCA (Table 3-5) suggest that the saturated hydraulic conductivity of 28.0 mm/yr and effective porosity of 5.9 percent measured from the single sample from UE-12t 1 are within the range of values that have been measured elsewhere at the NNSS, but both may be high relative to the median values of these parameters reported by Winograd and Thordarson (1975, Table 2). In addition to the data reported by Winograd and Thordarson (1975), Thordarson (1965) reported that

Table 3-6
Summary of Hydraulic Conductivity and Porosity Data from Winograd and Thordarson (1975)
(Page 1 of 2)

Unit	K_s (g/d/ft^2)	k_s (m^2)	K_s (mm/yr)	φ_{total} (%)	φ_{eff} (%)
LCA					
Number of samples	13	--	--	16	25
Low	2.00E-05	9.65E-19	0.30	0.4	0
High	0.1	4.83E-15	1,489.52	12.4	9
Median	8.00E-05	3.86E-18	1.19	5.5	1.1
Mean	0.01	4.83E-16	148.95	5.4	2.3
LCCU					
Argillite and Siltstone					
Number of samples	9	--	--	--	10
Low	7.00E-07	3.38E-20	0.01	--	0.7
High	7.00E-06	3.38E-19	0.10	--	3.6
Median	2.00E-06	9.65E-20	0.03	--	2
Mean	2.00E-06	9.65E-20	0.03	--	2
Quartzite					
Number of samples	9	--	--	--	10
Low	2.00E-06	9.65E-20	0.03	--	0.6
High	1.00E-04	4.83E-18	1.49	--	5
Median	1.00E-05	4.83E-19	0.15	--	1.4
Mean	2.00E-05	9.65E-19	0.30	--	1.9
Combined					
Number of samples	18	--	--	23	20
Low	7.00E-07	3.38E-20	0.01	0.2	0.6
High	1.00E-04	4.83E-18	1.49	10	5
Median	2.00E-06	9.65E-20	0.03	3.9	1.9
Mean	1.00E-05	4.83E-19	0.15	3.8	1.9
Zeolitic Tuff					
Number of samples	34	--	--	34	--
Low	5.00E-05	2.41E-18	0.74	19.8	--
High	6.00E-01	2.90E-14	8,937.11	48.3	--
Median	6.00E-03	2.90E-16	89.37	38.8	--
Mean	5.00E-02	2.41E-15	744.76	37.7	--

Table 3-6
Summary of Hydraulic Conductivity and Porosity Data from Winograd and Thordarson (1975)
(Page 2 of 2)

Unit	K_s (g/d/ft²)	k_s (m²)	K_s (mm/yr)	φ_{total} (%)	φ_{eff} (%)
Clayey Tuff and Clayey Sediments					
Number of samples	38	--	--	--	32
Low	2.00E-06	9.65E-20	0.03	--	1.8
High	0.4	1.93E-14	5,958.07	--	21.6
Median	6.00E-05	2.90E-18	0.89	--	10.4
Mean	0.02	9.65E-16	297.90	--	11

-- = Not applicable

measurements on four core samples from the LCA3 at Rainier Mesa provided effective porosities of 0.6 to 1.1 percent and permeabilities of 3.4E-18 to 9.7E-18 m^2, which are equivalent to hydraulic conductivities of 1 to 3 mm/yr. It is not known whether these measurements are included in the statistics reported by Winograd and Thordarson (1975). The relatively large permeability and effective porosity of the LCA3 sample from UE-12t 1 relative to the measurements reported by Thordarson (1965) could reflect the proximity of the UE-12t 1 sample to the weathered paleosurface that existed on the carbonate rock before the deposition of the tuffs. If this is the case, this sample could also be representative of the weathered LCA paleosurface beneath Yucca Flat.

The data for the LCCU originate from borehole UE-15d WW in northeast Yucca Flat and were subdivided by Winograd and Thordarson (1975, Table 4) into argillite and siltstone, quartzite, and combined-data categories (Table 3-6). Regardless of how the data are categorized, they indicate that the representative K_s of the LCCU (and, by inference, the LCCU1 and UCCU) elsewhere in Yucca Flat will probably be less than 1 mm/yr and that φ_{eff} will also be small (about 2 percent).

The data for the zeolitic tuffs summarized by Winograd and Thordarson (1975) and presented in Table 3-6 show a wide range in K_s values, but the median K_s of 89 mm/yr and φ_{total} of 39 percent are similar to the mean K_s and φ values calculated in Table 3-5 for the BRCU (19.5 mm/yr and 34.4 percent) and OSBCU (66.1 mm/yr and 30.0 percent). The data summarized in Winograd and Thordarson (1975) for clayey tuffs and sediments also span a wide range of values. The mean K_s for the ATCU of 212 mm/yr (Table 3-5) falls between the median and mean K_s values of 0.89 and 298 mm/yr reported by Winograd and Thordarson (1975), but the calculated φ_{eff} for the ATCU of

26.4 percent is higher than either the median or mean φ_{eff} reported for the clayey tuffs and sediments by these authors.

3.4.3.4.4 Tuff Matrix Hydraulic Properties from Yucca Mountain

An extensive matrix hydraulic properties dataset exists for tuffs at Yucca Mountain, located approximately 45 km to the southwest of Yucca Flat (Flint, 1998). The tuffs at Yucca Mountain that underwent hydrologic testing span a stratigraphic interval extending from the 13.25 Ma Bullfrog tuff (Tcb) to the 12.7 Ma Tiva Canyon tuff (Tcw). At Rainier Mesa and Yucca Flat, the tuffs range from the 15.25 Ma Redrock Valley tuff (Tor) to the 11.6 Ma Rainier Mesa tuff (Tmr) (Sawyer et al., 1994). Even though a unit-by-unit comparison is not possible, some comparisons between different general categories of tuffs can be made.

Densely welded tuffs at Yucca Mountain are characterized by small φ_{eff} and K_s. For instance, based on 405 measurements, densely welded tuffs of the Tiva Canyon tuff (Tcw) have a mean φ_{eff} of 6.60 ± 2.60 percent (1 SD) and a geometric mean K_s of 1.7 ± 0.16 mm/yr (1 SD) (Flint, 1998, Table 7). Based on 7 measurements of the moisture retention curve, the Tcw has a mean van Genuchten α of 0.00113 ± 0.0028 m^{-1} (1 SD) and a van Genuchten n of 1.300 ± 0.041 (1 SD) (Flint, 1998, Table 8).

Nonwelded vitric tuffs at Yucca Mountain have large φ_{eff} and high K_s. For example, based on 132 measurements, tuffs of the Pah Canyon tuff (Tpp) have a mean φ_{eff} of 46.9 ± 3.8 percent (1 SD) and a geometric mean K_s of 2.78E+04 ± 1.32E+04 mm/yr (1 SD) (Flint, 1998, Table 7). And, based on a single sample, the Pah Canyon tuff (Tpp) has a van Genuchten α of 0.335 ± 0.210 m^{-1} (1 SD) and a van Genuchten n of 1.427 ± 0.129 (1 SD) (Flint, 1998, Table 8).

Zeolitic tuffs at Yucca Mountain have moderate to large φ_{eff} and low K_s. For example, based on 293 measurements, zeolitic tuffs of the Calico Hills formation (CHz) have a mean φ_{eff} of 24.0 ± 4.9 percent (1 SD) and a geometric mean K_s of 1.4 ± 20.5 mm/yr (1 SD) (Flint, 1998, Table 7). Based on 3 samples, the Calico Hills formation (CHz) has a mean van Genuchten α of 0.0386 ± 0.0123 m^{-1} (1 SD) and a van Genuchten n of 1.290 ± 0.037 (1 SD) (Flint, 1998, Table 8). The geometric mean K_s for the Calico Hills formation (CHz) of 1.4 mm/yr is lower than the values of K_s reported in Table 3-5 for the BRCU (19.5 mm/yr) and the OSBCU (66.1 mm/yr).

The densely welded devitrified tuffs, nonwelded vitric tuffs, and nonwelded zeolitized tuffs constitute end members in tuff characteristics. Variations in welding and in the extent of zeolitization and other mineral alteration result in a spectrum of tuff properties that are intermediate between those summarized above. This spectrum of properties is reflected by the large standard deviations that exist in core-scale K_s for different tuff categories in recent data compilations produced by UGTA for the NNSS area (e.g., SNJV, 2006b, Table 6-6) and in the range of hydrologic properties of the cores collected from UE-12t 1 and U-12b.07c (Rainier Mesa Exploratory #1).

3.4.3.4.5 Hydraulic and Transport Properties Used in the Unsaturated-Zone Models for Yucca Flat

The matrix and bulk-fracture permeabilities used for different HSUs in the unsaturated-zone models are shown in Figure 3-25. All base-case hydraulic parameters are listed in Table 3-7, which also provides comments about the basis for the parameters. In general, matrix properties for HSUs for which very few or no measurements are available were based on measured properties from HSUs with similar lithologies for which measurements exist. For instance, the BRCU at Rainier Mesa and the LTCU in Yucca Flat are stratigraphically the same. The BRCU properties in Table 3-5 were assigned to the LTCU and other HSUs with similar lithology such as the UTCU. Likewise, the TM-LVTA properties were assigned to other vitric tuff aquifers such as the LVTA. Bulk fracture permeabilities for different HSUs were based on the overall propensity of the rocks to fracture (for tuffs, WTA > TCU > VTA; and for older rocks, LCA = UCA > LCA3 > LCCU = UCCU = MGCU), with additional guidance provided by the differences between permeability values at the laboratory and pumping-test scales in Table 3-4. These differences are interpreted to represent the contributions to bulk-rock permeability from fractures and faults. All HSUs except the AA, ATCU, and vitric tuff aquifers like the LVTA and TM-LVTA were assumed to contain some fractures and were assigned bulk-fracture permeabilities at least 1E-16 m^2. Bulk-fracture permeabilities for the LTCU (9.2E-16 m^2) and the OSBCU (5.2E-15 m^2) were based on the calibration of the saturated alluvial/volcanic aquifer system model to the dissipation of test-induced overpressures for an assumed background infiltration rate of 5 mm/yr (see Section 4.0).

An unknown aspect of the rock properties is the degree of anisotropy in permeabilities at the HSU scale. Based on the variability in the matrix permeabilities, and observations of layering and vertical welding transitions in many volcanic HSUs, the vertical-to-horizontal permeability ratio for the matrix could be less than unity in most volcanic HSUs. However, faults and fractures are usually

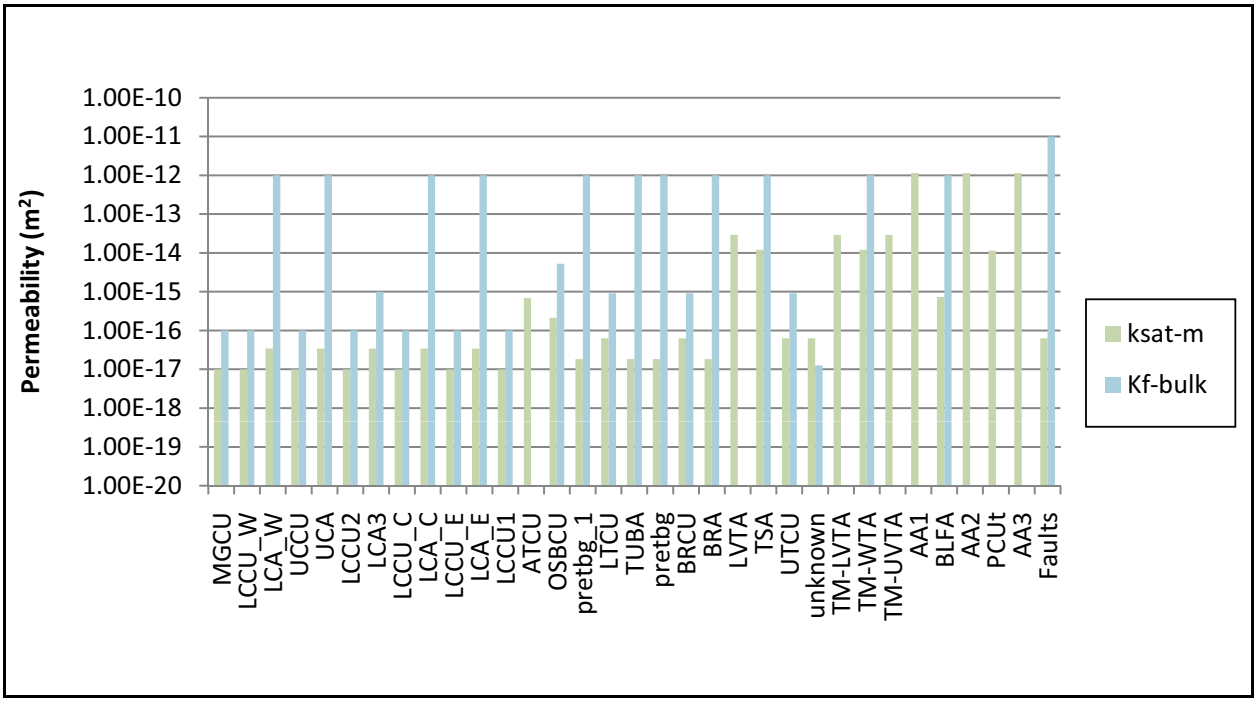

Figure 3-25
HSU Matrix and Fracture Continuum Permeabilities Used in the Unsaturated-Zone Models for Yucca Flat

Table 3-7
Base-Case Hydrologic Parameters Used in the Yucca Flat Unsaturated-Zone Models
(Page 1 of 2)

HSU	Matrix Properties					Fracture Properties [a]			Comment
	S_r	S_s	α (1/m)	n	K_s (m²)	α (1/m)	n	K_f (m²)	
MGCU	0.01	1.000	3.10E-02	1.580	1.00E-17	4.0	2.917	1.0E-16	Based on Table 3-6
LCCU	0.01	1.000	3.10E-02	1.580	1.00E-17	4.0	2.917	1.0E-16	Based on Table 3-6
LCA	0.01	0.999	2.90E-02	1.295	3.40E-17	4.0	2.917	1.0E-12	Based on Table 3-6
UCCU	0.01	1.000	3.10E-02	1.580	1.00E-17	4.0	2.917	1.0E-16	Assumed to be the same as LCCU
UCA	0.01	0.999	2.90E-02	1.295	3.40E-17	4.0	2.917	1.0E-12	Assumed to have LCA properties
LCCU2	0.01	1.000	3.10E-02	1.580	1.00E-17	4.0	2.917	1.0E-16	Assumed to be the same as LCCU
LCA3	0.01	0.999	2.90E-02	1.295	3.40E-17	4.0	2.917	1.0E-15	Smaller fracture permeability than LCA
LCCU1	0.01	1.000	3.10E-02	1.580	1.00E-17	4.0	2.917	1.0E-16	Assumed to be the same as LCCU
ATCU	0.01	1.000	5.50E-02	1.194	6.86E-16	N/A	N/A	N/A	Based on Table 3-5
OSBCU	0.016	1.000	5.20E-02	1.368	2.14E-16	4.0	2.917	5.2E-15	Based on Table 3-5

Table 3-7
Base-Case Hydrologic Parameters Used in the Yucca Flat Unsaturated-Zone Models
(Page 2 of 2)

HSU	Matrix Properties					Fracture Properties [a]			Comment
	S_r	S_s	α (1/m)	n	K_s (m²)	α (1/m)	n	K_f (m²)	
PRETBG1	0.001	1.000	9.52E-03	1.494	1.83E-17	4.0	2.917	1.0E-12	Lava-flow-assigned RVA properties in Table 3-5
LTCU	0.001	1.000	3.05E-02	1.308	6.32E-17	4.0	2.917	9.2E-16	Same as the BRCU in Table 3-5
TUBA	0.001	1.000	9.52E-03	1.494	1.83E-17	4.0	2.917	1.0E-12	Given RVA properties from Table 3-5
PRETBG	0.001	1.000	9.52E-03	1.494	1.83E-17	4.0	2.917	1.0E-12	Lava-flow-assigned RVA properties from Table 3-5
BRCU	0.001	1.000	3.05E-02	1.308	6.32E-17	4.0	2.917	9.2E-16	Based on Table 3-5
BRA	0.001	1.000	9.52E-03	1.494	1.83E-17	4.0	2.917	1.0E-12	Assigned RVA properties from Table 3-5
LVTA	0.062	1.000	4.71E-01	1.911	2.90E-14	N/A	N/A	N/A	Assigned TM-LVTA properties from Table 3-5
TSA	0.008	1.000	2.16E-01	1.384	1.20E-14	4.0	2.917	1.0E-12	Assigned TM-WTA properties from Table 3-5
UTCU	0.001	1.000	3.05E-02	1.308	6.32E-17	4.0	2.917	9.2E-16	Assigned BRCU properties from Table 3-5
Unknown [b]	0.01	1.000	3.10E-02	1.580	6.32E-17	4.0	2.917	1.3E-17	Assigned BRCU properties from Table 3-5
TM-LVTA	0.062	1.000	4.71E-01	1.911	2.90E-14	N/A	N/A	N/A	Unfractured; matrix properties from Table 3-5
TM-WTA	0.008	1.000	2.16E-01	1.384	1.20E-14	4.0	2.917	1.0E-12	Based on Table 3-5
TM-UVTA	0.062	1.000	4.71E-01	1.911	2.90E-14	N/A	N/A	N/A	Same as TM-LVTA
AA	0.175	0.999	3.54	1.740	1.14E-12	N/A	N/A	N/A	Unfractured, properties from Table 3-4
BLFA	0.008	1.000	2.16E-01	1.384	7.30E-16	4.0	2.917	1.0E-12	Same as TM-WTA
PCUT	0.175	0.999	2.54	1.740	1.14E-14	N/A	N/A	N/A	Unfractured; properties adjusted from AA
Faults	0.001	1.000	3.05E-02	1.308	6.32E-17	4.0	2.917	1.0E-11	LTCU matrix and high fracture permeability

[a] The same values of S_r and S_f were used for fractures in all HSUs (S_r = 0.01 and S_s = 1.0).
[b] The HSU was assigned BRCU properties based on its stratigraphic position.

N/A = Not applicable

steeply dipping, so the faults and fractures could result in an overall vertical-to-horizontal permeability ratio for the bulk-rock permeability greater than unity, depending on whether the fractures and faults are throughgoing or strata bound.

Faults were assumed to crosscut all but the alluvial and playa HSUs (AA and PCUT) and have hydrologic properties independent of the HSUs through which they passed. This simplification is slightly at odds with observations that suggest that faults have different characteristics through different HSUs and even within the same HSU, depending on the local strength and induration of the rock (Section 3.1.3.6). However, to provide opportunities for preferential flow to bypass low-permeability layers and to account for observations that even tuff and clastic confining units can have locally high permeabilities (e.g., SNJV, 2006b, Table 6-2), faults were assigned a bulk-rock fracture permeability of 1E-11 m^2. The high bulk-fracture permeability of the faults is intended to capture the increased number of fractures and small faults in the damage zone adjacent to the slip plane, whereas the low matrix permeability and associated unsaturated properties are intended to represent the gouge and fine-grained breccias that are often observed in the slip plane itself (Table 3-8).

Table 3-8
Matrix of Transport Model Sensitivity Cases
(Page 1 of 2)

Run	Run Number Code	Background Flux (mm/yr)	Anisotropy in AA (1.0,0.5,0.2)	Crater Infiltration (L,M,H)	TCU Effective Porosity	Anisotropy in TCU via zfperm (1.0,0.1,0.01)	Exchange Volume Radius (nR_c = 1,2,3)	Chimney (Y,N) [a]
1	1.2.1.2.1.2	1	0.5	L	0.25	1.0	2	N
2	1.2.3.2.1.2	1	0.5	H	0.25	1.0	2	N
3	1.3.1.2.3.3	1	0.2	L	0.25	0.01	3	N
4	1.3.1.2.3.3c	1	0.2	L	0.25	0.01	3	Y
5	1.3.1.3.3.3	1	0.2	L	0.35	0.01	3	N
6	1.3.2.2.3.3	1	0.2	M	0.25	0.01	3	N
7	2.1.1.2.1.2	5	1.0	L	0.25	1.0	2	N
8	2.1.2.2.1.2	5	1.0	M	0.25	1.0	2	N
9	2.1.3.2.1.2	5	1.0	H	0.25	1.0	2	N
10	2.2.1.1.1.2	5	0.5	L	0.15	1.0	2	N
11	2.2.1.2.1.1	5	0.5	L	0.25	1.0	1	N
12	2.2.1.2.1.2	5	0.5	L	0.25	1.0	2	N
13	2.2.1.2.1.2c	5	0.5	L	0.25	1.0	2	Y
14	2.2.1.2.1.3	5	0.5	L	0.25	1.0	3	N
15	2.2.1.3.1.2	5	0.5	L	0.35	1.0	2	N
16	2.2.2.2.1.1	5	0.5	M	0.25	1.0	1	N
17	2.2.3.2.1.1	5	0.5	H	0.25	1.0	1	N

Table 3-8
Matrix of Transport Model Sensitivity Cases
(Page 2 of 2)

Run	Run Number Code	Background Flux (mm/yr)	Anisotropy in AA (1.0,0.5,0.2)	Crater Infiltration (L,M,H)	TCU Effective Porosity	Anisotropy in TCU via zfperm (1.0,0.1,0.01)	Exchange Volume Radius (nR_c = 1,2,3)	Chimney (Y,N) [a]
18	2.2.3.2.1.2	5	0.5	H	0.25	1.0	2	N
19	2.2.3.2.1.2c	5	0.5	H	0.25	1.0	2	Y
20	2.2.3.2.1.3	5	0.5	H	0.25	1.0	3	N
21	2.2.3.2.2.2	5	0.5	H	0.25	0.1	2	N
22	2.3.1.2.1.2	5	0.2	L	0.25	1.0	2	N
23	2.3.1.2.3.2	5	0.2	L	0.25	0.01	2	N
24	2.3.3.2.3.2	5	0.2	H	0.25	0.01	2	N
25	2.3.3.2.3.2c	5	0.2	H	0.25	0.01	2	Y
26	3.1.3.2.1.1	10	1.0	H	0.25	1.0	1	N
27	3.2.1.2.1.2	10	0.5	L	0.25	1.0	2	N
28	3.2.2.2.1.2	10	0.5	M	0.25	1.0	2	N

Key to run numbers:
Level 1: Steady-state background flux. 1 = 1 mm/yr, 2 = 5 mm/yr, 3 = 10 mm/yr.
Level 2: Anisotropy (kv/kh) in AA. 1 = isotropic (no anisotropy), 2 = 0.5, 3 = 0.2.
Level 3: Crater infiltration. 1 = L (low), 2 = M (medium), 3 = H (high).
Level 4: TCU effective porosity. 1 = 0.15, 2 = 0.25, 3 = 0.35.
Level 5: Anisotropy in TCU. 1 = isotropic (1.0), 2 = 0.1, 3 = 0.01.
Level 6: Exchange volume radius. 1 = 1, 2 = 2, 3 = 3.

[a] Y denotes that the chimney was modeled. N denotes that the chimney was not modeled.

The effective porosities used in the transient flow and transport calculations are shown in Figure 3-26. A number of HSUs were assigned effective transport porosities of just 1 to 2 percent, because either the total porosity is itself small (e.g., MGCU, LCCU, UCCU), or flow through these HSUs has been observed to be dominated by fractures (e.g., TUBA, BRA, TSA, TM-WTA, BLFA, faults, chimneys), or both (e.g., LCA, LCA3, UCA). In the saturated alluvial/volcanic aquifer system and LCA transport models for Yucca Flat (Sections 4.0 and 6.0), an effective fracture porosity in the range of 1E-04 to 1E-02 is used, along with particle tracking and transport modules like PLUMECALC (Robinson et al., 2011) that simulate the effects of matrix diffusion that slow the transport of radionuclides. In the unsaturated-zone models, matrix diffusion is not explicitly modeled, but some of its effects are assumed to be accounted for by using effective transport porosities from the upper end of the fracture porosity range. For other HSUs where fracturing is sparse and fractures probably do not form a throughgoing network except in fault zones, the effective transport porosities are assumed to be

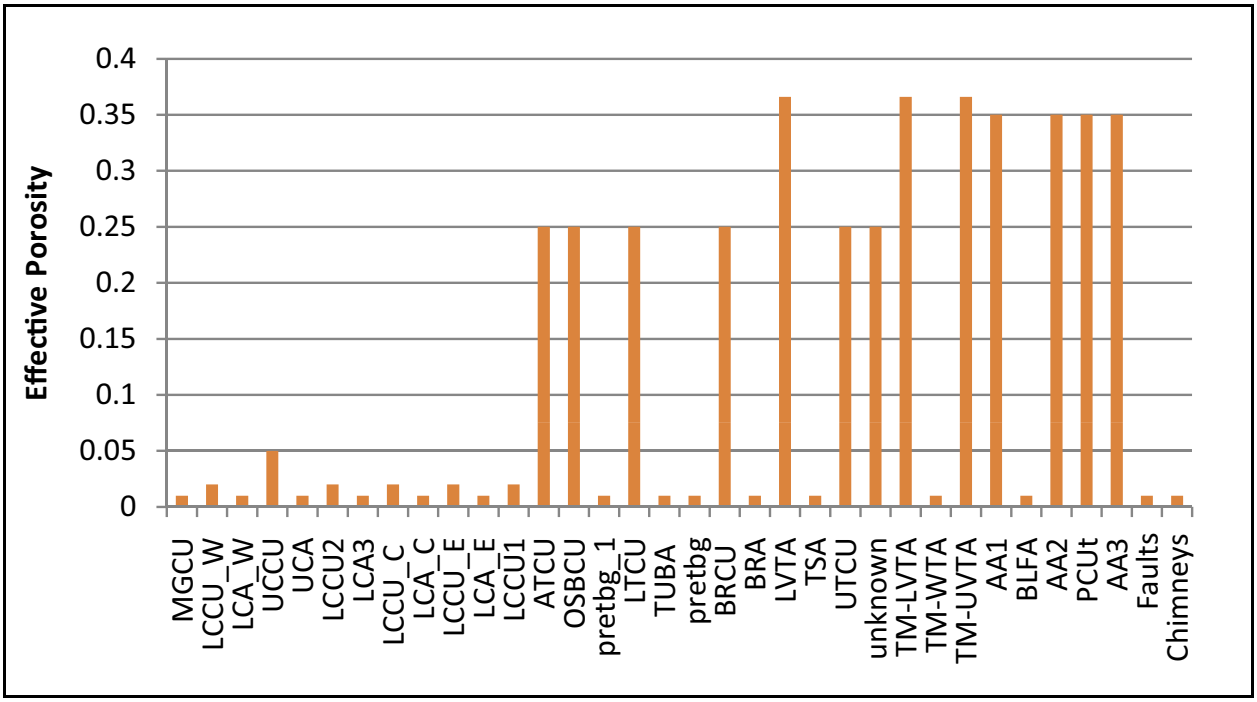

Figure 3-26
HSU Porosities Used in the Unsaturated-Zone Flow and Transport Models for Yucca Flat

equivalent to those of the rock matrix (ATCU, OSBCU, LTCU, BRCU, LVTA, UTCU, TM-LVTA, and TM-UVTA). Both fractures and faults are assumed to be entirely absent in the AA (subdivided in the HFM into AA1, AA2, and AA3) and PCUT, so the matrix porosity is used as the effective transport porosity in these HSUs.

3.5 Uncertainty and Sensitivity Approach

3.5.1 Sensitivity Matrix

The application of Monte Carlo techniques to develop probabilistic transport results for the unsaturated-zone models was not feasible because of the long model run times and the lack of data that would support the development of continuous parameter distributions for many of the hydrologic parameters used in the models. The long run times resulted from both the large size of the unsaturated-zone models (greater than one million nodes for several of the unsaturated-zone grids) and the highly nonlinear nature of the governing flow equations. Instead, the impact of uncertainty in selected hydrologic and transport parameters was investigated by more traditional sensitivity and uncertainty analysis in which uncertain parameters were varied through their possible ranges to assess

the impact of their uncertainty on the transport results. This was judged to be a reasonable approach during Phase I flow and transport model development, the primary goal of which was to produce a range of unsaturated-zone transport results consistent with model uncertainties that could bound the likely radionuclide input to the saturated-zone transport models described in Sections 4.0 and 6.0.

To characterize the impact of hydrologic and transport uncertainties on radionuclide transport to the water table, we performed a structured sensitivity analysis that examined how various combinations of parameters affect radionuclide arrivals at water table. Parameters and features that were examined included the following:

- Background infiltration rates
- Crater infiltration rates
- Sediment and tuff anisotropy
- Effective porosity of the tuff confining units (LTCU, OSBCU, and ATCU)
- The presence of high-permeability, low-porosity collapse chimneys in the volcanic units
- The size of the initial radionuclide exchange volume around each detonation working point.

A total of 28 different combinations of these parameters and processes were examined, as summarized in Table 3-8. Each model run is represented by a six-digit code that summarizes the parameter choices used in that run. For each model parameter, the parameter assumed either a low, medium, or high value, as indicated in the footnotes to Table 3-8. The table also includes results for model runs that end in *c*, such as run 2.2.3.2.1.2.c. The *c* at the end of the run number indicates that this run examined the effects of a high-permeability, low-porosity rubble zone in the non-alluvial portion of the chimney above the working point. For each model run, the same parameter combination was applied simultaneously to all 12 of the unsaturated-zone grids, and the graphical results associated with each run are usually presented as the aggregated results from all the grids.

An exhaustive examination of the possible combinations of six parameters each with three possible values would have resulted in $3^6 = 729$ possible runs. The runs summarized in Table 3-8, although far from exhaustive, were chosen so that the importance of individual parameters could be evaluated and, based on the model's sensitivity to that parameter (in terms of total fraction of the unsaturated-zone radionuclide inventory reaching the water table over the 1,000-year regulatory period) and the parameters uncertainty, that the probable range of model responses was spanned by the results.

3.5.2 Source-Term Simplification and the Rationale for Radionuclide Selection

In previous CAU-scale transport models constructed for Frenchman Flat (NNES, 2010b) and Pahute Mesa (SNJV, 2009b), separate so-called simplified source-term (SST) models external to the CAU models were used to estimate the radionuclide source terms at a plane of nodes downgradient of each detonation's exchange volume. This approach was taken so that relatively complex near-field processes such as melt-glass dissolution and the effects of the damage zone surrounding the cavity could be taken into account. The drawback in this approach is that the source term that is applied at the downgradient plane depends on water flux through the cavity, so that considerable effort has to be made each time the flow field in the CAU-scale model changes in order to ensure that the radionuclide flux from the SST model and the water flux in the CAU models are consistent. It would have been extremely difficult if not impossible to achieve this consistency in Yucca Flat given the extremely large number of detonations and the highly transient flow fields in both the unsaturated zone and the saturated alluvial/volcanic aquifer system models. In the unsaturated-zone models, the transient flow fields result from the presence of focused infiltration due to surface runoff into the craters, and the variability in crater infiltration rates due to differences in crater geometry and watershed areas (Section 3.3).

The approach used in the unsaturated-zone model was to take the radionuclide mass estimated to be associated with each detonation at the time of the detonation and distribute this mass uniformly around each detonation's working point directly in the unsaturated-zone models. The radionuclide mass was initially distributed in an exchange volume that was assumed to be equal to 1, 2, or 3 R_c, where the cavity radius R_c was estimated from the maximum announced yield of the detonation, its depth of burial, and overburden density according to the formula given by Pawloski (1999).

As in the previous CAU transport models for Frenchman Flat and Pahute Mesa, the estimated radionuclide mass associated with each detonation was based on the yield-weighted fraction of the unclassified radionuclide inventory of Bowen et al. (2001). However, some additional considerations arose because the definition of saturated-zone detonations in Bowen et al. (2001) includes detonations with working points in the unsaturated zone but within 100 m of the water table, whereas the unsaturated-zone model includes all detonations with working points above the water table. The yield-weighted fraction of the unsaturated-zone part of the Bowen et al. (2001) Yucca Flat inventory was used for all unsaturated-zone detonations with working points 100 m or more above the water table, whereas the yield-weighted fraction of the saturated-zone portion of the Bowen et al. (2001)

Yucca Flat inventory was used for all unsaturated-zone detonations with working points within 100 m of the water table.

After the yield-weighted fraction of the Yucca Flat unclassified radionuclide inventory had been estimated for each detonation, the radionuclide mass for each detonation that was immediately available for transport was further adjusted to account for the possible incorporation of some fraction of the radionuclide mass into the melt glass that typically forms at the bottom of the detonation cavities in silicate rocks and alluvium. For the 28 model runs presented in Table 3-8, the expected fraction of the radionuclide inventory that will become isolated in the melt glass is based on an IAEA (1998) study, which was produced with data from the NNSS (Table 3-9). The non-melt-glass fraction was assumed to be dissolved in pore water and immediately available for transport. For later model runs presented in Section 3.8, the non-melt-glass fractions were based on more recent analyses summarized in the HST report for Rainier Mesa (Tompson et al., 2011), as documented in Appendix C of this report.

Table 3-9
Radionuclides Considered in the Unsaturated-Zone Transport Models

Radionuclide	Half-Life (years)	Partitioning, in percent			
		Glass	Rubble	Gas	Water
^{3}H	12.32	0	0	2	98
^{14}C	5,730	0	10	80	10
^{36}Cl	3.01E+05	50	40	0	10
^{99}Tc	2.13E+05	80	20	0	0
^{129}I	1.57E+07	50	40	0	10
U (total)	--	90	10	0	0
^{237}Np	2.14E+06	95	5	0	0

Detonations with assumed exchange volumes that straddled the water table also required additional consideration. For detonations whose assumed exchange volumes straddled the water table, the unsaturated-zone fraction of the yield-weighted radionuclide inventory was distributed uniformly throughout the unsaturated-zone portion of the exchange volume. If the working point of the detonation was above the water table, there was generally sufficient grid resolution because the grids were designed to model transport from all detonations with working points above the water table. However, if the detonation had a working point below the water table, there was no guarantee that the

background grid resolution was sufficient to distribute this mass accurately within the unsaturated-zone portion of the assumed exchange volume. In any case, crater infiltration was not tracked in the unsaturated-zone models for detonations with working points below the water table, so ambient background fluxes were used to transport this portion of the unsaturated-zone inventory to the saturated zone. This issue, which affected the 28 simulations summarized in Table 3-8, is not significant to the overall results because most of the radionuclide mass remained in the saturated-zone model, where the appropriate mesh discretization existed. This outcome, not anticipated when the unsaturated-zone grids were originally designed, was circumvented in simulations presented in Section 3.8 that incorporated new source-term concepts by reassigning the unsaturated-zone portion of the inventory to the saturated-zone model where sufficient grid resolution exists near the working points of these detonations.

3.5.2.1 Selection of Radionuclide Species

Based on results from modeling studies at Pahute Mesa (SNJV, 2009b) and Frenchman Flat (NNES, 2010b), where contaminant boundaries in alluvium and volcanic rocks were defined by relatively few radionuclide species, we chose to focus the initial unsaturated-zone transport modeling effort on a few non-sorbing (^{3}H, ^{14}C, ^{36}Cl, ^{99}Tc, and ^{129}I) and weakly sorbing (^{237}Np and U isotopes) radionuclide species. Simulations presented later in Section 3.8 also considered the transport of ^{90}Sr and ^{137}Cs, which are strongly sorbed in the volcanic rocks and alluvium, but only weakly sorbed and thus readily transported in the LCA (SNJV, 2007). Radionuclide selection was also supported by the results of McNab (2008), which showed that unrealistically large crater infiltration rates were required to transport moderately or strongly sorbing radionuclides to the water table within 1,000 years (Section 3.1.3.7).

3.5.2.2 Assumptions and Simplifications

Radionuclide transport modeling in the unsaturated zone was further simplified by ignoring the later release of ^{36}Cl, ^{99}Tc, ^{129}I, ^{237}Np, and various U isotopes through melt-glass dissolution, which SNJV (2009b) estimated would be unimportant for unsaturated-zone detonations because the melt glass would be relatively dry soon after the detonation when the glass was hot and its solubility at its highest. The transport modeling effort was further simplified by assuming that ^{237}Np and U were non-sorbing rather than weakly sorbing. This allowed HSU-dependent variations in partition coefficient (K_d) values to be ignored for these radionuclide species and to simulate just a few tracers

(^{3}H and ^{14}C) from which the remaining radionuclide concentrations could be estimated. The ratios of radionuclides other than ^{3}H and ^{14}C were based on the average molar ratios of the radionuclide to ^{14}C in the combined unsaturated- and saturated-zone parts of the Bowen et al. (2001) radionuclide inventory for Yucca Flat, adjusted to account for the unavailability of their melt-glass fraction. Because ^{14}C was used to estimate the concentrations of other radionuclides, it was modeled as an ideal tracer rather than as a complex volatile species that partitions into and moves in the gas phase as well as sorbs to solid phases (SNJV, 2009b). The impact of gas-phase partitioning of ^{14}C on transport to the water table is investigated separately in Section 3.7.

3.6 Flow and Transport Model Results

3.6.1 Steady-State Flow Model

Despite strong evidence that current infiltration rates are zero or that water movement is upward in the upper several tens of meters of the unsaturated zone throughout much of alluvial filled parts of Yucca Flat (Walvoord, Phillips, et al., 2002; Walvoord, Plummer, et al., 2002; Kwicklis et al., 2006a), background infiltration rates in the inter-crater areas were assumed to be substantially higher. Higher background infiltration rates of 1, 5, and 10 mm/yr were uniformly applied to the tops of the 12 unsaturated grids to examine the effects of higher infiltration on radionuclide transport to the saturated zone. Although these higher present-day infiltration rates are considered unlikely, they were selected for consideration because of the following reasons: (1) no site-specific studies were available to characterize infiltration beneath arroyos, basin edges receiving runoff from the surrounding hills, or Yucca Lake playa, which are possibly areas of higher infiltration than the areas that have been studies for low-level waste deposal; (2) transient simulations of the evolution of the unsaturated-zone in Yucca Flat over the last several tens of thousands of years indicate that water that infiltrated during the late Pleistocene continues to drain to the water table at a low rate of as much as several tenths of a millimeter per year (Walvoord, Phillips, et al., 2002; Kwicklis et al., 2006); (3) temperature profiles from the lower part of the unsaturated zone and upper part of the saturated zone indicate cooler than expected temperatures in the center of the basin, suggestive of recent downward water movement of a magnitude inconsistent with negative infiltration rates; (4) moisture content and saturation data collected from exploratory boreholes and weapons emplacement holes in Yucca Flat show higher saturations at depth than those that characterized the shallow areas beneath the low-level radioactive waste sites; and (5) models of the saturated alluvial/volcanic aquifer system presented in Section 4.0

require relatively high recharge rates in order to match hydraulic heads when moderately high tuff confining unit permeabilities estimated from slug test and core data are used. Therefore, in order to qualitatively account for these observations, a broad range of background infiltration rates was considered in this study. A single additional model run is based on the USGS DVRFS infiltration model (with redistribution), which estimates net infiltration rates beneath most of the alluvial-filled parts of the basin to be less than 0.1 mm/yr and in the surrounding bedrock hills to be 1 to 10 mm/yr. The discussion of this model, which is considered plausible based on studies cited above in this section, is delayed until Section 3.8.2 after the results of the sensitivity analysis outlined in Table 3-9 are presented.

3.6.1.1 Recharge at the Water Table

Despite the uniform infiltration rates applied at the top of the unsaturated-zone models, the complex geology and contrasting hydrologic properties represented in the unsaturated-zone models creates complex patterns in groundwater recharge at the water table, even at steady-state (Figures 3-27 and 3-28). The highly nonuniform recharge at the water table reflects the non-vertical movement of water in the unsaturated zone toward features such as faults that facilitate drainage to the water table. These complex flow patterns would have gone unrecognized without the benefit of the three-dimensional models used in this study.

As an example, recharge at the water table is shown for a uniform 5-mm/yr infiltration rate at land surface that shows the impact of different assumed values of anisotropy in the alluvium (Figure 3-27) and in the tuff confining units (the LTCU, OSBCU, and ATCU) (Figure 3-28). Anisotropy in the alluvium has relatively little effect on steady-state recharge at the water table (Figure 3-27). This may be partly due to the assumption in these models that faults in the alluvium do not have hydrologic properties distinct from those in the surrounding alluvium. However, even when the permeabilities of the alluvium and tuff confining units are assumed to be isotropic (Figure 3-27a), recharge at the water table is highly nonuniform. Recharge in the faults tends to be higher than adjacent areas, where “shadow” zones of lower recharge exist because downward percolation has been intercepted by the dipping faults. Stronger anisotropy in the tuff confining units (smaller ratios of k_v/k_h) tends to create increasingly larger areas where the lateral diversion of percolation toward the faults reduces the downward flux to the water table within and beneath the tuff confining units (Figure 3-28).

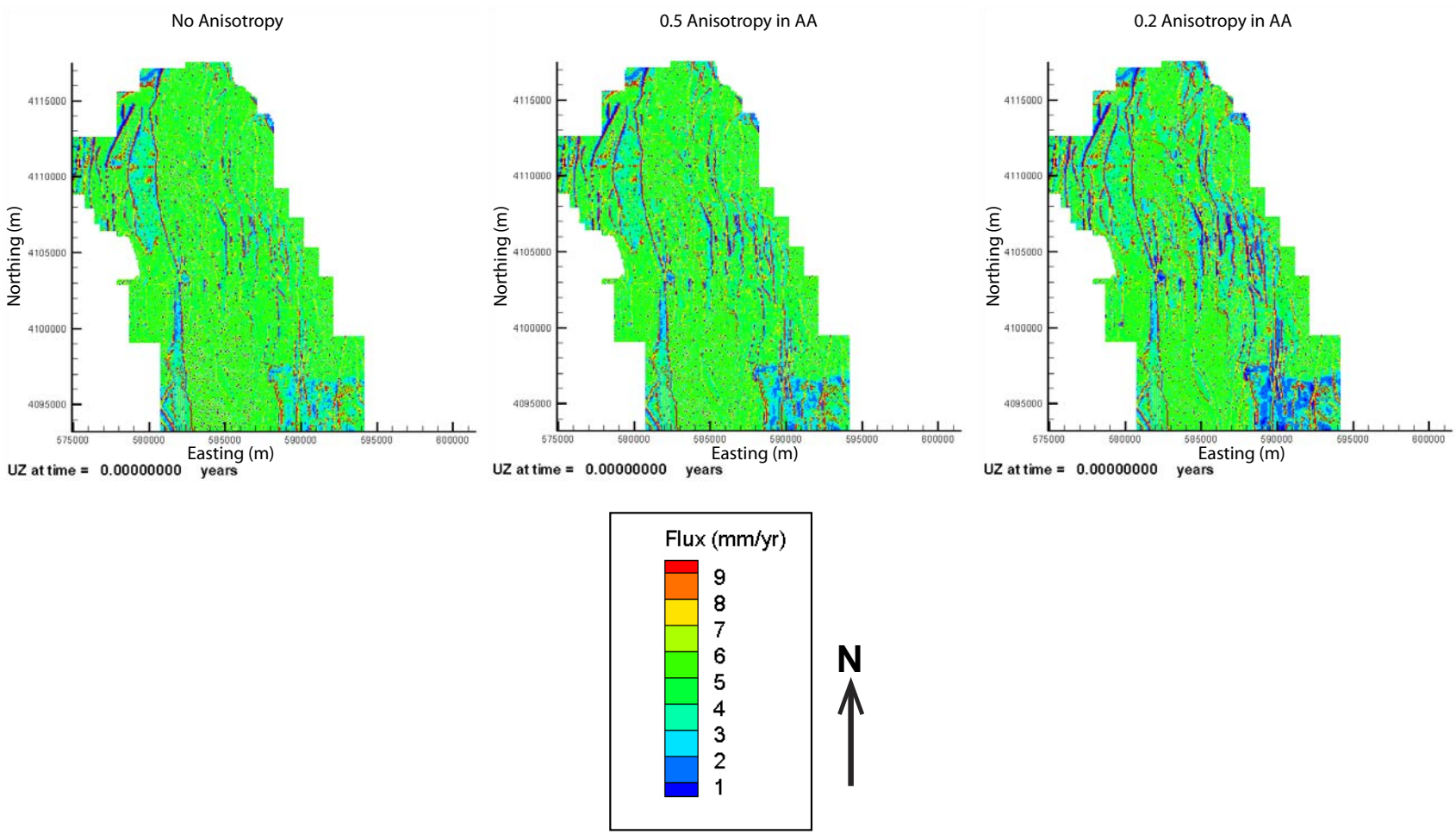

Figure 3-27
Effect of Sediment Anisotropy on Recharge at the Water Table Assuming a Uniform 5-mm/yr Background Infiltration Rate

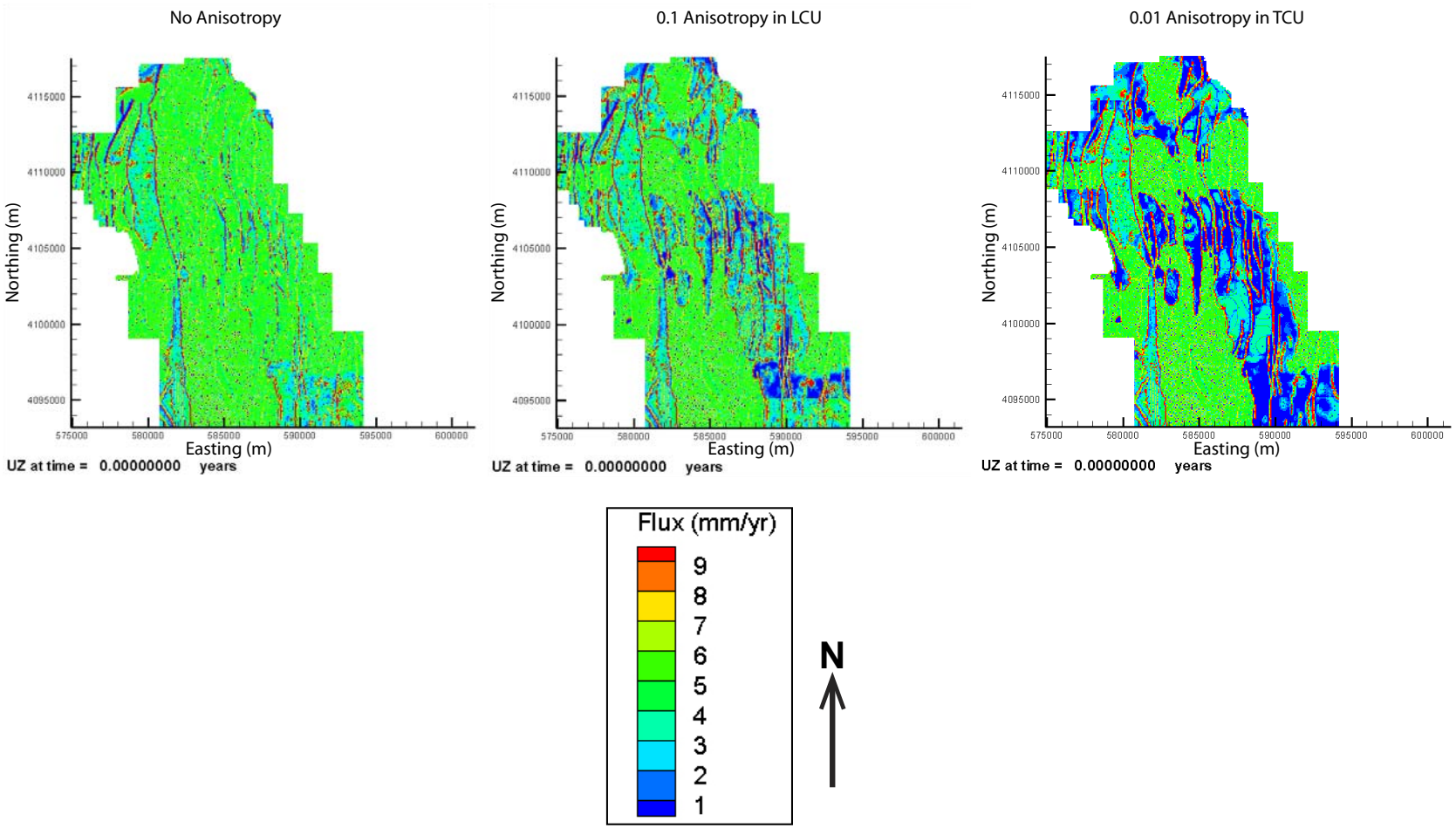

Figure 3-28
Effect of Anisotropy in the LTCU, OSBCU, and ATCU on Recharge at the Water Table Assuming a Uniform 5-mm/yr Background Infiltration Rate

3.6.2 Transient Flow and Transport Model Results: Examples from Runs 2.1.1.2.1.2 and 2.1.3.2.1.2.

Although it is not practical to visually present the results from each of the 12 grids for all 28 model runs, it is worthwhile to give a few examples of these results so that readers can get a sense of how these models functioned. Figures 3-29 to 3-31 show the simulated saturations and ^{14}C concentrations at the end of the 1,000-year regulatory period for run 2.1.1.2.1.2 for grids 2, 4, and 8, respectively. Run 2.1.1.2.1.2 is a case with a 5 mm/yr background flux, low crater infiltration rates, isotropic alluvium and tuff confining unit permeability, a tuff confining unit effective porosity of 0.25, and a 2 R_c exchange volume.

These plots indicate the tight clustering of the nuclear detonations. The saturation plots include close-ups of the grid refinement associated with the subsidence craters resulting from the detonations. These were areas of substantially higher infiltration, as discussed in Section 3.3 of this report. The ^{14}C concentrations are plotted on an exponential scale with an upper threshold of 3.21E-11 mol/L and a lower limit that is three orders of magnitude less (3.21E-14 mol/L). The upper limit of 3.21E-11 moles ^{14}C/L corresponds to the SDWA standard for beta-emitting radionuclides of 4 mrem/yr, so that all concentrations shown in red exceed the regulatory standard and other colors show concentrations that are lower, but within three orders of magnitude of the regulatory standard for ^{14}C. Areas with concentrations less than 3.21E-14 mol/L have been blanked out on these plots so that the distribution of ^{14}C concentrations close to the regulatory limit can be more clearly seen.

At the beginning of the transient transport simulations (December 3, 1961), radionuclide mass from all unsaturated-zone detonations conducted between 1957 and 1992 is instantaneously introduced and assumed to be distributed within a roughly spherical exchange volume of 1, 2, or 3 R_c centered on the working point. As infiltration moving through the crater floor percolates downward through the collapse chimney and reaches the exchange volume, it begins to flush radionuclides out of the exchange volume and downward toward the water table. Depending on the size of the crater bottom area relative to the exchange volume cross-sectional area, and the amount of lateral spreading that infiltration from the crater undergoes due to low permeability layers or sediment and rock anisotropy, radionuclides on the lateral edges of the exchange volume may extend beyond the zone that is flushed by the crater infiltration. The radionuclides on the periphery of the exchange volume can be transported at a much slower rate (by background infiltration) than those in directly beneath the crater floor. After 1,000 years, initially spherical radionuclide plumes associated with each detonation have

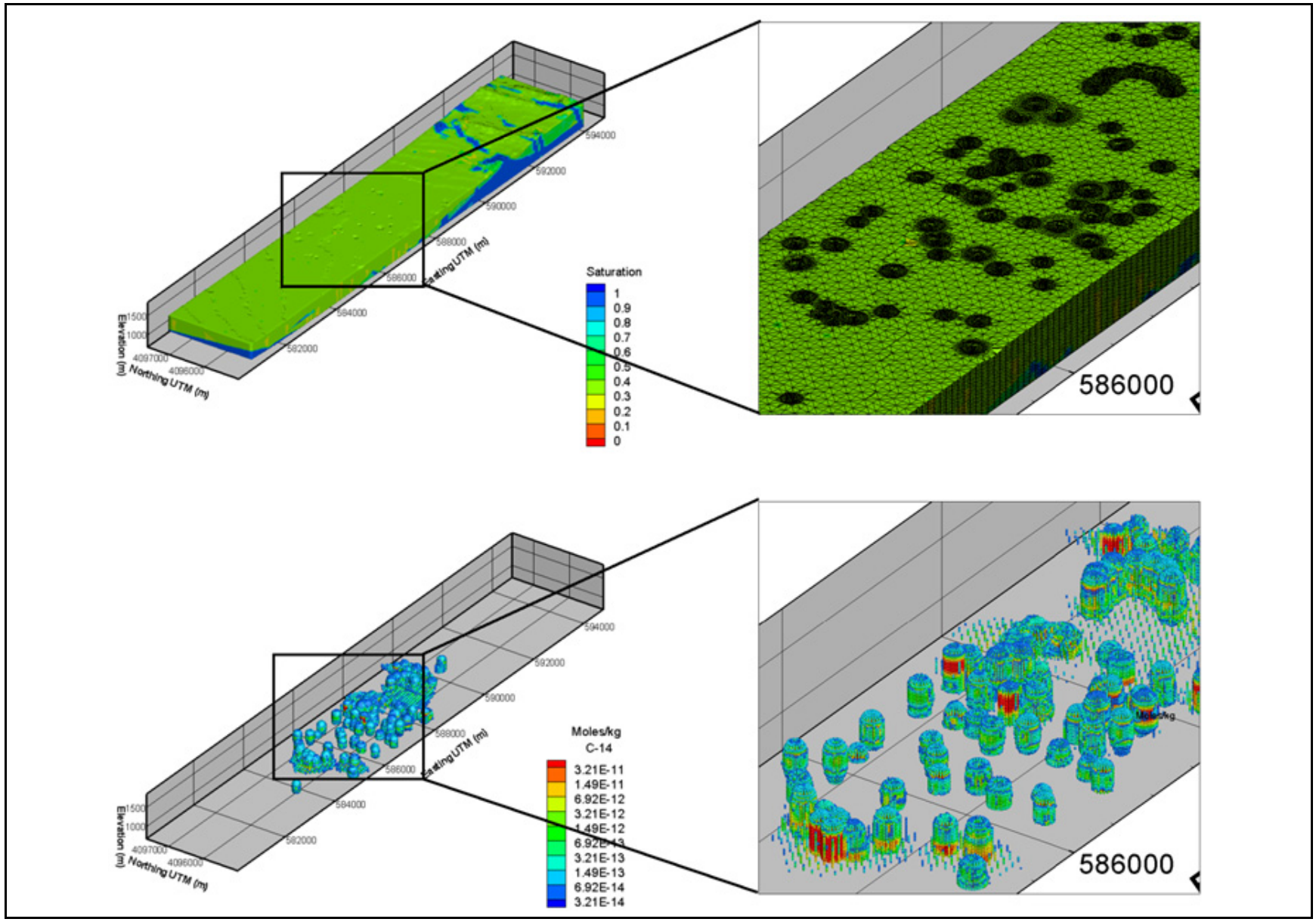

Figure 3-29
Water Saturations and ^{14}C Concentrations in Grid 2 at 1,000 Years for Run 2.1.1.2.1.2

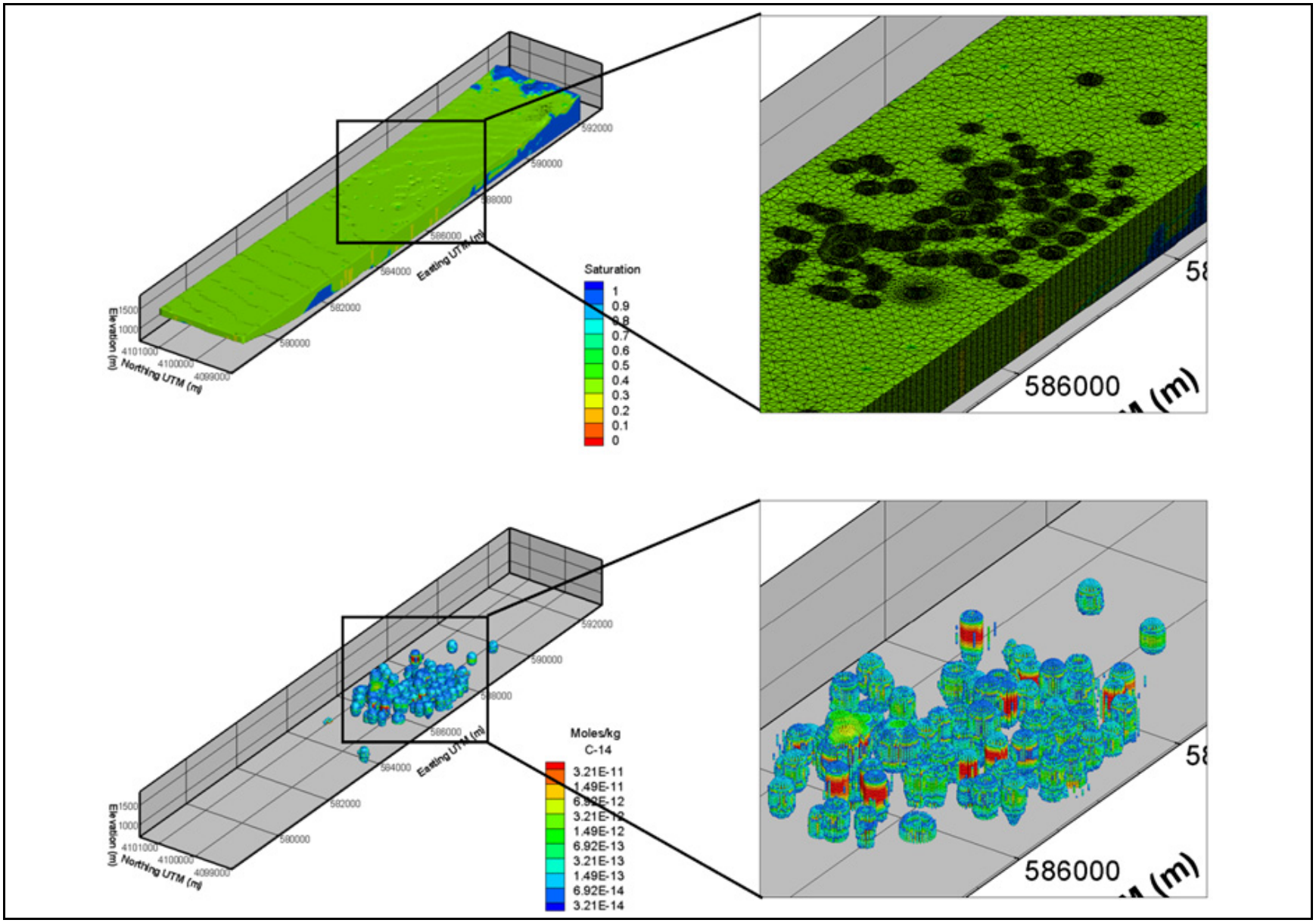

Figure 3-30
Water Saturations and ^{14}C Concentrations in Grid 4 at 1,000 Years for Run 2.1.1.2.1.2

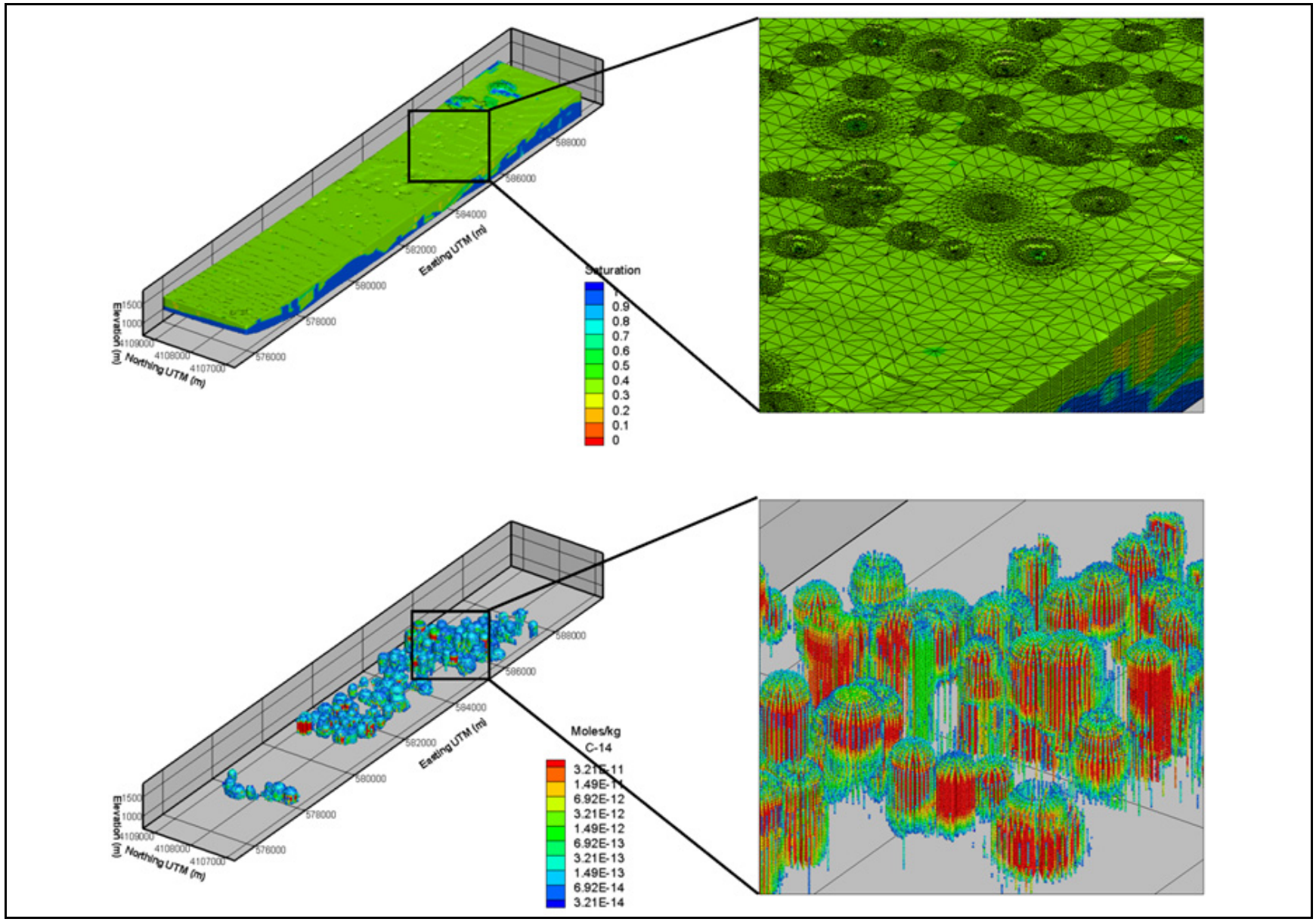

Figure 3-31
Water Saturations and ^{14}C Concentrations in Grid 8 at 1,000 Years for Run 2.1.1.2.1.2

become more cylindrical, reflecting the downward displacement and elongation of the plumes by crater infiltration. By the end of the 1,000-year simulation period, radionuclide concentrations at the water table have begun to reflect lateral spreading along the top of the water table itself, as shown in Figure 3-29 for grid 2.

The importance of fault zones as transport pathways varied from grid to grid and depended largely on the proximity of the detonation to a fault. Because faults in alluvium were not assigned properties different from that of the surrounding alluvium, only detonations in either vertical or lateral proximity to faults in the tuffs or pre-Tertiary rocks utilized the high-permeability, low-porosity faults as transport pathways. An example is shown for run 2.1.1.2.1.2 for grid 8, where all HSUs but the faults have been blanked (Figure 3-32). There are a large number of detonations, predominantly in the eastern half of the grid, where ^{14}C is being transported to the water table through fault zones.

3.6.3 ^{14}C Breakthrough at the Water Table

In order to compare the impact of different parameter combinations and infiltration rates on radionuclide transport from unsaturated-zone detonations, we plot the cumulative mass arrival of ^{14}C at the water table for different scenarios. As discussed earlier, it is assumed for the purpose of this comparison that ^{14}C behaves as an ideal liquid tracer and does not sorb to rocks or sediments, undergo radioactive decay, or partition into the gas phase. This helps to identify the importance of parameter and infiltration rate variations on other radionuclides for which these characteristics are also assumed to be valid.

3.6.3.1 All Results

The initial ^{14}C inventory in the unsaturated zone at the start of the transient 1,000-year simulation period is approximately 24 moles of ^{14}C. Figure 3-33 shows that for the 28 model runs listed in Table 3-8, the cumulative mass arrival by the end of the 1,000-year simulation period can vary between 1 and 12 moles of ^{14}C, or roughly between 4 and 50 percent of the initial ^{14}C inventory when the decay of ^{14}C is ignored. The mass of ^{14}C arriving at the water table would be about 13 percent lower at the end of 1,000 years had radioactive decay of ^{14}C been considered. However, to be able to extrapolate these results to other radionuclide species, it is convenient to ignore radioactive decay in these plots. Thus, from these plots, it can be inferred that between 4 and 50 percent of the non-melt-glass fraction of other long-lived, non-sorbing radionuclides would also arrive at the water

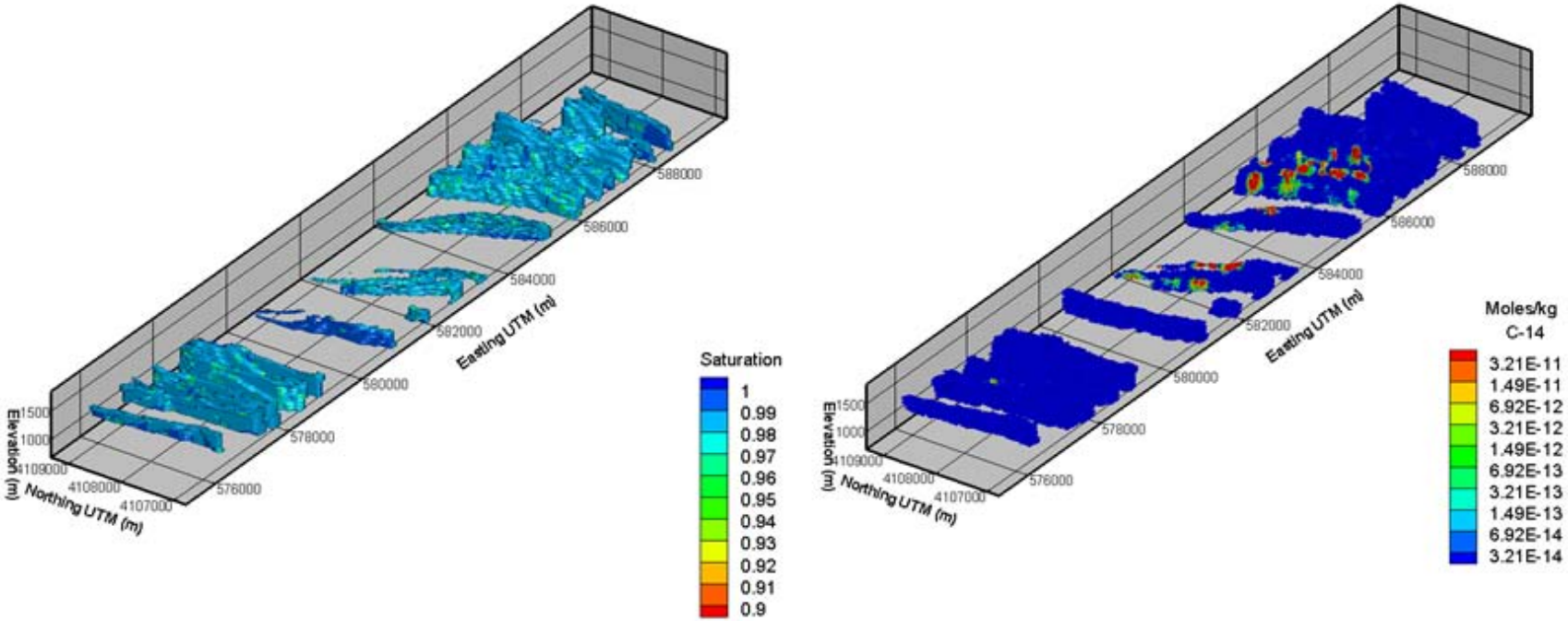

Figure 3-32
Results from Run 2.1.1.2.1.2 for Grid 8 at 1,000 Years

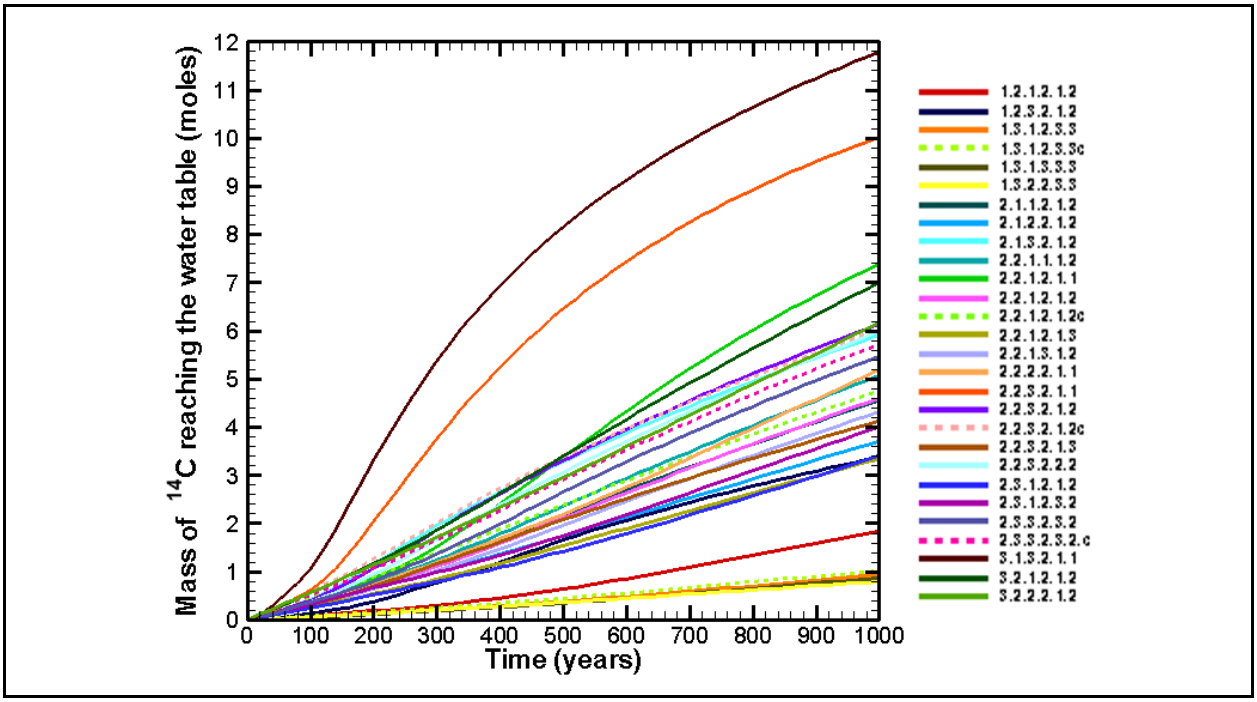

Figure 3-33
Cumulative Mass Arrival of ^{14}C at the Water Table—All Results

table, depending on the assumptions associated with the 28 individual breakthrough curves shown in Figure 3-33. The cases with the two highest cumulative mass arrivals are runs 3.1.3.2.1.1 and 2.2.3.2.1.1, both of which have high crater infiltration rates and a 1 R_c exchange volume. The importance of individual parameters and assumptions on transport behavior can be identified by comparing runs in which only a single parameter has been varied, as discussed in the following sections.

3.6.3.2 Effect of Background Infiltration

A comparison of model runs in which only the background infiltration rate is varied shows that transport to the water table increases with increasing background flux (Figure 3-34). Background infiltration rates of 10 mm/yr (run 3.2.1.2.1.2) produce about 7 moles ^{14}C at the water table, whereas background infiltration rates of 1 mm/yr (run 1.2.1.2.1.2) produce slightly less than 2 moles ^{14}C after 1,000 years. The higher background fluxes drive radionuclide transport to the water table before the crater infiltration pulses arrive at the exchange volume. A secondary effect may be that the higher background flux creates wetter initial conditions at the start of the transient flow period, so that wetting fronts associated with crater infiltration reach the exchange volume sooner.

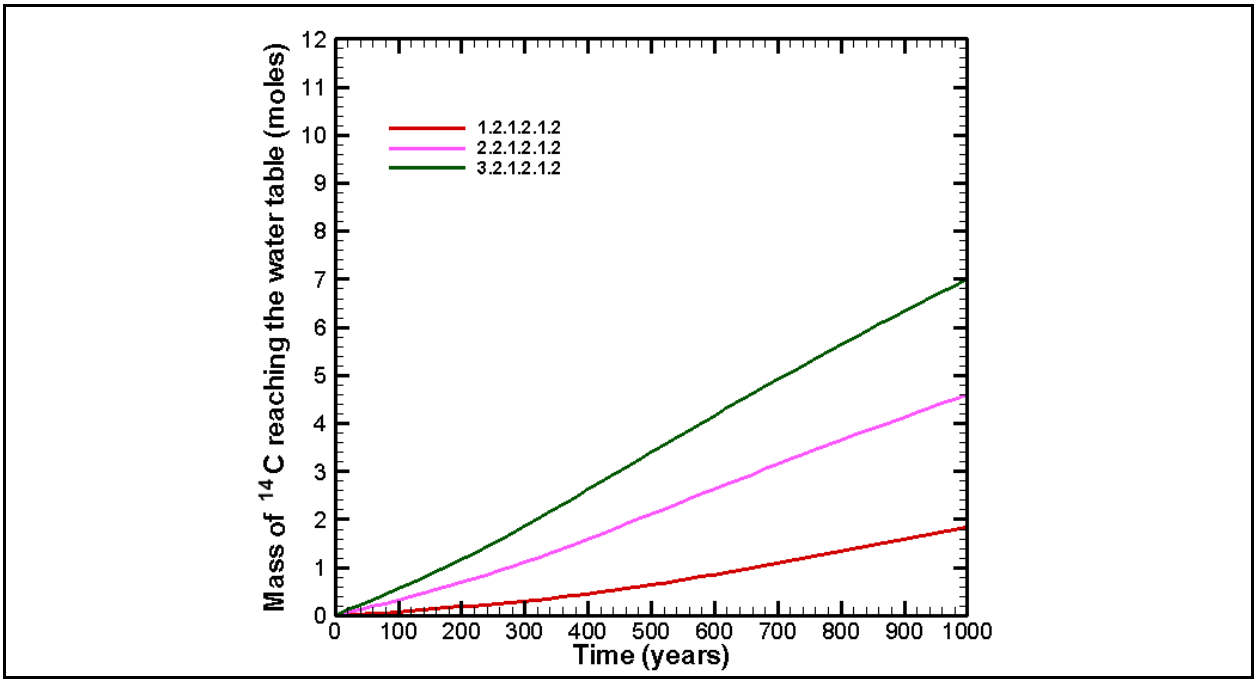

Figure 3-34
Cumulative Mass Arrival of ^{14}C at the Water Table—Effect of Background Infiltration Rates

3.6.3.3 Effect of Exchange Volume Radius

The effect of the initial exchange volume radius (1, 2, or 3 R_c) on the cumulative mass arrival of ^{14}C at the water table is shown for two different crater infiltration rates in Figure 3-35. Transport to the water table is greater when crater infiltration rates are high (solid lines) and when the radionuclide mass is assumed to be confined to a smaller exchange volume directly beneath the crater bottom (runs that end in .1) rather than dispersed across a larger volume that is only partially flushed by focused crater infiltration (runs that end in .3).

3.6.3.4 Effect of Crater Infiltration Rates

A comparison of model runs in which only the crater infiltration rates are varied and all other parameters are held constant shows that ^{14}C transport to the water table increases when crater infiltration rates are higher (Figure 3-36) (Note that infiltration for run 2.1.2.2.1.2 is less than for 2.1.1.2.1.2 or 2.1.3.2.1.2—see Figure 3-15). However, given the range of variability estimated in the crater infiltration rates, the effect of uncertainty in crater infiltration rates on ^{14}C mass arrival at the water table is relatively small, resulting in a total range in ^{14}C mass arrivals of only 2 moles.

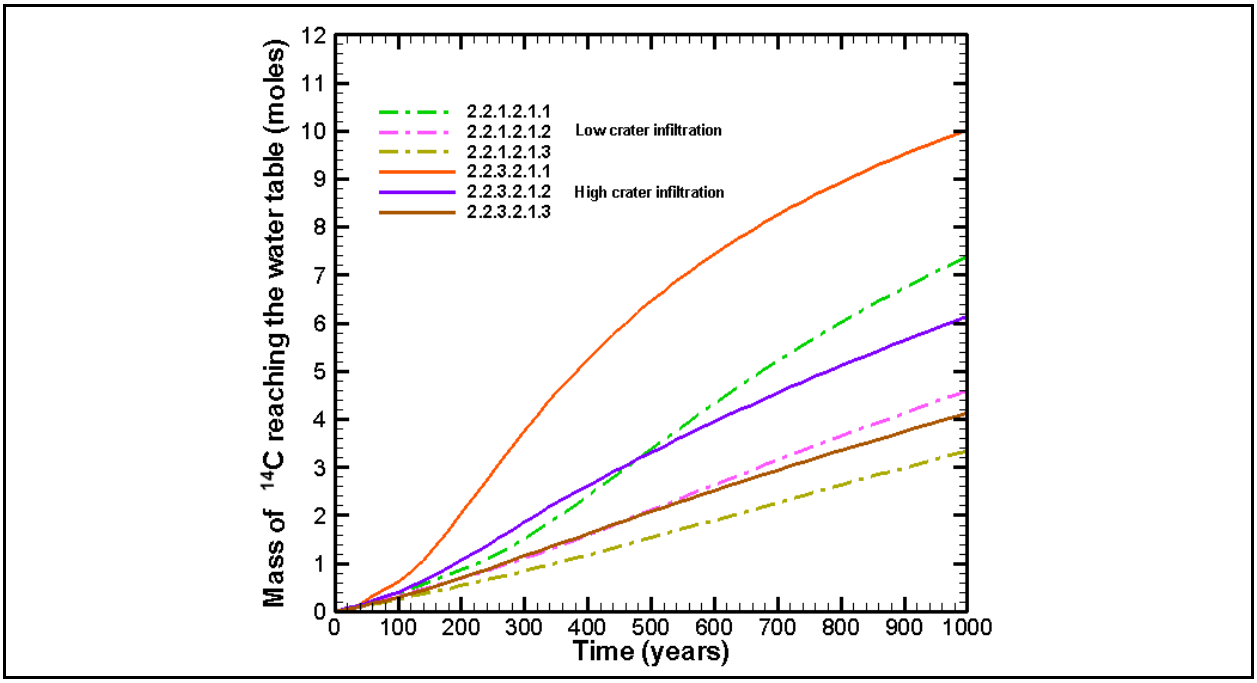

Figure 3-35
Cumulative Mass Arrival of ^{14}C at the Water Table—Effect of Exchange Volume Radius and Crater Infiltration Rates

3.6.3.5 Effect of Sediment Anisotropy

Sediment anisotropy was varied by decreasing the vertical permeability relative to a constant horizontal permeability of 1.12E-12 m^2. A decrease in k_v/k_h from 1.0 (run 2.1.1.2.1.2) to 0.5 (run 2.2.1.2.1.2) to 0.2 (run 2.3.1.2.1.2) results in only small decreases in the cumulated mass arrival of ^{14}C at the water table (Figure 3-37). The decrease in k_v/k_h from 1.0 to 0.5 appears to have a negligible effect, whereas the impact of decreasing k_v/k_h from 0.5 to 0.2 appears to have a relatively large effect. These results may be indicating that reductions in the vertical permeability of the sediments become important only when a certain threshold is crossed and vertical permeability begins to impede the downward flow of crater infiltration.

3.6.3.6 Effect of Tuff Confining Unit Anisotropy

Anisotropy in the permeability of the tuff confining units (the LTCU, OSBCU, and ATCU) were jointly varied by reducing their vertical permeability such that the ratios of vertical to horizontal permeability (k_v/k_h) varied from 1.0 (run 2.2.3.2.1.2) to 0.1 (run 2.2.3.2.2.2) to 0.01 (run 2.3.3.2.3.2). (Note that this last run—2.3.3.2.3.2—also incorporated a reduction in the k_v/k_h of the sediment from 0.5 to 0.2 compared with the other two runs.) The effect of reducing the vertical permeability of the

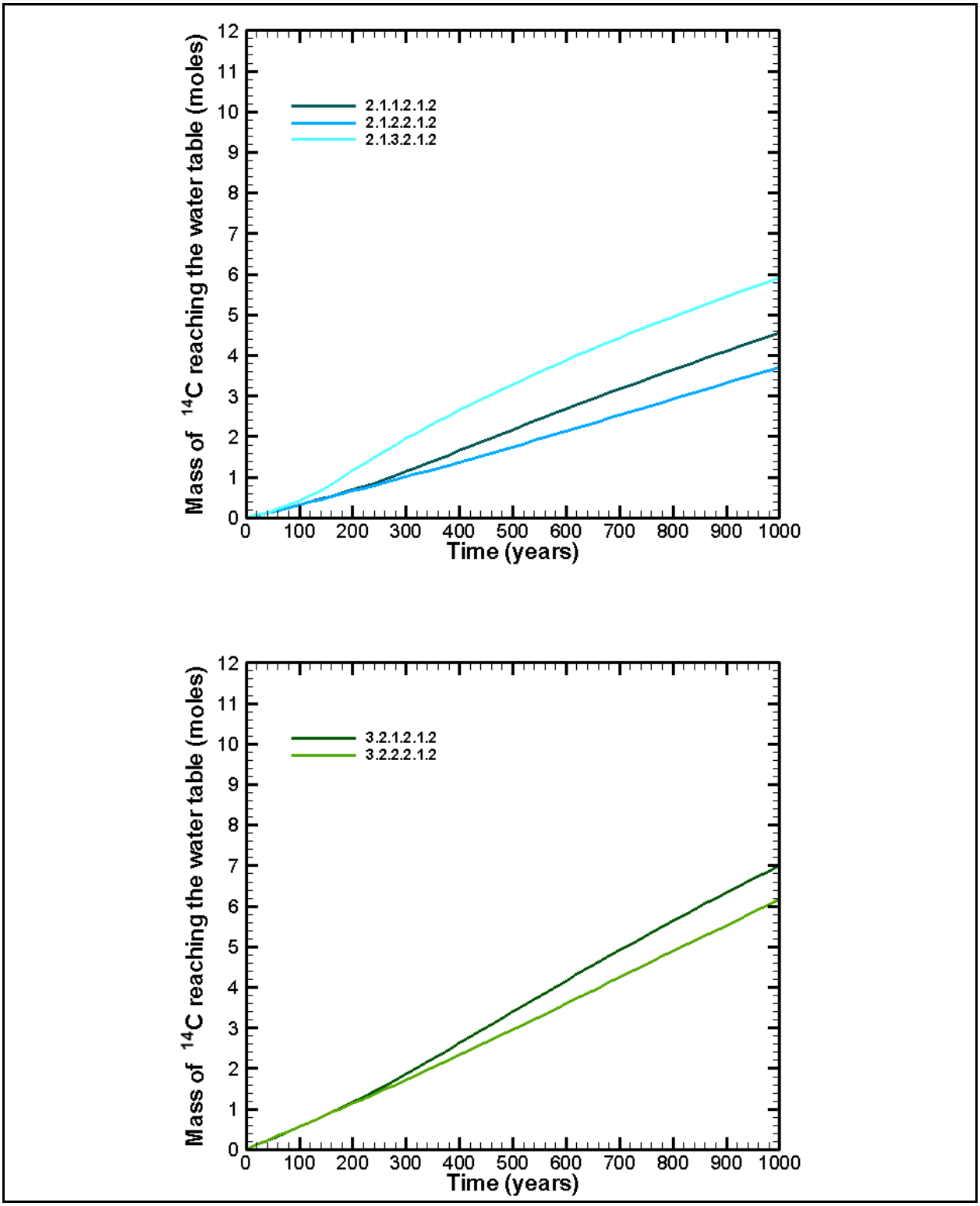

Figure 3-36
Cumulative Mass Arrival of ^{14}C at the Water Table—Effect of Crater Infiltration Rates

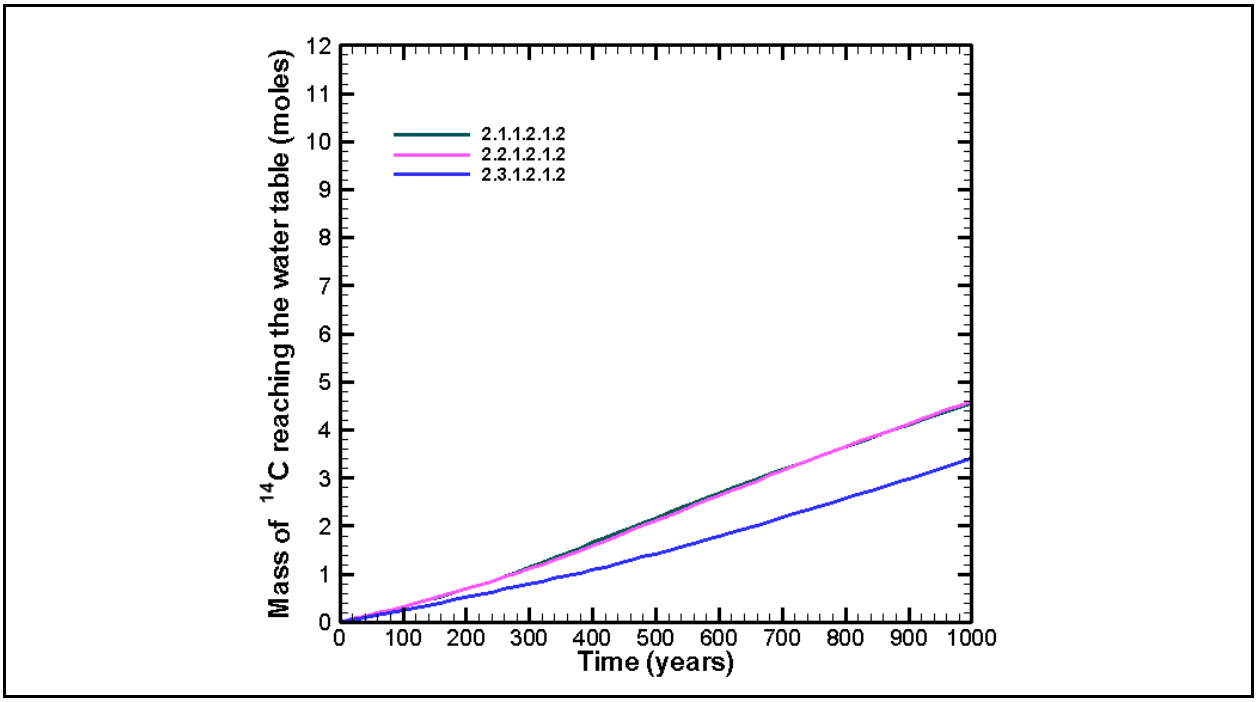

Figure 3-37
Cumulative Mass Arrival of ^{14}C at the Water Table—Effect of Sediment Anisotropy (k_v/k_h)

tuff confining units over two orders of magnitude produces a total range in cumulative mass arrival of ^{14}C of less than 1 mole after 1,000 years (Figure 3-38). The lack of sensitivity of ^{14}C mass arrival to tuff confining unit anisotropy may be because the interval of the unsaturated tuff confining units between the detonations and the water table is thin (or absent entirely) for many detonation locations that produce ^{14}C at the water table, so changes to the tuff confining unit properties have a negligible effect.

3.6.3.7 Effect of Tuff Confining Unit Porosity

The effect of reducing the effective transport porosity of the tuff confining units (the LTCU, OSBCU, and ATCU) from 0.35 (run 2.2.1.3.1.2) to 0.25 (run 2.2.1.2.1.2) to 0.15 (run 2.2.1.1.1.2) has a relatively minor effect on cumulative mass arrival of ^{14}C at the water table, producing a total range in mass arrival of ^{14}C of less than 1 mole after 1,000 years (Figure 3-39). The lack of sensitivity of these results to the effective transport porosity is probably for the same reason as the lack of sensitivity to tuff confining unit anisotropy, namely, the interval of the unsaturated tuff confining

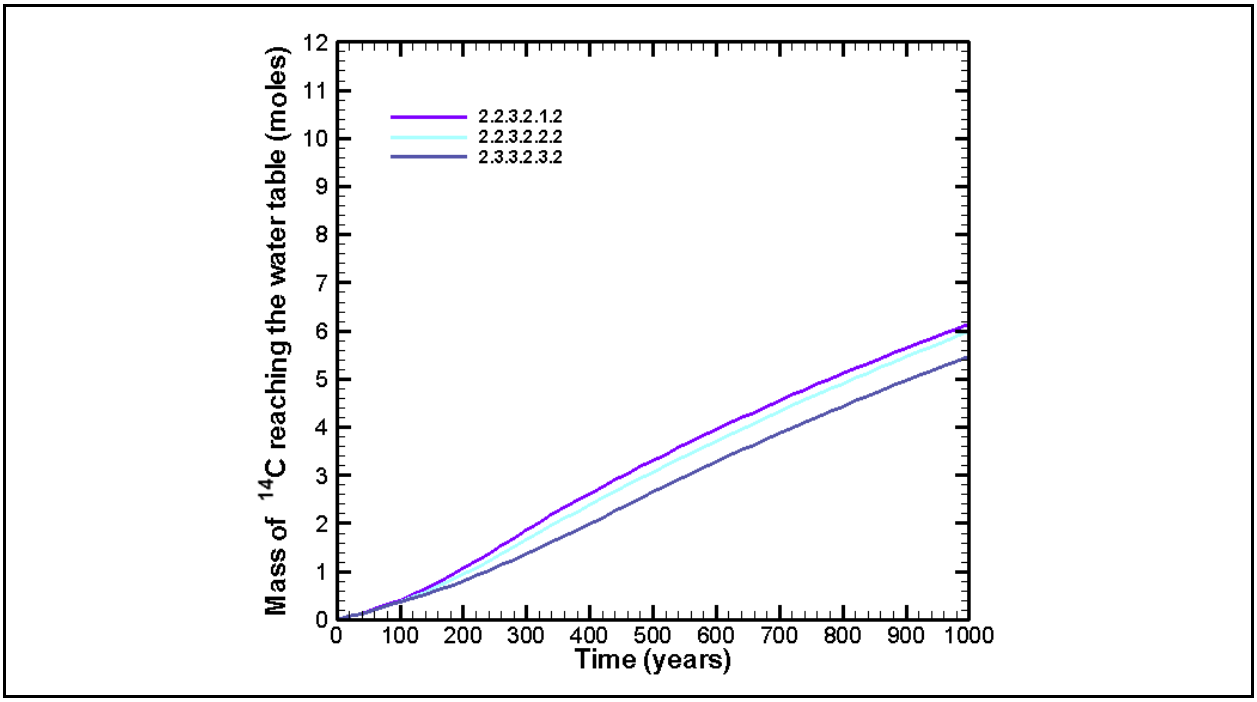

Figure 3-38
Cumulative Mass Arrival of ^{14}C at the Water Table—Effect of Tuff Confining Unit Anisotropy (k_v/k_h)

units between the detonations and the water table is thin or absent at most detonation locations that produce ^{14}C transport to the water table.

3.6.3.8 Effect of Collapse Chimneys

The impact of collapse chimneys on ^{14}C mass arrival at the water table was modeled by changing the properties of the tuffs in the chimney region between the bottom of the sediments and above the working point of the detonations at the start of the 1,000-year transient simulations. The tuffs within the collapse chimney were assigned properties roughly equivalent to those assigned to faults (effective porosities of 0.01 and permeabilities of 1E-11 m^2) to reflect the rubblized nature of the tuffs following chimney collapse. This was intended to allow for the faster movement of crater infiltration through the chimney collapse region and for the drainage of any perched water that may have been present above the working point prior to testing.

The impact of collapse chimneys in the tuffs was examined by comparing the results from four model runs that both included and ignored the presence of collapse chimneys under a range of assumed background and crater infiltration rates, exchange volume radii, and tuff confining unit anisotropy

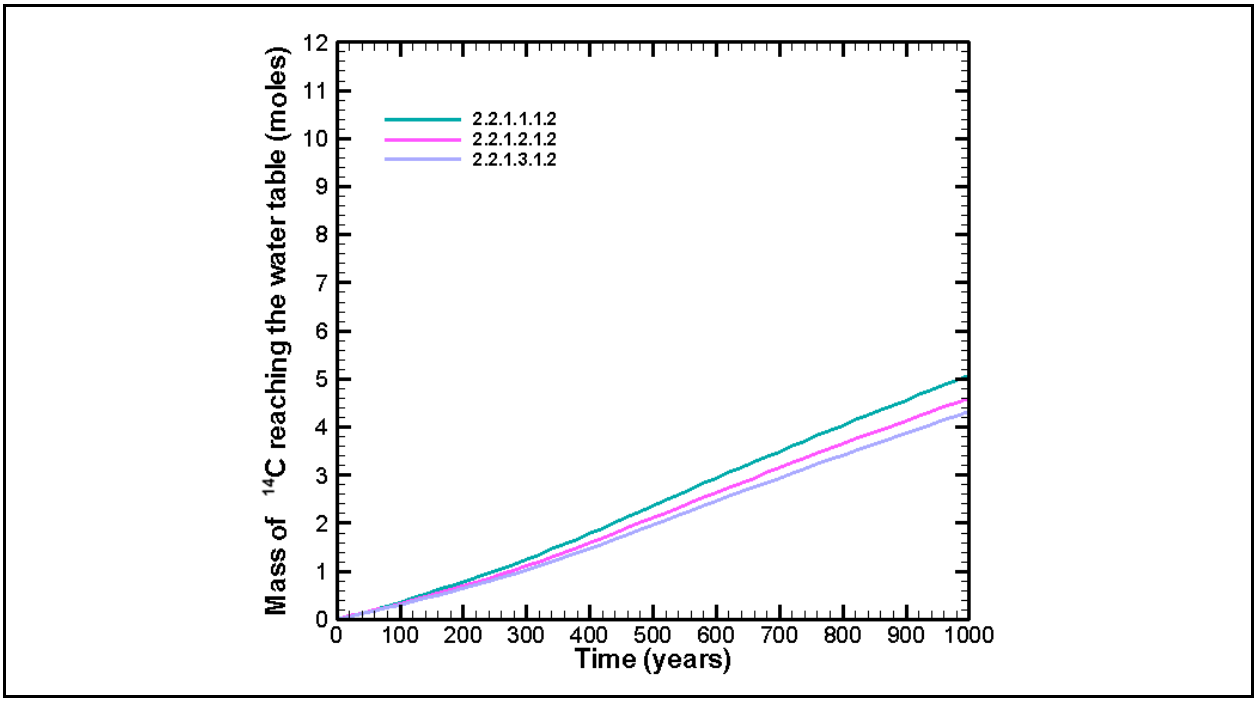

Figure 3-39
Cumulative Mass Arrival of ^{14}C at the Water Table—Effect of Tuff Confining Unit Transport Porosity

ratios (Figure 3-40). Excluding run 1.3.1.2.3.3, the presence of collapse chimneys did result in some early breakthrough relative to the results from the same run without the collapse chimney present. However, the effect of high-permeability, low-porosity collapse chimneys is small relative to the total variability in the results due to other factors. The small impact of including a collapse chimney in the tuffs above the working point again reflects the thinness or absence of tuffs above most unsaturated-zone detonations, as well as the absence of extensive perched water regions beneath Yucca Flat.

3.6.4 Estimation of Mass Arrival at the Water Table for Other Radionuclides

Figures 3-41 and 3-42 show the cumulative mass of radionuclides reaching the water table in the volcanic/alluvial aquifers and in the lower carbonate aquifer for model runs 2.1.1.2.1.2 and 2.1.3.2.1.2. As discussed in Section 3.5.2.2, only ^{14}C and ^{3}H were directly simulated in the unsaturated-zone models. All other radionuclides were estimated from simulated mass of ^{14}C reaching the water table using the relative mass of that radionuclide to ^{14}C in the Bowen et al. (2001) unclassified inventory for Yucca Flat, adjusted to account for differences in their radioactive half-lives and their melt-glass fractions. For both model runs, roughly an order of magnitude more ^{14}C

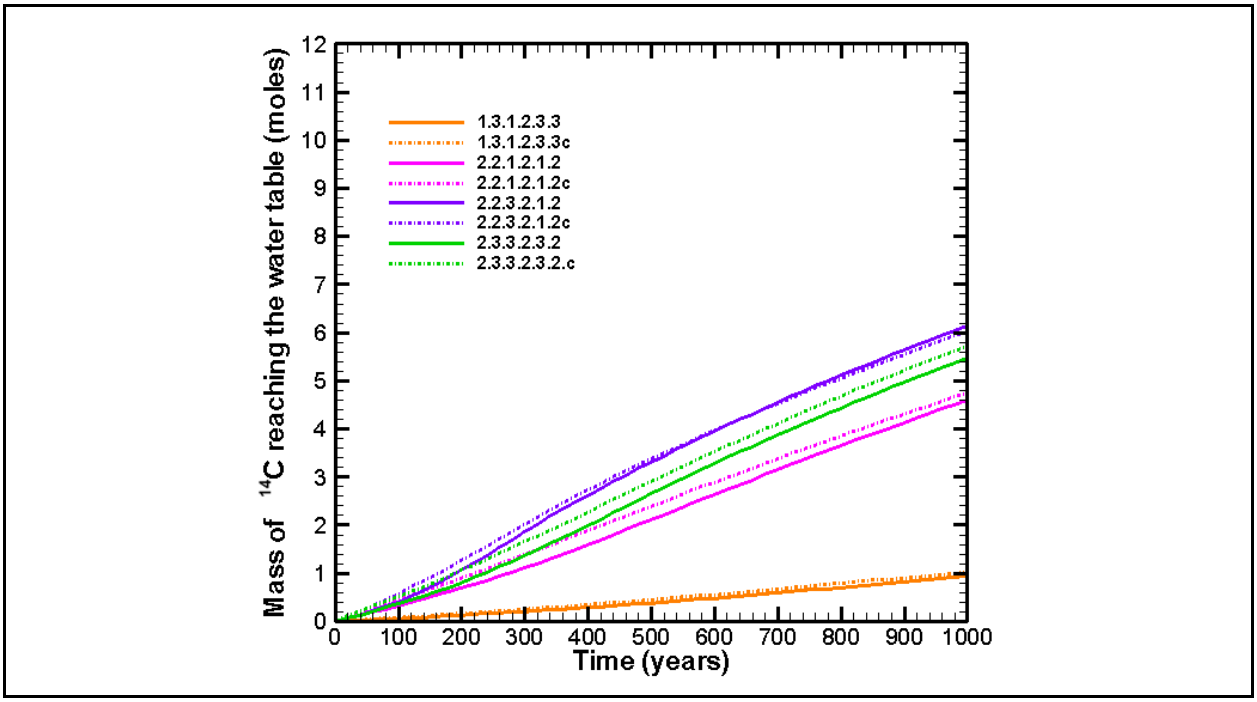

Figure 3-40
Cumulative Mass Arrival of ^{14}C at the Water Table—Effect of Collapse Chimneys

reaches the water table in the volcanic and alluvial aquifers than reaches the water table in the lower carbonate aquifer directly, and the other radionuclides scale proportionately. This is directly a consequence of the fact that most of the detonations were conducted in the center of the basin within or above the saturated volcanic rocks (Figure 3-2), whereas fewer detonations were conducted on the periphery of the basin above the LCA. Also noteworthy is the fact that ^{3}H in both model runs peaks at about 50 years, after which time relatively little additional ^{3}H arrives at the water table because of its short half-life (12.3 years).

Despite the fact that a far larger number of moles of uranium are estimated to reach the water table than any other radionuclide, it is the concentration of the radionuclide relative to its SDWA regulatory limit that determines if and where a radionuclide contaminates the groundwater from a regulatory perspective. The following sections show to what extent individual radionuclides present a contamination problem based on their regulatory limits.

3.6.5 Maps Showing Breakthrough of Selected Radionuclides at the Water Table

The following maps show the locations of radionuclide arrivals at the water table over time. In keeping with the concentration conventions established earlier, concentrations shown in red are at or above the regulatory limit (4 mrem/yr or the molar equivalent for beta-emitting

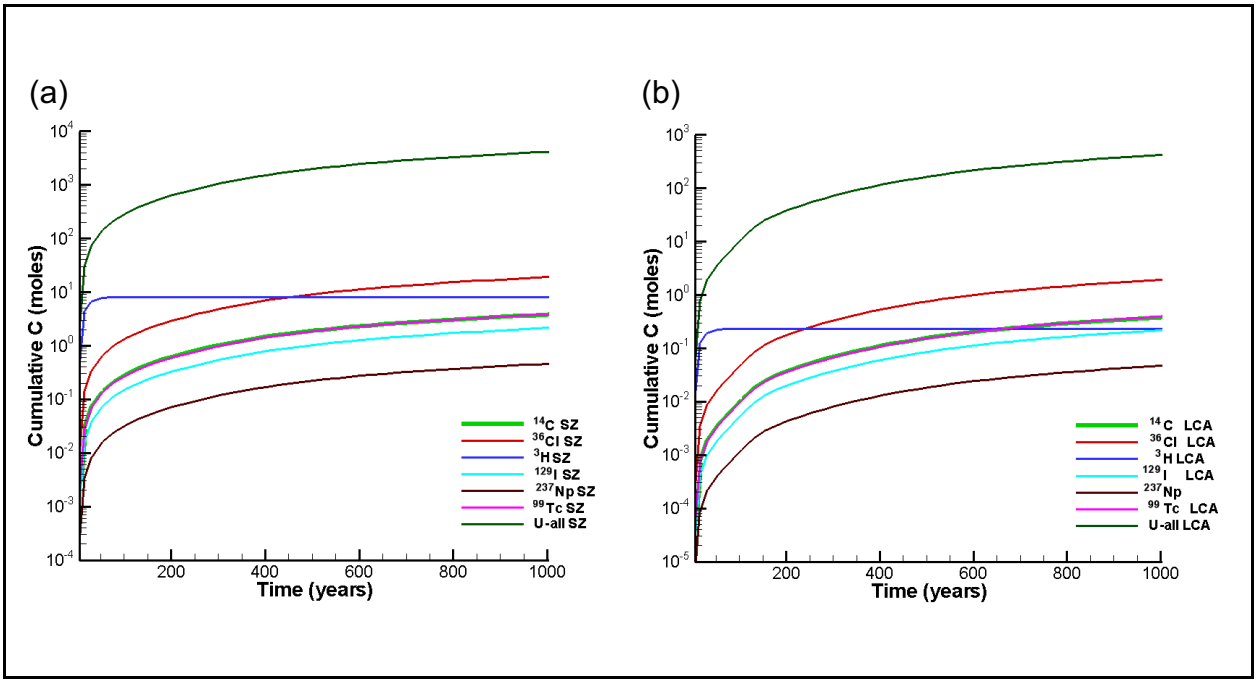

Figure 3-41
Cumulative Mass Arrival at the Water Table for Run 2.1.1.2.1.2
(a) to Volcanic Rocks and (b) to the LCA

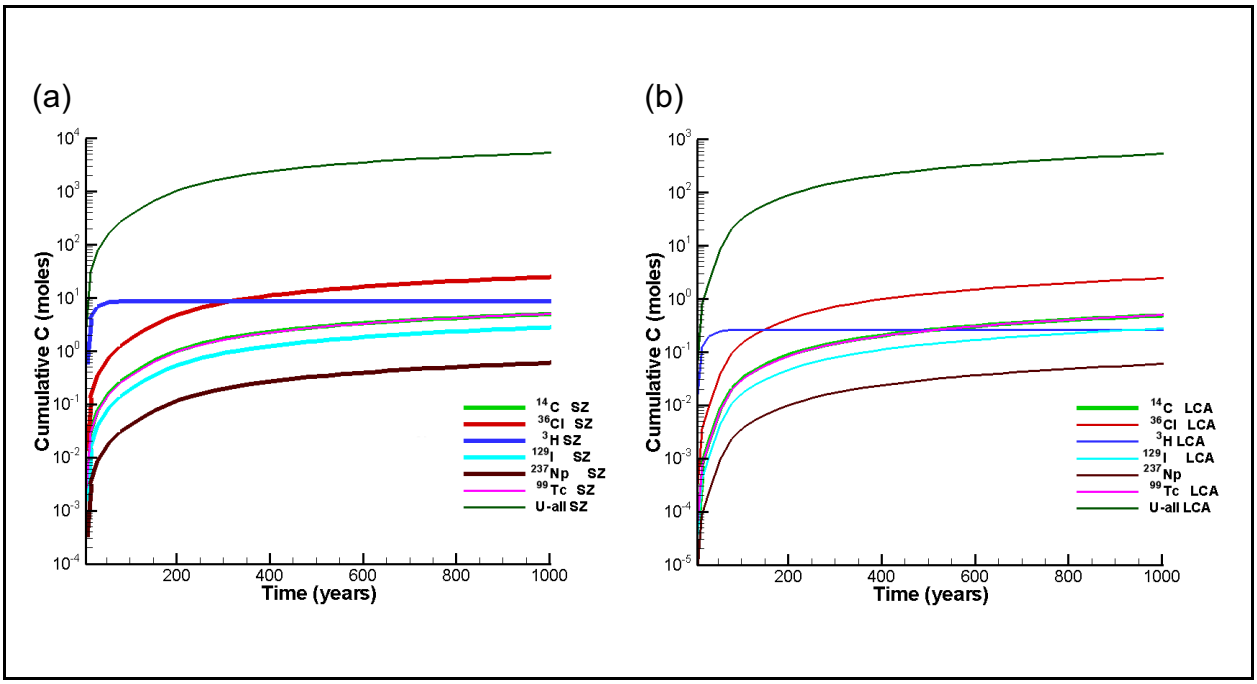

Figure 3-42
Cumulative Mass Arrival at the Water Table for Run 2.1.3.2.1.2
(a) to Volcanic Rocks and (b) to the LCA

radionuclides or 30 µg/L for uranium) and all other concentrations shown are within three orders of magnitude of the regulatory limit. Also shown in each figure is the outline of the saturated alluvial/volcanic aquifer system model that separates the outer areas of the map where radionuclides enter the LCA or LCA3 directly from inner areas where radionuclides must first pass through volcanic rocks. The water table concentrations were calculated directly in the unsaturated-zone model using the advection-dispersion equation.

3.6.5.1 Model Run 2.1.1.2.1.2

The concentrations of ^{14}C, ^{36}Cl, ^{129}I, ^{3}H, ^{99}Tc, ^{237}Np, and U in recharge arriving at the water table are shown in Figures 3-43 to 3-49 for model run 2.1.1.2.1.2 at various times during the 1,000-year transient simulation. The maps support the statement made earlier in connection with Figures 3-41 and 3-42 that most of the radionuclide mass arrives at the water table in the volcanic rocks and alluvium. An interesting feature of these maps is that only locations where the radionuclide concentrations are initially above the regulatory limit also exceed the limit at later times during the simulation. The fact that regulatory limits are exceeded at the very beginning of the simulation in some locations indicates that these are locations where the exchange volume intersects the water table. Although ^{14}C, ^{36}Cl, and ^{129}I reach the water table at many other locations over the course of the simulation, they reach the water table at concentrations that are below their individual regulatory limits (though they still may, in combination, exceed the regulatory limit of 4 mrem/yr for beta-emitting radionuclides). This is because each radionuclide's mass is initially distributed within the pore water of the exchange volume, and this water undergoes a significant amount of mixing and dilution from the radionuclide-free water infiltrating downward through the crater bottom and chimney system that eventually flushes the radionuclides in the exchange volume toward the water table.

Tritium (^{3}H) is slightly different from the other radionuclides in that there are locations where recharge concentrations exceed the SDWA standard for beta-emitting radionuclides that are not associated with exchange volumes that intersect the water table (Figures 3-46a and b). These tend to be located above carbonate aquifers on the perimeter of the basin where subsidence craters can have relatively large watersheds and infiltration rates. The difference between ^{3}H and other radionuclides is due to the fact that ^{3}H in the exchange volume tends to have concentrations that are several orders of magnitude greater than the SDWA standard (Section 2.0), so that even significant dilution by crater infiltration does not decrease the ^{3}H concentrations in recharge to levels below the SDWA standard.

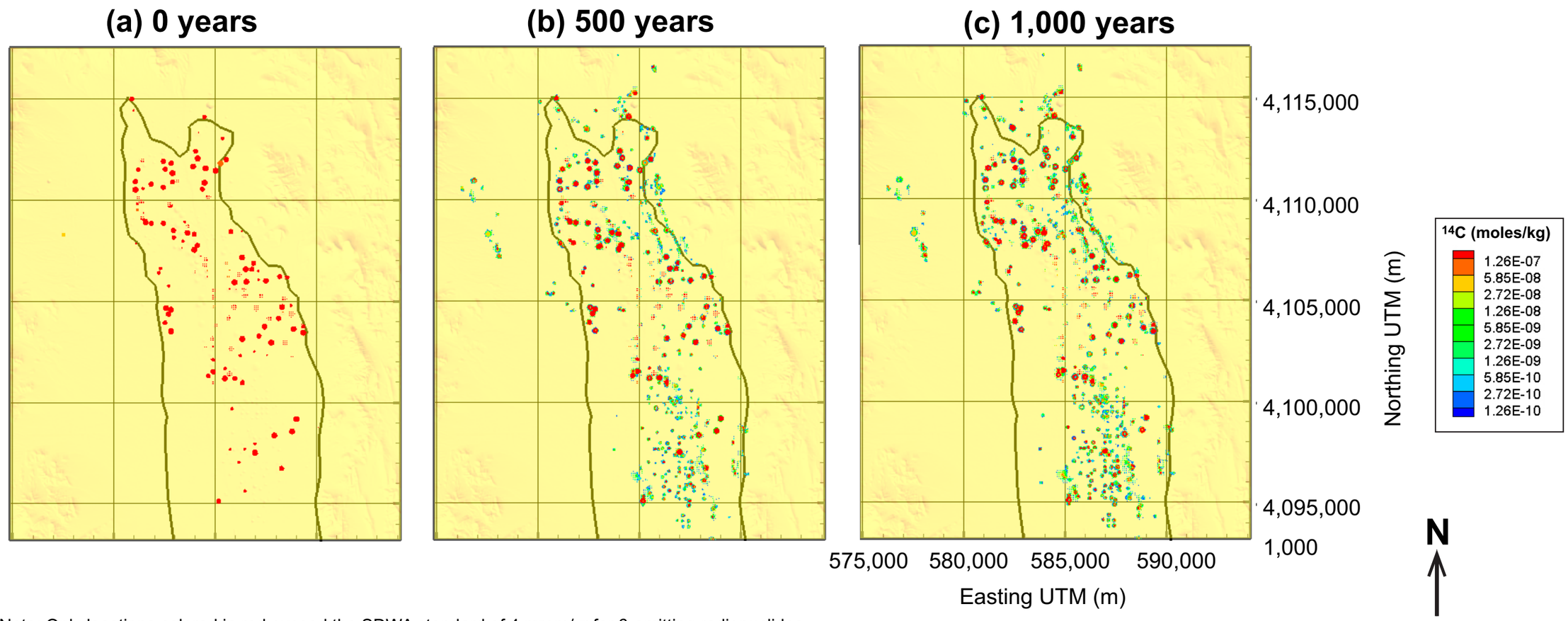

Note: Only locations colored in red exceed the SDWA standard of 4 mrem/yr for β-emitting radionuclides.
The outline of the saturated alluvial/volcanic system model is shown.

Figure 3-43
^{14}C Concentrations at the Water Table at Different Times for Case 2.1.1.2.1.2 (a) 0, (b) 500, and (c) 1,000 Years

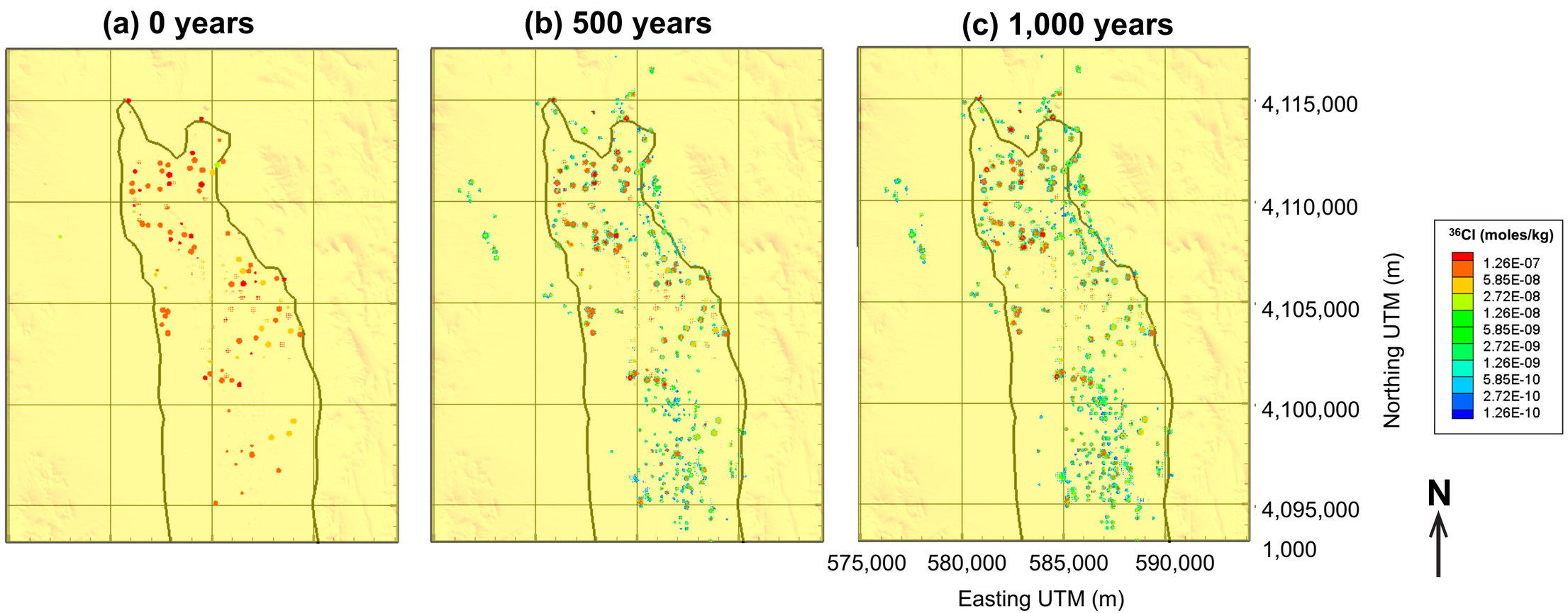

Note: Only locations colored in red exceed the SDWA standard of 4 mrem/yr for β-emitting radionuclides.
The outline of the saturated alluvial/volcanic system model is shown.

Figure 3-44
^{36}Cl Concentrations at the Water Table at Different Times for Case 2.1.1.2.1.2 (a) 0, (b) 500, and (c) 1,000 Years

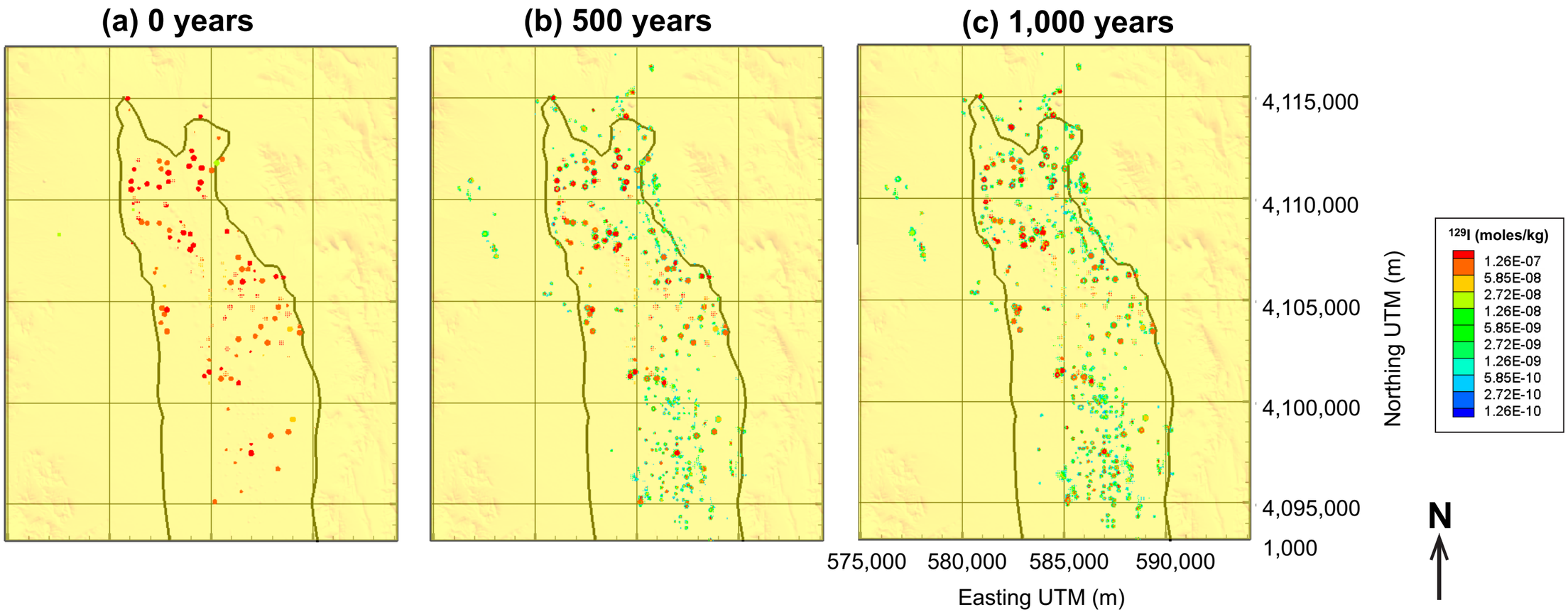

Note: Only locations colored in red exceed the SDWA standard of 4 mrem/yr for β-emitting radionuclides.
The outline of the saturated alluvial/volcanic system model is shown.

Figure 3-45
^{129}I Concentrations at the Water Table at Different Times for Case 2.1.1.2.1.2 (a) 0, (b) 500, and (c) 1,000 Years

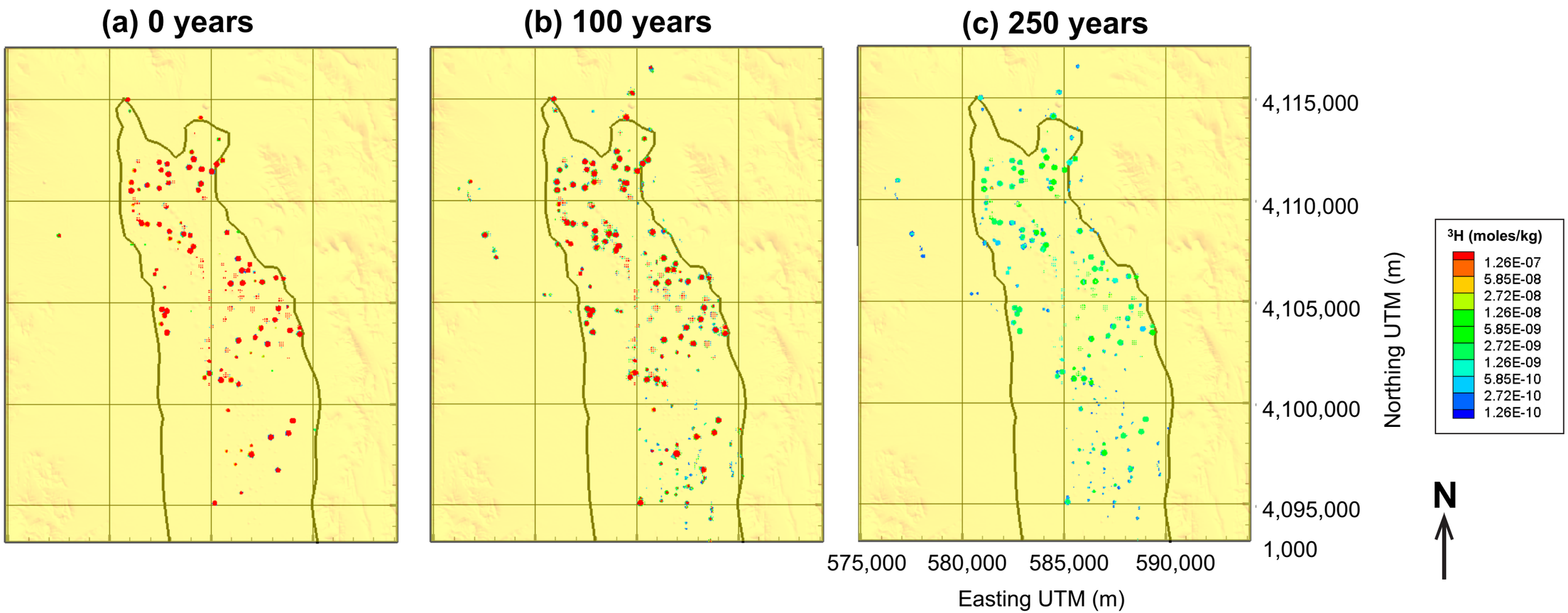

Note: Only locations colored in red exceed the SDWA standard of 4 mrem/yr for β-emitting radionuclides.
The outline of the saturated alluvial/volcanic system model is shown.

Figure 3-46
^{3}H Concentrations at the Water Table at Different Times for Case 2.1.1.2.1.2 (a) 0, (b) 100, and (c) 250 Years

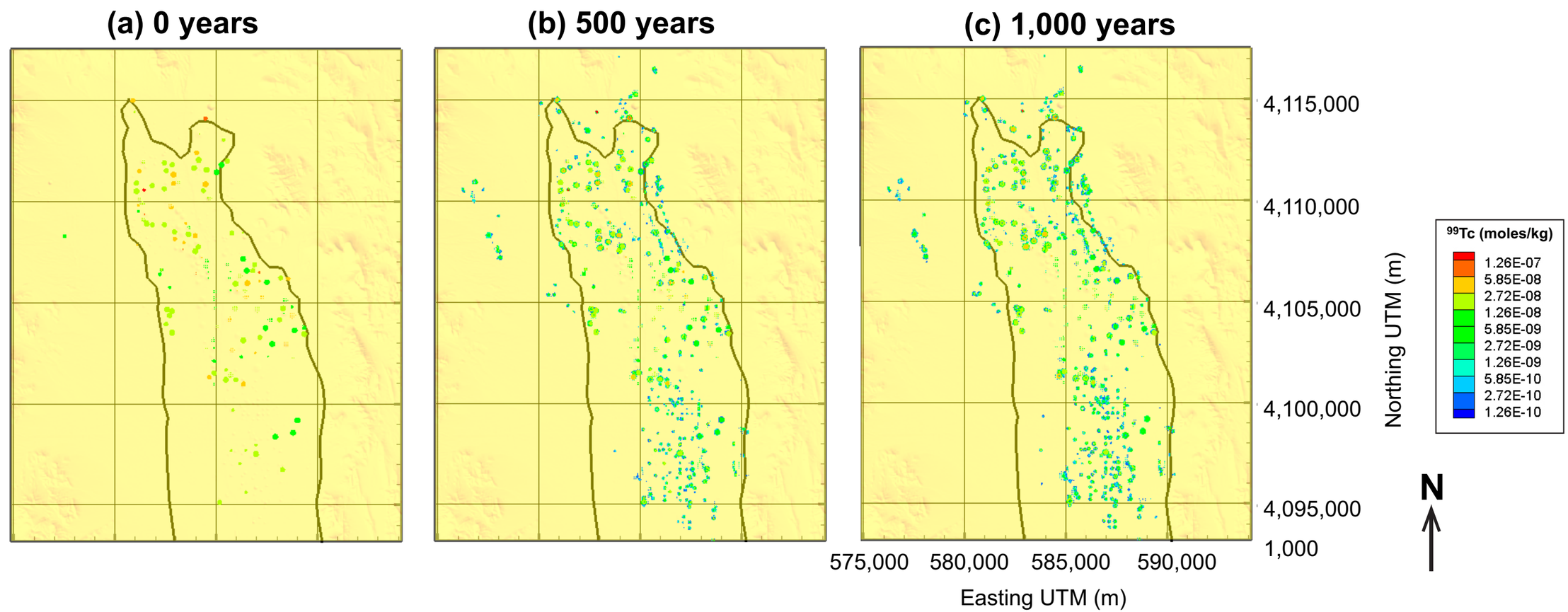

Note: Only locations colored in red exceed the SDWA standard of 4 mrem/yr for β-emitting radionuclides.
The outline of the saturated alluvial/volcanic system model is shown.

Figure 3-47
^{99}Tc Concentrations at the Water Table at Different Times for Case 2.1.1.2.1.2 (a) 0, (b) 500, and (c) 1,000 Years

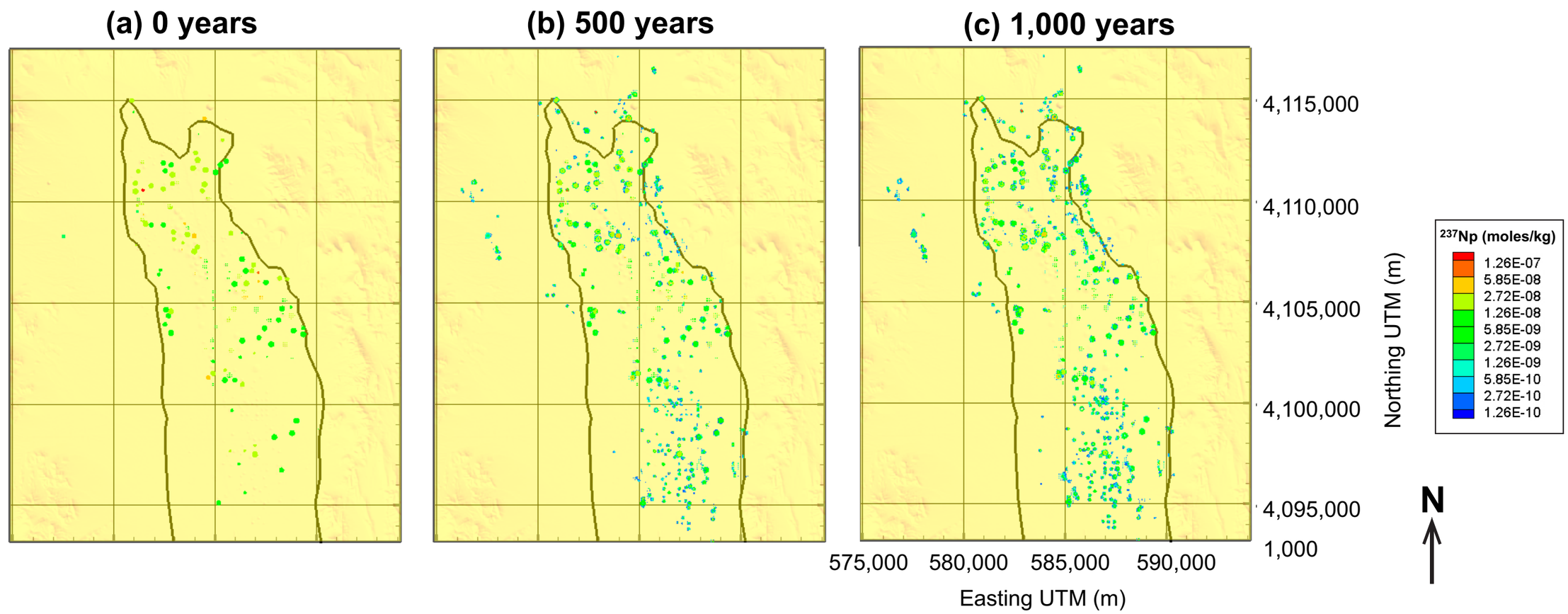

Note: Only locations colored in red exceed the SDWA standard of 4 mrem/yr for β-emitting radionuclides.
The outline of the saturated alluvial/volcanic system model is shown.

Figure 3-48
^{237}Np Concentrations at the Water Table at Different Times for Case 2.1.1.2.1.2 (a) 0, (b) 500, and (c) 1,000 Years

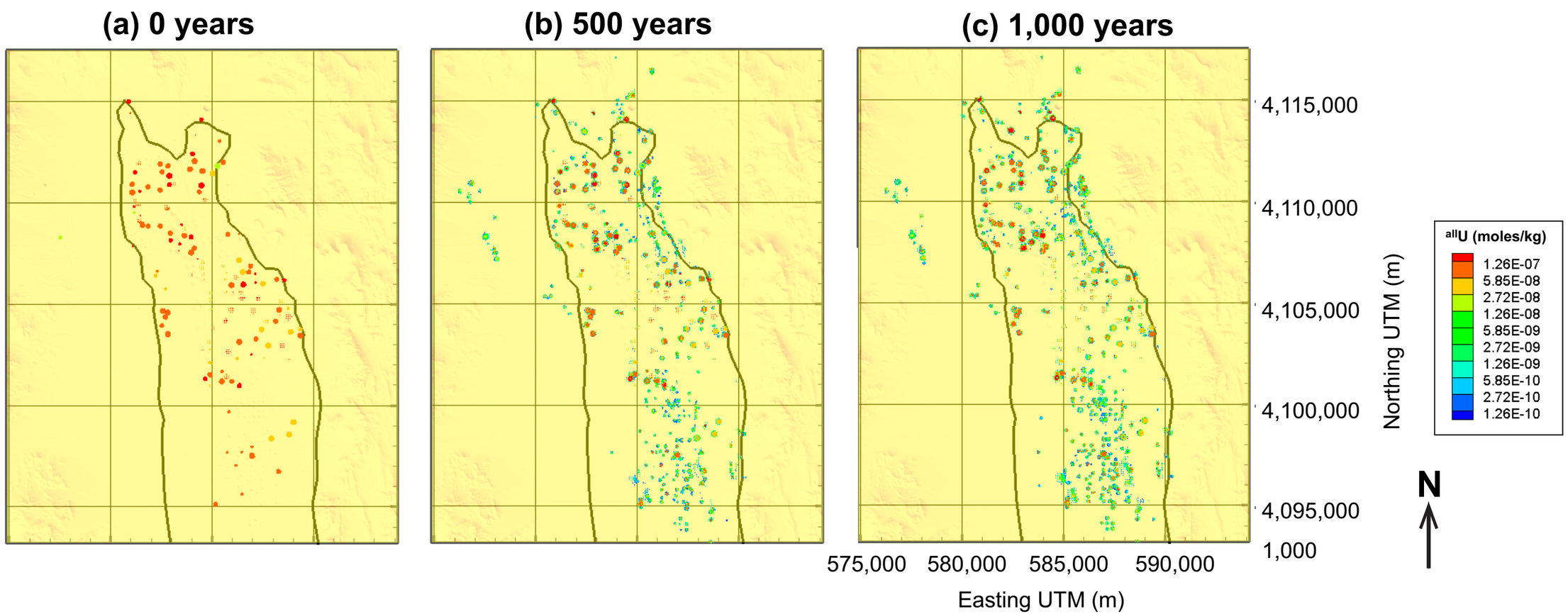

Note: Only locations colored in red exceed the SDWA standard of 4 mrem/yr for β-emitting radionuclides.
The outline of the saturated alluvial/volcanic system model is shown.

Figure 3-49
Total U Concentrations at the Water Table at Different Times for Case 2.1.1.2.1.2 (a) 0, (b) 500, and (c) 1,000 Years

Technetium-99 (^{99}Tc) concentration in recharge are shown in Figure 3-47. There are only three locations at the water table where initial ^{99}Tc concentrations exceed the 4-mrem/yr limit for beta-emitting radionuclides. All other initial water table concentrations as well as later recharge concentrations are below the 4-mrem/yr limit.

The concentrations of neptunium-237 (^{237}Np) at the water table are shown in Figure 3-48. ^{237}Np is an alpha-particle emitter with a regulatory limit of 15 pCi/L (which corresponds to a concentration of 8.98E-11 mol/L). Like ^{99}Tc, ^{237}Np is estimated to exceed the SDWA standard at a few scattered locations at the start of the transient simulation period, but almost all recharge at later times is below the regulatory limit for alpha emitters.

The concentrations of total uranium in recharge arriving at the water table are shown in Figure 3-49. Uranium is regulated based on its concentration rather than dose and has a 30-µg/L regulatory limit. Like several other radionuclide species, it exceeds its regulatory limit only at locations that are close to or intersect the water table.

3.6.5.2 Model Run 2.1.3.2.1.2

The distribution of ^{14}C, ^{36}Cl, ^{129}I, ^{3}H, ^{99}Tc, ^{237}Np, and U concentrations in recharge arriving at the water table are shown for model run 2.1.3.2.1.2 in Figures 3-50 to 3-56. These maps are quite similar in overall appearance to the maps for model run 2.1.1.2.1.2. However, Figure 3-36 shows that higher crater infiltration rates result in a greater cumulative mass of these radionuclides arriving at the water table after 100 years, though these subtle differences are not especially evident in maps of water table concentrations. Other observations and interpretations made in connection with model run 2.1.1.2.1.2 regarding the temporal and spatial distribution of radionuclide concentrations at the water table also pertain to the results of model run 2.1.3.2.1.2.

3.6.6 Water and Radionuclide Fluxes to the Saturated-Zone Models

One of the primary roles that the unsaturated-zone models play in the overall flow and transport modeling effort for Yucca Flat is to provide radionuclide and water fluxes to the saturated alluvial/volcanic aquifer system and LCA models. This required a substantial effort to identify which water table nodes in each of the 12 unsaturated-zone models mapped to which nodes at the top of each of the saturated-zone models. In general, the unsaturated-zone grids have as fine or finer grid resolution than either of the saturated-zone models. Therefore, one or more unsaturated-zone model

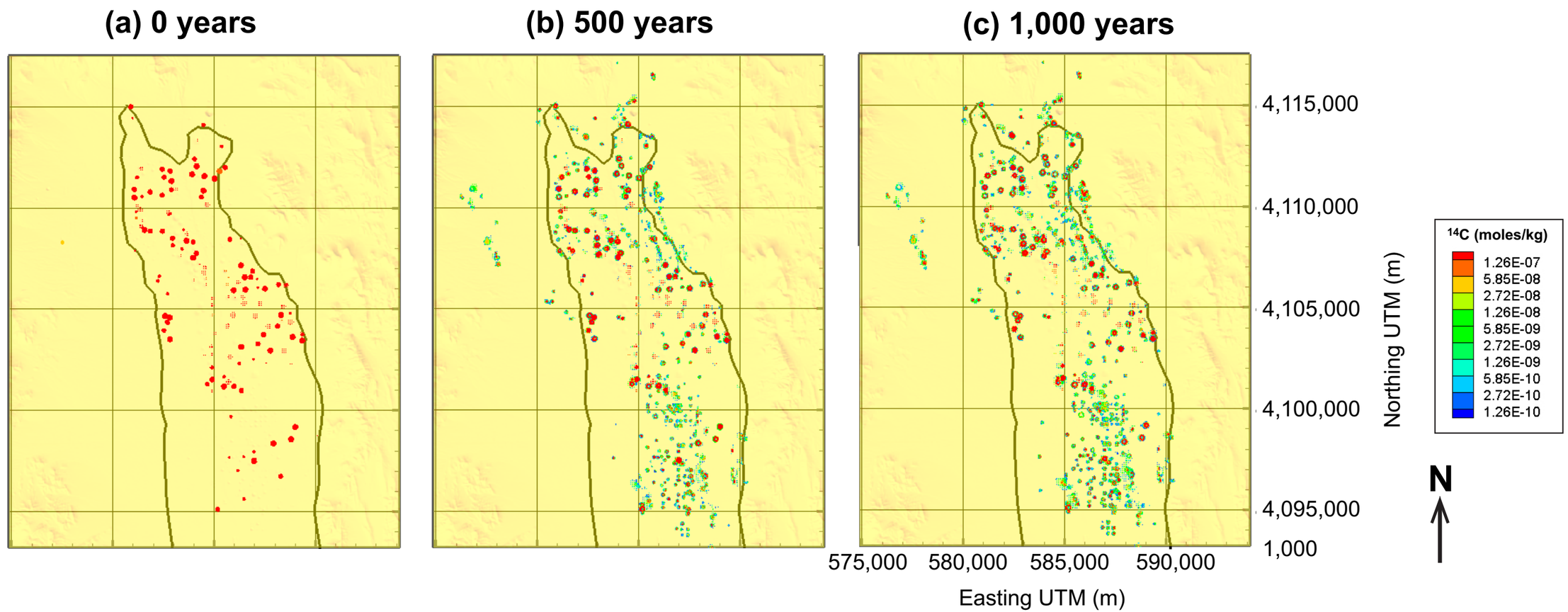

Note: Only locations colored in red exceed the SDWA standard of 4 mrem/yr for β-emitting radionuclides.
The outline of the saturated alluvial/volcanic system model is shown.

Figure 3-50
^{14}C Concentrations at the Water Table at Different Times for Case 2.1.3.2.1.2 (a) 0, (b) 500, and (c) 1,000 Years

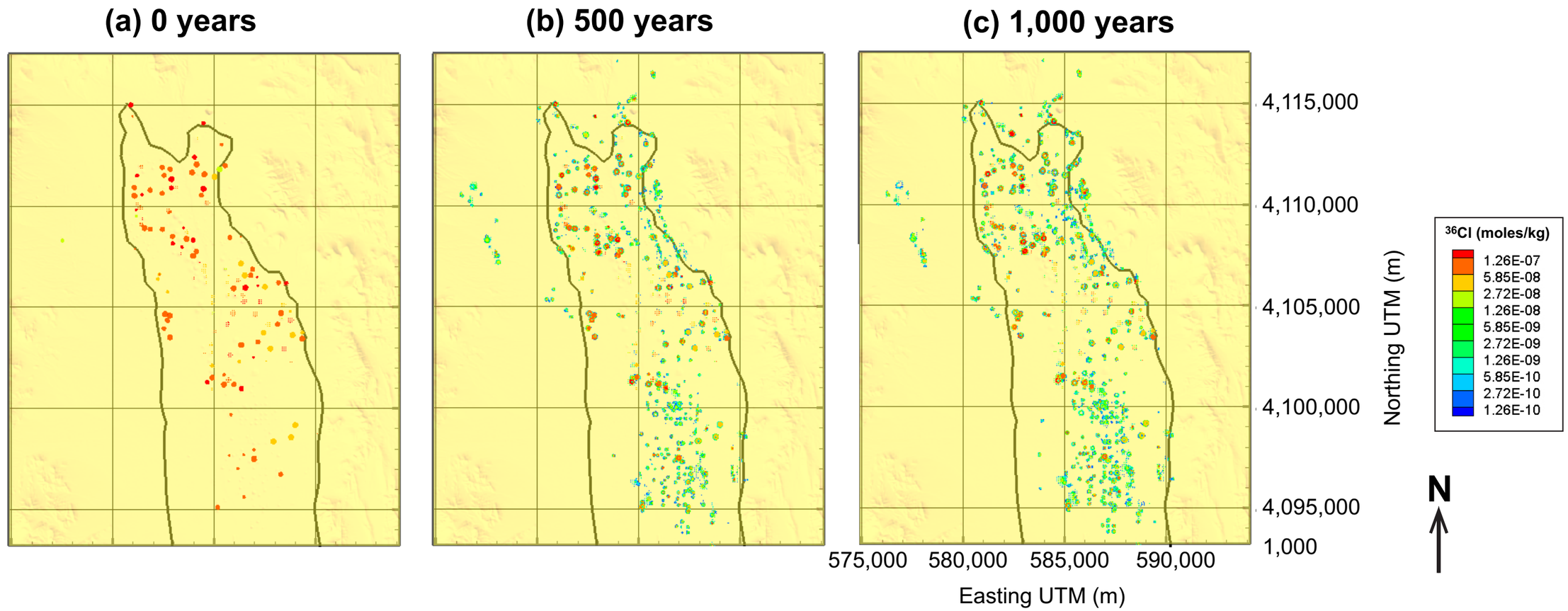

Note: Only locations colored in red exceed the SDWA standard of 4 mrem/yr for β-emitting radionuclides.
The outline of the saturated alluvial/volcanic system model is shown.

Figure 3-51
^{36}Cl Concentrations at the Water Table at Different Times for Case 2.1.3.2.1.2 (a) 0, (b) 500, and (c) 1,000 Years

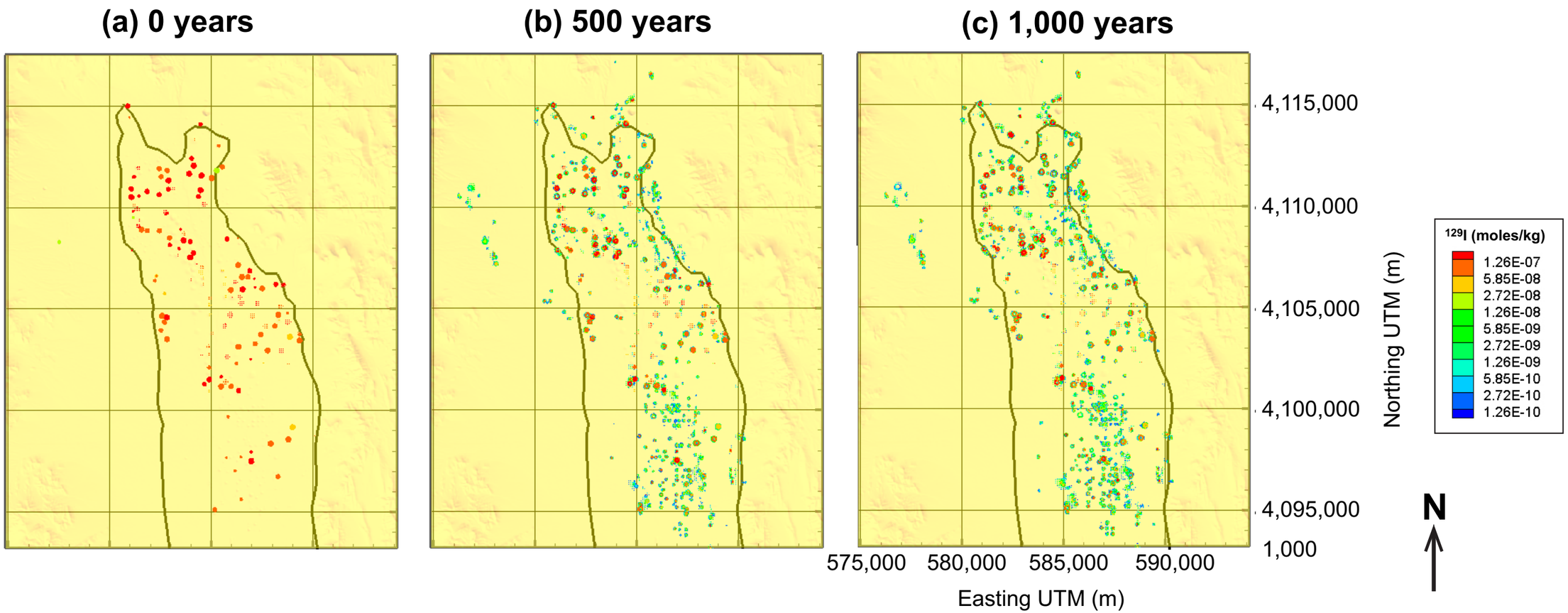

Note: Only locations colored in red exceed the SDWA standard of 4 mrem/yr for β-emitting radionuclides.
The outline of the saturated alluvial/volcanic system model is shown.

Figure 3-52
^{129}I Concentrations at the Water Table at Different Times for Case 2.1.3.2.1.2 (a) 0, (b) 500, and (c) 1,000 Years

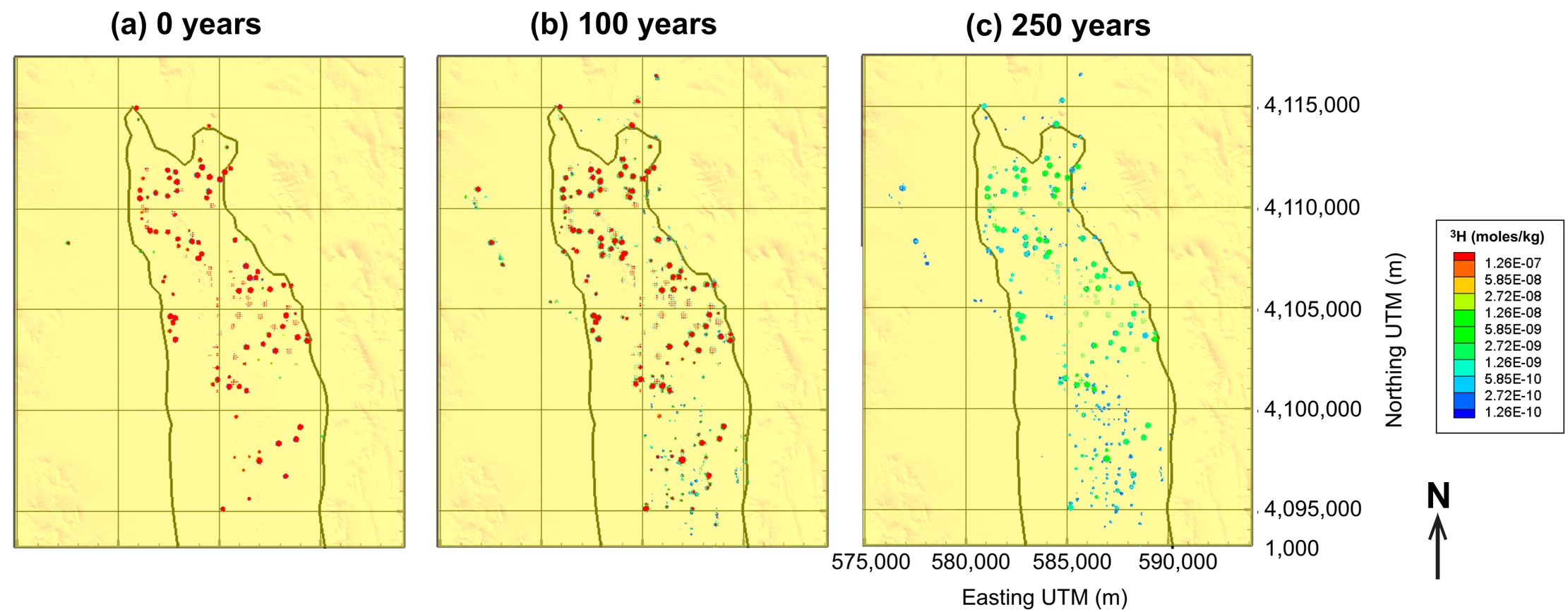

Note: Only locations colored in red exceed the SDWA standard of 4 mrem/yr for β-emitting radionuclides.
The outline of the saturated alluvial/volcanic system model is shown.

Figure 3-53
^{3}H Concentrations at the Water Table at Different Times for Case 2.1.3.2.1.2 (a) 0, (b) 100, and (c) 250 Years

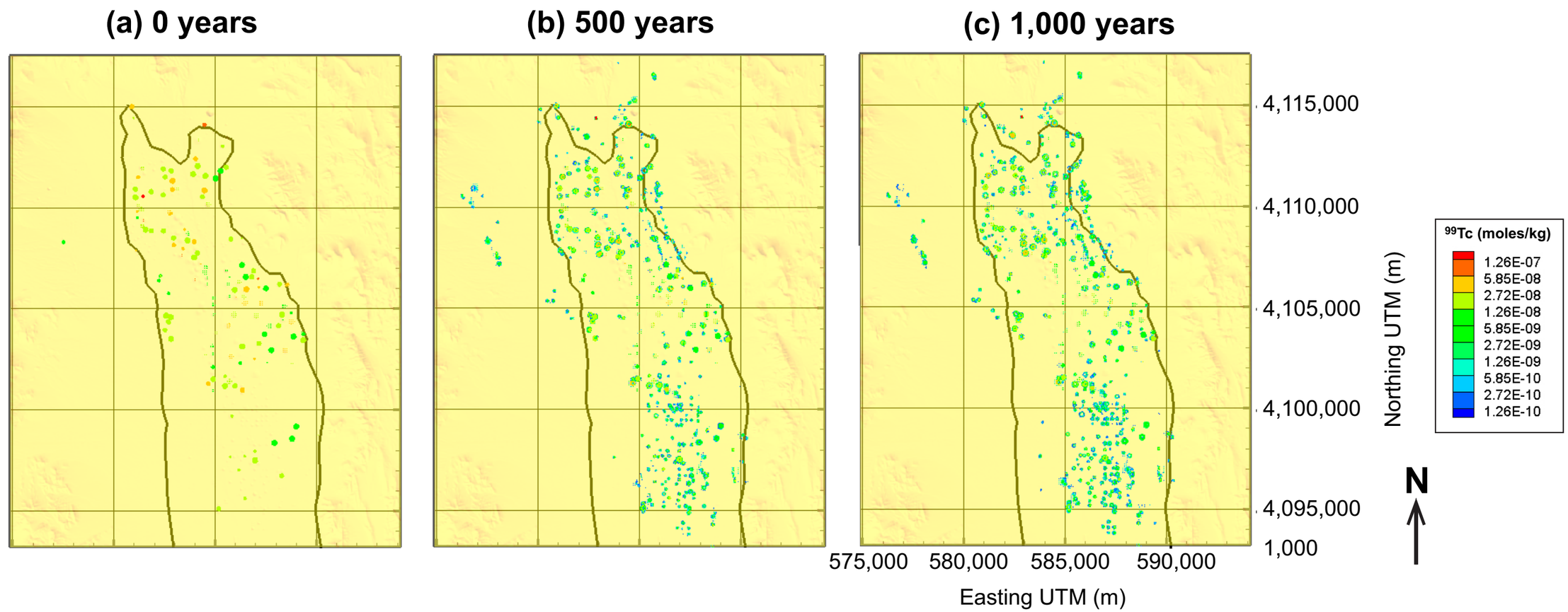

Note: Only locations colored in red exceed the SDWA standard of 4 mrem/yr for β-emitting radionuclides.
The outline of the saturated alluvial/volcanic system model is shown.

Figure 3-54
^{99}Tc Concentrations at the Water Table at Different Times for Case 2.1.3.2.1.2 (a) 0, (b) 500, and (c) 1,000 Years

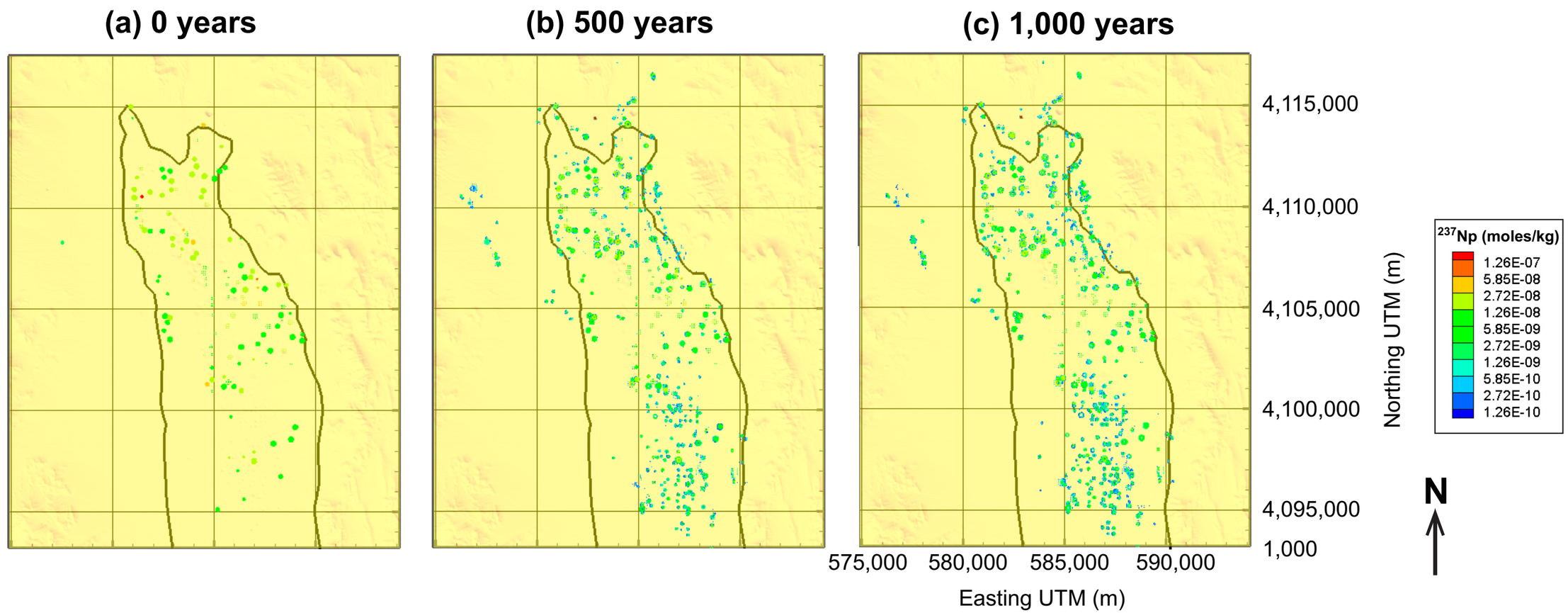

Note: Only locations colored in red exceed the SDWA standard of 4 mrem/yr for β-emitting radionuclides.
The outline of the saturated alluvial/volcanic system model is shown.

Figure 3-55
^{237}Np Concentrations at the Water Table at Different Times for Case 2.1.3.2.1.2 (a) 0, (b) 500, and (c) 1,000 Years

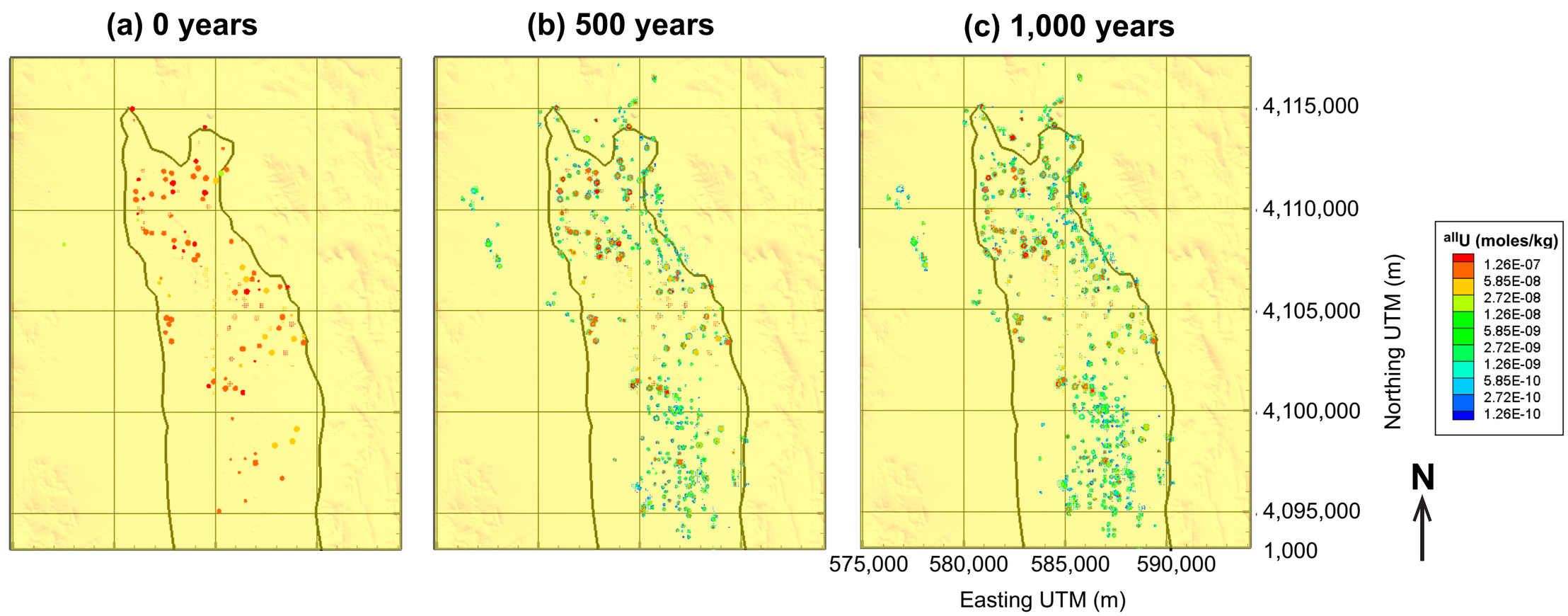

Note: Only locations colored in red exceed the SDWA standard of 4 mrem/yr for β-emitting radionuclides.
The outline of the saturated alluvial/volcanic system model is shown.

Figure 3-56
Total U Concentrations at the Water Table at Different Times for Case 2.1.3.2.1.2 (a) 0, (b) 500, and (c) 1,000 Years

nodes contributes water and radionuclide mass to a single saturated-zone model node (Figure 3-57). For steady-state flow, a FEHM *flow* macro was created for the saturated alluvial/volcanic aquifer system and LCA models in which each node at the top of the saturated-zone models was assigned the mass flux of water contributed by overlying nodes in the unsaturated-zone model. For transient flow, the water fluxes from the contributing nodes in the unsaturated-zone model were summed and assigned to the corresponding nodes in the saturated-zone models as function of time using the *boun* macro in FEHM. A separate table (or "model") in the *boun* macro was created for each node at the top of the saturated-zone models so that transients in flow due to crater infiltration could be represented for the 1,000-year regulatory period.

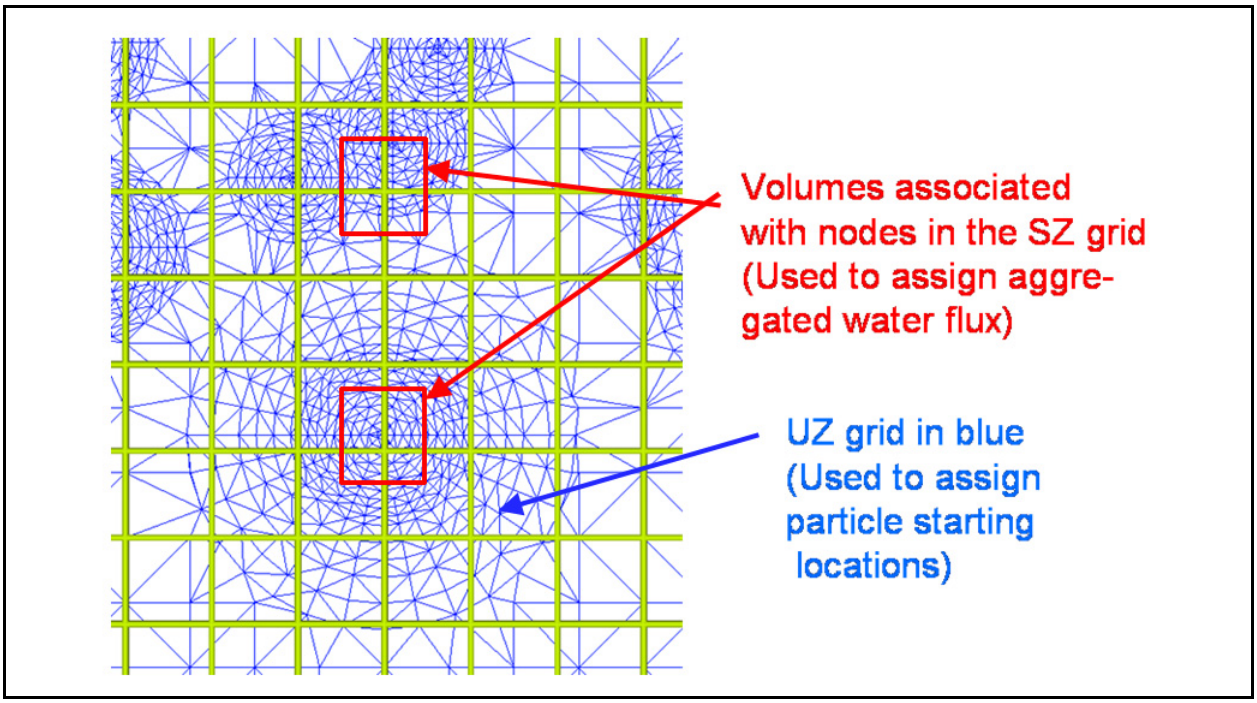

Figure 3-57
Schematic Diagram Showing How Multiple Nodes in the More Refined Unsaturated-Zone Grid Map onto a Single Node in the Coarser Saturated-Zone Model Grid

One limitation of the unsaturated-zone model grids is that they were not designed to accommodate crater recharge models for nuclear detonations whose working points were beneath the water table. Hence, water table nodes in the saturated-zone models beneath those craters did not have water flux histories that included the effects of transient infiltration into those craters. Of the 76 detonations with working points in the saturated zone, 64 had craters. Neglecting enhanced crater infiltration for the saturated-zone detonations is acceptable given that most of the radionuclide source associated with

these detonations is already in the saturated zone, and the great depth of these detonations (greater than 500 m bls) means that wetting fronts from crater infiltration would not arrive at the working points for several hundred years, long after short-lived radionuclides had decayed below levels of regulatory concern.

The unsaturated-zone models also produced a radionuclide flux versus time history for each node at the top of the saturated alluvial/volcanic aquifer system and saturated LCA models. Nodal radionuclide fluxes histories were calculated by multiplying the water flux in kg/s by the radionuclide concentration in mol/kg at multiple times throughout the 1,000-year regulator period. These radionuclide flux versus time histories were used by the saturated alluvial/volcanic aquifer system and saturated LCA models, along with PLUMECALC and the streamline particle tracking (sptr) methods in FEHM or with the Walkabout (Painter, 2011) particle-tracking code, to calculate radionuclide concentrations in the alluvial/volcanic aquifer system and LCA saturated-zone models. To help focus modeling efforts in the saturated-zone models on radionuclide fluxes likely to impact the contaminant boundary, only saturated-zone model nodes for which the aggregated concentrations exceeded one-thousandth of the MCL for any of the seven tracked radionuclides (^{3}H, ^{14}C, ^{36}Cl, ^{99}Tc, ^{129}I, ^{237}Np, or total U) were assigned a radionuclide flux history file. The saturated-zone modeling teams then made a determination regarding how to distribute the particles within the volume associated with each water table node (see, for example, Section 4.6.2).

Model outputs from 7 of the 28 unsaturated-zone models runs listed in Table 3-8, plus an additional case described in Section 3.8.2 (run 5.4.2.1.2.1), have been incorporated as inputs to the saturated alluvial/volcanic aquifer system model to test the effects of uncertainty in hydraulic and transport parameters, and the impacts of alternative testing effects conceptual models on radionuclide releases from the exchange volume. These included the following model runs:

- 1.2.1.2.1.2—representative of a low radionuclide mass flux from the unsaturated zone
- 2.1.1.2.1.2—representative of a medium radionuclide mass flux from the unsaturated zone
- 2.2.3.2.1.1—representative of a high radionuclide mass flux from the unsaturated zone (and small exchange volume case)
- 2.2.3.2.1.2—medium exchange volume case
- 2.2.3.2.1.3—large exchange volume case

- 2.3.1.2.3.2—highly anisotropic case (small k_v/k_h)
- 3.2.1.2.1.2—high background flux/permeability case
- 5.4.2.1.2.1—representative of a very low background infiltration case (0.1 mm/yr)

Of the eight sets of unsaturated-zone model output that were propagated through the saturated alluvial/volcanic aquifer system model, three sets were also used as direct inputs to the saturated-zone LCA flow and transport model where radionuclides from the unsaturated zone leaked directly into saturated, carbonate rock. Inputs to the LCA model from these three unsaturated-zone model runs were used to examine the impact of hydrologic and transport parameter uncertainty in the LCA model on the transport of radionuclides from the detonations with working points in the unsaturated zone. These three model runs included the following:

- 5.4.2.1.2.1—representative of very low infiltration case (0.1 mm/yr)
- 1.2.1.2.1.2—representative of medium radionuclide mass flux from the unsaturated zone
- 2.2.3.2.1.2—representative of high radionuclide mass flux from the unsaturated zone

The development of the low radionuclide mass flux case is described in Section 3.8.2. As discussed in Section 3.8.2, run 5.4.2.1.2 was developed to be consistent with most infiltration maps developed for Yucca Flat, which show negligible infiltration through the alluvium in the center of the basin.

3.6.7 Model Limitations

The unsaturated-zone models for Yucca Flat contain a number of known limitations. First, the models do not have grid refinement at craters and in collapse chimneys associated with detonations with working points below the water table. This affects the results of the unsaturated-zone model where detonations with working points below the water table have part of their exchange volumes in the unsaturated zone. The unsaturated-zone grids do not have the resolution to accurately model the movement of the radionuclide mass projected upward from detonations beneath the water table. However, because the radionuclide mass associated with these detonations is less than 1 percent of the radionuclide mass in the unsaturated-zone models, the effect of this conceptualization is small, especially in view of the fact that most of the mass associated with these detonations is already in the saturated-zone models where grids are adequately refined. In model runs presented in Section 3.8 that use new source-term concepts, this fraction of the inventory was applied directly to the top of the saturated-zone models. The absence of grid refinement near craters and chimneys of detonations with

working points beneath the water table also makes it impossible to accurately model crater infiltration above the saturated-zone detonations. Crater infiltration rates estimated for these detonations could be applied directly to the top of the saturated-zone models after allowing for a time delay through the unsaturated zone.

A second known limitation is that the unsaturated-zone models make use of an "effective porosity" concept to model radionuclide transport through fractured media rather directly model fracture/matrix exchange as in the saturated-zone models for the volcanic and carbonate rock. Faults, fractured-rock aquifers (tuffs and carbonate rock) and collapse chimneys each are assigned an effective porosity of 1 to 2 percent under the assumption that flow through fractures can be fast enough that only a small portion of the total matrix porosity is available to slow radionuclide movement. This approximation could tend to overestimate transport in welded-tuff aquifers and faults that cross the tuff confining units, where high matrix porosities and diffusion coefficients might result in greater attenuation than considered through these small effective porosities.

A third known limitation of the models is that liquid/gas partitioning of some radionuclides such as ^{14}C can result in accelerated diffusive transport in the gas phase. An attempt was made to investigate the transport of ^{14}C when gas/liquid partitioning according to Henry's law was involved. However, only partial success was possible for this computationally demanding simulation (see Section 3.7).

Fourth, the nonlinear nature of the equations governing unsaturated flow combined with the use of highly resolved grids that could represent both the complex hydrogeology and the near-field testing environment resulted in long computer run times. The long run times prevented a more complete analysis of the effects of parameter uncertainty on transport with traditional Monte Carlo approaches. The sensitivity analysis probably spanned the range of outcomes that would have been produced with a Monte Carlo analysis.

3.7 Evaluation of the Impact of Liquid-Gas Partitioning of ^{14}C and Sediment Heterogeneity on Radionuclide Transport

The model runs presented in the earlier sections of this report did not consider the impact of gas-phase partitioning of ^{14}C on its transport to the water table, allowing its use as a liquid tracer from which the concentrations of other radionuclide species could be estimated based on their relative mass in the Yucca Flat radionuclide inventory. However, SNJV (2009b) has demonstrated

that liquid-gas partitioning of ^{14}C is an important process affecting its concentration and arrival time at the water table. Section 3.7.1 examines the impact of this process on ^{14}C mass arrival times and concentration.

A second consideration addressed in this section is the likelihood that alluvium throughout the Yucca Flat basin has properties that are more variable than those represented in the models summarized in Table 3-8. In particular, sediments are, in general, likely to be more coarse-textured than the sands that dominate the alluvium in Area 3 near the RWMS, which formed the basis for the hydrologic property estimates applied to the alluvium in the models thus far. Section 3.7.2 examines the impact of hydrologic property variations on radionuclide arrival at the water table.

3.7.1 Effect of Liquid-Gas Partitioning on ^{14}C Transport to the Water Table

Simulations of ^{14}C transport described elsewhere in this report assume that ^{14}C migrates only in the liquid phase and that its movement is unaffected by sorption or exchange reactions with the soil or rock matrix. This idealized behavior was assumed earlier so that the movement of other radionuclides for which similar transport properties apply could be based on the ^{14}C simulation results. In fact, however, transport of ^{14}C in the gas phase and the possible sorption of ^{14}C to calcite in the soil are known to be important processes affecting ^{14}C transport in the unsaturated zone. For example, Walvoord et al. (2005) invoked gas- and liquid-phase transport as well as ^{14}C sorption in order to explain gas-phase ^{14}C profiles from boreholes penetrating the 110-m deep unsaturated zone at the USGS ADRS located 70 km southwest of Yucca Flat. Although the ^{14}C profile at the ADRS evolved under relatively unperturbed conditions as a result of ^{14}C moving downward from the soil zone and upward from groundwater de-gassing and calcite precipitation near the water table, SNJV (2009b) demonstrated how gas/liquid partitioning and sorption onto calcite would be likely to impact the transport of ^{14}C produced by nuclear detonations in the unsaturated-zone. The two-phase simulations performed by SNJV (2009b) demonstrated that when ^{14}C partitions and diffuses in the gas phase, peak ^{14}C concentrations arriving at the water table are reduced because ^{14}C is dispersed throughout a larger volume of the unsaturated zone and much of it spreads beyond the margins of the crater where it will not be entrained by infiltration moving downward through the crater bottom.

The impact of gas-phase partitioning of ^{14}C on its transport to the water table was examined in this study by comparing results from model run 2.2.1.2.1.1 both with and without gas/liquid partitioning. The partitioning of ^{14}C between the liquid and gas phases was modeled with Henry's law:

$$C_w = K_h \times P_{^{14}CO_2} \quad (3\text{-}4)$$

where C_w is the concentration of ^{14}C in the pore water (moles ^{14}C/kg H_2O), $P_{^{14}CO_2}$ is the partial pressure of $^{14}CO_2$ in the gas phase (atmospheres), and K_h is the Henry's law partitioning coefficient relating ^{14}C pore-water concentrations to $^{14}CO_2$ partial pressures. A value of 3.63E-03 mol ^{14}C kg^{-1} H_2O atm^{-1} was calculated by SNJV (2009b, p. 5-16) for a typical Yucca Flat groundwater composition assuming a pH of 7.0 and a temperature of 20 °C. This value is also used in the present study along with the effective liquid and gas-phase diffusivities of 4.12E-10 and 1.01 E-05 m^2 s^{-1} estimated for the alluvium by SNJV (2009b). The Millington-Quirk (1960) equation in FEHM is used to adjust these single-phase diffusivities to account for the effects of incomplete water or air saturations. The single-phase diffusivities estimated by SNJV (2009b) for alluvium were applied to all the HSUs in the model; any differences in the saturation-dependent values of air- and water-diffusivities for individual HSUs arose only because of differences in the saturations among the HSUs.

The two-phase Henry's law simulations proved to be computationally challenging and only 6 of the 12 grids ran to completion during the complete 1,000-year transient period (Figure 3-58). The effects of including Henry's law partitioning differed amongst the grids, producing considerably more transport of ^{14}C to the water table for grids 2 and 9, less ^{14}C transport to the water table in the case of grids 3, 5, and 6, and almost no differences in ^{14}C transport in the case of grid 1. The differences in behavior among the grids could be due to several factors, including (1) proximity of the detonations to the water table, which determines how quickly and at what concentration the ^{14}C in the gas phase reaches the water table, (2) whether a low-permeability layer with high water saturation and low gas-diffusivity lay between the detonation and the water table, and (3) whether crater infiltration rates are high and time for crater infiltration to reach the exchange volume are short relative to ^{14}C dilution by gaseous diffusion processes. The results shown in Figure 3-58 presumably integrate these effects over the many nuclear detonations in each grid.

Figures 3-59 and 3-60 show the effects of including Henry's law partitioning and gas-phase diffusion of ^{14}C on pore-water concentrations at the end of the 1,000-year transient simulation for grids 2 and 9. In both grids, gas/liquid partitioning and gas-phase diffusion promotes the outward spreading of ^{14}C from its initial distribution in the exchange volume with the result that pore water throughout much of the unsaturated zone has elevated ^{14}C concentrations. In contrast, without these processes, ^{14}C migrates downward with infiltrating water, but there is relatively little lateral or upward spreading

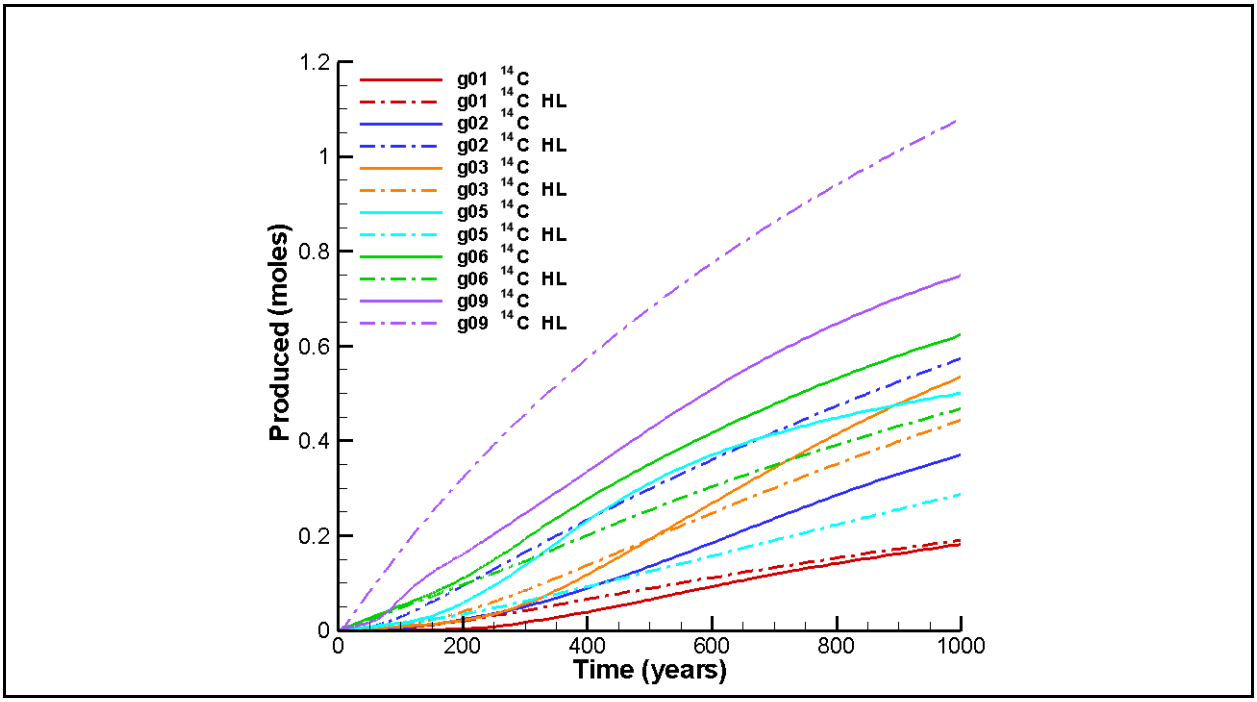

Figure 3-58
Effect of Henry's Law Partitioning of ^{14}C on Mass Transport to the Water Table in Grids 1, 2, 3, 5, 6, and 9 for Run 2.2.1.2.1.1

(compare the upper right and left panels of Figures 3-59 and 3-60). However, because gas-phase transport spreads ^{14}C throughout a much larger volume of the unsaturated zone, it generally dilutes the peak pore-water concentrations of ^{14}C relative to the case where transport occurs only in the liquid phase. This is evident from the lower right and left panels of Figures 3-59 and 3-60 which show that Henry's law partitioning and gas-phase diffusion of ^{14}C results in relatively few locations within the unsaturated zone where pore-water concentrations are greater the SDWA dose standard of 4 mrem/yr (equivalent to ^{14}C concentration of 3.21E-11 mol/L). This suggests that although a greater mass of ^{14}C reaches the water table in some cases when gas-phase transport is included, a smaller amount of the recharge has concentrations that are of regulatory concern. Therefore, the simulations presented in this report that ignore the effects of Henry's law partitioning and gas-phase diffusion tend to overestimate the impact of ^{14}C on the contaminant boundaries of the underlying aquifers. These results are consistent with those of SNJV (2009b), which looked at the combined effects of gas–water partitioning of $^{14}CO_2$ and sorption of liquid ^{14}C on ^{14}C transport to the water table in alluvium.

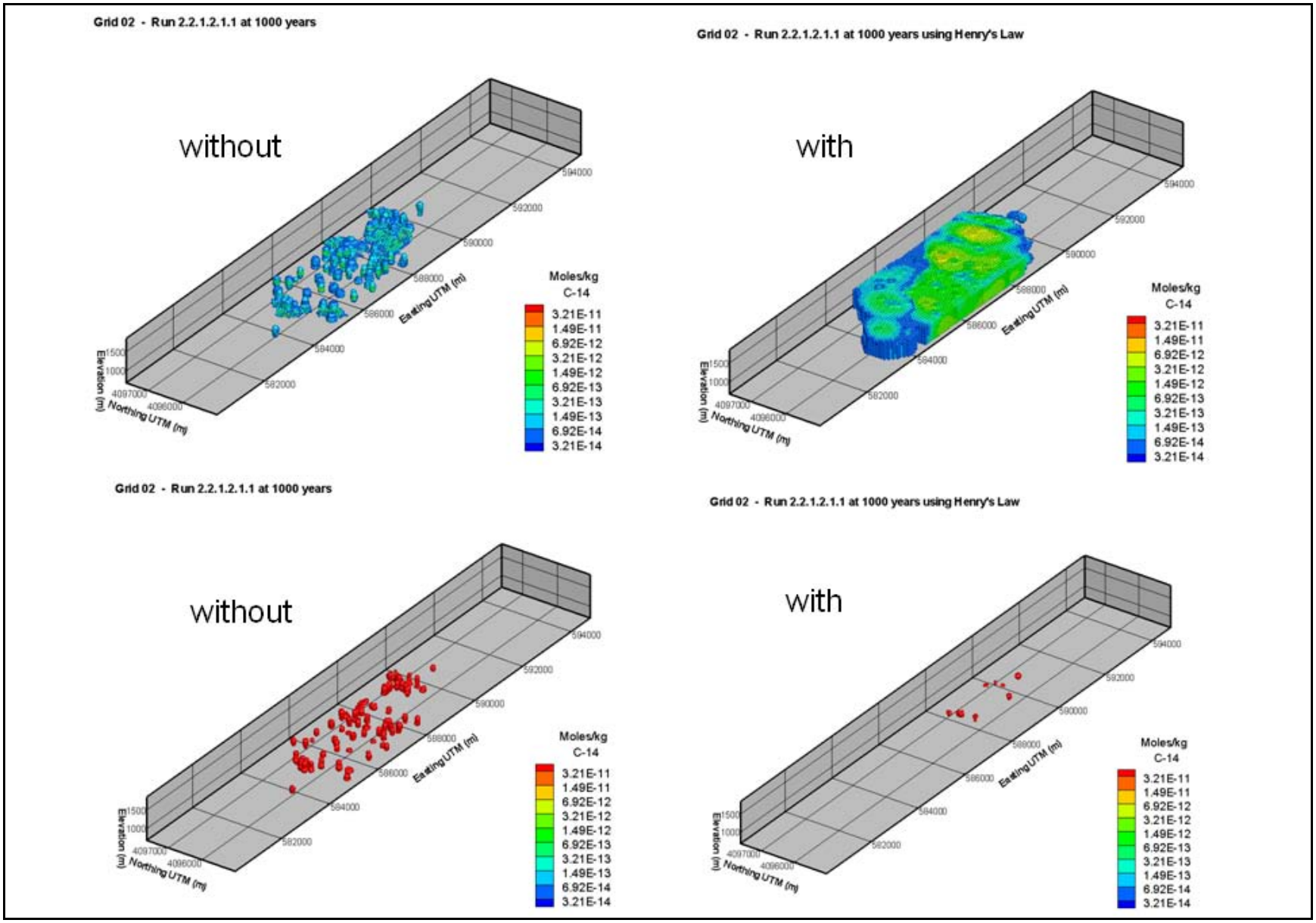

Figure 3-59
Effects of Henry's Law Partitioning of ^{14}C on Transport and Peak Concentrations in Grid 2 for Run 2.2.1.2.1.1

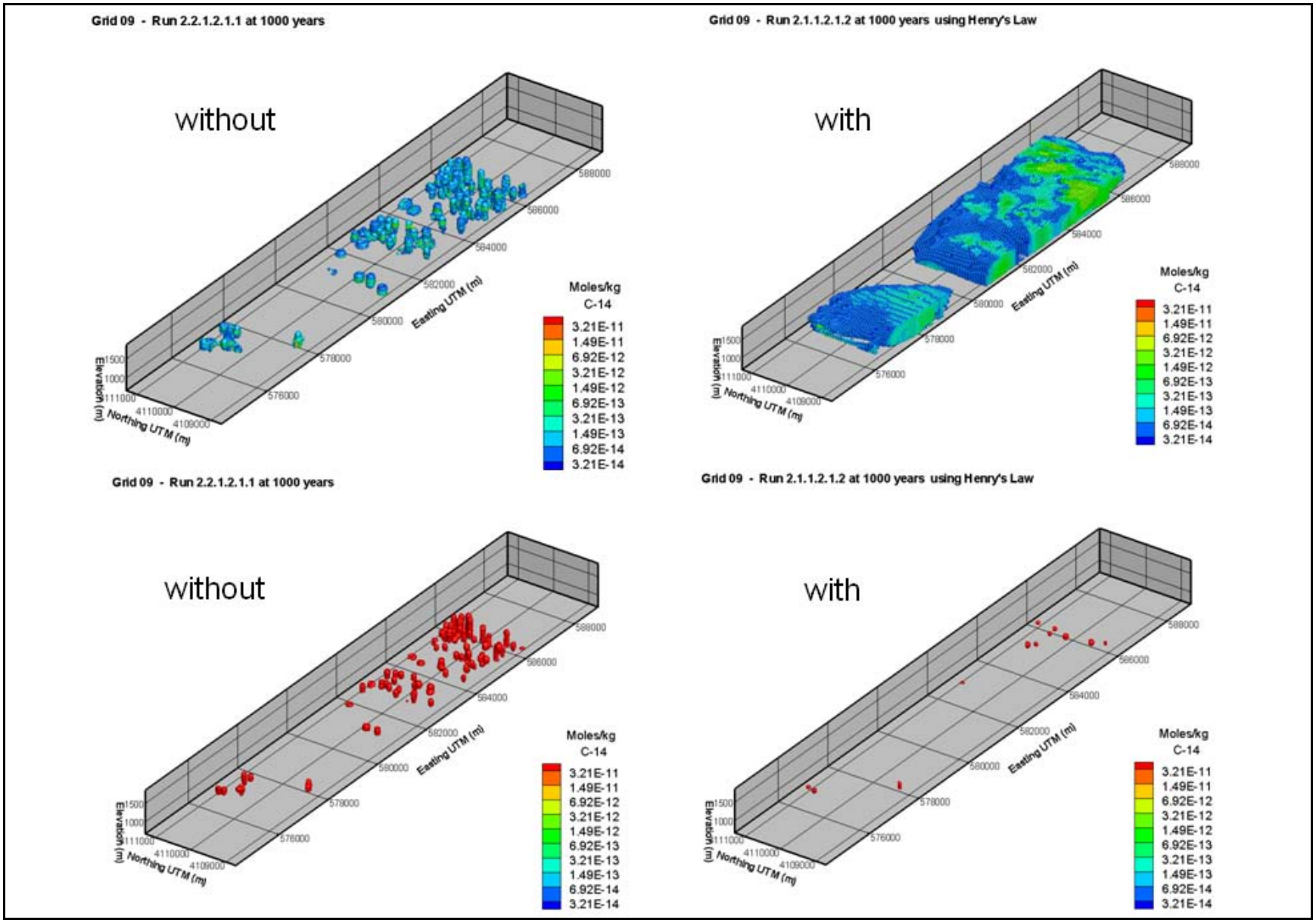

Figure 3-60
Effects of Henry's Law Partitioning of ^{14}C on Transport and Peak Concentrations in Grid 9 for Run 2.2.1.2.1.1

3.7.2 Effect of Alluvial Heterogeneity on Radionuclide Transport

Model runs presented earlier assumed that hydraulic properties for the alluvium were uniform throughout Yucca Flat and could be represented by the average alluvium properties measured adjacent to the subsidence craters at the RWMS in Area 3 (Section 3.4.3.3). Alluvial textures from the RWMS are relatively fine sands with minor silt and clay (Table 4-2). However, Sweetkind and Drake (2007b) analyzed qualitative descriptions of sediment textures from drillers logs and, based on these descriptions, created three-dimensional distributions of alluvial facies that include sediments with both coarse and finer textures. Twelve different textural classes were defined based on sediment descriptions from 1,430 intervals (over 90 percent of them some combination of sand and gravel) in 285 boreholes. Cross-sections and three-dimensional distributions of lithologic classes suggested the following (Figure 3-61):

- There is a progressive fining of sediment texture toward the basin center that reflects the decrease in depositional energy in the lower reaches of the coalescing alluvial fans that rim the basin.
- For similar reasons, there is a southward fining from gravel-dominated drill holes in the northern one-third of the model domain to more sand-dominated intervals in the central and southern parts of the domain.
- Coarse sediments on the west side of the basin could have their source in nearby alluvial fans, but possibly also could be derived from a major surface channel that drains Rainier Mesa that is responsible for gravel channel deposits in the northwest corner of Yucca Flat basin.
- A zone of relatively homogenous coarse and fine alluvial sand is present in Area 3 in the southeast part of the modeled domain.
- The far southern end of the model contains intervals of clay and limestone within the sand and gravel that represents the northernmost extent of the playa deposits.
- Although general textural trends exist, depositional facies within the coalescing alluvial fans that form most of the basin complicate textural relationships on a local scale.

These three-dimensional distributions were mapped onto the 12 unsaturated-zone grids and superimposed over the original alluvium where the more detailed information exists. This was done to investigate the sensitivity of the model to different sets of alluvial properties and to investigate the possible impacts that local variations in sediment textures would have on radionuclide transport to the water table. The conditions chosen to investigate the impact of sediment heterogeneity are those of run 2.1.3.2.1.2. This run has a 5-mm/yr background flux; isotropic sediment and tuff permeabilities;

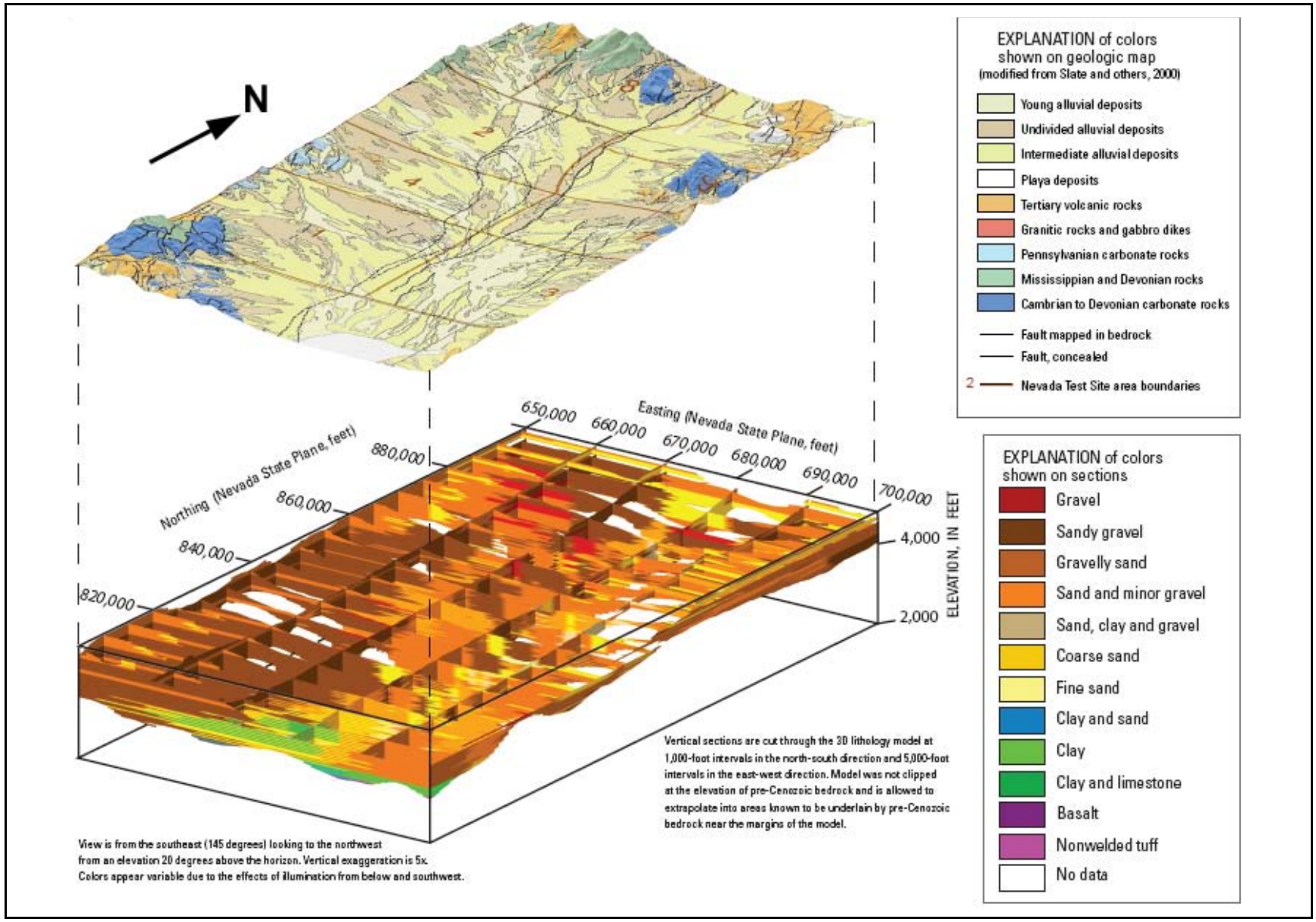

Figure 3-61
Figure Showing the Distribution of Alluvial Facies Based On Driller's Logs
Source: Sweetkind and Drake, 2007b

high crater infiltration rates; an effective porosity of 0.25 for the LTCU, OSBCU, and ATCU; and an exchange volume with 2 R_c

3.7.2.1 Sediment Hydrologic Properties

No hydrologic data were measured as part of the Sweetkind and Drake (2007b) study. Hydrologic properties for the different alluvial facies identified by Sweetkind and Drake (2007b) from driller's descriptions were estimated using various published data sources. Table 3-10 gives the estimated hydrologic properties for each of the alluvial facies identified by Sweetkind and Drake along with the sources of the hydrologic property data for each textural class. Although site-specific data are not available for most of the textural categories, the simulations are nonetheless instructive from the perspective of a sensitivity analysis. If large changes in temporal or spatial radionuclide fluxes to the water table are observed relative to the case with uniform alluvial properties because of sediment property variations, future data collection activities could be organized to collect the necessary data.

3.7.2.2 Steady-State Recharge at the Water Table

A comparison between the simulated steady-state recharge rates at the water table for a uniform infiltration rate of 5 mm/yr and either uniform or spatially variable alluvial properties is shown in Figure 3-62. Relative to the results for the uniform case, the recharge map simulated with heterogeneity included contains several areas in the western part of the basin were recharge is less than 1 mm/yr. These low recharge areas appear to be overlain by sandy gravel (Figure 3-61), suggesting that permeability contrasts between the sandy gravel and underlying sediments are redistributing infiltration elsewhere.

3.7.2.3 Transport Model Results for Heterogeneous Alluvium Model

The cumulative mass of ^{14}C leaving the unsaturated zone over time is shown in Figure 3-63 for run 2.1.3.2.1.2 both with uniform alluvium and with heterogeneous alluvium. Both simulations were done without liquid/gas partitioning of ^{14}C. The results are very similar until 300 years, after which time the cumulative mass arrival in the heterogeneous case begins to increase slightly relative to the homogeneous case. By 1,000 years, the cumulative mass of ^{14}C arriving at the water table is larger in the heterogeneous case by between one-half to one mole.Figure 3-64 shows the effects of heterogeneous alluvium on a grid-by-grid basis. Most of the overall increase in the cumulative mass

Table 3-10
Estimated Hydraulic Properties for the Sediment Textural Classifications in Sweetkind and Drake (2007b)
(Page 1 of 2)

Name	Description	Location	Category	Source	Description	θ_s [-]	θ_r [-]	α [1/cm]	n [-]	K_s [m/s]
Sweetkind and Drake (2007b) Classes										
Gravel	Cobble beds, boulder beds, and where gravel was reported as having no fine-grained matrix.	Hanford 200 Area	Coarse Gravel	Tokunaga et al., 2002	8–9.5 mm sieved fraction	0.28	0.0123	2.22	2.13	1.0E-02
Sandy gravel	Sand and gravel mixtures where gravel, clasts, or cobbles were 70% or more of the total	Hanford 200 Area	SG2	Khaleel and Freeman, 1995	Sandy gravel for which gravel content is ~>60% of the sample weight.	0.0761	0.002	0.0098	1.3465	1.40E-04
Gravelly sand	Sand and gravel mixtures where gravel, clasts, or cobbles were subequal in abundance to the sand component; used where sand was 30–70% of the total.	Hanford 200 Area	SG1	Khaleel and Freeman, 1995	Sandy gravel for which gravel content is ~<60% of the sample weight.	0.164	0.000	0.0594	1.2199	5.00E-05
Sand and minor gravel	Sand and gravel mixtures where the sand component was much more abundant than gravel, clasts, or cobbles; typically sand was 70–80% of the total, often >90% of the total.	Hanford 200 Area	GS	Khaleel and Freeman, 1995	Gravelly sand	0.2839	0.0123	0.0588	1.351	3.00E-05
Sand, clay, and gravel	Sand and gravel mixtures where silt or clay was identified as an additional important component. Typically these intervals are dominated by the sand-silt component with relatively minor gravels.	Hanford 200 Area	SSG	Khaleel and Freeman, 1995	Sand and gravel mixed with finer fraction	0.2407	0.000	0.0455	1.2003	1.50E-04

Table 3-10
Estimated Hydraulic Properties for the Sediment Textural Classifications in Sweetkind and Drake (2007b)
(Page 2 of 2)

Name	Description	Location	Category	Source	Description	θ_s [-]	θ_r [-]	α [1/cm]	n [-]	K_s [m/s]
Sweetkind and Drake (2007b) Classes										
Coarse sand	Used for sand sizes >0.5 mm, typically >1 mm, often with scattered pebbles up to 1 cm.	NNSS Area 5	Coarse Layer	Istok et al., 1994	Sand for which coarse size fraction (>0.5 mm) is ~>40% of the sample weight.	0.36	0.0725	0.044	2.27	4.34E-05
Fine sand	Used for sand sizes <0.5 mm, rare pebbles.	NNSS Area 3	Undisturbed properties Table 1-1	BN, 1998	Sand for which fine size fraction (<0.5 mm) is ~>50% of the sample weight.	0.38	0.067	0.0354	1.49	1.12E-05
Clay and sand	Used for intervals where sands are interbedded with clay layers. Typically explicitly interpreted in the description as alluvial material interbedded with playa deposits.	NA	S Clay	Schaap, 1999	Sandy clay: 45%–65% sand, 35%–55% clay	0.385	0.117	0.0334	1.208	1.31E-06
Clay	Used for intervals described as almost completely clay. Typically explicitly interpreted in the description as playa deposit.	NA	Clay	Schaap, 1999	>60% clay by weight	0.459	0.098	0.15	1.253	1.71E-06
		Amarillo, TX	Playa	Scanlon and Goldsmith, 1997	NA	NA	NA	NA	NA	2E-10
Clay and limestone	Used for intervals where clays are interbedded with thin-bedded limestone. Typically explicitly interpreted in the description as playa deposits.	NA	S Clay	Schaap, 1999	Approximate clay and limestone properties using Rosetta Sandy clay properties	0.385	0.117	0.0334	1.208	1.31E-06

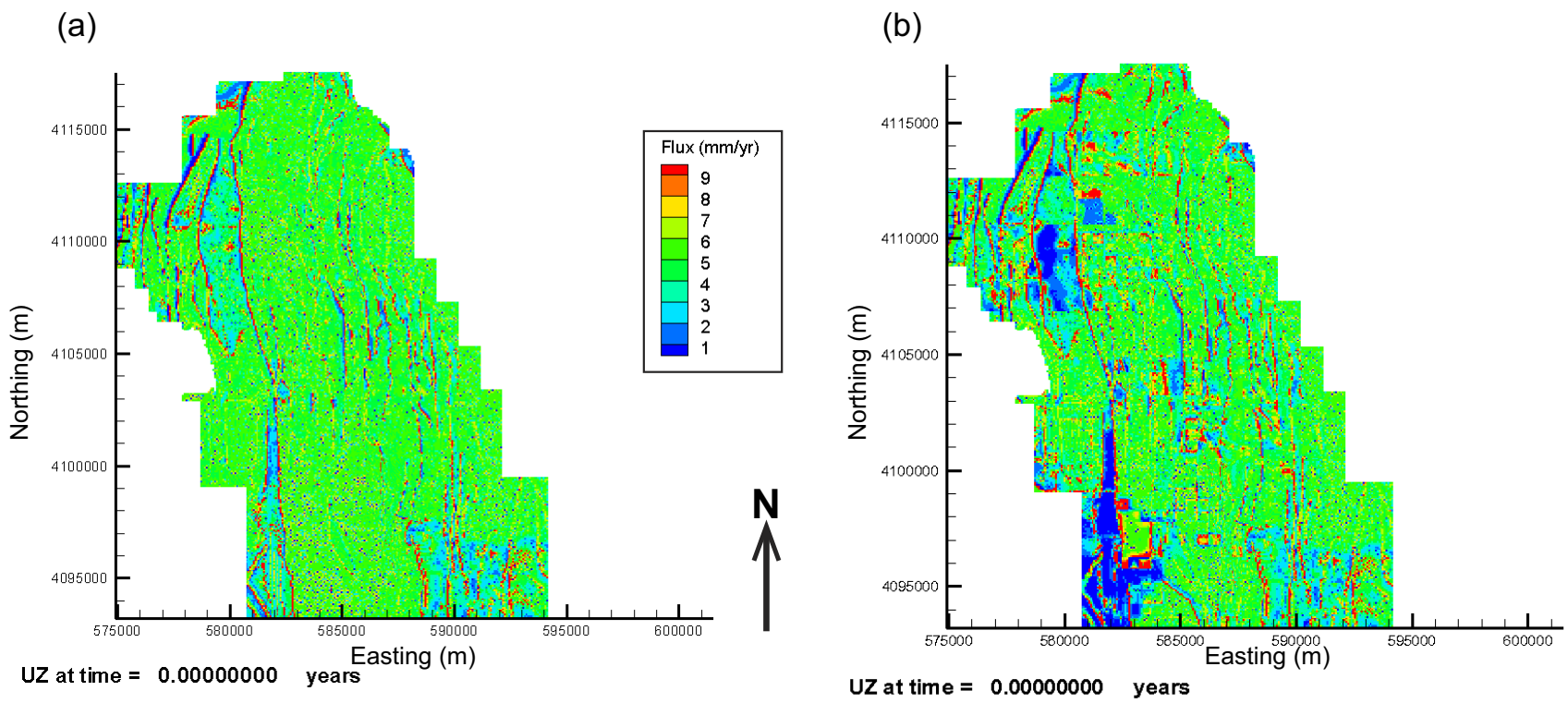

Figure 3-62
A Comparison between the Recharge Rates at the Water Table Simulated with a Uniform 5-mm/yr Infiltration Rate and Either (a) Uniform Alluvial Properties or (b) Spatially Variable Alluvial Properties

flux in the heterogeneous case is due to increases in grid 8 followed by grids 9 and 10. The overall increase in radionuclide transport in the heterogeneous case may be partly due to the smaller porosities estimated for sandy gravel (0.076), gravelly sand (0.164), and other sediment textural categories compared with the measured porosity of fine sand (0.38) assumed in the uniform alluvium case (Table 3-11). The smaller effective porosity allows both water and radionuclides to migrate faster for the same prescribed background and crater fluxes. The relatively large increases in cumulative ^{14}C flux for grids 8, 9, and 10 when heterogeneity is incorporated reflects the presence of these lower-porosity sediments above or below detonation locations in these grids. Overall, however, the difference between the homogeneous and heterogeneous cases are small relative to the variability due to other factors (Figure 3-33). The relatively small impact of sediment heterogeneity may be due to the fact that both background and crater infiltration rates in the model are prescribed, rather than a direct consequence of the hydrologic properties. As long as the permeability of the alluvium is sufficient to transmit those prescribed infiltration fluxes, transport is influenced mostly by the small differences in the moisture contents and porosity of the alluvium.

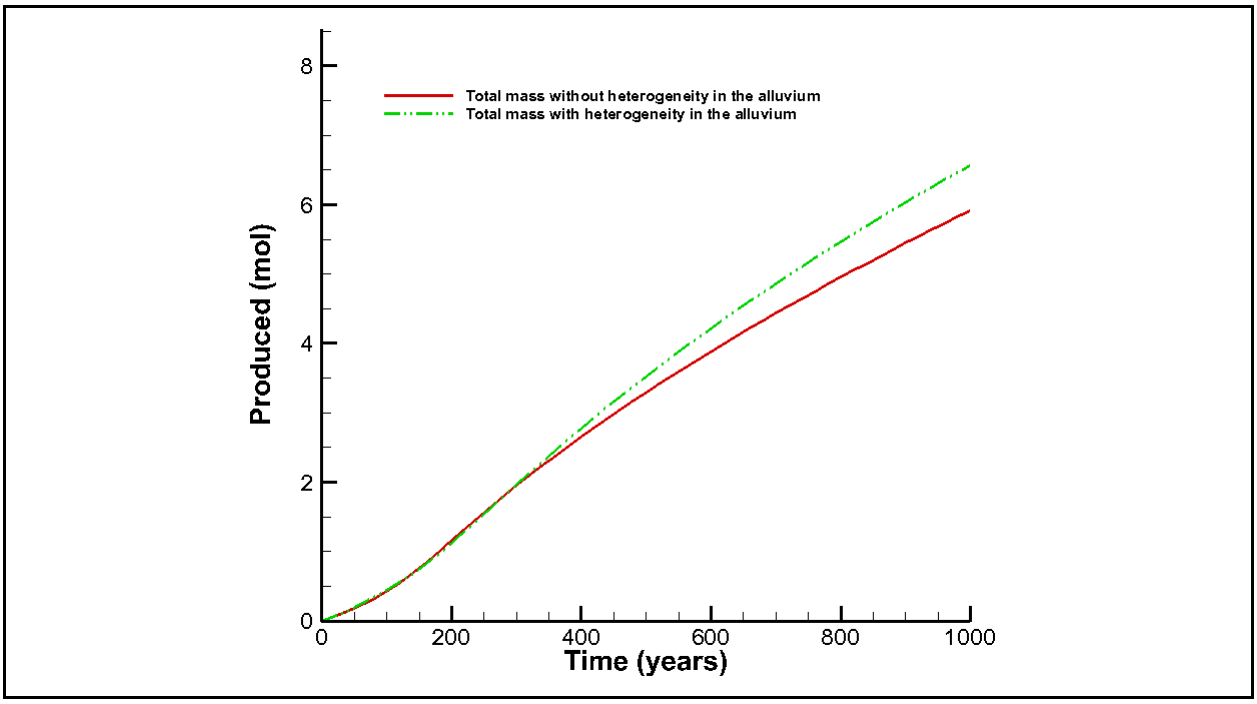

Figure 3-63
Cumulative Moles of ^{14}C Leaving the Unsaturated Zone over Time in Run 2.1.3.2.1.2 with Either Uniform or Heterogeneous Alluvium

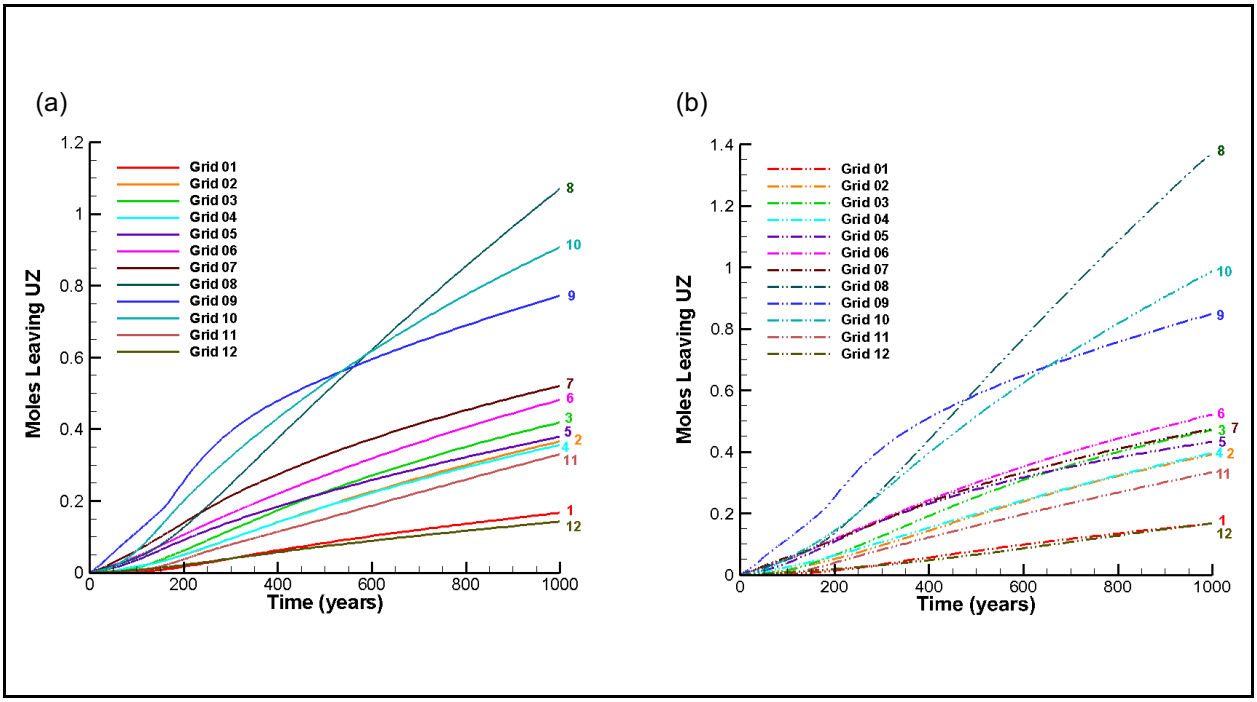

Figure 3-64
Cumulative Moles of ^{14}C Leaving the Unsaturated Zone over Time in Run 2.1.3.2.1.2 by Grid with Either (a) Uniform Alluvium or (b) Heterogeneous Alluvium

3.8 Unsaturated-Zone Models with Alternative HST Conceptualization

As described in Section 2.0, source-term conceptualization evolved from that described in Pawloski et al. (2008) and related reports over the course of the Yucca Flat modeling effort, primarily based on new source-term analyses from Rainier Mesa (Tompson et al., 2011) and Pahute Mesa (Rose et al., 2011). The changes to the conceptualization principally involve the recognition that different classes of radionuclides each have a different exchange volume radius, depending on whether they are volatile, have gaseous precursors, or are mostly incorporated into the melt-glass and cavity rubble, so that no single exchange volume radius simultaneously applies to all radionuclides. In this section, we present two additional model runs that incorporate these new source-term concepts. In the first implementation, an earlier model run (1.2.1.2.1.2) is repeated with the new model-dependent source-term allocations and radionuclide-specific exchange-volume concepts described in Section 2.0 to determine the impact of the new approach when all other aspects of the run are held constant. In the second implementation, the new HST concepts are applied to a case in which the USGS (with redistribution) infiltration map from SNJV (2007) is used as the upper boundary condition. This map is consistent with the concept that present-day infiltration through the

thick alluvial section is small (0.1 mm/yr or less), except where runoff near the basin margins or along arroyos takes place, and in bedrock hills bordering the basin.

As described in Section 2.0, the new source-term concepts differed from the original source term in several ways: (1) radionuclide mass was apportioned between models under the assumption of uniform concentrations within the exchange volume, rather than uniformly distributed mass; (2) exchange volume radii differed for different radionuclide classes, depending on whether the radionuclide in question was volatile, had a gaseous precursor, or was predominantly associated with the melt glass and rubble; and (3) because of lack of grid resolution in the unsaturated grids near saturated-zone detonations, radionuclide mass associated with detonations with working points below the water table was moved back to the top of the water table in the saturated alluvial/volcanic aquifer system and LCA models.

Because of the practical difficulties of implementing uniform concentrations in the unsaturated-zone models where moisture contents vary from detonation to detonation and from model to model, several approximations were made. First, radionuclide mass rather than concentration was assigned uniformly within the exchange volume of each detonation. Secondly, because the new conceptualization assumes a porosity of 0.40 in the glass and rubble of the cavity and a porosity of only 1E-03 in rock outside the cavity, more than 94 percent of the radionuclide mass is in the cavity, even if the radionuclide has an exchange volume radius of 3 R_c. Given the much larger uncertainty in the radionuclide inventory, in the assumption that radionuclide mass scales with maximum announced yield, and in the melt-glass partitioning factors, the assumption that all of the radionuclide mass was within the cavity is a reasonable approximation. Although this is a less accurate approximation for detonations hosted in alluvium, where the porosity is nearly equal to the glass/rubble zone and more of the inventory lies outside of the cavity, the earlier model runs summarized in Table 3-8 showed that for unsaturated-zone detonations, transport to the water table was highest for assumed exchange volumes of 1 R_c. Therefore, adopting this approximation conservatively bounds the problem for alluvium-hosted detonations.

3.8.1 Alternative Model Run 1.2.1.2.1.2'

In many ways, the new model runs with the new source term are more closely comparable to a 1 R_c exchange volume case. Unfortunately, a model run with a 1 R_c exchange volume and a background infiltration rate of 1 mm/yr was not among the existing model runs (Table 3-8). Therefore, we

compare the new model run to model run 1.2.1.2.1.2 and refer to it as model run 1.2.1.2.1.2'. A comparison of the model results with the two different source-term conceptualizations shows that ^{3}H transport to the saturated alluvial/volcanic aquifer system model is nearly identical in the two cases (Figure 3-65a), whereas slightly more mass breaks through for ^{14}C, ^{36}Cl, ^{129}I, ^{99}Tc, ^{237}Np, and total U (Figure 3-65b to g) in model run 1.2.1.2.1.2'. The slightly larger breakthrough for the 1.2.1.2.1.2' model is probably mostly attributable to the smaller exchange volume (effectively a 1 $R_c$exchange volume), which previous simulations have indicated leads to more transport in the unsaturated-zone models (Figure 3-35). However, larger breakthrough in the 1.2.1.2.1.2' model may also be related to the fact that whereas ^{36}Cl, ^{129}I, ^{99}Tc, ^{237}Np, and total U were scaled from ^{14}C using the average ratios from the unsaturated and saturated parts of the Bowen et al. (2001) inventory for Yucca Flat in the 1.2.1.2.1.2 model run, these radionuclides were directly simulated in the 1.2.1.2.1.2' model using source-term estimates that considered whether or not the individual detonations were within 100 m of the water table (Section 2.0). The comparison suggests that the initial scaling provided reasonably accurate estimates of mass flux for ^{36}Cl, ^{129}I, ^{99}Tc, ^{237}Np, and total U.

A comparison of the radionuclide mass transported to the LCA with the new 1.2.1.2.1.2' model and the original 1.2.1.2.1.2 models also shows that, except for ^{3}H, all radionuclides had slightly larger cumulative mass fluxes with the 1.2.1.2.1.2' model (Figure 3-66). Although the differences are larger in a relative sense for the LCA mass fluxes compared with the radionuclide fluxes to the volcanic rock, the much smaller overall mass fluxes to the LCA make this differences quite small in an absolute sense. For instance, whereas the mass of ^{36}Cl transport to the saturated alluvial/volcanic aquifer system model is between 10 and 30 moles after 1,000 years (Figure 3-65c), ^{36}Cl transport to the LCA is only 0.05 to 0.1 mole (Figure 3-66c).

The 1.2.1.2.1.2' model simulations also considered the transport of ^{90}Sr and ^{137}Cs, which the LCA model results showed could be important for defining the contaminant boundary in the LCA. The model simulations used median values for sorption coefficients (k_d) listed in SNJV (2007) for ^{90}Sr and ^{137}Cs (Table 3-11). As shown in Figure 3-67, breakthrough to the saturated alluvial/volcanic aquifer system model for these two radionuclides was on the order of 1E-05 moles or less. The relatively small breakthrough is attributable to both the large k_d values for most HSUs and the short (roughly 30 years) half-lives of ^{90}Sr and ^{137}Cs. Breakthrough of ^{90}Sr and ^{137}Cs to the LCA model did not occur, despite the zero k_d values assigned to faults and the LCA HSU in the unsaturated-zone models (Table 3-11).

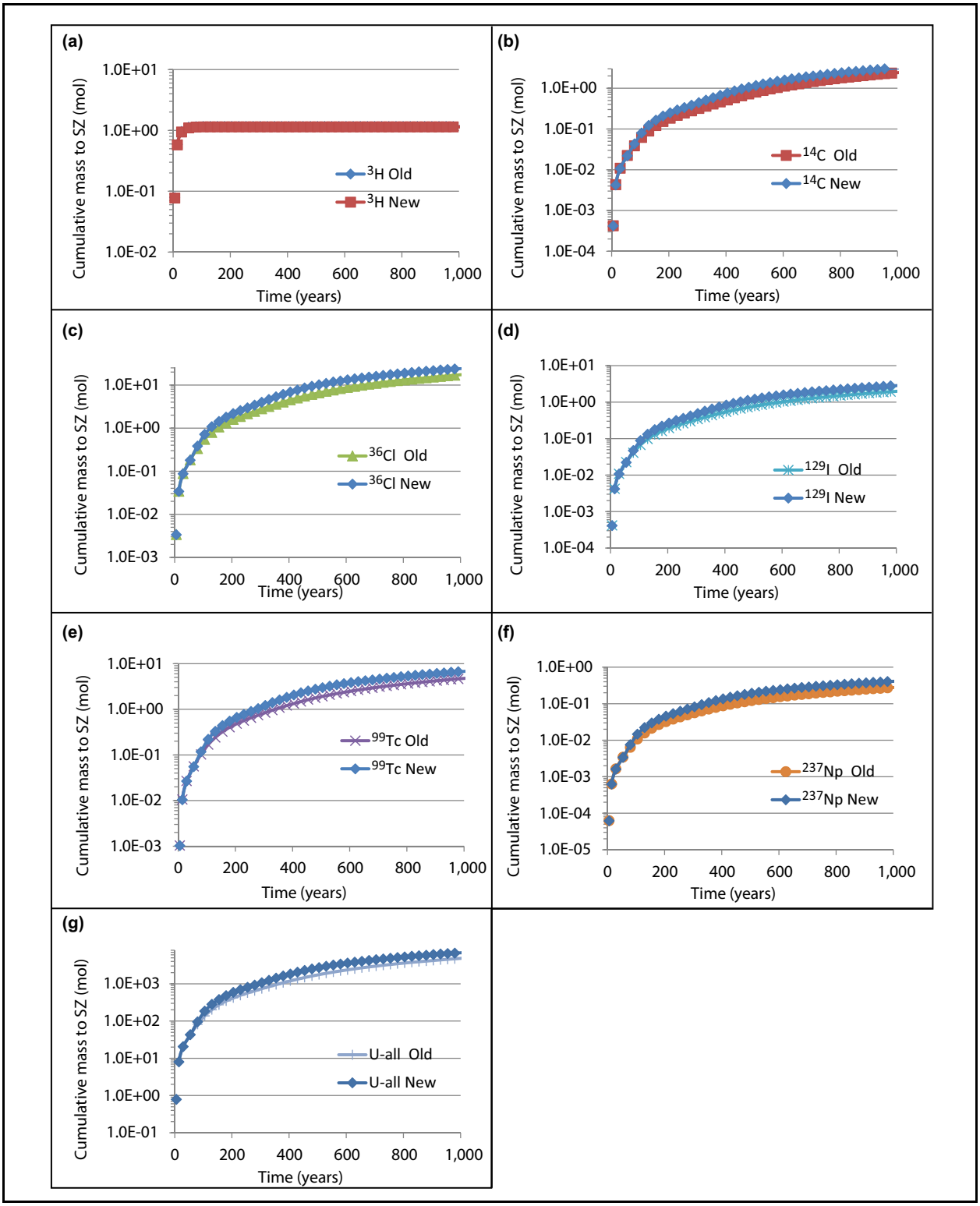

Figure 3-65
Comparison of Radionuclide Mass Flux to the Saturated Alluvial/Volcanic Aquifer System Model for Old and New Source-Term Conceptualizations for Runs 1.2.1.2.1.2 and 1.2.1.2.1.2': (a) ^{3}H, (b) ^{14}C, (c) ^{36}Cl, (d) ^{129}I, (e) ^{99}Tc, (f) ^{237}Np, and (g) Total U

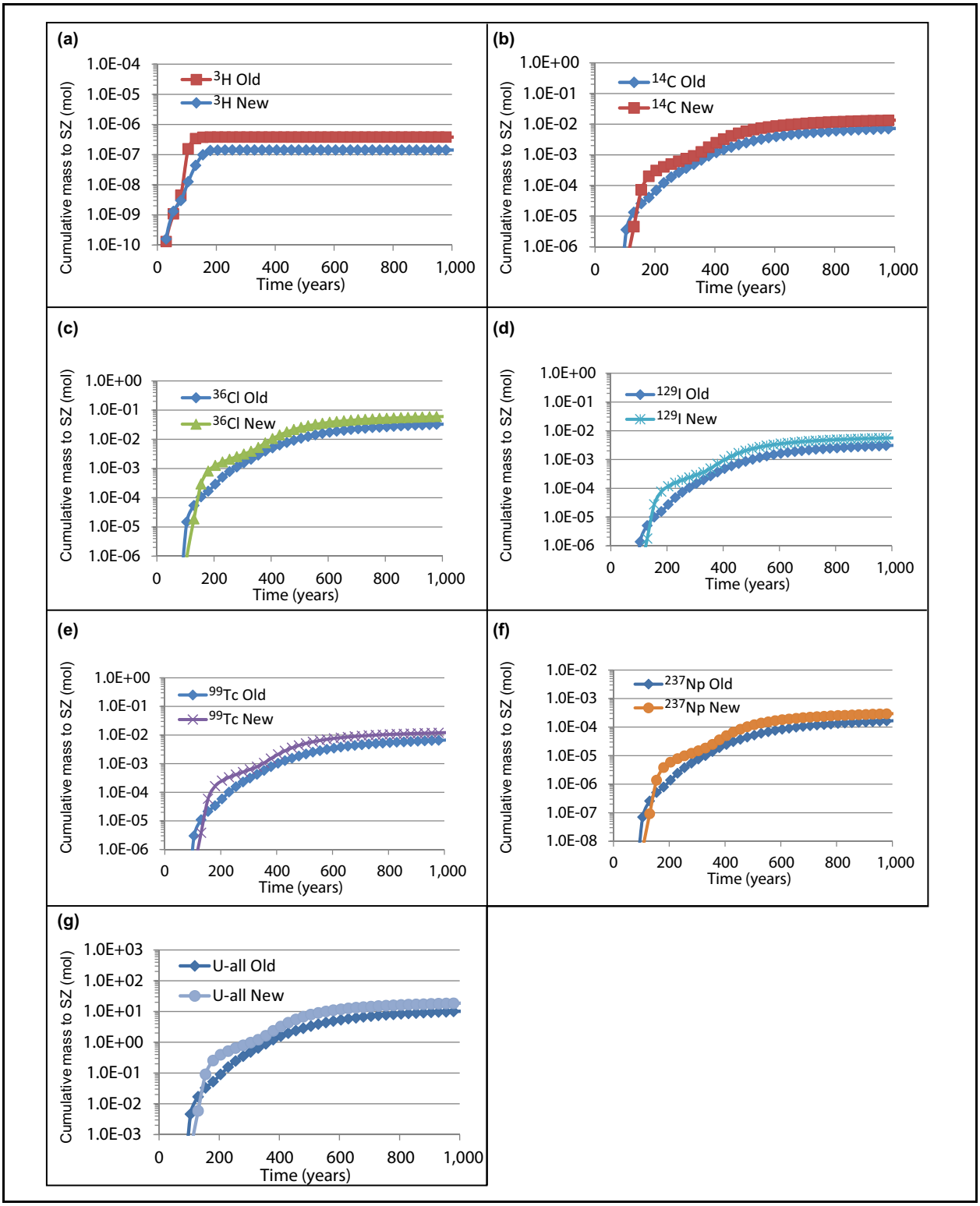

Figure 3-66
Comparison of Radionuclide Mass Flux to the Saturated Zone LCA Model for Old and New Source-Term Conceptualizations for Runs 1.2.1.2.1.2 and 1.2.1.2.1.2':
(a) ^{3}H, (b) ^{14}C, (c) ^{36}Cl, (d) ^{129}I, (e) ^{99}Tc, (f) ^{237}Np, and (g) Total U

Table 3-11
Sorption Coefficients (k_d) Used for ^{90}Sr and ^{137}Cs in Model Runs 1.2.1.2.1.2' and 5.4.2.1.2.1

HSU	^{90}Sr k_d (ml/g)	^{137}Cs k_d (ml/g)	Source
MGCU	60	350	SNJV,2007 (Fig. 11-4)
LCCU	60	350	SNJV, 2007 (Fig. 11-4)
LCA	0	0	Conservative assumption
UCCU	60	350	SNJV, 2007 (Fig. 11-4)
UCA	0	0	Conservative assumption
LCA3	0	0	Conservative assumption
ATCU	300	400	SNJV, 2007 (Fig. 11-5)
OSBCU	300	400	SNJV, 2007 (Fig. 11-5)
PRETBG	60	350	SNJV, 2007 (Fig. 11-4)
LTCU	300	400	SNJV, 2007 (Fig. 11-5)
TUBA	60	350	SNJV, 2007 (Fig. 11-4)
BRCU	300	400	SNJV, 2007(Fig. 11-5)
BRA	60	350	SNJV, 2007 (Fig. 11-4)
LVTA	100	600	SNJV, 2007 (Fig. 11-3)
TSA	60	350	SNJV, 2007 (Fig. 11-4)
UTCU	300	400	SNJV, 2007 (Fig. 11-5)
TM-LVTA	100	600	SNJV, 2007 (Fig. 11-3)
TM-WTA	60	350	SNJV, 2007 (Fig. 11-4)
TM-UVTA	100	600	SNJV, 2007 (Fig. 11-3)
AA	200	3,000	SNJV, 2007 (Fig. 11-1)
BLFA	60	350	SNJV, 2007 (Fig. 11-4)
PCUT	300	400	SNJV, 2007 (Fig. 11-5)
Fault zones	0	0	Conservative assumption

3.8.2 Model Run 5.4.2.1.2.1

Model run 5.4.2.1.2.1 uses the new source-term formulation described above for the 1.2.1.2.1.2' model run, along with USGS infiltration map with redistribution (Figure 3-68) and saturated permeabilities and vertical-to-horizontal anisotropy ratios for selected HSUs based on recalibration of the saturated alluvial/volcanic aquifer system model (Table 3-12) with this infiltration map.

A comparison of the radionuclide mass transported to the water table in the saturated alluvial/volcanic aquifer system and LCA for model run 5.4.2.1.2.1 (Figure 3-69) with that of 1.2.1.2.1.2' (Figures 3-65 and 3-66) shows that the mass fluxes of most radionuclides are reduced by one to two orders-of-magnitude in model run 5.4.1.2.1.2. Of interest is that neither ^{90}Sr nor ^{137}Cs

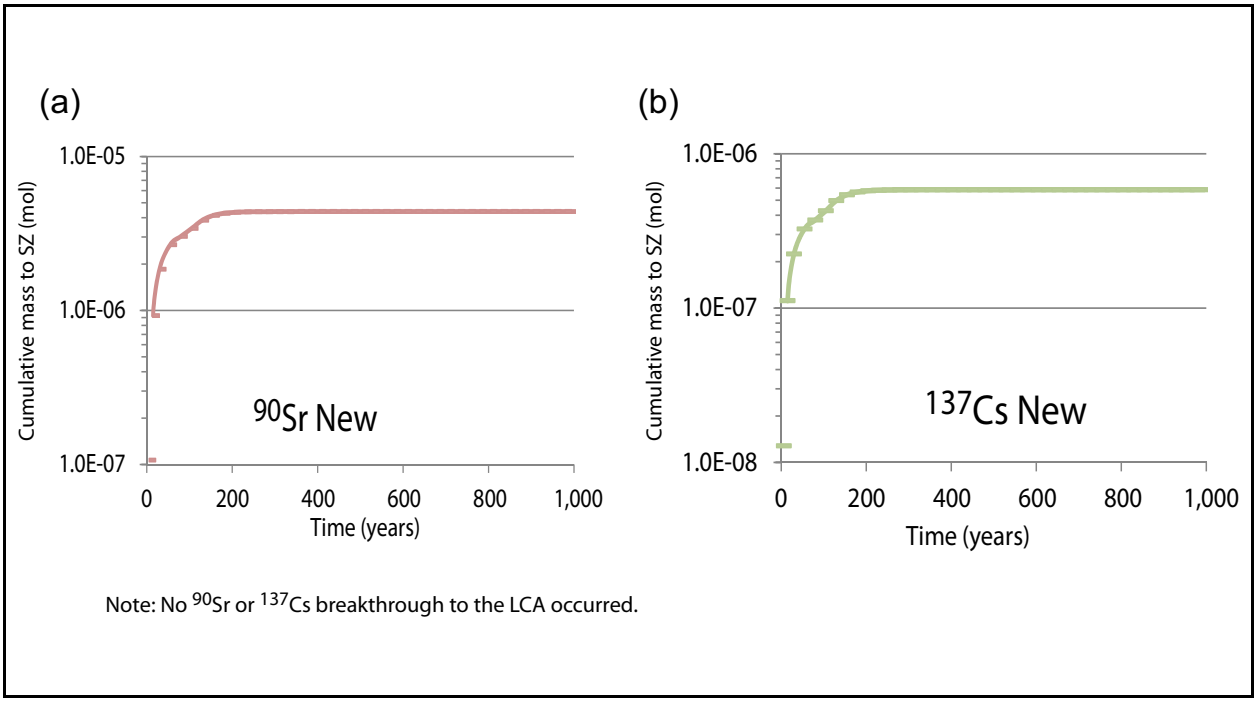

Figure 3-67
Cumulative Mass Flux from the 1.2.1.2.1.2' Model to the Saturated Alluvial/Volcanic Aquifer System Model: (a) ^{90}Sr, and (b) ^{137}Cs

breaks through to the LCA in 1,000 years due to a combination of low background flux, radioactive decay, and sorption in the volcanic rocks and alluvium. This is consistent with the results of the earlier model runs which demonstrated the importance of background flux on radionuclide transport to the water table before the arrival of the crater-bottom infiltration. Radionuclide breakthrough at the water table in the saturated alluvial/volcanic aquifer system model shows a break in slope after about 400 years. This break in slope appears to reflect the arrival at the water table of recharge associated with enhanced crater infiltration (Figure 3-70). It is especially evident in the breakthrough to the saturated volcanic rocks because of the extremely small background flux in the central part of the basin (Figure 3-68). Radionuclides arrive at the saturated LCA after about 200 years (Figure 3-69b), which appears to coincide with the arrival of crater infiltration at the LCA (Figure 3-70), so the break in slope associated with the arrival of crater infiltration to the volcanic rocks is not evident. As in model run 1.2.1.2.1.2', the cumulative mass transported to the saturated LCA by 1,000 years is orders-of-magnitude less than the mass transported to the saturated volcanic rocks. Although it may seem paradoxical that the radionuclide mass transported to the LCA is much smaller than to the volcanic rocks while the water flux is much higher to the LCA, this can be explained by the fact that the high background infiltration areas above the LCA do not necessarily coincide with detonation

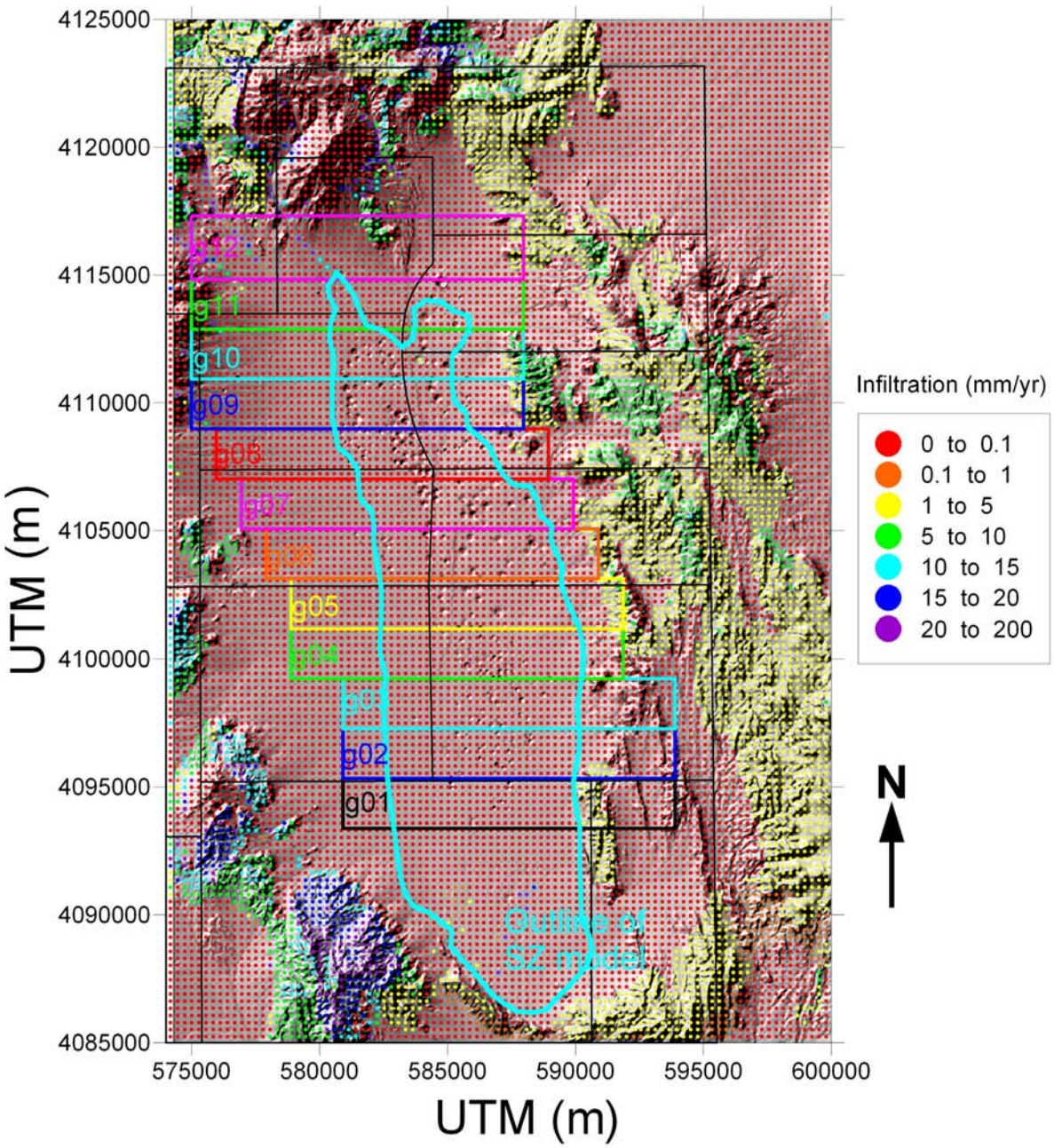

Note: Where the map indicates infiltration rates of 0.0 to 0.1 mm/yr, the model uses 0.1 mm/yr

Figure 3-68
Infiltration Rates from USGS DVRFS Model 1 (with Redistribution), along with Outlines for the 12 Unsaturated-Zone Model Grids and the Saturated Alluvial/Volcanic Aquifer System Model

Table 3-12
Modifications to Unsaturated-Zone Model Parameters Based on Saturated Alluvial/Volcanic Aquifer System Model Calibration to the USGS Infiltration Map with Runoff

HSU	Log Permeability (m^2)	Vertical to Horizontal Permeability Ratio k_v/k_h
ATCU	–14.7319	0.1
OSBCU	–16.7782	0.1
Pretbg_1	–12.000	0.1
LTCU	–15.7578	0.1
TUBA	–13.54	0.1
TSA	–12.4115	0.1
UTCU	–15.9913	0.1
TM-LVTA	–13.8627	0.1
TM-WTA	–15.000	0.1
TM-UVTA	–13.9278	0.1
AA1	–12.7173	0.1
AA2	–12.7173	0.1
AA3	–12.7173	0.1
Fault 14	–12.5125	1
Fault 45	–13.0000	1
Fault 47	–12.5125	1
Fault 48	–15.000	1
Fault 49	–13.599	1
Fault 54	–14.2792	1
Fault 60	–13.2111	1
Fault 63	–12.5125	1
Fault 69	–12.5125	1
Fault 71	–12.5125	1
Fault 77	–12.5125	1
Fault 78	–13.000	1
Fault 90	–13.000	1

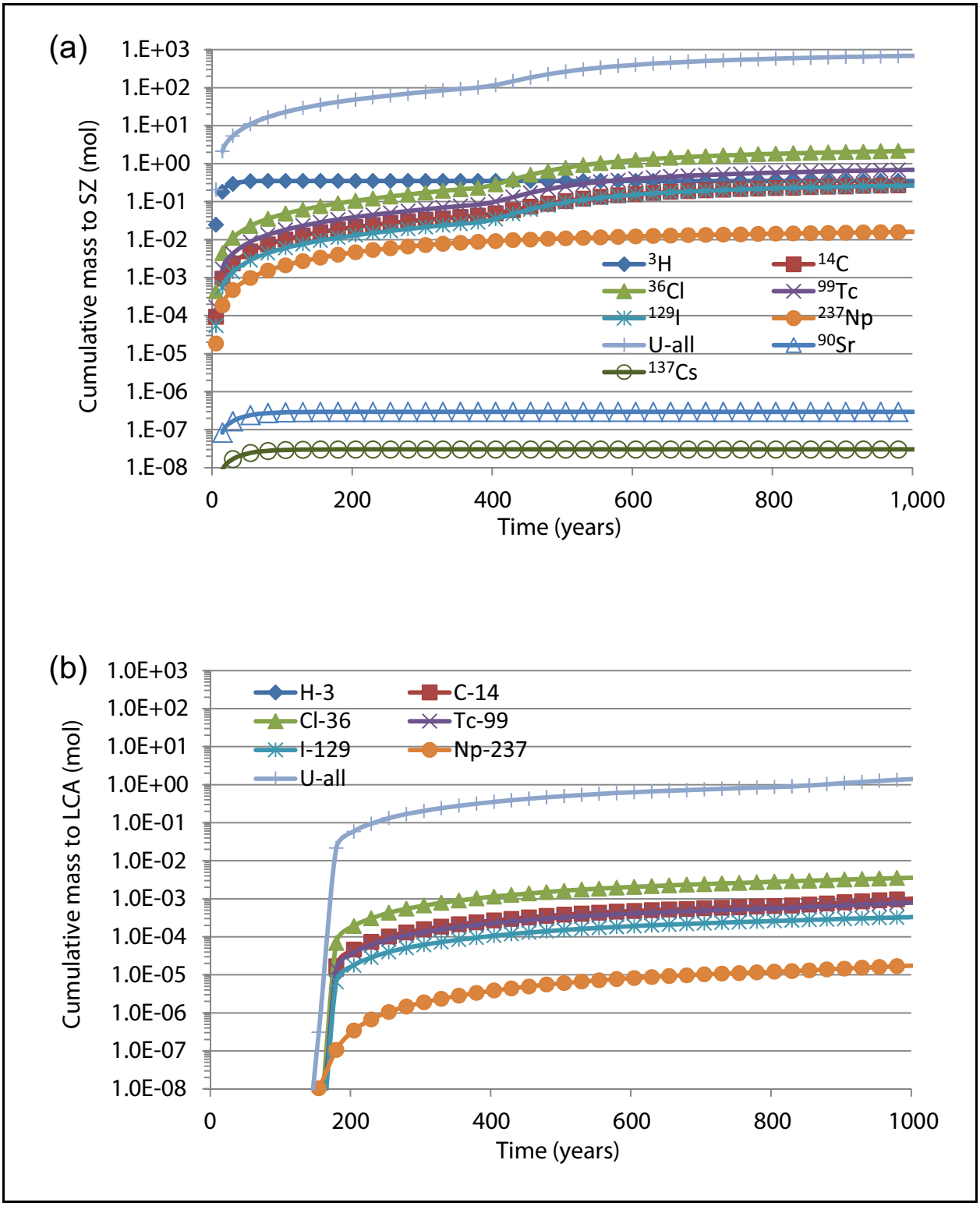

Figure 3-69
Cumulative Radionuclide Mass Reaching the Water Table during Unsaturated-Zone Model Run 5.4.2.1.2.1: (a) Saturated Alluvial/Volcanic Aquifer System Model, and (b) LCA Model

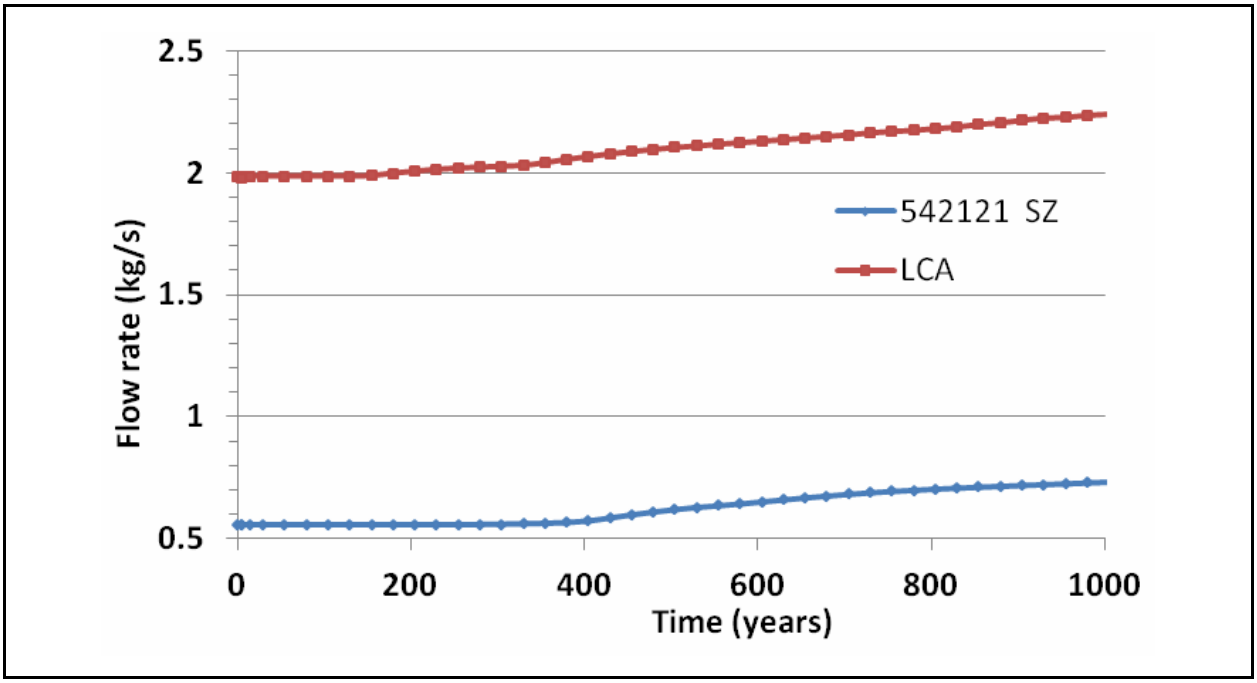

Figure 3-70
Water Flux Reaching the Saturated Alluvial/Volcanic Aquifer System and LCA Models in Unsaturated-Zone Model Run 5.4.2.1.2.1

locations, which are far fewer directly above the saturated LCA than the saturated volcanic rocks (Figure 3-2). The faster arrival times of crater infiltration at the saturated LCA reflect the fact that craters above the LCA on the perimeter of the basin generally have larger watersheds and higher crater infiltration rates than detonations above the saturated volcanic rock in the center of the basin (Figure 3-35).

3.9 Summary and Conclusions

A series of 12 three-dimensional numerical models of the unsaturated zone were created in order to simulate water flow and radionuclide transport from 668 nuclear detonations with working points above the water table. The models, which extended from land surface to the water table, covered a total area of Yucca Flat approximately 24 km by 13 km (312 km^2) and included all but two detonations with working points in the unsaturated zone. The models were based on high-resolution computational grids that were able to represent hundreds of faults, dipping hydrostratigraphic layers, and the details of the near-field test environment, including subsidence craters, collapse chimneys, and subsurface cavities formed by the heat and force of the detonation.

Hydraulic properties of the sediments came from unsaturated-zone characterization studies at the Area 3 RWMS in Yucca Flat. Rock matrix properties of the HSUs beneath Yucca Flat were based on laboratory measurements of a set of more than 60 cores from the same HSUs at Rainier Mesa, which borders Yucca Flat on the northwest. Fracture hydraulic properties were based on a variety of sources, including studies of fracture frequency and aperture in core samples from Yucca Flat, estimates of large-scale permeability resulting from calibration of the saturated alluvial/volcanic aquifer system model to hydrographs of test-induced hydraulic overpressures, and field observations regarding the tendency of different rock types at the NNSS to develop and maintain open fractures.

A prominent part of the development of the unsaturated-zone models for Yucca Flat involved characterizing the surface watersheds, geometry and long-term (1,000-year) infiltration rates for the 462 surface subsidence craters that have been identified in Yucca Flat. Focused infiltration into the bottoms of subsidence craters due to surface runoff and ponding following precipitation events has been observed and studied in a handful of craters in Yucca and Frenchman Flat. Developing sound estimates of long-term crater infiltration rates is essential for modeling radionuclide transport because it is infiltration from the crater bottom that will flow directly into the collapse chimney and cavity, and flush radionuclides within and near the cavity to the water table. Long-term infiltration rates at each of the 462 craters were calculated with a one-dimensional unsaturated-zone model that extended from land surface to the water table. The one-dimensional models used stochastically-generated daily precipitation records created for the next 1,000 years that were conditioned to the 55-year-long record from central Yucca Flat in a way that preserves the temporal clustering of wet and dry days during each season. Surface-water runoff volumes to each crater were estimated using the watershed area of the crater and a simple curve number approach that estimates the potential for runoff based on the soil's moisture status on the previous day. Moisture thresholds that determine whether or not a particular precipitation event produces surface runoff were identified by comparing model results to measured ponding depths in craters following specific rainfall events. ET estimates in the craters following runoff events were based on the calibration of the ET component of the models to 10-year-long records of weighing-lysimeter data from Frenchman Flat for both vegetated and unvegetated soils.

Long-term yearly infiltration rates for each crater were estimated from the sum of the total recharge and the net moisture-storage change in the model over the simulation period, divided by 1,000 years. Three sets of infiltration estimates for the 462 craters were made, including "preliminary" low and

high estimates, and a single set of final results. The “preliminary” estimates include the effects of a geometry error that affected the calculated ponding heights used in the one-dimensional crater infiltration models. Although runoff volumes were not affected, ponding heights were overestimated which in turn caused infiltration rates to be also overestimated. The preliminary “high” and “low” estimates otherwise differed in that the high estimates assumed no vegetation in the crater bottoms whereas the low estimates assumed all craters were vegetated, an assumption which led to larger ET losses. The high estimates also had slightly dryer antecedent moisture thresholds for surface runoff generation than the preliminary low estimates, which led to more surface-water runoff and infiltration. The “final” results were actually lower than the preliminary “low” estimates for most of the craters except for those on the periphery of the basin with large watersheds. The craters on the periphery of the basin with large upland watersheds tended to receive the largest volume of surface runoff and consequently had some of the largest infiltration rates. Craters in the interior of the basin were shielded by outlying craters from runoff generated in the bordering hills, and these interior craters often had watershed areas not much larger than the craters themselves. Whereas infiltration rates in the outlying craters can have infiltration rates in excess of 1 m/yr, craters in the interior of the basin typically have infiltration rates of 5 cm/yr or less.

The long-term infiltration rates calculated for each of the 462 individual craters were applied to the appropriate nodes representing the crater bottoms in one of the 12 three-dimensional models. These rates were then held constant throughout the duration of the 1,000-year transient flow and transport simulation. Initial moisture conditions for each transient simulation were generated by running each of the 12 models long enough that steady flow conditions were achieved for one of three uniform background infiltration rates: 1, 5, and 10 mm/yr. Existing water potential and chloride concentration data from interfluvial areas in Yucca and Frenchman Flats suggests that wide-spread present-day background infiltration rates of 5 and 10 mm/yr are highly unlikely, and that these infiltration rates are more typical of values that have not existed in alluvial basins in the American southwest since brief pluvial periods at the end of the last ice age. Nonetheless, these values were adopted to account for possibly larger (but as yet unmeasured) infiltration rates beneath arroyos and playas, possibly higher infiltration along the basin margins because of runoff from the surrounding hills, and the continued drainage of water that infiltrated during past pluvial periods at depth.

At the start of the transient 1,000-year simulation period (which coincides with the FISHER detonation on December 3, 1961, in the saturated alluvial/volcanic aquifer system model),

radionuclide mass from the entire testing period between 1957 and 1992 is instantaneously emplaced in spherical exchange volumes centered around the working point of each detonation. Each exchange volume is assumed to have a radius of 1, 2, or 3 times the cavity radius estimated from its maximum announced yield. The mass emplaced in each exchange volume is the fractional part of the total unclassified radionuclide inventory for Yucca Flat scaled according to the fractional yield of the detonation (i.e., the maximum announced yield of the detonation divided by the sum of the maximum announced yields of all detonations in Yucca Flat). The radionuclide mass is carried downward toward the water table by the ambient background flux as well as by diffusion and dispersion until the water infiltrating downward through the crater bottom arrives at the exchange volume. At this point, the contaminated pore water in the exchange volume mixes with and is diluted by the radionuclide-free water that infiltrated through the crater bottom, and the mixture is flushed toward the water table by continued infiltration from the crater bottom.

The pathways followed by radionuclides to the water table from the individual exchange volumes depends on the HSUs between the detonation and the water table, and the hydraulic properties of the HSUs assumed in different model runs. Some lateral flow occurs when the local crater infiltration rates exceed the vertical hydraulic conductivity of one or more of the HSUs. Lateral flow is intercepted by and redirected downward by faults in the model, which are assumed to be uniformly more permeable that the HSUs themselves. This assumption was adopted to create the potential for focused flow and rapid transport through faults in the bedrock.

Twenty-eight different combinations of background and crater infiltration rates, sediment and tuff anisotropy, tuff effective porosity, exchange volume size, and the existence or absence of high-permeability collapse chimneys were examined to determine their influence on the rates and magnitude of radionuclide transport to the water table. Carbon-14 (^{14}C) was modeled as a non-sorbing, non-decaying liquid tracer and used to evaluate the impact of changes in these variables on radionuclide mass arrival at the water table. The breakthrough of other radionuclides (^{36}Cl, ^{99}Tc, ^{129}I, ^{237}Np, and U) at the water table were estimated from the ^{14}C results assuming that their nodal molar concentrations scaled with the ratio of the radionuclide to ^{14}C in the combined saturated/unsaturated inventory estimated for Yucca Flat. Tritium (^{3}H) was modeled explicitly in the simulations because it did not appear to scale well with ^{14}C like the other radionuclides. The mass of individual radionuclides available for transport was in most cases less than the total mass of that radionuclide in the inventory because, except for ^{3}H and ^{14}C, the other radionuclides were

incorporated to varying extents in the melt glass and the melt-glass portions of the inventory were assumed to be immobile over the 1,000-year regulatory period.

The results of the sensitivity analysis indicated that between 4 and 50 percent of the ^{14}C inventory of approximately 25 moles initially in the unsaturated zone reaches the water table by 1,000 years. Excluding cases with one cavity-radii exchange volume, the ^{14}C mass reached the water table after 1,000 years is between about 4 to 25 percent. Because ^{14}C was modeled as a non-sorbing, non-decaying liquid phase tracer, the actual percentages of ^{14}C reaching the water table would be less than the percentages cited if radioactive decay had been included. Radionuclides with shorter half-lives like ^{3}H (12.3 years) would have an even smaller percentage of their initial mass reach the water table. Over the range of parameters examined, initial radionuclide exchange volumes and background flux caused the largest changes in radionuclide mass arrivals at the water table. Background flux determined the rate of transport at early times before crater infiltration reached the cavity. The exchange volume radius determined how much of each detonation's initial inventory lay directly beneath the crater where it could be mobilized by infiltration flowing from the crater bottom.

No formal uncertainty analyses were conducted with the 12 three-dimensional models, because the very long run times limited the number of model runs that could be completed, and parameter distributions for key model inputs were not available. However, structured sensitivity analyses were conducted that identified key model sensitivities. The structured sensitivity analyses indicated that the radionuclide mass arriving at the water table increases with increasing background and crater infiltration rates, smaller effective porosities in the tuff confining units, larger ratios of vertical to horizontal permeability in the tuffs and sediments, and smaller exchange volumes. The inclusion of high-permeability, low-porosity rubble zones associated with collapse chimneys results in some earlier breakthrough over 1,000 years when compared with identical cases where chimneys are assumed to be absent, but the overall effect is small compared with that caused by variability in other parameters. Likewise, changes in the effective porosity or vertical permeability in the tuffs produces relatively small changes in the radionuclide flux because the tuff confining units are either thin or absent between majority of the detonations and the water table.

Most (approximately 90 percent) of the radionuclide mass arriving at the water table reaches the saturated tuffs or alluvium rather than the saturated LCA. This is a consequence of the fact that most unsaturated-zone detonations are located near the center of the basin where the water table is in the

tuffs, rather than on the periphery of the basin where the water table is in the carbonate aquifer. As shown in Section 4.0, the saturated volcanic rocks provide an additional barrier that prevents radionuclides from most unsaturated-zone detonations from reaching the carbonate aquifer where they can be transported out of Yucca Flat. For ^{3}H, ^{14}C, ^{36}Cl, ^{129}I, and total U, most water table locations where recharge exceeds the SDWA standards for beta-emitting radionuclides are where the exchange volumes of the detonations essentially intersect the water table. Recharge at later times arrives at concentrations that are less than the SDWA standard because contaminated water initially in the exchange volume has been mixed with and diluted by radionuclide-free water moving downward from the crater bottom. For the cases with exchange volumes of 2 R_c or larger, neither ^{237}Np or ^{99}Tc appears to arrive at the water table at concentration exceeding the SDWA standards, even at locations where the exchange volumes intersect the water table.

Several additional model runs were conducted to examine the impact of specific processes or assumptions. Model run 2.2.1.2.1.1 was repeated for a subset of the 12 grids with gas/liquid partitioning of ^{14}C using Henry's law to assess the impact of gas-phase transport on ^{14}C breakthrough at the water table. ^{14}C transport to the water table increased for some grids and decreased for others, but the overall effect was to spread ^{14}C throughout the unsaturated zone, and thereby dilute the ^{14}C in pore water to below its MCL of 3.21E-11 mol/L. Another alternative model based on model run 2.1.3.2.1.2 considered the effects of sediment heterogeneity. In this case, sandy gravel and gravelly sand with a lower porosity than pure sand led to larger breakthrough of ^{14}C relative to the homogeneous case in grids where the sandy gravel was prominent. The impact of alternative source-term conceptual models and melt-glass partitioning ratios were investigated in model runs 1.2.1.2.1.2 and 1.2.1.2.1.2'. The impact for the unsaturated-zone models was relatively small compared with the effects of other factors. Model run 1.2.1.2.1.2' also considered the transport of ^{90}Sr and ^{137}Cs, which the LCA model indicated was imported for the contaminant boundary in the LCA. Using median ^{90}Sr and ^{137}Cs k_d values for different HSUs resulted in very low breakthrough to the saturated volcanic rock and no breakthrough to the LCA, thereby justifying the initial assumption that sorbing radionuclides could be excluded from the analysis. Finally, the USGS (with runoff) infiltration map was used in model run 5.4.2.1.2.1 along with the alternative source-term conceptual models and recalibrated permeability and anisotropy values from the saturated alluvial/volcanic aquifer system model to produce estimates of radionuclide breakthrough to the water table. The very low background infiltration rates throughout most of the testing area (0.1 mm/yr) resulted in very low rates of radionuclide transport to the water table relative to the other background infiltration rates

considered (uniform 1, 5 and 10 mm/yr). Transport of ^{90}Sr and ^{137}Cs to the saturated volcanic rocks and LCA was negligible.

Because unsaturated-zone pore water is not part of the calculated contaminant boundary for Yucca Flat, the primary role of the unsaturated-zone models are to estimate where, when and how much of the radionuclide inventory initially in the unsaturated zone reaches the water table. The mass of water and radionuclides reaching the water table is then post-processed and put into a format that can be used by the saturated-zone models for the volcanic and carbonate aquifers, so that these models can include the radionuclide sources from the unsaturated zone as well as their own radionuclide sources in their contaminant boundary calculations. The process required that nodes from the bottom of the unsaturated-zone models be mapped onto the appropriate nodes in either the saturated alluvial/volcanic aquifer system or LCA models. Three sets of unsaturated-zone model output have been produced as input to both saturated-zone models, representing low (run 5.4.2.1.2.1), medium (run 1.2.1.2.1.2) and high (run 2.2.3.2.1.2) transport cases. Other cases have been used by the saturated alluvial/volcanic aquifer system model to test the impact of assuming different (1, 2, or 3 R_c) exchange volumes (runs 2.2.3.2.1.1, 2.2.3.2.1.2, or 2.2.3.2.1.3) or to specifically examine the impact of background flux and permeability (run 3.2.1.2.1.2). The relative importance of radionuclides originating from detonations with working points in the unsaturated zone to the contaminant boundaries in the saturated alluvial/volcanic aquifer system and the LCA are discussed in Sections 4.0 and 6.0. Transport simulations presented in those sections show that, in general, radionuclide sources initially in the saturated zone are much more important than sources originating in the unsaturated zone for defining the contaminant boundaries in either the saturated alluvial/volcanic aquifer system model or the saturated LCA model.

4.0 YUCCA FLAT SATURATED ALLUVIAL/VOLCANIC AQUIFER SYSTEM FLOW AND TRANSPORT MODEL

4.1 Introduction

This section summarizes the conceptual and numerical models developed to represent the groundwater flow and contaminant transport within the saturated alluvial/volcanic aquifer system at Yucca Flat. This domain of Yucca Flat receives water and contaminant flux from the overlying unsaturated-zone model domain, and provides water and contaminant fluxes to the underlying saturated LCA model domain. This central portion of the Yucca Flat/Climax Mine CAU includes rocks lying below the water table and above the fractured carbonate aquifer.

Of the 747 detonations conducted at the Yucca Flat/Climax Mine CAU, 76 detonations have working points below the water table. An additional 90 detonations have exchange volumes that extend below the water table when a 2 R_c exchange volume radius is assumed for each detonation, even though the working point is above the water table. Many of these detonations have some of the larger announced yields in the Yucca Flat/Climax Mine CAU (e.g., BILBY, 249 kt; CARPETBAG, 220 kt). Detonations in this portion of Yucca Flat span the time period of 1962 to 1991.

Aspects of groundwater flow that most strongly impact radionuclide transport from the underground nuclear detonations and down into the lower carbonate aquifer were emphasized in the flow model development. These aspects include near-field testing effects (detonation-induced pressurization and rock damage) and transient flow. Equally strong consideration was given to developing modeling approaches that were sufficiently flexible so as to be able to accommodate a robust uncertainty analysis. This is critical for analysis of a system such as this, where the area of interest is quite deep (approximately 500 m bls in central Yucca Flat), hydrologic data are sparse, and the specific hydrologic and geochemical impact of each of the detonations is likely to have been unique and unknown so that it cannot be treated deterministically.

The saturated alluvial/volcanic aquifer system flow and transport model domain is illustrated in Figure 4-1, which includes the model boundary, subsidence craters at ground surface, and major faults.

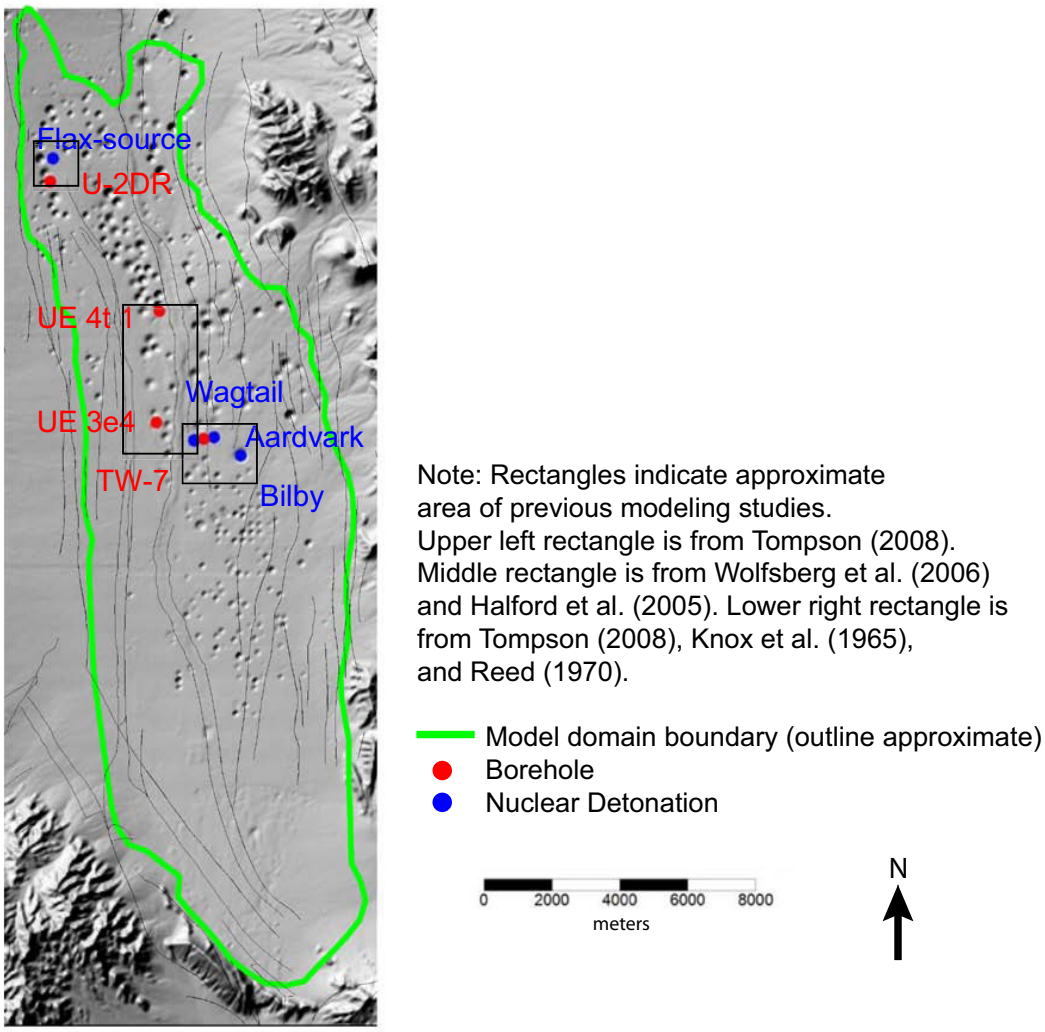

Figure 4-1
Saturated Alluvial/Volcanic Aquifer System Model Domain with Selected Wells and Previously Modeled Areas

Small portions of the saturated alluvial/volcanic aquifer system model domain have been simulated previously (see rectangles in Figure 4-1, which show the approximate extent of previous studies). Several early studies focused on the vicinity of the BILBY, AARDVARK, and WAGTAIL detonations (Knox et al., 1965; Garber and Wollitz, 1969; Reed, 1970; Davis, 1971) primarily to better understand the hydrogeologic impact of underground nuclear detonations. None of these were quantitatively evaluated against pressure data collected at nearby wells. Collectively, these early studies proposed quite a few different conceptual models that need to be considered.

The previously studied area near BILBY was modeled more quantitatively by Tompson (2008). The Tompson (2008) model considered both groundwater flow and contaminant transport. With this model, Tompson (2008) was able to match some aspects of measured hydrographs in the vicinity of BILBY, AARDVARK, and WAGTAIL. In addition, one area to the northwest was simulated, and excellent agreement was achieved with measurements at U-2dr. Based on simulating these two areas using a single conceptual testing-effects model (Model 2 in Section G.1.3.1), Tompson (2008) concluded that transient pressurization due to underground nuclear detonations, excluding those conducted in the "tuff pile" area, had only a minor effect on transport and could be ignored. Tompson (2008) also concluded that radionuclide transport away from detonations would likely be very slow.

The tuff pile area was simulated by Halford et al. (2005) (flow only) and by Wolfsberg et al. (2006) (flow and transport). Both studies included overpressurization due to detonations; Wolfsberg et al. (2006) also included rock damage. The conceptual model proposed by Wolfsberg et al. (2006) (Model 1 in Section G.1.3.1) differs from that proposed by Tompson (2008). The most significant difference expected to affect transport of radionuclides is that the Wolfsberg et al. (2006) model allows for the possibility of rocks outside the cavity and chimney area to fracture if pressures exceed lithostatic pressures, resulting in increased permeability zones. The Tompson (2008) model, in contrast, largely assumes permeability reduction outside the cavity area (in a compressed zone). The approach developed for this study considers both these end-member models and gradations between them using a flexible parameterization. Gradations are achieved by the use of parameters that can be easily varied in sensitivity and uncertainty analysis.

The present study developed and applied a range of testing-effects models because of the need to consider a much larger group of detonations than those considered by previous studies.

In summary, the flow model developed to support CAU-scale radionuclide transport simulations is larger in scale and considers a much larger number of underground nuclear detonations than previous saturated-zone modeling efforts at Yucca Flat. In addition, the model considers multiple alternative conceptual models of testing effects. This model is constrained by hydrographs at a larger number of wells than the previous efforts. Because of the large scale of the model, the degree of fidelity with individual hydrographs will not be as strong as could be achieved with smaller-scale modeling studies, such as those described above.

4.2 Hydrogeologic Conceptual Model

The conceptual model of flow in the saturated alluvial/volcanic aquifer system is based on discussions and data presented in previous studies (Fenelon, 2005; BN, 2006; SNJV, 2006b; Wolfsberg et al., 2006). The primary dataset supporting the conceptual model consists of measured hydraulic heads as compiled by Fenelon (2005). Many, if not most, hydraulic head data within the model domain were affected by underground nuclear detonations. The "natural" flow directions that would have characterized the system before 1958 and to which presumably the flow system will return after relaxing from the perturbations are therefore uncertain. The flow and transport analysis acknowledges this uncertainty.

4.2.1 Flow Directions

A fairly simple picture of groundwater flow in central Yucca Flat could be interpreted from a hydraulic head contour map developed by Winograd and Thordarson (1975). The map strongly suggests lateral flow from both the east and the west toward Yucca fault, which appears to be a drain. However, the head data used to develop this map were very sparse, particularly in the saturated volcanics (basin center), and thus this map largely represents a particular conceptual model rather than strict data contouring. This point is even more evident when present-day water-table data from the saturated volcanics is examined in close detail (Figure 4-2). Water-table elevations range from 735 to 775 m, and there is no tendency to follow the contours presented by Winograd and Thordarson (1975). The authors of SNJV (2006b) acknowledge the lack of clear trends by omitting contours entirely from their presentation of head data in Yucca Flat (Figure 4-2a). A relatively smooth contouring of the most recent available head data is shown in Figure 4-2b. Two interesting features are a relatively high water table in the northwestern section and a relatively low water table in the central section. They imply northerly flow in the northern portion of the volcanics, and both northerly and southerly flows in the southern portion. Even more complex flow directions were inferred from predevelopment water-level data by Fenelon et al. (2012) (Figure 1-11). Fenelon et al. (2012) provide separate contour lines for "alluvial volcanic aquifers" and "volcanic confining units." An interesting feature of the Fenelon et al. (2012) interpretation is that in the southern portion of the volcanics, both northerly and southerly flows are juxtaposed. Figures 4-2a and 4-2b can also be compared to Figure 3-20, which illustrates the elevations of water-table nodes in the unsaturated-zone model. The contours in Figure 4-2b and in Figure 3-20 are not identical. This is because there are insufficient data to illustrate the water-table surface as one unique interpretation.

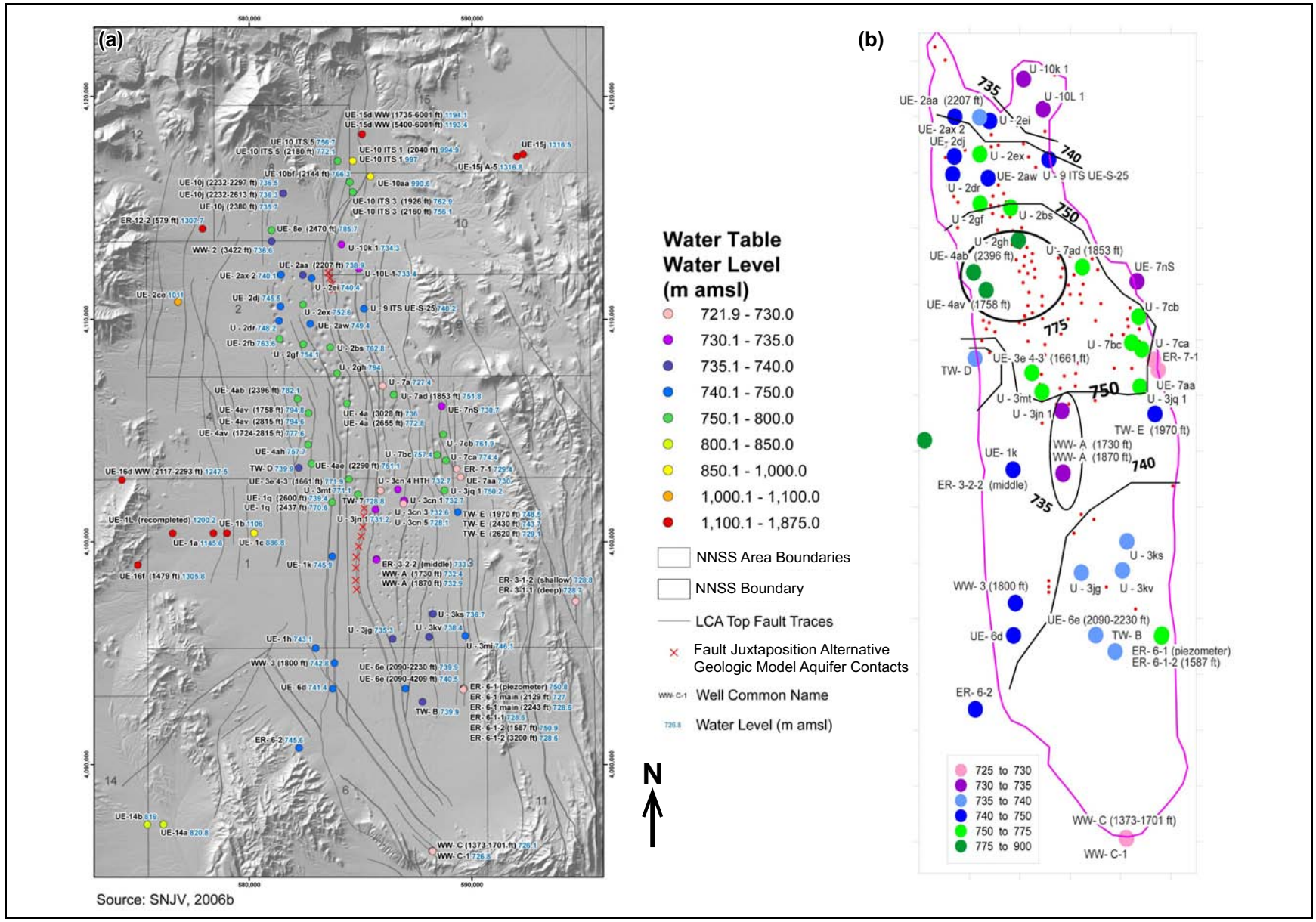

Figure 4-2
Water-Table Water Levels (SNJV, 2006b) and Interpreted Contours (This Study)

Based on interpretations provided by Fenelon (2005) of ubiquitous downward gradients, it is concluded that both before and during subsurface nuclear testing, there was a significant driving force for downward flow from the volcanics to the LCA. The average head difference is approximately 22 m. Therefore, it is reasonable to conclude that flow directions are primarily out of the volcanics and into the LCA. One possible exception to this is along the northern portion of Carpetbag fault, where Fenelon et al. (2012) postulate easterly flow from the LCA into the volcanics.

4.2.2 Predevelopment and Detonation-Induced Fluxes through the Saturated Volcanics

Pretesting Fluxes. There is project-wide consensus that modern pretesting infiltration rates in central Yucca Flat are very low (less than 0.1 mm/yr or net outflow because of ET). These infiltration rates have been enhanced by focused infiltration within surface craters, resulting in an infiltration rate of 10 mm/yr in many craters and up to 3 m/yr in a few craters (Section 3.0). There is less certainty, however, about the rate of deep recharge to the water table. Kwicklis et al. (2006a) argue that the deep vadose zone is still draining Pleistocene water at rates that are higher than modern infiltration rates but still very low (0.1 mm/yr).

Measured pretesting hydraulic heads were, on average, approximately 20 m higher in the saturated volcanics than in the permeable LCA below. Assuming a saturated thickness of 200 m and vertical flow, a steady-state flow field in equilibrium with a recharge rate of 0.1 mm/yr (or less) would correspond to an effective large-scale permeability of the volcanic rocks of 1E-17.5 m^2 (or less). This would presumably reflect the vertical layer with the lowest permeability in the sequence, the tuff confining unit. If one does not assume steady state, but rather a water table that has been slowly falling since abrupt reduction in recharge 8,000 years ago, the required large-scale effective permeability of the volcanic sequence would be no larger than 1E-16 m^2 (supporting calculations are presented in Appendix G).

It is notable that most hydrologic tests conducted in Yucca Flat suggest higher permeabilities for the tuff confining units. A compilation of 12 single-well hydraulic testing results from Yucca Flat for the tuff confining units shows a range of 1E-13.7 to 1E-18.4 m^2 with a geometric mean of 1E-15.2 m^2 and a harmonic mean of 1E-17.3 m^2 (Table 4-1). Hydraulic testing of 50 core samples from the tuff confining units at Yucca Flat (Section G.2.0) shows a range of 1E-11.3 m^2 to “below detection” with a geometric mean of 1E-14.6 m^2 and a harmonic mean of 1E-17.4 m^2 (assigning a value of 1E-18 m^2

Table 4-1
Compilation of 12 Single-Well Testing Results for the Tuff Confining Units

Well Above: UGTA Name Below: USGS Reporting Name	Date	*Hydraulic Conductivity* (m/day)	Permeability Log (m^2)	Comments
U-2bs U - 2bs [a]	01/28/1971	9.1E-04	–15.0	LTCU
U-2gh U - 2gh [a]	08/01/1988	2.4E-04	–15.5	LTCU
U-4t 1 U - 4t 1 [a]	06/04/1986	6.1E-06	–17.1	LTCU (per HFM)
U-7cd 1 U - 7cd 1 [a]	09/16/1992	2.4E-04	–15.5	LTCU
UE-4t 1 UE- 4t 1 (1906–2010 ft) [a]	11/02/1990	3.0E-07	–18.4	Air fall (Fenelon et al., 2010); LTCU (per HFM)
HTH E TW- E (1970 ft) [b]	08/02/1960	5.2E-04	–15.2	Zeolitized
HTH E TW- E (1970 ft) [c]	10/02/1960	1.3E-03	–14.8	Zeolitized
U-3cn-5 U - 3cn 5 [c]	01/03/1966	8.4E-03	–14.0	Fractured
U-3cn-5 U - 3cn 5 [c]	01/01/1966	1.6E-02	–13.7	Partly zeolitized, very fractured
U-3cn-5 U - 3cn 5 [d]	12/19/1965	1.7E-03	–14.7	Partly zeolitized
HTH-2 WW-2 (2045 ft) [d]	03/24/1961	3.6E-03	–14.4	Zeolitic, clayey
HTH-2 WW-2 (2045 ft) [b]	05/30/1961	4.3E-03	–14.3	Zeolitic, clayey

[a] Source: Halford et al., 2005
[b] Source: West and Thordarson, 1963; Dixon et al., 1973; Warren et al., 1998
[c] Source: Garber and Johnston, 1967; Dixon et al., 1973; Warren et al., 1998
[d] Source: Moore et al., 1963; Laczniak et al., 1996; Warren et al., 1998

to each of the 14 “below detection” results). These datasets hint that there might be high-permeability zones within the tuff confining units, which collectively might produce a higher-than-expected large-scale effective permeability. This, in turn, would suggest a higher rate of deep recharge.

The UGTA Activity has generally supported the conceptualization of a tuff confining unit with very low permeability and has noted that hydrologic testing results that indicate more permeable features in the tuff confining units are local anomalies. In previous studies, assigning very low permeability values to the tuff confining units in flow and transport simulations produced results with essentially no radionuclide transport away from even the largest detonations conducted in the tuff confining units

(Tompson, 2008). Results presented later in this section confirm this. However, to acknowledge both the uncertainty in rates of drainage of deep, older water across the water table and the possibility of higher effective permeability of the volcanic sequence, a wide range of recharge rates (0.1, 1, 5, and 10 mm/yr) and effective tuff confining unit permeabilities (1E-14.4 to 1E-15.8 m^2) also were used in the ensemble of flow and transport calculations. As shown later in this section (see Figure 4-12), this range of permeabilities is representative of measured values, although both higher and lower values have been measured at small scales.

Post-testing Fluxes. There are no direct measurements of post-testing fluxes to the water table. Unsaturated-zone simulations presented in Section 3.0 suggest that crater-focused infiltration (at ground surface) does not reach the water table until approximately 400 years after infiltrating. Given the large impact of subsurface detonations to the rocks and pore-water pressures in the saturated volcanics, it is reasonable to assume that fluxes out of the volcanics (into the LCA) might be different from pretesting rates. Increased pressure gradients, sustained for decades in some areas, suggest that the driving force for outflow may have been enhanced.

Keating et al. (2010) proposed that the measured ground surface subsidence from 1992 to 1997 (Vincent et al., 2003) provides a useful constraint on the total volume of water leaving the saturated volcanics as a result of depressurization during the early 1990s. The argument is simple: if it is assumed that ground surface subsidence represents a net decrease in aquifer volume and that water compressibility is much less than aquifer compressibility, then the ground surface subsidence integrated over the study area would be equal to the net volume of water leaving the system.
An extension of this argument is that simulations that approximately reproduce the total measured ground surface subsidence integrated over the study area produce approximately the correct amount of transient outflow from the model domain. Said another way, the ability to reproduce volume-integrated subsidence provides confidence in flux estimates in a specific way that the ability to reproduce a hydrograph does not.

There are, of course, several caveats to this argument. First, if at some locations, measured subsidence is partly due to compression in the unsaturated zone or LCA, this calculation would overestimate fluxes. However, spatial variation in subsidence levels appears to correlate strongly with locations of detonations conducted within the saturated volcanics and with measured declines in pore-water pressure (Halford et al., 2005), so it may be safe to presume that most of the compression occurs in

the saturated volcanics. Secondly, there may be water loss that does not produce measurable subsidence. For this reason, the interferometric synthetic aperture radar (InSAR)-based calculation may be an underestimate of net outflow.

The measured ground surface displacement for three time periods is shown in Figure 4-3. These data were interpolated onto a regular 100-m^2 grid to ease comparison with simulation results. For each grid block, total volume change for the time period was calculated. All positive values were summed. The totals are presented in Table 4-2.

These rates are large compared with inferred pretesting fluxes but integrated over the total period of relaxation; they represent only a very small fraction of the total volume of water in the system.

Considering uncertainty in aquifer and testing-effects parameters, Keating et al. (2010) generated an ensemble of simulations (each with a unique transient flux estimate), all roughly consistent with both measured hydrographs and spatially explicit variation in the subsidence data. Over the total simulation period (1961–2004), the "testing-enhanced" flux estimates (cumulative volume of water leaving the saturated zone because of testing) ranged from 2E+06 to 9E+06 m^3. Given that the InSAR datasets represent approximately15 percent of the total time period, these results are qualitatively reasonable.

The ensemble of simulations used to support the radionuclide transport simulations developed for this report were not compared to spatial variability in the InSAR data. This is partly due to the difficulty of making a spatially explicit comparison with simulations performed on an unstructured grid. It was possible, however, to easily compare total fluxes. The transient, detonation-induced outflow from the simulations presented below will be compared to the data shown in Table 4-2.

4.2.3 Hydrostratigraphy

There are five hydrogeologic units (HGUs) within the saturated alluvial/volcanic aquifer system flow and transport model domain: vitric-tuff aquifer (VTA), welded-tuff aquifer (WTA), alluvial aquifer (AA), tuff confining unit (TCU), and very small portions of the carbonate aquifer (CA). Although the large majority of the LCA in Yucca Flat is within the saturated LCA flow and model domain, small sections were retained within the saturated alluvial/volcanic aquifer system model to preserve relatively smooth model boundaries. Generally speaking, the tuff confining unit lies below the

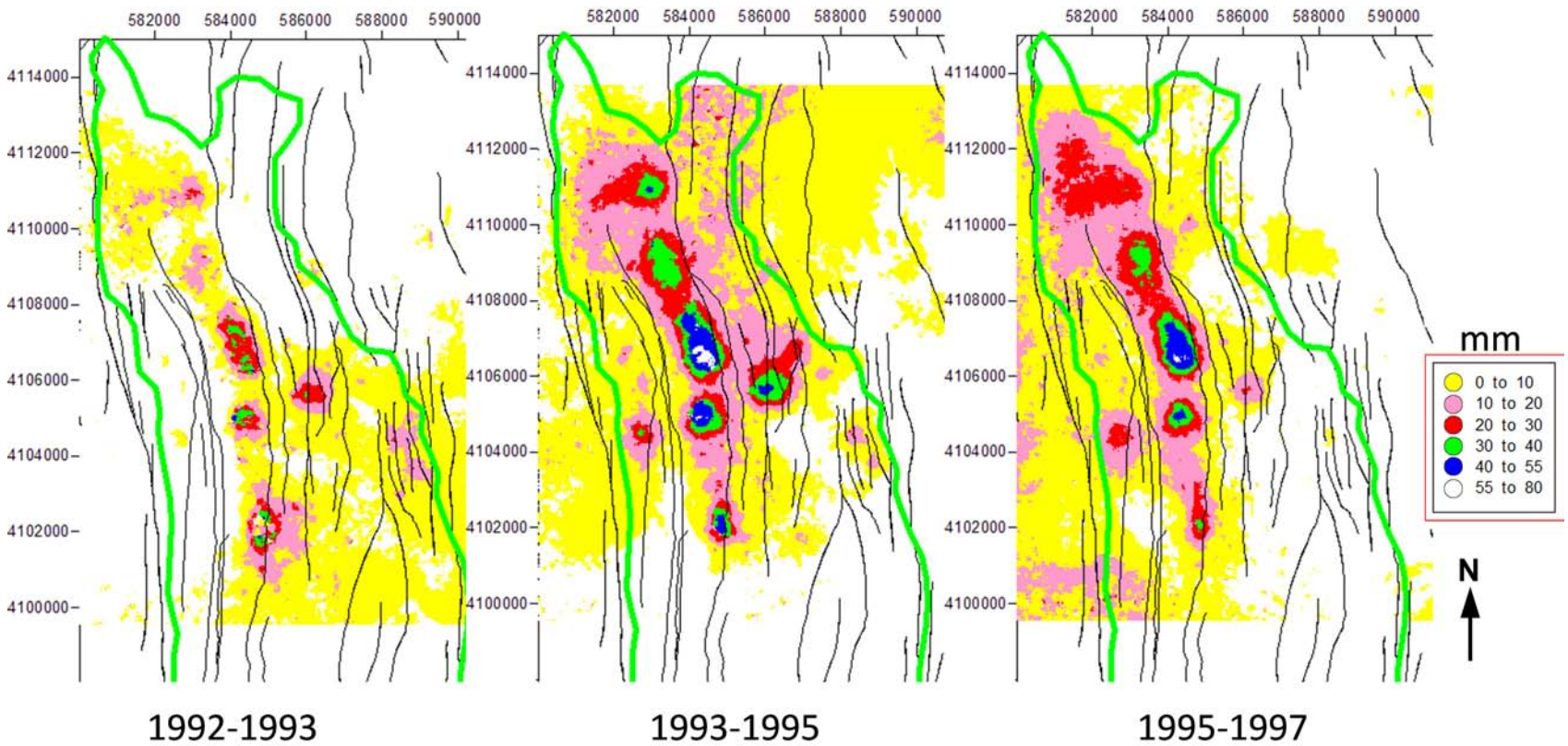

Figure 4-3
Measured Ground Surface Displacement for Three Time Periods Using InSAR Data

Table 4-2
Calculated Volume of Aquifer Compression from InSAR Data

Years	Total Volume (m^3)	Rate (kg/s) [a]
1992–1993	0.62E+06	16.8
1993–1995	1.30E+06	20.7
1995–1997	0.89E+06	14.1

[a] Rate is expressed as kilograms of water per second.

volcanic and alluvial aquifer units, although these units can be locally juxtaposed because of large-offset faults (Figure 4-4). Although generally the tuff confining unit is present between the detonation working points and the underlying LCA, there are factors that may allow for hydraulic communication between the overlying unsaturated zone or saturated alluvial/volcanic aquifer system and the underlying LCA. First, the tuff confining unit is not consistently present (at significant thickness) in all testing areas (Figure 4-4). Second, even in portions of the system where the tuff confining unit is thick, locally the LCA is in direct communication with more shallow, permeable volcanic aquifers because of large-offset faults. Finally, a number of detonations were conducted within the tuff confining unit, and therefore, because of rock damage, the protective characteristics of the tuff confining unit may have been compromised.

The distribution of rock types at the water table is shown in Figure 4-5. The volcanic aquifers include welded-tuff aquifers (TSA and TM-WTA) and vitric-tuff aquifers (TM-LTVA and TM-UVTA). In the welded-tuff aquifers, fractures are common, whereas in the vitric-tuff aquifers, fractures are rare (BN, 2006). The tuff confining units include the OSBCU, the ATCU, and the LTCU. The LTCU is massively zeolitized, but does contain fractures (Prothro, 1998). However, these fractures are considered to be poorly developed and disconnected; thus, they do not serve as the primary flow path for groundwater (SNJV, 2007; Drellack et al., 2010). The ATCU includes argillized volcanic rocks and tuffaceous sediments (Prothro, 2005). The OSBCU includes rocks with diverse lithology and mineralogy, and is potentially quite heterogeneous in its flow and properties. Fracturing in this unit is not thought to be significant. All of the tuff confining units, therefore, are assumed to be dominated by matrix flow.

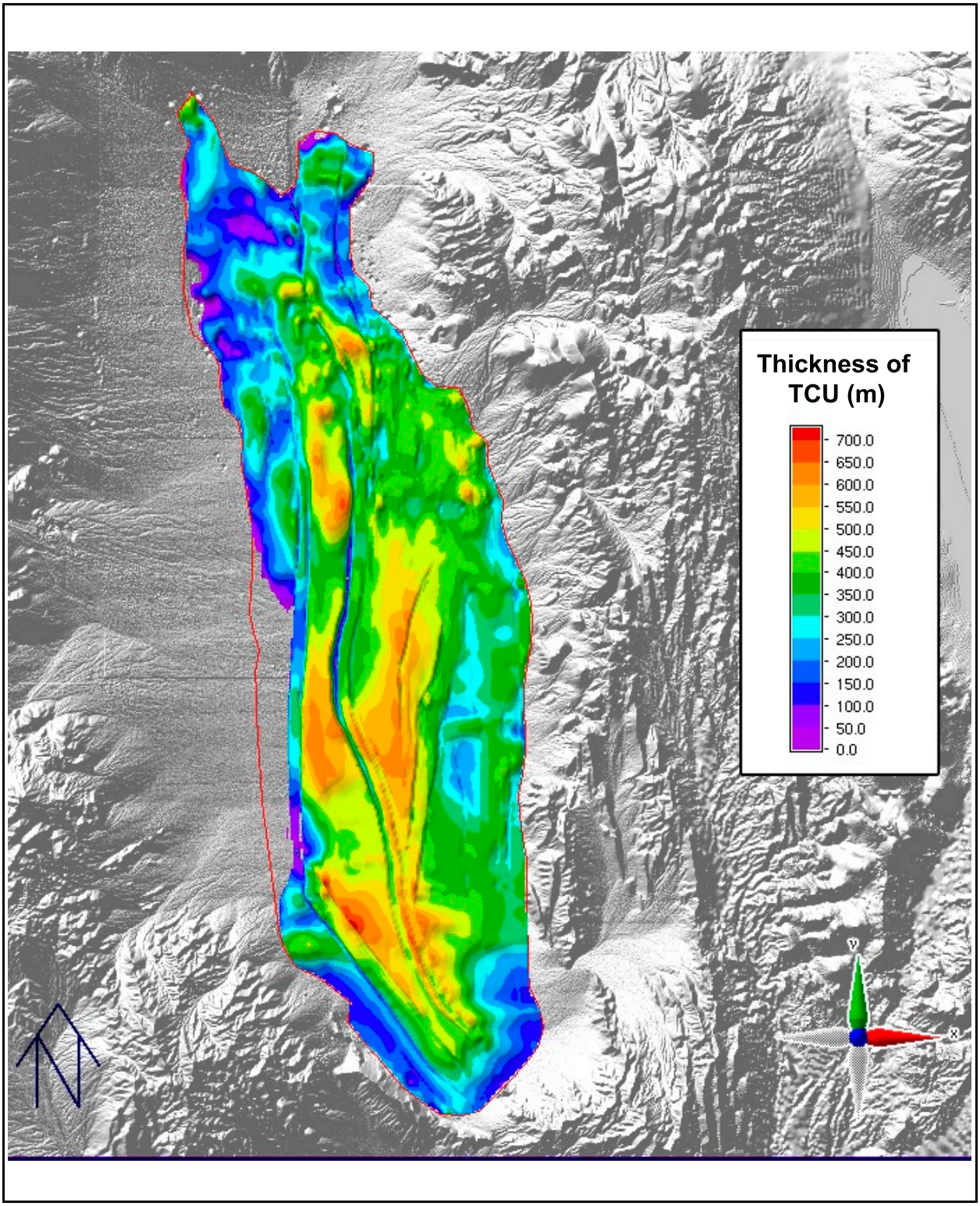

Figure 4-4
Thickness of the Tuff Confining Units

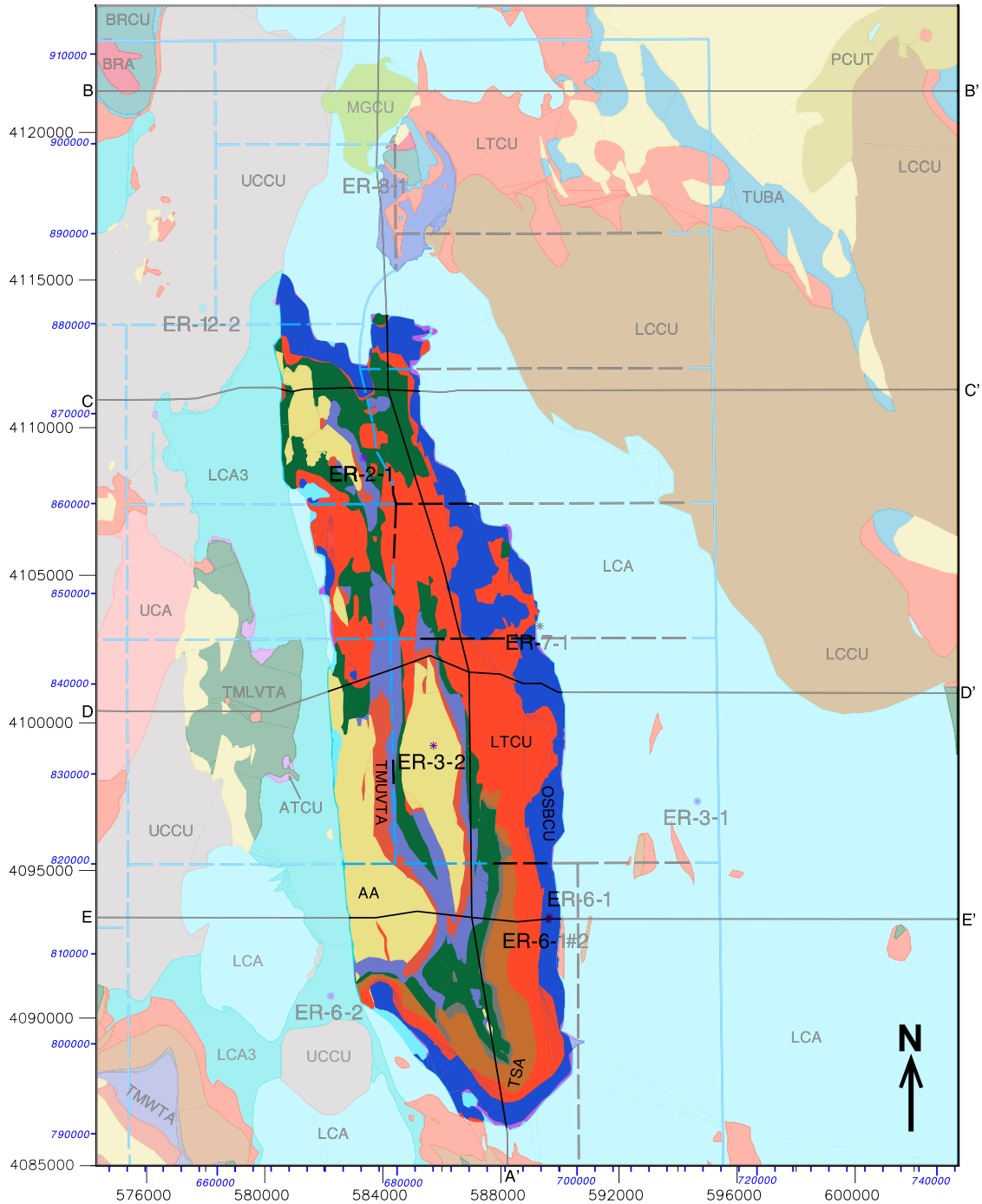

Note: Lighter shade background colors represent HSUs outside the saturated alluvial/volcanic aquifer system model domain. Darker shade represents HSUs within the saturated alluvial/volcanic aquifer system model domain. Distribution of HSUs at water table is illustrated in Figure 1-8.

Figure 4-5
Distribution of Rock Types at the Water Table
Source: Modified from BN, 2006

4.2.4 Hydraulic Properties

Although there is clearly evidence of heterogeneity within each of the major HSUs in the saturated alluvial/volcanic aquifer system model domain, and their average permeability and specific storage are uncertain, there is ample hydrologic evidence to support the conceptual model that, on average, the alluvial aquifer and volcanic aquifer units are much more permeable than the tuff confining units. Figure 6-3 in SNJV (2006b) illustrates this point. See Appendix G for a detailed summary of hydrologic data.

The hydrologic role of faults in the saturated alluvial and volcanic aquifer units is uncertain. Head and geochemical data within the saturated alluvial and volcanic aquifer units and nearby LCA wells are too sparse to provide information about which faults may act as drains or barriers. There have been no long-term pumping-scale aquifer tests that could be used to assess the possible role of faults. There is clear evidence that some faults were activated by underground nuclear detonations. Arguments can be made based on rock lithology that a single fault, such as Yucca fault, may have different hydrologic characteristics in each of the units. Brittle rocks such as the LCA and welded-tuff aquifers, for example, may have both enhanced (damage zone) and reduced (fault core) permeability within fault zones. In contrast, fault traces within deformable, soft rocks such as the LTCU or in alluvium may be "flow neutral." As a consequence, the modeling approach considers fault properties highly uncertain parameters. In the base-case calculations, it is assumed that most of the major faults are permeable (Wolfsberg et al., 2006) and provide a pathway for water to flow downward to the LCA. Alternative cases with faults with much lower permeability also are considered.

4.2.5 Hydrologic Connection to the LCA

There are many lines of evidence that water from the volcanics enters the LCA; however, the flux rate and the spatial distribution of this flux are uncertain. Based on relatively nonunique geochemical inverse modeling, SNJV (2006b) suggested that many of the wells completed in the LCA in Yucca Flat could contain a component of local recharge or drainage from the overlying volcanic rocks. However, groundwater ^{36}Cl/Cl ratios in the LCA provided some of the most direct evidence for drainage from the volcanic and alluvial aquifers to the LCA. It has been observed that groundwater in the LCA often has much lower ^{36}Cl/Cl ratios than modern precipitation (with estimated ^{36}Cl/Cl ratios of 500E-15) because of dissolution of low ^{36}Cl-bearing chloride contained in the carbonate rock matrix (Moran and Rose, 2003). It has also been noted from pack-rat midden studies (Plummer et al.,

1997) that before about 10,000 years ago, meteoric $^{36}Cl/Cl$ ratios were approximately twice as high as at present, so that $^{36}Cl/Cl$ ratios in groundwater significantly above 500E-15 are reflective of recharge during the late Pleistocene. Figure 4-6 shows $^{36}Cl/Cl$ ratios (× 1E+15) of groundwater by aquifer type. The overwhelming majority of groundwater samples from the volcanic and alluvial aquifers and from the UCCU and LCCU thrust plate have $^{36}Cl/Cl$ ratios well above 500E-15, consistent with an interpretation that they infiltrated during the late Pleistocene when meteoric $^{36}Cl/Cl$ ratios were elevated above their present levels (Figure 4-6a). Conversely, most of the groundwater samples from the LCA contain $^{36}Cl/Cl$ ratios well below modern values, consistent with the evidence in Moran and Rose (2003) that their $^{36}Cl/Cl$ ratios have been lowered by incorporating Cl from the 300 Ma carbonate rock matrix in which ^{36}Cl has largely decayed. Appendix L provides further evidence that groundwater from the LCA and some deep samples from the tuff confining units beneath the playa in Frenchman Flat have been affected by Cl dissolution.

Only wells UE-1c, TW D, and UE-1q have high $^{36}Cl/Cl$ ratios typical of groundwater from the alluvial and volcanic aquifers, suggesting relatively local drainage to the LCA from those aquifers (UE-1c was pumped from both the alluvium and LCA, so the high $^{36}Cl/Cl$ ratio could be attributed to the alluvial component). However, because of lateral flow in the LCA, the postulated drainage could have entered the LCA at upgradient (northern) locations rather than exactly at the locations of the wells themselves. Additionally, because of the relatively sparse sampling locations in the LCA, Figure 4-6 does not rule out the possibility that drainage could also be occurring along the many other faults beneath the volcanic rocks.

The primary conceptual model is that hydrologic communication between the volcanics and the LCA is limited spatially, and the most likely locations for outflow are along faults. This is supported by indications of confining conditions in the LCA beneath the volcanics during pumping of ER-6-1. There are a number of factors that could produce confining conditions, including low-permeability zeolized tuffs, clay-rich layers within the OBSCU, and paleosols filling the uppermost fractures of the carbonate aquifer. Finally, the substantial hydraulic head gradient between the volcanics and the LCA, even in the presence of very low recharge rates and relatively impermeable tuff confining units, is more easily explained if the hydraulic connection between the volcanics and LCA is limited.

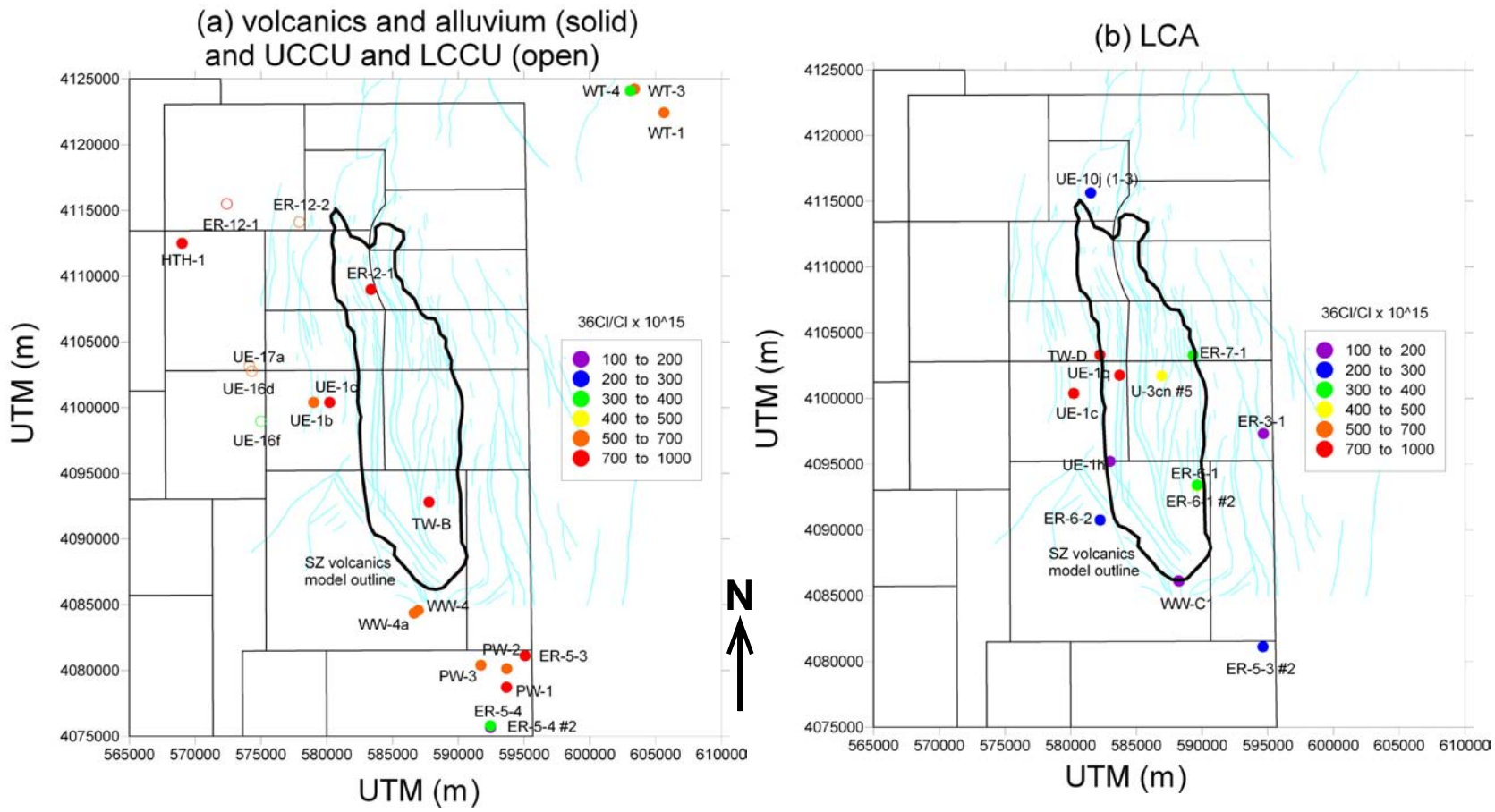

Note: Open circles in (a) indicate that groundwater was from the UCCU or LCCU thrust plate. Blue lines are faults in the Yucca Flat HFM (BN, 2006).

Figure 4-6
Groundwater ^{36}Cl/Cl Ratios (× 1E+15) of (a) Alluvial/Volcanic Aquifers and Clastic Confining Rocks and (b) the LCA

4.2.6 Testing Effects

The natural hydrologic system was affected greatly by underground nuclear testing. Pore-water pressures increased dramatically after testing. In some locations, pressures dissipated rapidly (days or less); in others, pressures remained elevated for decades (Figure 4-7). In addition to pore-water pressure perturbations, elastic and nonelastic changes in permeability and porosity of the rocks occurred. Because both pressurization effects and changes in rock properties are considered significant, capturing these effects at least to a first order is an important goal of model development. However, these aspects of the conceptual model are highly uncertain. This is because no direct measurements of near-field hydrologic properties have been made. Also, near-field water-pressure measurements (made before and after testing) are sparse (available at only four locations: Test Well 7 (HTH), U-9ca, U-7cb, and U-3cn 4 HTH). Detailed and varied conceptual models of the hydrogeologic effects of nuclear testing have been proposed; examples include Knox et al., 1965; Garber and Wollitz, 1969; Reed, 1970; Davis, 1971; Charlie et al., 1996; Laczniak et al., 1996; Cole et al., 1997; and Pawloski, et al., 2008. The analyses presented herein draw elements from many of these models. Appendix G includes further details of previous work on this topic.

It is generally agreed that chimney and cavity environments experienced dramatic changes; further near-field changes were more subtle but perhaps just as important from a radionuclide transport perspective. Types of nearly instantaneous changes to rock properties include creation of a compacted zone (with presumably lower permeability), creation of a chimney and cavity (with presumably higher permeability), and hydrofracturing (increasing permeability). In addition, pressures appear to increase in some zones (outside the cavity) and decrease within the cavity. The ability to model the details of all these changes at each detonation within a CAU-scale flow and model is limited. Instead, our approach considers detonation-specific characteristics as uncertain parameters that can be varied randomly in the context of sensitivity and uncertainty analysis. This approach should be capable of creating a robust ensemble of model predictions, bounding the “true” behavior of the system.

The following paragraph is from Tompson (2008, p. 7-3):

> In terms of **porosity** and **hydraulic conductivity**, slight to moderate increases would be expected in the cavity and chimney rubble zones of hard rock systems owing to bulking effects; decreases would be expected in the first several meters of the peripheral crushed zones owing to pulverization, at least, with some potential increases beyond that owing to increased fracturing; and, further out in the compressed

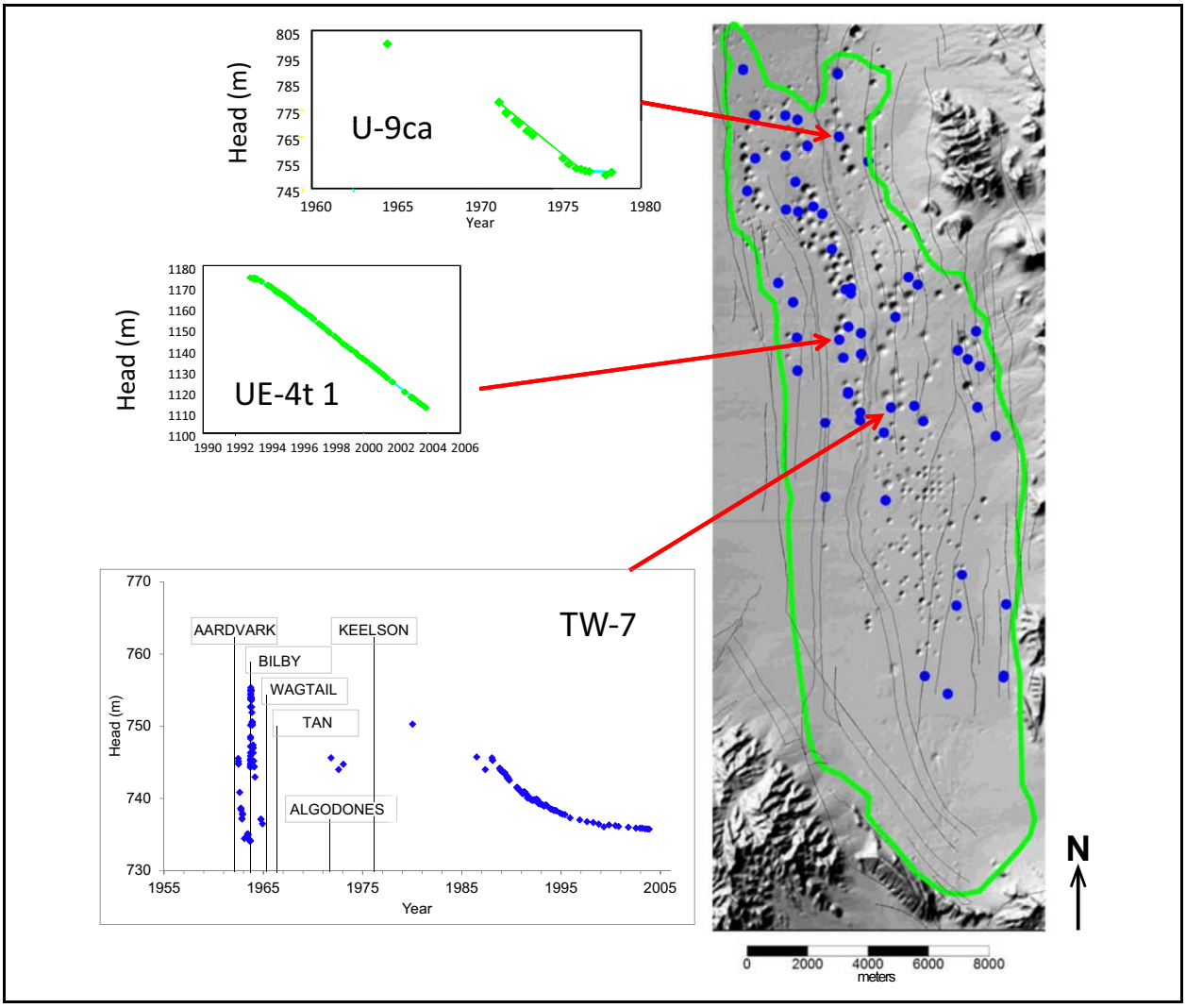

Figure 4-7
Wells with Completions in the Saturated Volcanics and Selected Hydrographs Showing Long-Term Effects of Testing

zones, slight to nil decreases may be observed (e.g., Chapter 5; Carle et al., 2008; Pawloski et al., 2001). In alluvial settings, smaller to no increases would be expected in the cavity areas owing to slumping or disorganized sorting effects caused during collapse (e.g., Carle et al., 2007); decreases would still be expected in the first several meters of the peripheral crushed zones, and would continue beyond that into the compressed zones, as there would be little possibility for fracturing-based increases.

These recommendations are only qualitative, which is appropriate considering the lack of near-field permeability or porosity measurements in Yucca Flat (before or after nuclear testing). Notably, Tompson (2008) gives recommendations for only “hard rock” and “alluvial” systems; which combined represent less than one-half the volume of the saturated alluvial/volcanic aquifer system model domain. As is documented in Appendix G and later in this section, rock property changes due

to testing can be parameterized by a numerical scheme to represent the qualitative trends described above. It is prudent, however, to also include scenarios where significant permeability increases occur beyond the cavity wall because of either explosion phenomenology or rock failure due to pressurization in excess of lithostatic (Wolfsberg et al., 2006). This broader view of possible testing effects may introduce faster radionuclide transport predictions to the ensemble of results; the consequences of this are discussed in Section 4.6.

The dataset compiled by Fenelon (2005) includes head data (single or time series) from 60 wells with a completion in the saturated alluvial/volcanic aquifer system. The locations of these wells are shown in Figure 4-7.

Conceptual Model Summary. In summary, groundwater inflow occurs as recharge at the water table and lateral inflow from the carbonate aquifer. The recharge rate is probably not at steady state and may be quite different from modern (shallow) infiltration rates. Under natural conditions, the recharge will tend to flow through shallow volcanic aquifers into permeable fault zones, flowing downward and discharging to the LCA (Figure 4-8). Because of underground nuclear detonations, flow directions could have been quite different from this simple behavior, at least for short periods of time. Initially, high-pressure zones developed around each detonation outside the margin of the gaseous cavity (Tompson, 2008). Immediately after the detonation, these high-pressure zones caused both radially outward and radially inward hydraulic gradients that dissipated quickly or slowly, depending on the local properties of the rock. Rock properties also were affected, but there is substantial uncertainty as to the extent and nature of the damage at each detonation.

4.3 Numerical Model Development

The goal of the numerical model development was to include as much detail as needed to honor the available quantitative hydrologic information and to build in sufficient flexibility to explicitly recognize the substantial uncertainty inherent in the conceptual model. A small number of uncertain factors were treated conservatively (e.g., fault permeability) so that potential errors due to conceptual model deficiencies would tend to result in overestimating contaminant transport (faster transport). The impact of these conservative assumptions was assessed by sensitivity analysis, as will be discussed below.

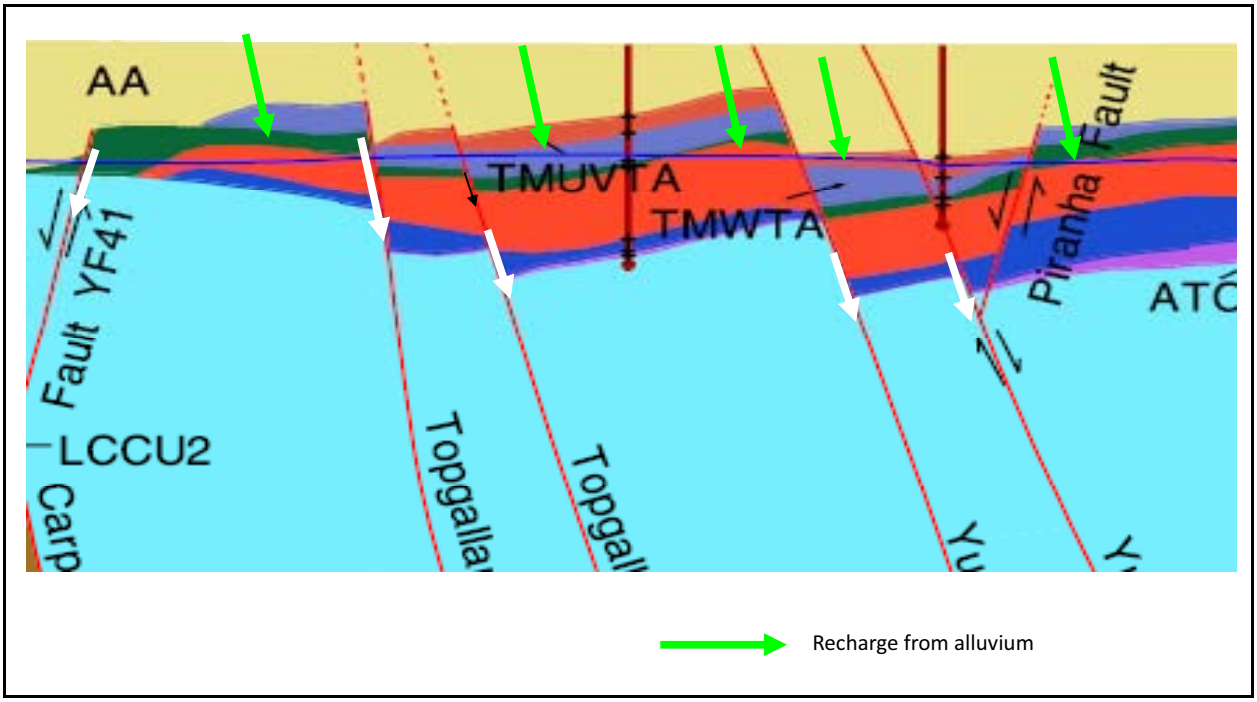

Figure 4-8
Conceptual Model of Flow from the Unsaturated Zone and Downward into the LCA along Faults

Model Extent. Lateral and lower model extent was defined strictly by stratigraphy and structure (faults) in the HFM (BN, 2006). The lateral model extent at the water table generally corresponds to the intersection of the saturated alluvial and volcanic rock units with the water table. The decision not to include the small areas of saturated alluvial and volcanic units outside the polygon was made for convenience and because no sources exist in these isolated areas. The model domain propagated to ground surface is illustrated in Figure 4-1.

The upper surface of the numerical model is defined by the water table. As mentioned above, present-day water-table elevations range from 735 to 775 m amsl, with complicated features such as mounding in the northern portion and sinks in the middle portion. Multiple lines of evidence suggest that the water table moved substantially during the period of interest (1950–1995) (Knox et al., 1965; Fenelon, 2005). Preliminary calculations were made that simulated a transient water table at great computational expense. It was determined that a simplification of establishing a flat and static water table (z = 750 m) was a reasonable compromise between accuracy and computational efficiency.

4.3.1 Numerical Mesh

Based on the model extent described above, orthogonal grids were developed with the EarthVision model (BN 2006; SNJV 2006b). Six numerical grids were used to provide a range of differing resolutions. A relatively coarse version (3b) was used for many preliminary flow model calculations, including calibration. This grid had a uniform horizontal resolution of 125 by 125 m and a vertical resolution varying from 500 m in deep layers to 50 m in the shallow layers. The resolution of this base grid is equivalent to the lower-resolution cells in the inset to Figure 4-9. Grid 3b was further enhanced to provide very high resolution in the vicinity of each detonation (12.5-by-12.5-by-12.5-m cubes). The locations of the high-resolution areas and an image of a resolved zone are shown in Figure 4-9.

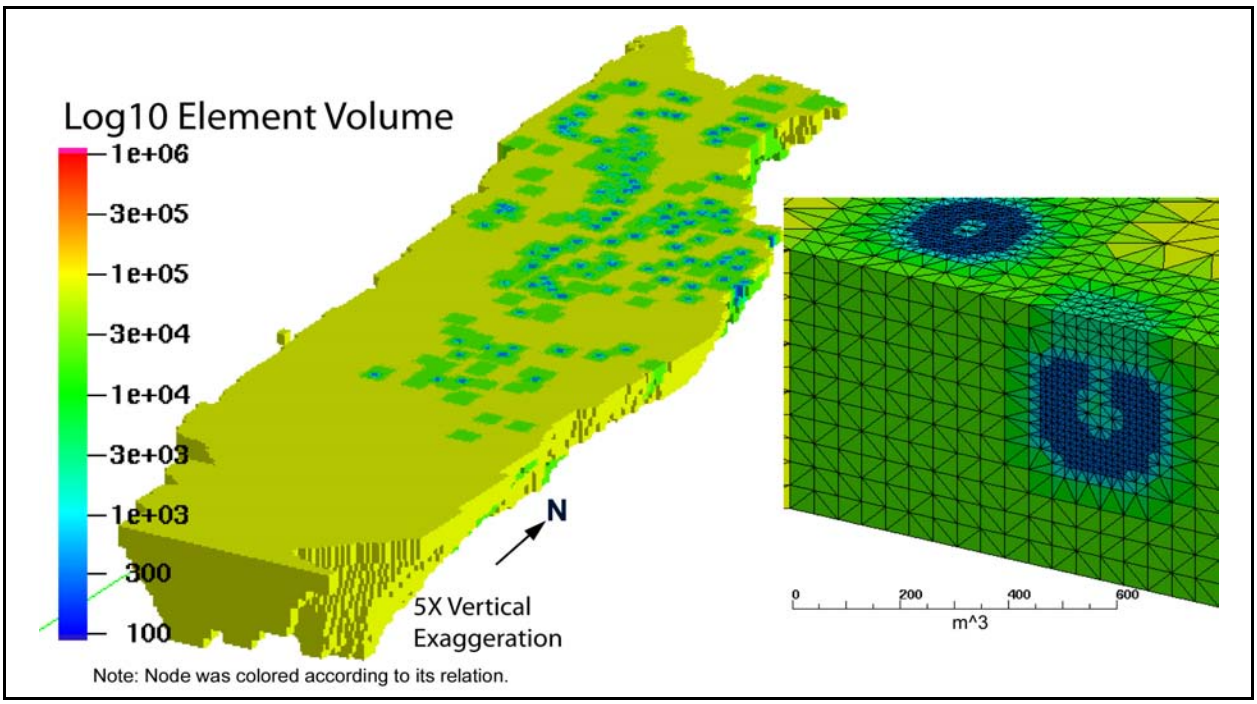

Figure 4-9
Locations of Increased Grid Resolution near Cavities

Each node was colored according to its relation to the HFM and the faults within the model domain. Figure 4-10 shows the spatial distribution of HSUs and faults as resolved by this grid.

Most of the LCA has been removed, except a thin rind along the edges (for the purpose of boundary condition application, described below) and a small section in the northwestern portion of the model domain. This latter section was retained to provide a geometrically smooth lateral boundary.

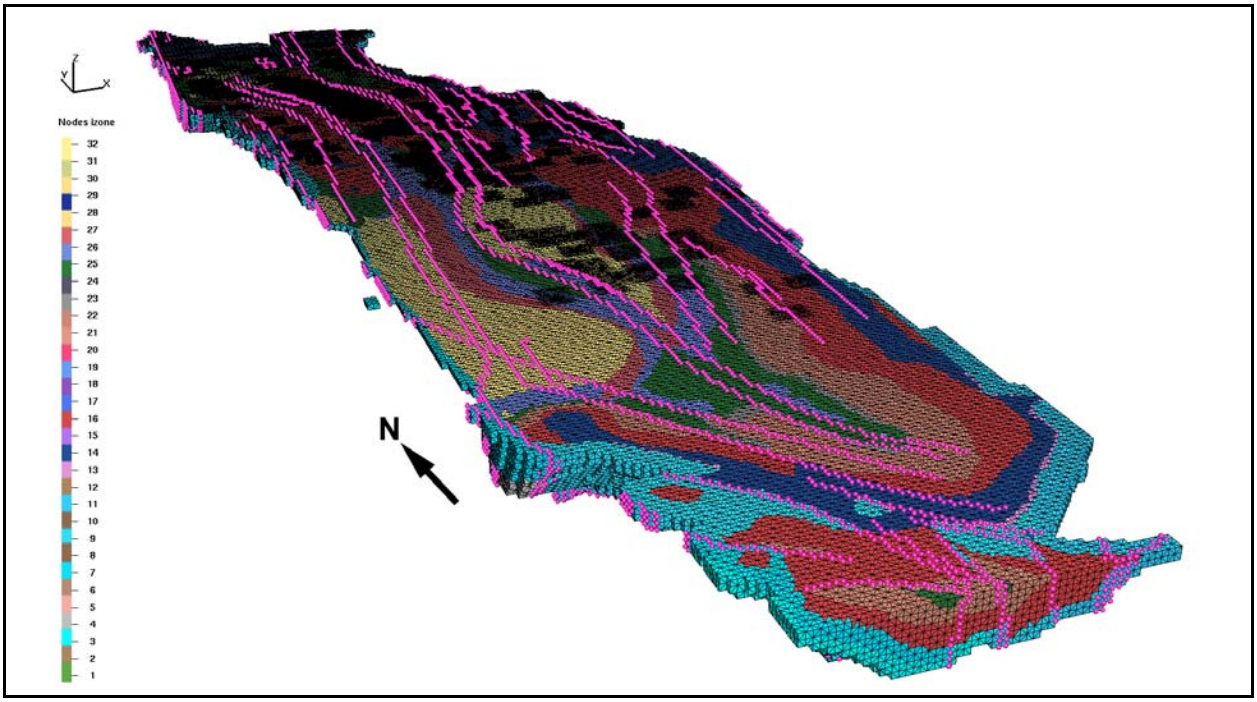

Figure 4-10
Numerical Mesh, Colored by HSUs and Faults (Pink Dots)

The number of nodes and fraction of total (active) model volume are shown in Table 4-3. The most important units (volumetrically) are the two confining units: the LTCU and OSBCU (56 percent total). The volcanic aquifers make up 12 percent and the alluvial aquifers 5 percent. The numerous faults make up 15 percent of the total model volume.

Table 4-3
Summary of Node Count and Total Volume of Each HSU (and Faults) within the Active Model Domain
(Page 1 of 2)

Zone	HSU Abbreviation	Node Count	Volume (m^3)	Fraction of Total Volume
7	LCA3	100	1.83E+07	0.00
9	LCA	2,888	6.64E+08	0.01
11	LCA	4	5.63E+05	0.00
13	ATCU	21,528	4.65E+09	0.07
14	OSBCU	146,161	2.29E+10	0.35
16	LTCU	189,549	1.41E+10	0.21
22	TSA	7,323	2.51E+09	0.04
23	UTCU	1,443	4.73E+08	0.01

Table 4-3
Summary of Node Count and Total Volume of Each HSU (and Faults) within the Active Model Domain
(Page 2 of 2)

Zone	HSU Abbreviation	Node Count	Volume (m^3)	Fraction of Total Volume
25	TM-LVTA	52,176	3.78E+09	0.06
26	TM-WTA	17,367	2.55E+09	0.04
27	TM-UVTA	8,080	1.21E+09	0.02
28	AA1	1,890	8.15E+08	0.01
30	AA2	998	3.92E+08	0.01
32	AA3	22,060	1.66E+09	0.03
114	Faults (all)	51,660	1.01E+10	0.15

Boundary Conditions. The water-table boundary was defined by constant, spatially variable flux (pretesting) and by transient, spatially variable flux after the beginning of testing. Pretesting and transient fluxes were determined on a node-by-node basis according to results produced by the unsaturated-zone models (beneath the footprint of the unsaturated-zone models) and spatially uniform rates elsewhere. The algorithm used to map fluxes across model boundaries strictly enforced mass conservation. The algorithm varied pretesting fluxes between 0.1 to 10 mm/yr (corresponding to infiltration rates used by the unsaturated-zone models) to capture a reasonable range of possible discrepancies between modern near-surface infiltration rates and deep unsaturated-zone recharge rates, without adding the computational burden of conducting a fully transient pretesting recharge model.

The lower and lateral boundaries were no-flow boundaries except along the lower surface of the model, where faults intersect the LCA. This is consistent with the conceptual model of the primary mechanism of hydrologic connection with lower aquifers described above in Section 4.2.5. Alternative modes of connection will be explored in sensitivity analyses described below. Those nodes where faults intersect the LCA are illustrated in Figure 4-11. They are shown as red dots.

These nodes were considered specified head outflow only. Heads were determined by interpolating simulated heads at the top of the LCA model. The “outflow only” specification was necessary to prevent water from short-circuiting, flowing in along one section of a fault (from the LCA), and discharging to an adjacent section. While these boundary conditions neglect lateral inflow from the

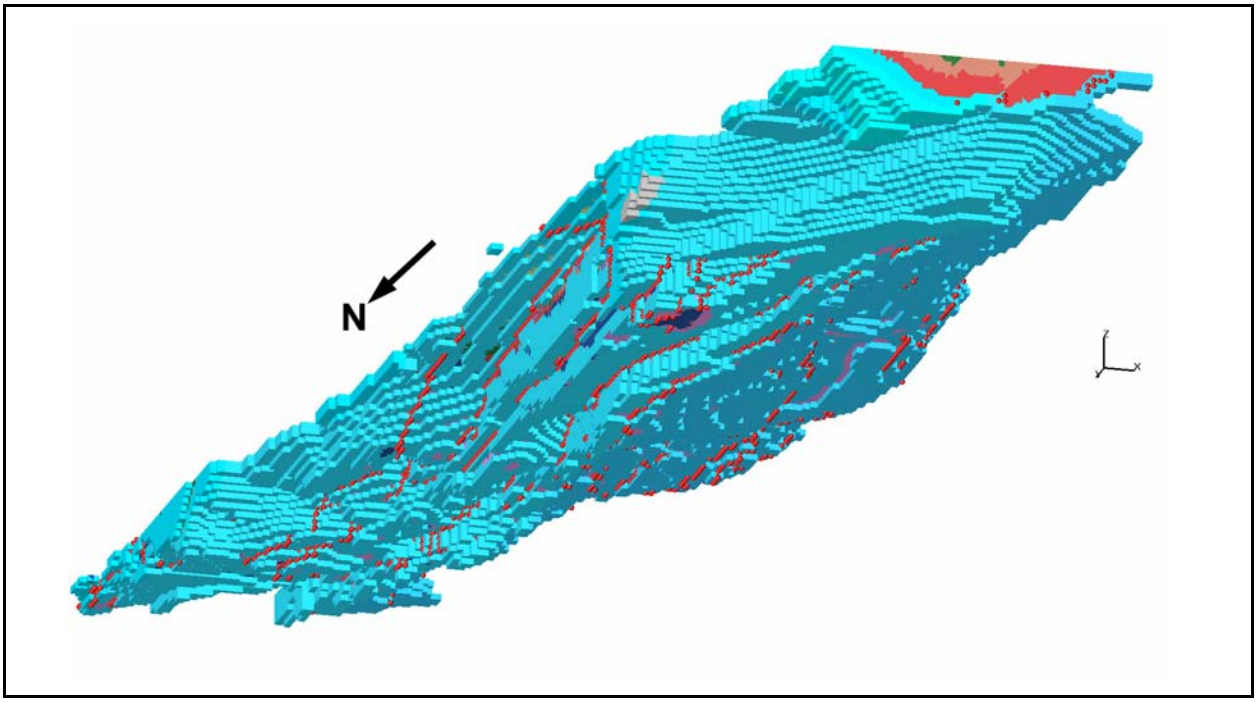

Figure 4-11
Constant Head Nodes at the Intersection of Faults and the Top of the LCA

LCA to the volcanics (as suggested by the Winograd and Thordarson [1975] map, Figure 2), this should not significantly impact radionuclide transport simulations because there are very few sources in the LCA. This strategy generally resulted in reasonable model results; however, in a few locations near the lateral boundaries of the model with few or no major faults mapped, this strategy did not provide sufficient drainage, and thus, simulations produced extremely high, unrealistic heads locally. As a remedy for this problem, several zones where the non-faulted top of the LCA is constant head (outflow only) were established. These are very small regions in the far north and a larger region including the southern end of the model.

Pretesting Rock Properties. Each node in the flow model was required to have the following properties defined: permeability (*x*, *y*, and *z* components), specific storage, and porosity. (Note: A dual-continuum model was assumed for some units in the transport phase of the calculations.) For permeability and specific storage, properties were assigned based on field testing (as compiled in Halford et al. [2005], discussed in detail in Appendix G) and the model calibration processes. Permeability values that represent large spatial scales and that were specifically collected in Yucca Flat were strongly emphasized (see “pumping-scale tests” and “slug tests” in Figure 4-12; purple diamonds are slug tests interpreted by Halford et al. [2005]). Model calibration

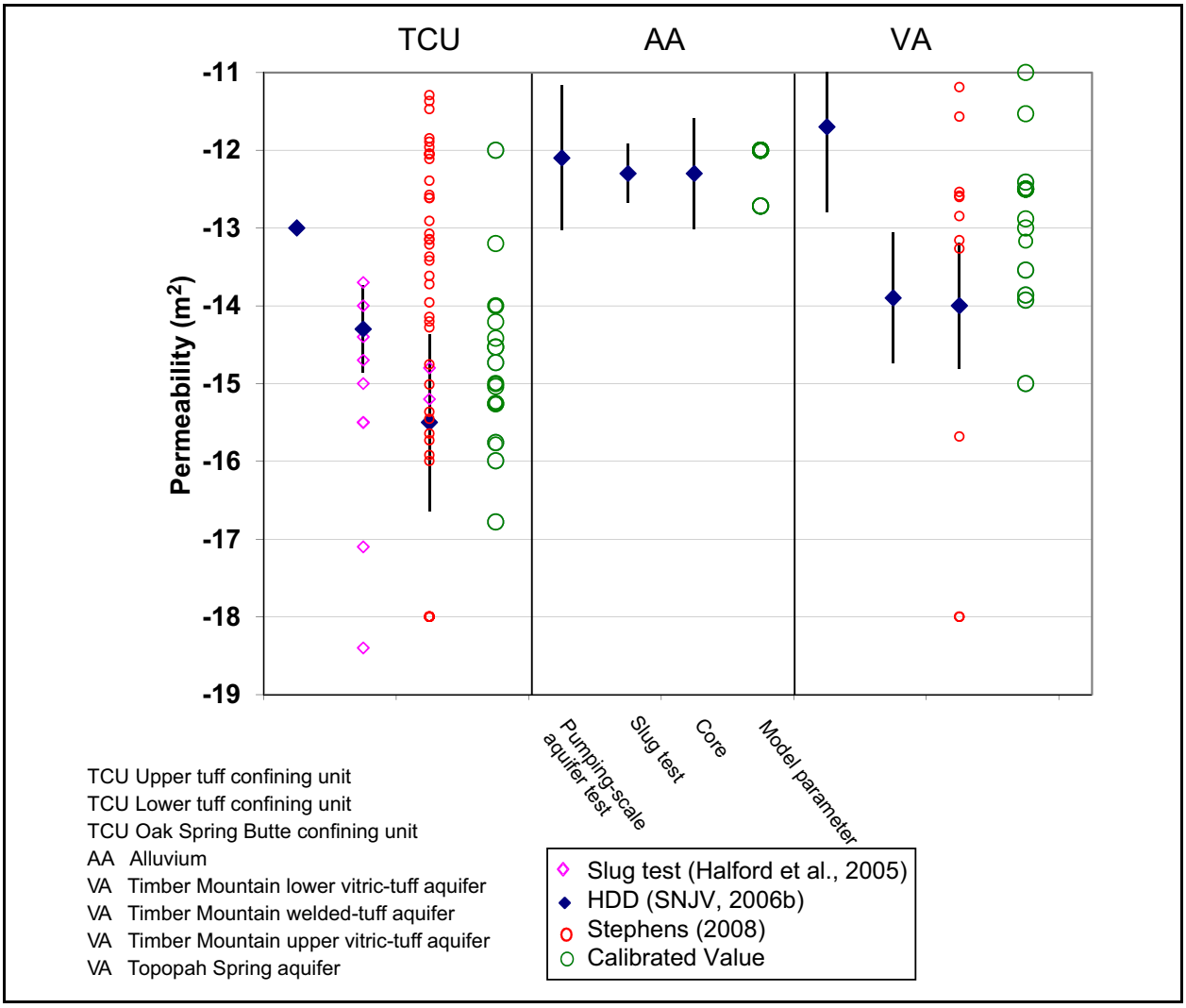

Figure 4-12
Results of Hydrologic Testing, Compared to Calibrated Values

provided additional information about values appropriate for the scale of grid cells. Several sets of permeability values were used in the analysis to explore uncertainty. These are shown in Table 4-4. As shown in Figure 4-12, these values are consistent with data collected previously at the site.

Specific storage values are presented in Table 4-5. A large range of values was reported for each HSU in SNJV (2006b), representing the observation that some areas of the tuff confining units are confined and some are not. The values used here fall well within previously estimated ranges. Both relatively low (representing confined conditions) and high (more similar to unconfined values) specific storage cases will be presented to test the sensitivity of the results to this parameter.

Table 4-4
Intrinsic Permeability Values (Log, m²)

HGU	HSU	Zone	Permeability Code (and Recharge) within Case Name (See Table 4-11)						
			11 (0.1 mm/yr)	12 (0.1 mm/yr)	5 (1 mm/yr)	1 (5 mm/yr)	7 (5 mm/yr)	8 (5 mm/yr)	6 (10 mm/yr)
CA	LCA	12	–12	–12	–12.5	–12	–12	–12	–12.5
TCU	ATCU	13	–14.73	–14.73	–14	–14	–14	–14	–13.2
TCU	OSBCU	14	–16.78	–16.78	–15.24	–14.53	–14.53	–14.53	–14.21
TCU	LTCU	16	–15.76	–15.76	–15.77	–15.04	–15.04	–15.04	–14.42
VTA	TSA	22	–12.41	–12.41	–13.17	–13	–13	–13	–11.53
TCU	UTCU	23	–15.99	–15.99	–15.26	–15.26	–15.26	–15.26	–15.26
VTA	TM-LVTA	25	–13.86	–13.86	–12.5	–12.88	–12.88	–12.88	–12.5
VTA	TM-WTA	26	–15	–15	–12.5	–12.5	–12.5	–12.5	–12.5
VTA	TM-UVTA	27	–13.93	–13.93	–12.5	–12.88	–12.88	–12.88	–12.5
AA	AA1	28	–12.72	–12.72	–12	–12	–12	–12	–12
AA	AA2	30	–12.72	–12.72	–12	–12	–12	–12	–12
AA	AA3	32	–12.72	–12.72	–12	–12	–12	–12	–12
Faults			–15	–13	–12	–12	–14	–15	–12

Table 4-5
Specific Storage Values (Log 1/m) Compared to Those Reported by SNJV (2006b)

HGU [a]	Number of Measurements	Average	Minimum	Maximum	Specific Storage Code within Case Name (See Table 4-11)		
					2	11	12
AA	22	–4.0	–6.9	–3.1	–3.9, –3.0	–6	–5
VA	72	–2.4	–14.4	–0.9	–3.9, –3.0	–6	–5
TCU	52	–4.2	–6.9	–3.1	–4.2, –4.0	–6	–6
LCA	162	–1.4	–8.3	–0.3	–4.0	–6	–6

[a] Specific storage data are categorized by HGU in SNJV (2006b). The Yucca Flat HGUs reported by SNJV (2006b) include the volcanic aquifer (VA) and lower carbonate aquifer (LCA) HGUs, in addition to the alluvial aquifer (AA) and tuff confining unit (TCU) HGUs.

For most of the units, effective porosity was assigned based on data compiled by SNJV (2006b). Because of its potential importance for both transient flow and transport calculations and the uncertainty in data in SNJV (2006b) for the Yucca Flat tuff confining units, 62 core samples were collected from the USGS NTS Core Library and analyzed for effective porosity. These data are tabulated in Section G.2.0. The majority of the samples were of zeolitized tuff; thus, these data were used to constrain the effective porosity for the LTCU and UTCU, as indicated in Table 4-6.

Table 4-6
Porosity Values
(Page 1 of 2)

HGU	HSU	Zone	Porosity Code within Case Name (See Table 4-11)		Source
			2	14	
CA	LCA	12	0.001	0.005	SNJV, 2006b
TCU	ATCU	13	0.15	0.34	SNJV, 2006b
TCU	OSBCU	14	0.15	0.38	SNJV, 2006b
TCU	LTCU	16	0.15	0.26	Stephens, 2008
VTA	TSA	22	0.001	0.003	SNJV, 2006b
TCU	UTCU	23	0.15	0.26	Stephens, 2008
VTA	TM-LVTA	25	0.15	0.43	SNJV, 2006b
VTA	TM-WTA	26	0.001	0.003	SNJV, 2006b
VTA	TM-UVTA	27	0.15	0.42	SNJV, 2006b
AA	AA1	28	0.15	0.34	SNJV, 2006b

Table 4-6
Porosity Values
(Page 2 of 2)

HGU	HSU	Zone	Porosity Code within Case Name (See Table 4-11)		Source
			2	14	
AA	AA2	30	0.15	0.41	SNJV, 2006b
AA	AA3	32	0.15	0.37	SNJV, 2006b
Faults			0.001	0.003	Assumed WTA properties

There is very little information about anisotropy of HSUs in Yucca Flat. Several possibilities, shown in Table 4-7, were considered. These range from assuming all HSUs are isotropic to assuming several key units (LTCU, OSBCU, and AA) are moderately to strongly anisotropic.

Table 4-7
Permeability Anisotropy Values

HGU	HSU	Zone	Permeability Anisotropy Code within Case Name (See Table 4-11)							
			1	2	3	4	5	6	7	8
CA	LCA	12	1	1	1	1	1	1	0.0014	0.1
TCU	ATCU	13	1	1	1	1	1	1	0.0014	0.1
TCU	OSBCU	14	1	1	1	1	0.1	1	0.0014	0.1
TCU	LTCU	16	1	1	1	1	0.1	1	0.0014	0.1
VTA	TSA	22	0.1	0.1	0.1	1	1	0.1	0.0014	0.1
TCU	UTCU	23	1	1	1	1	1	1	0.0014	0.1
VTA	TM-LVTA	25	0.1	0.1	0.1	1	1	0.1	0.0014	0.1
VTA	TM-WTA	26	0.1	0.1	0.1	1	1	0.1	0.0014	0.1
VTA	TM-UVTA	27	0.1	0.1	0.1	1	1	0.1	0.0014	0.1
AA	AA1	28	1	0.5	0.2	1	0.5	0.5	0.0014	0.1
AA	AA2	30	1	0.5	0.2	1	0.5	0.5	0.0014	0.1
AA	AA3	32	0.1	0.1	0.1	1	0.5	0.5	0.0014	0.1
Faults			1	1	1	1	1	1	1	1

4.3.2 Testing Effects

Of the 744 detonations in Yucca Flat, 180 had working points within 3 R_c of the saturated alluvial/volcanic aquifer system model domain and 108 within 1 R_c. Each of these detonations, regardless of whether the working point is within the model domain, is assumed to have the ability to potentially pressurize water and affect rock properties (permeability, porosity) within the model domain. Two mathematical models were developed that, when applied with a range of parameter values, span a large range of possible detonation-induced effects. Both models assume that an instantaneous cavity and chimney form, with relatively high porosity and permeability, and hydrostatic pressure. Both models assume that each detonation generated a unique degree of pressurization (possibly but not necessarily correlated with detonation yield), which in turn affected rock properties. The characteristics of the two models differ in the following ways: (1) the degree of pressurization/rock damage varies continuously with radial distance from the working point or only in a discrete zone, (2) detonation-induced rock damage tends to increase or decrease permeability, and (3) a critical pressure that, if exceeded, will lead to rock failure (and increased permeability) exists or does not exist. The details of the testing-effects models are presented in Appendix G.

A key parameter affecting both models is the maximum overpressurization (in meters) present just outside the cavity immediately following the detonation. This parameter in turn controls the degree and extent of rock damage. Undoubtedly, each detonation produced a unique level of overpressurization. Through model calibration, the likely levels of overpressurization for a small number of detonations could be constrained. For most detonations, there is no information on the level of overpressurization. The best calibrated set of overpressurization levels produced very low (less than 200 m) overpressurization levels for most detonations and very high levels (up to 1,200 m) for a small number of detonations (see set A in Figure 4-13). This set does produce a good calibration at the CAU scale, but is not unique. For the transport analysis portion of this section, the best calibrated values (set A) were used, along with two additional sets obtained with the relationship between announced yield and overpressurization developed by Wolfsberg et al. (2006) (sets B and C in Figure 4-13). According to recommendations in Tompson (2008), a set with only a few detonations in limited areas (the tuff pile area, Test Well 7 (HTH) area) having any pressurization at all also was used (Case D). The spatial distributions of these sets are shown in Figure 4-14. The variable Ho shown in the figure is the overpressurization at the working point, in meters (see Figure G-10 for details).

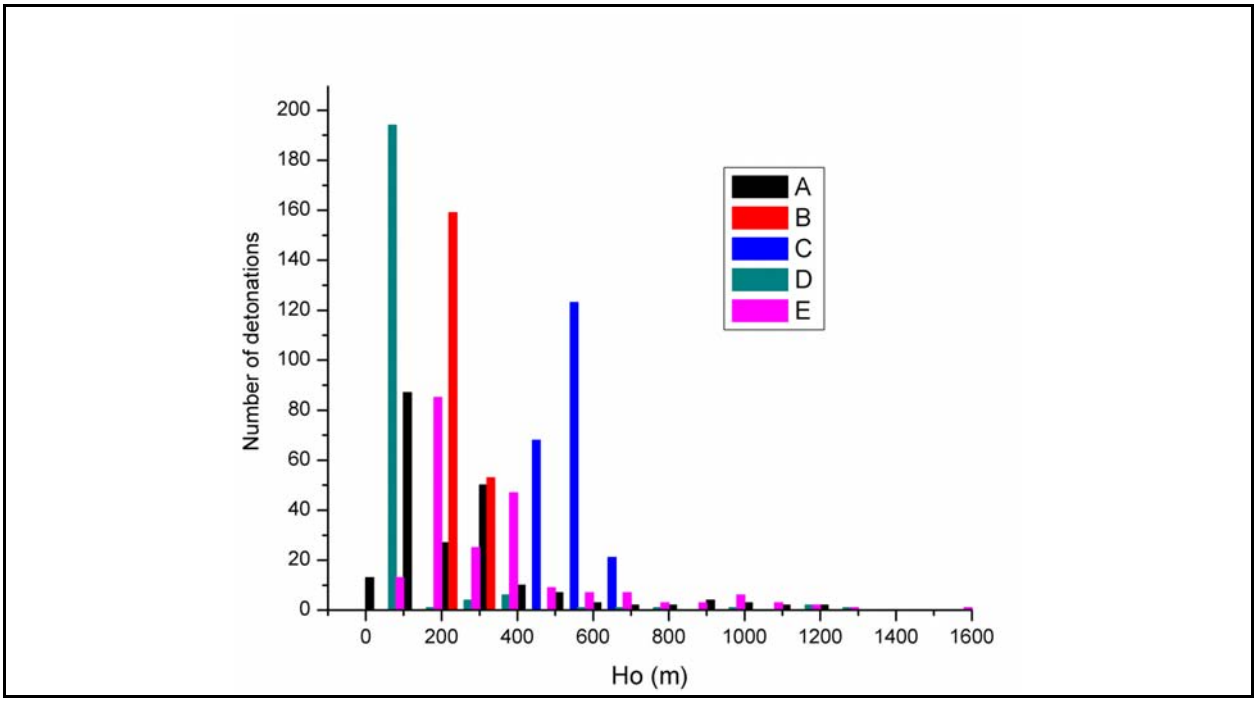

Figure 4-13
Distributions of Modeled Levels of Pressurization

The testing-effect model, presented in great detail in Appendix G, is a Fortran 90 code, and requires the following input: general testing-effects information (a flag indicating which mathematical model is assumed and all the parameter values required for that model); test-specific information (a flag indicating which test is being simulated, and the level of pressurization assumed for that test [H_o, in meters] and the cavity radius [R_c, in meters]); the initial fluid pressure, permeability, and porosity for every node in the model; and the HSU associated with each node. The output of the code is the post-testing fluid pressure, permeability, and porosity.

Because a single-phase (water-only) approximation is used, the initial period of cavity infilling is not considered. The impact of this omission is worthy of discussion. As pressures redistribute after the detonation, the infilling of the cavity will induce radial inward flow. If inward flow dominates for the entire period of depressurization (the tendency to return to pretesting pressures), "hydrologic containment" of radionuclides could occur, and possible outward transport due to pressurization-induced gradients could safely be neglected altogether. Tompson (2008, Section 6.3) explains this inward migration as follows: "This migration . . . is relatively small and short-lived, with maximum distances being on the order of 100 m. The importance of cavity refilling may be less important in areas where high pore-water pressures remain for long periods (e.g., on the order of

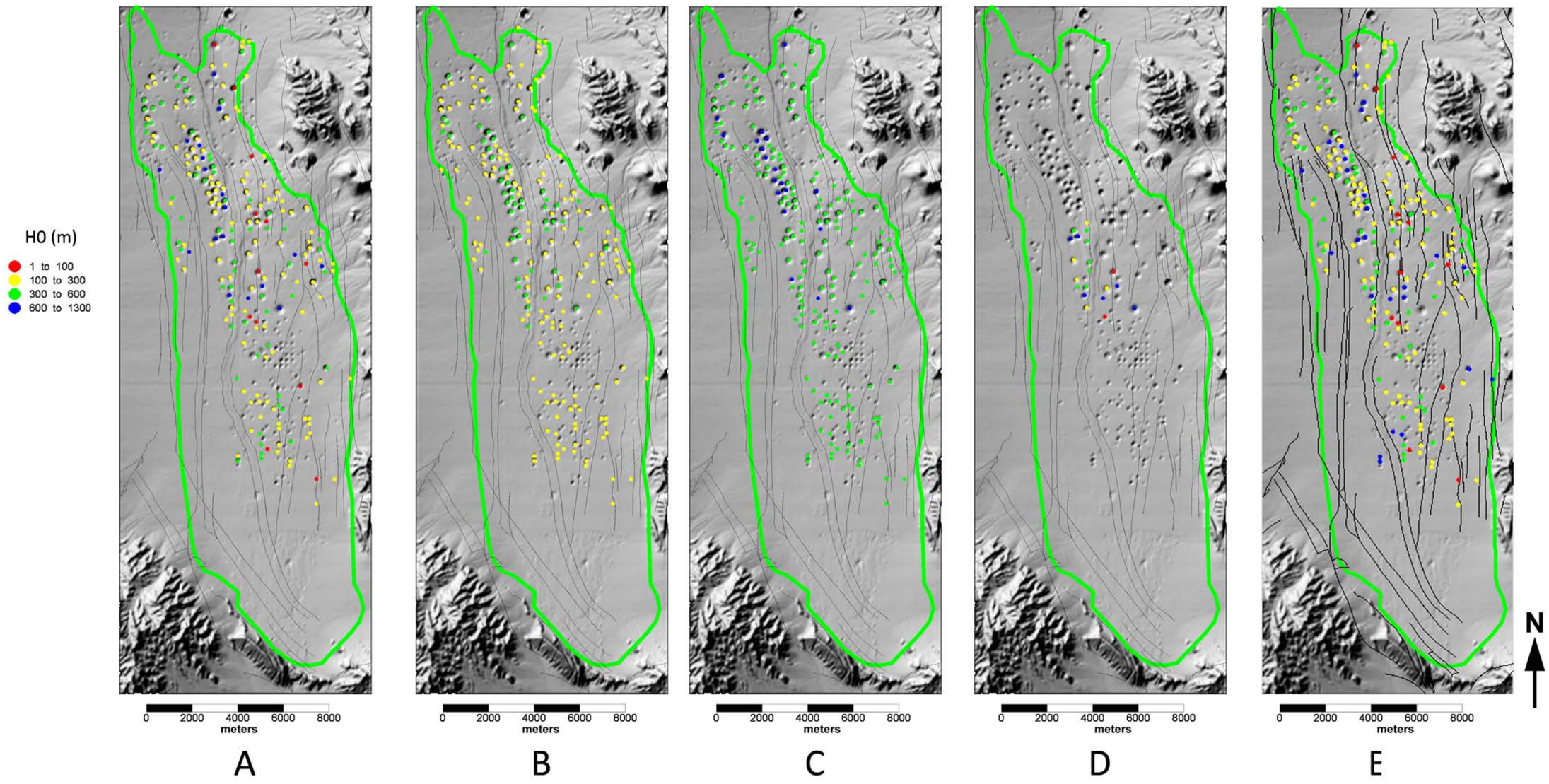

Figure 4-14
Spatial Distribution of Overpressurization Datasets for Sets A through E Shown in Figure 4-13

decades or more).” In order to confirm this assertion, a mass balance calculation was performed to assess the impact of neglecting the cavity infill. Inward flow due to cavity infilling was determined to be a very minor fraction (less than 5 percent) of the total water mass distribution expected to occur because of pore expansion and decompression. Most of that distribution is expected to be radially outward (or up the chimney), and thus, radionuclides will likely experience outward testing-induced gradients. It is important to note that, immediately after the detonation, as a pragmatic approximation, the cavity and chimney are set to hydrostatic conditions and that this does create inward transport of radionuclides for some period of time.

4.3.3 The Coupled Model

The testing-effects code is sequentially coupled to the FEHM groundwater flow model (Zyvoloski et al., 1997). Although the coupling could be applied after each detonation, for computational efficiency, the period from 1963 to 1995 was divided into 11 time periods, each including a number of detonations that are simulated simultaneously. First, FEHM is used to calculate a steady-state flow field, based on a pretesting recharge rate and pretesting rock properties. The pressures resulting from this calculation are input to the testing-effects code, which perturbs fluid pressures and rock properties for the group of detonations corresponding to that time period, and outputs the current pressure, permeability, porosity, and specific storage for every node in the model domain. FEHM uses the output from the testing-effects code as an initial condition for the first transient groundwater flow calculation (time period 1). This sequence repeats for each of the 11 time periods. Because of the assumed relation between pressure and porosity in FEHM (elastic storage), very minor changes occur to the porosity field during the groundwater flow simulations. All other rock property changes made by the testing-effects code are irreversible. The specific definition of the 11 time periods was based largely on the timing of hydrographs used for model calibration. The time periods began with FISHER (December 1961), AARDVARK, (May 1962), MERRIMAC (July 1962), BILBY (September 1963), WAGTAIL (March 1965), BUFF (December 1965), TAN (June 1966), COVE (February 1977), TURQUOISE (April 1983), ALEMAN (September 1986), and TEXARKANA (February 1989). Each time period included the pressurization due to that detonation and all the detonations afterwards until the next time period.

4.4 Model Calibration

The saturated alluvial/volcanic aquifer system groundwater flow model was calibrated to measured head data compiled by Fenelon (2005). This required not only selecting appropriate portions of the head dataset for model calibration, but also reducing the complexity of the coupled testing-effects/groundwater-flow model so that run times were sufficiently short to be coupled to the calibration software PEST (Doherty, 2004). These two processes are described briefly below. A more detailed description of the calibration process is provided in Appendix G.

4.4.1 Water-Level Data Selection

The electronic database compiled by Fenelon (2005) provides excellent notation on the conditions affecting various water-level measurements made in Yucca Flat since the 1950s. This database was screened to include water-level measurements that met the following two criteria: (1) the well was completed mostly within the saturated alluvial/volcanic aquifer system model domain, and (2) the notation accompanying the water-level measurement did not mention possible influence of drill-back operations. This latter criterion is important because many wells were drilled with the assistance of large volumes of water, and in some cases, water levels took a long time to equilibrate to representative aquifer conditions. Although Fenelon (2005) also made notes of whether the water levels were likely to be representative of background conditions or affected by nearby underground nuclear detonations, there was no presumed distinction between these two types of data.

There were 60 wells with head data that met these criteria. Table 4-8 lists these 60 wells and summarizes the available data. Figure 4-15 indicates the locations of the wells. Filled and inverted triangles indicate wells with repeated measurements over time (i.e., hydrographs). All others are shown as open triangles.

All the water-level data are compressed into a single plot and shown in Figure 4-16. These data range from 728 to 1,174 m. It is clear from this figure that the most complete hydrographs represent later times. During the time period of active testing, most wells were measured only once or a very few times.

Table 4-8
Wells Used for Calibration Purposes
(Page 1 of 3)

Well Above: UGTA Name Below: USGS Reporting Name	Easting (m)	Northing (m)	Ground Surface Elevation (m)	Depth to Top of Screen [a] (m)	Depth to Bottom of Screen (m)	Screen Length (m)
HTH-2 WW-2 (2045 ft)	581,005.6	4,113,499.5	1,362.3	485.9	623.3	137.5
UE-6e UE- 6e (2090–2230 ft)	587,012.5	4,093,408.7	1,200.3	637.0	679.7	42.7
UE-4t 1 UE- 4t 1 (1906–2010 ft)	584,575.5	4,106,066.8	1,262.2	580.9	612.6	31.7
UE-4av UE- 4av (1758 ft)	582,665.6	4,105,777.6	1,273.1	38.1	535.8	497.7
UE-4av UE- 4av (1724–2815 ft)	582,665.6	4,105,777.6	1,273.1	535.8	858.0	322.2
UE-4ae/Inst. UE- 4ae (2290 ft)	582,802.4	4,103,510.7	1,258.9	24.1	698.0	673.9
UE-4ab/Inst. UE- 4ab (2396 ft)	582,167.6	4,106,418.7	1,280.5	21.6	730.3	708.7
UE-4a (HTH) UE- 4a (2655 ft)	584,389.9	4,106,210.4	1,266.4	260.9	809.2	548.3
UE-3mf/Inst. UE- 3mf (1692–2395 ft)	584,886.0	4,101,847.2	1,239.3	515.7	730.0	214.3
UE-3mf/Inst. UE- 3mf (119–1692 ft)	584,886.0	4,101,847.2	1,239.3	36.3	515.7	479.5
UE-3e 4 UE- 3e 4-3 (1661 ft)	584,481.2	4,102,812.7	1,244.0	469.4	508.4	39.0
UE-3e 4 UE- 3e 4-2 (1919 ft)	584,480.9	4,102,812.7	1,244.0	558.4	587.0	28.7
UE-3e 4 UE- 3e 4-1 (2181 ft)	584,480.9	4,102,812.7	1,244.0	638.3	668.1	29.9
UE-2dj/Inst. UE- 2dj	581,406.3	4,110,575.6	1,323.1	23.5	716.3	692.8
UE-2b UE- 2b	581,137.8	4,109,485.4	1,313.7	36.6	1,070.5	1,033.9
UE-2ax 2 UE- 2ax 2	581,425.7	4,111,995.3	1,340.0	21.9	746.8	724.8
UE-2aw/Inst. UE- 2aw	582,743.7	4,109,794.4	1,302.1	23.5	709.6	686.1
UE-2ar Inst. UE- 2ar	582,831.3	4,108,811.2	1,292.6	24.7	716.6	691.9
UE-2aa UE- 2aa (2207 ft)	582,406.9	4,111,980.8	1,325.1	23.5	672.7	649.2
UE-1q UE- 1q (2437 ft)	583,722.6	4,101,777.6	1,244.0	24.4	742.8	718.4

Table 4-8
Wells Used for Calibration Purposes
(Page 2 of 3)

Well Above: UGTA Name Below: USGS Reporting Name	Easting (m)	Northing (m)	Ground Surface Elevation (m)	Depth to Top of Screen [a] (m)	Depth to Bottom of Screen (m)	Screen Length (m)
UE-1k UE- 1k	583,731.2	4,099,339.3	1,234.7	33.5	712.6	679.1
U-10k 1 Expl./Inst. U- 10k 1	584,148.3	4,113,350.6	1,302.2	685.8	693.4	7.6
U-9ca 1 U- 9ca 1	584,176.1	4,111,286.3	1,293.6	548.6	978.4	429.8
U-9 ITS UE-S-25 U - 9 ITS UE-S-25	585,153.5	4,110,463.7	1,286.9	24.1	618.1	594.1
U-7cd U - 7cd	584,903.0	4,104,066.6	1,254.2	36.6	495.3	458.7
U-7cc U - 7cc	586,784.1	4,106,359.2	1,306.5	171.0	487.7	316.7
U-7cb U - 7cb	588,718.6	4,104,823.3	1,306.5	94.5	563.9	469.4
U-7ca U - 7ca	588,835.4	4,103,654.0	1,293.6	83.8	548.6	464.8
U-7bz U-7bz (817–2188 ft)	586,041.5	4,105,290.2	1,272.8	263.7	666.9	403.3
U-7bd U - 7bd	588,106.3	4,104,182.9	1,287.3	36.0	609.6	573.6
U-7bc U - 7bc	588,432.1	4,103,893.8	1,289.0	36.3	685.8	649.5
U-7ba U - 7ba	584,900.5	4,104,756.9	1,258.6	35.7	458.4	422.8
U-7au U - 7au	584,324.4	4,103,942.8	1,252.9	35.7	490.4	454.8
U-7ad U-7ad (1965 ft)	586,483.3	4,106,603.9	1,306.2	34.4	598.9	564.5
U-4u U-4u (2112 ft)	584,497.2	4,104,964.6	1,255.6	36.6	643.7	607.2
U-4t 1 U - 4t 1	584,578.6	4,106,233.6	1,263.1	36.0	640.1	604.1
U-4r U - 4r	584,186.8	4,104,543.3	1,255.6	36.3	685.8	649.5
U-4au U - 4au	582,789.4	4,104,607.4	1,263.2	36.0	533.4	497.4
U-3mt U - 3mt	584,879.0	4,102,131.9	1,239.7	33.5	472.4	438.9
U-3mi U - 3mi	589,703.9	4,095,777.5	1,221.0	115.8	546.8	431.0

Table 4-8
Wells Used for Calibration Purposes
(Page 3 of 3)

Well Above: UGTA Name Below: USGS Reporting Name	Easting (m)	Northing (m)	Ground Surface Elevation (m)	Depth to Top of Screen [a] (m)	Depth to Bottom of Screen (m)	Screen Length (m)
U-3kz U - 3kz	584,481.3	4,1027,54.7	1,245.0	669.6	670.0	0.3
U-3kv U - 3kv	588,070.8	4,095,728.3	1,205.9	36.3	487.7	451.4
U-3ks U - 3ks	588,250.1	4,096,765.1	1,208.7	36.0	490.7	454.8
U-3jq Ex. 1/Inst. U - 3jq 1	588,764.0	4,102,312.9	1,272.4	36.0	677.9	641.9
U-3jn Ex. 1/Inst. U - 3jn 1	585,667.4	4,101,447.6	1,233.2	413.9	609.6	195.7
U-3cn 4 HTH U - 3cn 4 HTH	586,675.8	4,102,350.7	1,244.7	615.7	699.5	83.8
U-3cn 1 U - 3cn 1	586,973.6	4,101,828.0	1,241.8	609.6	749.8	140.2
U-2gh U - 2gh	583,945.6	4,107,567.0	1,273.2	36.3	548.9	512.7
U-2gf U - 2gf	582,426.9	4,108,875.7	1,295.0	36.6	551.7	515.1
U-2ex U - 2ex	582,414.8	4,110,652.2	1,314.1	36.6	612.3	575.8
U-2ei U - 2ei	582,803.5	4,111,845.1	1,319.0	36.0	640.1	604.1
U-2bs U - 2bs	583,637.6	4,108,733.8	1,288.2	25.6	585.2	559.6
U-2av U - 2av	583,141.9	4,110,977.7	1,310.0	24.4	668.4	644.0
HTH E TW- E (1970 ft)	589,361.9	4,101,336.4	1,271.6	176.8	600.5	423.7
Test Well B Ex. TW- B	587,779.9	4,092,816.0	1,198.4	509.0	510.5	1.5
Test Well 7 (HTH) TW- 7	585,901.0	4,102,301.2	1,236.8	614.8	692.5	77.7
ER-6-1-2 ER- 6-1-2 (1587 ft)	589,616.6	4,093,357.0	1,199.5	465.1	483.7	18.6
ER-6-1 ER- 6-1 piezometer	589,632.5	4,093,418.8	1,200.1	437.4	470.0	32.6
ER-3-2 ER- 3-2-1 (deep)	585,716.3	4,099,227.6	1,222.3	871.7	914.4	42.7
ER-2-1 ER- 2-1 (2559 ft)	583,334.6	4,108,978.3	1,285.0	705.0	792.5	87.5

[a] Or open interval

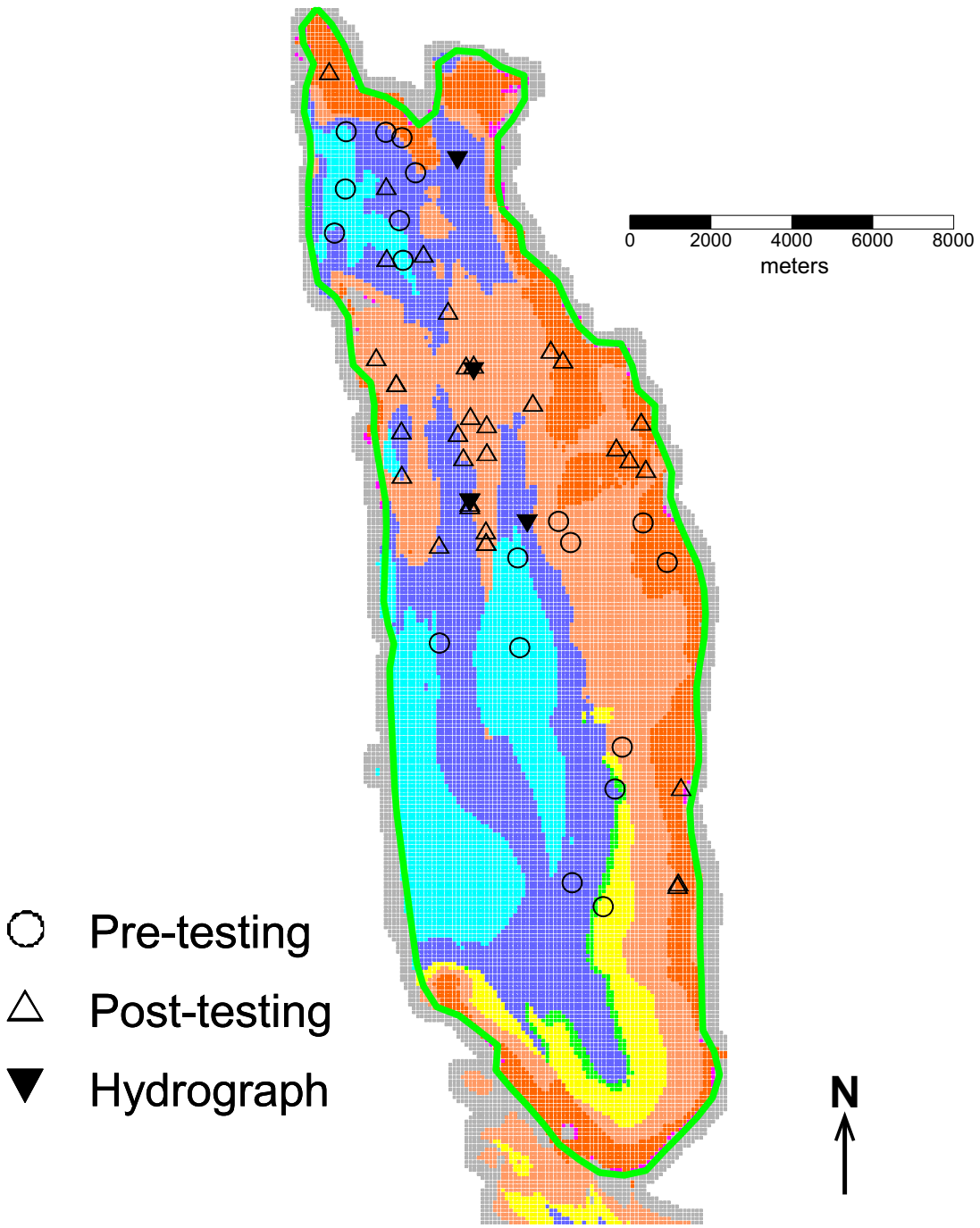

Note: Filled and inverted triangles are wells with repeated measurements over time. All others are shown as open triangles. Colors represent different HSUs at the water table. Warm colors are confining units; cool colors are aquifers.

Figure 4-15
Locations of Wells Used for Calibration

Figure 4-16
Water Levels Used for Evaluating Model Performance

4.4.2 Calibration and Model Uncertainty Assessment Process

The coupled model includes both testing-effects and groundwater-flow parameters. Depending on the conceptual model of testing effects, there are eight to ten test-independent parameters and one test-dependent parameter (e.g., one parameter for each test). The groundwater flow model has somewhat fewer parameters. In principle, each of the 27 HSUs and 57 faults could be assigned a unique permeability, two values of anisotropy (K_x/K_y, K_x/K_z), and storativity. All faults were assigned a single permeability and anisotropy value, and all HSUs were assigned a single storativity value. The resulting number of groundwater flow parameters to estimate was 25 (Table 4-9); the total number of coupled testing-effects/groundwater-flow parameters was 239.

The goal of the model calibration process was to produce a calibrated model and at the same time, establish the framework for the uncertainty assessment phase that followed. These two goals can sometimes be in conflict because traditional calibration methods fail when parameter dimensionality is large compared to data availability (the ill-posed inverse problem). Virtually all hydrogeologic problems are ill posed. The solution to this is usually to “fix” most model parameters and allow only a few to vary. Unfortunately, while this strategy can be successful in the model calibration (parameter estimation) phase, it can lead to greatly underrepresented uncertainty in the uncertainty assessment

Table 4-9
Parameters Used in Model Calibration

Parameter Type	Symbol	Number	Description
Testing Effects	H'	1	Pressure head threshold for rock damage
	f_{max}	1	Maximum extent of damage zone
	s	1	Slope of change in pressurization with radial distance
	H_o	212	Maximum overpressurization
Rock Properties	k	20	Permeability
	S_s	2	Specific storage
	K_{xy}/K_z	2	Anisotropy

phase (Hunt et al., 2007). As one example, reducing the dimensionality of the inverse problem can artificially lend "credence" to calibrated parameters. The singular value decomposition (SVD) calibration method (Tonkin and Doherty, 2009) available in the PEST software suite allows the user to calibrate a model with a large number of adjustable parameters in an ill-posed inverse problem. This approach was used for model calibration. Then, the large number of parameters that are not constrained by calibration data can be freely varied in the uncertainty analysis.

As described in Keating et al. (2010), a heuristic model was developed that demonstrates that the SVD method was capable of calibrating this model despite its strong nonlinearity and high parameter dimensionality. The SVD method was then applied to the calibration of the coupled testing-effects/groundwater-flow model, where a relatively coarse numerical mesh was used to increase computational efficiency. This calibration was performed in parallel on a LANL Beowulf Distributed Process Space (BProc) high performance computing machine (COYOTE). In the final calibration, approximately 150 parameters were varied simultaneously (a subset of the testing-effects parameter H_o, and permeability for all the major HSUs). The calibration was only performed for Testing-Effects Conceptual Model 1; however, the parameters were easily adapted for Testing-Effects Conceptual Model 2 through parameter translation where Conceptual Model 1-calibrated parameters were converted into a nearly equivalent set of parameters for Conceptual Model 2. Both models therefore were nearly equally well calibrated (see Appendix G).

One disadvantage of the SVD method is that it does not provide information about parameter uncertainty. As is shown clearly in Keating et al. (2010), the relation between model parameters and model outputs is strongly nonlinear; therefore, linear uncertainty estimates based on the covariance

matrix would be misleading. In Figure 4-17, sensitivity values are shown for permeability parameters and the most sensitive H_o parameters. These values provide a qualitative sense of which parameters are most constrained by the calibration dataset; that are summarized in Table 4-10. Of the permeability parameters, the most sensitive were the LTCU, OSBCU, TSA, and TM-LVTA. Of the H_o parameters, by far the most sensitive were BILBY, GASCON, and TECHADO. Other very sensitive parameters (not shown) were the slope of change in pressurization with radial distance (testing-effects parameter s), anisotropy (K_z/K_x), and specific storage (S_s).

A number of metrics for model goodness-of-fit were explored, most emphasizing the degree to which the model reproduced transient details in the water-level dataset. This is because the information content in hydrographs reflecting aquifer response to stress is generally much higher than steady-state data. For the purposes of this report, regression coefficients are computed and presented for all water levels (simulated versus measured; the number of water-level measurements n = 563). As with any statistical measure, regression coefficients can be misleading, particularly when variance is low and n is small (e.g., when n = 2, the regression coefficient is guaranteed to be 1.0). This dataset, however, has a very large variance, and n is quite large. As shown below, many of the models produce a regression coefficient greater than 0.9, suggesting that the numerical model can explain over 90 percent of the measured variability in the dataset. This result is remarkable given the almost certain fact that the model is much simpler than reality, particularly with respect to testing effects.

For the initial calibration, the pretesting 5-mm/yr recharge rate and associated permeability parameters used for the unsaturated-zone model case 211212 were used. Enhanced recharge due to testing effects was not explicitly included, because it is unlikely to arrive at the water table during the calibration period (1957–2002). Table 4-4 shows the permeability values obtained with a representative calibration. To estimate parameters for the 0.1-, 1-, and 10-mm/yr cases, the calibration process was not repeated; rather, the magnitude of the most sensitive parameters was manually adjusted. The parameters used for each of the four recharge scenarios are shown in Figure 4-12, with other permeability estimates also shown for comparison. It is clear from this figure that all the calibrated permeability values fall well within the range of *a priori* estimates from other Yucca Flat studies.

Figure 4-18 presents a comparison of measured and simulated hydrographs. In all simulations, some hydrographs were reproduced well and others poorly. This reflects the limitations of a large-scale

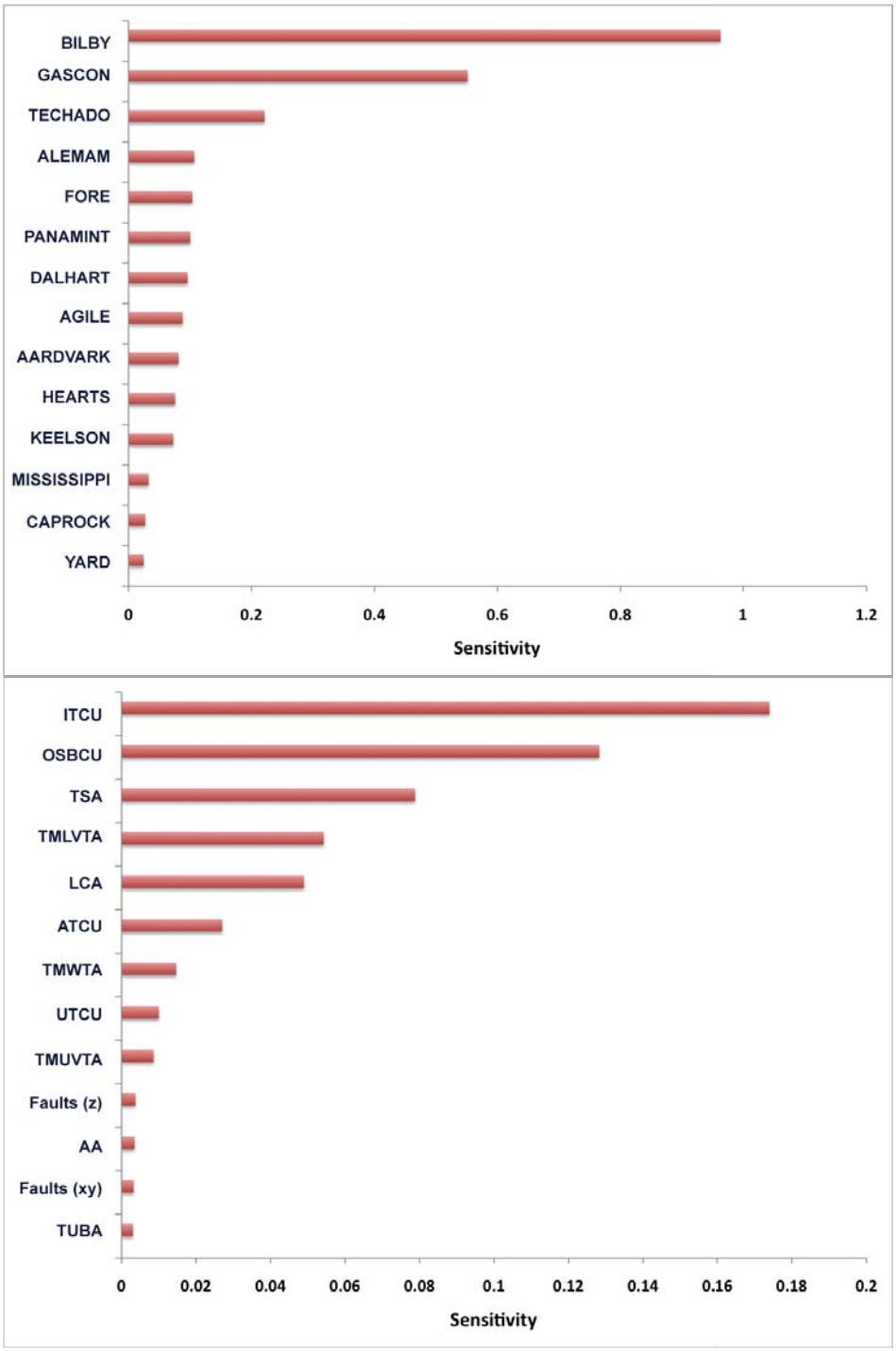

Figure 4-17
Sensitivity Coefficient for Model Parameters

Table 4-10
Parameters That Were Relatively Well Constrained by Model Calibration

Parameter	Type
s	Test Effects
K (OSBCU)	Permeability
ALEMAN	H_o
K (LTCU)	Permeability
TINDERBOX	H_o
SANDREEF	H_o
BILBY	H_o
HERMOSA	H_o
HEARTS	H_o

model to reproduce fine spatial and temporal details. Incorporating heterogeneity within HSUs might improve the performance.

Case names were assigned to each flow field according to the particular combination of parameters, boundary conditions, and testing-effects conceptual model. The case presented in Figure 4-18, for example, is 211212.1.14.5.1.2.N3.N2.s. Table 4-11 explains the meaning of case names.

4.5 Flow and Advective Transport

Because the goal of the overall project is to forecast radionuclide transport, advective transport simulations were conducted as part of the model evaluation process. This was, in part, to glean early information concerning which aspects of flow field uncertainty have the most impact on transport. This allowed the flow field uncertainty analysis to be guided so as to have the most impact on results of interest.

To accomplish this, particle tracking was used to simulate nonreactive, nondispersive tracers. These tracers do not represent specific radionuclides *per se*, but are used to evaluate potential advective transport. The particle-tracking methodology available in FEHM, which is based on the method of Pollock (1988), was utilized. Two sets of particles were utilized. The first set represents tracers entering the water table; these were introduced at discrete times spaced evenly over the 1,000-year simulation period. The second set represents tracers entering the exchange volume of each detonation; these were introduced as clouds of particles dispersed within the exchange volume at the

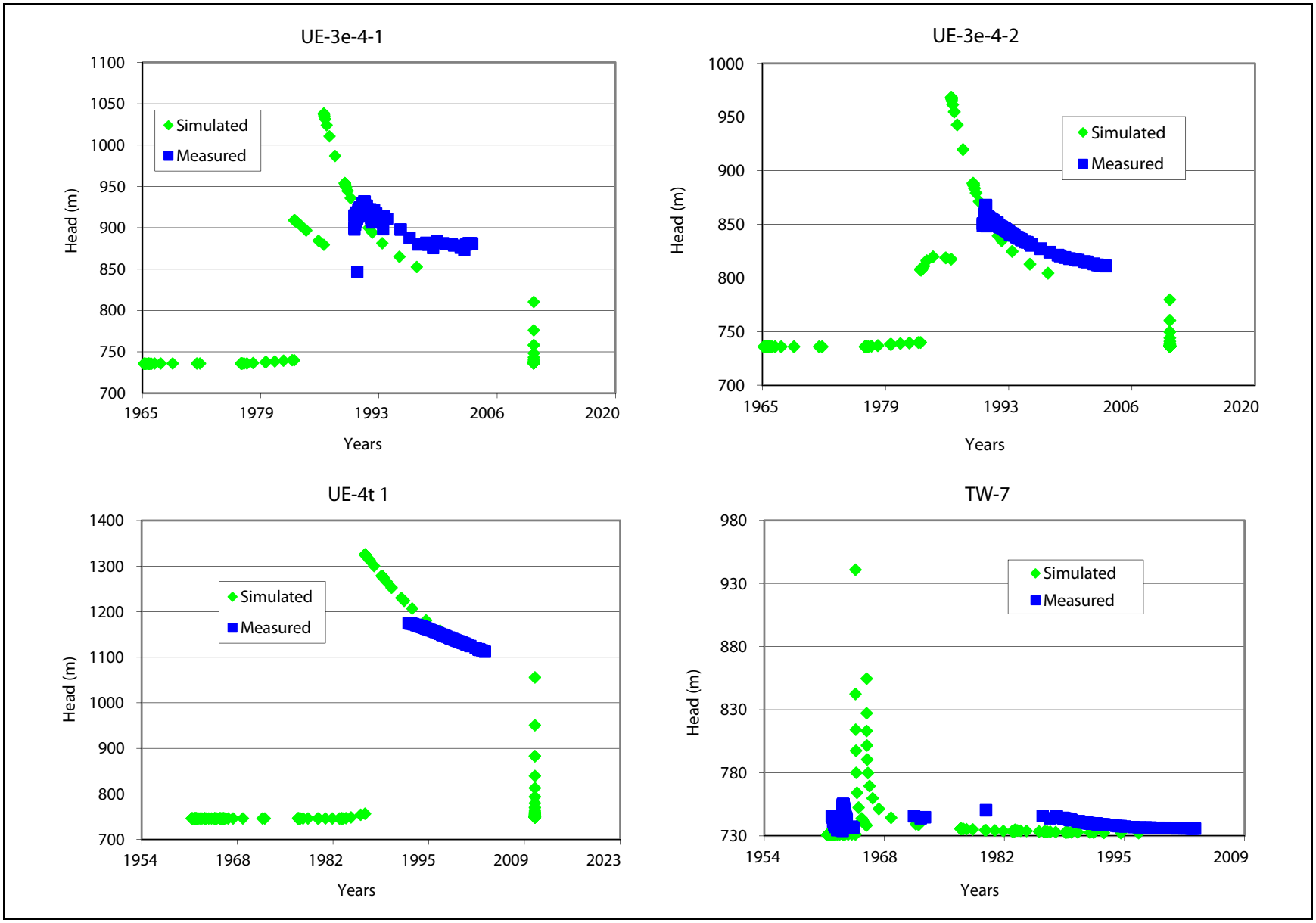

Figure 4-18
Example Comparisons of Simulated and Measured Hydrographs

Table 4-11
Description of Case Names

Example: 211212.1.14.5.4.2.2.N3.B2.v.1
UZcase.perm.porosity.anisotropy.pressurization.specific_storage.Exchange_volume. Perm_reduction.head_criterion.conceptual_model.perm_reduction
UZcase: 6-digit number, Section 3.0
Perm: permeability values for HSUs and fault zones (Table 4-4)
Porosity: porosity values for HSUs and fault zones (Table 4-6)
Anisotropy: anisotropy values for HSUs and fault zones (Table 4-7)
Pressurization: H_o values for each test (Figure 4-13; 1 = Case A; 2 = Case B; 3 = Case C; 4 = Case D; 13 = Case E)
Specific storage: S_s values for HSUs and fault zones (Table 4-5)
Exchange volume: If 1–3 (or absent), last digit in UZcase $\times$ R_c. If "4," thermal convection case
Permeability reduction/enhancement factor *F'* N1 = 50, N2 = 1.0, N3 = 0.02
Other Testing Effects Parameters Case; *H'*; *F'* (variables defined in Appendix G) B2: *H'* = 79 m, Testing Effects Conceptual Model 1 B3: *H'* = 790 m, Testing-Effects Conceptual Model 1 B5: Hydrofracture case 3, Testing-Effects Conceptual Model 2 (described as Case 3 in Section 4.6.5) B6: Hydrofracture case 4, Testing-Effects Conceptual Model 2 (described as Case 4 in Section 4.6.5) B7: Hydrofracture case 5, Testing-Effects Conceptual Model 2 (described as Case 5 in Section 4.6.5)
Conceptual model: v = Testing-Effects Conceptual Model 1; s = Testing-Effects Conceptual Model 2
Crushed/compressed zone permeability reduction/enhancement factors (Table 4-9) 1 = slight reduction, 2 = moderate reduction, 3 = enhanced

time of the detonation. Metrics such as the percentage of total particles leaving the model (entering the LCA) and the total percentage of particles released at each detonation that ultimately leave the system were recorded.

4.5.1 Representative Flow Field with Advective Transport

The calibrated flow field corresponding to the 5-mm/yr recharge rate produced a reasonable degree of goodness-of-fit with measured data, as shown in Figure 4-19. The correlation coefficient between measured and simulated heads for the 573 measurements is 0.94. Scatter around the best-fit line is evident. As discussed above, this is due to a variety of factors, including errors in the estimate of pressurization (H_o) at a particular detonation. On average, however, the model performs well and explains the great majority of the variance in the data.

The simulated head field is shown at a few representative times in Figure 4-20. The figure provides a sense for the creation of overpressurized zones, which gradually dissipate over time. It also provides a sense of the spatial resolution of the model in the vicinity of cavities. For example, a thin

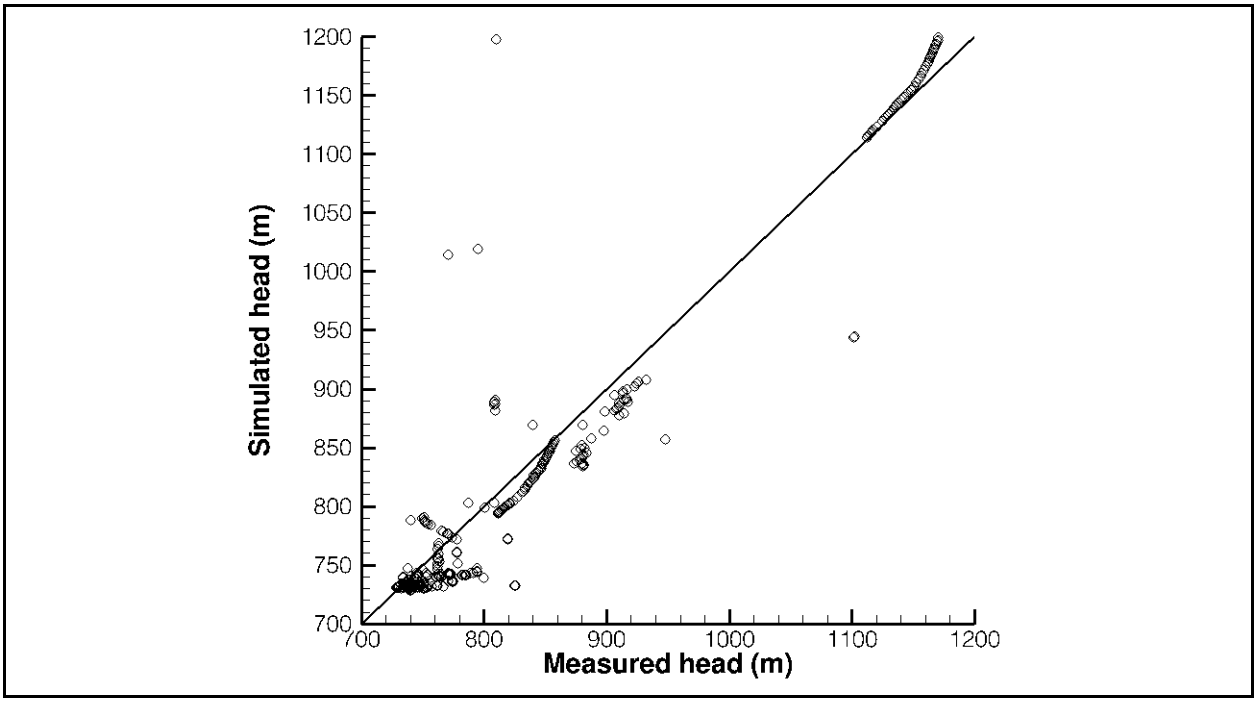

Figure 4-19
Measured versus Simulated Heads

zone of elevated pressures near the cavity exists near the northern end of the model in 1971. Near the southern end of the model, a large pressurization zone is evident, and the low-pressure cavity/chimney core can also be seen. Near the end of the simulation, most pressures have returned to hydrostatic.

The total amount of water leaving the lower boundary is shown in Figure 4-21. There are very short-lived, high spikes near the beginning of each set of detonations simulated. These are probably associated with a very small number of detonations very near model boundaries. Because of their short duration, these spikes do not contribute significantly to the total water flux leaving the model. Near the end of the simulation, outflow stabilizes at the pretesting (steady-state) values. The water flux that arrives at the water table for the case shown in Figure 4-21 has a steady increase over 1,000 years from about 24 to 27 kg/s, where the increase is a result of enhanced crater recharge reaching the water table (e.g., see Section 3.8.2 and Figure 3-70).

The spatial distribution of fluxes is shown in Figure 4-22. Water tends to leave the model at most lower boundary nodes, with the exception of the western edge (Topgallant fault). The lack of water leaving along the Topgallant fault is a result of the higher heads applied along the bottom of this fault

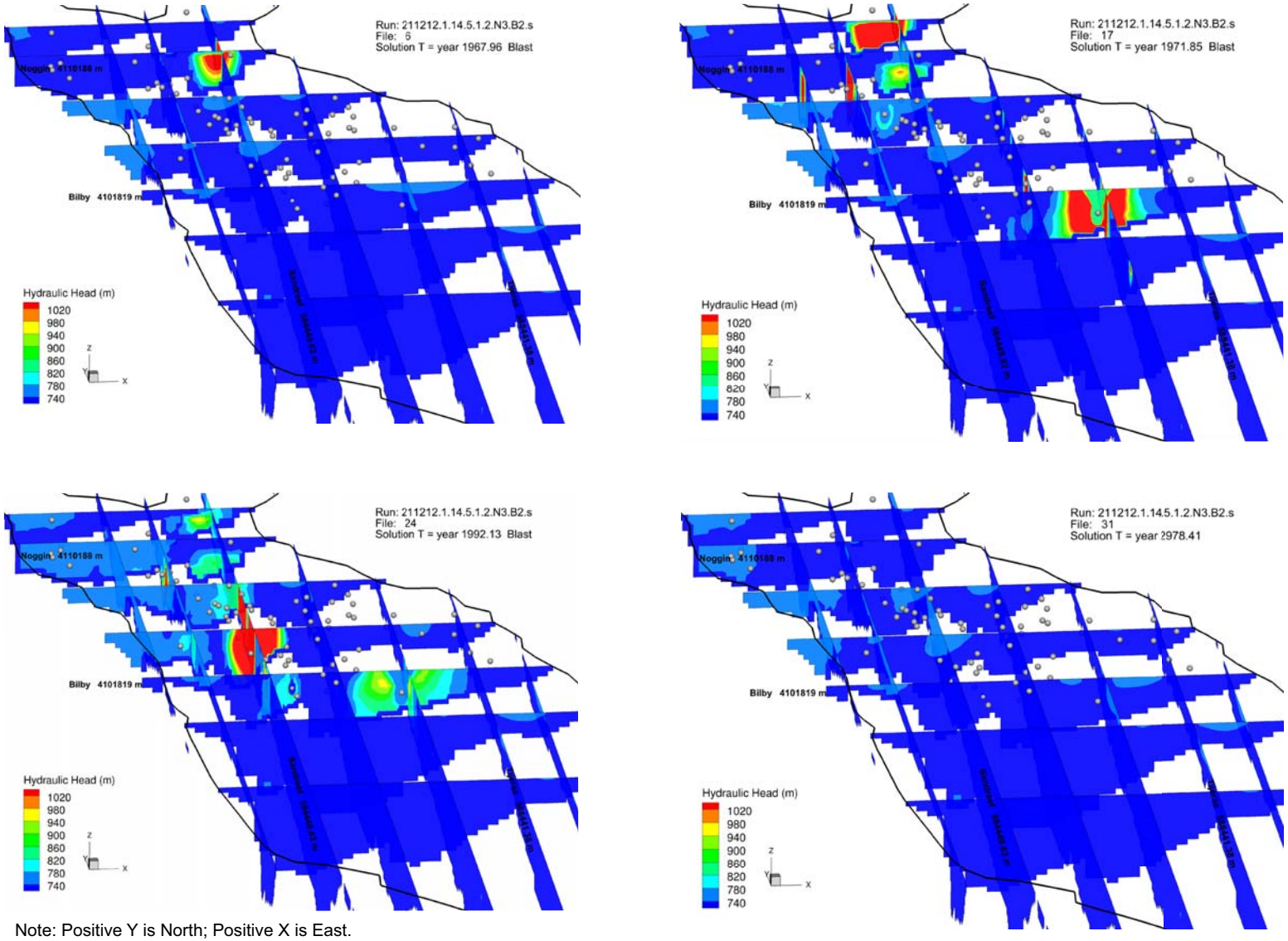

Note: Positive Y is North; Positive X is East.

Figure 4-20
Simulated Heads in Years 1967, 1971, 1992, and 2978

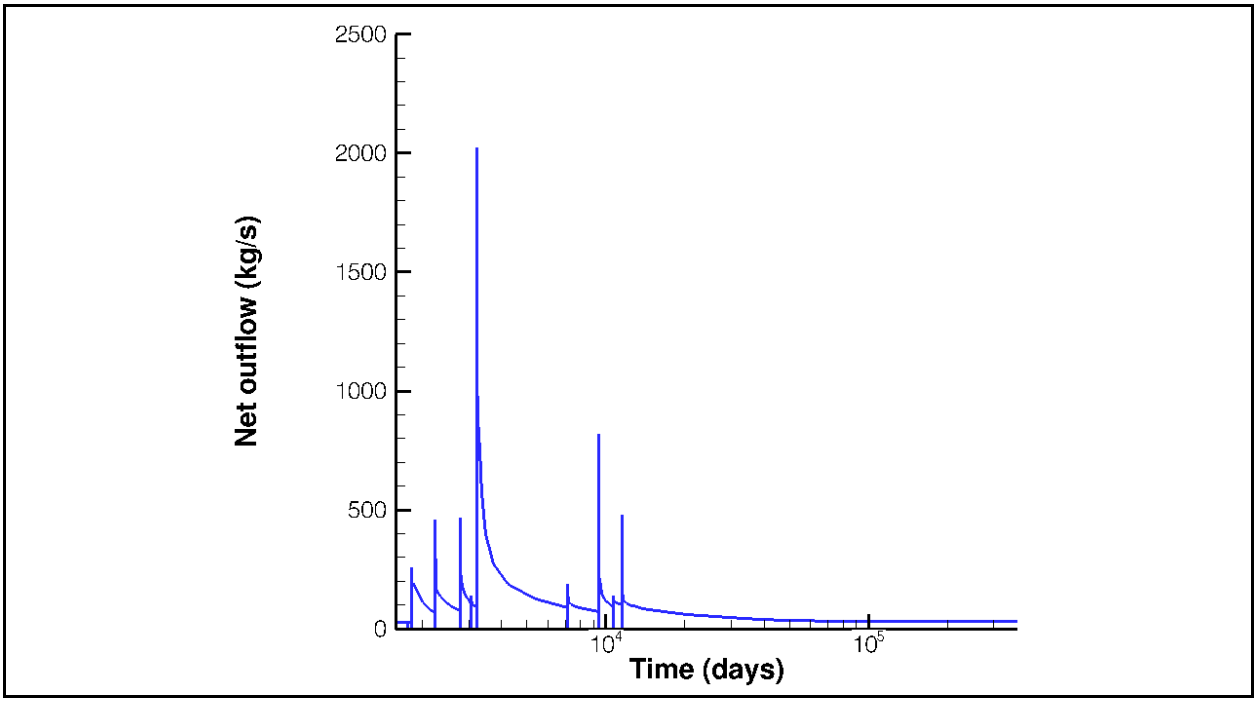

Figure 4-21
Total Flux of Water Leaving Model

(and derived from the LCA model), relative to heads along the other faults. Because there is no mechanism in the model for higher recharge along the western boundary and there are higher-permeability rocks (alluvium), the downward gradients necessary to produce outflow in this area were not achieved.

In early times, water is leaving along most of the faults at very small rates (royal blue color in Figure 4-22), with higher rates along Yucca fault near the center of the model domain. Over time, the area of relatively high discharge rates grows, particularly in the northwest. By the end of the simulation, very low discharge rates are evident in most locations, with a few exceptions in the southern portion of the model domain near the Topgallant fault. The total water exiting the system in excess of steady-state fluxes during the three time periods corresponding to InSAR measurements (listed in Table 4-12) are 0.48E+06, 1.31E+06, and 2.1E+06 m^3. These correspond reasonably well to the flux estimates derived from InSAR, well within an order of magnitude.

The results of the particle-tracking analysis of this flow field showed that 18 percent of the particles entering the water table and 24 percent of the particles entering the exchange volumes of saturated-zone detonations ultimately leave the model domain within the 1,000-year simulation.

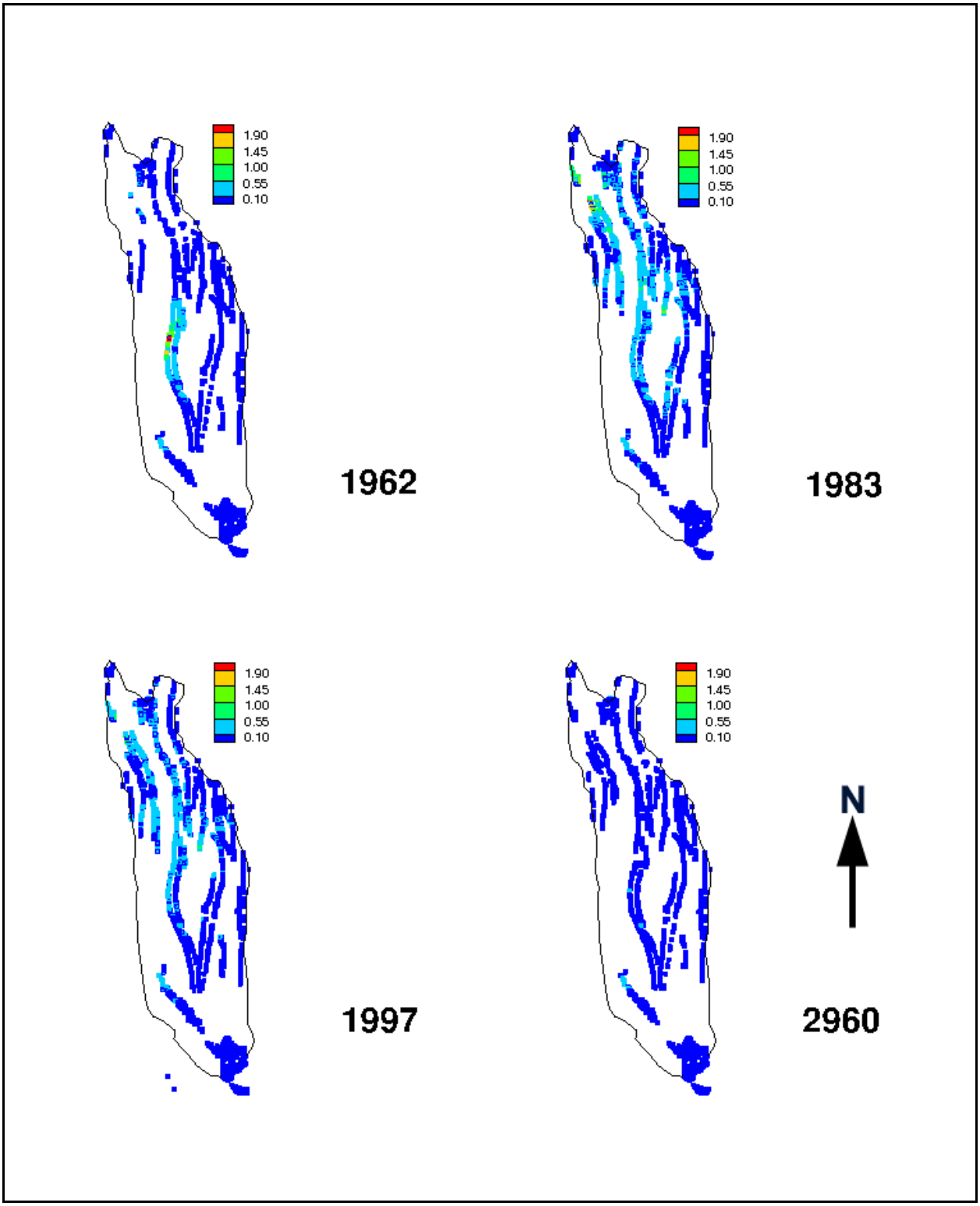

Figure 4-22
Spatial and Temporal Distributions of Outflow Fluxes (kg/s)
(Case 211212.1.14.5.1.2.N3.B2.s/)

Table 4-12
Total Volume of Water Outflow in Excess of Steady-State Flow
(Page 1 of 2)

Set	Case	Years		
		1992–1993	1993–1995	1995–1997
		(× 1E+06 m³)		
Measured InSAR Data		0.62	1.30	0.89
1	211212.1.14.4.1.2.N2.B3.s	0.97	2.50	3.74
	211212.1.14.4.1.2.N3.B2.s	0.94	2.46	3.75
	211212.1.14.4.1.2.N3.B3.s	0.99	2.56	3.85
	211212.1.14.5.1.2.N2.B2.s	0.91	2.41	3.70
	211212.1.14.5.1.2.N2.B3.s	0.91	2.41	3.70
	211212.1.14.5.1.2.N3.B2.s	0.87	2.31	3.60
	211212.1.14.5.1.2.N3.B3.s	0.93	2.46	3.77
	211212.1.14.6.1.2.N2.B2.s	0.97	2.52	3.76
	211212.1.14.6.1.2.N2.B3.s	0.97	2.52	3.76
	211212.1.14.6.1.2.N3.B2.s	0.94	2.48	3.78
	211212.1.14.6.1.2.N3.B3.s	1.00	2.58	3.87
	211212.1.14.5.2.2.N3.B2.s	0.05	0.14	0.22
	211212.1.14.5.3.2.N3.B2.s	0.69	1.81	2.75
	211212.1.14.4.1.2.N2.B2.s	0.97	2.50	3.74
2	211212.1.14.5.1.2.N2.B2.v.1	2.64	6.67	9.83
	211212.1.14.5.1.2.N2.B2.v.2	1.41	2.95	3.41
	211212.1.14.5.1.2.N2.B2.v.3	2.11	5.39	8.06
	211212.1.14.5.3.2.N2.B2.v.1	4.22	10.68	15.75
	211212.1.14.5.3.2.N2.B2.v.2	2.48	5.42	6.56
	211212.1.14.5.3.2.N2.B2.v.3	3.14	8.10	12.30
	211212.7.14.5.1.2.N2.B2.v.1	3.77	10.18	16.08
	211212.7.14.5.1.2.N2.B2.v.2	3.94	9.44	12.68
	211212.7.14.5.1.2.N2.B2.v.3	2.34	6.40	10.34
	211212.7.14.5.3.2.N2.B2.v.1	6.08	16.47	26.19
	211212.7.14.5.3.2.N2.B2.v.2	6.69	16.24	22.09
	211212.7.14.5.3.2.N2.B2.v.3	2.87	7.90	12.89
	211212.8.14.5.1.2.N2.B2.v.1	1.71	4.80	8.04
	211212.8.14.5.1.2.N2.B2.v.2	4.58	11.76	17.34
	211212.8.14.5.1.2.N2.B2.v.3	0.88	2.47	4.15
	211212.8.14.5.3.2.N2.B2.v.1	2.75	7.72	12.94
	211212.8.14.5.3.2.N2.B2.v.2	7.78	20.46	31.07
	211212.8.14.5.3.2.N2.B2.v.3	0.98	2.74	4.61

Table 4-12
Total Volume of Water Outflow in Excess of Steady-State Flow
(Page 2 of 2)

Set	Case	Years		
		1992–1993	1993–1995	1995–1997
		(× 1E+06 m³)		
3	121212.5.14.5.1.2.N3.B2.s	0.48	1.31	2.10
	131233.5.14.5.1.2.N3.B2.s	0.48	1.30	2.08
	131333.5.14.5.1.2.N3.B2.s	0.48	1.30	2.08
	213212.1.14.4.1.2.N3.B2.s	0.94	2.46	3.77
	221212.1.14.6.1.2.N3.B2.s	0.94	2.48	3.77
	223212.1.14.5.1.2.N3.B2.s	0.87	2.31	3.60
	231232.1.14.5.1.2.N3.B2.s	0.86	2.30	3.58
	321212.6.14.5.1.2.N3.B2.s	1.18	2.99	4.31
4	512212.5.11.2.7.1.11.2.N3.B2.s	0.02	0.04	0.07
	512212.5.12.2.8.1.11.2.N3.B2.s	0.02	0.04	0.06
	542121.12.2.8.1.11.2012_HST.N3.B2.s	0.02	0.04	0.06
	121212.5.14.5.13.2.2.N3.B2.s	0.61	1.65	2.61
	223212.1.14.5.13.2.2.N3.B2.s	1.03	2.73	4.21

Notes:
Dark gray shaded cells indicate cases where simulated values are far in excess of measured values.
Light gray shaded cells indicate cases with underestimate of outflow.

Examination of spatial trends showed that only particles entering the water table near faults eventually leave the lower boundary within 1,000 years. This has potentially important implications for radionuclide transport from unsaturated-zone sources. Additionally, only 74 of the 180 detonations had particles leaving the system, and 19 of these represented over 75 percent of the total number of particles leaving.

One interpretation of these particle-tracking results is that these are estimates of the maximum fraction of total radionuclide mass that could possibly exit the saturated volcanics. Processes not considered here, such as dispersion, radioactive decay, and diffusion into the matrix from fracture zones, will all tend to decrease the proportion of total mass leaving the system. All these processes are explicitly considered in simulations presented later in this section. As explained in Section 4.6.3, these processes collectively produce reduction factors ranging from 0.3 to 0.01, depending on model parameters.

4.5.2 Sensitivity Analysis

Three classes of flow model parameters were varied systematically to discern their effect on both model calibration criteria and advective transport to the LCA: (1) pretesting rock properties, (2) recharge rates, and (3) near-field testing effects. The pretesting rock properties considered were anisotropy, permeability of HSUs and faults, and specific storage. Recharge rates considered, as described above, include three pretesting background recharge rates followed by a transient rate produced by the unsaturated-zone model. The testing-effects parameters considered were maximum local pressurization caused by each detonation, testing-effects conceptual model, and the two or three parameters required by each model to enhance or reduce local permeability in response to the detonation. If anything, the resulting ensemble of simulations should overestimate uncertainty.

The expectation that measured vertical gradients should be honored imposes limits on reasonable combinations of recharge and permeability; as a result, these two factors were not varied independently. All other factors were varied independently.

The sensitivity cases are divided into four sets for ease of comparison. The first two sets of model cases correspond to the unsaturated-zone model results 211212 (corresponding to 5 mm/yr), and permeability, porosity, and specific storage values listed in Tables 4-4 to 4-7. The first set assumes Testing-Effects Conceptual Model 1, and examines sensitivity to permeability anisotropy and testing-effects model parameters. The second set assumes Testing-Effects Conceptual Model 2, and examines sensitivity to testing-effects model parameters and fault-zone permeability. The third set examines sensitivity to unsaturated-zone model results and corresponding permeability estimates. The last set examines the very low infiltration conceptual model (and corresponding low permeability values), low specific storage values, and alternative overpressurization combinations.

The results are compiled in Table 4-13. With few exceptions, the model calibration criteria of these sensitivity analysis cases are all reasonable (the regression coefficients are greater than 0.7). Very low correlations were obtained with Testing-Effects Conceptual Model 2 coupled with an enhanced permeability crushed zone. This is due to pressurization dissipating too quickly in most observation wells. Relatively low correlations were also seen with H_o sets 2 and 3, which were not calibrated.

Despite the intent to overestimate “true” uncertainty with this ensemble, the impact of these uncertainties on advective transport to the LCA shows remarkably little variation as indicated by the

Table 4-13
Sensitivity Analysis Models and Results [a]
(Page 1 of 3)

Parameters											Results		
Unsaturated-zone Model Case	Permeability	Porosity	Anisotropy	Pressurization	Specific Storage	Exchange Volume	Permeability Enhancement	Head Criterion	Conceptual Model	Crushed/ Zone Permeability Enhancement	Regression Coefficient	Fraction of Unsaturated-Zone Particles Leaving	Fraction of Saturated-Zone Particles Leaving
Set 1													
211212	1	14	4	1	2	2	N2	B3	v	N/A	0.82	0.15	0.23
	1	14	4	1	2	2	N3	B2	v	N/A	0.88	0.15	0.22
	1	14	4	1	2	2	N3	B3	v	N/A	0.84	0.15	0.23
	1	14	4	1	2	2	N2	B2	v	N/A	0.82	0.15	0.23
	1	14	5	1	2	2	N2	B2	v	N/A	0.90	0.17	0.25
	1	14	5	1	2	2	N2	B3	v	N/A	0.90	0.17	0.25
	1	14	5	1	2	2	N3	B2	v	N/A	0.94	0.18	0.24
	1	14	5	1	2	2	N3	B3	v	N/A	0.91	0.17	0.25
	1	14	6	1	2	2	N2	B2	v	N/A	0.83	0.16	0.24
	1	14	6	1	2	2	N2	B3	v	N/A	0.83	0.16	0.24
	1	14	6	1	2	2	N3	B2	v	N/A	0.88	0.16	0.23
	1	14	6	1	2	2	N3	B3	v	N/A	0.84	0.16	0.24
	1	14	5	2	2	2	N3	B2	v	N/A	0.33	0.16	0.18
	1	14	5	3	2	2	N3	B2	v	N/A	0.47	0.18	0.23

Table 4-13
Sensitivity Analysis Models and Results [a]
(Page 2 of 3)

Parameters											Results		
Unsaturated-zone Model Case	Permeability	Porosity	Anisotropy	Pressurization	Specific Storage	Exchange Volume	Permeability Enhancement	Head Criterion	Conceptual Model	Crushed/ Zone Permeability Enhancement	Regression Coefficient	Fraction of Unsaturated-Zone Particles Leaving	Fraction of Saturated-Zone Particles Leaving
Set 2													
211212	1	14	5	1	2	2	N2	B2	s	1	0.87	0.16	0.20
	1	14	5	1	2	2	N2	B2	s	2	0.00	0.18	0.21
	1	14	5	1	2	2	N2	B2	s	3	0.89	0.15	0.19
	1	14	5	3	2	2	N2	B2	s	1	0.85	0.19	0.26
	1	14	5	3	2	2	N2	B2	s	2	0.00	0.48	0.25
	1	14	5	3	2	2	N2	B2	s	3	0.79	0.18	0.23
	7	14	5	1	2	2	N2	B2	s	1	0.82	0.13	0.14
	7	14	5	1	2	2	N2	B2	s	2	0.00	0.13	0.13
	7	14	5	1	2	2	N2	B2	s	3	0.71	0.13	0.13
	7	14	5	3	2	2	N2	B2	s	1	0.76	0.15	0.18
	7	14	5	3	2	2	N2	B2	s	2	0.00	0.15	0.15
	7	14	5	3	2	2	N2	B2	s	3	0.58	0.15	0.16
	8	14	5	1	2	2	N2	B2	s	1	0.70	0.10	0.12
	8	14	5	1	2	2	N2	B2	s	2	0.00	0.10	0.10
	8	14	5	1	2	2	N2	B2	s	3	0.57	0.10	0.11
	8	14	5	3	2	2	N2	B2	s	1	0.61	0.12	0.17
	8	14	5	3	2	2	N2	B2	s	2	0.02	0.12	0.14
	8	14	5	3	2	2	N2	B2	s	3	0.48	0.11	0.11

Table 4-13
Sensitivity Analysis Models and Results [a]
(Page 3 of 3)

Parameters											Results		
Unsaturated-zone Model Case	Permeability	Porosity	Anisotropy	Pressurization	Specific Storage	Exchange Volume	Permeability Enhancement	Head Criterion	Conceptual Model	Crushed/ Zone Permeability Enhancement	Regression Coefficient	Fraction of Unsaturated-Zone Particles Leaving	Fraction of Saturated-Zone Particles Leaving
Set 3													
121212	5	14	5	1	2	2	N3	B2	s	N/A	0.95	0.10	0.20
131233	5	14	5	1	2	3	N3	B2	s	N/A	0.96	0.11	0.20
131333	5	14	5	1	2	3	N3	B2	s	N/A	0.96	0.11	0.20
213212	1	14	4	1	2	2	N3	B2	s	N/A	0.88	0.15	0.22
221212	1	14	6	1	2	2	N3	B2	s	N/A	0.88	0.16	0.23
223212	1	14	5	1	2	2	N3	B2	s	N/A	0.94	0.18	0.25
231232	1	14	5	1	2	2	N3	B2	s	N/A	0.94	0.15	0.22
321212	6	14	5	1	2	2	N3	B2	s	N/A	0.81	0.23	0.27
Set 4													
542121 [b]	11	11	7	1	2	1	N3	B2	s	N/A	0.76	0.08	0.15
542121 [b]	12	12	8	1	2	1	N3	B2	s	N/A	0.71	0.09	0.05
542121	12	14	8	1	2	1	N3	B2	s	N/A	0.71	0.06	0.07
121212	5	14	5	13	2	2	N3	B2	s	N/A	0.94	0.10	0.15
223212	1	14	5	13	2	2	N3	B2	s	N/A	0.92	0.14	0.16

[a] See Table 4-11 for detailed description of parameter code names.
[b] Recharge does not include crater-enhanced flow.

results of the sensitivity study. For set 1, the fraction of particles originally entering across the water table that exit into the LCA over 1,000 years only varies between 0.15 and 0.18. Likewise, the fraction of particles entering in the exchange volume of a saturated-zone nuclear detonation and exiting to the LCA varies consistently between 0.18 and 0.25. Qualitatively, this suggests that the model is fairly insensitive to uncertainty in testing-effects parameters for Testing-Effects Conceptual Model 1 and in permeability anisotropy. In set 2, the first six cases consider sensitivity to testing-effects parameters. Ignoring the two cases with enhanced permeability that produced very poor calibration (regression coefficients near zero), the range of results is almost identical to that for set 1 (Testing-Effects Conceptual Model 1). Collectively, these results suggest remarkably little sensitivity to the choice of testing-effects models, the parameters of the model used, and permeability anisotropy.

Cases 7 through 18 of set 2 analyze sensitivity to fault permeability. Compared to the base case (fault permeability = 1E-12 m^2), cases 7 through 12 assume a lower fault permeability of 1E-14 m^2, and cases 13 through 18 assume a fault permeability of 1E-15 m^2. Sensitivity is evident. The proportion of particles leaving does decrease as fault permeability decreases, but is only reduced from approximately 18 percent to approximately 10 percent. The trend is less clear with the particles originating at saturated-zone detonations. The proportion of particles leaving for the cases with lower fault permeability (1E-14 m^2) (14 to 16 percent) is moderately lower than that for the base case, and the proportion of particles leaving for the cases assuming a fault permeability of 1E-15 m^2 cases is again only moderately lower. Similarly, the effects of the unsaturated-zone fluxes (set 3) have only moderate impact on advective transport to the LCA.

Even though there are only moderate differences between the total number of particles leaving the system over 1,000 years, it is possible that there could be significant differences in the timing of the particle efflux. Particle breakthrough curves at the lower model boundary are shown in Figure 4-23. For all breakthrough curves shown in Figure 4-23, the simulations started with 18,139 particles entering the water table with 100 × 100 m spacing (× 4 time-varying segments [see Section 4.6.4.2]), and 450 particles per 179 saturated-zone detonations for a total of 153,106 particles. In Figure 4-23a, breakthrough curves for the set 1 cases are shown. For all cases, the largest incremental particle release is during the first 100 years, followed by a fairly steady rate of particle breakthrough. Most cases have fairly similar behavior, with the exception of case 13, which has fewer particles leaving

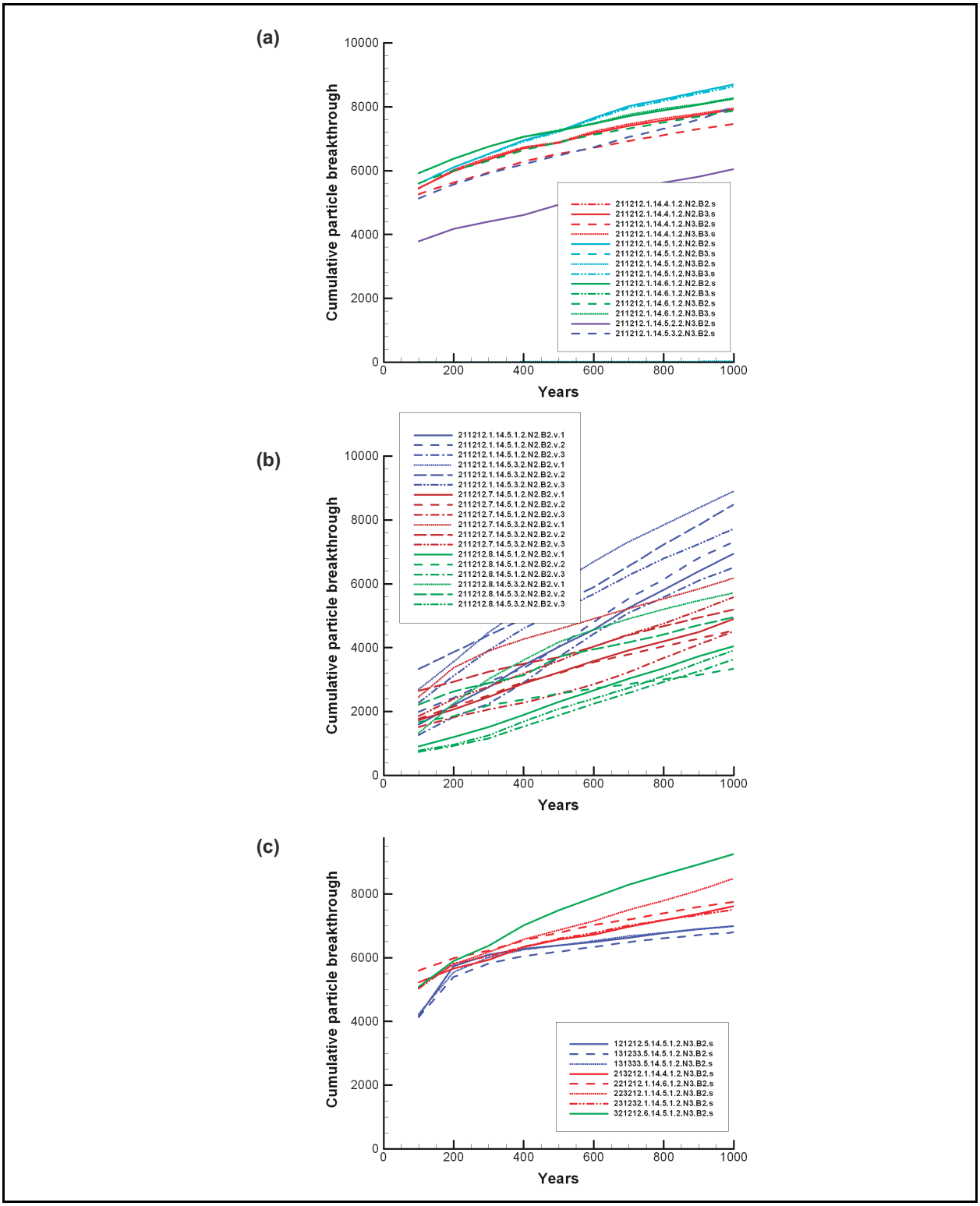

Figure 4-23
Particle Breakthrough at Lower Model Boundary

Note: Blue = High permeability; Red = Higher breakthrough than lower; Green = Lowest

the system than the other cases. This case, which has a high level of pressurization (level B), has relatively poor agreement with measured heads.

There is much larger range of total cumulative particle breakthrough in the set 2 cases (Figure 4-23b) (Testing-Effects Conceptual Model 2). All exhibit a fairly steady rate of particle breakthrough over the 1,000-year period. The effect of fault permeability can be seen, with high permeability (blue) showing higher breakthrough than lower (red) and lowest (green). For each permeability case, there is relatively small influence of the damage-zone characteristics (variations in the line types).

The variation in unsaturated-zone cases (and corresponding parameters in the saturated-zone model parameters) is shown in Figure 4-23c. The total cumulative particle breakthrough varies somewhat, but the basic shape of the curves is very similar. Of these parameters, background recharge rate or permeability has the greatest effect. Other parameters (cavity radius, anisotropy, and crater recharge) have less effect.

This analysis shows a fairly low sensitivity of cumulative particle breakthrough to presumed initial overpressures at detonations in the saturated zone (cases A, B, C, and E from Figure 4-14). This is not to say that there is not large variation in particle (mass) contributions from individual detonations. For example, particle breakthrough for mass originating at BILBY is very sensitive to the presumed overpressurization at BILBY. High-resolution model calibration studies (described in Appendix G) have been used to estimate the initial pressurization from BILBY. These estimates range from 200 to 400 m. Initial overpressurization in the crushed zone at BILBY was estimated by Tompson (2008) to be 8,000 m. A sensitivity study was performed with varying overpressurization at BILBY from 1,200 m to 800, 600, and 300 m. This resulted in 100, 8, 2, and 0 percent of the mass of BILBY leaving the model in the first 100 years. These percentages will be larger than total radionuclide transport because of retardation mechanisms such as fracture/matrix diffusion. When these processes are considered, the 1,200-m overpressurization case releases 36 percent of the initial BILBY ^{14}C inventory and 11 percent of the initial BILBY ^{3}H inventory to the LCA over 1,000 years. Despite this sensitivity to radionuclide transport from an individual detonation to overpressurization at that detonation, the *total* radionuclide transport from all detonations is fairly robust to uncertainty in overpressurization at individual detonations. This robust result will be discussed again after the transport section of this section.

Taking this ensemble of 40 cases, the detonations contributing most of the particles to the outflow to the LCA over 1,000 years were examined. These are shown in Figure 4-24. In Figure 4-24a, every detonation that contributes to the outflow in at least one of the 40 cases in parameter sensitivity sets 1 to 3 is shown as a colored symbol: orange indicates detonations that, on average, contribute less than 20 percent of the initial particles associated with the detonation; green dots contribute more than 20 to 40 percent of the initial particles associated with the detonation; and blue dots contribute more than 40 percent. In Figure 4-24b, median results from the parameter combinations listed in set 4 are shown. In this figure, the additional effect of ^{14}C mass associated with each particle is considered. All sources indicated that colored dots have at least 0.1 mole of ^{14}C breakthrough to the LCA. The most important detonations (set 4 cases) are labeled. Results from one particular case, 542121.12.2.8.1.11.2012_HST.N3.B2.s, are shown in Figure 4-24c. For this very low infiltration/low permeability case, the number of detonations contributing at least 0.1 mole of ^{14}C breakthrough to the LCA is much smaller.

4.5.3 Post-audit: InSAR

Ground surface subsidence was measured by USGS for three time periods (1992–1993, 1993–1995, and 1995–1997) (Vincent et al., 2003). The data from 1992 to 1993 are shown in Figure 4-3. Subsidence data provides a measure of the water released from elastic storage. The only portion of the flow domain where elastic storage release is expected to be important is the saturated zone; therefore, these measurements are particularly useful to this component of the CAU model. If the rock properties and the simulated fluxes to the LCA are approximately correct, the model should agree with the InSAR data at least to a first order. Because simulating ground surface subsidence accurately requires a coupled mechanical/hydrogeologic model with deformable media, it is not expected that the model will predict ground surface subsidence accurately.

A simple approximation was made for the purpose of making a first-order comparison of model results to measured subsidence. It is assumed that all pressure decreases cause a volume decrease determined exactly by the value of specific storage for any given rock, other than within cavities and chimneys where pressure changes are probably unrelated to elastic rock properties. Further, it is assumed that all volume decreases produce only vertical compression (no lateral compression). This is a first-order approximation that does not conserve rock mass and does not consider possible “inflation” due to pressure increases. Despite these many caveats, the comparison of simulated and

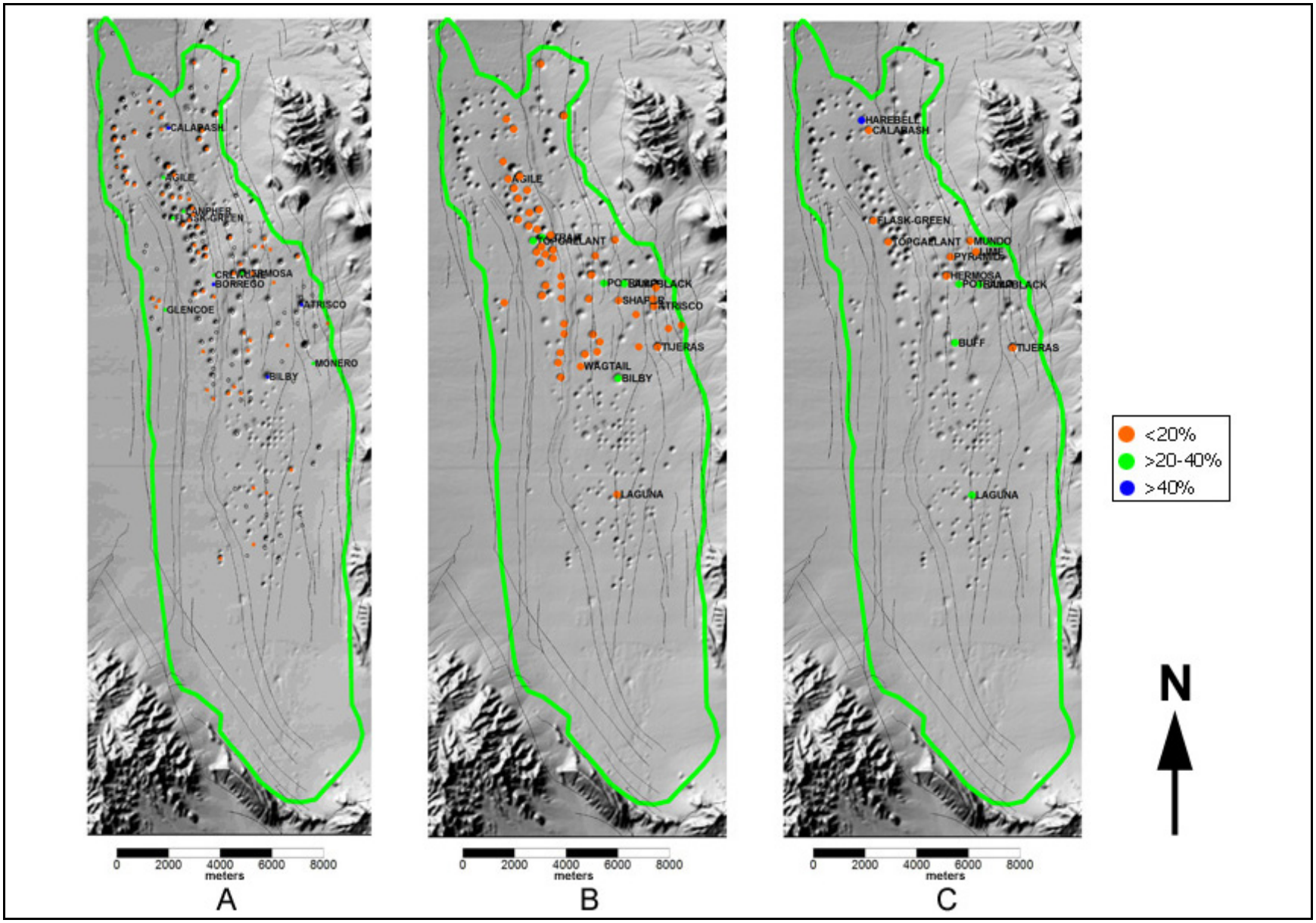

Figure 4-24
Detonations That Contribute to Significant Particle Outflow to the LCA

measured subsidence is reasonable. The model correctly simulates both the approximate range of measured subsidence and several key spatial trends, providing confidence in the simulated amount of water draining via release of elastic storage to the LCA and the estimated rock properties. There are a few locations where the model underestimates subsidence.

The simulated subsidence was compared to the observed subsidence for the time period 1992 to 1993 at each point in the model domain that overlaps with the subsidence data (the northern half of the model domain). Within this overlapping area, 10,000 comparisons between simulated and observed subsidence could be made. Of these, 85.6 percent of observations (±1 cm) fell between the minimum and maximum predictions as defined by the model cases based on the 64 sets of parameters generated by the use of the null-space Monte Carlo method. In Figure 4-25, a comparison between observed subsidence and model-generated uncertainty bounds of predicted subsidence is shown for a representative east–west cross section. The comparison, though not perfect, shows that predictive uncertainty bounds computed with the process model are able to span a range that largely includes observations that were not used in the model calibration process. This is quite remarkable and inspires confidence that the process model has been calibrated appropriately and provides estimates of uncertainty that appear reasonable when making the prediction of most interest to the present study, as this prediction is dependent on aspects of the system that are similar to those that lead to ground subsidence.

The consistency of each set of cases with the total volume of water outflow estimated with the InSAR data during three time periods in the 1990s is compiled in Table 4-12. A number of the simulations are quite close to the measured values, easily within a factor of 2 or 3. A few of the simulations significantly overestimate the amount of testing-induced water charge by slightly more than an order of magnitude (shown in dark gray shading), and some significantly underestimate the flux (light gray shading). These cases either are highly overpressurized (case C in Figure 4-13) or have reduced permeability of the fault zones, compared to the base case. The case C overpressurization cases are not propagated to the transport simulations described later in this section. The “low fault” permeability cases will be shown later to propagate very little radionuclide flux to the LCA, despite the apparent overestimate of testing-induced water flux.

The first three cases in set 4 all underestimate testing-induced flux of water to the LCA. The very low permeabilities and the very low specific storage values required to calibrate the model for these very

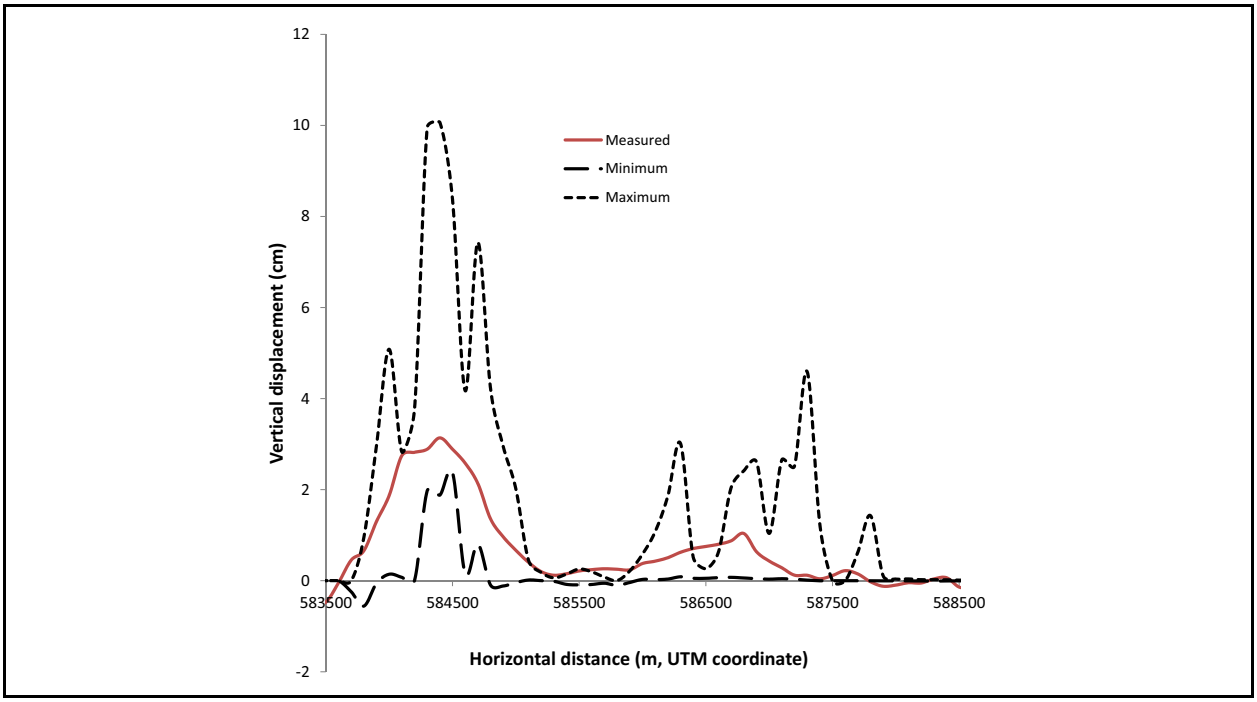

Figure 4-25
Comparison of Measured Subsidence and the Range of Predicted Subsidence for an Ensemble of Flow Models along an East–West Cross Section

low infiltration rates are contributing factors. The relatively low correlation coefficient for these cases (Table 4-3) is another reflection of this problem. As will be shown later in this section, these cases propagate almost no radionuclide flux to the LCA.

4.5.4 Flow Model Limitations

Not all the head variability in the Yucca Flat dataset is represented well by these models. This is due in large part to the inability of a large-scale model to reproduce in fine detail temporal and spatial trends in heads. Similar conclusions could be drawn about the InSAR/subsidence prediction comparisons.

4.6 Radionuclide Transport

4.6.1 Methodology

Particle-tracking methods have become popular for the study of flow and solute transport in groundwater modeling. PLUMECALC was developed based on the convolution-based particle tracking (CBPT) method for simulating resident or flux-averaged solute concentrations in

groundwater models. The method was originally developed for steady-state flow and linear transport processes such as sorption with a linear sorption isotherm, diffusion into matrix rock, and first-order decay, and later was extended to transport in transient flow conditions.

The PLUMECALC methodology was chosen for this project for two primary reasons. First, it relies on particle-tracking methodology, which has the advantage of minimizing numerical dispersion. Numerical dispersion is a serious issue for large-scale models (tens of kilometers) where it is impractical to use very small grid blocks everywhere. By avoiding numerical dispersion, artificial spreading and dilution of the source mass are avoided. Second, the PLUMECALC methodology allows very efficient calculations of radionuclide concentrations and mass flux from a particle-tracking simulation. In the context of uncertainty analysis, a large number of PLUMECALC realizations can be efficiently derived from a single flow-model run (particle-tracking result). This is advantageous because the flow model runs are computationally expensive.

As with any method, there are also limitations. Particle tracking in transient flow systems with complex boundary conditions is not a trivial problem, and few codes can accommodate the complexity required by this application. The code used here, FEHM_sptr, can accommodate this complexity, but is known to give unreliable results when dispersion is simulated in strongly heterogeneous flow fields. Dispersion was not simulated, so this problem does not affect the results. The impact of neglecting dispersion is discussed further below. A second known problem with FEHM_sptr is that the velocity interpolation scheme used is not accurate in outflow nodes, and, when used with PLUMECALC, will produce erroneously large concentrations in outflow nodes. As will be discussed below, those erroneous outflow node concentrations are excluded from the analysis.

The complete details of the numerical implementation are described in Srinivasan et al. (2010) and Robinson et al. (2010). For the calculation of resident concentration, using information from particle-tracking results can be accomplished in a variety of ways. The most efficient approach is to store information regarding the time history of the location of each particle and perform the contribution to the convolution integral on a particle-by-particle basis. The application of the numerical implementation is described Srinivasan et al. (2010).

To simulate radionuclide concentrations and mass flux with this method requires two steps: (1) develop particle tracks, and (2) run PLUMECALC. For the first step, we used the methodology described in Section 4.5 for advection-only transport calculations. The one difference is that here,

more particles were used at the water table to account for the transient arrival of mass flux from unsaturated-zone simulations.

The goal of selected flow-model/particle-tracking cases upon which to build transport simulations was to span a reasonable range of model outcomes and to determine the most sensitive parameters. The analysis presented in Section 4.5.2 allowed a relatively small set of flow models that meet this goal to be selected. On the backbone of these flow models, a large number of PLUMECALC realizations were generated in order to consider transport parameter uncertainty.

4.6.2 Implementation

4.6.2.1 Particle Trajectories

Two sets of particles were used to represent mass arriving at the water table (from unsaturated-zone simulations) and mass originating in sources internal to the saturated-zone volcanics. The particles representing mass arriving at the water table (from unsaturated-zone simulations) were inserted at a regular grid spacing (100 m) at the top of the model domain (z = 750 m). At each location, particles were released at multiple times (1,591, 81,591, 161,591, and 241,591 days). The initial particle locations are shown in Figure 4-26. Not all these particles were associated with radionuclide mass derived from unsaturated-zone simulations. The regular grid of particles was used so that a single FEHM_sptr run could be used, along with PLUMECALC, to evaluate multiple transport scenarios. In any given scenario, a different set of particles might be transporting mass.

For each detonation with an exchange volume at least partially within the model domain, 450 particles were used to represent the initial distribution of radionuclides. This number was a compromise between accuracy and computational efficiency. Particles were released into the flow field at the time of the detonation. The initial particle locations are shown at the full model scale and near one detonation in Figure 4-27. The exchange volume (1, 2, or 3 R_c) was used to define the maximum radius of particle shells.

The particle trajectories were calculated using FEHM with the sptr macro. No dispersion (caused by subgrid-scale physical heterogeneity) was assumed, although dispersion did effectively occur because of transient flow and grid-scale heterogeneity. To simulate subgrid-scale dispersion would have required a very large number of particles, and the process of relating each particle to its unique source

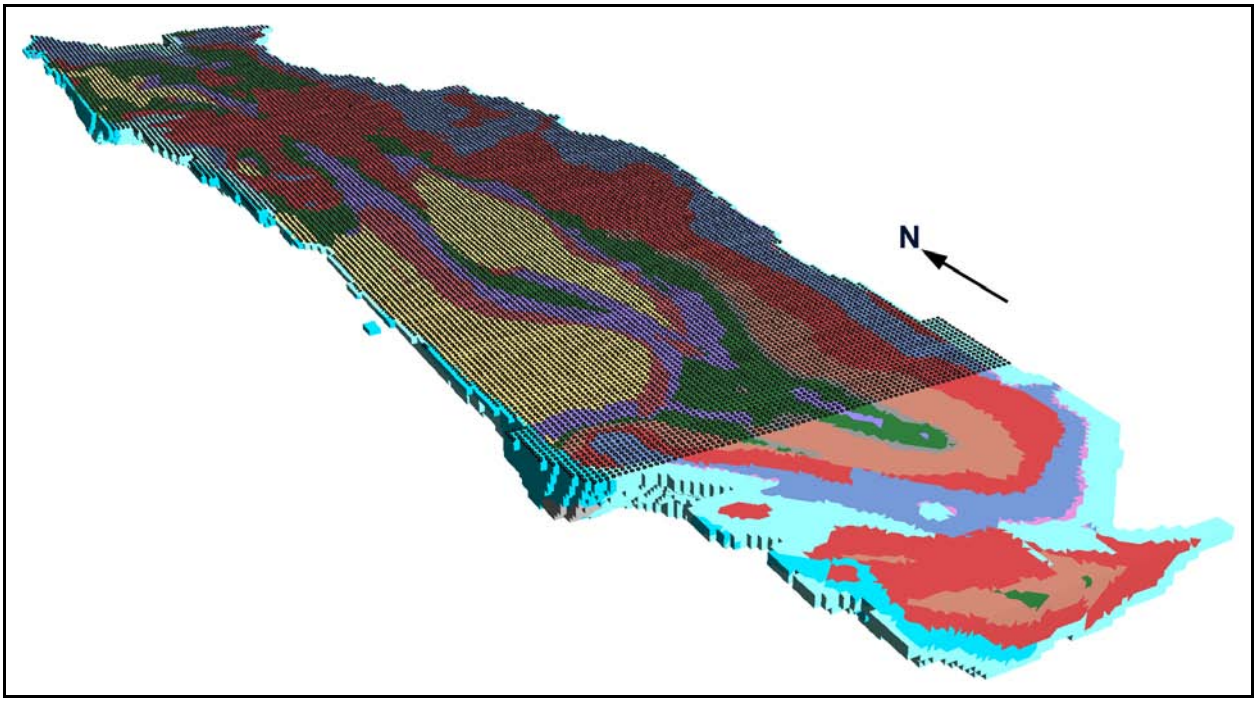

Figure 4-26
Distribution of Particles at the Water Table

(typically 70,000) would have been computationally demanding with little benefit. Additionally, there are constraints on the use of dispersion in a transient flow field when using FEHM_sptr. These constraints are limited to the transient saturated alluvial/volcanic flow field and are unrelated to other potential numerical resolution issues presented in Appendix K. Neglecting subgrid-scale dispersion introduces slight conservatism to the results in the sense that concentrations will be higher (as a result of less spreading). However, neglecting dispersion could have a nonconservative effect. For example, dispersion could cause earlier arrival times and, for radionuclides with short half-lives, result in higher mass flux to the model boundary.

4.6.2.2 Assigning Mass Flux to Each Particle

Mass Entering the Water Table. The time-varying mass arriving at the water table at each node at the base of the unsaturated-zone model was interpolated onto the regular grid described above and assigned to one of the particles shown in Figure 4-26. This method strictly enforces total mass conservation across the model boundaries and causes only slight degradation in spatial and temporal resolution of the fluxes. The result of this interpolation is a set of *mdot* files and a *sim* file suitable for PLUMECALC input.

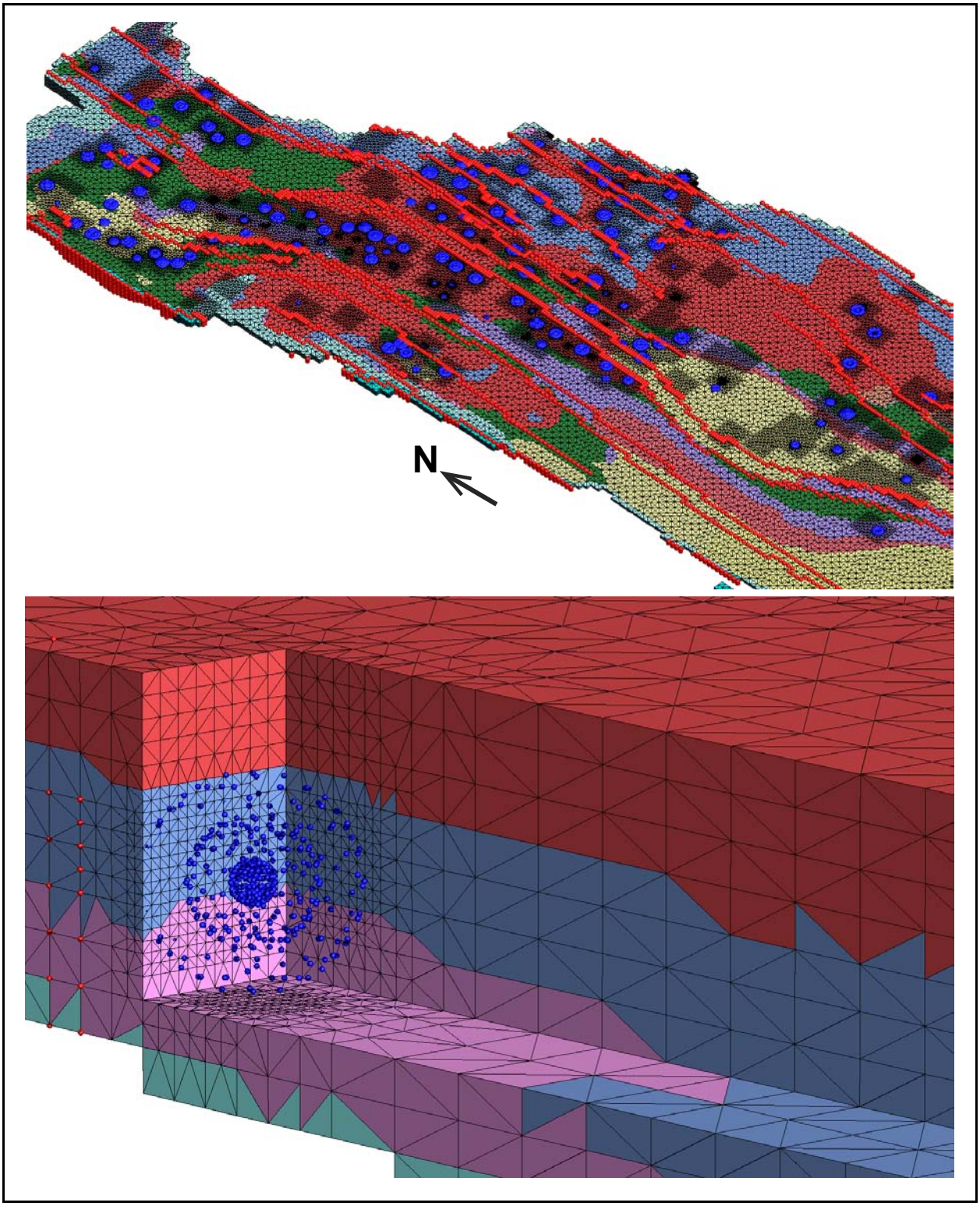

Figure 4-27
Distribution of Particles Representing Saturated-Zone Source Mass

Mass Representing Saturated-Zone Detonations. For each detonation with at least a portion of the exchange volume within the saturated zone, the radionuclide mass for that detonation was equally divided among all particles. This is approximately equivalent to a "uniform mass" distribution within the exchange volume. Particles were placed on three spherical shells around each detonation location, and the coordinates of all particles' initial locations on the shells were computed by LaGriT (LANL, 2011), a library of user-callable tools that provide mesh generation, mesh optimization, and dynamic mesh maintenance in two and three dimensions for a variety of applications. For the first three sets of flow and transport calculations (Table 4-13), exchange volume uncertainty was considered, and particle sphere radii were varied (1, 2, or 3 R_c). For all other simulations, an exchange volume corresponding to 1 R_c was assumed, in accordance with the HST described in Section 2.0.

Quite a few tests have exchange volumes that span the water table. The first three sets of flow and transport calculations (Table 4-13) relegate the mass within the exchange volume above the water table to the unsaturated-zone model. The remaining simulations consider a more conservative approximation, assuming all the mass from these detonations immediately enters the saturated zone, with particles assigned to an elevation of 745 m.

To ensure the consistency of our approach with the mass apportionment between model domains calculated by the HST (Section 2.0), we compared the source associated with each detonation. The comparison for a 1 R_c exchange volume, shown in Figure 4-28, is quite good.

In reality, not all the mass reported by Bowen et al. (2001) is immediately available for groundwater transport. A fraction of the mass is sequestered in melt glass, which slowly dissolves over time. In Table 4-14, the fractions considered to be sequestered for each radionuclide are listed. These range from 0 (^{3}H) to 95 percent (^{237}Np). The rate of glass dissolution depends on the flux rate of groundwater flowing through the cavity, dissolved glass constituent concentrations in the groundwater, and the temperature history. At Yucca Flat, the flux rate probably changed considerably over time, and these transient fluxes and temperatures were probably unique to each detonation. Mechanistically simulating these is beyond the scope of this project. Instead, the radionuclide mass in the melt glass was assumed to stay sequestered in the glass throughout the simulations, and sensitivity analyses were performed to assess the impact of the glass retention factor (g_{rn}) on transport results. A preliminary sensitivity analysis was performed to compare the base case (Table 4-14) with lower

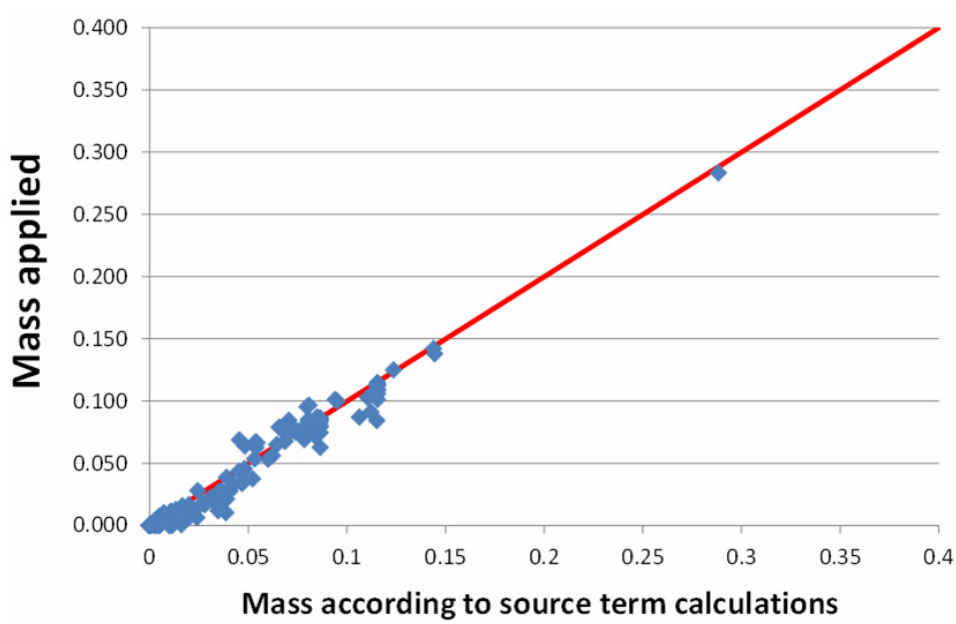

Figure 4-28
Comparison of Mass Release according to Uniform Mass-Based Allocation Method and Approximate Method

Table 4-14
Glass Retention Factors

Radionuclides	^{3}H	^{14}C	^{36}Cl	^{99}Tc	^{129}I	^{237}Np	U
Glass Retention Factor	0	0	0.5	0.8	0.5	0.95	0.9

retention factors $g_{rn}' = g_{rn} \times 0.94$. This analysis showed no sensitivity to g_{rn}. A more thorough sensitivity analysis considering a broader range of retention factors is presented later in this section.

The mobile mass available for groundwater transport ($M_{f,rn}$) for each radionuclide at each detonation was computed by

$$M_{f,\,rn} = M_{rn}(1 - g_{rn}) \qquad (4\text{-}1)$$

where

rn = any particular radionuclide of interest
M_{rn} = total mass of this radionuclide in this detonation
g_{rn} = glass retention factor (Table 4-14, derived from Table 4.1 in Tompson [2008])

4.6.2.3 Transport Properties of Rocks and Fault Zones

The HSUs were divided into two groups, depending on whether flow is thought to occur predominately in fractures or in porous rock matrix (Table 4-15). The groupings were made strictly based on recommendations in SNJV (2006b).

Table 4-15
Conceptual Model of Flow in Each HSU

Unit ID	HSU	Primary Flow
11	LCA	Fracture
13	ATCU	Matrix
14	OSBCU	Matrix
16	LTCU	Matrix
22	TSA	Fracture
23	UTCU	Matrix
25	TM-LVTA	Matrix
26	TM-WTA	Fracture
27	TM-UVTA	Matrix
28	AA1	Matrix
30	AA2	Matrix
32	AA3	Matrix

For each of the nine matrix flow units, the following transport parameters were assigned: effective (flowing) porosity ϕ, sorption coefficient k_d, and bulk rock density ρ_d. The bulk rock density is used to determine the matrix retardation factor $R = 1 + \rho_d K_d/\phi$. For each of the three fracture-flow units, a dual-continuum model was assumed, so both fracture and matrix properties were required. For the matrix properties in the dual-continuum model, in addition to effective porosity, sorption coefficient, and rock density, tortuosity must be defined. Matrix diffusion is related to tortuosity τ and the free-water diffusion coefficient D_0 as expressed by $D_m = \tau D_0$, where tortuosity depends solely on rock unit, whereas the free-water diffusion coefficient is a property of radioelement and is independent of rock units. The free-water diffusion coefficients for seven species are tabulated in Table 4-16.

For the dual-continuum model, the following fracture properties are also required: fracture porosity ϕ_f, sorption coefficient, and aperture b. The aperture is related to fracture porosity and spacing s by $\phi_f = b/s$.

Table 4-16
Free-Water Diffusion Coefficients

Species	*H*	C	Cl	Tc	I	Np	U
D_0 (m²/s)	2.40E-09	1.18E-09	2.03E-09	1.95E-09	2.05E-09	6.18E-10	6.64E-10

Radioactive decay for all but ^{3}H and ^{14}C was neglected in the analysis. This can be justified from the following analysis. Suppose at time t, the mass of a species in the system is $m(t)$. At time $t + \Delta t$, the mass in the system will change because of addition or removal of the mass: contribution of saturated-zone internal sources at a rate of $q_{in}^{(sz)}$ and contribution of the unsaturated-zone sources from the upper boundary at a rate of $q_{in}^{(uz)}$ left the system to the LCA model domain at a rate of $q_{out}^{(LCA)}$ and decay at a rate of $\lambda m(t)$. The change of mass can be described by the following equation:

$$\frac{dm}{dt} = -\lambda m + [q_{in}^{(uz)} + q_{in}^{(sz)} - q_{out}^{(LCA)}] \qquad (4\text{-}2)$$

The solution to this equation with the initial condition $m(0) = 0$ is

$$m(t) = \int_0^t [q_{in}^{(uz)} + q_{in}^{(sz)} - q_{out}^{(LCA)}] e^{-\lambda(t-\tau)} d\tau \qquad (4\text{-}3)$$

The total net mass into the system is

$$m_{net}(t) = \int_0^t [q_{in}^{(uz)} + q_{in}^{(sz)} - q_{out}^{(LCA)}] d\tau \qquad (4\text{-}4)$$

and the decayed mass is

$$m_{decayed}(t) = \int_0^t [q_{in}^{(uz)} + q_{in}^{(sz)} - q_{out}^{(LCA)}](1 - e^{-\lambda(t-\tau)}) d\tau \qquad (4\text{-}5)$$

For saturated-zone sources, because detonations are conducted at discrete times, $q_{in}^{(sz)} = \sum_{i=1}^{N} q_{in,i}^{(sz)} \delta(t - t_i)$, where δ is the Dirac delta function, the total saturated-zone source term can be computed as

$$Q_{in}^{(sz)} = \int_0^t q_{in}^{(sz)} (1 - e^{-\lambda(t-\tau)}) d\tau = \sum_{i=1}^{N} q_{in,i}^{(sz)} (1 - e^{-\lambda(t-t_i)}) \qquad (4\text{-}6)$$

where

$q_{in,i}^{(sz)}$ = mass of the ith detonation
t_i = detonation time of the ith detonation
N = number of saturated-zone detonations

The calculated total mass (in moles) decayed for case 211212.1.14.5.1.2.N3.B2.s is tabulated in Table 4-17. The results indicate that, except for ^{3}H and ^{14}C, the total decayed mass for all other radionuclides is very small for time up to 1,000 years, and it accounts for less than 0.2 percent of the total mass.

Table 4-17
Estimated Total Mass Decayed at 1,000 Years (in Moles)
(for the Base Case 211212.1.14.5.1.2.N3.B2.s)

	^{3}H	^{14}C	^{36}Cl	^{99}Tc	^{129}I	^{237}Np	U_{all}
Decay Constant (1/days)	1.54E-04	3.31E-07	6.31E-09	8.91E-09	1.21E-10	8.87E-10	4.25E-13
Internal Source (2 R_c)	1,803.7	7.42	53.30	12.25	6.53	1.76	11,133.0
Unsaturated-Zone Sources	11.22	3.87	18.95	3.84	2.14	0.46	4,109.9
Total Sources (Aqueous)	1,815.0	11.29	72.25	16.09	8.67	2.22	15,242.9
Internal Sources (Decayed)	1,803.7	0.831	0.120	3.91E-02	2.83E-04	5.58E-04	1.70E-03
Unsaturated-Zone Sources (Decayed)	11.22	0.221	0.021	6.01E-03	4.54E-05	7.17E-05	3.06E-04
Total Decayed	1,815.0	1.051	0.141	4.51E-02	3.28E-04	6.30E-04	2.00E-03

The available datasets for estimating all these parameters (and their inferred distributions, for the purpose of uncertainty analysis) are summarized in Table 4-18. Much of these data were collected in similar rocks collected at locations other than Yucca Flat (as described in SNJV [2006b]).
For effective porosity, only data measured on Yucca Flat core were used (Stephens, 2008).

Virtually all the data described in Table 4-18 were collected on very small samples. Extrapolating these values to large grid blocks requires considering the scale dependency of the property. It is well known that the parameter statistics computed from small-scale measurements should not be used directly to generate parameter samples at the grid scale. The parameter variance at a larger scale should have smaller variance. The method of Li et al. (2009) was used to upscale these datasets for the transport model application.

Generally, if there are measurements at scale T_1, but there is a need to compute the variance at scale T_2, this can be done by first calculating the variance function γ for each resolution. In fact, since $\sigma^2_{Y,T_1} = \sigma^2_Y \gamma(T_1)$ and $\sigma^2_{Y,T_2} = \sigma^2_Y \gamma(T_2)$, the variance at the grid scale T_2 can be estimated by

Table 4-18
Statistics of Datasets Used to Derive Parameters for PLUMECALC Simulations
(Page 1 of 2)

Parameters	HSU/HGU	Node Count	Mean	Standard Deviation	Minimum	Maximum	Distribution	Data Sources
Matrix Porosity (-)	AA	6,203	0.344	0.067	0.013	0.970	Normal	Table 7-3 on page 7-12 of SNJV (2007)
	AA2	113	0.409	0.060	0.298	0.503		
	AA3	6,090	0.373	0.066	0.013	0.970		
	LCA	26	0.022	0.014	0.004	0.060		
	OSBCU	958	0.381	0.062	0.007	0.580		
	TM-LVTA	2,290	0.432	0.075	0.009	0.708		
	TM-UVTA	428	0.421	0.064	0.083	0.631		
	TSA	31	0.376	0.084	0.178	0.510		
	TCU	50	0.259	0.109	0.004	0.574	Normal	Stephens (2008)
	WTA	6	0.213	0.126	0.047	0.407		
Density (kg/m^3)	ATCU	4	2,163.54	84.80	2,049.53	2,254.34	Normal	Computed from borehole data at Rainier Mesa area
	BRCU	13	1,640.45	121.30	1,414.71	1,809.56		
	LCA3	2	2,454.72	256.88	2,273.07	2,636.36		
	OSBCU	25	1,857.75	222.39	1,550.79	2,328.04		
	TM-LVTA	9	1,382.72	219.76	935.06	1,646.38		
	TM-WTA	3	2,098.15	321.55	1,727.73	2,305.43		
Tortuosity (10-based log)	LCA	20	–1.213	0.494	–2.097	–0.467	Lognormal	Computed from Appendix H, Matrix_diffusion_data set.xls, of SNJV (2007)
	WTA	45	–1.120	0.337	–1.678	–0.322		
Fracture Porosity	CA	--	5.0E-03		2.0E-04	2.0E-02	Triangular	Table 8-22, page 8-78, of SNJV (2007)
	WTA	--	3.0E-03		1.0E-04	6.0E-03		
Natural log Fracture Spacing (m)	LCA3	194	1.52	1.637	–5.79	3.18	Lognormal	Mean computed from ER-12-3 and ER-12-4, while standard deviation, minimum, and maximum were adopted from TCU data.
	WTA	6	1.548	0.0	1.548	1.548		Table 8-4 of SNJV (2007)

Table 4-18
Statistics of Datasets Used to Derive Parameters for PLUMECALC Simulations
(Page 2 of 2)

Parameters	HSU/HGU	Node Count	Mean	Standard Deviation	Minimum	Maximum	Distribution	Data Sources
K_d of Np (mL/g)	AA	1,417	2.9356	12.7296	0	198.376	Lognormal	Computed from Appendix I, Mechanistic_Kd_by_HSU.xls, of SNJV (2007)
	ATCU	322	3.9612	11.2223	0	91.640		
	TSA	57	0.012	0.028	0.000	0.103		
	TM-WTA	223	0.291	0.531	0.000	4.788		
	TM-UVTA	76	2.244	7.083	0.000	52.977		
	UTCU	60	0.046	0.061	0.000	0.288		
	LTCU	3,873	0.819	6.204	0.000	222.140		
	TM-LVTA	2,265	0.799	6.165	0.000	203.375		
K_d of U (mL/g)	AA	1,417	0.0011	0.0038	0	0.0488	Lognormal	Computed from Appendix I, Mechanistic_Kd_by_HSU.xls, of SNJV (2007)
	ATCU	322	0.0051	0.01	0	0.0501		
	TSA	57	0.0001	0.0003	0.0000	0.0014		
	TM-WTA	223	0.0009	0.0034	0.0000	0.0290		
	TM-UVTA	76	0.0014	0.0051	0.0000	0.0338		
	UTCU	60	0.0002	0.0006	0.0000	0.0038		
	LTCU	3,873	0.0008	0.0021	0.0000	0.0367		
	TM-LVTA	2,265	0.0010	0.0040	0.0000	0.0504		

kg/m³ = Kilograms per cubic meter

$\sigma^2_{Y,T_2} = \sigma^2_{Y,T_1}\gamma(T_2)/\gamma(T_1)$. The variance function depends on the correlation structure and correlation scales of the parameter, as well as the scale (resolution) of interest. In general, one can obtain the correlation structure and correlation scales from variogram analysis using spatially distributed samples, as long as the number of samples is reasonably sufficient. Because there is not enough information to infer the correlation structure and its correlation scales, in this study, it is assumed that all parameters have a (separable) exponential covariance function and that their correlation scales are similar to the grid size (T_2), which on average is about 100, 100, and 5 m in *x*, *y*, and *z* directions. There is not sufficient information about the measurement scales for these parameters. Therefore, it is assumed that most of these parameters (matrix porosity, sorption coefficient, matrix tortuosity, and bulk rock density) have a measurement scale of 0.1 m, while fracture porosity and fracture spacing have a measurement scale of meters. The fracture spacing in welded-tuff aquifers was an average spacing across the entire logged interval having good image quality (SNJV, 2007), so the measurement scale should be much larger. For the welded-tuff aquifer units, because the variability of fracture spacing is zero, upscaling does not affect this parameter.

In addition to upscaling that reduces parameter variance, there are two other mechanisms that will change both parameter mean and variance. First, for lognormally distributed random variable *V*, the moments of the log-transformed variable $U = \ln V$ can be computed from the moments of *V* as follows (e.g., Zhang, 2002):

$$\langle U \rangle = \ln \langle V \rangle - 0.5 \ln \left(1 + \sigma_V^2 / \langle V \rangle^2 \right) \tag{4-7}$$

$$\sigma_U^2 = \ln[1 + \sigma_V^2 / \langle V \rangle^2] \tag{4-8}$$

or conversely,

$$\langle V \rangle = \exp[\langle U \rangle + 0.5\sigma_U^2] \tag{4-9}$$

$$\sigma_V^2 = [\exp(\sigma_U^2) - 1]\exp[2\langle U \rangle + \sigma_U^2] \tag{4-10}$$

As a result, for a lognormally distributed random variable *V*, if the variance of log-transformed variable $U = \ln V$ is reduced because of upscaling, the mean of *V* will also be changed.

Some parameter statistics (mean and standard deviation) are calculated from a limited number of samples, and they highly depend on lower and upper bounds of samples. For correction, the distributions of these parameters are treated as truncated distributions and adjusted parameter statistics due to lower and upper bounds.

The resulting parameter values for each HSU are shown in Tables 4-19 to 4-26. For a small number of HSUs, no data were available so datasets from other similar units were used.

Three important zones are not mentioned in these tables: faults, cavities, and chimneys. For all the transport calculations, these zones are assumed to have the same properties as welded-tuff aquifers.

Table 4-19
Matrix Porosity

Unit ID	HSU	Proxy	Mean	Standard Deviation	Distribution
11	LCA	LCA	0.020	0.011	Normal
13	ATCU	TCU	0.258	0.078	Normal
14	OSBCU	OSBCU	0.381	0.044	Normal
16	LTCU	TCU	0.258	0.078	Normal
22	TSA	TSA	0.379	0.063	Normal
23	UTCU	TCU	0.258	0.078	Normal
25	TM-LVTA	TM-LVTA	0.432	0.053	Normal
26	TM-WTA	WTA	0.202	0.120	Normal
27	TM-UVTA	TM-UVTA	0.421	0.045	Normal
28	AA1	AA	0.344	0.047	Normal
30	AA2	AA2	0.411	0.046	Normal
32	AA3	AA3	0.373	0.047	Normal

Table 4-20
Bulk Rock Density

Unit ID	HSU	Proxy	Mean (kg/m^3)	Standard Deviation	Distribution
11	LCA	LCA3	2,454.7	181.4	Normal
13	ATCU	ATCU	2,163.5	59.9	Normal
14	OSBCU	OSBCU	1,839.7	178.0	Normal
16	LTCU	BRCU	1,649.5	99.4	Normal
22	TSA	TM-WTA	2,098.1	227.1	Normal
23	UTCU	BRCU	1,649.5	99.4	Normal
25	TM-LVTA	TM-LVTA	1,429.1	198.2	Normal
26	TM-WTA	TM-WTA	2,098.1	227.1	Normal
27	TM-UVTA	TM-LVTA	1,429.1	198.2	Normal
28	AA1	AVG	1,787.0	78.4	Normal
30	AA2	AVG	1,787.0	78.4	Normal
32	AA3	AVG	1,787.0	78.4	Normal

Table 4-21
Matrix Tortuosity

Unit ID	HSU	Proxy	Mean (log 10)	Standard Deviation	Distribution
11	LCA	LCA	–1.196	0.392	Lognormal
22	TSA	TSA	–1.128	0.249	Lognormal
26	TM-WTA	AVG	–1.143	0.184	Lognormal

AVG = Averaged properties

Table 4-22
Fracture Porosity

Unit ID	HSU	Proxy	Minimum	Mode	Maximum	Distribution
11	LCA	CA	2.00E-04	5.00E-03	2.00E-02	Triangular
22	TSA	WTA	1.00E-04	3.00E-03	6.00E-03	Triangular
26	TM-WTA	WTA	1.00E-04	3.00E-03	6.00E-03	Triangular

Table 4-23
Fracture Spacing

Unit ID	HSU	Proxy	Mean (m, ln)	Standard Deviation	Distribution
11	LCA	LCA3	1.520	1.295	Lognormal
22	TSA	WTA	1.548	1.138	Lognormal
26	TM-WTA	WTA	1.548	1.138	Lognormal

Table 4-24
K_d of Neptunium
(Page 1 of 2)

Unit ID	HSU	Proxy	Mean (mL/g, ln)	Standard Deviation	Distribution
11	LCA	AVG	–1.843	0.801	Lognormal
13	ATCU	ATCU	0.276	1.048	Lognormal
14	OSBCU	ATCU	0.276	1.048	Lognormal
16	LTCU	LTCU	–2.236	1.428	Lognormal
22	TSA	TSA	–5.598	1.200	Lognormal
23	UTCU	UTCU	–3.589	0.714	Lognormal
25	TM-LVTA	TM-LVTA	–2.281	1.436	Lognormal
26	TM-WTA	TM-WTA	–1.969	0.856	Lognormal
27	TM-UVTA	TM-UVTA	–0.389	1.093	Lognormal

Table 4-24
K_d of Neptunium
(Page 2 of 2)

Unit ID	HSU	Proxy	Mean (mL/g, ln)	Standard Deviation	Distribution
28	AA1	AA	–0.416	1.221	Lognormal
30	AA2	AA	–0.416	1.221	Lognormal
32	AA3	AA	–0.416	1.221	Lognormal

AVG = Averaged properties

Table 4-25
K_d of Uranium

Unit ID	HSU	Proxy	Mean (mL/g, ln)	Standard Deviation	Distribution
11	LCA	AVG	–8.143	0.608	Lognormal
13	ATCU	ATCU	–6.068	0.887	Lognormal
14	OSBCU	ATCU	–6.068	0.887	Lognormal
16	LTCU	LTCU	–8.164	1.015	Lognormal
22	TSA	TSA	–10.362	1.072	Lognormal
23	UTCU	UTCU	–9.669	1.072	Lognormal
25	TM-LVTA	TM-LVTA	–8.324	1.189	Lognormal
26	TM-WTA	TM-WTA	–8.376	1.166	Lognormal
27	TM-UVTA	TM-UVTA	–7.900	1.152	Lognormal
28	AA1	AA	–8.092	1.130	Lognormal
30	AA2	AA	–8.092	1.130	Lognormal
32	AA3	AA	–8.092	1.130	Lognormal

AVG = Averaged properties

Table 4-26
Mean Fracture Aperture

Unit ID	Mean Aperture (m)
11	2.78E-03
22	1.55E-03
26	1.55E-03
Faults	3.31E-03

Note: Calculated from porosity and fracture spacing.

4.6.3 Three Representative Results

The flow models 211212.1.14.5.1.2.N3.B2.s and *v.1 are representative flow simulations with good agreement between measured and simulated heads. The corresponding unsaturated-zone model, 211212, is an intermediate unsaturated-zone model result in terms of total radionuclide mass delivered to the water table. The flow model 542121.12.2.8.1.11.2012_HST.N3.B2.s was also selected as a representative flow simulation whose results are presented in detail below. This result was included because this model uses a recharge boundary condition of approximately 0.1 mm/yr and includes transient enhanced crater recharge (Section 3.0). However, the agreement between measured and simulated heads for this case (r^2 = 0.71) and between measured and simulated subsidence is not as good as for cases with higher infiltration. In this section, PLUMECALC results using the mean values for all the transport properties are presented.

In Figures 4-29a to f, the evolution over time of ^{14}C concentration within the saturated alluvial/volcanic aquifer system model domain, and ^{14}C fluxes to the LCA are shown for the three representative cases. Figures 4-29a and b show results from case 211212.1.14.5.1.2.N3.B2.s, Figures 4-29c and d show results from case 211212.1.14.5.1.2.N3.B2.v.1, and Figures 4-29e and f show results from case 542121.12.2.8,1,11,2012_HST.N3.B2.s. This series of figures shows a time series including four times at 20, 50, 100, and 1,000 years. One-time snapshot in three dimensions (at 50 years) is shown in Figure 4-30 for case 211212.1.14.5.1.2.N3.B2.s. The view is looking north from a perspective above the water table.

Figures 4-29a, c, and e illustrate ^{14}C concentrations within the saturated alluvial/volcanic aquifer system model domain with time. For all three of these figures, concentration can be seen to increase spatially with time. However, blue and purple colors indicate areas with concentrations at or below the SDWA upper limit of 3E-11 moles of ^{14}C/L. In Figure 4-29e, concentrations are shown to be more spatially isolated than in Figures 4-29a and c, which indicates that the low recharge case causes lower transport within the saturated alluvial/volcanic aquifer system model domain than the first two cases. It is evident in all three of these figures that most of the water with nonzero concentration is within or very close to cavities (near-field) and at relatively high concentration (warm colors). This is true at all times in the simulations. In the low infiltration/low permeability cases, very little contamination ever leaves the near field. In the other two cases, some transport away from the near field is evident; however, most of this water is below the SDWA (blue and purple colors).

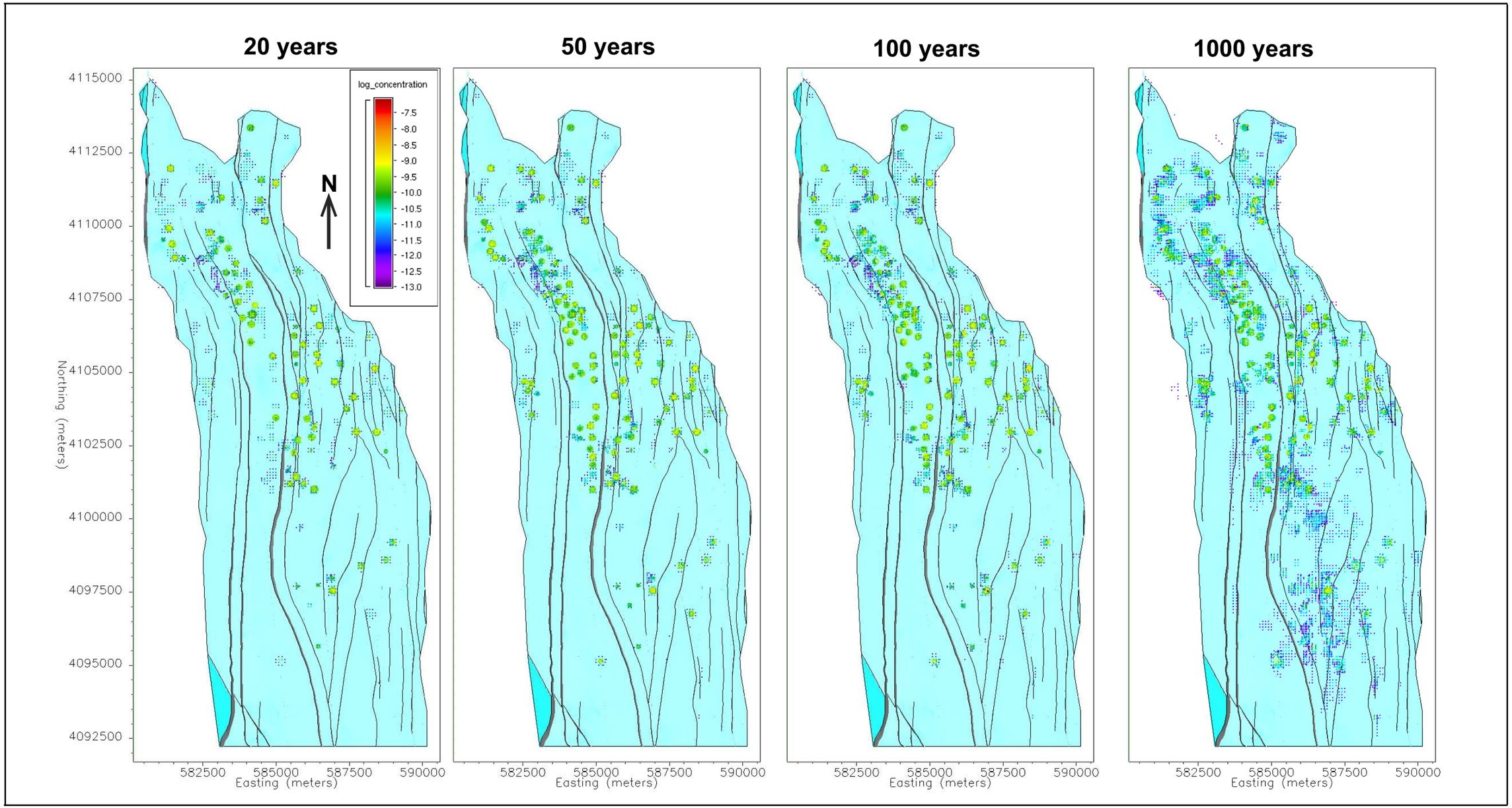

Figure 4-29a
Concentration of ^{14}C (mol/L) within Saturated Alluvial/Volcanic Aquifer System Model Domain at 20, 50, 100, and 1,000 Years (Case 211212.1.14.5.1.2.N3.B2.s)

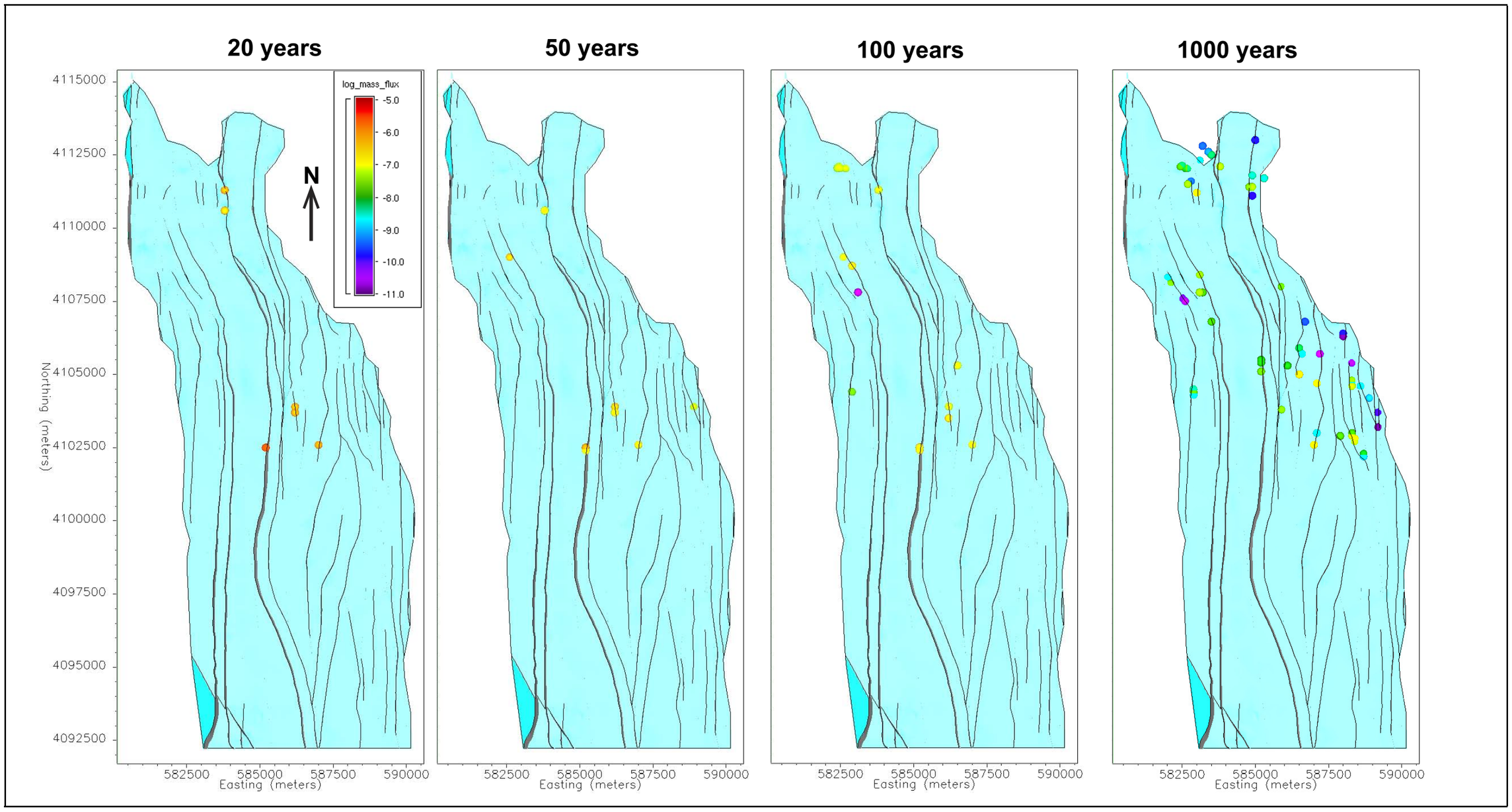

Figure 4-29b
Mass Flux of ^{14}C (mol/day) Transported to LCA from Saturated Alluvial/Volcanic Aquifer System Model Domain at 20, 50, 100, and 1,000 Years (Case 211212.1.14.5.1.2.N3.B2.s)

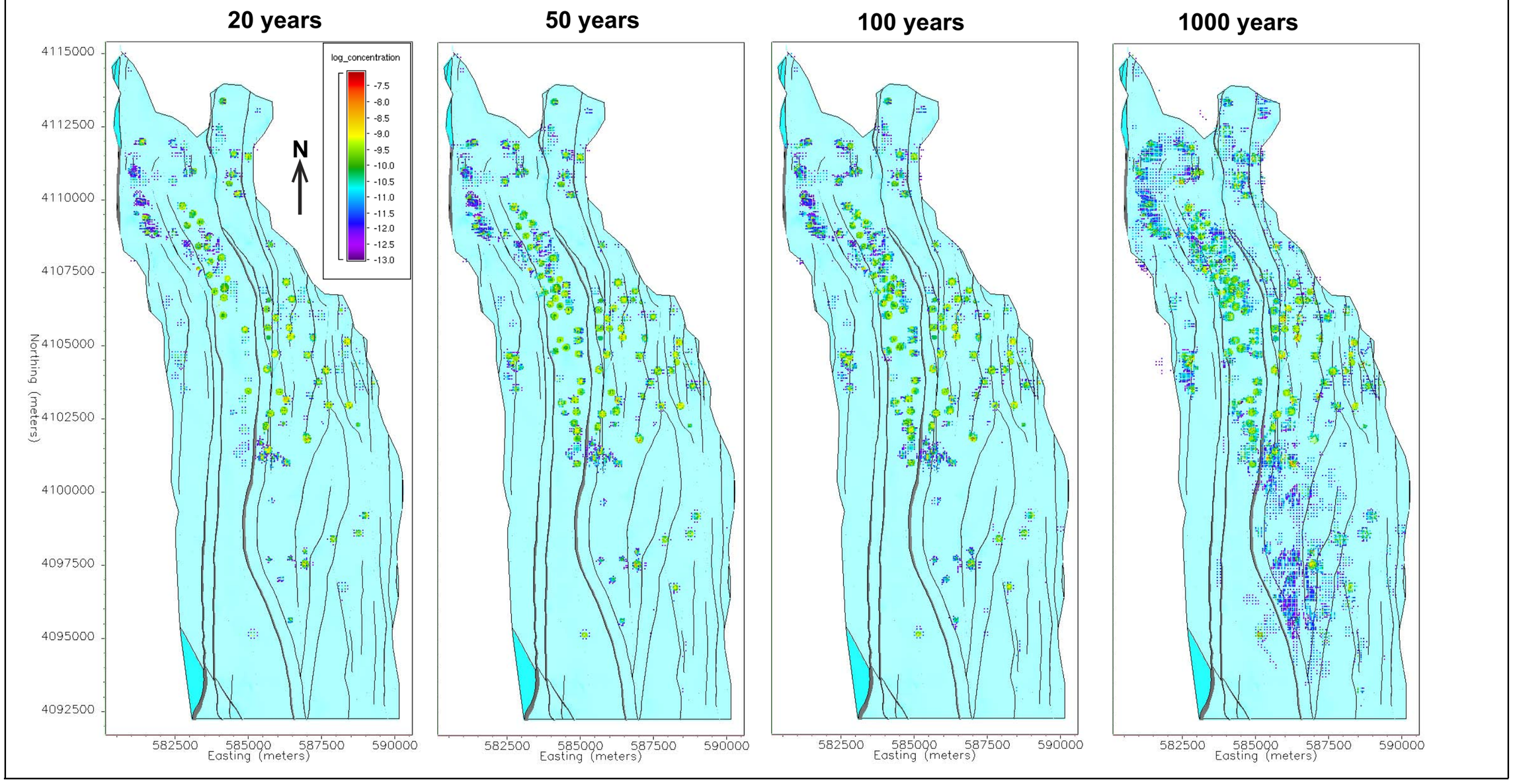

Figure 4-29c
Concentration of ^{14}C (mol/L) within Saturated Alluvial/Volcanic Aquifer System Model Domain at 20, 50, 100, and 1,000 Years (Case 211212.1.14.5.1.2.N3.B2.v.1)

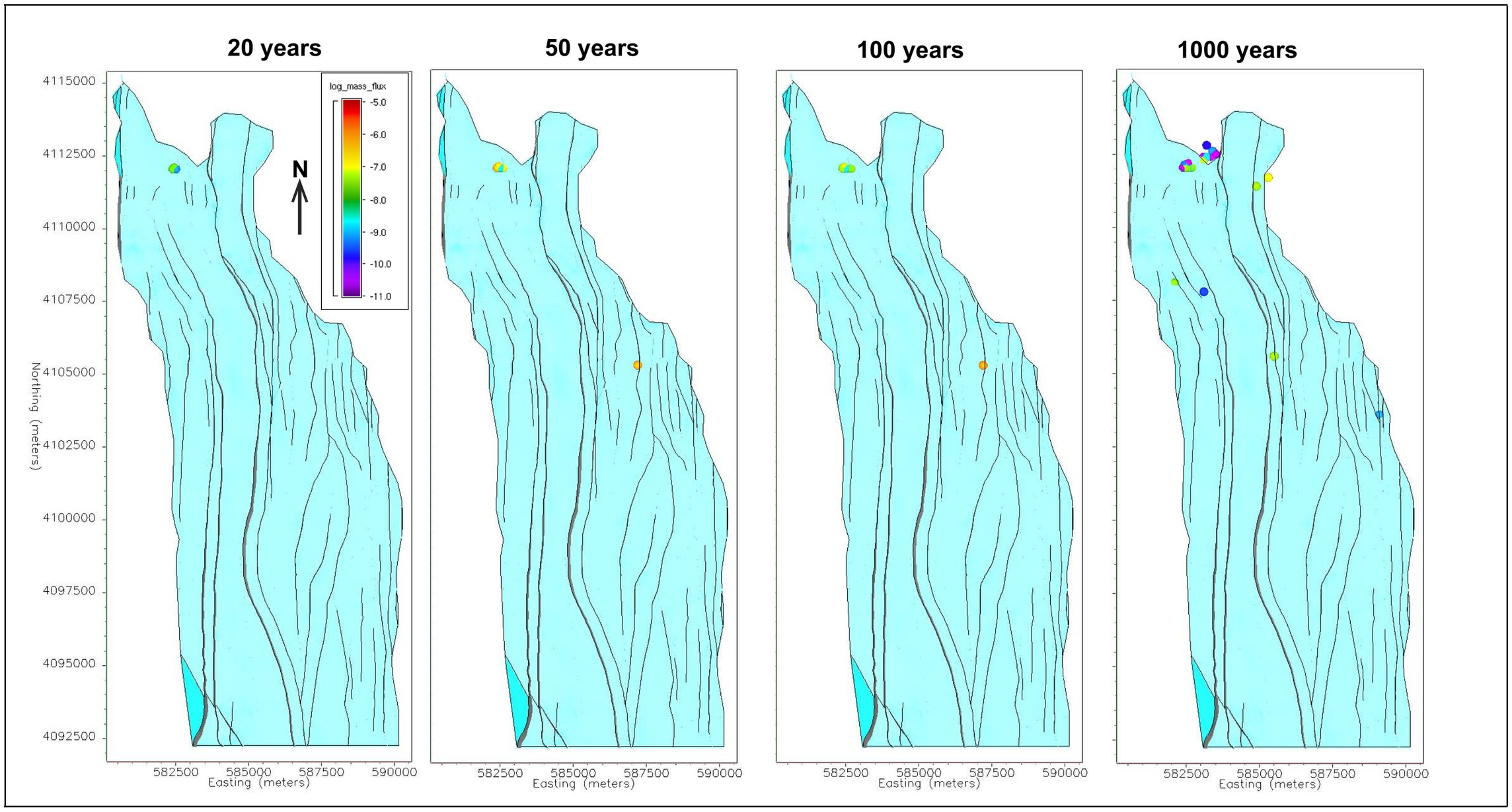

Figure 4-29d
Mass Flux of ^{14}C (mol/day) Transported to LCA from Saturated Alluvial/Volcanic Aquifer System Model Domain at 20, 50, 100, and 1,000 Years (Case 211212.1.14.5.1.2.N3.B2.v.1)

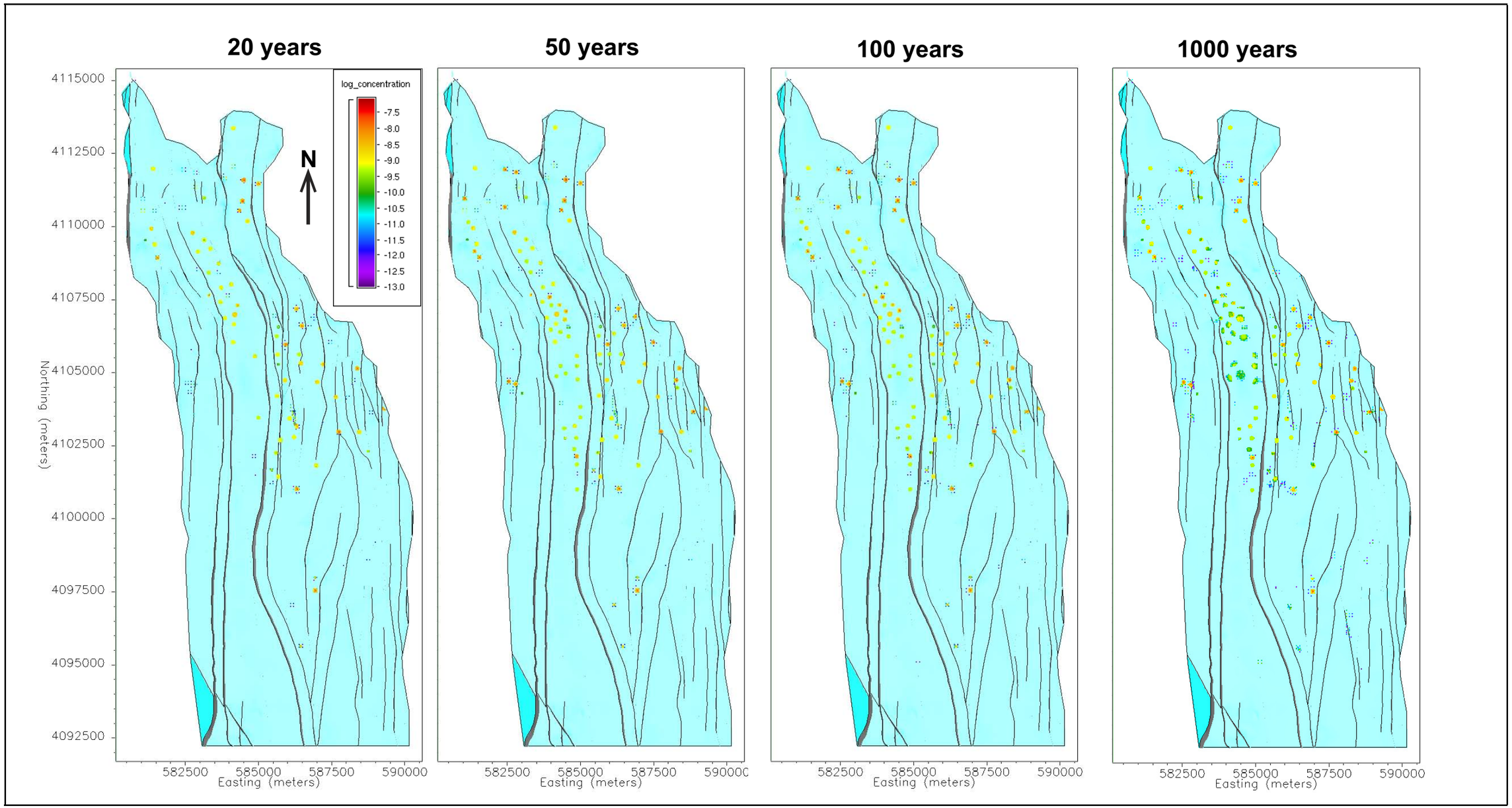

Figure 4-29e
Concentration of ^{14}C (mol/L) within Saturated Alluvial/Volcanic Aquifer System Model Domain at 20, 50, 100, and 1,000 Years (Case 542121.12.2.8.1.11.2012_HST.N3.B2.s)

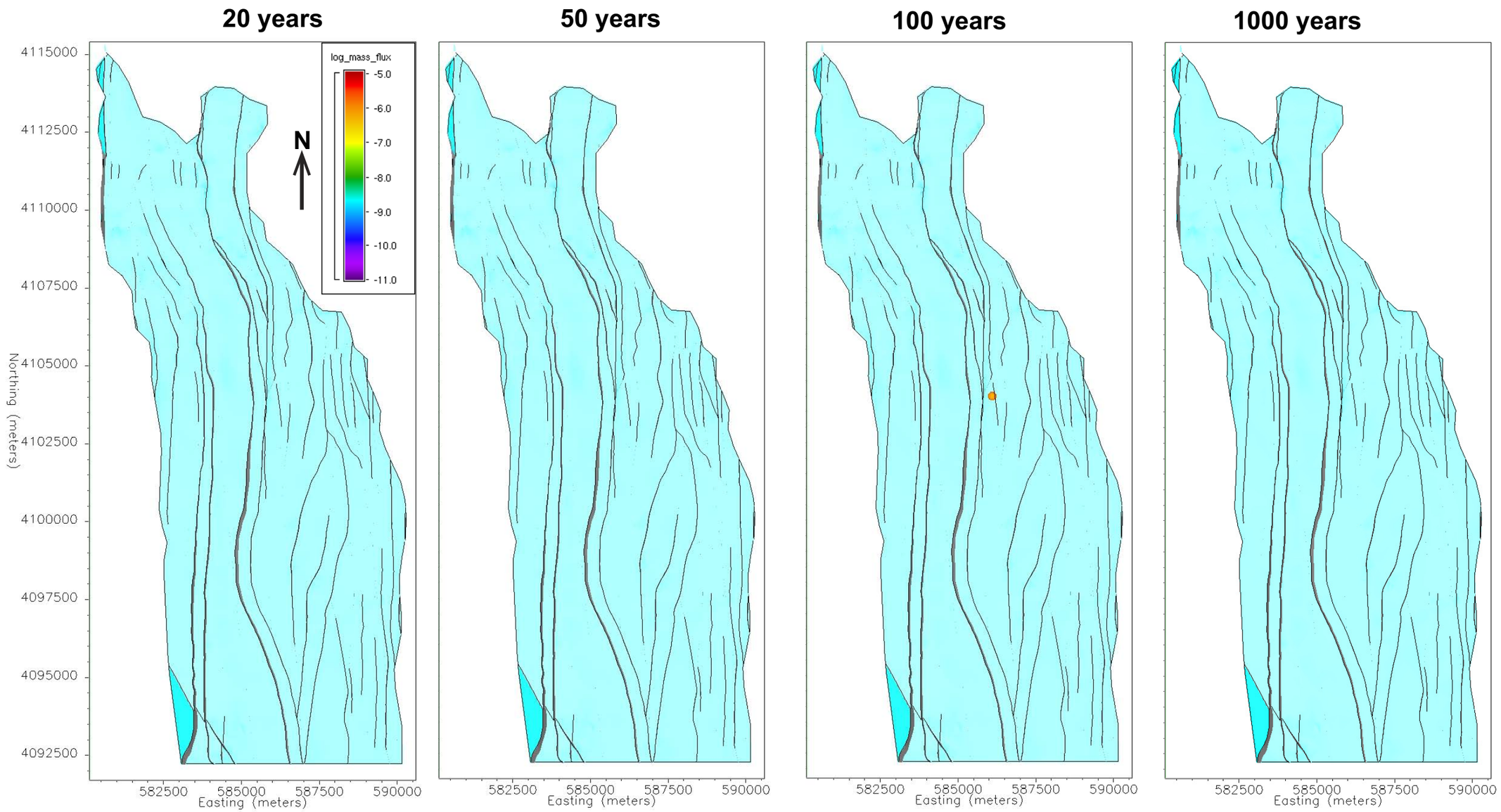

Figure 4-29f

Mass Flux of ^{14}C (mol/day) Transported to LCA from Saturated Alluvial/Volcanic Aquifer System Model Domain at 20, 50, 100, and 1,000 Years (Case 542121.12.2.8.1.11.2012_HST.N3.B2.s)

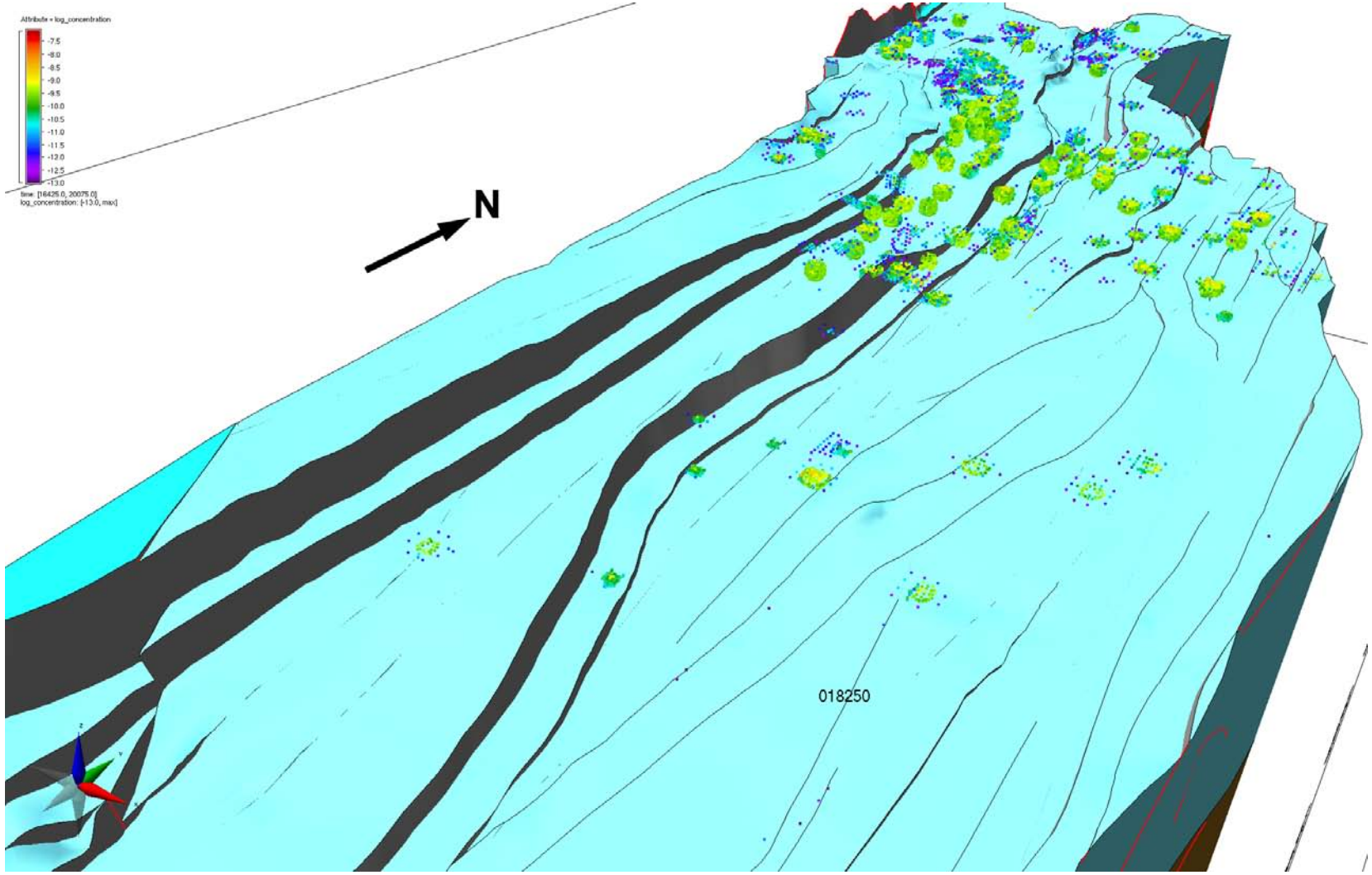

Figure 4-30
Three-Dimensional View of the ^{14}C Plume (in mol/L) within Saturated Alluvial/Volcanic Aquifer System Model Domain at Day 18,250 (50 Years) for Case 211212.1.14.5.1.2.N3.B2.s

As shown in Figures 4-29b, d, and f, only a small number of boundary nodes deliver radionuclide mass to the LCA. Of course, they are located along faults because of the conceptual and numerical models. Downward flux is heavily concentrated in the northern portion of the model domain for the first two cases. For the low recharge case, only one node appears that delivers mass to the LCA at 100 years.

The three-dimensional view shown in Figure 4-30 is provided for comparison purposes only (with Figure 4-29a, second panel) to illustrate the actual three-dimensionality of ^{14}C plume concentrations.

Figure 4-31 shows the exceedance volumes as functions of time for base-case model 211212.1.14.5.1.2.N3.B2.s. For this report, the exceedance volume, which is a scalar equivalent of the contaminant boundary, is calculated rather than an actual contaminant boundary. The exceedance volume is calculated according to regulatory limits based on the SDWA (CFR, 2012). All seven radionuclides are included (^{3}H, ^{14}C, ^{36}Cl, ^{99}Tc, ^{129}I, ^{237}Np, and U), each of which belongs to one of three groups: gross alpha particles (^{237}Np), beta emitters (^{3}H, ^{14}C, ^{36}Cl, ^{99}Tc, and ^{129}I), and uranium. The MCLs for these three groups are 15 pCi/L, 4 mrem/yr, and 30 µg/L. The exceedance volume is calculated as the total water volume that exceeds the MCL. Beta emitters dominate the exceedance volume at all times. The final cumulative exceedance volume is just under 4E+08 m^3. The exceedance volume at 1,000 years is 7.12E+07 m^3, or 0.37 percent of the total volume (1.92E+10 m^3) of groundwater in the saturated alluvial/volcanic aquifer system model domain.

In Figure 4-32, the cumulative mass leaving the model for each radionuclide is shown. The highest flux by far is ^{3}H (note that ^{3}H values are indicated on the right-hand vertical axis), but virtually all the mass is delivered early in the simulation. All these values, however, are much smaller than the amount of mass that enters the system (minus the amount presumed to have been held in the glass fraction) as either downward flux at the water table or mass released by saturated-zone detonations. These comparisons are made in Figure 4-33. The red bar indicates total mass input by sources within the model domain; the blue bars indicate total mass contributed from the unsaturated zone. The green and purple bars show total mass leaving the system by Testing-Effects Conceptual Models 1 and 2, respectively. This figure illustrates that for all radionuclides, a very small proportion of the total inventory leaves the saturated-zone model.

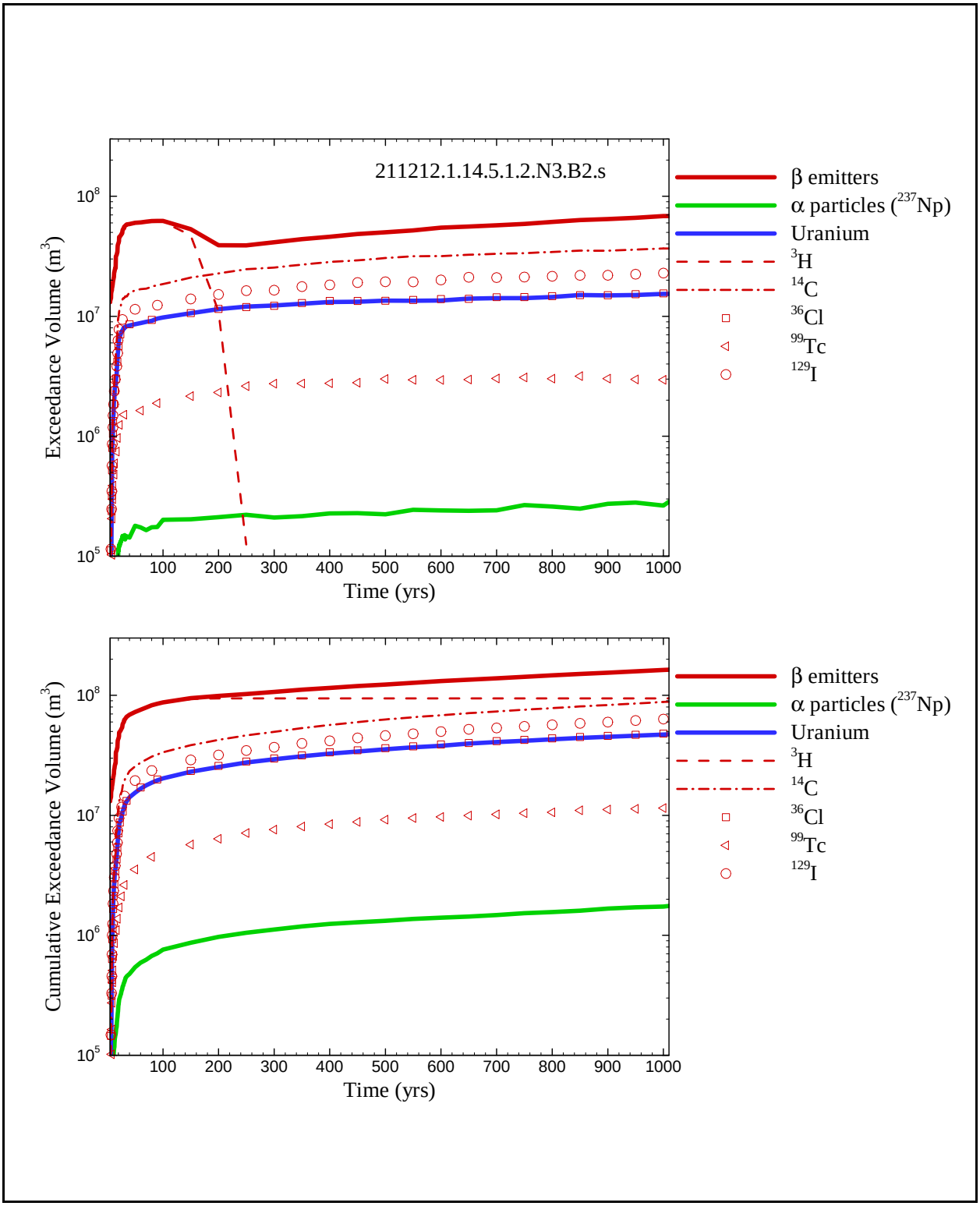

Figure 4-31
Exceedance Volume Calculations for Case 211212.1.14.5.1.2.N3.B2.s

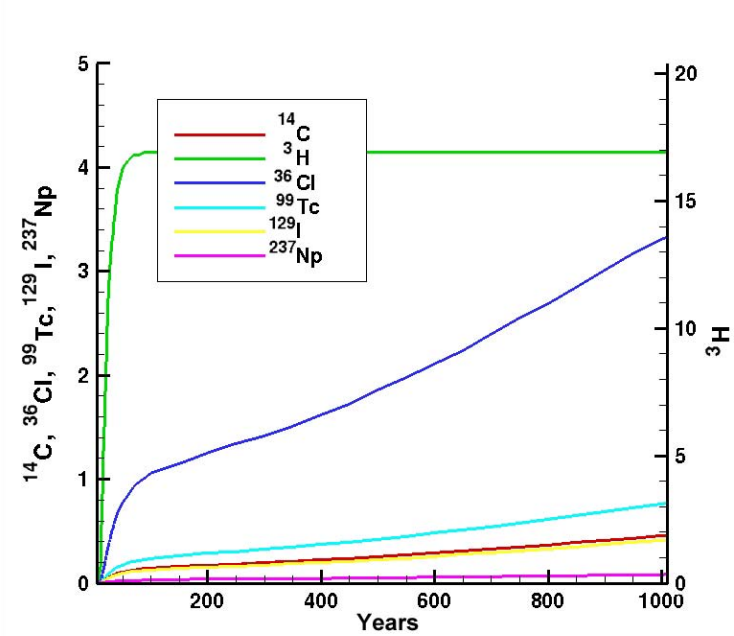

Figure 4-32
Cumulative Mass (Decay-Corrected) That Has Left the Model (in Moles)

In Figures 4-34 and 4-35, results for the same case, Testing-Effects Conceptual Model 2 (211212.1.14.5.1.2.N3.B2.v.1), are presented. The concentration figures are very similar to the previous case. Close inspection shows a slight increase in the number of nodes contaminated at very low levels. This is an interesting result, suggesting more dispersion due to flow-field transients and perhaps slower, focused flow toward the faults. Compared to the previous case for which images of mass flux at the lower model boundary are shown in Figures 4-29a to f, not only is the total mass flux less, but even fewer nodes are transmitting radionuclides downward. The exceedance volume calculation for this case reflects the increased volume of contamination, with the cumulative exceedance volume being twice the former case (Figure 4-34).

The cumulative mass flux delivered to the LCA from this model for each radionuclide is shown in Figure 4-35. All fluxes are lower than fluxes in the previous case.

To identify the relative contribution of different transport processes to the mass flux into the LCA model, four PLUMECALC simulations with different transport processes were run: with decay, matrix diffusion, and sorption; without matrix diffusion; without decay; and without sorption. For each of these model runs, the mass (mobile and immobile) staying in the system at 1,000 years and

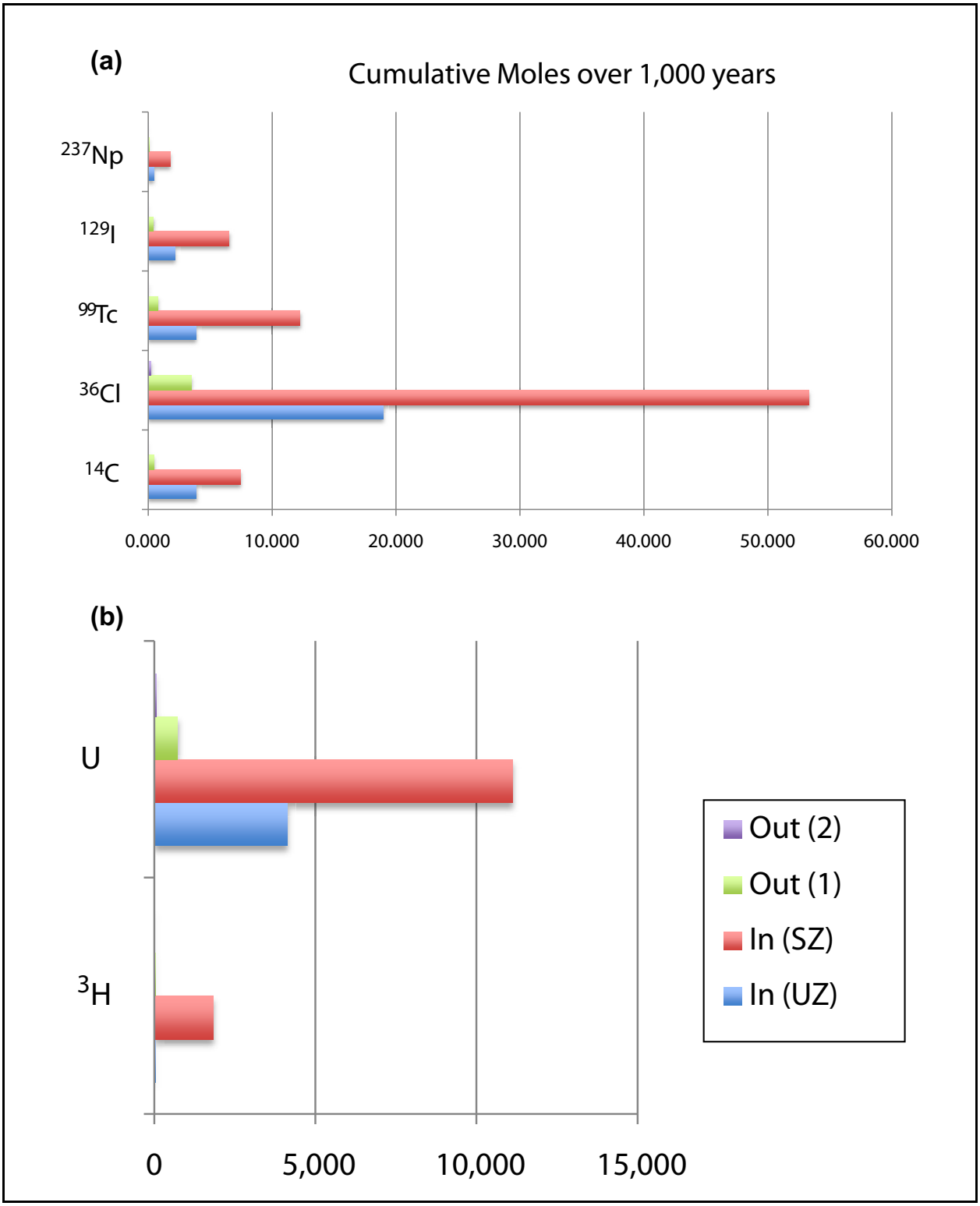

Figure 4-33
Inflow Mass from Internal (In (SZ)) and Unsaturated-Zone (In (UZ)) Sources, and Outflow Mass Calculated with Testing-Effects Conceptual Models 1 (Out (1)) and 2 (Out (2))

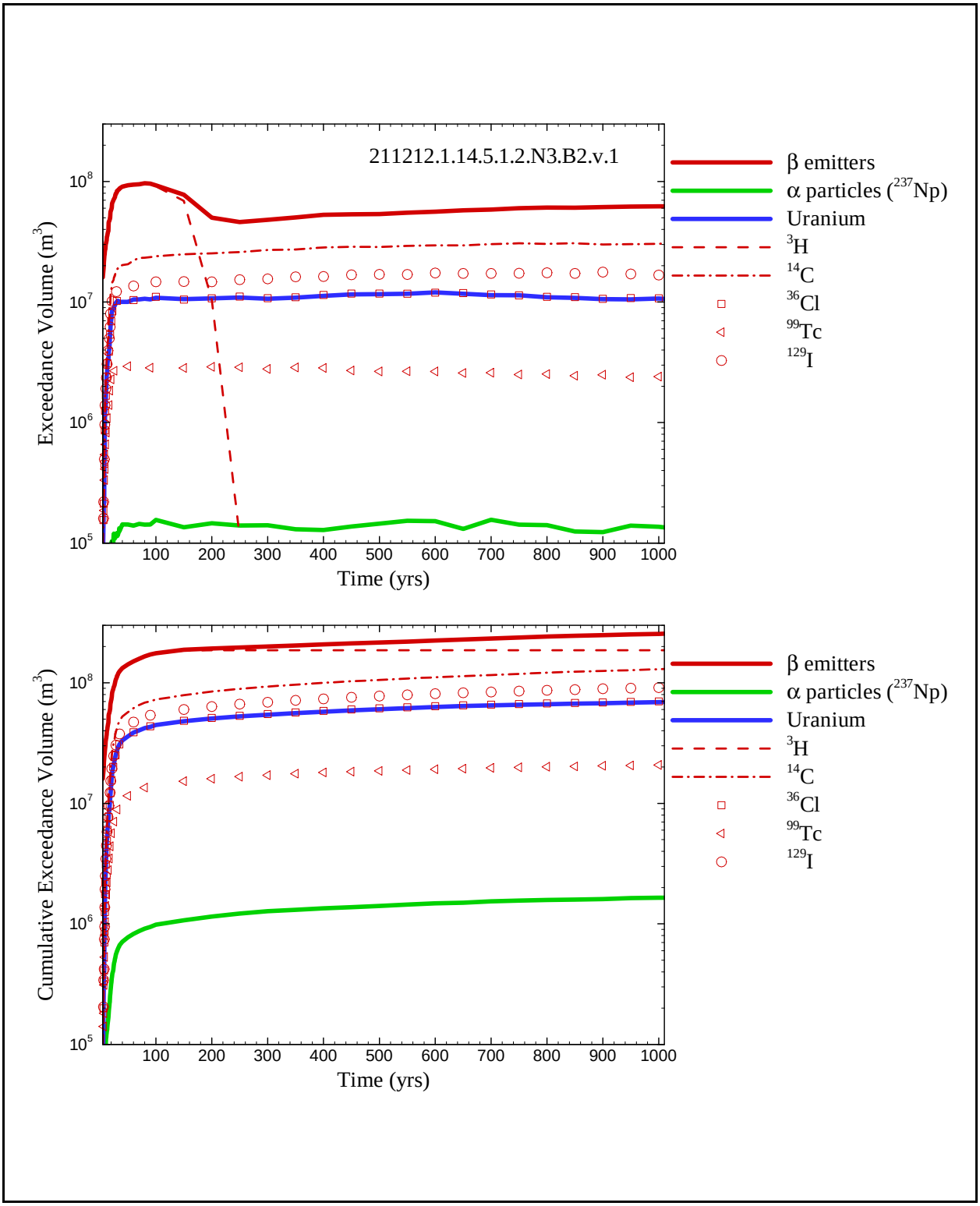

Figure 4-34
Exceedance Volume Calculations for Case 211212.1.14.5.1.2.N3.B2.v.1

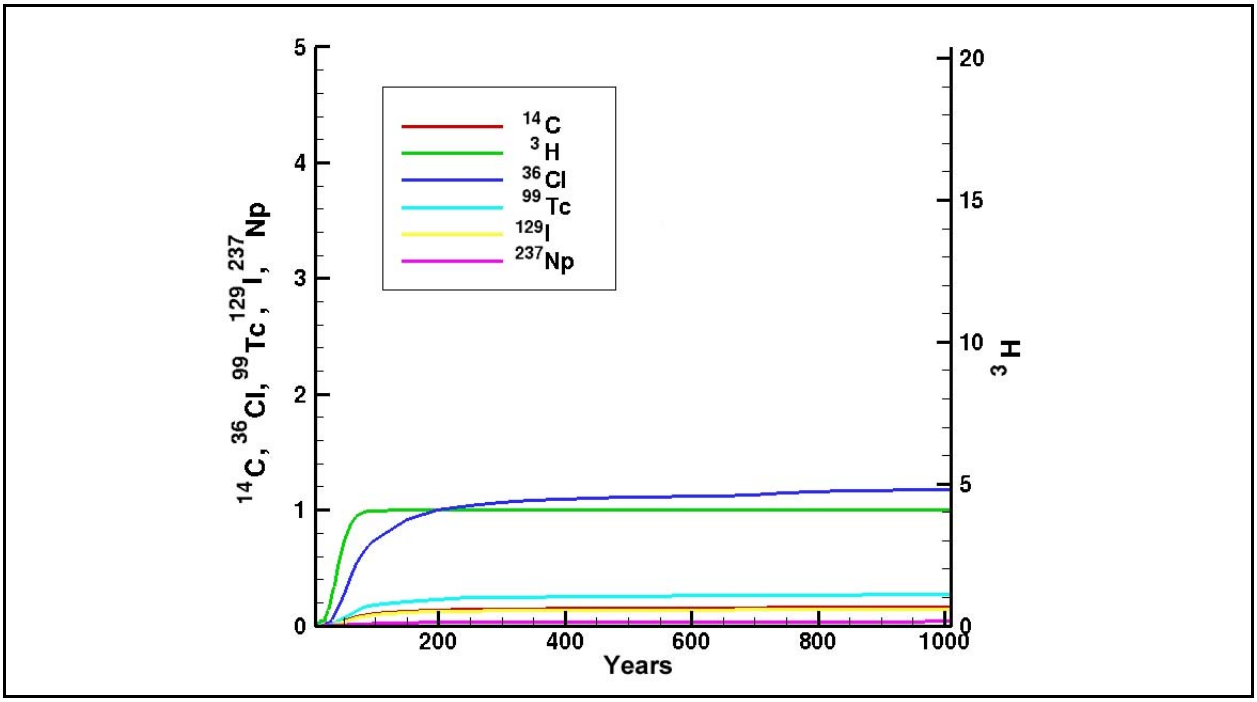

Figure 4-35
Cumulative Mass That Leaves the Model (in Moles)

the mass to the LCA model were computed. The results for these four simulations are tabulated in Table 4-27. First, the results indicate that matrix diffusion plays a significant role in the transport model. Without matrix diffusion, a much large portion of radionuclides would have entered the LCA model. While the total mass into the LCA model is almost the same for the cases with or without sorption, as expected, sorption does affect the distribution of the mass into the system. For example, without sorption, 1.37 moles of ^{237}Np stay in a mobile phase; this number reduces to 0.43 mole for the case with sorption. Given the relatively short simulation time (1,000 years), the effect of decay is significant only for ^{3}H, which has a half-life of 12.3 years.

Table 4-27
Evaluation of Importance of Various Transport Processes, Using Case 211212.1.14.5.1.2.N3.B2.s

Transport Sources/Processes	Mass	^{3}H	^{14}C	^{36}Cl	^{99}Tc	^{129}I	^{237}Np	U_{all}
		(mol)						
Unsaturated-zone sources (211212)	--	11.22	3.87	18.95	3.84	2.14	0.46	4,109.9
Saturated-zone internal sources (2 R_c)	--	1,803.7	7.42	53.30	12.25	6.53	1.76	11,133.0
Total sources	--	1,815.0	11.29	72.25	16.09	8.67	2.22	15,242.9
With decay, matrix diffusion, sorption	Stay in system (mobile)	0.000	6.522	45.215	10.026	5.406	0.429	9,508.425
	Immobile	0.000	2.912	20.253	4.487	2.417	1.602	4,317.140
	Stay in system (total)	0.000	9.434	65.468	14.513	7.823	2.031	13,825.565
	Left system	17.741	0.473	3.453	0.787	0.426	0.086	711.073
No matrix diffusion	Stay in system (mobile)	0.000	8.598	59.805	13.272	7.154	0.679	12,578.245
	Immobile	0.000	0.000	0.000	0.000	0.000	1.208	59.548
	Stay in system (total)	0.000	8.598	59.805	13.272	7.154	1.887	12,637.793
	Left system (7 steps)	103.764	1.277	8.523	1.916	1.029	0.217	1,790.398
No decay	Stay in system (mobile)	1,071.512	7.190	45.177	10.028	5.405	1.365	9,508.425
	Immobile	532.725	3.208	20.273	4.484	2.414	0.618	4,317.140
	Stay in system (total)	1,604.237	10.398	65.450	14.512	7.819	1.983	13,825.565
	Left system	139.896	0.494	3.453	0.787	0.426	0.086	711.073
No sorption	Stay in system (mobile)	0.000	6.519	45.177	10.028	5.405	1.371	9,564.000
	Immobile	0.000	2.910	20.273	4.484	2.414	0.611	4,245.620
	Stay in system (total)	0.000	9.429	65.450	14.512	7.819	1.982	13,809.620
	Left system	17.741	0.473	3.453	0.787	0.426	0.091	710.267

-- =No data

4.6.4 Impact of Numerical Approximations on Saturated Alluvial/Volcanic Aquifer System Flow and Transport Model

A number of numerical approximations were used in generating the results described in the previous sections. These were used for the purposes of computational efficiency. This section documents studies of the impact of these approximations on the results. As shown below, the impacts were generally insignificant.

Several analyses were conducted to investigate the accuracy of particle tracking and PLUMECALC methods used for the initial transport calculations. These analyses included (1) changing the position of particles at the water table, (2) increasing the number of time-varying segments, and (3) distributing particles in an exchange volume as three concentric shells versus uniform.

4.6.4.1 Position of Particles at the Water Table

In the initial transport calculations, particles representing unsaturated-zone sources at the water table were given initial positions at the upper edge of the top row of grid block volumes (z = 750 m). Because of the velocity interpolation method used by FEHM_sptr, velocities at edges of grid blocks may be artificially small (or even zero), so transport from unsaturated-zone sources might be underestimated. One analysis was conducted in which transport calculations for the base model case (211212.1.14.5.1.2.2.N3.B2) was repeated with particles placed at two lower-elevation z values (730 and 710 m). These elevations are well below the zone where velocities might be artificially low because of numerical inaccuracies. The results, shown in Table 4-28, demonstrate that using lower initial particle elevations does result in slightly higher mass outflow to the LCA. It is difficult to determine whether this is due to numerical inaccuracies (caused by artificially low velocities at control volume edges at z = 750 m) or whether deeper particles are simply closer to the outflow locations. In either case, the differences are minor when compared to the total inventory and are probably smaller than the overall accuracy of model results given all the inherent uncertainties.

Table 4-28
Sensitivity Analysis, Varying Starting Elevation of Particles Representing Unsaturated-Zone Sources

	^{3}H	^{14}C	^{36}Cl	^{99}Tc	^{129}I	^{237}Np	U_{all}
	Total Initial Mass (mol) [a]						
Elevation (m)	1,815.22	11.285	72.25	16.088	8.665	2.215	15,209.9
	Outflow to LCA (mol) at 1,000 Years						
750	3.93	0.39	2.77	0.63	0.34	0.07	582.46
730	4.23	0.44	3.12	0.70	0.38	0.07	660.35
710	4.47	0.41	2.82	0.64	0.35	0.07	599.45
	Fraction of Inventory (from Table 4-17) Leaving LCA						
750	0.002	0.035	0.038	0.039	0.040	0.031	0.038
730	0.002	0.039	0.043	0.044	0.044	0.032	0.043
710	0.002	0.036	0.039	0.040	0.040	0.032	0.039
	Fractional Difference of Outflow from Base Case (*Z* = 750 m)						
730	0.08	0.11	0.13	0.11	0.11	0.03	0.13
710	0.14	0.04	0.02	0.02	0.01	0.03	0.03

[a] Total initial mass includes saturated-zone inventory and unsaturated-zone sources for base-case scenario.

4.6.4.2 Increasing the Number of Time-Varying Segments

The PLUMECALC method involves a convolution of a time-varying mass source function with a pathline to compute concentrations. This method is applied to the unsaturated-zone sources by apportioning the unsaturated-zone sources to particles originating at a regular grid at the water table. The PLUMECALC theory assumes the pathline is independent of the time at which the particle enters the flow field. Because the flow field is transient, this assumption is violated. To correct this problem, time-varying mass source functions are divided into N time segments, which derive a pathline for each time segment (using FEHM_sptr) and convolve each time-varying mass source function segment with the corresponding pathline. If $N = 1$, the strength of the source term would vary in time, but the flow field would be assumed to be steady. In the initial transport calculations, N was set to 4, a significant improvement over the steady-state approximation. This assumption has been further justified by setting a larger number of transient times ($N = 9$). Table 4-29 presents model results comparing $N = 4$ and $N = 9$ for case 211212.1.14.5.1.2.N3.B2.s.

Table 4-29
Mass Distribution at 1,000 Years Using 4 or 9 Time Divisions to Approximate Transient Flow

Mass		^{3}H	^{14}C	^{36}Cl	^{99}Tc	^{129}I	^{237}Np	U_{all}
		(mol)						
Unsaturated-Zone Sources		11.22	3.87	18.95	3.84	2.14	0.46	4,109.9
Saturated-Zone Sources		1,804	7.415	53.300	12.248	6.525	1.755	11,100.000
Total Sources		1,815.22	11.285	72.250	16.088	8.665	2.215	15,209.900
N = 4	In system (mobile)	0.000	6.347	43.899	9.723	5.259	0.414	9,244.810
	In system (immobile)	0.000	3.243	22.756	5.051	2.728	1.653	4,865.603
	In system (total)	0.000	9.590	66.655	14.774	7.987	2.067	14,110.413
	Left system	3.927	0.394	2.768	0.633	0.343	0.068	582.460
N = 9	In system (mobile)	0.000	6.447	44.618	9.896	5.347	0.418	9,419.154
	In system (immobile)	0.000	3.147	22.046	4.882	2.646	1.649	4,683.787
	In system (total)	0.000	9.594	66.664	14.778	7.993	2.067	14,102.941
	Left system	3.913	0.373	2.686	0.609	0.323	0.066	568.206

The differences in simulated total mass leaving the system after more than doubling the number of time intervals is extremely small. A larger number of time intervals would be difficult to implement (given computational resources) and would probably result in very little or no improved accuracy.

Also performed was a comparison of the differences in the final (t = 1,000 years) locations of the particles released at water table using the two time discretization schemes. Only sets with all particles remaining in the model domain could be compared in this way; this comparison, therefore, cannot be used to assess impacts on transport to the LCA. In Figure 4-36, a comparison is made between the mean locations of the two sets. There are only very small differences in the lateral (xy) positions and slightly larger differences in elevation (z). Generally, the final position tends to be more shallow in the N = 9 case. Because the N = 4 case was used to calculate breakthrough to the LCA, this simplification results in additional small conservatism in model results.

In summary, the mass left in the system after 1,000 years appears to be in somewhat different spatial locations depending on the time discretization of the transient flow field. However, the total mass leaving the system is virtually identical in both cases. The conclusion of the analysis is that improved accuracy of mass transport to the LCA could not be accomplished with higher time discretization.

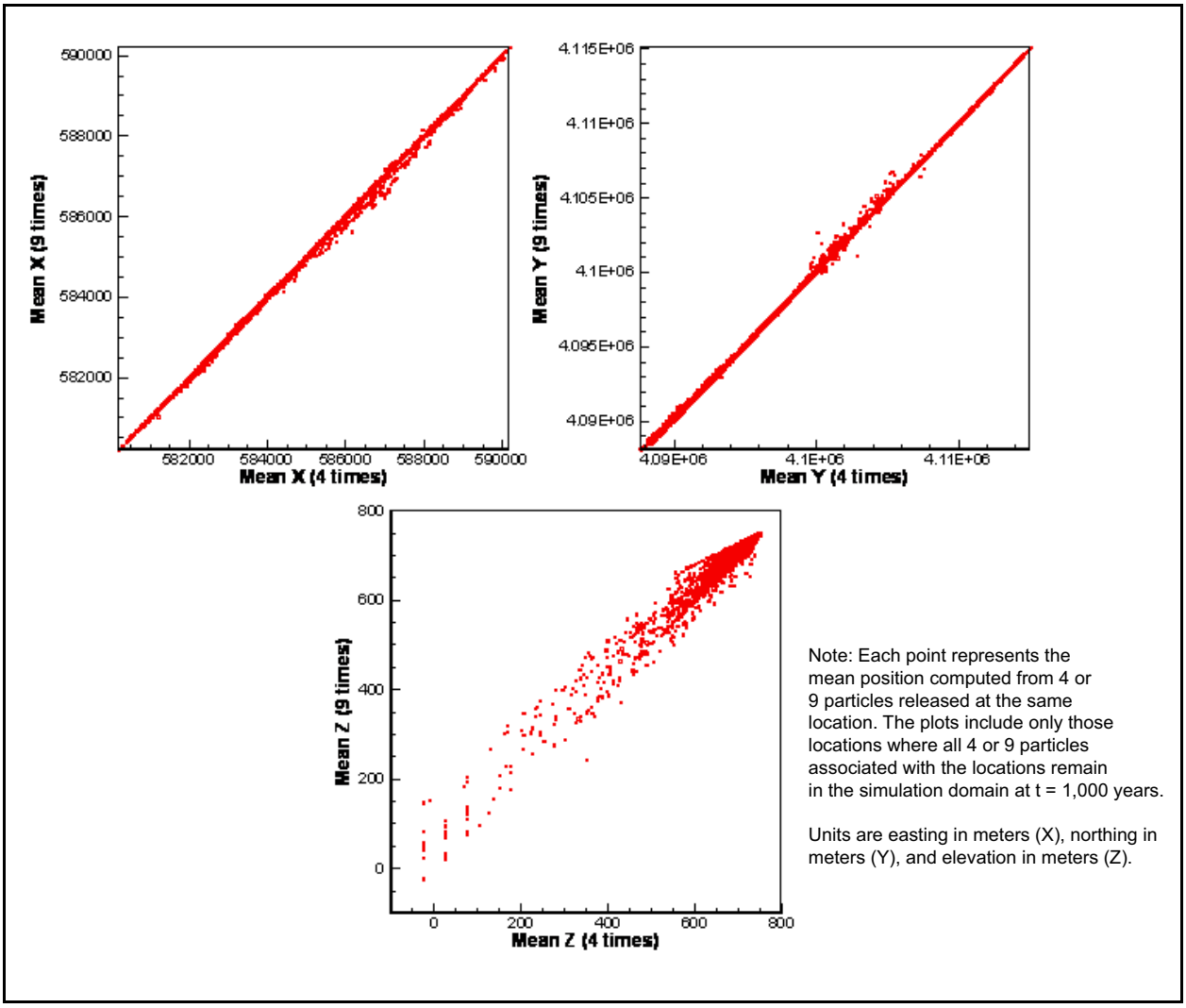

Figure 4-36
Particles Mean Positions for Two Cases

4.6.4.3 Uniform Distribution versus Three Shells of Particles

Each saturated-zone source was simulated as a sphere with 450 particles and a radius specified according to the exchange volume setting (i.e., 1 to 3 R_c). In the initial transport calculations, particles were distributed within an exchange volume as three concentric shells (Figure 4-37, red points). This method was chosen for practical reasons. Defining separate shells allows the analysis of differences in the long-term fate of radionuclides promptly injected to various discreet distances from the working point. This method also enables the assignment of the total number of particles used to represent the source term when dispersing them onto concentric shells rather than uniformly within a sphere. The concentric shell method resulted in a higher density of particles near the working point

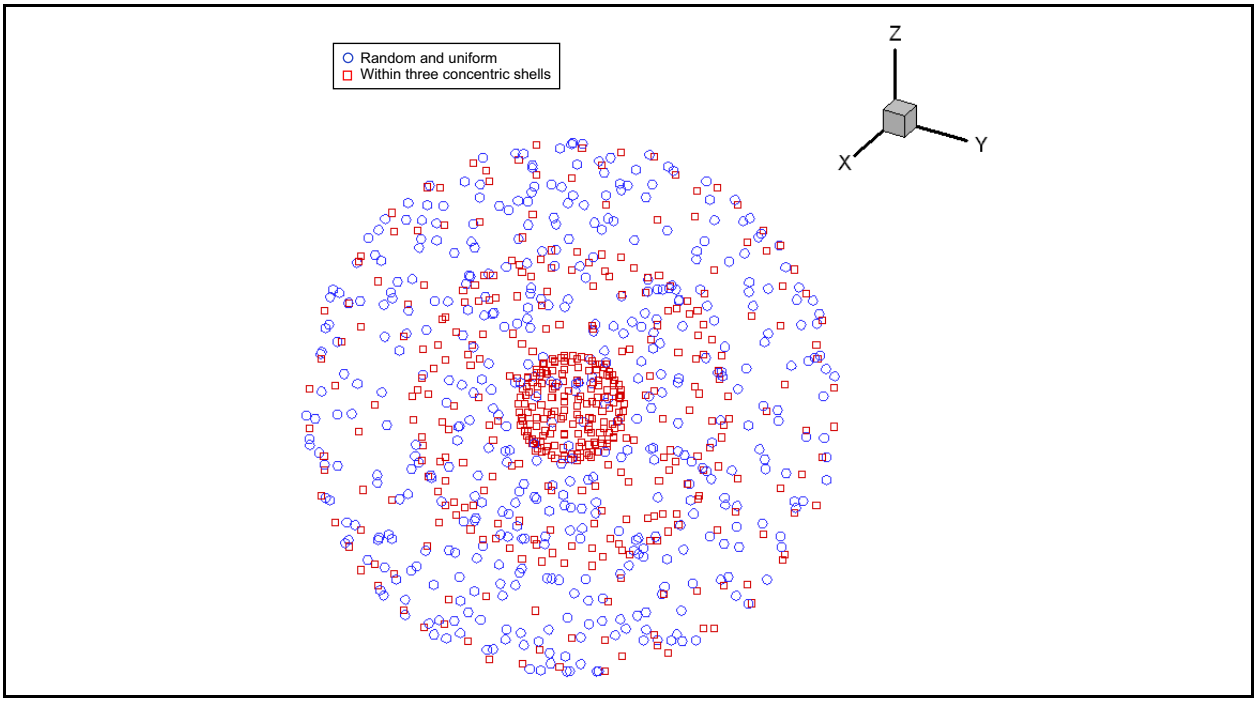

Figure 4-37
Distribution of Particles as Random and Uniform versus Within Three Concentric Shells

than at the maximum radius of the exchange volume. The effects of this simplification were investigated by conducting identical model runs with particles distributed randomly and uniformly within the exchange volume (Figure 4-37, blue points). For uniform and concentric shells, each had the same number of particles.

A comparison of total mass entering and leaving the system is presented in Table 4-30. Although there are differences in the total mass leaving the system, depending on the initial spatial distribution of particles, the mass leaving the system expressed as a fraction of the mass entering the system is very consistent. These numbers range from much less than 1 percent to 4 percent. There is a slight tendency for the uniform particle distribution runs to produce less mass transport to the LCA.

In summary, the spatial distribution of particles representing mass in the exchange volume does affect the simulation results, regardless of whether particles are distributed randomly or uniformly, or within three concentric shells, but this effect is relatively small.

Table 4-30
Comparison of Results Using Concentric Shells and Uniform Distribution of Particles for Case 211212.1.14.5.1.2.2.N3.B2.s

Mass		^{3}H	^{14}C	^{36}Cl	^{99}Tc	^{129}I	^{237}Np	U_{all}
		(mol)						
Unsaturated Zone		11.22	3.87	18.95	3.84	2.14	0.46	4,109.9
Saturated Zone, Internal		1,803.7	7.42	53.30	12.25	6.53	1.76	11,133.0
Total Sources		1,815.0	11.29	72.25	16.09	8.67	2.22	15,242.9
3 Shells	In system (mobile)	0.0	6.35	43.90	9.72	5.26	0.41	9,244.8
	In system (immobile)	0.0	3.24	22.76	5.05	2.73	1.65	4,865.6
	In system (total)	0.0	9.59	66.66	14.77	7.99	2.07	14,110.4
	Left system	3.9	0.39	2.77	0.63	0.34	0.07	582.4
Fraction of Total		0.00	0.03	0.04	0.04	0.04	0.03	0.04
Uniform	In system (mobile)	0.0	7.17	50.43	11.21	6.06	0.45	10,594.0
	In systems (immobile)	0.0	2.69	18.30	4.05	2.19	1.68	3,946.6
	In system (total)	0.0	9.86	68.73	15.26	8.24	2.13	14,540.5
	Left system	3.1	0.33	2.29	0.52	0.28	0.06	483.06
Fraction of Total		0.00	0.03	0.03	0.03	0.03	0.03	0.03

4.6.5 Sensitivity Analysis

The first step in examination of the impact of flow model and testing-effects uncertainty was to propagate a subset of the flow models described in Section 4.5.2 to full transport calculations. Variations that appeared to have very small effect on advective transport were not carried forward. Table 4-31 includes the 19 flow models selected to propagate to the full radionuclide transport analysis. These represent various combinations of background recharge rates and simulated radionuclide fluxes to the water table (generated from unsaturated-zone simulations), testing-effects assumptions (individual test overpressurization, damage zone characteristics), and permeability of HSUs and fault zones. For each of the seven sets of unsaturated-zone model results and corresponding saturated-zone parameters, Testing-Effects Conceptual Model 1 was run, with base-case damage zone properties and calibrated overpressurization estimates. For three of those models that show significant variation in radionuclide flux to the water table, Testing-Effects Conceptual Model 2 also was run for comparison. For the base unsaturated-zone model case (211212), variations in fault-zone permeability were analyzed.

Table 4-31
Transport Results for Variations in Flow Models
(Page 1 of 3)

Unsaturated-Zone Flow Field	Case	Cumulative Mass into Model or Out to LCA (mol)							Exceedance Volume (m^3)
		^{3}H	^{14}C	^{36}Cl	^{99}Tc	^{129}I	^{237}Np	U_{all}	
121212	Unsaturated-Zone Sources	2.5	1.6	7.7	1.6	0.9	0.2	1677.4	N/A
	Saturated Zone Internal Sources (2 R_c)	1,803.7	7.4	53.3	12.2	6.5	1.8	11,133.0	N/A
	Total Sources	1,806.5	9.0	61.0	13.8	7.4	1.9	12,810.4	N/A
	121212.5.14.5.1.2.N3.B2.s	8.4	0.2	1.6	0.4	0.2	0.0	338.4	1.596E+08
	121212.5.14.5.1.2.N3.B2.v.1	0.3	0.0	0.1	0.0	0.0	0.0	26.7	2.707E+08
	121212.5.14.5.1.2.2.N3.B2.s (SAE_2)	8.01	0.21	1.65	0.36	0.19	0.04	331.0	1.596E+08
	121212.5.14.5.13.2.2.N3.B2.s (SAE_5)	30.0	0.19	1.38	0.32	0.18	0.04	297.2	1.610E+08
	121212.5.14.5.1.2.2012_HST.N3.B2.s (SAE_8)	8.1	0.25	1.81	0.42	0.23	0.05	386.9	8.409E+07
211212	Unsaturated-Zone Sources	11.22	3.87	18.95	3.84	2.14	0.46	4,109.9	N/A
	Saturated-Zone Internal Sources (2 R_c)	1,803.7	7.42	53.30	12.25	6.53	1.76	11,133.0	N/A
	Total Sources	1,815.0	11.29	72.25	16.09	8.67	2.22	15,242.9	N/A
	211212.1.14.5.1.2.N3.B2.s	17.7	0.47	3.45	0.79	0.43	0.09	711.1	2.116E+08
	211212.1.14.5.1.2.N3.B2.v.1	0.7	0.04	0.23	0.05	0.03	0.01	47.9	3.257E+08
	211212.7.14.5.1.2.N3.B2.v.1	2.7	0.08	0.79	0.16	0.09	0.02	152.0	4.222E+08
	211212.8.14.5.1.2.N3.B2.v.1	3.0	0.23	1.32	0.28	0.15	0.02	281.5	5.516E+08
223211	Unsaturated-Zone Sources	15.4	8.63	41.84	8.49	4.72	1.02	9,071.9	N/A
	Saturated-Zone Internal Sources (1 R_c)	1,717.3	7.05	50.93	11.72	6.24	1.68	10,637.2	N/A
	Total Sources	1,732.6	15.68	92.77	20.21	10.96	2.70	19,709.1	N/A
	223211.1.14.5.1.2.N3.B2.s	24.8	0.77	5.38	1.23	0.65	0.12	1,119.9	1.612E+08
	223211.1.14.5.1.2.N3.B2.v.1	0.4	0.06	0.23	0.06	0.04	0.01	64.9	2.123E+08

Table 4-31
Transport Results for Variations in Flow Models
(Page 2 of 3)

Unsaturated-Zone Flow Field	Case	Cumulative Mass into Model or Out to LCA (mol)							Exceedance Volume (m^3)
		^{3}H	^{14}C	^{36}Cl	^{99}Tc	^{129}I	^{237}Np	U_{all}	
223212	Unsaturated-Zone Sources	12.0	5.21	25.42	5.16	2.87	0.62	5,510.7	N/A
	Saturated-Zone Internal Sources (2 R_c)	1,803.7	7.42	53.30	12.25	6.53	1.76	11,133.0	N/A
	Total Sources	1,816.0	12.62	78.72	17.40	9.39	2.37	16,643.7	N/A
	223212.1.14.5.1.2.N3.B2.s	17.8	0.54	3.85	0.86	0.47	0.09	801.7	2.406E+08
	223212.1.14.5.1.2.2.N3.B2.s (SAE_1)	18.5	0.53	3.84	0.87	0.46	0.09	815.4	2.413E+08
	223212.1.14.5.13.2.2.N3.B2.s (SAE_6)	36.9	0.57	3.99	0.92	0.50	0.10	843.3	2.411E+08
223213	Unsaturated-Zone Sources	9.0	3.42	16.73	3.40	1.89	0.41	3,628.2	N/A
	Saturated-Zone Internal Sources (3 R_c)	1,845.9	7.73	54.29	12.42	6.63	1.77	11,360.9	N/A
	Total Sources	1,854.9	11.15	71.02	15.81	8.51	2.17	14,989.2	N/A
	223213.1.14.5.1.2.N3.B2.s	14.5	0.45	3.17	0.71	0.39	0.08	670.2	4.220E+08
231232	Unsaturated-Zone Sources	12.6	3.35	16.44	3.34	1.85	0.40	3,564.7	N/A
	Saturated-Zone Internal Sources (2 R_c)	1,803.7	7.42	53.30	12.25	6.53	1.76	11,133.0	N/A
	Total Sources	1,816.6	10.77	69.74	15.58	8.38	2.15	14,697.7	N/A
	231232.1.14.5.1.2.N3.B2.s	17.9	0.48	3.53	0.80	0.44	0.09	727.7	1.988E+08
321212	Unsaturated-Zone Sources	20.7	5.83	28.52	5.79	3.22	0.69	6,184.1	N/A
	Saturated-Zone Internal Sources (2 R_c)	1,803.7	7.42	53.30	12.25	6.53	1.76	11,133.0	N/A
	Total Sources	1,824.7	13.24	81.82	18.03	9.74	2.45	17,317.1	N/A
	321212.6.14.5.1.2.N3.B2.s	15.4	0.64	4.61	1.04	0.55	0.11	961.5	2.648E+08
512212	Unsaturated-Zone Sources	2.27	1.14	5.67	1.15	0.64	0.14	1,229.9	N/A
	Saturated-Zone Internal Sources (2 R_c)	1,803.7	7.42	53.30	12.25	6.53	1.76	11,133.0	N/A
	Total Sources	1,806	8.55	58.95	13.40	7.17	1.90	12,362.9	N/A
	512212.5.12.2.8.1.11.2012_HST.N3.B2.s (SAE_9)	0.047	0.005	0.039	0.008	0.005	0.001	7.69	7.656E+07

Table 4-31
Transport Results for Variations in Flow Models
(Page 3 of 3)

Unsaturated-Zone Flow Field	Case	Cumulative Mass into Model or Out to LCA (mol)							Exceedance Volume (m^3)
		^{3}H	^{14}C	^{36}Cl	^{99}Tc	^{129}I	^{237}Np	U_{all}	
542121	Unsaturated-Zone Sources	0.35	0.27	2.18	0.69	0.27	0.09	331.05	N/A
	Saturated-Zone Internal Sources (1 R_c)	1,717.3	7.05	50.93	11.92	6.24	1.68	10,637.2	N/A
	Total Sources	1,717.6	7.33	53.11	12.41	6.51	1.77	10,968.3	N/A
	542121.12.2.8.1.11.2012_HST.N3.B2.s (SAE_12)	0.031	0.009	0.069	0.017	0.009	0.002	15.49	1.985E+07

Notes:
Shaded rows indicate inflow.
SAE_9 and SAE_12 are listed in this table. SAE_3 and SAE_4 were not run for transport.

N/A = Not applicable

Table 4-31 describes the results from these cases. For the base case (211212.s), the mass of radionuclides predicted to leave the model over 1,000 years, expressed as a fraction of total input (internal sources + mass arriving at the water table), range from 3 to 5 percent for radionuclides with long half-lives to less than 1 percent for ^{3}H which has a short half-life. These fractions do not vary significantly for the seven unsaturated-zone and corresponding saturated-zone parameter cases, and are slightly lower (around 1 percent or less) for the two reduced-permeability fault-zone cases.

Figure 4-38 shows the breakthrough of ^{14}C to the LCA for these sensitivity cases. A few trends are evident. First, as shown in Figure 4-38a, the presumed exchange volume is important. In this figure, the results are bounded by the red line, representing the lowest recharge rate and an exchange volume of 2 R_c, and the green line representing the medium recharge rate and an exchange volume of 1 R_c. The other lines represent medium recharge rates and variations in vadose zone parameters (permeability anisotropy and crater infiltration rates). With all other factors kept constant, transport to the LCA is highest for 1 R_c exchange volumes and lowest for 3 R_c exchange volumes. The biggest contributor to this effect is the reduced transport of ^{14}C to the water table for larger exchange volumes (see "Unsaturated-Zone Sources" tabulated in Table 4-31). This effect is larger, for example, than the difference between 5- and 10-mm/yr background recharge cases. A smaller exchange volume for an unsaturated-zone detonation causes increased radionuclide transport to the saturated-zone model because the source is completely within the zone of enhanced crater recharge (see Section 3.0 and Appendix G). Another important trend is that, if all other factors are kept constant, the breakthrough of ^{14}C to the LCA for the 5-mm/yr background recharge case is about twice that for the 1-mm/yr background recharge case. For a low infiltration rate of 0.1 mm/yr with or without enhanced crater recharge, breakthrough of ^{14}C to the LCA is at least one order of magnitude lower than for cases with the 1-mm/yr background recharge rate. The third important conclusion to be drawn from these sets of transport cases is evident in Figure 4-38b, which shows that Testing-Effects Conceptual Model 2 (dashed lines) always results in much lower breakthrough of ^{14}C to the LCA than Testing-Effects Conceptual Model 1 (solid lines). Figure 4-38c demonstrates the impact of uncertainty in the level of overpressurization. In this figure the line color indicates variation in recharge rates (red = low, blue/green = medium) and variations in UZ models with respect to permeability anisotropy and crater infiltration. This figure also shows the impact of changing the HST by moving the source term from the portion of the exchange volume above the water table immediately into the saturated-zone model and changing the exchange volume to 1 R_c. The results (solid blue line) are approximately double the previous results where this mass was assigned to the unsaturated-zone model. There are counteracting

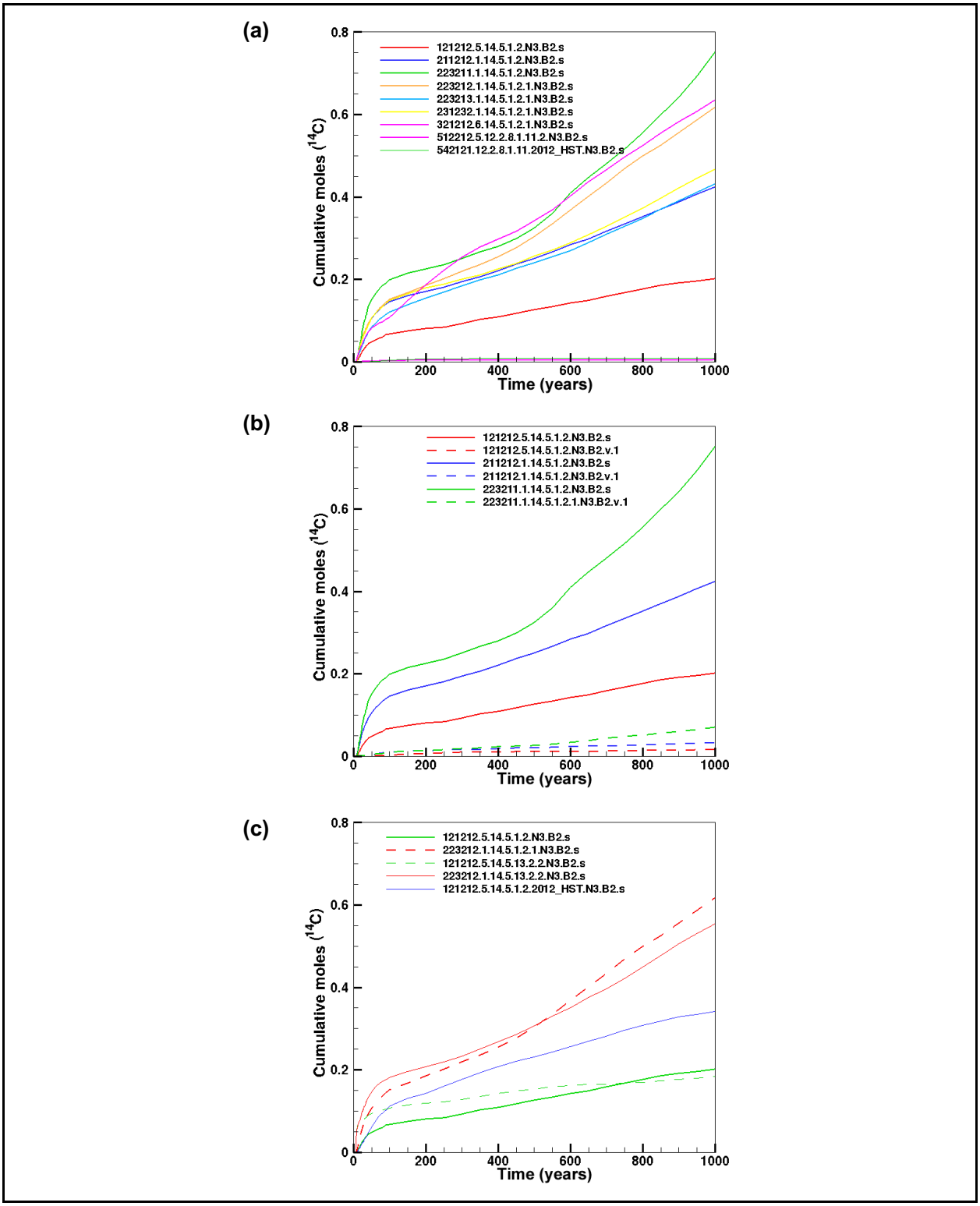

Figure 4-38
Cumulative breakthrough of ^{14}C to the LCA for Various Combinations of Simulations Comparisons: (a) Effects of Exchange Volume and Background Recharge, (b) Testing Effects of Conceptual Models, and (c) Effects of Overpressurization and HST Configuration

effects of changing the HST configuration. Moving particles to an elevation of 745 m results in increased radionuclide transport compared to the previous HST configuration, whereas moving the mass from 1, 2, or 3 R_c to 1 R_c exchange volume results in decreased transport.

Because of the large impact of testing effects (Figure 4-38b), additional simulations were conducted to better understand this sensitivity. Possible reasons for different results between the impacts of Testing-Effects Conceptual Models 1 and 2 include (1) presence or absence of hydrofracturing due to overpressurization, (2) size of overpressurization zone, and (3) magnitude of overpressurization. To test the importance of the first possible explanation, three new cases using Testing-Effects Conceptual Model 2 with the additional effect of hydrofracturing were developed. The criteria for hydrofracturing (relative head compared to lithostatic) were $H > 1 \times H_{crit}$ (case 3), $H > 10 \times H_{crit}$ (case 4), and $H >$ 1E+04 $\times H_{crit}$ except aquifers $H > 1 \times H_{crit}$ (case 5). Cumulative breakthrough of ^{14}C to the LCA is shown in Figure 4-39, with cases 1 and 2 repeated from Figure 4-38 for comparison. Hydrofracture case 3 results are intermediate between cases 1 and 2, strongly suggesting that the presence or absence of hydrofracturing is a major cause of different results between the two conceptual models. Hydrofracture cases 4 and 5 are much more similar to the base case (case 2), suggesting that allowing hydrofracturing only if pressures are ten times lithostatic or the rock type is welded tuff does not result in increased transport. A comparison of the time-varying ^{14}C mass flux delivery to the LCA model for each of these cases is shown in Figure 4-39. The solid red and blue lines show Testing-Effects Models 1 and 2, as presented previously (cases 1 and 2). The dotted pink line shows Testing-Effects Conceptual Model 2 with hydrofracturing (case 3). Hydrofracture cases 4 and 5 are indistinguishable from case 2. The comparison of results for the different testing-effects assumptions are tabulated in Table 4-32.

Two additional cases to test the impact of allowing detonations outside the tuff pile area to create overpressurization were developed. Tompson (2008) suggested that one conceptual model to consider was that only a very small number of tests created overpressurization. Using the saturated zone working point detonations with overpressures according to set A (Figure 4-13), cases B7 and B8 were generated, and results are shown in Table 4-34. These variation cases produce very little mass flux to the LCA. Additionally, they are very poorly calibrated (r^2 = 0.1 and 0.55, respectively).

Finally, a variation case was developed to determine the impact of neglecting possible buoyancy due to thermal effects. Using the HSU identification of each model grid node, and the geometric

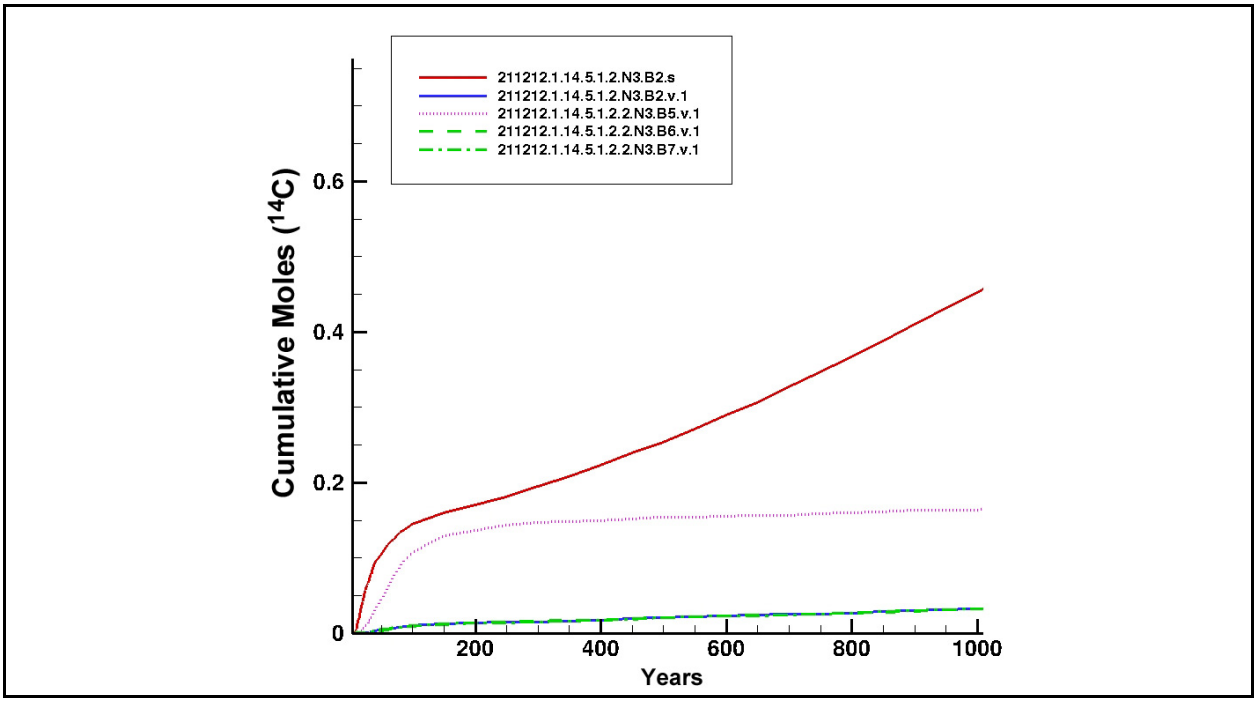

Figure 4-39
Cumulative Moles of ^{14}C Leaving the Model

Table 4-32
Impact of Testing-Effects Assumptions

Unsaturated-Zone Model Flow Field	Case	Hydrofracture Case	^{3}H	^{14}C	^{36}Cl	^{99}Tc	^{129}I	^{237}Np	U_{all}
211212	Unsaturated-Zone Sources (211212)		11.22	3.87	18.95	3.84	2.14	0.46	4,109.9
	Saturated-Zone Internal Sources (2 R_c)		1,803.7	7.42	53.30	12.25	6.53	1.76	11,133.0
	Total Sources		1,815.0	11.29	72.25	16.09	8.67	2.22	15,209.9
	211212.1.14.5.1.2.N3.B2.s	1	17.7	0.47	3.45	0.79	0.43	0.09	711.1
	211212.1.14.5.1.2.N3.B2.v.1	2	0.7	0.04	0.23	0.05	0.03	0.01	47.9
	211212.1.14.5.1.2.2.N3.B5.v.1	3	4.6	0.19	1.31	0.31	0.16	0.04	272.4
	211212.1.14.5.1.2.2.N3.B6.v.1	4	0.6	0.03	0.24	0.05	0.03	0.01	47.6
	211212.1.14.5.1.2.2.N3.B7.v.1	5	0.6	0.03	0.23	0.05	0.03	0.01	47.7
	211212.1.14.5.4.2.2.N3.B2.v.1	6	0.1	0.05	0.31	0.08	0.04	0.00	72.4

Note: Shaded rows indicate inflow.

determination of whether or not the nodes are within chimneys, the starting location of any particle within the cavity portion of the exchange volume of a detonation was moved to the highest aquifer node in the chimney. For this comparison, a 1 R_c exchange volume case was used to maximize the possible effect (223211). This caused upward displacement of particles in the 26 detonations listed in Table 4-33. This is a larger number than the 18 detonations suggested by Tompson (2008). Nevertheless, by comparing this case (case 9) to its base (nonthermal) case in Table 4-34, virtually no difference is observed.

Table 4-33
Detonations with Particles Moved Upward to Approximate Thermal Buoyancy

AGILE	MARSILLY
ALEMAN	NOGGIN
ALGODONES	OSCURO
CALABASH	PIRANHA
CARPETBAG	PORTMANTEAU
CHIBERTA	PUCE
COMMODORE	REBLOCHON
CREW-3RD	SANDREEF
DUMONT	STANYAN
FARALLONES	STARWORT
FLASK-GREEN	TAN
FLAX-TEST	TOPGALLANT
LANPHER	WAGTAIL

4.6.6 Breaching the Lower Model Boundary

Another important issue to be considered is the possibility that rock damage due to testing effects might breach the otherwise relatively impermeable boundary between the volcanics and upper LCA. To implement this conceptual model, we extended the rock-damage models described in Appendix G to allow direct outflow to the LCA under specified conditions. As described earlier, the lower boundary of the saturated alluvial/volcanic aquifer system model is “no flow” except where faults cross the boundary. Three cases were developed where these previously “no flow” boundary nodes were converted to constant-head boundaries instantaneously after each group of detonations, according to criteria summarized in Table 4-35. The three lower boundary breaching cases are designated as LBB_Case 1, LBB_Case 2, and LBB_Case 3 in Table 4-35. The locations of boundary

Table 4-34
Cases Considering Overpressurization in the Tuff Pile Area and Upward Buoyancy of the Source Term due to Thermal Effects

Unsaturated-Zone Model Flow Field	Case	Variation Case	^{3}H	^{14}C	^{36}Cl	^{99}Tc	^{129}I	^{237}Np	U_{all}
211212	Unsaturated-Zone Sources (211212)		11.22	3.87	18.95	3.84	2.14	0.46	4,109.9
	Saturated-Zone Internal Sources (2 R_c)		1,803.7	7.42	53.30	12.25	6.53	1.76	11,133.0
	Total Sources		1,815.0	11.29	72.25	16.09	8.67	2.22	15,209.9
	211212.1.14.5.1.2.N3.B2.s	1	17.7	0.47	3.45	0.79	0.43	0.09	711.1
	211212.1.14.5.1.2.N3.B2.v.1	2	0.7	0.04	0.23	0.05	0.03	0.01	47.9
	211212.1.14.5.4.2.2.N3.B2.s	7	0.0	0.04	0.33	0.08	0.04	0.01	68.8
	211212.1.14.5.4.2.2.N3.B2.v.1	8	0.1	0.05	0.31	0.08	0.04	0.00	72.4
223211	Unsaturated-Zone Sources (223211)		15.4	8.63	41.84	8.49	4.72	1.02	9,071.9
	Saturated-Zone Internal Sources (1 R_c)		1,717.3	7.05	50.93	11.72	6.24	1.68	10,637.2
	Total Sources		1,732.6	15.68	92.77	20.21	10.96	2.70	19,709.1
	223211.1.14.5.1.2.1.N3.B2.v.1	Base (non-isothermal)	0.4	0.07	0.43	0.10	0.05	0.01	104.4
	223211.1.14.5.1.2.4.N3.B2.v.1	9	0.5	0.07	0.43	0.10	0.05	0.01	104.2

Note: Shaded rows indicate inflow.

Table 4-35
Criteria for Lower Boundary Breaching Scenarios

Criteria	LBB_Case 1	LBB_Case 2	LBB_Case 3
Pressure at boundary node ≥ 0.7 × lithostatic	X	X	--
Boundary node is within 3 R_c of working point of detonation	--	X	X

-- = No data

nodes affected by these breaching cases are shown in Figure 4-40. In this figure, the color of the node indicates the time of the breach during the transient simulation. It is important to note that although the breach may be caused by a particular detonation, any detonation can subsequently contribute radionuclide flux to the outflow node.

The results for these three cases, compared to the original boundary condition, are shown in Figure 4-41. LBB_Case 2 and LBB_Case 3 are very similar, and produce approximately two-thirds as

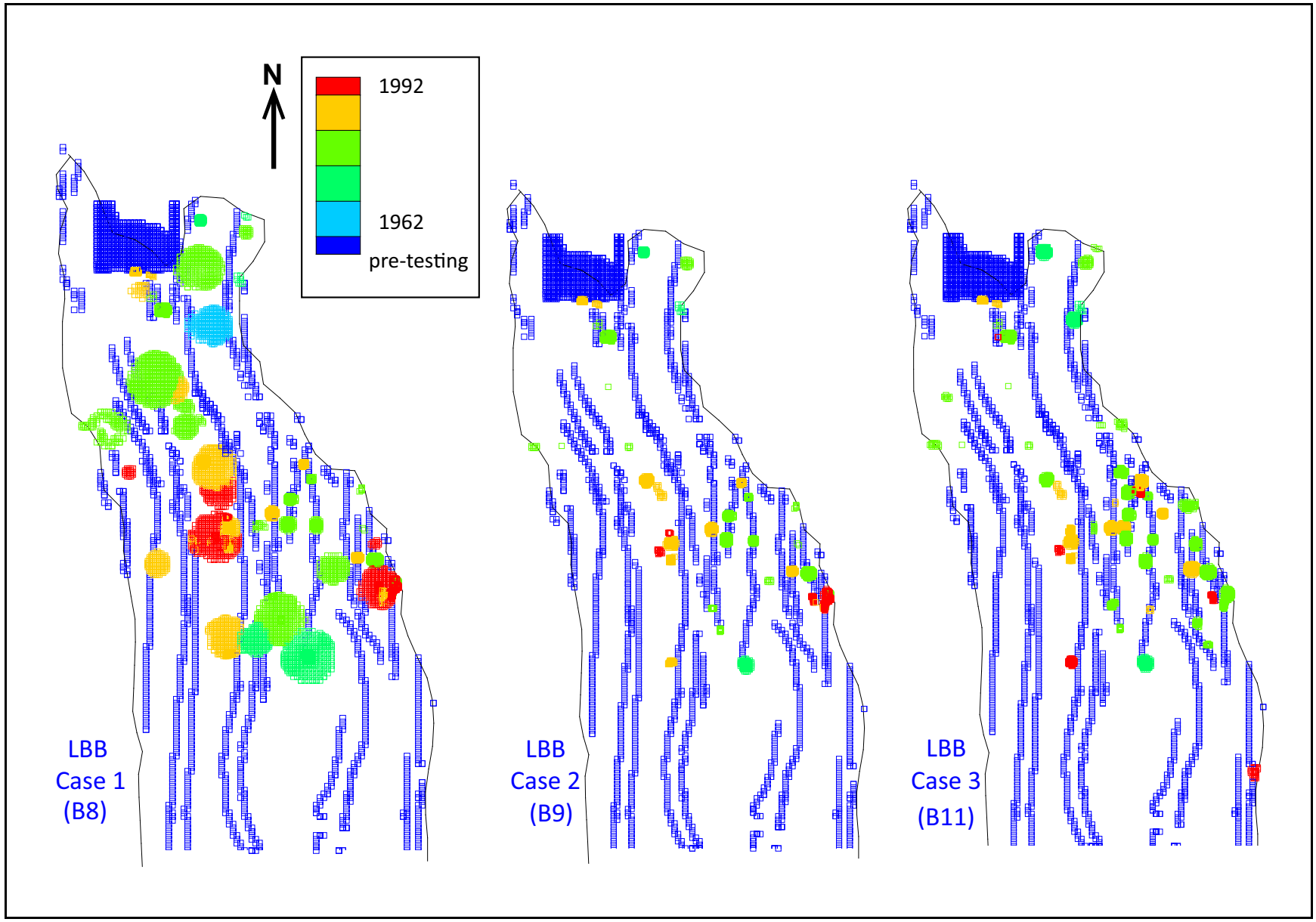

Figure 4-40
Locations of Boundary Nodes Affected by Lower Boundary Breaching Cases

Note: Color indicates year of breach, and symbol size indicates size of breach.

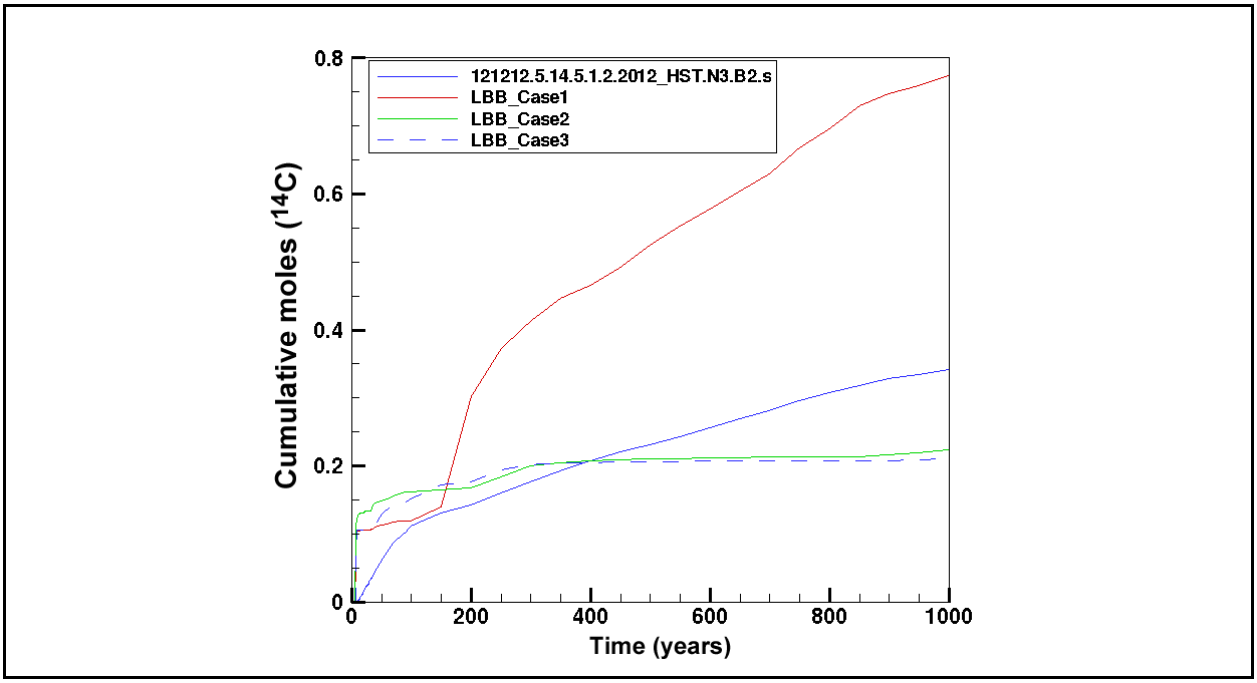

Figure 4-41
Cumulative Breakthrough of ^{14}C Flux to the LCA for Four Hydrofracturing Cases

much ^{14}C breakthrough as the unaltered base case (blue line). LBB_Case1 produces more than twice as much ^{14}C breakthrough as the unaltered base case, but still represents a very small fraction of the initial inventory (less than 2 percent).

4.6.7 Transport Parameter Sensitivity Analysis

A sensitivity analysis was conducted to identify some major factors that control the mass flux from the saturated alluvial/volcanic aquifer system model to the saturated LCA model. The effect of transport parameter uncertainty (parameters listed in Table 4-36) was investigated by the use of the variance-based sensitivity analysis theory (McKay, 1995, Saltelli et al., 2004). The theory is briefly described below.

The output Y from a simulator is a function of parameter vector $\boldsymbol{P} = (p_1, p_2, \ldots, p_K)^T$, where K is the number of parameters. Each parameter follows its own probability distribution, which is assumed to be known. The goal is to evaluate the sensitivity of these parameters and rank them based on their sensitivities. Suppose a set of model simulations is run with a fixed parameter at $p_j = \hat{p}_j$ and allow all the remaining parameters to vary in their probability spaces. The variance $V_{-j}(Y \mid p_j = \hat{p}_j)$ can be computed from this set of model runs, where the subscript in V_{-j} represents variance without

Table 4-36
Five Most Important Transport Parameters for Each Radionuclide Based on Sensitivity Analysis of 3,000 Realizations

^{3}H		^{14}C		^{36}Cl	
Parameter Name	**Sensitivity**	**Parameter Name**	**Sensitivity**	**Parameter Name**	**Sensitivity**
Matrix porosity of WTA	0.601	Matrix porosity of WTA	0.642	Matrix porosity of WTA	0.625
Fracture porosity of WTA	0.429	Fracture porosity of WTA	0.406	Fracture porosity of WTA	0.421
Tortuosity of TSA	0.050	Tortuosity of LTCU	0.041	Tortuosity of LTCU	0.041
Tortuosity of LTCU	0.041	Bulk density TM-WTA	0.040	Bulk density TM-WTA	0.040
Bulk density TM-WTA	0.040	Matrix porosity of LCA	0.039	Matrix porosity of LCA	0.039
^{99}Tc		^{129}I		^{237}Np	
Parameter Name	**Sensitivity**	**Parameter Name**	**Sensitivity**	**Parameter Name**	**Sensitivity**
Matrix porosity of WTA	0.623	Matrix porosity of WTA	0.624	K_d in TM-WTA	0.531
Fracture porosity of WTA	0.423	Fracture porosity of WTA	0.423	Fracture porosity of WTA	0.237
Tortuosity of LTCU	0.041	Tortuosity of LTCU	0.041	Matrix porosity of WTA	0.168
Bulk density TM-WTA	0.040	Bulk density TM-WTA	0.041	Bulk density TM-WTA	0.042
Bulk density (average)	0.039	Bulk density (average)	0.039	Fracture porosity of CA	0.041
U_{all}					
Parameter Name	**Sensitivity**				
Matrix porosity of WTA	0.619				
Fracture porosity of WTA	0.427				
K_d in TM-LVTA	0.046				
Tortuosity of LTCU	0.041				
Bulk density TM-WTA	0.040				

variability of parameter p_j. Because this variance is a conditional variance, the average (expectation) of this variance over all possible values of $\hat{p}_j$ in its probability space is $E_j[V_{-j}(Y \mid p_j = \hat{p}_j)]$, where E_j stands for the expectation over the parameter $\hat{p}_j$. As described in Saltelli et al. (2004), the total variance can be decomposed as

$$V = E_j[V_{-j}(Y \mid p_j)] + V_j[E_{-j}(Y \mid p_j)] \qquad (4\text{-}11)$$

The second term represents the main effect of parameter p_j on Y. Intuitively, if V_j is 0, the expectation $E_j(Y \mid p_j = \hat{p}_j)$ for any fixed p_j is the same, which means that this parameter does not have any effect on Y. In fact, V_j can be used to quantify the importance of this parameter:

$$S_j = \frac{V_j[E_{-j}(Y \mid p_j)]}{V} \tag{4-12}$$

It always gives the expected reduction of variance of output that would be obtained if one could fix an individual parameter.

In computing $V_j[E_{-j}(Y \mid p_j)]$, the operator E would call for an integral over all parameters but p_j, including the marginal distributions for these parameters, whereas the operator V would imply a further integral over p_j and it marginal distribution. The integrals can be estimated with Monte Carlo simulations.

Variances and thus the sensitivity measures can be estimated from a designed sample called a replicated Latin hypercube sample (rLHS). Each replicate in an rLHS corresponds to independent randomizations of the set of values for each parameter. An LHS of size N for K parameters is denoted by a sample matrix $\boldsymbol{P} = (p_1, p_2, \ldots, p_K)$ of dimension N rows and K columns. Each column vector $\boldsymbol{p}_j = [p_{1j}, p_{2j}, \ldots, p_{Nj}]^T$ contains N values, p_{ij}, $i = 1, ..., N$, sampled from equally probability intervals and randomized as to position in the vector. An rLHS is r replicates of the obtained as independent permutations of all of the columns of $\boldsymbol{P}_0$. The full design $\boldsymbol{P}$ is written as

$$\boldsymbol{P} = \begin{bmatrix} \boldsymbol{P}_1 \\ \boldsymbol{P}_2 \\ \vdots \\ \boldsymbol{P}_r \end{bmatrix}_{(r \times N) \times K}, \quad \boldsymbol{P}_m = [\boldsymbol{p}_{1m}, \boldsymbol{p}_{2m}, \ldots, \boldsymbol{p}_{Km}], \qquad m = 1, 2, \ldots, r$$

where vector $\boldsymbol{p}_{im}$ is an independent permutation of the rows of $\boldsymbol{p}_i$.

Since the full design matrix $\boldsymbol{P}$ has $r \times N$ rows and K columns, the total number of required model runs will be $r \times N$. In this design, the same N values for each parameter appear in each of r replicate design matrices, and the replicate design matrices differ in the parameter combinations by the rows of the matrix.

Denote the results from $r \times N$ model runs as y_{nk}, $n = 1, ..., N$, and $k = 1, ..., r$, each of the r replicates of an LHS yields an estimate of the variance of the prediction Y:

$$\hat{V}_k(Y) = \frac{1}{N-1} \sum_{n=1}^{N} (y_{nk} - \bar{y}_k)^2 \qquad (4\text{-}13)$$

where $\bar{y}_k = (1/N) \sum_{n=1}^{N} y_{nk}$ is the mean prediction over the kth replicate.

The total variance can be written as

$$\hat{V}(Y) = \frac{1}{rN} \sum_{k=1}^{r} \sum_{n=1}^{N} (y_{nk} - \bar{y})^2 = \frac{1}{rN} \sum_{k=1}^{r} \sum_{n=1}^{N} (y_{nk} - \bar{y}_k)^2 + \frac{1}{r} \sum_{k=1}^{r} (\bar{y}_k - \bar{y})^2 \qquad (4\text{-}14)$$

where $\bar{y} = (1/r) \sum_{n=1}^{N} y_k$ is the mean prediction over all r replicates.

The analysis generated 100 realizations based on the statistics tabulated in Tables 4-19 to 4-26 using the rLHS method with 30 replicates (Figure 4-42), yielding a total of 3,000 realizations. For each realization, a set of PLUMECALC runs with seven different radionuclides were conducted for one flow field (211212.1.14.5.1.2.N3.B2.s), and the total mass flux to the LCA model was calculated for each case.

The histograms for seven radionuclides derived from the 3,000 realizations are illustrated in Figure 4-42. The simple statistics for each radionuclide is also listed in the figure. Except for ^{237}Np, whose mass flux follows approximately a lognormal distribution, the distributions for the remaining six radionuclides may be approximated by normal distributions. There is a strong correlation ($r > 0.98$) among the mass flux of ^{3}H, ^{14}C, ^{36}Cl, ^{99}Tc, ^{129}I, and U, except for ^{237}Np, which has a correlation coefficient of about 0.58 with all other radionuclides.

For each radionuclide, the mass fluxes to the LCA model for all 3,000 realizations are considered as model results. For each parameter, because 3,000 realizations are derived from 100 parameter values with 30 replicates, the permutation of these 100 values is used to compute conditional variance of model results, and the first-order sensitivity is computed by the ratio of the conditional variance to the total variance. The sum of all sensitivities is not always equal to one, because of the possible correlation among parameters. As shown in Table 4-36, the most important parameters are matrix porosity and fracture porosity of welded-tuff aquifer units, which include fault zones, and chimneys

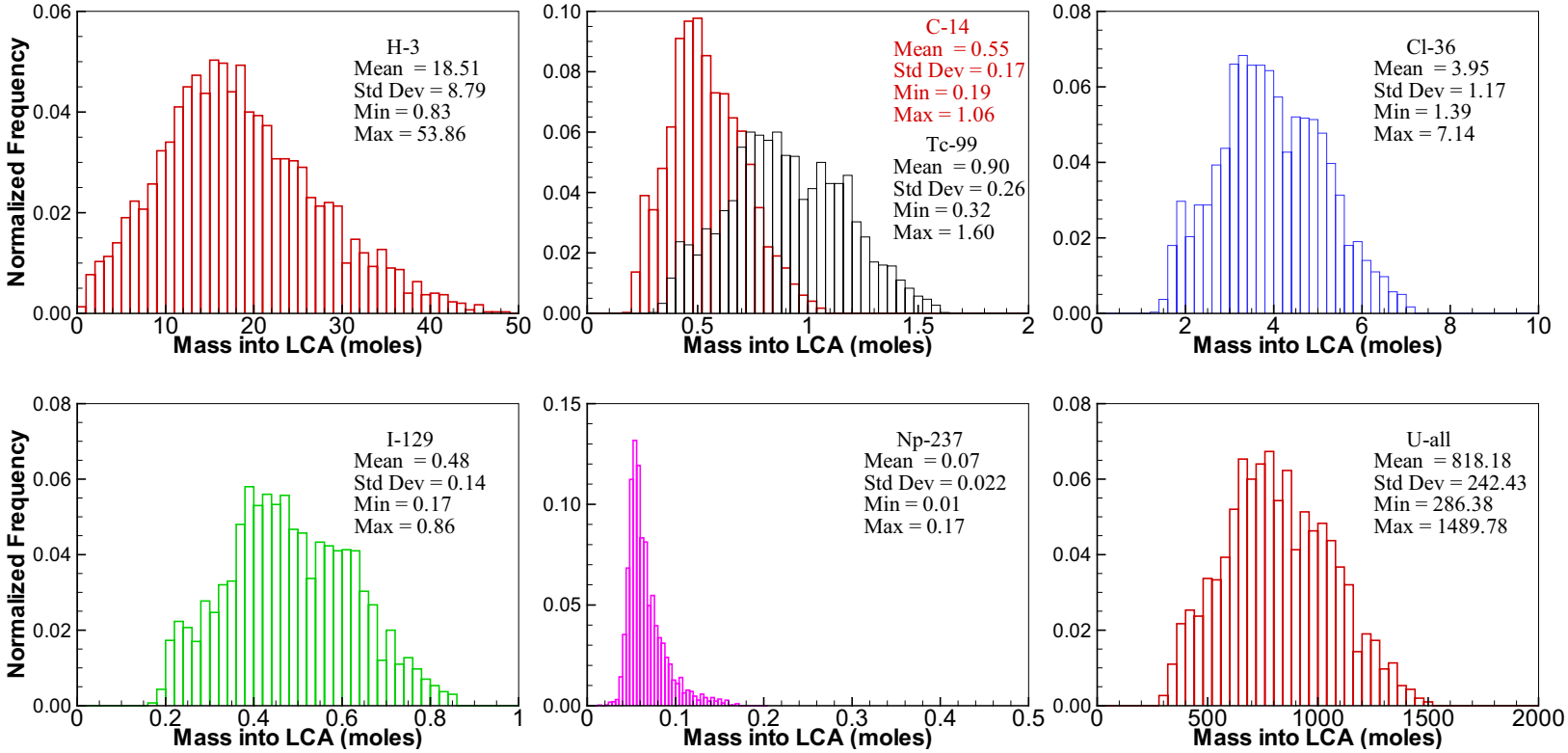

Figure 4-42
Histograms of Predictions of Mass Leaving the Model for Each Radionuclide

and cavities. For sorbing species (^{237}Np and U), the sorption coefficient (k_d) is also an important factor. In particular, K_d of ^{237}Np in the TM-WTA is the most important factor that controls the total mass flux into the LCA model. For each radionuclide, there are only two or three parameters that have a significant effect on the total mass flux of ^{237}Np into the LCA model. It should be noted that fracture spacing is not in the list of important parameters. One of the possible reasons is that the variability of fracture spacing for the welded-tuff aquifer unit was assumed to be zero, and fracture properties for this unit were adopted for some other units, faults, and chimney zones. In addition, the fracture aperture, a function of fracture porosity and spacing, is a direct input to PLUMECALC, and the variability of the fracture porosity is much larger than the variability of fracture spacing. For each radionuclide, there are only two or three parameters that have a significant effect on the total mass into the LCA model. The effect of the rest of the parameters is very small. This implies that, if we can substantially reduce the uncertainties in fracture porosity and matrix porosity of welded-tuff aquifers, fault zones, and chimney/cavities, the overall variability of the model results will be drastically reduced. A useful next step would be to conduct a sensitivity analysis to differentiate the impact of these different types of environments.

4.6.8 Transport Parameter Uncertainty Analysis

4.6.8.1 Effects of Source-Term Uncertainties

The effect of source-term uncertainty on the total mass transport from the saturated alluvial/volcanic aquifer system model to the saturated LCA model was investigated by allowing randomly varying source inventory and the melt-glass partitioning factors. This investigation used model 211212.1.14.5.1.2.N3.B2.s. The conclusion from this case is assumed to be applicable to other unsaturated-zone/saturated-zone cases. Only the variability of saturated-zone sources has been considered. This is justified because the contribution of unsaturated-zone sources to the LCA model through the saturated alluvial/volcanic aquifer system model is small (Table 4-37).

4.6.8.2 Source-Term Inventory Uncertainty

The distribution of RST for each radionuclide, shown in Table 4-38 was derived based on the qualitative uncertainty estimates provided in Bowen et al. (2001). The uncertainty is parameterized as a log-triangular distribution that is symmetric about the mean (or mode), with the ranges identified in

Table 4-37
Contribution of Unsaturated-Zone and Saturated-Zone Sources to LCA Model for Case 211212.1.14.5.1.2.N3.B2.s at 1,000 years (Decay-Corrected)

^{3}H	^{14}C	^{36}Cl	^{99}Tc	^{129}I	^{237}Np	U_{all}
Both Unsaturated-Zone and Saturated-Zone Sources (mol)						
17.74	0.47	3.45	0.79	0.43	0.086	711.07
Saturated-Zone Sources (mol)						
17.74	0.46	3.31	0.76	0.41	0.085	673.46
Saturated-Zone Sources (%)						
100	98	96	96	95	99	95
Unsaturated-Zone Sources (mol)						
0	0.01	0.14	0.03	0.02	0.001	37.61
Unsaturated-Zone Sources (%)						
0	2	4	4	5	1	5

Table 4-38
RST Uncertainty Distributions

Data	Fission Products Log RST Multiplier	Unspent Nuclear Fuel Log RST Multiplier	Nuclear Fuel Activation Products Log RST Multiplier	Tritium Log RST Multiplier
RST	^{99}Tc, ^{129}I	^{237}Np, U	^{14}C, ^{36}Cl	^{3}H
Distribution	Triangular	Triangular	Triangular	Triangular
Lower Bound	–0.1139	–0.07918	–1	–0.4772
Upper Bound	0.1139	0.07918	1	0.4772
Mean/Mode	0	0	0	0

Bowen et al. (2001) representing the minimum and maximum extent of the distributions. Table 4-38 presents the RST uncertainty distributions.

Figure 4-43 shows the histograms of the mass into the LCA model for all seven RST inventories based on 100 realizations; statistics are listed in Table 4-39. Larger variability is observed for ^{3}H, ^{14}C, and ^{36}Cl because of the larger variability on their log multipliers. Also shown in the figure and the table are the masses to the LCA from the base-case model with fixed source terms (the first row of Table 4-37). This base case is simulated deterministically (i.e., inventory multiplier 1.0, melt-glass partitioning factor f_0 as listed in Table 4-40, and realization '0') and the results are marked with "X" in the figure.

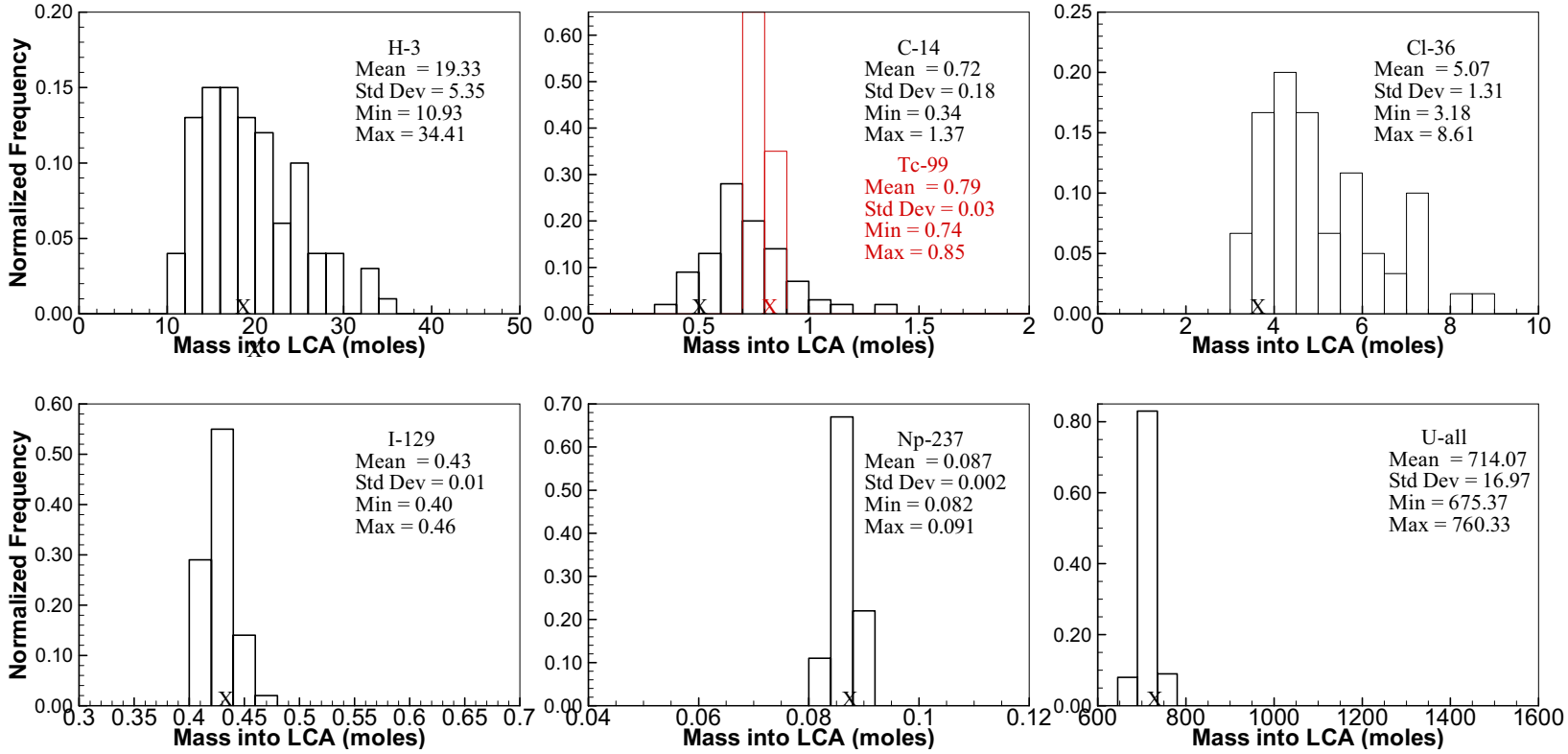

Note: "X" denotes base-case model.

Figure 4-43
Histograms of Masses to LCA Model

Table 4-39
Statistics of Mass into LCA Model due to Variability of Source-Term Inventory

Data	^{3}H	^{14}C	^{36}Cl	^{99}Tc	^{129}I	^{237}Np	U_{all}
	(mol)						
Mean	19.33	0.72	5.07	0.79	0.43	0.087	714.07
Standard Deviation	5.35	0.18	1.31	0.03	0.01	0.002	16.37
Minimum	10.93	0.34	3.18	0.74	0.40	0.082	675.37
Maximum	34.41	1.37	8.61	0.85	0.46	0.091	760.33
Base-case simulation with mean input	17.74	0.47	3.45	0.79	0.43	0.086	711.07
Increase	9%	53%	47%	0	0	1%	0.4%

Note: Results are based on 100 realizations.

Table 4-40
Distributions of the Melt-Glass Partitioning Factor (f)

Data	^{36}Cl, ^{129}I	^{237}Np	^{99}Tc	U_{all}
Distribution	Triangular	Triangular	Triangular	Triangular
Lower Bound	0	0.9	0.4	0.7
Upper Bound	0.5	1	0.8	0.9
Mode	0.25	0.95	0.6	0.8
Previous Values f_0	0.5	0.95	0.8	0.9
$(1 - \langle f \rangle)/(1 - f_0)$	1.5	1	2	2

It is interesting to note that, when the variability of the multiplier is small (e.g., ^{99}Tc, ^{129}I, ^{237}Np, and U_{all}), the mean mass from the saturated zone to the LCA model is very close to the mass calculated from mean source terms. On the other hand, when the variability of the multiplier is large (e.g., ^{14}C and ^{36}Cl), the mass to the LCA model derived from the simulation with mean source terms is always smaller than the mean mass computed from Monte Carlo simulations.

4.6.8.3 Uncertainty in Melt-Glass Partitioning Factor

Melt-glass partitioning factor is a random variable, and its distribution depends on species (Table 4-40). Note that, except for ^{237}Np, for which the previously used value was consistent with the mode of this triangular distribution, for all other species, previously used values are the upper bounds of their triangular distributions. As a result, the source terms in previous models have been underestimated by a factor of up to two (the last row of Table 4-40).

A total of 100 simulations were conducted with randomly sampled melt-glass partitioning factors for the four categories listed in Table 4-40. For each simulation, a sampled constant partition factor is applied to all 180 detonations within 3 R_c of the saturated zone. Figure 4-44 shows the histograms of the mass into the LCA model for five RST inventories based on 100 realizations; statistics are listed in Table 4-41. The ratio of the mean mass from Monte Carlo simulations to the mass reported in the base-case simulation with mean input is also compared in Table 4-41.

For the variability of the melt-glass partitioning factor, it is possible to calculate the mass to the LCA model without conducting PLUMECALC simulations. The reason is described below. For the jth RST, the mass from the saturated alluvial/volcanic aquifer system model to the LCA model may be written as

$$m_{LCA}^{(j)} = P(m_{UZ2SZ}^{(j)}) + \sum_{i=1}^{179} P(m_i^{(j)}) \tag{4-15}$$

where P is the PLUMECALC model; $m_{UZ2SZ}^{(j)}$ is the mass of the jth RST from the unsaturated-zone model to the saturated-zone model, which is assumed to be fixed for this study; $P(m_{UZ2SZ}^{(j)})$ is listed in the fifth row of Table 4-37; $m_i^{(j)}$ the mass of the jth RST at the ith detonation location.

The mass of the jth RST in the non-melt-glass phase at the ith detonation location can be written as

$$m_i^{(j)} = m_{i,total}^{(j)}(1 - f^{(j)}) \tag{4-16}$$

If mass is denoted in the previous deterministic model as $m_{i,0}^{(j)}$ and the melt-glass partitioning factor as $f_0^{(j)}$, then the mass in the new model can be related to the mass in the previous model as

$$m_i^{(j)} = \frac{1 - f^{(j)}}{1 - f_0^{(j)}} m_{i,0}^{(j)} \tag{4-17}$$

Substitute Equation (4-17) into Equation (4-15):

$$\begin{aligned} m_{LCA}^{(j)} &= P\left(m_{UZ2SZ}^{(j)}\right) + \sum_{i=1}^{179} P\left(\frac{1 - f^{(j)}}{1 - f_0^{(j)}} m_{i,0}^{(j)}\right) \\ &= P\left(m_{UZ2SZ}^{(j)}\right) + \frac{1 - f^{(j)}}{1 - f_0^{(j)}} \sum_{i=1}^{179} P\left(m_{i,0}^{(j)}\right) \end{aligned} \tag{4-18}$$

where $\sum_{i=1}^{179} P\left(m_{i,0}^{(j)}\right)$ for different species are listed in the third row of Table 4-37. For 100 realizations, the comparison of the mass to the LCA model calculated from Equation (4-18) with those derived

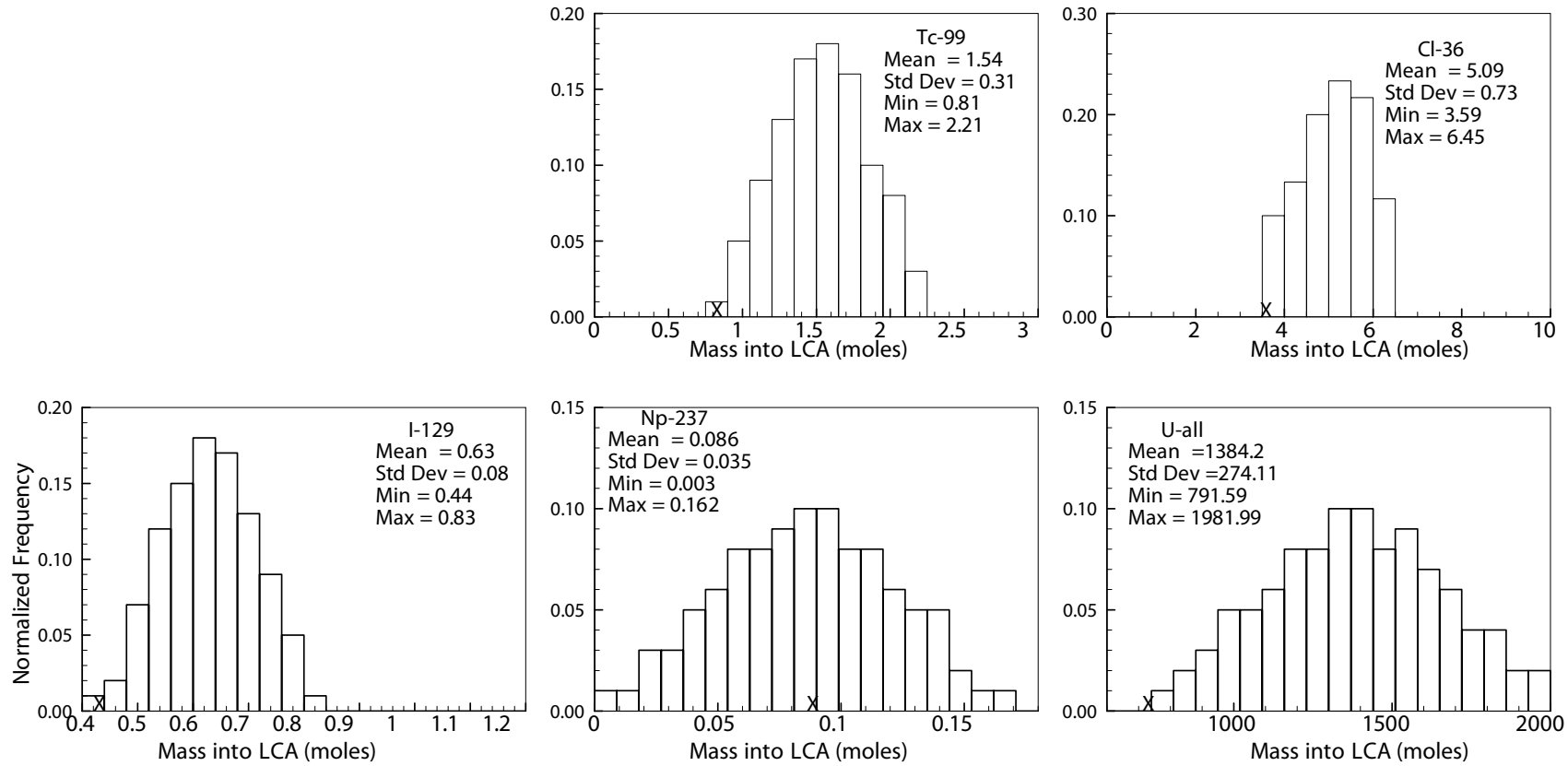

Note: "X" denotes base-case model.

Figure 4-44
Histograms of Mass into LCA Model Using Distributions of Melt-Glass Partitioning Factors Given in Table 4-40 with a Constant Melt-Glass Partitioning Factor Applied to All 179 Detonations in Each Realization (Based on 100 Model Runs)

Table 4-41
Statistics of Mass Into LCA Model due to Variability of Melt-Glass Partitioning Factors

Metric	^{36}Cl	^{99}Tc	^{129}I	^{237}Np	U_{all}
	(mol)				
$\left\langle m_{LCA}^{(j)} \right\rangle$ (Mean mass from Monte Carlo simulations)	5.09	1.540	0.63	0.086	1,384.20
Standard deviation	0.73	0.31	0.08	0.035	274.11
Minimum	3.59	0.81	0.44	0.003	791.59
Maximum	6.54	2.21	0.83	0.162	1,981.99
$m_{LCA,0}^{(j)}$ (Base-case simulation with mean input)	3.45	0.79	0.43	0.086	711.07
$\left\langle m_{LCA}^{(j)} \right\rangle / m_{LCA,0}^{(j)}$	1.48	1.95	1.47	1	1.95
$R^{(j)} = \left(1 - \left\langle f^{(j)} \right\rangle\right) / \left(1 - f_0^{(j)}\right)$	1.5	2	1.5	1	2

from PLUMECALC simulations shows that the results are identical, which means that PLUMECALC simulations are not required, and one can simply sample $f^{(j)}$ and then compute the mass to the LCA using Equation (4-18). The mass to the LCA computed from 10,000 samples of melt-glass partitioning factors is shown in Figure 4-45 where "X" in the figure represents the mass from the base-case model, and the statistics are tabulated in Table 4-42. The difference between results in Figures 4-44 and 4-45 is the number of samples. Note that here we have assumed that the partitioning factor varies from realization to realization, but a constant value is used for all 179 sources for any given realization and species. Also, the method is applicable only in the case that the melt-glass partitioning factor is the only source of source-term uncertainty. If there are other sources of uncertainties, one has to run transport simulation (PLUMECALC).

From Equation (4-18), the type of distribution of mass to the LCA model should be the same as the distributional type of the melt-glass partitioning factor, i.e., the triangular distribution, which is confirmed by the histograms in Figure 4-45.

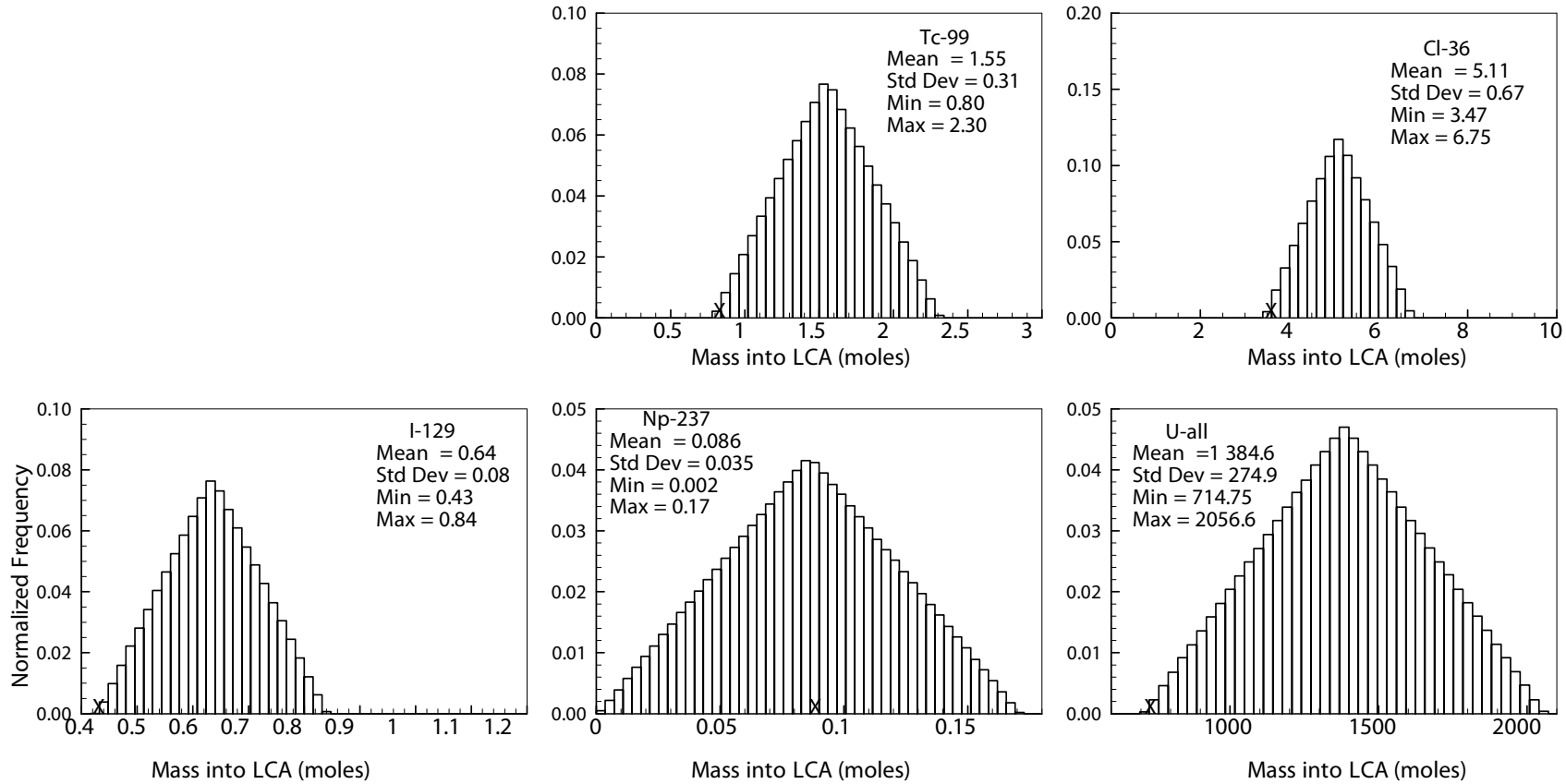

Note: "X" denotes base-case model.

Figure 4-45
Histograms of Mass into LCA Model Using Distributions of Melt-Glass Partitioning Factors Given in Table 4-40 with a Constant Melt-Glass Partitioning Factor Applied to All 179 Detonations in Each Realization (from Calculation with Equation (4-18) Based on 10,000 Samples)

Table 4-42
Statistics of Mass Into LCA Model due to Variability of Melt Glass Factors

Metric	^{36}Cl	^{99}Tc	^{129}I	^{237}Np	U_{all}
	(mol)				
Mean $\left\langle m_{LCA}^{(j)} \right\rangle$	5.11	1.55	0.64	0.086	1384.6
Standard deviation	0.67	0.31	0.08	0.035	274.9
Minimum	3.47	0.80	0.43	0.002	714.75
Maximum	6.75	2.30	0.84	0.17	2056.6
$m_{LCA,0}^{(j)}$	3.45	0.79	0.43	0.086	711.07
$\left\langle m_{LCA}^{(j)} \right\rangle / m_{LCA,0}^{(j)}$	1.48	1.96	1.49	1	1.95
$R^{(j)} = \left(1 - \left\langle f^{(j)} \right\rangle\right) / \left(1 - f_0^{(j)}\right)$	1.5	2	1.5	1	2
$\left\langle m_{LCA,MAX}^{(j)} \right\rangle / m_{LCA,0}^{(j)}$	1.96	2.91	1.95	1.98	2.89

It may be useful to derive the mean mass to the LCA model due to the variability of the melt-glass partitioning factor. Take the expectation of Equation (4-18):

$$\left\langle m_{LCA}^{(j)} \right\rangle = P\left(m_{UZ2SZ}^{(j)}\right) + \frac{1 - \left\langle f^{(j)} \right\rangle}{1 - f_0^{(j)}} \sum_{i=1}^{179} P\left(m_{i,0}^{(j)}\right) \tag{4-19}$$

where the mean $\left\langle f^{(j)} \right\rangle$ for triangular distributions is simply the average of lower bound, mode, and the upper bound. Because the lower and upper bounds are symmetric with respect to the mode, $\left\langle f^{(j)} \right\rangle$ is the same as the mode. The ratio of the mean mass from Monte Carlo simulations to the mass from the previous deterministic model will be

$$\frac{\left\langle m_{LCA}^{(j)} \right\rangle}{m_{LCA,0}^{(j)}} = \frac{P\left(m_{UZ2SZ}^{(j)}\right) + R^{(j)} \sum_{i=1}^{179} P\left(m_{i,0}^{(j)}\right)}{P\left(m_{UZ2SZ}^{(j)}\right) + \sum_{i=1}^{179} P\left(m_{i,0}^{(j)}\right)} \tag{4-20}$$

where $R^{(j)} = \left(1 - \left\langle f^{(j)} \right\rangle\right) / \left(1 - f_0^{(j)}\right)$ is listed in Table 4-42.

Because $R^{(j)} \geq 1$, it can be easily seen

$$1 \leq \frac{\left\langle m_{LCA}^{(j)} \right\rangle}{m_{LCA,0}^{(j)}} \leq R^{(j)} \tag{4-21}$$

Because the contribution of mass to the LCA model from unsaturated-zone sources through the saturated alluvial/volcanic aquifer system model is very small, Equation (4-20) can be approximated as

$$\frac{\left\langle m_{LCA}^{(j)} \right\rangle}{m_{LCA,0}^{(j)}} \approx R^{(j)} \tag{4-22}$$

Table 4-42 shows the ratio of the mean mass (and also the maximum mass) computed from Monte Carlo realizations to the mass reported previously based on a single value. The results indicate that the mean mass to the LCA model can be nearly doubled compared to the previously reported values, and the maximum mass could be almost tripled compared to the previously reported values.

4.6.8.4 Uncertainty in Source Term and Melt-Glass Partitioning Factor

To investigate the effect of uncertainties on both source inventory and the melt-glass partitioning factor, for each of the seven species, 100 realizations were run with 100 sets of inventory multipliers and 100 samples of the melt-glass partitioning factor as described above. The mass to the LCA from these realizations is shown in Figure 4-46, where “X” in the figure represents the mass from the base-case model, and the statistics are tabulated in Table 4-43.

From this source-term and melt-glass partitioning factor uncertainty investigation, one can make the following conclusions:

1. The effect of source inventory is significant only for ^{14}C and ^{36}Cl, and not important for the other radionuclides modeled including ^{3}H.

2. Variability of the melt-glass partitioning factor for ^{36}Cl, ^{99}Tc, ^{129}I, ^{237}Np, and U_{all} is much more important than that of their source inventory. The mean mass to the LCA model can be as large as twice the mass reported previously, because in the base-case model, the values of the melt-glass partitioning factor were taken from the upper bounds of their triangular distributions (except for ^{237}Np).

4.6.8.5 Uncertainty due to Source-Term Inventory, Partitioning Factor, and Transport Parameters

To investigate the uncertainty of mass from saturated alluvial/volcanic aquifer system model to the saturated LCA model due to uncertainties in source-term inventory, partitioning factor, and transport parameters, a set of Monte Carlo simulations with 400 realizations for case

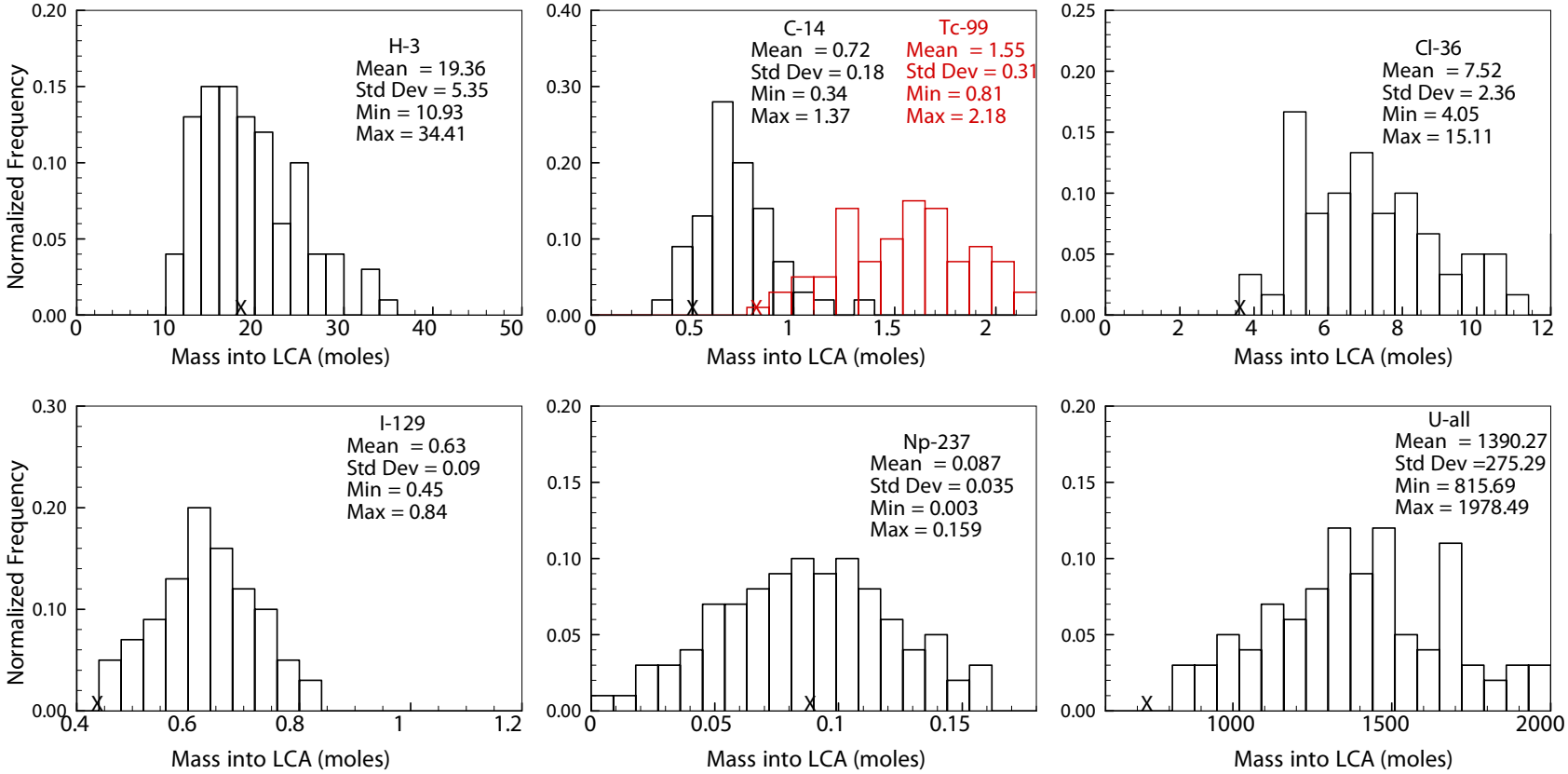

Note: "X" denotes base-case model.

Figure 4-46
Histograms of Mass into LCA Model due to Uncertainty in Both Source Inventory and Melt-Glass Partitioning Factor

Table 4-43
Statistics of Mass into LCA Model due to Variability on Both Source Inventory and Melt-Glass Partitioning Factor

Metric	^{3}H	^{14}C	^{36}Cl	^{99}Tc	^{129}I	^{237}Np	U_{all}
	(mol)						
Mean $\left\langle m_{LCA}^{(j)} \right\rangle$	19.36	0.72	7.52	1.55	0.63	0.087	1,390.27
Standard deviation	5.35	0.18	2.36	0.31	0.09	0.035	275.29
Minimum	10.93	0.34	4.05	0.81	0.45	0.003	815.69
Maximum	34.41	1.37	15.11	2.18	0.84	0.159	1,978.49
$m_{LCA,0}^{(j)}$	17.74	0.47	3.45	0.79	0.43	0.086	711.07
$\left\langle m_{LCA}^{(j)} \right\rangle / m_{LCA,0}^{(j)}$	1.09	1.53	2.18	1.96	1.47	1.01	1.96
$\left\langle m_{LCA,MAX}^{(j)} \right\rangle / m_{LCA,0}^{(j)}$	1.94	2.91	4.38	2.75	1.95	1.85	2.78

121212.5.14.5.1.2.2012_HST.N3.B2.s (SAE_13) were conducted. The distributions for the source inventory multiplier and the melt-glass partitioning factor are taken from Data Package LCVF087141, and the distributions of transport parameters are given in Section 4.6.2. The mass to the LCA model from these realizations is shown in Figure 4-47, and the statistics are listed in Table 4-44. Also shown in the figure (marked with 'X') are the masses simulated in the deterministic model (i.e., inventory multiplier 1.0, melt-glass partitioning factor f_0 as listed in Table 4-40, and realization '0'). The results indicate the following:

1. The distribution of solute mass into the LCA model shows a long-tail, lognormal-type distribution, which may be because both inventory multiplier and the melt-glass partitioning factor follow log-triangular distributions.

2. The uncertainty of mass into the LCA model depends on species, but in general, the uncertainty is very large. The coefficient of variation ranges from 40 to 72 percent.

3. Except for ^{3}H, ^{14}C, and ^{237}Np, the mass to the LCA in the deterministic model is much smaller than the mean mass from Monte Carlo simulations. This is because in the deterministic model, the value of the melt-glass partitioning factor f_0 was much larger than the mean or the mode of its distribution (Table 4-40). This means that, by taking a large value of the melt-glass partitioning factor f_0, the previous deterministic model may have greatly underestimated the mass into the LCA model. The mean mass computed from Monte Carlo simulations could be a few times larger than the mass from the deterministic model.

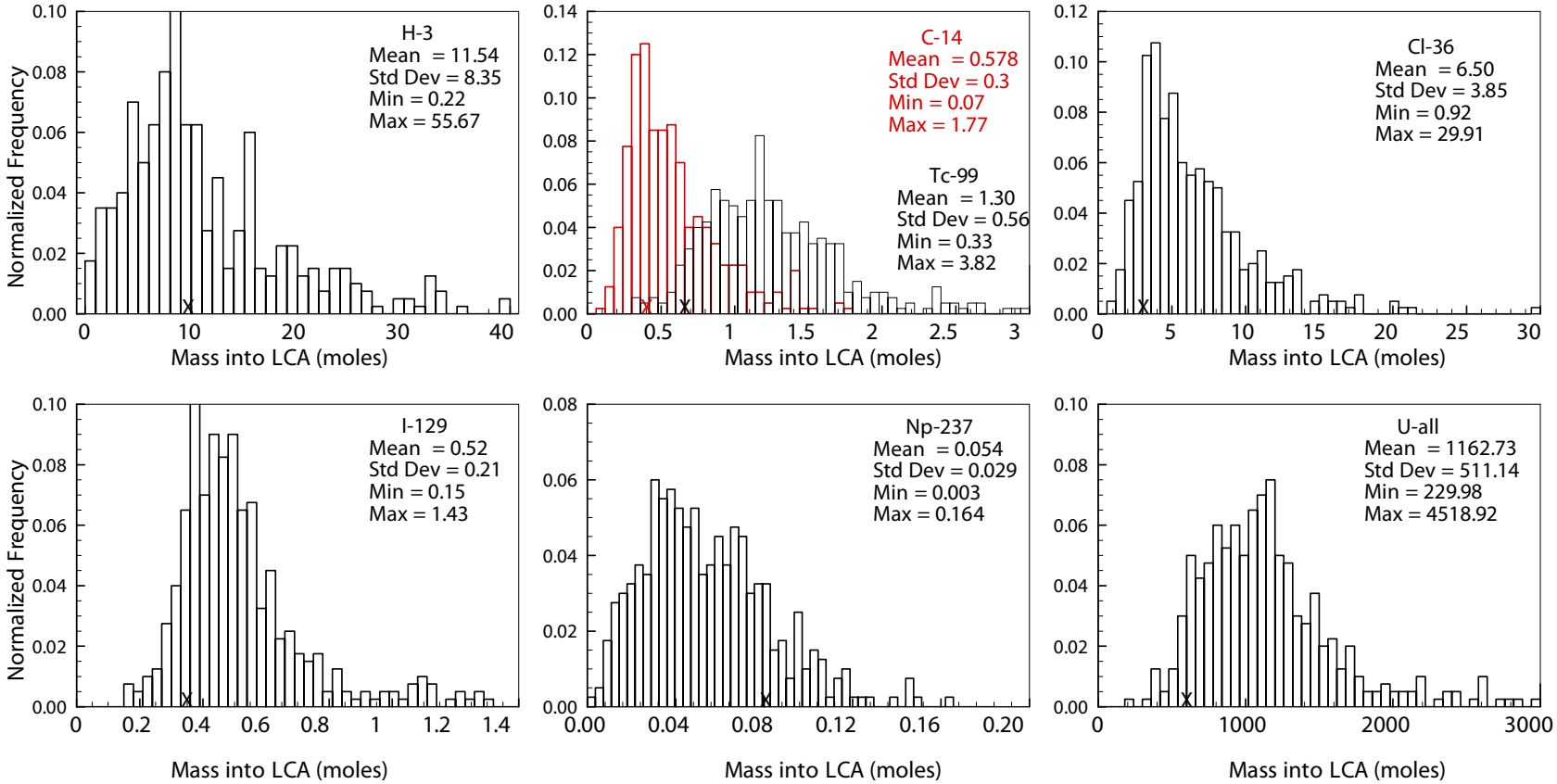

Note: "X" denotes base-case model.

Figure 4-47
Histograms of Mass into LCA Model due to Uncertainty in Source Inventory, the Melt-Glass Partitioning Factor, and Transport Parameters for Case 121212.5.14.5.1.2.2012_HST.N3.B2.s (SAE_13)

Table 4-44
Statistics of Mass into LCA Model due to Variability in Source Inventory, Melt-Glass Partitioning Factor, and Transport Parameters

Metric	^{3}H	^{14}C	^{36}Cl	^{99}Tc	^{129}I	^{237}Np	U_{all}
	(mol)						
Mean $\left\langle m_{LCA}^{(j)} \right\rangle$	11.54	0.58	6.498	1.30	0.52	0.054	1,162.73
Standard deviation	8.35	0.30	3.85	0.56	0.21	0.029	511.14
Coefficient of variation	72%	52%	59%	43%	40%	54%	44%
Minimum	0.223	0.07	0.919	0.33	0.15	0.003	229.98
Maximum	55.67	1.77	29.91	3.82	1.43	0.164	4,518.92
$m_{LCA,0}^{(j)}$ ("X" in Figure 4-47)	9.13	0.36	2.66	0.62	0.33	0.078	559.52
$\left\langle m_{LCA}^{(j)} \right\rangle / m_{LCA,0}^{(j)}$	1.26	1.61	2.44	2.10	1.58	0.69	2.08
$\left\langle m_{LCA,MAX}^{(j)} \right\rangle / m_{LCA,0}^{(j)}$	6.10	4.92	11.24	6.16	4.33	2.10	8.08

4.6.9 Comparison of Model Results to Measurement Data

It is informative to compare model prediction of radionuclide concentrations to laboratory measurements. The saturated alluvial/volcanic aquifer system flow and transport model was designed to calculate mass flux of radionuclides to the LCA, and its limitations in reproducing solute concentrations at a given point in time should be understood. Given the large spatial domain (approximately 24 by10 km), the CAU-scale model will be limited in its ability to accurately represent very fine-scale spatial variation in solution concentrations. Furthermore, a particle-based method can provide accurate concentrations only when the density of particles is large compared to the cell size. For the saturated alluvial/volcanic aquifer system model, this criterion is not met in the near field (near the cavity/chimney system). This is because the grid block size in the near field is very small so as to resolve the velocity field in these important regions.

There are 23 locations (at 20 wells) within the saturated alluvial/volcanic aquifer system model domain with a record of tritium measurements (Figure 4-48, Table 4-45). Measured tritium concentrations for most of these locations are below minimum detection limits (i.e., non-detect). Several locations have tritium concentrations that are above detection limits, but well below state and

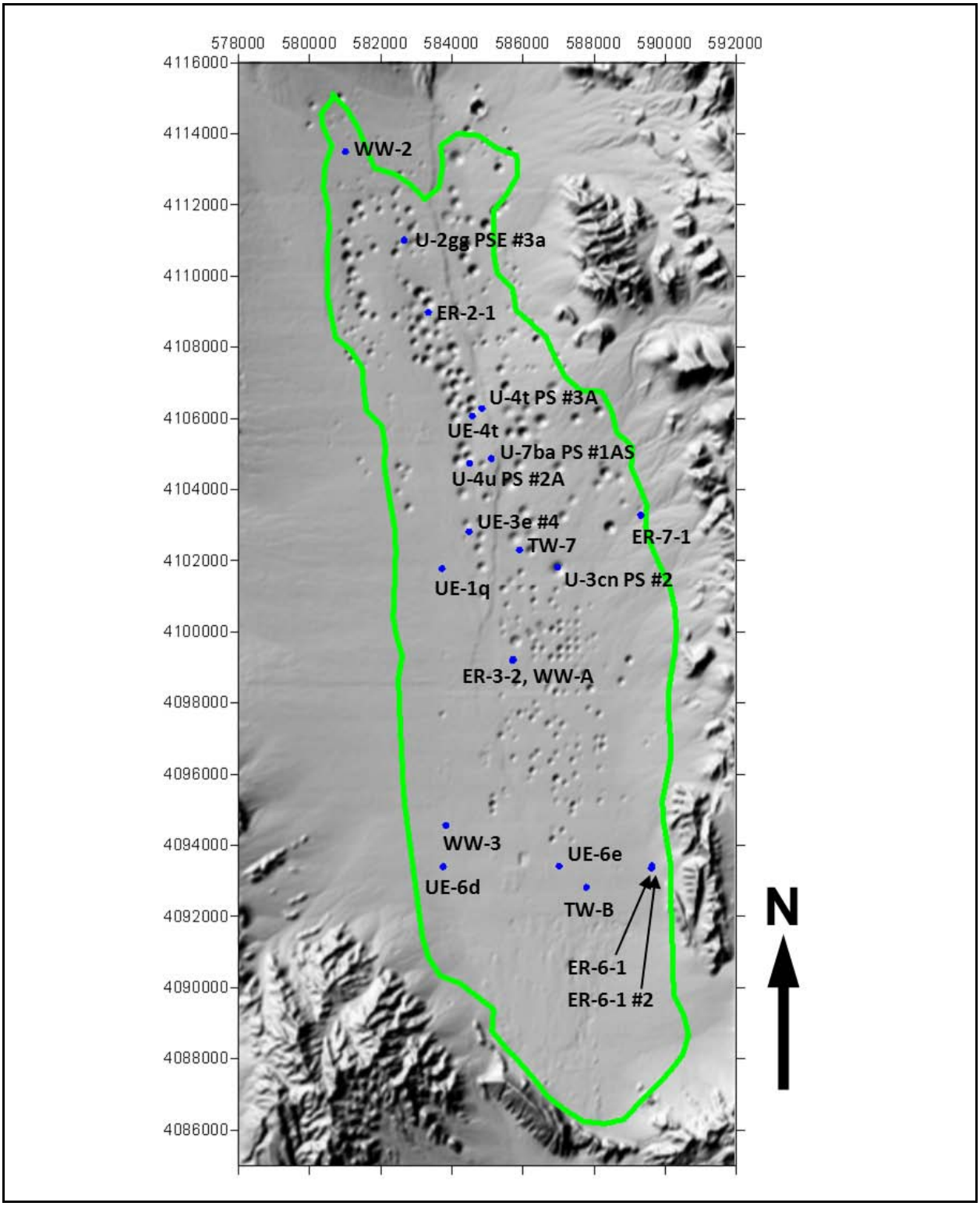

Figure 4-48
Locations of Wells with Tritium Measurements
in Saturated Alluvial/Volcanic Aquifer System Model

Table 4-45
Wells in Saturated Alluvial/Volcanic Aquifer System Model with Tritium Measurements
(Page 1 of 2)

Well Above: UGTA Name Below: USGS Reporting Name	Measured ^3H (pCi/L)		Easting	Northing
	Minimum	Maximum	(m, NAD27)	(m, NAD27)
ER-2-1 ER- 2-1	ND	228	583,334	4,108,978
ER-3-2 ER- 3-2	ND	ND	585,716	4,099,228
ER-6-1 ER- 6-1	ND	ND	589,633	4,093,419
ER-6-1-2 ER- 6-1-2 main	ND	ND	589,616	4,093,357
ER-7-1 ER- 7-1	ND	≤ 117	589,315	4,103,275
Test Well #7 (HTH) TW- 7	ND	ND	585,901	4,102,301
U-2gg PSE 3A U - 2gg PS E3A	5,440	7,570	582,657	4,111,010
U-3cn PS 2 U - 3cn PS 2	9.8E+05	2.70E+08	586,974	4,101,819
U-4t PS 3A U - 4t PS 3A	1,140	66,900	584,840	4,106,279
U-4u PS 2A U - 4u PS 2A	1.54E+07	5.83E+07	584,498	4,104,740
U-7ba PS 1AS U - 7ba PS 1AS	5.49E+06	4.30E+07	585,107	4,104,868
UE-1q UE- 1q (2600 ft)	ND	ND	583,723	4,101,778
UE-3e 4 UE- 3e 4 P1	3.30E+05	1.79E+07	584,481	4,102,813
UE-3e 4 UE- 3e 4 P2	2.19E+03	3.31E+06	584,481	4,102,813
UE-3e 4 UE- 3e 4 P3	1.39E+05	3.31E+06	584,481	4,102,813
UE-4t 1 UE- 4t 1 (1906–2010 ft)	ND	68	584,575	4,106,067
UE-4t 2 UE- 4t 2(1564–1754 ft)	ND	1,690	584,575	4,106,067
UE-6d UE- 6d	670	710	583,751	4,093,397
UE-6e UE- 6e	16	125	587,012	4,093,409

Table 4-45
Wells in Saturated Alluvial/Volcanic Aquifer System Model with Tritium Measurements
(Page 2 of 2)

Well Above: UGTA Name Below: USGS Reporting Name	Measured ^3H (pCi/L)		Easting	Northing
	Minimum	Maximum	(m, NAD27)	(m, NAD27)
Test Well B Ex. TW- B	44	260	587,780	4,092,816
WW A WW- A (1870 ft)	ND	573	585,714	4,099,194
HTH-2 WW-2 (3422 ft)	ND	ND	581,006	4,113,500
WW-3 WW- 3	ND	ND	583,828	4,094,555

Source: N-I, 2012

ND = Measurement below method detection limit (non-detect)

federal drinking water limits (20,000 pCi/L). These wells include UE-6d, UE-6e, Test Well B Ex., and WW A. The saturated alluvial/volcanic aquifer system model has very small grid cells in the vicinity of detonations in order to resolve the flow field, but with inadequate quantities of particles to properly simulate concentration (see Section 4.6.2.1). With the few exceptions of wells with low levels of measured tritium, only wells drilled in or in close proximity to working points have ever shown tritium concentrations above detection limits. The lack of detectable tritium in so many wells with screens completed in the saturated alluvial/volcanic aquifer system (the location of 180 detonations) is notable.

Table 4-46 shows the 23 locations listed in Table 4-45, sorted by far field (greater than or equal to 300 m to the closest detonation) and near field (less than 300 m to the closest test) with distance to the nearest detonation. Model results from three simulations were examined and compared to measured tritium concentrations at each of the 10 locations with tritium measurements sufficiently far from working points (i.e., far field) for the simulation results to be meaningful. Three representative models were selected that span the range of low, moderate, and high flux to the LCA (Table 4-47). In each of the three cases, the simulated tritium concentration was never above zero for any of the 10 locations at any time. This shows consistency with laboratory measurements for ER-3-2, ER-6-1, ER-6-1-2, UE-1q, HTH-2, and WW-3. However, this result underpredicts the low tritium concentrations at UE-6d, UE-6e, Test Well B Ex., and WW A. Given that the specified initial tritium

Table 4-46
Wells within Saturated Alluvial/Volcanic Aquifer System Model Domain with Tritium Measurements
(Page 1 of 2)

Well Above: UGTA Name Below: USGS Reporting Name	**Max Tritium Concentration (pCi/L)**	**Nearest Detonation**	**Distance**
Far Field (≥ 300m to the closest detonation)			
ER-2-1 ER- 2-1	228	INGOT	2 km
ER-3-2 ER- 3-2	ND	HAYMAKER	497 m
ER-6-1 ER- 6-1	ND	VILLITA	>2 km
ER-6-1-2 ER - 6-1-2 main	ND	VILLITA	>2 km
UE-1q UE- 1q	ND	BONARDA	>1 km
UE-6d UE- 6d	710	DUORO	>2 km
UE-6e UE- 6e	125	VILLITA	>1 km
HTH-2 WW-2	ND	FRISCO	944 m
Test Well B Ex. TW- B	260	VILLITA	>2 km
Far Field (≥ 300m to the closest detonation) (continued)			
WW A WW- A	573	HAYMAKER	640 m
WW-3 WW- 3	ND	DUORO	>1 km
Near Field (≤ 300 m to the closest detonation)			
UE-4t 1 UE - 4t 1	68	GASCON	170 m
UE-4t 2 UE - 4t 2	1,690	GASCON	170 m
ER-7-1 ER- 7-1	≤117	TORRIDO	200 m
Test Well 7 (HTH) TW- 7	ND	WAGTAIL	300 m
UE-3e 4 UE- 3e 4 P1	1.79E+07	ALEMAN	105 m
UE-3e 4 UE- 3e 4 P2	3.31E+06	ALEMAN	179 m

Table 4-46
Wells within Saturated Alluvial/Volcanic Aquifer System Model Domain with Tritium Measurements
(Page 2 of 2)

Well Above: UGTA Name Below: USGS Reporting Name	Max Tritium Concentration (pCi/L)	Nearest Detonation	Distance
Near Field (≤ 300 m to the closest detonation) (continued)			
UE-3e 4 UE- 3e 4 P3	3.31E+06	ALEMAN	275 m
U-3cn PS 2 U - 3cn PS 2	2.70E+08	BILBY	In chimney
U-4t PS 3A U - 4t PS 3A	6.69E+04	GASCON	54 m
U-2gg PSE 3A U - 2gg PS E3A	7,570	INGOT	65 m
U-7ba PS 1AS U - 7ba PS 1AS	4.30E+07	BASEBALL	cavity, chimney
U-4u PS 2A U - 4u PS 2A	5.83E+07	DALHART	In chimney

Source: N-I, 2012

ND = Measurement below method detection limit (non-detect)

Table 4-47
Simulations Used for Comparison to Tritium Measurements

Relative Flux to LCA	Simulation
Moderate	211212.1.14.5.1.2.N3.B2.v.1
High	121212.5.14.5.101.2.2012_HST.N3.B8.s (SAE_7)
Low	542121.12.2.8.1.11.2012_HST.N3.B2.s (SAE_12)

concentration in cavities was approximately 1E+09 pCi/L, it is not surprising that the model is not able to adequately represent concentrations six orders of magnitude lower. Perhaps by using much larger numbers of particles, the model would be capable of doing so.

Figure 4-49 illustrates the northern portion of the model grid showing locations of one far-field well (HTH-2, red) and two near-field wells (U-2gg PSE 3a and ER-2-1, blue), and the relative sizes of grid cells.

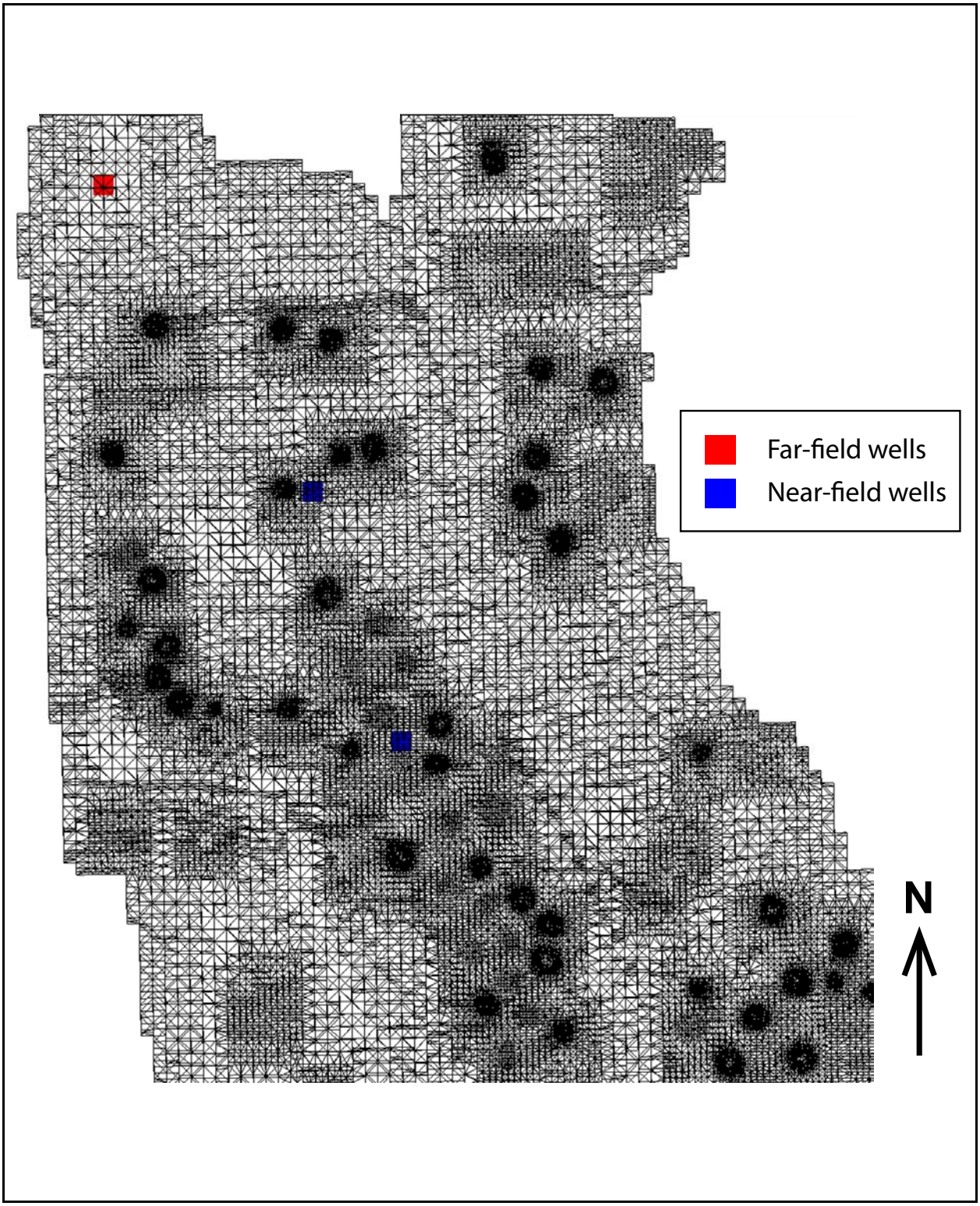

Figure 4-49
Northern Portion of Saturated Alluvial/Volcanic Aquifer System Model Showing Grid Size and Locations of Far-Field and Near-Field Wells

Although the tritium data at UE-3e 4 (P1, P2, and P3) are not useful for quantitative data/simulation comparison (because the well is very close to the ALEMAN detonation cavity), these data are worthy of discussion. A qualitative examination of simulation results shows that just north of the ALEMAN cavity (in the vicinity of UE-3e 4), the simulations generally show a very sharp gradient from the cavity, from approximately1E+09 to 0 pCi/L. The only exception to this is at the most shallow nodes (at the elevation of UE-3e 4 P3), where tritium leaves the cavity and moves a very short distance to the north. The simulations show no tritium migration toward the deeper elevations (UE-3e 4 P2 and P1). This result is in agreement with the hypothesis presented in SNJV (2007) that the shallow tritium at UE-3e 4 reflects groundwater transport and deeper tritium reflects prompt injection from SANDREEF (to the north) along fractures. However, the saturated alluvial/volcanic aquifer system model simulations do not include long-distance, prompt-injection mechanisms.

4.7 Summary and Conclusions

Given the currently available data to develop, calibrate, and evaluate numerical models of the saturated alluvial/volcanic aquifer system, an ensemble of model predictions have been provided to span a range of possible radionuclide transport scenarios. These calculations provide a range of contaminant fluxes to the underlying saturated LCA transport model presented in Section 6.0.

A number of flow and transport factors have been considered in the uncertainty analysis. Uncertain factors pertaining to the flow field include HSU permeability/recharge rate combinations, testing effects (test-dependent overpressurization and rock damage), fault-zone permeability, exchange volume, and effects of thermal buoyancy in the chimneys. Alternative rock-damage models were also used to generate breaching scenarios where hydraulic communication through the tuff confining units and the LCA model was considered. Transport factors considered include sorption coefficients, and for those units considered dual porosity, matrix porosity, tortuosity, and fracture aperture. Despite a fairly large range of factors considered, many aspects of the transport results are robust. In all cases, less than 11 percent of the total decay-corrected radionuclide mass (released by detonations within the saturated alluvial/volcanic aquifer system and radionuclide mass entering the water table from unsaturated-zone detonations) is predicted to leave the model domain within 1,000 years. In most cases, less than 5 percent is expected to leave. In some cases, only a very small percentage (much less than 1 percent) is predicted to leave. Given the wide range of hydrologic and testing-effects parameters considered, the robustness of the results is remarkable.

Figure 4-50 illustrates the range of source breakthrough expressed as a fraction of the total source term (saturated detonations + mass arriving at the water table). As expected, a lower fraction of tritium leaves the system than the other radionuclides because of radioactive decay. The breaching scenario LBB_Case1 allows about twice as much radionuclide mass to breakthrough as any other case. The impact of background recharge rate and permeability combinations is evident (colors reflect permeability variation, from high to low: red, blue, green, and yellow). Part of the reason for this effect is the strong influence of background recharge rate on fluxes of radionuclides to the water table (Table 4-31). The effect is not as linear in the saturated zone. It is evident that other factors such as testing-effects uncertainty, anisotropy, and exchange volume are equally or more important. For example, see large spread in results for blue symbols in Figure 4-50.

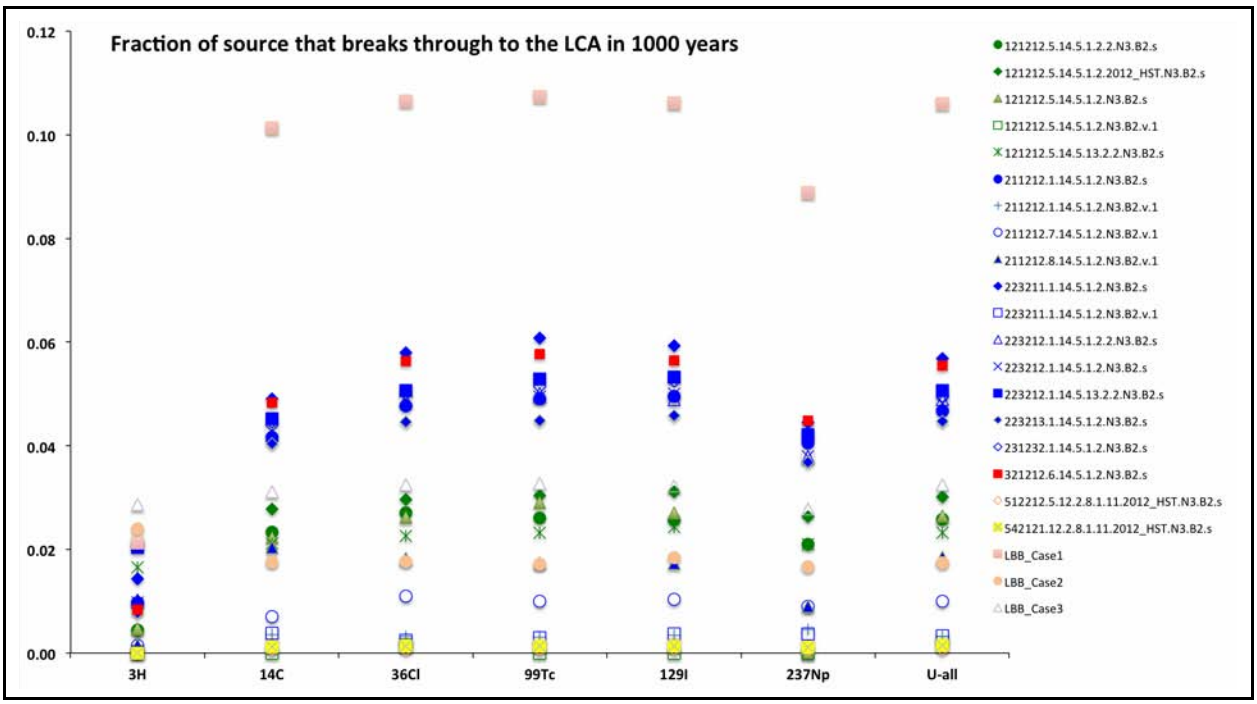

Figure 4-50
Fraction of Source That Breaks Through to the LCA in 1,000 Years

The very lowest level of breakthrough is represented by cases that consider very low infiltration rates and very low permeability or by Testing-Effects Conceptual Model 2, which assumes a very low permeability crushed zone around each cavity. These results are qualitatively consistent with Tompson (2008), who concluded that virtually no contaminant transport occurs away from detonations in the tuff confining units. It is noted that the low permeabilities in these cases are lower than most field-scale and core-scale hydrologic tests from Yucca Flat, which is the result of the

field-scale tests preferentially testing the higher permeability zones in the tuff-confining units (as shown in Figure 4-12).

The ensemble of results shown in Figure 4-50 is not meant to be a statistically meaningful sample. In other words, the mean of these results is not necessarily most likely. Given the uncertainty in net infiltration and hence recharge, it is difficult to define the set of model parameters presented here that reflects the “most likely” set of parameters. Given the high level of complexity in the real system and the necessary simplifications required for numerical modeling, it is concluded that the “true” behavior of the system falls somewhere within the range of the model results.

Although the mass that leaves the model domain is small compared to the total mass available, mass outflow occurs continuously over the 1,000-year simulation period. The largest fluxes occur early in the simulations because of overpressures related to testing, which relax at later times. Mass outflow tends to be strongly spatially focused, occurring only in a small number of locations. This is partly due to the conceptual model of fault zones acting as the sole conduits for outflow to the LCA. Even so, only certain locations along the fault zones actually transmit mass. The focusing of outflow is even more prominent in the lower boundary breaching scenarios. Evidently, the flow field is significantly altered when hydrologic sinks are created beneath certain detonations, and radionuclide flux that would otherwise discharge to the LCA along faults instead discharges at the location of breaching. Another characteristic of the ensemble of model simulations is that only relatively small numbers of detonations contribute mass to the LCA in any simulation and that these detonations tend to be important in all model cases. Figure 4-51 illustrates the contribution of mass to the LCA for each of the largest contributor detonations for case 211212.1.14.5.1.2.N3.B2.s. The seven largest contributors for this case are TAN, BILBY, TOPGALLANT, POTRILLO, TIJERAS, CALABASH, and ATRISCO.

There were interesting differences between individual simulations as well. It is clear that the issue of whether or not permeability enhancement (due to overpressurization exceeding lithostatic) occurred beyond the cavity has a significant impact on mass outflow to the LCA, as does the level of overpressurization associated with individual detonations. Also, the permeability of fault zones has significant impact.

Sensitivity analysis demonstrates that several testing-effects parameters significantly impact the total mass of radionuclides that leave the model domain. The most important are (1) level of

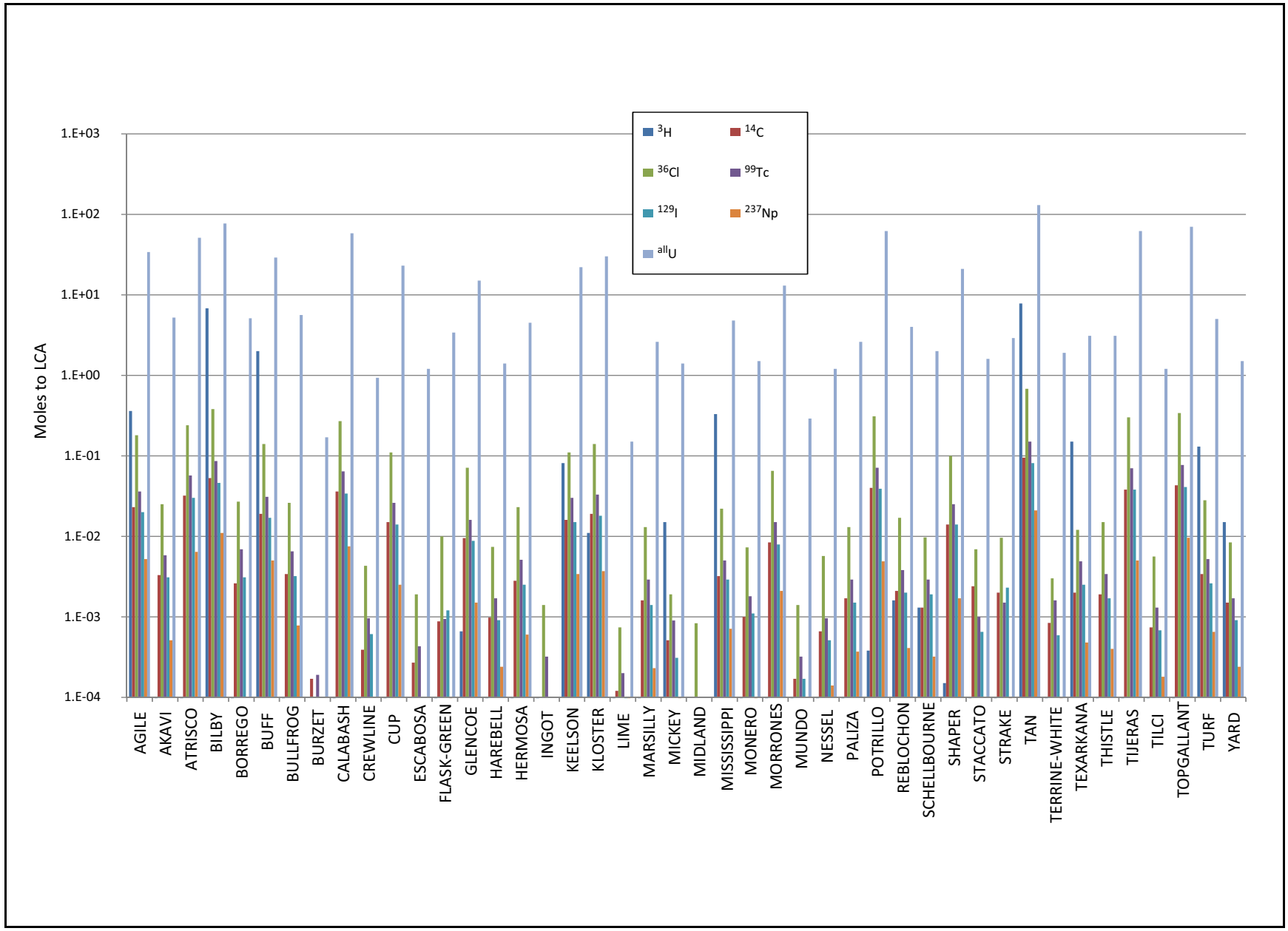

Figure 4-51
Contribution of Mass to the LCA Model from 44 Individual Detonations for Case 211212.1.14.5.1.2.N3.B2.s

overpressurization for individual detonations, (2) capacity for hydrofracturing due to overpressurization, and (3) size of overpressurization zones. For convenience, certain parameters have been grouped into two alternative conceptual models, but there is no implied assumption that either can be eliminated based on comparison with available data and with detailed geochemical analysis. Although each of these parameters has been varied, with the large number of detonations to consider (180), a complete sensitivity analysis for this problem has not been conducted. Very few parameter combinations can be eliminated based on comparison with available hydrologic or geochemical data.

From comparing advection-only transport results with reactive transport results (with decay, sorption, and fracture-matrix diffusion), it is clear that those detonations that have the potential for fast (less than 100 years) advective transport to the model boundaries dominate total mass flux in the 1,000-year reactive transport simulations.

Results of the Monte Carlo transport parameter uncertainty analysis indicate that when the variability of the source-term multiplier is small (e.g., ^{99}Tc, ^{129}I, ^{237}Np, and U_{all}), the mean mass transport from the saturated alluvial/volcanic aquifer system model to the LCA model is very close to the mass calculated using mean source terms. On the other hand, when the variability of the multiplier is large (e.g., ^{14}C and ^{36}Cl), the mean mass transport from the saturated alluvial/volcanic aquifer system model to the LCA model using mean source terms is always smaller than the mean mass computed from Monte Carlo simulations. The Monte Carlo results of melt-glass partitioning factor indicate that the mean mass transported to the LCA model can be nearly doubled and that the maximum mass could be almost tripled. In addition, the variability of the melt-glass partitioning factor for ^{36}Cl, ^{99}Tc, ^{129}I, ^{237}Np, and U_{all} is much more important than the uncertainty in their source inventories. With the exception of ^{3}H, ^{14}C, and ^{237}Np, the mass transport to the LCA in the deterministic model is smaller than the mean mass transport from the Monte Carlo simulations. This is because in the deterministic model, the value of the melt-glass partitioning factor was much larger than the mean or the mode of its distribution (Table 4-38).

Based on the sensitivity analysis, only a few transport parameters are influential. The most significant transport parameters are associated with fracture/matrix diffusion parameters for welded-tuff aquifers, fault zones, and cavity/chimneys. Additionally, sorption of Np in the TM-WTA is very important for that radionuclide.

Finally, some model results of tritium concentrations were compared to field data observations. There was generally good agreement between model results and observations for wells with measured tritium concentrations below detection limits (i.e., “clean” wells). In general, we can conclude that numerical modeling can reasonably estimate tritium concentrations in far-field locations (greater than 300 m from a detonation location).

5.0 YUCCA FLAT SATURATED LOWER CARBONATE AQUIFER FLOW MODEL

As described in Section 1.0, the LCA exists under the unsaturated zone and saturated alluvium/volcanic rocks throughout the Yucca Flat/Climax Mine CAU. The LCA is a regionally extensive aquifer that is generally conceptualized as having significant regional recharge to the north of Yucca Flat and discharge to the south of Yucca Flat in the general area of Ash Meadows. Although no underground nuclear detonations were conducted in the saturated section of the LCA at Yucca Flat, contaminants emanating from the detonations conducted in the overlying unsaturated zone or saturated alluvium/volcanic rocks may migrate downward into the LCA and then be transported laterally in the LCA during the 1,000-year FFACO time period.

This section presents the hydrogeologic background information and the technical basis for the groundwater flow model of the LCA at Yucca Flat. The saturated LCA flow model uses boundary water fluxes from the overlying unsaturated zone and saturated alluvial/volcanic aquifer system models and is used to develop the groundwater flow fields in the LCA for use in forecasting contaminant boundaries presented in Section 6.0. The result of implementing this flow model, along with uncertainties associated with contaminant sources and transport characteristics to forecast contaminant boundaries, is presented in Section 6.0.

The organization and content of this section is as follows:

- Section 5.1, “Introduction,” presents the overall modeling approach and the significant assumptions made during the development and calibration of the groundwater flow model.

- Section 5.2, “Background Hydrogeologic Data,” presents the most significant regional, NNSS, and Yucca Flat/Climax Mine CAU hydrogeologic data used to develop and calibrate the groundwater flow model. This section also presents the information used to develop the existing conceptual model of groundwater flow in the LCA, including analyses of the potentiometric surface and geochemical observations in the LCA at Yucca Flat.

- Section 5.3, “Previous Modeling Studies,” provides an overview of previous modeling efforts that contributed to the development of the Yucca Flat LCA flow model. Included in this overview are groundwater flow modeling studies done at the regional, CAU, and sub-CAU scales. The primary studies discussed in this section are the DVRFS model developed by USGS (Belcher et al., 2004), the Yucca Flat/Climax Mine CAU groundwater flow model by

Stoller-Navarro Joint Venture (SNJV) presented in the Yucca Flat/Climax Mine hydrologic data document (HDD) (SNJV, 2006b), and the Climax Mine sub-CAU groundwater flow models by DRI (Pohlmann et al., 2007; Pohlmann and Ye, 2012).

- Section 5.4, "LCA Groundwater Flow Model Construction," presents the development of the groundwater flow model, including the discretization of the LCA and identified faults that cut the LCA based on the HFM, the identification of the type and extent of appropriate boundary conditions, and the initial assignment of permeability values to the different regions of the LCA and faults.

- Section 5.5, "Flow Model Calibration," presents the calibration of the LCA groundwater flow model to the observed steady-state and transient heads given the constraints of the range of observed or inferred boundary fluxes and permeability. As with other CAU groundwater flow models, the model calibrations are performed with the parameter estimation software PEST. This section presents the base-case flow model used in the evaluation of contaminant transport from underground nuclear detonations presented in Section 6.0.

- Section 5.6, "Flow Model Uncertainty Analyses," presents the results of the calibration of alternative conceptual models and fixed parameters to develop a range of possible flow fields. The analyses presented in this section use the null-space Monte Carlo (NSMC) method to focus on reasonably constrained alternative flow models. The alternative flow models discussed in this section are used to evaluate the effect of flow model uncertainty on contaminant transport from underground nuclear tests presented in Section 6.0.

- Section 5.7, "Parameter Sensitivity Analysis," presents the results of local and global sensitivity analyses to define the significant flow model parameters influencing the calibration of the LCA flow model.

- Section 5.8, "Summary and Conclusions," presents a summary of the major results of the LCA groundwater flow model.

5.1 Introduction

The LCA is a regionally extensive aquifer that extends over several hydrographic basins in southern Nevada. The LCA has been the focus of a considerable characterization effort over the last several decades because of its significance as a water resource in southern Nevada and eastern California. This characterization has included regional evaluation of the potentiometric surface and general flow directions and rates, evaluation of the areas and amounts of regionally significant recharge and discharge rates, evaluation of regional geochemistry and regional temperature profiles as indicators of the regional flow paths, and modeling of the regional groundwater flow system in the Death Valley region. This regional information has been supplemented by additional characterization at the scale of the Yucca Flat/Climax Mine CAU, including evaluation of hydrologic properties from single-well

tests and a multiple-well aquifer test (MWAT), as well as a tracer test conducted in parallel to the MWAT. The information available to develop and calibrate the LCA groundwater flow model is summarized in the Yucca Flat/Climax Mine HDD (SNJV, 2006b). The development and calibration of the Yucca Flat LCA flow model is based on the hydrogeologic information available from the regional, NNSS, and CAU-specific characterization of the LCA.

The approach taken to develop and calibrate the LCA groundwater flow model is similar to the approach taken to develop and calibrate other CAU groundwater flow models, with the exception that the LCA flow model was developed separately from the overlying saturated alluvial/volcanic aquifer system flow model. The common boundary between the LCA and the overlying saturated HSUs is treated as a recharge boundary to the LCA. As noted in Section 4.0, the reason for decoupling these two flow models is that whereas the transient hydraulic effects of underground nuclear testing on the groundwater flow domain are significant to the calibration of the saturated alluvial/volcanic aquifer system model, they are not significant to the saturated LCA flow model. This is due to the much greater transmissivity of the LCA and the low permeability of the thick confining volcanic aquitard units—namely, from top to bottom, the LTCU, the OSBCU, the ATCU, and the volcaniclastic confining unit (VCU)—that hydrologically isolates the LCA from the overlying volcanic aquifers—namely, from top to bottom, the TM-WTA, the TM-LVTA, the TSA, and the LVTA. Although potentially significant hydrologic communication can exist between the overlying volcanic aquifers and the underlying LCA along the numerous north–south-trending normal faults that intersect the basin, the thick confining units isolate the flow systems in the volcanic aquifers from the LCA based on the differences in hydraulic potentials between these aquifers (Section 1.4).

The development of the LCA flow model starts with producing a model grid that honors the spatial extent of the LCA and associated faults identified in the HFM. The spatial extent of the saturated LCA of interest to the Yucca Flat/Climax Mine CAU flow and transport model is determined by the extent of the HFM along the southern, eastern, and western boundaries, as well as by where the LCA pinches out against the deeper confining units in the northeast and northwest portions of the model domain (Figures 1-4 and 1-9). Although the domain of the flow model of relevance may be less than or greater than that provided by the Yucca Flat/Climax Mine CAU HFM (BN, 2006), the HFM model extent was used along the southern boundary because it was believed to be far enough south to capture the reasonable extent of significant 1,000-year contaminant transport and it extended far enough east of the NNSS boundary to preclude significant boundary effects on the simulated flow

regime in central Yucca Flat. The northern model extent is also constrained by the extent of the HFM in northern Yucca Flat.

Although three model grids with increasing levels of refinement were developed for the LCA, the intermediate grid (with the finest resolution being about 125 m) was used as a compromise between model accuracy and computational efficiency, i.e., having sufficient model resolution to define the location and thickness of potentially significant features while maintaining computational complexity at a reasonable level. A refined model grid was used in a sensitivity analysis to evaluate the significance of the grid spacing on the calibrated flow field.

Once the model extent and spatial resolution of the numerical model has been developed, it is necessary to identify permeability zones. The LCA has been divided into three zones for the country rock and 106 faults. The three country-rock zones are (1) the areas east of the Yucca fault, where enhanced permeability is assumed because of the pervasiveness of unidentified small faults and fracture zones, (2) the area between the Yucca fault and the Carpetbag fault, and (3) the area west of the Carpetbag fault. The three major throughgoing faults in the study area are the Carpetbag, Topgallant, and Yucca faults, each consisting of two separate fault splays, which are treated as distinct features in the model. All other faults are treated as single discrete features, whose lateral and vertical extent is as defined in the HFM. In defining such large geographic extents within a similar permeability zone, the LCA flow model implicitly assumes that the permeability is homogeneous within that zone. In that sense, the modeled permeability is considered an effective homogeneous (but anisotropic) permeability. Within the fault zone, the modeled permeability distribution is divided into a core zone, which is generally one node wide in the center of the identified fault zone, and a damage zone on either side of the core, which is assumed to represent a zone of cataclastic deformation. Data within the LCA are insufficient to define a spatially heterogeneous permeability distribution. It should be noted that this approximation has been made in other models of the LCA at the NNSS, with the exception of the DVRFS model described in Belcher et al. (2004), in which large areas are assumed to have different permeability values based on geologic analogs.

The boundary fluxes in the LCA flow model consist of vertical recharge from the overlying volcanic and alluvial aquifers and from areas where the LCA subcrops along the basin margins, and lateral influx from areas to the west, north, northeast, and east of Yucca Flat. Although these boundary fluxes are derived from regional estimates, there is considerable uncertainty in these estimates as regional

models and regional synthesis reviews indicate different values with different bases, in particular for the influx from north of Yucca Flat. As a result, alternative analyses of different boundary influxes and vertical recharge have been considered in the model calibration. Alternative assumptions have been postulated for the lateral continuity of the LCA in northern Yucca Flat. These alternatives effectively yield different assumptions of the magnitude of the boundary influx along the northern boundary of the LCA flow model. To address this uncertainty, the alternative that assumes lateral continuity is used in the base-case model, while the alternative that assumes no lateral continuity is evaluated as an alternative model.

Maintaining consistency between the vertical recharge rate used in the LCA groundwater flow model and the infiltration rate used in the overlying unsaturated-zone flow model is desirable. However, the rates may differ for the following reasons: (1) the unsaturated-zone flow model extends over only a limited fraction of the LCA flow model (Figures 1-16 and 1-17); (2) the unsaturated-zone flow model extends over only areas of relatively thick alluvium and does not extend over areas along the basin margins, where the elevations are higher and there is less alluvium to limit the amount of water expected to recharge the deeper HSUs; and (3) the LCA flow model considers the vertical recharge estimates as initial guesses but then allows these values to adjust during the automated parameter estimation process included in PEST. While present-day infiltration and paleodrainage rates from the unsaturated zone to the water table range from less than 0.1 to about 1 mm/yr (as discussed in Section 3.0), the unsaturated-zone and saturated alluvial/volcanic aquifer system flow models assume discrete recharge rates of 0.1, 1, 5, and 10 mm/yr. As discussed in Sections 3.0 and 4.0, and summarized in Section 5.3, there is uncertainty in the spatial distribution and magnitude of net infiltration within the central portions and margins of the Yucca Flat basin. This uncertainty propagates to uncertainty in recharge to the LCA. Because of the significance of this uncertainty to contaminant transport from the contaminant sources in the unsaturated zone and saturated alluvial/volcanic units to the LCA, the unsaturated zone and saturated alluvial/volcanic aquifer system models conducted simulations with infiltration rates as high as 5 and 10 mm/yr, even though the regional estimates of average infiltration rates range from less than 0.1 to about 1 mm/yr. These analyses were conducted to ensure that contaminant releases to the LCA from these models were not underrepresented; they were not meant to imply that the expected recharge rate is as high as 5 to 10 mm/yr.

Each of the discrete features included in the LCA flow model is assigned an initial range of representative permeability estimates. This initial estimate range is used to constrain the upper and lower limits of the distribution used in the automated PEST calibration process. The approach used to define the initial estimates was to specify the range based on the overall range of observed permeability values.

Based on the initial estimates of permeability, boundary flux and recharge values, and the observed steady-state and transient water levels, the LCA flow model was calibrated with the automated routines included in the PEST software linked to FEHM. In addition to defining the expected range of properties and boundary conditions to be constrained by the flow model, the calibration required that appropriate weights be assigned to different observations. The approach taken was to first select an appropriate number of observed values from the transient MWAT and then develop weights that would allow approximately half of the objective function to be controlled by transient head residuals and the remaining half by steady-state head residuals. This calibration process resulted in an initial calibrated flow model.

Once the initial calibrated flow model was developed, alternative flow models were investigated to ensure that a reasonable range of alternative flow models was included in the assessment of potential contaminant migration from the Yucca Flat underground nuclear detonations. Two separate approaches were considered in the development of alternative calibrated flow fields. The first method involved utilizing the initial calibrated model as a base-case model from which over 80 alternative calibrated flow fields were derived using the NSMC method. This method is equivalent to evaluating the range of possible calibrated flow fields within the uncertainty of the calibrated parameter values for a given conceptual model. The second method focused on considering alternative conceptual models that may have a significant effect on contaminant transport in the LCA and then recalibrating the flow model for these alternative conceptualizations. One example of this second method is evaluating alternative fault-zone architectures. In addition, the two alternative HFMs identified as potentially affecting flow in the LCA at Yucca Flat (BN, 2006) were evaluated to determine whether these alternatives significantly affected the flow system. Finally, given the potential significance and large uncertainty in the boundary flux into the LCA in northern Yucca Flat, analyses using an alternative representation of this flux were conducted.

The net result of applying the uncertainty analysis approaches summarized above is a range of reasonably calibrated flow models. Although a “base-case” calibrated flow model was initially developed, this model is one of several reasonable alternatives that are consistent with the hydrologic observations. There is no presumed or inferred “best” or “most reasonable” flow model, and the “base case” should simply be regarded as a representative case with which other models and associated flow fields can be compared. The base-case flow model assumes that there is hydraulic communication between the LCA in northern Yucca Flat and the LCA in the western portion of the Groom Lake and Emigrant Valley hydrologic sub-basins. This is analogous to the assumption made in regional models of groundwater flow of the NNSS. An alternative flow model was developed assuming that there is limited hydraulic communication in northern Yucca Flat. This alternative model is consistent with recent conceptualizations developed by Fenelon et al. (2010) as illustrated in Figure 1-13, and the early work of Winograd and Thordarson (1975). The alternative conceptual model, called the alternative northern boundary flux model, results in lateral underflow rates of about one-hundredth of the underflow that results from the continuous LCA groundwater flow pathways of the base-case model. As a result, the base-case model may be considered conservative with respect to its potential effect on contaminant transport given that larger fluxes lead to higher velocities and hence greater transport.

5.2 Background Hydrogeologic Data

5.2.1 Introduction

The Yucca Flat/Climax Mine HDD (SNJV, 2006b) contains all geologic and hydrogeologic data necessary for construction of the Yucca Flat groundwater flow model. The key data required for construction and calibration of the flow model are briefly summarized below. For further details of the data and accompanying analysis or interpretation, the reader is referred to the Yucca Flat/Climax Mine HDD (SNJV, 2006b).

5.2.2 Yucca Flat Hydrostratigraphic Framework

The distribution of HSUs at the surface within the Yucca Flat/Climax Mine HFM area is shown in Figure 1-7. An important feature of this map is the outcropping of carbonate rocks at the surface in the east and the southwest. The outcropping may provide an avenue for enhanced recharge to the LCA as discussed further in Section 5.5. The distribution of HSUs at the water table is presented in

Figure 1-9. The top of the LCA is above the water table in the eastern portions of the study area, which results in unconfined hydrologic conditions in these areas. The central and western portions of the study area are under confined conditions as the water table is primarily in the overlying volcanic, clastic, and overthrust Paleozoic formations, which are separated from the underlying LCA by hydrologically confining units. A north–south hydrostratigraphic profile along the general direction of groundwater flow (A-A′) is provided in Figure 1-10b, and west–east hydrostratigraphic profiles (C-C′, D-D′, and E-E′) through central Yucca Flat are provided in Figure 1-10a. The areal location of the cross sections is provided in Figure 1-9.

The mass of LCA in the Yucca Flat flow model area is presented in Figure 5-1. As shown in Figure 1-4, the LCA pinches out in the east, north, and northwest, forming the eastern, northern, and northwestern boundaries of the LCA flow model shown in Figure 5-2. The central and southern edges of the western boundary coincide with the areal extent of the LCA3 overthrust carbonate plate associated with CP thrust faulting as shown in Figure 1-9.

Most of the structural elements in the base HFM are high-angle normal (basin-and-range) faults. The locations of these faults were based on mapped surface traces, drill-hole data, mapped surface effects from underground nuclear detonations, and geophysical evidence. Only the main surface faults were included in the model (Figures 5-2 and 5-3). These faults typically have apparent offsets greater than 60 m and appear to provide the main control on the structural fabric and outcrop patterns in the highlands bordering Yucca Flat. Most faults are modeled as single fault planes that extend to the base of the model. Some faults, however, terminate against other faults. Because the main basin-forming faults dip to the east in Yucca Flat, west-dipping faults in the model typically terminate against east-dipping faults.

Located in the center of the basin, the Yucca fault is the master basin-and-range-forming fault in the Yucca Flat/Climax Mine CAU. Figure 5-2 shows that there are two other large basin-forming faults in the CAU: the Carpetbag and Topgallant faults. These faults are associated with reactivation of the east-dipping, high-angle ramp structure of the CP thrust fault that resulted in the formation of the west-tilted Yucca Flat structural basin (BN, 2006). The basin-and-range faulting has acted to further complicate the hydrogeology, placing the various lithologic units in juxtaposition and blocking or enhancing the flow of groundwater in a variety of ways. The faults may act as conduits to

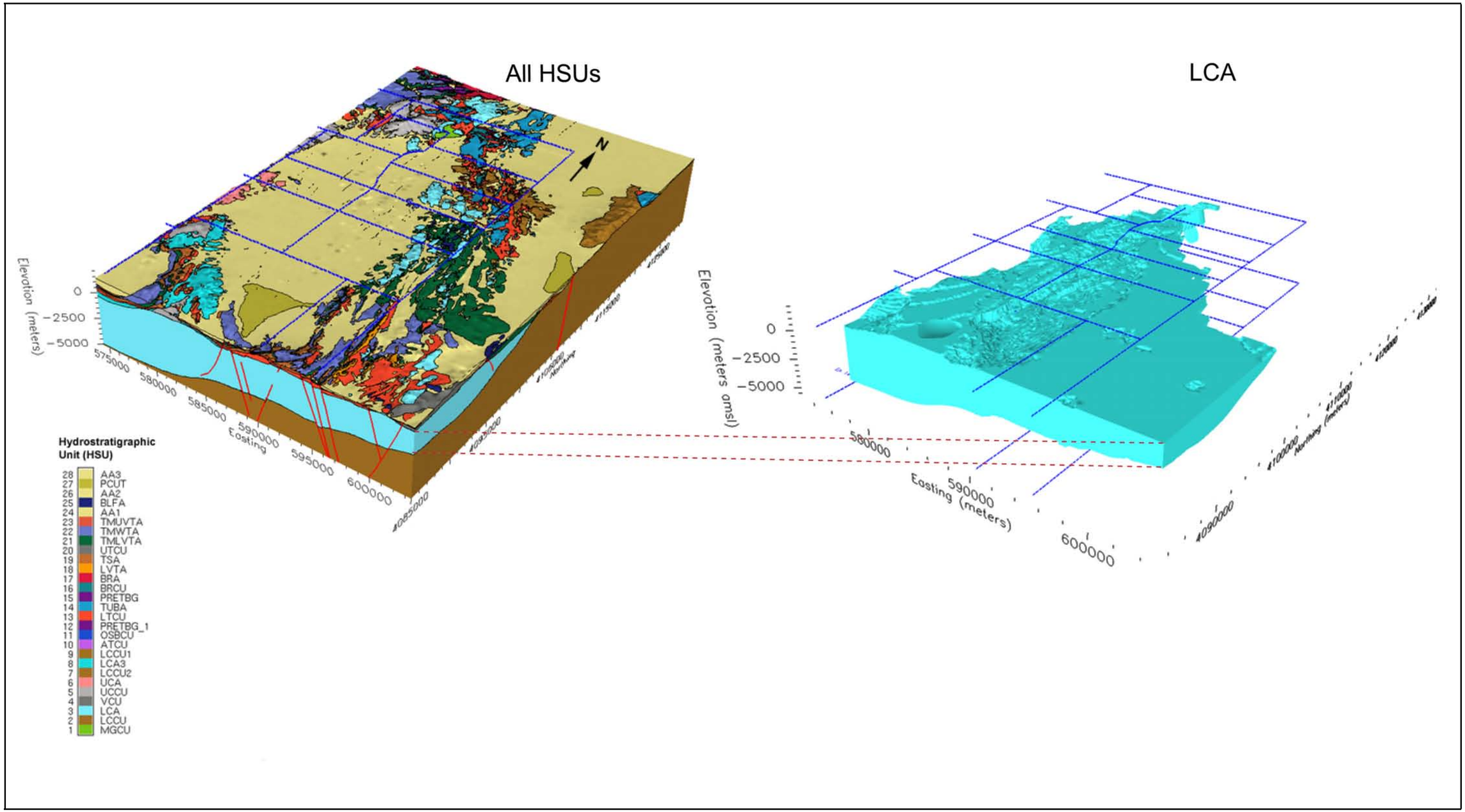

Figure 5-1
Mass of LCA in the Yucca Flat Groundwater Flow Model

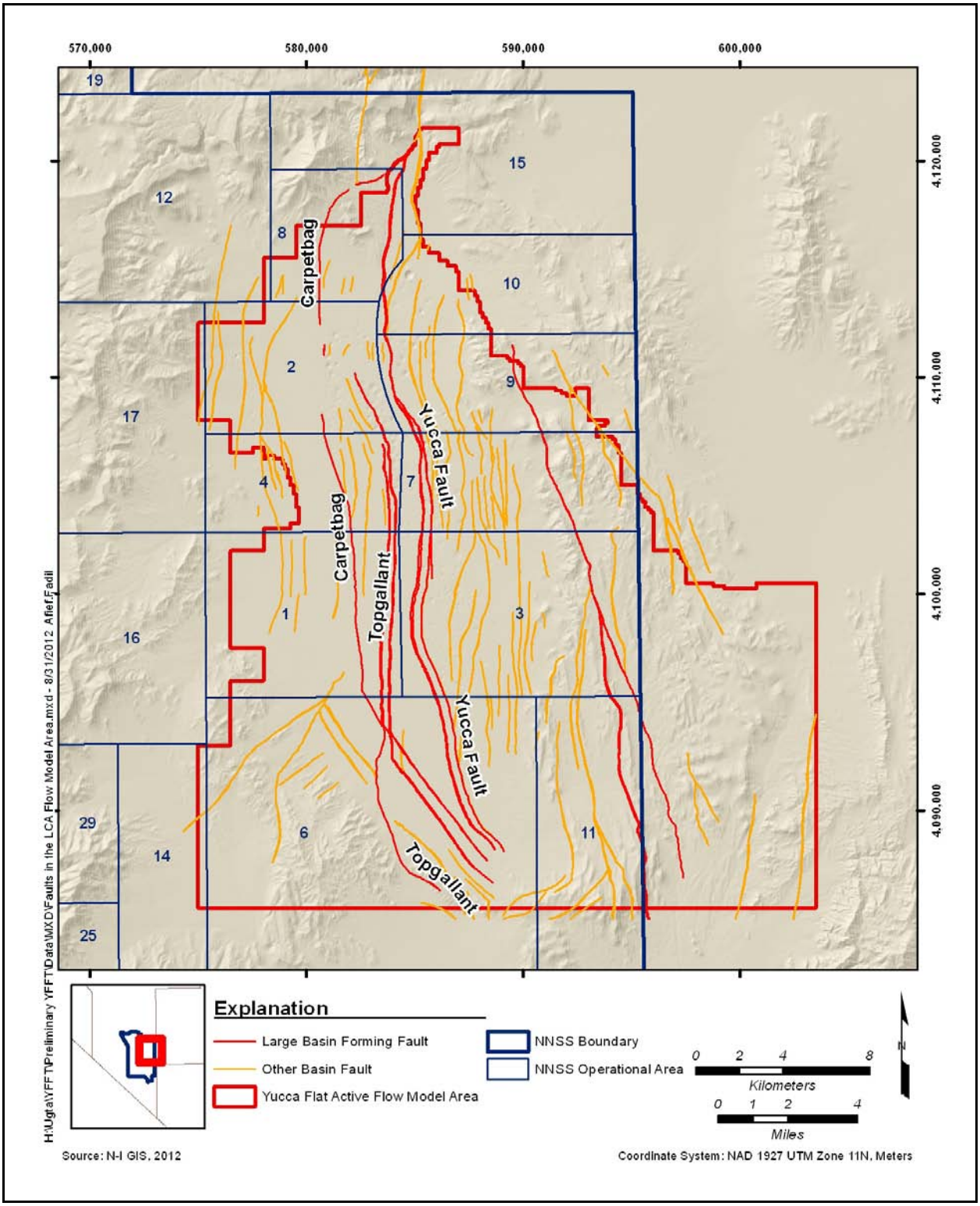

Figure 5-2
Faults in the Yucca Flat LCA Flow Model Area

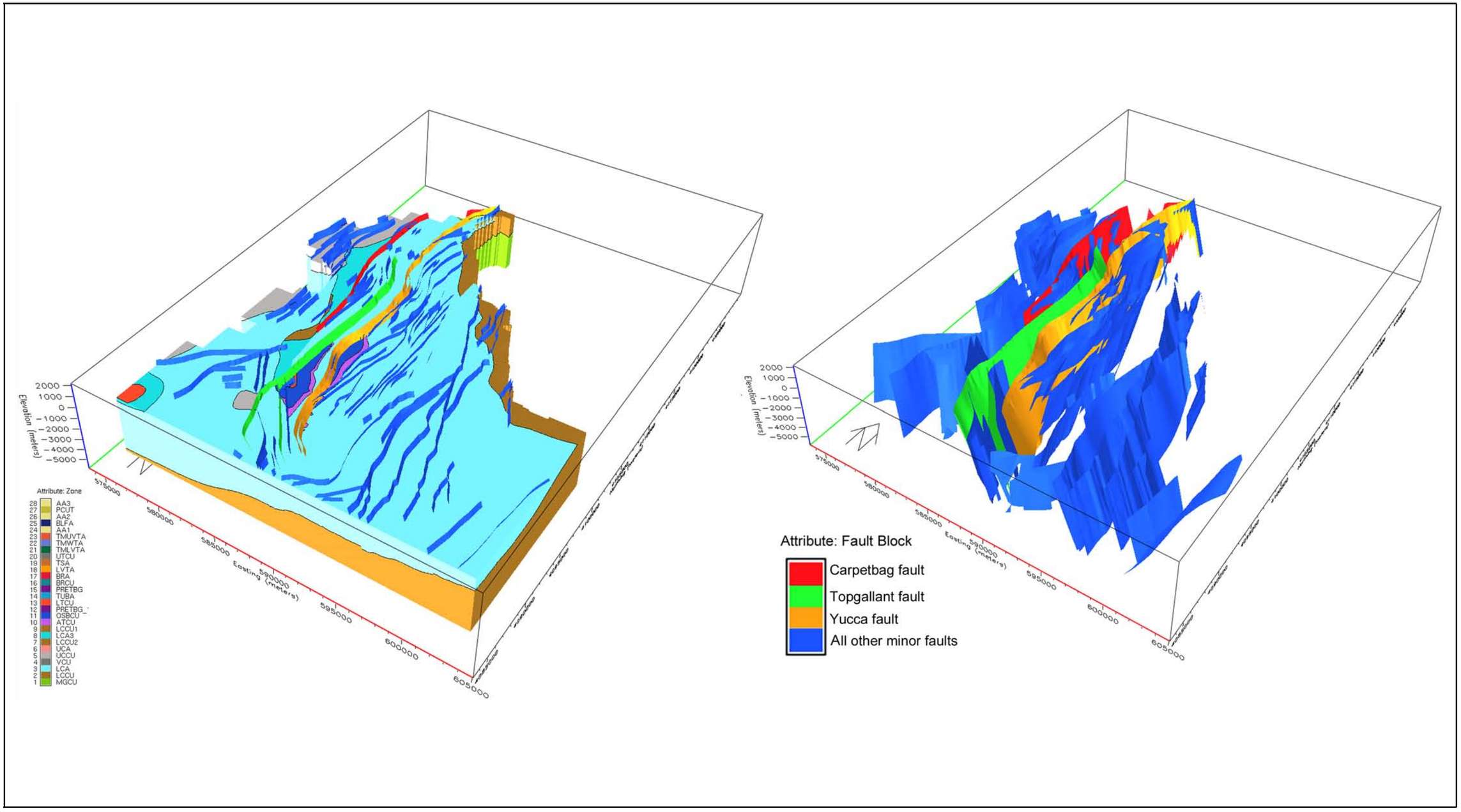

Figure 5-3
Three-Dimensional Representation of Faults in the Yucca Flat HFM and Groundwater Flow Model

groundwater flow along the fault plane and provide a barrier to cross flow because of the presence of fine-grained gouge along the fault plane.

5.2.3 Groundwater Discharge

Knowledge of discharges from the groundwater flow system is essential for proper calibration of a groundwater flow model. The sources of discharge may be natural (e.g., evapotranspiration, spring discharge) or anthropogenic (e.g., well production). In Yucca Flat, anthropogenic sources are the only significant discharges from the LCA, as there are no known surface or submerged springs in the LCA and the water table is several hundred meters below ground in areas where the LCA outcrops.

Water has been pumped from four LCA water supply wells for potable or industrial use and to support nuclear testing activities. The locations of water supply wells and the estimated withdrawal rates are presented in Figures 5-4 and 5-5, respectively. Well HTH-2 (WW-2) is located on the northern edge of Area 2 in Yucca Flat. The well was active from April 1962 through December 1990, and the average annual production was 37.4 million gallons. Well WW C is located in the southeastern part of Area 6. The well was used from September 1961 to July 1995, with an average annual production of 39.6 million gallons. Well WW-C-1 is located in the southeastern part of Area 6 in close proximity to WW C. The well started production in June 1962 and is still in use, with an average annual production of 24.7 million gallons. Well UE-1r (UE- 1r WW) is located on the eastern edge of Area 1 in Yucca Flat. The well was active from September 1984 to October 1988, and the average annual production was 6 million gallons.

Long-term groundwater production can remove significant volumes of water from the groundwater flow system, which can potentially affect hydraulic heads and flow rates in the formation. The largest withdrawal occurred during the early periods of nuclear testing in the 1960s and the 1970s. The total LCA production in the last 20 years is approximately 20 million gallons per year, or 2.4 kilograms per second (kg/s). As discussed in Section 5.5, this flow rate is small compared to the total estimated volumetric base flow of more than 100 kg/s, and consequently, the drawdowns associated with these long-term withdrawals are expected to be relatively small and stable. The historical pumpage and water levels at the two major LCA pumping wells (HTH-2 [WW-2] and WW-C-1) are presented in Figure 5-6. The figure shows that drawdowns are relatively minor over the reported period that spans approximately 40 years. Therefore, for model development and calibration purposes, the groundwater

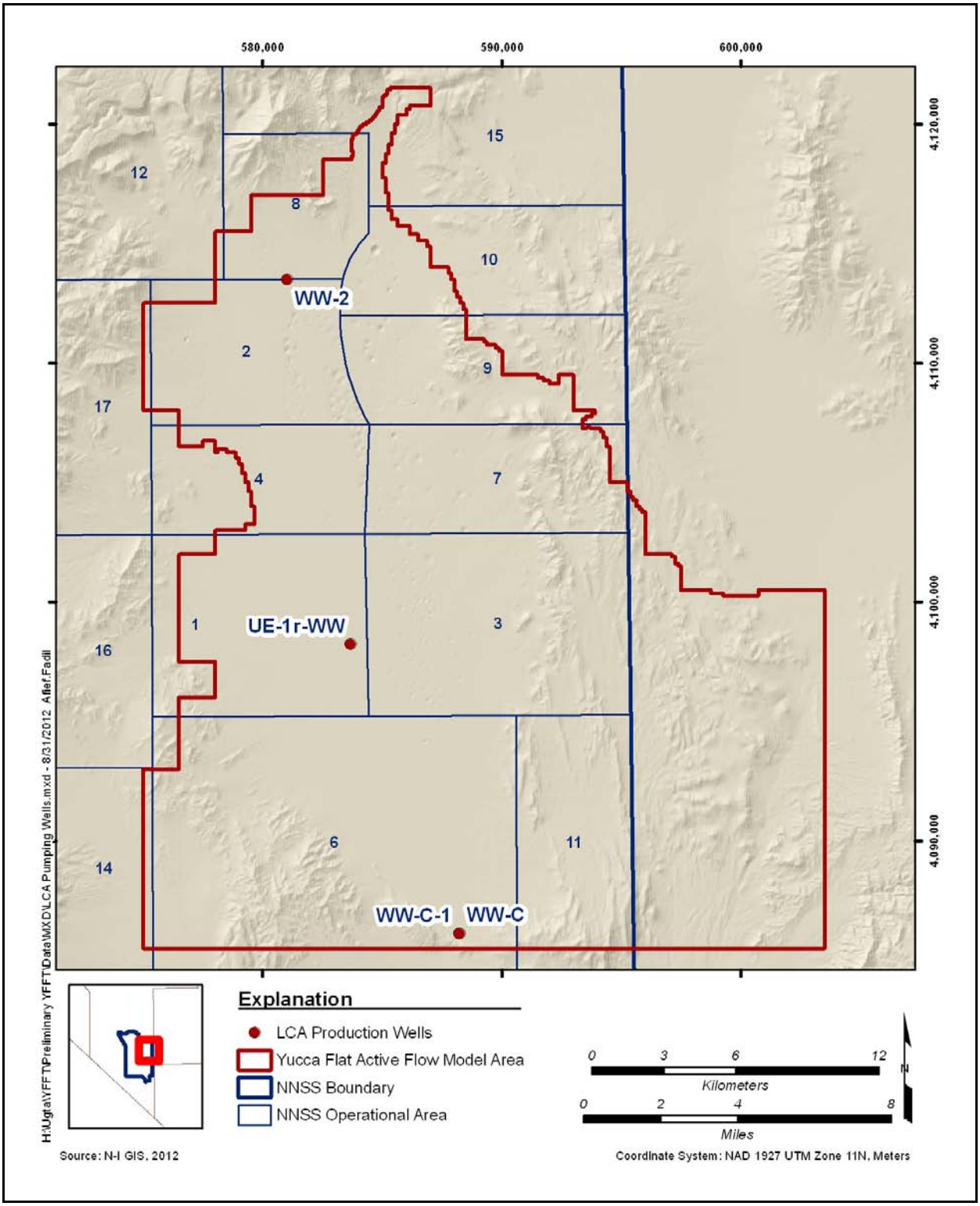

Figure 5-4
Locations of Groundwater Pumping Wells in the Yucca Flat/Climax Mine CAU

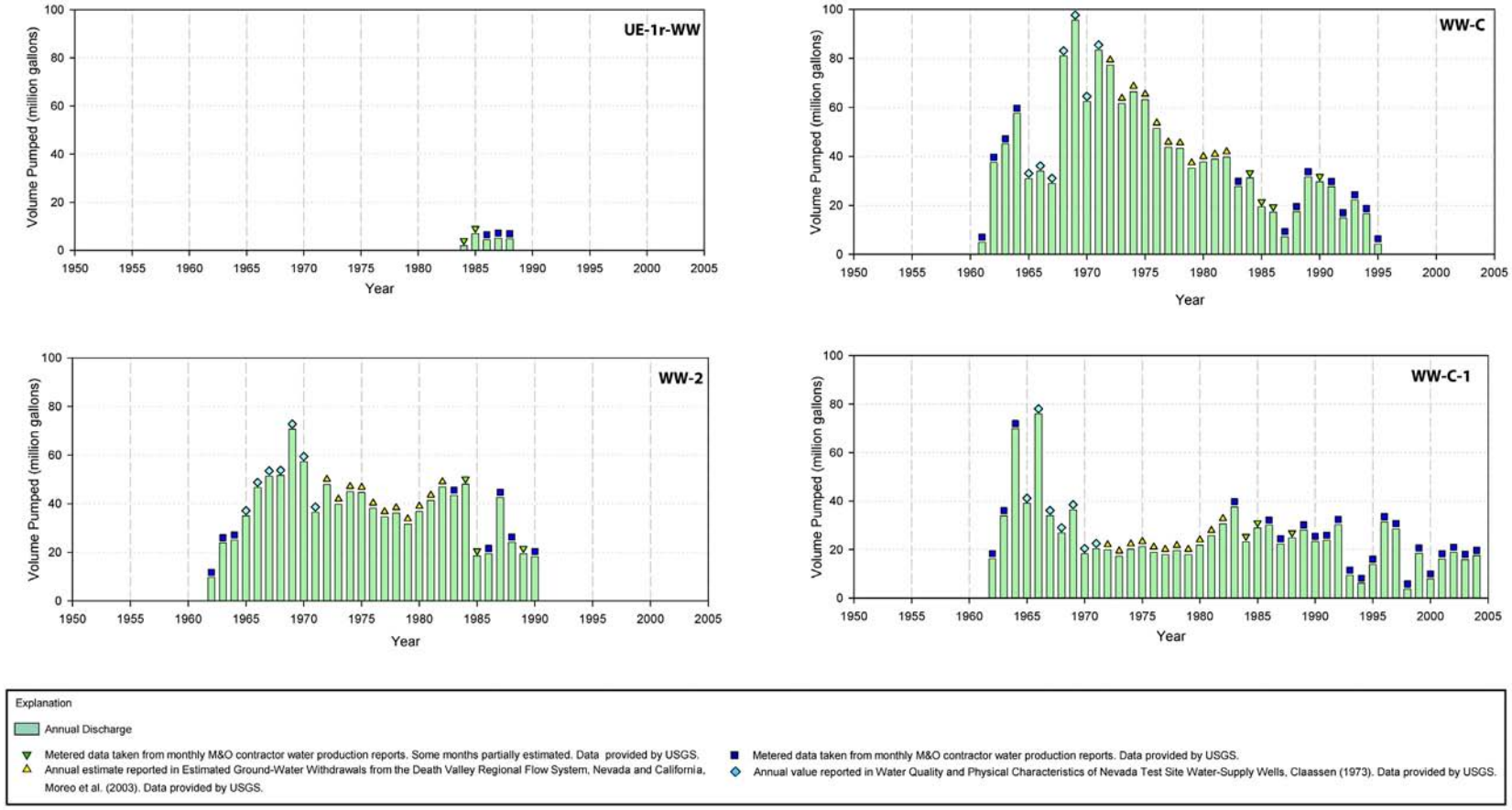

Figure 5-5
Production History for Yucca Flat Groundwater Pumping Wells
Source: Modified from SNJV, 2006b

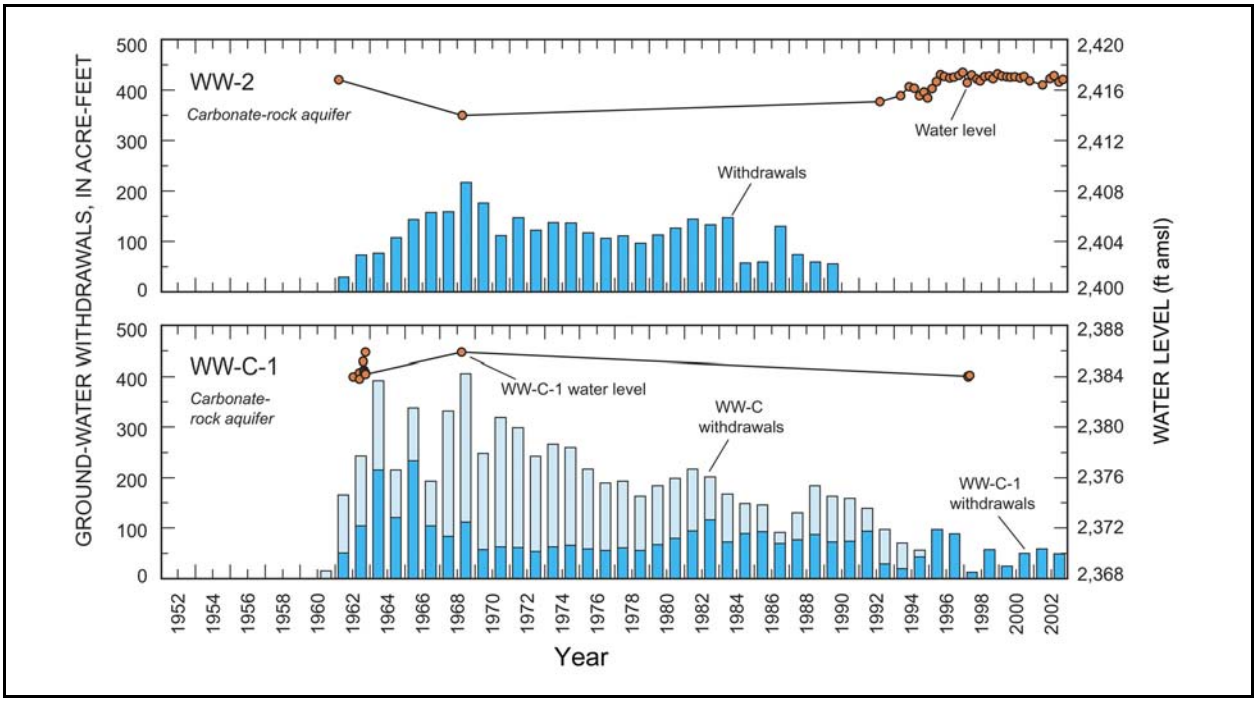

Figure 5-6
Annual Groundwater Production and Water Levels in LCA Wells HTH-2 (WW-2) and WW-C-1
Source: Modified from Fenelon, 2005

system in the LCA was assumed to be under steady-state conditions. Simulations were conducted to validate the reasonableness of this assumption, and the results are documented in Appendix I.

5.2.4 Hydraulic Heads

Hydraulic head is the most available hydrogeologic measurement used to constrain groundwater flow modeling. Hydraulic head information for the groundwater flow system in the Yucca Flat/Climax Mine CAU and vicinity was compiled and analyzed to support CAU-scale groundwater flow modeling. The primary objective was to determine representative steady-state hydraulic head values for the flow system that can serve as calibration targets during development of the steady-state flow model.

As stated in the Yucca Flat/Climax Mine HDD (SNJV, 2006b), water-level data historically have been collected in the Yucca Flat area on an *ad hoc* basis, as wells were drilled or recompleted, and for individual testing programs and projects. Consequently, the historical information generally does not provide complete, continuous records for most wells. A comprehensive water-level monitoring program was instituted by USGS in the early 1990s. These water-level measurements provide the best

basis for identifying the representative characteristics of modern-day water levels because of the completeness and consistency of the records. USGS compiled historical water-level data and data from its water-level monitoring program through calendar year 2003 (Fenelon, 2005). This study was the primary source of water-level data used for analysis of hydraulic head data for the Yucca Flat analyses.

Many of the observation wells that penetrate the LCA in the study area and for which water-level data are available are open over a large vertical extent that includes the lower portion of the tuff confining units. As a result, interpreting the water-level data is uncertain as there is insufficient information with which to confidently determine whether the measured water level is representative of the LCA or the overlying HSU. While it may be postulated that the LCA is generally more transmissive than the overlying confining units, and hence water levels in wells penetrating the LCA should be representative of the LCA, it is not uncommon for the upper portion of the LCA to be characterized by an argillic paleosol that has a very low permeability (Drellack et al., 2012). As a result, some water levels ascribed to the LCA by Fenelon et al. (2010) have not been used in the calibration of the LCA flow field. They include observations in Wells UE-10 ITS 3, UE-10 ITS 5, and UE-10bf in northern Yucca Flat.

The Yucca Flat/Climax Mine groundwater system is not in true steady state, nor was it in steady state before the advent of groundwater development in 1952. The analysis conducted for the present study (SNJV, 2006b) identifies heads that are considered to represent stable flow conditions consistent from historical to contemporary times. These heads were determined by evaluating hydrographs for each site record and supporting information about local groundwater conditions near each site to identify periods of records and/or individual measurements that reflect stability within overall measurement uncertainties, barometric pressure and variability caused by earth tides, and natural fluctuations and trends. Determination of such stability consequently required water-level records spanning long periods of time, preferably including the decades of extensive water-level production (from the 1960s to 1980s). This evaluation was conducted by USGS and is documented in the Yucca Flat water-level analysis report (Fenelon, 2005).

The water-level data for the available period of record are presented in Figure 5-7. The figure clearly shows that water-levels fluctuate over a narrow range for the period of record. The estimated steady-state water levels at 15 LCA observation well sites are presented in Figure 5-8. A key

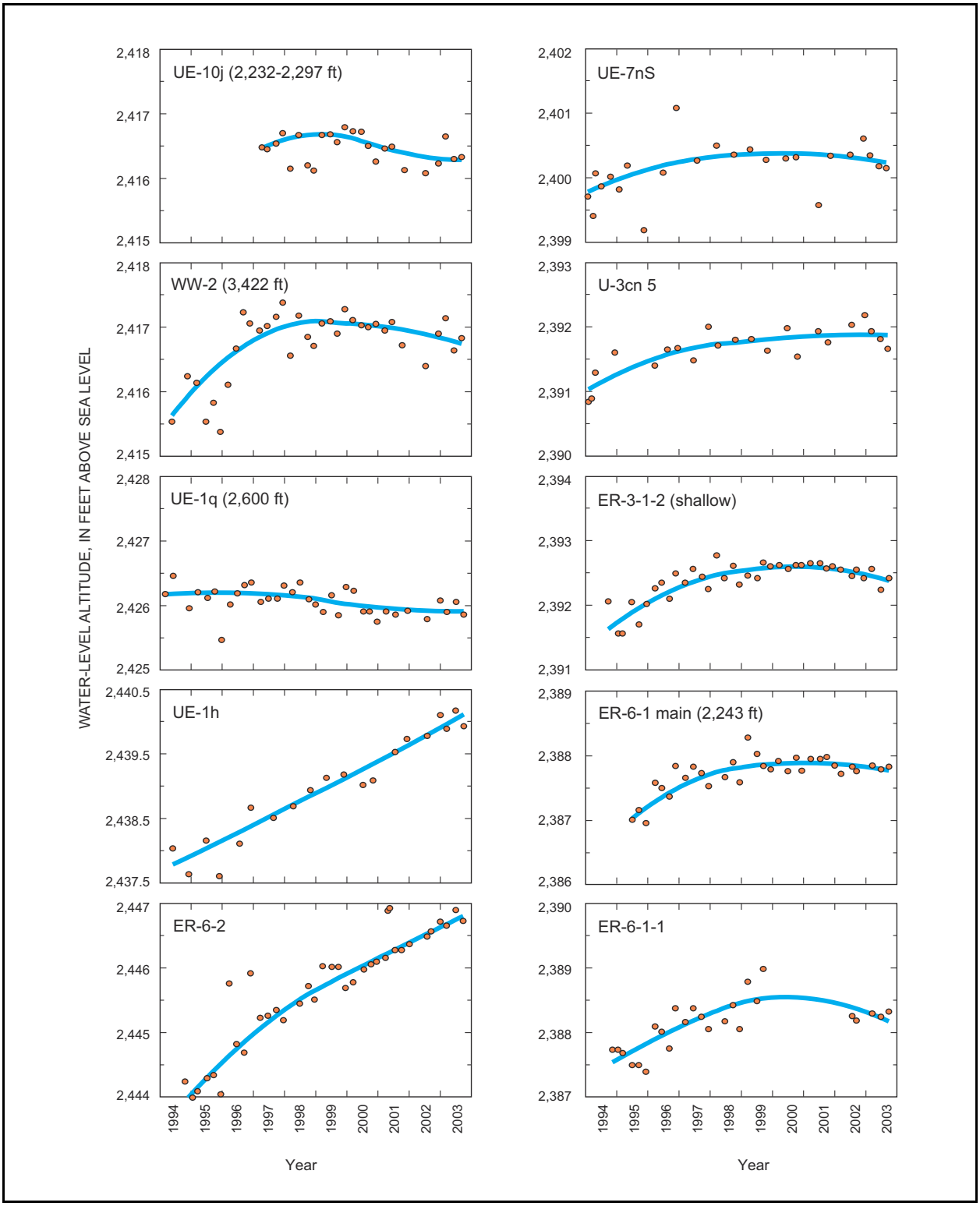

Figure 5-7
Historical Water Levels in LCA Observation Wells in Yucca Flat
Source: Modified from Fenelon, 2005

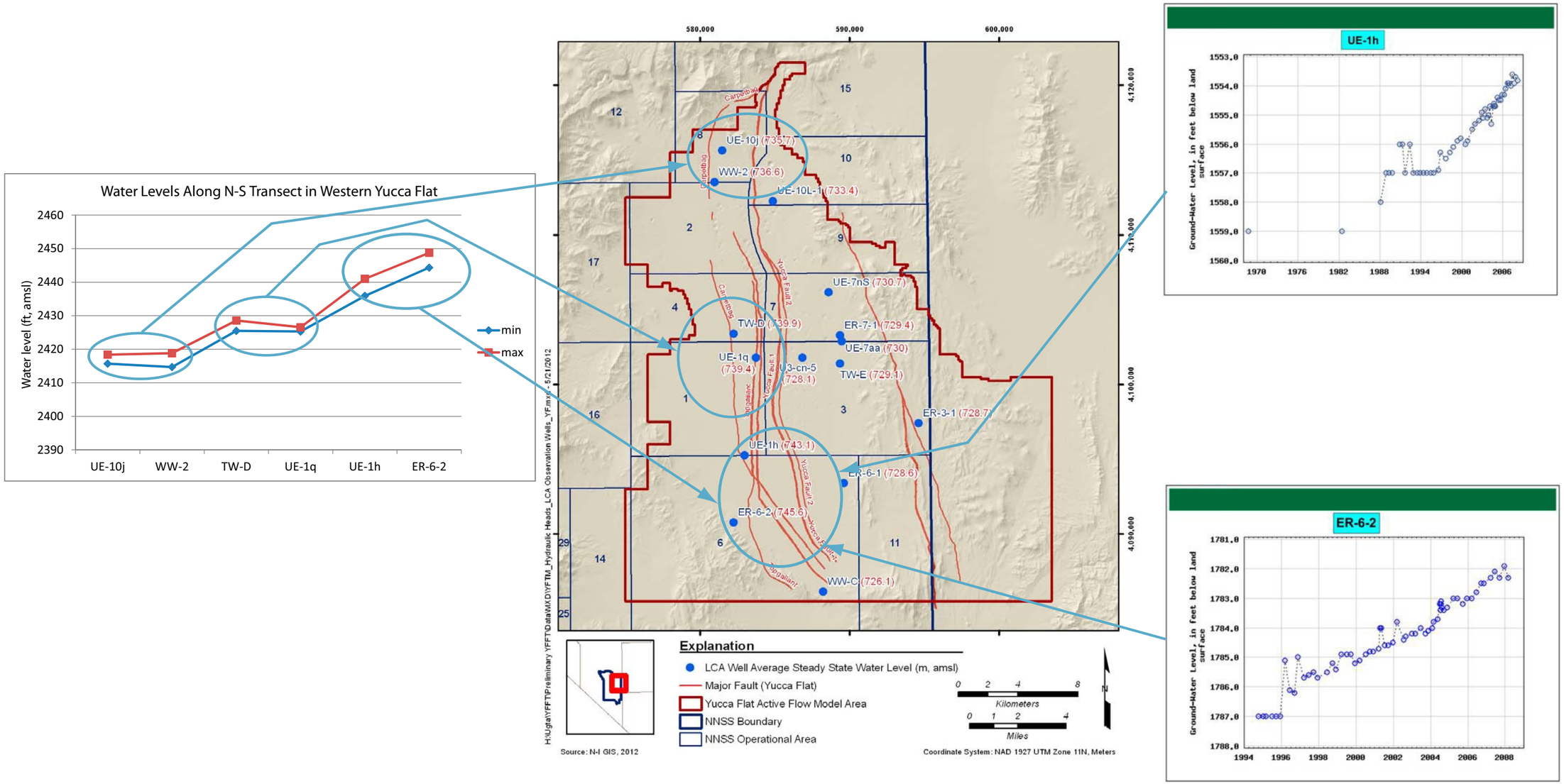

Figure 5-8
Hydraulic Heads at LCA Observation Wells in Yucca Flat

observation to note from Figure 5-8 is that heads in the western part of the basin are higher in the south than in the north. This trend has persisted over the entire period of record. Another noteworthy observation is that while most of the water levels have remained steady, water levels have shown a rise at ER-6-2 and UE-1h in recent years (Figure 5-7). The cause of this rise is not known with certainty but is attributed by Fenelon (2008) to be the result of climatic variations in recent years (Figure 5-9).

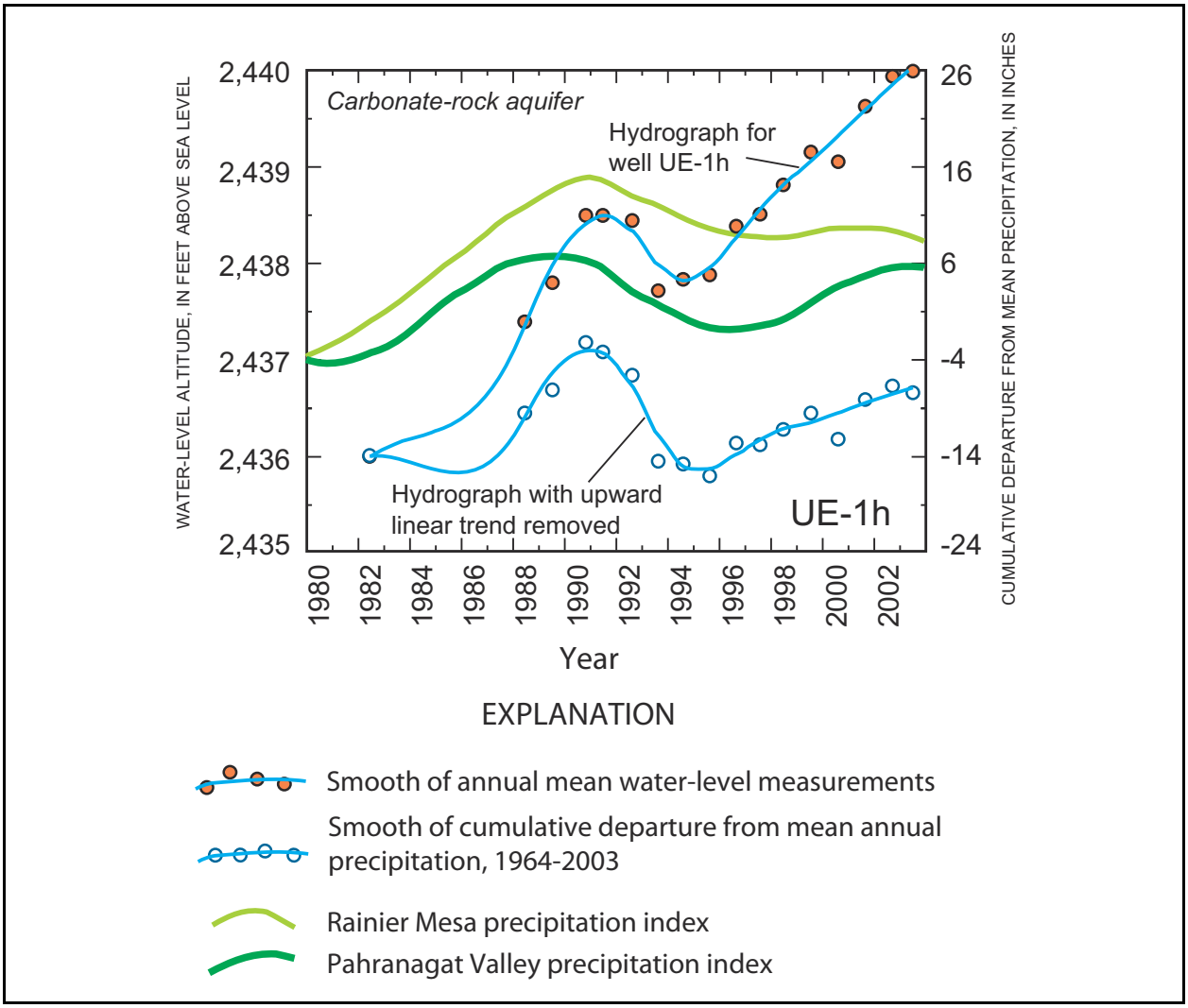

Figure 5-9
Historical Hydraulic Head at UE-1h and Precipitation Indices at Rainier Mesa and Pahranagat Valley
Source: Modified from Fenelon, 2005

The limited amount of head data precludes the construction of a unique potentiometric surface for the LCA. Specifically, the rising water-level trend at ER-6-2 and UE-1h, the observed south-to-north head gradient in the west, the presence of observation wells in the east and west sides of the basin at approximately the same longitude, and the presence of numerous structural features with offsets in excess of 100 m make it difficult to construct a potentiometric surface with confidence. Winograd and Thordarson (1975), however, were the first investigators to prepare a potentiometric surface map that depicts the movement of groundwater in the LCA at Yucca Flat. Groundwater from both the east and west sides of the basin is interpreted to move toward the center of the basin, where the major faults are located, and eventually exit Yucca Flat into the CP and Frenchman Flat basins before discharging in the network of springs at Ash Meadows (Figure 1-12). In more recent times, Fenelon et al. (2010) have interpreted groundwater flow in Yucca Flat to primarily follow a north–south trajectory as depicted in Figure 1-13. These interpretations of the potentiometric surface will be used to qualitatively assess the goodness of calibration discussed in Section 5.5.

In order to develop a dataset that provides large-scale information on the hydraulic structure of the Yucca Flat basin, a long-term MWAT was conducted in eastern Yucca Flat with pumpage at ER-6-1-2. The test is referred to in this study as the ER-6-1-2 MWAT. The objective of the aquifer test was to determine hydraulic properties for the LCA through long-term constant-rate pumping at ER-6-1-2 with monitoring of the formation response in a network of widely spaced wells (Figure 5-10). Continuous water-level responses were recorded at ER-7-1 and ER-3-1, and periodic water-level measurements were collected at UE-1h, UE-7nS, and U-3cn-5.

The ER-6-1-2 MWAT was conducted at an average pumping rate of 524 gallons per minute for a duration of 90 days, which provided significantly better diagnostic information for hydraulic properties than those historically collected from tests of shorter duration. The hydraulic response at the observation well sites is presented in Figure 5-10. The response in ER-7-1, which is aligned with ER-6-1-2 along the longitudinal axis of the faults, was prompt and substantial. The response at ER-3-1, which is closest to the pumped well but located transverse to the fault direction, was delayed and smaller than any well in the eastern part of the basin. Separated from the production well by several major faults with substantial offsets, UE-1h did not show any response to pumpage at ER-6-1-2. The drawdowns at UE-7nS and U-3cn-5 are of similar magnitude as those at ER-7-1. The ER-6-1-2 MWAT provides significant information for characterization of the LCA in Yucca Flat to

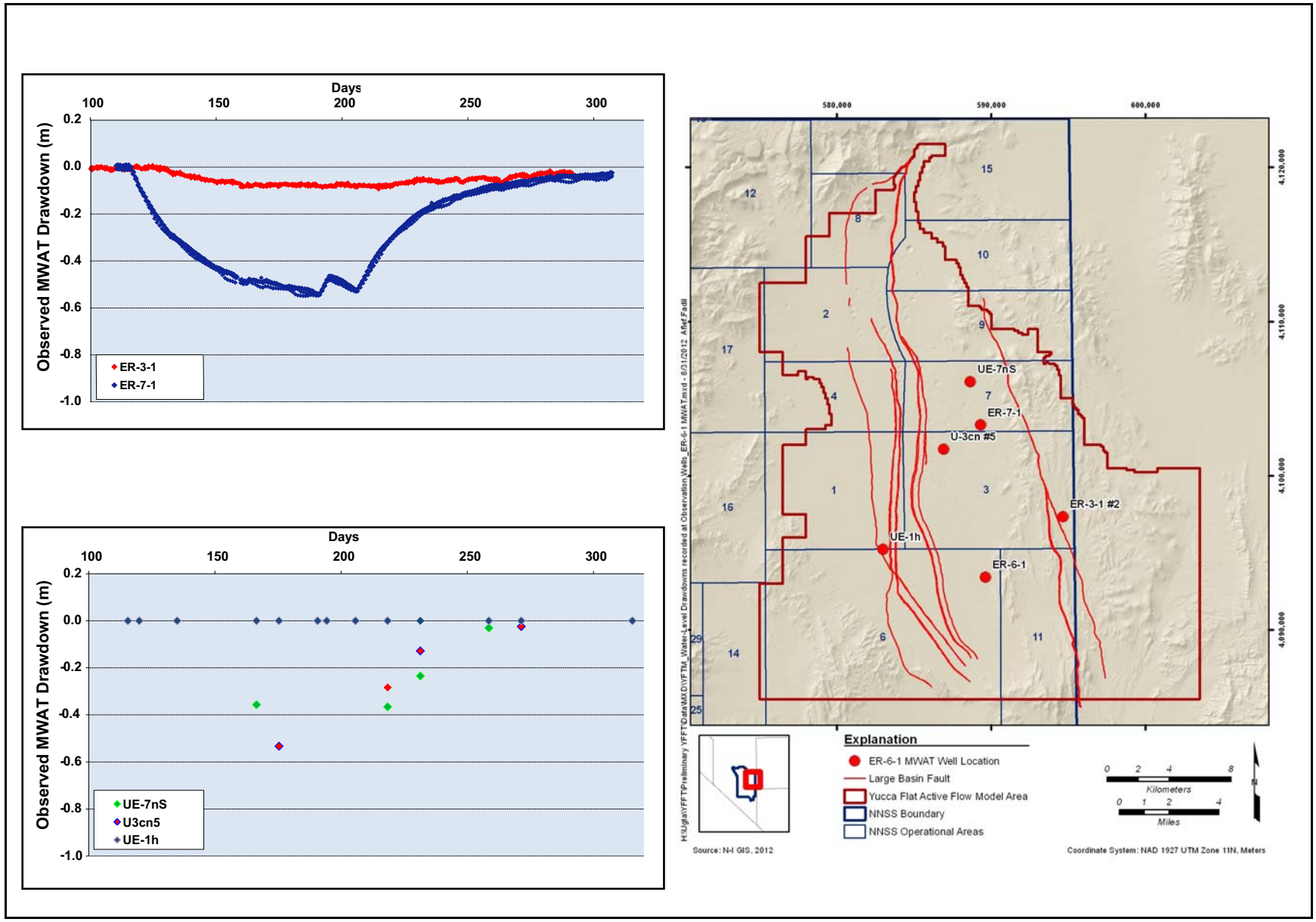

Figure 5-10
Water-Level Drawdowns Recorded at Observation Wells Monitored during ER-6-1-2 MWAT

an extent that is not possible with other tests of shorter duration or the general analysis of steady-state potentiometric data.

5.2.5 Hydraulic Properties of Saturated Media

As stated in the Yucca Flat/Climax Mine HDD (SNJV, 2006b), values used for the hydraulic properties of HSUs in the simulation of groundwater flow and transport should be consistent with available information to provide confidence in the simulation results. Specifically, hydraulic conductivity is a basic parameter for groundwater flow modeling that determines the volumetric flow rate. Representative hydraulic conductivities for the formations to be modeled at the scale over which the model is discretized are integral to producing defensible model predictions. Storage properties of the formations also are of interest as a basic hydraulic parameter needed for transient simulations of groundwater flow.

5.2.5.1 Hydraulic Conductivity Data

Analysis of the hydraulic conductivity data included separate evaluations of pumping-, slug-test-, and laboratory-scale data to determine statistics for hydraulic conductivity at each of these scales. Pumping-scale tests provide the most appropriate information for use in large-scale modeling, because they provide results representative of the greatest aquifer volume and are more likely to reflect high hydraulic conductivity structure in tested formations. Slug-test-scale and laboratory-scale tests provide less representative information, because they test smaller volumes of the formation and are more affected by local variability and effects related to drilling, construction, and test methods.

Figure 5-11 shows the results of the lognormality test for the Yucca Flat/Climax Mine LCA pumping-scale tests. The data span over five orders of magnitude. This range reflects variation in the formation, with larger values reflecting more fractured or faulted material and the lower end of the range representing the country-rock permeability.

5.2.5.2 Aquifer Storage Data

The storage coefficient (S) is defined as the volume of water that an aquifer releases from or takes into storage per unit surface area of the aquifer per unit change in head (Freeze and Cherry, 1979). It is a dimensionless variable that is generally smaller than 0.005 in confined aquifers. It is called the specific yield in unconfined aquifers. It is a measure of the drainable porosity and is typically less

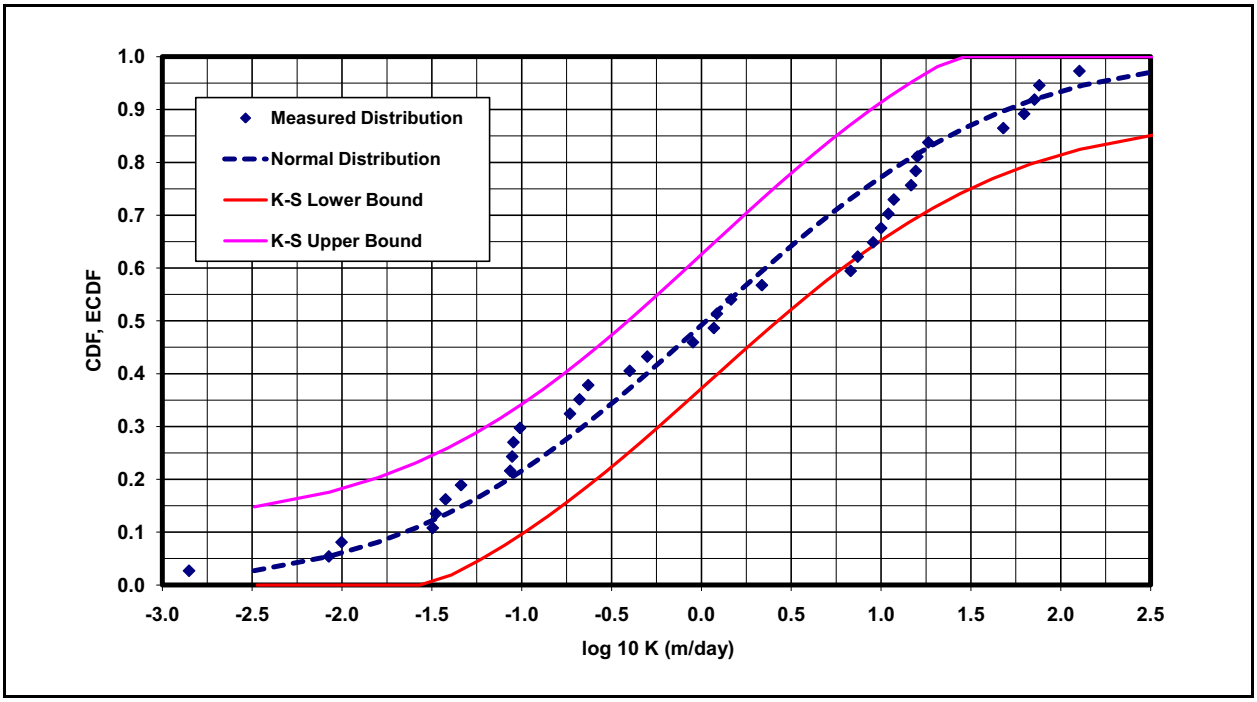

Figure 5-11
LCA Pumping-Scale Hydraulic Conductivity Probability Distribution for the Yucca Flat/Climax Mine CAU Dataset
Source: SNJV, 2006b

than 0.30. Specific storage (S_s) is the amount of water that an aquifer releases from or takes into storage per unit volume per unit decline in head. It is calculated by dividing the storage coefficient by the saturated thickness.

Figure 5-12 shows the distributions of the specific storage data in the Yucca Flat/Climax Mine CAU for various HSUs. The specific storage probability distribution for all data spans nearly nine orders of magnitude. The specific storage values that are greater than 1.0E-03 m^{-1} are, however, suspect because the associated storage coefficients would require excessively high porosity. These very high specific storage values are for the LCA from a location where the LCA is shallow and weathered and may have been dewatered during testing, in which case they actually represent the specific yield. It is unlikely that these data represent the conditions in the LCA for the central portion of the Yucca Flat/Climax Mine CAU because the LCA is deeply buried. When these values are ignored, the data span five orders of magnitude centered on approximately 5.0E-06 m^{-1}.

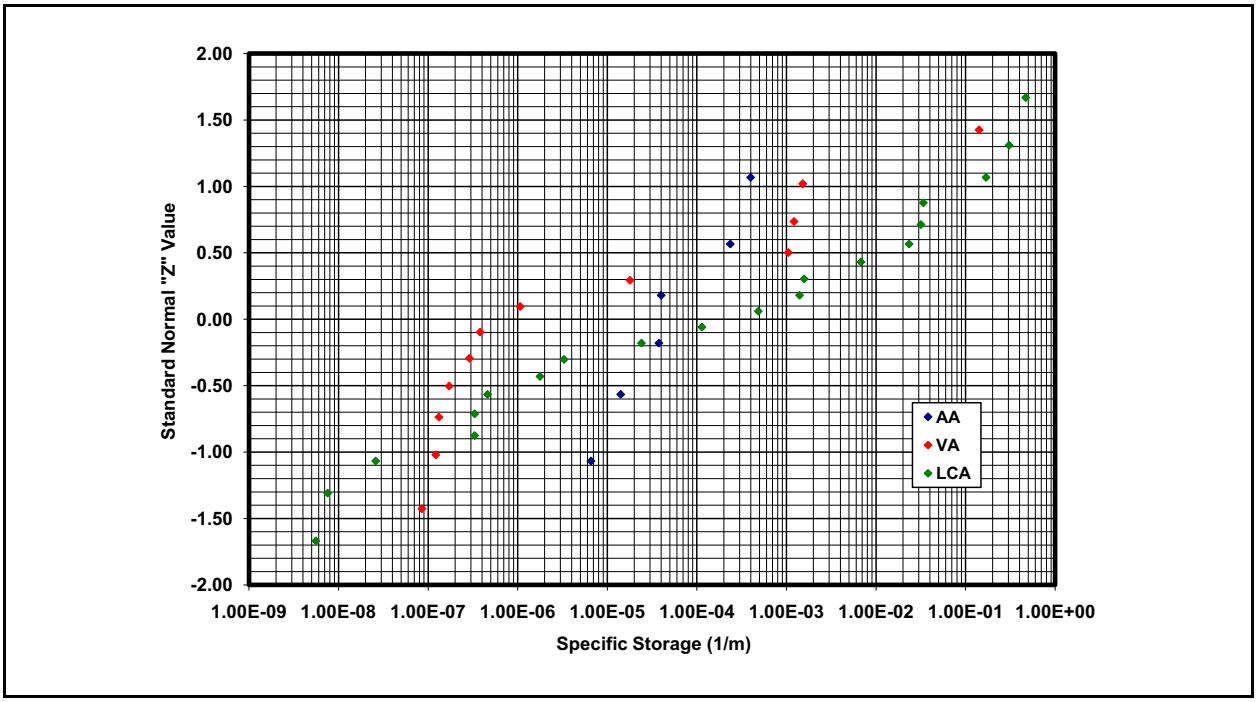

Figure 5-12
Specific Storage Data for the Yucca Flat/Climax Mine CAU Dataset
Source: SNJV, 2006b

5.2.5.3 Horizontal Anisotropy

Horizontal anisotropy is described as the ratio of the maximum to minimum hydraulic conductivity. It is a function of preferential orientation of some features that affect hydraulic conductivity. At the NNSS, this may be the orientation of large-scale fracturing and faults. The horizontal plane of anisotropy is usually closely aligned with the structural dip or bedding-plane dip of the formation.

Horizontal anisotropy can be determined at a scale appropriate for use in modeling from pumping-scale tests. The determination of horizontal anisotropy, however, requires data from multiple observation wells completed in the same depth interval as the pumping well during aquifer testing. Such data do not exist for the Yucca Flat/Climax Mine CAU. However, given the north–south trend of the faults, it would be reasonable to expect that north–south hydraulic conductivity (K_{n-s}) is greater than east–west hydraulic conductivity (K_{e-w}).

5.2.5.4 Vertical Anisotropy

Vertical anisotropy is defined as the ratio of vertical to horizontal hydraulic conductivity. The variability in hydraulic conductivity associated with vertical lithologic variations within a formation

is likely to cause hydraulic conductivity parallel to bedding to be higher than the hydraulic conductivity across the beds.

Vertical anisotropy can be determined from analysis of pumping tests with observation wells set at depths that differ from the pumped well. However, such analyses are difficult and uncertain, because the tests are affected by other factors that are poorly constrained. There are no analyses of pumping-scale tests in the Yucca Flat/Climax Mine CAU that provide vertical anisotropy information.

5.2.6 Groundwater Chemistry

5.2.6.1 Geochemical Modeling

As discussed in the Yucca Flat/Climax Mine HDD (SNJV, 2006b), groundwater chemistry data can be considered during evaluation of the groundwater flow system, because they provide a means for determining the origin, flow paths, and timescale of groundwater flow that is independent of estimates based on hydraulic flow analysis. Geochemical and hydraulic data reflect distinct but complementary aspects of a groundwater flow system and are considered in unison to develop a consistent, comprehensive, and defensible flow system.

Conceptual flow models were developed on the basis of observed hydraulic head relationships and broad distinctions in the geochemical character of groundwater in particular areas of the Yucca Flat basin. The flow paths evaluated during this investigation and the specific wells modeled for each flow path are illustrated in Figure 5-13. Five generalized conceptual groundwater flow paths through Yucca Flat in the LCA were evaluated: (1) groundwater moving from northern to southern Yucca Flat along the eastern side of the central fault structures (the eastern flow path), (2) groundwater entering Yucca Flat along the southeastern boundary and moving through southern Yucca Flat to Frenchman Flat (the southeastern flow path), (3) groundwater moving from north to south along the western side of Yucca Flat (the western flow path), (4) groundwater in west-central Yucca Flat (the west-central flow path), and (5) groundwater in northern Yucca Flat (the northern flow path).

Geochemical inverse models created with the NETPATH and PHREEQC software were used to identify the fractions of groundwater from different upgradient areas that could be present in groundwater at a downgradient location, taking into account mixing processes as well as water–rock

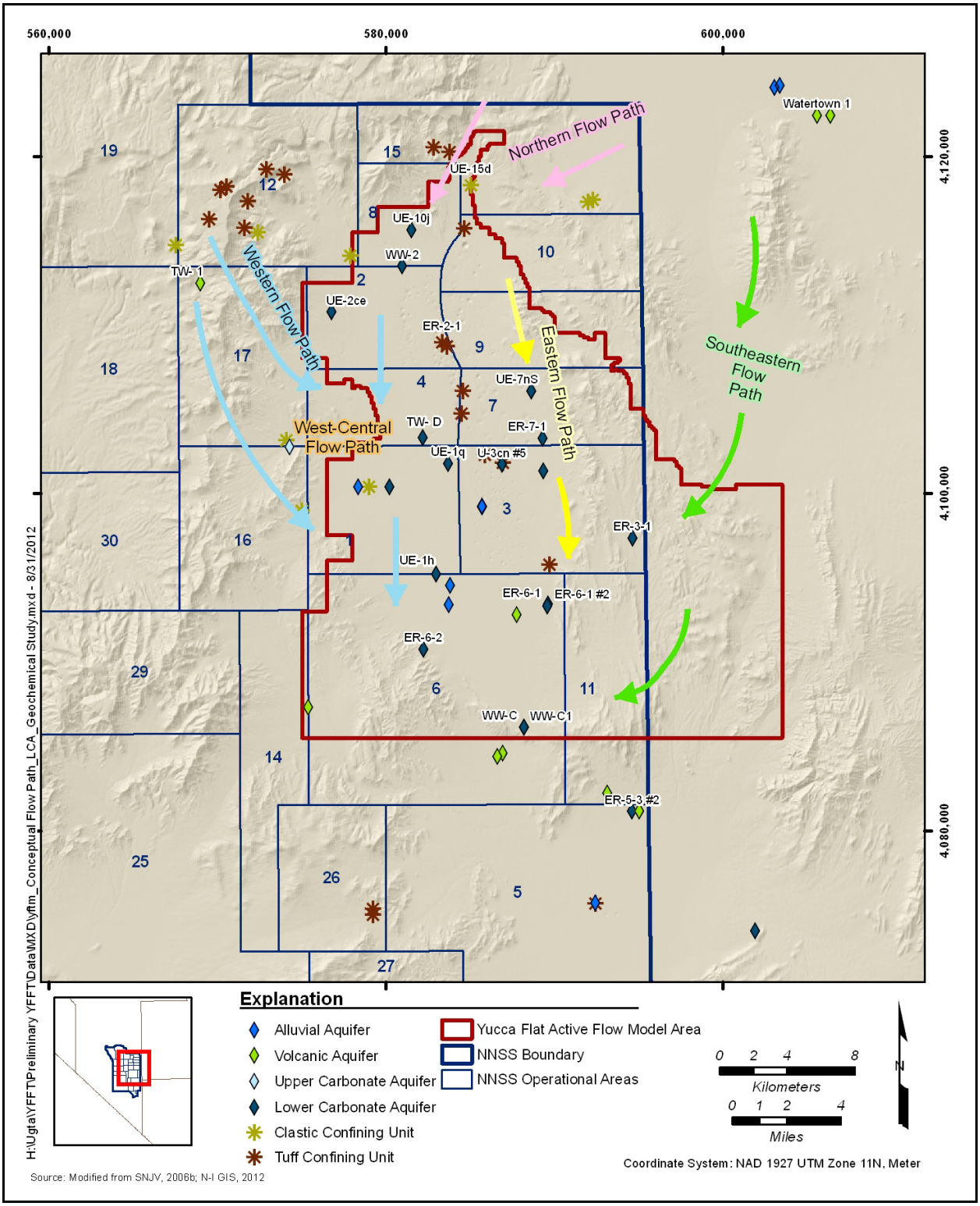

Figure 5-13
Conceptual LCA Flow Paths Evaluated in the Yucca Flat/Climax Mine CAU Geochemical Study

reactions that occur along the groundwater flow path. Groundwater flow estimates for each of the five conceptual flow paths are provided in the Yucca Flat/Climax Mine HDD (SNJV, 2006b) and are discussed below. As discussed in Appendix L, the interpretation of LCA groundwater velocity estimates derived from ^{14}C ages is uncertain because of the uncertainty in possible water-rock interactions that could result in an effective retardation of ^{14}C relative to other non-sorbing species. The velocity estimates summarized below assume ^{14}C is not sorbed, resulting in a potential underestimation of groundwater velocities.

Eastern Flow Path

Geochemical modeling indicated that if groundwater does flow from wells Watertown 1 WW to ER-7-1 beneath the Halfpint Range, groundwater velocities over the 25-km distance between these wells average between 3.2 and 4.2 m/yr. Similarly, the range of travel times of about 5,400 to 7,800 years estimated for flow between Wells UE-10j and ER-7-1 results in a groundwater velocity of 1.9 to 2.7 m/yr over the 15-km distance between these wells. Models for ER-6-1-2 estimated composite travel times of approximately 5,800 to 7,300 years over the 10-km distance between ER-7-1 and ER-6-1-2. These travel times result in a groundwater velocity in the LCA of between 1.4 and 1.7 m/yr between ER-7-1 and ER-6-1-2.

Overall, the relatively long transit times for flow in the LCA are attributed to the extremely small inflow of groundwater into the basin from the north, rather than low hydraulic conductivity in the highly faulted LCA.

Southeastern Flow Path

Three wells in southeastern Yucca Flat and northeastern Frenchman Flat (ER-3-1, WW C, and WWC-1) that produce LCA groundwater with a distinct set of geochemical characteristics were used in the analysis. The estimated groundwater travel times of approximately 16,000 to 24,000 years from UE-10j in northern Yucca Flat to WW C in southern Yucca Flat result in calculated groundwater velocities of approximately 1.3 to 1.9 m/yr over the 30-km distance between these wells.

There is some evidence that groundwater from east of Yucca Flat, characterized by groundwater from ER-3-1, becomes a prominent part of the groundwater system in the southernmost part of the Yucca Flat basin near WW C. Groundwater with the chemical and isotopic composition of ER-3-1 is prevented from entering the Yucca Flat basin farther to the north by the blocking effects of the LCCU,

but it sweeps southwestward into the basin toward the southern end of the Halfpint Range where the LCCU is absent. Groundwater flow from ER-3-1 to WW C in the southeastern part of Yucca Flat appears to preclude the possibility of groundwater leaving Yucca Flat by flowing to the southeast. The geochemical modeling indicates the possibility of relatively rapid flow from the vicinity of ER-3-1 to WW C. Travel times from ER-3-1 to WW C were estimated to be on the order of 1,000 to 3,000 years, resulting in groundwater flow velocities of 4.3 to 13 m/yr. The possibly rapid flow of groundwater from east of the basin into the southeastern part of Yucca Flat is consistent with the absence of the LCCU in the southeast portion of the basin and the relatively stagnant flow conditions in the upper portions of the Yucca Flat basin.

Western Flow Path

The geochemical evaluation of western Yucca Flat groundwater focused on developing models for three wells (UE-2ce, UE-1h, and ER-6-2). Because of extreme variability of geochemical signature in each of these wells, it was not possible to estimate the groundwater travel times and velocities in the western flow path. In general, however, models indicate that groundwater in western Yucca Flat may be derived predominantly from underflow through the LCA in northern Yucca Flat (represented by groundwater from UE-10j) and local recharge from the north and west of Yucca Flat. Models suggest that there may be additional contributions by groundwater flow from upper Fortymile Wash, which is located farther west outside the Yucca Flat CAU area.

Well UE-2ce was modeled as a mixture of local recharge and groundwater from northern Yucca Flat. Conservative tracers and PHREEQC models were in general agreement that local recharge was a significant component (up to 80 percent) of LCA groundwater at UE-2ce. The large component of local recharge estimated to exist in the LCA groundwater at UE-2ce could indicate that this well is located in a structurally isolated block of the LCA with limited regional LCA inflow, or it could reflect the relatively large recharge rates estimated for the high elevation areas at nearby Rainier Mesa.

Relative to other LCA groundwater in the rest of Yucca Flat, LCA water at UE-1h in western Yucca Flat has a distinct geochemical signature. Geochemical models for UE-1h were uncertain. Geochemical analysis indicates the water sources to be groundwater leakage from the west through the UCCU and vertical leakage from the tuff confining units. Meaningful groundwater travel times to

UE-1h could not be calculated because of problems with the ^{14}C data from UE-1h and because the actual mixing end members could not be identified.

Water at ER-6-2 appears to be chemically similar to other Yucca Flat LCA groundwater. Several of the geochemical models were in relatively good agreement that groundwater at ER-6-2 can be produced by mixing waters from the LCA in northern Yucca Flat, local paleoclimatic recharge groundwater like HTH 1 (TW- 1), and UCCU groundwater. Composite groundwater travel times for this mixture average about 15,000 years.

West-Central Flow Path

Geochemical modeling indicates that groundwater in the LCA at TW D and UE-1q did not originate primarily by flow through the LCA from the north. Alternative groundwater paths include vertical recharge through or around gaps in the tuff confining units created by faulting and easterly flow through the Eleana formation in western Yucca Flat. Strontium data support the presence of a component of groundwater from the UCCU in the western part the basin at UE-1q. Both TW D and UE-1q appear to contain a dominant mixing fraction derived from the volcanic HSUs, with a maximum LCA component of approximately 18 percent at TW D and approximately 35 percent at UE-1q. The relatively low amounts of LCA groundwater in TW D and UE-1q could reflect the relatively low rates of LCA inflow into the basin relative to local recharge, possibly coupled with the hydraulic isolation of the LCA block containing TW D and UE-1q from the regional LCA by block-bounding faults.

Northern Flow Path

The geochemical evaluation of groundwater in northern Yucca Flat groundwater focused on developing models for three wells (UE-10j, HTH-2 [WW-2], and UE-15d WW). In general, all models indicate that the shallower portions of UE-10j contain a dominant component of local recharge (between 70 and 80 percent) that has mixed with a much smaller percentage of groundwater inflow through the LCA. Models for HTH-2 (WW-2) suggest that only 4 percent or less of the groundwater at HTH-2 (WW-2) is derived from inflow through the LCA, with water principally derived from the mixing of volcanic and local perched water sources in northern Yucca Flat. A large component of local recharge for both UE-10j and HTH-2 (WW-2) is indicated by a large rise in water

levels beginning in late 2005 (USGS, 2006), which most likely resulted from the significant rainfall during the winter of 2004 to 2005.

Geochemical models were also developed to determine the source of water at UE-15d WW. The modeling results indicated that no more than 1 or 2 percent of Climax stock water is present at UE-15d WW. A significant proportion (37 to 74 percent) of water has a geochemical signature similar to that at Watertown 1 WW in Emigrant Valley. Smaller contributions of local recharge and water from the LCA west of the site were estimated at the site.

5.2.6.2 Carbon-Dating Analysis

In addition to estimating groundwater velocities using geochemical data as discussed above, LANL also estimated groundwater age using ^{14}C data (Kwicklis, 2010). (Additional details of the analysis and interpretation of ^{14}C data for the LCA at Yucca Flat are presented in Appendix L.) The estimated ages at various LCA wells are presented in Figure 5-14. The salient features of the age map are the presence of young water in the center of the basin, the relative similarity in age between the waters at ER-3-1 and WW C, and an age difference of approximately 15,000 years between waters in the northern and southern ends of the study area. The younger water in the center of the basin may likely be accounted for by rapid infiltration of groundwater via faults from the overlying volcanics in the center of the basin. The age difference of approximately 15,000 years in waters in the northern and southern ends of the study area is similar to the age difference estimated by geochemical modeling as discussed in Section 5.2.6.1.

The uncertainty in the use of groundwater ages derived from ^{14}C observations to assist in evaluating the reasonableness of groundwater velocities in the LCA in central Yucca Flat is analyzed in Appendix L. The analyses presented in Appendix L used two different methods to correct the measured ^{14}C activities, one based on the downgradient changes in the total dissolved inorganic carbon, and the other based on changes in the $\delta^{13}C$ relative to the estimated groundwater recharge. Although these correction methods account for the bulk dissolution of carbonate minerals and potential isotope exchange, there is still the potential for $H^{14}CO_3^-$ sorption onto the carbonate matrix or calcite fracture surfaces. If this sorption occurs, it would result in estimates of groundwater velocities that are too low. Although the analyses presented in Appendix L support the assumption that $H^{14}CO_3^-$ is not significantly sorbed, assuming such sorption does occur results in a conservative overestimation of effective transport velocities. For example, using the comparative analyses of the

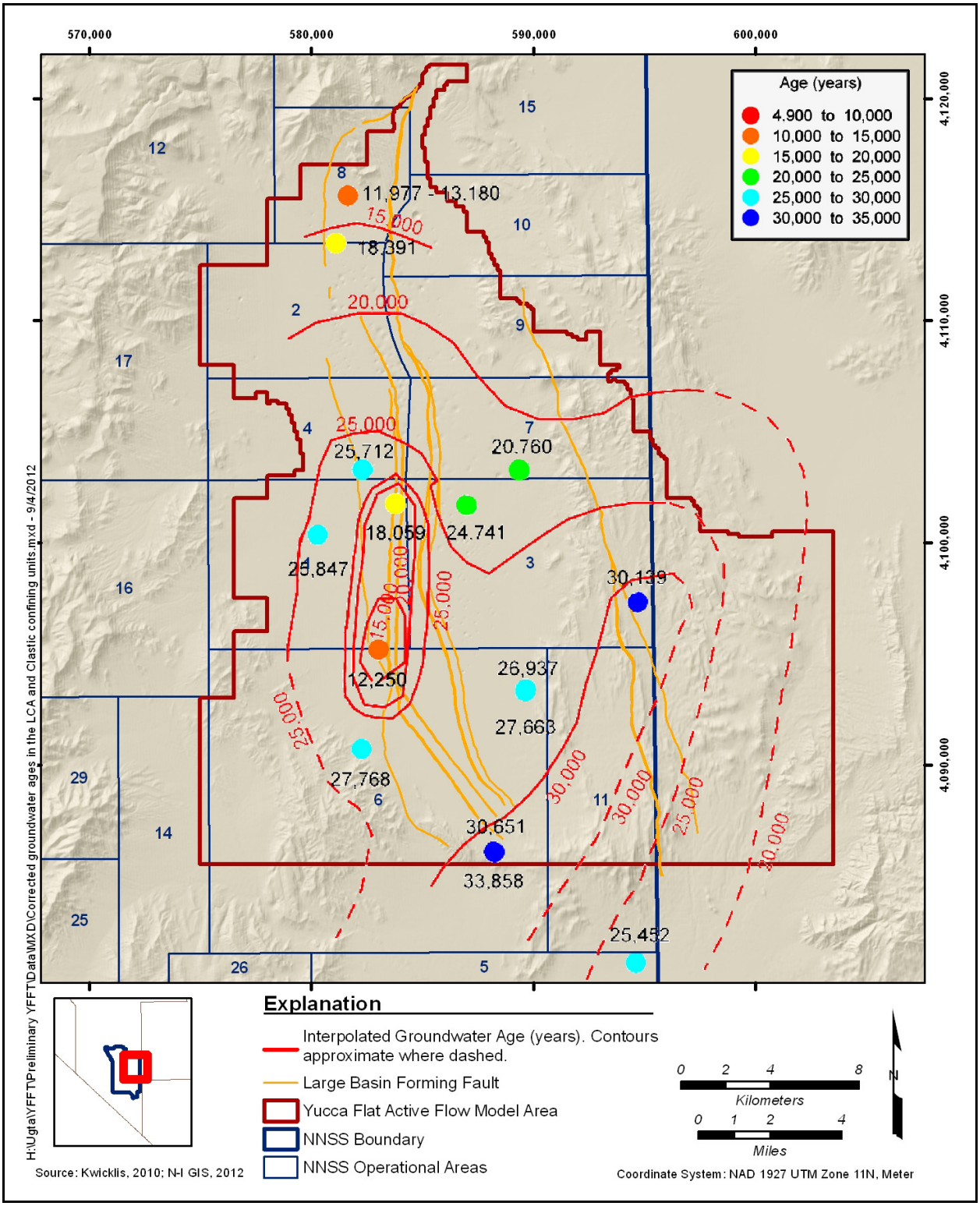

Figure 5-14
Estimated LCA Retarded Groundwater Ages Using ^{14}C Data

Devils Hole age dates that indicate a potential retardation of about a factor of 10 would result in an increase in the groundwater velocities by a factor of 10. Therefore, instead of the velocity range of 1 to 2 m/yr indicated above, the average velocity would be on the order of 10 to 20 m/yr. Given it is conservative to not underestimate the groundwater velocity, the flow model comparison assumes the velocities estimated from ^{14}C age dating are considered to represent retarded age dates and the unretarded age dates are reduced and velocity estimates increased.

5.2.6.3 Geochemical Analysis

Geochemical analysis of groundwater in the LCA was also conducted by Schoff and Moore (1964). They identified three types of groundwater at the NNSS and vicinity: (1) sodium and potassium bicarbonate, (2) calcium and magnesium bicarbonate, and (3) mixed. The sodium and potassium bicarbonate type is found in tuff aquifers and aquitards and in the valley-fill aquifers in Yucca Flat. The calcium and magnesium bicarbonate type is primarily found in Paleozoic carbonate aquifers. The groundwater chemistry and geochemical facies at the NNSS are presented in Figure 5-15. Based on the geochemical analysis of groundwater in the LCA, Schoff and Moore (1964) concluded that the water in the LCA is in part recharged by percolation downward either through tuff or through alluvium containing detrital tuff or both and that the water entering the carbonate rocks in this manner is generally a sodium-potassium type that, when added to the calcium-magnesium type already in the rocks, yields a water of mixed chemical character.

Winograd and Thordarson (1975) also recognized the unique geochemical signature of groundwater in the LCA at the NNSS and attributed it to recharge from the overlying tuff and alluvium units. They concluded that groundwater within the LCA beneath the NNSS and at Ash Meadows differs significantly from water in the LCA elsewhere in the study area and that the principal difference is in the milliequivalents per liter of sodium plus potassium and of sulfate plus chloride. Their study found that the principal source of sodium ions within the LCA beneath the NNSS is groundwater that originated in or passed through the Tertiary tuff aquifers and aquitards and that, in areas of downward cross flow beneath the NNSS, solution of the gypsum in the basal Tertiary strata adds important quantities of sulfate to water in the LCA.

It should be noted that evaluations of geochemical flow paths depend on sufficient data coverage, both laterally and vertically, within the study region. The wells with the parameter suite necessary to support analysis and characterization of geochemical flow paths are sparse and irregularly distributed

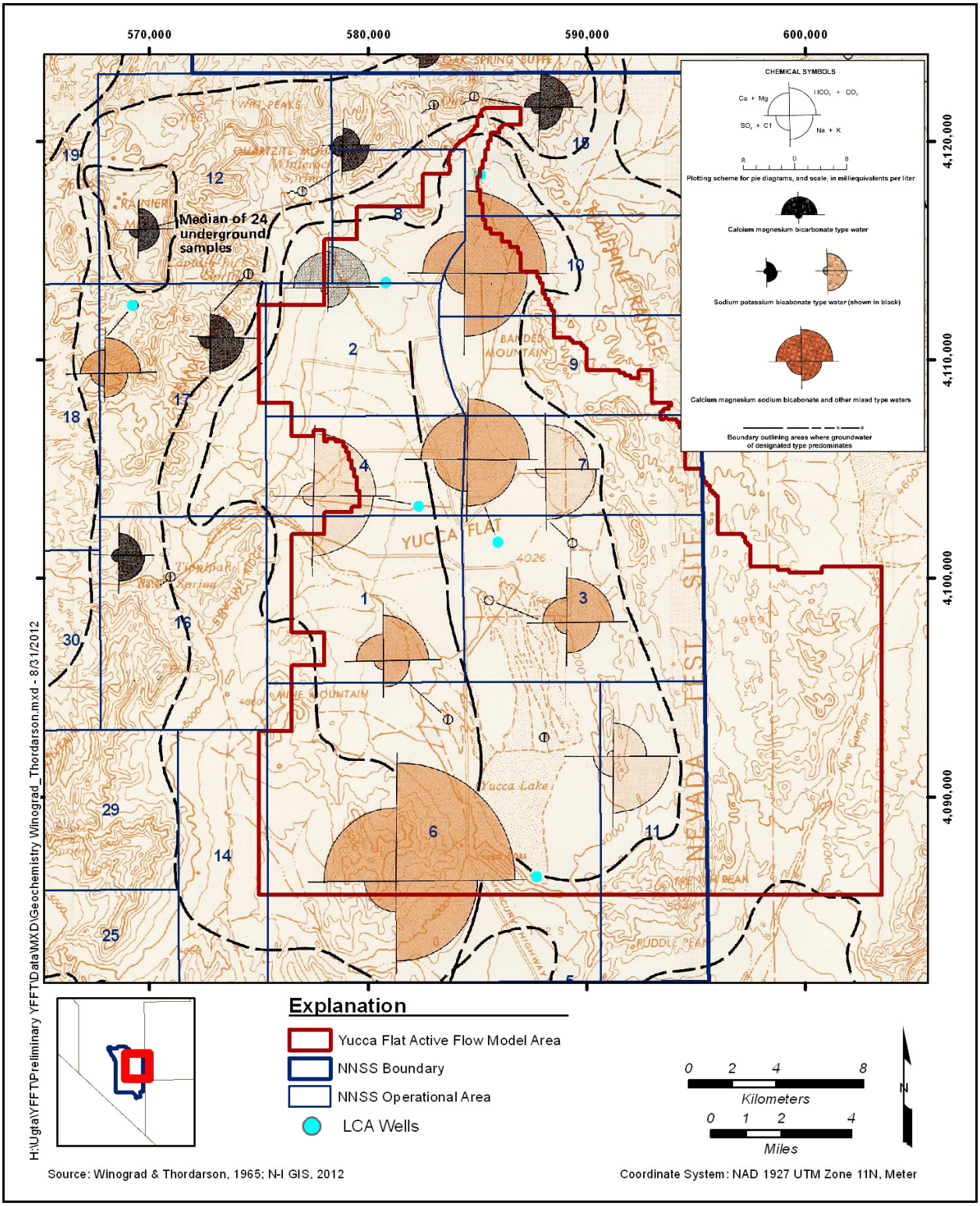

Figure 5-15
Groundwater Chemistry and Geochemical Facies at Yucca Flat

in the Yucca Flat/Climax Mine CAU. The geochemical reactions modeled are also limited by the availability of data that can be used to identify the minerals and gases that are present in the aquifer and the chemical compositions of groundwater along potential flow paths.

5.2.7 Groundwater Temperatures

The water table at Yucca Flat is approximately 450 m bls. There are no firm estimates of recharge to the water table or cross-boundary fluxes entering Yucca Flat. Estimates of water flowing through Yucca Flat vary widely from 13.7 kg/s (Winograd and Thordarson, 1975) to 1,024 kg/s (Pohlmann et al., 2007). Such a wide range of fluxes makes it difficult to use these estimates to corroborate model calibration results. It is well known that subsurface temperatures in the saturated zone can be used as a tracer of the groundwater flow regime (Bravo et al., 2002; Anderson, 2005) because groundwater flow alters the geothermal distribution that would exist solely because of heat conduction. Therefore, analyses were performed to determine whether the subsurface temperatures could potentially assist in identifying flow paths and quantities in the subsurface.

The temperature data within the saturated zone were collected at various locations in Yucca Flat by USGS (Reiner, 2007). The temperature distribution at the water table is presented in Figure 5-16, from which the following can be inferred:

- There is a cold trough in the center of the basin coinciding with the three major faults: Yucca, Topgallant, and Carpetbag faults. The center of the basin also corresponds to the area of the thick, insulating volcanic and alluvial materials, which would be expected to increase the temperature at depth, not decrease it as observed.
- The subsurface temperatures in the east are relatively high.
- No major temperature anomalies appear in the west and north, and therefore, heat transfer in these regions can, to a large degree, be explained by the process of heat conduction.

Based on the above observations, the following geothermal conceptualization was developed. Water from precipitation reaching the saturated volcanic units migrates laterally toward the major faults in the center of the basin. On reaching the faults, the cooler groundwater derived from the surface rapidly infiltrates into the LCA. This cooler groundwater captures heat deep in the subsurface and eventually transports heat out of Yucca Flat basin. This results in reduced temperature in the vicinity of the major faults (Figure 5-16). It is interesting to note that this conceptualization is similar to the one discussed in Section 5.2.6, in which it was hypothesized that the source of younger LCA

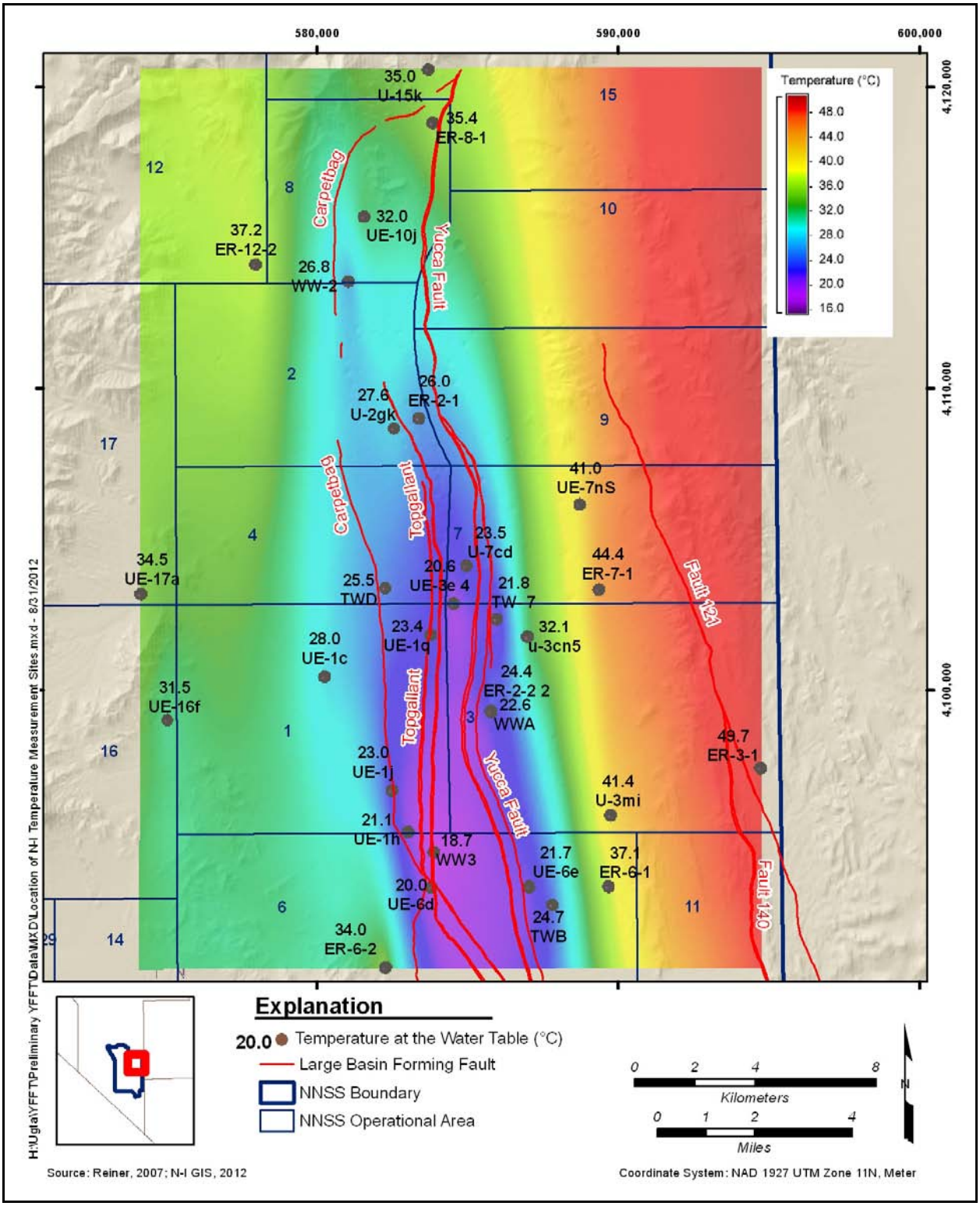

Figure 5-16
Temperature Distribution at the Water Table in Yucca Flat

water in the center of the basin is a consequence of groundwater from the volcanics moving rapidly into the LCA via faults in the center of the basin. The thermal data were used to estimate rates of LCA groundwater underflow and infiltration rates in Yucca Flat (Appendix H).

Following initial review of the thermal data in the saturated zone and recognizing the potential for subsurface temperatures to constrain groundwater model fluxes at Yucca Flat, additional thermal data were collected (NNES, 2010c). The goals of the additional data collection were to augment existing subsurface temperature data and to determine whether thermal data in the shallow unsaturated zone could be used to estimate groundwater flow rates deep in the saturated zone.

Combining the data from NNES (2010c) with the data presented in Reiner (2007) enabled construction of temperature profiles at various elevations above and below the water table (Figure 5-17). This figure is developed by using the available temperature data at the discrete depths (i.e., 17 data points at 450 m (1,500 ft) bls) and kriging the temperatures at these discrete locations using a north-south anisotropy. As shown in Figure 5-17, the same thermal distribution observed at the water table (located approximately 450 m (1,500 ft) bls) is present in both the shallow unsaturated zone and the saturated zone deep below the water table. This information not only has the potential for constraining model boundary fluxes but also strongly suggests the feasibility and viability of calibrating models in the deep saturated zone using shallow unsaturated-zone temperature data. The latter proposition has a significant cost-saving implication because shallow unsaturated-zone temperature data can be acquired for a small fraction of the cost required to obtain temperature data from deep (saturated-zone) monitoring wells.

5.2.8 LCA Flow Model Conceptualization

Based on available site-specific hydrogeologic, geochemical, and temperature data, in conjunction with regional information from areas outside the Yucca Flat/Climax Mine CAU, the following general conceptualization of groundwater flow in the LCA at Yucca Flat is developed:

- Recharge to the LCA in the Yucca Flat area occurs in the form of percolation through the overlying unsaturated-zone HSUs and drainage from the overlying saturated volcanic units.
- Lateral inflow to the LCA at Yucca Flat is the result of groundwater base flow along the northern, western, and eastern boundaries of the Yucca Flat area.

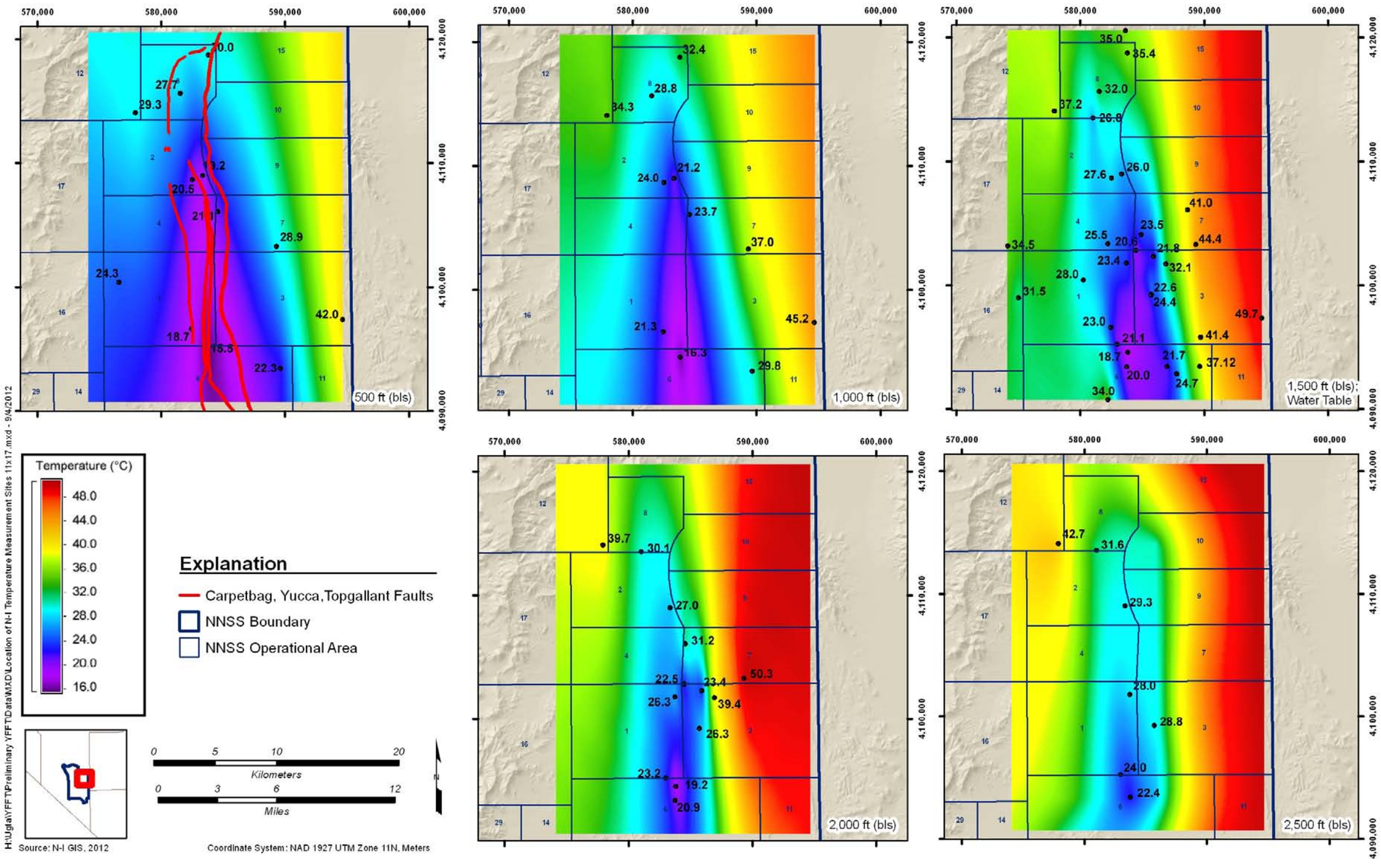

Figure 5-17
Temperature Distribution in Yucca Flat at Various Elevations

- Groundwater flow in the LCA is toward major faults in the center of the Yucca Flat basin and southward toward the Frenchman and CP basins.
- Groundwater flow is controlled to a large extent by high-permeability zones within the faults. The faults act as conduits for flow along the plane of the fault and provide a barrier to flow across the fault plane.
- The LCA heads in the eastern portion of the Yucca Flat basin are approximately 10 m lower than heads in the western portion of the basin in the central and southern parts of the basin.
- Water levels in the LCA have been fairly stable for the last two decades. Therefore, the groundwater flow system can be assumed to be in a state of quasi equilibrium for purposes of establishing the 1,000-year contaminant boundary.

This general conceptual model of groundwater flow in the LCA at Yucca Flat is consistent with the conceptual description developed by Winograd and Thordarson (1975) more than 35 years ago.

5.3 Previous Modeling Studies

As discussed in Section 1.0, implementation of the FFACO (1996, as amended) corrective action strategy requires the development of a representative CAU-scale groundwater flow and transport model. The development of a reliable model involves incorporating a number of interdependent models pertaining to geology, recharge, and hydrogeologic conceptualization at both the regional and CAU scales. The regional models provide the broad hydrogeologic context and data for the smaller CAU-scale models. The CAU-scale models incorporate (1) a local hydrostratigraphic framework that influences groundwater flow, (2) refined meshing in areas of interest in order to more accurately simulate the local flow field, and (3) alternative models that address site-scale uncertainty pertaining to hydrostratigraphy, boundary fluxes, heads, and recharge.

Over the past decade, regional models have been constructed by USGS, DRI, and SNJV. USGS and DRI completed their models in 2004 and 2007, respectively. DRI updated its model in 2012 to evaluate the effects of boundary condition uncertainty on the range of possible groundwater flow rates into northern Yucca Flat. Similarly, USGS has updated the 2004 DVRFS model to evaluate the effect of additional structural uncertainty. Summary descriptions of the all groundwater flow models (original and recently revised) are presented below in chronological order as follows:

- USGS 2004 DVRFS model
- SNJV 2006 Yucca Flat/Climax Mine CAU groundwater flow model

- DRI 2007 Climax Mine flow model
- DRI 2012 Climax Mine flow model
- USGS 2012 DVRFS model

5.3.1 USGS 2004 DVRFS Model

The DVRFS model (Belcher et al., 2004) was developed by USGS as an integrated regional modeling analysis tool in support of NNSA/NSO investigations at the NNSS and Yucca Mountain. The DVRFS model was developed by utilizing two previous regional-scale models and incorporating field data obtained since completion of the previous models. The two previous models are the UGTA regional flow model (DOE/NV, 1997a), which was developed to estimate potential for radionuclide transport from underground nuclear detonation sites on the NNSS, and the Yucca Mountain Project/Hydrologic Resource Management Program model (D'Agnese et al., 1997), which was developed to evaluate the groundwater flow field in the vicinity of Yucca Mountain.

The 2004 DVRFS model integrates a three-dimensional HFM and a three-dimensional groundwater flow model. The model incorporates regional geologic data and information (stratigraphy and structure) that capture the spatial geologic complexities within the model boundary. Twenty-seven HGUs are defined and incorporated into this model. Structural features that affect groundwater flow, such as faults, also were included in the model. The model represents Precambrian and Paleozoic crystalline and sedimentary rocks, Mesozoic sedimentary rocks, Mesozoic to Cenozoic intrusive rocks, Cenozoic volcanic tuffs and lavas, and late Cenozoic sedimentary deposits. The areal extent of the DVRFS model is presented in Figure 5-18. The Yucca Flat model domain lies in the eastern part of the DVRFS model domain as shown in Figure 5-18.

An apparent anomaly in the simulated 2004 DVRFS model steady-state flow field is the north-to-south flow field in Yucca Flat. This is in contradiction with the observed head data presented in Figure 5-8, which indicate that heads in the eastern part of the basin are approximately 10 m lower than heads in the west. The simulated LCA head residuals in Yucca Flat range from –30 to 7 m (Figure 5-19). This range is deemed fairly high for a groundwater system where the maximum difference in heads is less than 10 m.

The longitudinal (north–south) and lateral (east–west) steady-state flow rates simulated by the 2004 DVRFS model within the LCA (which is the primary HSU through which interbasin groundwater flow occurs) are presented in Figures 5-19 and 5-20. With the exception of local recharge within the

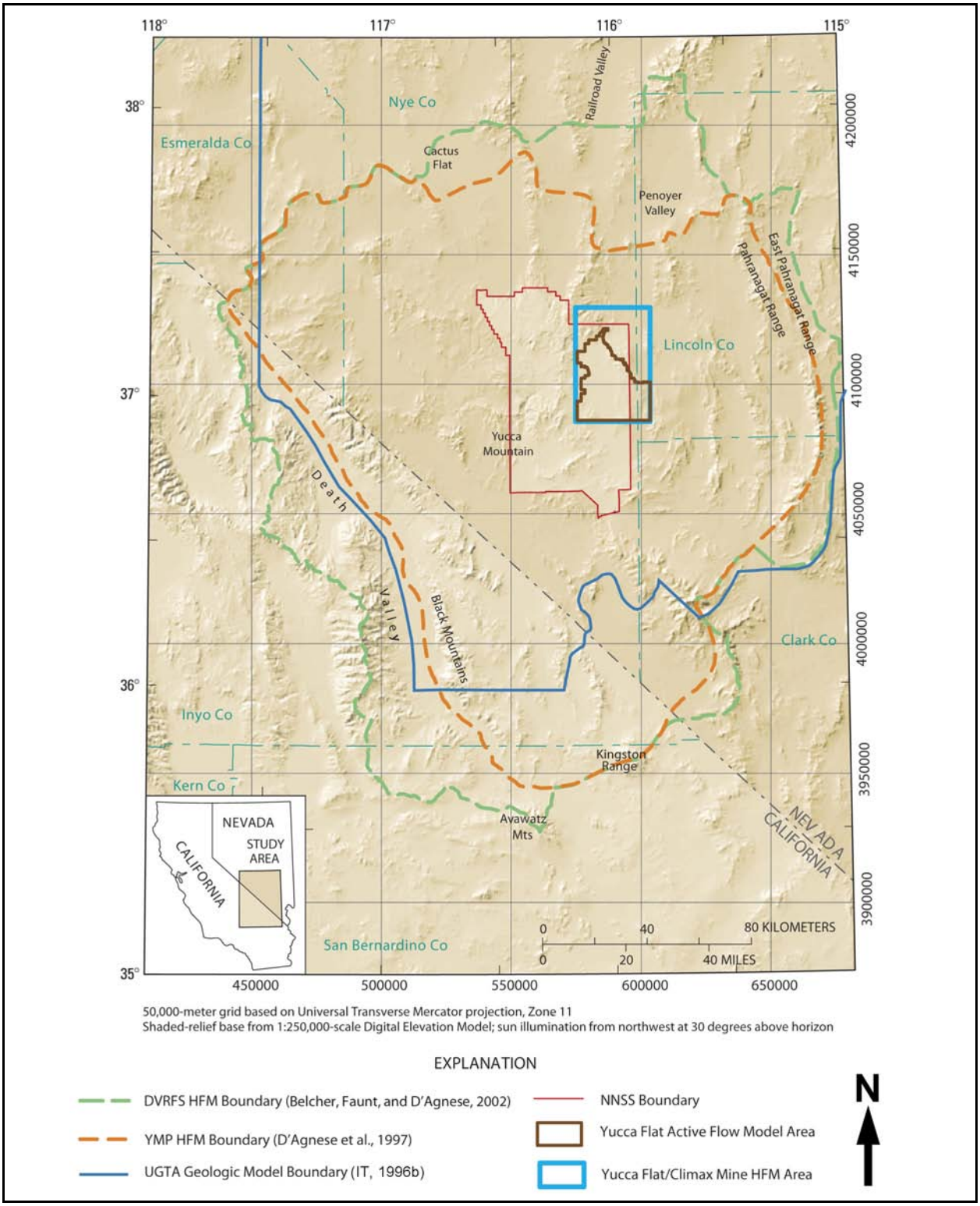

Figure 5-18
Delineations of Regional Groundwater Flow Models of the DVRFS Region
Source: Modified from Belcher et al., 2004

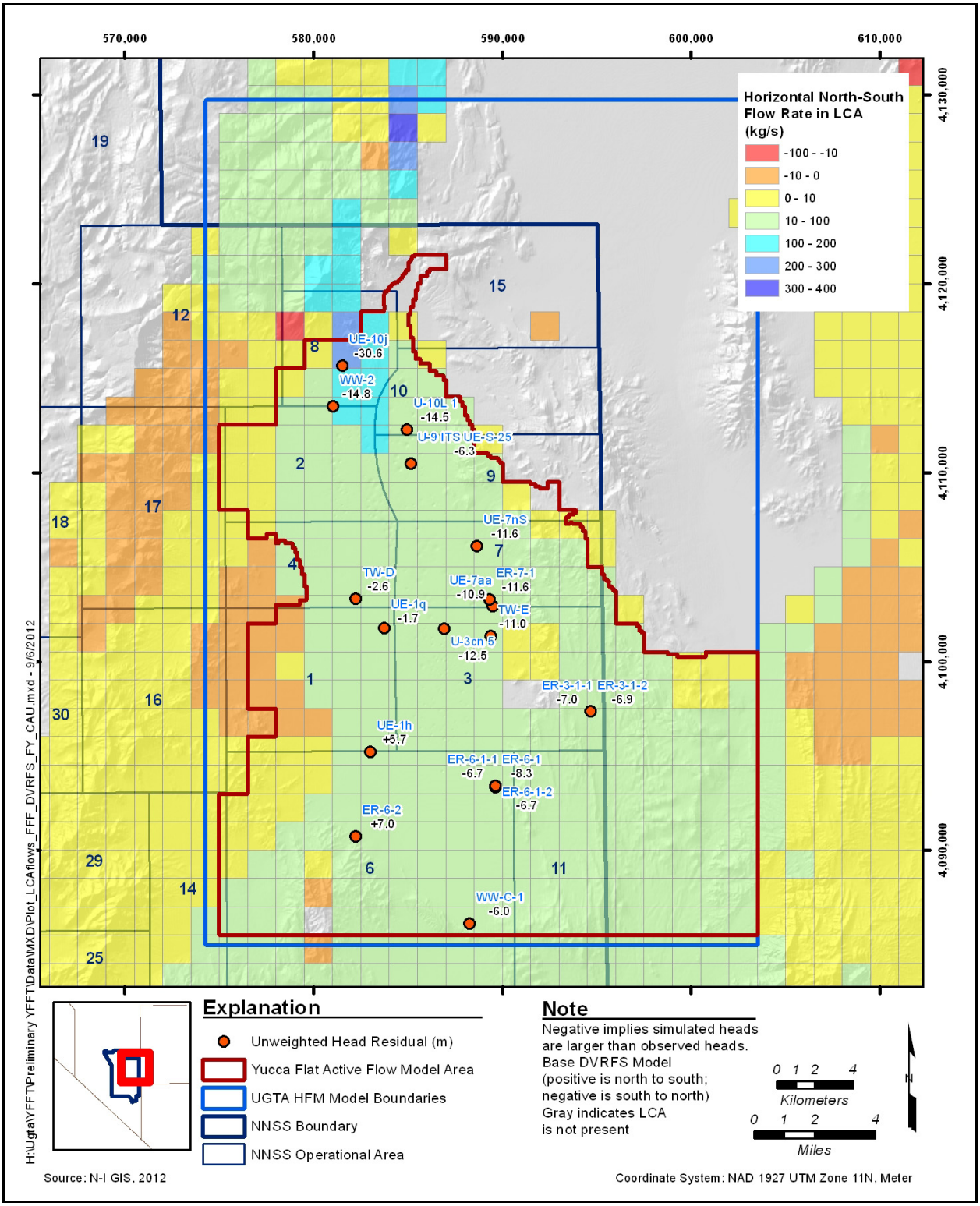

Figure 5-19
Simulated Steady-State Groundwater Flux in the LCA through the North–South Cell Face of the USGS 2004 DVRFS Model

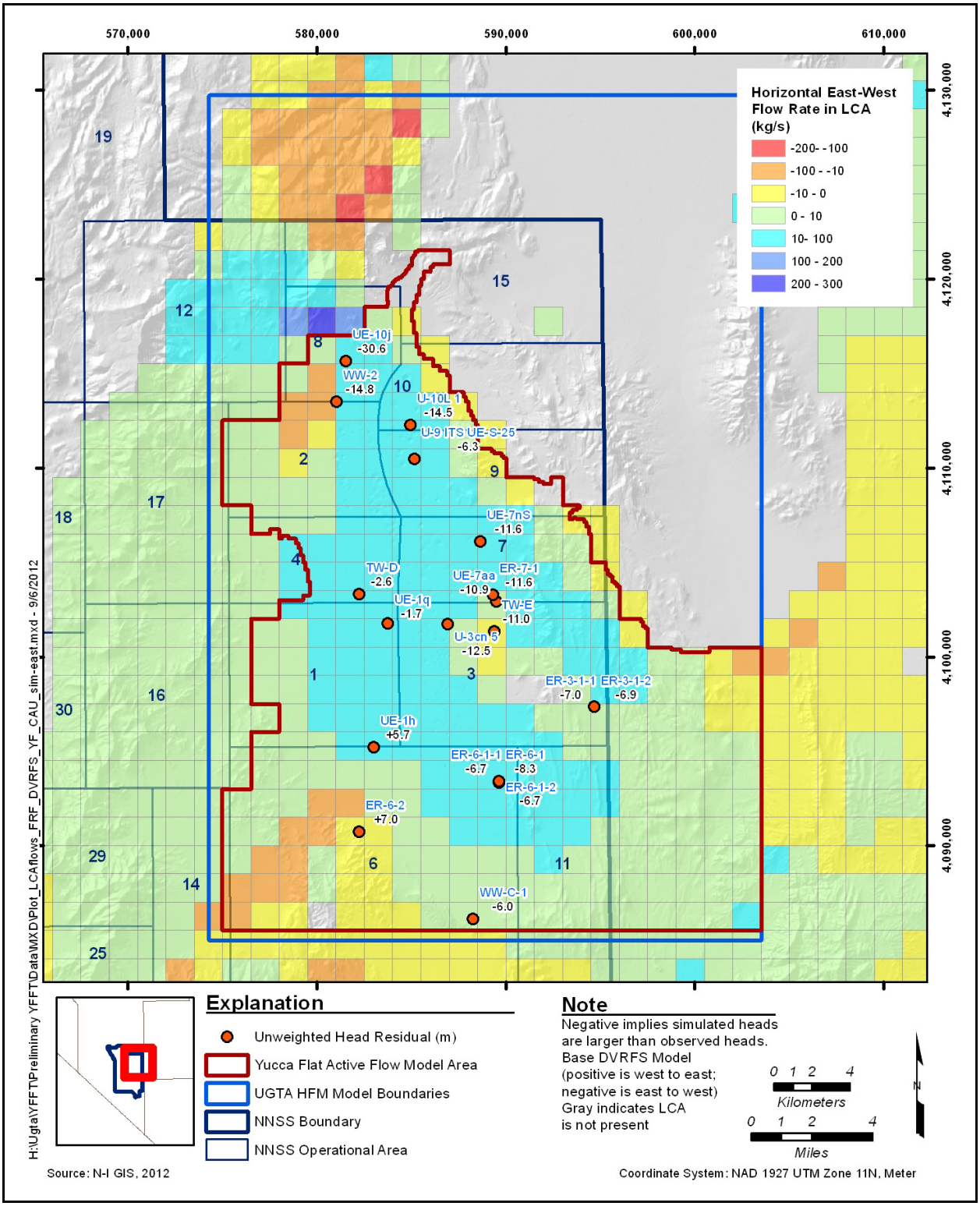

Figure 5-20
Simulated Steady-State Groundwater Flux in the LCA through the East–West Cell Face of the USGS 2004 DVRFS Model

Yucca Flat basin, the primary source of groundwater inflow into the Yucca Flat basin is inflow from the north. Approximately 48,000 cubic meters per day (m^3/day) (550 kg/s) of groundwater enters the Yucca Flat model domain from the north in the 2004 DVRFS Model. Yucca Flat lies within the Ash Meadows groundwater basin. The total discharge from the Ash Meadows basin is estimated to range between 61,000 and 71,000 m^3/day (700 and 820 kg/s) (Laczniak et al., 1999). This implies that approximately two-thirds of the discharge at Ash Meadows is modeled as groundwater entering Yucca Flat from the north. Such a large influx contrasts sharply with northern underflow estimates of less than 1 kg/s by Winograd and Thordarson (1975).

5.3.2 SNJV 2006 Yucca Flat/Climax Mine CAU Groundwater Flow Model

Inflow and outflow through the lateral boundaries of the SNJV 2006 Yucca Flat/Climax Mine CAU groundwater flow model constitute an important portion of the water budget of the flow and transport model. Using the steady-state version of the USGS 2004 DVRFS model described above, a total of 13 alternative CAU-scale flow models were developed and calibrated by SNJV in 2006 to capture the variability in the boundary fluxes resulting from differences in conceptualization of the Yucca Flat/Climax Mine CAU HFM and regional recharge distribution (SNJV, 2006b). The primary purpose of the SNJV study was to provide a range of lateral boundary fluxes that could be used as calibration guidelines for the Yucca Flat/Climax Mine CAU groundwater flow model. As discussed in the Yucca Flat/Climax Mine HDD (SNJV, 2006b), the alternative models allowed for boundary-flux calculations that encompassed the uncertainty associated with several plausible HFMs that honor site data and alternative recharge models.

The 2004 DVRFS model grid (Belcher et al., 2004) served as the base grid for all alternative HFMs. The first alternative is simply the DVRFS HFM (Belcher et al., 2004). The second alternative is referred to as the Yucca Flat/Climax Mine base HFM. This HFM was created by regridding the existing CAU-scale base HFMs for the Pahute Mesa-Oasis Valley (BN, 2002), Frenchman Flat (BN, 2005a), and Yucca Flat/Climax Mine (BN, 2006) areas, and inserting these HFMs into the corresponding DVRFS nodes in the regional model grid. Five additional alternative HFMs were developed by replacing the Yucca Flat/Climax Mine base HFM with each of the five Yucca Flat/Climax Mine CAU-specific alternative HFMs developed in BN (2006). The seven alternative HFMs developed for the Yucca Flat/Climax Mine CAU are listed in Table 5-1, along with the naming conventions used to refer to them.

Table 5-1
Naming Conventions for Alternative HFMs in the SNJV Yucca Flat/Climax Mine CAU Groundwater Flow Model

Abbreviation	Description
HDVR	DVRFS
HB	Yucca Flat/Climax Mine Base
HPZ	Yucca Flat/Climax Mine Partial Zeolitization
HCP	Yucca Flat/Climax Mine CP Thrust
HHB	Yucca Flat/Climax Mine Hydrologic Barrier
HCU	Yucca Flat/Climax Mine Contiguous UCCU
HFJ	Yucca Flat/Climax Mine Fault Juxtaposition

Source: SNJV, 2006b

In addition to uncertainty in the boundary flux conditions introduced by differences in conceptual geologic models (i.e., HFMs), the uncertainty associated with approximating recharge was considered by utilizing alternative recharge models. These alternative recharge models are based on an empirical mass-balance method and its derivatives, a deterministic distributed-parameter watershed method, a model calibration method, and a chloride mass-balance method. The alternative recharge models and the naming conventions used to refer to them are listed in Table 5-2.

Table 5-2
Naming Conventions for Alternative Recharge Models in the SNJV Yucca Flat/Climax Mine CAU Groundwater Flow Model

Abbreviation	Description
RUR	UGTA Revised
RUO	UGTA Original
RGSNO	USGS Model 1—with run-on infiltration included in recharge
RGSOF	USGS Model 2—without run-on infiltration included in recharge
RDVR	USGS Model 3—DVRFS calibrated recharge
RDRIAl	DRI Alluvial Mask
RDRIAlEl	DRI Alluvial and Elevation Mask

Source: SNJV, 2006b

Of the 49 possible alternative flow model combinations (7 recharge models and 7 HFMs), 13 combinations were selected for lateral boundary flux analyses. The selected combinations are listed in Table 5-3. The first seven combinations resulted from applying the seven alternative recharge

Table 5-3
Total Water Balance for the Alternative Flow Models of the Yucca Flat/Climax Mine CAU

Alternative Flow Model		Net Flow (m^3/day) [c]					% Difference in CAU-Specific Boundary Flux (Inflow + Recharge – Outflow)/Outflow	% Difference in DVRFS Regional Boundary Flux (Model Mass Balance Error)
Recharge Model	HFM	Northern Perimeter Boundary [a]	Southern Perimeter Boundary [b]	Eastern Perimeter Boundary	Western Perimeter Boundary	CAU-Specific Recharge		
RUR	HB	9,491	–21,428	31	–1,450	9,942	–15	0.34
RUO	HB	9,795	–18,229	–585	–852	13,507	18	0.12
RGSOF	HB	11,829	–15,695	–48	–2,269	6,325	1	0.77
RGSNO	HB	10,612	–16,762	–116	–1,465	7,805	0	0.97
RDRIAl	HB	7,207	–19,317	1,090	919	11,866	9	0.59
RDRIAlEl	HB	6,814	–20,428	828	927	10,129	–8	0.62
RDVR	HB	10,377	–16,450	525	–954	6,589	1	0.87
RDVR	HDVR	33,681	–56,843	–7,594	21,468	6,589	–4	–0.02
RDVR	HPZ	12,980	–21,950	–100	2,480	6,589	0	–0.02
RDVR	HCP	23,876	–36,047	–1,792	7,372	6,589	0	–0.02
RDVR	HHB	12,934	–21,853	–96	2,425	6,589	0	–0.02
RDVR	HCU	12,967	–21,848	–111	2,395	6,589	0	–0.02
RDVR	HFJ	12,978	–21,895	–101	2,423	6,589	0	–0.02

Source: SNJV, 2006b

[a] Flow into the HFM area
[b] Flow out of the HFM boundary
[c] To convert to kg/s, multiply by 0.0116.

models to the Yucca Flat/Climax Mine base HFM (HB). The remaining six combine the DVRFS calibrated recharge model (RDVR) with each of the alternative HFMs (excluding the HB because the combination of RDVR and HB was already accounted for when the first seven alternative models were selected). The use of these alternative models allowed determination of the sensitivity of the regional flow model to HFM variations and variations in recharge. The sensitivity to HFM variations was determined by varying the HFM while keeping the recharge model constant. Likewise, the sensitivity to variations in recharge was determined by varying the recharge model while keeping the HFM constant.

The simulated net inflows and outflows through each of the lateral boundaries of the alternative flow models are summarized in Table 5-3. The boundaries considered in this analysis were the northern, eastern, western, and southern boundaries of the Yucca Flat/Climax Mine HFM. The results indicate that the groundwater flow through the northern and southern boundaries is larger than that through the western and eastern boundaries. This is generally true for all combinations of recharge models and HFMs. The majority of this flow occurs in the regionally connected LCA, with the locally isolated alluvial and volcanic aquifers contributing very little to the boundary fluxes.

From Table 5-3, it is clear that variations in the HFM have a much larger impact on the water balance than variations in recharge. The DVRFS HFM has the highest north-to-south flow because there is a significant variation in thickness and cross-sectional profiles of the LCA and UCCU between the DVRFS and Yucca Flat/Climax Mine alternative HFMs. The Yucca Flat/Climax Mine base HFM has a thicker section of the UCCU and a relatively thinner section of the LCA in the center than the DVRFS HFM. As discussed in Section 9.0 of the Yucca Flat/Climax Mine HDD (SNJV, 2006b), the LCCU is raised in the northern parts of the DVRFS model. The HFM variation has the most significant effect on the western boundary flux. This is mainly due to variations of the UCCU thickness among the alternatives. Recharge model variation has the most significant impact on the northern and southern boundaries. The largest flux uncertainty is associated with the eastern and western boundaries. This result is generally consistent with the conceptual model of Yucca Flat and the limited data available to define the flow system in this area. The range in net boundary flux across each of the 13 alternative model boundaries is summarized in Table 5-4.

In evaluating the results of the regional model studies presented in SNJV (2006b), it is important to recognize that the fundamental modeling approach and constraints used were analogous to those

Table 5-4
Summary of Net Boundary Flux Ranges for Yucca Flat/Climax Mine Model Boundaries

Model Boundary	Net Inflow	Net Outflow
	(m^3/day)	
Northern	6,800–34,000	0
Southern	0	16,000–57,000
Eastern	30–1,100	50–7,600
Western	900–21,000	900–2,300
Recharge	6,300–14,000	0

Source: SNJV, 2006b

Note: Results are rounded to two significant figures. To convert to kg/s, multiply by 0.0116.

adopted in the USGS 2004 DVRFS model. This includes the definition of the targets for the regional-model lateral-boundary inflow and discharge estimates, as well as the calibration weights assigned to the observed and interpreted discharge and heads used in the calibration. These constraints lead to estimated Yucca Flat boundary flows that do not span possible reasonable alternative cases that include other sources of structural uncertainty, as have been recently explored in the USGS 2012 DVRFS model (see Section 5.3.5).

5.3.3 DRI 2007 Climax Mine Flow Model

Three underground nuclear detonations were conducted in the Climax stock between 1962 and 1966: HARD HAT, PILE DRIVER, and TINY TOT. The Climax Mine region is surrounded by granitic and volcanic rocks that outcrop at the surface (Figure 5-21). As shown in Figure 5-22, there is only a small sliver of the LCA in the vicinity of Climax Mine that creates a potential pathway for groundwater to flow into Yucca Flat from the north. DRI developed and refined a subsurface model that integrates a localized groundwater flow and transport model of northern Yucca Flat with the USGS regional model in order to estimate the amount of groundwater flux and radionuclide contamination entering the Yucca Flat basin. As discussed above, there are two versions of the model; the first completed in 2007 (Pohlmann et al., 2007) and the second in 2012 (Pohlmann and Ye, 2012). The original 2007 model is documented in this section. The revised 2012 model is documented in the following section. The bulk of the model development and calibration activities were completed during the initial modeling effort completed in 2007. The 2012 model involved incorporating updates

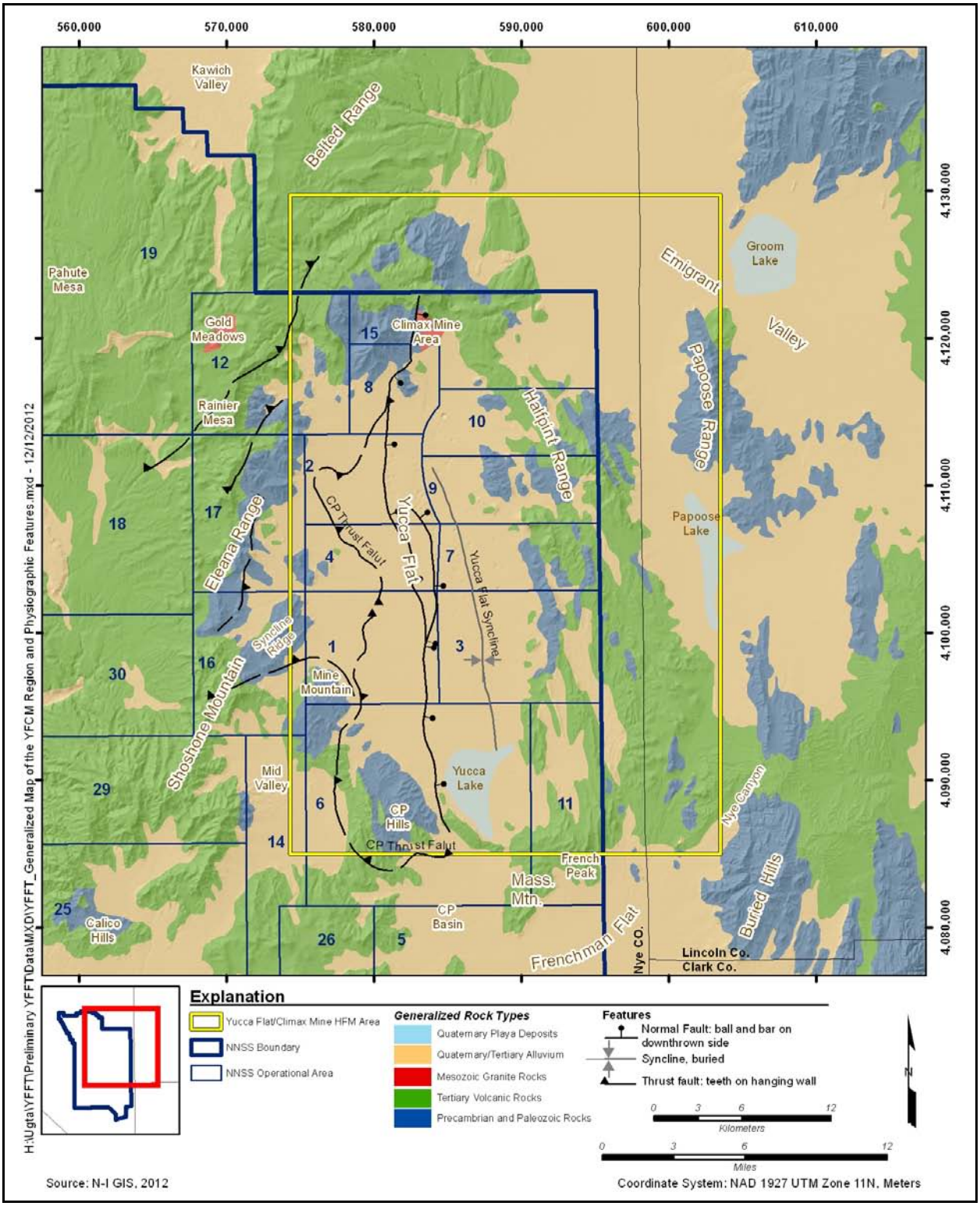

Figure 5-21
Map of the Major Rock Types Outcropping in the Region of Yucca Flat Showing the Climax Mine Granite Intrusion Being Exposed in the Extreme Northern End of Yucca Flat

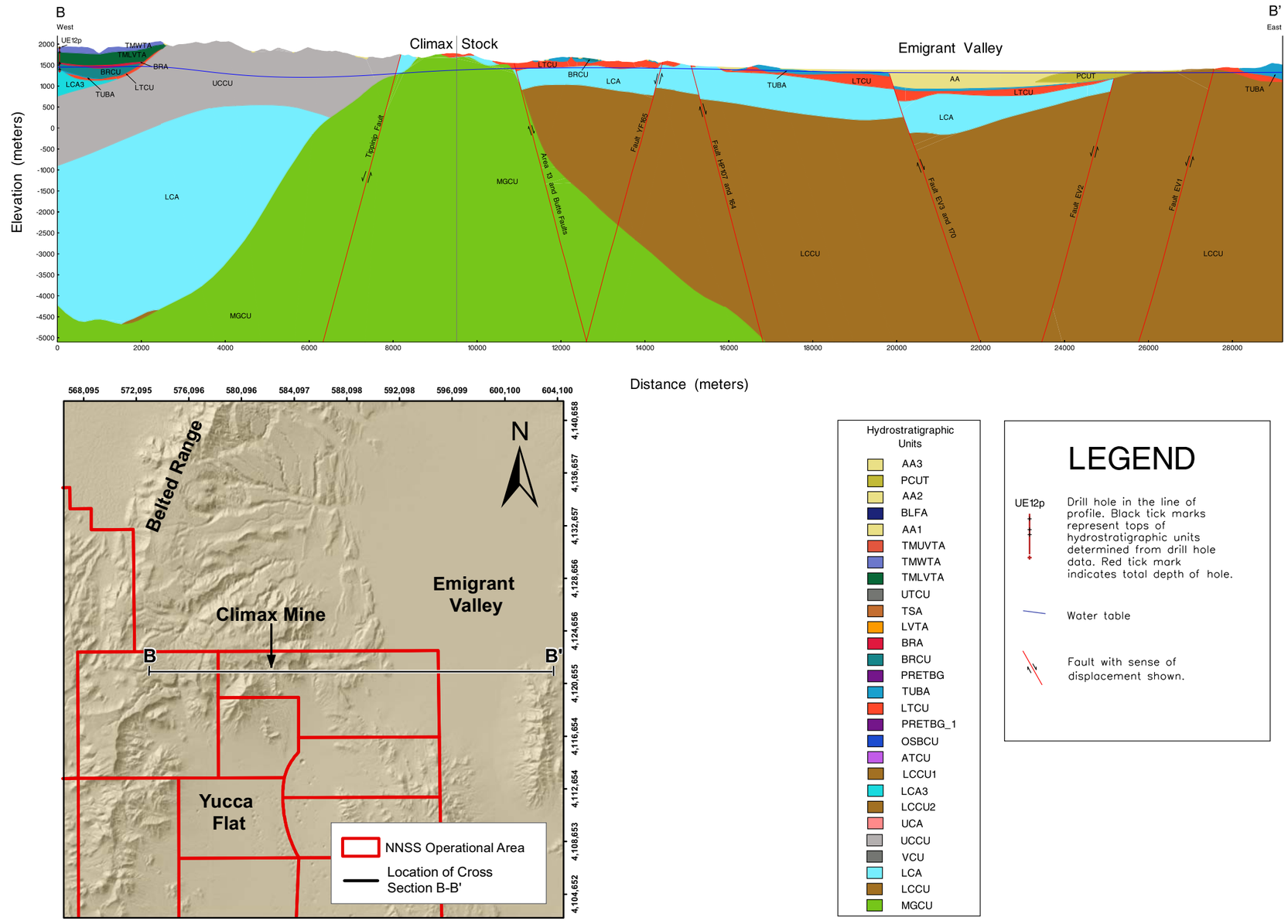

Figure 5-22
West–East Hydrogeologic Cross Section through the Climax Stock and the Adjacent Clastic Confining Units at the Northern End of Yucca Flat
Source: Modified from Pohlmann et al., 2007

to the HFM, recalibrating the revised model using a larger observation dataset, and readjusting calibration target weights to evaluate the sensitivity of the boundary inflow in northern Yucca Flat to the assumed calibration targets and weights.

The 2007 Climax Mine flow model was developed to provide (1) simulated heads and groundwater flows for the northern boundaries of the Yucca Flat/Climax Mine CAU model and (2) radionuclide fluxes from the three detonations conducted in the Climax stock by the use of modeling techniques that account for groundwater flow in fractured granite. The flow model features and results documented by Pohlmann et al. (2007) are summarized below.

The 2007 Climax Mine flow model is based on the 2004 DVRFS model (Belcher et al., 2004), but is extended through incorporation of multiple conceptual models of regional groundwater recharge and the local hydrostratigraphic framework. This was done in a manner similar to that described in Section 5.3.1, but at a more refined scale in the vicinity of Climax Mine. Although most aspects of the 2004 DVRFS model are preserved in the 2007 Climax Mine flow model, the 2004 DVRFS model was modified by refining the 1,500-m mesh in northern Yucca Flat to accommodate the highly resolved models of hydrostratigraphy (Figure 5-23).

Five alternatives of the HFM of northern Yucca Flat were considered in developing the 2007 Climax Mine flow model: one represents the configuration of HGUs in the entire DVRFS model (HFM 1), and the other four were developed for the Yucca Flat/Climax Mine CAU as part of the UGTA Activity (HFM 2 through 5). The four CAU-specific alternatives include a base model (HFM 2) and two alternatives that were developed to address uncertainty regarding particular features of the hydrostratigraphy that might be important to groundwater flow and contaminant transport in Yucca Flat (HFM 3 and HFM 4). HFM 3 incorporates a different interpretation of the configuration of HSUs with respect to the CP thrust fault, and HFM 4 postulates a barrier to groundwater flow on the east side of Climax stock. These two alternative models were merged to form a single alternative, which is the last of the five alternatives (HFM 5). These five alternative geologic models and the naming conventions used to refer to them are listed in Table 5-5.

In addition to the alternative geologic models, the 2007 Climax Mine flow model considered a set of alternative recharge models. The recharge model set includes five models that are based on three independent methodologies. The first model (R1) was developed based on a modification of the empirical Maxey-Eakin method, which estimates groundwater recharge as a function of precipitation

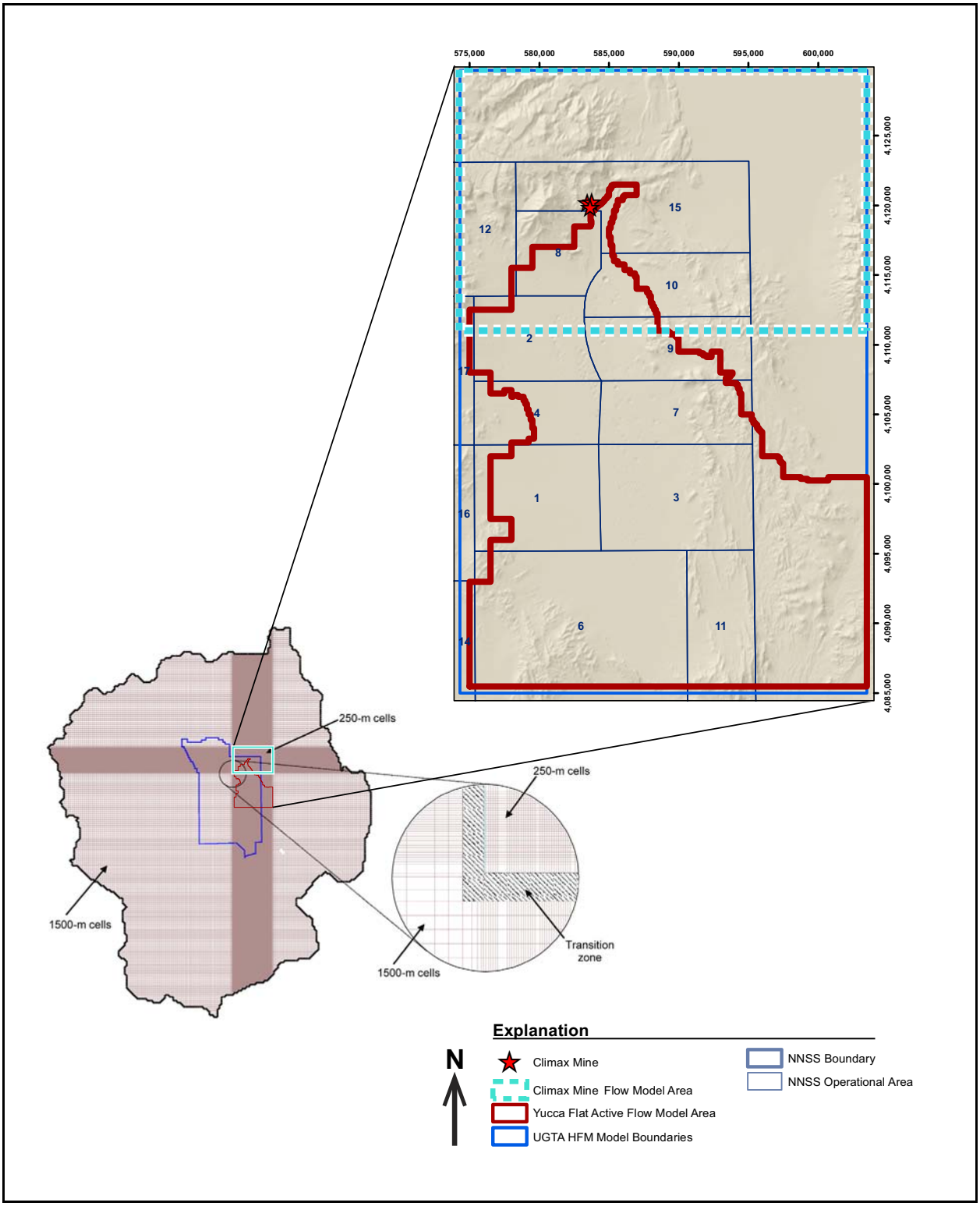

Figure 5-23
Plan View of the Climax Mine Flow Model Domain Showing Areas of Mesh Refinement
Source: Modified from Pohlmann et al., 2007; N-I GIS, 2012

Table 5-5
Naming Conventions for Alternative HFMs in the Climax Mine Flow Model

Abbreviation	Description
HFM 1 (USGS)	USGS DVRFS Model
HFM 2 (BAS)	UGTA Base Model
HFM 3 (CPT)	CP Thrust Alternative of the Base Model
HFM 4 (HB)	Hydrologic Barrier Model
HFM 5 (CPT+HB)	Combination of HFM 3 and HFM 4

Source: Pohlmann et al., 2007

for selected zones of elevation. The net infiltration method uses a distributed-parameter watershed model for estimating temporal and spatial distribution of net infiltration and potential recharge. Two recharge models were developed based on this methodology, one with a surface water run-on and runoff component (R2) and one without (R3). Estimates of chloride ion balances within hydrologic input and output components of individual hydrologic basins provide the basis for the third approach for estimating groundwater recharge. The chloride mass-balance methodology accounts for the elevation of precipitation and the limited quantities of recharge that are thought to occur on low-elevation alluvial surfaces and leads to two models of recharge, one that eliminates recharge in areas covered by alluvium (R4) and another that eliminates recharge in areas below a threshold elevation and areas covered by alluvium (R5). The five recharge models and the naming conventions used to refer to them are listed in Table 5-6.

Table 5-6
Naming Conventions for Alternative Recharge Models in the Climax Mine Flow Model

Abbreviation	Description
R1 (MME)	Modified Maxey-Eakin Model
R2 (DPW1)	Distributed-Parameter Watershed Model with Run-on and Runoff Component
R3 (DPW2)	Distributed-Parameter Watershed Model without Run-on and Runoff Component
R4 (CMB1)	Chloride Mass-Balance Model with Alluvial Mask
R5 (CMB2)	Chloride Mass-Balance Model with Alluvial and Elevation Masks

Source: Pohlmann et al., 2007

The composite prediction of groundwater flow in northern Yucca Flat was derived by incorporating uncertainty in multiple alternative input models of recharge and hydrostratigraphy using maximum likelihood Bayesian model averaging (MLBMA) methods. In addition, an assessment of the joint

predictive uncertainty of the input models was produced. During this process, predictions of the alternative models were weighted by their probability, which is the degree of belief that the model is correct given site measurements and prior information. The MLBMA utilized prior information and field measurements through both expert elicitation and parameter estimation inverse modeling to develop these probabilities. Prior probabilities for each of the alternative conceptual models were elicited from two panels of technical experts (one for the recharge models and one for the hydrostratigraphic models) based on the panelists' beliefs regarding the relative plausibility of each model considering its apparent consistency with available knowledge and data. Each elicitation panel evaluated the completeness of the sets of recharge and geologic models and ranked the models within each set.

The flow rates into northern Yucca Flat for 25 plausible alternative models are presented in Figure 5-24. The boundary chosen for these analyses is along the southern boundary of the Climax Mine flow model area indicated in Figure 5-23. These results are organized by recharge model and show the impacts of the alternative geologic models on each recharge model. Figure 5-24 shows that geologic models have a stronger influence on groundwater flow rate than recharge models. The total simulated flow rate varies between approximately 50,000 and 110,000 m^3/day (600 and 1,300 kg/s). According to Pohlmann et al. (2007), the two most likely flow models are the UGTA base model and CP thrust model based on their better fit to available observation data and the calibration methods incorporated in the DVRFS model. The most plausible alternative model is the CP thrust model, which provides a conduit for flow in the LCA in the area between Climax stock and the northwest Halfpint Range. Each alternative model, representing a combination of geologic and recharge conceptualization, has a unique flow field, which results in a different distribution of inflow into northern Yucca Flat. For example, the hydraulic head and flux along the southern Climax Mine model boundary for the UGTA base geologic and USGS run-on and runoff recharge combination is presented in Figure 5-25. The boundary flux into northern Yucca Flat is not uniform but varies laterally and vertically primarily because of the complex geology and associated permeability distribution in the underlying rocks.

5.3.4 DRI 2012 Climax Mine Flow Model

As discussed above, utilizing the 25 combinations of 5 HFMs and 5 regional recharge models, the DRI 2007 Climax Mine flow model simulated interbasin flow rates into northern Yucca Flat that far

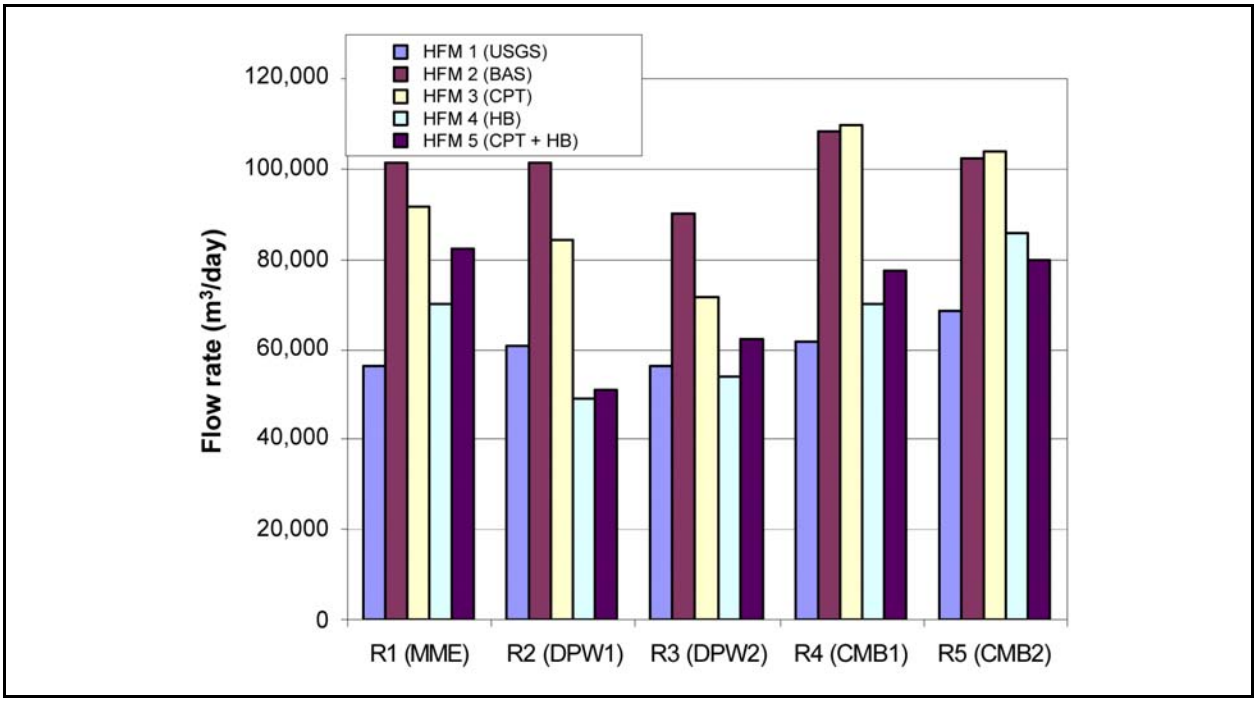

Figure 5-24
Total Flow Rate into Yucca Flat from the North (near Climax Mine)
Source: Modified from Pohlmann et al., 2007

exceeded the estimates reported by Winograd and Thordarson (1975), and Harrill et al. (1988), which were on the order of 90 and 1,700 m^3/day (1 and 20 kg/s), respectively. This difference is believed to be a result of structural uncertainty, including constraints imposed by the modeled boundary conditions and the juxtaposition of the LCA in northern Yucca Flat. According to Pohlmann and Ye (2012), "the higher flows simulated by the 2007 sub-CAU model resulted from a complex interplay between the configuration of hydrostratigraphic models in northern Yucca Flat and parameterization of the DVRFS model." DRI therefore revised the 2007 model with the goal of evaluating the feasibility of reducing interbasin groundwater flow into northern Yucca Flat to achieve inflow rates that are similar to other estimates, given available hydrogeologic models and new model parameterization (Pohlmann and Ye, 2012).

The 2012 model evaluation was accomplished through revisions to the 2007 model with particular emphasis on enhancements to the calibration process by focusing on parameters critical to interbasin flow into northern Yucca Flat. The approach involved using a global parameter sensitivity method to determine the most critical parameters for estimating northern influx into Yucca Flat. On selection of the parameters for each model, the Monte Carlo method was implemented to investigate the impact of parameter uncertainty on estimates of northern influx for each model. The two primary sources of

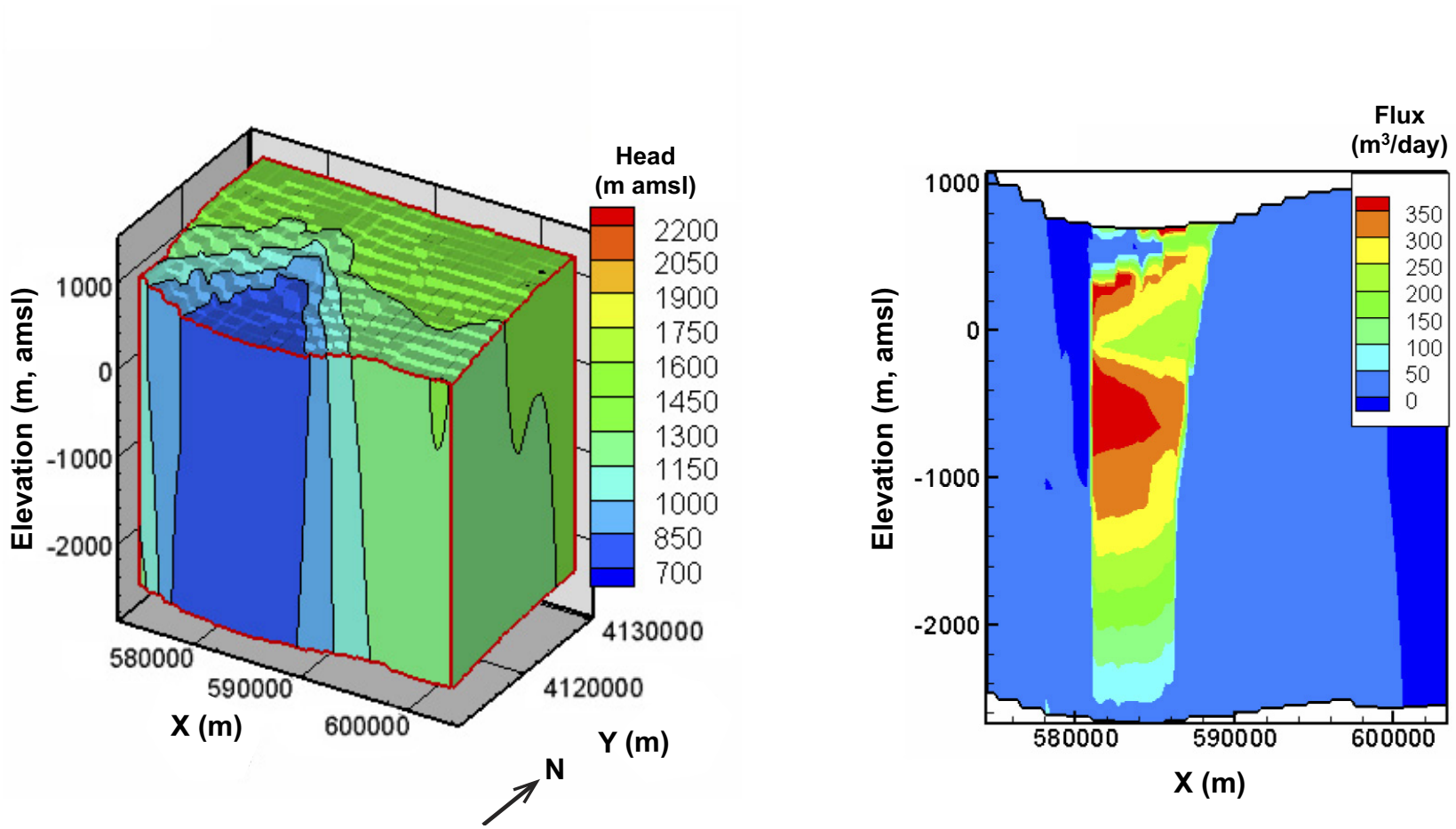

Figure 5-25
Hydraulic Head and Flux along Southern Boundary of Climax Mine Model for UGTA Base/USGS Run-On and Runoff Alternative
Source: Modified from Pohlmann et al., 2007

ambiguity within the DVRFS modeling framework are geologic conceptualization and parametric uncertainties. To address these uncertainties, a total of six models were considered in the 2012 revision that reflect uncertainty in conceptualizing the recharge process and in constructing the hydrostratigraphic framework in northern Yucca Flat.

The revised 2012 models provided calibrated values of northern influx into Yucca Flat ranging from about 28,000 to 60,000 m^3/day (320 to 700 kg/s). While these fluxes are lower than previous estimates of 50,000 to 110,000 m^3/day (580 to 1,300 kg/s), they are still higher than estimates reported in the previous studies cited above. DRI therefore utilized the Morris method to identify parameters that are highly sensitive to inflows into northern Yucca Flat and, using these parameters, conducted additional simulations to obtain model subsets that substantially reduce the northern influx into Yucca Flat without significantly worsening the calibration. The resulting estimates of interbasin flow into northern Yucca Flat range from 19,000 to 25,000 m^3/day (220 to 290 kg/s), which are substantially lower than the rates obtained during model calibration. According to Pohlmann and Ye (2012), “further reductions may only be possible by substantial modifications to other aspects of the model such as reducing the extent, continuity, or hydraulic conductivity of the lower carbonate aquifer north of Yucca Flat, increasing the weights of boundary flow observations, or revising selected boundary flow estimates.” The effect of these structural uncertainties is explored in the USGS 2012 DVRFS model discussed below.

5.3.5 USGS 2012 DVRFS Model

Since completion of the USGS DVRFS model in 2004, concerns pertaining to drawdown impacts of increased groundwater pumping in the southern Amargosa Desert and Pahrump Valley have resulted in the development of a local-scaled, fine-resolution groundwater flow model embedded in the regional model. During development of the local-scale model, it was also decided by USGS to refine the regional model with updated hydrostratigraphic information and revised estimates of boundary flow. An added benefit of the regional model revision is the development of refined flow estimates within the Yucca Flat model domain in order to support CAU-scale modeling activities at the NNSS. The revisions to the regional model are currently in progress; however, preliminary modeling results provided by USGS (Faunt et al., 2012) are summarized in this study in order to compare the revised estimates of groundwater underflow into Yucca Flat. For purposes of this report, the initial DVRFS

model is referred to as the 2004 DVRFS model, and the revised model is referred to as the 2012 DVRFS model.

Model revisions involve incorporating (1) an updated surface area of the top of Paleozoic strata based on results of gravity-derived depth-to-basement studies, (2) revised elevations of unit tops for Cenozoic HGUs based on reinterpretation of all borehole data in the Amargosa Desert area, (3) the modification of the LCCU elevation, which significantly reduced the amount of carbonate rocks in northern Yucca Flat, including Boundary fault (eastern Yucca Flat) and Cane Spring fault (south-central Yucca Flat) in the model, and allowed faults to act as dual barrier-conduit systems, and (4) a new three-dimensional lithology (and associated properties) in the upper part of Cenozoic basin fill (Faunt et al., 2012).

Based on the above enhancements to the model, preliminary results indicate a substantial reduction in groundwater influx into northern Yucca Flat. The longitudinal (north–south) and lateral (east–west) steady-state flow rates simulated by the 2012 DVRFS model within the LCA are presented in Figures 5-26 and 5-27. The net inflow from the groundwater basin north of Yucca Flat is estimated at about 4,700 m^3/day (approximately 55 kg/s). This is nearly an order of magnitude lower than the previous estimate of 550 kg/s derived from the 2004 DVRFS model. It should be noted that the 2012 DVRFS model is presently undergoing revision and that these estimates may potentially change as the model is documented and reviewed in the future.

5.3.6 Summary

This section reviewed five regional groundwater flow models that are relevant to evaluating potential boundary fluxes into the Yucca Flat LCA flow model. These are the USGS 2004 DVRFS and USGS 2012 DVRFS models, the SNJV 2006 Yucca Flat/Climax Mine CAU groundwater flow model, and the DRI 2007 and DRI 2012 Climax Mine flow models. The models used various HFMs and recharge models within the regional model to evaluate the range of possible groundwater flows into Yucca Flat. Because the SNJV Yucca Flat/Climax Mine CAU groundwater flow model and the two DRI Climax Mine models are fundamentally derived from the USGS 2004 DVRFS model, the limitations in the 2004 DVRFS model are also present in the SNJV Yucca Flat/Climax Mine CAU groundwater flow model and the DRI Climax Mine flow models. These limitations include the assumption that the evapotranspiration rates provide better constraints on the overall water budget than on the boundary

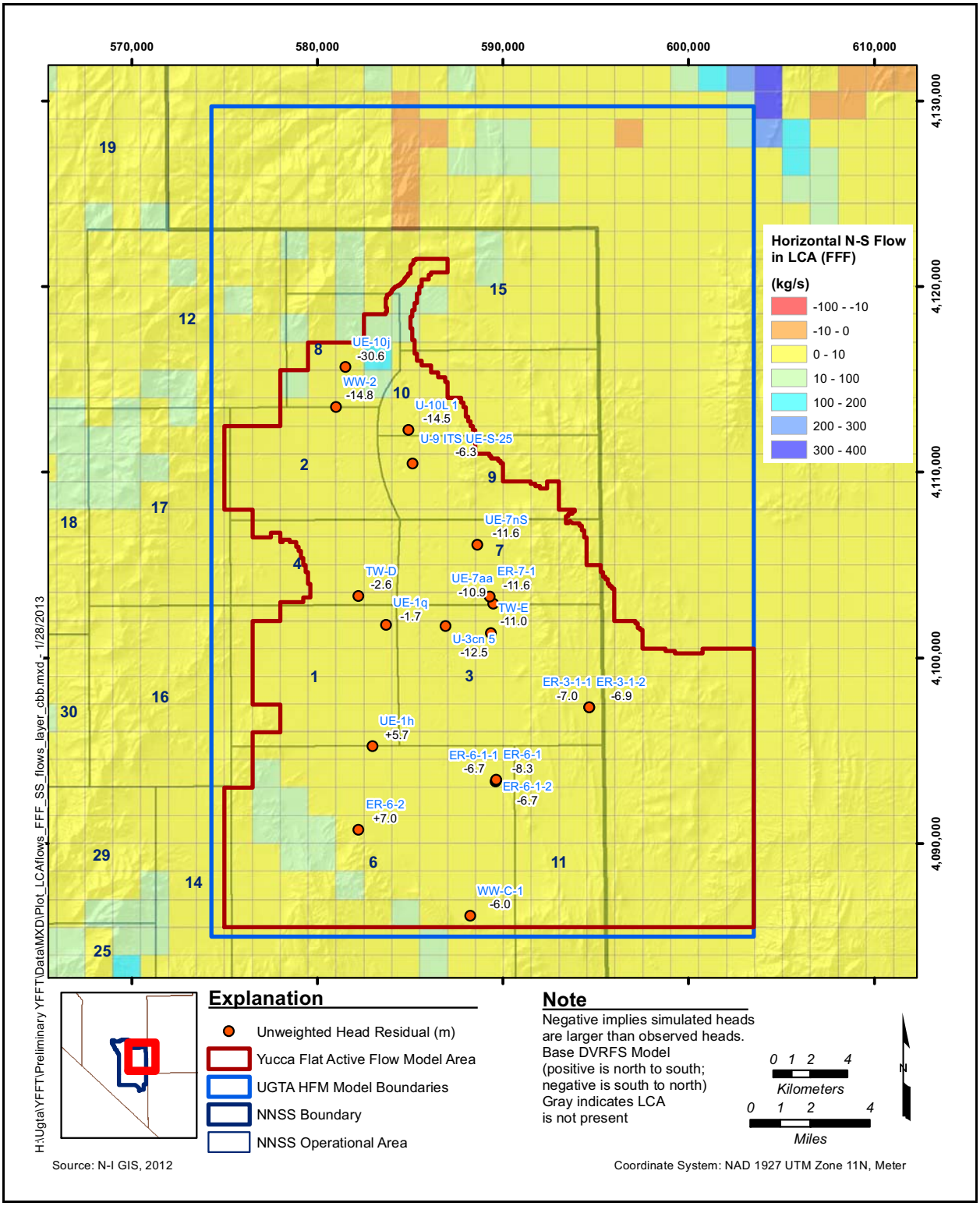

Figure 5-26
Simulated Steady-State Groundwater Flux in the LCA through the North–South Cell Face of the USGS 2012 DVRFS Model

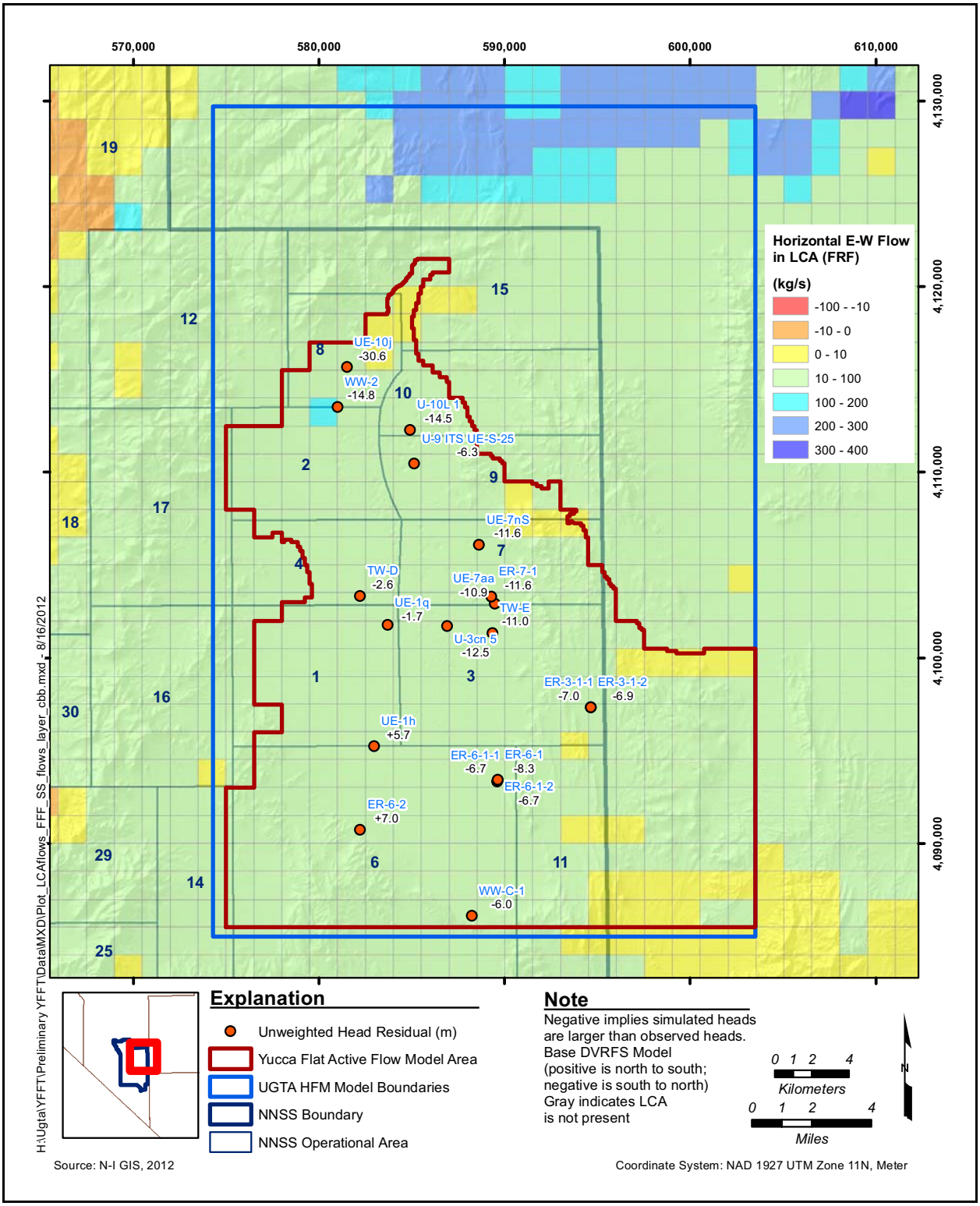

Figure 5-27
Simulated Steady-State Groundwater Flux in the LCA through the East–West Cell Face of the USGS 2012 DVRFS Model

flux or infiltration rates. The other assumption is that the underlying HFM structure in northern Yucca Flat incorporates significant lateral continuity of the LCA.

A summary of the northern inflow and total outflow along the southern boundary of the Yucca Flat model for all five regional models and other estimates of the boundary fluxes are presented in Table 5-7. In general, inflow along the northern model boundary is high in the regional models that are derived from the regional HFM and regional boundary conditions—approximately 550 kg/s in the 2004 DVRFS model, between about 80 and 390 kg/s in the SNJV Yucca Flat/Climax Mine CAU groundwater flow model, and between about 220 and 1,300 kg/s in the two DRI Climax Mine flow models. It is possible that these values may be on the high side considering that the granitic intrusion in the north virtually cuts off the LCA in the Yucca Flat basin from the LCA north of Yucca Flat. The value is reduced significantly in the recent USGS 2012 DVRFS model in large part because of a change in the lateral continuity of the LCA in northern Yucca Flat and a reinterpretation of some of the regional boundary influxes. This is also the conclusion reached by Winograd and Thordarson (1975), and Halford (2011, 2012). It is worth noting that a previous numerical flow model encompassing the NNSS and surrounding region (DOE/NV, 1997a) predicted approximately 300 kg/s entering Yucca Flat from the north. The thermal modeling results presented in Appendix H estimate northern influx of approximately 50 kg/s.

The total outflow from the LCA in southern Yucca Flat has also been estimated in regional models and other studies. This boundary flux consists of underflow from upgradient boundaries such as the northern boundary discussed above, vertical leakage through the overlying saturated alluvial/volcanic aquifer system, and local recharge in areas where the LCA subcrops along the margins of the Yucca Flat basin. As indicated in Table 5-7, there also is a wide disparity between the estimates derived from the regional models and other estimating methods. These differences are due to the differences in the estimates of influx into northern Yucca Flat discussed above and the differences in the estimates of local recharge to the LCA along the margins of the Yucca Flat basin.

Based on the above discussion, it appears that although previous modeling studies have been useful to gain some hydrogeologic understanding on a large basin-scale basis, the boundary fluxes derived from these models are uncertain. Therefore, in the present study, the boundary fluxes from these models are used as initial values and bounds during the calibration process, which rely on observed regional hydraulic heads and drawdowns recorded during the ER-6-1-2 MWAT as discussed in

Table 5-7
Estimated Fluxes (kg/s) along Northern and Southern Boundaries of Yucca Flat Flow Model

	Modeled Boundary Fluxes					Other Estimated Fluxes			
	USGS 2004 DVRFS	SNJV 2006 Yucca Flat/ Climax Mine CAU	DRI 2007 Climax Mine	DRI 2012 Climax Mine	USGS 2012 DVRFS	Winograd & Thordarson (1975)	Harrill et al. (1988)	Halford (2009, 2011, 2012) [b]	Buqo (2004)
Northern Inflow	550	80–390	600–1,300	220–290	55	1	<20 [a]	0.1	N/A
Southern Outflow	590	180–660	N/A	N/A	300	<40 [a]	<40 [a]	<80	27

[a] As quoted by K. Halford (USGS) in personal communication to A. Tompson (LLNL) dated August 5, 2011.
[b] Personal communication from K. Halford (USGS) to A. Tompson (LLNL), January 16, 2009, August 5, 2011, and October 9, 2012. The area of outflow corresponds to the central portion of the Yucca Flat boundary only.

Note: All fluxes are rounded to two significant figures.

Section 5.2. The range of boundary fluxes is considered uncertain, with the range assumed to be constrained by the range of regional model results. This results in a potential overestimation of influx from the northern boundary in comparison to the other interpretations presented in Table 5-7. In order to investigate the effects of this uncertainty on the calibrated flow field, a separate analysis was performed with the northern influx fixed at 1.0 kg/s to represent the alternative interpretations.

5.4 LCA Groundwater Flow Model Construction

This section describes the technical approach and methods implemented to construct the numerical groundwater flow model for the LCA at Yucca Flat. The key objective is to transform the conceptual model described in Section 5.2 into mathematical models that can simulate the groundwater flow system in areas surrounding Yucca Flat. The model construction process includes spatial discretization, definition of boundary conditions, and initial assignment of model parameters. As discussed in Section 1.0, the subsurface volume at Yucca Flat was divided into three separate models: (1) the unsaturated-zone model, which includes unsaturated portions of alluvium, tuffs, and carbonate rock; (2) the saturated alluvial/volcanic aquifer system model; and (3) the saturated LCA model. This section addresses the CAU-scale model as implemented within the saturated LCA model. The unsaturated zone and saturated alluvial/volcanic aquifer system models are described in Sections 3.0 and 4.0, respectively.

5.4.1 Model Area

The LCA numerical model is based on the HFM constructed for the Yucca Flat/Climax Mine area in BN (2006). The lateral model boundaries were selected so as to include all areas that can potentially capture and transport radionuclide contamination emanating from the underground nuclear detonation sites. This required extending model boundaries sufficiently far from contamination sources so that all relevant groundwater sources that govern flow direction and gradients in the LCA are included in the model domain. Because the modeling objective was to simulate groundwater flow in the carbonate aquifers, only those regions within the study area where the LCA, UCA, LCA3, and confining units separating these units were represented as active units in the flow model. Flow in the remaining (non-LCA) region was deactivated because of the low permeability or great depth of these units. The modeled LCA volume within Yucca Flat is presented in Figure 5-1.

The areal extent of the LCA flow and transport model is presented in Figure 5-2. The model lies within the Yucca Flat HFM domain. The model extends from –5,500 m amsl at the base to +1,500 m amsl at the top. The model spans approximately 36.0 km in the north–south direction and 28.5 km in the east–west direction. Wherever possible, the model boundaries are set to coincide with natural hydrologic boundaries. For example, a short segment of the extreme northwest portion of the boundary coincides approximately with the limit of the saturated LCA where it laps onto the intrusive MGCU. Grid nodes that are within the LCA in this segment are maintained in the active model region, and nodes that appear outside the LCA are rendered inactive in the modeling process. Similarly, no-flow boundaries were specified in the northern half of Yucca Flat where the LCA outcrops at the water table. In the southern portions of the model, the eastern model boundary was extended far enough so as to coincide with the eastern extent of the Frenchman Flat model. The western model boundary overlaps with the Rainier Mesa model boundary. Likewise, the southern model boundary of the Yucca Flat model overlaps the northern model boundary of the Frenchman Flat CAU model.

In most of Yucca Flat, the top of the model is set either at the water table or at the top of the LCA, whichever is lower in elevation. In some regions in the west where the LCA3 overlies the LCA, the topmost active node is within the LCA3. The LCA also forms the lower (active) model boundary, because the hydraulic conductivity of the LCCU underlying the LCA is extremely low, and therefore, the LCCU was conceptualized as an impermeable boundary for modeling purposes.

The areal extent of the saturated alluvial/volcanic aquifer system model and the unsaturated-zone model overlying the LCA is outlined in Figure 1-17, which depicts the several separate models that collectively make up the unsaturated-zone model.

5.4.2 Model Mesh

The model was constructed with the LANL FEHM groundwater flow modeling code, Version 3.23 (Zyvoloski et al., 1997). The flexibility of finite elements allows for the resolution of the grid to vary spatially to capture source areas and complex structures, such as faults with higher resolution than other areas where coarser discretization is sufficient. LANL developed the model mesh using the LaGriT mesh generation software (LANL, 2011). LaGriT is a library of user-callable tools that provide mesh generation, mesh optimization, and dynamic mesh maintenance in two and three dimensions.

Three model meshes representing three levels of refinement were generated. The primary difference between the meshes was the level of mesh refinement in the fault plane. The coarsest mesh had a 250-m-thick fault zone, and the finest mesh had 67.5-m-wide faults. The mid-level mesh, which was finally selected as a compromise between the need for simulation accuracy and computational expense, had a fault zone width of 125 m. A finer discretization in the vicinity of the faults allows fault geometry to be captured, provides transition between the faulted and unfaulted regions, and accounts for a relatively fast rate of contaminant transport in the faults (Figure 5-28). The mid-level mesh was discretized into 2,917,285 elements by 537,503 nodes. The refined mesh with 1,750,568 nodes was utilized as an alternative model to examine impacts of fault refinement on contaminant transport as discussed in Section 5.6.5.

The Yucca Flat mesh development used a balanced octree refinement approach on an orthogonal grid using the LaGriT meshing software (LANL, 2011). After the octree grid was built, some cells were removed from the bottom and top. The top surface was created by removing cells above the water table, and the bottom surface resulted from removing cells belonging to the LCCU. In order to allow correct specification of recharge rates, an area vector was computed for each exterior node. This area vector provides the area and normal vector associated with each exterior node. This allows one to convert a recharge map that provides information, for example, in units of millimeters per year into a per-node rate of kilograms per second.

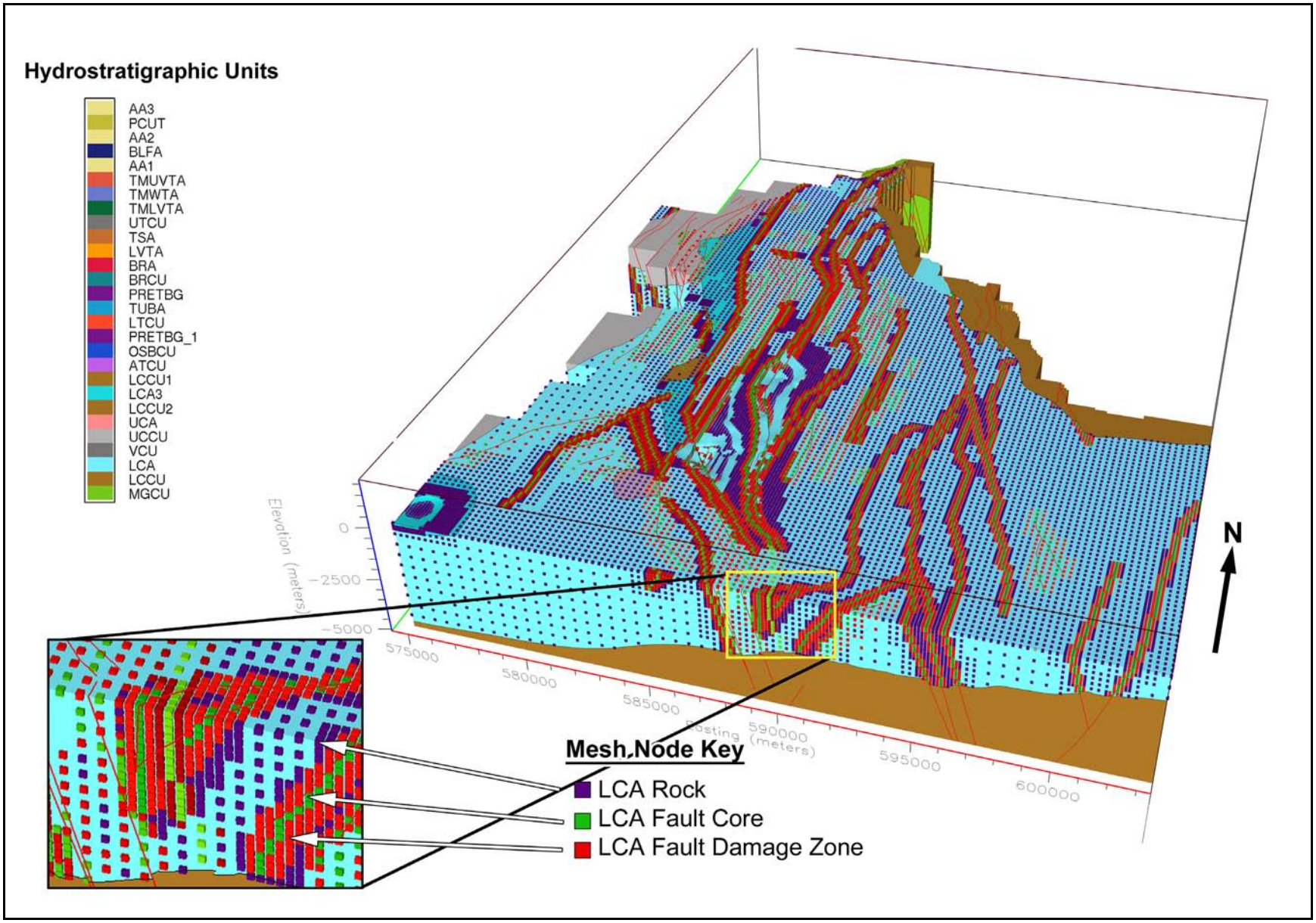

Figure 5-28
Mesh Discretization Highlighting Fault Core and Damage Zones

5.4.3 Material Assignment and Parameter Distribution

Yucca Flat lies within the basin-and-range extensional province in southern Nevada. The site is, therefore, highly faulted, with a total of 107 faults present in the model study area (Figure 5-29). The faults dip primarily to the east or west as indicated in Figure 5-3. The 107 faults include three dominant faults (Yucca, Topgallant, and Carpetbag faults), which are shown in Figure 5-29 as large basin-forming faults. These large dominant faults are expected to influence groundwater flow patterns in the area. For ease of identification, each of the 107 faults is referenced by a number between 101 and 217 as shown in Figure 5-30. The numbering system includes faults that are present in the HFM but do not extend into the LCA within the LCA model domain. The hydrogeologic properties in each fault were assumed to be uniform. In reality, however, the properties may vary along the fault extent. As discussed in Section 5.6.2, the NSMC uncertainty analysis is expected to encompass the hydrologic consequences of variable fault properties as the technique samples a large range for each hydrogeologic property, such as permeability, storativity, and anisotropy.

For modeling purposes, the entire study domain was divided into two regions—faulted and unfaulted. This enabled a discrete specification of hydraulic properties in each of these regions. A model node, therefore, represented either rock or fault material. The LCA was divided into several distinct units for the purposes of modeling: the LCA east (LCAe) refers to the LCA in the model area east of the Yucca fault, the LCA west (LCAw) refers to the LCA west of the Carpetbag fault, and the LCA central (LCAc) refers to the LCA in the area between the Yucca and Carpetbag faults (Figure 5-29). Of these three zones, the LCAe is conceptualized as highly faulted and fractured because it represents the “hanging” side of the basin-and-range extension, whereas the LCAw, which represents the footwall region, is expected to be the least impermeable of the three rock zones. The hydraulic properties were assumed to remain the same for all model nodes within each of these three zones. The base of the model corresponds to the bottom of the LCA because the underlying LCCU has very low permeability.

To the south of Yucca Flat lie the Frenchman Flat and CP basins. It is recognized that there is an “accommodation zone” between these two tectonic domains (i.e., the Yucca Flat and Frenchman Flat/CP basins; Figure 5-31) in which the subsurface rocks are likely to be more permeable than the host rock (Prothro, 2012). Therefore, a separate zone, referred to as the Yucca Flat accommodation zone, was specified in the LCA model along the south-central boundary as shown in Figure 5-29. The hydraulic permeability of this zone was an adjustable parameter during the model calibration process.

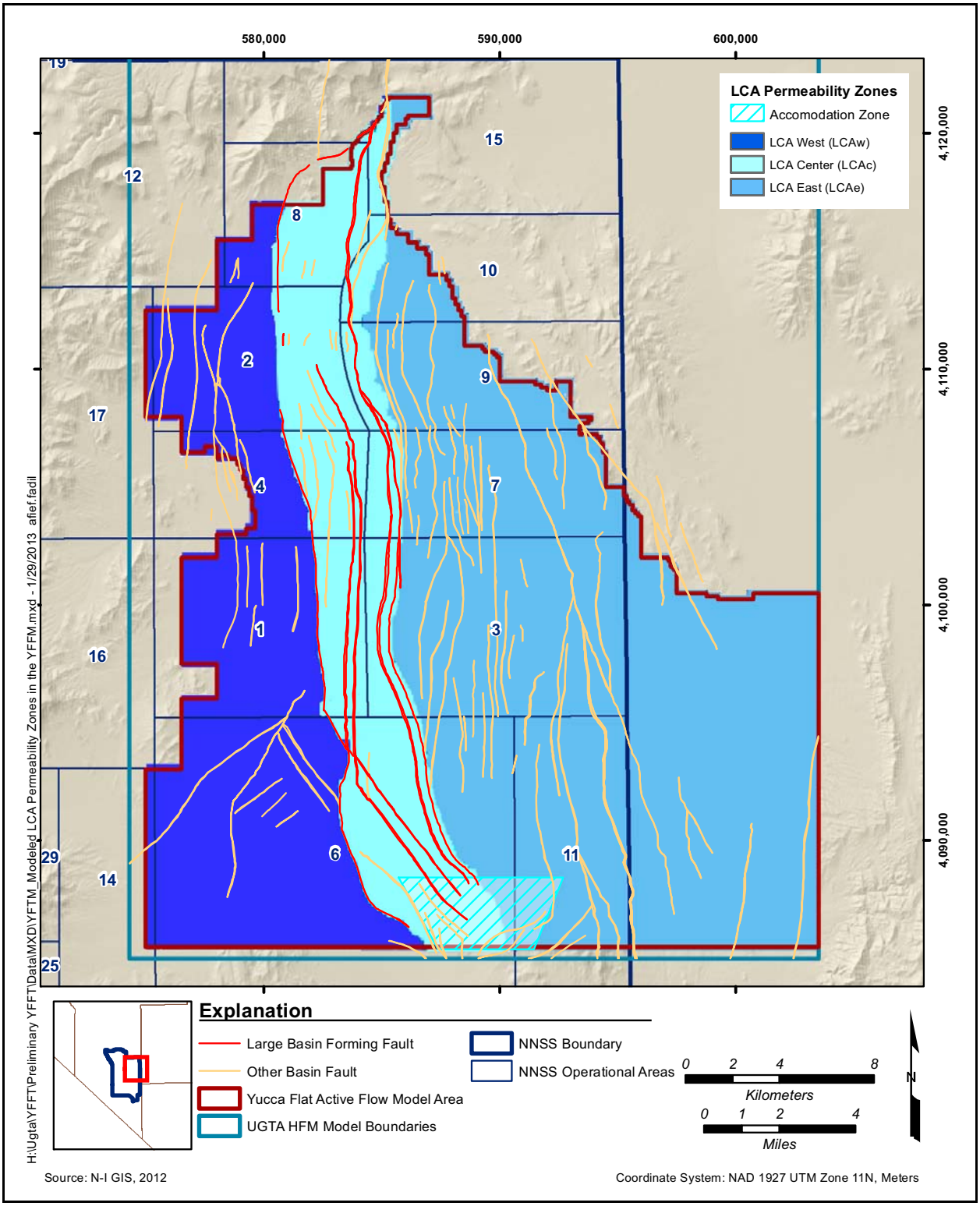

Figure 5-29
Modeled LCA Permeability Zones in the Yucca Flat Flow Model

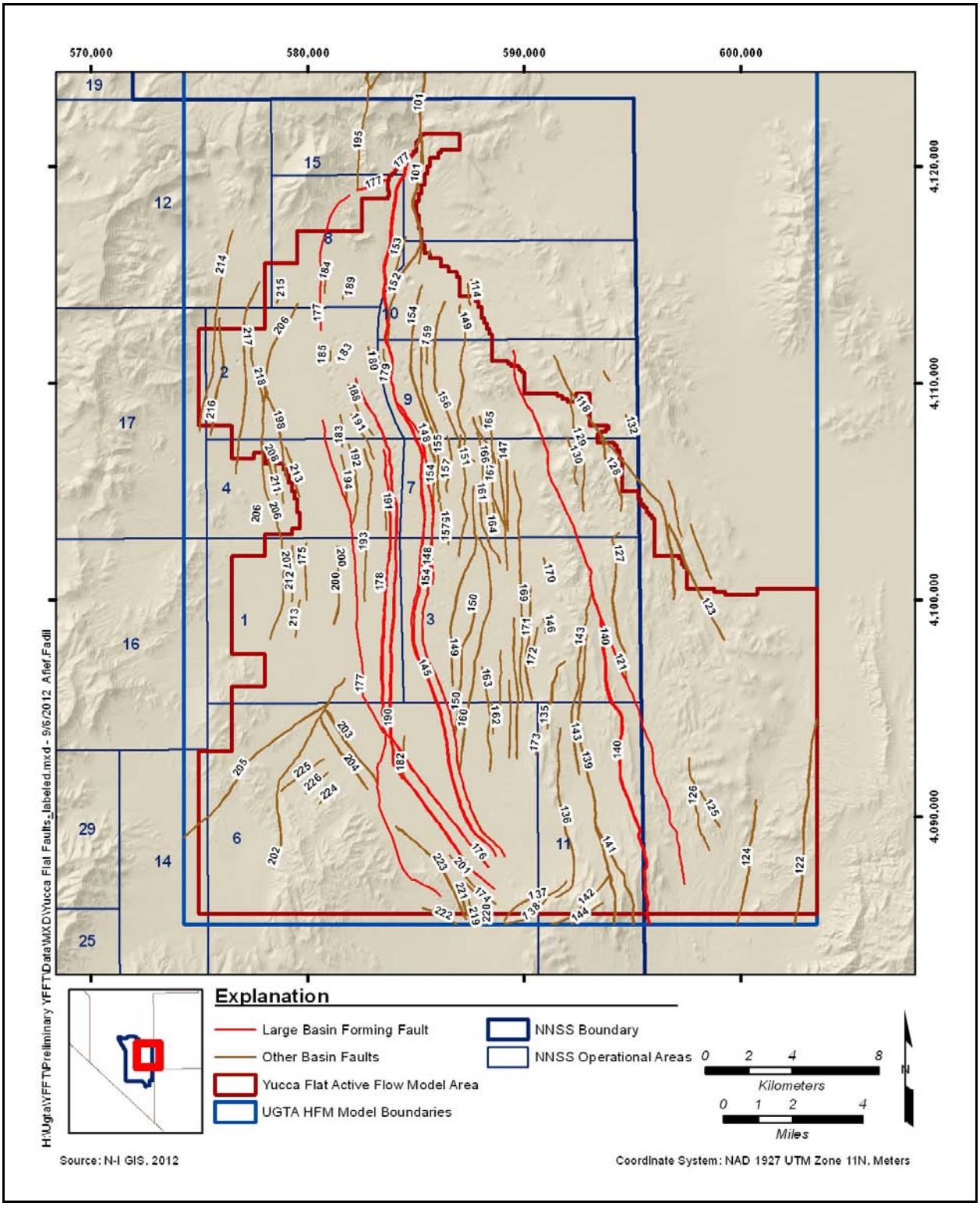

Figure 5-30
Faults Included in the Yucca Flat LCA Flow and Transport Model

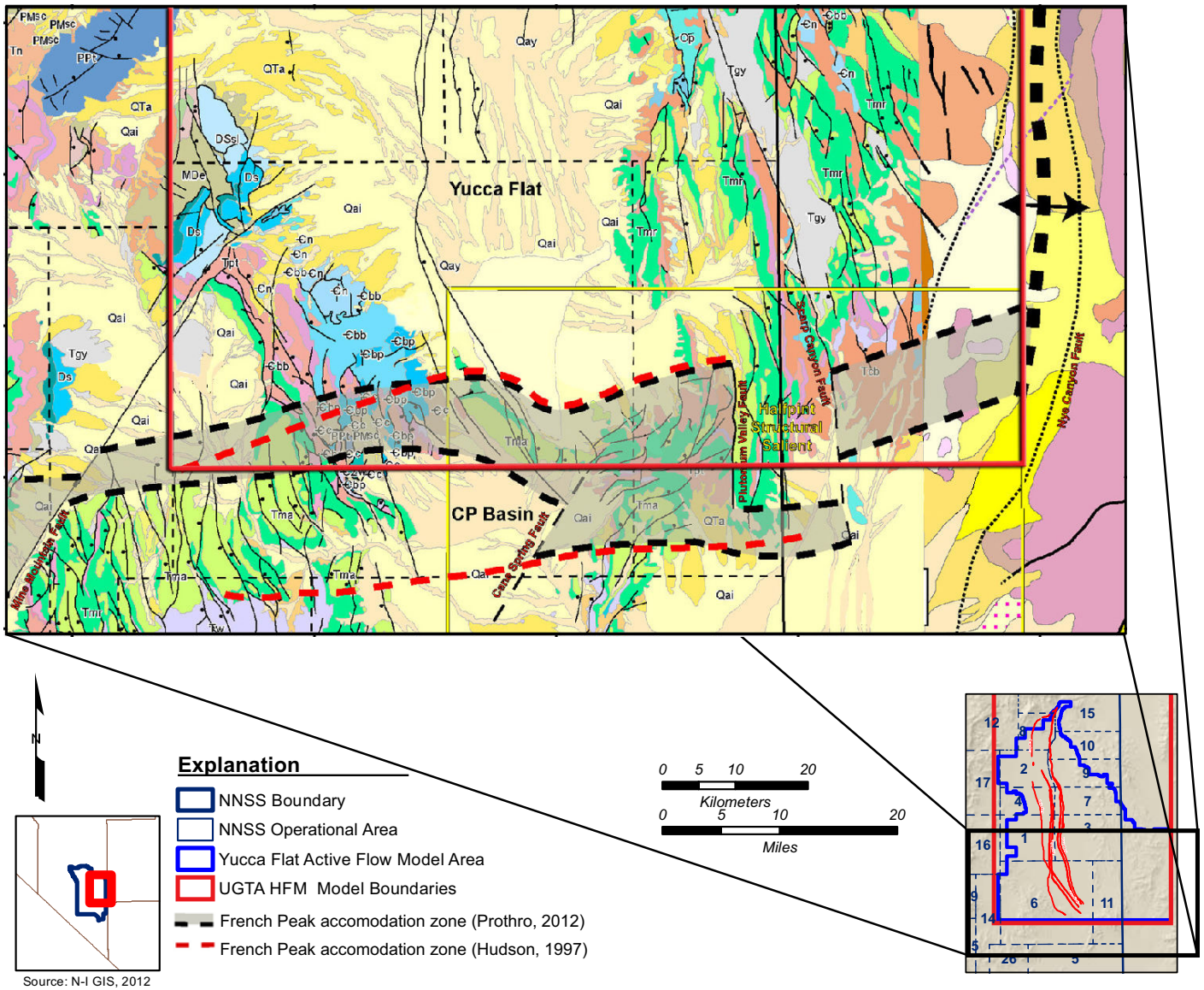

Source: N-I GIS, 2012

Figure 5-31
Geologic Map Showing French Peak Accommodation Zone
Sources: Prothro, 2012; Hudson, 1997; and N-I GIS, 2012

An alternative accommodation zone conceptualization was also implemented in which the width of the accommodation zone was much smaller and of the same order as the Yucca fault zone (i.e., core and damage zones). The spatial extent of this alternative accommodation zone is specified in Figure 5-74, and the associated flow and transport fields are analyzed and discussed in Section 5.6.5.

There is a general consensus among fault experts that, because of deformation stresses in play during fault formation, most faults have two permeability zones: a central core of low permeability and a damage zone of higher permeability (Caine et al., 1996; Evans et al., 1997). This conceptualization, which was implemented in the Yucca Flat model, is discussed in Appendix J and illustrated in Figure J-3. The fault core (adjacent to the fault plane) develops as a consequence of intense grinding caused by fault slippage. The intense grinding results in the formation of very fine particles that eventually solidify because of chemical alterations and create a hydraulic barrier normal to the fault plane. Adjacent to the core is the fault damage zone, which has significant fracturing in carbonate rock and thus enhanced permeability as compared to the host rock.

During the process of model calibration, the hydraulic conductivity in each of these two fault zones was estimated separately. The damage zone is conceptualized as anisotropic in both the lateral and vertical directions. The fault core is a highly consolidated medium with low permeability, and hence was assumed to be isotropic. Each fault zone was at least three nodes wide, with the center node representing the fault core and the peripheral nodes representing the damage zone surrounding the core (Figure 5-28).

5.4.4 Boundary Conditions

The solution of the groundwater flow equations requires that head and/or flow be specified at the model boundaries. As defined in Section 5.1, the extent of the LCA flow model domain is generally consistent with the extent of the HFM. As such, it extends far enough south to capture the possible extent of contaminant migration and far enough east to evaluate the potential for contaminant migration across the NNSS boundary. The northeast and western boundaries are selected to represent where the saturated LCA or LCA3 pinches out against low-permeability confining units such as the LCCU and UCCU.

In Yucca Flat, natural (no-flow) hydrologic boundaries exist only in the northern half of the model where the LCA and LCCU outcrop. In the southern portions, the model must account for regional

inflow and outflow that may be occurring along the lateral edges of the model. The model must also account for inflow due to recharge from the overlying unsaturated and saturated alluvial and volcanic units. There are no internal discharge locations within the Yucca Flat/Climax Mine CAU flow model domain.

Constant head and flux conditions were applied along the model boundaries. The system is conceptualized to receive cross-boundary flux along the western, northern, eastern, and northeastern boundaries; the cross-boundary flux along the northeastern boundary corresponds to the lateral influx across the confining units in the Halfpint Range (Figure 5-32). The estimates of the range of cross-boundary fluxes indicated in Figure 5-32 are derived from the regional models that are summarized in Section 5.3.

The top boundary receives recharge from the unsaturated zone and saturated alluvial/volcanic aquifer system models, as well as two areas to the west and east of the footprints of the unsaturated zone and saturated alluvial/volcanic aquifer system flow models. Therefore, three separate zones were assigned for the LCA model to receive recharge as shown in Figure 5-32. The zone in the center receives recharge from the unsaturated zone and saturated alluvial/volcanic aquifer system models, while the two separate zones in the east and west (called “top eastern” and “top western” in Figure 5-32) have recharge assigned based on the regional estimates of net infiltration. The amount of recharge in each of these zones is a calibration parameter. The range of acceptable recharge in the east and west zones was established using the results of five calibrated regional models, each representing the result of an alternative recharge conceptualization as discussed in the Yucca Flat/Climax Mine HDD (SNJV, 2006b). The recharge distribution in the USGS DVRFS calibrated model within the Yucca Flat/Climax Mine CAU model area and regionally is presented in Figure 5-33 for the steady-state calibrated DVRFS model. The recharge distribution at the Yucca Flat/Climax Mine CAU for four alternative regional models documented and discussed in the Yucca Flat/Climax Mine HDD (SNJV, 2006b) is presented in Figure 5-34, from which a fairly similar distribution can be noted in all models. A common feature in all five regional models is a region of zero to minimal recharge in the center of the basin coinciding with the alluvium and volcanic rocks modeled in the unsaturated zone and saturated alluvial/volcanic aquifer system models. The UGTA Revised model has a higher recharge rate in the center than the USGS or DRI models, but this model has largely been superseded by the USGS DVRFS model. In the USGS and DRI regional models, recharge in the center of the basin varies between approximately 2 to 4 kg/s, which is equivalent to a recharge rate of about 0.2 to

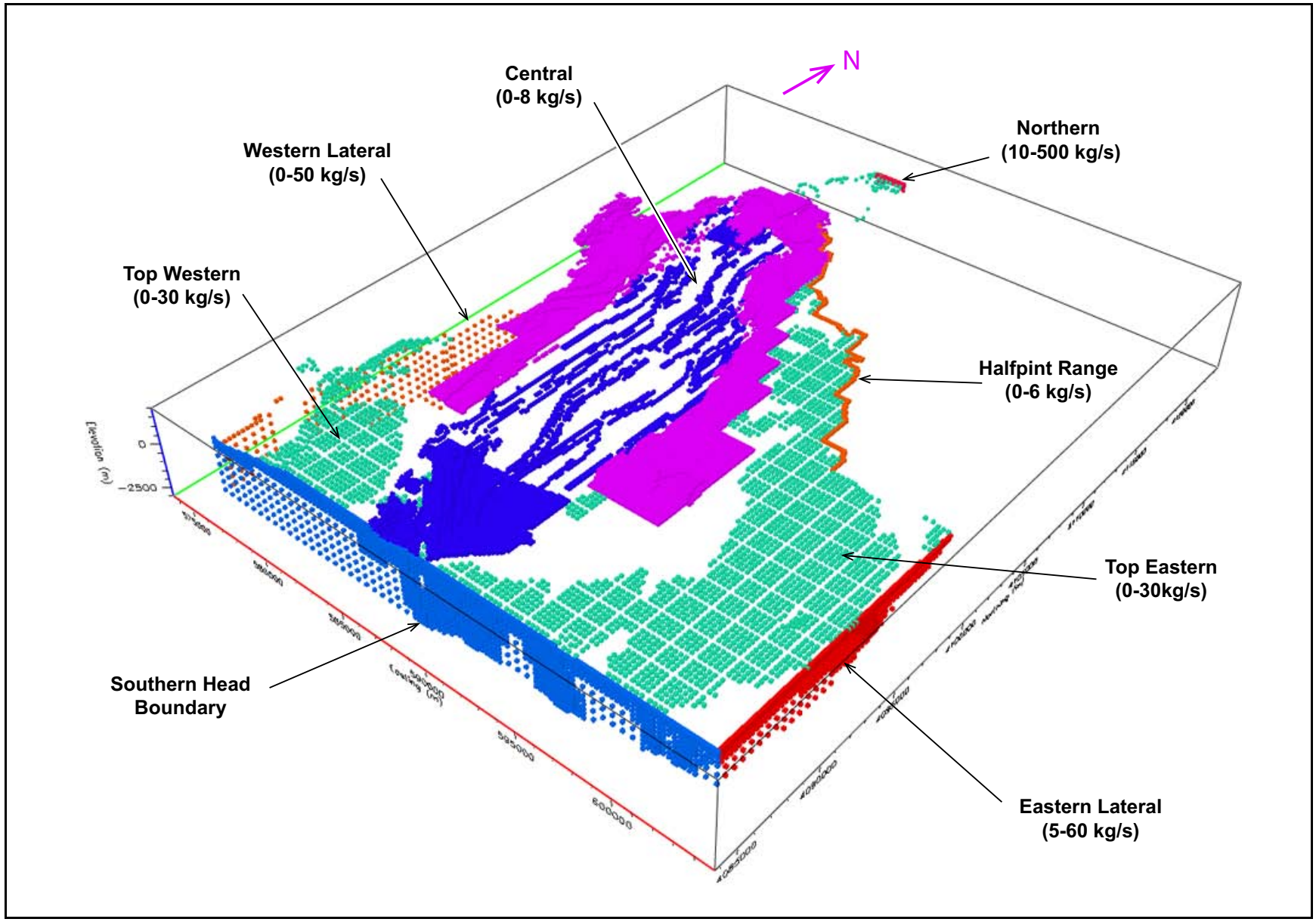

Figure 5-32
Boundary Types along the Lateral Edges and Top of the Yucca Flat LCA Model

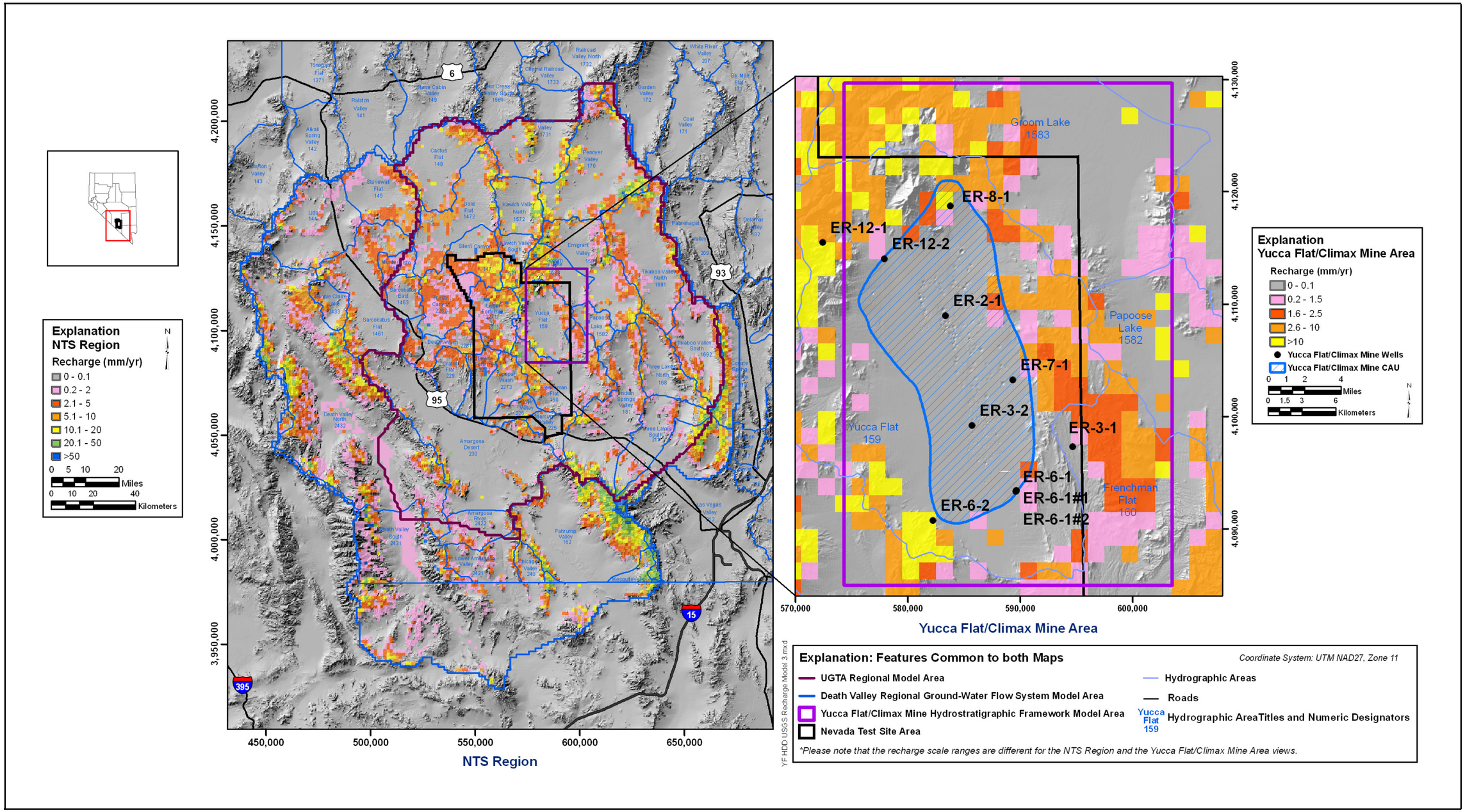

Figure 5-33
USGS Recharge Distribution in the Calibrated Steady-State Version of the DVRFS Model
Source: SNJV, 2006b

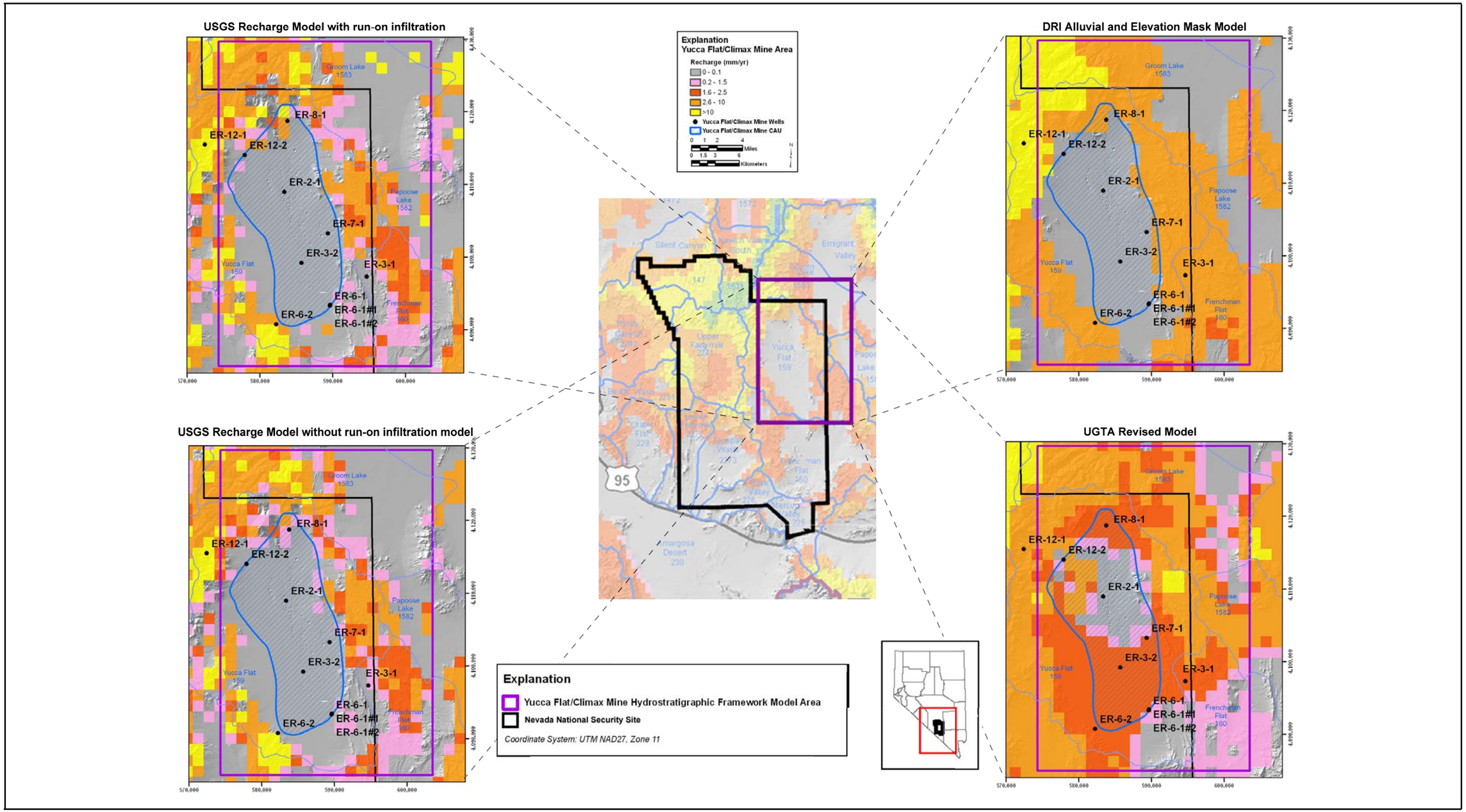

Figure 5-34
Recharge Distribution in USGS Alternative Regional Models
Source: Modified from SNJV, 2006b

0.4 mm/yr. Outside the center of the basin in areas where the LCA subcrops, the estimated recharge varies between 0.2 and 10 mm/yr. Recharge in the regional models was calculated for five zones in order to obtain bounds for the Yucca Flat model recharge zones specified in Figure 5-33. The total recharge in the west, north, and east zones, and the unsaturated zone and saturated alluvial/volcanic aquifer system model zones for the DVRFS base steady-state model is presented in Figure 5-35. Cumulative recharge for the four alternative USGS regional models is presented in Figure 5-36. In all five models, there is negligible recharge in the center of the basin, and approximately similar amounts of recharge in the west, north, and east. The cumulative infiltration in the five regional models varies between 61.5 and 95.1 kg/s.

In the Yucca Flat LCA groundwater flow model, the spatial distribution of the total recharge within each of the three recharge zones shown in Figure 5-35 honors the actual recharge distribution in each parent model: the unsaturated zone and saturated alluvial/volcanic aquifer system models in the center of the basin, and the USGS DVRFS base calibrated flow model (Belcher et al., 2004) in the east and west zones along the basin margins. Recharge to the LCA in the region of the saturated alluvial/volcanic aquifer system model is primarily along faults as shown in Figure 5-37, whereas almost the entire area underneath the unsaturated-zone model that is outside the saturated alluvial/volcanic aquifer system model area receives recharge. In the eastern and western peripheral zones, recharge primarily occurs in regions where the LCA either outcrops or subcrops. All lateral boundary fluxes and the top model recharge were specified as calibration parameters as discussed further in Section 5.5. The basis for the specified upper and lower limits for the boundary conditions is also discussed in Section 5.5.

Groundwater exits the model primarily along the southern boundary, which was specified as a constant-head boundary. Specified heads were used because they are better known than the magnitude and distribution of lateral boundary fluxes. The heads along the southern boundary were estimated from published potentiometric surface maps (Winograd and Thordarson, 1975; Laczniack et al., 1996; Fenelon, 2005; SNJV 2006b). The heads were estimated to drop linearly from 748 m amsl in the west and 729 m amsl in the east to 726 m amsl in the center of the basin.

5.5 Flow Model Calibration

The Yucca Flat LCA groundwater flow conceptual model described in Section 5.2 was transformed into a mathematical model in Section 5.4. The purpose of the Yucca Flat LCA groundwater flow

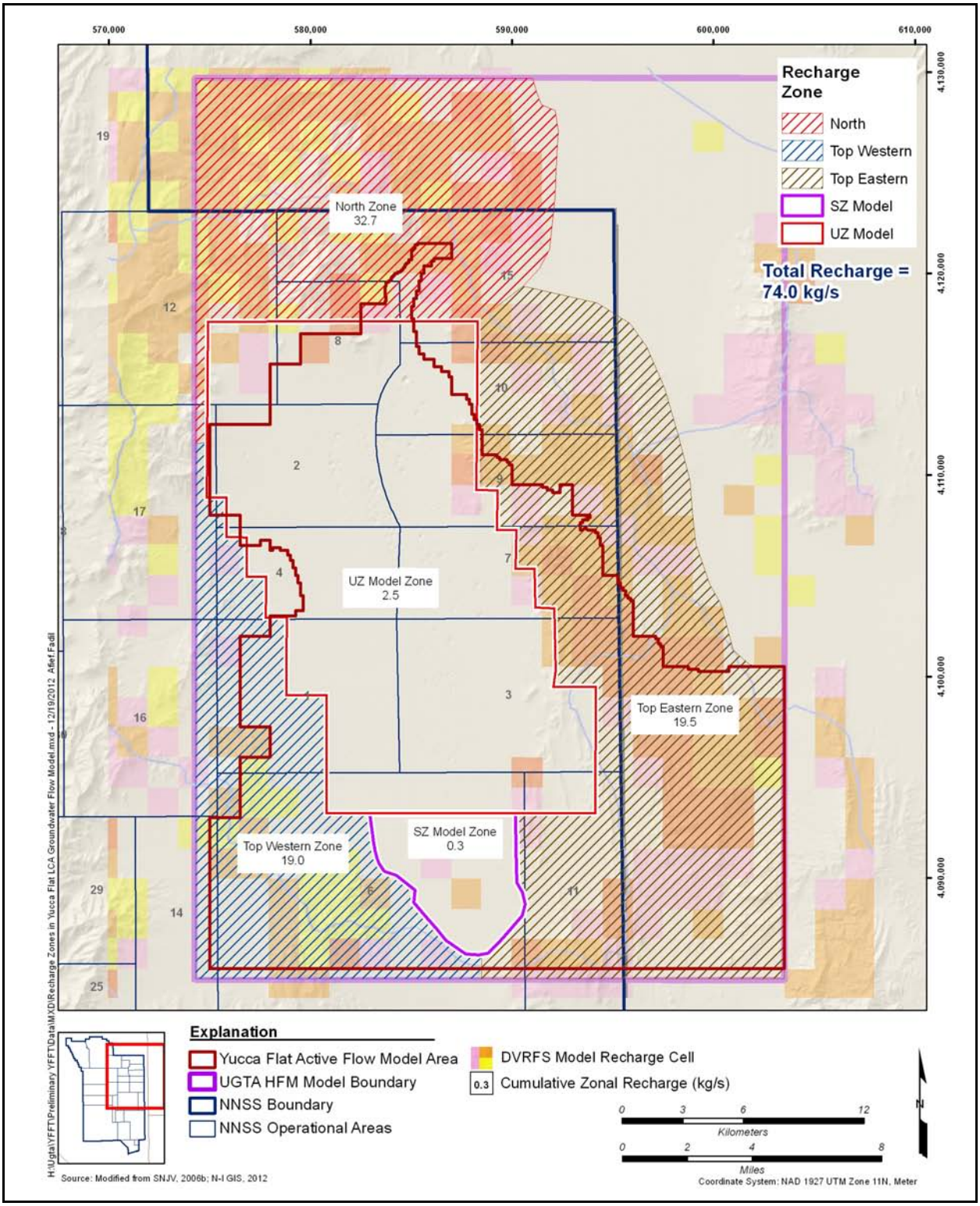

Figure 5-35
Cumulative Infiltration (kg/s) Corresponding to the DVRFS Calibrated Steady-State Model in Yucca Flat Recharge Zones

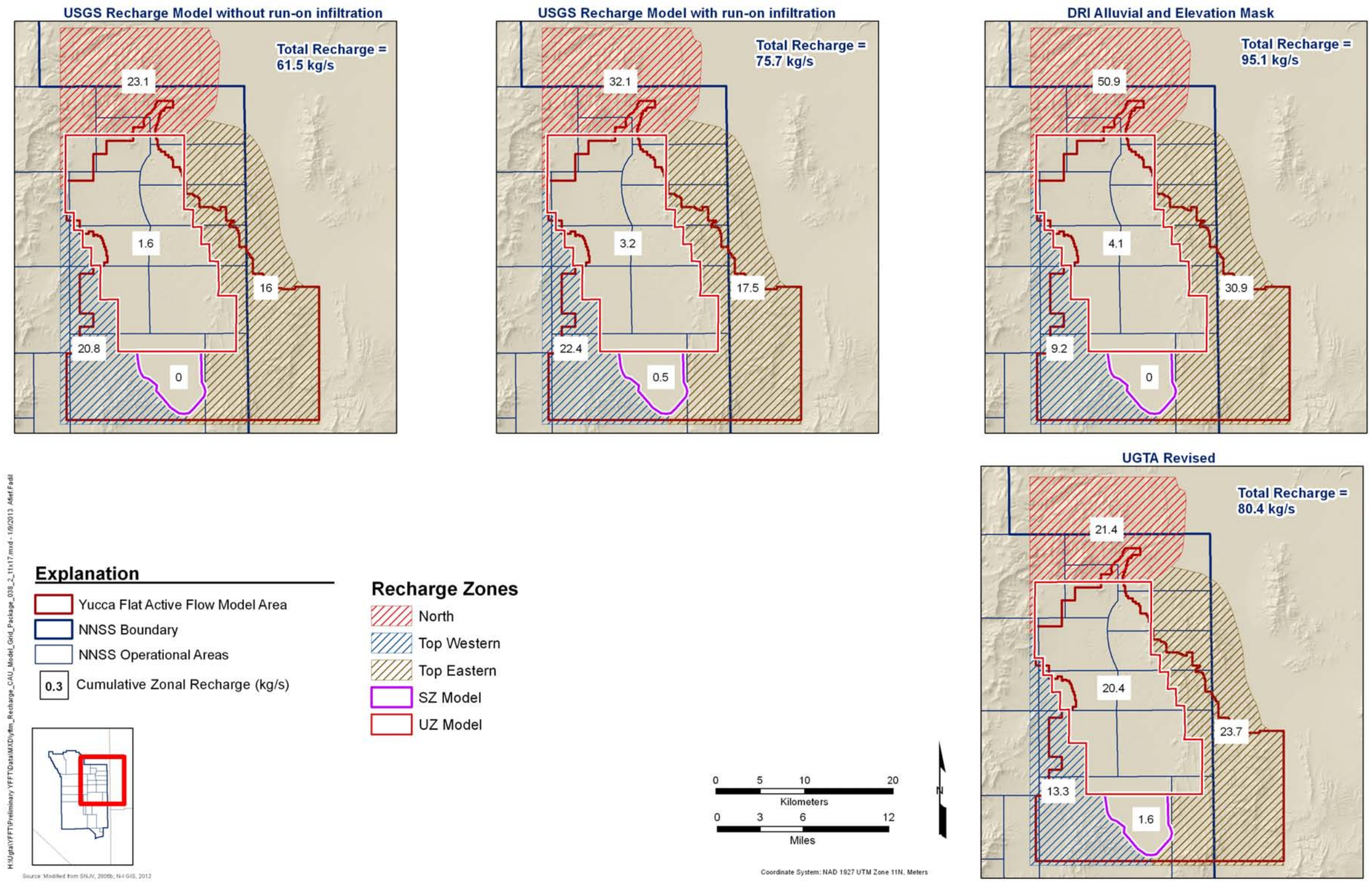

Figure 5-36
Cumulative Infiltration and Recharge in Individual Zones in the USGS Base and Alternative Models

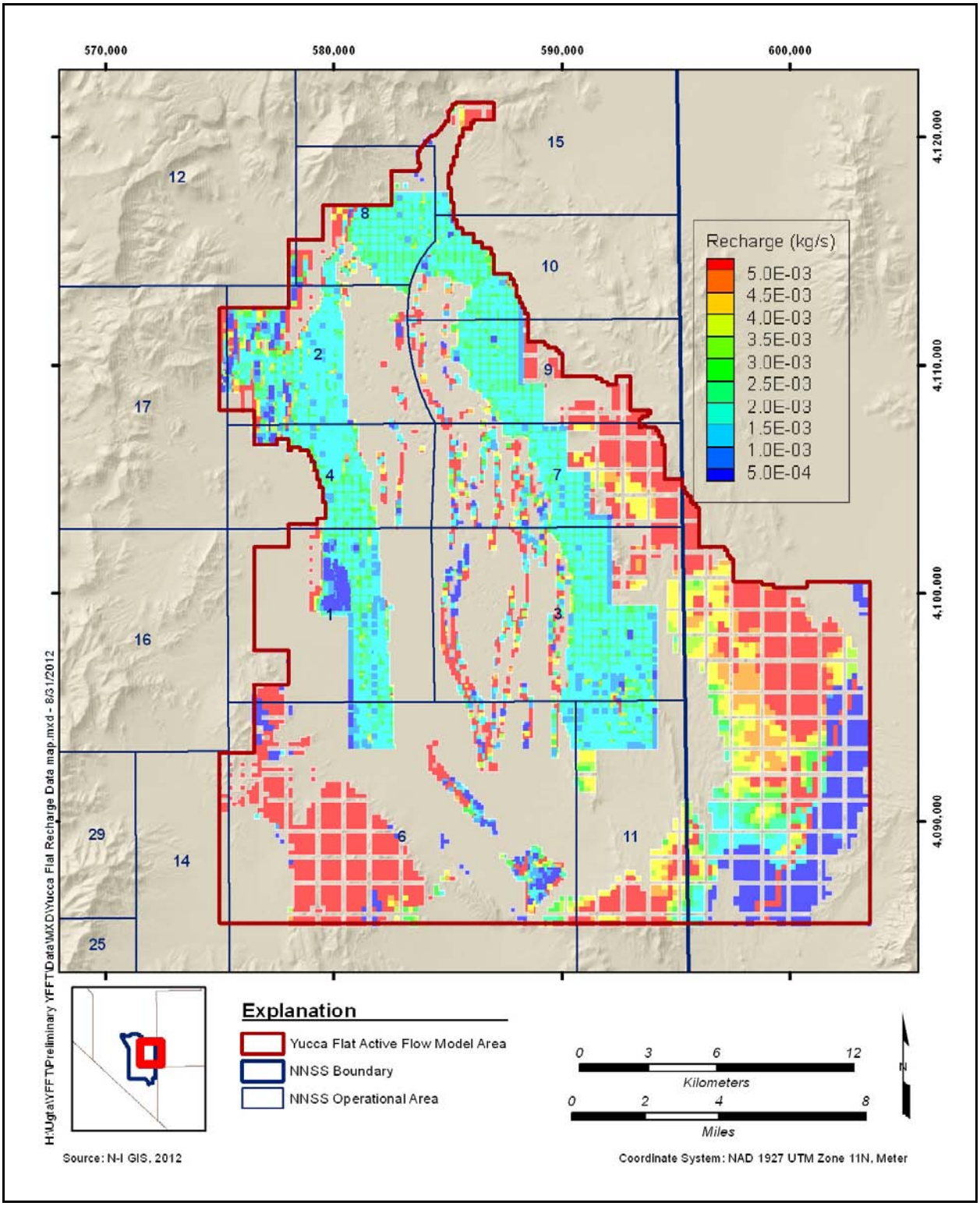

Figure 5-37
Spatial Distribution of Top Boundary Flux Corresponding to Recharge Rate of 5 mm/yr

model calibration is to reconcile model results with measured states of the aquifer system. This is accomplished through the guided adjustment of boundary fluxes and heads, and hydraulic properties for HSUs and faults within a hydrostratigraphic framework in order to match specified calibration targets. Targets included observed water-level, and drawdown and recovery data within the model boundaries. The flow model was used to develop particle trajectories from radionuclide source locations. The particle trajectories so developed were then used to conduct transport simulations for forecasting radionuclide migration for a period of 1,000 years.

This section describes the flow model calibration approach and the calibration results for the base HFM described in Section 5.2. The base HFM is the most viable model developed with existing data of the subsurface geology at Yucca Flat and is described in detail in BN (2006). Alternative models and their associated boundary conditions were investigated during the conceptual model uncertainty analysis phase, and the results are documented in Section 5.6. The results of flow model parameter sensitivity analyses are presented in Section 5.7.

5.5.1 Calibration Background

5.5.1.1 Calibration Metrics

The model calibration was conducted with the parameter estimation code PEST developed by Watermark Numerical Computing (Doherty, 2004). PEST was used to optimize hydraulic parameters and boundary conditions of the Yucca Flat LCA flow model in order to obtain a close match with observed heads and drawdowns. PEST uses an automated procedure where the unknown model parameters are automatically identified using an optimization scheme that minimizes the observation error (i.e., the difference, or the residual, between observed data and simulated results). The PEST code begins by perturbing each adjustable parameter by a certain amount and recording how the model residuals change. This sensitivity information is used by the Levenberg-Marquardt algorithm in PEST to compute parameter updates that improve model agreement with the observations.

The PEST code also includes a variety of statistical tools that help develop understanding of the model, and the representativeness and uniqueness of the calibration process within the constraints of the considered conceptual model and related assumptions. These features include (1) the singular value decomposition of the Jacobian matrix, (2) parameter identifiability information, and (3) the condition number of the covariance matrix. The use of these tools in PEST is summarized

in Doherty and Hunt (2010). The singular value decomposition of the Jacobian matrix estimates the extent of overparameterization of the model. The parameter identifiability module of PEST ranks the ability of the optimization method to uniquely identify each parameter. The condition number of the covariance matrix is useful for determining the optimal weights to apply to different aspects of the observations. Examples of implementing these tools during the model calibration of the LCA flow model are summarized in Section 5.5.1.4.

In addition to the tools used during calibration, sensitivity and related correlation coefficients provide useful information about the robustness of the parameter estimation. The sensitivity and correlation coefficients describe how much the model calibration changes relative to a change in parameter value and how parameters may influence one another. This is useful in testing the conceptual model to identify which parameters control model behavior and which parameters may act similarly on model results. In addition, these statistics allow parameters that may be important to model calibration to be quantitatively identified and considered in more detail. Sensitivity analyses for the parameters of the LCA flow model are summarized in Section 5.7.2.

ASTM Standard D5490, *Standard Guide for Comparing Ground-Water Flow Model Simulations to Site-Specific Information* (ASTM, 1993), describes several approaches for evaluating the agreement between a flow model and the observed system. These procedures were used to compare the results of flow model simulations to measured field data as part of the calibration process for the Yucca Flat LCA flow model. Comparisons were made that included qualitative and quantitative comparisons of model results with (1) measured steady-state heads at observation wells and (2) observed drawdowns during the transient MWAT conducted in 2006. These observation targets are described in detail in Section 5.2 and are further summarized below.

A variety of numerical and graphical tools are used to investigate flow model calibration. These include summary statistical measures such as the mean error, largest and smallest errors, standard deviation of error, and sum of weighted squared error.

The residual between the observed and computed head values is

$$r_{h,i} = H_i - h_i \tag{5-1}$$

where

$r_{h,i}$ = residual head
H_i = observed head at a given location
h_i = computed head at a given location

The mean error for head residuals is defined as

$$ME = \sum w_{h,i}\, r_{h,i} / n \tag{5-2}$$

where

ME = mean head error
$w_{h,i}$ = weight assigned to the head measurement H_i
n = number of computed and measured heads being compared

The standard deviation of the error is defined as

$$SD = [\sum w_{h,i}\,(r_{h,i} - ME)^2 / (n-1)]^{1/2} \tag{5-3}$$

where SD is the standard deviation.

The sum of the weighted squared error is defined as

$$\Phi = \sum (w_{h,i}\, r_{h,i})^2 + \sum (w_{d,i}\, r_{d,i})^2 \tag{5-4}$$

where

Φ = sum of the weighted squared error
$w_{d,i}$ = observation weight assigned to the drawdown target
$r_{d,i}$ = residual between the observed and computed drawdown values

During calibration, attempts were made to reduce the mean error to zero. The standard deviation, which describes the spread of the errors, also was used in the calibration process, because even though the mean error may be low, a large spread in the errors signifies that alternative models may be viable.

Statistical measures are useful for summarizing model behavior but do not readily give a sense for the spatial distribution of errors. To address this issue, plots of posted head residuals in plan view showing the spatial distribution of errors in the model were examined. This type of plot is useful for

examining whether the model errors are randomly distributed in space or clustered, with positive errors in some parts of the model and negative errors in others.

5.5.1.2 Model Parameterization

A total of 145 hydrogeologic properties and boundary conditions were specified as parameters in PEST. Of the 145 parameters, 98 were allowed to adjust during the calibration process. There are a total of 107 faults in the model, the traces of which at the top of the LCA vary from approximately 0.1 to 36 km. In order to reduce the problem dimensionality, it was decided to only allow faults with a trace larger than 3 km to vary independently. The hydrogeologic properties of faults with a trace less than 3 km were allowed to vary but in unison, i.e., the property values were tied as recommended in Doherty (2004), and Doherty and Hunt (2010). These small faults were broken into two groups: faults east of the Yucca fault and faults west of the Yucca fault. The hydrogeologic properties of all faults in each of these two groups were tied and varied jointly. All adjustable hydrogeologic parameters in PEST, along with their specified upper and lower limits, are specified in Table 5-8. All adjustable parameters were log transformed as the best convergence characteristics were observed with such a transformation.

Table 5-8
List of Adjustable Hydrogeologic Parameters and Boundary Conditions
(Page 1 of 3)

Adjustable Parameter	PEST Parameter Name	Lower Limit	Upper Limit
Boundary Flux		**kg/s**	
North	northflux	10	500
East	eastsoflux	5	60
Top LANL	top_lanl	0.01	8
Halfpint	hpflux	0.01	6
Top East	hevesi_east	0.01	30
Top West	hevesi_west	0.01	30
West	westflux	0.01	50
Storage		**1/m**	
Confined Rock Storage	aqc_con	1.0E-08	1.0E-05
Unconfined Rock Storage	aqc_unc	1.0E-06	1.0E-03
Fault Storage	aqc_flt	1.0E-08	1.0E-05

Table 5-8
List of Adjustable Hydrogeologic Parameters and Boundary Conditions
(Page 2 of 3)

Adjustable Parameter	PEST Parameter Name	Lower Limit	Upper Limit
Anisotropy		**Dimensionless**	
Faults	anisofaultx, aniso145x, aniso148x, aniso178x, aniso190x, aniso176x, aniso177x, anisofaultz, aniso145z, aniso148z, aniso178z, aniso190z, aniso176z, aniso177z	0.001	1
LCA Vertical	lcavniso	0.01	1
Rock Permeability		**m^2**	
LCA West Permeability	3_lcaw	1.0E-14	3.0E-11
LCA Central Permeability	9_lcac	1.0E-14	4.0E-11
LCA East Permeability	11_lcae	1.0E-14	1.0E-11
LCCU Rock Permeability	6_lccu2	1.0E-18	1.0E-08
LCA3 Rock Permeability	7_lca3	1.0E-18	1.0E-08
UCCU Rock Permeability	4_uccu	1.0E-18	1.0E-08
Fault Permeability		**m^2**	
Minor East Faults (Untied)	114_yf_91bn1, 118_hp112_16, 121_hp40, 122_rv60, 123_hp120, 124_hp10, 125_hp20, 126_hp30, 127_hp121, 128_hp116, 129_hp115, 132_hp108, 135_hp123, 136_yf_133, 137_yf_131, 139_hp72_yf1, 140_hp50_yf1, 141_hp60, 142_mm70, 143_hp124, 147_yf_103n1, 149_area3n9, 150_yf_embud, 151_yf_7r, 152_yf_55, 154_piranha, 155_yf_61a63, 156_yf_71, 160_area3eas, 161_yf_7y, 163_yf_97a, 167_yf_75, 169_yf_119n1, 171_yf_125, 223_yf_30,101_area13bu	1.0E-14	4.0E-10
Minor East Faults (Tied to Fault 126, i.e., 126_hp30)	115_yf_57, 116_yf_56, 130_hp125, 138_mm90, 144_mm20_60, 146_yf_129, 153_yf_54, 157_yf_69n67, 158_yf_62, 159_yf_61b, 162_yf_97b, 164_yf_95a, 165_yf_area7, 166_yf_80, 168_yf_93b, 170_hp122, 172_yf_127, 173_yf_126, 174_yf_wellc, 179_yf_48, 180_yf_46a, 181_yf_46b, 182_yf_50c, 183_yf_37n39, 184_yf_33b, 185_yf_34a, 186_yf_34b, 187_yf_44b, 188_yf_44c, 189_yf_35b, 191_yf_44a, 192_yf_40, 193_yf_41, 194_yf_38, 195_yf_tippi, 196_yf_baneb, 197_yf_33a, 219_cp20, 220_cp10, 221_cp30, 222_cp50	1.0E-14	4.0E-10
Minor West Faults (Untied)	175_yf_26egh, 217_yf_12, 218_yf_14n16	1.0E-14	1.0E-10
Minor West Faults (Tied to Fault 175, i.e., 75_yf_26egh)	198_yf_wgh, 200_yf_31, 201_yf_wellc, 202_yf_18, 203_yf_28a, 204_yf_28b, 205_yf_minem, 206_yf_u_2cm, 207_yf_u_2cm, 208_yf_23, 209_yf_22c, 210_yf_22d, 211_yf_22b, 212_yf_24, 213_yf_25n27, 214_yf_6a, 215_yf_16b, 216_yf_6b, 224_yf_20b, 225_yf_19, 226_yf_20a	1.0E-14	1.0E-10

Table 5-8
List of Adjustable Hydrogeologic Parameters and Boundary Conditions
(Page 3 of 3)

Adjustable Parameter	PEST Parameter Name	Lower Limit	Upper Limit
Fault Permeability (continued)		**m²**	
Yucca Fault	145_yf1, 148_yf2	1.0E-14	1.0E-09
Carpetbag Fault	176_yf_50b, 177_carpetba	1.0E-14	1.0E-09
Topgallant Fault	178_topgalla, 190_topgalla	1.0E-14	1.0E-09
Yucca Fault Accommodation Zone	yfsouthext	1.0E-14	1.0E-10
Fault Core Multiplier		**Dimensionless**	
Minor Faults	114_itfc, 207_itfc	0.1	1.0
Yucca Fault	145_itfc	1.0E-06	1.0
Carpetbag Fault	177_itfc	1.0E-05	1.0
Topgallant Fault	178_itfc	1.0E-05	1.0
North Fault 101	101_itfc	1.0E-05	1.0

The specified upper and lower limits for the parameters in Table 5-8 were based on information presented in the Yucca Flat/Climax Mine HDD (SNJV, 2006b). The upper limit of major fault permeability values was extended beyond the upper limit of observed values indicated in Figure 5-11 in order to ensure that the calibration space could accommodate the possibility of high values that may not have been sampled because of limited observations of fault properties.

As discussed in Section 5.3, the boundary fluxes, in particular the flux into Yucca Flat from the north, are uncertain. For example, flux estimates for the northern boundary in the existing literature range from less than 1 kg/s (Winograd and Thordarson, 1975) to more than 1,000 kg/s (Pohlmann et al., 2007). For the base-case model calibration, the lower and upper limits for this boundary were set at 10 and 500 kg/s, respectively. The upper bound of about 1,000 kg/s was deemed unreasonable because the entire discharge in the Ash Meadows basin (which includes contribution from several other sub-basins in addition to Yucca Flat) is estimated to be between 700 and 820 kg/s (Laczniack et al., 1999). The lower bound was set to 10 kg/s in order to avoid underestimating the potential for northern influx to the LCA and to capture the net infiltration that occurs to the LCA north of Yucca Flat and north of the NNSS boundary as illustrated in Figure 5-36.

A guiding criterion for specifying uncertain upper inflow limits at boundaries was developed based on the assumption that the total flow through Yucca Flat is not greater than 200 to 400 kg/s. This is

consistent with the range of influxes into northern Frenchman Flat evaluated in the Frenchman Flat CAU flow model (SNJV, 2006c). Therefore, an upper limit of between 50 and 60 kg/s was deemed reasonable at boundaries other than the north, where inflows are more uncertain. An upper limit of 50 kg/s was specified along the western boundary, whereas an upper limit of 60 kg/s was specified along the eastern boundary, where the materials are more permeable and the zone of groundwater contribution much larger than in the west. The LCA pinches out in the vicinity of the Halfpint Range, and consequently, there is little (if any) cross-boundary flow occurring along this boundary. Winograd and Thordarson (1975) estimated an influx of less than 1.5 kg/s to the LCA in this region. An upper limit of 6 kg/s was specified along this boundary. There are no firm estimates of recharge to the LCA from the overlying alluvial and volcanic units in the center of the basin, or along the eastern periphery of Yucca Flat where the LCA outcrops. As discussed in Section 5.4, there is a minimal recharge occurring in the central portion of the Yucca Flat basin in all USGS and DRI regional flow models (Figures 5-35 and 5-36), varying between 1.6 and 4.1 kg/s. In the UGTA revised regional model, approximately 20.4 kg/s of infiltration is estimated in the center of the basin; however, this model has been superseded by the USGS DVRFS model. Consequently, an upper recharge rate of 8 kg/s in the center of the basin was assumed in the LCA model, which honors the lower recharge rates in the DVRFS model while providing provision for higher recharge should the PEST require additional infiltration during the calibration process. An upper limit of 30 kg/s was selected for the two recharge zones in the east and west outside the unsaturated zone and saturated alluvial/volcanic aquifer system model areas based on the calibrated infiltration rates in the regional models as presented in Figure 5-36.

As shown in Figure 5-12 and discussed in Section 5.2.5.2, the estimated specific storage based on field tests varies between 1.0E-08 and 1.0E-03 m^{-1}. An upper limit of 1.0E-03 m^{-1} was deemed high as it can result in a storage coefficient of greater than 1 in areas of the basin with a thick section of the LCA. Therefore, the lower and upper limits for the specific storage in areas of the basin where the LCA is considered confined were specified at 1.0E-08 and 1.0E-05 m^{-1}, respectively. Although it is recognized that the minimum value is low given that the compressibility of water is slightly less than 5.0E-06 m^{-1}, the low values are representative of data presented in Figure 5-12. Specific storage in the areas of the basin that are considered unconfined was assumed to vary between 1.0E-06 and 1.0E-03 m^{-1}. Values at the low end of this range compensate for the uncertainty in the areal extent of the unconfined portions of the LCA.

As discussed in Sections 5.2.5.3 and 5.2.5.4, there are no data pertaining to anisotropy in the horizontal or vertical direction. Lower limits of 0.001 and 0.033 were assumed for the horizontal and vertical anisotropies in faults. The country rock was assumed isotropic in the horizontal direction as the faults were assumed to provide anisotropy to the combined faulted medium. The maximum vertical anisotropy was specified as 0.01.

Intrinsic permeability estimates for the LCA based on field tests vary between 1.0E-14 and 1.0E-10 m^2. This translates to a hydraulic conductivity range of 0.01 to 100.0 m/day (assuming an average groundwater temperature of 20 °C) as depicted in Figure 5-11. Such a wide span probably reflects variation in the formation, with larger values reflecting the permeability of more fractured or faulted material and the lower end of range representing the permeability of more host-rock material. Consequently, the LCA country rock permeability range was assumed to vary between 1.0E-14 and 4.0E-11 m^2. Because the LCA3 in the western portion of the modeled area is assumed to be less permeable than the LCA (based on field test conducted at ER-12-3 and ER-12-4), the lower limit of hydraulic permeability of the LCA3 was set at 1.0E-18 m^2, which is the same as the lower limit of the clastic confining units. The upper limit of both the clastic units and the LCA3 was initially set to 1.0E-08 m^2 in order to explore the tendency of these parameters to move toward either the lower or upper end of the specified ranges. In all cases, the tendency of these parameters was to gravitate toward the lower end of the specified (permeability) range.

The major faults (i.e., Yucca, Carpetbag, and Topgallant) were estimated to encompass the higher end of the observed data range, and consequently, an upper permeability limit of 1.0E-09 m^2 was specified for these faults. It should be noted that the basis for specifying an upper limit that is greater than the largest estimated field value is that there are no field tests that represent permeability values in the major faults. The Yucca fault accommodation zone had a slightly narrower permeability range than the major faults that varied between 1.0E-14 and 1.0E-10 m^2. The permeability of the other faults was assumed to vary between 1.0E-14 and 4.0E-10 m^2.

The development of the fault core and damage zones is a consequence of fault propagation. As displacement (offset) occurs, the fault length grows. The displacement causes fracturing in the vicinity of the fault plane, i.e., in the damage zone. There is also intense grinding of rock along the fault plane, which results in pulverization of the host rock that eventually leads to the development of a low-permeability zone called the fault core. The permeability of the fault core is expressed in PEST

as a multiplier of the damage-zone permeability and is referred to as the fault core multiplier or core permeability reduction factor. This multiplier was assumed to vary between 0.1 and 1.0 in the minor faults. The larger Carpetbag and Topgallant faults and the Yucca fault accommodation zone each have a minimum core permeability reduction factor of 1.0E-05 based on a five-order-of-magnitude difference in observed permeability between the fault core and damage zones documented in the literature (Figure J-4). A minimum fault core multiplier of 1.0E-06 is specified for the Yucca fault, the master basin-and-range fault with the longest length. The maximum fault core multiplier is set at 1.0 to reflect the possibility that the fault core permeability could be as high as the damage zone permeability, but not greater.

With regard to infiltration, water from precipitation within the central part of Yucca Flat infiltrates to the alluvium and the underlying volcanic aquifers. On reaching the saturated volcanic aquifers, groundwater moves laterally toward the faults and eventually through these faults into the LCA. In areas where the unsaturated zone and saturated alluvial/volcanic aquifer system models overlie the LCA model, recharge to the LCA is obtained directly from these two models. Recharge to the LCA outside the areas where the unsaturated zone and saturated alluvial/volcanic aquifer system models directly overlie the LCA is obtained from the calibrated DVRFS model.

Three uniformly distributed recharge rates of 0.1, 1, 5, and 10 mm/yr were applied to the unsaturated zone and saturated alluvial/volcanic aquifer system flow models. The upper values of this range were included in the analyses in order to ensure that the contaminant flux from the contaminant sources in these models was not underrepresented. This recharge reaches the LCA either through the unsaturated zone where the unsaturated-zone model directly overlies the LCA model or after traversing through the volcanic aquifer(s) in areas where the saturated alluvial/volcanic aquifer system model underlies the unsaturated-zone model. This results in a nonuniform distribution of recharge to the LCA model. Although the magnitude of recharge to the LCA varies with the assumed infiltration rate, the spatial distribution of recharge to the LCA remains approximately the same for all three recharge cases represented in the unsaturated zone and saturated alluvial/volcanic aquifer system models.

Because recharge to the LCA model is a calibration parameter, the approach implemented was to calibrate to the total top recharge rate while maintaining the same relative spatial recharge distribution to the LCA model as obtained by the unsaturated and saturated alluvial/volcanic aquifer system models. Recharge to the LCA model at the rate of 5 mm/yr is presented in Figure 5-37, from which it

is clear that recharge to the LCA was assumed to occur primarily through faults in most of the areas underlying the saturated alluvial/volcanic aquifer system model, whereas recharge from the unsaturated zone occurs over the entire contact surface between the LCA model and the unsaturated-zone model.

In areas outside the unsaturated zone and saturated alluvial/volcanic aquifer system models, recharge to the LCA occurs at locations that correspond to the calibrated DVRFS model. As illustrated in Figure 5-37, the recharge rate to the LCA in areas where the LCA subcrops along the western and eastern margins of the Yucca Flat basin is significantly greater than that in the central portion of the model domain. This spatial distribution is attributed to the generally higher elevations and lack of thick alluvium along the basin margins that tend to promote the possibility of recharge, as opposed to the lower elevations and thick alluvium in the center of the basin that tend to significantly limit the infiltration rate.

5.5.1.3 Calibration Data

As previously discussed, two types of information, or targets, were used for calibration of the Yucca Flat LCA flow model: steady-state hydraulic heads, and transient pumping-test drawdowns. Both of these targets are described in detail in Section 5.2. The key features of these datasets that affect the model calibration are summarized below.

Hydraulic Heads

- Water levels have remained fairly steady at observation wells in the LCA (Figure 5-7). The only exceptions were Wells ER-6-2 and UE-1h, where water levels have exhibited a rising trend for over a decade.
- The three major faults in the center of the basin coincide with a groundwater divide in Yucca Flat.
- Heads in the west are approximately 10 m higher than heads in the east at the same latitude.
- Heads in the eastern part of the basin drop approximately 9 m from the northern to southern end of Yucca Flat.
- Heads in the western half of the basin are higher in the south than in the north. This trend in water levels has persisted over the entire period of record (Figure 5-8).

Pumping-Test Drawdowns

- Well ER-6-1 was pumped at approximately 35 kg/s, resulting in a drawdown of approximately 1 m after 194 days of pumpage. The bulk of the pumping occurred in the first days of the test.
- Rapid drawdown was observed at Wells ER-7-1 and UE-7nS, which are observation wells located more than 10 km north of Well ER-6-1.
- Almost full recovery was noted at observation wells after 194 days of cessation of pumpage.
- There was no drawdown recorded at Well UE-1h, which is the second closest observation well to Well ER-6-1 and lies west of the three major faults in the center of the basin. This observation suggests that the major faults create a barrier to transverse flow because of either the low-permeability fault core, or the high-permeability damage zone on either side of the core, or both.
- There was also minimal drawdown recorded at Well ER-3-1, which is the closest observation well to Well ER-6-1 and lies east of the major range-bounding fault (fault 121 in Figure 5-30).

5.5.1.4 Calibration Approach

The Yucca Flat parameter estimation problem may be formulated as a weakly constrained inverse problem for two reasons. First, because there are 145 parameters to be identified with known water-level or drawdown information at only 15 observation sites, the LCA inverse model represents an overdetermined system. Second, because both the hydrogeologic properties and boundary conditions are unknown, the governing equations can be satisfied by more than a single parameter set. These two ill-posed conditions are not unique to Yucca Flat as most real-world inverse problems are of a similar nature. Therefore, a systematic approach consisting of the following steps was implemented to address uncertainties associated with the ill-posed problem:

- Conduct a singular value decomposition of the Jacobian matrix to establish the extent of overparameterization.
- Utilize the PEST identifiability module to rank ability of the optimization method to uniquely identify each parameter.
- Examine the condition number of Jacobian matrix for determining optimal distribution of weights between steady-state head and MWAT drawdowns.

The first issue of an overparameterized system can be addressed by fixing parameters, relating parameters (i.e., regularization), or conducting global uncertainty analysis (e.g., NSMC analysis).

All of these techniques were applied to the Yucca Flat inverse problem as described below. The second problem of simultaneously estimating hydrogeologic parameters and boundary conditions can be addressed by utilizing data corresponding to an alternative hydrologic stress field in which the boundary conditions are either known or unaffected by the alternative stress field. Fortunately, information about an alternative flow field exists at Yucca Flat because sufficient data were collected during the MWAT. The MWAT, however, only reduces parameter uncertainty over a limited region of the model as explained below.

To determine which parameters can be reasonably estimated by PEST, a singular value decomposition of the Jacobian matrix was conducted. The singular values that are obtained on decomposing the Jacobian matrix provide an indication as to how many and which parameters can be estimated in the parameter estimation process. Parameters corresponding to only the first *n* parameters can be reasonably estimated by the inverse problem, where *n* is the parameter at which the ratio of the highest (i.e., first) singular value to the nth singular value is approximately 1,000. The singular values for the Yucca Flat LCA flow model are presented in Figure 5-38. The 1st and 15th singular values have a ratio of approximately 1,000, which implies that approximately 15 parameters can be reasonably estimated. Note that this number is also the number of observation wells at the site. Most of the parameters have very small singular values, which implies that the majority of the parameters do not contribute to the solution of the inverse problem and therefore cannot be uniquely identified during the calibration process.

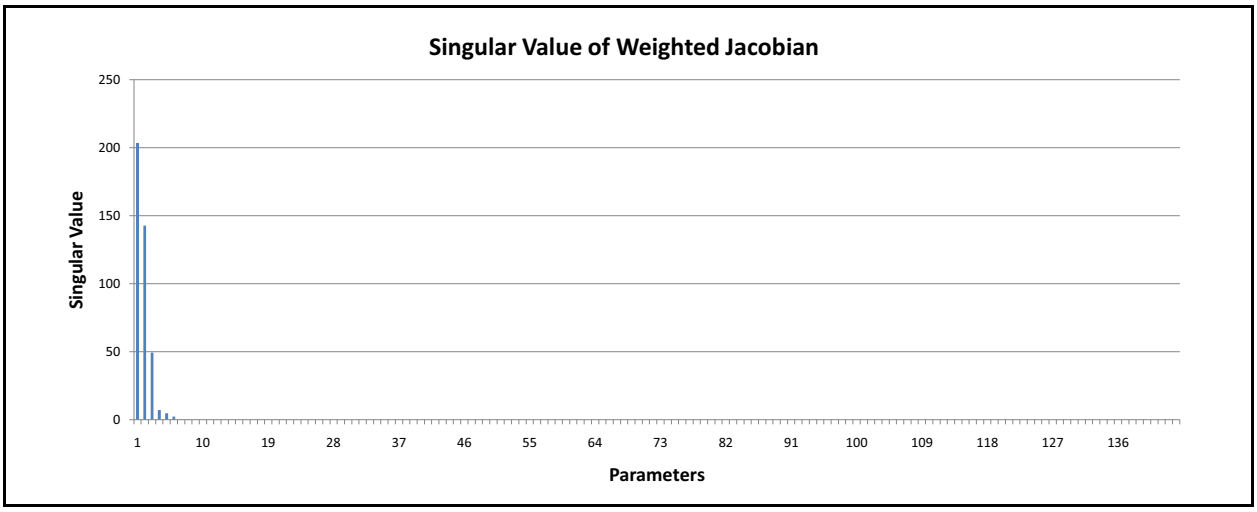

Figure 5-38
Singular Value of Jacobian Matrix for All Adjustable Parameters

Associated with the singular value decomposition is the PEST parameter identifiability index, which provides names of parameters that can be estimated during the inverse modeling process. The parameter identifiability index for each Yucca Flat LCA flow model parameter is presented in Figure 5-39. Identifiability ranges between 0 and 1, with parameters having an identifiability index of 1 being fully identifiable, and parameters having an identifiability index of 0 totally unidentifiable. As stated in the PEST manual (Doherty, 2004), only parameters with an identifiability index of 0.8 or greater can be reliably estimated. Accordingly, it is concluded that only about seven parameters can be reliably estimated.

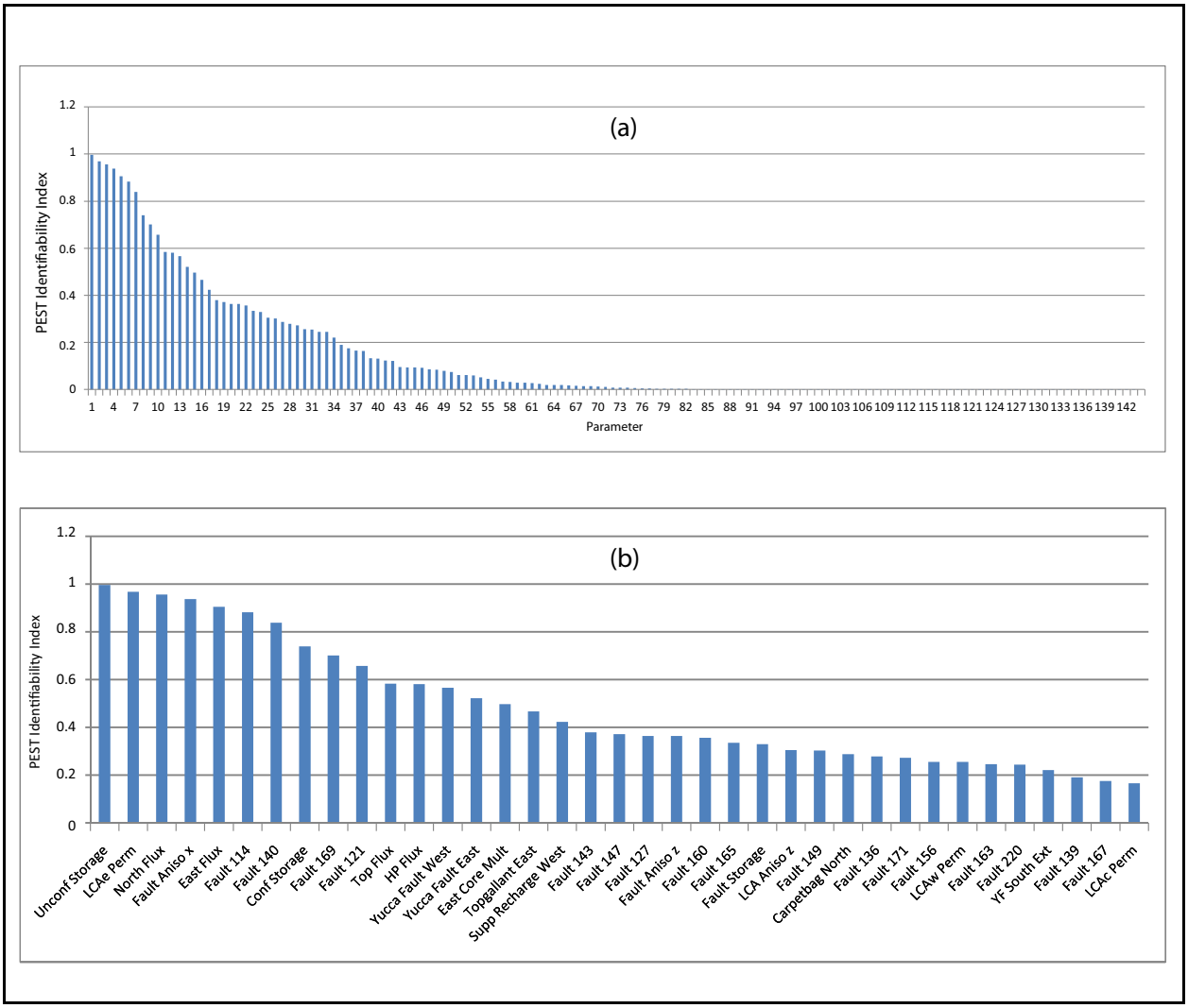

Figure 5-39
Identifiability Index for Adjustable Parameters: (a) All Parameters, and (b) Parameters with Identifiability Index Greater than or Equal to 0.16

A close examination of the identifiability index suggests that most of the highly identifiable parameters exist in the region of the modeled pumping-test influence shown in Figure 5-40. This conclusion can also be inferred from examining the identifiability of the longitudinal hydraulic conductivity of the faults as shown in Figure 5-41. Within the region of pumping-test influence, the identifiability of faults is the highest. Outside this region, the faults have low identifiability, with the exception of the Carpetbag and Topgallant faults, which have relatively high identifiability values because the large lateral extent of these faults influences the flow field fairly significantly.

Having established that the MWAT provides stability to the inversion process, a key question is how much weight should be assigned to the steady-state head targets and the MWAT drawdowns, both of which are part of the residual objective function. A single model run for PEST calibration involves two FEHM runs. The first is a steady-state run (without the MWAT), which yields simulated head values to compare with the steady-state head targets. The results of this run are taken as initial condition for simulating the MWAT. As discussed above, the steady-state solution does not constrain the hydrologic parameter estimation process, whereas the transient MWAT run does improve conditionality of the parameter estimation process. Therefore, if all the weights are assigned to the steady-state heads, then the problem is poorly constrained, as the steady-state heads can be reproduced by numerous combinations of parameters and boundary conditions, and consequently, the model rapidly converges in close proximity to initial estimates of the parameters. On the other hand, because the region of influence of the MWAT does not extend over the entire study area, imparting all weights to the MWAT would not allow all model parameters of interest to be estimated. Therefore, it is important to properly assign calibration weights to the steady-state head and transient drawdown targets so that the parameters are correctly identified.

The solution to the problem of proper weight assignment is to weigh the MWAT data sufficiently so that the inverse problem is transformed from the domain of an ill-posed calibration, as would be the case for only steady-state calibration targets, into a more well-posed calibration. This is achieved by examining the condition number of the Jacobian matrix. The condition number is a property of the matrix. A calibration problem with a low condition number is said to be well conditioned, whereas a problem with a high condition number is said to be ill conditioned. In context of the present problem, the steady-state problem is ill conditioned because the system of equations is not independent.

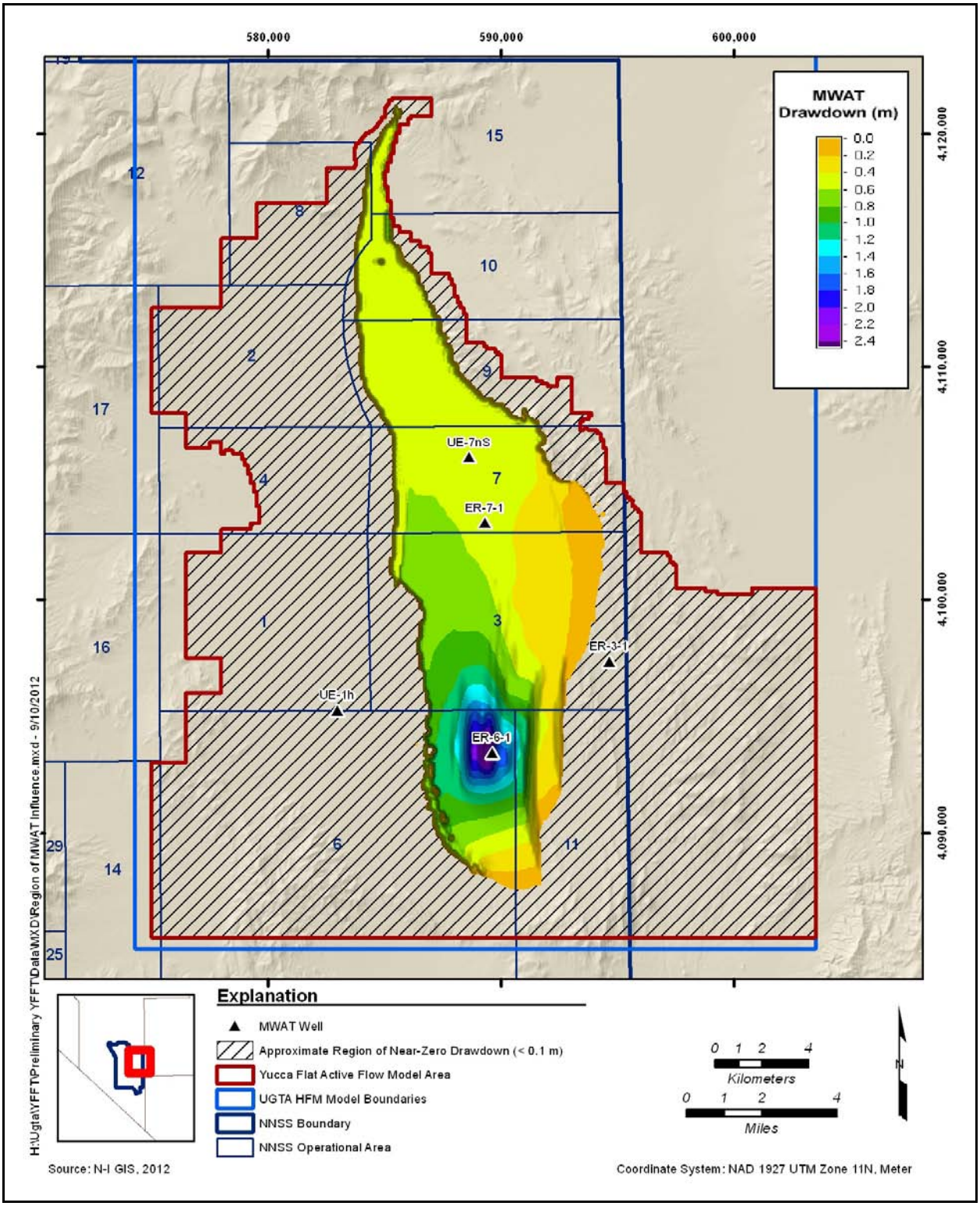

Figure 5-40
Modeled Region of MWAT Drawdown Influence

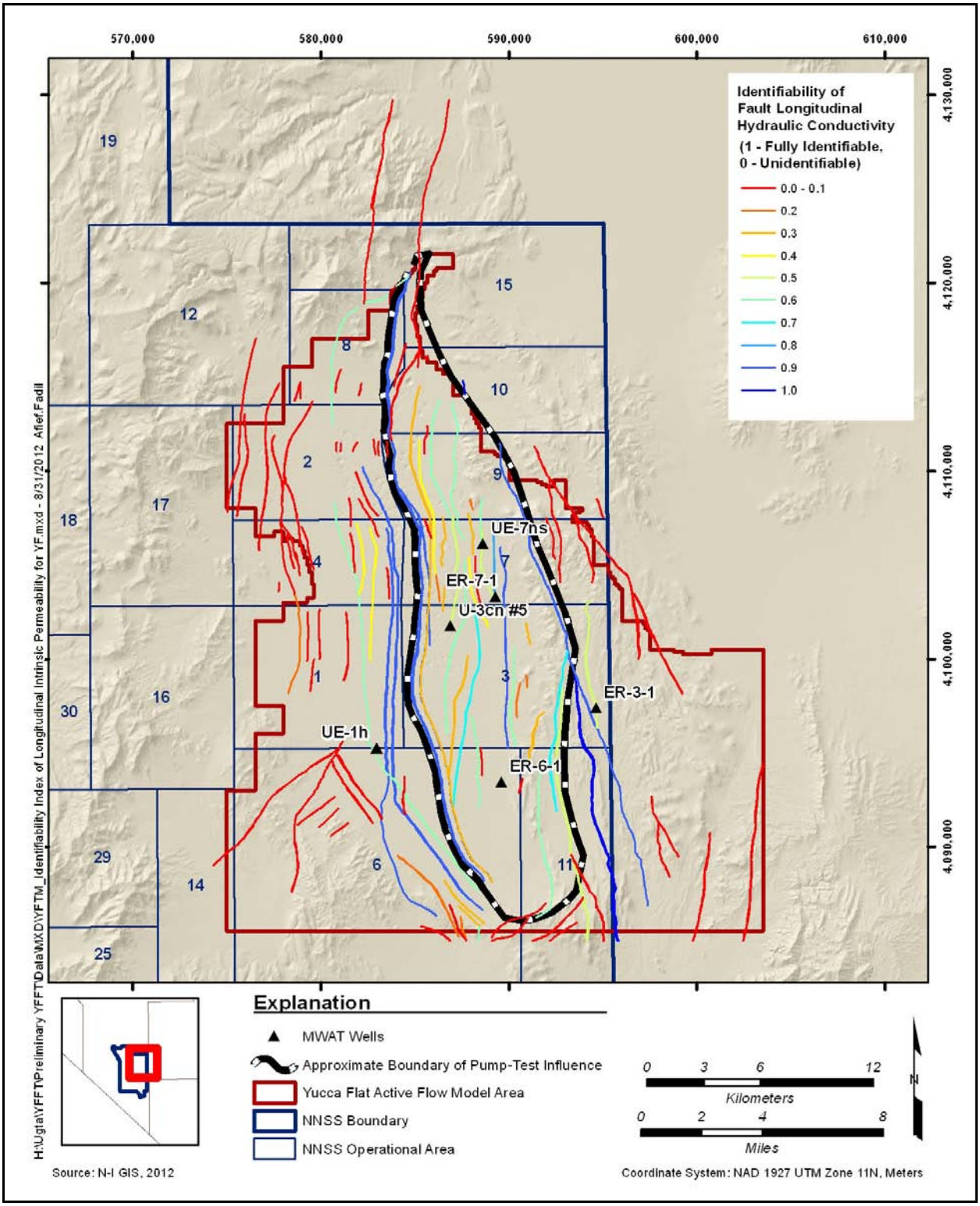

Figure 5-41
Identifiability Index of Longitudinal Permeability for Yucca Flat Modeled Faults

The matrix condition number as a function of the ratio of the MWAT drawdown weights to the steady-state head weights is depicted in Figure 5-42. The Jacobian has the highest condition number and thus is poorly conditioned for the steady-state problem, i.e., when the MWAT weights are zero. As the ratio of the MWAT to steady-state weights increases, the condition number decreases, i.e., the conditioning of the model improves. At a ratio of about 4, the condition number has substantially improved, with only marginal improvement noted at the next tested weight ratio of 10. As the ratio further increases, the problem conditionality worsens only marginally. It should be noted that, at a ratio of about 4, the residuals in the objective function contributed by the MWAT and steady-state heads were approximately the same, which also was the preferred outcome. Therefore, the MWAT observations were provided with a weight of 4, and the steady-state observations were provided with a weight of 1.

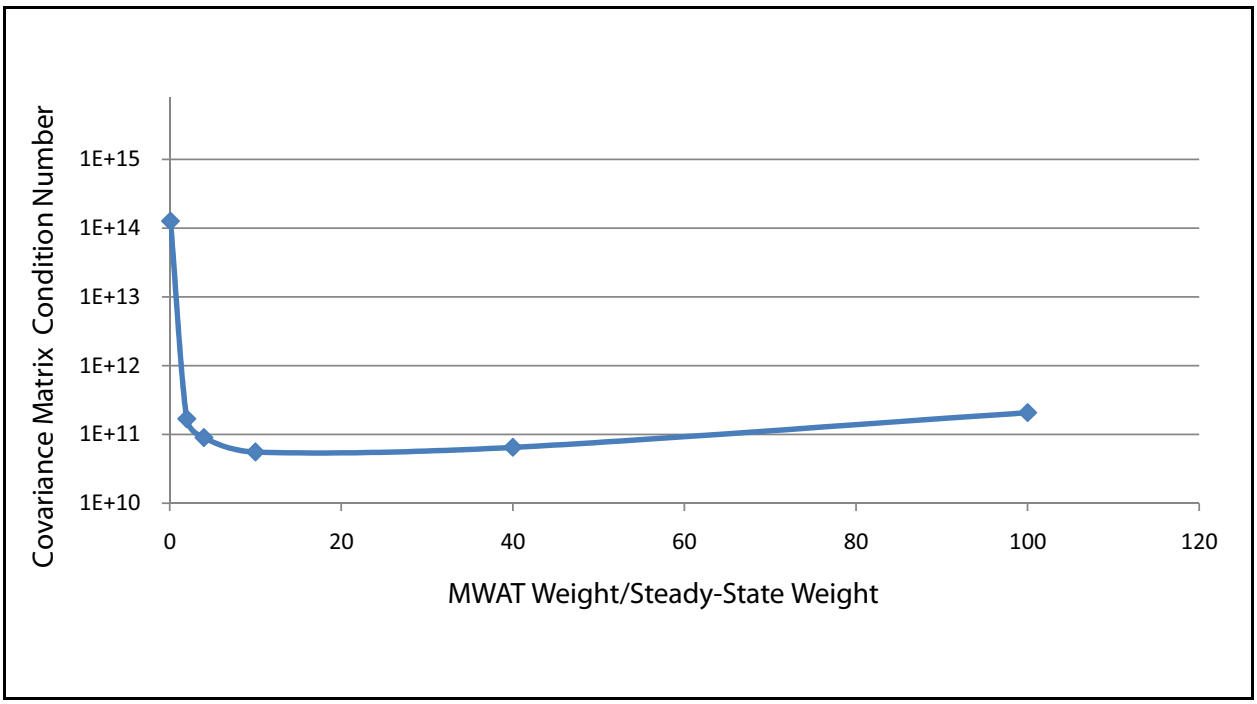

Figure 5-42
Matrix Condition Number as a Function of Steady-State Head and MWAT Drawdown Weights

As discussed above, a total of 146 hydrogeologic parameters and boundary conditions need to be estimated from head and drawdown observations at only 15 well sites. Therefore, the problem is overdetermined, which results in the need to regularize the system in order to impart stability to the parameter estimation process. The number of parameters that require estimation is large primarily

because there are 106 faults in the model for which the longitudinal, transverse, and vertical hydraulic conductivities need to be estimated. Of the 106 faults, however, there are only 3 large faults in the center of the basin—the Yucca, Topgallant, and Carpetbag faults (Figure 5-2)—and the rest are generally smaller faults to the east and west of the major faults. The inverse problem was, therefore, regularized by initially representing all small faults in the east in one permeability group and all small faults in the west to another permeability group. Every fault in these groups was assumed to have the same hydraulic property. This reduced the parameter dimensionality, and allowed PEST to proceed smoothly and the error objective function to drop precipitously. Once the objective function could not be lowered any further, the faults were allowed to vary independently, which allowed the parameter estimation process to lower the objective function even further.

5.5.2 Calibration Results

The flow model was calibrated simultaneously to the steady-state head targets specified in Figure 5-8 and the drawdowns specified in Figure 5-10. The FEHM model run cycle consisted of two simulations. The first was a steady-state FEHM run that provided the initial conditions for the subsequent transient MWAT FEHM run. For each PEST iteration, these two model runs were called in tandem, and all adjustable hydrogeologic parameters remained the same for the steady-state run and the transient MWAT run.

With the knowledge that the MWAT improves the conditioning of the inverse problem, a three-phase calibration approach was implemented in order to systematically guide the calibration process toward the final solution space. Initially, the MWAT information was the only data retained in the objective function. This resulted in moving toward close proximity of the final solution space for parameters in the region of pumping-test influence. Subsequently, the eastern steady-state heads were introduced. Finally, the western heads were added to the objective function because the western region is least constrained.

In addition to boundary fluxes, the calibration parameters were primarily the hydraulic permeability, anisotropy, and storage coefficient of the rock matrix and the faults. Each fault was conceptualized to contain two separate permeability zones: (1) a central core of low permeability, which can essentially act as a hydrologic barrier, and (2) a potentially highly permeable zone referred to as the damage zone (Figure 5-28). During the process of PEST model calibration, the hydraulic conductivities in these two zones were estimated separately and independently of each other. The damage zone is

conceptualized to be anisotropic in both the lateral and vertical directions. The fault core, on the other hand, is a highly consolidated medium with extremely low permeability and hence was assumed to be isotropic.

As mentioned above, all steady-state head and MWAT drawdown data were used as calibration targets, and PEST was invoked to estimate parameters and boundary conditions that minimize the objective function. The calibrated LCA potentiometric surface is presented in Figure 5-43. The head residuals and the simulated versus observed heads at the 15 observation wells are presented in Figures 5-44 and 5-45, respectively. As Figure 5-45 shows, the coefficient of determination (R^2) is greater than 0.99, indicating a good agreement between the observed and simulated values. The mean head residual is –0.02 m, and the weighted objective function for the entire dataset is 1.15 m^2. A summary of the calibration statistics is provided in Table 5-9. The calibrated recharge and cross-boundary fluxes are specified in Table 5-10. The difference of the total inflow minus the total outflow of 1.8 kg/s is acceptable and is the result of differences in inflow from the east and west lateral boundaries that outflow locally along the southern boundary.

The observed and simulated drawdowns at the MWAT sites are presented in Figure 5-46. As shown in Figure 5-46, the drawdowns at ER-3-1 and ER-7-1 during the MWAT were recorded nearly continuously. For calibration purposes, however, the simulated drawdown was compared with the observed drawdown at a few discrete times in order to minimize simulation time and output. As shown in Figure 5-46, the simulated output at 13 discrete times spans the entire pumping-test period fairly uniformly and therefore provides the necessary model output for comparison with the observed data in an efficient manner. The match between the observed and simulated drawdowns is fairly reasonable at all five observation well locations. The weighted square of residuals for the MWAT is only 0.55 m^2. The final calibrated value for each model parameter is presented in Table 5-11.

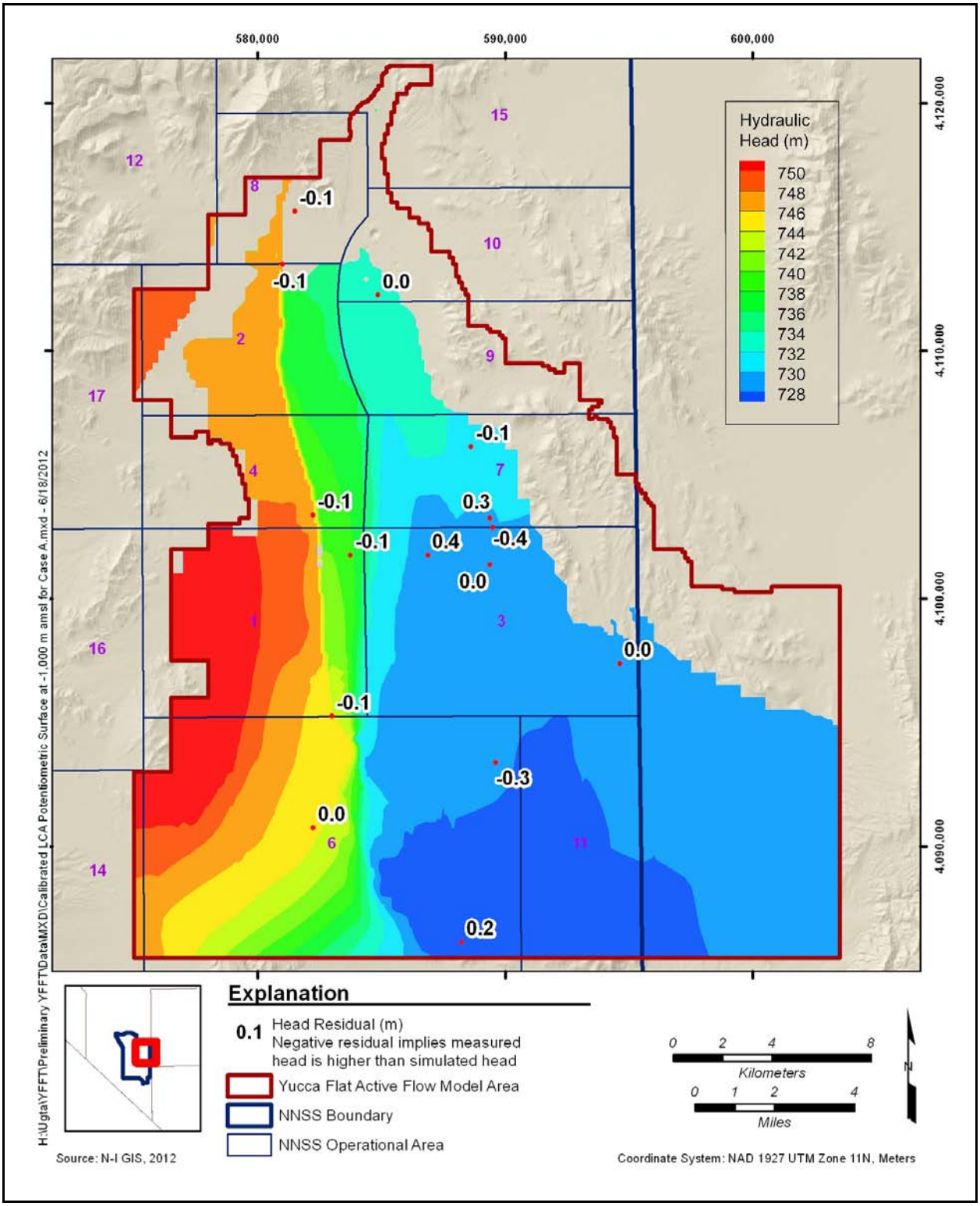

Figure 5-43
Calibrated LCA Potentiometric Surface at –1,000 m amsl and Associated Head Residuals at Steady-State Observation Wells

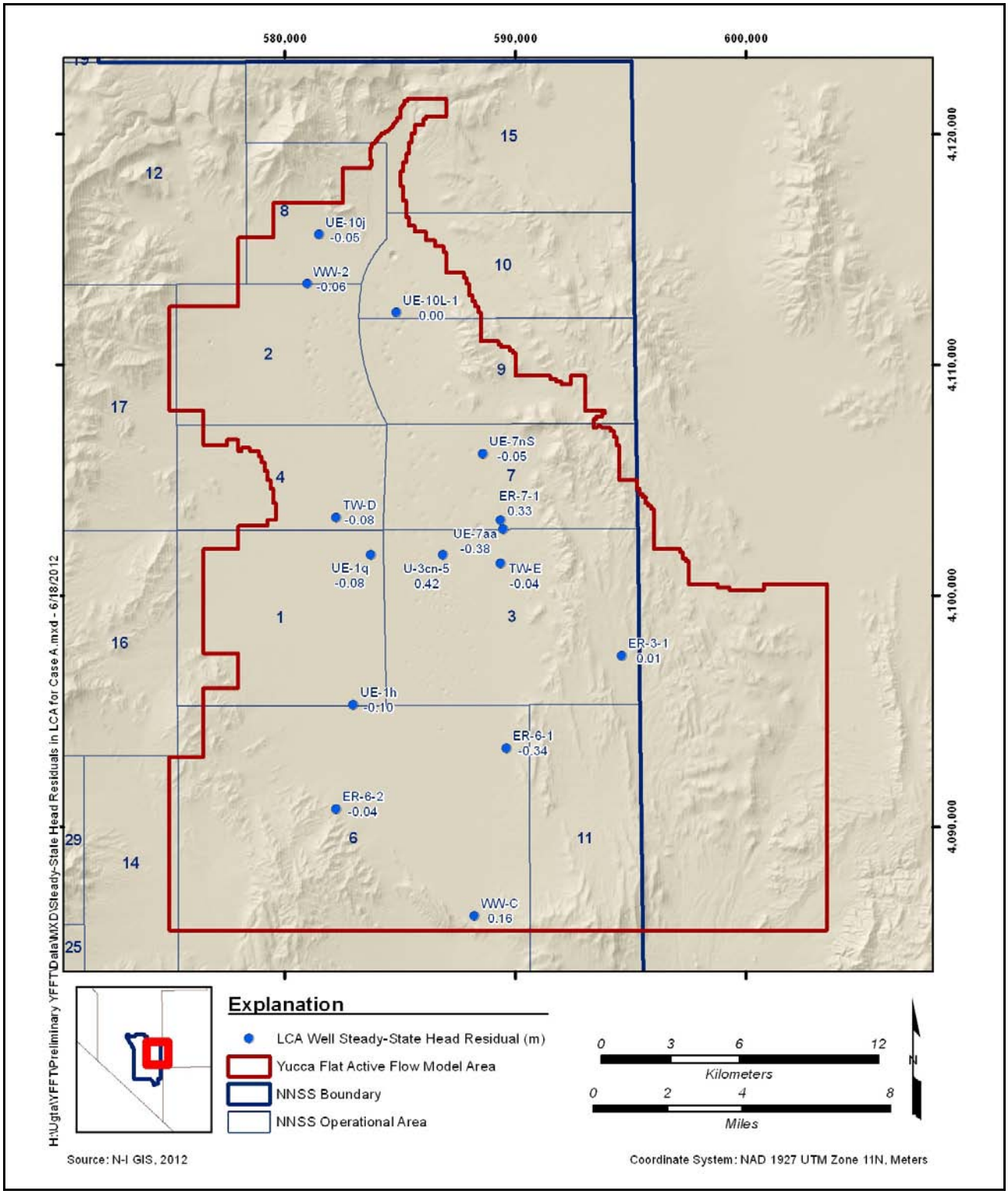

Figure 5-44
Steady-State Head Residuals in the LCA

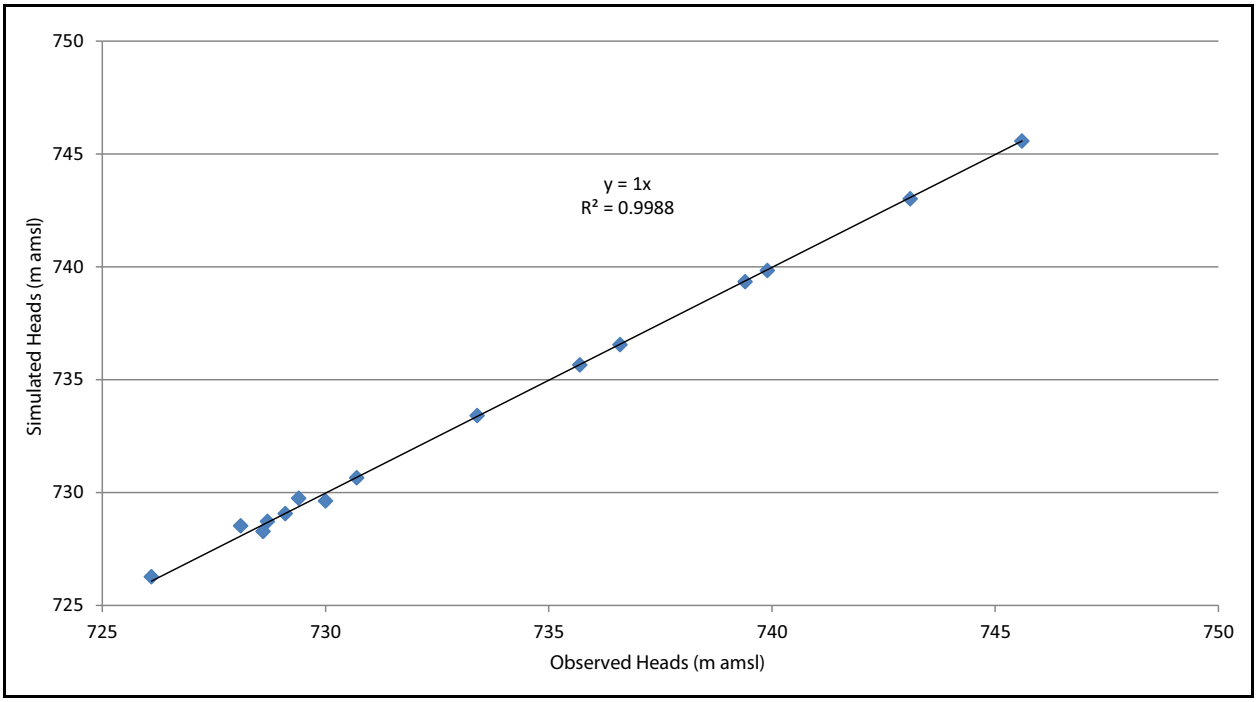

Figure 5-45
Observed and Simulated LCA Heads

Table 5-9
Summary of Calibration Statistics

Calibration Parameter (Unit)	Value
Number of Steady-State Head Observations	15
Minimum Steady-State Head Residual (m)	–0.41
Maximum Steady-State Head Residual (m)	0.38
Average Steady-State Head Residual (m)	0.01
Median Steady-State Head Residual (m)	0.05
Number of MWAT Drawdown Observations	45
Minimum Drawdown Residual (m)	–0.10
Maximum Drawdown Residual (m)	0.08
Average Drawdown Residual (m)	0.0
Median Drawdown Residual (m)	0.0

Table 5-10
Mass Balance Summary

Boundary	Net Inflow	Net Outflow
	(kg/s)	
North	130.0	0
East	59.3	0
West	24.3	0
Top Central	0.6	0
Top Eastern	30.0	0
Top Western	19.8	0
Halfpint Range	4.3	0
South	0	266.5
Total	**268.3**	**266.5**

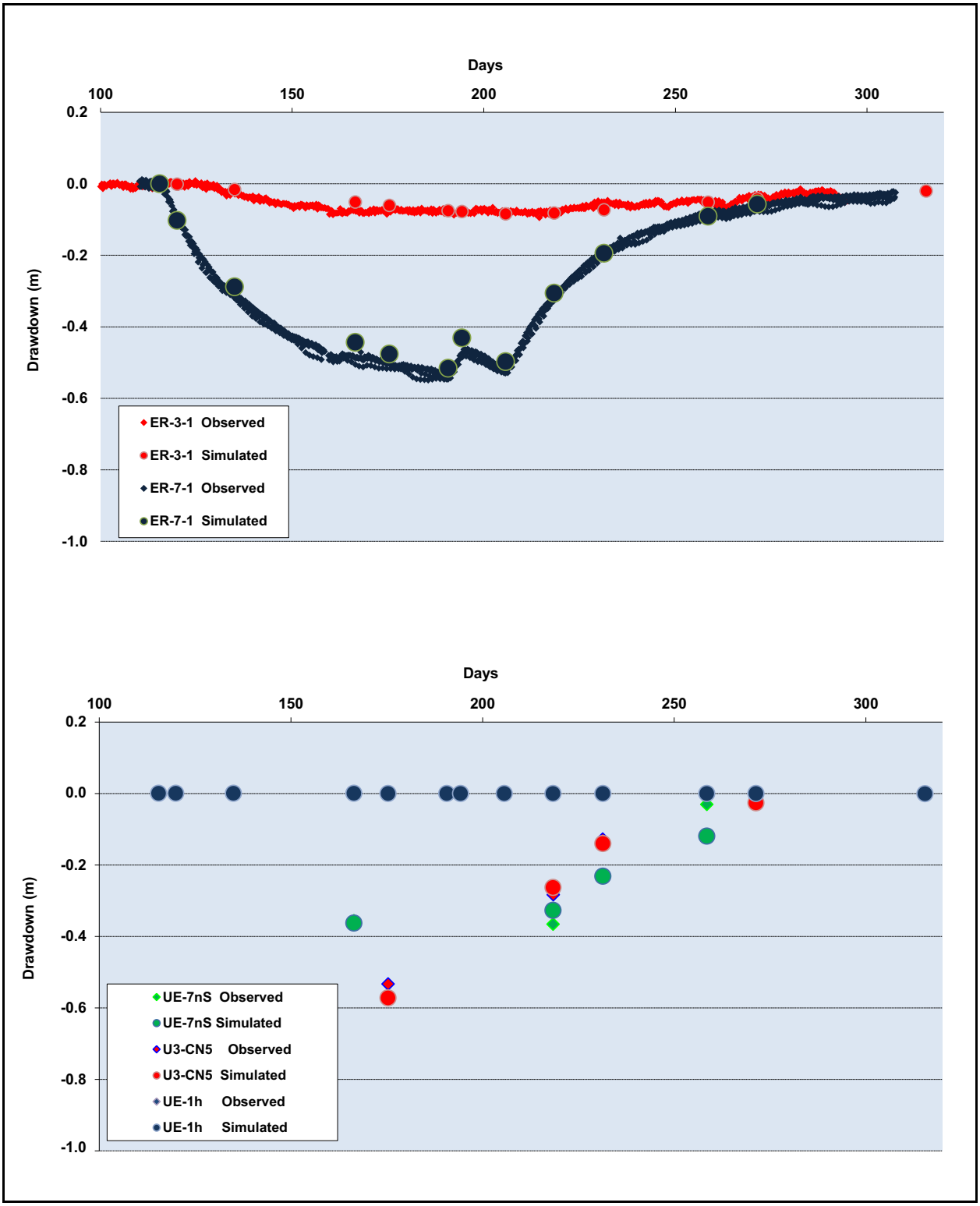

Figure 5-46
Simulated and Observed Drawdowns at the MWAT Sites

Table 5-11
Calibrated Model Parameter Values
(Page 1 of 3)

PEST Parameter Name	Calibrated Value	PEST Parameter Name	Calibrated Value
Boundary Flux	(kg/s)	Rock Permeability	(m^2)
northflux	130.0	6_lccu2	1.17E-16
westflux	24.3	7_lca3	8.08E-12
eastsoflux	59.4	4_uccu	1.88E-15
hevesi_east	30.0	Fault Permeability	(m^2)
hevesi_west	19.8	101_area13bu	6.41E-12
top_lanl	0.6	114_yf_91bn1	6.90E-12
hpflux	4.3	115_yf_57	4.38E-14
Storage	(1/m)	116_yf_56	4.38E-14
aqc_con	2.97E-08	118_hp112_16	7.37E-13
aqc_unc	1.70E-06	121_hp40	1.42E-12
aqc_flt	7.68E-07	122_rv60	7.04E-12
Anisotropy	Dimensionless	123_hp120	7.29E-13
anisofaultx	0.136	124_hp10	8.02E-13
anisofaultz	0.001	125_hp20	1.14E-12
aniso145x	0.262	126_hp30	4.38E-14
aniso145z	0.019	127_hp121	9.48E-13
aniso148x	0.011	128_hp116	7.84E-13
aniso148z	0.070	129_hp115	6.61E-13
aniso178x	0.018	130_hp125	4.38E-14
aniso178z	0.028	132_hp108	9.86E-13
aniso190x	0.003	135_hp123	5.89E-14
aniso190z	0.040	136_yf_133	3.01E-11
aniso176x	0.859	137_yf_131	1.07E-12
aniso176z	0.008	138_mm90	4.38E-14
aniso177x	0.026	139_hp72_yf1	2.41E-13
aniso177z	0.074	140_hp50_yf1	1.44E-11
lcavniso	1	141_hp60	9.64E-13
Rock Permeability	(m^2)	142_mm70	1.51E-12
3_lcaw	1.00E-14	143_hp124	2.32E-14
11_lcae	1.25E-12	144_mm20_60	4.38E-14
9_lcac	1.85E-14	145_yf1	6.77E-12

Table 5-11
Calibrated Model Parameter Values
(Page 2 of 3)

PEST Parameter Name	Calibrated Value	PEST Parameter Name	Calibrated Value
Fault Permeability	(m^2)	Fault Permeability	(m^2)
146_yf_129	4.38E-14	179_yf_48	4.38E-14
147_yf_103n1	4.00E-10	180_yf_46a	4.38E-14
148_yf2	9.02E-14	181_yf_46b	4.38E-14
149_area3n9	2.60E-10	182_yf_50c	4.38E-14
150_yf_embud	6.39E-12	183_yf_37n39	4.38E-14
151_yf_7r	9.21E-14	184_yf_33b	4.38E-14
152_yf_55	1.95E-12	185_yf_34a	4.38E-14
153_yf_54	4.38E-14	186_yf_34b	4.38E-14
154_piranha	1.03E-11	187_yf_44b	4.38E-14
155_yf_61a63	1.47E-12	188_yf_44c	4.38E-14
156_yf_71	2.21E-10	189_yf_35b	4.38E-14
157_yf_69n67	4.38E-14	190_topgalla	4.44E-13
158_yf_62	4.38E-14	191_yf_44a	4.38E-14
159_yf_61b	4.38E-14	192_yf_40	4.38E-14
160_area3eas	4.00E-10	193_yf_41	4.38E-14
161_yf_7y	1.00E-14	194_yf_38	4.38E-14
162_yf_97b	4.38E-14	195_yf_tippi	4.38E-14
163_yf_97a	4.00E-10	196_yf_baneb	4.38E-14
164_yf_95a	4.38E-14	197_yf_33a	4.38E-14
165_yf_area7	4.38E-14	198_yf_wgh	1.16E-13
166_yf_80	4.38E-14	200_yf_31	1.16E-13
167_yf_75	5.71E-12	201_yf_wellc	1.16E-13
168_yf_93b	4.38E-14	202_yf_18	1.16E-13
169_yf_119n1	1.80E-14	203_yf_28a	1.16E-13
170_hp122	4.38E-14	204_yf_28b	1.16E-13
171_yf_125	1.46E-12	205_yf_minem	1.16E-13
172_yf_127	4.38E-14	206_yf_u_2cm	1.16E-13
173_yf_126	4.38E-14	207_yf_u_2cm	1.16E-13
174_yf_wellc	4.38E-14	208_yf_23	1.16E-13
175_yf_26egh	1.16E-13	209_yf_22c	1.16E-13
176_yf_50b	2.92E-12	210_yf_22d	1.16E-13
177_carpetba	5.03E-13	211_yf_22b	1.16E-13
178_topgalla	9.36E-13	212_yf_24	1.16E-13

Table 5-11
Calibrated Model Parameter Values
(Page 3 of 3)

PEST Parameter Name	Calibrated Value	PEST Parameter Name	Calibrated Value
Fault Permeability	(m^2)	Fault Permeability	(m^2)
213_yf_25n27	1.16E-13	224_yf_20b	1.16E-13
214_yf_6a	1.16E-13	225_yf_19	1.16E-13
215_yf_16b	1.16E-13	226_yf_20a	1.16E-13
216_yf_6b	1.16E-13	yfsouthext	3.67E-11
217_yf_12	5.96E-13	Fault Core Multiplier	Dimensionless
218_yf_14n16	8.78E-13	114_itfc	7.43E-01
219_cp20	4.38E-14	145_itfc	1.00E-06
220_cp10	4.38E-14	177_itfc	2.81E-04
221_cp30	4.38E-14	178_itfc	9.45E-05
222_cp50	4.38E-14	207_itfc	1.64E-01
223_yf_30	1.16E-12	yfsouth_itfc	2.11E-05

The Darcy velocity vectors between elevations of –500 and +500 m amsl are presented in Figure 5-47 in order to illustrate the areal flow field in the LCA. Because the LCA is absent in the center of the basin at elevation above 0 m amsl, velocity vectors are presented for the interval of –500 and +500 m amsl. Vertical flow rates in the LCA are relatively small compared to lateral flow rates, and therefore the velocity at a particular location is quite similar throughout the 1,000-m depth.
As expected, groundwater flow in the eastern half of the basin is primarily southward. In the west, the flow is primarily eastward toward the major faults in the center of the basin with a slight northerly flow component in some areas. As discussed above, the northward flow results from the water levels in the west involve a head drop from 745.6 m at ER-6-2 in the south to a low of 735.7 m at UE-10j in the north.

The potential radionuclide migration pathways were evaluated with particle-tracking simulations. Source particles were released at 12 key locations where radionuclides either enter the LCA from the overlying unsaturated zone and saturated alluvial/volcanic aquifers or emanate from detonation locations that result in initial contamination within the LCA. These locations were chosen to be representative of the range of advective travel times within the LCA and do not account for the time of travel from the source location to the LCA through the overlying strata. The starting locations of

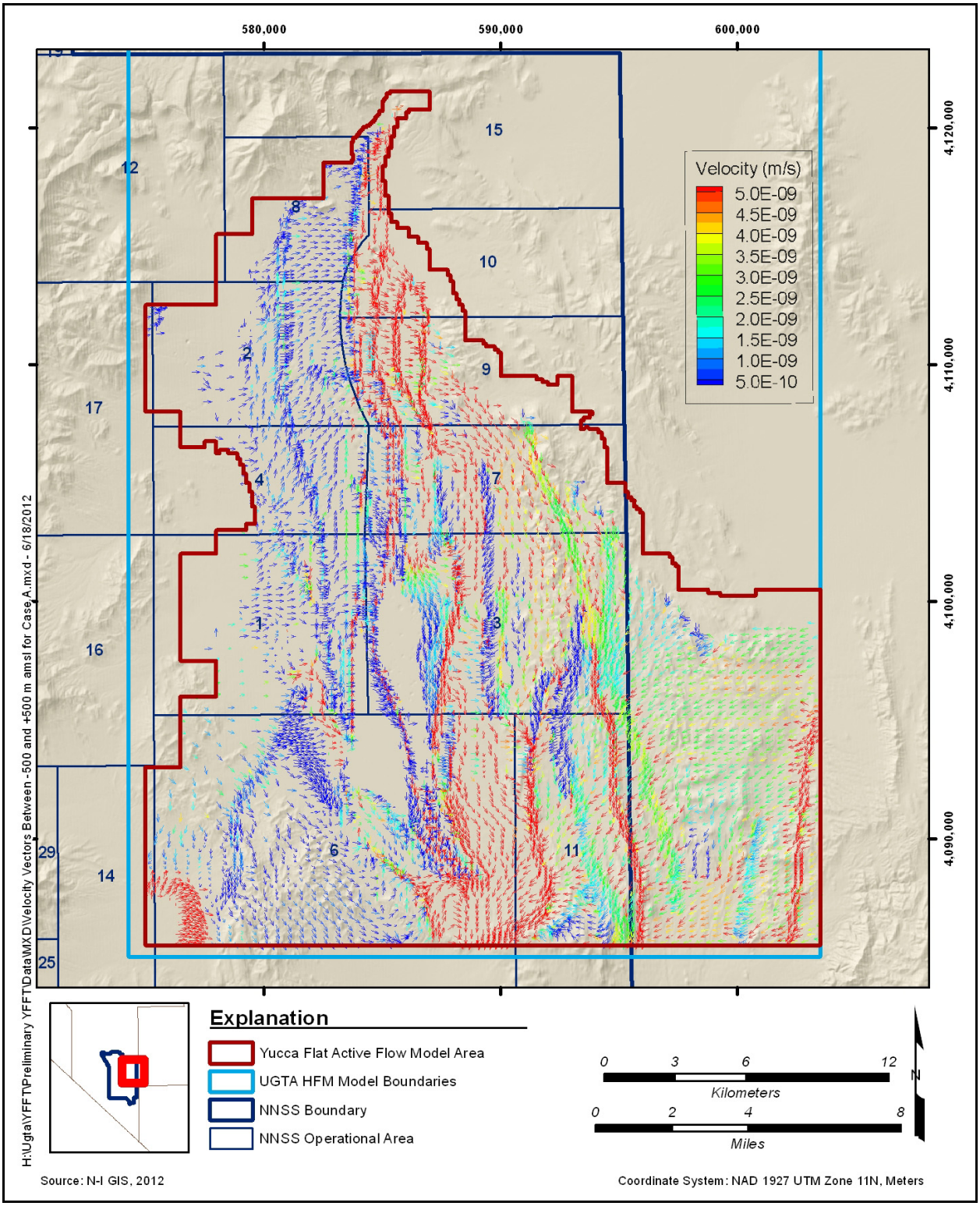

Figure 5-47
Velocity Vectors between –500 and +500 m amsl

the particles are shown in Figure 5-48. A total of 216 particles were released at each of the 12 locations. The simulation was conducted assuming that particles do not diffuse and that the medium porosity is uniformly 0.4 percent. This effective porosity value is chosen to reflect a central tendency of the fractured country rock that is used to evaluate radionuclide transport in Section 6.5.

The distance travelled from each of the 12 locations for the base-case calibration run is presented in Figure 5-49. These transport times are reflective of advective-only transport without considering the effects of matrix diffusion and sorption. The particle trajectory from 12 key detonation locations in east-central Yucca Flat described above is presented separately in Figure 5-50. The breakthrough curves at the northing location of 4,090,000 m (4.5 km from the southern boundary of the model) are presented in Figure 5-51. Almost all of the 216 particles released from locations 1, 2, 3, 4, 7, and 8 have reached the northing ordinate of 4,090,000 m within 1,000 years. Particles from locations 5, 10, and 12 travel fairly slowly, with only 0, 5, and 32 particles from these locations, respectively, reaching the southern reference location in 1,000 years. Particles from location 9 (the location of the NASH detonation) remain within the vicinity of this location because of the isolated nature of the LCA3 in this area.

5.5.3 Model Limitations

The Yucca Flat LCA flow model covers an area of 660 square kilometers (km^2) but has observed water-level data at only 15 sites. Thus, the overall density of data versus the size of the model suggests that the calibration data are sparse. Furthermore, observation wells in both the eastern and western parts of the basin are aligned in the north–south direction. Therefore, the head gradients in the east–west direction are not well constrained, and hence groundwater flow toward the major faults in the center of the basin cannot be estimated with certainty.

In addition to the uncertainty in heads and gradients, considerable uncertainty exists regarding fluxes along the boundaries of the model. As discussed in Section 5.3, there is large variation not only in boundary fluxes estimated in previous models but also between estimates obtained by numerical models and the hydrologic analysis conducted by Winograd and Thordarson (1975). Such wide variations and discrepancies impart uncertainty to the model.

The number of adjustable parameters in the model is large relative to the number of target observations sites. The large number of faults in the model makes it difficult to evaluate the values of

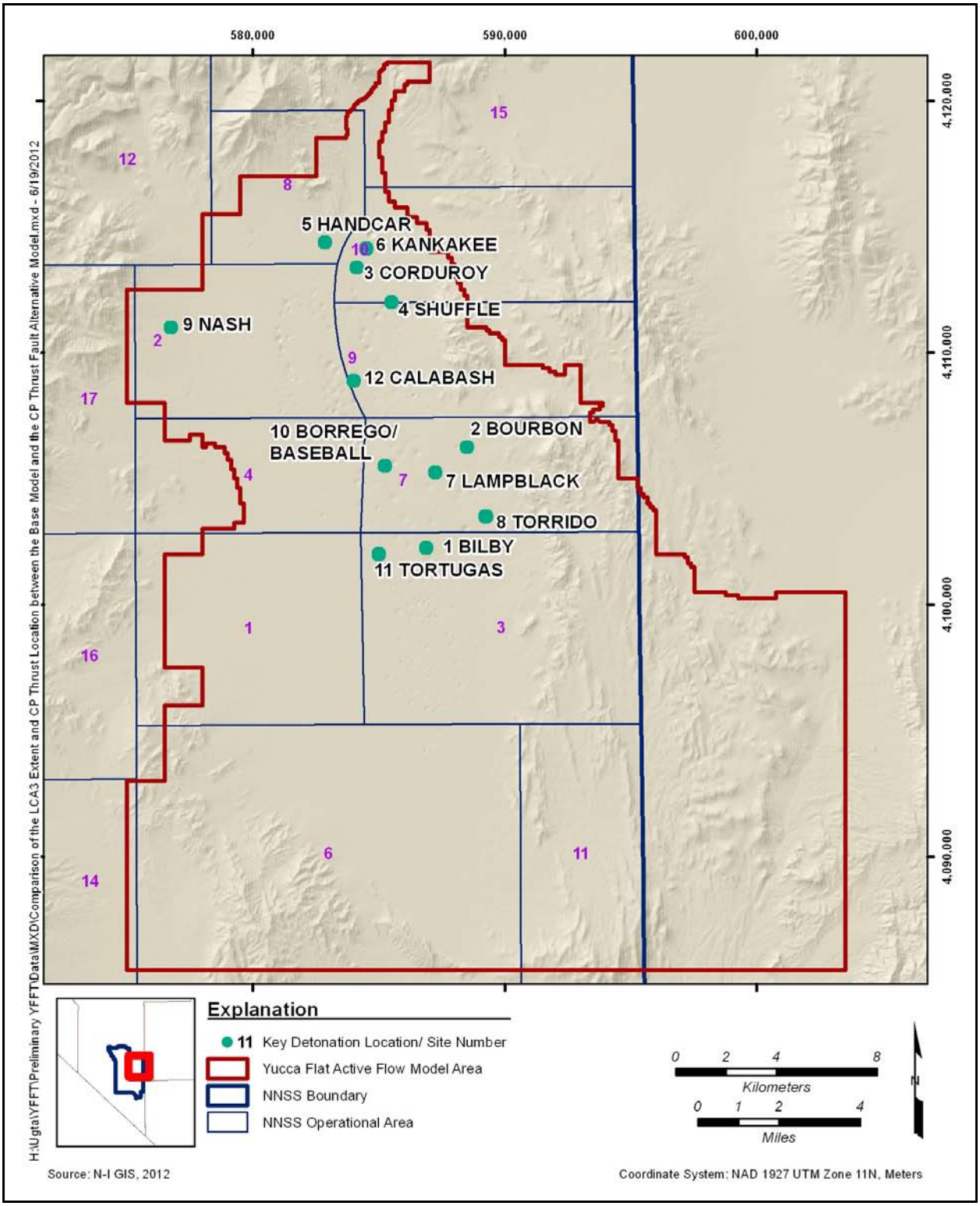

Figure 5-48
Key Locations Receiving Contamination from Sources in the Unsaturated Zone, Saturated Alluvial/Volcanic Aquifer System, and LCA

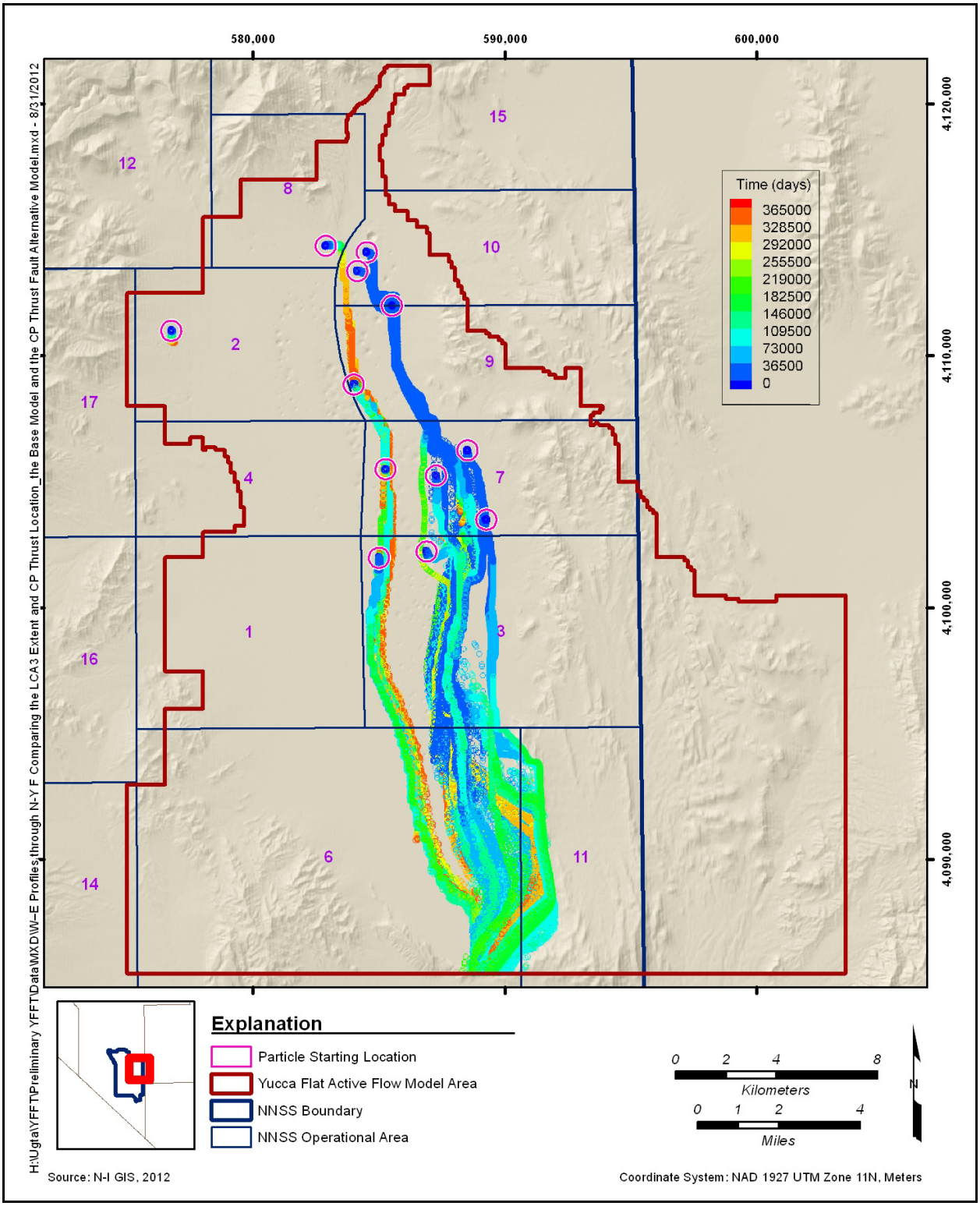

Figure 5-49
Particle Travel Paths and Times for Radionuclide Transport from 12 Key Locations for the Base-Case Calibration

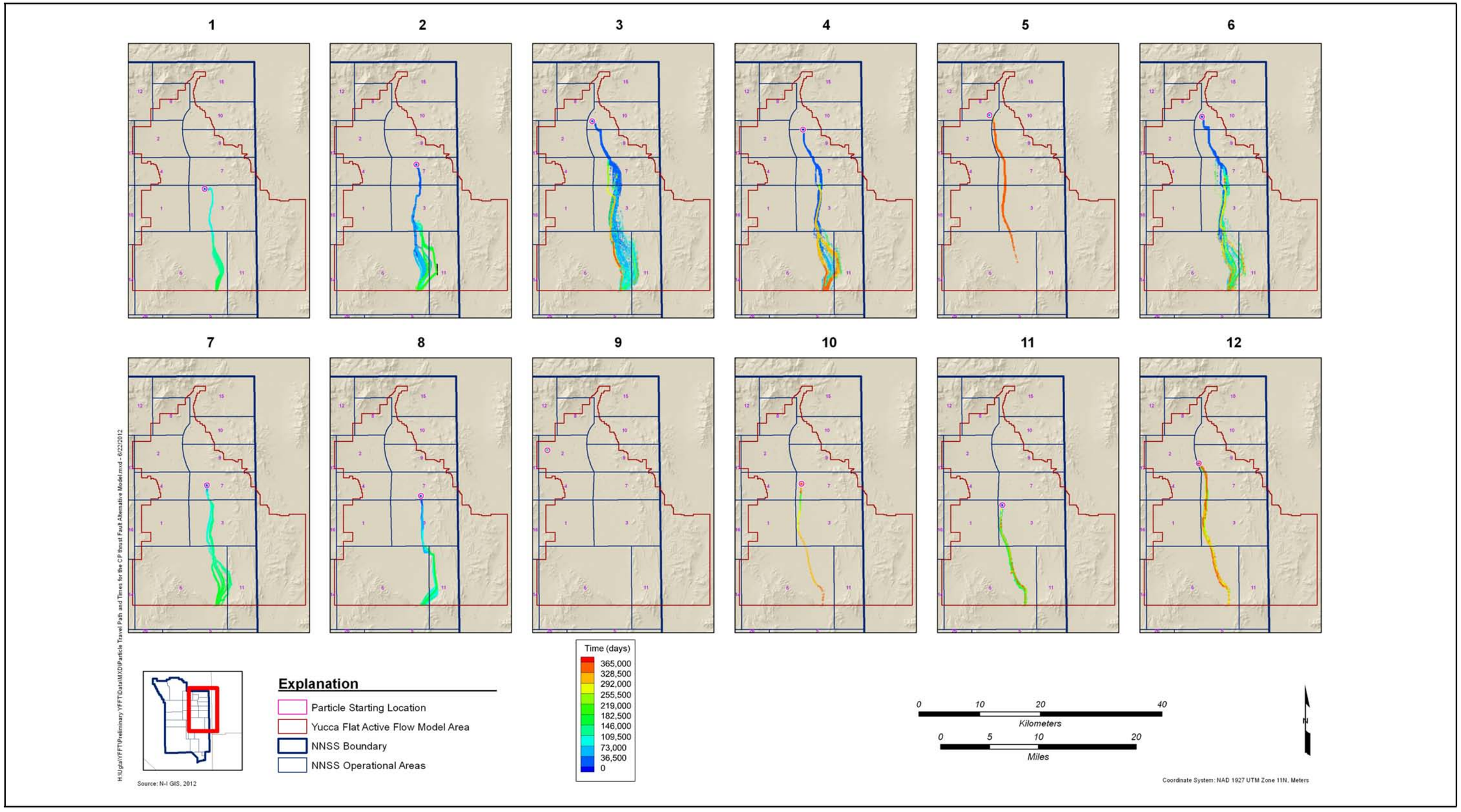

Figure 5-50
Particle Travel Paths and Times for Contamination Released at Each of the 12 Key Locations for the Base-Case Calibration

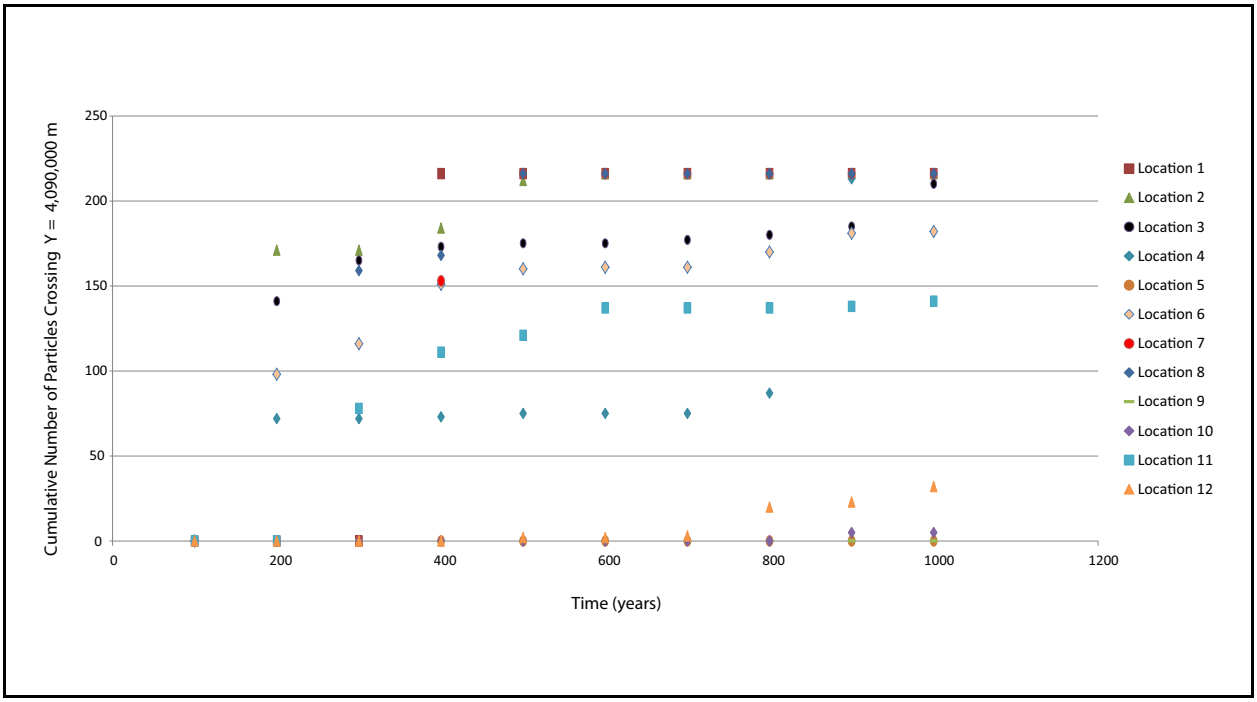

Figure 5-51
Breakthrough Curves at Model Northing Location 4,090,000 m for Particles Released at 12 Key Locations in the LCA

individual hydrologic parameters from the data alone without some subjective judgment as to which parameters can be appropriately grouped during calibration. Uncertain boundary fluxes, in conjunction with a high number of unknown hydrogeologic parameters, result in an overdetermined system. This uncertainty, however, is explored by conducting a rigorous global uncertainly analysis using the NSMC method and evaluating alternative model conceptualizations.

Another limitation pertains to parameterization of the LCA into three LCA zones: LCA east, LCA central, and LCA west. The hydraulic permeability distribution is expected to be quite complex. The LCA is most likely to be more permeable in the central parts of the basin, where the fault offsets are larger in the north where the faults terminate and the LCA thins out.

The Yucca Flat LCA flow model was calibrated to steady-state water-level conditions and therefore does not consider transient conditions associated with long-term climate change in the NNSS area. The higher heads in the volcanic units at Yucca Flat relative to the LCA could reflect the slow drainage from the volcanic units through the tuff confining units following the transition from pluvial to arid conditions approximately 10,000 years ago. Therefore, if these conditions do in fact exist, using a steady-state model would result in overestimation of recharge through the unsaturated zone.

However, as discussed further in Appendix I, the contribution of detonations conducted in the unsaturated zone to the lateral extent of contamination migration in the LCA is relatively small, and therefore, the assumption of steady-state conditions in all three CAU models and the DVRFS model appears to be reasonable.

5.6 Flow Model Uncertainty Analyses

5.6.1 Introduction

Modeling flow and transport in complex environmental systems requires quantification of uncertainty in model response due to uncertainty in model input. As stated in the *Addendum to Revision 1 of the Corrective Action Investigation Plan for Corrective Action Unit 98: Frenchman Flat, Nevada Test Site, Nevada* (NNSA/NV, 2001), the uncertainty analysis will include "alternative hydrostratigraphic models, boundary flux uncertainty, and parameter uncertainty for both flow and transport parameters," and "groundwater flow and transport model simulations with the range of parameter values will yield an assessment of the prediction uncertainty due to parameter uncertainty."
An important goal of the Yucca Flat LCA flow modeling is, therefore, to examine a range of permissible fits to the calibration data recognizing the nonunique nature of solutions obtained due to multiple conceptual models and parameter sets.

For the Yucca Flat LCA flow model, the uncertainty analyses conducted are grouped into the following three categories:

- **Global Uncertainty Analysis.** PEST, like most gradient-based parameter estimation software package, can find a calibrated parameter set that minimizes a user-defined objective function only in the vicinity of the specified initial conditions. Highly parameterized models, such as the Yucca Flat LCA flow model, have a non-convex objective function space, and therefore, it is necessary to examine the parameter set and associated groundwater flow field associated with different inflection points in the objective function space. PEST's NSMC method was applied to the base-case calibrated flow model in order to evaluate alternative flow fields, which have objective functions that are of similar magnitude as that of the base case.

- **Northern Boundary Flux Uncertainty.** Because of the large uncertainty in the hydraulic continuity and flow rates into the LCA in northern Yucca Flat (Table 5-7), an alternative model run was performed with the value fixed at an assumed low value indicative of the likelihood that the LCA in Yucca Flat is not hydraulically connected to the LCA flow system north of the NNSS boundary as illustrated in Figure 1-13.

- **HFM Uncertainty.** The primary goal of this type of assessment is to define the uncertainty in flow model responses associated with alternative HFMs. Based on recommendations in BN (2006), the significance of the two alternative HFMs that potentially affect flow in the LCA was evaluated.

- **Fault-Zone Parametric Uncertainty.** The analyses involves exploration of uncertainties in architecture of the fault zone that would lead to scenarios that may result in contaminant transport times (and extent) that are substantially longer (larger) or shorter (smaller) than those determined for the base case. The evaluation involves specifying alternative fault-zone parameters, recalibrating the alternative model(s), and evaluating the resulting flow and transport fields.

The combination of calibrated flow fields resulting from the uncertainty analyses conducted in this section was carried forward into transport modeling to evaluate the significance of model conceptualization and pathway variations on the contaminant boundary. The goal here is not to attempt to define all potential variations in flow paths and fluxes, but instead to capture a sufficient range of contaminant migration patterns and rates using multiple combinations of alternative conceptual models and parameter sets. Each of the four uncertainty analysis approaches is described below. The possible effects of these alternative models on flow paths and migration rates in the LCA at Yucca Flat are collectively examined in Section 5.6.5.

5.6.2 Global Uncertainty Analysis

The base-case results, including calibrated parameters and boundary conditions, are presented and discussed in Section 5.5. As discussed in Section 5.5, because of the large number of parameters and limited observation data, there is no guarantee that the calibrated solution is unique. There can be alternative calibration sets with alternative flow fields that could result in residuals that are equal to or lower than obtained for the initial calibration. The PEST identifiability index is a useful gauge to measure the uniqueness of the calibration.

A high identifiability (greater than 0.8) implies that the parameter can be uniquely determined (in conjunction with other parameters) during the parameter estimation process given the particular conceptual model. A nonunique solution will have a large number of adjustable parameters with a low identifiability index. It is recognized that the identifiability is conditioned on the conceptual model and that alternative conceptual models and parameter structures could have been modeled that lead to variation in the identifiability of each parameter.

The general approach adopted during model calibration was for parsimony in the model structure. For example, given the uncertainty in the spatial heterogeneity of hydraulic properties, initial analyses considered allowing the permeability of the LCA to vary spatially. This variability was implemented simply by defining three permeability zones in the eastern, central, and western portions of the basin based on geologic inference of structural damage. Similarly, although it is likely that the hydraulic characteristics of major faults would vary along the strike, especially in the northern portions of the basin that are less affected by the deformation than the center of the basin, it is assumed that a single permeability represents the average behavior of the fault damage and core zones. The lateral continuity of faults such as the Yucca, Topgallant, and Carpetbag faults is expected to favor results that allow for a greater influx of groundwater into northern Yucca Flat.

As shown in Figure 5-39, most of the parameters have a low identifiability, but there are several parameters that appear to be highly identifiable. For example, the northern boundary flux for the calibrated model has a high identifiability index of 0.99, which implies that the calibrated value of this parameter has a greater certainty. However, this interpretation has to be tempered by the knowledge that this assumes the conceptual model that allows for hydraulic continuity for the LCA in northern Yucca Flat, similar to what was assumed in the regional models. Alternative conceptualization for this area of the model indicates the potential for limited hydraulic continuity, which results in an alternative boundary flux. The evaluation of this alternative model is presented in Section 5.6.3.

To demonstrate, the PEST-derived value of the northern boundary influx during each iteration of the parameter estimation process is presented in Figure 5-52. For the base-case calibration discussed above, the northern flux, starting with an initial value of 50 kg/s, increases during each iteration, finally settling at approximately 130 kg/s. On completion of the calibration, an alternative run was conducted in which the initial value of the northern flux was perturbed to 250 kg/s. The path to convergence for this alternative case is also presented in Figure 5-52, which shows that the parameter tends to migrate toward the previously calibrated value of 130 kg/s, thereby providing confidence in the identifiability of this parameter given the conceptual model that allows for hydraulic communication to the areas north of Yucca Flat.

Not all parameters have a high identifiability index, and consequently, the solution space is non-convex. As an example, consider the variation in the least-squares error as a function of the

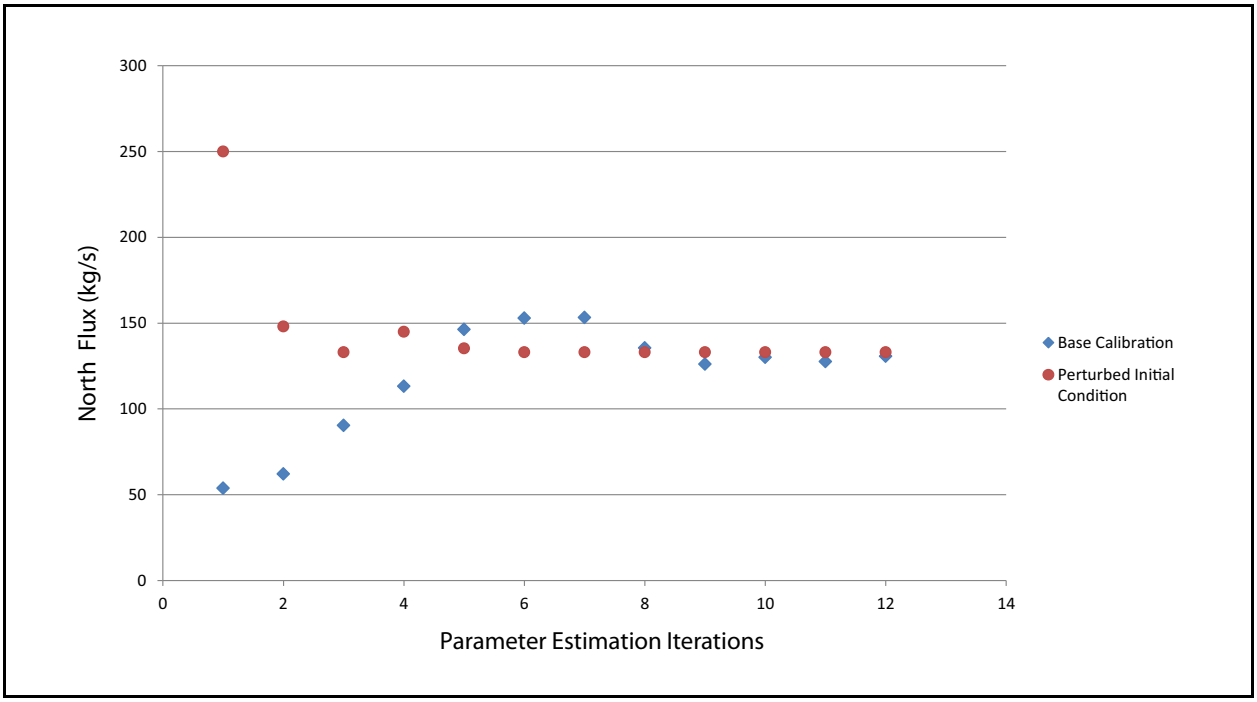

Figure 5-52
Calibration Convergence of Northern Boundary Model Influx

lateral flux along the western and southeastern boundaries (Figure 5-53). As is evident from the figure, there are multiple inflections points in the solution space, which would cause the (gradient-based) solution scheme used in PEST to be trapped in the multiple local minima. Because the number of adjustable parameters is large and the number of observation data limited, and additionally, because both the hydrogeologic parameters and the boundary conditions are estimated simultaneously, there is no unique solution to the parameter estimation problem. It is, therefore, necessary to rigorously account for uncertainty in the calibrated solution in order to determine alternative parameter sets that may provide as reasonable a solution as the base-case calibration discussed above.

PEST's NSMC method was applied to the base-case calibrated flow model in order to evaluate alternative flow fields that have acceptably low objective function. The NSMC method is emerging as a robust and efficient technique to explore alternative parameter sets and their impacts on the flow field (Tonkin and Doherty, 2009; Keating et al., 2010). The NSMC methodology allows a user to estimate the effect of many alternative models given a defined parameter set, conceptual model, and objective function. Each of these parameter fields may include a high level of detail that is well beyond what can be represented uniquely in a calibrated model. The method is efficient because once

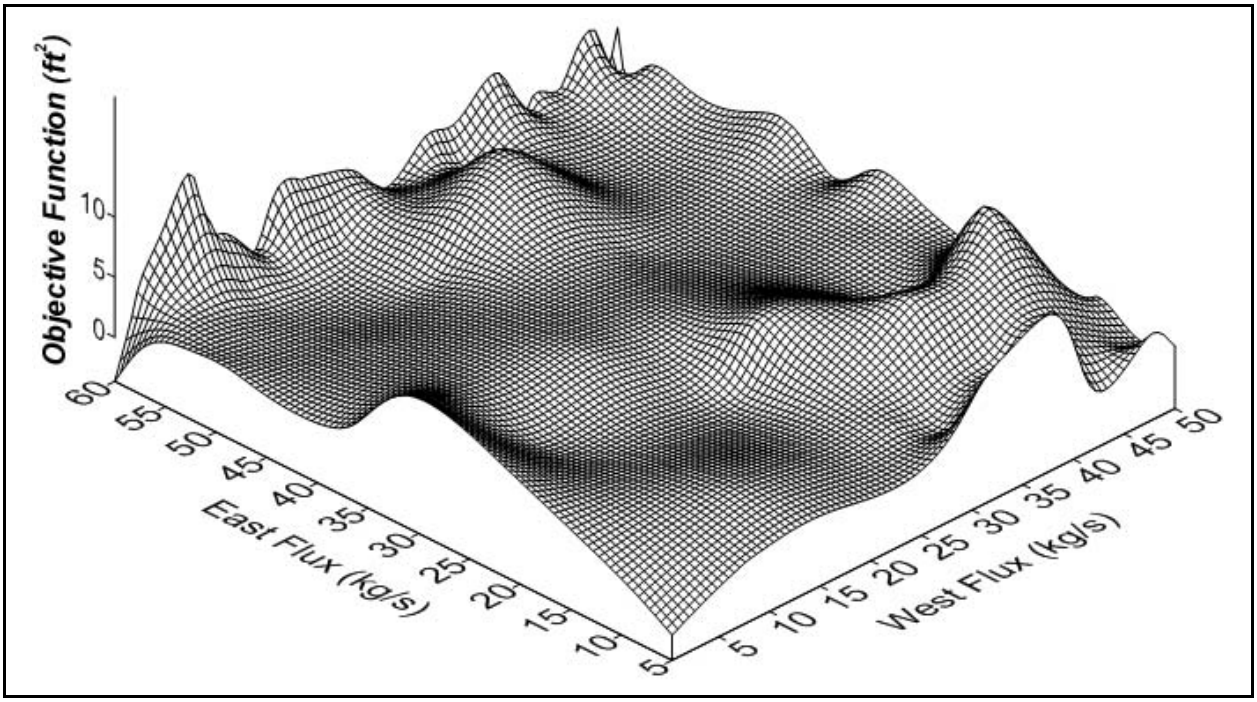

Figure 5-53
Calibration Objective Function as a Function of Lateral Western and Eastern Boundary Fluxes

a model has been calibrated, the numerical burden of recalibrating it many times using parameter fields of arbitrary complexity is generally minimal.

The hydrogeologic parameters and boundary conditions in the base-case model discussed above were varied over the estimated parameter range assuming a uniform distribution for each adjustable parameter. PEST's NSMC method uses a special technique to sample all parameters by utilizing information regarding the parameter and null spaces of the Jacobian matrix. This results in the NSMC method to be more efficient than the simple Monte Carlo method. Consequently, for a limited number of sampling, more information pertaining to parameter uncertainty is obtained by the NSMC method as compared to the traditional Monte Carlo method. The sampled parameters can then be used as an initial condition and full inverse recalibration of the model conducted for each parameter set.

A total of 100 sampled parameters sets were generated with the NSMC methodology, and the generated parameter sets were utilized as initial conditions for full PEST inversion. The 100 inversion runs were allowed to run for an allotted time during which 83 runs achieved an objective function of 10.0 or lower, which was selected as the maximum acceptable value for calibration purposes. The initial and final objective functions for these 83 runs are presented in Figures 5-54 and 5-55, from

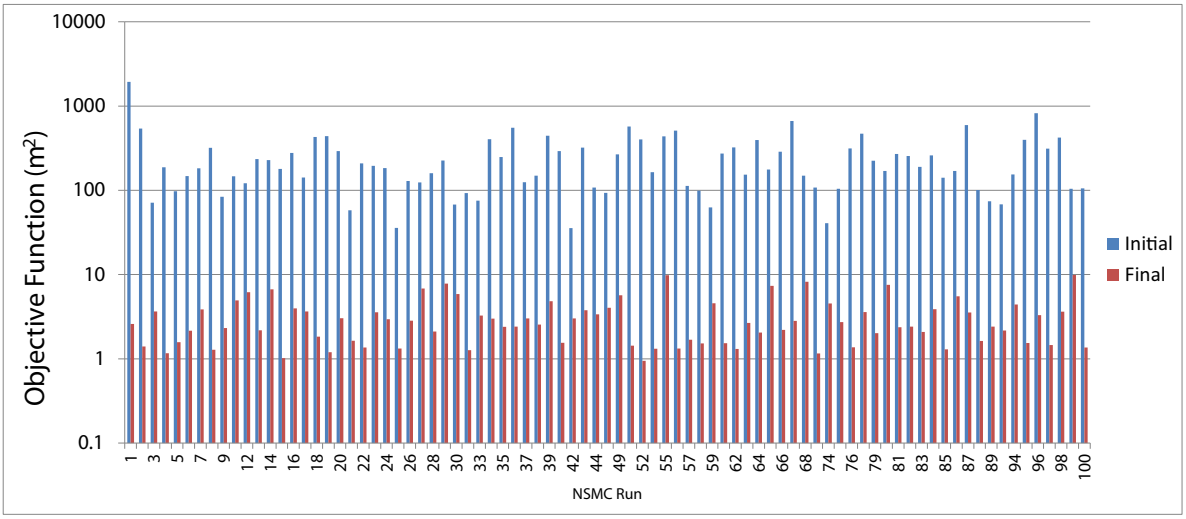

Note: Runs are ordered by run number from 1 to 100; missing run numbers represent the 17 model runs that did not converge.

Figure 5-54
Initial and Final Objective Functions for the Alternative NSMC Models

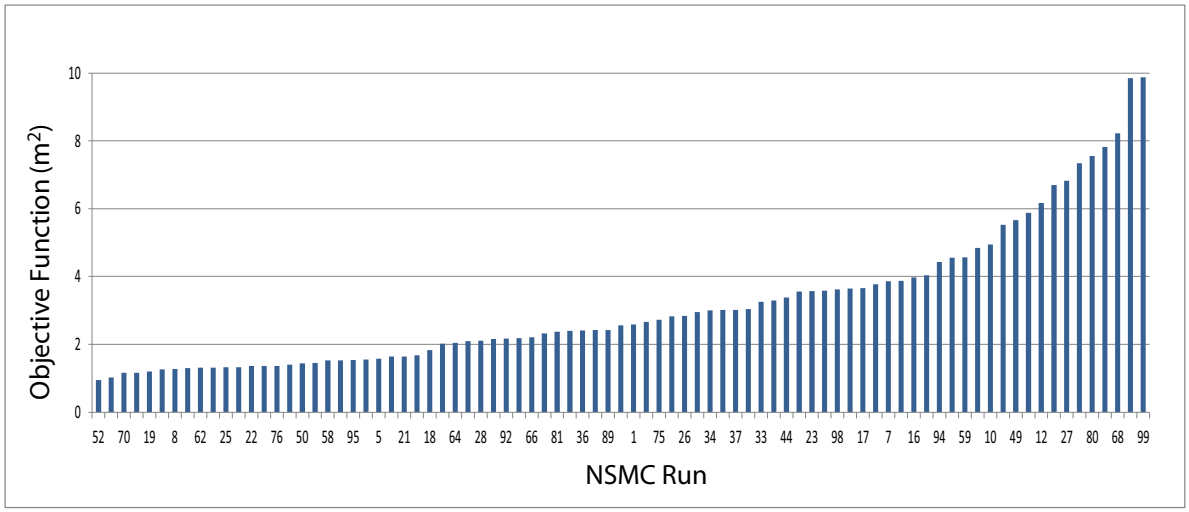

Note: Runs are sorted by objective function; missing run numbers represent the 17 model runs that did not converge.

Figure 5-55
Calibrated Objective Functions (Sorted) for the Alternative NSMC Models

which it can be inferred that PEST was able to substantially lower the objective function during the course of the parameter optimization. A subset of the alternative calibrated flow fields was eventually considered in the transport simulations discussed in Section 6.0. The basis for the selection of these alternative flow fields is discussed below.

Hydrogeologic parameters and boundary conditions vary in each of the 83 NSMC alternative flow fields. For example, inflow from the north ranges between 55.7 and 402.5 kg/s as shown by the cumulative distribution function (red curve) in Figure 5-56. The histogram for this parameter is also presented in Figure 5-56, from which a central tendency of approximately 150 kg/s can be noted. The calibrated value of northern flux for the base case, which may be considered an average case, is 130 kg/s. The recharge from the top in the center of the basin is much less than flux from the northern boundary. As shown in Figure 5-57, the top flux in the center of the basin varies from nearly 0 to 8 kg/s. The tendency is to remain close to the low end of the range. Approximately 70 percent of the NSMC runs had a recharge rate in the center of the basin of less than 1 kg/s. In addition to the north and center of the basin, the model receives groundwater inflow from lateral boundaries in the west, southeast, and Halfpint Range, as well as from the two top zones in the east and west as shown in Figure 5-32. The cumulative recharge from all inflow boundaries for the 83 NSMC runs is presented in Figure 5-58. The histogram and cumulative distribution (red curve) for this variable are presented in Figure 5-59. Interestingly, the total influx varies over a fairly narrow range, with a mean flux of about 250 kg/s and a standard deviation of about 56 kg/s. Such a narrow range implies that the combination of key hydrogeologic parameters should also vary over a narrow range.

As noted from the velocity vectors in Figure 5-47, a large proportion of groundwater in the LCA flows through three large basin-forming faults (Yucca, Topgallant, and Carpetbag), each of which has two splays. The distribution of the mean permeability of these three large faults varies over a narrow range, with an average value of 1.86E-12 m^2 (Figure 5-60). While the mean permeability of the major faults varies over a narrow range, the permeability variation in each fault is generally broader. For example, the permeability of the western splay of Topgallant fault (fault 190) varies over two orders of magnitude (Figure 5-61). Because most of the flow in the system is from north to south, and because the total flow varies over a narrow range, many alternative combinations of major fault permeability can transport the same amount of water through the system. Consequently, the average permeability of the major faults varies within a narrow range even though the permeability of each fault may vary over a large range. The flow field associated with each of these alternative

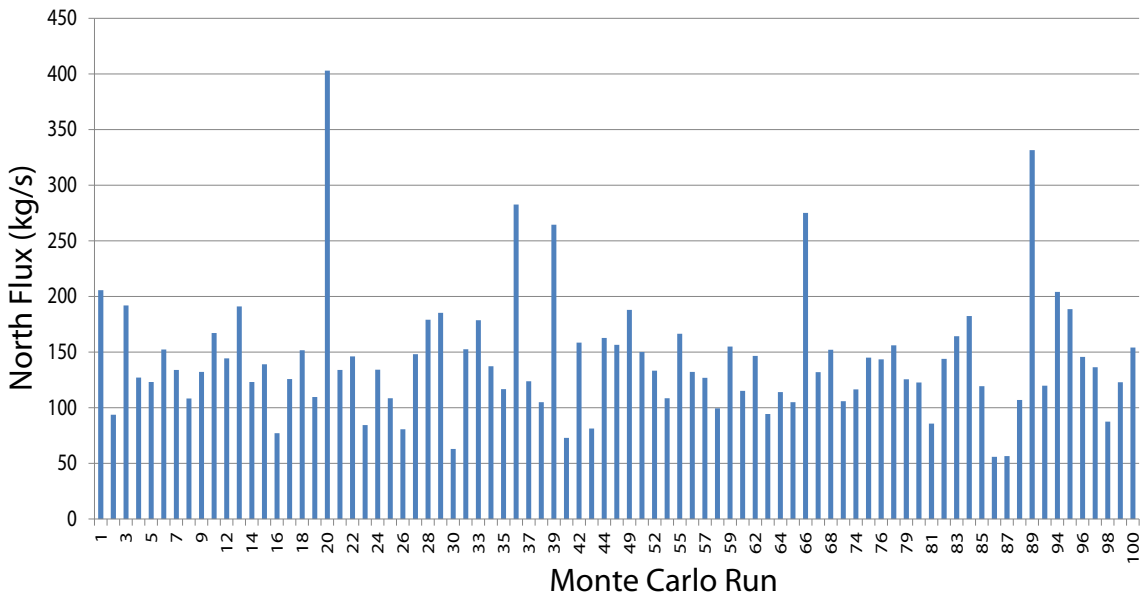

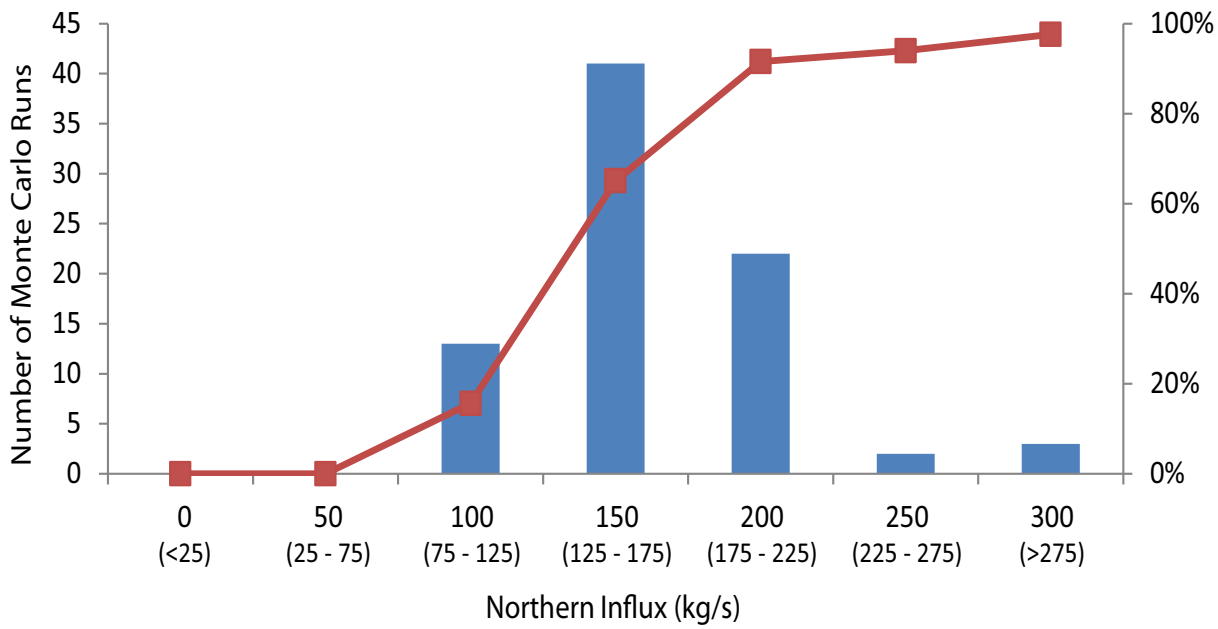

Note: Runs are ordered by run number from 1 to 100; missing run numbers represent the 17 model runs that did not converge.

Figure 5-56
Variation in Northern Boundary Inflow for the NSMC Simulations

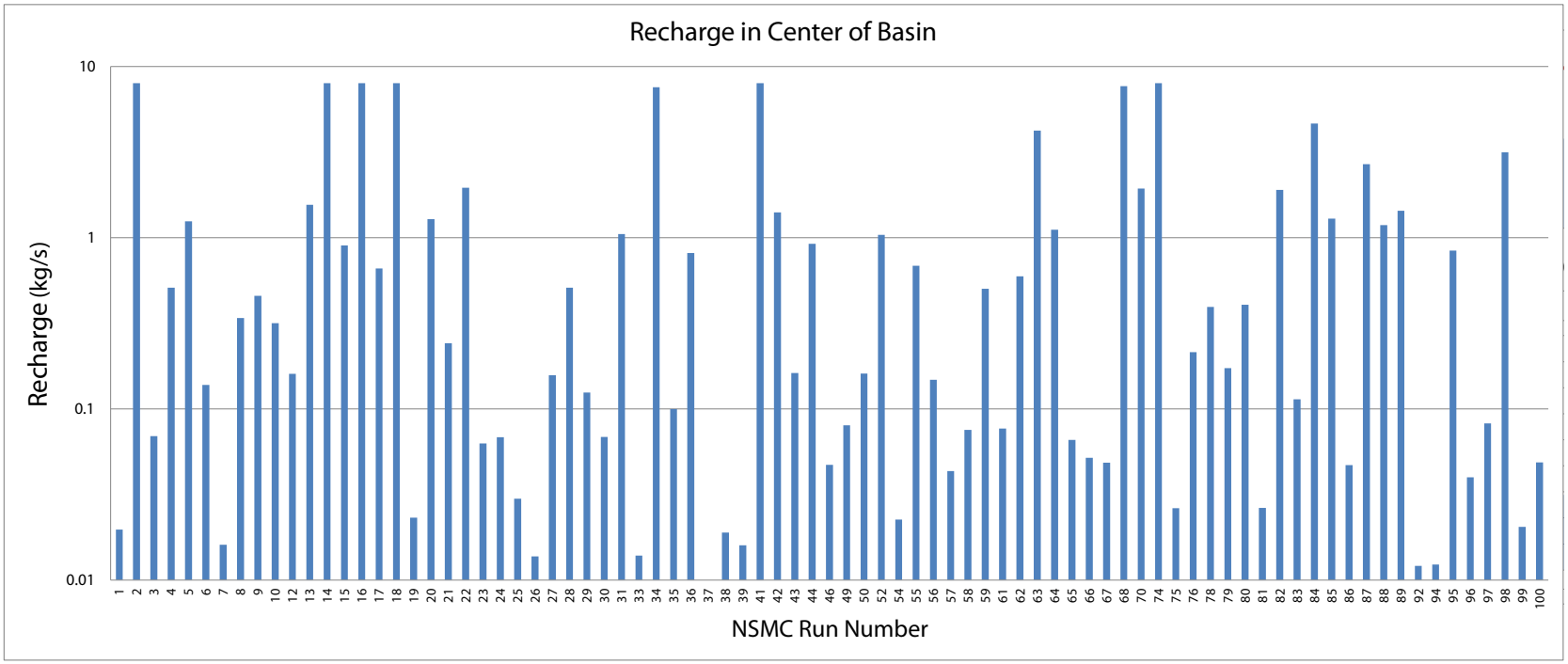

Note: Runs are ordered by run number from 1 to 100; missing run numbers represent the 17 model runs that did not converge.

Figure 5-57
Variation of Recharge in the Center of the Basin for the NSMC Simulations

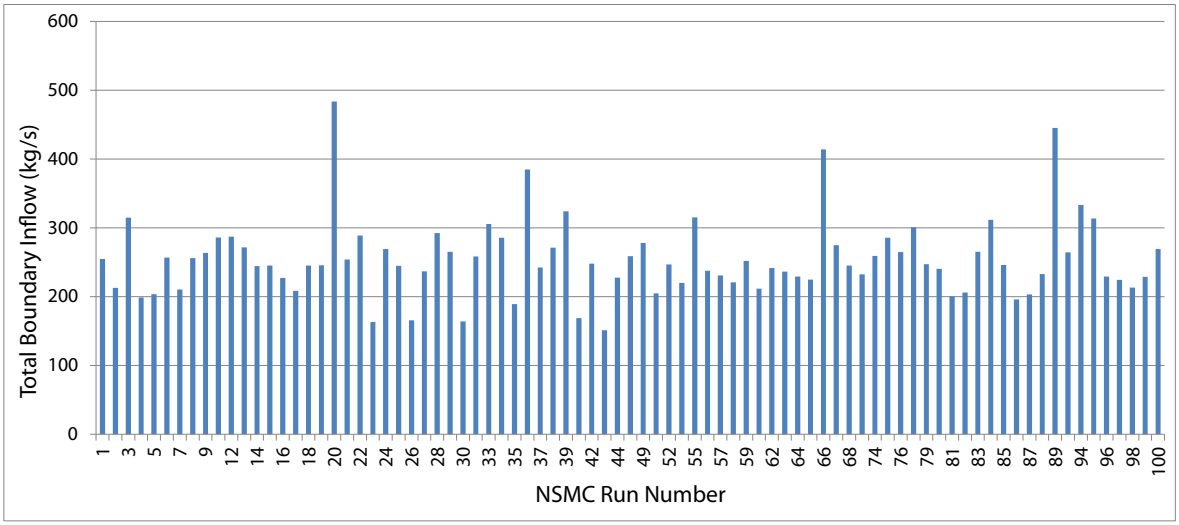

Note: Runs are ordered by run number from 1 to 100; missing run numbers represent the 17 model runs that did not converge.

Figure 5-58
Variation in Cumulative Boundary Inflows for the Alternative NSMC Simulations

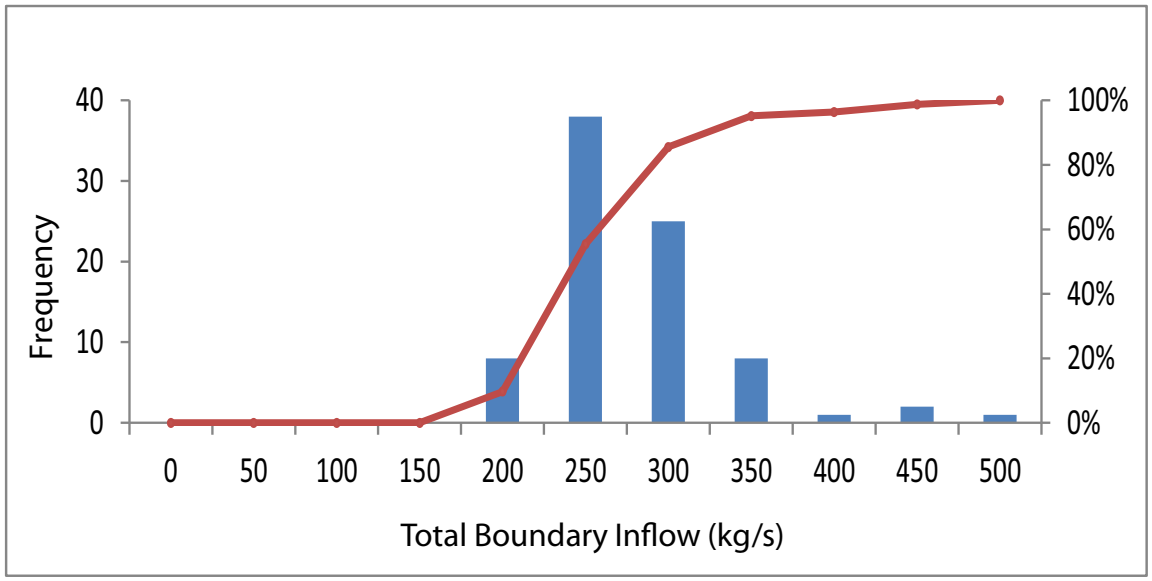

Note: Values represent the midpoints of bins.

Figure 5-59
Histogram and Cumulative Distribution Curve for Total Boundary Influx

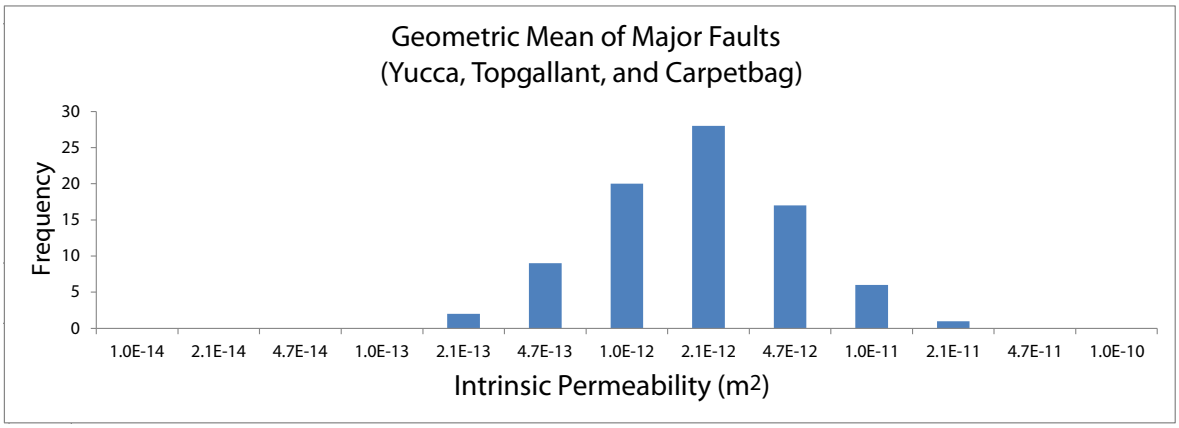

Note: Values represent the midpoints of bins.

Figure 5-60
Variation in Geometric Mean of Major Faults for the NSMC Simulations

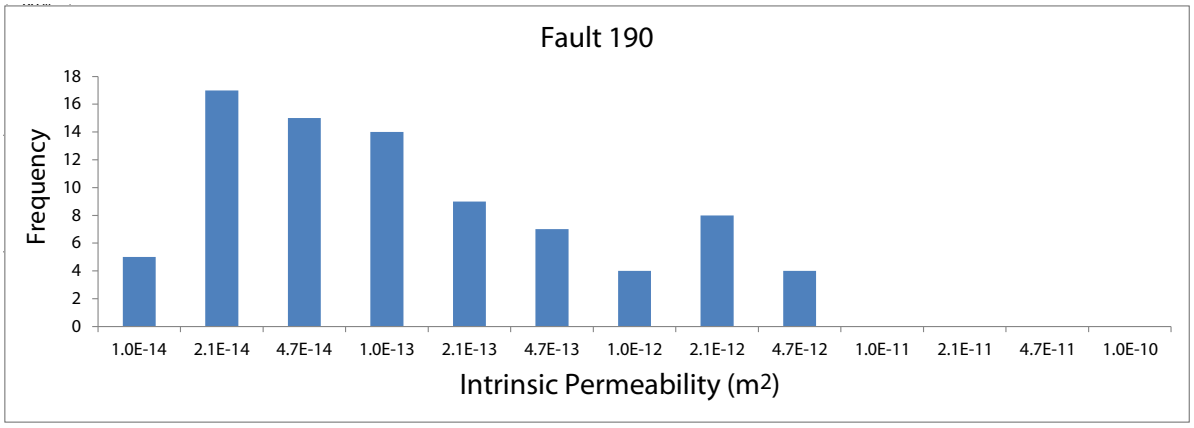

Note: Values represent the midpoints of bins.

Figure 5-61
Variation in Permeability of Western Splay of Topgallant Fault for the NSMC Simulations

combinations of permeabilities and other hydrologic parameters was systematically analyzed as discussed below, and three flow fields that encompass the range of flow rates were selected for transport simulations.

As expected, the least-squares error objective function was much less sensitive to the permeability of the smaller faults than to that of the major faults. For example, the longitudinal permeability of fault 210 (shown in Figure 5-30), which is only 2 km long, varies over four orders of magnitude (as shown in Figure 5-62). However, because of the small scale of this hydrologic feature, the overall solution is not significantly affected by large variations in its flow properties.

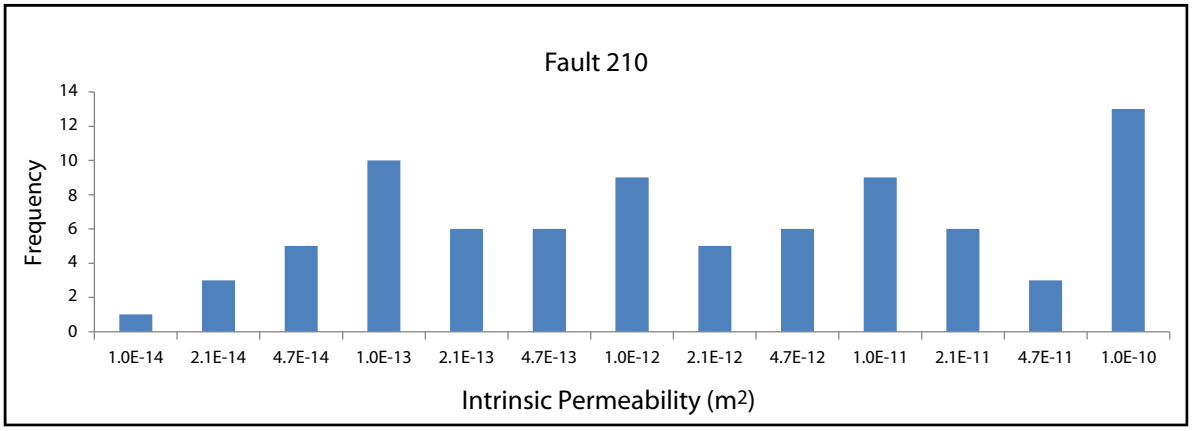

Note: Values represent the midpoints of bins.

Figure 5-62
Variation in Permeability of Fault 210 in Alternative NSMC Simulations

The storage coefficient of the faults and the rock are also identifiable parameters, and consequently, the calibrated values for these parameters vary over a narrow range (Figure 5-63). The average storage coefficient and standard deviation for faults are 3.2E-07 and 2.5E-07 m^{-1}, respectively. For the LCA rock, the average storage coefficient and standard deviation are 2.9E-06 and 1.6E-06 m^{-1}, respectively. These values are within the range of interpreted values presented in Figure 5-12.

The distributions of LCA rock permeability in the western and eastern halves of the model domain illustrated in Figure 5-64 indicate the permeability in the east is much higher than in the west, which

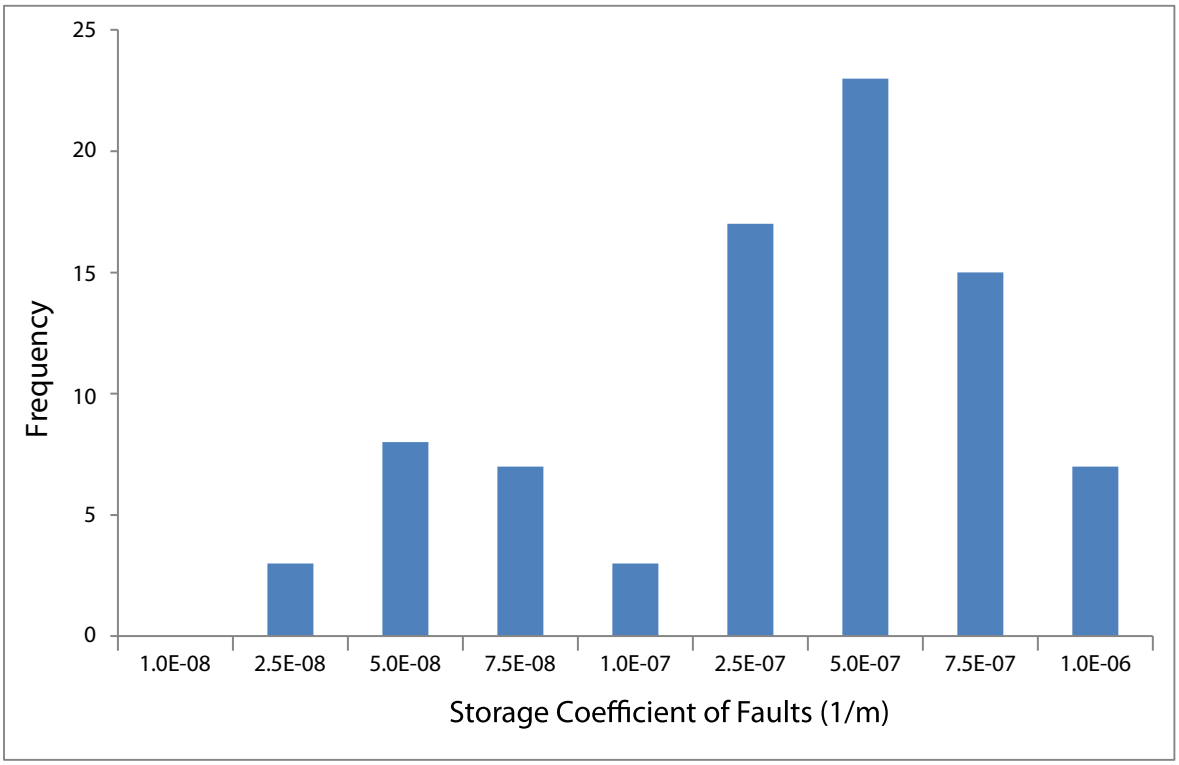

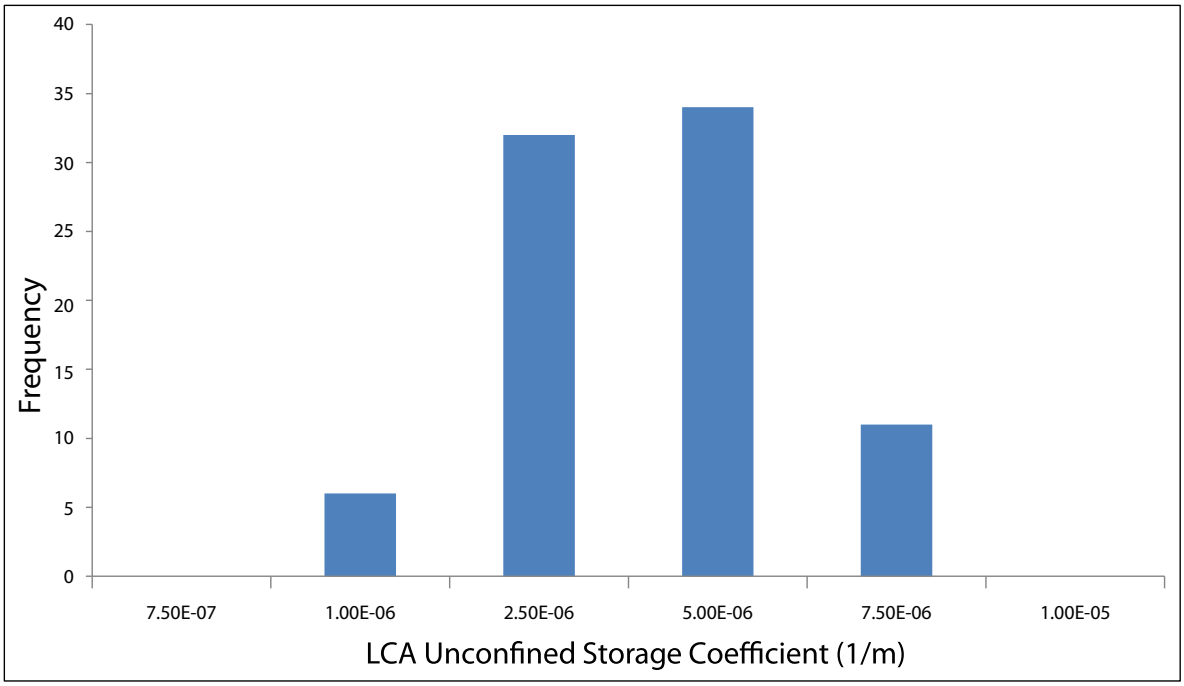

Note: Values represent the midpoints of bins.

Figure 5-63
Variation in Storage Coefficient for Alternative NSMC Simulations

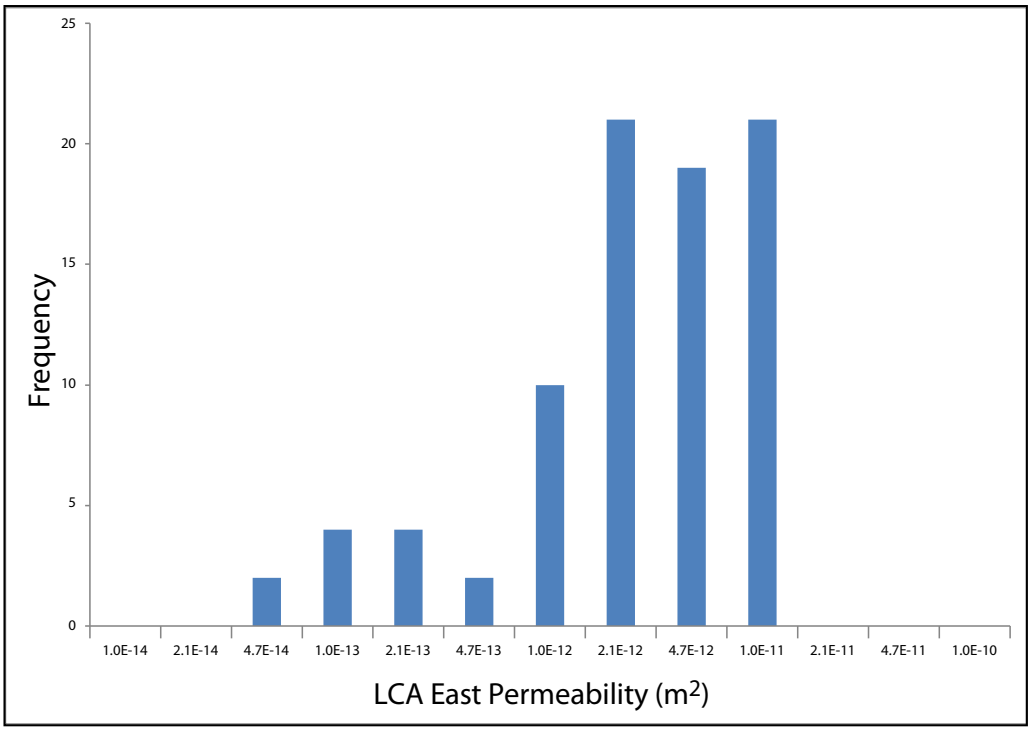

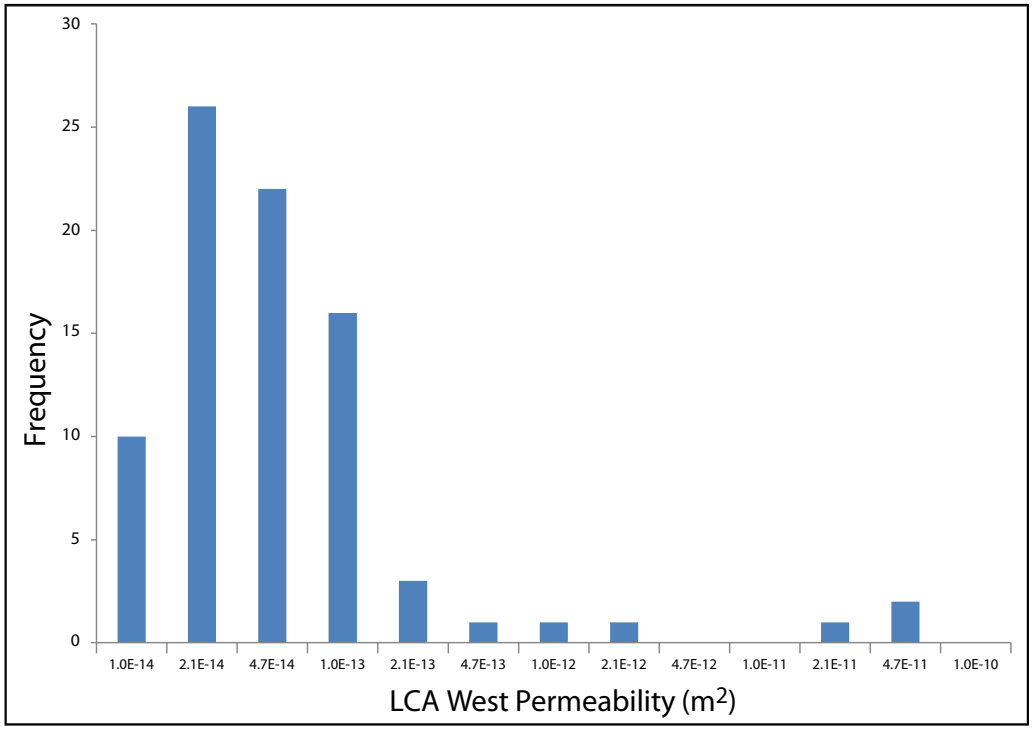

Note: Values represent the midpoints of bins.

Figure 5-64
Variation in Permeability of LCA East and LCA West in Alternative NSMC Simulations

is in conformity with the conceptualization that, on a basin-wide basis, the eastern half of Yucca Flat represents the "hanging" side of the basin-and-range extension, whereas the western half represents the "foot" side. The permeability range in eastern Yucca Flat generally range from 1.0E-13 to 1.0E-11 m^2, while the permeability in western Yucca Flat range from 1.0E-14 to 1.0E-13 m^2.

Particle-tracking simulations were conducted to estimate the potential for contaminant migration for each of the alternative NSMC models discussed above. Particle-tracking simulations were conducted to evaluate particle trajectory and travel times using a subsystem transport metric. The goal was not to attempt to define all potential variations in flow paths and fluxes, but instead to capture a sufficient range of contaminant migration patterns and transport rates using multiple realistic combinations of alternative models and parameter sets. This was necessary in order to select alternative flow fields for propagation to the transport model discussed in Section 6.0.

The particle trajectory for each of the 83 alternative NSMC runs (with an objective function of less than 10.0) was examined in order to select three flow fields that represent "fast," "medium," and "slow" particle-transport rates. This analysis identifies the potential range of advective transport times, with the aim of selecting runs that may be characterized as representing an "average" or "medium" behavior and runs that may result in a greater extent of contaminant transport (termed "fast") or a lesser extent of contaminant transport (termed "slow"). As discussed above and in Section 5.6.3, these determination of "fast," "medium," and "slow" are predicated on the base-case conceptual model that assumes significant lateral continuity of the LCA in northern Yucca Flat. As such, these runs are biased to the higher end of the possible boundary influx in northern Yucca Flat. The designators of "fast," "medium," and "slow" are used as convenient indicators of these flow fields. As presented below, the "medium" NSMC case provides advective transport times that are equivalent to those of the base-case model run presented in Section 5.5.2. As such, the base case model run is used to represent the "medium" flow model.

The number of particles reaching the southern reference location (northing 4,090,000 m) for each NSMC run is presented by the histogram and cumulative distribution (red curve) in Figure 5-65. Out of the 2,592 particles released at the 12 locations (216 at each location), there are 27 runs for which 1,750 particles have crossed the breakthrough location of northing 4,090,000 m. For two runs, only 500 particles have crossed the breakthrough location, while one run has 2,500 particles crossing the breakthrough location in 1,000 years. It is clear from the shape of the cumulative distribution that the

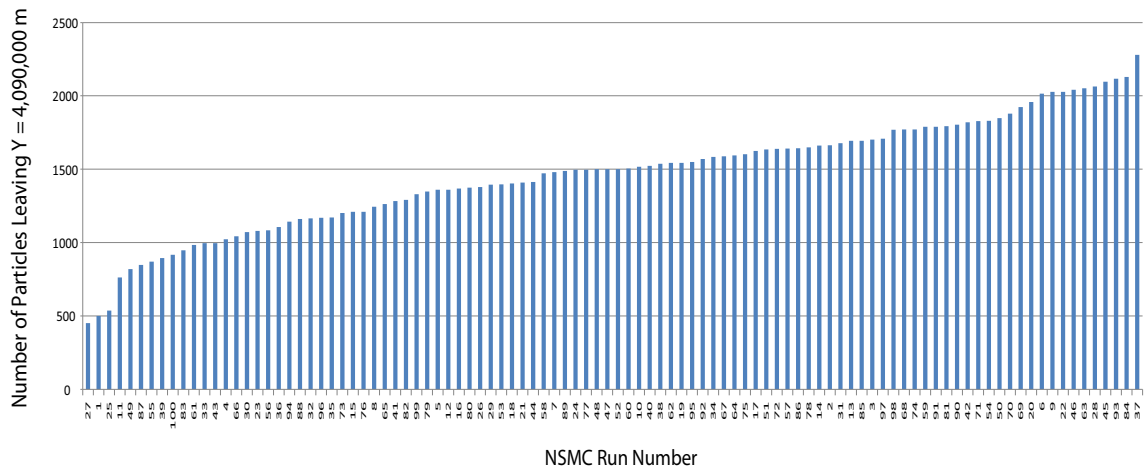

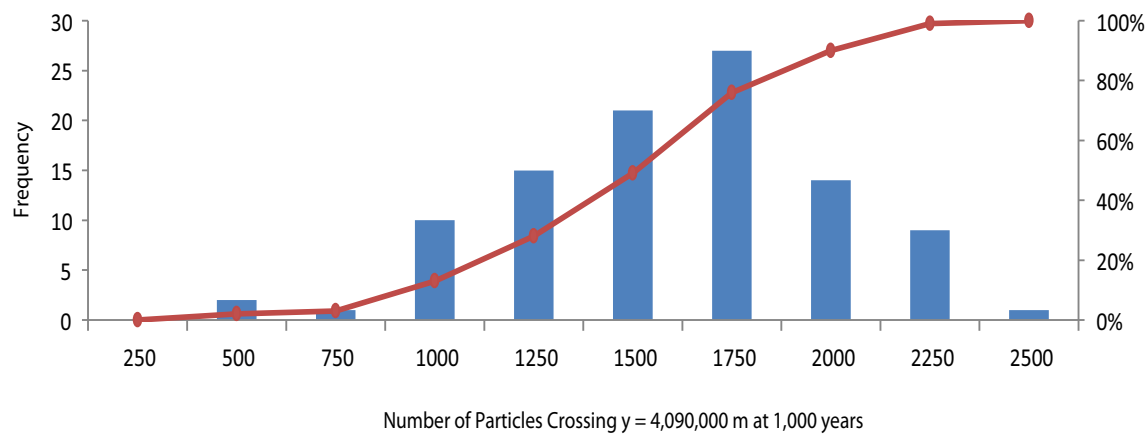

Note: Runs are ordered by run number from 1 to 100; missing run numbers represent the 17 model runs that did not converge. Values represent the midpoints of bins.

Figure 5-65
Distribution and Histogram for Total Number of Particles Reaching the Model Northing Location of 4,090,000 m from 12 Key Locations in the LCA

NSMC runs represent a wide range of flow conditions from which “slow,” “medium,” and “fast” flow fields can be selected for transport analysis.

Because the key detonations are located in the east-central portion of Yucca Flat, it was decided to select the “slow,” “medium,” and “fast” flow fields based on particle movement from the eastern locations (locations 1, 2, 7, 8, 10, 11, and 12 in Figure 5-48). The total number of particles starting from these locations for each NSMC run and reaching the breakthrough plane located at northing 4,090,000 m is presented in Figure 5-66. There is a fairly uniform distribution of particles reaching the breakthrough plane within the interval of 500 to 1,500 particles, which is also evident from the histogram and the cumulative distribution (red curve) presented in Figure 5-66. There are a few runs for which the total number of particles crossing the threshold location is less than 500. These runs, however, are associated with flow fields in which the interpreted velocity in the immediate vicinity of the detonation locations appears to be anomalously low. Therefore, these runs were not considered as candidates for the “slow” flow field.

Three runs representing “slow,” “medium,” and “fast” flow fields were selected for transport simulations. The criterion for selection was the number of particles crossing the threshold boundary (northing 4,090,000 m) in 1,000 years for detonation locations in east-central Yucca Flat. Runs with approximately 500, 1,000, and 1,500 particles crossing the threshold boundary were selected as representative “slow,” “medium,” and “fast” flow fields, respectively. The base-case calibration run presented in Section 5.5.2 has 1,042 particles crossing the threshold boundary, and consequently, this run was chosen as a representative “medium” flow case. NSMC runs 96 and 46, with 646 and 1,506 particles crossing the threshold boundary in 1,000 years, were chosen as the “slow” and “fast” cases. The particle migrations from selected locations for all three cases are presented in Figures 5-67 to 5-69 for illustrative purposes. The breakthrough curves for the “slow,” “medium,” and “fast” cases are presented in Figure 5-70, from which the relative rate of movement for each flow field can be readily noted.

5.6.3 Northern Boundary Flux Uncertainty

As discussed in Section 5.3.6, a wide range of boundary fluxes into northern Yucca Flat have been estimated. Generally, estimates derived from regional-scale models range from hundreds to about a thousand kilograms per second, while estimates derived from general hydrogeologic inferences of possible inflows into the LCA in this area range from less than one to tens of kilograms per second

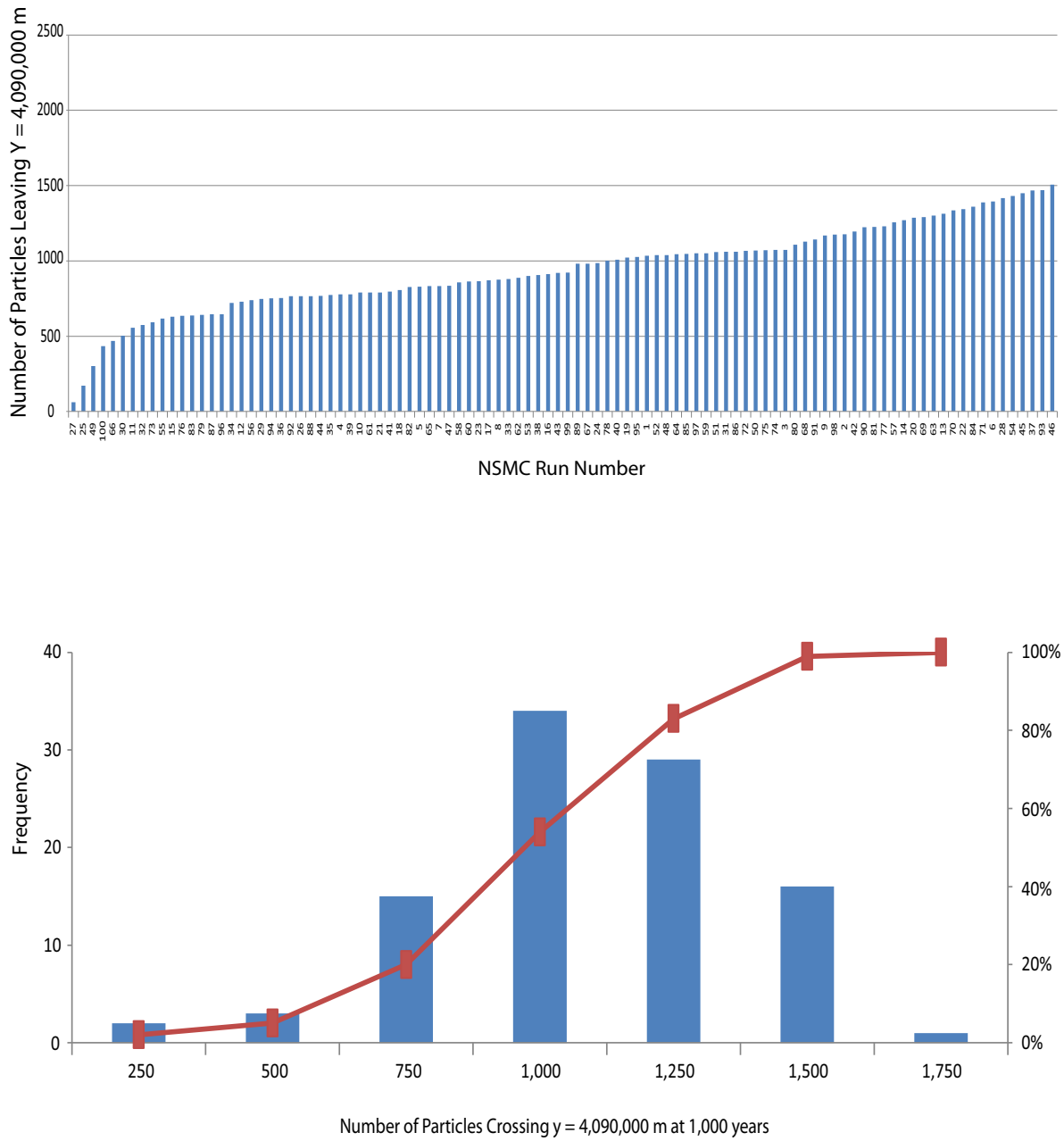

Note: Runs are ordered by run number from 1 to 100; missing run numbers represent the 17 model runs that did not converge. Values represent the midpoints of bins.

Figure 5-66
Distribution and Histogram for Total Number of Particles Reaching the Model Northing Location of 4,090,000 m from 7 Key Locations in the LCA

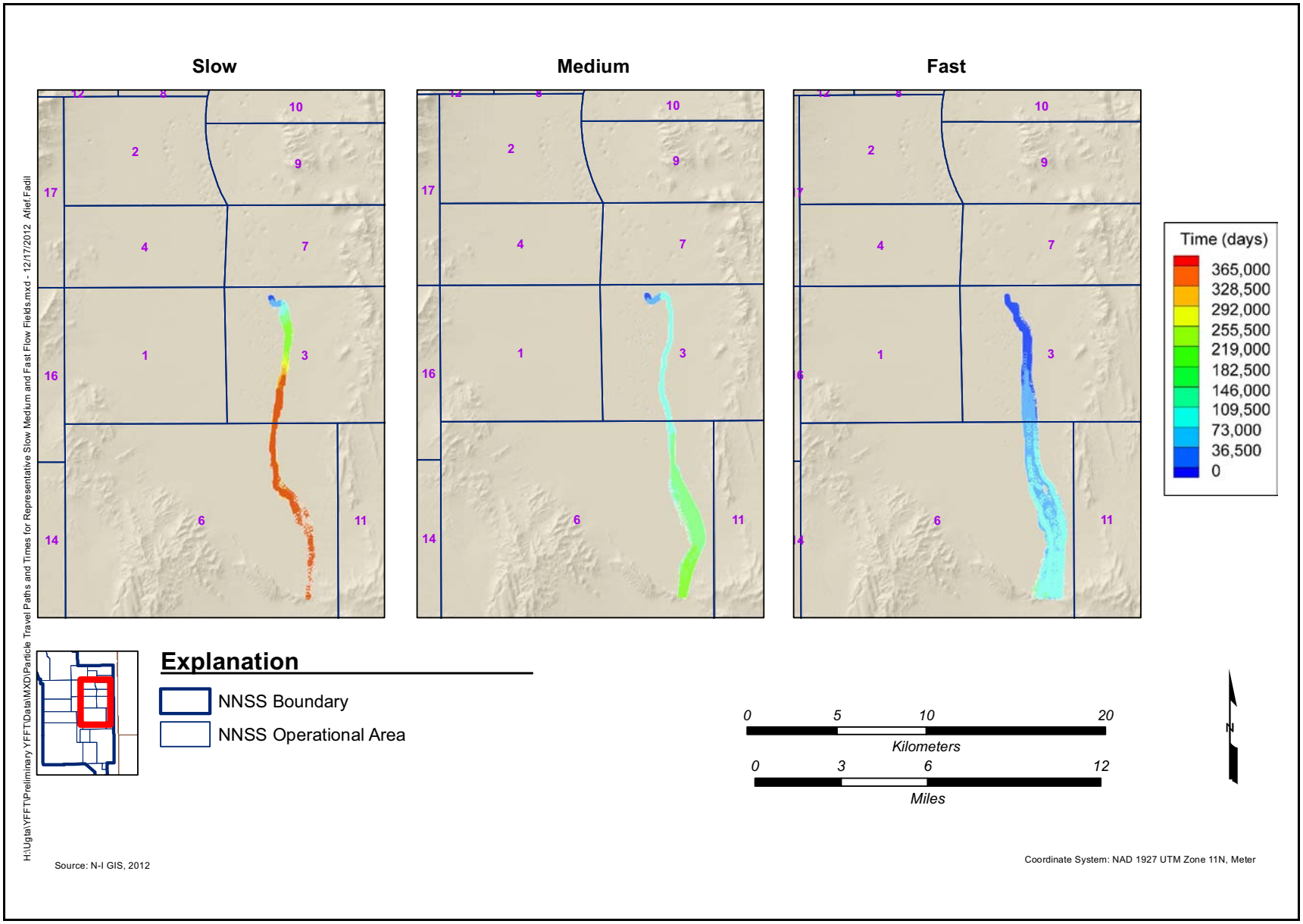

Figure 5-67
Advective Particle Travel Paths and Times for
Representative Slow, Medium, and Fast Flow Fields at Location 1 (BILBY)

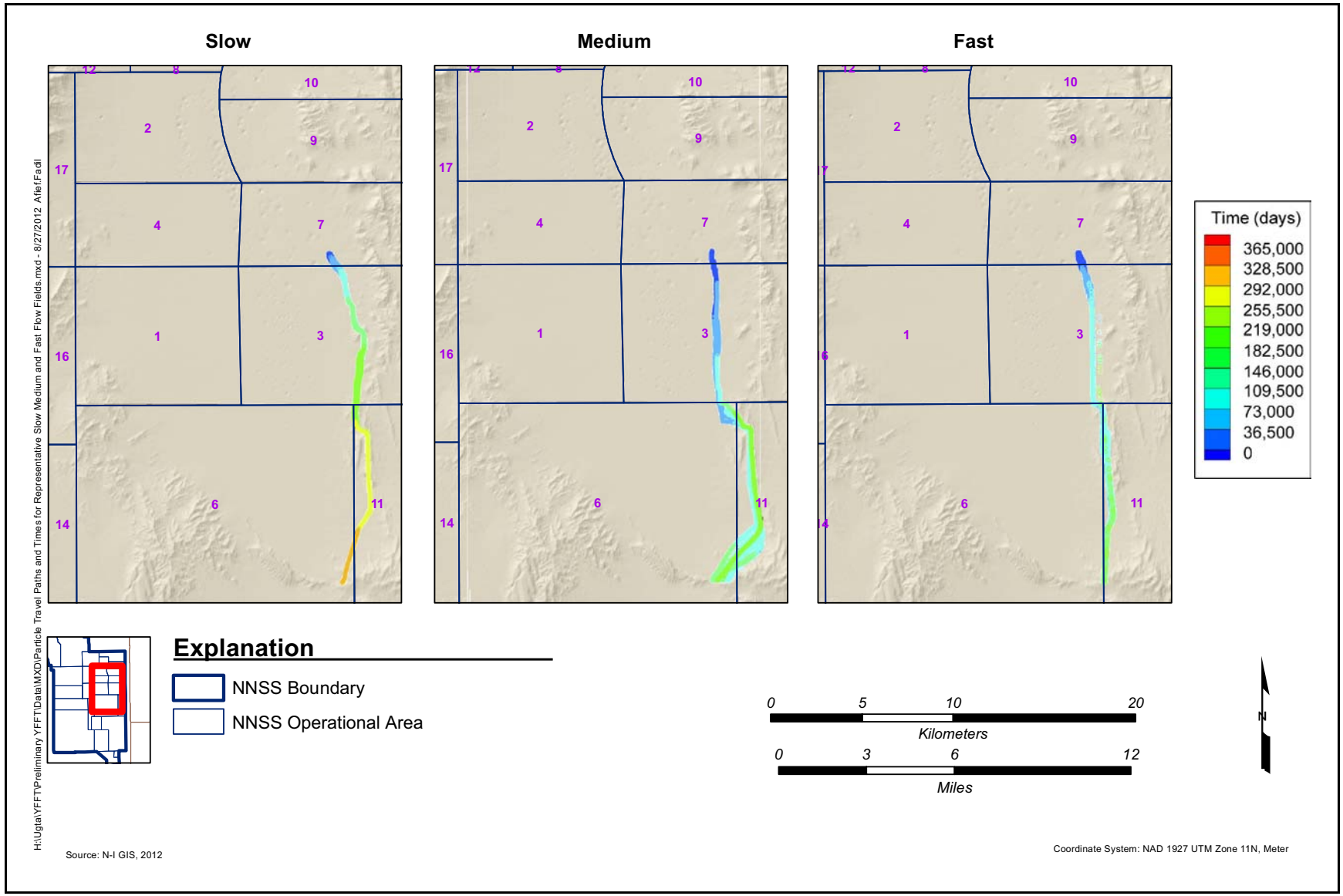

Figure 5-68
Advective Particle Travel Paths and Times for Representative Slow, Medium, and Fast Flow Fields at Location 8 (TORRIDO)

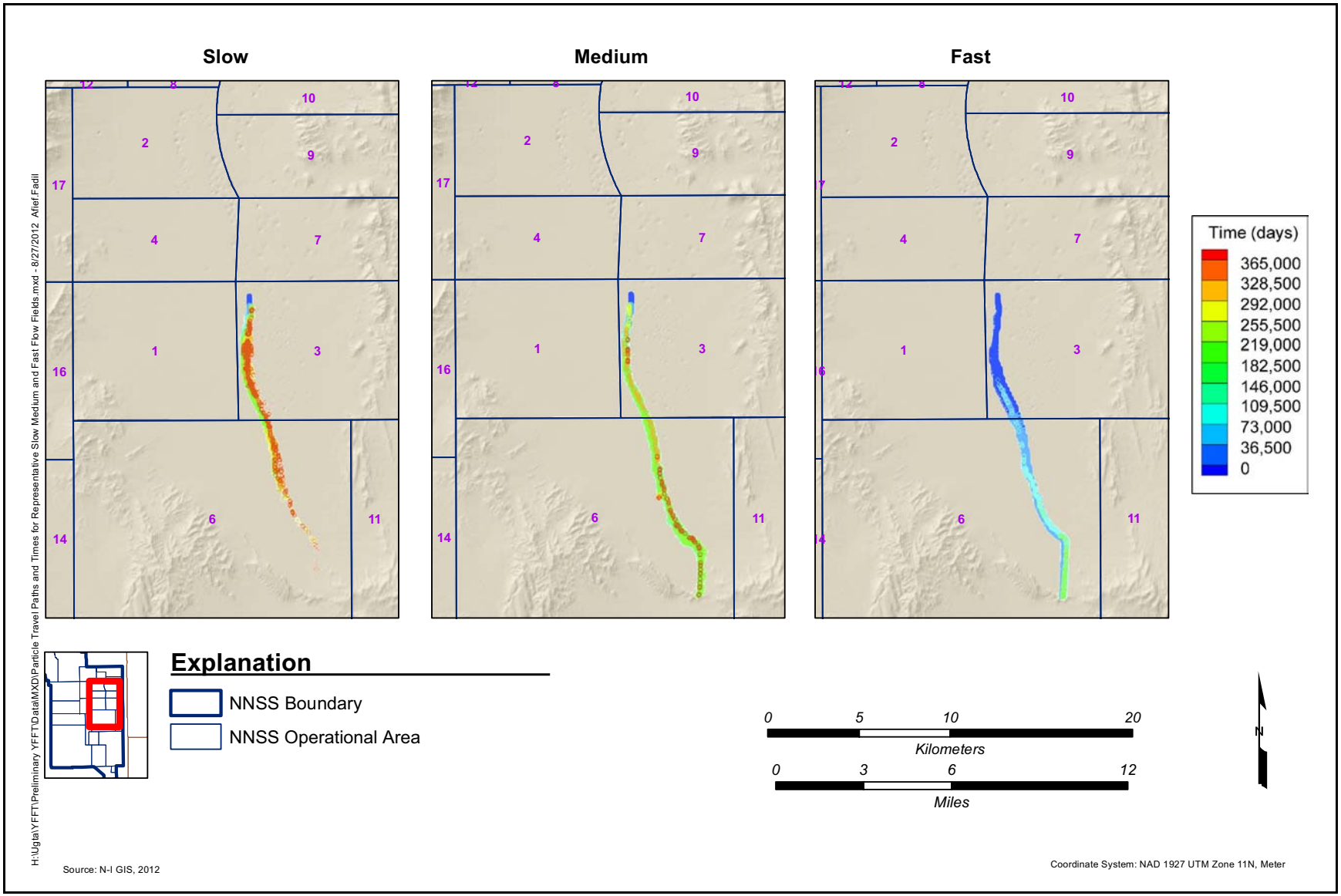

Figure 5-69
Advective Particle Travel Paths and Times for Representative Slow, Medium, and Fast Flow Fields at Location 11 (TORTUGAS)

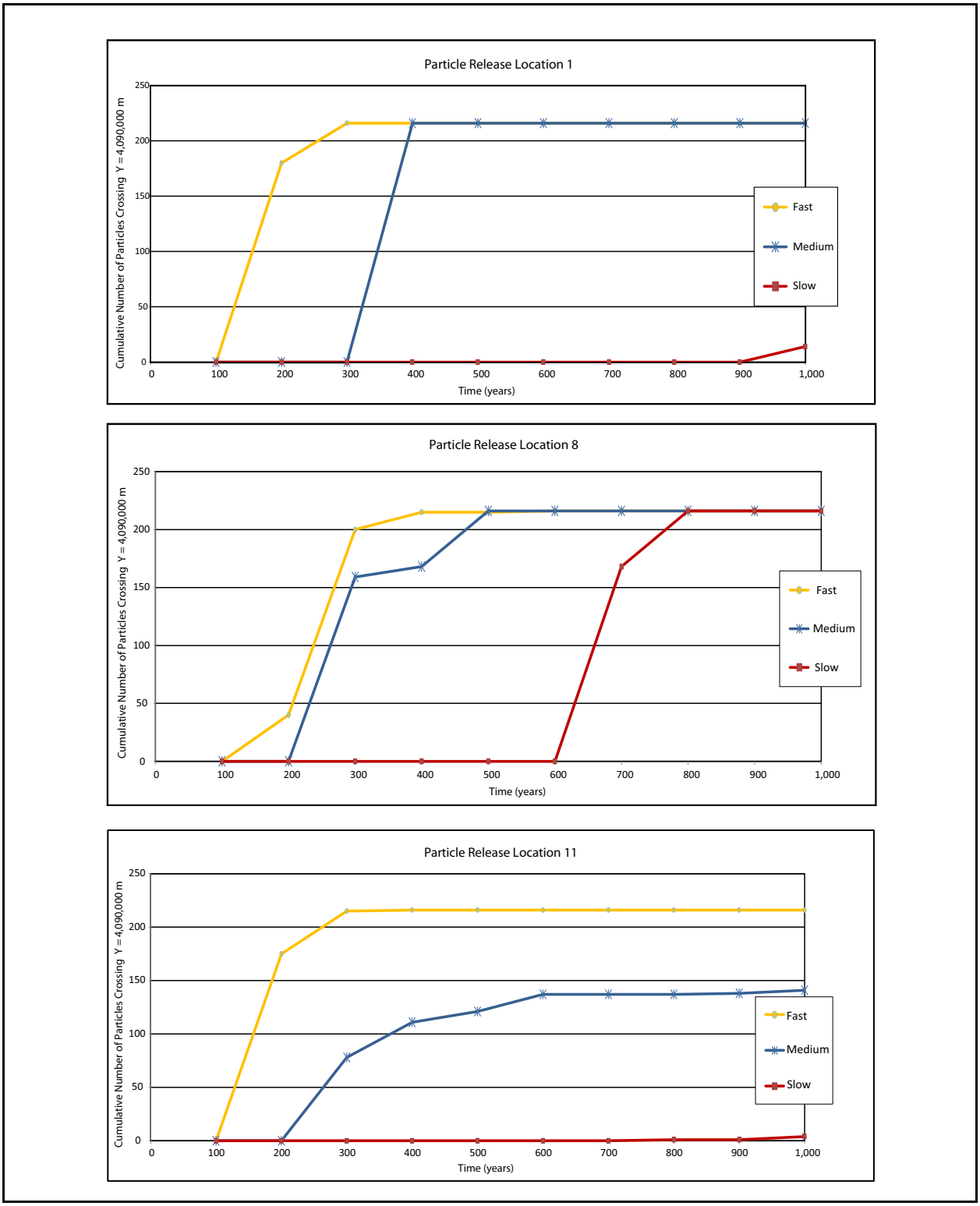

Figure 5-70
Breakthrough Curves for Particles Released at Three Representative Locations for Slow, Medium, and Fast Flow Fields

(Table 5-7). A recent revision of the DVRFS model developed by USGS has attempted to reconcile these differences by modifying the continuity of the LCA in this area, which has resulted in an estimated influx of about 55 kg/s (Faunt et al., 2012). Recent two-dimensional modeling has indicated that the flux could be as low as 0.1 kg/s and still generate a reasonably calibrated LCA flow model (Halford, 2012). The principal difference in these interpretations relates to the continuity and properties of the LCA in the vicinity of Climax stock, in particular, the continuity of the LCA between Climax stock and the low-permeability UCCU to the east of Climax stock, and the permeability of the LCA west of Climax stock (Figure 5-22). This structural uncertainty is similar to the HFM uncertainty identified in the alternative CP thrust HFM discussed in BN (2006) and Section 5.6.4.

A related uncertainty to the lateral underflow through the LCA in northern Yucca Flat is the uncertainty in the groundwater flow paths for waters that infiltrate north of Yucca Flat and north of the NNSS boundary illustrated in Figures 5-33 to 5-36. Waters are estimated to infiltrate at a rate of several tens to more than one hundred kilograms per second in the groundwater sub-basins north of Yucca Flat, notably, the western part of Emigrant Valley sub-basin 1581 and the western part of Groom Lake sub-basin 1583. A significant fraction of the infiltration in these sub-basins falls onto the subcrop of the LCA in these areas north of the NNSS. While it is possible that the groundwater in the LCA in these areas flows eastward and becomes part of the Belted Range tributary flow system (Fenelon et al., 2010), other conceptualizations included in the earlier regional models have this recharge contributing to the northern flux into the Yucca Flat tributary flow system.

The alternative flow models developed with the NSMC approach and presented in Section 5.6.2 have used the same constraints on northern influx as adopted in the base-case model, notably, a range from 10 to 500 kg/s. As a result, these NSMC alternatives do not explicitly capture the structural uncertainty associated with the lateral continuity of the LCA in the northern portion of the Yucca Flat basin. In addition, these alternatives do not capture the flow conceptualization in northern Yucca Flat developed by Fenelon et al. (2010) illustrated in Figure 1-13.

In order to address the likelihood that there is very limited influx of groundwater to the LCA in northern Yucca Flat, an alternative run was made. This run, called the alternative northern boundary flux model, fixed the northern influx (i.e., parameter “northflux”) at 1.0 kg/s, and allowed the constraints for all other boundary conditions and hydraulic properties to be exactly the same as the

base-case representation in Table 5-8.

The alternative northern boundary flux model resulted in a calibrated objective function of less than 3, which is equivalent to the calibration of the base-case and NSMC runs (Figure 5-55). To evaluate the impact of the alternative northern boundary flux model, particle-tracking results similar to those developed for the base-case and alternative NSMC cases are presented in Figures 5-71 to 5-73. When these results are compared to the corresponding results for the base case illustrated in Figure 5-49 and Figures 5-67 to 5-70, it is apparent that the reduced northern boundary influx leads to less advective transport of particles. To evaluate the impact of this alternative northern boundary flux on contaminant transport in the LCA, this alternative flow field was used with the LCA contaminant sources, and the results are presented in Section 6.5.6.

5.6.4 HFM Uncertainty

Because of geologic complexity and the inherent nonunique interpretation of geologic field data in the base HFM, it is necessary to develop and evaluate alternative flow models based on alternative HFMs. Based on analysis conducted by BN (2006), two alternative flow models, which were deemed to potentially impact groundwater flow, were evaluated: (1) the UCCU, and (2) the CP thrust fault alternative models:

Alternative 1—Contiguous UCCU in Southwestern Yucca Flat

Magnetotelluric (MT) data suggest that the UCCU is not continuous within the southwest portion of the model area. The data seem to indicate that much of the area is underlain by thick, highly resistive carbonate, and that the more electrically conductive Mississippian siliciclastic rocks that compose the UCCU are structurally broken up in this area and thus do not form a thick continuous sheet of clastic confining unit. This interpretation was incorporated into the base HFM. It is, however, difficult to interpret the MT data in this area with certainty, because data are sparse, and higher-resistance quartzite-rich units make it difficult to distinguish Mississippian siliciclastic rocks (i.e., UCCU) from older carbonate rocks. The UCCU alternative model was therefore developed that contains an extensive sheet of the UCCU overlying the regional LCA in the southwest portion of the model area. The hydrologic significance of this alternative is that it can potentially lower infiltration rates in the southwest and also cause a change in the flow field, allowing more water from the upper units to migrate eastward toward the center of the basin.

Alternative 2—CP Thrust Fault

Based on MT data and regional structural analysis, Mississippian siliciclastic rocks that compose the UCCU occur within the footwall of the CP thrust fault, which is modeled as steepening rapidly eastward and forming a ramp structure beneath

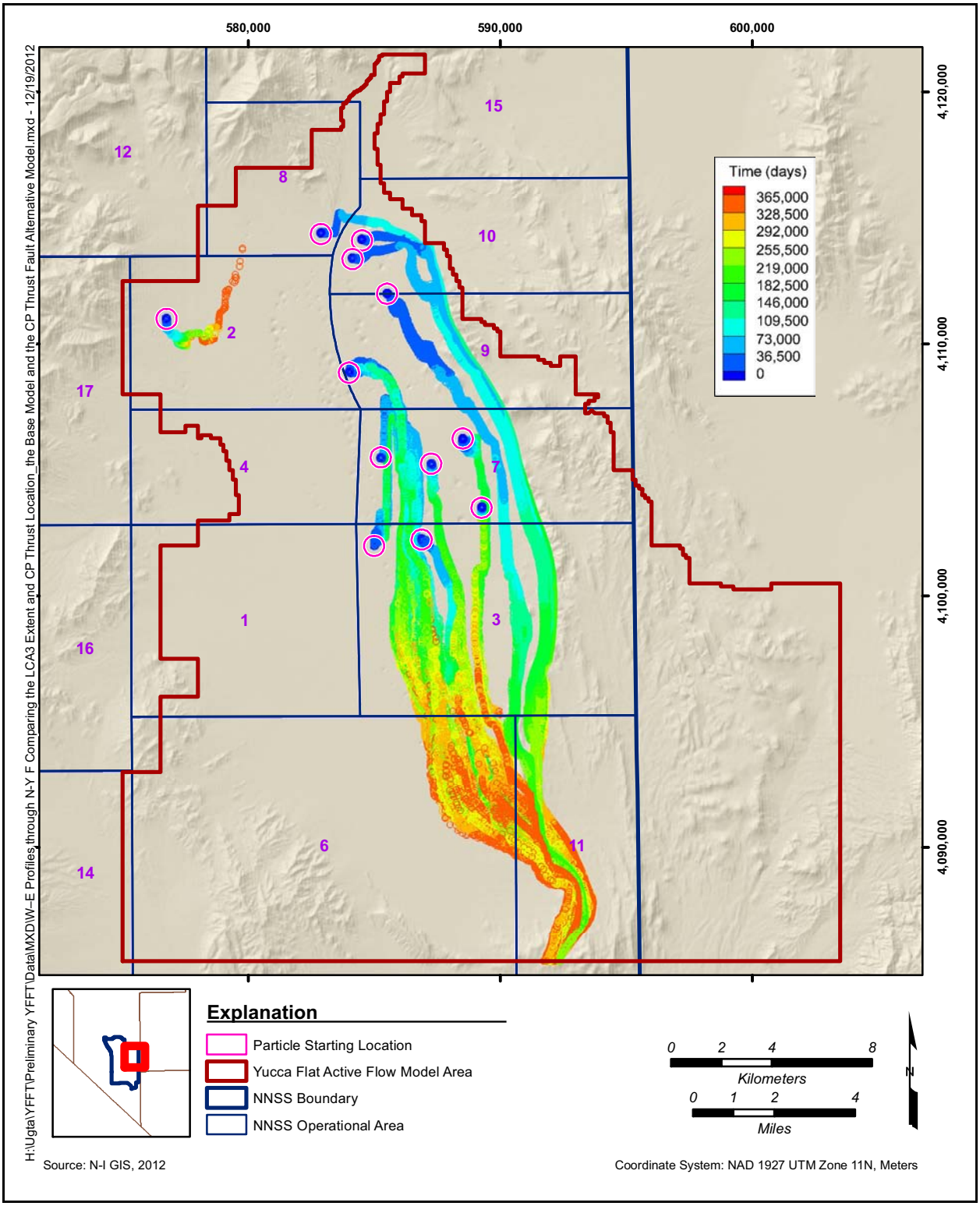

Figure 5-71
Advective Particle Travel Paths and Times from 12 Key Locations for the Alternative Northern Boundary Flux Model

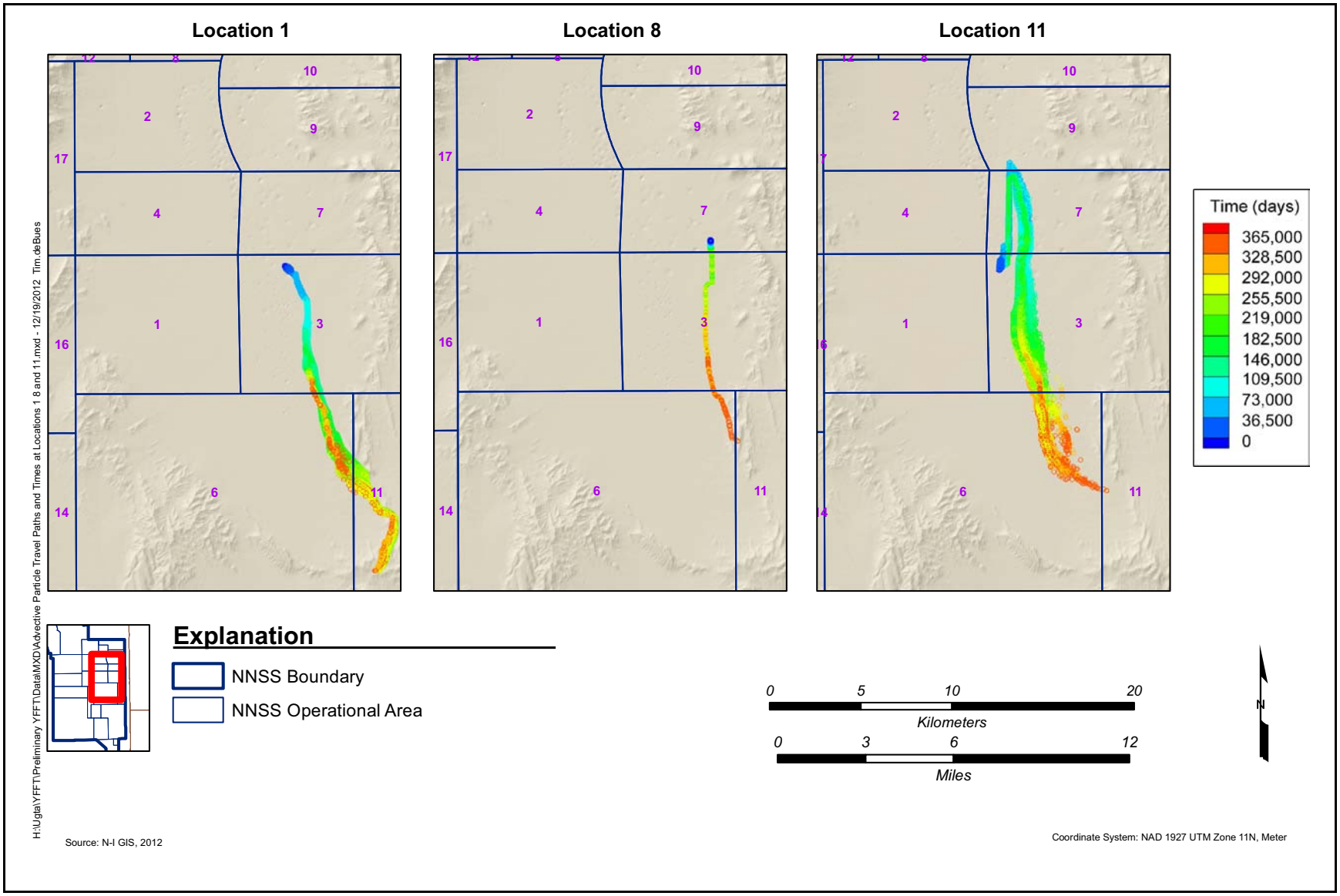

Figure 5-72
Advective Particle Travel Paths and Times at Locations 1, 8, and 11 (BILBY, TORRIDO, and TORTUGAS) for the Alternative Northern Boundary Flux Model

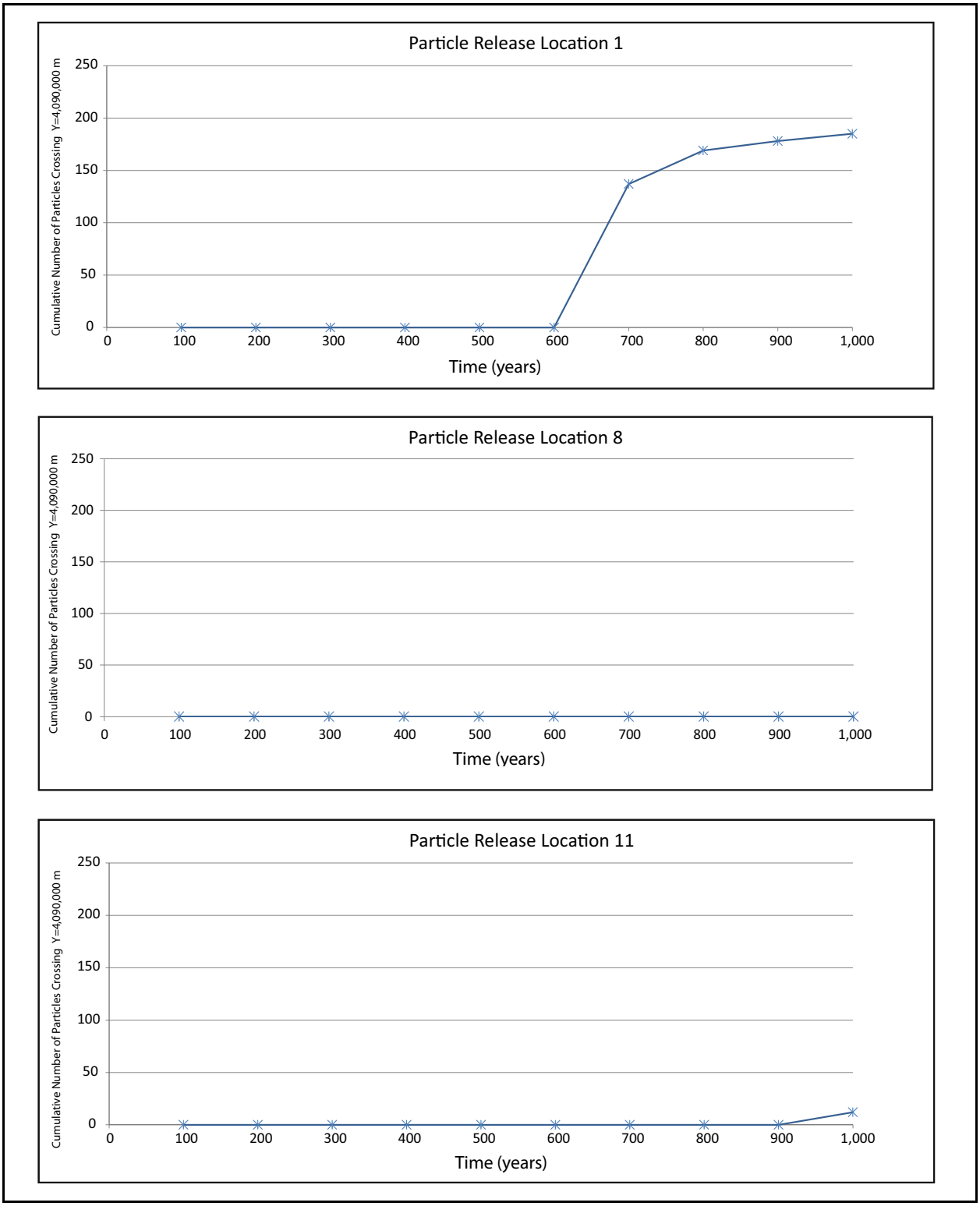

Figure 5-73
Breakthrough Curves for Particles Released at Locations 1, 8, and 11 (BILBY, TORRIDO, and TORTUGAS) for the Alternative Northern Boundary Flux Model

central Yucca Flat coincident with the Carpetbag-Topgallant fault system. As a result, the base HFM limits the UCCU to the western portion of the model area west of the Carpetbag-Topgallant fault system. However, MT data are sparse in northern Yucca Flat east of the Carpetbag fault, which results in poor constraint on the areal extent of the UCCU east of the Carpetbag fault. The CP thrust fault alternative scenario models the CP thrust ramp as being coincident with the Carpetbag-Topgallant fault system in the southern and central portions of Yucca Flat, but shifting to the east in northern Yucca Flat to become coincident with Yucca fault. The hydrologic significance of this alternative is that it can potentially lower the amount of northern influx into Yucca Flat.

Applying the calibrated base-case hydrogeologic parameters in the two alternative HFM models resulted in hydraulic heads that were nearly identical to the values for the base-case model at the observation wells. As a consequence, these alternative models did not require further calibration. Particle-tracking simulations were also conducted in order to determine differences in travel times and pathways between the base and alternative models. Particles were released at key locations in the study area where contamination either emanates from the LCA or arrives in the LCA from the overlying unsaturated zone and saturated alluvial/volcanic aquifer system model domains. Results of the particle-tracking simulations indicate no discernible differences in particle trajectories between the base and alternative models, suggesting that these alternative models do not significantly alter the transport pathways and travel times of radionuclides in Yucca Flat.

5.6.5 Fault-Zone Parametric Uncertainty

As discussed in Sections 5.4 and 5.5, two separate permeability zones, the core and damage zone, were specified in each Yucca Flat fault. The continuity and lateral extent of these two fault zones, however, are not sufficiently documented, and therefore, some uncertainty in the configuration of the faults exists. As with most models covering large areas with limited data, these uncertainties cannot be identified by the model calibration alone, and they may have significant effects on the resulting calculations made with the model. Therefore, simulations were conducted with different fault-zone configurations in order to obtain alternative flow fields associated with variations in the fault architecture. The primary goal was to explore alternative pathways for contaminant transport that could lead to significantly different contaminant transport times as compared to the base case. The following three alternative fault conceptualizations were examined: (1) uncertainty in fault permeability zones, (2) uncertainty in the southern accommodation zone, and (3) uncertainty in the Area3n9 fault.

Uncertainty in Fault Permeability Zones

As a consequence of the dual-zone fault architecture described above, significant quantities of groundwater flows through the damage zone of the calibrated model. Based on the severely limited data analyzed by site geologists, there is considerable uncertainty regarding the continuity and extent of these zones (Prothro et al., 2009). Wide damage zones have not been observed at the site, and there potentially may not be continuity in the fault core through the entire length of the fault (Prothro, NSTec, personal communication). The faults in Yucca Flat may therefore contain altered rock only along a narrow width on either side of the fault plane. It is also possible that the damage zone may be healed because of precipitation of calcite in fractured spaces or some other geochemical alterations that reduce the hydraulic permeability in this zone. Based on these possibilities, an alternative model was developed in which only a single narrow fault zone was specified that could function as either a low-permeability barrier or a high-permeability conduit as dictated during model calibration.

Uncertainty in Southern Accommodation Zone

The three major faults in Yucca Flat terminate north of the southern LCA flow model boundary, which is located approximately along the junction of the Frenchman Flat and Yucca Flat basins. Faults in the Yucca Flat basin are primarily normal faults formed by basin-and-range extension. Major faults in the Frenchman Flat basin are typically strike-slip faults; however, as illustrated in Figure 5-31, these faults do extend into Yucca Flat. Site geologists assume that a fairly wide accommodation zone exists along the boundary of the basins, and therefore, an independent permeability zone in the base case and NSMC models was specified between the two basins as shown in Figure 5-29. It is, however, possible that the accommodation zone is not as wide as assumed, and therefore, an alternative simulation was conducted with a narrower accommodation zone as indicated in Figure 5-74. This narrow zone, if present, can potentially result in different transport pathways within Yucca Flat.

Uncertainty in Area3n9 Fault

The Area3n9 fault in the vicinity of BILBY as mapped in the HFM is unusual as it is disconnected, containing two distinct limbs as shown in Figure 5-30 (fault 149). There is uncertainty regarding the continuity of the fault south of BILBY and also whether the hydrogeologic properties in the fault zones are similar in the two segments. In the base-case simulation, the fault architecture described above (with a core and damage zone) was specified, and the resulting hydrogeologic properties for the fault were obtained for the northern segment. Because of potential importance of the BILBY

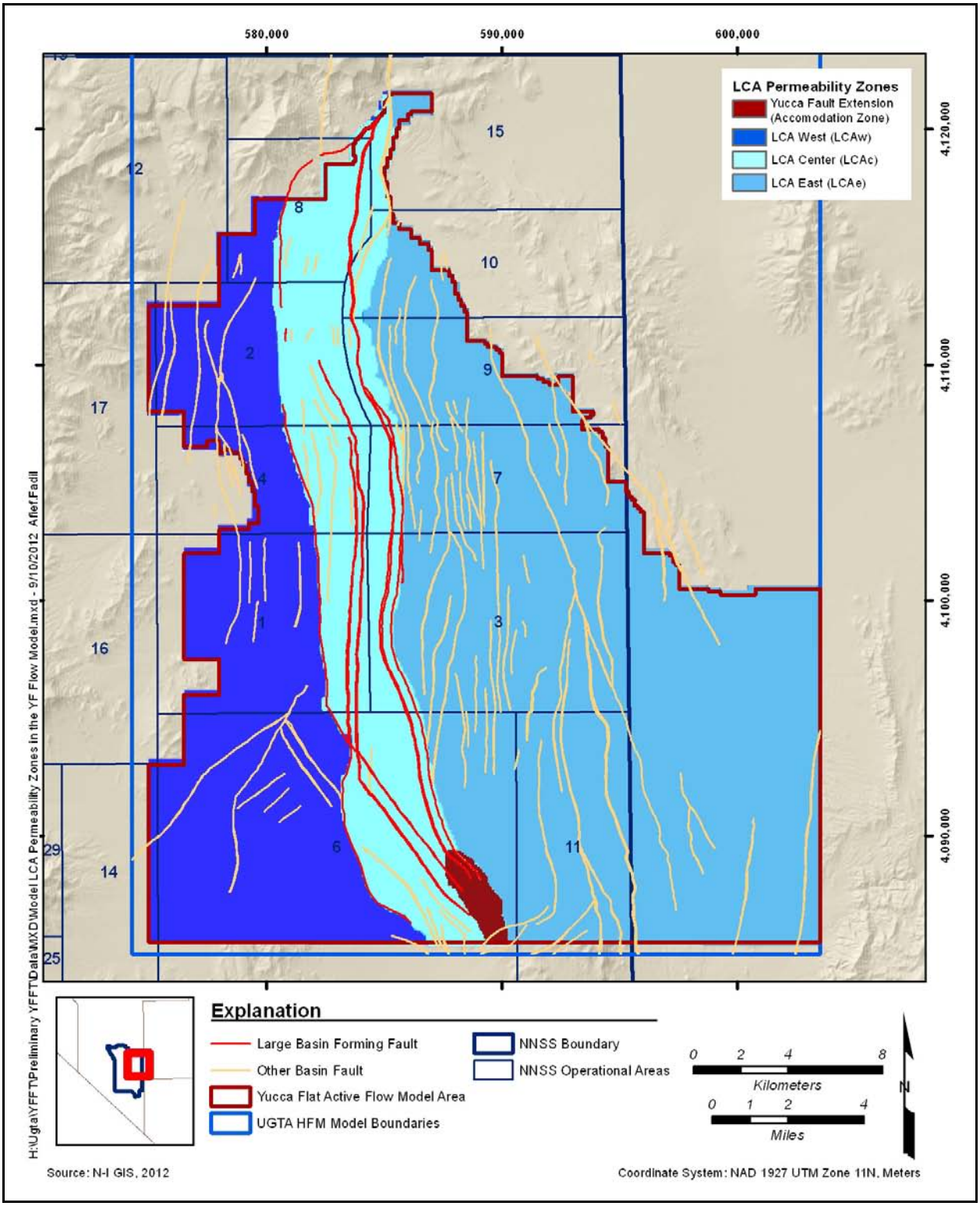

Figure 5-74
Modeled LCA Permeability Zones Showing Narrow Yucca Flat Accommodation Zone

detonation to overall radionuclide transport in Yucca Flat, an alternative run was conducted with both segments of the fault tied (i.e., having the same permeability), which essentially results in the Area3n9 fault acting as a single fault even though the fault limbs are disconnected.

All three alternative models described above were calibrated with PEST, resulting in low objective functions of 2.8, 3.4, and 7.7 for the thin accommodation zone, Area3n9 fault, and no damage zone alternative models, respectively. The contaminant transport breakthrough metric for these alternative runs is presented in Figure 5-75, along with the slow, medium, and fast NSMC flow-field cases discussed in Section 5.6.2. As can be inferred from the figure, the breakthrough curves for all three alternative cases are contained within the range of transport for the slow and fast flow-field cases. Consequently, it can be deduced that the alternative fault models would not result in radionuclide migration rates that are outside the bounds obtained from the slow and fast cases. Transport simulations involving radionuclide migration with advection, dispersion, sorption, and other geochemical reactions for the base and alternative cases are discussed in Section 6.0.

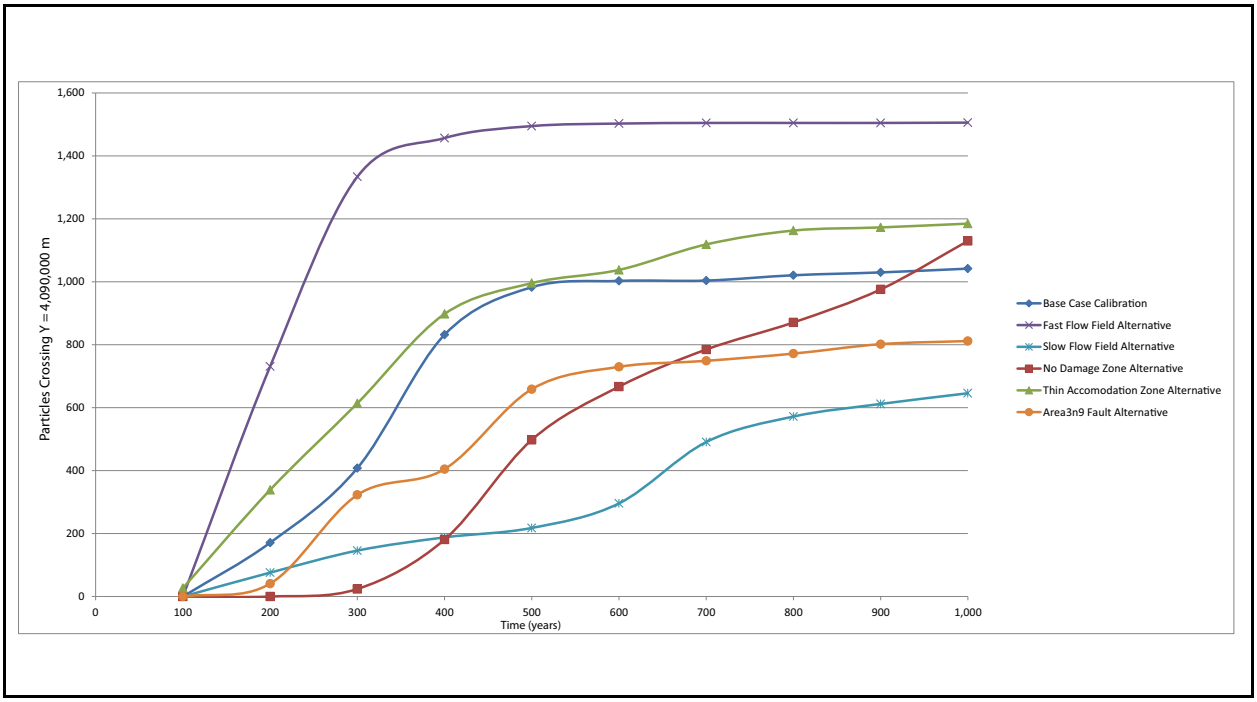

Figure 5-75
Breakthrough Curves at Model Northing Location 4,090,000 m for Alternative Fault Models

Because of the importance of the BILBY detonation, the Area3n9 fault alternative model results are discussed further. As can be noted from Figure 5-75, approximately 200 fewer particles exit the threshold boundary (y = 4,090,000m) for this alternative case compared to the base case. This difference, however, is entirely due to faster migration from BILBY for the base-case run. To illustrate, the particle trajectory from the BILBY detonation for the base case and the Area3n9 fault alternative run is presented in Figure 5-76. As is evident from the figure, tying the permeabilities of the southern and northern segments of the fault results in the particles remaining in the Area3n9 fault rather than migrating eastward to the higher-permeability fault 160 as in the base case and traveling at a slower rate than for the base case. By the end of 1,000 years, all 216 particles released at BILBY have reached the threshold boundary for the base case, while for the Area3n9 sensitivity case, only 14 particles have reached the threshold boundary. It is therefore concluded that the base calibration run and the associated alternative NSMC runs constructed with the base-case fault representation provide more conservative results with respect to radionuclide migration potential from BILBY.

5.6.6 Narrower Fault Zone Alternative Model (Level 3 Mesh)

As discussed in Section 5.4, three meshes (levels 1, 2, and 3) with increasing levels of refinement were developed. Level 1 is the coarsest and level 3 the finest mesh. The mid-level mesh (level 2) was selected as a compromise between the need for simulation accuracy and computational expense. Each fault in the mesh is represented by one core node and at least two damage-zone nodes on either side of the core. The nodal spacing in the level 2 and level 3 meshes is 125 and 75 m, respectively. The fault width is therefore typically twice as wide in the level 2 mesh as the level 3 mesh. A sensitivity run was therefore conducted with the level 3 mesh to evaluate the impact of specifying a narrower fault on contaminant transport.

The final calibrated hydrologic parameters and boundary conditions for the base case (level 2) mesh discussed in Section 5.5 were specified in the level 3 mesh. Particles were released at the same 12 locations (shown in Figure 5-48) for evaluating particle transport times for the alternative level 3 models. These locations represent locations of greatest contamination either emanating in the LCA or infiltrating into the LCA from the overlying unsaturated zone and saturated alluvial/volcanic aquifer system model domains. At each location, a total of 216 particles were released within a cube spanning 100 m in the x, y, and z directions. Because of the finer level 3 mesh, the particles were

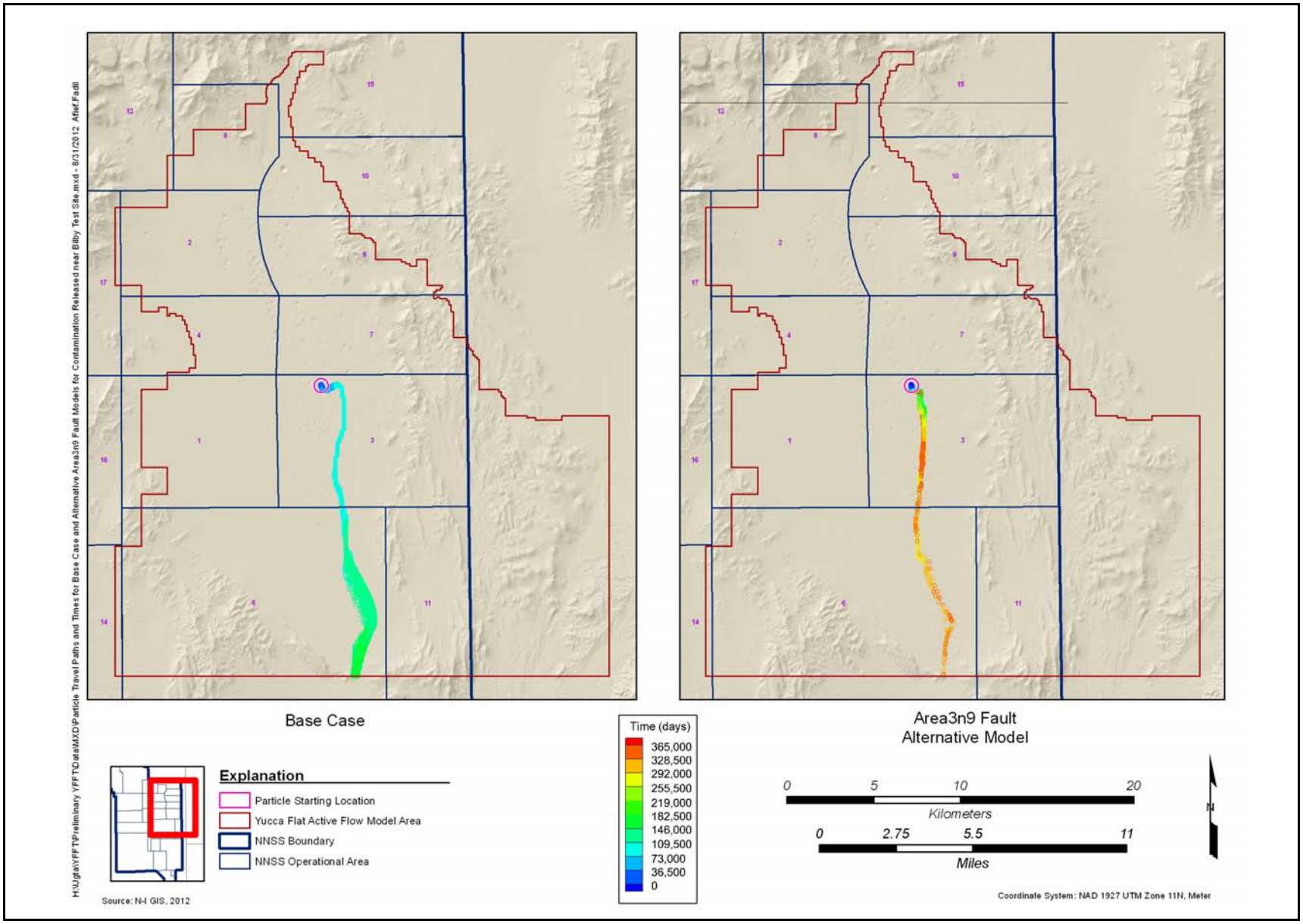

Figure 5-76
Particle Travel Paths and Times for Base Case and Alternative Area3n9 Fault Models for Contamination Released near BILBY

released over a smaller region in order to ensure that the particles follow approximately the same path as with the level 2 mesh.

The breakthrough curves (at the northing boundary of 4,090,000 m) for particles released at locations 1, 8, and 11, which were used to examine the trajectory for the fast, medium, and slow NSMC cases, are presented in Figure 5-77. The particles released at location 1 arrive at the threshold boundary within a time frame that is in between the travel time for the medium and fast NSMC cases. At location 8, the particles arrive only slightly faster than for the fastest NSMC case. At location 11, the particles in the level 3 mesh arrive slower than for the fast and medium NSMC cases. The particle trajectories at these three locations are presented in Figure 5-78, along with the trajectory for the base (medium) case, in order to illustrate the generally similar particle pathways for the level 2 and level 3 meshes. Based on the results presented in Figures 5-77 and 5-78, it is evident that there is not a significant difference in the particle paths and travel times simulated with the level 2 and level 3 meshes, and that the bounding level 2 models (i.e., the fast and slow NSMC cases) will generally encompass the extent of contaminant transport emanating from the detonation locations.

5.7 Parameter Sensitivity Analysis

5.7.1 Background

Generally accepted practice for the assessment of groundwater model calibration includes sensitivity analysis (ASTM, 1995). The purpose of sensitivity analysis is to examine the sensitivity of model outputs to model inputs for assessing the adequacy of the model with respect to its intended function and to provide an understanding of the level of confidence in model results (ASTM, 1994, 2004).

Two approaches to local parameter sensitivity analysis were implemented for the Yucca Flat LCA flow model. The first approach uses PEST (Doherty, 2004), a nonlinear parameter estimation code, to evaluate parameter sensitivity and correlations. The PEST code calculates a sensitivity coefficient for each parameter with respect to all weighted observations. This analysis is termed “local” because it investigates parameter values near the base calibrated value using only slight changes to parameter values. The second approach involves perturbing each of the parameters over a range, one at a time, from a reference value and computing the corresponding change in the model output (Anderson and Woessner, 1992). Because of the wider range of parameter space that is explored by this approach, the technique is more “global” in nature.

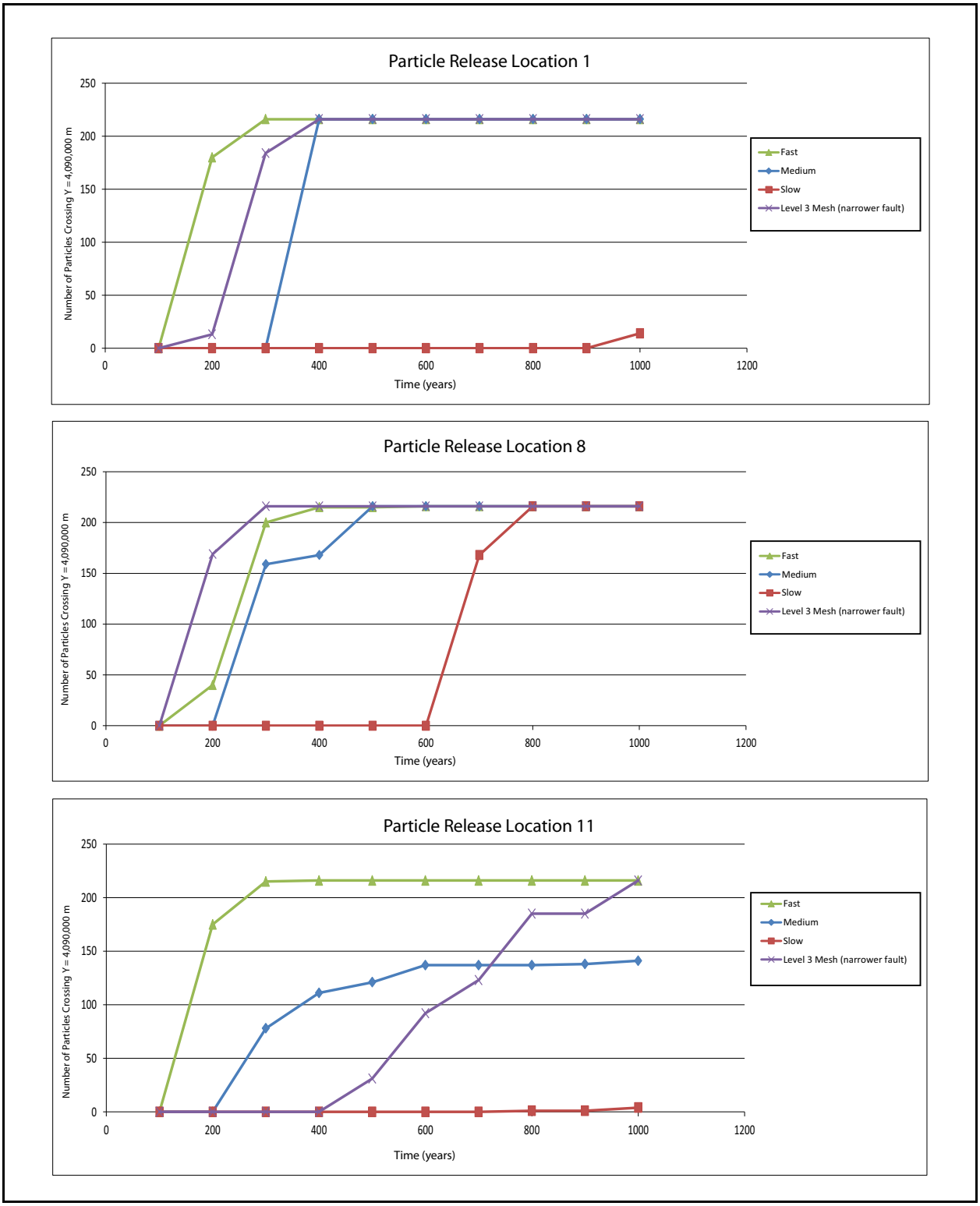

Figure 5-77
Particle Breakthrough Curves at Northing Location of 4,090,000 m for the Level 3 Mesh, and the Fast, Medium, and Slow Level 2 Mesh Cases

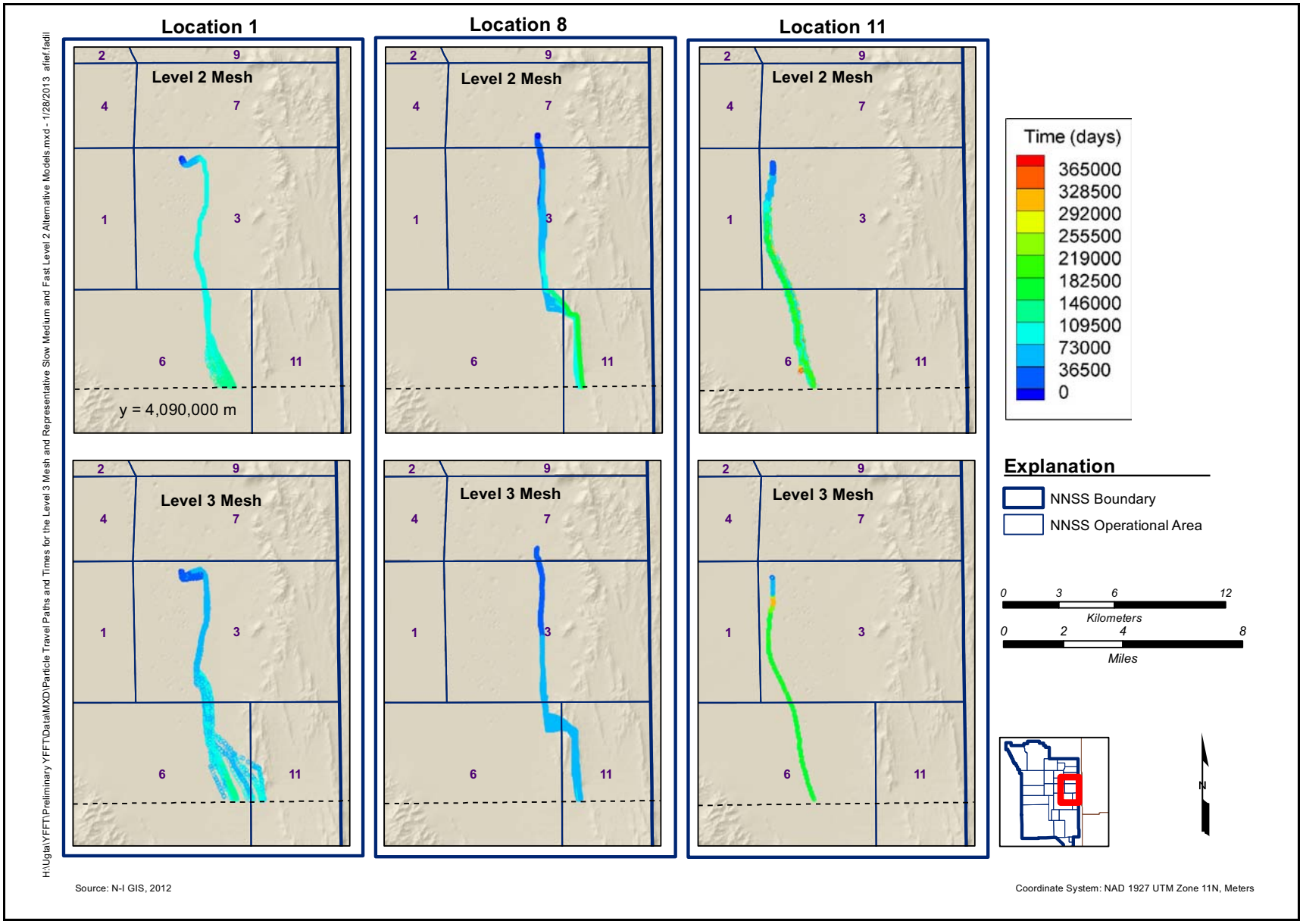

Figure 5-78
Particle Travel Paths and Times for the Level 3 Mesh, and Representative Slow, Medium, and Fast Level 2 Mesh Alternative Models

The sensitivity of the parameters will be examined with respect to the goodness-of-fit calibration metric termed the objective function. As discussed in Section 5.5, the objective function is the sum of the squares of the weighted residuals:

$$\Phi = \sum_{i=1}^{m} (w_i r_i)^2 \qquad (5\text{-}5)$$

where

Φ = sum of the squares of the weighted residuals, or the objective function
w_i = observation weight for a given observation
r_i = residual or difference between the simulated and measured values for a given observation
m = number of observations

The residuals are calculated for both the steady-state heads and the MWAT drawdowns. The sensitivity analysis conducted with the Yucca Flat flow model and presented in this section was instrumental in developing the calibrated model documented in Section 5.5.2.

5.7.2 Parameter Sensitivity Analysis

As described in Doherty et al. (2010), and the Frenchman Flat modeling report (SNJV, 2006c), sensitivity coefficients relate change in output over the change in input around a reference input value. If the reference point is the calibrated parameter value, then the sensitivity coefficient represents parameter sensitivity in the vicinity of the calibrated parameter set. These sensitivities can be obtained quantitatively from the output of PEST. In the process of optimizing a nonlinear model, PEST calculates the Jacobian matrix. The Jacobian matrix relates the model-calculated observations to the model input parameters where any element of the Jacobian matrix, J_{ij}, describes the derivative of the ith observation with respect to the jth parameter. Based on the Jacobian matrix, PEST calculates the composite sensitivity of each parameter with respect to all weighted observations. The composite sensitivity of parameter i is defined as follows:

$$s_i = \frac{\sqrt{J^t Q J_{ij}}}{m} \qquad (5\text{-}6)$$

where

s_i = composite sensitivity of parameter i
J^t = transpose of the Jacobian matrix
Q = cofactor matrix, and m-dimensional, square, diagonal matrix consisting of the squared observation weights
J_{ij} = Jacobian matrix
m = number of observations of nonzero weight.

The sensitivity coefficient for a given parameter is therefore the weighted average of the derivatives of all the observations with respect to that parameter. It should be noted that the sensitivity coefficient is locally derived and applies only to the parameter range over which the input-output relationship is linear. The composite sensitivities of all adjustable parameters are presented in Figures 5-79 and 5-80 from which it is apparent that the sensitivities in general are quite low and that the objective function is highly sensitive to only a few parameters. Most of the highly sensitive parameters (e.g., the north influx, LCA rock permeability in the east, and the LCA unconfined storage) are located in the east because most of the observation data are in this region of the model. For example, the sensitivity coefficient of the LCA rock permeability in the east (LCA east) is more than seven times the sensitivity of the LCA rock permeability in the west (LCA west). Assuming that there is a linear relationship between the sensitivities and that the intrinsic rock permeability is 1E-13 m^2 in both regions, for a given perturbation of one order of magnitude, the objective function changes by 3.38 m^2 for the LCA east versus only 0.44 m^2 for the LCA west.

With regard to fluxes, the north flux is the most sensitive boundary condition. This is because groundwater entering Yucca Flat from the northern boundary moves into the eastern portions of the study area where most of the observation wells are located. The supplemental west recharge boundary is the next most sensitive flux parameter. The relatively high sensitivity of this parameter appears to be due to head buildup with increasing value of this flux, which causes more water from the north to be diverted to the east. The top, east, supplemental southwest, and Halfpint fluxes all have low sensitivities. The top and Halfpint fluxes have low sensitivities because of their relatively small magnitude. The sensitivities of the eastern and supplemental west influxes are low because there are few wells in direct flow path between these two boundaries and the southern boundary. The objective function is also fairly sensitive to the aquifer storage parameters. The unconfined storage sensitivity is the largest because the MWAT in the eastern portions of the study area is in a region where the water table is below the top of the LCA. As expected, the major faults are much more sensitive than the smaller faults because of their larger spatial extent. However, given that the large faults are not in the zone of the MWAT influence, the relative sensitivity magnitude of the major faults is not particularly high.

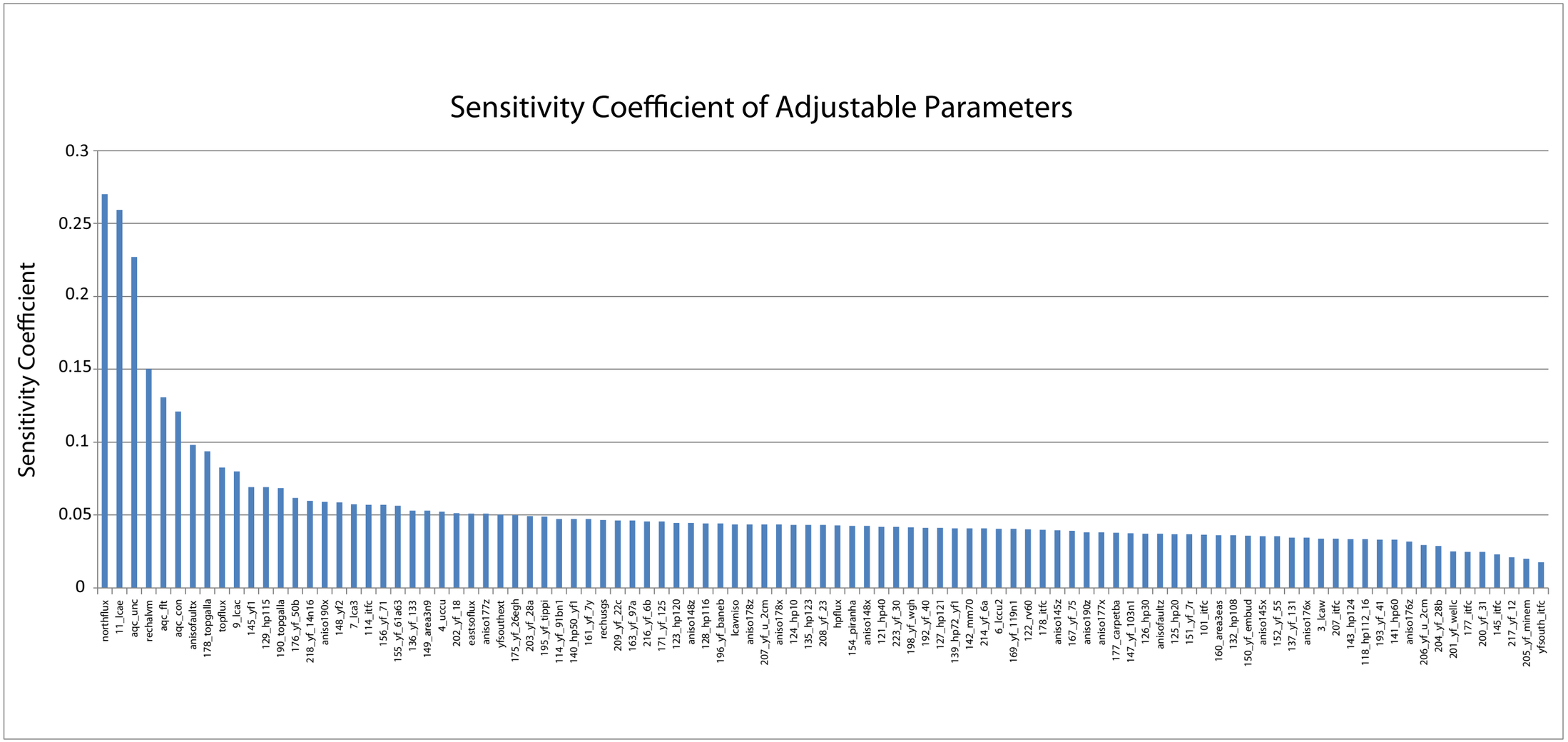

Figure 5-79
Sensitivity Coefficients of Model Adjustable Parameters

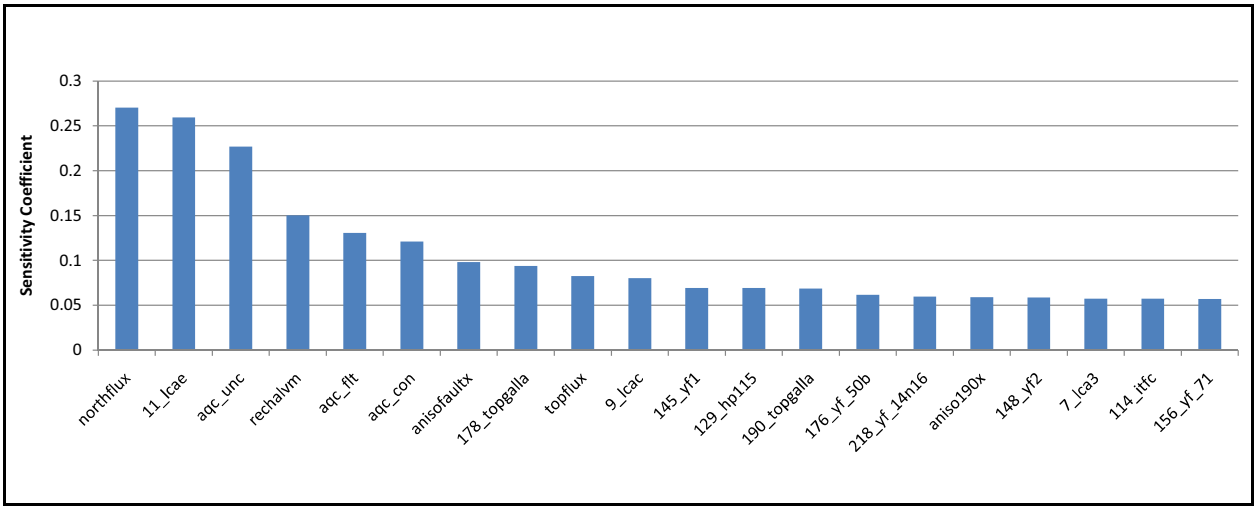

Figure 5-80
Sensitivity Coefficients of 20 Highest Sensitive Parameters

5.7.3 Parameter Perturbation Analysis

A sensitivity analysis was performed by perturbing one parameter at a time over a specified range of values and computing the corresponding change in the model output from the base model. The perturbation is around the base calibrated parameter values. The change in model output as a result of parameter perturbation was evaluated by the use of the objective function defined above and in Section 5.5. The objective function was divided into three components representing changes in (1) drawdown targets during the MWAT, (2) head values at steady-state head targets, and (3) a composite of the MWAT and steady-state targets. These metrics are identified on plots as "MWAT_phi," "SS_phi," and "sum_phi," respectively. Key input parameters were systematically increased and decreased by a set multiplier from the calibrated parameter value. The results of these perturbations are presented and discussed below. Most parameters perturbations were varied with multiplicative factors of 0.1, 0.5, 5, and 10 times the calibrated parameter value.

Over the entire range of parameter values examined, influx along the northern model boundary and several of the Topgallant fault permeability parameters had a significant impact on the objective function, as did the permeability of the LCA in the east, the horizontal anisotropy of the LCA, and the specific storage of the unconfined portions of the LCA. The most sensitive parameter is flux across the LCA along the northern model boundary (Figure 5-81). Changes in this parameter affect both steady-state head residuals and MWAT drawdown residuals. The response of the objective function to parameter perturbation is asymmetrical; larger values of the flux result in larger magnitude changes in

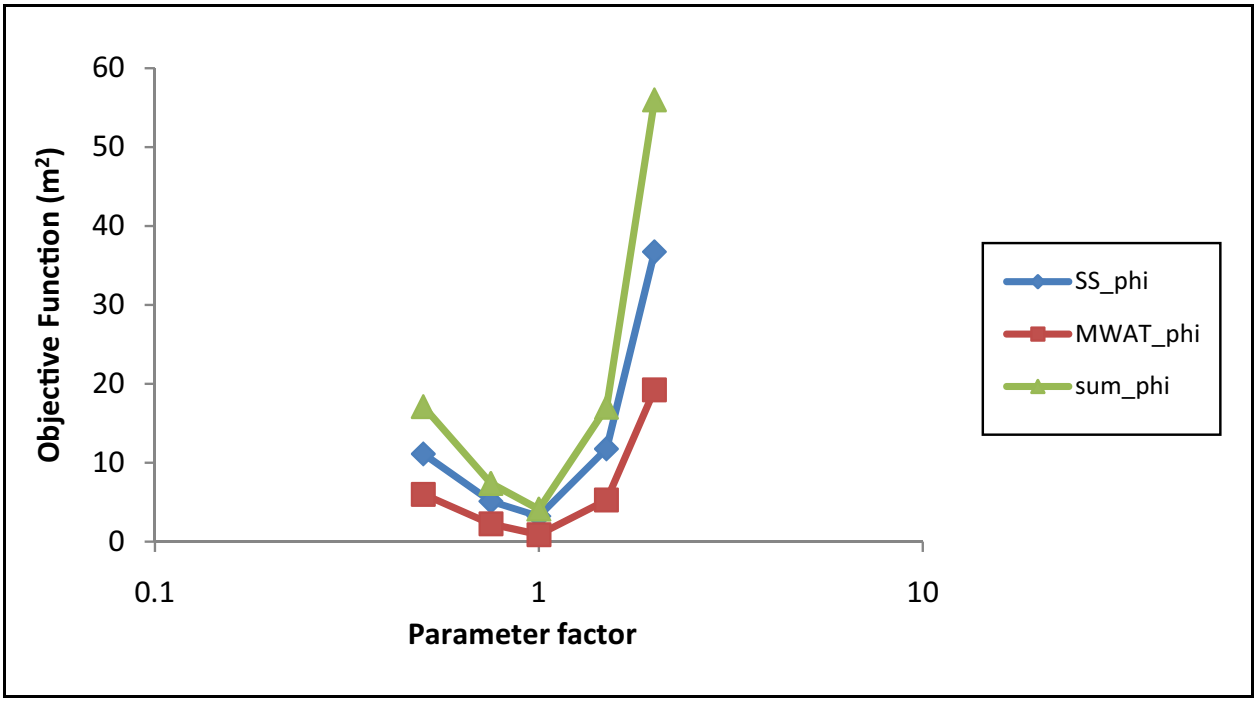

Figure 5-81
Sensitivity Analysis for Northern Boundary Flux

the objective function. The reason for such a response is the tendency of the model to channelize water entering the model domain from the north toward the east, where most of the steady-state head targets and all of the MWAT drawdown targets are located. This is the only flux boundary condition that is substantially sensitive to the objective function.

Three intrinsic fault permeability parameters have similar responses: Carpetbag (fault 176), Topgallant (fault 178), and Topgallant (fault 190) influence the flow field because of the spatial extent of the faults. The perturbation results show that these parameters almost exclusively influence the steady-state head residuals and not the MWAT head change residuals, as these parameters are located outside the area of influence of the aquifer test (Figure 5-82).

Faults 145 and 148 are two of the most conductive fault splays in the Yucca fault system. Fault 145 represents the western splay, and fault 148 represents the eastern splay. These splays exhibit asymmetric sensitivity to the fault permeability parameters. The objective function is more responsive to increases than decreases in fault permeability. As shown in Figure 5-83 most changes in the objective function value occur in the steady-state head residuals and not in the MWAT head change residuals, as the fault permeability parameters are located outside the area of influence of the aquifer test. The minor faults had negligible influence on the objective function.

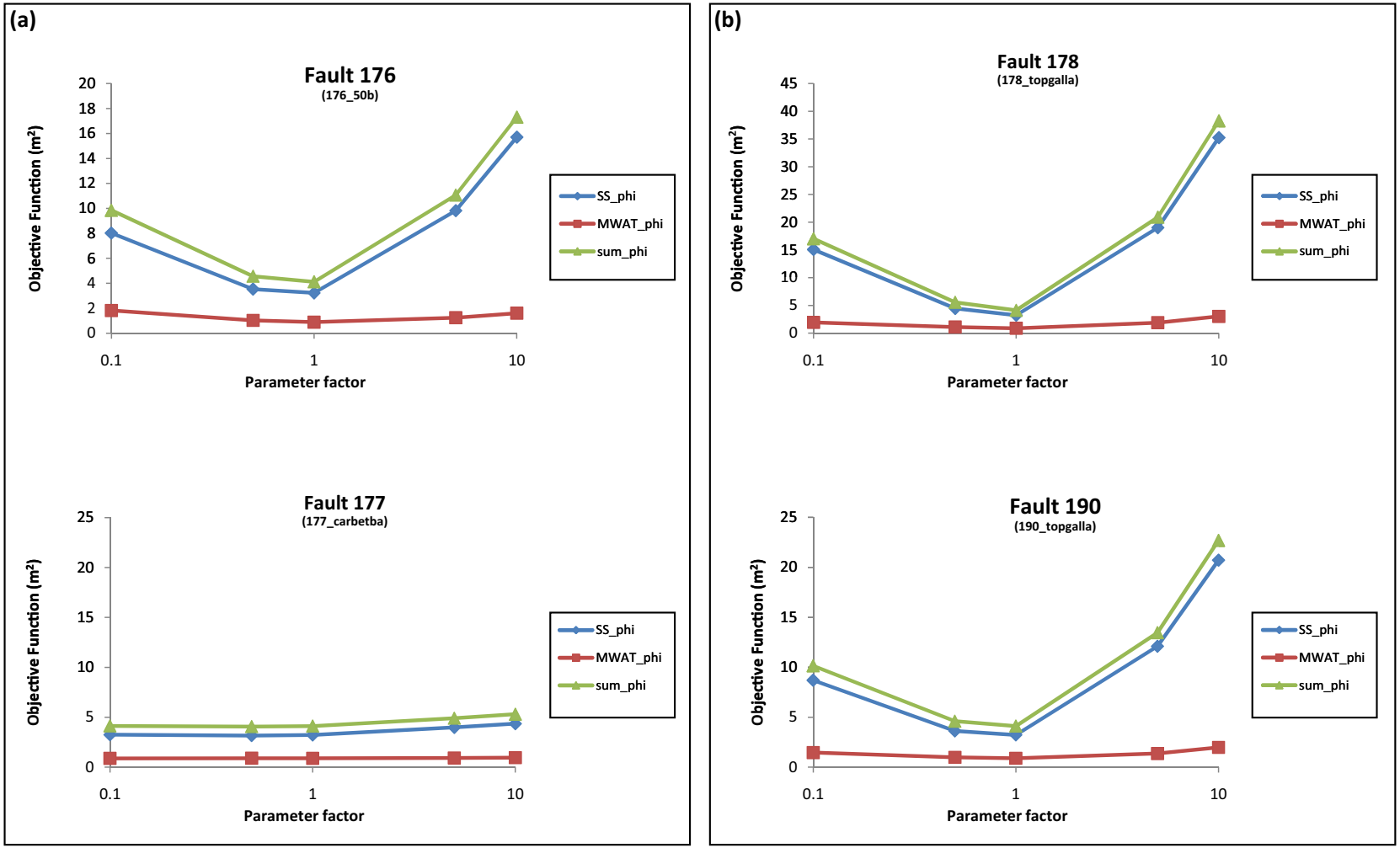

Figure 5-82
Sensitivity Analysis for (a) Carpetbag Fault (Faults 176 and 177) and (b) Topgallant Fault (Faults 178 and 190)

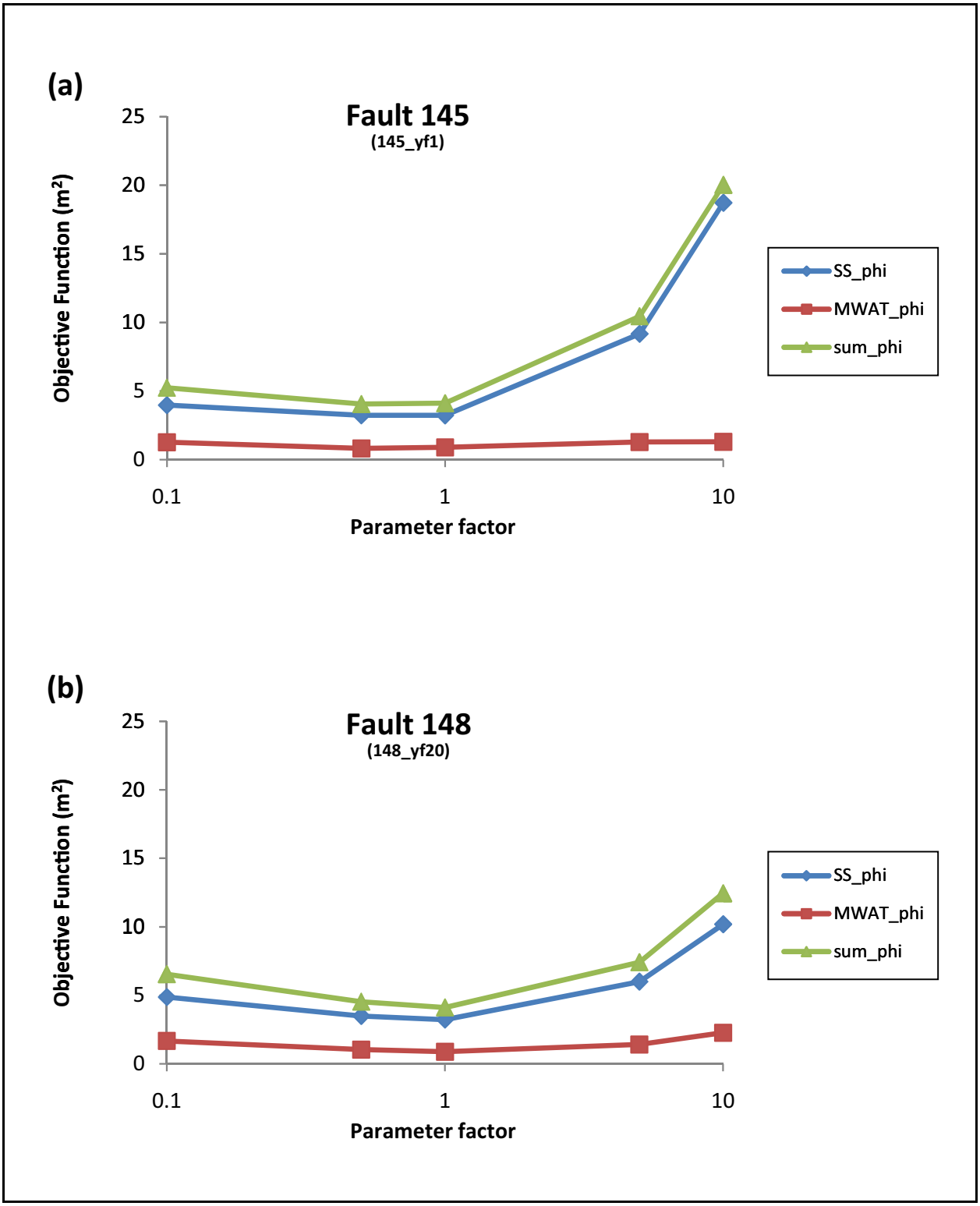

Figure 5-83
Sensitivity Analysis for Yucca Fault: (a) Fault 145, and (b) Fault 148

Figure 5-84 shows that the intrinsic permeability of the LCA rock matrix in the east (11_lcae) has a much greater impact on simulated heads than the intrinsic permeability of the LCA rock matrix in the central region (9_lcac) for the range of parameter values considered. As these two permeability parameter values increase, the contribution to the overall objective function consists primarily of the steady-state head residuals. As these values decrease, the MWAT head change residuals contribute more to the overall objective function value than the steady-state head residuals. In general, over the parameter perturbation ranges considered, the intrinsic permeability parameters are more sensitive than the anisotropy ratio parameters to changes in the objective function value. Figure 5-85 shows that the horizontal anisotropy ratio of the LCA (lcahniso) had much greater sensitivity to reductions than to increases in the anisotropy ratio. For this parameter, there is a large contribution from the MWAT residuals to the overall value of the objective function. As illustrated in Figure 5-85, perturbation analysis of the anisotropy ratio of the minor LCA faults (anisofaultx) and the anisotropy of the Topgallant fault (aniso178x) showed low sensitivity.

As expected, the specific storage parameters showed a large contribution from the MWAT residuals to the overall objective function value (Figure 5-86). Of the three specific storage parameters, the specific storage of the unconfined regions of the rock matrix (aqc_unc) had the largest impact on the objective function value. In particular, a value of specific storage of the unconfined rock matrix equal to one-tenth of the calibrated parameter value resulted in a large objective function. Increasing the specific storage of the confined regions of the rock matrix (aqc_con) and the specific storage values of the faults (aqc_flt) resulted in an increase in the objective function, whereas parameter values less than the calibrated parameter values resulted in objective function values similar to those of the calibrated parameter values.

5.7.4 Global Velocity Sensitivity

In addition to the effect of parameter perturbations on the objective function value, the effect on velocity magnitude was considered. Velocity was selected as a simple proxy for advective radionuclide migration in the groundwater system. Darcy velocities were examined at locations in the LCA corresponding to particular underground nuclear detonations of interest. These locations are identified in Table 5-12 and shown in Figure 5-87. Simulated velocity at a single node, or in some cases two nodes, is a more localized metric than the objective function value, which integrates information about hydraulic head throughout Yucca Flat. Consequently, the response of parameter

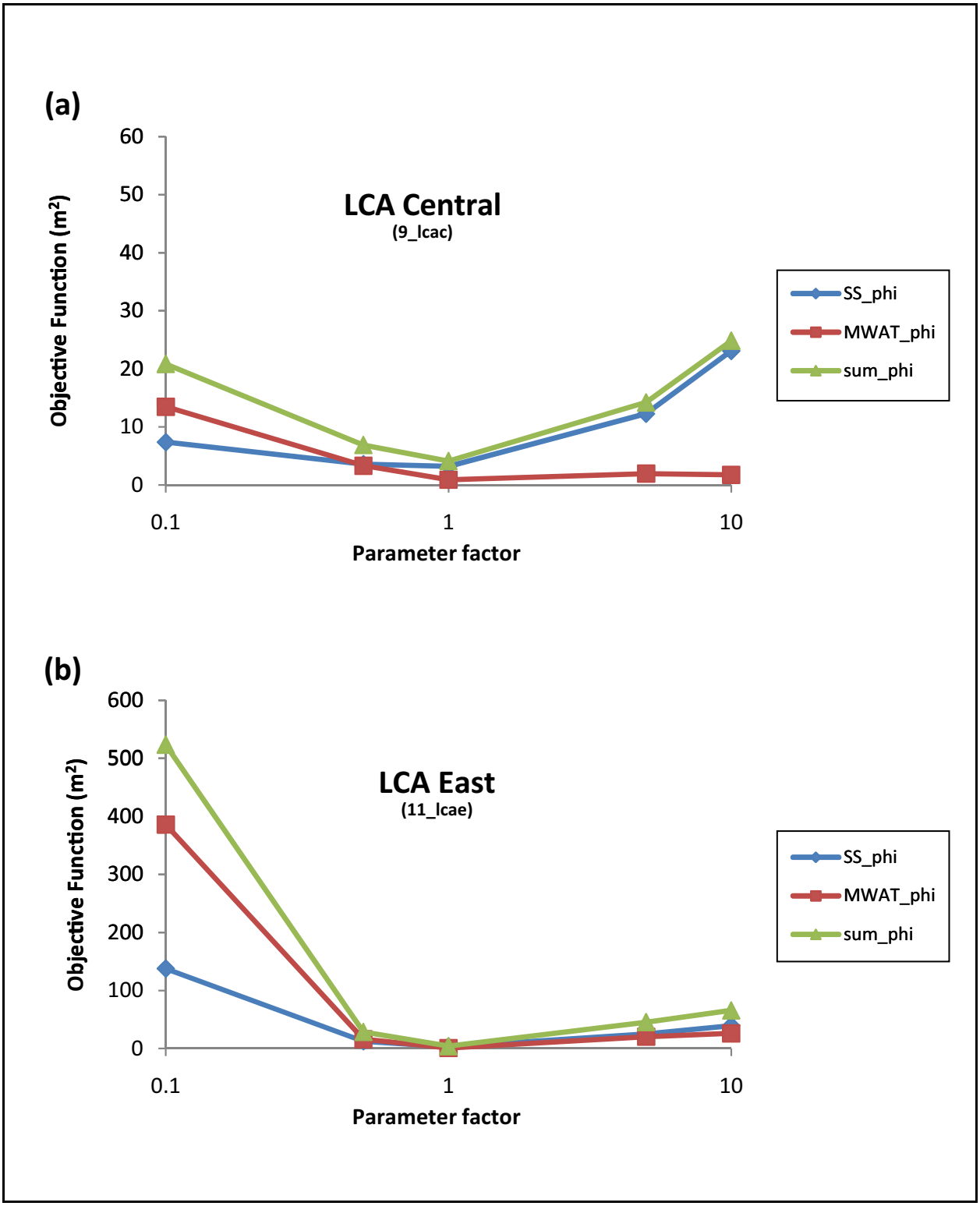

Figure 5-84
Sensitivity Analysis of LCA Rock Permeabilities for (a) LCA Central and (b) LCA East

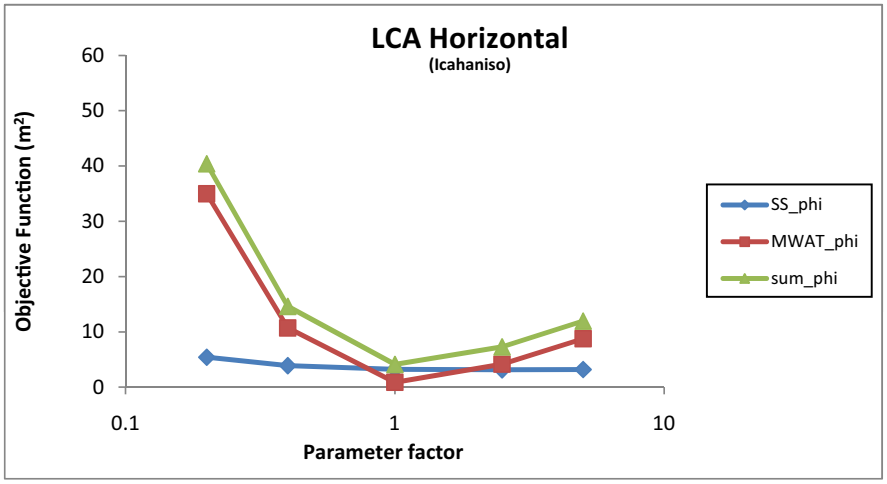

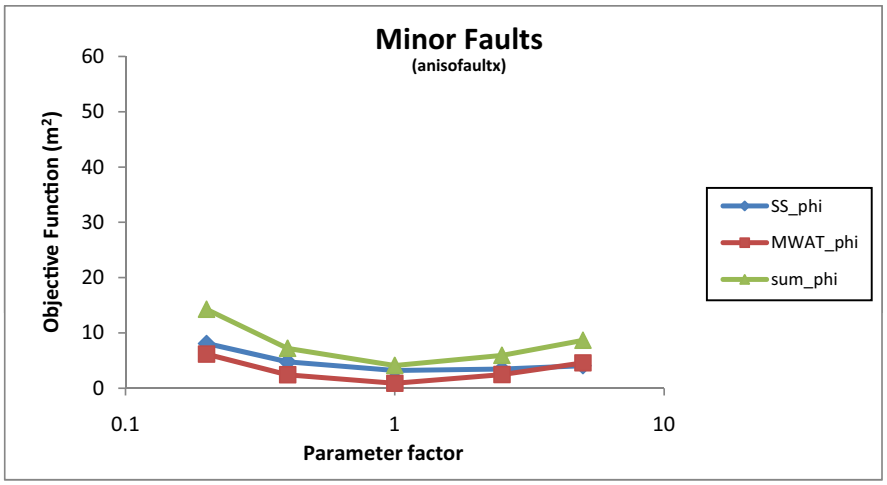

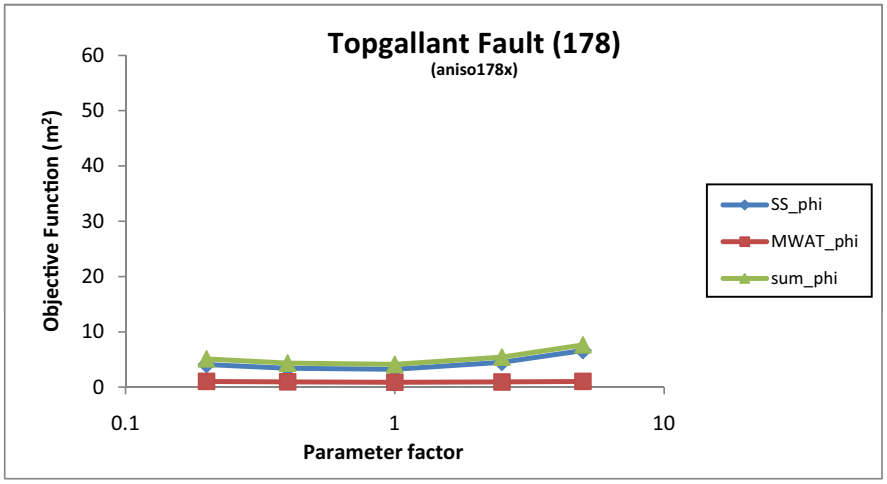

Figure 5-85
Sensitivity Analysis of LCA Rock and Fault Anisotropies

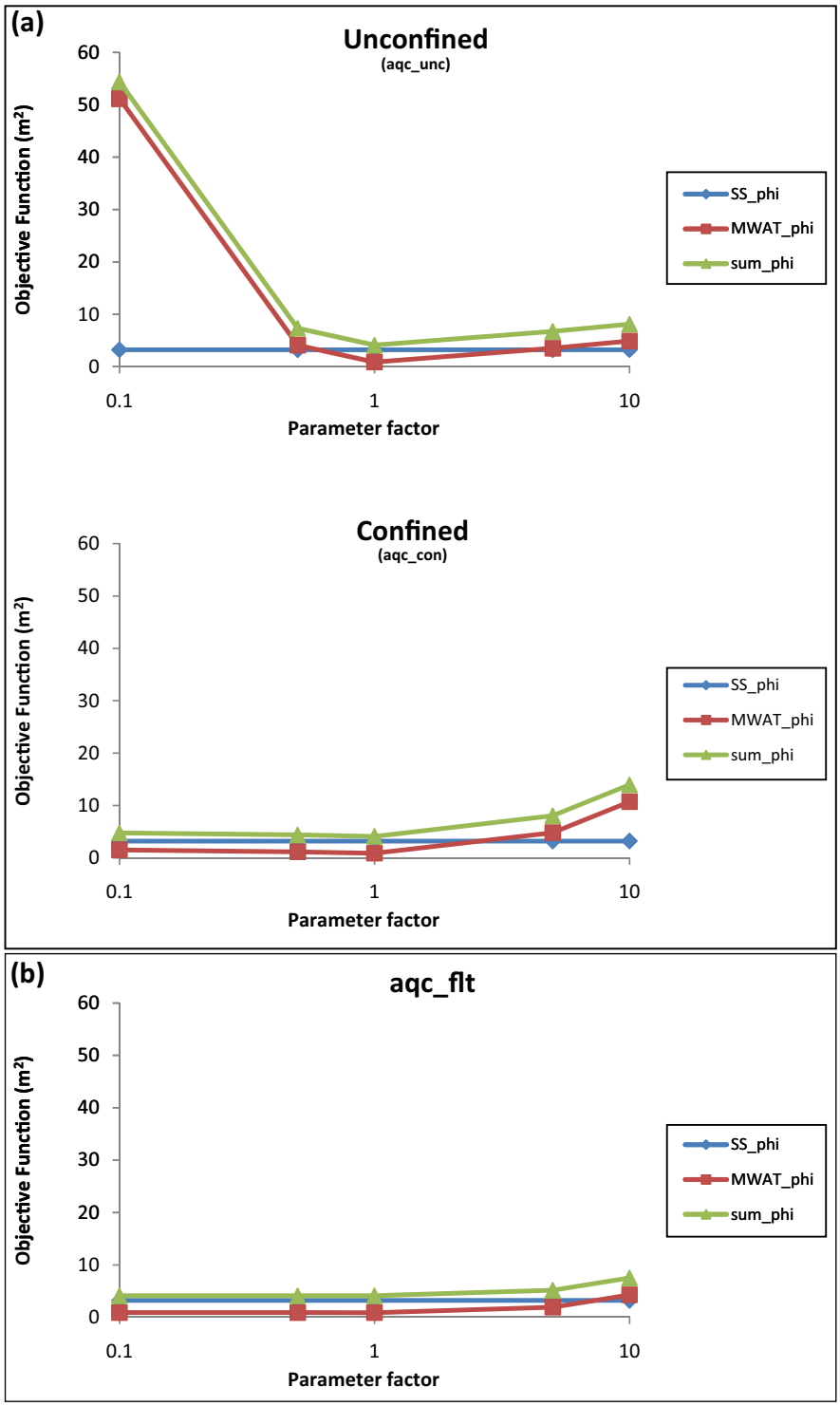

Figure 5-86
Sensitivity Analysis for Storativity of Fault and Rock: (a) Rock Matrix, and (b) Faults

Table 5-12
Detonation Locations of Interest for Velocity Sensitivity Analysis

Detonation Name	FEHM Node(s)	NNSS Area	Location Relative to Yucca Fault
BILBY	408436 408361	3	East of Yucca Fault
BOURBON	505252	7	East of Yucca Fault
CORDUROY	446204	10	East of Yucca Fault
HANDCAR	511336 511335	8	West of Yucca Fault
KANKAKEE	511203 511202	10	East of Yucca Fault
LAMPBLACK	471756 471755	7	East of Yucca Fault
TORRIDO	503100	7	East of Yucca Fault

perturbation on the objective function value and the velocity magnitude can be different. Oftentimes, there is no change in velocity, although there is a change in the objective function value reflecting the extremely local nature of the velocity metric. Or, conversely, parameter perturbations of parameters with low sensitivity coefficients, in particular, parameters controlling fault conductivity at detonation locations adjacent to the associated fault, can result in large impacts on local velocities at underground nuclear detonation locations.

The results of sensitivity analyses for key hydrogeologic parameters are presented in Figures 5-88 to 5-91. In general, a high sensitivity to velocity was found for the most sensitive parameters as defined by the sensitivity coefficient. For example, flux along the northern model boundary (northflux) was the most sensitive parameter for both the sensitivity coefficient and velocity parameter perturbation analyses. Increasing the amount of water flowing in at the northern boundary increased velocity at all nodes of interest except at HANDCAR. At HANDCAR, the velocity remained constant because HANDCAR is located west of where most of the water emanating from the northern boundary flows in eastern Yucca Flat. Figure 5-88 also shows the general trend in the relative magnitude of velocities: velocities are the lowest at HANDCAR, followed by LAMPBLACK, TORRIDO, BILBY, BOURBON, KANKAKEE, and CORDUROY, in that order. The parameters most sensitive to velocity will be discussed in a sequence that moves from north to south for the underground detonations of interest in the model domain.

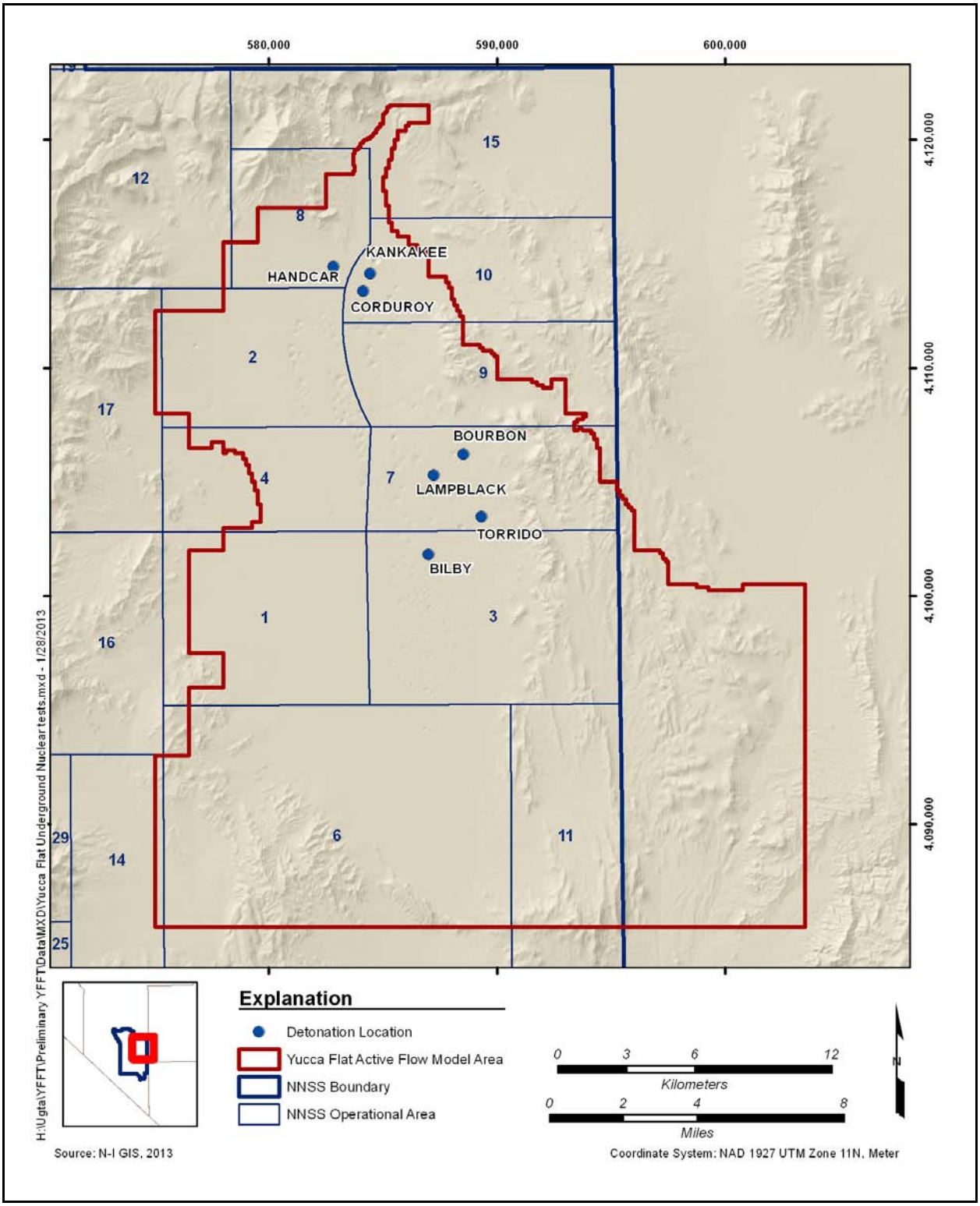

Figure 5-87
Detonation Locations Where Sensitivity to Darcy Velocity Was Estimated

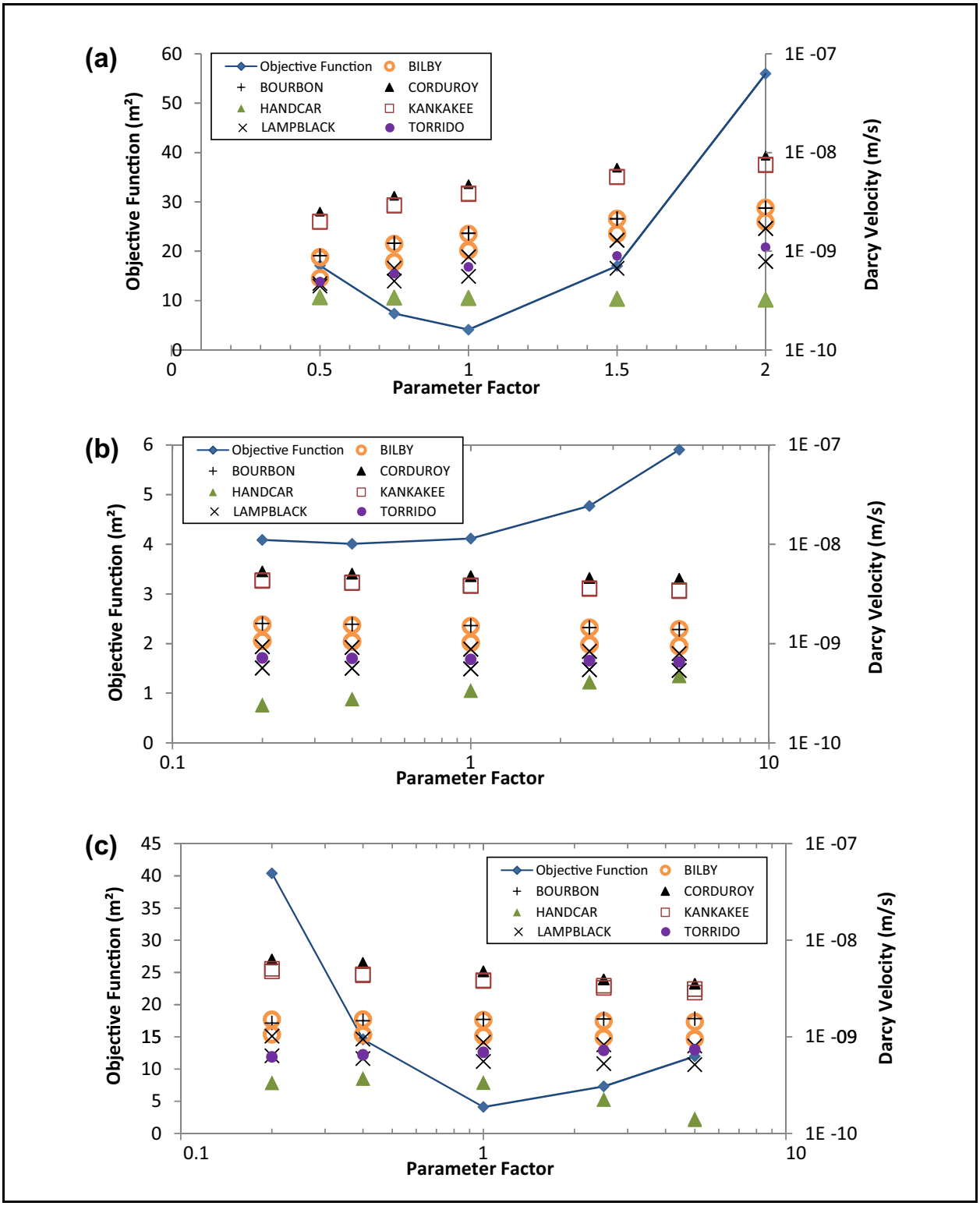

Figure 5-88
Velocity Sensitivity Analysis: (a) North Flux, (b) Yucca Fault Horizontal Anisotropy, and (c) LCA Horizontal Anisotropy

Note: There are two FEHM nodes corresponding to the BILBY and LAMPBLACK detonations.

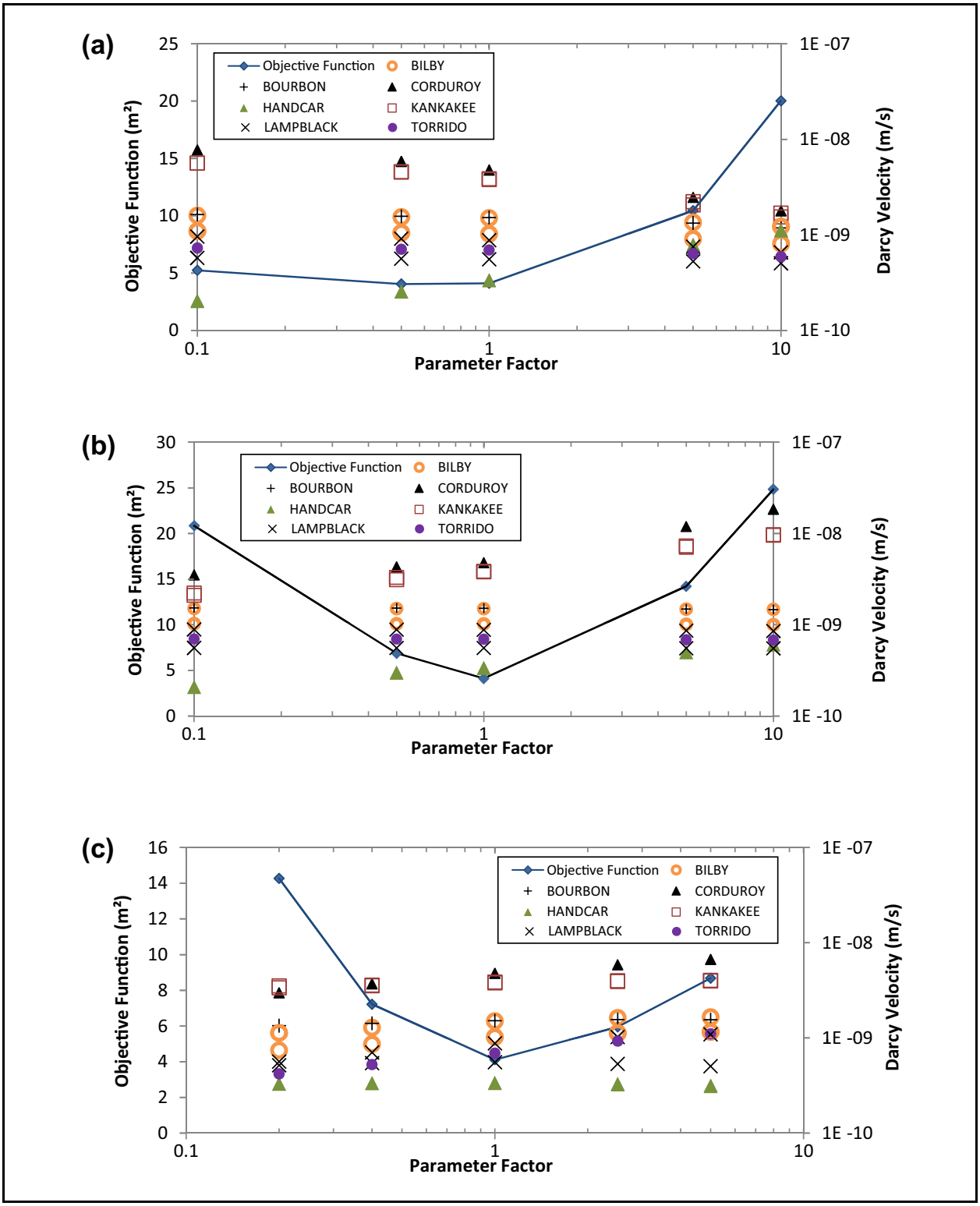

Figure 5-89
Velocity Sensitivity Analysis: (a) Permeability of the Western Splay of Yucca Fault, (b) Permeability of LCA Central, and (c) Horizontal Anisotropy of Minor Faults

Note: There are two FEHM nodes corresponding to the BILBY and LAMPBLACK detonations.

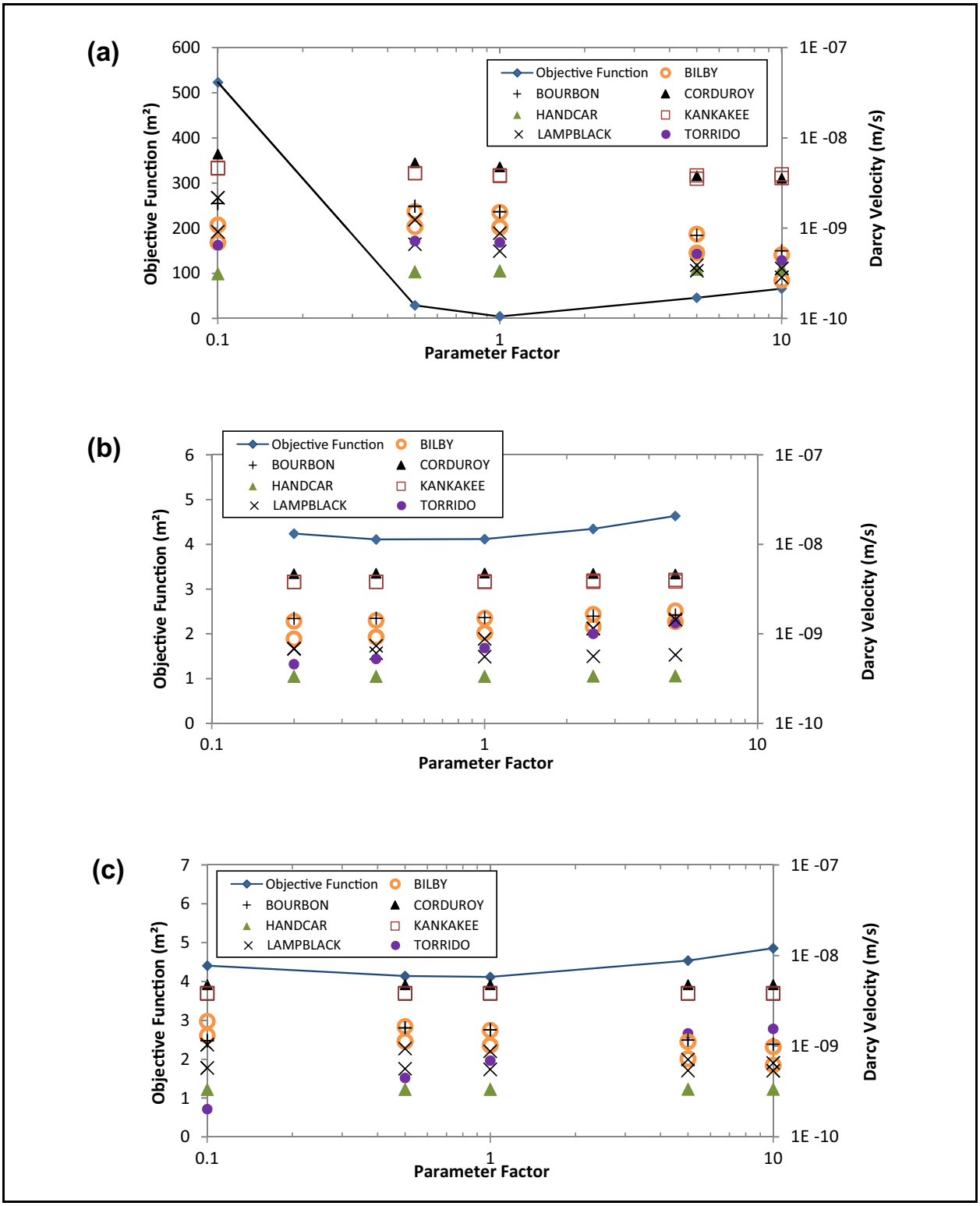

Figure 5-90
Velocity Sensitivity Analysis: (a) Permeability of LCA East, (b) Vertical Anisotropy of Minor Faults, and (c) Permeability of Fault 114

Note: There are two FEHM nodes corresponding to the BILBY and LAMPBLACK detonations.

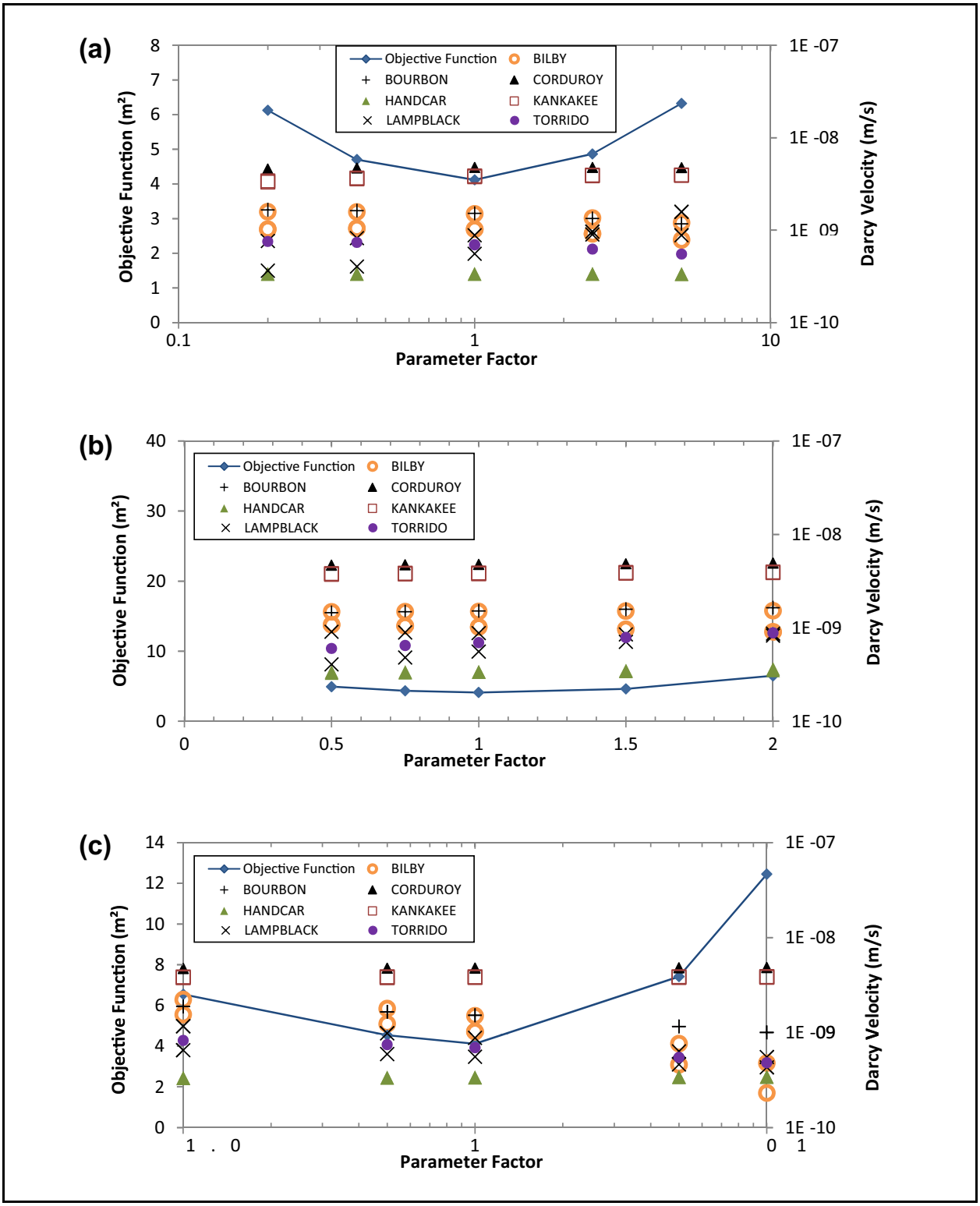

Figure 5-91
Velocity Sensitivity Analysis for Lateral Barrier: (a) All Minor East Faults, (b) Top Flux, and (c) Permeability of Eastern Splay of Yucca Fault

Note: There are two FEHM nodes corresponding to the BILBY and LAMPBLACK detonations.

HANDCAR was the only detonation location of interest west of the Yucca fault, which is the master basin-and-range fault in Yucca Flat. Velocities at HANDCAR are most sensitive to parameters associated with the conductivity of the Yucca fault (because of the physical proximity of HANDCAR to the fault): the Yucca fault horizontal anisotropy (aniso145x), and the hydraulic conductivity of the western splay of the Yucca fault (145_yf1). Velocity in the vicinity of HANDCAR is sensitive to the horizontal anisotropy of the LCA (lcahniso). As the parameter values of the Yucca fault horizontal anisotropy (aniso145x) and the hydraulic conductivity of the western splay of the Yucca fault (145_yf1) increase, the velocity also increases. The opposite effect is seen with the horizontal anisotropy of the LCA (lcahniso): as the anisotropy increases, the velocity decreases.

KANKAKEE and CORDUROY are located within 1,800 m of HANDCAR but on the east side of the Yucca fault. Two parameters that had a strong effect on changes in simulated velocity are the hydraulic conductivity of the western splay of the Yucca fault (145_yf1) and the hydraulic conductivity of the LCA central (9_lcac). At KANKAKEE and CORDUROY, as the hydraulic conductivity of the western splay of the Yucca fault (145_yf1) decreases, more water is focused on the east side of the Yucca fault, and the velocity consequently increases, an opposite effect of what is observed at HANDCAR on the west side of the fault. As the hydraulic conductivity of the LCA central (9_lcac) increases, the velocity also increases. As the horizontal anisotropy of minor faults (anisofaultx) increases, the velocity increases for one of the two nodes of interest at CORDUROY; no similar effect occurs at KANKAKEE, where velocity remains approximately constant.

BOURBON, LAMPBLACK, TORRIDO, and BILBY are located east of the Yucca fault in Areas 7 and 3 of the NNSS. Velocities at BOURBON show sensitivity to the hydraulic conductivity of the LCA east (11_lcae), the parameter with the second-highest sensitivity coefficient. This parameter, however, shows limited sensitivity at the nearby CORDUROY and TORRIDO. BOURBON shows less sensitivity than CORDUROY and TORRIDO to many other parameters, such as the horizontal and vertical anisotropy and permeability of minor faults (anisofaultx, anizofaultz, and 114_yf_91bn1).

LAMPBLACK is sensitive to the recharge parameter (topflux): increases in recharge correspond to increases in velocity. Oftentimes, for parameters such as the horizontal and vertical anisotropy of minor faults (anisofaultx and anisofaultz) and the core hydraulic permeability multiplier of the east faults (114_itfc), one of the two FEHM nodes representing LAMPBLACK shows sensitivity while

the velocity of the other node remains constant. The parameter with the second-highest sensitivity coefficient, the hydraulic conductivity of the LCA east (11_lcae), shows inverse relationships between conductivity and velocity.

Velocity at TORRIDO is sensitive to the horizontal and vertical anisotropy and conductivity of minor faults (anisofaultx, anisofaultz, and 114_yf_91bn1). Increased velocities are associated with increases in these parameter values. BOURBON and TORRIDO have different magnitude velocity responses to perturbation of these three parameters: velocities at TORRIDO are more sensitive than those at BOURBON.

BILBY, the southernmost underground detonation of interest, shows velocity sensitivity to the hydraulic conductivity of the LCA east (11_lcae): as the conductivity increases, the velocity decreases. BILBY also shows velocity sensitivity to the conductivity of the eastern splay of the Yucca fault (148_yf2): as the fault conductivity increases, the velocity decreases. Other detonation locations in the vicinity, BOURBON, LAMPBLACK, and TORRIDO, show a decreased sensitivity to this parameter.

5.7.5 Sensitivity Summary

The problem of overparameterization discussed in Section 5.5 is evident in the sensitivity analysis conducted in this section. Due to the large number of adjustable parameters and the relatively few head and drawdown observations, the sensitivity coefficients of most parameters are fairly low. In general, with the exception of the northern boundary flux, both the boundary fluxes and hydraulic properties have relatively low influence on the objective function. As expected, the spatial extent of a parameter and the proximity of the parameter to the observed data greatly influence the sensitivities. For example, the permeability of the LCA rock in eastern Yucca Flat and the unconfined aquifer storativity are two of the most sensitive hydraulic properties. Both these parameters are located in the eastern part of the basin, which is in the region of MWAT influence and where the number of steady-state head observations is the largest. Similarly, the north flux is the most sensitive boundary flux. This is because it is the only adjustable boundary parameter that influences the MWAT and because inflows from this boundary migrate into eastern Yucca Flat.

In light of the low parameter sensitivities discussed above, the uncertainty analyses conducted in Section 5.6 are very useful in examining alternative flow fields. The NSMC simulations discussed in

Section 5.6 explore numerous alternative flow fields, a majority of which have acceptable (calibration) objective functions. Similarly, the discrete parameter uncertainty analyses conducted in Section 5.6 evaluate likely scenarios that would lead to contaminant transport times (and extent) that are substantially longer (larger) or shorter (smaller) than those determined for the base case. The evaluations are accomplished by selecting certain flow model parameters and boundary conditions that are deemed critical and could not be uniquely established during model calibration because of limited data. A good example of such parameters or conditions would be the permeability of the major faults. This parameter strongly impacts contaminant migration but has relatively low sensitivities; consequently, it cannot be established with high certainty because of lack of observation data along the fault plane.

Sensitivity of parameters to magnitude of velocity was also analyzed in addition to the effects of parameter perturbation on the objective function. The radionuclide migration times and pathways are strongly influenced by the velocity field. Darcy velocities were examined at locations in the LCA corresponding to underground nuclear detonation locations at which radionuclide release to the LCA was the largest. In general, a high sensitivity to velocity was found for the most sensitive parameters as defined by the sensitivity coefficient.

5.8 Summary and Conclusions

This section discussed three-dimensional finite element groundwater flow modeling conducted to understand the potential for lateral and vertical migration of radionuclides within the LCA at Yucca Flat. The modeling approach accounted for conceptual and parametric uncertainties by examining alternative HFMs, recharge models, hydrologic boundary conditions, and hydrogeologic properties in order to propagate uncertainties associated with these elements into flow fields for conducting transport simulations. This approach resulted in several flow fields that were consistent with site-specific data and conceptual understanding of the Yucca Flat groundwater flow system.

5.8.1 Summary of Hydrogeology and Conceptual Model

Yucca Flat is a topographically closed basin with a playa at its southern end. Faulted and tilted blocks of Tertiary-age volcanic rocks and underlying Paleozoic and Precambrian sedimentary rocks form low mountain ranges surrounding the Yucca Flat basin. The Tertiary volcanic rocks are covered in the Yucca Flat area by late Tertiary and Quaternary surficial deposits, such as alluvium, colluvium,

eolian deposits, spring deposits, basalt lavas, lacustrine, and playa deposits, that may aggregate to more than several hundred meters in overall thickness. Underlying the Tertiary volcanic rocks are Paleozoic and Proterozoic sedimentary and metasedimentary rocks, including dolomite, limestone, quartzite, and argillite. The Paleozoic rocks form interbasin hydrologic continuity with adjacent sub-basins to the southeast, south, and southwest of Yucca Flat. Whether there is hydrologic continuity of the LCA to the north of Yucca Flat is uncertain. As a result, alternative conceptual models to address this uncertainty have been developed and implemented during the flow model calibration.

The Yucca Flat basin was formed in response to basin-and-range extension during the Cenozoic age. Large-scale normal faulting began in the Yucca Flat area in response to regional extension near the end of this period of volcanism. Most of the structural elements in the base HFM are high-angle normal faults with the Yucca fault in the center of the basin being the master (basin-and-range) fault. Two other large faults—the Carpetbag and Topgallant faults—are associated with reactivation of the east-dipping high-angle ramp structure of the CP thrust fault that resulted in the formation of the west-tilted Yucca Flat structural basin.

Yucca Flat is located within the Great Basin hydrographic province, which is characterized by internal drainage and consists of closed hydrographic basins such as Yucca Flat. Groundwater flows between sub-basins within a thick sequence of Paleozoic carbonate rocks that extends throughout the subsurface of much of central and southeastern Nevada. This carbonate aquifer, termed the LCA, extends beneath much of Yucca Flat, although the regional connection of the aquifer to the northwest, north, and northeast of Yucca Flat is limited by the geologic structure, notably, the presence of the intrusive Mesozoic volcanics. Local recharge due to precipitation occurs in Yucca Flat, with larger quantities infiltrating into the subsurface along the higher elevations on the basin margins and minimal recharge occurring in the lower elevations in the central valley.

Water has been pumped from four LCA water supply wells for potable or industrial use and to support nuclear testing activities. The total LCA production, however, is low, and in the last 20 years, the average withdrawal rate has been about 20 million gallons per year or 2.4 kg/s. As discussed in Section 5.5, such a flow rate is small compared to the total estimated volumetric base flow of several hundred kilograms per second. Consequently, drawdowns associated with these long-term withdrawals are insignificant.

Water levels at most LCA wells in Yucca Flat have fluctuated over a narrow range in the past decades. Based on local potentiometric observations and geochemical inferences, groundwater in the basin generally moves southward or southwestward. Paradoxically, heads in the western parts of the basin are higher in the south than in the north. This trend has persisted over the entire period of sampling record spanning several decades. Another noteworthy observation is that while most of the water levels have remained steady, water levels at observation wells in the southwest (Wells ER-6-2 and UE-1h) have exhibited an increasing trend in the past two decades. The cause of this rise has been attributed to climatic variations in recent years (Fenelon et al., 2012).

In order to develop a dataset that provides large-scale information on the hydraulic structure of the Yucca Flat basin, a long-term MWAT was conducted in eastern Yucca Flat with pumping at ER-6-1-2. The objective of the aquifer test was to determine hydraulic properties for the LCA through long-term constant-rate pumping at ER-6-1-2, while monitoring formation response in a network of five widely spaced observation wells. The response in observation wells aligned with ER-6-1-2 along the dominant north–south fault orientation was prompt. The response at observation wells located transverse to the fault alignment was delayed and significantly muted. The faults, therefore, appear to form a hydraulic barrier to flow normal to their strike and a conduit to flow parallel to their strike.

Groundwater age in the LCA was estimated with ^{14}C data. The salient features of the groundwater age distribution in Yucca Flat are the presence of young water in the center of the basin and the approximately 15,000-year apparent age difference between water in the northern and southern ends of the study area. The younger LCA water in the center of the basin is conceptualized as reflecting downward drainage of groundwater via faults through the overlying volcanics in the center of the basin. Groundwater temperature data also suggest that there is downward drainage of cooler groundwater to the LCA from the overlying volcanics in the center of the basin. This inference is based on the presence of a cold trough in the center of the basin coinciding with the three major faults—the Carpetbag, Topgallant, and Yucca faults.

5.8.2 Summary of LCA Flow Model Calibration

The goal of the LCA groundwater flow model is to develop a range of reasonable groundwater flow fields that reproduce the observed steady-state and transient water-level observations given uncertainties pertaining to the hydrogeologic properties of the LCA and vertical/lateral influx into the model study area. Uncertainty exists in all aspects of the LCA flow model. Therefore, it is not

possible to uniquely identify a preferred or expected flow field during model calibration. The uncertainties, however, were evaluated by developing a range of reasonable alternative flow models. The alternative flow models were developed by considering a range of likely parameter and boundary values. These alternative models share the same basic assumptions, namely, (1) within a geologic feature or permeability zone, the properties are homogeneous; (2) each model fault contains three hydraulic zones—a central gouge zone (fault core) and two damage zones on either side of the central gouge zone; (3) the faults are expected to have much greater permeability parallel to their strike and low permeability perpendicular to their strike because of the presence of higher permeability in the fault damage zone and low permeability in the fault core zones; (4) the flow system is in steady state; (5) the spatial resolution of permeability contrasts is limited to the grid scale analyzed, which has a minimum spacing of about 125 m; and (6) the spatial distribution of vertical recharge is as identified in the unsaturated zone and saturated alluvial/volcanic aquifer system models presented in Sections 3.0 and 4.0, and in the DVRFS model in areas of the LCA not directly overlain by either of these two models.

The calibration of the LCA flow model utilized both the steady-state heads and transient drawdowns observed during the MWAT to support estimation of the boundary fluxes and permeability of the faults and the LCA country rock. The LCA country rock was divided into three distinct zones: the LCA east of the Yucca fault, the LCA west of the Carpetbag fault, and the LCA between the Carpetbag and Yucca faults. In order for the steady-state head and MWAT drawdown data to contribute approximately equally to the model calibration, the transient drawdowns were weighted four times as much as the steady-state heads. This was done so that the permeability and boundary fluxes could be reasonably constrained by the calibration process.

The technical approach implemented was to initially constrain the hydrologic properties and boundary fluxes within the area of influence of the ER-6-1-2 pumping well by the MWAT and then estimate parameters in the other portions of the model domain based on their consistency with the steady-state observations. Parameters in the areas of the LCA flow model outside the area constrained by the MWAT have a much larger uncertainty, are less identifiable, and have a lower sensitivity to the objective function. Therefore, while the parameter estimation process in general yields residual uncertainty in some important aspects of the flow field, the most identifiable and therefore greatest confidence in the properties occurs in the area of influence of the MWAT, which generally coincides with the area underlying the largest fraction of underground nuclear detonations in the

Yucca Flat/Climax Mine CAU. The MWAT resulted in significant drawdown being observed along the major north–south trending faults, while little to no drawdown was detected in observation wells located across the strike of these faults. This compartmentalization of the LCA flow system is consistent with the general conceptual model of a spatially variable permeability controlled by fracture and fault zone structures (Laczniak et al., 1996).

A range of vertical recharge estimates has been developed for the Yucca Flat area in previous modeling studies. It ranges from almost no vertical recharge in the central portions of Yucca Flat in areas with thick (on the order of 500 m) unsaturated alluvium, to significant recharge in areas of higher elevation in the northwest and northeast margins of the basin. The unsaturated zone and saturated alluvial/volcanic aquifer system models presented in Sections 3.0 and 4.0 implemented a uniform recharge over the entire surface area by fixing the infiltration rates at spatially averaged values corresponding to 0.1, 1, 5 and 10 mm/yr. During calibration of the base-case LCA model, recharge was specified as an adjustable parameter, which calibrated to a value of 0.6 kg/s (approximately 0.06 mm/yr) in the center of the basin.

A range of lateral influxes to the LCA have been estimated by the regional models for the Yucca Flat area. These estimates typically encompass a fairly wide range of fluxes. In particular, the influx from the north varies from greater than 200 kg/s based on published regional model estimates to as low as 1 kg/s based on other published hydrogeologic interpretations. The range of values accommodated in the alternative NSMC flow models encompasses the expected range of fluxes in existing regional models. In addition, given the significant conceptual uncertainty in the flux into Yucca Flat from the north, a separate calibrated model was developed assuming the flux was at the low end of the possible range, i.e., 1 kg/s.

While the range of reasonable permeabilities identified for the LCA fault zones has been developed from single-well aquifer tests conducted across the NNSS, it is possible to compare the calibrated values to other modeling studies performed to analyze the response of pumpage from ER-6-1-2 during the MWAT. Two models were developed to test this possibility, namely,
(1) a three-dimensional finite-difference groundwater flow model that explicitly includes the most significant faults (defined as those with a vertical offset greater than 60 m) identified in the Yucca Flat/Climax Mine and Frenchman Flat CAUs, and (2) a separate strip model that conceptualized a fault zone of variable width that extends northward from the ER-6-1-2 pumping well to

Well ER-7-1, an observation well located about 10 km to the north. The calibrated results of the three-dimensional model indicated fault-zone hydraulic conductivities on the order of 100 m/day (corresponding to a permeability of about 1E-10 m^2) for assumed fault widths of approximately several hundred meters (SNJV, 2006e, Figure 3-22). The calibrated results of the strip model indicated a fault-zone width of about 1,000 m and a hydraulic conductivity of about 200 m/day (assuming a transmissive thickness of about 300 m). These permeability values are about an order of magnitude greater than the major fault permeability values used in the base-case calibrated model, but are approximately the same as those developed in several of the NSMC runs, implying that the range of calibrated models encompasses the range of observed permeability derived from alternative analyses of the MWAT.

Another means of evaluating the reasonableness of the range of calibrated LCA flow models is to evaluate the average velocities inferred from geochemical observations, radiotracer observations, or the natural gradient portion of the MWAT tracer test. The geochemical observations indicate velocities on the order of 1.4 to 1.7 m/yr between Well UE-10j in northern Yucca Flat to Well WW C in southern Yucca Flat (SNJV, 2007). As noted in Appendix L, corrected ^{14}C observations have been used to infer an average velocity of about 2.0 m/yr. Considering that ^{14}C is possibly retarded by reaction with the carbonate rocks in the LCA by a factor of about 10 (see Section L.2.0), these retarded velocities would correspond to unretarded velocities of about 10 to 20 m/yr. This is similar to the range estimated by Hershey and Acheampong (1997), and is consistent with the advective transport times from key locations calculated with the base-case flow model and NSMC alternatives. In addition, the natural gradient test during the MWAT was interpreted to provide a local ambient velocity of about 24 m/yr (SNJV, 2007).

The uncertainty in the use of groundwater ages derived from ^{14}C observations to assist in evaluating the reasonableness of groundwater flow rates in the LCA in central Yucca Flat is analyzed in Appendix L. The analyses presented in Appendix L used two different methods to correct the measured ^{14}C activities, one based on the downgradient changes in the total dissolved inorganic carbon, and the other based on changes in the $\delta^{13}C$ relative to the estimated groundwater recharge. Although these correction methods account for the bulk dissolution of carbonate minerals and potential isotope exchange, there is still the potential for $H^{14}CO_3^-$ sorption onto the carbonate matrix or calcite fracture surfaces. If this sorption occurs, it would result in estimates of groundwater velocities that are too low. Although the analyses presented in Appendix L support the assumption

that $H^{14}CO_3^-$ is not significantly sorbed, assuming such sorption occurs results in a conservative overestimation of effective transport velocities. Given that the goal of the modeling in the Yucca Flat/Climax Mine CAU is to not underrepresent the possible extent of contaminant migration, overestimating the transport velocities is appropriate.

Calibrations of the alternative flow models reflect the range in possible flow fields given the steady-state and transient head observations, and the constraints provided by uncertainty in the ranges of hydraulic properties, as well as boundary fluxes and average net infiltration rates developed from regional model estimates. Significant structural uncertainty exists in the hydraulic continuity of the LCA in the northern portion of the Yucca Flat basin. As a result of this uncertainty, two alternatives were explored in the calibration. The base-case calibration conservatively assumed that there was hydraulic continuity in this area of the model, and the calibrated boundary fluxes were found to range from about 50 to about 400 kg/s (with the base-case value of 130 kg/s). The alternative northern boundary flux model, which is more consistent with the conceptual model presented in Fenelon et al. (2010) and Fenelon et al. (2012), and inferences from thermal hydrologic modeling presented in Appendix H, used a fixed northern influx of 1.0 kg/s based on the early work of Winograd and Thordarson (1975). Both of these alternatives were reasonably calibrated, and both have been propagated in Section 6.5 to evaluate their impact on potential contaminant transport. The base-case model is more conservative in that it potentially overestimates the northern influx and hence results in a conservative estimate of groundwater flux and velocity in the central portions of the basin where contaminant transport is most significant.

5.8.3 Conclusions

Based on the above summary, it is concluded that the LCA flow models developed and calibrated in this section are reasonable representation of the range of possible flow conditions that could potentially affect the extent of contaminant transport in Yucca Flat. The key findings that support this conclusion are summarized below:

- Two alternative conceptual models of the hydraulic continuity of the saturated LCA in northern Yucca Flat were evaluated. The base-case conceptual model assumes the LCA is laterally continuous in this area as assumed in the regional groundwater flow models. The alternative conceptual model assumes there is limited hydraulic communication in northern Yucca Flat. The base-case model was chosen for conservatism, i.e., avoid

underestimating the groundwater flux, and therefore, avoid underestimating the possible extent of groundwater contamination.

- The lateral influx from the north in the base-case flow model was calibrated to be about 130 kg/s with a range from 50 to 400 kg/s and is within the range of regional groundwater flow estimates derived by USGS and DRI.

- The alternative calibrated model of northern boundary flux, assuming limited hydraulic communication, used a fixed value of 1.0 kg/s, which is similar to fluxes estimated by Winograd and Thordarson (1975) and Harrill et al. (1988).

- The lateral influxes from other model boundaries are generally less sensitive to the calibration of the flow in the central portion of Yucca Flat and are also less significant from the perspective of evaluating flow and transport from the sources of potential contamination into the LCA.

- The vertical recharge to the LCA in the central portions of the modeled area overlain by the unsaturated zone model and saturated alluvial/volcanic aquifer system models are on the order of 0.1 mm/yr.

- The vertical recharge to the LCA in the western and eastern portions of the modeled area where the LCA subcrops and the surface elevation is higher is significantly greater, on the order of 1 to 10 mm/yr. Several organizations have independently developed recharge estimates in these portions of the modeled domain using different approaches, and these estimates are reasonably consistent with the values developed for the regional DVRFS model.

- The modeled flux leaving the Yucca Flat LCA flow model (about 260 kg/s for the base-case model, and about 160 kg/s for the alternative northern boundary flux model) is in the range of calibrated values used in the Frenchman Flat CAU flow model (SNJV, 2006c), which also are derived from regional model estimates.

- The modeled flux leaving the Yucca Flat LCA flow model is consistent with the relative flow rates for different flow systems that can be estimated based on the relative flow volume arrow widths indicated in Fenelon et al. (2010) illustrated in Figure 1-13. Although the intent of the arrow widths presented in Fenelon et al. (2010) was to identify tributary groundwater flow systems with “less” or “more” flow, the relative arrow widths can be used qualitatively to estimate possible flow amounts. Based on the relative arrow widths presented in Fenelon et al. (2010), it can be inferred that the LCA flow in the Yucca Flat tributary flow system is less than the flow in either the Ash Meadows flow system or the Spring Mountains tributary flow system. If the total Ash Meadows annual discharge is about 740 kg/s (19,000 acre-feet per year [acre-ft/yr]) (Laczniak et al., 1999), the inferred flow rate in the Yucca Flat tributary flow system would be smaller, as is simulated in the base-case and alternative northern boundary flux model. This is also consistent with recent interpretation by Fenelon et al. (2012) who state that “the total amount of groundwater flow through Yucca Flat is relatively minor and estimated to be 1,000 acre-ft/yr or less.”

- The calibrated spatially averaged fault and country rock permeability of the LCA falls within the permeability distribution observed during the pumping tests (Figure 5-13).
  The pumping-test data are more representative of the scale of interest. The higher end of the observed permeability distribution is considered more representative of fault permeability in the damage zone, whereas the middle of the distribution is considered to represent the permeability of the host (unfractured) carbonate rock.

- Although the widths of the fault zones are unknown, the minimum width of 125 m assumed for the damage zone is consistent with alternative models developed of the MWAT. Fault damage zones are considered to accommodate both the breccia zones and smaller, unmapped faults (i.e., faults with offsets less than 60 m).

- Transient effects from underground nuclear testing have an insignificant and short-lived effect on the simulated flow field in the LCA. This is a result of the large transmissivity of the LCA combined with the short duration (decades) of the predicted transient hydrologic impacts from the testing effects in the overlying volcanic HSUs.

The following general aspects of the LCA flow conceptual model have been reproduced in all of the calibrated flow fields:

- Flow is generally southward along the trace of the major structural discontinuities. Flow directions and rates are controlled by the transmissive properties of the major fault zones.

- The overall flux in the LCA is made up of portions of lateral influx into the basin and vertical recharge into the LCA from the overlying HSUs, notably, along the basin margins. The limited vertical recharge in the center of the basin is conceptualized as being concentrated along major discontinuities that cut the thick tuff confining units between the welded-tuff and vitric-tuff aquifer units and the underlying LCA.

- Although the identified alternative HFMs do not significantly affect the flow regime in the LCA, a range of flow directions and rates are possible given the uncertainty in the calibrated flow properties and boundary conditions.

- Short-term (decades) transient pressure responses in the overlying tuff aquifers do not significantly affect flow in the LCA because of the large transmissivity of the LCA.

5.8.4 Model Limitations

While the general aspects of the LCA flow model are consistent with the flow system conceptualization inferred by others, there are some particular aspects that are uncertain. These aspects either have been addressed within the context of the uncertainty analyses or are not significant contributors to the forecast extent of contaminant transport for the following reasons:

- **Homogeneous versus spatially heterogeneous permeability distributions.** The focus of the model calibration was on developing spatially averaged flow directions and rates based on uncertain permeability distributions and boundary fluxes, rather than attempting to determine the spatial variability of flow rates due to small-scale heterogeneity. By incorporating a range of boundary fluxes and alternative calibrated permeability fields, it is assumed that the average transport over the scale of 10 km or more is approximated. A similar issue occurs in the identification of appropriate parameter distributions and scale dependency of the transport parameters that affect the forecast extent of contaminant migration.

- **Inability to reproduce the rising heads in the southwestern portion of the model domain and the low heads observed in the northern part of the model domain.** It is difficult to reproduce the transient rising heads at ER-6-2 and UE-1h and the low heads at UE-10j and HTH-2 (WW-2) while maintaining the general conceptual north-to-south flow field. The high heads in the southern portion of the model domain may represent local recharge in areas where the LCA crops out on the western portion of the model. Although the cause of these anomalies has not been identified, these observations lie to the west of the principal flow regime of interest to the east of the Topgallant and Yucca faults, where most of the underground nuclear detonations that are close to faults or the saturated LCA reside. As a result, this uncertainty does not significantly affect the flow paths and flow rates of greatest significance to contaminant transport within the Yucca Flat/Climax Mine CAU.

- **Consistency of hydraulic continuity and flow rates into northern Yucca Flat.** Significant uncertainty exists in the continuity of the LCA and the associated boundary flux in northern Yucca Flat. Regional groundwater flow models have assumed the LCA is continuous in northern Yucca Flat, while recent analyses (Fenelon et al., 2012) support the alternative conceptual model of limited hydraulic continuity of the LCA in northern Yucca Flat. To accommodate this uncertainty, both conceptual models have been used. The case assuming hydraulic continuity is called the base case because it maximizes flow into the Yucca Flat basin, hence leading to a conservative estimate of flow in the LCA.

- **Consistency of structural discontinuities and flow rates from Yucca Flat to Frenchman Flat.** Uncertainty exists in the hydrologic continuity along major structural features at the southern end of Yucca Flat. As a result, the continuity of the hydrologic flow system in the LCA within the accommodation zone beneath Massachusetts Mountain also is uncertain. However, the hydraulic heads within the LCA in both Yucca Flat and Frenchman Flat are of similar magnitude, thereby suggesting hydrologic continuity within this geologic unit. The modeled boundary fluxes out of the southern boundary of the Yucca Flat LCA flow

model are also similar to the boundary fluxes into the northern boundary of the Frenchman Flat flow model (about 200 and 400 kg/s, respectively). The boundary flux along the southern boundary is also consistent with the general flow amounts estimated by Fenelon et al. (2010). This region is sufficiently far south of the possible sources of contamination in the LCA, so that uncertainty in the definition of the flow rates in the accommodation zone does not significantly affect the forecast extent of contamination.

6.0 YUCCA FLAT SATURATED LOWER CARBONATE AQUIFER TRANSPORT MODEL

Contaminants released from underground nuclear detonations conducted in either the unsaturated zone or the saturated alluvial/volcanic aquifer system may be transported to the LCA because of the generally vertical downward flow in the Yucca Flat area. In addition, some underground detonations were conducted with working points close to or below the interface between the saturated and unsaturated portions of the LCA. Therefore, evaluating contaminant transport within the LCA due to these potential sources is an important part of the Yucca Flat/Climax Mine CAU transport analysis and evaluation.

As described in Section 5.0, the LCA is a regionally extensive aquifer at the NNSS and in the DVRFS. Therefore, in order to reasonably forecast the potential contaminant migration within the LCA in the Yucca Flat/Climax Mine CAU, a detailed process model of LCA flow and transport is developed. This section describes the LCA transport model and the associated parameters used in the LCA transport model. The discussion is divided into a general description of the LCA transport conceptual model, followed by the general modeling approach, and then the parameters used in the model to calculate contaminant transport. This is followed by a description of how the LCA transport model is integrated with inputs from the LCA flow model described in Section 5.0, the LCA source terms described in Section 2.0, and the contaminant source inputs to the LCA from the overlying unsaturated zone and saturated alluvium/volcanic aquifer system models described in Sections 3.0 and 4.0, respectively. Finally, Section 6.5 presents the result of forecasting contaminant transport in the LCA using the LCA transport model based on these inputs and the uncertainty in the LCA transport parameters.

The radionuclide source inputs to the LCA consist of vertical downward transport from the overlying unsaturated alluvium, tuff, and carbonate units, and the overlying saturated alluvium and tuff units, as well as the sources that are the results of detonations with exchange volumes extending into the saturated LCA. Section 2.0 presents the results of radionuclide contaminant sources at the time of the nuclear detonations; i.e., the fraction of the inventory within a detonation's exchange volume that intersects the saturated LCA and is directly input to the saturated LCA transport model. Section 3.0

presents the results of radionuclide contaminant sources from the overlying unsaturated alluvium, tuff, and carbonate rocks. Section 4.0 presents the results of radionuclide contaminant sources from the overlying saturated alluvium and volcanic rocks.

Determination of a stochastic contaminant boundary is the ultimate objective of the CAI phase of the UGTA FFACO strategy. The FFACO (1996, as amended) defines this boundary as follows:

> A ***contaminant boundary*** is formally defined as a probabilistic model-forecast perimeter and a lower hydrostratigraphic unit (HSU) boundary that delineates the extent of radionuclide-contaminated groundwater from underground testing over 1,000 years. The contaminated groundwater is a volume (3-D), and this volume is projected upward to the ground surface to define a two-dimensional ***contaminant boundary*** perimeter. Contaminated groundwater is defined as water exceeding the radiological standards of the SDWA. Simulation modeling of contaminant transport will be used to forecast the location of ***contaminant boundaries*** within 1,000 years and must show the 95th percentile of the model results (boundary outside of which only 5 percent of the simulations exceed the SDWA standards).

Based on this definition, the lower contaminated HSU is the LCA. The contaminated volume is the volume of saturated rock (in contrast to the volume of water) that has a 5 percent or greater probability of exceeding the SDWA MCL within 1,000 years. The two-dimensional contaminant boundary is the vertical projection of the perimeter of the lateral extent of contamination having a 5 percent or greater probability of exceeding the SDWA MCL within 1,000 years.

The purpose of the present study focuses on understanding the behavior of radionuclide migration in the Yucca Flat/Climax Mine CAU and to define, both qualitatively and quantitatively, the sensitivity of such behavior to uncertainty in the flow and transport model conceptualization and parameterization. Therefore, multiple conditional contaminant boundaries are forecast to identify the range of possible contaminant migration. These contaminant boundaries are conditioned on alternative assumptions associated with (1) HST scenarios, (2) groundwater flow conceptual models, and (3) flow and radionuclide transport parameter ranges. Evaluating the effects of alternative scenarios and models is appropriate in order to identify the full range of potential forecast contaminant migration.

As discussed in Section 1.7, the modeling strategy adopted for the Yucca Flat/Climax Mine CAU has been to evaluate the effects of alternative conceptual models and parameter ranges in such a way as to ensure that the possible extent of contaminant migration is not underrepresented. This strategy is

particularly relevant to the LCA transport model. The base case results presented in Section 6.5.2 include conservative assumptions related to (1) the use of the maximum announced yield of each detonation as discussed in Section 2.0, (2) the LCA flow field that assumes lateral hydraulic continuity of the LCA in northern Yucca Flat as discussed in Section 5.0, (3) no sorption of several significant radionuclides as discussed in Section 6.3.5, and (4) fracture transport characteristics of the fault damage zones that minimize the effect of matrix diffusion as discussed in Section 6.3.6. The significance of these compounded conservative assumptions is to purposely bias the transport results in a way to maximize the extent of contaminant transport. Alternative, less conservative assumptions are evaluated to determine the significance of the conservative assumptions on the forecast extent of the contaminant boundary.

While probability maps, which represent the perimeter of the model nodes that have a 5 percent or greater probability of exceeding the MCL, provide qualitative information pertaining to the global behavior of radionuclide migration over all Monte Carlo simulations, the maps are difficult to characterize quantitatively because they represent a spatial geometry. To alleviate this difficulty and to provide a scalar metric that can be used to quantitatively evaluate the significance of uncertain conceptual models and parameters, two metrics are developed. The first metric is the exceedance volume, which is the total volume of model nodes that have a 5 percent or greater probability of exceeding the MCL when considering all radionuclides at any time up to 1,000 years. The second metric is the maximum extent of southern contaminant migration, defined by the most southerly node in the model that has a 5 percent or greater probability of exceeding the MCL when considering all radionuclides at any time up to 1,000 years. The exceedance volume and maximum southern extent of contamination, which are scalar equivalents of the contaminant boundary, are calculated based on the results of the conditional contaminant boundary perimeters (probability maps).

6.1 Transport Conceptual Model and Parameters

The LCA contaminant transport conceptual model is divided into two general subjects: (1) contaminant release, and (2) contaminant migration. The release mechanism for the Yucca Flat/Climax Mine CAU consists of multiple point sources that represent either the locations of underground nuclear detonations performed adjacent to the saturated LCA or releases from detonations performed in overlying HSUs that are subsequently transported to the saturated LCA. Migration from the source area is controlled through physical processes that are a function of the

hydrogeologic and geochemical properties of the rocks. The details of the processes considered in contaminant release from the source areas are discussed in Section 2.0 and Appendix C. The processes that result in the release of contaminants to the LCA include those directly released to the LCA because of the extent of the cavity and exchange volume intersecting the saturated LCA, as well as the flow and transport processes considered in the unsaturated-zone flow and transport model and the saturated alluvial/volcanic aquifer system flow and transport model presented in Sections 3.0 and 4.0, respectively.

Radionuclide migration in the LCA is affected by multiple physical and chemical processes that depend on either the hydrogeologic system and its properties or the specific properties of the radionuclides. These processes include radioactive decay of the species, advection in both porous and fractured media, diffusion from fracture water into matrix water, sorption onto immobile minerals, sorption onto mobile colloidal minerals, and attachment and detachment of colloids from immobile surfaces. The components of the conceptual model are listed below, with discussion regarding assumptions and simplifications as related to the development of the Yucca Flat LCA transport model. The parameterization of the processes associated with the conceptual model is discussed in Section 6.3.

6.1.1 Advective and Dispersive Transport

Radionuclides advect and disperse in the flow system as they move through porous and fractured media. The advection at any location is governed by the groundwater flux estimates developed from the flow model, with the velocity, v, being a linear scaling of the flux, Q, by effective porosity, n_{eff}, and the cross-sectional area perpendicular to flow, A, as

$$v = Q/(A \times n_{eff}) \qquad (6\text{-}1)$$

In fractured media such as the LCA, the effective porosity used for advection is the fracture volume fraction. Thus, for the same flux, simulated velocities are much higher for fractured rock than they are for porous media because of the small fracture volume. The advective flow paths correspond with the groundwater flux; the velocity simply determines the rate of movement along flow paths.

The Yucca Flat transport model includes the HSUs as zoned in the HFM. However, these zones are coarse, and material heterogeneities and features not explicitly zoned in the HFM exist at smaller scales. In addition, the Yucca Flat LCA flow model does not consider the potential spatial

heterogeneity within a unit across the basin, with the exception of the different LCA country rock regions in the east, central, and western portions of the model domain. These heterogeneities can cause divergence and/or convergence of flow paths within the zones of single material properties. For example, faults with offsets greater than 60 m are included in the model; other faults that may provide potential pathways for contaminant migration are not explicitly represented in the model domain but are indirectly incorporated in the fault damage zones that are conceptualized as including smaller offset antithetic and synthetic faults. The presence of faults within an otherwise homogeneous zone could increase the tortuous nature of flow within that zone over the scale of hundreds of meters to kilometers. At even smaller scales (meters to tens of meters), velocities may differ along flow paths between different fracture networks. None of these processes are accounted for explicitly in the Yucca Flat transport model. Rather, dispersion coefficients are assigned in order to create spreading along and transverse to the advective flow paths as described by SNJV (2007). This is practically accomplished with random-walk displacements in the particle-tracking simulations and the use of discrete values for longitudinal, transverse, and vertical dispersivities.

6.1.2 Matrix Diffusion

In fractured rock zones, fluid flow occurs principally in fractures and immobile fluid resides in the saturated rock matrix. This enables using the dual-porosity conceptual model in which solutes interact between fracture and matrix water through the matrix diffusion coefficient (D_m). As described in the Frenchman Flat transport model (NNES, 2010b) and the Pahute Mesa transport model (SNJV, 2009a), numerous theoretical, laboratory, and field studies support the validity of the matrix diffusion conceptual and numerical model.

Matrix diffusion is conceptualized with a model of uniform flow and transport in a system with equally spaced fractures. Solutes diffuse out of fractures and into the matrix according to concentration gradients and the surface-area-to-volume ratio of the fractures from which they diffuse. Diffusion is limited by the volume of matrix material into which diffusion occurs. This volume is determined by the spacing between fractures. Over time, the concentrations of solutes in the matrix increase, thus reducing the concentration gradient driving diffusion out of the fractures if they still have higher concentration. For limited-duration source releases, the fractures may be flushed of solutes, and then when the concentration gradient is reversed, diffusion back into the fractures could occur from matrix storage. Because the matrix porosity of a few percent is much greater than the

fracture porosity of a few tenths to hundredths of a percent, the total contaminant mass in the matrix may be significantly greater than the fraction of the mass in the fractures for a range of matrix diffusion coefficients.

The above matrix diffusion conceptual model is a simplification of the actual processes that occur in complex fracture networks where fractures intersect and are of variable length and aperture. Diffusion out of some fractures can actually lead to interference of diffusion or enhancement of concentrations in other fractures. However, at the scale of the Yucca Flat LCA transport model, an abstraction is appropriate and designed to capture the net effect of fracture-matrix interactions with modeled grid-block-scale parameters. The diffusion parameters are uncertain, driven by the uncertainty in the tortuosity of the matrix, which is addressed in stochastic sampling of fracture properties in the Monte Carlo simulation approach.

Although there is evidence that the matrix diffusion process may be scale dependent (SNJV, 2007, Section 10.5), for the purposes of contaminant transport in the LCA at Yucca Flat, this scale dependency is not included in the base-case transport analyses. The potential effect of scale-dependent matrix diffusion is investigated in a sensitivity analysis (see Section 6.5).

6.1.3 Matrix and Fracture Sorption

The conceptual and numerical models allow for reactions between mobile solutes and immobile matrix and fracture material. In porous media, the reactions occur as the solute comes into contact with the immobile minerals along the flow paths between the grains. In fractured media such as the LCA, the solute may be sorbed either directly on the fracture wall because of the presence of clay and other sorptive minerals on the fracture surface or by the matrix after the solute diffuses out of the fracture and into the matrix.

Sorption reactions can be characterized with both thermodynamic and kinetic formulations. The processes may involve surface complexation and ion exchange. These are discussed in great detail in the Frenchman Flat transport model (NNES, 2010b) and Pahute Mesa transport model (SNJV, 2009a), as well as the Yucca Flat/Climax Mine transport data document (TDD) (SNJV, 2007). In the Yucca Flat transport model, all sorption reactions are assumed to occur under equilibrium conditions and are characterized either with distribution coefficients, K_d, for the matrix or with a retardation factor for sorption on the linings of the fractures. The equilibrium sorption formulation

has been found appropriate to characterize contaminant transport at the scale of 100 m to 1 km, because the sorption process is dependent on the resident-time contact, and at the field scale, the solutes have more time to come into contact with the reactive minerals than they do in short-time laboratory experiments.

6.1.4 Colloid-Facilitated Transport

Whereas matrix diffusion of all solutes and matrix sorption of reactive solute species serve to reduce their mobility, colloidal processes can increase the mobility of a reactive solute. The conceptual model for colloid-facilitated transport in the Yucca Flat LCA transport model is that reactive species entering the Yucca Flat LCA transport model domain from the LCA source regions can be partitioned irreversibly onto naturally occurring mobile colloids. Those colloids then can potentially migrate, experiencing only the reversible processes of attachment and detachment to immobile surfaces on fractures or filtration at variable aperture fracture surfaces. Colloids do not diffuse out of fractures, and the species sorbed onto colloids are conservatively assumed to not desorb and then react with immobile minerals. Colloids onto which reactive species are partitioned at the source region also are assumed to never be removed irreversibly from the flow system. This conceptual model, therefore, is highly sensitive to the amount of solute that partitions onto mobile colloids.

It has been found that the significance of colloid-facilitated transport on the extent of the forecast contaminant boundary is minor, in large part because of the lateral extent of contamination associated with more mobile and dose-significant radionuclides over the time period of interest. Analyses presenting these comparisons for contaminant transport from the BOURBON underground nuclear detonation are presented in Appendix M. As a result of these analyses, colloid-facilitated transport was screened out of the analyses of contaminant migration in the LCA at Yucca Flat.

6.1.5 Radioactive Decay Chains

All of the radionuclide species emanating from the source locations experience radioactive decay. Kersting et al. (2003) examined all of the potential decay chains associated with the RST for underground nuclear detonations and identified the most important chain to be $^{241}Pu \rightarrow {}^{241}Am \rightarrow {}^{237}Np$. Field-scale simulations led to the conclusion that, because of the large quantity of Np in the initial source, coupled with its high mobility and low activity, inclusion of this decay chain did not change predictive results when compared to simply eliminating mass as a result

of decay. As discussed in Section 2.0, the initial ^{237}Np inventory for each detonation is the 1992 inventory documented in Bowen et al. (2001); ^{237}Np was not decay corrected to the time of the detonation as was done for the other radionuclides because the Yucca Flat testing period spanned approximately two ^{241}Pu half-lives. The 1992 inventory is the composite of all detonations performed during the testing period and provides an imprecise radionuclide amount for each individual detonation. Because including the decay chain would not significantly change the calculated results, decay chains and their daughter products are not explicitly included in the radioactive decay process as simulated in the Yucca Flat LCA transport model.

6.2 Numerical Model Approach

Two numerical codes are used to simulate flow and transport processes in the LCA at Yucca Flat: FEHM (Zyvoloski et al., 1997) and PLUMECALC (Robinson et al., 2011). As described in Section 5.0, simulation of groundwater flow is performed with FEHM, which is linked to the parameter estimation code PEST through input and output files.

Transport modeling is performed with FEHM and PLUMECALC. FEHM uses a particle-tracking algorithm, called sptr, to determine flow paths and particle trajectories from the velocity field of the flow model. This particle-tracking algorithm defines the temporal and spatial distribution of advective-dispersive particle trajectories along the forecast travel paths derived from the velocity fields developed in FEHM. PLUMECALC is a convolution-based transport code that uses the particle-track information generated by FEHM to calculate the mobile resident solute concentration by superposition of solute flux over the particles. The solute flux from each source considered whether the source was existent in the LCA at the time of the detonation or whether the source was the result of transport from detonations conducted in the overlying unsaturated zone or saturated alluvium and volcanic aquifers. For detonations with exchange volumes that extend into the saturated LCA, the source contaminant mass flux is determined by applying the portion of the inventory contained in the saturated LCA at the day of the detonation as presented in Section 2.0. For detonations conducted in the overlying units, the mass flux to the saturated LCA is calculated by the models presented in Sections 3.0 and 4.0 for the unsaturated zone and saturated alluvial/volcanic aquifer system, respectively.

Transport parameters include fracture properties (fracture porosity and fracture spacing or fracture aperture), matrix porosity, matrix diffusion (D_m), dispersivity, fracture retardation, and matrix

sorption (K_d). Knowledge of fracture properties is critical to understanding fracture-matrix transfer functions and flow velocity fields. Because of uncertainty of the transport parameters, a stochastic approach was used for simulating transport. In this approach, for a given calibrated groundwater flow field and particle trajectories that are calculated for the given advective flow field with a given dispersivity, multiple realizations of transport are projected with the remaining transport parameters (effective [e.g., fracture] porosity, matrix porosity, fracture aperture, matrix diffusion, fracture retardation, matrix adsorption) being sampled from relevant uncertainty distributions.

Because the same numerical modeling approach was used during the Frenchman Flat Phase II transport analyses and the Pahute Mesa Phase I transport analyses, only a brief summary is presented here, with greater details provided in NNES (2010b) and SNJV (2009a).

The appropriateness and representativeness of the sptr algorithm and PLUMECALC are evaluated in Appendix K. In addition, an algorithm called Walkabout (Painter, 2011) has recently been proposed as an alternative to sptr. Testing of Walkabout is also presented in Appendix K. Given the potential that the two particle-tracking algorithms could create different contaminant transport results, a representative modeling case was run with both particle-tracking routines to evaluate the potential difference. These results are presented in Section 6.5.

6.2.1 Introduction

The Yucca Flat LCA transport model was designed to efficiently simulate the movement of reactive and nonreactive solutes in the fractured LCA of the Yucca Flat model domain. The following functionality was required:

- Simulate radionuclide concentration histories at all locations in the model domain.
- Function in Monte Carlo mode, sampling from distributions of uncertain transport parameters, in order to evaluate the probability of MCL exceedance and develop the required contaminant boundary.
- Accommodate spatially distributed sources.
- Accommodate uncertain radionuclide release at each of the different source locations.

- Accommodate different radionuclides, each with potentially different transport parameter values such as sorption and matrix diffusion coefficients.
- Simulate transport in zones conceptualized as fractured media.

The development and implementation of the Yucca Flat LCA transport modeling framework used FEHM (Zyvoloski et al., 1997) and PLUMECALC (Robinson et al., 2011). The Yucca Flat LCA flow model is implemented in FEHM, which has particle-tracking capability. Particle-track information from FEHM for the calibrated steady-state flow models for instantaneous or transient releases from all source locations provides input to PLUMECALC for transport modeling. PLUMECALC uses convolution integrals to convert the transient source-release functions for all unsaturated zone and saturated volcanic sources and instantaneous release for all sources with exchange volumes extending into the saturated LCA into concentration histories at each model node. The results from each individual source are superposed to generate concentrations at each grid cell from all sources. PLUMECALC calculates three-dimensional concentration profiles for all radionuclides through the 1,000-year regulatory time frame of the simulations.

The following sequence describes transport simulation within this framework:

1. FEHM particle tracking for each steady-state flow model
   - Simulate 10,000 particles per LCA source with FEHM using the flag to output particle information for input to PLUMECALC. This number of particles was found to provide an adequate level of numerical accuracy based on similar analyses at Frenchman Flat (NNES, 2010b).
   - Simulate 500 particles for each source node receiving mass flux from the overlying unsaturated-zone model (Section 3.0) and the saturated alluvial/volcanic aquifer system model (Section 4.0). The significance of the number of particles per source node was evaluated to ensure that 500 particles provided a reasonably stable result.
2. PLUMECALC Monte Carlo transport simulations
   - For each Monte Carlo transport simulation, sample uncertain transport parameter values from parameter distributions, including source-release concentrations for each radionuclide.
   - For each radionuclide, simulate transport for 1,000 years for each source.

This method is efficient because transport simulations with PLUMECALC are fast relative to FEHM simulations, which would have substantial time overhead related to particle-tracking and time-stepping simulations.

6.2.2 FEHM Particle Tracking

Particle-track information is determined by the use of FEHM. The particle-tracking method in FEHM is based upon Pollock (1988) and documented in more detail in Robinson et al. (2011). Although the particle tracking implemented in FEHM is capable of dual-porosity matrix diffusion, linear sorption, and radionuclide decay, those processes are modeled with PLUMECALC as described in Section 6.2.3, thereby reducing FEHM particle tracking to advective and dispersive processes only.

For the LCA transport analyses presented in Section 6.5, the random-walk dispersion implemented in the particle-tracking module requires longitudinal, transverse, and vertical dispersivities. For each calibrated steady-state flow model, a dispersion tensor is specified, and particle tracking is simulated with particles released at each source location. As discussed in Section 6.5, 500 particles are used to represent each source location for transient source fluxes into the LCA from the overlying unsaturated zone or saturated alluvial/volcanic aquifer system, while 10,000 particles are used for each of the source locations that have exchange volumes that extend into the saturated LCA.

Advective transport is computed with the minimum flowing porosity, which is adjusted in PLUMECALC simulations using the unit-specific porosity input. This computation results in additional residence time similar to residence time computed for linear sorption isotherms or for matrix diffusion coefficients. The PLUMECALC-required input is then read into the Monte Carlo simulator, for which PLUMECALC is run for each transport realization.

6.2.3 PLUMECALC

The PLUMECALC software developed for this project (Robinson et al., 2011) is a convolution-based particle-tracking (CBPT) method for simulating flux-averaged or resident solute concentrations in groundwater models through superposition of solute flux onto particle-track information. The flux-averaged solute concentration is the flux of solute divided by the flux of groundwater in a control volume. The resident concentration is either the total mass of solute within a cell volume divided by the total volume of the cell (termed the total resident concentration) or the total mobile solute mass

within a cell divided by the effective porosity of the cell (called the mobile resident concentration). The approach adopted in this study is the mobile resident concentration.

One of the difficulties addressed by this study is simulating *in situ* concentrations at any location in space that account for transient source releases as spatially distributed sources. This is accomplished in PLUMECALC with a novel convolution integral method coupled with the principle of superposition. Superposition enables efficient additive impacts of multiple sources to be represented at a single location in space. Invoking superposition entails assuming that species' concentrations do not interfere with one another and that the concentrations are small enough that immobile sorption site concentrations far exceed the concentrations of the aqueous reactive species.

The PLUMECALC method is valid for steady-state flow and linear transport processes, including sorption with linear sorption isotherms, diffusion into matrix rock, and first-order decay. Implementation of these processes and associated assumptions is addressed in Robinson et al. (2011). The principles of superposition of multiple solute sources and numerical convolution are used to integrate results for multiple time-varying sources. In FEHM particle tracking, a pulse of particles is introduced at each source location, and movement is simulated through time. Particle departure times are recorded from each cell encountered as particles move through the system. The CBPT technique used in PLUMECALC incorporates the time variation of each input source function, taking advantage of the ability of particle-based FEHM simulations to maintain sharp fronts where advection dominates, such as in the high-flux zones of the Yucca Flat LCA flow models. The theory for the CBPT method in PLUMECALC is discussed in Section 2 of the PLUMECALC user's manual (Robinson et al., 2011).

The algorithm for carrying out the convolution and superposition calculation from the FEHM particle-tracking results is efficient. For each calibrated steady-state flow model (in FEHM), PLUMECALC is used to simulate transport incorporating source-term variability, decay, and spatially variable sorption and matrix diffusion. To change the flow field or dispersion parameters, FEHM must be run to determine new particle-track information. For each steady-state flow field considered and for a fixed set of dispersivities, FEHM is run only once, and the Monte Carlo transport simulation set is conducted with only PLUMECALC.

6.3 Parameters

The LCA at Yucca Flat is a fractured rock. The conceptual model of the LCA in the transport analysis is that of a classic double-porosity medium defined by advective solute transport through the fractures, solute mass transfer between the fractures and the matrix (or unfractured rock) via the mechanism of diffusion, and diffusive transport within the matrix. Modeling of transport in the LCA at Yucca Flat assumed that the fractures can be characterized as a single set of parallel fractures. As discussed in Wolfsberg et al. (2002), in the mathematical representation of a double-porosity system with a single set of parallel fractures, the parameters defining the fractures are mutually dependent as given by

$$\phi_f = \frac{b}{s} \tag{6-2}$$

where

ϕ_f = fracture (effective) porosity (unitless)
b = fracture aperture (length [L])
s = fracture spacing (L)

The properties defining mass transfer in the matrix in the double-porosity model are (1) matrix porosity and (2) matrix diffusion parameters, which are matrix tortuosity and the free-water diffusion coefficient of the solutes.

Advective-dispersive solute transport through fractures in the LCA at Yucca Flat is a function of the groundwater velocity and mechanical dispersion, which arises from the complex and heterogeneous movement of water and solute particles through the intricate network of fractures in the LCA. Groundwater velocity is calculated as the Darcy flux divided by the fracture porosity. The effect of dispersion is the spreading of solute over a volume that is larger than would be predicted based on estimates of the mean groundwater velocity. The dispersion coefficient included in the advective-dispersive transport equation is calculated as dispersivity times the groundwater velocity. Dispersivity is generally a scale-dependent parameter because of the varying scales of heterogeneity and increases with increased transport distance.

In the Yucca Flat LCA transport model, radionuclide retardation via sorption is considered for reactions with immobile minerals in both the fracture and matrix materials. Sorption can occur on the mineral coatings lining the fracture walls or after solutes diffuse out of the fractures into the immobile water in the matrix continuum. For the purposes of LCA transport, both fracture retardation and

equilibrium matrix sorption are considered. Sorption is much more significant in the matrix materials than within fractures because of the much larger surface area involved.

Modeling of transport in the LCA at Yucca Flat uses two numerical codes: the particle-tracking method in FEHM as discussed in Section 6.2.2, and PLUMECALC as discussed in Section 6.2.3. The input parameters related to simulation of transport in the fractured LCA are listed below:

- FEHM
  - Groundwater velocity distribution determined from the calibrated groundwater flow models using FEHM
  - Dispersivity
- PLUMECALC
  - Porosity of the medium, which is the effective matrix porosity for a porous medium and the fracture porosity for a fractured medium
  - Fracture aperture in the primary porosity (i.e., fractures) for a fractured medium
  - Matrix porosity, which is the total porosity in the matrix for a fractured medium
  - Matrix diffusion coefficient in the rock matrix (equals the product of the matrix tortuosity and the solute free-water diffusion coefficient)
  - Sorption coefficient in the matrix
  - Sorption coefficient in the primary porosity (i.e., fractures)
  - Retardation factor in the fracture system

Use of these parameters by FEHM and PLUMECALC is described in the respective user's guides (Zyvoloski et al., 1997, and Robinson et al., 2011).

Values for the transport parameters were, when possible, derived from field- and/or laboratory-scale data. Values for all of the parameters are uncertain. Therefore, a statistical distribution was derived for each parameter with the data used to define the distributions designed to represent the full range of parameter variability. Multiple sets of parameter values were selected for 400 Monte Carlo realizations through random sampling of the parameter distributions. Each of the 400 parameter sets presents a unique realization for the Yucca Flat LCA transport model. The goal of using multiple sets

of input parameter values in the Monte Carlo transport simulations was to capture heterogeneity and uncertainty in the transport parameters by sampling from the defined parameter distributions for multiple realizations. Statistical analysis of the Monte Carlo realizations identifies levels of parametric uncertainty influence and output sensitivity.

As discussed in Section 1.7, the base-case simulation of transport in the LCA was designed to produce conservative results (i.e., the simulations were implemented in a manner that does not underestimate the possible extent of contaminant migration). Therefore, the distributions for the transport parameters were developed with the objective of conservatism. That is, parameters were developed with the intent of biasing the results to more significant fracture transport and less matrix diffusion. In addition to the base-case simulation, an alternative simulation, which used transport parameter distributions that are more representative of the LCA fracture characteristics and more closely match the conceptualization of the LCA, was conducted. The alternative simulation is referred to as the alternative LCA parameterization simulation. In the following, the transport parameter distributions developed for the base-case simulation are presented first, followed by those developed for the alternative simulation. Organization of the discussion of the transport parameters developed for simulating transport in the LCA at Yucca Flat is as follows:

- Section 6.3.1, Fracture Parameters
  - Section 6.3.1.1, Fracture Porosity
  - Section 6.3.1.2, Fracture Aperture
  - Section 6.3.1.3, Fracture Spacing
  - Section 6.3.1.4, Summary Discussion of Fracture Parameters
- Section 6.3.2, Matrix Porosity
- Section 6.3.3, Matrix Diffusion Coefficient Parameters
  - Section 6.3.3.1, Matrix Tortuosity
  - Section 6.3.3.2, Free-Water Diffusion Coefficients
- Section 6.3.4, Dispersivity
- Section 6.3.5, Fracture Retardation and Matrix Sorption
- Section 6.3.6, Input Parameters for the Alternative LCA Parameterization Simulation

Although fracture spacing is not a PLUMECALC input parameter, it is inherently part of the model because it is related to fracture porosity and fracture aperture as indicated by Equation (6-2). Therefore, the input values developed for fracture porosity and fracture aperture were used to calculate the corresponding fracture spacing values. This was done in order to present the fracture spacing for the simulations.

The following sections present a general overview of the transport parameters as they are incorporated in the transport modeling, discuss supplemental information, present the parameter distributions used for the transport modeling, and discuss limitations. Development of the parameter distributions for the alternative LCA parameterization simulation is provided in Section 6.3.6. The distributions for the source data and the methods used to develop model distributions for the fracture parameters, matrix porosity, and matrix diffusion parameters are tabulated in Table 6-1 for both the base-case simulation and the alternative LCA parameterization simulation. The fracture retardation and matrix sorption distributions are tabulated in Tables 6-2 and 6-3, respectively.

6.3.1 Fracture Parameters

For modeling flow and transport, the LCA was simulated as either faulted or unfaulted, with the faulted portion referred to as the fault zones and the unfaulted portion referred to as the country rock. Fault zones are conceptualized as consisting of damage zones and core zones. The core zones consist of fault gouge and are generally considered to be of low permeability and not significant pathways for groundwater flow or contaminant transport. For the purposes of transport model parameter specification within the CAU model domain, the core zones are conservatively treated the same as the damage zones. That is, the core zones are not considered separate and distinct transport features, aside from the role they play in affecting the groundwater flow regime and associated particle trajectory paths and fluxes, but are assumed to be fractured like the damaged zones even though their hydraulic conductivity is lower than that of the damaged zones.

The conceptual model characterizes the LCA fault zones as more highly fractured than the LCA country rock. Therefore, different distributions were developed for the fracture parameters describing these two zones. This conceptualization is supported by an analysis of flowing features in the LCA at Yucca Flat (Appendix J). That analysis indicates that the LCA flowing fracture system is complex and shows evidence of both large, regional-scale flowing features and smaller-scale flowing features. The large-scale flowing features likely represent major faults and their associated damage zones, whereas the smaller-scale flowing features likely represent fractured and jointed country rock.

The Yucca Flat LCA transport model considers a fracture geometry consisting of a single set of equally spaced, parallel fractures consistent with the implementation within PLUMECALC. Each of the fractures is assumed to have a constant aperture across its entire extent, and all fractures in the set are assumed to have the same aperture. In summary, this conceptualized geometry assumes that

Table 6-1
Source Data Distributions and Methodology for Developing Fracture Parameters, Matrix Porosity, and Tortuosity Distributions
(Page 1 of 3)

Parameter	Mean [a]	Standard Deviation [a]	Lower Bound [b]	Most Likely [c]	Upper Bound [b]	Distribution Type	Comments	Source
Fracture Porosity (unitless), ϕ_f (PLUMECALC Input Parameter)								
CR (BC)	N/A	N/A	2E-04	N/A	2E-02	Log Uniform	Sampled lower 2/3 of full distribution	SNJV (2007) and Section 6.3.1.1
FZ (BC)	N/A	N/A	2E-04	N/A	2E-02	Log Uniform	Sampled upper 2/3 of full distribution	SNJV (2007) and Section 6.3.1.1
CR (Alt)	N/A	N/A	2E-04	N/A	2E-02	Log Uniform	Sampled lower 2/3 of full distribution (same as base-case simulation)	SNJV (2007) and Section 6.3.6.1
FZ (Alt)	N/A	N/A	2E-04	N/A	2E-02	Log Uniform	Sampled upper 1/3 of full distribution	SNJV (2007) and Section 6.3.6.1
Log Hydraulic Conductivity (m/day), *K* (Used in Calculation of Fracture Aperture)								
CR (BC & Alt)	0.16	1.34	N/A	N/A	N/A	Lognormal	Sampled lower 2/3 of full distribution	SNJV (2006a), and Sections 6.3.1.2 and 6.3.6.1
FZ (BC & Alt)	0.16	1.34	N/A	N/A	N/A	Lognormal	Sampled upper 2/3 of full distribution	SNJV (2006a), and Sections 6.3.1.2 and 6.3.6.1
Fracture Aperture Multiplier (unitless) (Used in Calculation of Fracture Aperture)								
CR (BC & Alt)	N/A	N/A	2	5	10	Triangular	Derived from assessment of hydraulic and tracer apertures	Sections 6.3.1.2 and 6.3.6.1
FZ (BC & Alt)	N/A	N/A	5	10	20	Triangular	Derived from assessment of hydraulic and tracer apertures	Sections 6.3.1.2 and 6.3.6.1
Tracer Fracture Aperture (m), *b* (PLUMECALC Input Parameter)								
CR & FZ (BC)	N/A	N/A	N/A	N/A	N/A	N/A	Calculated from sampled hydraulic conductivity and sampled fracture aperture multiplier	Section 6.3.1.2
CR (Alt)	N/A	N/A	N/A	N/A	N/A	N/A	Hydraulic aperture calculated using Equation (6-4) with sampled hydraulic conductivity and assumed fracture spacing of 3 m; tracer aperture used in model calculated from hydraulic aperture and sampled fracture aperture multiplier (same as base-case simulation)	Section 6.3.6.1

Table 6-1
Source Data Distributions and Methodology for Developing Fracture Parameters, Matrix Porosity, and Tortuosity Distributions
(Page 2 of 3)

Parameter	Mean [a]	Standard Deviation [a]	Lower Bound [b]	Most Likely [c]	Upper Bound [b]	Distribution Type	Comments	Source
FZ (Alt)	N/A	N/A	N/A	N/A	N/A	N/A	Hydraulic aperture calculated using Equation (6-4) with sampled hydraulic conductivity and assumed fracture spacing of 0.5 m; tracer aperture used in model calculated from hydraulic aperture and sampled fracture aperture multiplier	Section 6.3.6.1
Model Fracture Spacing (m), *s* (Not a PLUMECALC Input Parameter; Calculated to Show Values Associated with Input Values of Fracture Porosity and Fracture Tracer Aperture)								
CR & FZ (BC & Alt)	N/A	N/A	N/A	N/A	N/A	N/A	Calculated from sampled fracture porosity and calculated tracer fracture aperture using Equation (6-5)	Sections 6.3.1.3 and 6.3.6.1
Total Matrix Porosity (unitless), ϕ_m (PLUMECALC Input Parameter)								
CR & FZ (BC)	0.0263	0.0163	N/A	N/A	N/A	Normal	From porosity data	SNJV (2007) and Section 6.3.2
CR (Alt)	0.0263	0.0163	N/A	N/A	N/A	Normal	Calculated as the sampled porosity data developed just as for the base-case simulation multiplied by a sampled matrix porosity reduction factor	SNJV (2007) and Section 6.3.6.2
FZ (Alt)	0.0263	0.0163	N/A	N/A	N/A	Normal	From porosity data (same as base-case simulation)	SNJV (2007) and Section 6.3.6.2
Matrix Porosity Reduction Factor (unitless) (Used to Calculate Total Matrix Porosity in the Country Rock for the Alternative LCA Parameterization Simulation)								
CR (Alt)	N/A	N/A	0.2	N/A	0.8	Uniform	Developed from results of flowing feature analysis presented in Appendix J	Section 6.3.6.2 and Appendix J
Tortuosity (unitless), τ (Used to Calculate Matrix Diffusion Coefficient)								
CR & FZ (BC & Alt)	N/A	N/A	N/A	N/A	N/A	N/A	Correlated with matrix porosity: $\log \tau = 20.38\ \phi_m - 2.13$	Sections 6.3.3 and 6.3.6.3

Table 6-1
Source Data Distributions and Methodology for Developing Fracture Parameters, Matrix Porosity, and Tortuosity Distributions
(Page 3 of 3)

Parameter	Mean [a]	Standard Deviation [a]	Lower Bound [b]	Most Likely [c]	Upper Bound [b]	Distribution Type	Comments	Source
Free-Water Diffusion Coefficient (m^2/s) D_o (Used to Calculate Matrix Diffusion Coefficient)								
CR & FZ (BC & Alt)	N/A	N/A	N/A	3E-10 & 2.24E-09	N/A	N/A	Value of 3E-10 m^2/s used for radionuclides with an atomic mass greater than 137, and value of 2.24E-09 m^2/s used for radionuclides with an atomic mass less than or equal to 137	Sections 6.3.3.2 and 6.3.6.3
Matrix Diffusion Coefficient (m^2/s) (PLUMECALC Input Parameter)								
CR & FZ (BC & Alt)	N/A	N/A	N/A	N/A	N/A	N/A	Calculated as the matrix tortuosity multiplied by the radionuclide free-water diffusion coefficient using Equation (6-6)	Sections 6.3.3 and 6.3.6.3

[a] Applicable for lognormal and normal distributions only
[b] Applicable for log-uniform and triangular distributions only
[c] Applicable for triangular distributions only

Alt = Alternative LCA parameterization simulation
BC = Base-case simulation
CR = Country rock
FZ = Fault zones
N/A = Not applicable

Table 6-2
LCA Transport Model Fracture Retardation Distributions

Radionuclide	Fracture Retardation Parameter Distribution (mL/g)				Source
	Lower Bound	Upper Bound	Mode	Shape	
^{90}Sr	1	2.5	1.75	Triangular	SNJV, 2007 (Table 12-3)
$^{135/137}Cs$	1.8	320	160.9	Triangular	SNJV, 2007 (Table 12-3)
^{237}Np	1	10	5.5	Triangular	SNJV, 2007 (Table 12-3)
U	1	1.6	1.3	Triangular	SNJV, 2007 (Table 12-3)
$^{239/240/242}Pu$	2.4	50	26.2	Triangular	SNJV, 2007 (Table 12-3)

Note: All other radionuclides are considered to be non-sorbing on fracture surfaces.

Table 6-3
LCA Transport Model Matrix Sorption (K_d) Distributions

Radionuclide	Matrix Sorption Parameter Distribution (mL/g)				Source
	Lower Bound	Upper Bound	Mode	Shape	
U	0.03	30	15	Triangular	Rechards and Tierney, 2005
$^{239/240/242}Pu$	900	20,000	10,450	Triangular	Rechards and Tierney, 2005
Alternative Distributions Used in Sensitivity Analyses					
^{14}C	1	20	10.5	Triangular	Zavarin, 2012
^{63}Ni	5	16	10.5	Triangular	Zavarin, 2012
^{90}Sr	5	16	10.5	Triangular	Zavarin, 2012
$^{135/137}Cs$	0.2	6.8	3.5	Triangular	Zavarin, 2012

Note: All other radionuclides of potential significance are considered to be non-sorbing in the matrix.

fractures are equally spaced and hydraulically connected with a constant aperture across the entire model domain. This conceptualization is a simplification of the variability in spacing and aperture observed in nature. An objective of simulating transport using multiple realizations of parameter sets is to incorporate the uncertainty in simulated transport distance resulting from the simplified conceptualization of complex, uncertain, and spatially variable transport properties.

As indicated by Equation (6-2), the fracture parameters in the mathematical model of a double-porosity system with a single set of parallel fractures are interdependent. If values for two of the parameters are known, the value for the third parameter can be calculated. For the Yucca Flat LCA transport model, the two fracture parameters chosen for development of input distributions were fracture porosity and fracture aperture. These are also the PLUMECALC input parameters, but the

decision to develop input distributions for these two parameters rather than one of these and fracture spacing was made for several reasons unrelated to the PLUMECALC input requirements. First, the observed data for fracture porosity is considered to be more representative of CAU-scale transport than the observed data for fracture spacing. Second, literature data related to the investigation of porosity in fractured systems is available to inform and augment the observed data in developing the range of fracture porosity values likely representative of the LCA. Third, the underlying hydraulic data used to develop the fracture aperture are considered to be more comprehensive and relevant than the observed fracture spacing data. Each of these points is discussed in more detail below.

The approach to developing the input values for fracture porosity and fracture aperture for the 400 Monte Carlo realizations involved several steps. The steps involved in developing the 400 input values for fracture porosity in the fault zones and the country rock, which are described in Section 6.3.1.1, consisted of the following:

- Define a distribution of fracture porosity based on observed data.
- Determine how that distribution would be sampled for both the fault zones and the country rock.
- Sample the distribution to obtain the input values for the fault zones and the country rock.

Development of the input values for tracer fracture aperture used a mathematical relationship between fracture aperture and hydraulic conductivity, and an assessment of differences in hydraulic fracture apertures and tracer fracture apertures. The steps involved in developing the 400 input values for tracer fracture aperture for the fault zones and the country rock, which are discussed in Section 6.3.1.2, consisted of the following:

- Define a distribution of hydraulic conductivity based on observed data.
- Determine how that distribution would be sampled for both the fault zones and the country rock.
- Sample the hydraulic conductivity distribution to obtain values for both the fault zones and the country rock.
- Calculate the hydraulic fracture aperture values for the fault zones and the country rock from the sampled hydraulic conductivity values.
- Assess the relationship between hydraulic fracture aperture and tracer fracture aperture.

- Develop a distribution for an aperture multiplier that accounts for tracer fracture apertures that are larger than hydraulic fracture apertures.
- Determine how the aperture multiplier distribution would be sampled for both the fault zones and the country rock.
- Sample the aperture multiplier distribution to obtain values for both the fault zones and the country rock.
- Calculate the tracer fracture aperture values from the calculated hydraulic fracture apertures and the sampled aperture multiplier for both the fault zones and the country rock.

As previously stated, fracture spacing is not a PLUMECALC input parameter. However, it is intrinsic to the transport model because of its relationship to the PLUMECALC input parameters fracture porosity and fracture aperture. Therefore, the values of fracture spacing for the fault zones and the country rock were calculated with Equation (6-2). This was done in order to show the fracture spacing values that correspond to the input values for fracture porosity and fracture aperture. Section 6.3.1.3 contains the fracture spacing discussion.

6.3.1.1 Fracture Porosity

Fracture porosity is the primary parameter for converting flux, as simulated in the Yucca Flat LCA flow model, to velocity. As described in Domenico and Schwartz (1990),

$$v = \frac{Q}{A\phi_e} \tag{6-3}$$

where
v = groundwater velocity (length per time [L/t])
Q= Darcy flux (L^3/t)
A= cross-sectional area (L^2)
ϕ_e= effective or fracture porosity (unitless)

In fractured media, the effective porosity is a measure of the interconnectedness of open fractures available for flow. Many fractures may dead-end and not participate in flow at any scale, whereas other fractures may participate at the scale of tens of meters, but not at hundreds of meters or several kilometers. The percentage of fractures interconnected at the CAU scale will be much smaller than the percentage of those interconnected at the scales of tens of meters and those observed in boreholes. From observations at the borehole scale, the interconnectedness of fractures beyond the borehole

cannot be determined. In addition, the degree to which fractures interconnected at the tracer-test scale (tens of meters) are also interconnected at the CAU scale is unknown.

Values for fracture porosity on a scale of tens of meters can be estimated by several methods. Assuming plug flow transport, a fracture porosity can be estimated using peak-concentration arrival time from tracer tests for pathways along which advective transport dominates over diffusion into the matrix. Fracture porosity can also be estimated using interpreted hydraulic conductivity values and observed fracture spacing data where both types of data are available. Both of these methods are described in Section 8.0 of SNJV (2007). Values can also be estimated through numerical interpretation of breakthrough curve data from tracer tests for pathways dominated by advective transport. The fracture porosity values estimated by all three of these methods are uncertain as described in SNJV (2007).

Fracture porosity estimates for the LCA in the NNSS investigation area have been determined through evaluation of data from tracer tests at WW C and WW-C-1, and the ER-6-1 Well Cluster, and from hydraulic conductivity, fracture aperture, and fracture spacing data at ER-6-1-2 and ER-7-1. The ER-6-1 Well Cluster consists of three wells—ER-6-1, ER-6-1-1, and ER-6-1-2. Well ER-7-1 and the ER-6-1 Well Cluster are located in Yucca Flat, and Wells WW C and WW-C-1 are located between Yucca Flat and Frenchman Flat. Additional estimates related to carbonate sediments have been obtained through evaluation of data from tracer tests in a fracture dolomite at three locations at the Waste Isolation Pilot Plant (WIPP) site located near Carlsbad, New Mexico. Development of the estimated values of fracture porosity from these field data and the recommended distribution for use in the Yucca Flat transport model are presented in SNJV (2007). SNJV (2007) recommended a skewed log-triangular distribution for the fracture porosity of the LCA at Yucca Flat with minimum, most likely, and maximum values of –3.7, –3.0, and –1.7 (corresponding to 2E-04, 5E-03, and 2E-02), respectively. SNJV (2007) discussed that fracture porosities determined by the use of hydraulic conductivities will be biased low and, therefore, were given a lower probability. The higher values in this distribution are associated with those determined from tracer testing at ER-6-1, which is located in a faulted area of the LCA. This distribution was developed during a time period when the fracture characteristics in the LCA were considered to be consistent across the Yucca Flat area without separate specification of parameters for fault zones and country rock. The distribution was skewed toward the higher fracture porosity values to enable higher values consistent with faulted areas to be sampled more frequently than lower values considered to be associated with a less faulted

LCA. Since that time, a revised conceptualization of the LCA has been developed in which fracture characteristics in the fault zones are considered different from those in the country rock, with the fault zones being more highly fractured than the country rock. Therefore, two new distributions were developed using the fracture porosity data reported in SNJV (2007).

Few data regarding the fracture porosity of the LCA at Yucca Flat are available. As a result, a log-uniform distribution from the lowest value of 2E-04 to the highest value of 2E-02 reported in SNJV (2007) was used for the LCA. The fault zones in the LCA will have a higher fracture porosity than the country rock for the conceptualization that the fault zones are more highly fractured than the country rock. To account for this difference, the fracture porosity for the country rock was sampled from the lower two-thirds of the distribution, and the fracture porosity for the fault zones was sampled from the upper two-thirds of the distribution. The distribution of fracture porosity data sampled is shown in Figure 6-1a, and the sampled fracture porosities for the country rock and faults zones used in the transport model are shown in Figure 6-1b.

The major limitations associated with the fracture (effective) porosity distribution for the LCA at Yucca Flat are sparse data, uncertainty in the data inputs and methods used to estimate fracture porosity, and the issue of scaling borehole and hydraulic/tracer-test values to values representative at the CAU scale. The LCA within the Yucca Flat model encompasses a domain of about 36.0 km in the north–south direction and 28.5 km in the east–west direction, with north–south paths along the largest faults of about 25 to 35 km. The actual effective porosity in such a large area will be heterogeneous, varying both in the lateral and vertical directions. Determining values for effective porosity that capture this heterogeneity would require extensive data collection at time and spatial scales that are impractical.

These limitations result in uncertainty in the fracture porosity used in the transport model and a lack of knowledge regarding a representative mean value. In addition, the sparse data result in an inability to capture the heterogeneous nature of the fracture porosity and its effect on contaminant movement. The use of a distribution and multiple simulations using different values from the distribution is the method implemented to attempt to incorporate the heterogeneity and uncertainty in fracture porosity.

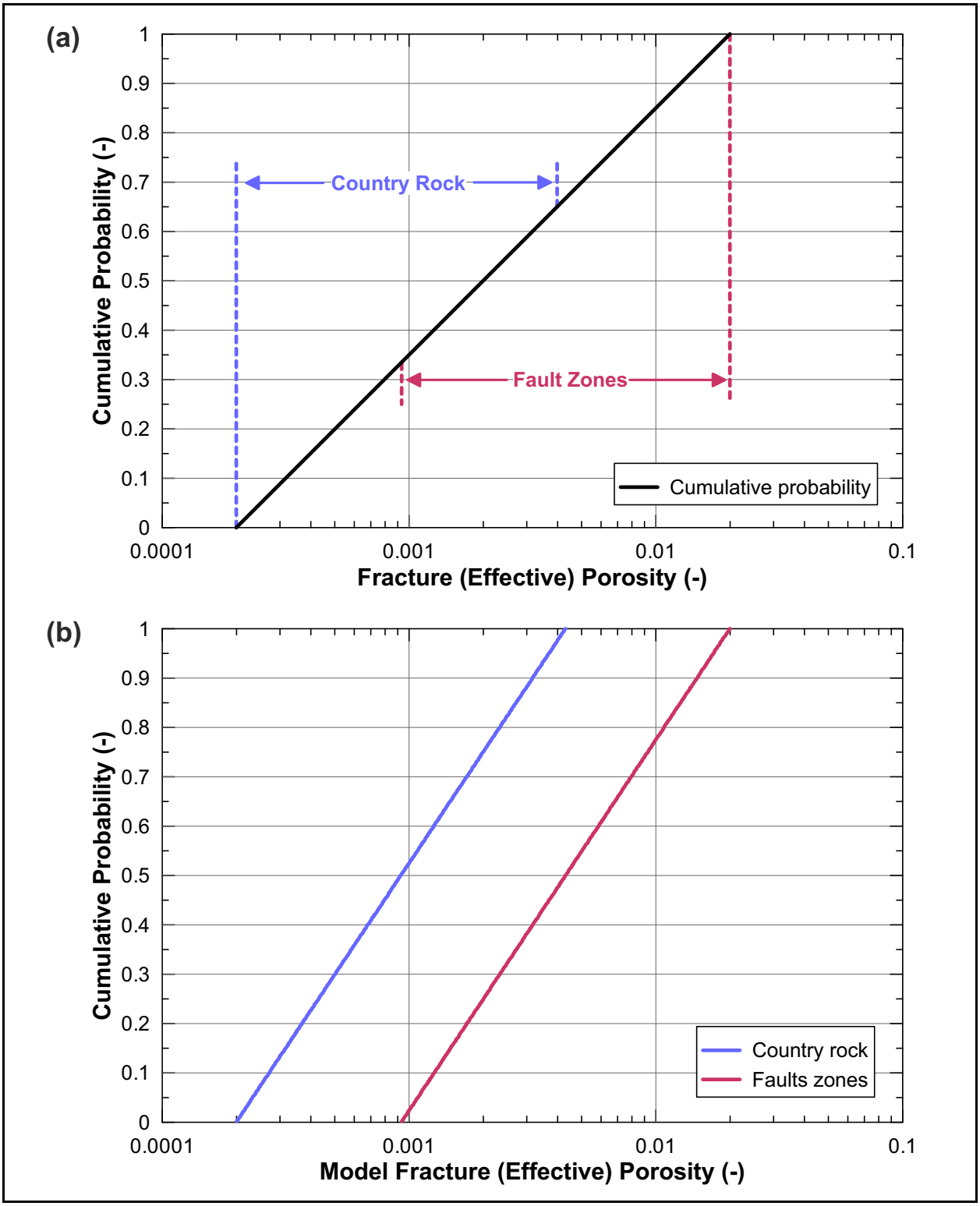

Figure 6-1
Fracture Porosity: (a) Distribution Sampled, and (b) Distribution of the Model Values for the Country Rock and Fault Zones

6.3.1.2 Fracture Aperture

Although fracture aperture can be observed in borehole core and borehole image logs, Berkowitz (2002) states that mechanical measurements of fracture aperture are of little value in characterizing fractures for flow and transport because they do not capture the influence of the internal geometry of the fracture plane on hydraulic resistance to flow and effective fracture aperture for transport. Therefore, fracture aperture was calculated from hydraulic conductivity and fracture spacing by the use of the cubic law as described in Freeze and Cherry (1979):

$$b = (k \times 12 \times s)^{0.333} \qquad (6\text{-}4)$$

where k is the permeability (L^2). This equation requires a permeability. Therefore, the sampled hydraulic conductivities were converted to permeability. The parameter values used for the conversion were a fluid density of 997 kg/m^3, a fluid viscosity of 8.91E-04 kg/(m·s), and a gravitational acceleration of 9.81 m/s. Fracture apertures that are calculated with Equation (6-4) are termed hydraulic fracture apertures.

SNJV (2006b) indicates that hydraulic conductivity data for the LCA in the NNSS investigation area based on 77 pumping-scale aquifer tests can be represented by a lognormal distribution with a mean of 0.16 and a standard deviation of 1.34 in units of meters per day. Because the LCA is conceptualized as having a lower hydraulic conductivity in the country rock than in the fault zones, the lower two-thirds of the hydraulic conductivity distribution was sampled for calculation of the hydraulic fracture aperture in the country rock, and the upper two-thirds was sampled for calculation of the hydraulic fracture aperture in the fault zones (Figure 6-2a). The sampled hydraulic conductivity distributions for the country rock and fault zones are shown in Figure 6-2b.

Calculation of fracture aperture with Equation (6-4) also requires a value for fracture spacing. Available fracture spacing data for the LCA from analyses of borehole image logs conducted in Wells ER-6-1-2 and ER-7-1 (SNJV, 2005b) were used to estimate a single value of fracture spacing for use in the calculation. A cumulative probability distribution of the fracture spacing data from these two wells indicates a spacing of 2.54 m at the 50th percentile (Figure 6-3). This spacing was rounded to a value of 3 m and used along with the sampled hydraulic conductivity values to calculate estimates for hydraulic fracture aperture. Note that this spacing of 3 m was used only for this calculation and is not the fracture spacing used in the LCA transport model. See Section 6.3.1.3 for

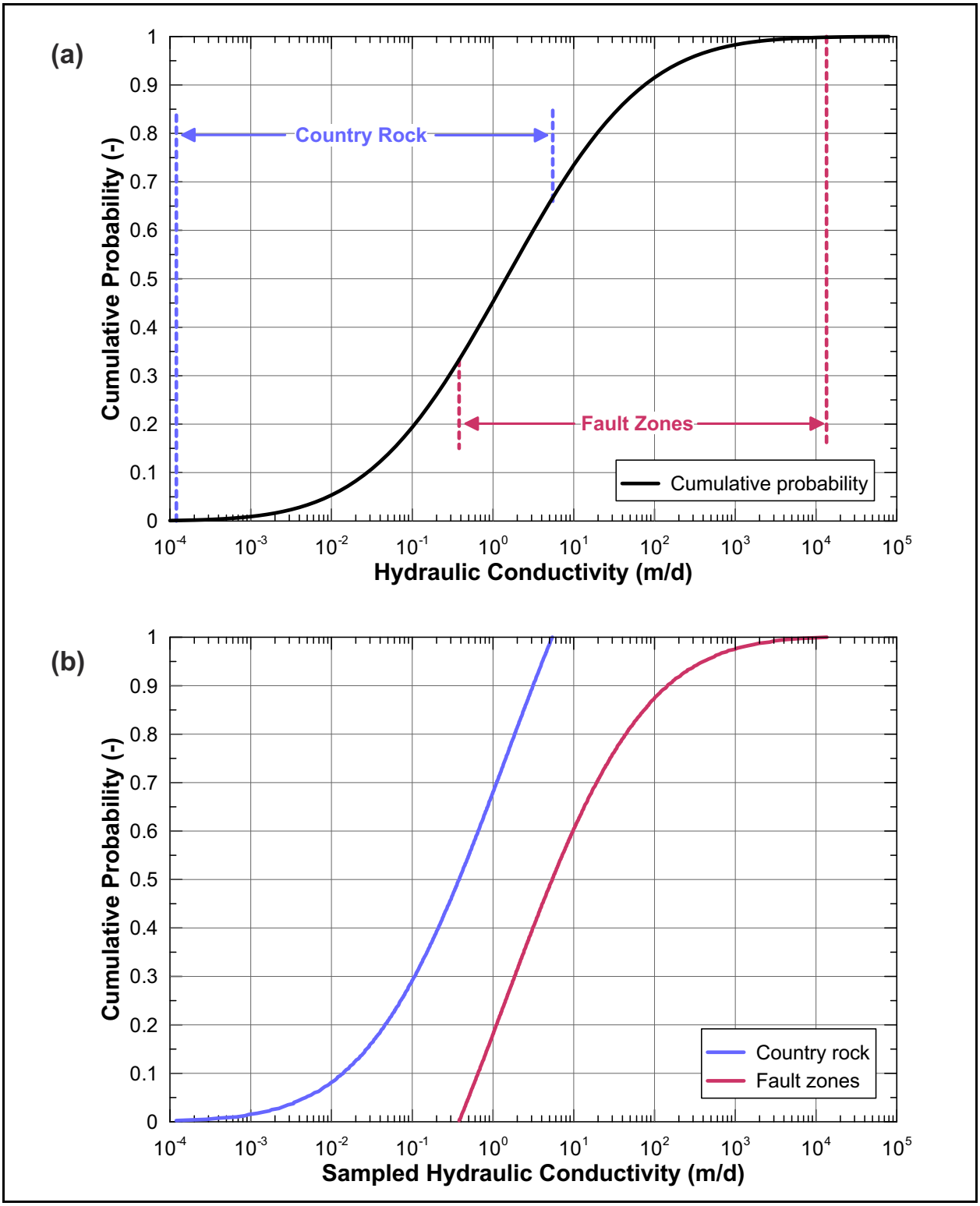

Figure 6-2
Hydraulic Conductivity: (a) Distribution Sampled, and (b) Distribution of the Sampled Values Used to Calculate Hydraulic Fracture Aperture for the Country Rock and Fault Zones

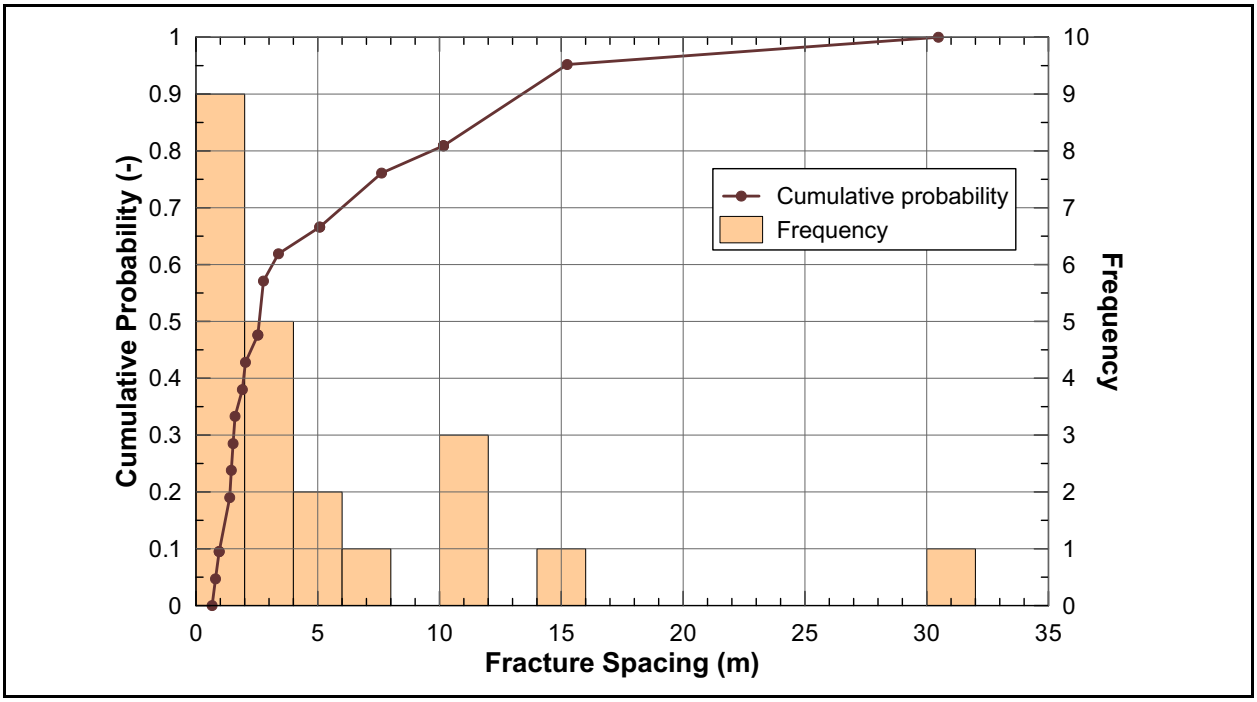

Figure 6-3
Cumulative Probability and Frequency for Fracture Spacing Data in the LCA from Analyses of Borehole Image Logs Conducted in Wells ER-6-1-2 and ER-7-1

the discussion of the fracture spacing distributions that were calculated from the fracture porosity and fracture aperture values and input in the model.

The available fracture spacing data are not sufficient to estimate a different fracture spacing for the fault zones and the country rock. Although the LCA is conceptualized as having more fractures, which corresponds to smaller fracture spacing, in the fault zones than in the country rock, the same value was used to calculate the fracture aperture for the fault zones and the country rock in the base-case model in order to simulate conservative transport in the fault zones. The use of a larger fracture spacing in Equation (6-4) results in larger fracture apertures, and larger fracture apertures lead to larger transport distances. The alternative LCA parameterization simulation uses a smaller fracture spacing in the fault zones than in the county rock for this calculation, as discussed in Section 6.3.6.1, which is more consistent with the LCA conceptualization.

Fracture apertures can also be calculated from the fracture porosity determined from tracer tests and the fracture spacing by applying Equation (6-2). The reason that Equation (6-4) was used to calculate fracture aperture rather than Equation (6-2) is because the underlying dataset for hydraulic conductivity in the LCA is much larger than the underlying dataset for fracture porosities determined

from tracer tests. The hydraulic conductivity dataset is based on 77 pumping-scale aquifer tests, whereas there are only two fracture porosity values determined from a tracer test conducted in the LCA at the ER-6-1 Well Cluster.

A disadvantage of calculating fracture aperture from hydraulic tests and fracture spacing, referred to as the hydraulic aperture, is that this computation method yields values that are consistently lower than those calculated with fracture porosity determined from peak-concentration arrival times from tracer tests and fracture spacing, referred to as the tracer aperture. This difference is a function of the portion of the aperture distribution within the fracture that participates during hydraulic and tracer tests. The effective aperture for hydraulic tests will be most impacted by the smaller aperture regions because those are the areas that offer the most resistance to flow while the arithmetic mean of the fracture apertures controls migration during tracer tests (Tsang, 1992). Tsang (1984) also discusses the reasoning for the larger apertures derived from tracer tests as compared to hydraulic tests. The following paragraphs provide examples of comparisons of hydraulic and tracer fracture apertures from several field investigations and a laboratory experiment. The parameter values and results associated with these comparisons are summarized in Table 6-4.

The difference in magnitude between hydraulic apertures and tracer apertures can be illustrated in the LCA at Yucca Flat based on hydraulic and tracer data from the ER-6-1 Well Cluster. Tracers were injected into ER-6-1-1 and into the upper and lower completion intervals of ER-6-1, and recovered from ER-6-1-2 during the MWAT tracer test (SNJV, 2006b). Data for the tracers injected into ER-6-1-1 exhibited a large amount of noise because of measured concentrations near the detection limit. Therefore, a fracture porosity was not interpreted from those data (SNJV, 2007). Fracture porosities were estimated at 1.7E-02 and 4.7E-03 based on interpretation of breakthrough data for the tracers injected into the upper and lower intervals of ER-6-1 using the peak-concentration arrival time observed in ER-6-1-2. Using those fracture porosities and observed fracture spacings of 2.7 and 1.2 m for the upper and lower intervals in Equation (6-2) yields tracer apertures of 4.6E-02 and 5.7E-03 m for the upper and lower intervals. Hydraulic conductivity data are available along the ER-6-1-2 borehole based on analysis of spinner flow meter log results (SNJV, 2005a). Using those data, a weighted average hydraulic conductivity was calculated for the intervals corresponding to the upper and lower intervals in the tracer test. Using the weighted average hydraulic conductivities and fracture spacings of 2.7 and 1.2 m for the upper and lower intervals in Equation (6-4) yields hydraulic apertures of 1.6E-03 and 1.1E-03 m for the upper and lower intervals. A comparison of the tracer

Table 6-4
Comparison Summary of Hydraulic and Tracer Fracture Apertures Determined from Field Investigations and a Laboratory Experiment

Site	Test Interval or Pathway	Lithology	Spacing (s) [a] (m)	Hydraulic Conductivity (K) [b] (m/s)	Calculated Hydraulic Aperture (b_{hyd}) [c] (m)	Fracture Porosity (ϕ_f) [d]	Calculated Tracer Aperture (b_{tr}) [e] (m)	Calculated Aperture Ratio [f]
ER-6-1 Well Cluster	Upper	LCA	2.7	1.2E-03	1.6E-03	1.7E-02	4.6E-02	29
	Lower	LCA	1.2	9.9E-04	1.1E-03	4.7E-03	5.7E-03	5
BULLION	ER-20-6-1 to ER-20-6-3	LFA	3	2.3E-05	4.4E-04	6.8E-03	2.0E-02	45
	ER-20-6-2 to ER-20-6-3	LFA	3	1.5E-05	3.8E-04	4.9E-03	1.5E-02	39
C-holes	Lower Bullfrog Tuff	Tuff	3	5.2E-04	1.2E-03	3.0E-03	9.0E-03	8
	Prow Pass Tuff	Tuff	3	2.2E-05	4.3E-04	1.8E-03	5.4E-03	13
WIPP	H-3b1 to H-3b3	Dolomite	1.23	3.4E-07	6.4E-05	1.9E-03	1.2E-03	19
	H-6b to H-6a	Dolomite	0.41	5.1E-06	1.1E-04	3.1E-03	6.4E-04	6
	H-11b3 to H-11b1	Dolomite	0.32	4.1E-06	9.3E-05	1.0E-03	1.6E-04	2
Kamaishi mine	Single fractures	Granodiorite	NR [g]	NR [g]	NR [g]	NR [g]	2E-04 to 1E-03	~10
Laboratory experiments	Three synthetic single fractures	N/A	N/A	N/A	4.0E-04 to 6.0E-04	NR [h]	7.9E-04 to 1.93E-03	2.0 to 3.2

[a] Site-specific value or assumed value of 3 m.
[b] Source is hydraulic-test interpretations.
[c] Calculated as $b_{hyd} = (12 \times s \times K\mu/\rho g)^{1/3}$ using K from hydraulic testing.
[d] Value interpreted from tracer-peak arrival time.
[e] Calculated as $b_{tr} = \phi_f \times s$ using ϕ_f from tracer test.
[f] Calculated as b_{tr}/b_{hyd}.
[g] Not reported in Sawada et al. (2001).
[h] Not reported in Zheng et al. (2008).

Note: Data derived from non-QAPP compliant analyses are used for corroboration only; they are not directly relied upon for developing the tracer aperture to hydraulic aperture ratio comparison in the Yucca Flat analysis.

LFA = Lava-flow aquifer
N/A = Not applicable
NR = Not reported

apertures and hydraulic apertures indicates that the tracer aperture is larger than the hydraulic aperture by a factor of about 29 for the upper interval and about 5 for the lower interval (Table 6-4).

The ER-6-1 MWAT tracer test provides a unique data set to define the tracer to hydraulic fracture aperture ratio for use in the LCA transport model. However, these data which are representative of the fault damage zone in the vicinity of ER-6-1 are not expected to be representative of the LCA country rock away from fault damage zones. To evaluate the range of tracer to hydraulic aperture ratios potentially applicable to the undamaged LCA country rock, additional *in situ* and laboratory investigations were reviewed. These data are analyzed in the following paragraphs to inform the assumed distribution of this ratio. While it is recognized that these are not Yucca Flat or LCA specific data sets, they provide useful insights into the possible range of aperture ratios.

A comparison of hydraulic and tracer apertures can be made at several other locations including the lava-flow aquifer near BULLION, a fractured volcanic tuff at the Yucca Mountain C-holes Complex, the fractured Culebra dolomite at the WIPP site in New Mexico, and a fractured granodiorite in Japan. Tracer transport data are available for two travel paths from the BULLION forced-gradient experiment (IT, 1998). Both paths are aligned with the orientation of the major fracture system, with the path from ER-20-6-2 to ER-20-6-3 being about two-thirds as long as the path from ER-20-6-1 to ER-20-6-3. Fracture spacing data are not available for the lava-flow aquifer at this site, so a value of 3 m was used based on analogy with other site information. Using the fracture porosities calculated from the peak arrival times for the tracers and a fracture spacing of 3 m yields tracer fracture apertures of 2.0E-02 and 1.5E-02 m for the long and short travel paths, respectively. The hydraulic conductivity for each tracer injection well was estimated as the average of the available transmissivity data divided by the gravel pack thickness. Using those values and a fracture spacing of 3 m yields hydraulic fracture apertures of 4.4E-04 and 3.8E-04 m for the far and near injection wells, respectively. A comparison of the calculated apertures from the BULLION forced-gradient experiment indicates that the tracer apertures are a factor of about 45 and 39 larger than the hydraulic apertures for the long and short travel paths, respectively (Table 6-4).

Tracer tests were conducted in the lower Bullfrog Tuff and Prow Pass Tuff at the C-holes Complex at the Yucca Mountain site. Fracture spacing data are not available for these formations at the C-holes Complex, so a value of 3 m was used based on analogy with other site information. Using the fracture porosity calculated from the tracer peak arrival times and a fracture spacing of 3 m yields tracer

fracture apertures of 9.0E-03 and 5.4E-03 m for the lower Bullfrog Tuff and Prow Pass Tuff, respectively. Minimum and maximum hydraulic conductivities are available for these two formations at the C-holes Complex (Bechtel SAIC, 2004). Using the arithmetic average of those values and a fracture spacing of 3 m yields hydraulic fracture apertures of 1.2E-03 and 4.3E-04 m for the lower Bullfrog Tuff and Prow Pass Tuff, respectively. The differences between the tracer and hydraulic fracture apertures at this site are a factor of 8 based on data for the lower Bullfrog Tuff and a factor of 13 based on data for the Prow Pass Tuff (Table 6-4).

Numerous tracer tests have been conducted in the Culebra dolomite member of the Rustler Formation at the WIPP site in New Mexico. SNJV (2007) calculated fracture porosities at three of these sites using the peak tracer arrival times along the fastest transport paths. Using these fracture porosities and site-specific fracture spacings reported in Jones et al. (1992) yields calculated tracer fracture apertures of 1.2E-03 m at the H-3 hydropad, 6.4E-04 m at the H-6 hydropad, and 1.6E-04 m at the H-11 hydropad. Transmissivity and average Culebra thickness data are available for each hydropad in Cauffman et al. (1990) and Jones et al. (1992), respectively. Those data were used to calculate a hydraulic conductivity for each hydropad. Using those values and the site-specific fracture spacing data yields hydraulic fracture apertures of 6.4E-05, 1.1E-04, and 9.3E-05 m at the H-3, H-6, and H-11 hydropads, respectively. A comparison of the calculated apertures for each hydropad shows that the tracer fracture apertures are larger than the hydraulic fracture apertures by a factor of 2 to 19 (Table 6-4).

Sawada et al. (2001) conducted hydraulic and tracer tests in the fractured granodiorite of the Kamaishi mine in Japan. Tracer tests conducted in two isolated, single fractures yielded tracer fracture apertures of 2E-04 and 1E-03 m. They also calculated the hydraulic fracture apertures for these two fractures from the observed flow rates using the cubic law. Although Sawada et al. (2001) do not report the values they calculated for the hydraulic apertures, they state that a comparison of the hydraulic and tracer apertures indicated that the tracer fracture apertures are about a factor of 10 larger than the hydraulic fracture apertures (Table 6-4).

Zheng et al. (2008) conducted an investigation of hydraulic and tracer fracture apertures and presented a comparison of apertures for laboratory experiments on each of three synthetic fractures at three flow rates. The ratios of tracer fracture aperture to hydraulic fracture aperture ranged from 2.0 to 3.2 with the ratio increasing with larger flow rates. They concluded that the tracer

aperture (termed the mass balance aperture) is the only equivalent aperture appropriate for describing solute transport in single variable-aperture fractures (Table 6-4).

Because the hydraulic apertures reflect the small aperture regions that control hydraulic responses, they are not representative for modeling solute transport. Solute transport will be a function of the mean fracture apertures, which are better reflected by tracer fracture apertures. Therefore, an aperture multiplier was applied to the hydraulic apertures calculated using Equation (6-4) to obtain tracer apertures for input to the transport model. A triangular distribution for the aperture multiplier was used with minimum, most likely, and maximum values of 2, 5, and 10, respectively, for the country rock, and 5, 10, and 20, respectively, for the fault zones (Table 6-1). A larger range was selected for the fault zones distribution than for the country rock distribution because the fault zones are considered to not only have more fractures than the country rock but also have larger variability in fracture apertures than the country rock. The range in the aperture multiplier for the fault zones is consistent with the range found for Well ER-6-1, which has a hydraulic conductivity that falls near the upper end of the sampled hydraulic conductivities for the fault zones. This comparison suggests that the selected aperture multiplier range is appropriate for the fault zones.

In summary, the development of fracture apertures for the Yucca Flat LCA transport model involved using several steps. Note that each of these steps was conducted separately for the fault zones and the country rock. First, the hydraulic conductivity distribution was sampled. Second, hydraulic apertures were calculated with Equation (6-4), and the sampled hydraulic conductivities and a fracture spacing of 3 m. Third, the aperture multiplier was sampled. Fourth, tracer apertures were calculated as the hydraulic aperture multiplied by the sampled aperture multiplier. The calculated tracer fracture apertures were then used in the Yucca Flat LCA transport model. For each of the 400 model realizations developed from the sampling, one fracture aperture is used throughout the entire extent of the fault zones in the model, and another single fracture aperture is used throughout the entire extent of the country rock in the model. The resultant aperture distributions used in the model are shown in Figure 6-4a, and the relationship between apertures in the faults zones and apertures in the country rock in the 400 model realizations is shown in Figure 6-4b. This latter plot shows that, in general, the fracture apertures for the fault zones, which range from 1.6E-03 to 7.9E-02 m, are around a half order of magnitude larger than the fracture apertures for the country rock, which range from 1.0E-04 to 5.4E-03 m. A scatterplot of the fracture porosity and fracture aperture in the country rock and fault zones for the model realizations is shown in Figure 6-5. The scatterplot shows the paired values for

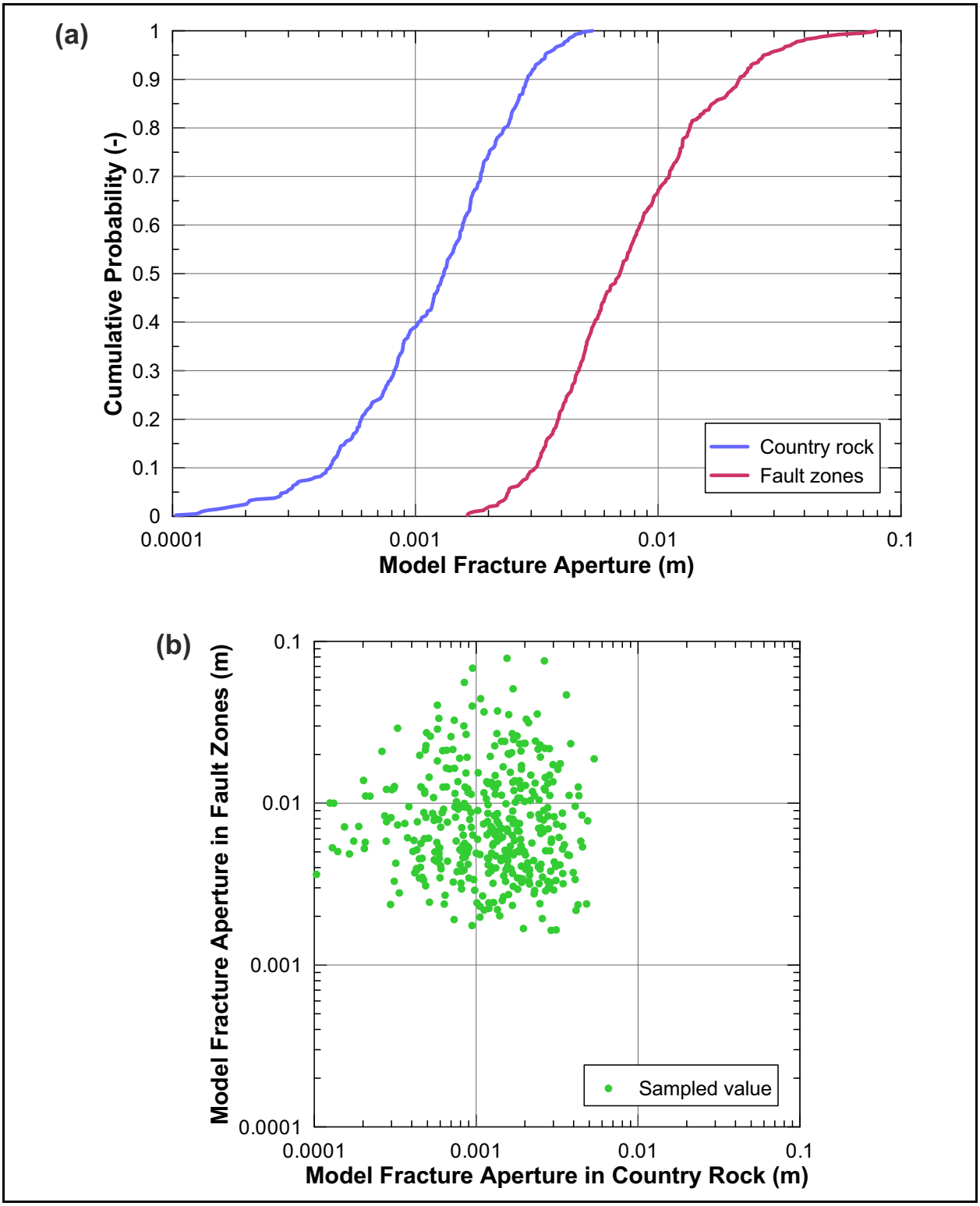

Figure 6-4
Fracture Aperture: (a) Distribution of Model Values for the Country Rock and Fault Zones, and (b) Scatterplot of Paired Model Values in the Country Rock and Fault Zones for the 400 Realizations

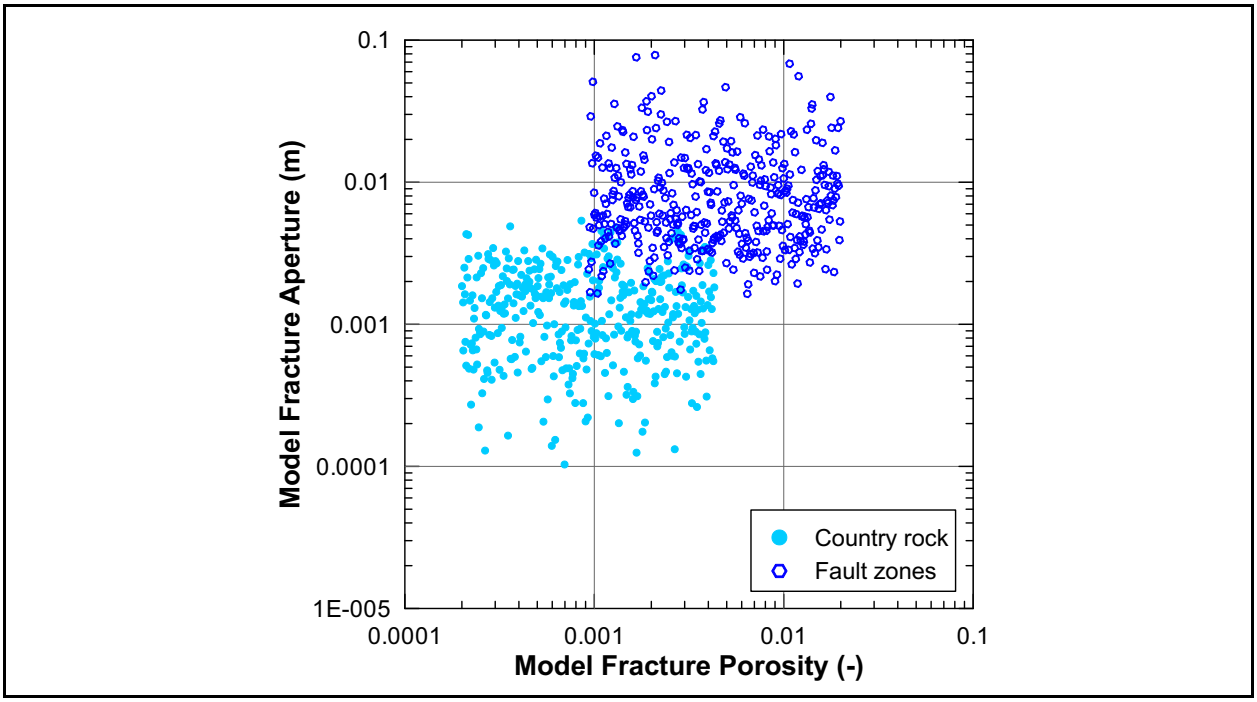

Figure 6-5
Scatterplot of Model Fracture Aperture and Model Fracture Porosity for the Country Rock and Fault Zones for the 400 Realizations

the fracture aperture and fracture porosity in the country rock for the 400 model realizations as solid light-blue circles, and the paired values for the fracture aperture and fracture porosity in the fault zones for the 400 model realizations as open dark-blue circles. Each circle represents the paired values for one realization. Therefore, there are 400 circles for the country rock and 400 circles for the fault zones.

The major limitations associated with the fracture aperture distribution for the LCA at Yucca Flat are a function of the limitations in quantification of the parameters used to calculate the aperture. In summary, these are the hydraulic conductivity and fracture spacing used to calculate the hydraulic aperture and the aperture multiplier used to calculate the tracer aperture. Limitations in the hydraulic conductivity data are discussed in SNJV (2006a) and include the following: data are available for a limited number of locations scattered across the investigation area, and as such, complete, comprehensive characterization across the extent of the Yucca Flat model area is not provided, and there is a sampling bias toward more productive testing intervals. In fractured media, bias is also introduced because the tested portion of the formation does not intersect all fractures that participate in regional-scale flow.

A limitation in the fracture spacing data is the inability to collect data consistent with the scale of the pumping tests that yield the hydraulic conductivity data. Fracture spacing data have been obtained at the NNSS in two ways: observations from borehole cores, and analysis of borehole image logs. Both of these methods are subject to inaccuracies because of damage to cores and borehole walls as a result of the coring and/or drilling process. In addition, these types of data are only available at a few locations and do not provide comprehensive coverage of the entire LCA at Yucca Flat. Observations in outcrops allow more detailed areal evaluation but are not likely representative of the rock fracturing at depth. In addition, an analysis of spinner flow log data and borehole image log data showed limited or no correlation between the most productive intervals in a borehole and observed fractures (see Appendix J). Fracture spacing data are also limited by four biases that affect estimation of fracture size and frequency through data collection: length bias, orientation bias, truncation bias, and censoring (Berkowitz, 2002). Small fractures will be underrepresented, as there is a lower probability of intersecting smaller fractures than larger fractures (length bias). Fractures parallel to the sampling plane will also be underrepresented (orientation bias). Fractures shorter than a predetermined length are usually not mapped (truncation bias). A censoring bias is introduced because the sample area is finite, and the fracture traces may not be completely visible (Baecher et al., 1977). Unfortunately, censoring bias is most important for longer fractures, which are assumed to be the more conductive fractures.

Limitations in the aperture multiplier distributions are related to a limited amount of data with which to quantify the difference between the hydraulic and tracer apertures. Data are available from several field tests and one laboratory experiment that clearly show larger fracture tracer apertures than hydraulic apertures. Only one of these tests was conducted in the LCA at Yucca Flat and, therefore, does not provide comprehensive coverage for the entire LCA at Yucca Flat.

These limitations result in uncertainty associated with the fracture aperture used in the model. In an effort to incorporate this uncertainty in the simulation results, distributions of hydraulic conductivity and the aperture multiplier were used along with multiple simulations using different values from the distributions.

Simulated matrix diffusion decreases and fracture transport increases as fracture aperture increases. Therefore, the large fracture apertures developed for the fault zones in the base-case simulation are consistent with the objective of biasing the results to more significant fracture transport than matrix

diffusion. Less conservative fracture apertures for the fault zones are used in the alternative LCA parameterization simulation as discussed in Section 6.3.6.1.

6.3.1.3 Fracture Spacing

Fracture spacing is not a direct input parameter for the PLUMECALC simulations. However, the fracture spacing is an inherent component of the simulations because of its relationship to the fracture input parameters through the mathematical representation given by Equation (6-2). Therefore, the fracture spacing values associated with the input values for fracture porosity and fracture aperture were calculated.

The fracture spacing parameter affects the estimation of mass transfer from the fractures to the matrix by defining the volume of storage for solutes diffusing into the matrix and the surface area across which diffusion occurs. The fracture spacing distributions for the country rock and fault zones associated with the model input values of fracture porosity and fracture aperture are shown in Figure 6-6a, and a scatterplot of fracture spacing in the country rock versus fracture spacing in the fault zones for the 400 model realizations is shown in Figure 6-6b. Both of these figures show that the fracture spacing for the country rock and fault zones is similar, with the overall distribution of fracture spacing in the fault zones slightly larger than in the country rock.

Fracture spacing that is larger in the fault zones than in the county rock is inconsistent with the conceptualization that the more highly fractured fault zones have smaller fracture spacing than the county rock. Use of input parameter values that correspond to larger fracture spacing in the fault zones provides for conservatism in the base-case simulation because it results in less matrix diffusion and greater transport than if input parameter values that correspond to smaller fracture spacing were used. The impact of using input parameter values that correspond to smaller fracture spacing in the fault zones than in the country rock consistent with the conceptualization of the LCA is assessed with the alternative LCA parameterization simulation. The fracture parameters for the alternative LCA parameterization simulation are discussed in Section 6.3.6.1. Scatterplots of the fracture aperture and fracture spacing, and fracture porosity and fracture spacing, in the country rock and fault zones for the 400 model realizations are shown in Figures 6-7 and 6-8, respectively. In both figures, the values for the country rock are given by solid light-blue circles, and the values for the fault zones are given by open dark-blue circles. Each circle shows the paired values for one realization. Both figures illustrate that the range of fracture spacing for the 400 realizations is about the same for the country rock and

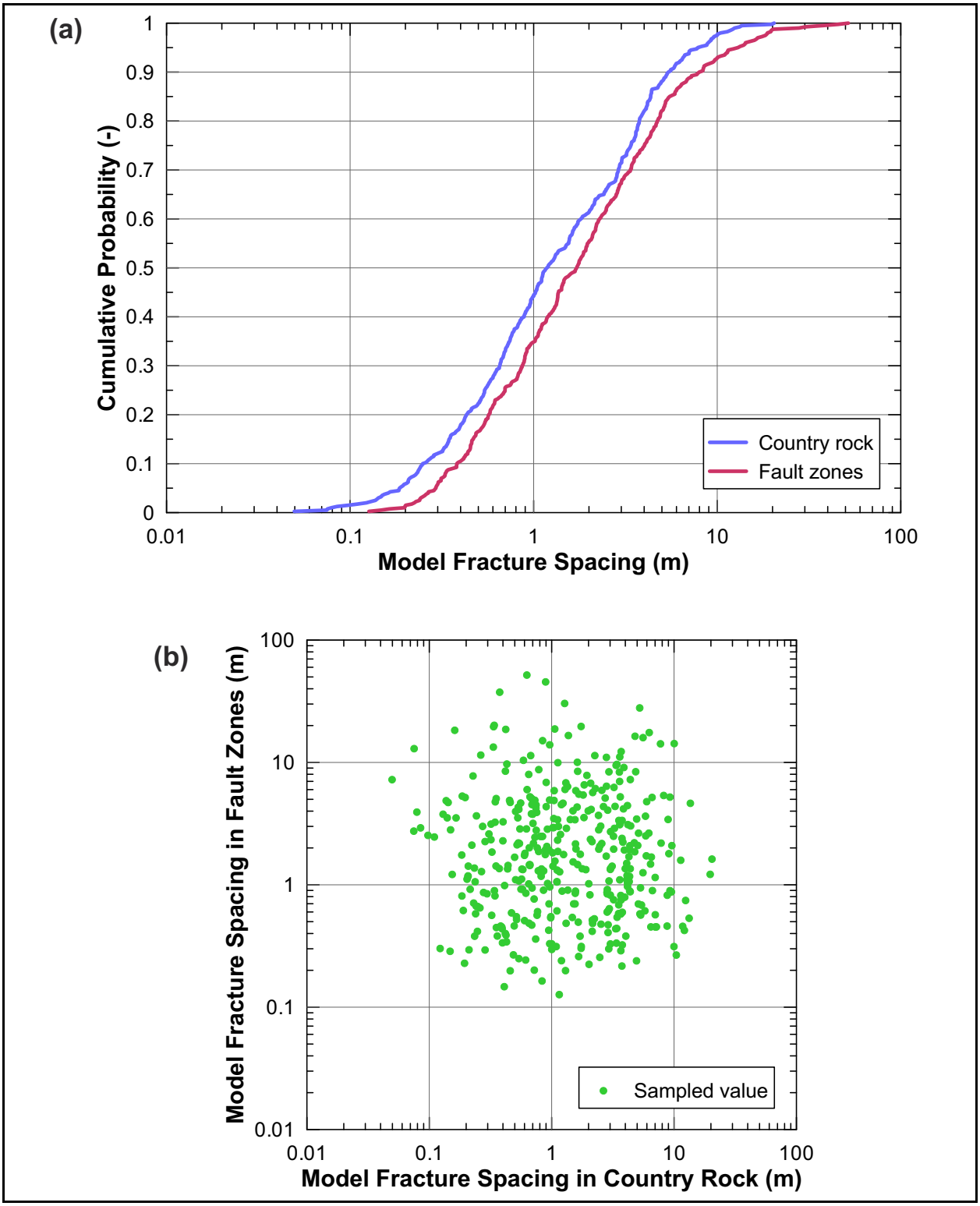

Figure 6-6
Fracture Spacing: (a) Distribution of Model Values for the Country Rock and Fault Zones, and (b) Scatterplot of Model Values in the Country Rock and Fault Zones for the 400 Realizations

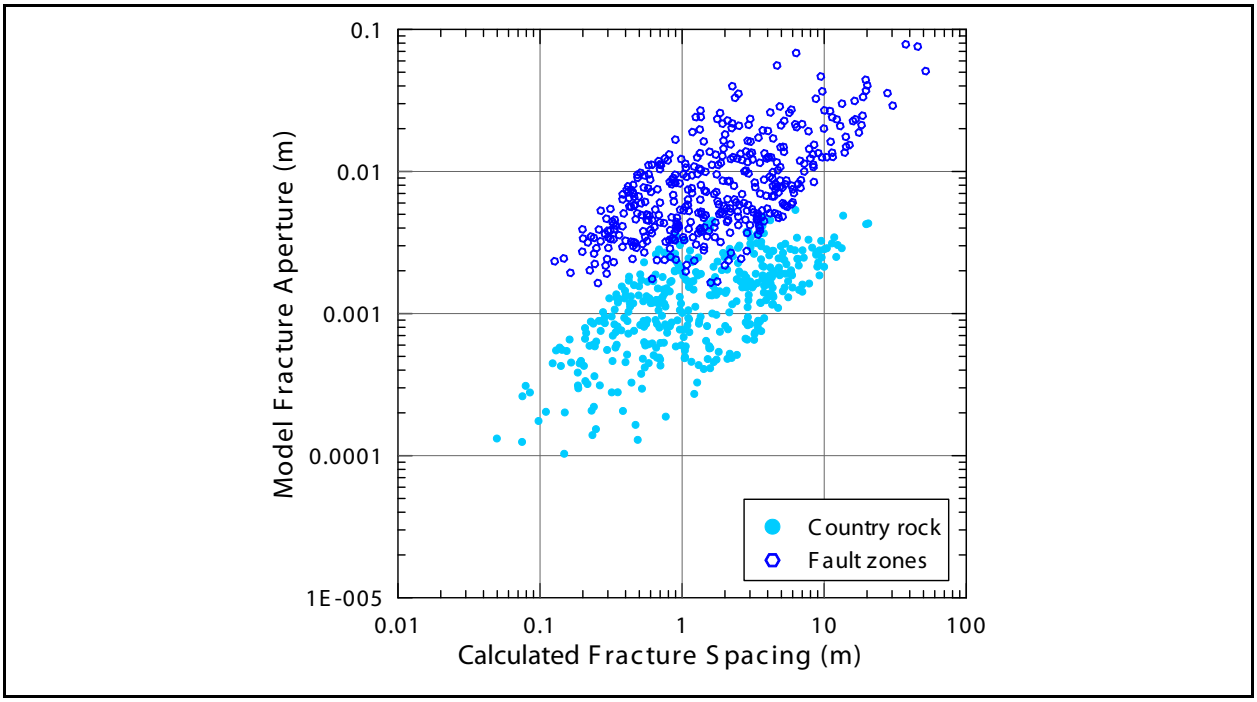

Figure 6-7
Scatterplot of Model Fracture Aperture and Calculated Fracture Spacing for the Country Rock and Fault Zones for the 400 Realizations

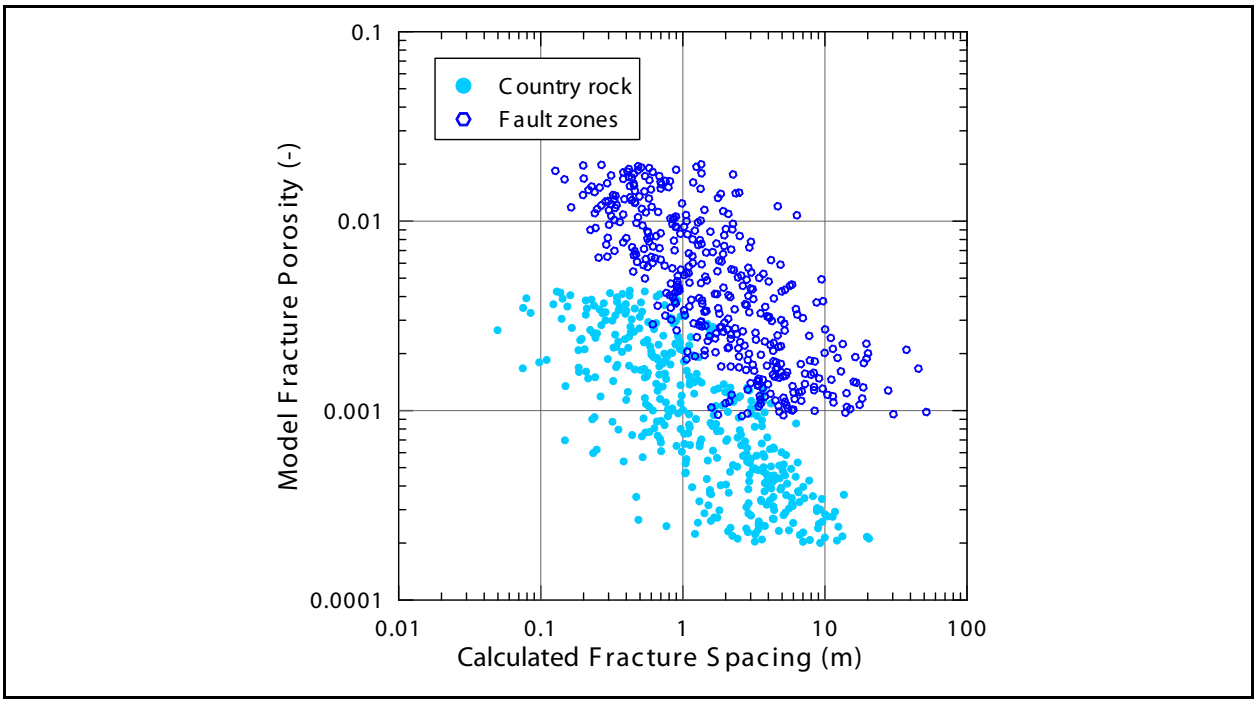

Figure 6-8
Scatterplot of Model Fracture Porosity and Calculated Fracture Spacing for the Country Rock and Fault Zones for the 400 Realizations

fault zones. Figure 6-7 shows that the fracture aperture values for the fault zones are generally about an order of magnitude larger than those for the country rock, and Figure 6-8 shows that the fracture porosity values for the fault zones are generally about half an order of magnitude larger than those for the country rock.

Across the CAU scale of the model, the actual fracture spacing in the LCA will be heterogeneous in both the lateral and vertical directions. Obtaining observed data on fracture spacing that capture this heterogeneity would require extensive data collection at spatial scales that are impractical. In addition, the conceptual model for representing fractures consists of a single set of parallel fractures. This conceptualization requires the use of one fracture spacing for the country rock and one fracture spacing for the fault zones throughout the entire model domain for each model realization. Consequently, heterogeneity cannot be incorporated into the individual model runs beyond the difference in spacing between the fault zones and country rock. The wide range in fracture spacing calculated for the model realizations (about 0.05 to 20 m for the country rock, and about 0.1 to 52 m for the fault zones) is designed to incorporate the effects of heterogeneity in fracture spacing on simulated transport results.

The limitations in fracture spacing are derived from the limitations in fracture porosity (Section 6.3.1.1) and fracture aperture (Section 6.3.1.2) from which fracture spacing was calculated. Another limitation in fracture spacing is a function of representing the fracture system assuming a single set of parallel fractures. For this assumption, the fracture parameters of porosity, aperture, and spacing are related as shown in Equation (6-2). Rearranging this equation gives

$$s = \frac{b}{\phi_f} \tag{6-5}$$

The LCA is conceptualized as consisting of fault zones and the country rock, with the fault zones being more highly fractured than the country rock. Because the fault zones are considered to be more fractured, the fracture porosity will be higher in the fault zones than in the country rock. The conceptualization used here also assumes that the fractures in the fault zones will be larger than those in the country rock because of the greater tectonic deformation, and therefore, will have larger apertures. For the condition that the fracture porosity and fracture aperture are higher in the fault zones than in the country rock, the fracture spacing calculated for the fault zones using Equation (6-5) will also be higher than that calculated for the country rock. This result is inconsistent with the conceptualization that the fault zones are more fractured, which would be represented by a smaller

fracture spacing. Because there was an overlap in the portion of the distribution sampled for the fault zones and country rock fracture porosity (Section 6.3.1.1), and hydraulic conductivity and aperture multiplier (Section 6.3.1.2), the calculated fracture spacing for the fault zones is smaller than that for the country rock for 42 percent of the realizations. For the other 58 percent of the realizations, the fracture spacing in the fault zones is larger than that in the country rock. Overcoming this limitation would require modeling the fractures in the LCA using a very complex discrete fracture network modeling approach where the geometry of each fracture in the fault zones and country rock is explicitly defined. However, the ability to develop such a model is not supported by the available data.

The approach to incorporating fracture spacing into models of the Yucca Mountain site consisted of using flowing interval spacing rather than fracture spacing (Bechtel SAIC, 2004). Flowing intervals or features were defined using results of borehole flowmeter surveys, and each flowing interval was assumed to consist of a single fracture. This was done because the number of fractures in the flowing intervals was unknown and the flowing interval spacing was less than an order of magnitude smaller than the model grid block size. This approach underestimates the effects of matrix diffusion because it represents a network of fractures in a flowing feature as a single fracture, thus, significantly reducing the surface area across which matrix diffusion occurs, and effectively reducing the amount of accessible storage in the matrix in a performance period of interest. For this reason, using a similar approach of assigning the flowing feature spacing as the fracture spacing was not considered appropriate for the Yucca Flat LCA transport model. Evaluation of the impact of flowing features is discussed later in the context of defining parameters for the alternative LCA parameterization simulation (see Section 6.3.6).

6.3.1.4 Summary Discussion of Fracture Parameters

The conceptualization of the fracture parameters and development of the input distributions honor the interrelationship between fracture porosity, fracture aperture, and fracture spacing as given by Equation (6-2). Distributions were developed for the PLUMECALC input parameters fracture porosity and fracture aperture. The associated fracture spacing values were also calculated. The parameterization approach developed was based on results/analyses of field tracer and hydraulic tests, and was designed to be conservative by biasing results to more significant fracture transport and less matrix diffusion.

The hydraulic and tracer test results/analyses provided the data from which a distribution of fracture porosity was developed. The upper two-thirds of that distribution was sampled for the fault zones, and the lower two-thirds was sampled for the country rock. The tracer test results/analyses also provided insight into development of the distributions for the fracture aperture multiplier.

Analyses of hydraulic tests provided the data from which a distribution of hydraulic conductivity was developed. The hydraulic conductivity distribution was necessary because it provided the underlying data from which the fracture aperture was developed. The upper two-thirds of the hydraulic conductivity distribution was sampled for the fault zones, and the lower two-thirds was sampled for the country rock. A hydraulic fracture aperture was calculated from the hydraulic conductivity and a fracture spacing of 3 m. The tracer fracture apertures used in the model were calculated from the hydraulic apertures using the sampled aperture multipliers.

6.3.2 Matrix Porosity

In a double-porosity medium, solutes diffuse from the fractures into the matrix where the matrix porosity provides the storage in immobile matrix water for the diffusing solutes. The matrix porosity was considered to be the same for the fault zones and the country rock because the mechanisms that produce faulting are not expected to alter the unfractured (matrix) portion of the LCA.

The observed matrix porosity data for the LCA can be represented by a normal distribution with a mean of 0.0264 and a standard deviation of 0.0163 (SNJV, 2007). In order to avoid sampling negative porosities or porosities higher than expected for the LCA at Yucca Flat, the sampled distribution was truncated at the minimum and maximum observed values of 0.0035 and 0.0595, respectively (SNJV, 2007). The resultant distribution of sampled model values for matrix porosity is shown in Figure 6-9.

6.3.3 Matrix Diffusion Coefficient Parameters

Matrix diffusion has the effect of attenuating the concentration and increasing the travel time of solute contaminants moving through saturated fractured rock. The matrix diffusion process involves the diffusion of contaminants out of flowing water in fractures and into the relatively stagnant or immobile water in the pores of the surrounding matrix (and vice versa).

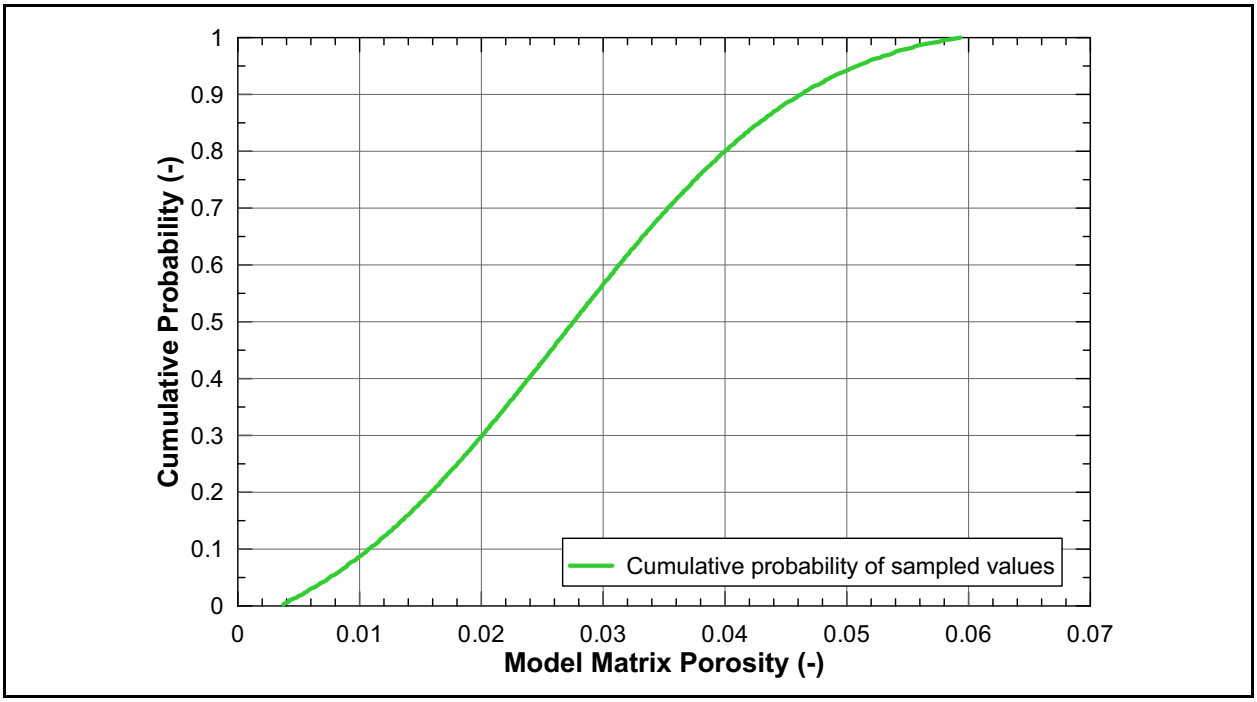

Figure 6-9
Distribution of Model Values of Matrix Porosity

From a numerical modeling perspective, the product of the matrix porosity and matrix diffusion coefficient effectively serves as a lumped parameter to account for matrix diffusion. The matrix diffusion coefficient is directly related to the tortuosity of the porosity media and the solute free-water diffusion coefficient using the relationship presented in Bear (1972) and Freeze and Cherry (1979):

$$D_m = \tau D_o \qquad (6\text{-}6)$$

where
D_m = matrix diffusion coefficient (L^2/t)
τ = matrix tortuosity (unitless)
D_o = solute free-water diffusion coefficient (L^2/t)

The following subsections discuss these two parameters that are used to calculate the matrix diffusion coefficient.

6.3.3.1 Matrix Tortuosity

Tortuosity can be defined as a bulk measure of the constrictive and tortuous nature of the interconnected pore space through which diffusion occurs. These factors result in variation in pore channel diameters and path lengths as the diffusing solute migrates through the interconnected

porosity. Smaller tortuosities are indicative of longer diffusional path lengths and greater resistance to diffusion through the medium. Typically, a relationship can be found between tortuosity and porosity, which is advantageous because porosity data are oftentimes more readily available than tortuosities or matrix diffusion coefficients. Therefore, the tortuosity and porosity data for carbonate rock presented in SNJV (2007) were investigated for developing a tortuosity-porosity functional relationship for the Yucca Flat LCA model.

The porosity and tortuosity data from laboratory tracer diffusion experiments in carbonate rock as provided in SNJV (2007) are shown in Figure 6-10. The diffusion experiments for these data are documented in Hershey et al. (2003) and Reimus et al. (2006). The tortuosity values from the Hershey et al. (2003) experiments appear to be uncharacteristically large for the low-porosity rock samples (Figure 6-10) in comparison to other diffusion cell experiments on LCA samples and from other diffusion experiments published in the literature. A review of Hershey et al. (2003) indicates that the diffusion cells were set on a vibrating platform that was operated daily for 15 minutes to keep the reservoir solution mixed. Vibration of the diffusion cells was not a component of the experiments documented in Reimus et al. (2006). Potentially, the vibration in the Hershey et al. (2003) experiments may have enhanced tracer migration and resulted in the larger interpreted tortuosities. Therefore, the data from Hershey et al. (2003), displayed as open purple circles in Figure 6-10, were not included in the dataset from which the tortuosity-porosity relationship for the LCA at Yucca Flat was developed.

Reimus et al. (2006) present results for diffusion experiments on wafers from LCA core samples with fluorobenzoate and halide tracers. Development of matrix diffusion parameters in SNJV (2007) considered results from one flourobenzoate tracer and one halide tracer. Therefore, the data from Reimus et al. (2006) plotted in Figure 6-10 contain two tortuosity values, one for each tracer, associated with each porosity value. A review of Figure 6-10 shows that the data from Reimus et al. (2006) indicate a large range in tortuosity for the experiments on the samples with the lowest porosities (i.e., porosities of 0.009 to 0.013). In addition, the data with the lowest tortuosities (i.e., log values less than –1.5) associated with the lowest porosity samples show good correlation with the tortuosity data for samples with higher porosities (i.e., greater than 0.03). Therefore, the Reimus et al. (2006) data for samples with the higher tortuosities of greater than –1.5 and the lower porosities of 0.013, shown as solid purple circles in Figure 6-10, were not considered when the tortuosity-porosity relationship was developed. Omitting these data for development of the

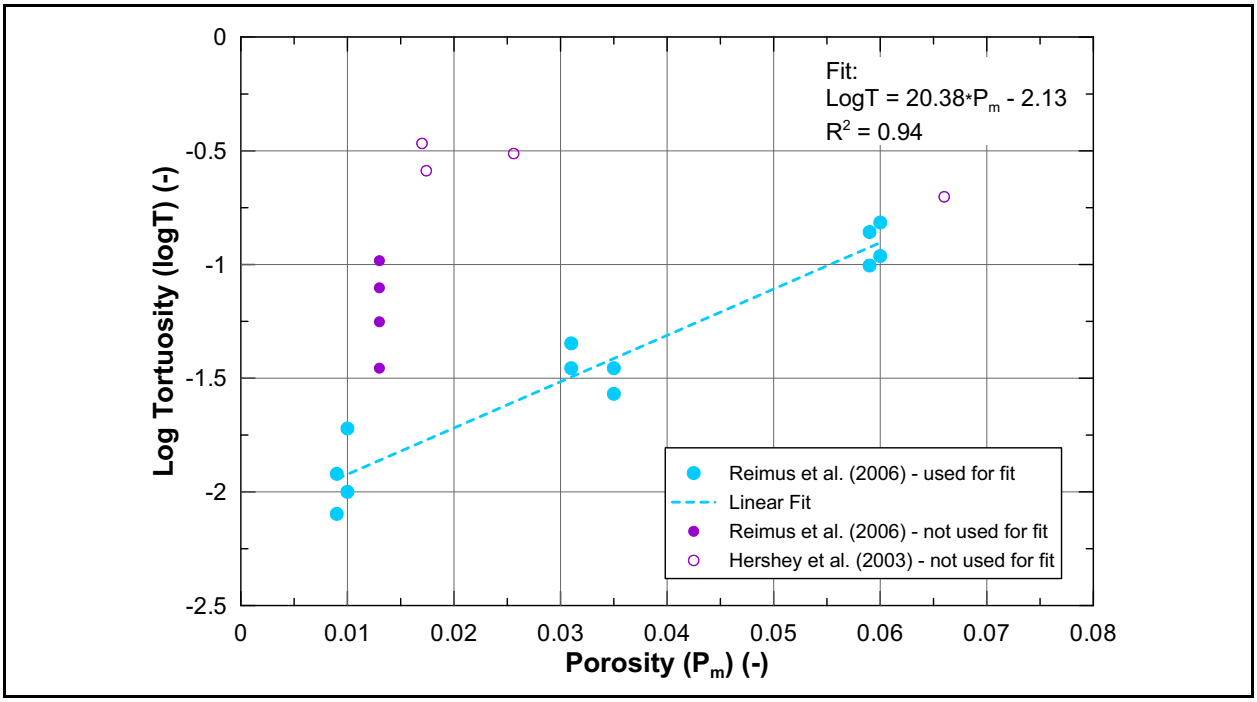

Figure 6-10
Log Tortuosity versus Porosity from Laboratory Tracer Diffusion Experiments in Carbonate Rock

porosity-tortuosity relationship is consistent with the assumption that lower tortuosities are expected at lower porosities. Using the remaining data from Reimus et al. (2006), shown as solid blue circles in Figure 6-10, results in a correlation between tortuosity and matrix porosity of

$$\text{Log } \tau = 20.38\phi_m - 2.13 \qquad (6\text{-}7)$$

where

ϕ_m = matrix porosity (unitless)

Using this correlation, shown as a dashed line in Figure 6-10, the matrix tortuosity was calculated from the sampled matrix porosity. The resultant distribution of calculated matrix tortuosities for the Yucca Flat LCA model is as illustrated in Figure 6-11 and ranges from a minimum of 0.0088 to a maximum of 0.12.

6.3.3.2 Free-Water Diffusion Coefficients

The free-water diffusion coefficient is a function of fluid temperature and the ionic radius of the solute. While it is possible to have a discrete value for each radionuclide simulated with the Yucca Flat LCA model, the approach taken here is similar to that adopted in the Frenchman Flat transport

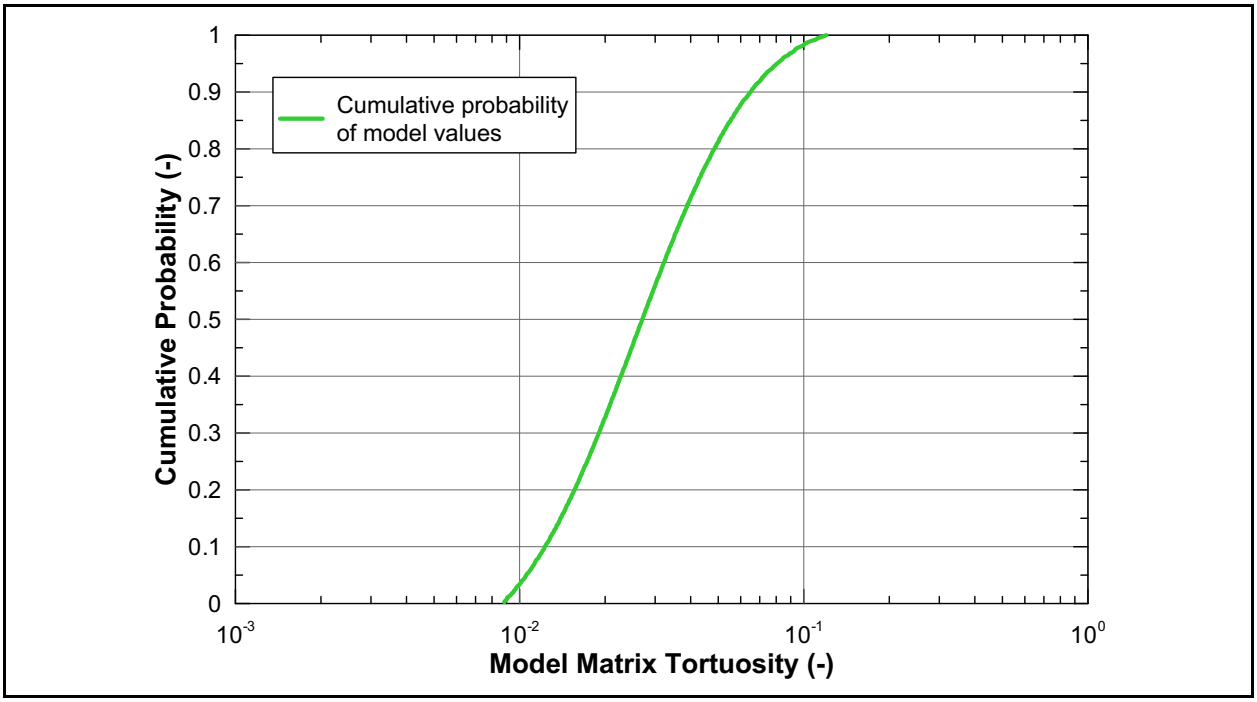

Figure 6-11
Distribution of Model Values of Matrix Tortuosity

model (NNES, 2010b). Radionuclides with an atomic mass greater than 137 (e.g., ^{237}Np and U) were assigned a free-water diffusion coefficient of 3.0E-10 m^2/s and those with an atomic mass less than or equal to 137 were assigned a free-water diffusion coefficient of 2.24E-09 m^2/s.

6.3.4 Dispersivity

The effect of dispersion during transport of solutes in geologic systems is commonly quantified in terms of longitudinal and transverse dispersivities. Longitudinal dispersivity is defined relative to the direction of flow, whereas transverse dispersivity is defined relative to directions normal to the flow direction.

Dispersivity is generally considered to be dependent on the scale of transport. A review of the literature on scale-dependent dispersion and the development of various relationships between longitudinal dispersivity and transport scale is presented in SNJV (2007). Given possible transport scales on the order of 10 km or more in the Yucca Flat/Climax Mine CAU, a longitudinal dispersivity of 20 m was selected. The transverse horizontal dispersivity is considered to be one order of magnitude less than the longitudinal dispersivity, and the transverse vertical dispersivity is considered

to be two orders of magnitude less than the longitudinal dispersivity. In summary, the dispersivities selected as inputs to the Yucca Flat LCA transport model for all transport cases are as follows:

- Longitudinal dispersivity: 20 m
- Transverse horizontal dispersivity: 2.0 m
- Transverse vertical dispersivity: 0.2 m

6.3.5 Fracture Retardation and Matrix Sorption

In the Yucca Flat LCA transport model, radionuclide retardation via sorption is considered for reactions with immobile minerals in both fracture and matrix material. First, sorption may occur on the mineral coatings lining the fracture walls, and second, radionuclides may diffuse into the rock matrix and sorb to the bulk mineralogy of the LCA rock. For the LCA transport model, fracture sorption is parameterized with retardation coefficients derived from laboratory experiment data, and matrix sorption is parameterized with distribution coefficients (K_d) derived from the literature. This section develops the retardation factor and K_d distributions used in LCA transport modeling.

6.3.5.1 Fracture Retardation

The LCA mineralogy along fracture walls consists of clays, iron oxide, zeolites, and other minerals, along with the underlying dolomite and calcite that are the primary minerals of the carbonate rock. Fracture retardation is considered for radionuclides of the following elements: nickel, strontium, cesium, neptunium, uranium, and plutonium.

No direct experimental data are available for estimating nickel retardation, and the estimates are based on an understanding of the thermodynamic properties of nickel as compared to strontium and cesium. The cesium and strontium retardation data indicate that aluminosilicate clays play a pivotal role in the fracture retardation of radionuclides. Nickel ion exchange to smectite mineral is known to be stronger than strontium but weaker than cesium. Nickel sorption to the calcite mineral is predicted to be stronger than strontium and Cesium (Zavarin, 2012). A conservative approach is used to assign nickel fracture retardation equivalent to that of strontium.

The LANL fracture transport experiments summarized in SNJV (2007) are used to select the strontium, cesium, neptunium, uranium, and plutonium fracture retardation distributions used for the

LCA transport modeling. The retardation factors are selected based on the following review of the LANL data:

- The range of strontium fracture retardation reported is 1 to greater than 30. However, 16 of the 20 data points have retardation factors less than 2.5, and a range of retardation factors from 1 to 2.5 is selected.
- The range of cesium retardation factors not associated with colloid transport is 1.8 to 320, and this range is selected.
- The range of neptunium retardation factors is 1 to greater than 50. However, 18 of the 32 data points are less than 10, and a range of 1 to 10 is selected.
- The range of uranium retardation factors is 1 to 2.7. However, only 1 of 24 data points is greater than 1.6, and a range of 1 to 1.6 is selected.
- The range of plutonium retardation factors not associated with colloid transport is 2.4 to 50, and this range is selected.

The retardation factor distributions are considered to be triangular and symmetric about the mode value. The mode has been estimated by using the arithmetic average of the upper and lower limit values. The reported ranges of retardation values are representative of spatial heterogeneity in measured values. At the large spatial scales used in the LCA model, the average retardation values will tend to be more representative of the overall retardation of radionuclides. Thus, the distributions of retardation should reflect the fact that median or mode values are more likely than the minimum or maximum measured values. Table 6-2 presents the fracture retardation factor distributions.
An example fracture retardation distribution used in the Yucca Flat LCA transport model is illustrated in Figure 6-12 for strontium.

6.3.5.2 Matrix Sorption

The LCA rock is dominated by dolomite and calcite minerals with only trace amounts of silicate and iron oxide. Sorption in the matrix is considered to be controlled by calcite and dolomite surface chemistry. The LCA rock surface area accessible to sorption is very low, and experimental sorption/desorption data may need to be adjusted by the surface area of the LCA rock (Zavarin, 2012). Matrix sorption is considered for radionuclides of uranium and plutonium in the base-case analysis, and for radionuclides of carbon, strontium, cesium, and nickel in a sensitivity analysis.

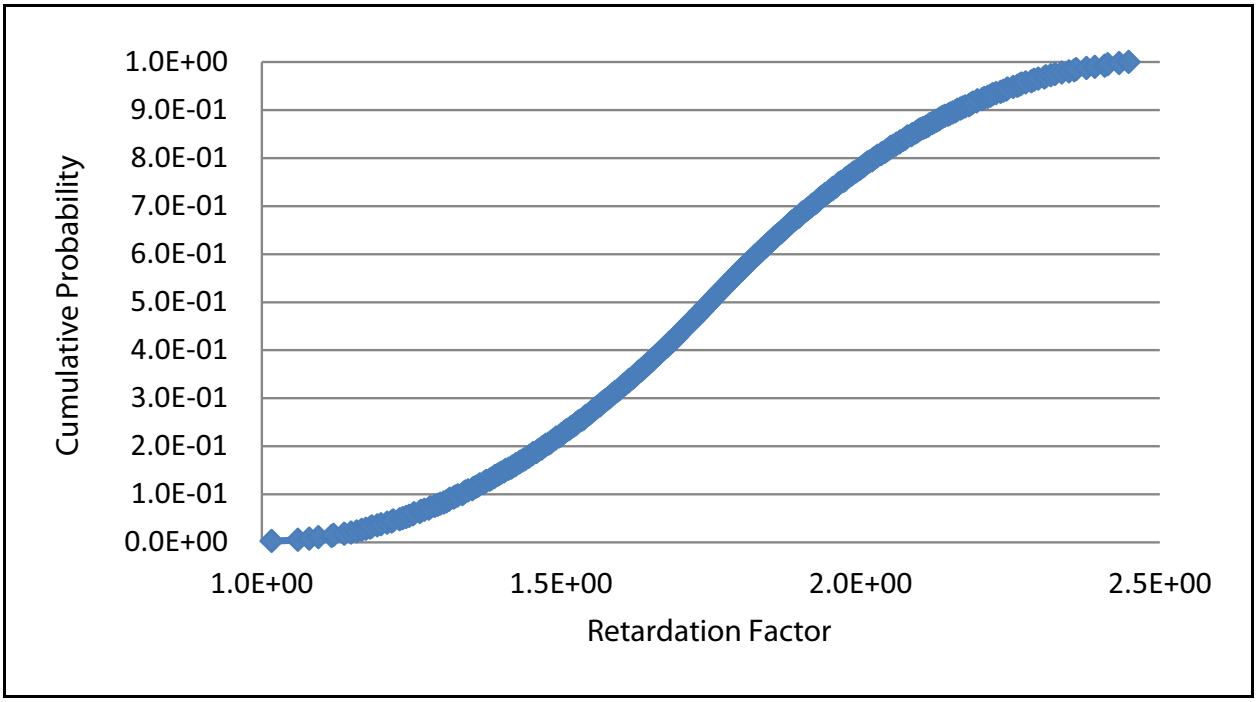

Figure 6-12
Strontium Fracture Retardation Distribution of the LCA

The uranium and plutonium K_d distributions are from transport studies for the WIPP (Rechards and Tierney, 2005). These data are representative of the LCA in Yucca Flat, and the significance of the data uncertainty is presented in Section 6.5.9.

Appendix L investigates whether the groundwater age estimates from naturally occurring ^{14}C can be used to constrain the migration velocities of test-derived ^{14}C and other test-generated radionuclides, such as ^{36}Cl and ^{129}I, that are considered to move as tracers through the LCA at Yucca Flat. The investigation concluded that groundwater ^{14}C is moving without retardation relative to the dissolved ^{36}Cl and that ^{14}C K_d values are likely very small. The investigation also concluded that large K_d values for ^{14}C are incompatible with the observed rates of ^{14}C migration and expected hydrologic and transport properties. Therefore, the base-case analysis assumes that ^{14}C matrix K_d values are zero.

The alternative K_d values used in the sensitivity study are generally taken from guidance provided by LLNL (Zavarin, 2012). This guidance, using additional sources of non-QAPP compliant data, is used

as a sensitivity analysis and not used directly in the base-case contaminant boundary forecasts. The alternative K_d values are selected by the following review of the LLNL guidance:

- Sutton (2009) performed a literature review of distribution coefficients for carbonate minerals and reported a carbon K_d values range from 0 to 199.5 mL/g. However, the LLNL guidance considers these values unrepresentative of the LCA, because the values may have been a result of calcite dissolution/precipitation reactions, and the values do not consider the low reactive surface area of LCA rock. The LLNL guidance reviewed additional batch fracture flow experiment data from Hershey et al. (2003) and recommended a K_d range of 1 to 20 mL/g. The recommended range is selected for the sensitivity analysis.

- Dosch and Lynch (1980) summarized Culebra dolomite K_d values and reported a strontium K_d range of 5 to 16 mL/g, which is recommended by the LLNL guidance and is selected for the sensitivity analysis.

- The LLNL guidance identified a cesium K_d range of 0.2 to 6.8 mL/g from sorption/desorption experiments and recommended reducing these values to 0.002 to 0.68 mL/g to account for the low LCA rock surface area. The base-case cesium K_d of 0.0 mL/g, conservatively reflects the recommended reduced values which are close to zero. The sorption/desorption experiment K_d values with a range of 0.2 to 6.8 mL/g have been used in the sensitivity analysis to explore the parameter's potential significance.

- The LLNL guidance identified nickel partitioning onto calcite to be one to two orders of magnitude greater than that for strontium and recommended using the strontium values for conservatism. The strontium K_d range of 5 to 16 mL/g is selected for the sensitivity analysis.

The K_d distributions are considered to be triangular and symmetric about the mode value. The mode has been estimated by using the arithmetic average of the upper and lower limit values. Table 6-3 presents the K_d distributions used in the base case and the sensitivity case. An example matrix K_d distribution used in the Yucca Flat LCA transport model is illustrated in Figure 6-13 for uranium.

6.3.6 Input Parameters for the Alternative LCA Parametrization Simulation

Analysis of spinner flow logs conducted in boreholes ER-6-1, ER-6-1-2, ER-6-2, and ER-7-1 located in Yucca Flat suggests that the thickness of the LCA across which flow occurs is less than the entire LCA thickness (see Appendix J). In addition, flow within the LCA can be described as occurring in separate flowing features. Flowing features are defined as zones across which preferential flow occurs, and are conceptualized as zones of increased transmissivity associated with increased fracturing relative to adjacent zones having little to no flow. A derivative analysis of the spinner flow log data from ER-6-1-2 indicates the presence of both large- and smaller-scale flowing features. The

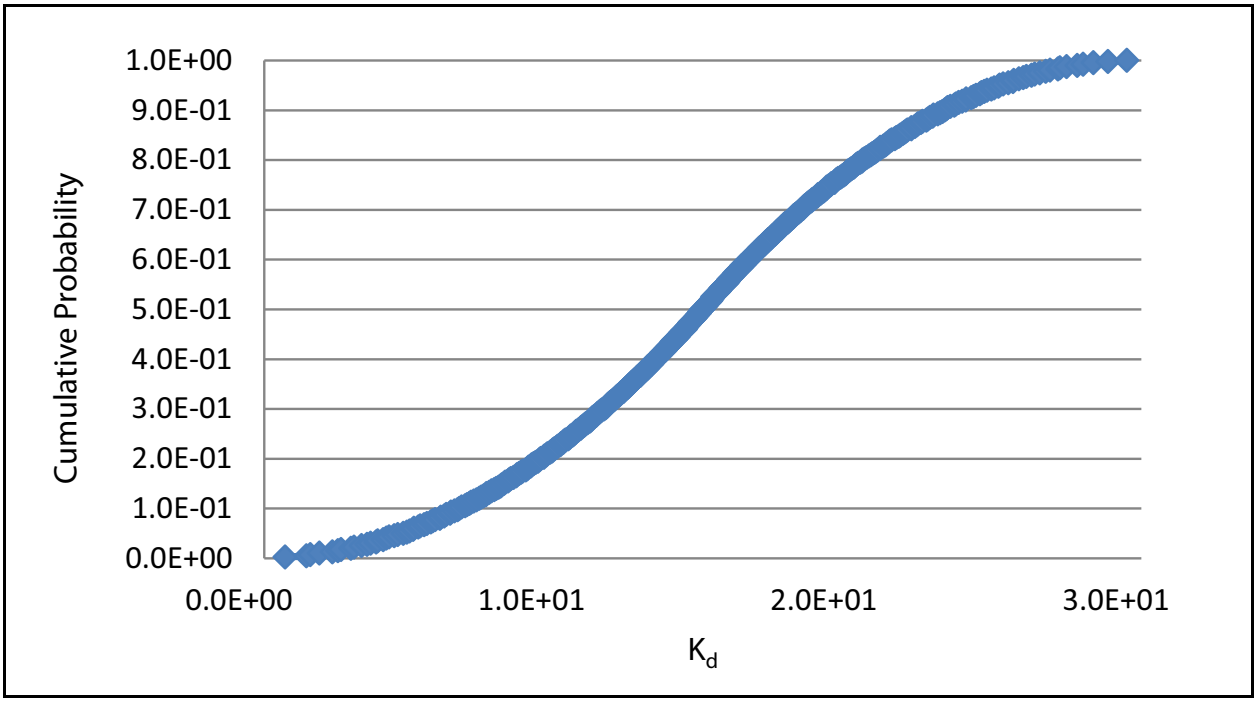

Figure 6-13
Uranium Matrix Sorption (K_d) Distribution of the LCA

large-scale features are attributed to fault zones, and the smaller-scale features are attributed to flowing zones within the country rock. The alternative parameter values for the fault zones (i.e., the portion of the LCA with large-scale flowing features) are a higher fracture porosity and a smaller fracture spacing than were used for the conservative base-case model presented above. The alternative parameter values for the country rock (i.e., the portion of the LCA with smaller-scale flowing features) result in conditions representing flow through a portion of the country rock rather than across the entire thickness of the country rock. No changes were made to the fracture parameter values for the country rock in the alternative simulation. Rather, the alternative parameterization of the country rock relates to the fraction of the LCA that participates in flow, which is accounted for most simply through a reduction in the available matrix porosity for diffusion. The intent of the alternative LCA parameterization simulation was to assign input parameter values to the LCA that were guided by the findings from the flowing feature analysis and more consistent with the conceptualization of the LCA than those used for the conservative base-case simulation. The discussions in the following subsections describe development of the transport parameter values for the alternative LCA parameterization simulation.

6.3.6.1 Alternative Fracture Parameter Values

The alterative LCA parameterization simulation includes revisions to the input values for the fracture parameters for the fault zones. Because this alternative simulation considers the fault zones to be more highly fractured than the conservative base-case simulation, the fault zones in the alternative simulation have a higher fracture porosity and a smaller fracture spacing than the fault zones in the conservative base-case simulation. The alternative LCA parameterization simulation does not include revisions to the input values for the fracture parameters for the country rock. However, the parameters for the country rock used to develop the fracture parameter values were resampled, along with the parameters for the fault zones, in order to create the paired parameter sets for the 400 model realizations used for the alternative simulation. This resampling resulted in fracture parameter values for the county rock for the alternative simulation that are slightly different from those used for the base-case simulation. All figures for fracture parameters shown below include the input distributions for both the fault zones and country rock for both the base-case and alternative simulations.

As discussed in Section 6.3.1.1, the upper two-thirds of the fracture porosity distribution (from 9.4E-04 to 2E-02) was sampled for the fault zones in the base-case simulation. For the alternative simulation, the upper one-third of the fracture porosity distribution (from 4.3E-03 to 2E-02) was selected for sampling in order to capture more fracturing in the fault zones than was represented in the base-case simulation. The revised input distribution of fracture porosity in the fault zones for the alternative simulation is shown in Figure 6-14. Also shown in this figure is the sampled distribution of fracture porosity in the country rock used for the alternative simulation, which is identical to that used for the base-case simulation.

The other fracture input parameter for PLUMECALC is fracture aperture. As discussed in Section 6.3.1.2, the fracture aperture of the fault zones for the base-case simulation was determined by sampling the upper two-thirds of the hydraulic conductivity distribution, calculating a hydraulic fracture aperture from that hydraulic conductivity using Equation (6-4) and a fracture spacing of 3 m, and then calculating a tracer fracture aperture from the hydraulic fracture aperture and a sampled aperture multiplier. This same approach was used to develop the fracture aperture in the fault zones for the alternative simulation, but the fracture spacing was reduced from 3 to 0.5 m. This was done to obtain a smaller value of fracture spacing for the fault zones in the alternative simulation than was used in the conservative base-case simulation. The alternative fracture spacing values are consistent with the conceptualization of the LCA that the fault zones are more highly fractured than the country

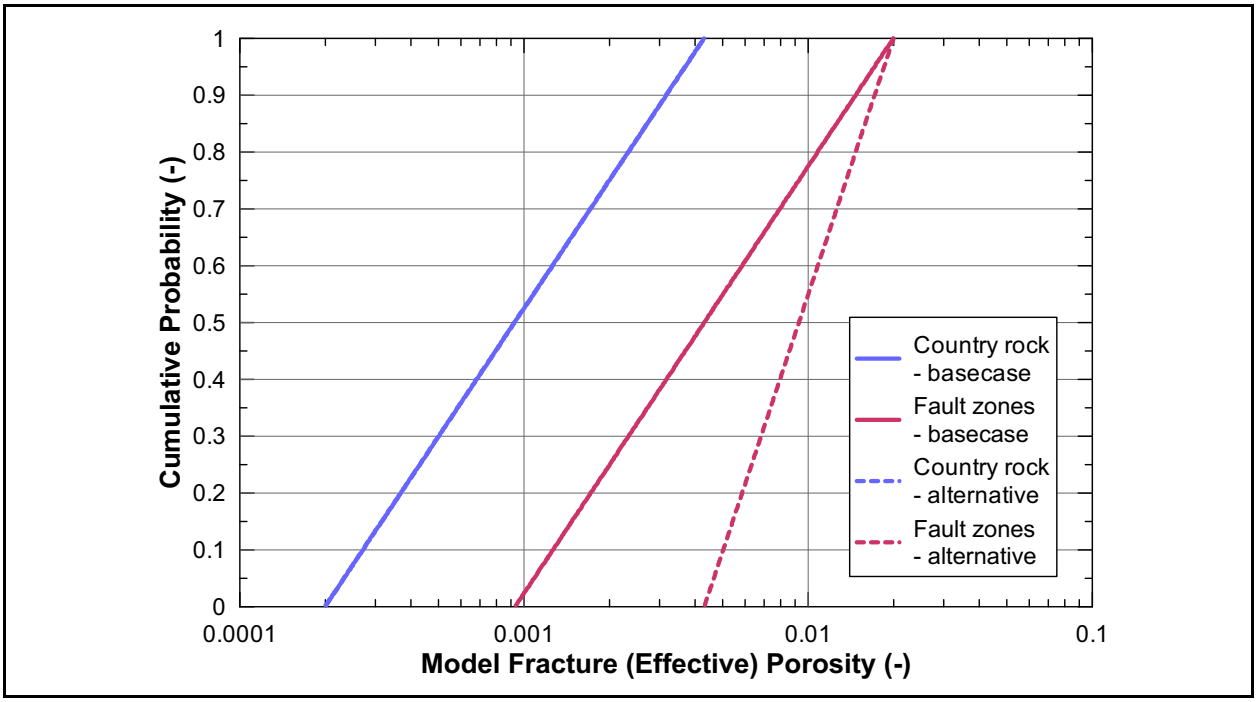

Figure 6-14
Distributions of Model Values of Fracture Porosity in the Country Rock and Fault Zones for the Base-Case and Alternative Models

rock. The resultant input distribution of fracture aperture for the fault zones in the alternative simulation, shown in Figure 6-15, ranges from 8.4E-04 to 8.1E-02 m. These values are about a factor of 3 less than the values for the base-case simulation. Fracture aperture of the country rock for the alternative simulation was developed identical to that described in Section 6.3.1.2, including use of a 3-m fracture spacing for calculation of the hydraulic fracture aperture. The resultant fracture aperture input distribution for the country rock is essentially the same as that for the base-case simulation as shown in Figure 6-15.

The fracture porosities and fracture apertures for the alternative simulation were used to calculate the corresponding fracture spacings using Equation (6-2). As shown in Figure 6-16, the fracture spacing for the fault zones is less for the alternative simulation than was used for the base-case simulation, which is consistent with the conceptualization that the fault zones in the LCA are more fractured than the country rock. Therefore, the alternative simulation provides a more realistic representation of the difference in fracture density between the fault zones and country rock than does the conservative base-case simulation. Because of resampling effects, the fracture spacing for the country rock is slightly different between the alternative and base-case simulations.

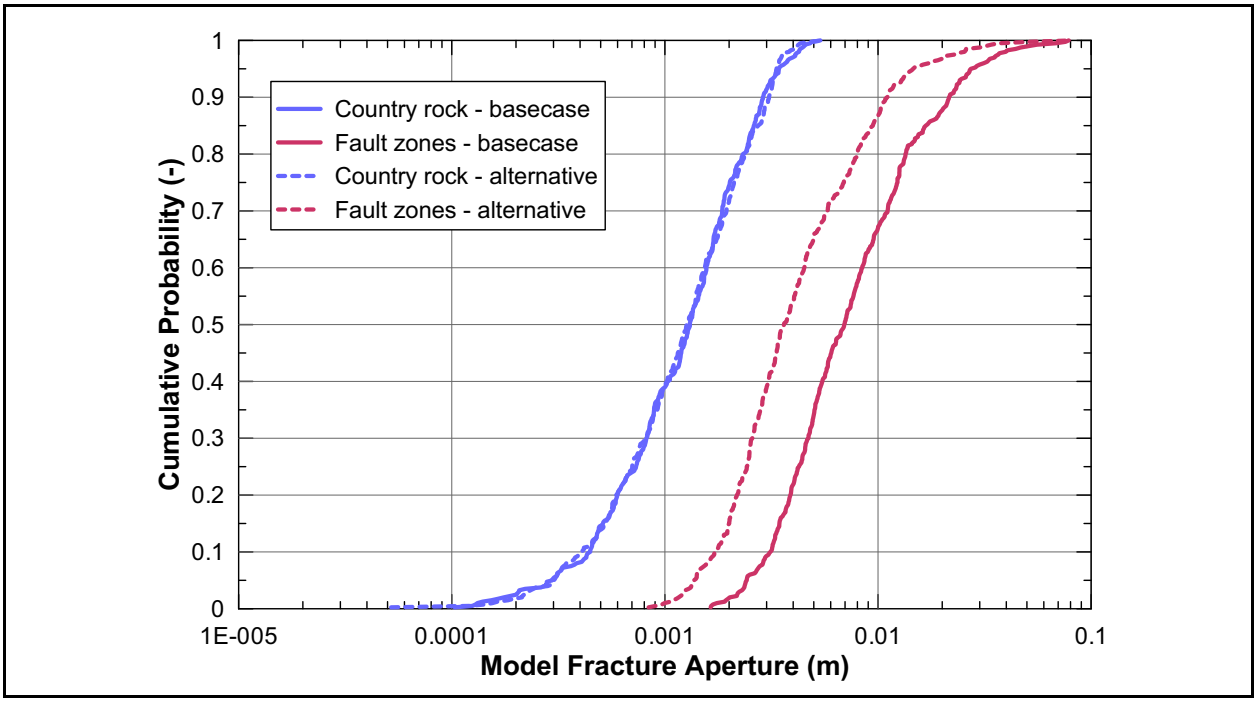

Figure 6-15
Distributions of Model Values of Fracture Aperture in the Country Rock and Fault Zones for the Base-Case and Alternative Models

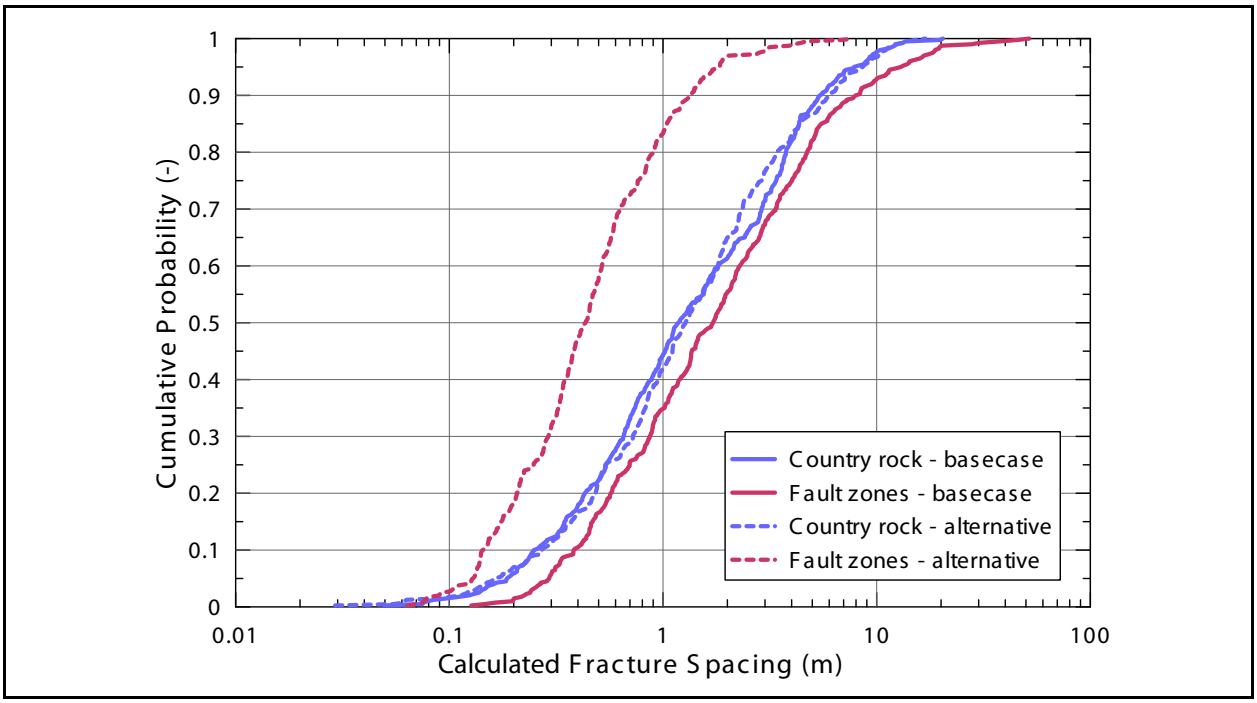

Figure 6-16
Distributions of Calculated Values of Fracture Spacing in the Country Rock and Fault Zones for the Base-Case and Alternative Models

Scatterplots of fracture aperture versus fracture porosity, fracture aperture versus fracture spacing, and fracture porosity versus fracture spacing for the alternative simulation are shown in Figures 6-17 to 6-19, respectively. In these figures, the 400 sampled values for the country rock are shown as solid light-blue circles, and the 400 sampled values for the fault zones are shown as open dark-blue circles. Figures 6-17 and 6-19 illustrate that the fracture porosity for the fault zones is, in general, about an order of magnitude higher than the fracture porosity for the country rock, and Figures 6-17 and 6-18 illustrate that the fracture aperture for the fault zones is, in general, about half an order of magnitude higher than the fracture aperture for the country rock. Figures 6-18 and 6-19 illustrate that the fracture spacing for the fault zones is, in general, about a factor of 3 less than the fracture spacing in the country rock.

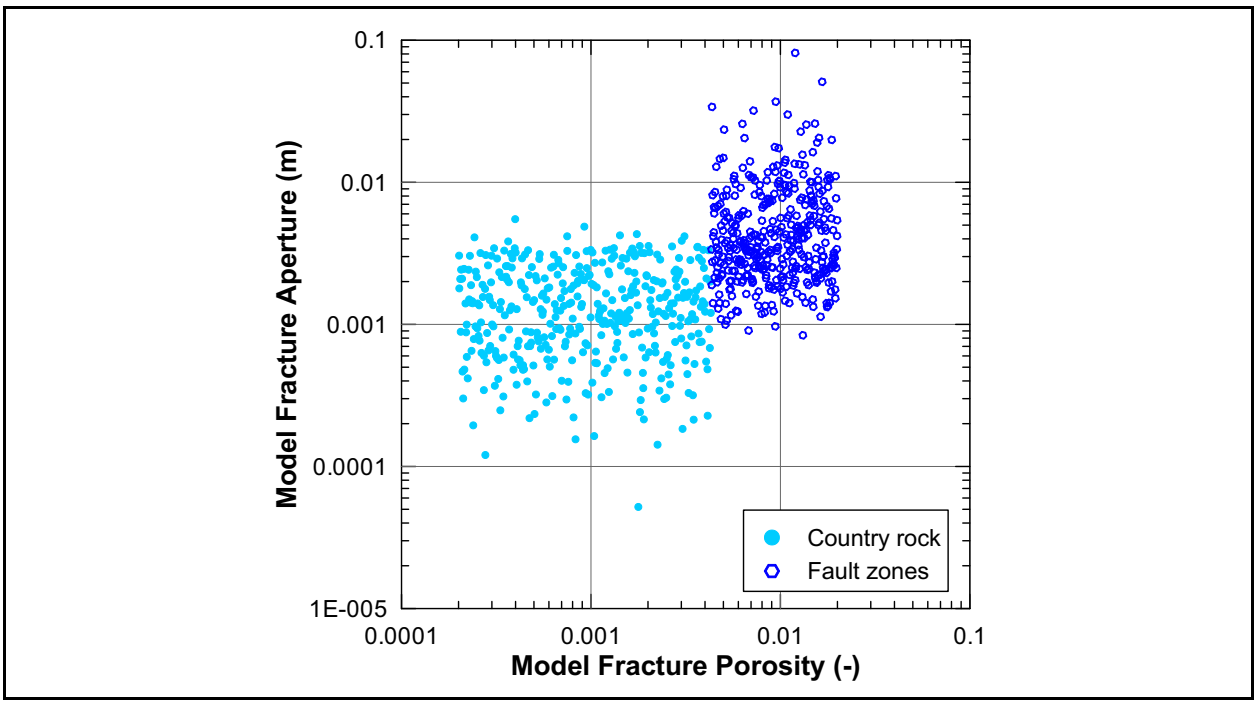

Figure 6-17
Scatterplot of Model Fracture Aperture and Model Fracture Porosity for the Country Rock and Fault Zones for the 400 Alternative Model Realizations

6.3.6.2 Alternative Matrix Porosity Values

The flowing feature analysis presented in Appendix J suggests that flow does not occur across the entire extent of the LCA country rock, but rather occurs across only portions of the country rock in flowing features. The alternative LCA parameterization simulation was designed to incorporate this reduction in flow area in the country rock. The characteristics of the fractures in the flowing features

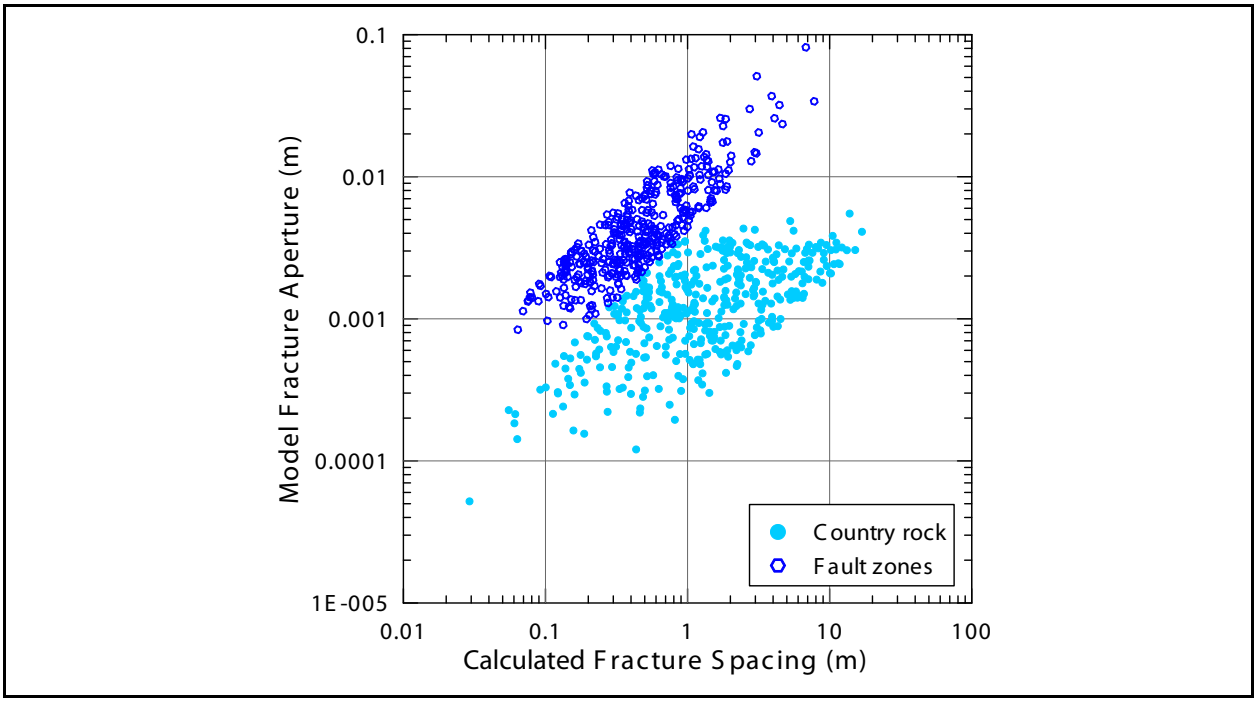

Figure 6-18
Scatterplot of Model Fracture Aperture and Calculated Fracture Spacing for the Country Rock and Fault Zones for the 400 Alternative Model Realizations

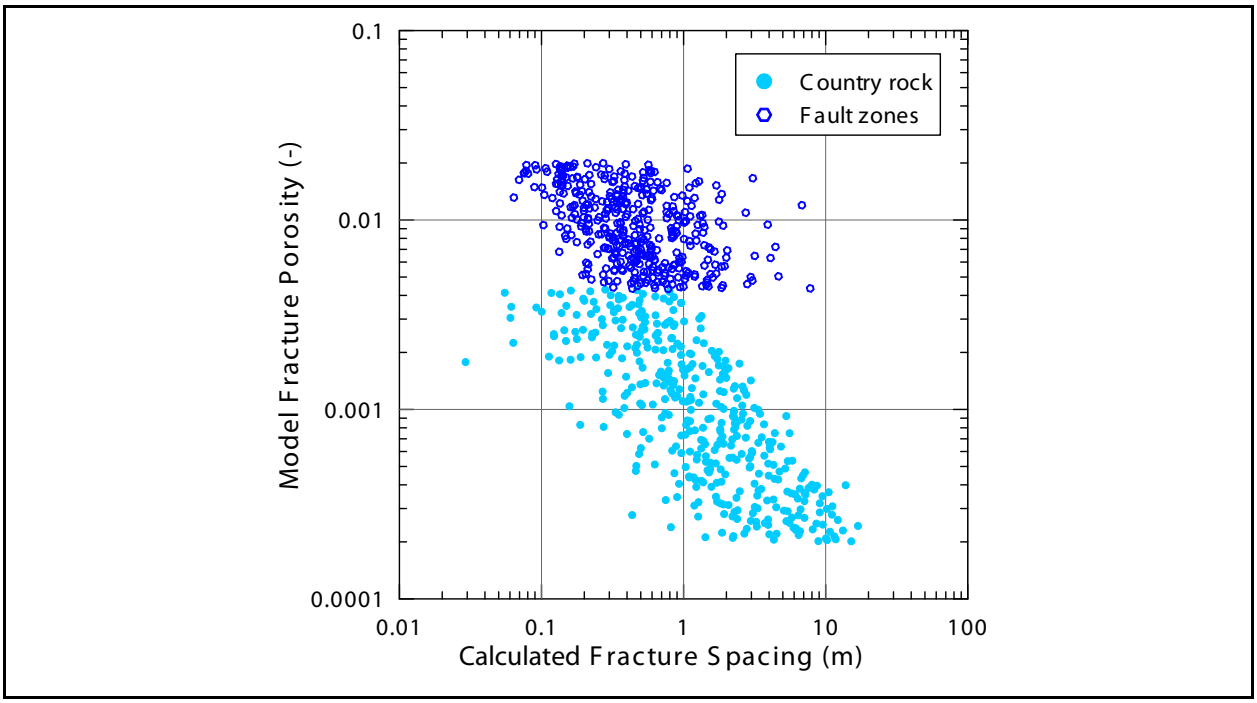

Figure 6-19
Scatterplot of Model Fracture Porosity and Calculated Fracture Spacing for the Country Rock and Fault Zones for the 400 Alternative Model Realizations

in the country rock are assumed to be the same as those for the base-case conceptualization of the LCA country rock. The result of having flow across a portion of the LCA country rock rather than across the entire extent is a reduction in the volume of matrix available for solute diffusion from the fractures into the matrix and vice versa. That is, the amount of storage in the immobile matrix water for the diffusing solutes is reduced. This reduction can be accounted for in transport simulations simply by reducing the matrix porosity in the country rock.

The reduction in storage can be estimated through examination of the range in volumes of rock containing or not containing flowing features. The derivative of the smoothed spinner flow log data for ER-6-1-2 (see Figure J-13 in Appendix J) indicates that smaller-scale flowing features make up about 40 percent of the logged interval not associated with large-scale flowing features. Derivative curves are not included in Appendix J for the spinner flow log data from ER-7-1, ER-6-1, and ER-6-2. However, the flow percentage data shown in Figures J-8 to J-10 in Appendix J were used to estimate the percentages of the logged LCA that contain smaller-scale flowing intervals. This was done by disregarding the intervals with large flow percentages, which correspond to large-scale flowing features, and comparing the thickness of all other intervals with nonzero flow to the logged LCA interval. This comparison shows that the percentage of the LCA with flow, disregarding the intervals with large flow percentages, is about 56, 84, and 17 percent in ER-7-1, ER-6-1, and ER-6-2, respectively. These percentages, along with that found for ER-6-1-2, suggest that, for the portion of the LCA associated with the country rock, the thickness with flow can be approximated to range from about 20 to 80 percent of the total thickness.

The alternative parameterization for the country rock consists of a matrix porosity reduction to account for the observation that flow does not occur across the entire thickness of the LCA country rock. The distribution for this reduction is considered to be uniform and range from 0.2 to 0.8 (Figure 6-20) based on the percentages of the LCA country rock containing flowing features estimated from the spinner flow log data for ER-6-1-2, ER-6-1, ER-6-2, and ER-7-1. The use of a distribution and multiple simulations using different values from the distribution is the method selected to attempt to incorporate the uncertainty associated with the matrix porosity reduction factor. Therefore, the matrix porosity reduction factor was sampled and used to modify the matrix porosities from the base-case simulation to obtain the modified matrix porosities for the country rock used in the alternative simulation as shown in Figure 6-21. No change was made in development of the input distribution of matrix porosity for the fracture zones in the alternative simulation, which is also shown

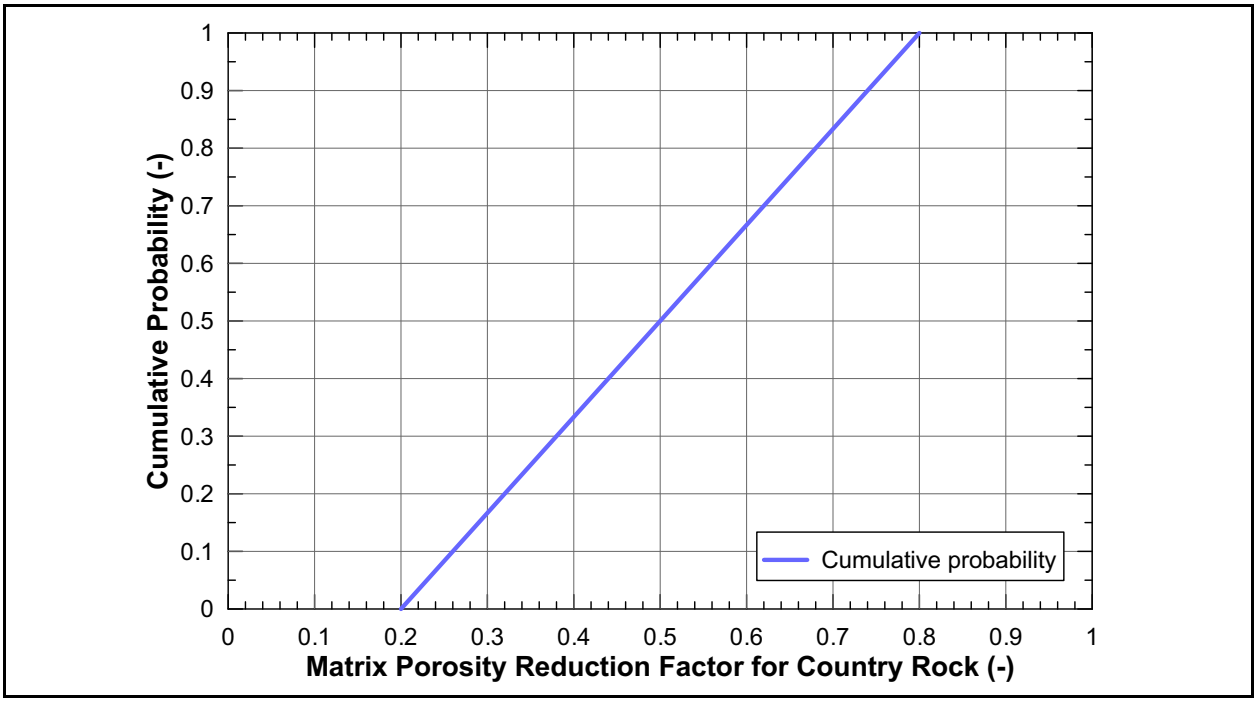

Figure 6-20
Distribution of Matrix Porosity Reduction Factor for the Country Rock

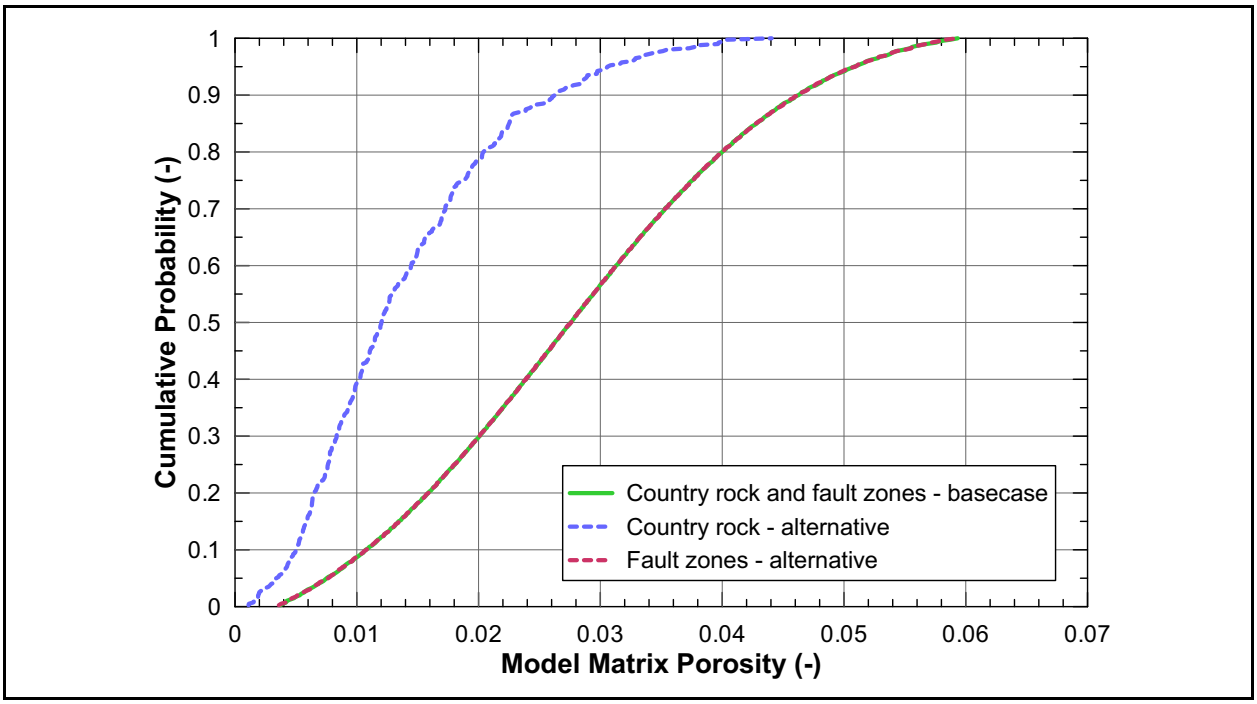

Figure 6-21
Distributions of Model Values of Matrix Porosity for the Country Rock and Fault Zones for the Base-Case and Alternative Models

in Figure 6-21. The distribution of matrix porosity for the fault zones in the alternative simulation (dashed red line in Figure 6-21) is the same as that in the base-case simulation (solid green line in Figure 6-21).

6.3.6.3 Alternative Matrix Diffusion Coefficient Values

For the base-case model, the matrix tortuosity was calculated from the matrix porosity using Equation (6-7). Because the matrix porosity was the same for the fault zones and country rock in the base-case model, the matrix tortuosity also was the same. Although the matrix porosity for the country rock was modified for the alternative simulation to represent reduced flow participation, the matrix tortuosity for the country rock was not considered to change. Therefore, the matrix tortuosity for the fault zones and country rock in the alternative simulation also was the same, and was calculated from the matrix porosity for the fault zones, which did not change from the base-case model, by the use of Equation (6-7). The input distribution of matrix tortuosity for the country rock and fault zones for the alternative simulation is identical to that shown in Figure 6-11 for the base-case simulation.

The free-water diffusion coefficients for the radionuclides in the alternative LCA parameterization simulation were the same as those used in the base-case simulation. The base-case values are provided in Section 6.3.3.2.

6.4 Integration of the LCA Flow Model and HST Inputs to the LCA Transport Model

The goal of the LCA transport model is to calculate the contaminant concentration within the LCA downgradient along the likely groundwater travel paths from the contaminant sources.
The PLUMECALC code is used for all of the contaminant transport calculations in the LCA.
The appropriateness of this code for the intended purpose of evaluating contaminant transport and determining an initial estimate of the extent of the contaminant boundary is presented in Appendix K.

There are three principal inputs to PLUMECALC: (1) the particle transport paths and minimum travel times for each LCA flow model calculated with the sptr routine within FEHM, (2) the initial contaminant mass in place in the sources that intersect the LCA as well as the spatial and temporal variation in contaminant mass influx to the LCA from the overlying unsaturated zone and the saturated alluvial/aquifer system, and (3) the LCA transport parameters. The LCA transport

parameters used as input to the LCA transport model are described in Section 6.3. The approach used to simulate particle transport and the particle-tracking results are presented in Section 6.4.1. The contaminant mass flux inputs to the LCA transport model from the unsaturated-zone contaminant sources are presented in Section 6.4.2. The contaminant mass flux inputs to the LCA transport model from the source locations in the saturated alluvial/volcanic aquifer system are presented in Section 6.4.3. The contaminant mass in place in the LCA from those sources with exchange volumes that intersect the LCA at the time of the detonations is presented in Section 6.4.4. Based on these inputs, LCA transport calculations for representative sources are presented in Section 6.4.5.

The presentation of mass fluxes into the LCA or initial mass in place in the LCA in this section provides representative illustrations of the inputs. These illustrations focus on a few representative cases to provide an indication of the differences in the spatial and temporal mass fluxes and the integration of the output from the unsaturated zone and saturated alluvial/volcanic aquifer system models used as input to the LCA transport model.

6.4.1 LCA Flow Model Particle-Tracking Results

The LCA transport model uses the velocity fields generated from the calibrated flow fields described in Section 5.0. The development of these velocity fields used the same finite element mesh and the associated control volumes used in FEHM. These velocity fields are used in the sptr subroutine of FEHM to determine the particle trajectories and minimum advective transport times along these trajectories. Although issues have been identified in the use of sptr in complex heterogeneous flow fields such as those at Yucca Flat, as discussed in Appendix K, these issues do not significantly affect the use of this subroutine for evaluating contaminant transport in a steady-state flow field and determining the extent of the contaminant boundary.

This section presents the details of modifications in the flow model output that were necessary to accommodate the sptr algorithm in FEHM, and defines how the particle starting points for LCA sources are identified and implemented in the finite element mesh. It also presents the particle-tracking results for representative source locations. These particle-tracking results and the resulting minimum travel times are used in PLUMECALC with the transport parameters described in Section 6.3 and the source mass fluxes described in Sections 6.4.2 to 6.4.4 to generate multiple realizations of radionuclide transport that forecast the contaminant migration downgradient of the contaminant sources. These results are presented in Section 6.5.

The LCA transport model uses the same finite element mesh refinement that is used in the LCA flow model. In order to approximate the transport in the vicinity of source regions and major faults (defined in the HFM as those with vertical offset of 60 m [200 ft] or greater), the LCA flow model has a refined mesh in the upper 200 m of the saturated LCA, and in the damaged and core zones of the major faults. Representative depictions of the detailed mesh in the upper few hundred meters of the saturated LCA in the vicinity of the CORDUROY detonation are given in Figure 6-22. Representative depictions of the detailed mesh in the vicinity of the Yucca fault near the BOURBON detonation are given in Figure 6-23.

One distinction between the LCA flow model and LCA transport model meshes warrants discussion. The initial mesh developed for the Yucca Flat flow and transport model was developed from the HFM for the Yucca Flat/Climax Mine CAU (BN, 2006). The HFM extends from –5,000 m amsl to the land surface (which ranges from a low of 1,195 m amsl at Yucca Lake to a high of 1,463 m amsl in the northern portions of the valley) and includes low-permeability HSUs underlying the LCA, as well as the alluvial and volcanic HSUs overlying the LCA.

The LCA flow model mesh took advantage of a feature in FEHM that allows for the definition of inactive nodes. Inactive nodes were assigned to low-permeability units that were assumed to represent aquicludes that underlie the LCA within the Yucca Flat transport model, most notably, the LCCU. In addition, because all of the HSUs overlying the LCA and the LCA3 are included in either the unsaturated zone or saturated alluvial/volcanic aquifer system model domain, these HSUs were also represented as inactive nodes in the LCA flow model. Therefore, before the particle paths and advective-dispersive particle transport times were evaluated, the inactive nodes were made active with a sufficiently low permeability to not affect the simulated flow field and model calibration. The flow fields resulting from the use of low-permeability nodes for previously inactive nodes were equivalent to the calibrated flow model generated using inactive nodes.

All contaminant source nodes in the LCA transport model—whether the contamination is the result of an exchange volume that extends into the saturated LCA at the time of the detonation, or the result of contaminant mass influx from either the overlying unsaturated zone or the saturated alluvial/volcanic aquifer system—are active nodes and are used as the starting points for calculating particle trajectories. There is the possibility that particle trajectories may propagate from higher-permeability active nodes to low-permeability active nodes that were previously considered inactive. For example,

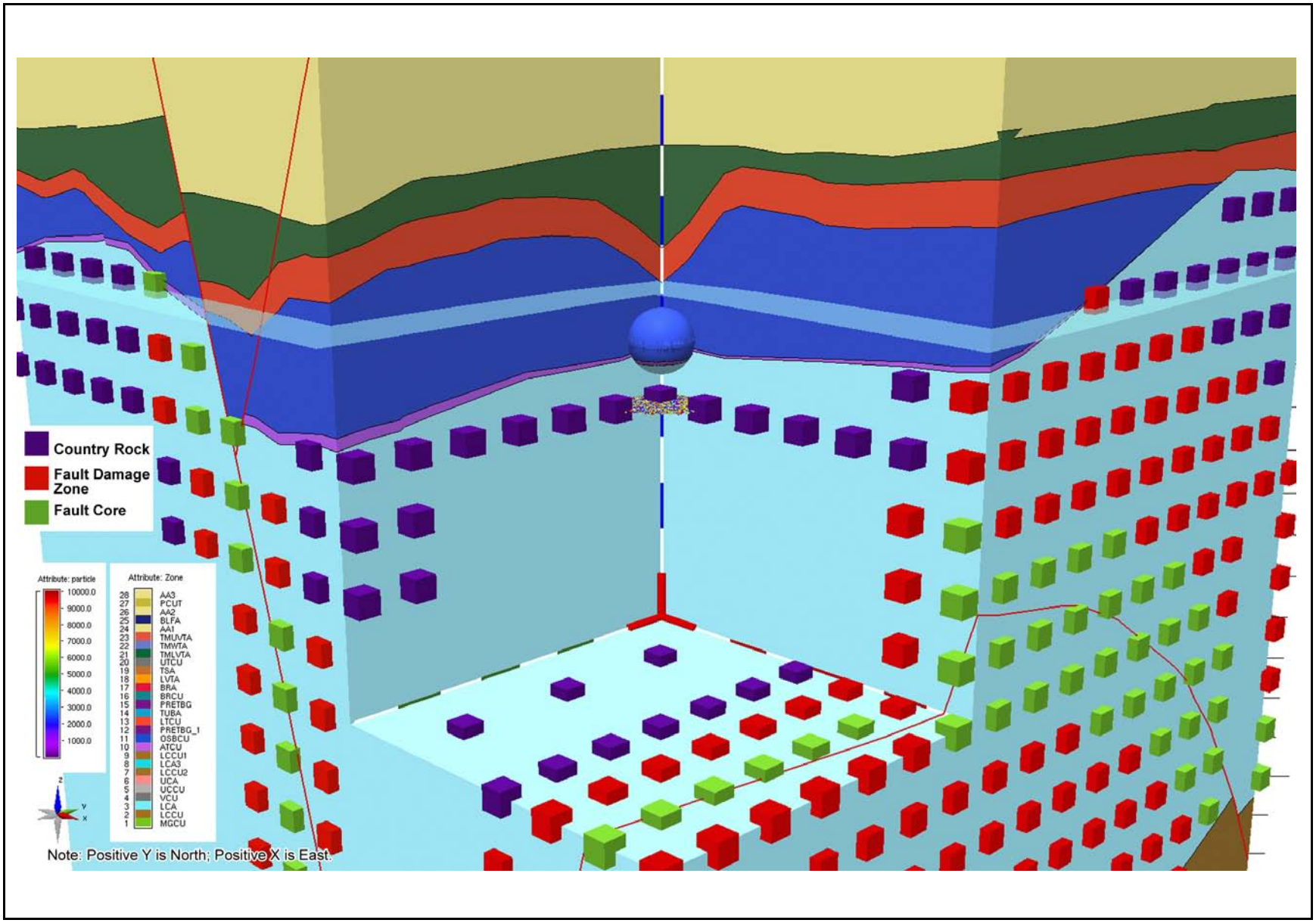

Figure 6-22
Perspective View of Particle Starting Locations for the Portion of the CORDUROY Detonation Intersecting the Saturated LCA

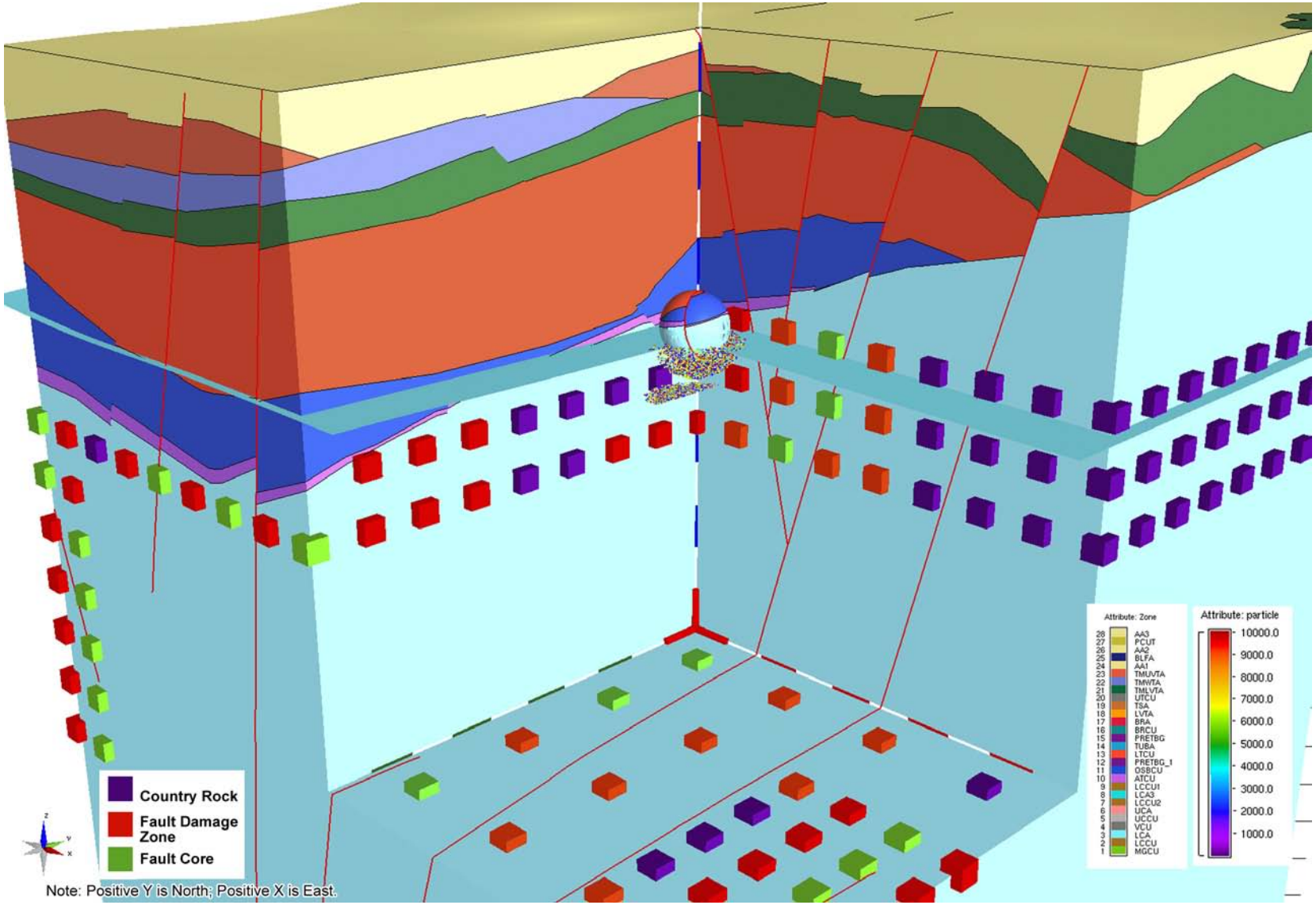

Figure 6-23
Perspective View of Particle Starting Locations for the Portion of the BOURBON Detonation Intersecting the Saturated LCA

particles in a horizontal flow field may pass horizontally from the LCA to stratigraphically overlying volcanic units that are juxtaposed with the LCA along the downthrown side of a fault. These particles would essentially be lost from the LCA model domain. In order to evaluate the potential significance of this loss of particles (and therefore contaminant mass), an evaluation of particle trajectories that propagate into previously inactive low-permeability nodes was performed. This analysis determined that the loss of mass due to the lack of sufficient grid refinement generally affected less than 0.3 percent of the total contaminant mass in the LCA. In the case of ^{3}H, the lack of mass conservation was on the order of 1.6 percent of the mass entering the LCA from the overlying volcanic units; however, this is insignificant in comparison to the amount of ^{3}H that is initially in place in the LCA for the 12 detonations with exchange volumes that are 2 R_c.

The PLUMECALC code uses the particle-tracking results (both particle travel paths and minimum travel times) derived from the sptr routine of FEHM as an input to the transport forecast. The approach used in the particle tracking distributed particles randomly in a volume of rock corresponding to the source dimensions. The source dimensions differ from detonation to detonation and between source nodes that correspond to an underground nuclear detonation with an exchange volume intersecting the saturated LCA and source nodes that correspond to nodes with an influx of contamination from the overlying unsaturated zone or saturated alluvial/volcanic aquifer system transport model. Each of these source-node particle-tracking approaches is discussed below.

There are 12 underground nuclear detonations with exchange volumes that intersect the saturated LCA when an exchange volume radius of 2 R_c is assumed. For an exchange volume radius of 1 R_c, the number of detonations intersecting the saturated LCA is 4, and for an exchange volume radius of 3 R_c, the number of detonations intersecting the saturated LCA is 39 (Figures 2-2 and 2-3). Depending on the exact locations of these detonations and the fraction of the exchange volume that intersects the saturated LCA, these detonations may correspond to one or several nodes in the saturated LCA transport model. For each detonation location that intersects the saturated LCA, the particle tracking was performed with 10,000 particles distributed uniformly within the volume of the spherical cap portion of the exchange volume below the top of the saturated LCA. This number of particles was selected because it was found to be sufficient to represent contaminant transport in the Frenchman Flat Phase II transport model (NNES, 2010b). In order to minimize the effect of particle trajectories exiting the active nodes, the top of the semisphere of particles was placed one-quarter of the nodal spacing or about 31 m below the top of the saturated LCA. An example of the initial distribution of

the 10,000 particles for the CORDUROY and BOURBON detonations are illustrated in Figures 6-22 and 6-23, respectively.

The number and locations of LCA nodes receiving significant contaminant mass flux from the overlying unsaturated zone or saturated alluvial/volcanic aquifer system model are a function of the modeled conditions used in the overlying models. In order to ensure that the more significant contaminant influx was included in the saturated LCA transport model, all nodes receiving a contaminant concentration of at least 1 percent of the MCL at any time during the 1,000-year simulation period were included as sources in the LCA. Analysis of the effect of this approximation determined that over 99.9 percent of the total mass coming into the LCA from the overlying models was included in the sources. The number of source nodes meeting this criterion varies for the modeling case and, as discussed in Sections 3.0 and 4.0, is highly dependent on the background infiltration rate. In addition, as discussed in Section 4.0, the spatial distribution of contaminant flux locations to the saturated LCA is significantly affected by the conceptualization of the extent and permeability changes associated with altered zones, especially for those detonations with working points near the base of the tuff confining units immediately above the saturated LCA. Because of the significance of the background infiltration rate on the number and distribution of locations with contaminant flux exceeding the 1 percent of the MCL criterion, two separate illustrations of this distribution are provided in Figure 6-24 and Figure 6-25 for infiltration rates of 0.1 mm/yr and 1 mm/yr, respectively. These distributions are for combined runs 542121 and SAE_12 for the 0.1-mm/yr case and runs 121212 and SAE_2 for the 1-mm/yr case.

In order to determine the appropriate number of particles to use to develop a numerically stable result, a series of calculations were performed using 100, 500, or 2,500 particles for each source node receiving contaminant mass from the overlying unsaturated zone and saturated alluvial/volcanic aquifer system models. Based on these analyses (see Section 6.5), it was determined that 500 particles per source node provided reasonably stable results. These particles were randomly placed in a square area around the node receiving the mass influx. An example of the initial distribution of the 500 particles for the source node with the highest mass influx of ^{129}I from the overlying saturated alluvial/volcanic aquifer system model is illustrated in Figure 6-26.

Once the particles are initially placed, the sptr algorithm in FEHM calculates how those particles would move in the advective flow system within the calibrated LCA flow model. In order to ensure

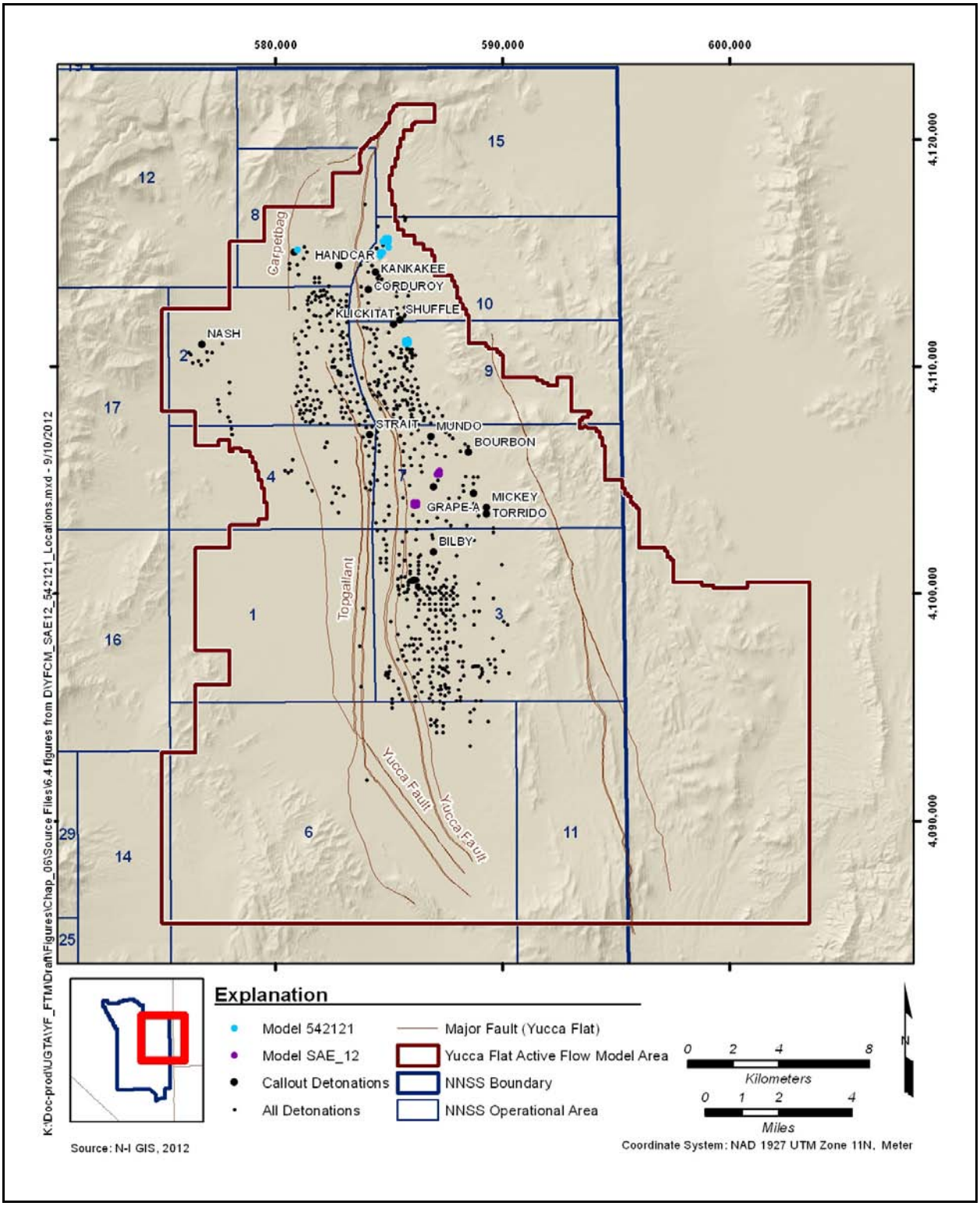

Figure 6-24
Locations of LCA Source Nodes Associated with Contaminant Influx from the Unsaturated Zone and Saturated Alluvial/Volcanic Aquifer System Models for Infiltration Rate of 0.1 mm/yr

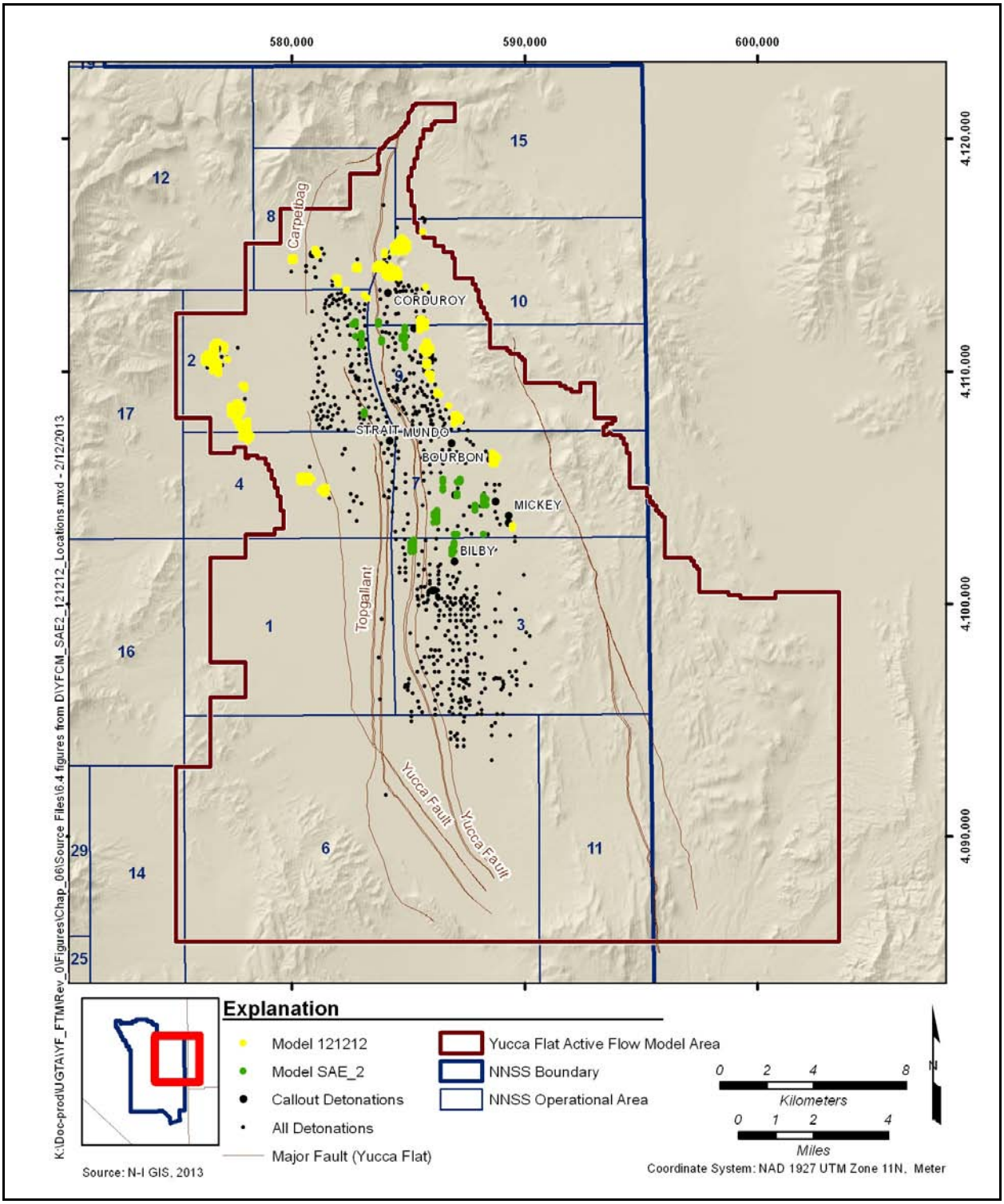

Figure 6-25
Locations of LCA Source Nodes Associated with Contaminant Influx from the Unsaturated Zone and Saturated Alluvial/Volcanic Aquifer System Models for Infiltration Rate of 1 mm/yr

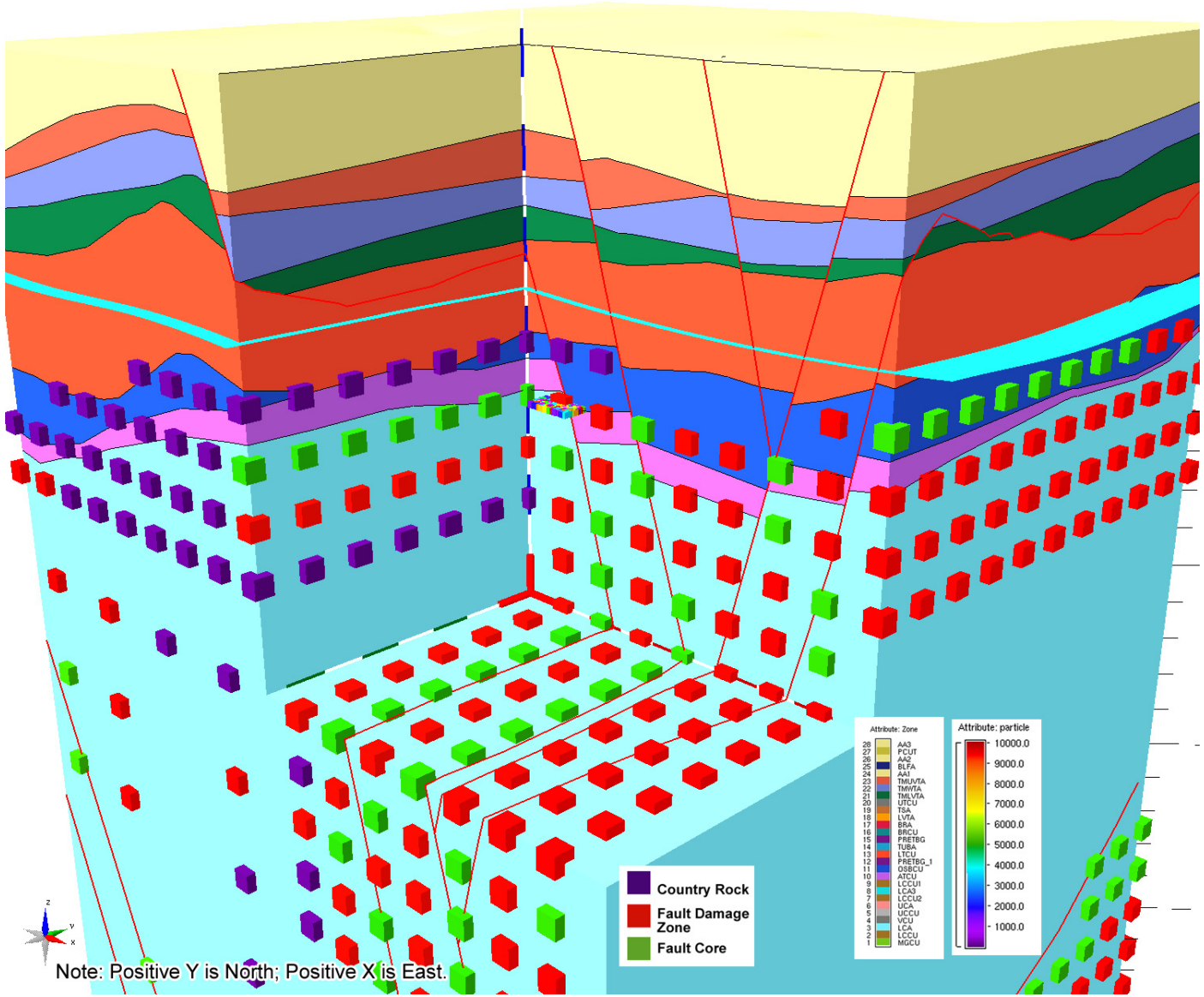

Figure 6-26
Perspective View of Particle Starting Locations for a Typical Node Receiving Mass Input from the Overlying Saturated Alluvial/Volcanic Aquifer System Model

that all possible travel trajectories are computed, the particle tracking uses the minimum effective porosity of each of the different LCA country rock units or faults along each travel path. The actual effective porosity is sampled from the distributions presented in Section 6.3 for each PLUMECALC realization of contaminant transport.

Particle trajectories are calculated assuming no dispersion for the two representative distributions of particle starting locations depicted in Figures 6-22 and 6-23. Figure 6-22 depicts a distribution of particle starting locations for the portion of the CORDUROY detonation intersecting the LCA, and Figure 6-23 depicts a distribution of particle starting locations for the portion of the BOURBON detonation intersecting the LCA. The calculated particle trajectories for these distributions are illustrated in Figures 6-27 and 6-28, respectively. The color coding used to distinguish the individual particle trajectories illustrated in these and other similar figures are arbitrary and chosen to illustrate the range of the particle trajectories. As expected, without dispersion, the flow trajectories are reasonably confined to a narrow path and are dominated by flow within the more permeable damaged zones of the major north–south-trending normal faults.

Calculated particle trajectories from the source node in the LCA that corresponds to one of the highest influx of contaminants from the overlying saturated alluvial/volcanic aquifer system transport model are illustrated in Figure 6-29. This figure also depicts the underground nuclear detonations conducted in the vicinity of this source node and the proximity of the source node to the major faults that allow contaminants to migrate from the overlying tuff units to the LCA.

The simulated particle trajectories from the three representative starting locations—CORDUROY, BOURBON, and the source node with one of the most significant fluxes from the overlying alluvial/volcanic aquifer system flow and transport model—to the southern boundary of the LCA flow model are illustrated in Figure 6-30. This figure illustrates that all particles are transported in a generally southerly direction along the trace of the major faults and exit the southern boundary. These trajectories are implemented with the minimum effective porosity, and do not represent 1,000-year transport times, which are significantly affected by matrix diffusion, dispersion, retardation, and decay as presented in Section 6.5.

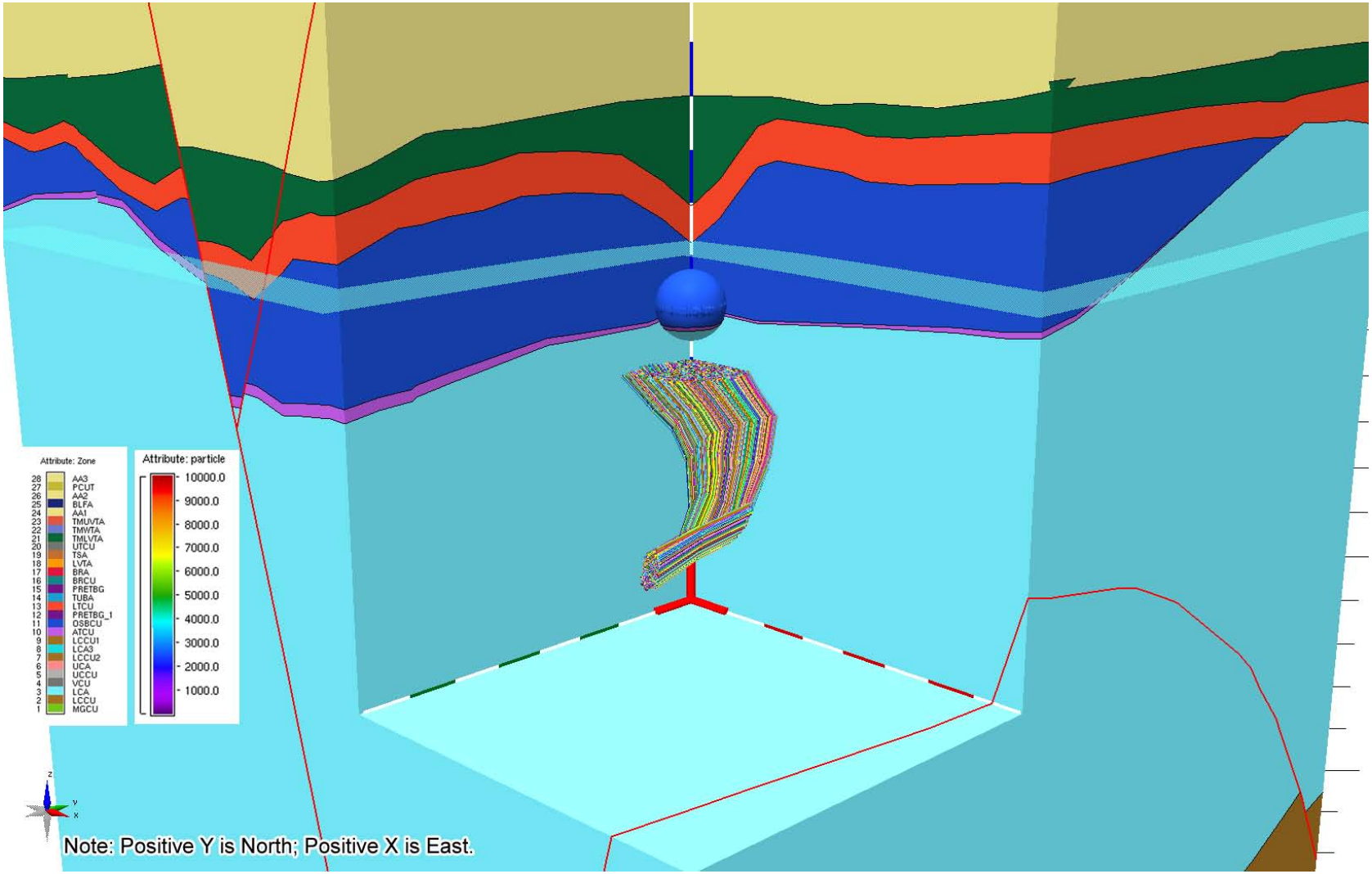

Figure 6-27
Perspective Plot of LCA Particle Trajectories from the CORDUROY Detonation

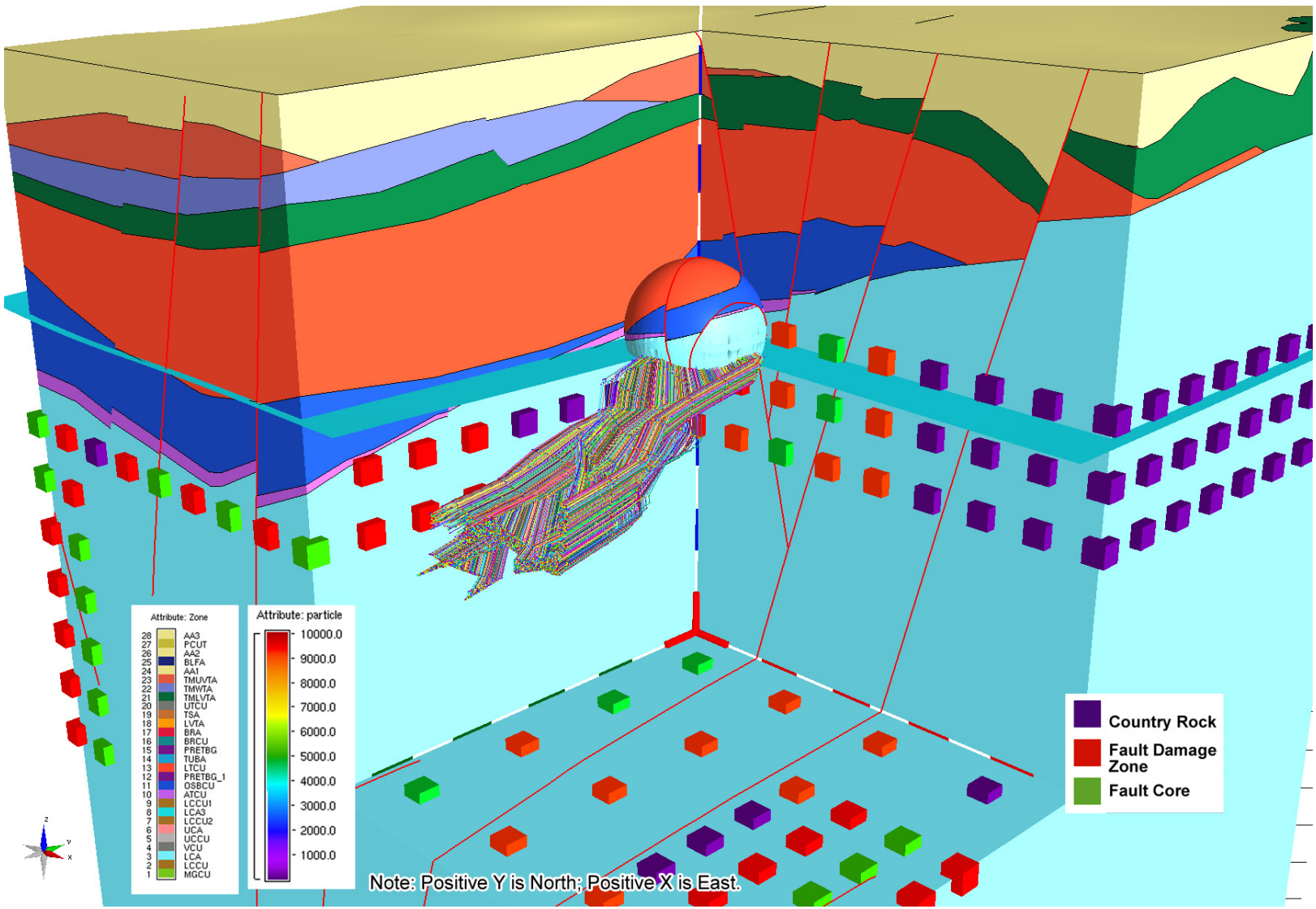

Figure 6-28
Perspective Plot of LCA Particle Trajectories from the BOURBON Detonation

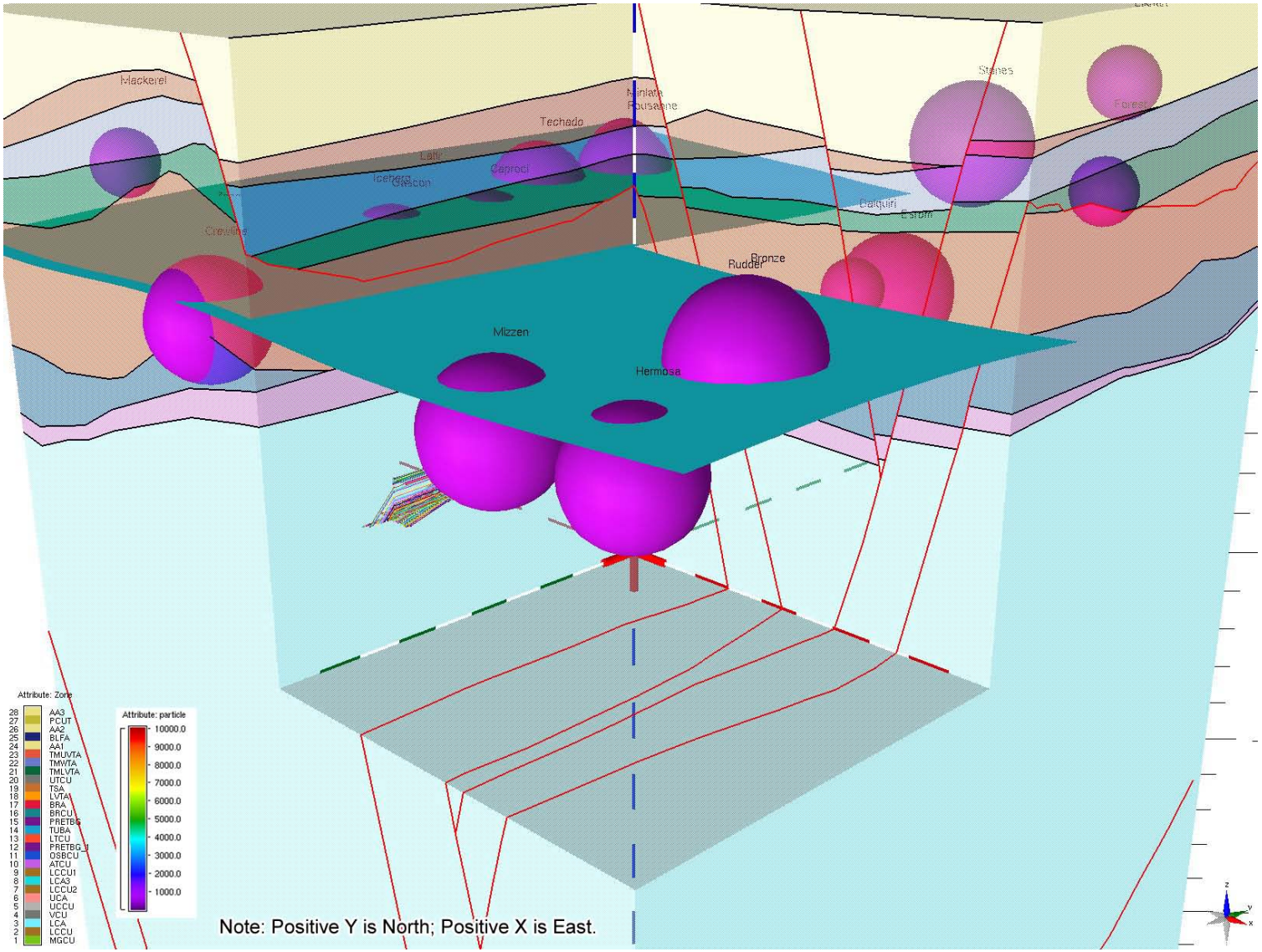

Note: Grey surface is the top of the water table in the alluvial/volcanic aquifer system. Spheres represent 2 R_c exchange volumes based on cavity radius calculated using the maximum of the yield range in DOE/NV (2000b) and the equation in Pawloski (1999).

Figure 6-29
Perspective Plot of LCA Particle Trajectories near Representative Nodes Receiving Contaminant Influx from the Saturated Alluvial/Volcanic Aquifer System Model

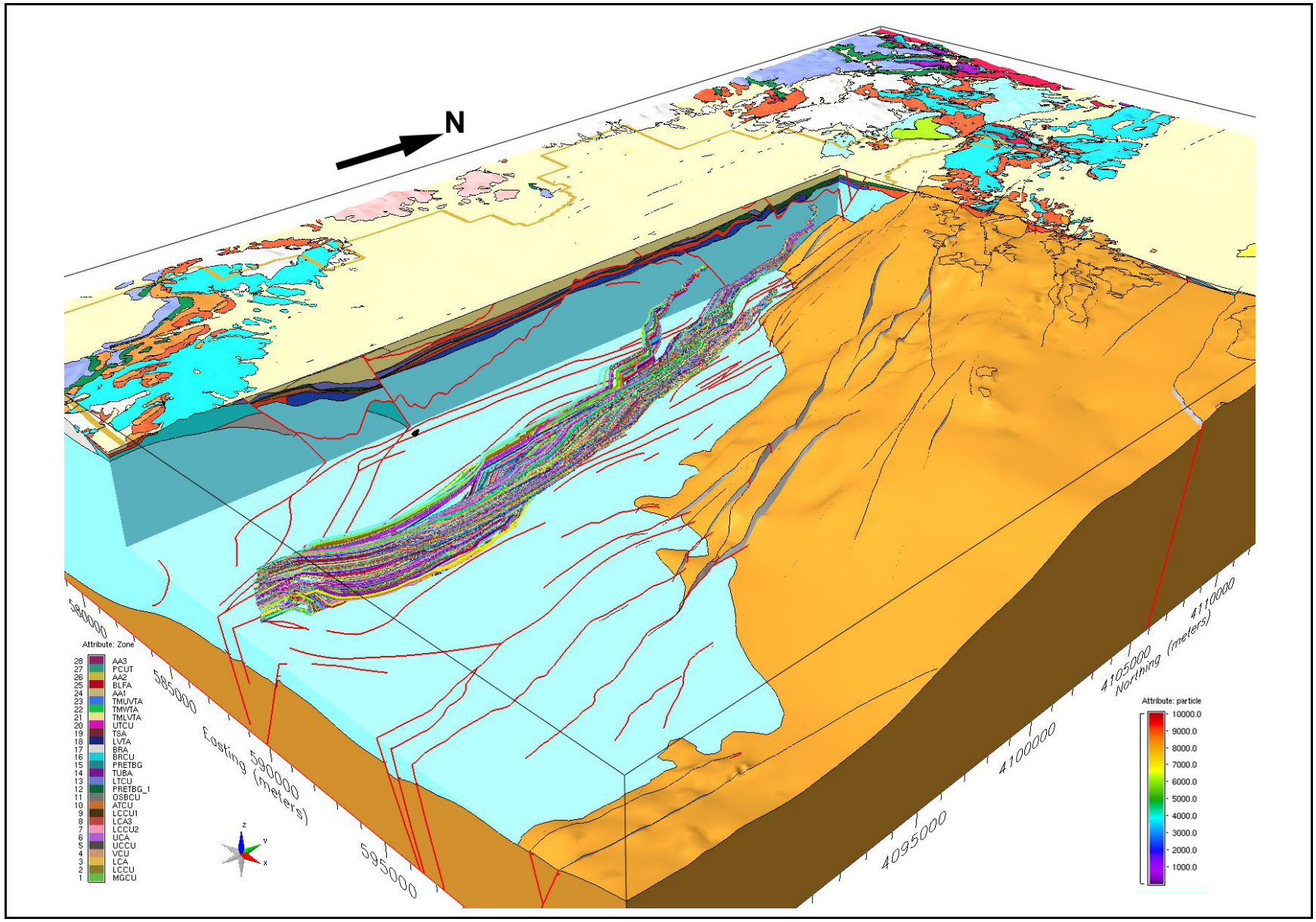

Figure 6-30
Perspective Plot of LCA Particle Trajectories from Representative Source Nodes

6.4.2 Unsaturated-Zone Source Inputs to the LCA Transport Model

The contaminant sources to the saturated LCA may be provided from one of three potential sources: (1) lateral and vertical contaminant migration from underground nuclear detonations conducted in unsaturated alluvial, volcanic, or carbonate rocks immediately above the water table in the LCA, (2) lateral and vertical contaminant migration from underground nuclear detonations conducted in saturated alluvial or volcanic rocks immediately above the saturated LCA, or (3) the fraction of underground nuclear detonation exchange volume inventory that is assumed to directly intersect the saturated LCA at the time of the detonation. The first two of these contaminant sources are provided from the output of the contaminant transport models of the unsaturated zone and saturated alluvial/volcanic aquifers system described in Sections 3.0 and 4.0, respectively.

For contaminant influx to the LCA emanating from contamination due to underground nuclear detonations conducted in either the unsaturated zone or the saturated alluvial/volcanic aquifer system overlying the LCA, the source input to the LCA is a mass flux (in moles per day [mol/day]) of individual radionuclide species at specified nodes in the LCA at discrete times. As discussed in Sections 3.0 and 4.0, the radionuclides that are considered in the unsaturated zone and saturated alluvial/volcanic aquifer system models to most significantly affect the extent of the contaminant boundary in the saturated LCA are ^{3}H, ^{99}Tc, ^{14}C, ^{36}Cl, ^{129}I, U, and ^{237}Np. As noted in Section 3.8, the unsaturated and saturated alluvial/volcanic aquifer contaminant flux of other screened radionuclides, such as ^{90}Sr and ^{137}Cs, that have a high initial concentration in the saturated LCA because of their low sorption potential in carbonate rocks is insignificant due to the large sorption of these radionuclides on non-carbonate rocks. The spatial and temporal distribution of this input flux varies for different scenarios and realizations of the unsaturated-zone and saturated-zone parameters. The discrete times are based on the time steps used in the unsaturated zone and saturated alluvial/volcanic aquifer system models, which in turn are related to the timing of individual detonations or groups of detonations, or a uniform time step for time periods after the 1992 moratorium on nuclear testing.

The inputs provided for the case of the unsaturated-zone sources consist of the spatial and temporal distribution of contaminant mass fluxes. As noted in Section 3.0, a number of different cases have been analyzed to explore a reasonable range of uncertainty in the unsaturated-zone flow and transport that could affect release rates from the unsaturated zone to the LCA, and hence the extent of contaminant migration in the LCA. The results below focus on two unsaturated-zone modeling cases, one that considers a background infiltration rate of 0.1 mm/yr, and the other that considers a higher

value of 1 mm/yr. The cases selected are denoted as cases 542121 and 121212, respectively. Other background infiltration and recharge rates were analyzed in the unsaturated zone and saturated alluvial/volcanic aquifer system models presented in Sections 3.0 and 4.0, respectively, notably, 5 and 10 mm/yr. The results of using an infiltration rate of 5 mm/yr are evaluated in a sensitivity analysis presented in Section 6.5.4. As discussed in Sections 3.0 and 4.0, the 10-mm/yr case is considered not likely and has not been propagated to evaluate the potential effects on LCA transport. Although there are other characteristics of unsaturated-zone flow and transport that differ in these two cases, as noted in Section 3.0, the principal factor affecting the forecast contaminant flux from the unsaturated-zone detonations to the saturated zone (whether the saturated alluvial/volcanic aquifer system or the saturated LCA) is the background average infiltration rate. As a result, choosing these two cases provides a reasonable bound on the expected conditions.

Representative spatial distributions of the total contaminant mass flux to the LCA from unsaturated-zone sources within 1,000 years for ^{3}H are illustrated in Figures 6-31 and 6-32. Figure 6-31 assumes an infiltration rate of 0.1 mm/yr, and Figure 6-32 assumes an infiltration rate of 1 mm/yr. Representative spatial distributions of the total contaminant mass flux to the LCA from unsaturated-zone sources within 1,000 years for ^{129}I, assuming infiltration rates of 0.1 and 1 mm/yr, are illustrated in Figures 6-33 and 6-34. A 1,000-year time window is selected to ensure that the total mass flux to the LCA that may affect the determination of the contaminant boundary is represented, even though the ^{3}H influx occurs principally in the first few decades after the underground nuclear testing. These figures illustrate that only a few locations significantly affect the cumulative mass flux into the LCA because they provide a significant fraction of the total contamination.

The temporal distributions of contaminant flux from the unsaturated-zone transport model to the saturated LCA model for ^{3}H and ^{129}I for an infiltration rate of 1 mm/yr (corresponding to run 121212) are illustrated in Figures 6-35 and 6-36. Similar figures assuming an infiltration rate of 0.1 mm/yr (corresponding to run 542121) are illustrated in Figures 6-37 and 6-38. The time zero corresponds to the initial time used in the unsaturated-zone transport model presented in Section 3.0. These results again reinforce the significant effect that the average infiltration rate has on the timing and rate of contaminant flux to the LCA as discussed in Section 3.0.

The most significant unsaturated-zone contaminant influx to the saturated LCA is contributed from a few underground nuclear detonations: BOURBON, TORRIDO (combined with a nearby detonation

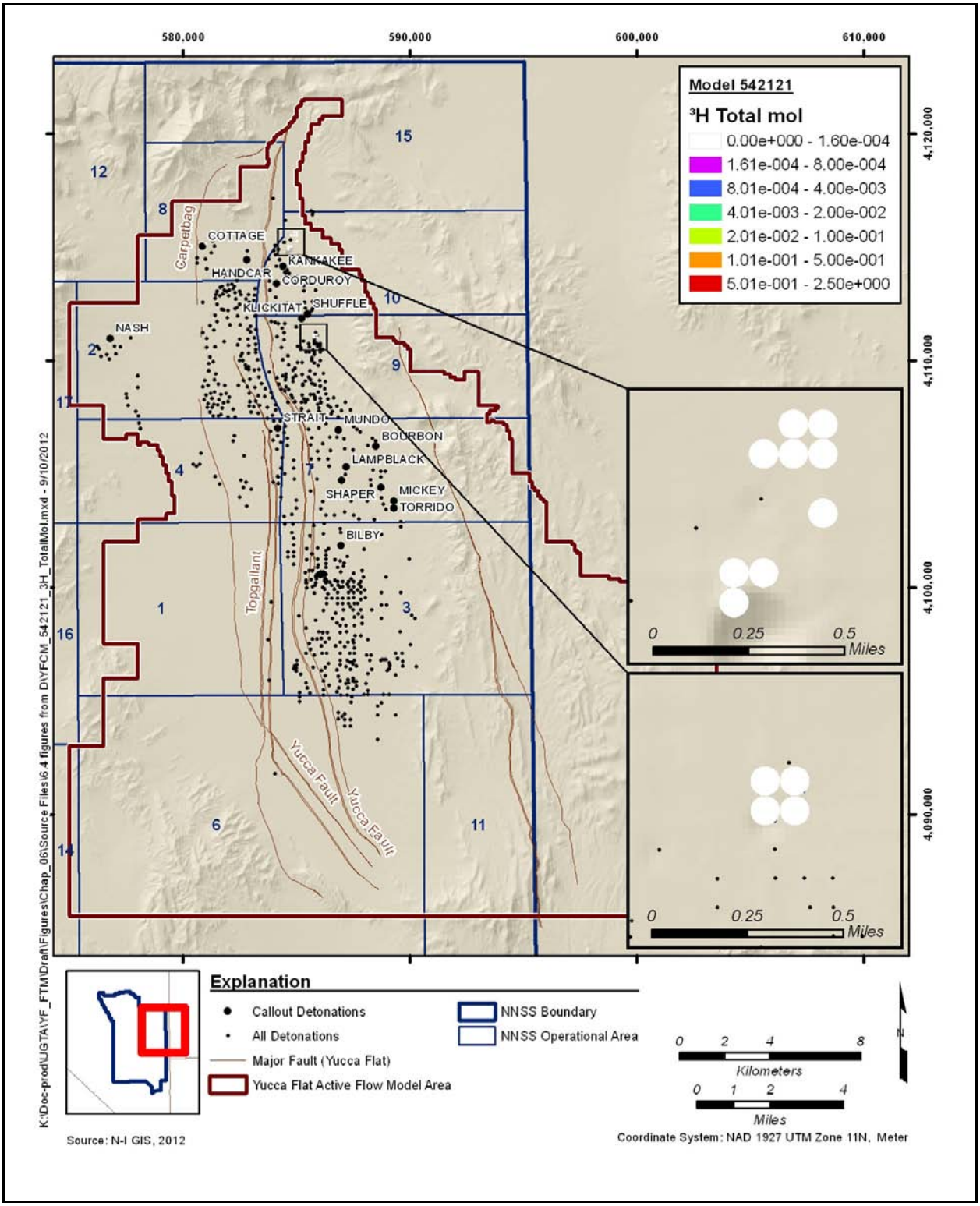

Figure 6-31
Map of Total ³H Flux to the LCA from Unsaturated-Zone Sources for Infiltration Rate of 0.1 mm/yr

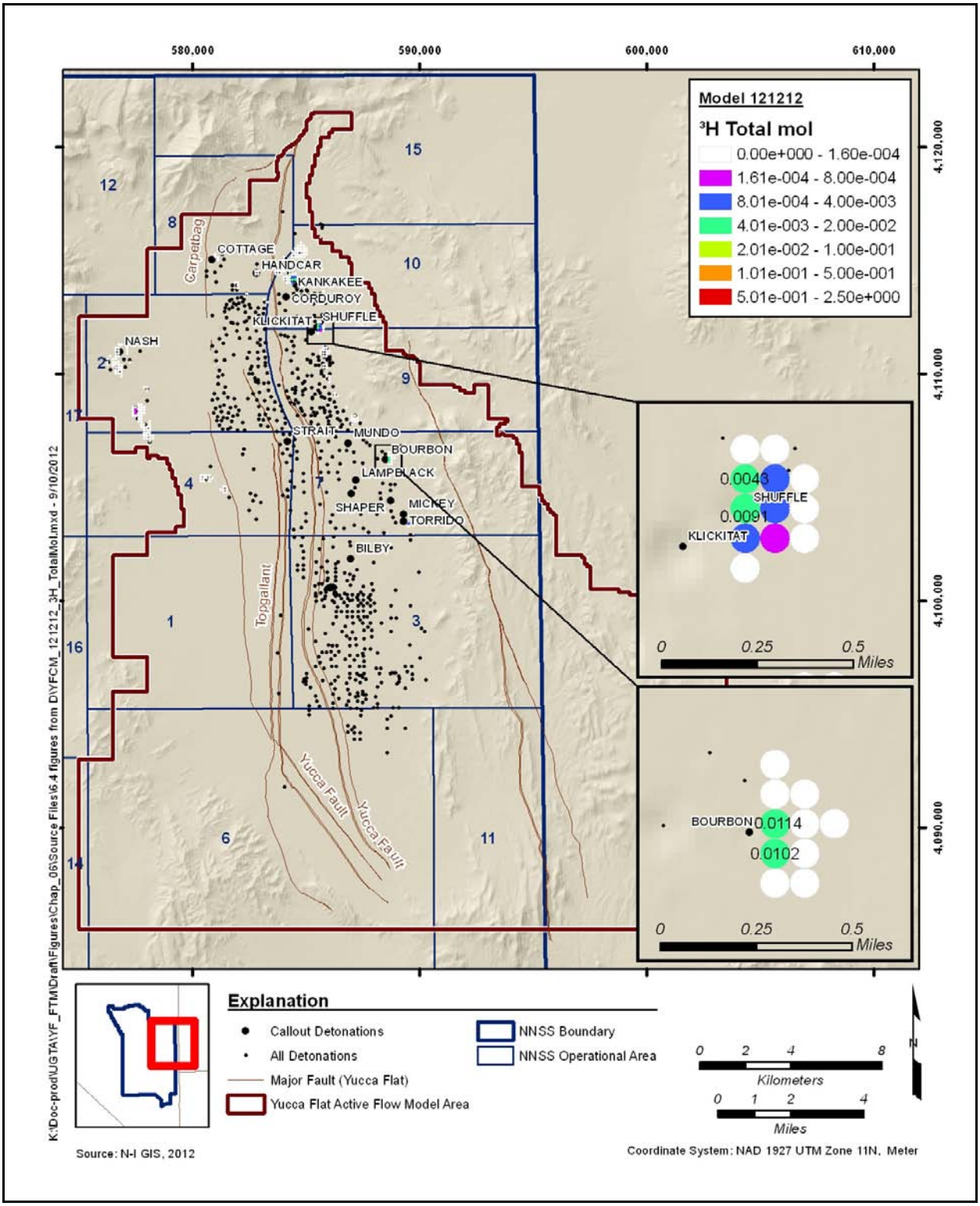

Figure 6-32
Map of Total ³H Flux to the LCA from Unsaturated-Zone Sources for Infiltration Rate of 1 mm/yr

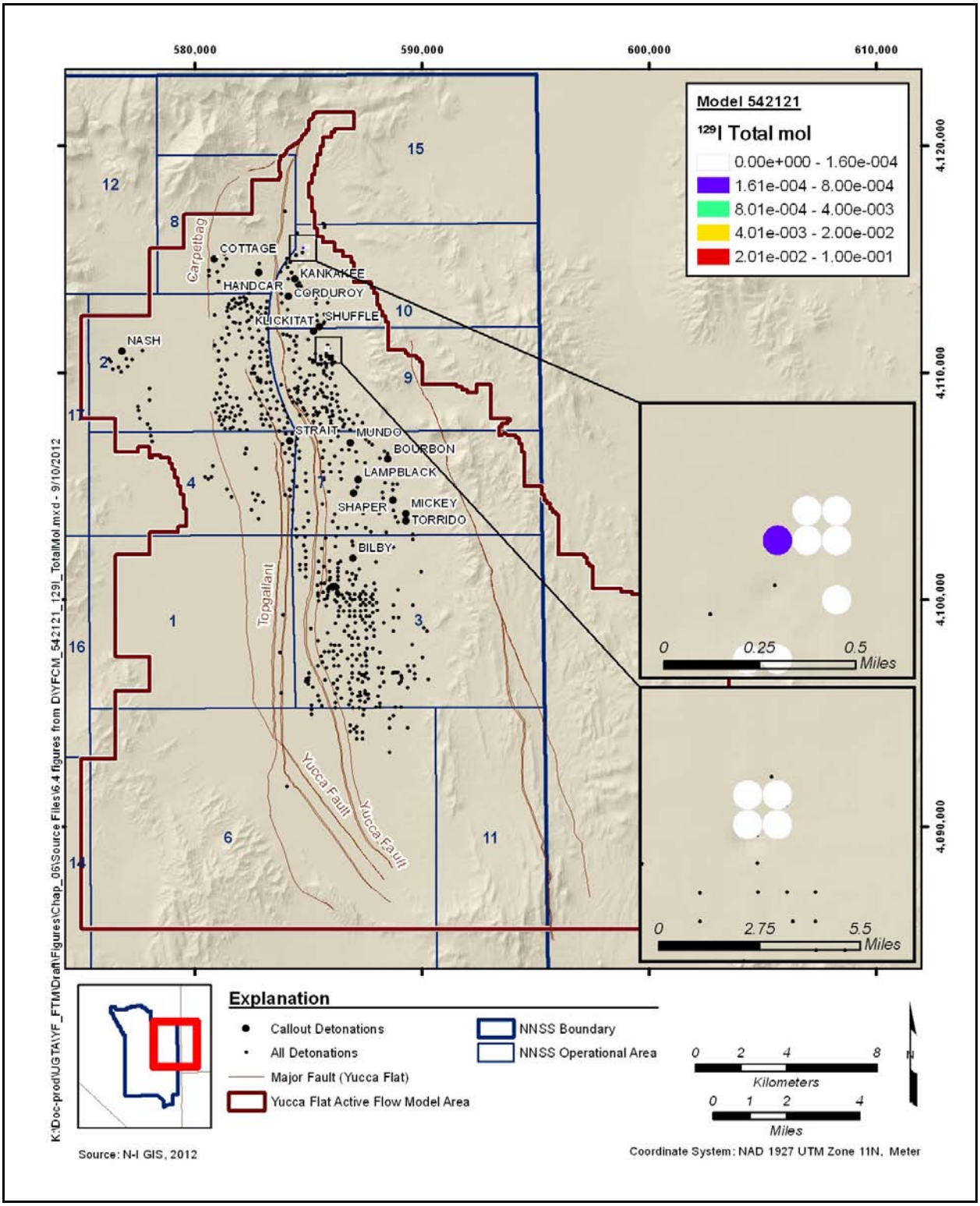

Figure 6-33
Map of Total ^{129}I Flux to the LCA from the Unsaturated-Zone Sources for Infiltration Rate of 0.1 mm/yr

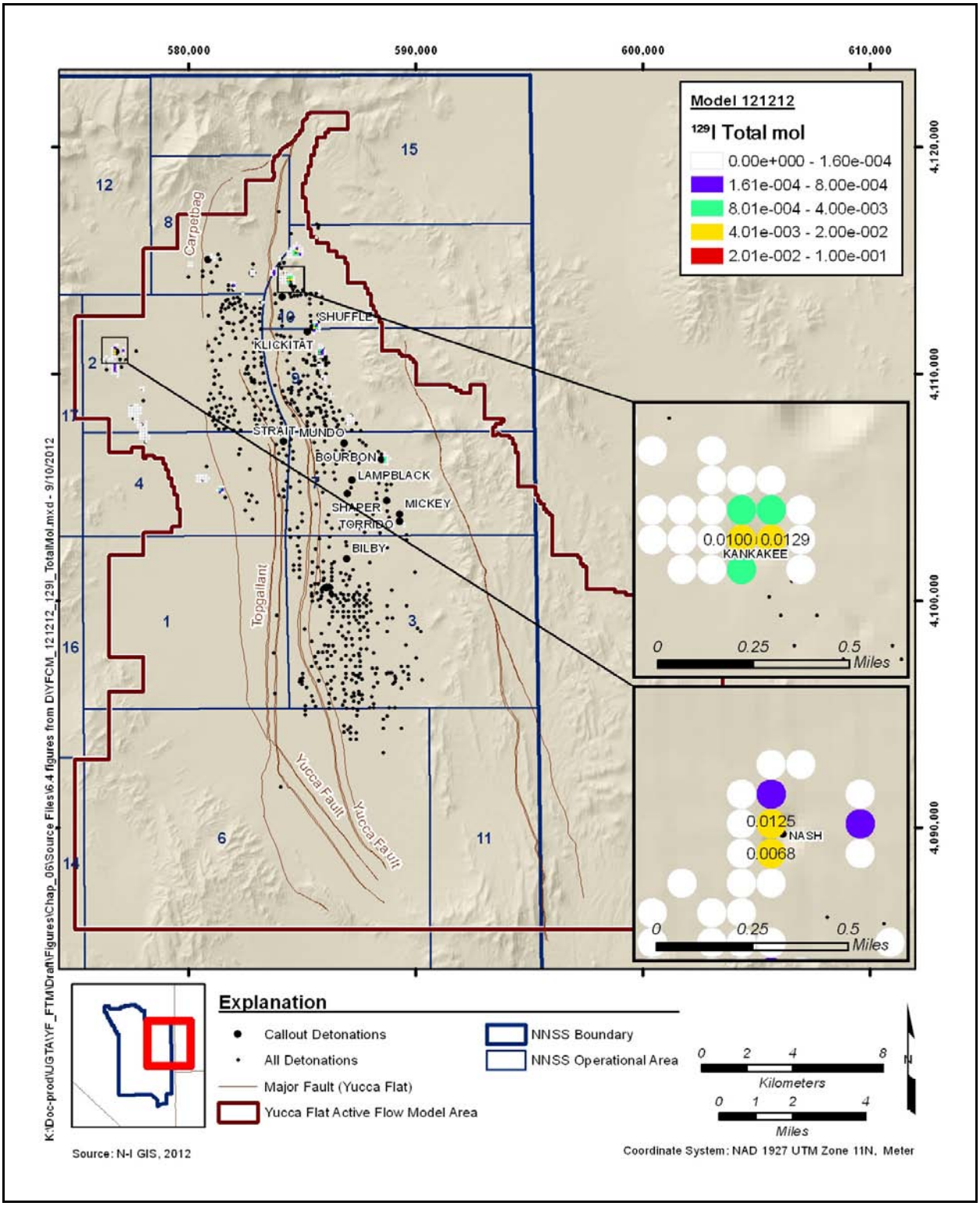

Figure 6-34
Map of Total ^{129}I Flux to the LCA from the Unsaturated-Zone Sources for Infiltration Rate of 1 mm/yr

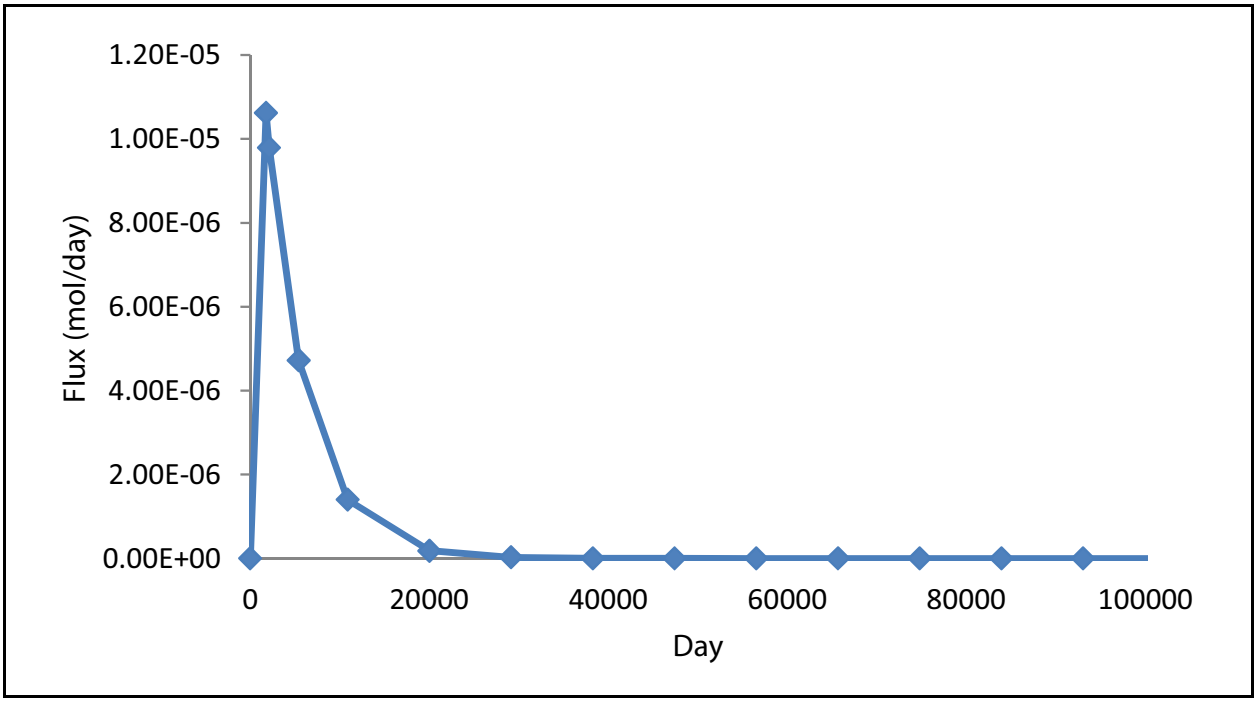

Figure 6-35
Time History of ^{3}H Flux to the LCA from Unsaturated-Zone Sources for Recharge Rate of 1 mm/yr

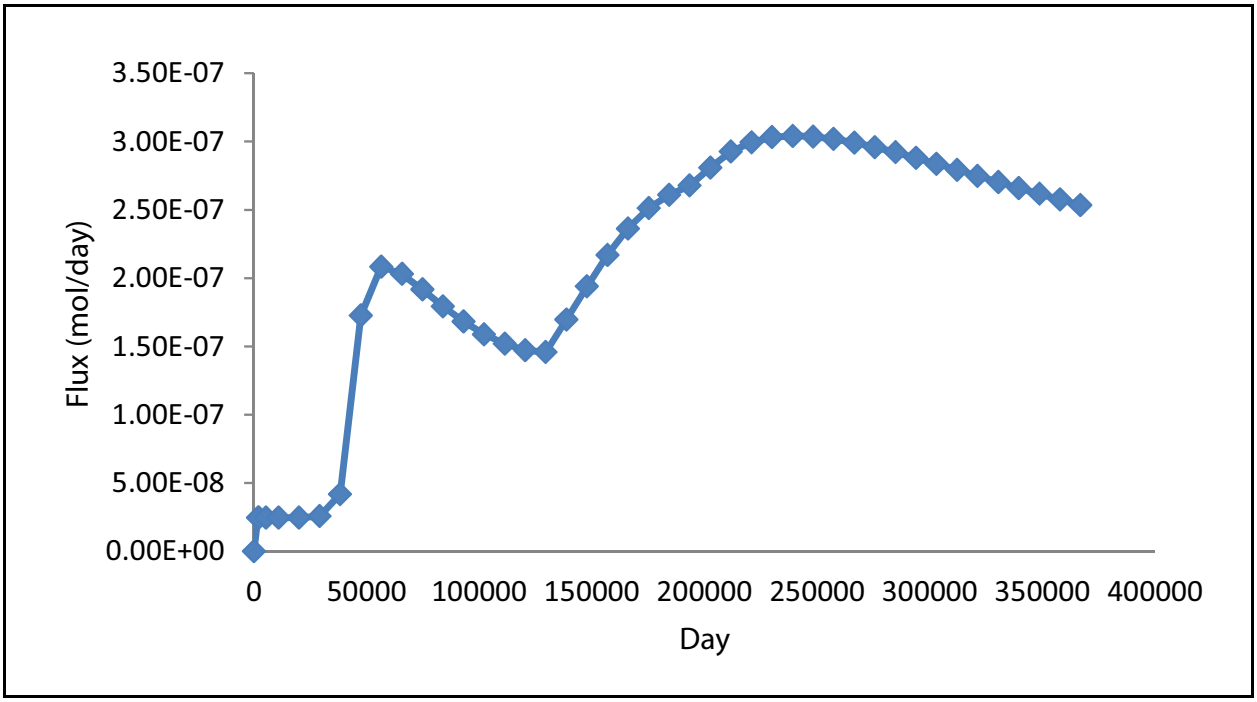

Figure 6-36
Time History of ^{129}I Flux to the LCA from Unsaturated-Zone Sources for Recharge Rate of 1 mm/yr

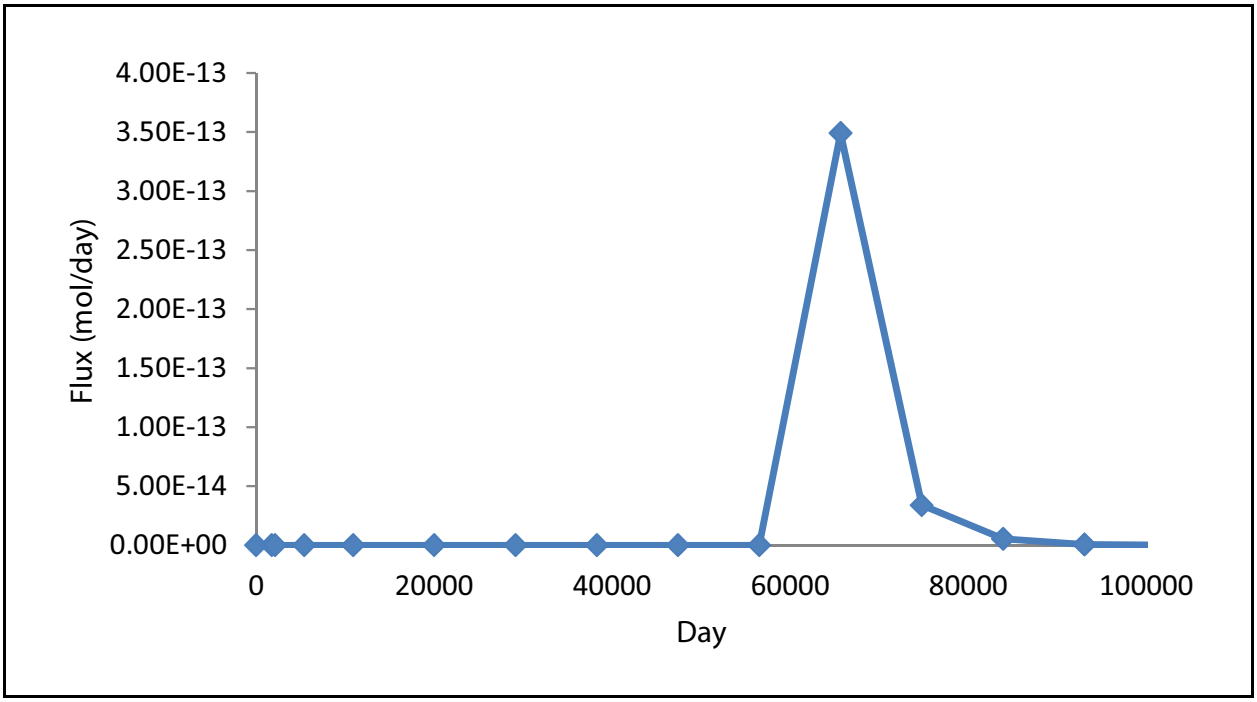

Figure 6-37
Time History of ^{3}H Flux to the LCA from Unsaturated-Zone Sources for Recharge Rate of 0.1 mm/yr

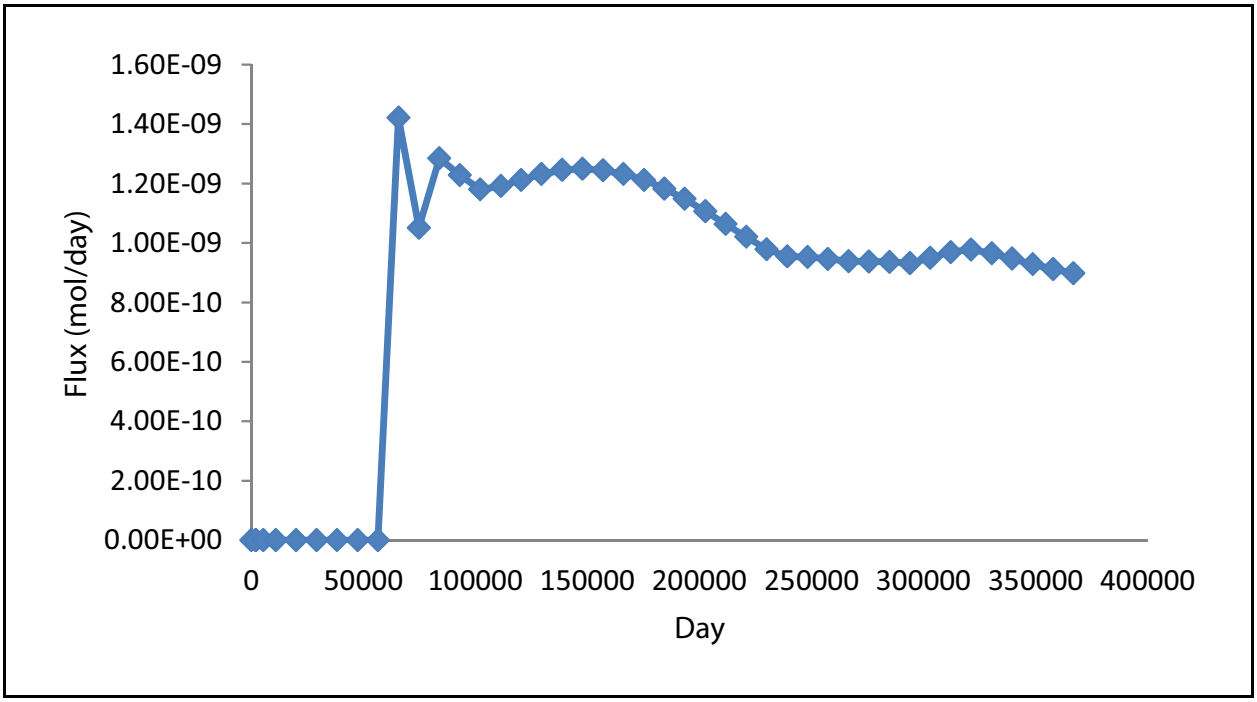

Figure 6-38
Time History of ^{129}I Flux to the LCA from Unsaturated-Zone Sources for Recharge Rate of 0.1 mm/yr

MICKEY), KANKAKEE, SHUFFLE (combined with a nearby detonation KLICKITAT), NASH, and HANDCAR. The temporal variations in contaminant fluxes from these source locations to the saturated LCA derived from the 1-mm/yr infiltration rate unsaturated-zone case 121212 are illustrated in Figures 6-39 and 6-40 for ^{3}H and ^{129}I, respectively.

The detonations that provide some significant contaminant flux to the saturated LCA very soon after the detonations were conducted include BOURBON, TORRIDO, KANKAKEE, and SHUFFLE. This is because these detonations have working points that are sufficiently close to the water table in the LCA (when the maximum announced yield of these detonations is considered) that the portion of contamination in the exchange volume immediately above the water table is calculated to enter the saturated zone soon after return to ambient flow conditions. NASH and HANDCAR are located sufficiently above the water table; thus, it takes several decades for contaminants to reach the water table from the edge of the exchange volume. KANKAKEE has the most significant fraction of the ^{129}I inventory released to the saturated LCA.

The temporal variation in the cumulative mass flux from all sources in the overlying unsaturated zone to the LCA for ^{3}H and ^{129}I is also illustrated in Figures 6-35 and 6-36, respectively. As expected, the most significant rate of ^{3}H input occurs in the first few decades following the detonation and then drops off as the ^{3}H decays. In contrast, the ^{129}I influx is minimal in the first few decades, but then the flux rate significantly increases as a result of the crater-enhanced recharge water and contaminant flux reaching the saturated LCA. About half of the total ^{129}I influx from the unsaturated-zone working-point detonations to the saturated LCA occurs in the first 200 years, and then the influx rate levels off over the next 800 years. This is primarily the result of the rapid transport of the fraction of the total inventory contained in the unsaturated-zone working-point detonation cavities and exchange volumes that are near or straddle the saturated LCA, or with cavities underlying the craters with the greatest crater-enhanced recharge, followed by the slower transport of the remainder of the initial unsaturated-zone inventory that exists either outside the crater areas or under craters with less crater-enhanced recharge. As illustrated in Figures 6-39 and 6-40, the most significant unsaturated-zone working-point source transport to the water table occurs from detonations with cavities or exchange volumes that straddle the LCA water table. As a result, of the total 1,000-year contaminant mass flux to the LCA from the unsaturated-zone working points, most is contributed by a few source nodes.

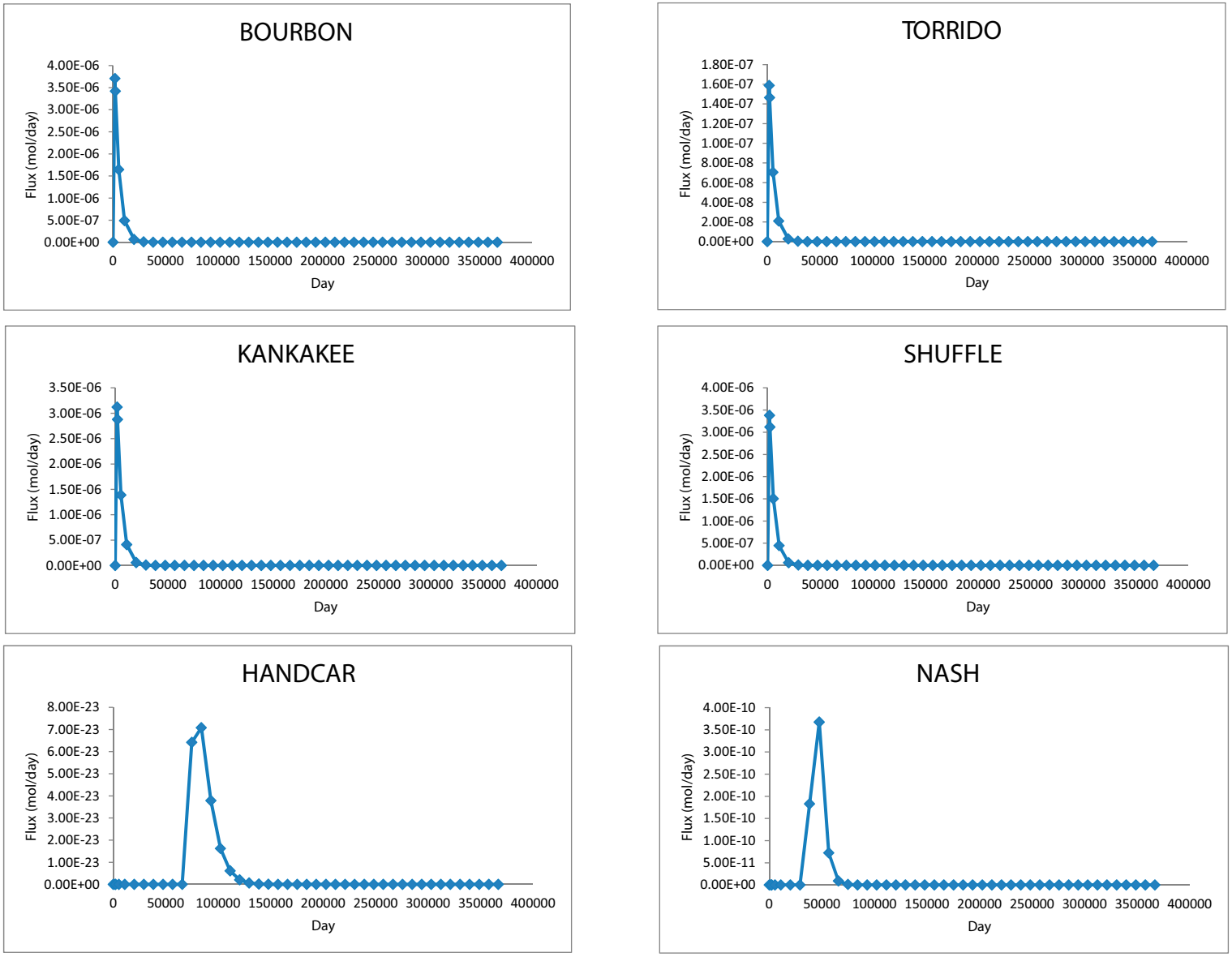

Figure 6-39
Temporal Variation in ^3H Flux to the LCA from Key Unsaturated-Zone Working-Point Detonations for Recharge Rate of 1 mm/yr

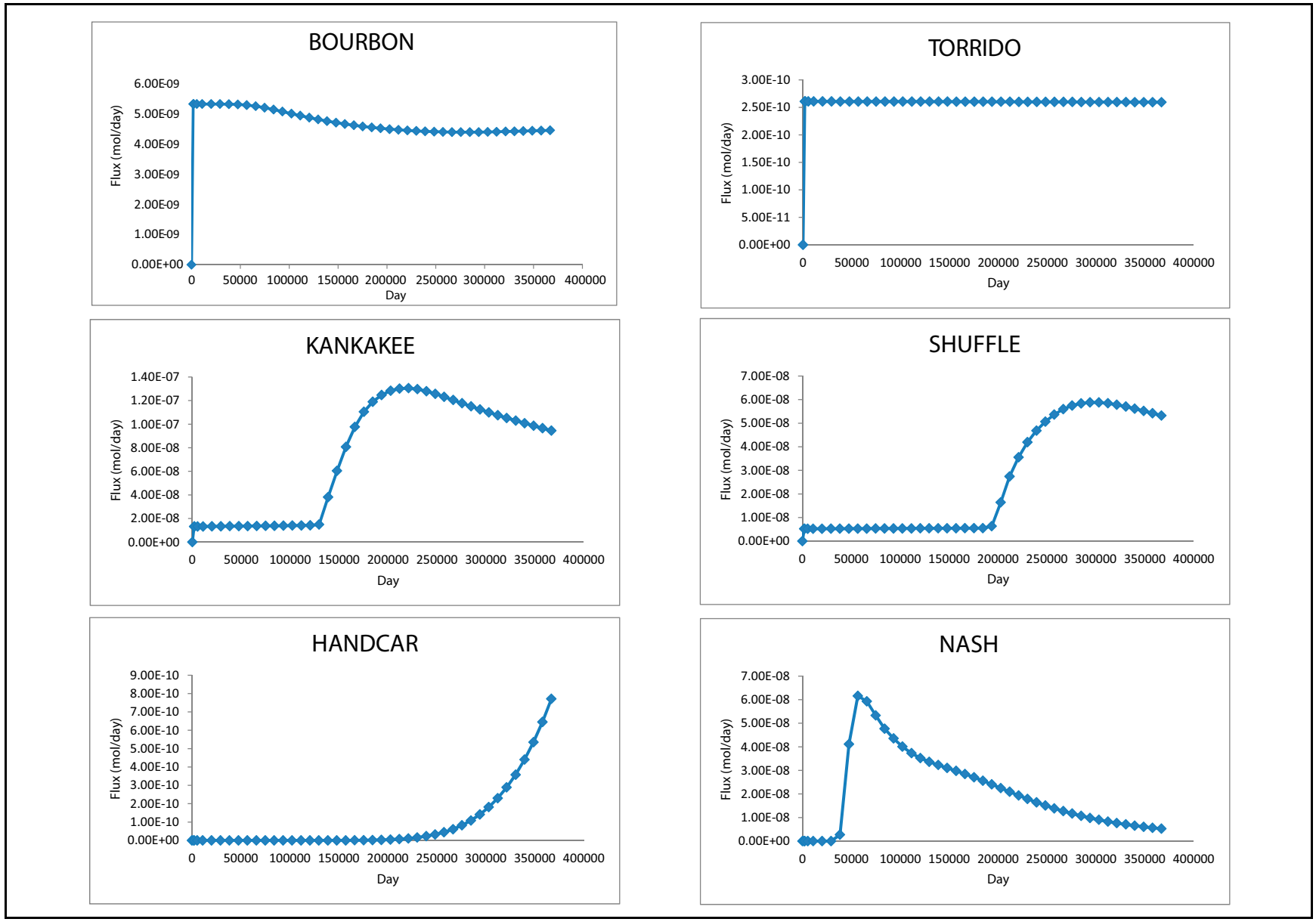

Figure 6-40
Temporal Variation in ^{129}I Flux to the LCA from Key Unsaturated-Zone Working-Point Detonations for Recharge Rate of 1 mm/yr

6.4.3 Saturated-Zone Source Inputs to the LCA Transport Model

The saturated alluvial/volcanic aquifer system immediately overlies the saturated LCA in the central portion of the Yucca Flat area. As described in Section 4.0, water that infiltrates through the unsaturated zone provides a spatially variable recharge to this aquifer system. Given the basinal structure of the volcanic units in Yucca Flat, groundwater flow and contaminant transport through the saturated alluvial/volcanic aquifer system eventually provides groundwater recharge and a contaminant mass flux to the saturated LCA.

The results presented in this section are based on results available from the saturated alluvial/volcanic aquifer system model presented in Section 4.0.

The groundwater recharge and associated contaminant transport to the saturated LCA from the overlying saturated alluvial/volcanic aquifer system is uncertain. As noted in Section 4.0, a number of different cases have been analyzed to explore a reasonable range of uncertainty in the saturated alluvial/volcanic aquifer system flow and transport that could affect release rates from the saturated zone to the LCA, and hence the extent of contaminant migration in the LCA. The results below focus on two saturated-zone modeling cases, one that uses a recharge corresponding to an infiltration rate of 0.1 mm/yr (run SAE_12), and one that uses a recharge corresponding to an average infiltration rate of 1 mm/yr (run SAE_2).

Based on the contaminant sources initially in place in the saturated alluvial/volcanic aquifer system as well as the contaminant influx to the saturated zone from the sources initially in the overlying unsaturated zone, contaminants can be transported through the saturated alluvial/volcanic aquifer system to the underlying LCA. Figures 6-41 and 6-42 illustrate the spatial distribution of the 1,000-year cumulative contaminant mass flux to the LCA from the overlying alluvial/volcanic aquifer system for ^{3}H for net infiltration rates of 0.1 and 1 mm/yr, respectively. Figures 6-43 and 6-44 illustrate the spatial distribution of the 1,000-year cumulative contaminant mass flux to the LCA from the overlying alluvial/volcanic aquifer system for ^{129}I for net infiltration rates of 0.1 and 1 mm/yr, respectively. As described in Section 4.0, the contaminant influx to the LCA is concentrated along major fault discontinuities through the thick low-permeability tuff confining units. As anticipated and discussed in Section 4.0, the cumulative contaminant mass flux is much greater for the 1-mm/yr infiltration rate case than for the 0.1-mm/yr infiltration rate case.

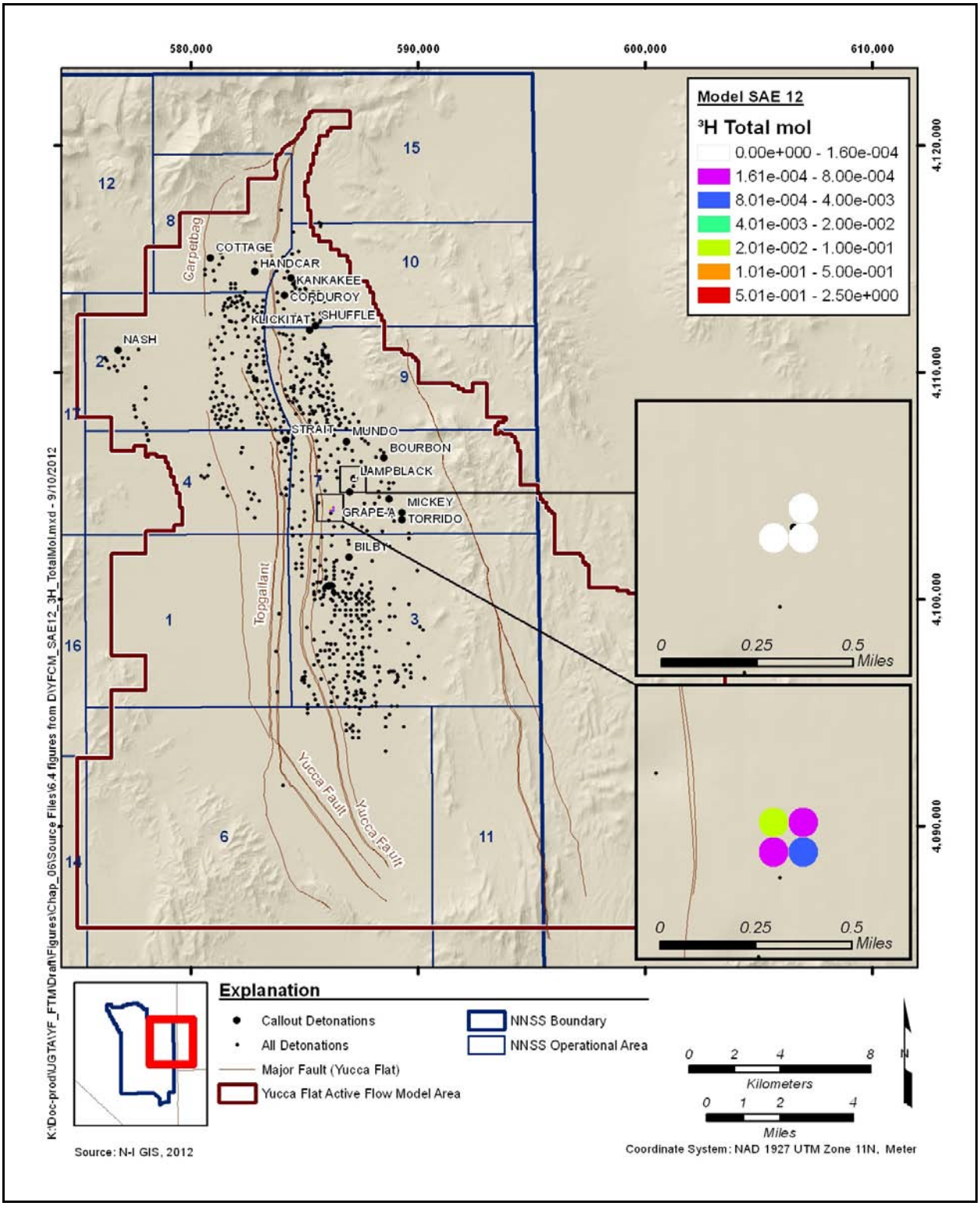

Figure 6-41
Map of 1,000-Year Cumulative ³H Mass Flux from the Saturated Alluvial/Volcanic Aquifer System to the LCA for Infiltration Rate of 0.1 mm/yr

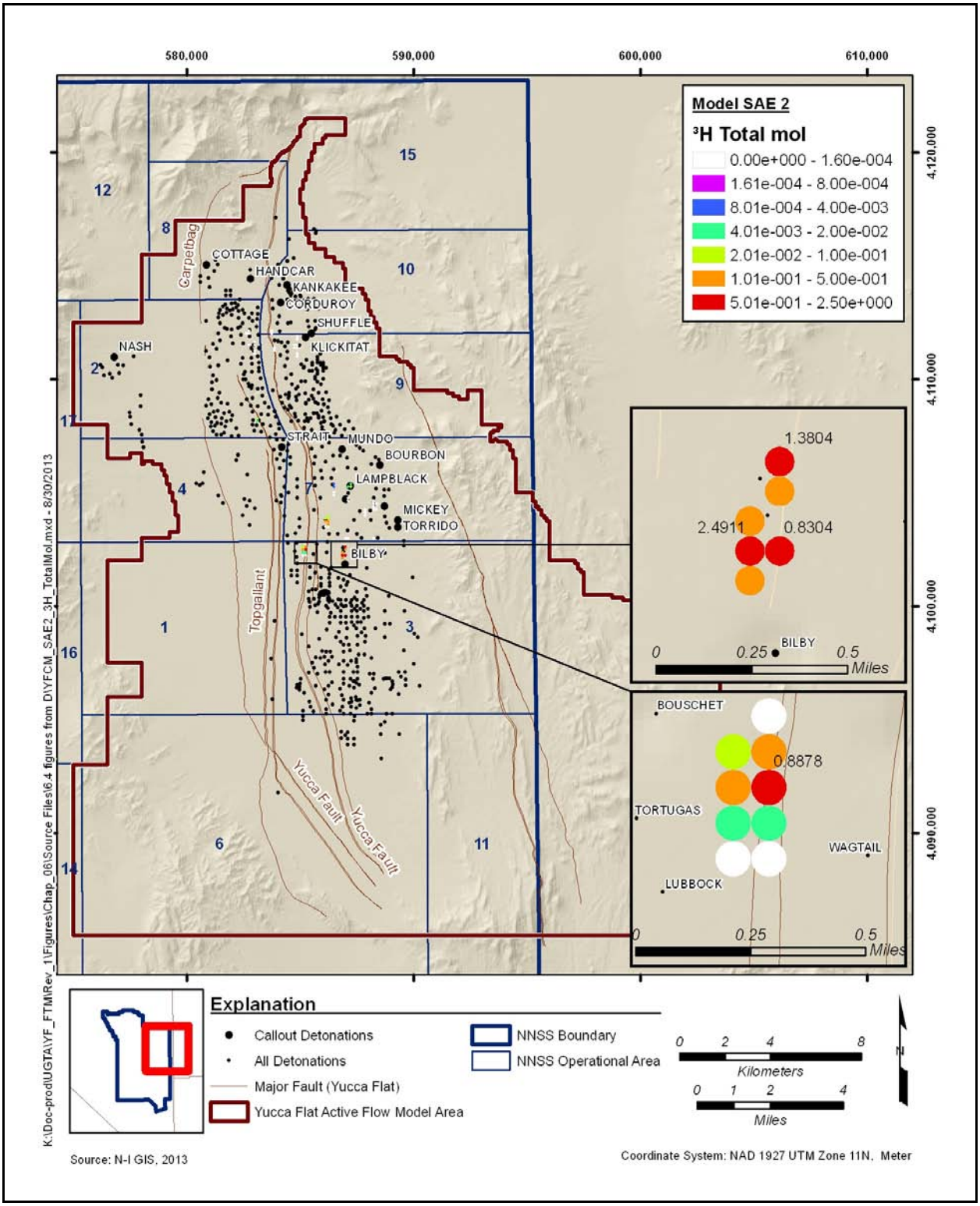

Figure 6-42
Map of 1,000-Year Cumulative ^{3}H Mass Flux from the Saturated Alluvial/Volcanic Aquifer System to the LCA for Infiltration Rate of 1 mm/yr

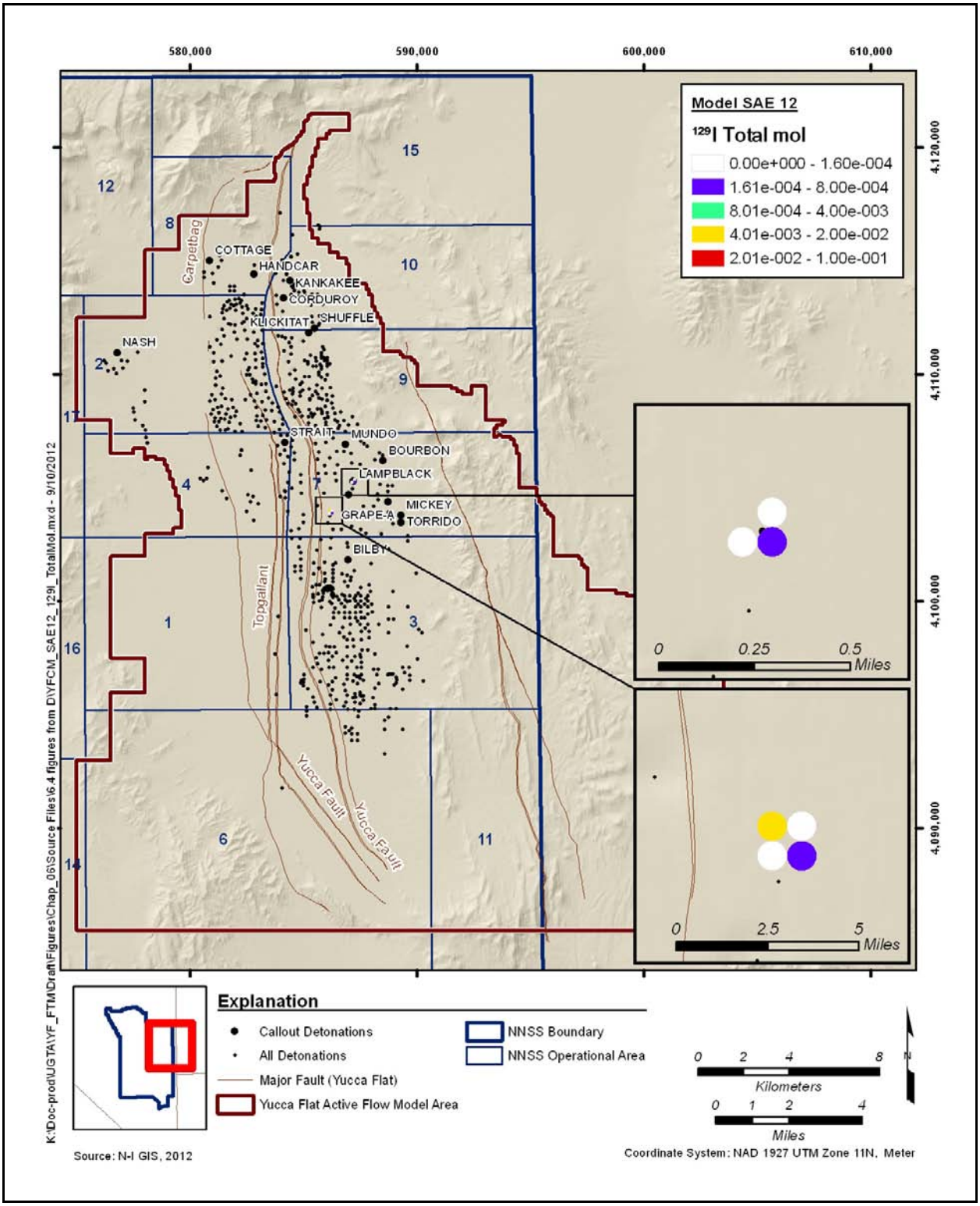

Figure 6-43
Map of 1,000-Year Cumulative ^{129}I Mass Flux from the Saturated Alluvial/Volcanic Aquifer System to the LCA for Infiltration Rate of 0.1 mm/yr

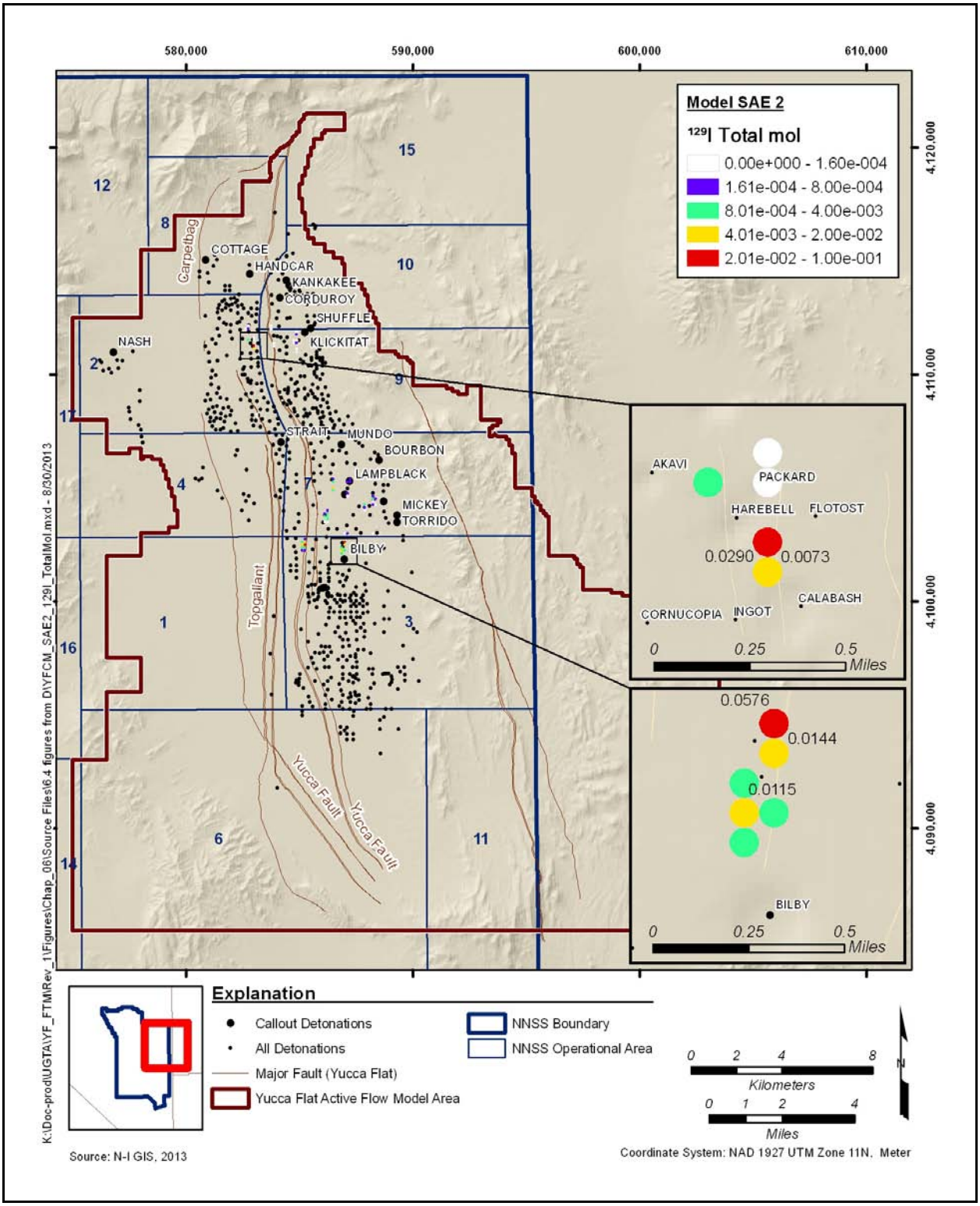

Figure 6-44
Map of 1,000-Year Cumulative ^{129}I Mass Flux from the Saturated Alluvial/Volcanic Aquifer System to the LCA for Infiltration Rate of 1 mm/yr

As a result of the significant transient flow regime caused by the underground nuclear testing, the temporal distribution of the total contaminant mass flux from the saturated alluvial/volcanic aquifer system to the LCA is variable as illustrated in Figures 6-45 and 6-46 for ^{3}H and ^{129}I, respectively. As in the case of the unsaturated-zone working-point detonations, this variability is dominated by a small fraction of the total source locations as illustrated in Figures 6-42 and 6-44 for ^{3}H and ^{129}I, respectively.

As in the case of the unsaturated-zone working-point detonations, it is useful to examine the time rate of contaminant mass flux from the saturated alluvial/volcanic aquifer system to the saturated LCA. Figures 6-45 to 6-48 illustrate the time rate of flux of ^{3}H and ^{129}I to the saturated LCA for infiltration rates of 1 and 0.1 mm/yr. The total flux of ^{3}H to the LCA is dominated by the influx in the first few decades during the underground nuclear testing. In contrast, the total flux of ^{129}I is small at early times, and increases with time for the first few hundred years and then decreases with time to 1,000 years. Again, this is the result of the significant decay of ^{3}H given its 12.3-year half-life and the releases from cavities that are closest to major faults.

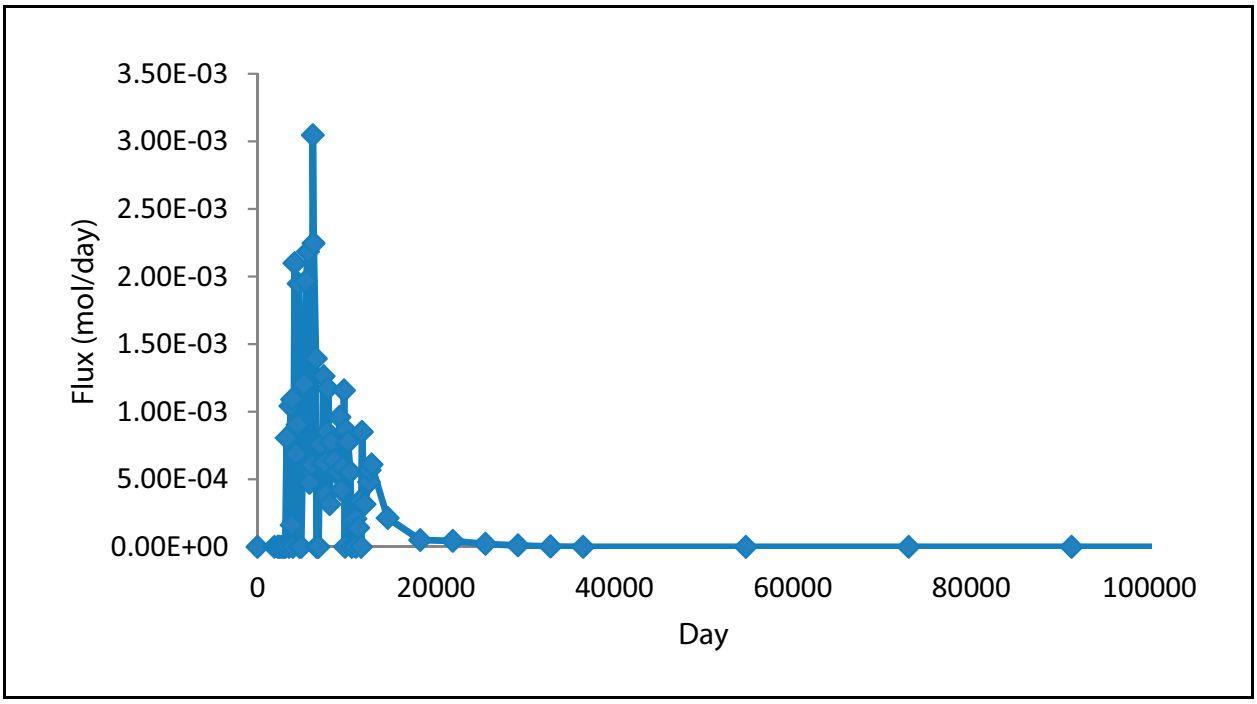

Figure 6-45
Time History of Total ^{3}H Mass Flux from the Saturated Alluvial/Volcanic Aquifer System to the LCA for Recharge Rate of 1 mm/yr

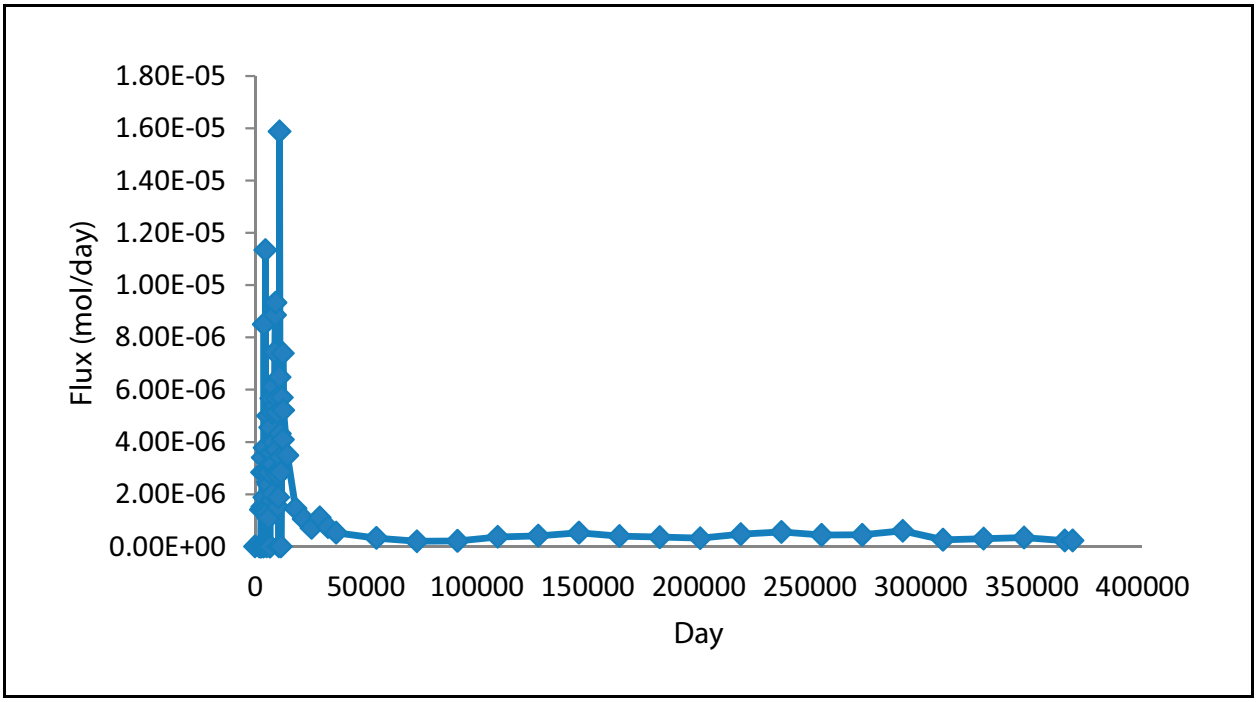

Figure 6-46
Time History of Total ^{129}I Mass Flux from the Saturated Alluvial/Volcanic Aquifer System to the LCA for Recharge Rate of 1 mm/yr

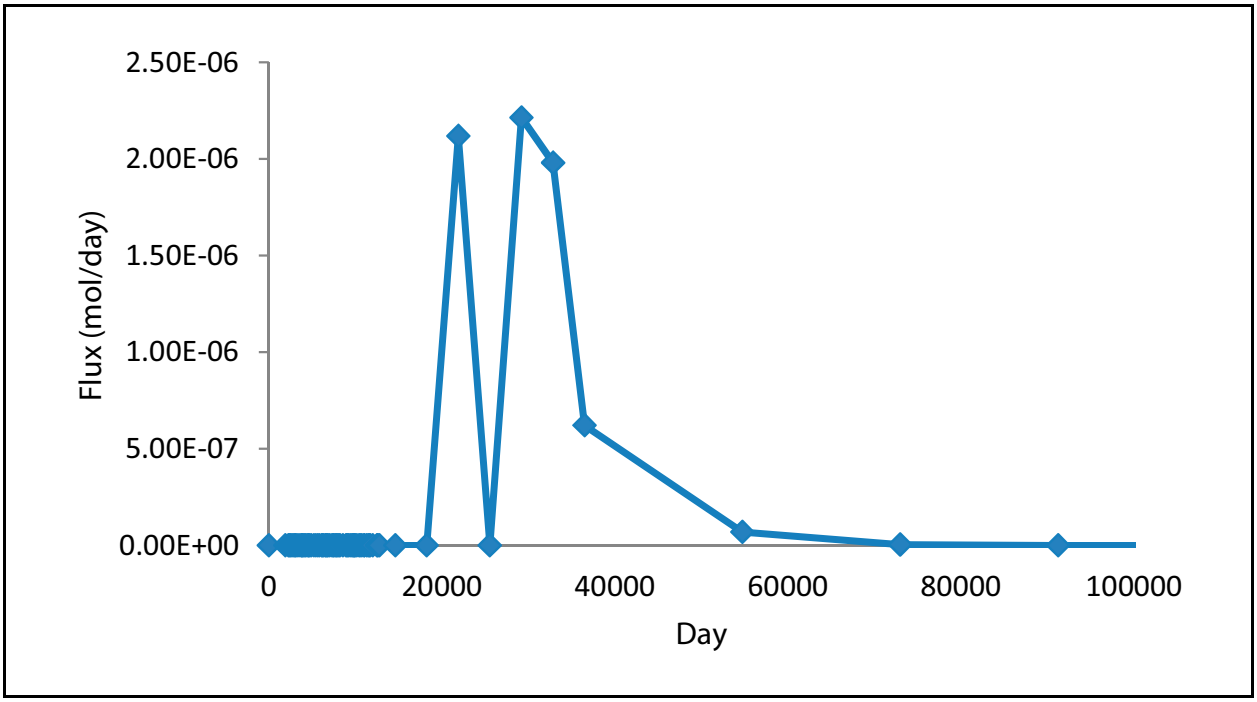

Figure 6-47
Time History of Total ^{3}H Mass Flux from the Saturated Alluvial/Volcanic Aquifer System to the LCA for Recharge Rate of 0.1 mm/yr

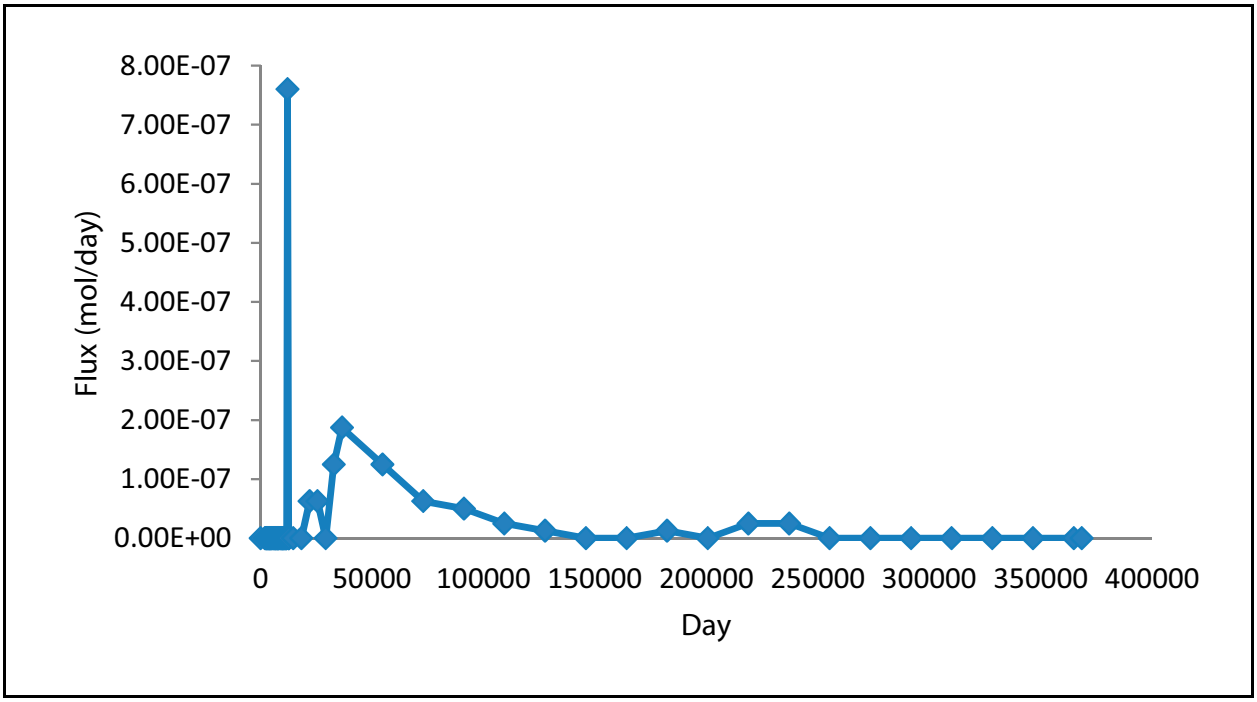

Figure 6-48
Time History of Total ^{129}I Mass Flux from the Saturated Alluvial/Volcanic Aquifer System to the LCA for Recharge Rate of 0.1 mm/yr

The spatial variability in ^{14}C contaminant mass flux from the saturated alluvial/volcanic aquifer system to the LCA is illustrated at several discrete times in Section 4.0. The spatial variability illustrates that the most significant source inputs to the LCA vary with time (because of different detonations conducted at different times) and reconfirms that only a few of the source-node locations contribute significantly to the total contaminant mass flux to the LCA. For example, of the total 1,000-year contaminant mass flux to the LCA from the saturated alluvial/volcanic aquifer system (which is principally associated with underground nuclear detonations with saturated-zone working points) for the 1-mm/yr infiltration rate case, 99.6 percent of the total 1,000-year ^{3}H flux of 8.35 mol and 93.8 percent of the total ^{129}I flux of 0.196 mol are contributed by the top 20 source locations (Figures 6-49 and 6-50). The different colors on these plots represent different source-node locations. These cumulative flux releases to the LCA can be compared to the initial mobile inventories in place in the portion of the exchange volumes that intersect the saturated alluvial/volcanic aquifer system of 2,090 and 7.45 mol for ^{3}H and ^{129}I, respectively, for the 2 R_c uniform-mass-based HST allocation method.

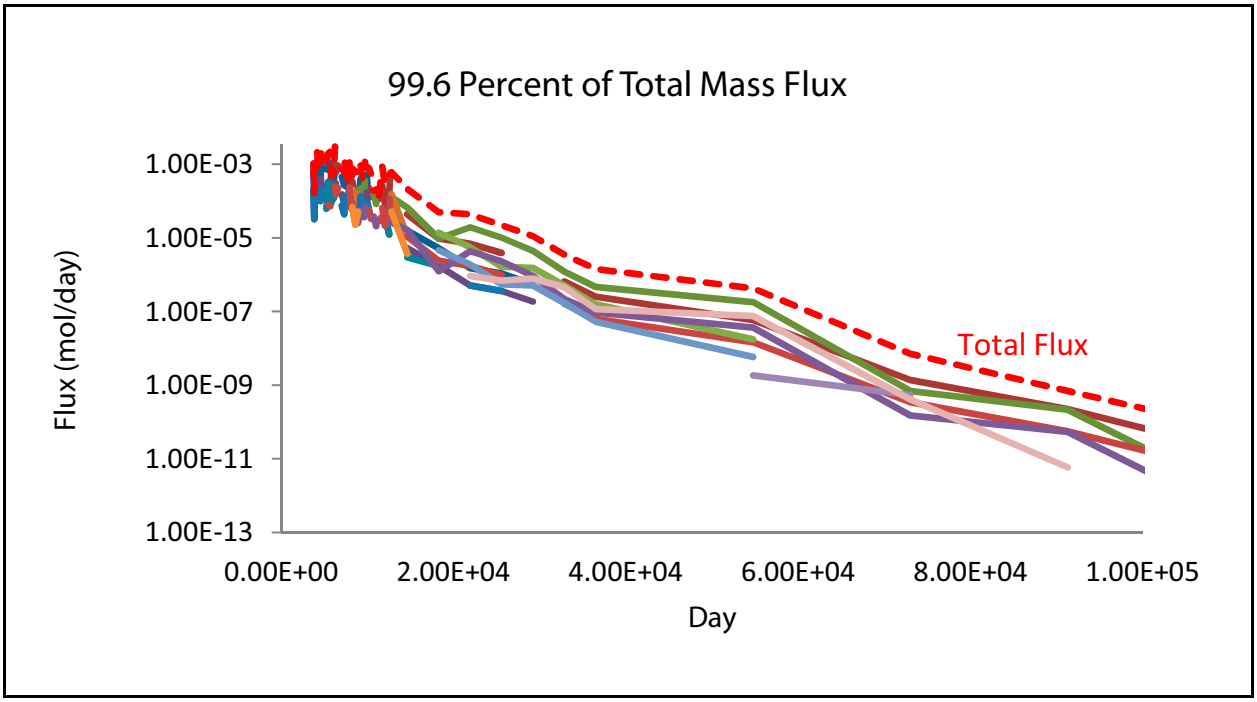

Figure 6-49
Time History of ^{3}H Mass Flux from the Top 20 Saturated Alluvial/Volcanic Aquifer System Source Nodes to the LCA for Recharge Rate of 1 mm/yr

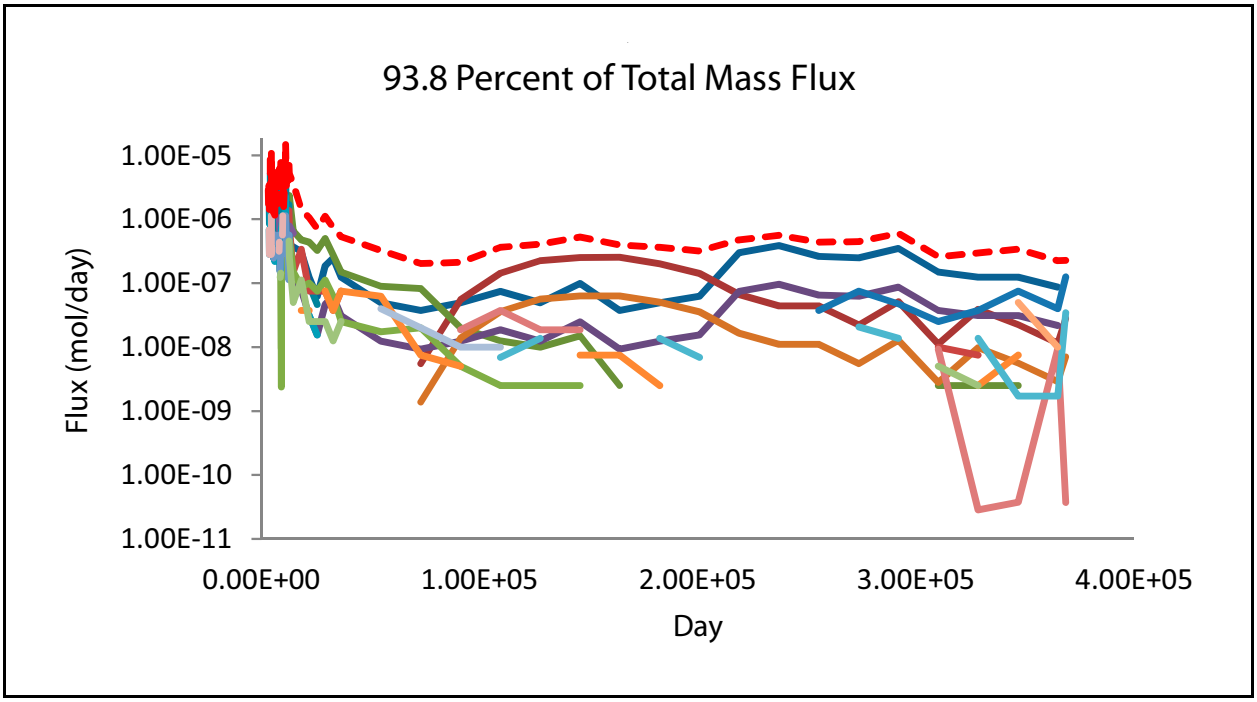

Figure 6-50
Time History of ^{129}I Mass Flux from the Top 20 Saturated Alluvial/Volcanic Aquifer System Source Nodes to the LCA for Recharge Rate of 1 mm/yr

The most significant source areas for saturated alluvial/volcanic aquifer system releases to the LCA are associated with the following underground detonations: BILBY (in northwest Area 3), TORTUGAS (in northwest Area 3), and LAMPBLACK (in Area 7). Temporal variations in contaminant fluxes from these source areas are illustrated in Figures 6-51 and 6-52 for ^{3}H and ^{129}I, respectively. Additional locations of significance that are not illustrated include STARWORT (in southeast Area 2), and BARREGO/BASEBALL (in southwest Area 7). These are not illustrated because the LCA nodes receiving contamination near these sources are distributed areally, and determining the precise source of the contamination is difficult. These detonations with working points in the saturated alluvial/volcanic aquifer system provide a significant fraction of the contaminant source to the saturated LCA because of their proximity to faults that either directly intersect the exchange volumes of the detonations or intersect aquifers that in turn intersect the exchange volumes.

6.4.4 LCA Source Inputs to the LCA Transport Model

The number of underground nuclear detonations with exchange volumes that are likely to intersect the saturated LCA is a function of the assumed radius of the exchange volume. Because uncertainty exists in the exchange volume radius and in the fraction of the inventory that may be present in the LCA for those detonations with exchange volumes that straddle the LCA, a range of different assumptions of initial source input to the LCA have been developed as discussed in Section 2.3.2.

Based on the Bowen inventory (Bowen et al., 2001) decay corrected to the time of the detonation, the initial distribution of contaminant mass (in moles) for ^{3}H, ^{14}C, ^{129}I, and ^{90}Sr in the saturated LCA at the 12 detonations with a 2 R_c exchange volume radius that intersects the saturated LCA is presented in Table 6-5.

As expected, the largest fraction of the initial inventory in place in the LCA is associated with those detonations that have a larger pore volume fraction intersecting the saturated LCA, such as BOURBON, CORDUROY, and TORRIDO.

6.4.5 Comparison of Source Inputs to the LCA Transport Model

Comparing the input mass flux from the unsaturated- and saturated-zone source regions, it is apparent that even though almost 61 percent of the total radionuclide inventory is initially within the

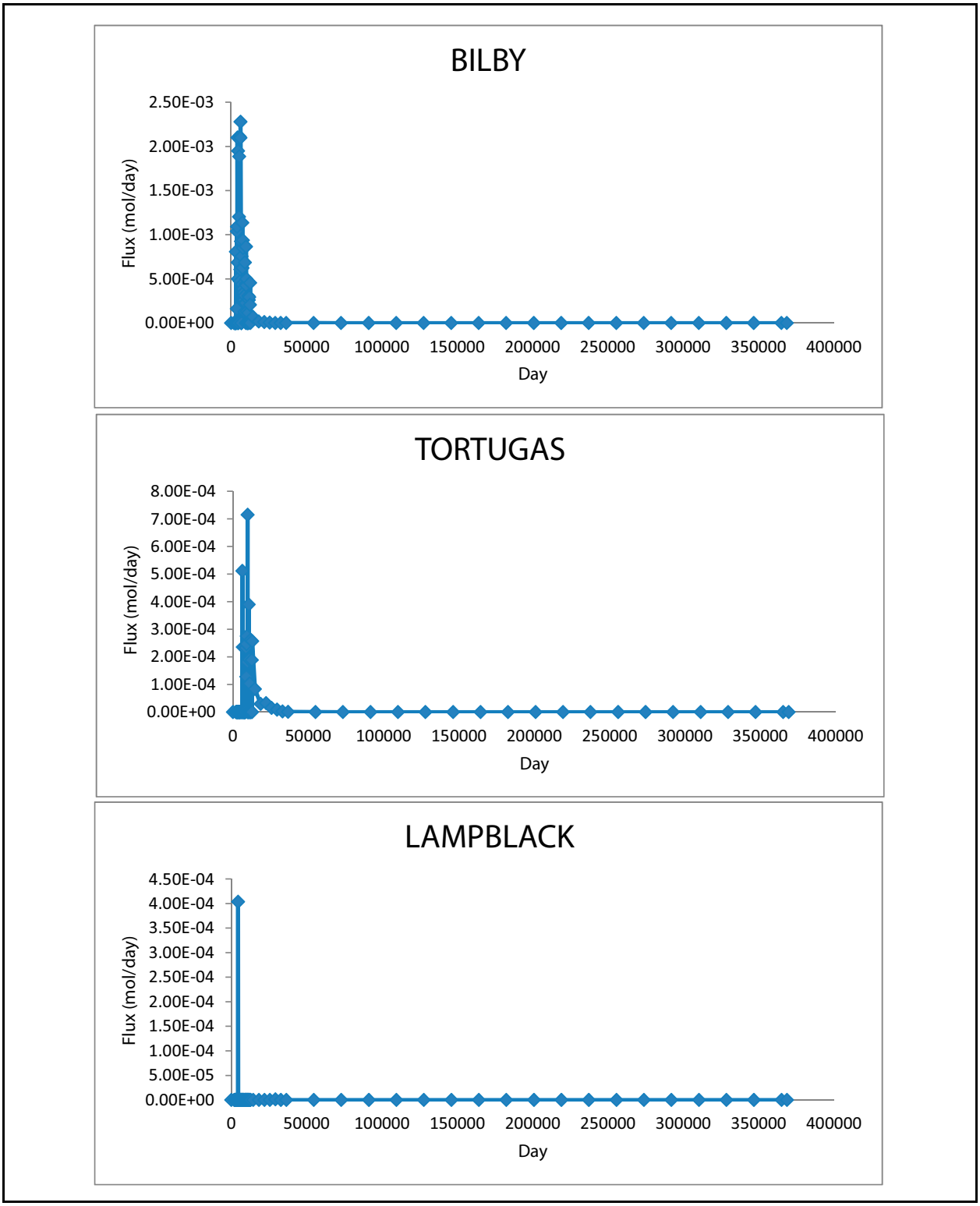

Figure 6-51
Temporal Variation in ^3H Flux to the LCA from Key Saturated-Zone Working-Point Detonations for Recharge Rate of 1 mm/yr

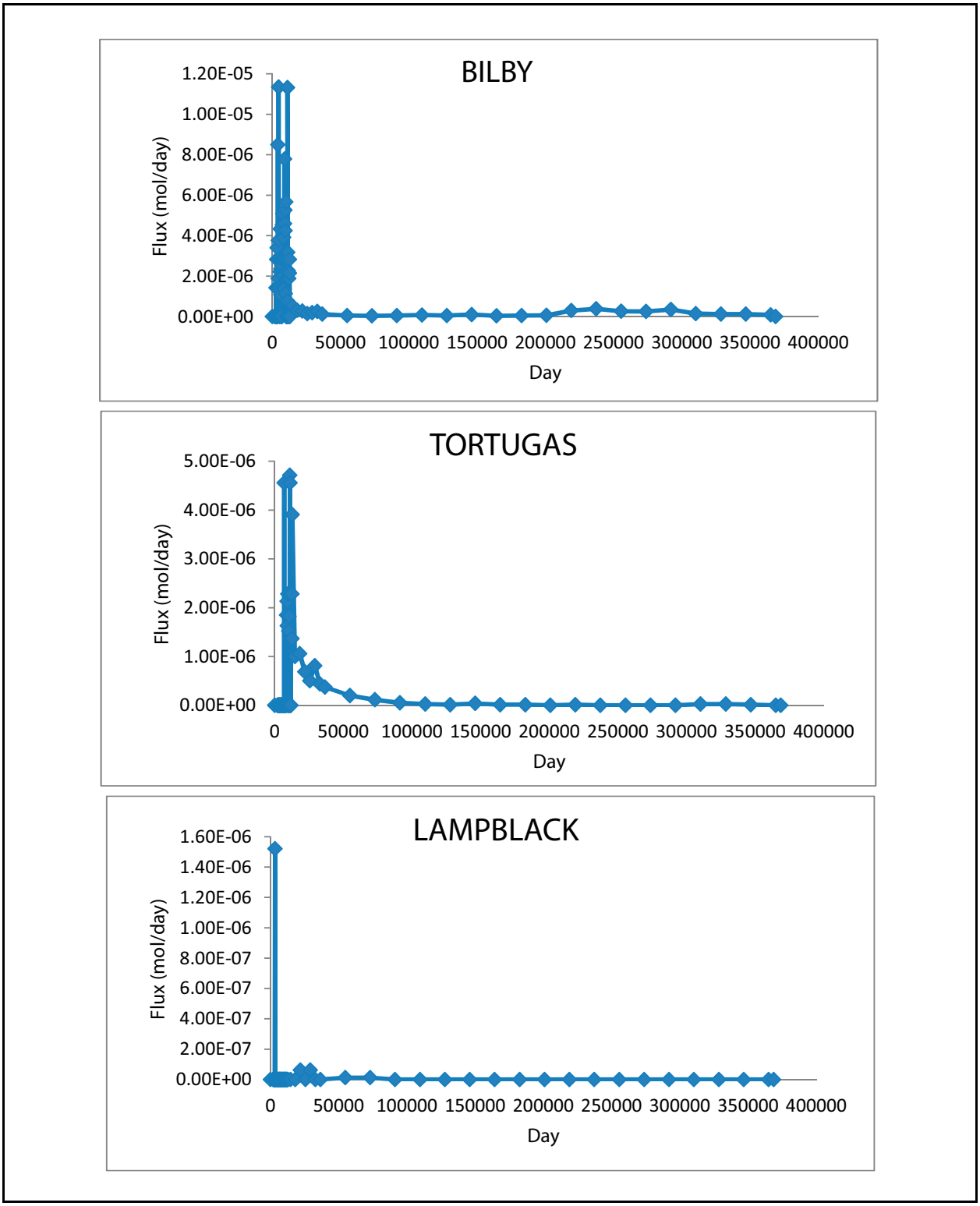

Figure 6-52
Temporal Variation in ^{129}I Flux to the LCA from Key Saturated-Zone Working-Point Detonations for Infiltration Rate of 1 mm/yr (Case SAE_2)

Table 6-5
Mobile Initial Inventory in the Saturated LCA for ^{3}H, ^{14}C, ^{129}I, and ^{90}Sr

Detonation Name	Maximum Announced Yield (kt)	Uniform Mass Allocation [a] and 2 R_c Exchange Volume Radius					Uniform Concentration Allocation [a] and Mean Exchange Volume Radius				
		Fraction of Exchange Volume	^{3}H (mol)	^{14}C (mol)	^{129}I (mol)	^{90}Sr (mol)	Fraction of Exchange Volume	^{3}H (mol)	^{14}C (mol)	^{129}I (mol)	^{90}Sr (mol)
BOURBON [b]	200	0.0394	1.64E+00	4.55E-03	4.03E-03	2.27E-02	0.4301	1.79E+01	4.97E-02	6.60E-02	1.65E-01
CORDUROY	200	0.0555	2.46E+00	6.42E-03	5.68E-03	3.29E-02	0.1582	7.03E+00	1.83E-02	2.43E-02	6.25E-02
COTTAGE	150	0.0010	7.36E-03	1.73E-04	4.34E-05	8.25E-05	0.0031	2.28E-02	5.36E-04	2.02E-04	1.70E-04
GRAPE-A	200	0.0002	7.08E-03	2.31E-05	2.05E-05	1.07E-04	0.0008	2.83E-02	9.24E-05	1.23E-04	2.87E-04
KLICKITAT	70	0.0030	5.16E-02	1.21E-04	1.07E-04	6.49E-04	0.0074	1.27E-01	2.99E-04	3.97E-04	1.07E-03
LAMPBLACK	200	0.0134	5.91E-01	1.55E-03	1.37E-03	7.91E-03	0.0087	3.84E-01	1.01E-03	1.34E-03	3.42E-03
MICKEY	200	0.0086	3.52E-01	9.94E-04	8.80E-04	4.92E-03	0.0155	6.35E-01	1.79E-03	2.38E-03	5.91E-03
MUNDO	150	0.0097	1.15E-01	8.39E-04	7.44E-04	2.77E-03	0.0099	1.17E-01	8.57E-04	1.14E-03	1.88E-03
SHAPER	200	0.0016	5.58E-02	1.85E-04	1.64E-04	8.54E-04	0.0019	6.62E-02	2.20E-04	2.92E-04	6.76E-04
SHUFFLE	200	0.0132	5.13E-01	1.53E-03	1.35E-03	7.38E-03	0.0234	9.09E-01	2.70E-03	3.59E-03	8.73E-03
STRAIT	500	0.0010	6.22E-02	2.89E-04	2.56E-04	1.16E-03	0.0011	6.84E-02	3.18E-04	4.22E-04	8.47E-04
TORRIDO	200	0.0362	1.32E+00	4.18E-03	3.70E-03	1.97E-02	0.3604	1.32E+01	4.16E-02	5.53E-02	1.31E-01
		Total	**7.18E+00**	**2.09E-02**	**1.83E-02**	**1.01E-01**	**Total**	**4.05E+01**	**1.17E-01**	**1.55E-01**	**3.82E-01**

[a] Mobile inventories for the uniform mass allocation of ^{129}I and ^{90}Sr are considered to be 50 and 60 percent of the respective initial total inventories per the Yucca Flat HST (Pawloski et al., 2008) and the remaining fraction in the melt glass. The mobile inventories for the uniform concentration allocation of ^{129}I and ^{90}Sr use the Appendix C mean melt-glass fractions and are 75 and 40 percent of the respective initial total inventories.

[b] BOURBON is a detonation with a working point located in the unsaturated LCA. This detonation is included above because the 2 R_c exchange volume intersects the saturated LCA. Although the BOUBRBON detonation was conducted in carbonate rock, it is assumed to have a silicate glass puddle because of the intersection of the cavity with overlying tuff confining units (Carle et al., 2008).

unsaturated zone (a percent that is dominated by the activity of ^{3}H), the saturated-zone sources make up a more significant fraction of the total mass input to the LCA. This is because of the large fraction of the nuclear detonations with their exchange volumes initially in the unsaturated zone overlying the saturated alluvial/volcanic aquifer system in the center of Yucca Flat. The additional time it takes for the radionuclides from these source zones to reach the LCA minimizes their impact on contaminant flux to the LCA.

While only a very small fraction of the underground nuclear detonations have exchange volumes that intersect the saturated LCA (e.g., 12 detonations out of 744 assuming an exchange volume radius of 2 R_c), the different transport characteristics of the carbonate rocks and the significance of horizontal transport within the LCA make the inventory in these detonations potentially significant to the determination of the extent of contaminant migration in the Yucca Flat/Climax Mine CAU. To compare the significance of the inventory derived from the different source regions, the results of mass inflows to the LCA from a single representative case are tabulated in Table 6-6 for four radionuclides of potential interest. It is relevant to note that the cumulative initial mass in place for these radionuclides in the three different model domains is different from the fractions indicated in Section 2.0 because these values include the different amounts of above and below the water table inventory allocations defined in Bowen et al. (2001), and the radionuclide inventories are decay corrected from September 23, 1992, to the actual time of the detonation. The radionuclides are chosen for the following reasons:

- The radionuclide ^{3}H has the greatest fraction of the total initial mobile activity and is unretarded by sorption, which tends to significantly affect the early-time cumulative volume of rock with water exceeding the SDWA MCLs.

- The radionuclide ^{14}C has been shown to significantly affect the time-cumulative volume of rock exceeding the SDWA MCLs at other CAUs and has been used as an indicator of contaminant transport in the unsaturated zone and saturated alluvial/volcanic aquifer system transport models.

- The radionuclide ^{90}Sr has a large total initial mobile activity in the LCA, which combined with its low SDWA MCL, can lead to very high initial concentrations in the cavity, especially for the carbonate-breaching detonations. Although ^{90}Sr is significantly retarded in the saturated alluvial and volcanic rock units, sorption in the carbonate LCA is very low and uncertain.

- The radionuclide ^{129}I has a very long half-life and is an unretarded species that may persist in the environment for a long time.

Table 6-6
Summary of Mass Distribution of ^{3}H, ^{14}C, ^{129}I, and ^{90}Sr between Different Model Components of the Yucca Flat/Climax Mine CAU Assuming an Exchange Volume of 2 R_c and Base-Case Unsaturated- and Saturated-Zone Flow and Transport Properties

	^{3}H	^{14}C	^{129}I	^{90}Sr
	Mass (mol)			
Total mass at t_o	5.15E+03	3.17E+01	3.29E+01	1.14E+02
Mobile mass in place in UZ at t_o	3.05E+03	2.32E+01	8.96E+00	3.32E+01
Mass released from unsaturated zone to LCA in 1,000 years with recharge rate of 0.1 mm/yr	3.55E-09	1.01E-03	3.29E-04	NA
Mass released from unsaturated zone to LCA in 1,000 years with recharge rate of 1 mm/yr	6.20E-02	1.38E-01	7.93E-02	NA
Mobile mass in place in saturated zone at t_o	2.09E+03	8.45E+00	7.45E+00	3.52E+01
Mass released from saturated zone to LCA in 1,000 years with recharge rate of 0.1 mm/yr	3.12E-02	9.82E-03	9.42E-03	NA
Mass released from saturated zone to LCA in 1,000 years with recharge rate of 1 mm/yr	8.35E+00	2.09E-01	1.96E-01	NA
Mobile mass in place in LCA at t_o	7.18E+00	2.09E-02	1.83E-02	1.01E-01

Notes:

Total radionuclide mass and mass of each radionuclide initially in place are corrected to the time of each nuclear detonation starting with the September 23, 1992, inventory presented in Bowen et al. (2001). For short-lived radionuclides such as ^{3}H, this increases the total mass from the decay-corrected September 23, 1992, values.

The ratios of total mass placed above and below the water table is different from those specified in Bowen et al. (2001), because the estimated location of the water table is used to allocate mass between models instead of a point 100 m above the water table as discussed in Section 2.3.3.

Even though the LCA contamination sources make up on the order of 0.1 percent of the total initial inventory of ^{3}H for a 2 R_c exchange volume radius, the initial inventory of ^{3}H in the LCA is more than four times the mass of ^{3}H that is forecast to enter the LCA from the overlying unsaturated and saturated zones. This is indicative of the significant decay of ^{3}H that occurs as it is transported through the overlying tuff and alluvial units to the underlying LCA.

In contrast, the amount of ^{129}I that is initially in place in the LCA, assuming an exchange volume radius of 2 R_c, is about 3 percent of the mass that enters the LCA from the overlying saturated zone. Although the mass that enters the LCA from the overlying saturated zone occurs over a 1,000-year time period, the long-lived nature of ^{129}I implies that the entire mass is still in place in the LCA at the end of the time period and can therefore contribute to defining the extent of contamination.

Of particular interest to the determination of the extent of contamination in the Yucca Flat/Climax Mine CAU is the distinct difference in the retardation characteristics of ^{90}Sr (and ^{137}Cs and ^{63}Ni) in the alluvial and tuff units as compared to the LCA. The ^{90}Sr that is initially in the HST of the unsaturated zone and the saturated alluvial/volcanic aquifer system, which comprises about 99.9 percent of the total ^{90}Sr inventory in the Yucca Flat/Climax Mine CAU, is retarded and decayed sufficiently in these zones (with a K_d of more than 100 mL/g and a half-life of 29 years); therefore, essentially none of the ^{90}Sr enters the LCA within 1,000 years. However, even the small fraction of ^{90}Sr that is initially in the saturated LCA (about 0.1 percent of the total inventory for the 12 detonations that intersect the LCA with an exchange volume of 2 R_c) can have a significant impact on the extent of contaminant migration. This is because the initial concentration in the exchange volume is more than 100,000 times the MCL (Table 2-7), and there is assumed to be no sorption of ^{90}Sr on the carbonate minerals in the LCA. The effect of including sorption of ^{90}Sr (and ^{137}Cs and ^{63}Ni) in the LCA is evaluated in a sensitivity analysis presented in Section 6.5.7.

The specific distribution of initial mass for each of the 12 detonations with a 2 R_c exchange volume that intersect the saturated LCA and the 3 other detonations with working points in the unsaturated LCA is summarized in Table 6-7 for ^{3}H and Table 6-8 for ^{129}I. Note that, in these tables, the BOURBON detonation meets both of these criteria and is included in the 2 R_c breaching category for convenience. In addition to presenting the initial distribution of these radionuclides for each of the 15 detonations in the different models (the unsaturated-zone model, the saturated alluvial/volcanic aquifer system model, and the saturated LCA model), these tables summarize the cumulative release from the unsaturated-zone detonations to the nearest source nodes in the LCA model for a representative run.

As illustrated in Figures 6-39 and 6-40, there is a strong correlation between several of the detonations with exchange volumes that straddle the interface between the unsaturated zone and saturated LCA and the contaminant flux to the LCA. This is also evident in the columns of Tables 6-7 and 6-8, which summarize the cumulative contaminant flux to the LCA from the detonations that straddle the interface between the unsaturated zone and saturated LCA.

The temporal rate of contaminant mass flux calculated by the representative unsaturated zone and saturated alluvial/volcanic aquifer system models for selected detonations is illustrated in Figures 6-39, 6-40, 6-51, and 6-52. As noted in Table 6-5, six unsaturated-zone detonations

Table 6-7
Initial ^3H Inventory for Selected LCA Significant Detonations

Detonation	Initial Mobile Inventory Allocation [a]				Integrated 1,000-Year Release to Saturated LCA		
	Total (mol)	Unsaturated Zone (mol)	Saturated Alluvial/Volcanic Aquifer System (mol)	Saturated LCA (mol)	0.1 mm/yr Infiltration Rate (mol)	1 mm/yr Infiltration Rate (mol)	5 mm/yr Infiltration Rate (mol)
Detonations with Working Points within 2 R_c of Saturated LCA							
BOURBON [b]	4.17E+01	4.00E+01	0.00E+00	1.64E+00	0.0	2.16E-02	8.52E-02
CORDUROY [c]	4.44E+01	0.00E+00	4.19E+01	2.46E+00	N/A	N/A	N/A
COTTAGE	7.36E+00	7.35E+00	0.00E+00	7.36E-03	4.20E-17	4.21E-05	1.53E-04
GRAPE-A	3.54E+01	0.00E+00	3.54E+01	7.08E-03	N/A	N/A	N/A
KLICKITAT	1.72E+01	1.71E+01	0.00E+00	5.16E-02	N/A	N/A	N/A
LAMPBLACK	4.41E+01	0.00E+00	4.35E+01	5.91E-01	6.19E-15	6.50E-02	2.11E-01
MICKEY	4.10E+01	3.89E+01	1.70E+00	3.52E-01	N/A	N/A	N/A
MUNDO	1.18E+01	8.36E+00	3.34E+00	1.15E-01	N/A	N/A	N/A
SHAPER	3.49E+01	0.00E+00	3.48E+01	5.58E-02	N/A	N/A	N/A
SHUFFLE	3.89E+01	3.83E+01	0.00E+00	5.13E-01	0.0	1.97E-02	9.93E-2
STRAIT	6.22E+01	0.00E+00	6.22E+01	6.22E-02	N/A	N/A	N/A
TORRIDO	3.65E+01	3.52E+01	0.00E+00	1.32E+00	0.0	9.25E-04	4.67E-03
Subtotal	4.15E+02	1.85E+02	2.23E+02	7.18E+00	6.23E-15	1.07E-01	4.01E-01
Detonations with Working Points in Unsaturated LCA							
HANDCAR	1.85E+00	1.85E+00	0.00E+00	0.00E+00	0.0	1.81E-18	3.21E-09
KANKAKEE	2.82E+01	2.82E+01	0.00E+00	0.00E+00	0.0	1.82E-02	7.27E-02
NASH	5.32E+00	5.32E+00	0.00E+00	0.00E+00	0.0	5.79E-06	5.70E-03
Subtotal	3.54E+01	3.54E+01	0.00E+00	0.00E+00	0.0	1.82E-02	7.84E-02
All Other Detonations	4.70E+03	2.83E+03	1.86E+03	0.00E+00	3.12E-02	8.29E+00	1.76E+01
Total	5.15E+03	3.05E+03	2.09E+03	7.18E+00	3.12E-02	8.41	18.1

[a] As discussed in Section 2.0, the initial Bowen inventory (Bowen et al., 2001) presented in this table has been decay corrected to the time of the detonation. As discussed in Section 3.0, the initial Bowen inventory used in the unsaturated-zone transport model has been decay corrected to December 3, 1961, the time of the FISHER detonation.

[b] BOURBON is a detonation with a working point located in the unsaturated LCA. However, because the 2 R_c exchange volume of BOURBON intersects the saturated LCA, this detonation is included above.

[c] Although the CORDUROY detonation also straddles the unsaturated zone, as discussed in Section 2.0, the unsaturated-zone portion of the initial inventory was placed in the underlying saturated zone to account for processes not included in the model, notably, drilling fluid lost during drill-back operation.

Table 6-8
Initial Mobile ^{129}I Inventory for Selected LCA Significant Detonations

Detonation	Initial Mobile Inventory Allocation [a]				Integrated 1,000-Year Release to Saturated LCA		
	Total (mol)	2 R_c Initial Inventory in Unsaturated Zone (mol)	2 R_c Initial Inventory in Saturated Zone (mol)	2 R_c Initial Inventory in Saturated LCA (mol)	0.1 mm/yr Infiltration Rate (mol)	1 mm/yr Infiltration Rate (mol)	5 mm/yr Infiltration Rate (mol)
Detonations with Working Points within 2 R_c of Saturated LCA							
BOURBON [b]	1.02E-01	9.83E-02	0.00E+00	4.03E-03	0.0	1.74E-03	4.87E-03
CORDUROY [c]	1.02E-01	0.00E+00	9.66E-02	5.68E-03	N/A	N/A	N/A
COTTAGE	4.34E-02	4.34E-02	0.00E+00	4.34E-05	0.0	1.56E-04	3.27E-04
GRAPE-A	1.02E-01	0.00E+00	1.02E-01	2.05E-05	N/A	N/A	N/A
KLICKITAT	3.58E-02	3.57E-02	0.00E+00	1.07E-04	N/A	N/A	N/A
LAMPBLACK	1.02E-01	0.00E+00	1.01E-01	1.37E-03	4.56E-04	1.22E-03	5.86E-03
MICKEY	1.02E-01	9.72E-02	4.26E-03	8.80E-04	N/A	N/A	N/A
MUNDO	7.67E-02	5.43E-02	2.17E-02	7.44E-04	N/A	N/A	N/A
SHAPER	1.02E-01	0.00E+00	1.02E-01	1.64E-04	N/A	N/A	N/A
SHUFFLE	1.02E-01	1.01E-01	0.00E+00	1.35E-03	0.0	9.54E-03	3.59E-02
STRAIT	2.56E-01	0.00E+00	2.56E-01	2.56E-04	N/A	N/A	N/A
TORRIDO	1.02E-01	9.86E-02	0.00E+00	3.70E-03	0.0	9.53E-05	4.82E-04
Sub Total	1.23E+00	5.28E-01	6.83E-01	1.83E-02	4.56E-04	1.27E-02	4.74E-02
Other Detonations with Working Points in the Unsaturated LCA							
HANDCAR	3.47E-03	3.47E-03	0.00E+00	0.00E+00	0.0	3.29E-05	2.59E-02
KANKAKEE	5.79E-02	5.79E-02	0.00E+00	0.00E+00	0.0	2.71E-02	7.43E-02
NASH	1.13E-02	1.13E-02	0.00E+00	0.00E+00	0.0	8.02E-03	1.13E-02
Subtotal	7.26E-02	7.26E-02	0.00E+00	0.00E+00	0.0	3.51E-02	1.11E-01
All Other Detonations	1.51E+01	8.36E+00	6.77E+00	0.00E+00	9.29E-03	2.28E-01	6.07E-01
Total	1.64E+01	8.96E+00	7.45E+00	1.83E-02	9.74E-03	2.76E-01	7.66E-01

[a] Inventory presented is the mobile fraction that is considered to be 50 percent of the total ^{129}I based on the Bowen inventory (Bowen et a., 2001).

[b] BOURBON is a detonation with a working point located in the unsaturated LCA. However, because the 2 R_c exchange volume of BOURBON intersects the saturated LCA, this detonation is included above.

[c] Although the CORDUROY detonation also straddles the unsaturated zone, as discussed in Section 2.0, the unsaturated-zone portion of the initial inventory was placed in the underlying saturated zone to account for processes not included in the model, notably, drilling fluid lost during drill-back operation.

(BOURBON, SHUFFLE, KLICKITAT, TORRIDO, MICKEY, and KANKAKEE) contribute about 78 percent of the total ^{3}H contaminant input and about 50 percent of the total ^{129}I contaminant input to the LCA from the 668 detonations with working points above the water table. In contrast, the saturated-zone working-point detonations contribute contaminant flux to the LCA in a more areally distributed fashion, with a few exceptions such as BILBY where the contaminant source and location of contaminant flux to the LCA are closely correlated. The spatial correlation between the few unsaturated-zone working-point detonations that straddle the saturated LCA and the contaminant flux to the LCA is as expected as the initial inventory in these detonations would be transported to the water table in the LCA with either the ambient percolation flux or the increased flux associated with the crater-enhanced recharge for those detonations with surface craters.

In contrast, there is very little spatial correlation between the locations of detonations with exchange volumes that straddle the interface between the saturated alluvial/volcanic aquifer system and the LCA and the contaminant flux to the LCA. This is as expected given the low-permeability confinement provided by the LTCU and OSBCU, in which these detonations were conducted. Contaminants in the exchange volumes of these detonations generally must be transported laterally several cavity radii before they enter transmissive faults that allow vertical transport into the LCA.

Climax Mine Source Input to LCA Transport Model

In addition to the radionuclide sources associated with detonations with working points in the unsaturated zone and saturated alluvial/volcanic aquifer system, the Yucca Flat/Climax Mine CAU must consider the potential contamination associated with the three underground nuclear detonations performed in the granite stock at Climax Mine. The yield-weighted inventory of these three detonations (TINY TOT, PILE DRIVER, and HARD HAT) contribute a small fraction of the total Yucca Flat/Climax Mine CAU inventory (e.g., 0.35, 0.25, and 0.2 percent for ^{3}H, ^{129}I, and ^{14}C, respectively). Nevertheless, as noted in Pohlmann et al. (2007), unretarded radionuclides may be transported through the low-permeability granite stock to the surrounding aquifers, most notably, the LCA, and hence to the northern boundary of the Yucca Flat LCA transport model within the 1,000-year time period of relevance to determining the extent of the contaminant boundary.

Contaminant release rates and cumulative release amounts have been calculated by Pohlmann et al. (2007) for a range of uncertain flow and transport properties. Considering three representative non-sorbing radionuclides ^{3}H, ^{14}C, and ^{129}I, the peak calculated 95th percentile release rates are about

2E-04, 5E-05, and 3E-05 moles per year (mol/yr), respectively (Pohlmann et al., 2007, Figures 5-36, 5-33, and 5-45). The cumulative mass released at the boundary of the granite stock for ^{3}H, ^{14}C, and ^{129}I are about 0.01, 0.03, and 0.02 mol, respectively, for the same 95th percentile release rates. These cumulative release amounts are only 3 to 4 percent of the cumulative release amounts from the saturated alluvial/volcanic aquifer system (Table 6-5) and therefore are insignificant to the determination of the extent of the Yucca Flat/Climax Mine CAU contaminant boundary.

6.4.6 LCA Transport Model Contaminant Concentrations

Given (1) the particle trajectories and transport times developed from the LCA flow model (presented in Section 6.4.2), (2) input mass fluxes as a function of time and space (due to either influx from overlying units or influx at the time of the detonation for LCA sources), and (3) transport parameter values (e.g., effective porosity, fracture aperture, matrix porosity), PLUMECALC calculates the contaminant concentration in each finite element cell at specified times from the start of testing at the Yucca Flat/Climax Mine CAU (July 26, 1957). For purposes of the Yucca Flat LCA transport analyses, in order to define the maximum extent of significant contaminant migration, the discrete times chosen for analysis are at 10, 50, 100, 200, 300, 400, 500, 600, 700, 800, 900, and 1,000 years. Because the definition of the extent of contamination in the FFACO (1996, as amended) requires forecasting the maximum extent at any time within 1,000 years, the early-time results are used to ensure that the contaminant plumes associated with short-lived radionuclides such as ^{3}H, ^{90}Sr, ^{137}Cs, and ^{63}Ni are captured, and the later-time results are used to ensure that the longer-lived radionuclides such as ^{129}I, ^{99}Tc, and ^{36}Cl are appropriately addressed.

The approach taken to identify the extent of contaminant migration is to perform transport simulations for all sources and all significant radionuclides over a range of uncertain transport parameter values and to evaluate the probability of exceeding the MCLs for each modeled radionuclide within each grid cell. These fractional exceedance values are summed over all modeled radionuclides to determine a probability of exceeding the MCL within each grid cell.

The principal performance metric used in the contaminant transport analyses is the probability that any grid cell is likely to exceed the SDWA MCL concentration. This probability is determined based on multiple realizations of the transport model sampled over the range of possible transport parameter values considering the range and uncertainty in the different source representations and alternative

LCA flow models. The results of the contaminant boundary forecasts based on multiple realizations are presented in Section 6.5.

To understand the underlying basis of the probabilistic results, it is useful to examine the concentrations developed for a single realization using fixed transport parameters for a single radionuclide contaminant. Examples of such analyses have used the single realization corresponding to the median value of the exceedance volume distribution results. These analyses are presented in Section 6.5.2.

The results of analyses of the different sources of contamination in the LCA are presented in Section 6.5, considering that those radionuclides can potentially contribute to the extent of the contaminant boundary over the probabilistic range of transport parameter values. These results use the different source-term scenarios identified in Section 2.0, the range of contaminant influx from the detonations with contamination initially residing in the unsaturated zone as presented in Section 3.0, the range of contaminant influx from the detonations with contamination initially residing in the saturated alluvial/volcanic aquifer system as presented in Section 4.0, a range of alternative LCA groundwater flow models as documented in Section 5.0 and the associated particle trajectories presented in Section 6.4.1, and the range of LCA transport parameter values presented in Section 6.3. These results are developed with the same approach used to develop the results in the Phase II Frenchman Flat CAU transport model document (NNES, 2010b).

6.5 LCA Transport Model Results

Using the LCA transport model described in Section 6.2, along with the transport parameter distributions described in Section 6.3 and source mass fluxes described in Section 6.4, a range of uncertainty and sensitivity analyses were performed to evaluate the extent of possible contamination in the LCA. As defined in the FFACO, the ultimate goal of the transport modeling is to define the contaminant boundary or a composite range of possible contaminant boundaries that can then be used by NNSA/NSO and NDEP to negotiate the use restriction and regulatory boundaries. The determination of the contaminant boundary requires quantifying the probability that the volume of rock downgradient of the contamination sources exceeds the maximum permissible contaminant levels (i.e., MCLs) of the SDWA. Determining this probability for the LCA transport model requires multiple simulations of contaminant transport incorporating the uncertainty in alternative flow models, alternative source-term representations, alternative transport parameters, and alternative

inputs from contaminant sources in the overlying unsaturated zone and the saturated alluvial/volcanic aquifer system.

The LCA results addressing the above uncertainties are presented in this section. Following an introductory discussion that summarizes all of the modeling performed, the results are presented in the following groupings:

- Base-case results (Section 6.5.2)
- Alternative LCA source-term results (Section 6.5.3)
- Alternative unsaturated zone and saturated alluvial/volcanic aquifer system model inputs for different infiltration rates (Section 6.5.4)
- Alternative saturated alluvia/volcanic aquifer system flow and transport model results (Section 6.5.5)
- Alternative LCA flow model results (Section 6.5.6)
- Alternative LCA transport parameter results (Section 6.5.7)
- LCA transport model uncertainty importance results (Section 6.5.9)

6.5.1 Introduction

Significant sources of uncertainty potentially affect the forecast extent of contamination in the LCA in the Yucca Flat/Climax Mine CAU. In order to evaluate the range of forecast contamination extent as well as the principal uncertainties affecting the forecast extent, a spectrum of model runs were performed during the analysis. Table 6-9 categorizes the different runs performed during the LCA transport modeling to evaluate the significance of the different sources of uncertainty.

Before presenting the range of possible results, this section identifies a base-case representation. This allows the significance of alternative models or parameter distributions to be compared to a representative case. The “base case” should not be construed as a “most likely” or “expected” or “mean” case, but is simply a modeling case to which other cases may be compared to determine the relative significance of the uncertainty being evaluated. The “base case” transport model run represents an infiltration rate on the order of 0.1 mm/yr in the center of the Yucca Flat basin and higher values (on the order of several to more than 10 mm/yr) along the basin margins. These rates have been estimated from a range of different observations and conceptualizations, including regional infiltration estimates and estimates of pluvial drainage. The “base case” run also corresponds to the

Table 6-9
Summary of LCA Transport Model Analyses
(Page 1 of 2)

Section #/ Title	Description	Shorthand Designator	Contaminant Sources	Time-Varying Probability of Exceeding MCL	Time-Cumulative Probability of Exceeding MCL	CDF of Cumulative Exceedance Volume	CDF of Maximum Southern Extent of Contaminant Migration	Fractional Exceedance Volume
Section 6.5.2 Base Case	0.1 mm/yr infiltration rate, uniform concentration HST	542121	Unsaturated zone	Concentrations do not exceed MCL				
		SAE_12	Saturated zone	X (50, 100, 300, 1,000)	X	X	X	X
		Base case	LCA	X (50, 100, 300, 1,000)	X			X
Section 6.5.3 Alternative LCA HSTs	Alternative LCA HSTs	Initial $2R_c$ uniform mass HST	LCA	--	X	X (combine with base case)	X (combine with base case)	--
		Alternative HST scenario	LCA	--	X			--
Section 6.5.4 Alternative Infiltration Rates	1 and 5 mm/yr infiltration rate cases	121212	Unsaturated zone	--	X	X (combine with SAE_12)	X (combine with SAE_12)	X
		SAE_2	Saturated zone	--	X			X
		223212	Unsaturated zone	--	X			--
		SAE_1	Saturated zone	--	X			--
Section 6.5.5 Alternative Saturated Alluvial/Volcanic Aquifer System Flow and Transport Models	Alternative cases of hydraulic communication and overpressure effects	SAE_5	Saturated zone	--	X	X (combine with SAE_2)	X (combine with SAE_2)	--
		SAE_7	Saturated zone	--	X			--
		SAE_10	Saturated zone	--	X			--
		SAE_11	Saturated zone	--	X			--
	400 realizations	SAE_13	Saturated zone	--	X	X (combine with SAE_2)	X (Combine with SAE_2)	--

Table 6-9
Summary of LCA Transport Model Analyses
(Page 2 of 2)

Section #/ Title	Description	Shorthand Designator	Contaminant Sources	Time-Varying Probability of Exceeding MCL	Time-Cumulative Probability of Exceeding MCL	CDF of Cumulative Exceedance Volume	CDF of Maximum Southern Extent of Contaminant Migration	Fractional Exceedance Volume
Section 6.5.6 Alternative LCA Flow Fields	NSMC cases	Lower bound NSMC	LCA	--	X	X (combine with base case)	X (combine with base case)	--
		Upper bound NSMC	LCA	--	X			--
	Alternative northern boundary flux		LCA	--	X			--
Section 6.5.7 Alternative LCA Transport Parameters	Alternative matrix sorption for Sr, Cs, C, and Ni		LCA	X (50, 100, 300, 1,000)	X	X (combine with base case)	X (combine with base case)	X
	Scale-dependent matrix diffusion		LCA	--	X			--
	Alternative fault fracture porosity		LCA	--	X			--
	Walkabout vs. sptr		LCA	--	X			--
	Combined alternative flow and transport		LCA	--	X			--
Section 6.5.8 Combined Transport Models	0.1 mm/yr combined sources	542121+SAE_12+ Base case	All	--	X	--	--	--
	1 mm/yr combined sources	121212+SAE_2+ Base case	All	--	X	--	--	--
	5 mm/yr combined sources	223212+SAE_1+ Base case	All	--	X	--	--	--
Section 6.5.9 Sensitivity Uncertainty Importance Sensitivity Analyses	N/A	N/A	N/A	N/A	N/A	X	X	N/A
Section 6.5.10 Composite Contaminant Boundary	Composite contaminant boundary	N/A	LCA	--	X	--	--	--

Note: X indicates that a figure or figures illustrating the results of the analysis are presented in the indicated section, and -- indicates that no figure is presented to illustrate the results of the analysis.

base-case LCA flow model that assumes hydraulic continuity of the LCA in northern Yucca Flat. As presented in Section 5.6.3, the alternative LCA flow model that assumes limited hydraulic continuity of the LCA in northern Yucca Flat has a significantly reduced northern boundary flux from the base-case model.

In order to capture the probability of exceedance performance metric, 400 realizations for each alternative scenario are performed. This approach is the same as the approach adopted for the Phase II Frenchman Flat contaminant transport analyses.

Different graphical representations of the results are possible to evaluate the potential significance of the uncertainties. The relative and absolute differences in forecast model results can be evaluated by examining several graphical displays of the results. Several common methods used to evaluate the results include (1) the time-cumulative maps of the probability of exceeding the MCLs, (2) CDFs of the volume of rock exceeding the MCLs for each of the 400 realizations, and (3) CDFs of the maximum southern extent of the volume of rock exceeding the MCLs for each of the 400 realizations. The 5 percent probability of exceedance contour indicated on the time-cumulative probability exceedance map represents a two-dimensional areal depiction of the extent of contamination that corresponds to the 95th percentile of the exceedance volume CDF. The effect of the differences in forecast model results is also evaluated by identifying the more significant parameters using a range of uncertainty importance analyses (e.g., sensitivity analyses) presented in Section 6.5.9. Table 6-9 indicates the types of result figures used to illustrate the significance of the uncertainties being evaluated.

6.5.2 Base Case

As discussed in Section 6.4, there are three principal sources of contaminant influx to the LCA within the Yucca Flat/Climax Mine CAU: (1) sources that are the result of flow and transport from contaminated sources that are initially in the unsaturated zone, (2) sources that are the result of flow and transport from contaminated sources that are initially in the saturated alluvial/volcanic aquifer system, and (3) sources that are the result of underground nuclear detonations with exchange volumes that intersect the saturated LCA. Because of the varied spatial locations of these sources and because of the need to break up the total solution into discrete calculations, these three source inputs were modeled separately, with the integrated results developed to show the combined effect of the different sources.

This section presents the base-case representation of contaminant transport in the LCA. This representation includes uncertainty in LCA source-term inputs and LCA transport parameters, and uses a discrete single representation of the LCA flow model and discrete source inputs from the overlying unsaturated zone and saturated alluvial/volcanic aquifer system models. As discussed in Sections 2.0 and 6.3, respectively, the uncertainty in LCA source-term inputs and LCA transport parameters is treated stochastically by conducting Latin Hypercube Sampling (LHS) over the range of uncertain inputs. Such a direct method of propagating parameter uncertainty is not practicable for uncertainties associated with other aspects of the source-term model (notably, the source term used in the unsaturated zone and saturated alluvial/volcanic aquifer system models), the unsaturated-zone flow and transport model, the saturated alluvial/volcanic aquifer system flow and transport model, or the LCA flow model, as well as the uncertainty in dispersivity in the LCA transport model. As a result, rather than sampling from uncertain probabilistic distributions, the approach has been to develop discrete cases that capture the range of expected conditions and to propagate the discrete cases to the LCA transport model to evaluate the impact they have on the forecast contaminant boundary in the LCA.

A representative and important case in point that illustrates the role of discrete cases to capture the range of expected behavior on transport in the LCA is the effect of the net infiltration rate on the percolation flux through the unsaturated-zone flow and transport model, and the corresponding saturated-zone fluxes in the saturated alluvial/volcanic aquifer system flow and transport model. As presented in Sections 3.0 and 4.0, the steady-state pretesting infiltration rate has a significant effect on contaminant releases to the LCA, due principally to the observation that flow in these two models is dependent on the infiltration rate because there is insignificant lateral flow into these models from perched water systems. As discussed in Sections 1.0, 3.0, 4.0, and 5.0, the average infiltration rate in the central portion of Yucca Flat, where all of the detonations in the Yucca Flat/Climax Mine CAU were performed, is very low, less than 0.1 mm/yr. However, there is uncertainty in this infiltration rate. There is also uncertainty in the spatial distribution of the infiltration rate over the domain of the unsaturated-zone model. Developing an uncertainty distribution to represent the uncertainty in the infiltration rate and the spatial distribution of the infiltration rate would be subject to a number of subjective decisions or other difficult-to-quantify uncertainties if, for example, one were to develop alternative infiltration distributions using an infiltration model. As a result, the practicable solution is to develop discrete alternative average infiltration rates that bound the possible effects of this important process on contaminant transport. Spatially averaged net infiltration rates of 1 and 5 mm/yr

were chosen to capture the upper bounds of possible infiltration rates in the center of the Yucca Flat basin. Although analyses in Sections 3.0 and 4.0 also use a value of 10 mm/yr, the 5-mm/yr value is a very unlikely bound as discussed in Sections 3.0 and 5.0. However, it is included in the analyses below to ensure the contaminant releases to the LCA are bounded.

The case presented below is developed using the 0.1-mm/yr infiltration rate case for the unsaturated zone and saturated alluvial/volcanic aquifer system models in the central portion of Yucca Flat. The base-case LCA flow model is the calibrated LCA flow model described in Section 5.5. The inputs from the unsaturated-zone sources are generated from run 542121, which corresponds to a background infiltration rate of 0.1 mm/yr, no anisotropy of the alluvial HSU, low crater recharge rate, medium porosity of the tuff confining unit, no anisotropy in the tuff confining unit, and an exchange volume of 1 R_c. The inputs from the saturated-zone sources are generated from run SAE_12 with a mean value of the sampled saturated alluvial/volcanic aquifer system transport parameters combined with flow assumptions that are consistent with unsaturated-zone run 542121, namely, a background infiltration rate of 0.1 mm/yr, no anisotropy in the alluvial aquifer, low crater recharge rate, medium porosity of the tuff confining unit, no anisotropy in the tuff confining unit, and an exchange volume of 1 R_c. The inputs from the LCA sources (i.e., the portions of the exchange volume that are assumed to intersect the saturated LCA; see Section 6.4) assume that a portion of inventory mass is in the exchange volume with a radionuclide-dependent exchange volume radius that intersects the saturated LCA and that portion of the inventory concentration is uniformly distributed in the saturated LCA around the source location.

An important component of the analyses is the identification of the numerical precision of the results. In the case of contaminant transport at Yucca Flat, this numerical precision is in part due to the number of particles used in FEHM to model the advective transport from the key sources, and the number of realizations used to evaluate the uncertainty in the forecast contaminant migration that is relevant in determining the probability of exceeding the SDWA MCLs at any point downgradient of the contaminant sources. The technical rationale for the base-case model representation is presented in the following paragraphs.

As noted in Section 6.4, the particle-tracking algorithm in FEHM is used to project the advective component of contaminant transport from each of the radionuclide source locations. Previous analyses at other CAUs have determined that 10,000 particles for source nodes with initial

contaminant mass is sufficient to capture the range of advective and dispersive flow paths and transport times. As a result, 10,000 particles were used for the contaminant migration from sources that intersect the saturated LCA. This degree of resolution is appropriate for the small number of detonations that have exchange volumes intersecting the saturated LCA, 12 detonations for an exchange volume radius of two times the cavity radius (2 R_c) and 39 detonations for an exchange volume radius of three times the cavity radius (3 R_c).

There can be several hundred source nodes receiving contaminant mass from the overlying unsaturated- and saturated-zone contaminant sources, and using 10,000 particles per source node provides a computational constraint, as the amount of computational effort is directly proportional to the number of particles per source node times the number of source nodes. In order to evaluate the stability of the results to a reasonable range of possible particle distributions per source node, a series of calculations were performed with 100, 500, and 2,500 particles per source node using the upper bound saturated-zone sources as inputs. The results of these analyses indicate that 500 particles are sufficient to provide a reasonably stable result. The number of particles for a stable result from the sources with a time-varying contaminant influx, such as from the overlying unsaturated- and saturated-zone contaminant sources, is less than the number necessary for those nodes with an initial contaminant mass, because the time rate of change of contaminant input is small and spreads over decades or centuries, rather than the immediate prompt injection that occurs in seconds or minutes following a detonation.

The FFACO requirements specify that the contaminant boundary is determined as a probability of exceeding the SDWA MCLs. This probability has been determined by conducting multiple realizations of possible contaminant migration from sampled transport parameter uncertainty distributions for multiple discrete groundwater flow conceptual models and multiple discrete unsaturated and saturated zone flow and transport models. In previous applications, the probability of the discrete groundwater flow and transport models has not been quantified, but the ensemble of possible contaminant plumes has been forecast and combined into a composite contaminant boundary. This composite contaminant boundary includes contaminant boundary forecasts using alternative conceptual models to define the intent of composite contaminant boundaries.

A similar approach is taken for the Yucca Flat/Climax Mine CAU transport modeling. A number of discrete alternative inputs to the LCA transport model are evaluated. These include discrete unsaturated-zone flow and transport model source inputs, discrete saturated alluvial/volcanic aquifer system flow model and source inputs, and discrete LCA flow model boundary conditions and fault conceptual models. These discrete, unweighted inputs are combined with sampled transport parameter uncertainty to develop conditional contaminant boundaries unweighted by the probability of the scenario. These probabilities are considered conditional because they are each conditioned on the discrete, unweighted alternative models and input parameters.

As in other CAUs, it is useful to determine the number of sampled transport parameter realizations that is necessary to provide reasonably stable results for each of the discrete cases being evaluated. To evaluate this, analyses were performed with 200, 400, and 800 realizations for each of the three principal radionuclide source zones. The results of these analyses indicate that 400 realizations provide reasonably stable results for determining the 95th percentile of the volume of rock forecast to exceed the SDWA MCL. The use of 400 multiple realizations to define the range of the possible forecast extent of contaminant migration is for consistency with other CAUs. The evaluation of parameter and model significance could have been accomplished with fewer discrete realizations, but using a set number of consistent parameter realizations allows for the post-processing of the results to quantify the significance of the parameter uncertainty and to evaluate the extent to which the significance of the parameter uncertainty is impacted by the sampled parameter distributions.

Based on the analyses presented in Section 6.4, it is possible to define a representative case against which the result of assuming alternative models and parameters can be compared. For unsaturated-zone sources, this case is defined by unsaturated-zone flow and transport model run 542121. For saturated-zone sources, this case is defined by saturated-zone flow and transport model run SAE_12, which represents the mean value of the transport parameter distribution combined with the unsaturated-zone flow and transport assumptions included in unsaturated-zone run 542121. For LCA sources, this case is defined by the run that assumes that each detonation intersecting the saturated LCA has an uncertain radionuclide-dependent exchange volume radius and that the concentration is uniformly distributed within the exchange volume.

For unsaturated-zone sources, the base-case results indicate no breakthrough exceeds the MCL in the saturated LCA. This is directly attributable to the extremely low contaminant flux to the LCA from

unsaturated-zone sources due to the low background percolation flux, and the large time delay for the enhanced crater recharge flux to reach the contaminant sources and the additional time delay for those contaminants to be transported to the saturated LCA.

For saturated-zone sources, the base-case results are illustrated by the following figures:

- Forecast ^{3}H concentrations at 50 and 100 years for the median realization (Figure 6-53)
- Forecast ^{129}I concentration at 300 and 1,000 years for the median realization (Figure 6-54)
- Forecast probability of exceedance of SDWA MCLs including all modeled radionuclides at 50, 100, 300, and 1,000 years (Figures 6-55 and 6-56)
- Forecast time-cumulative probability of exceedance of alpha-emitter and beta- and photon-emitter MCLs (Figure 6-57). The time-cumulative probability of exceedance uses the probability of exceeding the MCL at each node for each individual modeled time step (10, 50, 100, 150, 200, 300, 400, 500, 600, 700, 800, 900, and 1,000 years) and identifies the maximum probability of MCL exceedance at each node regardless of the time that maximum occurs.
- Forecast 95th percentile fractional exceedance volume (Figure 6-58)

The following observations can be made from these results:

- ^{3}H dominates the extent of contaminant migration, but due to the short half-life, the maximum extent of contamination decreases significantly during the next few hundred years.
- ^{129}I (combined with ^{36}Cl and ^{99}Tc) dominates the extent of contaminant migration once the ^{3}H plume has decayed.
- ^{14}C is an insignificant contributor to the extent of contaminant migration in the LCA.
- The extent of contamination is affected by only a few saturated-zone source locations. The most significant saturated-zone source detonations are associated with contaminant flux derived from the BILBY detonation, with less significant contributions from STARWORT, HAREBELL/INGOT/CALABASH, and LUBBOCK/TAHOKA detonations.
- Less mobile contaminants (including alpha emitters like ^{237}Np or U) are insignificant contributors to the extent of contaminant migration.
- The extent of contamination for saturated-zone sources is significantly greater than that for unsaturated-zone sources.

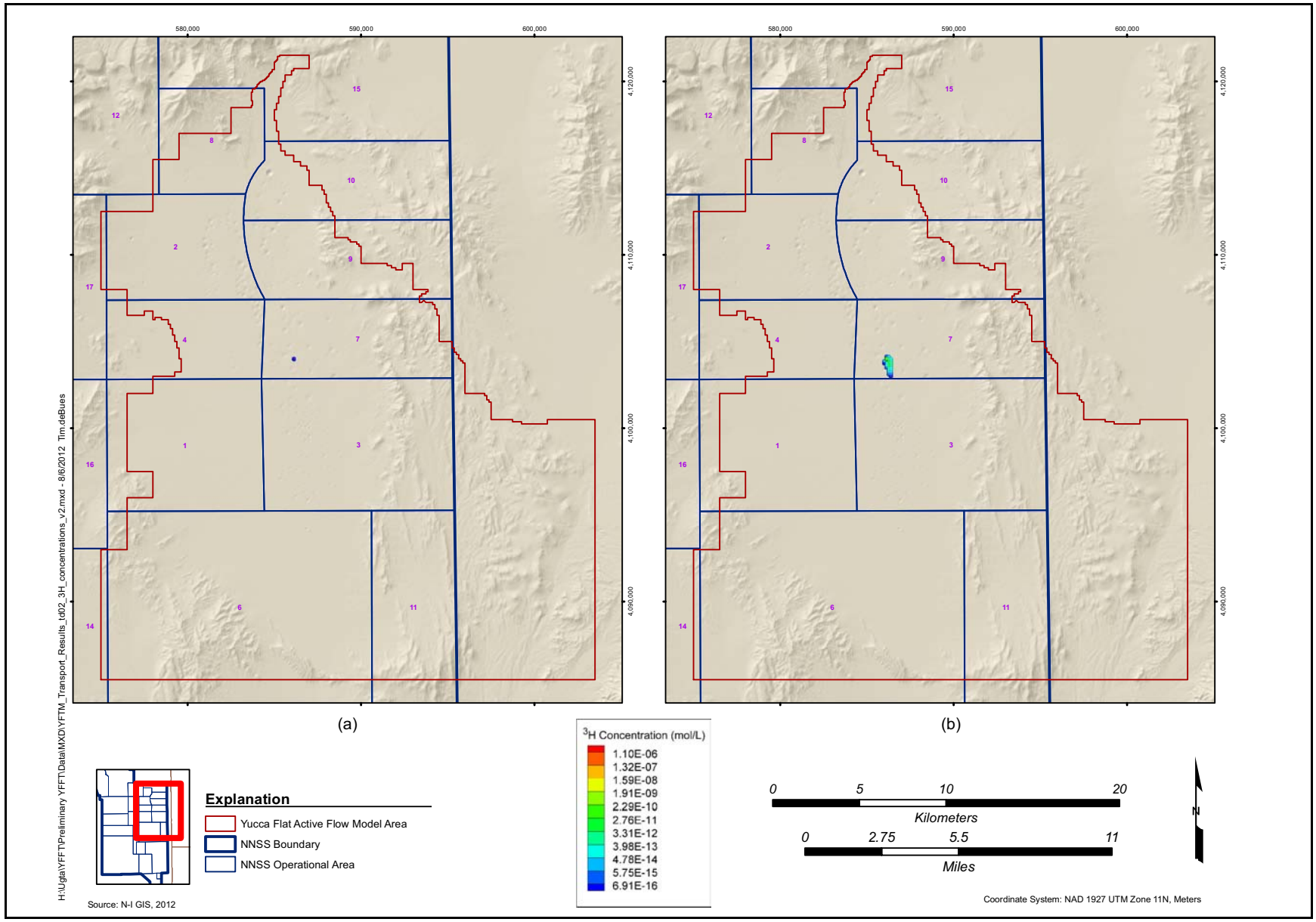

Figure 6-53
Base-Case Representative ^{3}H Concentrations for Saturated-Zone Sources: (a) 50 Years, and (b) 100 Years

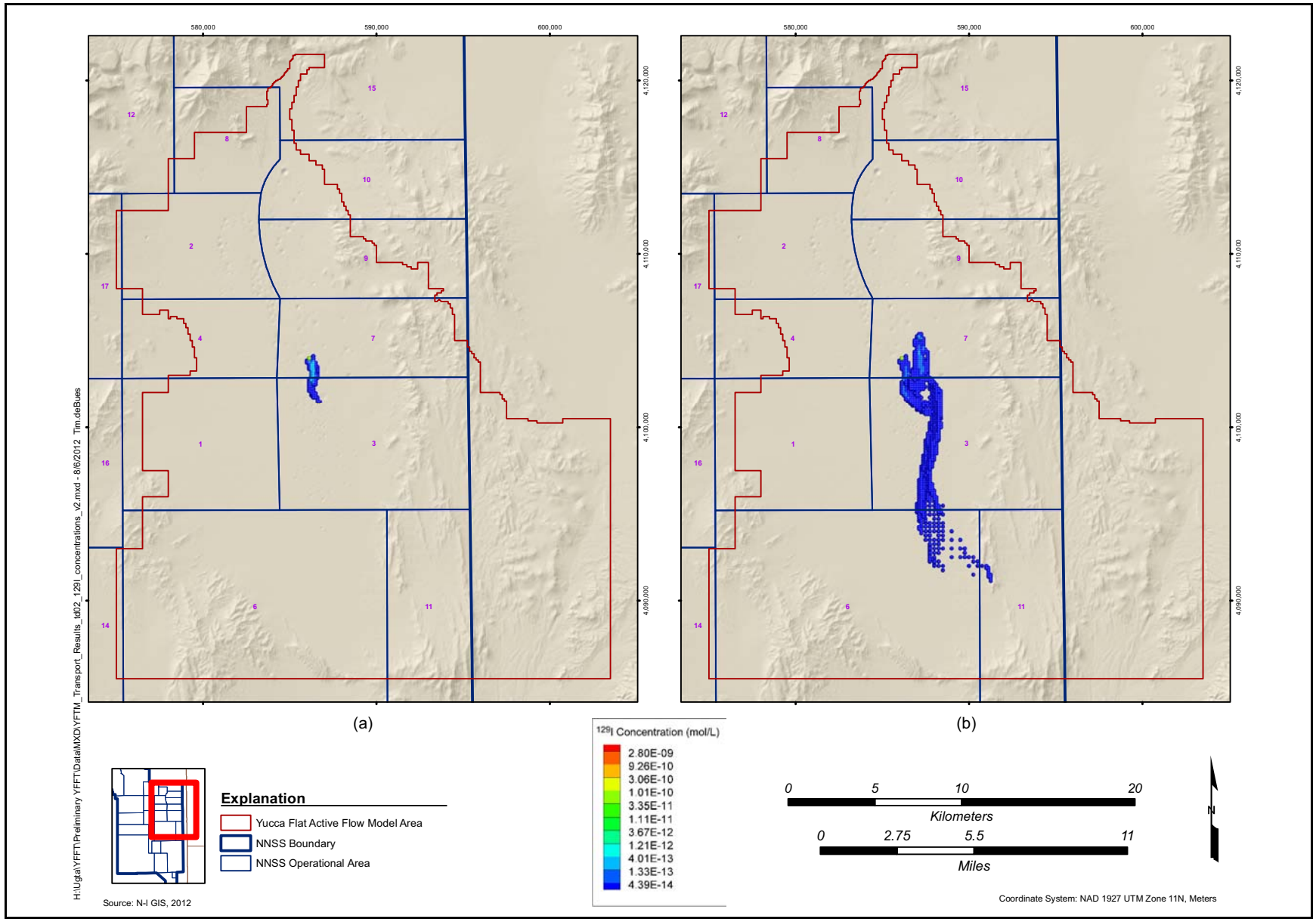

Figure 6-54
Base-Case Representative ^{129}I Concentrations for Saturated-Zone Sources: (a) 300 Years, and (b) 1,000 Years

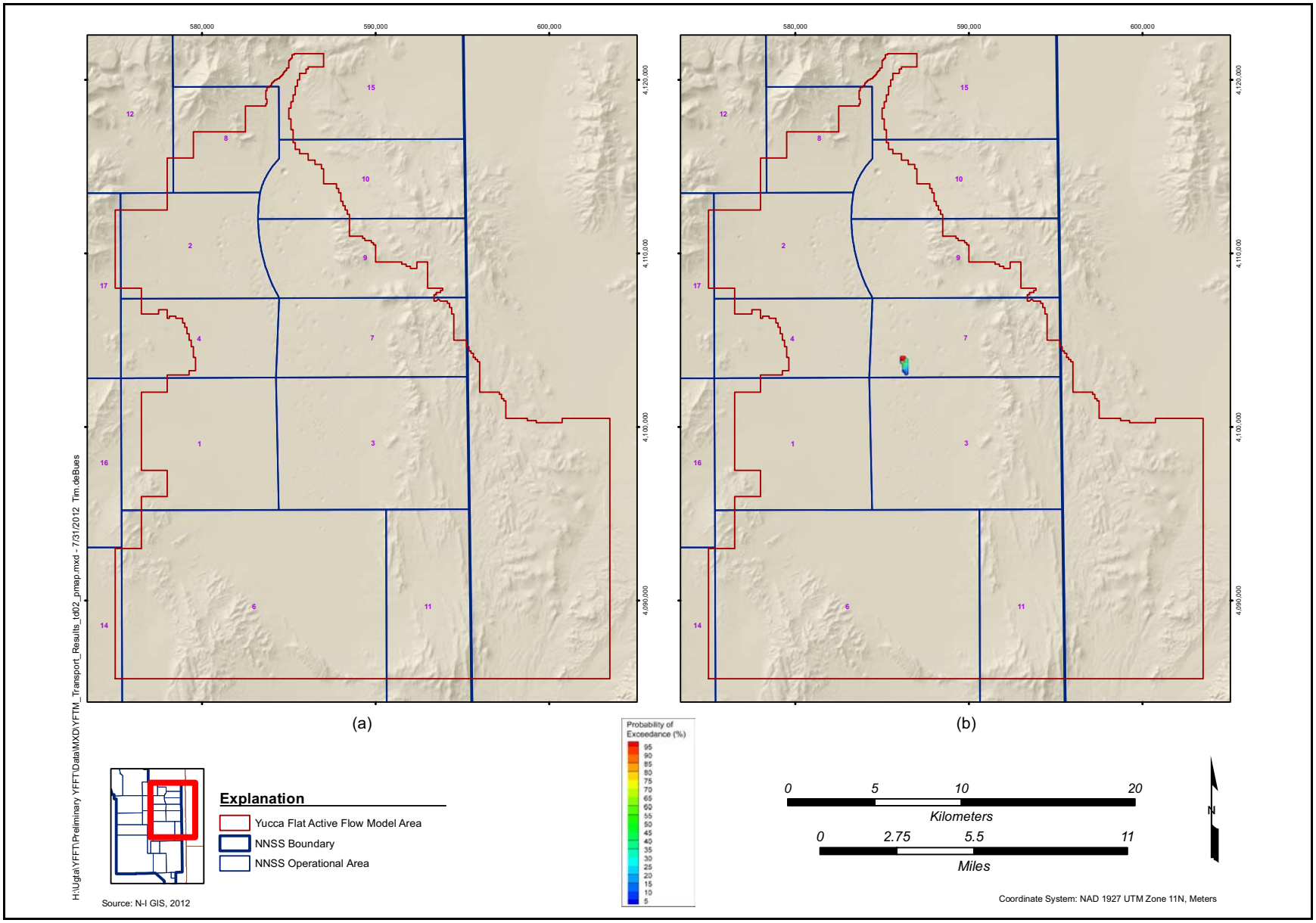

Figure 6-55

Base-Case Probability of Exceedance of MCL for Saturated-Zone Sources: (a) 50 Years, and (b) 100 Years

Note: Based on base-case saturated-zone run SAE_12 (542121.12.2.8.1.11.2012_HST.N3.B2.s)

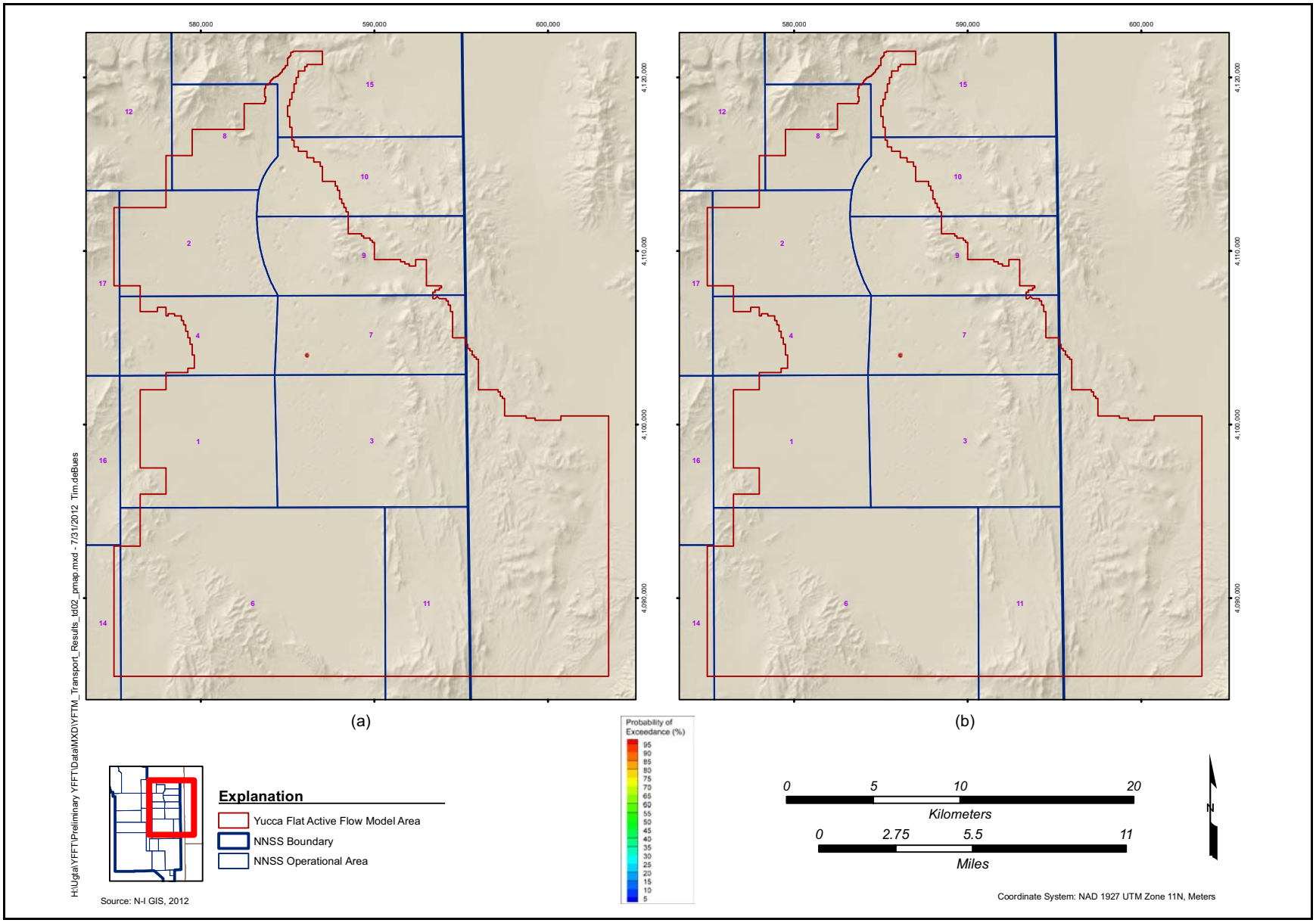

Figure 6-56

Base-Case Probability of Exceedance of MCL for Saturated-Zone Sources: (a) 300 Years, and (b) 1,000 Years

Note: Based on base-case saturated-zone run SAE_12 (542121.12.2.8.1.11.2012_HST.N3.B2.s)

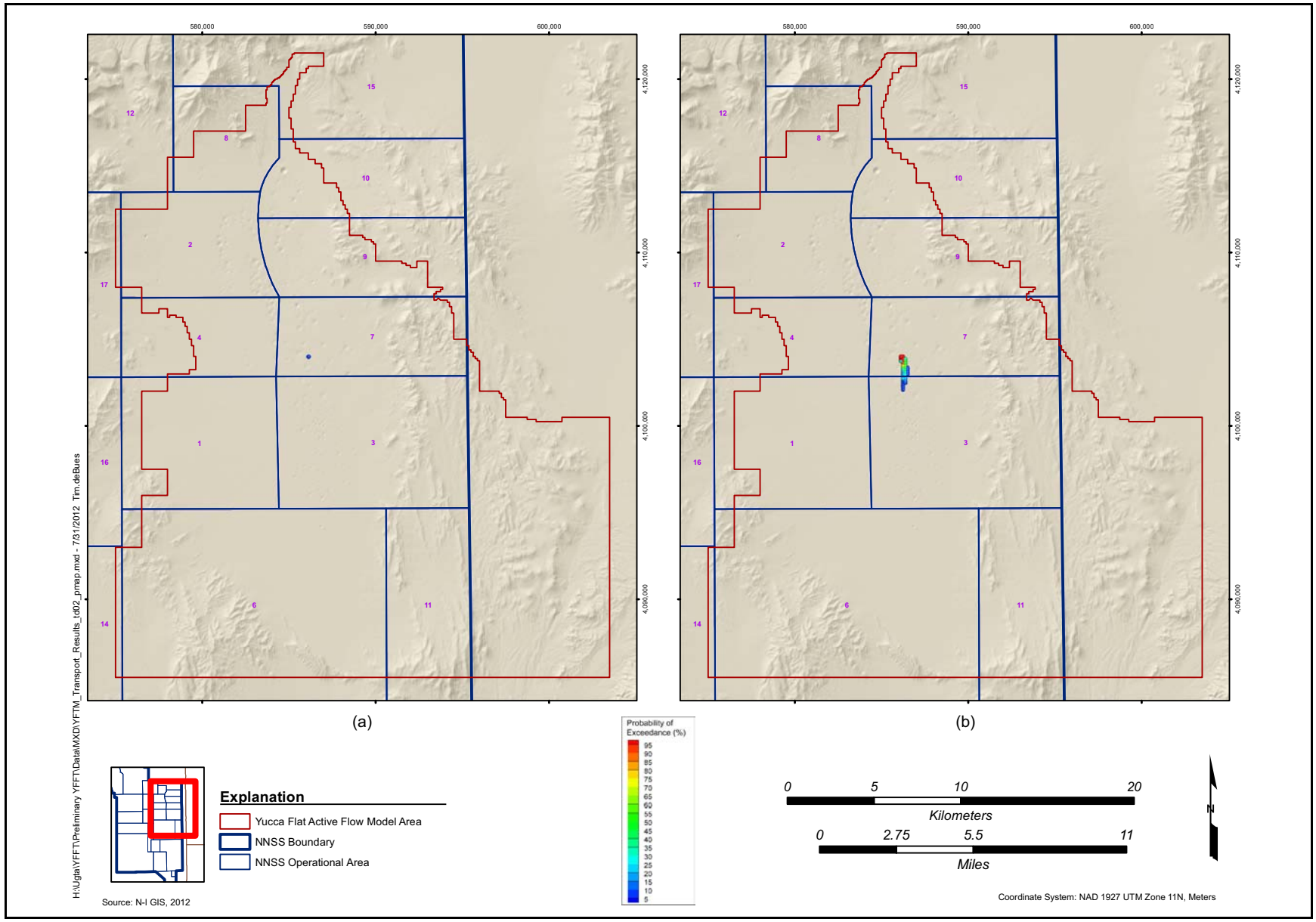

Figure 6-57
Base-Case Time-Cumulative Probability of Exceedance of MCLs for Saturated-Zone Sources: (a) Alpha-Emitter MCLs, and (b) Beta- and Photon-Emitter MCLs

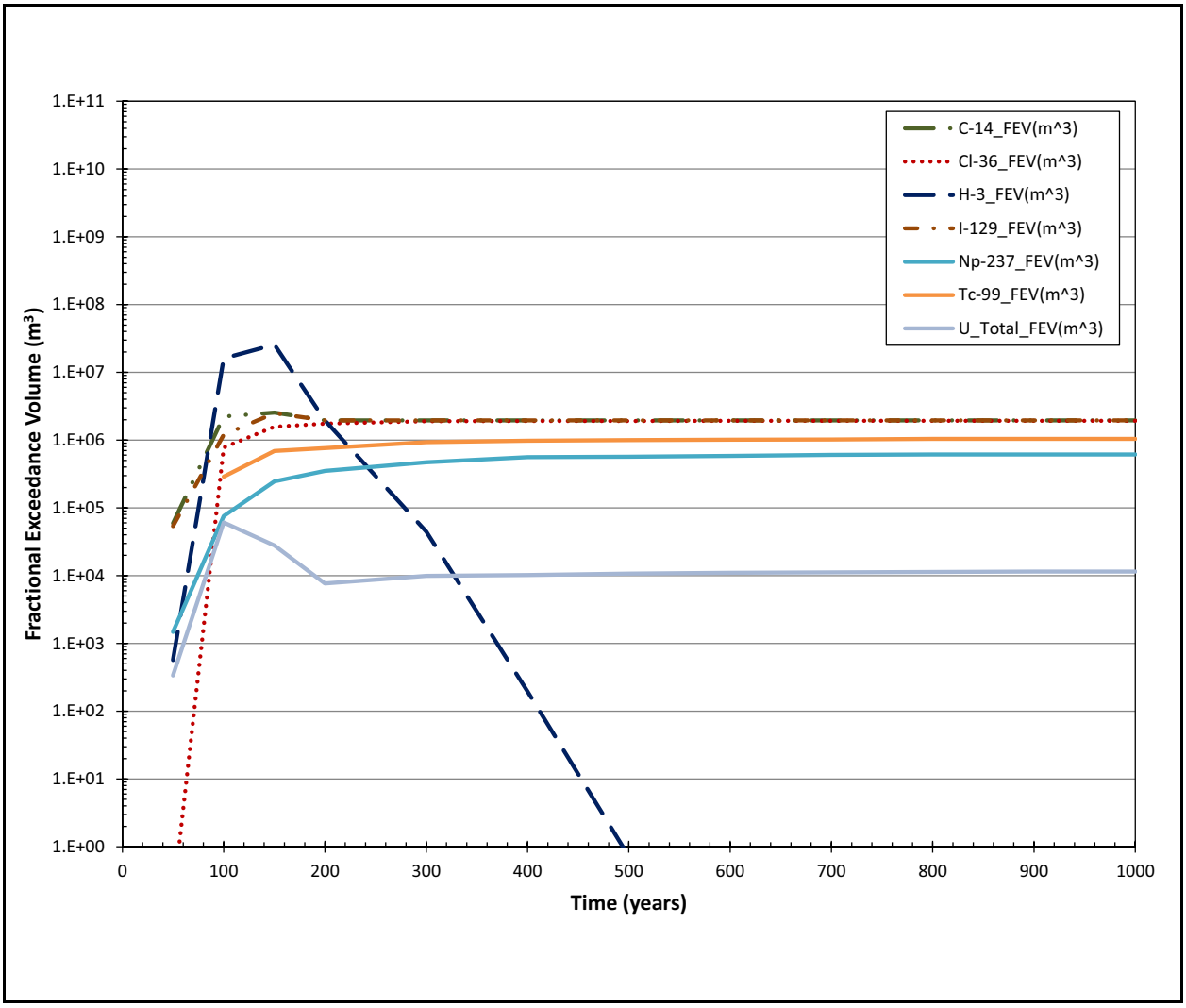

Figure 6-58
Base-Case Fractional Exceedance Volume for Saturated-Zone Sources

- The extent of contamination is dominated by a few saturated-zone sources that occur along the fault north of the BILBY detonation and along the Yucca fault east of the Tuff Pile.

Groundwater sampling and contaminant concentration analyses have been performed at observation wells located near several detonations of potential significance to contaminant migration from unsaturated zone and saturated alluvial/volcanic aquifer system sources. The analyses associated with the near-field "hot well" sampling program and other observation locations are summarized in Appendix D.

An observation well of particular relevance to the unsaturated-zone results are the observations in UE-2ce located 183 m from the NASH detonation. These observations indicate significant

contamination in the saturated LCA that can be directly attributable to the NASH detonation. The results of the base representation (of essentially no contamination near NASH) are not consistent with this observation. As noted in Carle et al. (2008), there may be significant chimney drainage of perched water or injection of drill-back fluids that could explain the discrepancy. Alternatively, it is possible that the local average and crater-enhanced infiltration and associated percolation in the vicinity of the NASH detonation are underestimated in the base representation. To address this, an alternative source-term representation was used, the results of which are presented in Section 6.5.3. Regardless of the source of the discrepancy, the lateral transport from the NASH detonation presented in Section 6.5.3 is insignificant.

An observation well of particular relevance to the saturated alluvial/volcanic aquifer system model results are the observations in Well U-3cn-5, completed in the LCA 129 m downgradient of the BILBY detonation. This observation well indicates minimal contamination in the saturated LCA. The results of the base representation are not significantly different from these observations at 50 years, equivalent to the present.

For LCA sources, the base-case results are illustrated by the following figures:

- Forecast ^{3}H concentrations at 50 and 100 years for the median realization (Figure 6-59). Note that the SDWA MCL for ^{3}H is 6.9E-13 mol/L.
- Forecast ^{129}I concentrations at 300 and 1,000 years for the median realization (Figure 6-60). Note that the SDWA MCL for ^{129}I is 4.4E-11 mol/L.
- Forecast ^{90}Sr concentrations at 50 and 300 years for the median realization (Figure 6-61). Note that the SDWA MCL for ^{90}Sr is 6.3E-16 mol/L.
- Forecast probability of exceedance of SDWA MCLs at 50, 100, 300, and 1,000 years (Figures 6-62 and 6-63).
- Forecast time-cumulative probability of exceedance of alpha-emitter and beta- and photon-emitter MCLs (Figure 6-64).
- Forecast 95th percentile fractional exceedance volume (Figure 6-65).
- CDFs for cumulative MCL exceedance volume and maximum southern extent of MCL exceedance (Figure 6-66).

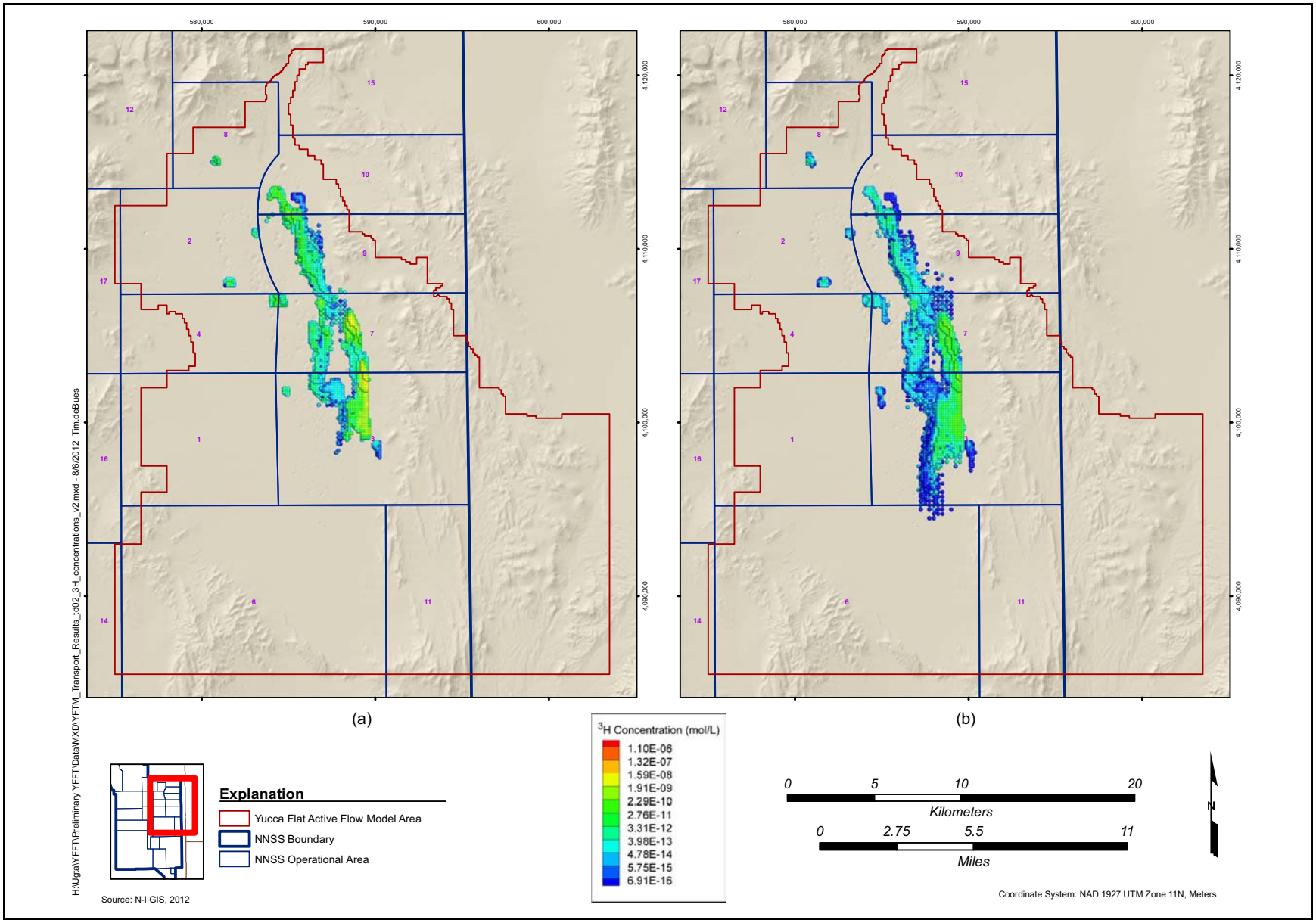

Figure 6-59
Base-Case Representative ^{3}H Concentrations for LCA Sources: (a) 50 Years, and (b) 100 Years

Note: Base-case LCA flow model and median realization

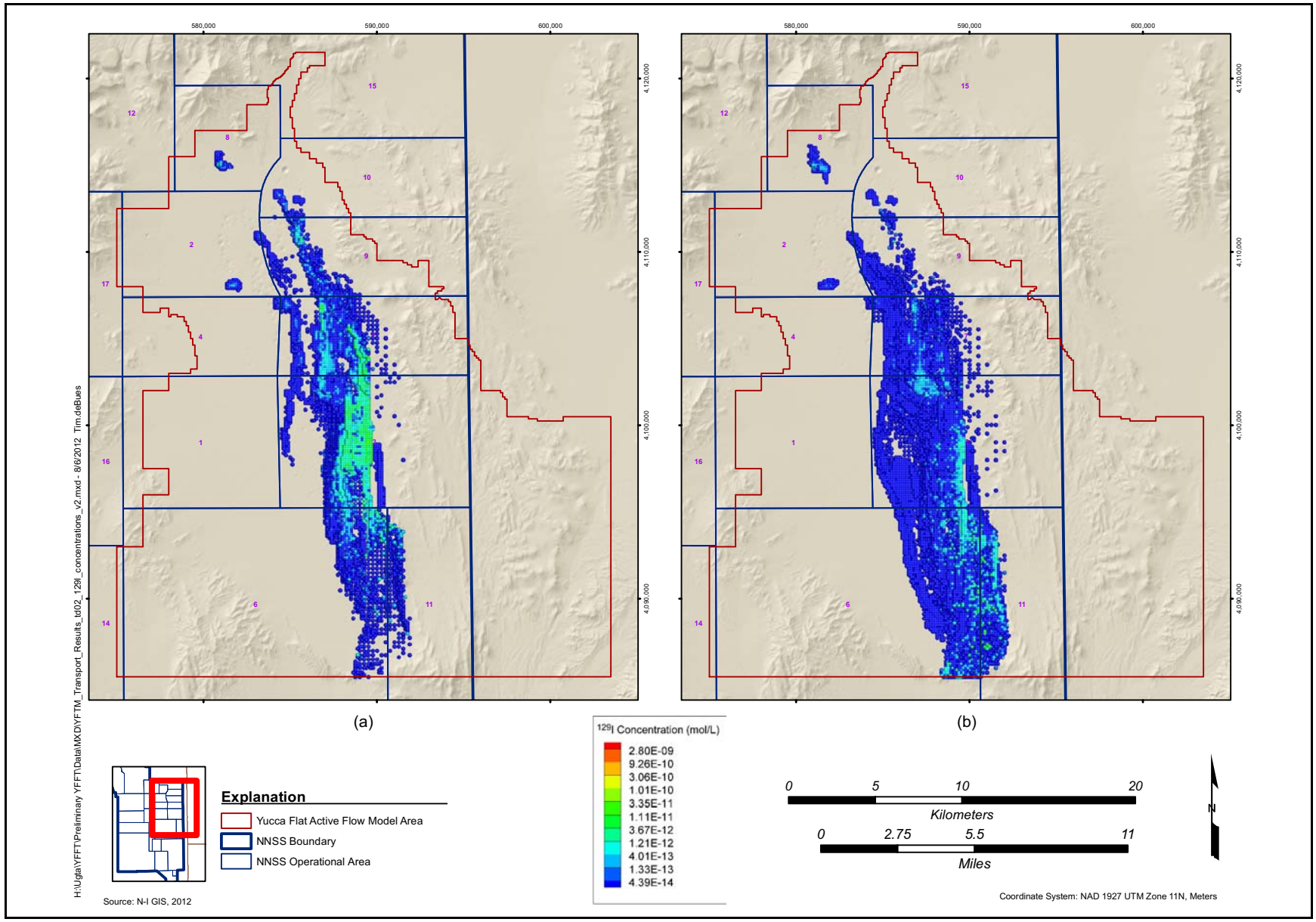

Figure 6-60

Base-Case Representative ^{129}I Concentrations for LCA Sources: (a) 300 Years, and (b) 1,000 Years

Note: Base-case LCA flow model and median realization

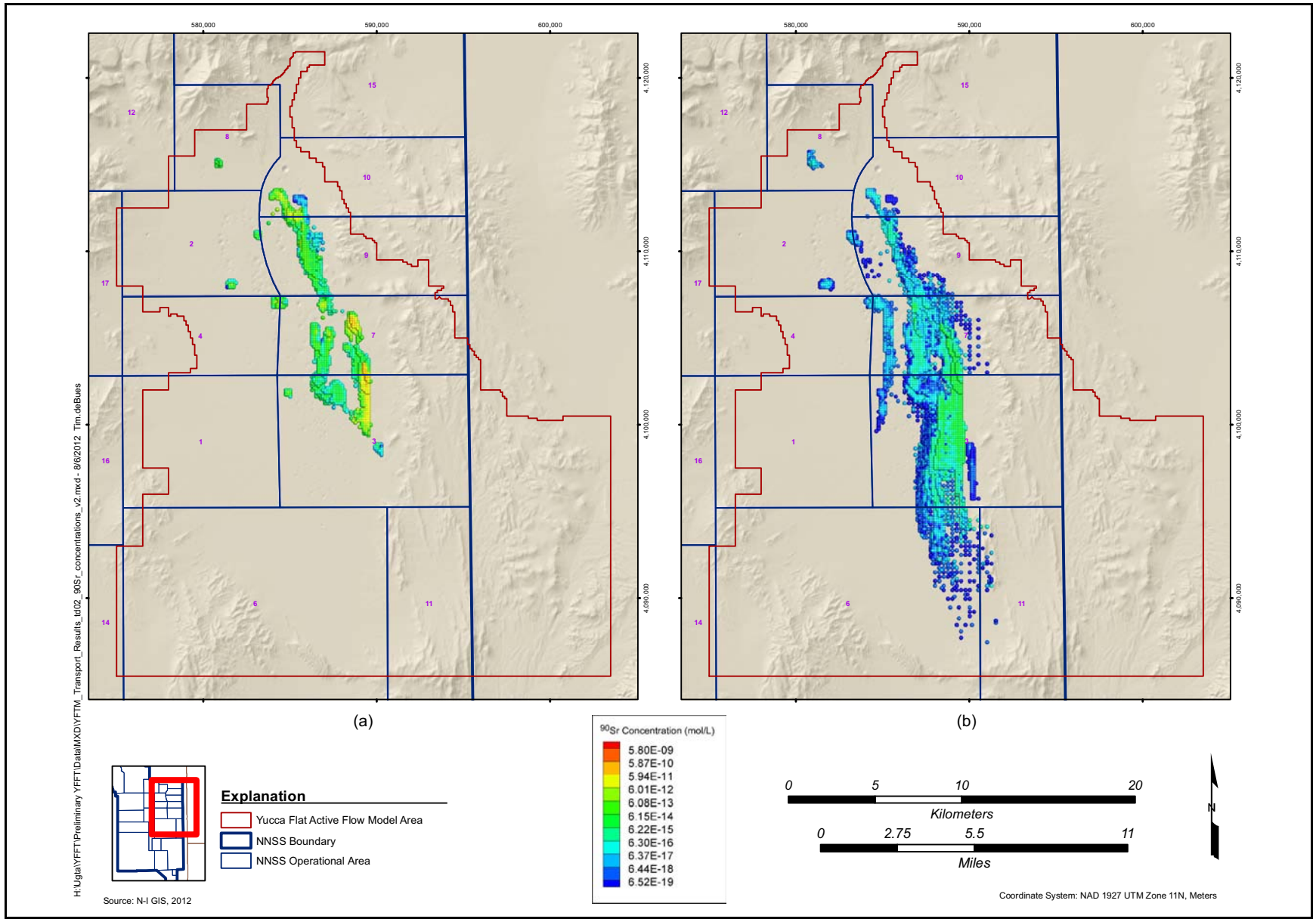

Figure 6-61
Base-Case Representative ^{90}Sr Concentrations for LCA Sources: (a) 50 Years, and (b) 300 Years

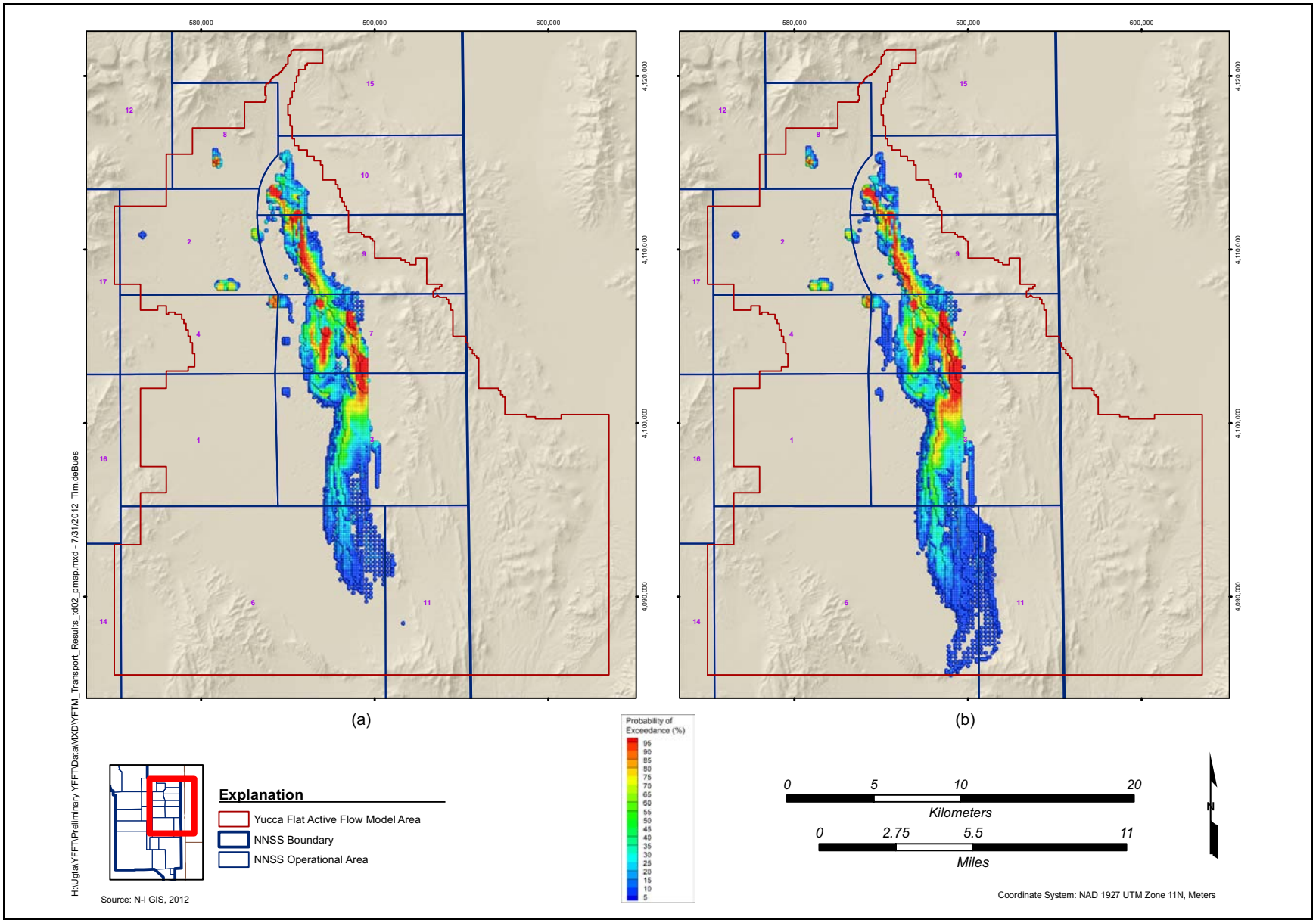

Figure 6-62
Base-Case Probability of Exceedance of MCL for LCA Sources: (a) 50 Years, and (b) 100 Years

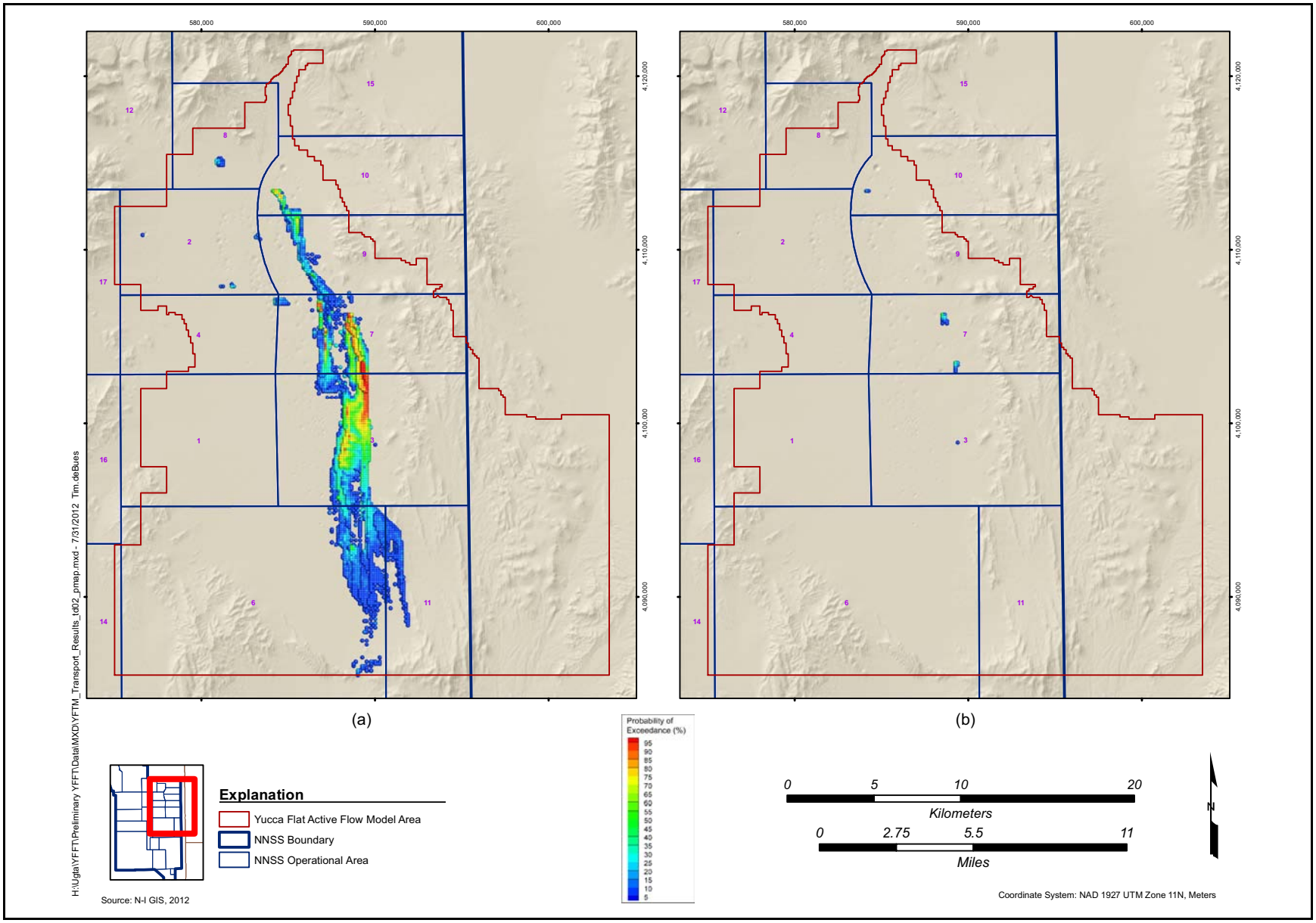

Figure 6-63
Base-Case Probability of Exceedance of MCL for LCA Sources: (a) 300 Years, and (b) 1,000 Years

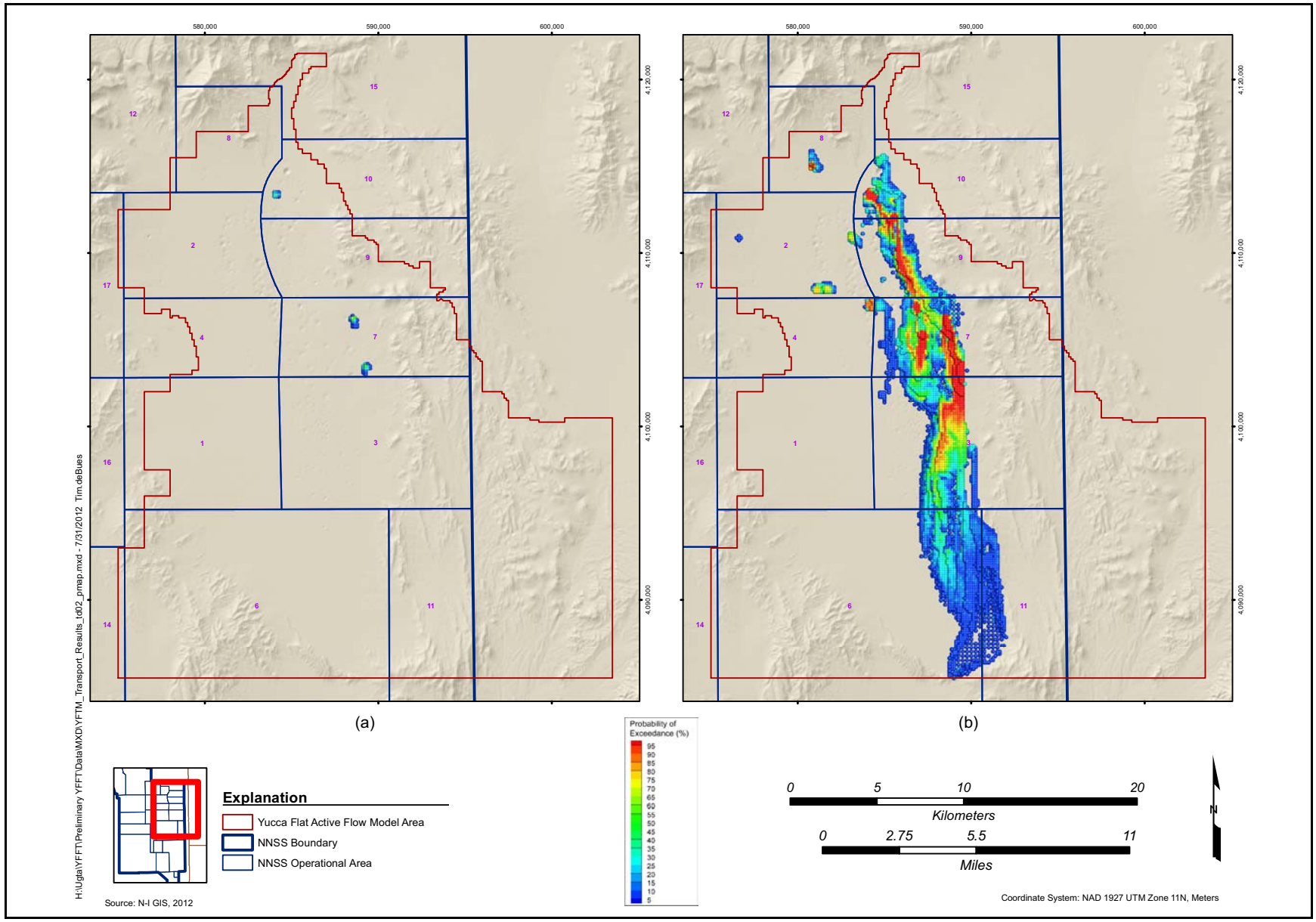

Figure 6-64
Base-Case Time-Cumulative Probability of Exceedance of MCLs for LCA Sources: (a) Alpha-Emitter MCLs, and (b) Beta- and Photon-Emitter MCLs

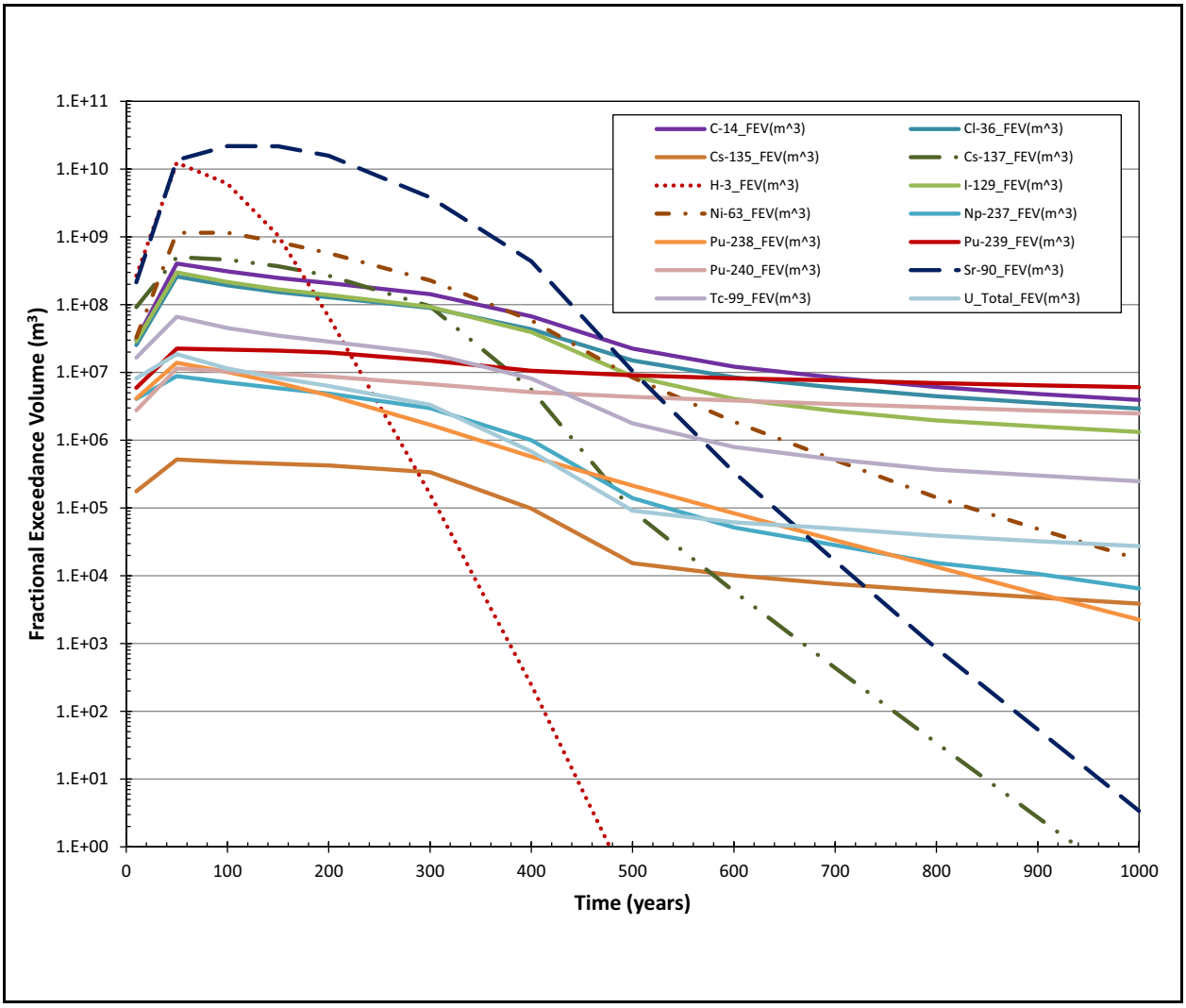

Figure 6-65
Base-Case Fractional Exceedance Volume for LCA Sources

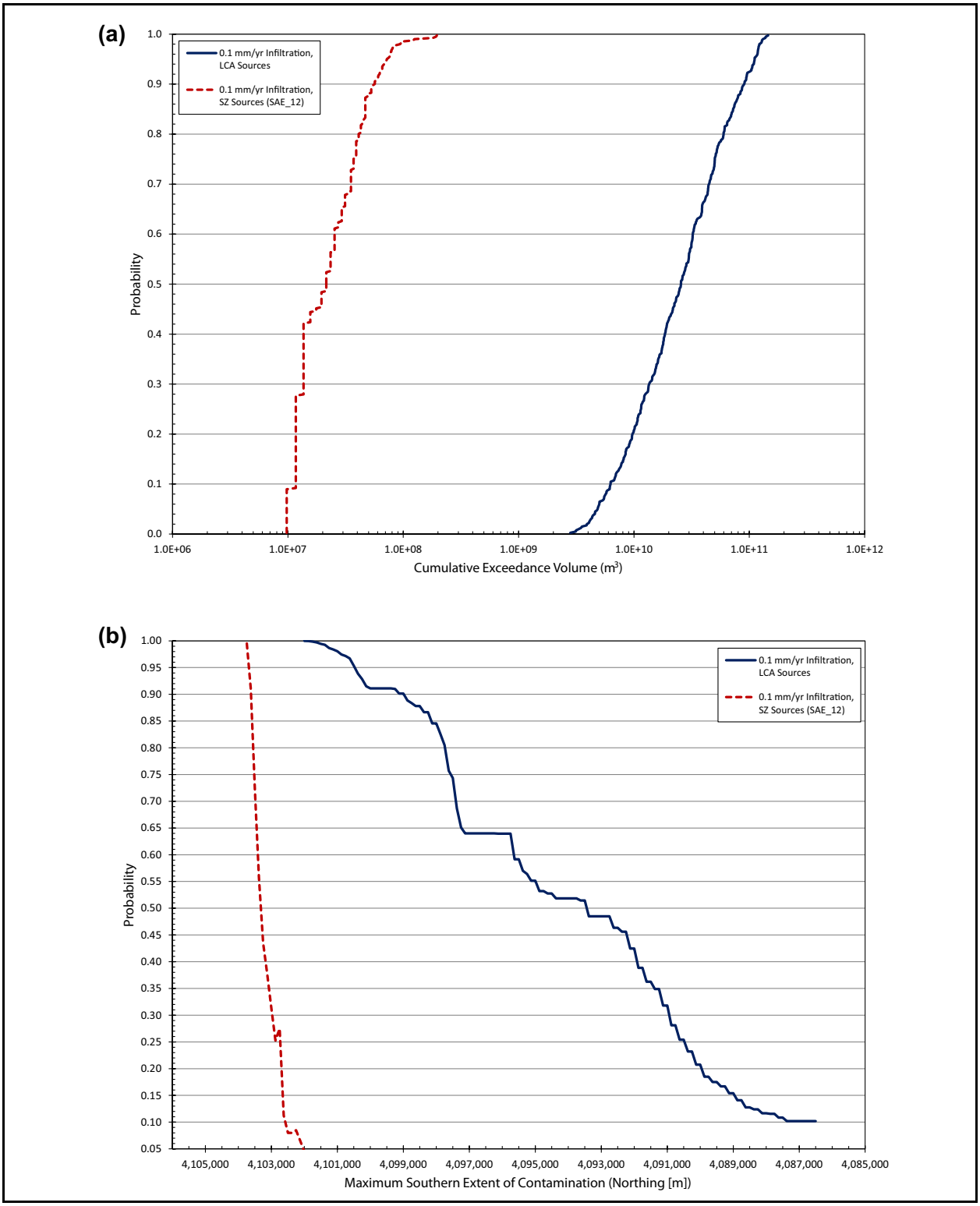

Figure 6-66
Base-Case CDFs for Saturated Zone and LCA Sources: (a) Cumulative MCL Exceedance Volume, and (b) Maximum Southern Extent of MCL Exceedance

The following observations can be made from these results:

- ^{3}H and ^{90}Sr dominate the extent of contaminant migration, but due to their short half-lives, the maximum extent of contamination decreases significantly during the next few hundred years. This is particularly noted in Figure 6-63, where the extent of contaminant migration decreases significantly between 300 and 1,000 years as the ^{90}Sr decays.

- ^{129}I (combined with ^{36}Cl and ^{99}Tc) dominates the extent of contaminant migration once the ^{3}H plume has decayed.

- The extent of contaminant migration is controlled by the beta- and photon-emitter radionuclides. Less mobile contaminants (including alpha emitters like ^{237}Np and U) are insignificant contributors to the extent of contaminant migration.

- The most significant LCA sources affecting the extent of contamination are the BOURBON, TORRIDO, CORDUROY, SHUFFLE, and STRAIT underground nuclear detonations.

- The extent of contamination from LCA sources is significantly greater than that from saturated-zone sources, even though the initial contamination in place in the saturated-zone sources is significantly greater. This is a result of the significant initial contaminant concentration in the LCA, especially from ^{3}H and ^{90}Sr, which have initial concentrations that can be 1E+05 to 1E+07 times the MCL as depicted in Section 2.0.

- There is a low probability that contamination exceeding the SDWA MCL may extend to the southern modeled boundary located at a northing of 4,085,500 m. This is apparent in Figures 6-64b and 6-66b. Although this probability exceeds the 5th percentile of the FFACO, this model run is noted to include several specific conservative assumptions, the combined effect of which results in a low probability that the MCL may be exceeded. Alternative model runs presented in Sections 6.5.6 and 6.5.7 illustrate the significance of these conservative assumptions. Even if contaminants exceeding the MCL extend south of the southern boundary, they would likely be retained in the LCA in Frenchman Flat.

Contaminant concentrations have been measured in observation wells drilled in the near-field vicinity of several of the perceived significant detonations with working points near the saturated LCA. These include Well UE-7nS located 137 m downgradient of the BOURBON working point and Well ER-7-1 located several hundred meters downgradient of the TORRIDO and MICKEY detonations. As discussed in Appendix D, observations of ^{3}H contamination at UE-7nS indicate concentrations of about 10,000 pCi/L, less than the MCL of 20,000 pCi/L, while observations of ^{3}H contamination at ER-7-1 indicate concentrations less than the minimum detection limit. These observations are significantly different than the transport model results illustrated in Figures 6-59a and 6-61a, which indicate significant contamination should be present at these two locations. The model indicates 50-year concentrations (corresponding to about 2015) well above the SDWA MCLs of ^{3}H and ^{90}Sr of

6.9E-13 mol/L and 6.5E-16 mol/L, respectively. In addition, the 50-year map of the probability of exceeding the MCLs at these two locations illustrated in Figure 6-62a indicates probabilities of MCL exceedance above 90 percent. This discrepancy may be the result of these observation wells not intersecting permeable flowing features that provide hydraulic communication between the exchange volume and the observation well (as postulated in SNJV, 2007, and Buddemeier and Isherwood, 1985). However, it is also likely that the assumed exchange volume does not extend into the saturated LCA, as is assumed by using the maximum announced yield of 200 kt for these detonations. Given the reported range in yield for these detonations is from 20 to 200 kt, the actual yield could result in a smaller cavity radius, and thus a smaller exchange volume and a smaller likelihood that the exchange volume would intersect the saturated LCA, as is postulated when using the maximum of the announced yield.

In addition to the two wells drilled near the two key detonations with exchange volumes that are likely to extend into the saturated LCA (notably, BOURBON and TORRIDO), WW C and WW-C-1 located in the southern portion of Yucca Flat have been monitored since the early 1960s. Based on the modeling results, contamination is not expected to reach these wells until several hundred years. As discussed in Appendix D, these wells have had measurable ^{3}H of about 100 pCi/L and currently show a downward trend. The presence of ^{3}H in these wells and the downward trend have been attributed by Lyles (1990) to be the result of an interrupted tracer experiment conducted by USGS in 1964 in which about 0.1 to 0.2 Ci of ^{3}H was introduced into WW-C-1. Although the current trend of ^{3}H concentration is decreasing in WW-C-1, it is not clear whether an increased trend would indicate transport from upgradient underground nuclear testing contaminant sources or the return of contamination introduced in these wells during the interrupted tracer experiment.

6.5.3 Alternative LCA HSTs

As discussed in Section 2.0, three alternative LCA source-term scenarios have been identified. The base-case LCA source term used to generate the results presented in Section 6.5.2 is derived from the uniform concentration-based source-term allocation approach presented in Appendix C and Section 2.3.3 wherein the LCA initial inventory allocation is based on radionuclide-specific exchange volumes with uncertainty and a uniform concentration in the exchange volume.

Two alternative source terms were developed that use different initial inventory allocations. In the first alternative (called the Preliminary 2 R_c HST or Initial 2 R_c HST case in subsequent figures), a

fixed 2 R_c exchange volume is used for all radionuclides and all detonation exchange volumes that intersect the saturated LCA, with 2 representing the midpoint of the range of variability expected in exchange volume radii between 1 and 3. In this alternative source-term scenario, a uniform-mass distribution was assigned to the exchange volume, as compared to the uniform concentration used in the base-case allocation method.

The second alternative (called the Alternative Bounding or 3 R_c Alternative HST in subsequent figures) used the same allocation as the base-case allocation, except at the following discrete detonations where all of the initial inventory was placed in the saturated LCA:

- BOURBON—to account for the potential effects of cavity/chimney drainage and drill-back fluid losses
- HANDCAR—to account for the potential effects of cavity/chimney drainage and drill-back fluid losses
- KANKAKEE—to account for the potential effects of cavity/chimney drainage and drill-back fluid losses
- NASH—to account for the potential effects of cavity/chimney drainage and drill-back fluid losses
- CORDUROY—to account for the potential effects of hydraulic communication to the LCA through test-altered zones and drill-back fluid losses
- TORRIDO—to account for the potential effects of hydraulic communication to the LCA through test-altered zones and drill-back fluid losses
- LAMPBLACK—to account for the potential effects of hydraulic communication to the LCA through test-altered zones and drill-back fluid losses
- CALABASH—to account for the potential effects of chimney drainage due to diverted flow from the overlying volcanic aquifers to the underlying LCA

The results for these alternative LCA source-term scenario are illustrated in the following figures:

- Time-cumulative probability of exceeding the MCL (Figure 6-67)
- CDFs of time-cumulative MCL exceedance volume and maximum southern extent of contamination (Figure 6-68). The two alternative LCA source term scenarios are compared to the base-case scenario (called the 3 R_c HST on this figure).

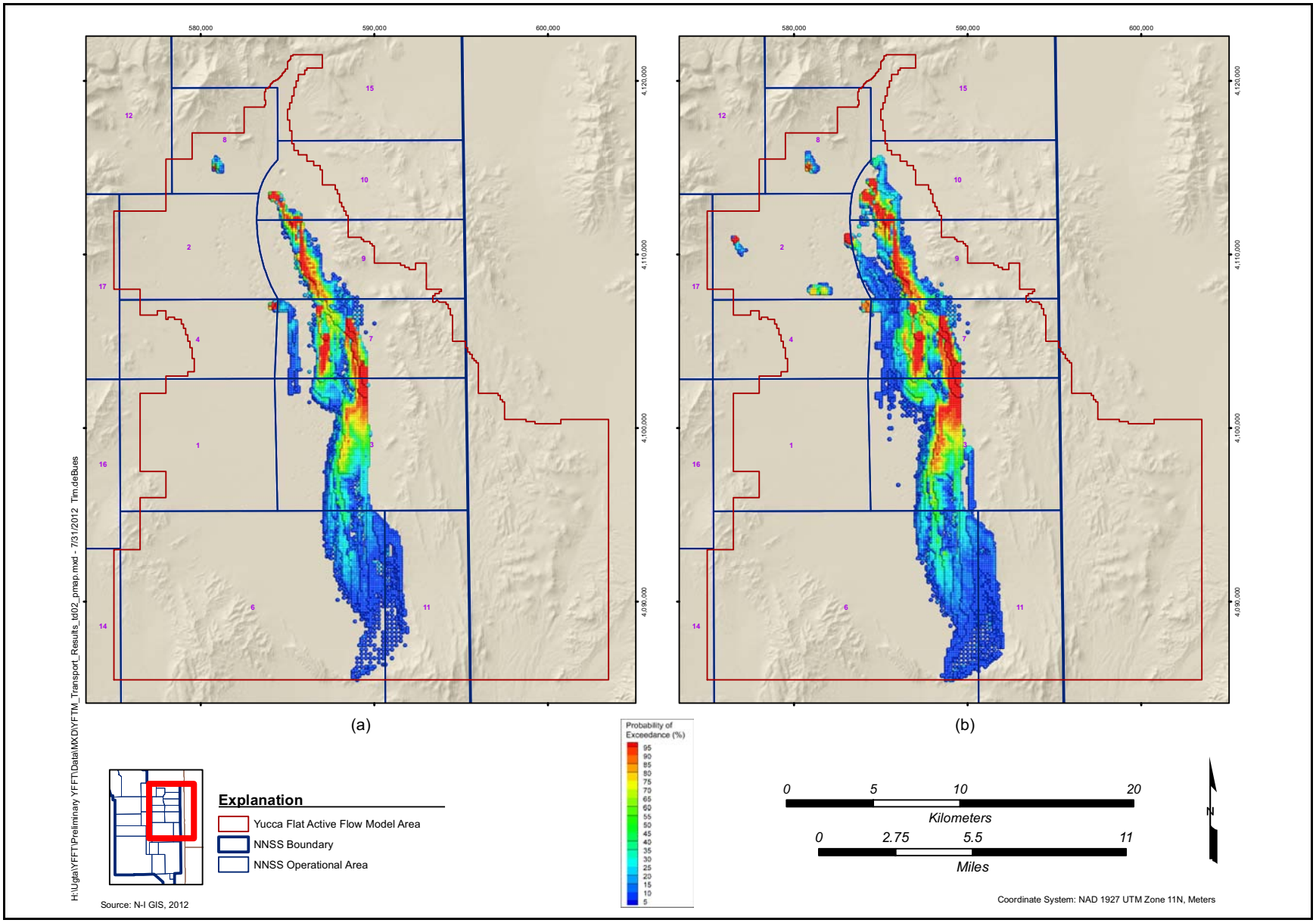

Figure 6-67
Time-Cumulative Probability of Exceedance of MCLs for Alternative LCA Sources: (a) Preliminary 2 R_c, and (b) Alternative Bounding HST

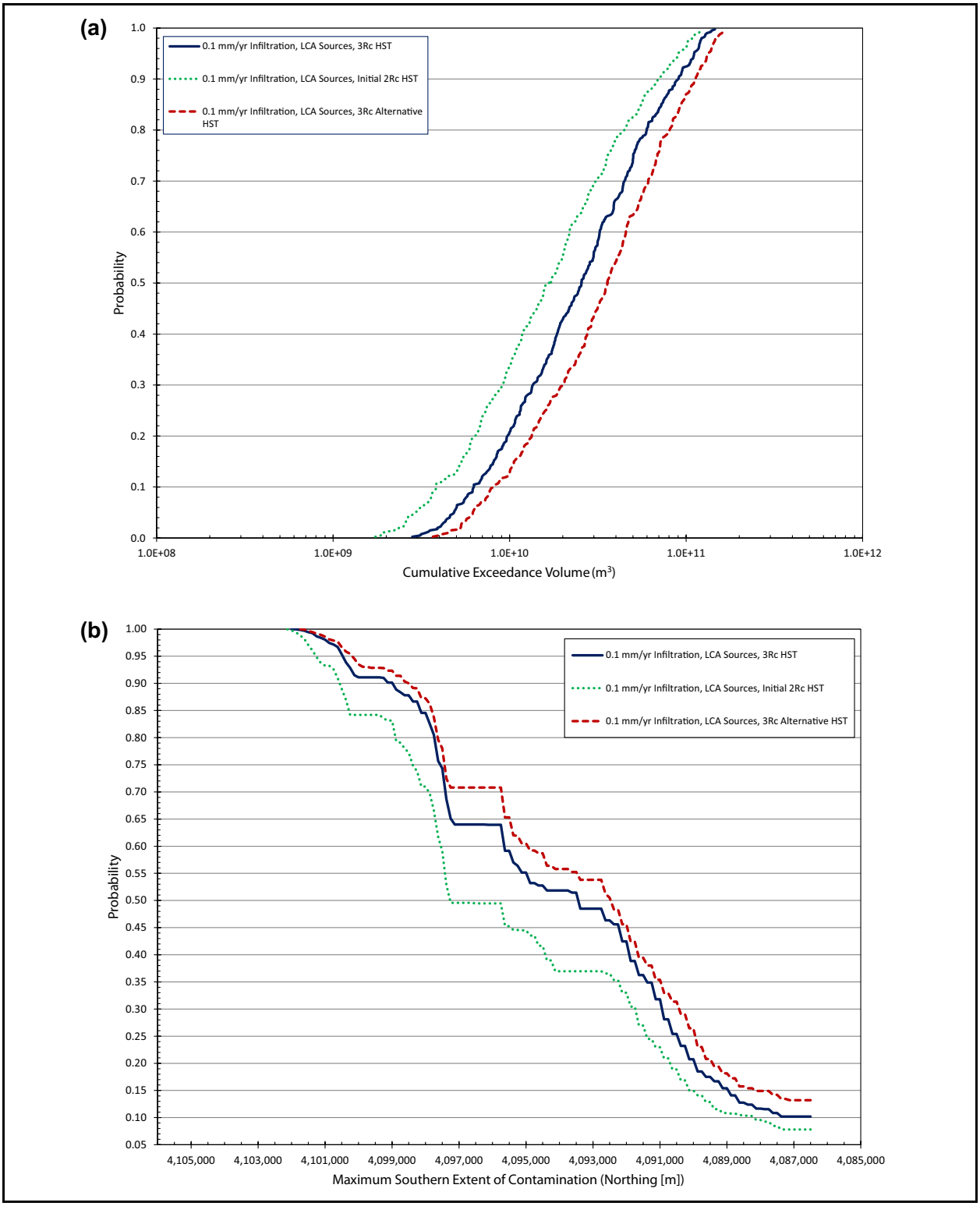

Figure 6-68
CDFs for LCA Sources with Alternative HSTs: (a) Cumulative MCL Exceedance Volume, and (b) Maximum Southern Extent of MCL Exceedance

The following observations can be made from these results:

- The base-case uniform-concentration-based LCA source term yields a greater extent of contamination than the alternative uniform-mass-based LCA source term. This result could have been predetermined by examining the significant difference in initial mass in place for the base-case source term, in particular, the increase at BOURBON (about tenfold), TORRIDO (about tenfold), and CORDUROY (about threefold). As presented in Table 2-7, these three detonations comprise about 95 percent of the initial inventory in the saturated LCA.

- The alternative source-term scenario developed to investigate the potential effects of cavity/chimney drainage, hydraulic communication in test-altered zones, and drill-back fluid losses results in an increased extent of contamination, again due to the increase in initial mass and concentration in place in the saturated LCA.

- In the vicinity of the NASH detonation, the calculated concentrations of the alternative source-term scenario assuming significant cavity/chimney drainage are representative of the contaminant concentration observations in UE-2ce.

- Although not illustrated, the extent of contamination is most significantly influenced by the non-sorbing radionuclides that initially have concentrations of 1E+04 to 1E+07 times the MCL, notably, ^{90}Sr, ^{3}H, and ^{137}Cs.

6.5.4 Alternative Infiltration Rates

As discussed in Sections 3.0, 4.0, and 5.0, the long-term steady-state infiltration rate in the Yucca Flat area is both spatially variable and uncertain. This uncertainty affects the modeled percolation flux through the unsaturated-zone flow model as well as the calibrated specific discharge through the saturated alluvial/volcanic aquifer system flow model. Although there is significant evidence to support the conceptualization that the infiltration rate in the central part of Yucca Flat, corresponding to the area of most active underground nuclear testing, is extremely small (with an average infiltration rate on the order of 0.1 mm/yr), to address the potential effect of lateral drainage, pluvial drainage, and alternative recharge scenarios, alternative rates were used as sensitivity analyses in different unsaturated zone and saturated alluvial/volcanic aquifer system model transport runs. These alternative analyses included values of 1, 5, and 10 mm/yr.

To analyze the potential effects of these alternative scenarios, the mass releases from both the 1- and 5-mm/yr transport results presented in Sections 3.0 and 4.0 were propagated to the LCA. These cases used the uniform-mass source-term allocation that places more of the initial mass in the

unsaturated zone. The following figures illustrate the effects of these alternative scenarios on transport in the LCA:

- Time-cumulative probability of exceeding MCLs from unsaturated-zone sources (Figure 6-69)
- Time-cumulative probability of exceeding MCLs from saturated alluvial/volcanic aquifer system sources (Figure 6-70)
- Forecast probability of exceedance of SDWA at 50, 100, 300, and 1,000 years (Figures 6-71 and 6-72)
- Fractional exceedance volume for unsaturated-zone sources (Figure 6-73)
- Fractional exceedance volume for saturated-zone sources (Figure 6-74)
- CDFs for cumulative MCL exceedance volume and maximum southern extent of MCL exceedance (Figure 6-75)

The following observations can be made from these results:

- The unsaturated-zone releases are insignificant in comparison to the releases from the saturated alluvial/volcanic aquifer system (compare Figures 6-69 and 6-70).
- Releases at 1 mm/yr are significantly greater than releases at 0.1 mm/yr. Similarly, releases at 5 mm/yr are much greater than releases at 1 mm/yr (compare Figures 6-57, 6-69, and 6-70).
- The contaminant extent is dominated by the mobile species, notably, ^{3}H, ^{14}C, ^{36}Cl, and ^{129}I (see Figures 6-73 and 6-74).
- The contaminant extent from LCA sources, regardless of the LCA source-term allocation method, is significantly greater than the extent due to unsaturated zone or saturated alluvial/volcanic aquifer system sources (compare Figures 6-64, 6-69, and 6-70).
- The contaminant extent associated with unsaturated zone and saturated alluvial/volcanic aquifer system sources is dominated by a few detonations that are close to either the saturated LCA or faults that provide hydraulic communication to the saturated LCA (Section 6.4).

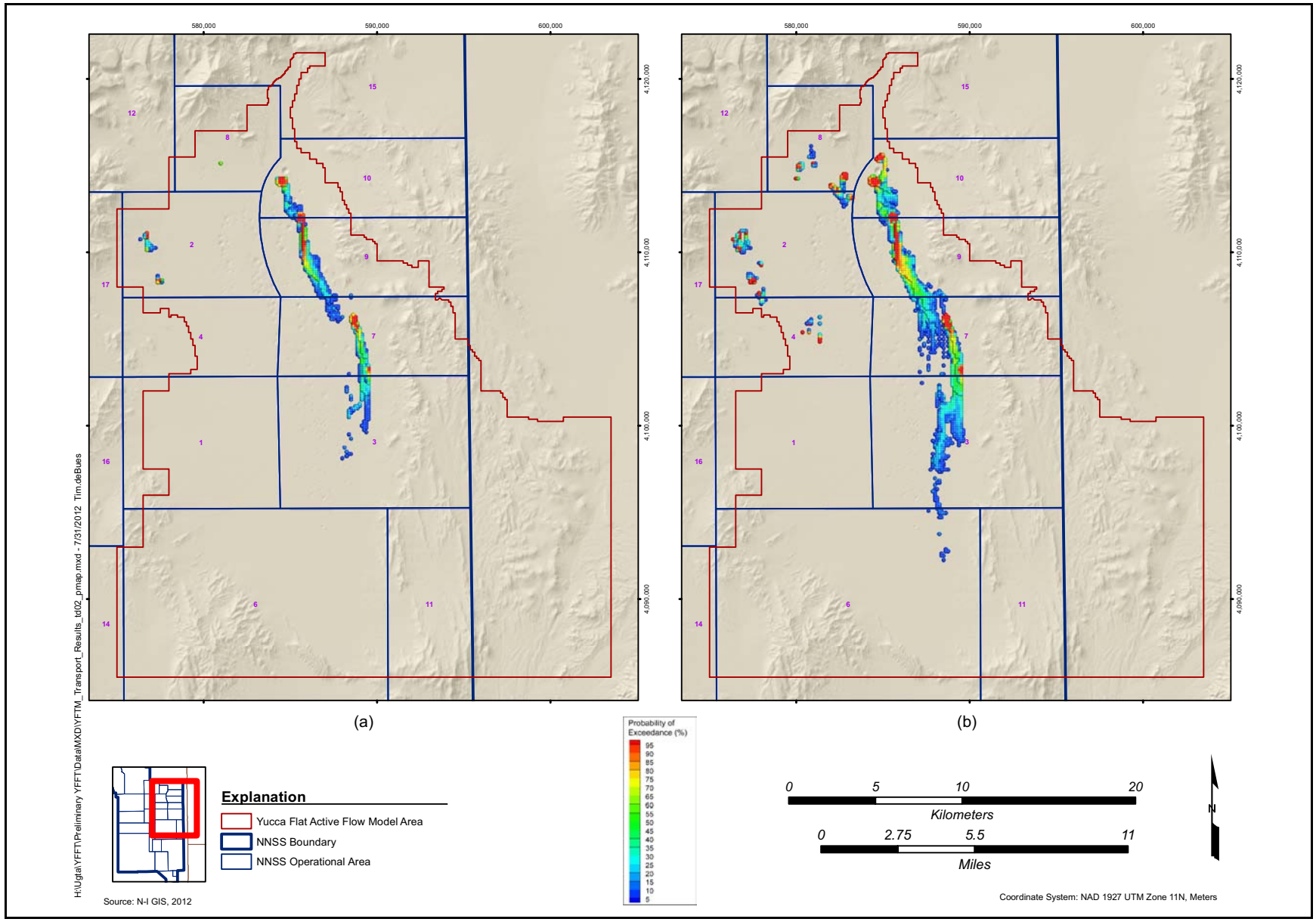

Figure 6-69
Time-Cumulative Probability of Exceedance of MCLs for Unsaturated-Zone Sources with Alternative Infiltration Rates: (a) 1 mm/yr, and (b) 5 mm/yr

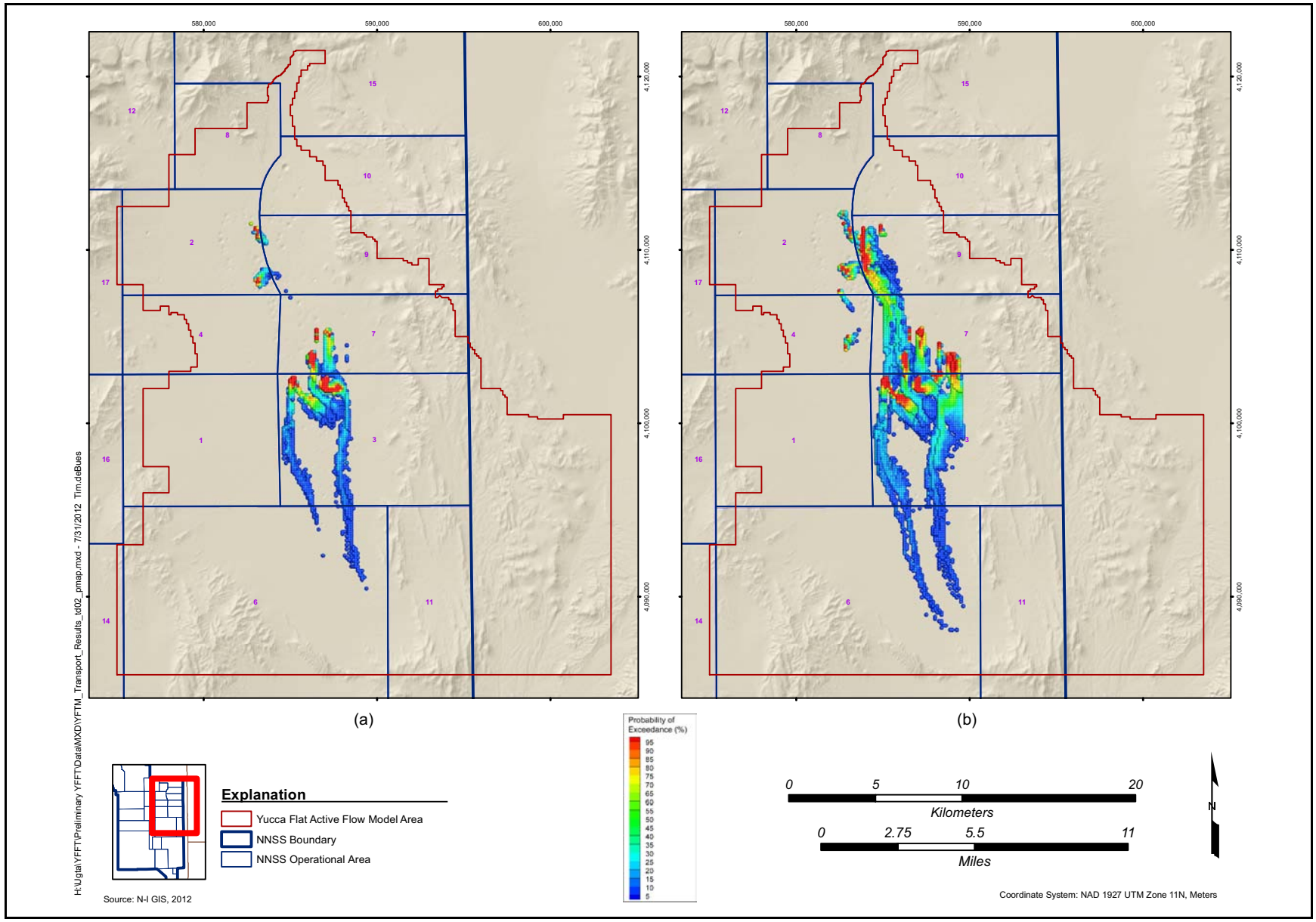

Figure 6-70
Time-Cumulative Probability of Exceedance of MCLs for Saturated-Zone Sources with Alternative Infiltration Rates: (a) 1 mm/yr, and (b) 5 mm/yr

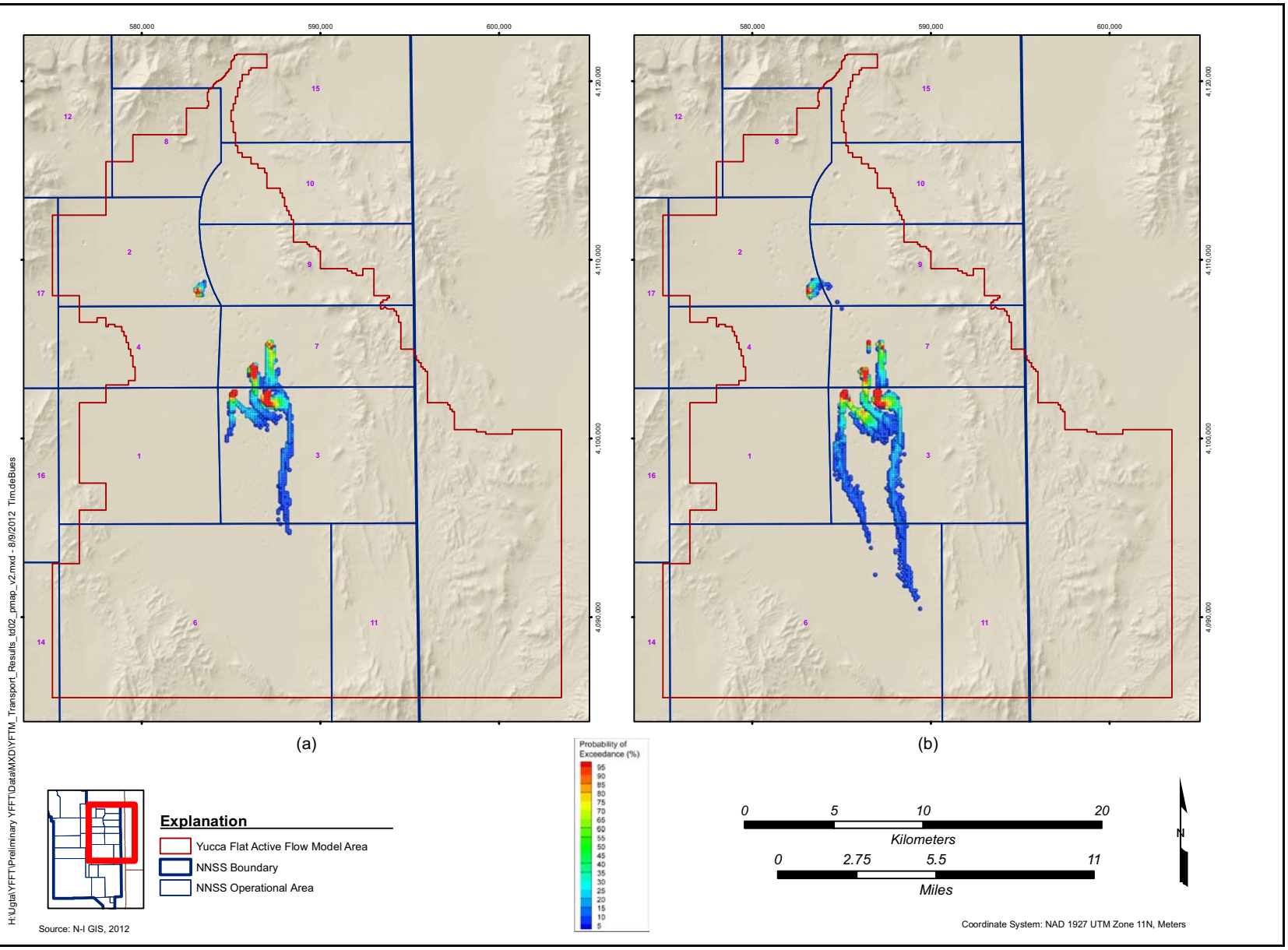

Figure 6-71
Probability of Exceeding MCL for Saturated-Zone Sources with Infiltration Rate of 1 mm/yr: (a) 50 Years, and (b) 100 Years

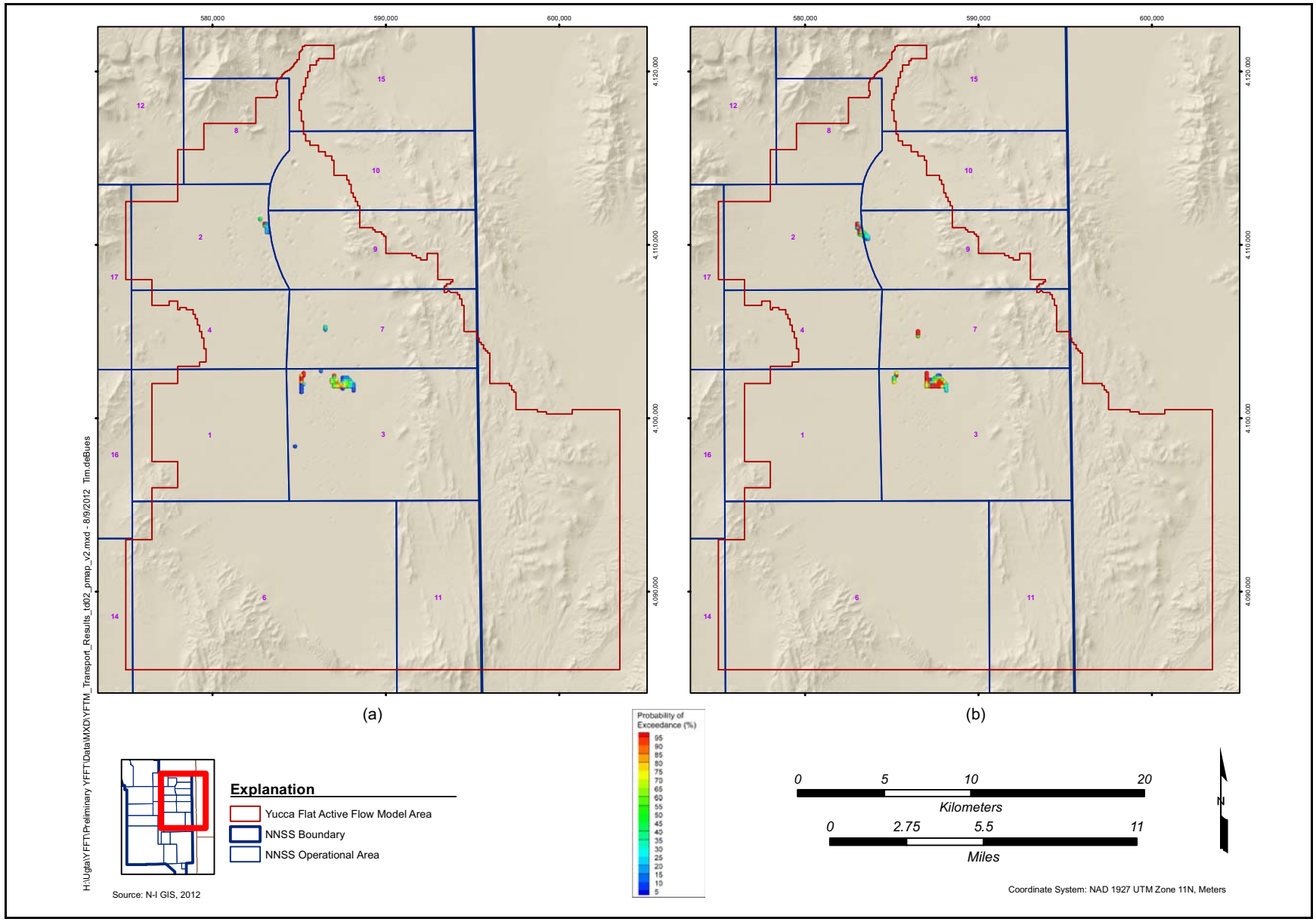

Figure 6-72
Probability of Exceeding MCL for Saturated-Zone Sources with Infiltration Rate of 1 mm/yr: (a) 300 Years, and (b) 1,000 Years

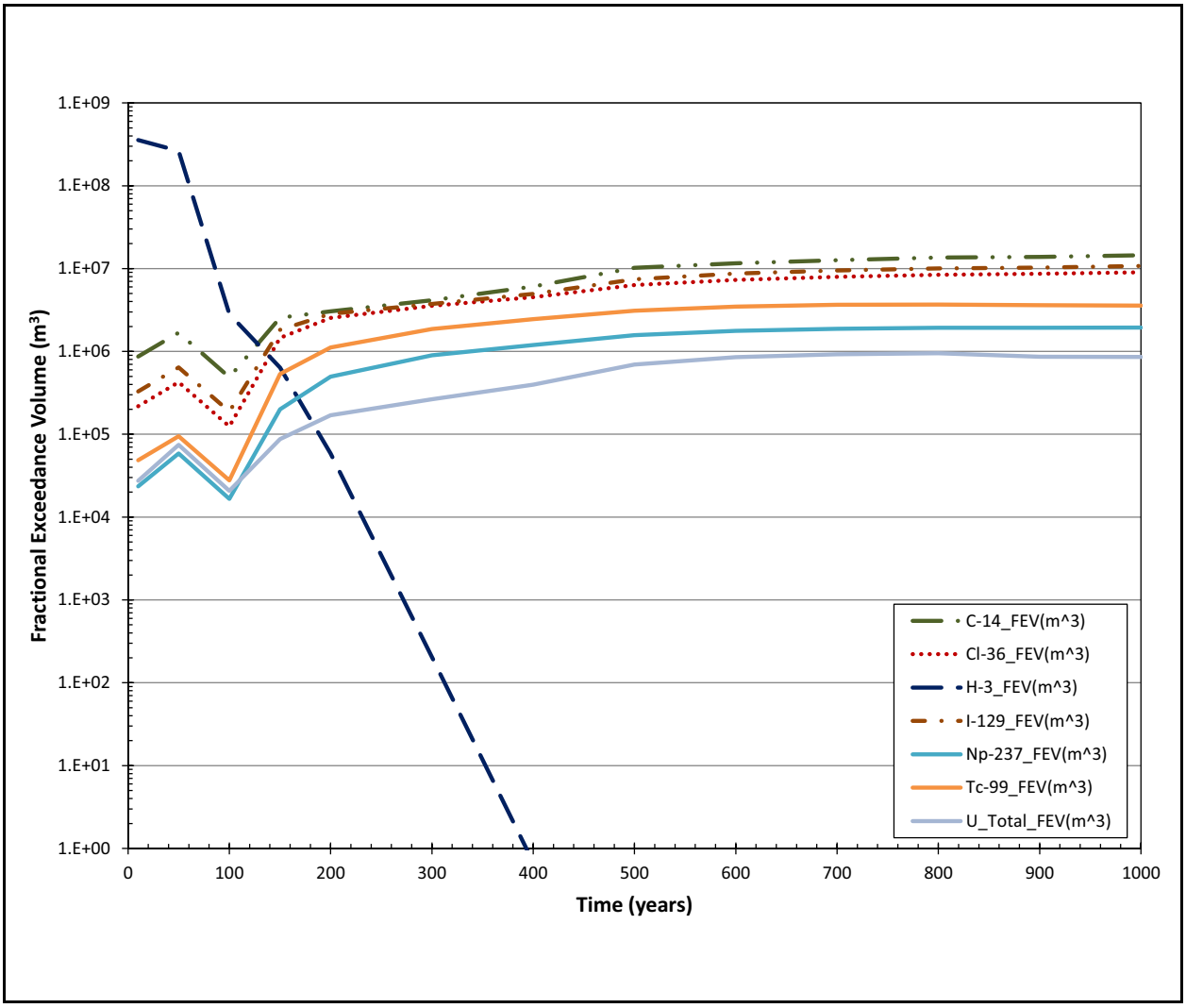

Figure 6-73
Fractional Exceedance Volume for Unsaturated-Zone Sources with Infiltration Rate of 1 mm/yr

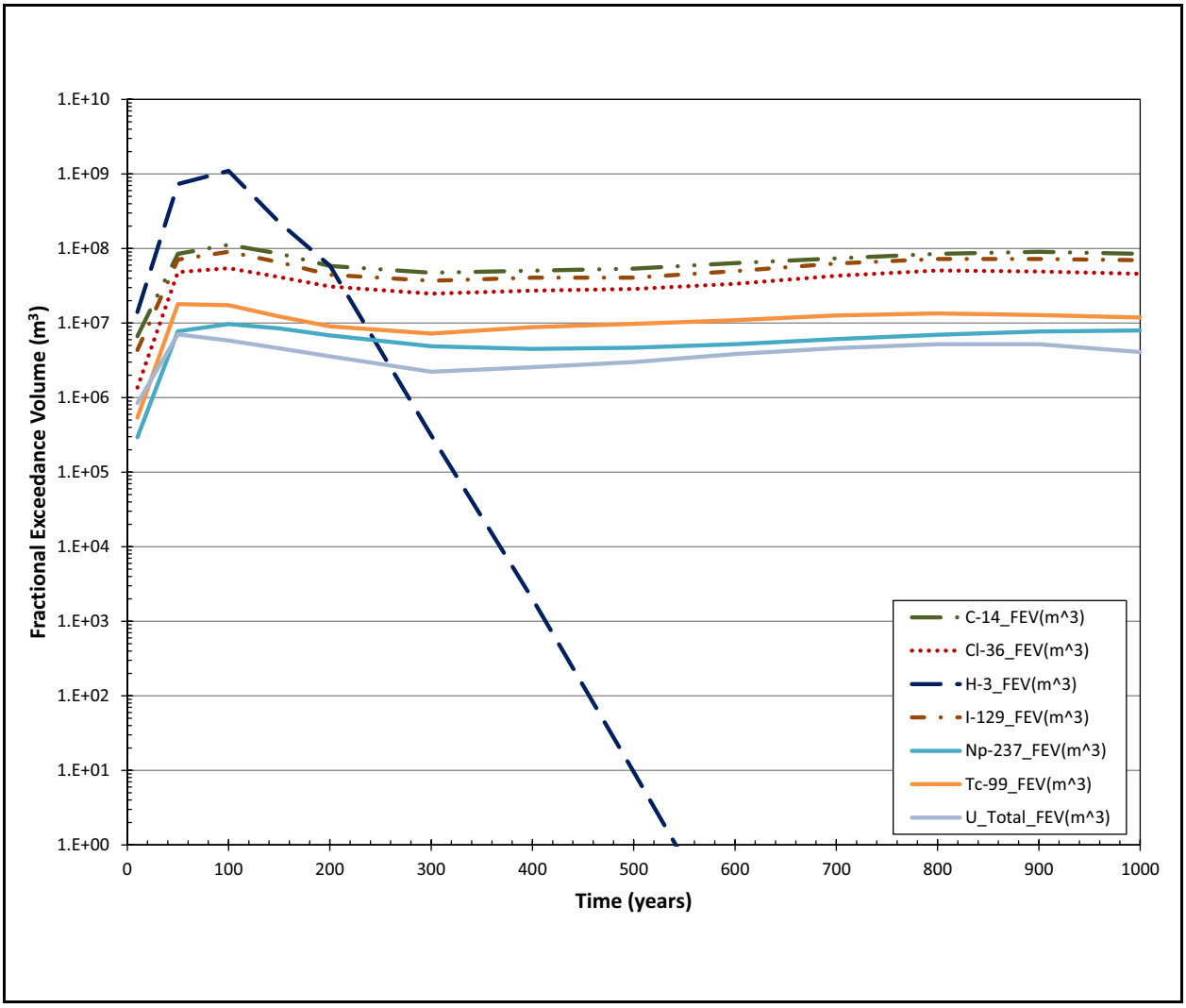

Figure 6-74
Fractional Exceedance Volume for Saturated-Zone Sources with Infiltration Rate of 1 mm/yr

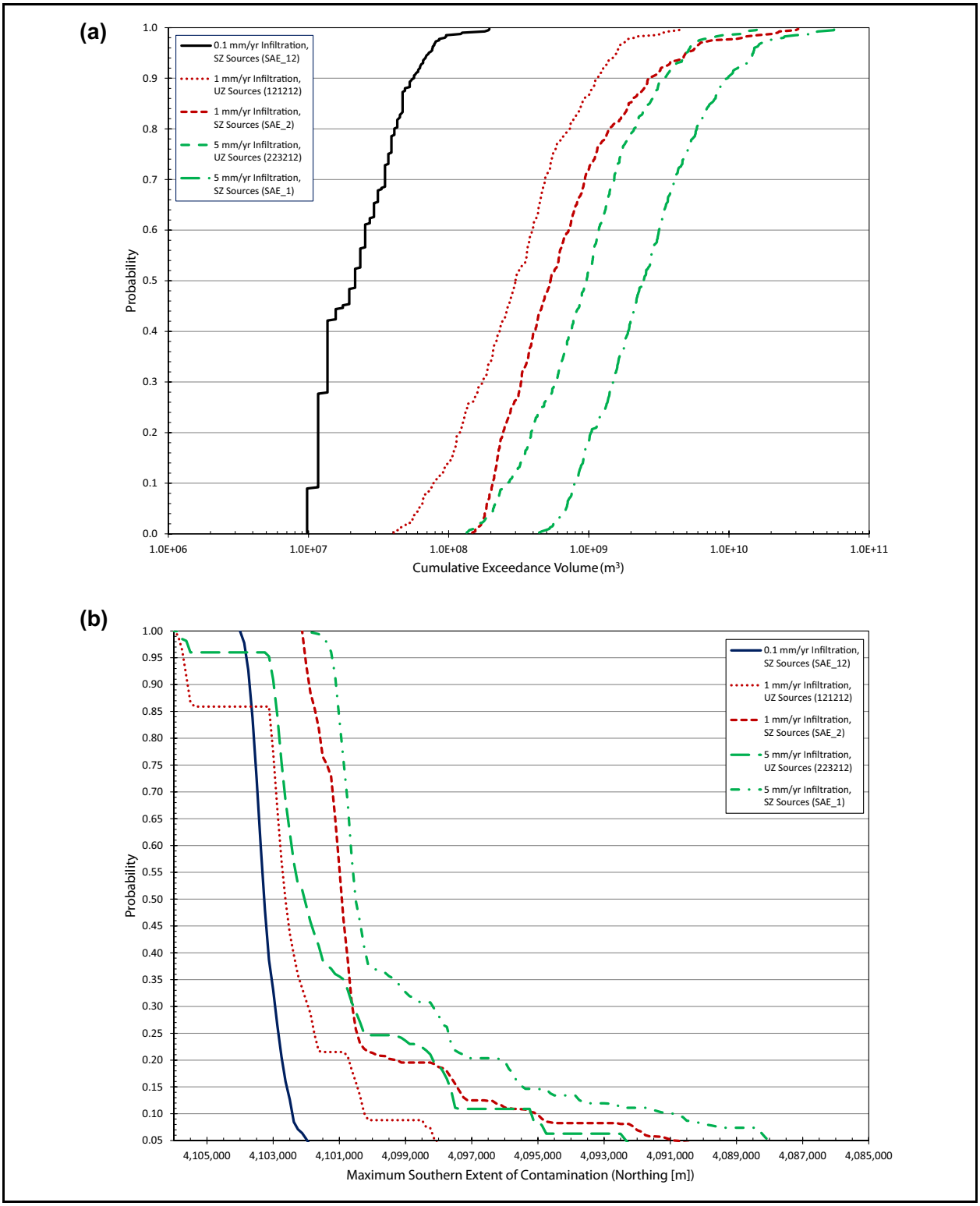

Figure 6-75
CDFs for Unsaturated-Zone and Saturated-Zone Sources with Alternative Infiltration Rates: (a) Cumulative MCL Exceedance Volume, and (b) Maximum Southern Extent of MCL Exceedance

6.5.5 Alternative Saturated Alluvial/Volcanics Aquifer System Flow and Transport Models

As discussed in Section 4.0, in addition to the uncertainty in the ambient steady-state recharge rate, there is uncertainty associated with the groundwater flow regime in the saturated alluvial/volcanic aquifer system caused by the uncertainty in the effects induced by underground nuclear detonations. These potential effects include significantly increased fluid pressures near some detonations expended in the low-permeability tuff confining units as well as modified permeabilities in altered zones around the detonation cavity. In addition, uncertainty in saturated alluvial/volcanic aquifer system transport parameters could affect the calculated release of contaminants to the saturated LCA.

To evaluate the effect of these uncertainties on mass flux to the saturated LCA and the resultant contaminant transport in the LCA, a number of alternative representations were propagated to the LCA, including the alternative overpressurization model (run SAE_5) and alternative hydraulic communication cases (runs SAE_7, SAE_10, and SAE_11). In addition, 400 Monte Carlo transport runs (run SAE_13) incorporating uncertainty in saturated alluvial/volcanic aquifer system transport parameters were propagated to the LCA. Each of these runs used a background infiltration rate of 1 mm/yr. These alternative runs are described in Section 4.0. The results of these alternative runs when propagated to the LCA are illustrated in the following figures:

- Time-cumulative probability of MCL exceedance for runs SAE_5 and SAE_7 (Figure 6-76)
- Time-cumulative probability of MCL exceedance for runs SAE_10 and SAE_11 (Figure 6-77)
- Time-cumulative probability of MCL exceedance for uncertain saturated alluvial/volcanic aquifer system transport parameters (Figure 6-78)
- CDFs for cumulative MCL exceedance volume and maximum southern extent of contamination for alternative saturated alluvial/volcanic aquifer system flow models (Figure 6-79)
- CDFs for cumulative MCL exceedance volume and maximum southern extent of contamination for alternative saturated alluvial/volcanic aquifer system transport parameters (Figure 6-80)

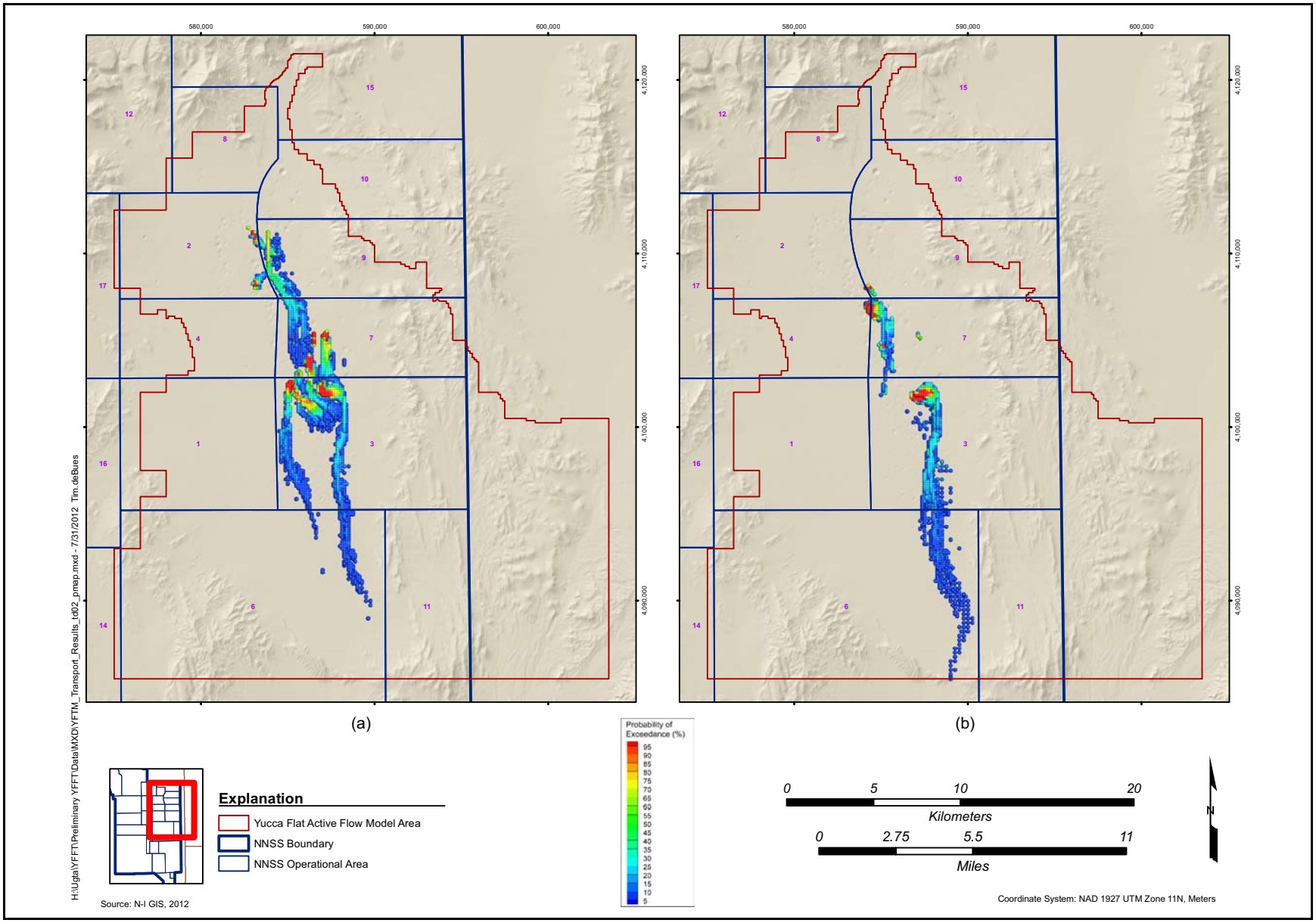

Figure 6-76
Time-Cumulative Probability of Exceedance of MCLs for Saturated-Zone Sources with (a) Alternative Overpressurization Model (SAE_5), and (b) Alternative Hydraulic Communication Model (SAE_7)

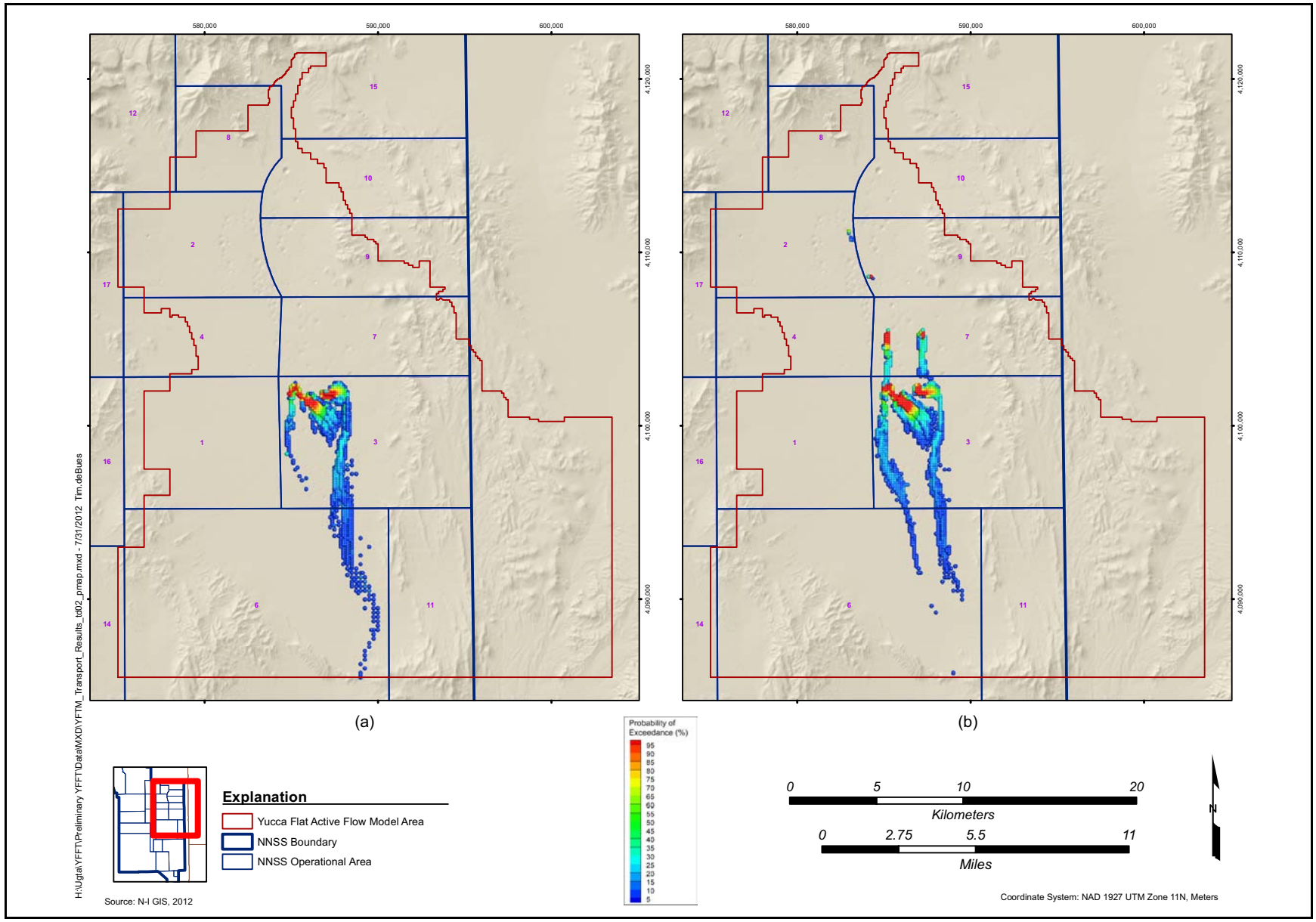

Figure 6-77
Time-Cumulative Probability of Exceedance of MCLs for Saturated-Zone Sources with Alternative Hydraulic Communication Models: (a) SAE_10, and (b) SAE_11

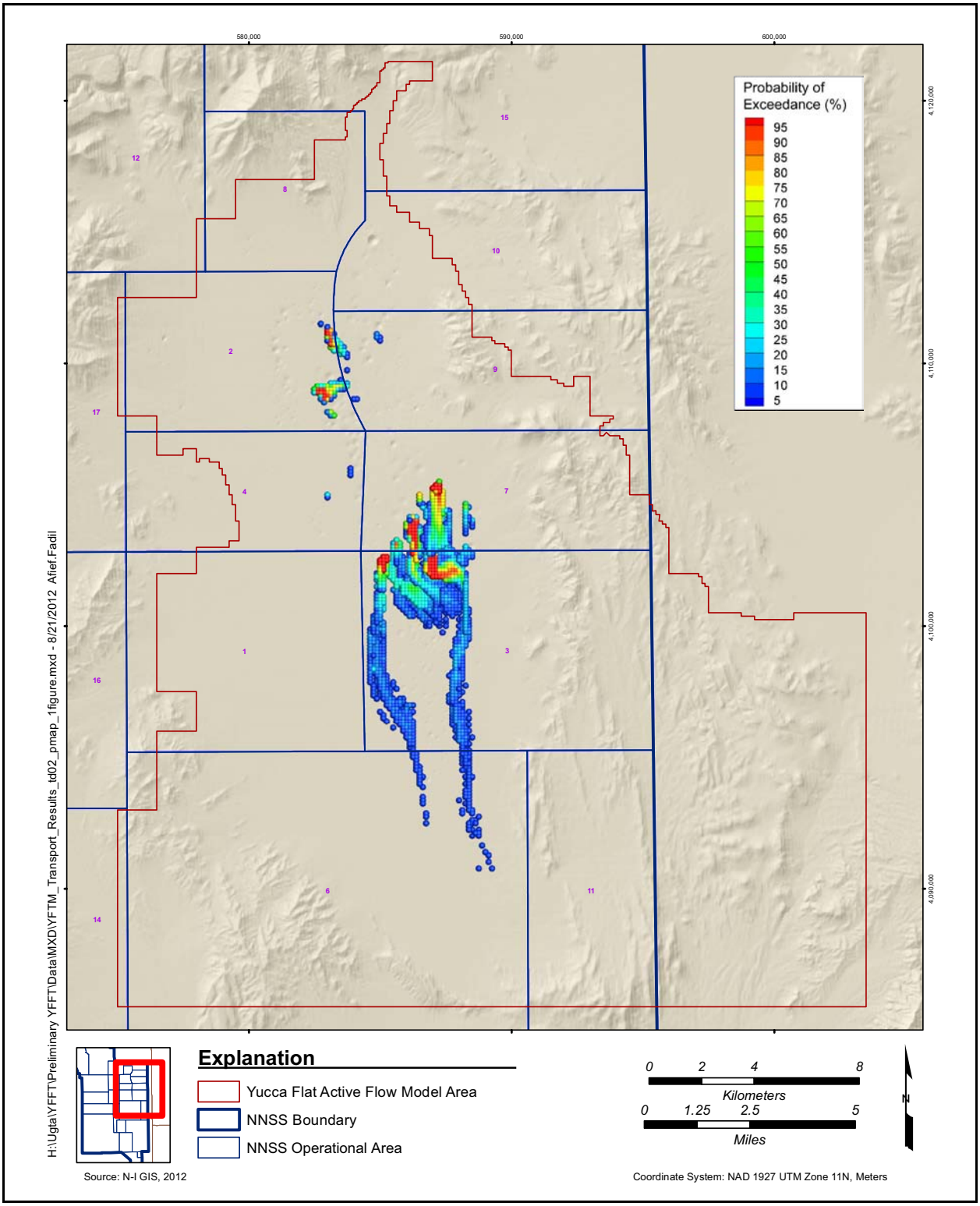

Figure 6-78
Time-Cumulative Probability of Exceedance of MCLs for Saturated-Zone Sources, 400 Realizations

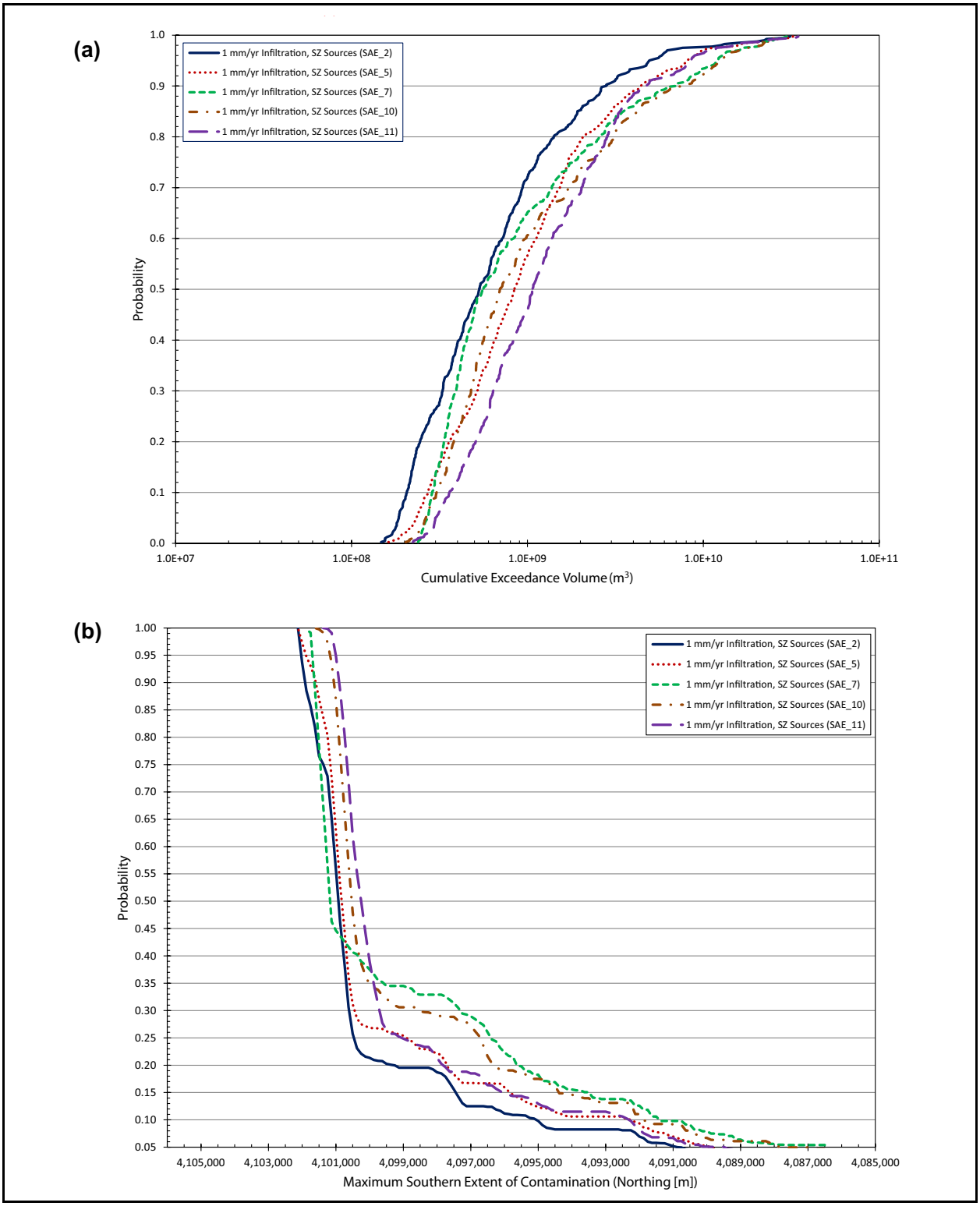

Figure 6-79
CDFs for Saturated-Zone Sources with Alternative Hydraulic Communication and Overpressure Effects: (a) Cumulative MCL Exceedance Volume, and (b) Maximum Southern Extent of MCL Exceedance

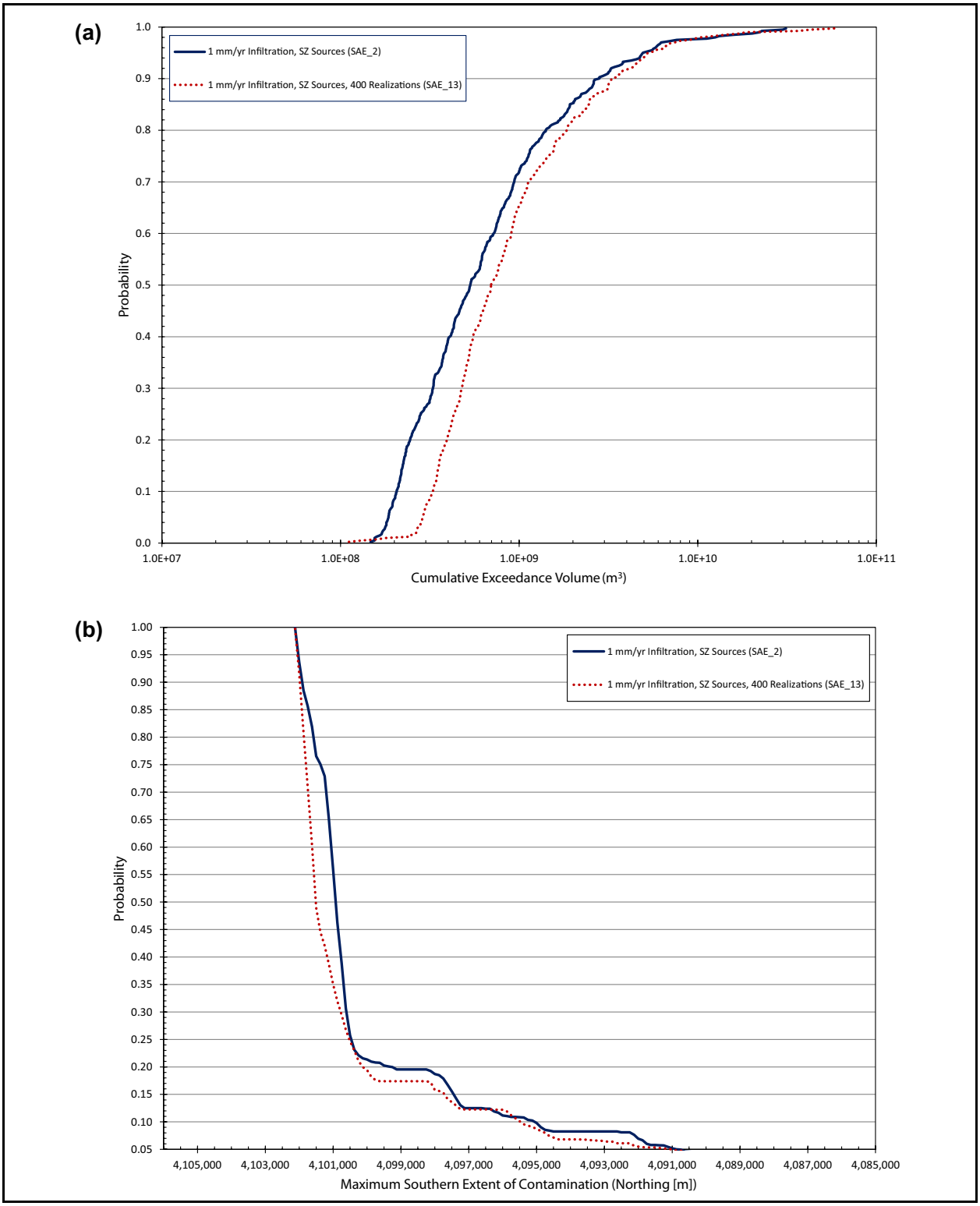

Figure 6-80
CDFs for Saturated-Zone Sources, 400 Realizations: (a) Cumulative MCL Exceedance Volume, and (b) Maximum Southern Extent of MCL Exceedance

The following observations can be made from these results:

- The alternative representations of overpressures and altered-zone hydraulic properties have a noted effect on the extent of contamination within the LCA commensurate with the effect these changes have on mass flux from saturated volcanic sources to the LCA (compare Figure 6-70a with Figures 6-76 and 6-77).

- Although the effects are as expected, in no case did the effects, even with a bound of background infiltration of 1 mm/yr, exceed the extent of contamination associated with LCA sources (compare Figure 6-64b with Figures 6-76 and 6-77).

- The spatial distribution of contamination is changed for the alternative altered-zone hydraulic property cases because the source of contamination has changed from being located along major faults to being located near areas where hydraulic communication is allowed with the saturated LCA (compare Figure 6-70a with Figures 6-76 and 6-77). However, the overall extent of contamination is not significantly changed.

- The incorporation of uncertainty in the saturated alluvial/volcanic aquifer system transport model parameters, although changing the shape of the resultant exceedance volume CDF did not change the range of results, implies that the uncertainty in LCA transport parameters more significantly controls the uncertainty in the extent of the forecast contaminant boundary (compare Figure 6-78 with Figure 6-70a). This observation is confirmed in the sensitivity analyses presented in Section 6.5.9.

6.5.6 Alternative LCA Flow Fields

As discussed in Section 5.6, a range of alternative LCA flow fields can be reasonably calibrated given the uncertainty in the boundary fluxes, hydraulic properties, and limited steady-state and transient head observations in the LCA at Yucca Flat. To evaluate this uncertainty in the LCA flow model parameters and conceptual models, NSMC methods were used to generate 83 alternative calibrated flow fields. Based on particle-tracking analyses from several discrete locations of interest presented in Section 5.6.2, “fast” and “slow” flow fields were identified and propagated to evaluate their effect on transport in the LCA. In these analyses, the base-case LCA source term was used for comparison purposes because it has a more significant effect on the extent of the contaminant boundary than the other sources. The “fast” and “slow” alternative flow fields are representative of flow fields that are expected to provide greater and lesser amounts of contaminant transport, respectively, based on the advective particle-tracking results from seven significant starting locations as presented in Section 5.6.2.

As discussed in Section 5.6.3, the alternative NSMC flow fields are based on the conservative conceptual model that assumes the LCA in northern Yucca Flat is in hydraulic communication with the LCA north of Yucca Flat and north of Climax Mine. In order to evaluate the significance of this conceptual model, an alternative model assuming there is no hydraulic communication of the LCA in northern Yucca Flat was developed and calibrated. This model is termed the alternative northern boundary flux model because the model was implemented by specifying the northern boundary flux at 1.0 kg/s. The flow fields and velocities resulting from this model were used in the transport model to evaluate the significance of this alternative to the extent of contaminant transport in the LCA. Again, the LCA HST was used for the source term because of its significance in controlling the extent of the contaminant boundary.

The results of these analyses using alternative LCA flow fields for contaminant transport in the LCA are presented in the following figures:

- Probability of exceeding MCLs for alternative NSMC runs (Figure 6-81)
- Probability of exceeding MCLs for the alternative northern boundary flux model (Figure 6-82)
- CDFs of cumulative MCL exceedance volume and maximum southern extent of MCL exceedance (Figure 6-83)

The following observations can be made from these results:

- The “slow” NSMC flow field yielded significantly less extent of contamination in the LCA than the base-case flow field. This is as expected given that this case also illustrated less extensive advective transport based on the particle-tracking results presented in Section 5.6.
- The “fast” NSMC flow field yielded slightly less contamination in the LCA than the base case. This result is unexpected given that the particle-tracking results for this case implied that there would be greater advective transport from the selected locations of interest. The difference may be because locations other than those selected also contribute significantly to the extent of contaminant migration.
- The alternative northern boundary flux model yielded significantly less transport in the LCA than the base-case model. This was anticipated as the boundary flux was reduced from about 130 kg/s to 1.0 kg/s, effectively reducing the total volumetric flow through the basin by about one-half. This illustrates the conservative nature of the base-case model that assumes hydraulic communication of the LCA in northern Yucca Flat.

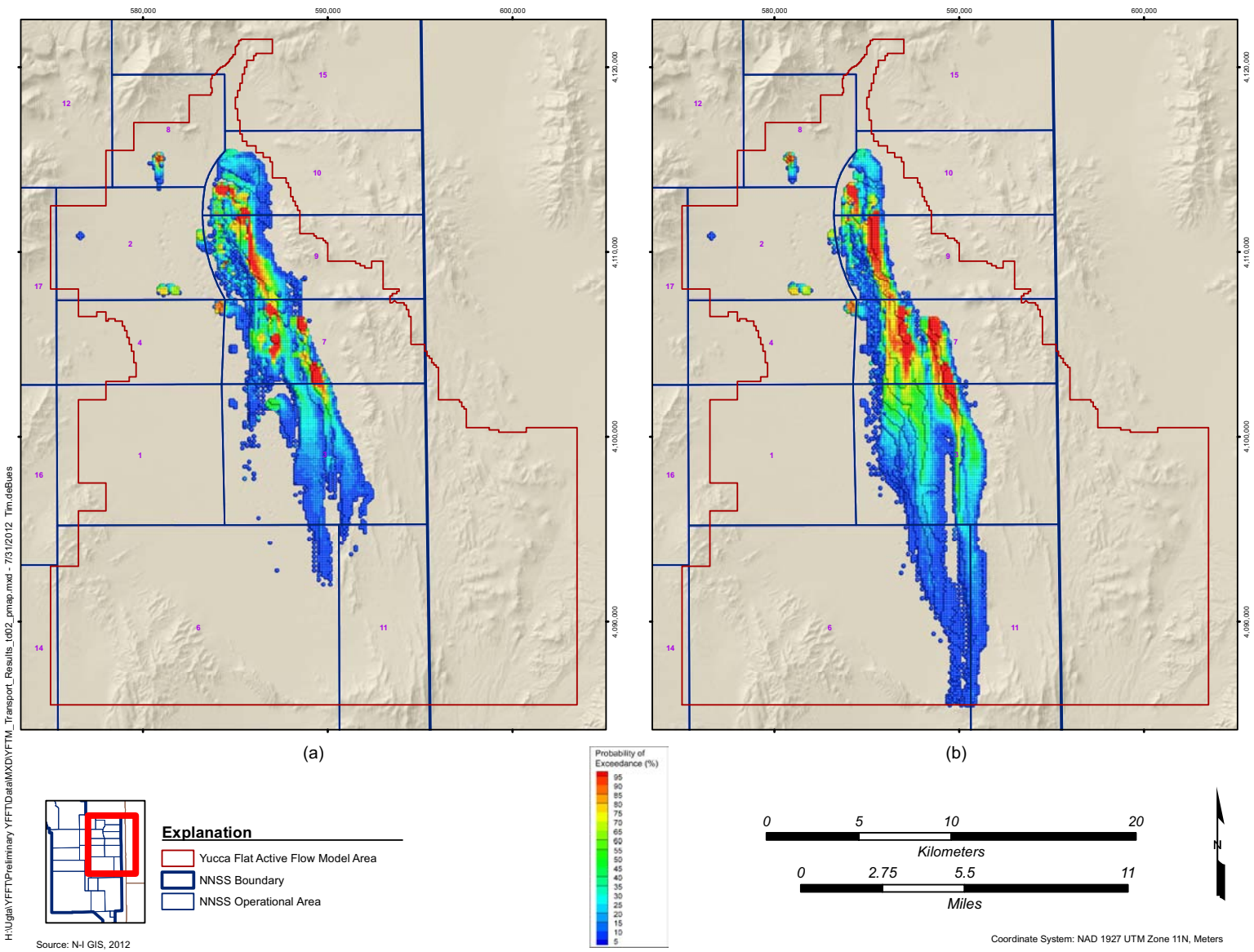

Figure 6-81
Time-Cumulative Probability of Exceedance of MCLs for LCA Sources with Alternative NSMC LCA Flow Fields: (a) NSMC Slow, and (b) NSMC Fast

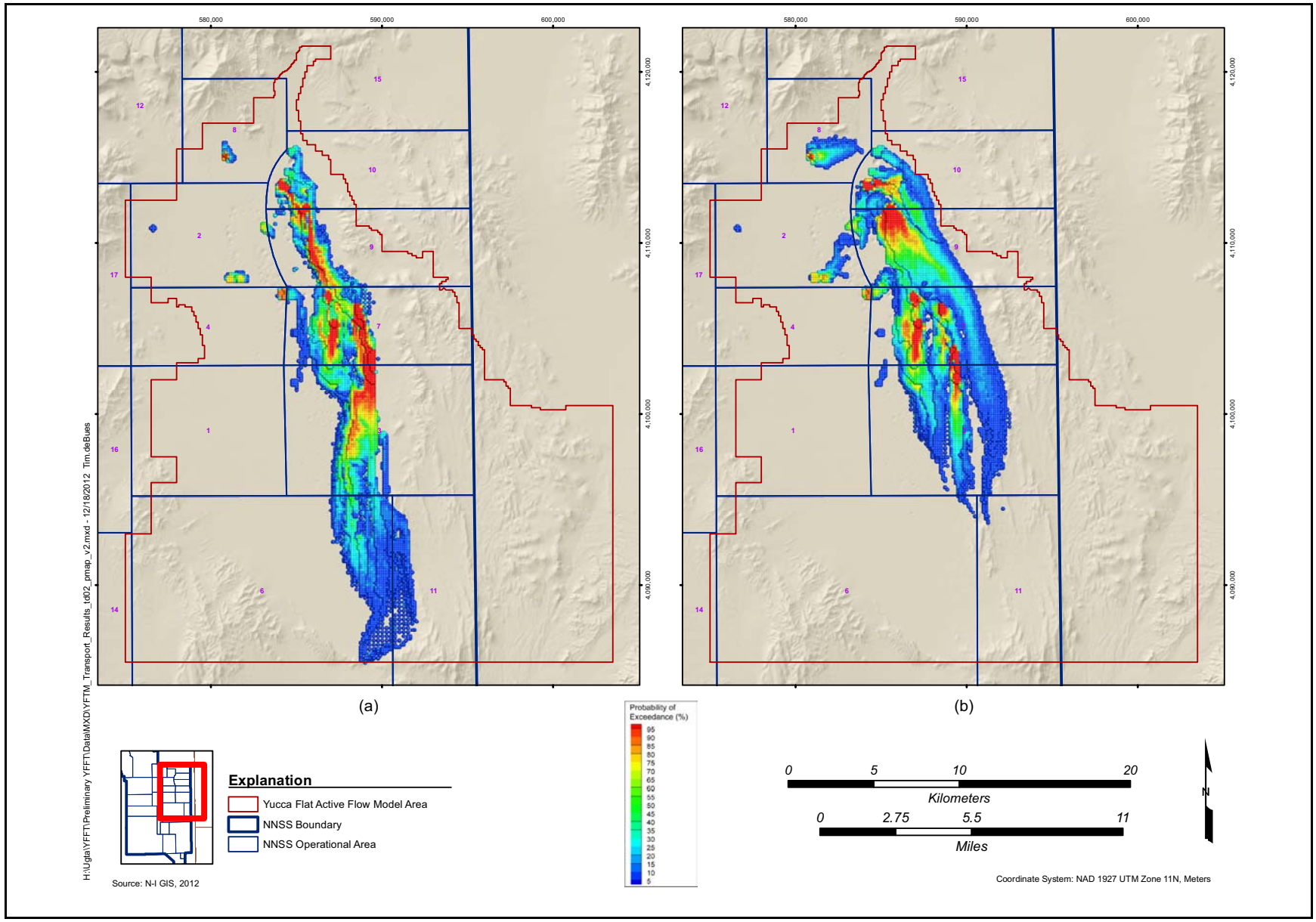

Figure 6-82
Time-Cumulative Probability of Exceedance of MCLs for LCA Sources with Alternative LCA Flow Fields: (a) Base Case, and (b) Alternative Northern Boundary Flux Model

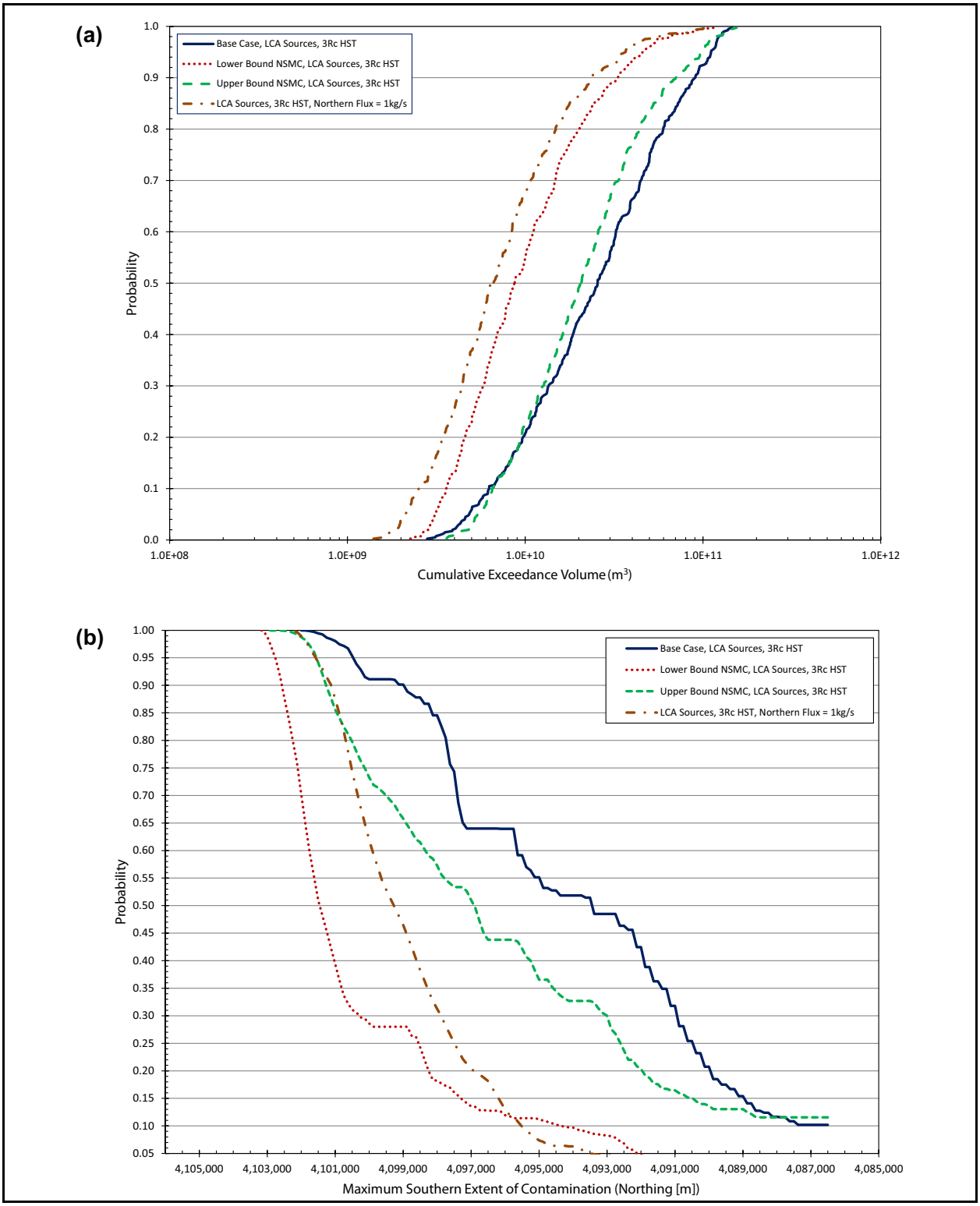

Figure 6-83
CDFs for LCA Sources with Alternative NSMC LCA Flow Fields: (a) Cumulative MCL Exceedance Volume, and (b) Maximum Southern Extent of MCL Exceedance

6.5.7 Alternative LCA Transport Parameters

Similar to alternative LCA groundwater flow models, reasonable alternative transport parameter distributions can also significantly affect the extent of the forecast contaminant boundary. While parameter uncertainty itself is evaluated in the 400 Monte Carlo multiple realizations, the uncertainty addressed in this section relates to uncertainty in the distributions of parameter uncertainty. The uncertainties evaluated include the following:

- Alternative matrix sorption of Ni, Cs, C, and Sr
- Alternative scale-dependent matrix diffusion
- Alternative fracture aperture and effective porosity distribution in fault damage zones

As discussed in Section 6.3 and the Yucca Flat/Climax Mine TDD (SNJV, 2007), there is very limited information with which to develop K_d distributions for Ni, Cs, C, and Sr in carbonate rocks. As a result, in the base analyses, these radionuclides are assumed to be non-sorbed (i.e., K_d = 0.0 mL/g) in the LCA. In order to evaluate the potential significance of this assumption, alternative K_d distributions presented in Table 6-3 have been applied to the LCA transport model for LCA contaminant sources. Only LCA sources are evaluated because there is significant sorption of these radionuclides in the unsaturated zone and the saturated alluvium/volcanic aquifer system to preclude significant transport of these radionuclides to the LCA from the overlying sources.

As noted in Section 6.3, there is analog information which suggests that matrix diffusion may be a scale-dependent process. Although it is not clear whether the scale dependency is more related to fracture characteristics (e.g., distributions of fracture porosity or fracture aperture), the possibility of scale-dependent matrix diffusion was evaluated by using an alternative distribution based on Liu et al. (2007), as suggested in SNJV (2006b).

As discussed in Section 6.3 and Appendix J, an alternative approach to identifying fracture characteristics, notably, fracture porosity and fracture spacing or aperture, has been proposed related to the concept of flowing features. This approach is analogous to the approach proposed by Kuzio (2004) and used in the saturated-zone transport modeling at the potential repository site at Yucca Mountain.

As discussed in Section 6.2, the transport model used for evaluating contaminant boundaries in the LCA uses a particle-tracking methodology that consists of a combination of a particle-tracking software to evaluate the advective-dispersive transport of mass from discrete source locations and

a transport algorithm that includes the effects of matrix diffusion, matrix and fracture sorption, and radionuclide decay. The transport algorithm is presented in PLUMECALC (Robinson et al., 2011). As discussed in Appendix K, two software tools are available for particle tracking, the sptr subroutine of FEHM and Walkabout (Painter, 2011). Although both of these software have been determined to provide adequate representations of advective-dispersive transport, the base-case analyses have used the sptr subroutine in FEHM. To evaluate the impact of potential differences in this software on the results, an analysis was performed using Walkabout.

Finally, a run was made using the alternative LCA matrix sorption and fault damage zone fracture parameters, in combination with the alternative LCA flow field presented in Section 5.6.3, based on the alternative northern boundary flux model. The purpose of this run was to evaluate the significance of the combined effects of conservative assumptions used in the base-case model.

The results of evaluating alternative transport parameter distributions and software are presented in the following figures:

- Time-cumulative probability of exceeding MCLs for alternative matrix sorption and matrix diffusion parameters (Figure 6-84)
- Time-cumulative probability of exceeding MCLs for alternative fracture transport parameters and Walkabout (Figure 6-85)
- Time-cumulative probability of exceeding MCLs for combined alternative LCA flow field and transport parameters (Figure 6-86)
- Fractional exceedance volume for alternative matrix sorption parameters (Figure 6-87)
- CDFs of cumulative MCL exceedance volumes and maximum southern extent of MCL exceedance (Figure 6-88)

The following observations can be made from these results:

- Including sorption for Ni, Cs, C, and Sr significantly reduces the lateral and longitudinal extent of contamination as well as the total time-cumulative exceedance volume associated with LCA sources. This is expected because these radionuclides, in particular, ^{90}Sr and ^{137}Cs, significantly contribute to the extent of the contaminant migration in the LCA from LCA sources (Figure 6-84).

- Even when significant sorption is included for Ni, Cs, C, and Sr, ^{90}Sr and ^{137}Cs significantly contribute to the exceedance volume in the LCA because, as illustrated in Section 2.0, the initial concentrations of these radionuclides in the exchange volume far exceed the MCLs.

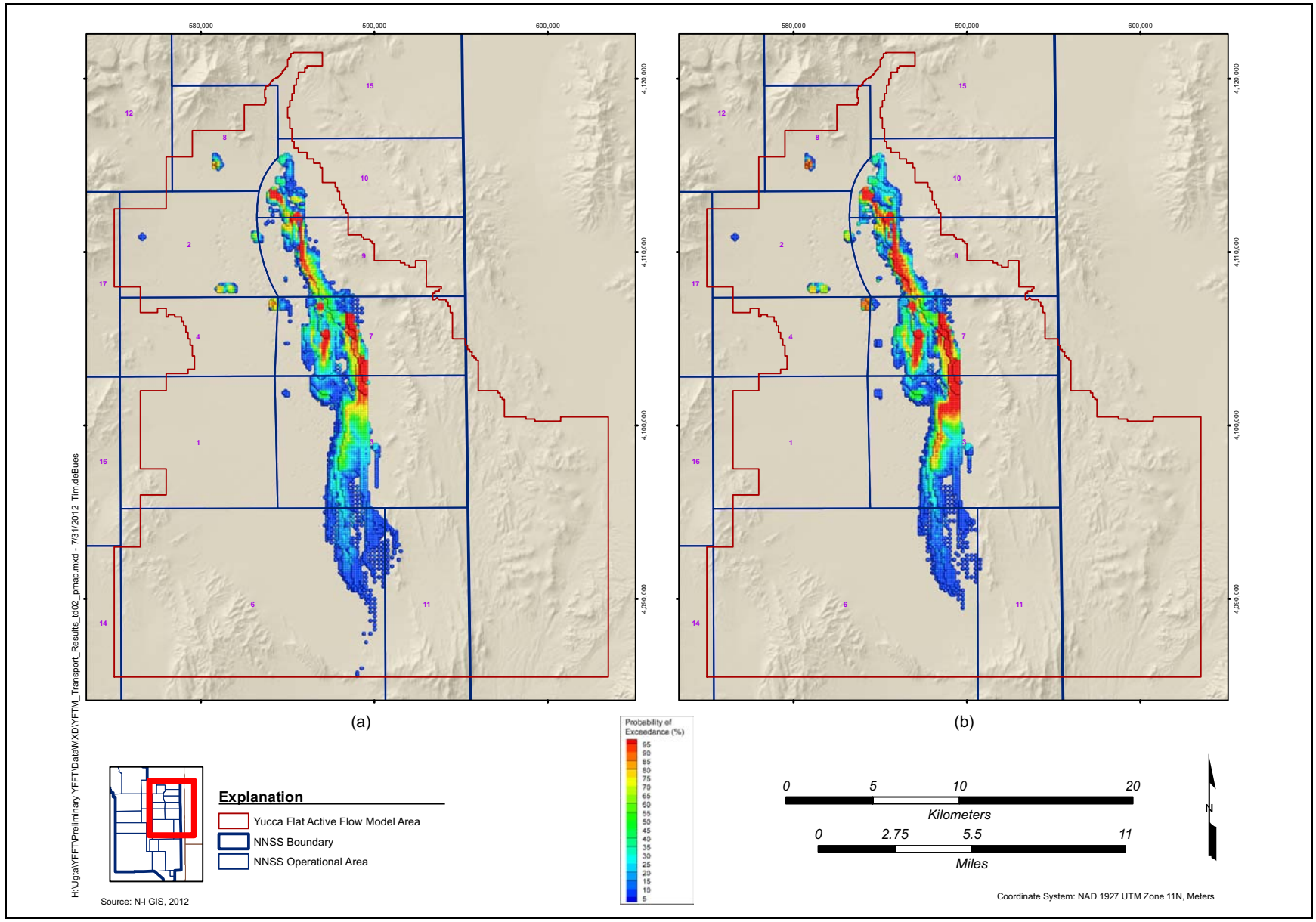

Figure 6-84
Time-Cumulative Probability of Exceedance of MCLs for LCA Sources with Alternative LCA Transport Parameters: (a) Alternative Matrix Sorption for Sr, Cs, C, and Ni, and (b) Scale-Dependent Matrix Diffusion

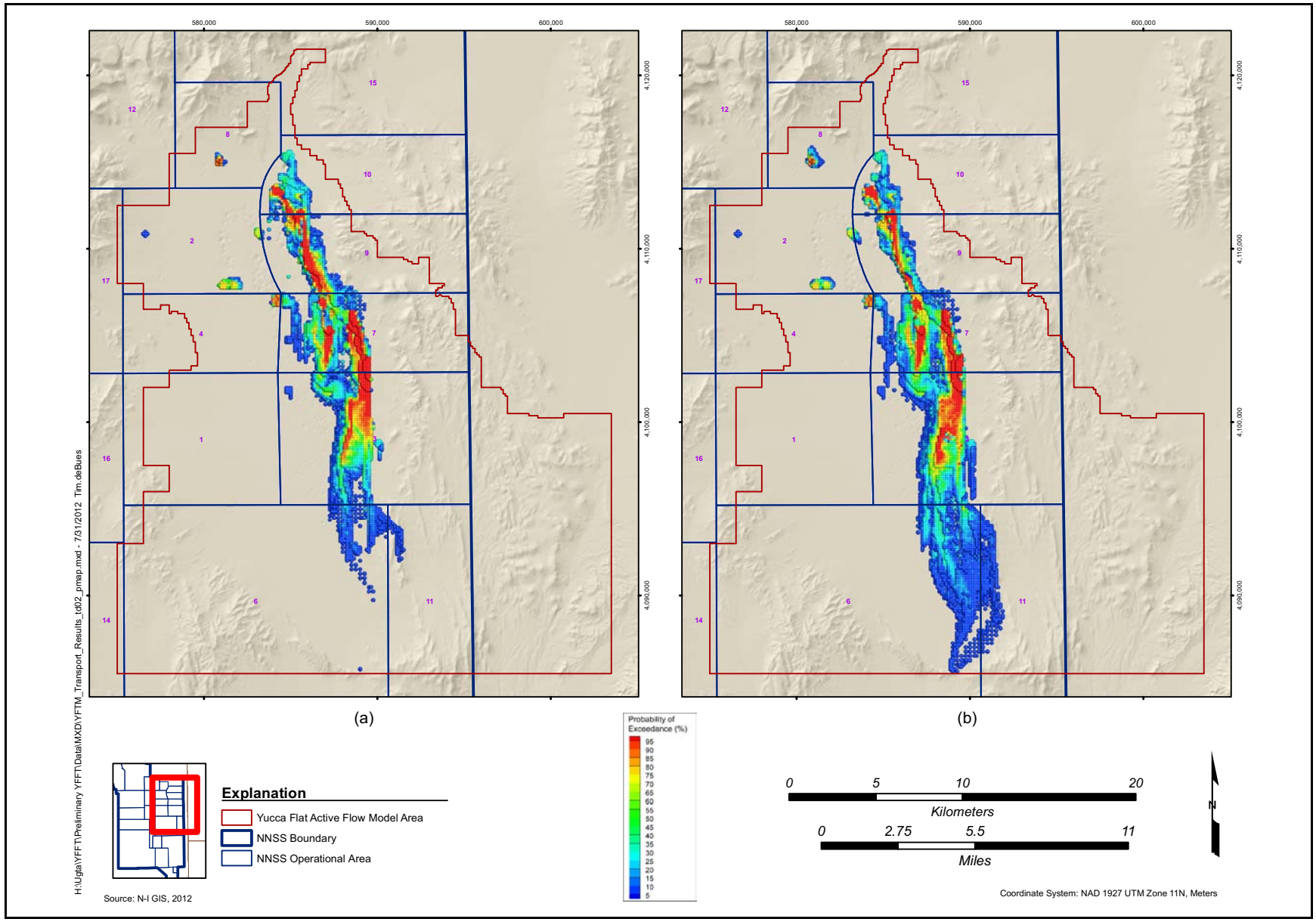

Figure 6-85
Time-Cumulative Probability of Exceedance of MCLs for LCA Sources with Alternative LCA Transport Parameters: (a) Alternative Fault Fracture Porosity, and (b) Walkabout

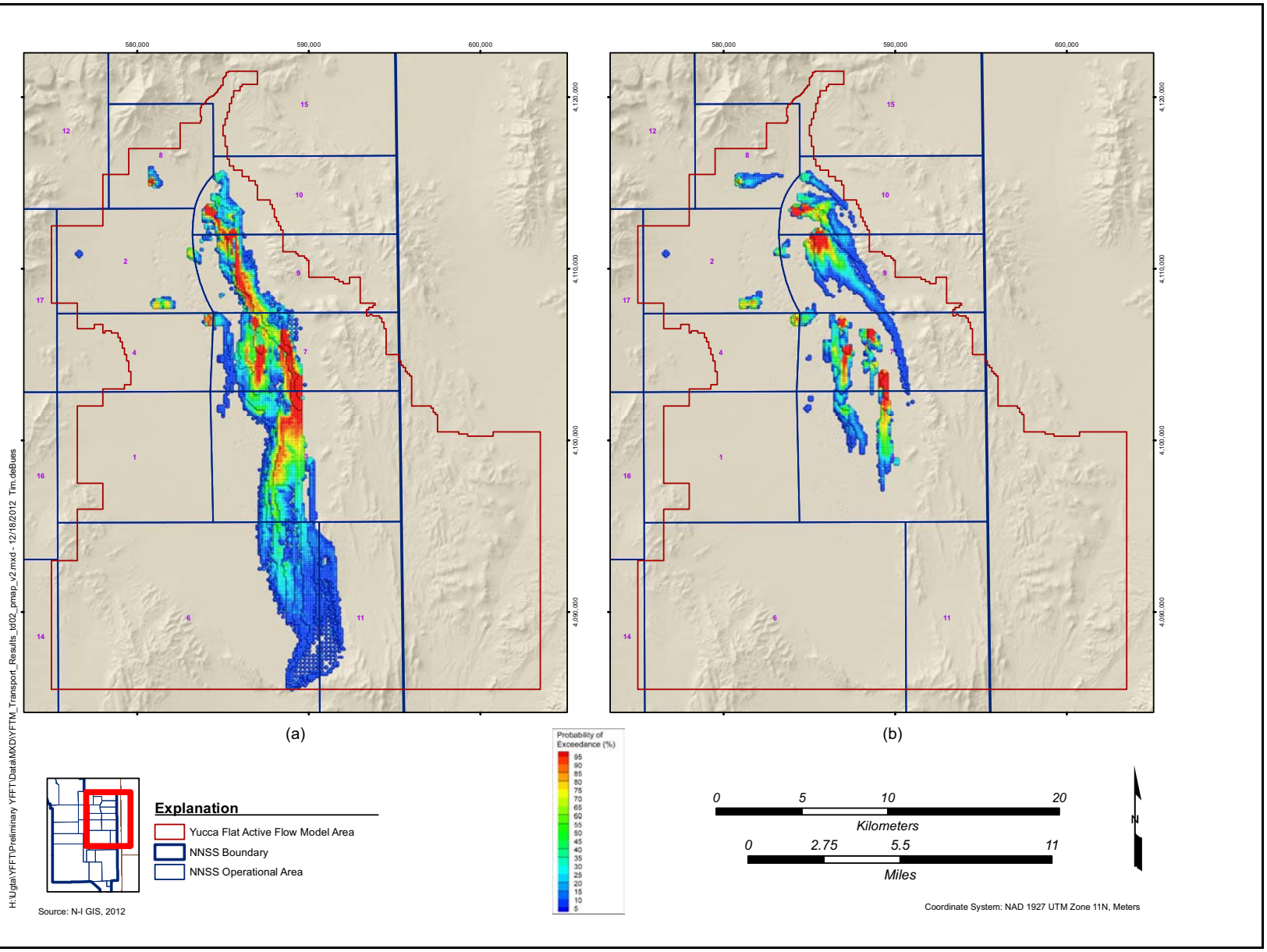

Figure 6-86
Time-Cumulative Probability of Exceedance of MCLs for LCA Sources: (a) Base Case, and (b) Alternative Northern Boundary Flux Model with Alternative LCA Transport Parameters

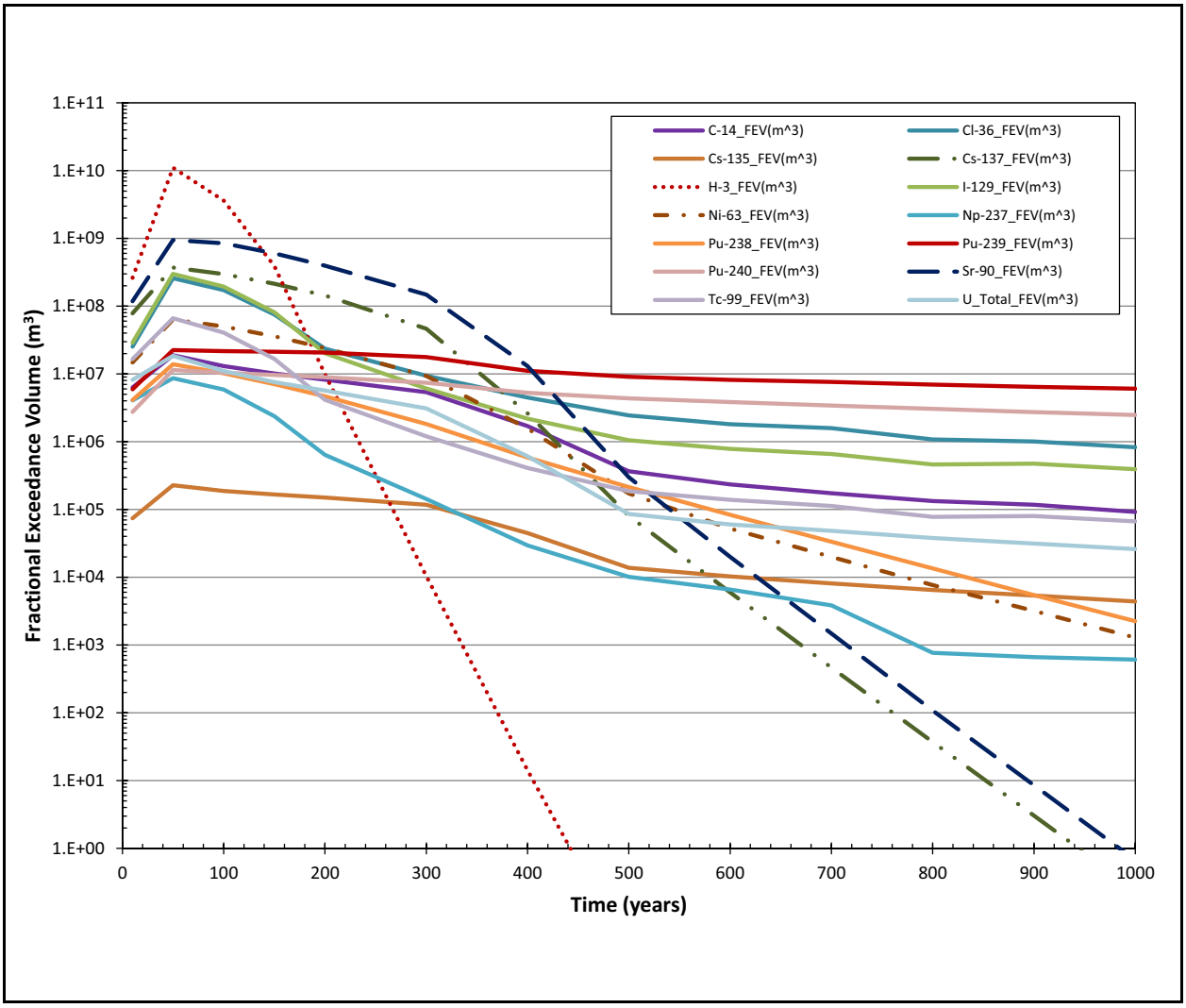

Figure 6-87
Fractional Exceedance Volume for LCA Sources with Alternative Matrix Sorption for Sr, Cs, C, and Ni

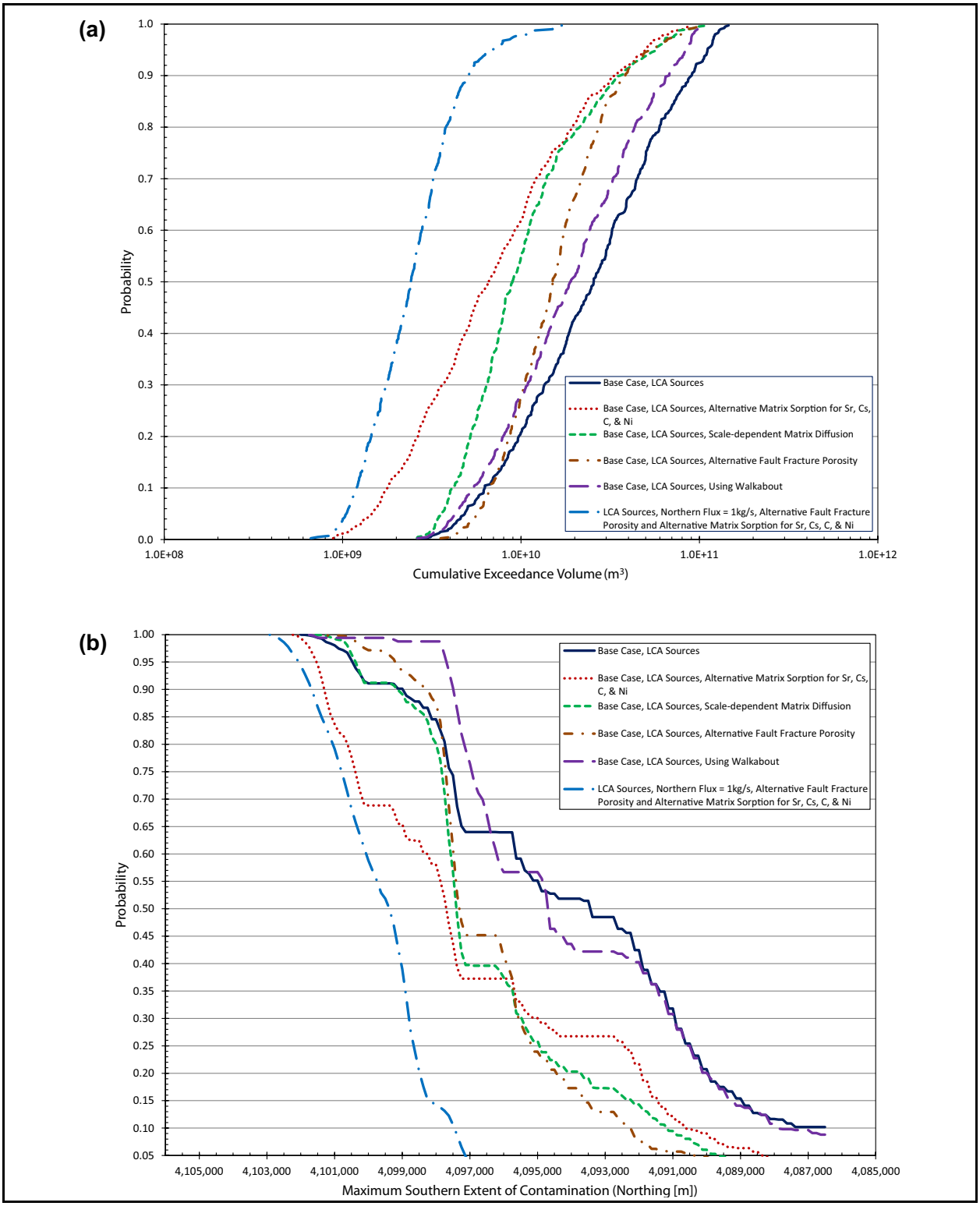

Figure 6-88
CDFs for LCA Sources with Alternative LCA Transport Parameters: (a) Cumulative MCL Exceedance Volume, and (b) Maximum Southern Extent of MCL Exceedance

- Scale-dependent matrix diffusion as conceptualized in the alternative model significantly reduces the exceedance volume (Figure 6-88). However, scale-dependent matrix diffusion minimally reduces the forecast extent of contaminant migration as represented by the contaminant boundary, which is defined by the 95th percentile of the exceedance volume. This is a result of the observation that the contaminant boundary is most impacted by low fracture porosity combined with high fracture aperture, both of which tend to minimize the effects of matrix diffusion. As a result, modifying the matrix diffusion model does not significantly affect the forecast contaminant boundary.

- The alternative fracture porosity and aperture distribution conceptual model significantly reduces the forecast extent of contaminant migration in the LCA. This is likely due to the decrease in fracture porosity for this scenario.

- The use of Walkabout instead of FEHM_sptr, although yielding slightly different results, did not significantly affect the forecast extent of contaminant migration in the LCA. However, it is interesting to note that the use of Walkabout did eliminate the small anomalous concentration that occurs along the southern boundary (compare Figures 6-85b and 6-64b).

- Combining the model with the reduced northern boundary flux with the transport parameters that allow for sorption of Sr, Cs, Ni, and C, and the revised damage-zone fracture properties results in significantly less contaminant transport. This combined effect emphasizes the magnitude of the conservatism included in the base-case model.

6.5.8 Combined Transport Model Runs

The results presented in the above analyses have considered a single contaminant source domain to the LCA, i.e., (1) sources that emanate from the overlying unsaturated-zone model domain, (2) sources that emanate from the overlying saturated alluvial/volcanic aquifer system model domain, or (3) the portion of the HST from detonations that have exchange volumes intersecting the LCA. This was done to facilitate the modeling and to illustrate the significance of the different source domains to the forecast contaminant boundary. While it is possible to visually examine the resulting figures to conclude that the contaminant sources initially in the LCA are much more significant than contaminant sources that enter the LCA as a result of flow and transport from the overlying domains, in order to more directly evaluate the potentially additive effect of the different sources, the results of the different individual sources were summed to develop combined model results.

As discussed in Sections 3.0 and 4.0, the principal uncertainty affecting the magnitude of contaminant flux from the overlying unsaturated zone and saturated alluvial/volcanic aquifer system to the LCA is the background steady-state infiltration rate. Although the present-day estimated infiltration rate is less than 0.1 mm/yr in the central portions of the Yucca Flat basin, even considering the transient

effects of run-on and runoff, simulations have been conducted assuming 1, 5, and 10 mm/yr. The upper end of this range has been included to ensure that the extent of contaminant migration is not underrepresented. The results of using contaminant fluxes of 0.1, 1, and 5 mm/yr are summarized in Sections 6.5.2 and 6.5.4. These results are combined with the base-case LCA source contaminant transport summarized in Section 6.5.2.

The results of evaluating the effects of combined contaminant sources are presented in the following figures:

- Time-cumulative probability of exceeding MCLs for the background infiltration rate of 0.1 mm/yr for combined unsaturated zone, saturated alluvial/volcanic aquifer system, and base-case LCA sources (Figure 6-89)
- Time-cumulative probability of exceeding MCLs for the background infiltration rate of 1 mm/yr for combined unsaturated zone, saturated alluvial/volcanic aquifer system, and base-case LCA sources (Figure 6-90)
- Time-cumulative probability of exceeding MCLs for the background infiltration rate of 5 mm/yr for combined unsaturated zone, saturated alluvial/volcanic aquifer system, and base-case LCA sources (Figure 6-91)
- CDFs of cumulative MCL exceedance volumes for combined unsaturated zone, saturated alluvial/volcanic aquifer system, and base-case LCA sources (Figure 6-92)

The following observations can be made from these results:

- The combined time-cumulative extent of contaminant migration is dominated by the LCA sources, even when conservatively assuming background infiltration rates as high as 5 mm/yr. The Base-Case LCA sources plots of the time-cumulative probability of exceeding MCLs do not change for the different background infiltration rates because they use the same calibrated flow field and the same source term. This conclusion is in part a function of the conservative transport parameters used in the base-case transport model, in particular the assumption that Sr, Cs, and Ni are not sorbed in the LCA.

6.5.9 Sensitivity Importance Analyses

Contaminant transport from underground nuclear detonations conducted in the Yucca Flat/Climax Mine CAU is uncertain. This uncertainty is due in part to alternative conceptual models that describe groundwater flow and contaminant transport in the LCA as described in Sections 5.5 and 6.2, and uncertainty in conceptual models of contaminant mass influx to the LCA from sources with exchange volumes that either intersect the saturated LCA or are provided by transport from sources in the

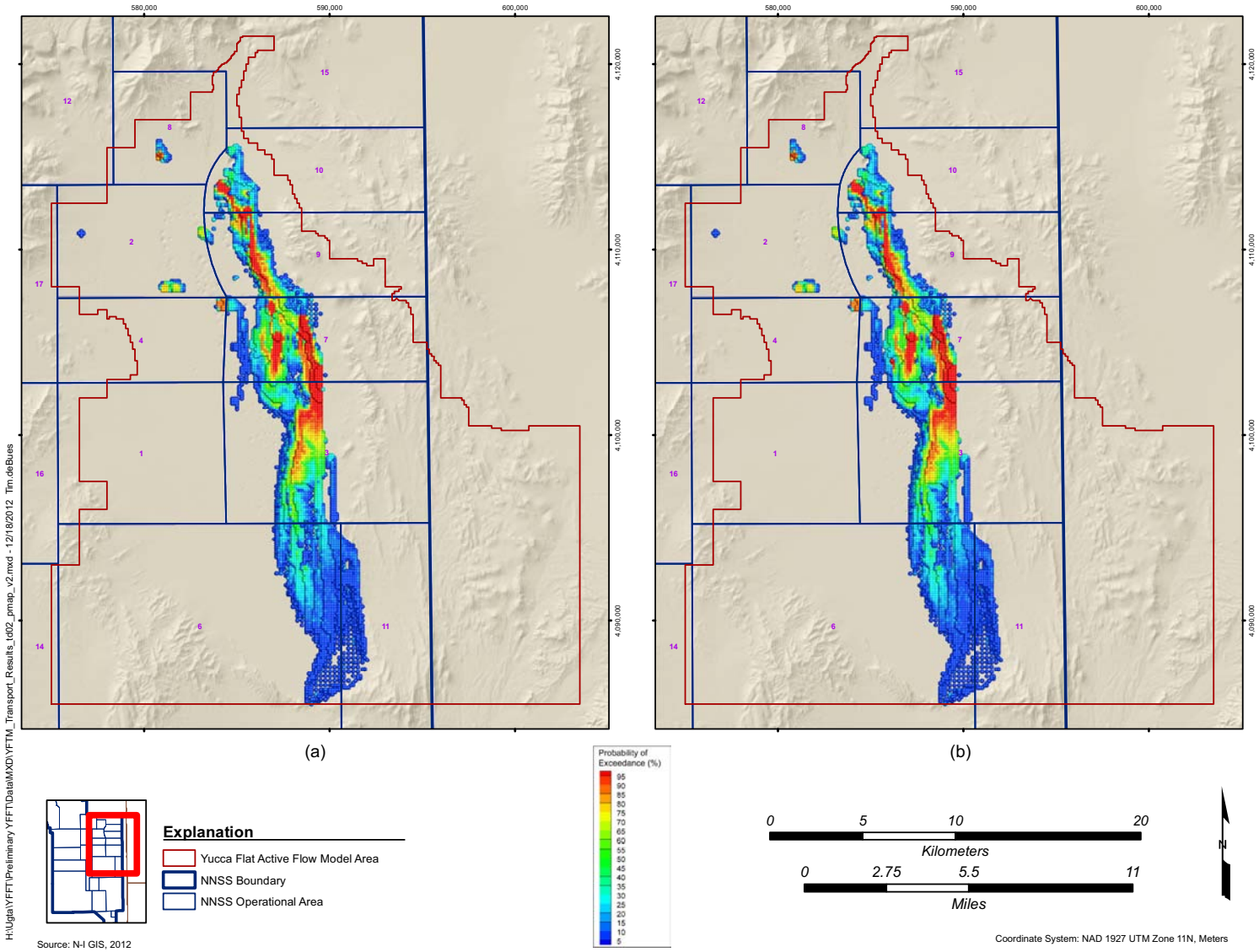

Figure 6-89
Time-Cumulative Probability of Exceedance of MCLs for Infiltration Rate of 0.1 mm/yr: (a) Base-Case LCA Sources, and (b) Combined Unsaturated-Zone, Saturated-Zone, and LCA Sources

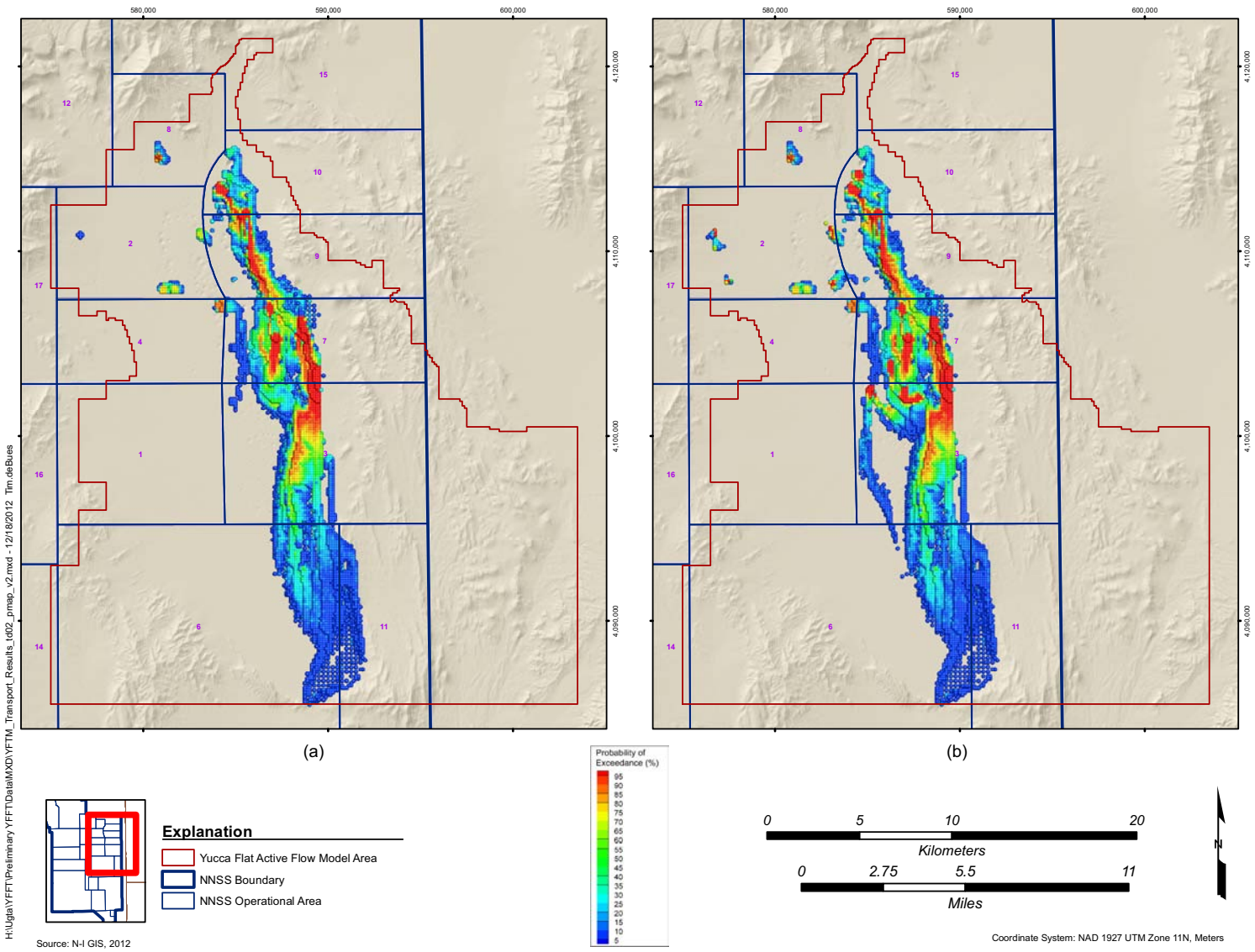

Figure 6-90
Time-Cumulative Probability of Exceedance of MCLs for Infiltration Rate of 1 mm/yr: (a) Base-Case LCA Sources, and (b) Combined Unsaturated-Zone, Saturated-Zone, and LCA Sources

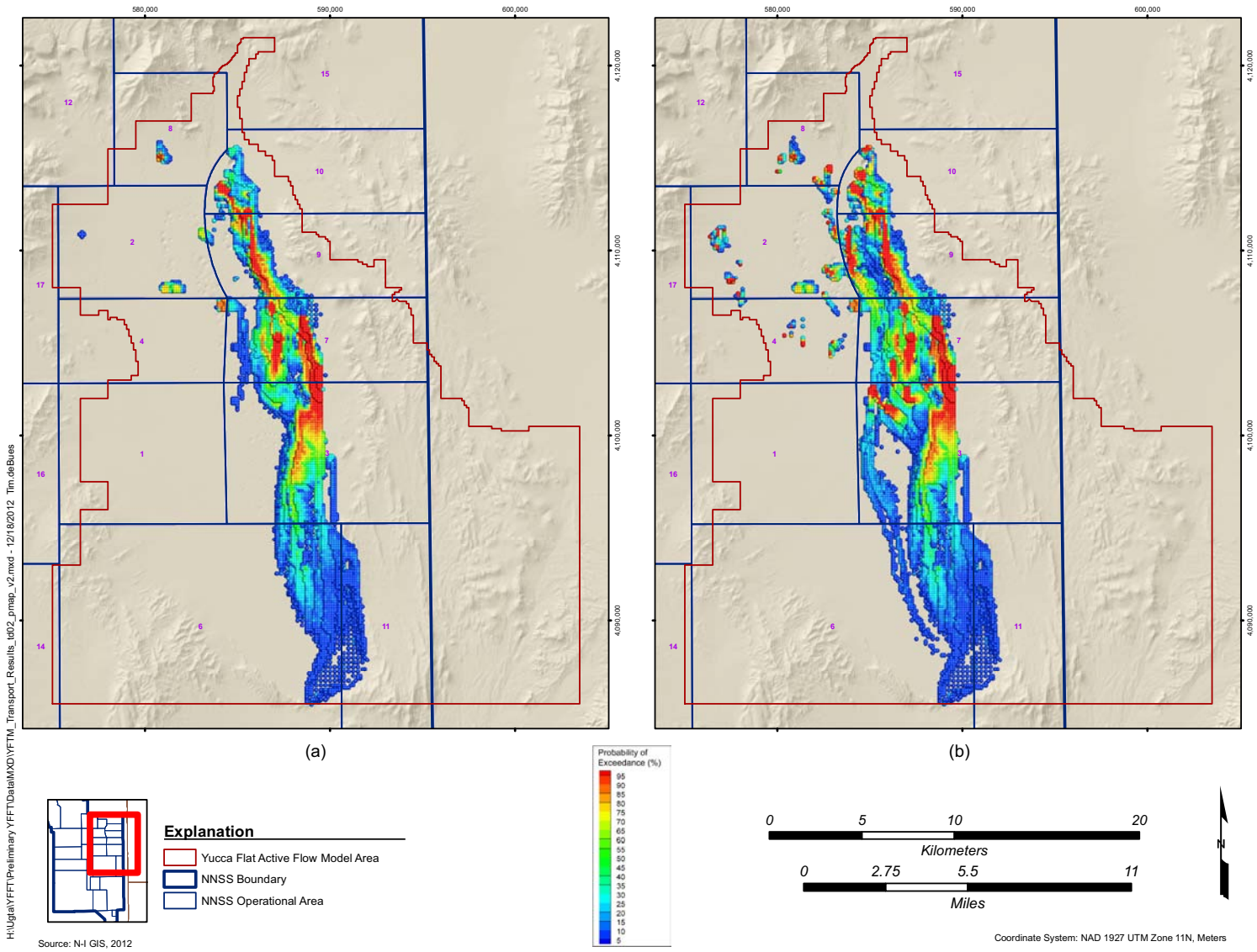

Figure 6-91
Time-Cumulative Probability of Exceedance of MCLs for Infiltration Rate of 5 mm/yr: (a) Base-Case LCA Sources, and (b) Combined Unsaturated-Zone, Saturated-Zone, and LCA Sources

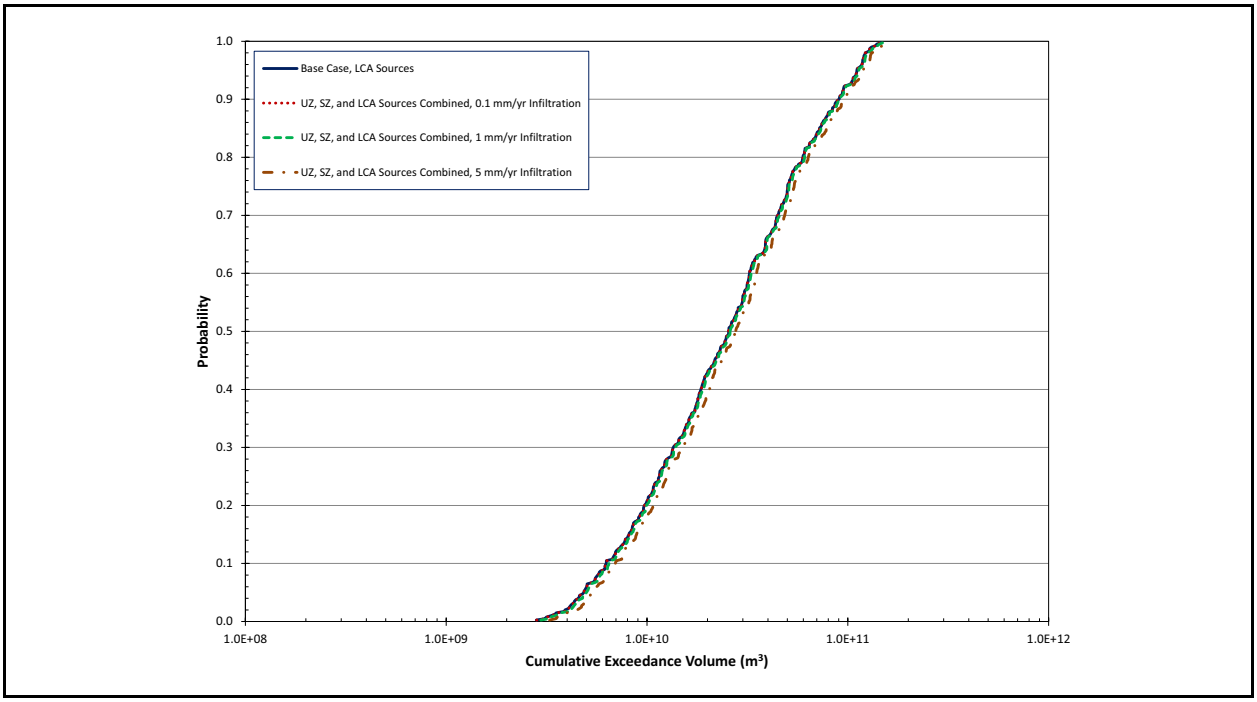

Figure 6-92
CDFs of Cumulative MCL Exceedance Volume for Combined Unsaturated-Zone, Saturated-Zone, and LCA Sources

overlying unsaturated zone or saturated alluvium/volcanic aquifer system. In addition, the uncertainty in the forecast contaminant boundary is due to uncertainty in the transport parameter values used in the LCA transport model.

This section quantifies the relative importance of the transport parameters used in the LCA transport model with respect to metrics relevant to the lateral and vertical extent of the contaminant boundary. Although the contaminant boundary is generally portrayed as a map of the 1,000-year time-cumulative probability of exceeding the SDWA MCLs, the extent of contaminant migration in the LCA can also be characterized as a discrete performance metric to provide a consistent means of evaluating parameter sensitivity. Two performance metrics have been selected for analysis, namely, (1) the time-cumulative exceedance volume (corresponding to the bulk volume of the LCA that is forecast to contain groundwater having at least a 5 percent probability of exceeding the SDWA MCLs at any time in the next 1,000 years), and (2) the maximum southern extent of the LCA that is forecast to have at least a 5 percent probability of exceeding the SDWA MCLs at any time in the next 1,000 years.

6.5.9.1 Approach

A range of techniques may be used to evaluate the significance of parameter uncertainty to the forecast extent of the contaminant boundary. The sensitivity analysis techniques that have been found informative for other UGTA CAUs are (1) stepwise regression analysis, (2) maximum entropy analysis, and (3) classification tree analysis (SNJV, 2009a; NNES, 2010b). Stepwise regression provides a measure of the monotonic response sensitivity to each input parameter. Maximum entropy analysis provides a measure of mutual information in non-monotonic, nonlinear systems. Classification tree is a categorical approach that evaluates the causes of the extreme ends of a behavior. The following sections provide brief descriptions of these approaches and representative results for a single model run for the discrete contaminant boundary performance metrics. The most significant parameters identified using the different methods for some select alternative model cases are presented in Section 6.5.9.5.

The representative run used to illustrate the significant parameters affecting the forecast extent of contaminant migration is the base-case LCA transport model using the LCA source term. This case is selected because it controls the maximum extent of contamination. The results of this model run are illustrated in Figure 6-63. Before presenting the more quantitative statistical analysis of the sensitivity of the parameter uncertainty, it is useful to illustrate the dependence using scatterplots that simply cross-plot the resulting performance metric and the parameter. Scatterplots for the more important parameters are illustrated in Figure 6-93 for the time-cumulative MCL exceedance volume metric. A list of the abbreviations for the most significant parameters is presented in Table 6-10. These scatterplots illustrate that as the effective porosity of the fault damage zone (EFFPOR_FA) decreases, the cumulative exceedance volume increases because of the increase in advective-dominated transport. In contrast, as the matrix diffusion parameter (DM_AM_CC) increases, the cumulative exceedance volume decreases because of the increased significance of matrix diffusion in delaying the contaminant transport. Other parameters, such as the effective porosity of the country rock (EFFPOR_CA) and the aperture of the fault damage zone (AP_FA), show only limited correlation.

6.5.9.2 Stepwise Regression Analysis Results

Stepwise regression models are developed by performing a forward regression such that at each step, a parameter is sequentially added to the model starting with the parameter that is most likely to reduce the variability in the model output. In each subsequent step, the next most significant parameter is

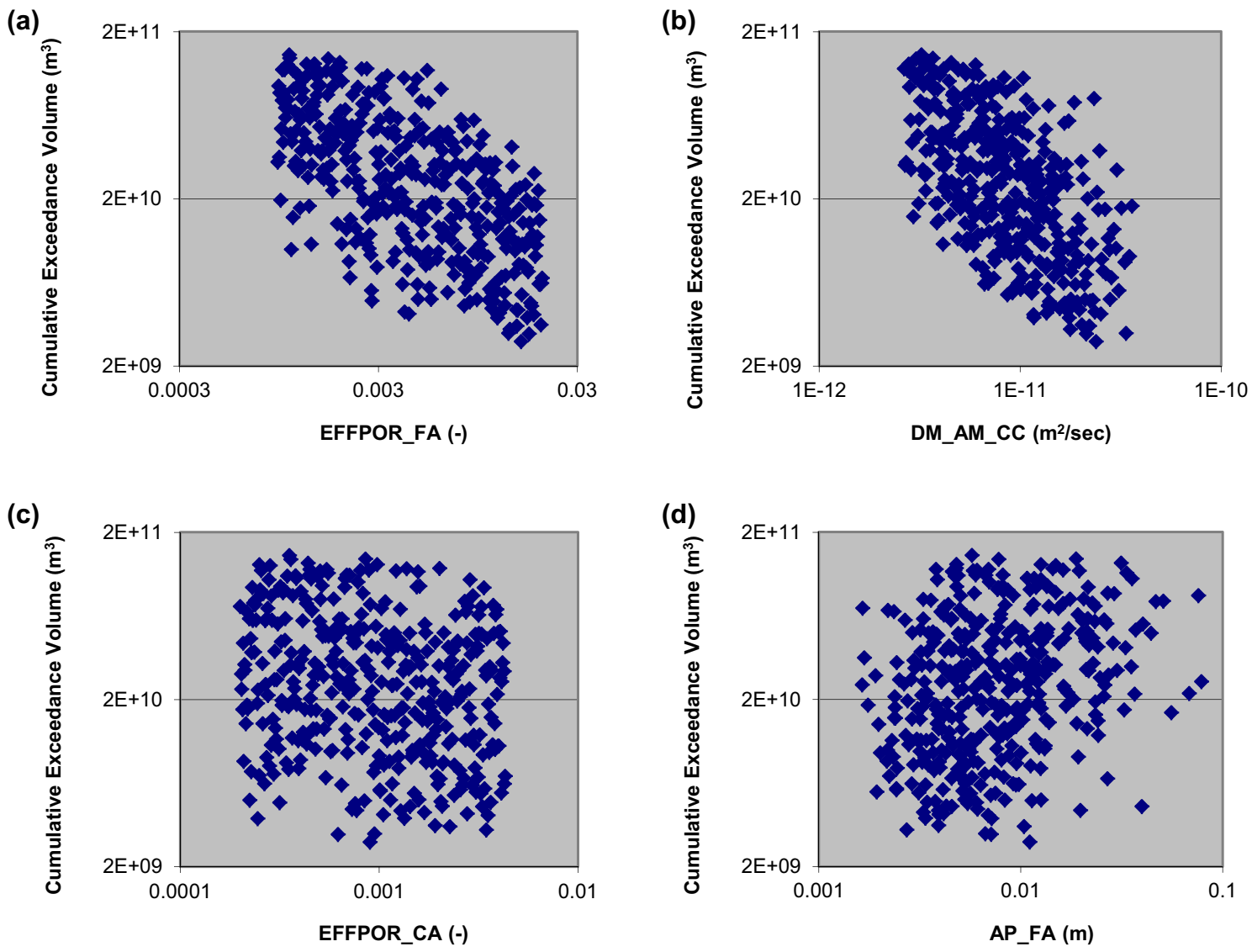

Figure 6-93
Scatterplots for Time-Cumulative MCL Exceedance Metric for the Base-Case LCA HST

Table 6-10
Significant LCA Contaminant Transport Parameter Abbreviations and Descriptions

Parameter Abbreviation	Parameter Description
DM_AM_CC	Matrix diffusivity for radionuclides with atomic numbers greater than 137
DM_H3_CC	Matrix diffusivity for radionuclides with atomic numbers less than or equal to 137
EFFPOR_FA	Effective (fracture) porosity of fault damage zone
AP_FA	Fracture aperture of fault damage zone
MATPOR_CA	Matrix porosity of carbonate country rock
EFFPOR_CA	Effective (fracture) porosity of carbonate country rock
AP_CA	Fracture aperture of carbonate country rock
FR_Sr_CC	Fracture retardation coefficient for ^{90}Sr
FR_U_CC	Fracture retardation coefficient for U
KD_C_CC_CA	Matrix sorption coefficient for ^{14}C

added to the preceding parameter(s) such that the output variance is maximally reduced at each step. This analysis identifies those parameters that contribute, in descending order of importance, to output variability through a rank-transformed linear model. The measure of uncertainty importance is represented by the standard regression coefficient (SRC). The square of the SRC is the fractional contribution of variance to the model as each parameter is added. It is expressed as the variance loss (approximately the R^2 loss) if a parameter were to be removed from the model.

A summary of the stepwise regression results for the base-case model and the saturated alluvial/volcanic aquifer system contaminant sources is presented in Table 6-11 for the two performance metrics describing the contaminant boundary. Based on these results, one can make the following observations:

- The most significant parameters relate to the transport characteristics, notably, the fracture porosity and fracture aperture of the disturbed zone of faults, as well as the matrix diffusion.
- The importance of the matrix diffusion parameter, although noted as parameter DM_AM_CC, is actually the result of parameter DM_H3_CC or MATPOR_CA. These three parameters are directly related and are fundamentally developed from the sampled values of matrix porosity (MATPOR_CA), because the diffusion coefficients for radionuclides with atomic numbers greater than 137 (DM_AM_CC), or less than or equal to 137 (DM_H3_CC), are determined by the tortuosity-matrix porosity relationship presented in Section 6.3. Because it is only low atomic number radionuclides that control the extent of the contaminant plume (notably, ^{90}Sr, ^{3}H, and ^{137}Cs), the parameter DM_H3_CC is more relevant than parameter DM_AM_CC. The significance of parameter DM_AM_CC should be interpreted as the significance of parameter DM_H3_CC because of the perfect correlation between these parameters.

Table 6-11
Ranked Stepwise Regression Analysis for Contaminant Boundary Performance Metrics for the Base-Case LCA HST Model

Regression Step	Variable	Standard Regression Coefficient	R^2 Loss	Total R^2
Time-Cumulative Exceedance Volume				
1	EFFPOR_FA	–0.661	0.436	0.393
2	DM_AM_CC	–0.619	0.380	0.772
3	EFFPOR_CA	–0.277	0.076	0.853
4	AP_FA	0.239	0.056	0.904
5	AP_CA	0.165	0.027	0.930
Southern Extent of Maximum Contamination				
1	EFFPOR_FA	–0.611	0.373	0.333
2	DM_AM_CC	–0.553	0.303	0.628
3	EFFPOR_CA	–0.331	0.109	0.744
4	AP_FA	0.194	0.037	0.779
5	AP_CA	0.162	0.026	0.805

- Increasing the fracture porosity of the disturbed zone of faults tends to decrease the exceedance volume and the southern extent of contamination. This is a result of the effect of fracture porosity on the advective transport of a significant fraction of the contaminant sources that enters the disturbed zone of faults from the overlying saturated alluvial/volcanic aquifer system.

- Increasing the fracture aperture (or spacing) of the disturbed zone of faults tends to increase the exceedance volume and the southern extent of contamination. This is a result of the effect of fracture aperture on advective contaminant transport in the LCA.

- Increasing the matrix porosity of the LCA rock matrix tends to decrease the exceedance volume and the southern extent of contamination. This is a result of the effect of matrix porosity on the magnitude of matrix diffusion along the transport path.

6.5.9.3 Entropy Analysis Results

Entropy analysis (also referred to as contingency table) is used to determine the strength of association between the input variables and the output response. This method has been found to be particularly useful for determining the strength of input-output association for any general nonlinear, non-monotonic relationship, as compared to stepwise regression analyses, which fail under such conditions.

The information-theoretic concept of entropy has been found to be a useful metric for the characterization of uncertainty (or information) in the univariate case and redundancy (or mutual information) in the multivariate case. For the multivariate case addressed here, a measure of the importance on the basis of mutual information is defined by the R-statistic. A chi-square test is used to determine whether or not the association between input and output variables is nonrandom. The chi-square statistic is calculated by summing over the differences between observed and expected entries for each binned input-output combination in the table. The larger the chi-square value is, the higher the correlation between the dependent and independent variables is.

Entropy analysis results are commonly visualized using a "bubble plot." The contingency table is organized such that the quantiles of the independent variable (input) increase from top to bottom, and those of the dependent variable increase from left to right with the size of the bubble corresponding to how many observations fall into each quantile-quantile box.

A summary of the entropy analysis results for the base-case model and the saturated alluvial/volcanic aquifer system contaminant sources is presented in Table 6-12 for the two performance metrics describing the contaminant boundary. Note that the four top ranked variables are the same for both metrics; however, the ranking between the third and fourth variables is reversed. Bubble plots for the performance metrics for this modeling case are illustrated in Figures 6-94 and 6-95. Note the four ranked variables presentation order in Figures 6-94 and 6-95 bubble plots is the same as presented in Table 6-12 for the two metrics. Based on these results, one can make the following observations:

- The most sensitive parameter is the fracture porosity of the disturbed zone of faults. This is a result of the large uncertainty in this parameter and the significant effect this parameter has on the advective transport of contaminants within these fault zones.
- The entropy statistics confirm that the parameters related to the sampled matrix porosity (MATPOR_CA) all have the same R-statistic, chi-squared and chi-squared probability. This indicates they are all directly correlated. As a result, the matrix diffusion parameter has the same importance as the matrix porosity, as expected given the correlation between these two parameters.
- The bubble plots confirm the trend and significance of the fault and country rock transport parameters, with high and low effective porosities of the fault zones correlating to low and high extents of the contaminant boundary.
- The bubble plots confirm the trend and significance of the matrix diffusion coefficient, with increases in matrix diffusion (which are correlated to increases in matrix porosity) correlating with decreases in the volume and extent of contamination (Figures 6-94 and 6-95, respectively).

Table 6-12
Ranked Entropy Analysis for Contaminant Boundary Performance Metrics for the Base-Case LCA HST Model

Rank	Variable	R-Statistic	Chi-Squared	Chi-Square Probability
Time-Cumulative Exceedance Volume				
1	EFFPOR_FA	0.607	156.	0
2	DM_AM_CC, DM_H3_CC, MATPOR_CA, MATPOR_FA	0.601	167.	0
3	AP_FA	0.328	42.	0.0004
4	EFFPOR_CA	0.316	39.	0.001
Southern Extent of Maximum Contamination				
1	EFFPOR_FA	0.591	167.	0
2	DM_AM_CC, DM_H3_CC, MATPOR_CA, MATPOR_FA	0.535	129.	0
3	EFFPOR_CA	0.382	57.	1.58E-06
4	AP_FA	0.262	27.	0.042

Note: Only R-statistic greater than 0.2 and chi-square probabilities less than 0.05 are indicated. The chi-square limitation indicates a less than 5 percent chance that the associations are random.
The parameters DM_AM_CC, DM_H3_CC, and MATPOR_FA are all directly correlated to parameter MATPOR_CA.

6.5.9.4 Classification Tree Analysis Results

Classification tree analysis has been shown to be a useful tool for analyzing which variables or a combination of variables leads to extreme values of the output distribution. A binary decision tree is at the heart of classification tree analysis. The decision tree is generated by recursively finding the variable splits that best separate the output into groups where a single category dominates. The degree by which a single category dominates is called the split purity. For each successive fork of the binary decision tree, the algorithm searches through the variables one by one to find the purest split within each variable. The splits are then compared among all the variables to find the best split for that fork. The process is repeated until all groups contain a single category or until a specified level of purity is reached. Tree-based models are attractive because (1) they are adept at capturing nonadditive behavior, (2) they can handle more general interactions between predictor variables, and (3) they are invariant to monotonic transformations of the input variables.

A summary of representative classification tree results for the base-case model and the base-case LCA source-term allocation is presented in Figure 6-96 for the maximum MCL exceedance volume and maximum southern extent of contaminant migration performance metrics. These results confirm

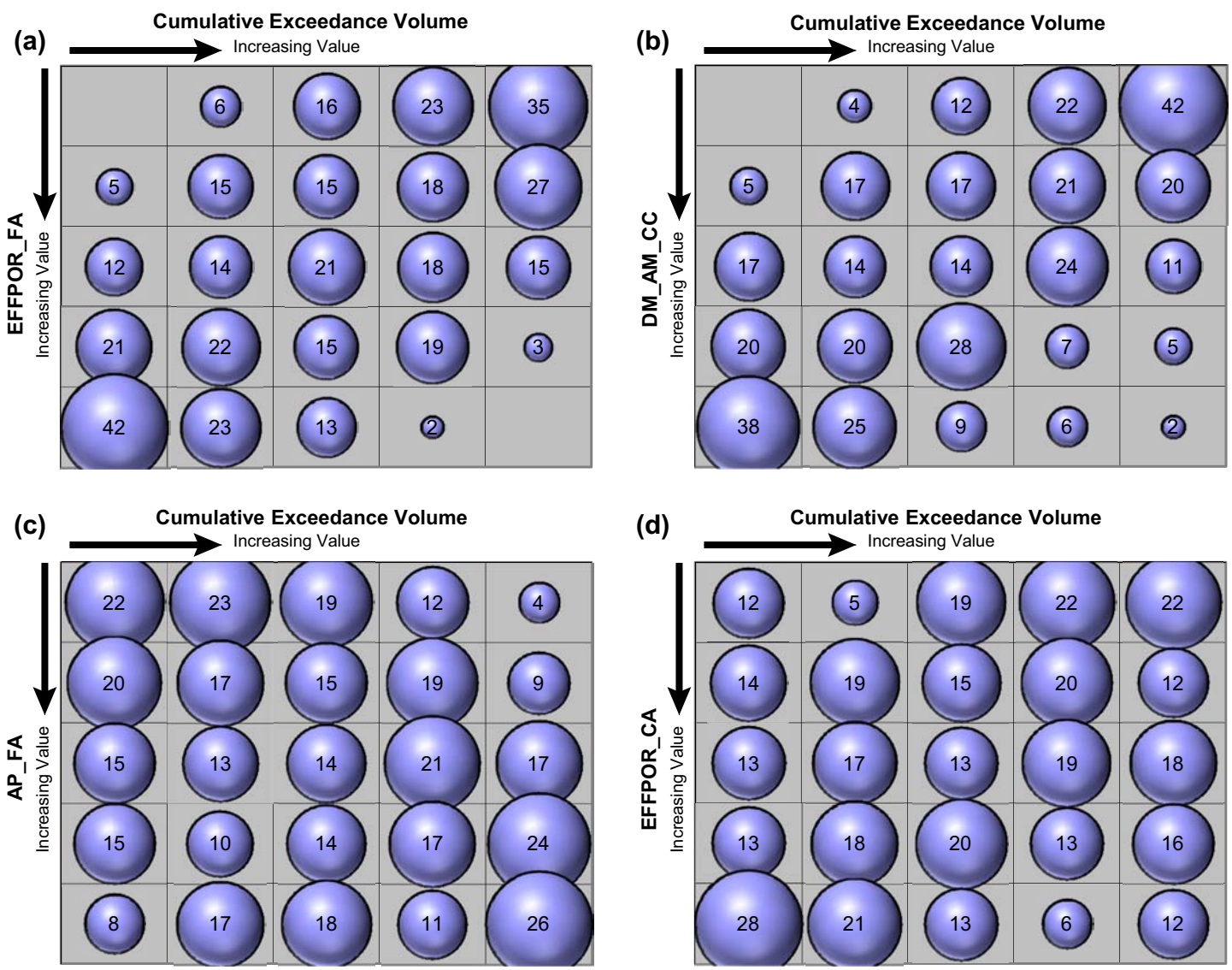

Figure 6-94
Contingency Tables for Time-Cumulative Probability of MCL Exceedance Volume Sensitivity to Transport Parameter Uncertainty for the Base-Case LCA HST

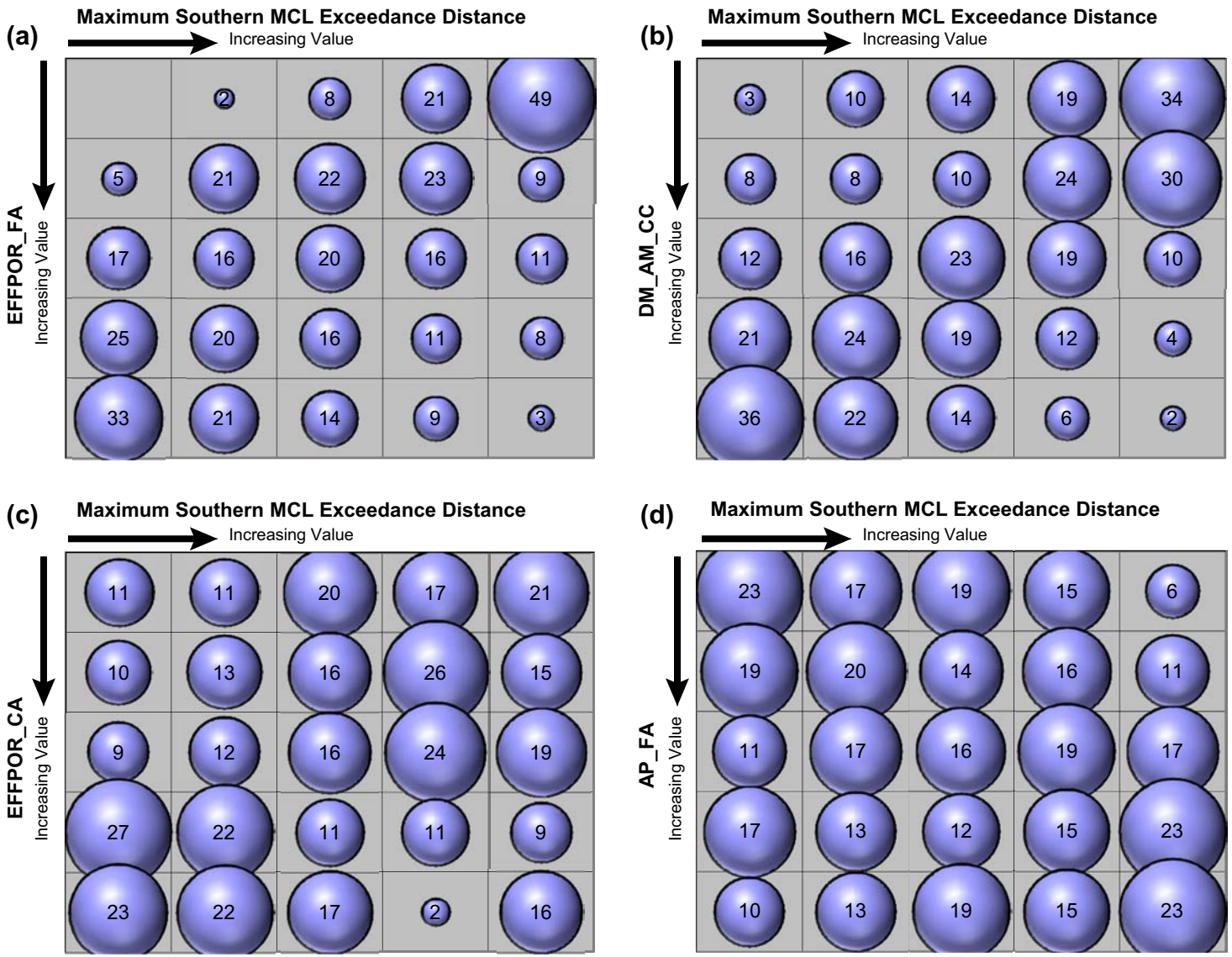

Figure 6-95
Contingency Tables of Southern Extent of Maximum Concentration Sensitivity to Transport Parameter Uncertainty for the Base-Case LCA HST

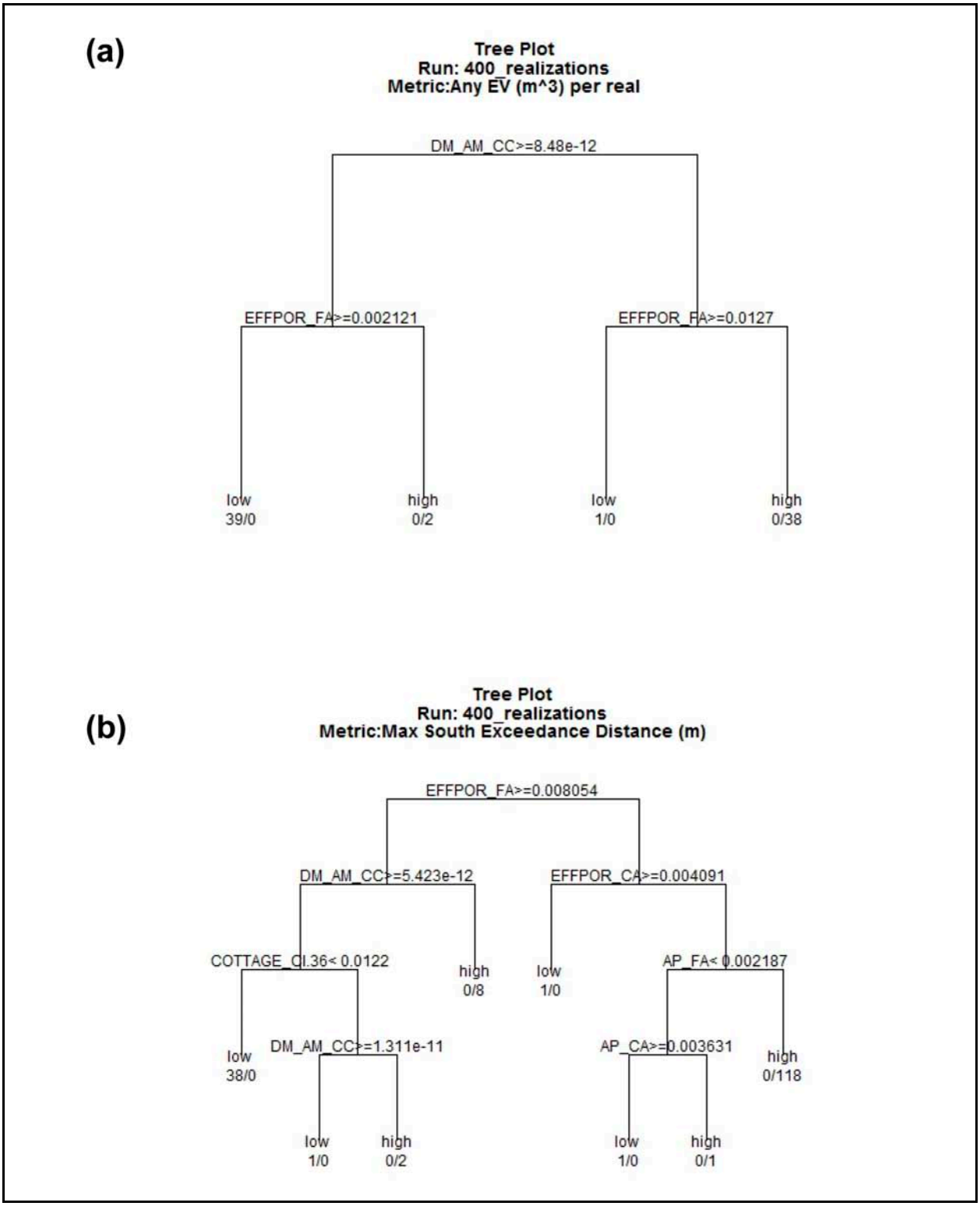

Figure 6-96
Classification Tree for Time-Cumulative Exceedance Volume for the Base-Case LCA HST

the significance of the fracture porosity and fracture aperture of the fault zones in controlling the high and low exceedance volume forecasts.

Classification tree plots are a visual representation of a binary regression model for a dataset. In a binary regression model, data are recursively divided based on the explanatory power of splitting the dataset across a parameter input value. The parameter chosen as the basis for the first split has the most explanatory power, with each successive split based on parameters of ever-decreasing explanatory power. So the parameter(s) at the top of the tree most explain the low and high values of the results; the maximum MCL exceedance volume (EV) and the maximum southern extent of contaminant migration in Figure 6-96(a) and (b), respectively. The parameters that most distinguish the low and high values is DM_AM_CC (the matrix diffusion coefficient) in the case of the maximum exceedance volume and EFFPOR_FA (the effective porosity of the fault damage zones) in the case of the maximum southern exceedance distance. In the case of the maximum MCL exceedance volume, values of DM_AM_CC greater than or equal to 8.48E-12 m^2/s explain 39 of the 40 lowest maximum MCL exceedance values (i.e., the left hand side of Figure 6-96[a]) while values of DM_AM_CC that are not greater than 8.48E-12 m^2/s explain 38 of the 40 highest values (i.e., the right hand side of Figure 6-96[a]).

This classification is repeated with the subset that falls to each branch of the tree. For the left hand branch of the maximum MCL exceedance volume classification tree (Figure 6-96[a]), the second parameter that can best classify the results is EFFPOR_FA; with EFFPOR_FA values greater than or equal to 0.002121 explaining 39 of the 40 lowest values of the maximum MCL exceedance volume. For the right hand branch of the maximum MCL exceedance volume classification tree (Figure 6-96[a]), the second parameter than can best classify the results is also the EFFPOR_FA; with EFFPOR_FA values less than 0.0127 explaining 38 of the highest values of the maximum MCL exceedance volume. It is interesting that the same parameter, is used in both the left and right branches of the maximum MCL exceedance volume classification tree, although with different values on each branch. This again illustrates the significance of this uncertain parameter in controlling both the high and low values of the forecast maximum MCL exceedance volume.

Additional displays of the top and bottom 10 percent of the results are presented in partition plots illustrated in Figure 6-97. The blue squares represent the highest 40 realizations, while the red squares represent the lowest 40 realizations. These plots are analogous to the two first classification bins on

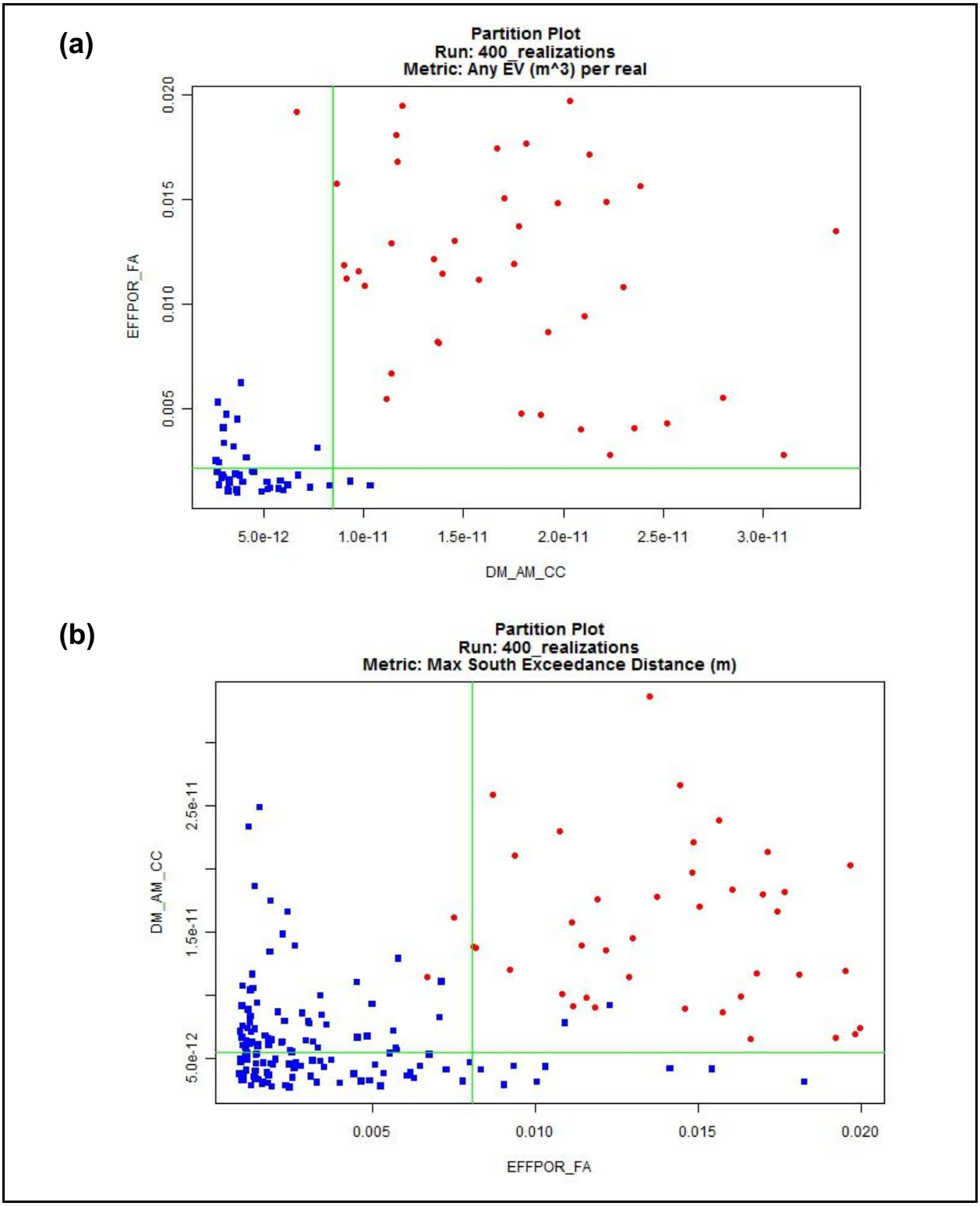

Figure 6-97
Partition Plots for Base-Case LCA Sources Transport Model: (a) Time-Cumulative MCL Exceedance Volume, and (b) Maximum Southern Extent of MCL Exceedance

the left hand side of the classification trees illustrated in Figure 6-96. For example, the 39 low values of the maximum MCL exceedance volume indicated by following the "yes" branches of the tree plot in Figure 6-96(a), are the 39 red squares indicated in the upper right quadrant of Figure 6-97(a), with DM_AM_CC values greater than 8.48E-12 m^2/s and EFFPOR_FA values greater than 0.002121. The propensity of the highest realizations to cluster near low fracture porosities and low matrix diffusion coefficients (which also correlate to low matrix porosities) is expected as both of these parameters lead to greater advective transport and less matrix diffusion, both of which tend to maximize the forecast MCL exceedance volume and southern extent of contamination.

Still further analyses of the upper 10 percent of the realizations are possible by developing boxplots that identify the range of the key parameters affecting these realizations. These analyses indicate that, again, the most significant parameters are the effective fracture porosity and fracture aperture in the fault damage zones (Figure 6-98). As expected, it is the lower percentiles of the fault zone fracture porosity and matrix porosity distributions, and the higher percentiles of the fracture aperture distribution that control the highest 10 percent of the forecast exceedance volumes.

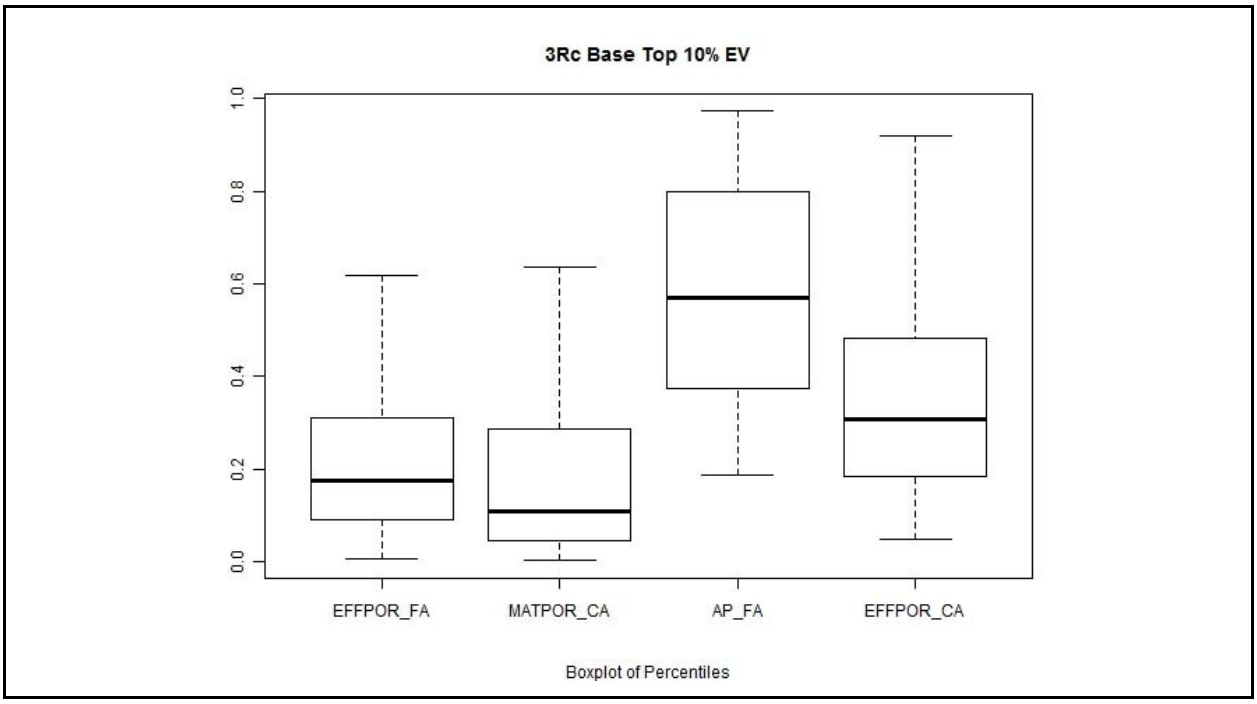

Figure 6-98
Boxplot of Transport Parameters for Top 10 Percent of Cumulative Exceedance Volume Distribution for the Base-Case LCA HST Model

6.5.9.5 Results of Uncertainty Importance/Sensitivity Analyses for Alternative Modeling Scenarios

The previous uncertainty importance/sensitivity analyses focus on the base-case run with saturated LCA HST sources. Additional analyses are performed using two additional modeling cases in this section, notably, the run with LCA HST sources and the alternative matrix sorption parameters for ^{90}Sr, ^{14}C, ^{137}Cs, and ^{61}Ni, and the run using 400 realizations of the saturated alluvial/volcanic aquifer system transport model (run SAE_13 from Section 4.0). The results of the ranked transport parameter significance based on stepwise regression, entropy, and classification tree sensitivity analyses for the time-cumulative exceedance volume and maximum southern extent of contaminant migration performance metrics for all three modeling cases are tabulated in Table 6-13. Based on these results, one can make the following observations:

- The fault damage zone fracture porosity and fracture aperture as well as the matrix diffusion parameter are consistently the most significant transport parameters controlling the two performance metrics. As noted above, this is likely due to the large uncertainty in these parameters as presented in Section 6.3, as well as the importance of these parameters in affecting the advective transport along the trace of the faults and the extent of matrix diffusion (with larger apertures corresponding to larger fracture spacings and hence less matrix diffusion for longer-lived radionuclides).

- The fault damage zone fracture porosity and fracture aperture are important parameters regardless of whether the contaminant source is initially assumed to be in the saturated LCA or whether it enters the LCA from the detonations with working points in the overlying saturated alluvial/volcanic aquifer system.

- There is marked consistency in the most significant parameters. However, occasionally another parameter can be used to develop classification trees. For example, the uncertainty in the initial contaminant concentration of Cs at the MICKEY detonation was found to be important in the modeling case when matrix retardation was assumed for Sr, Cs, C, and Ni.

- The LCA transport parameter uncertainty is more significant than the uncertainty in saturated alluvial/volcanic aquifer system transport parameters. This is evident because the same LCA transport parameters are determined as the most significant for the 400 realization saturated-zone sources modeling cases.

Table 6-13
Summary of Ranked LCA Transport Parameter Significance Based on Regression, Entropy, and Classification Tree Sensitivity Analyses

Modeling Case	Sensitivity Analyses of Time-Cumulative Exceedance Volume			Sensitivity Analyses of Maximum Southern Extent of Contamination		
	Regression	Entropy	Classification Tree	Regression	Entropy	Classification Tree
Base Case, LCA Sources	EFFPOR_FA	EFFPOR_FA	DM_AM_CC, DM_H3_CC, MATPOR_FA, MATPOR_CA	EFFPOR_FA	EFFPOR_FA	EFFPOR_FA
	DM_AM_CC, DM_H3_CC, MATPOR_FA, MATPOR_CA	DM_AM_CC, DM_H3_CC, MATPOR_FA, MATPOR_CA	EFFPOR_FA	DM_AM_CC, DM_H3_CC, MATPOR_FA, MATPOR_CA	DM_AM_CC, DM_H3_CC, MATPOR_FA, MATPOR_CA	AP_FA
	EFFPOR_CA	AP_FA	--	EFFPOR_CA	EFFPOR_CA	EFFPOR_CA
	AP_FA	EFFPOR_CA	--	AP_FA	AP_FA	--
	AP_CA	--	--	AP_CA	--	--
Alternative LCA Transport Parameters, LCA Sources	DM_AM_CC, DM_H3_CC, MATPOR_FA, MATPOR_CA	DM_AM_CC, DM_H3_CC, MATPOR_FA, MATPOR_CA	DM_AM_CC, DM_H3_CC, MATPOR_FA, MATPOR_CA	EFFPOR_CA	DM_AM_CC, DM_H3_CC, MATPOR_FA, MATPOR_CA	DM_AM_CC, DM_H3_CC, MATPOR_FA, MATPOR_CA
	EFFPOR_FA	EFFPOR_FA	AP_CA	DM_AM_CC, DM_H3_CC, MATPOR_FA, MATPOR_CA	EFFPOR_CA	EFFPOR_FA
	EFFPOR_CA	FR_Sr_CC	--	EFFPOR_FA	EFFPOR_FA	MICKEY_Cs
	AP_FA	EFFPOR_CA	--	AP_FA	AP_CA	AP_CA
	AP_CA	--	--	MATPOR_CA	--	--
Base Case, Saturated Zone Sources and Uncertainty	DM_AM_CC, DM_H3_CC, MATPOR_FA, MATPOR_CA	DM_AM_CC, DM_H3_CC, MATPOR_FA, MATPOR_CA	DM_AM_CC, DM_H3_CC, MATPOR_FA, MATPOR_CA	DM_AM_CC, DM_H3_CC, MATPOR_FA, MATPOR_CA	DM_AM_CC, DM_H3_CC, MATPOR_FA, MATPOR_CA	EFFPOR_FA
	EFFPOR_FA	EFFPOR_FA	EFFPOR_FA	EFFPOR_FA	EFFPOR_FA	EFFPOR_CA
	AP_FA	AP_FA		AP_FA	AP_FA	AP_FA
	EFFPOR_CA	EFFPOR_CA		EFFPOR_CA	EFFPOR_CA	AP_CA
	AP_CA	--		AP_CA	--	--

6.5.10 Composite Contaminant Boundaries and Conclusions

A range of alternative LCA groundwater flow and transport models have been evaluated to determine their potential significance to the possible extent of contaminant migration from underground nuclear detonations conducted in the Yucca Flat/Climax Mine CAU. Each of these alternative models has been analyzed over a range of possible LCA transport parameter values in order to determine the extent of the contaminant boundary, which requires evaluating the probability of contamination exceeding the SDWA MCLs within the next 1,000 years. The approach taken in the uncertainty analyses has been to explore a wide range of alternative conceptual models to fully explore the range of possible contaminant transport.

A necessary output of the contaminant transport modeling is the forecast contaminant boundary. The uncertainty in the flow and transport conceptual models is treated deterministically because it is not possible to quantify the probability of the alternative models. As a result, a range of possible contaminant boundaries have been developed and illustrated in the previous sections. In order to provide an integrated view of the range of possible results, composite contaminant boundaries have been developed for the different runs that are representative of the range of results. The runs included in these analyses are (1) base-case, (2) uniform concentration-based HST, (3) alternative sorption for Cs, Sr, Ni, and C, (4) alternative scale-dependent matrix diffusion, (5) alternative fault damage zone fracture characteristics, (6) slow NSMC flow field, (7) alternative northern boundary flux model, and (8) alternative northern boundary flux model combined with alternative matrix sorption for Cs, Sr, Ni, and C, and alternative damage zone fracture characteristics. The runs not included in the development of composite contaminant boundaries are the alternative source-term scenario and the fast NSMC flow field because the are less likely.

The results of the combined contaminant boundaries are presented in the following figures:

- Time-cumulative composite contaminant boundaries (Figure 6-99)
- Temporal variation of the composite contaminant boundaries (Figures 6-100 and 6-101)
- Extent of contamination for varying probabilities (Figures 6-102 and 6-103)

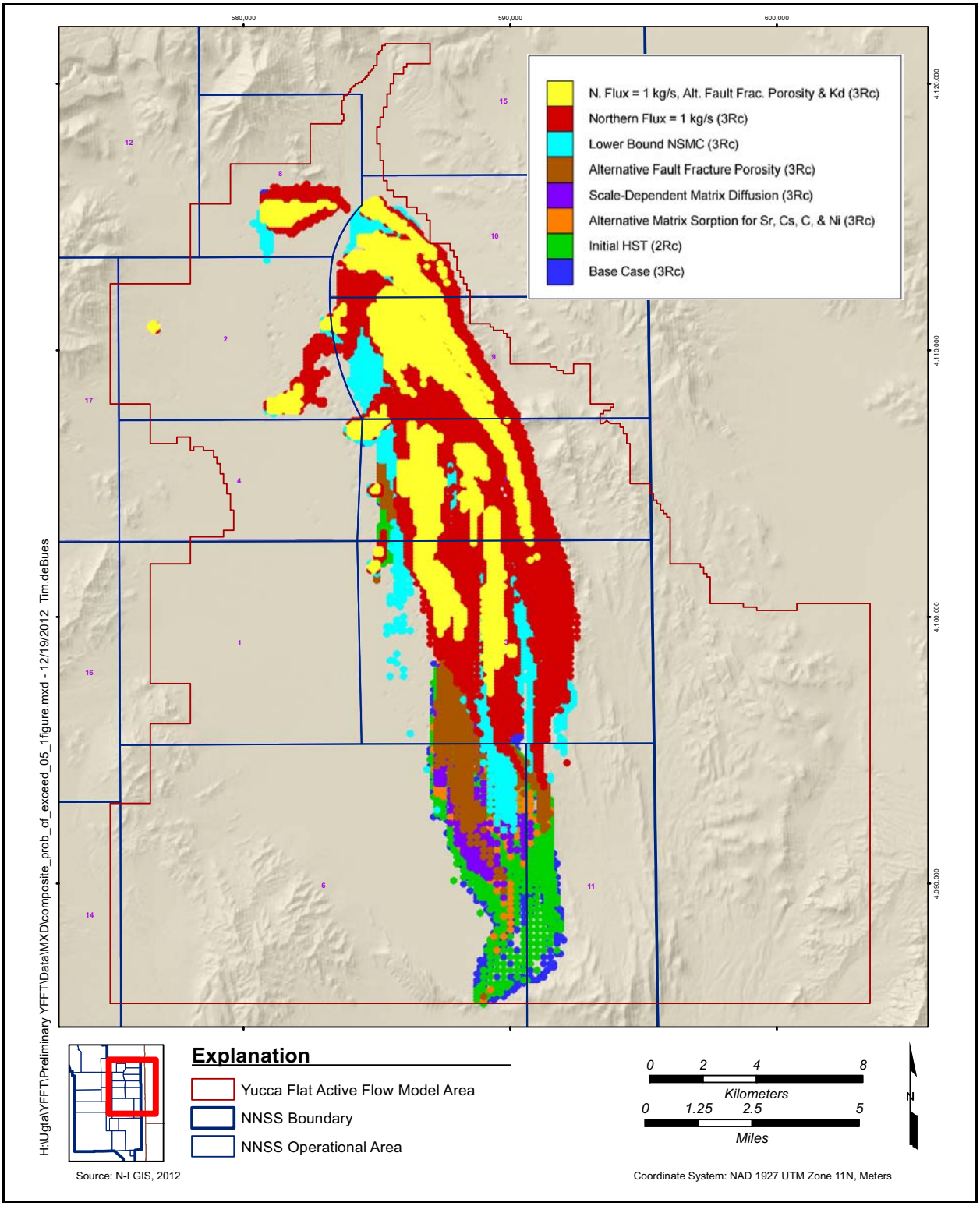

Figure 6-99
Time-Cumulative Composite Contaminant Boundaries

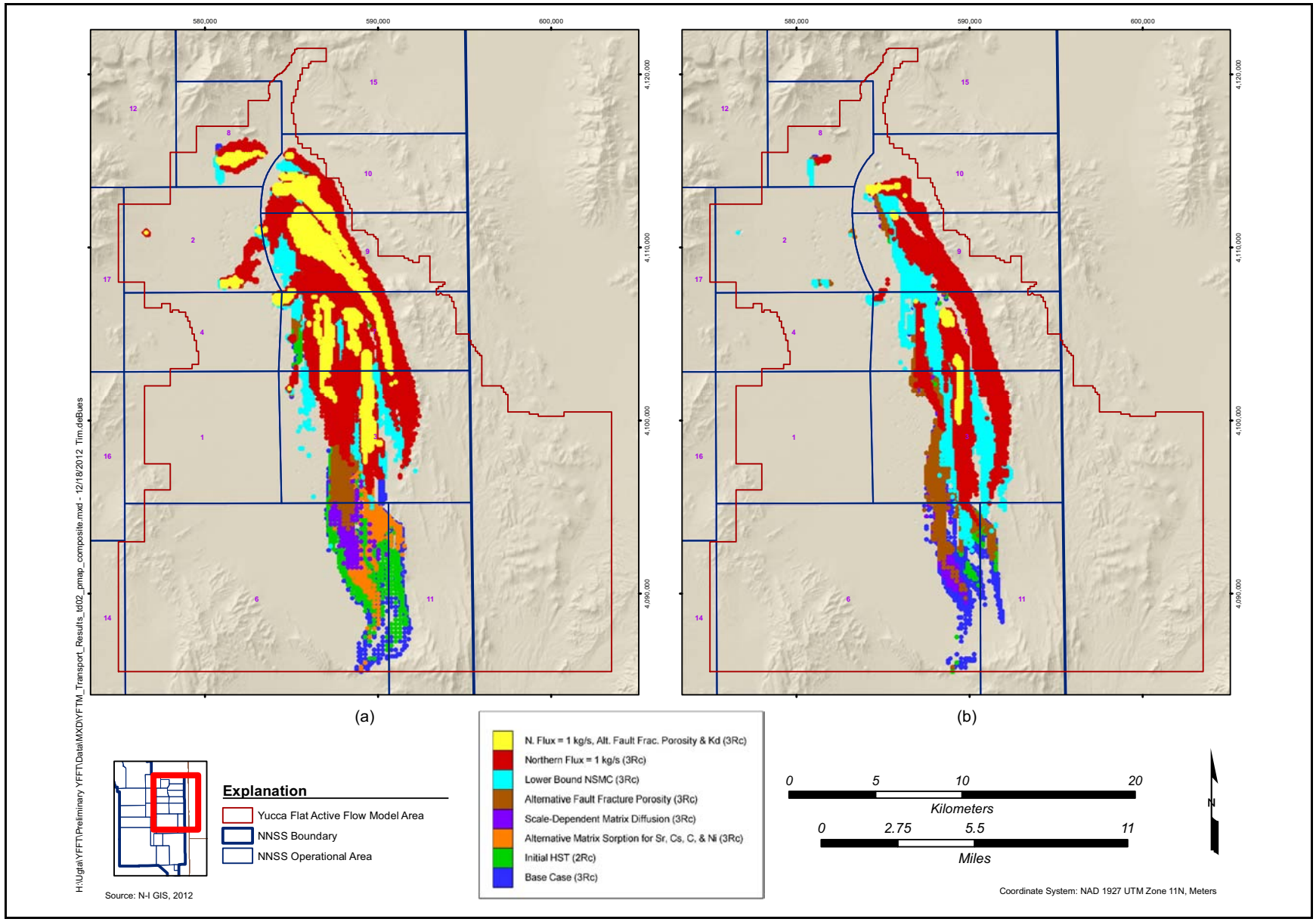

Figure 6-100
Temporal Variation of the Composite Contaminant Boundaries: (a) 100 Years, and (b) 300 Years

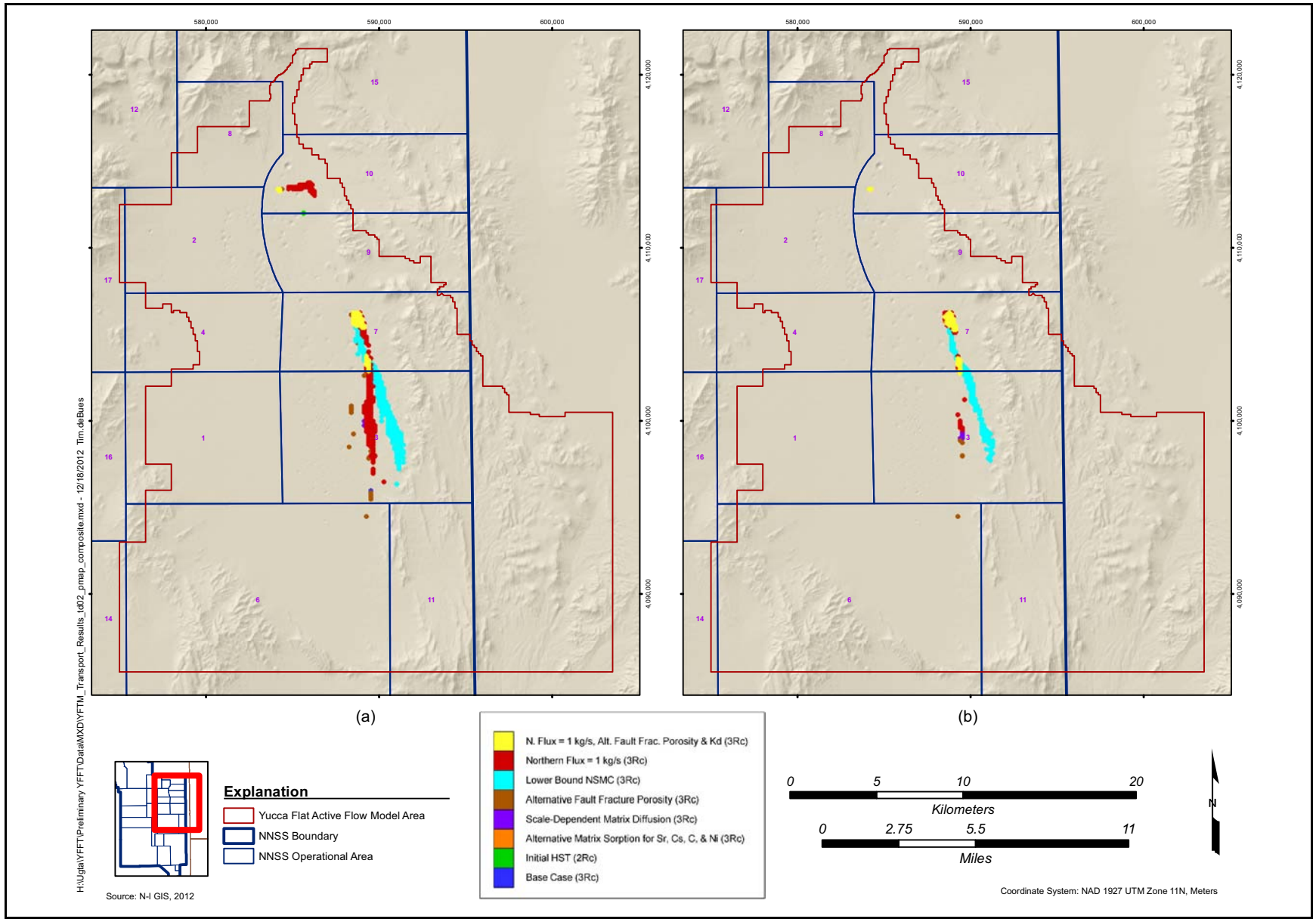

Figure 6-101
Temporal Variation of the Composite Contaminant Boundaries: (a) 500 Years, and (b) 1,000 Years

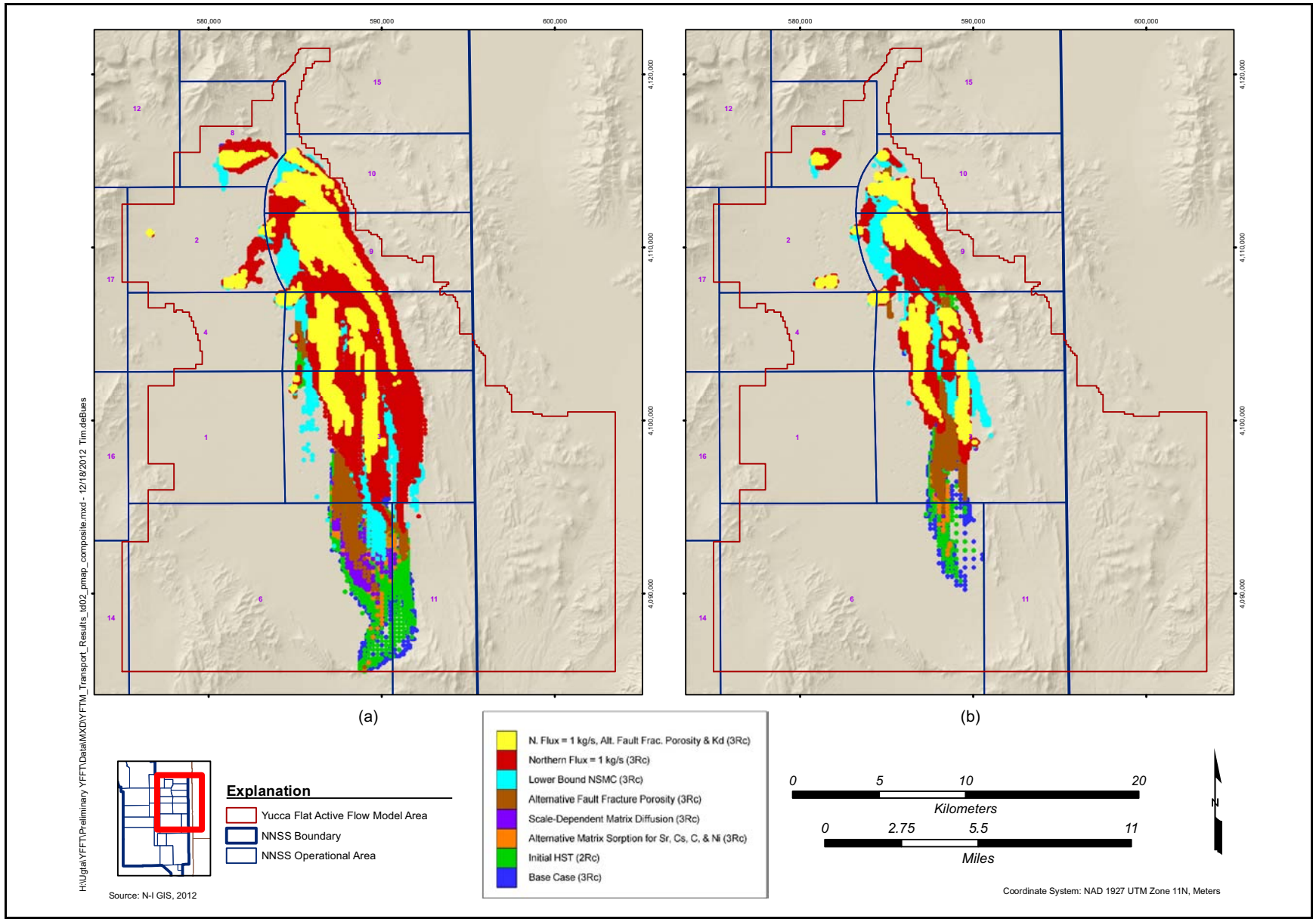

Figure 6-102
Extent of Contamination for Varying Probabilities: (a) 5 Percent, and (b) 25 Percent

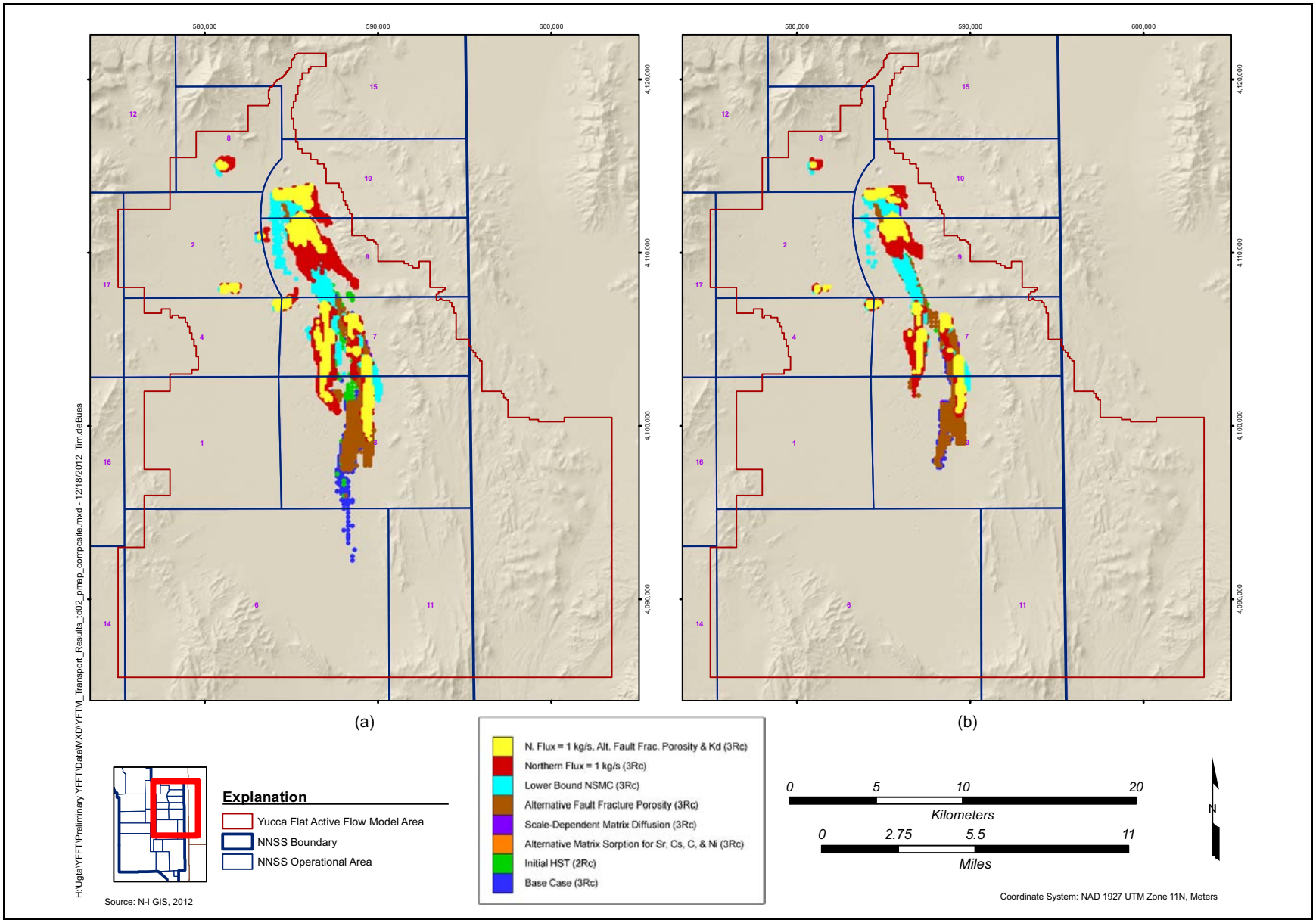

Figure 6-103
Extent of Contamination for Varying Probabilities: (a) 50 Percent, and (b) 75 Percent

The above results confirm the conservative nature of the base-case flow and transport model representation used in the base case and uniform concentration-based HST case because all other alternative models result in a less extensive forecast contaminant boundary. The time variation in the extent of the contaminant boundary confirms the observation that it is the shorter-lived radionuclides, notably, ^{3}H, ^{90}Sr, and ^{137}Cs, that control the extent of the contaminant boundary in the LCA and that beyond about 300 years, there is only a limited contaminant boundary.

The above results confirm the conservative nature of the 5 percent probability threshold for the contaminant boundary. Using higher probability thresholds results in a significant reduction in the extent of contaminant migration. This illustrates that it is the tails of the contaminant transport parameter distributions that most significantly affect the contaminant boundary extent. The tails of the transport parameter distributions are less well defined than the central tendency of the parameters. In addition, because the conceptual model assumes that the distributions are applicable over large spatial distances (i.e., there is no spatial variability in transport parameters), the tails of the distributions can more significantly affect the results. The 50 percent probability of SDWA MCL exceedance is more representative of the central tendency in the results, which would include the possibility of spatial variability in transport properties.

Although the contaminant boundary may extend to the southern modeled boundary of the Yucca Flat/Climax Mine CAU, this possibility results from the conservative nature of the base-case conceptual model. The alternative plausible contaminant boundaries result in less extensive transport. These alternatives may be considered more representative given that the model results are not reproduced at several observation wells downgradient from LCA sources, including Well WW C. In addition, even if the 5 percent probability of SDWA MCL exceedance does extend to the southern modeled boundary, this is a transient phenomenon and would decay with the 12-year half-life of ^{3}H, the 29-year half-life of ^{90}Sr, and the 30-year half-life of ^{137}Cs.

These composite contaminant boundaries can be used by NNSA/NSO to identify initial use restriction areas and by NDEP to identify an initial regulatory objective as required in the FFACO. Although the analyses are notably conservative, they also serve the purpose of developing the CADD/CAP requirements, including the model evaluation plans, if the CAU moves to the CADD/CAP stage of the FFACO UGTA strategy.

Because the contaminant boundary is based on the 95th percentile time-cumulative extent of contamination (i.e., the lateral and vertical extent of contamination that is forecast to have at least a 5 percent probability of exceeding the SDWA MCL), a useful means of comparing the multiple modeling cases is to use the 95th percentile of the cumulative exceedance volume performance metric. In addition, because of the potential significance of the lateral extent of contamination, an additional useful metric is the maximum southern extent of the SDWA MCL exceedance probability. Because the results are generated separately for the different sources providing contaminant flux to the LCA, the comparisons are grouped by contaminant source, namely, the unsaturated-zone sources, the saturated alluvial/volcanic aquifer system sources, and the sources with exchange volumes that are assumed to intersect the saturated LCA.

The differing unsaturated zone, saturated alluvium/volcanic aquifer system, and LCA contaminant source results for both the cumulative exceedance volume and maximum southern concentration performance metrics are illustrated in Figures 6-104 and 6-105. The following observations can be made from these results:

- The unsaturated-zone sources are insignificant contributors to the extent of contaminant migration in the LCA in comparison to the saturated-zone or LCA sources, even though about 56 to 61 percent of the initial inventory is in the unsaturated-zone exchange volume (depending on the source-term conceptual model). This is a result of the significant delay, decay, and retardation in contaminant flux reaching the saturated LCA from these sources. This conclusion is confirmed by the analyses presented in McNab (2008).

- The volumetric extent of contamination is significantly greater for LCA sources. This is controlled by the short-lived radionuclides, notably, ^{90}Sr, ^{3}H, and ^{137}Cs, that have very high initial concentrations and are non-sorbed in the LCA. The southern extent of contamination in the LCA transport model are also most significantly affected by these short-lived, non-sorbing radionuclides.

- Higher background infiltration rates, such as 1 or 5 mm/yr, which are considered unlikely as discussed in Sections 3.0 and 5.0, significantly increase the extent of contaminant migration in the LCA. This is in large part due to the significant increase in contaminant mass influx from the overlying saturated alluvial/volcanic aquifer system sources for the higher infiltration rates. However, even for the higher infiltration rates, the contaminant extent due to the initial contamination assumed to be in place in the LCA dominates the overall extent of contamination.

- The uncertainty in the extent of contaminant migration is not significantly affected by uncertainty in the unsaturated zone or saturated alluvial/volcanic aquifer system conceptual model or parameter ranges.

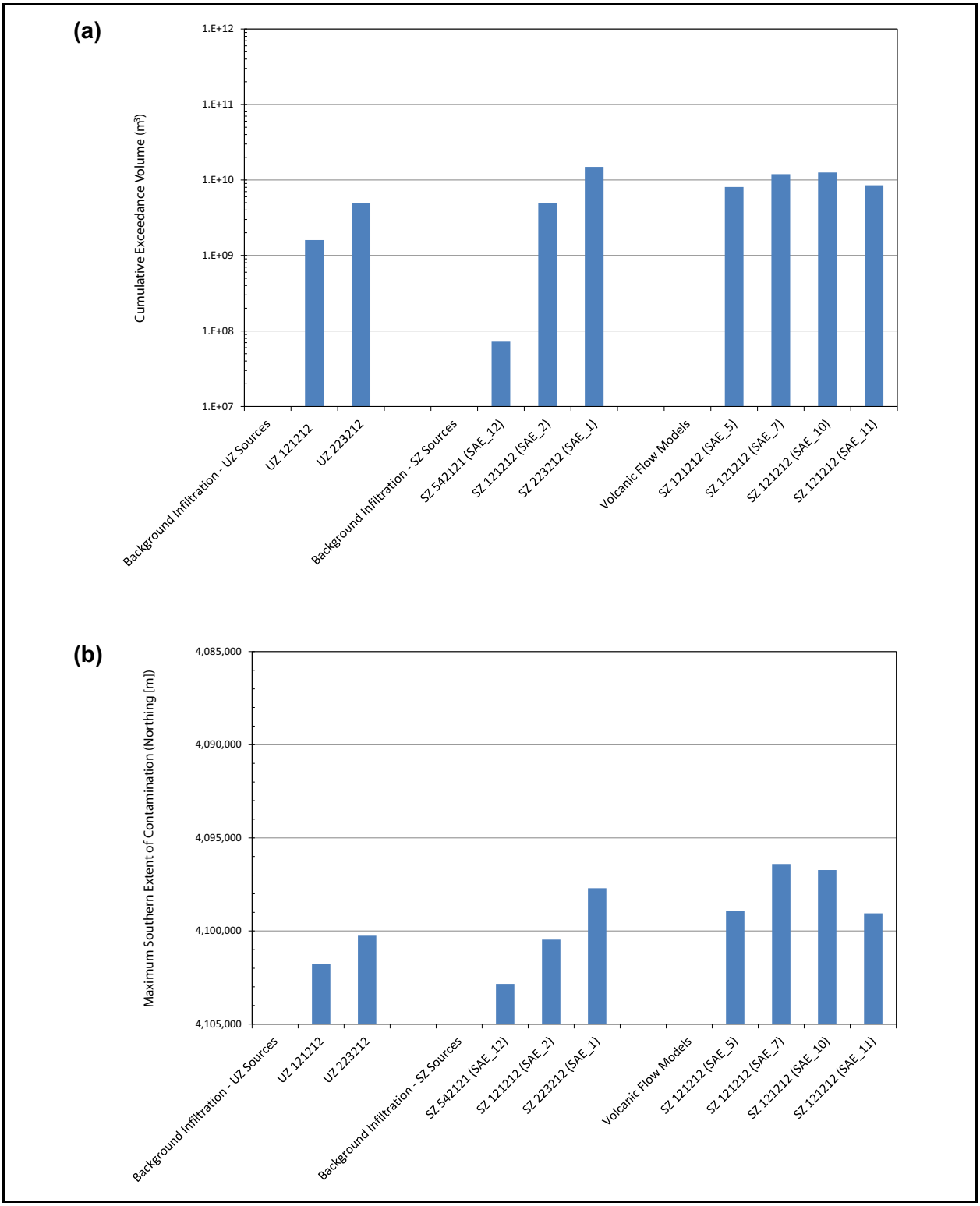

Figure 6-104
Summary of 95th Percentile Results for Unsaturated-Zone and Saturated-Zone Sources: (a) Cumulative MCL Exceedance Volume, and (b) Maximum Southern Extent of MCL Exceedance

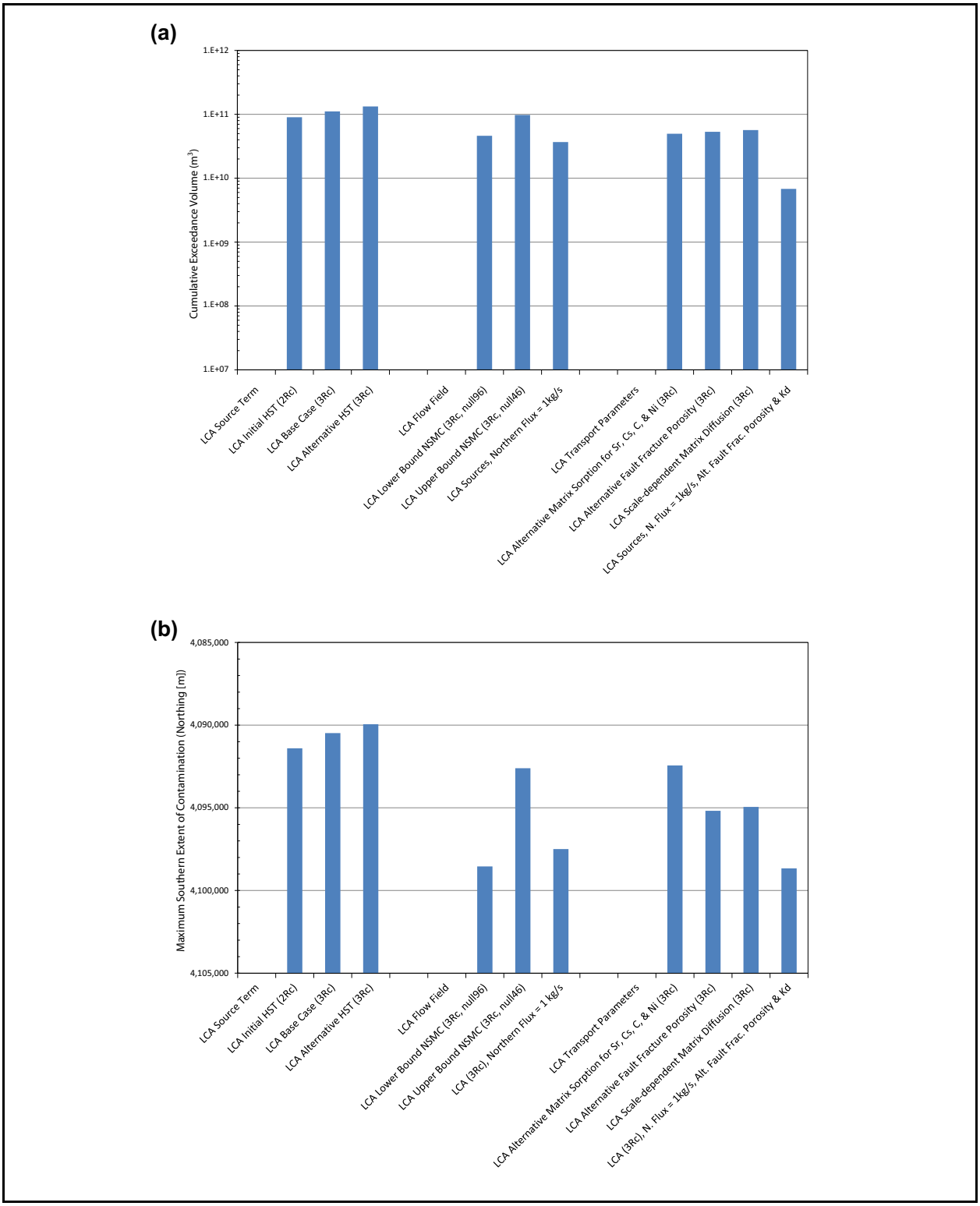

Figure 6-105
Summary of 95th Percentile Results for LCA Sources: (a) Cumulative MCL Exceedance Volume, and (b) Maximum Southern Extent of MCL Exceedance

6.6 Summary and Conclusions

The transport model used for evaluating the effects of contamination either assumed to initiate in the saturated LCA (due to the assumption the exchange volume intersects the saturated LCA, and the contaminant mass or concentration is uniformly distributed in the exchange volume) or calculated to enter the saturated LCA from the overlying unsaturated zone or saturated alluvial/volcanic aquifer system is fundamentally based on the same conceptual model used for the Frenchman Flat CAU analyses with the distinction that faults in the LCA are conceptualized of consisting of a high-permeability damage zone. The conceptual distinction between the fault damage zones and the nonfaulted country rock is based on available data compiled in the Yucca Flat/Climax Mine HDD (SNJV, 2006b) and TDD (SNJV, 2007). As discussed in these documents and summarized in Section 6.3 and Appendix J, these data have been used to develop the parameter ranges and distributions used in the transport model for the fracture transport characteristics, notably, the effective or fracture porosity, the fracture spacing and aperture, and the matrix porosity used to develop the matrix diffusion parameter. These data are appropriate to develop appropriate parameter distributions for evaluating contaminant transport in the LCA.

The available laboratory and field data have been used in the development of the source term and transport parameter distributions. These distributions have been used to calculate 400 realizations of potential contaminant transport. In addition, while the available hydrologic and transport data are adequate to estimate appropriate parameter distributions for contaminant transport analyses, alternative conceptualizations and parameter distributions are possible given the uncertainty in several of the parameters. As a result, alternative distributions have been used to evaluate the significance of this uncertainty to the contaminant transport. These alternatives include (1) alternative flowing feature and fracture aperture distributions, (2) alternative matrix sorption distributions for several key radionuclides, (3) alternative scale-dependent matrix diffusion distributions, and (4) alternative calibrated flow models. These alternatives illustrate the conservative nature of the base-case model representation.

A wide range of uncertainty and uncertainty importance analyses have been conducted to explore the potential range in contaminant migration in the LCA resulting from underground nuclear detonations conducted in the Yucca Flat/Climax Mine CAU. Although the greatest percentage of the total contamination resides initially in the overlying unsaturated zone (comprising about 61 to 56 percent of the total initial inventory depending on the source-term allocation model) and saturated

alluvial/volcanic aquifer system (comprising most of the remaining 39 to 43 percent of the total initial inventory), the small fraction of the inventory initially assumed to be in the saturated LCA (depending on the size of the exchange volume and the distribution of contaminant mass in the exchange volume), when combined with a limited influx from the overlying units, results in a forecast preliminary contaminant boundary in the LCA.

In evaluating the different sources of contaminant mass to the LCA presented in Section 6.4, the alternative calibrated groundwater flow models for the LCA presented in Section 5.6, and the uncertainty in the LCA contaminant transport parameter values presented in Section 6.3, a range of possible contaminant extents are forecast. While it is possible to develop a composite contaminant boundary by simply combining the individual contaminant boundaries forecast for each modeling case, it is informative to compare and contrast the different model forecasts to develop general conclusions on the possible extent of contaminant migration and the significant uncertainties that contribute to those forecasts.

The following summarizes the significant aspects of the contaminant transport results considering the uncertainty in inputs that affect those results:

- Underground nuclear detonations conducted in the Yucca Flat/Climax Mine CAU are forecast to have contaminated a portion of the LCA within the CAU boundary.
- The source of this contamination is dominated by a small number of detonations with exchange volumes that intersect the saturated LCA. Of particular importance are the BOURBON and TORRIDO detonations, each of which has a maximum announced yield of 200 kt, and depending on the radionuclide, has about 40 percent of the initial inventory assumed to be in the saturated LCA.
- Observations of radionuclide concentrations in the saturated LCA downgradient from BOURBON and TORRIDO, at Wells UE-7nS and ER-7-1, respectively, do not confirm the forecast contaminant extent. At UE-7nS, the observed ^{3}H concentration is near the MCL, while the model forecasts concentrations far exceed the MCL. At ER-7-1, the ^{3}H concentration is below the minimum detection level, while again the model forecasts concentrations are well above the MCL. It is possible that this discrepancy is a result of the observation wells not intersecting flowing features that are hydraulically connected to the source of contamination (as postulated in SNJV, 2006b, and Buddemeier and Isherwood, 1985). However, it is very possible that the assumed extent of initial contamination, which is based on the maximum unclassified yield of these and all of the other 747 detonations in the Yucca Flat/Climax Mine CAU, overstates the actual classified extent of contamination.

- Observations of significant contamination at UE-2ce completed in the LCA3 183 m downgradient from NASH are not consistent with the representation of essentially no contamination at this location using an infiltration rate of 0.1 mm/yr. This inconsistency could be the result of (1) the lack of inclusion of drill-back fluid losses or chimney drainage, (2) underestimating the enhanced-crater recharge, or (3) underestimating the local infiltration at this location. Alternative cases using higher local infiltration or drill-back fluid losses and chimney drainage reasonably reproduce the observed concentrations.

- Observations of minimal contamination at Well U-3cn-5 completed in the LCA 129 m southeast from BILBY are consistent with the representation of essentially no contamination at this location using an infiltration rate of 0.1 mm/yr. However, alternative cases with higher background recharge rates of 1, 5, and 10 mm/yr result in significant contaminant flux to the LCA at this location (generally due to transient flow and transport down the fault located a few hundred meters north of the working point). These results imply the lower infiltration rate case is more reasonable, although it cannot be ruled out that Well U-3cn-5 did not intersect permeable features that could provide hydraulic connection to the faulted area to the north.

- Contaminants that have an initial source in the unsaturated zone and saturated alluvial/volcanic aquifer system are significantly retained in those units because of their low vertical flux and limited lateral extent. A small fraction of the initial inventory in the overlying unsaturated zone and saturated alluvial/volcanic aquifer system is transported downward to the saturated LCA. The rate of transport to the LCA is directly controlled by the ambient percolation flux and recharge to the saturated units, which in turn is controlled by the net infiltration rate at the surface.

- Within the LCA, the contaminant transport is in a southerly direction consistent with the general regional trends of the LCA. The extent of contaminant migration in the LCA is dependent on the flow and transport model, and parameter values in the LCA, as well as the distribution and amount of contaminant influx to the LCA.

- Contaminant migration in the saturated LCA is generally southerly from central Yucca Flat toward Frenchman Flat and CP basin. Although the hydrologic characteristics of the LCA structures in the accommodation zone between Yucca Flat and Frenchman Flat are uncertain, this uncertainty does not significantly affect the flow directions or velocities in central Yucca Flat, which is the source of a large fraction of the Yucca Flat/Climax Mine CAU contamination and lies about 15 km north of the accommodation zone.

- There is a low probability that contamination emanating from underground nuclear detonations conducted in the Yucca Flat/Climax Mine CAU will be transported outside the southern model boundary at concentrations with a probability of 5 percent or greater of exceeding the SDWA MCLs. This conclusion reflects the compound conservative assumptions made in the base-case model. Alternative models have been run to explore the significance of the conservative assumptions. These alternatives may be more representative of expected conditions. For example, the northern flux alternative model is more consistent with recent analyses of LCA flow presented in Fenelon et al. (2012).

- The forecast extent of contaminant migration in the LCA is controlled by the presence of, and hydrologic and transport characteristics of, faults that intersect the LCA and the overlying tuff confining units. The damage zones of these faults provide preferential groundwater flow paths for water flow in the LCA. These faults also are considered to provide the hydraulic connection to the tuff aquifers through the intervening tuff confining units, and therefore, provide the pathway for contaminants emanating from the overlying units to enter the LCA. Finally, the transport properties of the fault zones, in particular the fracture porosity and fracture aperture in the damage zones of the major faults, control the extent of lateral migration in the LCA.

- The forecast extent of contaminant migration in the LCA, as defined by either the time-cumulative exceedance volume or the southern extent of contaminant migration, is controlled by contaminant sources that are initially in place in the saturated LCA.

- The extent of contamination in the LCA associated with LCA sources is the result of short-lived mobile radionuclides such as ^{90}Sr, ^{137}Cs, and ^{3}H. After a few hundred years, these radionuclides decay to concentrations that are insignificant in comparison to the SDWA MCLs. The longer-lived radionuclides that initiate in the LCA, such as ^{129}I, ^{99}Tc, ^{36}Cl, and ^{14}C, are generally at concentrations that do not significantly contribute to the extent of contaminant migration.

- The extent of contamination in the LCA associated with saturated alluvial/volcanic aquifer system sources is also the result of short-lived mobile radionuclides, notably, ^{3}H, and to a lesser extent, the long-lived mobile radionuclides such as ^{129}I, ^{99}Tc, and ^{36}Cl. These radionuclides come into the saturated LCA along permeable faults that penetrate the impermeable tuff confining units through most of the 1,000-year time period of interest to the FFACO. Although ^{3}H influx to the LCA from sources in the overlying units is significant, these sources are small in comparison to the initial concentrations of ^{90}Sr and ^{137}Cs. In addition, the ^{3}H decays within about 100 years to levels below the SDWA MCL.

- The uncertainty in the forecast extent of contaminant migration in the LCA is dominated by uncertainty in (1) LCA source initial concentrations, and (2) fracture porosity and aperture of fault damage zones.

- Uncertainty in source inputs to the LCA, whether the uncertainty is in the contaminant flux from the overlying saturated units or the contaminants initially in place in the LCA, does not significantly affect the uncertainty in the extent of contaminant migration in the LCA given that the size of the exchange volume is based on the maximum announced yield of each detonation.

- The extent of contaminant migration is significantly affected by the parameter distributions for the fracture porosity and fracture aperture for the damage zone of faults that intersect the LCA. The maximum extent of contaminant migration is controlled by low fracture porosities and high fracture apertures (the latter corresponding to high fracture spacings).

- Sampled parameter values are assumed to be applicable over the entire spatial domain of the modeled feature. For example, if a low fracture porosity of the fault damage zones is sampled, this value is applied to each fault with a damage zone, and the same value is applied along the entire length of the fault damage zone. This essentially assumes an infinite correlation of the parameter values within each feature, which, when combined with the uncertainty distributions, may overestimate the effect of the tails of the distributions on the tails of the results. Because it is the tails of the forecast results that are the performance metric of interest to determine the FFACO-defined contaminant boundary (i.e., a probability of greater than or equal to 5 percent of exceeding the SDWA MCLs), the assumption of spatial uniformity and the lack of scale dependence tends to overpredict the lateral extent of the contaminant boundary.

The LCA transport model is a reasonable representation of the expected behavior of contaminant migration in the Yucca Flat/Climax Mine CAU given the philosophy to not underrepresent the possible extent of the contaminant boundary. A range of alternative forecast contaminant boundaries have been developed to illustrate the significance of structural uncertainty in conceptual models. However, all contaminant boundaries use the maximum announced detonation yields and the corresponding exchange volume sizes.

7.0 SUMMARY AND CONCLUSIONS

The Yucca Flat/Climax Mine CAU contains 747 underground nuclear detonations, 90 percent of the total number of subsurface detonations conducted at the NNSS. These detonations comprise about 39 percent of the total radionuclide activity at the NNSS (when decay corrected to September 23, 1992), which is dominated by ^{3}H (Bowen et al., 2001). These detonations comprise about 43 percent of the total NNSS underground nuclear test inventory of long-lived mobile radionuclides such as ^{129}I and about 80 percent of the total inventory of long-lived immobile radionuclides such as ^{239}Pu. The majority of the tests in the Yucca Flat/Climax Mine CAU were performed in the unsaturated zone, i.e., with working points above the water table. Assuming an exchange volume of 2 R_c and the uniform-mass allocation method, the fraction of the Yucca Flat/Climax Mine CAU initial inventory contained in the unsaturated zone is about 61 percent. Over 99 percent of the remaining inventory is initially in the exchange volume of the saturated alluvial/volcanic rock units.

In order to capture the relevant and significant aspects of the contaminant sources as well as groundwater flow and contaminant transport processes that affect the migration of the radionuclide contaminants within the Yucca Flat/Climax Mine CAU, four separate flow and transport models have been developed:

- Climax Mine flow and transport model
- Yucca Flat unsaturated-zone flow and transport model
- Yucca Flat saturated alluvial/volcanic aquifer system flow and transport model
- Yucca Flat saturated LCA flow and transport model

The results of the Climax Mine flow and transport model analyses have been used to determine the mass flux that may be expected to be released from the granitic stock at Climax Mine to the permeable LCA that intersects and surrounds the granitic stock. As discussed in Section 6.4, the contaminant flux to the LCA from the three detonations conducted in the Climax Mine is insignificant in comparison to the inventory initially in place in the LCA or that is forecast to be transported to the LCA from the overlying unsaturated zone and saturated alluvial/volcanic rock units. Therefore, the Climax Mine detonations were not explicitly included in the transport models for Yucca Flat proper.

The contaminants forecast to be transported from their source in the unsaturated zone either directly to the underlying saturated LCA (in those areas in the western, northern, and eastern portions of Yucca Flat where the water table is in the LCA) or to the saturated alluvial/volcanic rock units (in those areas in central Yucca Flat where the water table is in the alluvium or volcanic rocks) are presented in Section 3.0 based on the source terms presented in Section 2.0. As discussed in Sections 3.0 and 6.4, the contaminant flux from the unsaturated zone to the LCA is concentrated under those detonations with exchange volumes that are close to the water table in the LCA. Most of the contamination from the unsaturated-zone sources is retained in the unsaturated zone because of the slow transport through this zone except in the vicinity of cavities underlying craters with significant crater recharge or for those cavities with exchange volumes close to the water table. Contaminant flux from the unsaturated-zone sources to the water table is generally insignificant in comparison to the mass of contaminants assumed to be initially in place in the saturated LCA or those contaminants that enter the LCA from the overlying saturated alluvial/volcanic rock units. This conclusion is particularly germane for the lower infiltration rate of 0.1 mm/yr in central Yucca Flat, where there is essentially no transport of contamination from the unsaturated-zone sources to the water table.

The contaminants forecast to be transported from their source in the saturated alluvial/volcanic rock units in the central portion of Yucca Flat are presented in Section 4.0 based on the source terms presented in Section 2.0 and the contaminants that are transported to the saturated alluvial/volcanic rock units from the overlying unsaturated-zone sources. As discussed in Sections 4.0 and 6.4, the contaminant flux from the saturated alluvial/volcanic rock units to the LCA is considered to be concentrated along the major faults in the central portion of Yucca Flat. This is a result of the thick tuff confining units between the working points and the LCA and/or the presence of clays and paleosols sealing fractures at the top of the LCA that preclude contaminants from migrating directly from the exchange volumes to the LCA. Instead, for those detonations with exchange volumes that directly intersect the fault damage zones, which are a small subset of the total saturated alluvial/volcanic rock detonations, the transport can occur directly down the fault to the LCA, which has a lower potentiometric surface than the overlying saturated volcanic rock units. A representative example of this phenomenon occurs near the BILBY detonation. For those detonations with exchange volumes that do not directly intersect faults, the contaminants are projected to migrate laterally in the aquifer until the travel path intersects the nearest fault, at which point the transport occurs downward

through the transmissive fault to the LCA. Even though it is possible to identify the areas with the greatest contaminant mass influx from the overlying saturated alluvial/volcanic rock units to the LCA as presented in Section 6.4, identifying the detonation(s) that most significantly contribute to the mass influx is only possible in the context of the results presented in Section 4.0.

The model results presented in this document provide a reasonable expectation that contaminants that originate from underground nuclear testing in the Yucca Flat/Climax Mine CAU are generally projected to be confined to the Yucca Flat basin. This is especially true for greater than 99 percent of the initial inventory that is contained in the closed hydrologic basin consisting of the unsaturated zone and the saturated alluvial/volcanic aquifer system. The hydrologic and transport data are sufficient to demonstrate the efficacy of flow and transport conceptual and numerical models in limiting releases to the regionally continuous LCA. For those contaminants that may enter the LCA, the vast majority of these are also retained in the Yucca Flat basin. The most significant of these contaminants, notably ^{3}H, ^{90}Sr, and ^{137}Cs, are naturally attenuated by decay in the next few hundred years. Other contaminants are contained within the Yucca Flat basin and have a low likelihood of being transported off of the NNSS. As a result of the above, the data and models are sufficient to allow estimation of the extent of contaminant migration in the Yucca Flat/Climax Mine CAU.

The following discussion summarizes the major results and conclusions of the flow and transport models presented in this document. This discussion is broken into the following topics:

- Source-term model
- Unsaturated-zone flow model
- Saturated alluvial/volcanic aquifer system flow model
- Saturated LCA flow model
- Unsaturated-zone transport model
- Saturated alluvial/volcanic aquifer system transport model
- Saturated LCA transport model
- Overall conclusions

The conclusions of the source-term model presented in this document (Section 2.0) may be summarized as follows:

- The conceptual model of the geometry of the test-altered zones of the exchange volume and data on radionuclide distribution within the exchange volume are appropriate to define the initial contaminant distribution for sources with working points in the different hydrogeologic domains (unsaturated zone, saturated alluvial/volcanic rock units, and saturated LCA).

- Initial contaminant concentrations in the cavities of underground nuclear detonations in Yucca Flat, as well as the their values relative to the radionuclide-specific SDWA MCLs, are significantly dependent on the radionuclides and whether the cavities extend into the saturated LCA. Initially, the concentration of ^{3}H in the cavity is about 10,000 times the MCL; however, this concentration decreases to about 10 times the MCL in 150 years. Initially, the ^{90}Sr concentration is about 500 times the MCL in the volcanic and alluvial units and about 2,000,000 times the MCL in the LCA. This dramatic difference is due to the difference in sorption behavior of ^{90}Sr in silicic versus carbonate rocks. The ^{90}Sr concentration decreases to 10 times the MCL in 200 years for the silicic sources and about 500 years for the LCA sources.

- Two alternative conceptual models, referred to as the uniform-mass allocation method and the uniform-concentration allocation method, have been developed. These alternatives address HST conceptual model uncertainty. The HST allocation method uncertainty, in combination with parametric uncertainty related to exchange volume sizes, glass fraction, and radionuclide inventory variability, provides an appropriate representation of HST uncertainty.

- Alternative conceptual models have been implemented for radionuclide allocation between the different HSUs. This conceptual uncertainty results in different fractions of the total initial inventory being assigned to the three model components. The uniform-mass allocation method results in 75 percent of the initial inventory in the unsaturated-zone domain, 25 percent in the saturated alluvial/volcanic aquifer system model domain, and less than 0.1 percent in the saturated LCA. The uniform-concentration allocation method results in about 58 percent of the initial volatile radionuclide (e.g., ^{3}H, ^{36}Cl, ^{90}Sr, ^{99}Tc, ^{129}I, ^{137}Cs) inventory in the unsaturated-zone domain, 41 percent in the saturated alluvial/volcanic aquifer system model domain, and about 1 percent in the saturated LCA. Uncertainty in the initial spatial distribution of contaminants for the uniform-mass allocation is developed considering the uncertainty in the size of the exchange volume based on the maximum unclassified yield range and resulting uncertainty in the geometric relationship of the vertical extent of the exchange volume in comparison to the elevations of the hydrostratigraphic surfaces and the water table.

- Uncertainty in the initial inventory has been addressed in the LCA source-term model by sampling from recommended distributions in Bowen et al. (2001). The Bowen et al. (2001) inventory was redistributed to reflect the actual working point and exchange volume location with respect to the water table, as opposed to apportioning the inventory based on an arbitrary surface located 100 m above the water table. These uncertainties can have a notable effect on the initial concentration at any particular detonation. For example, at BOURBON, the initial ^{3}H mass (or concentration) in the LCA can vary from a factor of 0.13 to 1.3 times the mass (or concentration).

- Uncertainty in the initial distribution of volatile precursors of mobile radionuclides has been evaluated by using a range of exchange volume sizes that are radionuclide dependent. The potential dilution associated with gaseous transport of volatile precursors, which would

tend to lower the initial contaminant concentration, has not been included in the base representations.

- Releases from the portion of the inventory initially in the melt glass are a small fraction of the total mobile inventory and are insignificant in defining the contaminant boundary even for bounding estimates of glass degradation rates. Uncertainty in the melt-glass fraction and the melt-glass dissolution rates is insignificant in comparison to uncertainty in the initial yield-weighted inventory assigned to an individual detonation.

The conclusions of the unsaturated-zone flow model presented in this document (Section 3.0) may be summarized as follows:

- The available data are used to define the hydrogeologic properties and boundary fluxes for determining the rate of water flux through the vadose zone.

- A prominent part of the development of the unsaturated-zone models for Yucca Flat involved characterizing the surface watersheds, geometry, and long-term (1,000-year) infiltration rates for the 459 surface subsidence craters that have been identified in Yucca Flat. Focused infiltration into the bottoms of subsidence craters due to surface runoff and ponding following precipitation events has been observed in a handful of craters in Yucca Flat and Frenchman Flat. These observations were used to calibrate the models of crater infiltration developed for the unsaturated-zone models.

- The craters on the periphery of the basin with large upland watersheds tend to receive the largest volume of surface runoff and consequently had some of the largest infiltration rates. Craters in the interior of the basin are shielded by outlying craters from runoff generated in the bordering hills, and these interior craters often have watershed areas not much larger than the craters themselves. Whereas infiltration rates in the outlying craters are modeled to have infiltration rates in excess of 1 m/yr, craters in the interior of the basin typically have modeled infiltration rates of 5 cm/yr or less.

- The long-term infiltration rates calculated for each of the 459 individual craters were applied to the appropriate nodes representing the crater bottoms in each of the 12 three-dimensional models used to represent the unsaturated zone of Yucca Flat in the testing areas. These rates were then held constant throughout the duration of the 1,000-year transient flow and transport simulation. Initial moisture conditions for each transient simulation were generated by running each of the 12 models long enough such that steady flow conditions were achieved for one of four uniform background infiltration rates: 0.1, 1, 5, and 10 mm/yr.

- The background or ambient infiltration rate most consistent with regional estimates derived with alternative methods (elevation-dependent chloride mass balance, modified Maxey-Eakin, and a distributed soil water budget model) and local evaluations of soil moisture profiles is less than 0.1 mm/yr. A value of 0.1 mm/yr was selected to represent this case. Alternative recharge rates of 1, 5, and 10 mm/yr were used to explore the potential effect of discrete

transient events or long-term pluvial responses. Although these background infiltration rates are larger than the rates that current models or measurements suggest are reasonable in the deep, alluvium-filled parts of the basin, these values were adopted to account for possibly larger (but as yet unmeasured) infiltration rates beneath arroyos and playas, possibly higher infiltration along the basin margins because of runoff from the surrounding hills, and the continued drainage of water that infiltrated during past pluvial periods at depth. The higher values are also consistent with other lines of evidence in the saturated-zone modeling.

- Because of differences in the hydrologic properties of HSUs and faults within the unsaturated-zone models, the estimated distribution of steady-state recharge at the water table is spatially variable even when infiltration is assumed to be uniform. Recharge at the water table becomes focused along faults with a resultant “rain shadow” effect downgradient from the faults when the ratio of vertical to horizontal permeability decreases in the tuff confining units. Low-permeability confining units also divert water laterally when crater infiltration rates exceed their vertical permeability.

- A range of alternative flow models have been developed and propagated to the evaluation of contaminant transport to reflect the uncertainty in properties (notably, anisotropy of the alluvium and tuff confining units) and boundary conditions (notably, infiltration rate and enhanced crater recharge). Alternative enhanced crater recharge models have been used to evaluate the significance of uncertainty in this process to contaminant transport.

The conclusions of the saturated alluvial/volcanic aquifer system flow model presented in this document (Section 4.0) may be summarized as follows:

- The saturated alluvial/volcanic aquifer system flow model has been calibrated to over 500 head measurements at 60 wells and has been used to explain over 90 percent of the variability in the observed heads.

- The available data have been used to develop alternative calibrated saturated-zone flow models that reproduce relevant observations, including post-testing transient water-level declines resulting from the dissipation of excess pressures that occurred due to the underground nuclear testing.

- A range of recharge rates may be used to develop reasonably calibrated flow models. This range extends from the present-day background infiltration rate of about 0.1 mm/yr to higher values of 1, 5, and 10 mm/yr to bound the potential effects associated with paleodrainage and local recharge events in arroyos. The higher values are consistent with calibrated values of permeability and independent lines of evidence such as the observed post-detonation subsidence in central Yucca Flat.

- A paleodrainage conceptual model has been developed as an alternative cause for the observed present-day potential difference between the saturated alluvial/volcanic aquifer system and the LCA. This alternative model results in an aquitard permeability of

about 1E-17 to 1E-16 m^2, which is consistent with values derived for a steady-state infiltration of about 0.1 mm/yr. As a result, this alternative would yield transport results similar to those simulated with this lower background infiltration rate.

- The presence of the test-induced overpressures and the subsequent slow decline in overpressures in the vicinity of some of the detonations with working points in the tuff confining units is indicative of the low permeability of the tuff confining units.

- An ensemble of alternative saturated-zone flow models have been developed to address uncertainty in the background percolation flux from the base of the overlying vadose zone, and hydrologic properties of the tuff confining units and volcanic aquifers. The alternative flow models consider a range of testing effects (damage zone extent and properties, and the magnitude and extent of test-induced overpressurization).

- The uncertain flow fields consider the faults to provide a hydraulic connection through the thick tuff confining units and assume that the lowermost confining units and/or paleosols at the top of the LCA are sufficiently impermeable to not allow water or contaminants to discharge to the underlying LCA except at the faults.

- The ensemble of saturated alluvial/volcanic aquifer system model results were corroborated by comparison to observed ground surface subsidence. Although no model reproduced the data in all locations, the range of model results bounded the observed data over a majority of the model domain.

- While it is noted that for detonations conducted in vitric-tuff aquifers and alluvial materials, the permeability in test-altered zones is generally reduced, and in welded-tuff aquifers and carbonate rocks, the permeability in test-altered zones is generally increased, there is uncertainty in the hydrologic properties of the test-altered zones for detonations conducted in zeolitic tuff confining units. To address this uncertainty, two alternative conceptualizations have been evaluated, one in which the altered zone in the zeolitic tuffs is considered to have an increased permeability, and the other in which the altered zone in the zeolitic tuffs is considered to have a reduce permeability. Both conceptualizations have been analyzed to evaluate the full spectrum of possible flow fields even though it is acknowledged that differences are likely to be detonation specific. That is, differences are likely to be due to, for example, different size detonations, different lithologies, or different depths.

- In addition to uncertainty in the hydrologic properties of the test-altered zones, there is uncertainty in the degree of overpressurization in the vicinity of cavities for detonations conducted in the tuff confining units. This uncertainty was addressed by using a range of overpressures in the saturated alluvial/volcanic aquifer system flow model.

- The saturated alluvial/volcanic rock units, although continuous outside the Yucca Flat basin, are offset by bounding faults of the basin. As a result, the groundwater flow from these units ultimately discharges into the LCA underneath Yucca Flat. This conceptualization is consistent with the early work on the hydrogeology of the Yucca Flat area by Winograd and

Thordarson (1975), more recent geochemical information indicating the presence of alluvial/volcanic water in the underlying LCA, and the conceptual model developed by Fenelon et al. (2012).

- Particle trajectories developed with the ensemble of saturated alluvial/volcanic aquifer system flow models indicate that there were slight differences in the distribution of cumulative particle arrivals to the underlying LCA; however, these analyses indicate that the degree of overpressurization significantly affected the particle outflow rate at specific detonation locations (e.g., BILBY).

- Although the thick tuff confining units above the LCA in most of the saturated section of Yucca Flat basin allow only the potential for insignificant diffuse leakage to the LCA except along throughgoing faults, alternative cases were developed to explore the possibility that test-induced permeability changes in the test-altered zones could allow for hydraulic connections to the LCA. In these cases, the post-detonation flow field is modified.

- Groundwater ^{14}C ages in the LCA indicate values generally ranging from 12,000 years in northern Yucca Flat to 30,000 years in southern Yucca Flat with the exception of younger ages in the vicinity of major crosscutting faults in the center of the basin. These younger ages, combined with other geochemical characteristics, are consistent with downward leakage through the faults cutting the tuff confining units.

- The post-detonation steady-state water flux to the LCA ranges from less than one to several tens of kilograms per second depending on the background recharge rate. The transient fluxes to the LCA associated with test-induced overpressures can be several tens of kilograms per second during the time of active testing. These values are consistent with observed subsidence data if it is assumed the subsidence is the result of consolidation of the saturated tuff confining units as opposed to consolidation of the overlying unsaturated alluvium.

The conclusions of the saturated LCA flow model presented in this document (Section 5.0) may be summarized as follows:

- Although limited direct observations exist of the groundwater flow regime in the LCA at Yucca Flat, the available steady-state and transient heads have been used with inferred ranges of hydraulic properties to develop groundwater flow models that are consistent with the observed ranges of properties and boundary fluxes.

- Groundwater flow directions and flow rates in the LCA flow model are generally consistent with inferred regional trends. The modeled flow directions are southerly approximately parallel to the strike of the major structural features.

- Groundwater flow directions are also consistent with inferred mixing relationships developed from analyses of LCA geochemical signatures. For example, the possible presence of mixed

tuff and carbonate waters in central Yucca Flat is consistent with the possible influx of tuff groundwater to the LCA along major faults that intersect the tuff confining units.

- The total volumetric flow out of the LCA, out of the Yucca Flat basin to the south (into the Frenchman Flat or CP basin) is consistent with the volumetric flow rates used in the Frenchman Flat CAU flow model even though significant uncertainty exists in the flow properties of the structural features in the accommodation zone between Yucca Flat and Frenchman Flat. The absence of a significant head decline across the accommodation zone indicates a good hydraulic connection between the Yucca Flat and Frenchman Flat basins.

- The calibrated boundary fluxes and hydraulic properties are consistent with inferences developed from other observations such as thermal and geochemical tracer information. Although there is uncertainty in the lateral influx to the LCA from north of Yucca Flat, with some researchers (notably, Belcher et al., 2004; Pohlmann et al., 2007) concluding this influx could be substantial (several hundred kilograms per second), while others (notably, Winograd and Thordarson, 1975; Halford, 2009) concluding there is very limited influx from north of Yucca Flat (on the order of a few kilograms per second), recent analyses including a draft revision of the DVRFS model (Faunt et al., 2012) and thermal analyses (Appendix H) indicate the lateral inflow into northern Yucca Flat is closer to the lower end of the inferred range, i.e., about 50 kg/s. The calibrated LCA groundwater flow model, which relies significantly on the calibration to the MWAT data, provides calibrated boundary influx values from northern Yucca Flat consistent with these values, i.e., about 50 to 100 kg/s.

- A spatial distribution of recharge to the saturated LCA has been used that is consistent with regional net infiltration data and associated estimates. This distribution consists of very low recharge rates (a few kilograms per second) in the central portion of the basin overlain by the saturated alluvial/volcanic aquifer system and higher recharge rates (on the order of 30 to 40 kg/s) in the southeast and southwest portions of the LCA model domain. The recharge in the central portion of the basin is consistent with the lower end of the average infiltration rates used in the unsaturated-zone flow model.

- The calibrated boundary fluxes in the groundwater flow model, in particular the influxes from the north and the vertical recharge along the major faults in central Yucca Flat, are consistent with values derived from analyses of the available temperature data, as presented in Appendix H.

- The alternative HFMs did not significantly affect the groundwater flow regime in the LCA. However, the postulated hydrologic significance of the proposed alternative HFMs has been incorporated through the use of alternative hydrologic boundary conditions. In essence, this implies that the uncertainty in groundwater flow within the LCA at Yucca Flat that has been postulated to be due to HFM uncertainty can be addressed through the use of alternative boundary conditions.

- The transmissive characteristics of the major faults in central Yucca Flat are consistent with general inferences of fault hydrogeologic characteristics derived from other faulted carbonate

rocks, namely, a disturbed zone of higher permeability on the hanging and footwalls of the fault and a low-permeability central "core." These characteristics are also consistent with the observed hydrologic response during the MWAT at ER-6-1, where the drawdowns induced by the pumping propagated rapidly along the strike of the faults and did not propagate across the strike.

- Available data have been used to define the geometric characteristics of the major and minor faults and to parameterize the fault properties. The faults have been modeled as relatively wide fault zones, with a central low-permeability core surrounded by a permeable disturbed zone. Uncertainty in the fault geometry has been explored with several alternative representations, including (1) a thinner damage zone and no core zone, (2) a thinner damage zone with core zones, and (3) a thinner accommodation zone in southern Yucca Flat.

- Although the infiltration rate across Yucca Flat has been determined to be spatially variable, with very low values in central Yucca Flat and higher values along the higher elevation margins of the basin, a uniform distribution has been adopted for use in the unsaturated-zone flow model. The percolation flux at the base of the unsaturated-zone model (equivalent to the recharge flux at the top of the water table) is spatially variable because of lateral flow resulting from anisotropy and structural features included in the unsaturated-zone flow model. However, recharge to the LCA is constrained to occur along the major faults that cut the tuff confining units. Therefore, the actual surficial spatial distribution does not significantly affect the results because the volumetric water flux is applied consistently across the model domain boundaries.

- Although significant groundwater discharge has occurred from the LCA in Yucca Flat in the past, notably, during the time of significant underground nuclear tests in the 1960s to 1980s, and the LCA is still a source of groundwater for some limited NNSS uses, these groundwater withdrawals do not significantly affect the groundwater flow direction or rates in Yucca Flat. It may be that the significant pumping in the past may have affected the potentiometric surface during the pumping, but there were insufficient head observations made during that time period with which to constrain the flow model.

- As presented in Section 4.0, transient test-induced phenomena are significant in the evaluation of groundwater flow and contaminant transport in the saturated volcanic rock units above the LCA. There were time periods during testing that the calculated water influx to the LCA from the saturated volcanic rock units from a single test or a series of tests exceeded the average vertical recharge across the entire basin. Although short lived (on the order of a few years at any particular location and a total duration of a few decades during the time period of intense underground nuclear testing), this transient water influx does not significantly affect the overall flow regime in the LCA because of the relatively short duration of the transient pulse and the high permeability of the LCA. After the period of underground nuclear testing, the recharge rate returned to essentially the pretesting rates, with the exception of the increased local recharge under some craters. These transient fluxes were found to not significantly affect the groundwater flow regime in the LCA.

- It is interesting to note that the calculated cumulative water influx to the LCA associated with underground nuclear testing is of the same order of magnitude as the groundwater withdrawal from the LCA in the Yucca Flat area during the three decades of underground nuclear testing. Regardless, neither of these impacts on the LCA water budget during the decades of underground nuclear testing has resulted in any observed changes in the potentiometric surface, and neither of the impacts has had any lasting effects on the modeled LCA flow regime.

- The increased recharge associated with crater-enhanced recharge evaluated in Section 3.0, while affecting the migration of some radionuclides from some underground cavities to the LCA, does not significantly alter the recharge to the LCA. The long-term steady-state recharge when averaged over the entire modeled domain was calculated to increase by less than 5 percent from the pretesting conditions. This small increase is a function of the small area encompassed by the crater footprints.

The conclusions of the unsaturated-zone transport model presented in this document (Section 3.0) may be summarized as follows:

- The available data of effective transport properties have been used to characterize the amount of contaminants that are possible to be transported to the saturated zone underlying Yucca Flat, considering the uncertainty in these transport parameters and their significance to the calculated contaminant flux. Uncertainty in the water flux is more significant than uncertainty in transport properties in affecting the calculated contaminant flux.

- Because unsaturated-zone pore water is not part of the calculated contaminant boundary for Yucca Flat, the primary role of the unsaturated-zone models is to estimate where, when, and how much of the radionuclide inventory initially in the unsaturated zone reaches the water table. The mass of water and radionuclides reaching the water table is then post-processed and put into a format that can be used by the saturated-zone models for the volcanic and carbonate aquifers so that these models can include the radionuclide sources from the unsaturated zone as well as their own radionuclide sources in their contaminant boundary calculations.

- Combinations of background and crater infiltration rates, sediment and tuff anisotropy, tuff effective porosity, exchange volume size, and the existence or absence of high-permeability collapse chimneys were examined to determine their influence on the rates and magnitude of radionuclide transport to the water table.

- Contaminant releases from the unsaturated zone to the water table are insignificant for the expected infiltration rate of 0.1 mm/yr. Even for higher background infiltration rates, the fraction of initial inventory that is retained or decays in the unsaturated zone yields only a small fraction of the initial inventory being released to the water table in either the saturated alluvial/volcanic aquifer system or the saturated LCA.

- The sensitivity analysis indicated that the radionuclide mass arriving at the water table increases with increasing background and crater infiltration rates, smaller effective porosities in the tuff confining units, larger ratios of vertical to horizontal permeability in the tuffs and sediments, and smaller exchange volumes. The inclusion of high-permeability, low-porosity rubble zones associated with collapse chimneys results in some earlier breakthrough over 1,000 years when compared with identical cases where chimneys are assumed to be absent, but the overall effect is small compared with that caused by variability in other parameters. Likewise, changes in the effective porosity or vertical permeability in the tuffs produce relatively small changes in the radionuclide flux because the tuff confining units are either thin or absent between majority of the detonations and the water table.

- Most (approximately 90 percent) of the radionuclide mass arriving at the water table for any particular unsaturated-zone flow case reaches the saturated tuffs or alluvium rather than the saturated LCA. This is a consequence of the fact that most unsaturated-zone detonations are located near the center of the basin where the water table is in the tuffs, rather than on the periphery of the basin where the water table is in the carbonate aquifer.

- For ^{3}H, ^{14}C, ^{36}Cl, ^{129}I, and total U, most water-table locations where recharge exceeds the SDWA standards for beta-emitting radionuclides are where the exchange volumes of the detonations essentially intersect the water table. Recharge at later times arrives at concentrations that are less than the SDWA standards because contaminated water initially in the exchange volume has been mixed with and diluted by radionuclide-free water moving downward from the crater bottom. For the cases with exchange volumes of 2 R_c or larger, neither ^{237}Np nor ^{99}Tc is modeled to arrive at the water table at concentrations exceeding the SDWA standards, even at locations where the exchange volumes intersect the water table.

- For the uniform-mass allocation method, the detonations and resulting exchange volumes that intersect the water table generally provide the most significant flux to the water table because of their close proximity to the water table and the assumed background percolation flux. These detonations include BOURBON, TORRIDO, KANKAKEE, and SHUFFLE. Although significant downward percolation flux can exist under craters with enhanced recharge, there are few craters with sufficient enhanced recharge to significantly increase the rate of contaminant flux to the water table during the 1,000-year regulatory time period.

- Most of the contaminants initially in place in the unsaturated zone remain or are decayed within the unsaturated zone during the next 1,000 years. More mobile, longer-lived radionuclides are transported to the water table where they may contribute to the forecast contaminant boundary in the alluvial/volcanic aquifer system and the LCA.

- The contaminant release from the unsaturated zone directly to the LCA is insignificant in comparison to the contaminant release from the saturated alluvial/volcanic aquifer system.

- Transport of ^{90}Sr and ^{137}Cs is significantly retarded in the unsaturated zone so that the release of these radionuclides to the saturated LCA is insignificant. This is in contrast to the concentrations of these radionuclides initially in place in the saturated LCA.

- The use of an effective transport porosity as opposed to a dual porosity conceptual model with matrix diffusion is deemed appropriate given the goal of calculating the mass flux to the underlying saturated HSUs.

- Uncertainty in contaminant transport to the water table is considered by evaluating a range of alternative flow models, source terms, and transport parameters. The transport parameters evaluated include the effective porosity of the tuff confining units.

The conclusions of the saturated alluvial/volcanic aquifer system transport model presented in this document (Section 4.0) may be summarized as follows:

- The available transport data have been used to define a range of forecast contaminant boundaries and contaminant fluxes to the underlying LCA.

- Contaminants that are initially within the saturated alluvial/volcanic rock units or that enter the saturated zone by downward percolation from the overlying unsaturated-zone sources generally remain within the saturated zone. This is especially relevant for the expected recharge rate of 0.1 mm/yr.

- Mobile, longer-lived radionuclides may be transported downward to the underlying LCA along major faults that intersect the aquifers and confining units; however, these releases are generally insignificant. Generally, less than 5 percent of the mass fraction that is initially in place in the saturated zone or that enters the saturated zone from the vadose zone is transported to the LCA in 1,000 years even for the extreme bounded recharge rates. There is remarkably little variation in this total fraction estimate given the wide range of parameters and conceptual models considered. Additionally, in most cases, only a small subset of the detonations contributes significantly to the contaminant flux to the LCA (see below).

- Only a small number of detonations contribute significantly to contaminant flux from the saturated alluvial/volcanic aquifer system to the underlying LCA. Generally, the contaminants that are transported to the underlying LCA are from underground nuclear detonations with exchange volumes that are close to or intersect the faults that are assumed to provide hydraulic connection through the tuff confining units. These detonations include BILBY, LUBBOCK, TORTUGAS, WAGTAIL, and CALABASH. Most of the contaminants in detonations that are several hundred meters away from faults have sufficiently long residence times in the aquifers or tuff confining units, so they decay or are retained in the saturated alluvial/volcanic rock units.

- Uncertainty in contaminant flux rate from the saturated alluvial/volcanic rock units to the LCA has been evaluated. The most significant uncertainties are the conceptual model and hydraulic characteristics of the damage zone around the underground nuclear detonation, the recharge rate from the overlying unsaturated-zone flow model, the hydraulic properties of the tuff confining units, and the fracture porosity of the welded-tuff aquifers. Considering the spatial distribution of detonations contributing to contaminant flux, these uncertainties are

generally irreducible. That is, even if additional information is acquired in the vicinity of a specific detonation, the extrapolation of this information (e.g., characteristics of the damage zone) to other detonation locations would be uncertain, and this uncertainty would need to be included in the assessment of contaminant transport.

- Comparisons of measured and modeled ^{3}H were made for wells that were completed in the saturated zone and were sufficiently far (approximately 300 m) from the cavity/chimney systems for the simulation results to be meaningful. For the seven wells meeting these criteria, simulation results and measurements agreed quite well.

The conclusions of the saturated LCA transport model presented in this document (Section 6.0) may be summarized as follows:

- A range of contaminant boundaries in the LCA compliant with the FFACO requirements have been developed that incorporate uncertainties in the LCA flow model, LCA source term, contaminant influx to the LCA from the overlying unsaturated zone and saturated alluvial/volcanic rock units, and LCA transport parameters. These contaminant boundaries indicate that the contamination is generally contained within the Yucca Flat/Climax Mine CAU.

- The model results indicate a generally southerly migration of contaminants that may enter the LCA from detonations with exchange volumes that are close to or straddle the saturated LCA or that are near faults with assumed hydraulic connection to the LCA. The extent of contaminant migration is a function of the uncertainty in the fracture properties of the major faults and the conceptualization of the LCA flow field.

- Comparisons of the spatial distribution of ^{14}C ages and $^{36}Cl/Cl$ ratios in LCA groundwater indicate that the ^{14}C is generally not sorbed and is considered to be transported conservatively with other non-sorbing species such as ^{36}Cl. The rate of transport is about 2 m/yr. This rate of transport is consistent with the lower end of the permeability and flow rate distributions in the LCA. However, in order to evaluate a wide range of possible hydrologic conditions and groundwater velocities, the groundwater velocities estimated by ^{14}C ages were not used to constrain the LCA groundwater flow and transport models.

- Although some realizations indicate the potential for contaminants in excess of the SDWA MCLs to leave the southern boundary of the Yucca Flat/Climax Mine CAU, the probability of this is generally less than 10 percent. These realizations represent the low-probability (less than 10%) tails of the key transport parameters for the more conservative modeling cases such as the base case. Less conservative conceptual models such as the alternative northern boundary flux LCA flow model and the LCA transport models using either alternative Sr and Cs sorption coefficients, alternative fault damage zone fracture porosities, or alternative scale-dependent matrix diffusion do not result in contaminants in excess of the SDWA MCLs leaving the southern boundary of the model domain. These low-probability (i.e., less than 10 percent) realizations indicate the low possibility of some contaminants in excess of the

SDWA MCLs entering the Frenchman Flat CAU, as the flow system in the LCA is considered to be continuous across the accommodation zone under Massachusetts Mountain. However, it is noted that the MCL exceedance is dominated by short-lived radionuclides, notably, ^{90}Sr, that decay to insignificant values in a few hundred years.

- The potential significance of colloidal transport of ^{239}Pu was evaluated and determined to be insignificant in comparison to the extent of contamination associated with non-sorbing radionuclides such as ^{3}H, ^{90}Sr, and ^{137}Cs.

- Several assumptions in the LCA flow and transport models tend to overestimate the extent of contaminant migration in the LCA. For example, the assumption that there is no spatial scaling of transport properties and that uniform properties exist throughout the model domain overemphasizes the importance of the tails of the distributions. This assumption maximizes the probability that the forecast contaminant concentration will exceed the SDWA MCL.

- Even though the groundwater flow regime in the LCA is continuous from Yucca Flat to the presumed discharge of the LCA groundwater in the Ash Meadows flow system and/or the Alkali Flat-Furnace Creek Ranch flow system (Fenelon et al., 2010), contaminant levels in excess of the SDWA MCLs are not expected to extend south of the Yucca Flat/Climax Mine CAU model boundary. However, contaminants are likely to be transported in the LCA flow system from Yucca Flat to Frenchman Flat to the Rock Valley fault zone, and ultimately to the discharge, albeit at concentrations below the SDWA MCLs.

- Although contamination from underground nuclear testing conducted in the Yucca Flat/Climax Mine CAU is forecast to extend into the LCA and then be transported in a generally southerly direction in the LCA, the vast majority of contamination initially in place in the CAU is modeled as being retained in the unsaturated zone and saturated alluvial/volcanic rock units above the LCA. The cause of this is principally the result of the immobility of a large fraction of the inventory in the melt glass as well as the slow release and transport of the mobile fraction of the inventory due to (1) the large distance between the exchange volumes and the water table in the LCA, (2) the low permeability and significant thickness of the tuff confining units between the exchange volumes and the LCA and (3) the low amount of water flux through the unsaturated zone and the saturated alluvial/volcanic rock units.

- The forecast contaminant boundary in the LCA has three principal components associated with the three different sources of contaminant flux to the LCA. The first component relates to contaminant sources from detonations with exchange volumes that are assumed to initially extend into the saturated LCA. The contaminant boundary associated with these sources is controlled by the mobility of ^{3}H, ^{90}Sr, ^{137}Cs, and ^{63}Ni. The second component relates to contaminant sources from detonations with exchange volumes in the saturated alluvial/volcanic rock units that are close to major faults that intersect the tuff confining units. The contaminant boundary associated with these sources is controlled by the mobility of short-lived ^{3}H and long-lived ^{129}I, ^{99}Tc, and ^{36}Cl. Contaminant sources from detonations with

exchange volumes in the unsaturated zone that overlies the water table in the LCA are insignificant contributors to the extent of the forecast contaminant boundary in the LCA.

- Contaminants forecast to be released from the Climax Mine nuclear tests and transported to the LCA that surrounds the Climax stock are an insignificant contributor to contaminant migration in the LCA in Yucca Flat. This is a result of their low initial inventory and the slow release of the non-sorbing radionuclides through the fractured granitic stock.

- If alternative assumptions are made about the potential sorption of ^{90}Sr, ^{137}Cs, and ^{63}Ni on the carbonate minerals and other impurities in the LCA, then the forecast extent of contamination associated with LCA sources would be reduced. However, the magnitude of the reduction is not significant given the presence of the ^{3}H fractional contaminant exceedance that dominates when ^{90}Sr, ^{137}Cs, and ^{63}Ni are assumed to be sorbed. Based on the low concentrations of these radionuclides in near-field contaminated wells that penetrate the LCA (e.g., the NASH satellite well at UE-2ce), one might conclude that these radionuclides should be considered sorbed in the LCA.

- The total contaminant exceedance volume in the LCA is most affected by underground nuclear detonations with exchange volumes that are assumed to intersect the saturated LCA as well as detonations with working points in the saturated alluvial/volcanic rock units. The unsaturated-zone sources, although comprising about 61 percent of the total inventory in the Yucca Flat/Climax Mine CAU for the uniform-mass allocation method, have little significance to the extent of the contaminant boundary in the LCA. The exceedance volume is most affected by mobile short-lived radionuclides such as ^{3}H, ^{90}Sr, and ^{137}Cs.

- The forecast contaminant boundary in the LCA is controlled by less than 10 of the 747 underground nuclear detonations conducted in the Yucca Flat/Climax Mine CAU as discussed in the following bullets.

- For the LCA sources, the forecast LCA contaminant exceedance volume is controlled by the SHUFFLE, CORDUROY, TORRIDO, and BOURBON detonations, and the forecast southern extent of contamination is controlled by the TORRIDO and BOURBON detonations. The significance of these detonations is related to the larger fraction of their exchange volumes that are assumed to breach the water table in the LCA.

- For the saturated alluvial/volcanic rock unit sources, the forecast LCA contaminant exceedance volume and southern extent of contamination are controlled by releases from a few detonations located within a few hundred meters of the Yucca fault, including CALABASH, LUBBOCK, and TORTUGAS, and nearby faults, such as BILBY. The significance of these detonations is related to their proximity to the major throughgoing faults that provides for hydraulic connection across the tuff confining units.

- For the unsaturated-zone sources, the forecast LCA contaminant exceedance volume is controlled by the releases from the KANKAKEE and BOURBON detonations. The significance of these detonations is related to their proximity to the water table in the LCA.

- Detonations conducted in the unsaturated zone, even though they comprise about 61 percent of the total inventory assuming the uniform-mass allocation method, contribute little to the extent of contamination in the LCA. This is a result of the relatively long transit times through the unsaturated zone except in the few cases with either a high crater recharge or the working point of the detonation close to the LCA water table. The long transit times allow for significant decay of ^{3}H prior to release to the LCA. In addition, for the portion of the unsaturated-zone sources that are released to the water table in the alluvial/volcanic rock units in the central portion of the Yucca Flat, the additional transit time in these units delays and disperses the releases to the LCA. The volcanic rocks and alluvium strongly adsorb radionuclides such as ^{90}Sr and ^{137}Cs that may be mobile in the LCA.

- Alternative calibrated LCA flow models were developed to explore the potential impacts of flow model uncertainty on contaminant transport in the LCA. The alternative flow models did not significantly affect the lateral extent of contamination in the LCA.

- Fracture porosity and fracture aperture (or spacing) were determined to be the LCA transport parameters that most significantly affected the likelihood that the forecast contaminant concentration would exceed the SDWA MCL along the likely groundwater travel paths. This is a result of the uncertainty in these parameters and the fact that these parameters control the degree of advective transport and amount of matrix diffusion along the contaminant travel path (decreased fracture porosities increase the advective transport, and increased fracture apertures or spacings decrease the amount of matrix diffusion).

- Major faults control the extent of contaminant migration in the LCA. This is a result of the significant groundwater flux and relatively high velocities in the damage zone of faults that tend to increase the lateral extent of contaminant migration, as well as the contaminant flux that occurs through these same faults that provide a hydraulic communication through the tuff confining units. Uncertainty in the fault-zone flow and transport characteristics, such as permeability, fracture porosity, and fracture aperture, significantly affects the forecast contaminant boundary.

- The forecast contaminant concentrations in the vicinity of the NASH underground nuclear detonation are similar to the observed concentrations in the NASH satellite well at UE-2ce and the detailed source-term modeled results for the case when the NASH inventory was assumed to be transported rapidly to the LCA because of drainage in the chimney/cavity region. The observed ^{3}H concentration at UE-2ce ranges from several thousand to several hundred times the SDWA MCL of 20,000 pCi/L for several years following the detonation performed in 1967 (SNJV, 2006b, Figures 6-11 to 6-13). The results illustrated in Figure 6-69 indicate concentrations exceeding the SDWA MCLs in the vicinity of the NASH detonation up to 50 years after the completion of the detonation.

- The forecast contaminant concentrations in the vicinity of the BILBY underground nuclear detonation are consistent with the observed minimal concentrations in the satellite well that penetrates the LCA in the vicinity of this detonation, U-3cn-5 for the infiltration case of 0.1 mm/yr. However, for cases with higher infiltration rates, the forecast contaminant

concentrations for several key radionuclides, including ^{3}H and ^{129}I, significantly exceed the SDWA MCLs at the location of the satellite well, far in excess of the observed concentrations. While it is possible that these differences could be an indication that the lower infiltration rate case is more reasonable, it is also possible that U-3cn-5 did not intersect permeable features in the LCA that are more likely to transport the contaminants away from the detonation location. This could be a result of the fact that this well penetrates only the upper 60 m of the LCA, and the fractures and other discontinuities in the upper portion of the LCA are sealed by alteration products developed in this portion of the LCA, or that the permeable features are essentially vertical and have been missed in this borehole.

- The forecast contaminant concentrations in the vicinity of the BOURBON underground nuclear detonation are not consistent with the observed concentrations in the satellite well that penetrates the LCA in the vicinity of this detonation, UE-7nS. The forecast contaminant concentrations for several key radionuclides, including ^{3}H, ^{90}Sr, and ^{137}Cs, significantly exceed the SDWA MCLs at the location of the satellite well, while the observed concentrations are significantly less than the SDWA MCLs (with the exception of ^{3}H) (SNJV, 2007, Figure 6-15; Tompson, 2008, Figure B.4, Appendix D). While it is possible that these differences could be an indication of the unreasonableness of the transport model in the vicinity of this detonation, it is also possible that the satellite well did not intersect permeable features in the LCA that are more likely to transport the contaminants away from the detonation location. This could be a result of the fact that this well penetrates only the upper 170 m of the LCA, and the fractures and other discontinuities in the upper portion of the LCA are sealed by alteration products developed in this portion of the LCA, or that the permeable features are essentially vertical and have been missed in this borehole.

- Composite contaminant boundaries have been developed for the range of likely alternative conceptual models. The time-cumulative contaminant boundary is most significantly affected by the contaminant transport from non-sorbing, short-lived radionuclides, notably, ^{3}H, ^{90}Sr, and ^{137}Cs. Once these radionuclides decay, the extent of the boundary is significantly reduced. The contaminant boundaries are also reflective of the tails of uncertain contaminant transport parameter distributions. The range of contaminant boundaries confirm the assertion that the identified base case conservatively maximizes the extent of contaminant transport as the other flow and transport models result in boundaries that do not extend to the southern modeled boundary.

Based on the above, the overall conclusions that can be drawn from the analyses presented herein may be summarized as follows:

- The strategy adopted in the Yucca Flat/Climax Mine CAU flow and transport modeling was to not underrepresent the possible extent of contaminant migration. This strategy was adopted to address the uncertainty in conceptual models and parameter distributions. The impacts of the conservative assumptions were evaluated to determine their significance to the forecast contaminant boundary.

- Although uncertainty exists in the source term, as well as the flow and transport models and the associated flow and transport parameter values, there are sufficient data to define the expected range of possible forecast contaminant boundaries. These data include CAU-specific information on geologic and hydrogeologic conditions developed from observations made during and after the underground nuclear tests in the Yucca Flat/Climax Mine CAU, as well as inferences derived from other areas of the NNSS and analog information from other sites, such as WIPP. Of particular importance have been the large-scale tests performed at the ER-6-1 MWAT and the transient potentiometric observations in the Tuff Pile.

- Although there is uncertainty in the flow and transport from the contaminant sources in the Climax Mine, which comprise less than 0.1 percent of the total contaminant inventory in the CAU, a range of contaminant fluxes have been calculated from the Climax Mine model (Pohlmann et al., 2007). These calculated fluxes are insignificant in comparison to other sources of contamination in the saturated LCA transport model and therefore do not affect the forecast of the contaminant boundary.

- Although there is uncertainty in the flow and transport from the contaminant sources in the unsaturated zone, which comprise about 61 percent of the total contaminant inventory in the CAU for the uniform-mass allocation method and 56 percent of the total contaminant inventory for the uniform-concentration allocation method, a range of contaminant fluxes have been calculated from the unsaturated-zone model. These calculated fluxes are appropriate for use in saturated-zone models (of the alluvial/volcanic aquifer system and the LCA) used to forecast the contaminant boundary. The calculated fluxes err on the side of overprediction, in particular with respect to the background infiltration rate, the crater recharge rate, and the size of the exchange volume for volatile radionuclide precursors.

- For the low infiltration rate cases (on the order of 0.1 mm/yr), essentially no contaminants are released from the unsaturated zone to the water table. Even for higher infiltration rates (on the order of 1 to 10 mm/yr), insignificant amounts of contaminants are released from the unsaturated zone to the water table. The unsaturated-zone sources, therefore, do not contribute to the forecast contaminant boundary extent.

- Although there is uncertainty in the flow and transport from the contaminant sources in the saturated alluvial/volcanic rock units, which comprise about 39 percent of the total contaminant inventory in the CAU for the uniform-mass allocation method and 43 percent of the total contaminant inventory for the uniform-concentration allocation method, a range of contaminant fluxes to the saturated LCA have been calculated. Even for the highest modeled recharge rate, most (about 90 percent) of the contaminant mass is retained in the saturated alluvial/volcanic aquifer system. Except at infiltration rates of 5 mm/yr or larger, the contaminant transport from the saturated alluvial/volcanic rock units to the LCA is insignificant in comparison to the mass assumed to initially be in place in the LCA.

- The presence and characteristics of faults that intersect the tuff confining units and provide a potential hydrologic connection to the underlying LCA are significant contributors to the likelihood and amount of contaminant flux into the LCA. Because of the unique setting of the

saturated alluvial/volcanic rock units in the Yucca Flat basin, there is no hydrologic communication possible outside the basin. That is, the only process by which contaminants in the saturated alluvial/volcanic rock units can exit the Yucca Flat basin is by downward flow and transport to the underlying LCA, and the subsequent lateral flow and transport in the LCA to the south/southwest.

- The conceptual model of LCA groundwater flow and contaminant transport is appropriate to define the extent of contaminant transport in the LCA in the Yucca Flat/Climax Mine CAU. Uncertainty in the conceptual model has been addressed by the use of alternative representations of the LCA groundwater flow and contaminant transport parameter distributions. The base-case representation was conservatively chosen to ensure that the forecast contaminant boundary was not underestimated. Alternative models indicate less extensive contaminant boundaries.

- Significant uncertainty exists in the hydraulic continuity of the LCA in northern Yucca Flat. As a result, two end-member conceptual models have been evaluated, one assuming lateral hydraulic continuity (as assumed in the DVRFS model developed by Belcher et al. [2004]), and the other assuming limited lateral hydraulic continuity (as inferred from the early work of Winograd and Thordarson [1975], and the more recent conceptual model described in Fenelon et al. [2012]). The significance of these alternatives has been evaluated. Again, because the conceptual model that assumes lateral hydraulic continuity leads to a more laterally extensive contaminant boundary, it is conservatively included in the base-case representation.

- Only a handful of detonations significantly affect the extent of contaminant migration and the forecast contaminant boundary in the LCA. Of greatest significance are a few detonations with exchange volumes that extend below the top of the saturated LCA, notably, BOURBON, TORRIDO, SHUFFLE, and CORDUROY. Of lesser significance are detonations near faults or near the top of the saturated LCA, or detonations assumed to have a high initial overpressure, notably, BILBY, CALABASH, LUBBOCK, and TORTUGAS. Of even lesser significance are detonations with working points in the unsaturated zone, except for those detonations in the unsaturated LCA, notably, BOURBON and KANKAKEE.

- Observation wells have been placed downgradient from several of the important detonations noted above. In particular, UE-7nS is 137 m from BOURBON, ER-7-1 is 200 m from TORRIDO and 500 m from MICKEY, U-3cn-5 is 129 m southeast of BILBY, and UE-2ce is 183 m from NASH. Observed radionuclide concentrations in these boreholes (see Table D-1) tend to support the models of flow and transport for certain cases as follows:

  - UE-7nS indicates slight contamination (several hundred to several thousand picocuries per liter of ^{3}H), while the model results indicate contamination at this location of greater than the MCL 20,000 pCi/L for ^{3}H. This discrepancy could be because the actual exchange volume size is less than the modeled exchange volume size based on the maximum announced test yield or because conductive features in the LCA have been missed by this borehole.

- ER-7-1 indicates no contamination, while the model results indicate contamination at this location of greater than the MCL of 20,000 pCi/L for ^{3}H. This discrepancy again could be because the actual exchange volume size is less than the modeled exchange volume size based on the maximum announced test yield or because conductive features in the LCA have been missed by this borehole.

- U-3cn-5 indicates no contamination, which is consistent with the model results when a recharge rate of 0.1 mm/yr is assumed or when the BILBY overpressures are assumed minimal. However, alternative modeling cases that assume high overpressures for the BILBY detonation and a high value for the recharge rate (i.e., 1, 5, or 10 mm/yr) yield significant contamination (above the MCL for ^{3}H) at U-3cn-5. This discrepancy may be indicative that the recharge rate of 0.1 mm/yr is most reasonable; however, it cannot be ruled out that conductive features in the LCA have been missed by this borehole.

- UE-2ce indicates significant contamination (5 to 10 times the ^{3}H MCL), which is consistent with the model results when local recharge rates are set high (1 mm/yr or greater) or when the effects of drill-back fluid losses and chimney drainage are included in the model. These results could indicate that the infiltration rate near NASH is at the higher end of the distribution (which may be because of the higher elevation and presence of arroyos near NASH) or that local drainage of perched zones down the NASH chimney or drill-back fluid losses are more significant at this location.

- ER-2-1 is located in close proximity to a number of detonations with working points in the tuff confining units. The lack of any significant contamination at this observation well supports the limited lateral contaminant transport from these detonations.

- It is noted that in almost all cases, routine sampling focused on what were believed to be a few key radionuclides that would act as tracers of potential contamination, most notably, ^{3}H. It has been rare to sample other potentially significant radionuclides such as ^{90}Sr and ^{137}Cs.

- There are other wells in Yucca Flat that penetrate areas of interest and may be suitable for model evaluation or monitoring, for example, WW A, HTH-2 (WW-2), Test Well B Ex. (TW-B), TW D, WW C, and WW-C-1. Slightly elevated ^{3}H measurements (about 10 to 100 pCi/L) have been observed at WW A, Test Well B Ex. (TW-B), WW C, and WW-C-1. The source of these elevated values cannot be determined with certainty. However, it is likely that, for example, the elevated values at WW C and WW-C-1 are the result of a terminated tracer test initiated by USGS in 1964 where 0.1 to 0.2 Ci of ^{3}H was released into WW C.

As noted in Section 1.0, the purpose of this document is to address the FFACO requirements related to the CAI phase of the UGTA corrective action strategy. As noted in the Appendix VI, Revision No. 4, of the FFACO (1996, as amended), the UGTA corrective action strategy consists of a technical basis for achieving the strategy, discrete goals to be achieved by the flow and transport models,

definitions of the necessary outputs of the contaminant transport models, technical requirements for the development and implementation of the flow and transport models, and roles and responsibilities of NNSA/NSO and NDEP in the use of the flow and transport model results for regulatory decisions. Each of these requirements has been addressed through the process of developing and implementing the flow and transport models for the Yucca Flat/Climax Mine CAU as documented in this report. Table 7-1 summarizes the FFACO requirements and how each requirement has been addressed in this document or related supporting documents. In addition, Appendix A provides a summary of the quality assurance requirements of the UGTA Quality Assurance Project Plan (NNSA/NSO, 2011) and how those requirements have been addressed in the work products supporting this document.

The specific requirements for the CAU flow and transport models as identified in the FFACO (1996, as amended) and where they are addressed in this document are presented in the Table 7-1.

Table 7-1
Addressing FFACO UGTA Corrective Action Strategy Requirements for CAU Flow and Transport Models in the Yucca Flat/Climax Mine CAU Flow and Transport Model Document
(Page 1 of 5)

FFACO (1996, as amended) Requirement	How the FFACO Requirement is Addressed
The technical basis for achieving the UGTA strategy is through an evaluation of each CAU using a combination of approaches, including the following: 1. Data collection consisting of, but not limited to, drilling exploration, hydrologic testing, and field and laboratory studies designed to characterize the hydrogeological setting 2. Modeling of the hydrogeological setting, the radiological source term, and flow and contaminant transport to forecast areas of current and future contamination for 1,000 years 3. Iterative model evaluations and monitoring of groundwater near and downgradient of areas of past underground testing 4. Identification and documentation of land-use policies (institutional controls) designed to restrict future public access to groundwater contaminated by underground testing	The data collection aspect related to the Yucca Flat/Climax Mine CAU is summarized in the Yucca Flat/Climax Mine hydrologic data document (HDD) (SNJV, 2006b) and the Yucca Flat/Climax Mine transport data document (TDD) (SNJV, 2007), and has been supplemented by additional data and analyses presented in this document. The data related to the hydrogeologic and hydrostratigraphic units in the Yucca Flat/Climax Mine CAU as well as the modeling of the hydrogeologic setting are documented in BN (2006). Modeling of the RST and HST is documented in McNab (2008), Pawloski et al. (2008), Tompson (2008), and SNJV (2009b), and has been supplemented by additional analyses presented in this document. Modeling of the hydrogeologic setting, and groundwater flow and contaminant transport to forecast areas of current and future contamination for 1,000 years is presented in this document. The subsequent approaches, namely, iterative model evaluations, monitoring of groundwater, and the identification of institutional controls to restrict future public access, are activities that are planned to commence in the CADD/CAP phase of the UGTA strategy.
The goal of the four combined approaches is to provide the data, model forecasts, and confidence in the model results to facilitate informed regulatory decisions by NDEP and NNSA/NSO. The goal of regulatory decisions is to protect the public and the environment from the risk of radiologically contaminated groundwater. Risk to human health and safety in this context is defined as the combined probability of exposure to groundwater contamination, which is identified through model forecasts of probabilistic contaminant boundaries, and the consequences of this exposure. The consequences of exposure will be based on the radiological standards of the SDWA, which may or may not be supplemented with radiological dose calculations using acceptable exposure scenarios.	Model forecasts of probabilistic contaminant boundaries have been presented in Section 6.0. The probabilistic analyses are based on the radiological standards of the SDWA. There are no plans to supplement these analyses with radiological dose calculations. As note in Section 6.0 and the related sections, a range of model forecasts have been developed to ensure the forecast contaminant boundary is not underrepresented.

Table 7-1
Addressing FFACO UGTA Corrective Action Strategy Requirements for CAU Flow and Transport Models in the Yucca Flat/Climax Mine CAU Flow and Transport Model Document
(Page 2 of 5)

FFACO (1996, as amended) Requirement	How the FFACO Requirement is Addressed
The modeling forecasts of contaminant transport provide the fundamental basis for identifying contaminant boundaries, and for establishing access restrictions to contaminated groundwater and a regulatory boundary for each CAU. The term ***forecast*** is used instead of ***prediction*** to denote the methods and uncertainty of evaluating contaminant boundaries. Transport modeling simulations are used to compute radionuclide concentrations in time and space within a CAU. These three-dimensional (3-D) concentration data are integrated into probabilistic forecasts of the likelihood of groundwater exceeding or remaining below the radiological standards of the SDWA. . . . Contaminant boundaries are not discrete ***predictions*** of the location or concentration of contaminants but instead are spatial representations of the probability of exceeding the SDWA radiological standards. The ***forecasts*** provide planning tools to facilitate regulatory decisions designed to protect the health and safety of the public.	Modeling forecasts of contaminant transport are documented in Sections 3.0, 4.0, and 6.0, as well as in the Climax Mine flow and transport model document (Pohlmann et al., 2007). The transport modeling simulations are used to compute radionuclide concentrations and fluxes in time and space within the CAU. The transport model results are integrated into probabilistic forecasts of the likelihood of groundwater exceeding or remaining below the radiological standards of the SDWA. The forecasts provide planning tools to facilitate regulatory decisions, including the identification of potential use restriction boundaries and regulatory boundaries. In adopting the philosophy of not underrepresenting the possible extent of contaminant transport in the LCA, it is recognized that less conservative representations may be more appropriate for evaluating model results in the CADD/CAP stage, developing use restriction and regulatory boundaries, and siting locations for long-term monitoring. This is particularly noticeable in the observation that existing wells downgradient from potential contaminant sources at BOURBON, TORRIDO, and BILBY have not observed significant contamination. This observation is in stark contrast to the forecast contamination at these locations.
A ***contaminant boundary*** is formally defined as a probabilistic model-forecast perimeter and a lower hydrostratigraphic unit (HSU) boundary that delineates the extent of radionuclide-contaminated groundwater from underground testing over 1,000 years. The contaminated groundwater is a volume (3-D), and this volume is projected upward to the ground surface to define a two-dimensional ***contaminant boundary*** perimeter. Contaminated groundwater is defined as water exceeding the radiological standards of the SDWA. Simulation modeling of contaminant transport will be used to forecast the location of ***contaminant boundaries*** within 1,000 years and must show the 95th percentile of the model results (boundary outside of which only 5 percent of the simulations exceed the SDWA standards).	The probabilistic model-forecast perimeter for the LCA, which is the lower HSU boundary in the Yucca Flat/Climax Mine CAU, is presented in Section 6.0. The three-dimensional volume of contaminated groundwater is projected upward to the ground surface to define a two-dimensional contaminant boundary perimeter. The boundary shows the location outside of which 5 percent of the simulations exceed the SDWA standards.

Table 7-1
Addressing FFACO UGTA Corrective Action Strategy Requirements for CAU Flow and Transport Models in the Yucca Flat/Climax Mine CAU Flow and Transport Model Document
(Page 3 of 5)

FFACO (1996, as amended) Requirement	How the FFACO Requirement is Addressed
The CAU models will use the inventory and inventory uncertainty from the *Nevada Test Site Radionuclide Inventory, 1951–1992* (Bowen et al., 2001) as the initial radiological source term used to predict the hydrological source term incorporated into transport models. The complex geological setting and groundwater pathways for the NNSS combined with limitations in obtaining characterization data for these systems results in significant uncertainty in the model studies and forecasts of ***contaminant boundaries***. The uncertainty includes both statistical (variability and parametric or knowledge uncertainty) and structural uncertainty (numerical model and conceptual model uncertainty). The multiple components of uncertainty will be evaluated through development of multiple alternative model approaches that are integrated with Monte Carlo simulations of contaminant transport. These multiple alternative approaches will require multiple sets of Monte Carlo transport simulations and produce an ensemble of ***contaminant boundary*** forecasts for each CAU. Additional results showing individual radionuclide contributions to the SDWA standard, the contaminant boundary configurations at different time intervals and other percentiles of exceeding the SDWA standards (e.g., 50th or 75th percentiles) may also be used.	The CAU models use the inventory and inventory uncertainty identified in Bowen et al. (2001) as the initial RST. The statistical and structural uncertainty in conceptual models and parameters are presented in Sections 2.0 to 6.0. As a result, multiple alternative models have been developed and multiple sets of Monte Carlo transport simulations performed to produce an ensemble of contaminant boundary forecasts in Section 6.5.10. Additional results showing individual radionuclide contributions to the exceedance volume, as well as the contaminant boundary configurations at different times and other percentiles of exceeding the SDWA standards, have been presented.
NNSA/NSO will develop flow and transport models for each CAU that incorporate the eight major topics described in Section 3.2.1 of Appendix VI [of the FFACO]. NNSA/NSO will provide periodic briefings to NDEP as work progresses. The flow and transport results may be written as two reports or incorporated into a single report. NDEP will review and provide written comments on the modeling report(s), and NNSA/NSO will provide responses to resolve the comments. Flow and transport models for each CAU will be constructed and will consider the following, at a minimum: 1. Alternative hydrological framework models of the CAU modeling domain 2. Uncertainty in the radiological and hydrological source term 3. Alternative models of recharge	These requirements have been addressed as follows: 1. Alternative HFMs have been evaluated in Sections 4.0 and 5.0. 2. Uncertainty in the RST and HST has been evaluated in Section 2.0 and Appendix C. 3. Alternative models of recharge have been evaluated in Sections 3.0 to 5.0.

Table 7-1
Addressing FFACO UGTA Corrective Action Strategy Requirements for CAU Flow and Transport Models in the Yucca Flat/Climax Mine CAU Flow and Transport Model Document
(Page 4 of 5)

FFACO (1996, as amended) Requirement	How the FFACO Requirement is Addressed
4. Alternative boundary conditions and groundwater flows	4. Alternative boundary conditions and groundwater flows have been evaluated in Sections 4.0 and 5.0.
5. Multiple permissive sets of calibrated flow models	5. Multiple permissive sets of calibrated flow models have been addressed in Sections 3.0 to 5.0.
6. Probabilistic simulations of transport using plausible sets of alternative framework and recharge models, and boundary and groundwater flows from calibrated flow models	6. Probabilistic simulations of transport have been addressed in Sections 4.0 and 6.0.
7. Ensembles of forecasts of contaminant boundaries for the CAU	7. Ensembles of contaminant boundary forecasts have been addressed in Section 6.0.
8. Sensitivity and uncertainty analysis of the model outputs	8. Sensitivity and uncertainty analyses of model output have been addressed in Sections 3.0 to 6.0.
Alternative definitions of probability values from Figures 3-3 and 3-4 [of Appendix VI of the FFACO] can be used to define ***contaminant boundaries*** dependent on the degree of certainty required by decision makers for identifying contaminated and uncontaminated groundwater. ***Contaminant boundaries*** will be assembled for individual underground detonations (Figure 3-3) or for a composite of underground detonations (Figure 3-4).	Contaminant boundaries are assembled using a composite of all underground detonations in the Yucca Flat/Climax Mine CAU. The composite contaminant boundaries based on alternative conceptual models illustrate the effect of assuming alternative definitions of the probability values for exceedance of the SDWA MCLs; notably, values of 5 percent (the definition used for the FFACO contaminant boundary), and 25, 50, and 75 percent. These results illustrate the significance of the tails of the distributions, with the expected case being more commensurate with the 50 percent probability value. Even these results are tempered by the considered structural uncertainties, some of which are irreducible such as the use of the maximum announced yield for each detonation.

Table 7-1
Addressing FFACO UGTA Corrective Action Strategy Requirements for CAU Flow and Transport Models in the Yucca Flat/Climax Mine CAU Flow and Transport Model Document
(Page 5 of 5)

FFACO (1996, as amended) Requirement	How the FFACO Requirement is Addressed
Use restriction boundaries will be negotiated and established by NNSA/NSO and NDEP for each CAU where the ***use restriction boundaries*** are established from a combination of assessments of ***contaminant boundary*** forecasts, requirements for protection of worker health and safety, and required administrative policies designed to restrict access to contaminated groundwater. These areas of potentially contaminated groundwater *inside* the ***use restriction boundaries*** are expected to require institutional controls to restrict access to contaminated groundwater.	The composite contaminant boundary forecasts may be used as one of the inputs to support the NNSA/NSO and NDEP negotiations of use restriction boundaries.
During the CADD/CAP and CR stages, NDEP and NNSA/NSO will negotiate and establish two regulatory-based requirements (Figure 3-2). The first are ***CAU regulatory boundary objectives*** for individual CAUs, and the second is a ***regulatory boundary***; both requirements are designed to enhance protection of the public and environment.	The required regulatory boundary objectives and regulatory boundary will be negotiated by NNSA/NSO and NDEP.
Model ***acceptance*** by NDEP is required at two decision points of the UGTA strategy (Figure 3-2 [of Appendix VI of the FFACO]) for each CAU. Model ***acceptance*** is defined as a joint decision by NNSA/NSO and NDEP that there is sufficient credibility/reliability of model studies to use the transport modeling forecasts as the basis for regulatory decisions leading to protection of the health and safety of the public. The second major decision point of Figure 3-2 is a joint NNSA/NSO and NDEP decision of the adequacy of the data and results for the flow and transport model, a judgment whether there is sufficient confidence in the model results to progress to the third stage of the UGTA strategy. The model results and data will be evaluated jointly by NDEP and NNSA/NSO to assess whether there is sufficient confidence in the model results to proceed with the UGTA corrective action strategy. If both NNSA/NSO and NDEP agree that the model results and data are **adequate**, the answer to this question is yes. If either party determines that the model results and/or data are **not adequate**, the answer is no.	This document provides input to the NNSA/NSO and NDEP decisions related to the model and data adequacy to support the UGTA strategy, and the model acceptance for use in the CADD/CAP stage of the UGTA strategy.

8.0 REFERENCES

ASTM, see ASTM International.

Allen, B.M., S.L. Drellack Jr., and M.J. Townsend. 1997. *Surface Effects of Underground Nuclear Explosions*, DOE/NV/11718-122. Las Vegas, NV: Bechtel Nevada.

Anderson, M.P. 2005. "Heat as a Ground Water Tracer." *Ground Water* 43 (6): 951–968. doi:10.1111/j.1745-6584.2005.00052.x.

Anderson, M.P., and W.W. Woessner. 1992. *Applied Groundwater Modeling*. San Diego, CA: Academic Press.

ASTM International. 1993 (reapproved 2008). *Standard Guide for Comparing Ground-Water Flow Model Simulations to Site-Specific Information*, ASTM Standard D5490 - 93(2008). West Conshohocken, PA.

ASTM International. 1994 (reapproved 2008). *Standard Guide for Conducting a Sensitivity Analysis for a Ground-Water Flow Model Application*, ASTM Standard D5611 - 94(2008). West Conshohocken, PA.

ASTM International. 1995 (reapproved 2006). *Standard Guide for Documenting a Ground-Water Flow Model Application*, ASTM Standard D5718 - 95(2006). West Conshohocken, PA.

ASTM International. 2004 (reapproved 2010). *Standard Guide for Application of a Ground-Water Flow Model to a Site-Specific Problem*, ASTM Standard D5447 - 04(2010). West Conshohocken, PA.

Bechtel SAIC, see Bechtel SAIC Company, LLC.

BN, see Bechtel Nevada.

Baecher, B.G., N.A. Lanney, and H.H. Einstein. 1977. "Statistical Descriptions of Rock Properties and Sampling." In *Proceedings of the 18th U.S. Symposium on Rock Mechanics*. American Institute of Mining Engineers.

Bear, J. 1972. *Dynamics of Fluids in Porous Media*. New York, NY: Elsevier Publishing Co.

Bechtel Nevada. 1998. *Hydrogeologic Characterization of the Unsaturated Zone at the Area 3 Radioactive Waste Management Site*, DOE/NV/11718-210. Prepared for the U.S. Department of Energy, Nevada Operations Office. Las Vegas, NV.

Bechtel Nevada. 2002. *A Hydrostratigraphic Model and Alternatives for the Groundwater Flow and Contaminant Transport Model of Corrective Action Units 101 and 102: Central and Western Pahute Mesa, Nye County, Nevada*, DOE/NV/11718--706. Prepared for the U.S. Department of Energy, National Nuclear Security Administration Nevada Operations Office. Las Vegas, NV.

Bechtel Nevada. 2005a. *A Hydrostratigraphic Framework Model and Alternatives for the Groundwater Flow and Contaminant Transport Model of Corrective Action Unit 98: Frenchman Flat, Clark, Lincoln, and Nye Counties, Nevada*, DOE/NV/11718--1064. Prepared for the U.S. Department of Energy, National Nuclear Security Administration Nevada Site Office. Las Vegas, NV.

Bechtel Nevada. 2005b. *Site Characterization Data from the U3ax/bl Exploratory Boreholes at the Nevada Test Site*, DOE/NV/11718--003-REV.1. Prepared for the U.S. Department of Energy, National Nuclear Security Administration Nevada Site Office. Las Vegas, NV.

Bechtel Nevada. 2006. *A Hydrostratigraphic Model and Alternatives for the Groundwater Flow and Contaminant Transport Model of Corrective Action Unit 97: Yucca Flat-Climax Mine, Lincoln and Nye Counties, Nevada*, DOE/NV/11718--1119. Prepared for the U.S. Department of Energy, National Nuclear Security Administration Nevada Site Office. Las Vegas, NV.

Bechtel SAIC Company, LLC. 2004. *Saturated Zone In-Situ Testing*, ANL-NBS-HS-0020039 Rev 01. Las Vegas, NV.

Becker, N., Los Alamos National Laboratory. 2012. Email to E. Kwicklis (LANL), R. Andrews (N-I), and S. Marutzky (N-I). Subject: "Notes on Use of Drill-Back Fluids," 23 February. Los Alamos, NM.

Belcher, W.R., J.B. Blainey, F.A. D'Agnese, C.C. Faunt, M.C. Hill, R.J. Laczniak, G.M. O'Brien, C.J. Potter, H.M. Putnam, C.A. San Juan, and D.S. Sweetkind. 2004. *Death Valley Regional Ground-Water Flow System, Nevada and California—Hydrogeologic Framework and Transient Ground-Water Flow Model*, Scientific Investigations Report 2004-5205. Reston, VA: U.S. Geological Survey.

Berkowitz, B. 2002. "Characterizing Flow and Transport in Fractured Geological Media: A Review." *Advances in Water Resources* 25 (8–12): 861–884. doi:10.1016/S0309-1708(02)00042-8.

Blainey, J., INTERA, Inc. 2012. Email to T. Birdie (N-I) titled "Regional Model Shapefiles," 18 July. Austin, TX.

Blankennagel, R.K., and J.E. Weir, Jr. 1973. *Geohydrology of the Eastern Part of Pahute Mesa, Nevada Test Site, Nye County, Nevada*, Professional Paper 712-B. Denver, CO: U.S.Geological Survey.

Boardman, C.R. 1970. "Engineering Effects of Underground Nuclear Explosives." In *Proceedings of Symposium on Engineering with Nuclear Explosives*, CONF-700101, 43–67. Las Vegas, NV, 14–16 January.

Bodvarsson, G.S., H.H. Liu, C.F. Ahlers, Y.-S. Wu, E. Sonnenthal. 2001. "Parameterization and Upscaling in Modeling Flow and Transport in the Unsaturated Zone of Yucca Mountain." In *Conceptual Models of Flow and Transport in the Fractured Vadose Zone*, by U.S. National Committee for Rock Mechanics, Panel on Conceptual Models of Flow and Transport in the Fractured Vadose Zone, 335–366. Washington, DC: National Academy Press.

Bowen, S.M., D.L. Finnegan, J.L. Thompson, C.M. Miller, P.L. Baca, L.F. Olivas, C.G. Geoffrion, D.K. Smith, W. Goishi, B.K. Esser, J.W. Meadows, N. Namboodiri, and J.F. Wild. 2001. *Nevada Test Site Radionuclide Inventory, 1951–1992*, LA-13859-MS. Los Alamos, NM: Los Alamos National Laboratory.

Bravo, H.R., F. Jiang, and R.J. Hunt. 2002. "Using Groundwater Temperature Data to Constrain Parameter Estimation in a Groundwater Flow Model of a Wetland System." *Water Resources Research* 38 (8): 1153. doi:10.1029/2000WR000172.

Buddemeier, R.W., and D. Isherwood comps. 1985. *Radionuclide Migration Project 1984 Progress Report*, UCRL-53628. Livermore, CA: Lawrence Livermore National Laboratory.

Buqo, T.S. 2004. *Nye County Water Resources Plan*. Prepared for the Nye County Department of Natural Resources and Federal Facilities. Pahrump, NV.

CFR, see *Code of Federal Regulations*.

Caine, J.S., J.P. Evans, and C.B. Forster. 1996. "Fault Zone Architecture and Permeability Structure." *Geology* 24 (11): 1025–1028.

Carle, S.F., R.M. Maxwell, and G.A. Pawloski. 2003. *Impact of Test Heat on Groundwater Flow at Pahute Mesa, Nevada Test Site*, UCRL-ID-152599. Livermore, CA: Lawrence Livermore National Laboratory.

Carle, S.F., R.M. Maxwell, G.A. Pawloski, D.E. Shumaker, A.F.B. Tompson, and M. Zavarin. 2007. *Evaluation of the Transient Hydrologic Source Term for the Cambric Underground Nuclear Test at Frenchman Flat, Nevada Test Site*, UCRL-TR-226916. Livermore, CA: Lawrence Livermore National Laboratory.

Carle, S.F., M. Zavarin, Y. Sun, and G.A. Pawloski. 2008. *Evaluation of Hydrologic Source Term Processes for Underground Nuclear Tests in Yucca Flat, Nevada Test Site: Carbonate Tests*, LLNL-TR-403485. Livermore, CA: Lawrence Livermore National Laboratory.

Cauffman, T.L, A.M. LaVenue, and J.P. McCord. 1990. *Ground-Water Flow Modeling of the Culebra Dolomite, Volume II: Database*, SAND89-7068/2, Albuquerque, NM: Sandia National Laboratories.

Charlie, W.A., G.E. Veyera, D.S. Durnford, and D.O. Doehring. 1996. "Porewater Pressure Increases in Soil and Rock from Underground Chemical and Nuclear Explosions." *Engineering Geology* 43 (4): 225–236. doi:10.1016/S0013-7952(96)00032-4.

Code of Federal Regulations. 2012. Title 40 CFR, Part 141, "National Primary Drinking Water Regulations." Washington, DC: U.S. Government Printing Office.

Cole, J.C., A.G. Harris, and R.R. Wahl. 1997. *Sub-crop Geologic Map of Pre-Tertiary Rocks in the Yucca Flat and Northern Frenchman Flat Areas, Nevada Test Site, Southern Nevada*, Open-File Report 97-678. Denver, CO: U.S. Geological Survey.

Conca, J.L., D.G. Levitt, P.R. Heller, T.J. Mockler, and M.J. Sully. 1999. "Direct UFA Measurements of the Unsaturated Hydraulic Conductivity; Comparisons to van Genuchten/Mualem Estimations, and Applications to Recharge Mapping in Arid Regions." In *Characterization and Measurement of the Hydraulic Properties of Unsaturated Porous Media*, edited by M. Th. van Genuchten, F.J. Leij, and L. Wu. Riverside, CA: University of California.

DOE/NV, see U.S. Department of Energy, Nevada Operations Office.

D'Agnese, F.A., C.C. Faunt, A.K. Turner, and M.C. Hill. 1997. *Hydrogeologic Evaluation and Numerical Simulations of the Death Valley Regional Ground-Water Flow System, Nevada and California*, Water-Resources Investigations Report 96-4300. Denver, CO: U.S. Geological Survey.

Davis, S.N. 1971. "Discussion of Paper by Walter E. Reed, 'Transport of Water away from a Buried Heat Source with Special Reference to Hydrologic Phenomena Observed at Aardvark Nuclear Detonation.'" *Journal of Geophysical Research* 76 (2): 630–632. doi:10.1029/JB076i002p00630.

Dixon, G.L., K.A. Sargent, and R.W. Spengler. 1973. *Lithologic Logs and Stratigraphic Identification of Exploratory and Emplacement Drill Holes in Area 3, Nevada Test Site*, USGS-474-151; NTS-244. U.S. Geological Survey.

Doherty, J. 2004. *PEST: Model-Independent Parameter Estimation, User Manual, 5th Edition*, Brisbane, Australia: Watermark Numerical Computing.

Doherty, J.E., and R.J. Hunt. 2010. *Approaches to Highly Parameterized Inversion: A Guide to Using PEST for Groundwater-Model Calibration*, Scientific Investigations Report 2010-5169. Reston, VA: U.S. Geological Survey.

Doherty, J.E., R.J. Hunt, and M.J. Tonkin. 2010. *Approaches to Highly Parameterized Inversion: A Guide to Using PEST for Model-Parameter and Predictive-Uncertainty Analysis.* Scientific Investigations Report 2010-5211. Reston, VA: U.S. Geological Survey.

Domenico, P.A., and F.W. Schwartz. 1990. *Physical and Chemical Hydrology.* New York, NY: John Wiley & Sons.

Dosch, R.G., and A.W. Lynch. 1980. "Radionuclide Transport in a Dolomite Aquifer." In *Scientific Basis for Nuclear Waste Management*, Vol. 2, edited by C.J.M. Northrup Jr., 617–624. New York, NY: Plenum Press.

Doty, G.C., and F.E. Rush. 1985. *Inflow to a Crack in Playa Deposits of Yucca Lake, Nevada Test Site, Nye County, Nevada*, Water-Resources Investigations Report 84-4296. Denver, CO: U.S. Geological Survey.

Drellack, S.L., Jr., L.B. Prothro, J.L. Gonzales, and J.M. Mercadante. 2010. *The Hydrogeologic Character of the Lower Tuff Confining Unit and the Oak Spring Butte Confining Unit in the Tuff Pile Area of Central Yucca Flat*, DOE/NV/25946--544. Las Vegas, NV: National Security Technologies, LLC.

Drellack, S.L., L.B. Prothro, J.L. Gonzales, J.M. Mercadante, and D.N. Haugstad. 2012. Written communication. Subject: *Low Water Production from Carbonate Aquifers at Rainier Mesa: Implications for the Distribution of Hydraulic Conductivity within the Lower Carbonate Aquifer, Nevada Test Site and Vicinity.* Las Vegas, NV: National Security Technologies, LLC.

EPA, see U.S. Environmental Protection Agency.

Eakin, T.E., G.B. Maxey, T.W. Robinson, J.C. Fredericks and O.J. Loeltz. 1951. "Contributions to the Hydrology of Eastern Nevada." In *Water Resources Bulletin*, No. 12. Carson City, NV: State of Nevada, Office of the State Engineer/U.S. Geological Survey.

Evans, J.P., C.B. Forster, and J.V. Goddard. 1997. "Permeability of Fault-Related Rocks, and Implications for Hydraulic Structure of Fault Zones." *Journal of Structural Geology* 19 (11): 1393–1404.

FFACO, see *Federal Facility Agreement and Consent Order.*

Faunt, C.C, D.S. Sweetkind, M.C. Hill, M.T. Pavelko, and W.R. Belcher. 2012. Written communication. Subject: *Update of the Death Valley Regional Groundwater Flow System Transient Model, Nevada and California*. U.S. Geological Survey.

Federal Facility Agreement and Consent Order. 1996 (as amended March 2010). Agreed to by the State of Nevada; U.S. Department of Energy, Environmental Management; U.S. Department of Defense; and U.S. Department of Energy, Legacy Management. Appendix VI, which contains the Underground Test Area Strategy, was last modified May 2011, Revision No. 4.

Fenelon, J.M. 2005. *Analysis of Ground-Water Levels and Associated Trends in Yucca Flat, Nevada Test Site, Nye County, Nevada, 1951–2003*, Scientific Investigations Report 2005-5175. Carson City, NV: U.S. Geological Survey.

Fenelon, J.M., U.S. Geological Survey. 2008. Personal communication to T. Birdie (N-I) regarding Wells ER-6-2 and UE-1h, 23 July. Henderson, NV.

Fenelon, J.M., D.S. Sweetkind, P.E. Elliot, and R.J. Laczniak. 2012. *Conceptualization of the Predevelopment Groundwater Flow System and Transient Water-Level Responses in Yucca Flat, Nevada National Security Site, Nevada*, Scientific Investigations Report 2012-5196. Reston, VA: U.S. Geological Survey.

Fenelon, J.M., D.S. Sweetkind, and R.J. Laczniak. 2010. *Groundwater Flow Systems at the Nevada Test Site, Nevada: A Synthesis of Potentiometric Contours, Hydrostratigraphy, and Geologic Structures*, Professional Paper 1771. Reston, VA: U.S. Geological Survey.

Flint, L.E. 1998. *Characterization of Hydrogeologic Units Using Matrix Properties, Yucca Mountain, Nevada*, Water-Resources Investigations Report 97-4243. Denver, CO: U.S. Geological Survey.

Freeze, R.A., and J.A. Cherry. 1979. *Groundwater.* Englewood Cliffs, NJ: Prentice Hall.

French, R.H., T.L. Buchanan, S.L. Hokett, and S. Curtis. 1999. "Calibration of a Hybrid Rainfall-Runoff Model in an Arid Environment." In *Proceedings of the 28th IAHR Congress, Graz, Austria*. Also included as Appendix 8 of R.H. French and S. Curtis, *The Precipitation Event of 23–24 February 1998, Analysis of a Design Level Event*, DOE/NV/11508--48; Publication No. 45170. Las Vegas, NV: Desert Research Institute.

Garber, M.S., and R.H. Johnston. 1967. *A Summary of Lithologic Data, Aquifer Tests, and Construction of Hydraulic Test Well U3cn-5, Nevada Test Site*. U.S. Geological Survey.

Garber, M.S., and L.E. Wollitz. 1969. "Measuring Underground-Explosion Effects on Water Levels in Surrounding Aquifers." *Ground Water* 7 (4): 3–7. doi:10.1111/j.1745-6584.1969.tb01283.x.

Grasso, D.N. 2000. *Geologic Surface Effects of Underground Nuclear Testing, Yucca Flat, Nevada Test Site, Nevada*, Open-File Report 00-176. Denver, CO: U.S. Geological Survey.

Grasso, D.N. 2001. *GIS Surface Effects Archive of Underground Nuclear Detonations Conducted at Yucca Flat and Pahute Mesa, Nevada Test Site, Nevada*, Open-File Report 2001-272. Denver, CO: U.S. Geological Survey.

Halford, K., U.S. Geological Survey. 2009. Personal communication to A. Tompson (LLNL) regarding groundwater flow estimates for the Yucca Flat/Climax Mine CAU. 16 January

Halford, K., U.S. Geological Survey. 2011. Personal communication to A. Tompson (LLNL) regarding groundwater flow estimates for the Yucca Flat/Climax Mine CAU. 5 August 5.

Halford, K., U.S. Geological Survey. 2012. Personal communication to A. Tompson (LLNL) regarding groundwater flow estimates for the Yucca Flat/Climax Mine CAU. 9 October.

Halford, K.J., R.J. Laczniak, and D.L. Galloway. 2005. *Hydraulic Characterization of Overpressured Tuffs in Central Yucca Flat, Nevada Test Site, Nye County, Nevada*, Scientific Investigations Report 2005-5211. Carson City, NV: U.S. Geological Survey.

Harrill, J.R., J.S. Gates, and J.M. Thomas. 1988. *Major Groundwater Flow Systems in the Great Basin Region of Nevada, Utah and Adjacent States*. Hydrological Investigation Atlas HA-694-C, scale 1:1,000,000. Denver, CO: U.S. Geological Survey.

Hawkins, W., and K. Wohletz. 1997. *Visual Inspection for CTBT Verification*, LA-13244-MS. Los Alamos, NM: Los Alamos National Laboratory.

Hershey, R.L., and S.Y. Acheampong. 1997. *Estimation of Groundwater Velocities from Yucca Flat to the Amargosa Desert Using Geochemistry and Environmental Isotope*, DOE/NV.11508-26, UC-703; Publication No. 45157. Las Vegas, NV: Desert Research Institute.

Hershey, R.L., W. Howcroft, and P.W. Reimus. 2003. *Laboratory Experiments to Evaluate Diffusion of ^{14}C into Nevada Test Site Carbonate Aquifer Matrix*, DOE/NV/11508-55; Publication No. 45180. Las Vegas, NV: Desert Research Institute.

Hevesi, J.A., A.L. Flint, and L.E. Flint. 2003. *Simulation of Net Infiltration and Potential Recharge Using a Distributed-Parameter Watershed Model for the Death Valley Region, Nevada and California*, Water-Resources Investigations Report 03-4090. Sacramento, CA: U.S. Geological Survey.

Hokett, S.L., and R.H. French. 1998. *Evaluation of Recharge Potential at Crater U5a (WISHBONE)*, DOE/NV/11508-32; Publication No. 45160. Las Vegas, NV: Desert Research Institute, Water Resources Center.

Hokett, S.L., and D.R. Gillespie. 1996. *Preliminary Evaluation of Recharge Potential at Subsidence Crater U5A in Frenchman Flat, Nevada Test Site*, DOE/NV/11508-15; Publication No. 45147. Las Vegas, NV: Desert Research Institute.

Hokett, S.L., D.R. Gillespie, G.V. Wilson, and R.H. French. 2000. *Evaluation of Recharge Potential at Subsidence Crater U10i, Northern Yucca Flat, Nevada Test Site*, DOE/NV/11508-53; Publication No. 45174. Las Vegas, NV: Desert Research Institute.

Hudson, M.R. 1997. *Structural Geology of the French Peak Accommodation Zone, Nevada Test Site, Southwestern Nevada*, Open-File Report 97-56. Denver, CO: U.S. Geological Survey.

Hunt, R.J., J. Doherty, and M.J. Tonkin. 2007. “Are Models Too Simple? Arguments for Increased Parameterization.” *Ground Water* 45 (3): 254–262. doi:10.1111/j.1745-6584.2007.00316.x.

IAEA, see International Atomic Energy Agency.

IT, see IT Corporation.

International Atomic Energy Agency. 1998. *The Radiological Situation at the Atolls of Mururoa and Fangataufa, Technical Report, Volume 3: Inventory of Radionuclides Underground at the Atolls*, IAEA-MFTR-3. In *Proceedings of an IAEA Conference, Vienna, 30 June–3 July.* Vienna, Austria.

Istok, J.D., D.O. Blout, L. Barker, K.R. Johnejack, and D.P. Hammermeister. 1994. "Spatial Variability in Alluvium Properties at a Low-Level Nuclear Waste Site." *Soil Scientists Society of America* 58: 1040–1051.

IT Corporation. 1996a. *Regional Geologic Model Data Documentation Package (Underground Test ARea Subproject Phase I Data Analysis Task, Volume I, Parts 1 and 2)*, ITLV/10972--181. Prepared for the U.S. Department of Energy, Nevada Operations Office. Las Vegas, NV.

IT Corporation. 1996b. *Groundwater Recharge and Discharge Data Documentation Package (Underground Test Area Subproject Phase I Data Analysis Task, Volume III)*. Prepared for the U.S. Department of Energy, Nevada Operations Office. Las Vegas, NV.

IT Corporation. 1999. *Value of Information Analysis for Corrective Action Unit 97: Yucca Flat, Nevada Test Site, Nevada*, DOE/NV/13052--079; ITLV/13052--079. Las Vegas, NV.

Jones, T.L., V.A. Kelley, J.F. Pickens, D.T. Upton, R.L. Beauheim, and P.B. Davies. 1992. *Integration of Interpretation Results of Tracer Tests Performed in the Culebra Dolomite at the Waste Isolation Pilot Plant Site*, SAND92-1579, UC-721. Sandia, NM: Sandia National Laboratories.

Keating, E.H., J. Doherty, J.A. Vrugt, and Q. Kang. 2010. "Optimization and Uncertainty Assessment of Strongly Nonlinear Groundwater Models with High Parameter Dimensionality." *Water Resources Research* 46: W10517. doi:10.1029/2009WR008584.

Kersting, A.B., D.L. Finnegan, A.F.B. Tompson, B.K. Esser, D.K. Smith, M. Zavarin, C.J. Bruton, and G.A. Pawloski. 2003. *Radionuclide Decay and In-Growth Technical Basis Document*, UCRL-ID-153798. Livermore, CA: Lawrence Livermore National Laboratory.

Khaleel, R., and E.J. Freeman. 1995. *Variability and Scaling of Hydraulic Properties for 200 Area Soils, Hanford Site*, WHC-EP-0883. Richland, WA: Westinghouse Hanford Company.

Knox, J.B., D.E. Rawson, and J.A. Korver. 1965. "Analysis of a Groundwater Anomaly Created by an Underground Nuclear Explosion." *Journal of Geophysical Research* 70 (4): 823–835. doi:10.1029/JZ070i004p00823.

Kuzio, S. 2004. *Probability Distribution for Flowing Interval Spacing*, ANL-NBS-MD-000003 REV. 01. Las Vegas, NV: Yucca Mountain Project.

Kwicklis, E., Los Alamos National Laboratory. 2010. PowerPoint presentation presented to the Yucca Flat Preemptive Review Committee. 17 November. Los Alamos, NM.

Kwicklis, E.M., and R.W. Healy. 1993. "Numerical Investigation of Steady Liquid Water Flow in a Variably Saturated Fracture Network." *Water Resources Research* 29 (12): 4091–4102.

Kwicklis, E.M., F. Thamir, R.W. Healy, and D. Hampson. 1998. *Numerical Simulation of Air- and Water-Flow Experiments in a Block of Variably Saturated, Fractured Tuff from Yucca Mountain, Nevada*, Water-Resources Investigations Report 97-4274. Denver, CO: U.S. Geological Survey.

Kwicklis, E.M., G. WoldeGabriel, and M. Sully. 2008. Written communication. Subject: *Analysis of Core-Scale Hydrologic and Mineralogic Data from Boreholes UE12t #1 and RME#1 at Rainier Mesa, Nevada Test Site*. Los Alamos, NM: Los Alamos National Laboratory.

Kwicklis, E.M., A.V. Wolfsberg, P.H. Stauffer, M.A. Walvoord, and M.J. Sully. 2006a. "Multiphase, Multicomponent Parameter Estimation for Liquid and Vapor Fluxes in Deep Arid Systems Using Hydrologic Data and Natural Environmental Tracers." *Vadose Zone Journal* 5 (3): 934–950.

Kwicklis, E.M., A.V. Wolfsberg, P.H. Stauffer, M.A. Walvoord, and M.J. Sully. 2006b. *Numerical Evaluation of Liquid and Vapor Fluxes at the Nevada Test Site Area 3 Radioactive Waste Management Site Using Hydrologic Data and Natural Environmental Tracers*, LA-UR-06-1212. Los Alamos, NM: Los Alamos National Laboratory.

LANL, see Los Alamos National Laboratory.

Laczniak, R.J., J.C. Cole, D.A. Sawyer, and D.A. Trudeau. 1996. *Summary of Hydrogeologic Controls on Ground-Water Flow at the Nevada Test Site, Nye County, Nevada*, Water-Resources Investigations Report 96-4109. Carson City, NV: U.S. Geological Survey.

Laczniak, R.J., G.A. DeMeo, S.R. Reiner, J.L. Smith, and W.E. Nylund. 1999. *Estimates of Ground-Water Discharge as Determined from Measurements of Evapotranspiration, Ash Meadows Area, Nye County, Nevada*, Water-Resources Investigations Report 99-4079. Carson City, NV: U.S. Geological Survey.

Li, C., Z. Lu, T. Ma, and X. Zhu. 2009. "A Simple Kriging Method Incorporating Multiscale Measurements in Geochemical Survey." *Journal of Geochemical Exploration* 101: 147–154. doi:10.1016/j.gexplo.2008.06.003.

Liu, H.H., Y.Q. Zhang, and F.J. Molz. 2007. "Scale Dependence of the Effective Matrix Diffusion Coefficient: Some Analytical Results." *Vodose Zone Journal* 6 (3): 679–683. doi:10.2136/vzj2006.0140.

Los Alamos National Laboratory. 2011. *LaGriT Los Alamos Grid Toolbox* website. As accessed at http://lagrit.lanl.gov/.

Lyles, B.F. 1990. *Tritium Variations in Groundwater on the Nevada Test Site*, DOE/NV/10384-38; Publication No. 45086. Las Vegas, NV: Desert Research Institute, Water Resources Center.

Maxey, G.B., and T.E. Eakin. 1949. "Groundwater in White River Valley, White Pine, Nye and Lincoln Counties, Nevada." In *Water Resources Bulletin*, No. 8. Carson City, NV: State of Nevada, Office of the State Engineer/U.S. Geological Survey.

McKay, M.D. 1995. *Evaluating Prediction Uncertainty*, NUREG/CR-6311; LA-12915-MS. Prepared for the U.S. Nuclear Regulatory Commission, Office of Nuclear Regulatory Research. Washington, DC.

McNab, W.W. 2008. *Evaluation of Hydrologic Source Term Processes for Underground Nuclear Tests in Yucca Flat, Nevada Test Site: Unsaturated Tests and the Impact of Recharge*, LLNL-TR-403360. Livermore, CA: Lawrence Livermore National Laboratory.

Millington, R.J. and J.P. Quirk. 1960. "Transport in Porous Media." In *Transactions of the Seventh International Congress of Soil Science*, Vol. 1, 97–106. Amsterdam, The Netherlands: Elsevier.

Montazer, P.M., and W.E. Wilson. 1984. *Conceptual Hydrologic Model of Flow in the Unsaturated Zone, Yucca Mountain, Nevada*, Water-Resources Investigations Report 84-4345. Denver, CO: U.S. Geological Survey.

Moore, J.E., A.C. Doyle, G.E. Walker, and R.A. Young. 1963. *Ground-Water Test Well 2, Nevada Test Site, Nye County, Nevada*, with a section on geophysical logs by R.D. Carroll, Open-File Report TEI-836. U.S. Geological Survey.

Moran, J.E., and T.P. Rose. 2003. "A Chlorine-36 Study of Regional Groundwater Flow and Vertical Transport in Southern Nevada." *Environmental Geology* 43 (5): 592–605.

N-I, see Navarro-Intera, LLC.

N-I GIS, see Navarro-Intera Geographic Information Systems.

NNES, see Navarro Nevada Environmental Services, LLC.

NNSA/NSO, see U.S. Department of Energy, National Nuclear Security Administration Nevada Site Office.

NNSA/NV, see U.S. Department of Energy, National Nuclear Security Administration Nevada Operations Office.

NSTec, see National Security Technologies, LLC.

National Security Technologies, LLC. 2007. *Characterization Report Area 3 Radioactive Waste Management Site, Nevada Test Site, Nevada*, DOE/NV/25946--080. Prepared for the U.S. Department of Energy, National Nuclear Security Administration Nevada Site Office. Las Vegas, NV.

National Security Technologies, LLC. 2008. *Analysis of Fractures in Cores from the Tuff Confining Unit beneath Yucca Flat, Nevada Test Site*, DOE/NV/25946--351. Prepared by L.B. Prothro for the U.S. Department of Energy, National Nuclear Security Administration Nevada Site Office. Las Vegas, NV.

Navarro-Intera Geographic Information Systems. 2012. ESRI ArcGIS Software.

Navarro-Intera Geographic Information Systems. 2013. ESRI ArcGIS Software.

Navarro-Intera, LLC. 2012. Written communication. Subject: "UGTA Geochemistry Database," UGTA Technical Data Repository Database Identification Number UGTA-4-129. Las Vegas, NV. As accessed on 1 September.

Navarro Nevada Environmental Services, LLC. 2010a. *Phase II Documentation Overview of Corrective Action Unit 98: Frenchman Flat, Nevada Test Site, Nye County, Nevada*, Rev. 1, N-I/28091--007. Las Vegas, NV.

Navarro Nevada Environmental Services, LLC. 2010b. *Phase II Transport Model of Corrective Action Unit 98: Frenchman Flat, Nevada Test Site, Nye County, Nevada*, Rev. 1, N-I/28091--004, S-N/99205--122. Las Vegas, NV.

Navarro Nevada Environmental Services, LLC. 2010c. *Yucca Flat Well Temperature Profile Study Data Report*, Rev. 0, N-I/28091--008. Las Vegas, NV.

Painter, S.L. 2011. *User's Manual for Walkabout V1.0*, LA-UR-11-01952. Los Alamos, NM: Los Alamos National Laboratory.

Pawloski, G.A. 1999. *Development of Phenomenological Models of Underground Nuclear Tests on Pahute Mesa, Nevada Test Site—BENHAM and TYBO*, UCRL-ID-136003. Livermore, CA: Lawrence Livermore National Laboratory.

Pawloski, G.A., A.F.B. Tompson, and S.F. Carle. 2001. *Evaluation of the Hydrologic Source Term from Underground Nuclear Tests on Pahute Mesa at the Nevada Test Site: CHESHIRE Test*, UCRL-ID-147023. Livermore, CA: Lawrence Livermore National Laboratory.

Pawloski, G.A., A.F.B. Tompson, S.F. Carle, R.L. Detwiler, Q. Hu, S. Kollet, R.M. Maxwell, W.W. McNab, S.K. Roberts, D.E. Shumaker, Y. Sun, and M. Zavarin. 2008. *Evaluation of Hydrologic Source Term Processes for Underground Nuclear Tests in Yucca Flat, Nevada Test Site: Introduction and Executive Summary*, LLNL-TR-403428. Livermore, CA: Lawrence Livermore National Laboratory.

Peters, R.R., and E.A. Klavetter. 1988. "A Continuum Model for Water Movement in an Unsaturated Fractured Rock Mass." *Water Resources Research* 24 (3): 416–430. doi:10.1029/WR024i003p00416.

Plummer, M.A., F.M. Phillips, J. Fabryka-Martin, H.J. Turin, P.E. Wigand, and P. Sharma. 1997. "Chlorine-36 in Fossil Rat Urine: An Archive of Cosmogenic Nuclide Deposition during the Past 40,000 Years." Science 277 (5325): 538–541. doi:10.1126/science.277.5325.538.

Pohll, G.M., J.J. Warwick, and S.W. Tyler. 1996. "Coupled Surface–Subsurface Hydrologic Model of a Nuclear Subsidence Crater at the Nevada Test Site." *Journal of Hydrology* 186 (1–4): 43–62. doi:10.1016/S0022-1694(96)03033-8.

Pohlmann, K., and M. Ye. 2012. *Numerical Simulation of Inter-basin Groundwater Flow into Northern Yucca Flat, Nevada National Security Site, Using the Death Valley Regional Flow System Model*, DOE/NV/26383-18; Publication No. 45235. Las Vegas, NV: Desert Research Institute, Division of Hydrologic Sciences.

Pohlmann, K., M. Ye, D. Reeves, D. Decker, J. Chapman, and M. Zavarin. 2007. *Modeling of Groundwater Flow and Radionuclide Transport at the Climax Mine Sub-CAU, Nevada Test Site*, DOE/NV/26383-06; Publication No. 45226. Las Vegas, NV: Desert Research Institute.

Pollock, D.W. 1988. "Semianalytical Computation of Path Lines for Finite-Difference Models." *Ground Water* 26 (6): 743–750.

Prothro, L.B. 1998. Written communication. Subject: *Analysis of Fractures in Cores from the Tuff Confining Unit beneath Yucca Flat, Nevada Test Site*. Las Vegas, NV: Bechtel Nevada.

Prothro, L.B. 2005. *Mineralogic Zonation within the Tuff Confining Unit, Yucca Flat, Nevada Test Site*, DOE/NV/11718--995. Las Vegas, NV: Bechtel Nevada.

Prothro, L.B., National Security Technologies, LLC. 2012. Email to R. Andrews (N-I), Subject: "Frenchman Flat Accommodation Zone," 25 January. Las Vegas, NV.

Prothro, L.B., S.L. Drellack Jr., D.N. Haugstad, H.E. Huckins-Gang, and M.J. Townsend. 2009. *Observations on Faults and Associated Permeability Structures in Hydrogeologic Units at the Nevada Test Site*, DOE/NV/25946--690. Las Vegas, NV: National Security Technologies, LLC.

Pruess, K., and Y.W. Tsang. 1990. "On Two-Phase Relative Permeability and Capillary Pressure of Rough-Walled Rock Fractures." *Water Resources Research* 26 (9): 1915–1926.

REECO, see Reynolds Electrical & Engineering Co., Inc.

RSN, see Raytheon Services Nevada.

Raytheon Services Nevada. 1991. *Nevada Test Site Drilling & Mining Summary through December 1990*. Prepared for the U.S. Department of Energy, Nevada Operations Office. Mercury, NV.

Rechard, R.P., and M.S. Tierney. 2005. "Assignment of Probability Distributions for Parameters in the 1996 Performance Assessment for the Waste Isolation Pilot Plant, Part 2: Application of Process." *Reliability Engineering and System Safety* 88 (1): 33–80.

Reed, W.E. 1970. "Transport of Water Away from a Buried Heat Source with Special Reference to Hydrologic Phenomena Observed at Aardvark Nuclear Detonation." *Journal of Geophysical Research* 75 (2): 415–430. doi:10.1029/JB075i002p00415.

Reimus, P.W., R.L. Hershey, D. Decker, S.D. Ware, C. Papelis, S. Earman, A. Abdel-Fattah, M. Haga, D. Counce, S. Chipera, and C. Sedlacek. 2006. *Tracer Transport Properties in the Lower Carbonate Aquifer of Yucca Flat*, LA-UR-06-0486. Los Alamos, NM: Los Alamos National Laboratory.

Reiner, S.R. 2007. *Ground-Water Temperature Data, Nevada Test Site and Vicinity, Nye, Clark, and Lincoln Counties, Nevada, 2000–2006*, Data Series 269. Carson City, NV: U.S. Geological Survey.

Reynolds Electrical & Engineering Co., Inc. 1994. *Site Characterization and Monitoring Data from Area 5 Pilot Wells, Nevada Test Site, Nye County, Nevada*, DOE/NV/11432-74. Las Vegas, NV.

Robinson, B.A., Z.V. Dash, and G. Srinivasan. 2010. "A Particle Tracking Transport Method for the Simulation of Resident and Flux-Averaged Concentration of Solute Plumes in Groundwater Models." *Computational Geosciences* 14 (4): 779–792. doi:10.1007/s10596-010-9190-6.

Robinson, B.A., Z.V. Dash, and S.L. Painter. 2011. *User's Guide for the PLUMECALC Application with Subgridding*, LA-UR-11-02090. Los Alamos, NM: Los Alamos National Laboratory.

Rose, T.P., Q. Hu, P. Zhao, C.L. Conrado, R. Dickerson, G.F. Eaton, A.B. Kersting, J.E. Moran, G. Nimz, B.A. Powell, E.C. Ramon, F.J. Ryerson, R.W. Williams, P.T. Wooddy, and M. Zavarin. 2011. *Radionuclide Partitioning in an Underground Nuclear Test Cavity*, LLNL-TR-409817. Livermore, CA: Lawrence Livermore National Laboratory.

Russell, C.E., and T. Minor. 2002. *Reconnaissance Estimates of Recharge Based on an Elevation-Dependent Chloride Mass-Balance Approach*, DOE/NV/11508-37; Publication No. 45164. Las Vegas, NV: Desert Research Institute, Water Resources Center.

Shaw, see Shaw Environmental, Inc.

SNJV, see Stoller-Navarro Joint Venture.

Saltelli, A., S. Tarantola, F. Campolongo, and M. Ratto. 2004. *Sensitivity Analysis in Practice: A Guide to Assessing Scientific Models*. West Sussex, England: John Wiley & Sons, Ltd.

Sawada, A., M. Uchida, M. Shimo, H. Yamamoto, H. Takahara, and T.W. Doe. 2001. "Anisotropy, Reversibility and Scale Dependence of Transport Properties in Single Fracture and Fractured Zone—Non-sorbing Tracer Experiment at the Kamaishi Mine." In *Proceedings from the 4th International Seminar Aspo, September 9–11, 2000*, SKB Technical Report TR-01-24, 151–164. Svensk Karnbranslehantering AB.

Sawyer, D.A., R.J. Fleck, M.A. Lanphere, R.G. Warren, D.E. Broxton, and M.R. Hudson. 1994. "Episodic Caldera Volcanism in the Miocene Southwestern Nevada Volcanic Field: Revised Stratigraphic Framework, $^{40}Ar/^{39}Ar$ Geochronology, and Implications for Magmatism and Extension." *Geological Society of America Bulletin* 106 (10): 1304–1318.

Scanlon, B.R., and R.S. Goldsmith. 1997. "Field Study of Spatial Variability in Unsaturated Flow beneath and adjacent to Playas." *Water Resources Research* 33 (10): 2239–2252. doi:10.1029/97WR01332.

Scanlon, B.R., K. Keese, R.C. Reedy, J. Simunek, and B.J. Andraski. 2003. "Variations in Flow and Transport in Thick Desert Vadose Zones in Response to Paleoclimatic Forcing (0–90 kyr): Field Measurements, Modeling, and Uncertainties." *Water Resources Research* 39 (7): 1179. doi:10.1029/2002WR001604.

Schaap, M.G. 1999. *Rosetta, Version 1.0, Class Average Hydraulic Parameters*. Riverside, CA: U.S. Department of Agriculture, Agricultural Research Service, U.S. Salinity Laboratory.

Schoff, S.L., and J.E. Moore. 1964. *Chemistry and Movement of Groundwater, Nevada Test Site*, Trace Elements Investigations Report 838. Denver, CO: U.S. Geological Survey.

Shaw Environmental, Inc. 2003. *Modeling Approach/Strategy for Corrective Action Unit 97, Yucca Flat and Climax Mine*, Rev. 0, Shaw/13052-205. Las Vegas, NV.

Smith, D.K. 1995. *Challenges in Defining a Radiologic and Hydrologic Source Term for Underground Nuclear Test Centers, Nevada Test Site, Nye County, Nevada*, UCRL-JC-120389. Livermore, CA: Lawrence Livermore National Laboratory.

Smith, D.K., D.L. Finnegan, and S.M. Bowen. 2003. "An Inventory of Long-Lived Radionuclides Residual from Underground Nuclear Testing at the Nevada Test Site, 1951–1992." *Journal of Environmental Radioactivity* 67 (1): 35–51. doi:10.1016/S0265-931X(02)00146-7.

Spaulding, W.G. 1990. "Vegetational and Climatic Development of the Mojave Desert: The Last Glacial Maximum to the Present." In *Packrat Middens: The Last 40,000 Years of Biotic Change*, edited by T.R. Van Devender, P.S. Martin, and J.L. Betancourt, 166–199. Tuscon, AZ: University of Arizona Press.

Spaulding, W.G., and L.J. Graumlich. 1986. "The Last Pluvial Climatic Episodes in the Deserts of Southwestern North America." *Nature* 320: 441–444. doi:10.1038/320441a0.

Srinivasan, G., D.M. Tartakovsky, M. Dentz, H. Viswanathan, B. Berkowitz, and B.A. Robinson. 2010. "Random Walk Particle Tracking Simulations of Non-Fickian Transport in Heterogeneous Media." *Journal of Computational Physics* 229: 4304–4314. doi:10.1016/j.jcp.2010.02.014.

Stephens, D.B. 2008. *Moisture Retention Testing for TCU, VTA, and WTA Samples*. Laboratory report prepared for Los Alamos National Laboratory. Los Alamos, NM.

Stoller-Navarro Joint Venture. 2005a. *Analysis of Hydraulic Responses from the ER-6-1 Multiple-Well Aquifer Test, Yucca Flat FY 2004 Testing Program, Nevada Test Site, Nye County, Nevada*, Rev.0, S-N/99205--051. Las Vegas, NV.

Stoller-Navarro Joint Venture. 2005b. *Underground Test Area Fracture Analysis Report for Yucca Flat Wells ER-2-1, ER-6-1#2, ER-7-1, and ER-12-2, Nevada Test Site, Nevada*. S-N/99205-040. Las Vegas, NV.

Stoller-Navarro Joint Venture. 2006a. *Geochemical and Isotopic Evaluation of Groundwater Movement in Corrective Action Unit 97: Yucca Flat/Climax Mine, Nevada Test Site, Nevada*, Rev. 0, S-N/99205--070. Las Vegas, NV.

Stoller-Navarro Joint Venture. 2006b. *Phase I Hydrologic Data for the Groundwater Flow and Contaminant Transport Model of Corrective Action Unit 97: Yucca Flat/Climax Mine, Nevada Test Site, Nye County, Nevada*, Rev. 0, S-N/99205--077. Las Vegas, NV.

Stoller-Navarro Joint Venture. 2006c. *Phase II Groundwater Flow Model of Corrective Action Unit 98: Frenchman Flat, Nevada Test Site, Nye County, Nevada*, Rev. 0, S-N/99205--074. Las Vegas, NV.

Stoller-Navarro Joint Venture. 2006d. *Underground Test Area Fracture Analysis Report for Rainier Mesa Wells ER-12-3 and ER-12-4, and Shoshone Mountain Well ER-16-1, Nevada Test Site, Nevada*, S-N/99205--085. Las Vegas, NV.

Stoller-Navarro Joint Venture. 2006e. *Well ER-6-1 Tracer Test Analysis: Yucca Flat, Nevada Test Site, Nye County, Nevada*, Rev. 0, S-N/99205--084. Las Vegas, NV.

Stoller-Navarro Joint Venture. 2007. *Phase I Contaminant Transport Parameters for the Groundwater Flow and Contaminant Transport Model of Corrective Action Unit 97: Yucca Flat/Climax Mine, Nevada Test Site, Nye County, Nevada*, Rev. 0, S-N/99205--096. Las Vegas, NV.

Stoller-Navarro Joint Venture. 2009a. *Phase I Transport Model of Corrective Action Units 101 and 102: Central and Western Pahute Mesa, Nevada Test Site, Nye County, Nevada*, S-N/99205--111. Las Vegas, NV.

Stoller-Navarro Joint Venture. 2009b. *Unclassified Source Term and Radionuclide Data for Corrective Action Unit 97: Yucca Flat/Climax Mine, Nevada Test Site, Nevada*, Rev. 2, S-N/99205--114. Las Vegas, NV.

Stonestrom, D.A., D.E. Prudic, R.J. Laczniak, K.C. Akstin, R.A. Boyd, and K.K. Henkelman. 2003. *Estimates of Deep Percolation Beneath Native Vegetation, Irrigated Fields, and the Amargosa-River Channel, Amargosa Desert, Nye County, Nevada*, Open-File Report 2003-104. Carson City, NV: U.S. Geological Survey.

Sutton, M. 2009. *Review of Distribution Coefficients for Radionuclides in Carbonate Minerals*, LLNL-SR-415700. Livermore, CA: Lawrence Livermore National Laboratory.

Sweetkind, D.S., and R.M. Drake II. 2007a. *Characteristics of Fault Zones in Volcanic Rocks near Yucca Flat, Nevada Test Site, Nevada*, Open-File Report 2007-1293. Reston, VA: U.S. Geological Survey.

Sweetkind, D.S., and R.M. Drake II. 2007b. *Geologic Characterization of Young Alluvial Basin-Fill Deposits from Drill-Hole Data in Yucca Flat, Nye County, Nevada*, Scientific Investigations Report 2007-5062. Reston, VA: U.S. Geological Survey.

Teller, E., W.K. Talley, G.H. Higgins, and G.W. Johnson. 1968. *The Constructive Uses of Nuclear Explosives*. New York, NY: McGraw-Hill.

Thordarson, W. 1965. *Perched Ground Water in Zeolitized-Bedded Tuff, Rainier Mesa and Vicinity, Nevada Test Site, Nevada*, TEI-862. Denver, CO: U.S. Geological Survey.

Tokunaga, T.K., J. Wan, and K.R. Olson. 2002. "Saturation-Matric Potential Relations in Gravel." *Water Resources Research* 38 (10): 1214. doi:10.1029/2001WR001242.

Tompson, A.F.B., ed. 2008. *Evaluation of Hydrologic Source Term Processes for Underground Nuclear Tests in Yucca Flat, Nevada Test Site: Saturated Tests*, LLNL-TR-403429. Livermore, CA: Lawrence Livermore National Laboratory.

Tompson, A.F.B., M. Zavarin, W.W. McNab, S.F. Carle, D.E. Shumaker, C. Lu, Y. Sun, G.A. Pawloski, Q. Hu, and S.K. Roberts. 2011. Written communication. Subject: *Hydrologic Source Term Processes and Models for Underground Nuclear Tests at Rainier Mesa and Shoshone Mountain, Nevada National Security Site*. Livermore, CA: Lawrence Livermore National Laboratory.

Tonkin, M., and J. Doherty. 2009. "Calibration-Constrained Monte Carlo Analysis of Highly Parameterized Models Using Subspace Techniques." *Water Resources Research* 45 (1): W00B10. doi:10.1029/2007WR006678.

Tsang, Y.W. 1984. "The Effect of Tortuosity on Fluid Flow through a Single Fracture." *Water Resources Research* 20 (9): 1209–1215. doi:10.1029/WR020i009p01209.

Tsang, Y.W. 1992. "Usage of 'Equivalent Apertures' for Rock Fractures as Derived from Hydraulic and Tracer Tests." *Water Resources Research* 28 (5): 1451–1455. doi:10.1029/92WR00361.

Tyler, S.W., J.B. Chapman, S.H. Conrad, D.P. Hammermeister, D.O. Blout, J.J. Miller, M.J. Sully, and J.M. Ginanni. 1996. "Soil-Water Flux in the Southern Great Basin, United States: Temporal and Spatial Variations over the Last 120,000 Years." *Water Resources Research* 32 (6): 1481–1499. doi:10.1029/96WR00564.

Tyler, S.W., W.A. McKay, J.W. Hess, R.L. Jacobson, and K. Taylor. 1986. *Effects of Surface Collapse Structures on Infiltration and Moisture Redistribution*, DOE/NV/10384-04; Publication No. 45045. Las Vegas, NV: Desert Research Institute, Water Resources Center.

Tyler, S.W., W.A. McKay, and T.M. Mihevc. 1992. "Assessment of Soil Moisture Movement in Nuclear Subsidence Craters." *Journal of Hydrology* 139 (1–4): 159–181. doi:10.1016/0022-1694(92)90200-F.

USGS, see U.S. Geological Survey.

U.S. Department of Energy, National Nuclear Security Administration Nevada Operations Office. 2001. *Addendum to Revision 1 of the Corrective Action Investigation Plan for Corrective Action Unit 98: Frenchman Flat, Nevada Test Site, Nevada*, Rev. 1, DOE/NV–478-REV. 1-ADD. Las Vegas, NV.

U.S. Department of Energy, National Nuclear Security Administration Nevada Site Office. 2011. *Underground Test Area Quality Assurance Project Plan, Nevada National Security Site, Nevada*, DOE/NV--1450. Las Vegas, NV.

U.S. Department of Energy, Nevada Operations Office. 1997a. *Regional Groundwater Flow and Tritium Transport Modeling and Risk Assessment of the Underground Test Area, Nevada Test Site, Nevada*, DOE/NV--477, UC-700. Las Vegas, NV.

U.S. Department of Energy, Nevada Operations Office. 1997b. *Shaft and Tunnel Nuclear Detonations at the Nevada Test Site: Development of a Primary Database for the Estimation of Potential Interactions with the Regional Groundwater System*, DOE/NV--464, UC-400. Las Vegas, NV.

U.S. Department of Energy, Nevada Operations Office. 2000a. *Corrective Action Investigation Plan for Corrective Action Unit 97: Yucca Flat/Climax Mine, Nevada Test Site, Nevada*, DOE/NV--659. Las Vegas, NV.

U.S. Department of Energy, Nevada Operations Office. 2000b. *United States Nuclear Tests, July 1945 through September 1992*, DOE/NV--209-REV 15. Las Vegas, NV.

U.S. Environmental Protection Agency. 1991. "National Primary Drinking Water Regulations; Radionuclides; Proposed Rule." *Federal Register* 56:138 (18 July).

U.S. Geological Survey. 2006. "USGS Groundwater Data for Nevada." As accessed at http://nwis.waterdata.usgs.gov/nv/nwis/gw on 5 June.

van Genuchten, M. Th. 1980. "A Closed-Form Equation for Predicting the Hydraulic Conductivity of Unsaturated Soils." *Soil Science Society of America Journal* 44 (5): 892–898.

Vincent, P., S. Larsen, D. Galloway, R.J. Laczniak, W.R. Walter, W. Foxall, and J.J. Zucca. 2003. "New Signatures of Underground Nuclear Tests Revealed by Satellite Radar Interferometry." *Geophysical Research Letters* 30 (22): 2141. doi:10.1029/2003GL018179.

Walvoord, M.A., F.M. Phillips, S.W. Tyler, and P.C. Hartsough. 2002. "Deep Arid System Hydrodynamics 2, Application to Paleohydrologic Reconstruction Using Vadose Zone Profiles from the Northern Mojave Desert." *Water Resources Research* 38 (12): 1291. doi:10.1029/2001WR000825.

Walvoord, M.A., M.A. Plummer, F.M. Phillips, and A.V. Wolfsberg. 2002. "Deep Arid System Hydrodynamics 1, Equilibrium States and Response Times in Thick Desert Vadose Zones." *Water Resources Research* 38 (12): 1308. doi:10.1029/2001WR000824.

Walvoord, M.A., D.A. Stonestrom, B.J. Andraski, and R.G. Striegl. 2004. "Constraining the Inferred Paleohydrologic Evolution of a Deep Unsaturated Zone in the Amargosa Desert." *Vadose Zone Journal* 3 (2): 502–512. doi:10.2136/vzj2004.0502.

Walvoord, M.A., R.G. Striegl, D.E. Prudic, and D.A. Stonestrom. 2005. "CO_2 Dynamics in the Amargosa Desert: Fluxes and Isotopic Speciation in a Deep Unsaturated Zone." *Water Resources Research* 41: W02006. doi:10.1029/2004WR003599.

Warren, R.G., D.A. Sawyer, F.M. Byers Jr., and J.C. Cole. 1998. A Petrographic/Geochemical Database and Stratigraphic and Structural Framework for the Southwestern Nevada Volcanic Field. Boulder, CO: National Oceanic and Atmospheric Administration, National Geophysical Data Center.

West, L.R., and W. Thordarson. 1963. *Summary of Hydraulic Data, Water Chemistry, and Abridged Lithologic Log of Ground-Water Test Well 8, Nye County, Nevada*, Technical Letter NTS-47. U.S. Geological Survey.

Wilson, G.V., D.M. Ely, S.L. Hokett, and D.R. Gillespie. 2000. "Recharge from a Subsidence Crater at the Nevada Test Site." *Soil Scientists Society of America Journal* 64 (5): 1570–1581. doi:10.2136/sssaj2000.6451570x.

Winograd, I.J., and W. Thordarson. 1975. *Hydrogeologic and Hydrochemical Framework, South-Central Great Basin, Nevada-California, with Special Reference to the Nevada Test Site*, Professional Paper 712-C. U.S. Geological Survey.

Wolfsberg, A., J. Boryta, E. Keating, P. Stauffer, C. Gable, and S. Kelkar. 2006. Written communication regarding *Analysis and Evaluation of Elevated Groundwater Heads and Their Impact on Flow and Solute Transport in the Tuff Pile: Areas 3, 4, and 7 of the Nevada Test Site, Nye County, Nevada*. Los Alamos, NM: Los Alamos National Laboratory.

Wolfsberg, A., L. Glascoe, G. Lu, A. Olson, P. Lichtner, M. McGraw, T. Cherry, and G. Roemer. 2002. *TYBO/BENHAM: Model Analysis of Groundwater Flow and Radionuclide Migration from Underground Nuclear Tests in Southwestern Pahute Mesa, Nevada*, LA-13977. Los Alamos, NM: Los Alamos National Laboratory.

Wood, D.B. 2007. *Digitally Available Interval-Specific Rock-Sample Data Compiled from Historical Records, Nevada Test Site and Vicinity, Nye County, Nevada*, Data Series 297. Reston, VA: U.S. Geological Survey.

Zavarin, M. Lawrence Livermore National Laboratory. 2012. Personal communication regarding LCA radionuclide sorption coefficients. 16 March. Livermore, CA.

Zavarin, M., M.R. Johnson, S.K. Roberts, R. Pletcher, T.P. Rose, A.B. Kersting, G. Eaton, Q. Hu, E. Ramon, J. Walensky, and P. Zhao. 2005. *Radionuclide Transport in Tuff and Carbonate Fractures from Yucca Flat, Nevada Test Site*, UCRL-TR-219836. Livermore, CA: Lawrence Livermore National Laboratory.

Zavarin, M., S. Roberts, P. Reimus, and M. Johnson. 2007. *Summary of Radionuclide Reactive Transport Experiments in Fractured Tuff and Carbonate Rocks from Yucca Flat, Nevada Test Site*, UCRL-TR-225271. Livermore, CA: Lawrence Livermore National Laboratory.

Zhang, D. 2002. *Stochastic Methods for Flow in Porous Media: Coping with Uncertainties*. San Diego, CA: Academic Press, A Division of Harcourt, Inc.

Zheng, Q., S.E. Dickson, and Y. Guo. 2008. "On the Appropriate 'Equivalent Aperture' for the Description of Solute Transport in Single Fractures: Laboratory-Scale Experiments." *Water Resources Research* 44, W04502. doi:10.1029/2007WR005970.

Zyvoloski, G.A., B.A. Robinson, Z.V. Dash, and L.L. Trease. 1997. *Summary of the Models and Methods for the FEHM Application—A Finite-Element Heat- and Mass-Transfer Code*, LA-13307-MS. Los Alamos, NM: Los Alamos National Laboratory.

Appendix A

Quality Assurance Project Plan Implementation

A.1.0 Implementation of QAPP Requirements in Yucca Flat/Climax Mine CAU Flow and Transport Model

The *Underground Test Area Quality Assurance Project Plan* (QAPP), *Nevada National Security Site, Nevada*, was revised to incorporate new requirements and issued in May 2011 (NNSA/NSO, 2011). An implementation plan was developed to ensure that UGTA participants achieve compliance with the requirements of the QAPP by the end of the fiscal year 2012 (N-I, 2011a). Gap analyses were compiled, and both project-wide and participant-specific gaps were identified (N-I, 2011b).

The *Yucca Flat/Climax Mine CAU Flow and Transport Model* is meant to be compliant with the QAPP and associated FFACO requirements (FFACO, 1996, as amended in 2010). This appendix summarizes how the QAPP modeling and software requirements and the data management requirements have been addressed in the activities supporting the development of the *Yucca Flat/Climax Mine CAU Flow and Transport Model*. To ease the presentation and to provide a uniform means of comparing how the requirements have been addressed, the same tabular format as presented in the gap analysis (N-I, 2011b) has been used. The modeling and software requirements are addressed in Table A-1, and the data management requirements are addressed in Table A-2.

As indicated in these tables, all QAPP requirements have been met either in this document or in products and activities supporting this product. NNSA/NSO intends to perform an assessment to determine the adequacy of the QAPP implementation for the Yucca Flat/Climax Mine CAU. This assessment is planned to be performed in fiscal year 2013.

The QAPP (NNSA/NSO, 2011) has been revised to reflect NDEP comments and other suggested clarifications of requirements (NDEP, 2011). The revised plan, the *Underground Test Area Activity Quality Assurance Plan, Nevada National Security Site, Nevada*, Rev. 1 (NNSA/NSO, 2012), was completed subsequent to the work performed to develop the *Yucca Flat/Climax Mine CAU Flow and Transport Model* document. Therefore, the requirements in effect are related to the QAPP (NNSA/NSO, 2011), and the following tables map the QAPP requirements documented in NNSA/NSO (2011) to their implementation in project products.

Table A-1
Implementation of QAPP Modeling and Software Requirements in the Yucca Flat/Climax Mine CAU Flow and Transport Model
(Page 1 of 12)

QAPP Requirement [a]	How the QAPP Requirement Is Addressed for the Yucca Flat/Climax Mine CAU	Where QAPP Requirement Is Addressed
SECTION A		
A.9 Computer Software and Codes		
Participants shall develop and implement procedures for the development (if necessary), modification, verification, and control of computer software codes.	The software and codes used in the calculation of contaminant transport from the contaminant sources in the four Yucca Flat/Climax Mine model domains (Climax Mine, Yucca Flat unsaturated zone, Yucca Flat saturated alluvial/volcanic aquifer system, and Yucca Flat saturated LCA) have been verified and controlled using project participants procedures. These software include FEHM, PLUMECALC, and Walkabout.	Records packages developed and maintained by each participant document the participant procedures related to development, modification, verification, and control of computer software.
Acquisition of commercially available off-the-shelf software shall be controlled through the procurement process.	Off-the-shelf software (e.g., Microsoft Excel, TecPlot, and other data processing software) were acquired through the procurement process at each UGTA participant organization.	Records packages developed and maintained by each participant document the participant procedures related to COTS software procurement.
A.9.1 Selection		
Participants shall identify the required and desirable attributes of a code before procurement, acquisition, or development.	The required attributes of codes were identified in the corrective action planning process, including the CAIP.	CAIP (DOE/NV, 2000)
Participants shall evaluate codes based on the identified attributes, and those without the required attributes shall be eliminated from consideration.	Code evaluation of Walkabout conducted by N-I using N-I software installation and checkout procedure.	Records packages developed and maintained by each participant.
Participants shall document the code selected for the groundwater flow and transport model and the selection criteria in the CAIP.	Codes selected for groundwater flow and radionuclide transport were identified in the CAIP.	CAIP (DOE/NV, 2000)
If a code change is required after publication of the CAIP, justification for the change and the potential codes shall be submitted to the Federal Sub-Project Director for approval.	A Record of Technical Change to the CAIP for use of PLUMECALC was submitted to the Activity Lead (referred to as the Federal Sub-Project Director in the QAPP [NNSA/NSO, 2011]). Other software used (Walkabout, MODFLOW/MT3DMS, Feflow, and FracMan/MAFIC) are for corroboration purposes.	Records packages developed and maintained by each participant.

Table A-1
Implementation of QAPP Modeling and Software Requirements in the Yucca Flat/Climax Mine CAU Flow and Transport Model
(Page 2 of 12)

QAPP Requirement [a]	How the QAPP Requirement Is Addressed for the Yucca Flat/Climax Mine CAU	Where QAPP Requirement Is Addressed
A.9.1 Selection (continued)		
The justification shall incorporate, at the minimum, a justification for the change, code attributes, testing results against the above criteria, and a comparison between available codes.	The justification for the proposed change from FEHM_sptr to Walkabout for particle tracking was to address identified numerical inaccuracies in FEHM_sptr when used in a highly heterogeneous flow field. As documented in Appendix K, these inaccuracies are inherent.	Code testing and justification is provided in Robinson et al. (2011). Additional testing and code justification is documented in Appendix K.
Upon approval, either a CAIP addendum or record of technical change shall be submitted to NDEP for approval.	N/A	N/A
Participants shall document other code selection within a record package.	Other codes have been documented in participant data packages.	Records packages developed and maintained by each participant.
A.9.2 Development		
Participants developing code or software shall ensure that the purpose and requirements of the code are clearly and precisely documented before development.	No code development was necessary. Walkabout was developed by LANL following LANL procedures.	Records packages developed and maintained by each participant.
Developed software shall be uniquely identified, and documentation shall include the following, at a minimum: • Input and output requirements (including the range of acceptable inputs) • Functional requirements including the operating system(s) • Assumptions • Identification of any limitations on applications • Identification of the compiler and its version • Instructions adequate for installation and execution of the software • Description and equations, algorithms, and numerical solution techniques, as applicable	No code development was necessary. Walkabout was developed by LANL following LANL procedures.	Records packages developed and maintained by each participant. Additional documentation of Walkabout in Painter (2011).
The developer shall develop a test case for software intended for multiple users.	No code development was necessary. Walkabout was developed and tested by LANL following LANL procedures. Additional testing was performed by N-I as documented in Appendix K.	Records packages developed and maintained by each participant.

Table A-1
Implementation of QAPP Modeling and Software Requirements in the Yucca Flat/Climax Mine CAU Flow and Transport Model
(Page 3 of 12)

QAPP Requirement [a]	How the QAPP Requirement Is Addressed for the Yucca Flat/Climax Mine CAU	Where QAPP Requirement Is Addressed
A.9.2 Development (continued)		
The test case shall be provided for installation testing to ensure that the software is functioning as intended and that results are consistent with those observed by the code developer.	No code development was necessary. Walkabout was developed by LANL following LANL procedures and installation testing performed by N-I.	Records packages developed and maintained by each participant.
The test case shall be provided to the users and shall include acceptance criteria for the results.	No code development was necessary. Test case for Walkabout was provided to users along with acceptance criteria.	Records packages developed and maintained by each participant.
Test case documentation shall include any necessary instructions and input data to execute (clearly identifying the specific application[s] tested).	No code development was necessary. Test case results for Walkabout were developed.	Records packages developed and maintained by each participant. Summaries of the testing results are included in Appendix K.
A.9.3 Verification		
Once code development is complete, the code developer, or designee, shall verify and document that the code performs the intended functions correctly and that the documentation identified in Section A.9.2 of this table is complete.	No code development was necessary. Verification testing performed by developer (Painter, 2011).	Records packages developed and maintained by each participant. Additional documentation in Painter (2011).
The verification required shall depend on the complexity, risk, and uniqueness of the code.	No code development was necessary. Verification testing performed on Walkabout was commensurate with complexity, risk, and uniqueness of the code.	Records packages developed and maintained by each participant. Additional documentation in Painter (2011).
Code modifications shall be verified according to the same requirements as the original code.	Code modifications to PLUMECALC verified by LANL.	Records packages developed and maintained by each participant. Additional documentation in Robinson et al. (2011).
Verification documentation shall describe the testing and results.	Verification testing results are documented.	Records packages developed and maintained by each participant. Additional documentation in Robinson et al. (2011) and Appendix K.

Table A-1
Implementation of QAPP Modeling and Software Requirements in the Yucca Flat/Climax Mine CAU Flow and Transport Model
(Page 4 of 12)

QAPP Requirement [a]	How the QAPP Requirement Is Addressed for the Yucca Flat/Climax Mine CAU	Where QAPP Requirement Is Addressed
A.9.4 Installation Testing		
Upon installation of software or code on a computer, operational checks (i.e., test cases provided by code developer) shall be performed to verify that the software is functioning as intended.	Installation testing performed by N-I.	Records packages developed and maintained by each participant.
Installation testing results must agree within the test-specified acceptance criteria before code application proceeds.	Installation testing results compared to acceptance criteria.	Records packages developed and maintained by each participant.
Installation testing shall be conducted when operation and hardware system configurations change.	Installation testing conducted when changes in operating and hardware system.	Records packages developed and maintained by each participant. Example of some additional tests presented in Section 4.0.
A.9.5 Code Review		
Code reviews shall be performed and documented to ensure that codes, and code applications, are technically adequate and properly documented, and satisfy established technical and quality requirements.	Code reviews occur during the development and testing of the codes and are conducted by each participant responsible for code development.	Records packages are developed and maintained by each participant.
Reviewers shall possess the appropriate technical expertise and shall not have participated in the development or installation testing of the code.	Independent reviewers are responsible for code reviews.	Records packages indicating the independent reviewers are developed and maintained by each participant.
The reviewer(s) shall address the following elements, as applicable: • Is the code appropriate for its intended application? • Are the assumptions reasonable and valid? • Are the mathematical model and mathematical operations correct? • Do the methods conform to accepted and published concepts? • Are results consistent with known data using either visual or quantitative measures? • Is documentation sufficient to reproduce development or testing, as applicable? • Is verification adequate to ensure confidence in the software/code?	These criteria are embodied in procedures of the participant responsible for code development. Code development may be single-use routines and codes intended for multiple applications.	Records package with review criteria, and review comments and comment resolutions are maintained as records by each participant.

Table A-1
Implementation of QAPP Modeling and Software Requirements in the Yucca Flat/Climax Mine CAU Flow and Transport Model
(Page 5 of 12)

QAPP Requirement [a]	How the QAPP Requirement Is Addressed for the Yucca Flat/Climax Mine CAU	Where QAPP Requirement Is Addressed
A.9.6 Configuration Control		
Participants shall maintain an inventory of computer software and codes used and develop and implement a system for identifying, revising, and controlling hardware/software configurations in accordance with DOE Order 200.1A, *Information Technology Management* (DOE, 2008).	Software configuration control is maintained by each participant developing and using software.	Records packages containing configuration control hardware and software are maintained by each participant.
The configuration of software shall be controlled and documented so traceability is maintained until software retirement.	Software configuration control is maintained by each participant developing and using software.	Records packages containing software configuration are maintained by each participant.
Codes shall undergo maintenance, verification, and instruction manual updates by the participant responsible for the code development and/or configuration control.	Code maintenance, verification, and manual updates are controlled by each participant.	Records packages containing maintenance, verification, and instruction manuals are maintained by each participant.
Participants shall obtain documentation for commercially available or acquired software.	Code documentation is controlled by each participant.	Records packages containing documentation for commercial or acquired software are maintained by each participant.
This documentation should contain reference material, operational test records, and user-oriented information, as available, and shall be maintained as records.	Code reference materials are controlled by each participant.	Records packages containing reference materials are maintained by each participant.
Configuration items include, but are not limited to, the following: • Operating system components • Runtime libraries, if applicable • Software executables • Source code files, if available • Users documentation, including software requirements and designs • Test plans and procedures • Software development and quality planning documents • Documentation of technical reviews	Software configuration items are controlled by each participant.	Records packages containing software configuration items are maintained by each participant.

Table A-1
Implementation of QAPP Modeling and Software Requirements in the Yucca Flat/Climax Mine CAU Flow and Transport Model
(Page 6 of 12)

QAPP Requirement [a]	How the QAPP Requirement Is Addressed for the Yucca Flat/Climax Mine CAU	Where QAPP Requirement Is Addressed
SECTION B		
B.5 Groundwater Flow and Transport Modeling		
Flow and transport modeling shall be documented in report(s) produced by the responsible participant.	This report and included references contain the flow and transport modeling produced by the responsible participants. The responsible participants are identified in the Acknowledgement to this document.	This document contains the documentation of the flow and transport modeling. Additional records packages are maintained by each participant.
B.5.1 Model Parameters		
The documentation of processing, calculating, characterizing, or applying data shall be included in the documents described in the following subsections.	See below.	N/A
B.5.1.1 Hydrostratigraphic Framework Model		
The M&O contractor is responsible for developing the HFM documents. These documents describe how the HFM and alternatives were developed, describe the models, and document the data sources.	Addressed in the HFM document.	BN, 2006
B.5.1.2 Hydrologic Data		
A CAU-specific hydrologic data document presents hydrologic data and the supporting information used to develop the groundwater flow and transport model; data quality assessments; data analyses to derive expected values or probability distributions; and hydrologic-parameter uncertainty estimates.	Addressed in the Yucca Flat/Climax Mine HDD.	SNJV, 2006
B.5.1.3 Transport Parameters		
A CAU-specific transport parameter document describes transport parameters and the supporting information used to develop the groundwater flow and transport model; data quality assessments; data analyses to derive expected values or probability distributions; and transport-parameter uncertainty estimates.	Addressed in the Yucca Flat/Climax Mine TDD.	SNJV, 2007

Table A-1
Implementation of QAPP Modeling and Software Requirements in the Yucca Flat/Climax Mine CAU Flow and Transport Model
(Page 7 of 12)

QAPP Requirement [a]	How the QAPP Requirement Is Addressed for the Yucca Flat/Climax Mine CAU	Where QAPP Requirement Is Addressed
B.5.1.4 Source Term Data		
A source term document is prepared for each CAU that describes development of simplified models or the conceptual models used for implementing source terms for the flow and transport models.	Addressed in HST documents and unclassified HST report.	Pawloski et al., 2008; Tompson, 2008; McNab, 2008; Carle et al., 2008; and SNJV, 2009. Additional analyses presented in Appendix C.
B.5.2 Model Parameter Preparation		
Data used to derive model parameter values for flow and transport models shall be evaluated for quality before use (Section A.8.2 of this table).	Data quality evaluated in supporting data documents. Additional data evaluated for quality in participant data packages and summarized in this document.	SNJV, 2006 and SNJV, 2007
Non-direct data shall be evaluated for acceptability before use (Section A.8.1 of this table).	Non-direct data evaluated in supporting data documents. Additional data evaluated for acceptability in participant data packages and summarized in this document.	SNJV, 2006 and SNJV, 2007
Data collected from a location outside of the model area shall be evaluated for transferability before use (Section A.8.3 of this table).	Transferability of data evaluated in supporting data documents. Additional data evaluated for transferability in participant data packages and summarized in this document.	SNJV, 2006 and SNJV, 2007
During the CADD/CAP stage, changes to parameters shall be documented in an addendum or, if requesting movement to the CR stage, in a summary report.	N/A at this stage of implementing the UGTA strategy.	N/A
Changes during the CR stage shall be documented in a summary report or CR addendum.	N/A at this stage of implementing the UGTA strategy.	N/A

Table A-1
Implementation of QAPP Modeling and Software Requirements in the Yucca Flat/Climax Mine CAU Flow and Transport Model
(Page 8 of 12)

QAPP Requirement [a]	How the QAPP Requirement Is Addressed for the Yucca Flat/Climax Mine CAU	Where QAPP Requirement Is Addressed
B.5.3 Model Calibration		
The calibration process is documented in the groundwater flow and transport model document, or subsequent modeling report developed during the CADD/CAP or CR stage.	Flow model calibration for the saturated alluvial/volcanic aquifer system and saturated LCA consists of comparisons to steady-state and transient data.	Sections 4.0 and 5.0
Documentation shall include the following: • Specific approaches used for model calibration • Rationale for selecting particular model calibration approaches • Calibration results • Comparison of initial versus final unit properties (e.g., porosity, permeability) • How the final properties relate to the conceptual model	Approaches and results of model calibration for the saturated alluvial/volcanic aquifer system and saturated LCA have used steady-state and transient data. Additional confirmation provided by comparisons to subsidence data (InSAR) and thermal data.	Sections 4.0 and 5.0
In addition, the model developer shall document why the model is a reasonable approximation of the *in situ* conditions.	Documentation of reasonableness of models includes comparison to alternative lines of evidence. Uncertainty in calibration is addressed using a range of alternative calibrations and NSMC approaches.	Sections 4.0 and 5.0
B.5.4 Sensitivity Analysis		
Sensitivity analysis will consider the purpose of the analysis and focus on the hypothesis to be tested.	Sensitivity analyses have been performed to identify the most significant parameters. Alternative flow models have been developed to investigate a reasonable range of calibrated models. Range of alternative contaminant boundary forecasts are developed to evaluate significance of model and parameter uncertainty.	Sections 3.0 to 6.0
The sensitivity analysis approach selected by the modeler shall be described and justified with respect to the model purpose in the flow and transport model document (or subsequent modeling documents).	The sensitivity analysis approach is described and justified.	Sections 3.0 to 6.0

Table A-1
Implementation of QAPP Modeling and Software Requirements in the Yucca Flat/Climax Mine CAU Flow and Transport Model
(Page 9 of 12)

QAPP Requirement [a]	How the QAPP Requirement Is Addressed for the Yucca Flat/Climax Mine CAU	Where QAPP Requirement Is Addressed
B.5.5 Uncertainty Analysis		
The method applicability to the uncertainty type shall be described and justified by the modeler with respect to the model purpose.	Uncertainty analyses have been performed to evaluate the effect of uncertainty in source term, unsaturated-zone flow and transport properties, saturated alluvial/volcanic aquifer system flow and transport properties, and saturated LCA flow and transport properties.	Sections 3.0 to 6.0
B.5.6 Contaminant Boundary Calculations		
The contaminant boundary calculation procedure involves the following steps:		
1. Selecting a groundwater flow model (which may include HFM and/or parameterization alternatives) (NNES, 2010).	Groundwater flow models in the saturated alluvial/volcanic aquifer system and the saturated LCA have been developed considering a range of uncertainty HFM alternatives and parameter uncertainty.	Sections 4.0 and 5.0
2. Assigning the hydrologic source term(s) using consistent groundwater flow rates observed in the selected flow model—if the test is not completely in the unsaturated zone (NNES, 2010).	Two alternative HSTs have been developed. Within each alternative, uncertainties in HST parameters (e.g., size of exchange volume, properties of altered zones, inventory) have been included in the model.	Section 2.0 and Appendix C Implementation is presented in Sections 3.0, 4.0, and 6.0.
3. Executing radionuclide transport calculations for flow model results, including consideration of source term and transport uncertainties (NNES, 2010).	Transport calculations have been conducted for sources in the unsaturated zone, saturated alluvial/volcanic aquifer system, and the saturated LCA.	Sections 3.0, 4.0, and 6.0.
4. Collecting contaminant concentration distributions (in space) at regular, specified output times over a 1,000-year period, for all simulations of the transport model (Daniels and Tompson, 2003; NNES, 2010).	Transport calculations are provided at 10, 50, 100, 150, 200, 300, 400, 500, 600, 700, 800, 900, and 1,000 years.	Section 6.5
5. Converting contaminant concentration distributions to the radiological standards of the SDWA (CFR, 2010) for each transport model result (Daniels and Tompson, 2003; NNES, 2010).	Contaminant concentrations are normalized to SDWA MCLs, and fractional exceedance of MCLs are added to determine the probability the MCL will be exceeded from all radionuclides considered.	Section 6.5

Table A-1
Implementation of QAPP Modeling and Software Requirements in the Yucca Flat/Climax Mine CAU Flow and Transport Model
(Page 10 of 12)

QAPP Requirement [a]	How the QAPP Requirement Is Addressed for the Yucca Flat/Climax Mine CAU	Where QAPP Requirement Is Addressed
B.5.6 Contaminant Boundary Calculations (continued)		
6. Determining spatial locations and times where radiological standards are exceeded for each transport model result (Daniels and Tompson, 2003; NNES, 2010).	Spatial locations where MCL is forecast to be exceeded are determined.	Section 6.5
7. Logging the frequency that radiological standards are exceeded at each model element location, regardless of time, over the entire series of transport model simulations (Daniels and Tompson, 2003; NNES, 2010).	Time cumulative probabilities of exceeding the MCL have been determined for each modeling case simulated.	Section 6.5
8. Identifying model element locations where the frequency that radiological standards are exceeded is greater than 5% of the total number of transport simulations. Elements meeting this criterion are then considered within the contaminant boundary at 95th percentile; elements not meeting this criterion are considered outside the boundary (Daniels and Tompson, 2003; NNES, 2010).	Time cumulative probabilities of exceeding the MCL have been determined for each modeling case, allowing for determining the frequency that radiological standards are exceeded in at least 5% of the realizations.	Section 6.5
9. Repeating the described procedural steps for multiple alternative models.	Alternative source term models, alternative infiltration/recharge models, alternative LCA flow models, and alternative representations of LCA transport parameter distributions have been repeated to develop multiple representations of the probability of areas exceeding the MCL.	Section 6.5

Table A-1
Implementation of QAPP Modeling and Software Requirements in the Yucca Flat/Climax Mine CAU Flow and Transport Model
(Page 11 of 12)

QAPP Requirement [a]	How the QAPP Requirement Is Addressed for the Yucca Flat/Climax Mine CAU	Where QAPP Requirement Is Addressed
B.6 Model Evaluation		
During this stage, additional data will be gathered to increase confidence in the conceptual model and flow and transport model results reliability.	Model evaluation occurs during the CADD/CAP stage of the UGTA strategy. As such, this requirement is not explicitly addressed in this document. However, the conclusions summarized in Section 7.0 identify likely candidate observation locations that could be used to evaluate the reasonableness of model results with particular focus on near-field wells located downgradient from likely significant contaminant sources to the LCA.	Additional data will be collected during the CADD/CAP stage of the UGTA strategy to evaluate the representativeness of key processes likely to affect contaminant transport from underground nuclear detonations conducted in the Yucca Flat/Climax Mine CAU. These data collection activities will be identified in the CADD/CAP.
Refinements to the model will be documented as addenda to the CADD/CAP or in a summary report.	N/A at this stage of implementing the UGTA strategy.	N/A
These evaluations will be documented as addenda to the CR or in a summary report.	N/A at this stage of implementing the UGTA strategy.	N/A
B.7 Configuration Control		
Models accepted by NDEP (before the CADD/CAP and CR stages) shall be archived and placed under configuration control (Section A.9.6 of this table). The model documentation shall be sufficient to ensure traceability and reproducibility.	N/A at this stage of implementing the UGTA strategy. Model documentation is traceable and reproducible.	Model documentation data packages are retained as records by the participants.
Documentation shall include the following: • Input data and source identification • Identification of model assumptions and limitations (e.g., valid ranges of model application, spatial and temporal scaling) • Model executable codes, including pre- and post-processors • Computer calculations, and basis to permit traceability of inputs and outputs • Final results and output data files • Identification of the originator(s) and reviewer(s)	This documentation is included in data packages prepared by the participants supporting the modeling of the Yucca Flat/Climax Mine CAU in accordance with their applicable procedures.	This documentation is retained as records by the individual participants.

Table A-1
Implementation of QAPP Modeling and Software Requirements in the Yucca Flat/Climax Mine CAU Flow and Transport Model
(Page 12 of 12)

QAPP Requirement [a]	How the QAPP Requirement Is Addressed for the Yucca Flat/Climax Mine CAU	Where QAPP Requirement Is Addressed
SECTION C		
C.4.1 Input to Other Participant Documents		
When transmitting information, professional judgment, data, code, models, or inputs to another participant, the originating participant shall ensure that the source(s) of the transmittal is identified and traceable.	Input provided by LANL, LLNL, and DRI to N-I identifies the source of the material.	Material sources for all inputs are identified in the document. Additional documentation of inputs is retained as record by individual participants.
The originating participant shall also identify any limitations or qualifiers for the data or information to the receiving entity.	Originating participant has identified limitations and qualifiers on information provided.	Documentation of limitations and qualifiers is retained as record by sending and receiving participants.

[a] Modified from N-I (2011b)

Table A-2
Implementation of QAPP Data Management Requirements in the Yucca Flat/Climax Mine CAU Flow and Transport Model
(Page 1 of 8)

QAPP Requirement [a]	How the QAPP Requirement Is Addressed for the Yucca Flat/Climax Mine CAU	Where QAPP Requirement Is Addressed
SECTION A		
A.8 Data Management		
Participants shall ensure that processes are in place for the management, control, and transfer of data.	Data management, control, and transfer are addressed by individual participant procedures.	Records packages containing data management, control, and transfer are maintained by each participant.
The processes shall include provisions for gathering, manipulating, and distributing data, and shall address the following:	Processes for gathering, manipulating, and distributing data are addressed by individual participant procedures.	Records packages containing processes for gathering, manipulating, and distributing data are maintained by each participant.
1. Participants shall verify that transcription and transfer of data are performed correctly by: • reviewing a representative sample of sufficient data points to provide confidence that data have been transcribed or transferred properly; • documenting the method of verification and verification results; and • documenting the transfer of data to software applications, including software application name and version number.	Processes for verifying transcription and transfer of data are addressed by individual participant procedures.	Records packages containing processes for verifying transcription and transfer of data are maintained by each participant.
2. Data used in reports, analyses, models, or interpretive works are traceable to their source.	Processes for evaluating data traceability are addressed by individual participant procedures.	Records packages containing processes for data traceability are maintained by each participant. Data used in this document are traceable to their source.
3. Data that have been manipulated are checked to ensure the manipulation process was performed as intended.	Processes for checking data manipulation are addressed by individual participant procedures.	Records packages containing processes for checking data manipulation are maintained by each participant.
4. Data are maintained during the lifetime of the project using backup and archival processes.	Data are maintained using backup and archival processes.	Records packages containing processes for maintaining data during the project lifetime are maintained by each participant.
5. Data used in reports, analyses, models, or interpretive works are maintained as records in accordance with Section A.7 of this table.	Data are maintained using processes addressed in individual participant procedures.	Records packages containing data used in reports, analyses, and models are maintained by each participant.

Table A-2
Implementation of QAPP Data Management Requirements in the Yucca Flat/Climax Mine CAU Flow and Transport Model
(Page 2 of 8)

QAPP Requirement [a]	How the QAPP Requirement Is Addressed for the Yucca Flat/Climax Mine CAU	Where QAPP Requirement Is Addressed
A.8 Data Management (continued)		
6. Access to databases, datasets, and files is controlled so that unauthorized modifications or deletions are not allowed.	Database access is controlled.	Access to databases is controlled by N-I database procedures.
7. Data source(s), extraction criteria, and data quality are documented or referenced, and maintained with the dataset extracted from a database.	Databases identify data sources and data quality.	Databases maintained and controlled by N-I identify data sources and data quality.
8. Data not acquired in compliance with this QAPP are evaluated for acceptability (see Section A.8.1 of this table) before use. Acceptance will be established before entry into a database, when possible. If data are incorporated into a database before documenting acceptance, the data shall be flagged and clearly identified as "preliminary."	Data not acquired in accordance with the requirements of the QAPP that are entered into the N-I database are flagged as "preliminary" until they have been qualified.	N-I databases indicate the quality of the data.
9. Data are evaluated for quality as described in Section A.8.2 of this table.	See Section A.8.2 of this table.	Records packages containing processes for evaluating data quality are maintained by each participant.
10. Data collected from a location outside of the model area shall be evaluated for transferability before use (see Section A.8.3 of this table).	See Section A.8.3 of this table.	Records packages containing processes for evaluating data transferability are maintained by each participant.
A.8.1 Data Source Acceptance		
Data not acquired in compliance in accordance with the requirements of the QAPP (e.g., non-direct data) shall be evaluated for acceptance before use by the Sub-Project.	Data used in this analysis have been generally acquired in accordance with the requirements of the QAPP.	Most data are summarized in the Yucca Flat/Climax Mine HDD (SNJV, 2006) and the Yucca Flat/Climax Mine TDD (SNJV, 2007). Additional data, also developed in compliance with the QAPP, are presented in Appendices E, G, and J. Additional data have been evaluated for acceptability in participant data packages and summarized in this document (Sections 3.2 and 6.3). Data acquired by recognized national organizations such as the National Oceanic and Atmospheric Administration (NOAA) and USGS have been determined to be acceptable.

Table A-2
Implementation of QAPP Data Management Requirements in the Yucca Flat/Climax Mine CAU Flow and Transport Model
(Page 3 of 8)

QAPP Requirement [a]	How the QAPP Requirement Is Addressed for the Yucca Flat/Climax Mine CAU	Where QAPP Requirement Is Addressed
A.8.1 Data Source Acceptance (continued)		
Data obtained from a peer-reviewed journal shall be considered acceptable and shall not require a source acceptance evaluation.	Peer review journal information was used to corroborate qualified data and to support the parameter distributions developed based on qualified data.	N/A
A.8.1.1 Approach		
A subject matter expert or Topical Committee shall evaluate non-direct data sources (e.g., defense projects, Yucca Mountain Project, databases) to determine the appropriateness of the methods and the correctness of the resulting dataset or data source.	Non-direct data are generally used in a corroborative sense and are not directly relied upon for the saturated-zone flow and transport models. Non-direct data sources have been used for some of the unsaturated-zone data, including analysis of crater recharge, and unsaturated-zone flow and transport properties. These data are determined to be appropriate by the participant.	Data appropriateness for most datasets is evaluated in the Yucca Flat/Climax Mine HDD (SNJV, 2006) and the Yucca Flat/Climax Mine TDD (SNJV, 2007). Records packages associated with the appropriateness of additional data sources are maintained by each participant.
The expert or committee shall address one or more of the following as applicable: • The equipment and procedures used to collect and analyze the data are technically adequate (e.g., typical of scientific and industry standards). • The extent to which the data demonstrate the properties of interest (e.g., physical, chemical, geologic, and mechanical) is reasonable given the range of inherent variability for the property. • Conditions under which the data were obtained, if germane to the data quality, are acceptable. • Measurements were performed in accordance with sound technical or administrative practices or procedures. • Data have been used in similar applications. • Data and their results have undergone prior peer or other professional review. • A sufficient quantity of corroborating data is available to demonstrate comparability.	Because other non-direct data are generally used in a corroborative sense and are not directly relied upon for the flow and transport model, these requirements are not applicable. Other datasets are determined to be appropriate by the participant.	Data appropriateness for most datasets is evaluated in the Yucca Flat/Climax Mine HDD (SNJV, 2006) and the Yucca Flat/Climax Mine TDD (SNJV, 2007). Records packages associated with the appropriateness of additional data sources are maintained by each participant.

Table A-2
Implementation of QAPP Data Management Requirements in the Yucca Flat/Climax Mine CAU Flow and Transport Model
(Page 4 of 8)

QAPP Requirement [a]	How the QAPP Requirement Is Addressed for the Yucca Flat/Climax Mine CAU	Where QAPP Requirement Is Addressed
A.8.1.2 Documentation		
The expert or committee shall develop a data acceptance report and address the following, as applicable: • Description of data, its source, rationale for its selection, and its intended uses • Extent and reliability of the documentation associated with the data • Discussion of attributes described above (Section A.8.1.1 of this table) • Prior uses of the data and associated verification processes • Dataset(s) used for corroboration, rationale for selection, and justification of inferences drawn • Data acquisition, collection, or development records • DQIs (i.e., accuracy, precision, representativeness, completeness, and comparability) • Impact of use or nonuse of data • Uncertainties and restrictions, if any • Assumptions, constraints, bounds, or limits on the data or source • Data flags to be assigned to the data	Because non-direct data are generally used in a corroborative sense and are not directly relied upon for the flow and transport model, there is no need to develop a data acceptance report.	Data acceptance for most datasets is evaluated in the Yucca Flat/Climax Mine HDD (SNJV, 2006) and the Yucca Flat/Climax Mine TDD (SNJV, 2007). Records packages associated with the acceptance of additional data sources are maintained by each participant.
A.8.1.3 Documentation Review		
If the acceptance evaluation was not performed by a committee, an independent reviewer shall review the document for the following items: • The content of the report is technically adequate, complete, and correct. • Uncertainties and restrictions are discussed. • The assumptions, constraints, bounds, or limits on the data are identified.	Because non-direct data are only used in a corroborative sense and are not directly relied upon for the flow and transport model, there is no need to develop a data acceptance report.	Data acceptance for most datasets is evaluated in the Yucca Flat/Climax Mine HDD (SNJV, 2006) and the Yucca Flat/Climax Mine TDD (SNJV, 2007). Records packages associated with the appropriateness of additional data sources are maintained by each participant.

Table A-2
Implementation of QAPP Data Management Requirements in the Yucca Flat/Climax Mine CAU Flow and Transport Model
(Page 5 of 8)

QAPP Requirement [a]	How the QAPP Requirement Is Addressed for the Yucca Flat/Climax Mine CAU	Where QAPP Requirement Is Addressed
A.8.2 Data Quality Evaluation		
Participants shall ensure that data are evaluated with respect to quality before use in reports, analyses, interpretive works, or models.	Data quality is evaluated by each participant responsible for collecting or developing data before their use in models, analyses, interpretive works, or reports.	Records packages containing processes for data quality evaluations are maintained by each participant. Principal data quality evaluations are contained in the Yucca Flat/Climax Mine HDD (SNJV, 2006) and the Yucca Flat/Climax Mine TDD (SNJV, 2007). Additional data have been evaluated for acceptability in participant data packages and summarized in this document (Sections 3.2 and 6.3). Data acquired by recognized national organizations such as NOAA and USGS have been determined to be acceptable.
Data quality flags shall be assigned and documented for each individual data record or group of similar records to indicate the quality or suitability for the intended usage.	Data quality flags are applied to data prior to their use in accordance with applicable participant procedures.	Records packages containing processes for indicating data quality are maintained by each participant
Reports, models, or interpretive works shall indicate the quality of the data being used.	The data used in this report, other than those used in corroborative analyses, are direct data and have been generated using processes compliant with the QAPP or have been qualified in other project documents.	Records packages containing processes for indicating the quality of data are maintained by each participant. The Yucca Flat/Climax Mine HDD (SNJV, 2006) and the Yucca Flat/Climax Mine TDD (SNJV, 2007) document the quality of data used in the flow and transport models.

Table A-2
Implementation of QAPP Data Management Requirements in the Yucca Flat/Climax Mine CAU Flow and Transport Model
(Page 6 of 8)

QAPP Requirement [a]	How the QAPP Requirement Is Addressed for the Yucca Flat/Climax Mine CAU	Where QAPP Requirement Is Addressed
A.8.3 Data Transferability		
Participants shall determine the transferability of data using the following steps:		
1. Establish acceptance criteria based on the use of the parameter and its importance. These criteria are established before the modeling simulations and the uncertainty and parameter sensitivity evaluations are performed. Changes in the criteria might be expected as the CAU investigations and modeling progress. Thus, if it is determined that more restrictive criteria are needed for a particular parameter, it will be necessary to repeat the transferability evaluation. If the previously used criteria are restrictive enough, it will not be necessary to re-perform the evaluation.	Acceptance criteria for most data used in the Yucca Flat/Climax Mine CAU models have been used in the data reports. Additional data transferability is evaluated with applicable participant procedures.	Data transferability for most datasets is evaluated in the Yucca Flat/Climax Mine HDD (SNJV, 2006) and the Yucca Flat/Climax Mine TDD (SNJV, 2007). Records packages associated with the transferability of additional data sources are maintained by each participant.
2. Evaluate whether geologic, geochemical, hydrologic, or other factors would disqualify the measurement for use by the Sub-Project.	Factors potentially affecting the transferability of data are addressed in the data documents.	The effect of identified factors on data transferability for most datasets is evaluated in the Yucca Flat/Climax Mine HDD (SNJV, 2006) and the Yucca Flat/Climax Mine TDD (SNJV, 2007). Records packages associated with the transferability of additional data sources are maintained by each participant.
3. Document the process and data used in sufficient detail that others can understand and repeat the process. This information should be incorporated either directly or by reference.	Data used in the models and analyses have been documented in this document or supporting documents.	The principal data evaluation documents supporting the models in the current document are the Yucca Flat/Climax Mine HDD (SNJV, 2006) and the Yucca Flat/Climax Mine TDD (SNJV, 2007).

Table A-2
Implementation of QAPP Data Management Requirements in the Yucca Flat/Climax Mine CAU Flow and Transport Model
(Page 7 of 8)

QAPP Requirement [a]	How the QAPP Requirement Is Addressed for the Yucca Flat/Climax Mine CAU	Where QAPP Requirement Is Addressed
A.8.3 Data Transferability (continued)		
The approach for implementing the data transfer process shall be parameter specific and shall consider the following, if applicable: • Parameter characteristics, including underlying dependencies on other parameters • Similarity of geologic setting and other relevant characteristics • Type of measurement and/or interpretative technique, including measurement scale • Modeling approach, including conceptual models and model scale • Heterogeneity • Range in values • Sensitivity of contaminant boundary to parameter value • Reports, models, or interpretive works shall describe the transferability of the data being used	Data transferability approach is described in the data documents. Additional data transferability is addressed in this document and related participant procedures.	Data transferability is documented in the Yucca Flat/Climax Mine HDD (SNJV, 2006) and the Yucca Flat/Climax Mine TDD (SNJV, 2007). Additional data transferability for unsaturated-zone data sources is documented in participant's records packages and summarized in Section 3.2 based on the similarity of geologic setting and HSU characteristics.
SECTION B		
B.4 Non-direct Data		
The source of these data shall be evaluated for acceptability before their use.	See specific requirements in Section A of this table.	See documents above in Section A of this table.
The approach, documentation, and review associated with this evaluation are described in Sections A.8.1.1 to A.8.1.3 of this table. After the data source is accepted, data records shall be managed in accordance with Section A.7 of this table. Data shall be evaluated with respect to quality as described in Section A.8.2 of this table; and if used and not collected from within the CAU of interest, data shall be evaluated for transferability as described in Section A.8.3 of this table.	See specific requirements in Section A of this table.	See documents in Section A of this table.

Table A-2
Implementation of QAPP Data Management Requirements in the Yucca Flat/Climax Mine CAU Flow and Transport Model
(Page 8 of 8)

QAPP Requirement [a]	How the QAPP Requirement Is Addressed for the Yucca Flat/Climax Mine CAU	Where QAPP Requirement Is Addressed
SECTION C		
C.4.1 Input to Other Participant Documents		
When transmitting information, professional judgment, data, code, models, or inputs to another participant, the originating participant shall ensure that the source(s) of the transmittal is identified and traceable.	Input provided by LANL, LLNL, and DRI to N-I identifies the source of the material.	Material sources for all inputs are identified in the document. Additional documentation of inputs is retained as record by individual participants.
The originating participant shall also identify any limitations or qualifiers for the data or information to the receiving entity.	Originating participant has identified limitations and qualifiers on information provided.	Documentation of limitations and qualifiers is retained as record by sending and receiving participants.

[a] Modified from N-I (2011b)

A.2.0 REFERENCES

BN, see Bechtel Nevada.

Bechtel Nevada. 2006. *A Hydrostratigraphic Model and Alternatives for the Groundwater Flow and Contaminant Transport Model of Corrective Action Unit 97: Yucca Flat-Climax Mine, Lincoln and Nye Counties, Nevada*, DOE/NV/11718--1119. Prepared for the U.S. Department of Energy, National Nuclear Security Administration Nevada Site Office. Las Vegas, NV.

CFR, see *Code of Federal Regulations*.

Carle, S.F., M. Zavarin, Y. Sun, and G.A. Pawloski. 2008. *Evaluation of Hydrologic Source Term Processes for Underground Nuclear Tests in Yucca Flat, Nevada Test Site: Carbonate Tests*, LLNL-TR-403485. Livermore, CA: Lawrence Livermore National Laboratory.

Code of Federal Regulations. 2010. Title 40 CFR, Part 141, "National Primary Drinking Water Regulations." Washington, DC: U.S. Government Printing Office.

DOE, see U.S. Department of Energy.

DOE/NV, see U.S. Department of Energy, Nevada Operations Office.

Daniels, J.I., and A.F.B. Tompson. 2003. *Technical Basis for Also Using Health-Risk Assessment To Establish Contaminant Boundaries for Corrective Action Units (CAUs) of the Underground Test Area (UGTA) at the Nevada Test Site (NTS)*, UCRL-TR-201702. Livermore, CA: Lawrence Livermore National Laboratory.

FFACO, see *Federal Facility Agreement and Consent Order*

Federal Facility Agreement and Consent Order. 1996 (as amended March 2010). Agreed to by the State of Nevada; U.S. Department of Energy, Environmental Management; U.S. Department of Defense; and U.S. Department of Energy, Legacy Management. Appendix VI, which contains the Underground Test Area strategy, was last modified May 2011, Revision No. 4.

McNab, W.W. 2008. *Evaluation of Hydrologic Source Term Processes for Underground Nuclear Tests in Yucca Flat, Nevada Test Site: Unsaturated Tests and the Impact of Recharge*, LLNL-TR-403360. Livermore, CA: Lawrence Livermore National Laboratory.

NDEP, see Nevada Division of Environmental Protection.

N-I, see Navarro-Intera, LLC.

NNES, see Navarro Nevada Environmental Services, LLC.

NNSA/NSO, see U.S. Department of Energy, National Nuclear Security Administration Nevada Site Office.

Navarro-Intera, LLC. 2011a. Written communication. Subject: Transmittal of the Underground Test Area Sub-Project Implementation Plan for the Quality Assurance Project Plan. May. Las Vegas, NV.

Navarro-Intera, LLC. 2011b. Written communication. Subject: Transmittal of the Underground Test Area Quality Assurance Project Plan (QAPP) Gap Analysis. September. Las Vegas, NV.

Navarro Nevada Environmental Services, LLC. 2010. *Phase II Transport Model of Corrective Action Unit 98: Frenchman Flat, Nevada Test Site, Nye County, Nevada*, Rev.1, N-I/28091--004, S-N/99205--122. Las Vegas, NV.

Nevada Division of Environmental Protection. 2011. Written communication. Subject: Underground Test Area Quality Assurance Plan, Nevada National Security Site, Nevada, Revision No. 0, May 2011, Federal Facility Agreement and Consent Order. June. Las Vegas, NV.

Painter, S.L. 2011. *User's Manual for Walkabout V1.0*, LA-UR-11-01952. Los Alamos, NM: Los Alamos National Laboratory.

Pawloski, G.A., A.F.B. Tompson, S.F. Carle, R.L. Detwiler, Q. Hu, S. Kollet, R.M. Maxwell, W.W. McNab, S.K. Roberts, D.E. Shumaker, Y. Sun, and M. Zavarin. 2008. *Evaluation of Hydrologic Source Term Processes for Underground Nuclear Tests in Yucca Flat, Nevada Test Site: Introduction and Executive Summary*, LLNL-TR-403428. Livermore, CA: Lawrence Livermore National Laboratory.

Robinson, B.A., Z.V. Dash, and S.L. Painter. 2011. *User's Guide for the PLUMECALC Application with Subgridding*, LA-UR-11-02090. Los Alamos, NM: Los Alamos National Laboratory.

SNJV, see Stoller-Navarro Joint Venture.

Stoller-Navarro Joint Venture. 2006. *Phase I Hydrologic Data for the Groundwater Flow and Contaminant Transport Model of Corrective Action Unit 97: Yucca Flat/Climax Mine, Nevada Test Site, Nye County, Nevada*, Rev. 0, S-N/99205--077. Las Vegas, NV.

Stoller-Navarro Joint Venture. 2007. *Phase I Contaminant Transport Parameters for the Groundwater Flow and Contaminant Transport Model of Corrective Action Unit 97: Yucca Flat/Climax Mine, Nevada Test Site, Nye County, Nevada*, Rev. 0, S-N/99205--096. Las Vegas, NV.

Stoller-Navarro Joint Venture. 2009. *Unclassified Source Term and Radionuclide Data for Corrective Action Unit 97: Yucca Flat/Climax Mine, Nevada Test Site, Nevada*, Rev. 2, S-N/99205--114. Las Vegas, NV.

Tompson, A.F.B., ed. 2008. *Evaluation of Hydrologic Source Term Processes for Underground Nuclear Tests in Yucca Flat, Nevada Test Site: Saturated Tests*, LLNL-TR-403429. Livermore, CA: Lawrence Livermore National Laboratory.

U.S. Department of Energy. 2008. *Information Technology Management*, DOE Order 200.1A. Washington, DC.

U.S. Department of Energy, National Nuclear Security Administration Nevada Site Office. 2011. *Underground Test Area Quality Assurance Project Plan, Nevada National Security Site, Nevada*, DOE/NV--1450, Rev. 0. Las Vegas, NV.

U.S. Department of Energy, National Nuclear Security Administration Nevada Site Office. 2012. *Underground Test Area Quality Assurance Plan, Nevada National Security Site, Nevada*, DOE/NV--1450, Rev. 1. Las Vegas, NV.

U.S. Department of Energy, Nevada Operations Office. 2000. *Corrective Action Investigation Plan for Corrective Action Unit 97: Yucca Flat/Climax Mine, Nevada Test Site, Nevada*, DOE/NV--659. Las Vegas, NV.

Appendix B

Yucca Flat/Climax Mine CAU Detonation Characteristics

B.1.0 YUCCA FLAT/CLIMAX MINE CAU DETONATION CHARACTERISTICS

The available information on the depth-related characteristics of the 747 Yucca Flat/Climax Mine CAU detonations are documented in Table B-1. This table presents information available in other UGTA Activity controlled documents and databases, including DOE/NV (1997 and 2000), Grasso (2001), SNJV (2009), Pawloski et al. (2008) and BN (2006). This table is organized alphabetically.

The characteristics of the detonations in the Yucca Flat/Climax Mine CAU can be visualized in many ways. A number of these graphical depictions are included in Sections 1.0 and 2.0 of this document. An additional means of visualizing this information is to develop cross plots of the detonations using metrics of potential relevance to the fate and transport of radionuclides that are in the initial inventory. One such depiction is illustrated in Figure B-1. This figure identifies the detonations that are within both 5 R_c of a fault and 5 R_c of the saturated LCA. The symbols on this figure illustrate whether the detonation has a working point that is above or below the water table. The size of each symbol on this graphic indicates the size of the exchange volume of each detonation. Because most of the detonations have announced maximum yields of 200 kt, the sizes are commensurate with that magnitude of detonation. The color scheme indicates the amount of enhanced crater recharge associated with the crater overlying each of the indicated detonations, if there is a crater at that location. It is not surprising that the detonations that have working points closest to the saturated LCA and are close to faults are also those detonations that have been determined to most significantly contribute to the extent of the contaminant boundary as evaluated in Section 6.5, notably the BOURBON, TORRIDO and MICKEY detonations.

Table B-1
Yucca Flat/Climax Mine Detonation Characteristics
(Page 1 of 23)

Detonation Name	Emplacement Hole Name	CAS	UTM Easting	UTM Northing	Date Expended	Announced Yield (kt)[a]	Cavity Radius (m)[b]	Land Surface Elevation (m amsl)	Depth to Working Point (m)	Working Point HSU	Estimated Depth to Steady State Water Level (m)	Saturated Working Point	Estimated Depth to Saturated LCA or LCA3 (m)	Number of R_c from WP to Saturated LCA or LCA3
AARDVARK	U-3am(s)	03-57-013	586202.6	4102340.7	05/12/1962	40	43	1,240.8	434	LTCU	503	No	921	11.3
ABEYTAS	U-3gx	03-57-162	587894.0	4098394.1	11/05/1970	20 to 200	76	1,215.2	393	TM-LVTA	481	No	773	5.0
ABILENE	U-3mn	03-57-270	585020.7	4096555.6	04/07/1988	<20	40	1,214.6	245	TM-UVTA	481	No	1082	20.9
ABO	U-3mc	03-57-263	585707.0	4100718.6	10/30/1985	<20	42	1,229.0	196	AA	495	No	1232	24.7
ABSINTHE	U-3ep	03-57-110	587232.8	4100114.5	05/26/1967	<20	47	1,225.9	119	AA	492	No	936	17.4
ACE	U-2n	02-57-145	582057.1	4111553.6	06/11/1964	3	20	1,326.8	266	AA	579	No	814	26.2
ACUSHI	U-3bg	03-57-033	587049.5	4100234.7	02/08/1963	Low	39	1,225.9	261	AA	492	No	975	18.3
ADZE	U-3fw	03-57-137	589379.6	4096098.6	05/28/1968	<20	40	1,215.2	240	TSA	475	No	666	10.7
AGILE	U-2v	02-57-151	582934.9	4109148.8	02/23/1967	20 to 200	65	1,297.2	733	TM-LVTA	543	Yes	1025	4.5
AGOUTI	U-3ao	03-57-015	585868.6	4100346.4	01/18/1962	6.4	26	1,227.4	261	AA	494	No	1257	36.9
AGRINI	U-2ev	02-57-122	581343.1	4111306.7	03/31/1984	<20	37	1,330.8	320	AA	584	No	855	14.5
AHTANUM	U-2l	02-57-143	581628.7	4113187.9	09/13/1963	Low	40	1,346.9	226	AA	604	No	606	9.5
AJAX	U-9al	09-57-035	584394.3	4110007.1	11/11/1966	<20	40	1,280.8	238	AA	537	No	902	16.6
AJO	U-3gd	03-57-144	585851.5	4098524.0	01/30/1970	<20	37	1,218.6	304	AA	486	No	1329	27.7
AKAVI	U-2es	02-57-119	582515.1	4111539.4	12/03/1981	20 to 150	65	1,320.4	494	TM-LVTA	576	No	776	4.3
AKBAR	U-10ax	10-57-028	585846.5	4113082.3	11/09/1972	<20	39	1,321.9	267	TM-LVTA	588	No	588	8.2
ALEMAN	U-3kz	03-57-240	584481.3	4102754.6	09/11/1986	<20	33	1,245.1	503	TM-LVTA	475	Yes	1020	15.7
ALGODONES	U-3jn	03-57-208	585682.5	4101447.6	08/18/1971	20 to 200	71	1,233.2	528	TM-UVTA	497	Yes	1140	8.7
ALIGOTE	U-7bg	07-57-028	588499.6	4106431.8	05/29/1981	<20	37	1,337.5	320	LTCU	606	No	606	7.7
ALIMENT	U-3gj	03-57-150	590293.1	4096467.7	05/15/1969	<20	40	1,234.1	241	OSBCU	503	No	503	6.6
ALLEGHENY	U-9x	09-57-113	585931.2	4108050.1	09/29/1962	Low	41	1,297.8	211	TM-WTA	564	No	736	12.8
ALPACA	U-2a	02-57-001	581991.1	4113320.2	02/12/1965	0.33	10	1,341.7	225	AA	604	No	604	37.9
ALUMROOT	U-9cj	09-57-081	584359.2	4111408.7	02/14/1973	<20	43	1,291.4	183	AA	546	No	856	15.7
ALVA	U-2j	02-57-142	581415.3	4112702.6	08/19/1964	4.4	26	1,347.2	166	AA	602	No	766	23.1
ALVISO	U-2du	02-57-099	582300.9	4107470.5	06/11/1975	<20	43	1,287.8	183	AA	523	No	655	11.0
ANACOSTIA	U-9i	09-57-098	586258.2	4108733.8	11/27/1962	5.2	26	1,300.9	228	TM-LVTA	569	No	569	13.2
ANCHOVY	U-3bq	03-57-042	587295.9	4099504.2	11/14/1963	Low	39	1,221.3	260	AA	488	No	977	18.4
ANGUS	U-3jg	03-57-201	586440.9	4095646.4	04/25/1973	<20	34	1,207.6	453	AA	472	No	1272	24.1
APODACA	U-3gs	03-57-158	589680.9	4096739.6	07/21/1971	<20	40	1,221.9	241	LTCU	487	No	615	9.3
APSHAPA	U-9ai	09-57-031	585282.1	4108928.5	06/06/1963	Low	51	1,281.4	89	AA	544	No	678	11.5
ARABIS-BLUE	U-9itsz26	09-57-018	586037.8	4110591.9	03/06/1970	<20	49	1,303.0	101	TM-LVTA	571	No	571	9.6
ARABIS-GREEN	U-9itsx28	09-57-011	585793.4	4110834.8	03/06/1970	<20	39	1,297.2	259	TM-LVTA	565	No	565	7.8
ARABIS-RED	U-9itsv26	09-57-003	585550.2	4110590.2	03/06/1970	<20	39	1,291.7	250	TM-LVTA	558	No	558	7.9
ARIKAREE	U-9r	09-57-108	584540.2	4109246.4	05/10/1962	Low	44	1,281.4	166	AA	538	No	921	17.2

Table B-1
Yucca Flat/Climax Mine Detonation Characteristics
(Page 2 of 23)

Detonation Name	Emplacement Hole Name	CAS	UTM Easting	UTM Northing	Date Expended	Announced Yield (kt)[a]	Cavity Radius (m)[b]	Land Surface Elevation (m amsl)	Depth to Working Point (m)	Working Point HSU	Estimated Depth to Steady State Water Level (m)	Saturated Working Point	Estimated Depth to Saturated LCA or LCA3 (m)	Number of R_c from WP to Saturated LCA or LCA3
ARMADA	U-9cs	09-57-089	586856.5	4107486.5	04/22/1983	<20	39	1,322.5	265	LTCU	590	No	590	8.3
ARMADILLO	U-3ar	03-57-018	585464.2	4099935.1	02/09/1962	7.1	28	1,225.0	240	AA	492	No	1353	39.7
ARNICA-VIOLET	U-2dd3	02-57-081	581366.4	4108055.4	06/26/1970	<20	39	1,298.8	264	AA	558	No	584	8.2
ARNICA-YELLOW	U-2dd2	02-57-080	581193.9	4107698.2	06/26/1970	<20	37	1,296.9	309	TM-LVTA	554	No	554	6.6
ARSENATE	U-9ci	09-57-080	585965.9	4108579.5	11/09/1972	<20	39	1,295.1	250	TM-LVTA	562	No	640	10.0
ARTESIA	U-7x	07-57-060	588155.6	4106241.4	12/16/1970	20 to 200	72	1,328.9	485	LTCU	595	No	639	2.1
ASCO	U-10bc	10-57-033	585712.3	4112251.5	04/25/1978	<20	43	1,312.2	183	TM-LVTA	579	No	579	9.2
ASIAGO	U-2ar	02-57-016	582842.2	4108821.8	12/21/1976	<20	37	1,292.0	330	AA	545	No	1032	19.0
ATARQUE	U-3ht	03-57-188	587626.0	4096508.4	07/25/1972	<20	38	1,209.1	294	AA	474	No	893	15.8
ATRISCO	U-7bp	07-57-035	588299.3	4104471.7	08/05/1982	138	59	1,294.8	640	OSBCU	538	Yes	764	2.1
AUGER	U-3fx	03-57-138	588938.2	4100424.2	11/15/1968	<20	40	1,248.8	241	TM-LVTA	507	No	687	11.2
AUK	U-7b	07-57-024	588134.1	4103773.3	10/02/1964	<20	34	1,281.1	452	LTCU	529	No	753	8.9
AUSTIN	U-6e	06-57-003	588587.7	4094337.5	06/21/1990	<20	36	1,201.5	351	TM-LVTA	458	No	756	11.2
AVENS-ALKERMES	U-9itsu24	09-57-002	585429.5	4110346.3	12/16/1970	<20	37	1,288.4	306	TM-LVTA	554	No	554	6.7
AVENS-ANDORRE	U-9itst28	09-57-001	585305.9	4110833.1	12/16/1970	<20	35	1,291.1	380	LTCU	555	No	555	5.0
AVENS-ASAMLTE	U-9itsw21	09-57-006	585674.2	4109981.4	12/16/1970	<20	37	1,290.5	308	LTCU	557	No	557	6.7
AVENS-CREAM	U-9itsx29	09-57-012	585793.3	4110956.4	12/16/1970	<20	38	1,298.4	293	LTCU	566	No	566	7.2
AZUL	U-2em	02-57-113	583216.9	4110319.0	12/14/1979	<20	41	1,302.4	205	AA	556	No	838	15.4
BACCARAT	U-7ax	07-57-022	587818.7	4106819.5	01/24/1979	<20	37	1,337.8	326	OSBCU	606	No	606	7.6
BACKGAMMON	U-3jh	03-57-202	586841.3	4094444.2	11/29/1979	<20	40	1,203.4	229	AA	466	No	1211	24.5
BACKSWING	U-9aw	09-57-043	585382.4	4108119.5	05/14/1964	<20	44	1,284.1	163	AA	547	No	1046	20.1
BALTIC	U-9itss25	09-57-099	585185.3	4110467.0	08/06/1971	<20	35	1,286.9	412	TM-LVTA	547	No	598	5.3
BANDICOOT	U-3bj	03-57-035	587052.7	4099503.4	10/19/1962	12.5	34	1,221.6	241	AA	489	No	1030	23.2
BANEBERRY	U-8d	08-57-010	580000.4	4114255.1	12/18/1970	10	30	1,394.2	278	TM-LVTA	649	No	649	12.4
BANON	U-2dz	02-57-103	581549.5	4108930.9	08/26/1976	20 to 150	64	1,302.4	537	AA	544	No	818	4.4
BARBEL	U-3bx	03-57-049	587539.6	4099505.1	10/16/1964	<20	39	1,221.3	259	AA	488	No	924	17.1
BARRACUDA	U-3cr	03-57-061	587842.7	4099993.7	12/04/1963	Low	39	1,228.6	263	AA	495	No	800	13.8
BARRANCA	U-3he	03-57-168	587209.7	4098010.8	08/04/1971	<20	39	1,214.3	271	AA	481	No	941	17.2
BARSAC	U-3gc	03-57-143	586266.6	4097550.4	03/20/1969	<20	37	1,213.7	304	AA	480	No	1248	25.5
BASEBALL	U-7ba	07-57-025	584900.6	4104756.9	01/15/1981	20 to 150	63	1,258.5	564	LTCU	458	Yes	727	2.6
BAY LEAF	U-3gq	03-57-156	586238.9	4100326.6	12/12/1968	<20	46	1,226.2	130	AA	493	No	1204	23.4
BEEBALM	U-3fn	03-57-131	586404.5	4101679.9	05/01/1970	<20	35	1,235.7	390	TM-WTA	503	No	972	16.6
BELEN	U-3br	03-57-043	585461.5	4101204.6	02/04/1970	20 to 200	75	1,232.9	421	AA	497	No	1178	10.2
BELLOW	U-4ac	04-57-004	580586.7	4105316.2	05/16/1984	<20	41	1,292.7	207	TM-LVTA	418	No	418	5.1

Table B-1
Yucca Flat/Climax Mine Detonation Characteristics
(Page 3 of 23)

Detonation Name	Emplacement Hole Name	CAS	UTM Easting	UTM Northing	Date Expended	Announced Yield (kt)[a]	Cavity Radius (m)[b]	Land Surface Elevation (m amsl)	Depth to Working Point (m)	Working Point HSU	Estimated Depth to Steady State Water Level (m)	Saturated Working Point	Estimated Depth to Saturated LCA or LCA3 (m)	Number of R_c from WP to Saturated LCA or LCA3
BERNAL	U-3jy	03-57-218	586788.9	4096333.3	11/28/1973	<20	38	1,209.8	285	AA	475	No	1191	23.8
BERNALILLO	U-3n	03-57-272	585974.7	4100603.9	09/17/1958	0.015	4	1,227.7	139	AA	495	No	1201	265.5
BEVEL	U-3fu	03-57-135	587062.4	4100920.4	04/04/1968	<20	40	1,232.3	241	AA	498	No	1001	19.0
BIGGIN	U-9bz	09-57-072	585248.2	4109887.9	01/30/1969	<20	40	1,283.8	242	TM-LVTA	545	No	650	10.2
BILBY	U-3cn	03-57-058	586983.0	4101819.0	09/13/1963	249	70	1,241.8	715	OSBCU	509	Yes	865	2.2
BILGE	U-3kc	03-57-221	586791.4	4095358.2	02/19/1975	<20	37	1,206.1	318	AA	470	No	1219	24.4
BILLET	U-7an	07-57-015	584996.6	4103457.6	07/27/1976	20 to 150	61	1,249.7	636	LTCU	487	Yes	994	5.9
BIT-A	U-3gt	03-57-159	586304.5	4100326.9	10/31/1968	<20	45	1,225.9	148	AA	493	No	1194	23.3
BIT-B	U-3gt	03-57-159	586304.5	4100326.9	10/31/1968	<20	48	1,225.9	118	AA	493	No	1194	22.9
BITTERLING	U-3cu	03-57-063	587844.3	4099445.5	06/12/1964	<20	42	1,231.1	193	AA	497	No	799	14.4
BLACK	U-9p	09-57-106	585485.6	4108243.2	04/27/1962	Low	41	1,285.3	218	AA	549	No	992	18.9
BLENTON	U-7p	07-57-053	587645.2	4104167.5	04/30/1969	20 to 200	70	1,281.7	558	LTCU	536	Yes	751	2.8
BOBAC	U-3bl	03-57-037	586805.8	4100233.5	08/24/1962	Low	41	1,225.6	206	AA	492	No	1140	22.8
BOBSTAY	U-3jb	03-57-196	587484.4	4095964.2	10/26/1977	<20	35	1,207.3	381	TM-WTA	471	No	975	17.0
BOGEY	U-9au	09-57-041	585828.9	4108360.5	04/17/1964	<20	47	1,291.7	119	AA	557	No	720	12.8
BONARDA	U-3gv	03-57-161	584638.4	4101323.3	09/25/1980	20 to 150	70	1,236.6	381	TM-WTA	490	No	910	7.7
BONEFISH	U-3bt	03-57-045	585947.4	4101693.8	02/18/1964	<20	38	1,234.4	301	AA	498	No	1012	18.7
BOOMER	U-3aa	03-57-001	585854.2	4100467.6	10/01/1961	Low	49	1,227.7	101	AA	495	No	1241	23.3
BORATE	U-2ge	02-57-137	581824.2	4110807.4	10/23/1987	20 to 150	64	1,321.3	543	AA	573	No	890	5.5
BORDEAUX	U-3dr	03-57-086	585721.7	4096451.4	08/18/1967	<20	37	1,210.1	332	AA	477	No	1292	25.9
BORREGO	U-7br	07-57-036	584883.7	4105224.3	09/29/1982	<150	63	1,261.0	564	LTCU	493	Yes	736	2.7
BOURBON	U-7n	07-57-051	588521.7	4106212.5	01/20/1967	20 to 200	53	1,333.2	560	LCA	601	No	601	0.8
BOUSCHET	U-3la	03-57-241	584857.3	4102756.2	05/07/1982	20 to 150	63	1,244.5	563	LTCU	479	Yes	956	6.2
BOWIE	U-3mk	03-57-268	589600.8	4102651.0	04/06/1990	<20	41	1,297.5	213	TM-LVTA	568	No	568	8.7
BOWL-1	U-2bo1	02-57-041	581808.8	4113091.3	06/26/1969	<20	42	1,343.3	198	AA	603	No	603	9.6
BOWL-2	U-2bo2	02-57-154	581763.8	4112901.9	06/26/1969	<20	40	1,341.7	229	AA	600	No	631	10.0
BRACKEN	U-10aq	10-57-022	585881.2	4113350.0	07/09/1971	<20	37	1,323.4	305	LTCU	585	No	585	7.6
BRANCO	U-2ew	02-57-123	583900.0	4108548.8	09/21/1983	<20	38	1,282.9	293	AA	520	No	873	15.3
BRANCO-HERKIMER	U-2ew	02-57-123	583900.0	4108548.8	09/21/1983	<20	34	1,282.9	427	TM-WTA	520	No	873	13.1
BRAZOS	U-9d	09-57-092	584494.4	4108644.4	03/08/1962	8.4	29	1,280.5	259	AA	535	No	1066	27.8
BRETON	U-4ar	04-57-013	582552.3	4104689.0	09/13/1984	20 to 150	66	1,264.6	483	TM-LVTA	503	No	830	5.3
BRIE	U-10cc	10-57-042	585645.9	4116576.5	06/18/1987	<20	41	1,345.1	203	LTCU	326	No	326	3.0
BRISTOL	U-4av	04-57-017	582680.7	4105777.6	11/26/1991	<20	34	1,273.1	457	LTCU	482	No	810	10.4
BRONZE	U-7f	07-57-044	585932.4	4105959.3	07/23/1965	20 to 200	71	1,284.1	531	LTCU	548	No	837	4.4

Table B-1
Yucca Flat/Climax Mine Detonation Characteristics
(Page 4 of 23)

Detonation Name	Emplacement Hole Name	CAS	UTM Easting	UTM Northing	Date Expended	Announced Yield (kt)[a]	Cavity Radius (m)[b]	Land Surface Elevation (m amsl)	Depth to Working Point (m)	Working Point HSU	Estimated Depth to Steady State Water Level (m)	Saturated Working Point	Estimated Depth to Saturated LCA or LCA3 (m)	Number of R_c from WP to Saturated LCA or LCA3
BRUSH	U-3eq	03-57-111	587690.7	4099871.0	01/24/1968	<20	48	1,225.6	118	AA	492	No	872	16.0
BUFF	U-3dh	03-57-077	586307.9	4103157.5	12/16/1965	20 to 200	72	1,250.3	501	LTCU	515	No	839	4.8
BULKHEAD	U-7am	07-57-014	586391.0	4105626.1	04/27/1977	20 to 150	62	1,286.0	594	OSBCU	551	Yes	731	2.2
BULLFROG	U-4au	04-57-016	582789.3	4104607.5	08/30/1988	<150	65	1,263.4	489	TM-WTA	500	No	852	5.6
BUNKER	U-9bb	09-57-050	585952.6	4109752.0	02/13/1964	<20	40	1,296.6	227	TM-LVTA	564	No	564	8.5
BURZET	U-4ai	04-57-007	582669.8	4104386.5	08/03/1979	20 to 150	67	1,262.5	450	AA	501	No	854	6.1
BYE	U-10i	10-57-048	584741.3	4115308.7	07/16/1964	20 to 200	76	1,321.3	391	LTCU	566	No	566	2.3
CABOC	U-2cp	02-57-067	577928.4	4107733.7	12/16/1981	<20	37	1,374.6	335	TM-LVTA	522	No	522	5.1
CABRESTO	U-7h	07-57-046	586153.4	4103766.4	05/24/1973	<20	42	1,255.2	198	AA	519	No	777	13.8
CABRILLO	U-2dr	02-57-096	581340.0	4109927.8	03/07/1975	20 to 200	68	1,314.6	601	AA	566	Yes	978	5.6
CALABASH	U-2av	02-57-020	583141.8	4110977.8	10/29/1969	110	55	1,310.0	625	LTCU	569	Yes	733	2.0
CAMPOS	U-9cp	09-57-086	586012.8	4109098.3	02/13/1978	<20	37	1,296.3	320	TM-LVTA	564	No	564	6.6
CANFIELD	U-3kx	03-57-238	587228.5	4101332.3	05/02/1980	<20	36	1,237.5	351	TM-LVTA	504	No	895	15.1
CAN-GREEN	U-2dd1	03-57-072	581554.1	4107528.9	04/21/1970	20 to 200	83	1,293.3	274	AA	554	No	581	3.7
CANJILON	U-3fq	03-57-132	586673.3	4103158.8	12/16/1970	<20	37	1,254.6	302	TM-LVTA	522	No	710	10.7
CANNA-LIMOGES	U-9itsyz26	09-57-100	585942.1	4110591.5	11/17/1972	<20	41	1,300.0	213	TM-LVTA	568	No	568	8.7
CANNA-UMBRINUS	U-9itsyz26	09-57-100	585942.1	4110591.5	11/17/1972	<20	43	1,300.0	183	TM-LVTA	568	No	568	9.0
CAN-RED	U-2dd4	03-57-073	581725.0	4107886.6	04/21/1970	20 to 200	76	1,295.1	399	LTCU	554	No	554	2.1
CANVASBACK	U-3cp	03-57-060	587529.6	4102369.5	08/22/1964	<20	34	1,253.6	448	LTCU	515	No	815	10.8
CAPITAN	U-3jj	03-57-204	587017.0	4094295.5	06/28/1972	<20	46	1,202.7	134	AA	465	No	1162	22.4
CAPROCK	U-4q	04-57-031	584589.6	4106533.9	05/31/1984	20 to 150	62	1,263.7	600	LTCU	493	Yes	788	3.0
CARMEL	U-2h	02-57-141	581705.2	4112238.6	02/21/1963	Low	44	1,338.1	163	AA	599	No	777	14.0
CARNELIAN	U-4af	04-57-005	580782.8	4105880.6	07/28/1977	<20	41	1,291.7	209	AA	492	No	492	6.9
CARP	U-3cb	03-57-052	587540.2	4099261.3	09/27/1963	Low	37	1,219.8	330	AA	486	No	932	16.3
CARPETBAG	U-2dg	02-57-084	581456.2	4109387.3	12/17/1970	220	69	1,311.2	661	TM-LVTA	552	Yes	948	4.2
CARRIZOZO	U-3hr	03-57-186	585419.6	4095780.0	12/03/1970	<20	38	1,210.1	279	TM-WTA	477	No	1070	20.8
CASHMERE	U-2ad	02-57-004	583355.4	4109585.1	02/04/1965	<20	40	1,297.2	232	AA	550	No	1016	19.6
CASSELMAN	U-10g	10-57-047	584198.8	4111604.7	02/08/1963	Low	37	1,294.5	303	AA	549	No	859	14.6
CASSOWARY	U-3bn	03-57-039	586808.3	4099502.8	12/16/1964	<20	45	1,220.7	150	AA	488	No	1048	19.9
CATHAY	U-9ch	09-57-079	585530.1	4107725.7	10/08/1971	<20	35	1,288.1	378	TM-LVTA	552	No	976	17.1
CEBOLLA	U-3jc	03-57-197	587278.0	4095916.3	08/09/1972	<20	38	1,207.6	287	AA	472	No	1043	19.9
CEBRERO	U-9cw	09-57-091	587572.4	4107446.1	08/14/1985	<20	43	1,342.6	183	TM-LVTA	611	No	611	10.0
CENTAUR	U-2ak	02-57-009	582595.3	4110305.5	08/27/1965	<20	43	1,310.3	172	AA	561	No	906	17.1
CERISE	U-3eu	03-57-115	588010.7	4099872.1	11/18/1966	<20	41	1,228.6	211	AA	494	No	776	13.8

Table B-1
Yucca Flat/Climax Mine Detonation Characteristics
(Page 5 of 23)

Detonation Name	Emplacement Hole Name	CAS	UTM Easting	UTM Northing	Date Expended	Announced Yield (kt)[a]	Cavity Radius (m)[b]	Land Surface Elevation (m amsl)	Depth to Working Point (m)	Working Point HSU	Estimated Depth to Steady State Water Level (m)	Saturated Working Point	Estimated Depth to Saturated LCA or LCA3 (m)	Number of R_c from WP to Saturated LCA or LCA3
CERNADA	U-3kk	03-57-227	586852.1	4096059.6	09/24/1981	<20	41	1,208.2	213	AA	473	No	1185	23.7
CERRO	U-3lf	03-57-245	587562.6	4097311.1	09/02/1982	<20	40	1,211.6	229	AA	478	No	868	16.0
CHAENACTIS	U-2dl	02-57-090	580879.2	4108806.6	12/14/1971	20 to 200	79	1,307.9	331	AA	565	No	718	4.9
CHAMITA	U-3lz	03-57-261	585146.9	4095352.4	08/17/1985	<20	37	1,208.2	332	TM-UVTA	475	No	1112	21.1
CHANTILLY	U-2di	02-57-087	581107.5	4108868.1	09/29/1971	<20	37	1,307.0	331	AA	562	No	705	10.1
CHARCOAL	U-7g	07-57-045	587402.8	4103770.5	09/10/1965	20 to 200	73	1,271.6	455	LTCU	533	No	762	4.2
CHATTY	U-2bn	02-57-040	582052.4	4113070.5	03/18/1969	<20	42	1,339.3	195	AA	601	No	601	9.7
CHEEDAM	U-2et	02-57-120	583164.7	4113141.5	02/17/1983	<20	36	1,320.4	343	TM-LVTA	585	No	585	6.7
CHENILLE	U-9bg	09-57-055	586140.4	4107469.1	04/22/1965	<20	45	1,303.3	141	TM-WTA	569	No	701	12.4
CHESS	U-7at	07-57-019	587513.1	4107062.2	06/20/1979	<20	36	1,336.2	335	LTCU	604	No	604	7.3
CHEVRE	U-10ay	10-57-029	584102.8	4114137.0	11/23/1976	<20	37	1,304.8	317	AA	572	No	572	6.9
CHIBERTA	U-2ek	02-57-111	583361.2	4109241.7	12/20/1975	20 to 200	65	1,291.4	716	LTCU	540	Yes	998	4.3
CHINCHILLA	U-3ag	03-57-007	586296.4	4100551.1	02/19/1962	1.9	20	1,228.3	150	AA	495	No	1161	50.6
CHINCHILLA II	U-3as	03-57-019	585643.3	4100306.6	03/31/1962	Low	46	1,227.1	137	AA	494	No	1295	25.2
CHIPMUNK	U-3ay	03-57-025	586098.9	4100544.6	02/15/1963	Low	57	1,227.7	59	AA	495	No	1192	20.2
CHOCOLATE	U-3es	03-57-113	585627.5	4097243.7	04/21/1967	<20	40	1,212.8	241	AA	480	No	1327	27.2
CIMARRON	U-9h	09-57-096	584537.9	4109387.2	02/23/1962	11.9	31	1,282.6	305	AA	539	No	960	21.1
CINNAMON	U-3dm	03-57-082	586200.5	4098951.9	03/07/1966	<20	47	1,219.2	120	AA	487	No	1296	25.0
CLAIRETTE	U-3kr	03-57-232	586103.7	4096315.6	02/05/1981	<20	36	1,209.4	354	AA	475	No	1305	26.4
CLARKSMOBILE	U-2as	02-57-017	583612.8	4108400.9	05/17/1968	20 to 200	73	1,285.6	473	TM-LVTA	515	No	940	6.5
CLUB	U-2aa	02-57-002	582544.6	4110183.5	01/30/1964	<20	43	1,309.4	180	AA	559	No	910	17.0
CLYMER	U-9ce	09-57-076	584147.2	4111027.4	03/12/1966	<20	35	1,293.0	397	AA	546	No	938	15.5
COALORA	U-3lo	03-57-253	584882.1	4101324.1	02/11/1983	<20	38	1,236.9	274	TM-UVTA	492	No	871	15.7
COBBLER	U-7u	07-57-057	585690.7	4105288.4	11/08/1967	<20	31	1,269.2	667	LTCU	531	Yes	849	5.9
CODSAW	U-9g	09-57-095	585533.3	4109241.7	02/19/1962	Low	41	1,285.3	212	TM-WTA	550	No	589	9.2
COFFER	U-2de	02-57-082	581126.4	4109837.8	03/21/1969	<100	58	1,317.7	465	AA	569	No	932	8.0
COGNAC	U-3fm	03-57-130	585402.3	4100624.5	10/25/1967	<20	40	1,229.6	241	AA	495	No	1233	24.8
COLFAX	U-3k	03-57-219	585883.8	4100523.5	10/05/1958	0.0055	3	1,228.0	107	AA	495	No	1228	373.7
COLMOR	U-3hv	03-57-190	587188.9	4096465.7	04/26/1973	<20	39	1,209.4	246	AA	475	No	1006	19.0
COMMODORE	U-2am	02-57-011	583146.8	4109545.6	05/20/1967	250	70	1,297.8	745	LTCU	549	Yes	1042	4.3
CONCENTRATION	U-3kn	03-57-229	586798.4	4098405.5	12/01/1978	<20	39	1,216.5	248	AA	483	No	1091	21.2
CORAZON	U-3ha	03-57-164	585604.0	4095323.5	12/03/1970	<20	40	1,207.3	241	AA	474	No	1050	20.2
CORDUROY	U-10k	10-57-049	584139.0	4113364.3	12/03/1965	20 to 200	66	1,302.4	679	OSBCU	568	Yes	712	0.5
CORMORANT	U-3df	03-57-075	586329.3	4097063.0	07/17/1964	<20	38	1,211.6	272	AA	478	No	1242	24.9

Table B-1
Yucca Flat/Climax Mine Detonation Characteristics
(Page 6 of 23)

Detonation Name	Emplacement Hole Name	CAS	UTM Easting	UTM Northing	Date Expended	Announced Yield (kt)[a]	Cavity Radius (m)[b]	Land Surface Elevation (m amsl)	Depth to Working Point (m)	Working Point HSU	Estimated Depth to Steady State Water Level (m)	Saturated Working Point	Estimated Depth to Saturated LCA or LCA3 (m)	Number of R_c from WP to Saturated LCA or LCA3
CORNICE-GREEN	U-10ap3	10-57-021	585340.7	4113063.8	05/15/1970	20 to 200	74	1,312.5	444	LTCU	580	No	583	1.9
CORNICE-YELLOW	U-10ap1	10-57-020	585634.7	4113511.3	05/15/1970	20 to 200	76	1,319.5	390	OSBCU	584	No	584	2.6
CORNUCOPIA	U-2ga(s)	02-57-135	582496.6	4110908.2	07/24/1986	<20	35	1,314.3	380	AA	566	No	803	12.1
CORREO	U-3lw	03-57-260	588279.8	4096993.7	08/02/1984	<20	37	1,209.1	334	TM-LVTA	475	No	708	10.1
COSO-BRONZE	U-4an	04-57-012	582279.4	4106647.7	03/08/1991	<20	37	1,281.4	333	TM-WTA	500	No	721	10.5
COSO-GRAY	U-4an	04-57-012	582279.4	4106647.7	03/08/1991	<20	34	1,281.4	442	LTCU	500	No	721	8.2
COSO-SILVER	U-4an	04-57-012	582279.4	4106647.7	03/08/1991	<20	33	1,281.4	475	LTCU	500	No	721	7.2
COTTAGE	U-8j	08-57-005	580872.6	4115022.7	03/23/1985	20 to 150	65	1,388.7	515	OSBCU	627	No	627	1.8
COULOMMIERS	U-2ei	02-57-110	582803.6	4111845.1	09/27/1977	20 to 150	64	1,318.9	530	TM-LVTA	579	No	742	3.3
COURSER	U-3do	03-57-084	587526.8	4103161.8	09/25/1964	0	0	1,264.3	359	LTCU	523	No	762	No Rc
COVE	U-3ki	03-57-225	586181.9	4095843.9	02/16/1977	<20	37	1,207.9	335	AA	474	No	1285	25.7
COWLES	U-3hx	03-57-191	587249.9	4095237.9	02/03/1972	<20	37	1,205.5	302	AA	468	No	1100	21.0
COYPU	U-3af	03-57-006	586227.0	4100523.4	04/10/1963	Low	53	1,227.7	75	AA	495	No	1176	20.8
CREMINO	U-8e	08-57-004	581041.3	4114029.9	09/27/1978	<20	41	1,367.9	210	AA	588	No	727	12.6
CREMINO-CAERPHILLY	U-8e	08-57-004	581041.3	4114029.9	09/27/1978	<20	34	1,367.9	420	TM-LVTA	588	No	727	8.8
CREPE	U-2q	02-57-147	584097.7	4107781.6	12/05/1964	20 to 200	76	1,278.6	404	TM-LVTA	498	No	885	6.4
CRESTLAKE-BRIAR	U-2dw	02-57-101	581277.2	4108289.7	07/18/1974	<20	36	1,301.2	374	AA	560	No	701	9.1
CRESTLAKE-TANSAN	U-2dw	02-57-101	581277.2	4108289.7	07/18/1974	<20	38	1,301.2	272	AA	560	No	701	11.0
CREW	U-2db	02-57-073	581142.7	4109533.4	11/04/1968	20 to 200	78	1,314.3	359	AA	561	No	1033	8.8
CREW-2ND	U-2db	02-57-073	581142.7	4109533.4	11/04/1968	<20	36	1,314.3	359	AA	561	No	1033	18.7
CREW-3RD	U-2db	02-57-073	581142.7	4109533.4	11/04/1968	<20	31	1,314.3	603	TM-LVTA	561	Yes	1033	13.4
CREWLINE	U-7ap	07-57-017	584882.5	4105559.8	05/25/1977	20 to 150	63	1,264.3	564	LTCU	498	Yes	759	3.1
CROCK	U-10ak	10-57-014	585695.3	4112557.4	05/08/1968	<20	43	1,315.8	182	AA	583	No	583	9.3
CROWDIE	U-2fe	02-57-132	580886.0	4111213.7	05/05/1983	<20	35	1,335.9	390	AA	590	No	806	11.9
CRUET	U-2cn	02-57-065	577488.7	4108504.9	10/29/1969	11	32	1,398.7	264	TM-WTA	523	No	523	8.1
CUCHILLO	U-3jt	03-57-213	587279.6	4095535.1	08/09/1972	<20	42	1,206.1	199	AA	469	No	1068	20.7
CULANTRO-A	U-3hia	03-57-172	588707.2	4096766.6	12/10/1969	<20	46	1,208.2	134	AA	472	No	614	10.4
CULANTRO-B	U-3hib	03-57-173	588859.5	4096789.7	12/10/1969	<20	45	1,209.1	149	AA	473	No	629	10.7
CUMARIN	U-3gz	03-57-163	588972.9	4099205.2	02/25/1970	20 to 200	75	1,232.9	408	LTCU	498	No	673	3.5
CUMBERLAND	U-2e	02-57-104	582495.2	4112453.8	04/11/1963	Low	40	1,326.5	227	AA	588	No	629	10.1
CUP	U-9cb	09-57-074	584998.0	4111471.6	03/26/1965	20 to 200	70	1,293.9	541	LTCU	554	No	676	1.9
CYATHUS	U-8b	08-57-002	580631.5	4114259.8	03/06/1970	8.7	28	1,379.8	294	TM-LVTA	611	No	702	14.1
CYCLAMEN	U-3cx	03-57-065	585554.7	4100717.3	05/05/1966	12	31	1,230.2	305	AA	496	No	1200	28.0
DAIQUIRI	U-7o	07-57-052	585686.5	4106568.5	09/23/1966	<20	32	1,287.2	561	LTCU	550	Yes	877	9.9

Table B-1
Yucca Flat/Climax Mine Detonation Characteristics
(Page 7 of 23)

Detonation Name	Emplacement Hole Name	CAS	UTM Easting	UTM Northing	Date Expended	Announced Yield (kt)[a]	Cavity Radius (m)[b]	Land Surface Elevation (m amsl)	Depth to Working Point (m)	Working Point HSU	Estimated Depth to Steady State Water Level (m)	Saturated Working Point	Estimated Depth to Saturated LCA or LCA3 (m)	Number of R_c from WP to Saturated LCA or LCA3
DALHART	U-4u	04-57-035	584497.3	4104964.6	10/13/1988	<150	61	1,255.8	640	LTCU	477	Yes	898	4.2
DAMAN I	U-3be	03-57-031	586238.7	4099886.0	06/21/1962	Low	39	1,224.1	260	AA	491	No	1261	25.7
DANABLU	U-2eu	02-57-121	580872.2	4112542.3	06/09/1983	<20	37	1,353.6	320	AA	607	No	810	13.2
DAUPHIN	U-9cq	09-57-087	587191.7	4107487.7	11/14/1980	<20	37	1,332.6	320	LTCU	600	No	600	7.6
DEAD	U-9k	09-57-102	586040.0	4108309.5	04/21/1962	Low	42	1,298.8	194	AA	566	No	700	12.0
DECK	U-3kd	03-57-222	587120.5	4097370.5	11/18/1975	<20	37	1,206.4	326	AA	472	No	945	16.7
DELPHINIUM	U-2dp	02-57-094	581221.5	4108524.1	09/26/1972	15	34	1,303.3	296	AA	562	No	751	13.4
DEXTER	U-3hs	03-57-187	587503.6	4096587.2	06/23/1971	<20	47	1,209.4	120	AA	475	No	932	17.3
DIANTHUS	U-10at	10-57-025	583792.8	4113467.9	02/17/1972	<20	37	1,306.1	305	AA	572	No	737	11.7
DISCUS THROWER	U-8a	08-57-001	580092.9	4114839.3	05/27/1966	22	38	1,406.7	337	TM-LVTA	661	No	661	8.5
DIVIDER	U-3ml	03-57-269	590030.7	4097442.0	09/23/1992	<20	36	1,234.7	340	LTCU	503	No	531	5.3
DOFINO	U-10ba	10-57-031	584072.7	4114634.8	03/08/1977	<20	43	1,309.4	183	AA	575	No	575	9.1
DOFINO-LAWTON	U-10ba	10-57-031	584072.7	4114634.8	03/08/1977	<20	38	1,309.4	282	AA	575	No	575	7.7
DOLCETTO	U-7bi	07-57-030	588930.9	4105098.7	08/30/1984	<20	36	1,318.0	365	LTCU	568	No	620	7.1
DORMOUSE	U-3aq	03-57-017	585413.8	4100297.2	01/30/1962	Low	36	1,227.1	363	AA	493	No	1276	25.4
DORMOUSE PRIME	U-3az	03-57-026	586834.7	4100052.0	04/05/1962	10.6	31	1,224.1	261	AA	490	No	1160	28.1
DOVEKIE	U-3cd	03-57-053	587542.6	4098651.5	01/21/1966	<20	37	1,216.5	333	AA	483	No	883	14.9
DRAUGHTS	U-7al	07-57-013	587130.2	4103312.7	09/27/1978	20 to 150	67	1,261.6	442	OSBCU	526	No	646	3.0
DRILL (SOURCE-LOWER)	U-2ai	02-57-008	582627.0	4109970.4	12/05/1964	3.4	42	1,306.4	219	AA	557	No	937	31.2
DRILL (TARGET-UPPER)	U-2ai	02-57-008	582627.0	4109970.4	12/05/1964	<20	22	1,306.4	188	AA	557	No	937	18.3
DRIVER	U-9ar	09-57-039	585259.1	4108440.8	05/07/1964	<20	45	1,280.2	148	AA	543	No	976	18.4
DUB	U-10a	10-57-001	583769.3	4114435.6	06/30/1964	11.7	33	1,308.5	259	AA	575	No	575	9.6
DUFFER	U-10ds	10-57-043	585375.1	4113516.1	06/18/1964	<20	34	1,314.3	447	LTCU	580	No	580	3.9
DUMONT	U-2t	02-57-149	583702.8	4107414.5	05/19/1966	20 to 200	67	1,278.6	671	LTCU	486	Yes	958	4.4
DUORO	U-3lv	03-57-259	585147.6	4095139.1	06/20/1984	20 to 150	70	1,207.3	381	TM-UVTA	474	No	1140	11.0
DUTCHESS	U-7bm	07-57-033	588957.9	4103410.3	10/24/1980	<20	34	1,291.7	427	LTCU	534	No	637	6.2
EAGLE	U-9av	09-57-042	584928.9	4109631.1	12/12/1963	5.3	28	1,281.1	165	AA	541	No	860	24.8
EBBTIDE	U-3kt	03-57-234	585104.5	4098734.7	09/15/1977	<20	35	1,220.7	380	AA	487	No	1368	28.2
EDAM	U-2dy	02-57-102	581080.2	4107892.3	04/24/1975	20 to 200	75	1,299.4	412	TM-LVTA	556	No	556	1.9
EEL	U-9m	09-57-104	584642.4	4108698.3	05/19/1962	4.5	25	1,280.2	218	AA	536	No	1040	32.9
EFFENDI	U-2ap	02-57-015	583203.9	4110475.2	04/27/1967	<20	41	1,305.8	221	AA	560	No	845	15.2
ELIDA	U-3hy	03-57-192	586183.3	4095234.1	12/19/1973	<20	35	1,205.5	381	AA	471	No	1225	24.1
ELKHART	U-9bs	09-57-066	585774.9	4107421.8	09/17/1965	<20	41	1,293.9	220	TM-WTA	558	No	921	17.1
EMBUDO	U-3hd	03-57-167	587724.9	4098804.8	06/16/1971	<20	37	1,218.0	303	AA	484	No	806	13.2

Table B-1
Yucca Flat/Climax Mine Detonation Characteristics
(Page 8 of 23)

Detonation Name	Emplacement Hole Name	CAS	UTM Easting	UTM Northing	Date Expended	Announced Yield (kt)[a]	Cavity Radius (m)[b]	Land Surface Elevation (m amsl)	Depth to Working Point (m)	Working Point HSU	Estimated Depth to Steady State Water Level (m)	Saturated Working Point	Estimated Depth to Saturated LCA or LCA3 (m)	Number of R_c from WP to Saturated LCA or LCA3
EMERSON	U-2al	02-57-010	583203.7	4110703.5	12/16/1965	<20	39	1,307.3	260	AA	564	No	816	14.2
ERMINE	U-3ab	03-57-002	585930.0	4100474.6	03/06/1962	Low	54	1,227.7	73	AA	495	No	1229	21.4
ESCABOSA	U-7ac	07-57-004	586063.2	4103430.9	07/10/1974	20 to 200	67	1,250.3	639	LTCU	513	Yes	837	3.0
ESROM	U-7ak	07-57-012	585529.5	4106927.3	02/04/1976	20 to 200	67	1,285.0	655	LTCU	548	Yes	925	4.0
ESTACA	U-3ja	03-57-195	587650.3	4095832.9	10/17/1974	<20	37	1,206.7	321	TM-UVTA	470	No	887	15.3
FADE	U-9be	09-57-053	586292.9	4107438.8	06/25/1964	<20	41	1,307.0	205	TM-LVTA	574	No	699	12.0
FAHADA	U-7bh	07-57-029	588352.9	4106547.1	05/26/1983	<20	35	1,338.7	384	OSBCU	606	No	606	6.3
FAJY	U-2fc	02-57-130	581039.6	4110940.3	06/28/1979	20 to 150	64	1,330.1	536	AA	584	No	848	4.9
FALLON	U-2dv	02-57-100	581826.7	4108876.7	05/23/1974	20 to 200	73	1,302.7	466	AA	548	No	887	5.8
FARALLONES	U-2fa	02-57-128	581179.6	4110132.3	12/14/1977	20 to 150	60	1,317.3	667	AA	570	Yes	903	3.9
FAWN	U-3eo	03-57-109	586939.7	4101148.2	04/07/1967	<20	39	1,233.5	271	AA	500	No	977	18.1
FENTON	U-2m1	02-57-144	581433.6	4112871.8	04/23/1966	1.4	18	1,348.1	167	AA	601	No	745	32.1
FERRET	U-3bf	03-57-032	586309.5	4101581.4	02/08/1963	Low	37	1,235.0	326	TM-UVTA	502	No	995	18.1
FERRET PRIME	U-3by	03-57-050	586809.2	4099258.7	04/05/1963	Low	40	1,219.8	241	AA	487	No	1085	21.1
FILE	U-3gb	03-57-142	5857801.0	4097000.1	10/31/1968	<20	40	1,212.2	229	AA	479	No	1326	27.4
FINFOOT	U-3du	03-57-089	586321.6	4099257.0	03/07/1966	<20	42	1,220.4	196	AA	488	No	1277	25.7
FISHER	U-3ah	03-57-008	586464.9	4100198.2	12/03/1961	13.4	31	1,225.3	364	AA	492	No	1194	26.8
FIZZ	U-3fr	03-57-133	586277.2	4100363.0	03/10/1967	<20	48	1,225.9	118	AA	493	No	1192	22.4
FLASK-GREEN	U-2az1	02-57-026	583308.9	4107656.6	05/26/1970	105	57	1,277.7	529	TM-UVTA	497	Yes	896	6.4
FLASK-RED	U-2az3	02-57-028	582917.7	4107966.4	05/26/1970	0.035	5	1,286.3	152	AA	518	No	833	136.2
FLASK-YELLOW	U-2az2	02-57-027	583194.3	4108184.0	05/26/1970	0.09	6	1,286.3	335	AA	516	No	917	96.9
FLAX-BACKUP	U-2dj	02-57-088	581421.8	4110588.1	12/21/1972	<20	34	1,323.1	445	AA	577	No	908	13.6
FLAX-SOURCE	U-2dj	02-57-088	581421.8	4110588.1	12/21/1972	<20	30	1,323.1	688	TM-LVTA	577	Yes	908	7.3
FLAX-TEST	U-2dj	02-57-088	581421.8	4110588.1	12/21/1972	20 to 200	74	1,323.1	436	AA	577	No	908	6.4
FLORA	U-3lg	03-57-246	586182.6	4095447.4	05/22/1980	<20	36	1,206.4	335	AA	472	No	1226	24.1
FLOTOST	U-2ao	02-57-014	583203.2	4111355.9	08/16/1977	<20	38	1,310.9	275	AA	569	No	753	12.6
FLOYDADA	U-7cb	07-57-042	588718.6	4104823.3	08/15/1991	<20	33	1,306.7	503	OSBCU	545	No	688	5.6
FOB-BLUE	U-9iy27	09-57-013	585916.0	4110713.0	01/23/1970	<20	49	1,299.7	101	TM-LVTA	567	No	567	9.5
FOB-GREEN	U-9iv27	09-57-005	585549.8	4110712.0	01/23/1970	<20	40	1,293.0	244	TM-LVTA	560	No	560	7.9
FOB-RED	U-9iv24	09-57-004	585551.0	4110346.7	01/23/1970	<20	39	1,289.9	266	TM-LVTA	556	No	556	7.4
FORE	U-9ao	09-57-036	584452.2	4110875.8	01/16/1964	20 to 200	72	1,289.6	491	TM-LVTA	545	No	867	5.2
FOREFOOT	U-3kf	03-57-223	586695.7	4101208.6	06/02/1977	<20	42	1,233.5	194	AA	500	No	1012	19.5
FOREST	U-7a	07-57-001	585989.4	4107000.2	10/31/1964	<20	35	1,296.9	387	LTCU	562	No	813	12.2
FREEZEOUT	U-3kw	03-57-237	587403.4	4094918.5	05/11/1979	<20	36	1,204.3	335	AA	466	No	1016	18.4

Table B-1
Yucca Flat/Climax Mine Detonation Characteristics
(Page 9 of 23)

Detonation Name	Emplacement Hole Name	CAS	UTM Easting	UTM Northing	Date Expended	Announced Yield (kt)[a]	Cavity Radius (m)[b]	Land Surface Elevation (m amsl)	Depth to Working Point (m)	Working Point HSU	Estimated Depth to Steady State Water Level (m)	Saturated Working Point	Estimated Depth to Saturated LCA or LCA3 (m)	Number of R_c from WP to Saturated LCA or LCA3
FRIJOLES-DEMING	U-3jw	03-57-216	587513.1	4097518.2	09/22/1971	<20	45	1,212.2	150	AA	478	No	876	16.1
FRIJOLES-ESPUELA	U-3ju	03-57-214	587500.5	4097640.0	09/22/1971	<20	45	1,212.8	149	AA	479	No	872	16.1
FRIJOLES-GUAJE	U-3hf	03-57-169	587591.2	4097829.3	09/22/1971	<20	39	1,213.1	257	AA	479	No	834	14.8
FRIJOLES-PETACA	U-3hz	03-57-193	587272.2	4097553.9	09/22/1971	<20	40	1,213.1	226	AA	479	No	908	17.0
FRISCO	U-8m	08-57-008	580981.3	4114444.1	09/23/1982	20 to 150	67	1,373.7	451	OSBCU	583	No	672	3.3
FUNNEL	U-3ga	03-57-141	586239.2	4100250.4	06/25/1968	<20	47	1,226.2	119	AA	493	No	1216	23.3
FUTTOCK	U-3eh	03-57-102	586950.5	4102397.9	06/18/1975	<20	42	1,247.9	187	AA	514	No	797	14.5
GALENA-GREEN	U-9cv	09-57-090	586059.4	4108855.0	06/23/1992	<20	35	1,295.7	401	OSBCU	563	No	563	4.7
GALENA-ORANGE	U-9cv	09-57-090	586059.4	4108855.0	06/23/1992	<20	35	1,295.7	380	OSBCU	563	No	563	5.2
GALENA-YELLOW	U-9cv	09-57-090	586059.4	4108855.0	06/23/1992	<20	38	1,295.7	290	LTCU	563	No	563	7.2
GARDEN	U-9aj	09-57-032	586075.5	4108091.1	10/23/1964	<20	45	1,301.2	150	TM-LVTA	568	No	706	12.4
GASCON	U-4t	04-57-034	584590.7	4106233.8	11/14/1986	20 to 150	62	1,263.1	593	LTCU	490	Yes	877	4.6
GAZOOK	U-2do	02-57-093	581110.4	4108068.2	03/23/1973	<20	37	1,300.9	326	AA	558	No	618	7.9
GERBIL	U-3bp	03-57-041	587294.7	4099748.0	03/29/1963	Low	38	1,222.9	280	AA	489	No	958	17.8
GIBSON	U-3ew	03-57-117	587850.6	4097830.2	08/04/1967	<20	40	1,213.1	241	AA	479	No	788	13.7
GILROY	U-3ex	03-57-118	587084.7	4098985.4	09/15/1967	<20	40	1,218.6	241	AA	485	No	1038	19.9
GLENCOE	U-4i	04-57-025	583012.9	4104285.0	03/22/1986	29	36	1,260.7	610	OSBCU	493	Yes	821	5.9
GORBEA	U-2cq	02-57-068	578034.8	4107531.7	01/31/1984	20 to 150	69	1,371.3	388	TM-LVTA	521	No	546	2.3
GOUDA	U-2ef	02-57-107	583290.9	4110007.8	10/06/1976	<20	42	1,298.4	200	AA	552	No	851	15.5
GOURD-AMBER	U-2bf	02-57-033	581716.8	4113255.2	04/24/1969	<20	43	1,346.6	181	AA	606	No	606	9.9
GOURD-BROWN	U-2bl	02-57-038	581611.7	4112809.7	04/24/1969	<20	40	1,343.9	227	AA	600	No	689	11.6
GRAPE A	U-7s	07-57-055	588741.4	4104384.9	12/17/1969	20 to 200	70	1,300.9	551	OSBCU	539	Yes	683	1.9
GRAPE B	U-7v	07-57-058	586511.3	4105992.2	02/04/1970	20 to 200	70	1,296.3	554	LTCU	563	No	716	2.3
GREYS	U-9ax	09-57-044	584827.1	4108332.3	11/22/1963	Intermediate	81	1,274.7	301	AA	533	No	1063	9.4
GROVE	U-2ds	02-57-097	582208.3	4107805.4	05/22/1974	<20	37	1,291.1	314	TM-LVTA	537	No	558	6.6
GRUNION	U-3bz	03-57-051	587052.9	4099259.6	10/11/1963	Low	39	1,219.8	261	AA	487	No	1041	20.0
GRUYERE	U-9cg	09-57-078	584451.4	4111195.7	08/16/1977	<20	41	1,289.9	207	AA	545	No	821	15.0
GRUYERE-GRADINO	U-9cg	09-57-078	584451.4	4111195.7	08/16/1977	<20	37	1,289.9	320	AA	545	No	821	13.5
GUANAY	U-3di	03-57-078	586939.0	4097065.2	09/04/1964	<20	39	1,211.6	261	AA	478	No	1099	21.5
GUNDI	U-3bm	03-57-038	586807.8	4099746.3	11/15/1962	Low	40	1,222.2	241	AA	489	No	1158	22.9
GUNDI PRIME	U-3db	03-57-070	587535.8	4100602.1	05/09/1963	Low	38	1,232.3	272	AA	498	No	841	14.6
HADDOCK	U-3dl	03-57-081	586920.1	4102550.5	08/28/1964	<20	36	1,248.8	364	LTCU	515	No	769	11.3
HANDCAR	U-10b	10-57-030	582825.0	4114420.1	11/05/1964	12	21	1,333.5	403	LCA	598	No	598	9.2
HANDICAP	U-9ba	09-57-049	585600.0	4109517.7	03/12/1964	<20	45	1,287.8	144	AA	554	No	590	9.9

Table B-1
Yucca Flat/Climax Mine Detonation Characteristics
(Page 10 of 23)

Detonation Name	Emplacement Hole Name	CAS	UTM Easting	UTM Northing	Date Expended	Announced Yield (kt)[a]	Cavity Radius (m)[b]	Land Surface Elevation (m amsl)	Depth to Working Point (m)	Working Point HSU	Estimated Depth to Steady State Water Level (m)	Saturated Working Point	Estimated Depth to Saturated LCA or LCA3 (m)	Number of R_c from WP to Saturated LCA or LCA3
HAPLOPAPPUS	U-9itsw22	09-57-021	585689.3	4110103.1	06/28/1972	<20	42	1,291.4	184	TM-LVTA	558	No	558	8.9
HARD HAT	U-15a	15-57-001	583452.9	4120183.5	02/15/1962	5.7	19	1,558.7	287	MGCU	222	Yes	No LCA	No LCA
HAREBELL	U-2br	02-57-046	582872.3	4111349.9	06/24/1971	20 to 200	71	1,314.3	519	TM-LVTA	572	No	762	3.4
HARKEE	U-3bv	03-57-047	5875387.9	4099992.9	05/17/1963	Low	40	1,225.9	241	AA	492	No	896	16.4
HARLINGEN-A	U-6g	06-57-004	587387.5	4094141.3	08/23/1988	<20	38	1,202.4	290	AA	463	No	1014	19.1
HARLINGEN-B	U-6h	06-57-005	587388.8	4093867.1	08/23/1988	<20	38	1,201.8	290	AA	462	No	1021	19.2
HATCHET	U-3fz	03-57-140	587178.3	4098284.9	05/03/1968	<20	40	1,215.2	241	AA	482	No	975	18.4
HATCHIE	U-9e	09-57-093	585399.2	4109074.5	02/08/1963	Low	56	1,282.6	61	AA	546	No	618	9.9
HAVARTI	U-10bg	10-57-037	585685.2	4112160.0	08/05/1981	<20	42	1,310.0	200	TM-LVTA	578	No	578	9.0
HAYMAKER	U-3au(s)	03-57-021	586022.4	4099759.4	06/27/1962	67	52	1,223.5	408	AA	491	No	1294	17.0
HAZEBROOK-APRICOT	U-10bh	10-57-038	584467.8	4115187.7	02/03/1987	<20	39	1,317.3	262	AA	571	No	571	7.9
HAZEBROOK-CHECKERBERRY	U-10bh	10-57-038	584467.8	4115187.7	02/03/1987	<20	40	1,317.3	226	AA	571	No	571	8.6
HAZEBROOK-EMERALD	U-10bh	10-57-038	584467.8	4115187.7	02/03/1987	<20	42	1,317.3	186	AA	571	No	571	9.2
HEARTS	U-4n	04-57-028	584185.3	4104863.2	09/06/1979	140	60	1,258.8	638	LTCU	473	Yes	1069	7.2
HEILMAN	U-2cg	02-57-059	577034.6	4110254.9	04/06/1967	<20	45	1432.3	153	AA	531	No	531	8.4
HERMOSA	U-7bs	07-57-037	585994.6	4105624.7	04/02/1985	20 to 150	61	1,277.7	640	LTCU	541	Yes	771	2.2
HOD-A (GREEN)	U-9itsx23	09-57-008	585795.6	4110225.6	05/01/1970	<20	40	1,294.8	241	TM-LVTA	562	No	562	8.0
HOD-B (RED)	U-9itsx20	09-57-007	585797.2	4109859.7	05/01/1970	<20	39	1,293.0	265	TM-LVTA	560	No	560	7.6
HOD-C (BLUE)	U-9iz25	09-57-017	586038.5	4110470.0	05/01/1970	<20	49	1,302.4	101	TM-LVTA	570	No	570	9.6
HOGNOSE	U-3ai	03-57-009	586168.2	4099984.8	03/15/1962	Low	40	1,225.0	240	AA	492	No	1260	25.5
HOOK	U-9bc	09-57-051	586179.3	4109411.5	04/14/1964	<20	41	1,302.7	204	TM-LVTA	571	No	571	9.0
HOOPOE	U-3cf	03-57-054	585968.1	4100478.0	12/16/1964	<20	54	1,227.1	70	AA	494	No	1223	21.3
HOOSIC	U-9j	09-57-101	585824.9	4108896.8	03/28/1962	3.4	23	1,290.8	187	TM-LVTA	557	No	557	16.1
HOREHOUND	U-3gm	03-57-153	589385.8	4094331.2	08/27/1969	<20	37	1,201.5	332	LTCU	460	No	646	8.5
HOSPAH	U-3je	03-57-199	586356.6	4097977.3	12/14/1971	<20	37	1,215.2	302	AA	482	No	1248	24.9
HUDSON	U-9n	09-57-105	584845.4	4109204.2	04/12/1962	Low	45	1,280.2	151	AA	539	No	832	15.1
HULA	U-9bu	09-57-068	585210.3	4107663.6	10/29/1968	<20	42	1,280.8	198	AA	543	No	1055	20.4
HULSEA	U-2bx	02-57-051	583106.7	4112288.0	03/14/1974	<20	42	1,316.4	195	AA	577	No	577	9.1
HUPMOBILE	U-2y	02-57-153	582976.7	4111227.4	01/18/1968	7.4	28	1,313.7	247	AA	573	No	706	16.4
HURON KING	U-3ky	03-57-239	585915.7	4097689.3	06/24/1980	<20	37	1,214.6	320	AA	481	No	1298	26.4
HUTCH	U-2df	02-57-083	581050.2	4110535.3	07/16/1969	20 to 200	70	1,327.1	548	AA	581	No	888	4.9
HUTIA	U-3bc	03-57-029	585694.3	4100015.8	06/06/1963	Low	46	1,225.0	135	AA	492	No	1319	25.7
HYRAX	U-3bh	03-57-034	587050.7	4099990.9	09/14/1962	Low	41	1,224.4	217	AA	491	No	996	19.0
ICEBERG	U-4g	04-57-023	584315.6	4106380.6	03/23/1978	20 to 150	61	1,265.5	640	LTCU	485	Yes	922	4.6

Table B-1
Yucca Flat/Climax Mine Detonation Characteristics
(Page 11 of 23)

Detonation Name	Emplacement Hole Name	CAS	UTM Easting	UTM Northing	Date Expended	Announced Yield (kt)[a]	Cavity Radius (m)[b]	Land Surface Elevation (m amsl)	Depth to Working Point (m)	Working Point HSU	Estimated Depth to Steady State Water Level (m)	Saturated Working Point	Estimated Depth to Saturated LCA or LCA3 (m)	Number of R_c from WP to Saturated LCA or LCA3
ILDRIM	U-2au	02-57-019	583943.4	4108335.6	07/16/1969	20 to 200	75	1,282.9	410	TM-WTA	514	No	892	6.4
IMP	U-2bj	02-57-037	581937.1	4113015.3	08/09/1968	<20	43	1,340.8	179	AA	602	No	602	9.8
INGOT	U-2gg	02-57-139	582867.7	4110922.0	03/09/1989	20 to 150	65	1,307.3	500	TM-WTA	564	No	715	3.3
IPECAC-A	U-3hka	03-57-175	588768.4	4096797.3	05/27/1969	<20	47	1,208.5	124	AA	472	No	627	10.7
IPECAC-B	U-3hkb	03-57-176	588950.9	4096782.7	05/27/1969	<20	47	1,209.4	124	AA	473	No	649	11.2
ISLAY	U-2er	02-57-118	582885.3	4112872.3	08/27/1981	<20	38	1,323.4	294	TM-LVTA	587	No	587	7.7
IZZER	U-9bp	09-57-064	585682.0	4107863.3	07/16/1965	<20	44	1,299.7	164	AA	565	No	968	18.3
JACKPOTS	U-3kj	03-57-226	586113.6	4097397.5	06/01/1978	<20	37	1,212.8	304	AA	479	No	1266	26.0
JAL	U-3hh	03-57-171	586945.1	4095236.8	03/19/1970	<20	37	1,205.5	301	AA	469	No	1207	23.8
JARA	U-3hp	03-57-099	586883.1	4095541.3	06/06/1974	<20	35	1,207.0	378	AA	471	No	1209	23.8
JARLSBERG	U-10ca	10-57-040	585732.9	4116509.2	08/27/1983	<20	42	1,344.5	200	TM-LVTA	325	No	325	3.0
JERBOA	U-3at	03-57-020	586571.4	4100049.9	03/01/1963	Low	37	1,224.1	301	AA	491	No	1196	23.6
JIB	U-3hb	03-57-165	588834.1	4095243.7	05/08/1974	<20	43	1,204.3	180	TM-UVTA	463	No	658	11.1
JICARILLA	U-3jm	03-57-207	587494.2	4095854.9	04/19/1972	<20	45	1,207.0	148	AA	470	No	971	18.3
JORNADA	U-4j	04-57-026	584319.7	4105223.0	01/28/1982	139	60	1,260.0	639	LTCU	477	Yes	968	5.6
KANKAKEE	U-10p	10-57-052	584440.2	4114121.4	06/15/1966	20 to 200	53	1,308.2	455	LCA	575	No	575	2.3
KARA	U-2dh3	02-57-086	581340.7	4107540.3	05/11/1972	<20	39	1,294.5	259	AA	554	No	554	7.6
KARAB	U-4ah	04-57-006	581625.6	4104512.0	03/16/1978	<20	37	1,274.7	331	LTCU	525	No	525	5.2
KASHAN	U-10av	10-57-026	583820.0	4113082.8	05/24/1973	<20	39	1,303.9	265	AA	567	No	741	12.2
KAWEAH	U-9ab	09-57-025	584777.9	4108442.2	02/21/1963	3	21	1,276.2	227	AA	534	No	1035	38.5
KAWICH A-BLUE	U-8n	08-57-009	580630.7	4114503.8	12/09/1988	<20	35	1,384.4	384	OSBCU	540	No	725	9.7
KAWICH A-WHITE	U-8n	08-57-009	580630.7	4114503.8	12/09/1988	<20	36	1,384.4	369	LTCU	540	No	725	9.9
KAWICH-BLACK	U-2cu	02-57-072	577996.1	4109283.8	02/24/1989	<20	34	1,379.5	431	TM-LVTA	551	No	551	3.5
KAWICH-RED	U-2cu	02-57-072	577996.1	4109283.8	02/24/1989	<20	36	1,379.5	370	TM-LVTA	551	No	551	5.0
KEEL	U-3hu	03-57-189	587398.0	4096373.8	12/16/1974	<20	37	1,208.8	305	AA	473	No	975	18.1
KEELSON	U-7ai	07-57-010	586217.5	4102791.8	02/04/1976	20 to 200	67	1,244.8	640	LTCU	508	Yes	862	3.3
KENNEBEC	U-2af	02-57-005	582780.2	4109651.9	06/25/1963	Low	40	1,303.0	226	AA	554	No	1039	20.3
KERMET	U-2c	02-57-054	582493.4	4113032.5	11/23/1965	<20	42	1,331.4	196	AA	594	No	594	9.5
KESTI	U-9cn	09-57-085	587373.1	4107793.1	06/16/1982	<20	38	1,338.4	288	LTCU	606	No	606	8.4
KESTREL	U-3dd	03-57-071	586935.2	4097979.3	04/05/1965	<20	34	1,214.6	447	AA	481	No	1056	17.9
KHAKI	U-3et	03-57-114	587414.8	4100342.9	10/15/1966	<20	40	1,228.6	233	AA	495	No	886	16.3
KINIBITO	U-3me	03-57-264	584883.3	4101004.2	12/05/1985	20 to 150	63	1,235.0	579	LTCU	496	Yes	925	5.6
KLICKITAT	U-10e	10-57-045	585241.1	4111838.4	02/20/1964	70	51	1,300.3	492	LTCU	568	No	568	1.5
KLOSTER	U-2eo	02-57-115	582422.6	4111935.2	02/15/1979	20 to 150	64	1,324.1	536	TM-LVTA	584	No	745	3.3

Table B-1
Yucca Flat/Climax Mine Detonation Characteristics
(Page 12 of 23)

Detonation Name	Emplacement Hole Name	CAS	UTM Easting	UTM Northing	Date Expended	Announced Yield (kt)[a]	Cavity Radius (m)[b]	Land Surface Elevation (m amsl)	Depth to Working Point (m)	Working Point HSU	Estimated Depth to Steady State Water Level (m)	Saturated Working Point	Estimated Depth to Saturated LCA or LCA3 (m)	Number of R_c from WP to Saturated LCA or LCA3
KNIFE A	U-3fb	03-57-122	587908.0	4098653.1	09/12/1968	<20	37	1,217.4	332	TM-LVTA	483	No	775	12.0
KNIFE B	U-3dz	03-57-093	585990.5	4098006.5	11/15/1968	<20	36	1,215.2	363	AA	482	No	1294	25.9
KNIFE C	U-3er	03-57-112	589586.5	4098019.1	10/03/1968	<20	37	1,228.3	301	LTCU	495	No	652	9.2
KNOX	U-2at	02-57-018	584072.8	4108017.9	02/21/1968	20 to 200	67	1,279.9	645	LTCU	504	Yes	895	3.7
KOHOCTON	U-9ak	09-57-034	585690.0	4108966.8	08/23/1963	Low	39	1,300.6	255	TM-LVTA	566	No	592	8.6
KOOTANAI	U-9w	09-57-111	585615.8	4108481.7	04/24/1963	Low	43	1,287.8	182	AA	552	No	797	14.3
KRYDDOST	U-2co	02-57-066	577568.2	4107987.2	05/06/1982	<20	36	1,390.5	335	TM-LVTA	516	No	543	5.6
KYACK-A	U-2bq1	02-57-044	582780.2	4112686.1	09/20/1969	<20	42	1,323.4	192	AA	586	No	600	9.7
KYACK-B	U-2bq2	02-57-045	582920.0	4112540.3	09/20/1969	<20	42	1,320.1	186	AA	582	No	582	9.4
LABAN	U-2ff	02-57-133	580942.1	4108258.1	08/03/1983	<20	37	1,303.0	326	AA	561	No	667	9.2
LABIS	U-10an	10-57-019	585340.2	4113290.2	02/05/1970	25	37	1,313.1	442	LTCU	580	No	608	4.5
LAGOON	U-10ar	10-57-023	584056.7	4115032.4	10/14/1971	<20	37	1,312.8	305	AA	575	No	575	7.3
LAGUNA	U-3fd	03-57-124	586937.0	4097552.4	06/23/1971	20 to 200	73	1,213.4	455	TM-WTA	480	No	1075	8.5
LAMPBLACK	U-7i	07-57-049	587212.2	4105292.2	01/18/1966	20 to 200	70	1,294.2	561	OSBCU	560	Yes	629	1.0
LANPHER	U-2x	02-57-152	583723.9	4107906.7	10/18/1967	20 to 200	65	1,282.0	715	LTCU	498	Yes	927	3.3
LAREDO	U-3mh	03-57-267	590070.9	4098752.1	05/21/1988	<150	71	1,247.2	351	LTCU	515	No	520	2.4
LATIR	U-4d	04-57-020	584162.6	4106654.3	02/27/1974	20 to 200	67	1,270.1	641	LTCU	486	Yes	888	3.7
LEDOUX	U-1a.01	01-57-001	583791.1	4095876.4	09/27/1990	<20	38	1,217.7	291	AA	479	No	1104	21.4
LEXINGTON	U-2bm	02-57-039	582204.5	4113122.6	08/24/1967	<20	40	1,336.9	227	AA	599	No	599	9.3
LEYDEN	U-9cm	09-57-084	587165.1	4108127.5	11/26/1975	<20	37	1,329.8	326	LTCU	597	No	597	7.3
LIME	U-7j	07-57-047	587088.1	4106511.9	04/01/1966	<20	32	1,318.6	561	OSBCU	585	No	666	3.3
LINKS	U-9bf	09-57-054	586002.4	4107727.0	07/23/1964	<20	47	1,300.0	120	AA	566	No	670	11.7
LIPTAUER	U-2eh	02-57-109	581499.3	4111689.4	04/03/1980	20 to 150	68	1,331.4	417	AA	585	No	839	6.2
LONGCHAMPS	U-2dm	02-57-091	581388.9	4108588.7	04/19/1972	<20	37	1,303.0	326	AA	560	No	779	12.3
LOVAGE	U-3fe	03-57-125	586942.7	4095846.3	12/17/1969	<20	35	1,207.9	378	AA	472	No	1166	22.5
LOWBALL	U-7av	07-57-021	584995.6	4103823.6	07/12/1978	20 to 150	63	1,252.4	565	LTCU	490	Yes	932	5.8
LUBBOCK	U-3mt	03-57-271	584879.0	4102131.9	10/18/1991	20 to 150	67	1,239.6	457	LTCU	468	No	807	5.3
LUNA	U-3m	03-57-262	585925.1	4100568.1	09/21/1958	0.0015	1	1,227.7	148	AA	495	No	1214	533.2
MACKEREL	U-4b	04-57-018	584360.3	4105698.8	02/18/1964	<20	37	1,263.4	334	TM-LVTA	484	No	937	16.3
MAD	U-9a	09-57-023	584500.3	4109136.9	12/13/1961	0.5	12	1,281.4	182	AA	537	No	951	64.1
MALLET	U-3fv	03-57-136	588164.0	4095241.4	01/31/1968	<20	40	1,204.3	240	AA	465	No	801	14.0
MANATEE	U-9af	09-57-029	585284.7	4108882.8	12/14/1962	Low	56	1,280.8	60	AA	543	No	705	11.5
MANTECA	U-4al	04-57-010	582496.0	4103966.9	12/10/1982	20 to 150	68	1,263.1	412	AA	505	No	715	4.5
MANZANAS	U-3gr	03-57-157	589681.8	4096496.1	05/21/1970	<20	40	1,221.6	241	TSA	485	No	623	9.6

Table B-1
Yucca Flat/Climax Mine Detonation Characteristics
(Page 13 of 23)

Detonation Name	Emplacement Hole Name	CAS	UTM Easting	UTM Northing	Date Expended	Announced Yield (kt)[a]	Cavity Radius (m)[b]	Land Surface Elevation (m amsl)	Depth to Working Point (m)	Working Point HSU	Estimated Depth to Steady State Water Level (m)	Saturated Working Point	Estimated Depth to Saturated LCA or LCA3 (m)	Number of R_c from WP to Saturated LCA or LCA3
MARIBO	U-2cs	02-57-070	577997.8	4108796.2	06/26/1985	<20	35	1,379.5	381	TM-LVTA	547	No	581	5.7
MARSH	U-3kb	03-57-220	586433.6	4097734.1	09/06/1975	<20	34	1,214.0	427	AA	480	No	1230	23.6
MARSILLY	U-2el	02-57-112	583306.2	4108418.4	04/05/1977	20 to 150	60	1,286.3	689	LTCU	520	Yes	970	4.7
MARVEL	U-10ds1	10-57-044	585381.5	4113496.4	09/21/1967	2.2	21	1,314.3	176	AA	580	No	580	19.2
MATACO	U-3bk	03-57-036	587293.9	4100235.9	06/14/1963	Low	42	1,227.1	196	AA	493	No	914	17.1
MAUVE	U-3dp	03-57-085	585415.1	4097059.5	08/06/1965	<20	37	1,212.5	321	AA	479	No	1294	26.3
MAXWELL	U-9br	09-57-065	586397.6	4108003.3	01/13/1966	<20	43	1,310.0	183	TM-LVTA	578	No	663	11.2
MEMORY	U-3kq	03-57-231	585411.2	4098187.3	03/14/1979	<20	36	1,217.7	365	AA	485	No	1366	27.8
MERIDA	U-2dn	02-57-092	581263.2	4107916.4	06/07/1972	<20	41	1,297.8	204	AA	556	No	559	8.7
MERLIN	U-3ct	03-57-062	586803.3	4100843.3	02/16/1965	10.1	30	1,230.8	296	AA	497	No	1049	25.1
MERRIMAC	U-3bd	03-57-030	585946.0	4101214.5	07/13/1962	Intermediate	75	1,231.7	413	AA	498	No	1098	9.1
MESCALERO	U-3gu	03-57-160	586298.9	4100174.2	01/05/1972	<20	47	1,225.3	120	AA	492	No	1220	23.4
MESITA	U-3jd	03-57-198	587541.9	4095817.0	05/09/1973	<20	45	1,207.0	149	AA	470	No	954	17.9
METROPOLIS	U-2gh	02-57-140	583945.8	4107567.1	03/10/1990	20 to 150	66	1,273.1	469	TM-LVTA	479	No	903	6.6
MICKEY	U-7m	07-57-050	589307.3	4103777.5	05/10/1967	20 to 200	72	1,304.5	500	LTCU	573	No	583	1.2
MIDLAND	U-7by	07-57-040	586783.4	4106602.6	07/16/1987	20 to 150	65	1,310.6	487	OSBCU	577	No	662	2.7
MIERA	U-7ad	07-57-005	586483.2	4106603.9	03/08/1973	20 to 200	69	1,306.1	569	OSBCU	573	No	723	2.3
MINERO	U-3lt	03-57-257	584988.3	4096420.8	12/20/1984	<20	40	1,214.6	245	TM-UVTA	481	No	1096	21.3
MINIATA	U-2bu	02-57-048	584282.2	4107306.5	07/08/1971	83	53	1,273.8	529	LTCU	494	Yes	861	6.4
MINK	U-3ae	03-57-005	586157.6	4100495.8	10/29/1961	Low	42	1,227.7	192	AA	495	No	1191	23.8
MINNOW	U-3cv	03-57-064	587843.5	4099749.6	05/15/1964	<20	40	1,225.9	241	AA	492	No	791	13.8
MISSISSIPPI	U-9ad	09-57-027	584347.0	4110555.5	10/05/1962	115	60	1,290.5	494	TM-LVTA	546	No	961	7.9
MIZZEN	U-7ah	07-57-009	585660.0	4105623.5	06/03/1975	20 to 200	67	1,274.1	637	LTCU	536	Yes	863	3.4
MOA	U-3ed	03-57-097	587692.9	4099261.8	09/01/1965	<20	42	1,220.7	194	AA	487	No	827	15.1
MOGOLLON	U-3li	03-57-248	584869.0	4096387.5	04/20/1986	<20	39	1,214.6	259	TM-UVTA	481	No	1124	22.2
MONAHANS-A	U-3lk	03-57-250	587113.8	4094139.8	11/09/1988	<20	38	1,202.1	290	AA	463	No	1133	22.2
MONAHANS-B	U-6i	06-57-006	587114.5	4093866.1	11/09/1988	<20	38	1,201.5	290	AA	462	No	1154	22.7
MONERO	U-3jq	03-57-210	588748.7	4102312.8	05/19/1972	<20	32	1,272.5	537	OSBCU	522	Yes	675	4.3
MONTEREY	U-4aj	04-57-008	582197.9	4106418.6	07/29/1982	20 to 150	69	1,280.2	400	TM-LVTA	495	No	783	5.6
MORRONES	U-3ei	03-57-103	587740.8	4102979.7	05/21/1970	20 to 200	72	1,264.3	483	LTCU	518	No	795	4.3
MUDPACK	U-10n	10-57-051	582823.3	4114801.0	12/16/1964	2.7	23	1,336.9	152	TM-LVTA	602	No	602	19.6
MUGGINS	U-3ls	03-57-256	584899.0	4096509.5	12/09/1983	<20	40	1,215.2	244	TM-UVTA	482	No	1110	21.6
MULESHOE	U-7bk	07-57-031	587666.5	4106941.6	11/15/1989	<20	40	1,338.4	244	LTCU	606	No	606	9.1
MULLET	U-2ag	02-57-006	582878.8	4109587.4	10/17/1963	Low	56	1,301.5	60	AA	552	No	1053	17.7

Table B-1
Yucca Flat/Climax Mine Detonation Characteristics
(Page 14 of 23)

Detonation Name	Emplacement Hole Name	CAS	UTM Easting	UTM Northing	Date Expended	Announced Yield (kt)[a]	Cavity Radius (m)[b]	Land Surface Elevation (m amsl)	Depth to Working Point (m)	Working Point HSU	Estimated Depth to Steady State Water Level (m)	Saturated Working Point	Estimated Depth to Saturated LCA or LCA3 (m)	Number of R_c from WP to Saturated LCA or LCA3
MUNDO	U-7bo	07-57-034	586866.8	4106899.7	05/01/1984	20 to 150	63	1,319.2	566	OSBCU	586	No	637	1.1
MUSCOVY	U-3dx	03-57-091	589376.5	4097073.4	04/23/1965	<20	43	1,216.5	180	TM-WTA	482	No	652	11.0
MUSHROOM	U-3ef	03-57-100	588026.9	4099506.8	03/03/1967	<20	43	1,225.0	180	AA	491	No	771	13.7
MUSTANG	U-9at	09-57-040	584660.2	4109770.1	11/15/1963	Low	44	1,283.8	166	AA	542	No	867	15.9
NAMA-AMARYLIS	U-9itsxy31	09-57-020	585853.1	4111200.7	08/05/1971	<20	38	1,300.3	273	LTCU	568	No	568	7.8
NAMA-MEPHISTO	U-9itsz27	09-57-019	586037.6	4110713.8	08/05/1971	<20	40	1,303.0	244	TM-LVTA	571	No	571	8.2
NARRAGUAGUS	U-2f	02-57-127	582284.4	4112241.0	09/27/1963	Low	45	1,328.9	150	AA	589	No	658	11.3
NASH	U-2ce	02-57-058	576803.9	4110955.3	01/19/1967	39	29	1,452.1	364	LCA3	527	No	441	2.6
NATCHES	U-9ak1	09-57-033	585702.2	4108966.8	08/23/1963	Low	57	1,288.4	59	AA	554	No	577	9.2
NATOMA	U-10aw	10-57-027	583987.3	4114820.4	04/05/1973	<20	40	1,309.7	244	AA	574	No	574	8.3
NAVATA	U-3lb	03-57-242	587107.3	4101042.4	09/29/1983	<20	43	1,233.8	183	AA	500	No	972	18.4
NESSEL	U-2ep	02-57-116	582922.5	4108524.0	08/29/1979	20 to 150	66	1,286.6	464	AA	532	No	931	7.1
NEWARK	U-10u	10-57-057	584694.2	4113804.8	09/29/1966	<20	40	1,306.1	229	AA	573	No	573	8.6
NIGHTINGALE	U-2ey	02-57-125	582371.1	4113504.4	06/22/1988	<150	78	1,336.2	238	AA	600	No	600	4.6
NIPPER	U-3gl	03-57-152	588163.4	4095423.9	02/04/1969	<20	40	1,204.9	241	AA	466	No	775	13.4
NIZA	U-9cr	09-57-088	585829.0	4109372.2	07/10/1981	<20	36	1,293.0	341	LTCU	560	No	560	6.1
NOGGIN	U-9bx	09-57-070	584631.9	4110188.0	09/06/1968	20 to 200	69	1,286.3	582	TM-LVTA	543	Yes	832	3.6
NOOR	U-2be	02-57-032	581797.0	4112191.7	04/10/1968	20 to 200	76	1,336.5	382	AA	596	No	760	5.0
NORBO	U-8c	08-57-003	581390.6	4115024.5	03/08/1980	<20	39	1,376.2	271	OSBCU	639	No	639	9.4
NORMANNA	U-10cb	10-57-041	585704.1	4116403.1	07/12/1984	<20	42	1,342.3	200	LTCU	350	No	350	3.6
NUMBAT	U-3bu	03-57-046	587537.7	4100236.7	12/12/1962	Low	40	1,228.3	232	AA	494	No	876	16.1
OAKLAND	U-2bi	02-57-036	581489.4	4113032.0	04/04/1967	<20	44	1,348.1	166	AA	601	No	701	12.2
OARLOCK	U-3km	03-57-228	586422.3	4096606.3	02/16/1977	<20	37	1,210.1	318	AA	476	No	1248	25.1
OBAR	U-7ag	07-57-008	586293.8	4107185.6	04/30/1975	20 to 200	69	1,306.4	569	OSBCU	573	No	741	2.5
OCATE	U-3jp	03-57-209	587651.1	4095621.1	03/30/1972	<20	41	1,206.4	210	AA	469	No	894	16.7
OCHRE	U-3ec	03-57-096	586928.6	4099960.0	04/29/1966	<20	47	1,223.2	126	AA	490	No	1037	19.4
OCONTO	U-9ay	09-57-045	585607.7	4109127.7	01/23/1964	10.5	31	1,286.6	265	TM-LVTA	552	No	579	10.1
OFFSHORE	U-3ks	03-57-233	588250.1	4096765.0	08/08/1979	20 to 150	69	1,208.8	397	LTCU	472	No	646	3.6
ONAJA	U-3js	03-57-212	587187.2	4095725.1	03/30/1972	<20	38	1,207.0	279	AA	471	No	1066	20.7
ORGANDY	U-9bo	09-57-063	586778.3	4107958.6	06/11/1965	<20	43	1,320.4	173	TM-LVTA	588	No	588	9.7
ORKNEY	U-10be	10-57-035	583958.3	4117105.7	05/02/1984	<20	41	1,378.3	210	AA	606	No	722	12.5
OSCURO	U-7z	07-57-062	585633.6	4104206.1	09/21/1972	20 to 200	70	1,252.1	560	LTCU	513	Yes	893	4.8
OTERO	U-3q	03-57-274	586089.4	4100642.4	09/12/1958	0.038	5	1,229.0	146	AA	496	No	1179	172.1
PACA	U-3ax	03-57-024	586701.4	4100279.2	05/07/1962	Low	39	1,225.6	259	AA	492	No	1139	22.6

Table B-1
Yucca Flat/Climax Mine Detonation Characteristics
(Page 15 of 23)

Detonation Name	Emplacement Hole Name	CAS	UTM Easting	UTM Northing	Date Expended	Announced Yield (kt)[a]	Cavity Radius (m)[b]	Land Surface Elevation (m amsl)	Depth to Working Point (m)	Working Point HSU	Estimated Depth to Steady State Water Level (m)	Saturated Working Point	Estimated Depth to Saturated LCA or LCA3 (m)	Number of R_c from WP to Saturated LCA or LCA3
PACKARD	U-2u	02-57-150	582975.8	4111486.5	01/15/1969	10	31	1,315.2	247	AA	575	No	784	17.3
PACKRAT	U-3aw	03-57-023	585432.6	4100172.0	06/06/1962	Low	39	1,225.9	262	AA	492	No	1290	26.4
PAISANO	U-9w1	09-57-112	585625.0	4108474.1	04/24/1963	Low	57	1,287.8	58	AA	553	No	797	13.0
PAJARA	U-3ji	03-57-203	586842.2	4094169.9	12/12/1973	<20	38	1,202.4	278	AA	465	No	1218	24.7
PALISADE-1	U-4at	04-57-015	578112.7	4106968.3	05/15/1989	<20	36	1,365.2	335	TM-LVTA	490	No	537	5.5
PALISADE-2	U-4at	04-57-015	578112.7	4106968.3	05/15/1989	<20	35	1,365.2	390	TM-LVTA	490	No	537	4.2
PALISADE-3	U-4at	04-57-015	578112.7	4106968.3	05/15/1989	<20	35	1,365.2	404	TM-LVTA	490	No	537	3.8
PALIZA	U-7bd	07-57-026	588106.2	4104182.8	10/01/1981	20 to 150	66	1,287.5	472	LTCU	533	No	710	3.6
PAMPAS	U-3al	03-57-012	586380.7	4099687.8	03/01/1962	9.5	28	1,222.9	363	AA	490	No	1256	31.9
PANAMINT	U-2gb	02-57-136	583468.9	4108952.6	05/21/1986	<20	33	1,286.0	480	TM-WTA	529	No	959	14.5
PANCHUELA	U-3mg	03-57-266	585148.3	4094941.0	06/30/1987	<20	37	1,206.1	319	AA	473	No	1192	23.6
PAR	U-2p	02-57-146	581965.5	4111857.4	10/09/1964	38	43	1,331.4	406	AA	586	No	839	10.1
PARNASSIA	U-2bc	02-57-030	582555.9	4112872.7	11/30/1971	<20	37	1,328.9	331	TM-LVTA	592	No	600	7.3
PARROT	U-3dk	03-57-080	587846.5	4098988.1	12/16/1964	1.3	17	1,219.5	180	AA	486	No	794	36.1
PASCAL-A	U-3j	03-57-194	585947.3	4100849.8	07/26/1957	Slight	45	1,229.3	152	AA	496	No	1172	22.7
PASCAL-B	U-3d	03-57-068	585902.7	4100547.6	08/27/1957	Slight	45	1,227.7	152	AA	495	No	1221	23.8
PASCAL-C	U-3e	03-57-094	586176.6	4100648.5	12/06/1957	Slight	53	1,228.6	76	AA	496	No	1164	20.5
PASSAIC	U-9l	09-57-103	584931.9	4108150.8	04/06/1962	Low	40	1,275.0	234	AA	536	No	1122	22.2
PEBA	U-3bb	03-57-028	586311.4	4101215.8	09/20/1962	Low	40	1,232.3	241	AA	499	No	1049	20.2
PEDERNAL	U-3hg	03-57-170	588312.5	4096353.9	09/29/1971	<20	35	1,207.3	379	TM-LVTA	470	No	635	7.3
PEKAN	U-3bw	03-57-048	587539.1	4099748.9	08/12/1963	Low	37	1,223.8	302	AA	490	No	912	16.0
PENASCO	U-3hl	03-57-181	587549.3	4096762.6	11/19/1970	<20	39	1,209.8	271	AA	475	No	903	16.2
PERA	U-10bd	10-57-034	585407.4	4112296.1	09/08/1979	<20	42	1,307.3	200	TM-LVTA	575	No	575	8.9
PERSIMMON	U-3dn	03-57-083	587548.2	4097067.6	02/23/1967	<20	38	1,210.7	299	AA	476	No	873	15.1
PETREL	U-3dy	03-57-092	587416.2	4099870.0	06/11/1965	1.3	17	1,224.1	181	AA	490	No	924	43.7
PICCALILLI	U-3fc	03-57-123	588761.4	4098595.2	11/21/1969	20 to 200	76	1,222.2	394	LTCU	489	No	656	3.4
PIKE	U-3cy	03-57-066	587901.4	4100724.6	03/13/1964	<20	48	1,237.5	115	AA	501	No	774	13.7
PILE DRIVER	U-15a.01	15-57-002	583511.6	4119950.0	06/02/1966	62	45	1,551.4	463	MGCU	185	Yes	No LCA	No LCA
PINEAU	U-7ao	07-57-016	587154.5	4104958.3	07/16/1981	<20	41	1,286.3	207	TM-UVTA	552	No	678	11.5
PINEDROPS-BAYOU	U-10as	10-57-024	584266.4	4114406.9	01/10/1974	<20	36	1,310.0	343	TM-LVTA	576	No	576	6.5
PINEDROPS-SLOAT	U-10as	10-57-024	584266.4	4114406.9	01/10/1974	<20	41	1,310.0	213	AA	576	No	576	8.9
PINEDROPS-TAWNY	U-10as	10-57-024	584266.4	4114406.9	01/10/1974	<20	38	1,310.0	282	TM-LVTA	576	No	576	7.7
PIPEFISH	U-3co	03-57-059	586564.5	4099501.4	04/29/1964	<20	39	1,221.0	262	AA	488	No	1243	25.1
PIRANHA	U-7e	07-57-043	585905.9	4104740.6	05/13/1966	20 to 200	70	1,263.7	549	LTCU	526	Yes	806	3.7

Table B-1
Yucca Flat/Climax Mine Detonation Characteristics
(Page 16 of 23)

Detonation Name	Emplacement Hole Name	CAS	UTM Easting	UTM Northing	Date Expended	Announced Yield (kt)[a]	Cavity Radius (m)[b]	Land Surface Elevation (m amsl)	Depth to Working Point (m)	Working Point HSU	Estimated Depth to Steady State Water Level (m)	Saturated Working Point	Estimated Depth to Saturated LCA or LCA3 (m)	Number of R_c from WP to Saturated LCA or LCA3
PITON-A	U-9itsy30	09-57-014	585914.5	4111079.0	05/28/1970	<20	40	1,300.9	237	TM-LVTA	568	No	568	8.3
PITON-B	U-9itsx27	09-57-010	585794.5	4110712.6	05/28/1970	<20	40	1,296.9	230	TM-LVTA	564	No	564	8.4
PITON-C	U-9itsaa25	09-57-116	586160.7	4110470.4	05/28/1970	<20	49	1,305.8	101	TM-LVTA	573	No	573	9.6
PLAID II	U-2r	02-57-148	582660.9	4109086.8	02/03/1966	<20	39	1,298.4	269	AA	546	No	1011	19.0
PLANER	U-3el	03-57-106	586939.8	4096760.4	11/21/1969	<20	35	1,210.4	378	AA	476	No	1107	20.8
PLATYPUS	U-3ad	03-57-004	586086.1	4100469.3	02/24/1962	Low	57	1,227.1	58	AA	494	No	1206	20.1
PLAYER	U-9cc	09-57-075	585230.1	4108118.6	08/27/1964	<20	51	1,280.5	90	AA	543	No	1075	19.3
PLEASANT	U-9ah	09-57-030	584973.0	4109304.9	05/29/1963	Low	41	1,279.6	211	AA	540	No	815	14.7
PLIERS	U-3gn	03-57-154	585566.0	4097487.0	08/27/1969	<20	40	1,214.3	239	AA	481	No	1341	27.6
PLOMO	U-3ff	03-57-126	590224.1	4098600.6	05/01/1974	<20	45	1,253.9	149	TM-LVTA	522	No	522	8.3
POD-A	U-2ch	02-57-063	577225.1	4110576.5	10/29/1969	16.7 (total)	36	1,424.0	267	TM-LVTA	540	No	540	7.6
POD-B	U-2ci	02-57-060	576218.3	4110593.9	10/29/1969		37	1,491.7	249	TM-LVTA	444	No	2246	54.0
POD-C	U-2cj	02-57-061	576388.4	4110138.7	10/29/1969		41	1,474.9	171	AA	466	No	2460	55.8
POD-D	U-2ck	02-57-062	576745.9	4110032.1	10/29/1969		35	1,451.2	312	TM-LVTA	512	No	512	5.7
POLKA	U-10ai	10-57-008	584091.8	4112756.8	12/06/1967	<20	42	1,299.4	195	AA	558	No	766	13.6
POLYGONUM	U-2by	02-57-052	582313.0	4112686.0	10/02/1973	<20	41	1,330.8	213	AA	592	No	599	9.4
POMMARD	U-3ee	03-57-098	587962.8	4100420.7	03/14/1968	1.5	17	1,235.4	209	AA	501	No	778	33.5
PONGEE	U-2ah	02-57-007	582887.3	4109696.8	07/22/1965	<20	46	1,301.5	134	AA	553	No	1018	19.2
PONIL	U-7bv	07-57-039	588717.6	4105097.9	09/27/1985	<20	36	1,310.6	365	LTCU	556	No	689	9.0
PORTMANTEAU	U-2ax	02-57-022	581401.3	4111977.3	08/30/1974	20 to 200	67	1,340.2	655	TM-LVTA	600	Yes	865	3.1
PORTOLA	U-10bb	10-57-032	584194.6	4114881.4	02/06/1975	<20	42	1,312.2	198	AA	575	No	575	9.0
PORTOLA-LARKIN	U-10bb	10-57-032	584194.6	4114881.4	02/06/1975	<20	38	1,312.2	275	AA	575	No	575	7.9
PORTULACA	U-2bv	02-57-049	581181.7	4111525.2	06/28/1973	20 to 200	73	1,337.5	466	AA	591	No	830	5.0
POTRERO	U-2eb	02-57-106	582007.9	4112814.4	04/23/1974	<20	41	1,337.2	211	AA	597	No	629	10.2
POTRILLO	U-7af	07-57-007	586452.7	4105321.5	06/21/1973	20 to 200	69	1,282.3	567	OSBCU	548	Yes	711	2.1
PRATT	U-3hq	03-57-185	586270.5	4096453.4	09/25/1974	<20	37	1,210.1	314	AA	476	No	1277	26.0
PRESIDIO	U-6d	06-57-002	588591.5	4093261.8	04/22/1987	<20	37	1,198.5	320	TM-LVTA	458	No	811	13.3
PUCE	U-3bs	03-57-044	585459.2	4101692.1	06/10/1966	<20	33	1,235.4	486	AA	493	No	1103	18.7
PUDDLE	U-3kg	03-57-224	587981.2	4095240.4	11/26/1974	<20	42	1,219.8	184	AA	481	No	859	15.7
PURPLE	U-3ds	03-57-087	588160.5	4096154.9	03/18/1966	<20	37	1,206.7	334	TM-WTA	469	No	721	10.5
PUYE	U-3jl	03-57-206	585717.6	4097700.5	08/14/1974	<20	34	1,215.2	430	AA	482	No	1325	26.3
PYRAMID	U-7be	07-57-027	586148.4	4106326.1	04/16/1980	20 to 150	63	1,292.7	579	OSBCU	557	Yes	772	3.1
QUARGEL	U-2fb	02-57-129	581380.9	4109135.7	11/18/1978	20 to 150	64	1,301.8	542	TM-LVTA	539	Yes	791	4.0
QUESO	U-10bf	10-57-036	584525.4	4116147.8	08/11/1982	<20	41	1,337.2	216	AA	571	No	676	11.2

Table B-1
Yucca Flat/Climax Mine Detonation Characteristics
(Page 17 of 23)

Detonation Name	Emplacement Hole Name	CAS	UTM Easting	UTM Northing	Date Expended	Announced Yield (kt)[a]	Cavity Radius (m)[b]	Land Surface Elevation (m amsl)	Depth to Working Point (m)	Working Point HSU	Estimated Depth to Steady State Water Level (m)	Saturated Working Point	Estimated Depth to Saturated LCA or LCA3 (m)	Number of R_c from WP to Saturated LCA or LCA3
QUINELLA	U-4l	04-57-027	583986.5	4106455.6	02/08/1979	20 to 150	63	1,267.7	579	LTCU	484	Yes	907	5.3
RACCOON	U-3ajs	03-57-010	585861.6	4100165.0	06/01/1962	Low	44	1,225.6	164	AA	493	No	1278	25.3
RACK	U-9ap	09-57-037	584551.1	4108818.9	08/15/1968	<20	42	1,280.5	200	AA	536	No	1045	20.1
RARITAN	U-9u	09-57-109	584853.6	4109551.9	09/06/1962	Low	44	1,281.4	156	AA	540	No	896	16.8
REBLOCHON	U-2en	02-57-114	583164.7	4108799.1	02/23/1978	20 to 150	61	1,288.1	658	LTCU	534	Yes	966	5.1
REDMUD	U-7ab	07-57-003	588743.0	4103928.1	12/08/1976	<20	34	1,295.7	427	LTCU	533	No	720	8.6
REO	U-10m	10-57-050	585360.5	4112541.0	01/22/1966	<20	41	1,309.4	208	AA	577	No	654	10.9
RHYOLITE	U-2ey	02-57-126	582371.1	4113504.4	06/22/1988	<150	81	1,336.2	207	AA	600	No	600	4.9
RIB	U-3jv	03-57-215	587365.6	4097067.0	12/14/1977	<20	41	1,211.0	213	AA	477	No	922	17.3
RINGTAIL	U-3ak	03-57-011	586678.0	4099901.2	12/17/1961	Low	36	1,223.5	363	AA	490	No	1169	22.4
RIOLA	U-2eq	02-57-117	583107.7	4107931.4	09/25/1980	1.07	13	1,281.1	424	AA	508	No	832	31.4
RIVET I	U-10aa	10-57-002	584653.8	4113411.8	01/18/1967	<20	45	1,302.4	152	AA	567	No	676	11.7
RIVET II	U-10z	10-57-061	584519.9	4113374.8	01/26/1967	<20	42	1,300.6	198	AA	563	No	692	11.8
RIVET III	U-10y	10-57-060	584461.9	4113493.1	03/02/1967	<20	38	1,301.5	274	AA	567	No	675	10.6
RIVOLI	U-2eg	02-57-108	582905.9	4110296.9	05/20/1976	<20	42	1,305.8	200	AA	559	No	881	16.2
ROANOKE	U-9q	09-57-107	584322.4	4108706.0	10/12/1962	Low	44	1,279.6	155	AA	530	No	998	19.1
ROMANO	U-2ex	02-57-124	582414.6	4110652.3	12/16/1983	20 to 150	65	1,314.0	515	TM-UVTA	561	No	880	5.7
ROQUEFORT	U-4as	04-57-014	578066.1	4107227.1	10/16/1985	20 to 150	68	1,367.9	415	TM-LVTA	508	No	535	1.8
ROUSANNE	U-4p	04-57-030	584501.4	4107089.7	11/12/1981	20 to 150	64	1,269.8	517	LTCU	499	Yes	793	4.3
ROVENA	U-10s	10-57-055	584541.8	4113804.2	08/10/1966	<20	42	1,304.8	194	AA	572	No	572	9.0
RUDDER	U-7aj(s)	07-57-011	585622.1	4106251.4	12/28/1976	20 to 150	61	1,281.7	639	OSBCU	544	Yes	896	4.2
RUMMY	U-7au	07-57-020	584324.5	4103942.8	09/27/1978	20 to 150	61	1,253.0	640	LTCU	489	Yes	1077	7.2
RUSSET	U-6a	06-57-001	584046.3	4091762.8	03/05/1968	<20	47	1,197.9	120	AA	459	No	840	15.3
SABADO	U-3lc	03-57-243	588744.6	4094877.4	08/11/1983	<20	37	1,202.7	320	UTCU	461	No	665	9.3
SACRAMENTO	U-9v	09-57-110	584629.8	4108118.6	06/30/1962	Low	45	1,273.1	149	AA	527	No	816	14.8
SAN JUAN	U-3p	03-57-273	586030.1	4100629.1	10/20/1958	Zero	0	1,228.0	71	AA	495	No	1189	No Rc
SANDREEF	U-7aq	07-57-018	584449.6	4103090.0	11/09/1977	20 to 150	60	1,247.9	701	LTCU	479	Yes	1082	6.4
SANTEE	U-10f	10-57-046	584053.6	4111651.4	10/27/1962	Low	37	1,296.6	319	AA	551	No	875	15.0
SAPELLO	U-3ge	03-57-145	585035.3	4096753.8	04/12/1974	<20	43	1,215.8	181	AA	482	No	1072	20.7
SAPPHO	U-2dh2	02-57-085	581666.9	4107605.1	03/23/1972	<20	42	1,292.7	198	AA	552	No	552	8.4
SARDINE	U-3ch	03-57-056	586320.5	4099500.8	12/04/1963	Low	39	1,221.3	262	AA	489	No	1273	25.9
SATSOP	U-2g	02-57-134	581994.9	4112161.9	08/15/1963	Low	40	1,332.9	225	AA	590	No	735	12.7
SATZ	U-2dq	02-57-095	581995.9	4107469.5	07/07/1978	<20	37	1,289.9	315	TM-LVTA	536	No	613	8.0
SAXON	U-2cc	02-57-056	576988.3	4110605.5	07/28/1966	1.2	17	1,438.4	154	TM-LVTA	536	No	2533	140.0

Table B-1
Yucca Flat/Climax Mine Detonation Characteristics
(Page 18 of 23)

Detonation Name	Emplacement Hole Name	CAS	UTM Easting	UTM Northing	Date Expended	Announced Yield (kt)[a]	Cavity Radius (m)[b]	Land Surface Elevation (m amsl)	Depth to Working Point (m)	Working Point HSU	Estimated Depth to Steady State Water Level (m)	Saturated Working Point	Estimated Depth to Saturated LCA or LCA3 (m)	Number of R_c from WP to Saturated LCA or LCA3
SAZERAC	U-3fa	03-57-121	586598.4	4098618.4	10/25/1967	<20	37	1,217.7	301	AA	485	No	1185	23.3
SCANTLING	U-4h	04-57-024	584008.0	4107293.7	08/19/1977	20 to 150	60	1,272.5	701	OSBCU	482	Yes	940	4.0
SCAUP	U-3da(s)	03-57-069	587973.7	4101654.6	05/14/1965	<20	34	1,249.1	427	LTCU	507	No	780	10.4
SCHELLBOURNE	U-2gf	02-57-138	582427.0	4108875.8	05/13/1988	<150	66	1,295.1	463	AA	541	No	966	7.6
SCISSORS	U-3gh	03-57-148	585481.1	4095536.4	12/12/1968	<20	40	1,208.5	241	AA	475	No	1063	20.6
SCREAMER	U-3dg	03-57-076	588155.5	4097678.9	09/01/1965	<20	37	1,211.6	302	TM-WTA	478	No	674	9.8
SCREE-ACAJOU	U-9itsx24	09-57-009	585795.1	4110353.3	10/13/1970	<20	39	1,296.0	249	TM-LVTA	563	No	563	8.1
SCREE-ALHAMBRA	U-9itsz21	09-57-015	586040.2	4109982.7	10/13/1970	<20	42	1,300.0	192	TM-LVTA	568	No	568	9.0
SCREE-CHAMOIS	U-9itsz24	09-57-016	586038.9	4110344.7	10/13/1970	<20	49	1,301.8	101	TM-LVTA	569	No	569	9.6
SCUPPER	U-3hj	03-57-174	586146.5	4097062.4	08/19/1977	<20	34	1,211.9	450	AA	478	No	1271	24.1
SCUTTLE	U-2bh	02-57-035	582143.2	4113332.6	11/13/1969	1.7	19	1,339.3	165	AA	602	No	602	23.0
SEAFOAM	U-2ea	02-57-105	582304.4	4112975.4	12/13/1973	<20	42	1,333.2	198	AA	595	No	595	9.5
SEAMOUNT	U-3kp	03-57-230	586724.9	4097399.0	11/17/1977	<20	36	1,212.8	370	AA	479	No	1141	21.4
SEAWEED B	U-3hkd	03-57-177	589119.4	4096533.4	10/16/1969	<20	47	1,211.9	119	AA	474	No	659	11.5
SEAWEED-C	U-3hke	03-57-179	589089.1	4096405.3	10/01/1969	<20	47	1,211.6	119	AA	473	No	655	11.4
SEAWEED-D	U-3hkf	03-57-180	589005.6	4096302.6	10/01/1969	<20	47	1,210.4	119	AA	472	No	652	11.3
SEAWEED-E	U-3hkc	03-57-178	589088.2	4096661.3	10/01/1969	<20	47	1,211.3	124	AA	474	No	657	11.3
SECO	U-8l	08-57-007	581288.4	4115240.2	02/25/1981	<20	42	1,383.2	200	OSBCU	646	No	646	10.6
SEERSUCKER	U-9bm	09-57-061	586089.7	4108118.3	02/19/1965	<20	45	1,301.2	144	TM-LVTA	568	No	708	12.5
SEPIA	U-3en	03-57-108	586956.6	4100661.0	11/12/1965	<20	40	1,229.3	241	AA	496	No	1038	19.9
SEVILLA	U-3fk	03-57-129	589611.2	4099756.1	06/25/1968	<20	36	1,253.0	359	TM-LVTA	516	No	703	9.5
SEYVAL	U-3lm	03-57-252	586098.4	4097732.6	11/12/1982	<20	36	1,214.3	366	AA	481	No	1271	25.1
SHALLOWS	U-3jf	03-57-200	587543.9	4098286.2	02/26/1976	<20	40	1,215.2	245	AA	481	No	838	14.8
SHAPER	U-7r	07-57-054	587003.8	4104683.3	03/23/1970	20 to 200	70	1,278.6	561	OSBCU	545	Yes	674	1.6
SHAVE	U-3gk	03-57-151	589468.7	4096860.4	01/22/1969	<20	40	1,218.0	241	UTCU	483	No	641	10.0
SHREW	U-3ac	03-57-003	586005.9	4100481.8	09/16/1961	Low	50	1,227.4	98	AA	494	No	1217	22.4
SHUFFLE	U-10t	10-57-056	585514.7	4112021.9	04/18/1968	20 to 200	72	1,306.1	494	ATCU	574	No	574	1.1
SIDECAR	U-3ez	03-57-120	588334.1	4098989.5	12/13/1966	<20	40	1,222.2	240	TM-WTA	489	No	686	11.2
SIENNA	U-3cj	03-57-057	587296.4	4099260.1	01/18/1966	<20	38	1,220.1	275	AA	487	No	987	18.7
SILENE	U-9ck	09-57-082	585209.7	4107846.4	06/28/1973	<20	42	1,280.8	198	AA	543	No	1098	21.4
SIMMS	U-10w	10-57-058	584589.5	4113947.6	11/05/1966	2.3	20	1,306.4	199	AA	573	No	573	18.7
SNUBBER	U-3ev2s	03-57-116	589971.4	4101236.8	04/21/1970	12.7	31	1,279.9	344	LTCU	551	No	562	7.0
SOLANO	U-3jx	03-57-217	587489.8	4095476.1	08/09/1972	<20	46	1,206.1	134	AA	468	No	966	18.1
SOLANUM	U-9itsw24.5	09-57-022	585733.9	4110423.2	12/14/1972	<20	43	1,294.2	183	TM-LVTA	561	No	561	8.6

Table B-1
Yucca Flat/Climax Mine Detonation Characteristics
(Page 19 of 23)

Detonation Name	Emplacement Hole Name	CAS	UTM Easting	UTM Northing	Date Expended	Announced Yield (kt)[a]	Cavity Radius (m)[b]	Land Surface Elevation (m amsl)	Depth to Working Point (m)	Working Point HSU	Estimated Depth to Steady State Water Level (m)	Saturated Working Point	Estimated Depth to Saturated LCA or LCA3 (m)	Number of R_c from WP to Saturated LCA or LCA3
SOLENDON	U-3cz	03-57-067	586313.5	4101389.8	02/12/1964	<20	45	1,233.2	150	AA	500	No	1020	19.3
SPAR	U-3jr	03-57-211	587291.6	4095759.1	12/19/1973	<20	45	1,207.0	148	AA	471	No	1048	20.0
SPIDER-A	U-2bp1	02-57-042	583144.6	4112855.9	08/14/1969	<20	41	1,318.6	213	AA	582	No	582	9.0
SPIDER-B	U-2bp2	02-57-043	583130.8	4112627.6	08/14/1969	<20	40	1,318.3	228	AA	581	No	581	8.8
SPOON	U-9bd	09-57-052	586581.4	4107729.0	09/11/1964	<20	43	1,315.5	180	TM-LVTA	583	No	625	10.3
SPRIT	U-3hc	03-57-166	587388.7	4099108.4	11/10/1976	<20	43	1,219.2	183	AA	486	No	969	18.3
SPUD	U-3fy	03-57-139	589078.2	4095244.0	07/17/1968	<20	40	1,205.8	240	TM-LVTA	464	No	666	10.7
ST. LAWRENCE	U-2b	02-57-029	582280.6	4113243.5	11/09/1962	Low	44	1,336.2	166	AA	599	No	599	9.8
STACCATO	U-10ah	10-57-007	584012.5	4112436.3	01/19/1968	20 to 200	73	1,298.8	444	AA	559	No	807	5.0
STANLEY	U-10q	10-57-053	584495.7	4111592.0	07/27/1967	20 to 200	72	1,291.4	484	TM-LVTA	547	No	818	4.6
STANYAN	U-2aw	02-57-021	582749.8	4109788.0	09/26/1974	20 to 200	69	1,301.8	573	TM-WTA	554	Yes	995	6.1
STARWORT	U-2bs	02-57-047	583637.5	4108733.7	04/26/1973	90	53	1,288.1	564	LTCU	525	Yes	951	7.3
STILLWATER	U-9c	09-57-073	584153.6	4109205.1	02/08/1962	3.07	23	1,282.9	181	AA	537	No	1030	36.9
STILT	U-3fh	03-57-127	588759.6	4099204.6	12/15/1967	<20	37	1,230.8	333	TM-LVTA	497	No	658	8.8
STOAT	U-3ap	03-57-016	585809.3	4100056.4	01/09/1962	5.1	24	1,225.6	302	AA	493	No	1297	41.4
STODDARD	U-2cms	02-57-064	577514.9	4108322.2	09/17/1968	31	39	1,396.9	468	TM-LVTA	522	No	528	1.6
STONES	U-9ae	09-57-028	585378.8	4107420.1	05/22/1963	Intermediate	76	1,284.1	393	TM-LVTA	547	No	942	7.2
STRAIT	U-4a	04-57-001	584191.6	4106990.5	03/17/1976	200 to 500	87	1,270.7	782	OSBCU	484	Yes	932	1.7
STRAKE	U-7ae	07-57-006	588267.9	4104733.7	08/04/1977	20 to 150	64	1,300.3	518	LTCU	546	No	817	4.7
STURGEON	U-3bo	03-57-040	587294.8	4099991.8	04/15/1964	<20	45	1,225.0	150	AA	491	No	936	17.5
STUTZ	U-2ca	02-57-055	576304.6	4110491.9	04/06/1966	<20	40	1,485.0	226	TM-LVTA	466	No	466	6.0
SUEDE	U-9bk	09-57-060	586490.8	4107916.7	03/20/1965	<20	45	1,312.8	143	TM-LVTA	581	No	660	11.5
SUNDOWN-A	U-1d	01-57-003	583883.6	4099324.7	09/20/1990	<20	39	1,233.5	270	AA	495	No	969	17.9
SUNDOWN-B	U-1d	01-57-003	583883.6	4099324.7	09/20/1990	<20	39	1,233.5	256	AA	495	No	969	18.3
SUTTER	U-2bw	02-57-050	583168.9	4111930.2	12/21/1976	<20	42	1,314.3	200	AA	573	No	662	11.0
SWITCH	U-9bv	09-57-069	586287.3	4109038.6	06/22/1967	3.1	20	1,303.6	302	LTCU	572	No	572	13.5
TAHOKA	U-3mf	03-57-265	584880.3	4101857.7	08/13/1987	20 to 150	61	1,239.6	639	LTCU	487	Yes	796	2.6
TAJIQUE	U-7aa	07-57-002	589600.0	4102864.3	06/28/1972	<20	37	1,300.6	332	LTCU	571	No	571	6.5
TAJO	U-7bl	07-57-032	587486.3	4106026.0	06/05/1986	20 to 150	64	1,315.8	518	LTCU	582	No	704	2.9
TAN	U-7k	07-57-048	585761.0	4102698.5	06/03/1966	20 to 200	70	1,240.5	561	TM-LVTA	499	Yes	1037	6.9
TANGERINE	U-3eb	03-57-095	586318.1	4100247.1	08/12/1966	<20	51	1,225.6	88	AA	492	No	1206	21.9
TANYA	U-2dt	02-57-098	581536.8	4108016.4	07/30/1968	20 to 200	77	1,297.5	381	AA	558	No	557	2.3
TAPESTRY	U-2an	02-57-013	582505.7	4109969.7	05/12/1966	<20	39	1,307.9	249	AA	557	No	953	18.1
TAPPER	U-3go	03-57-155	586271.8	4096087.7	06/12/1969	<20	37	1,208.5	303	AA	475	No	1289	25.9

Table B-1
Yucca Flat/Climax Mine Detonation Characteristics
(Page 20 of 23)

Detonation Name	Emplacement Hole Name	CAS	UTM Easting	UTM Northing	Date Expended	Announced Yield (kt)[a]	Cavity Radius (m)[b]	Land Surface Elevation (m amsl)	Depth to Working Point (m)	Working Point HSU	Estimated Depth to Steady State Water Level (m)	Saturated Working Point	Estimated Depth to Saturated LCA or LCA3 (m)	Number of R_c from WP to Saturated LCA or LCA3
TARKO	U-2fd	02-57-131	580969.6	4109096.1	02/28/1980	<20	36	1,306.7	369	AA	561	No	699	9.2
TAUNTON	U-9aa	09-57-024	584387.9	4109300.1	12/04/1962	Low	40	1,282.9	228	AA	539	No	968	18.5
TECHADO	U-4o	04-57-029	584466.8	4106807.4	09/22/1983	<150	64	1,267.7	533	LTCU	493	Yes	787	4.0
TEE	U-2ab	02-57-003	582895.8	4110647.9	05/07/1965	7	30	1,309.7	190	AA	564	No	872	22.7
TEJON	U-3cg	03-57-055	586045.8	4100469.2	05/17/1963	Low	53	1,227.1	75	AA	494	No	1213	21.5
TELEME	U-9cl	09-57-083	586977.4	4107776.4	02/06/1975	<20	37	1,327.1	305	LTCU	594	No	594	7.8
TEMESCAL	U-4ab	04-57-003	580723.6	4105392.9	11/02/1974	<20	39	1,290.5	263	AA	445	No	445	4.7
TEMPLAR	U-9bt	09-57-067	586061.7	4107680.9	03/24/1966	0.37	12	1,301.8	150	TM-WTA	568	No	656	42.2
TENAJA	U-3lh	03-57-247	588082.0	4096993.0	04/17/1982	<20	36	1,204.6	356	TM-LVTA	470	No	731	10.4
TENDRAC	U-3ba	03-57-027	586313.0	4100849.8	12/07/1962	Low	37	1,229.3	303	AA	496	No	1110	21.2
TERN	U-3dw	03-57-090	587750.8	4100115.3	01/29/1965	<20	41	1,229.0	211	AA	495	No	845	15.5
TERRINE-WHITE	U-9bi1	09-57-057	585749.6	4108470.0	12/18/1969	20 to 200	73	1,290.8	457	TM-LVTA	556	No	703	3.4
TERRINE-YELLOW	U-9bi2	09-57-058	586297.1	4108498.7	12/18/1969	20 to 200	75	1,303.9	418	LTCU	572	No	621	2.7
TEXARKANA	U-7ca	07-57-041	588835.4	4103653.9	02/10/1989	20 to 150	65	1,293.6	504	OSBCU	519	No	700	3.0
THISTLE	U-7t	07-57-056	588372.8	4105145.1	04/30/1969	20 to 200	70	1,307.9	561	OSBCU	556	Yes	741	2.6
THROW	U-2bg	02-57-034	581491.1	4112444.2	04/10/1968	<20	40	1,343.6	231	AA	601	No	768	13.4
TICKING	U-9bj	09-57-059	586536.1	4107607.3	08/21/1965	<20	41	1,314.9	210	TM-LVTA	582	No	619	10.0
TIJERAS	U-7y	07-57-061	588441.4	4102969.9	10/14/1970	20 to 200	70	1,276.2	561	OSBCU	523	Yes	760	2.9
TILCI	U-4ak	04-57-009	582802.2	4103541.3	11/11/1981	20 to 150	67	1,259.1	445	AA	492	No	724	4.2
TINDERBOX	U-9az	09-57-046	585062.8	4110618.9	11/22/1968	<20	34	1,287.8	440	LTCU	547	No	638	5.8
TINY TOT	U-15e	15-57-003	583635.8	4119815.4	06/17/1965	<20	26	1,530.7	111	MGCU	228	No	No LCA	No LCA
TIOGA	U-9f	09-57-094	585254.4	4109360.5	10/18/1962	Low	57	1,281.1	59	AA	543	No	720	11.8
TOMATO	U-3ek	03-57-105	589650.8	4097075.0	04/07/1966	<20	40	1,222.2	226	TM-LVTA	489	No	601	9.4
TOPGALLANT	U-4e	04-57-021	583857.1	4106866.9	02/28/1975	20 to 200	65	1,271.9	713	LTCU	483	Yes	999	4.4
TOPMAST	U-7ay	07-57-023	587120.4	4106085.7	03/23/1978	<20	34	1,309.4	458	OSBCU	576	No	681	6.6
TORCH	U-3fj	03-57-128	588757.4	4099753.1	02/21/1968	<20	40	1,237.2	241	TM-WTA	501	No	643	10.1
TORNERO	U-3ll	03-57-251	584991.2	4096281.3	02/11/1987	<20	38	1,213.4	298	TM-WTA	480	No	1105	21.2
TORNILLO	U-9aq	09-57-038	585832.6	4108278.0	10/11/1963	0.38	12	1,293.6	150	AA	559	No	735	48.7
TORRIDO	U-7w	07-57-059	589308.4	4103472.4	05/27/1969	20 to 200	71	1,297.2	515	OSBCU	566	No	566	0.7
TORTUGAS	U-3gg	03-57-147	584787.0	4102390.0	03/01/1984	20 to 150	61	1,243.3	639	LTCU	474	Yes	889	4.1
TOYAH	U-9ac	09-57-026	584855.0	4109054.6	03/15/1963	Low	46	1,279.2	131	AA	538	No	848	15.6
TRANSOM	U-4f	04-57-022	584199.5	4104826.1	05/10/1978	Zero	0	1,258.5	640	LTCU	472	Yes	1075	No Rc
TRAVELER	U-2cd	02-57-057	576639.2	4110223.7	05/04/1966	<20	42	1,457.2	198	AA	497	No	497	7.1
TREBBIANO	U-3lj	03-57-249	584637.3	4101536.6	09/04/1981	<20	37	1,238.1	305	TM-UVTA	486	No	888	15.8

Table B-1
Yucca Flat/Climax Mine Detonation Characteristics
(Page 21 of 23)

Detonation Name	Emplacement Hole Name	CAS	UTM Easting	UTM Northing	Date Expended	Announced Yield (kt)[a]	Cavity Radius (m)[b]	Land Surface Elevation (m amsl)	Depth to Working Point (m)	Working Point HSU	Estimated Depth to Steady State Water Level (m)	Saturated Working Point	Estimated Depth to Saturated LCA or LCA3 (m)	Number of R_c from WP to Saturated LCA or LCA3
TROGON	U-3dj	03-57-079	587842.1	4100237.5	07/24/1964	<20	42	1,231.1	193	AA	497	No	813	14.8
TRUCHAS-CHACON	U-3hn	03-57-184	587366.7	4096674.8	10/28/1970	<20	47	1,209.4	119	AA	475	No	957	17.8
TRUCHAS-CHAMISAL	U-3ho	03-57-182	587427.7	4096675.3	10/28/1970	<20	48	1,209.4	118	AA	475	No	945	17.6
TRUCHAS-RODARTE	U-3hm	03-57-183	587244.5	4096761.5	10/28/1970	<20	39	1,210.1	266	AA	476	No	975	18.2
TRUMBULL	U-4aa	04-57-002	580449.3	4105391.9	09/26/1974	<20	39	1,295.7	263	TM-LVTA	400	No	400	3.5
TUB-A	U-10ajc	10-57-011	585011.6	4113677.3	06/06/1968	<20	42	1,308.8	189	AA	575	No	575	9.2
TUB-B	U-10ajb	10-57-010	584929.5	4113446.3	06/06/1968	<20	42	1,306.1	189	AA	573	No	647	10.9
TUB-C	U-10ajf	10-57-013	585174.5	4113447.5	06/06/1968	<20	42	1,310.0	189	AA	577	No	589	9.5
TUB-D	U-10ajd	10-57-012	584806.4	4113620.2	06/06/1968	<20	38	1,305.2	273	TM-LVTA	572	No	601	8.6
TUB-F	U-10aja	10-57-009	585051.1	4113621.3	06/06/1968	<20	42	1,308.8	189	AA	575	No	575	9.2
TULIA	U-4s	04-57-033	583979.3	4104612.0	05/26/1989	<20	35	1,257.3	398	TM-UVTA	471	No	906	14.5
TULOSO	U-3gi	03-57-149	587055.0	4098589.2	12/12/1972	<20	39	1,216.5	271	AA	483	No	1028	19.4
TUNA	U-3de	03-57-074	585950.0	4100962.2	12/20/1963	Low	35	1,229.9	414	AA	497	No	1155	21.2
TUN-A	U-10am1	10-57-015	581745.8	4113669.8	12/10/1969	<20	42	1,350.0	200	AA	611	No	611	9.8
TUN-B	U-10am2	10-57-016	581744.8	4113867.8	12/10/1969	<20	42	1,351.5	194	AA	613	No	613	10.0
TUN-C	U-10am3	10-57-017	581943.6	4113670.1	12/10/1969	<20	42	1,345.7	194	TM-LVTA	608	No	608	9.9
TUN-D	U-10am4	10-57-018	581943.5	4113868.2	12/10/1969	<20	39	1,347.2	256	OSBCU	610	No	610	9.1
TURF	U-10c	10-57-039	583885.9	4111681.3	04/24/1964	20 to 200	71	1,317.3	506	TM-LVTA	553	No	929	6.0
TURNSTONE	U-3dt	03-57-088	586734.5	4098831.9	10/16/1964	<20	47	1,218.0	126	AA	485	No	1102	20.8
TURQUOISE	U-7bu	07-57-038	584809.2	4103174.8	04/14/1983	<150	64	1,246.0	533	LTCU	480	Yes	1024	7.7
TWEED	U-9bn	09-57-062	586381.4	4108261.9	05/21/1965	<20	38	1,308.2	284	TM-LVTA	576	No	668	10.1
TYG-A	U-2dc1e	02-57-077	581681.5	4108467.9	12/12/1968	<20	40	1,300.0	228	AA	556	No	751	13.1
TYG-B	U-2dc2d	02-57-078	581773.6	4108110.1	12/12/1968	<20	39	1,296.6	251	AA	555	No	596	8.8
TYG-C	U-2dc3c	02-57-076	581980.0	4108163.0	12/12/1968	<20	40	1,295.1	228	AA	551	No	677	11.2
TYG-D	U-2dc4a	02-57-075	581887.9	4108520.7	12/12/1968	<20	41	1,298.8	207	AA	553	No	798	14.4
TYG-E	U-2dc5b	02-57-074	582037.2	4108368.6	12/12/1968	<20	42	1,296.6	198	AA	551	No	789	14.1
TYG-F	U-2dc6f	02-57-079	581579.9	4108250.8	12/12/1968	<20	39	1,299.7	265	AA	559	No	611	8.9
UMBER	U-3em	03-57-107	586934.2	4098284.7	06/29/1967	10	29	1,215.5	310	AA	482	No	1054	24.8
VALENCIA	U-3r	03-57-275	586269.3	4100609.8	09/26/1958	0.002	2	1,228.0	148	AA	495	No	1155	503.5
VALISE	U-9by	09-57-071	585189.3	4110534.6	03/18/1969	<20	51	1,287.8	91	AA	548	No	605	10.1
VAT	U-9cf	09-57-077	585065.4	4109887.0	10/10/1968	<20	42	1,282.6	195	AA	543	No	675	11.4
VAUGHN	U-3lr	03-57-255	584881.4	4101537.4	03/15/1985	20 to 150	68	1,238.1	426	TM-LVTA	489	No	831	6.0
VELARDE	U-3jk	03-57-205	587114.1	4094413.1	04/25/1973	<20	38	1,203.4	277	AA	465	No	1132	22.5
VERDELLO	U-3ku	03-57-235	586940.5	4096562.4	07/31/1980	<20	36	1,210.1	366	AA	476	No	1134	21.3

Table B-1
Yucca Flat/Climax Mine Detonation Characteristics
(Page 22 of 23)

Detonation Name	Emplacement Hole Name	CAS	UTM Easting	UTM Northing	Date Expended	Announced Yield (kt)[a]	Cavity Radius (m)[b]	Land Surface Elevation (m amsl)	Depth to Working Point (m)	Working Point HSU	Estimated Depth to Steady State Water Level (m)	Saturated Working Point	Estimated Depth to Saturated LCA or LCA3 (m)	Number of R_c from WP to Saturated LCA or LCA3
VERMEJO	U-4r	04-57-032	584186.7	4104543.2	10/02/1984	<20	36	1,255.5	350	TM-UVTA	467	No	1083	20.4
VICTORIA	U-3kv	03-57-236	588070.9	4095728.3	06/19/1992	<20	40	1,205.8	244	AA	468	No	789	13.6
VIDE	U-8k	08-57-006	581247.8	4114733.3	04/30/1981	<20	37	1,373.4	323	OSBCU	635	No	635	8.4
VIGIL	U-10ad	10-57-004	584492.2	4113883.3	11/22/1966	<20	50	1,304.8	94	AA	572	No	572	9.4
VILLE	U-4am	04-57-011	581416.3	4104858.4	06/12/1985	<20	38	1,276.8	291	TM-LVTA	520	No	520	6.0
VILLITA	U-3ld	03-57-244	587433.1	4095131.9	11/10/1984	<20	36	1,204.6	372	AA	467	No	985	17.0
VISE	U-3ej	03-57-104	586315.4	4101024.4	01/30/1969	20 to 200	73	1,230.8	454	TM-LVTA	498	No	1080	8.6
VITO	U-10ab	10-57-003	584797.3	4113427.6	07/14/1967	<20	50	1,304.5	97	AA	571	No	659	11.2
VULCAN	U-2bd	02-57-031	582390.6	4112300.5	06/25/1966	25	40	1,327.1	322	AA	588	No	631	7.7
WACO	U-3lu	03-57-258	588586.3	4094734.0	12/01/1987	<20	43	1,202.7	183	AA	461	No	730	12.7
WAGTAIL	U-3an	03-57-014	585598.6	4102259.1	03/03/1965	20 to 200	65	1,237.5	750	LTCU	492	Yes	989	3.7
WALLER	U-2bz	02-57-053	582787.2	4112149.8	10/02/1973	<20	37	1,320.7	311	AA	582	No	658	9.4
WARD	U-10x	10-57-059	584599.3	4113678.0	02/08/1967	<20	39	1,303.9	260	AA	571	No	592	8.5
WASHER	U-10r	10-57-054	584598.9	4112476.1	08/10/1967	<20	34	1,297.5	468	LTCU	553	No	766	8.8
WELDER	U-3fs	03-57-134	586280.6	4100270.4	10/03/1968	<20	48	1,225.9	118	AA	493	No	1207	22.7
WEMBLEY	U-3ey	03-57-119	587511.0	4098986.9	06/05/1968	<20	40	1,218.6	238	AA	485	No	944	17.7
WEXFORD	U-2cr	02-57-069	577687.2	4110989.1	08/30/1984	<20	37	1,403.3	314	TM-LVTA	558	No	2702	64.5
WHITE	U-9b	09-57-048	584215.2	4108940.6	05/25/1962	Low	42	1,280.5	193	AA	534	No	1068	20.8
WHITEFACE-A	U-3lp	03-57-254	586173.7	4097977.7	12/20/1989	<20	42	1,214.6	197	AA	481	No	1268	25.5
WHITEFACE-B	U-3lp	03-57-254	586173.7	4097977.7	12/20/1989	<20	43	1,214.6	183	AA	481	No	1268	25.2
WICHITA	U-9y	09-57-114	583810.8	4109475.1	07/27/1962	Low	45	1,292.0	150	AA	547	No	949	17.7
WINCH	U-3gf	03-57-146	585205.0	4096144.9	02/04/1969	<20	40	1,212.2	241	TM-WTA	479	No	1078	21.0
WOLVERINE	U-3av	03-57-022	586027.4	4100518.2	10/12/1962	Low	54	1,227.4	74	AA	494	No	1207	21.4
WOOL	U-9bh	09-57-056	586640.0	4108317.7	01/14/1965	<20	41	1,313.7	216	TM-LVTA	582	No	582	8.9
WORTH	U-10ag	10-57-006	584481.7	4112435.8	10/25/1967	<20	42	1,295.7	197	AA	548	No	764	13.5
YANNIGAN-BLUE	U-2ay3	02-57-025	583000.6	4107701.8	02/26/1970	20 to 200	78	1,284.4	364	AA	510	No	879	6.7
YANNIGAN-RED	U-2ay1	02-57-023	583384.8	4107989.6	02/26/1970	20 to 200	76	1,284.4	392	AA	508	No	963	7.5
YANNIGAN-WHITE	U-2ay2	02-57-024	582938.3	4108172.4	02/26/1970	20 to 200	76	1,288.4	395	AA	523	No	897	6.6
YARD	U-10af	10-57-005	584113.4	4112079.2	09/07/1967	20 to 200	71	1,297.5	521	TM-LVTA	555	No	802	4.0
YERBA	U-1c	01-57-002	583737.0	4097662.4	12/14/1971	<20	37	1,228.6	332	AA	490	No	1098	20.7

Table B-1
Yucca Flat/Climax Mine Detonation Characteristics
(Page 23 of 23)

Detonation Name	Emplacement Hole Name	CAS	UTM Easting	UTM Northing	Date Expended	Announced Yield (kt)[a]	Cavity Radius (m)[b]	Land Surface Elevation (m amsl)	Depth to Working Point (m)	Working Point HSU	Estimated Depth to Steady State Water Level (m)	Saturated Working Point	Estimated Depth to Saturated LCA or LCA3 (m)	Number of R_c from WP to Saturated LCA or LCA3
YORK	U-9z	09-57-115	585333.2	4108261.3	08/24/1962	Low	40	1,282.6	227	AA	546	No	1012	19.7
ZAZA	U-4c	04-57-019	584134.2	4106044.8	09/27/1967	20 to 200	67	1,267.4	667	LTCU	488	Yes	961	4.5
ZINNIA	U-2dk	02-57-089	581030.2	4108432.1	05/17/1972	<20	37	1,304.2	323	AA	563	No	726	10.9

Sources: DOE/NV, 1997 and 2000; FFACO, 1996, as amended, August 2006; BN, 2006

[a] The number reported is yield in kilotons (kt) and is the maximum reported yield as identified in DOE/NV (2000).
[b] Calculated for non-LCA/LCA3 working-point detonations as $R_c = 70.2 * Y^{1/3} / [rho_{ob} * WP]^{1/4}$ (Pawloski, 1999) where Y is the maximum announced yield (kt), (DOE/NV, 2000) rho_{ob} is the overburden density (Mg/m^3), and WP is the working-point depth (m). Calculated cavity radius for carbonate rock working-point tests KANKAKEE and BOURBON, R_c = [in m $9.05 * Y^{1/3}$ (kt)], from Boardman (1970). Cavity radius for the carbonate rock working-point tests HANDCAR and NASH is the measured value from Carle et al. (2008). Cavity radii for the Climax Mine detonations HARD HAT, PILE DRIVER, and TINY TOT are from Pohlmann et al. (2007). Detonations with a yield reported as "low" or "slight" are assumed to have a 20 kt yield.

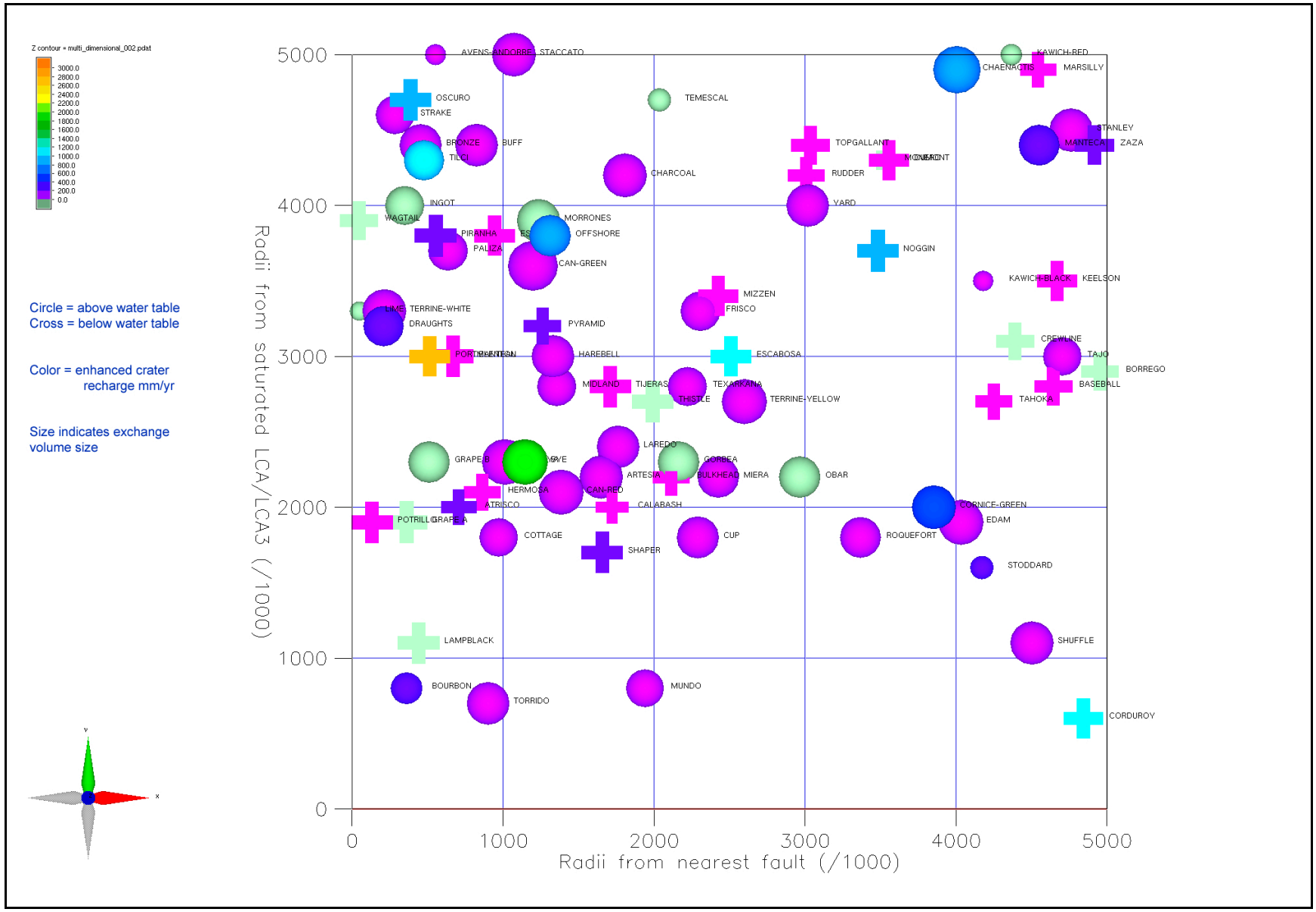

Figure B-1
Identification of Yucca Flat/Climax Mine CAU Detonations within 5 R_c of the LCA and Faults

B.2.0 REFERENCES

BN, see Bechtel Nevada.

Bechtel Nevada. 2006. *A Hydrostratigraphic Model and Alternatives for the Groundwater Flow and Contaminant Transport Model of Corrective Action Unit 97: Yucca Flat-Climax Mine, Lincoln and Nye Counties, Nevada*, DOE/NV/11718--1119. Prepared for the U.S. Department of Energy, National Nuclear Security Administration Nevada Site Office. Las Vegas, NV.

Boardman, C.R. 1970. "Engineering Effects of Underground Nuclear Explosives." In *Proceedings of Symposium on Engineering with Nuclear Explosives*, CONF-700101, 43–67. Las Vegas, NV, 14–16 January.

DOE/NV, see U.S. Department of Energy, Nevada Operations Office.

Federal Facility Agreement and Consent Order. 1996 (as amended March 2010). Agreed to by the State of Nevada; U.S. Department of Energy, Environmental Management; U.S. Department of Defense; and U.S. Department of Energy, Legacy Management. Appendix VI, which contains the Underground Test Area Strategy, was last modified May 2011, Revision No. 4.

Grasso, D.N. 2001. *GIS Surface Effects Archive of Underground Nuclear Detonations Conducted at Yucca Flat and Pahute Mesa, Nevada Test Site, Nevada*, Open-File Report 01-272. Denver, CO: U.S. Geological Survey.

Pawloski, G.A. 1999. *Development of Phenomenological Models of Underground Nuclear Tests on Pahute Mesa, Nevada Test Site—BENHAM and TYBO*, UCRL-ID-136003. Livermore, CA: Lawrence Livermore National Laboratory.

Pawloski, G.A., A.F.B. Tompson, S.F. Carle, R.L. Detwiler, Q. Hu, S. Kollet, R.M. Maxwell, W.W. McNab, S.K. Roberts, D.E. Shumaker, Y. Sun, and M. Zavarin. 2008. *Evaluation of Hydrologic Source Term Processes for Underground Nuclear Tests in Yucca Flat, Nevada Test Site: Introduction and Executive Summary*, LLNL-TR-403428. Livermore, CA: Lawrence Livermore National Laboratory.

Pawloski, G.A., G. WoldeGabriel, and I. Farnham. 2005. Written communication regarding *Categorization of Underground Nuclear Tests on Yucca Flat and Climax Mine, Nevada Test Site, for Use in Radionuclide Transport Models*. Livermore, CA: Lawrence Livermore National Laboratory; Los Alamos, NM: Los Alamos National Laboratory; and Las Vegas, NV: Stoller-Navarro Joint Venture.

SNJV, see Stoller-Navarro Joint Venture.

Stoller-Navarro Joint Venture. 2007. *Phase I Contaminant Transport Parameters for the Groundwater Flow and Contaminant Transport Model of Corrective Action Unit 97: Yucca Flat/Climax Mine, Nevada Test Site, Nye County, Nevada*, Rev. 0, S-N/99205--096. Las Vegas, NV.

Stoller-Navarro Joint Venture. 2009. *Unclassified Source Term and Radionuclide Data for Corrective Action Unit 97: Yucca Flat/Climax Mine, Nevada Test Site, Nevada*, Rev. 2, S-N/99205--114. Las Vegas, NV.

DOE, see U.S. Department of Energy, Nevada Operations Office

U.S. Department of Energy, Nevada Operations Office. 1997. *Shaft and Tunnel Nuclear Detonations at the Nevada Test Site: Development of a Primary Database for the Estimation of Potential Interactions with the Regional Groundwater System*, DOE/NV--464. Las Vegas, NV.

U.S. Department of Energy, Nevada Operations Office. 2000. *United States Nuclear Tests, July 1945 through September 1992*, DOE/NV--209-REV 15. Las Vegas, NV.

Appendix C

Yucca Flat/Climax Mine CAU Hydrologic Source Term Allocation and Screening

C.1.0 INTRODUCTION

This appendix documents the technical basis for the initial HST allocation between the three CAU-scale models and the HST screening. As discussed in Section 2.3.3, many of the Yucca Flat detonations have exchange volumes that span across two or more of the models, and allocating the initial HST between the models requires estimation of the spatial distribution of radionuclides in the post-detonation environment. The relatively recent and improved conceptual understanding of radionuclide physical and chemical partitioning developed for the Rainier Mesa HST by Tompson et al. (2011) enables an estimation of the initial spatial distribution that is more accurate than the distribution estimated for the Yucca Flat HST by Pawloski et al. (2008).

The Bowen et al. (2001) inventory (referred to as the “Bowen inventory” in this appendix) includes only those radionuclides with sufficient abundance to have concentrations above one-tenth (0.1) of the EPA drinking water MCLs in a fully saturated cavity 100 years from 1992. The Bowen et al. (2001) screening, however, did not consider radionuclide extent beyond the cavity, radionuclide incorporation into melt glass, or radionuclide sorption processes. As a result, many of the radionuclides included in the Bowen inventory are unlikely to contribute to the contaminant boundary. The improved understanding of radionuclide partitioning by Tompson et al. (2011) also enables a screening of radionuclides that is more accurate than the screening performed for the Yucca Flat HST by Pawloski et al. (2008).

C.2.0 OBJECTIVES

The objectives of this appendix are as follows:

- Briefly review the definition and nature of the HST, and the steps used to develop models of HST behavior for use in larger-scale (CAU) models. (These are described more thoroughly in a series of LLNL reports published in 2008 that evaluated HST processes for underground nuclear detonations conducted in Yucca Flat: Carle et al., 2008; McNab, 2008; Pawloski et al., 2008; and Tompson, 2008.)

- Provide additional details of, and adjustments made to, several of the steps in this process that have evolved since the release of the 2008 LLNL Yucca Flat HST documents, specifically with respect to the hydrologic screening process for identifying the most important radionuclides for inclusion in CAU models.

- Present the initial HST allocation fractions between the three CAU-scale models (developed in Section 2.3.3) for each of the 744 detonations conducted at Yucca Flat proper.

C.3.0 HYDROLOGIC SOURCE TERM CONCEPTUAL MODEL

Briefly stated, the HST represents the transient release of residual radioactivity into groundwater from underground nuclear detonations. An HST model seeks to quantitatively calculate this release from mathematical representations of the release processes, and physical and chemical data and information related to the detonation and the altered detonation environment.

In general, the development of an HST model requires the following:

- A **phenomenological understanding** of underground detonation effects and their role in altering the physical and chemical environment surrounding a detonation location
- An estimate of the abundance, physical form, and spatial distribution of radioactivity—the **radiologic source term** (or RST)—in the post-detonation environment
- Consideration of **complex mechanisms and processes** that serve to transfer radioactive compounds into groundwater or to moisture in the vadose zone as a result of (1) the immediate impacts of the detonation, (2) residual transient effects lingering after a detonation, and (3) ambient, longer-term processes occurring well after a detonation

Simplified representations of the HST model are required for use in populating individual source regions in larger-scale models of groundwater flow and contaminant transport within the entire Yucca Flat/Climax Mine CAU. By necessity, such models must abstract and generalize many of the complicated release mechanisms from a large number of detonations conducted in the CAU. Although detailed models of the HST for certain detonations have been and continue to be developed in order to gain insights into these mechanisms, they cannot be developed for every detonation in every CAU.

As summarized in Pawloski et al. (2008) and DOE/NV (2000), 659 underground nuclear tests were conducted in the Yucca Flat/Climax Mine CAU—656 in Yucca Flat proper, and 3 in the Climax Mine stock just north of Yucca Flat. These tests were associated with 747 unique nuclear detonations with announced yields or yield ranges (DOE/NV, 2000), reflecting the fact that some of these tests included multiple detonations. Of the 747 detonations, 170 were conducted below or within 100 m of the static water level, and the remaining 577 were conducted greater than 100 m above the static water level (Pawloski et al., 2008).

C.3.1 Phenomenology

An underground nuclear explosion will release an immense amount of thermal and mechanical energy (Germain and Kahn, 1968; Borg et al., 1976; OTA, 1989; IAEA, 1998a, 1998b, 1998c). The explosion will produce high temperatures and pressures in the geologic materials surrounding the detonation location (i.e., the working point), and generate a compressive shock wave that moves radially away from it. Vaporization and compression of the geologic media (including water) will generate and expand an open, approximately spherical cavity volume centered at the working point (Figure C-1). The cavity size (or radius) will reach a maximum approximately 500 milliseconds after detonation. The actual shape of the cavity may be nonspherical, but a spherical approximation is generally consistent with observations obtained in detonation-cavity drill-back holes. The maximum radius of the cavity can be estimated as a function of the energy (yield) of the explosion, its depth of burial, and the strength of the overlying geologic media (Borg, et al., 1976).

During cavity growth, the temperature and pressure of the gas inside will decrease. Components of the gas will condense in an order determined by their relative vapor pressures. First among these are the rock and heavier radionuclide isotopes that, along with molten rock lining the cavity walls, tend to accumulate into a melt glass puddle at the bottom of the cavity. The remaining gases include high-pressure steam, air, and lighter radionuclide isotopes, which condense as final temperature and pressure conditions reestablish in the cavity before collapse.

The shock wave and cavity expansion will serve to crush, fracture, compress, or otherwise alter intact rock that extends beyond the cavity wall, and high gas pressures will maintain an open cavity volume. Post-detonation observations often reveal that a crush zone of permanently pulverized and compressed rock is formed in a zone extending radially away from the cavity wall, beyond which the materials may be compressed, but not otherwise broken or fractured, for some additional radial distance. Hydrofractures outside the cavity region can form when cavity pressure is high. Liquid interstitial water in the rock next to the cavity may also boil if close to the wall, but will otherwise undergo compression along with the bulk rock surrounding the cavity.

Within minutes to days after detonation, the rock overlying the cavity collapses into the cavity and creates a rubblized column or chimney that may extend to the ground surface where a crater is formed. The collapsed material will have altered physical properties and a variable degree of saturation dependent on pre-collapse conditions. Depending on the timing of collapse, rubble may

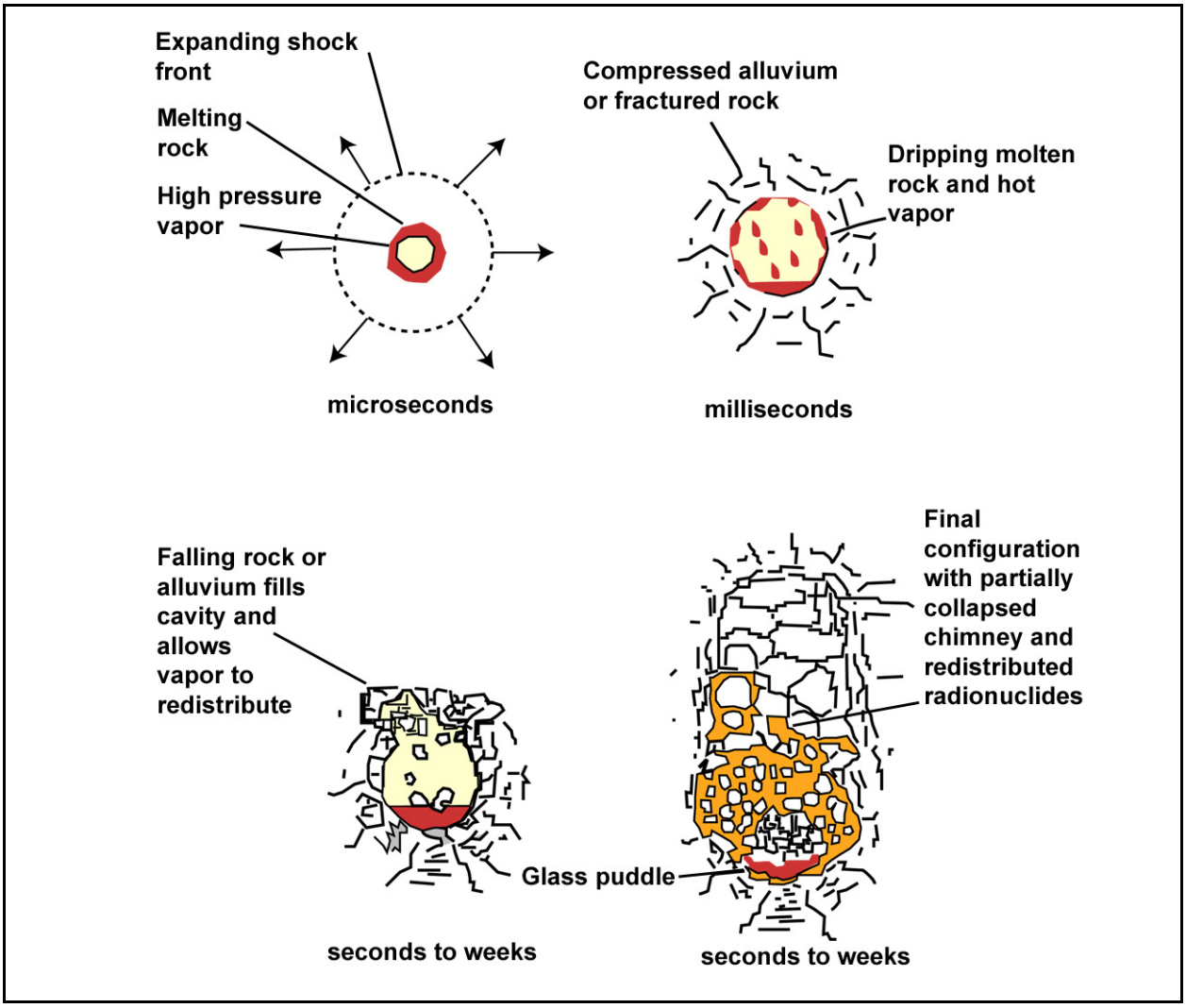

Figure C-1
Phenomenology of an Underground Nuclear Explosion Showing Accretion of Melt Glass, Redistribution of More Volatile Radionuclides, Initially as Gases, Later as Condensates, and Collapse of the Chimney
Source: Tompson et al., 1999

become dispersed in the melt glass if the glass is still liquid, or remain fairly well intact if it has become more solidified.

For detonations conducted below the water table, groundwater in the rock adjacent to the cavity will be pressurized, or compressed, as a result of the explosion and cavity expansion processes, and will otherwise return to the cavity as saturation levels in the collapsed material dictate. Pressure dissipation can lead to localized groundwater mounding effects near the explosion site that usually relax over time (Knox et al., 1965; Borg et al., 1976; Burkhard and Rambo, 1991;

Halford et al., 2005; Wolfsberg et al., 2006; Tompson, 2008). These effects, when limited in extent, were not seen to produce significant enhanced radionuclide migration away from detonation cavities (Tompson, 2008). However, more extensive pressurization effects may develop from the impacts of multiple detonations conducted in close proximity or from broader overburden subsidence effects associated with testing (Vincent et al., 2003). Depending on larger-scale geological conditions, these effects may produce possibilities for enhanced radionuclide migration away from detonation cavities.

High residual temperatures associated with the detonation will be manifested in the melt glass and neighboring media, and can last many years (Carle et al., 2003). Returning groundwater will serve to quench some of the higher temperatures and may convect heat away in buoyancy-driven flow to the extent that permeability conditions allow (e.g., Pawloski et al., 2001).

For detonations conducted above the water table, or for detonations whose mechanical impacts extend to areas above the water table, static interstitial moisture or other perched zones of water above the water table may become mobile as a result of altered moisture retention characteristics in the formation. In addition, due to a lack of returning groundwater to a previously unsaturated setting, cooling will be limited to thermal conductive processes only (e.g., without the contribution of groundwater convection). Circulation of cavity gases may occur in the chimney of an unsaturated-zone detonation and possibly extend to the ground surface.

C.3.2 Altered Zones

The hydrodynamic and mechanical impacts from the nuclear explosion produce permanently altered zones such as cavity, nuclear melt glass, crush, compressed, and rubblized collapse chimney zones. The geometries of these zones are dependent on explosion phenomenology, rock type, saturation, and the yield of the detonation. Transient groundwater flow effects may be created as a result of groundwater condensation and return to the cavity, relaxation of elevated pore water pressures in saturated areas surrounding the cavity, and convective flow processes driven by residual detonation heat. These effects may be short-lived (months) or last longer (years) depending on the particulars of a given near-field system.

The general configuration of detonation-altered zones and properties is largely based on information compiled in OTA (1989) with respect to multiples of cavity radii (R_c):

- Detonation-enhanced fracture permeability extends to 3 R_c (OTA, 1989).
- Detonation-enhanced microfracturing in rocks extends to 2 R_c (OTA, 1989).
- *In situ* rock properties do not change beyond 3 R_c, except in the chimney (OTA, 1989).

A schematic diagram for geometry of detonation-altered zones is shown in Figure C-2. Typical concepts used to define the detonation-altered zones include the following:

- ***Cavity.*** Idealized sphere of radius 1.0 R_c representing the maximum extent of the detonation cavity. The conceptualized cavity at HST t_0 is composed of the melt glass puddle that coalesces at the bottom and the in-fallen, rubblized chimney.

- ***Melt glass.*** A zone at the bottom of the cavity where vaporized and melted material accumulates due to gravity. The volume of melt glass can be calculated, and this volume may also contain in-fallen rubble.

- ***Chimney.*** An idealized cylinder of rubble that falls into the collapsed cavity void, with a radius set to the cavity radius. The chimney zone may extend to the ground surface or stop before that, dependent on the yield of the detonation and the strength of the overlying rock.

- ***Crush zone.*** A zone within 1.3 R_c that is more intensely fractured or "pulverized" as described in Borg (1973) and Borg et al. (1976). The material in this zone has failed mechanically and permanently lost porosity due to the compressional shock wave.

- ***Altered matrix to 2.0 R_c.*** Matrix permeability is assumed enhanced to 2.0 R_c as a result of microfracturing (OTA, 1989).

- ***Altered fractures to 3.0 R_c.*** Fracture permeability and porosity in *in situ* rock is enhanced between 1.0 and 3.0 R_c, with increasing fracture permeability closer to the working point (Boardman and Skrove, 1966; OTA, 1989).

C.3.3 Radiologic Source Term

The RST for an underground nuclear detonation represents the residual, post-detonation inventory of radioactivity associated with that detonation. The residual inventory is derived from the original materials in the test device, nuclear reactions connected with the explosion, and activation products created in the geologic medium. Complex dynamic processes occurring in the seconds to weeks after detonation control the initial chemical nature, spatial distribution, and physical partitioning of the

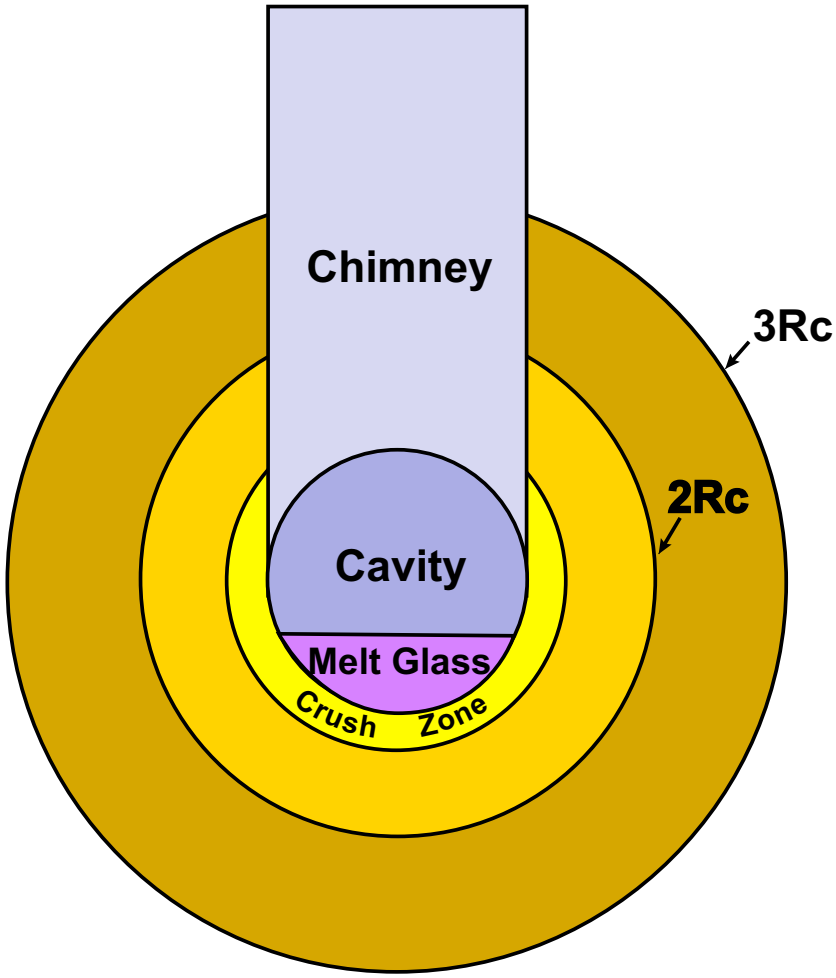

Note: All detonation-altered zones are assumed radially symmetric about the vertical axis.

Figure C-2
Schematic Diagram for Geometry of Detonation-Altered Zones
Source: Modified from Tompson et al., 2011

RST onto rubble or into melt glass, gas, or water phases found in the cavity and chimney areas surrounding the detonation.

RST Composition. The composition and magnitude of the RST are generally determined from diagnostic samples of water and rock extracted from detonation areas and from knowledge of test design. In general, RST data for individual detonations are classified. With the exception of a few unclassified RST estimates at specific detonations and related unclassified observations of radionuclides in water drawn from scattered wells at the NNSS, the most complete unclassified source of radionuclide inventories for detonations conducted at the NNSS are the aggregate data tabulated in Bowen et al. (2001) and Smith et al. (2003). Bowen et al. (2001) provide aggregate

information on the abundance, or inventory, of 43 specific, long-lived radioactive isotopes deemed pertinent to CAU studies (Table C-1). At Yucca Flat, the aggregated inventories are associated with either above-water-table (unsaturated) or below-water-table (saturated) group of detonations. The data are decay corrected to September 23, 1992, the date of the last underground nuclear test. The Bowen inventory data include only those isotopes whose half-lives are greater than 10 years, even though shorter-lived radionuclides are produced in nuclear detonations. As a result, it does not include some short-lived radionuclides that may otherwise have been measured or observed in groundwater at the NNSS.

Table C-1
Long-Lived Radioactive Isotopes Deemed Pertinent to CAU Studies
(Page 1 of 2)

Bowen RST Radionuclide [a]	Potentially Relevant Radionuclides at 0.1 MCL after ^{3}H Decay [b]			
	All Detonations	Models		
		Unsaturated Zone	Saturated Alluvial/ Volcanic Aquifer System	Saturated LCA
^{3}H				
^{14}C				
^{26}Al [c]	<0.1 MCL	<0.1 MCL	<0.1 MCL	<0.1 MCL
^{36}Cl				
^{39}Ar [d]	<0.1 MCL	<0.1 MCL	<0.1 MCL	<0.1 MCL
^{40}K [c]	<0.1 MCL	<0.1 MCL	<0.1 MCL	<0.1 MCL
^{41}Ca [c]	<0.1 MCL	<0.1 MCL	<0.1 MCL	[e]
^{59}Ni [c]	<0.1 MCL	<0.1 MCL	<0.1 MCL	<0.1 MCL
^{63}Ni [c]	<0.1 MCL	<0.1 MCL	<0.1 MCL	
^{85}Kr [d]	<0.1 MCL	<0.1 MCL	<0.1 MCL	<0.1 MCL
^{90}Sr				
^{93}Zr	<0.1 MCL	<0.1 MCL	<0.1 MCL	<0.1 MCL
^{93m}Nb	<0.1 MCL	<0.1 MCL	<0.1 MCL	<0.1 MCL
^{94}Nb	<0.1 MCL	<0.1 MCL	<0.1 MCL	<0.1 MCL
^{99}Tc				
^{107}Pd [c]	<0.1 MCL	<0.1 MCL	<0.1 MCL	<0.1 MCL
^{113m}Cd [c]	<0.1 MCL	<0.1 MCL	<0.1 MCL	<0.1 MCL
^{121m}Sn [c]	<0.1 MCL	<0.1 MCL	<0.1 MCL	<0.1 MCL
^{126}Sn [c]	<0.1 MCL	<0.1 MCL	<0.1 MCL	<0.1 MCL
^{129}I				

Table C-1
Long-Lived Radioactive Isotopes Deemed Pertinent to CAU Studies
(Page 2 of 2)

Bowen RST Radionuclide [a]	Potentially Relevant Radionuclides at 0.1 MCL after ^{3}H Decay [b]			
	All Detonations	Models		
		Unsaturated Zone	Saturated Alluvial/ Volcanic Aquifer System	Saturated LCA
^{135}Cs	<0.1 MCL	<0.1 MCL	<0.1 MCL	
^{137}Cs	<0.1 MCL	<0.1 MCL	<0.1 MCL	
^{151}Sm	<0.1 MCL	<0.1 MCL	<0.1 MCL	<0.1 MCL
^{150}Eu [c]	<0.1 MCL	<0.1 MCL	<0.1 MCL	<0.1 MCL
^{152}Eu	<0.1 MCL	<0.1 MCL	<0.1 MCL	<0.1 MCL
^{154}Eu	<0.1 MCL	<0.1 MCL	<0.1 MCL	<0.1 MCL
^{166m}Ho [c]	<0.1 MCL	<0.1 MCL	<0.1MCL	<0.1 MCL
^{232}Th	<0.1 MCL	<0.1 MCL	<0.1 MCL	<0.1 MCL
^{232}U	<0.1 MCL	<0.1 MCL	<0.1 MCL	<0.1 MCL
^{233}U	<0.1 MCL	<0.1 MCL	<0.1 MCL	<0.1 MCL
^{234}U	<0.1 MCL	<0.1 MCL	<0.1 MCL	<0.1 MCL
^{235}U	<0.1 MCL	<0.1 MCL	<0.1 MCL	
^{236}U	<0.1 MCL	<0.1 MCL	<0.1 MCL	<0.1 MCL
^{238}U				
^{237}Np	<0.1 MCL	<0.1 MCL		[e]
^{238}Pu				
^{239}Pu				
^{240}Pu				
^{241}Pu	<0.1 MCL	<0.1 MCL	<0.1 MCL	<0.1 MCL
^{242}Pu	<0.1 MCL	<0.1 MCL	<0.1 MCL	<0.1 MCL
^{241}Am	<0.1 MCL	<0.1 MCL	<0.1 MCL	<0.1 MCL
^{243}Am	<0.1 MCL	<0.1 MCL	<0.1 MCL	<0.1 MCL
^{244}Cm	<0.1 MCL	<0.1 MCL	<0.1 MCL	<0.1 MCL

[a] Bowen et al., 2001.
[b] Shaded cells indicate radionuclides that are determined in the screening analysis in Section C.4.0 to be potentially relevant to the calculation of contaminant boundaries (using the 0.1 MCL limit after ^{3}H decay).
[c] No published EPA MCL (dose equivalent).
[d] As a gas, no published EPA MCL (dose equivalent).
[e] At the margin of inclusion.

RST Allocation. In HST and CAU model calculations, the aggregate unclassified RST isotope inventories reported in Bowen et al. (2001) for a given geographic testing area are apportioned to individual detonations using a yield-weighting algorithm. The "yield" for each detonation is either the announced yield (in kilotons) or the maximum of the announced yield range, as tabulated in DOE/NV (2000). The yield-weighting process can proceed in one of two ways:

- In the *traditional approach*, equivalent fractions of the aggregate 1992 inventory are apportioned to equivalent-yield detonations as of 1992. When scaled back to different detonation t_0 times, equivalent-yield detonations will have different t_0 inventories. This approach has been used in previous HST analyses, including the 2008 LLNL Yucca Flat HST reports (Carle et al., 2008; McNab, 2008; Pawloski et al., 2008; and Tompson, 2008).

- In a *newer approach*, developed recently for the HST tunnel models at Rainier Mesa (Tompson et al., 2011), the aggregate 1992 inventory is apportioned to individual detonations in such a way that equivalent-yield detonations have equivalent inventories at their individual t_0 times. When corrected to 1992, equivalent-yield detonations will have different inventories, yet will still sum in the aggregate to the totals cited in Bowen et al. (2001). (At Rainier Mesa, this method was deemed important for understanding contributions from multiple closely located detonations over time to observations of tunnel effluent concentrations.) The difference between this and the traditional approach is more significant for short-lived radionuclides (e.g., tritium), yet may be overshadowed by intrinsic uncertainties in the RST itself (see below). The newer approach was not considered in the 2008 LLNL Yucca Flat HST reports, and is described here for completeness.

Zero-Yield Detonations. To properly apply the aggregate RST inventory associated with Yucca Flat/Climax Mine detonations (Bowen et al., 2001), the inventory should be divided among all detonations with announced, nonzero yields. This means that the SAN JUAN, COURSER, and TRANSOM detonations should not appear as unique source-release points and that the inventory should be divided among 744 (instead of 747) detonations. These three detonations occurred near other detonations, and contaminant transport paths should merge or be close. This approach is consistent with classification advice, permits allocation of all Bowen inventory, and removes no unique source-release points from the model. More specifically, this means that the unsaturated Bowen inventory for the Yucca Flat/Climax Mine detonations should be divided among 575 detonations (removing SAN JUAN and COURSER) and that the saturated inventory should be divided among 169 (removing TRANSOM).

Slight-Yield Detonations. The announced yields of the following three detonations in Yucca Flat—PASCAL A, PASCAL B, and PASCAL C—were designated in DOE/NV (2000) as "slight."

Recent DOE guidance indicates that the term "slight" should be interpreted as "less than 20 kt." Thus, yield-weighted allocations of the RST to these detonations should be based upon a maximum yield of 20 kt for each of these detonations.

Uncertainty in the RST. Different methodologies have been used for estimating the quantities of nuclides that appear in the Bowen inventory, and there are uncertainty or accuracy limitations associated with each method. The general limitations reported by Bowen et al. (2001) include accuracies for fission products (approximately 10 to 30 percent for most), unspent fuel materials (approximately 20 percent or better), fuel activation products (approximately 50 percent or better), residual tritium (approximately 300 percent or better), and activation products (approximately a factor of 10). As noted by Bowen et al. (2001), additional differences from these general results apply in some specific cases. The uncertainties are based upon classified RST estimates for individual detonations. They cannot—and should not—be interpreted to represent a relationship between unclassified yield-weighted RSTs and their classified detonation-specific counterparts. The uncertainties used in unclassified calculations can only be used to evaluate the extent to which RST uncertainty may affect contaminant boundary calculations if classified RSTs were used.

As a rule, any quantifiable uncertainty in the RST should be propagated into the HST, simplified HST, and CAU model calculations. Additional discussion of this concern is included in the discussion of HST screening in Section C.4.0.

Screening of the RST. An HST screening activity was developed to identify a subset of the 43 Bowen radionuclides that are anticipated to have the most significant impact on groundwater contamination—or, in other words, eliminate or exclude radionuclides that are not expected to significantly contribute to the contaminant boundary calculations in the CAU model from the 43 Bowen radionuclides. As described in Section C.4.0, the screening approach is based upon an analysis of the expected initial aqueous concentrations for Yucca Flat/Climax Mine detonations, and folds together a myriad of parameters and uncertainties in the following:

- Magnitude of the RST inventories for each radionuclide
- Ranges of exchange volume radii for particular radionuclides (see below)

- Ranges in the melt-glass partitioning percentage for pertinent radionuclides, including melt-glass release rates
- Porosity, saturation, and sorption characteristics of the cavity and chimney host rock

The screening analysis was conducted for all Yucca Flat/Climax Mine detonations and for subsets of detonations with cavities in the unsaturated zone, saturated alluvial/volcanic aquifer system, and saturated LCA model domains. Specific results are shown in Table C-1. Differences arise primarily because specific sorption conditions in the LCA promote higher concentrations and mobilities for some radionuclides that, in turn, increase their regulatory relevancy. Because of the general trend for downward migration of radionuclides, from the unsaturated zone to the saturated alluvial/volcanic aquifer system and to the saturated LCA, the structure of these results is consistent with the inclusion of more radionuclides at detonations later in the overall progression—in the saturated LCA model—than in the saturated alluvial/volcanic aquifer system model and the unsaturated-zone model.

C.3.4 Physical Partitioning and Spatial Distribution of the RST

Melt Glass, Water, Gas, and Rubble. Following an underground nuclear detonation, radionuclides are generally expected to partition into one or more *melt glass*, *water*, *gas*, or *rubble* phases distributed in and about the cavity and altered zones. Their physical partitioning and spatial distribution are governed by thermodynamic properties of the radionuclides, detonation-related phenomenological effects, and other conditions in the rock media where the detonation took place. Specifically, melt glass, water, gas, and rubble fractions have the following characteristics:

- *Melt glass* fractions are concentrated in the bottom half of the cavity, and typically include between 95 and 100 percent of the actinides in the RST and significant amounts of all other radionuclides (with the exception of ^{3}H, ^{14}C, and ^{85}Kr).
- *Water* fractions, initially, contain large fractions of the ^{3}H inventory and smaller amounts of ^{14}C, ^{36}Cl, ^{39}Ar, ^{85}Kr, and ^{129}I that show up in condensed steam.
- *Gas* fractions include significant fractions of noncondensable species such as ^{14}C, ^{39}Ar, and ^{85}Kr remaining after steam condensation.
- *Rubble* fractions include other condensable species that do not fall out with water.

Because most previous HST models focused on saturated-zone detonations, it was common to merge the water, gas, and rubble fractions of the RST into a common aqueous distribution. These concepts are discussed more thoroughly in IAEA (1998a, 1998b, 1998c), in the 2008 LLNL Yucca Flat HST

reports (Carle et al., 2008; McNab, 2008; Pawloski et al., 2008; and Tompson, 2008), in the more recent studies of Rose et al. (2011) and Tompson et al. (2011), and in Section C.4.0.

Exchange Volume. The exchange volume is defined as the volume of rock that encompasses the immediate extent of non-melt-glass radioactive contamination following an underground nuclear detonation.

In previous HST modeling efforts, including parts of the 2008 LLNL Yucca Flat HST studies, the exchange volume was conceptualized as a spherical region centered on the detonation working point—with a radius ranging from 1.5 to 3 R_c—into which all non-melt-glass RST radionuclides were homogeneously distributed in available groundwater. This conceptualization was supported by basic phenomenological arguments and limited radionuclide distribution data obtained in several detonation cavity drill-back holes, and by a desire for parsimony in the overall approach. Because most previous HST models focused on saturated-zone detonations, the merged water, gas, and rubble fractions of the RST were introduced into a common aqueous distribution within the saturated portions of the exchange volume. Depending on the radionuclide, the aqueous species would also be subject to sorption interactions (e.g., aqueous complexation or ion exchange reactions) with the solid-phase minerals composing the rock in the exchange volume.

Recent HST model development activities at Rainier Mesa (Tompson et al., 2011) have attempted to address the concept that radionuclides are actually heterogeneously distributed within an exchange volume, that the exchange volume may be nonspherical, and that the size or extent of an exchange volume can be both variable and radionuclide dependent. This concept is supported by the following data and analyses:

- Additional data available at Rainier Mesa for unsaturated-zone detonations—specifically from the mine-back activities conducted at the RAINIER detonation (U-12b) (e.g., Wadman and Richards, 1961; Essington and Forslow, 1971)
- New cavity data obtained at CHANCELLOR (U-19ad) (Rose et al., 2011)
- Updated modeling analyses (Carle et al., 2008; Tompson, 2008) that address gas- and liquid-phase radionuclide migration in unsaturated environments (such as those at Yucca Flat)—whose results imply that broader and more disparate aqueous-phase distributions may exist for some radionuclides (say, to 5 R_c in the short term) along with more transient, “shifting” exchange volume dimensions.

Exchange Volume Size. As a practical means to address these issues, the recommended approach for specifying the exchange volume size involves the use of a spherical volume whose diameter is drawn from a radionuclide-specific range inside of which the pertinent radionuclide species are uniformly distributed. This is seen as a reasonable approximation to represent differing realities and situations characterized by nonspherical radionuclide distributions, nonuniform radionuclide distributions, and/or radionuclide-specific distributions with (essentially) one degree of freedom to represent uncertainty or detonation-to-detonation variability (the R_c multiplier). One of the principal ideas in this simplification is that it will allow for the generation of concentration distributions that are fairly consistent with observations, the phenomenological conceptualization, and our modeling results. Secondary considerations, such as the inclusion of an explicit chimney to distribute recirculating radionuclides originally in the cavity, may be implemented in the HST. Specific guidance regarding exchange volume size includes the following:

- To determine the appropriate exchange volume size, the following simple criteria are recommended:
  - If a radionuclide partitions into glass at greater than or equal to 90 percent, its exchange volume range is 1 to 1.5 R_c.
  - If a radionuclide partitions into glass at less than 90 percent but greater than 0 percent, its exchange volume range is 1.5 to 3 R_c.
  - If a radionuclide partitions into glass at 0 percent, its exchange volume range is 3 to 5 R_c.
  - For ^{3}H, an exchange volume range is 1.5 to 3 R_c.
  - For ^{14}C, the above-water-table exchange volume range is 3 to 5 R_c, or an adjusted range based on additional detonation-specific or condition-specific evidence.
  - For carbonate detonations, ^{90}Sr and ^{137}Cs have ranges that are higher than shown in earlier Yucca Flat HST studies.
- Uncertainty in exchange volume diameter should be based on a triangular distribution symmetric about the mean of the minimum and maximum diameter exchange volume.
- For model grid constraints that limit the exchange volume size to 1.5 or 2.5 R_c, use 2.5 R_c in place of 3 R_c.
- For transport models based upon particle algorithms, attempt to honor the table limits regardless of grid and material property constraints.

- For exchange volumes that cross model boundaries (i.e., boundaries between the unsaturated zone and saturated alluvial/volcanic aquifer system models, or between the saturated alluvial/volcanic aquifer system and saturated LCA models), we recommend splitting assignments according to the table.
  - Reapportioning mass from one model side into another (as in "breaching" cases in earlier Yucca Flat models) is not recommended.
  - In cases where the recommended process cannot be followed, explicit recognition of all such instances in a summary table or section with appropriate discussion or justification of process should be followed.
- For potentially relevant radionuclides, it is not recommended that any radionuclide mass identified in the Bowen inventory for the CAU be excluded from the model.
  - In cases where the recommended process cannot be followed, explicit recognition of all such instances in a summary table or section with appropriate discussion or justification of process should be followed.

Recommended ranges of exchange volume diameters for the radionuclides that are identified in Table C-1 as potentially relevant to the calculation of contaminant boundaries are summarized in Table C-2.

On the Distribution of Non-glass Radionuclide Inventory in a Model Exchange Volume. As a practical means to address this process, the following guidelines are provided.

To distribute the non-glass inventory inside an exchange volume for an included radionuclide, follow the guidelines provided below:

- Identify radionuclide mass (*M*) from (1) Bowen et al. (2001), (2) yield-weighted allocation process, and (3) glass-partitioning criteria.
- Identify an appropriate range of exchange volume radii from Table C-2.
- Assume a uniform degree of (significant and increased) altered-zone fracturing, unless material is alluvium.
- Assume an effective cavity zone porosity of 0.2 to 0.4, inclusive of matrix and rubble/fracture portions.
- Above the water table, consider nonzero water saturation in altered-zone fractures derived from condensed steam derived from pore water originally in cavity rock that was melted.

Table C-2
Recommended Ranges of Exchange Volume Radius Multipliers for the Radionuclides Identified as Potentially Relevant to the Calculation of Contaminant Boundaries in Table C-1

Radionuclide	Exchange Volume Radius (in terms of R_c) [a]					
	Unsaturated Zone		Saturated Zone		Unsaturated Zone LCA	
	Minimum	Maximum	Minimum	Maximum	Minimum	Maximum
^{3}H	1.5	3	1.5	3	1.5	3
^{14}C	3	5	3	5	3	5
^{36}Cl	1.5	3	1.5	3	1.5	3
^{41}Ca	1.5	3	1.5	3	1.5	3
^{63}Ni	1	1.5	1	1.5	1	1.5
^{90}Sr	1.5	3	1.5	3	3	5
^{99}Tc	1.5	3	1.5	3	1.5	3
^{129}I	1.5	3	1.5	3	1.5	3
^{135}Cs	1.5	3	1.5	3	1.5	3
^{137}Cs	1.5	3	1.5	3	3	5
^{235}U	1	1.5	1	1.5	1	1.5
^{238}U	1	1.5	1	1.5	1	1.5
^{237}Np	1	1.5	1	1.5	1	1.5
^{238}U	1	1.5	1	1.5	1	1.5
^{239}Pu	1	1.5	1	1.5	1	1.5
^{240}Pu	1	1.5	1	1.5	1	1.5

[a] Shaded entries represent changes from previous Yucca Flat HST report recommendations. Multipliers are applied to R_c, which is detonation dependent. R_c (in meters) is calculated for non-carbonate working-point detonations as $R_c = 70.2Y^{1/3}/(\rho_b \times DOB)^{1/4}$ (Pawloski, 1999), where Y is the maximum announced yield (kt) (DOE/NV, 2000), ρ_b is the overburden density (g/cm^3), and DOB is the depth of burial (working-point depth) (m). R_c is calculated for carbonate-rock working-point detonations KANKAKEE and BOURBON as $R_c = 9.05 \times Y^{1/3}$ from Boardman (1970).

- Determine concentration $C = M/V$, where V is the eligible water volume (see below).
- Identify eligible water volume (V) inside the exchange volume radius: V = total effective cavity-zone pore water + total altered-zone fracture water. Include altered-zone pore water in alluvium. Exclude altered-zone matrix water.
- Assign mass (M) to eligible water volume (V) in the exchange volume to ensure constant value of concentration (C).

- Below the water table, consider the redistribution of cavity mass for ^{3}H, ^{14}C, and ^{36}Cl into the chimney zone, but no farther than water table.

- Above the water table, consider the redistribution of cavity mass for ^{14}C into the chimney zone.

C.4.0 HYDROLOGIC SOURCE TERM SCREENING

C.4.1 Purpose

The HST screening activity was developed to identify radionuclides that have a significant impact on groundwater contamination. The screening is intended to identify radionuclides that are likely to significantly contribute to the contaminant boundary calculation and focus CAU transport models on those radionuclides.

C.4.2 Conceptual Model and Basis

The conceptual model is based on simplified parameterization of the phenomenological model described above. The screening is based on radionuclide concentrations (and associated MCLs) in the exchange volume before advective transport. To ensure that the effect of glass dissolution on radionuclide concentrations is conservatively estimated, the first 100 years of glass dissolution and radionuclide release are included in the initial exchange volume concentration. Thus, the screening is based on the highest plausible radionuclide concentration that may be encountered in the near field.

C.4.3 Approach

The screening begins with the 43 radionuclides identified by Bowen et al. (2001). Based on the parameter uncertainties defined below, 59,760 Monte Carlo realizations of the initial radionuclide concentration in the exchange volume were run (80 realizations per detonation in the Yucca Flat/Climax Mine CAU). Based on the concentration of each radionuclide in these realizations, the following screening criteria are applied at the 95 percent confidence interval:

- The radionuclide is predominantly of natural origin.[1]
- The radionuclide concentration is less than 0.1 of its MCL.
- The radionuclide will decay to less than 0.1 of its MCL before the decay of tritium to less than 0.1 of its MCL.

1. The natural origin criterion is not based on a 95 percent confidence interval. It is intended to remove natural ^{40}K and ^{232}Th from further consideration. However, these radionuclides would also be screened out based on the less than 0.1 MCL limit.

The 0.1 MCL criterion was used to ensure that additive contribution of radionuclides to risk would remain below a total of 1.0 MCL at the 95 percent confidence interval. Because the prevailing conditions in each of the three Yucca Flat models differ significantly in some cases (e.g., percent saturation in unsaturated versus saturated models), the screening is grouped into detonations whose working points fall within 3 R_c of each of the three Yucca Flat models.

C.4.4 Simplifications

As described in the following sections, a number of pragmatic simplifications are used in support of this analysis. Given the scale of these simplifications, the accuracy of this analysis should be considered accordingly. The screening analysis is not intended to provide an exact initial radiologic composition of the near field at each detonation. Instead, it is meant to broadly screen for relevance of radionuclides with respect to contaminant boundary calculations. The conservative nature of this analysis ensures that only those radionuclides that pose very little risk are excluded from further analysis. This argument is strengthened by comparing the lists of screened radionuclides to groundwater sampling and analysis data from near-field “hot well” samples. Based on this comparison, all radionuclides found to exist above their respective MCLs in “hot wells” were correctly identified as relevant to contaminant boundary calculations. However, the conservative nature of this analysis has also resulted in the inclusion of some radionuclides that have, to date, never been measured above their respective MCLs at the NNSS.

The MCLs were taken directly from 4-mrem/yr values published by EPA. However, certain radionuclides included in the Bowen inventory have no published EPA MCLs. In those cases, dose conversion factors from International Commission on Radiological Protection (ICRP) Publication 72, *Age-Dependent Doses to the Members of the Public from Intake of Radionuclides Part 5, Compilation of Ingestion and Inhalation Coefficients* (ICRP, 1996), were used. These values were taken from a database compilation located in the RESRAD code developed jointly by DOE and U.S. Nuclear Regulatory Commission. The radionuclides for which ICRP dose conversion factors were used were ^{26}Al, ^{40}K, ^{41}Ca, ^{93m}Nb, ^{107}Pd, ^{113m}Cd, ^{121m}Sn, ^{126}Sn, ^{150}Eu, and ^{166m}Ho. For each of these radionuclides, the 4-mrem/yr MCL was based on a consumption rate of 2 liters per day and 365.25 days per year. Two radionuclides, ^{39}Ar and ^{85}Kr, had no reported MCLs. Both radionuclides are gases, and there is no reasonable pathway to ingestion (i.e., both radionuclides rapidly degas from water).

C.4.5 Parameter Distributions and Basis Used in HST Screening

RST. The RST for each detonation was based on yield weighting of the Bowen inventory using the traditional approach. The difference in radionuclide distribution patterns using the traditional and new approaches for short-lived radionuclides is not appreciably greater than the RST uncertainty already identified in Bowen et al. (2001) (Figure C-3). Thus, the choice of yield-weighting methodology will not affect these analyses. Bowen et al. (2001) subdivided Yucca Flat detonations into those considered "saturated" and "unsaturated." The RST for each detonation accounted for this categorization.

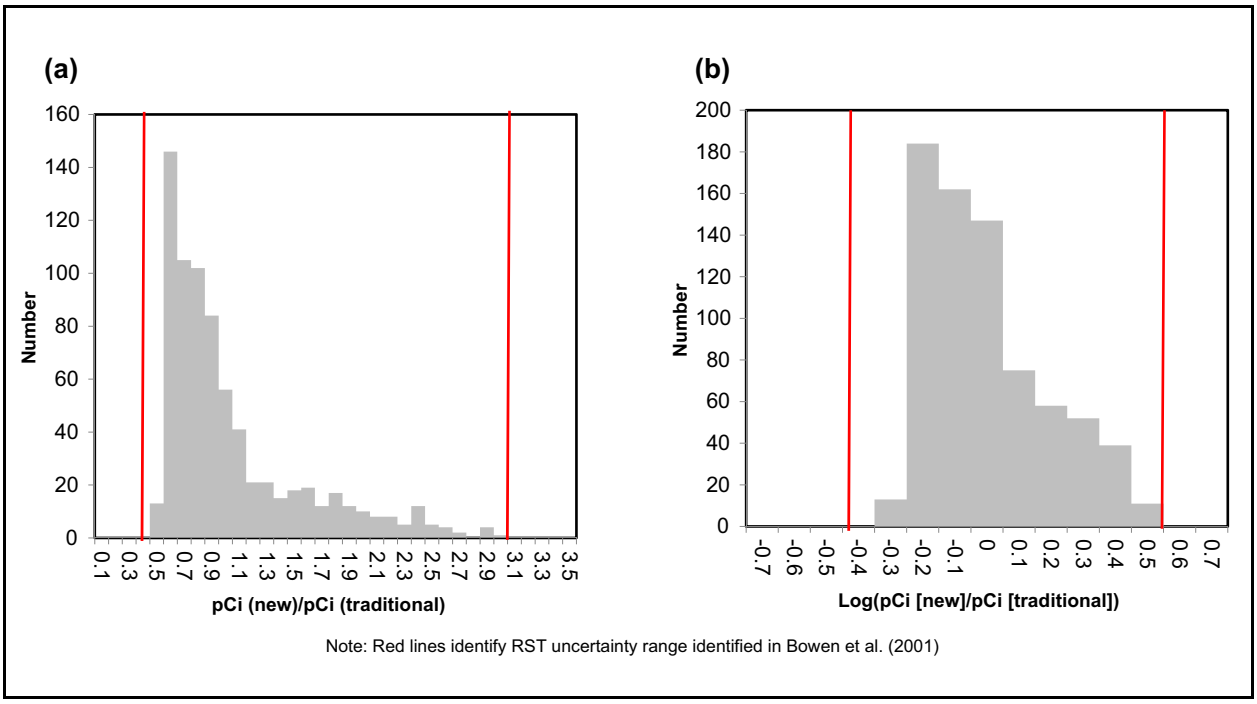

Figure C-3
Comparison of (a) ^{3}H and (b) ^{90}Sr RSTs at t_0 for All Yucca Flat Detonations Using the New versus Traditional Yield-Weighting Methods

Uncertainty in the RST followed the methodology identified in Rainier Mesa HST analysis (Tompson et al., 2011), which was based on the uncertainties identified in Bowen et al. (2001). Uncertainty in the RST was assumed to follow a log-triangular form. The applied uncertainty was geometric rather than arithmetic because (1) an arithmetic application would result in negative RSTs in many cases, and (2) discussions with weapons-testing radiochemists indicated that a geometric distribution was phenomenologically more appropriate. A triangular distribution was used because it established the geometric mean concentration as most likely. In the context of the accumulated uncertainties from all

parameters, Rainier Mesa HST screening calculations (Tompson et al., 2011) indicated that uniform or triangular RST distributions yield the same set of dominant radionuclides.

Cavity Radius. As discussed in Section 2.3, cavity radius (in meters) was calculated based on Pawloski (1999):

$$R_c = \frac{70.2Y^{1/3}}{(\rho_b DOB)^{1/4}} \qquad (C\text{-}1)$$

where

Y = maximum announced yield (kt) identified in DOE/NV-209, Rev. 15
ρ_b = overburden density (g/cm^3)
DOB = depth of burial (working-point depth) (m)

Values were taken directly from Pawloski et al.(2005). Uncertainty in the cavity radius was not addressed.

Exchange Volume Radius. The exchange volume radius was radionuclide specific and fell into one of three categories: 1 to 1.5 R_c, 1.5 to 3 R_c, or 3 to 5 R_c. The categorization of radionuclides into these three bins was based on observations at Rainier Mesa (Tompson et al., 2011), and the known volatility of each radionuclide and its precursors. For example, plutonium is a refractory element that is deposited primarily in the nuclear melt glass. Its exchange volume radius was estimated to be between 1 and 1.5 R_c (average 1.25 R_c). Noble gases (e.g., ^{85}Kr) and $^{14}CO_2$ are likely to migrate away from the cavity as gases at early times. Thus, their exchange volume radius will be significantly larger, 3 to 5 R_c (average 4 R_c). However, as was shown in the Rainier Mesa HST calculations (Tompson et al., 2011), the scale of the exchange volume for gaseous radionuclides is spatially heterogeneous and time dependent. Thus, the range of 3 to 5 R_c should be considered an approximate snapshot of the gaseous radionuclide exchange volume at early times.

Glass Partitioning. Each radionuclide was partitioned between nuclear melt glass and the water in the exchange volume. Partitioning was based on IAEA (1998a) recommendations and adjusted, when appropriate, based on direct evidence from the NNSS. The direct evidence came primarily from two sources: The Rainier Mesa HST analysis (Tompson, et al., 2011), and the summary of radionuclide partitioning based on sampling efforts at the CHANCELLOR site (Rose et al., 2011). Uncertainty in the glass partitioning is not well known. However, comparison of IAEA (1998a) recommendations, combined with radionuclide distribution information from the RAINIER and CHANCELLOR

detonations, provides a qualitative representation of partitioning uncertainty. All glass partitioning uncertainty is based on a triangular distribution. For each Monte Carlo iteration, partitioning into the other materials (gas, water, rubble) was adjusted based on the fraction assigned to glass partitioning. Partitioning falls into the following categories:

- All gases (^{3}H, ^{14}C, ^{85}Kr, ^{39}Ar): 0 percent in glass
- All refractory radionuclides identified by IAEA (1998a) as 95 or 98 percent in the glass (^{26}Al, ^{59}Ni, ^{63}Ni, ^{93}Zr, ^{93}Nb, ^{94}Nb, ^{151}Sm, ^{150}Eu, ^{152}Eu, ^{154}Eu, ^{166}Ho, ^{232}Th, ^{237}Np, $^{238,239,240,241,242}Pu$, $^{241,243}Am$, ^{244}Cm): 95–100 percent in glass
- All uranium ($^{232–236,238}U$): 70–90 percent in glass
- ^{36}Cl and ^{129}I: 10–50 percent in glass
- ^{40}K, ^{41}Ca, ^{107}Pd, ^{113}Cd, ^{126}Sn: 30–70 percent in glass
- ^{90}Sr and ^{99}Tc: 40–80 percent in glass
- ^{121}Sn: 20–60 percent in glass
- ^{135}Cs: 20–70 percent in glass
- ^{137}Cs: 25–40 percent in glass

Glass Release Fraction. The fraction of glass released was based on the four categories developed as part of the Rainier Mesa HST analysis (Tompson et al., 2011). The initial glass mass (700 tons per kiloton yield), temperature, and associated cooling history will control the extent of glass dissolution. As a result, detonations were categorized by yield, which correlates with glass volume and initial temperature. Yields were categorized as less than 0.1 kt, 0.1 to 1 kt, 1 to 20 kt, and greater than 20 kt based on reported yields or maximum announced yields identified in DOE/NV (2000). Glass dissolution parameter uncertainties yielded percent, glass dissolution ranges of 0.0013 to 0.11, 0.0018 to 0.14, 0.0052 to 0.67, and 0.017 to 2.6, respectively, for the first 100 years of glass dissolution. Uncertainties were based on a log-triangular distribution. Details can be found in the Rainier Mesa HST report (Tompson et al., 2011).

Cavity and Exchange Volume Porosity. The cavity and exchange volume porosity at each detonation was based on the average porosity of the HSU located at the working point. Bulking effects were not taken into account, and parameter uncertainty was not included. Importantly, for this exercise, it was

assumed that the entire porosity of the exchange volume was accessible to radionuclides. While this may not be the case in fractured exchange volumes outside the cavity at t_0, simulations performed as part of the Rainier Mesa HST effort (Tompson et al., 2011) suggest that diffusion into the matrix within the exchange volume will occur relatively rapidly. Thus, this homogeneous distribution of radionuclides in the exchange volume may be more representative of t + 1 year rather than a true distribution at t_0.

Saturation. Saturation at each detonation was based on an estimate of the average saturation of the HGU located at the working point. Uncertainty in this parameter was not addressed. Saturations values were 0.25, 0.45, 0.45, 0.8, 0.8, and 1.0 for detonations located in the AA, VTA, WTA, TCU, CA, and GCU, respectively.

K_d by HSU. Radionuclide K_d values were simulated based on the component additivity approach reported in a number of project documents (e.g., Carle et al., 2002, 2007; Tompson et al., 2005). Radionuclide-mineral sorption behavior is dependent on water chemistry. Thus, parameters were established based on four individual water chemistries (alluvium, tuff, carbonate, and granite water chemistries) that were calculated from well data at the NNSS. Uncertainties in K_d values were based solely on the uncertainty in surface complexation/ion exchange parameters and not the uncertainty in the water chemistry; surface complexation/ion exchange uncertainties are substantially larger than the effects of water chemistry. K_d values at individual detonations were based on the average mineralogy of the HSU at the working-point location.

C.4.6 Results

Figure C-4 summarizes the distribution of initial activity of all radionuclides and all Yucca Flat/Climax Mine CAU detonations relative to their respective MCLs. It is a summary of 59,760 Monte Carlo realizations based on parameterization and uncertainties identified above. It is clear that many of the 43 radionuclides listed in Bowen et al. (2001) are unlikely to contribute to health risk because their concentrations fall well below their respective MCLs. At the 95 percent confidence interval, only the following radionuclides may be found above 0.1 MCL: ^{3}H, ^{14}C, ^{36}Cl, ^{90}Sr, ^{99}Tc, ^{129}I, ^{137}Cs, ^{152}Eu, ^{154}Eu, ^{238}U, and ^{238,239,240,241}Pu.

Of these, ^{137}Cs, ^{152}Eu, ^{154}Eu, and ^{241}Pu will decay to below 0.1 MCL before ^{3}H. Thus, contamination by ^{3}H will always contribute more to the contaminant boundary calculation than these radionuclides.

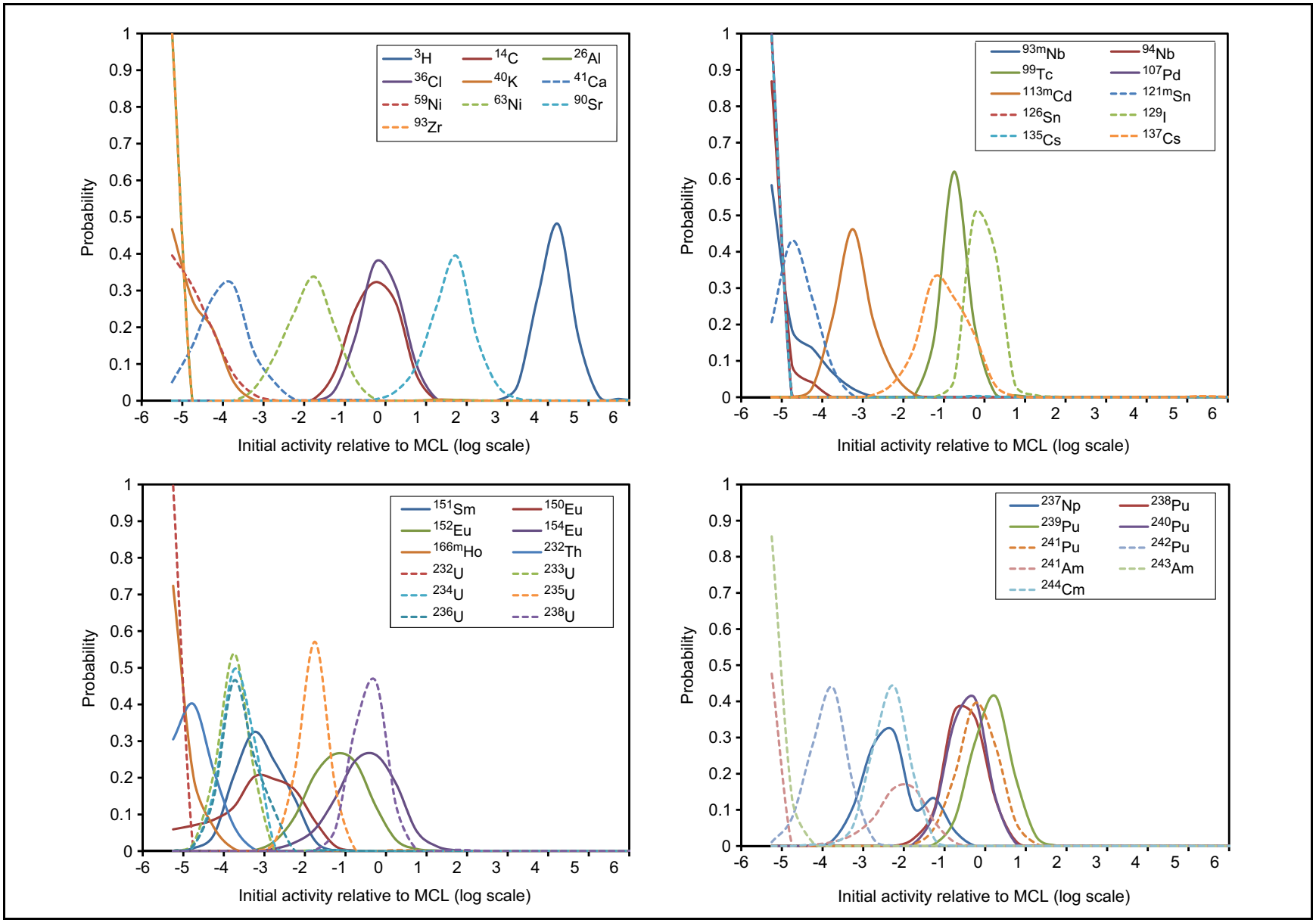

Figure C-4
Probability Distributions of Initial Radionuclide Concentrations (Relative to MCLs) in All Detonations within the Yucca Flat/Climax Mine CAU

Based on this analysis, the contaminant boundary calculations can be limited further to the following radionuclides: ^{3}H, ^{14}C, ^{36}Cl, ^{90}Sr, ^{99}Tc, ^{129}I, ^{238}U, and $^{238,239,240}Pu$.

However, given the unique nature of detonation and geochemical conditions in the three model domains (unsaturated zone, saturated alluvial/volcanic aquifer system, and saturated LCA), radionuclide screening by model domain is warranted. When the radionuclide screening is performed for detonations within each of the three model domains separately, we find that the screening is dependent on the characteristics (e.g., mineralogy, saturation) of the models (Table C-1). The major result is the inclusion of ^{41}Ca, ^{63}Ni, ^{135}Cs, ^{137}Cs, ^{235}U, and ^{237}Np in the saturated LCA model and ^{237}Np in the saturated alluvial/volcanic aquifer system model. However, it should be noted that the ^{41}Ca and ^{237}Np 95th percentiles were very near the 0.1 MCL limit in all Yucca Flat models. The primary reason for the increased number of relevant radionuclides in the saturated LCA model was the lower radionuclide K_d values predicted for carbonate rocks.

C.4.7 Conclusions

The screening analysis identified radionuclides that are likely to contribute to contaminant boundaries and pose a potential risk to the environment and the public. Of the 43 radionuclides listed in Bowen et al. (2001), only 10 radionuclides are likely to contribute to contaminant boundary calculations in all three Yucca Flat models. Five additional radionuclides may contribute to contaminant boundary calculations in some but not all models.

Of the 16 radionuclides that may to some extent contribute to contaminant boundary calculations, 5 are considered non-sorbing tracers (^{3}H, ^{14}C, ^{36}Cl, ^{99}Tc, and ^{129}I). Of the remaining radionuclides, ^{90}Sr, ^{135}Cs, and ^{137}Cs are very strongly sorbing in both alluvium and tuff. Thus, they are likely to be transported downstream only in the carbonate aquifer. Similarly, ^{63}Ni may be transported downstream at relevant concentrations only in the carbonate aquifer; its presence (or absence) has never been evaluated at the NNSS. The ^{237}Np 95th percentile concentration was found to be very near 0.1 MCL in all models. Thus, ^{237}Np is unlikely to contribute significantly to contaminant boundary estimates. A recent survey of neptunium concentrations in “hot wells” from the NNSS indicates that neptunium concentrations are well below its MCL. The uranium isotopes ^{235}U and ^{238}U are identified as potentially contributing to contaminant boundaries. However, it should be noted that these uranium isotopes are primarily (but not entirely) of natural origin. Groundwater from clean wells at the NNSS commonly contains uranium concentrations within an order of magnitude of the uranium MCL

(30 µg/L). The isotopes of plutonium ($^{238,239,240}Pu$) are strongly sorbing. However, the plutonium inventory is very large, and MCL is quite low, leading to the conclusion that it may contribute to contaminant boundary. In practice, plutonium activities in groundwater have been detected above the MCL of 16 pCi/L at only two “hot well” locations (U-19ad and U-12t). At several other sites, plutonium concentrations may be within an order of magnitude of the MCL. Plutonium is believed to migrate primarily associated with colloids. Thus, its transport velocity in fractured rock may be quite high. However, although there are not many wells located downstream of underground nuclear detonations, the few that exist do not suggest plutonium colloid-facilitated transport at concentrations above its MCL. Nevertheless, its contribution to contaminant boundary calculations cannot be eliminated using the screening methods described here.

C.5.0 HYDROLOGIC SOURCE TERM ALLOCATION BETWEEN MODELS

Many of the Yucca Flat detonations have exchange volumes that span across the models. This section presents the initial HST allocation fractions between the three Yucca Flat models (developed in Section 2.3.3) for each of the 744 detonations conducted at Yucca Flat proper. Two methods are used to allocate the initial inventory between the three Yucca Flat transport models. These two methods are considered to capture conceptual uncertainty in the extent of the exchange volume and initial distribution of radionuclides within the exchange volume.

The first allocation method assumes that the exchange volume has a uniform radius of 1, 2, or 3 R_c and that radionuclides in the exchange volume are allocated by the fraction of total (fracture and matrix) pore space within each model domain. The second allocation method implements the recent conceptual understanding of the radionuclide physical and chemical partitioning described in Section C.3.4. This second allocation method assumes that radionuclide concentration in the water within the exchange volume is uniform. It considers the extent of the exchange volume beyond the cavity that is specific to each radionuclide, but places the majority of the radionuclides in the high-porosity cavity. These two allocation methods are referred to as the “uniform-mass” and “uniform-concentration” allocation methods within this document.

Table C-3 presents, for each of the 744 detonations conducted at Yucca Flat proper, the detonation name, maximum yield-weighted fraction of the total Bowen inventory, and the initial HST fraction for each Yucca Flat model for each of the two allocation methods. The initial RST is assigned to specific detonations within each model in the following steps: (1) determine the individual detonation inventory by multiplying the Bowen RST by the maximum yield-weighted fraction, (2) decay correct the individual detonation inventory from September 23, 1992, to the time of each detonation (t_0) (see Section 2.3), (3) remove the melt-glass inventory fraction presented in Tables 2-6 and 2-7 from individual detonation inventory, and (4) multiply the remaining RST by detonation-specific allocation fraction presented in Table C-3.

Table C-3
Initial RST Fractions for Detonations in the Unsaturated Zone, Saturated Alluvial/Volcanic Aquifer System, and Saturated LCA Models
(Page 1 of 34)

Detonation Name [a]	Maximum Yield-Weighted Fraction of Total Inventory [b]	Uniform-Mass Inventory Fraction (2 R_c Exchange Volume)			Uniform-Concentration Inventory Fraction (^3H)		
		Unsaturated Zone	Saturated Alluvial/Volcanic Aquifer System	Saturated LCA	Unsaturated Zone	Saturated Alluvial/Volcanic Aquifer System	Saturated LCA
AARDVARK	0.00102	0.9735	0.0265	0.0000	0.9922	0.0078	0.0000
ABEYTAS	0.00512	0.8877	0.1123	0.0000	0.9849	0.0151	0.0000
ABILENE	0.00051	1.0000	0.0000	0.0000	1.0000	0.0000	0.0000
ABO	0.00051	1.0000	0.0000	0.0000	1.0000	0.0000	0.0000
ABSINTHE	0.00051	1.0000	0.0000	0.0000	1.0000	0.0000	0.0000
ACE	0.00008	1.0000	0.0000	0.0000	1.0000	0.0000	0.0000
ACUSHI	0.00051	1.0000	0.0000	0.0000	1.0000	0.0000	0.0000
ADZE	0.00051	1.0000	0.0000	0.0000	1.0000	0.0000	0.0000
AGILE	0.00512	0.0000	1.0000	0.0000	0.0000	1.0000	0.0000
AGOUTI	0.00016	1.0000	0.0000	0.0000	1.0000	0.0000	0.0000
AGRINI	0.00051	1.0000	0.0000	0.0000	1.0000	0.0000	0.0000
AHTANUM	0.00051	1.0000	0.0000	0.0000	1.0000	0.0000	0.0000
AJAX	0.00051	1.0000	0.0000	0.0000	1.0000	0.0000	0.0000
AJO	0.00051	1.0000	0.0000	0.0000	1.0000	0.0000	0.0000
AKAVI	0.00384	0.9058	0.0942	0.0000	0.9949	0.0051	0.0000
AKBAR	0.00051	1.0000	0.0000	0.0000	1.0000	0.0000	0.0000
ALEMAN	0.00051	0.1923	0.8077	0.0000	0.0000	1.0000	0.0000
ALGODONES	0.00512	0.3095	0.6905	0.0000	0.0000	1.0000	0.0000
ALIGOTE	0.00051	1.0000	0.0000	0.0000	1.0000	0.0000	0.0000
ALIMENT	0.00051	1.0000	0.0000	0.0000	1.0000	0.0000	0.0000
ALLEGHENY	0.00051	1.0000	0.0000	0.0000	1.0000	0.0000	0.0000
ALPACA	0.00001	1.0000	0.0000	0.0000	1.0000	0.0000	0.0000

Table C-3
Initial RST Fractions for Detonations in the Unsaturated Zone, Saturated Alluvial/Volcanic Aquifer System, and Saturated LCA Models
(Page 2 of 34)

Detonation Name [a]	Maximum Yield-Weighted Fraction of Total Inventory [b]	Uniform-Mass Inventory Fraction (2 R_c Exchange Volume)			Uniform-Concentration Inventory Fraction (^3H)		
		Unsaturated Zone	Saturated Alluvial/Volcanic Aquifer System	Saturated LCA	Unsaturated Zone	Saturated Alluvial/Volcanic Aquifer System	Saturated LCA
ALUMROOT	0.00051	1.0000	0.0000	0.0000	1.0000	0.0000	0.0000
ALVA	0.00011	1.0000	0.0000	0.0000	1.0000	0.0000	0.0000
ALVISO	0.00051	1.0000	0.0000	0.0000	1.0000	0.0000	0.0000
ANACOSTIA	0.00013	1.0000	0.0000	0.0000	1.0000	0.0000	0.0000
ANCHOVY	0.00051	1.0000	0.0000	0.0000	1.0000	0.0000	0.0000
ANGUS	0.00051	0.6957	0.3043	0.0000	0.5406	0.4594	0.0000
APODACA	0.00051	1.0000	0.0000	0.0000	1.0000	0.0000	0.0000
APSHAPA	0.00051	1.0000	0.0000	0.0000	1.0000	0.0000	0.0000
ARABIS-BLUE	0.00051	1.0000	0.0000	0.0000	1.0000	0.0000	0.0000
ARABIS-GREEN	0.00051	1.0000	0.0000	0.0000	1.0000	0.0000	0.0000
ARABIS-RED	0.00051	1.0000	0.0000	0.0000	1.0000	0.0000	0.0000
ARIKAREE	0.00051	1.0000	0.0000	0.0000	1.0000	0.0000	0.0000
ARMADA	0.00051	1.0000	0.0000	0.0000	1.0000	0.0000	0.0000
ARMADILLO	0.00018	1.0000	0.0000	0.0000	1.0000	0.0000	0.0000
ARNICA-VIOLET	0.00051	1.0000	0.0000	0.0000	1.0000	0.0000	0.0000
ARNICA-YELLOW	0.00051	1.0000	0.0000	0.0000	1.0000	0.0000	0.0000
ARSENATE	0.00051	1.0000	0.0000	0.0000	1.0000	0.0000	0.0000
ARTESIA	0.00512	0.9625	0.0375	0.0000	0.9928	0.0070	0.0002
ASCO	0.00051	1.0000	0.0000	0.0000	1.0000	0.0000	0.0000
ASIAGO	0.00051	1.0000	0.0000	0.0000	1.0000	0.0000	0.0000
ATARQUE	0.00051	1.0000	0.0000	0.0000	1.0000	0.0000	0.0000
ATRISCO	0.00353	0.0136	0.9864	0.0000	0.0000	0.9999	0.0001

Table C-3
Initial RST Fractions for Detonations in the Unsaturated Zone, Saturated Alluvial/Volcanic Aquifer System, and Saturated LCA Models
(Page 3 of 34)

Detonation Name [a]	Maximum Yield-Weighted Fraction of Total Inventory [b]	Uniform-Mass Inventory Fraction (2 R_c Exchange Volume)			Uniform-Concentration Inventory Fraction (^3H)		
		Unsaturated Zone	Saturated Alluvial/Volcanic Aquifer System	Saturated LCA	Unsaturated Zone	Saturated Alluvial/Volcanic Aquifer System	Saturated LCA
AUGER	0.00051	1.0000	0.0000	0.0000	1.0000	0.0000	0.0000
AUK	0.00051	1.0000	0.0000	0.0000	1.0000	0.0000	0.0000
AUSTIN	0.00051	1.0000	0.0000	0.0000	1.0000	0.0000	0.0000
AVENS-ALKERMES	0.00051	1.0000	0.0000	0.0000	1.0000	0.0000	0.0000
AVENS-ANDORRE	0.00051	1.0000	0.0000	0.0000	1.0000	0.0000	0.0000
AVENS-ASAMLTE	0.00051	1.0000	0.0000	0.0000	1.0000	0.0000	0.0000
AVENS-CREAM	0.00051	1.0000	0.0000	0.0000	1.0000	0.0000	0.0000
AZUL	0.00051	1.0000	0.0000	0.0000	1.0000	0.0000	0.0000
BACCARAT	0.00051	1.0000	0.0000	0.0000	1.0000	0.0000	0.0000
BACKGAMMON	0.00051	1.0000	0.0000	0.0000	1.0000	0.0000	0.0000
BACKSWING	0.00051	1.0000	0.0000	0.0000	1.0000	0.0000	0.0000
BALTIC	0.00051	1.0000	0.0000	0.0000	1.0000	0.0000	0.0000
BANDICOOT	0.00032	1.0000	0.0000	0.0000	1.0000	0.0000	0.0000
BANEBERRY	0.00026	1.0000	0.0000	0.0000	1.0000	0.0000	0.0000
BANON	0.00384	0.5286	0.4714	0.0000	0.3657	0.6343	0.0000
BARBEL	0.00051	1.0000	0.0000	0.0000	1.0000	0.0000	0.0000
BARRACUDA	0.00051	1.0000	0.0000	0.0000	1.0000	0.0000	0.0000
BARRANCA	0.00051	1.0000	0.0000	0.0000	1.0000	0.0000	0.0000
BARSAC	0.00051	1.0000	0.0000	0.0000	1.0000	0.0000	0.0000
BASEBALL	0.00384	0.0181	0.9819	0.0000	0.0000	1.0000	0.0000
BAY LEAF	0.00051	1.0000	0.0000	0.0000	130.00	1.0000	0.0000
BEEBALM	0.00051	1.0000	0.0000	0.0000	1.0000	0.0000	0.0000

Table C-3
Initial RST Fractions for Detonations in the Unsaturated Zone, Saturated Alluvial/Volcanic Aquifer System, and Saturated LCA Models
(Page 4 of 34)

Detonation Name [a]	Maximum Yield-Weighted Fraction of Total Inventory [b]	Uniform-Mass Inventory Fraction (2 R_c Exchange Volume)			Uniform-Concentration Inventory Fraction (^3H)		
		Unsaturated Zone	Saturated Alluvial/Volcanic Aquifer System	Saturated LCA	Unsaturated Zone	Saturated Alluvial/Volcanic Aquifer System	Saturated LCA
BELEN	0.00512	0.8355	0.1645	0.0000	0.9971	0.0029	0.0000
BELLOW	0.00051	1.0000	0.0000	0.0000	1.0000	0.0000	0.0000
BERNAL	0.00051	1.0000	0.0000	0.0000	1.0000	0.0000	0.0000
BERNALILLO	<0.00000	1.0000	0.0000	0.0000	1.0000	0.0000	0.0000
BEVEL	0.00051	1.0000	0.0000	0.0000	1.0000	0.0000	0.0000
BIGGIN	0.00051	1.0000	0.0000	0.0000	1.0000	0.0000	0.0000
BILBY	0.00638	0.0000	1.0000	0.0000	0.0000	1.0000	0.0000
BILGE	0.00051	1.0000	0.0000	0.0000	1.0000	0.0000	0.0000
BILLET	0.00384	0.0000	1.0000	0.0000	0.0000	1.0000	0.0000
BIT-A	0.00051	1.0000	0.0000	0.0000	1.0000	0.0000	0.0000
BIT-B	0.00051	1.0000	0.0000	0.0000	1.0000	0.0000	0.0000
BITTERLING	0.00051	1.0000	0.0000	0.0000	1.0000	0.0000	0.0000
BLACK	0.00051	1.0000	0.0000	0.0000	1.0000	0.0000	0.0000
BLENTON	0.00512	0.3887	0.6113	0.0000	0.0000	1.0000	0.0000
BOBAC	0.00051	1.0000	0.0000	0.0000	1.0000	0.0000	0.0000
BOBSTAY	0.00051	1.0000	0.0000	0.0000	1.0000	0.0000	0.0000
BOGEY	0.00051	1.0000	0.0000	0.0000	1.0000	0.0000	0.0000
BONARDA	0.00384	0.9672	0.0328	0.0000	0.9943	0.0057	0.0000
BONEFISH	0.00051	1.0000	0.0000	0.0000	1.0000	0.0000	0.0000
BOOMER	0.00051	1.0000	0.0000	0.0000	1.0000	0.0000	0.0000
BORATE	0.00384	0.6323	0.3677	0.0000	0.8700	0.1300	0.0000
BORDEAUX	0.00051	1.0000	0.0000	0.0000	1.0000	0.0000	0.0000

Table C-3
Initial RST Fractions for Detonations in the Unsaturated Zone, Saturated Alluvial/Volcanic Aquifer System, and Saturated LCA Models
(Page 5 of 34)

Detonation Name [a]	Maximum Yield-Weighted Fraction of Total Inventory [b]	Uniform-Mass Inventory Fraction (2 R_c Exchange Volume)			Uniform-Concentration Inventory Fraction (^3H)		
		Unsaturated Zone	Saturated Alluvial/Volcanic Aquifer System	Saturated LCA	Unsaturated Zone	Saturated Alluvial/Volcanic Aquifer System	Saturated LCA
BORREGO	0.00384	0.1279	0.8721	0.0000	0.0000	1.0000	0.0000
BOURBON	0.00512	0.9606	0.0000	0.0394	0.5699	0.0000	0.4301
BOUSCHET	0.00384	0.0709	0.9291	0.0000	0.0000	1.0000	0.0000
BOWIE	0.00051	1.0000	0.0000	0.0000	1.0000	0.0000	0.0000
BOWL-1	0.00051	1.0000	0.0000	0.0000	1.0000	0.0000	0.0000
BOWL-2	0.00051	1.0000	0.0000	0.0000	1.0000	0.0000	0.0000
BRACKEN	0.00051	1.0000	0.0000	0.0000	1.0000	0.0000	0.0000
BRANCO	0.00051	1.0000	0.0000	0.0000	1.0000	0.0000	0.0000
BRANCO-HERKIMER	0.00051	1.0000	0.0000	0.0000	1.0000	0.0000	0.0000
BRAZOS	0.00022	1.0000	0.0000	0.0000	1.0000	0.0000	0.0000
BRETON	0.00384	0.5884	0.4116	0.0000	0.7991	0.2009	0.0000
BRIE	0.00051	1.0000	0.0000	0.0000	1.0000	0.0000	0.0000
BRISTOL	0.00051	0.7646	0.2354	0.0000	0.8322	0.1678	0.0000
BRONZE	0.00512	0.5952	0.4048	0.0000	0.2221	0.7779	0.0000
BRUSH	0.00051	1.0000	0.0000	0.0000	1.0000	0.0000	0.0000
BUFF	0.00512	0.5814	0.4186	0.0000	0.1713	0.8287	0.0000
BULKHEAD	0.00384	0.2552	0.7448	0.0000	0.0000	1.0000	0.0000
BULLFROG	0.00384	0.5494	0.4506	0.0000	0.3515	0.6485	0.0000
BUNKER	0.00051	1.0000	0.0000	0.0000	1.0000	0.0000	0.0000
BURZET	0.00384	0.7624	0.2376	0.0000	0.9705	0.0295	0.0000
BYE	0.00512	1.0000	0.0000	0.0000	1.0000	0.0000	0.0000
CABOC	0.00051	1.0000	0.0000	0.0000	1.0000	0.0000	0.0000

Table C-3
Initial RST Fractions for Detonations in the Unsaturated Zone, Saturated Alluvial/Volcanic Aquifer System, and Saturated LCA Models
(Page 6 of 34)

Detonation Name [a]	Maximum Yield-Weighted Fraction of Total Inventory [b]	Uniform-Mass Inventory Fraction (2 R_c Exchange Volume)			Uniform-Concentration Inventory Fraction (^3H)		
		Unsaturated Zone	Saturated Alluvial/Volcanic Aquifer System	Saturated LCA	Unsaturated Zone	Saturated Alluvial/Volcanic Aquifer System	Saturated LCA
CABRESTO	0.00051	1.0000	0.0000	0.0000	1.0000	0.0000	0.0000
CABRILLO	0.00512	0.3019	0.6981	0.0000	0.0000	1.0000	0.0000
CALABASH	0.00282	0.1623	0.8377	0.0000	0.0000	0.9997	0.0003
CAMPOS	0.00051	1.0000	0.0000	0.0000	1.0000	0.0000	0.0000
CANFIELD	0.00051	1.0000	0.0000	0.0000	1.0000	0.0000	0.0000
CAN-GREEN	0.00512	1.0000	0.0000	0.0000	1.0000	0.0000	0.0000
CANJILON	0.00051	1.0000	0.0000	0.0000	1.0000	0.0000	0.0000
CANNA-LIMOGES	0.00051	1.0000	0.0000	0.0000	1.0000	0.0000	0.0000
CANNA-UMBRINUS	0.00051	1.0000	0.0000	0.0000	1.0000	0.0000	0.0000
CAN-RED	0.00512	1.0000	0.0000	0.0000	0.9998	0.0000	0.0002
CANVASBACK	0.00051	0.9998	0.0002	0.0000	0.9989	0.0011	0.0000
CAPITAN	0.00051	1.0000	0.0000	0.0000	1.0000	0.0000	0.0000
CAPROCK	0.00384	0.0137	0.9863	0.0000	0.0000	1.0000	0.0000
CARMEL	0.00051	1.0000	0.0000	0.0000	1.0000	0.0000	0.0000
CARNELIAN	0.00051	1.0000	0.0000	0.0000	1.0000	0.0000	0.0000
CARP	0.00051	1.0000	0.0000	0.0000	1.0000	0.0000	0.0000
CARPETBAG	0.00563	0.0267	0.9733	0.0000	0.0000	1.0000	0.0000
CARRIZOZO	0.00051	1.0000	0.0000	0.0000	1.0000	0.0000	0.0000
CASHMERE	0.00051	1.0000	0.0000	0.0000	1.0000	0.0000	0.0000
CASSELMAN	0.00051	1.0000	0.0000	0.0000	1.0000	0.0000	0.0000
CASSOWARY	0.00051	1.0000	0.0000	0.0000	1.0000	0.0000	0.0000
CATHAY	0.00051	1.0000	0.0000	0.0000	1.0000	0.0000	0.0000

Table C-3
Initial RST Fractions for Detonations in the Unsaturated Zone, Saturated Alluvial/Volcanic Aquifer System, and Saturated LCA Models
(Page 7 of 34)

Detonation Name [a]	Maximum Yield-Weighted Fraction of Total Inventory [b]	Uniform-Mass Inventory Fraction (2 R_c Exchange Volume)			Uniform-Concentration Inventory Fraction (^3H)		
		Unsaturated Zone	Saturated Alluvial/Volcanic Aquifer System	Saturated LCA	Unsaturated Zone	Saturated Alluvial/Volcanic Aquifer System	Saturated LCA
CEBOLLA	0.00051	1.0000	0.0000	0.0000	1.0000	0.0000	0.0000
CEBRERO	0.00051	1.0000	0.0000	0.0000	1.0000	0.0000	0.0000
CENTAUR	0.00051	1.0000	0.0000	0.0000	1.0000	0.0000	0.0000
CERISE	0.00051	1.0000	0.0000	0.0000	1.0000	0.0000	0.0000
CERNADA	0.00051	1.0000	0.0000	0.0000	1.0000	0.0000	0.0000
CERRO	0.00051	1.0000	0.0000	0.0000	1.0000	0.0000	0.0000
CHAENACTIS	0.00512	1.0000	0.0000	0.0000	1.0000	0.0000	0.0000
CHAMITA	0.00051	1.0000	0.0000	0.0000	1.0000	0.0000	0.0000
CHANTILLY	0.00051	1.0000	0.0000	0.0000	1.0000	0.0000	0.0000
CHARCOAL	0.00512	0.8657	0.1343	0.0000	0.9823	0.0177	0.0000
CHATTY	0.00051	1.0000	0.0000	0.0000	1.0000	0.0000	0.0000
CHEEDAM	0.00051	1.0000	0.0000	0.0000	1.0000	0.0000	0.0000
CHENILLE	0.00051	1.0000	0.0000	0.0000	1.0000	0.0000	0.0000
CHESS	0.00051	1.0000	0.0000	0.0000	1.0000	0.0000	0.0000
CHEVRE	0.00051	1.0000	0.0000	0.0000	1.0000	0.0000	0.0000
CHIBERTA	0.00512	0.0000	1.0000	0.0000	0.0000	1.0000	0.0000
CHINCHILLA	0.00005	1.0000	0.0000	0.0000	1.0000	0.0000	0.0000
CHINCHILLA II	0.00051	1.0000	0.0000	0.0000	137.00	1.0000	0.0000
CHIPMUNK	0.00051	1.0000	0.0000	0.0000	1.0000	0.0000	0.0000
CHOCOLATE	0.00051	1.0000	0.0000	0.0000	1.0000	0.0000	0.0000
CIMARRON	0.00030	1.0000	0.0000	0.0000	1.0000	0.0000	0.0000
CINNAMON	0.00051	1.0000	0.0000	0.0000	1.0000	0.0000	0.0000

Table C-3
Initial RST Fractions for Detonations in the Unsaturated Zone, Saturated Alluvial/Volcanic Aquifer System, and Saturated LCA Models
(Page 8 of 34)

Detonation Name [a]	Maximum Yield-Weighted Fraction of Total Inventory [b]	Uniform-Mass Inventory Fraction (2 R_c Exchange Volume)			Uniform-Concentration Inventory Fraction (^3H)		
		Unsaturated Zone	Saturated Alluvial/Volcanic Aquifer System	Saturated LCA	Unsaturated Zone	Saturated Alluvial/Volcanic Aquifer System	Saturated LCA
CLAIRETTE	0.00051	1.0000	0.0000	0.0000	1.0000	0.0000	0.0000
CLARKSMOBILE	0.00512	0.6984	0.3016	0.0000	0.8855	0.1145	0.0000
CLUB	0.00051	1.0000	0.0000	0.0000	1.0000	0.0000	0.0000
CLYMER	0.00051	1.0000	0.0000	0.0000	1.0000	0.0000	0.0000
COALORA	0.00051	1.0000	0.0000	0.0000	1.0000	0.0000	0.0000
COBBLER	0.00051	0.0000	1.0000	0.0000	0.0000	1.0000	0.0000
CODSAW	0.00051	1.0000	0.0000	0.0000	1.0000	0.0000	0.0000
COFFER	0.00256	0.9924	0.0076	0.0000	0.8921	0.1079	0.0000
COGNAC	0.00051	1.0000	0.0000	0.0000	1.0000	0.0000	0.0000
COLFAX	<0.00000	1.0000	0.0000	0.0000	1.0000	0.0000	0.0000
COLMOR	0.00051	1.0000	0.0000	0.0000	1.0000	0.0000	0.0000
COMMODORE	0.00640	0.0000	1.0000	0.0000	0.0000	1.0000	0.0000
CONCENTRATION	0.00051	1.0000	0.0000	0.0000	1.0000	0.0000	0.0000
CORAZON	0.00051	1.0000	0.0000	0.0000	1.0000	0.0000	0.0000
CORDUROY	0.00512	0.0247	0.9198	0.0555	0.0000	0.8418	0.1582
CORMORANT	0.00051	1.0000	0.0000	0.0000	1.0000	0.0000	0.0000
CORNICE-GREEN	0.00512	0.9986	0.0013	0.0000	0.9978	0.0004	0.0017
CORNICE-YELLOW	0.00512	1.0000	0.0000	0.0000	1.0000	0.0000	0.0000
CORNUCOPIA	0.00051	1.0000	0.0000	0.0000	1.0000	0.0000	0.0000
CORREO	0.00051	1.0000	0.0000	0.0000	1.0000	0.0000	0.0000
COSO-BRONZE	0.00051	1.0000	0.0000	0.0000	1.0000	0.0000	0.0000
COSO-GRAY	0.00051	0.9846	0.0154	0.0000	0.9961	0.0039	0.0000

Table C-3
Initial RST Fractions for Detonations in the Unsaturated Zone, Saturated Alluvial/Volcanic Aquifer System, and Saturated LCA Models
(Page 9 of 34)

Detonation Name [a]	Maximum Yield-Weighted Fraction of Total Inventory [b]	Uniform-Mass Inventory Fraction (2 R_c Exchange Volume)			Uniform-Concentration Inventory Fraction (^3H)		
		Unsaturated Zone	Saturated Alluvial/Volcanic Aquifer System	Saturated LCA	Unsaturated Zone	Saturated Alluvial/Volcanic Aquifer System	Saturated LCA
COSO-SILVER	0.00051	0.7664	0.2336	0.0000	0.8320	0.1680	0.0000
COTTAGE	0.00384	0.9990	0.0000	0.0010	0.9969	0.0000	0.0031
COULOMMIERS	0.00384	0.7842	0.2158	0.0000	0.7987	0.2013	0.0000
COURSER	0.0	0.0000	0.0000	0.0000	0.0000	0.0000	0.0000
COVE	0.00051	1.0000	0.0000	0.0000	1.0000	0.0000	0.0000
COWLES	0.00051	1.0000	0.0000	0.0000	1.0000	0.0000	0.0000
COYPU	0.00051	1.0000	0.0000	0.0000	1.0000	0.0000	0.0000
CREMINO	0.00051	1.0000	0.0000	0.0000	1.0000	0.0000	0.0000
CREMINO-CAERPHILLY	0.00051	1.0000	0.0000	0.0000	1.0000	0.0000	0.0000
CREPE	0.00512	0.9082	0.0918	0.0000	0.9928	0.0072	0.0000
CRESTLAKE-BRIAR	0.00051	1.0000	0.0000	0.0000	1.0000	0.0000	0.0000
CRESTLAKE-TANSAN	0.00051	1.0000	0.0000	0.0000	1.0000	0.0000	0.0000
CREW	0.00512	1.0000	0.0000	0.0000	1.0000	0.0000	0.0000
CREW-2ND	0.00051	1.0000	0.0000	0.0000	1.0000	0.0000	0.0000
CREW-3RD	0.00051	0.0684	0.9316	0.0000	0.0000	1.0000	0.0000
CREWLINE	0.00384	0.1450	0.8550	0.0000	0.0000	1.0000	0.0000
CROCK	0.00051	1.0000	0.0000	0.0000	1.0000	0.0000	0.0000
CROWDIE	0.00051	1.0000	0.0000	0.0000	1.0000	0.0000	0.0000
CRUET	0.00028	1.0000	0.0000	0.0000	1.0000	0.0000	0.0000
CUCHILLO	0.00051	1.0000	0.0000	0.0000	1.0000	0.0000	0.0000
CULANTRO-A	0.00051	1.0000	0.0000	0.0000	1.0000	0.0000	0.0000
CULANTRO-B	0.00051	1.0000	0.0000	0.0000	1.0000	0.0000	0.0000

Table C-3
Initial RST Fractions for Detonations in the Unsaturated Zone, Saturated Alluvial/Volcanic Aquifer System, and Saturated LCA Models
(Page 10 of 34)

Detonation Name [a]	Maximum Yield-Weighted Fraction of Total Inventory [b]	Uniform-Mass Inventory Fraction (2 R_c Exchange Volume)			Uniform-Concentration Inventory Fraction (^3H)		
		Unsaturated Zone	Saturated Alluvial/Volcanic Aquifer System	Saturated LCA	Unsaturated Zone	Saturated Alluvial/Volcanic Aquifer System	Saturated LCA
CUMARIN	0.00512	0.8995	0.1005	0.0000	0.9860	0.0140	0.0000
CUMBERLAND	0.00051	1.0000	0.0000	0.0000	1.0000	0.0000	0.0000
CUP	0.00512	0.5838	0.4161	0.0000	0.3003	0.6989	0.0008
CYATHUS	0.00022	1.0000	0.0000	0.0000	1.0000	0.0000	0.0000
CYCLAMEN	0.00031	1.0000	0.0000	0.0000	1.0000	0.0000	0.0000
DAIQUIRI	0.00051	0.3729	0.6271	0.0000	0.0000	1.0000	0.0000
DALHART	0.00384	0.0000	1.0000	0.0000	0.0000	1.0000	0.0000
DAMAN I	0.00051	1.0000	0.0000	0.0000	260.00	1.0000	0.0000
DANABLU	0.00051	1.0000	0.0000	0.0000	1.0000	0.0000	0.0000
DAUPHIN	0.00051	1.0000	0.0000	0.0000	1.0000	0.0000	0.0000
DEAD	0.00051	1.0000	0.0000	0.0000	1.0000	0.0000	0.0000
DECK	0.00051	1.0000	0.0000	0.0000	1.0000	0.0000	0.0000
DELPHINIUM	0.00038	1.0000	0.0000	0.0000	1.0000	0.0000	0.0000
DEXTER	0.00051	1.0000	0.0000	0.0000	1.0000	0.0000	0.0000
DIANTHUS	0.00051	1.0000	0.0000	0.0000	1.0000	0.0000	0.0000
DISCUS THROWER	0.00056	1.0000	0.0000	0.0000	337.00	1.0000	0.0000
DIVIDER	0.00051	1.0000	0.0000	0.0000	1.0000	0.0000	0.0000
DOFINO	0.00051	1.0000	0.0000	0.0000	1.0000	0.0000	0.0000
DOFINO-LAWTON	0.00051	1.0000	0.0000	0.0000	1.0000	0.0000	0.0000
DOLCETTO	0.00051	1.0000	0.0000	0.0000	1.0000	0.0000	0.0000
DORMOUSE	0.00051	1.0000	0.0000	0.0000	1.0000	0.0000	0.0000
DORMOUSE PRIME	0.00027	1.0000	0.0000	0.0000	261.00	1.0000	0.0000

Table C-3
Initial RST Fractions for Detonations in the Unsaturated Zone, Saturated Alluvial/Volcanic Aquifer System, and Saturated LCA Models
(Page 11 of 34)

Detonation Name [a]	Maximum Yield-Weighted Fraction of Total Inventory [b]	Uniform-Mass Inventory Fraction (2 R_c Exchange Volume)			Uniform-Concentration Inventory Fraction (^3H)		
		Unsaturated Zone	Saturated Alluvial/Volcanic Aquifer System	Saturated LCA	Unsaturated Zone	Saturated Alluvial/Volcanic Aquifer System	Saturated LCA
DOVEKIE	0.00051	1.0000	0.0000	0.0000	1.0000	0.0000	0.0000
DRAUGHTS	0.00384	0.9102	0.0898	0.0000	0.9875	0.0125	0.0000
DRILL (SOURCE-LOWER)	0.00009	1.0000	0.0000	0.0000	1.0000	0.0000	0.0000
DRILL (TARGET-UPPER)	0.00051	1.0000	0.0000	0.0000	1.0000	0.0000	0.0000
DRIVER	0.00051	1.0000	0.0000	0.0000	1.0000	0.0000	0.0000
DUB	0.00030	1.0000	0.0000	0.0000	1.0000	0.0000	0.0000
DUFFER	0.00051	1.0000	0.0000	0.0000	1.0000	0.0000	0.0000
DUMONT	0.00512	0.0000	1.0000	0.0000	0.0000	1.0000	0.0000
DUORO	0.00384	0.9288	0.0712	0.0000	0.9967	0.0033	0.0000
DUTCHESS	0.00051	1.0000	0.0000	0.0000	1.0000	0.0000	0.0000
EAGLE	0.00014	1.0000	0.0000	0.0000	1.0000	0.0000	0.0000
EBBTIDE	0.00051	1.0000	0.0000	0.0000	1.0000	0.0000	0.0000
EDAM	0.00512	0.9999	0.0000	0.0000	0.9992	0.0000	0.0008
EEL	0.00012	1.0000	0.0000	0.0000	1.0000	0.0000	0.0000
EFFENDI	0.00051	1.0000	0.0000	0.0000	1.0000	0.0000	0.0000
ELIDA	0.00051	1.0000	0.0000	0.0000	1.0000	0.0000	0.0000
ELKHART	0.00051	1.0000	0.0000	0.0000	1.0000	0.0000	0.0000
EMBUDO	0.00051	1.0000	0.0000	0.0000	1.0000	0.0000	0.0000
EMERSON	0.00051	1.0000	0.0000	0.0000	1.0000	0.0000	0.0000
ERMINE	0.00051	1.0000	0.0000	0.0000	1.0000	0.0000	0.0000
ESCABOSA	0.00512	0.0027	0.9973	0.0000	0.0000	1.0000	0.0000
ESROM	0.00512	0.0291	0.9709	0.0000	0.0000	1.0000	0.0000

Table C-3
Initial RST Fractions for Detonations in the Unsaturated Zone, Saturated Alluvial/Volcanic Aquifer System, and Saturated LCA Models
(Page 12 of 34)

Detonation Name [a]	Maximum Yield-Weighted Fraction of Total Inventory [b]	Uniform-Mass Inventory Fraction (2 R_c Exchange Volume)			Uniform-Concentration Inventory Fraction (^3H)		
		Unsaturated Zone	Saturated Alluvial/Volcanic Aquifer System	Saturated LCA	Unsaturated Zone	Saturated Alluvial/Volcanic Aquifer System	Saturated LCA
ESTACA	0.00051	1.0000	0.0000	0.0000	1.0000	0.0000	0.0000
FADE	0.00051	1.0000	0.0000	0.0000	1.0000	0.0000	0.0000
FAHADA	0.00051	1.0000	0.0000	0.0000	1.0000	0.0000	0.0000
FAJY	0.00384	0.7497	0.2503	0.0000	0.7100	0.2900	0.0000
FALLON	0.00512	0.8543	0.1457	0.0000	0.9978	0.0022	0.0000
FARALLONES	0.00384	0.0239	0.9761	0.0000	0.0000	1.0000	0.0000
FAWN	0.00051	1.0000	0.0000	0.0000	1.0000	0.0000	0.0000
FENTON	0.00004	1.0000	0.0000	0.0000	1.0000	0.0000	0.0000
FERRET	0.00051	1.0000	0.0000	0.0000	1.0000	0.0000	0.0000
FERRET PRIME	0.00051	1.0000	0.0000	0.0000	241.00	1.0000	0.0000
FILE	0.00051	1.0000	0.0000	0.0000	1.0000	0.0000	0.0000
FINFOOT	0.00051	1.0000	0.0000	0.0000	1.0000	0.0000	0.0000
FISHER	0.00034	1.0000	0.0000	0.0000	1.0000	0.0000	0.0000
FIZZ	0.00051	1.0000	0.0000	0.0000	1.0000	0.0000	0.0000
FLASK-GREEN	0.00269	0.2935	0.7065	0.0000	0.0000	1.0000	0.0000
FLASK-RED	<0.00000	1.0000	0.0000	0.0000	1.0000	0.0000	0.0000
FLASK-YELLOW	<0.00000	1.0000	0.0000	0.0000	1.0000	0.0000	0.0000
FLAX-BACKUP	0.00051	1.0000	0.0000	0.0000	1.0000	0.0000	0.0000
FLAX-SOURCE	0.00051	0.0000	1.0000	0.0000	0.0000	1.0000	0.0000
FLAX-TEST	0.00512	0.9984	0.0016	0.0000	0.9348	0.0652	0.0000
FLORA	0.00051	1.0000	0.0000	0.0000	1.0000	0.0000	0.0000
FLOTOST	0.00051	1.0000	0.0000	0.0000	1.0000	0.0000	0.0000

Table C-3
Initial RST Fractions for Detonations in the Unsaturated Zone, Saturated Alluvial/Volcanic Aquifer System, and Saturated LCA Models
(Page 13 of 34)

Detonation Name [a]	Maximum Yield-Weighted Fraction of Total Inventory [b]	Uniform-Mass Inventory Fraction (2 R_c Exchange Volume)			Uniform-Concentration Inventory Fraction (^3H)		
		Unsaturated Zone	Saturated Alluvial/Volcanic Aquifer System	Saturated LCA	Unsaturated Zone	Saturated Alluvial/Volcanic Aquifer System	Saturated LCA
FLOYDADA	0.00051	0.9141	0.0859	0.0000	0.9854	0.0146	0.0000
FOB-BLUE	0.00051	1.0000	0.0000	0.0000	1.0000	0.0000	0.0000
FOB-GREEN	0.00051	1.0000	0.0000	0.0000	1.0000	0.0000	0.0000
FOB-RED	0.00051	1.0000	0.0000	0.0000	1.0000	0.0000	0.0000
FORE	0.00512	0.7581	0.2419	0.0000	0.9189	0.0811	0.0000
FOREFOOT	0.00051	1.0000	0.0000	0.0000	1.0000	0.0000	0.0000
FOREST	0.00051	1.0000	0.0000	0.0000	1.0000	0.0000	0.0000
FREEZEOUT	0.00051	1.0000	0.0000	0.0000	1.0000	0.0000	0.0000
FRIJOLES-DEMING	0.00051	1.0000	0.0000	0.0000	1.0000	0.0000	0.0000
FRIJOLES-ESPUELA	0.00051	1.0000	0.0000	0.0000	1.0000	0.0000	0.0000
FRIJOLES-GUAJE	0.00051	1.0000	0.0000	0.0000	1.0000	0.0000	0.0000
FRIJOLES-PETACA	0.00051	1.0000	0.0000	0.0000	1.0000	0.0000	0.0000
FRISCO	0.00384	1.0000	0.0000	0.0000	0.9991	0.0009	0.0000
FUNNEL	0.00051	1.0000	0.0000	0.0000	1.0000	0.0000	0.0000
FUTTOCK	0.00051	1.0000	0.0000	0.0000	1.0000	0.0000	0.0000
GALENA-GREEN	0.00051	1.0000	0.0000	0.0000	1.0000	0.0000	0.0000
GALENA-ORANGE	0.00051	1.0000	0.0000	0.0000	1.0000	0.0000	0.0000
GALENA-YELLOW	0.00051	1.0000	0.0000	0.0000	1.0000	0.0000	0.0000
GARDEN	0.00051	1.0000	0.0000	0.0000	1.0000	0.0000	0.0000
GASCON	0.00384	0.0205	0.9795	0.0000	0.0000	1.0000	0.0000
GAZOOK	0.00051	1.0000	0.0000	0.0000	1.0000	0.0000	0.0000
GERBIL	0.00051	1.0000	0.0000	0.0000	1.0000	0.0000	0.0000

Table C-3
Initial RST Fractions for Detonations in the Unsaturated Zone, Saturated Alluvial/Volcanic Aquifer System, and Saturated LCA Models
(Page 14 of 34)

Detonation Name [a]	Maximum Yield-Weighted Fraction of Total Inventory [b]	Uniform-Mass Inventory Fraction (2 R_c Exchange Volume)			Uniform-Concentration Inventory Fraction (^{3}H)		
		Unsaturated Zone	Saturated Alluvial/Volcanic Aquifer System	Saturated LCA	Unsaturated Zone	Saturated Alluvial/Volcanic Aquifer System	Saturated LCA
GIBSON	0.00051	1.0000	0.0000	0.0000	1.0000	0.0000	0.0000
GILROY	0.00051	1.0000	0.0000	0.0000	1.0000	0.0000	0.0000
GLENCOE	0.00074	0.0000	1.0000	0.0000	0.0000	1.0000	0.0000
GORBEA	0.00384	0.9992	0.0008	0.0000	0.9978	0.0022	0.0000
GOUDA	0.00051	1.0000	0.0000	0.0000	1.0000	0.0000	0.0000
GOURD-AMBER	0.00051	1.0000	0.0000	0.0000	1.0000	0.0000	0.0000
GOURD-BROWN	0.00051	1.0000	0.0000	0.0000	1.0000	0.0000	0.0000
GRAPE A	0.00512	0.4450	0.5549	0.0002	0.0000	0.9992	0.0008
GRAPE B	0.00512	0.5566	0.4434	0.0000	0.2810	0.7190	0.0000
GREYS	0.00512	1.0000	0.0000	0.0000	1.0000	0.0000	0.0000
GROVE	0.00051	1.0000	0.0000	0.0000	1.0000	0.0000	0.0000
GRUNION	0.00051	1.0000	0.0000	0.0000	1.0000	0.0000	0.0000
GRUYERE	0.00051	1.0000	0.0000	0.0000	1.0000	0.0000	0.0000
GRUYERE-GRADINO	0.00051	1.0000	0.0000	0.0000	1.0000	0.0000	0.0000
GUANAY	0.00051	1.0000	0.0000	0.0000	1.0000	0.0000	0.0000
GUNDI	0.00051	1.0000	0.0000	0.0000	1.0000	0.0000	0.0000
GUNDI PRIME	0.00051	1.0000	0.0000	0.0000	272.00	1.0000	0.0000
HADDOCK	0.00051	1.0000	0.0000	0.0000	1.0000	0.0000	0.0000
HANDCAR	0.00031	1.0000	0.0000	0.0000	1.0000	0.0000	0.0000
HANDICAP	0.00051	1.0000	0.0000	0.0000	1.0000	0.0000	0.0000
HAPLOPAPPUS	0.00051	1.0000	0.0000	0.0000	1.0000	0.0000	0.0000
HAREBELL	0.00512	0.7678	0.2322	0.0000	0.9151	0.0849	0.0000

Table C-3
Initial RST Fractions for Detonations in the Unsaturated Zone, Saturated Alluvial/Volcanic Aquifer System, and Saturated LCA Models
(Page 15 of 34)

Detonation Name [a]	Maximum Yield-Weighted Fraction of Total Inventory [b]	Uniform-Mass Inventory Fraction (2 R_c Exchange Volume)			Uniform-Concentration Inventory Fraction (^3H)		
		Unsaturated Zone	Saturated Alluvial/Volcanic Aquifer System	Saturated LCA	Unsaturated Zone	Saturated Alluvial/Volcanic Aquifer System	Saturated LCA
HARKEE	0.00051	1.0000	0.0000	0.0000	1.0000	0.0000	0.0000
HARLINGEN-A	0.00051	1.0000	0.0000	0.0000	1.0000	0.0000	0.0000
HARLINGEN-B	0.00051	1.0000	0.0000	0.0000	1.0000	0.0000	0.0000
HATCHET	0.00051	1.0000	0.0000	0.0000	1.0000	0.0000	0.0000
HATCHIE	0.00051	1.0000	0.0000	0.0000	1.0000	0.0000	0.0000
HAVARTI	0.00051	1.0000	0.0000	0.0000	1.0000	0.0000	0.0000
HAYMAKER	0.00172	0.9720	0.0280	0.0000	0.8065	0.1935	0.0000
HAZEBROOK-APRICOT	0.00051	1.0000	0.0000	0.0000	1.0000	0.0000	0.0000
HAZEBROOK-CHECKERBERRY	0.00051	1.0000	0.0000	0.0000	1.0000	0.0000	0.0000
HAZEBROOK-EMERALD	0.00051	1.0000	0.0000	0.0000	1.0000	0.0000	0.0000
HEARTS	0.00359	0.0000	1.0000	0.0000	0.0000	1.0000	0.0000
HEILMAN	0.00051	1.0000	0.0000	0.0000	1.0000	0.0000	0.0000
HERMOSA	0.00384	0.0304	0.9696	0.0000	0.0000	1.0000	0.0000
HOD-A (GREEN)	0.00051	1.0000	0.0000	0.0000	241.00	1.0000	0.0000
HOD-B (RED)	0.00051	1.0000	0.0000	0.0000	265.00	1.0000	0.0000
HOD-C (BLUE)	0.00051	1.0000	0.0000	0.0000	101.00	1.0000	0.0000
HOGNOSE	0.00051	1.0000	0.0000	0.0000	1.0000	0.0000	0.0000
HOOK	0.00051	1.0000	0.0000	0.0000	1.0000	0.0000	0.0000
HOOPOE	0.00051	1.0000	0.0000	0.0000	1.0000	0.0000	0.0000
HOOSIC	0.00009	1.0000	0.0000	0.0000	1.0000	0.0000	0.0000
HOREHOUND	0.00051	1.0000	0.0000	0.0000	1.0000	0.0000	0.0000
HOSPAH	0.00051	1.0000	0.0000	0.0000	1.0000	0.0000	0.0000

Table C-3
Initial RST Fractions for Detonations in the Unsaturated Zone, Saturated Alluvial/Volcanic Aquifer System, and Saturated LCA Models
(Page 16 of 34)

Detonation Name [a]	Maximum Yield-Weighted Fraction of Total Inventory [b]	Uniform-Mass Inventory Fraction (2 R_c Exchange Volume)			Uniform-Concentration Inventory Fraction (^3H)		
		Unsaturated Zone	Saturated Alluvial/Volcanic Aquifer System	Saturated LCA	Unsaturated Zone	Saturated Alluvial/Volcanic Aquifer System	Saturated LCA
HUDSON	0.00051	1.0000	0.0000	0.0000	1.0000	0.0000	0.0000
HULA	0.00051	1.0000	0.0000	0.0000	1.0000	0.0000	0.0000
HULSEA	0.00051	1.0000	0.0000	0.0000	1.0000	0.0000	0.0000
HUPMOBILE	0.00019	1.0000	0.0000	0.0000	1.0000	0.0000	0.0000
HURON KING	0.00051	1.0000	0.0000	0.0000	320.00	1.0000	0.0000
HUTCH	0.00512	0.6590	0.3410	0.0000	0.5041	0.4959	0.0000
HUTIA	0.00051	1.0000	0.0000	0.0000	1.0000	0.0000	0.0000
HYRAX	0.00051	1.0000	0.0000	0.0000	1.0000	0.0000	0.0000
ICEBERG	0.00384	0.0000	1.0000	0.0000	0.0000	1.0000	0.0000
ILDRIM	0.00512	0.9299	0.0701	0.0000	0.9963	0.0037	0.0000
IMP	0.00051	1.0000	0.0000	0.0000	1.0000	0.0000	0.0000
INGOT	0.00384	0.8278	0.1722	0.0000	0.9903	0.0097	0.0000
IPECAC-A	0.00051	1.0000	0.0000	0.0000	1.0000	0.0000	0.0000
IPECAC-B	0.00051	1.0000	0.0000	0.0000	1.0000	0.0000	0.0000
ISLAY	0.00051	1.0000	0.0000	0.0000	1.0000	0.0000	0.0000
IZZER	0.00051	1.0000	0.0000	0.0000	1.0000	0.0000	0.0000
JACKPOTS	0.00051	1.0000	0.0000	0.0000	1.0000	0.0000	0.0000
JAL	0.00051	1.0000	0.0000	0.0000	1.0000	0.0000	0.0000
JARA	0.00051	1.0000	0.0000	0.0000	1.0000	0.0000	0.0000
JARLSBERG	0.00051	1.0000	0.0000	0.0000	1.0000	0.0000	0.0000
JERBOA	0.00051	1.0000	0.0000	0.0000	1.0000	0.0000	0.0000
JIB	0.00051	1.0000	0.0000	0.0000	1.0000	0.0000	0.0000

Table C-3
Initial RST Fractions for Detonations in the Unsaturated Zone, Saturated Alluvial/Volcanic Aquifer System, and Saturated LCA Models
(Page 17 of 34)

Detonation Name [a]	Maximum Yield-Weighted Fraction of Total Inventory [b]	Uniform-Mass Inventory Fraction (2 R_c Exchange Volume)			Uniform-Concentration Inventory Fraction (^3H)		
		Unsaturated Zone	Saturated Alluvial/Volcanic Aquifer System	Saturated LCA	Unsaturated Zone	Saturated Alluvial/Volcanic Aquifer System	Saturated LCA
JICARILLA	0.00051	1.0000	0.0000	0.0000	1.0000	0.0000	0.0000
JORNADA	0.00356	0.0000	1.0000	0.0000	0.0000	1.0000	0.0000
KANKAKEE	0.00512	1.0000	0.0000	0.0000	1.0000	0.0000	0.0000
KARA	0.00051	1.0000	0.0000	0.0000	1.0000	0.0000	0.0000
KARAB	0.00051	1.0000	0.0000	0.0000	1.0000	0.0000	0.0000
KASHAN	0.00051	1.0000	0.0000	0.0000	1.0000	0.0000	0.0000
KAWEAH	0.00008	1.0000	0.0000	0.0000	1.0000	0.0000	0.0000
KAWICH A-BLUE	0.00051	1.0000	0.0000	0.0000	384.00	1.0000	0.0000
KAWICH A-WHITE	0.00051	1.0000	0.0000	0.0000	369.00	1.0000	0.0000
KAWICH-BLACK	0.00051	1.0000	0.0000	0.0000	1.0000	0.0000	0.0000
KAWICH-RED	0.00051	1.0000	0.0000	0.0000	1.0000	0.0000	0.0000
KEEL	0.00051	1.0000	0.0000	0.0000	1.0000	0.0000	0.0000
KEELSON	0.00512	0.0004	0.9996	0.0000	0.0000	1.0000	0.0000
KENNEBEC	0.00051	1.0000	0.0000	0.0000	1.0000	0.0000	0.0000
KERMET	0.00051	1.0000	0.0000	0.0000	1.0000	0.0000	0.0000
KESTI	0.00051	1.0000	0.0000	0.0000	1.0000	0.0000	0.0000
KESTREL	0.00051	0.8302	0.1698	0.0000	0.9937	0.0063	0.0000
KHAKI	0.00051	1.0000	0.0000	0.0000	1.0000	0.0000	0.0000
KINIBITO	0.00384	0.0731	0.9269	0.0000	0.0000	1.0000	0.0000
KLICKITAT	0.00179	0.9970	0.0000	0.0030	0.9926	0.0000	0.0074
KLOSTER	0.00384	0.7699	0.2301	0.0000	0.8381	0.1619	0.0000
KNIFE A	0.00051	1.0000	0.0000	0.0000	332.00	1.0000	0.0000

Table C-3
Initial RST Fractions for Detonations in the Unsaturated Zone, Saturated Alluvial/Volcanic Aquifer System, and Saturated LCA Models
(Page 18 of 34)

Detonation Name [a]	Maximum Yield-Weighted Fraction of Total Inventory [b]	Uniform-Mass Inventory Fraction (2 R_c Exchange Volume)			Uniform-Concentration Inventory Fraction (^3H)		
		Unsaturated Zone	Saturated Alluvial/Volcanic Aquifer System	Saturated LCA	Unsaturated Zone	Saturated Alluvial/Volcanic Aquifer System	Saturated LCA
KNIFE B	0.00051	1.0000	0.0000	0.0000	363.00	1.0000	0.0000
KNIFE C	0.00051	1.0000	0.0000	0.0000	301.00	1.0000	0.0000
KNOX	0.00512	0.0000	1.0000	0.0000	0.0000	1.0000	0.0000
KOHOCTON	0.00051	1.0000	0.0000	0.0000	1.0000	0.0000	0.0000
KOOTANAI	0.00051	1.0000	0.0000	0.0000	1.0000	0.0000	0.0000
KRYDDOST	0.00051	1.0000	0.0000	0.0000	1.0000	0.0000	0.0000
KYACK-A	0.00051	1.0000	0.0000	0.0000	1.0000	0.0000	0.0000
KYACK-B	0.00051	1.0000	0.0000	0.0000	1.0000	0.0000	0.0000
LABAN	0.00051	1.0000	0.0000	0.0000	1.0000	0.0000	0.0000
LABIS	0.00064	1.0000	0.0000	0.0000	1.0000	0.0000	0.0000
LAGOON	0.00051	1.0000	0.0000	0.0000	1.0000	0.0000	0.0000
LAGUNA	0.00512	0.6080	0.3920	0.0000	0.7949	0.2051	0.0000
LAMPBLACK	0.00512	0.5925	0.3941	0.0134	0.0000	0.9913	0.0087
LANPHER	0.00512	0.0000	1.0000	0.0000	0.0000	1.0000	0.0000
LAREDO	0.00384	1.0000	0.0000	0.0000	1.0000	0.0000	0.0000
LATIR	0.00512	0.0000	1.0000	0.0000	0.0000	1.0000	0.0000
LEDOUX	0.00051	1.0000	0.0000	0.0000	1.0000	0.0000	0.0000
LEXINGTON	0.00051	1.0000	0.0000	0.0000	1.0000	0.0000	0.0000
LEYDEN	0.00051	1.0000	0.0000	0.0000	1.0000	0.0000	0.0000
LIME	0.00051	0.7687	0.2313	0.0000	0.8700	0.1300	0.0000
LINKS	0.00051	1.0000	0.0000	0.0000	1.0000	0.0000	0.0000
LIPTAUER	0.00384	1.0000	0.0000	0.0000	1.0000	0.0000	0.0000

Table C-3
Initial RST Fractions for Detonations in the Unsaturated Zone, Saturated Alluvial/Volcanic Aquifer System, and Saturated LCA Models
(Page 19 of 34)

Detonation Name [a]	Maximum Yield-Weighted Fraction of Total Inventory [b]	Uniform-Mass Inventory Fraction (2 R_c Exchange Volume)			Uniform-Concentration Inventory Fraction (^{3}H)		
		Unsaturated Zone	Saturated Alluvial/Volcanic Aquifer System	Saturated LCA	Unsaturated Zone	Saturated Alluvial/Volcanic Aquifer System	Saturated LCA
LONGCHAMPS	0.00051	1.0000	0.0000	0.0000	1.0000	0.0000	0.0000
LOVAGE	0.00051	1.0000	0.0000	0.0000	1.0000	0.0000	0.0000
LOWBALL	0.00384	0.1065	0.8935	0.0000	0.0000	1.0000	0.0000
LUBBOCK	0.00384	0.5611	0.4389	0.0000	0.0795	0.9205	0.0000
LUNA	<0.00000	1.0000	0.0000	0.0000	1.0000	0.0000	0.0000
MACKEREL	0.00051	1.0000	0.0000	0.0000	1.0000	0.0000	0.0000
MAD	0.00001	1.0000	0.0000	0.0000	1.0000	0.0000	0.0000
MALLET	0.00051	1.0000	0.0000	0.0000	1.0000	0.0000	0.0000
MANATEE	0.00051	1.0000	0.0000	0.0000	1.0000	0.0000	0.0000
MANTECA	0.00384	0.9352	0.0648	0.0000	0.7926	0.2074	0.0000
MANZANAS	0.00051	1.0000	0.0000	0.0000	1.0000	0.0000	0.0000
MARIBO	0.00051	1.0000	0.0000	0.0000	1.0000	0.0000	0.0000
MARSH	0.00051	0.9654	0.0346	0.0000	0.8738	0.1262	0.0000
MARSILLY	0.00384	0.0000	1.0000	0.0000	0.0000	1.0000	0.0000
MARVEL	0.00006	1.0000	0.0000	0.0000	1.0000	0.0000	0.0000
MATACO	0.00051	1.0000	0.0000	0.0000	1.0000	0.0000	0.0000
MAUVE	0.00051	1.0000	0.0000	0.0000	1.0000	0.0000	0.0000
MAXWELL	0.00051	1.0000	0.0000	0.0000	1.0000	0.0000	0.0000
MEMORY	0.00051	1.0000	0.0000	0.0000	1.0000	0.0000	0.0000
MERIDA	0.00051	1.0000	0.0000	0.0000	1.0000	0.0000	0.0000
MERLIN	0.00026	1.0000	0.0000	0.0000	1.0000	0.0000	0.0000
MERRIMAC	0.00512	0.8710	0.1290	0.0000	0.9974	0.0026	0.0000

Table C-3
Initial RST Fractions for Detonations in the Unsaturated Zone, Saturated Alluvial/Volcanic Aquifer System, and Saturated LCA Models
(Page 20 of 34)

Detonation Name [a]	Maximum Yield-Weighted Fraction of Total Inventory [b]	Uniform-Mass Inventory Fraction (2 R_c Exchange Volume)			Uniform-Concentration Inventory Fraction (^3H)		
		Unsaturated Zone	Saturated Alluvial/Volcanic Aquifer System	Saturated LCA	Unsaturated Zone	Saturated Alluvial/Volcanic Aquifer System	Saturated LCA
MESCALERO	0.00051	1.0000	0.0000	0.0000	1.0000	0.0000	0.0000
MESITA	0.00051	1.0000	0.0000	0.0000	1.0000	0.0000	0.0000
METROPOLIS	0.00384	0.5519	0.4481	0.0000	0.0000	1.0000	0.0000
MICKEY	0.00512	0.9498	0.0416	0.0086	0.9805	0.0039	0.0155
MIDLAND	0.00384	0.9372	0.0628	0.0000	0.9897	0.0103	0.0000
MIERA	0.00512	0.5345	0.4655	0.0000	0.2362	0.7638	0.0000
MINERO	0.00051	1.0000	0.0000	0.0000	1.0000	0.0000	0.0000
MINIATA	0.00213	0.2573	0.7427	0.0000	0.0000	1.0000	0.0000
MINK	0.00051	1.0000	0.0000	0.0000	1.0000	0.0000	0.0000
MINNOW	0.00051	1.0000	0.0000	0.0000	1.0000	0.0000	0.0000
MISSISSIPPI	0.00294	0.8025	0.1975	0.0000	0.9468	0.0532	0.0000
MIZZEN	0.00512	0.0422	0.9578	0.0000	0.0000	1.0000	0.0000
MOA	0.00051	1.0000	0.0000	0.0000	1.0000	0.0000	0.0000
MOGOLLON	0.00051	1.0000	0.0000	0.0000	1.0000	0.0000	0.0000
MONAHANS-A	0.00051	1.0000	0.0000	0.0000	1.0000	0.0000	0.0000
MONAHANS-B	0.00051	1.0000	0.0000	0.0000	1.0000	0.0000	0.0000
MONERO	0.00051	0.3337	0.6663	0.0000	0.0000	1.0000	0.0000
MONTEREY	0.00384	0.9404	0.0596	0.0000	0.9928	0.0072	0.0000
MORRONES	0.00512	0.6859	0.3141	0.0000	0.5690	0.4310	0.0000
MUDPACK	0.00007	1.0000	0.0000	0.0000	1.0000	0.0000	0.0000
MUGGINS	0.00051	1.0000	0.0000	0.0000	1.0000	0.0000	0.0000
MULESHOE	0.00051	1.0000	0.0000	0.0000	1.0000	0.0000	0.0000

Table C-3
Initial RST Fractions for Detonations in the Unsaturated Zone, Saturated Alluvial/Volcanic Aquifer System, and Saturated LCA Models
(Page 21 of 34)

Detonation Name [a]	Maximum Yield-Weighted Fraction of Total Inventory [b]	Uniform-Mass Inventory Fraction (2 R_c Exchange Volume)			Uniform-Concentration Inventory Fraction (^{3}H)		
		Unsaturated Zone	Saturated Alluvial/Volcanic Aquifer System	Saturated LCA	Unsaturated Zone	Saturated Alluvial/Volcanic Aquifer System	Saturated LCA
MULLET	0.00051	1.0000	0.0000	0.0000	1.0000	0.0000	0.0000
MUNDO	0.00384	0.7073	0.2830	0.0097	0.3725	0.6176	0.0099
MUSCOVY	0.00051	1.0000	0.0000	0.0000	1.0000	0.0000	0.0000
MUSHROOM	0.00051	1.0000	0.0000	0.0000	1.0000	0.0000	0.0000
MUSTANG	0.00051	1.0000	0.0000	0.0000	1.0000	0.0000	0.0000
NAMA-AMARYLIS	0.00051	1.0000	0.0000	0.0000	1.0000	0.0000	0.0000
NAMA-MEPHISTO	0.00051	1.0000	0.0000	0.0000	1.0000	0.0000	0.0000
NARRAGUAGUS	0.00051	1.0000	0.0000	0.0000	1.0000	0.0000	0.0000
NASH	0.00100	1.0000	0.0000	0.0000	1.0000	0.0000	0.0000
NATCHES	0.00051	1.0000	0.0000	0.0000	1.0000	0.0000	0.0000
NATOMA	0.00051	1.0000	0.0000	0.0000	1.0000	0.0000	0.0000
NAVATA	0.00051	1.0000	0.0000	0.0000	1.0000	0.0000	0.0000
NESSEL	0.00384	0.8545	0.1455	0.0000	0.6108	0.3892	0.0000
NEWARK	0.00051	1.0000	0.0000	0.0000	1.0000	0.0000	0.0000
NIGHTINGALE	0.00384	1.0000	0.0000	0.0000	1.0000	0.0000	0.0000
NIPPER	0.00051	1.0000	0.0000	0.0000	1.0000	0.0000	0.0000
NIZA	0.00051	1.0000	0.0000	0.0000	1.0000	0.0000	0.0000
NOGGIN	0.00512	0.3003	0.6997	0.0000	0.0000	1.0000	0.0000
NOOR	0.00512	1.0000	0.0000	0.0000	1.0000	0.0000	0.0000
NORBO	0.00051	1.0000	0.0000	0.0000	1.0000	0.0000	0.0000
NORMANNA	0.00051	1.0000	0.0000	0.0000	1.0000	0.0000	0.0000
NUMBAT	0.00051	1.0000	0.0000	0.0000	1.0000	0.0000	0.0000

Table C-3
Initial RST Fractions for Detonations in the Unsaturated Zone, Saturated Alluvial/Volcanic Aquifer System, and Saturated LCA Models
(Page 22 of 34)

Detonation Name [a]	Maximum Yield-Weighted Fraction of Total Inventory [b]	Uniform-Mass Inventory Fraction (2 R_c Exchange Volume)			Uniform-Concentration Inventory Fraction (^3H)		
		Unsaturated Zone	Saturated Alluvial/Volcanic Aquifer System	Saturated LCA	Unsaturated Zone	Saturated Alluvial/Volcanic Aquifer System	Saturated LCA
OAKLAND	0.00051	1.0000	0.0000	0.0000	1.0000	0.0000	0.0000
OARLOCK	0.00051	1.0000	0.0000	0.0000	1.0000	0.0000	0.0000
OBAR	0.00512	0.5283	0.4717	0.0000	0.2179	0.7821	0.0000
OCATE	0.00051	1.0000	0.0000	0.0000	1.0000	0.0000	0.0000
OCHRE	0.00051	1.0000	0.0000	0.0000	1.0000	0.0000	0.0000
OCONTO	0.00027	1.0000	0.0000	0.0000	1.0000	0.0000	0.0000
OFFSHORE	0.00384	0.8687	0.1313	0.0000	0.9815	0.0185	0.0000
ONAJA	0.00051	1.0000	0.0000	0.0000	1.0000	0.0000	0.0000
ORGANDY	0.00051	1.0000	0.0000	0.0000	1.0000	0.0000	0.0000
ORKNEY	0.00051	1.0000	0.0000	0.0000	1.0000	0.0000	0.0000
OSCURO	0.00512	0.2648	0.7352	0.0000	0.0000	1.0000	0.0000
OTERO	<0.00000	1.0000	0.0000	0.0000	1.0000	0.0000	0.0000
PACA	0.00051	1.0000	0.0000	0.0000	1.0000	0.0000	0.0000
PACKARD	0.00026	1.0000	0.0000	0.0000	1.0000	0.0000	0.0000
PACKRAT	0.00051	1.0000	0.0000	0.0000	1.0000	0.0000	0.0000
PAISANO	0.00051	1.0000	0.0000	0.0000	1.0000	0.0000	0.0000
PAJARA	0.00051	1.0000	0.0000	0.0000	1.0000	0.0000	0.0000
PALISADE-1	0.00051	1.0000	0.0000	0.0000	1.0000	0.0000	0.0000
PALISADE-2	0.00051	1.0000	0.0000	0.0000	1.0000	0.0000	0.0000
PALISADE-3	0.00051	1.0000	0.0000	0.0000	1.0000	0.0000	0.0000
PALIZA	0.00384	0.8258	0.1742	0.0000	0.9651	0.0349	0.0000
PAMPAS	0.00024	1.0000	0.0000	0.0000	1.0000	0.0000	0.0000

Table C-3
Initial RST Fractions for Detonations in the Unsaturated Zone, Saturated Alluvial/Volcanic Aquifer System, and Saturated LCA Models
(Page 23 of 34)

Detonation Name [a]	Maximum Yield-Weighted Fraction of Total Inventory [b]	Uniform-Mass Inventory Fraction (2 R_c Exchange Volume)			Uniform-Concentration Inventory Fraction (^3H)		
		Unsaturated Zone	Saturated Alluvial/Volcanic Aquifer System	Saturated LCA	Unsaturated Zone	Saturated Alluvial/Volcanic Aquifer System	Saturated LCA
PANAMINT	0.00051	0.9516	0.0484	0.0000	0.9723	0.0277	0.0000
PANCHUELA	0.00051	1.0000	0.0000	0.0000	1.0000	0.0000	0.0000
PAR	0.00097	1.0000	0.0000	0.0000	1.0000	0.0000	0.0000
PARNASSIA	0.00051	1.0000	0.0000	0.0000	1.0000	0.0000	0.0000
PARROT	0.00003	1.0000	0.0000	0.0000	1.0000	0.0000	0.0000
PASCAL-A	0.00051	1.0000	0.0000	0.0000	1.0000	0.0000	0.0000
PASCAL-B	0.00051	1.0000	0.0000	0.0000	1.0000	0.0000	0.0000
PASCAL-C	0.00051	1.0000	0.0000	0.0000	1.0000	0.0000	0.0000
PASSAIC	0.00051	1.0000	0.0000	0.0000	1.0000	0.0000	0.0000
PEBA	0.00051	1.0000	0.0000	0.0000	1.0000	0.0000	0.0000
PEDERNAL	0.00051	1.0000	0.0000	0.0000	1.0000	0.0000	0.0000
PEKAN	0.00051	1.0000	0.0000	0.0000	1.0000	0.0000	0.0000
PENASCO	0.00051	1.0000	0.0000	0.0000	1.0000	0.0000	0.0000
PERA	0.00051	1.0000	0.0000	0.0000	1.0000	0.0000	0.0000
PERSIMMON	0.00051	1.0000	0.0000	0.0000	1.0000	0.0000	0.0000
PETREL	0.00003	1.0000	0.0000	0.0000	1.0000	0.0000	0.0000
PICCALILLI	0.00512	0.9107	0.0893	0.0000	0.9850	0.0150	0.0000
PIKE	0.00051	1.0000	0.0000	0.0000	1.0000	0.0000	0.0000
PINEAU	0.00051	1.0000	0.0000	0.0000	1.0000	0.0000	0.0000
PINEDROPS-BAYOU	0.00051	1.0000	0.0000	0.0000	1.0000	0.0000	0.0000
PINEDROPS-SLOAT	0.00051	1.0000	0.0000	0.0000	1.0000	0.0000	0.0000
PINEDROPS-TAWNY	0.00051	1.0000	0.0000	0.0000	1.0000	0.0000	0.0000

Table C-3
Initial RST Fractions for Detonations in the Unsaturated Zone, Saturated Alluvial/Volcanic Aquifer System, and Saturated LCA Models
(Page 24 of 34)

Detonation Name [a]	Maximum Yield-Weighted Fraction of Total Inventory [b]	Uniform-Mass Inventory Fraction (2 R_c Exchange Volume)			Uniform-Concentration Inventory Fraction (^3H)		
		Unsaturated Zone	Saturated Alluvial/Volcanic Aquifer System	Saturated LCA	Unsaturated Zone	Saturated Alluvial/Volcanic Aquifer System	Saturated LCA
PIPEFISH	0.00051	1.0000	0.0000	0.0000	1.0000	0.0000	0.0000
PIRANHA	0.00512	0.3805	0.6195	0.0000	0.0000	1.0000	0.0000
PITON-A	0.00051	1.0000	0.0000	0.0000	1.0000	0.0000	0.0000
PITON-B	0.00051	1.0000	0.0000	0.0000	1.0000	0.0000	0.0000
PITON-C	0.00051	1.0000	0.0000	0.0000	1.0000	0.0000	0.0000
PLAID II	0.00051	1.0000	0.0000	0.0000	269.00	1.0000	0.0000
PLANER	0.00051	1.0000	0.0000	0.0000	1.0000	0.0000	0.0000
PLATYPUS	0.00051	1.0000	0.0000	0.0000	1.0000	0.0000	0.0000
PLAYER	0.00051	1.0000	0.0000	0.0000	1.0000	0.0000	0.0000
PLEASANT	0.00051	1.0000	0.0000	0.0000	1.0000	0.0000	0.0000
PLIERS	0.00051	1.0000	0.0000	0.0000	1.0000	0.0000	0.0000
PLOMO	0.00051	1.0000	0.0000	0.0000	1.0000	0.0000	0.0000
POD-A	0.00011	1.0000	0.0000	0.0000	1.0000	0.0000	0.0000
POD-B	0.00011	1.0000	0.0000	0.0000	1.0000	0.0000	0.0000
POD-C	0.00011	1.0000	0.0000	0.0000	1.0000	0.0000	0.0000
POD-D	0.00011	1.0000	0.0000	0.0000	1.0000	0.0000	0.0000
POLKA	0.00051	1.0000	0.0000	0.0000	1.0000	0.0000	0.0000
POLYGONUM	0.00051	1.0000	0.0000	0.0000	1.0000	0.0000	0.0000
POMMARD	0.00004	1.0000	0.0000	0.0000	1.0000	0.0000	0.0000
PONGEE	0.00051	1.0000	0.0000	0.0000	1.0000	0.0000	0.0000
PONIL	0.00051	1.0000	0.0000	0.0000	1.0000	0.0000	0.0000
PORTMANTEAU	0.00512	0.1855	0.8145	0.0000	0.0000	1.0000	0.0000

Table C-3
Initial RST Fractions for Detonations in the Unsaturated Zone, Saturated Alluvial/Volcanic Aquifer System, and Saturated LCA Models
(Page 25 of 34)

Detonation Name [a]	Maximum Yield-Weighted Fraction of Total Inventory [b]	Uniform-Mass Inventory Fraction (2 R_c Exchange Volume)			Uniform-Concentration Inventory Fraction (^3H)		
		Unsaturated Zone	Saturated Alluvial/Volcanic Aquifer System	Saturated LCA	Unsaturated Zone	Saturated Alluvial/Volcanic Aquifer System	Saturated LCA
PORTOLA	0.00051	1.0000	0.0000	0.0000	1.0000	0.0000	0.0000
PORTOLA-LARKIN	0.00051	1.0000	0.0000	0.0000	1.0000	0.0000	0.0000
PORTULACA	0.00512	0.9855	0.0145	0.0000	0.8589	0.1411	0.0000
POTRERO	0.00051	1.0000	0.0000	0.0000	1.0000	0.0000	0.0000
POTRILLO	0.00512	0.4036	0.5964	0.0000	0.0000	0.9998	0.0002
PRATT	0.00051	1.0000	0.0000	0.0000	1.0000	0.0000	0.0000
PRESIDIO	0.00051	1.0000	0.0000	0.0000	1.0000	0.0000	0.0000
PUCE	0.00051	0.5379	0.4621	0.0000	0.8503	0.1497	0.0000
PUDDLE	0.00051	1.0000	0.0000	0.0000	1.0000	0.0000	0.0000
PURPLE	0.00051	1.0000	0.0000	0.0000	1.0000	0.0000	0.0000
PUYE	0.00051	0.9625	0.0375	0.0000	0.7913	0.2087	0.0000
PYRAMID	0.00384	0.3751	0.6249	0.0000	0.0000	1.0000	0.0000
QUARGEL	0.00384	0.4578	0.5422	0.0000	0.0000	1.0000	0.0000
QUESO	0.00051	1.0000	0.0000	0.0000	1.0000	0.0000	0.0000
QUINELLA	0.00384	0.0398	0.9602	0.0000	0.0000	1.0000	0.0000
RACCOON	0.00051	1.0000	0.0000	0.0000	1.0000	0.0000	0.0000
RACK	0.00051	1.0000	0.0000	0.0000	1.0000	0.0000	0.0000
RARITAN	0.00051	1.0000	0.0000	0.0000	1.0000	0.0000	0.0000
REBLOCHON	0.00384	0.0000	1.0000	0.0000	0.0000	1.0000	0.0000
REDMUD	0.00051	1.0000	0.0000	0.0000	1.0000	0.0000	0.0000
REO	0.00051	1.0000	0.0000	0.0000	1.0000	0.0000	0.0000
RHYOLITE	0.00384	1.0000	0.0000	0.0000	1.0000	0.0000	0.0000

Table C-3
Initial RST Fractions for Detonations in the Unsaturated Zone, Saturated Alluvial/Volcanic Aquifer System, and Saturated LCA Models
(Page 26 of 34)

Detonation Name [a]	Maximum Yield-Weighted Fraction of Total Inventory [b]	Uniform-Mass Inventory Fraction (2 R_c Exchange Volume)			Uniform-Concentration Inventory Fraction (^3H)		
		Unsaturated Zone	Saturated Alluvial/Volcanic Aquifer System	Saturated LCA	Unsaturated Zone	Saturated Alluvial/Volcanic Aquifer System	Saturated LCA
RIB	0.00051	1.0000	0.0000	0.0000	1.0000	0.0000	0.0000
RINGTAIL	0.00051	1.0000	0.0000	0.0000	1.0000	0.0000	0.0000
RIOLA	0.00003	1.0000	0.0000	0.0000	1.0000	0.0000	0.0000
RIVET I	0.00051	1.0000	0.0000	0.0000	152.00	1.0000	0.0000
RIVET II	0.00051	1.0000	0.0000	0.0000	198.00	1.0000	0.0000
RIVET III	0.00051	1.0000	0.0000	0.0000	274.00	1.0000	0.0000
RIVOLI	0.00051	1.0000	0.0000	0.0000	1.0000	0.0000	0.0000
ROANOKE	0.00051	1.0000	0.0000	0.0000	1.0000	0.0000	0.0000
ROMANO	0.00384	0.7439	0.2561	0.0000	0.9471	0.0529	0.0000
ROQUEFORT	0.00384	0.9524	0.0476	0.0000	0.9816	0.0184	0.0000
ROUSANNE	0.00384	0.3953	0.6047	0.0000	0.0000	1.0000	0.0000
ROVENA	0.00051	1.0000	0.0000	0.0000	1.0000	0.0000	0.0000
RUDDER	0.00384	0.0347	0.9653	0.0000	0.0000	1.0000	0.0000
RUMMY	0.00384	0.0000	1.0000	0.0000	0.0000	1.0000	0.0000
RUSSET	0.00051	1.0000	0.0000	0.0000	1.0000	0.0000	0.0000
SABADO	0.00051	1.0000	0.0000	0.0000	1.0000	0.0000	0.0000
SACRAMENTO	0.00051	1.0000	0.0000	0.0000	1.0000	0.0000	0.0000
SAN JUAN	0.0	0.0000	0.0000	0.0000	71.00	0.0000	0.0000
SANDREEF	0.00384	0.0000	1.0000	0.0000	0.0000	1.0000	0.0000
SANTEE	0.00051	1.0000	0.0000	0.0000	1.0000	0.0000	0.0000
SAPELLO	0.00051	1.0000	0.0000	0.0000	1.0000	0.0000	0.0000
SAPPHO	0.00051	1.0000	0.0000	0.0000	1.0000	0.0000	0.0000

Table C-3
Initial RST Fractions for Detonations in the Unsaturated Zone, Saturated Alluvial/Volcanic Aquifer System, and Saturated LCA Models
(Page 27 of 34)

Detonation Name [a]	Maximum Yield-Weighted Fraction of Total Inventory [b]	Uniform-Mass Inventory Fraction (2 R_c Exchange Volume)			Uniform-Concentration Inventory Fraction (^3H)		
		Unsaturated Zone	Saturated Alluvial/Volcanic Aquifer System	Saturated LCA	Unsaturated Zone	Saturated Alluvial/Volcanic Aquifer System	Saturated LCA
SARDINE	0.00051	1.0000	0.0000	0.0000	1.0000	0.0000	0.0000
SATSOP	0.00051	1.0000	0.0000	0.0000	1.0000	0.0000	0.0000
SATZ	0.00051	1.0000	0.0000	0.0000	1.0000	0.0000	0.0000
SAXON	0.00003	1.0000	0.0000	0.0000	1.0000	0.0000	0.0000
SAZERAC	0.00051	1.0000	0.0000	0.0000	1.0000	0.0000	0.0000
SCANTLING	0.00384	0.0000	1.0000	0.0000	0.0000	1.0000	0.0000
SCAUP	0.00051	1.0000	0.0000	0.0000	1.0000	0.0000	0.0000
SCHELLBOURNE	0.00384	0.8817	0.1183	0.0000	0.9979	0.0021	0.0000
SCISSORS	0.00051	1.0000	0.0000	0.0000	1.0000	0.0000	0.0000
SCREAMER	0.00051	1.0000	0.0000	0.0000	1.0000	0.0000	0.0000
SCREE-ACAJOU	0.00051	1.0000	0.0000	0.0000	1.0000	0.0000	0.0000
SCREE-ALHAMBRA	0.00051	1.0000	0.0000	0.0000	1.0000	0.0000	0.0000
SCREE-CHAMOIS	0.00051	1.0000	0.0000	0.0000	1.0000	0.0000	0.0000
SCUPPER	0.00051	0.7949	0.2051	0.0000	0.5627	0.4373	0.0000
SCUTTLE	0.00004	1.0000	0.0000	0.0000	1.0000	0.0000	0.0000
SEAFOAM	0.00051	1.0000	0.0000	0.0000	1.0000	0.0000	0.0000
SEAMOUNT	0.00051	1.0000	0.0000	0.0000	1.0000	0.0000	0.0000
SEAWEED B	0.00051	1.0000	0.0000	0.0000	119.00	1.0000	0.0000
SEAWEED-C	0.00051	1.0000	0.0000	0.0000	1.0000	0.0000	0.0000
SEAWEED-D	0.00051	1.0000	0.0000	0.0000	1.0000	0.0000	0.0000
SEAWEED-E	0.00051	1.0000	0.0000	0.0000	1.0000	0.0000	0.0000
SECO	0.00051	1.0000	0.0000	0.0000	1.0000	0.0000	0.0000

Table C-3
Initial RST Fractions for Detonations in the Unsaturated Zone, Saturated Alluvial/Volcanic Aquifer System, and Saturated LCA Models
(Page 28 of 34)

Detonation Name [a]	Maximum Yield-Weighted Fraction of Total Inventory [b]	Uniform-Mass Inventory Fraction (2 R_c Exchange Volume)			Uniform-Concentration Inventory Fraction (^3H)		
		Unsaturated Zone	Saturated Alluvial/Volcanic Aquifer System	Saturated LCA	Unsaturated Zone	Saturated Alluvial/Volcanic Aquifer System	Saturated LCA
SEERSUCKER	0.00051	1.0000	0.0000	0.0000	1.0000	0.0000	0.0000
SEPIA	0.00051	1.0000	0.0000	0.0000	1.0000	0.0000	0.0000
SEVILLA	0.00051	1.0000	0.0000	0.0000	1.0000	0.0000	0.0000
SEYVAL	0.00051	1.0000	0.0000	0.0000	1.0000	0.0000	0.0000
SHALLOWS	0.00051	1.0000	0.0000	0.0000	1.0000	0.0000	0.0000
SHAPER	0.00512	0.4298	0.5686	0.0016	0.0000	0.9981	0.0019
SHAVE	0.00051	1.0000	0.0000	0.0000	1.0000	0.0000	0.0000
SHREW	0.00051	1.0000	0.0000	0.0000	1.0000	0.0000	0.0000
SHUFFLE	0.00512	0.9868	0.0000	0.0132	0.9766	0.0000	0.0234
SIDECAR	0.00051	1.0000	0.0000	0.0000	1.0000	0.0000	0.0000
SIENNA	0.00051	1.0000	0.0000	0.0000	1.0000	0.0000	0.0000
SILENE	0.00051	1.0000	0.0000	0.0000	1.0000	0.0000	0.0000
SIMMS	0.00006	1.0000	0.0000	0.0000	1.0000	0.0000	0.0000
SNUBBER	0.00033	1.0000	0.0000	0.0000	1.0000	0.0000	0.0000
SOLANO	0.00051	1.0000	0.0000	0.0000	1.0000	0.0000	0.0000
SOLANUM	0.00051	1.0000	0.0000	0.0000	1.0000	0.0000	0.0000
SOLENDON	0.00051	1.0000	0.0000	0.0000	1.0000	0.0000	0.0000
SPAR	0.00051	1.0000	0.0000	0.0000	1.0000	0.0000	0.0000
SPIDER-A	0.00051	1.0000	0.0000	0.0000	1.0000	0.0000	0.0000
SPIDER-B	0.00051	1.0000	0.0000	0.0000	1.0000	0.0000	0.0000
SPOON	0.00051	1.0000	0.0000	0.0000	1.0000	0.0000	0.0000
SPRIT	0.00051	1.0000	0.0000	0.0000	1.0000	0.0000	0.0000

Table C-3
Initial RST Fractions for Detonations in the Unsaturated Zone, Saturated Alluvial/Volcanic Aquifer System, and Saturated LCA Models
(Page 29 of 34)

Detonation Name [a]	Maximum Yield-Weighted Fraction of Total Inventory [b]	Uniform-Mass Inventory Fraction (2 R_c Exchange Volume)			Uniform-Concentration Inventory Fraction (^3H)		
		Unsaturated Zone	Saturated Alluvial/Volcanic Aquifer System	Saturated LCA	Unsaturated Zone	Saturated Alluvial/Volcanic Aquifer System	Saturated LCA
SPUD	0.00051	1.0000	0.0000	0.0000	1.0000	0.0000	0.0000
ST. LAWRENCE	0.00051	1.0000	0.0000	0.0000	166.00	1.0000	0.0000
STACCATO	0.00512	0.9692	0.0308	0.0000	0.9988	0.0012	0.0000
STANLEY	0.00512	0.8162	0.1838	0.0000	0.9326	0.0674	0.0000
STANYAN	0.00512	0.3717	0.6283	0.0000	0.0000	1.0000	0.0000
STARWORT	0.00230	0.2492	0.7508	0.0000	0.0000	1.0000	0.0000
STILLWATER	0.00008	1.0000	0.0000	0.0000	1.0000	0.0000	0.0000
STILT	0.00051	1.0000	0.0000	0.0000	1.0000	0.0000	0.0000
STOAT	0.00013	1.0000	0.0000	0.0000	1.0000	0.0000	0.0000
STODDARD	0.00079	0.9747	0.0253	0.0000	0.9816	0.0184	0.0000
STONES	0.00512	1.0000	0.0000	0.0000	0.9994	0.0006	0.0000
STRAIT	0.01280	0.0000	0.9990	0.0010	0.0000	0.9989	0.0011
STRAKE	0.00384	0.6685	0.3315	0.0000	0.5232	0.4768	0.0000
STURGEON	0.00051	1.0000	0.0000	0.0000	1.0000	0.0000	0.0000
STUTZ	0.00051	1.0000	0.0000	0.0000	1.0000	0.0000	0.0000
SUEDE	0.00051	1.0000	0.0000	0.0000	1.0000	0.0000	0.0000
SUNDOWN-A	0.00051	1.0000	0.0000	0.0000	1.0000	0.0000	0.0000
SUNDOWN-B	0.00051	1.0000	0.0000	0.0000	1.0000	0.0000	0.0000
SUTTER	0.00051	1.0000	0.0000	0.0000	1.0000	0.0000	0.0000
SWITCH	0.00008	1.0000	0.0000	0.0000	1.0000	0.0000	0.0000
TAHOKA	0.00384	0.0000	1.0000	0.0000	0.0000	1.0000	0.0000
TAJIQUE	0.00051	1.0000	0.0000	0.0000	1.0000	0.0000	0.0000

Table C-3
Initial RST Fractions for Detonations in the Unsaturated Zone, Saturated Alluvial/Volcanic Aquifer System, and Saturated LCA Models
(Page 30 of 34)

Detonation Name [a]	Maximum Yield-Weighted Fraction of Total Inventory [b]	Uniform-Mass Inventory Fraction (2 R_c Exchange Volume)			Uniform-Concentration Inventory Fraction (^3H)		
		Unsaturated Zone	Saturated Alluvial/Volcanic Aquifer System	Saturated LCA	Unsaturated Zone	Saturated Alluvial/Volcanic Aquifer System	Saturated LCA
TAJO	0.00384	0.8471	0.1529	0.0000	0.9816	0.0184	0.0000
TAN	0.00512	0.1767	0.8233	0.0000	0.0000	1.0000	0.0000
TANGERINE	0.00051	1.0000	0.0000	0.0000	1.0000	0.0000	0.0000
TANYA	0.00512	1.0000	0.0000	0.0000	1.0000	0.0000	0.0000
TAPESTRY	0.00051	1.0000	0.0000	0.0000	1.0000	0.0000	0.0000
TAPPER	0.00051	1.0000	0.0000	0.0000	1.0000	0.0000	0.0000
TARKO	0.00051	1.0000	0.0000	0.0000	1.0000	0.0000	0.0000
TAUNTON	0.00051	1.0000	0.0000	0.0000	1.0000	0.0000	0.0000
TECHADO	0.00384	0.2791	0.7209	0.0000	0.0000	1.0000	0.0000
TEE	0.00018	1.0000	0.0000	0.0000	1.0000	0.0000	0.0000
TEJON	0.00051	1.0000	0.0000	0.0000	1.0000	0.0000	0.0000
TELEME	0.00051	1.0000	0.0000	0.0000	1.0000	0.0000	0.0000
TEMESCAL	0.00051	1.0000	0.0000	0.0000	1.0000	0.0000	0.0000
TEMPLAR	0.00001	1.0000	0.0000	0.0000	1.0000	0.0000	0.0000
TENAJA	0.00051	1.0000	0.0000	0.0000	1.0000	0.0000	0.0000
TENDRAC	0.00051	1.0000	0.0000	0.0000	1.0000	0.0000	0.0000
TERN	0.00051	1.0000	0.0000	0.0000	1.0000	0.0000	0.0000
TERRINE-WHITE	0.00512	0.9338	0.0662	0.0000	0.9903	0.0097	0.0000
TERRINE-YELLOW	0.00512	1.0000	0.0000	0.0000	0.9994	0.0006	0.0000
TEXARKANA	0.00384	0.5913	0.4087	0.0000	0.3320	0.6680	0.0000
THISTLE	0.00512	0.4789	0.5211	0.0000	0.0000	1.0000	0.0000
THROW	0.00051	1.0000	0.0000	0.0000	1.0000	0.0000	0.0000

Table C-3
Initial RST Fractions for Detonations in the Unsaturated Zone, Saturated Alluvial/Volcanic Aquifer System, and Saturated LCA Models
(Page 31 of 34)

Detonation Name [a]	Maximum Yield-Weighted Fraction of Total Inventory [b]	Uniform-Mass Inventory Fraction (2 R_c Exchange Volume)			Uniform-Concentration Inventory Fraction (^3H)		
		Unsaturated Zone	Saturated Alluvial/Volcanic Aquifer System	Saturated LCA	Unsaturated Zone	Saturated Alluvial/Volcanic Aquifer System	Saturated LCA
TICKING	0.00051	1.0000	0.0000	0.0000	1.0000	0.0000	0.0000
TIJERAS	0.00512	0.3036	0.6964	0.0000	0.0000	1.0000	0.0000
TILCI	0.00384	0.7230	0.2770	0.0000	0.9597	0.0403	0.0000
TINDERBOX	0.00051	1.0000	0.0000	0.0000	1.0000	0.0000	0.0000
TIOGA	0.00051	1.0000	0.0000	0.0000	1.0000	0.0000	0.0000
TOMATO	0.00051	1.0000	0.0000	0.0000	1.0000	0.0000	0.0000
TOPGALLANT	0.00512	0.0000	1.0000	0.0000	0.0000	1.0000	0.0000
TOPMAST	0.00051	1.0000	0.0000	0.0000	1.0000	0.0000	0.0000
TORCH	0.00051	1.0000	0.0000	0.0000	1.0000	0.0000	0.0000
TORNERO	0.00051	1.0000	0.0000	0.0000	1.0000	0.0000	0.0000
TORNILLO	0.00001	1.0000	0.0000	0.0000	1.0000	0.0000	0.0000
TORRIDO	0.00512	0.9638	0.0000	0.0362	0.6396	0.0000	0.3604
TORTUGAS	0.00384	0.0000	1.0000	0.0000	0.0000	1.0000	0.0000
TOYAH	0.00051	1.0000	0.0000	0.0000	1.0000	0.0000	0.0000
TRANSOM	0.0	0.0000	0.0000	0.0000	0.0000	0.0000	0.0000
TRAVELER	0.00051	1.0000	0.0000	0.0000	1.0000	0.0000	0.0000
TREBBIANO	0.00051	1.0000	0.0000	0.0000	1.0000	0.0000	0.0000
TROGON	0.00051	1.0000	0.0000	0.0000	1.0000	0.0000	0.0000
TRUCHAS-CHACON	0.00051	1.0000	0.0000	0.0000	1.0000	0.0000	0.0000
TRUCHAS-CHAMISAL	0.00051	1.0000	0.0000	0.0000	1.0000	0.0000	0.0000
TRUCHAS-RODARTE	0.00051	1.0000	0.0000	0.0000	1.0000	0.0000	0.0000
TRUMBULL	0.00051	1.0000	0.0000	0.0000	1.0000	0.0000	0.0000

Table C-3
Initial RST Fractions for Detonations in the Unsaturated Zone, Saturated Alluvial/Volcanic Aquifer System, and Saturated LCA Models
(Page 32 of 34)

Detonation Name [a]	Maximum Yield-Weighted Fraction of Total Inventory [b]	Uniform-Mass Inventory Fraction (2 R_c Exchange Volume)			Uniform-Concentration Inventory Fraction (^3H)		
		Unsaturated Zone	Saturated Alluvial/Volcanic Aquifer System	Saturated LCA	Unsaturated Zone	Saturated Alluvial/Volcanic Aquifer System	Saturated LCA
TUB-A	0.00051	1.0000	0.0000	0.0000	1.0000	0.0000	0.0000
TUB-B	0.00051	1.0000	0.0000	0.0000	1.0000	0.0000	0.0000
TUB-C	0.00051	1.0000	0.0000	0.0000	1.0000	0.0000	0.0000
TUB-D	0.00051	1.0000	0.0000	0.0000	1.0000	0.0000	0.0000
TUB-F	0.00051	1.0000	0.0000	0.0000	1.0000	0.0000	0.0000
TULIA	0.00051	1.0000	0.0000	0.0000	0.9998	0.0002	0.0000
TULOSO	0.00051	1.0000	0.0000	0.0000	1.0000	0.0000	0.0000
TUNA	0.00051	1.0000	0.0000	0.0000	1.0000	0.0000	0.0000
TUN-A	0.00051	1.0000	0.0000	0.0000	1.0000	0.0000	0.0000
TUN-B	0.00051	1.0000	0.0000	0.0000	1.0000	0.0000	0.0000
TUN-C	0.00051	1.0000	0.0000	0.0000	1.0000	0.0000	0.0000
TUN-D	0.00051	1.0000	0.0000	0.0000	1.0000	0.0000	0.0000
TURF	0.00512	0.7328	0.2672	0.0000	0.9439	0.0561	0.0000
TURNSTONE	0.00051	1.0000	0.0000	0.0000	1.0000	0.0000	0.0000
TURQUOISE	0.00384	0.2075	0.7925	0.0000	0.0000	1.0000	0.0000
TWEED	0.00051	1.0000	0.0000	0.0000	1.0000	0.0000	0.0000
TYG-A	0.00051	1.0000	0.0000	0.0000	1.0000	0.0000	0.0000
TYG-B	0.00051	1.0000	0.0000	0.0000	1.0000	0.0000	0.0000
TYG-C	0.00051	1.0000	0.0000	0.0000	1.0000	0.0000	0.0000
TYG-D	0.00051	1.0000	0.0000	0.0000	1.0000	0.0000	0.0000
TYG-E	0.00051	1.0000	0.0000	0.0000	1.0000	0.0000	0.0000
TYG-F	0.00051	1.0000	0.0000	0.0000	1.0000	0.0000	0.0000

Table C-3
Initial RST Fractions for Detonations in the Unsaturated Zone, Saturated Alluvial/Volcanic Aquifer System, and Saturated LCA Models
(Page 33 of 34)

Detonation Name [a]	Maximum Yield-Weighted Fraction of Total Inventory [b]	Uniform-Mass Inventory Fraction (2 R_c Exchange Volume)			Uniform-Concentration Inventory Fraction (^3H)		
		Unsaturated Zone	Saturated Alluvial/Volcanic Aquifer System	Saturated LCA	Unsaturated Zone	Saturated Alluvial/Volcanic Aquifer System	Saturated LCA
UMBER	0.00026	1.0000	0.0000	0.0000	1.0000	0.0000	0.0000
VALENCIA	<0.00000	1.0000	0.0000	0.0000	1.0000	0.0000	0.0000
VALISE	0.00051	1.0000	0.0000	0.0000	1.0000	0.0000	0.0000
VAT	0.00051	1.0000	0.0000	0.0000	1.0000	0.0000	0.0000
VAUGHN	0.00384	0.8247	0.1753	0.0000	0.9433	0.0567	0.0000
VELARDE	0.00051	1.0000	0.0000	0.0000	1.0000	0.0000	0.0000
VERDELLO	0.00051	1.0000	0.0000	0.0000	1.0000	0.0000	0.0000
VERMEJO	0.00051	1.0000	0.0000	0.0000	1.0000	0.0000	0.0000
VICTORIA	0.00051	1.0000	0.0000	0.0000	1.0000	0.0000	0.0000
VIDE	0.00051	1.0000	0.0000	0.0000	1.0000	0.0000	0.0000
VIGIL	0.00051	1.0000	0.0000	0.0000	1.0000	0.0000	0.0000
VILLE	0.00051	1.0000	0.0000	0.0000	1.0000	0.0000	0.0000
VILLITA	0.00051	1.0000	0.0000	0.0000	1.0000	0.0000	0.0000
VISE	0.00512	0.6969	0.3031	0.0000	0.8523	0.1477	0.0000
VITO	0.00051	1.0000	0.0000	0.0000	1.0000	0.0000	0.0000
VULCAN	0.00064	1.0000	0.0000	0.0000	1.0000	0.0000	0.0000
WACO	0.00051	1.0000	0.0000	0.0000	1.0000	0.0000	0.0000
WAGTAIL	0.00512	0.0000	1.0000	0.0000	0.0000	1.0000	0.0000
WALLER	0.00051	1.0000	0.0000	0.0000	1.0000	0.0000	0.0000
WARD	0.00051	1.0000	0.0000	0.0000	1.0000	0.0000	0.0000
WASHER	0.00051	1.0000	0.0000	0.0000	1.0000	0.0000	0.0000
WELDER	0.00051	1.0000	0.0000	0.0000	1.0000	0.0000	0.0000

Table C-3
Initial RST Fractions for Detonations in the Unsaturated Zone, Saturated Alluvial/Volcanic Aquifer System, and Saturated LCA Models
(Page 34 of 34)

Detonation Name [a]	Maximum Yield-Weighted Fraction of Total Inventory [b]	Uniform-Mass Inventory Fraction (2 R_c Exchange Volume)			Uniform-Concentration Inventory Fraction (^3H)		
		Unsaturated Zone	Saturated Alluvial/Volcanic Aquifer System	Saturated LCA	Unsaturated Zone	Saturated Alluvial/Volcanic Aquifer System	Saturated LCA
WEMBLEY	0.00051	1.0000	0.0000	0.0000	1.0000	0.0000	0.0000
WEXFORD	0.00051	1.0000	0.0000	0.0000	1.0000	0.0000	0.0000
WHITE	0.00051	1.0000	0.0000	0.0000	1.0000	0.0000	0.0000
WHITEFACE-A	0.00051	1.0000	0.0000	0.0000	1.0000	0.0000	0.0000
WHITEFACE-B	0.00051	1.0000	0.0000	0.0000	1.0000	0.0000	0.0000
WICHITA	0.00051	1.0000	0.0000	0.0000	1.0000	0.0000	0.0000
WINCH	0.00051	1.0000	0.0000	0.0000	1.0000	0.0000	0.0000
WOLVERINE	0.00051	1.0000	0.0000	0.0000	1.0000	0.0000	0.0000
WOOL	0.00051	1.0000	0.0000	0.0000	1.0000	0.0000	0.0000
WORTH	0.00051	1.0000	0.0000	0.0000	1.0000	0.0000	0.0000
YANNIGAN-BLUE	0.00512	0.9980	0.0020	0.0000	0.9996	0.0004	0.0000
YANNIGAN-RED	0.00512	0.9574	0.0426	0.0000	0.9991	0.0009	0.0000
YANNIGAN-WHITE	0.00512	0.9789	0.0211	0.0000	0.9994	0.0006	0.0000
YARD	0.00512	0.6832	0.3168	0.0000	0.7574	0.2426	0.0000
YERBA	0.00051	1.0000	0.0000	0.0000	1.0000	0.0000	0.0000
YORK	0.00051	1.0000	0.0000	0.0000	1.0000	0.0000	0.0000
ZAZA	0.00512	0.0000	1.0000	0.0000	0.0000	1.0000	0.0000
ZINNIA	0.00051	1.0000	0.0000	0.0000	1.0000	0.0000	0.0000

[a] The three detonations conducted in the Climax Mine area of the CAU—HARDHAT, PILEDRIVER and TINYTOT—are excluded.
[b] Maximum of announced yield identified in DOE/NV-209, Rev.15.

C.6.0 REFERENCES

Boardman, C.R. 1970. "Engineering Effects of Underground Nuclear Explosives." In *Proceedings of Symposium on Engineering with Nuclear Explosives*, CONF-700101, 43–67. Las Vegas, NV, 14–16 January.

Boardman, C.R., and J. Skrove. 1966. "Distribution in Fracture Permeability of a Granitic Rock Mass Following a Contained Nuclear Explosion." *Journal of Petroleum Technology* 18 (5): 619–623. doi:10.2118/1358-PA.

Borg, I.Y. 1973. *Comparison of Shock Effects in Granitic Rock Recovered from the Monique Event, Algeria, and the Piledriver Event, Nevada Test Site*, UCRL-51349. Livermore, CA: Lawrence Livermore Laboratory.

Borg, I.Y., R. Stone, H.B. Levy, and L.D. Ramspott. 1976. *Information Pertinent to the Migration of Radionuclides in Ground Water at the Nevada Test Site, Part 1: Review and Analysis of Existing Information*, UCRL-52078. Livermore, CA: Lawrence Livermore National Laboratory.

Bowen, S.M, D.L. Finnegan, J.L. Thompson, C.M. Miller, P.L. Baca, L.F. Olivas, C.G. Geoffrion, D.K. Smith, W. Goishi, B.K. Esser, J.W. Meadows, N. Namboodiri, J.F. Wild. 2001. *Nevada Test Site Radionuclide Inventory, 1951–1992*, LA-13859-MS. Los alamos, NM: Los Alamos National Laboratory.

Burkhard, N.R., and J.T. Rambo. 1991. "One Plausible Explanation For Groundwater Mounding." In *Proceedings of the 6th Symposium on the Containment of Underground Nuclear Explosions*, CONF-9109114, Vol. 2. Livermore, CA: Lawrence Livermore National Laboratory.

Carle, S.F., R.M. Maxwell, and G.A. Pawloski. 2003. *Impact of Test Heat on Groundwater Flow at Pahute Mesa, Nevada Test Site*, UCRL-ID-152599. Livermore, CA: Lawrence Livermore National Laboratory.

Carle, S. F., R.M. Maxwell, G.A. Pawloski, D.E. Shumaker, A.F.B. Tompson, and M. Zavarin. 2007. *Evaluation of the Transient Hydrologic Source Term for the Cambric Underground Nuclear Test at Frenchman Flat, Nevada Test Site*, UCRL-TR-226916. Livermore, CA: Lawrence Livermore National Laboratory.

Carle, S.F., M. Zavarin, and G.A. Pawloski. 2002. *Geostatistical Analysis of Spatial Variability of Mineral Abundance and K_d in Frenchman Flat, NTS, Alluvium*, UCRL-ID-150200. Livermore, CA: Lawrence Livermore National Laboratory.

Carle, S.F., M. Zavarin, Y. Sun, and G.A. Pawloski. 2008. *Evaluation of Hydrologic Source Term Processes for Underground Nuclear Tests in Yucca Flat, Nevada Test Site: Carbonate Tests*, LLNL-TR-403485. Livermore, CA: Lawrence Livermore National Laboratory.

DOE/NV, see U.S. Department of Energy, Nevada Operations Office.

Essington, E.H. and E.J. Forslow. 1971. *Distribution of Radioactivity in and near the Rainier Rubble Chimney*, NVO-1229-180. Las Vegas, NV: Teledyne Isotopes, Nevada Operations.

Germain, L.S., and J.S. Kahn. 1968. *Phenomenology and Containment of Underground Nuclear Explosions*, UCRL-50482; TID-4500, UC-2. Livermore, CA: Lawrence Livermore National Laboratory.

Halford, K.J., R.J. Laczniak, and D.L. Galloway. 2005. *Hydraulic Characterization of Overpressured Tuffs in Central Yucca Flat, Nevada Test Site, Nye County, Nevada*, Scientific Investigations Report 2005-5211. Carson City, NV: U.S. Geological Survey.

IAEA, see International Atomic Energy Agency.

ICRP, see International Commission on Radiological Protection.

International Atomic Energy Agency. 1998a. T*he Radiological Situation at the Atolls of Mururoa and Fangataufa, Technical Report, Volume 3: Inventory of Radionuclides Underground at the Atolls*, IAEA-MFTR-3. In *Proceedings of an IAEA Conference, Vienna, 30 June–3 July.* Vienna, Austria.

International Atomic Energy Agency. 1998b. *The Radiological Situation at the Atolls of Mururoa and Fangataufa, Technical Report, Volume 4: Releases to the Biosphere of Radionuclides from Underground Nuclear Weapons Tests at the Atolls*, IAEA-MFTR-4. In *Proceedings of an IAEA Conference, Vienna, 30 June–3 July.* Vienna, Austria.

International Atomic Energy Agency. 1998c. *The Radiological Situation at the Atolls of Mururoa and Fangataufa, Technical Report, Volume 6: Dose due to Radioactive Materials Present in the Environment or Released form the Atolls*, In *Proceedings of an IAEA Conference, Vienna, 30 June–3 July.* Vienna, Austria.

International Commission on Radiological Protection. 1996. *Annals of the ICRP, Vol. 26(1): ICRP Publication 72: Age-Dependent Doses to the Members of the Public from Intake of Radionuclides Part 5, Compilation of Ingestion and Inhalation Coefficients*.

Knox, J.B., D.E. Rawson, and J.A. Korver. 1965. “Analysis of a Groundwater Anomaly Created by an Underground Nuclear Explosion.” *Journal of Geophysical Research* 70 (4): 823–835. doi:10.1029/JZ070i004p00823.

McNab, W.W. 2008. *Evaluation of Hydrologic Source Term Processes for Underground Nuclear Tests in Yucca Flat, Nevada Test Site: Unsaturated Tests and the Impact of Recharge*, LLNL-TR-403360. Livermore, CA: Lawrence Livermore National Laboratory.

OTA, see U.S. Congress, Office of Technology Assessment.

Pawloski, G.A. 1999. *Development of Phenomenological Models of Underground Nuclear Tests on Pahute Mesa, Nevada Test Site—BENHAM and TYBO*, UCRL-ID-136003. Livermore, CA: Lawrence Livermore National Laboratory.

Pawloski, G.A., A.F.B. Tompson, and S.F. Carle. 2001. *Evaluation of the Hydrologic Source Term from Undrground Nuclear Tests on Pahute Mesa at the Nevada Test Site: CHESHIRE Test*, UCRL-ID-147023. Livermore, CA: Lawrence Livermore National Laboratory.

Pawloski, G.A., A.F.B. Tompson, S.F. Carle, R.L. Detwiler, Q. Hu, S. Kollet, R.M. Maxwell, W.W. McNab, S.K. Roberts, D.E. Shumaker, Y. Sun, and M. Zavarin. 2008. *Evaluation of Hydrologic Source Term Processes for Underground Nuclear Tests in Yucca Flat, Nevada Test Site: Introduction and Executive Summary*, LLNL-TR-403428. Livermore, CA: Lawrence Livermore National Laboratory.

Pawloski, G.A., G. WoldeGabriel, and I. Farnham. 2005. Written communication regarding *Categorization of Underground Nuclear Tests on Yucca Flat and Climax Mine, Nevada Test Site, for Use in Radionuclide Transport Models*. Livermore, CA: Lawrence Livermore National Laboratory; Los Alamos, NM: Los Alamos National Laboratory; and Las Vegas, NV: Stoller-Navarro Joint Venture.

Rose, T.P., Q. Hu, P. Zhao, C.L. Conrado, R. Dickerson, G.F. Eaton, A.B. Kersting, J.E. Moran, G. Nimz, B.A. Powell, E.C. Ramon, F.J. Ryerson, R.W. Williams, P.T. Wooddy, and M. Zavarin. 2011. *Radionuclide Partitioning in an Underground Nuclear Test Cavity*, LLNL-TR-409817. Livermore, CA: Lawrence Livermore National Laboratory.

Smith, D.K., D.L. Finnegan, and S. M.Bowen. 2003. "An Inventory of Long-Lived Radionuclides Residual from Underground Nuclear Testing at the Nevada Test Site, 1951–1992." *Journal of Environmental Radioactivity* 67 (1): 35–51. doi:10.1016/S0265-931X(02)00146-7.

Tompson, A.F.B., ed. 2008. *Evaluation of Hydrologic Source Term Processes for Underground Nuclear Tests in Yucca Flat, Nevada Test Site: Saturated Tests*, LLNL-TR-4003429. Livermore, CA: Lawrence Livermore National Laboratory.

Tompson, A.F.B., C.J. Bruton, and G.A. Pawloski, eds. 1999. *Evaluation of the Hydrologic Source Term from Underground Nuclear Tests in Frenchman Flat at the Nevada Test Site: The CAMBRIC Test*, UCRL-ID-132300. Livermore, CA: Lawrence Livermore National Laboratory.

Tompson, A.F.B., R.M. Maxwell, S.F. Carle, M. Zavarin, G.A. Pawloski, and D.E. Shumaker. 2005. *Evaluation of the Non-Transient Hydrologic Source Term from the CAMBRIC Underground Nuclear Test in Frenchman Flat, Nevada Test Site*, UCRL-TR-217191. Livermore, CA: Lawrence Livermore National Laboratory.

Tompson, A.F.B., M. Zavarin, W.W. McNab, S.F. Carle, D.E. Shumaker, C. Lu, Y. Sun, G.A. Pawloski, Q. Hu, and S.K. Roberts. 2011. Written communication. Subject: *Hydrologic Source Term Processes and Models for Underground Nuclear Tests at Rainier Mesa and Shoshone Mountain, Nevada Test Site*. Livermore, CA: Lawrence Livermore National Laboratory.

U.S. Congress, Office of Technology Assessment. 1989. *The Containment of Underground Explosions*, OTA-ISC-414. Washington, DC: U.S. Government Printing Office.

U.S. Department of Energy, Nevada Operations Office. 2000. *United States Nuclear Tests, July 1945 through September 1992*, DOE/NV--209-REV 15. Las Vegas, NV.

Vincent, P., S. Larsen, D. Galloway, R.J. Laczniak, W.R. Walter, W. Foxall, and J.J. Zucca. 2003. "New Signatures of Underground Nuclear Tests Revealed by Satellite Radar Interferometry" *Geophysical Research Letters* 30 (22): 2141. doi:10.1029/2003GL018179.

Wadman R.E., and W.D. Richards. 1961. *Postshot Geologic Studies of Excavations below Rainier Ground Zero*, UCRL-6586. Livermore, CA: Lawrence Livermore National Laboratory.

Wolfsberg, A., J. Boryta, E. Keating, P. Stauffer, C. Gable, and S. Kelkar. 2006. Written communication regarding *Analysis and Evaluation of Elevated Groundwater Heads and Their Impact on Flow and Solute Transport in the Tuff Pile: Areas 3, 4, and 7 of the Nevada Test Site, Nye County, Nevada*. Los Alamos, NM: Los Alamos National Laboratory.

Appendix D

Contamination Observations in Yucca Flat Wells

D.1.0 INTRODUCTION

D.1.1 Background

This appendix summarizes the information available from observation wells in the Yucca Flat area, whether drilled explicitly to evaluate the near field contaminant extent (i.e., the hot wells) or for related characterization activities that have been sampled for in situ contamination. The information in this appendix is derived from the analyses summarized in the Yucca Flat Transport Parameter Document (SNJV, 2007) and analyses of data available in the geochemistry database as of September 2012 (N-I, 2012).

Although post-detonation drilling and sampling occurred in a significant fraction of the underground nuclear tests conducted in the Yucca Flat/Climax Mine CAU, the information generated from these activities is generally classified and focussed on retrieving information on the melt glass constituents and therefore is not relevant for evaluating contaminant migration. However, there have been a number of post-detonation exploratory drill holes that provided useful information for determining HST contamination extent and post-detonation contaminant transport. In addition, other drill holes encountered contamination presumed to originate from the nuclear tests in the Yucca Flat/Climax Mine CAU.

D.1.2 Purpose/objectives

The phenomenology of post-detonation geochemical and hydrogeologic conditions and the near- and far-field radionuclide distribution are determined in part by observations made from water samples. Summaries of relevant radiochemical information available from near-field wells (i.e., wells located near nuclear tests) through about 2006 have been documented in the Yucca Flat Transport Parameter Document (SNJV, 2007). The Transport Parameter Document did not include other observation wells in the Yucca Flat area, therefore this appendix provides a more comprehensive summary of all available radiochemistry data.

The protocol for determining the radiochemical constituents to analyze for in a particular sampling event is dependent on the sampling objectives. While ^{3}H is usually included in the analysis due to its large initial inventory and mobility, other radiochemical isotopes are only sporadically analyzed.

In many cases, the reported concentration is less than the minimum detection limit (MDL). Reporting the value as the MDL would be misleading. As a result, only values that exceed the MDL are reported in the following discussion. The following discussion notes if the isotope was analyzed for and was found to be below the MDL, but the actual MDL, which vary for different sampling and analytical protocols, are not always reported. Although the contaminant boundary can be determined by the concentration of any of the 43 radionuclides identified in the Bowen inventory (Bowen et al., 2001), this section focuses on the subset that contributes most significantly to the probability of contaminant concentrations exceeding the maximum contaminant level (MCL), notably, ^{3}H, ^{14}C, ^{36}Cl, ^{63}Ni, ^{90}Sr, ^{99}Tc, ^{129}I, ^{137}Cs, ^{237}Np, and ^{239}Pu (see Figures 2-6 to 2-8).

D.1.3 Observation wells in Yucca Flat

The number of near-field wells in the vicinity of test cavities in Yucca Flat is limited because of the logistical complexities associated with accessing the underground testing environment (i.e., most of the nuclear tests were conducted between 300 and 1,400 m bgs) and the difficult and costly well construction and development at these sites. Approximately half of the near-field wells used for groundwater sampling were completed opportunistically in post-test, re-entry holes. The remaining wells were drilled specifically for near-field groundwater characterization purposes for the Hydrologic Resources Management Program (HRMP), Long-Term Hydrologic Monitoring Program (LTHMP), Radionuclide Migration (RNM) Program, Routine Radiological Monitoring Program (RREMP), or UGTA Activity.

As noted in Pawloski et al. (2008), many of the Yucca Flat/Climax Mine CAU detonations had post shot drill backs into the cavities to extract melt glass and other constituents to diagnose test performance. Most of these wells were backfilled and sealed over the decades. However, a few wells were retained by the UGTA Activity to allow contaminant migration monitoring. The wells currently available and included in water sampling in Yucca Flat are shown in Figure D-1.

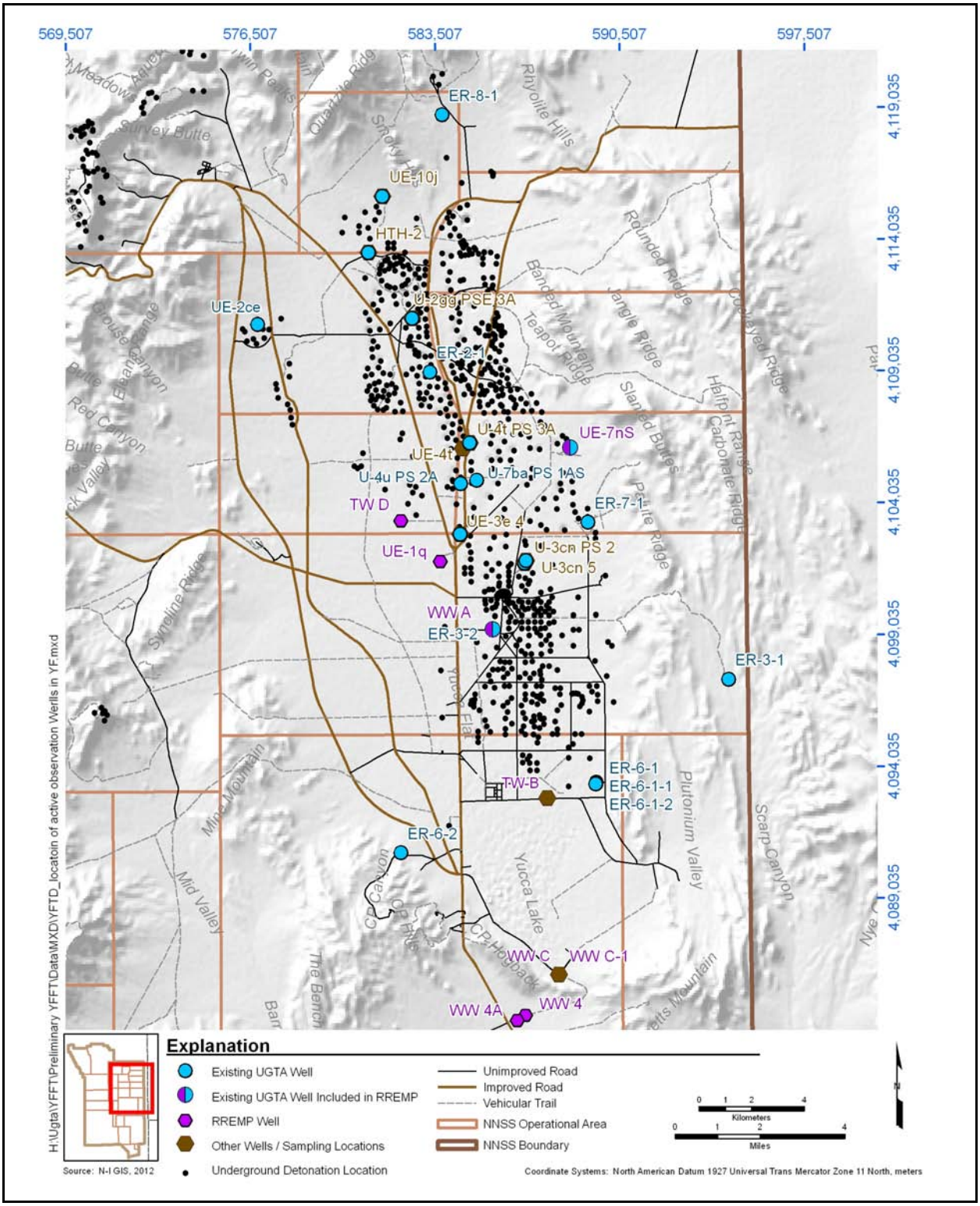

Figure D-1
Location of Observation Wells in Yucca Flat

D.1.4 Sampling of observation wells in Yucca Flat

The observation wells indicated in Figure D-1 have undergone periodic sampling. The sampling dates, sampled radioisotopes, collection methods, and corresponding results are identified in Table D-1. There have been significant differences in sampling and analytical protocols over the years; hence, caution should be used when comparing data from different wells. Samples collected using downhole submersible pumps are more likely to be representative of the bulk fluid composition in the near-field environment. Several of the wells, particularly those that have been converted from post-test re-entry holes, consist of a small diameter (7.3-cm) carbon-steel piezometer tube. In most cases, these wells have only been sampled using wireline bailers. Given that the standing fluid in these piezometers does not circulate freely with the sampled formation and that thorough purging could not be accomplished, samples collected from these wells tend to be of lower quality than those from pumped wells.

Groundwater samples from near-field or post-test wells have been collected at eight locations in the Yucca Flat/Climax Mine CAU. Details regarding these wells are compiled in Table D-2. Several of the sites have (or had) more than one sampling well, providing data at different depth intervals relative to the detonation working point. Many were drilled at a slant to access the cavity from outside the collapse crater. True vertical depth is provided unless otherwise specified (Table D-2).

Unclassified data used to characterize the Yucca Flat/Climax Mine CAU near-field environment are summarized in the following sections.

D.1.5 Contents of Appendix

This appendix contains visual displays of radiochemical data at observation wells in Yucca Flat. To allow a consistent means to compare contaminant levels at different sampling events and locations, the concentration data have been normalized to the MCL. In cases where measured concentrations are less than the MDL, the concentrations are not explicitly illustrated.

The appendix is arranged by (1) well locations in the saturated units above the LCA that are generally associated with underground nuclear detonations conducted in or above the saturated alluvial/volcanic aquifer system and (2) well locations associated with underground nuclear detonations conducted in or above the saturated LCA. The former provide results that can be compared to contaminant fluxes and concentrations in the saturated alluvial/volcanic aquifer system

Table D-1
Sampling Dates and Radioisotopes for Sampled Observations Wells in Yucca Flat
(Page 1 of 5)

Well	NNSS Area	HSU Open to Well	Sample Dates	Radioisotopes Analyzed and Corresponding Results
ER-2-1	2	TM-WTA, TM-LVTA, LTCU	09/03/2003 (pumped), 09/05/2003 (564 m-bgs bailed)	• For the 09/03/2003 sample, ^{3}H was reported as 228 pCi/L, ^{14}C as 0.04 pCi/L, and ^{36}Cl as 1.0E-04 pCi/L; ^{137}Cs, ^{90}Sr, ^{129}I, and Pu were below the MDL; ^{99}Tc was reported as 12 ± 4 pCi/L and 8 ± 4 pCi/L for duplicates (these values are near the 6 pCi/L MDL and considered highly uncertain). • For the 09/05/2003 sample, ^{3}H, ^{14}C, ^{137}Cs, and Pu were reported below the MDL.
ER-3-1	3	LCA	1995, 1996 (pumped)	• ^{3}H was reported below the MDL (181 - 283 pCi/L) for both samples. • Pu was analyzed in both samples and ^{137}Cs was analyzed in the 11/09/1995 sample. Reported results were below the MDL. • For the 11/09/1995 sample, ^{90}Sr and ^{99}Tc were reported below the MDL (0.6 and 25 pCi/L, respectively), and as 0.27 ± 0.13 and 3.2 ± 1.4 pCi/L, respectively for the 10/16/1996 sample; values are near the MDLs (0.2 and 2.2 pCi/L, respectively) and considered highly uncertain.
ER-3-2	3	AA	1995, 1999, 2000 (451 and 774 m-bgs bailed)	• ^{3}H was reported below the MDL (10 - 164 pCi/L) for all samples. • Pu was only analyzed in the 02/25/1999 sample and was reported below the MDL (0.05 pCi/L).
ER-6-1	6	LCA	10/09/1992, 11/23/1992, 1999 to 2004 (bailed annually), 01/28/2004 (pumped)	• ^{3}H was reported below the MDL (0.96 - 360 pCi/L) for all samples. • ^{14}C, ^{90}Sr, ^{99}Tc, ^{129}I, ^{137}Cs, and Pu were reported below the MDL throughout the sampling period; these radionuclides were not analyzed in all samples. • ^{36}Cl was reported as 1.3E-04 pCi/L for the 11/23/1992 sample.
ER-6-1-2	6	LCA	2003 (pumped), 2004 (701 m-bgs bailed)	• For the 2003 sample, ^{3}H was reported as ≤30.8 pCi/L; ^{14}C as 7.4E-03 pCi/L ^{36}Cl as 1.4E-04 pCi/L; and ^{90}Sr, ^{99}Tc, ^{129}I, ^{137}Cs, ^{237}Np, and Pu were reported below the MDL. • For the 2004 sample, ^{3}H, ^{14}C, ^{137}Cs, and Pu were reported below the MDL.
ER-6-2	6	LCA3	07/20/2004 (823 m-bgs bailed), 08/04/2004 (pumped)	• For the 07/20/2004 sample, ^{3}H, ^{14}C, ^{137}Cs, and Pu were reported below the MDL. • For the 08/04/2004 sample, ^{3}H was reported as 92 pCi/L, ^{14}C as 8.1E-03 pCi/L, and ^{36}Cl as 1.6E-04 pCi/L; ^{90}Sr, ^{99}Tc, ^{129}I, ^{137}Cs, and Pu were reported below the MDL.
ER-7-1	7	LCA	07/02/2003 (719 m-bgs bailed), 07/17/2003 (pumped)	• For the 07/02/2003 sample, ^{3}H, ^{14}C, ^{137}Cs, and Pu were reported below the MDL. • For the 7/17/2003 sample, ^{3}H was reported as ≤117 pCi/L, ^{14}C as 1.6E-02 pCi/L and ^{36}Cl as 1.2E-04 pCi/L; ^{90}Sr, ^{99}Tc, ^{129}I, ^{137}Cs, and Pu were reported below the MDL.
ER-8-1	8	MGCU	None	• A sample was not collected because fill within the borehole obstructed access to the water table.
HTH 2	8	LCA	1962, 1989 to 2006 (monthly to annually)	• For a 2006 sample, ^{3}H and ^{36}Cl were reported as <1 and 1.5E-04 pCi/L, respectively. • Gamma emitters, ^{3}H, ^{14}C, ^{90}Sr, ^{99}Tc, and Pu were reported below or near the MDL (values reported near the MDL are likely to be nondetects). Samples were primarily analyzed for ^{3}H; other radionuclides were analyzed less frequently. The ^{3}H MDLs ranged from 1 to 900 pCi/L.
TW B	6	TSA	1963, 1965, bailed monthly from 1976 to 1987, 1990, 1993, 1998	• ^{90}Sr was reported below the MDL (0.4 pCi/L) for the 1963 sample and ^{3}H was reported as a nondetect for the 1965 sample. • ^{3}H was reported to decrease from 260 pCi/L to 158 pCi/L for the monthly samples, and was reported as 109 and 44 pCi/L for the 1990 and 1998 samples, respectively. • For the 1993 sample, ^{36}Cl, ^{99}Tc, and ^{137}Cs were reported as 6.8E-04, <5, and <0.7 pCi/L, respectively.

Table D-1
Sampling Dates and Radioisotopes for Sampled Observations Wells in Yucca Flat
(Page 2 of 5)

Well	NNSS Area	HSU Open to Well	Sample Dates	Radioisotopes Analyzed and Corresponding Results
TW D	4	LCA	1965, bailed 1973 to 1987 (biannually) and 1993 to 2010 (annually).	• ^{3}H, ^{14}C, ^{90}Sr, ^{99}Tc, ^{90}Sr, ^{137}Cs, and Pu were reported below or near the MDL (values reported near the MDL are likely to be nondetects). Samples were primarily analyzed for ^{3}H; other radionuclides were analyzed much less frequently. • For a 1993 sample, ^{3}H was reported as 3.8±1.3 pCi/L and ^{99}Tc was reported as <5.
U-2gg PSE 3A	2	TM-LVTA	09/21/1994 (597 m-bgs bailed), 09/22/1994 (587 m-bgs bailed) (see Section D.2.5 for more details)	• For the 09/21/1994 sample, ^{3}H was reported as 5.4E+03 and 7.6E+03 pCi/L,^{14}C as 6.0E+03 pCi/L, ^{137}Cs as 2.7 pCi/L, and Pu as <2.7E-03 pCi/L. • For the 09/22/1994 sample, ^{3}H was reported as 6,490 pCi/L, ^{14}C as 19,900 pCi/L, and ^{137}Cs as 0.9 pCi/L, and Pu as <3.1E-03 pCi/L.
U-3cn 5	3	LCA	Samples were collected frequently during 1965 to 1973 hydraulic testing. Additional sampling in 1980, 1981, 1997, 1998, 2000, 2011 (see Section D.3.1 for more details).	• During 1965-1973 hydraulic tests, ^{3}H ranged from less than 1.3E+03 to 1.3E+08 pCi/L (671–727 m); 1.6E+06 to 3.2E+06 pCi/L (604–655 m); 1.6E+06 to 8.5E+06 pCi/L (560–604 m); and <1.3E+03 to 9.4E+04 pCi/L (863–893 m). • ^{3}H was reported below the MDL (10.9 to 1,200 pCi/L) for most samples following the hydraulic tests; ^{3}H was reported as 2.9 pCi/L for 1980 sample and as 10.4 pCi/L for 1981 sample. ^{137}Cs was reported as 0.003 pCi/L for the 1980 sample and below the MDL (0.001 to 101 pCi/L) for subsequent samples (1981 to 2000); ^{90}Sr was reported as 7.0E-04 pCi/L for the 1980 sample, as 4.6E-04 pCi/L for the 1981 sample, and below the MDL (0.29 and 0.59 pCi/L, respectively) for 1997 and 2000 samples; ^{99}Tc was reported below the MDL (2.1 pCi/L) for 1997 sample; and Pu was reported as 2.3E-04 pCi/L for 1980 sample and below the MDL (0.07 and 0.01 pCi/L, respectively) for 1997 and 2000 samples. • For the 2011 sample, ^{3}H was reported below the MDL (192 pCi/L), ^{14}C as 0.033 pCi/L, ^{129}I as 1.1E-06 pCi/L, and ^{137}Cs as <0.04 pCi/L.
U-3cn PS 2	3	OSBCU	Samples were collected frequently during 1964 to 1966 hydraulic testing, 1977, 1981, 1982, 1983, 1985, 1997, 2001, 2004, and 2007 (see Section D.3.1 for more details).	• During 1964–1966 hydraulic tests, ^{3}H ranged from 2.1E+08 to 2.7E+08 pCi/L, ^{90}Sr was reported as 0.4 pCi/L, and ^{137}Cs ranged from 3 to 5 pCi/L at 579–792 m; ^{3}H ranged from 9.8E+05 to 9.5E+07 pCi/L at 512–527 m (no ^{137}Cs or ^{90}Sr results were reported for this sampling interval). • ^{3}H in subsequent samples ranged from 7.7E+06 pCi/L (2007) to 4.6E+07 pCi/L (1981), ^{14}C from 171 pCi/L (1997) to 372 pCi/L (2004), ^{36}Cl from 0.3 pCi/L (1997) to 63 pCi/L (2004), ^{90}Sr from 0.06 pCi/L (1983) to 2.4 pCi/L (1997), ^{99}Tc from 36 pCi/L (2007) to 80 pCi/L (1997), ^{129}I from 0.2 pCi/L (2007) to 0.5 pCi/L (1997), ^{137}Cs from 1.1 pCi/L (1997) to 3.7 pCi/L (1977), and Pu from 2E-03 pCi/L (1985) to 6E-02 pCi/L (2007).
U-4t PS 3A	7	LTCU	1993 and 2008 (bailed; see Section D.2.4 for more details).	• For the 1993 samples (311 and 322 m), a high variability in ^{3}H (1.1E+03 to 6.7E+04 pCi/L) was observed. • For the 2008 sample, ^{3}H was reported as 3.0E+03 pCi/L, ^{14}C as 0.87 pCi/L, ^{36}Cl as <4.9E-03 pCi/L, ^{129}I as 2.5E-04, and Pu as <1.5E-03 pCi/L.

Table D-1
Sampling Dates and Radioisotopes for Sampled Observations Wells in Yucca Flat
(Page 3 of 5)

Well	NNSS Area	HSU Open to Well	Sample Dates	Radioisotopes Analyzed and Corresponding Results
U-4u PS 2A	7	LTCU	1992, 1993, 1997, 1998, 1999, 2003, 2008 (bailed at 472, 484, and 504 m depths; see Section D.2.3 for more details).	• For the 1992 samples, ^{3}H was reported as 5.8E+07 pCi/L (504 m). • For the 1993 samples, ^{3}H ranged from 4.9E+07 pCi/L (533 m) to 5.3E+07 pCi/L (484 m), ^{137}Cs from 2.0 pCi/L (533 m) to 600 pCi/L (504 m), and Pu was 0.14 pCi/L (533 m). • For the 1997 samples, ^{3}H was reported as 1.6E+07 pCi/L (472, 484, and 512 m); ^{14}C was reported as 47 pCi/L, ^{90}Sr as 3.1 pCi/L, ^{137}Cs as 66 pCi/L, and $^{239/240}$Pu as 0.2 pCi/L for samples collected at 512 m. • For the 1998 samples, ^{3}H was reported as 1.5E+07 to 2.2E+07 pCi/L, ^{14}C as 238 pCi/L, ^{36}Cl as 8.5 pCi/L, ^{99}Tc as 16 pCi/L,^{137}Cs as 43 to 75 pCi/L, and $^{239/240}$Pu as 0.12 pCi/L. • For the 1999 samples, ^{3}H was reported as 1.6E+07 pCi/L,^{14}C as 229 pCi/L, ^{36}Cl as 8.5 pCi/L, and $^{239/240}$Pu as 1.2 pCi/L. • For the 2003 samples, ^{3}H was reported as 2.7E+07 pCi/L, ^{14}C as 326 pCi/L, ^{36}Cl as 29 pCi/L, ^{129}I as 0.13 pCi/L, ^{99}Tc as 35 pCi/L, and $^{239/240}$Pu as 0.32 pCi/L. • For the 2008 samples, ^{3}H was reported as 2.4E+07 pCi/L, ^{14}C as 402 pCi/L, ^{36}Cl as 19 pCi/L, ^{129}I as 0.15 pCi/L, ^{99}Tc as 26 pCi/L, and $^{239/240}$Pu as 0.44 pCi/L.
U-7ba PS 1AS	7	LTCU	07/19/1995 (bailed at 366, 427, 488, 549, and 584 m depths; see Section D.2.2 for more details).	• ^{3}H increased with depth (5.5E+06 pCi/L to 4.3E+07 pCi/L). • ^{137}Cs was reported as 65 pCi/L (366 m), 4.7E+04 pCi/L (427 m), 6.9E+04 pCi/L (488 m), 3.4E+04 pCi/L (549 m), and 1.3E+05 pCi/L (584 m).
UE-10j	10	LCA	05/25/1965 (bailed 728 m), 04/30/1993 (680–796 m) 03/17/1997 (760–796 m; Zone 1) 03/20/1997 (721–741 m; Zone 2) 03/24/1997 (680–700 m; Zone 3)	• For the 1965 sample, ^{90}Sr was reported below the MDL (0.3 pCi/L). • For the 1993 sample, ^{3}H, ^{90}Sr, ^{99}Tc, and ^{137}Cs, were reported below MDLs (2, 0.5, 4.5, and 0.6 pCi/L, respectively); and ^{36}Cl was reported as 2E-04 pCi/L. • For the 1997 samples, ^{3}H and ^{137}Cs were reported below MDLs (90 to 190 and 6.8 pCi/L, respectively.)
UE-1q	1	LCA	1992 and bailed annually from 1999 to present	• ^{3}H was reported near or below the MDL (1 - 34 pCi/L) for all samples indicating its absence (values reported near the MDL are likely to be nondetects). • Gamma emitters, ^{14}C, ^{90}Sr, ^{99}Tc, and Pu were reported below the MDL throughout the sampling period; these radionuclides were not analyzed in all samples. • ^{36}Cl was reported as 1.4E-04 pCi/L in 1992 samples.
UE-2ce	2	LCA3	Frequent pumped samples between 1977 to 1984; bailed in 1993, 2001, 2005; pumped in 2008 (see Section D.3.3 for more details)	• ^{3}H ranged from 1.6E+04 to 3.4E+07 pCi/L, ^{90}Sr ranged from 0.08 to 5.1 pCi/L, and ^{137}Cs ranged from <4.5E-03 to 1.7 pCi/L in early samples (1977 to 1984). • ^{3}H ranged from 9.3E+04 to 1.5E+05 pCi/L, and Pu was below the MDL (0.04 to 0.09 pCi/L) in 1993, 2001, and 2005 bailed samples; ^{137}Cs was <0.3 pCi/L in 1993 sample; and ^{14}C, ^{36}Cl, ^{99}Tc, ^{129}I were 0.8, 0.4, <0.002, 0.02 pCi/L, respectively in the 2005 sample. • For the 2008 samples, ^{3}H ranged from 1.2E+5 to 2.7E+5 pCi/L; ^{14}C ranged from 0.88 to 1.11 pCi/L; and ^{36}Cl, ^{99}Tc, ^{129}I were 1.3, 0.002, 0.01 pCi/L, respectively.
UE-3e 4 P1	3	LTCU	1990, 1991, 1992, 1993, 1998, and 2009 (bailed; see Section D.2.1 for more details).	• ^{3}H ranged from 3.3E+05 to 1.8E+07 pCi/L. • For the 1993 samples, ^{14}C and ^{239,240}Pu were reported below the MDL (3,200 and 0.06 pCi/L, respectively). • For the 2009 samples, ^{14}C was reported as 1.3 pCi/L, ^{36}Cl as 0.73 pCi/L, ^{99}Tc as 2.1 pCi/L, ^{129}I as 6.8E-03 pCi/L, and ^{239,240}Pu as <3.1E-04 pCi/L.

Table D-1
Sampling Dates and Radioisotopes for Sampled Observations Wells in Yucca Flat
(Page 4 of 5)

Well	NNSS Area	HSU Open to Well	Sample Dates	Radioisotopes Analyzed and Corresponding Results
UE-3e 4 P2	3	LTCU	1990, 1991, 1992, 1993, 1998, and 2009 (bailed; see Section D.2.1 for more details).	• ^{3}H decreased from 3.3E+06 to 2.2E+03 pCi/L from 1990 to 2009. • For the 1993 sample, ^{14}C, ^{137}Cs, and ^{239,240}Pu were reported below the MDL (3,200, 0.28, and 0.08 pCi/L, respectively). • For the 2009 sample, ^{14}C was reported as 0.012 pCi/L, ^{36}Cl as 3.6E-04 pCi/L, ^{99}Tc as 1.9 pCi/L, and ^{129}I as 1.7E-04 pCi/L.
UE-3e 4 P3	3	TM-LVTA	1990, 1991, 1992, 1993, 1998, and 2009 (bailed; see Section D.2.1 for more details).	• ^{3}H decreased from 3.3E+06 to 1.4E+05 pCi/L from 1990 to 2009. • For the 1993 sample, ^{14}C was reported as 4.8E+03 pCi/L; and ^{137}Cs and ^{239,240}Pu were reported below the MDL (0.47 and 0.08 pCi/L, respectively). • For the 2009 samples, ^{14}C was reported as 0.11 pCi/L, ^{36}Cl as 6.6E-02 pCi/L, ^{129}I as 5.6E-04 pCi/L, and ^{239,240}Pu as <3.1E-04 pCi/L.
UE-4t 1	7	LTCU	1990, 1992, 2000, and 2008 (bailed; see Section D.2.4 for more details).	• ^{3}H was reported below or near MDLs (8.4 to 1,080 pCi/L) for the 1990, 1992, and 2000 samples. • For the 2008 sample, ^{3}H was reported as 68 pCi/L, ^{14}C as 0.097 pCi/L, ^{36}Cl as 2.7E-04 pCi/L, and ^{129}I as 3.4E-05 pCi/L.
UE-4t 2	7	LTCU	2000 and 2008 (bailed; see Section D.2.4 for more details).	• For the 2000 sample, ^{3}H activities was reported below the MDL (10.4 pCi/L). • For the 2008 sample, ^{3}H was reported as 1.7E+03 pCi/L, ^{14}C as 0.061 pCi/L, ^{36}Cl as 5.1E-04 pCi/L, and ^{129}I as 4.2E-04 pCi/L.
UE-7nS	7	LCA	Samples were collected between 1977 and 1984 at multiple depths (sampling information incomplete). Samples were collected at 620 m bgs by RREMP annually between 1994 and 2010, and in 1993, 2001, and 2005 by LLNL and LANL. (see Section D.3.2 for more details)	• A general increasing trend in ^{3}H activities (13 pCi/L to 2,850 pCi/L) was reported for samples collected between 1977 and 1984; sampling information including depth was not reported for the earliest samples. • RREMP analyses included ^{3}H, ^{14}C, ^{90}Sr, ^{99}Tc, ^{137}Cs, and Pu. ^{3}H decreased from 550 pCi/L in 1995 to 41 pCi/L in 2010. All other radionuclides were below the MDL. • For the 1993 samples, ^{3}H was reported as 457 pCi/L, ^{14}C as <3,200 pCi/L, ^{137}Cs as < 0.2 pCi/L, and ^{239,240}Pu as < 0.04 pCi/L. • For the 2001 samples, ^{3}H was reported as 4,600 pCi/L, ^{14}C as 0.14 pCi/L, ^{36}Cl as 1.4E-03 pCi/L, ^{129}I as 6.1E-04 pCi/L, and ^{239,240}Pu as <0.04 pCi/L by LLNL. LANL reported ^{3}H as 386 to 3,320 pCi/L. • For the 2005 samples, ^{3}H was reported as 132 pCi/L, ^{14}C as 0.14 pCi/L, ^{36}Cl as 2.4E-04 pCi/L, ^{99}Tc as <0.04 pCi/L, ^{129}I as 4.1E-05 pCi/L, and ^{239,240}Pu as <0.04 pCi/L.
WW 4	6	TM-WTA	1983 to 2010 (monthly to biannually) (Pumped)	• For a 1993 sample, ^{3}H was reported as 0.96 pCi/L, ^{36}Cl as 3.1E-4 pCi/L, and ^{99}Tc as <5 pCi/L. • ^{3}H, ^{14}C, ^{90}Sr, ^{99}Tc, ^{137}Cs, and Pu were reported below or near the MDL (values reported near the MDL are likely to be nondetects). Samples were primarily analyzed for ^{3}H; other radionuclides were analyzed less frequently. The ^{3}H MDLs ranged from 10 to 900 pCi/L.
WW 4A	6	TM-WTA	1994 and 1995 to 2010 (quarterly) (Pumped)	• ^{3}H, ^{14}C, ^{90}Sr, ^{99}Tc, ^{137}Cs, and Pu were reported below or near the MDL (values reported near the MDL are likely to be nondetects). Samples were primarily analyzed for ^{3}H; other radionuclides were analyzed less frequently. The ^{3}H MDLs ranged from 1.5 to 754 pCi/L.

Table D-1
Sampling Dates and Radioisotopes for Sampled Observations Wells in Yucca Flat
(Page 5 of 5)

Well	NNSS Area	HSU Open to Well	Sample Dates	Radioisotopes Analyzed and Corresponding Results
WW A	3	AA	1961, 1962, monthly between 1972 and 1987, 1990, and annually from 2000 to 2010	• For the 1961 and 1962 samples, ^{90}Sr was reported below the MDL (0.4 pCi/L). • ^{3}H was reported near or below the MDL for the majority of the monthly 1972 to 1987 samples. ^{3}H was reported as 37 pCi/L for the final 1987 sample and as 170 pCi/L for the 1990 sample. • ^{3}H decreased from 573 to 342 pCi/L between 2001 and 2010. Gamma emitters, ^{14}C, ^{90}Sr, ^{99}Tc, and ^{239,240}Pu were reported near or below the MDL indicating their absence (values reported near the MDL are likely to be nondetects).
WW C	6	LCA	1961, 1962, nearly monthly between 1972 and 1995 (pumped)	• For the 1961 and 1962 samples, ^{90}Sr was reported below the MDL (0.4 and 0.5 pCi/L, respectively). • ^{3}H ranged from approximately 100 pCi/L in 1972 to less than 50 pCi/L in 1987; the initial elevated ^{3}H was attributed to a 1964 tracer test (Lyles, 1990). • For the 1993 sample, ^{3}H was reported as 11.5 pCi/L, ^{36}Cl as 2.4E-04 to 2.6E-04 pCi/L, and ^{99}Tc as <5 pCi/L. • ^{90}Sr and Pu was reported below the MDL for samples collected between 1989 and 1995 (these radionuclides were not reported for earlier samples).
WW-C-1	6	LCA	1962, pumped 1973 to 1987 (biannually) and 1989 to 2010 (monthly).	• ^{3}H decreased from about 100 pCi/L in 1973 samples to less than the MDL in the 1987 samples. Initial high ^{3}H was attributed to a ^{3}H tracer introduced into this well in the early 1960s (Lyles, 1990). ^{3}H was reported below MDLs (10 to 30 pCi/L) for subsequent analyses. • ^{14}C, ^{90}Sr, ^{99}Tc, ^{137}Cs, and Pu were reported below or near the MDL for samples collected between 1989 and present (values reported near the MDL are likely to be nondetects). • For the 1993 sample, ^{36}Cl was reported as 2.4E-04 pCi/L.

Note: Concentrations reported with a “<” are less than the MDL (the MDL follows the “<”).

Table D-2
Summary of Near Field Wells and Associated Underground Nuclear Detonations in Yucca Flat/Climax Mine CAU

Detonation Characteristics									Near Field or Hot Well Characteristics			
Detonation Name	**Hole Name**	**Announced Yield (kt)**	**Surface Elevation [a] (m)**	**Working Point Depth (m)**	**R_c [b] (m)**	**Working Point HSU**	**Water Level Depth (m)**	**Working Point SZ or UZ**	**Name**	**Open Interval HSU**	**Location**	**Orientation**
ALEMAN	U-3kz	<20	1,245	503	33	TM-LVTA	475	SZ	UE-3e 4 P1	LTCU	105 m north	Slant
									UE-3e 4 P2	LTCU	179 m north	
									UE-3e 4 P3	TM-LVTA	275 m north	
BASEBALL	U-7ba	20–150	1,259	564	63	LTCU	458	SZ	U-7ba PS 1 AS	LTCU	Cavity, Chimney	Slant
BILBY	U-3cn	249	1,242	714	70	OSBCU	509	SZ	U-3cn PS 2	OSBCU	Chimney	Vertical
									U-3cn 5	LCA	129 m southeast	Vertical
BOURBON	U-7n	20–200	1,333	560	53	LCA	601	UZ	UE-7ns	LCA	137 m from working point	Vertical
DALHART	U-4u	<150	1,256	640	61	LTCU	477	SZ	U-4u PS 2A	LTCU	Chimney	Slant
GASCON	U-4t	20–150	1,263	593	62	LTCU	490	SZ	U-4t PS 3A	LTCU	54 m from cavity	Slant
									UE-4t 1 UE-4t 2	LTCU	170 m south	Vertical
INGOT	U-2gg	20–150	1,307	500	65	TM-WTA	564	UZ	U-2gg PSE 3A	TM-LVTA	65 m below working point	Slant
NASH	U-2ce	39	1,452	364	29	LCA3	527	UZ	UE-2ce	LCA3	183 m from working point	Vertical
TORRIDO	U-7w	20–200	1,297	515	71	OSBCU	566	UZ	ER-7-1	LCA	200 m from working point	Vertical

Source: DOE/NV, 1997 and 2000; FFACO, 1996, as amended; BN, 2006

[a] Modified from information in DOE/NV, 2000

[b] Calculated for non-LCA/LCA3 working point detonations as $R_c = 70.2 * Y^{1/3} / [rho_{ob} * WP]^{1/4}$ (Pawloski, 1999) where Y is the maximum announced yield (kt), (DOE/NV, 2000) rho_{ob} is the overburden density (Mg/m^3), and WP is the working point depth (m). Calculated cavity radius for carbonate rock working point test BOURBON, $R_c = [in\ m\ 9.05 * Y^{1/3}\ (kt)]$, from Boardman (1970). Cavity radius for the carbonate rock working point test NASH is the measured value from Carle et al. (2008)

model presented in Section 4.5 while the later are relevant for comparison to the contaminant concentrations calculated in the saturated LCA transport model presented in Section 6.5.

D.2.0 Observation Wells Completed in Saturated Alluvial-Volcanic Aquifer System Near Underground Nuclear Detonations

Observation wells have been completed in the saturated alluvial/volcanic aquifer system near the ALEMAN, SANDREEF, BASEBALL, DALHART and GASCON underground nuclear detonations. The hydrogeologic conditions and observed radioisotope concentrations at wells near these locations are discussed below.

D.2.1 ALEMAN and SANDREEF

ALEMAN was detonated in 1986 with an announced yield of less than 20 kt (Table D-2). The ALEMAN detonation was located at a depth of 503 m bgs in tuff; the water table was reported to be 475 m (Table D-2). The SANDREEF detonation (1977) with an announced yield of 20 to 150 kt and a working point depth of 701 m bgs was located about 350 m from the ALEMAN detonation. In 1985 and 1986, when the ALEMAN emplacement hole (U-3kz) was being installed, radionuclides were found in water pumped from the hole. The origin of the radionuclides was determined to be the SANDREEF detonation (Thompson et al., 1999). The ALEMAN and SANDREEF detonations (illustrating a 2 R_c estimation from Pawloski, 1999) are shown in Figure D-2.

Hole UE-3e 4 was completed 58 m from the ALEMAN working point with three piezometer tubes accessing depths 655 to 662 m (tube 1), 575 to 582 m (tube 2), and 493 to 500 m (tube 3) (SNJV, 2007). ^{137}Cs was found at an approximate depth of 650 m in UE-3e 4 sidewall samples and was determined to likely come from the SANDREEF detonation (SNJV, 2007). Although sampling was preceded by several bailer swabs in an attempt to clean the piezometer tubes, samples indicated significant quantities of cement and a corresponding high pH. Radionuclide activities measured in samples collected from the three piezometer tubes normalized to the MCL are shown in Figure D-3. From Figure D-3 it is apparent that only ^{3}H exceeds the MCL in these samples and that the other detected radionuclides are present at levels more than two orders of magnitude lower than the MCL. Samples from the deepest interval consistently had higher ^{3}H concentrations than in the other two tubes. It is possible that measured ^{3}H is also influenced by the SANDREEF detonation.

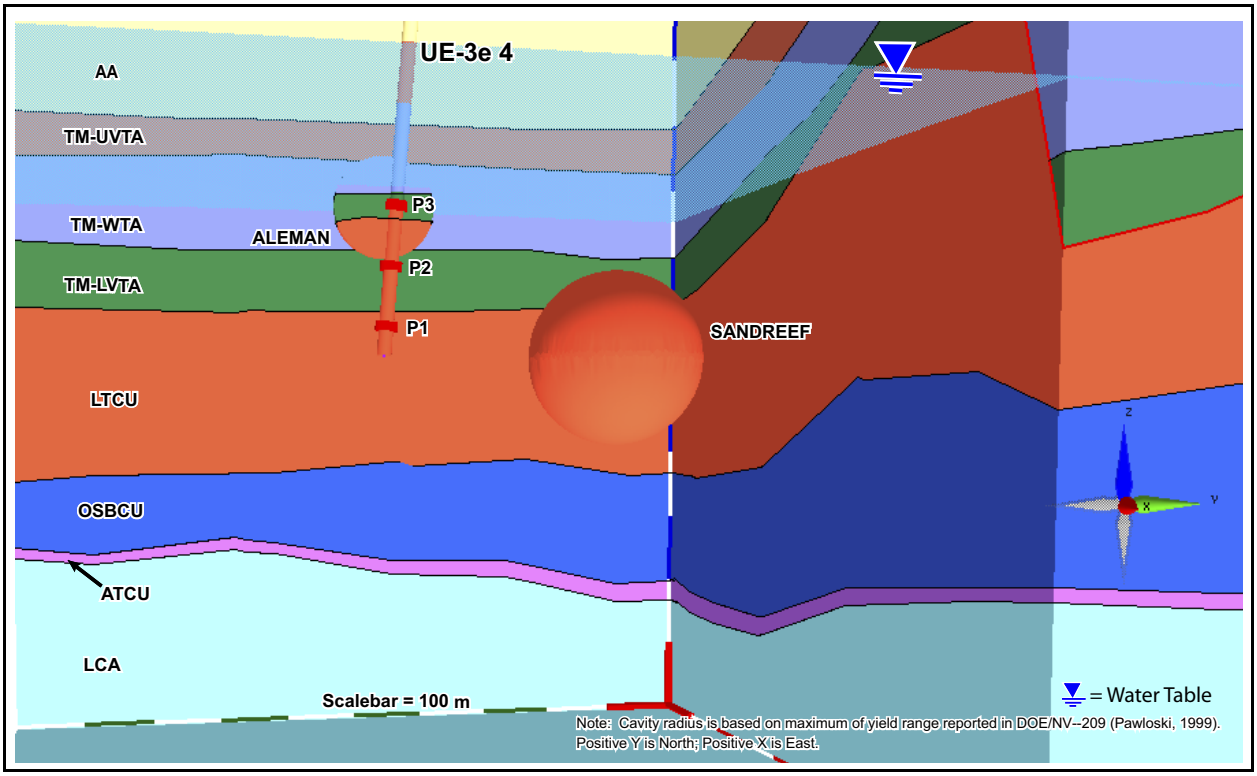

Figure D-2
Perspective View of ALEMAN and SANDREEF (2 R_c) and Well UE-3e 4

D.2.2 BASEBALL

BASEBALL was detonated in 1981 with an announced yield of 20 to 150 kt (Table D-2). The BASEBALL working point was at a 564-m depth in saturated tuff and at106 m below the local volcanic aquifer water table (Table D-2). Different water levels measured pre- and post-testing indicate the water levels may have been affected by testing (SNJV, 2007).

In 1994, the U-7ba PS 1AS post-test hole was drilled into the BASEBALL cavity. The BASEBALL detonation (illustrating a 2 R_c estimation from Pawloski, 1999) and the U-7ba PS 1AS post-test hole are shown in Figure D-4. During post-test drilling, radiation levels in the upper part of the cavity were measured using a high-sensitivity gamma detector. The results showed extremely heterogeneous radionuclide deposition in the cavity region. An extreme variability of radionuclide content exists in samples taken from locations close to one another even at the same depth (SNJV, 2007).

In July 1995, bailed samples were taken at several intervals in U-7ba PS 1AS; however, the borehole was never cleaned out and it is possible that little or no communication occurred between the water in the casing and the formation water since the time the hole was drilled. Notably, the ^{3}H activities in the

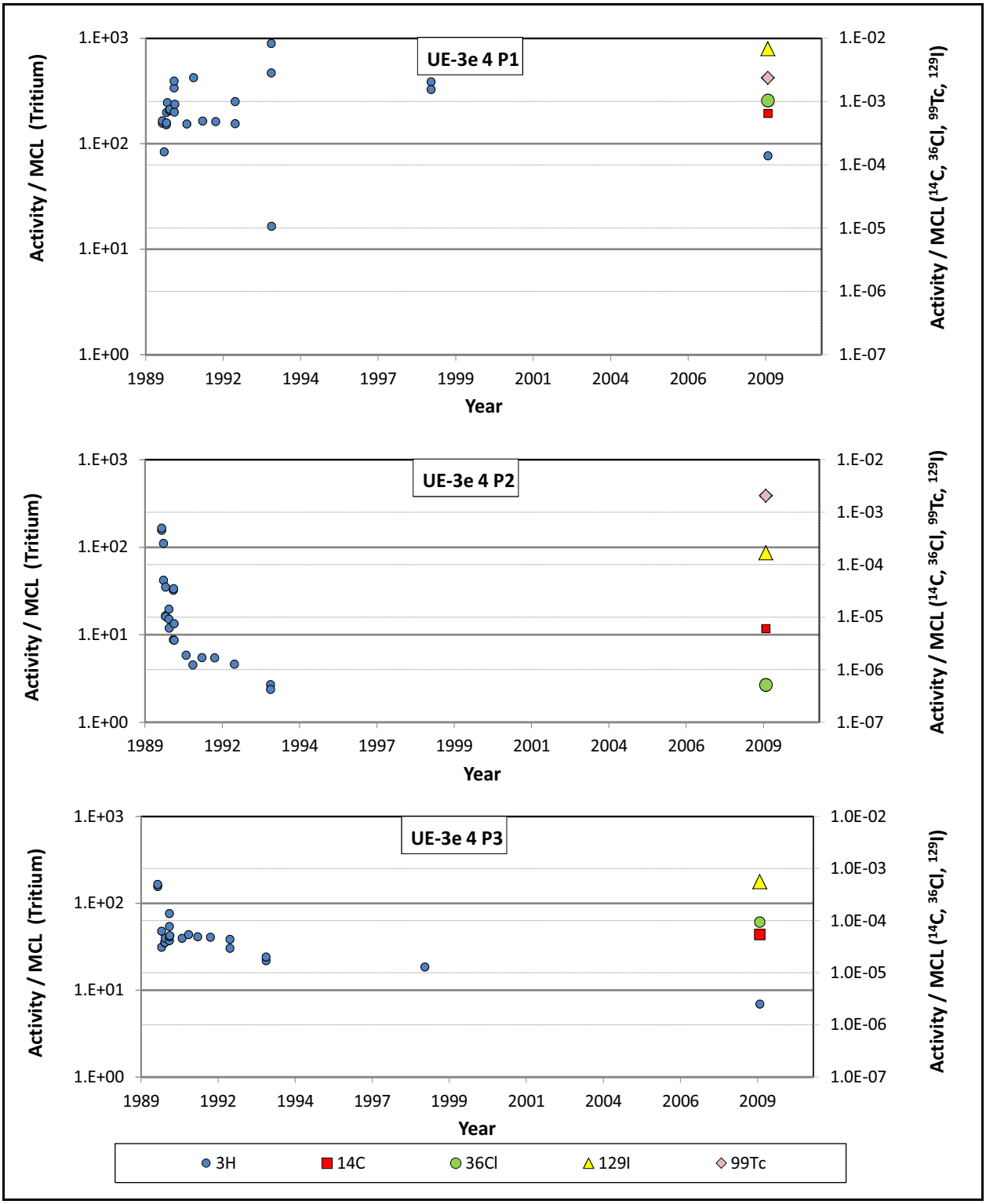

Figure D-3
Radionuclide Activity Relative to MCL for Well UE-3e 4

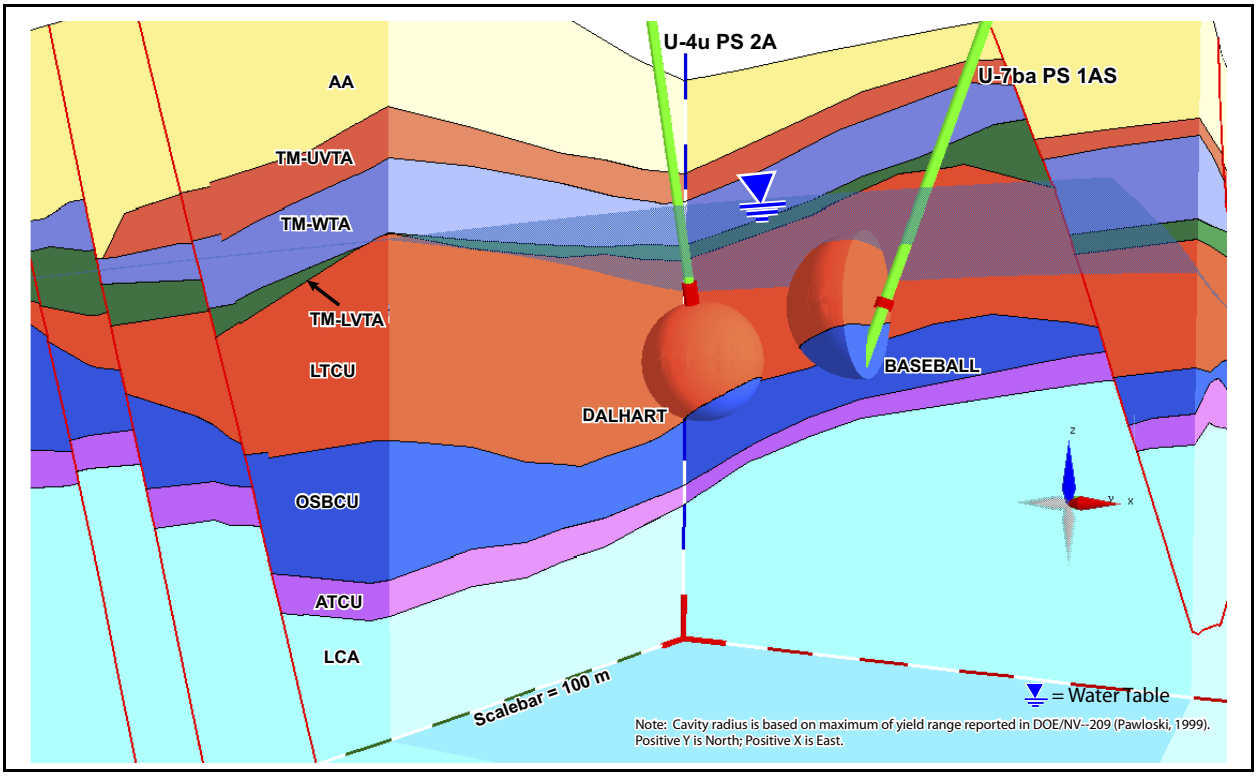

Figure D-4
Perspective View of BASEBALL and DALHART Detonations (2 R_c) and Wells U-4u PS 2A and U-7ba PS 1AS

bailed samples (5.5×10^6 to 4.3×10^7 pCi/L) is consistent with the ^{3}H concentrations found in water from earlier core samples (10^6 to 10^8 pCi/L). Both the ^{3}H and ^{137}Cs measured in these samples exceed the MCL (Table D-1).

Radionuclides appear to have remained where originally deposited during the formation of the BASEBALL cavity and chimney. During a 13-year span from the detonation and drill backs, there appears to have been little vertical or horizontal migration of ^{3}H. Gamma activity was not detected above the water table or significantly outside the cavity radius.

D.2.3 DALHART

DALHART was conducted in 1988 with an announced yield of less than 150 kt (Table D-2). The working point was at a depth of 640 m bgs in saturated zeolitized tuff; the water level was at a depth of 477 m bgs (Table D-2).

In 1990, the post-test drillback U-4u PS 2A was completed with a slotted interval between 472 and 501 m (Figure D-4); 139 to 168 m above the working point (2.25 to 2.75 R_c). Radioactivity in drilling fluids was first encountered at 532 m bgs. ^{137}Cs was detected in core samples from 525 m bgs, 115 m above the working point (1.9 R_c). No radioactivity was observed in the vadose zone (SNJV, 2007).

Although water samples have been collected intermittently at this site since 1992, the well had not been thoroughly cleaned out until 2003. Early samples had a significant particulate load resulting from drilling mud. Samples were collected in 2003 and 2008 using a low-flow coil pump after purging 26.7 m^3 (2003) and 21.5 m^3 (2008) of water from the well.

Both non-sorbing and colloid-associated radionuclides (e.g., Pu) migrated at least 2 to 3 R_c vertically in the DALHART chimney over the 20-year period following detonation. The detected radioisotopes normalized to the MCL are presented in Figure D-5. Figure D-5 shows that only ^{3}H exceeds the MCL; even though the ^{14}C activity at DALHART is the highest recent measurement made by LLNL for all of the NNSS wells, it is still below the 2,000 pCi/L MCL (Zavarin, 2009a). The ^{3}H activities, decay corrected to the time of test, are quite similar between the 2003 (6.2E+07 pCi/L) and 2008 (7.1E+07 pCi/L) samples. Although filtration experiments showed that the majority of the Pu in the 2008 sample is associated with colloids that are 40 nanometers (nm) or greater in size, approximately 35 percent of the Pu was either aqueous or associated with colloids that are 10 to 40 nm in size.

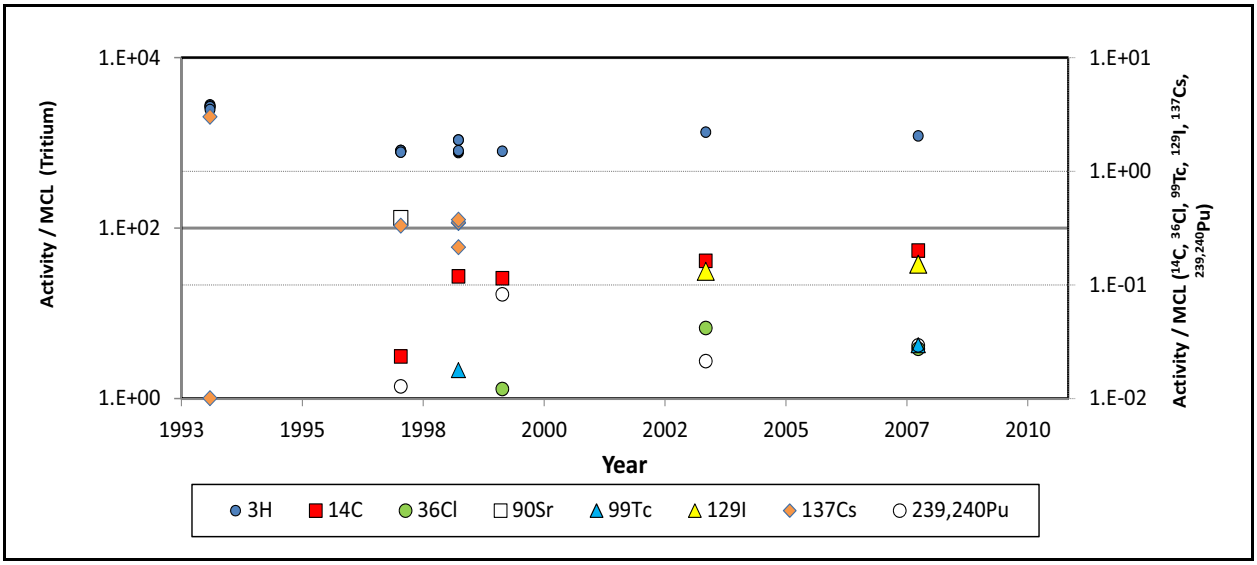

Figure D-5
Radionuclide Activity Relative to MCL for U-4u PS 2A

D.2.4 GASCON

GASCON was a 20- to 150-kt detonation conducted in 1986 (Table D-2). The working point was at a depth of 593 m bgs in the LTCU. In 1987, a vertical exploratory hole (UE-4t) was drilled 170 m south-southwest of the GASCON emplacement hole to a depth of 736 m. The hole includes two piezometer tubes perforated at 581 to 607 m bgs (UE-4t 1) and 477 to 526 m bgs (UE-4t 2). In May 1993, a post-test hole (U-4t PS 3A) was drilled to within 54 m of the cavity wall and extended underneath the cavity (Figure D-6).

^{3}H activities below or near the MDL (8.4 to 1,080 pCi/L) were reported for UE-4t 1 samples collected in 1990, 1992, 2000 and a UE-4t 2 sample collected in 2000. In 2008, samples were collected from both UE-4t piezometers and Well U-4t PS 3A. No radioisotopes were detected above the MCL in these samples (Table D-1). The ^{3}H activity in all three samples was low; the highest activity was reported for the U-4t PS 3A sample (2,970 pCi/L) followed by the upper piezometer, UE-4t 2 (1,690 pCi/L). The very low ^{3}H activity in the lower piezometer, UE-4t 1 (68 pCi/L), is consistent with the high water levels in this interval which suggests that the completion zone is not hydraulically connected to the post-shot nearfield (Zavarin, 2009b).

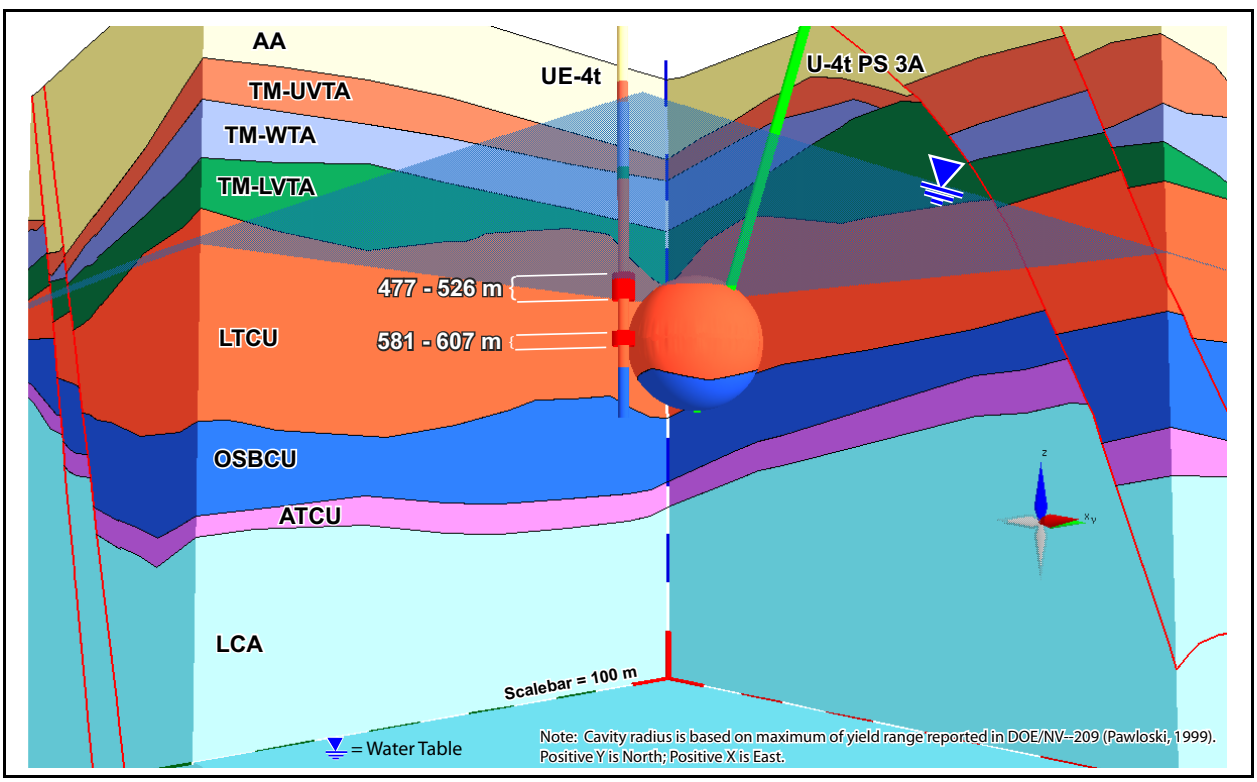

Figure D-6
Perspective View of GASCON Detonation (2 R_c) and Wells U-4t PS 3A and UE-4t

D.2.5 INGOT

INGOT was detonated in 1989 with an announced yield of 20 to 150 kt (Table D-2). The working point was located at a depth of 500 m bgs in unsaturated tuff about 250 m above the Paleozoic carbonates and about 64 m above the water table (Table D-1). A drill back hole, U-2gg PSE 3A, was slant-drilled to pass within 10 m of the edge of the cavity at the working point level (i.e., a total depth 46 m below the water table). The INGOT detonation (illustrating a 2 R_c estimation from Pawloski, 1999) and U-2gg PSE 3A are shown in Figure D-7. The drillback results show that in addition to ^{3}H, gaseous fission daughter products are abundant and may be encountered 10 m or more from the cavity edge. Late-time gaseous transport of ^{137}Xe and ^{90}Kr is believed to be responsible for dispersion and subsequent deposition of ^{137}Cs and ^{90}Sr (SNJV, 2007).

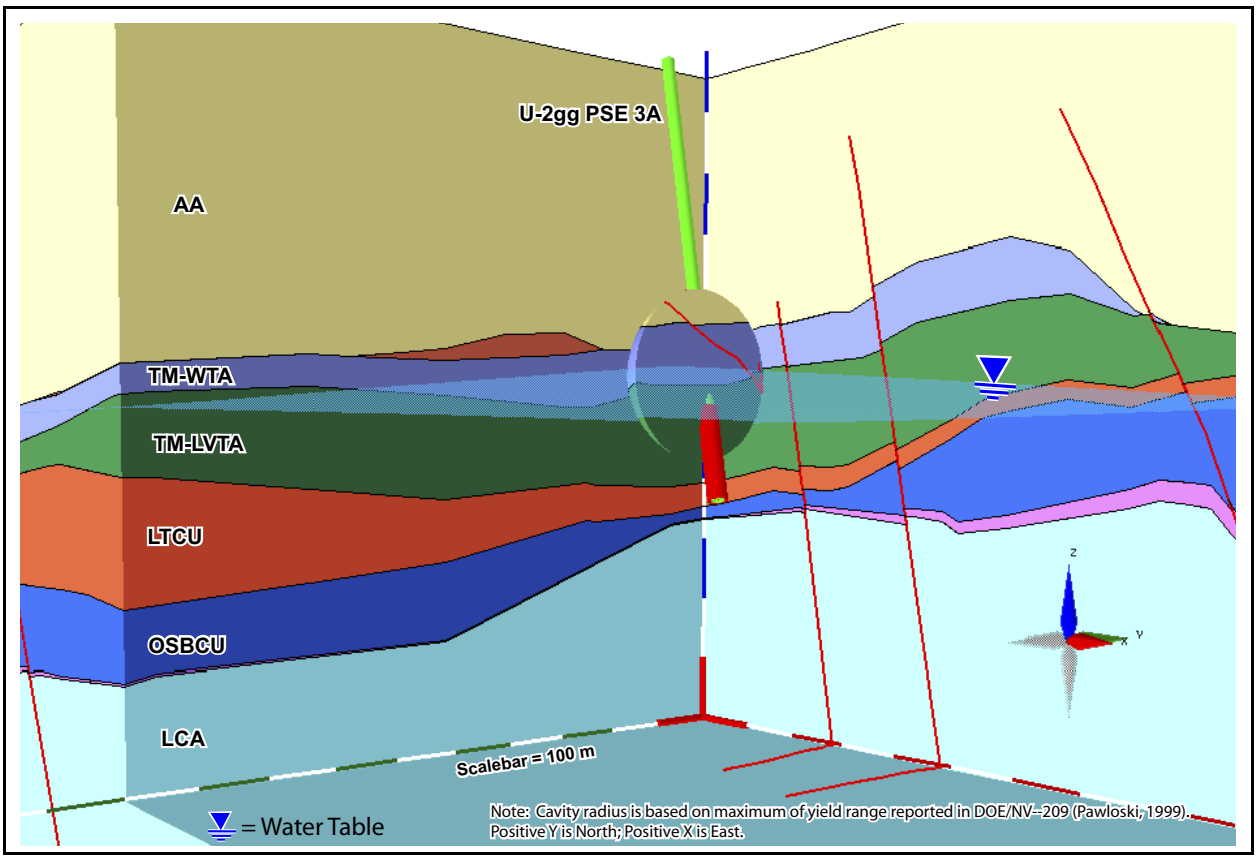

Figure D-7
Perspective View of INGOT Detonation (2 R_c) and Well U-2gg PSE 3A

Samples were collected from U-2gg PSE 3A in 1994. Measured ^{3}H activities are on the order of 5,000 to 7,500 pCi/L (Table D-1), below the 20,000 pCi/L MCL. The ^{137}Cs and ^{85}Kr activities were less than 10 pCi/L and 20 pCi/L, respectively. This can be compared to the 1E+03 to 3E+06 picocuries per kilogram (pCi/kg) measured in rubble material located approximately 10 m from the INGOT cavity edge. The ^{14}C activity was reported to be as high as 20,000 pCi/L; however, the value was reported only once (SNJV, 2007).

In summary, bailed groundwater samples collected from below the INGOT cavity suggests that very little radioactivity reached the water table.

D.3.0 Observation Wells Completed in Saturated Lower Carbonate Aquifer Near Underground Nuclear Detonations

Observation wells have been completed in the saturated LCA near the BILBY, BOURBON, NASH and TORRIDO/MICKEY underground nuclear detonations. While the working point for the BILBY detonation is in the saturated tuff confining unit and the working point for the TORRIDO and MICKEY detonations are in the unsaturated tuff confining unit above the LCA, these working points are close to the saturated LCA and close to where nearby observation wells are located so they are included in this section. The hydrogeologic conditions and observed radioisotope activities at wells near these locations are discussed below.

D.3.1 BILBY

The BILBY detonation (249 kt, 70-m cavity radius) was emplaced in zeolitized tuff at a depth of 714 m within about 150 m of the LCA. The bottom of the BILBY cavity is estimated to be approximately 60 m from the tuff-carbonate contact.

A post-shot diagnostic hole, Well U-3cn PS 2, was drilled into the BILBY chimney and cavity (Figure D-8). Its construction began on September 23, 1963, ten days after the BILBY detonation. It reached a maximum depth of 793 m, close to the bottom of the cavity. Well U-3cn PS 2 has perforations approximately 200 m above the working point and is open to the cavity, but crimping below the perforations prevented sampling at the lower level. A development and testing chronology for this well is given in Table B.1 of Tompson (2008).

Between 1964 and 1966, a series of five aquifer tests were conducted in Well U-3cn PS 2, extracting water from two distinct intervals. One was located in a 213-m stretch at the bottom of the hole, crossing the cavity, and the other was in a 15-m, packed-off interval just below the water table at a 512-m depth (Figure D-8). ^{3}H activities from the first three tests, near the cavity, were between 2E+08 and 3E+08 pCi/L, about 10,000 times the MCL (Figure D-9). ^{3}H activities for samples collected during the latter two tests from the chimney region above the cavity were between 1E+06 and 1E+08 pCi/L. Additional samples were obtained from well U-3cn PS 2 between 1977

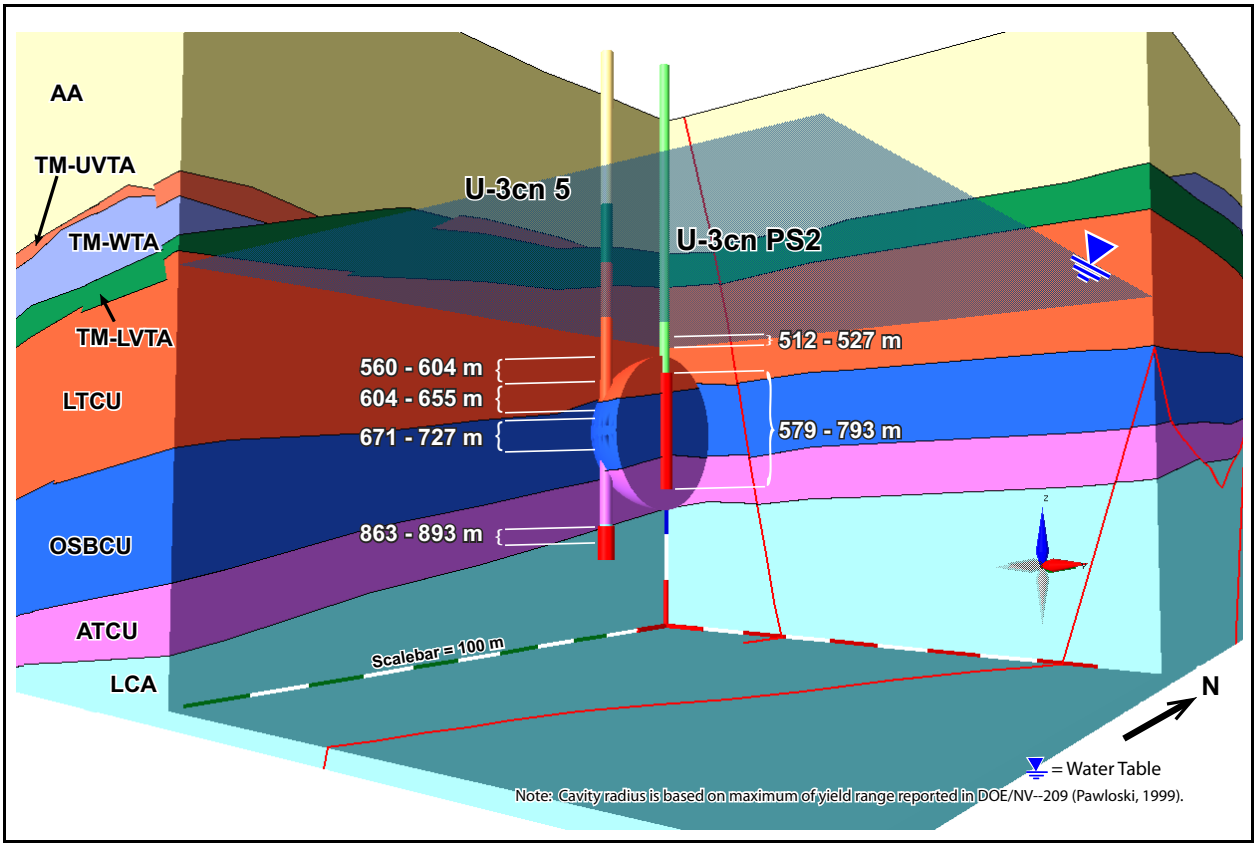

Figure D-8
Perspective View of BILBY Detonation (2 R_c) and Wells U-3cn 5 and U-3cn PS2

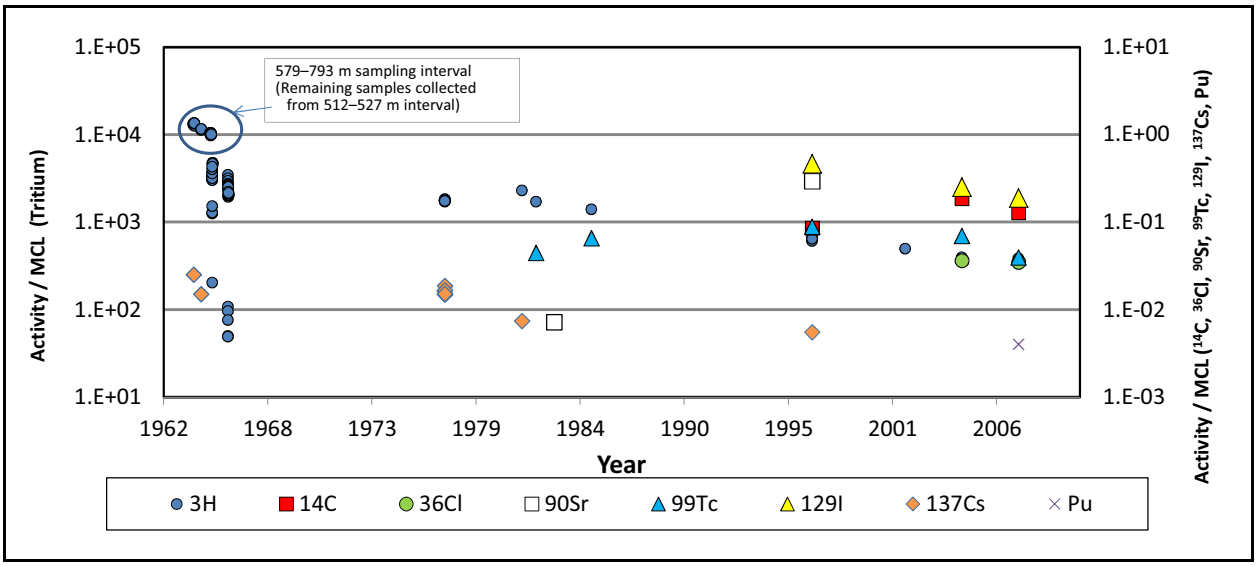

Figure D-9
Radionuclide Activity Relative to MCL for U-3cn PS 2

and 2007 using a new pump located at the upper interval near the water table. Radioisotope measurements in these samples indicated the presence of ^{3}H, ^{14}C, ^{36}Cl, ^{90}Sr, ^{99}Tc, ^{106}Ru, ^{129}I, ^{137}Cs, ^{234}U, ^{235}U, ^{238}U, and $^{239+240}Pu$.

Drill hole U-3cn 5 is a satellite well located approximately 121 m from U-3cn PS 2. Its construction began on September 24, 1965, and it was drilled to a depth of over 900 m to a point well below the BILBY cavity (Figure D-8). The satellite well was drilled to evaluate the connectivity between the tuff confining unit and carbonate aquifer. Water levels in the satellite well completed in the LCA are 15.8 m lower than the post-test hole. Thus, the groundwater gradient is from the tuff to the carbonate.

A U-3cn 5 development and testing chronology is given in Tompson (2008). Between 1965 and 1973, a series of hydraulic tests were conducted, extracting water from several distinct intervals located at, above, and below the general cavity elevation (Figure D-8). Hydraulic tests were successful in drawing water from intervals 560 to 604 m, 604 to 655 m, 671 to 727 m, 863 to 893 m, and 863 to 922 m. Hydraulic testing at the 863 to 922 m interval was continued for an additional 2.5 years.

^{3}H activities measured in these tests, normalized to the MCL, are shown in (Figure D-10). Notably, the activities were highest in the test of the 671 to 727 m interval, and only after a period of steady pumping did they rise to 1.3E+08 pCi/L. In tests of intervals 604 to 655 m and 560 to 604 m, ^{3}H activities were in the range of 2.7E+06 to 8.1E+06 pCi/L. ^{3}H activities were much smaller (i.e., less than 1.3E+03 to 1.4E+05pCi/L) for the 863 to 893 m interval. All but the first three samples collected from the 863 to 922 m interval (tested from November 21 to 23, 1966 and March, 1967 to September, 1969) were below the 1.5E+03 pCi/L MDL.

Between 1980 and 2000, additional samples were obtained, first from the 863 to 922-m interval (1980 to 1982) and later from a shallower interval between 691 and 688 m (1997 to 2000). Radioisotope measurements in these samples indicated the presence of ^{3}H, ^{14}C, ^{137}Cs, ^{155}Eu, ^{234}U, ^{235}U, ^{238}U, and $^{239+240}Pu$. ^{3}H levels were in the range of 135 to 270 pCi/L. In addition, numerous other isotopes are indicated in this region of the altered system.

In summary, the observation wells drilled in the vicinity of the BILBY detonation offer a unique opportunity to evaluate not only the contamination in the detonation cavity vicinity in the tuff confining unit, but also the potential effect of an exchange volume that could extend into the saturated LCA, given the working point is located within about 1.7 R_c of the saturated LCA. The data indicate

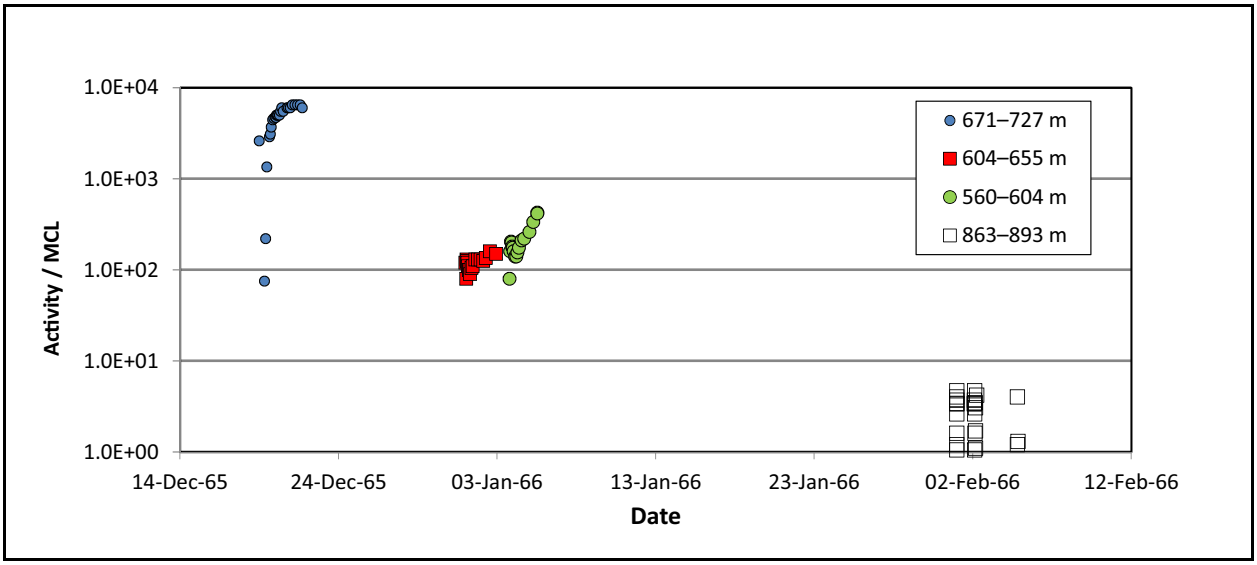

Figure D-10
Tritium Activity Relative to MCL for U-3cn 5

initial contamination within a distance of 2.5 R_c of the working point in the tuff confining unit. It appears from these analyses that upward migration of radionuclides into the chimney (possibly as a result of test-induced heat) has occurred (SNJV, 2007). Although some contamination of the underlying LCA has occurred, the concentrations are significantly lower than those observed in the overlying units. Pumping rates of 50 gpm were used in the satellite well which may not have provided a sufficient gradient to draw the BILBY cavity or exchange volume contaminants to the satellite well. Due to the spatially heterogeneous nature of fracture flow in the carbonate aquifer, contamination of the carbonate aquifer cannot be ruled out based on sampling of U-3cn 5 (SNJV, 2007).

D.3.2 BOURBON

BOURBON was detonated in 1967 at a depth of 560 m, with an announced yield of 20 to 200 kt (Table D-2). The rock at the working point was a silty limestone and located very close to the tuff-Paleozoic carbonate boundary. The water table depth is reported as 601 m (Table D-2). Thus, the bottom of the BOURBON cavity is likely located in the saturated LCA.

A satellite well, UE-7nS, was drilled in 1976 to a depth of 672 m with the bottom 62 m slotted. The satellite well is located 137 m southeast of the emplacement hole (Figure D-11). A fault was identified at 594 m, very close to the water table. A pump was installed in the satellite well, but the yield was too low to adequately clean out the well. Groundwater has been sampled at this well

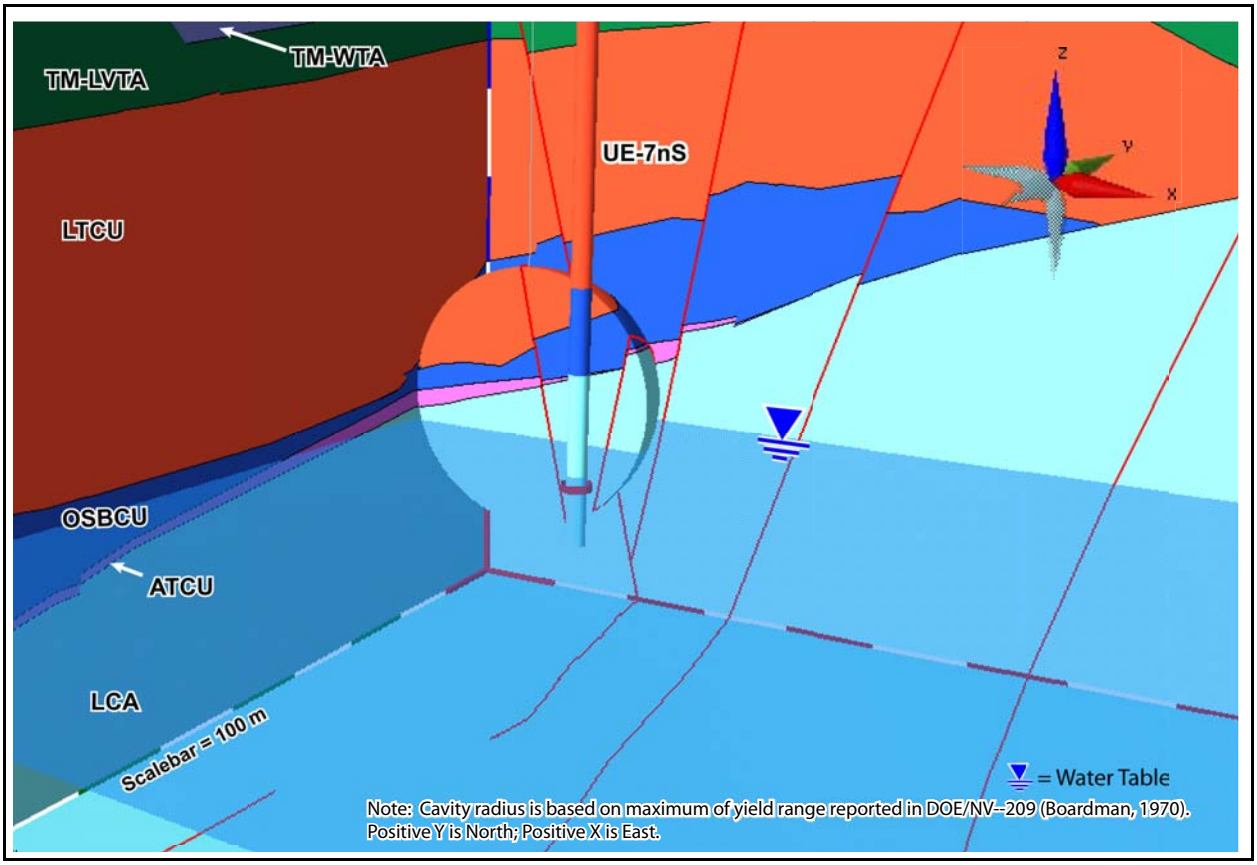

Figure D-11
Perspective View of BOURBON Detonation (2 R_c) and Nearby Observations Wells

periodically by HRMP, LLHRMP. RREMP, and UGTA for a variety of radionuclides (Table D-1). The detected radionuclides, relative to the MCL, are presented in Figure D-12. The ^{14}C activity in the 2001 and 2004 samples are essentially the same, while a decrease in ^{3}H (4,600 to 132 pCi/L), ^{36}Cl (1.4E-03 to 2.4E-04 pCi/L), and ^{129}I (6.1E-04 to 4.1E-05 pCi/L) was observed over this time period. Pu was not detected. The analytical results suggest poor communication between the BOURBON cavity and the satellite well (Zavarin, 2006). This well was not purged prior to sampling so it is possible that these decreases are a sampling artifact.

D.3.3 NASH

NASH was detonated in 1967 with an announced yield of 39 kt (Table D-2). The NASH detonation was located at a depth of 365 m bgs in the LCA3. The NASH working point was above the water table. The tuff-carbonate contact is located at 340 m.

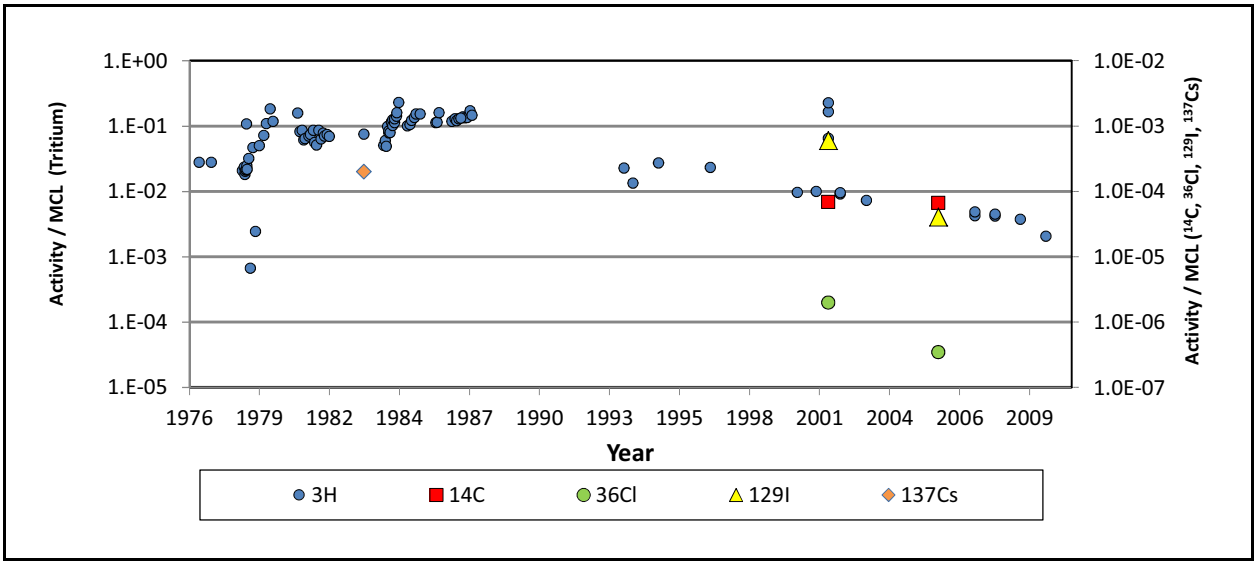

Figure D-12
Radionuclide Activity Relative to MCL for UE-7ns

A satellite well, UE-2ce, was completed in 1977 to a total depth of 503 m with the bottom 73 m slotted in the LCA3. Well UE-2ce is located approximately 183 m south of the NASH working point (Figure D-13). A long-term pumping experiment was performed at the NASH site that was meant to be analogous to the radionuclide migration pumping experiment performed at the Frenchman Flat CAMBRIC site. Pumping at Well UE-2ce began in 1977. The ^{3}H concentrations rose with the cumulative volume of water pumped from the well. By late 1977, a few thousand cubic meters of water had been pumped, and the ^{3}H concentration had begun to level off at approximately 10^{7} to 10^{8} pCi/L, decay corrected to the time of the detonation. The pump in UE-2ce failed in 1984, after pumping approximately 42,000 m^{3}. Bailed samples were collected between 1993 and 2005 and the ^{3}H activities were approximately two orders of magnitude lower than in the earlier pumped samples (Table D-1). A new pump was installed in 2008 and multiple samples were collected over a 1-week period and analyzed for ^{3}H and ^{14}C; a final sample was collected on July 2 and analyzed for a larger suite of analytes (Table D-1). The ^{3}H activity decay corrected to the time of the detonation in the 2008 samples (2.8×10^{6} pCi/L) was substantially greater than the 2005 samples (8.3×10^{5} pCi/L) but still much lower than the pumped samples collected in 1984 (~5×10^{7} pCi/L). The approximate volume of groundwater purged in 2008 was 150 m^{3} so it is possible that additional pumping would increase ^{3}H activities at UE-2ce further (Zavarin, 2010).

The detected radioisotopes normalized to the MCL are presented in Figure D-14. Although non-sorbing and some sorbing radionuclides have been transported from the working point to the

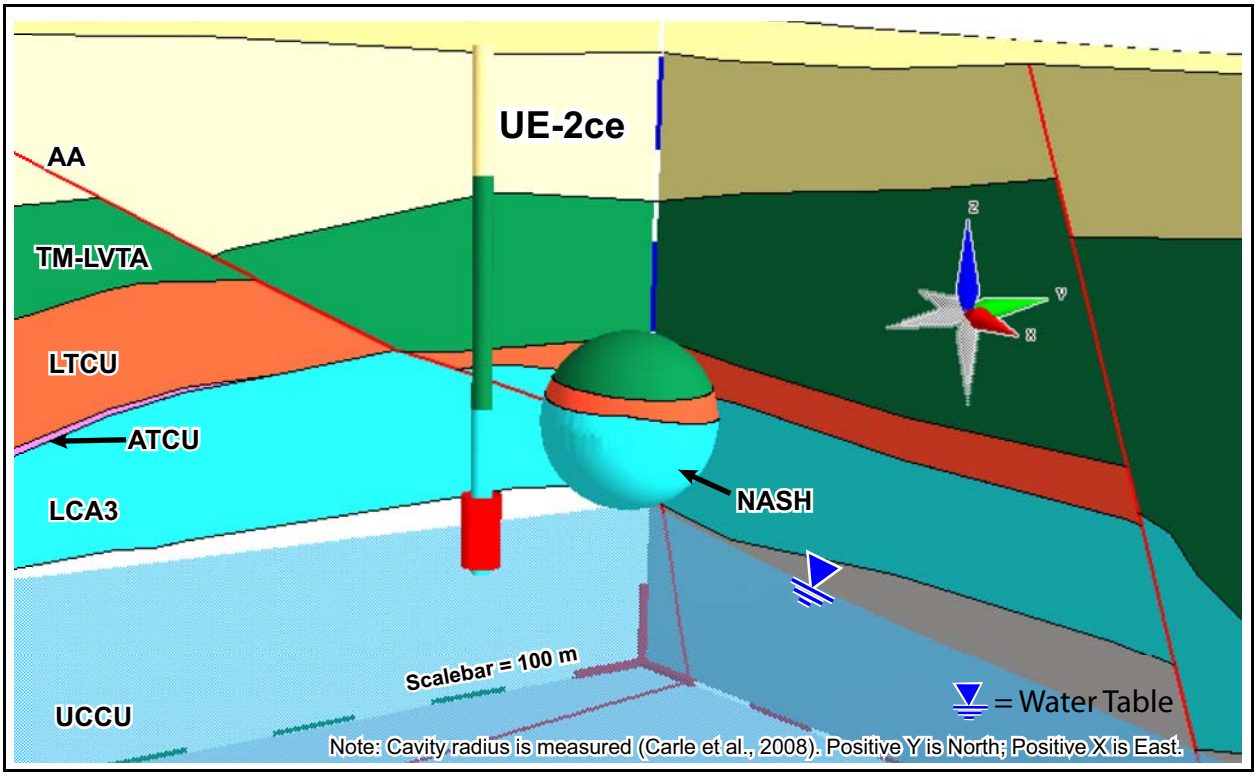

Figure D-13
Perspective View of NASH Detonation (2 R_c) and Well UE-2ce

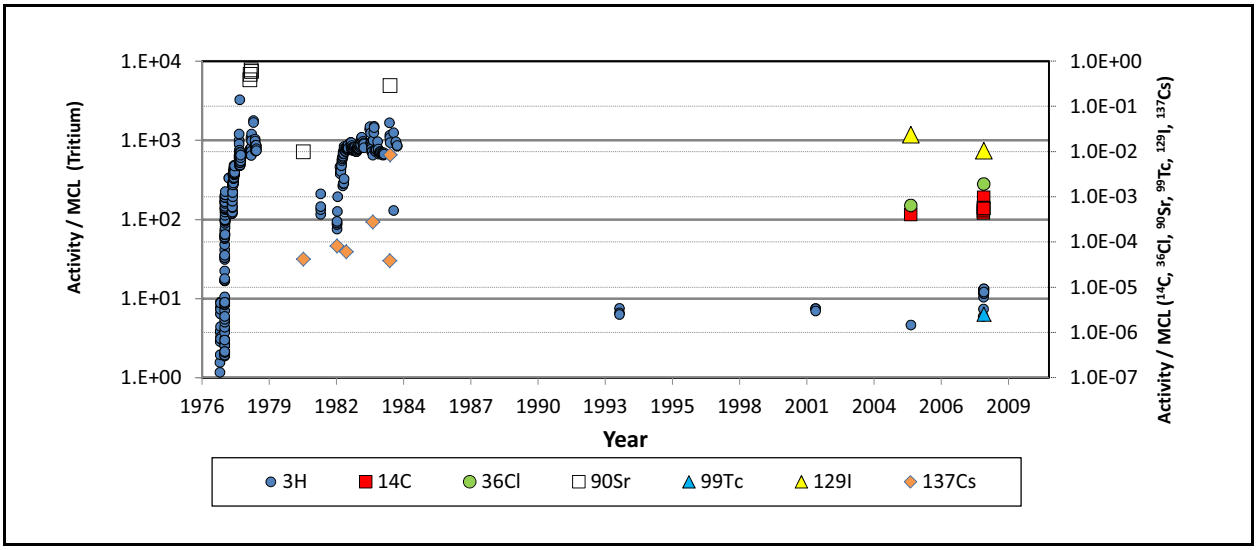

Figure D-14
Radionuclide Activity Relative to MCL for UE-2ce

satellite well in the carbonate aquifer, only ^{3}H exceeds the MCL (Figure D-14). Well UE-2ce is an important site because it is the only case in which it is clear that radionuclides from a nuclear test at the NNSS are present in the carbonate aquifer. Based on pumping data, it is estimated that only 0.7 to 1.3 percent of the ^{3}H source term has reached the NASH satellite well (Carle et al., 2008). It is not known whether this fraction represents prompt injection, intersection of the exchange volume with the water table, recharge through the vadose zone cavity, or a combination of these processes.

D.3.4 MICKEY and TORRIDO

MICKEY and TORRIDO were 20- to 200-kt detonations that took place in 1967 and 1969, respectively. The MICKEY working point was at a depth of 500 m bgs in the LTCU and the TORRIDO working point was at a depth of 515 m bgs in the OSBCU. These detonations were located about 200 m and 500 m downgradient from well ER-7-1 (Figure D-15). Even though contamination was initially estimated to be encountered in the LCA at ER-7-1, little detectable activity in the ER-7-1 groundwater was observed (Table D-1). ^{3}H was reported as 117.2 ± 4.3 pCi/L which was considered to be an upper limit due to possible post-sampling contamination.

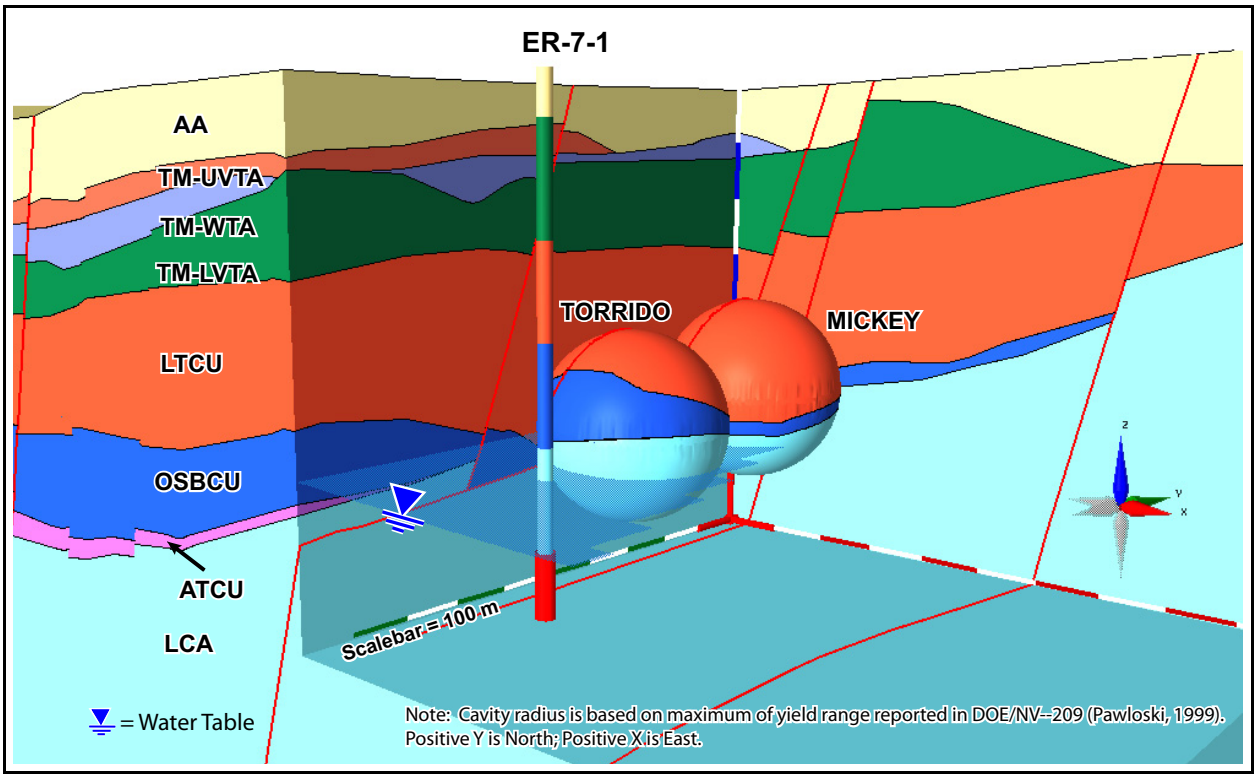

Figure D-15
Perspective View of TORRIDO and MICKEY Detonations (2 R_c) and Well ER-7-1

D.4.0 SUMMARY AND CONCLUSIONS

This appendix summarizes the currently available contaminant concentration information in the significant observation wells located in the vicinity of underground nuclear detonations conducted in Yucca Flat as well as other observation wells in Yucca Flat. These data provide a useful baseline for future model evaluation and monitoring.

D.5.0 REFERENCES

Bechtel Nevada. 2006. *A Hydrostratigraphic Model and Alternatives for the Groundwater Flow and* Contaminant Transport Model of Corrective Action Unit 97: Yucca Flat-Climax Mine, Lincoln *and Nye Counties, Nevada*, DOE/NV/11718--1119. Prepared for the U.S. Department of Energy, National Nuclear Security Administration Nevada Site Office. Las Vegas, NV.

BN, see Bechtel Nevada.

Boardman, C.R. 1970. "Engineering Effects of Underground Nuclear Explosives." In *Proceedings of Symposium on Engineering with Nuclear Explosives*, CONF-700101, 43–67. Las Vegas, NV, 14–16 January.

Bowen, S.M., D.L. Finnegan, J.L. Thompson, C.M. Miller, P.L. Baca, L.F. Olivas, C.G. Geoffrion, D.K. Smith, W. Goishi, B.K. Esser, J.W. Meadows, N. Namboodiri, and J.F. Wild. 2001. *Nevada Test Site Radionuclide Inventory, 1951–1992*, LA-13859-MS. Los Alamos, NM: Los Alamos National Laboratory.

Carle, S.F., M. Zavarin, Y. Sun, and G.A. Pawloski. 2008. *Evaluation of Hydrologic Source Term Processes for Underground Nuclear Tests in Yucca Flat, Nevada Test Site: Carbonate Tests*, LLNL-TR-403485. Livermore, CA: Lawrence Livermore National Laboratory.

DOE/NV, see U.S. Department of Energy, Nevada Operations Office.

Federal Facility Agreement and Consent Order. 1996 (as amended March 2010). Agreed to by the State of Nevada; U.S. Department of Energy, Environmental Management; U.S. Department of Defense; and U.S. Department of Energy, Legacy Management. Appendix VI, which contains the Underground Test Area Strategy, was last modified May 2011, Revision No. 4.

Lyles, B.F. 1990. *Tritium Variations in Groundwater on the Nevada Test Site*, DOE/NV/10384-38; Publication No. 45086. Las Vegas, NV: Desert Research Institute, Water Resources Center.

N-I, see Navarro-Intera, LLC.

Navarro-Intera Geographic Information Systems. 2012. ESRI ArcGIS Software.

Navarro-Intera, LLC. 2012. Written communication. Subject: "UGTA Geochemistry Database," UGTA Technical Data Repository Database Identification Number UGTA-4-129. Las Vegas, NV. As accessed on 1 September.

Pawloski, G.A. 1999. *Development of Phenomenological Models of Underground Nuclear Tests on Pahute Mesa, Nevada Test Site—BENHAM and TYBO*, UCRL-ID-136003. Livermore, CA: Lawrence Livermore National Laboratory.

Pawloski, G.A., A.F.B. Tompson, S.F. Carle, R.L. Detwiler, Q. Hu, S. Kollet, R.M. Maxwell, W.W. McNab, S.K. Roberts, D.E. Shumaker, Y. Sun, and M. Zavarin. 2008. Evaluation of Hydrologic Source Term Processes for Underground Nuclear Tests in Yucca Flat, Nevada Test Site: Introduction and Executive Summary, LLNL-TR-403428. Livermore, CA: Lawrence Livermore National Laboratory.

SNJV, see Stoller-Navarro Joint Venture.

Stoller-Navarro Joint Venture. 2007. *Phase I Contaminant Transport Parameters for the Groundwater Flow and Contaminant Transport Model of Corrective Action Unit 97: Yucca Flat/Climax Mine, Nevada Test Site, Nye County, Nevada*, Rev. 0, S-N/99205--096. Las Vegas, NV.

Thompson, J.L. 1999. *Laboratory and Field Studies Related to Radionuclide Migration at the Nevada Test Site: October 1, 1997-September 30, 1998*, LA-13576-PR. Los Alamos, NM: Los Alamos National Laboratory.

Tompson, A.F.B., ed. 2008. Evaluation of Hydrologic Source Term Processes for Underground Nuclear Tests in Yucca Flat, Nevada Test Site: Saturated Tests, LLNL-TR-403429. Livermore, CA: Lawrence Livermore National Laboratory.

U.S. Department of Energy, Nevada Operations Office. 1997. *Shaft and Tunnel Nuclear Detonations at the Nevada Test Site: Development of a Primary Database for the Estimation of Potential Interactions with the Regional Groundwater System*, DOE/NV--464, UC-400. Las Vegas, NV.

U.S. Department of Energy, Nevada Operations Office. 2000. *United States Nuclear Tests, July 1945 through September 1992*, DOE/NV--209-REV 15. Las Vegas, NV.

Zavarin, M., Lawrence Livermore National Laboratory. 2006. Memorandum to B. Wilborn (NNSA/NSO) titled “Isotopic Analyses: Monitoring Well UE-7ns,” 8 November.

Zavarin, M., Lawrence Livermore National Laboratory. 2009a. Memorandum to B. Wilborn (NNSA/NSO) titled “Isotopic Analyses: Monitoring Well U-4u PS#2 (Dalhart),” 22 December.

Zavarin, M., Lawrence Livermore National Laboratory. 2009b. Memorandum to B. Wilborn (NNSA/NSO) titled “Isotopic Analyses: Monitoring Wells U-4t PS#3a and UE-4t (Gascon),” 22 December.

Zavarin, M., Lawrence Livermore National Laboratory. 2010. Memorandum to B. Wilborn (NNSA/NSO) titled “Isotopic Analyses: Monitoring Well UE-2ce,” 24 August.

Appendix E

Enhanced Crater Recharge Model and Analyses

E.1.0 INTRODUCTION

A number of field and modeling studies in Yucca Flat and Frenchman Flat provide compelling evidence that surface runoff can be focused into nuclear subsidence craters and result in crater infiltration rates that are substantially higher than those in areas adjacent to the craters. Subsidence crater infiltration studies in Yucca Flat include those associated with the LAGUNA test at U-3fd in Area 3 (Tyler, McKay, and Mihevc, 1992; Pohll, Warwick, and Tyler, 1996), the BYE test at U-10i (French and Curtis, 1999; Hokett et al., 2000), and the HYRAX test at U3-bh (Kwicklis et al., 2006). Other studies characterized crater infiltration at the WISHBONE test at U-5a in central Frenchman Flat (Hokett and French, 1998; Wilson et al., 2000). Evidence for enhanced crater infiltration rates are based on differences in moisture content and water potential profiles from boreholes drilled within and adjacent to the craters, direct observations of ponding within the craters following rainfall events (U-10i, U-5fd), sediment deposits (U-10i, U-5a), and modeling.

Based on these studies, it was recognized that a GIS-based study of craters in Yucca Flat to characterize their dimensions (depth, surface and bottom diameters), contributing watershed areas, and evidence for past water transport (erosion features, playa deposits, and anomalous vegetation) would be invaluable for generalizing the results of the detailed crater infiltration studies cited above and for providing the fundamental data that would allow estimation of infiltration rates at the 462 subsidence craters that were eventually catalogued in Yucca Flat. Of these, three are related to detonations that are not relevant to UGTA, notably SEDAN, EES and UNCLE, leaving 459 subsidence craters of relevance to the unsaturated zone flow and transport model, The overall objective of the geographic information system (GIS) task was to characterize the craters in Yucca Flat. Characterization includes: (1) defining crater extents, bottoms, and depth; (2) associating different test events with the potential craters they produced; and (3) delineation of surface drainage and catchment areas for those craters that act as hydrologic sinks where rain and other surface water potentially infiltrates into the subsurface environment.

The net infiltration rate in non-cratered areas of Yucca Flat is very small (generally less than 0.1 mm/yr) or negative (moisture flux is upward) from ground surface to a depth of about 63 m below ground surface (Kwicklis et al., 2006). However, nuclear subsidence craters can intercept surface

water runoff and result in large infiltration volumes (Tyler, McKay, and Mihevc, 1992; Pohll, Warwick, and Tyler, 1996; Hokett et al., 2000; and Wilson et al., 2000). This section describes calculations that were conducted to estimate average annual infiltration into all 462 nuclear subsidence craters in Yucca Flat, Nevada.

This appendix summarizes the data and methods used to develop and calibrate models of surface runoff and infiltration into nuclear subsidence craters in Yucca Flat. The data inputs, parameters and calibration approach is presented in Section E.4.0 along with the actual calculation algorithms used to convert surface-water runoff volumes into ponding depths for use in 1-D models of crater infiltration.

Crater catchment areas were determined using ArcGIS spatial analyst tools. Calculations of surface water runoff volumes were conducted using the U.S. Department of Agriculture (USDA) Soil Conservation Service Curve Number (SCS-CN) method described in detail in USDA NRCS (2004), USDA NRCS (1986), Mishra and Singh (2003), and Hawkins et al. (2009). Runoff volumes from contributing catchments and from crater side walls were converted into a pond depth based on the crater geometry and assuming all craters can be approximated by a frustum. Daily calculations of precipitation plus pond height were then used as input to HYDRUS-1D (Šimůnek, van Genuchten, and Šejna, 2005) to calculate average annual infiltration. This approach is unique in that surface soil water potential was simulated for a 1,000-year period using HYDRUS-1D (calibrated to weighing lysimeter data) in order to calculate curve number on a daily basis. Surface soil water potential thresholds that separate antecedent runoff conditions (ARCs) I, II, and III were estimated during model calibration using ponding depth data, and soil moisture data from a handful of craters located in Yucca Flat and Frenchman Flat.

Calculations of long-term average annual net infiltration into all craters were conducted using stochastically generated 1,000-year daily precipitation records.

E.2.0 METHODS AND PARAMETERS

E.2.1 Crater Catchment Delineation

Crater catchment areas were estimated using satellite imagery and Geographic Information Systems (GIS) tools. Crater characterization included: 1) defining crater top and bottom diameters and depths; and 2) delineation of surface drainage and catchment areas for those craters that act as hydrologic sinks. All data processing was conducted using a combination of ENVI Ver. 4.3 and Arc/Info ArcGIS Ver. 9.2. A detailed digital elevation map (DEM) for Yucca Flat was created using DEMs from the USGS (http://seamless.usgs.gov), and from the Space Shuttle Radar Topography Mission (SRTM). The USGS DEM represents 1983 elevations while the SRTM represents 2000 elevations. The GIS analyses are presented in Section E.3.0.

E.2.2 Precipitation Data

All precipitation data were downloaded from the NNSS Air Resources Laboratory website (http://www.sord.nv.doe.gov/home_climate_rain.htm). Daily precipitation data were downloaded for stations BJY, PHS, and W5B. Data collection began in 1960, 1964, and 1963, for BJY, PHS, and W5B, respectively. Annual precipitation for these three stations is shown in Figure E-1. Average annual precipitation is 16.8, 19.1, and 12.6 cm/year, for BJY, PHS, and W5B, respectively, for the time period of 1965–2007 (43 years).

Ten replicates of daily rainfall records for 1,000 years were generated for the BJY station using the Stochastic Climate Library daily rainfall model (Srikanthan, Chiew, and Frost, 2007). The synthetic records were based on a 46 year record (1961–2006) of daily observations of 24 hour rainfall at BJY. Cumulative distribution functions (CDFs) of the annual precipitation totals for the 1,000-year synthetic precipitation records are shown in Figure E-1.

E.2.3 Potential Evapotranspiration

PET was calculated for a 10-year period of 1995–2004 using meteorological inputs from the Area 5 weighing lysimeter site and using the method of Hargreaves and Allen (2003). In order to generate a 1,000-year PET record, a sine curve was fit through the 10-year record of calculated PET, and PET

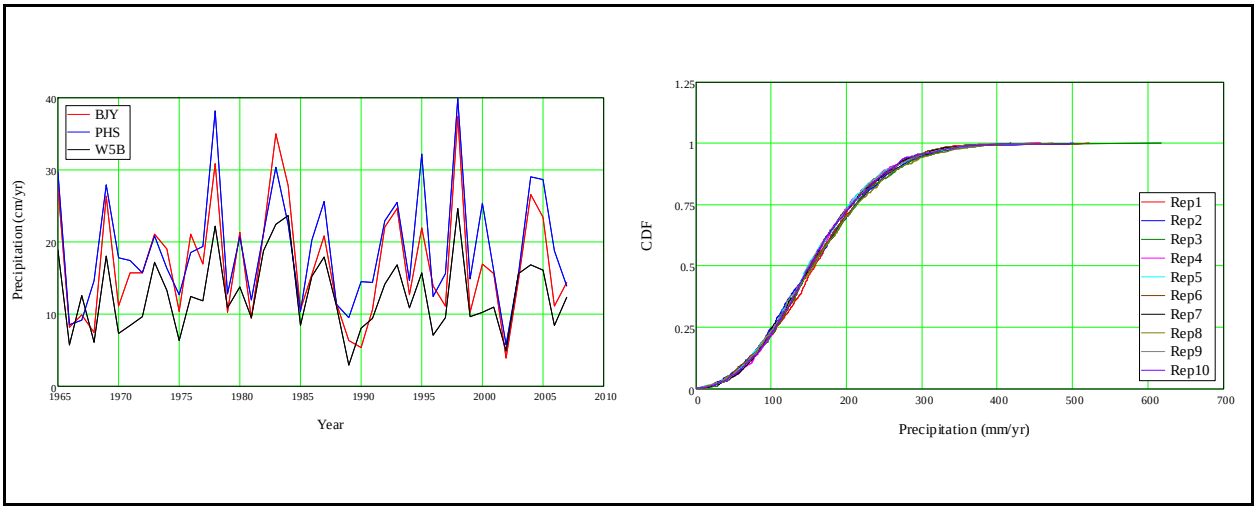

Figure E-1
43-Year Precipitation Record from BJY, PHS, and W5B (Left) and
CDFs of Annual Precipitation from 1,000-Year Synthetic Precipitation Record (Right)

was reduced by 50 percent during any day with measurable precipitation. Figure E-2 shows calculated PET and sine curve fitted PET.

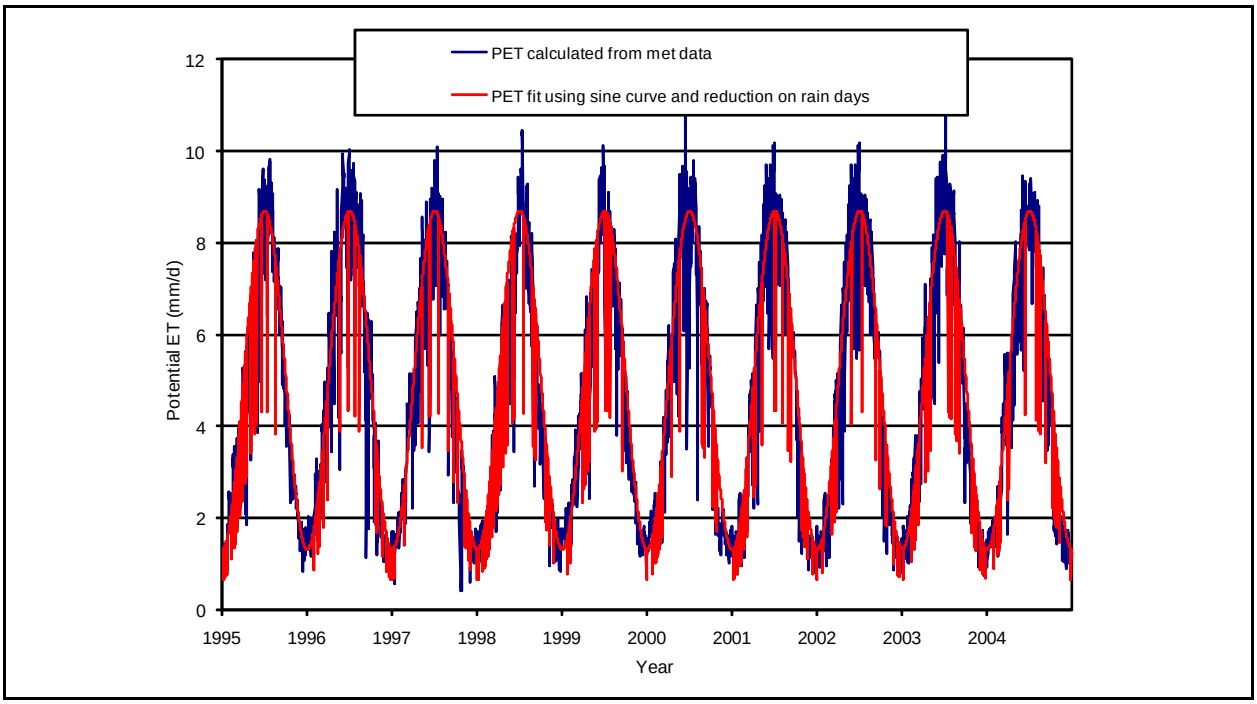

Figure E-2
Calculated and Sine Curve Fitted PET

E.2.4 Calibration of HYDRUS-1D to Lysimeter Data

Two weighing lysimeters, one vegetated and the other nonvegetated, were installed about 400 m west of the Area 5 Radioactive Waste Management Site (RWMS) at the north end of Frenchman Flat at the NNSS. A schematic diagram of the lysimeter design, and a photo of the nonvegetated lysimeter are shown in Figure E-3.

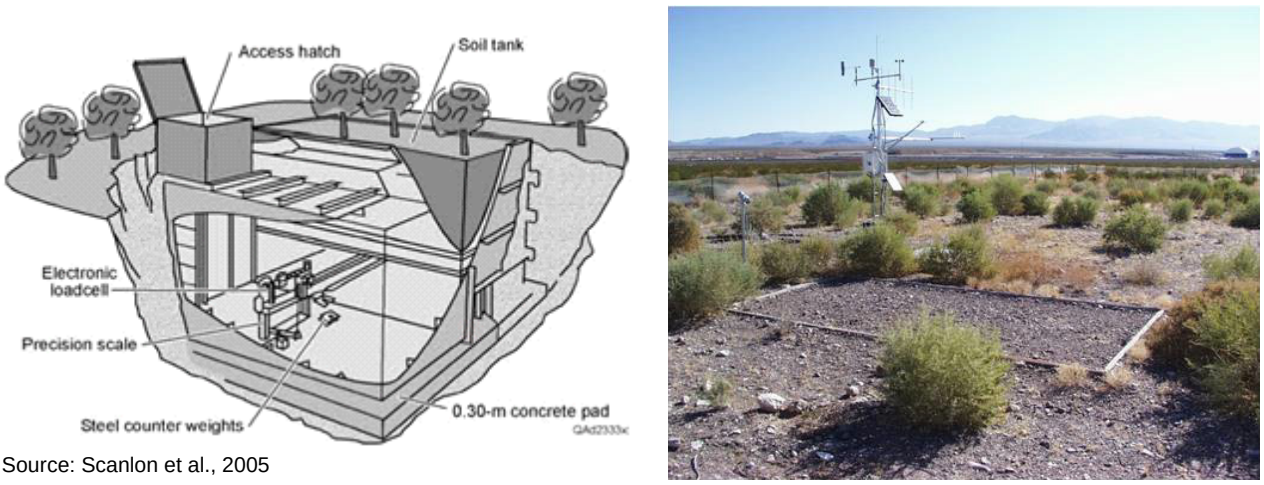

Source: Scanlon et al., 2005

Figure E-3
Schematic Diagram of Weighing Lysimeter (Left) and Photo of Area 5 Non-vegetated Weighing Lysimeter (Right)

Calibration of the HYDRUS-1D (H1D) model (Šimůnek, van Genuchten, and Šejna, 2005) was achieved by comparing HYDRUS-1D output to total soil water storage measurements in the lysimeters using a 10-year data record (1995–2004). Site-specific precipitation, PET, and soil properties data were used as model input. H1D requires inputs of potential evaporation (PE) and potential transpiration (PT). These two inputs were calculated from PET and scaled until measured and modeled soil water storage had similar results. Although Yucca Flat is located about 20 km north of, and about 250 m higher than Frenchman Flat (location of the lysimeters), the calibration to Area 5 data was assumed to be appropriate for Yucca Flat. Results of the calibrated H1D model compared to lysimeter soil water storage measurements are shown in Figure E-4.

E.2.5 Soil Conservation Service Curve Number (SCS-CN) Method

The SCS-CN method is a simple rainfall-runoff method that provides rainfall excess, but not rates. The SCS-CN method is often used to generate input to flood peak methodologies, but is not by itself

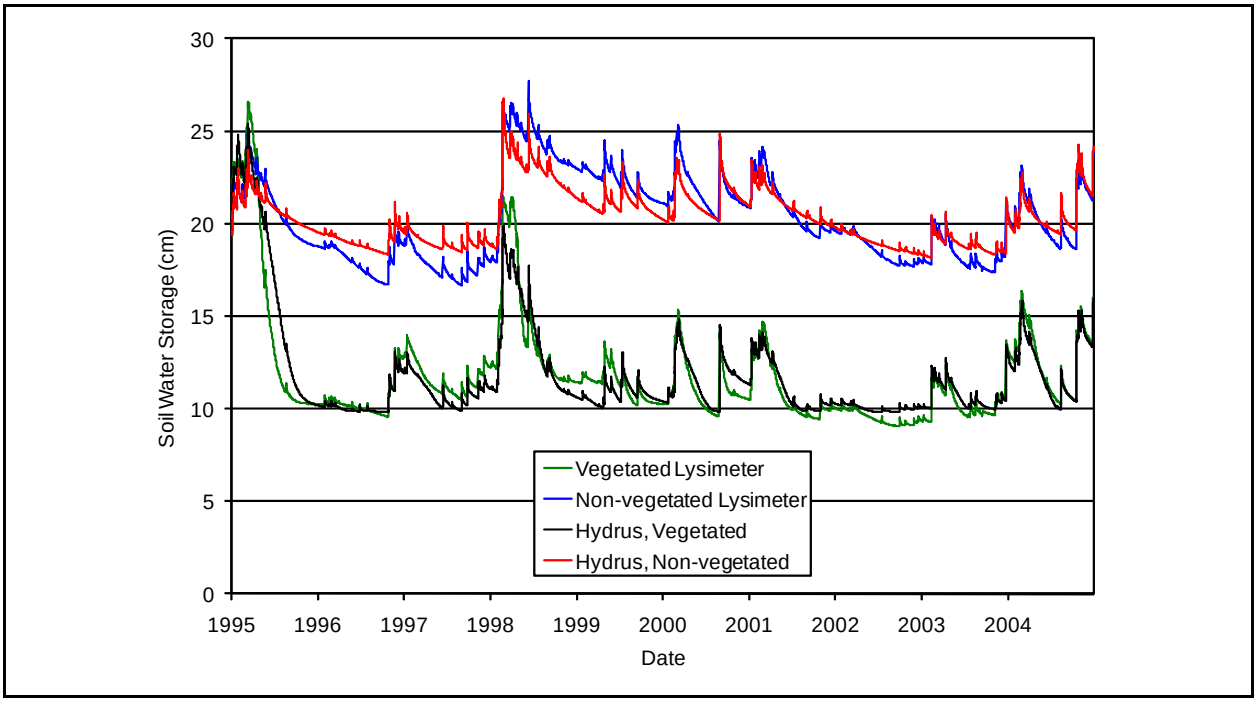

Figure E-4
Calibration of H1D to Weighing Lysimeter Soil Water Storage Data

a flood peak method (Hawkins et al., 2009). Therefore, the methodology does not account for rainfall duration or intensity, and for all practical purposes, rainfall occurs on a daily timestep. The derivation of the curve number equation is highly empirical and not physically based, but it does satisfy conservation of mass. The derivation of the curve number equation is provided in USDA NRCS (2004, 630.1001). For details on the SCS-CN method, refer to USDA NRCS (2004, 630.1001), Mishra and Singh (2003) and Hawkins et al. (2009).

The initial curve number for Yucca Flat crater calculations was selected from Table 9-2 of USDA NRCS (2004, Part 630, Chapter 9), based on a land use classification of arid shrubland, hydrologic soil group consisting of sand, loamy sand, or sandy loam soil texture (hydrologic soil group A), and a hydrologic condition of less than 30 percent ground cover. The curve number for these conditions is 63. Curve numbers for ARCI and ARCIII conditions were selected from USDA NRCS (2004, Chapter 10, Table 10-1). These curve numbers are 43 and 80 for ARC I and III, respectively. Slope adjustments were made for all ARC conditions based on the methods of Neitsch et al. (2002) and Williams and Izaurralde (2005). Crater slopes were calculated using satellite imagery estimates of crater depth, crater area, and crater floor area, and assuming that all crater are frustums.

The basis of the approach for calculating runoff into all 462 Yucca Flat craters described in this report, and the methodology that is unique and, to our knowledge, has not be previously attempted, is to relate ARC to soil surface water potential calculated on a daily timestep using H1D. In this approach, we used the surface water potential on the previous day to determine ARC where ARCI, II, and III conditions are defined by water potential thresholds calculated during model calibration.

Simulations of the local water balance for a location representing Yucca Flat were conducted using (calibrated) H1D and both the 43-year and 1,000-year precipitation and PET records. The model depth was set to 2 m, and hydraulic properties were taken from Table 12 of NSTec (2007). Figure E-5 shows the calculated surface soil water potential for the first 2,000 days of the H1D 43-year simulation using precipitation data from BJY. Figure E-5 also includes the water potential thresholds calculated during model calibration. Threshold values of -3 and -20 m potentials were found to work well for all calibration datasets.

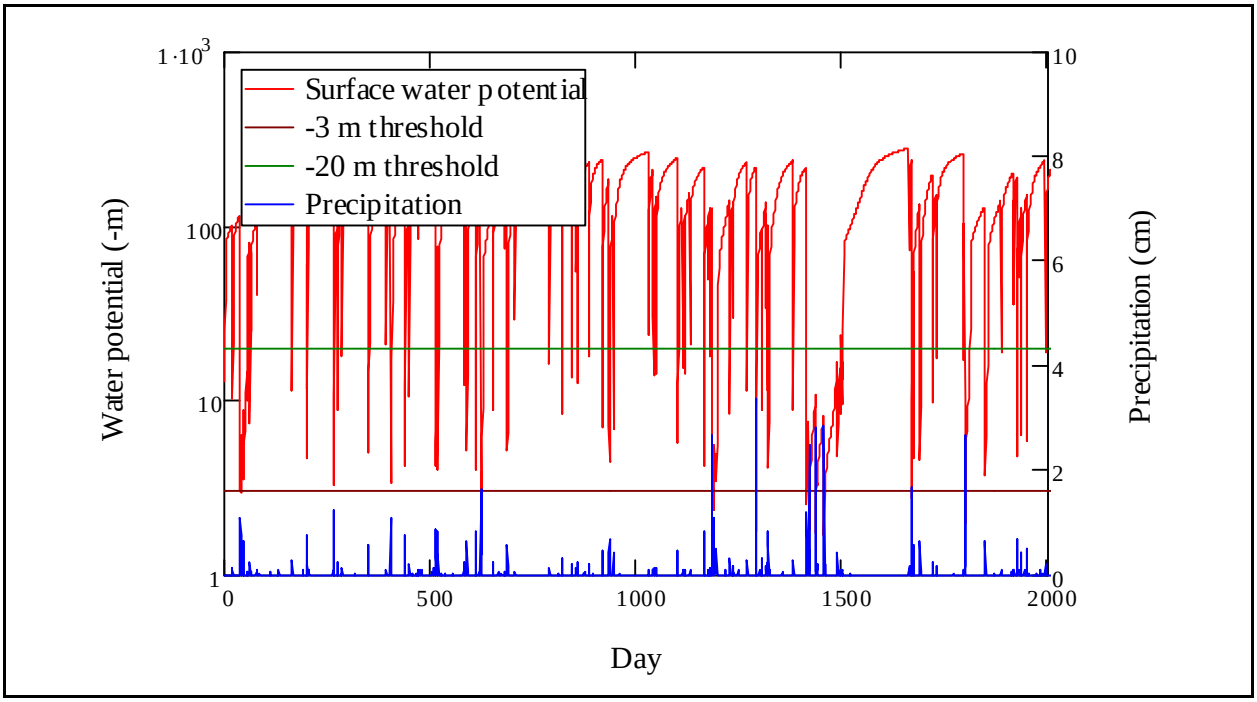

Figure E-5
Surface Soil Water Potential, Calibrated Water Potential Thresholds, and Daily Precipitation for First 2,000 Days of 43-Year Record

For every crater, runoff volumes from contributing catchment areas are calculated (for 312 craters that have a contributing area) using the CN methodology with slope corrections. Calculations were

made using the 43-year precipitation record for model calibration, and using the 1,000-year synthetic precipitation record for predictions of long-term average net infiltration.

Once runoff depth and volume from a catchment area (which includes the crater area minus the bottom area) has been calculated using the CN methods described above, that volume is converted into a ponding depth within a crater using the crater's geometry (top and bottom area and depth). One major assumption inherent in these calculations is that all 462 Yucca Flat craters can be approximated using a frustum geometry.

E.3.0 GIS ANALYSES

GIS products necessary to analyze crater recharge include an Environmental Systems Research Institute, Inc. (ESRI) formatted geodatabase containing all GIS files created and used in the analysis complete with metadata descriptions. This report documents the methodologies used to create the GIS files including descriptive statistics of key attributes generated.

E.3.1 GIS Analysis Files

Several GIS data files resulted from the different GIS characterization and analysis tasks performed and are listed in Table E-1. The coordinate system for all GIS data files is Universal Transverse Mercator (UTM) Zone 11N, North American Datum 1927 (NAD 27), and units are in meters. All data processing was conducted using a combination of ENVI Ver. 4.3 and Arc/Info ArcGIS Ver. 9.2.

Table E-1
List of GIS Files Used and Created for Completion of Project Tasks
(Page 1 of 2)

GIS Filename	Description
usgs_utm_10m	10m resolution USGS digital elevation model
srtm_utm_10m	10m resolution Shuttle Radar Topography Mission derived digital elevation model
yf_DEM_raw	Non-hydrologically corrected digital elevation model
yf_DEM_final	Combined SRTM and USGS hydrologically corrected digital elevation model
yf_DEM_hs	Shaded relief grid for the Yucca Flat Basin
yf_playa	Playa feature at south end of Yucca Flat Basin
flow_dir	Surface flow direction derived from digital elevation model
yf_watershed	Drainage basin defining Yucca Flat Basin
flow_accum	Surface flow accumulation derived from digital elevation model
yf_basins_grd	The watersheds of the Yucca Flat Basin in Arc/Info Grid format
yf_basins	The watersheds of the Yucca Flat Basin as vector based polygons
yf_drainages	Drainage system of the Yucca Flat Basin
sink_areas	The sink areas in the Yucca Flat basin as delineated by digital elevation model
nts_roads	Roads in and around the Nevada National Security Site
yf_mosaic_123 - R	Mosaic of visible wavelength spectral bands from the QuickBird satellite
yf_mosaic_132 - S	Mosaic of visible wavelength spectral bands from the QuickBird satellite – drainage enhanced band combination

Table E-1
List of GIS Files Used and Created for Completion of Project Tasks
(Page 2 of 2)

GIS Filename	Description
yf_mosaic_432 - T	Mosaic of visible wavelength spectral bands from the QuickBird satellite – vegetation enhanced band combination
yf_craters_usgs	Yucca Flat Craters derived from USGS
yf_craters	Yucca Flat Craters derived from USGS and on screen digitization from DEM and Satellite data sources
yf_bottoms	The crater bottom surface areas for each of the craters in the Yucca Flat Basin
eventlocations	Nuclear test event locations in the Yucca Flat basin
nts_boundaries	Operational area boundaries of Nevada National Security Site

USGS Digital Elevation Model

In order to calculate surface flow and runoff, an accurate hydrologically correct digital elevation model (DEM) is needed. The United States Geological Survey (USGS) DEMs were examined for use in our surface flow analysis. The usgs_utm_10m dataset was created by extracting a section of USGS National Elevation Dataset (NED) digital elevation model (DEM) data surrounding Yucca Flat basin from the USGS Seamless Data Distribution System (http://seamless.usgs.gov) and re-projected from GCS 1983, NAD 83, to UTM meters, zone 11, NAD 27. The USGS DEM was found to be insufficient to create an accurate hydrologically correct DEM without supplement. Subsurface tests performed after the creation of the USGS DEM were not present in the USGS DEM. Consequently, it was decided that we would augment the USGS DEM with the Shuttle Radar Topography Mission (SRTM) derived DEM but keep the resolution of the combined DEM at 10 m to capture all craters of interest at a sufficient resolution.

Shuttle Radar Topography Mission Digital Elevation Model

The srtm_utm_10m dataset was created by extracting a section of SRTM data surrounding Yucca Flat basin from the USGS Seamless Data Distribution System (http://seamless.usgs.gov) and clipped to the boundary of an existing USGS 10 meter NED DEM. The SRTM data were reprojected from WGS 1984 to UTM meters, zone 11, NAD 27 and resampled to 10 m cell size to match the USGS 10 meter DEM.

Non-Hydrologically Corrected Digital Elevation Model

The yf_DEM_raw DEM was created by combining the derived USGS NED digital elevation data and SRTM derived digital elevation data. In locations where craters were missing in the older USGS data but visibly present in the SRTM data, the SRTM data for the crater's sink area was copied into the USGS data (replacing the USGS data) to create this combined DEM that contains all visible craters from both sources of data. Combining the two source DEMs was done by creating a filter of just those craters present in the SRTM DEM then reclassifying the SRTM DEM retaining the elevation data for those craters but changing the values of all other cells to zero then combining the two DEMs.
The unique craters from the SRTM data are preserved while ensuring that only elevations from the SRTM data that are lower than the values in the USGS data for the same cell locations are transferred to avoid creating erroneous raised elevations.

Combined Hydrologically Corrected Digital Elevation Model

In an effort to remove artificial areas of depression that may have been introduced in the creation of the input DEMs the yf_DEM_final dataset was created by processing the yf_DEM_raw dataset with the ArcGIS Spatial Analyst fill tool with a fill threshold set at 3 m. This threshold retained the majority of the craters while eliminating all sink errors within the Yucca Flat basin study area boundary resulting in the yf_DEM_final dataset - a hydrologically correct DEM. Although this process of filling in sink errors might have artificially filled some crater areas – crater areas were masked from the fill to ensure that crater depths were maintained. Higher resolution DEMs are preferred and would allow for a much higher threshold further improving on a hydrologically corrected DEM better preserving crater morphology.

Shaded Relief Grid for the Yucca Flat Basin

The yf_DEM_final DEM was processed into a shaded relief raster dataset named yf_DEM_hs using the ArcGIS Spatial Analyst hillshade tool. The shaded relief raster was used to visually inspect the DEM and observe and identify the various shaded ares created by craters. Default values for azimuth (315), altitude (45), and z factor (1) were used, shadows were not modeled.

Yucca Flat Basin Playa

The yf_playa ArcGIS vector polygon dataset represents the playa feature at the south end of the Yucca Flat basin of the NNSS. The playa region in the south of the Yucca Flat basin is extremely flat

and most computer algorithms that compute overland flow poorly represent the surface flow in the vicinity in and around the playa. The yf_playa file was created to improve the ArcGIS overland flow direction and accumulation calculations.

The yf_playa GIS file was created in the following manner: The playa feature was extracted from the yf_DEM_final DEM by first subtracting the original DEM from a completely sink filled version to derive a grid of just the sink areas then classifying the sink areas into 1 m elevation bands and selecting the elevation band (and those of greater depth in the playa region) that matched the outline of the playa boundary as visually indicated on a shaded relief grid derived from the original DEM. The playa grid feature was converted to a polygon shapefile, using the ArcGIS raster to polygon tool, and imported into the Yucca Flat Infiltration geodatabase as a polygon feature class. The playa has a perimeter of approximately 26,000 m and encompasses an area 14,563,900 m^2.

Flow Direction GIS Grid Derived from Digital Elevation Model

One of the essential elements to deriving hydrologic characteristics about a surface is the ability to determine the direction of flow from every cell in the gridded dataset. The ArcGIS flow direction function was used to process the yf_DEM_final dataset and create the flow_dir dataset showing the direction of flow out of each cell in the grid. There are eight valid output directions relating to the eight adjacent cells into which flow could travel. This approach is commonly referred to as an eight direction (D8) flow model and follows an approach presented in Jenson and Domingue (1988).

The direction of flow is determined by finding the direction of steepest descent, or maximum drop, from each cell. This is calculated as:

$$\text{Maximum drop} = \text{change in z-value} / \text{distance}$$

The distance is determined between cell centers. Therefore if the cell size is one, the distance between two orthogonal cells is one and the distance between two diagonal cells is 1.414216, the square root of two. If the maximum descent to several cells is the same, the neighborhood is enlarged until the steepest descent is found. When a direction of steepest descent is found, the output cell is coded with the value representing that direction. If all neighbors are higher than the processing cell, the processing cell is a sink and has an undefined flow direction.

Yucca Flat Watershed

The yf_watershed polygon dataset represents the drainage basin or watershed of the Yucca Flat basin in the NNSS and defines the study area boundary of the Yucca Flat infiltration project as illustrated in Figure E-6. The Yucca Flat hydrologic basin is approximately 25,000 m wide and 36,000 m long encompassing an area approximately 774,112,092 m^2.

The flow direction grid flow_dir was processed using the ArcGIS basin function. The derived basin grid was converted to a polygon shapefile using the ArcGIS raster to polygon tool. The Yucca Flat watershed was visually selected in the polygon shapefile, all internal sub-basins merged, and external basins deleted leaving just the Yucca Flat basin. The polygon ESRI shapefile was then imported into the Yucca Flat Infiltration ESRI geodatabase as a polygon dataset.

Flow Accumulation GIS Grid Derived from Digital Elevation Model

Flow accumulation is calculated as the accumulated weight of all of the cells flowing into each downslope cell in the output dataset. Cells in the dataset with a high flow accumulation denote areas of concentrated flow and are used to identify stream channels. The flow_dir dataset was used as input into the ArcGIS Flow Accumulation function to produce the flow_accum dataset.

Drainage System in the Yucca Flat Basin Area

The yf_drainages dataset represents the drainage system of the Yucca Flat basin area in the NNSS. The yf_craters_usgs vector file was created in the following manner. First, the flow accumulation grid dataset flow_accum was used to create a stream grid where stream cells were assigned for areas of a minimum 10,000 m^2 area of contribution (where flow accumulation was greater than 100×100 cells). Next, the flow accumulation grid and stream grid (stream_grd) were input into the ESRI ArcGIS Stream Order function to create a Strahler ordered drainage grid. The drainage grid was processed with the ESRI ArcGIS Spatial Analyst stream to feature tool to create a polyline drainage dataset imported into the Yucca Flat Infiltration ESRI geodatabase. Figure E-7 illustrates an example of surface drainage in and around craters in Yucca Flat.

GIS Grid of Yucca Flat Basins

The yf_basins_grd dataset represents the hydrological basins or watersheds of the Yucca Flat basin at NNSS in ArcGIS grid format (Figure E-6). Basins delineate the hydrologic divides based on

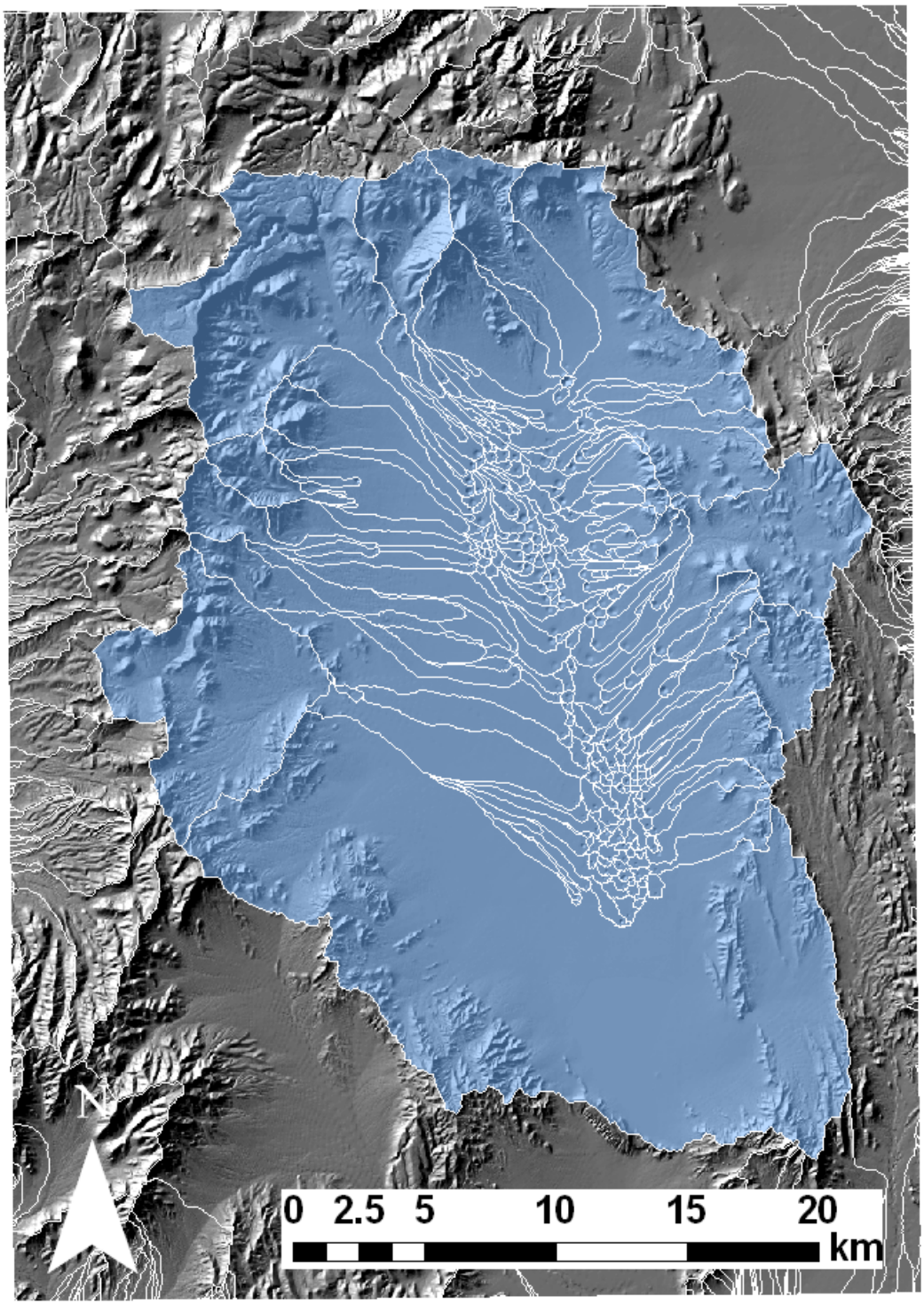

Figure E-6
Yucca Flat Hydrologic Basin Overlaid on Shaded Relief Map Derived from the Combined USGS and SRTM DEMs

Note: Crater catchment outlines are shown as white lines.

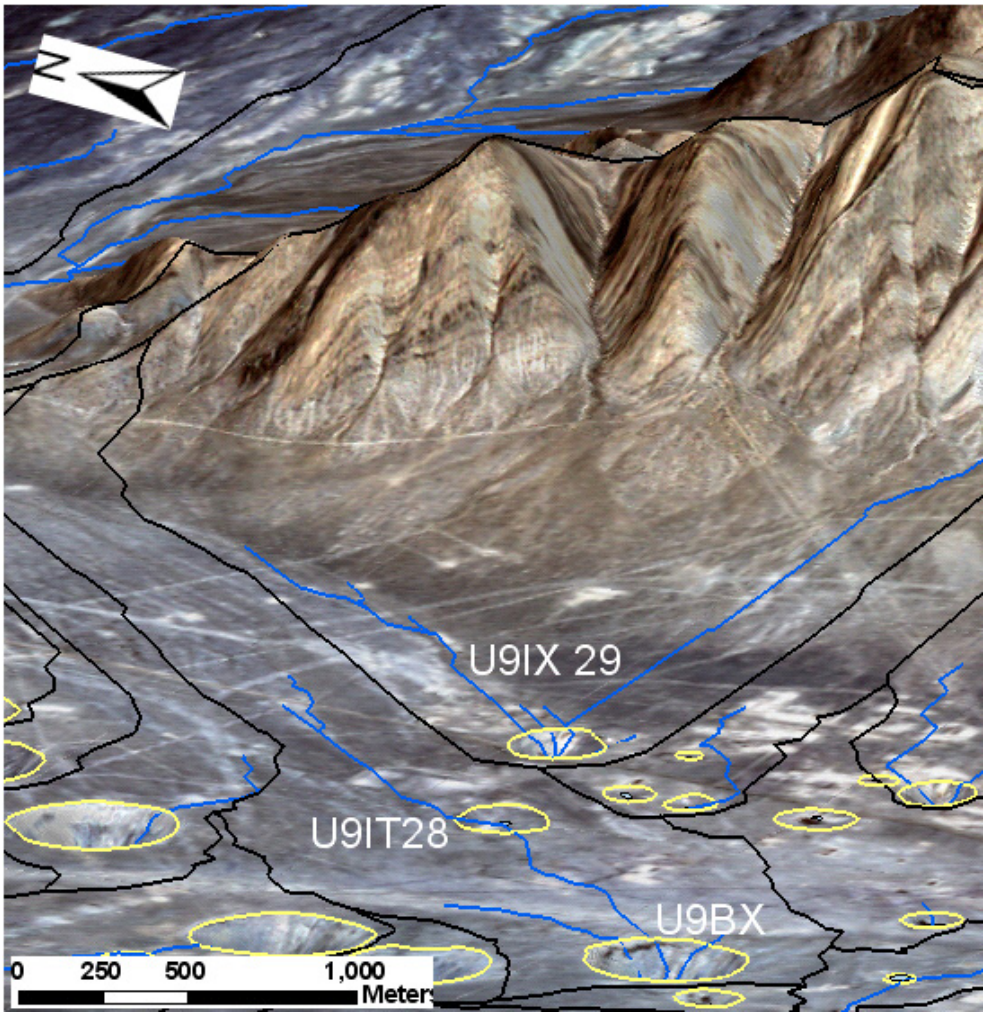

Figure E-7
3D High Oblique View Illustrates how Drainage Lines (Blue) Either Flow through Craters (Yellow) Not Acting as Hydrologic Sinks (U9IT28) and Craters that Act as Hydrologic Sinks (U9BX)

Note: Crater catchment outlines are shown as black lines.

a given contribution area where all of the water within the basin flows to a particular outlet or pour point. The pour point is usually the lowest point where water flows out of a particular basin or catchment. The flow_dir dataset was processed using the ArcGIS basin function to derive the yf_basins_grd dataset.

Yucca Flat Basins

The yf_basins vector polygon dataset represents the hydrological basins or watersheds of the Yucca Flat basin at NNSS. The yf_basins dataset was created by converting the yf_basins_grd dataset from

ESRI grid format to an ESRI vector polygon dataset that was then imported into the Yucca Flat Infiltration ESRI geodatabase. Converting the yf_basins_grd grid dataset into a vector dataset provided a means to more easily associate attributes to each basin and represent the basins in cartographic form.

Sink Area GIS Grid Derived from Digital Elevation Model

The sink areas were extracted from a combination 10 meter USGS and 30 meter SRTM DEM by subtracting the original DEM from a completely sink filled version to derive a grid of just the sink areas called sink_areas. Delineating the sink areas allowed for better preservation of crater sink areas as a result of filling the DEM as previously mentioned. The resulting grid was subsequently imported into the Yucca Flat Infiltration ESRI geodatabase. Figure E-7 illustrates the extent of crater areas that act as hydrologic sinks and those that do not.

Digital Orthophoto Mosaic Datasets

Digital orthophotos for the majority of the Yucca Flat basin were acquired from Digital Globe's QuickBird satellite. Four spectral bands were purchased, three in the visible spectrum (red, green, blue) and one in near-infrared. Three different mosaics were created by combining each of the four bands in different ways to help distinguish particular features on the ground. The yf_mosaic_123 dataset (not illustrated) was used to help identify crater morphology, roads, and ground features related to the craters in the Yucca Flat basin. The yf_mosaic_132 dataset (Figure E-8) highlights and enhances how surface drainage appears thus making it easier to identify surface erosional features in and around the Yucca Flat craters. The yf_mosaic_432 dataset (Figure E-9) uses the near-infrared band to help identify vegetation and vegetation health which is used as another indicator as to whether or not a crater receives surface runoff. The ground sample distance for each of the mosaics was 2.4 m per pixel.

Nevada National Security Site Roads

The nts_roads dataset represents roads within the vicinity of NNSS. It was determined that roads may act as preferred channels where surface flow might follow and consequently flow into a crater. The original vector polyline file was provided by Bechtel Nevada in ESRI Arc/Info .e00 interchange format and was imported into an ESRI Arc/Info coverage file format. The attribute fields "source" and "desc" were added and populated. The coverage file version was exported to ESRI shapefile

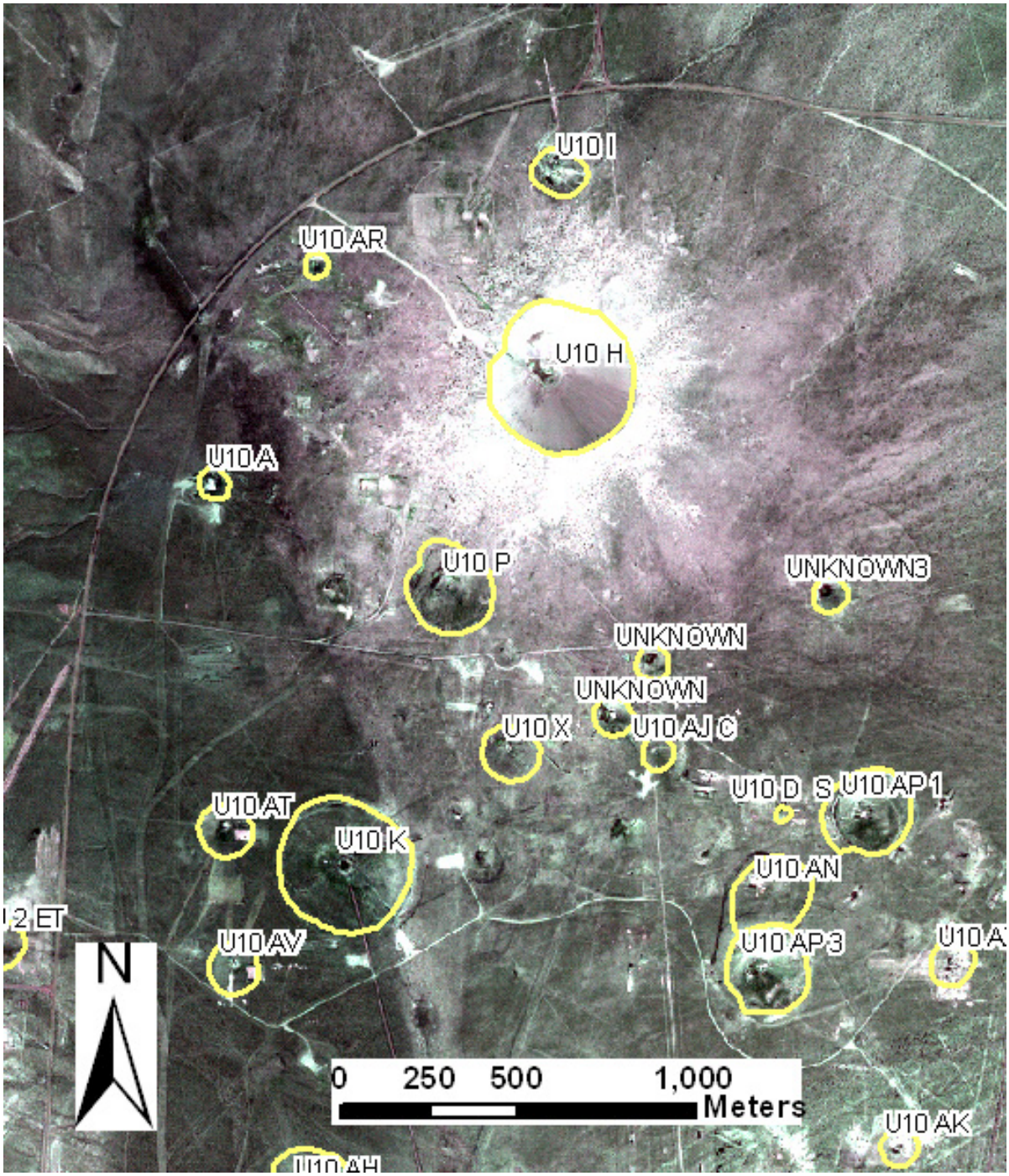

Figure E-8
QuickBird Satellite Image 132 Band Combination Used to Help Analyze Drainage Patterns in and Around Craters

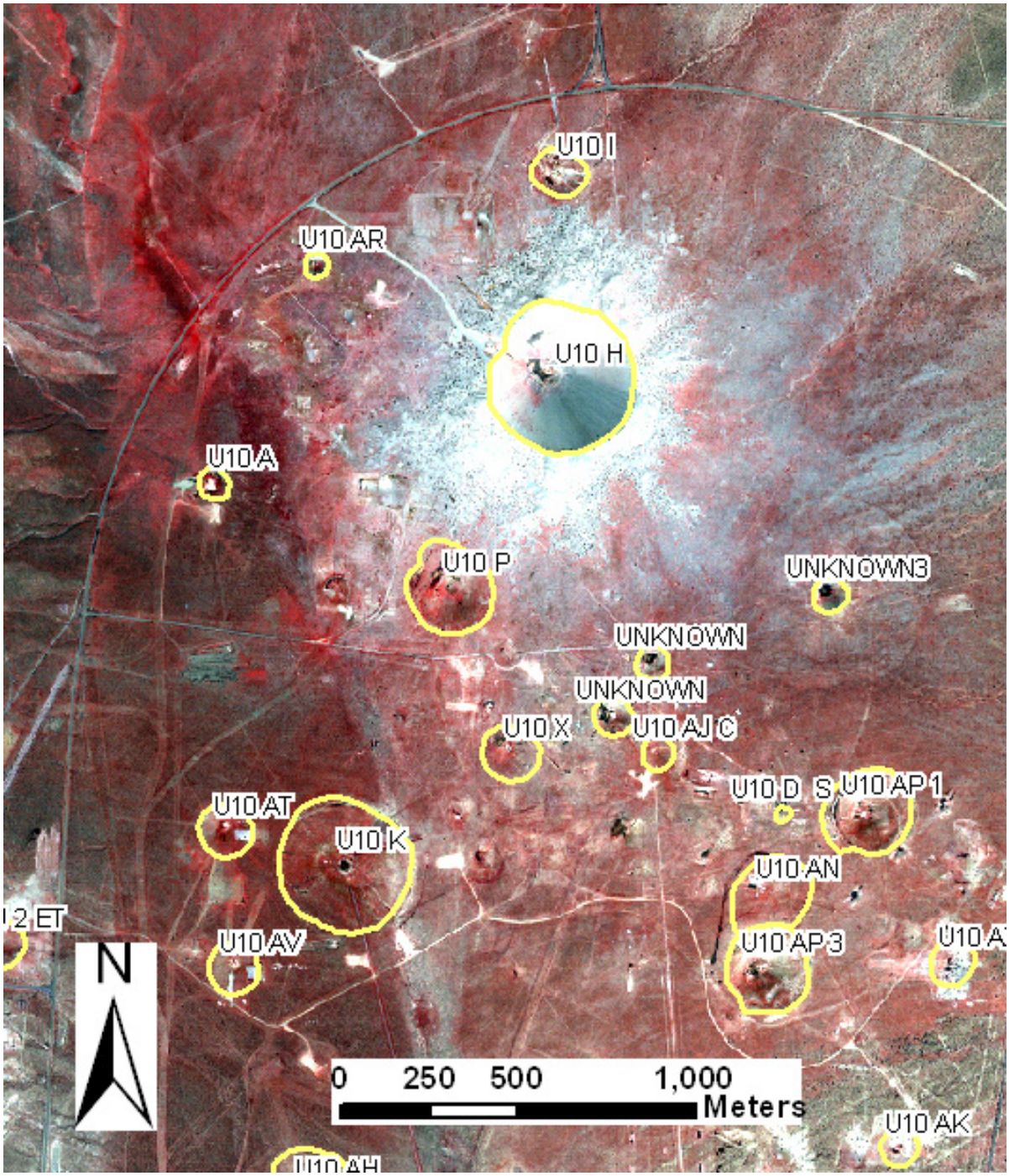

Figure E-9
QuickBird Satellite Image 432 Band Combination Highlighting Vegetation Health in Proximity To Crater Rims

format, re-projected from Nevada State Plane, NAD 27, to UTM zone 11, NAD 27, and subsequently imported as a dataset into the Yucca Flat infiltration ESRI geodatabase.

USGS Derived Yucca Flat Craters

The USGS completed an effort to map the concentric fracture rings around the craters at NNSS. It was determined that the USGS data files could be used to aid in the digitization of crater outlines that would need to be created for the project. The yf_craters_usgs dataset is derived from the USGS Yucca Flat Surface Effects Map Database developed by Grasso (2001). The yf_craters_usgs dataset was created in the following manner: Crater features were extracted from the yfse_n27f USGS surface effects ESRI geodatabase file by selecting for attribute “feature” = “Sink” and exporting the results to a new ESRI shapefile. All non-crater rim features less than 200 m in length were removed from the new ESRI shapefile leaving just the crater rim fractures. The polyline crater rim features were converted to polygon using the ESRI ArcGIS feature to polygon function with a 2 m open node connection tolerance. The resulting polygons were edited on screen to produce clean polygon crater areas and the file was imported as a dataset into the Yucca Flat infiltration ESRI geodatabase.

Yucca Flat Craters

The yf_craters dataset represents craters created by underground nuclear tests in the Yucca Flat basin of the NNSS. The yf_craters_usgs dataset was copied to create the yf_craters dataset. The polygon crater areas were moved and edited on screen to match the apparent crater rims as indicated on the shaded relief grid derived from a combination 10 meter USGS and 30 meter SRTM DEM. Additional craters indicated on the DEM not in the Yucca Flat Surface Effects Map Database were digitized on screen as polygon features and added to the dataset. Attributes for the hole name were transferred from the “event_locations” GIS data file during editing. The shapefile dataset was then imported into the Yucca Flat Infiltration geodatabase as a polygon feature class.

Each of the craters in the yf_craters shapefile was analyzed for rim erosion, vegetation change within the crater, and presence of alluvial fans using an overlay of the yf_craters data file on the QuickBird satellite imagery collected at NNSS with a 1/2/3 (red, green, blue) band combination showing the visible wavelength, a drainage enhanced 1/3/2 (red, blue, green) band combination, and a vegetation enhanced 4/3/2 (near-IR/blue/green) band combination. The 4/3/2 band combination allows vegetation to be enhanced in a false color for the QuickBird image. In such a band combination, sand

(silicon dioxide) will appear white, healthy vegetation bright red, stressed or dying vegetation dark red, and water or metal roofs of man-made features black. Health of vegetation in desert environments is a proxy for determining where water is flowing subsurface. Analysis was a three step process:

First, the imagery was viewed in ENVI 4.3 image analysis software and ESRI ArcMap GIS software to get a general idea of the extent of each crater feature. Display of the imagery in ENVI provided somewhat better resolution of erosional features and individual shrubs and trees. Second, each of the three characteristics of interest was defined and added as attribute fields to the GIS data file. Crater erosion was defined as being the presence (rim_erosion attribute set to “y”) or absence (rim_erosion attribute set to “n”) of visible arroyos, gullies and other erosional features within the bounds of or on the outer slopes of the crater. Vegetation change was defined as either the increased (veg_change attribute set to “y”) or decreased (veg_change attribute set to “n”) presence of vegetation within the crater boundary as compared with the surrounding image. Alluvial fans were defined as being present (alluvial_fan attribute set to “y”) or absence (alluvial_fan attribute set to “n”) either within or on the outer rim of the crater. Finally, the “yf_craters” attribute table was edited and the exact nature of the features seen for each crater was detailed in the “erosion_desc” attribute.

The craters were then analyzed for the presence of related topographic sink features and for intersections with roads. Sink features, which are topographic depressions that could capture surface water, were determined by overlaying the crater boundaries with the sink_areas dataset. Road intersections with crater boundaries, which could act as a pathway for surface water into a crater, were determined through a simple spatial selection for intersection between the crater boundaries and road vector features provided by the nts_roads dataset. More detailed determination of road and crater intersections from imagery was not performed. Attributes of “sink” and “road” were calculated as yes or no for the presence or absence of a sink depression and the presence or absence of one or more road and crater boundary intersections for each crater feature.

Next the yf_basins file and the yf_craters file was analyzed using ArcGIS software. A definition query was defined as 'sink' = y to show only craters which acted as sinks. Columns were added to the attribute table labeled Basin_ObjectID and Basin_Area respectively. The two tables for craters and basins were then joined in order to associate a basin with each crater acting as a sink. If a crater was acting as a sink within a basin, the basin object ID and basin catchment area from the yf_basins file

were added to the appropriate columns in the yf_craters file. If a crater was located within a basin but not acting as a sink, the basin object ID was added to the appropriate column in the yf_craters file but a value of 0 was assigned to the Basin_Area attribute. Any crater not acting as a sink is only associated with a basin object ID, but craters acting as sinks are associated with both a basin object ID and basin area; therefore, multiple craters can be located in only one basin.

Yucca Flat Crater Bottoms

The yf_bottoms dataset represents the bottom surface area for each of the surface craters created by underground nuclear tests in the Yucca Flat basin of the NNSS to asses the geometry of the crater extent relative to the crater bottom it encompassed. The file was created in the following manner: The ESRI ArcGIS Spatial Analyst tools 'slope' and 'contour' were first applied to the yf_craters file; this made it easier to determine where the crater walls were steep and where the walls began to flatten out in the bottom of the crater. For larger craters with obvious bottoms (i.e., where the contour lines began to be more widely spaced or where the slope was less than 5 percent) the best-fit contour line was selected to represent the crater bottom. The contour lines were then converted into polygons using the ESRI ArcGIS 'Feature to Polygon' tool, and then the area and perimeter of each crater bottom was calculated. Figure E-10 illustrates the concentric nature of crater bottoms and size relative to crater extents.

The Slope and Contour functions did not work well for the smaller and shallower craters, so each of the remaining craters was inspected individually to determine the crater bottom. Using the yf_mosaic_432 dataset and the outlines of each crater rim, a polyline was digitized within each crater in the area that best represented each crater bottom. This was done using the ESRI ArcGIS Editor tool and Create New Feature function. The polylines were then exported and converted into polygons using the ESRI ArcGIS 'Feature to Polygon' tool. The perimeter and areas were then calculated for each crater.

Event Locations

A GIS file called “event_locations” represents nuclear test event locations at the Nevada National Security Site and was constructed from a spreadsheet of test event locations and test attributes at the Nevada National Security Site. The file was exported to a comma delimited format and attribute field names renamed to conform to ESRI geodatabase field name requirements. The exported file was

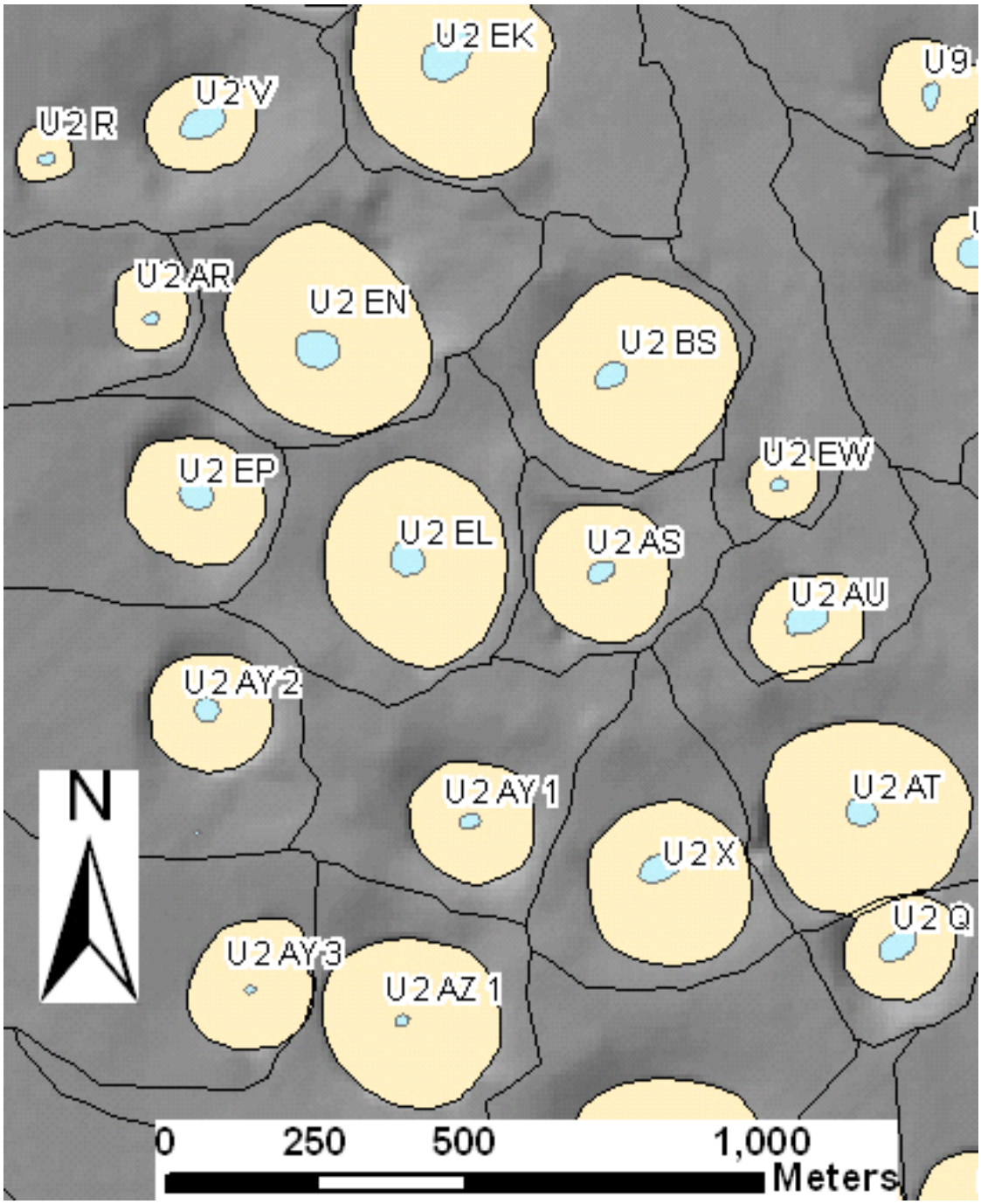

Figure E-10
Concentric Nature and Size of Crater Bottoms (Blue) Relative to the Extent of Each Crater (Tan)

Note: Catchment areas for each crater are depicted in gray and separated by black lines.

imported into ESRI ArcMap software as a table then converted to a vector point feature class using the coordinates listed for each event from the utm_e_top and utm_n_top attributes contained in the file. Those test events that geographically fell outside of the Yucca Flat basin were removed from the dataset.

In addition to the original attributes from the spreadsheet two attributes where calculated and added to the event_locations file. The first attribute called w_table was derived and calculated using the dbwt_m attribute which indicates the relative height of test burial above or below water table in meters. If the test was above the water table the w_table was assigned a value of “above” and if the test was below the water table the w_table attr.ibute was assigned a value of “below.”

The second attribute added to the event_locations was labeled “crater” and indicates whether or not the test event produced a crater. Each area on the land surface above where a test event took place was analyzed using a combination of the DEM, derived hill-shade of the DEM, slope analysis of the DEM, and visual inspection of the land surface using high resolution imagery in the visible wavelength. If a crater could be seen through any of the analysis methods described, then the crater attribute for the corresponding test event geographically located within the crater would be assigned a value of “yes” otherwise the crater attribute would be assigned a value of “no.” However, there was a lack of information on how to differentiate multiple test events that produced a crater that had the same or similar geographic coordinates at the surface but were either conducted at different times or at different depths. It was decided that all of the multiple test events residing geographically in a crater would be assigned a “yes” or “no” attribute depending on whether a crater was identified or not. Thus, there are 462 craters identified in Yucca Flat, three of which are not related to UGTA relevant detonations. Depending on the size of the surface test it is possible that some of the surface tests may have produced craters which may be incorrectly associated with a subsurface test. Based on the lack of information regarding surface testing we cannot rule out the possibility that some craters were caused by surface tests.

The final compilation of the 462 Yucca Flat craters has 362 craters with a non-zero depth while 100 craters have a depth listed as zero.

Nevada National Security Site Boundaries

The nts_boundaries dataset represents the operational area boundaries of NNSS and was only used for cartographic purposes. The original file was provided by Bechtel Nevada in ESRI Arc/Info .e00 interchange format and was imported into an ESRI Arc/Info coverage file format. The file was tested for topological correctness and topological relationships were constructed for each of the polygons defining the NNSS boundaries. Each polygon was verified for no label or dangling node errors and the attribute field “source” was added and populated. The Arc/Info coverage version was then exported to ESRI shapefile format, re-projected from Nevada State Plane, NAD 27, to UTM zone 11, NAD 27, and subsequently imported as a feature class into the Yucca Flat infiltration geodatabase.

E.3.2 GIS Analysis Results

E.3.2.1 Crater Dimensions

As described above, 462 craters have been identified in Yucca Flat. The GIS analysis results were used to quantify the crater dimensions, catchment areas, and evidence for water movement associated with these 462 craters.

Crater dimensions including depths, and top and bottom diameters are shown in Figure E-11 as sorted parameters. The craters having the largest depth, top diameter, and bottom diameter are associated with the SEDAN, BILBY, and HAYMAKER tests, respectively. Figure E-12 shows a cumulative distribution function (CDF) plot of volume of all Yucca Flat craters, calculated using a frustum geometry for all craters. Table E-2 lists the basic statistics for the depths and diameters of all craters. Recall that the final compilation of the 462 Yucca Flat craters has 362 craters with a non-zero depth while 100 craters have a depth listed as zero. All craters with a depth of zero were assigned a depth of 1 m for this summary, and for the runoff and infiltration modeling. .

E.3.2.2 Watershed Areas

One of the most important products of the GIS study was the identification of the watershed areas that contribute surface runoff to each of the subsidence craters (Figure E-6). As discussed in Section E.4.0, these watershed areas were used directly in the calculation of surface runoff volumes to the craters over the 1,000 year regulatory time frame. Of the 462 subsidence craters identified in Yucca Flat, 312 had watershed areas greater than the area of the crater itself and the remaining craters

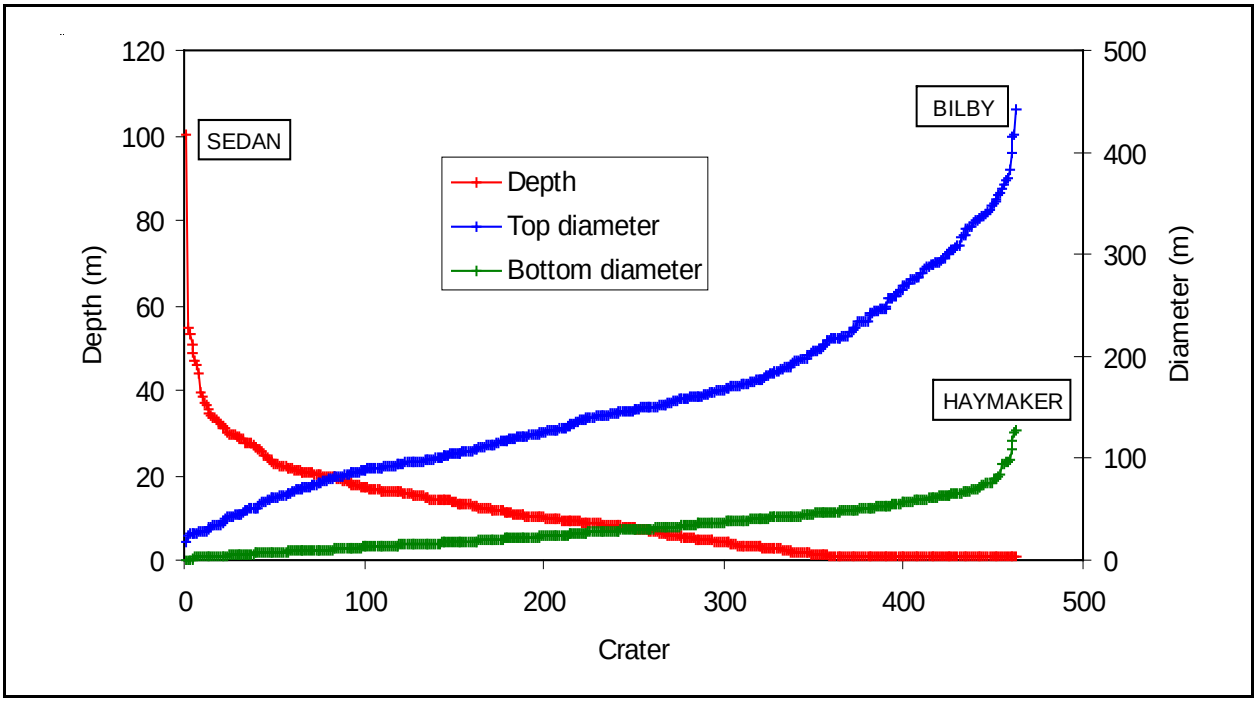

Figure E-11
Sorted Crater Depths and Sorted Top and Bottom Diameters

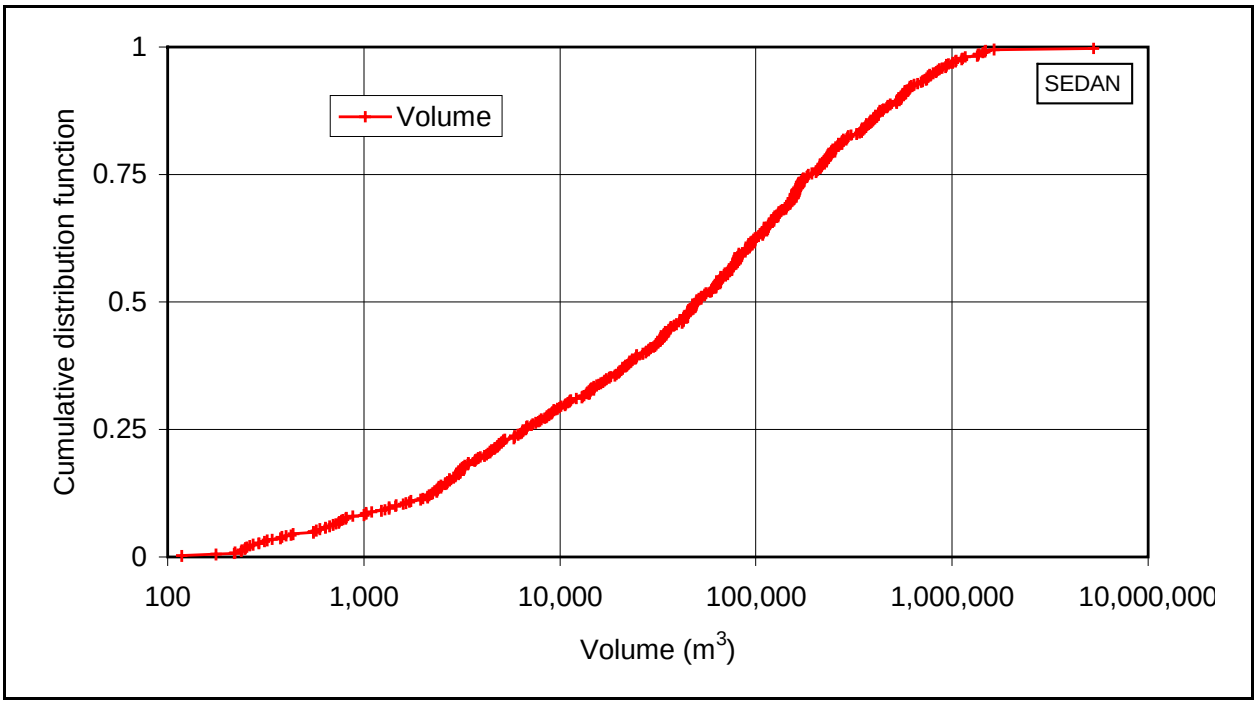

Figure E-12
CDF of Crater Volumes Calculated using Frustum Geometry

Table E-2
Statistics of Yucca Flat Crater Dimensions and Catchment Sizes

Statistics	Depth	Diameter		Catchment	
		Top	Bottom	Volume	Area
	(m)			(m^2)	
Minimum	1.0	19.2	0.0	118	0.04
Median	8.6	142	28.4	49,826	0.27
Mean	10.9	156	32.3	179,289	1.60
Maximum	100	442	127	5,265,349	59.3

had contributing watershed areas that did not extend beyond the crater boundaries. Craters with larger watershed areas are more at risk for flooding than those with smaller watershed areas, and hence likely to have higher infiltration rates to drive radionuclide movement to the water table, assuming all other factors such as crater bottom areas being equal. Most of the largest watershed areas are associated with craters on the perimeter of the basin (Figure E-6). Tests in the center of the basin tend to be shielded from runoff by outlying tests and often have watershed areas not much larger than the dimensions of the craters themselves.

Of the 462 Yucca Flat craters, 312 have catchment areas greater than the area of the crater while 151 craters have no catchments greater than their own crater area. Figure E-13 shows a cumulative distribution function plot of catchment size for these 312 craters. Catchment areas range from 0.04 to 59.3 km^2 and appear to be log-normally distributed, with median and mean areas of 0.27 and 1.60 km^2, respectively (Table E-2). As shown in Figure E-13, 50 percent of all craters have catchment sizes between 0.14 and 0.87 km^2, and 90 percent of the craters have catchment areas less than 3 km^2. There are only 11 craters with catchment areas greater than 10 km^2.

E.3.2.3 Crater Characteristics

In addition to crater catchment sizes, a knowledge of the crater depth, crater area, and crater bottom areas proved critical for estimating long-term crater infiltration rates. The geometric information associated with each crater allowed the volumes of each crater to be identified and pond heights associated with runoff volumes to be calculated for hydrologic models with using an idealized conical (frustum) geometry (see Section 3.0). The crater bottom areas, identified in the GIS study from slope breaks at the bottoms of the crater walls, determine the cross-sectional areas across which the ponded

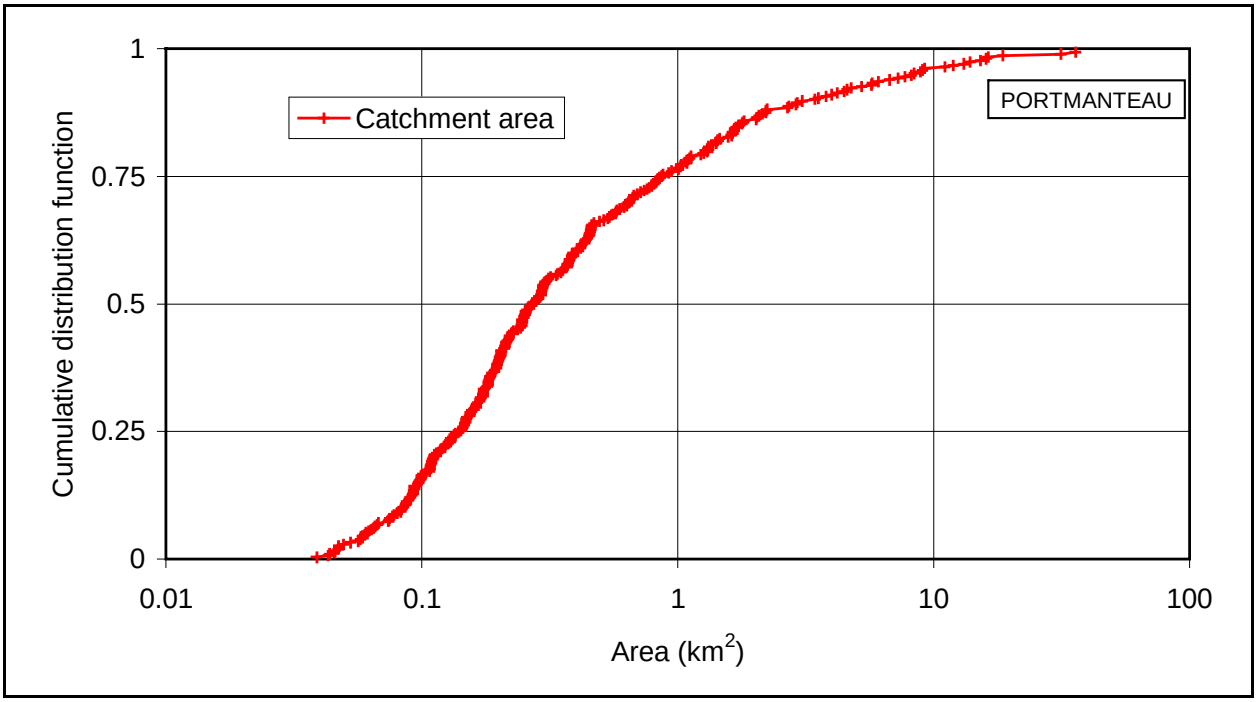

Figure E-13
CDF of Catchment Areas of Yucca Flat Craters

runoff volumes will infiltrate, and hence influence the infiltration rates calculated with the 1-D Hydrus models described in the following section. These crater bottom areas were also used directly in the large-scale 3-D models to apply the long-term infiltration rates calculated with the 1-D Hydrus models. The portion of the Yucca Flat basin from Area 2 shown in Figure E-10 illustrates the relationship between catchment areas, crater areas and crater bottom areas. The crater bottom areas are very small compared to the crater catchment areas even for this set of tightly clustered tests in the center of the basin, indicating how surface runoff can become focused into much small areas at the crater bottoms.

Correlations between crater catchment size and crater attributes were investigated. For example, one might expect craters with the largest catchments to have the most healthy vegetation, standing water, erosional features, or sand deposits at the crater bottom, as a result of focused runoff into crater bottoms. The only possible correlation between catchment size and a crater attribute was the appearance of sand in the crater bottom. Figure E-14 (center left) shows catchment size versus observations of sand and no sand for all craters, and observations of sand appear to occur in craters with catchment sizes greater than 0.83 km^2, which is the upper 25 percent of the CDF shown in Figure E-13. Other than the appearance of sand, we found no obvious correlations between catchment

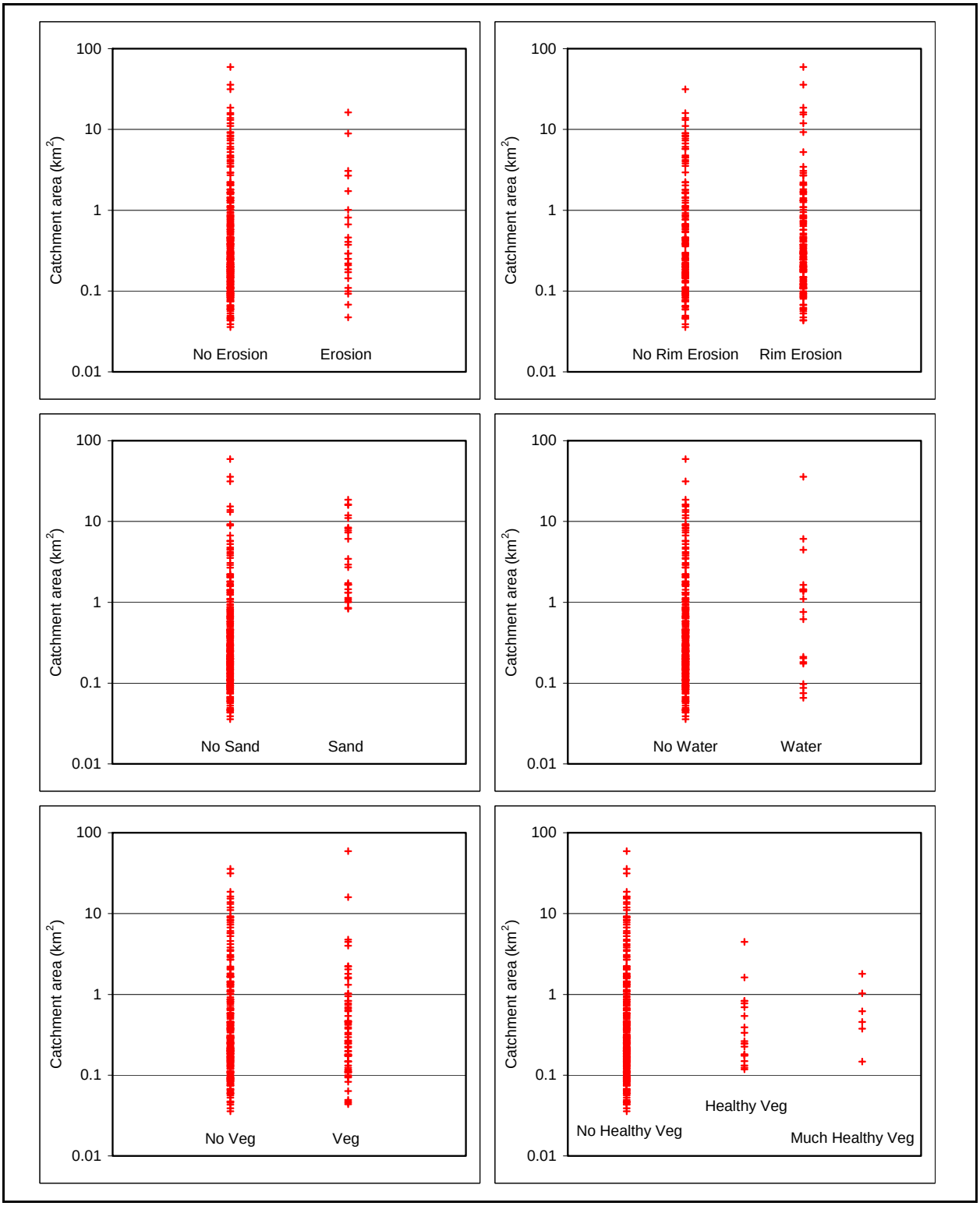

Figure E-14
Crater Attributes versus Catchment Area for All Craters

size and crater attribute. Figure E-14 show various crater attributes, such as evidence of sand, or erosion, versus catchment size.

As discussed above, QuickBird imagery was used to identify vegetation, and the presence of standing water in craters. It is notable that standing water, or apparent water (which could be metal structures), was observed in 23 of the 462 craters. While standing water is considered to be relatively rare in the arid environment of Yucca Flat, the QuickBird data were measured on April 4, 2003, and on April 9, 2006. Between March 27 and April 9, 2006 (a period of 13 days), there was 27 and 51 mm of precipitation at BJY and PHS rain gauges, respectively. Therefore, the QuickBird data likely captured a rare period of sustained rainfall at Yucca Flat.

Observations of either stressed or unstressed vegetation were noted for 90 (19 percent) of the 462 craters while observations of “healthy” vegetation were noted for only 37 (8 percent) of the craters, and observations of “lots of healthy vegetation” were noted for only 6 (1.3 percent) of the craters. Therefore, despite the occasional focusing of runoff into craters as evidenced by standing water observations, vegetation does not appear to flourish in craters as a result of focused runoff into craters. This is likely due to the timing of this additional water in the form of flood waters rather than frequent inputs like precipitation.

E.4.0 Coupled Runoff and Infiltration Model Calibration for Enhanced Crater Recharge

The first calibration conducted as part of this study was the calibration of H1D to weighing lysimeter data (previously discussed). However, another important calibration of this study was the determination of surface soil water potential thresholds to determine the slope-adjusted values of CNI, CNII, and CNIII. These thresholds were adjusted until runoff reasonably matched the direct observations of ponded water in craters U-10i (Hokett et al., 2000) and U-3fd (Pohll, Warwick, and Tyler, 1996), and the inferred ponded volumes in crater U-5a (Wilson et al., 2000). In addition, the thresholds were adjusted until H1D simulations of water content and water potential profiles reasonably matched the observed profiles beneath craters U-3fd (Tyler, McKay, and Mihevc, 1992) and U-3bh (BN, 1998). In the case of U-3fd, both ponded water depths and moisture profiles were matched. Since no ponded water was ever observed in U-3bh, only moisture profiles were matched for this crater.

The following sections describe results of model calibration to ponding height and/or subsurface moisture data from several craters. Model calibration was conducted in two phases, a preliminary phase and a final phase. For each phase a different set of assumptions were used to define the geometry of a frustum. For the final calibration cases, one set of surface soil water potential thresholds were used while for the preliminary phase two sets of surface water potential thresholds were used to represent an upper and lower bound. These thresholds are provided in Table E-3.

Table E-3
Calibration Surface Soil Water Potential Thresholds and PET Multipliers for Preliminary and Final Results

	Water Potential Thresholds (m)				PET Multipliers		
	Dry/Med	Med/Wet	Dry/Med	Med/Wet			
	Upper Bound		Lower Bound		Upper Bound	Lower Bound	
Preliminary Results	-20	-3	-10	-2	PE=PET/2 (no veg)	PE=PET/3	PT+PET×0.15
Final Results	Single Set				Single Set		
	-20	-3			PE=PET/2 (no veg)		

E.4.1 Crater U-10i (BYE)

Crater U-10i is located in Area 10, at the northern end of Yucca Flat, just north of Sedan crater. Crater U-10i was created by the BYE test on July 16, 1964 and has the fourth largest catchment area (18.6 km^2) of the Yucca Flat craters. Hokett et al. (2000) describe a runoff and ponding event that occurred on February 23 and 24, 1998 and resulted in 2.4 m of ponded water in U-10i. A photograph of U-10i following the February 23-24, 1998 ponding event is shown in Figure E-15. Hokett et al. (2000) also report evidence of multiple ponding events by analysis of the crater floor sediment deposits. They conclude that the sediment deposits suggest six distinct pond events, with two of the six being much larger events than the other four events.

Figure E-15
Photo of U-10i Crater after the February 23–24, 1998, Ponding Event
Source: Hokett et al., 2000

The modeled runoff volume from the catchment for February 23, 1998, was 11,147 m^3. This is very close to the total runoff volume of 11,350 m^3 reported by French et al. (1999). Modeled ponding depth, without infiltration, was 4.4 m (Figure E-16). During the flood event, some of this volume of water infiltrated into the crater floor and side walls. The depth of infiltrated water was estimated by French et al. (1999) to be 1.14 m during the event. Table 2 of Hokett et al. (2000) provides an average value of saturated hydraulic conductivity (K_{sat}) from cores from a borehole drilling in the crater floor

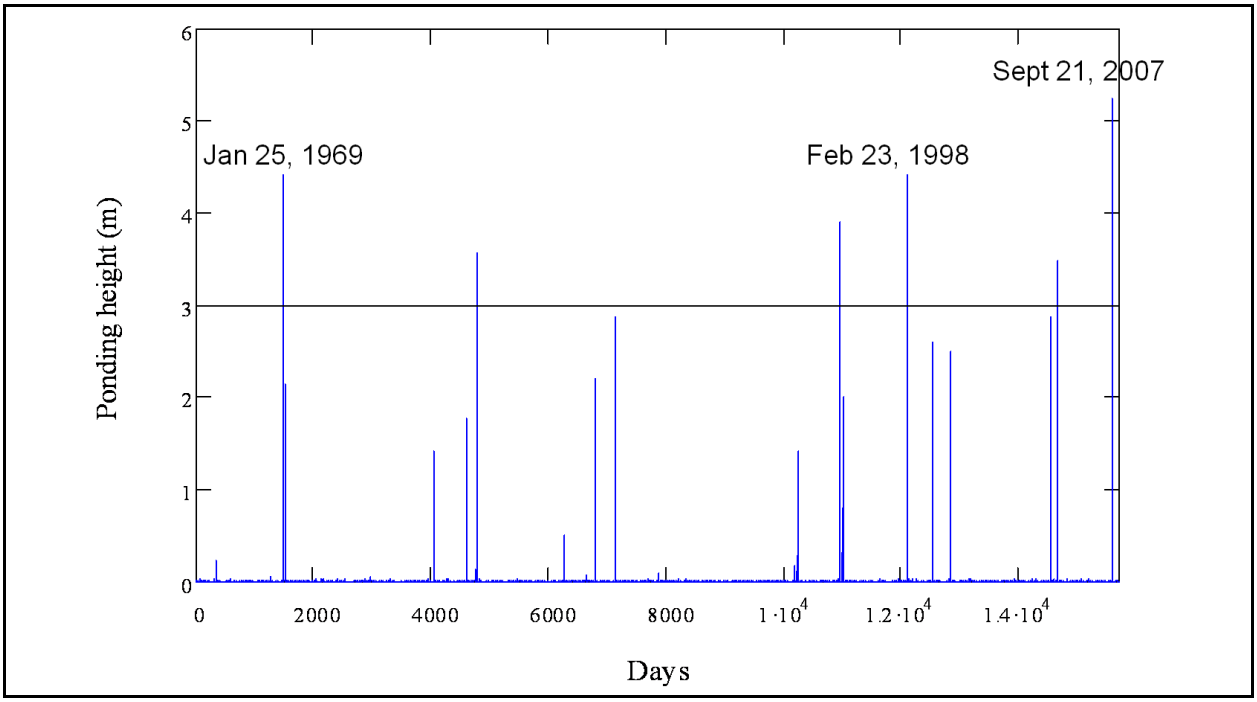

Figure E-16
Calculated Pond Height for U-10i for 43-Year Record

equal to about 2.0 m/day. Ignoring the effects of higher K_{sat} values on side walls than in crater floors, and ignoring the effects of pressure head on infiltration rates, infiltration can be roughly approximated as equal to the average K_{sat} of 2 m/day. Therefore, after one day of runoff and infiltration, the calculated pond depth should be runoff – infiltration = 4.4 m – 2.0 m = 2.4 m, which exactly matches the observed pond depth. With regard to the six ponding events evident in the sediment deposition record, Figure E-16 shows all ponding events with a line at 3 m pond depth. Although the last two events that are greater than 3 m occurred after 2000 when Hokett et al. (2000) was published, there remain four large events that loosely corroborate the hypothesis of six large deposition events in Hokett et al. (2000).

E.4.2 Crater U-3fd (LAGUNA)

Crater U-3fd is located in Area 3 in the central part of Yucca Flat and has a small catchment area of less than 0.20 km^2. Pohll, Warwick, and Tyler (1996) describe two series of ponding events that occurred in 1983 in U-3fd. The larger of the two series is presented as a 50-day period between August and October, 1983 (Pohll, Warwick, and Tyler, 1996, Figure 6), and the smaller of the two series is presented as a 100-day period between January and May, 1983 (Pohll, Warwick, and Tyler, 1996, Figure 8). Although Pohll, Warwick, and Tyler (1996) do not provide exact dates of

ponding events, the peak pond events can be correlated to precipitation records from station BJY. Figure 6 in Pohll, Warwick, and Tyler (1996) indicates a maximum ponding depth of about 0.41 m which occurred about 17 days into the 50-day period (and a ponding depth of about 0.25 m for the day with the highest precipitation). The maximum 24-hour rain total (58.4 mm) for the entire period of record occurred on August 18, 1983 which appears to match the timing of maximum ponding shown in Figure 6 of Pohll, Warwick, and Tyler (1996). Figure E-17 shows a photo of U-3fd taken in March 1995 following a ponding event.

Source: Photo by Greg Pohl

Figure E-17
Photo of U-3fd Crater Taken in March 1995

Runoff volumes from the catchment area for crater U-3fd, plus runoff from the crater itself were calculated using the methods described previously, and using the precipitation record from BJY. Model results indicate that the maximum ponding event occurred on Aug. 18, 1983, with a calculated pond depth of 2.1 m. As was done for U-10i crater, infiltration can be approximated using measured K_{sat}. Tyler, McKay, and Mihevc (1992) report soil K_{sat} values for cores from boreholes drilled within U-3fd (N1) and next to U-3fd (N2). The N1 borehole is located in the crater floor where fine sediments have been deposited. However, only the crater floor is expected to have deposition of fine sediments. Therefore, for large pond events (such as the one described here), much of this relatively flat crater will be covered with water, including areas that do not have fine sediment deposition.

Therefore, we calculated the average K_{sat} value for all the N1 and N2 core samples (1.8 m/day). Calculated pond depth after infiltration reduced to 2.1 m – 1.8 m = 0.3 m, which matches the measured depth of 0.25 m reasonably well. Calculated and measured pond height from Pohll, Warwick, and Tyler (1996, Figure 6) are shown in Figure E-18.

The "verification" event described in Pohll, Warwick, and Tyler (1996, Figure 8) occurred between January and May 1983. Although exact dates are not given in Pohll, Warwick, and Tyler (1996), calculated runoff of 0.47 m occurs between March 1 and 4, 1983. After accounting for some infiltration, this value matches either of the two ponding periods shown in Figure 8 of Pohll, Warwick, and Tyler (1996) reasonably well. However, as shown in Figure E-18, the runoff model only predicts one period of ponding while Pohll, Warwick, and Tyler (1996) show two periods.

For U-3fd, the runoff model was also calibrated by calculating water content and water potential profiles and comparing them to measured profiles in Tyler, McKay, and Mihevc (1992). Calculated and measured profiles are shown in Figure E-19, where t = 0 corresponds to the time of crater formation and t = 14 years corresponds to the time of drilling. Infiltration flux was calculated as change in storage divided by time which yields an average flux rate of 0.5 m/year. This rate compares well to the rate of 0.6 m/yr reported by Tyler, McKay, and Mihevc (1992) and Pohll, Warwick, and Tyler (1996).

E.4.3 Crater U-3bh (HYRAX)

Crater U-3bh is located in Area 3 in the central part of Yucca Flat, and is within the Area 3 RWMS. This crater was created during the HYRAX test on September 14, 1962. No ponded water has ever been documented for this crater. However, there are subsurface water content and potential data from two boreholes drilled into U-3bh. These two boreholes were drilled into the floor of U-3bh in 1996 in order to characterize the subsurface, prior to this crater being used for waste disposal. The crater has been used for waste disposal since 1996 to present. Figure E-20 shows a photo of U-3bh taken in approximately 1998. Borehole U-3bh-C1 was drilled from Jan. 1, 1996, through February 8, 1996, and borehole U-3bl-C2 was drilled from February 12, 1996, through February 22, 1996 (BN, 1998). For the H1D simulations, February 10, 1996, was selected as the time of drilling for both boreholes. Therefore, simulation time was set to 12,203 days (33.41 years).

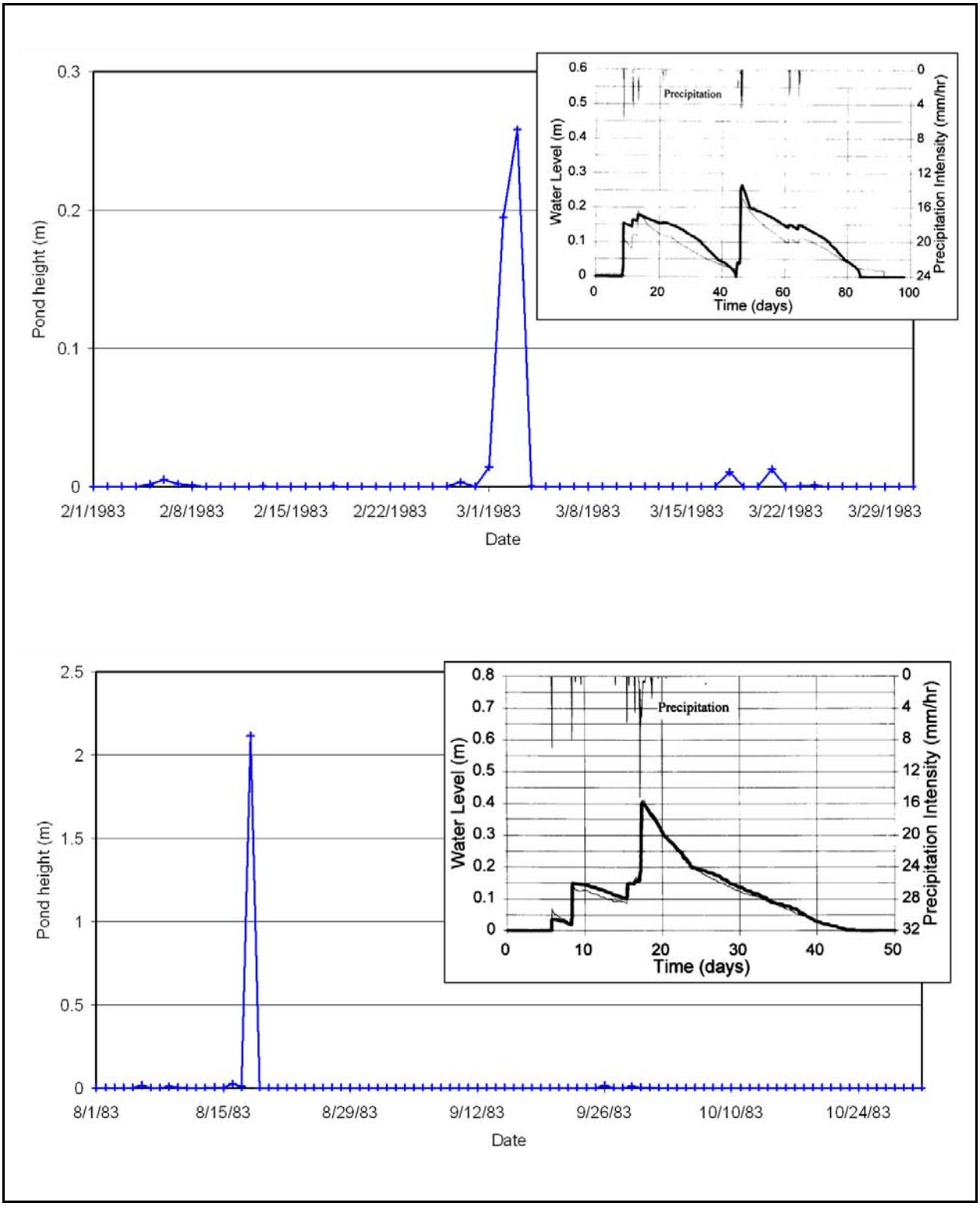

Figure E-18
Calculated Pond Height for U-3fd in March (Top) and August (Bottom) 1983 and Measured Values from Pohll, Warwick, and Tyler (1996)

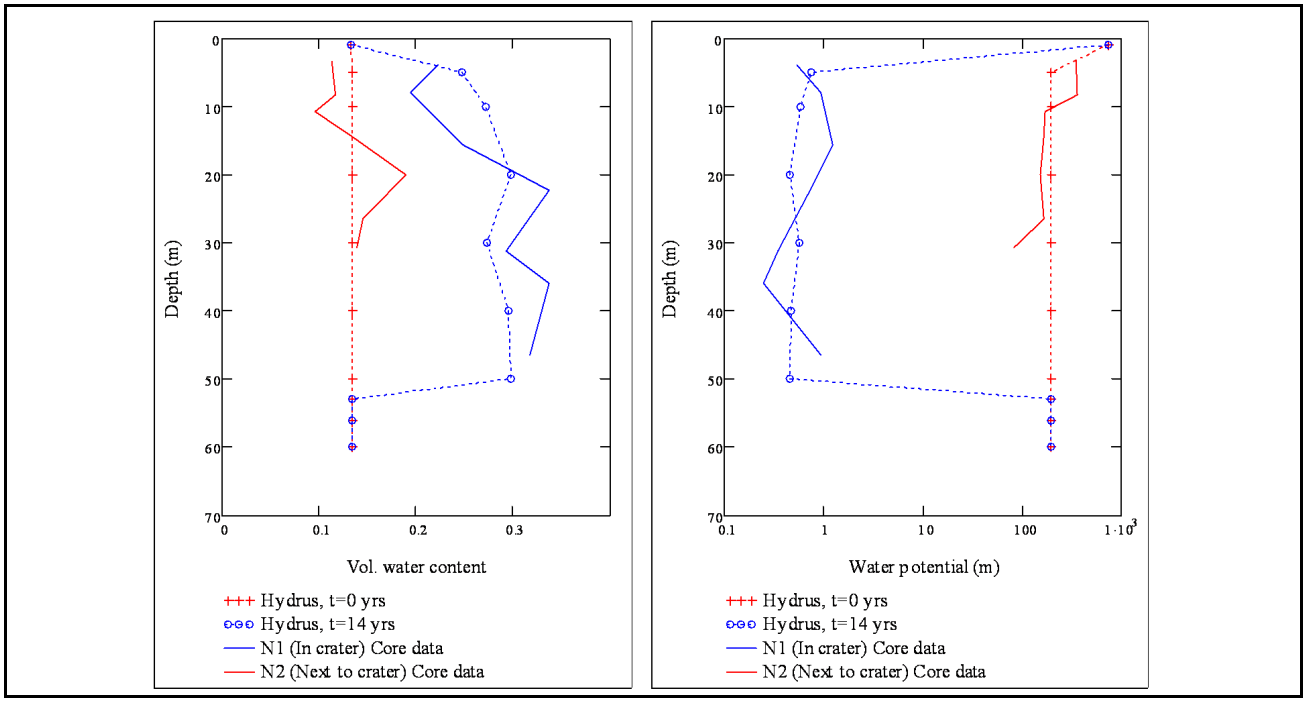

Figure E-19
Calculated and Measured Soil Water Content (Left) and Potential (Right) at U-3fd

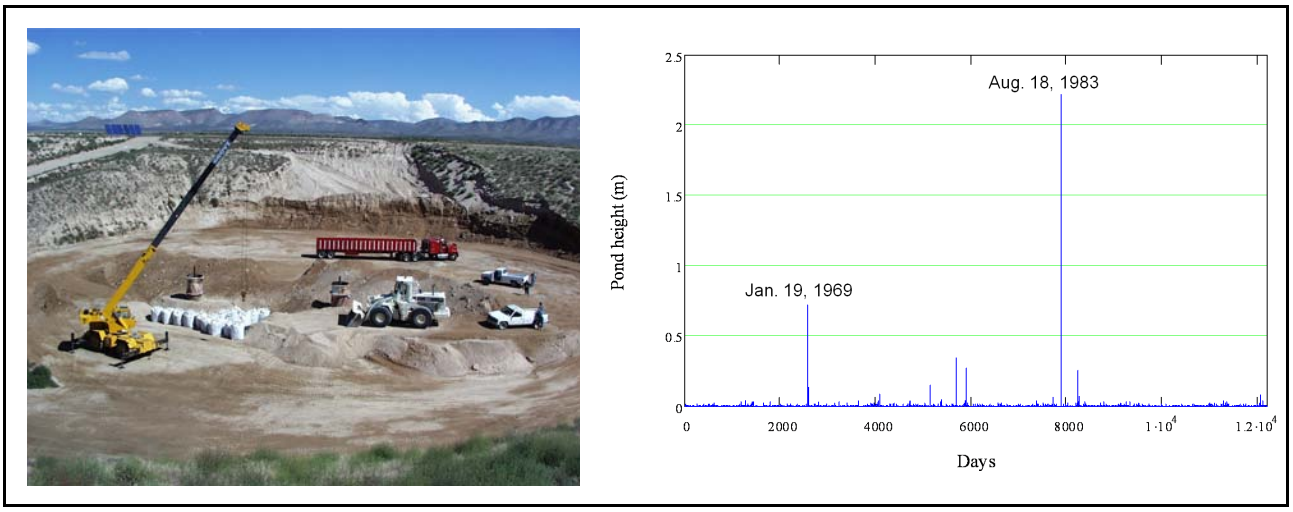

Figure E-20
Photo of U-3bh Taken in 1998 (Left) and
Calculated Pond Height for U-3bh Crater for 33-Year Simulation Period (Right)

Figure E-20 shows the calculated pond depths for U-3bh for the 33-year simulation period. The maximum ponding event corresponds to the storm of Aug. 18, 1983, that was discussed previously for crater U-3fd. This storm caused a pond height of 2.2 m (without any infiltration) in U-3bh. The second largest pond height (0.72 m) occurred on Jan. 19, 1969.

The runoff model was also calibrated to U-3bh subsurface data by calculating water content and water potential profiles and comparing them to measured profiles in BN (1998) and in NSTec (2007). Calculated and measured profiles are shown in Figure E-21, where t = 0 corresponds to the time of crater formation and t = 33 years corresponds to the time of borehole drilling. Infiltration flux was calculated as change in storage divided by time which yields an average flux rate of 0.076 m/year. This compares well to the average flux of 0.077 m/yr estimated from the difference in the moisture contents beneath and adjacent to the crater above the depth of the wetting front (55 m) and dividing by 33 years.

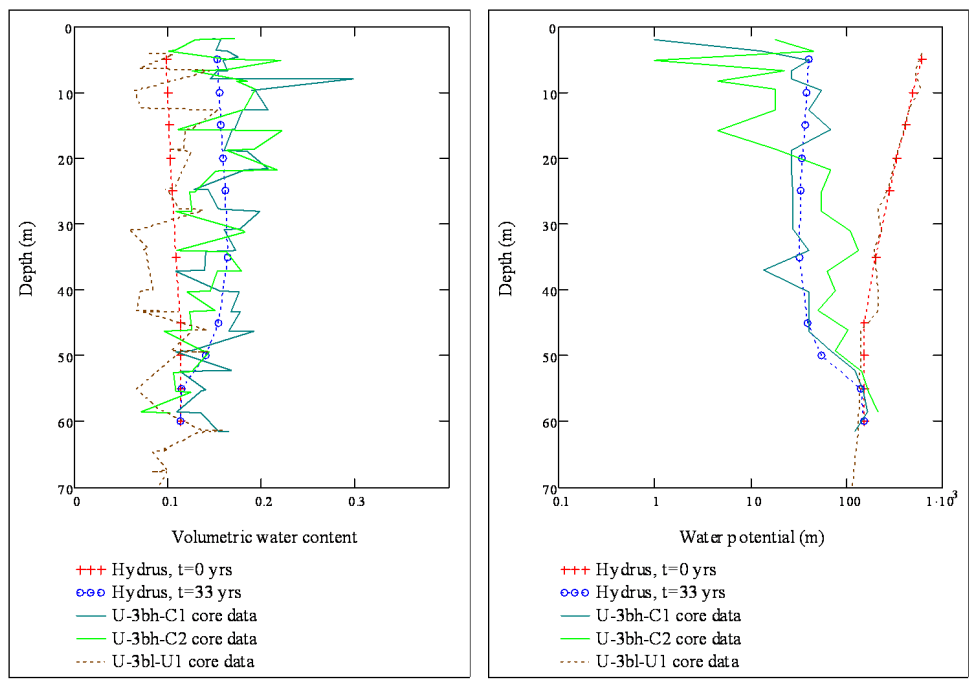

Figure E-21
Calculated and Measured Soil Water Content (Left) and Potential (Right) at U-3bh

E.4.4 Crater U-5a (WISHBONE)

Crater U-5a is located in Area 5 of the NNSS, just north of the Frenchman Flat playa, and 4 km south of the Area 5 RWMS. Crater U-5a was created during the WISHBONE test in 1965. Although this crater is not located in Yucca Flat, Frenchman Flat is located only 20 km from Yucca Flat. Although there are no direct measurements of pond depths or volumes in crater U-5a, Wilson et al. (2000) provide indirect evidence for their hypothesis that as much as 14.6 m of sediment were deposited in the U-5a crater during a single flood event. Wilson et al. (2000) estimate that a ponding volume of 63,000 m^3 was required to leave these high water marks.

Runoff was calculated for crater U-5a using the precipitation record from station W5B, and using a catchment area of 14.5 km^2 that is cited by Wilson et al. (2000) and Hokett and French (1998) as the active contributing catchment to U-5a, known as Barren Wash. Calculated pond height is shown in Figure E-22, where one single runoff event stands out sharply. This event occurred on July 22, 1984, and is the most likely date for the single large flood event hypothesized by Wilson et al. (2000). After consideration of infiltration, which was probably very high given the large pressure head caused by virtually filling this crater, then pond height is reasonably consistent with that reported by Wilson et al. (2000).

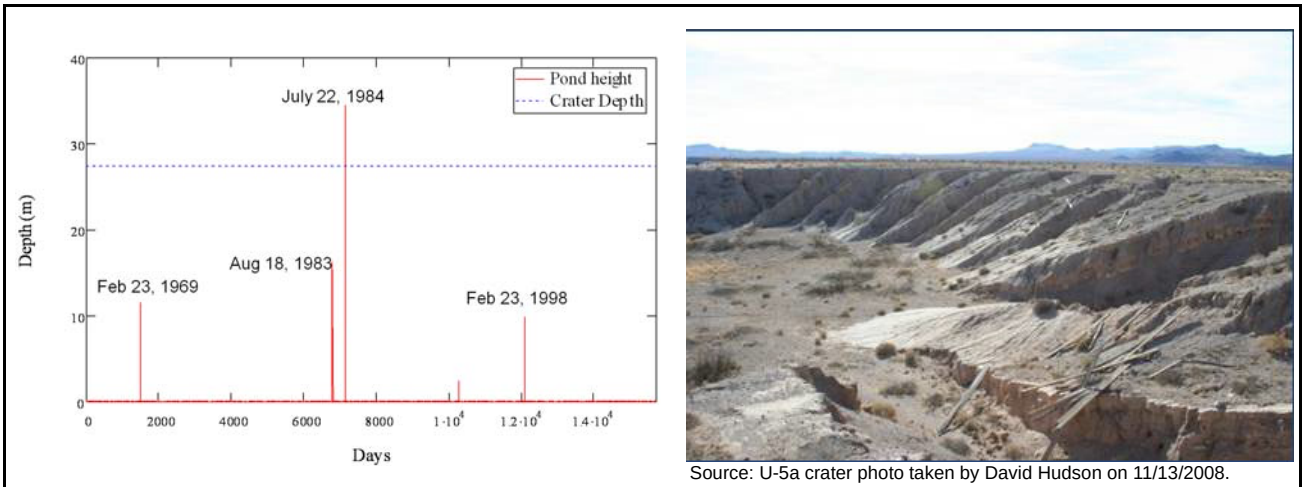

Source: U-5a crater photo taken by David Hudson on 11/13/2008.

Figure E-22
Calculated Pond Heights for U-5a Crater (Left), and Photo of U-5a (Right)

Photos taken of U-5a in 2008 support the hypothesis that this crater has received large amounts of runoff (and sediment) from the upstream catchment. Figure E-22 includes a photo taken on Nov. 13, 2008. These photos clearly show the crater is much shallower than the original depth of 27.4 m. This photo suggests that given enough time and runoff events, many of the Yucca Flat craters may become partially or completely filled with sediment. In the case of U-5a, the crater was 53 percent filled (in terms of height not volume) within a period of only 19 years, from the test date to the date of the single large flood event in 1984, if the crater was filled in one event as hypothesized by Wilson et al. (2000).

E.5.0 RESULTS

Surface water runoff and infiltration into all Yucca Flat craters was calculated using the SCS-CN method with H1D. The runoff model was calibrated by adjusting surface soil water potential thresholds that separate curve number antecedent runoff conditions, until runoff and infiltration model results best matched ponding data and subsurface moisture conditions for three craters in Yucca Flat, and one crater in Frenchman Flat. Long-term (1,000-year) one-dimensional simulations of infiltration were then conducted for all 462 craters, where infiltration is calculated as recharge plus change in soil water storage.

The methods used to make these crater recharge calculations include many assumptions, the largest of which include uniform precipitation over large catchment areas, no transmission losses over large catchment areas, and the assumption that craters have frustum geometries. However, model calibration to data collected at U-10i, U-3fd, U-3bh, and U-5a all provide confidence in the model results, and model results are consistent with the conclusions of other researchers with regard to ponding volumes, and infiltration fluxes (Tyler, McKay, and Mihevc, 1992; Pohll, Warwick, and Tyler, 1996; French et al., 1999; Wilson et al., 2000; and Hokett et al., 2000).

This work clearly shows that nuclear subsidence craters are potential groundwater recharge points, if the crater catchment area is relatively large. Model results and observations made at the U-5a crater suggest that craters with large catchments areas will also fill with sediment, eventually eliminating a groundwater pathway. Crater infiltration was calculated for all 462 craters using the 1,000-year synthetic precipitation record and H1D, where average annual infiltration is the sum of recharge out of the model domain and change in storage, divided by 1,000 years.

Figure E-23 shows the preliminary and final results of sorted infiltration for all craters. Model results indicate that the median and mean infiltration for all craters was 62 and 206 mm/year, respectively. As discussed previously, the preliminary results included an upper and lower bound and use an alternative relationship between crater dimensions and recharge while the final results include one set of results and the frustrum relationship for crater dimensions. Table E-4 provides some statistics on the preliminary and final results.

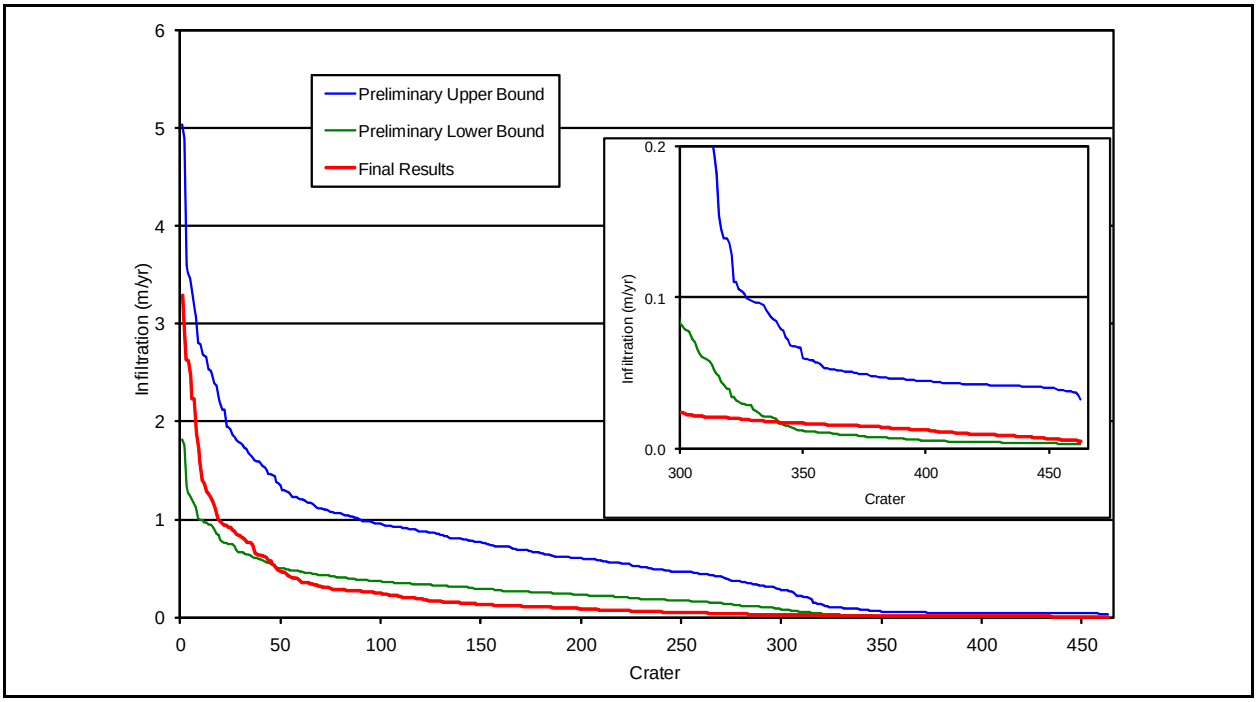

Figure E-23
Final and Preliminary Infiltration Results

Table E-4
Statistics for Final and Preliminary Infiltration Results

	Final (m/yr)	Preliminary (m/yr)	
		Upper Bound	Lower Bound
Minimum	0.005	0.032	0.003
Median	0.062	0.512	0.189
Mean	0.206	0.648	0.240
Maximum	3.288	5.035	1.818

Figure E-24 shows a map of Yucca Flat with crater catchment areas, and infiltration flux for all 462 craters. Crater catchment areas, and therefore infiltration rates, tend to be largest on the north and west sides of Yucca Flat rather than on the east side, or in the center of Yucca Flat.

The details of the enhanced crater recharge results that are used in the unsaturated zone flow and transport model are presented in Table E-5.

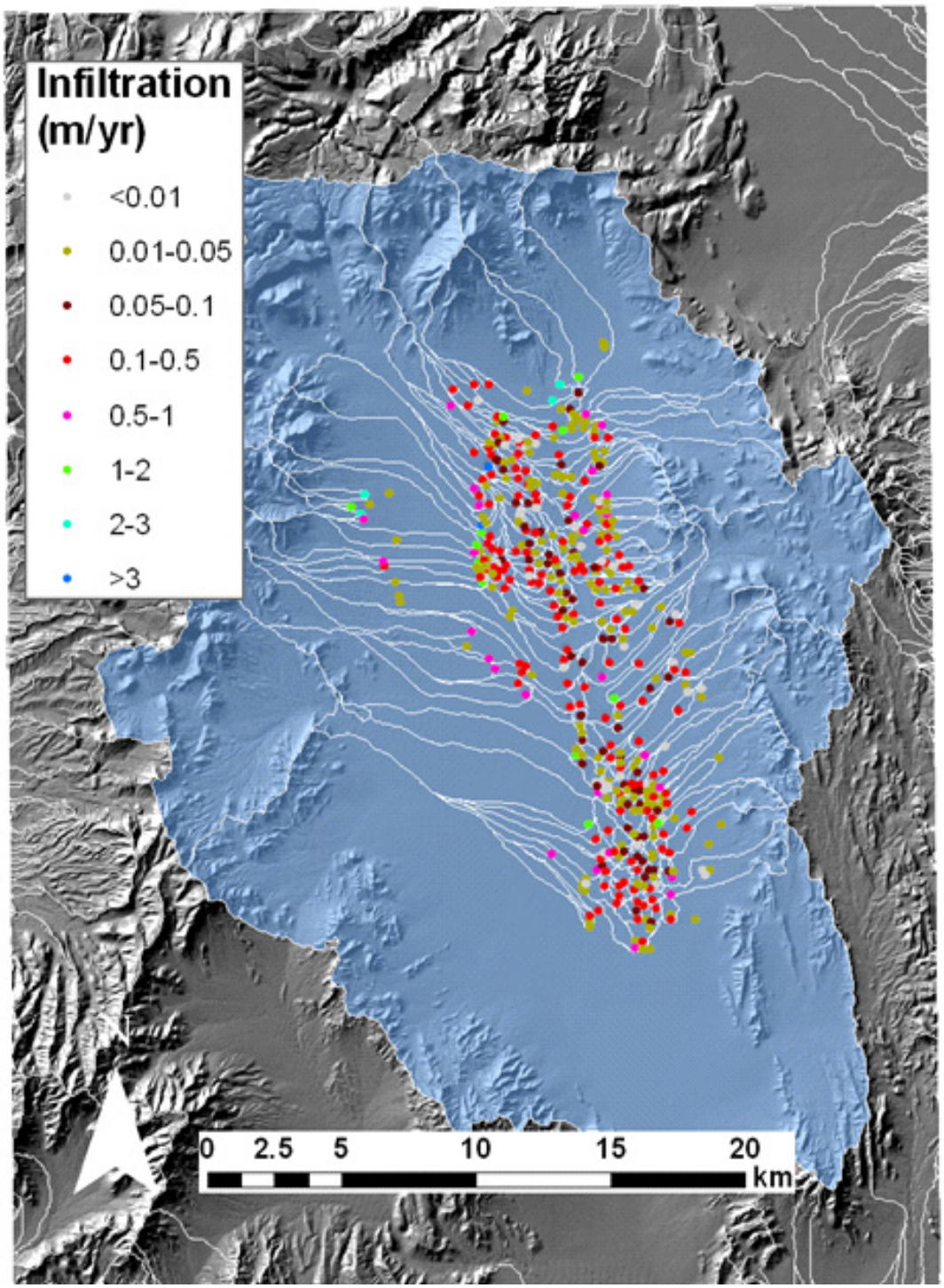

Figure E-24
Map Showing Crater Catchment Areas and Infiltration Flux for Each Crater

Table E-5
Yucca Flat/Climax Mine Surface Crater Characteristics
(Page 1 of 23)

Detonation Name	Presence of Surface Crater (Y/N)	Size and Nonzero Depth Surface Craters (m)	Surface Crater (m^2)		Modeled Catchment Area of Surface Crater (km^2)	Modeled Enhanced Crater Recharge (m/yr)
			Top Area	Bottom Area		
AARDVARK	Y	14.41	57989.072	3508.448	0.45	0.06
ABEYTAS	Y	23.16	34976.185	1730.133	1.26	0.276
ABILENE	Y	<1	7688.091	505.538	<0.04	0.008
ABO	N	--	--	--	--	--
ABSINTHE	N	--	--	--	--	--
ACE	Y	<1	633.401	7.508	<0.04	0.024
ACUSHI	Y	14.1	24232.281	3074.527	0.83	0.118
ADZE	N	--	--	--	--	--
AGILE	Y	5.46	24480.072	3169.412	0.72	0.085
AGOUTI	Y	8.6	13609.964	1933.423	0.2	0.046
AGRINI	Y	<1	1481.690	16.574	<0.04	0.021
AHTANUM	Y	8.05	1808.422	114.668	0.04	0.123
AJAX	Y	9.55	11025.872	621.468	0.1	0.068
AJO	Y	18.7	21728.101	446.065	0.7	0.406
AKAVI	Y	14.88	18690.576	484.351	0.19	0.153
AKBAR	Y	4.87	12539.856	398.604	0.43	0.204
ALEMAN	N	--	--	--	--	--
ALGODONES	Y	5.86	60884.225	2499.232	0.58	0.076
ALIGOTE	N	--	--	--	--	--
ALIMENT	N	--	--	--	--	--
ALLEGHENY	Y	<1	8022.318	237.289	<0.04	0.011
ALPACA	N	--	--	--	--	--
ALUMROOT	N	--	--	--	--	--
ALVA	Y	4.82	8509.594	948.612	0.53	0.17
ALVISO	N	--	--	--	--	--
ANACOSTIA	Y	8.57	15968.772	1310.654	0.51	0.143
ANCHOVY	Y	17.66	21614.327	1690.398	0.06	0.022
ANGUS	N	--	--	--	--	--
APODACA	N	--	--	--	--	--
APSHAPA	N	--	--	--	--	--
ARABIS-BLUE	N	--	--	--	--	--
ARABIS-GREEN	N	--	--	--	--	--
ARABIS-RED	Y	3.77	6580.286	46.883	0.44	0.357
ARIKAREE	Y	<1	2045.737	54.538	<0.04	0.014

Table E-5
Yucca Flat/Climax Mine Surface Crater Characteristics
(Page 2 of 23)

Detonation Name	Presence of Surface Crater (Y/N)	Size and Nonzero Depth Surface Craters (m)	Surface Crater (m^2)		Modeled Catchment Area of Surface Crater (km^2)	Modeled Enhanced Crater Recharge (m/yr)
			Top Area	Bottom Area		
ARMADA	Y	2.9	17984.688	1040.012	<0.04	0.011
ARMADILLO	Y	6.1	18035.894	351.085	8.42	0.944
ARNICA-VIOLET	Y	10.92	1918.659	173.891	0.05	0.112
ARNICA-YELLOW	Y	29.62	12100.831	841.036	2.93	1.001
ARSENATE	N	--	--	--	--	--
ARTESIA	Y	21.15	59499.121	3714.974	0.5	0.064
ASCO	N	--	--	--	--	--
ASIAGO	Y	9.8	15315.009	370.045	0.19	0.157
ATARQUE	Y	<1	14636.347	1306.757	<0.04	0.007
ATRISCO	Y	28.46	101692.361	3199.207	2.72	0.311
AUGER	N	--	--	--	--	--
AUK	N	--	--	--	--	--
AUSTIN	N	--	--	--	--	--
AVENS-ALKERMES	N	--	--	--	--	--
AVENS-ANDORRE	Y	2.98	21602.982	369.379	<0.04	0.022
AVENS-ASAMLTE	Y	1.53	10807.500	244.203	<0.04	0.015
AVENS-CREAM	Y	17.43	22285.392	1248.073	2.89	0.611
AZUL	N	--	--	--	--	--
BACCARAT	Y	<1	4256.228	49.261	<0.04	0.017
BACKGAMMON	Y	<1	10856.145	368.259	<0.04	0.01
BACKSWING	Y	9.93	8898.821	1269.324	0.07	0.026
BALTIC	N	--	--	--	--	--
BANDICOOT	Y	29.72	27623.455	749.180	0.11	0.085
BANEBERRY	Y	22.68	16752.728	188.635	0.92	0.764
BANON	Y	26.74	42957.244	345.427	0.25	0.269
BARBEL	Y	10.65	16231.979	2734.957	0.08	0.016
BARRACUDA	N	--	--	--	--	--
BARRANCA	N	--	--	--	--	--
BARSAC	Y	14.79	21169.994	1758.543	0.17	0.048
BASEBALL	Y	14.55	35585.610	2006.338	0.29	0.068
BAY LEAF	N	--	--	--	--	--
BEEBALM	N	--	--	--	--	--
BELEN	Y	18.85	47738.982	5019.303	0.31	0.032
BELLOW	Y	<1	2126.315	20.319	<0.04	0.021

Table E-5
Yucca Flat/Climax Mine Surface Crater Characteristics
(Page 3 of 23)

Detonation Name	Presence of Surface Crater (Y/N)	Size and Nonzero Depth Surface Craters (m)	Surface Crater (m^2)		Modeled Catchment Area of Surface Crater (km^2)	Modeled Enhanced Crater Recharge (m/yr)
			Top Area	Bottom Area		
BERNAL	Y	16.71	17804.706	718.239	0.18	0.112
BERNALILLO	N	--	--	--	--	--
BEVEL	N	--	--	--	--	--
BIGGIN	N	--	--	--	--	--
BILBY	Y	20.64	153314.260	7298.784	5.24	0.262
BILGE	N	--	--	--	--	--
BILLET	N	--	--	--	--	--
BIT-A	N	--	--	--	--	--
BIT-B	N	--	--	--	--	--
BITTERLING	Y	4.71	4001.452	1380.749	0.1	0.032
BLACK	Y	14.31	9101.044	158.390	0.22	0.342
BLENTON	Y	<1	42962.613	767.525	<0.04	0.012
BOBAC	Y	6.69	8859.245	91.398	0.15	0.242
BOBSTAY	Y	14.12	27561.408	675.886	0.25	0.14
BOGEY	N	--	--	--	--	--
BONARDA	Y	6.77	20030.150	628.466	13.17	1.085
BONEFISH	Y	15.76	26764.009	3696.688	1.09	0.129
BOOMER	N	--	--	--	--	--
BORATE	Y	15.09	31782.283	1680.156	0.11	0.037
BORDEAUX	Y	17.53	19948.895	671.060	0.18	0.119
BORREGO	N	--	--	--	--	--
BOURBON	Y	10.44	3403.489	125.807	0.11	0.244
BOUSCHET	Y	14.52	43132.444	1440.835	0.2	0.069
BOWIE	N	--	--	--	--	--
BOWL-1	Y	<1	6385.960	93.246	<0.04	0.015
BOWL-2	Y	7.32	4497.753	289.796	0.06	0.082
BRACKEN	N	--	--	--	--	--
BRANCO	Y	7.31	11407.343	474.803	0.16	0.113
BRANCO-HERKIMER	N	--	--	--	--	--
BRAZOS	Y	5.68	16433.037	1298.397	0.1	0.033
BRETON	Y	10.85	36501.625	3413.285	2.04	0.214
BRIE	Y	<1	11822.635	141.287	<0.04	0.015
BRISTOL	N	--	--	--	--	--
BRONZE	Y	15.8	75014.246	12458.442	0.18	0.011

Table E-5
Yucca Flat/Climax Mine Surface Crater Characteristics
(Page 4 of 23)

Detonation Name	Presence of Surface Crater (Y/N)	Size and Nonzero Depth Surface Craters (m)	Surface Crater (m^2)		Modeled Catchment Area of Surface Crater (km^2)	Modeled Enhanced Crater Recharge (m/yr)
			Top Area	Bottom Area		
BRUSH	N	--	--	--	--	--
BUFF	Y	8.86	52265.675	3182.410	1.02	0.116
BULKHEAD	Y	<1	64357.615	425.589	<0.04	0.016
BULLFROG	Y	4.43	43122.955	549.536	1.11	0.216
BUNKER	Y	1.11	12130.562	105.729	<0.04	0.018
BURZET	Y	7.95	22873.943	1108.313	0.46	0.137
BYE	Y	12.08	15838.437	1101.204	18.62	1.727
CABOC	Y	<1	771.043	11.770	<0.04	0.021
CABRESTO	N	--	--	--	--	--
CABRILLO	Y	10.52	26963.753	3718.499	0.15	0.021
CALABASH	Y	13.06	52924.855	1458.422	0.42	0.113
CAMPOS	N	--	--	--	--	--
CANFIELD	Y	6.28	37337.380	446.954	4.58	0.574
CAN-GREEN	Y	8.79	7124.304	1355.965	0.09	0.031
CANJILON	N	--	--	--	--	--
CANNA-LIMOGES	N	--	--	--	--	--
CANNA-UMBRINUS	N	--	--	--	--	--
CAN-RED	Y	22.21	19965.388	732.270	0.16	0.107
CANVASBACK	N	--	--	--	--	--
CAPITAN	N	--	--	--	--	--
CAPROCK	Y	31.27	46473.156	2036.824	1.42	0.28
CARMEL	Y	8.59	6971.808	99.980	<0.04	0.059
CARNELIAN	Y	3.54	7457.035	125.308	5.72	0.765
CARP	N	--	--	--	--	--
CARPETBAG	Y	26.12	88491.154	2861.369	0.67	0.114
CARRIZOZO	N	--	--	--	--	--
CASHMERE	Y	8.99	10956.739	1776.530	0.3	0.073
CASSELMAN	Y	16.99	13051.528	633.934	<0.04	0.021
CASSOWARY	N	--	--	--	--	--
CATHAY	Y	4.1	48090.243	687.607	0.45	0.112
CEBOLLA	N	--	--	--	--	--
CEBRERO	N	--	--	--	--	--
CENTAUR	Y	<1	522.507	54.186	<0.04	0.009
CERISE	Y	9.34	16796.158	2018.535	1.66	0.277

Table E-5
Yucca Flat/Climax Mine Surface Crater Characteristics
(Page 5 of 23)

Detonation Name	Presence of Surface Crater (Y/N)	Size and Nonzero Depth Surface Craters (m)	Surface Crater (m^2)		Modeled Catchment Area of Surface Crater (km^2)	Modeled Enhanced Crater Recharge (m/yr)
			Top Area	Bottom Area		
CERNADA	N	--	--	--	--	--
CERRO	N	--	--	--	--	--
CHAENACTIS	Y	11.86	9629.153	803.083	2.69	0.74
CHAMITA	Y	4.69	21271.024	989.517	1.45	0.263
CHANTILLY	Y	<1	625.694	20.266	<0.04	0.015
CHARCOAL	Y	7.57	57054.767	1385.906	0.44	0.099
CHATTY	Y	3.68	3068.236	182.649	0.39	0.314
CHEEDAM	Y	8.71	14216.968	428.619	0.45	0.251
CHENILLE	Y	9.79	5284.420	5.705	0.04	0.414
CHESS	N	--	--	--	--	--
CHEVRE	Y	<1	4172.919	152.076	<0.04	0.011
CHIBERTA	Y	34.23	97123.879	5280.764	0.25	0.031
CHINCHILLA	Y	1.28	7237.538	3097.083	<0.04	0.005
CHINCHILLA II	Y	<1	5226.053	421.498	<0.04	0.008
CHIPMUNK	N	--	--	--	--	--
CHOCOLATE	Y	5.83	11863.458	333.939	0.08	0.077
CIMARRON	Y	<1	19647.876	601.060	<0.04	0.01
CINNAMON	N	--	--	--	--	--
CLAIRETTE	N	--	--	--	--	--
CLARKSMOBILE	Y	19.67	42990.860	1218.497	0.09	0.051
CLUB	Y	1.52	4644.292	290.799	<0.04	0.01
CLYMER	Y	<1	5862.452	174.382	<0.04	0.011
COALORA	Y	<1	846.232	14.018	<0.04	0.02
COBBLER	N	--	--	--	--	--
CODSAW	Y	<1	6041.142	49.045	1.64	0.222
COFFER	Y	28.61	11637.514	163.991	11.07	3.288
COGNAC	N	--	--	--	--	--
COLFAX	N	--	--	--	--	--
COLMOR	Y	<1	2656.526	37.291	<0.04	0.017
COMMODORE	Y	39.65	91891.038	1048.739	0.41	0.205
CONCENTRATION	Y	2.06	3188.111	109.977	<0.04	0.017
CORAZON	N	--	--	--	--	--
CORDUROY	Y	19.58	109820.237	3295.227	35.86	1.396
CORMORANT	N	--	--	--	--	--

Table E-5
Yucca Flat/Climax Mine Surface Crater Characteristics
(Page 6 of 23)

Detonation Name	Presence of Surface Crater (Y/N)	Size and Nonzero Depth Surface Craters (m)	Surface Crater (m^2)		Modeled Catchment Area of Surface Crater (km^2)	Modeled Enhanced Crater Recharge (m/yr)
			Top Area	Bottom Area		
CORNICE-GREEN	Y	43.93	46831.821	265.075	0.38	0.461
CORNICE-YELLOW	Y	31.28	47788.325	1400.618	4.76	0.847
CORNUCOPIA	Y	4.84	17651.897	374.642	0.18	0.113
CORREO	Y	4.4	32489.314	1120.015	0.06	0.023
COSO-BRONZE	Y	<1	6620.627	151.315	<0.04	0.013
COSO-GRAY	N	--	--	--	--	--
COSO-SILVER	N	--	--	--	--	--
COTTAGE	Y	10.06	66678.434	1619.909	0.46	0.101
COULOMMIERS	Y	24.94	37498.305	717.332	0.22	0.143
COURSER	N	--	--	--	--	--
COVE	Y	8.2	15664.753	1796.855	1.41	0.257
COWLES	Y	4.63	20353.813	3108.608	0.17	0.024
COYPU	N	--	--	--	--	--
CREMINO	N	--	--	--	--	--
CREMINO-CAERPHILLY	N	--	--	--	--	--
CREPE	Y	13.09	26079.213	2511.819	0.06	0.016
CRESTLAKE-BRIAR	Y	9.6	2815.792	77.312	<0.04	0.035
CRESTLAKE-TANSAN	N	--	--	--	--	--
CREW	Y	16.73	10665.262	392.965	3.79	1.288
CREW-2ND	N	--	--	--	--	--
CREW-3RD	N	--	--	--	--	--
CREWLINE	N	--	--	--	--	--
CROCK	Y	3.83	8124.486	352.316	<0.04	0.016
CROWDIE	Y	13.23	8907.102	246.316	0.79	0.582
CRUET	Y	4.7	11701.334	423.423	7.73	0.842
CUCHILLO	N	--	--	--	--	--
CULANTRO-A	N	--	--	--	--	--
CULANTRO-B	N	--	--	--	--	--
CUMARIN	Y	16.15	34821.116	669.170	0.65	0.281
CUMBERLAND	Y	10.01	11898.362	2245.587	0.59	0.113
CUP	Y	54.91	66132.601	2080.949	0.63	0.157
CYATHUS	Y	7.63	4449.339	217.004	0.25	0.284
CYCLAMEN	Y	13.61	17077.024	2221.388	0.15	0.033
DAIQUIRI	N	--	--	--	--	--

Table E-5
Yucca Flat/Climax Mine Surface Crater Characteristics
(Page 7 of 23)

Detonation Name	Presence of Surface Crater (Y/N)	Size and Nonzero Depth Surface Craters (m)	Surface Crater (m^2)		Modeled Catchment Area of Surface Crater (km^2)	Modeled Enhanced Crater Recharge (m/yr)
			Top Area	Bottom Area		
DALHART	Y	20.27	71112.592	1571.184	0.11	0.051
DAMAN I	Y	13.26	22890.953	783.199	0.26	0.13
DANABLU	Y	6.04	10077.841	1462.718	0.67	0.161
DAUPHIN	Y	8.48	13358.233	622.792	0.09	0.064
DEAD	Y	<1	9372.695	3645.106	<0.04	0.005
DECK	Y	11.5	22987.972	863.309	0.18	0.088
DELPHINIUM	Y	15.34	11414.246	330.322	0.09	0.12
DEXTER	N	--	--	--	--	--
DIANTHUS	Y	5.61	17429.093	1056.157	0.42	0.123
DISCUS THROWER	Y	12.29	16968.071	303.332	0.41	0.311
DIVIDER	N	--	--	--	--	--
DOFINO	N	--	--	--	--	--
DOFINO-LAWTON	N	--	--	--	--	--
DOLCETTO	Y	<1	15362.990	238.961	<0.04	0.013
DORMOUSE	Y	2.72	6831.194	1218.655	<0.04	0.007
DORMOUSE PRIME	Y	26.06	21521.867	632.548	0.06	0.063
DOVEKIE	Y	3.24	10022.360	617.622	0.09	0.05
DRAUGHTS	Y	15.92	62727.828	261.152	0.37	0.29
DRILL (SOURCE-LOWER)	Y	1.78	3852.585	758.671	<0.04	0.007
DRILL (TARGET-UPPER)	N	--	--	--	--	--
DRIVER	N	--	--	--	--	--
DUB	Y	11.5	5730.636	519.869	16.3	2.237
DUFFER	Y	1.43	1400.922	24.749	<0.04	0.023
DUMONT	Y	22.85	83859.522	2166.081	0.57	0.122
DUORO	Y	20.06	24560.871	1854.941	0.17	0.048
DUTCHESS	N	--	--	--	--	--
EAGLE	Y	19.07	16831.382	96.844	1.1	0.919
EBBTIDE	Y	7.43	9989.365	190.728	15.3	1.592
EDAM	Y	11.45	29042.578	2893.878	1.31	0.174
EEL	Y	<1	3751.102	16.893	<0.04	0.023
EFFENDI	Y	2.44	6429.723	592.609	<0.04	0.009
ELIDA	N	--	--	--	--	--
ELKHART	Y	3.81	16245.734	2171.069	0.08	0.018

Table E-5
Yucca Flat/Climax Mine Surface Crater Characteristics
(Page 8 of 23)

Detonation Name	Presence of Surface Crater (Y/N)	Size and Nonzero Depth Surface Craters (m)	Surface Crater (m^2)		Modeled Catchment Area of Surface Crater (km^2)	Modeled Enhanced Crater Recharge (m/yr)
			Top Area	Bottom Area		
EMBUDO	Y	18.61	19427.562	966.650	7.29	1.276
EMERSON	Y	10.67	6640.591	192.513	0.1	0.169
ERMINE	N	--	--	--	--	--
ESCABOSA	Y	14.34	95227.015	1524.132	31.37	1.364
ESROM	Y	48.68	47068.482	3051.941	0.85	0.136
ESTACA	N	--	--	--	--	--
FADE	Y	5.13	11283.278	2678.043	0.29	0.046
FAHADA	Y	<1	26438.053	1115.941	<0.04	0.009
FAJY	Y	34.55	45634.623	200.244	0.25	0.405
FALLON	Y	23.75	29513.905	783.978	0.25	0.143
FARALLONES	Y	20.64	72755.605	5025.745	0.32	0.034
FAWN	Y	10.08	17865.374	3765.058	0.11	0.016
FENTON	Y	<1	635.956	14.983	<0.04	0.018
FERRET	N	--	--	--	--	--
FERRET PRIME	Y	20.94	18549.277	1061.966	0.09	0.045
FILE	Y	13.13	15851.187	299.517	0.25	0.238
FINFOOT	Y	7.74	15974.042	283.309	0.15	0.141
FISHER	Y	11.69	20816.641	1742.674	0.39	0.094
FIZZ	N	--	--	--	--	--
FLASK-GREEN	Y	38.43	67722.366	349.774	0.21	0.291
FLASK-RED	Y	<1	587.194	54.116	<0.04	0.009
FLASK-YELLOW	N	--	--	--	--	--
FLAX-BACKUP	Y	27.88	25661.636	462.107	0.22	0.203
FLAX-SOURCE	N	--	--	--	--	--
FLAX-TEST	N	--	--	--	--	--
FLORA	N	--	--	--	--	--
FLOTOST	Y	3.19	3216.302	460.598	0.05	0.04
FLOYDADA	N	--	--	--	--	--
FOB-BLUE	N	--	--	--	--	--
FOB-GREEN	Y	<1	7124.254	442.009	<0.04	0.008
FOB-RED	Y	1.55	15517.171	235.582	<0.04	0.017
FORE	Y	33.12	74147.581	1083.782	1.01	0.33
FOREFOOT	N	--	--	--	--	--
FOREST	N	--	--	--	--	--

Table E-5
Yucca Flat/Climax Mine Surface Crater Characteristics
(Page 9 of 23)

Detonation Name	Presence of Surface Crater (Y/N)	Size and Nonzero Depth Surface Craters (m)	Surface Crater (m^2)		Modeled Catchment Area of Surface Crater (km^2)	Modeled Enhanced Crater Recharge (m/yr)
			Top Area	Bottom Area		
FREEZEOUT	Y	9.26	29965.914	2544.731	0.12	0.025
FRIJOLES-DEMING	Y	1.69	4729.102	78.283	<0.04	0.021
FRIJOLES-ESPUELA	Y	1.73	6535.043	259.892	<0.04	0.012
FRIJOLES-GUAJE	N	--	--	--	--	--
FRIJOLES-PETACA	N	--	--	--	--	--
FRISCO	Y	<1	17946.128	1784.592	<0.04	0.007
FUNNEL	N	--	--	--	--	--
FUTTOCK	N	--	--	--	--	--
GALENA-GREEN	N	--	--	--	--	--
GALENA-ORANGE	N	--	--	--	--	--
GALENA-YELLOW	N	--	--	--	--	--
GARDEN	N	--	--	--	--	--
GASCON	Y	20.62	89684.263	3648.931	0.17	0.031
GAZOOK	Y	<1	638.180	7.797	<0.04	0.024
GERBIL	Y	12.38	23131.153	1504.175	0.12	0.04
GIBSON	Y	14.98	9652.668	812.357	0.19	0.103
GILROY	N	--	--	--	--	--
GLENCOE	Y	<1	452.972	9.982	<0.04	0.02
GORBEA	N	--	--	--	--	--
GOUDA	N	--	--	--	--	--
GOURD-AMBER	Y	<1	1594.832	100.527	<0.04	0.01
GOURD-BROWN	Y	1.82	4417.516	89.956	<0.04	0.02
GRAPE A	Y	8.6	71542.737	1752.601	1.78	0.23
GRAPE B	Y	24.61	106716.085	5646.571	1.72	0.136
GREYS	Y	5.13	8693.915	678.901	2.02	0.478
GROVE	Y	12.53	3045.985	92.922	0.22	0.487
GRUNION	Y	15.14	17926.196	1935.690	0.06	0.018
GRUYERE	N	--	--	--	--	--
GRUYERE-GRADINO	N	--	--	--	--	--
GUANAY	Y	17.48	12919.386	546.380	0.15	0.118
GUNDI	Y	<1	5069.063	92.419	<0.04	0.014
GUNDI PRIME	Y	8.38	20908.640	4675.315	2.21	0.189
HADDOCK	N	--	--	--	--	--
HANDCAR	N	--	--	--	--	--

Table E-5
Yucca Flat/Climax Mine Surface Crater Characteristics
(Page 10 of 23)

Detonation Name	Presence of Surface Crater (Y/N)	Size and Nonzero Depth Surface Craters (m)	Surface Crater (m^2)		Modeled Catchment Area of Surface Crater (km^2)	Modeled Enhanced Crater Recharge (m/yr)
			Top Area	Bottom Area		
HANDICAP	Y	<1	2160.225	28.509	<0.04	0.018
HAPLOPAPPUS	N	--	--	--	--	--
HARD HAT	N	--	--	--	--	--
HAREBELL	Y	15.43	67259.374	1291.161	0.3	0.101
HARKEE	Y	3.59	8051.026	1721.274	0.07	0.018
HARLINGEN-A	Y	2.74	12425.001	256.637	<0.04	0.021
HARLINGEN-B	N	--	--	--	--	--
HATCHET	Y	10.32	18799.561	2148.156	0.26	0.053
HATCHIE	N	--	--	--	--	--
HAVARTI	Y	<1	965.349	24.158	<0.04	0.016
HAYMAKER	Y	18.24	59526.084	12694.237	0.35	0.015
HAZEBROOK-APRICOT	N	--	--	--	--	--
HAZEBROOK-CHECKERBERRY	N	--	--	--	--	--
HAZEBROOK-EMERALD	N	--	--	--	--	--
HEARTS	N	--	--	--	--	--
HEILMAN	N	--	--	--	--	--
HERMOSA	Y	36.6	114424.255	2460.552	0.13	0.052
HOD-A (GREEN)	Y	18.09	16527.817	224.091	0.95	0.664
HOD-B (RED)	Y	9.41	17828.593	1028.233	1.32	0.334
HOD-C (BLUE)	N	--	--	--	--	--
HOGNOSE	Y	11.42	15067.516	1263.278	<0.04	0.012
HOOK	Y	1.39	6209.758	96.081	<0.04	0.018
HOOPOE	N	--	--	--	--	--
HOOSIC	Y	1.1324	6379.331	95.342	<0.04	0.016
HOREHOUND	N	--	--	--	--	--
HOSPAH	Y	8.96	22858.153	3933.340	0.39	0.041
HUDSON	N	--	--	--	--	--
HULA	Y	<1	3228.056	49.124	<0.04	0.016
HULSEA	N	--	--	--	--	--
HUPMOBILE	Y	2.2	2002.048	21.736	<0.04	0.037
HURON KING	Y	20.37	19521.357	476.383	2.08	0.81
HUTCH	Y	45.84	55176.665	3921.810	8.2	0.769
HUTIA	Y	1.12	6766.315	1938.260	<0.04	0.006
HYRAX	Y	20.05	21128.091	1202.086	0.197	0.079

Table E-5
Yucca Flat/Climax Mine Surface Crater Characteristics
(Page 11 of 23)

Detonation Name	Presence of Surface Crater (Y/N)	Size and Nonzero Depth Surface Craters (m)	Surface Crater (m^2)		Modeled Catchment Area of Surface Crater (km^2)	Modeled Enhanced Crater Recharge (m/yr)
			Top Area	Bottom Area		
ICEBERG	Y	21.77	64866.151	2322.580	0.11	0.034
ILDRIM	Y	4.89	26593.455	3003.991	0.09	0.015
IMP	Y	<1	1258.563	81.905	<0.04	0.01
INGOT	N	--	--	--	--	--
IPECAC-A	N	--	--	--	--	--
IPECAC-B	N	--	--	--	--	--
ISLAY	Y	5.63	11602.434	782.039	0.09	0.046
IZZER	N	--	--	--	--	--
JACKPOTS	N	--	--	--	--	--
JAL	Y	5.27	15082.139	1242.121	0.38	0.104
JARA	Y	5.72	20168.931	727.232	0.24	0.099
JARLSBERG	Y	<1	7751.317	212.777	<0.04	0.012
JERBOA	Y	25.66	24637.947	1097.237	0.08	0.044
JIB	N	--	--	--	--	--
JICARILLA	N	--	--	--	--	--
JORNADA	Y	20.75	70821.844	2722.516	2.23	0.286
KANKAKEE	Y	19.68	48451.069	2051.647	0.25	0.062
KARA	N	--	--	--	--	--
KARAB	Y	7.65	8686.428	241.656	3.07	0.914
KASHAN	Y	4.28	16347.619	1910.679	0.08	0.02
KAWEAH	Y	<1	9436.000	198.050	<0.04	0.013
KAWICH A-BLUE	N	--	--	--	--	--
KAWICH A-WHITE	N	--	--	--	--	--
KAWICH-BLACK	Y	<1	554.488	15.751	<0.04	0.017
KAWICH-RED	N	--	--	--	--	--
KEEL	Y	16.07	20476.414	572.490	0.34	0.206
KEELSON	Y	3.59	98384.173	10670.384	0.29	0.013
KENNEBEC	Y	10.15	8780.230	58.690	0.1	0.279
KERMET	Y	<1	6710.450	356.639	<0.04	0.009
KESTI	N	--	--	--	--	--
KESTREL	Y	0	5225.462	393.855	<0.04	0.008
KHAKI	N	--	--	--	--	--
KINIBITO	Y	6.15	36689.747	786.095	0.17	0.071
KLICKITAT	Y	31.46	59793.786	4110.505	11.93	0.893

Table E-5
Yucca Flat/Climax Mine Surface Crater Characteristics
(Page 12 of 23)

Detonation Name	Presence of Surface Crater (Y/N)	Size and Nonzero Depth Surface Craters (m)	Surface Crater (m^2)		Modeled Catchment Area of Surface Crater (km^2)	Modeled Enhanced Crater Recharge (m/yr)
			Top Area	Bottom Area		
KLOSTER	Y	16.52	37446.800	205.197	0.22	0.27
KNIFE A	N	--	--	--	--	--
KNIFE B	N	--	--	--	--	--
KNIFE C	Y	<1	7266.700	97.479	<0.04	0.015
KNOX	Y	30.06	89015.554	1928.684	0.27	0.087
KOHOCTON	N	--	--	--	--	--
KOOTANAI	Y	3.54	9952.814	2953.199	<0.04	0.006
KRYDDOST	N	--	--	--	--	--
KYACK-A	Y	<1	1618.594	112.523	<0.04	0.009
KYACK-B	Y	<1	1630.926	60.519	<0.04	0.012
LABAN	Y	<1	1555.071	14.298	<0.04	0.022
LABIS	Y	3.23	37484.823	648.907	<0.04	0.021
LAGOON	Y	16.02	3663.827	13.402	3.54	2.627
LAGUNA	Y	4.92	28249.034	833.327	0.2	0.072
LAMPBLACK	N	--	--	--	--	--
LANPHER	Y	11.7	60532.759	2314.035	0.15	0.035
LAREDO	Y	<1	905.416	12.010	<0.04	0.021
LATIR	Y	20.82	55186.363	1002.606	0.13	0.081
LEDOUX	N	--	--	--	--	--
LEXINGTON	Y	<1	12709.111	2315.688	<0.04	0.006
LEYDEN	N	--	--	--	--	--
LIME	N	--	--	--	--	--
LINKS	N	--	--	--	--	--
LIPTAUER	Y	21.68	30847.469	504.678	0.14	0.138
LONGCHAMPS	Y	16.92	4172.435	305.885	<0.04	0.014
LOVAGE	Y	33.53	33907.411	367.198	0.2	0.237
LOWBALL	Y	17.75	33350.046	37.677	0.15	0.46
LUBBOCK	Y	<1	1061.948	14.771	<0.04	0.02
LUNA	N	--	--	--	--	--
MACKEREL	N	--	--	--	--	--
MAD	N	--	--	--	--	--
MALLET	Y	11.61	12718.933	1474.393	0.47	0.131
MANATEE	N	--	--	--	--	--
MANTECA	Y	9.02	23211.712	484.967	0.68	0.284

Table E-5
Yucca Flat/Climax Mine Surface Crater Characteristics
(Page 13 of 23)

Detonation Name	Presence of Surface Crater (Y/N)	Size and Nonzero Depth Surface Craters (m)	Surface Crater (m^2)		Modeled Catchment Area of Surface Crater (km^2)	Modeled Enhanced Crater Recharge (m/yr)
			Top Area	Bottom Area		
MANZANAS	N	--	--	--	--	--
MARIBO	N	--	--	--	--	--
MARSH	Y	6.68	29863.453	1100.613	0.14	0.052
MARSILLY	Y	21.09	82758.758	2794.351	0.18	0.042
MARVEL	N	--	--	--	--	--
MATACO	Y	1.79	15897.179	3326.771	<0.04	0.006
MAUVE	Y	19.73	20195.656	878.015	2.14	0.628
MAXWELL	N	--	--	--	--	--
MEMORY	Y	9.68	24785.621	807.753	1.36	0.357
MERIDA	Y	2.56	6693.773	893.438	<0.04	0.008
MERLIN	Y	12.12	17513.411	2016.104	0.13	0.031
MERRIMAC	Y	12.18	31949.73	598.787	0.3	0.165
MESCALERO	N	--	--	--	--	--
MESITA	N	--	--	--	--	--
METROPOLIS	N	--	--	--	--	--
MICKEY	Y	<1	2932.907	249.741	<0.04	0.008
MIDLAND	Y	<1	11431.723	70.831	<0.04	0.019
MIERA	Y	4.91	87467.302	1403.155	0.2	0.042
MINERO	Y	<1	11609.235	76.735	<0.04	0.018
MINIATA	Y	29.53	45977.328	1475.979	0.19	0.073
MINK	N	--	--	--	--	--
MINNOW	Y	3.54	12256.245	2582.414	0.09	0.016
MISSISSIPPI	Y	32.37	56775.658	782.257	0.25	0.163
MIZZEN	Y	29.25	74441.036	2541.889	0.2	0.051
MOA	Y	8.57	8555.938	632.652	0.09	0.06
MOGOLLON	Y	<1	5761.223	67.907	<0.04	0.017
MONAHANS-A	Y	<1	5689.659	60.694	<0.04	0.017
MONAHANS-B	N	--	--	--	--	--
MONERO	N	--	--	--	--	--
MONTEREY	Y	<1	3685.918	95.734	<0.04	0.013
MORRONES	N	--	--	--	--	--
MUDPACK	Y	<1	5315.322	66.883	<0.04	0.016
MUGGINS	Y	<1	7303.375	43.040	<0.04	0.02
MULESHOE	N	--	--	--	--	--

Table E-5
Yucca Flat/Climax Mine Surface Crater Characteristics
(Page 14 of 23)

Detonation Name	Presence of Surface Crater (Y/N)	Size and Nonzero Depth Surface Craters (m)	Surface Crater (m^2)		Modeled Catchment Area of Surface Crater (km^2)	Modeled Enhanced Crater Recharge (m/yr)
			Top Area	Bottom Area		
MULLET	N	--	--	--	--	--
MUNDO	Y	9.21	95940.036	7022.759	0.08	0.01
MUSCOVY	Y	<1	4837.067	739.159	<0.04	0.006
MUSHROOM	Y	5.67	8184.829	434.886	0.82	0.345
MUSTANG	Y	1.29	2681.484	1141.460	<0.04	0.005
NAMA-AMARYLIS	N	--	--	--	--	--
NAMA-MEPHISTO	N	--	--	--	--	--
NARRAGUAGUS	Y	<1	617.869	29.436	<0.04	0.013
NASH	Y	50.69	30805.879	0.00	0.88	2.625
NATCHES	N	--	--	--	--	--
NATOMA	N	--	--	--	--	--
NAVATA	N	--	--	--	--	--
NESSEL	Y	23.61	39961.958	2192.514	0.28	0.064
NEWARK	Y	<1	3970.304	30.924	<0.04	0.02
NIGHTINGALE	N	--	--	--	--	--
NIPPER	Y	<1	5889.870	203.069	<0.04	0.011
NIZA	Y	6.46	8954.436	57.058	0.04	0.152
NOGGIN	Y	53.19	69164.030	751.854	1.64	0.651
NOOR	Y	9.27	9373.516	735.469	0.16	0.091
NORBO	Y	3.7	3216.711	110.379	0.16	0.223
NORMANNA	Y	<1	11333.590	290.922	<0.04	0.011
NUMBAT	Y	10.11	25642.621	3450.586	0.21	0.029
OAKLAND	N	--	--	--	--	--
OARLOCK	Y	17.31	20587.609	422.920	0.35	0.26
OBAR	N	--	--	--	--	--
OCATE	Y	6.65	7227.646	375.278	0.11	0.101
OCHRE	N	--	--	--	--	--
OCONTO	Y	4.22	16364.618	1619.767	<0.04	0.009
OFFSHORE	Y	15.54	33332.503	2543.587	6.09	0.641
ONAJA	Y	19.4	15242.256	143.642	0.07	0.204
ORGANDY	N	--	--	--	--	--
ORKNEY	N	--	--	--	--	--
OSCURO	Y	22.02	137249.858	175.291	1.62	0.637
OTERO	N	--	--	--	--	--

Table E-5
Yucca Flat/Climax Mine Surface Crater Characteristics
(Page 15 of 23)

Detonation Name	Presence of Surface Crater (Y/N)	Size and Nonzero Depth Surface Craters (m)	Surface Crater (m^2)		Modeled Catchment Area of Surface Crater (km^2)	Modeled Enhanced Crater Recharge (m/yr)
			Top Area	Bottom Area		
PACA	Y	7.07	12702.378	202.978	0.15	0.171
PACKARD	Y	2.82	7347.169	359.754	<0.04	0.013
PACKRAT	Y	6.98	18338.767	2831.801	0.54	0.078
PAISANO	N	--	--	--	--	--
PAJARA	Y	33.75	19304.882	180.931	1.01	0.939
PALISADE-1	Y	<1	7998.012	154.990	<0.04	0.013
PALISADE-2	N	--	--	--	--	--
PALISADE-3	N	--	--	--	--	--
PALIZA	Y	9.83	60426.067	1182.098	0.3	0.091
PAMPAS	Y	8.75	25199.854	1252.344	0.06	0.028
PANAMINT	N	--	--	--	--	--
PANCHUELA	Y	8.12	23679.974	868.911	0.05	0.032
PAR	Y	19.91	17756.771	1498.450	0.17	0.056
PARNASSIA	Y	17.79	17420.895	213.963	0.2	0.271
PARROT	Y	2.85	6247.038	1671.223	<0.04	0.006
PASCAL-A	N	--	--	--	--	--
PASCAL-B	N	--	--	--	--	--
PASCAL-C	N	--	--	--	--	--
PASSAIC	Y	19.1	18342.015	1135.642	0.25	0.102
PEBA	Y	19.51	21868.528	2540.163	0.29	0.051
PEDERNAL	N	--	--	--	--	--
PEKAN	Y	12.97	16951.664	114.214	0.12	0.252
PENASCO	Y	10.36	15518.276	1761.092	0.1	0.028
PERA	Y	1.5	6337.557	198.640	<0.04	0.013
PERSIMMON	Y	4.39	14270.635	1534.731	0.46	0.099
PETREL	N	--	--	--	--	--
PICCALILLI	Y	13.85	37996.213	1225.506	2.21	0.427
PIKE	Y	7.47	7208.450	587.891	0.36	0.194
PILE DRIVER	N	--	--	--	--	--
PINEAU	N	--	--	--	--	--
PINEDROPS-BAYOU	N	--	--	--	--	--
PINEDROPS-SLOAT	N	--	--	--	--	--
PINEDROPS-TAWNY	N	--	--	--	--	--
PIPEFISH	Y	16.19	16746.331	1349.914	0.2	0.07

Table E-5
Yucca Flat/Climax Mine Surface Crater Characteristics
(Page 16 of 23)

Detonation Name	Presence of Surface Crater (Y/N)	Size and Nonzero Depth Surface Craters (m)	Surface Crater (m^2)		Modeled Catchment Area of Surface Crater (km^2)	Modeled Enhanced Crater Recharge (m/yr)
			Top Area	Bottom Area		
PIRANHA	Y	16.05	83097.583	3227.182	1.82	0.2
PITON-A	N	--	--	--	--	--
PITON-B	Y	<1	1615.420	39.614	<0.04	0.015
PITON-C	N	--	--	--	--	--
PLAID II	Y	2.37	7180.325	474.106	<0.04	0.01
PLANER	N	--	--	--	--	--
PLATYPUS	N	--	--	--	--	--
PLAYER	N	--	--	--	--	--
PLEASANT	N	--	--	--	--	--
PLIERS	Y	7.8	12593.866	256.549	0.12	0.14
PLOMO	N	--	--	--	--	--
POD-A	N	--	--	--	--	--
POD-B	N	--	--	--	--	--
POD-C	N	--	--	--	--	--
POD-D	Y	13.23	5512.317	0.00	0.07	0.887
POLKA	N	--	--	--	--	--
POLYGONUM	N	--	--	--	--	--
POMMARD	N	--	--	--	--	--
PONGEE	N	--	--	--	--	--
PONIL	Y	<1	13989.052	101.064	<0.04	0.018
PORTMANTEAU	Y	28.64	66165.690	1304.118	59.28	3.045
PORTOLA	N	--	--	--	--	--
PORTOLA-LARKIN	N	--	--	--	--	--
PORTULACA	Y	29.81	24065.262	939.956	0.62	0.264
POTRERO	Y	<1	977.756	71.982	<0.04	0.01
POTRILLO	Y	1.79	87799.001	3478.874	<0.04	0.01
PRATT	Y	10.55	22199.797	443.119	0.13	0.112
PRESIDIO	N	--	--	--	--	--
PUCE	N	--	--	--	--	--
PUDDLE	N	--	--	--	--	--
PURPLE	Y	8.99	13929.914	1562.433	4.18	0.621
PUYE	Y	<1	16840.486	1459.680	<0.04	0.007
PYRAMID	Y	11.42	92894.037	73.400	0.22	0.265
QUARGEL	Y	21.73	40987.570	1005.803	0.21	0.106

Table E-5
Yucca Flat/Climax Mine Surface Crater Characteristics
(Page 17 of 23)

Detonation Name	Presence of Surface Crater (Y/N)	Size and Nonzero Depth Surface Craters (m)	Surface Crater (m^2)		Modeled Catchment Area of Surface Crater (km^2)	Modeled Enhanced Crater Recharge (m/yr)
			Top Area	Bottom Area		
QUESO	N	--	--	--	--	--
QUINELLA	Y	26.44	78666.769	1434.815	0.65	0.193
RACCOON	Y	2.96	6327.368	1801.667	<0.04	0.006
RACK	Y	5.26	6461.606	293.630	0.05	0.059
RARITAN	Y	1.85	3406.679	16.342	<0.04	0.04
REBLOCHON	Y	22.43	91057.807	3825.297	0.21	0.035
REDMUD	Y	<1	5869.377	34.877	<0.04	0.02
REO	Y	<1	7521.535	158.817	<0.04	0.013
RHYOLITE	N	--	--	--	--	--
RIB	Y	4.25	7241.899	350.652	0.09	0.079
RINGTAIL	Y	<1	3888.114	283.379	<0.04	0.008
RIOLA	N	--	--	--	--	--
RIVET I	N	--	--	--	--	--
RIVET II	Y	<1	7661.714	138.629	<0.04	0.014
RIVET III	Y	<1	18349.043	175.367	<0.04	0.016
RIVOLI	N	--	--	--	--	--
ROANOKE	N	--	--	--	--	--
ROMANO	Y	27.41	37648.870	2101.535	0.37	0.088
ROQUEFORT	Y	1.9	22949.887	448.196	<0.04	0.016
ROUSANNE	Y	17.73	43275.560	692.363	0.1	0.085
ROVENA	Y	<1	951.449	67.277	<0.04	0.01
RUDDER	Y	8.16	104398.948	9235.430	0.29	0.016
RUMMY	Y	13.82	125653.087	7400.218	8.89	0.359
RUSSET	N	--	--	--	--	--
SABADO	N	--	--	--	--	--
SACRAMENTO	Y	12.66	12720.961	935.627	0.38	0.157
SAN JUAN	N	--	--	--	--	--
SANDREEF	Y	15.5	30514.826	226.421	0.81	0.498
SANTEE	Y	3.5	4702.296	51.585	<0.04	0.044
SAPELLO	Y	2.45	4994.807	116.243	<0.04	0.021
SAPPHO	N	--	--	--	--	--
SARDINE	Y	16.87	19539.081	2062.335	0.12	0.03
SATSOP	Y	10.18	8447.279	1171.334	0.05	0.021
SATZ	Y	9.31	2133.020	204.606	0.2	0.308

Table E-5
Yucca Flat/Climax Mine Surface Crater Characteristics
(Page 18 of 23)

Detonation Name	Presence of Surface Crater (Y/N)	Size and Nonzero Depth Surface Craters (m)	Surface Crater (m^2)		Modeled Catchment Area of Surface Crater (km^2)	Modeled Enhanced Crater Recharge (m/yr)
			Top Area	Bottom Area		
SAXON	Y	<1	1508.504	73.925	<0.04	0.011
SAZERAC	Y	11.83	19958.206	1834.740	0.33	0.08
SCANTLING	Y	24.16	66049.155	1906.431	0.11	0.044
SCAUP	Y	<1	30184.912	2846.944	<0.04	0.007
SCHELLBOURNE	Y	16.28	38155.393	715.083	0.15	0.101
SCISSORS	Y	9.19	12186.080	872.711	1.23	0.371
SCREAMER	Y	14.43	17689.010	2973.702	0.82	0.122
SCREE-ACAJOU	Y	<1	3463.000	32.900	<0.04	0.019
SCREE-ALHAMBRA	Y	<1	2617.974	57.771	<0.04	0.014
SCREE-CHAMOIS	N	--	--	--	--	--
SCUPPER	N	--	--	--	--	--
SCUTTLE	N	--	--	--	--	--
SEAFOAM	N	--	--	--	--	--
SEAMOUNT	Y	12.53	23462.654	589.078	0.27	0.162
SEAWEED B	N	--	--	--	--	--
SEAWEED-C	N	--	--	--	--	--
SEAWEED-D	N	--	--	--	--	--
SEAWEED-E	N	--	--	--	--	--
SECO	N	--	--	--	--	--
SEERSUCKER	N	--	--	--	--	--
SEPIA	Y	10.73	17913.774	817.429	0.2	0.099
SEVILLA	N	--	--	--	--	--
SEYVAL	Y	5.83	17170.946	86.611	0.2	0.222
SHALLOWS	Y	9.01	14928.046	1470.500	0.16	0.048
SHAPER	Y	14.41	88832.149	845.655	1.66	0.357
SHAVE	Y	<1	13026.050	979.258	<0.04	0.008
SHREW	N	--	--	--	--	--
SHUFFLE	Y	10.2	52082.863	4432.036	0.77	0.073
SIDECAR	Y	2.97	7377.094	307.040	<0.04	0.015
SIENNA	Y	7.78	18992.748	187.301	0.08	0.125
SILENE	N	--	--	--	--	--
SIMMS	Y	<1	2901.051	41.513	<0.04	0.017
SNUBBER	Y	<1	7321.490	90.878	<0.04	0.016
SOLANO	N	--	--	--	--	--

Table E-5
Yucca Flat/Climax Mine Surface Crater Characteristics
(Page 19 of 23)

Detonation Name	Presence of Surface Crater (Y/N)	Size and Nonzero Depth Surface Craters (m)	Surface Crater (m^2)		Modeled Catchment Area of Surface Crater (km^2)	Modeled Enhanced Crater Recharge (m/yr)
			Top Area	Bottom Area		
SOLANUM	N	--	--	--	--	--
SOLENDON	Y	<1	809.780	14.885	<0.04	0.019
SPAR	N	--	--	--	--	--
SPIDER-A	Y	<1	605.207	66.196	<0.04	0.008
SPIDER-B	N	--	--	--	--	--
SPOON	Y	<1	290.094	9.967	<0.04	0.017
SPRIT	N	--	--	--	--	--
SPUD	Y	<1	8433.348	113.216	<0.04	0.015
ST. LAWRENCE	N	--	--	--	--	--
STACCATO	Y	10.21	52899.494	4289.063	1.8	0.155
STANLEY	Y	12.42	48193.243	7099.778	0.74	0.048
STANYAN	Y	16.11	38261.119	2672.356	0.55	0.092
STARWORT	Y	16.21	85729.865	1774.503	0.15	0.051
STILLWATER	Y	8.08	24505.926	983.717	0.37	0.124
STILT	N	--	--	--	--	--
STOAT	Y	<1	10982.565	1077.371	<0.04	0.007
STODDARD	Y	16.14	39189.193	625.106	1.13	0.399
STONES	Y	19.75	54071.053	3411.292	0.29	0.044
STRAIT	Y	28.95	47302.377	2781.318	0.14	0.032
STRAKE	Y	1.34	30733.502	1197.315	<0.04	0.01
STURGEON	Y	2.1	3946.046	156.250	<0.04	0.015
STUTZ	Y	20.64	7691.625	0.00	0.09	1.188
SUEDE	N	--	--	--	--	--
SUNDOWN-A	N	--	--	--	--	--
SUNDOWN-B	N	--	--	--	--	--
SUTTER	N	--	--	--	--	--
SWITCH	N	--	--	--	--	--
TAHOKA	Y	16.25	67436.558	1565.163	0.13	0.051
TAJIQUE	N	--	--	--	--	--
TAJO	Y	16.33	72846.145	2512.737	0.13	0.034
TAN	Y	20.13	109501.755	1439.579	1.69	0.317
TANGERINE	N	--	--	--	--	--
TANYA	Y	<1	571.282	9.678	<0.04	0.021
TAPESTRY	Y	3.51	7404.115	395.666	<0.04	0.014

Table E-5
Yucca Flat/Climax Mine Surface Crater Characteristics
(Page 20 of 23)

Detonation Name	Presence of Surface Crater (Y/N)	Size and Nonzero Depth Surface Craters (m)	Surface Crater (m^2)		Modeled Catchment Area of Surface Crater (km^2)	Modeled Enhanced Crater Recharge (m/yr)
			Top Area	Bottom Area		
TAPPER	Y	21.7	23718.840	1168.355	0.3	0.118
TARKO	Y	10.88	8610.979	1514.884	9.05	1.232
TAUNTON	N	--	--	--	--	--
TECHADO	N	--	--	--	--	--
TEE	Y	8.91	10234.366	1451.837	0.23	0.066
TEJON	N	--	--	--	--	--
TELEME	Y	8.45	24055.739	1963.186	1.43	0.23
TEMESCAL	N	--	--	--	--	--
TEMPLAR	N	--	--	--	--	--
TENAJA	Y	9.19	27953.640	1448.159	0.21	0.062
TENDRAC	Y	22.95	20418.969	761.263	0.26	0.153
TERN	Y	3.64	6496.185	156.631	13.83	0.959
TERRINE-WHITE	Y	11.61	51713.370	4512.026	1.57	0.137
TERRINE-YELLOW	Y	1.2	27916.501	1872.098	<0.04	0.008
TEXARKANA	Y	3.15	57509.165	4162.212	0.04	0.009
THISTLE	N	--	--	--	--	--
THROW	Y	15.42	4084.810	237.036	0.09	0.158
TICKING	N	--	--	--	--	--
TIJERAS	Y	46.95	79688.773	2176.794	0.43	0.111
TILCI	Y	16.43	38383.905	684.505	4	0.806
TINDERBOX	N	--	--	--	--	--
TINY TOT	N	--	--	--	--	--
TIOGA	N	--	--	--	--	--
TOMATO	Y	<1	10085.195	83.855	<0.04	0.017
TOPGALLANT	Y	14.27	64916.600	670.224	0.42	0.191
TOPMAST	N	--	--	--	--	--
TORCH	N	--	--	--	--	--
TORNERO	Y	<1	15849.846	162.201	<0.04	0.016
TORNILLO	Y	<1	1957.571	30.960	<0.04	0.017
TORRIDO	Y	<1	39376.893	204.142	<0.04	0.018
TORTUGAS	Y	12.63	69074.802	7732.990	0.13	0.012
TOYAH	Y	<1	1353.916	279.458	<0.04	0.006
TRANSOM	Y	27.87	79846.081	4430.595	1.3	0.135
TRAVELER	Y	10.67	5365.648	0.00	6.72	2.47

Table E-5
Yucca Flat/Climax Mine Surface Crater Characteristics
(Page 21 of 23)

Detonation Name	Presence of Surface Crater (Y/N)	Size and Nonzero Depth Surface Craters (m)	Surface Crater (m^2)		Modeled Catchment Area of Surface Crater (km^2)	Modeled Enhanced Crater Recharge (m/yr)
			Top Area	Bottom Area		
TREBBIANO	Y	<1	946.618	25.438	<0.04	0.016
TROGON	N	--	--	--	--	--
TRUCHAS-CHACON	N	--	--	--	--	--
TRUCHAS-CHAMISAL	N	--	--	--	--	--
TRUCHAS-RODARTE	Y	3.63	13105.031	451.321	0.1	0.065
TRUMBULL	N	--	--	--	--	--
TUB-A	Y	2.83	6877.468	267.693	<0.04	0.016
TUB-B	Y	<1	10304.640	164.461	<0.04	0.014
TUB-C	N	--	--	--	--	--
TUB-D	N	--	--	--	--	--
TUB-F	N	--	--	--	--	--
TULIA	N	--	--	--	--	--
TULOSO	N	--	--	--	--	--
TUNA	N	--	--	--	--	--
TUN-A	Y	1.99	5949.947	38.314	<0.04	0.034
TUN-B	Y	3.23	4932.148	368.565	0.17	0.122
TUN-C	Y	4.2	5299.220	758.046	0.11	0.056
TUN-D	Y	8.33	4424.114	425.579	16	1.883
TURF	Y	14.52	84235.547	4411.956	0.46	0.047
TURNSTONE	N	--	--	--	--	--
TURQUOISE	Y	14.49	40960.385	303.050	0.46	0.311
TWEED	Y	36.97	26987.963	571.775	0.76	0.448
TYG-A	Y	<1	2040.597	116.555	<0.04	0.01
TYG-B	Y	21.09	5509.033	185.792	0.08	0.177
TYG-C	Y	7.55	2813.187	68.777	0.11	0.302
TYG-D	Y	4.84	3027.672	252.122	0.05	0.068
TYG-E	Y	8.75	6128.176	244.327	0.11	0.147
TYG-F	Y	32	9823.268	189.227	0.07	0.171
UMBER	Y	16.78	22628.596	1105.176	0.11	0.052
VALENCIA	N	--	--	--	--	--
VALISE	N	--	--	--	--	--
VAT	Y	8.63	8885.706	1181.399	0.63	0.197
VAUGHN	N	--	--	--	--	--
VELARDE	Y	17.23	12949.181	772.148	0.57	0.268

Table E-5
Yucca Flat/Climax Mine Surface Crater Characteristics
(Page 22 of 23)

Detonation Name	Presence of Surface Crater (Y/N)	Size and Nonzero Depth Surface Craters (m)	Surface Crater (m^2)		Modeled Catchment Area of Surface Crater (km^2)	Modeled Enhanced Crater Recharge (m/yr)
			Top Area	Bottom Area		
VERDELLO	Y	9.55	21794.341	1878.737	0.17	0.041
VERMEJO	Y	<1	2385.440	135.616	<0.04	0.01
VICTORIA	N	--	--	--	--	--
VIDE	N	--	--	--	--	--
VIGIL	N	--	--	--	--	--
VILLE	Y	6.55	11312.388	1060.121	9.246	0.978
VILLITA	Y	13.17	28116.628	830.609	0.18	0.095
VISE	Y	<1	8430.542	274.208	<0.04	0.011
VITO	N	--	--	--	--	--
VULCAN	Y	16.45	23286.170	1933.807	3.44	0.54
WACO	N	--	--	--	--	--
WAGTAIL	N	--	--	--	--	--
WALLER	N	--	--	--	--	--
WARD	Y	2.35	20102.041	370.591	<0.04	0.019
WASHER	N	--	--	--	--	--
WELDER	N	--	--	--	--	--
WEMBLEY	Y	6.65	14881.863	146.079	0.06	0.117
WEXFORD	Y	<1	1486.002	44.873	<0.04	0.014
WHITE	Y	5.25	15744.485	2417.050	0.24	0.038
WHITEFACE-A	N	--	--	--	--	--
WHITEFACE-B	N	--	--	--	--	--
WICHITA	Y	1.13	12166.823	100.826	<0.04	0.018
WINCH	N	--	--	--	--	--
WOLVERINE	N	--	--	--	--	--
WOOL	Y	13.21	13426.535	443.009	0.37	0.254
WORTH	N	--	--	--	--	--
YANNIGAN-BLUE	Y	27.22	37273.608	209.465	0.31	0.396
YANNIGAN-RED	Y	35.42	34164.717	643.148	0.17	0.141
YANNIGAN-WHITE	Y	27.87	33428.231	1268.779	0.28	0.11
YARD	Y	17.26	100368.930	5145.388	0.87	0.077

Table E-5
Yucca Flat/Climax Mine Surface Crater Characteristics
(Page 23 of 23)

Detonation Name	Presence of Surface Crater (Y/N)	Size and Nonzero Depth Surface Craters (m)	Surface Crater (m^2)		Modeled Catchment Area of Surface Crater (km^2)	Modeled Enhanced Crater Recharge (m/yr)
			Top Area	Bottom Area		
YERBA	Y	10.34	10327.053	327.728	1.03	0.534
YORK	Y	19.67	20343.770	555.819	0.05	0.061
ZAZA	Y	22.23	62846.255	1702.926	1.31	0.27
ZINNIA	Y	10.57	8665.736	829.950	5.77	1.13

-- = Not Applicable

E.6.0 REFERENCES

BN, see Bechtel Nevada.

Bechtel Nevada, 1998. Hydrogeologic Characterization of the Unsaturated Zone at the Area 3 Radioactive Waste Management Site. DOE Report No. DOE/NV/11718--210.

DOE, see U.S. Department of Energy.

French, R.H., T.L. Buchanan, S.L. Hokett, and S. Curtis, 1999. Calibration of a Hybrid Rainfall-Runoff Model in an Arid Environment. Proceedings of the XXVIII IAHR Congrass, Graz, Austria. ,Also included as Appendix 8 of French, R.H. and S. Curtis, The Precipitation Event of 23-24 February 1998, Analysis of a Design Level Event. Desert Research Institute Publication No. 45170. DOE Report No. DOE/NV/11508-48.

French, R.H. and S. Curtis, 1999. *The Precipitation Event of 23-24 February 1998, Analysis of a Design Level Event.* Desert Research Institute Publication No. 45170. DOE Report No. DOE/NV/11508-48.

Grasso, D.N. 2001. *GIS Surface Effects Archive of Underground Nuclear Detonations Conducted at Yucca Flat and Pahute Mesa, Nevada Test Site, Nevada*. Open-File Report 2001-272. Denver, CO: U.S. Geological Survey.

Hargreaves, G.H. and Allen, R.G. 2003. *History and Evaluation of Hargreaves Evapotranspiration Equation.* Journal of Irrigation and Drainage Engineering, 129, (1), 53-63. Reston, Virginia: American Society of Civil Engineers.

Hawkins, R.H., T.J. Ward, D.E. Woodward, and J.A. Van Mullem, 2009. Curve Number Hydrology; State of the Practice. American Society of Civil Engineers.

Hokett, S.L. and R.H. French, 1988. Evaluation of Recharge Potential at Subsidence Crater U19b, Central Pahute Mesa, Nevada Test Site. Desert Research Institute Publication No. 45161. DOE Report No. DOE/NV/11508-33.

Hokett, S.L., D.R. Gillespie, G.V. Wilson, and R.H. French, 2000. Evaluation of Recharge Potential at Subsidence Crater U10i, Northern Yucca Flat, Nevada Test Site. Desert Research Institute Publication No. 45174. DOE Report No. DOE/NV/11508-53.

Jenson, S.K., and J.O. Domingue. 1988. “Extracting Topographic Structure from Digital Elevation Data for Geographical Information System Analysis.” *Photogrammetric Engineering and Remote Sensing* 54 (11): 1593–1600.

Kwicklis, E.M., A.V. Wolfsberg, P.H. Stauffer, M.A. Walvoord, and M.J. Sully, 2006. Multiphase, Multicomponent Parameter Estimation for Liquid and Vapor Fluxes in Deep Arid Systems Using Hydrologic Data and Natural Environmental Tracers. Vadose Zone Journal 5:934-950.

Mishra, S.K. and V. P. Singh, 2003. Soil Conservation Service Curve Number (SCS-CN) Methodology. Kluwer Academic Publishers: Dordrecht, The Netherlands.

NOAA, see National Oceanic and Atmospheric Administration.

National Oceanic and Atmospheric Administration, 2008a, Air Resources Laboratory, Special Operations and Research Division (ARL SORD). http://www.sord.nv.doe.gov/home_climate_rain.htm, Accessed Sept. 2, 2008.

NSTec, see National Security Technologies.

National Security Technologies, 2007. Characterization Report Area 3 Radioactive Waste Management Site, Nevada Test Site, Nevada. DOE Report No. DOE/NV/25946--080.

Nietsch, S. L., J.G. Arnold, R.G. Kiniry, J.R. Williams, and K.W. King, 2002. Soil and water assessment tool (SWAT): theoretical documentation, version 2000. Texas Water Resources Institute, College Station, Texas, TWRI Report TR-191.

Pohll, G.H., J.J. Warwick, and S.W. Tyler, 1996. Coupled Surface-Subsurface Hydrologic Model of a Nuclear Subsidence Crater at the Nevada Test Site. Journal of Hydrology 186: 43-62.

Scanlon, B.R., D.G. Levitt, R.C. Reedy, K.E. Keese, and M.J. Sully, 2005. Ecological Controls on Water Cycle Response to Climate Variability in Deserts. Proceedings of the National Academy of Sciences, vol. 102, no. 17, 6033-6038.

Šimunek, J., M.Th. van Genuchten, and M. Šejna. 2005. The HYDRUS-1D Software Package for Simulating the One-Dimensional Movement of Water, Heat, and Multiple Solutes in Variably-Saturated Media - Version 3.0. Department of Environmental Sciences. University of California, Riverside. Riverside, California.

Srikanthan, S., F. Chiew, and A. Frost. 2007. Stochastic Climate Library: User Guide. Cooperative Research Centre for Catchment Hydrology. Australia.

Tyler, S.W., W.A. McKay, and T.M. Mihevc, 1992. Assessment of Soil Moisture Movement in Nuclear Subsidence Craters. Journal of Hydrology 139: 159-181.

USACE, see U.S. Army Corps of Engineers.

U.S. Army Corps of Engineers, Hydrologic Engineering Center, 1990. Flood Hydrograph Package, HEC-1. Davis, California.

USDA, see U.S. Department of Agriculture.

U.S. Department of Agriculture, 2004. Natural Resources Conservation Service (NRCS), National Engineering Handbook, Part 630, Hydrology. http://www.info.usda.gov/viewerFS.aspx?hid=21422

Williams, J.R., and R.C. Izaurralde. The APEX Model. ftp://ftp-fc.sc.egov.usda.gov/NHQ/nri/ceap/brcreport_2005.pdf

Wilson, G.V., D.H. Ely, S.L. Hokett, and D.R. Gillespie, 2000. Recharge from a Subsidence Crater at the Nevada Test Site. Soil Sci. Soc. Am. J. 64: 1570-1581.

Appendix F

Saturated Zone Pluvial Drainage Model

F.1.0 Alternative Conceptual Models and Parameters of Saturated Volcanic Rock Units at Yucca Flat

F.1.1 Evaluating the 'Slow Drainage' Hypothesis

In most locations where head data have been collected at multiple depths in Yucca Flat there is a strong indication of a downward gradient from the saturated volcanics towards the lower carbonate aquifer (Fenelon ,2005; Fenelon et al., 2012). There are two possible causes of this trend: (1) testing-induced pressure gradients, and (2) "natural" downward gradients due to local recharge. Inspection of the data indicates that these downward gradients have been measured in wells several kilometers from the nearest test (TW-E and ER-6-1) and so, at least in some locations, this gradient is probably natural and reflects local recharge. The gradient is somewhat subtle (see Table F-1) and generally overwhelmed by testing-induced gradients and so accurately reproducing the gradient in the flow model may be of secondary importance to reproducing testing-induced gradients. However, calibration of the flow model to this gradient under "pre-testing" conditions could be an important constraint on large-scale effective aquifer permeabilities and recharge, thus careful attention to this issue is warranted.

Table F-1
Measured Head Differences between the Volcanic Rocks and the Carbonate Aquifer
(Page 1 of 2)

Well	Year	HSU	Head	Tos (m)	Bos (m)	Δh (m)	Nearest Previous Detonation
TW-E (1,970)	1960	LTCU	748.5	748.5	671.2	21.8	RINGTAIL (1961), 3,044 m
TW-E (2,620)	1962	LCA	726.7	502.6	473.1		
ER-6-1 (piezometer)	1992	OSBCU	750.5	756	730	23.5	HOREHOUND (1969), 0.94 km [a]
ER-6-1 (main, 2,129)	1992	LCA	727.0	644.8	550.4		
ER-6-1-2 (1,587)	2002	TSA	751	751	716	22.5	HOREHOUND* (1969), 1.0 km
ER-6-2 (3,200)	2002	LCA	728.5	658.6	224.13		

Table F-1
Measured Head Differences between the Volcanic Rocks and the Carbonate Aquifer
(Page 2 of 2)

Well	Year	HSU	Head	Tos (m)	Bos (m)	Δh (m)	Nearest Previous Detonation
WW-2 (2,535)	1961	LTCU	761.1	--	--	26.6	MISSISSIPPI (1962), 4,453 m
WW-2 (3,422)	1962	LCA	734.5	--	--		

[a] Above 850 m

Note: ( ) indicates depth of well in feet

Tos = Top of open section in m asl
Bos = Bottom of open section in m asl

-- = Not applicable

The infiltration regime at the NNSS changed approximately 9,500 years ago due to a combination of vegetation and climate change (Spaulding and Graumlich, 1986; Spaulding et al., 1990; Forester et al., 1999; Tyler et al., 1996; Walvoord et al., 2002a,b; Kwicklis et al., 2006). Perhaps most important for infiltration, vegetation changed from a juniper-pinyon woodland to a desert shrub assemblage (xerophytes) that included creosote and saltbrush, which are efficient at a scavenging soil moisture. Estimates of infiltration prior to this change, based on deep pore-water chloride concentrations below the shallow chloride bulge in the root zone, have suggested paleo-infiltration rates of 2.3 to 7.6 mm/yr in Yucca Flat (Walvoord, Phillips, et al. 2002; Kwicklis et al., 2006) and 4.4 mm/yr for brief pluvial periods in Frenchman Flat (Walvoord, Phillips, et al. [2002]; Section 3.1.3.2). Since about 10,000 years ago, net infiltration has been estimated to be approximately zero, and paleo-infiltration has continued to drain to the water table at rates of several tenths of a millimeter per year in these basins [Walvoord, Phillips, et al. (2002); Kwicklis et al. (2006)].

Groundwater ^{14}C ages calculated in Appendix L are consistent with the concept that the last significant recharge in Yucca Flat occurred during the late Pleistocene/early Holocene. Groundwater ages in the alluvial volcanic aquifer system in Yucca Flat are predominantly in the range of 8,000 to 12,000 years old. The groundwater ^{14}C ages in the LCA are generally older and increase from about 12,000 years in the northern part of the basin to more than 30,000 years in the southern part of the basin, except for an area near major faults where younger ^{14}C ages as well as other groundwater characteristics indicate downward leakage from the overlying aquifers. Thus, the relative ages of

groundwater in the alluvial/volcanic aquifer system and the LCA are consistent with the concept of paleodrainage from the volcanic to the LCA.

Most of the evidence that water tables were once higher is based on spring deposits, including both tufa (Winograd and Doty, 1980; Szabo et al., 1994) and fine-grained sediments trapped by phreatophytes (Quade et al., 1995; Forester et al., 1999) that suggest regional water levels were higher in the past. Winograd and Doty (1980) estimated water table elevations in the LCA beneath Frenchman Flat were less than 30 m higher during the last pluvial period based on hydrologic calculations and the distribution of tufas in Ash Meadows, which were later dated at between 500,000 and 750,000 years old (Szabo et al., 1994). Szabo et al. (1994) dated calcite deposits in Devils Hole over the past 120,000 years and estimated that water levels there had declined rapidly by about 9 m beginning about 20,000 years ago. Quade et al. (1995) estimated water levels at the end of the Pleistocene in several areas in Las Vegas Valley east of the NNSS were between 25 and 70 m higher than today, and were up to 115 m higher in the volcanic units at Yucca Mountain based on the distribution then undated of spring deposits at the southern end of Yucca Mountain. Forester et al. (1999) concluded from ^{230}Th/U dates of surface deposits near Yucca Mountain that discharge activity ceased at about 15 to 12 ka at upgradient sites near Yucca Mountain (including those examined by Quade et al., 1995), and later (about 9 ka) at downgradient sites at lower elevations, similar to the cessation of spring activity in Las Vegas and Pahrump Valleys (Quade et al., 1995). The cessation of spring activity from the LCA in Las Vegas and Pahrump Valleys at around 9 ka is consistent with the evidence from unsaturated-zone studies that infiltration underwent a dramatic decline at this time.

Yucca Mountain was studied for almost three decades as a potential high-level nuclear waste repository, and provides an interesting analog for the transient drainage hypothesis that is the subject of this appendix. Geochemical and isotopic data from the unsaturated-zone at Yucca Mountain show that the widespread perched water with a significant component of late-Pleistocene infiltration exists hundreds of meters above the water table atop zeolitic tuff confining units similar to the LTCU and OSBCU in Yucca Flat the (Yang et al., 1996; Flint et al., 2002). This analog provides support to the argument that the LTCU and OSBCU could have large-scale properties that inhibit the drainage of groundwater from the tuffs to the LCA in Yucca Flat.

While none of the aforementioned studies directly estimates water level increases in the tuffs of Yucca Flat, the similarity in δ^{13}C compositions of shallow calcite from the alluvium in the UE-1a

complex with deeper fracture-lining calcite from the TCU suggest the TCU calcite originated from downwardly percolating fluids and not groundwater from the underlying LCA (Dickerson et al., 2004). This is in agreement with the position of Winograd and Doty (1980), that gradients between the tuff and LCA in Yucca Flat have always been downward, even during pluvial periods.

The basic premise of the transient drainage hypothesis is that due to its higher permeability, water levels in the LCA equilibrated relatively quickly when climate and vegetation changed roughly 10,000 years ago, but that present water levels in the lower permeability tuff confining units are in part a relic of past wetter conditions. This model implies that the water table in the tuffs will continue to fall until it reaches equilibrium with the lower LCA, in the absence of modern local recharge. This model is presented as an alternative conceptual model to the one presented in the main body of the report, which assumes that the tuff aquifer and confining units have already equilibrated to modern recharge rates. That conceptual model requires at least small amounts of modern local recharge.

Discriminating between these two possibilities by conducting comprehensive studies of modern and paleo-recharge with the 3D model presented in Section 4.0 would be difficult and costly; and it is unlikely that definitively eliminating one model would be possible. The purpose of this analysis is twofold. First, identify what combinations of hydraulic properties and assumptions about past water table heights are compatible with the transient drainage hypothesis, thereby possibly providing an alternative means of calibrating the large-scale properties of the tuff confining units. Second, develop simple strategies for incorporating conceptual model uncertainty into flow model development, avoiding (if possible) the need to carry forward fully-transient paleo-recharge models into the suite of flow models used for transport simulations.

F.1.2 Numerical Models and Supporting Data

To evaluate the plausibility of these two conceptual models, 2-D numerical models were developed representing a simple layered aquifer (see Figure F-1) bounded at the top by a free water table surface and below by an “infinite reservoir”, the lower carbonate aquifer, whose head is specified at 740 m. Vertical faults coincide with lateral boundaries. The thickness of the volcanic aquifer (approximately 250 m) is similar to that measured at observation wells TW-E, WW-2, and ER-6-1.

The magnitude of downward gradients is constrained by data from 4 wells (Table F-1). Two of these (TW-E and WW-2) were measured at times when the nearest previous test in the volcanic aquifer was

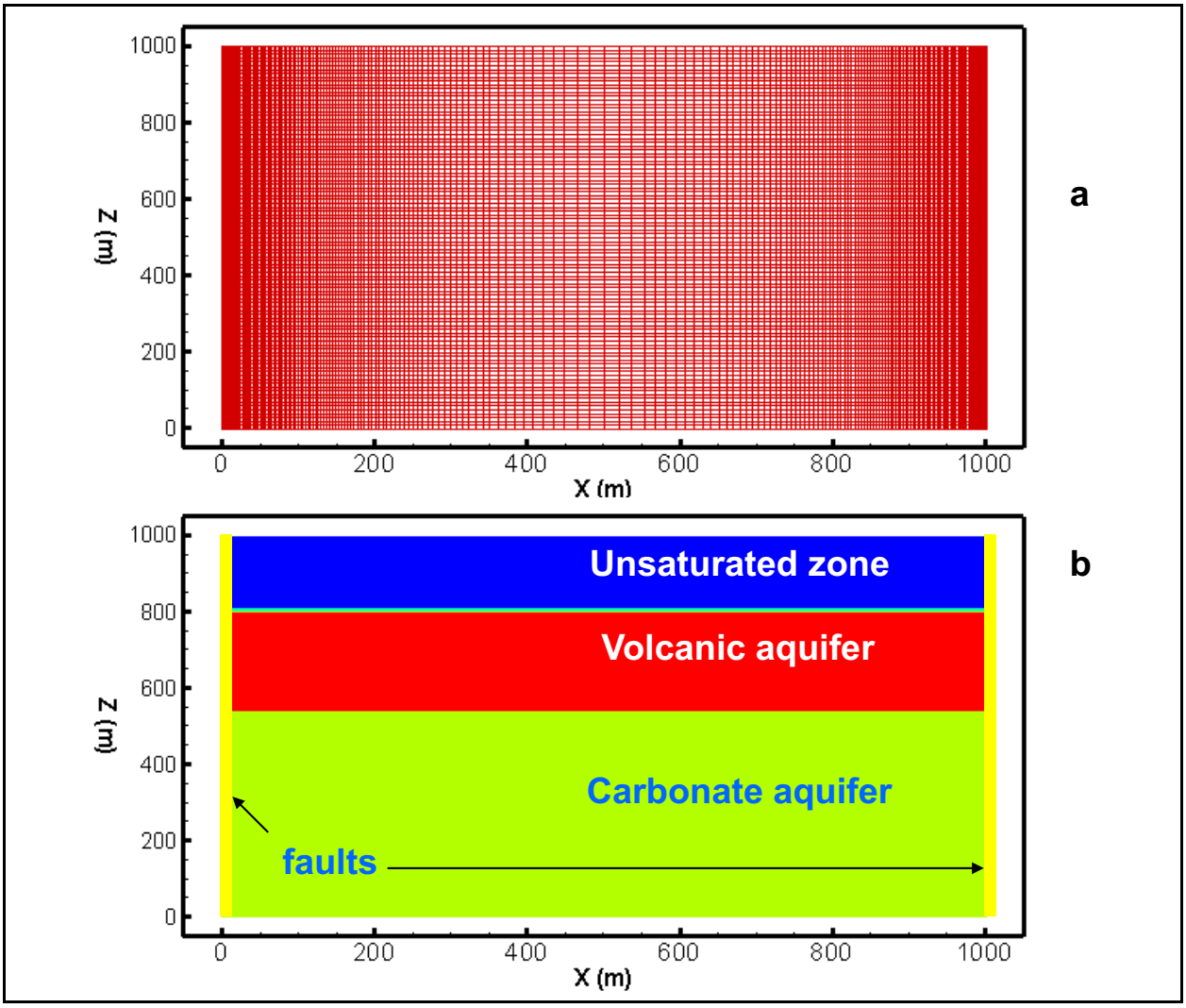

Figure F-1
Simplified Models (a) Computational Grid, (b) Features

over 3,000 m away. Two others, ER-6-1 and ER-6-2, were measured 1 km away from a test conducted 5 years previous to the measurement. Measured head differences in these four wells were remarkably consistent, only ranging from 21.8 to 26.6. Numerical experiments were designed to address the question, given available estimates of aquifer properties and recharge rates, are these gradients consistent with both conceptual models? Table F-2 presents ranges of aquifer property estimates for the lower tuff confining unit at Yucca Flat (SNJV, 2006).

F.1.3 Transient Simulations

Transient simulations were conducted assuming an initial water table height 8,000 years before present. Water table drainage was simulated under condition of constant recharge (or zero recharge)

Table F-2
Aquifer Parameters and Recharge Estimates

Parameter	Count	Minimum	Maximum	Mean	Source
Specific storage log (1/m)	36	-6.8	-3.1	-4.1	TCU, SNJV, 2006 (p. 6-50)
Fracture specific storage	7	-6.2	-4.6	-5.2	TCU, SNJV, 2006 (p. 6-50)
LogPermeability (m^2)	34	-17.93	-13.48	-15.50	TCU, lab-scale SNJV, 2006 (Table 6-1)
	10	-15.21	-13.29	14.31	TCU, slug-test-scale SNJV, 2006 (Table 6-1)
Porosity - lab transport	8	.27	.37	--	LTCU, lab transport experiments, SNJV, 2007 (p. 7-5)
Porosity - all data	2,828	.075	.694	.403	LTCU, all data, SNJV, 2007 (p.7-13)
Modern recharge (mm/yr)	--	0	10 [a]	--	SNJV, 2006
Paleo-drainage (mm/yr)	--	0.13	0.4	--	Kwicklis et al., 2006; Walvoord et al., 2002b

[a] All seven infiltration maps except UGTA original (later superseded by UGTA revised) had much lower infiltration rates in the alluvium (SNJV, 2006).

-- = Not applicable

for 9,000 years. The final 1,000 years of the simulations were used to address the issue of how predicted head gradients might change during the 1,000 year period of transport simulations required for the UGTA radionuclide transport calculations. During the entire 9,000 years, the lower carbonate aquifer (LCA) is held at a head of 740 m, in accordance with the conceptual model that the LCA rapidly equilibrated to the modern climate regime (8,000 years before present).

A single-phase (water only) formulation in FEHM was used for the simulations. Simulating drainage under conditions of a free water table surface is a difficult numerical problem and so validation of the FEHM algorithm for this particular model was undertaken. To test the accuracy of the FEHM formulation it was compared to a 2-phase (water-air) simulation which is numerically intensive and has been validated in a wide range of hydrologic test cases. Several comparisons of the single-phase and two-phase results are presented in Keating and Zyvoloski (2009); the comparison is quite good.

The following parameters were varied to provide information on the sensitivity of the result (present day head gradients) to parameter uncertainty: modern recharge (R, mm/yr), the height of the water table 8,000 years ago, the hydraulic conductivity (K) and porosity (η) of the aquifer. First single parameter sensitivity studies were conducted (holding all other parameters constant). Finally, a more comprehensive Monte-Carlo type analysis was conducted. Measured head differences between the

volcanic rocks and the carbonate aquifer were calculated and the corresponding aquifer parameters and recharge values recorded.

F.1.3.1 Sensitivity Analysis Results

Assuming a value of specific storage of 10^{-4} m^{-1}, a porosity of 0.3, and a permeability of 10^{-16} m^2, we simulated a draining water table under zero recharge conditions. Figure F-2a shows these results for three different initial water table elevations. Regardless of the initial height of the water table, in all simulations equilibrium with the lower carbonate aquifer was achieved within approximately 6,000 years from the time of the lowering of recharge. Head differences of 20 m (as are observed today) were reached in 3,000 years or less. None of these simulations are consistent, therefore, with the conceptual model of 8,000 years of draining resulting in a 20 m head difference.

We used a similar method to address sensitivity to uncertainty in aquifer porosity. Assuming the same model parameters as listed above and an initial water table height of 800 m, we simulated transient drainage with varying values of porosity (0.03–0.3). Results are shown in Figure F-2b. Under low porosity conditions, the water table drops rapidly, achieving equilibrium within 1,000 years of recharge reduction. None of these simulations are consistent with modern head gradients that have been observed.

Sensitivity to assumptions of modern recharge rate and aquifer permeability were tested by varying permeability between 10^{-17} m^2 and 10^{-13} m^2 and modern recharge from 0 to 3 mm/yr. Two types of metrics were used to evaluate each transient simulation: 1) predicted present-day head difference between the volcanic aquifer and the LCA, and 2) number of years after climate change (8,000 years ago) steady-state was reached. The results are presented in Figure F-3. Blue hatched regions in this figure indicate regions of simulation agreement with measured heads and with a slowly draining aquifer (steady-state has not yet been reached). In Figure F-3a it is evident that many of the low permeability simulations, particularly those involving recharge rates of 3 mm/yr, resulted in head gradients much larger than measured gradients. In Figure F-3b, it is evident that *only* the low permeability simulations require the necessary long-time period (approximately 8,000 years of draining) to be consistent with the draining conceptual model. This analysis clearly demonstrates that only a small set of parameter combinations will produce simulations consistent with measurements and with the slowly-draining conceptual model, suggesting that this simple conceptual model holds

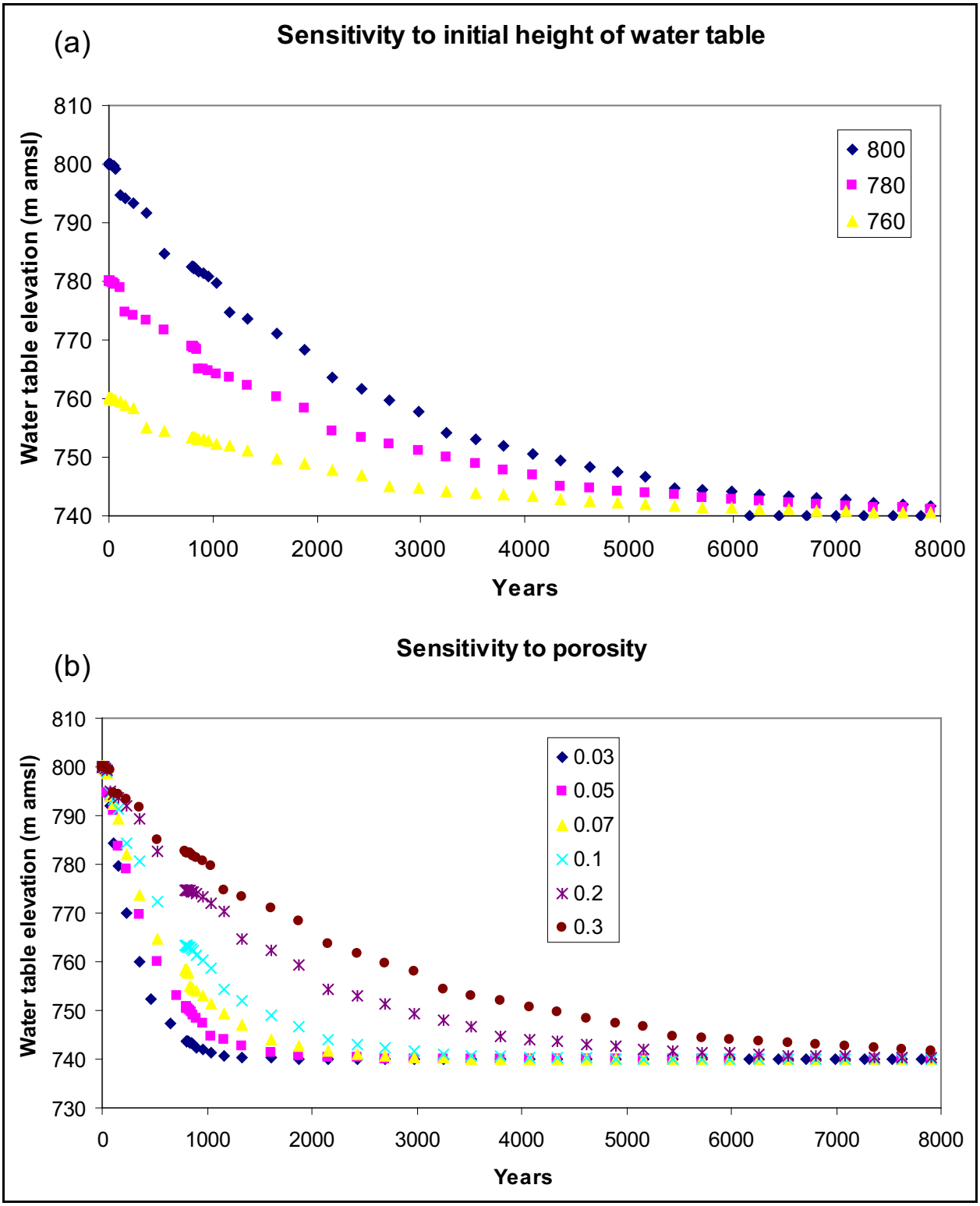

Figure F-2
Sensitivity of Simulated Water Table Elevations to Uncertainty in (a) Initial Height of Water Table and (b) Aquifer Porosity

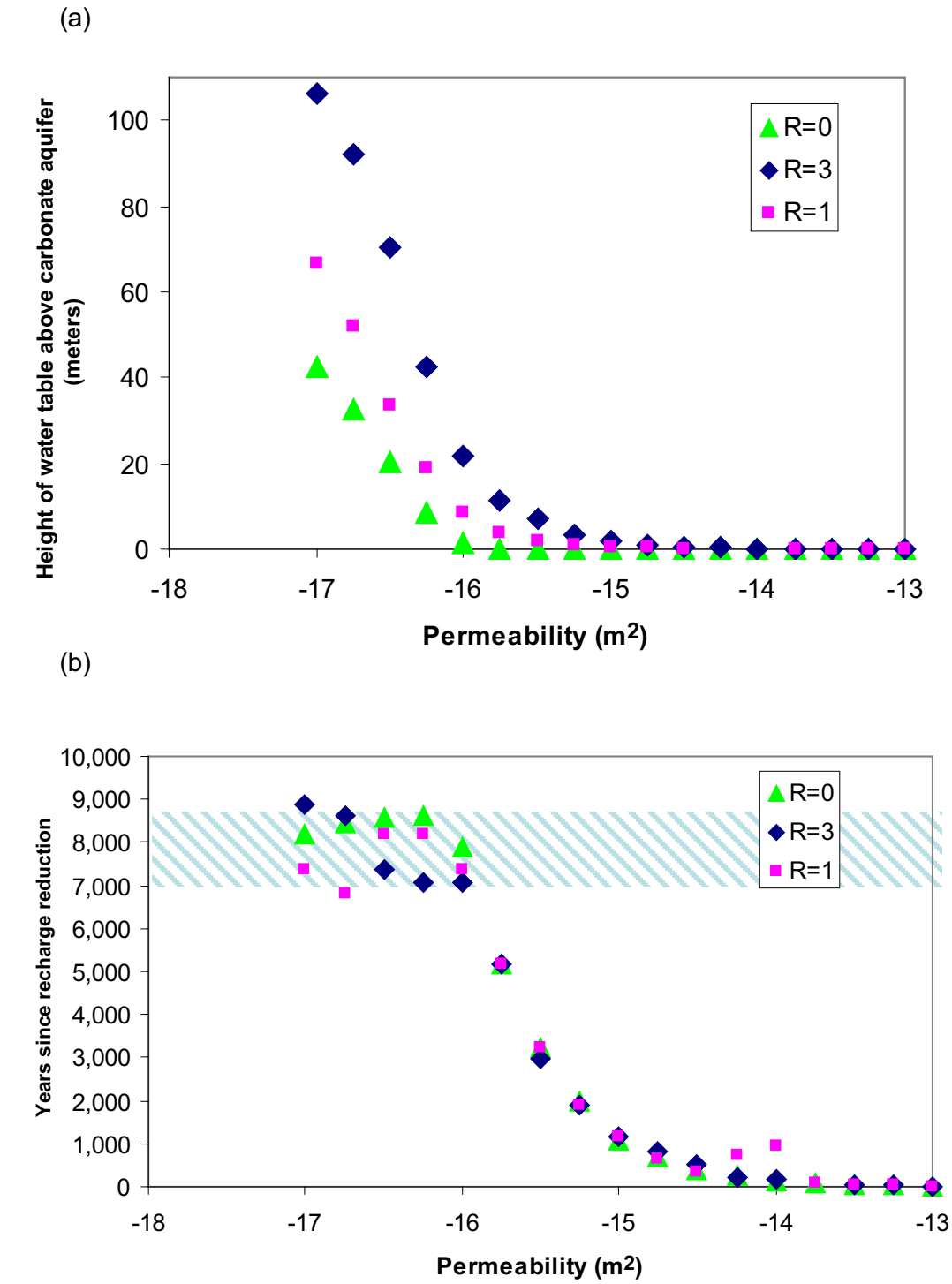

Note: "R" indicates recharge rate in mm/yr.

Figure F-3
Relationship between Aquifer Permeability and (a) Height of Present Water Table after 8,000 Years of Drainage, and (b) Time to Reach Equilibrium with Lower Recharge Rate

promise for constraining the large-scale aquifer properties. For this reason, a more comprehensive uncertainty analysis was undertaken.

Using a matrix of parameter combinations shown in Table F-3, all 500 parameter combinations were tested. Of these, 30 combinations (6 percent) resulted in transient simulations consistent with a 20 m modern head gradient. The results are shown in Figure F-4, where a red symbol indicates an incompatible result (modern head gradient either much larger or much smaller than observed gradients) and a green symbol indicates a compatible result (roughly consistent with observed gradients). Because the plots are bivariate, multiple symbols are overlain at each parameter combination. Informative trends are evident. First, no parameter combinations associated with intrinsic permeabilities lower than 10^{-17} m^2 or higher than 10^{-16} m^2 are compatible with the transient drainage hypothesis. The low permeability simulations drained much too slowly or even rose over time when recharge rates were relatively high; the high permeability simulations drained much too quickly. All parameter combinations associated with porosities lower than 0.1 were also rejected. All modern recharge rates higher than 3 mm/yr were rejected. In general, results compatible with the transient drainage hypothesis were characterized by effective porosity that range from 0.1 to 0.4, low recharge rates, and permeability between 10^{-16} and 10^{-17} m^2.

Table F-3
Values used to Create 500 Unique Parameter Combinations for Uncertainty Analysis

Modern Recharge (mm/yr)	0	3.1	6.3	9.4	
Porosity	.01	.108	.206	.304	.402
Permeability (log m^2)	-17.5	-17.0	-16.5	-16.0	-15.5
Initial Water Table Height (m)	800	820	840	860	880

It could be argued that all of these “favorable” parameter combinations are physically plausible and consistent with available data. There are two possible reasons this might not be the case. First, many of the permeability estimates in the Yucca Flat/Climax Mine HDD (SNJV, 2006), the recent core-scale data, and the pumping-scale aquifer test data from Yucca Flat are significantly higher than the 10^{-17} m^2 suggesting a possible inconsistency. Second, while a subset of the available matrix property data for the TCU do have relatively large effective porosities and low permeabilities, many more of the data have both large effective porosities and moderate to large permeabilities (see, for example, Figures F-5 and F-6). (Effective porosity here is measured as the volume of water that

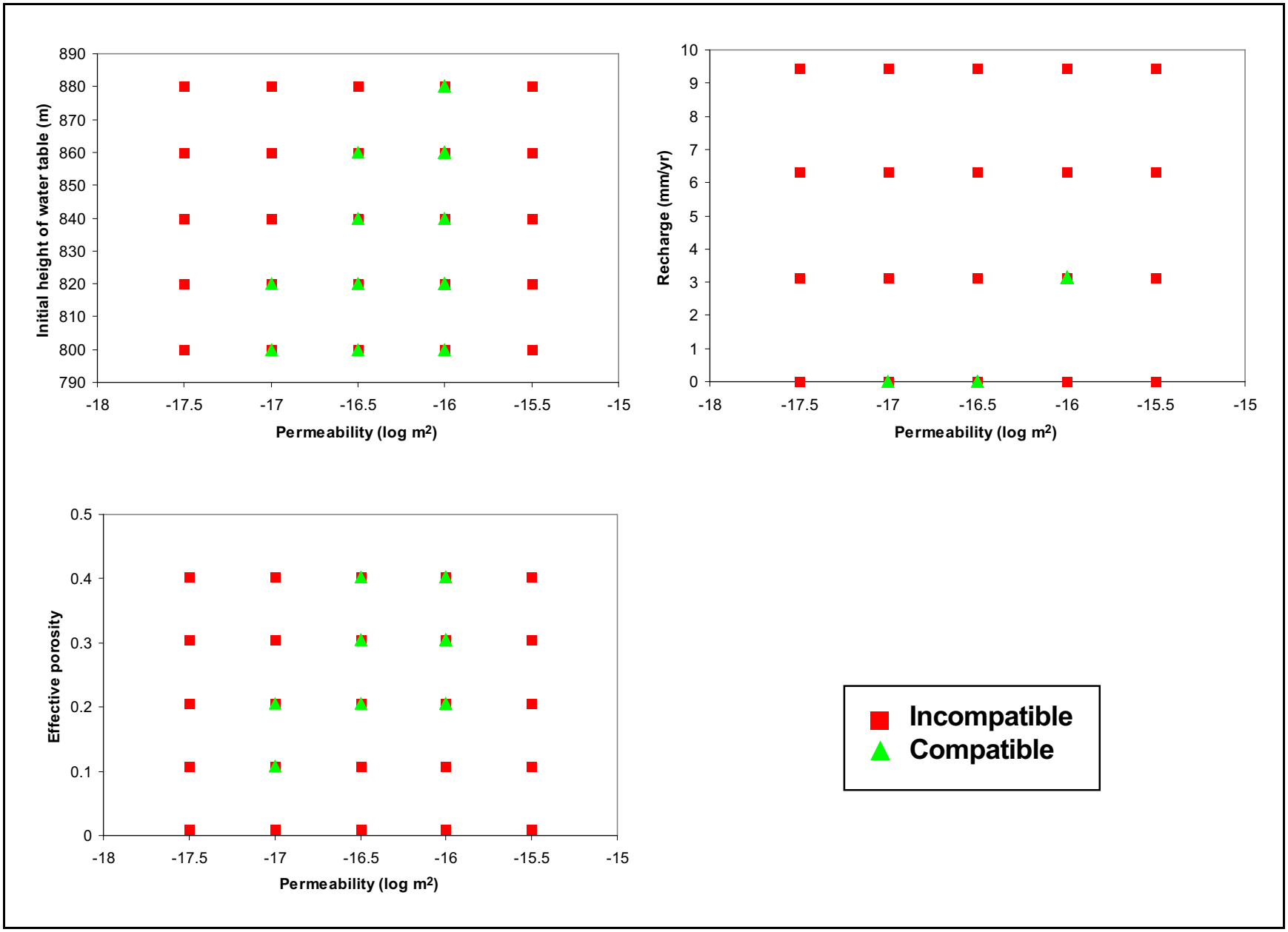

Figure F-4
Results of 500 Transient Simulations, Showing which Parameter Combinations were Incompatible and Compatible with the Draining Conceptual Model

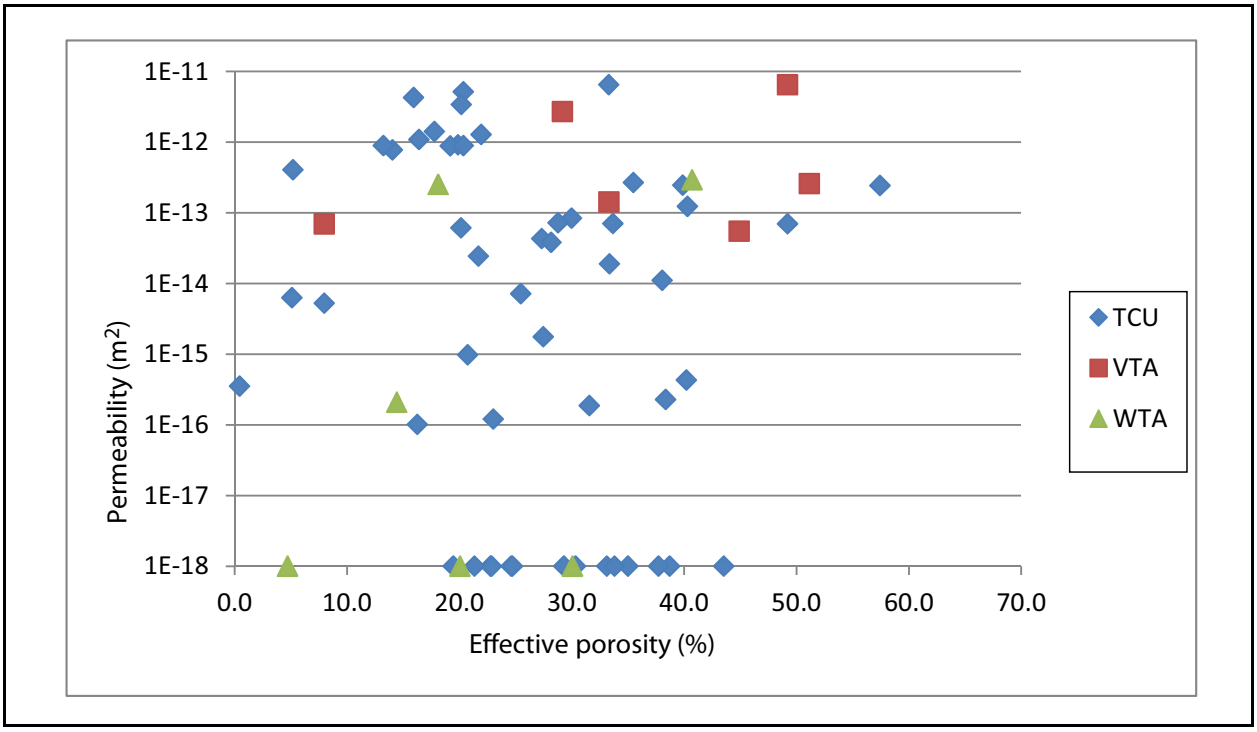

Figure F-5
Matrix Permeabilities versus Porosities for Tuff Confining Units (TCUs), Vitric Tuff Aquifers (VTAs) and Welded Tuff Aquifers (WTAs)

drains from the sample at -15 bars of suction per unit volume of saturated rock). Clearly, there is no simple relationship between effective porosity and permeability for the TCU (Figure F-5), and other factors, possibly the extent and type of mineral alteration, must be influencing permeability. The Yucca Flat/Climax Mine HDD (SNJV, 2006) defines only two types of porosity: fracture and matrix porosity. For non-fractured rocks, such as the zeolitized lower tuff confining unit, no differentiation between total and effective porosity is made. The new matrix porosity data show that, although there is nearly a one-to-one relationship for the WTA and VTA lithologies, the TCU samples have effective porosities that are much less than total porosity. This could be due to the fact that the total porosity measurements include the effects of structurally bound water in the zeolites.

F.1.3.2 Implications for Flow and Transport Modeling

The simulations provide useful constraints on the range of aquifer properties and recharge rates that are 1) consistent with the transient draining hypothesis or 2) are consistent with a conceptual model of steady state. Although most of the parameter combinations tested support the steady state conceptual model, some combinations (very low permeability, very high porosity, very low recharge rate)

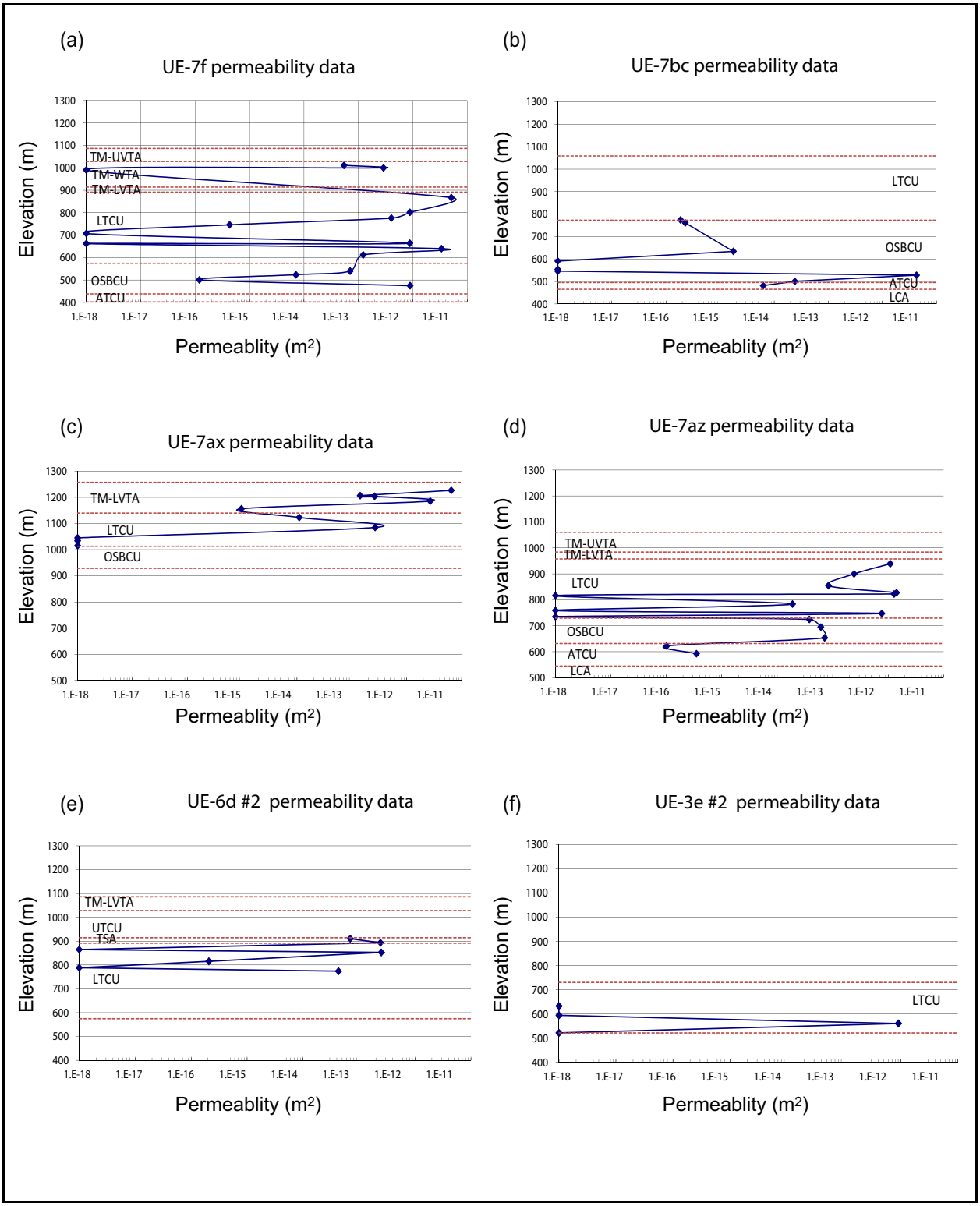

Figure F-6
Matrix Permeability versus Elevation Profiles from Boreholes (a) UE-7f (b) UE-7bc (c) UE-7ax (d) UE-7az (e) UE-6d #2 and (f) UE-3e #2
Source: Modified from Stephens, 2008

support the transient conceptual model. Although this combination of permeabilities and porosities is plausible and often typical of zeolitic tuffs (Figure F-5), recently collected data from Yucca Flat also show that the matrix permeabilities of the zeolitic tuffs can be considerably higher (Figure F-6). There is a high degree of heterogeneity within HSUs considered as homogeneous in the models, with matrix permeabilities ranging from 10^{-18} m^2 to almost 10^{-11} m^2 within the tuff confining units. This is probably because the HFM sometimes groups diverse lithologies and characterizes them based on the dominant lithology within the HSU, while not explicitly recognizing thin or minor lithologies that may be present (BN, 2006). The data in Figure F-6 suggest that lithologic layering within the tuff confining units may result in a pronounced anisotropy, depending on the lateral extent of these apparent layers, with horizontal permeability dominated by the high-permeability layers and vertical permeability dominated by the low permeability layers. The vertical permeability may exert the dominant control on drainage from the tuffs to the LCA. Mild to strong anisotropy is assumed for these units in the CAU-scale flow and transport results presented in Section 4.0.

An important conclusion is that none of the simulations predict significant head changes over the next 1,000 years (the time frame required for contaminant boundary calculations). The thirty simulations mentioned above predict an average of 1.3 m head decline over the next 1,000 years (maximum of 5.6 m). This is a very small head decrease compared to the large measured testing-induced pressure fluctuations, and so it is reasonable to neglect this small effect.

A potentially more important effect might be over-estimating permeability and/or modern recharge rates by calibrating a steady-state flow model to pre-testing gradients.

To account for this possible bias in parameter uncertainty estimates derived from model calibrations, the range of plausible parameters should be at least as large as the space defined by the red symbols in Figure F-4. The parameters found to be consistent with the paleo-drainage hypothesis identified in Figure F-4 are similar to those calibrated under steady-state conditions with a 0.1 mm/yr infiltration rate. Therefore, no additional simulations were done as a result of the transient drainage analysis.

F.2.0 REFERENCES

BN, see Bechtel Nevada.

Bechtel Nevada. 2006. A Hydrostratigraphic Model and Alternatives for the Groundwater Flow and Contaminant Transport Model of Corrective Action Unit 97: Yucca Flat-Climax Mine, Lincoln and Nye Counties, Nevada. DOE/NV/11718-1119.Dickerson, R., T. T. Rose, and G. Eaton, 2004. Letter Report: Underground Test Area Project, Mineralogical and Isotopic Analysis of Fracture-Coating and Alteration Minerals in the Yucca Flat Tuff Confining Unit, Nevada Test Site, Stoller-Navarro Joint Venture.

Dickerson, R., T. Rose, and G. Eaton. 2004. *Letter Report: Underground Test Area Project, Mineralogical and Isotopic Analysis of Fracture-Coating and Alteration Minerals in the Yucca Flat Tuff Confining Unit, Nevada Test Site.* Prepared by Stoller-Navarro Joint Venture Underground Test Area Project for the U.S. Department of Energy.

Fenelon, J.M. 2005. *Analysis of Ground-Water Levels and Associated Trends in Yucca Flat, Nevada Test Site, Nye County, Nevada, 1951–2003*, Scientific Investigations Report 2005-5175. Carson City, NV: U.S. Geological Survey. (p. 33).

Fenelon, J.M., D.S. Sweetkind, P.E. Elliott, and R.J. Laczniak. 2012. C*onceptualization of the Predevelopment Groundwater Flow System and Transient Water-Level Responses in Yucca Flat, Nevada National Security Site, Nevada*, Scientific Investigations Report 2012-5196. Reston, VA: U.S. Geological Survey.

Flint, A.L., L.E. Flint, E.M. Kwicklis, J.T. Fabryka-Marin, and G.S. Bodvarsson. 2002. Estimating recharge at Yucca Mountain, Nevada, USA: comparison of methods, Hydrogeology Journal 10:180-204.

Forester, R.M. J.P. Bradbury, C. Carter, A.B. Elvidge-Tuma, M.L. Hemphill, S.C. Lundstrom, S.A. Mahan, B.D. Marshall, L.A. Neymark, J.B. Paces, S.E. Sharpe, J.F. Whelan, and P.E. Wigand. 1999. The Climatic and Hydrologic History of Southern Nevada During the Late Quaternary, U.S. Geological Survey Open-File Report 98-635, Denver, CO.

Kwicklis, E.M., A.V. Wolfsberg, P.H. Stauffer, M.A. Walvoord, and M.J. Sully. 2006. “Multiphase, Multicomponent Parameter Estimation for Liquid and Vapor Fluxes in Deep Arid Systems Using Hydrologic Data and Natural Environmental Tracers.” *Vadose Zone Journal 5 (3): 934–950*.

Quade, J., M.D. Mifflin, W.L. Pratt, W. McCoy, and L. Burckle. 1995. Fossil spring deposits in the southern Great Basin and their implications for changes in water-table levels near Yucca Mountain, Nevada, during Quaternary time, Geological Society of America Bulletin 1995: 107, no. 2:213-230.

Spaulding, W.G., and L.J. Graumlich. 1986. "The Last Pluvial Climatic Episodes in the Deserts of Southwestern North America." In *Nature*, v. 320: 441-444.

Spaulding, W.G. 1990. Vegetational and climatic development of the Mojave Desert: The Last Glacial Maximum to the Present, p. 166-199. In J.L. Betancourt et al. (ed.) Packrat middens: the Last 40,000 years of biotic change. Univ. of Ariz. Press, Tucson.

Stephens, D.B. 2008. *Moisture Retention Testing for TCU, VTA, and WTA Samples*. Laboratory report prepared for Los Alamos National Laboratory. Los Alamos, NM.

Stoller-Navarro Joint Venture. 2006. *Phase I Hydrologic Data for the Groundwater Flow and Contaminant Transport Model of Corrective Action Unit 97: Yucca Flat/Climax Mine, Nevada Test Site, Nye County, Nevada*, Rev. 0, S-N/99205--077. Las Vegas, NV.

Stoller-Navarro Joint Venture. 2007. *Phase I Contaminant Transport Parameters for the Groundwater Flow and Contaminant Transport Model of Corrective Action Unit 97: Yucca Flat/Climax Mine, Nevada Test Site, Nye County, Nevada*, Rev. 0, S-N/99205--096. Las Vegas, NV.

Szabo, B.J., P.T. Kolesar, A.C. Riggs, I.J. Winograd, and K.R. Ludwig, 1994. Paleoclimatic inferences from a 120,000-yr calcite record of water-table fluctuation in Browns Room of Devils Hole, Nevada, Quaternary Research (41), p. 59-69.

Tompson, A.F.B., ed. 2008. *Evaluation of Hydrologic Source Term Processes for Underground Nuclear Tests in Yucca Flat, Nevada Test Site: Saturated Tests*, LLNL-TR-403429. Livermore, CA: Lawrence Livermore National Laboratory.

Tyler, S.W., J.B. Chapman, S.H. Conrad, D.P. Hammermeister, D.O. Blout, J.J. Miller, M.J. Sully, and J.M. Ginanni. 1996. "Soil-Water Flux in the Southern Great Basin, United States: Temporal and Spatial Variations Over the Last 120,000 Years." In *Water Resources Research*, v. 32: 1481-1499.

Walvoord, M.A., M.A. Plummer, F.M. Phillips, and A.V. Wolfsberg. 2002a. "Deep Arid System Hydrodynamics 1: Equilibrium States and Response Times in Thick Desert Vadose Zones." In *Water Resources Research*, v. 38: 15.

Walvoord, M.A., F.M. Phillips, S.W. Tyler, and P.C. Hartsough. 2002b. "Deep Arid System Hydrodynamics 2: Application to Paleohydrologic Reconstruction Using Vadose-Zone Profiles from the Northern Mojave Desert." In *Water Resources Research*, v. 38: 12.

Winograd, I.J., and G.C. Doty. 1980. Paleohydrology of the southern Great Basin, with special reference to water table fluctuations beneath the Nevada Test Site during the Late (?) Pleistocene. U.S. Geological Survey Open-File Report 80-569, Reston, VA.

Yang, I.C. G.W. Rattray, Y. Pei. 1996. Interpretation of chemical and isotopic data from boreholes in the unsaturated zone at Yucca Mountain, Nevada. USGS Water-Resources Investigations Report 96-4058, 58 p.

Appendix G

Saturated Volcanic Aquifer System Test-Induced Overpressure Conceptual Model and Characteristics

G.1.0 Simulating Underground Nuclear Testing Effects within the CAU-Scale Model

G.1.1 Rationale

Underground nuclear tests create significant changes in the physical properties of the surrounding rocks and create overpressurization in the groundwater. For an overview of the hydrologic effects and the causative mechanisms, see Laczniak et al. (1996), Tompson (2008), and Halford et al. (2005). Because testing-induced changes have the potential to significantly affect radionuclide transport at multiple scales, it is important to consider these effects in the CAU model. At other NNSS sites (Pahute Mesa, Frenchman Flat), these processes were accounted for in the HST, not in the CAU-scale flow and transport models. One reason is that there was very little evidence of pressurization effects in the far field at these sites. In the saturated zone in Yucca Flat, however, there is ample evidence of pressurization in the far field, in some cases long after the test was conducted. It is important to note that this phenomenon has been measured both within the Tuff Pile area (e.g., UE-4e1,2 and U-4t) and locations to the east (TW-7) and north (e.g., U-7cb).

As shown in Figure G-1, there are complex physical changes that occur in the vicinity of an underground nuclear detonation, perhaps as far field as 6 cavity radii (R_c). In some zones, both permeability enhancement (due to fracturing) and permeability decreases (due to compaction/crushing) can occur; the net effect on large-scale effective permeability change in these zones is unknown. At least a portion of the mechanical effects, particular in the far field, are elastic.

Unfortunately, during the testing period at Yucca Flat (1957–1992) relevant to UGTA, virtually no direct hydrologic measurements were made, other than occasional measurements of water levels in wells. In particular, porosity and permeability were never directly measured. Inferences have been made, however, based on geochemical principles, visual observations of fracturing, measurements of tracer migration in the near field at a very small number of tests, and ground surface motion data (App and Brunish, 1991). Some of these inferences have been directly integrated into hydrologic models (e.g., Wolfsberg et al., 2006; Halford et al., 2005; Tompson, 2008) in studies of small portions of Yucca Flat. However, none of these inferences have been confirmed with near-field hydrologic testing. Since this CAU-scale model is required to simulate radionuclide transport for over 100 tests,

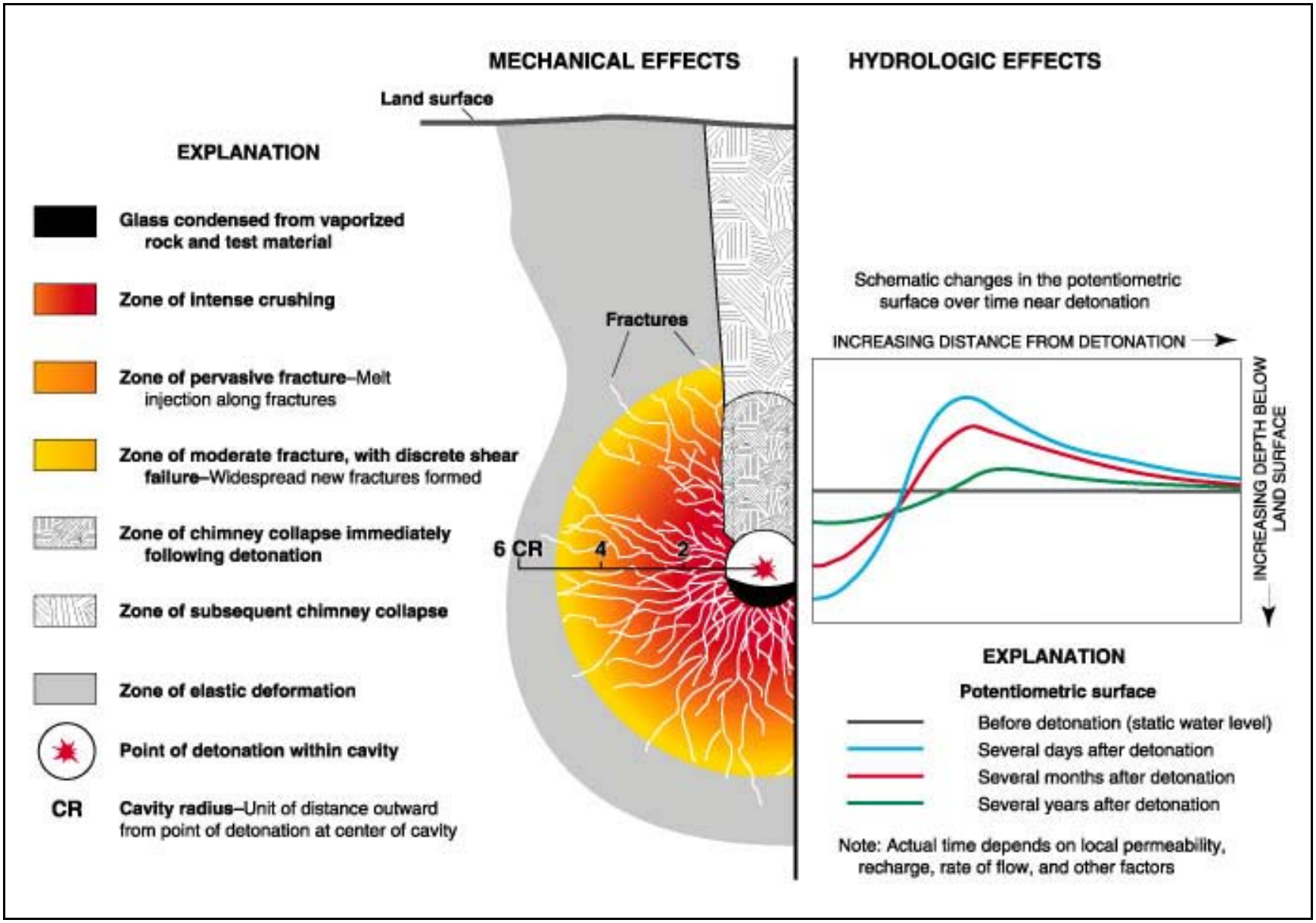

Figure G-1
Illustration of Mechanical and Hydrologic Effects from an Underground Nuclear Detonation
Source: Laczniak et al., 1996

the large majority of which have virtually no near- or far-field data from which to infer the hydrologic impact of the test, it was necessary to build a flexible modeling framework that could explicitly acknowledge this uncertainty.

G.1.2 Approach

Two models were developed as the backbone for the testing-effect simulation strategy. One model was based largely on the conceptual and numerical models presented in Tompson (2008). Beyond the cavity/chimney, this model assumes two discrete zones—a crushed zone and a compressed zone (see Figures G-2 and G-3b)—each with a uniform level of permeability/porosity change and overpressurization. The other model was based largely on processes and modeling strategies proposed by Wolfsberg et al. (2006) and Halford et al. (2005). Beyond the cavity/chimney, this model assumes a continuous gradient in rock property changes and overpressurization (as shown in Figure G-3a). According to the Yucca Flat HST, both these conceptual models are physically reasonable, and neither can be discounted given the paucity of detailed data (Tompson, 2008, p. 3-5). By adjusting parameter input values of each of these two conceptual/numerical models, the models can behave either very differently or quite similarly from each other, and are collectively capable of producing a wide variety of testing effects, including permeability reduction, permeability enhancement, discrete zones of damage and overpressurization, and continuous gradations of damage and overpressurization. For the large majority of tests, for which very little hydrologic data are available, the uncertainty represented by consideration of these various models and parameterization is believed to be, practically speaking, irreducible.

It is reasonable to assume that each test at Yucca Flat had unique hydrologic impacts according to the characteristics of the nuclear test, the mechanical properties of the rocks near the tests, and the proximity of hydrologic/geochemical boundaries such as the water table, major faults, and so on. The impact of stratigraphy alone could be quite complex, given that many (if not most) tests included several rock types and at least one such boundary within 1 to 2 R_c. For these reasons, rather than attempting to customize a model to each test, for each realization, the same model is applied to every test. The only test-dependent parameter is the level of overpressurization. Several other parameters relating to changes in rock properties are dependent on the level of overpressurization. Collectively, this set of test-dependent parameters does provide a substantial spatial variability.

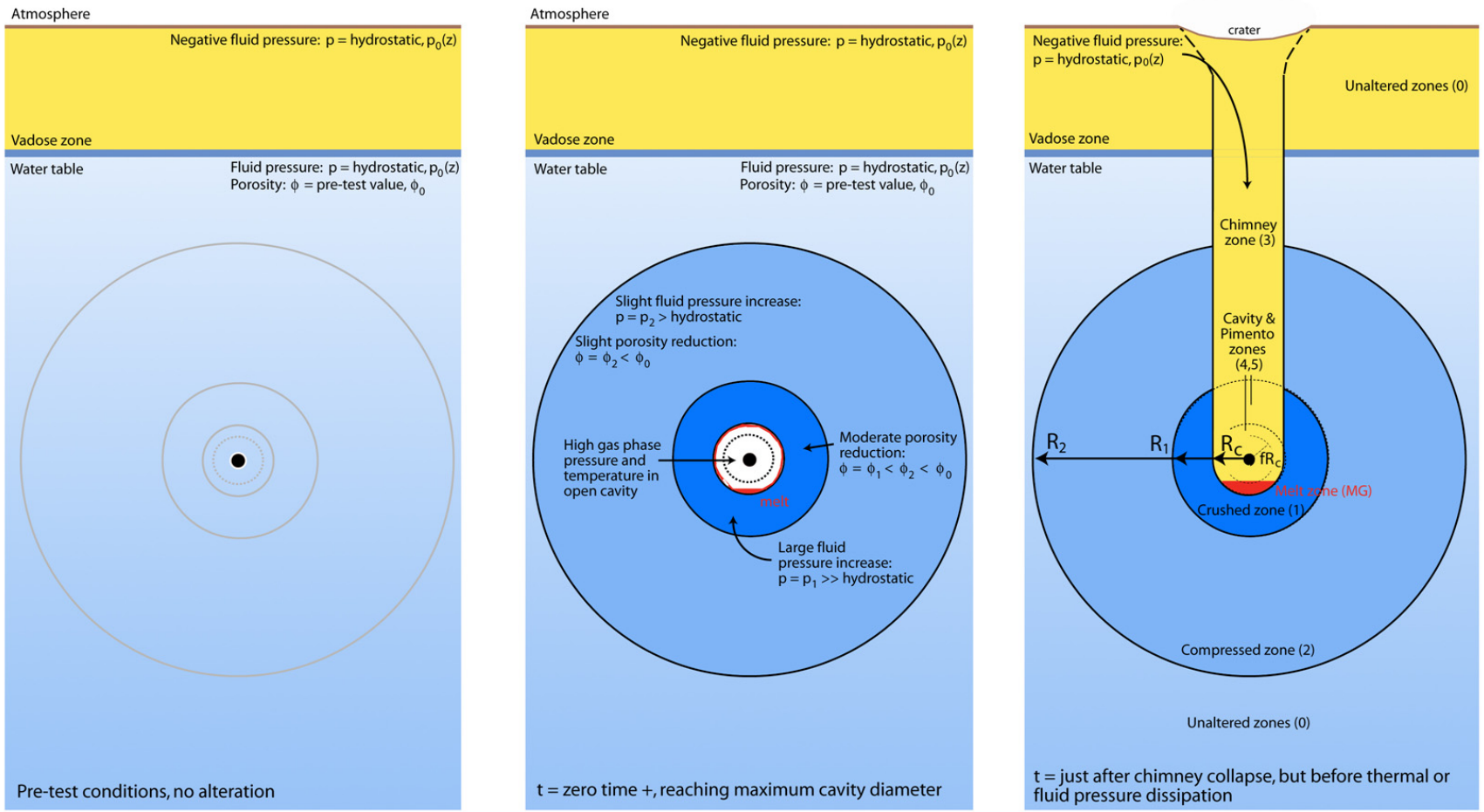

Figure G-2
Definition of Crushed and Compressed Zones
Source: Tompson, 2008

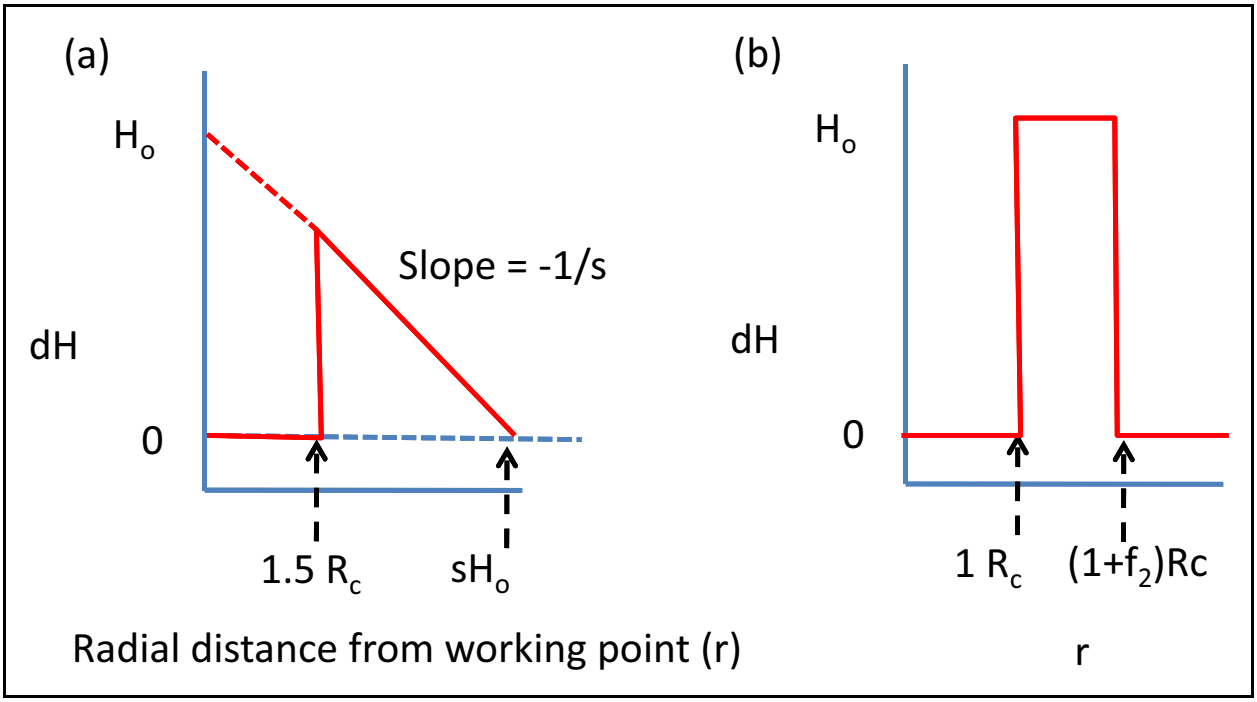

Figure G-3
Overpressure (dH) as a Function of Radial Distance from the Working Point (r), according to Two Conceptual Models: (a) Model 1, and (b) Model 2

G.1.3 Numerical Model Details

As described above, these models consider three zones: the chimney (A); the cavity (B); and a zone of overpressurization, and permeability and porosity reduction or enhancement (C) (Figure G-4). In the case of Model 2, Zone C is subdivided further into two discrete zones: a crushed zone (from R_1 to R_2), and a compressed zone (from R_2 to R_3).

G.1.3.1 Pressurization

Model 1, building on the approaches proposed by Halford et al. (2005) and Wolfsberg et al. (2006), assumes that immediately after the test, overpressurization decreases smoothly with radial distance from the working point, from a maximum value, H_o, to zero at some distance away. The approach developed by Wolfsberg et al. (2006) was based on field measurements of peak radial particle velocity (*Vp*) made by App and Brunish (1991) in the Tuff Pile area during testing. These velocities were converted to estimates of stress, which in turn were converted to overpressurization (*dp*, in megapascals [MPa]) using a skempton coefficient. The resulting relationship between overpressurization (*dp*) and the radial distance from the working point (*r*) was exponential. Using this

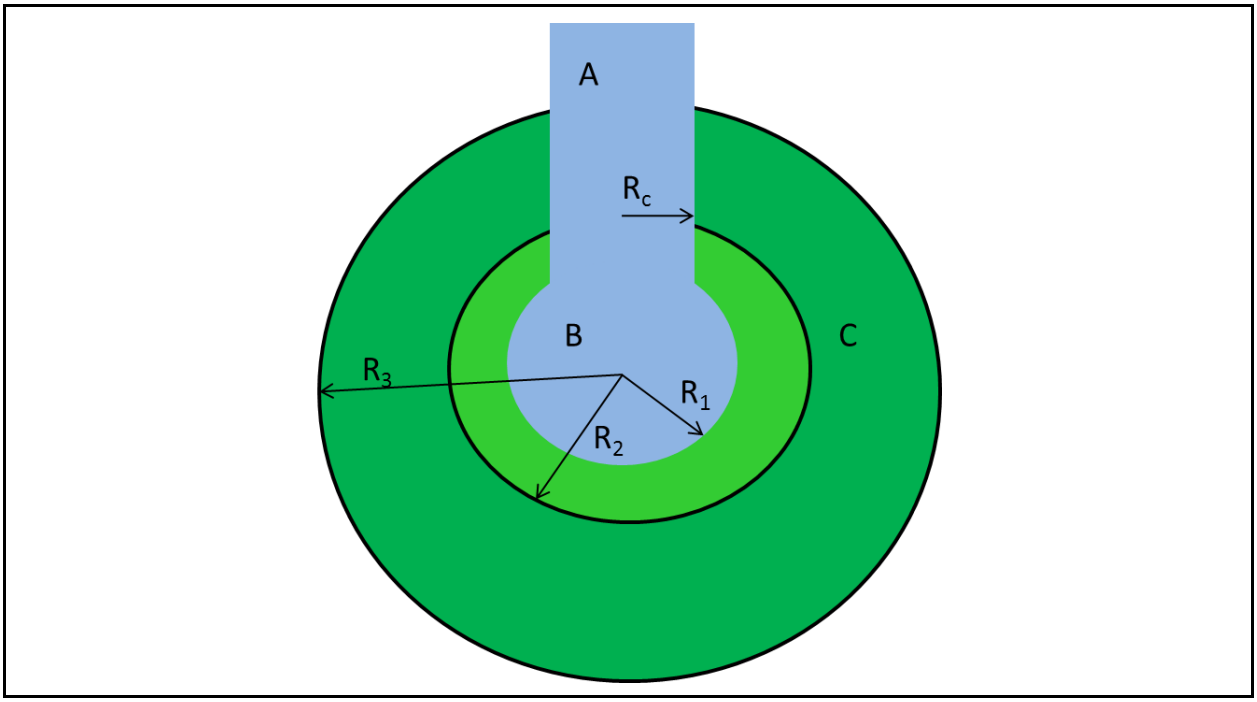

Figure G-4
Definition of Chimney, Cavity, and Overpressurized Zones

approach, a very good calibration to hydrologic data in the Tuff Pile was obtained. Halford et al. (2005) simulated transient groundwater flow in the Tuff Pile area using a very similar exponential relationship and also a simpler linear relationship. Halford et al. (2005) concluded that both models perform equally well. For this study, we assume the simple linear relationship proposed by Halford et al. (2005).

Model 2, building on approaches proposed in Tompson (2008), assumes a very highly overpressurized, narrow crushed zone (expressed as meters of increased head, dH_{cr}, more than 10,000 m in some cases) and a slightly overpressurized (dH_{co}), larger compressed zone. Although Tompson (2008) simulated a dry cavity immediately after the blast, since the CAU-scale flow model is single phase, hydrostatic conditions are applied in the cavity.

As shown in Figure G-1, overpressures will be high at early times and confined to short radial distances. At later times, pressures will dissipate and affect a broader area. Model 2 attempts to capture the overpressures at very early times, whereas Model 1 is a reasonable approximation to later times. Since the time scale of the simulations is days, not microseconds, capturing the behavior of very early times is not plausible.

G.1.3.2 Rock Property Changes due to Testing

Permeability

The model proposed by Tompson (2008) suggested that permeability in the crushed zone would tend to be affected only very slightly; permeability in the compressed zone might change more. The calibrated values of permeability in the compressed zone at WAGTAIL (which include LTCU, TM-LVTA, and TM-WTA rocks) were very low (6.0E-17 m^2); at FLAX-SOURCE, the compressed zone included the TM-LVTA and AA, and calibrated values of permeability were low (1.8E-15 m^2). At BILBY, some attempt was made to adjust the crushed-zone permeability according to the pretesting rock type: for the OSBCU, the permeability was reduced by a factor of 0.2; and for the LTCU, the permeability was increased by a factor of 133.

In both conceptual models, the numerical implementation applies a permeability modification factor, α, which is linearly related to the degree of overpressurization (*dH*). To accurately reflect the reality that there are no permeability data to base the assumptions upon, both permeability enhancement and reduction are allowed to occur in the course of sensitivity analysis. The exact relation between permeability change and overpressurization differs slightly between the two models. The factor α is not rock-type specific.

Model 1

$dH = H_o - r/s$ for $r \geq R_c$

$\alpha = F\,(1.0 - (H_o - dH)/H_o)$

If $dH > H'$ and $(r/R_c) \leq f_{max}$, $K = K_o \times \alpha$

where

s = adjustable parameter = $-\,dr/dH$

r = distance from working point

dH = change in head (m)

H_o = maximum dH (see Figure G-3)

sH_o = maximum distance of overpressurization

F = a proportionality factor relating overpressurization to permeability change

f_{max} = the number of R_c over which permeability change occurs

K_o = pretest permeability

Model 2

Crushed zone only

$dH = H_o$

Crushed and compressed zones

$\alpha = C_{min} + \gamma\,(C_{max} - C_{min})$

$\gamma = (H_{max} - H_n)/(H_{max} - H_{min})$

where H_{max} and H_{min} constants are used to normalize the impact on permeability of a particular test by the relation between its overpressurization relative to all other tests. C_{min} and C_{max} are used to adjust the range of permeability enhancement or decrease.

In Model 1, there is an additional mechanism for permeability change. As implemented by Wolfsberg et al. (2006), the ratio of pore water pressure to lithostatic pressure is calculated at every node, and if a critical ratio (F) is exceeded, rock failure is simulated by an instantaneous increase in permeability and decrease in porosity. This represents a significant difference between the two models.

In both models, the permeability of the cavity and chimney is assumed to be high (1E-12 m^2).

Porosity

Model 1 assumes no porosity change, unless the pressure exceeds a critical ratio (F) of lithostatic. When that occurs, porosity is reduced to Φ. This adjustable parameter, Φ, was set to 0.01 for all simulations presented here.

Model 2 calculates porosity reduction in the crushed zone from the degree of overpressurization, according to compressibility of water. For crushed zone, porosity reduction is calculated given the original pore space (θ_0), the compressibility of water (β), and the overpressure (dp_1).

The resulting crushed zone porosity (θ_1) is

$$\theta_1 = \frac{(\theta_0 - \beta\, dp_1 \theta_0)}{1 - \beta\, dp_1 \theta_0} \qquad \textit{(G-1)}$$

The pores are compressed to 10 percent of the amount of compression in the crushed zone; the resulting compressed zone porosity (θ_2) is $0.9\theta_0 + 0.1\theta_1$.

The resulting pressure increase in the compressed zone (dp_2) is

$$dp_2 = \left(1 - \frac{\theta_1}{\theta_2}\right) / \beta \qquad \textit{(G-2)}$$

Geometry of Pressurization and Damage Zones

Model 1

$R_1 = 1.5\ R_c$

Maximum extent of pressurization and permeability reduction/enhancement: sH_o

Model 2

$R_1 = 1.0\ R_c$

Crushed zone: $R_2 = (1 + f_2) \times R_c$; $f_2 = f_{min1} + \alpha\ (f_{max1} - f_{min1})$; f_2 ranges from 2.5 to 3.0

Compressed zone: $R_3 = f_3 \times R_c$; $f_3 = f_{min2} + \alpha\ (f_{max2} - f_{min2})$; f_3 ranges from 19 to 21

Parameter Values

The strategy described above provides a number of model parameters that can be varied to produce a range of testing effects, including permeability reduction (rock crushing), permeability enhancement (due to fracturing), and a range of levels of overpressurization. The model calibration process was able to provide some information for a small number of parameters; most were varied widely in the uncertainty analysis. Table G-1 describes the base case for Testing-Effects Model 1; Table G-2 describes the three cases considered for Testing-Effects Model 2.

Table G-1
Base-Case Model Parameters for Model 1
(8 Test Independent, 1 Test Dependent)

Parameter	Value
H_n	27–1,229 m
s	1.6531
f_{max}	7.5
H'	79
K'	1E-12 m^2
Φ'	0.01
F	50
K_c	1E-12 m^2
Φ_c	0.01 m^2

Table G-2
Base-Case Model Parameters for Model 2
(10 Test Independent, 1 Test Dependent)

Overpressure Zone	Parameter	Value	Enhanced v. 3	Reduced v. 2	Base v. 1
Pressurization in Crushed Zone	H_n	0–1,267 m	--	--	--
	H_{max}	1,267 m	--	--	--
	H_{min}	0	--	--	--
Crushed Zone	f_{max}	3	--	--	--
	f_{min}	2.5	--	--	--
	C_{max}	--	2	1	1
	C_{min}	--	1	0.1	0.5
Compressed Zone	f_{max}	21	--	--	--
	f_{min}	19	--	--	--
	C_{max}	--	1.5	1	1
	C_{min}	--	1	0.5	0.9

Note: Physical characteristics and total source mass for underground nuclear tests with a nonzero fraction.

These parameters can be compared to the damage-zone characteristics presented in Tompson (2008). For each of the four detonations examined (WAGTAIL, AARDVARK, BILBY, and FLAX-SOURCE), the crushed zone was assigned a uniform permeability value unique to that detonation (–14.0, –16.2, –14.0, and –14.2, respectively), achieved by calibration. (Note that for BILBY, two values of crushed-zone permeability were used: –16.3 for the LTCU, and –14.0 for the others.) Since each detonation had several HSUs present in the crushed zone, the ratio of initial to final permeability varied between 5E-04 and 0.7, depending on the detonation and the HSU. High-permeability HSUs tend to experience the largest permeability reduction (much less than 0.1), whereas confining units tend to experience relatively moderate reduction (greater than 0.1). The base and reduced cases allow reduction between 1 and 0.5 (or 1 and 0.1), respectively. The reduction is applied to all HSUs, and the degree of reduction varies from detonation to detonation, not based on individual calibration (which is impossible at the CAU scale) but on the relative degree of overpressurization for an individual detonation compared to all detonations.

Given the potential importance of these testing-induced gradients to radionuclide transport and the (generally irreducible) uncertainty in levels of overpressurization for most tests, the levels of pressurization were varied for each test as part of the uncertainty process. The levels of

overpressurization varied from 27 to 1,229 m, and the radius over which pressurization occurred varied from 16.33 to 743 m.

Examples of testing-effects model outcomes are illustrated in Figures G-5 to G-12. These figures illustrate the simulated head and permeability changes associated with a test with a cavity radius of 75 m and a pretesting ambient background head of 780 m. The upper figure in each set shows changes in permeability. Yellow indicates no change, dark blue indicates change to crater/chimney permeability (defined in the flow model independently), and other color shades indicate changes calculated by the testing-effects model as a function of overpressurization. The lower figure in each set illustrates post-test head. In all models, the crater/chimney nodes immediately become hydrostatic (740 m).

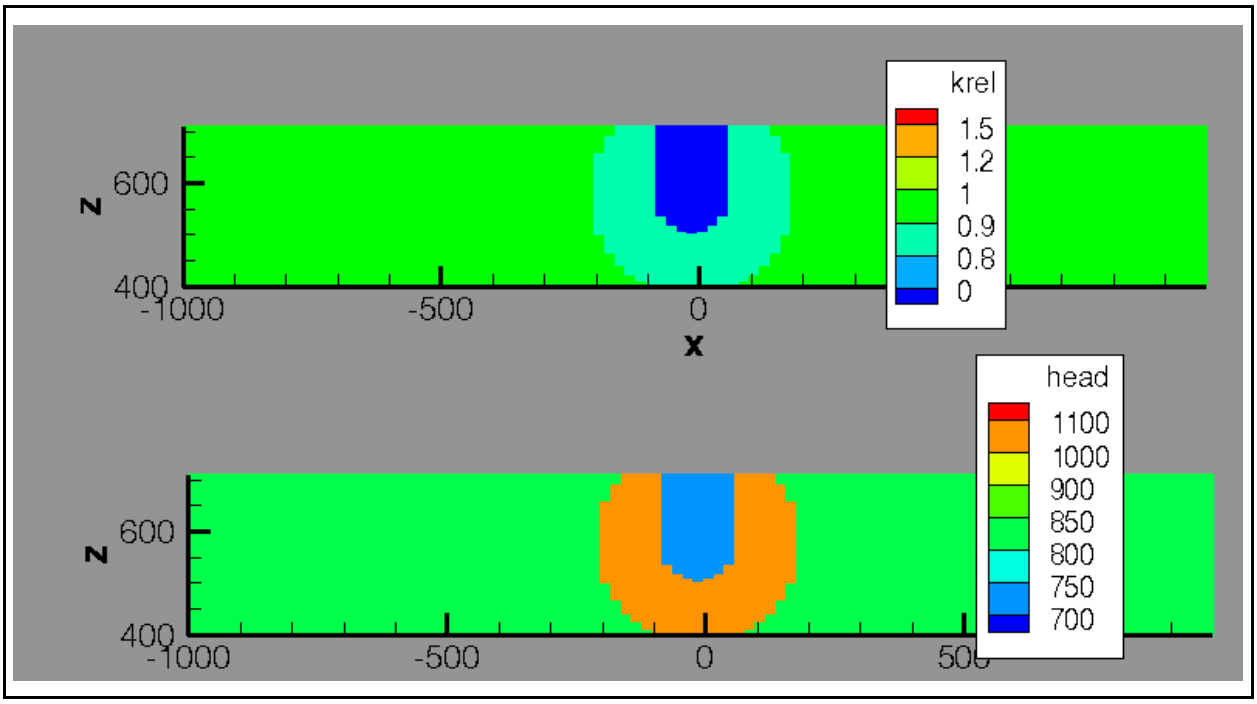

Figure G-5
Example Initial Permeability and Head Assumed for Model 2
(dH = 300 m; Mild Permeability Reduction)

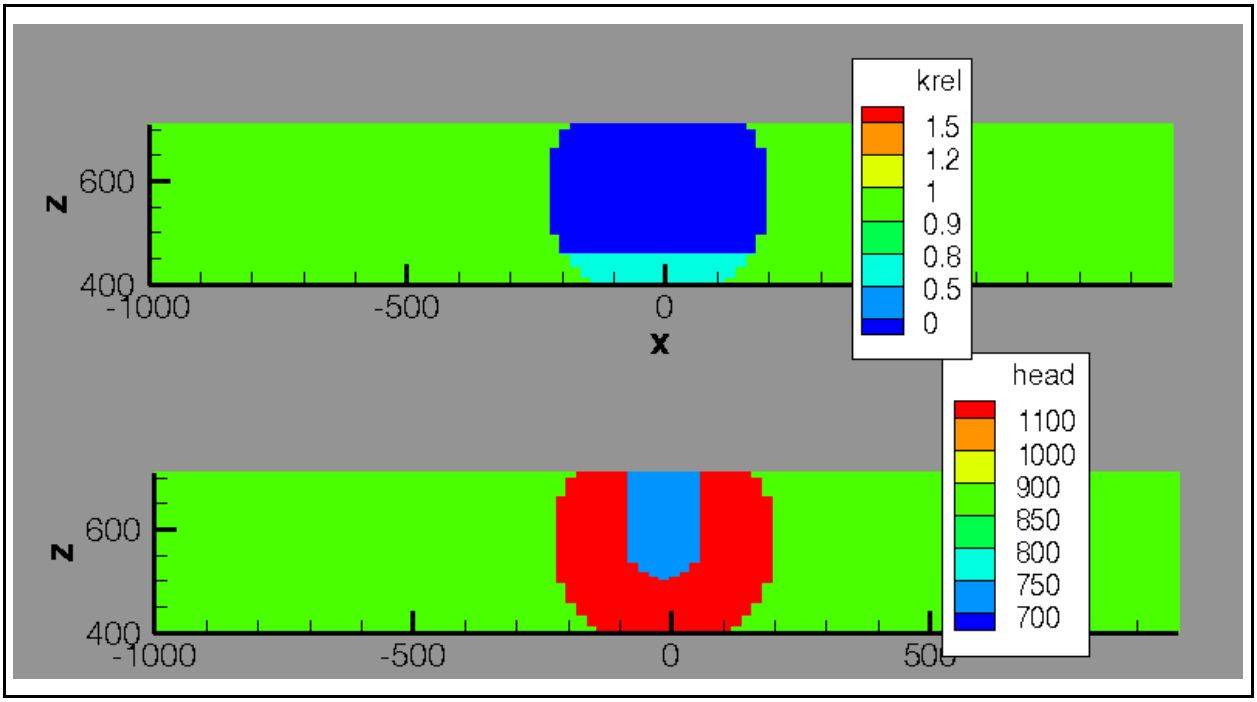

Figure G-6
Example Initial Permeability and Head Assumed for Model 2
(dH = 1,000 m; Mild Permeability Reduction)

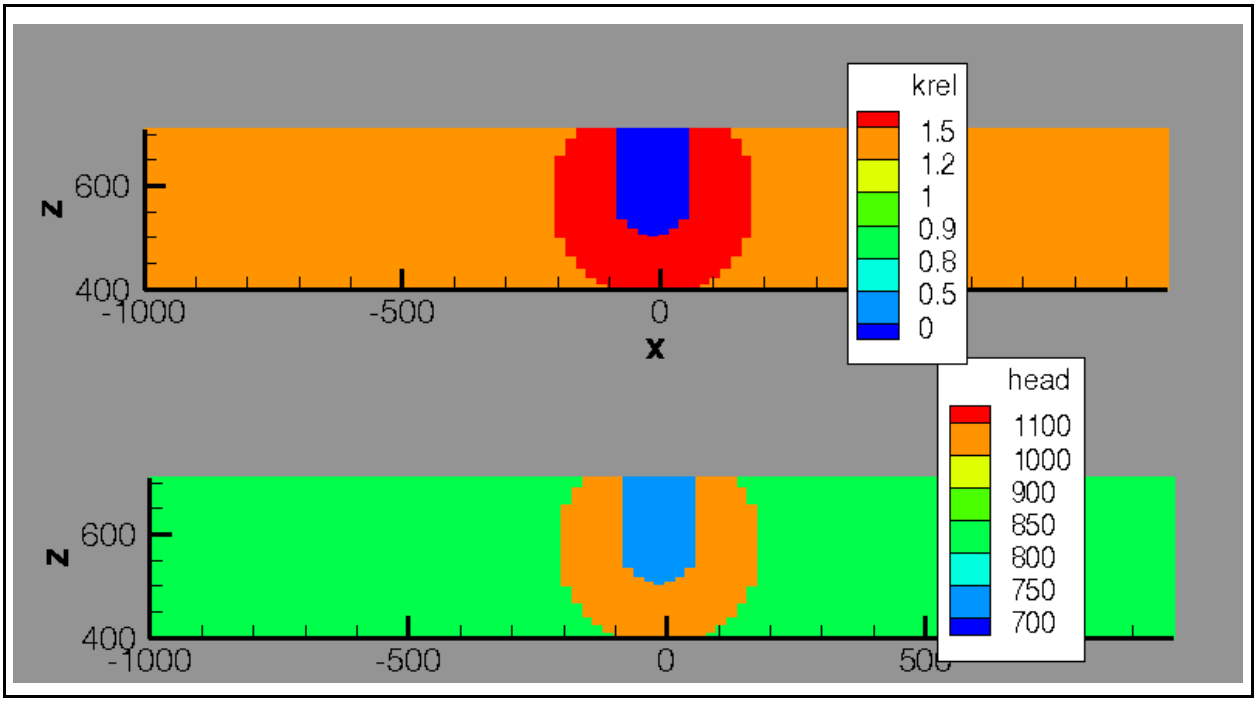

Figure G-7
Example Initial Permeability and Head Assumed for Model 2
(dH = 300 m; Enhanced Permeability)

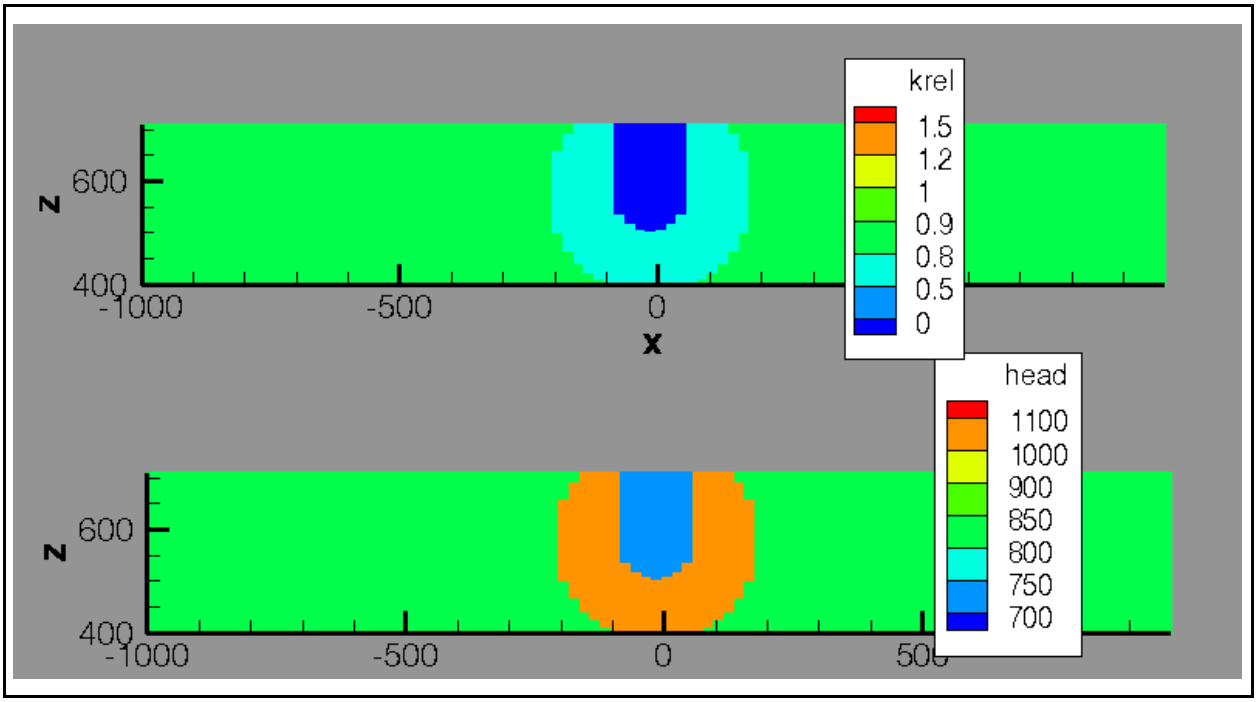

Figure G-8
Example Initial Permeability and Head Assumed for Model 2
(dH = 300 m; Strong Permeability Reduction)

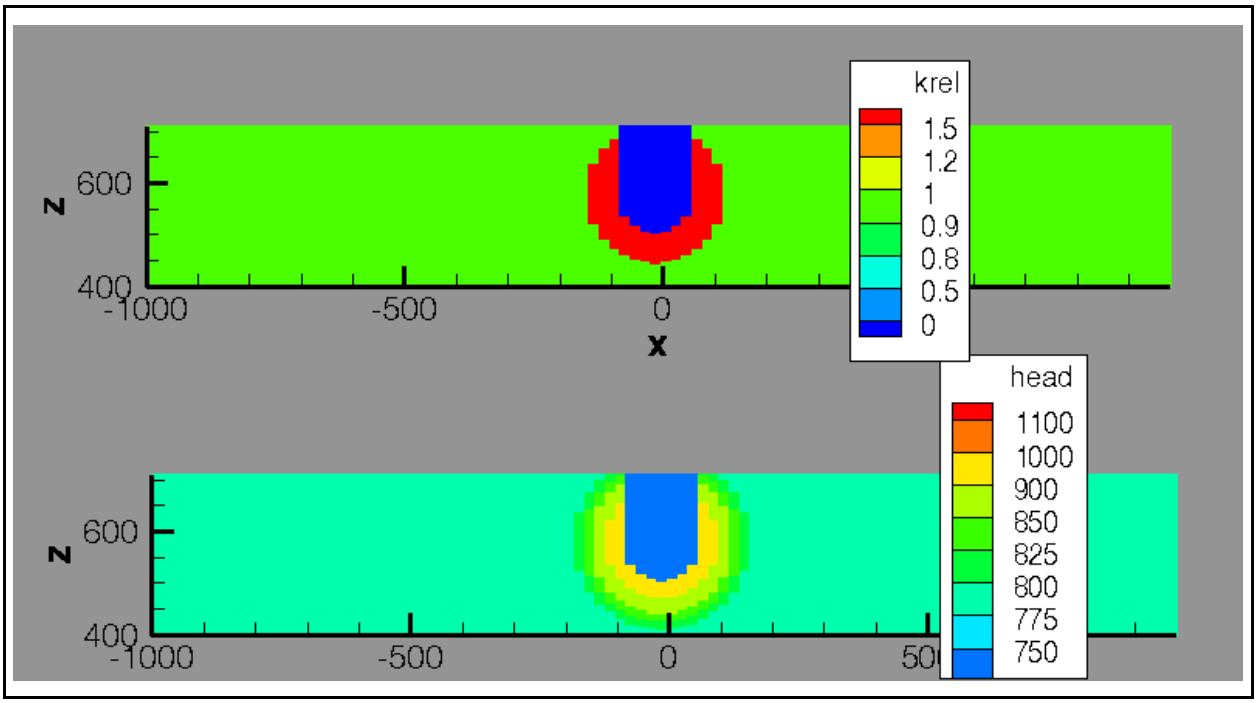

Figure G-9
Example Initial Permeability and Head Assumed for Model 1
(H_o = 300 m; Permeability Enhanced 50 ×, Low Head Criteria)

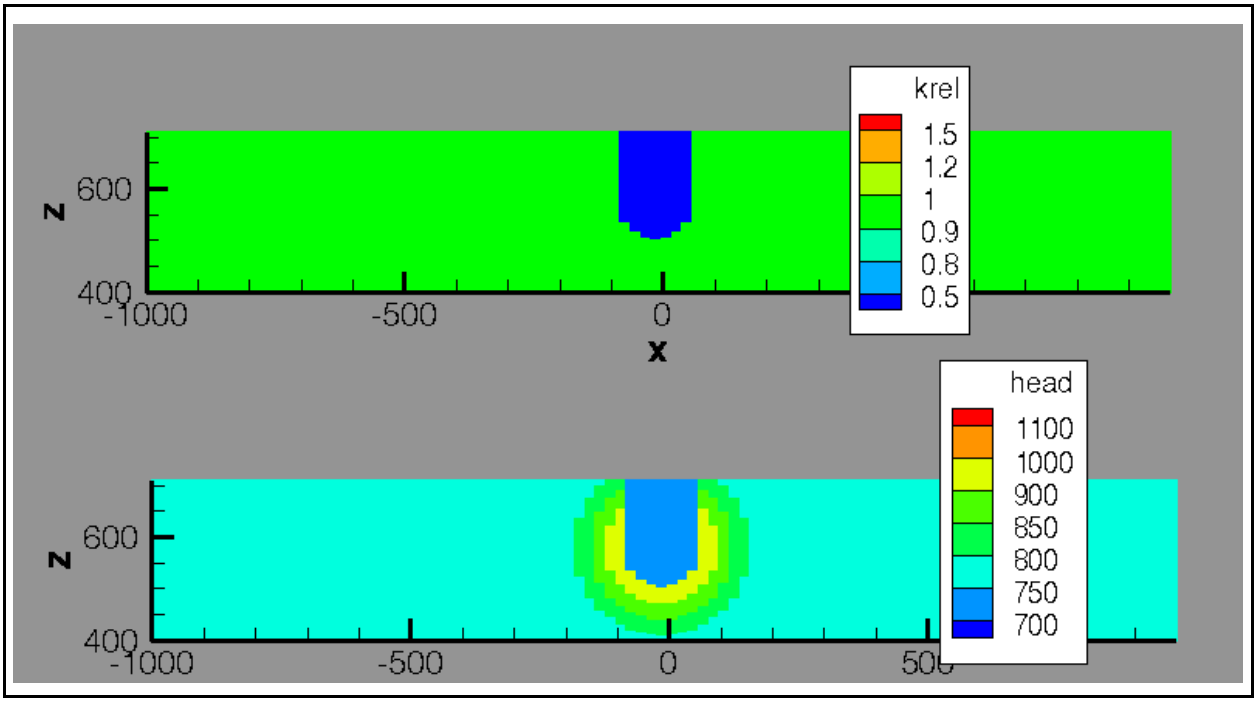

Figure G-10
Example Initial Permeability and Head Assumed for Model 1
(H_o = 300 m; Permeability Enhanced 50 ×, High Head Criteria)

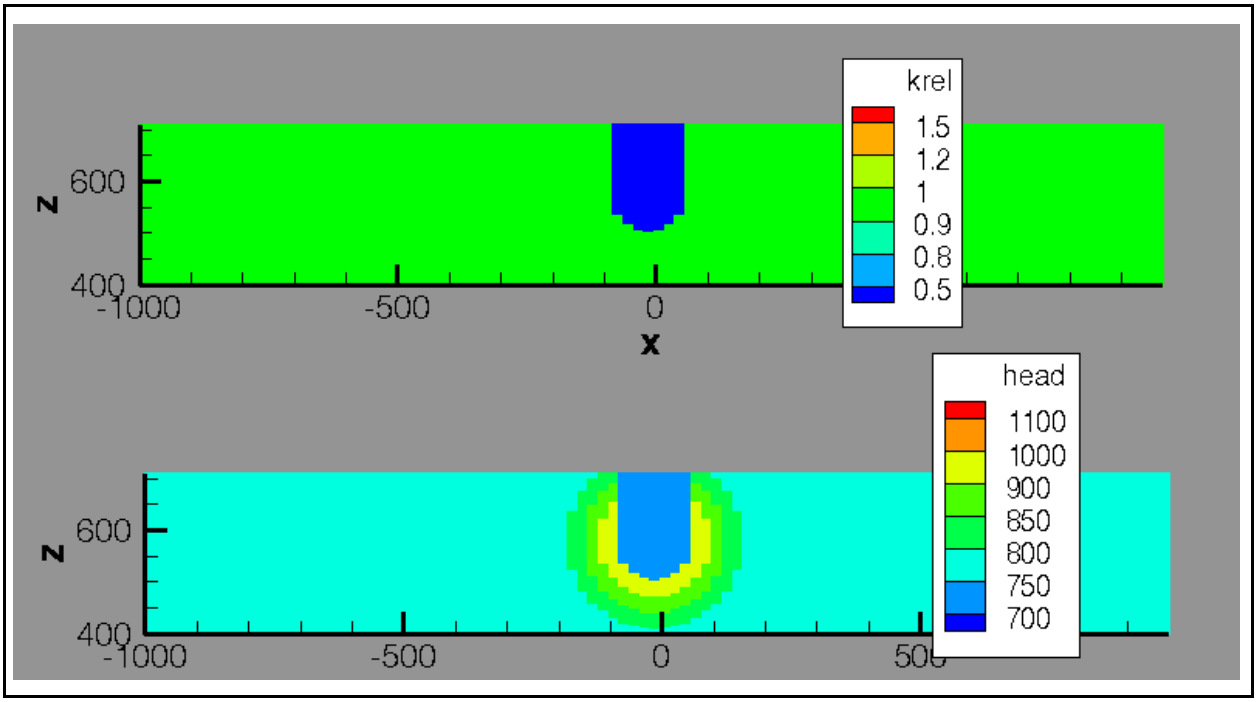

Figure G-11
Example Initial Permeability and Head Assumed for Model 1
(H_o = 300 m; No Permeability Change, Low Head Criteria)

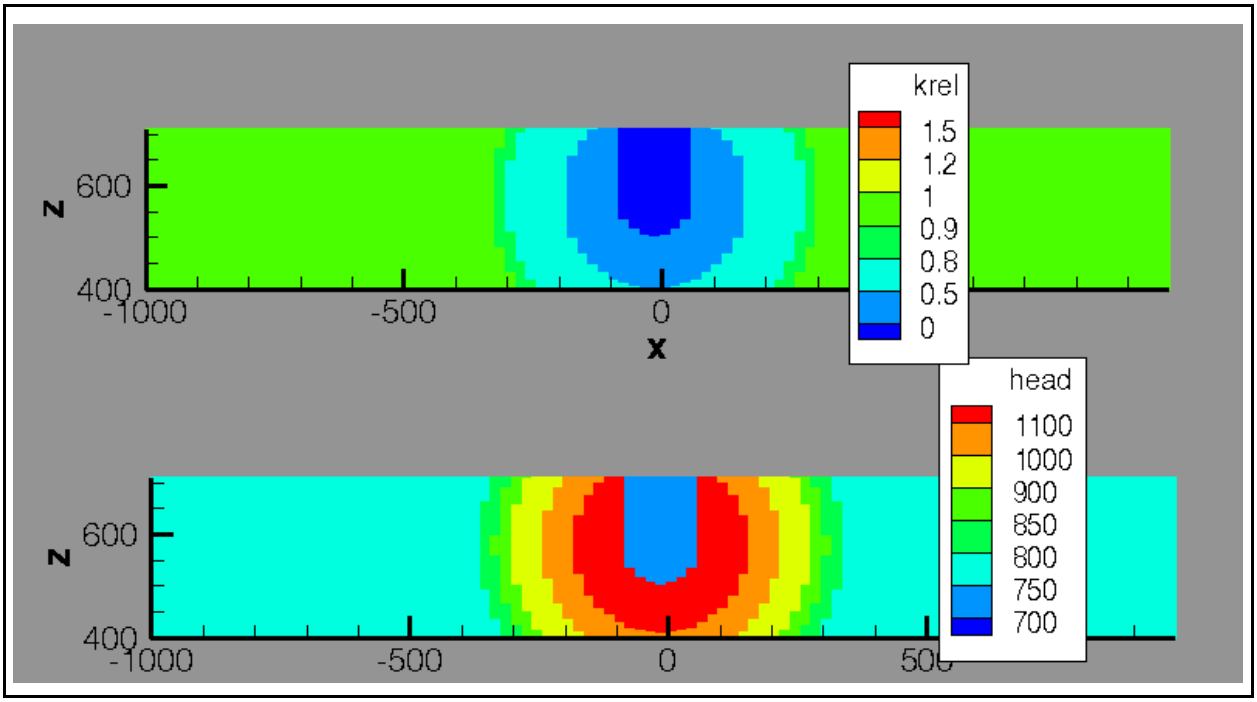

Figure G-12
Example Initial Permeability and Head Assumed for Model 1
(H_o = 600 m; Permeability Reduction × 0.02, Low Head Criteria)

Figures G-5 to G-8 show variations produced using Testing-Effects Conceptual Model 2, as summarized in Table G-3. These variations are produced by varying *dH*, C_{min} (crushed zone), C_{min} (compressed zone), C_{max} (crushed zone), and C_{max} (compressed zone).

Table G-3
Example Realizations of Conceptual Model 2

Variation	*dH* (m)	Crushed and Compressed Zones
1 (Figure G-5)	300	Mild permeability reduction (v.1)
2 (Figure G-6)	1,000	Mild permeability reduction (v.1)
3 (Figure G-7)	300	Enhanced permeability (v.3)
4 (Figure G-8)	300	Strong permeability reduction (v.2)

Immediately after the test, the cavity and chimney revert to hydrostatic head (740 m). In the first case (Figure G-5), there is a thin zone of elevated head surrounding the cavity. Most of the flow domain experiences no change in permeability (green color); a moderate reduction in permeability is present in the overpressurized zone. Figure G-6 shows a much higher level of overpressurization that exceeds the lithostatic pressure, causing an increase in permeability throughout the overpressurized

zone. Figure G-7 illustrates the enhanced permeability case, where moderate overpressurization leads to moderate permeability enhancement. Figure G-8 shows a relatively strong permeability reduction case.

Figures G-9 to G-12 illustrate variations in Testing-Effects Conceptual Model 1; parameter variations are summarized in Table G-4. In each of these figures, it is clear that *dH* varies with distance from the working point, and the zone of overpressurization can be quite large if H_0 is large (Figure G-12). Depending on the values of two parameters, the nature of permeability change (enhanced, reduced, or neutral) and the degree of overpressurization necessary to cause permeability change, a wide variety of behaviors can be produced. Permeability in the overpressurized zone can be enhanced (Figure G-9), unaffected (Figures G-10 and G-11), or dramatically changed due to pressures exceeding the lithostatic pressure (Figure G-12). Even though the potential for permeability enhancement exists in Case 6, the heads never exceed H'.

Table G-4
Representative Cases for Model 1

Variation	H_o	*K* Change (*F*)	Head Criteria (*H'*)
5 (Figure G-9)	300	Permeability enhancement (× 50) (N1)	Low (B2)
6 (Figure G-10)	300	Permeability enhancement (× 50) (N1)	High (B3)
7 (Figure G-11)	300	No permeability change (N2)	N/A
8 (Figure G-12)	600	Permeability reduction (× 0.02) (N3)	Low (B2)

N/A = Not applicable

G.1.4 Comparison of Model Results to Measured Heads at TW-7

Hydrographs measured at TW-7 provide some of the most detailed information available concerning hydrologic impacts of underground nuclear tests at Yucca Flat. This section examines what (if any) information about either testing effects or rock properties can be derived from the TW-7 hydrographs. This section also demonstrates the consistency of the approaches described above with the measurements at this test well.

Observations at TW-7. TW-7 was drilled in 1954 in Area 3 at Yucca Flat to a total depth of 686 m (552 m amsl). Static water table was found at a depth of approximately 509 m (728 m amsl). Water levels measured at this well are shown in Figures G-13 and G-14.

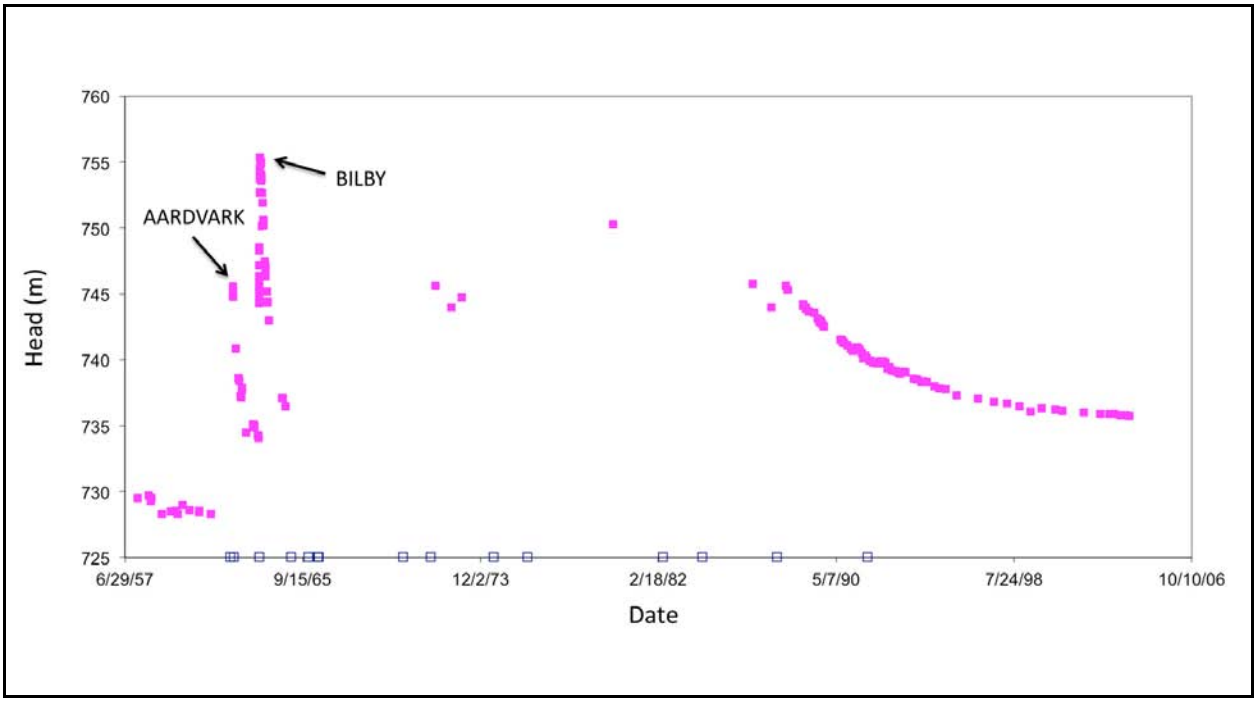

Figure G-13
Water Levels at TW-7 for the Entire Period of Record

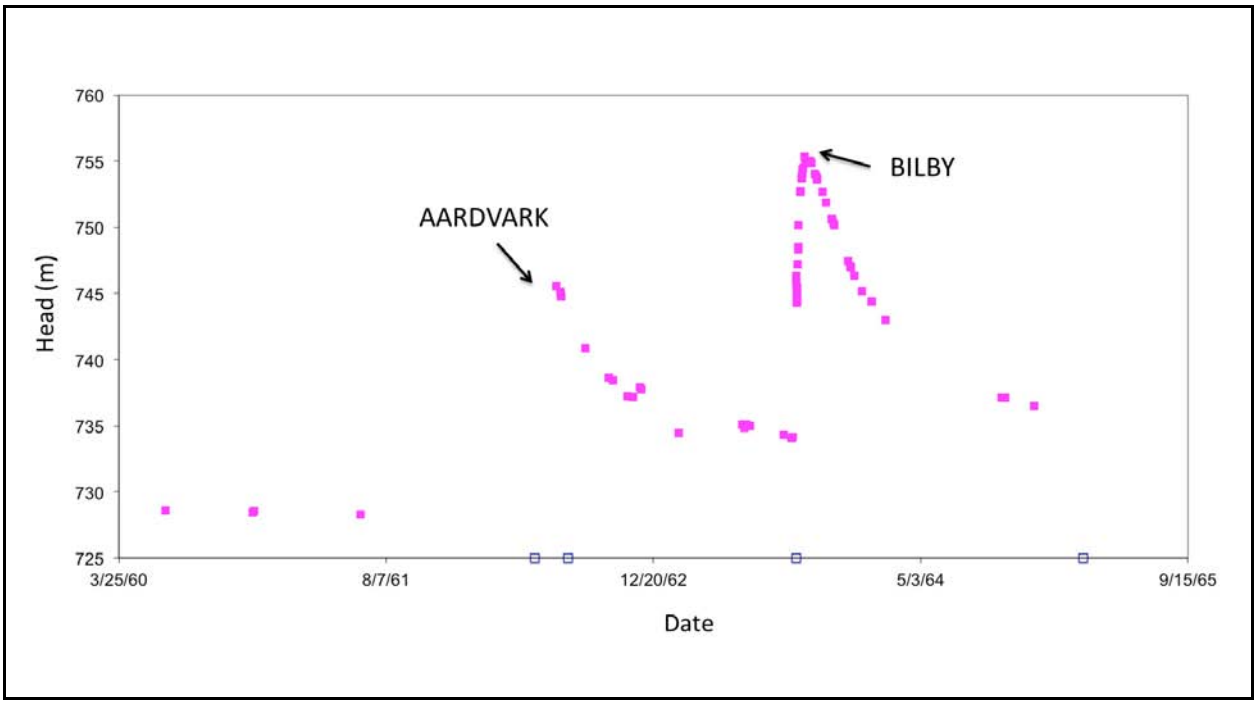

Figure G-14
Water Levels at TW-7, Emphasizing the Pre-1965 Record

There are several characteristics of this hydrograph that can be used to infer both testing effects and rock properties. One is the magnitude of the highest heads measured after AARDVARK and BILBY. The measured maximum is probably lower than the true maximum due to infrequent sampling. The second characteristic is the rate of pressure dissipation after tests, which should be entirely controlled by hydrodynamics (either by rock properties or by evolution of hydraulic gradients). It is significant that pressures dissipated much more quickly after AARDVARK and BILBY than after subsequent detonations. The third measure is the "quasi-static" water levels to which the heads appear to be trending after tests. It is significant that the quasi-static water level appears to be higher at the end of testing (approximately 736 m) compared to the pretesting level (approximately 728 m). Possible reasons include addition of new water from the vadose zone and activation of a fault that allows a hydraulic connection with a distal, higher pressure zone (Garber, 1963).

The final characteristic analyzed is the time delay between the moment of the detonation and the peak pressure. This is only available for the BILBY detonation, and is illustrated in Figure G-15. The peak water level was measured approximately 15 days after the BILBY detonation. One final and potentially significant observation at this well is that the top of the 11¾-inch casing was 1.63 ft lower on June 21, 1962, than it had been a year earlier. Garber (1963) noted that both the AARDVARK and HAYMAKER detonations had a measurable effect on the Yucca fault, with AARDVARK having the larger impact.

G.1.4.1 Previous Studies of TW-7 Response

The effect of the AARDVARK detonation on water pressures at TW-7 has been analyzed in great detail by Garber (1963), Knox et al. (1965), Reed (1970), and Davis (1971). One conclusion that might be drawn from these studies is that multiple conceptual models can be invoked to explain the data.

Garber (1963) noted that hydraulic tests performed in the well before and after AARDVARK showed no change in hydraulic conductivity due to the detonation. He proposed three theories to explain the water-level responses: (1) introduction of new water (released from the vadose zone); (2) new fractures caused directly by the explosion, which provide hydraulic connection between TW-7 and a distant zone of higher heads; and (3) new fractures caused by movement of Yucca fault, which provide hydraulic connection between TW-7 and a distant zone of higher heads. He did not attempt to use any quantitative methods to test these hypotheses via comparison with TW-7 data.

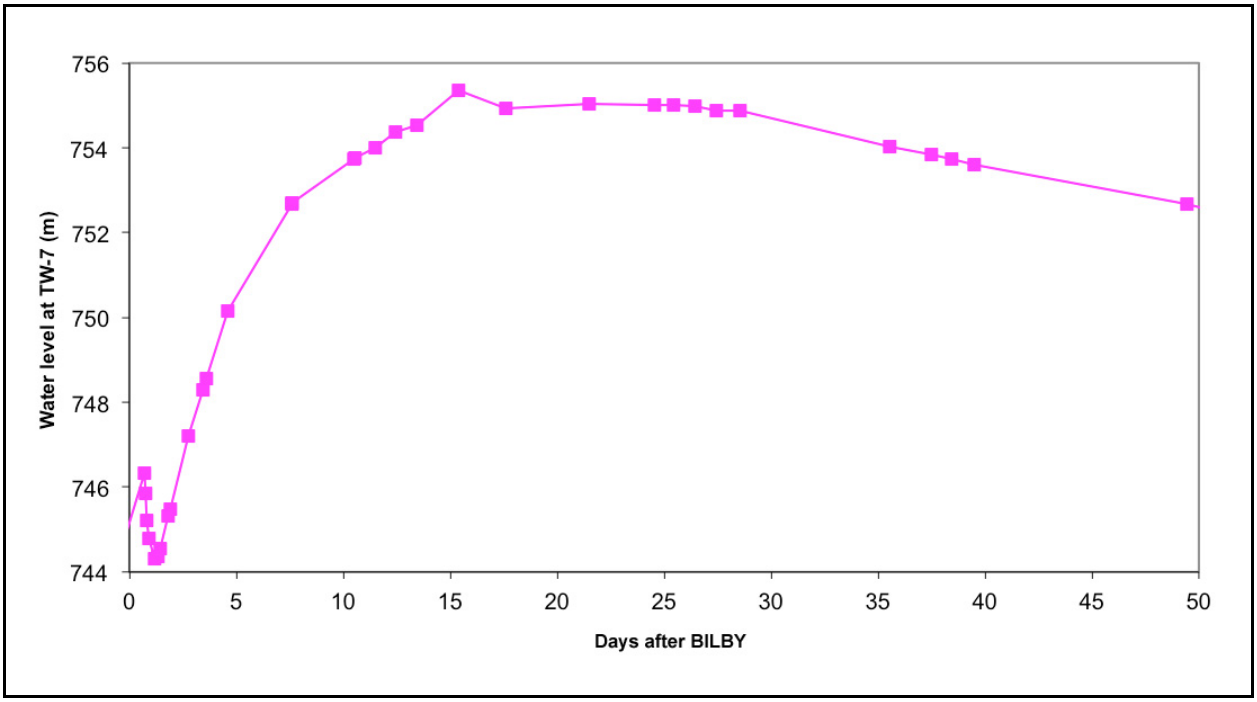

Figure G-15
Water Levels at TW-7 Immediately After the BILBY Detonation

Knox et al. (1965) suggested that the AARDVARK detonation caused a compaction zone, 24 m thick, just outside the cavity radius. The size of the compaction zone was constrained by an earlier estimate by Carlson and Roberts (1963) that over 30 percent of the cavity volume may be accounted for by compaction. In the vadose zone, this created an almost instantaneous elevated water-table mound (approximately 200 m high and 200 m wide), which then moved hydrodynamically toward TW-7, causing a peak arrival in agreement with the measured data. Interestingly, their models predicted faster pressure dissipation (approximately 200 days) than was measured (more than 400 days). The authors make a distinction between an early time period (less than 1.5 days) when both inward and outward flow occurs and a later time period (1.5 to 396 days), when all flow is outward radially away from the cavity. During this time period, testing-induced flow is less than pretesting background flow.

Reed (1970) challenged this analysis by first claiming the proposed model was overly complex. He also took issue with the notion that compaction (and thus also *reduced* permeability) occurred near the cavity and noted that the only published dataset documents *increased* permeability near the cavity. He proposed, instead, a thermo-electric-kinetic model. Davis (1971) published a reply to this paper. He dismissed Reed's model as mathematically flawed and emphasized that mechanical compaction (a similar model, but not identical to that proposed by Knox et al., 1965) is the most

important factor that causes water levels to rise. He additionally suggested that hydrodynamic propagation of pressures toward TW-7 could have occurred under “more or less confined conditions” rather than propagating along the water table as a large mound.

Tompson (2008) calibrated a high-resolution transient three-dimensional flow model of testing-induced impacts at WAGTAIL, AARDVARK, and BILBY to measured water levels at TW-7. Tompson (2008) noted that assigning a low permeability to the LTCU and anisotropy to the OSBCU was necessary for a good match. Another interesting conclusion of this work is that matching post-BILBY water levels at TW-7 required overpressurization not only in the crushed zone but also in the compressed zone out to approximately 20 R_c.

G.1.4.2 Radial Flow Model

A very simple radial flow model was developed to attempt to match the post-BILBY hydrograph at TW-7. The aquifer extends from r = 0 to 2,000 m and z = 500 (the top of the LCA) to 800 m. The working point is at r = 0 m and z = 527 m. Heads at nodes representing TW-7 (r = 1,185 m, 544 m < z < 622 m) are evaluated. At time zero, hydrostatic conditions are applied. Then, to represent the overpressurization due to the BILBY detonation, an instantaneous increase in head occurs. Change in head (dh) ranges from a maximum value at $r = 1\ R_c$ (cavity radius, 70 m) and decays radially at a constant rate, dh/dr (Halford et al., 2005).

$$dh(r) = H_o - r(dh/dr) \qquad \text{(G-3)}$$

Four parameters were adjusted to attempt to reproduce the measured water levels at TW-7: aquifer permeability, specific storage, H_o, and dh/dr. A number of parameter combinations, shown in Table G-5, were used to generate hydrographs shown in Figure G-16.

Table G-5
Parameters used in Radial Flow Model [a]
(Page 1 of 2)

Parameter Combination Scenario	Permeability (log 10 m²) [b]	Specific Storage (1/m)	H_o (m)	dh/dr (-)
A	–14.2	–6	211.4	0.19
B	–14	–6.2	211.4	0.19
C	–15	–6	211.4	0.19

Table G-5
Parameters used in Radial Flow Model [a]
(Page 2 of 2)

Parameter Combination Scenario	Permeability (log 10 m²) [b]	Specific Storage (1/m)	H_o (m)	dh/dr (-)
D	–14	–5	211.4	0.19
E	–15	–7	211.4	0.19
F	–14	–6	111	0.19
G	–14	–6	211.4	0.605
H	–14	–6	411.4	0.605

[a] Results are shown in Figure G-16
[b] Permeability of the entire volcanic pile. In this area, the volcanics are dominated by the OSBCU and LTCU.

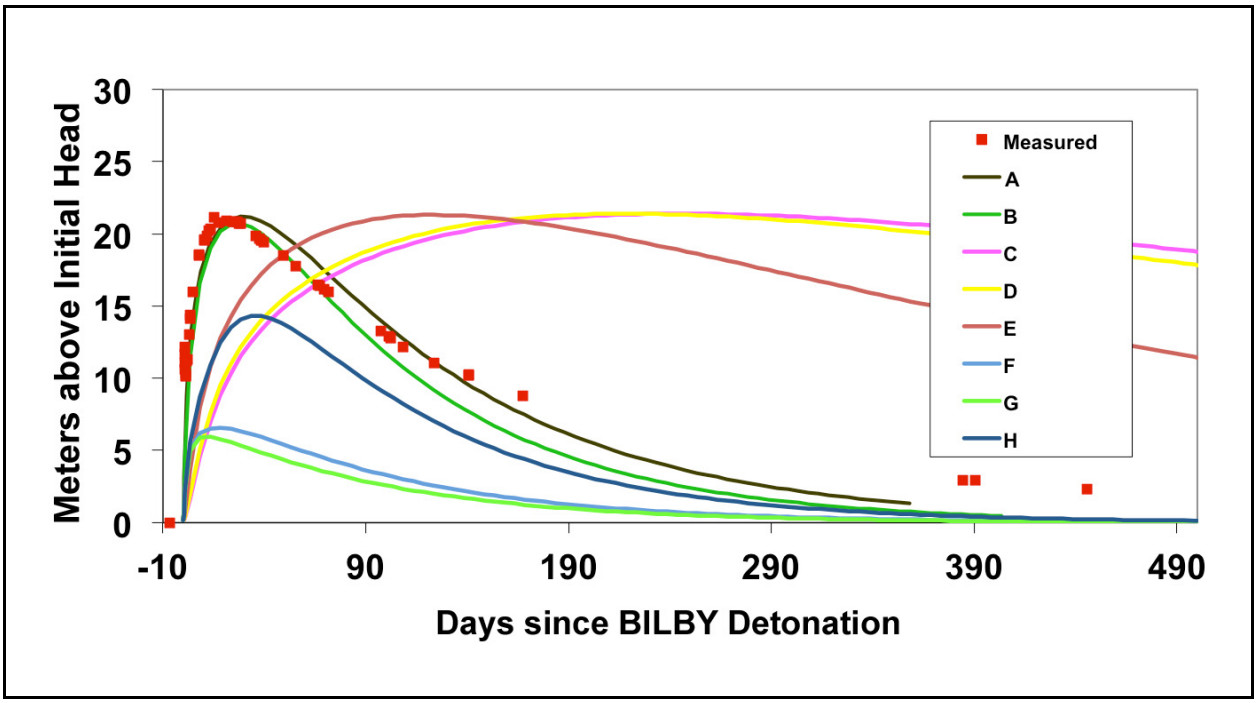

Figure G-16
Simulated and Measured Water Levels at TW-7 Immediately After the BILBY Detonation, Using Radial Model and Parameters Listed in Table G-5

This sensitivity analysis demonstrates a few key points. First, the time of arrival of the peak head (approximately 15 days) is very sensitive to permeability, and the only reasonably good fits were obtained with fairly high permeability (1E-14 m²). Lower permeability values (C, E), regardless of assumed specific storage value, result in delayed pressure breakthrough. The height of the

hydrograph is also very sensitive to H_o and dh/dr. The best-fit combinations (A, B) assume a value of H_o that corresponds to a maximum overpressure of approximately 200 m at 1 R_c and extending out approximately 1,000 m from the working point. Starting with higher values of H_o and smaller spatial extent (e.g., Case H) results in too small a peak overpressure.

G.1.4.3 Three-Dimensional Flow Models

Using hydrostratigraphy as determined by the EarthVision model, a high-resolution model was developed for the vicinity of BILBY (Figure G-17). A similar exercise was conducted to verify the consistency of both conceptual models with the measured hydrographs.

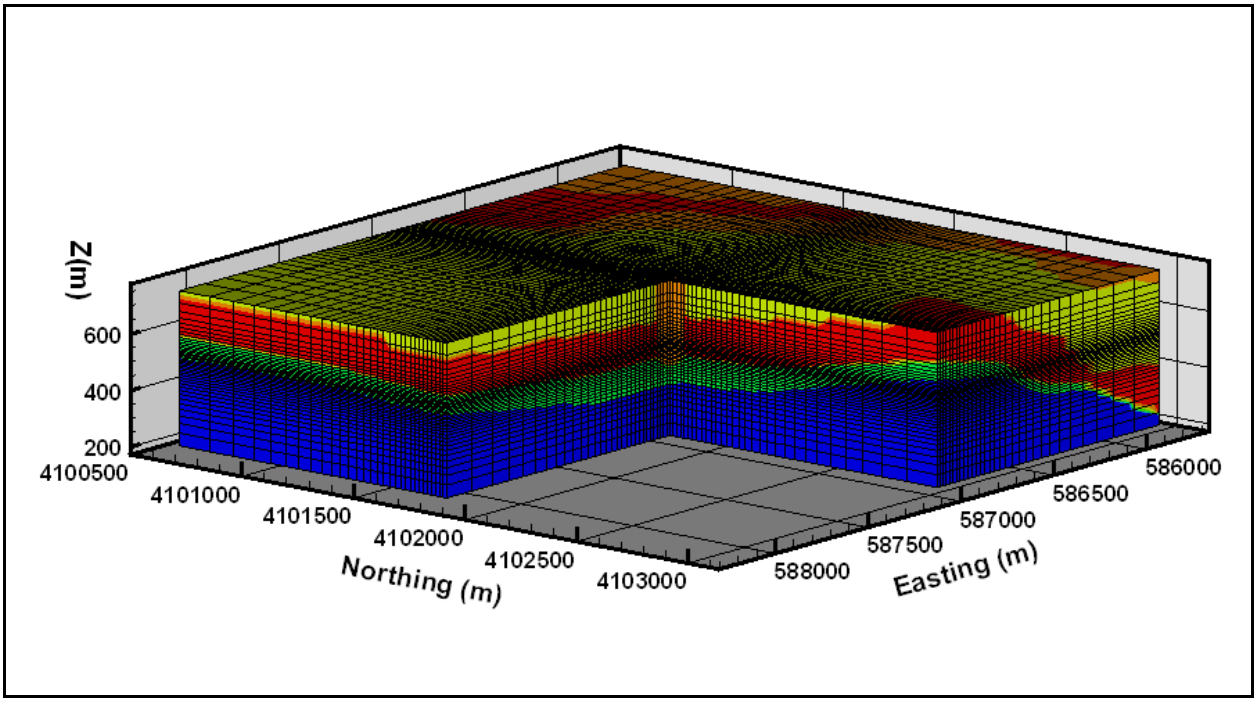

Figure G-17a
High-Resolution Three-Dimensional Model of the BILBY Detonation
Note: Colors indicate HSU layers.

The model parameters used for this analysis are shown in Table G-6. The results for this analysis are shown in Figure G-18. For comparison, the parameters used in Tompson (2008) for BILBY are also shown.

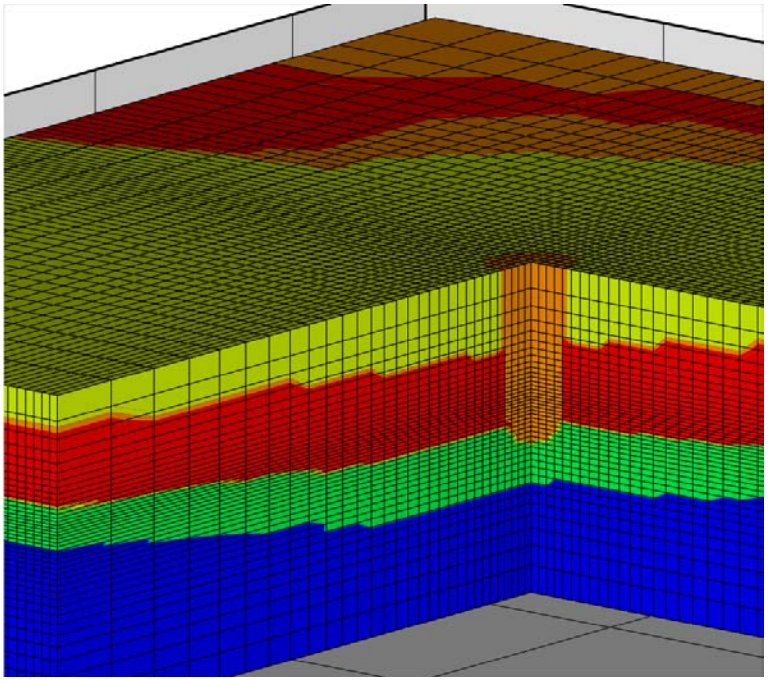

Figure G-17b
High-Resolution Three-Dimensional Model of the BILBY Detonation (Inset)
Note: Colors indicate HSU layers.

The most important conclusion emerging from this analysis is that both testing-effects conceptual models are reasonably consistent with water-level data response at TW-7 to BILBY. The parameters required by the models are very sensitive to the TW-7 data. The parameters required by the models were generally similar to those derived by Tompson (2008), with the notable exception of LTCU properties (Tompson [2008] used a much lower value than the models here). The difference in this parameter may explain the poor fit shown in the best calibrated model. (See the simulated time-to-peak overpressure and the peak overpressure value illustrated in Case 63 in Figure 5.6 of Tompson [2008].) The parameters used, however, were also calibrated to hydrographs at other wells (U-3cn #4 HTH) and other detonations (AARDVARK and WAGTAIL). There are clearly compromises that must be made to simultaneously fit a broader set of data. For all the models shown in Table G-6, the maximum radial distance for initial overpressurization extends at least 13 R_c.

In summary, a simple radial flow model was used to show the constancy of the testing-effects models with hydrologic data at TW-7. The three-dimensional high-resolution model incorporating complex hydrostratigraphy produced similar results and furthermore supported the notion that multiple

Table G-6
Testing-Effects Parameters and Rock Properties Used for Three-Dimensional Model [a]

Rock Property	Testing Effects	Conceptual Model	Tompson, 2008
***dh* (m)**			
N/A	1	2	N/A
N/A	311	-- [b]	8,000
Radius (multiples of R_c)			
Overpressurized Zone	13.3		N/A
Crushed Zone	--	1.48	2.5
Compressed Zone	--	13.69	20
Porosity Decrease Factor			
Crushed Zone	0.91	0.85	N/A
Compressed Zone	0.99	1.00	N/A
Permeability Decrease Factor			
Crushed Zone	0.95	1.00	0.2 (OSBCU), 133(LTCU)
Compressed Zone	1.02	0.99	1.0
Porosity			
Matrix Flow Units	0.3	0.3	N/A
Fracture Flow Units	1.00E-03	1.00E-03	N/A
Specific Storage (1/m)			
Matrix Flow Units	–5.08	–5.01	–6.4
Fracture Flow Units	–6.45	–6.45	N/A
Permeability (log m²)			
Cavity	–11.90	–11.90	–12.2
LCA	–14.00	–14.00	–12.23
ATCU	–15.00	–15.00	–16.23
OSBCU	–12.38	–11.04	–13.23
LTCU	–13.48	–13.96	–16.05
TSA	–15.00	–15.00	N/A
TM-LVTA	–12.83	–12.69	–12.45
TM-WTA	–11.09	–11.40	–12.45
TM-UVTA	–12.00	–12.00	–12.45
TUBA	–12.52	–12.52	N/A
AA	–12.10	–12.10	–12.93

[a] Results are shown in Figure G-18.
[b] Calculated internally according to specified porosity decrease.

N/A = Not applicable

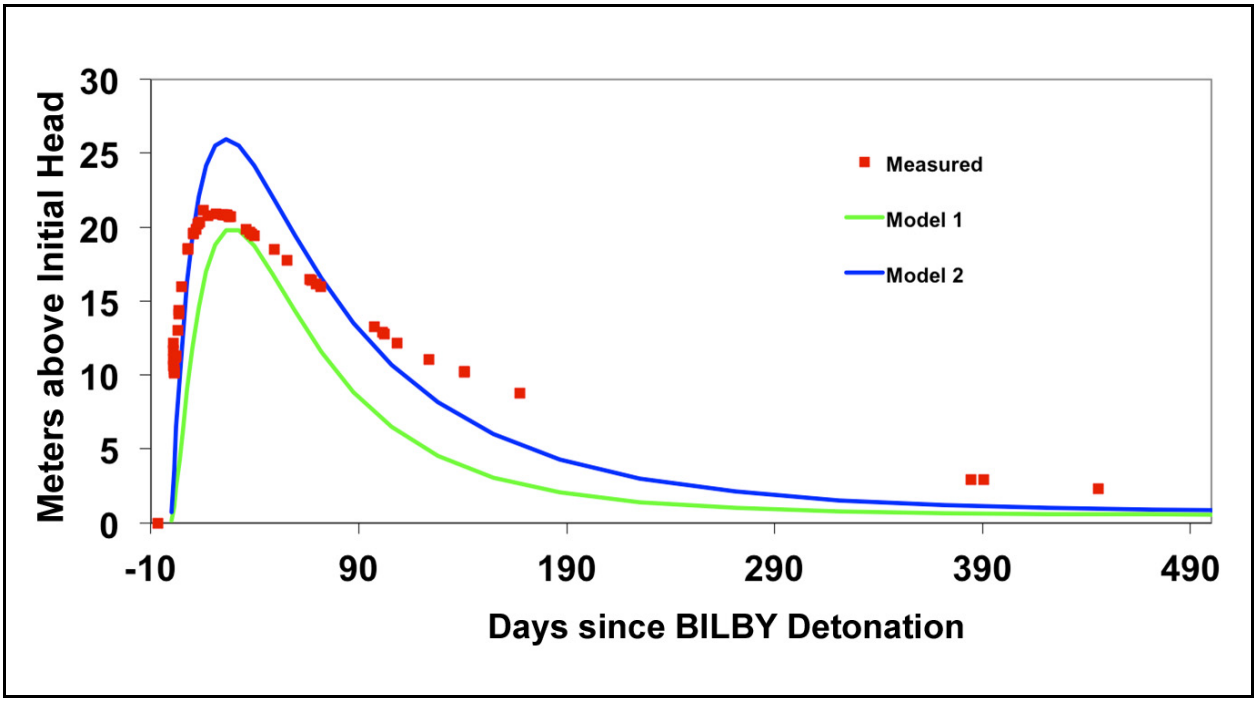

Figure G-18
Simulated and Measured Water Levels at TW-7
Immediately After the BILBY Detonation, Using Three-Dimensional Model

conceptual models are consistent with the data at TW-7. Therefore, multiple conceptual models (and gradations between them) are carried forward in the flow and transport uncertainty analyses.

G.2.0 HYDROLOGIC ANALYSIS OF CORE FROM YUCCA FLAT

The following tables (Tables G-7 and G-8) list data reported for laboratory analysis of core collected in Yucca Flat holes. Other types of data were measured on these cores as well. For a complete description of the data and laboratory methods, see Stephens (2008).

Table G-7
Total and Effective Porosity
(Page 1 of 3)

Well	Porosity (%)		HSU
	Total	Effective	
UE3e#2 (2,007.6–2,007.9 ft)	25.7	22.8	TCU
UE3e#2 (2,133.5–2,133.8 ft)	39.6	33.1	TCU
UE3e#2 (2,243.7–2,244 ft)	43.8	19.9	TCU
UE3e#2 (2,370.7–2,371.0 ft)	28.1	22.9	TCU
UE6d#2 (1,000.7–1,001.2 ft)	58.9	57.4	TCU
UE6d#2 (1,095.0–1,095.4 ft)	27.2	20.0	WTA
UE6d#2 (1,133.4–1,134 ft)	20.4	18.1	WTA
UE6d#2 (1,256.7–1,257.1 ft)	14.7	14.4	WTA
UE6d#2 (1,345.6–1,346.0 ft)	37.7	30.1	WTA
UE6d#2 (1,391.5–1,391.9 ft)	36.2	27.3	TCU
UE6d#2 (944.9–945.2 ft)	50.6	49.2	VTA
UE7ax (1,060.0–1,060.4 ft)	44.9	38.7	TCU
UE7ax (365.6–366.0 ft)	38.3	33.3	TCU
UE7ax (431.0–431.4 ft)	52.5	51.1	VTA
UE7ax (440.1–440.5 ft)	39.2	29.2	VTA
UE7ax (499.8–500.3 ft)	49.1	44.9	VTA
UE7ax (596.3–596.7 ft)	31.0	20.7	TCU
UE7ax (704.9–705.3 ft)	44.9	38.0	TCU
UE7ax (829.8–830.2 ft)	44.2	35.5	TCU
UE7ax (960.1–960.5 ft)	38.9	30.3	TCU
UE7ax (998.0–998.5 ft)	41.5	35.0	TCU
UE7az (1,137.7–1,138.1 ft)	41.9	16.4	TCU
UE7az (1,266.3–1,266.7 ft)	47.9	39.9	TCU
UE7az (1,415.1–1,415.5 ft)	41.4	30.0	TCU

Table G-7
Total and Effective Porosity
(Page 2 of 3)

Well	Porosity (%)		HSU
	Total	Effective	
UE7az (1,503.8–1,504.2 ft)	40.4	17.8	TCU
UE7az (1,519.6–1,520.0 ft)	46.4	21.9	TCU
UE7az (1,540.4–1,540.9 ft)	42.3	37.7	TCU
UE7az (1,647.4–1,647.8 ft)	44.2	33.3	TCU
UE7az (1,729.1–1,729.5 ft)	30.9	24.6	TCU
UE7az (1,766.0–1,766.4 ft)	38.1	14.0	TCU
UE7az (1,841.1–1,841.5 ft)	34.7	28.1	TCU
UE7az (1,939.4–1,939.8 ft)	27.5	20.1	TCU
UE7az (2,073.6–2,074.0 ft)	32.5	28.8	TCU
UE7az (2,176.8–2,177.2 ft)	21.6	16.2	TCU
UE7az (2,275.4–2,275.8 ft)	10.2	0.4	TCU
UE7az (1,807.3–1,807.7 ft)	25.7	19.4	TCU
UE7bc (1,683.4–1,683.8 ft)	37.7	31.5	TCU
UE7bc (1,728.1–1,728.5 ft)	43.4	38.4	TCU
UE7bc (2,144.5–2,144.8 ft)	29.8	27.5	TCU
UE7bc (2,286.4–2,286.7 ft)	49.4	43.5	TCU
UE7bc (2,407.8–2,408.2 ft)	31.6	21.3	TCU
UE7bc (2,433.2–2,433.7 ft)	29.9	24.7	TCU
UE7bc (2,493.2–2,493.6 ft)	34.3	15.9	TCU
UE7bc (2,582.3–2,582.6 ft)	35.1	21.7	TCU
UE7bc (2,644.9–2,645.2 ft)	20.0	5.1	TCU
UE7f (1,278.8–1,279.1 ft)	42.3	20.3	TCU
UE7f (1,492.9–1,493.2 ft)	40.0	13.2	TCU
UE7f (1,578.3–1,578.7 ft)	26.9	5.2	TCU
UE7f (1,676.5–1,676.9 ft)	45.3	40.2	TCU
UE7f (1,803.0–1,803.4 ft)	33.3	29.3	TCU
UE7f (1,946.4–1,946.8 ft)	40.4	19.2	TCU
UE7f (1,950.5–1,951.0 ft)	38.1	33.8	TCU
UE7f (2,025.6–2,026.0 ft)	33.6	20.2	TCU
UE7f (2,117.3–2,117.7 ft)	46.8	40.3	TCU
UE7f (2,352.7–2,353.0 ft)	40.8	33.7	TCU
UE7f (2,406.0–2,406.4 ft)	31.3	25.5	TCU

Table G-7
Total and Effective Porosity
(Page 3 of 3)

Well	Porosity (%)		HSU
	Total	Effective	
UE7f (2,481.0–2,481.4 ft)	26.9	23.0	TCU
UE7f (2,566.6–2,567.0 ft)	36.2	20.3	TCU
UE7f (2,632.2–2,632.6 ft)	25.3	8.0	TCU
UE7f (806.9–807.4 ft)	50.2	49.0	VTA
UE7f (843.1–843.6 ft)	42.3	40.7	WTA
UE7f (873.5–873.9 ft)	5.0	4.7	WTA

Table G-8
Saturated Hydraulic Conductivity
(Page 1 of 3)

Sample Number	K_{sat} (cm/s)
UE3e#2 (2,007.6–2,007.9 ft)	1.0E-04
UE3e#2 (2,133.5–2,133.8 ft)	3.2E-09
UE3e#2 (2,243.7–2,244 ft)	8.9E-04
UE3e#2 (2,370.7–2,371.0 ft)	1.2E-08
UE6d#2 (944.9–945.2 ft)	6.8E-05
UE6d#2 (1,000.7–1,001.2 ft)	2.4E-04
UE6d#2 (1,095.0–1,095.4 ft)	7.3E-09
UE6d#2 (1,133.4–1,134 ft)	2.5E-04
UE6d#2 (1,256.7–1,257.1 ft)	2.0E-07
UE6d#2 (1,345.6–1,346.0 ft)	7.2E-08
UE6d#2 (1,391.5–1,391.9 ft)	4.2E-05
UE7ax (365.6–366.0 ft)	6.4E-03
UE7ax (431.0–431.4 ft)	1.4E-04
UE7ax (440.1–440.5 ft)	2.5E-04
UE7ax (499.8–500.3 ft)	2.6E-03
UE7ax (596.3–596.7 ft)	9.5E-07
UE7ax (704.9–705.3 ft)	1.1E-05
UE7ax (829.8–830.2 ft)	2.6E-04

Table G-8
Saturated Hydraulic Conductivity
(Page 2 of 3)

Sample Number	K_{sat} (cm/s)
UE7ax (960.1–960.5 ft)	3.2E-09
UE7ax (998.0–998.5 ft)	1.3E-08
UE7ax (1,060.0–1,060.4 ft)	3.7E-09
UE7az (1,137.7–1,138.1 ft)	1.1E-03
UE7az (1,266.3–1,266.7 ft)	2.4E-04
UE7az (1,415.1–1,415.5 ft)	8.2E-05
UE7az (1,503.8–1,504.2 ft)	1.4E-03
UE7az (1,519.6–1,520.0 ft)	1.3E-03
UE7az (1,540.4–1,540.9 ft)	3.3E-07
UE7az (1,647.4–1,647.8 ft)	1.9E-05
UE7az (1,729.1–1,729.5 ft)	8.8E-09
UE7az (1,766.0–1,766.4 ft)	7.6E-04
UE7az (1,807.3–1,807.7 ft)	1.8E-08
UE7az (1,841.1–1,841.5 ft)	3.7E-05
UE7az (1,939.4–1,939.8 ft)	6.0E-05
UE7az (2,073.6–2,074.0 ft)	7.0E-05
UE7az (2,176.8–2,177.2 ft)	9.9E-08
UE7az (2,275.4–2,275.8 ft)	3.4E-07
UE7bc (1,683.4–1,683.8 ft)	1.8E-07
UE7bc (1,728.1–1,728.5 ft)	2.2E-07
UE7bc (2,144.5–2,144.8 ft)	1.7E-06
UE7bc (2,286.4–2,286.7 ft)	4.6E-08
UE7bc (2,407.8–2,408.2 ft)	6.4E-08
UE7bc (2,433.2–2,433.7 ft)	3.7E-08
UE7bc (2,493.2–2,493.6 ft)	4.2E-03
UE7bc (2,582.3–2,582.6 ft)	2.4E-05
UE7bc (2,644.9–2,645.2 ft)	6.2E-06
UE7f (806.9–807.4 ft)	5.3E-05
UE7f (843.1–843.6 ft)	2.8E-04

Table G-8
Saturated Hydraulic Conductivity
(Page 3 of 3)

Sample Number	K_{sat} (cm/s)
UE7f (873.5–873.9 ft)	1.7E-08
UE7f (1,278.8–1,279.1 ft)	5.0E-03
UE7f (1,492.9–1,493.2 ft)	8.7E-04
UE7f (1,578.3–1,578.7 ft)	4.0E-04
UE7f (1,676.5–1,676.9 ft)	4.2E-07
UE7f (1,803.0–1,803.4 ft)	6.5E-08
UE7f (1,946.4–1,946.8 ft)	8.6E-04
UE7f (1,950.5–1,951.0 ft)	4.0E-08
UE7f (2,025.6–2,026.0 ft)	3.3E-03
UE7f (2,117.3–2,117.7 ft)	1.2E-04
UE7f (2,352.7–2,353.0 ft)	6.9E-05
UE7f (2,406.0–2,406.4 ft)	7.0E-06
UE7f (2,481.0–2,481.4 ft)	1.2E-07
UE7f (2,566.6–2,567.0 ft)	8.8E-04
UE7f (2,632.2–2,632.6 ft)	5.1E-06

G.3.0 REFERENCES

App, F.N., and W.M. Brunish. 1991. *Stress Wave Calculations of Four Selected Underground Nuclear Tests: MERLIN, HEARTS, PRESIDIO and MISTY ECHO*, EES-NTC-91-03. Los Alamos, NM: Los Alamos National Laboratory.

Carlson, R.H., and W.A. Roberts. 1963. *Project SEDAN, Mass Distribution and Throwout Studies*, PNE-217F. Seattle, WA: Boeing Company.

Davis, S.N. 1971. "Discussion of Paper by Walter E. Reed, 'Transport of Water away from a Buried Heat Source with Special Reference to Hydrologic Phenomena Observed at Aardvark Nuclear Detonation.'" *Journal of Geophysical Research* 76 (2): 630–632. doi:10.1029/JB076i002p00630.

Garber, M.S., 1963. Large Rise and Following Decline of Water Level in Well 7, Area 3, Nevada Test Site—An Effect from the Aardvark Underground Nuclear Explosion, Technical Letter Yucca-48. Denver, CO: U.S. Geological Survey.

Halford, K.J., R.J. Laczniak, and D.L. Galloway. 2005. *Hydraulic Characterization of Overpressured Tuffs in Central Yucca Flat, Nevada Test Site, Nye County, Nevada*, Scientific Investigations Report 2005-5211. Carson City, NV: U.S. Geological Survey.

Knox, J.B., D.E. Rawson, and J.A. Korver. 1965. "Analysis of a Groundwater Anomaly Created by an Underground Nuclear Explosion." *Journal of Geophysical Research* 70 (4): 823–835. doi:10.1029/JZ070i004p00823.

Laczniak, R.J., J.C. Cole, D.A. Sawyer, and D.A. Trudeau. 1996. *Summary of Hydrogeologic Controls on Ground-Water Flow at the Nevada Test Site, Nye County, Nevada*, Water-Resources Investigations Report 96-4109. Carson City, NV: U.S. Geological Survey.

Reed, W.E. 1970. "Transport of Water Away from a Buried Heat Source with Special Reference to Hydrologic Phenomena Observed at Aardvark Nuclear Detonation." *Journal of Geophysical Research* 75 (2): 415–430. doi:10.1029/JB075i002p00415.

Stephens, D.B. 2008. *Moisture Retention Testing for TCU, VTA, and WTA Samples*. Laboratory report prepared for Los Alamos National Laboratory. Los Alamos, NM.

Tompson, A.F.B., ed. 2008. *Evaluation of Hydrologic Source Term Processes for Underground Nuclear Tests in Yucca Flat, Nevada Test Site: Saturated Tests*, LLNL-TR-403429. Livermore, CA: Lawrence Livermore National Laboratory.

Wolfsberg, A., J. Boryta, E. Keating, P. Stauffer, C. Gable, and S. Kelkar. 2006. Written communication regarding *Analysis and Evaluation of Elevated Groundwater Heads and Their Impact on Flow and Solute Transport in the Tuff Pile: Areas 3, 4, and 7 of the Nevada Test Site, Nye County, Nevada*. Los Alamos, NM: Los Alamos National Laboratory.

Appendix H

Thermohydrologic Flow Model and Analyses

H.1.0 INTRODUCTION

The water table at Yucca Flat is approximately 450 m bls. There is uncertainty in the estimates of recharge to the water table and lateral interbasin underflow entering the Yucca Flat/Climax Mine CAU. Estimates of groundwater flowing through Yucca Flat vary from 13.7 kg/s (Winograd and Thordarson, 1975) to 1,024 kg/s (Pohlmann et al., 2007). Subsurface temperatures can be used to estimate groundwater fluxes (Bravo et al., 2002; Anderson, 2005). This appendix uses observed subsurface temperature information to provide an alternative estimate of groundwater fluxes in Yucca Flat, accounting for the perturbation of the thermal regime due to groundwater flow in the basin. In addition, this appendix proposes that the thermal information in the shallow unsaturated zone can be used to estimate groundwater flow deep in the saturated zone.

Temperature data within the saturated zone were collected at various locations in Yucca Flat by Reiner (2007) (Figure H-1). Based on available data, a temperature distribution map at the water table was constructed with the Kriging interpolation technique and is presented in Figure H-2. The salient features of the thermal map include the following:

- A cold trough coinciding with the three major faults—Carpetbag, Topgallant, and Yucca faults—exists in the center of the basin.
- Subsurface temperatures in the east are relatively high (Thompson, 1991).
- No major temperature anomalies appear in the west and north, and therefore, heat transfer in these regions can, to a large degree, be explained by the process of heat conduction.

Based on the above observations, this appendix proposes the following geothermal conceptualization:

Water from precipitation in the saturated volcanic aquifers migrates laterally toward the major faults in the center of the basin. On reaching the faults, groundwater rapidly infiltrates into the LCA, which captures and eventually transports deep-seated heat out of the Yucca Flat basin. This results in reduced heat flux and temperatures near the surface in the vicinity of the major faults (Figure H-3).

- In the west and north, the observed temperatures and geothermal gradient can be accounted for, to a large degree, by heat conduction with very low vertical groundwater flow rates to perturb the ambient geothermal gradient.

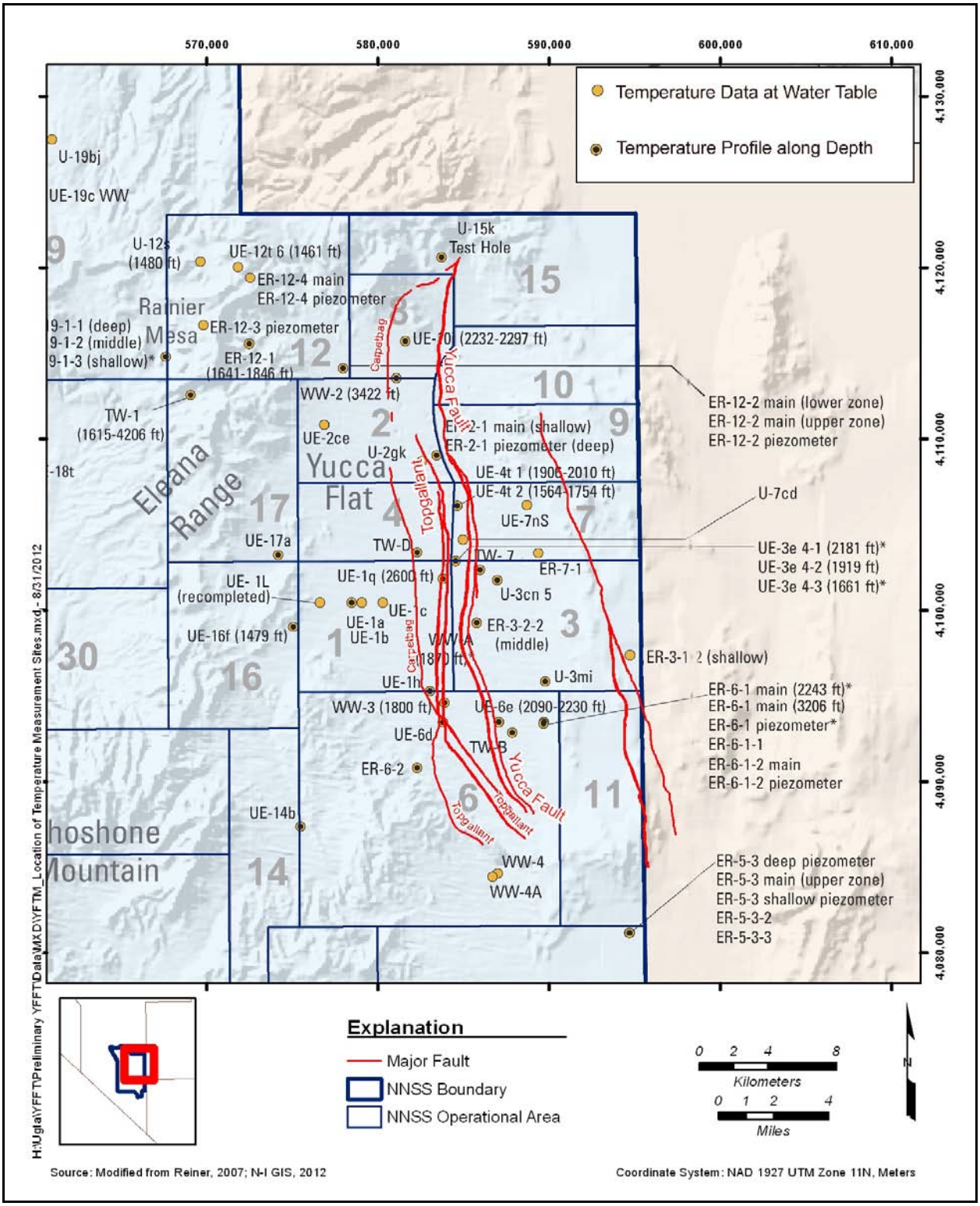

Figure H-1
Temperature Measurement Sites in Reiner (2007)

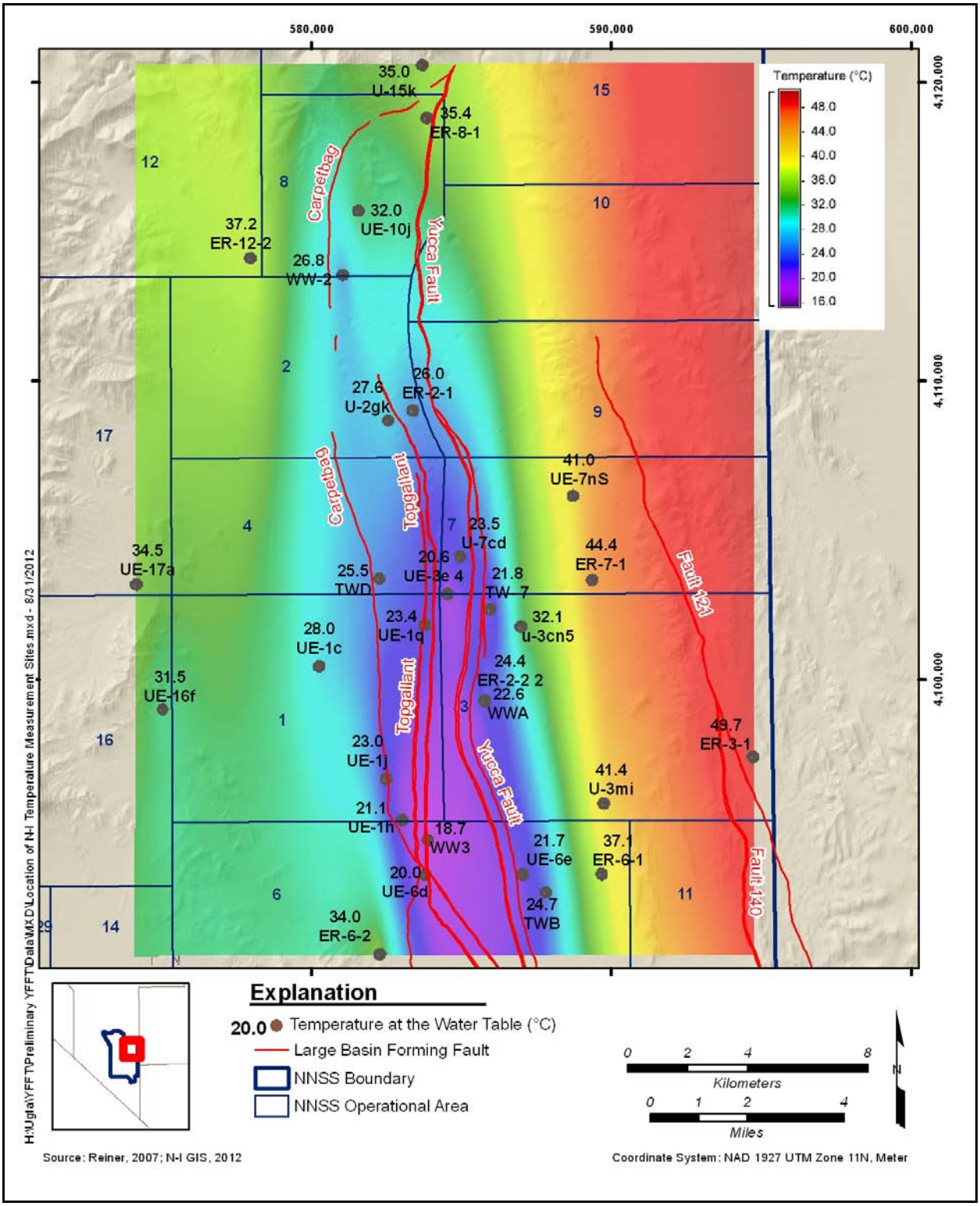

Figure H-2
Temperature Distribution at the Water Table in Yucca Flat

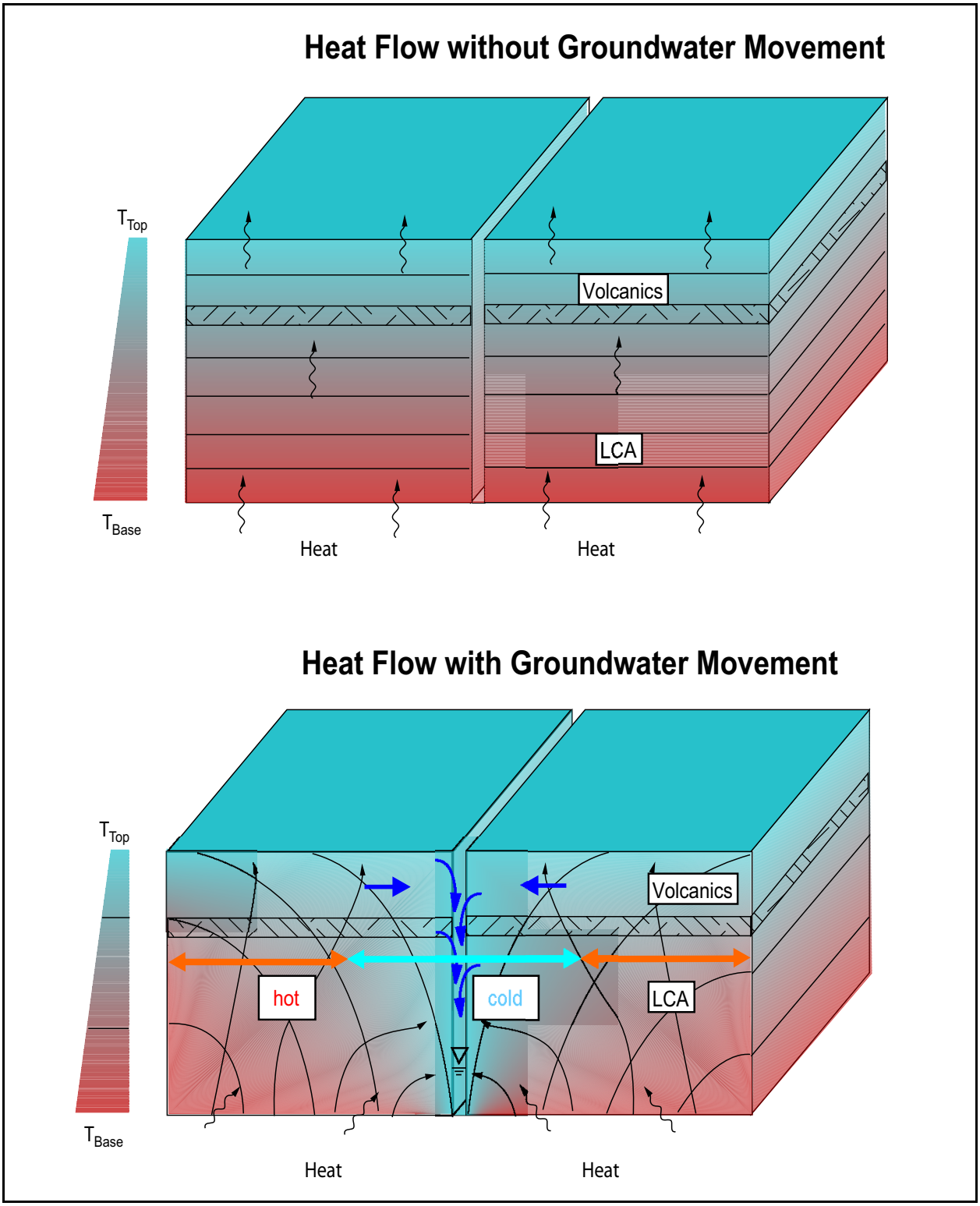

Figure H-3
Conceptual Model of Geothermal Transport in Central Yucca Flat

Note: Blue arrows indicate water flow and black arrows indicate heat flow.

Following initial review of the thermal data in the saturated zone and recognizing the potential for subsurface temperatures to constrain groundwater model fluxes at the NNSS, it was decided to collect additional thermal data at Yucca Flat. This initiative is referred to in this appendix as the Navarro Nevada Environmental Services (NNES) study, and its results are documented in NNES (2010). The goal of the NNES study was to achieve the following:

- Augment existing subsurface temperature data in Yucca Flat.
- Determine whether thermal data in the shallow unsaturated zone have a temperature distribution similar to that observed in the deeper saturated zone.
- Ensure data quality by performing an extensive calibration of the instrumentation at each well site. Additionally, establish sampling procedures that ensure steady-state temperatures at each well site.

The locations of the NNES study well sites are presented in Figure H-4, along with a typical temperature log at Well ER-8-1, an observation well located in Area 8 of the NNSS. Note that the temperature profiles extend in the unsaturated zone and show a gradient change at the intersection of the LCA and the overlying volcanic unit. There is a slight kink at the water table, but it does not significantly alter the geothermal gradient.

As indicated by Gillespie (2005), the heat flux at the intersection of two geologic units should be the same in both units for conduction-dominated systems. That is, the ratio of the thermal gradient in adjacent geologic units should be proportional to the ratio of the thermal conductivities of the units. From Figure H-4, the ratio of the carbonate-to-volcanic thermal gradient at Well ER-8-1 is approximately 2.4. The thermal conductivity of carbonate rock can be assumed to vary between 4 and 5.25 watts per meter kelvin (W/(m·K)) (Robertson, 1979; Clauser and Huenges, 1995; Gillespie, 2005). The thermal conductivity of volcanic rocks varies between 1.5 and 2.0 W/(m·K) (Gillespie, 2005). Assuming an average thermal conductivity of 4.5 W/(m·K) for carbonate rock and 1.75 W/(m·K) for volcanic rock results in a carbonate-to-volcanic ratio of 2.6, which, as expected, is similar to the ratio of the geothermal gradient of 2.4 at the intersection of the two geologic units at Well ER-8-1. At the junction of the LCA and granite rocks, the variation in the geothermal gradient is much less pronounced, indicating that thermal conductivity of granite is not significantly different from that of carbonate rock.

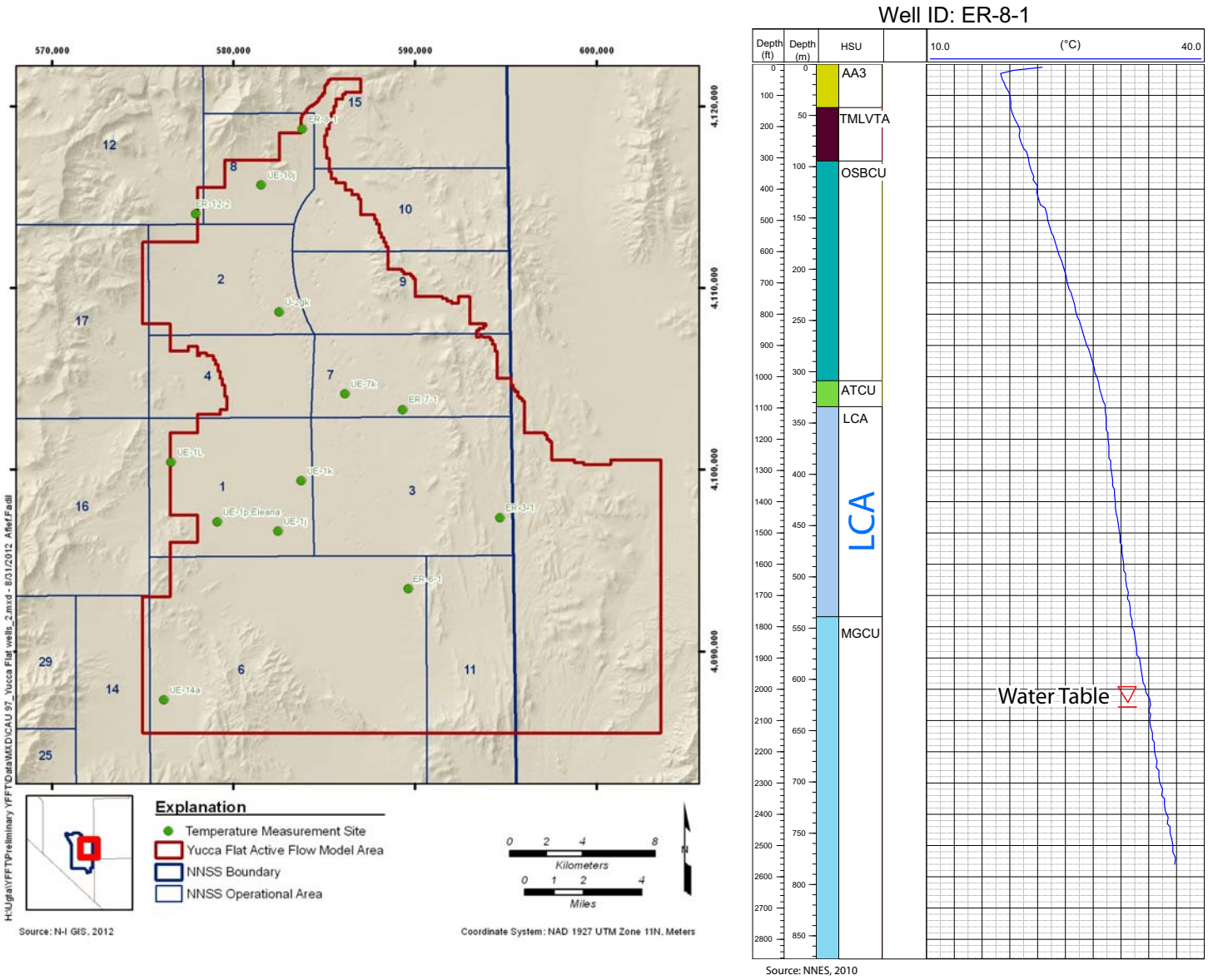

Figure H-4
Locations of NNES Temperature Measurement Sites and Temperature Log at Observation Well ER-8-1

Based on an extensive laboratory testing of granite samples, Cho et al. (2009) estimated an average thermal conductivity of 3.62 W/(m·K). This implies that an approximate ratio of thermal conductivities in carbonate and granitic rocks is about 1.25. From the temperature log in Figure H-4, it can be deduced that the ratio of geothermal gradients to the carbonate and granite rocks is approximately 1.4. This ratio also is remarkably close to the estimated thermal conductivity ratio of 1.25 in the two materials.

Combining the data provided in NNES (2010) with the data provided in Reiner (2007) enabled construction of temperature profiles at various elevations above and below the water table (Figure 5-17). This figure was developed by using the available temperature data at the discrete depths (for example 17 data points at 450 m (1,500 ft) bls) and kriging the temperatures at these discrete locations using a north-south anisotropy. As expected, the same thermal distribution observed at the water table (approximately 450 m/1,500 ft bls) is present in both the shallow unsaturated zone and the saturated zone deep below the water table. This information has the potential for constraining boundary fluxes in the flow model, and also suggests the feasibility of acquiring temperature data more economically from shallow (unsaturated zone) monitoring wells than from deep (saturated zone) monitoring wells.

H.2.0 SIMPLIFIED GEOTHERMAL MODELS

The extent and magnitude of radionuclide migration within the LCA in Yucca Flat is influenced by vertical recharge along the margins and central portion of the Yucca Flat basin and lateral groundwater inflow from the northern and eastern boundaries of the basin. To investigate the potential magnitude of the volumetric flux associated with vertical recharge and lateral boundary inflow from in northern Yucca Flat, two separate thermohydrologic models were developed to evaluate a range of volumetric influx, thermal conductivity, and basal heat flux. These models are referred to as the central box and northern thermal models in this appendix. The FEHM computer code (Zyvoloski et al., 1999) was used for model simulations.

The primary goal of the central box model is to determine whether the coolness observed in the LCA in the center of the basin is a consequence of focused vertical recharge along the major faults located in the center of the basin. As explained below, this hypothesis was tested by simulating flow in the alluvial/volcanic aquifer system toward the faults that extends into the underlying LCA.

The northern thermal model was developed primarily to test alternative hypotheses of lateral inflow from the north to the LCA in Yucca Flat. A secondary objective was to estimate the rate of inflow into Yucca Flat along the northern Yucca Flat boundary.

To some extent, both thermal models represent a simplification of the complex hydrogeology in the area. It should be noted that the primary goal of the models was to simulate the geothermal field to test a few key hypotheses and was not an attempt to calibrate the model to the hydraulic head data. Because the boundary fluxes were specified explicitly by using a range of possible boundary fluxes, and the contrast between the confining units and the aquifers is very large, the simulation results are not significantly influenced by the specific magnitude of hydrogeologic flow parameters. Additionally, because both these models are steady-state models, the thermal simulation results are not affected by the material porosity.

H.2.1 Central Box Model

Calibration of the saturated Yucca Flat alluvial/volcanic aquifer system model discussed in Section 4.0 required recharge from the alluvial/volcanic aquifer system to the underlying LCA to occur only through faults with the largest quantity of recharge occurring via the Yucca fault. Analysis of ^{14}C data in the LCA presented in Figure H-5 suggests that groundwater in the center of the Yucca Flat basin, where the three major faults are located, is the youngest. The temperature distribution at the water table (Figure H-2) also suggests focused recharge to the LCA in the center of the basin coinciding with the major faults. Therefore, the geochemical and temperature data, along with the hydrologic modeling results, indicate a rapid exchange of groundwater between the LCA and the overlying alluvial/volcanic aquifer system in the center of the basin.

The objective of the central box model is to reproduce the thermal trough observed in the center of the basin based on data collected from 15 wells in the area. Data from all of these wells indicate cooling in the center of the basin. It is unlikely that the extreme cooling observed in the center of the basin is a consequence of instrumentation errors or inappropriate data acquisition methodology. Therefore, the data quality was deemed sufficient for the objective of the central box model.

The hypothesis that the cold trough observed in the center of the basin occurs because of exchange of water through the major faults located in the area was tested by developing a hypothetical but representative simplified box model of central Yucca Flat consisting of a single large fault. As shown in Figure H-6aa, the model is 30 km long, 6.5 km wide, and 4.5 km deep, and consists of approximately 650 m of permeable alluvium and volcanics at the top that is underlain by a tuff confining unit that is approximately 550 m. A 2,300-m-thick LCA unit underlies the tuff confining unit. The LCA rests on a 1,500-m clastic confining unit that forms the basement rock at the NNSS. A 20-m-wide fault is located on the right side of the model. This box model approximates the geologic strata and structure in the center of the basin. The top 1,000 m of the model is discretized by 14 equal layers. The bottom 3,500 m is discretized by 18 equal layers. A finer discretization was applied to the top regions of the model because the thermal data in most wells are limited to shallow depths.

A uniform recharge rate was specified along the top surface of the model. A discharge flux was set equal to the cumulative recharge at the top and was uniformly distributed along the southern boundary of the fault. This is in conformity with the saturated alluvial/volcanic aquifer system model,

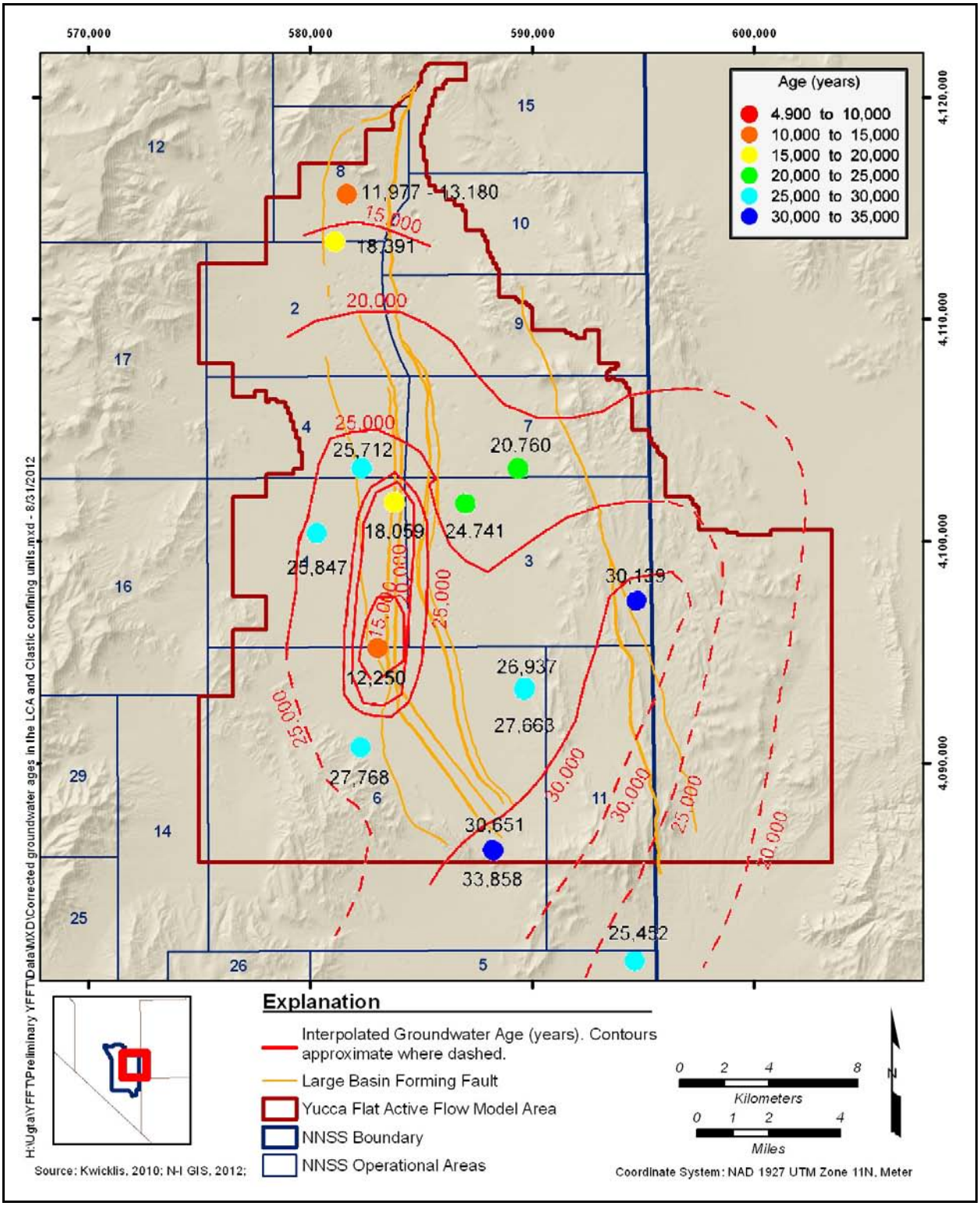

Figure H-5
Interpreted Groundwater Age in the LCA Using ^{14}C Data

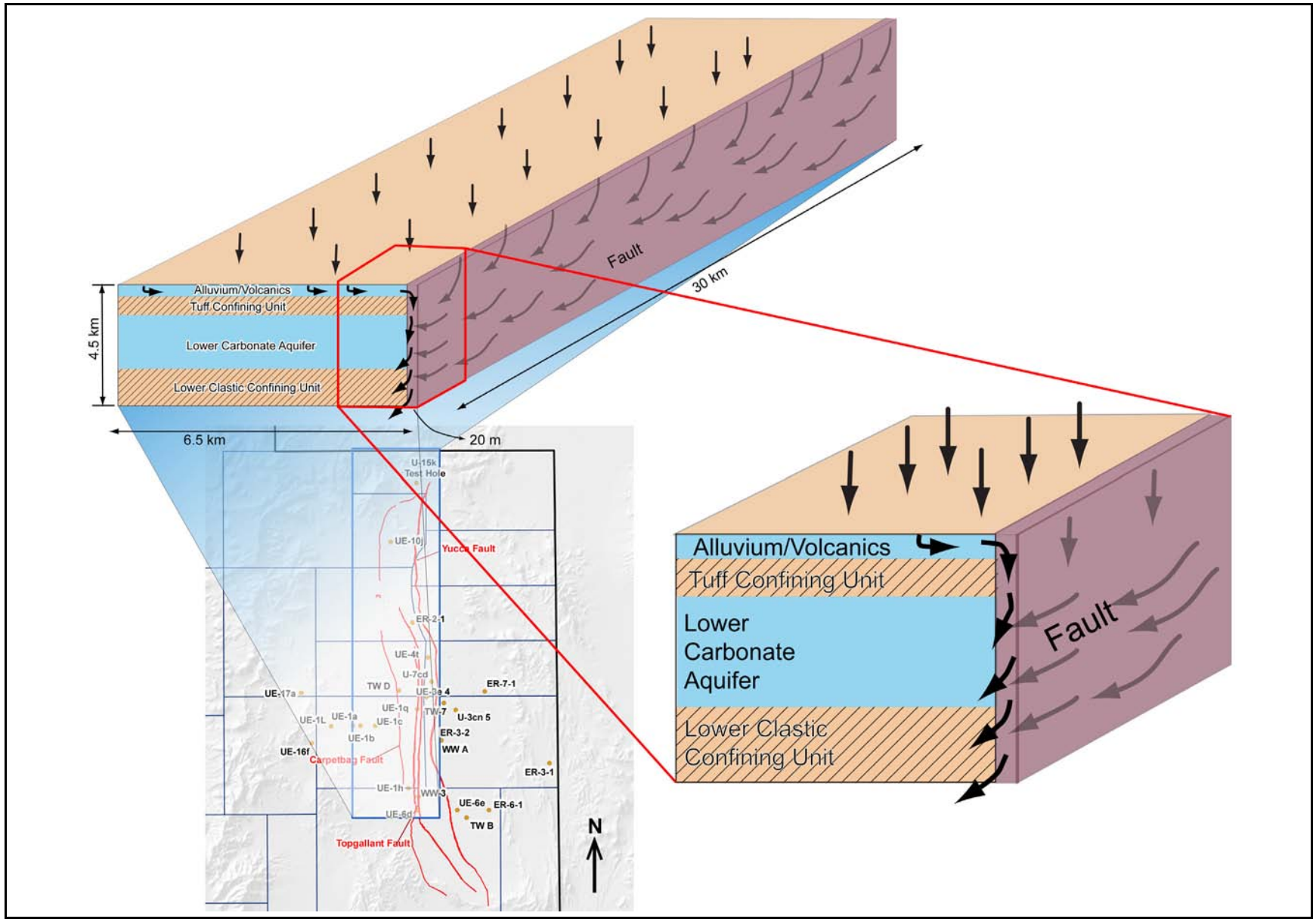

Figure H-6a
Schematic Representation of Central Box Model Showing Groundwater Pathways

in which recharge from the alluvial/volcanic aquifer system to the LCA occurs only via faults, and groundwater on reaching the LCA exits the southern boundary primarily through faults. Intrinsic conductivities in the LCA, alluvial aquifer, volcanic aquifer, tuff confining unit, and clastic confining unit were specified to be 1E-15, 1E-15, 5E-14, 1E-16, and 1E-16 m^2, respectively. The hydraulic conductivity in the fault was set to 1E-12 m^2. Because steady-state simulations are of interest, the solution is independent of the material porosity for both flow and thermal transport. Note that all the boundary specifications are of the Cauchy (i.e., flux) type. Thus, the thermal solution is influenced more by the contrast in hydraulic conductivity (which channelizes water to the fault) than by the magnitude of hydraulic conductivity in the individual HSUs. Recharge on reaching the volcanic aquifer moves laterally toward the fault in both the saturated alluvial/volcanic aquifer system model and the simplified central box model.

Subsurface temperatures at a depth on the order of five meters from the land surface remain approximately uniform throughout the year at the average surface temperature (Figure H-6bb). Therefore, the thermal boundary condition along the top of the box model was specified as the average surface temperature in the Yucca Flat basin. Based on data obtained from the DRI temperature gauge A3S in Yucca Flat (WRCC, 2009), the average surface temperature in the Yucca Flat valley was specified along the top model boundary and was estimated at 14.5 °C. A uniform heat flux of 65 mW/m^2 was specified at the base of the model. This value is a representative value of heat flux in the area (Sass et al., 1976). Sensitivity simulations involving variations of this basal heat flux are discussed below. The thermal conductivities of alluvium, volcanic rocks, the LCA, and the clastic confining unit were specified as 1.25, 1.25, 4.00, and 2.25 W/(m·K), respectively, based on the estimates provided by Robertson (1979), Clauser and Huenges (1995), Gillespie (2005), and SNJV (2006). As discussed below, the solution in the vicinity of the faults is not significantly sensitive to the specified value of thermal conductivity.

Because the recharge rate to the modeled groundwater flow system is unknown, a set of three simulations with total volumetric influx rates of 10, 20, and approximately 30 kg/s was performed. The volumetric influx rate of 30 kg/s corresponds to a recharge rate of 5 mm/yr. The volumetric influx rates of 10 and 20 kg/s correspond to recharge rates of 1.6 and 3.2 mm/yr, respectively. The simulated temperature distributions at the water table (i.e., 500 m bls) for the three cases are presented in Figure H-7. As expected, higher influx rates induce more cooling. A qualitative comparison of the simulated results with the observed geothermal distribution presented in

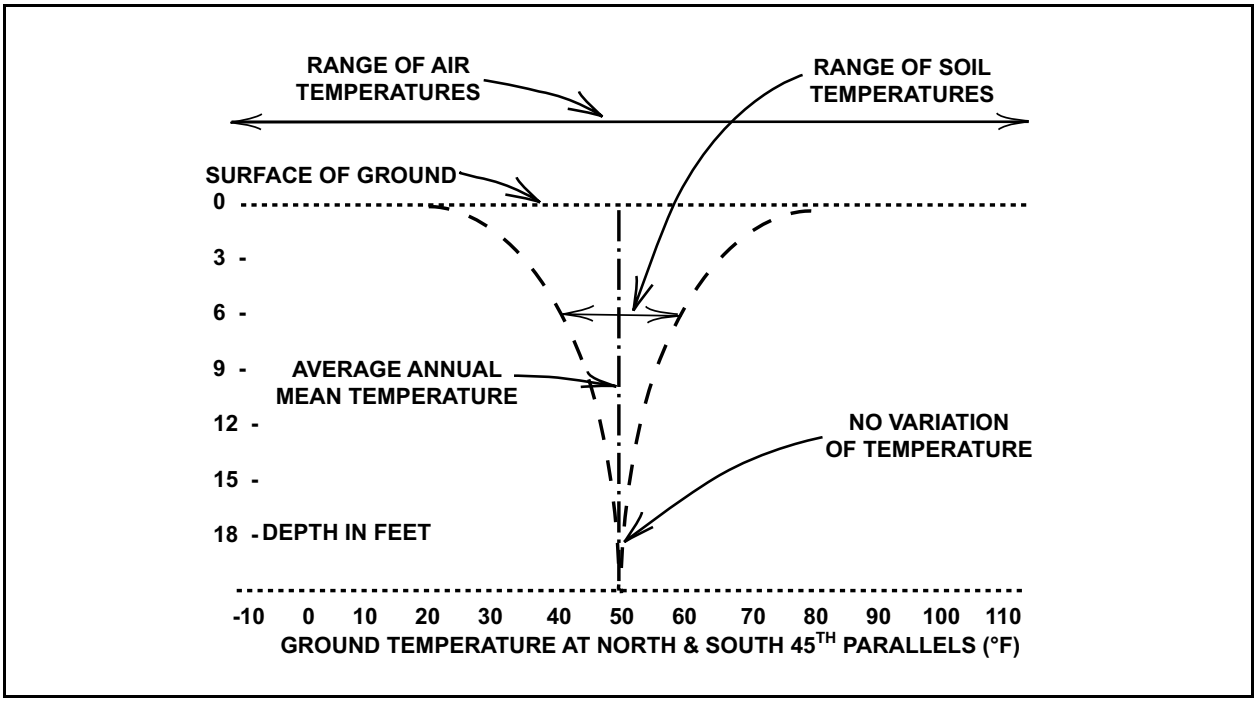

Figure H-6b
Near-Surface Temperature Variation as a Function of Depth
Source: Post, 2011

Figure H-2 suggests that the recharge at the low end of the specified range is unlikely. A higher influx rate of 30 kg/s provides a better match with the observed temperature distribution at the water table.

Temperature profiles at three (east–west) cross sections located 1, 3, and 10 km from the southern boundary of the box model are presented in Figure H-8. The figure clearly shows that the temperature distributions at all three cross sections are similar at various latitudes along the fault. At all three locations, the temperature increases from about 22 °C at the fault to 35 °C at the western boundary of the box model, where the geothermal gradient appears to be unaffected by groundwater flow. As can be inferred from Figure H-1, the observation wells in the center of the basin are within 1 km of the three major faults in Yucca Flat—the Carpetbag, Topgallant, and Yucca faults. Therefore, for purposes of comparison, the observed temperature at each well was compared to the simulated temperatures 500 m from the fault and 3 km from the southern boundary.

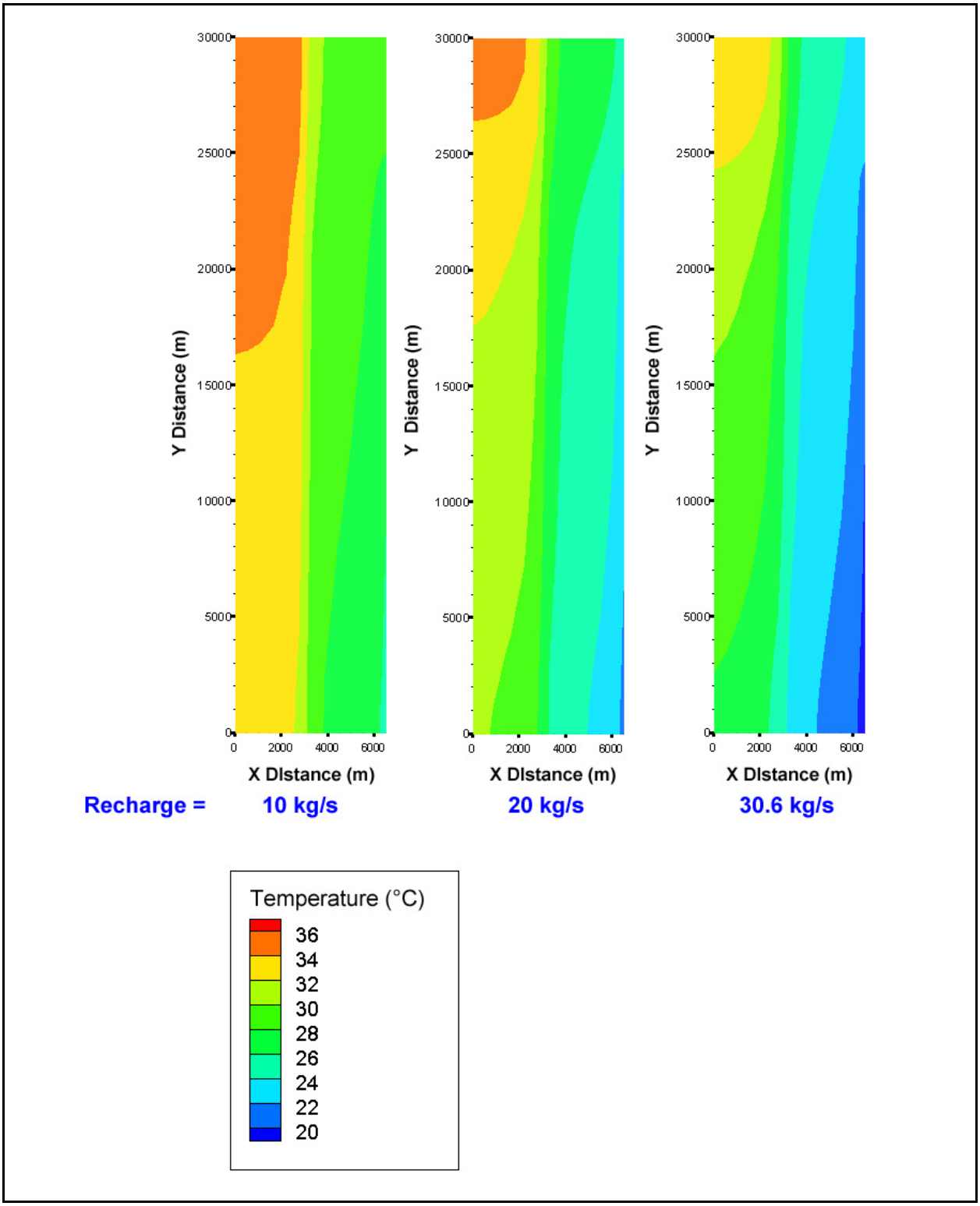

Figure H-7
Simulated Temperatures at 500 m bls with Basal Heat Flux of 55 mW/m² and Base-Case Thermal Conductivities

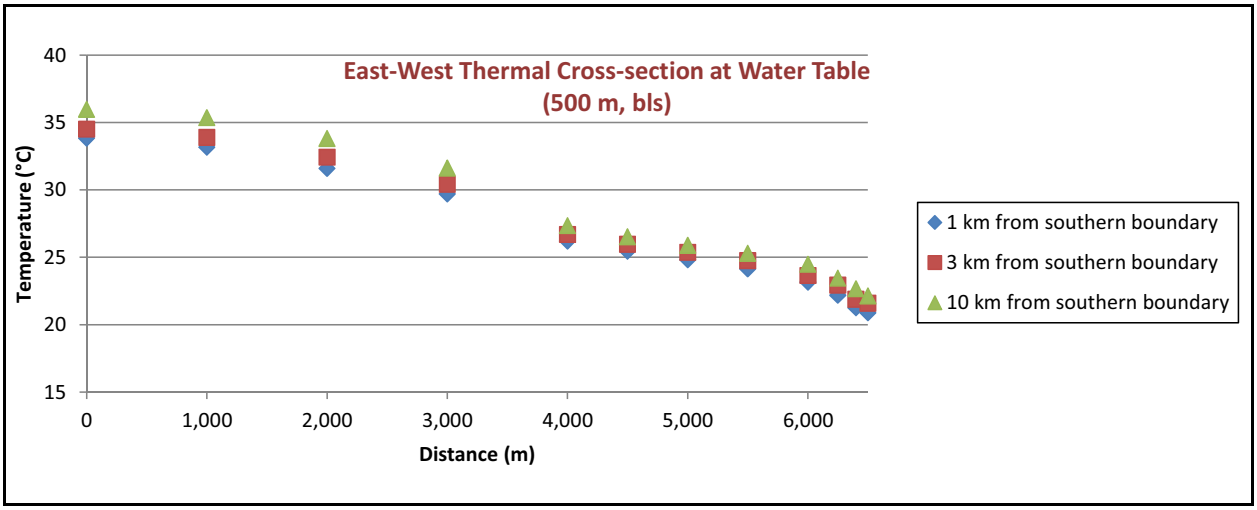

Figure H-8
Temperatures at the Water Table along Three East–West Cross Sections

The simulated and observed temperatures for model influx rates of 10.0, 20.0, and 30.6 kg/s are provided in Figure H-9. The observed temperature data were obtained from Reiner (2007). At most sites, a good match between observed and simulated temperatures is noted with an influx rate between 20.0 and 30.6 kg/s. The exceptions are Wells UE-6d and UE-1h, where the influx rates appear to be much larger because of potential influx along faults in the western part of the basin.

The primary parametric and boundary condition uncertainties are the thermal conductivities of the various HSUs and the heat flux along the base of the model. Therefore, two sets of sensitivity simulations were conducted to address potential uncertainties in these parameters.

In the first set of sensitivity simulations, the thermal conductivities of the LCA, volcanic rocks, and clastic confining unit were varied by 15 to 20 percent from their base-case values as indicated in Figure H-10 for Well ER-3-2. Well ER-3-2 can be viewed as a surrogate well for all the other observation wells in the center of the basin. Unlike hydraulic conductivity, which can vary over several orders of magnitude, the thermal conductivities of most geologic materials are fairly well known, and there is generally a small variability in this property at a site. For example, as can be deduced from Figure H-11, the variance of thermal conductivity in the volcanic material at the NNSS is less than 20 percent. Simulation results (with the influx rate of 30 kg/s) for the case presented in Figure H-10 indicate that varying the thermal conductivity from the base case has a minor impact on the simulation results.

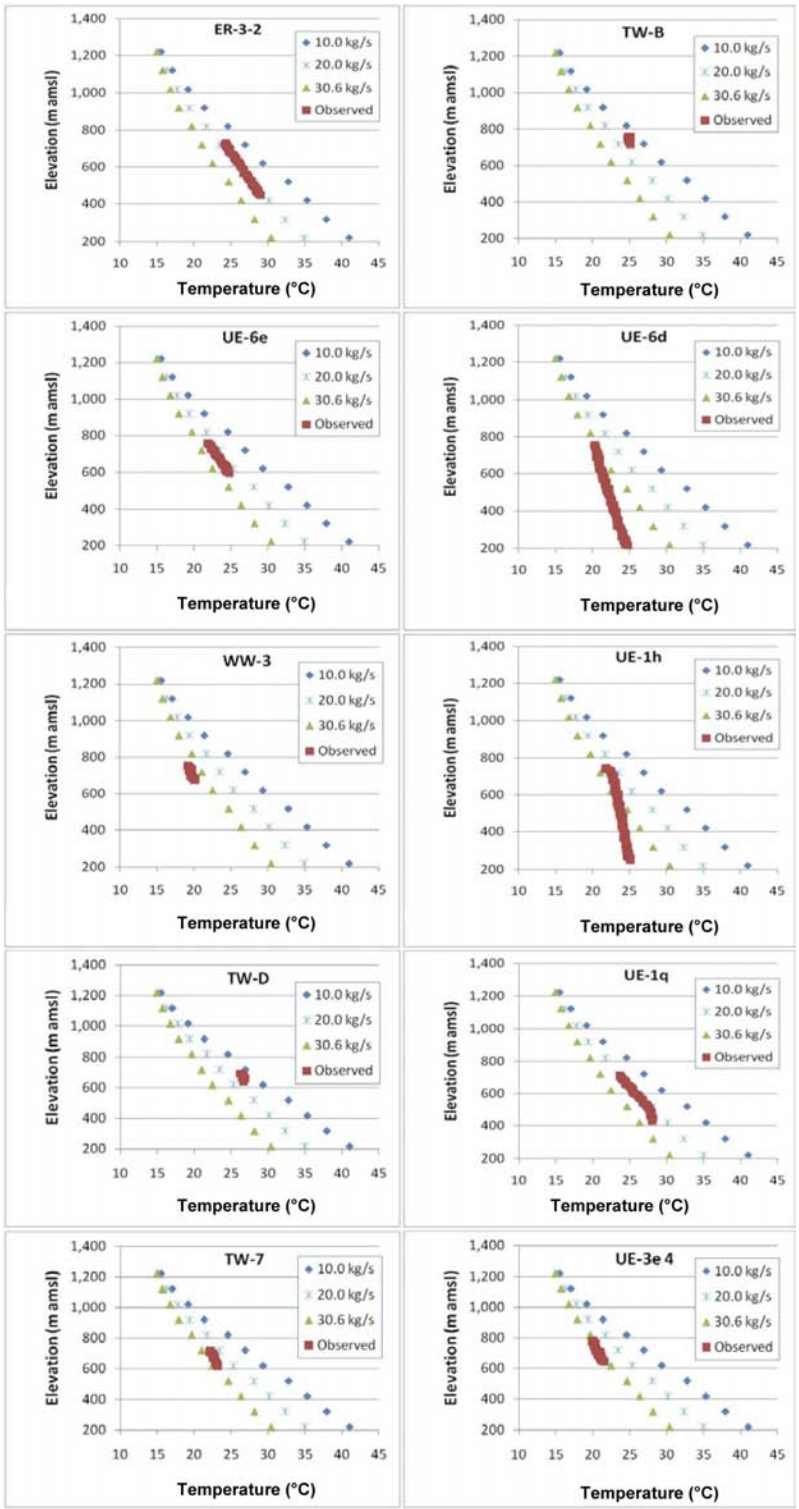

Figure H-9
Simulated and Observed Geothermal Gradients for the Central Box Model

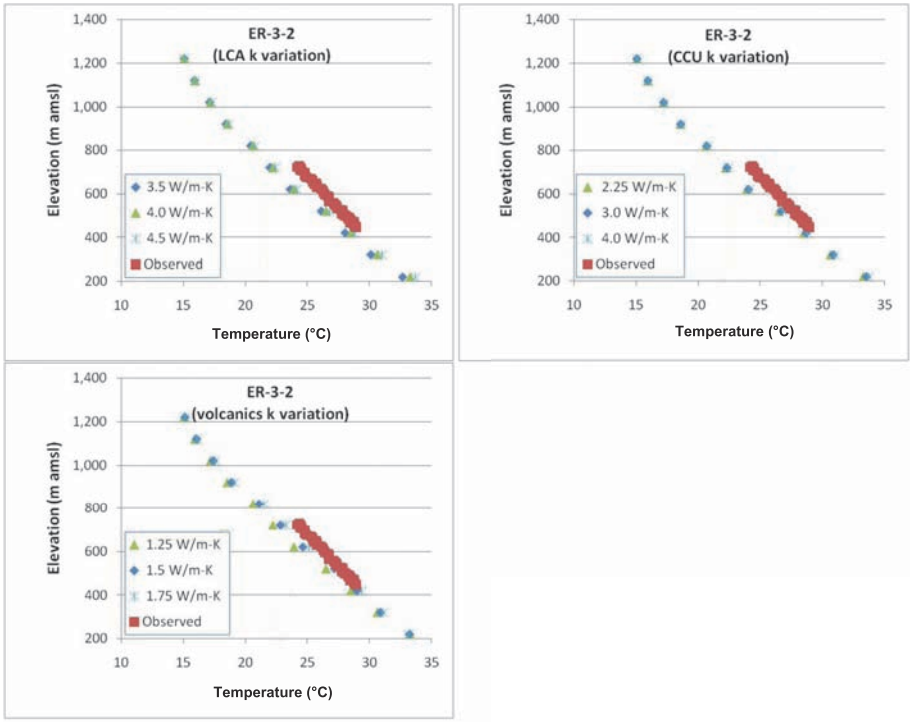

Figure H-10
Sensitivity Simulations Involving Variations in Modeled Thermal Conductivity

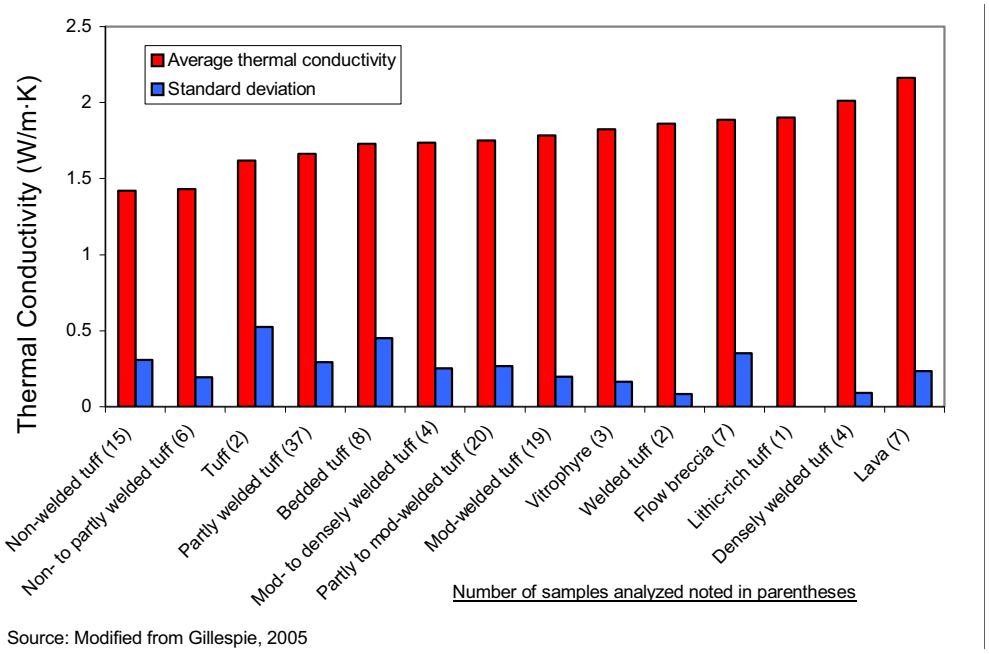

Figure H-11
Variation in Laboratory-Derived Values of Thermal Conductivity in Tuff Material at the NNSS

In the second set of sensitivity simulations, the heat flux along the base was varied between 55 and 75 mW/m^2 (assuming the influx rate of 30 kg/s) to account for uncertainties in this parameter (Figure H-12). This resulted in a variation of simulated temperature at the water table of approximately 2.5 °C between 55 and 75 mW/m^2.

The sensitivity results provide a useful measure of the impact of variations in key parameters on the simulated temperatures, and therefore, can be used to approximately bound the solution. For example, from Figure H-9, it can be estimated that an increase or decrease of 10 kg/s in the influx rate causes temperature variation at the water table of about 3.5 °C. Similarly, the basal heat flux sensitivity results shown in Figure H-12 indicate that a change in basal heat flux of 20 mW/m^2 results in a variation of about 2.5 °C at the water table. Therefore, if the basal heat flux were assumed to be higher by about 20 mW/m^2, an increase in the influx rate of about 7 to 8 kg/s would be required to reproduce the same simulated temperatures in the subsurface. The sensitivity results, therefore, suggest that the parametric uncertainties can be addressed within a stochastic framework and that the solution can be bounded within a relatively narrow range if a formal model calibration of flow and heat transport is attempted.

It should be noted that the influx rate in the central box model applies to roughly half of the Yucca Flat basin underlying the saturated alluvial/volcanic aquifer system model area because the central box model simulates flow in only one side of the center of the basin. Therefore, if the simulated influx rate of 30 kg/s is assumed to reasonably reproduce the observed temperatures, then the total influx to the LCA in Yucca Flat will be at twice the rate in the central box model, i.e., 60 kg/s. It is worth mentioning that influx from the top could potentially be occurring outside the basin valley along topographic highs in the east and west, moving laterally toward the center of the basin in the saturated alluvium and volcanics. During model calibration, it was determined that influx from the top could be infiltrating into the subsurface at a rate of up to 60 kg/s in these regions and eventually moving toward the center of the basin. Note that the unsaturated zone and saturated alluvial/volcanic aquifer system models also simulate a scenario in which recharge at a high rate of 5 mm/yr infiltrates into the subsurface in the center of the basin. Such a high recharge rate would also result in the low subsurface temperatures observed in the center of the basin.

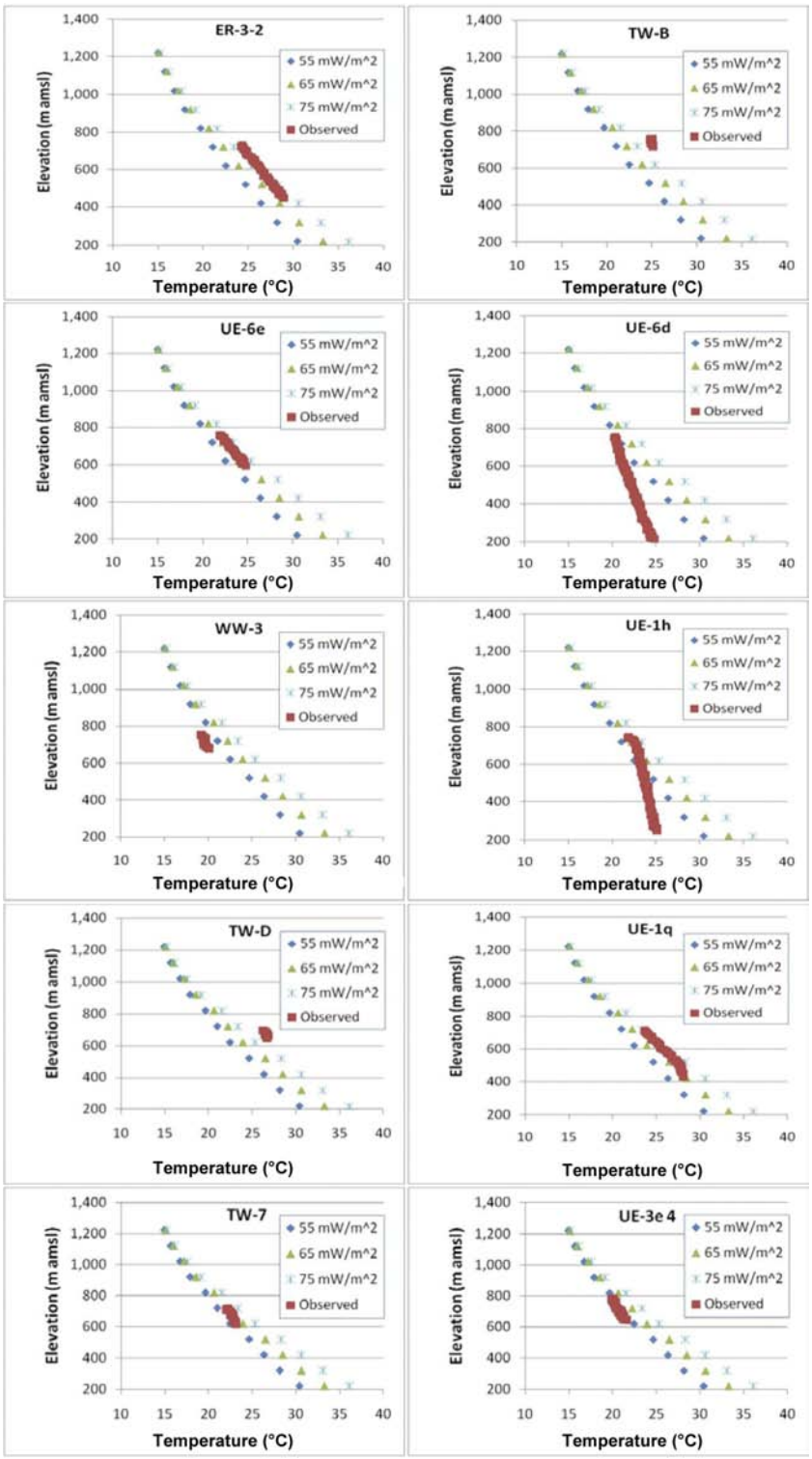

Figure H-12
Sensitivity Simulations Involving Variations in Modeled Base Heat Flux

H.2.2 Northern Thermal Model

The rate at which groundwater is entering the LCA from Climax Mine in northern Yucca Flat is uncertain. Recent modeling studies have suggested that the inflow rates could be as high as 1,024 kg/s (Pohlmann et al., 2007). Such an inflow rate, however, is inconsistent with other interpretations (e.g., Winograd and Thordarson, 1975) and exceeds the total estimated outflow from the Ash Meadows regional groundwater basin, of which the Yucca Flat basin is only a part. The northern thermal model, therefore, was developed to determine whether large northern fluxes in the regional models (Belcher et al., 2004; Pohlmann et al., 2007) entering Yucca Flat are compatible with geothermal observations and to obtain an estimate of groundwater influx through the northern Yucca Flat model boundary (Figure H-13a).

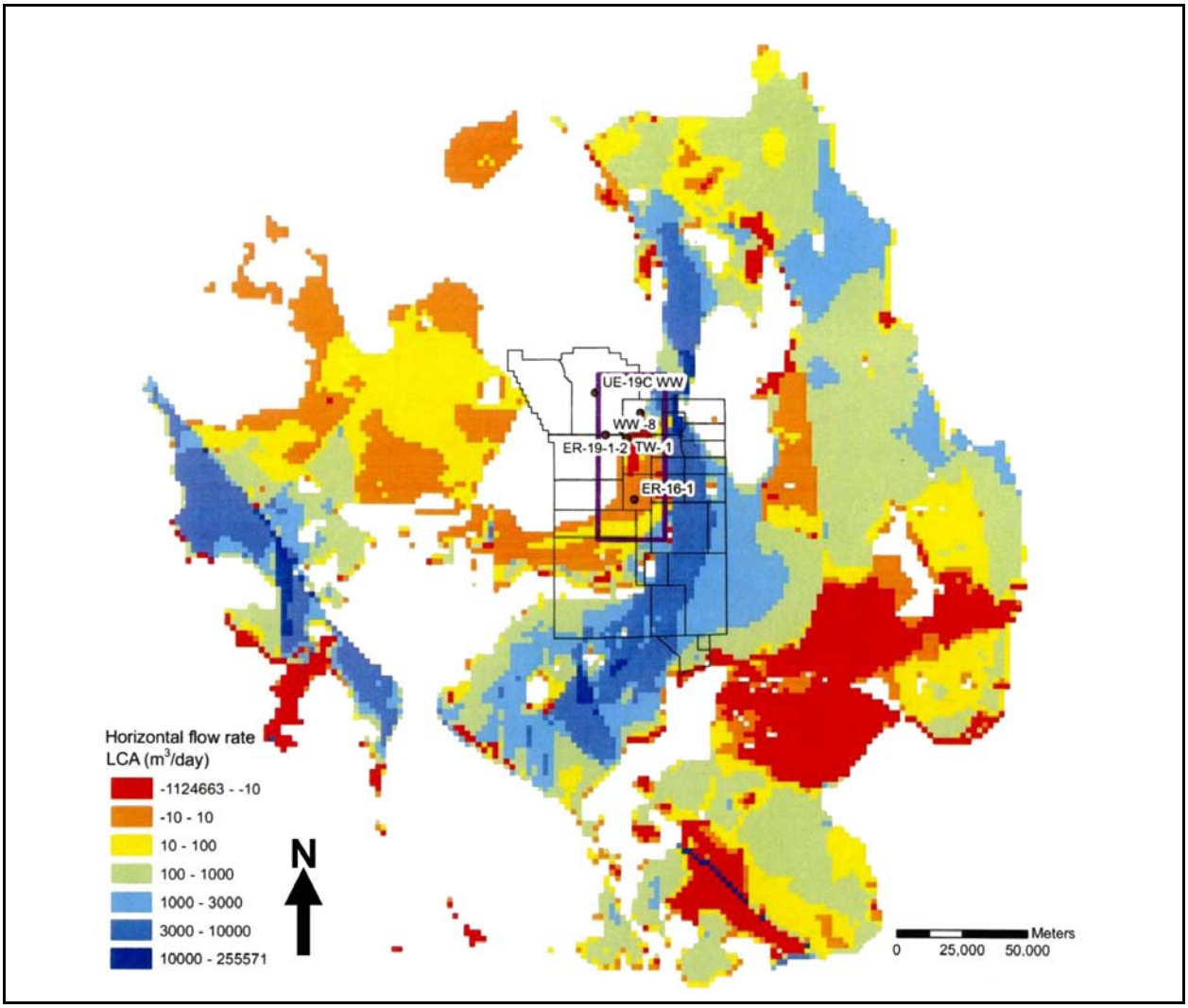

Figure H-13a
Groundwater Flow Rates within the Regional Model Domain

The flux estimates were obtained by conducting sensitivity simulations with various boundary flow, thermal conductivity, and basal heat flux values. The goal was not necessarily to reproduce the observed thermal and head data in the wells, but was primarily to determine, given hydrogeologic settings and boundary conditions similar to those in the regional model, whether it is possible for a large northern flux to coexist with the observed temperatures in northern Yucca Flat. The modeling area of interest is, therefore, only a few kilometers south of the Yucca Flat northern boundary, and only water influx from the north was considered. Recharge from precipitation in the northern thermal model was neglected for the following reasons:

- Recharge in the northern neck of the study area is minimal based on recharge in the DVRFS model (Belcher et al., 2004).
- The goal of this model is to demonstrate that the observed temperatures would be much colder if large amounts of water were flowing from the northern boundary. If recharge from precipitation was included in the model, then the amount of flux from the northern boundary needed to match the observed temperatures would be even lower.
- Based on the recharge versus temperature relationship for a one-dimensional column derived by Bredehoeft and Papadopulos (1965), the amount of cooling induced at a depth of 1 km below the surface in volcanic rock for a recharge rate of, say, 5 mm/yr is less than 1 °C (Figure H-13b).

Note that the northern thermal model does not have any faults, because the regional model does not have any fault in the vicinity of the northern boundary, and also because faults were modeled as barriers in the regional model rather than dual conduit-barrier features. As shown in Figure H-14, there are two wells (ER-8-1 and UE-10j) that penetrate the LCA near the northern boundary. Strictly speaking, only Well ER-8-1 is situated sufficiently close to the northern boundary to function as a reliable observation well to estimate volumetric influx from the north. However, because there are no other observation wells in the area, the temperatures in both Wells ER-8-1 and UE-10j were used to estimate groundwater flux entering Yucca Flat through the northern boundary. More reliance, however, was placed on simulation results at Well ER-8-1. The thermal logs at Wells ER-8-1 and UE-10j obtained by NNES (2010) also are presented in Figure H-14. The logs show a smooth continuity of temperatures at the water table (i.e., at the intersection of the saturated and unsaturated zones). However, at Well UE-10j, there is an anomalous kink in the geothermal gradient starting at the water table (approximately 625 m bls) and extending to about 675 m bls, after which the

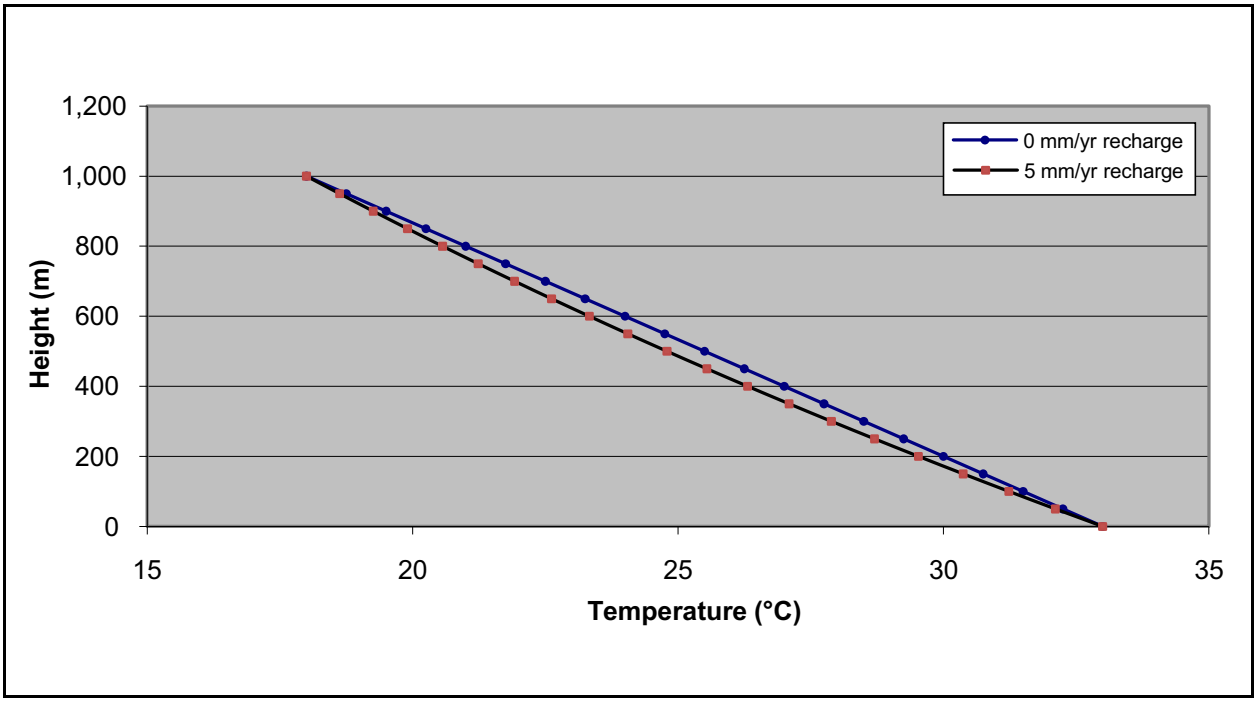

Figure H-13b
Thermal Profile in a One-Dimensional Vertical Volcanic Column Subjected to Recharge Rates of 0 and 5 mm/yr

geothermal gradient observed in the LCA above the water table resumes. It is not clear what may be causing this kink because the geothermal gradient below the water table should have steepened and not flattened. However, as expected, there is a sharp break in the thermal profile at the intersection of the LCA and overlying volcanic units in both wells.

As a check of data integrity, temperatures in the saturated zone at Well UE-10j were spot checked to ensure that there is reasonable agreement between the data obtained by Reiner (2007) and NNES (2010). The temperature at an elevation of 704.4 m amsl is 32.6 °C in Reiner (2007), and the temperature at an elevation of 705.2 m amsl is 32.7 °C in NNES (2010), indicating that the two datasets have reasonably similar data. It should be noted that Well UE-10j was deemed to contain reliable data, and therefore, also used by Gillespie (2005). The data reported by Reiner (2007) do not include temperature data at Well ER-8-1, and therefore, a data comparison could not be conducted at this site.

The northern thermal model extends over the entire HFM of Yucca Flat (Figure H-15). For purposes of estimating northern influx, the model could have been terminated approximately 5 to 7 km from the northern boundary, but the entire extent of the Yucca Flat HFM was considered because the model

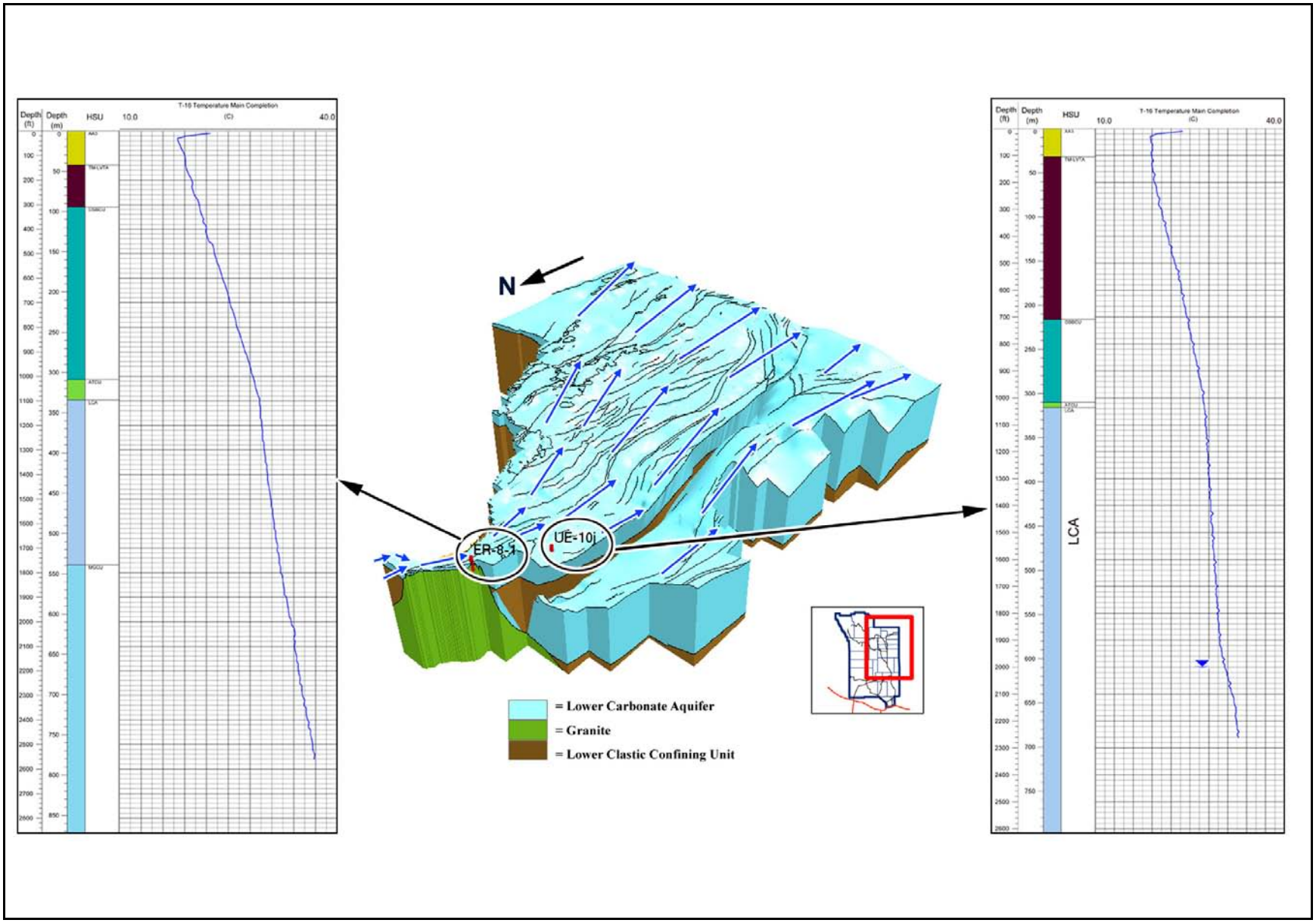

Figure H-14
Areal Extent of the Contiguous Portion of the LCA in Yucca Flat and the Locations of Wells ER-8-1 and UE-10j near Climax Mine

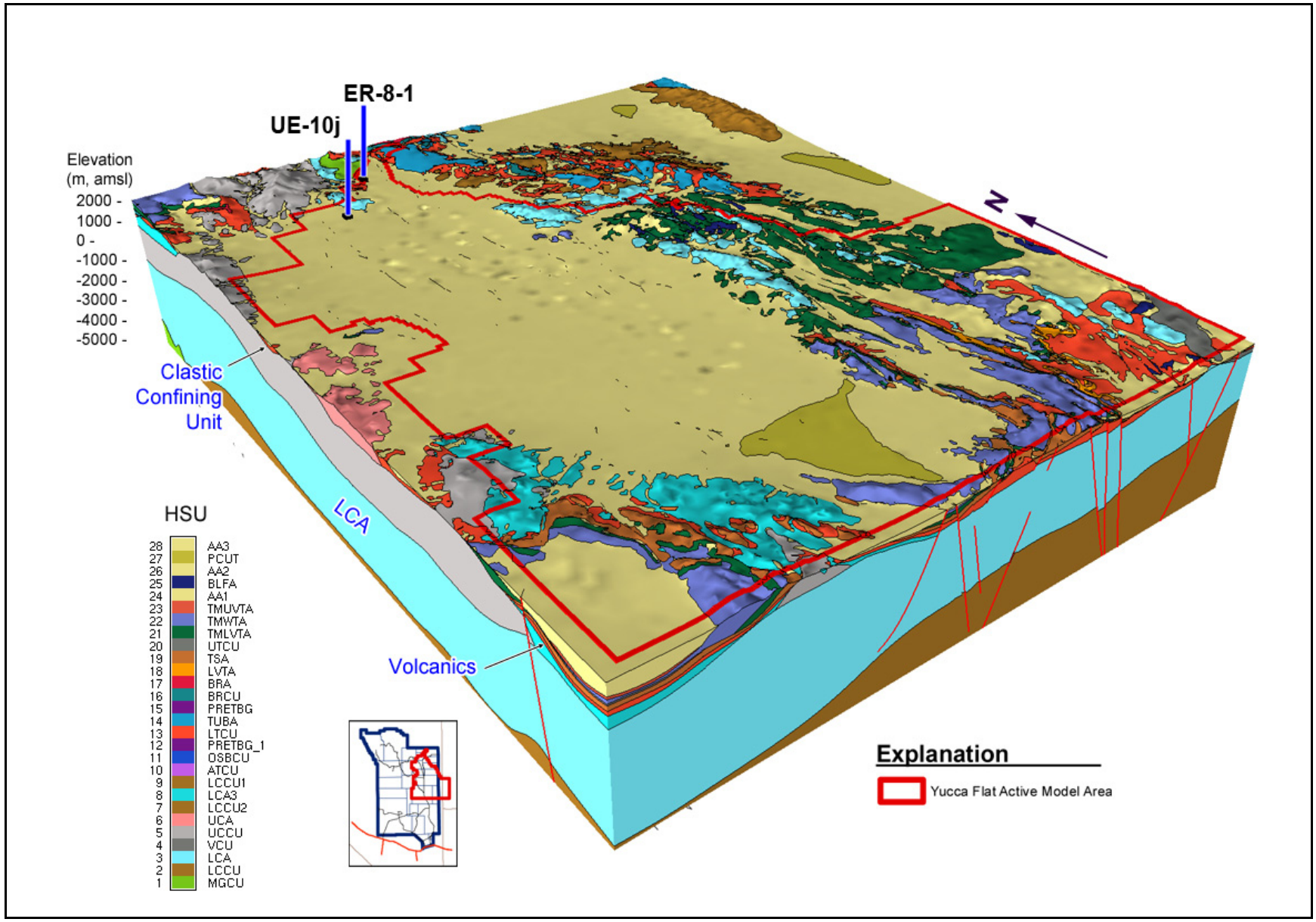

Figure H-15
Areal Extent of the Entire Yucca Flat Northern Thermal Model

was readily available. The top of the model shown in Figure H-15 represents the various HSUs of the Yucca Flat HFM. The LCCU is the bottommost unit in the model. The extent of the LCA in the Yucca Flat model area is presented in Figure H-14, from which it is clear that there is a small sliver of the LCA in the north where groundwater enters the Yucca Flat basin. A flux boundary was specified along this segment of the LCA. A flux of equal magnitude was specified along the southern boundary in order to simulate north–south movement of groundwater through Yucca Flat as represented in the DVRFS model (Belcher et al., 2004). The volumetric influx was distributed uniformly in the small sliver of the LCA along the northern boundary. Similarly, the specified outflow was distributed uniformly along the southern boundary.

The thermal logs collected by NNES (2010) suggest that the surface temperature in the central Yucca Flat basin is approximately 15 °C. In the northern areas of Yucca Flat near Climax Mine, surface temperatures are approximately 19 °C. Therefore, a surface temperature of 15 °C was specified for areas within the Yucca Flat valley, whereas a surface temperature of 19 °C was specified for areas in the north. These temperatures were specified as both initial and boundary conditions.

Intrinsic permeabilities in the carbonate, alluvial/volcanic, clastic, and granite units were specified to be 1E-12, 1E-13, 1E-16, and 5E-15 m^2, respectively. These are typical values for the corresponding units based on Yucca Flat model calibration. Because the granitic stock was not present in the Yucca Flat model, the permeability of this unit was estimated from the Pahute Mesa Phase I modeling study (SNJV, 2006). A mean intrinsic permeability of 3.7E-15 m^2 was derived from SNJV (2006) for the granitic stock. Thermal conductivities of 4.50, 2.26, 3.90, 1.75, and 1.50 W/(m·K) were specified for the carbonate, granite, clastic, volcanic, and alluvial HSUs, respectively. The thermal conductivity of carbonate rock was estimated from Robertson (1979), Clauser and Huenges (1995), and Gillespie (2005). The thermal conductivities of volcanic and alluvial rocks were derived from Gillespie (2005). The thermal conductivities of the LCCU and granitic stock were estimated from SNJV (2006).

A uniform heat flux of 55 mW/m^2 was specified along the base of the model based on analysis conducted by Gillespie (2005) at Well U-15k immediately west of Climax Mine. An inlet groundwater temperature of 25 °C in the LCA along the northern boundary at Climax Mine was estimated as follows. The elevation at Climax Mine is approximately 1,500 m amsl, and the temperature at the land surface was estimated at 17.5 °C. According to Gillespie (2005), the heat flux

at Well U-15k (in the granitic stock) is approximately 55 mW/m^2. Because granite has a thermal conductivity of approximately 3.62 W/(m·K) (Cho et al., 2009), the thermal gradient at the site was estimated at 15.2 degrees Celsius per kilometer (°C/km). Depth to water at Climax Mine is approximately 500 m (0.5 km) bls in the LCA sliver next to Climax Mine, resulting in an average inlet temperature estimate of 25 °C.

$$\begin{aligned}\text{Inlet temperature} &= \text{temperature at land surface} + \text{thermal gradient} \times \text{depth to water}\\ &= 17.5\ °\text{C} + 15.2\ °\text{C/km} \times 0.5\ \text{km}\\ &= 25\ °\text{C}\end{aligned}$$

As shown in Figure H-16, groundwater velocities between elevations of 0 and +500 m amsl are typically high in the north because of the limited lateral extent of the LCA in the area. The groundwater velocity is, therefore, expected to strongly impact temperatures in the north, with high flow rates causing cooler temperatures than low flow rates. Simulations were conducted with four rates of groundwater flux entering northern Yucca Flat: 0, 50, 100, and 300 kg/s. The simulated and observed geothermal gradients are presented in Figures H-17a to d for Well ER-8-1 and Figures H-18a to d for Well UE-10j.

Figure H-17a shows the base-case results for Well ER-8-1. The simulation results indicate the inflow rate of between 0 and 50 kg/s. The base-case results for Well UE-10j are shown in Figure H-18a, from which the northern influx can also be estimated to be between 0 and 50 kg/s. At both well sites, the geothermal profile resulting from a groundwater influx greater than 100 kg/s is in contradiction with the observed temperature profile.

To account for variability in the thermal material properties and the basal heat flux, three separate sensitivity simulations were conducted. The base heat flux was increased from 55 to 75 mW/m^2, and a set of low and high values of thermal conductivity was specified for each HSU as indicated in Table H-1. From the data presented in Figure H-11, the thermal conductivity of volcanic material varies in a narrow range from 1.4 to 2.15 W/(m·K). The ranges of thermal conductivities for the alluvial and clastic units are based on the Pahute Mesa Phase I modeling study (SNJV, 2006). The specified range of 3.95 to 5.95 W/(m·K) for the carbonate unit is slightly larger than the range of 4.67 to 5.23 W/(m·K) specified in SNJV (2006). A wider range was specified to examine the effects of thermal conductivity in this key unit because all of the lateral flow occurs in northern Yucca Flat

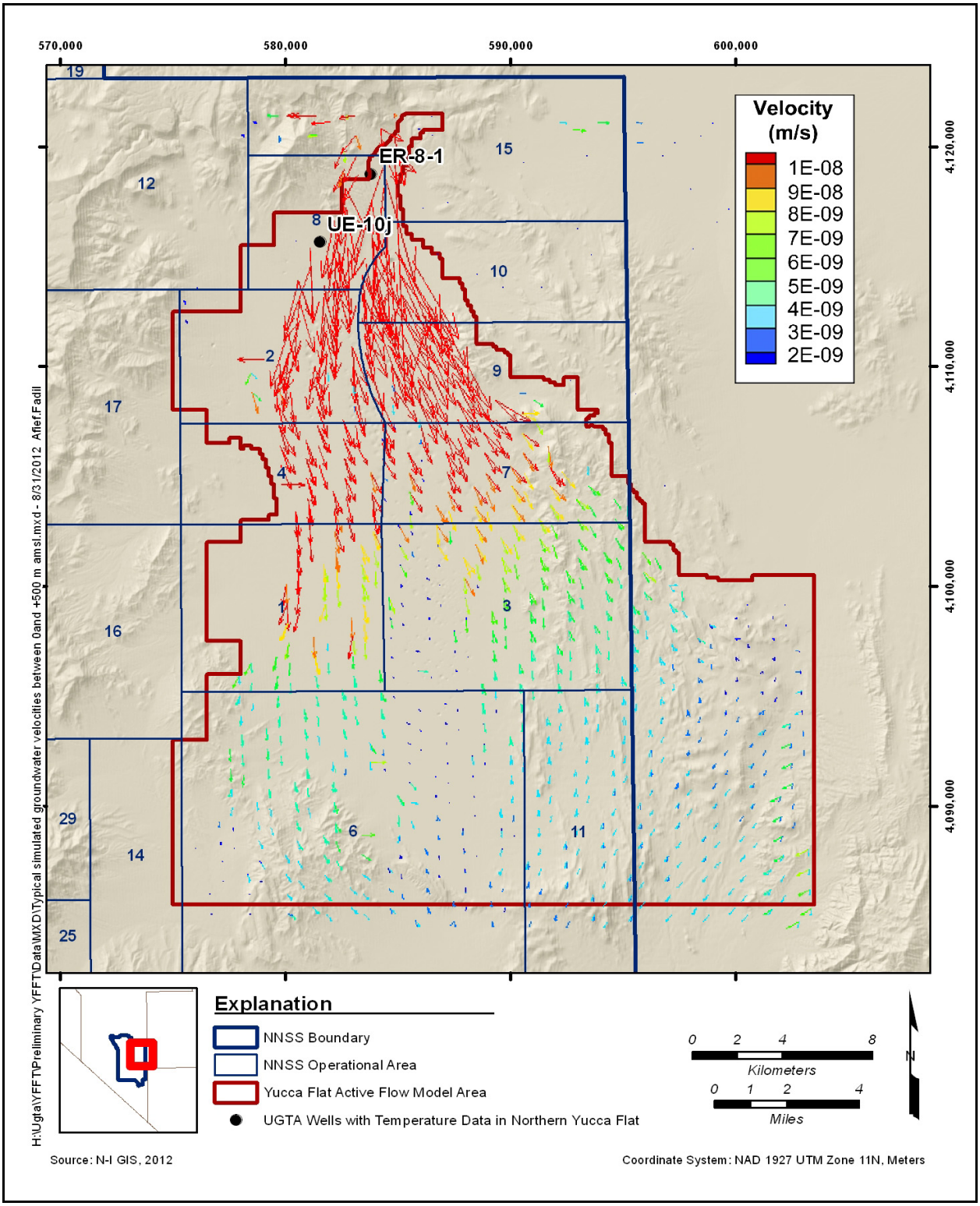

Figure H-16
Typical Simulated Groundwater Velocities between 0 and +500 m amsl in the Northern Thermal Model

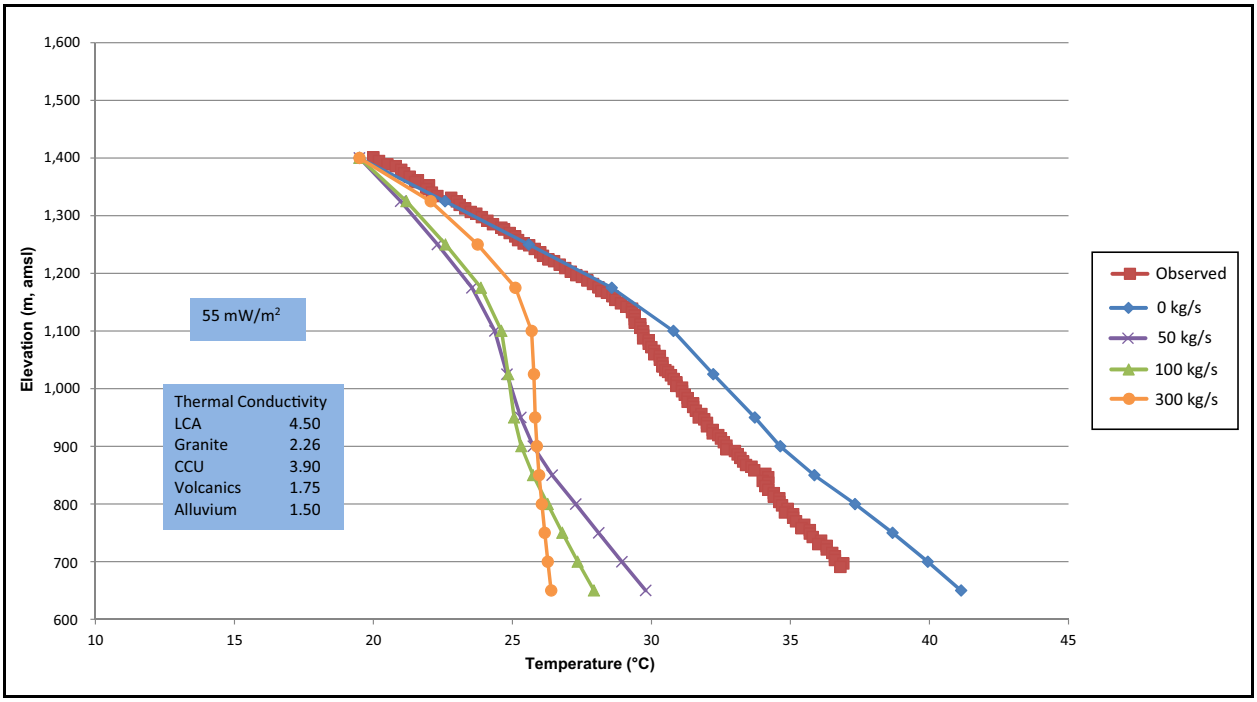

Figure H-17a
Simulated and Observed Temperatures at Well ER-8-1—Base Case

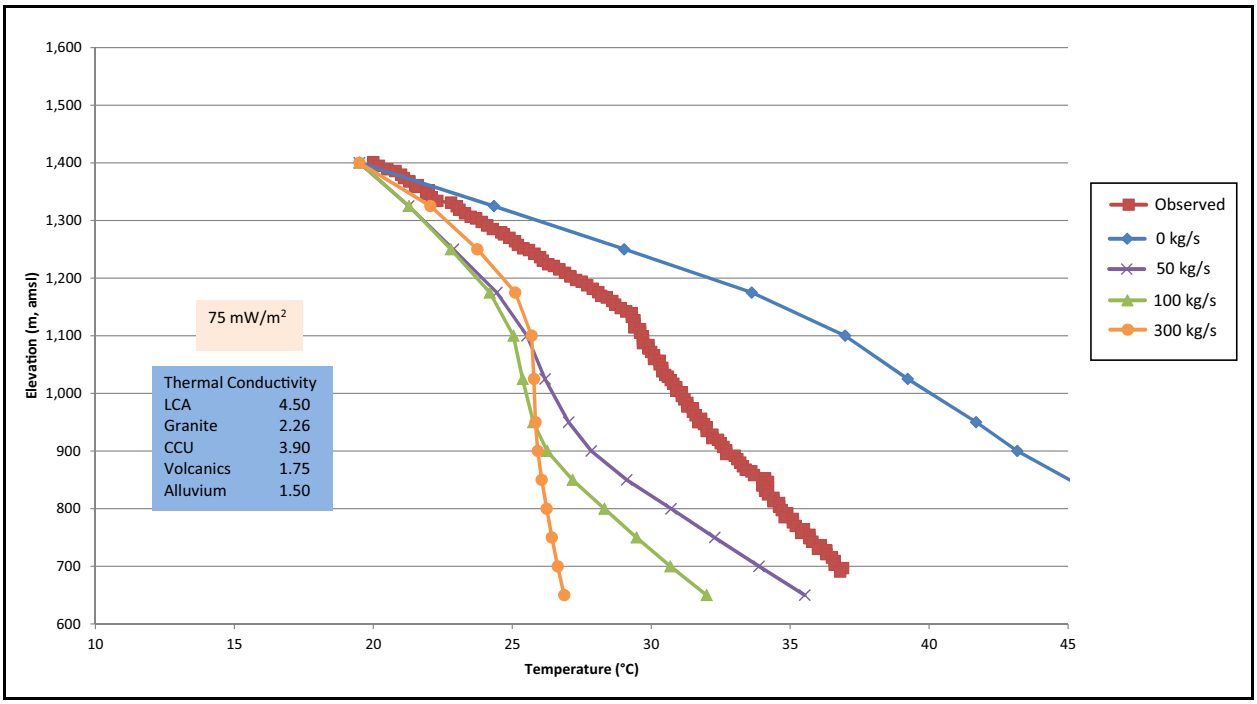

Figure H-17b
Simulated and Observed Temperatures at Well ER-8-1—High Basal Heat Flux Case

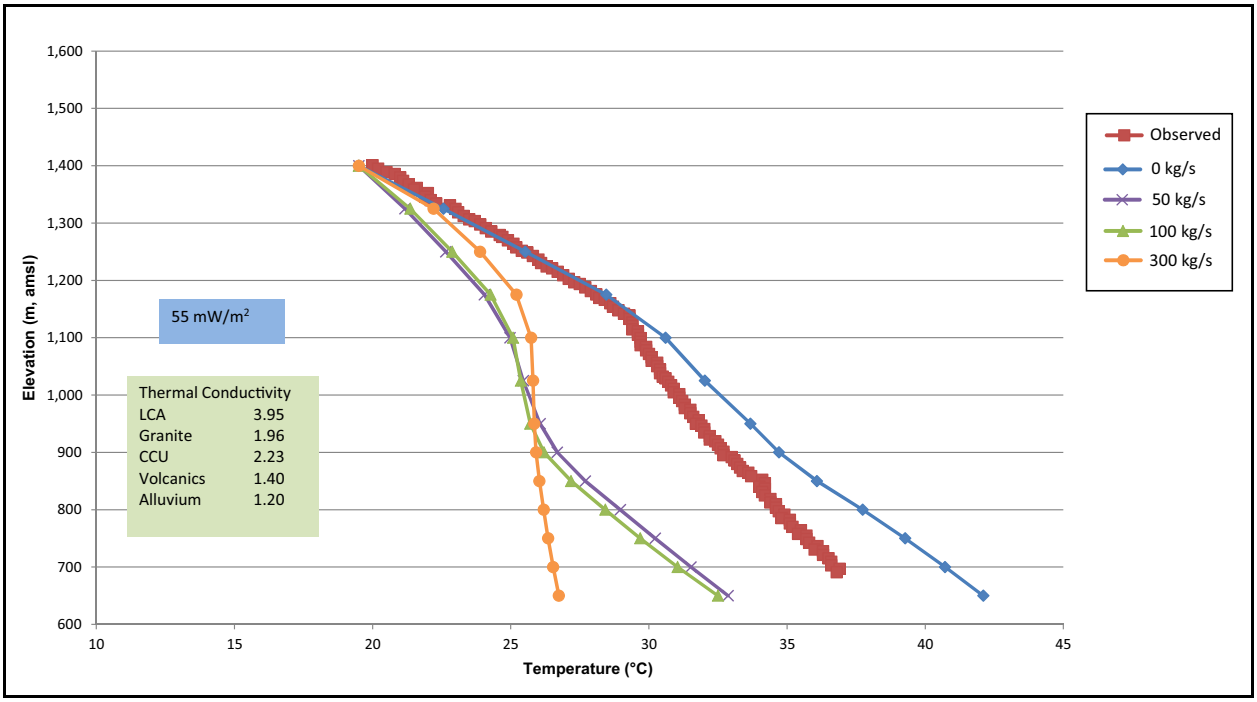

Figure H-17c
Simulated and Observed Temperatures at Well ER-8-1—Low Thermal Conductivity Case

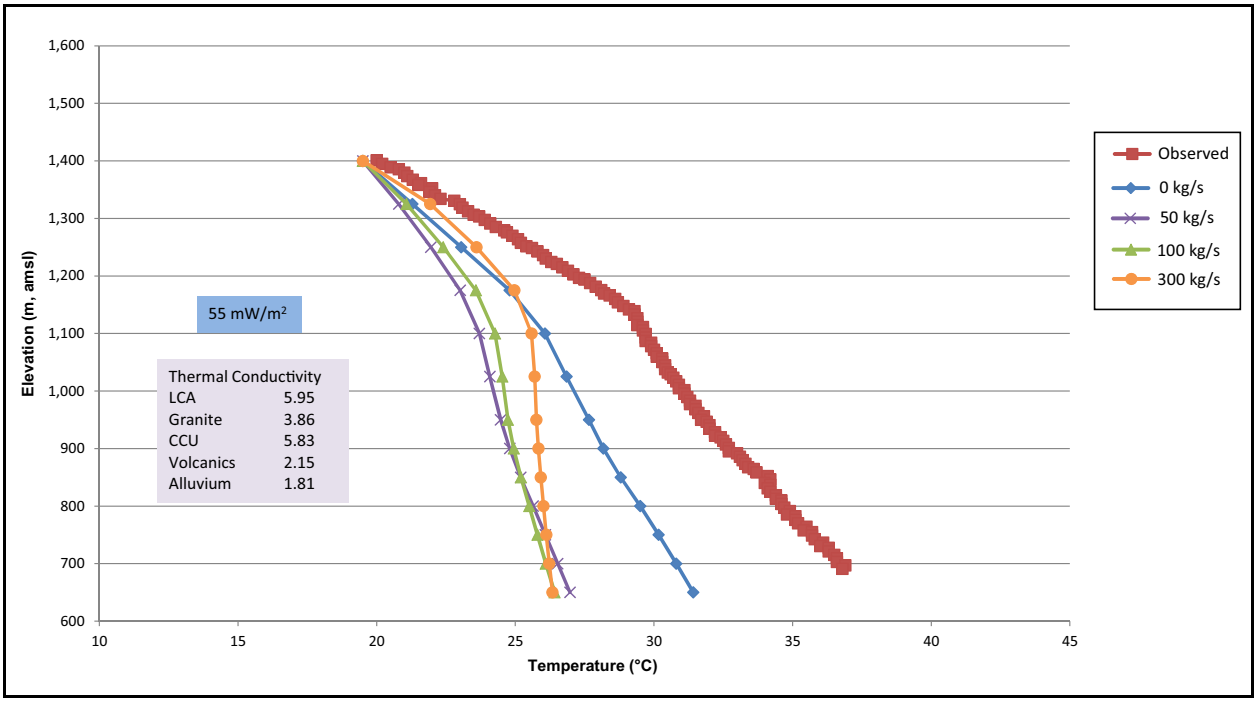

Figure H-17d
Simulated and Observed Temperatures at Well ER-8-1—High Thermal Conductivity Case

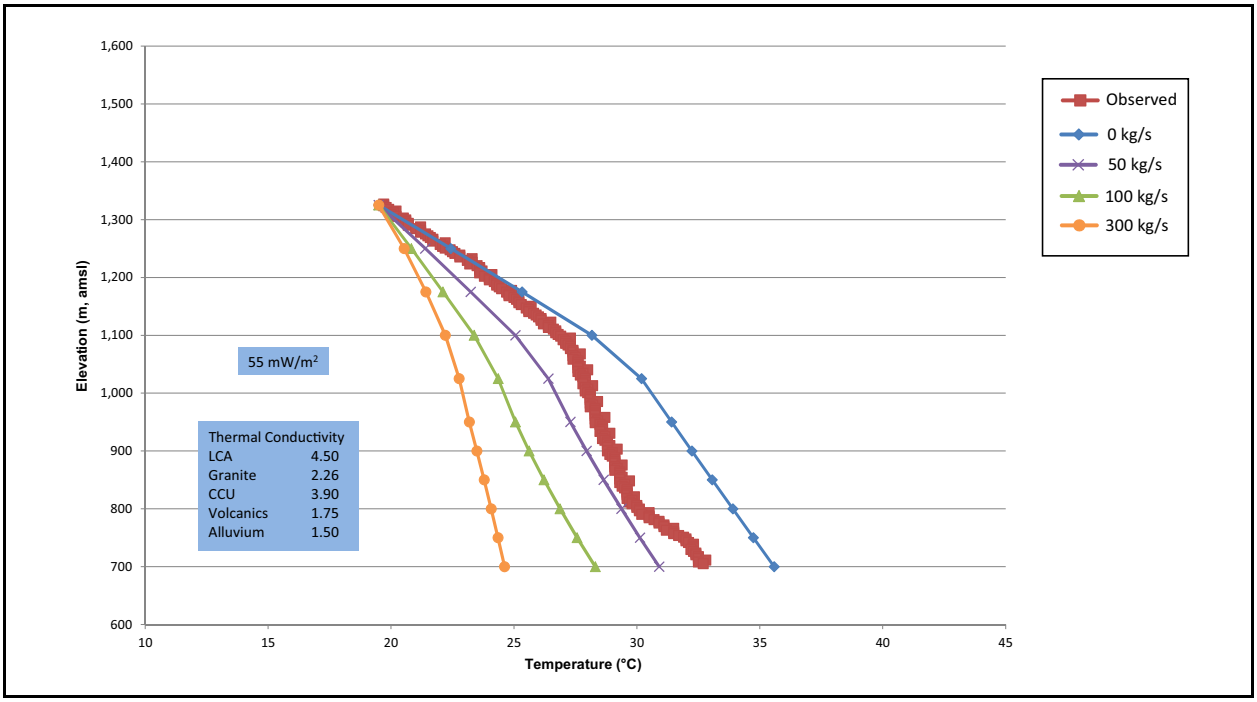

Figure H-18a
Simulated and Observed Temperatures at Well UE-10j—Base Case

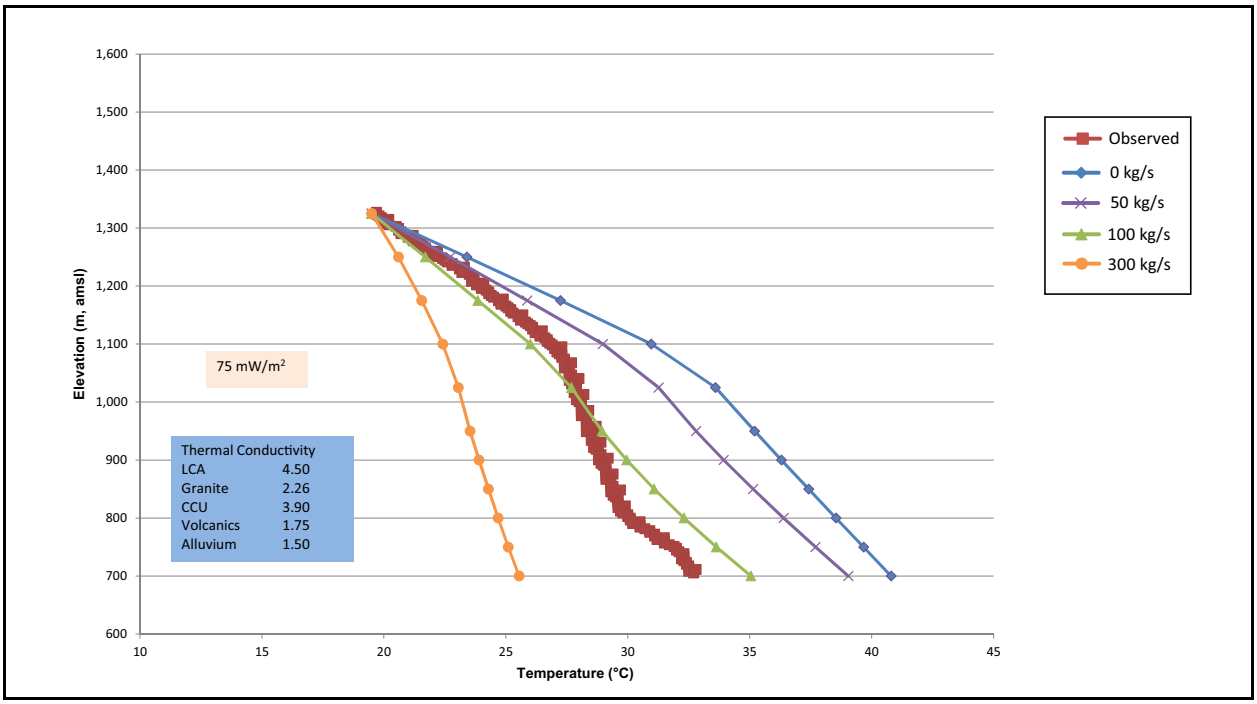

Figure H-18b
Simulated and Observed Temperatures at Well UE-10j—High Basal Heat Flux Case

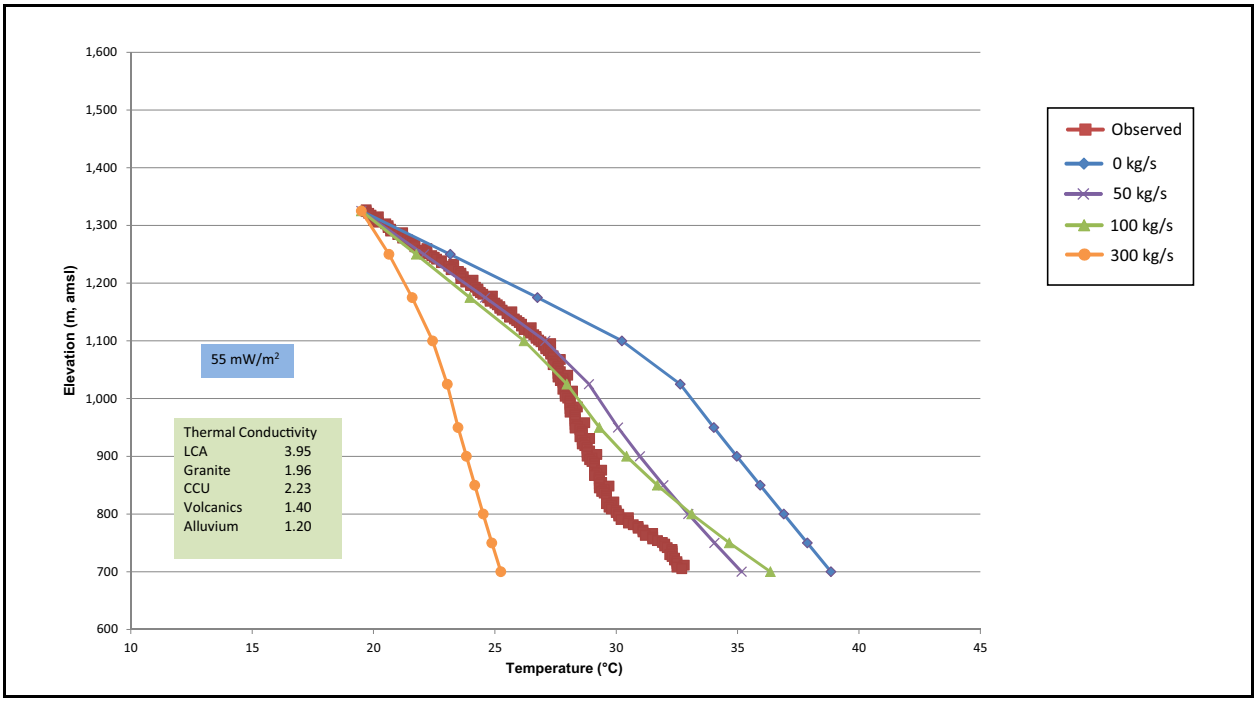

Figure H-18c
Simulated and Observed Temperatures at Well UE-10j—Low Thermal Conductivity Case

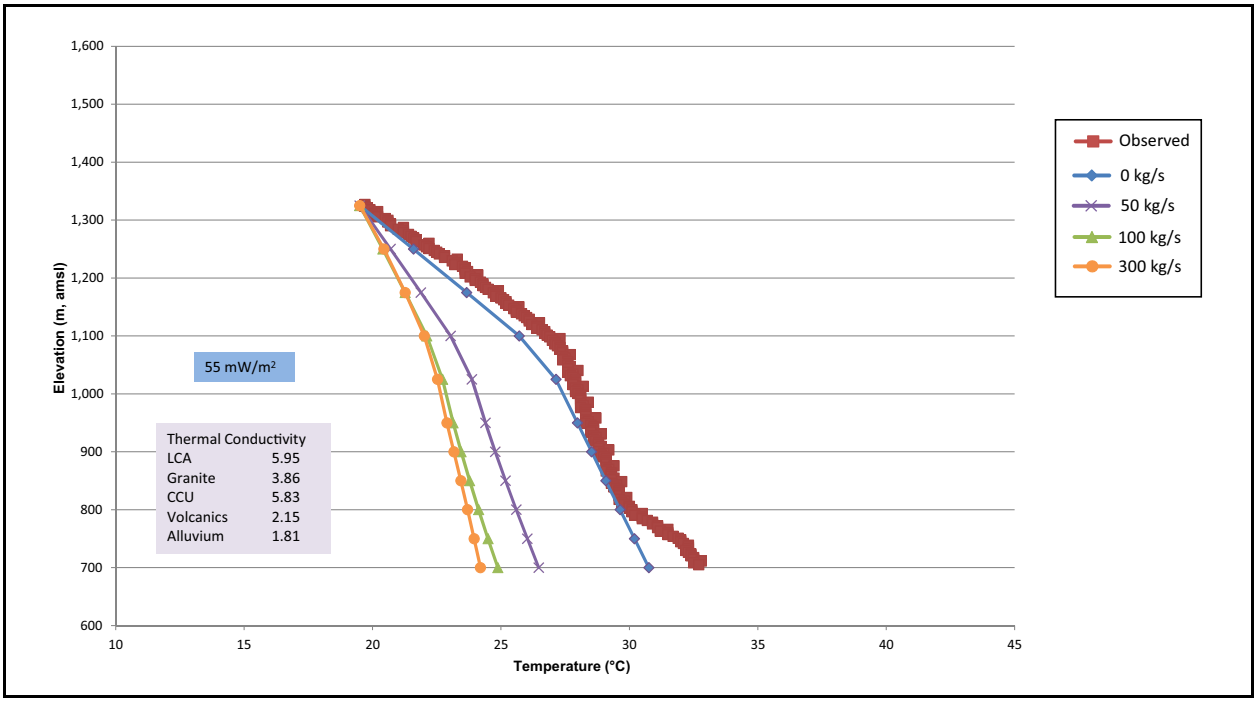

Figure H-18d
Simulated and Observed Temperatures at Well UE-10j—High Thermal Conductivity Case

Table H-1
Ranges of Thermal Conductivities for Volcanic, Alluvial, Carbonate, Granite, and Clastic Units

HSU	Thermal Conductivity (W/(m·K))		
	Low	Base Case	High
Volcanic [a]	1.4	1.75	2.15
Alluvial	1.2 [b]	1.5 [c]	1.81 [c]
Carbonate [b]	3.95	4.5	5.95
Granite [d]	1.96	2.26	3.86
Clastic	2.23	3.9	5.83

[a] Source: Gillespie, 2005
[b] Source: SNJV, 2006
[c] Estimated by author
[d] Source: Table H-2

through this unit. The sources listed in Table H-2 were reviewed for purposes of estimating the range of thermal conductivity for the granitic stock.

Table H-2
Range of Thermal Conductivity for the Granitic Stock

Thermal Conductivity (W/(m·K))		Source
Low	High	
1.96	3.86	Kim et al., 2007
2.26	2.6	SNJV, 2006
2.1	2.1	Monachos, 2001

The simulation results for the sensitivity runs are presented in Figures H-17b to d for Well ER-8-1 and Figures H-18b to d for Well UE-10j. Based on the results, it appears that the observed geothermal gradients at Wells ER-8-1 and UE-10j are incompatible with high northern flux rates in the regional models (Belcher et al., 2004; Pohlmann et al., 2007) which assume hydraulic continuity of the LCA in northern Yucca Flat. This assumption of hydraulic continuity was used in the base case flow model and the NSMC cases presented in Section 5.0 which result in a northern influx rate of 130 kg/s and a range from about 50 to 400 kg/s. The limited hydraulic communication alternative flow model presented in Section 5.6, with a specified northern model boundary influx of 1 kg/s, would provide a thermohydrologic response that is more consistent with the observed thermal profiles in this area.

H.3.0 REFERENCES

Anderson, M.P. 2005. "Heat as a Ground Water Tracer." *Ground Water* 43 (6): 951–968. doi:10.1111/j.1745-6584.2005.00052.x.

Belcher, W.R., J.B. Blainey, F.A. D'Agnese, C.C. Faunt, M.C. Hill, R.J. Laczniak, G.M. O'Brien, C.J. Potter, H.M. Putnam, C.A. San Juan, and D.S. Sweetkind. 2004. *Death Valley Regional Ground-Water Flow System, Nevada and California—Hydrogeologic Framework and Transient Ground-Water Flow Model*, Scientific Investigations Report 2004-5205. Reston, VA: U.S. Geological Survey.

Bravo, H.R., F. Jiang, and R.J. Hunt. 2002. "Using Groundwater Temperature Data to Constrain Parameter Estimation in a Groundwater Flow Model of a Wetland System." *Water Resources Research* 38 (8): 1153. doi:10.1029/2000WR000172.

Bredehoeft, J.D., and I.S. Papadopulos. 1965. "Rates of Vertical Groundwater Movement Estimated from the Earth's Thermal Profile." *Water Resources Research* 1 (2): 325–328. doi:10.1029/WR001i002p00325.

Cho, W.J., S. Kwon, and J.W. Choi. 2009. "The Thermal Conductivity for Granite with Various Water Contents." *Engineering Geology* 107 (3–4): 167–171. doi:10.1016/j.enggeo.2009.05.012.

Clauser, C., and E. Huenges. 1995. "Thermal Conductivity of Rocks and Minerals." In *Rock Physics and Phase Relations: A Handbook of Physical Constants*, edited by T.J. Ahrens, 105–126. Washington, DC: American Geophysical Union.

Gillespie, D. 2005. *Temperature Profiles and Hydrologic Implications from the Nevada Test Site Area*, DOE/NV/13609-40; Publication No. 45211. Las Vegas, NV: Desert Research Institute.

Kim, J., Y. Lee, and M. Koo. 2007. "Thermal Properties of Granite from Korea." Abstract #T11B-0576. American Geophysical Union, Fall Meeting.

Kwicklis, E., Los Alamos National Laboratory. 2010. Power Point presentation presented to the Yucca Flat Preemptive Review Committee. 17 November. Los Alamos, NM.

Monachos, G. 2001. "Conductivity Table for Various Materials." Monachos Engineering. As accessed at http://www.monachos.gr/en/resources/Thermo/conductivity.asp on 7 February 2011.

N-I GIS, see Navarro-Intera Geographic Information Systems.

NNES, see Navarro Nevada Environmental Services, LLC.

Navarro-Intera Geographic Information Systems. 2012. ESRI ArcGIS Software.

Navarro Nevada Environmental Services, LLC. 2010. *Yucca Flat Well Temperature Profile Study Data Report*, Rev. 0, N-I/28091--008. Las Vegas, NV.

Pohlmann, K., M. Ye, D. Reeves, D. Decker, J. Chapman, and M. Zavarin. 2007. *Modeling of Groundwater Flow and Radionuclide Transport at the Climax Mine Sub-CAU, Nevada Test Site*, DOE/NV/26383-06; Publication No. 45226. Las Vegas, NV: Desert Research Institute.

Post, P.C. 2011. "Low-Level and Deep Geothermal Energy." Innovative Environmental Energy Concepts, Inc. As accessed at http://www.ieeconcepts.com/geothermal on 3 January.

Reiner, S.R. 2007. *Ground-Water Temperature Data, Nevada Test Site and Vicinity, Nye, Clark, and Lincoln Counties, Nevada, 2000–2006*, Data Series 269. Carson City, NV: U.S. Geological Survey.

Robertson, E.C. 1979. *Thermal Conductivities of Rocks*, Open-File Report 79-356. Reston, VA: U.S. Geological Survey.

SNJV, see Stoller-Navarro Joint Venture.

Sass, J.H., W.H. Diment, A.H. Lachenbruch, B.V. Marshall, R.J. Munroe, T.H. Moses Jr., and T.C. Urban. 1976. *A New Heat-Flow Contour Map of the Conterminous United States*, Open-File Report 76-756. Reston, VA: U.S. Geological Survey.

Stoller-Navarro Joint Venture. 2006. *Groundwater Flow Model of Corrective Action Units 101 and 102: Central and Western Pahute Mesa, Nevada Test Site, Nye County, Nevada*, Rev. 0, S-N/99205--076. Las Vegas, NV.

Thompson, P.H., Raytheon Services Nevada. 1991. Memorandum to K. Hahn (LANL) titled "Geothermal Investigations of LANL Areas of Yucca Flat," GEO-1223. Las Vegas, NV.

WRCC, see Western Regional Climate Center.

Western Regional Climate Center. 2009. "A-3 South (NTS) Nevada Climate Data." As accessed at http://www.nts.dri.edu/cgi-bin/rawMAIN.pl?nve03s on 17 September.

Winograd, I.J., and W. Thordarson. 1975. *Hydrogeologic and Hydrochemical Framework, South-Central Great Basin, Nevada-California, with Special Reference to the Nevada Test Site*, Professional Paper 712-C. U.S. Geological Survey.

Zyvoloski, G.A., B.A. Robinson, Z.V. Dash, and L.L. Trease. 1999. *Models and Methods Summary for the FEHM Application*, FEHM MMS SC-194. Los Alamos, NM: Los Alamos National Laboratory.

Appendix I

Transient Flow Model for the Lower Carbonate Aquifer in Yucca Flat

I.1.0 INTRODUCTION

Groundwater flow in the subsurface is in a state of constant flux owing to climatic variations and anthropogenic factors. However, if the natural or anthropogenic stresses are not significantly consequential to modeling objectives within the time frame of interest, the assumption of a steady-state system may be appropriate and preferred because of the associated simplicity in model input requirements and minimization of computational burden. Consequently, the following steady-state assumptions were implemented during the development and calibration of the Yucca Flat saturated LCA flow model:

- The boundary conditions specified for the simulation of the transient multi-well aquifer test (MWAT) are temporally invariant.
- The predevelopment (i.e., before groundwater pumpage) flow field at Yucca Flat is hydrologically steady.
- The flow field in the LCA during (and following) nuclear testing at Yucca Flat remains steady.

The objective of this appendix is to demonstrate and document that these underlying assumptions are reasonable for Yucca Flat saturated LCA flow and transport simulations. This appendix validates these assumptions by comparing steady-state and transient calibration results and associated particle-tracking simulations. The analyses conducted to address each of the three assumptions listed above are presented separately in the following sections.

I.2.0 EFFECT OF ALTERNATIVE BOUNDARY CONDITIONS ON THE SIMULATED LCA FLOW MODEL DURING THE MWAT

I.2.1 Background and Objectives

Constant-head boundary conditions were prescribed along the southern boundary of the Yucca Flat saturated LCA flow model because the amount of flux exiting the model along the southern boundary is unknown. Assigning constant-head boundary conditions to the model's southern boundary allows any amount of model inflows from the top, western, northern, and eastern boundaries to discharge out of the model without specifying (*a priori*) model outflow rates. However, because of the proximity of the southern boundary to Well ER-6-1 (the pumping well for the MWAT conducted in 2004), sensitivity analyses were conducted to determine whether the specification of constant-head boundary conditions along the southern boundary was impacting model calibration results.

Flux boundary conditions were specified along the southern boundary as alternative boundary conditions, and a simulation was run to obtain an alternative set of calibrated parameter values. The alternative model was constructed with an intermediate calibrated model before completion of the base-case model documented in Section 5.5, and the results of the alternative model were compared with those of the calibrated parent model. The hypothesis to be tested was that the resulting difference in the calibrated parameter and boundary fluxes between the two models would be of a magnitude that the alternative Monte Carlo simulations conducted separately to address parameter uncertainty would encompass. The objective did not include evaluating the potential significance of the limited hydraulic communication conceptual model evaluated as a separate sensitivity analysis in Section 5.6.

I.2.2 Technical Approach

The technical approach used in the alternative simulation involved using the base-case calibrated model and specifying the resulting *steady-state* fluxes along the southern boundary. Because fluxes out of the southern boundary during the aquifer test would be less for the case with constant-head boundary conditions than for the case with fixed-flux boundary conditions, specification of flux along the southern boundary is expected to provide an upper bound on drawdowns (i.e., induce larger

drawdowns). Conversely, the base calibrated model (with constant-head boundary conditions) provides a lower-bound (or minimum) drawdown because constant heads allow for additional recharge (or alternatively, a reduced discharge) to flow into the model domain without incurring any drawdown along the boundary. Collectively, the base case and the alternative model capture the range of drawdowns and the associated calibrated parameter space given that the conceptual model that assumes the LCA in northern Yucca Flat is in hydraulic communication with the LCA in areas north of Yucca Flat. The automatic parameter estimation package PEST described in Section 5.0 was used for model calibration.

I.2.3 Simulation Results and Conclusions

The details of the MWAT are described in SNJV (2006). Drawdowns were recorded at observation wells ER-3-1, ER-7-1, UE-1h, UE-7nS, and U-3cn-5. The observed and model-calibrated drawdowns at observation wells ER-3-1 and ER-7-1 are presented in Figure I-1 for both the base case and the alternative model. The model-calibrated drawdowns for both cases are very similar and also match the observed drawdowns. The apparent drawdown traces observed at ER-3-1 and ER-7-1 represent the effects of diurnal earth tides. Similar conclusions can be drawn at observation wells UE-1h, UE-7nS, and U-3cn-5 (Figure I-2).

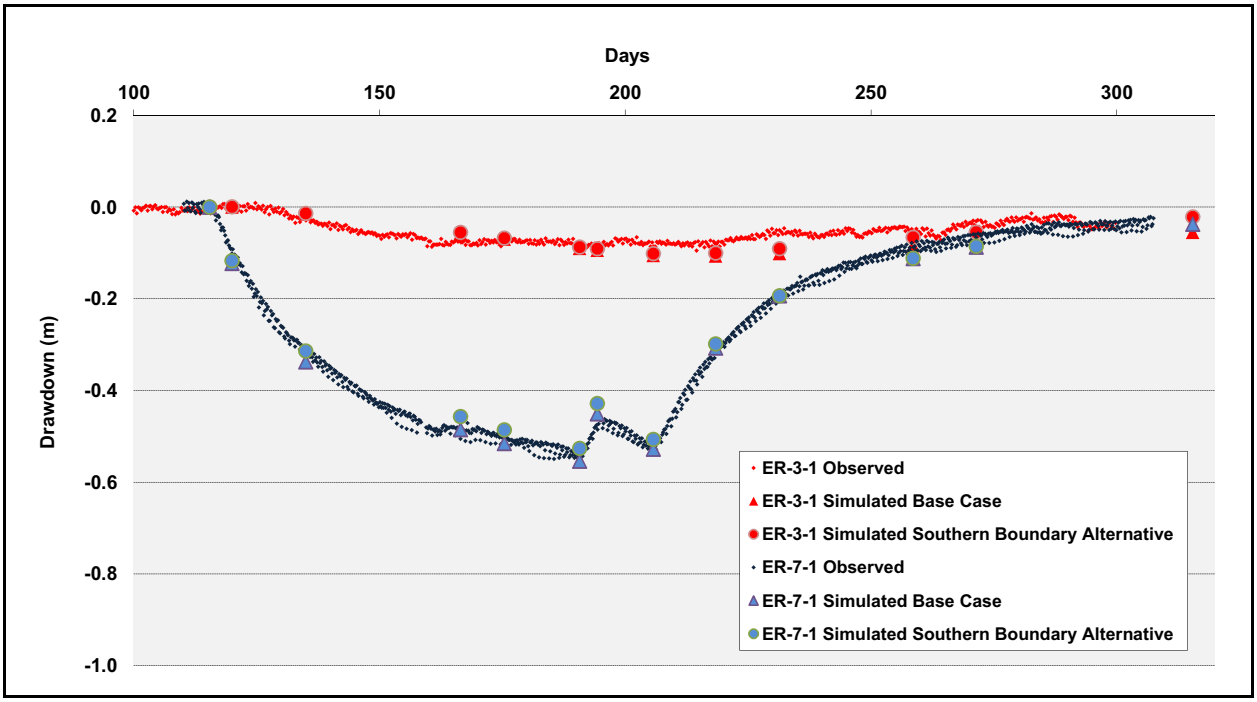

Figure I-1
Observed and Simulated Drawdowns at Observation Wells ER-3-1 and ER-7-1

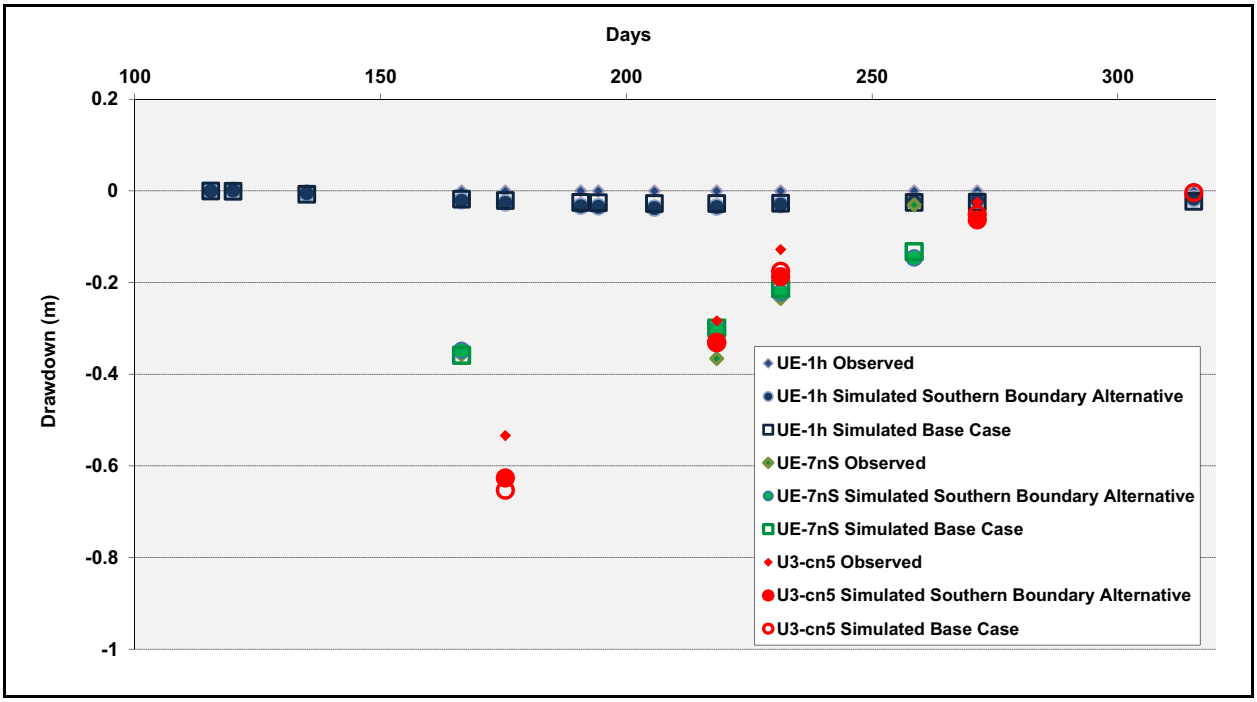

Figure I-2
Observed and Simulated Drawdowns
at Observation Wells UE-1h, UE-7nS, and U-3cn-5

The model-calibrated parameters for the base and alternative cases are presented in Table I-1. The difference in net flux into the model domain is on the order of 15 percent for the most significant boundaries, which results in an increase in the estimated permeability of the LCA in the eastern portion of the model domain also by 15 percent. These differences are small in comparison to the range of parameter values estimated with null-space Monte Carlo methods (Figures 5-56 to 5-58), confirming that the choice of boundary conditions along the southern boundary of the model domain does not significantly affect the calibrated flow model. It is therefore concluded that using constant-head boundary conditions for the MWAT simulations is a reasonable approximation.

Table I-1
Calibrated Parameters for Base and Alternative Cases of Southern Boundary Conditions
(Page 1 of 5)

Parameter	Alternative Case	Base Case	Difference (%) [a]
Flux Boundary Conditions (kg/s)			
northflux	30.1	25.5	15
westflux	50	50	0
eastsoflux	43.9	38.4	12
topflux	35.1	31.5	10
hpflux	4.7	4.5	3
rechusgs	11.1	11.7	-5
rechalvm	24.0	20.1	16
Storativity (1/m)			
aqc_con	2.11E-07	2.16E-07	-2
aqc_unc	1.45E-05	1.22E-05	16
aqc_flt	8.50E-08	6.22E-08	27
Anisotropy Ratio (dimensionless)			
anisofaultx	6.40E-02	3.74E-02	41
anisofaultz	3.36E-02	4.20E-02	-25
aniso145x	1.58E-02	1.39E-02	12
aniso145z	3.48E-02	3.54E-02	-2
aniso148x	2.09E-02	3.04E-02	-45
aniso148z	0.230	0.225	2
aniso178x	1.02E-02	1.13E-02	-11
aniso178z	4.25E-02	4.13E-02	3
aniso190x	3.71E-02	2.14E-02	42
aniso190z	0.164	0.135	18
aniso176x	0.785	0.958	-22
aniso176z	7.32E-02	7.56E-02	-3
aniso177x	0.327	0.273	17
aniso177z	0.261	0.219	16
lcahniso	1	1	0
lcavniso	1	0.9	9

Table I-1
Calibrated Parameters for Base and Alternative Cases of Southern Boundary Conditions
(Page 2 of 5)

Parameter	Alternative Case	Base Case	Difference (%) [a]
Permeability of Country Rock and Faults (m^2)			
3_lcaw	1.25E-13	6.96E-14	44
11_lcae	6.86E-13	6.07E-13	12
9_lcac	2.67E-13	3.33E-13	-25
6_lccu2	1.20E-16	1.38E-16	-15
7_lca3	1.19E-13	1.10E-13	8
4_uccu	2.42E-15	2.25E-15	7
114_yf_91bn1	2.80E-12	2.55E-12	9
115_yf_57	3.75E-12	3.10E-12	17
116_yf_56	3.75E-12	3.10E-12	17
118_hp112_16	1.00E-12	1.00E-12	0
121_hp40	1.00E-12	1.01E-12	-1
122_rv60	1.00E-12	1.20E-12	-20
123_hp120	1.63E-12	1.72E-12	-5
124_hp10	1.34E-12	1.53E-12	-14
125_hp20	1.69E-12	1.75E-12	-3
126_hp30	3.75E-12	3.10E-12	17
127_hp121	1.16E-12	1.00E-12	13
128_hp116	1.18E-12	1.22E-12	-3
129_hp115	2.28E-12	2.49E-12	-9
130_hp125	3.75E-12	3.10E-12	17
132_hp108	2.59E-12	2.48E-12	4
135_hp123	1.16E-12	1.22E-12	-5
136_yf_133	1.72E-12	1.97E-12	-15
137_yf_131	1.02E-12	1.18E-12	-16
138_mm90	3.75E-12	3.10E-12	17
139_hp72_yf1	2.33E-12	1.47E-12	37
140_hp50_yf1	1.76E-12	1.85E-12	-5
141_hp60	1.73E-12	1.81E-12	-5
142_mm70	1.36E-12	1.42E-12	-4
143_hp124	1.15E-12	1.00E-12	13
144_mm20_60	3.75E-12	3.10E-12	17

Table I-1
Calibrated Parameters for Base and Alternative Cases of Southern Boundary Conditions
(Page 3 of 5)

Parameter	Alternative Case	Base Case	Difference (%) [a]
Permeability of Country Rock and Faults (m²) (continued)			
145_yf1	1.26E-11	1.00E-11	20
146_yf_129	3.75E-12	3.10E-12	17
147_yf_103n1	1.07E-11	5.82E-12	45
148_yf2	1.00E-11	1.05E-11	-5
149_area3n9	2.39E-12	2.21E-12	8
150_yf_embud	1.09E-12	1.19E-12	-9
151_yf_7r	1.05E-12	1.17E-12	-12
152_yf_55	1.23E-12	1.29E-12	-5
153_yf_54	3.75E-12	3.10E-12	17
154_piranha	1.25E-12	1.00E-12	20
155_yf_61a63	1.00E-12	1.09E-12	-9
156_yf_71	1.00E-12	1.32E-12	-32
157_yf_69n67	3.75E-12	3.10E-12	17
158_yf_62	3.75E-12	3.10E-12	17
159_yf_61b	3.75E-12	3.10E-12	17
160_area3eas	3.57E-12	2.71E-12	24
161_yf_7y	2.46E-12	1.72E-12	30
162_yf_97b	3.75E-12	3.10E-12	17
163_yf_97a	1.48E-12	1.44E-12	2
164_yf_95a	3.75E-12	3.10E-12	17
165_yf_area7	3.75E-12	3.10E-12	17
166_yf_80	3.75E-12	3.10E-12	17
167_yf_75	1.00E-12	1.03E-12	-3
168_yf_93b	3.75E-12	3.10E-12	17
169_yf_119n1	3.02E-12	2.81E-12	7
170_hp122	3.75E-12	3.10E-12	17
171_yf_125	1.29E-12	1.45E-12	-13
172_yf_127	3.75E-12	3.10E-12	17
173_yf_126	3.75E-12	3.10E-12	17
174_yf_wellc	3.75E-12	3.10E-12	17
175_yf_26egh	6.08E-13	5.21E-13	14

Table I-1
Calibrated Parameters for Base and Alternative Cases of Southern Boundary Conditions
(Page 4 of 5)

Parameter	Alternative Case	Base Case	Difference (%) [a]
Permeability of Country Rock and Faults (m^2) (continued)			
176_yf_50b	2.78E-12	3.61E-12	-30
177_carpetba	6.77E-12	6.13E-12	9
178_topgalla	5.00E-12	5.00E-12	0
179_yf_48	3.75E-12	3.10E-12	17
180_yf_46a	3.75E-12	3.10E-12	17
181_yf_46b	6.08E-13	5.21E-13	14
182_yf_50c	6.08E-13	5.21E-13	14
183_yf_37n39	3.75E-12	3.10E-12	17
184_yf_33b	3.75E-12	3.10E-12	17
185_yf_34a	3.75E-12	3.10E-12	17
186_yf_34b	3.75E-12	3.10E-12	17
187_yf_44b	3.75E-12	3.10E-12	17
188_yf_44c	3.75E-12	3.10E-12	17
189_yf_35b	3.75E-12	3.10E-12	17
190_topgalla	1.15E-11	1.23E-11	-7
191_yf_44a	3.75E-12	3.10E-12	17
192_yf_40	1.07E-12	1.29E-12	-20
193_yf_41	1.00E-12	1.00E-12	0
194_yf_38	3.75E-12	3.10E-12	17
195_yf_tippi	1.00E-12	1.00E-12	0
196_yf_baneb	1.28E-12	1.78E-12	-39
197_yf_33a	3.75E-12	3.10E-12	17
198_yf_wgh	6.59E-13	6.07E-13	8
200_yf_31	4.34E-13	5.16E-13	-19
201_yf_wellc	1.35E-12	1.72E-12	-28
202_yf_18	1.06E-12	1.28E-12	-21
203_yf_28a	6.84E-13	8.02E-13	-17
204_yf_28b	6.19E-13	8.95E-13	-45
205_yf_minem	5.10E-13	7.22E-13	-42
206_yf_u_2cm	7.26E-13	9.79E-13	-35
207_yf_u_2cm	9.67E-13	9.18E-13	5

Table I-1
Calibrated Parameters for Base and Alternative Cases of Southern Boundary Conditions
(Page 5 of 5)

Parameter	Alternative Case	Base Case	Difference (%) [a]
Permeability of Country Rock and Faults (m^2) (continued)			
208_yf_23	6.26E-13	6.31E-13	-1
209_yf_22c	4.99E-13	6.07E-13	-22
210_yf_22d	6.08E-13	5.21E-13	14
211_yf_22b	6.08E-13	5.21E-13	14
212_yf_24	6.08E-13	5.21E-13	14
213_yf_25n27	6.08E-13	5.21E-13	14
214_yf_6a	8.97E-13	1.07E-12	-19
215_yf_16b	6.08E-13	5.21E-13	14
216_yf_6b	7.76E-13	1.11E-12	-43
217_yf_12	6.17E-13	9.12E-13	-48
218_yf_14n16	1.16E-12	1.08E-12	7
219_cp20	3.75E-12	3.10E-12	17
220_cp10	3.75E-12	3.10E-12	17
221_cp30	3.75E-12	3.10E-12	17
222_cp50	3.75E-12	3.10E-12	17
223_yf_30	1.62E-12	1.52E-12	6
224_yf_20b	6.08E-13	5.21E-13	14
225_yf_19	6.08E-13	5.21E-13	14
226_yf_20a	6.08E-13	5.21E-13	14
yfsouthext	8.81E-10	8.27E-10	6
101_itfc	1	5.65E-01	43
114_itfc	1.90E-01	1.40E-01	26
145_itfc	1.55E-06	1.78E-06	-15
177_itfc	2.22E-03	3.57E-03	-61
178_itfc	6.86E-05	6.46E-05	6
207_itfc	6.34E-01	4.12E-01	35
yfsouth_itfc	1.90E-05	1.72E-05	9

[a] Difference (%) = {(Alternative case value – Base case value)/Alternative case value} × 100

I.3.0 EFFECT OF LONG-TERM GROUNDWATER DISCHARGE ON THE LCA FLOW FIELD

I.3.1 Background and Objectives

Based on the LCA groundwater potentiometric data analyzed for the study, transient water-level fluctuations are minimal in most wells (Figure 5-9). However, a water-level monitoring program was not implemented until the mid-1990s, and therefore, most of the water-level data are for more recent times. As shown in Figures 5-6 and 5-7, the majority of LCA groundwater withdrawals occurred between 1960 and 1990 to support nuclear testing and research activities. Therefore, this section evaluates, through comparison of transient and steady-state simulations, the impact of neglecting LCA anthropogenic discharge and assuming steady-state conditions on the flow model results. The evaluation consists of conducting transient simulations for the period from 1962 to 2008 and demonstrating that drawdowns due to pumping in the model area are minimal.

I.3.2 Technical Approach

The technical approach involved conducting transient simulations for the period from 1962 to 2008, during which groundwater was extracted from the four LCA wells shown in Figure 5-5. The model was initially run for an extended period of approximately 330,000 years assuming that no pumping of groundwater from the LCA occurred during this period. This initial run was performed to reach steady-state conditions before commencement of pumping in 1962.

I.3.3 Simulation Results and Conclusions

The observed and simulated heads at LCA observation wells are presented in Figures I-3 to I-6. The "calibration target" lines on these figures represent the values used in the steady-state model calibration presented in Section 5.5. The simulation results clearly show that fluctuations in the water levels due to pumping remained within a narrow range in all these wells. Additionally, water levels in the production wells appear to have recovered completely to pre-1962 levels very shortly after decline/cessation of pumping. This is an indication that the amount of recharge, as well as lateral boundary flow in the LCA, is substantially larger than the amount of groundwater withdrawal that occurred during nuclear testing. Based on these observations and simulation results, it is concluded

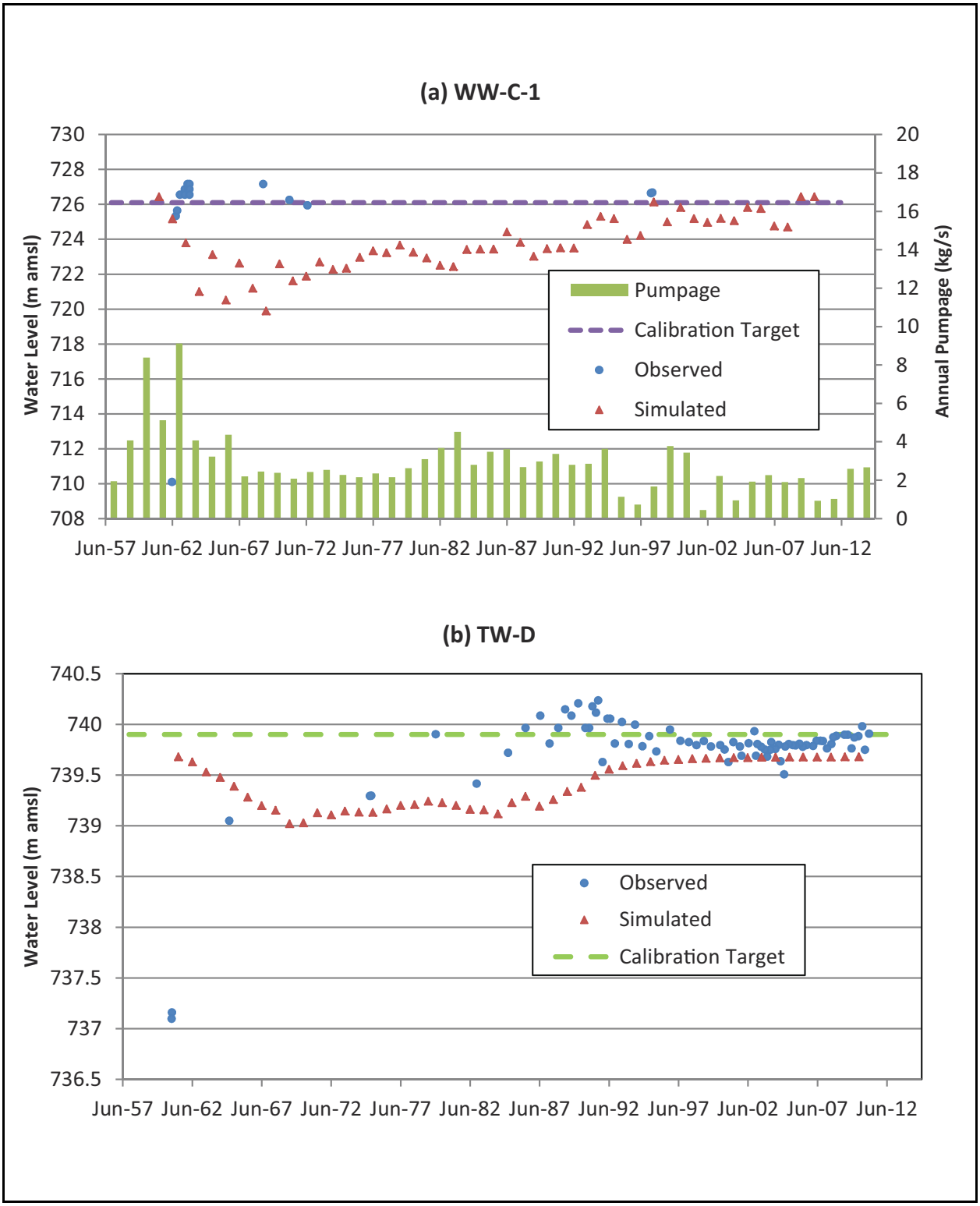

Figure I-3
Transient Simulated and Observed Water Levels at Well Sites
(a) WW-C-1 and (b) TW-D

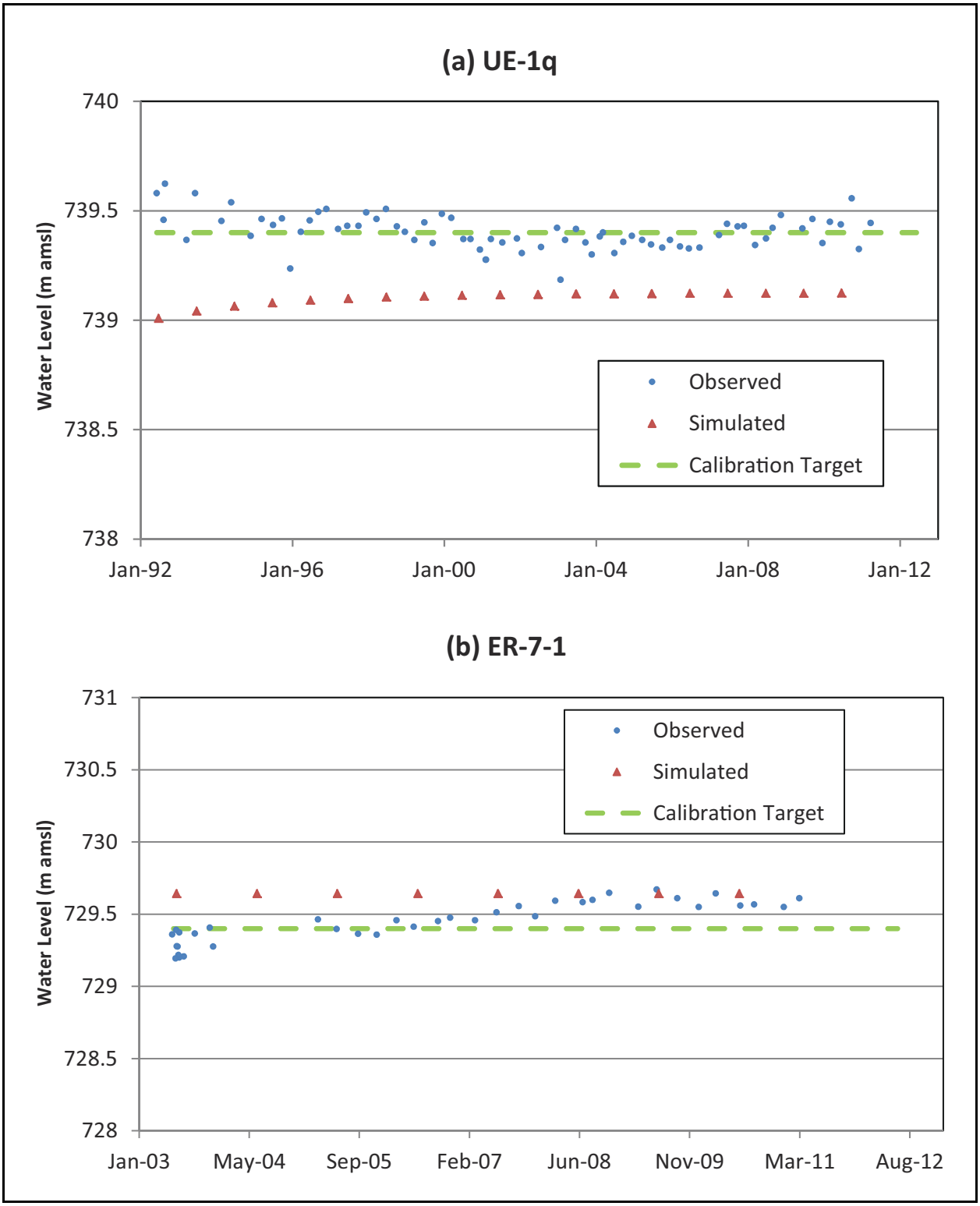

Figure I-4
Transient Simulated and Observed Water Levels at Well Sites
(a) UE-1q and (b) ER-7-1

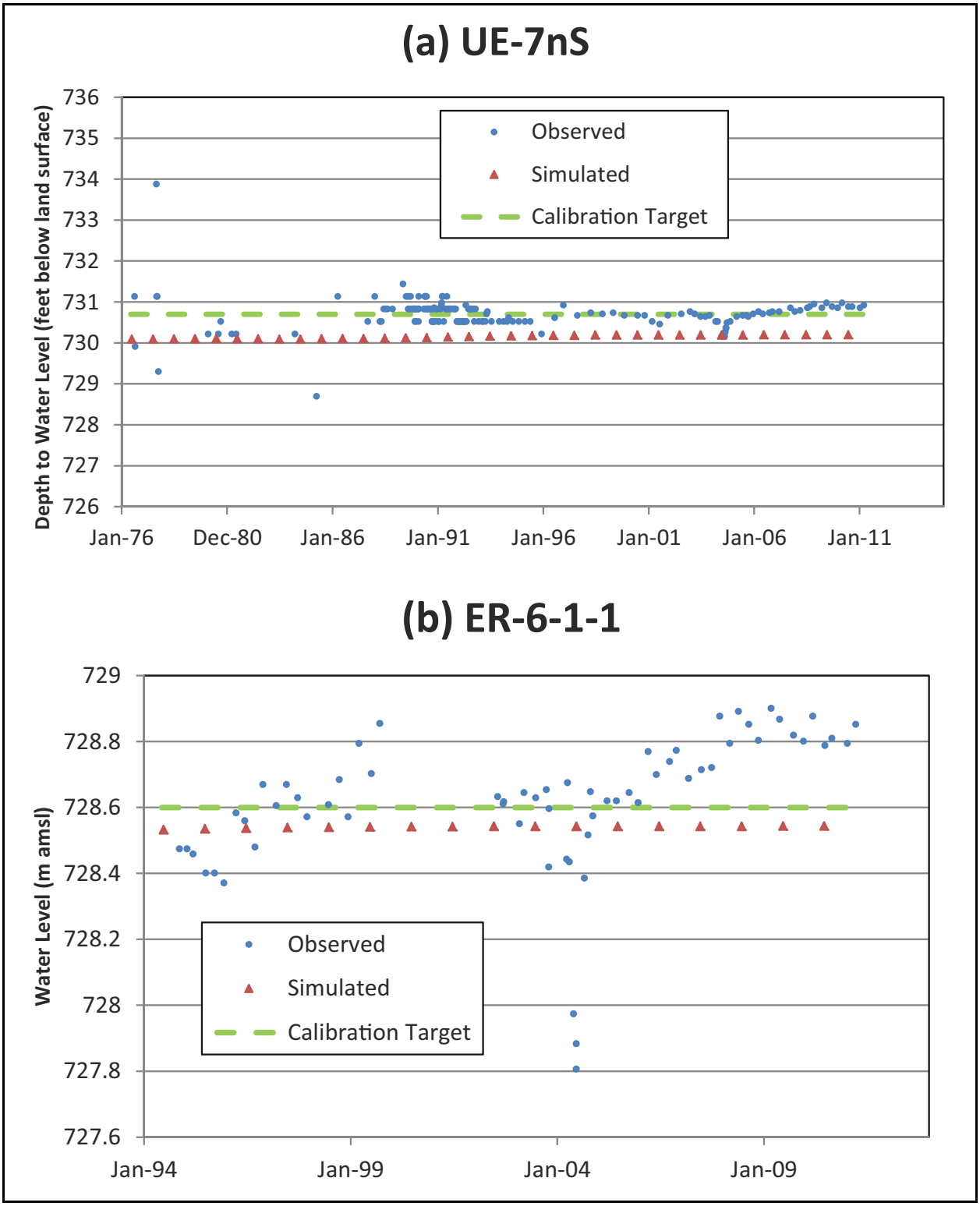

Figure I-5
Transient Simulated and Observed Water Levels at Well Sites
(a) UE-7nS and (b) ER-6-1-1

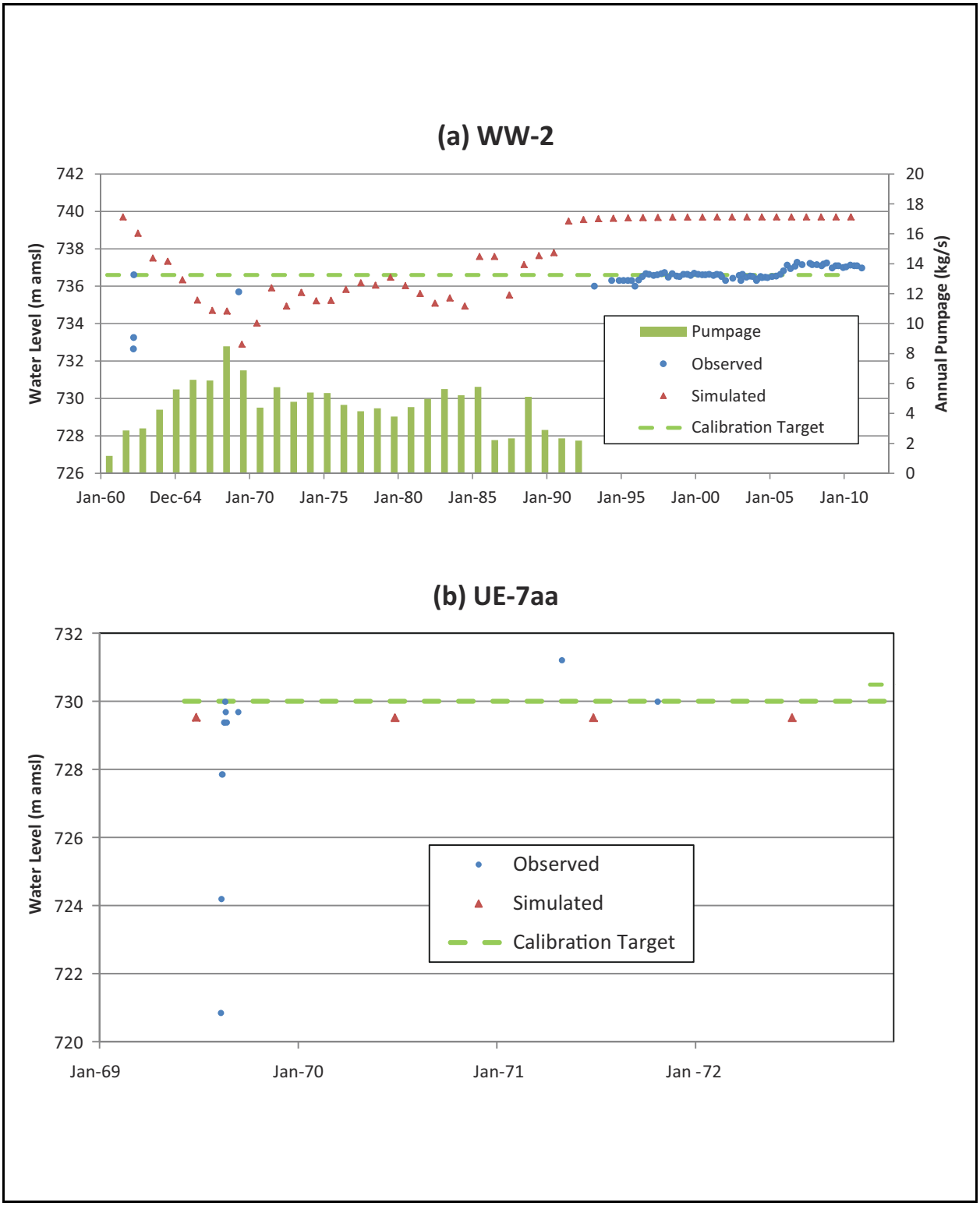

Figure I-6
Transient Simulated and Observed Water Levels at Well Sites
(a) WW-2 and (b) UE-7aa

that neglecting pumping in the LCA flow simulations during the period of maximum groundwater withdrawal is reasonable. It should be noted that continued pumpage at Well WW-C-1, which is the only active LCA well, should not impact water levels at Yucca Flat during the 1,000-year simulation period. This is because the average production rate in this well is slightly greater than 2 kg/s, which is a small fraction of the rate (266 kg/s) at which water is entering the Yucca Flat model domain from the top and lateral boundaries for the base-case model discussed in Section 5.5. This production rate is also substantially smaller than the total influx range of 151 to 483 kg/s estimated from the 84 null-space Monte Carlo uncertainty runs discussed in Section 5.6.2 and presented in Figure 5-58.

I.4.0 EFFECT OF POST-DETONATION TRANSIENT RECHARGE TO THE LCA FROM THE OVERLYING UNSATURATED ZONE AND SATURATED ALLUVIAL/VOLCANIC AQUIFER SYSTEM

The saturated LCA groundwater flow model used in the contaminant transport calculations presented in Section 6.0 is a steady-state flow model. In contrast, the unsaturated zone and saturated alluvial/volcanic aquifer system models presented in Sections 3.0 and 4.0, respectively, simulate a transient flow field. This section evaluates the significance of the post-detonation transient recharge to the saturated LCA from the overlying unsaturated zone and saturated alluvial/volcanic aquifer system to confirm the appropriateness of implementing a steady-state flow field in the LCA.

I.4.1 Effect of Transient Recharge from the Unsaturated Zone

Before underground nuclear testing began in Yucca Flat, the percolation flux through the unsaturated zone is considered to have been in steady state. Although long-term transient flows associated with pluvial drainage are possible, the analysis presented in Appendix F indicates that these long-term transient flows do not significantly affect the steady-state percolation flux through the unsaturated zone.

As a result of underground nuclear detonations conducted in Yucca Flat, the hydrologic conditions in the unsaturated zone have changed. Detonation-induced changes in the hydrologic conditions have resulted from the following:

- Alteration of topography and drainage that potentially changes infiltration rates and patterns near the detonation site
- Alteration of hydrologic conditions in the vicinity of the detonation
- Creation of chimneys and altered alluvium and rock zones around the detonation cavity
- Possible change in hydraulic communication between perched zones near the detonation site

These changes alter the percolation flux distribution in the unsaturated zone, which in turn affects recharge to the water table. Because the water table in Yucca Flat can represent either the top of the

saturated alluvial/volcanic aquifer system or the top of the saturated LCA, the recharge to both of these model domains may be impacted by the post-detonation transient drainage changes in the unsaturated zone. As discussed in Section 4.0, the saturated alluvial/volcanic aquifer system model is transient to account for the changes in the hydrogeologic properties and fluid pressures associated with the underground nuclear detonations in Yucca Flat. As a result, this model uses, as direct input, the transient changes in recharge from the unsaturated-zone model. In contrast, the saturated LCA flow model presented in Section 5.0 is a steady-state model. Therefore, it is necessary to evaluate the potential significance of the changes in recharge to the saturated LCA from the unsaturated zone that overlies the LCA.

As noted in Section 3.0, a number of different modeling cases have been analyzed to explore a reasonable range of uncertainty in the unsaturated-zone flow and transport properties that could affect release rates from the unsaturated zone to the LCA and hence the extent of contaminant migration in the LCA. The comparison below uses an unsaturated-zone modeling case that assumes an average infiltration rate of 5 mm/yr, no vertical anisotropy in the alluvial aquifer, a minimum crater-enhanced recharge rate, a median effective porosity of the tuff confining unit of 0.25, no vertical anisotropy of the tuff confining unit, and an exchange volume radius of 2 R_c. This case represents a bound on the expected net infiltration to the unsaturated-zone model and thus bounds the likely impact of post-detonation impacts.

Figure I-7 presents the initial, pre-detonation steady-state water flux at the base of the unsaturated-zone flow model. The base of the unsaturated-zone model is conceptualized to directly overlie the saturated LCA. Figure I-8 presents the same information at 1,000 years, illustrating the maximum effect of post-detonation effects caused by changes in hydrologic properties and crater-enhanced recharge. These figures illustrate the generally insignificant post-detonation effects on increasing water flux to the LCA given that most of the area has the same water flux at 1,000 years as the pre-detonation steady-state water flux. This observation is supported by the pre- and post-detonation cumulative flux rates presented in Figure I-9, which illustrates the time rate of change of the total water flux to the LCA from the overlying unsaturated-zone model domain over time. At the end of the next 1,000 years, the total water flux to the LCA from the unsaturated zone for this modeling case is about 24.0 kg/s, which may be compared to an integrated water flux of about 23.6 kg/s in the 1,000 years preceding nuclear testing in Yucca Flat (assuming the same background infiltration rate of 5 mm/yr). Although there may be areas of locally increased water flux that may

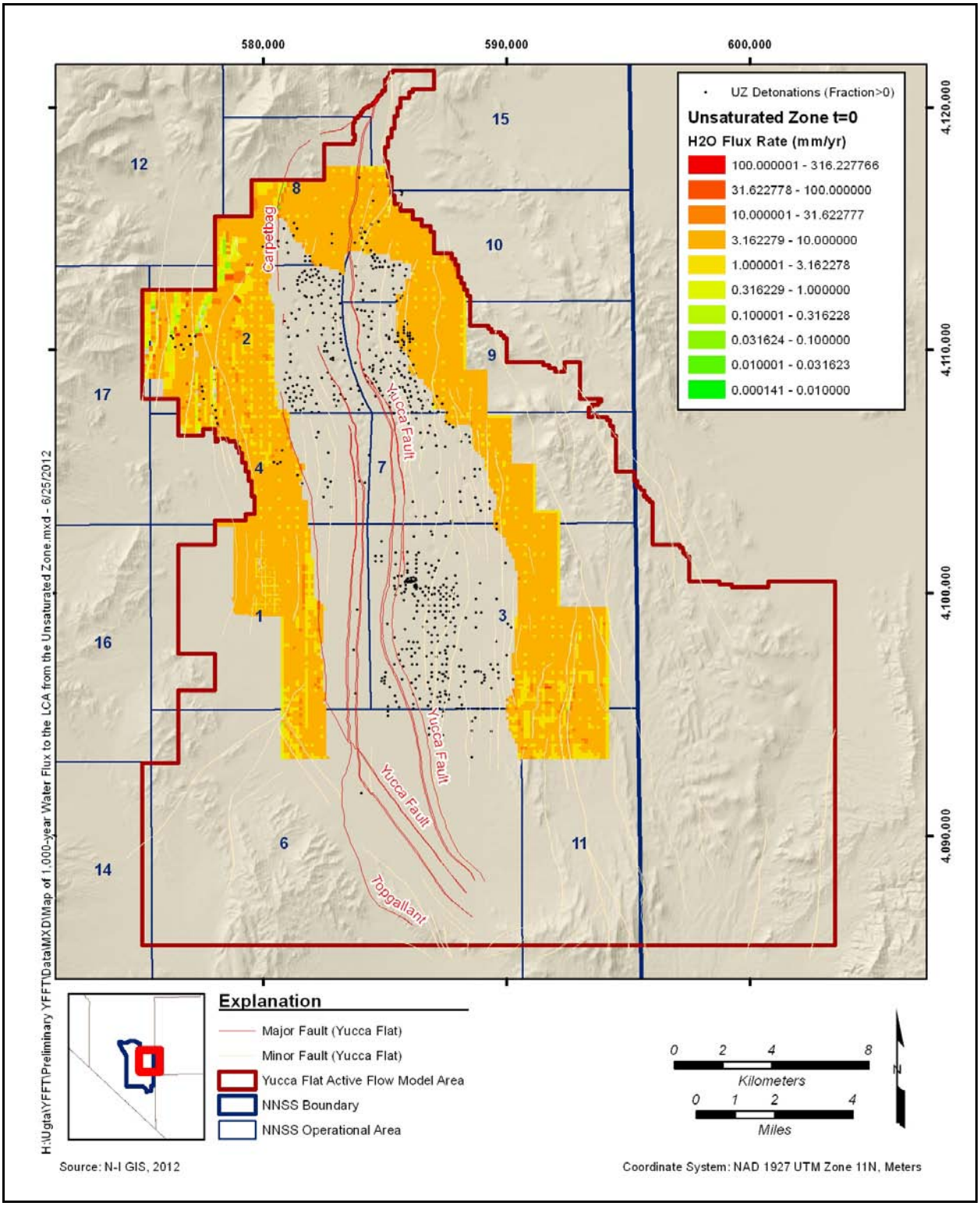

Figure I-7
Map of Pre-detonation Steady-State Water Flux to the LCA from the Unsaturated-Zone Model Domain with an Assumed Net Infiltration Rate of 5 mm/yr

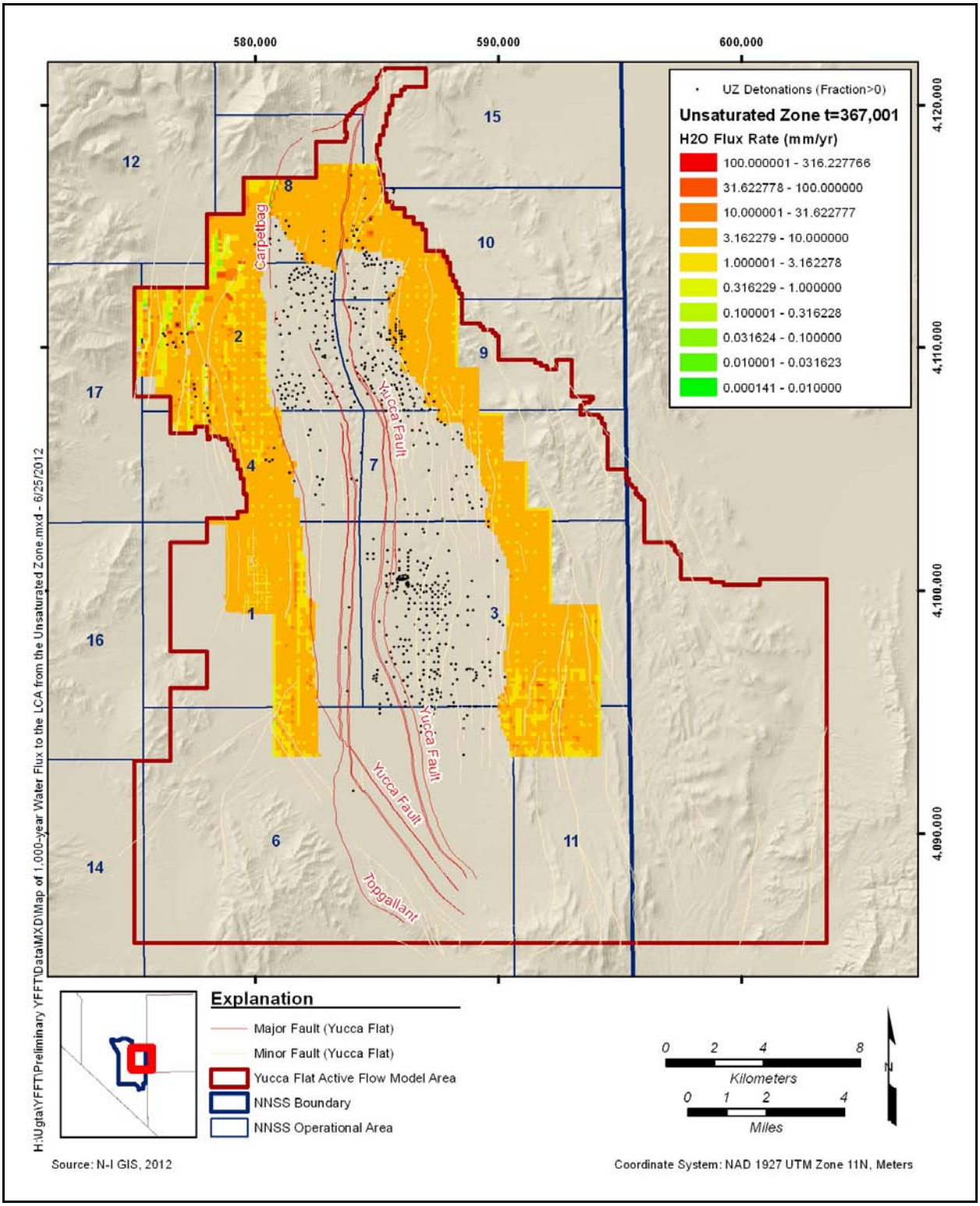

Figure I-8
Map of 1,000-Year Water Flux to the LCA from the Unsaturated-Zone Model Domain with an Assumed Net Infiltration Rate of 5 mm/yr

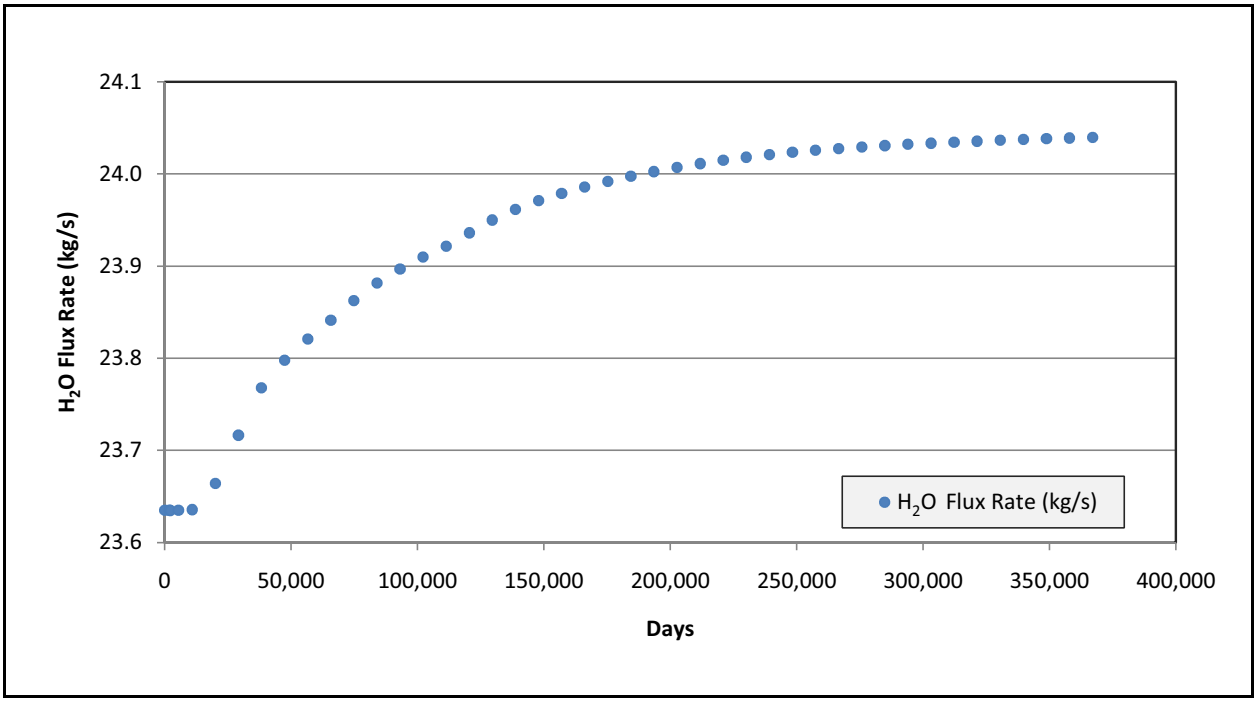

Figure I-9
Time History of Total Water Flux to the LCA from the Unsaturated-Zone Model Domain with an Assumed Net Infiltration Rate of 5 mm/yr

accelerate the timing and rate of release of some contaminants to the water table from the detonation sites in the unsaturated zone, the cumulative water flux to the LCA is not significantly impacted by the transient crater-enhanced recharge, in part because of the small areas of the craters.

I.4.2 Effect of Transient Recharge from the Saturated Alluvial/Volcanic Aquifer System

The groundwater recharge to the saturated LCA from the overlying saturated alluvial/volcanic aquifer system is uncertain. As noted in Section 4.0, a number of different cases have been analyzed to explore a reasonable range of uncertainty in the saturated alluvial/volcanic aquifer system flow and transport properties that could affect release rates from the saturated alluvial/volcanic aquifer system to the LCA and hence the extent of contaminant migration in the LCA. The results below use a saturated alluvial/volcanic aquifer system modeling case that assumes an average infiltration rate of 5 mm/yr, no vertical anisotropy in the alluvial aquifer, a minimum crater-enhanced recharge rate, a median effective porosity of the tuff confining unit of 0.25, no vertical anisotropy of the tuff confining unit, and an exchange volume radius of 2 R_c. This case represents an upper bound on the

expected recharge to the saturated alluvial/volcanic aquifer system model and thus bounds the likely impact of post-detonation impacts.

Assuming a spatially averaged infiltration rate of 5 mm/yr, Figure I-10 presents a map of the steady-state pre-detonation water flux to the LCA from the saturated alluvial/volcanic aquifer system. The transient effects associated with underground nuclear detonations and the changes in total recharge associated with additional crater-enhanced recharge result in a temporal variation in the total volumetric flux into the LCA from the overlying saturated alluvial/volcanic aquifer system as illustrated in Figure I-11. This figure illustrates the modeled changes in the total volumetric flux to the LCA in the 50-year time period since the underground nuclear testing in the Yucca Flat saturated alluvial/volcanic aquifer system commenced on July 26, 1957. The spatial distribution of the modeled volumetric flux to the LCA at discrete times during the height of the underground nuclear testing in Yucca Flat is illustrated in Figures I-12 and I-13 (corresponding to October 12, 1965, and December 3, 1978); Figure I-14 illustrates the spatial distribution of the modeled volumetric flux to the LCA after the cessation of nuclear testing (corresponding to July 26, 2007). A comparison of Figures I-10 and I-14, as well as the temporal distribution of the total flux to the LCA in Figure I-11, shows that a steady-state flow field is created after the cessation of testing and that the spatial distribution is similar to the steady-state distribution of recharge that existed before testing, except that the flux rate is increased by about 10 percent.

The modeled temporal distribution of the total water flux from the saturated alluvial/volcanic aquifer system to the LCA indicates that during the decades of underground nuclear testing in Yucca Flat, there was a significant increase in the annual recharge to the LCA. This increase has been attributed to the amount of water released from storage in the high-porosity, low-permeability confining units immediately after the nuclear detonations. As illustrated in Figures I-12 and I-13, these transient pulses are spatially limited to areas immediately adjacent to the detonations. For example, the large influx of water to the LCA modeled around day 3,000 may be attributed to the CORDUROY and BILBY detonations (with announced yields of less than 200 and 249 kt, respectively) and other detonations in northwest Area 3, whereas the large influx of water to the LCA modeled around day 7,800 may be attributed to the BASEBALL, TORTUGAS (announced yields of 20 to 150 kt), and BORREGO (announced yield less than 150 kt) detonations, and the STARWORT detonation (with an announced yield of 90 kt).

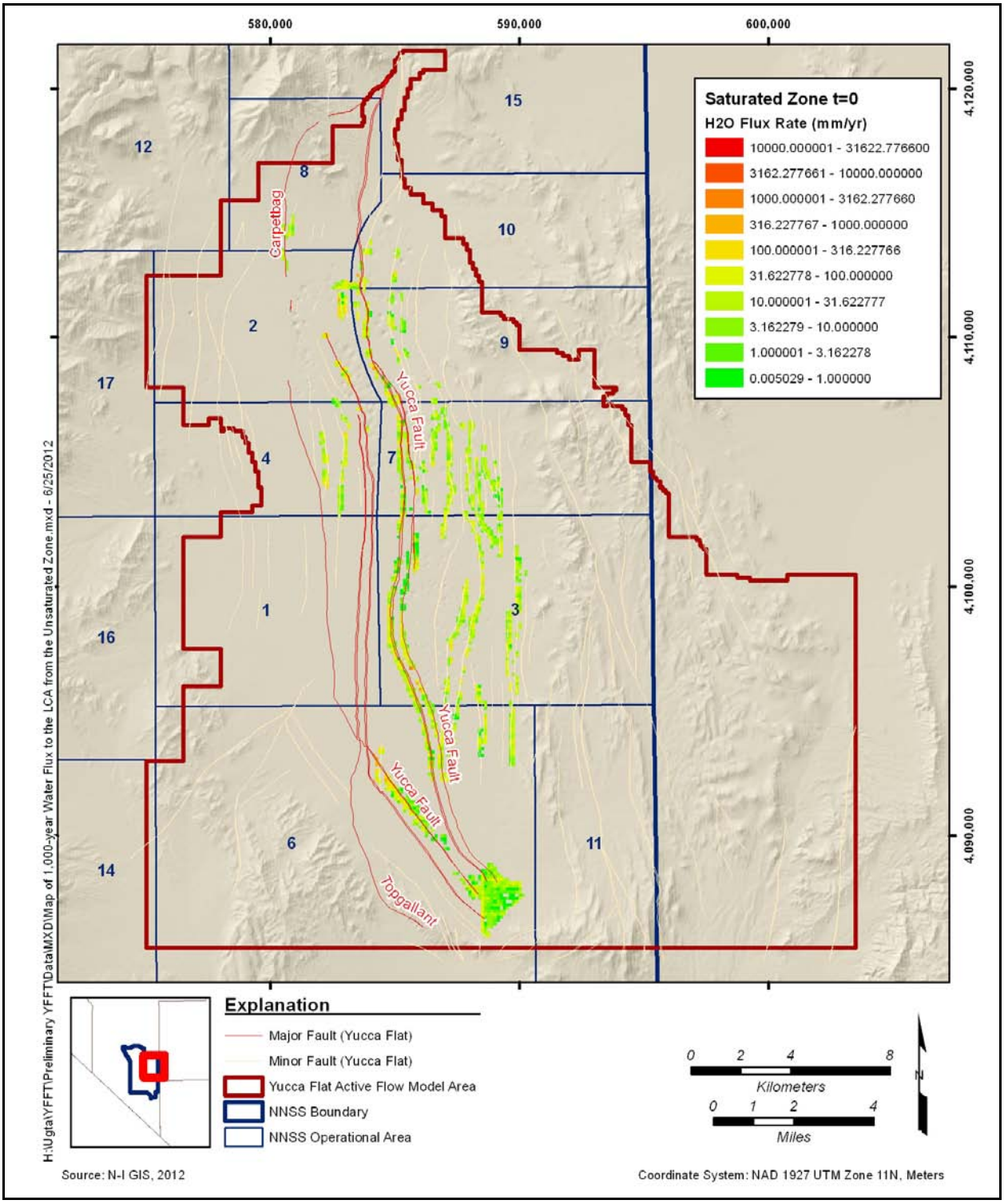

Figure I-10
Map of Pre-detonation Steady-State Water Flux to the LCA from the Saturated Alluvial/Volcanic Aquifer System with an Assumed Infiltration Rate of 5 mm/yr

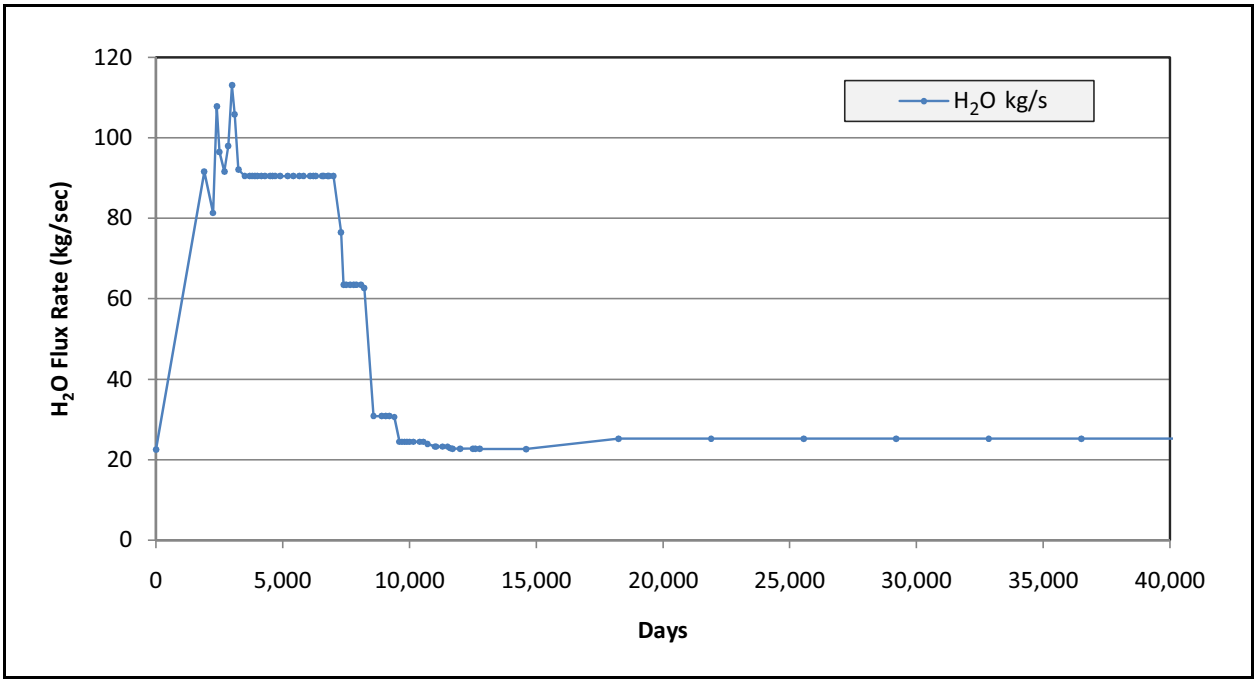

Figure I-11
Time History of Total Water Flux to the LCA from the Saturated Alluvial/Volcanic Aquifer System with an Assumed Infiltration Rate of 5 mm/yr

As described in Section 5.0, the LCA flow model is a steady-state flow model that has been calibrated to a range of spatially distributed recharge rates. As noted by Fenelon et al. (2012), with the exception of the NASH detonation in northwest Yucca Flat, there has been no direct observation of the impacts of detonation-induced transient effects on hydraulic heads in the LCA. This is perhaps because (1) nuclear testing preceded the ability to perform continual water-level monitoring, (2) the observation locations are across faults that act as hydrologic barriers to detonation-induced transient effects, (3) the transmissive and storage properties of the LCA are such that no discernible effect would be generated, or (4) the modeled transient pulses from the overlying saturated alluvial/volcanic aquifer system are conservatively overestimated. In addition, it is possible that the modeled transient recharge to the LCA (Figure I-11) is of a similar magnitude to the water withdrawn from the LCA during the time of active underground testing (Figure I-14), thus cancelling any potential effect even though the areas of groundwater withdrawal are spatially different from the areas of active testing.

The extent to which the modeled transient recharge pulses to the LCA could affect the LCA flow field and hence contaminant transport in the LCA has been evaluated through a transient LCA flow model. The evaluation began with calibrating a steady-state flow field to the infiltration rate of 5 mm/yr.

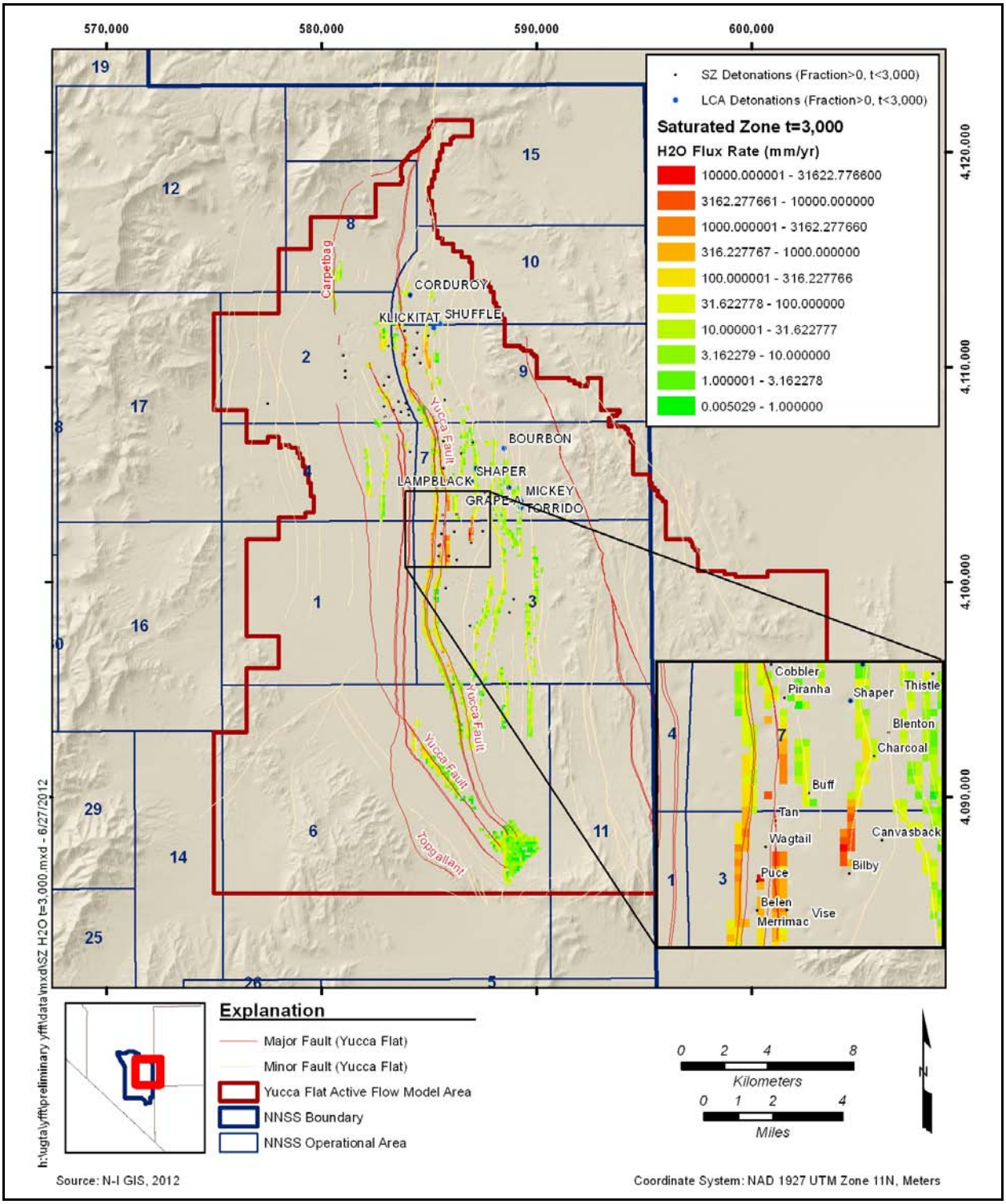

Figure I-12
Map of Modeled Water Flux to the LCA from the Saturated Alluvial/Volcanic Aquifer System at Day 3,000 (October 12, 1965) with an Assumed Infiltration Rate of 5 mm/yr

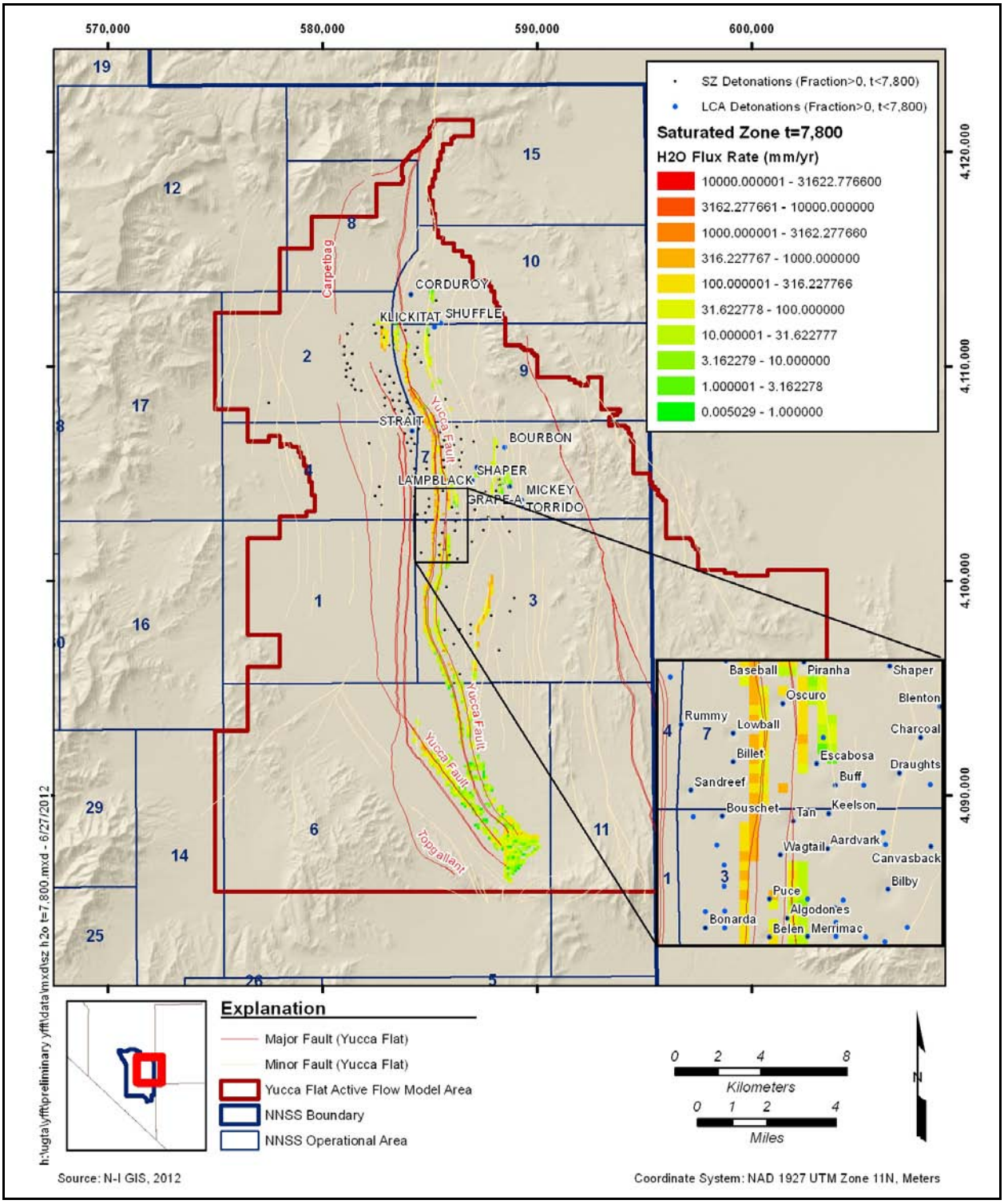

Figure I-13
Map of Modeled Water Flux to the LCA from the Saturated Alluvial/Volcanic Aquifer System at Day 7,800 (December 3, 1978) with an Assumed Infiltration Rate of 5 mm/yr

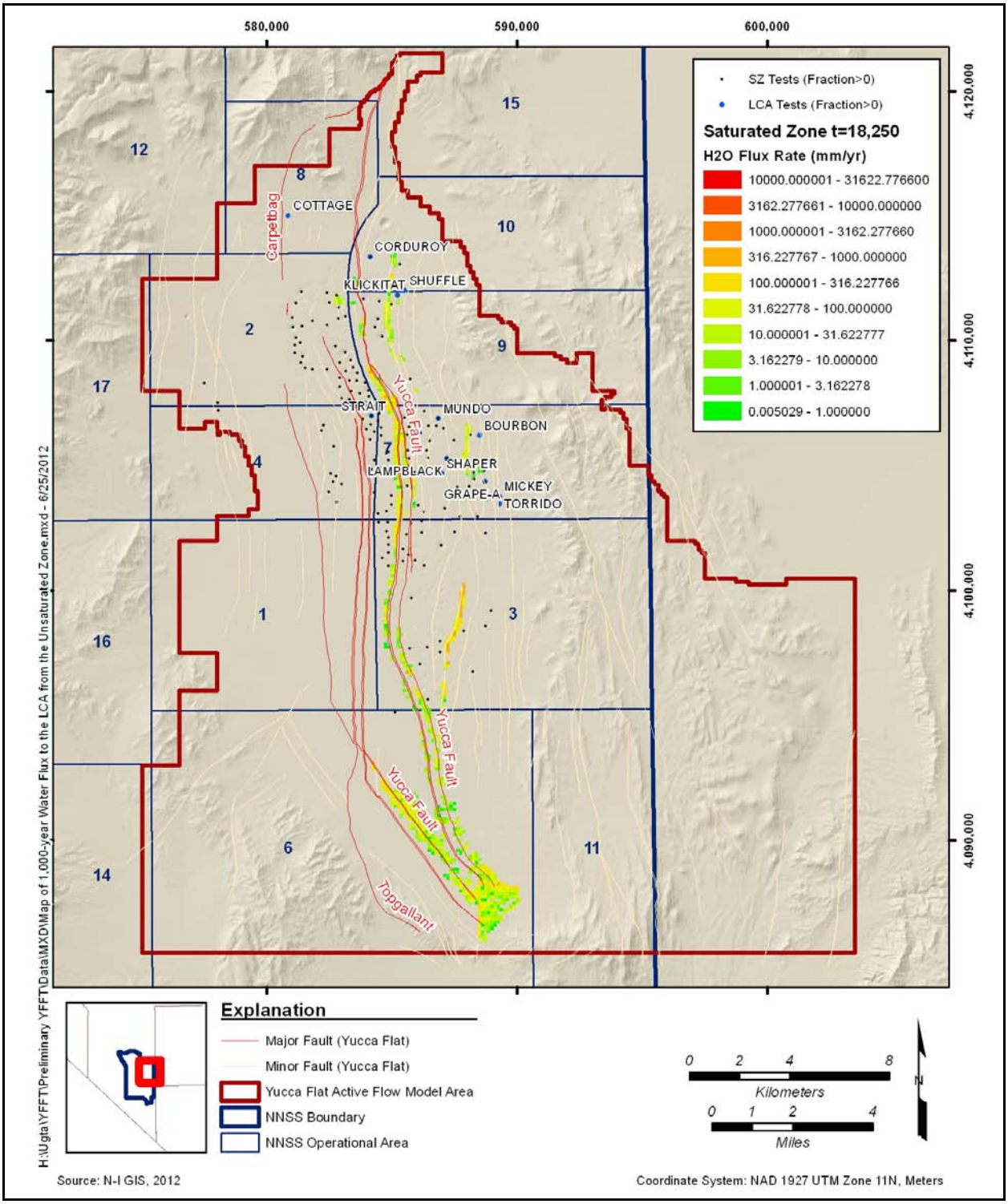

Figure I-14
Map of Modeled Water Flux to the LCA from the Saturated Alluvial/Volcanic Aquifer System from Day 18,250 (July 26, 2007) to Day 365,250 (July 26, 2957) with an Assumed Infiltration Rate of 5 mm/yr

Transient recharges were then applied based on the changes in the modeled recharge rate illustrated in Figure I-11. The results of the enhanced recharge rates are illustrated in Figures I-15 and I-16 for time periods corresponding to 8.5, 12.5, 18, and 31 years after the commencement of nuclear testing in Yucca Flat. The early time periods show an area of increased heads in northern Yucca Flat of up to 5 m above the pre-detonation levels; however, these increased heads are predicted to decline to near steady-state values within about a decade after the cessation of significant testing. The return to pre-detonation conditions is a result of the cessation of the testing and the transmissive and storage properties of the LCA.

Although the LCA flow field in the later 970 years of the 1,000-year time period of interest for establishing contaminant boundaries is unaffected by the transient water influx that occurred in the 30 years of underground nuclear testing in the saturated rocks of Yucca Flat (from 1962 to 1991), the potential transient effects of local recharge on tritium transport during the first 30 years may be significant. This effect was evaluated by applying particle tracking to the transient flow field for the first 30 years. The particle tracking started at several nodes that were determined to provide significant tritium influx from saturated-zone sources during this time period (notably, the BILBY, STARWORT, BORREGO, and BASEBALL detonations).

Two sets of simulations were conducted to estimate the impact of steady-state and transient flow fields on particle transport. The first simulation was a full transient run that used the 5-mm/yr calibrated flow field, whereas the second simulation used the pre-detonation steady-state flow field for the calibrated 5-mm/yr case. The particle travel distances in the LCA for the first 30 years of nuclear testing are presented in Figure I-17 for the steady-state and transient recharge cases. A fracture effective porosity of 0.0045 was used for the simulations. Most of the particles remain close to their source locations. The largest migration is near the BILBY detonation location, where the change in water flux (from pre-detonation steady-state conditions) also is calculated to be the largest as indicated in Figure I-12. A comparison of the steady-state and transient particle trajectories in Figure I-17 suggests that the particle travel distances are similar for the steady-state and transient flow fields except in the vicinity of the BILBY detonation site, where the particles traveled approximately 800 m farther for the transient case.

The modeled transient case is a bound on possible net infiltration rates given that the calibrated saturated alluvial/volcanic aquifer system model with a 5-mm/yr infiltration rate tends to maximize

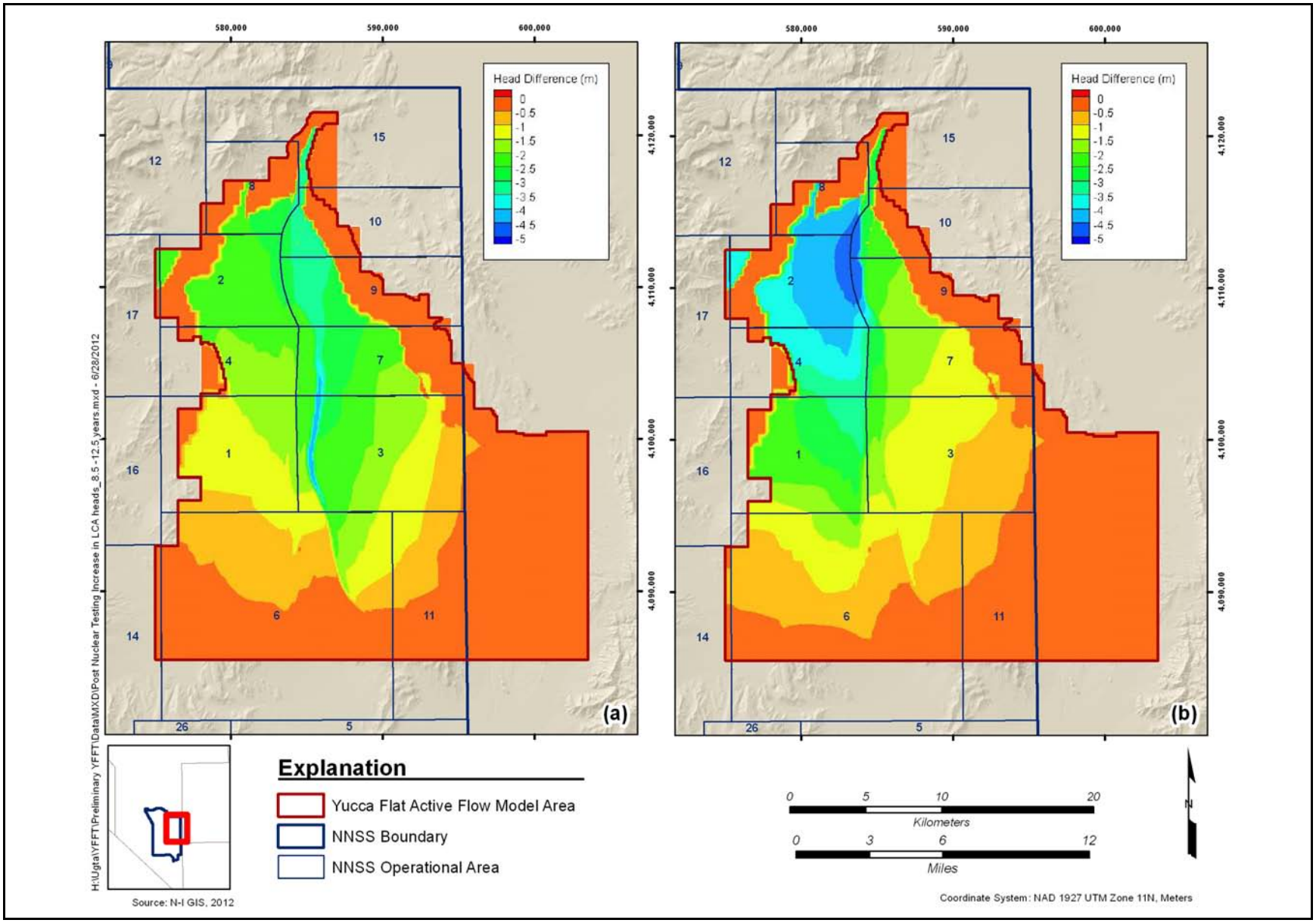

Figure I-15
Calculated Increase in LCA Potentiometric Surface due to Underground Nuclear Testing: (a) 8.5 Years, and (b) 12.5 Years (with an Assumed Recharge Rate of 5 mm/yr)

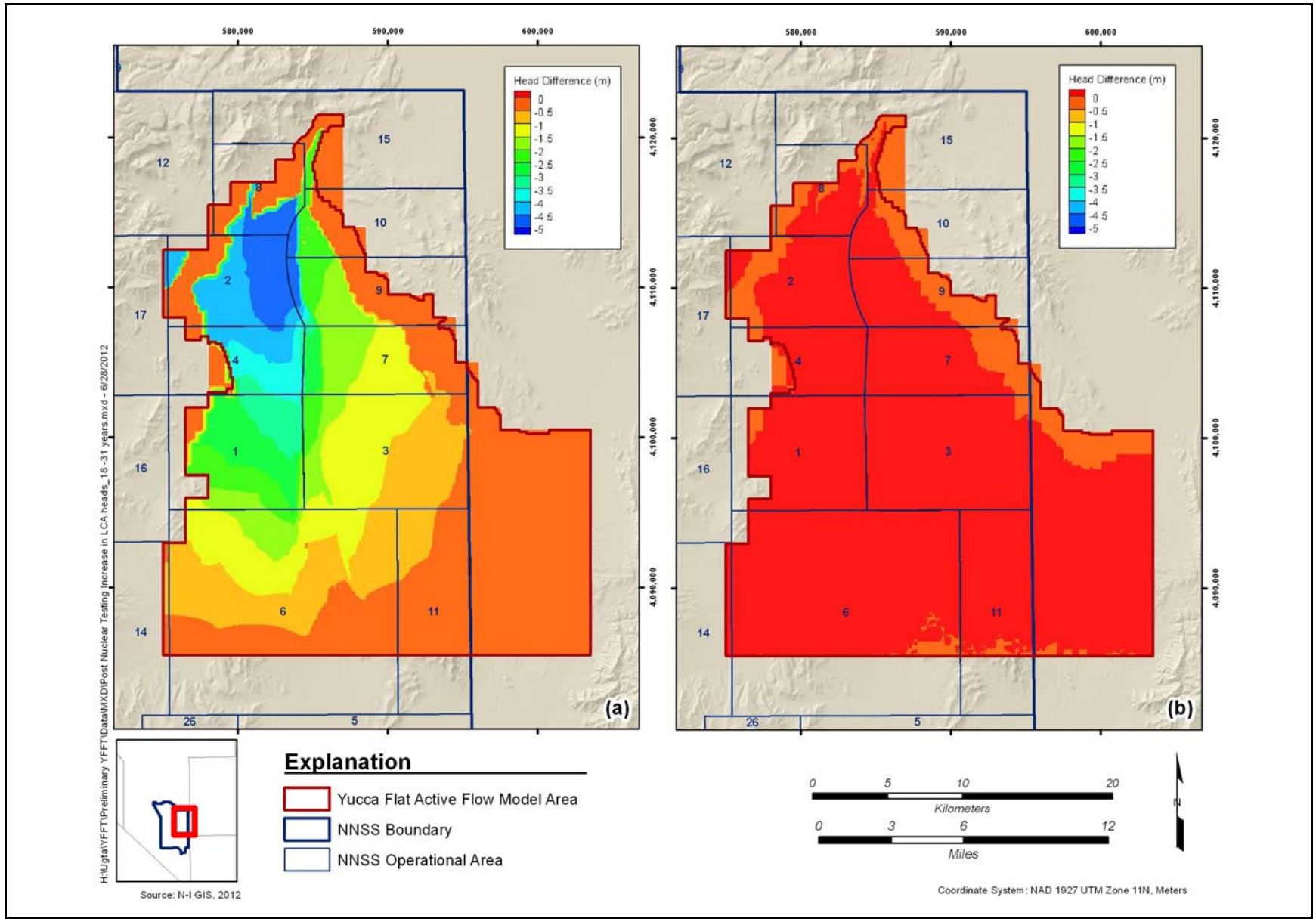

Figure I-16
Calculated Increase in LCA Potentiometric Surface due to Underground Nuclear Testing: (a) 18 Years, and (b) 31 Years (with an Assumed Recharge Rate of 5 mm/yr)

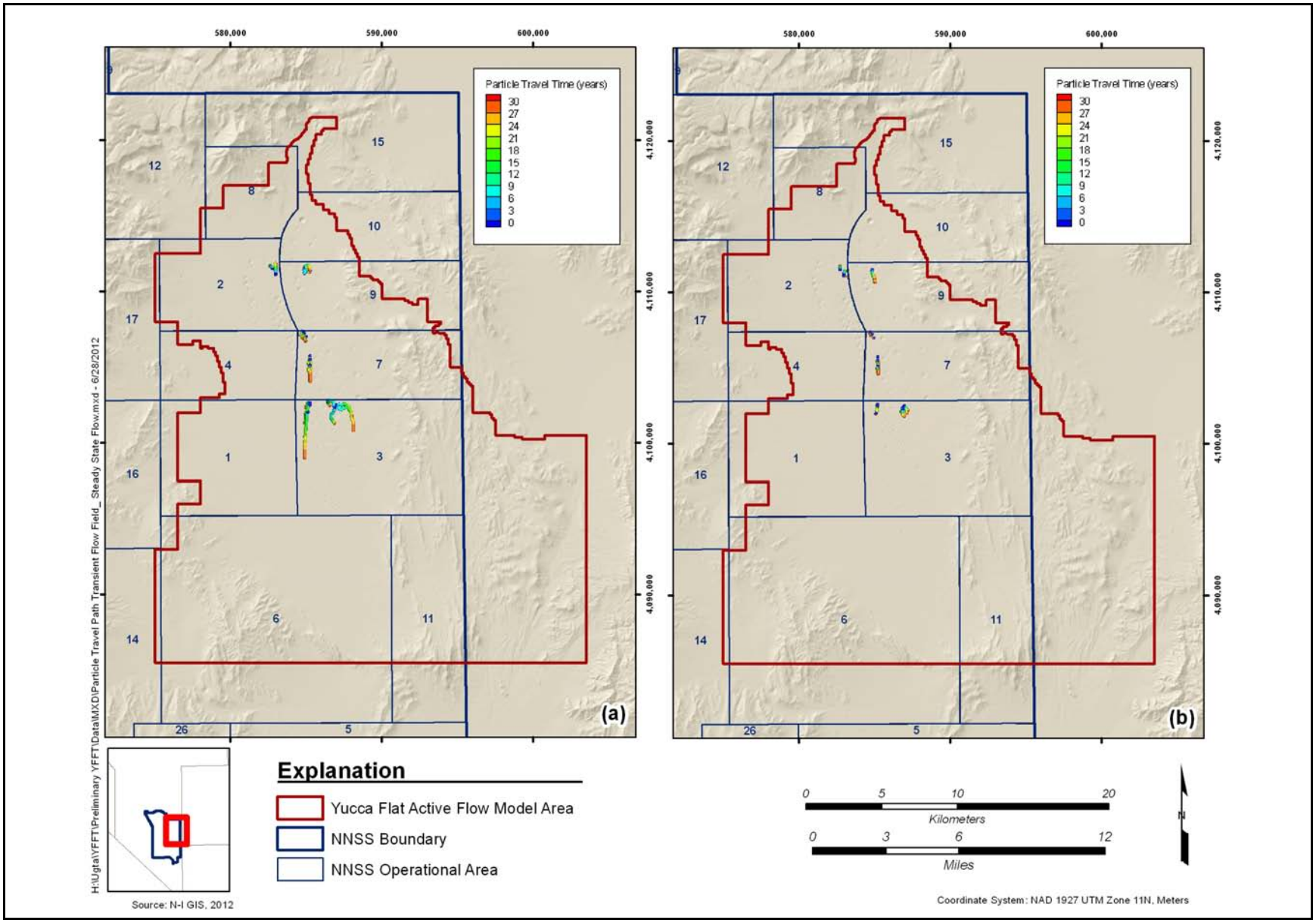

Figure I-17
Calculated Particle Travel Times from Representative Contaminant Source Nodes: (a) Transient Flow Field due to Underground Nuclear Testing, and (b) Steady-State Flow Field (with an Assumed Recharge Rate of 5 mm/yr and Fracture Effective Porosity of 0.0045)

the permeability of the tuff confining units as presented in Section 4.0. As a result, the actual magnitude of transient drainage associated with underground nuclear detonations is expected to be much less significant than this modeled case suggests. Based on the above simulations, the consequence of using a steady-state flow field for conducting LCA transport simulation is reasonable because the contaminant boundary would not be significantly affected by the transient transport in the LCA.

I.5.0 CONCLUSIONS

The analyses presented in this appendix demonstrate that invoking the assumption of steady-state boundary conditions during the development and calibration of the Yucca Flat saturated LCA flow model does not significantly impact flow and transport modeling results. In addition, neglecting groundwater pumpage from the LCA does not appreciably affect the simulated flow field. Assuming steady-state boundary conditions when simulating the MWAT does not significantly impact the simulated drawdowns or calibrated aquifer properties that are in part based on the observed drawdowns during the transient MWAT. Additionally, the results of the analyses presented in Section I.4.0 indicate that assuming steady-state recharge from the overlying unsaturated zone and saturated alluvial/volcanic aquifer system (and thereby neglecting post-detonation transient recharge) to the LCA does not appreciably impact radionuclide transport or the ability to predict the extent of contaminant migration in the 1,000-year FFACO period even for the net infiltration rate of 5 mm/yr. More representative estimates of net infiltration from the unsaturated zone and saturated alluvial/volcanic aquifer system model domains (e.g., values in the range of 0.1 to 1.0 mm/yr) would lead to even less of a transient impact on the LCA flow field. This conclusion is also supported by Fenelon et al. (2012), who show that there is no direct correlation between the potential effects of nuclear testing and changes in the LCA flow field, with the exception of the NASH detonation.

Based on the above analyses, it is concluded that using a steady-state LCA flow model is appropriate for conducting calculations of both groundwater flow and contaminant transport in Yucca Flat.

I.6.0 REFERENCES

Fenelon, J.M., D.S. Sweetkind, P.E. Elliott, and R.J. Laczniak. 2012. *Conceptualization of the Predevelopment Groundwater Flow System and Transient Water-Level Responses in Yucca Flat, Nevada National Security Site, Nevada*, Scientific Investigations Report 2012-5196. Reston, VA: U.S. Geological Survey.

SNJV, see Stoller-Navarro Joint Venture.

Stoller-Navarro Joint Venture. 2006. *Phase I Hydrologic Data for the Groundwater Flow and Contaminant Transport Model of Corrective Action Unit 97: Yucca Flat/Climax Mine, Nevada Test Site, Nye County, Nevada*, Rev. 0, S-N/99205--077. Las Vegas, NV.

Appendix J

LCA Fault Zone Conceptual Model and Characteristics

J.1.0 INTRODUCTION

The prevalence of the generally north-south trending normal faults is an important characteristic of the geologic and hydrogeologic framework of the alluvial-volcanic aquifer system and LCA in the central testing area of Yucca Flat. Although the underground nuclear testing program attempted to avoid these faults when locating working points for underground detonations, the close spacing of the faults, uncertainty in the size of the anticipated detonation cavity as well as the possibility that faults were initially undetected under the thick alluvial blanket resulted in a number of detonation cavities or exchange volumes intersecting fault planes. These faults have been recognized to provide a potential vertical hydraulic communication through the lower tuff confining units to the underlying LCA as well as to provide a potential lateral conduit for groundwater flow in the LCA along the strike of the faults.

Recognizing the significance that faults have on the transport of contaminants from underground nuclear detonations to and within the regional carbonate aquifer system, this appendix summarizes the existing data and interpretations used to define the basis for the conceptual model of fault zone flow and transport in the LCA. In addition, the interpretation of hydrogeologic information developed from direct testing of fault zones in boreholes drilled in central Yucca Flat is presented as it provides a basis for the fault zone parameter distributions used in the LCA transport model.

J.1.1 Objectives

The characterization of the fault zones in Yucca Flat has resulted in a significant amount of geologic and hydrogeologic data that are relevant to the development and application of groundwater flow and contaminant transport models. The data and related interpretations form the basis for the conceptual model of faults in Yucca Flat.

This appendix summarizes the relevant data and observations and provides additional analyses of this information to support the conceptual model and parameter values used in the flow and transport models presented in Sections 4.0 to 6.0. The principal focus of this appendix is on the transport characteristics of the faults in the LCA because of the significance fault damage zone transport properties have on the forecast extent of contaminant migration. This focus is derived from the

importance of the LCA as a regionally-contiguous aquifer in the eastern half of the NNSS (Winograd and Thordarson 1975; Fenelon et al 2012).

J.1.2 General Description of LCA Fault Zones

Faults are ubiquitous at the NNSS and include normal, reverse, thrust, and strike-slip faults formed by both compressional and extensional forces. Normal faults, related to generally east-west-directed, basin-and-range extension during the past 11 million years, are dominant structural features in the eastern and southern portions of the NNSS. These faults control much of the topographic character in the area, and played significant roles in the development of structural basins such as Yucca Flat. Normal faults range in size from small to large basin-forming faults such as the Yucca, Topgallant, and Carpetbag faults that have more than 300 meters of offset. The hydrologic framework model of the Yucca Flat/Climax Mine CAU includes faults with greater than a 60 m offset (BN, 2006). Most normal faults in the NNSS region strike in a general north-south direction and dip steeply either to the east or west, reflecting the general east-west extensional stress direction.

The architectural components recognized in NNSS faults include the fault core, damage zones and protolith (Prothro et al., 2009) (Figure J-1). The fault core is the relatively narrow zone where most of the fault offset is accommodated through slippage along one or more closely spaced and linked fault planes (Caine and Forster, 1999). This slippage is usually accompanied by collapse of *in situ* matrix porosity and fragmentation and granulation of the wall rock, and results in the formation of fault-core material ranging from coarse breccia and sand-sized, granulated material to very fine-grained, clay-rich fault gouge. Extending out and away from the fault core in both the hanging wall and footwall rocks of most faults is a damage zone containing deformation features related to movement along the fault. Fault-related deformation features in damage zones include shattered and brecciated zones, fractures, smaller-scale antithetic and synthetic faults, deformation bands, and fault-related folding referred to as fault drag or drag folding (Figure J-1). Structural features within damage zones tend to enhance permeability generally by the formation of additional fracture networks. The protolith is the country rock beyond the damage zone, which exhibits little or no fault-related damage.

J.1.3 Summary of Geologic Information/Interpretations of LCA Fault Zones

Over the decades of underground nuclear testing and subsequent characterization activities at the NNSS significant geological and geophysical investigations of the fault systems in Yucca Flat have

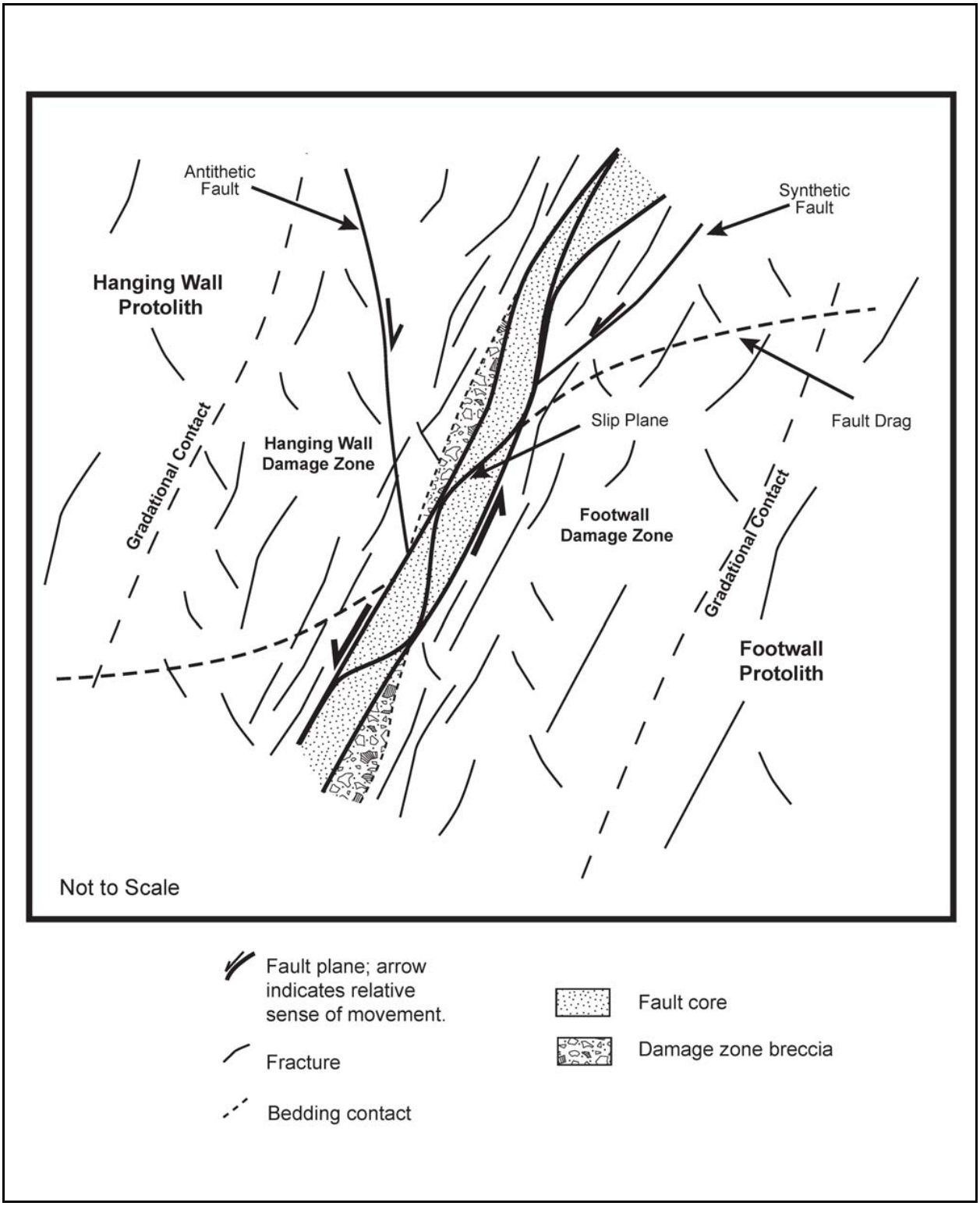

Figure J-1
Schematic Cross-Sectional View Across a Fault Zone Showing Architectural Components and Associated Structural Features
Source: Prothro et al., 2009

occurred. The location and offsets of faults in the Yucca Flat basin have been determined by detailed surface geologic mapping, abundant drill-hole observations used to evaluate the offset of Cenozoic volcanic units and geophysical investigations used to define the offsets within the Paleozoic bedrock. The results of these investigations are summarized in a number of USGS and other contractor documents.

Recent investigations have focussed on evaluating the geologic characteristics of the fault zones in the alluvial/volcanic aquifer system and the LCA. Sweetkind and Drake (2007) summarize the geologic mapping and fault zone data collected at surface locations west and northwest of Yucca Flat where the volcanic section that exists at depth beneath Yucca Flat is exposed at the surface. Descriptive field data were collected at 14 surface outcrop locations and from three drill cores. Field investigations concentrated on describing fault geometry (number of splays, fault curvature, and linkage) and fault zone architecture (fault trace length, width of fault core and damage zones, asymmetry of damage in hanging wall and footwall) in welded, nonwelded, and zeolitized tuff.

At each outcrop location, fault-related rocks were subdivided into three classes: (1) a fault core that is adjacent to the slip plane and composed of clay-rich gouge, highly pulverized rock, or matrix-supported breccia; (2) a damage zone of clast-supported breccia and fractured rock surrounding the fault core; and (3) a protolith of relatively undamaged rock at some distance from the fault. Fault cores were described by the core zone width, matrix material, degree of cementation, alteration or mineralization, presence of clay gouge, and the nature of contacts with damage zone. Damage zones were described by the width in hanging wall and footwall of fault, nature of contacts with fault core and protolith, changes in fracture orientation and intensity, presence of fault splays or offset in hanging wall and footwall of fault, and the presence of breccia. The protolith was described by noting the degree of welding. This study determined that total displacement, among other variables, was an important factor in the development of fault zones. Faults with large amounts of displacement typically developed wider damage zones than faults with modest amounts of displacement (Sweetkind and Drake, 2007).

Results of studies at Yucca Mountain and Yucca Flat by Dickerson and Drake (2003) and Sweetkind and Drake (2007), respectively, show that the ratio of total offset to total width of the damage zone ranges from 10:1 to 1:6, with an average value around 2:1. As the amount of offset increases, the total amount of collateral damage to the rocks adjacent to the plane of the fault also tends to increase. Field

observations made at Yucca Mountain has revealed that increasing amounts of offset along faults not only increases the overall width of fault damage zone, but also increases the degree and extent of fracturing and brecciation associated with these damage zones. An important conclusion from these investigations is the general relationship between fault displacement and the width of the fault damage zone reproduced as Figure J-2.

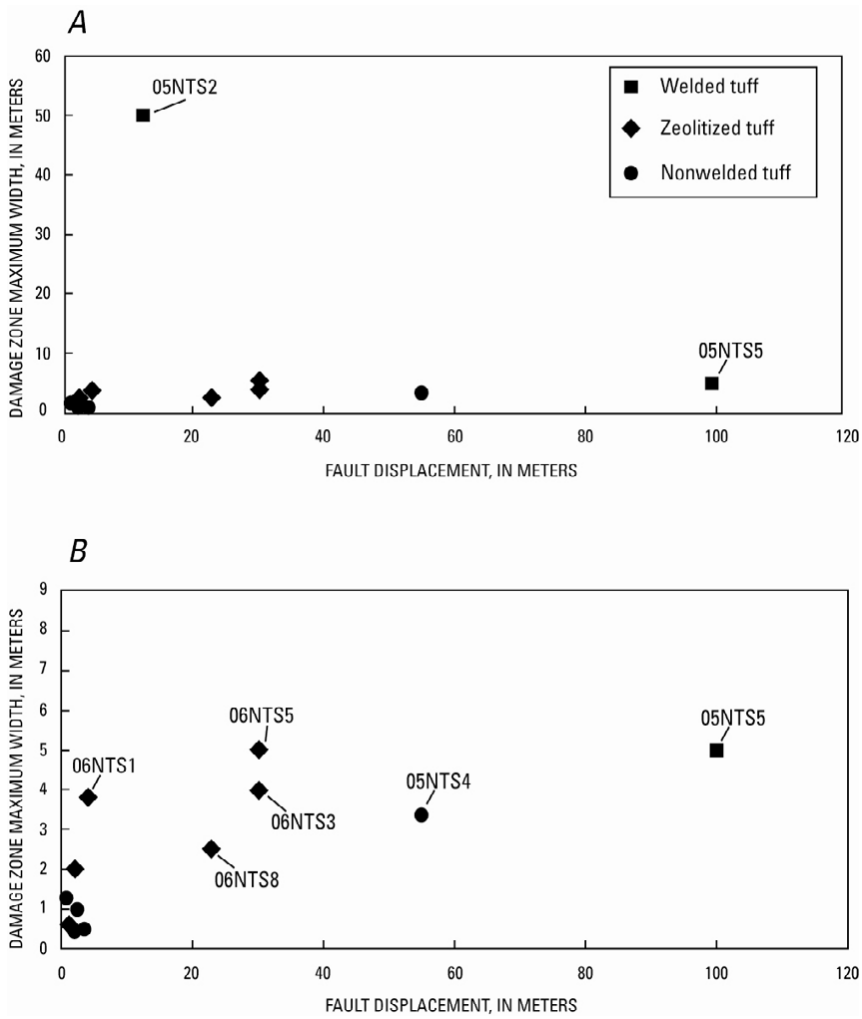

Figure J-2
Relationship Between Fault Displacement and Damage Zone Width for the Nevada National Security Site
Source: Sweetkind and Drake, 2007

Additional detailed geophysical characterization across several inferred faults was performed by Asch et al (2008) to develop a detailed understanding of the geometry and physical properties of fault zones in Yucca Flat and to characterize fault geometry, the presence of fault splays, and the fault-zone

width. The investigations performed by Asch et al (2008) included a suite of electrical geophysical surveys in combination with ground magnetic surveys. These surveys resulted in high-resolution subsurface data that portray subsurface fault geometry at two sites and identify structures not readily apparent from surface geologic mapping. The results of these investigations confirmed that the Yucca Flat fault is sinuous, probably as the result of en-echelon linked segments. Geophysical profiles were conducted at a variety of scales to characterize individual fault segments and to identify the extent of damage zones associated with fault offset.

J.1.4 Summary of Hydrogeologic Information/Interpretations of LCA Fault Zones

The hydrogeologic characterization of fault zones in Yucca Flat has been the subject of a number of studies. The relationship of permeability structures and related observations of faults has been summarized by Prothro et al (2009). Some of the key conclusions related to the effect of faults on the hydrogeologic characteristics of the LCA synthesized from these studies are enumerated below:

> Numerous exposures of faulted CA were studied, and all showed fault-related permeability features consistent with strong and well consolidated rock units. Most of the faults studied were basin-and-range normal faults, but one may represent an older reverse fault. Damage zone characteristics included enhanced fracture development, with fracture intensity increasing towards the fault core. Cemented breccia was common adjacent to the fault core, but most damage zone fractures were open, with little secondary mineralization observed.
>
> Fault zones within CA at the NTS likely create important zones of enhanced permeability. Permeability enhancement is the result of an increase in fracturing within the damage zones of faults cutting CA. Although fault cores likely form zones of low permeability, they are relatively narrow and thus probably have little overall influence on the permeability of fault zones within CA. However, the presence of the fault core and the tendency of fractures to strike parallel to the fault likely create anisotropy with regard to flow properties within CA fault zones. Flow properties are probably most enhanced in a direction parallel to the strike of the fault.
>
> Faults are complex, profound, and dominant geologic features at the NTS, so it is reasonable to assume that faults are also important, yet complex, hydrologic features. Comparing and contrasting observations of fault zones at the NTS with observations and data from other studies strongly suggests that faults at the NTS form discrete zones of enhanced fracture permeability within those HGUs susceptible to enhanced fracture development. It should be remembered that UGTA CAU-scale HFMs are geologically simplified and, thus, include only a small portion of the faults present. These are typically the larger normal faults. Therefore, portions of HSUs between model faults likely have, in reality, many more faults, albeit smaller, with associated

fault zones not included in the model. The effect of the faults not captured in the HFMs on the flow properties of HSUs should be considered during flow modeling and HSU parameterization. (Prothro et al, 2009)

The identification of faults in the subsurface in Yucca Flat is based on a number of direct and indirect borehole observations. Indirect observations include breakouts in the borehole, unstable borehole conditions, and water inflow zones. Direct observations include fracture mapping in image logs. Detailed characterization of fracture zones in the vicinity of faulted LCA is presented in SNJV (2005a). The hydraulic and tracer testing at ER-6-1 was analyzed to evaluate the role of the fault intersected by the borehole and the lateral extent of faults in SNJV (2006). These analyses included estimating the hydraulic conductivity along the major faults in the HFM to reproduce the observed response due to the MWAT (Figure J-3). Additional details and interpretations associated with the characterization of the fracture transport parameters in fault damage zones are presented in Section J.3.0.

J.1.5 Geologic and Hydrogeologic Information/Interpretations of Analog Fault Zones

The study of the hydrogeologic characteristics of faulted domains in carbonate rocks is not unique to the LCA at the NNSS. Hydrogeologic characterization of fault zones in carbonate rock domains has been the subject of a number of studies in the scientific literature. These studies confirm the general conceptual model of strike-slip and normal faults consisting of a core zone of lower permeability and higher permeability damage zones in the hanging and footwalls. These studies also confirm the general observation that the damage zone width increases with fault length or fault offset, similar to the observations made at the NNSS. A few representative examples are presented below.

Agosta (2008) conducted field and laboratory investigations of thrust and normal faults in the Fucino Basin in central Italy to determine the relationship between hydraulic properties (e.g., permeability and porosity) and related fault architecture characteristics. The investigations illustrated a 10,000 fold increase in permeability in the fault damage zone compared to the country rock.

Vermilye and Scholz (1998) evaluated the correlation between process (e.g., damage) zone width and fault length. For faults with lengths on the order of 10 km (similar to the length of the major faults in Yucca Flat), the process zone width was about 100 m.

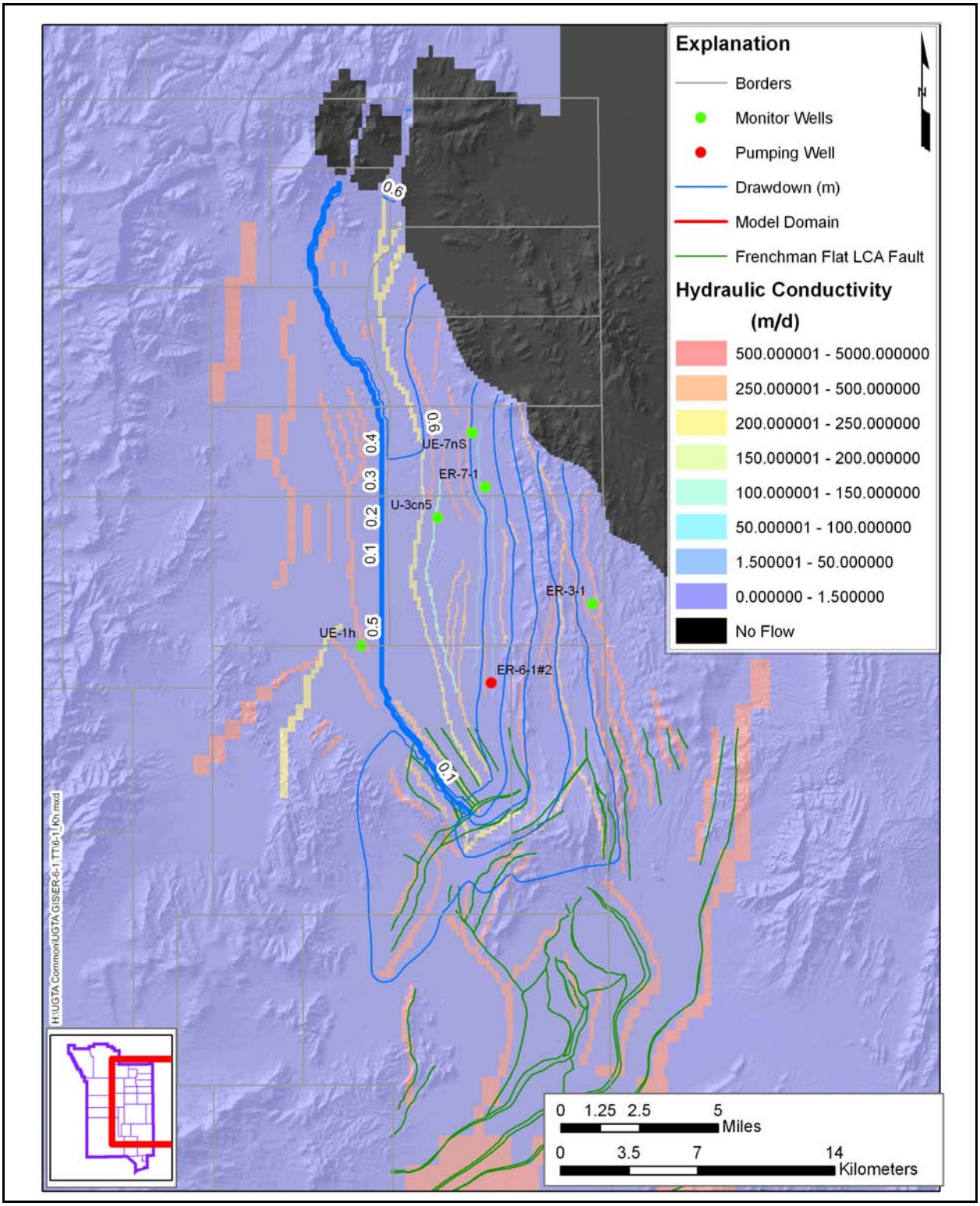

Figure J-3
Estimated Hydraulic Conductivity of Faults in Yucca Flat Derived from Analyses of ER-6-1 MWAT
Source: Modified from SNJV, 2006

Boutareaud et al (2008) evaluated the correlation between permeability and fault zone structures and determined the permeability of the central gouge in the core zone was on the order of 10 to 10,000 times less permeable than the protolith (e.g., country rock) and the permeability of the damage zone was on the order of 10 times more permeable than the protolith.

Micarelli et al (2006) studied near surface normal fault zones in the calcarenites of the Hybleau Plateau of Sicily. They studied the relationship between the size and characteristics of fault core and damage zones to the amount of fault displacement. For displacements less than 1 m, there was no fault core; for displacements from 1 to 5 m were observed to have discontinuous cores and faults with greater than a 5 m offset were observed to have a continuous core consisting of cataclastic rocks. Damage zone was observed to increase with fault displacement with the greatest rate of change occurring in faults with displacements less than between 1.5 and 5 m.

In summary, observations from geologic and hydrogeologic settings that are similar to the structural setting of the LCA in Yucca Flat indicate that fault zones can be reasonably conceptualized as consisting of a fault core of reduced permeability and a fault damage zone of increase permeability in comparison to the country rock. These studies also indicate that fault damage zone width is on the order of 1/100th of the fault length based on the correlation of these two properties for the same fault.

J.2.0 LOWER CARBONATE AQUIFER FLOWING FEATURE ANALYSIS

J.2.1 Introduction

Groundwater flow at the NNSS is controlled in part by flow in the Lower Carbonate Aquifer (LCA), which is composed of a thick sequence of marine sediments that accumulated during the Paleozoic and has been intensively fractured by late Cenozoic tectonic activity. On the NNSS, regional movement of water through the LCA is controlled by variations in fracture transmissivity and by structural juxtaposition of this aquifer with the lower clastic confining unit (Winograd and Thordarson, 1975). While solution cavities are present, large-scale faults and smaller-scale fractures are the primary control on groundwater flow within the LCA at the NNSS (Laczniak et al., 1996).

This section reviews the available fracture and spinner flow log data for wells completed into the LCA in Yucca Flat at the NNSS with an emphasis on summarizing what can be estimated about how flow occurs in the LCA. Specifically, the objective was to evaluate the LCA fracture database and evaluate flowing features in the LCA at Yucca Flat.

This section is organized as follows: Section J.2.2 reviews the fracture characterization data available for LCA boreholes. Section J.2.3 discusses the general approach used in the flowing feature analysis documented herein. Section J.2.4presents a synthesis of the available fracture characterization data for the LCA in Yucca Flat and provides a conceptual model or basis for the flowing feature analysis. Section J.2.5 presents the flowing feature analysis and describes a potential conceptual model that may be relevant for defining and modeling flowing features in the LCA in Yucca Flat.

J.2.2 LCA Fracture Database – Yucca Flat

As part of the Underground Test Area (UGTA) Program, a fracture characterization database has been developed with the cooperation of agencies participating in ongoing evaluation and characterization activities, under contract with the U.S. Department of Energy, National Nuclear Security Administration Nevada Site Office (NNSA/NSO). One purpose of this study was to review the LCA properties available in the existing fracture database (a distributed Microsoft Access copy of

Fracture07.mdb) for their applicability for developing a discrete fracture model of the LCA that might be up-scaled to CAU models.

A review of fracture data for wells located in Yucca Flat and completed into the LCA was conducted to determine the availability of data for evaluating flowing features in the LCA. Boreholes located in Yucca Flat and completed to the LCA are ER-6-1, ER-6-1#2, ER-6-2, and ER-7-1 (Figure J-4). summarizes the LCA interval and completion interval in each borehole. Note that the completion interval includes over 85 percent of the LCA in boreholes ER-6-1 and ER-6-1#2 and about 40 percent of the LCA in ER-6-2 and ER-7-1.

The database and reports relied upon in this analysis include:

- Fracture Characterization Database for the NNSS and Vicinity (SNJV, 2007) – Fracture07.mdb.
- Underground Test Area Fracture Analysis Report for Yucca Flat Wells ER-2-1, ER-6-1#2, ER-7-1 and ER-12-2 (SNJV, 2005a)
- Wells ER-6-1 and ER-6-2 Core Fracture Analyses and Geophysical Log Comparisons (IT Corporation, 1996).

A brief summary of the data is provided below.

Core fracture analyses were conducted in ER-6-1 and ER-6-2. The results of those analyses are presented in IT (1996). That report also provides a brief summary of borehole televiewer interpretations for these two boreholes. Neither the core fracture analyses data nor the data from the televiewer interpretations are included in the NNSS fracture characterization database (fracture07.mdb). The quality of the core for ER-6-1 was generally poor resulting in uncertain interpretations of fractures. About 877 ft of good quality core was obtained from the bottom 74 percent (2,006 to 2,883 ft bgs) of the LCA in ER-6-2. Use of fracture information for these two boreholes required conversion of the hard copy information in figures in the report to electronic data. In addition, the upper limit in fracture density for ER-6-1 given in the report is up to 60 fractures per 5 ft. This is significantly higher than the density given for ER-6-2 and observed in ER-6-1#2 and ER-7-1 discussed below. It is likely that these densities are artificially high due to the shattered nature of the core and significant numbers of coring-induced fractures.

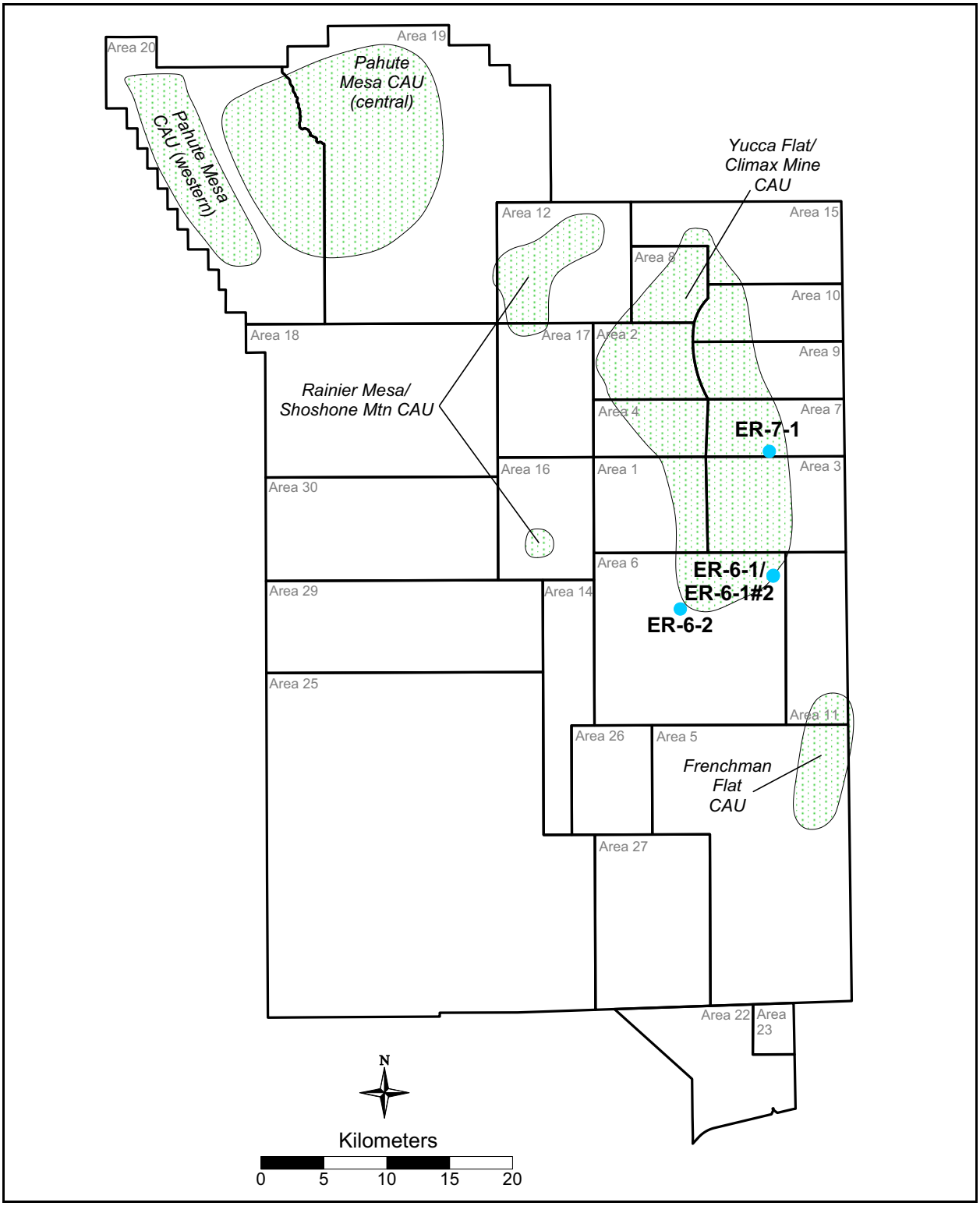

Figure J-4
Location of Environmental Characterization Boreholes Completed into the LCA in Yucca Flat

Electric micro imager (EMI) logs were conducted in boreholes ER-6-1#2 and ER-7-1. The analyses of those logs are provided in SNJV (2005a) and all data from those analyses (location, configuration, aperture, percent open, orientation, and dip) are included in the NNSS fracture characterization database. Data regarding the type of mineral filling in these fractures are not available from the EMI logs. Table J-1 summarizes the available fraction of LCA in the completion intervals for boreholes ER-6-1, ER-6-1#2, ER-6-2, and ER-7-1.

Table J-1
LCA Interval and Completion Interval for Boreholes in Yucca Flat

Borehole	LCA Interval (ft bgs)	Completion Interval (ft bgs)	Percentage of LCA in Completion Interval
ER-6-1	1,770–3,086	1,795–3,206	98
ER-6-1#2	1,770–3,030	1,949–3,200	86
ER-6-2	1,900–2,883	1,740–3,430	41
ER-7-1	1,700–>2,500	2,181–2,479	<40

Table J-2 shows the fracture data available for the LCA in Yucca Flat boreholes. One can see that fractures are mapped and identified and in all cases information on aperture and orientation is available. Spinner flow (SFM) log data is also available for all boreholes and is probably the most relevant dataset with regards to flowing feature analyses.

Table J-2
Availability of LCA Interval Fracture Data in Yucca Flat Boreholes

Borehole	Fracture Aperture	Fracture Orientation & Dip	Coating	Mineral Phase	Spinner Flow Log
ER-6-1	Yes	No	No	No	Yes
ER-6-1#2	Yes	Yes	No	No	Yes
ER-6-2	Yes	No	No	No	Yes
ER-7-1	Yes	Yes	No	No	Yes

J.2.3 Approach to Flowing Feature Analysis

Based upon the available LCA fracture data described in Section J.2.2, an approach was developed for conducting the flowing feature analysis which attempted to synthesize and use the available data

and which would result in both a conceptual understanding (qualitative) and, to the degree possible, a quantitative description of flowing features.

Studies of flow in fractured systems as well as at nearby Yucca Mountain have found that fracture characteristics such as density and aperture do not correlate well with the identification of flowing features (Kuzio et al., 2004). Berkowitz (2002) noted in his review of characterization of flow and transport in fractured media that the magnitude of permeability estimates is critically dependent on the values assigned to fracture transmissivity. He went on to say that mechanical measurements of fracture aperture are of little value in this regard, as they do not capture the influence of the internal geometry of the fracture plane on the hydraulic resistance to flow. The observed fracture pattern may not be strongly related to the equivalent permeability if, for example, a significant percentage of the fractures are sealed by mineral precipitates or are closed owing to the stress regime. Berkowitz (2002) noted in his review that it is typical in fractured systems that a significant proportion of the fractures may be nonconductive. This may be because they are closed, sealed by mineral precipitates or simply poorly interconnected at the scale of interest. A model based on fracture occurrence without accounting for fractures that are nonconductive will vastly overestimate interconnectivity.

Estimation of flowing features requires knowledge of individual feature transmissivity which can only be obtained with focused straddle packer testing or flow logging where flow rates are assumed to be a proxy for transmissivity. There are no focused straddle packer tests available; therefore the best information available for defining flowing features is the SFM datasets. Therefore, though the approach developed reviews the other available data, the methodology relies almost entirely on the SFM data.

The approach used was a phased approach. The initial analysis phase synthesizes the SFM flow data along with the other available fracture data for the boreholes in an effort to: draw conclusions regarding the correlation between measured fracture properties and flow; determine the distribution of flow in the LCA within the available boreholes; and develop a conceptual understanding of flowing features within the LCA which could be used to guide a more quantitative analysis. This phase of the analysis is simply referred to as a data synthesis phase.

The principal methodology employed in the first phase is graphical depiction of SFM interval flow rate versus other fracture property data collected in each borehole. Assuming negligible vertical gradients within the logged intervals, interval flow rate is reasonably correlated to interval

transmissivity. Through these techniques one can determine how flow is contributed across the logged interval and also see if other measured data such as aperture correlates with flow intervals.

The second phase is a detailed quantitative analysis of the SFM logs to attempt to: define flowing features and to discriminate large-scale versus smaller-scale flowing features. The methodology used in this phase takes advantage of the fact that changes in the SFM signal (converted to velocity and then flow rate) represents a change in the flow rate in the borehole. This assumes the SFM data has negligible noise, is not affected by tool characteristics, and that the diameter of the logged interval is known. By direct inspection of the flow logs and by calculating the derivative of the flow rate in the borehole, inflowing features can be isolated. The objective of the detailed analysis was to develop an approach for accessing the distribution of flowing features across the LCA at Yucca Flat.

Further details regarding the methodology are described in the analysis section below.

J.2.4 LCA Flowing Feature Analysis

The flowing feature analysis is discussed below. The more qualitative synthesis of the data is discussed first followed by the more quantitative detailed flowing feature analysis.

J.2.4.1 Synthesis of Available LCA Fracture Data

This section presents the available data on LCA fracture character and attempts to synthesize the datasets to better understand how fracture characteristics may relate to flow potential.

The interval logged and percentage of LCA logged are summarized in Table J-3. Flow percentages determined from the SFM logs are illustrated in Figure J-5.

Table J-3
LCA, Completion, and SFM Log Intervals for Boreholes in Yucca Flat

Borehole	LCA Interval (ft bgs)	Completion Interval (ft bgs)	Percentage of LCA in Completion Interval	SFM Log Interval (ft bgs)	Percentage of LCA Logged with SFM Log
ER-6-1	1,770–3,086	1,795–3,206	98	1,553–2,940	87
ER-6-1#2	1,770–3,030	1,949–3,200	86	1,850–3,025	85
ER-6-2	1,900–2,883	1,740–3,430	41	2,030–3,375	31
ER-7-1	1,700–>2,500	2,181–2,479	<40	2,181–2,479	<40

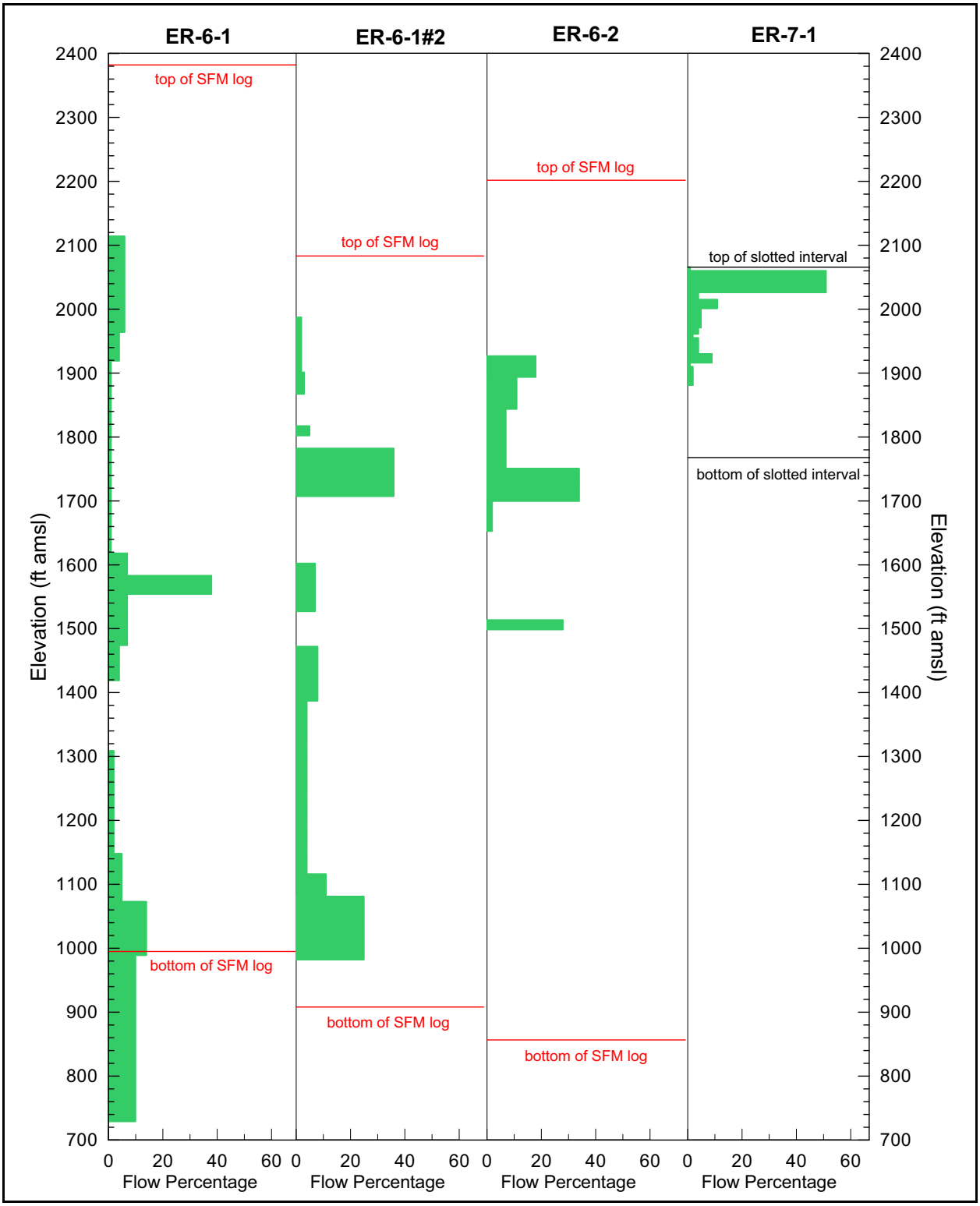

Figure J-5
Flow Percentage Data from Analysis of SFM Logs
Source: SNJV, 2005b and 2005c

A review of Figure J-5 shows that the flow into these boreholes is focused at specific features which can be separated by large intervals of borehole. Figure J-6 shows flow accumulation as percent of the total flow within each of the four boreholes in Table J-3. This figure shows that the fluid logging results indicate that 50 percent or greater of the total flow from the LCA originates in a relatively small percentage of the borehole LCA interval (7 to 12 percent). From a review of the other available data, it is noted that typically these high flow features correlate to washouts, breakouts, breccias, and temperature/pH shifts. The following plots show some of these relationships.

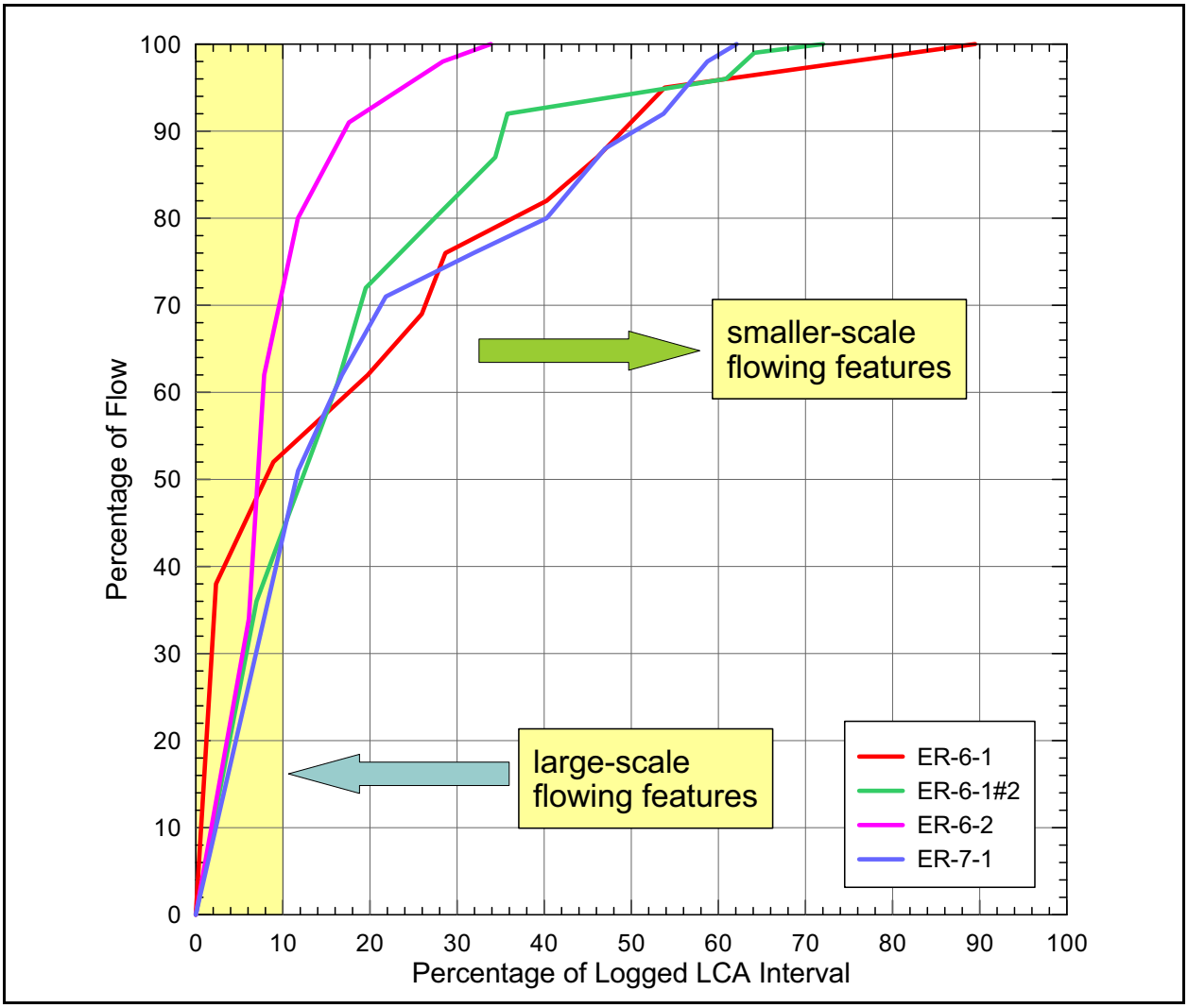

Figure J-6
Accumulation of Flow from SFM Logs

Figures J-7 to J-10 show the borehole lithology, SFM interpreted flow zones and percentages, fracture density at a 5-ft interval, fracture aperture, fracture orientation, fracture dip, and locations of washouts and breakouts for boreholes ER-6-1#2, ER-7-1, ER-6-1 and ER-6-2, respectively. A review of these plots shows little correlation between fracture density and SFM interpreted flow percentages.

The plots do indicate that LCA borehole flow is dominated by a few high flowing features. These are poorly correlated to fracture aperture, orientation, dip and even density. Any conceptual development of flowing features should recognize that the *entire* LCA was not characterized with either SFM or EMI logs in any of the boreholes. Therefore, any developed conceptualization will be based on data from only a portion of the LCA and there may be significant features within the LCA that have been missed. For example, the EMI log in ER-6-1#2 shows a zone with six large aperture (greater than 100 mm) fractures located at a depth above the top of the SFM logging interval. If this zone could have been included in the SFM log, it may have been found to have the highest flow percentages. This interval of ER-6-1#2 is behind the borehole liner and could not be logged. The contribution of these fractures to flow in the borehole is unknown.

The ER-7-1 SFM log interpretation is likely the most unreliable. SNJV (2004) provides an analysis of both static and pumping conditions within ER-7-1. SNJV (2004) concluded that static flow in the borehole is from the top of the slotted section through to a depth of approximately 2,400 ft and deeper. Two SFM logs were run in ER-7-1 under two pumping rates (121 and 156 gpm). Under both conditions, the drawdown in the well was not enough to overcome vertical gradients within the borehole. The depth at which flow changed from up the borehole to down the borehole for the 121 gpm logging run was approximately 2,290 ft. The depth at which flow changed from up the borehole to down the borehole for the 156 gpm logging run was 2,375 ft. The data suggest that there is a major transmissive zone at a depth of approximately 2,400 ft which thieves groundwater from higher in the LCA. This flow cell extends below a depth of 2,400 ft. The bottom line is that the flow log depicted in Figure J-8 cannot be considered reliable. It is very likely that very transmissive zones exist between 2,300 and 2,400 ft of depth and below. These are not identified in the SFM flow percentage shown in Figure J-8.

Additional information regarding flowing intervals is available for boreholes ER-6-1 and ER-6-1#2 from thermal flow meter (TFM) logs and tracer test data (SNJV, 2005b, 2006). Interpretation of the TFM logs conducted under conditions of pumping indicate that the intervals in these two wells most

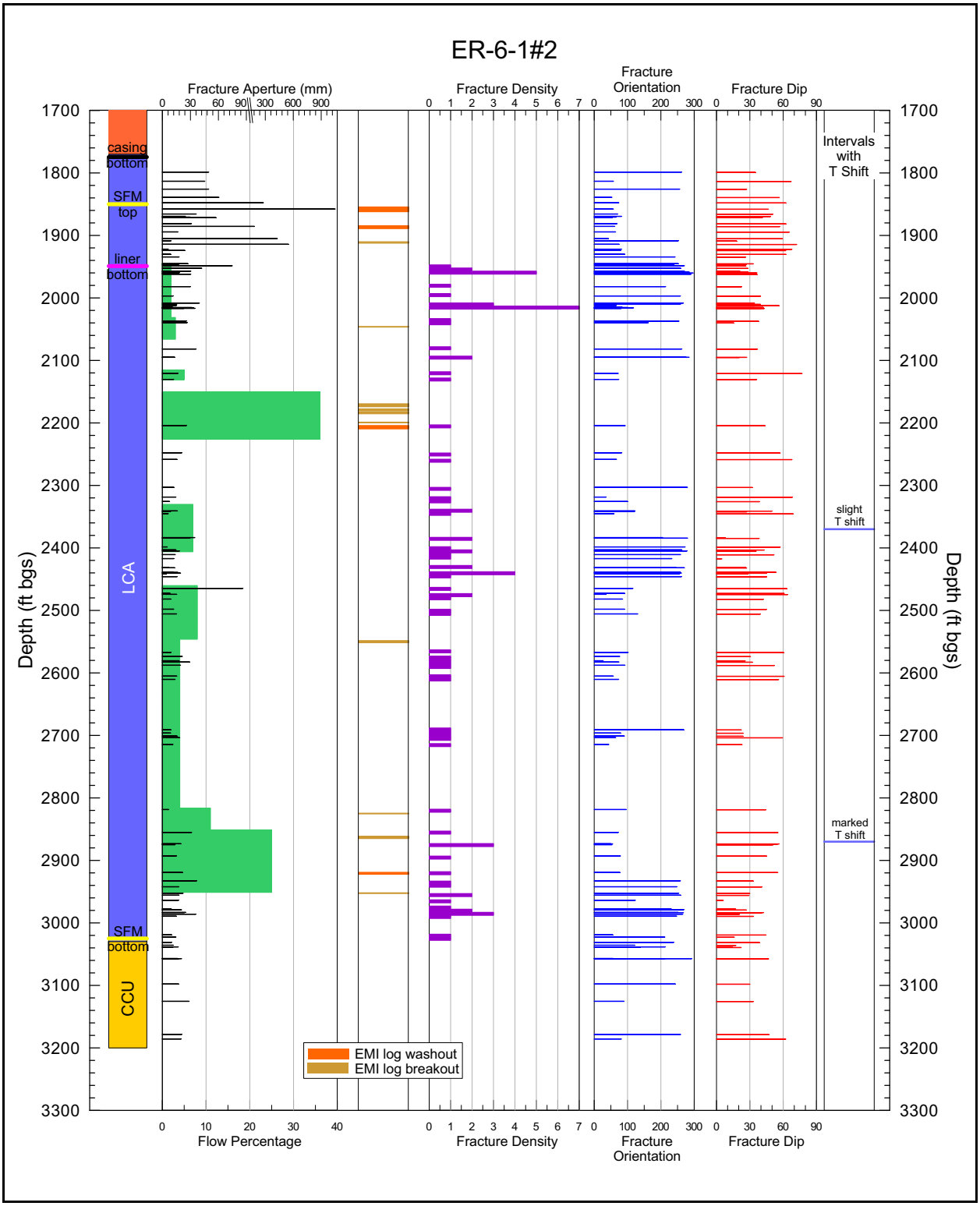

Figure J-7
Flow Percentage and Fracture Data for ER-6-1#2
Source: SNJV, 2005a, 2005b, and 2007

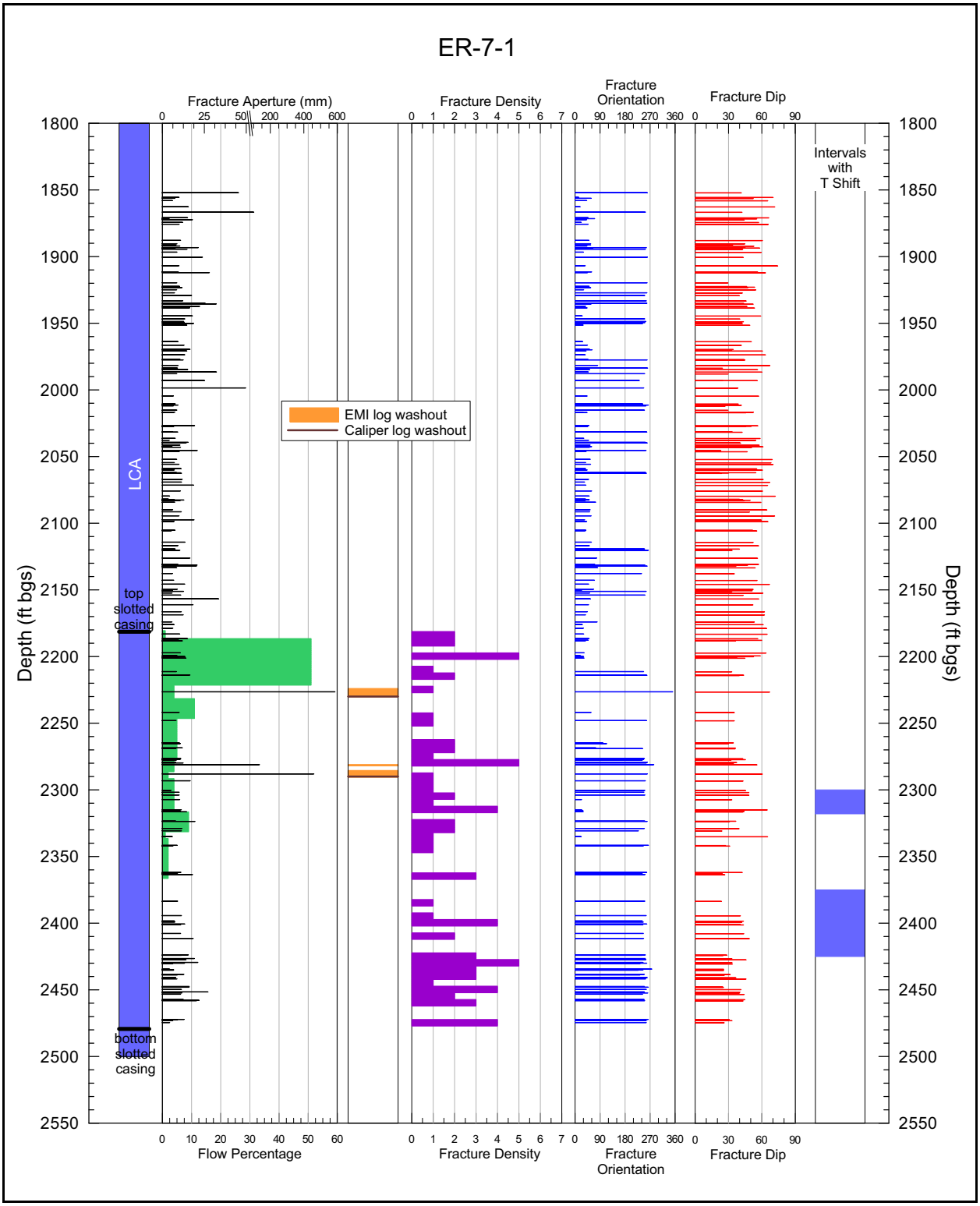

Figure J-8
Flow Percentage and Fracture Data for ER-7-1
Source: SNJV, 2005a, 2005b, and 2007

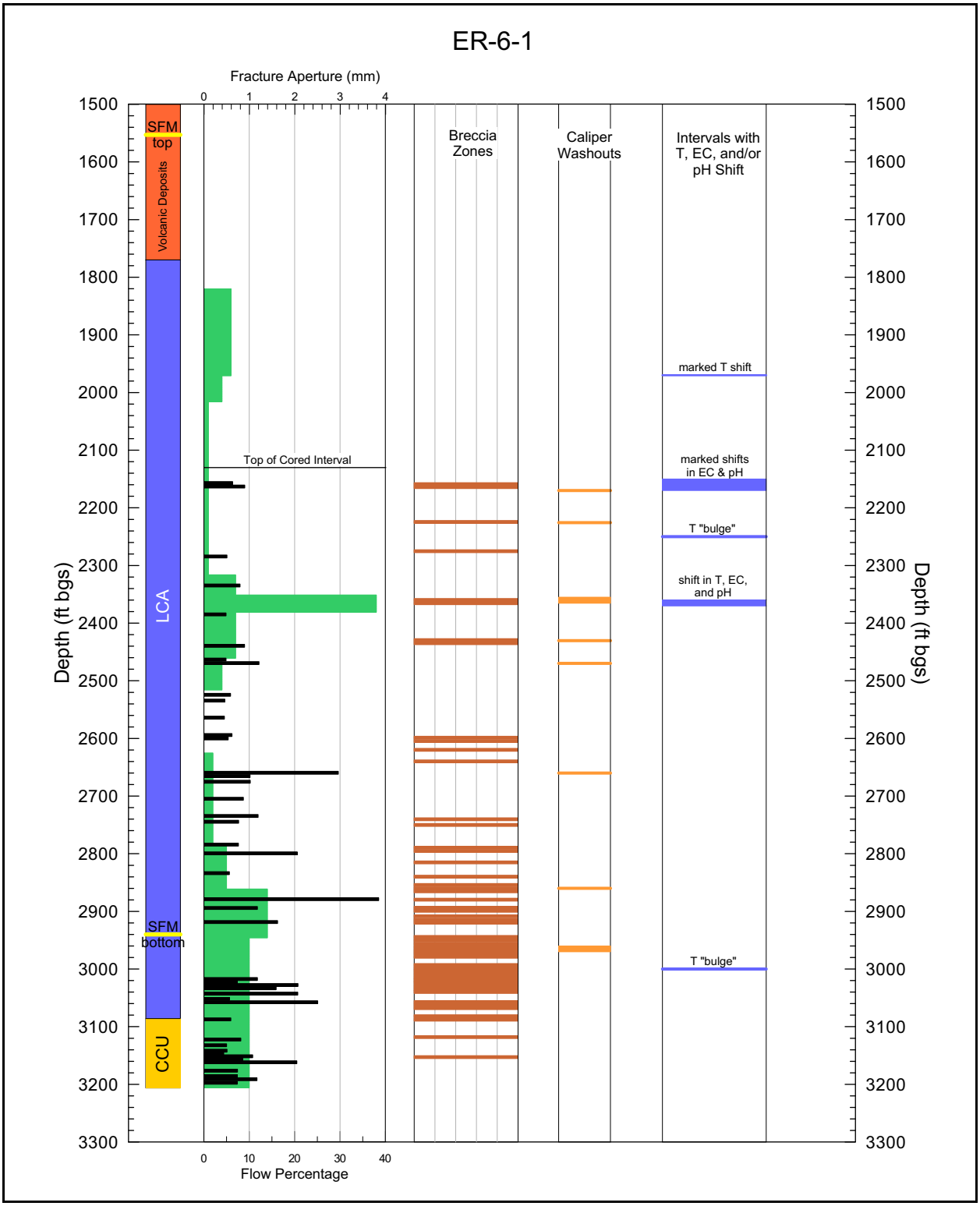

Figure J-9
Flow Percentage and Fracture Data for ER-6-1
Source: IT, 1996; SNJV, 2005b

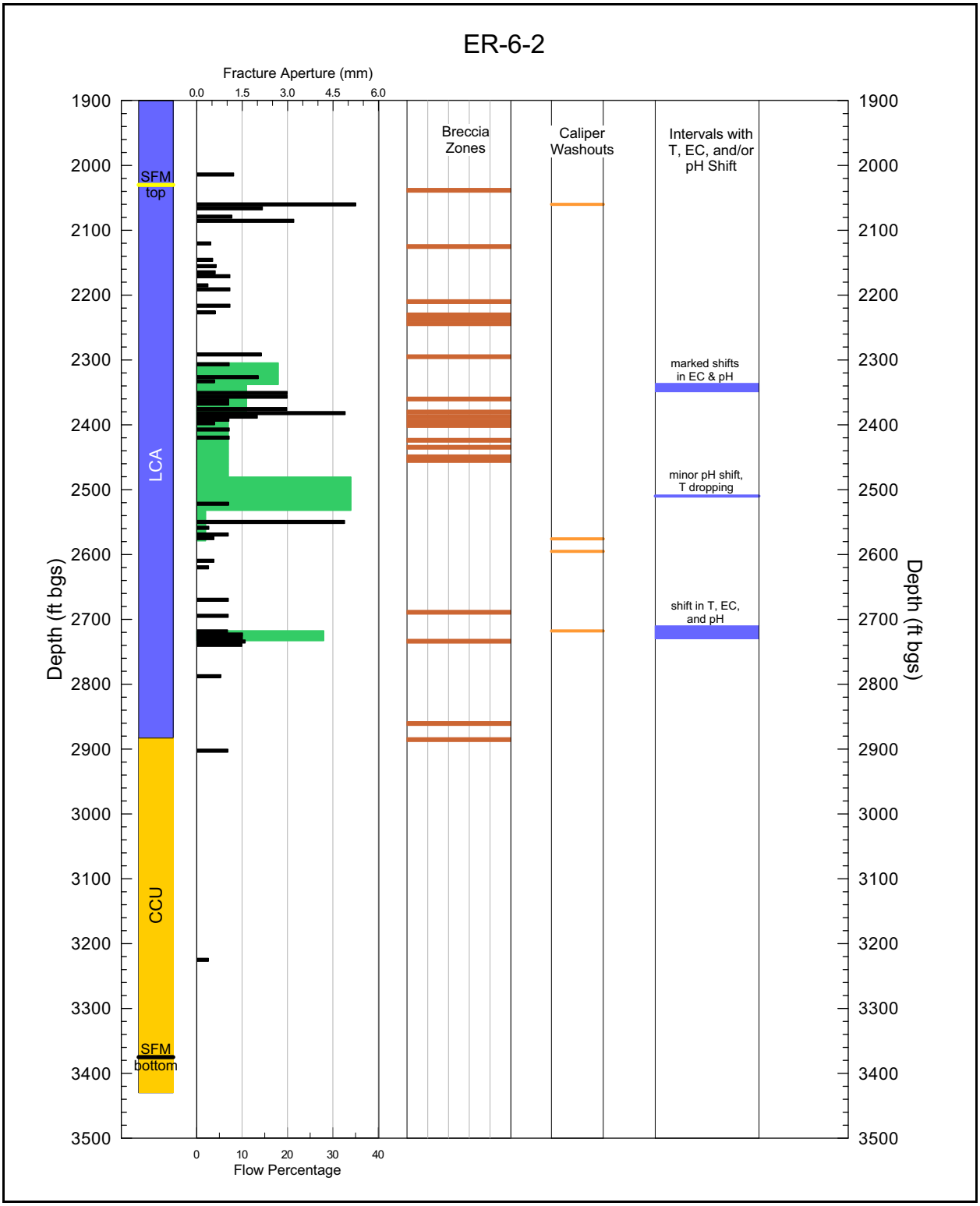

Figure J-10
Flow Percentage and Fracture Data for ER-6-2
Source: SNJV, 2005a, 2005b, and 2007

connected to the other well are not adjacent to the high flow intervals determined from the SFM logs (Figure J-11). This lack of correlation between transmissivity and connectivity has been observed in many fractured settings and was well documented in Kelley et al. (1991) based upon cross-hole experiments in the Grimsel Test Site in Switzerland.

Observations at distal wells during the ER-6-1 multi-well aquifer test showed no response at a well located about 4.3 miles to the northwest, a response delayed about 10 days at a well located about 4 miles to the northeast, and an almost immediate response at a well (ER-7-1) located about 6.2 miles to the north. These data indicate that the interconnectedness of flowing faults in the LCA is very directional.

The key conclusions that can be reached from the review of the available data are:

1. The LCA can be conceptualized to be comprised of major faults and their associated damage zones and these are probably the large-scale flowing features seen in the SFM logs.

2. The “country rock” also has fractures and joints that contribute to flow into boreholes and presumably contribute to LCA connectivity at some unknown scale.

3. Based upon a very limited dataset of four boreholes, the split of groundwater flow (and by analog transmissivity) between LCA major fault features to smaller fault/joint flow features is approximately 50 to 70 percent. That is, major large-scale flowing features would comprise 50 to 70 percent of the borehole flow with smaller-scale features making up the difference. The quantitative basis for this split derives from the analysis in the flowing section.

J.2.4.2 Detailed Analysis of SFM and Fracture Data

Based upon the observations in Section J.2.4.1, a detailed analysis approach for the SFM logs was developed. Assumptions are inherent in the analysis due to the limited amount of data available for analysis. That said, the conceptual hypothesis for the detailed analysis is: (1) the larger the aperture, the larger the flow rate (transmissivity); (2) the larger the fracture intensity, the larger the flow rate (transmissivity); (3) the current stress field impacts fracture flow potential where one would expect the higher potential for fractures oriented parallel to the minimum compressive stress; and (4) damage zones are zones of enhanced fracturing and, hence, transmissivity.

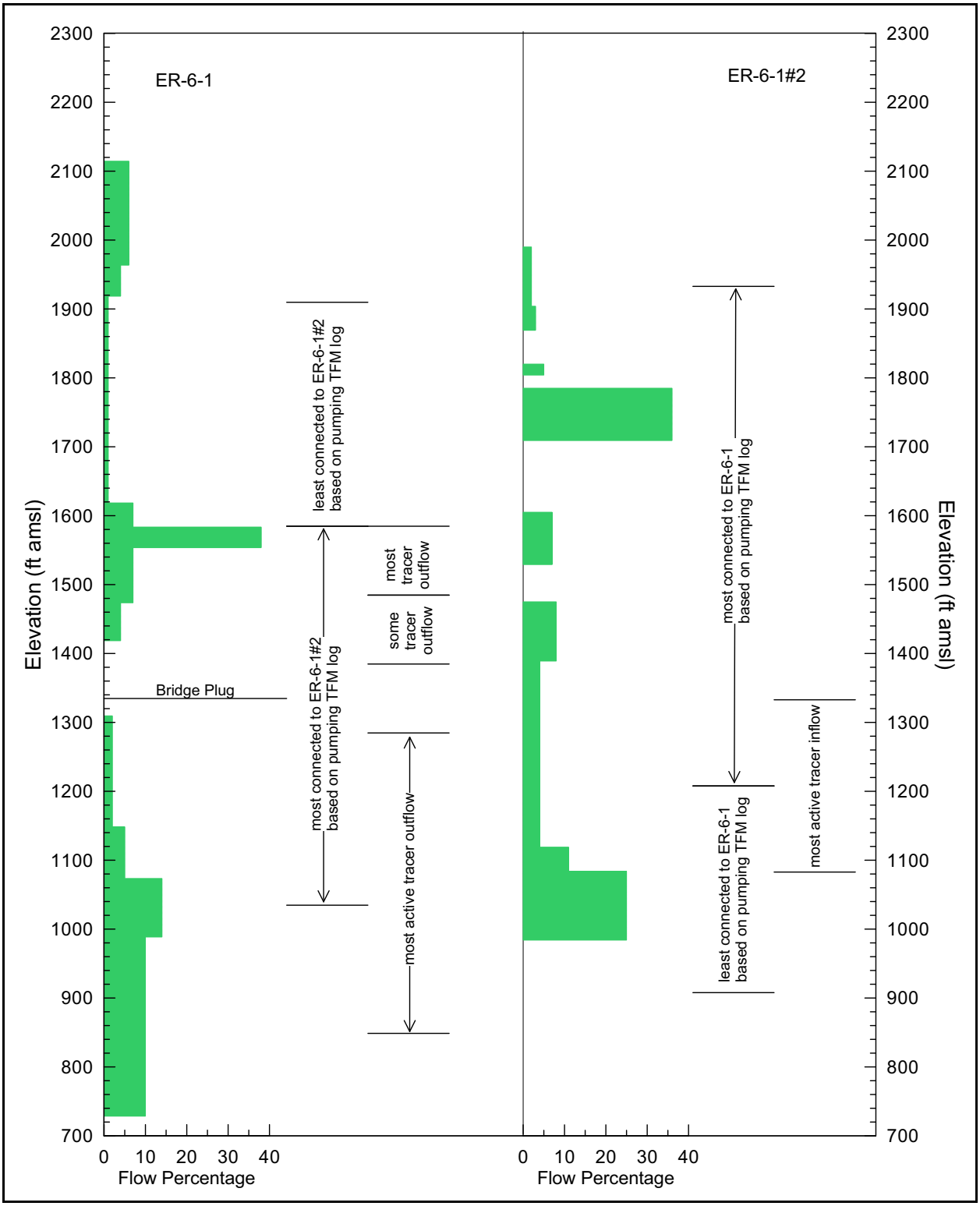

Figure J-11
Comparison of Flow Percentages from SFM Logs and Analyses of Pumping TFM Logs and Tracer Test Observations

J.2.4.3 Detailed Analysis of SFM Data to Discriminate Large- versus Smaller-Scale Flowing Features

While large-scale flowing features (faults and fault zones) that may represent lineaments of shear zones are intersected by LCA boreholes, the definition of their extent using vertical boreholes is not possible. Specifically, these features are expected to be high angle and they can occur at a scale commensurate with the LCA intervals being logged. Through geologic mapping of the structure of the top of the LCA, it can be concluded that large-scale fault spacing range from 0.4 to 0.75 km (400 to 750 m) (Drellack, 2012) in Yucca Flat.

Because of the inability to sample large-scale faults with vertical boreholes, the analysis focused on defining a method to discriminate smaller-scale features from large-scale features. The methodology employed is subjective though it may be useful as an alternate approach to conceptualizing and implementing flowing features in the LCA.

To determine the occurrence of smaller-scale features, the following steps were employed:

1. Smoothed the raw SFM data with a spline curve to remove noise;
2. Calculated the numerical derivative of the spline-smoothed data at each measurement interval;
3. Estimated a derivative magnitude above which the result would be considered a flowing feature;
4. Identified the smaller-scale flowing features through an analysis of the derivative peaks.

Figure J-12 plots the raw and smoothed SFM log for borehole ER-6-1#2. The significant changes in flow observed in this figure are inferred as a flowing feature. To better isolate where flowing features might reside, a derivative of the smoothed flow log data was calculated as shown in Figure J-13. Figure J-13 shows two large scale flow features at approximately 2,200 and 2,900 ft depth below measuring point. These features are interpreted to be large-scale flowing features that one would associate with large fault zones, lineaments, and shear zones. The smaller derivative peaks are inferred to be smaller-scale flowing features.

A similar analysis was performed for boreholes ER-6-1, ER-6-2 and ER-7-1. ER-7-1 did not yield meaningful results. This is to be expected given the complex inter-borehole flow regime (see

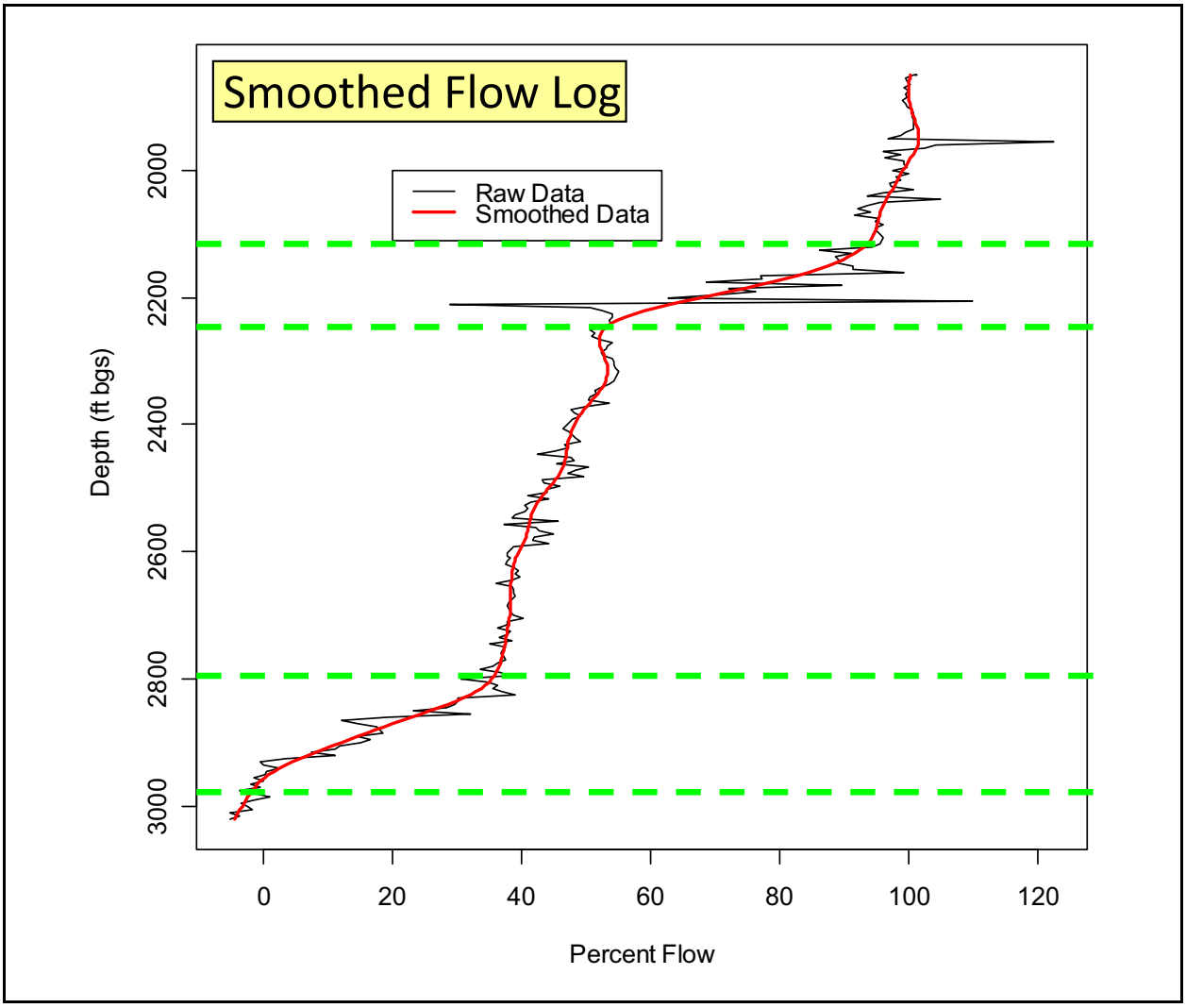

Figure J-12
Raw and Smoothed SFM Log Data for ER-6-1#2

Section J.2.4.1). Figure J-14a plots the empirical cumulative density function for smaller-scale flowing features in the LCA based upon the three borehole SFM logs analyzed and the underlying assumptions in smoothing and censoring. The distribution is log-normal (Figure J-14b) with a good fit to the theoretical distribution (where the data has been linearized based on the log-normal assumption). The median mean of the spacing of the smaller-scale flowing features is 94 ft. Figure J-15a plots the fracture spacing determined from EMI-logs for boreholes ER-6-1 and ER-7-1. The median spacing is 2.5 ft. For comparison, Figure J-15b shows the empirical cumulative distribution function shown in Figure J-15a, where the median distance between the centers of the derivative peaks that represent smaller-scale flowing features is 94 ft.

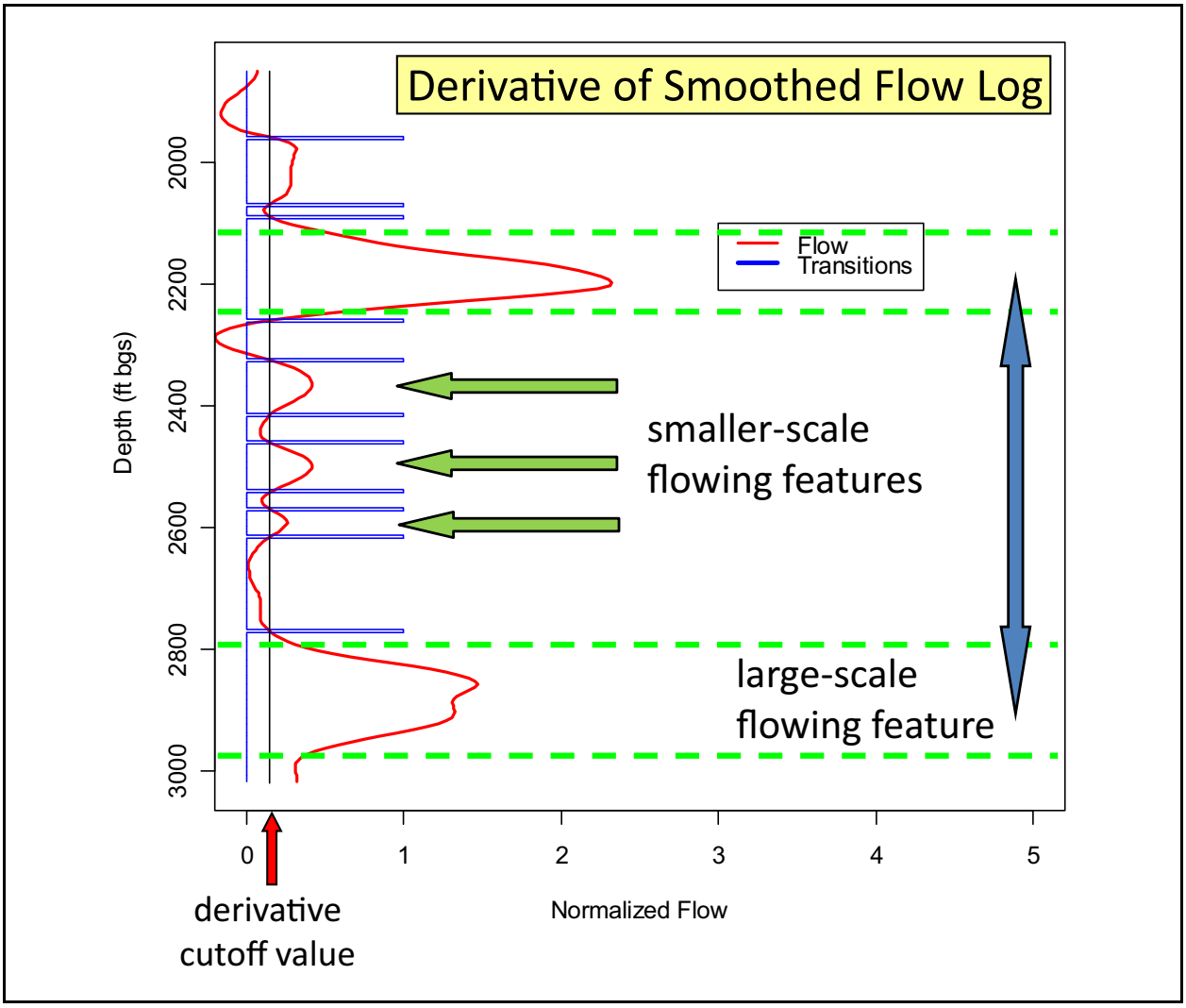

Figure J-13
Derivative of Smoothed SFM Data and Flowing Feature Identification for ER-6-1#2

J.2.4.4 Analysis of Smaller-Scale Features and the Correlation Between Measured Properties and Flow Rate

Once the locations and flow rates of smaller-scale flowing features were determined, the correlation between flow rate and other fracture properties that have been collected for some boreholes at the site was evaluated. The two boreholes with the most fracture information in the LCA are ER-6-1#2 and ER-7-1. The analysis for ER-6-1#2 is presented below in addition to a brief discussion of the results from ER-7-1. Note that the analyzed flow rates are for those intervals considered to be smaller-scale flowing features. Data for the large-scale flowing feature intervals (faults) were excluded from the analysis.

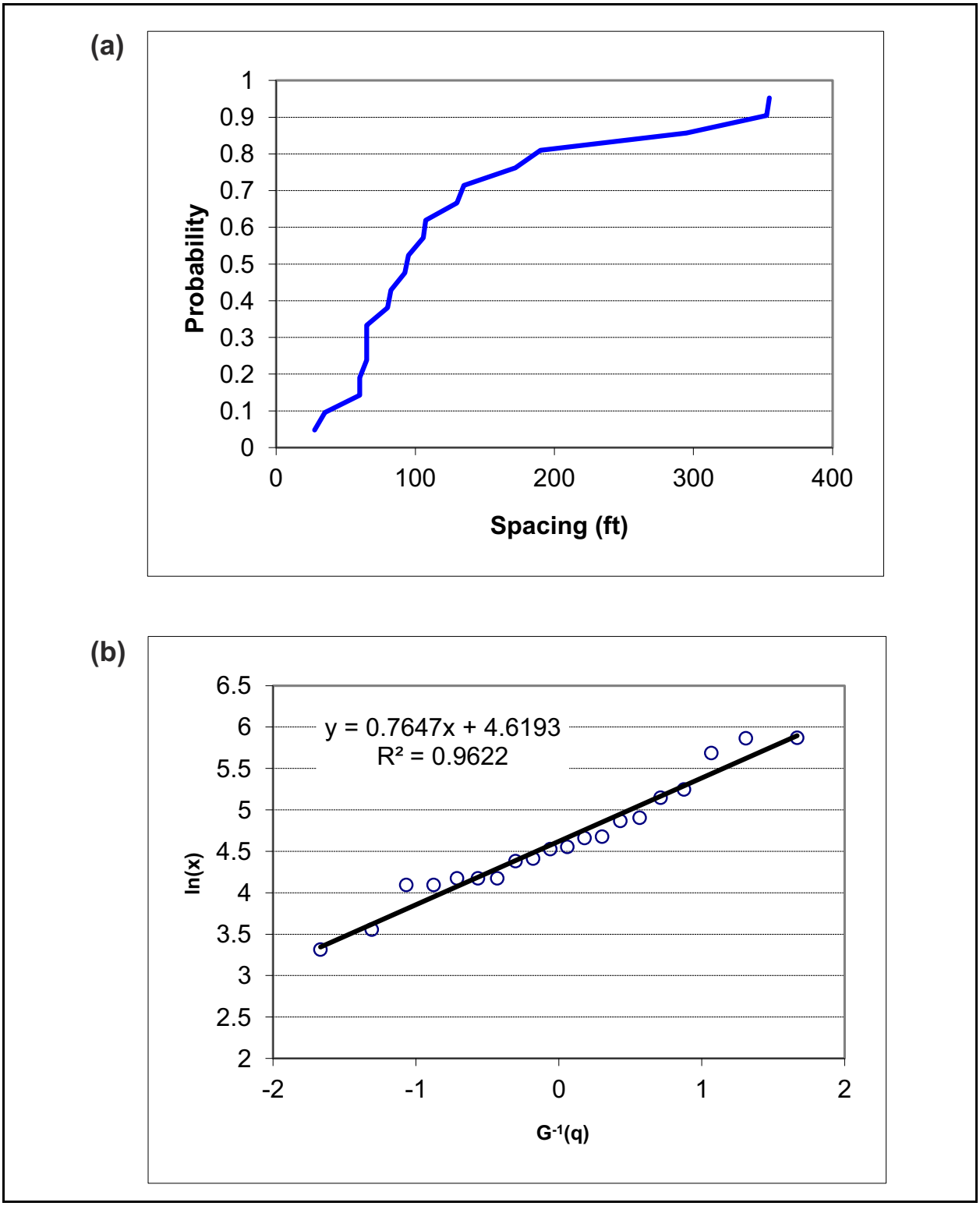

Figure J-14
Spacing between Smaller-scale Flowing Features for Boreholes ER-6-1, ER-6-1#2, and ER-6-2 (a) Distribution (b) Fit

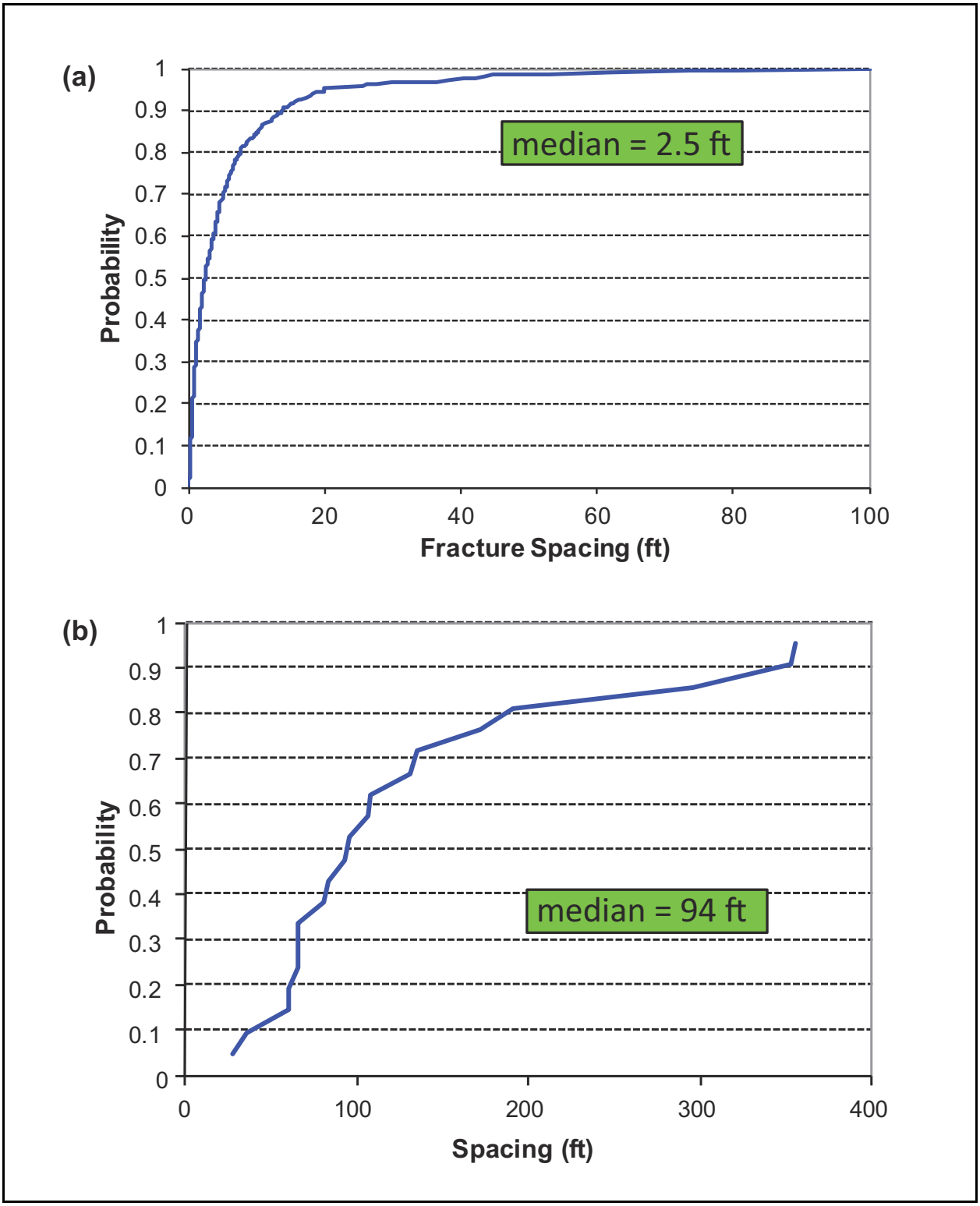

Figure J-15
Cumulative Distribution Function (a) EMI Fracture Spacing for ER-6-1 and ER-7-1, (b) Spacing between Smaller-scale Flowing Features for ER-6-1, ER-6-1#2, and ER-6-2

The statistical package R was used to develop scatter-plots matrices to investigate the correlation of fracture properties to flow as determined by the SFM flow logs. Because there has been some inference that east dipping fractures may behave hydraulically different than west dipping fractures, the fractures were binned into two sets for analysis, west dipping and east dipping. Figure J-16 shows the results for west-dipping fractures in borehole ER-6-1#2. The scatter-plot matrix shows rank correlation between flow and other measured fracture variables. For the west-dipping fractures, the following can be observed: (1) a positive correlation between flow rate and aperture and (2) a negative correlation between flow rate and depth. Figure J-17 shows the same scatter-plot matrix for east-dipping fractures. For east-dipping fractures there are no apparent relationships. The similar analysis for borehole ER-7-1 was largely non-instructive with a weak correlation between flow and aperture.

In conclusion, this analysis shows that the limited datasets do not provide definitive relationships. However, some correlation between west dipping fractures and smaller-scale feature flow rates was observed as well as some correlation between aperture and flow rate. Because the volcanic aquifers have larger fracture datasets, this type of analysis may be fruitful for them.

J.2.5 Study Conclusions and Potential for Application

Conceptually, the LCA flowing fracture system is complex with evidence for large regional-scale flowing features (faults) and smaller-scale flowing features (interpreted as fracture zones with significant flow). In a simplistic sense, one could conceptualize the LCA flowing features as a composite distribution that may look something like that illustrated in Figure J-18. It would be composed of large regional features that could extend miles and smaller-scale features that have an average spacing of approximately 100 ft and occur across a portion of the LCA not associated with large-scale features. The reality is probably that the fracture sets are fractal in nature. In comparison, the YMP Project median flowing feature spacing was approximately 64 ft (Kuzio et al, 2004).

The large-scale features dominate flow regionally. These are features that may intersect a borehole once, twice, or not at all. Because these features will not necessarily be encountered in vertical boreholes, one must depend upon detailed geologic work to define their location and characteristics. One expects that 50 percent or greater of flow in the LCA flow model should move through these large-scale features.

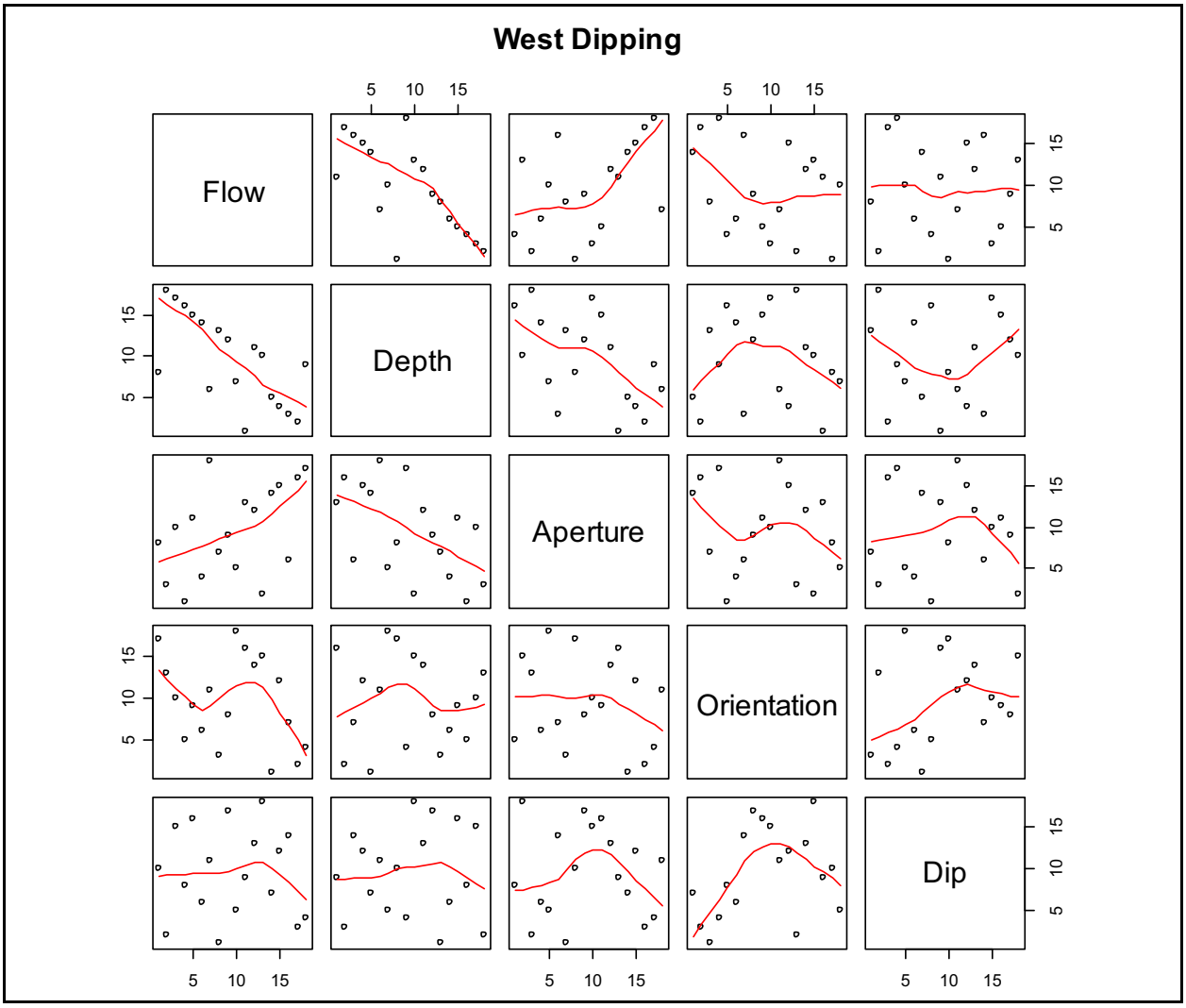

Figure J-16
Correlation Cross Plot, West Dipping Fractures for ER-6-1#2

The smaller-scale flowing features are also important sometimes contributing up to 50 percent of borehole transmissivity and these features can be sampled with boreholes, while recognizing the limitations of one-dimensional sampling. Smaller-scale flowing features do have large potential for double-porosity. These features can be better characterized with straddle-packer testing and continued fluid logging campaigns at multiple pumping rates.

Figure J-19 shows a conceptual picture of how the LCA may behave. The “country rock” would be represented by smaller-scale flowing features and a distribution of the fraction of LCA with flowing features could be sampled. Fracture porosities in the smaller-scale flowing features would be representative of typical secondary porosity systems (0.02 to 0.0002). The large-scale features are

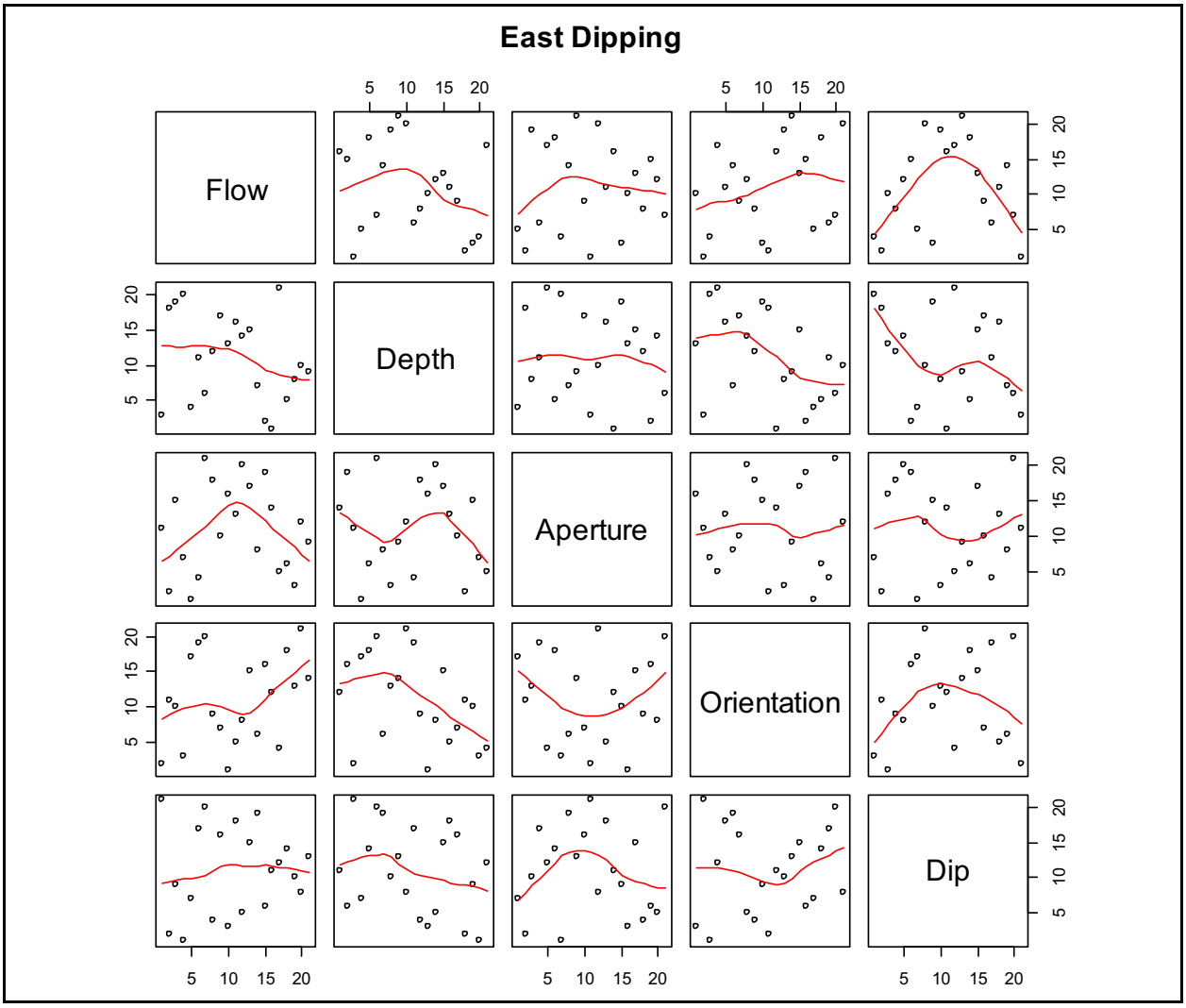

Figure J-17
Correlation Cross Plot, East Dipping Fractures for ER-6-1#2

modeled discretely from the geologic model. These units may have higher porosities than typical fractures because of their complexity in terms of shear and damage zones with porosities that could range from 1 to several percent.

Based upon observations of Winograd and Pearson (1976) and hydraulic responses seen in long-term aquifer tests, one would expect that transport in the larger-scale features should be quicker than in the smaller-scale features.

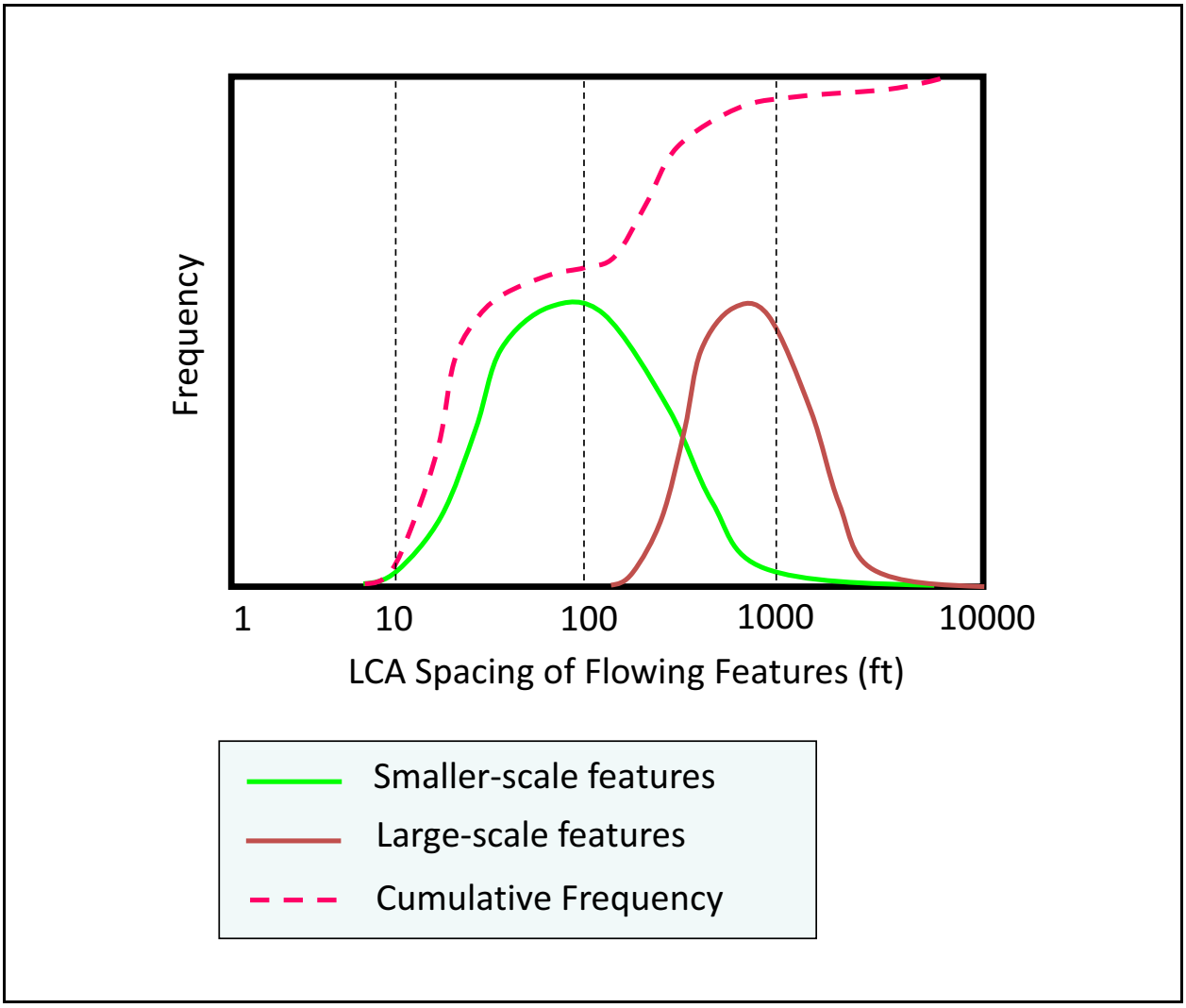

Figure J-18
Conceptual Composite Distribution of LCA Flowing Features

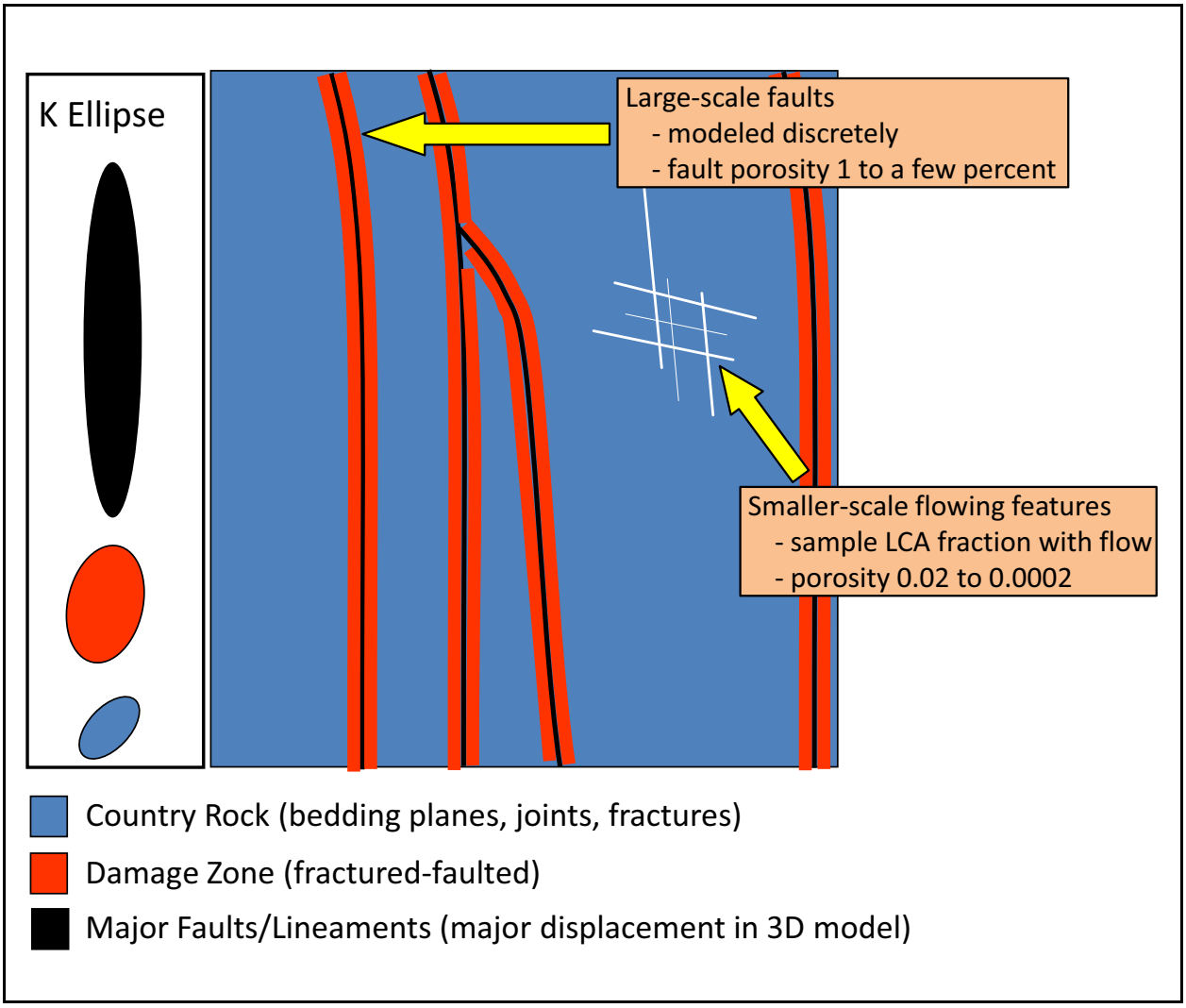

Figure J-19
Application to CAU Transport - LCA Hydrostructural Domains

J.3.0 SUMMARY

The observations of fault zones in the NNSS region and Yucca Flat area indicate the propensity for faults to have a core zone of low permeability perpendicular to the strike of the fault surrounded by damage zones of higher permeability parallel to the strike of the fault. In general, there is evidence to support the conceptual model that the width of fault damage zones is positively correlated with the length or offset along the fault. Given some of the faults in Yucca Flat have offsets of several hundred meters and lengths of several 10's of kilometers, it would not be unexpected to have damage zones with widths of 100 m or more, although this is not directly observed.

The hydraulic and transport testing from boreholes drilled into the LCA in Yucca Flat provide useful data to develop flow and transport properties of the fault damage zones and unfaulted country rock. A range of flow and transport properties have been observed from the testing performed. This range may be attributable to either spatial variability or uncertainty.

A useful means of characterizing the flow and transport characteristics of the LCA is to use the concept of "flowing features", similar to the approach adopted in the saturated zone modeling of the volcanic aquifers at Yucca Mountain (Kuzio et al., 2004). Using such an approach with the fluid logging data allows for the development of the spacing of "flowing features" within the country rock which provides a basis for identifying the likely portion of the country rock that takes part in matrix diffusion. To evaluate the impact of this conceptualization, an alternative LCA transport model case is developed in Section 6.3, with the results presented in Section 6.5.7.

J.4.0 REFERENCES

Agosta, F. 2008. *Fluid flow properties of basin-bounding normal faults in platform carbonates, Fucino Basin, central Italy,* in The Internal Structure of Fault Zones: Implications for Mechanical and Fluid-Flow Properties, 299, 277-291. The Geological Society of London.

Asch, T.H., D.S. Sweetkind, B.L. Burton, E.L. Wallin, 2008. *Detailed Geophysical Fault Characterization in Yucca Flat, Nevada Test Site, Nevada.* USGS Open File Report 2008-1346.

BN, see Bechtel Nevada.

Baecher, B.G., N.A. Lanney and H.H. Einstein. 1977. Statistical descriptions of rock properties and sampling: Proceedings of the 18th U.S. Symposium on Rock Mechanics, Topical Mechanics, American Institute of Mining Engineers.

Bechtel Nevada. 2006. *A Hydrostratigraphic Model and Alternatives for the Groundwater Flow and Contaminant Transport Model of Corrective Action Unit 97: Yucca Flat-Climax Mine, Lincoln and Nye Counties, Nevada,* DOE/NV/11718--1119. Prepared for the U.S. Department of Energy, National Nuclear Security Administration Nevada Site Office. Las Vegas, NV.

Berkowitz, B. 2002. Characterizing flow and transport in fractured geologic media: A review. Advances in Water Resources, Volume 25, p. 861-884.

Boutareaud, S., Wibberly, C., Fabbri, O., and Shimamoto, T. 2008. *Permeability structure and co-seismic thermal pressurization on fault branches: insights from the Usukidani fault, Japan,* in The Internal Structure of Fault Zones: Implications for Mechanical and Fluid-Flow Properties, 299, 341-361. The Geological Society of London.

Caine, J.S., and Forster, C.B. 1999. *Fault zone architecture and fluid flow - insights from field data and numerical modeling* in Haneberg, W.C., Mozely, P.S., Moore, J.C., and Goodwin, L.B., eds., Faults and subsurface fluid flow in the shallow crust: Geophysical Monograph 113, p. 101-127.

Dickerson, R.P., and Drake, R.M. II. 2003. Geologic map of south-central Yucca Mountain, Nye County, Nevada; U.S. Geological Survey Miscellaneous Field Studies Map MF-2422.

Drellack, S.L., Jr. National Security Technologies, LLC. 2012. Personal communication to R. Andrews (N-I) regarding comments about the INTERA memo on Yucca Flat LCA Flowing Feature Analysis. 18 March. Las Vegas, NV.

Fenelon, J.M., D.S. Sweetkind, P.E. Elliott, and R.J. Laczniak. 2012. *Conceptualization of the Predevelopment Groundwater Flow System and Transient Water-Level Responses in Yucca Flat, Nevada National Security Site, Nevada*, Scientific Investigations Report 2012-5196. Reston, VA: U.S. Geological Survey.

IT, see IT Corporation.

IT Corporation. 1996. *Wells ER-6-1 and ER-6-2 Core Fracture Analyses and Geophysical Log Comparisons*. ITLV/10972--171.

Kelley, V.A., J.M. Lavanchy, and S. Loew. 1991. Transmissivities and Heads Derived From Detailed Analysis of Siblingen 1989 Fluid Logging Data. National Cooperative for the Disposal of Radioactive Waste (NAGRA), Technical Report NTB 90-09, 184 p. Wettingen, Switzerland.

Kuzio, S., K. Rehfeldt, J. Gebhart, B. Arnold, and M. Zhu. 2004. Probability Distribution for Flowing Interval Spacing, Prepared for the US Department of Energy Office of Civilian Radioactive Waste Management by Bechtel SAIC Company, LLC, 48 p.

Laczniak, R.J., J.C. Cole, D.A. Sawyer, and D.A. Trudeau. 1996. Summary of Hydrogeologic Controls on Ground-Water Flow at the Nevada Test Site, Nye County, Nevada. U.S. Geological Survey Water-Resources Investigations Report 96-4109.

Micarelli, L., A. Benedicto, and C.A.J. Wibberley. 2006. *Structural evolution and permeability of normal fault zones in highly porous carbonate rocks*, Journal of Structural Geology, 28(7), pp. 1214-1227.

Prothro, L.B., S.L. Drellack, D.N. Haugstad, H.E. Huckins-Gang, and M.J. Townsend. 2009. *Observations on Faults and Associated Permeability Structures in Hydrogeologic Units at the Nevada Test Site*, DOE/NV/25946--690. Las Vegas, NV: National Security Technologies, LLC.

SNJV, see Stoller-Navarro Joint Venture.

Stoller-Navarro Joint Venture. 2004. Analysis of Well ER-7-1 Testing, Yucca Flat FY 2003 Testing Program, Nevada Test Site, Nevada. S-N/99205--021. Las Vegas, NV.

Stoller-Navarro Joint Venture. 2005a. Underground Test Area Fracture Analysis Report for Yucca Flat Wells ER-2-1, ER-6-1#2, ER-7-1, and ER-12-2 Nevada Test Site, Nevada. S-N/99205-040. Las Vegas, NV.

Stoller-Navarro Joint Venture. 2005b. Analysis of Hydraulic Responses from the ER-6-1 Multiple-Well Aquifer Test, Yucca Flat FY 2004 Testing Program, Nevada Test Site, Nye County, Nevada. S-N/99205--051. Las Vegas, NV.

Stoller-Navarro Joint Venture. 2005c. Analysis of Well ER-6-2 Testing, Yucca Flat FY 2004 Testing Program, Nevada Test Site, Nye County, Nevada, S-N/99205--053. Las Vegas, NV.

Stoller-Navarro Joint Venture. 2006. Well ER-6-1 Tracer Test Analysis: Yucca Flat, Nevada Test Site, Nye County, Nevada. S-N/99205--084. Las Vegas, NV.

Stoller-Navarro Joint Venture. 2007. Fracture07.mdb Fracture Characterization Database for the Nevada Test Site and Vicinity. Las Vegas, NV.

Sweetkind, D.S., and R.M. Drake II. 2007. *Characteristics of Fault Zones in Volcanic Rocks near Yucca Flat, Nevada Test Site, Nevada*, Open-File Report 2007-1293. Reston, VA: U.S. Geological Survey.

Vermilye, J.M., and Scholz, C.H. 1998. *A microstructural view of fault growth*, Journal of Geophysical Research, 103(B6):12,223-12,237.

Winograd, I.J. and F.J. Pearson. 1976. Major Carbon 14 Anomaly in a Regional Carbonate Aquifer: Possible Evidence for Mega-scale Channeling, South Central Great Basin. Water Resources Research, Volume 12, No. 6, pp. 1125-1143.

Winograd, I.J., and W. Thordarson. 1975. *Hydrogeologic and Hydrochemical Framework, South-Central Great Basin, Nevada-California, with Special Reference to the Nevada Test Site*, U.S. Geological Survey Professional Paper 712-C.

Appendix K

Technical Basis for Transport Model Software Selection

K.1.0 INTRODUCTION

The computer software selected to calculate contaminant transport over the next 1,000 years must meet technical and quality requirements. The need for appropriate selection criteria and a clear basis for the selection of such software was recently identified in a U.S. Government Accountability Office (GAO) review of the approach DOE uses to select computer models that support environmental cleanup decisions (GAO, 2011). Although the GAO report focuses on software used to support cleanup decisions at the Hanford and Savannah River sites, and there is no planned cleanup—other than natural attenuation—of the residual contamination resulting from underground nuclear testing at the NNSS, the GAO recommendation for documenting the technical basis for software selected to model contaminant transport is deemed relevant to the software used by UGTA at the NNSS.

This appendix presents the justification for the use of FEHM_sptr, Walkabout V1.2, and PLUMECALC V2.3.3 for contaminant transport modeling in the Yucca Flat/Climax Mine CAU. FEHM_sptr is a subroutine in FEHM (Zyvoloski et al., 1999). It calculates particle trajectories and advective particle transport times using a velocity field developed with the FEHM software. Walkabout V1.2 (Painter, 2011) is stand-alone software that also calculates particle trajectories and advective particle transport times using velocity fields developed with FEHM. PLUMECALC V2.3.3 (Robinson et al., 2011) is software that uses particle trajectories and advective particle transport times developed with either FEHM_sptr or Walkabout V1.2 to calculate contaminant concentrations downgradient from contaminant sources. It incorporates the effects of matrix diffusion, fracture and matrix sorption, and radionuclide decay. The computational efficiency of PLUMECALC V2.3.3 makes it ideally suited for the multiple Monte Carlo realizations required to forecast the contaminant boundary for the Yucca Flat/Climax Mine CAU.

Contaminant boundary forecasts developed in Section 6.5 are based on FEHM_sptr and PLUMECALC V2.3.3. For comparison, contaminant transport results generated when Walkabout V1.2, instead of FEHM_sptr, is used are also presented in Section 6.5. Appendix N compares contaminant transport results obtained by the use of alternative corroborative software with the results presented in Section 6.5. This comparison provides additional confidence in the projection of contaminant migration.

K.1.1 FFACO and QAPP Software Requirements

Modeling groundwater flow and radionuclide transport in order to forecast contaminant boundaries associated with underground nuclear testing requires software that can appropriately approximate features and processes affecting contaminant transport. The requirements for software selection are provided in the FFACO (1996, as amended) and UGTA QAPP (NNSA/NSO, 2011).

The software requirement in the FFACO requires that models used to forecast contaminant boundaries be verified, where "model verification" is defined as including "evaluations to ensure the code is programmed correctly and the algorithms are implemented properly with no assumption errors or program bugs."

The software selection requirements in the QAPP are as follows:

> Participants shall identify the required and desirable attributes of a code before procurement, acquisition, or development. These attributes may be identified in procurement, installation, or technical review documents. Participants shall evaluate codes based on the identified attributes, and those without the required attributes shall be eliminated from consideration. A test problem may be created to evaluate candidate codes. The tests or documentation should compare simulation results with published analytical solutions and/or other code results. If no available code performs to the required attributes, the participant may develop the needed code.
>
> Participants shall document the code selected for the groundwater flow and transport model and the selection criteria in the CAIP. If a code change is required after publication of the CAIP, justification for the change and the potential codes shall be submitted to the Federal Sub-Project Director for approval. The justification shall incorporate, at the minimum, a justification for the change, code attributes, testing results against the above criteria, and a comparison between available codes. Upon approval, either a CAIP addendum or record of technical change shall be submitted to NDEP for approval. Participants shall document other code selection within a record package.

The Yucca Flat/Climax Mine CAU CAIP (DOE/NV, 2000) identified the approach to code selection:

> The selection of the model (code) to use for the CAU simulations is an important decision. The selected code will be used to predict the migration of contaminants within the CAU-scale model boundary. To establish confidence in the CAU model, the process to select the code will be outlined and justified. The selection process will ensure that the selected code will simulate the migration of the potential contaminants in groundwater and allow for an assessment of the uncertainty in the predictions.

> The selection process will follow one of two tracks depending on the acceptability of the code FEHM, which was chosen to simulate the Pahute Mesa groundwater flow system. . . . The first step . . . is an assessment of how well FEHM performed in the simulation of radionuclide transport in groundwater of the Pahute Mesa CAUs. If the FEHM performance is deemed acceptable, then an example problem representing conditions in the Yucca Flat/Climax Mine area will be created to test FEHM for applicability to the Yucca Flat/Climax Mine CAU. If the test is successful, then FEHM will be chosen as the code for simulating the flow and transport in the Yucca Flat/Climax Mine area. However, if FEHM is deemed unacceptable, then the code selection process will move into a second phase with the identification of candidate codes and the selection of the three best-qualified codes based on the set of code attributes identified in Section 5.1.2.2. These three codes will then be tested by application to an example problem designed to simulate conditions in the Yucca Flat/Climax Mine area and the final code selection will be made.

The performance of FEHM was deemed acceptable (Shaw, 2003). An example problem representing the conditions in the Yucca Flat/Climax Mine area was developed by the use of FEHM and related transport software (FEHM_sptr combined with PLUMECALC). The related transport software was developed explicitly to efficiently evaluate contaminant concentrations with a convolution-based particle-tracking algorithm. The example problem was similar to the application of FEHM_sptr and PLUMECALC to the Frenchman Flat contaminant transport modeling described in NNES (2010). Because of the acceptable performance of FEHM, and the successful application of FEHM_sptr and PLUMECALC to the preliminary Yucca Flat transport analyses and the Frenchman Flat transport model, the code selection process did not need to move into the second phase.

K.1.2 Software Selection Criteria and Approach

The software selection criteria and approach for UGTA flow and transport models are documented in the modeling approach document for the Yucca Flat/Climax Mine CAU (Shaw, 2003) and in the modeling approach and Phase I flow model documents for the Central and Western Pahute Mesa CAUs (SNJV, 2004, 2006). The general attributes of the code selection criteria are as follows:

- Fully three-dimensional
- Large numbers of nodes capability
- Multiple boundary condition options
- Transient capability
- Efficient solver
- Acceptable numerical accuracy
- Minimal numerical dispersion

- Acceptable verification and validation
- Access to source code

The groundwater flow model attributes of the code selection criteria are as follows:

- Saturated groundwater flow
- Heterogeneous and anisotropic hydraulic conductivity
- Point and distributed sources and sinks of water
- Temperature dependence
- Simulate complex geology

The transport model attributes of the code selection criteria are as follows:

- Advection, dispersion, sorption, and matrix diffusion
- Radioactive decay
- Daughter products

The desirable attributes of the code selection criteria are as follows:

- Finite-element formulation
- Steady-state capability
- Double-porosity/double-permeability formulation
- Multiple solutes
- Established pre- and post-processors

Based on these criteria and attributes, it was determined that FEHM was a suitable code for modeling groundwater flow at the Yucca Flat/Climax Mine CAU (Shaw, 2003). The use of FEHM as a code suitable for contaminant transport calculations was not explicitly addressed in the Yucca Flat/Climax Mine CAU CAIP (DOE/NV, 2000). However, the Phase I contaminant transport model developed for Pahute Mesa provided a justification for the use of the convolution-based particle-tracking method that combines FEHM_sptr with PLUMECALC to calculate advective-dispersive contaminant concentrations in a dual-porosity domain (SNJV, 2009). As a result, it was determined that FEHM, when used in conjunction with FEHM_sptr and PLUMECALC to calculate resident mobile contaminant concentrations, including the effects of matrix diffusion, fracture retardation, matrix sorption, and radionuclide decay, is acceptable for use in CAU-scale transport modeling required by the FFACO for UGTA.

K.1.3 UGTA Software Selection Background

As documented in the Yucca Flat/Climax Mine CAU modeling strategy document (Shaw, 2003), rather than developing a specific Yucca Flat/Climax Mine CAU software test to evaluate the ability of the flow and transport code to meet the specified attributes and criteria, the similarities in the key attributes, features, and processes between the Central and Western Pahute Mesa CAUs and the Yucca Flat/Climax Mine CAU allowed for the software testing performed for TYBO and BENHAM detonations to be used. Shaw (2003) used the successful testing results as a basis for determining that FEHM adequately met the selection criteria.

FEHM has been used for groundwater flow modeling at each of the previously completed UGTA CAUs—CAU 98, Frenchman Flat (NNES, 2010), and CAUs 101 and 102, Central and Western Pahute Mesa (SNJV, 2006). The history of successful use of this software for UGTA CAUs, combined with the testing performed on this software as part of the Yucca Mountain program (Dash et al., 1997 and Dash, 2003a, 2003b), provides confidence in the ability of this code to adequately simulate groundwater flow in the unsaturated and saturated HSUs at Yucca Flat.

As noted in the Frenchman Flat transport model document (NNES, 2010), the development of multiple forecasts of contaminant transport to evaluate the uncertainty in contaminant migration as specified in the FFACO requires a very efficient means of calculating concentrations downgradient from contaminant sources. To support the need for an efficient radionuclide transport software, the code PLUMECALC was developed. PLUMECALC uses the advective-dispersive particle-tracking results developed from the sptr subroutine of FEHM to calculate a cell-based contaminant concentration that includes the effects of matrix diffusion, fracture sorption, matrix sorption, and radioactive decay. PLUMECALC V2.2 was used for the transport calculations presented in the Frenchman Flat CAU transport model document (NNES, 2010).

Subsequent to the analyses of contaminant transport at Frenchman Flat, software errors were discovered in PLUMECALC V2.2. These errors were believed to result in an overprediction of contaminant concentrations. Additional issues were identified with the particle-tracking algorithm used in the sptr subroutine of FEHM.

As a result of the above errors, an evaluation of the appropriateness of these software tools, notably FEHM_sptr to calculate advective-dispersive particle trajectories and PLUMECALC to calculate

contaminant concentrations, was undertaken. This appendix summarizes the results of software testing conducted on FEHM_sptr and a proposed replacement to FEHM_sptr called Walkabout as well as PLUMECALC. FEHM V3.0, Walkabout V1.2 (Painter, 2011), and PLUMECALC V2.3.3 (Robinson et al., 2011) were used in the testing.

The testing results documented in this appendix provide the basis for selecting FEHM_sptr and PLUMECALC V2.3.3 as appropriate codes for modeling contaminant transport in the Yucca Flat/Climax Mine CAU. The focus of the testing documented in this appendix is on the use of FEHM_sptr (or Walkabout V1.2) and PLUMECALC V2.3.3 for developing forecasts of the contaminant boundary in the lower carbonate aquifer in Yucca Flat presented in Section 6.5. FEHM_sptr (or Walkabout V1.2) and PLUMECALC V2.3.3 are also used to model contaminant transport in the saturated alluvial/volcanic aquifer system presented in Section 4.6. Both FEHM_sptr and Walkabout V1.2 have been determined to suitably develop particle path trajectories and advective-dispersive transport times.

K.1.4 Contents of Appendix K

This appendix summarizes the results of testing of the transport codes used to calculate contaminant concentrations that are subsequently used to develop forecasts of contaminant boundaries as required in the FFACO. The approach to the testing is to (1) compare the results of the numerical software with analytical solutions for one-dimensional transport problems over a range of parameters similar to what are expected to be sampled in the transport analyses, and (2) make code-to-code comparisons in three dimensions using flow and transport properties and scales relevant to the Yucca Flat/Climax Mine CAU.

The particle-tracking algorithm is used to develop particle trajectories and advective-dispersive transport times. They are then used as input to the transport software used to calculate contaminant concentrations. As such, testing of the particle-tracking routines—FEHM_sptr and Walkabout V1.2—is presented in Section K.2.0 before the results of testing of the transport software—PLUMECALC V2.3.3—are presented in Section K.3.0.

K.2.0 PARTICLE-TRACKING SOFTWARE SELECTION BASIS

K.2.1 Introduction to FEHM_sptr and Walkabout

Random-walk particle-tracking methods are an attractive approach for evaluating advective-dispersive contaminant transport because in advective-dominated systems, traditional finite difference or finite element methods are prone to numerical dispersion. Methods for interpolating the velocity within numerical grid cells for structured grids with rectangular-shaped control volume cells are presented in Pollock (1988). Particle-tracking methods reduce the possibility of artificial solute spreading in groundwater transport simulations. The use of particle tracking also allows methods to be implemented in which the time variable is a stochastic variable to allow diffusion into the rock matrix to be modeled (Robinson et al., 2010).

Particle-tracking methods have significant computational advantages in many situations, especially in advection-dominated systems, but require accurate methods for calculating groundwater velocity. The difficulty arises because numerical solution to the flow equation typically provides flow velocities at specific locations; flow velocity at any location within the computational domain of interest must then be reconstructed from the solution at these discrete locations.

The particle-tracking technique also has a few drawbacks. LaBolle et al. (1996) showed that care must be taken to minimize local mass conservation errors in systems with contrasting transport velocities as random-walk displacements can result in excessive trapping of particles in low-velocity zones unless specialized methods are introduced. The use of particles to simulate the aqueous concentration of a solute requires that enough particles be used to minimize jaggedness in the computed concentration field. This issue is especially relevant for nonpoint sources and for source terms that vary over time.

The sptr subroutine of FEHM performs random-walk particle tracking using the method of Pollock (1988) and LaBolle et al. (1996). The sptr routine uses a residence time transfer function to determine the residence time of each particle within each cell and moves each particle randomly based on the proportion of mass flow rate from the resident cell to each downgradient cell (Zyvoloski et al., 1999).

Walkabout performs random-walk particle-tracking simulations of solute transport based on groundwater flow solutions that use fully unstructured control volume grids (Painter, 2011). Walkabout is designed to work within the FEHM code system (Zyvoloski, 2007), and accepts groundwater flow solutions from FEHM and computational mesh descriptions from Los Alamos Grid Toolbox, LaGriT (LANL, 2011). A typical workflow for Walkabout within the FEHM system would use LaGriT to generate unstructured grids. FEHM then provides a discretized representation of the steady-state flow field to Walkabout. Given this discrete solution, Walkabout then reconstructs a groundwater flow field and performs the random-walk particle-tracking calculation. Output is provided in a form compatible with the PLUMECALC software. PLUMECALC may be used to efficiently post-process the particle-tracking results from Walkabout to add effects of retention/retardation and arbitrary source histories. An option exists to also record particle positions versus time, thus allowing other post-processing codes or visualization systems to be used.

K.2.2 Comparisons to Analytical Solutions and Alternative Software

The Walkabout user's manual presents comparisons of particle trajectory results and first- and second-moment theoretical results for a range of advective-dispersive conditions (Painter, 2011). An example comparison assuming longitudinal, transverse horizontal, and transverse vertical dispersivities of 1.0, 0.1, and 0.01 m, respectively, is presented in Figures K-1 and K-2. Red and blue dots in the left hand of Figure K-1 correspond to the first- and second-moment results for the x-position of particles, respectively, from Walkabout, and the blue lines represent the analytical results. Red and blue dots in the right hand of Figure K-1 correspond to the horizontal transverse and vertical transverse second-moment particle locations, respectively, from Walkabout, and the blue lines represent the analytical results. The left side of Figure K-2 is a top-down view illustrating the dispersion of particles in the x- and y-directions for the verification test 1a used in Figure K-1. The right side of Figure K-2 is a 3-D rendering illustrating the dispersion of particles in the x- and z-directions for this verification test.

In addition to the verification of the numerical algorithm to theoretical solutions, additional verification tests were performed by the use of simple three-dimensional flow and transport models that include heterogeneous flow fields. The additional model verification was accomplished by comparing the results of FEHM_sptr and Walkabout to those of alternative particle-tracking routines such as RWHet (LaBolle, 2005). The approach taken was to start with a three-dimensional flow

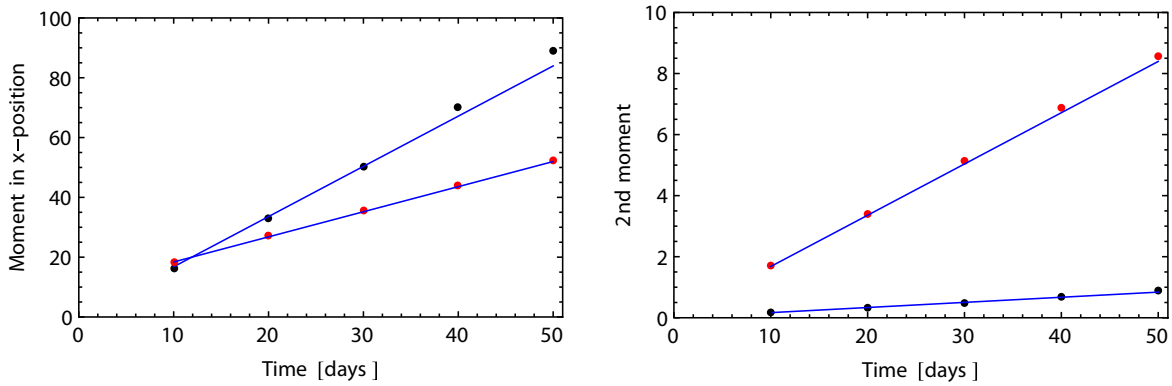

Source: Painter, 2011

Note: Particle tracking results for Verification Test 1a in Painter (2011) corresponding to 3-D transport in a homogeneous and isotropic flow field with dispersivity of 1.0 m, 0.1 m and 0.01 m in the x-, y-, and z-direction, respectively.

Figure K-1
Comparison of Walkabout Particle-Tracking Results at Discrete Times with Theoretical Curves

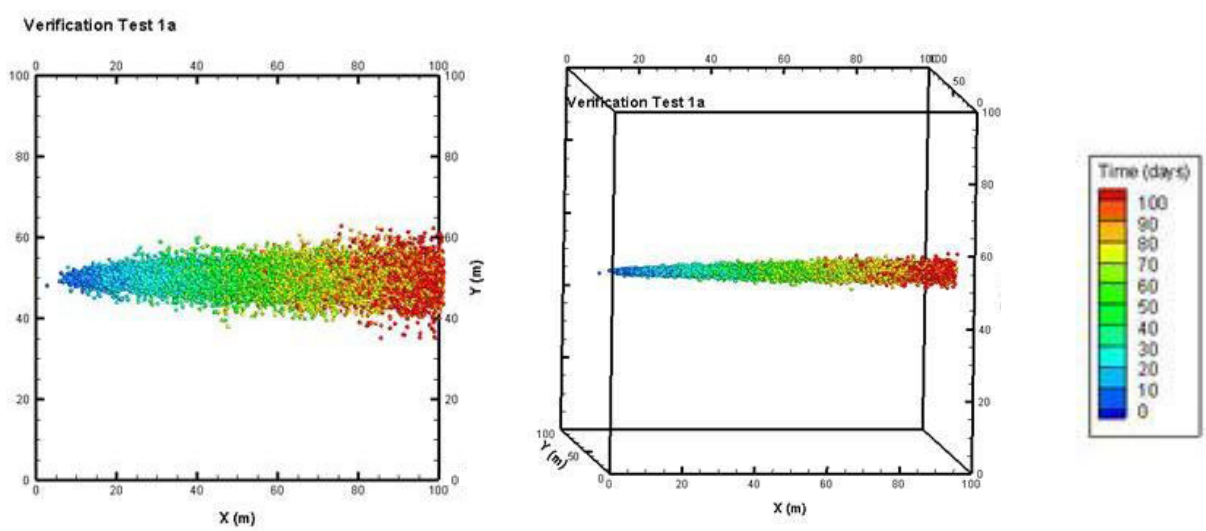

Note: Particle tracking results for Verification Test 1a in Painter (2011) corresponding to 3-D transport in a homogeneous and isotropic flow field with dispersivity of 1.0 m, 0.1 m and 0.01 m in the x-, y-, and z-direction, respectively.

Figure K-2
Walkabout Particle-Tracking Results for Verification Test 1a of Painter (2011)

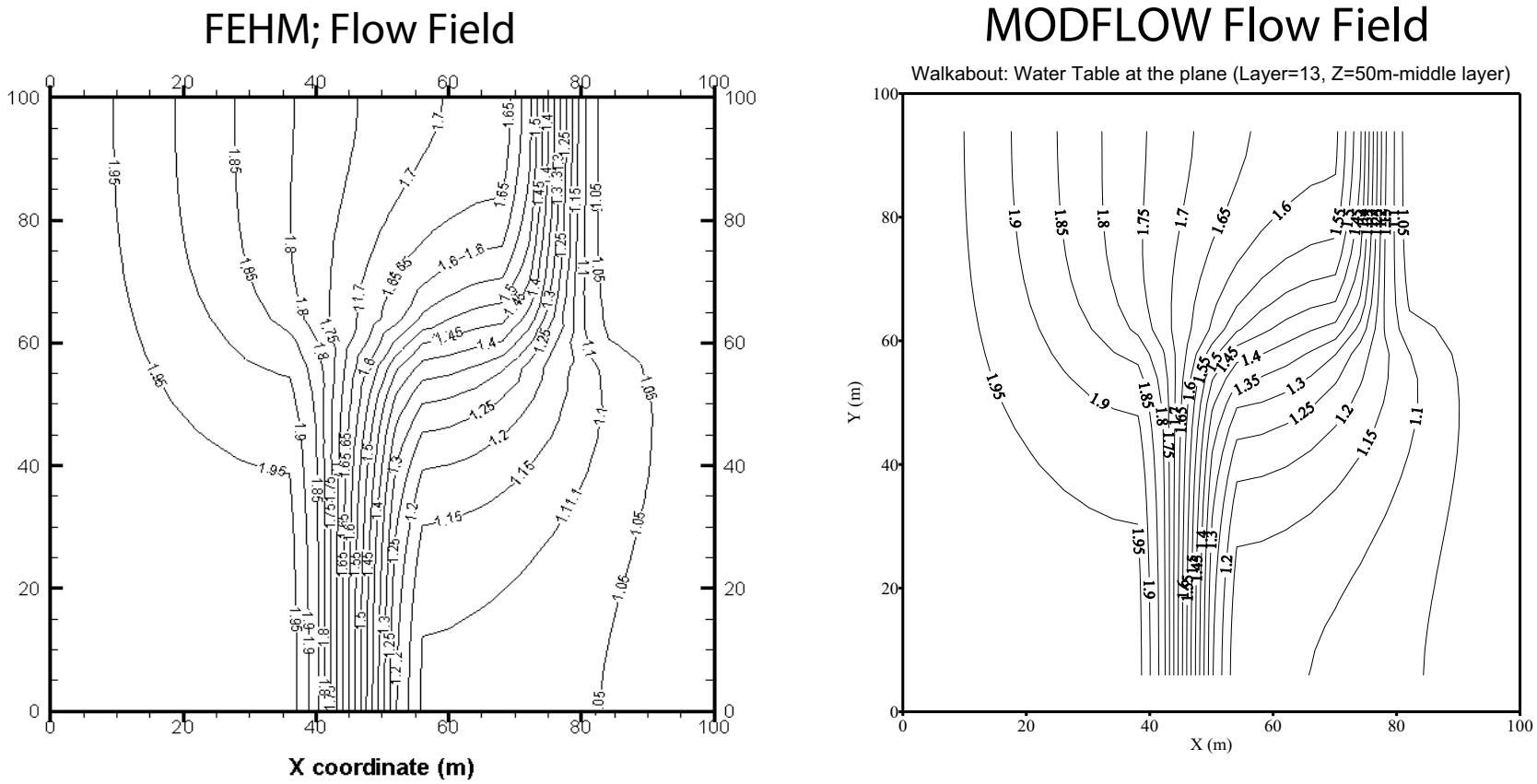

Figure K-3
Comparison of Potentiometric Surfaces of FEHM and MODFLOW for Walkabout Verification Test

domain with horizontal flow around two barriers that are 100,000 times less permeable than the aquifer and to develop flow fields using FEHM and MODFLOW. As illustrated in Figure K-3, very similar flow fields were generated by the use of the two methods. These flow fields were then used to track particles with Walkabout and RWHet for a longitudinal dispersivity of 1.0 m with no transverse dispersivity. The resulting particle tracks generated with Walkabout are illustrated in Figure K-4. The Walkabout and RWHet comparison is illustrated in Figure K-5, which indicates very similar particle trajectories and transport times. It is also notable that very few particles were inappropriately trapped in the low-permeability barrier, a problem noted by LaBolle et al. (1996) as being characteristic of particle-tracking methods.

To evaluate a flow field that could result in particle trajectories that are inappropriately trapped, a revised case was developed with the permeability contrast of the flow barrier of 100 instead of 10,000. The particle-tracking results for FEHM/Walkabout and MODFLOW/RWHet are illustrated in Figures K-6 and K-7 for longitudinal, transverse horizontal, and transverse vertical dispersivities of 1.0, 0.1, and 0.0 m. Resulting particle breakthrough times from the three starting locations are illustrated in Figure K-8. These figures again identify the similarity in the results of the two flow and particle-tracking codes. The more disperse breakthrough of the particles from the middle starting location in RWHet is probably due to some particles being delayed in the low permeability barrier.

The above particle-tracking results were generated with Walkabout and RWHet. Because the sptr subroutine in FEHM has also been successfully applied to develop particle trajectories and advective dispersive transport times, a comparison between FEHM_sptr and FEHM/Walkabout was performed as well. Figure K-9 illustrates the particle trajectories for no dispersivity, and Figure K-10 illustrates resulting nodal-based normalized concentrations based on particle-tracking results. The results compare well.

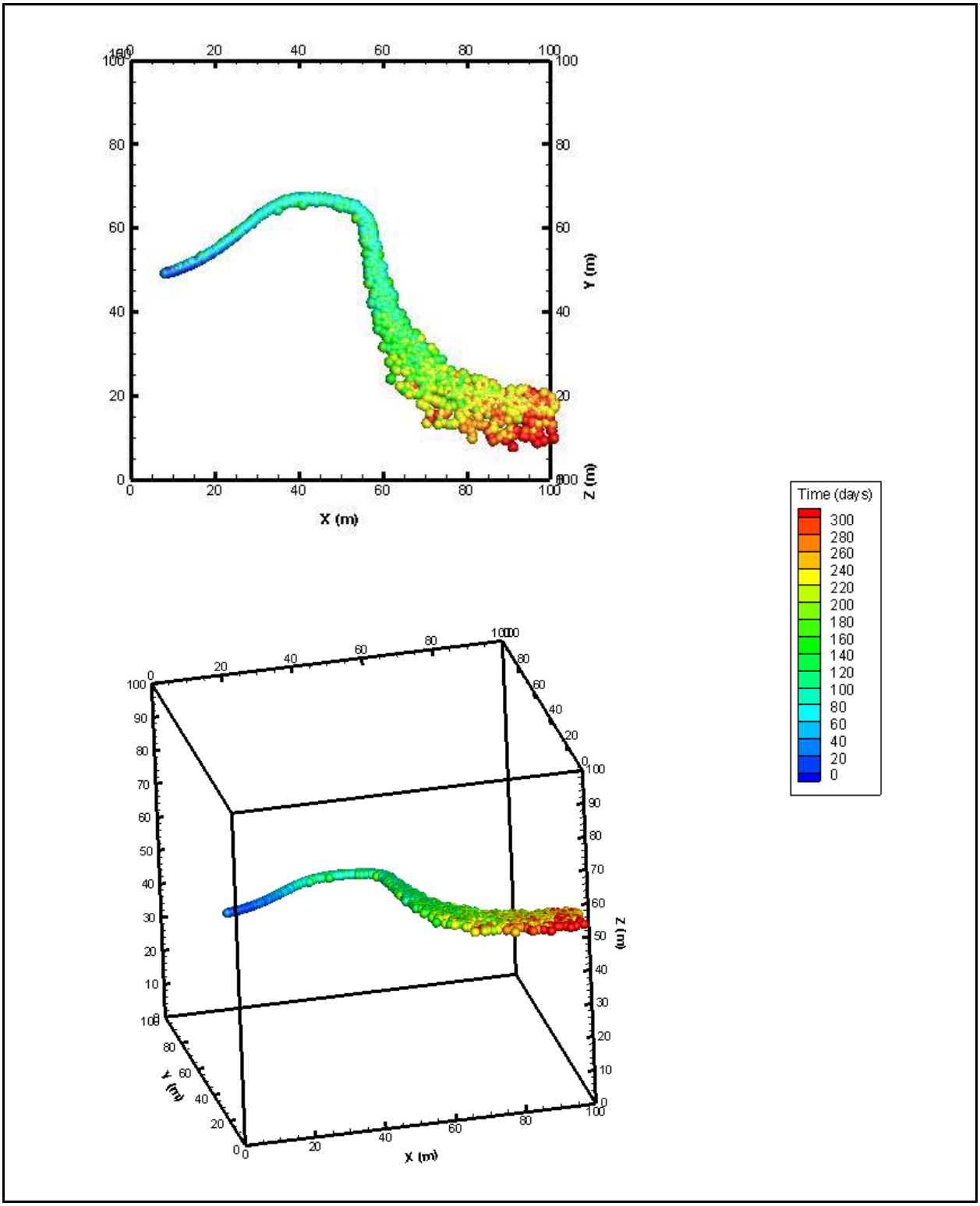

Figure K-4
Walkabout Particle Transport Times for Verification Test
(1.0 m Longitudinal Dispersivity)

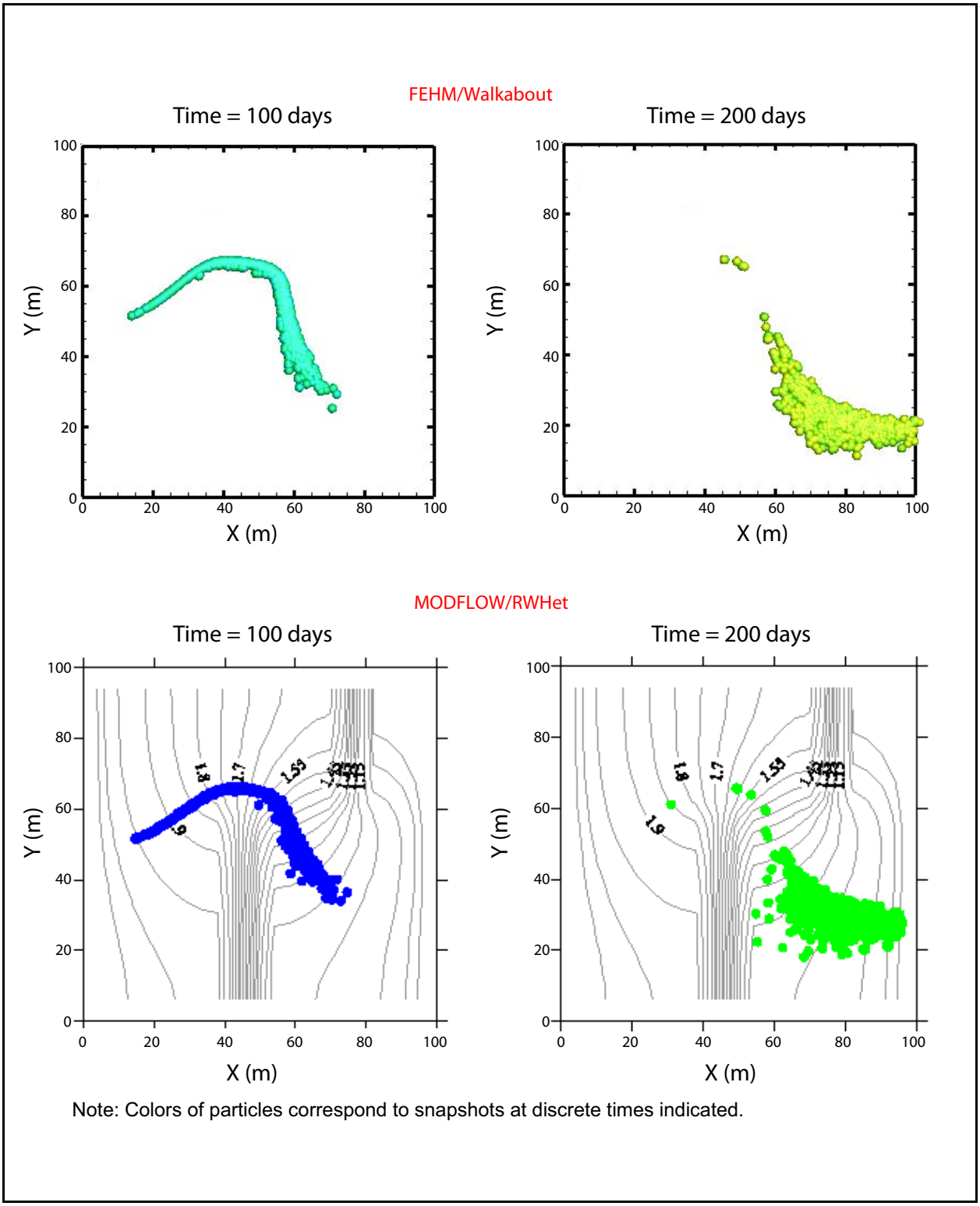

Figure K-5
Comparison of Particle-Tracking Results for Walkabout and RWHet for Verification Test (1.0 m Longitudinal Dispersivity)

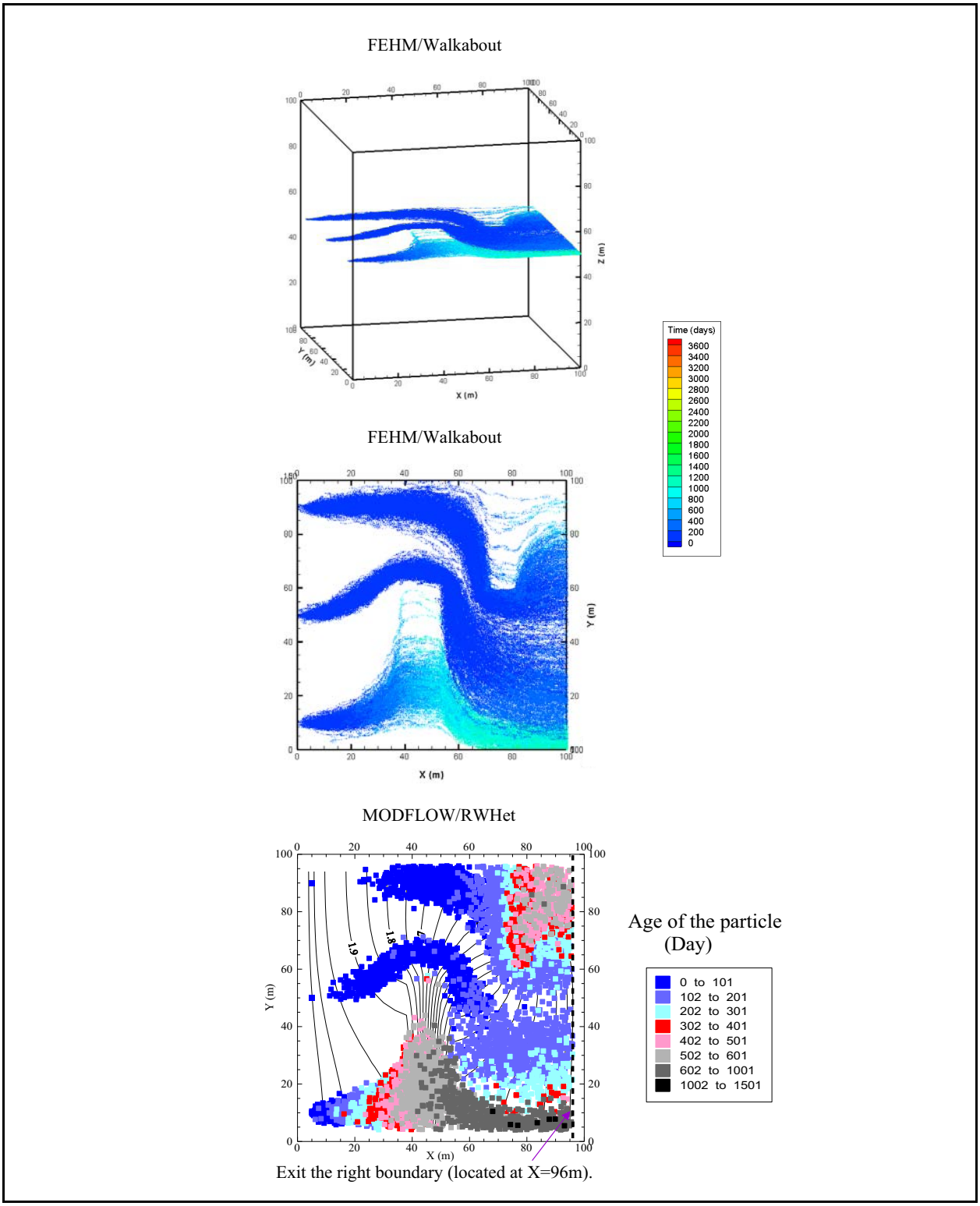

Figure K-6
Comparison of Particle-Tracking Results for FEHM/Walkabout and MODFLOW/RWHet for Dispersivities of 1.0, 0.1, and 0.0 m

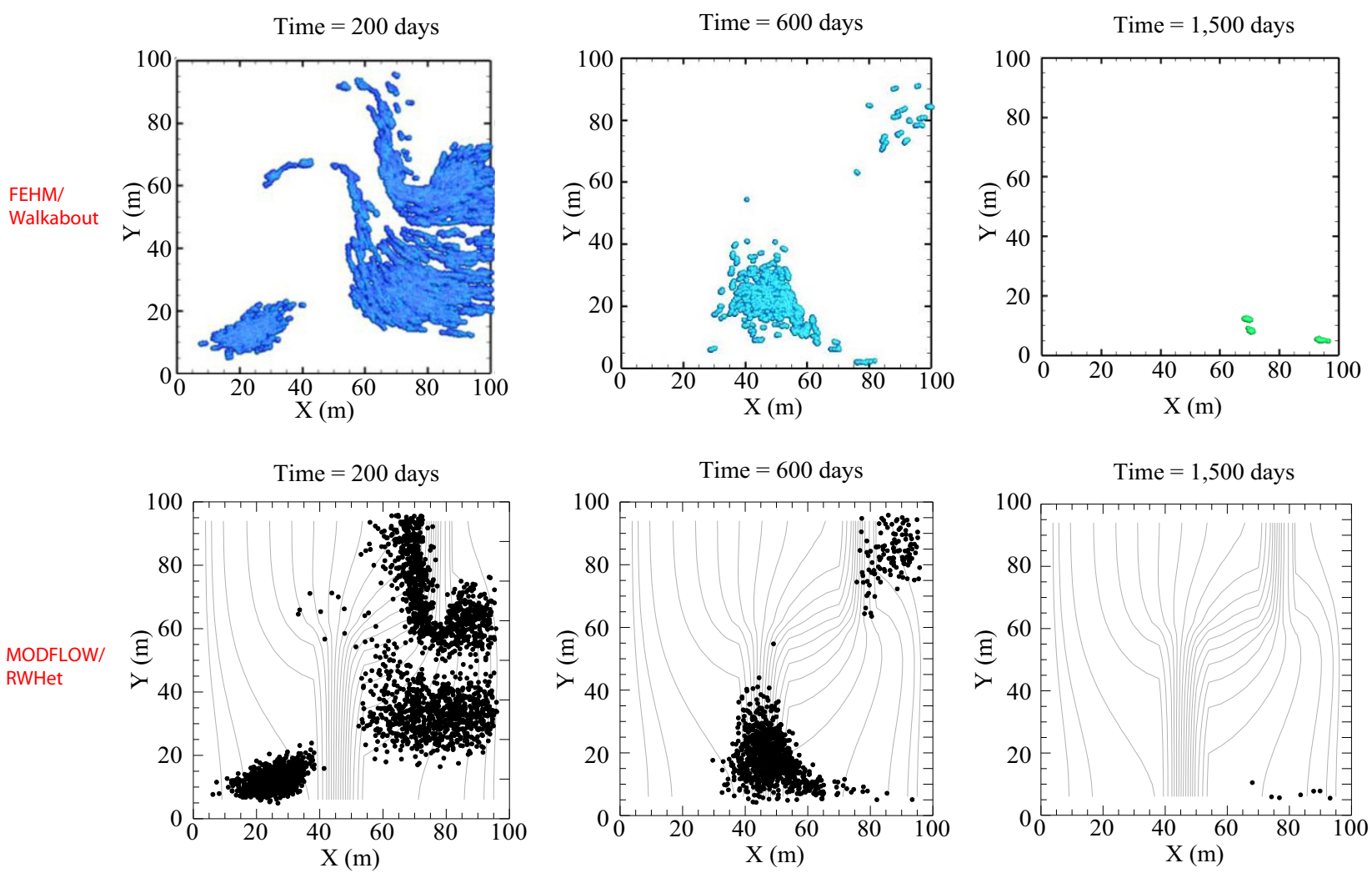

Note: Particle colors are coded to discrete-time snapshots for FEHM/Walkabout results but not for MODFLOW/RWHet.

Figure K-7
Comparison of Particle-Tracking Results at Discrete Times for FEHM/Walkabout and MODFLOW/RWHet for Dispersivities of 1.0, 0.1, and 0.0 m

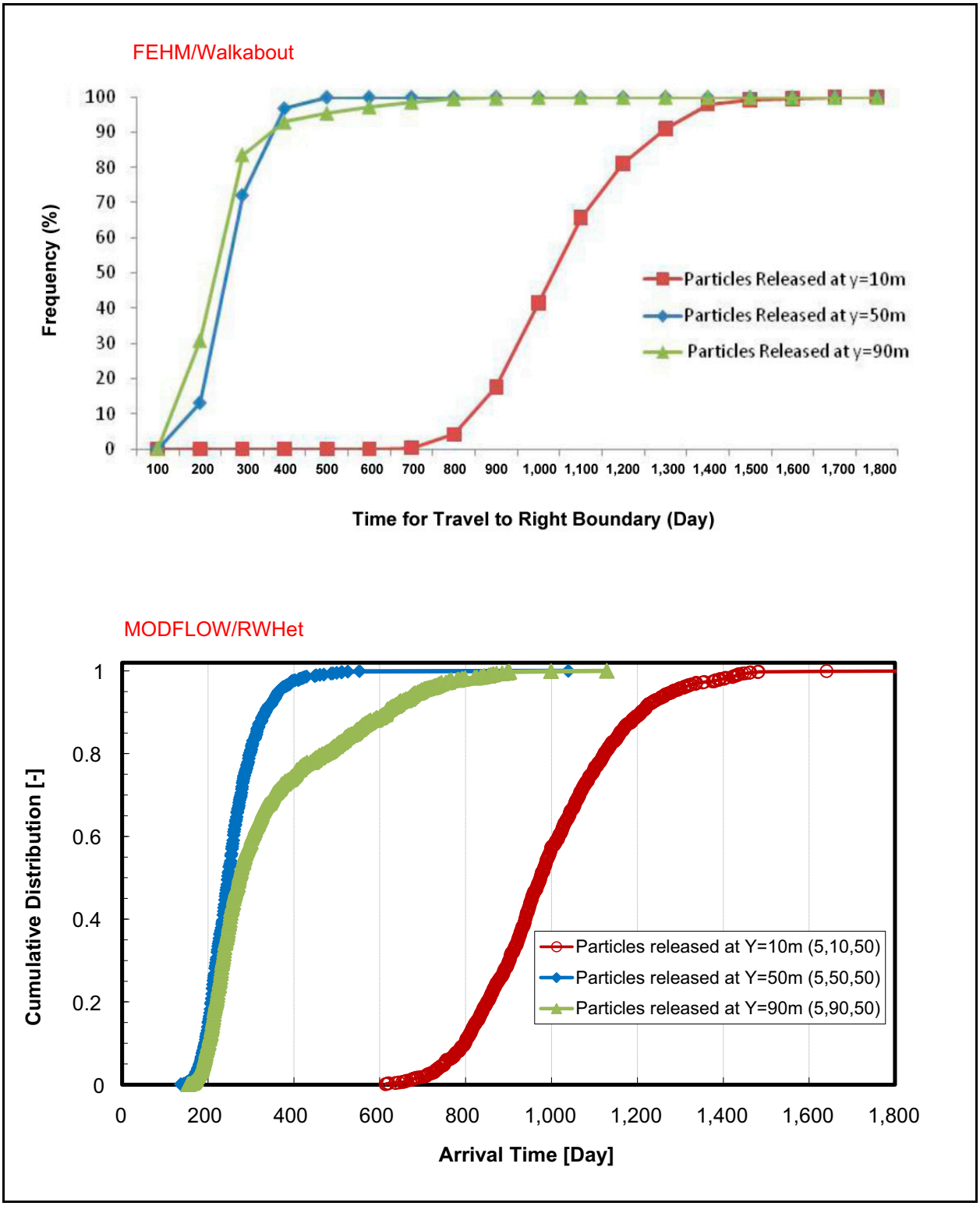

Figure K-8
Comparison of Particle-Tracking Breakthrough Times for FEHM/Walkabout and MODFLOW/RWHet for Dispersivities of 1.0, 0.1, and 0.0 m

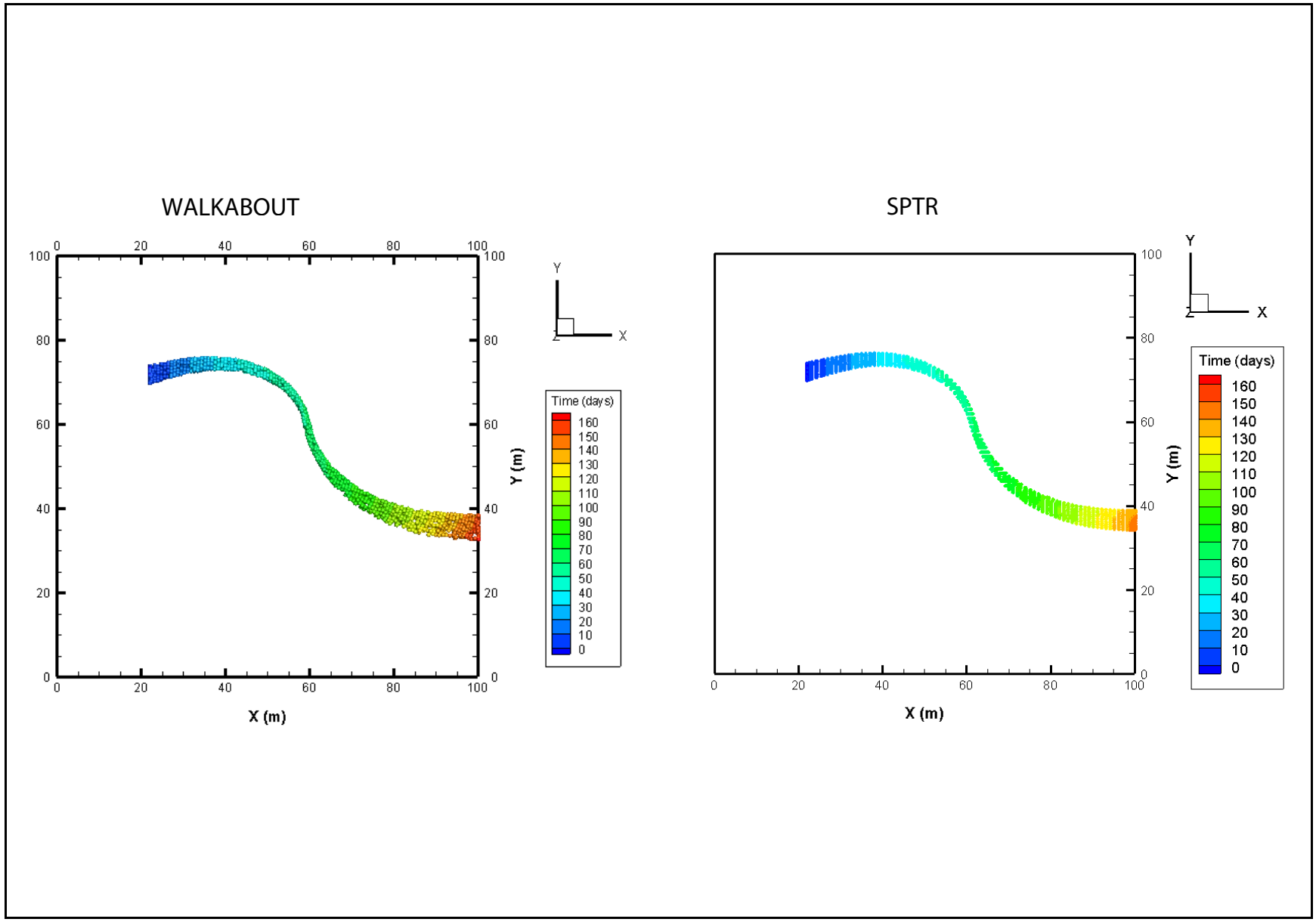

Figure K-9
Comparison of FEHM_sptr and Walkabout Particle Transport Times

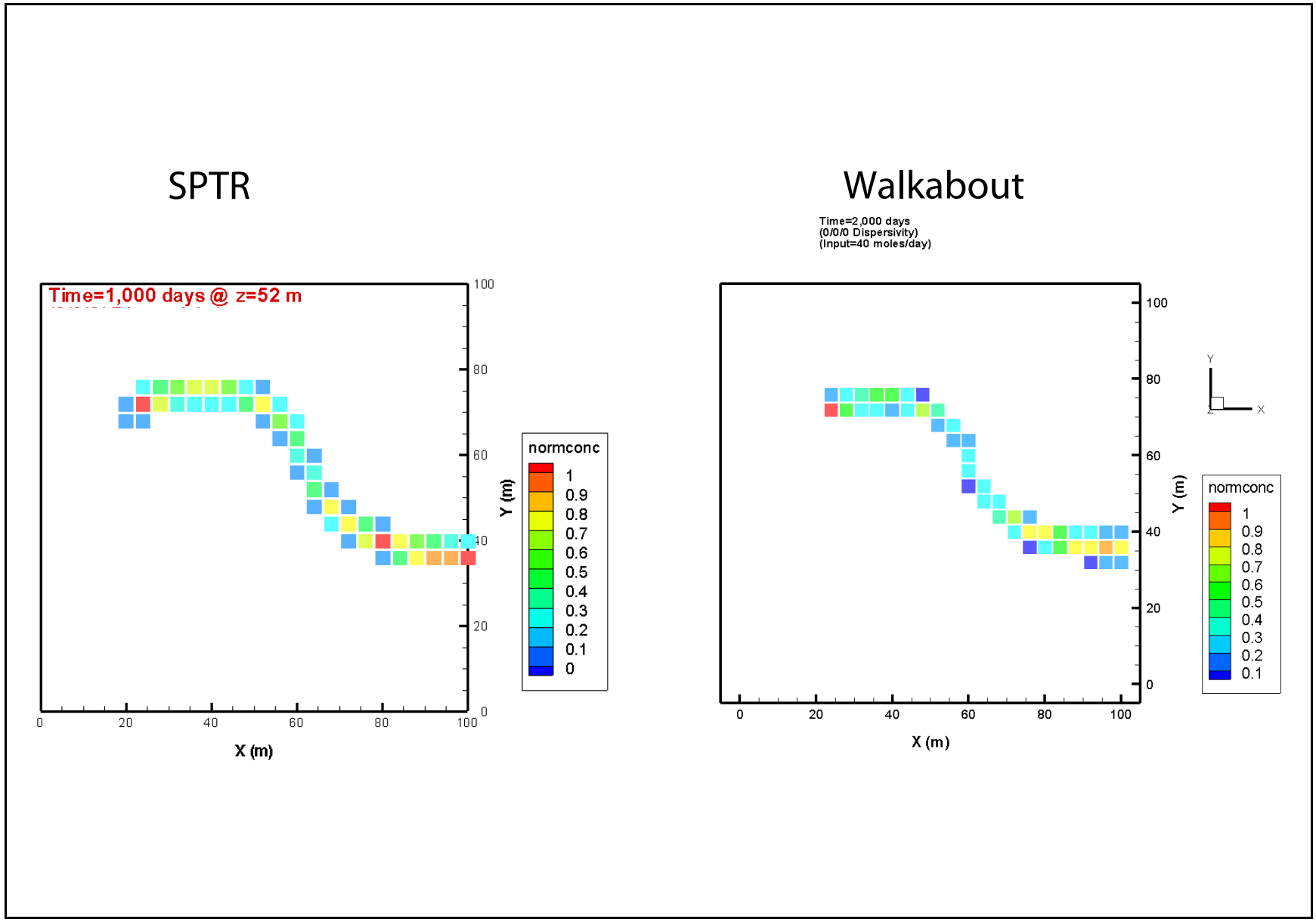

Figure K-10
Comparison of FEHM_sptr and Walkabout Normalized Steady-State Concentrations

K.3.0 TRANSPORT MODEL SOFTWARE SELECTION BASIS

K.3.1 Introduction to PLUMECALC

PLUMECALC is based on a convolution-based particle-tracking method that uses the principle of superposition in space and time to take advantage of efficiencies that can be gained under the assumption of linearity. PLUMECALC uses a methodology similar to that adopted in the convolution integral modeling approach included in the SZ_Convolute software applied to saturated zone transport modeling of the Yucca Mountain repository (Arnold et al., 2003 and Bechtel SAIC, 2005). The method is valid for linear transport processes and steady-state flow. PLUMECALC uses this method and the system response to an instantaneous pulse (or pulses for multiple solute sources) of particles to compute plume concentration for an arbitrary solute mass input function. Two different approaches may be used to calculate concentrations with PLUMECALC V2.3.3, notably the resident concentration, which is the average concentration of fluid in a control volume (either the mobile or the total control volume), and the flux-averaged concentration, which is the average concentration in the fluid weighted by the relative fluid flux. The metric of interest to UGTA is the resident mobile concentration, which is the average concentration in the fracture (i.e., mobile) fluid domain.

The conceptual and numerical basis for PLUMECALC is presented in Robinson et al. (2011) and is based on methods initially presented by Parker and van Genuchten (1984). PLUMECALC has been tested with example problems and validation tests by the code developers (Robinson et al., 2011). Additional tests of PLUMECALC have been performed over a range of conditions that are relevant to the Yucca Flat transport model. These tests include one-dimensional comparisons to analytical solutions presented by Ogata and Banks (1961), and Sudicky and Frind (1982), and three-dimensional comparisons to alternative industry-standard software.

K.3.2 One-Dimensional Comparisons to Analytical Solutions

The verification tests of PLUMECALC have considered both single-porosity tests that are compared to analytical solutions presented by Ogata and Banks (1961), and dual-porosity tests that are compared to analytical solutions presented by Sudicky and Frind (1982). The test comparisons presented in this appendix are based on PLUMECALC V2.3.2; however, these tests are also relevant

for PLUMECALC V2.3.3, which was used in the calculation of contaminant transport that provided the basis for developing the contaminant boundary forecasts presented in Section 6.0.

Example single-porosity verification comparisons are presented in Figure K-11. Example dual-porosity verification comparisons are presented in Figure K-12. PLUMECALC was also verified by conducting tests over a wider range of key transport parameters, such as fracture porosity, fracture aperture, and matrix diffusion, as illustrated in Figure K-13. These results indicate the excellent agreement between PLUMECALC and the analytical solutions. The discrepancy at early times is a result of how the boundary condition is assigned in PLUMECALC, which is overcome by constraining contaminant sources to be a few grid cells downgradient from influx zones.

K.3.3 Three-Dimensional Comparisons to Alternative Corroborative Software

Numerical approximations are associated with both particle-tracking-based or continuum-based transport algorithms used in numerical software. Of particular interest in contaminant transport approximations are complexities associated with heterogeneous flow and velocity fields. As a result of these approximations, additional verification tests were designed to evaluate the effects that heterogeneous velocity fields might have on the results. The heterogeneous velocities may be the result of either permeability or porosity contrasts along the likely contaminant transport pathways. To evaluate the effect of the numerical approximations included in FEHM_sptr or Walkabout and PLUMECALC, a number of three-dimensional cases were run with the results compared to an industry-standard continuum-based solution approach as included in MODFLOW (Harbaugh et al., 2000) and MT3D (Zheng, 1990).

The comparison of FEHM_sptr/PLUMECALC and MODFLOW/MT3D results is illustrated in Figure K-14. The comparison of Walkabout/PLUMECALC and MODFLOW/MT3D results is illustrated in Figure K-15. The code comparison test illustrated in these figures corresponds to a 20,000 m × 400 m × 400 m grid, in the x-, y- and z-directions, respectively, with nodes that are 40 m on a side. The flow field is specified along the x-direction, with no flow boundaries along the y- and z- boundaries. The permeability in all nodes is the same except for a 40-m thick high permeability layer from Z = - 20 m to Z = 20 m) from X = 0 m to X = 12,000 m that has a permeability of 100 times the background permeability. This layer mimics the effect of a high-permeability fault damage zone within otherwise homogeneous, less permeable country rock. The fracture porosity in all nodes is 1E-03. The x-, y-, and z-dispersivities used in the test model are 30 m, 3 m and 0.3 m,

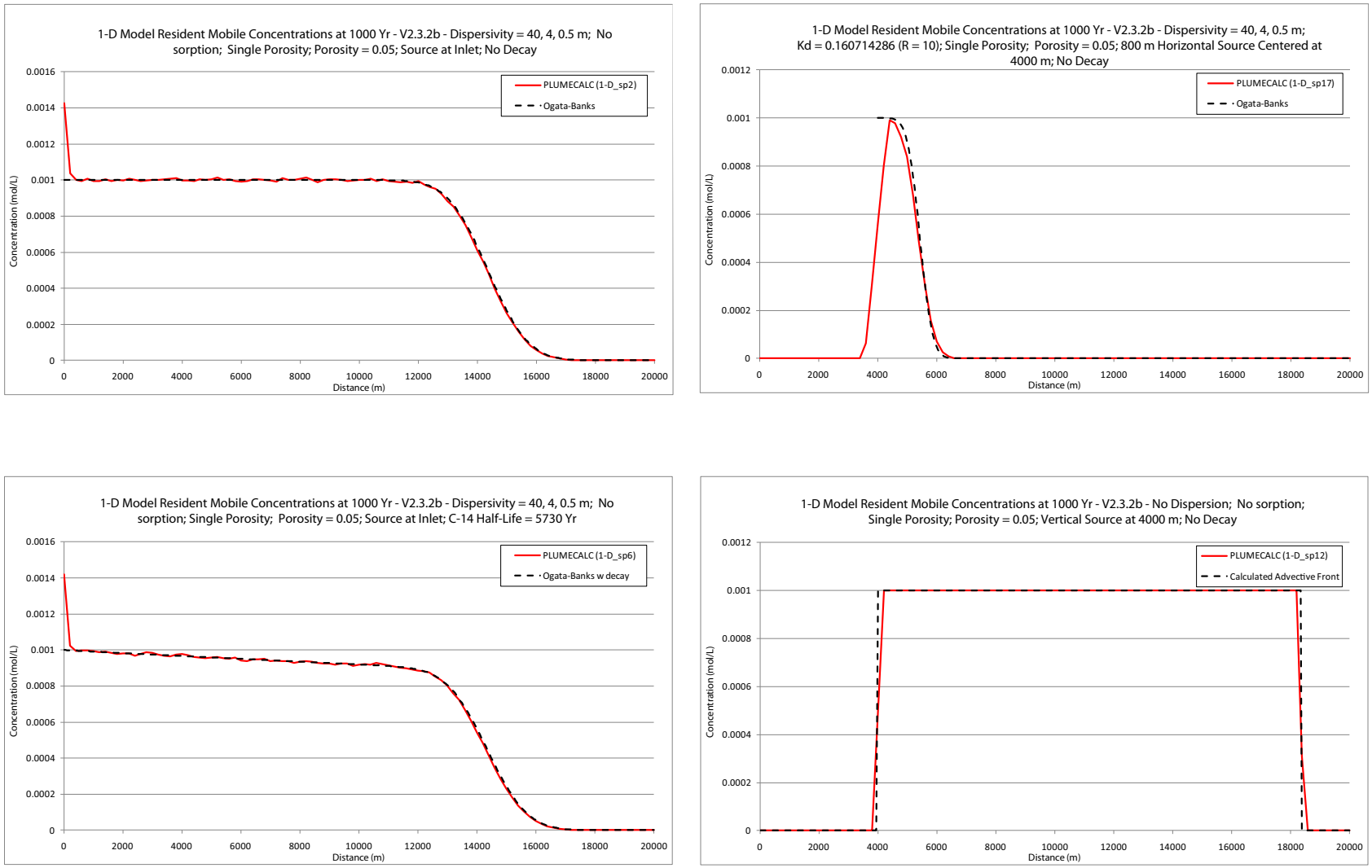

Figure K-11
Single-Porosity Verification of PLUMECALC Comparison to Analytical Solution

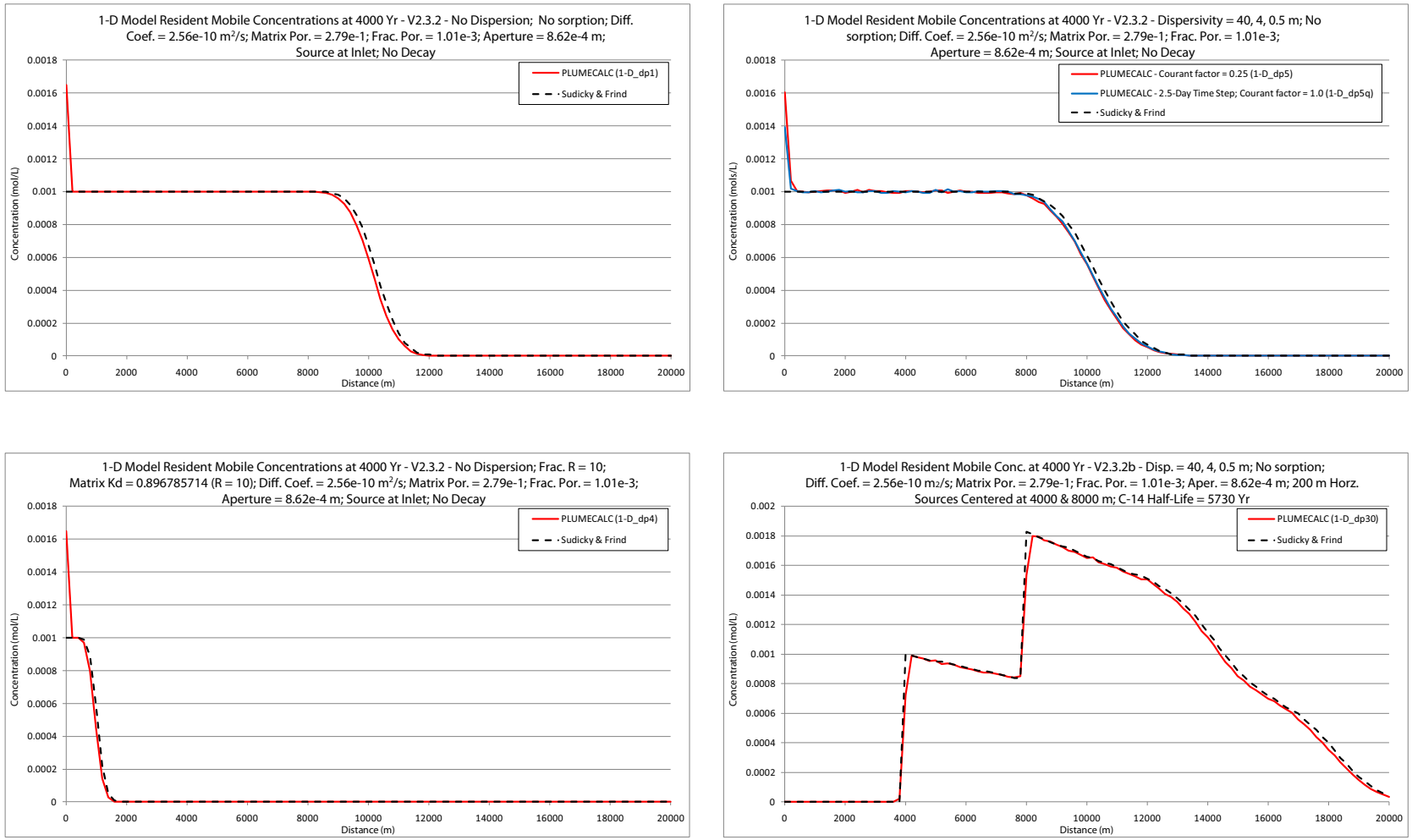

Figure K-12
Dual-Porosity Verification of PLUMECALC Comparison to Analytical Solution

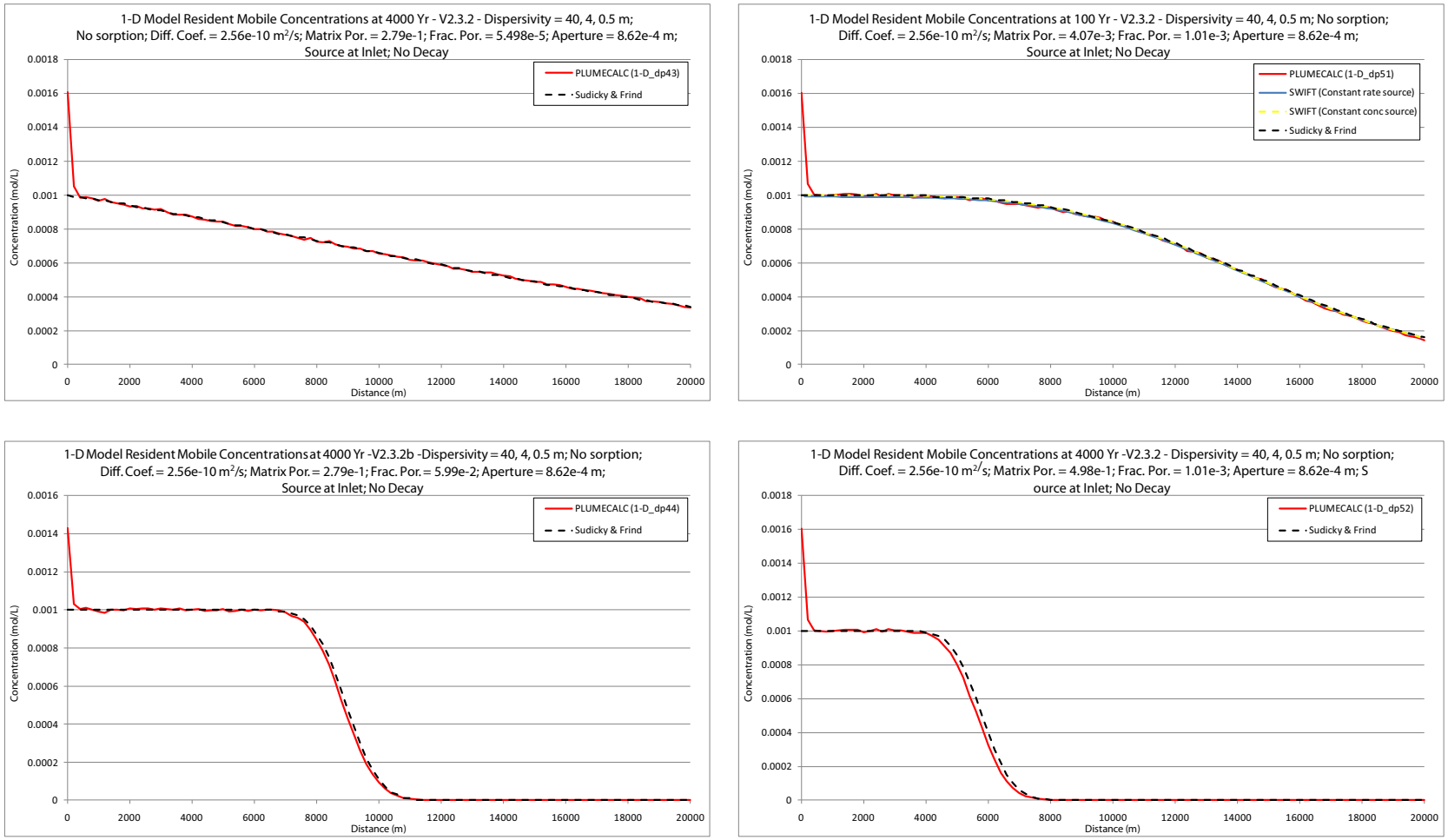

Figure K-13
Dual-Porosity Verification of PLUMECALC Comparison to Analytical Solution for a Range of Transport Parameters

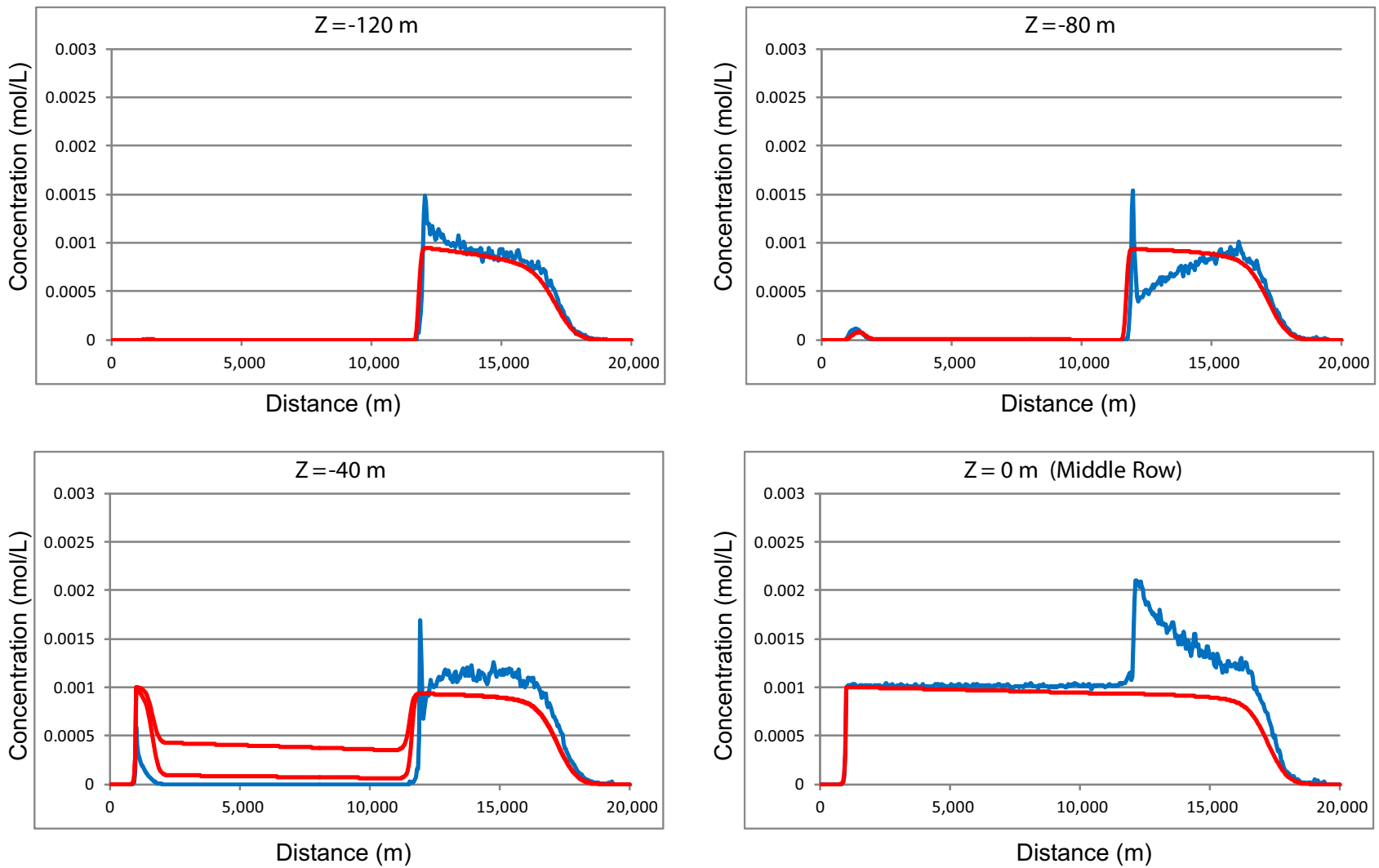

Note: Red curves are MODFLOW/MT3D, and blue curves are FEHM_sptr/PLUMECALC.

Figure K-14
Comparison of FEHM_sptr/PLUMECALC and MODFLOW/MT3D for Heterogeneous Permeability Field

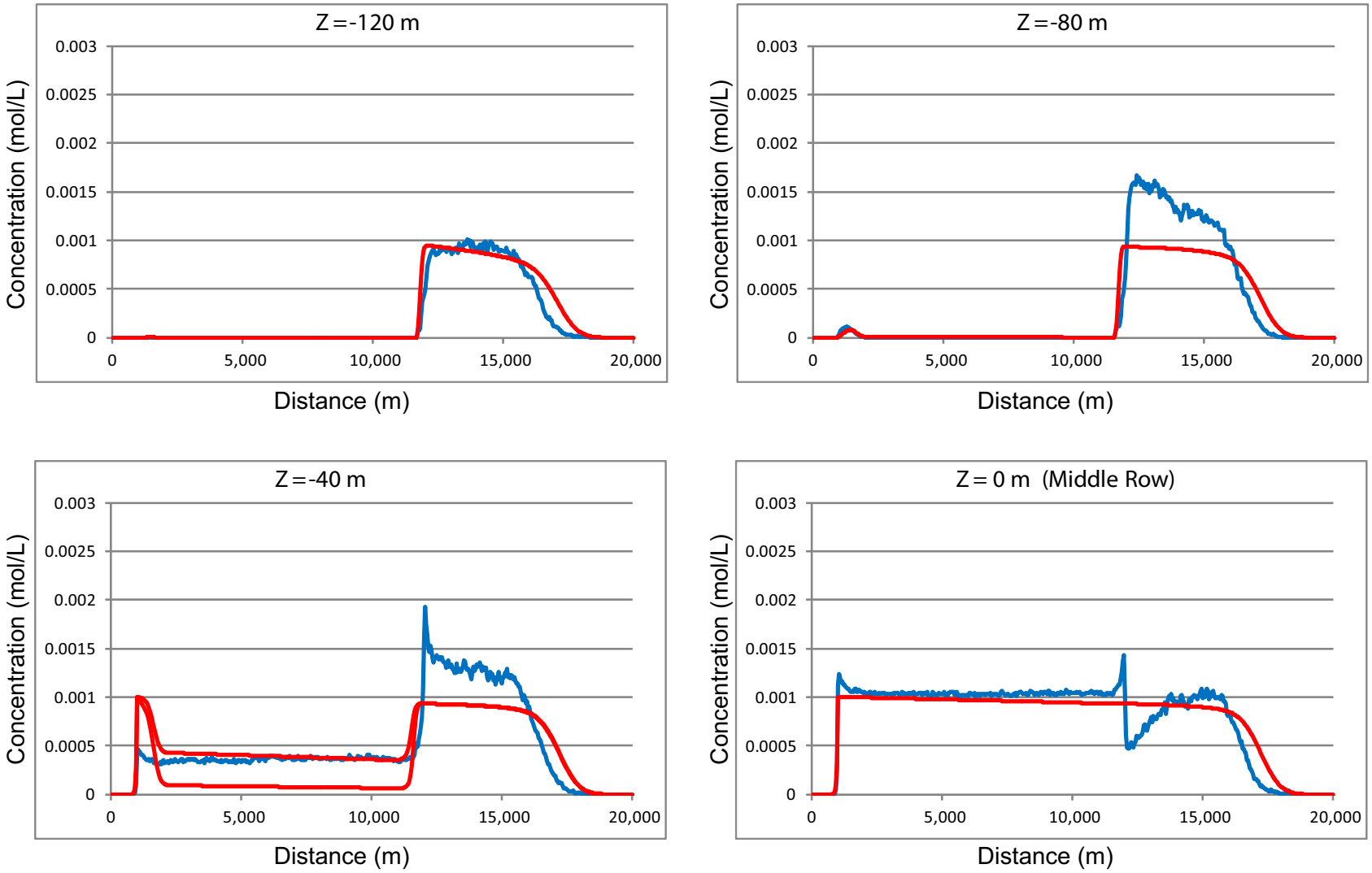

Note: Red curves are MODFLOW/MT3D, and blue curves are Walkabout/PLUMECALC.

Figure K-15
Comparison of Walkabout/PLUMECALC and MODFLOW/MT3D for Heterogeneous Permeability Field

respectively which mimics a greater longitudinal dispersivity and a smaller transverse dispersivity perpendicular to the plane of the high permeability zone. The initial concentration is specified with 15,000 uniformly distributed particles at x = 1,000 m and y from -198 m to 198 m and z from -59.2 m to + 59.2 m. The simulation is run to 1,500 days to capture the leading edge of the plume. The test is performed with both FEHM_sptr/PLUMECALC and Walkabout/PLUMECALC to evaluate the effect of the different particle tracking approximations. The MODFLOW/MT3D model split Layer 5 into 4 sub-layers to better approximate the results at Z = - 40 m for comparison to the particle tracking methods. As a result, two layer elevations are illustrated for MODFLOW/MT3D, one at Z = -49.34 m and the other at Z = -33.34 m, resulting in two red lines in Figures K-14 and K-15 from about X = 1,000 m to X = 12,000 m where the results converge at the end of the high permeability zone. These results indicate the possibility of undershoots or overshoots for the particle-based methods, but the extent of contaminant migration at the leading edge of the plume is reasonably approximated.

Additional three-dimensional comparisons of Walkabout/PLUMECALC and MODFLOW/RWHet are made for a heterogeneous flow field with single porosity transport as illustrated in Figures K-16 and K-17. Additional comparisons including an unstructured FEHM mesh and MODFLOW/MT3DMS are illustrated in Figure K-18. Although these plots use the same scales, they use different color schemes for the legends. These figures again illustrate excellent agreement between the different software.

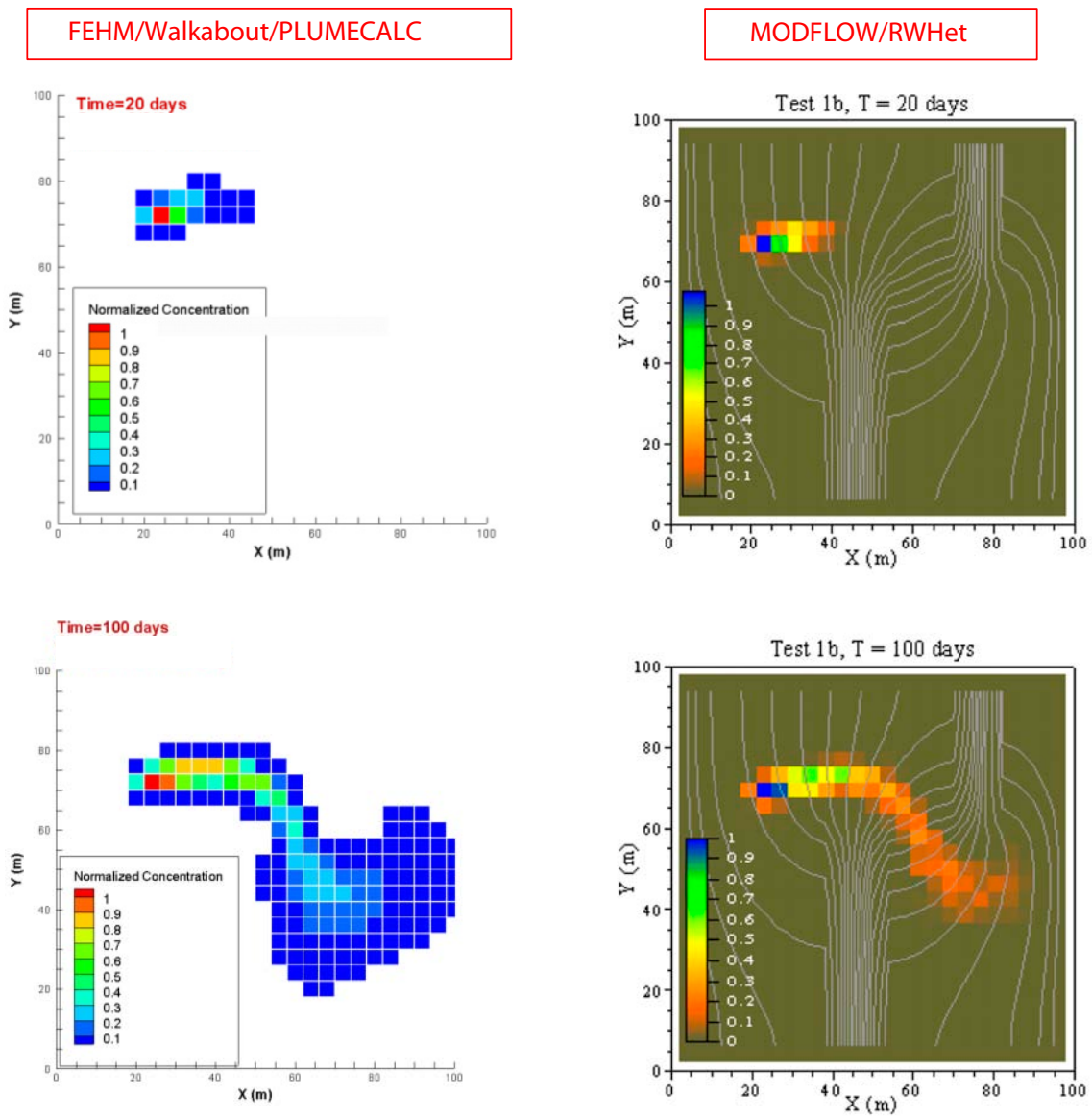

Figure K-16
Comparison of Walkabout/PLUMECALC and MODFLOW/RWHet for Heterogeneous Flow Field at 20 and 100 Days

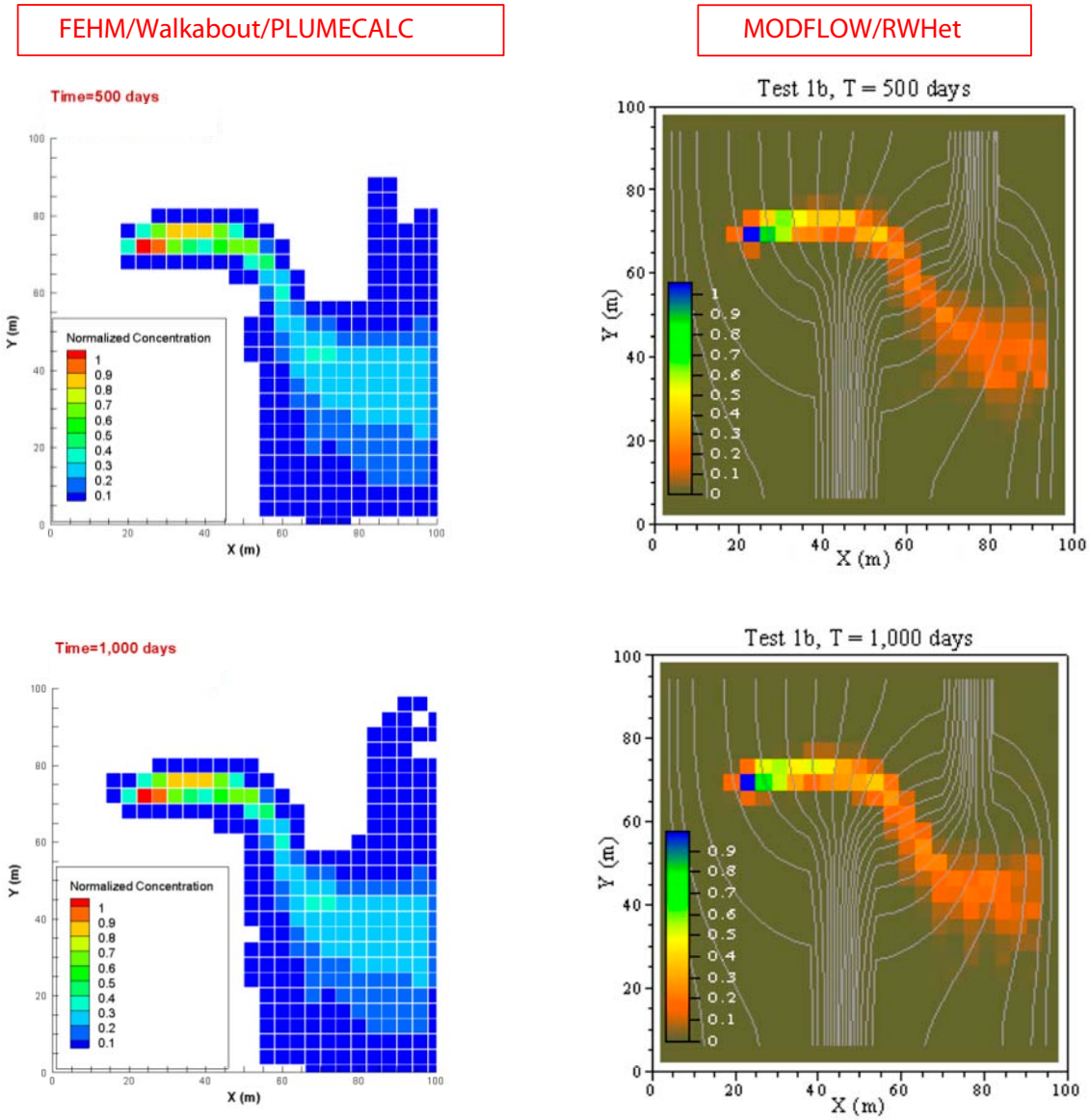

Figure K-17
Comparison of Walkabout/PLUMECALC and MODFLOW/RWHet for Heterogeneous Flow Field at 500 and 1,000 Days

FEHM/
Walkabout
PLUMECALC

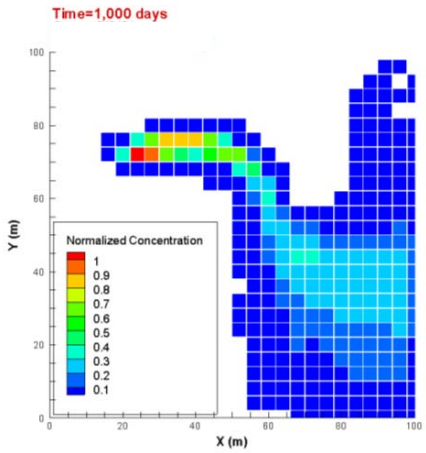

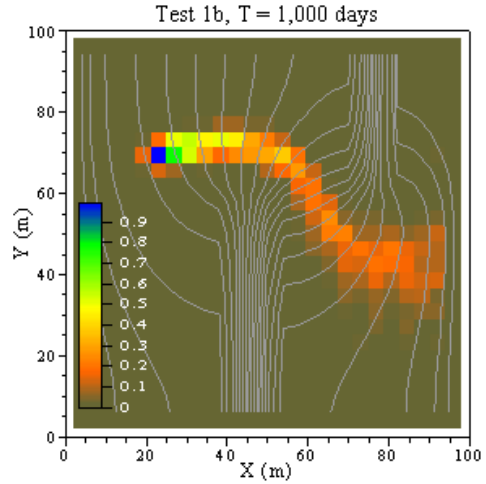

MODFLOW/
RWHet

MODFLOW/
MT3D

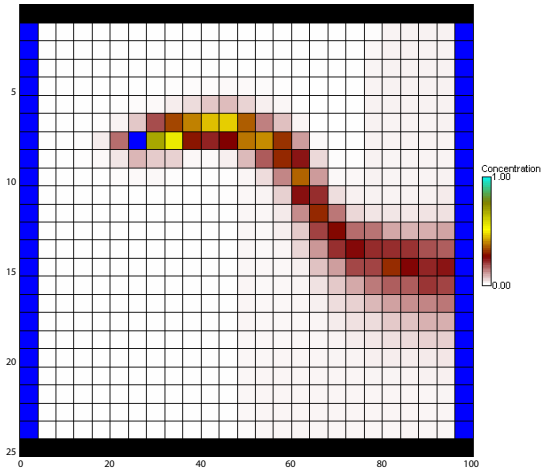

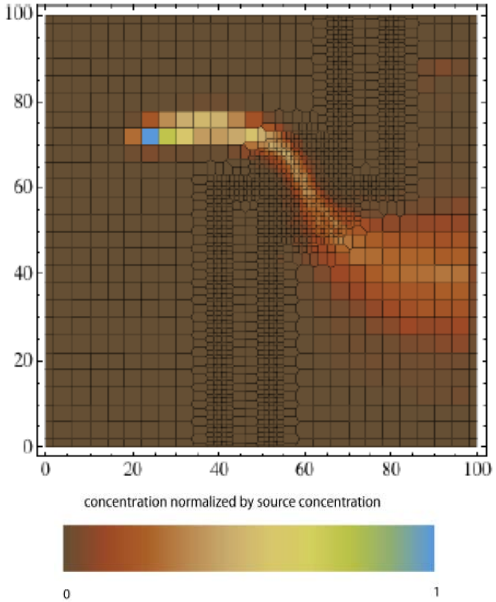

FEHM/Walkabout
Unstructured Mesh

Figure K-18
Comparison of Walkabout/PLUMECALC, MODFLOW/RWHet, MODFLOW/MT3D, and FEHM/Walkabout for Heterogeneous Flow Field

K.4.0 CONCLUSIONS

Based on the suite of analytical and code-to-code verification tests, both FEHM_sptr and Walkabout V1.2 have been found to be suitable codes for evaluating advective-dispersive particle trajectories in steady-state heterogeneous flow fields. There are advantages and disadvantages of both solution methods, and they can yield different results that should be investigated to determine their impact on the results and conclusions. In addition, user-specified solution constraints, such as the VRATIO in FEHM_sptr and the Courant factor in Walkabout, need to specified at values to minimize inappropriate particle accumulation in low-permeability cells.

Similarly, based on the suite of analytical and code-to-code verification tests over a wide range of parameter values, PLUMECALC V2.3.3, when used in the resident mobile concentration mode, has been found to be a suitable code for evaluating contaminant concentrations in saturated fractured or porous media. For fractured rocks, PLUMECALC assumes flow occurs in parallel fractures and diffusion occurs into stagnant water in the matrix. As a result, for UGTA applications, PLUMECALC V2.3.3 is suitable for evaluating contaminant concentrations over the next 1,000 years that result from contaminant sources associated with underground nuclear testing. Again, constraints on the use of PLUMECALC have been developed as a result of the testing, and there is a need to evaluate the stability of the results with the number of particles used in either FEHM_sptr or Walkabout.

Additional confidence in the representativeness of the transport results is demonstrated in Appendix N, where the results of FEHM_sptr and PLUMECALC are compared to those of corroborative software MODFLOW/MT3DMS, Feflow, and FracMan/MAFIC within a subarea of the Yucca Flat/Climax Mine CAU. Simple one-dimensional analyses that use an analytical solution and an alternative transport algorithm in FEHM also are described in Appendix N.

K.5.0 REFERENCES

Arnold, B.W., S.P. Kuzio, and B.A. Robinson. 2003. "Radionuclide Transport Simulation and Uncertainty Analyses with the Saturated-Zone Site-Scale Model at Yucca Mountain, Nevada." *Journal of Contaminant Hydrology* 62–63: 401–419. doi:10.1016/S0169-7722(02)00158-4.

Bechtel SAIC, see Bechtel SAIC Company, LLC.

Bechtel SAIC Company, LLC. 2005. *Saturated Zone Flow and Transport Model Abstraction*, MDL-NBS-HS-000021 REV 03. Prepared for the U.S. Department of Energy, Office of Civilian Radioactive Waste Management. Las Vegas, NV.

DOE/NV, see U.S. Department of Energy, Nevada Operations Office.

Dash, Z.V. 2003a. *Software Users Manual (UM) for the FEHM Application Version 2.21*, STN: 10086-2.21-00, Rev. No. 00, Document ID: 10086-UM-2.21-00. Los Alamos, NM: Los Alamos National Laboratory.

Dash, Z.V. 2003b. *Validation Test Plan (VTP) for the FEHM Application Version 2.21*, STN: 10086-2.21-00, Rev. No. 00, Document ID: 10086-VTP-2.21-00. Los Alamos, NM: Los Alamos National Laboratory.

Dash, Z.V., B.A. Robinson, and G.A. Zyvoloski. 1997. *Software Requirements, Design, and Verification and Validation for the FEHM Application—A Finite-Element Heat- and Mass-Transfer Code*, LA-13305-MS. Los Alamos, NM: Los Alamos National Laboratory.

FFACO, see *Federal Facility Agreement and Consent Order.*

Federal Facility Agreement and Consent Order. 1996 (as amended March 2010). Agreed to by the State of Nevada; U.S. Department of Energy, Environmental Management; U.S. Department of Defense; and U.S. Department of Energy, Legacy Management. Appendix VI, which contains the Underground Test Area Strategy, was last modified May 2011, Revision No. 4.

GAO, see U.S. Government Accountability Office

Harbaugh, A.W., E.R. Banta, M.C. Hill, and M.G. McDonald. 2000. *MODFLOW-2000, The U.S. Geological Survey Modular Ground-Water Model—User Guide to Modularization Concepts and the Ground-Water Flow Process*, Open-File Report 2000-92. Reston, VA: U.S. Geological Survey.

LANL, see Los Alamos National Laboratory.

LaBolle, E.M. 2005. *RWHet: Random Walk Particle Model for Simulating Transport in Heterogeneous Permeable Media Version 3.2: User's Manual and Program Documentation*.

LaBolle, E.M., G.E. Fogg, and A.F.B. Tompson. 1996. "Random-Walk Simulation of Transport in Heterogeneous Porous Media: Local Mass-Conservation Problem and Implementation Methods." *Water Resources Research* 32 (3): 583–593. doi:10.1029/95WR03528.

Los Alamos National Laboratory. 2011. *LaGriT Los Alamos Grid Toolbox* website. As accessed at http://lagrit.lanl.gov/.

NNES, see Navarro Nevada Environmental Services, LLC.

NNSA/NSO, see U.S. Department of Energy, National Nuclear Security Administration Nevada Site Office.

Navarro Nevada Environmental Services, LLC. 2010. *Phase II Transport Model of Corrective Action Unit 98: Frenchman Flat, Nevada Test Site, Nye County, Nevada*, Rev. 1, N-I/28091--004, S-N/99205--122. Las Vegas, NV.

Ogata, A., and R.B. Banks. 1961. *A Solution of the Differential Equation of Longitudinal Dispersion in Porous Media*, Professional Paper 411-A. Washington, DC: U.S. Geological Survey.

Painter, S.L. 2011. *User's Manual for Walkabout V1.0*, LA-UR-11-01952. Los Alamos, NM: Los Alamos National Laboratory.

Parker, J.C., and M. Th. van Genuchten. 1984. "Flux-Averaged and Volume-Averaged Concentrations in Continuum Approaches to Solute Transport." *Water Resources Research* 20 (7): 866–872. doi:10.1029/WR020i007p00866.

Pollock, D.W. 1988. "Semianalytical Computation of Path Lines for Finite-Difference Models." *Ground Water* 26 (6): 743–750.

Robinson, B.A., Z.V. Dash, and S.L. Painter. 2011. *User's Guide for the PLUMECALC Application with Subgridding*, LA-UR-11-02090. Los Alamos, NM: Los Alamos National Laboratory.

Robinson, B.A., Z.V. Dash, and G. Srinivasan. 2010. "A Particle Tracking Transport Method for the Simulation of Resident and Flux-Averaged Concentration of Solute Plumes in Groundwater Models." *Computational Geosciences* 14 (4): 779-792. doi:10.1007/s10596-010-9190-6.

Shaw, see Shaw Environmental, Inc.

SNJV, see Stoller-Navarro Joint Venture.

Shaw Environmental, Inc. 2003. *Modeling Approach/Strategy for Corrective Action Unit 97, Yucca Flat and Climax Mine*, Rev. 0, Shaw/13052-205. Las Vegas, NV.

Stoller-Navarro Joint Venture. 2004. *Modeling Approach/Strategy for Corrective Action Units 101 and 102: Central and Western Pahute Mesa*, Rev. 0, S-N/99205--008. Las Vegas, NV.

Stoller-Navarro Joint Venture. 2006. *Groundwater Flow Model of Corrective Action Units 101 and 102: Central and Western Pahute Mesa, Nevada Test Site, Nye County, Nevada*, Rev. 0, S-N/99205--076. Las Vegas, NV.

Stoller-Navarro Joint Venture. 2009. *Phase I Transport Model of Corrective Action Units 101 and 102: Central and Western Pahute Mesa, Nevada Test Site, Nye County, Nevada*, Rev. 1, S-N/99205--111. Las Vegas, NV.

Sudicky, E.A., and E.O. Frind. 1982. "Contaminant Transport in Fractured Porous Media: Analytical Solutions for a System of Parallel Fractures." *Water Resources Research* 18 (6): 1634–1642. doi:10.1029/WR018i006p01634.

U.S. Department of Energy, National Nuclear Security Administration Nevada Site Office. 2011. *Underground Test Area Quality Assurance Project Plan, Nevada National Security Site, Nevada*, DOE/NV--1450. Las Vegas, NV.

U.S. Department of Energy, Nevada Operations Office. 2000. *Corrective Action Investigation Plan for Corrective Action Unit 97: Yucca Flat/Climax Mine, Nevada Test Site, Nevada*, DOE/NV--659. Las Vegas, NV.

U.S. Government Accountability Office. 2011. *Nuclear Waste: DOE Needs a Comprehensive Strategy and Guidance on Computer Models that Support Environmental Cleanup Decisions.* GAO-11-143, Washington, DC.

Zheng, C. 1990. *MT3D: A Modular Three-Dimensional Transport Model for Simulation of Advection, Dispersion and Chemical Reaction of Contaminants in Groundwater Systems*. Prepared for the U.S. Environmental Protection Agency, Robert S. Kerr Environmental Research Laboratory. Rockville, MD: S.S. Papadopulos & Associates, Inc.

Zyvoloski, G.A. 2007. *FEHM: A Control Volume Finite Element Code for Simulating Subsurface Multi-phase Multi-fluid Heat and Mass Transfer*, LA-UR-07-3359. Los Alamos, NM: Los Alamos National Laboratory.

Zyvoloski, G.A., B.A. Robinson, Z.V. Dash, and L.L. Trease. 1999. *Models and Methods Summary for the FEHM Application*, FEHM MMS SC-194. Los Alamos, NM: Los Alamos National Laboratory.

Appendix L

Groundwater ^{14}C Ages and Velocity Estimates for the Lower Carbonate Aquifer in Yucca Flat

L.1.0 INTRODUCTION

The purpose of this appendix is to investigate whether the groundwater age estimates from naturally occurring carbon-14 (^{14}C) can be used to constrain the migration velocities of not only test-derived ^{14}C, but also other test-generated radionuclides, such as chlorine-36 (^{36}Cl) and iodine-129 (^{129}I), that are believed to move as tracers through the lower carbonate aquifer (LCA) in Yucca Flat. To accomplish this purpose, the ^{14}C ages of groundwater are first corrected with simple correction techniques to account for the dissolution and isotopic exchange with carbonate minerals. Then, the temporal variations of naturally occurring ^{36}Cl in groundwater are compared with terrestrial records of meteoric ^{36}Cl variability recorded in pack-rat midden data over the past 40,000 years. The goal of this comparison is to verify the reasonableness of the groundwater ^{14}C ages and the hypothesis that ^{14}C is migrating in groundwater at the same rate as a conservative tracer like ^{36}Cl. Finally, a simple one-dimensional dual-porosity model of groundwater flow and transport in the LCA is presented to demonstrate that tracer migration velocities of 2 m/yr or less are possible for combinations of hydrologic and transport parameters that are well within their measured ranges.

L.1.1 Previous Geochemical Analyses

SNJV (2006a) conducted an analysis of geochemical and isotopic variations in Yucca Flat groundwater using graphical methods and geochemical inverse modeling. This was done to help understand groundwater flow directions, mixing proportions, and velocities in the LCA in Yucca Flat. One of the major findings of the analysis was that a large proportion of the groundwater in the LCA is derived from local recharge within the basin rather than from regional underflow, as evidenced primarily from a large component of relatively dilute groundwater with characteristics of tuff aquifers or tuffaceous alluvium in the LCA. The analysis thus confirmed a similar conclusion made earlier by Winograd and Thordarson (1975) on the basis of the major ion chemistry and fewer available wells.

The characteristics identified in SNJV (2006a) as indicative of the presence of volcanic aquifer water in the LCA included dilute groundwater with high ^{36}Cl to total chloride ($^{36}Cl/Cl$) ratios near the Yucca, Carpetbag, and Topgallant fault systems (Figure L-1). The high $^{36}Cl/Cl$ ratios indicate that this dilute water was paleorecharge that had infiltrated in the late Pleistocene when meteoric $^{36}Cl/Cl$ ratios

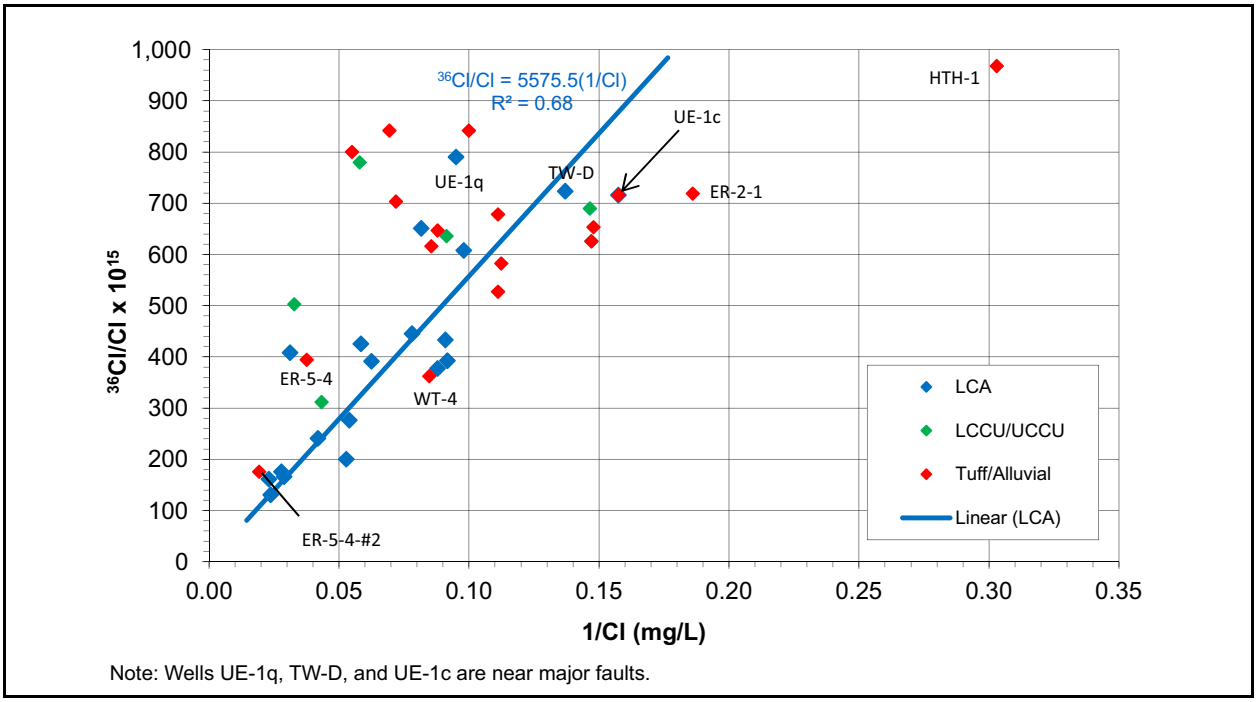

Figure L-1
Relation between the Groundwater ^{36}Cl/Cl Ratios and Inverse Cl Concentrations

were roughly twice the modern-day ratios (Plummer et al., 1997; SNJV, 2006a). Elsewhere in the LCA, groundwater ^{36}Cl/Cl ratios were lower than present-day meteoric levels (roughly 500E-15), and the trend in the LCA data was toward zero ^{36}Cl/Cl ratios at infinite Cl concentrations (0 L/mg inverse chloride). These suggest that chloride with a low ^{36}Cl/Cl ratio had been added by reactions between the LCA groundwater and the carbonate rock matrix, which contains about 22 to 93 parts per million (ppm) of leachable chloride (Kenneally, 1995). Although the data were too sparse to rule out the possibility that drainage from the alluvial/volcanic aquifer system to the LCA was occurring along other faults, they highlighted the potential for such drainage to occur where stratigraphic offsets along faults are especially large and where the tuff confining units have been thinned or removed entirely by faulting, thus bringing the volcanic aquifers directly into contact with the LCA.

The local prominence of groundwater from the alluvial/volcanic aquifer system in the LCA supports the long-held position that groundwater flow into Yucca Flat is limited by the low-permeability clastic and granitic rocks that bound the basin on its northeastern, northern, and northwestern sides (Winograd and Thordarson, 1975). The basis for this interpretation is that modern infiltration rates are relatively low compared to those that existed at the end of the ice ages roughly 10,000 years ago; infiltration rates presently range from near zero or negative in the alluvial-filled parts of the basin to

as much as a few millimeters per year in the bedrock hills bordering the basin (Tyler et al., 1996; Walvoord, Phillips, et al., 2002; Walvoord, Plummer, et al., 2002; Kwicklis et al., 2006; SNJV, 2006b). Therefore, for the relatively small amounts of dilute groundwater draining from the alluvial/volcanic aquifer system to exert a prominent influence on groundwater chemistry in the upper part of the LCA, the regional groundwater flow entering the LCA in Yucca Flat must also be relatively small.

SNJV (2006a) estimated groundwater velocities between upgradient and downgradient wells in the LCA using geochemical inverse models such as NETPATH (Plummer et al., 1994) and PHREEQC (Parkhurst and Appelo, 1999) that accounted for the water–rock interactions affecting ^{14}C activities along the flow path. In principle, these models allowed the decreases in ^{14}C activities due to radioactive decay to be isolated from those caused by other processes, such as carbonate dissolution/precipitation reactions and isotopic exchange, so that travel times and velocities between wells could be calculated. Based on these models, SNJV (2006a) estimated groundwater velocities of 2 m/yr or less for most parts of the basin, with the exception being a possible southwest-oriented flow path between Wells ER-3-1 and WW-C-1, where the velocities were substantially higher (4.3 to 13 m/yr).

L.1.2 Factors Affecting Estimates of Groundwater Velocity Derived from ^{14}C Observations

If ^{14}C sorbs to the carbonate rock, as indicated by many laboratory and field studies (e.g., Mozeto et al., 1984; Maloszewski and Zuber, 1991; Ware et al., 2005; Reimus et al., 2006), interpretations derived from NETPATH and PHREEQC inverse models would underestimate transport velocities because these models cannot identify and correct for sorption. In this case, the slow migration velocities of naturally occurring ^{14}C will underestimate the rates of movement of non-sorbing, test-generated radionuclides such as ^{36}Cl and ^{129}I, even though they will provide a good estimate of the future long-term migration velocities of test-generated ^{14}C.

Some studies have pointed out that matrix diffusion of ^{14}C will also affect ^{14}C age dating of groundwater (e.g., Sanford, 1997). Various studies have attempted to correct groundwater ^{14}C ages at the NNSS and other sites for the effects of these diffusive processes (e.g., Maloszewski and Zuber, 1991; Sanford, 1997; Hershey et al., 2003). Because diffusion arising from Brownian motion affects all molecular species including water (as would be evident if tritiated water [hydrogen tritium oxide,

or HTO] or "heavy" water [hydrogen deuterium oxide, or HDO] had been used as tracers in these experiments), the migration of $H^{14}CO_3^-$ in Yucca Flat as interpreted through the calculated groundwater ages and velocities provides a useful analog regarding the migration of other dissolved species if its sorption and exchange behavior is understood.

This appendix reevaluates the various processes that could potentially affect the interpretation of ^{14}C ages in the LCA and determines the representativeness of groundwater velocities inferred from the ^{14}C observations.

L.2.0 ANALYSES OF GROUNDWATER ^{14}C AGES

This appendix uses the dataset used in SNJV (2006a) and additional data from alluvial and volcanic aquifer wells in northern and central Frenchman Flat that were not included in the original study (UE5PW-1, UE5PW-2, UE5PW-3, and ER-5-4). Sampling locations used in the present analysis are shown in Figure L-2.

The geochemical data used in SNJV (2006a) and the present analysis were collected over decades by different investigators for different purposes and vary widely in terms of which chemical species and isotopes were analyzed. Typically, more recent water samples are more complete in terms of isotope compositions, particularly for species like ^{36}Cl and ^{14}C. Therefore, this analysis tends to focus on a smaller subsample of the wells and springs shown in Figure L-2.

The groundwater ^{14}C versus $\delta^{13}C$ data from Yucca Flat and the surrounding areas are shown in Figure L-3. The figure shows a general trend of decreasing ^{14}C with increasing $\delta^{13}C$, which is consistent with the concept that groundwater recharge with an initially high ^{14}C activity and isotopically light $\delta^{13}C$ signature acquired from biogenic CO_2 in the soil zone of the recharge area has been progressively affected by the incorporation of ^{14}C-free, isotopically heavy $\delta^{13}C$ acquired through water–rock interaction downgradient of the recharge area. Clark and Fritz (1997) indicate that a simple correction can be made to the standard radioactive decay equation to account for the effects of water–rock interactions on calculated groundwater ^{14}C age:

$$t_{years} = (1/\lambda) \cdot \ln(^{14}C_{rech} \cdot q / {}^{14}C_{well}) \qquad (L\text{-}1)$$

where t_{years} is the groundwater ^{14}C age in years, λ is the decay constant for ^{14}C (1.21E-04 per year), $^{14}C_{rech}$ is the ^{14}C activity of recharge, $^{14}C_{well}$ is the ^{14}C activity of groundwater at a well, and q is an adjustment factor less than one that accounts for the decrease in ^{14}C activity that occurs downgradient from the recharge area because of the incorporation of ^{14}C-free carbon through water–rock interaction. This factor is used to adjust the initial ^{14}C activity ($^{14}C_{rech}$) in the decay equation so that the calculated age reflects only the ^{14}C decrease associated with radioactive decay and not decreases in ^{14}C caused by water–rock interaction.

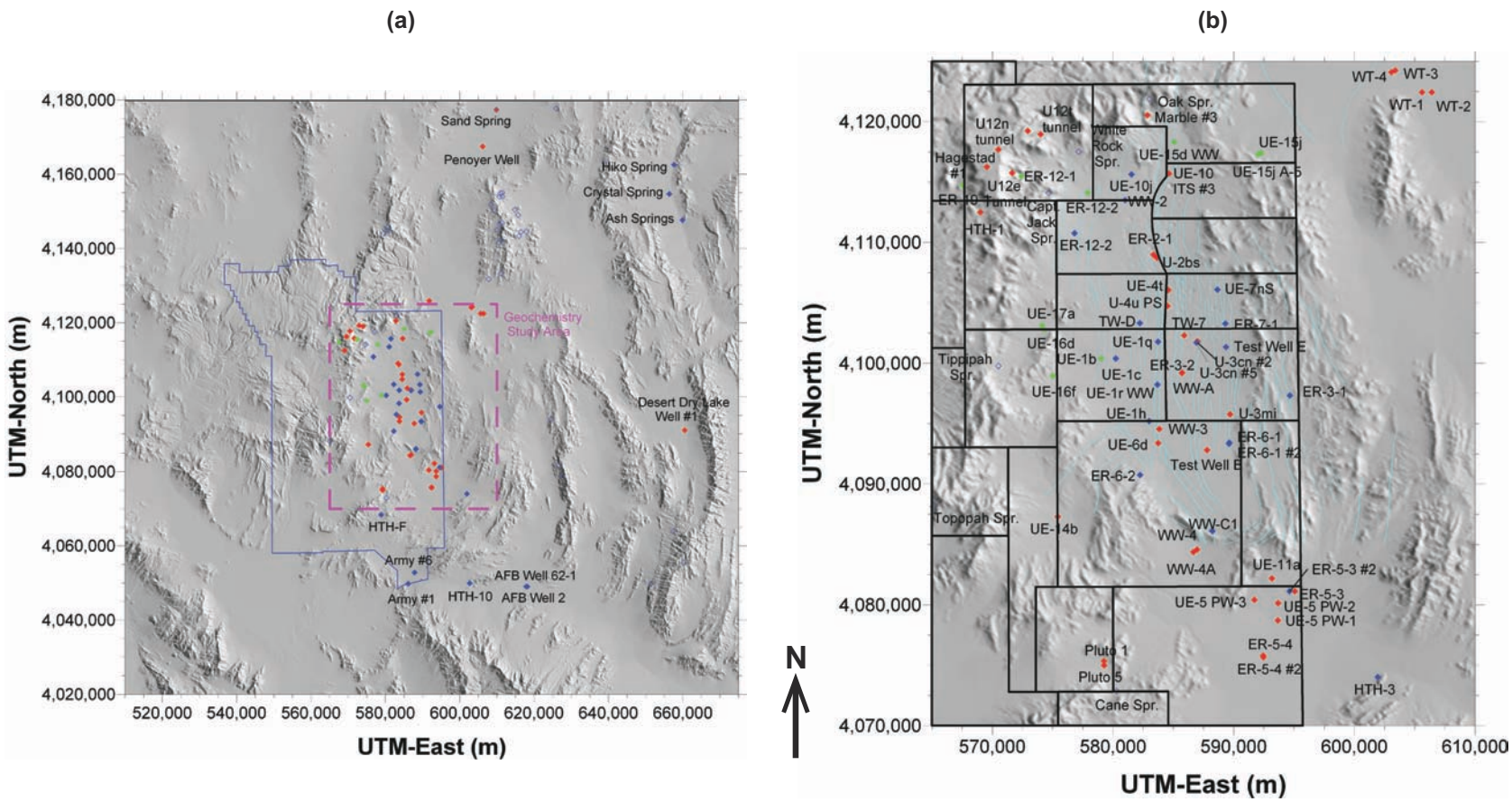

Explanation: Open blue diamonds represent samples from perched springs, solid blue diamonds represent samples from the LCA, red diamonds represent samples from the alluvial and volcanic aquifers, and green diamonds represent samples from the clastic confining units. Light cyan lines represent fault locations at the water table in the Yucca Flat HFM.

Source: BN, 2006

Figure L-2
Distribution of Sampling Locations
(a) within and Adjacent to the Yucca Flat Study Area of SNJV (2006a) and (b) within the Yucca Flat Study Area

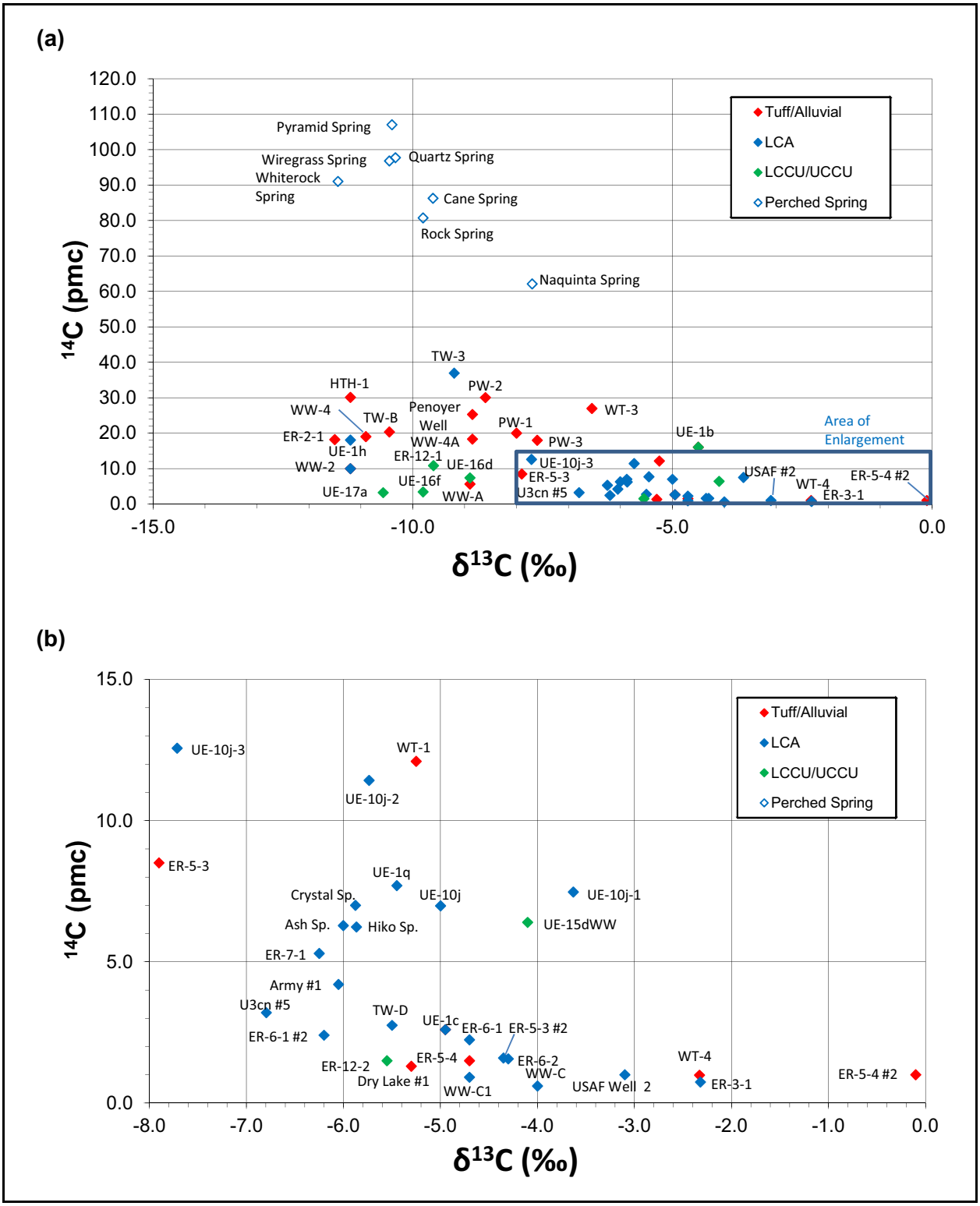

Figure L-3
Relationship between ^{14}C and $\delta^{13}C$:
(a) All Data, and (b) Isotopically Heavy Data with Low ^{14}C

In this analysis, it is assumed that $^{14}C_{rech}$ is 100 percent modern carbon (pmc), which is broadly consistent with the data from perched springs (Figure L-3a). The ^{14}C activity is reported as percent modern carbon, where modern carbon activity is defined as the approximate ^{14}C activity of wood grown in 1890 (13.56 disintegrations per minute per gram of carbon) before the dilution of ^{14}C in the atmosphere by the burning of fossil fuels or later ^{14}C inputs from atmospheric nuclear weapons tests. With the possible exception of groundwater sampled near nuclear tests and some perched springs, most of the groundwater in the Yucca Flat area is old enough that its ^{14}C is unaffected by either industrial activities or atmospheric nuclear testing. In the more distant past, the rates of ^{14}C production and its removal from the atmosphere by dissolution in the oceans, terrestrial burial, and radioactive decay were in approximate equilibrium, so atmospheric levels of ^{14}C varied only slightly over most of the past 10,000 years (e.g., Reimer et al., 2004). However, between 12,000 and 40,000 years ago, atmospheric ^{14}C concentrations were as much as 50 percent higher than "modern" levels because of changes in natural ^{14}C production associated with the strength of the earth's geomagnetic field and changes in the earth's carbon cycle (e.g., Reimer et al., 2004; van der Plicht et al., 2004). Like many hydrologic studies, the present analysis does not consider these variations in atmospheric ^{14}C activities, because their influence is usually small compared to other processes that could affect groundwater ages, and their inclusion would not normally change the fundamental conclusions regarding the flow system. However, it is worth noting that higher atmospheric ^{14}C activities in the past could add as much as one ^{14}C half-life (5,730 years) to the groundwater ages calculated in this appendix when the calculated ages are greater than 25,000 years.

As described in Clark and Fritz (1997), the adjustment factor q can be calculated in several ways. One method uses the downgradient increase in groundwater dissolved inorganic carbon (DIC) relative to recharge water to estimate the total fraction of the groundwater DIC that was acquired since recharge. This fraction (q_{DIC}) is calculated as follows:

$$q_{DIC} = DIC_{rech} / DIC_{well} \qquad (L\text{-}2)$$

where DIC_{rech} is the DIC in recharge water and DIC_{well} is the DIC in a groundwater sample from a downgradient well. Groundwater DIC includes dissolved CO_2(aq), bicarbonate (HCO_3^-), and CO_3^{2-}, and is essentially equivalent to alkalinity (the sum of milliequivalents per liter [meq/L] HCO_3 and meq/L CO_3^{2-}) at the neutral to slightly alkaline pH values typical of groundwater in the Yucca Flat basin (SNJV, 2006a). Thus, alkalinity increases can be used to approximate the DIC increases between the recharge and downgradient groundwaters.

A second correction method uses the differences in the $\delta^{13}C$ of recharge and of calcite in the aquifer to estimate an analogous dilution factor:

$$q_{\delta^{13}C} = (\delta^{13}C_{well} - \delta^{13}C_{carbonate}) / (\delta^{13}C_{rech} - \delta^{13}C_{carbonate}) \qquad (L\text{-}3)$$

where the subscript *carbonate* refers to carbonate minerals, such as limestone, dolomite, and calcite, that may have interacted with the groundwater. Changes in the $\delta^{13}C$ of the groundwater since it was recharged, as expressed in the dilution factor $q_{\delta^{13}C}$, reflect the effects of both carbonate dissolution and isotope exchange during carbonate recrystallization on the ^{14}C originally in the recharge water. The dilution factor $q_{\delta^{13}C}$ is used in an identical manner to q_{DIC} in Equation (L-1).

The age adjustments assumed slightly different values for $\delta^{13}C_{rech}$, $\delta^{13}C_{carbonate}$, and DIC_{rech}, depending on whether the sample came from the tuff and alluvial aquifers, the LCA, or the LCCU/UCCU (Table L-1). The assumed values were based on the range of alkalinities measured in groundwater from different aquifer groups and the overall trend in the $\delta^{13}C$ versus inverse alkalinity plot shown in Figure L-4. This figure shows that, in general, groundwater with low alkalinity (high inverse alkalinity) has relatively light $\delta^{13}C$, whereas groundwater with relatively high alkalinity (low inverse alkalinity) has relatively heavy $\delta^{13}C$. This overall trend is due to the dominance of isotopically light soil-zone CO_2 at low alkalinities and the increasing influence of isotopically heavier calcite, limestone, and dolomite at higher alkalinities. Data presented in SNJV (2006a, Table 3-2) indicate that alluvium in Yucca Flat contains calcite and caliche with a mean $\delta^{13}C$ of –3.1 ± 1.7 per mil (1 SD), the tuff confining units contain calcite with a mean $\delta^{13}C$ of –2.9 ± 2.1 per mil (1 SD), and the LCA includes dolomite, limestone, and calcite with a mean $\delta^{13}C$ of +0.6 ± 1.8 per mil (1 SD). The values within each of these groups range from about 6 to 8 per mil, which may explain the scatter around any single possible trend line in Figure L-4 both within and among the aquifer groups. Variability in the $\delta^{13}C$ and alkalinity of recharge may also play a role in producing some of the scatter. The $\delta^{13}C$ of soil zone CO_2 in the southern Great Basin becomes lighter with increasing surface elevation because of elevation-dependent changes in plant types and precipitation (Quade et al., 1989). Therefore, it is expected that variability in the $\delta^{13}C$ of recharge would exist as well, reflecting the difference in recharge elevations. It has also been proposed that the $\delta^{13}C$ of soil-gas CO_2 was lighter during the late Pleistocene, when vegetation types and moisture and temperature conditions that today exist only at high elevations had moved downward toward the valley floors (Quade and Cerling, 1990). Therefore, some of the variability in groundwater $\delta^{13}C$ could reflect the effects of long-term climate change within a given recharge location. In spite of the scatter, the simple correction methods used in this

Table L-1
$\delta^{13}C$ and Alkalinity Values Used in the Groundwater ^{14}C Age Corrections

Aquifer	$\delta^{13}C_{rech}$ (‰)	$\delta^{13}C_{carbonate}$ (‰)	DIC_{rech} (mg/L as HCO_3^-)	SNJV (2006a) Values for $\delta^{13}C_{carbonate}$ (‰)
Tuff/Alluvial	–12.0	0	110	–2.9 ± 2.1/–3.1 ± 1.7
LCA	–11.0	+1.0	170	+0.6 ± 1.8
LCCU/UCCU	–12.0	0	170	--

-- = No values are provided in SNJV (2006a).

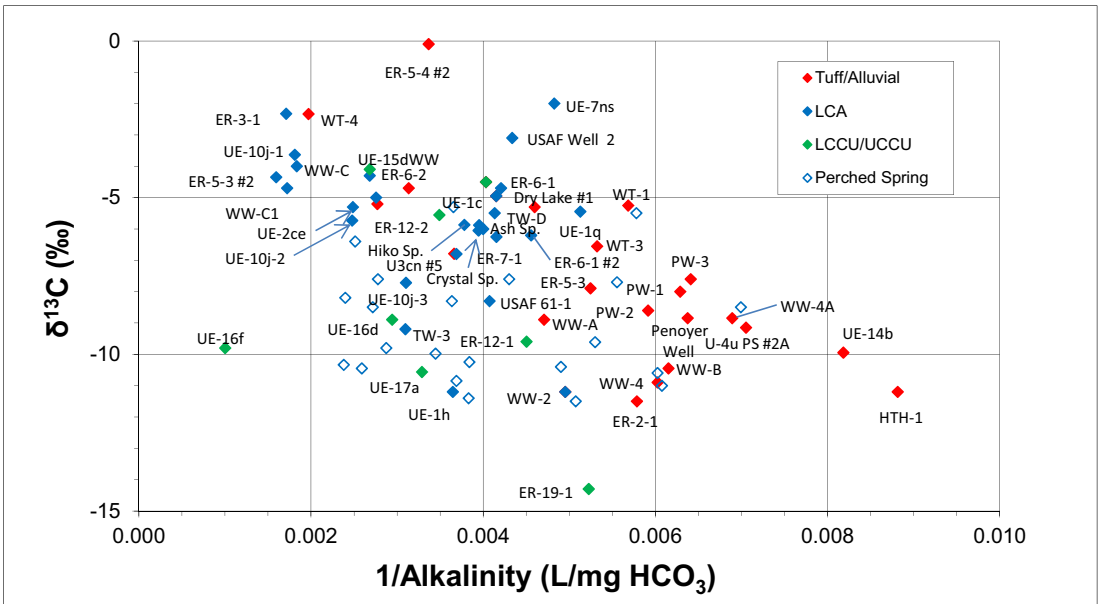

Note: ER-19-1 had a pH of 10.7, probably because of interaction with cement used to complete the well. It was sampled only with a low-yield pump and was never properly purged, rendering its data suspect. Laboratory measurements of alkalinity are shown in this plot because field measurements were unavailable for most samples. However, where both field and laboratory data are reported, the alkalinity values are highly correlated with no systematic bias.

Figure L-4
$\delta^{13}C$ and Inverse Alkalinity in Yucca Flat Area Groundwater

study require estimates of the end-member compositions for each aquifer group, and these were estimated based on the isotopic data in SNJV (2006a, Table 3-2), the data shown in Figure L-4, and other considerations, as described in the following paragraph.

The measured groundwater $\delta^{13}C$ values in Figure L-4 are as light as –12 per mil and as heavy as 0 per mil, suggesting these as end-member values for $\delta^{13}C_{rech}$ and $\delta^{13}C_{carbonate}$, respectively. The dilute groundwater from Well HTH 1 from recharge areas on Rainier Mesa suggests an alkalinity as low as 110 mg/L for the alluvial/volcanic aquifer system, whereas none of the groundwater from the LCA or

from the LCCU/UCCU has an alkalinity less than about 170 mg/L as HCO_3^-. The end-member values in Table L-1 were also chosen with the goal of minimizing any discrepancy between the groundwater ages calculated with the corrections represented in Equations (L-2) and (L-3). Figures L-5 to L-7 compare the ages calculated with the two correction methods for wells tapping different aquifers or aquifer groups. As indicated by the proximity of the data to the one-to-one lines (black) and the high R^2 values of the regression lines (red) with the slopes close to unity and the intercepts close to zero, the two methods provide reasonably consistent age estimates for the groundwater from the alluvial/volcanic aquifer system (Figure L-5) and in the LCA (Figure L-6). For groundwater from the LCCU/UCCU group (Figure L-7), however, the two methods produce less satisfactory agreement, indicating a higher level of uncertainty in the accuracy of the age corrections for groundwaters from these low-permeability confining HSUs. The poor correlation for the LCCU/UCCU group is mostly because of data from Well UE-16f, which had an alkalinity of 996 mg/L HCO_3^- and an uncharacteristically light $\delta^{13}C$ value of –9.8 per mil.

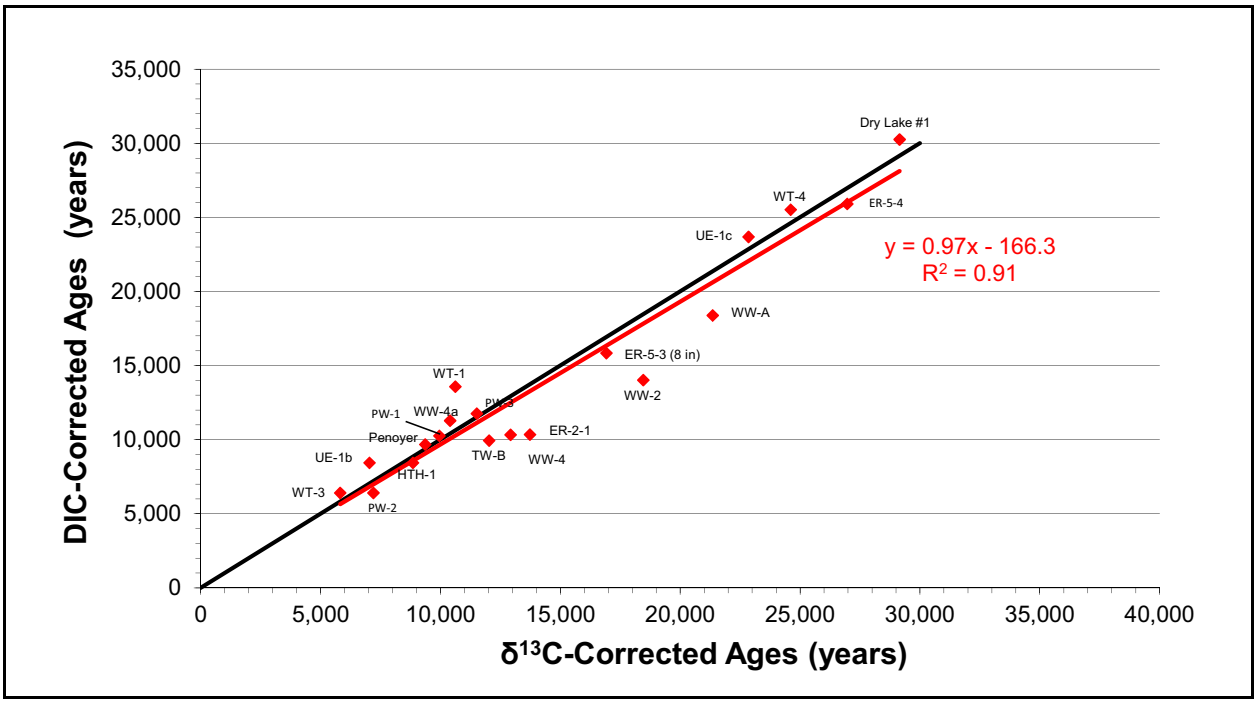

Figure L-5
Comparison of δ13C-Corrected versus DIC-Corrected Groundwater Ages for the Alluvial/Volcanic Aquifer System

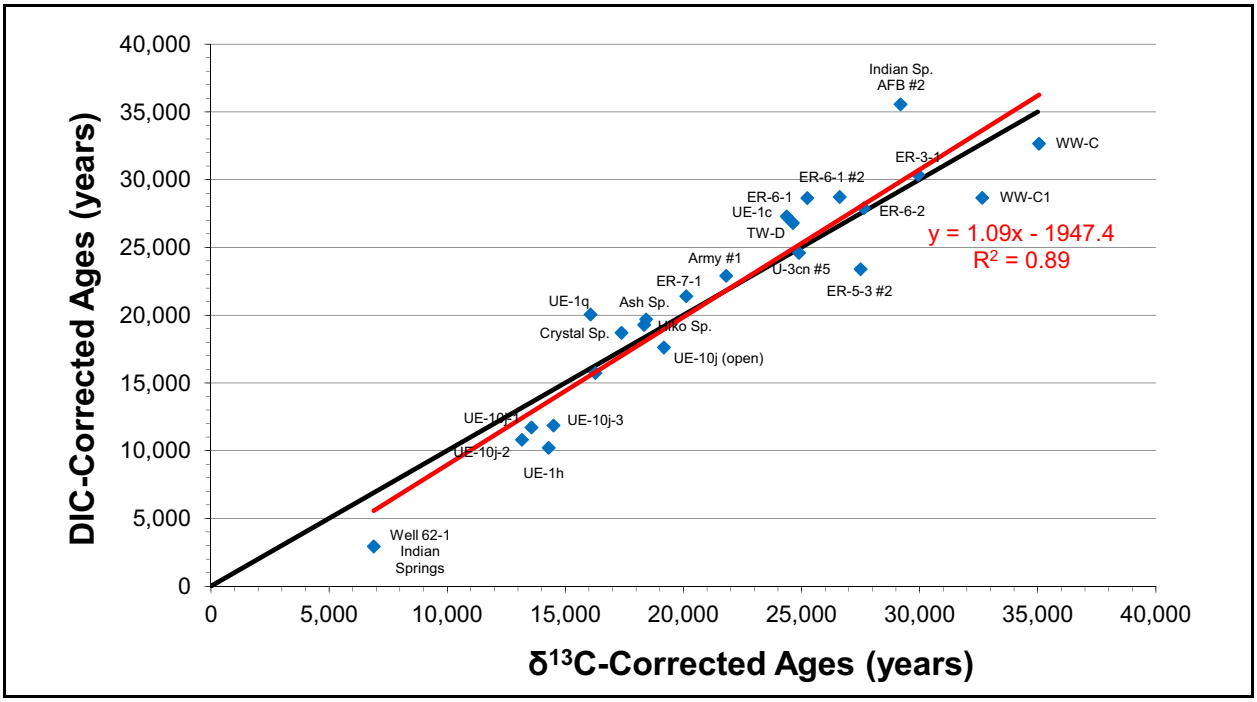

Figure L-6
Comparison of δ13C-Corrected versus DIC-Corrected Groundwater Ages for the LCA

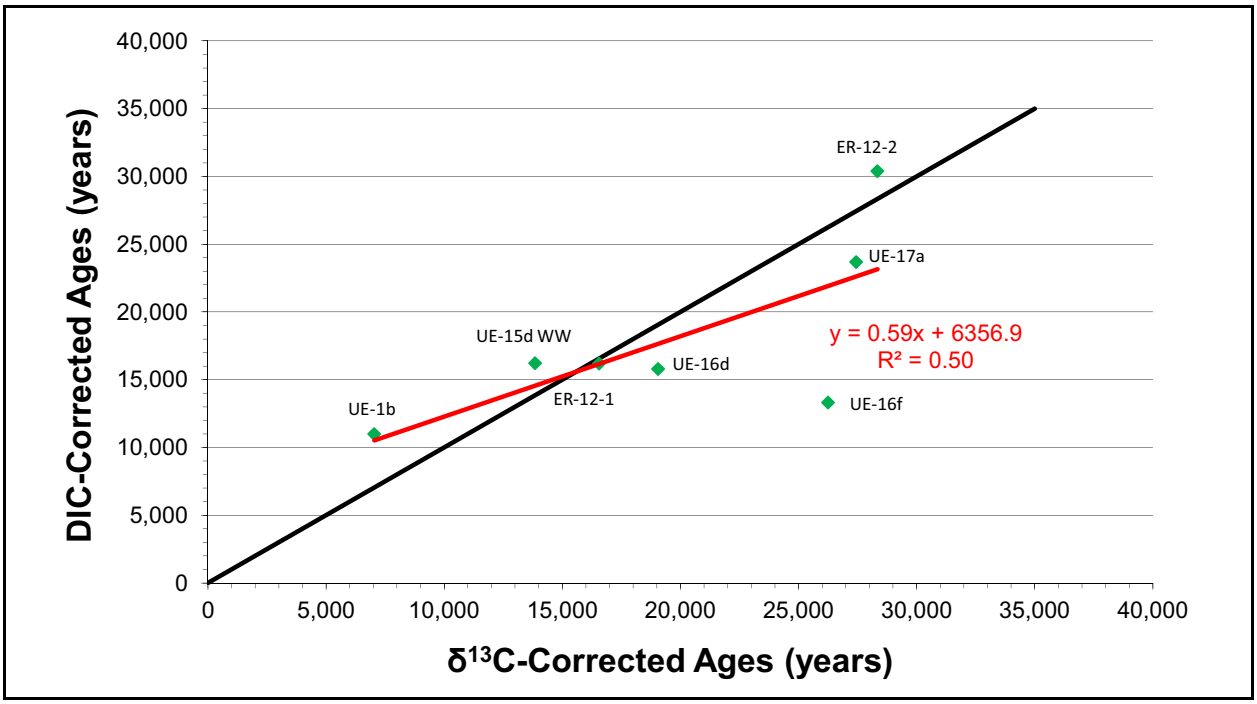

Figure L-7
Comparison of δ13C-Corrected versus DIC-Corrected Groundwater Ages for the LCCU and UCCU

L.2.1 Maps of Groundwater ^{14}C Ages

The average of the $\delta^{13}C$-corrected and DIC-corrected groundwater ^{14}C ages was calculated and plotted on the maps shown in Figure L-8. The maps show the portion of the NNSS containing Yucca Flat, along with the NNSS areas within the model boundary and the major faults in the area. The groundwater ^{14}C ages for the alluvial/volcanic aquifer system in Yucca Flat (Figure L-8 [b]) are mostly from the late Pleistocene or early Holocene (12,000 to 8,000 years ago). This is consistent with the conclusions from unsaturated-zone studies that infiltration through the thick alluvium in Yucca Flat ceased about 10,000 years ago and that, as a consequence, today only negligibly small rates of infiltration from the late Pleistocene result in recharge to the water table (Walvoord, Phillips, et al., 2002; Kwicklis et al., 2006). No attempt was made to infer more about the flow system from the sparse groundwater ^{14}C ages for the alluvial/volcanic aquifer system in Yucca Flat.

The groundwater ^{14}C ages for the LCA (circles) and the LCCU/UCCU (squares) in Yucca Flat are shown in Figure L-8 (a). The groundwater ^{14}C age contours shown in the figure were hand drawn for the LCA portion of the flow system. The following general concepts about flow patterns in the LCA presented in SNJV (2006a) were used as guidance in developing the contours:

1. Because groundwater flow in the LCA is dominantly north to south, groundwater ages should increase toward the southern end of the basin.

2. Higher-permeability zones exist along the Topgallant and Yucca faults in the center of the basin; as a result, flow converges (and age contours bend) toward those features.

3. Groundwater from the overlying alluvial/volcanic aquifer system drains into the LCA along the major faults in the center of the basin, as evidenced by the dilute groundwater with high $^{36}Cl/Cl$ ratios near these faults.

Figure L-8 (a) shows that groundwater ^{14}C ages in the LCA at this location are younger than elsewhere in the LCA and similar to those in the overlying alluvial/volcanic aquifer system, supporting the contention that the LCA communicates with these aquifers along these faults. The figure also indicates that there is a zone of older groundwater between Well ER-3-1 east of Yucca Flat and Wells WW C and WW-C-1 in southern Yucca Flat toward which groundwater flow converges from both the northwest and southeast. This is consistent with the relatively rapid flow path estimated to exist between Wells ER-3-1 and WW C based on the similar chemistry of these wells (SNJV, 2006a). This inferred flow path does not appear to be aligned with the fault orientations shown in

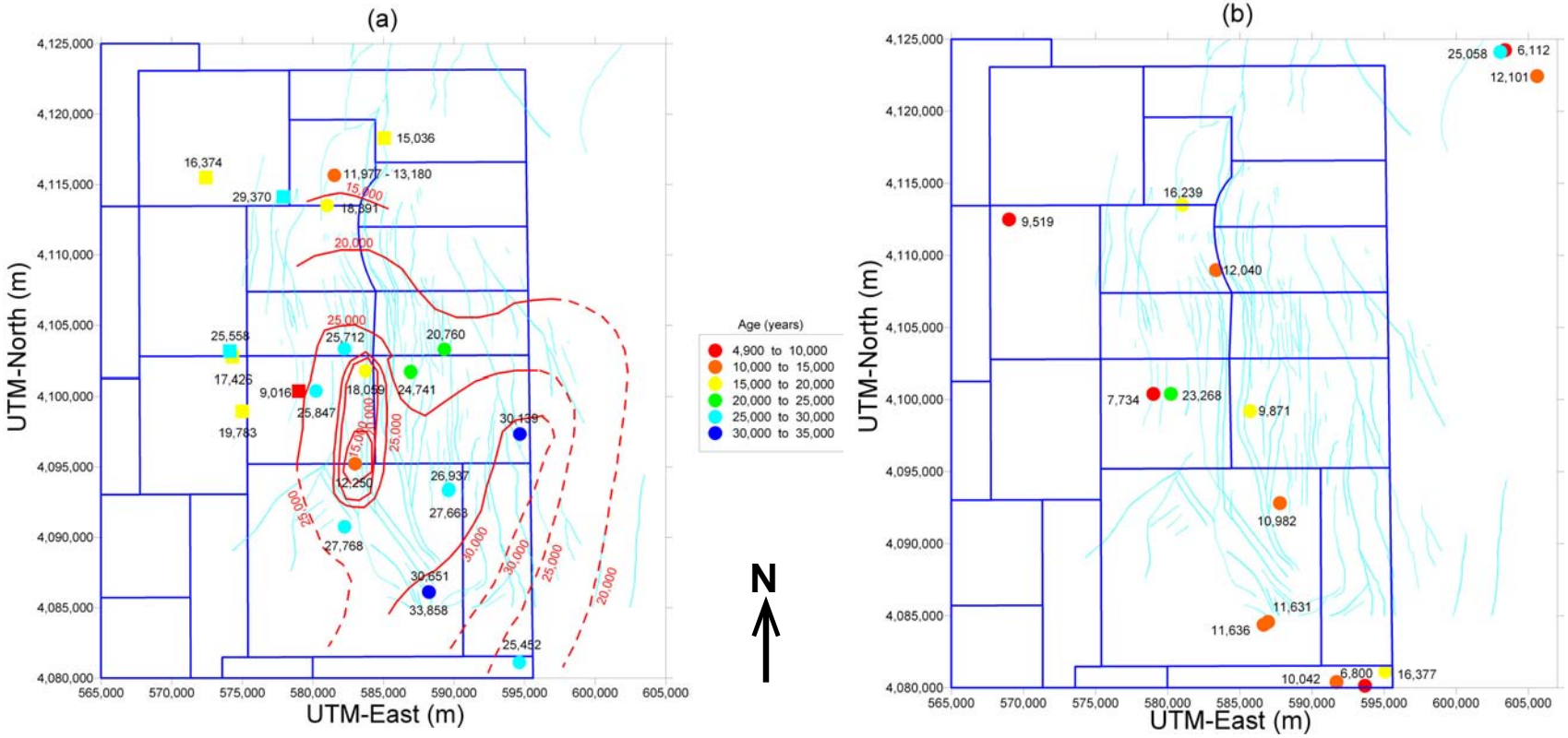

Note: For the pre-Tertiary rocks, corrected groundwater ^{14}C ages are for both the LCA (circles) and clastic confining units (squares). Contours are for the LCA only.

Figure L-8
Groundwater ^{14}C Ages for (a) Pre-Tertiary Rocks and (b) Alluvial/Volcanic Aquifer System in Yucca Flat

Figure L-8, so other causes must be invoked to explain its existence. One explanation presented in SNJV (2006a) is that the shallow, low-permeability clastic rocks of the LCCU, which limit inflow along the eastern edge of the Yucca Flat to the north, become more deeply buried beneath the saturated LCA toward the south, thereby allowing hydraulic communication between the LCA within Yucca Flat and the regional flow system to the northeast. The contour map of groundwater ^{14}C ages for the LCA emphasizes this hydraulic connection between Well ER-3-1 and Wells WW C and WW-C-1.

L.2.2 Comparison of ^{14}C Ages with LCA Groundwater Flow Regime

Overall, the younger ^{14}C ages in the alluvial/volcanic aquifer system and older ^{14}C ages in the underlying carbonate rocks show relationships that are consistent with interpretations of the flow system based on the estimated predevelopment hydraulic head data (Fenelon et al., 2012). These data indicate that heads in the alluvial/volcanic aquifer system before nuclear testing and pumping for water supply were elevated by between 6 and 30 m above the regional carbonate aquifer and that, therefore, there is a potential for downward flow from the alluvial/volcanic aquifer system to the carbonate aquifer. Fenelon et al. (2012) also inferred that this head difference can be attributed to the effects of long-term climate change and the presence of low-permeability zeolitized tuff confining units between the alluvial/volcanic aquifer system and the LCA, which has prevented the complete drainage of late Pleistocene recharge from the alluvial/volcanic aquifer system to the LCA. Both the relative and absolute ages of the water in the alluvial/volcanic aquifer system and the LCA support this interpretation. Fenelon et al. (2012) also proposed that lateral flow directions in the alluvial and tuff aquifers depend on local connections between these aquifers, which are, as recognized from the hydrogeologic framework model for Yucca Flat (BN, 2006), highly compartmentalized by faults and tuff confining units.

A key feature of the Fenelon et al. (2012) interpretation is that local communication between the alluvial/volcanic aquifer system and the LCA occurs at a relatively few locations where the tuff confining unit has been thinned, removed, or broken by faulting. The primary location for hydraulic communication between the alluvial/volcanic aquifer system and the LCA was hypothesized by Fenelon et al. (2012) to be in the center of the basin in the vicinity of Test Well 7 (HTH). No geochemical data exist for Test Well 7 (HTH), but Well UE-1q, which is about 2.5 km to the west of Test Well 7 (HTH) near the Topgallant fault, has characteristics that support overall hydraulic

connection between the shallow and deep aquifers in this area. Together, the data from Wells UE-1q and UE-1h suggest that local drainage to the LCA from the alluvial/volcanic aquifer system can occur near major faults in the area, such as the Topgallant and Carpetbag faults (Figure L-8 [a]). The absence of data from Test Well 7 (HTH) prevents an evaluation of whether drainage also occurs along the Yucca fault farther to the east.

The predevelopment hydraulic head contours for the LCA presented in Fenelon et al. (2012, Plate 4) indicate overall north–south flow through the LCA in Yucca Flat, with flow from the west and the northeast converging in a highly faulted corridor just to the east of the Yucca fault. In the Fenelon et al. (2012) interpretation, flow from the west, north, and east converges along the eastern margin of the NNSS in the southeast corner of Yucca Flat. While also indicating overall north–south flow through much of Yucca Flat, the ^{14}C age contours for the LCA appear to preclude flow off the NNSS toward the southeast. However, the sparseness of both head and ^{14}C data in the southeast corner of Yucca Flat makes it difficult to definitively rule out or confirm either flow path. Alternative hydraulic head contours in this data-poor area presented in Fenelon et al. (2012, Plate 4) allow for this possibility.

L.2.3 Laboratory ^{14}C Sorption and Diffusion Studies

A number of laboratory studies have been conducted to investigate radionuclide sorption and diffusion properties in the LCA at Yucca Flat, including those of ^{14}C (as $H^{14}CO_3^-$) (Hershey et al., 2003; Zavarin et al., 2005; Ware et al., 2005; Reimus et al., 2006; Zavarin et al., 2007; Reimus et al., 2008). Of particular interest for this appendix is the report by Zavarin et al. (2007), which used a consistent modeling approach to interpret through-flow experiments involving ^{14}C, ^{3}H, and other radionuclides in LCA cores with either natural fractures (Ware et al., 2005) or induced (slotted) fractures (Zavarin et al., 2005) parallel to the core axis. The primary difference between the two sets of experiments was the possible presence of fracture coatings in the naturally fractured cores. Transport parameters, such as fracture and matrix sorption, matrix diffusion coefficients, and dispersivity, were determined by first modeling the transport of ^{3}HHO to fix a subset of flow and transport parameters unrelated to sorption and then identifying parameters related to sorption based on the breakthrough of specific radionuclides from the cores. The negligible matrix diffusion estimated from ^{3}HHO breakthrough measured over the relatively short duration of the experiments led Zavarin et al. (2007) to infer that radionuclide sorption, if it occurred, was primarily due to

sorption on the fracture walls rather than matrix sorption. In the case of ^{137}Cs and ^{90}Sr, this interpretation was supported by the fact that sorption was negligible for the induced fractures and affected breakthrough to varying degrees in the natural fractures. For $H^{14}CO_3^-$, fracture retardation factors of between 1 (no retardation) and 5 were estimated for the naturally fractured cores, which had nearly identical matrix compositions. The differences in the modeled fracture retardation factors in the presence of nearly identical matrix compositions implied that differences in mineral coatings were the cause. It should be noted, however, that repeat experiments at different flow rates in each of six LCA cores with natural fractures never resulted in consistent estimates of fracture retardation factors for $H^{14}CO_3^-$, even for the same core (Zavarin et al., 2007, Table 6). In most cases, the experiments at low flow rates (where one would expect fracture sorption to be more identifiable) yielded no evidence of fracture sorption, suggesting that the inferred fracture sorption in the experiments at high flow rates could be due to other experimental artifacts. As pointed out by Hershey et al. (2003, p. 23), who modeled similar through-flow experiments, any ^{14}C lost to the atmosphere by degassing or by exchange before entering or after exiting the fracture would have resulted in an erroneously high estimates of the retardation factors. For their experiments, model matches to $H^{14}CO_3^-$ breakthrough yielded matrix sorption coefficients of 4.2 to 30 mL/g.

A number of batch experiments have also been conducted to study the sorption behavior of $H^{14}CO_3^-$ and $H^{13}CO_3^-$ onto crushed carbonate material from the LCA, including rock matrix (Hershey et al., 2003), fracture coatings (Ware et al., 2005), and pure calcite or dolomite (Reimus et al., 2008). These experiments involve measuring the decrease in $H^{14}CO_3^-$ and $H^{13}CO_3^-$ solution concentrations over time in a vial containing a crushed rock or mineral sample while continuously agitating the solution to promote reactions. These studies concluded that $H^{14}CO_3^-$ uptake onto newly crushed material is initially rapid, consistent with equilibrium sorption of $H^{14}CO_3^-$ over minutes to hours; that the initial uptake is followed by longer-term, kinetically controlled precipitation/dissolution reactions that effectively serve to exchange $H^{14}CO_3^-$ and $H^{13}CO_3^-$ initially in solution into freshly precipitated mineral layers; and that there is an accompanying increase in $H^{12}CO_3^-$ as preexisting carbonate is simultaneously dissolved. Hershey et al. (2003) estimated matrix K_d values of 14.8 and 18.4 mL/g based on two 210-day batch experiments involving LCA rock. However, Hershey et al. (2003) acknowledged that initial crushing of the samples and continued abrasion during shaking may have created fresh sorption sites that would not ordinarily be available to groundwater. Reimus et al. (2008) demonstrated that increased aging of pure calcite or dolomite material by exposing it to LCA water for longer periods reduces the rate and duration of the initial

and overall $H^{14}CO_3^-$ uptake. There was consistently more $H^{14}CO_3^-$ uptake onto freshly ground calcite than onto calcite that had been soaked in LCA groundwater because of the "annealing" of new high-energy surface sites created during the crushing process. However, the $H^{14}CO_3^-$ that was lost is mostly unrecoverable when the sample is flushed with unspiked LCA water. Reimus et al. (2008) also showed that $H^{14}CO_3^-$ uptake by dolomite is much less than that by calcite. This is in agreement with Mozeto et al. (1984), who noted that $H^{13}CO_3^-$ uptake is inhibited at higher magnesium concentrations.

L.2.4 Inferences from Devils Hole

Devils Hole is a cavern bordering Ash Meadows approximately 60 km south of Yucca Flat, where 40 cm of vein calcite deposited in layers have been retrieved from 130 m below the water table (Landwehr and Winograd, 2012). The layers have been precisely dated with uranium-series dating, and oxygen-18 ($\delta^{18}O$) ratios of the calcite have been measured to provide a 560,000-year record of climate variations in southern Nevada (Winograd et al., 1992; Winograd et al., 2006). In addition, $\delta^{13}C$ variations have been measured in the calcite as a function of time (Coplen et al., 1994; Coplen, 2007). The measured $\delta^{13}C$ variations reflect either climate-controlled changes in the density of vegetation in the adjacent Spring Mountains recharge area or changes in ratios of carbon isotopes in the atmosphere. The relevance of the Devils Hole data to the present study is that, as stated in the online supplemental materials to Winograd et al. (2006), the groundwater travel time from the Spring Mountains recharge area to Devils Hole is no more than 7,000 years and possibly as little as 2,000 years. A variety of evidence is given for this range of groundwater travel times, perhaps the most compelling of which is that groundwater $\delta^{18}O$ variations recorded in the calcite vein do not lag behind climatically induced $\delta^{18}O$ variations recorded in deep-sea sediments and ice cores by more than a few thousand years. The range of groundwater residence times implies a transport velocity for ^{18}O of 11.4 to 40 m/yr (including the effects of matrix diffusion) over a distance of roughly 80 km.

The larger hydraulic gradient near the Spring Mountains recharge area and different structural setting near Devils Hole make a direct comparison with transport velocities in Yucca Flat difficult. The principal value of the Devils Hold data for the Yucca Flat study is that the groundwater travel times estimated from the $\delta^{18}O$ variations provide an independent way to evaluate the estimates of groundwater age obtained from the groundwater ^{14}C activities at Devils Hole and the correction methods described previously. This could provide a large-scale, long-term perspective on the

importance of fracture or matrix sorption or isotope exchange of $H^{14}CO_3^-$ in the LCA under natural conditions.

Groundwater at Devils Hole has an alkalinity of 310 mg/L HCO_3^-, a $\delta^{13}C$ of –5.0 per mil, and a ^{14}C activity of 2.8 pmc, consistent with nearby springs in the Ash Meadows area (Winograd and Pearson, 1976). Using the same values for DIC_{rech}, $\delta^{13}C_{rech}$, and $\delta^{13}C_{carbonate}$ as for other LCA groundwater (DIC_{rech} = 170 mg/L HCO_3^-, $\delta^{13}C_{rech}$ = –11 per mil, and $\delta^{13}C_{carbonate}$ = 0 per mil) in Equations (L-1) to (L-3) yields an average ^{14}C age of about 24,000 years for groundwater at Devils Hole. This is about a factor of 10 older than the age implied by the lag in the $\delta^{18}O$ variations relative to other records and evidence, and suggests a retardation factor of about 10 for ^{14}C relative to ^{18}O, which moves as part of the water molecule $H_2{}^{18}O$. Using data from Winograd and Pearson (1976) for Trout Springs high in the Spring Mountains recharge area (DIC_{rech} = 179 mg/L HCO_3^-, and $\delta^{13}C_{rech}$ = –8 per mil) increases the calculated ^{14}C age of Devils Hole groundwater to more than 25,000 years. These discrepancies clearly point to the need to evaluate the groundwater ^{14}C ages in Yucca Flat using other independent evidence.

L.3.0 ASSESSMENT OF GROUNDWATER ^{14}C AGES IN YUCCA FLAT USING TERRESTRIAL AND GROUNDWATER ^{36}CL /CL RATIOS

As described in the previous section, the pattern of groundwater ^{14}C ages for the LCA and its relation to overlying groundwater in the saturated alluvial/volcanic aquifer system can be interpreted in a coherent way based on an understanding of the hydrogeology and paleohydrology of the basin. While this lends support to the validity of the calculated groundwater ^{14}C ages, the general hydrologic literature and NNSS-specific studies contain well-documented evidence that groundwater ^{14}C ages in carbonate rocks can be overestimated and groundwater velocities underestimated because of sorption of ^{14}C onto the carbonate matrix or calcite fracture coatings (e.g., Maloszewski and Zuber, 1991; Hershey et al., 2003).

To investigate whether retardation of ^{14}C in LCA groundwater due to sorption or isotope exchange has occurred in Yucca Flat, it is useful to compare the movement of ^{14}C against that of other diffusing, isotopic species that are known not to sorb onto carbonate rocks. Following an approach outlined in SNJV (2006c) for the alluvial and volcanic aquifers in Frenchman Flat, the temporal variations of $^{36}Cl/Cl$ ratios in meteoric water recorded over the last 40,000 years in pack-rat urine preserved in pack-rat middens and ^{14}C dated with organic material incorporated into the middens (Plummer et al., 1997) were compared with the temporal variations $^{36}Cl/Cl$ ratios preserved in the groundwater record. The underlying hypothesis was that if the calculated groundwater ^{14}C ages are accurate and if the ^{14}C in the groundwater is moving conservatively along with the dissolved Cl, the temporal variations in the $^{36}Cl/Cl$ ratios from the terrestrial and groundwater records should be synchronous. Long-term temporal variations in the $^{36}Cl/Cl$ ratios of meteoric water were attributed by Plummer et al. (1997) to a combination of variations in the strength of the earth's magnetic field and to paleoclimatic processes affecting the position of the jet stream and high-altitude mixing in the troposphere. The variations in the $^{36}Cl/Cl$ ratios of pack-rat urine measured in widely scattered middens throughout Nevada were normalized relative to the modern $^{36}Cl/Cl$ ratios near the middens, and the normalized variations were scaled to values appropriate for the NNSS area by assuming a modern $^{36}Cl/Cl$ ratio of 500E-15 as estimated by Fabryka-Martin et al. (1993) for the Yucca Mountain area.

To allow for a comparison between the groundwater and terrestrial records of past meteoric $^{36}Cl/Cl$ ratios, it was first necessary to adjust the $^{36}Cl/Cl$ ratios of groundwater that had obviously been influenced by the incorporation of ^{36}Cl-free chloride through water–rock interaction. These groundwater samples are those with measured $^{36}Cl/Cl$ ratios less than the assumed $^{36}Cl/Cl$ ratio of present-day meteoric water (500E-15) that lie along a linear trend toward the origin in the plot of $^{36}Cl/Cl$ versus inverse chloride (Figure L-1). Groundwater with $^{36}Cl/Cl$ ratios greater than 500E-15 was assumed to not have been significantly affected by Cl dissolution, so the $^{36}Cl/Cl$ ratios were not adjusted. To estimate the $^{36}Cl/Cl$ ratios of the LCA groundwater at the time of recharge $(^{36}Cl/Cl)_0$, the measured groundwater $^{36}Cl/Cl$ ratios were adjusted as follows:

$$(^{36}Cl/Cl)_0 = (^{36}Cl/Cl) \cdot (Cl/Cl_0) \qquad (L\text{-}4)$$

where Cl is the measured Cl concentration of the sample, and Cl_0 is the estimated Cl concentration at the time of recharge. Although the LCA groundwater originated at various times and probably at various locations, including outside the Yucca Flat basin, for simplicity, it was assumed that paleorecharge had an average concentration of 7 mg/L. This assumed value is based on the mean Cl concentration of seeps from the tuff confining layers penetrated in tunnels at Rainier Mesa, a major recharge area on the northwestern margin of Yucca Flat. Present-day spring data from perched springs north of Yucca Flat were considered but dismissed, because most of the spring data appeared, from their delta deuterium (δD) versus $\delta^{18}O$ signature, to have been significantly affected by evaporation. This is indicated by their departure from the Global Meteoric Water Line (GMWL) along a trend with a slope near 4 (Clark and Fritz, 1997). In contrast, most of the groundwater and tunnel data plot near or parallel to the GMWL (Figure L-9).

The calculated $(^{36}Cl/Cl)_0$ ratios of groundwater were compared with the pack-rat midden data in Figure L-10. Figure L-10 (a) shows the LCA groundwater data, and Figure L-10 (b) contains data from the alluvial/volcanic aquifer system. The pack-rat midden data (represented by blue circles on these plots) show peaks in the meteoric $^{36}Cl/Cl$ ratios at about 33,000, 23,000, and 11,500 years ago, and values near or below present-day meteoric values (500E-15) since about 9,000 years ago. Relative lows appear in the pack-rat midden data about 26,000 and possibly 20,000 years ago. In general, the reconstructed LCA groundwater $(^{36}Cl/Cl)_0$ ratios track the pack-rat midden data very well, with a few exceptions. Well U-3cn-5 was drilled to monitor possible radionuclide migration from the BILBY test, and although high levels of radioactivity were not detected, there may have been some relatively minor effects from the test on groundwater $^{36}Cl/Cl$ ratios due to the proximity of

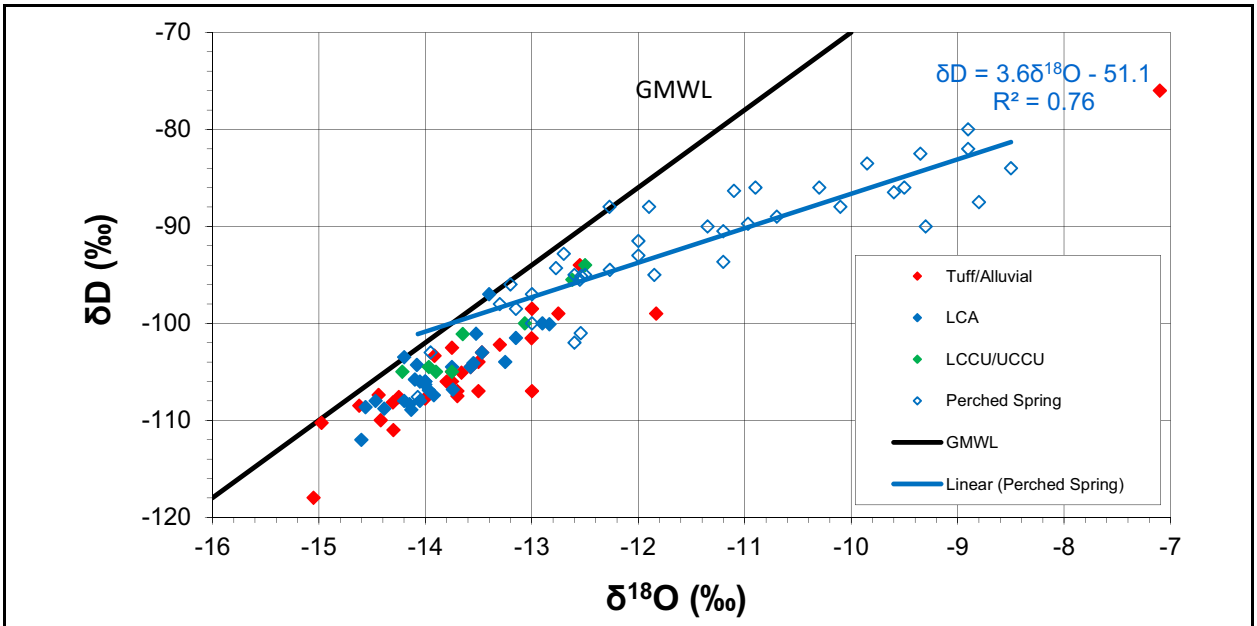

Note: GMWL indicates the Global Meteoric Water Line ($\delta D = 8 \cdot \delta^{18}O + 10$), and the regression line follows the evaporation trend of the data for the perched springs.

Figure L-9
δD versus δ¹⁸O for Yucca Flat Area Groundwater and Perched Springs

the well screen to the BILBY working point (122 m) (SNJV, 2007). After adjustment, groundwater from Well ER-5-3-2 in Frenchman Flat (with a measured $^{36}Cl/Cl$ ratio of 229E-15) also has an anomalously high $(^{36}Cl/Cl)_0$ ratio of 1,251E-15 relative to both other LCA samples of similar age and the pack-rat midden data. However, if a value for Cl_0 of 12 mg/L is used, similar to the values applied to alluvial and volcanic aquifer water in Frenchman Flat in SNJV (2006c), the estimated value of $(^{36}Cl/Cl)_0$ decreases to 729E-15, consistent with the pack-rat midden data. This alternative value is plotted for Well ER-5-3-2 in Figure L-10 (c). Overall, however, temporal variations in the estimates of meteoric $^{36}Cl/Cl$ ratios provided by the LCA groundwater data appear to be synchronous with those provided by the pack-rat midden data, suggesting both that the estimated groundwater ^{14}C ages are reasonably accurate and that the groundwater ^{14}C is moving without retardation relative to the dissolved ^{36}Cl. Thus, the migration velocities of naturally occurring ^{14}C should provide reasonable estimates of migration velocity of not only test-derived ^{14}C but also other non-sorbing radionuclide species such as ^{36}Cl, ^{99}Tc, and ^{129}I. These radionuclide migration velocities appear to be on the order of 2 m/yr (SNJV, 2006a), or 2 km in 1,000 years.

The groundwater record of meteoric $^{36}Cl/Cl$ variations from the alluvial/volcanic aquifer system has a high level of agreement with the terrestrial record provided by the pack-rat midden data

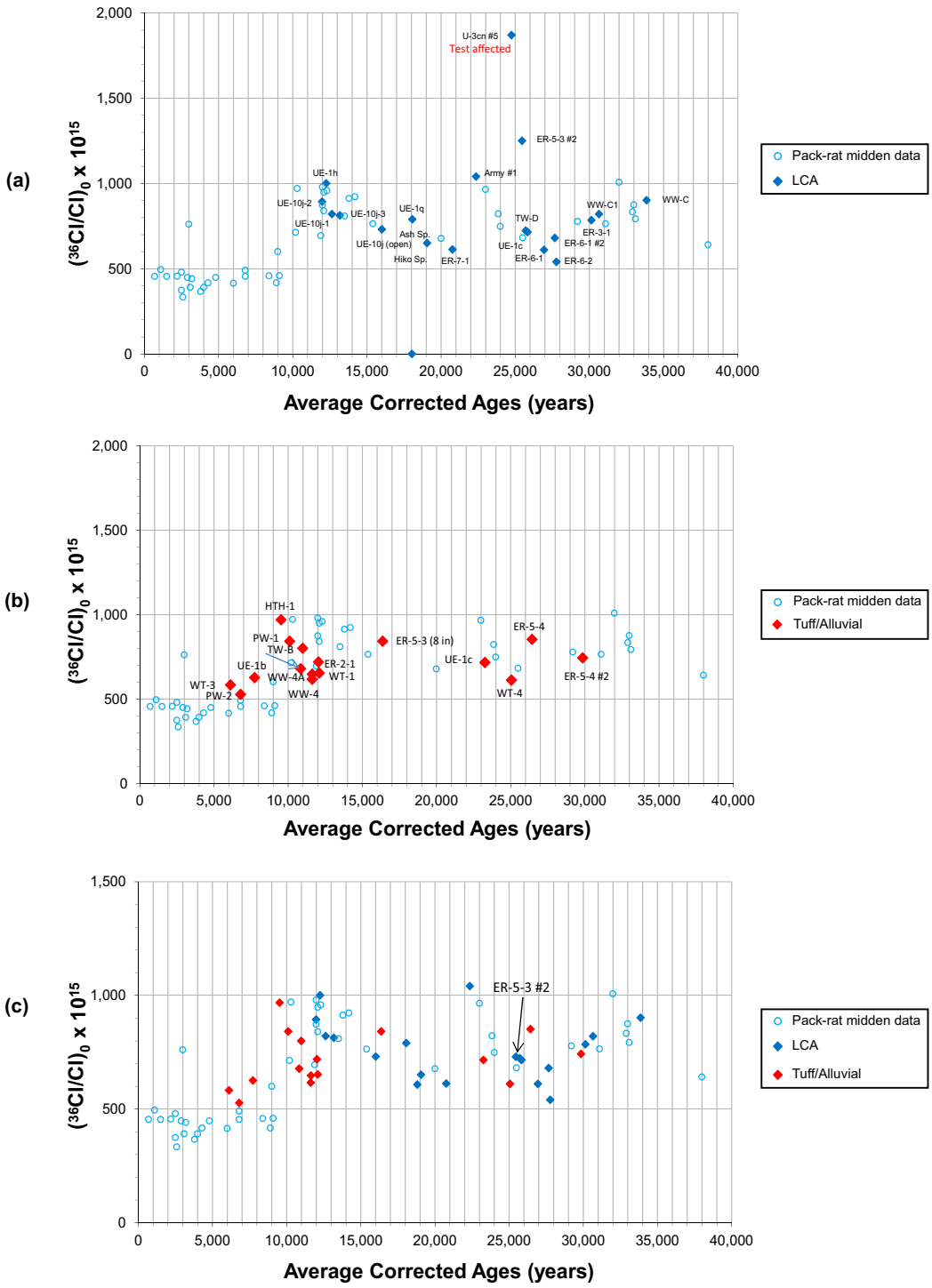

Note: Pack-rat midden data from Plummer et al. (1997).

Figure L-10
Comparison of Groundwater and Terrestrial $^{36}Cl/Cl$ versus ^{14}C Age:
(a) LCA Groundwater, (b) Alluvial/Volcanic Aquifer System Groundwater, and
(c) LCA Groundwater and Alluvial/Volcanic Aquifer System Groundwater

(Figure L-10 [b]) and, together with the groundwater data from the LCA, provides a reasonably consistent record of $^{36}Cl/Cl$ variations through time (Figure L-10 [c]). For this dataset, only the measured $^{36}Cl/Cl$ ratios from Watertown 4 WW (WT-4)and a deep well from Frenchman Flat (ER-5-4-2) were scaled with Equation (L-4) based on their plotting positions relative to the trend in Figure L-1. Watertown 4 WW underwent the same scaling as the LCA wells, whereas Well ER-5-4-2 used a value for Cl_0 of 12.3 mg/L, which was the average of other shallow Frenchman Flat groundwaters and used previously for the same purpose in SNJV (2006a). The groundwater data from the alluvial/volcanic aquifer system reflect the decrease in $^{36}Cl/Cl$ ratios between 12,000 and 9,000 years ago, and the lower $^{36}Cl/Cl$ ratios since that time.

L.4.0 EVALUATION OF GROUNDWATER ^{14}C VELOCITIES WITH A ONE-DIMENSIONAL FLOW AND TRANSPORT MODEL

If the solute migration velocities of roughly 2 m/yr estimated from the ^{14}C data (SNJV, 2006a) are reflective of those of other non-sorbing radionuclide species as indicated by the comparison between the terrestrial and groundwater $^{36}Cl/Cl$ ratios in the preceding section, the question naturally follows as to whether combinations of hydrologic and transport properties can be found that are consistent with the available hydrologic and transport datasets for Yucca Flat (SNJV, 2006b; 2007) such that non-sorbing tracers will migrate at approximately 2 m/yr. To investigate this question, a simple one-dimensional dual-porosity flow model was created for the LCA in Yucca Flat. The model is 10 km long and has a head difference of 4 m between the upgradient and downgradient boundaries for an average gradient of 0.0004 m/m. This is consistent with an average head gradient of 0.0003 m/m between Well UE-10j (735.8 m) at the northern end of Yucca Flat and Well WW C (726.64 m) at the southern end of Yucca Flat over a distance of 30.3 km (Fenelon et al., 2012). For the transport part of the model, the initial concentrations within the model domain were set to zero, and the concentration along the inflow boundary was set to 1.0 for time greater than zero and held constant for the duration of the simulation (10,000 years).

The flow and transport model described in this section uses the generalized dual-porosity model (GDPM) capability in FEHM (Zyvoloski et al., 2008). The GDPM approach assumes that regional flow and advective transport takes place only within the fracture system but that matrix diffusion takes place between the fracture and matrix domains via a one-dimensional series of matrix nodes that communicate with each other and with the adjacent fracture node, but not with matrix nodes associated with neighboring fracture nodes. This approach has been shown to accurately match analytical solutions for tracer breakthrough in dual-porosity systems (e.g., Sudicky and Frind, 1982). In this application, unless noted otherwise, the fractures are assumed to be parallel, and the matrix blocks are approximated as tabular blocks with a fracture half-spacing of 1 m, with 10 nodes placed at distances of 0.001, 0.002, 0.008, 0.016, 0.032, 0.064, 0.128, 0.256, 0.512, and 1.0 m from the fracture surface to accurately capture the diffusive gradients. Alternatively, for a system of orthogonal fractures, the matrix blocks could have been approximated as spherical.

The base case assumes a permeability of 1E-12 m^2, an effective matrix porosity of 0.03, a hydrodynamic dispersivity of 40 m (α = 40 m), and an effective fracture porosity of 0.001. A comparison of these values with the distributions summarized in Table L-2 shows that these are near the mean values for these parameters (SNJV, 2006b; 2007). Using the base-case parameters as a starting point, the simulations examined the effect of changing various model parameters on tracer breakthrough at the downstream boundary.

Table L-2
Comparison of Model Parameters with Estimated Distributions

Parameter	Model Value (Base Case)	Estimated Mean	Estimated Standard Deviation or (Range)	Distribution	Source
Log Hydraulic Conductivity (m/day) [a]	–0.07	0.03	1.31	Lognormal	SNJV, 2006b (Table 6-1)
Dispersivity (m)	40	40	10	Normal	SNJV, 2007 (Chapter 9)
Matrix Porosity	0.03	0.022	0.014	Normal	SNJV, 2007 (Table 7-3)
Effective Fracture Porosity	0.001	5E-03	2E-04 to 2E-02	Log triangular	SNJV, 2007 (Figure 8-6)
Effective Matrix Diffusion ($D_{eff} = D_0\tau$) (m^2/s)	5E-11	1.25E-11 [b]	N/A	Tortuosity correlated with matrix porosity ($\tau = \phi_m^{1.33}$)	SNJV, 2007 (Figure 10-13)
Log Fracture Spacing (m) [c]	0.30	–0.418	0.365	Lognormal	SNJV, 2007
Log Fracture Aperture (m) [d]	–2.70	N/A	N/A	Lognormal	SNJV, 2007

[a] A permeability of 1E-12 m^2 corresponds to a hydraulic conductivity of 0.85 m/day at 25 °C.
[b] The estimated mean assumes a free-water diffusion coefficient of 2E-09 m^2/s, a mean matrix porosity of 0.022, and a calculated tortuosity value of 0.0062.
[c] The base-case fracture spacing in the model was 2 m. The fracture spacing in SNJV (2007) ranged from 0.5 to 13.9 m, with a mean of 2.6 m.
[d] The base-case fracture aperture was 0.002 m.

Figure L-11 shows the influence of different assumed values for the effective diffusion coefficient ($D_{eff} = D_0\tau$), where D_0 is the free-water diffusion coefficient (m^2/s) and τ is the tortuosity, which is defined as the net molecular displacement divided by the actual path length (L/L). The results of the sensitivity analysis show that although the mean normalized breakthrough (C/C_0 = 0.5) is relatively unaffected by the assumed value of D_{eff} when D_{eff} is 5E-10 or greater, smaller values of D_{eff} can produce breakthrough that is much more dispersive, with both earlier breakthrough and longer tails.

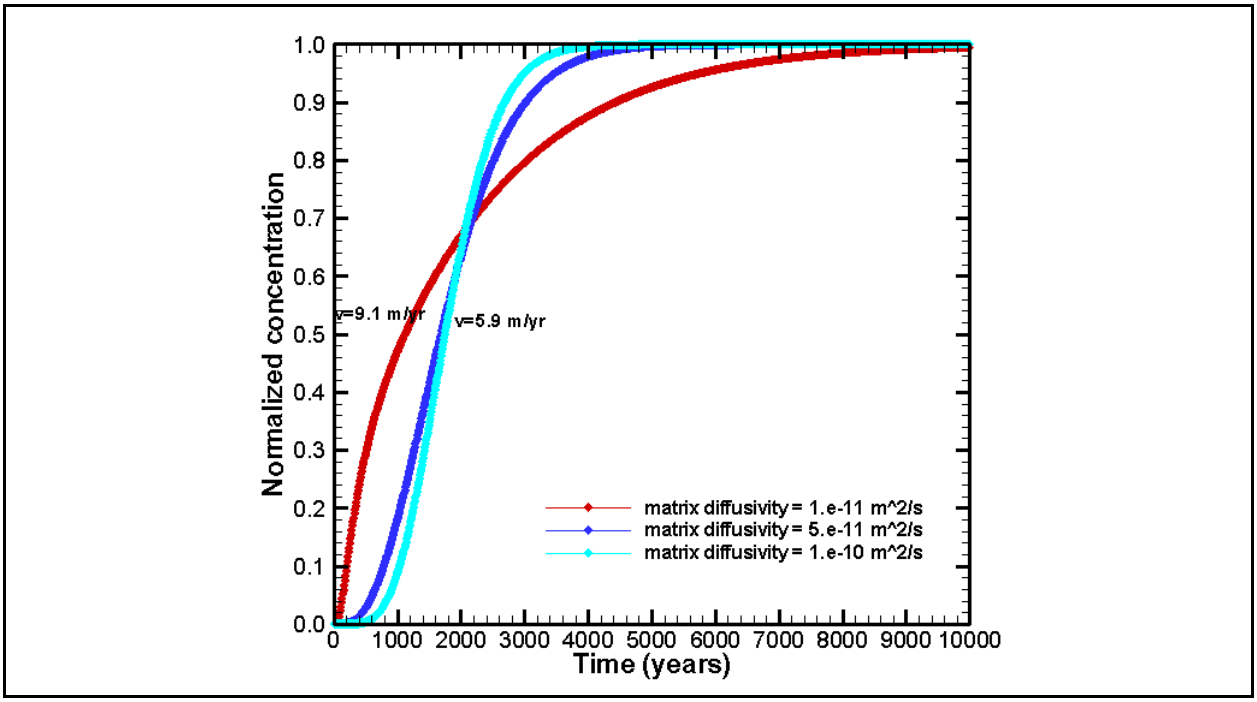

Figure L-11
Effect of Matrix Diffusivity on Tracer Breakthrough

The larger apparent dispersion in the breakthrough curves at smaller values of D_{eff} is because it is more difficult for the tracer to diffuse into the matrix (resulting in earlier breakthrough) and to diffuse back out of the matrix (resulting in longer "tails" in the breakthrough curve). Based on the mean breakthrough time at about 1,100 years and the model length of 10 km, a mean transport velocity of about 9.1 m/yr is calculated for D_{eff} = 1.0E-11 m^2/s. The mean transport velocity decreases to 5.9 m/yr for D_{eff} values of 5.0E-11 and 1.0E-10 m^2/s. Because D_{eff} is probably not larger than 1.0E-10 m^2/s, these results suggest that other parameters need to be adjusted to reduce the mean breakthrough velocity from 5.9 m/yr to the value of 2 m/yr indicated by the ^{14}C data.

Figure L-12 shows that a relatively small reduction in the permeability of the LCA from 1E-12 to 3.5E-13 m^2 is sufficient to reduce the transport velocities of the simulated tracer to 2 m/yr. A permeability of 3.5E-13 m^2 is well within the range of observed values (Table L-2). The cumulative probability distribution of pumping-scale hydraulic conductivity values reported for the LCA in Yucca Flat (SNJV, 2006b, Figure 6-19) indicates that a permeability of 3.5E-13 m^2 (corresponding to a hydraulic conductivity of 0.3 m/day) is greater than or equal to approximately 33 percent of the measured values. Thus, a large-scale permeability of 3.5E-13 m^2 is not only plausible based on the available hydraulic conductivity data but also compatible with a tracer migration velocity of 2 m/yr.

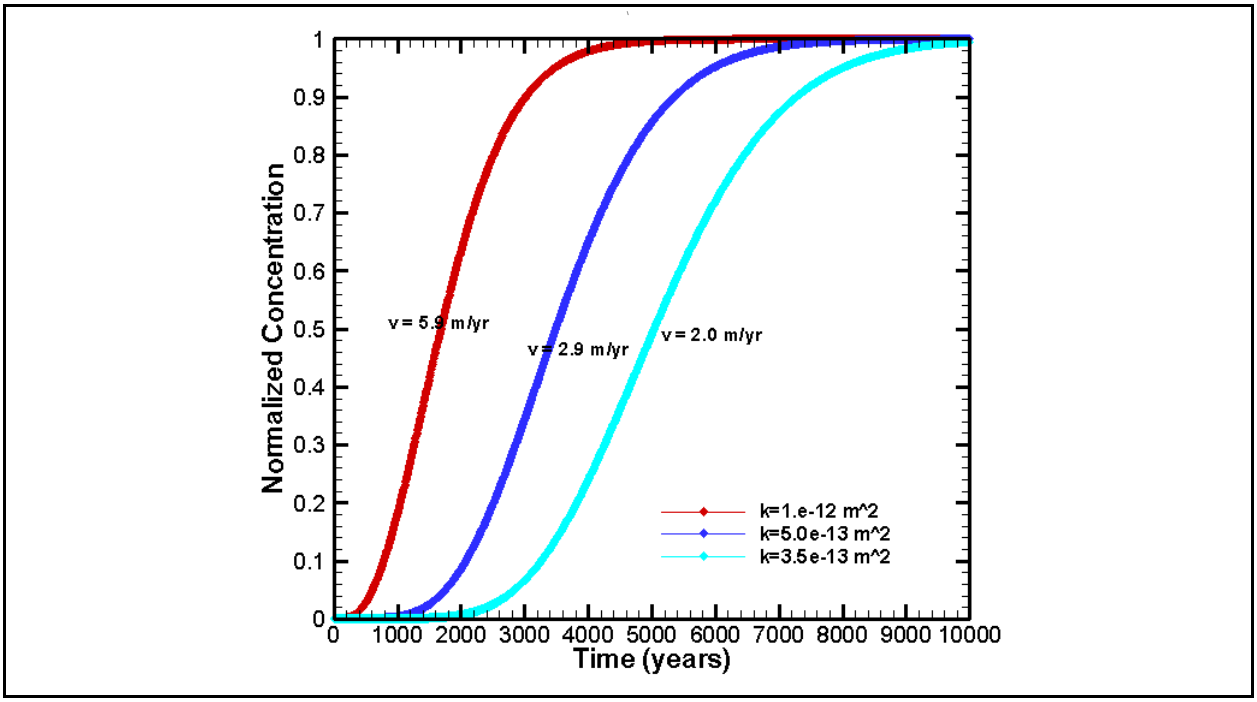

Figure L-12
Effect of Saturated Hydraulic Conductivity on Tracer Breakthrough

Additionally, the impact of effective fracture porosity on solute migration velocities was investigated. Figure L-13 shows that tracer breakthrough is extremely sensitive to effective fracture porosity when the latter is varied between 1E-04 and 1E-02. In these examples, effective porosity was varied by keeping the aperture constant at 1E-03 m and adjusting the fracture spacing between 20 and 0.2 m. Aperture, spacing, and fracture porosity are related by

$$\phi_f = b / s_f \qquad (L\text{-}5)$$

where ϕ_f is the fracture porosity, b is the aperture (m), and s_f is the fracture spacing (m). For a constant fracture aperture of 0.002 m, ϕ_f increases from 1E-04 to 1E-02 as s_f decreases from 20 to 0.2 m. As can be seen from Figure L-13, the effect of fracture porosity and spacing on tracer breakthrough is impressive, with migration velocities estimated from mean breakthrough ($C/C_0 = 0.5$) of 143 m/yr at ϕ_f of 1E-04 and 5.3 m/yr at ϕ_f of 1E-02. Migration velocities are higher at smaller fracture porosities and larger fracture spacings because advective groundwater velocities ($v = q/\phi_f$) are higher when fracture porosity is smaller, and the matrix block surface area available for diffusion is smaller when fracture spacing becomes larger. Moreover, the results show that as fracture spacing increases, the tails of the breakthrough curves become more extensive because it takes longer for the tracer that has diffused into the matrix to diffuse out again when fracture spacing is larger. At smaller fracture

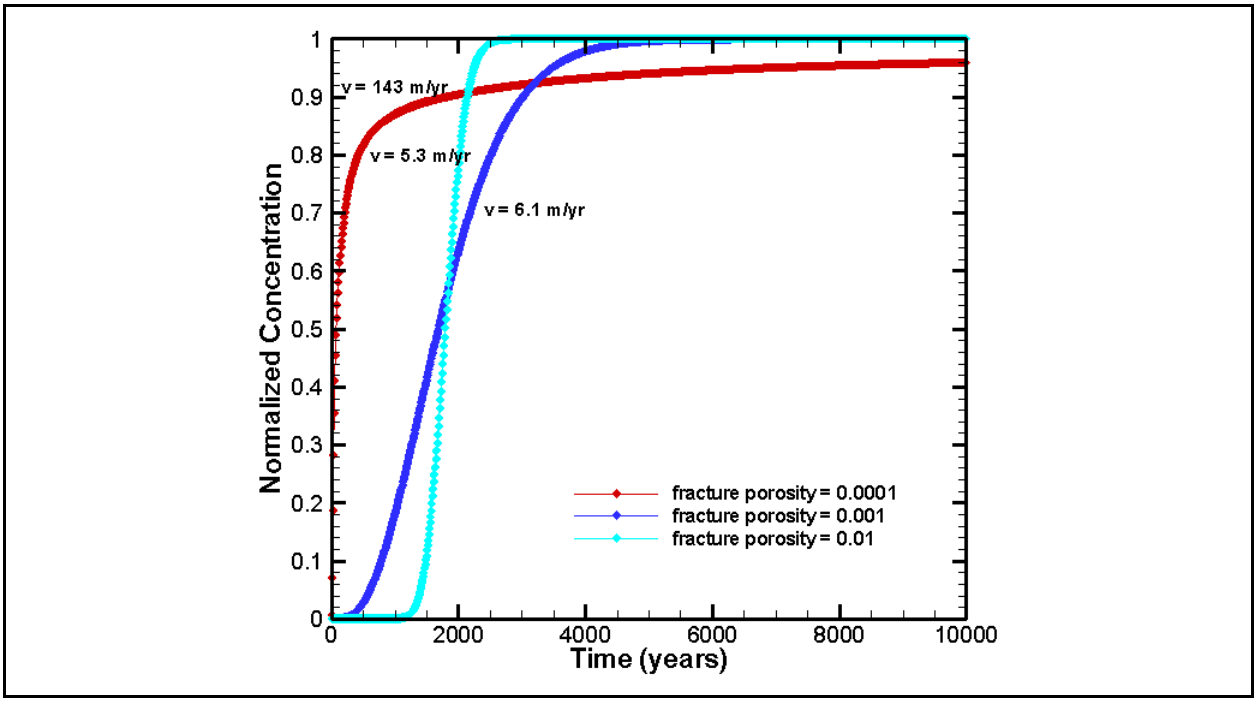

Figure L-13
Effect of Fracture Porosity (and Fracture Spacing) on Tracer Breakthrough

spacings (e.g., s_f = 0.2 m, ϕ_f = 1E-02), tracer breakthrough becomes more pluglike, as would be the case for transport in a single porosity medium. Because fracture porosity is unlikely to be much greater than 1E-02 or fracture spacing less than 0.2 m, large fracture porosity or small fracture spacing can hardly be the cause of the estimated 2-m/yr migration velocity of naturally occurring ^{14}C.

Based on the ^{36}Cl/Cl analysis, the previous models have assumed no sorption of ^{14}C to the LCA matrix. However, to investigate the magnitude of the linear sorption parameter (K_d) for the rock matrix that would be required to reduce the mean transport velocity from 5.9 to roughly 2 m/yr, a range of K_d values were investigated (Figure L-14). The results show that for base-case values of permeability, D_{eff}, and ϕ_f, a value for K_d of 0.05 or 0.1 mL/g would be more than sufficient to reduce transport velocities to roughly 2 m/yr or less. This has important implications. First, it suggests that if ^{14}C sorption is the cause of the small inferred ^{14}C velocities in the LCA, these small velocities can be achieved with very small K_d values, and that much larger K_d values for ^{14}C are incompatible with the observed rates of ^{14}C migration. Secondly, the sensitivity of ^{14}C transport velocities to matrix K_d implies similarly slow velocities for other weakly sorbing radionuclides with small K_d values, such as ^{237}Np and U, and possibly ^{137}Cs or ^{90}Sr.

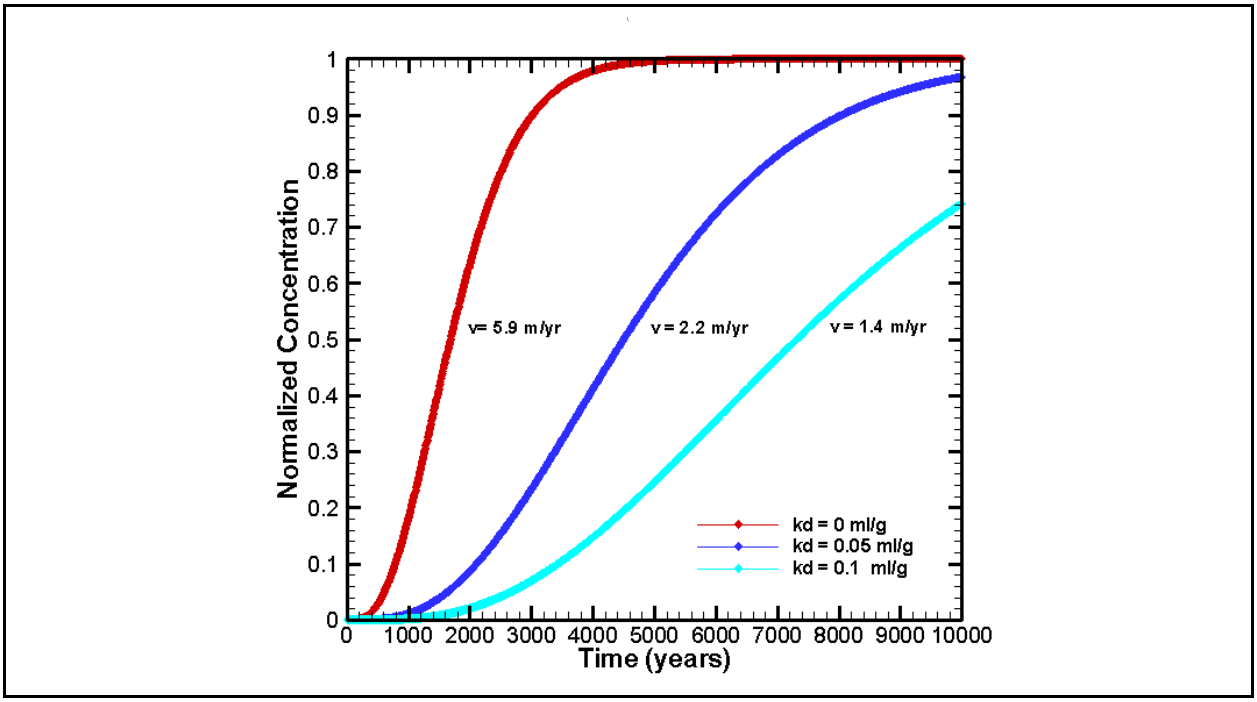

Figure L-14
Effect of Matrix K_d on Tracer Breakthrough

In summary, although small sorption coefficients (K_d = 0.05 to 0.1 mL/g) would be sufficient to decrease rates of ^{14}C movement in the LCA to 2 m/yr or less, these velocities can also be achieved with a large-scale permeability value of 3.5E-12 m^2. This permeability value is larger than about one-third of the measured field-scale values (SNJV, 2006b) and thus provides a large-scale permeability value that is compatible with both the permeability data and the rates of ^{14}C migration when ^{14}C is assumed not to sorb.

L.5.0 SUMMARY AND CONCLUSIONS

Groundwater ^{14}C ages were calculated for Yucca Flat and nearby areas. The calculation used measured ^{14}C activities and two analytical correction methods based on the downgradient changes in total DIC and changes in the $\delta^{13}C$ relative to the estimated groundwater recharge. These correction methods accounted for bulk dissolution of carbonate, and in the case of the $\delta^{13}C$-based corrections, also isotope exchange; however, they may not have fully accounted for $H^{14}CO_3^-$ sorption onto the carbonate matrix or calcite fracture surfaces if these processes occurred. These are processes that have been identified in laboratory experiments as having possible effects on $H^{14}CO_3^-$ transport in carbonate rocks, and if they occurred, they would result in estimates of groundwater age that are too large and groundwater velocities that are too low. For these reasons, the transport behavior of $H^{14}CO_3^-$ was evaluated by comparing it against Cl, which is widely regarded as a conservative, non-sorbing tracer. Specifically, the temporal history of meteoric $^{36}Cl/Cl$ variations recorded in pack-rat midden data for southern Nevada over the past 40,000 years was compared to the temporal record of meteoric $^{36}Cl/Cl$ variations in groundwater in the Yucca Flat area as interpreted from the measured groundwater $^{36}Cl/Cl$ ratios and the estimated groundwater ^{14}C ages. The good agreement between the temporal $^{36}Cl/Cl$ record provided by the pack-rat midden data and the groundwater record indicated that the groundwater ^{14}C ages were reasonable and that $H^{14}CO_3^-$ was moving conservatively along with ^{36}Cl in groundwater in both the alluvial/volcanic aquifer system and the LCA. The apparently conservative behavior of $H^{14}CO_3^-$ in the LCA could be because any calcite fracture coatings, unlike crushed calcite samples in laboratory studies, have had millions of years to “age” and achieve a stable crystal morphology in which recrystallization is minimal. Crushed calcite samples in laboratory studies are not aged for more than a year in representative groundwater.

The corrected ^{14}C ages in the shallow alluvial/volcanic aquifer system in Yucca Flat are predominantly in the range of 8,000 to 12,000 years old, which is consistent with interpretations from unsaturated-zone studies that local recharge in Yucca Flat ceased about 10,000 years ago, except for small rates of infiltration in the low bedrock hills bordering the basin. The ^{14}C ages in the LCA are generally older and increase from about 12,000 years in the northern part of the basin to more than 30,000 years in the southern part of the basin, except for an area near major faults where younger ^{14}C ages and other groundwater characteristics indicate downward leakage from the overlying

aquifers. Overall, the groundwater ^{14}C ages are consistent with interpretations of the flow system based on geologic and hydrologic data, as well as previous studies of the geochemistry and isotope hydrology of the site that suggested solute migration velocities on the order of 2 m/yr. A simple one-dimensional dual-porosity flow and transport model of the LCA was created to demonstrate that migration velocities of this magnitude can be achieved by using hydraulic and transport properties typical of the LCA, with hydraulic conductivities slightly lower than average.

L.6.0 REFERENCES

BN, see Bechtel Nevada.

Bechtel Nevada. 2006. *A Hydrostratigraphic Model and Alternatives for the Groundwater Flow and Contaminant Transport Model of Corrective Action Unit 97: Yucca Flat–Climax Mine, Lincoln and Nye Counties, Nevada*. DOE/NV/11718--1119. Prepared for the U.S. Department of Energy, National Nuclear Security Administration Nevada Site Office. Las Vegas, NV.

Clark, I., and P. Fritz. 1997. *Environmental Isotopes in Hydrogeology.* Boca Raton, FL: CRC Press.

Coplen, T.B. 2007. "Calibration of the Calcite–Water Oxygen-Isotope Geothermometer at Devils Hole, Nevada, a Natural Laboratory." *Geochimica et Cosmochimica Acta* 71 (16): 3948–3957. doi:10.1016/j.gca.2007.05.028.

Coplen, T.B., I.J. Winograd, J.M. Landwehr, and A.C. Riggs. 1994. "500,000-Year Stable Carbon Isotopic Record from Devils Hole, Nevada." *Science* 263 (5145): 361–365. doi:10.1126/science.263.5145.361.

Fabryka-Martin, J., S.J. Wightman, W.J. Murphy, M.P. Wickham, M.W. Caffee, G.J. Nimz, J.R. Southon, and P. Sharma. 1993. *Distribution of Chlorine-36 in the Unsaturated Zone at Yucca Mountain: An Indicator of Fast Transport Paths.* Paper presented at FOCUS '93 Site Characterization and Model Validation. Las Vegas. NV.

Fenelon, J.M., D.S. Sweetkind, P.E. Elliot, and R.J. Laczniak. 2012. *Conceptualization of the Predevelopment Groundwater Flow System and Transient Water-Level Responses in Yucca Flat, Nevada National Security Site, Nevada*, Scientific Investigations Report 2012-5196. Reston, VA: U.S. Geological Survey.

Hershey, R.L., W. Howcroft, and P.W. Reimus. 2003. *Laboratory Experiments to Evaluate Diffusion of ^{14}C into Nevada Test Site Carbonate Aquifer Matrix*, DOE/NV/11508-55; Publication No. 45180. Las Vegas, NV: Desert Research Institute.

Kenneally, J. 1995. Written communication. Subject: *Preliminary Report Evaluating the Use of Strontium and Chloride Concentrations and $^{87}Sr/^{86}Sr$ Ratios as Analogs for the Dissolution of Inorganic Carbon.* Livermore, CA: Lawrence Livermore National Laboratory.

Kwicklis, E.M., A.V. Wolfsberg, P.H. Stauffer, M.A. Walvoord, and M.J. Sully. 2006. "Multiphase, Multicomponent Parameter Estimation for Liquid and Vapor Fluxes in Deep Arid Systems Using Hydrologic Data and Natural Environmental Tracers." *Vadose Zone Journal* 5 (3): 934–950. doi:10.2136/vzj2006.0021.

Landwehr, J.M., and I.J. Winograd. 2012. *Devils Hole, Nevada—A Primer,* Fact Sheet 2012-3021. U.S. Geological Survey.

Maloszewski, P. and A. Zuber. 1991. "Influence of Matrix Diffusion and Exchange Reactions on Radiocarbon Ages in Fissured Carbonate Aquifers." *Water Resources Research* 27 (8): 1937–1945. doi:10.1029/91WR01110.

Mozeto, A.A., P. Fritz, and E.J. Reardon. 1984. "Experimental Observations on Carbon Isotope Exchange in Carbonate-Water Systems." *Geochimica et Cosmochimica Acta* 48 (3): 495–504.

Parkhurst, D.L., and C.A.J. Appelo. 1999. *User's Guide to PHREEQC (Version 2)—A Computer Program for Speciation, Batch-Reaction, One-Dimensional Transport, and Inverse Geochemical Calculations*, Water-Resources Investigations Report 99-4259. Denver, CO: U.S. Geological Survey.

Plummer, L.N., E.C. Prestemon, and D.L. Parkhurst. 1994. *An Interactive Code (NETPATH) for Modeling Net Geochemical Reactions along a Flow Path, Version 2.0*, Water-Resources Investigations Report 94-4169. Denver, CO: U.S. Geological Survey.

Plummer, M.A., F.M. Phillips, J. Fabryka-Martin, H.J. Turin, P.E. Wigand, and P. Sharma. 1997. "Chlorine-36 in Fossil Rat Urine: An Archive of Cosmogenic Nuclide Deposition during the Past 40,000 Years." *Science* 277 (5325): 538–541. doi:10.1126/science.277.5325.538.

Quade, J., and T.E. Cerling. 1990. "Stable Isotopic Evidence for a Pedogenic Origin of Carbonates in Trench 14 near Yucca Mountain, Nevada," *Science* 250 (4987): 1549–1552. doi:10.1126/science.250.4987.1549.

Quade, J., T.E. Cerling, and J.R. Bowman. 1989. "Systematic Variations in the Carbon and Oxygen Isotopic Composition of Pedogenic Carbonate along Elevation Transects in the Southern Great Basin, United States." *Geological Society of America Bulletin* 101 (4): 464–475. doi:10.1130/0016-7606(1989)101<0464:SVITCA>2.3.CO;2.

Reimer, P.J., M.G.L. Baillie, E. Bard, A. Bayliss, J.W. Beck, C.J.H. Bertrand, P.G. Blackwell, C.E. Buck, G.S. Burr, K.B. Cutler, P.E. Damon, R.L. Edwards, R.G. Fairbanks, M. Friedrich, T.P. Guilderson, A.G. Hogg, K.A. Hughen, B. Kromer, G. McCormac, S. Manning, C.B. Ramsey, R.W. Reimer, S. Remmele, J.R. Southon, M. Stuiver, S. Talamo, F.W. Taylor, J. van der Plicht, and C.E. Weyhenmeyer. 2004. "IntCal04 Terrestrial Radiocarbon Age Calibration, 0-26 cal kyr BP." *Radiocarbon* 46 (3): 1029–1058.

Reimus, P.W., R.L. Hershey, D.L. Decker, E. Garcia, S. Earman, J. Ryu, R.C. Roback, and G. Pohll. 2008. *Laboratory Experiments of ^{14}C Uptake and Release on Calcite and Dolomite to Support Groundwater Radionuclide Transport Modeling for the Nevada Test Site Underground Test Area Program*, LA-UR-08-0427. Los Alamos, NM.: Los Alamos National Laboratory.

Reimus, P.W., R.L. Hershey, D.L. Decker, S.D. Ware, C. Papelis, S. Earman, A. Abdel-Fattah, M. Haga, D. Counce, S. Chipera, C. Sedlacek. 2006. *Tracer Transport Properties in the Lower Carbonate Aquifer of Yucca Flat*, LA-UR-06-0486. Los Alamos, NM: Los Alamos National Laboratory.

SNJV, see Stoller-Navarro Joint Venture.

Sanford, W.E. 1997. "Correcting for Diffusion in Carbon-14 Dating of Ground Water." *Groundwater* 35 (2): 357–361. doi:10.1111/j.1745-6584.1997.tb00093.x.

Stoller-Navarro Joint Venture. 2006a. *Geochemical and Isotopic Evaluation of Groundwater Movement in Corrective Action Unit 97: Yucca Flat/Climax Mine, Nevada Test Site, Nevada*, Rev. 0, S-N/99205--070. Las Vegas, NV.

Stoller-Navarro Joint Venture. 2006b. *Phase I Hydrologic Data for the Groundwater Flow and Transport Model of Corrective Action Unit 97: Yucca Flat/Climax Mine, Nevada Test Site, Nye County, Nevada*, Rev. 0, S-N/99205--077. Las Vegas, NV.

Stoller-Navarro Joint Venture. 2006c. *Phase II Groundwater Flow Model of Corrective Action Unit 98: Frenchman Flat, Nevada Test Site, Nye County, Nevada*, Rev. 0, S-N/99205--074. Las Vegas, NV.

Stoller-Navarro Joint Venture. 2007. *Phase I Contaminant Transport Parameters for the Groundwater Flow and Contaminant Transport Model of Corrective Action Unit 97: Yucca Flat/Climax Mine, Nevada Test Site, Nye County, Nevada*, Rev. 0, S-N/99205--096. Las Vegas, NV.

Sudicky, E.A., and E.O. Frind. 1982. "Contaminant Transport in Fractured Porous Media: Analytical Solutions for a System of Parallel Fractures." *Water Resources Research* 18 (6): 1634–1642. doi:10.1029/WR018i006p01634.

Tyler, S.W., J.B. Chapman, S.H. Conrad, D.P. Hammermeister, D.O. Blout, J.J. Miller, M.J. Sully, and J.M. Ginanni. 1996. "Soil-Water Flux in the Southern Great Basin, United States: Temporal and Spatial Variations over the Last 120,000 Years." *Water Resources Research* 32 (6): 1481–1499.

van der Plicht, J., J.W. Beck, E. Bard, M.G.L. Baillie, P.G. Blackwell, C.E. Buck, M. Friedrich, T.P. Guilderson, K.A. Hughen, B. Kromer, F.G. McCormac, C.B. Ramsey, P.J. Reimer, R.W. Reimer, S. Remmele, D.A. Richards, J.R. Southon, M. Stuiver, and C.E. Weyhenmeyer. 2004. "NotCal04—Comparison/Calibration ^{14}C Records 26-50 cal kyr BP." *Radiocarbon* 46 (3): 1225–1238.

Walvoord, M.A., F.M. Phillips, S.W. Tyler, and P.C. Hartsough. 2002. "Deep Arid System Hydrodynamics 2. Application to Paleohydrologic Reconstruction Using Vadose-Zone Profiles from the Northern Mojave Desert." *Water Resources Research* 38 (12): 1291. doi:10.1029/2001WR000825.

Walvoord, M.A., M.A. Plummer, F.M. Phillips, and A.V. Wolfsberg. 2002. "Deep Arid System Hydrodynamics 1. Equilibrium States and Response Times in Thick Desert Vadose Zones." *Water Resources Research* 38 (12): 1308. doi:10.1029/2001WR000824.

Ware, S.D., A. Abdel-Fattah, M. Ding, P.W. Reimus, C. Sedlacek, M.J. Haga, E. Garcia, and S. Chipera. 2005. *Radionuclide Sorption and Transport in Fractured Rocks of Yucca Flat, Nevada Test Site*, LA-UR-05-9279, Los Alamos, NM: Los Alamos National Laboratory.

Winograd, I.J., T.B. Coplen, J.M. Landwehr, A.C. Riggs, K.R. Ludwig, B.J. Szabo, P.T. Kolesar, and K.M. Revesz. 1992. "Continuous 500,000-Year Climate Record from Vein Calcite in Devils Hole, Nevada." *Science* 258 (5080): 255–260. doi:10.1126/science.258.5080.255.

Winograd, I.J., J.M. Landwehr, T.B. Coplen, W.D. Sharp, A.C. Riggs, K.R. Ludwig, and P.T. Kolesar. 2006. "Devils Hole, Nevada, $\delta^{18}O$ Record Extended to the Mid-Holocene." *Quaternary Research* 66 (2): 202–212. doi:10.1016/j.yqres.2006.06.003.

Winograd, I.J., and F.J. Pearson Jr. 1976. "Major Carbon 14 Anomaly in a Regional Carbonate Aquifer: Possible Evidence for Megascale Channeling, South Central Great Basin." *Water Resources Research* 12 (6): 1125–1143. doi:10.1029/WR012i006p01125.

Winograd, I.J., and W. Thordarson. 1975. *Hydrogeologic and Hydrochemical Framework, South-Central Great Basin, Nevada-California, with Special Reference to the Nevada Test Site*, Professional Paper 712-C. Denver, CO: U.S. Geological Survey.

Zavarin, M., M.R. Johnson, S.K. Roberts, R. Pletcher, T.P. Rose, A.B. Kersting, G. Eaton, Q. Hu, R. Ramon, J. Walensky, and P. Zhao. 2005. *Radionuclide Transport in Tuff and Carbonate Fractures from Yucca Flat, Nevada Test Site*, UCRL-TR-219836. Livermore, CA: Lawrence Livermore National Laboratory.

Zavarin, M., S.K. Roberts, P.W. Reimus, and M.R. Johnson. 2007. *Summary of Radionuclide Reactive Transport Experiments in Fractured Tuff and Carbonate Rocks from Yucca Flat, Nevada Test Site*, UCRL-TR-225271. Livermore, CA: Lawrence Livermore National Laboratory.

Zyvoloski, G.A, B.A. Robinson, and H.S. Viswanathan. 2008. "Generalized Dual Porosity: A Numerical Method for Representing Spatially Variable Sub-Grid Scale Processes." *Advances in Water Resources* 31 (3): 535–544. doi:10.1016/j.advwatres.2007.11.006.

Appendix M

Evaluation of the Importance of Colloid Transport in the Lower Carbonate Aquifer in Yucca Flat

M.1.0 INTRODUCTION

The primary purpose of this appendix is develop a detailed process-level model of colloid-facilitated plutonium and europium transport in the LCA in Yucca Flat so that their importance relative to other radionuclides for defining the contaminant boundary can be assessed. A secondary goal is to provide a basis for simplifying colloid-facilitated transport in the CAU-scale models for the LCA in Yucca Flat. Currently, these models rely on computationally efficient particle-based solute-transport simulations to deal effectively with dozens of distributed source locations, and the large space and timescales needed to assess the contaminant boundary at the CAU scale. The particle-tracking-based models require certain linear assumptions and equilibrium chemistry, and assume no interaction among migrating radionuclide and colloid species (Robinson et al., 2011); therefore, these models cannot simulate the competitive radionuclide sorption between colloids and immobile minerals, which is central to the issue of colloid-facilitated transport. The one-dimensional model presented in this appendix not only allows this competitive sorption process to be simulated in detail using the standard advection-dispersion formulation for transport, but also explicitly simulates matrix diffusion using a dual-porosity formulation, thus providing a basis for both simplifying and comparing simulation results produced with particle-based approaches.

The one-dimensional model extends 30 km southward from the BOURBON detonation into Frenchman Flat (Figure M-1). The BOURBON detonation was the southernmost of only four underground nuclear detonations in Yucca Flat with working points in the LCA, all of which were emplaced within the unsaturated zone near the water table. Unlike Carle et al. (2008), who considered detailed near-field processes such as CO_2 generation and temperature effects to look at redistribution of radionuclides following the detonation, the present analysis ignores unsaturated-zone and multiphase aspects of the problem and focuses on radionuclide transport processes once the radionuclides have reached the saturated LCA. The present analysis assumes that the radionuclide inventory associated with the BOURBON detonation lies entirely below the water table and that the radionuclide inventory (minus the melt-glass fraction) is emplaced in the saturated fractures of the LCA lying between one and three times the cavity radius and thus immediately available for transport through groundwater flow. The analysis evaluates the importance of colloidal plutonium (Pu-Col) and colloidal europium (Eu-Col) transport by comparing their contaminant

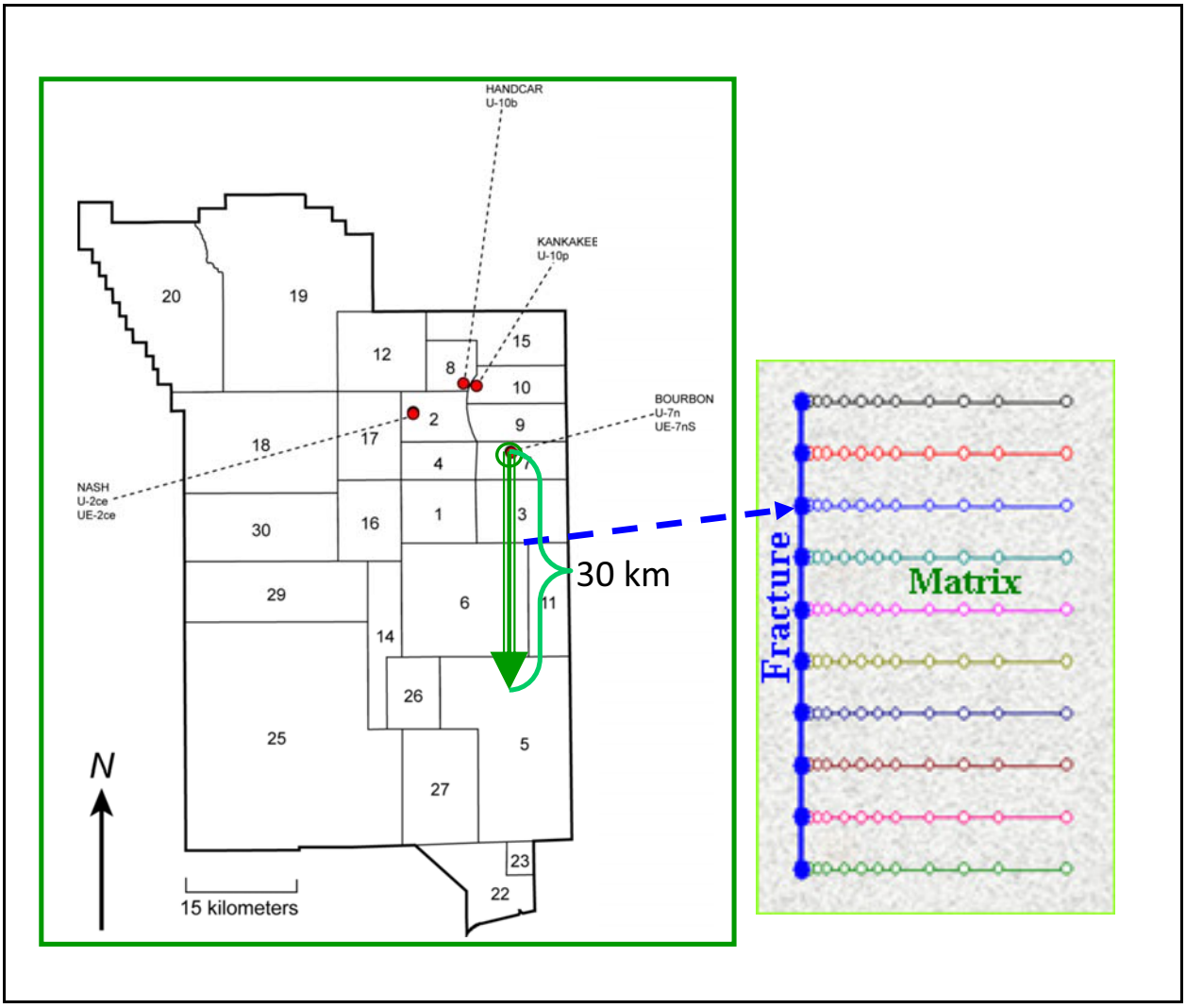

Figure M-1
The One-Dimensional Streamtube Model Extending Southward from the BOURBON Detonation

lengths (the distances along which plutonium and europium concentrations are above their regulatory limits) against the contaminant lengths defined by the dissolved radionuclide species. The analysis, therefore, examines the factors that affect the transport of other radionuclide species, such as ^{3}H, ^{14}C, ^{36}Cl, ^{59}Ni, ^{63}Ni, ^{99}Tc, ^{129}I, ^{237}Np, U, ^{90}Sr, and ^{137}Cs, in addition to ^{152}Eu, ^{154}Eu, ^{238}Pu, ^{239}Pu, ^{240}Pu, ^{241}Pu, and ^{242}Pu. Note that unlike the three-dimensional transport models in Section 6.0, these one-dimensional models do not consider the ^{135}Cs transport which is estimated to have an initial concentration less than its MCL whereas the Section 6.0 models initial ^{137}Cs concentrations in the LCA are about one hundred thousand times its MCL [see Figures 2-6, 2-7, and 2-8]).The reactive transport model described here is developed within a Monte Carlo framework and includes

a stochastic treatment of solute advection and dispersion in a fractured continuum, mass transfer between fractures and rock matrix by diffusion, and kinetic or equilibrium sorption of plutonium and europium onto colloids and fracture or matrix minerals. By simultaneously considering hydrologic, source-term, and transport parameter uncertainties, the present analysis attempts to develop an integrated picture of the factors affecting the migration of plutonium and europium in the LCA relative to other radionuclide species. For plutonium and europium, the model considers competitive sorption between the dissolved, colloidal, and sorbed parts of the inventory to allow transport to be simulated without making *a priori* assumptions concerning what fraction of the initial inventory is associated with colloids. The analysis presented in this appendix includes the following steps:

- Characterize the uncertainty distributions of the effective flow and transport parameters, such as fracture porosity, aperture and spacing, fracture retardation coefficients, matrix diffusion, and sorption coefficients, for each of the 18 radionuclide species considered.
- Develop a methodology for estimating the initial radionuclide concentration uncertainty given the uncertainties in radionuclide inventory, exchange volume radius, and fracture porosity.
- Develop a one-dimensional dual-porosity streamtube model extending 30 km southward from the BOURBON detonation.
- Run 800 Monte Carlo realizations of flow and transport while considering flow, transport, and source-term uncertainties.
- Calculate the contaminant lengths of each radionuclide at different times and the concentration profiles at 1,000 years.
- Analyze the plutonium transport behavior to estimate the fraction of the initial plutonium source that is likely to undergo long-range transport by colloids (i.e., a plutonium reduction factor).
- Summarize the distributions of the calculated contaminant lengths and concentration profiles for individual radionuclides to develop estimates of the contaminant boundaries at the 5th, 50th, and 95th percentiles.
- Perform global sensitivity analysis of the computed contaminant lengths for each of the 18 radionuclide species to identify the most sensitive parameters affecting the transport lengths.

M.2.0 EFFECTIVE FLOW AND TRANSPORT PARAMETERS

This section presents flow and transport parameters that are expected to influence radionuclide transport and the probability distributions that characterize their uncertainties.

M.2.1 Fracture Parameters, Flow Rate, and Matrix Porosity

Recent field-scale tracer-test interpretations by Reimus et al. (2003), Reimus, Ware, et al. (2006), and Dai et al. (2012) highlighted the significance of fracture apertures in governing mass transfer between fractures and matrix, particularly when the field-scale fractures in which solute flows may have different apertures than those used in laboratory columns. In dual-porosity transport modeling with the generalized dual-porosity model (GDPM), particle-tracking models, and analytical solutions, fracture aperture affects matrix diffusion by setting the effective wetted surface per unit fracture water volume. For a fixed porosity, wetted surface area increases as fracture aperture decreases, because more fractures are necessary to provide that porosity. Fracture aperture is related to fracture porosity through the fracture spacing term (see below) and thus can also affect groundwater velocities.

In the present analysis, fracture spacing (S_f) in the LCA is sampled from a lognormal distribution, and fracture porosity (ϕ_f or porF) is sampled from a log-triangular distribution, as defined in SNJV (2006, Table 6-6, Figure 6-21). The effective fracture aperture (*fb*) is computed from sampled fracture porosity and fracture spacing with the following equation:

$$fb = S_f \phi_f \qquad (M\text{-}1)$$

The matrix porosity ($\phi_m$or porM), which affects matrix diffusion and concentration gradients away from the fractures, is sampled from a normal distribution as defined in SNJV (2007, Table 7-3). Table M-1 lists the statistics of the basic flow and transport parameters for the LCA at Yucca Flat.

Table M-1
Statistics of the Flow and Transport Parameters for the LCA at Yucca Flat

Parameter (unit)	Symbol	Lower	Upper	Mean	Standard Deviation	Distribution	Reference
Log Fracture Porosity (-)	ϕ_f or porF	-3.7	-2.0 [a]	-2.3	N/A	Log Triangular	SNJV, 2007 (Table 8-22, Figure 8-6)
Matrix Porosity	ϕ_m or porM	0.004	0.06	0.022	0.014	Normal	SNJV, 2007 (Table 7-3)
Log Conductivity (m/day)	K_{eff}	N/A	N/A	0.16	1.34	Lognormal	SNJV, 2006 (Table 6-1)
Log Fracture Aperture (m)	*fb*	-4.0	-2.0	N/A	N/A	Equation (M-1)	Computed
Log Fracture Spacing (m)	S_f	-0.295	1.142	0.418	0.362	Lognormal	SNJV, 2006 (Table 6-6, Figure 6-21)
Inflow Rate (m^3/day or kg/s)	*Q* or flowr	N/A	N/A	N/A	N/A	Equation (M-2)	Computed

[a] The upper bound for log fracture porosity of -1.7 reported in SNJV (2007, Table 8-22) is truncated at -2.0.

M.2.2 Conductivity and Inflow Rate

With a lognormal distribution of the effective hydraulic conductivity taken from SNJV (2006, Table 6-1), the inflow rate into a streamtube can be calculated from Darcy's law:

$$Q = K_{eff} A G_h \qquad (M\text{-}2)$$

where Q is the inflow rate (m^3/day), A is the cross section or area available for flow (m^2), G_h is the hydraulic gradient, and K_{eff} is the effective hydraulic conductivity of the LCA (m/day) (Bear, 1972).

The inflow rate Q (or flowr) is computed from Equation (M-2) with the cross-section area computed from the thickness of the LCA and the sampled fracture spacing, the sampled hydraulic conductivity, and an assumed hydraulic gradient of 3.33E-04. The hydraulic gradient is assumed known and is calculated from the approximately 10-m difference in hydraulic head between Wells UE-10j and WW C (30.2 km apart) in Yucca Flat.

M.2.3 Matrix Diffusion Coefficient and Fracture Dispersivity

Previous UGTA studies of radionuclide migration in fractured rock have applied a mass transfer coefficient to describe the rate at which a solute moves between fractures and the rock matrix by

diffusion (Robinson, 1994; Wolfsberg et al., 2002; Reimus et al., 2003; Dai et al., 2007). The mass transfer coefficient depends on the matrix diffusion coefficient (D_m), fracture aperture (fb), and matrix porosity (ϕ_m) according to the following function:

$$\text{Mass transfer coefficient} = \frac{\phi_m}{fb}\sqrt{D_m} \qquad (M\text{-}3)$$

The matrix diffusion coefficient, fracture aperture, and matrix porosity are the key parameters that describe a critical component of contaminant transport in fractured rock systems (advection and dispersion in fractures are the other critical components). The diffusion coefficients (D_0) of ^{3}H and ^{14}C in free water at 25 ºC are 2.44E-09 and 1.1E-09 m^2/s, respectively (Reimus, Ware, et al., 2006). The diffusion coefficients of other radionuclides are found in literature (e.g., Li and Gregory, 1974; Lide, 2000) and listed in Table M-2. The matrix diffusion coefficients of different radionuclides can be computed as $D_{m_i} = \omega D_{0_i}$, where i represents different radionuclides, and ω is the matrix tortuosity. The free-water diffusion coefficients for plutonium and europium are somewhat uncertain given that they depend on the speciation of these radionuclides and that the species-specific diffusion coefficients are not known. However, it is assumed that this uncertainty is small relative to other factors affecting diffusion, such as fracture aperture and spacing, and matrix porosity and tortuosity. In the LCA, ω is assumed to be correlated with matrix porosity by $\log\omega = -2.468 + 21.25\phi_m$ (SNJV, 2007, Figure 10-4). It is also assumed that colloid and Pu-Col diffusion into matrix is negligible (a value of 1E-30 m^2/s is used) because of their large molecular size relative to the smaller matrix pore size.

Dispersion in fractured rocks is an expected transport process in the LCA (SNJV, 2007). As shown in Table M-2, a mean longitudinal dispersivity of 40 m is assumed for a normal distribution with a standard deviation of 10 m.

M.2.4 Sorption Distribution Coefficients

The sorption coefficients of the radionuclides are different for different reactive mineral classes. The distributions of the sorption coefficients in fracture and matrix for the sorbing species are given in Table M-3. The data given in Table M-3 are based on available data that include the documented parameter distributions for the LCA in Yucca Flat in Reimus, Hershey, et al. (2006). The sources from which these statistics are derived are referenced in the table. As Zavarin (2012a) suggested, the fracture and matrix sorption parameters for ^{59}Ni and ^{63}Ni are assumed the same as those for ^{90}Sr.

Table M-2
Diffusion Coefficients and Dispersivity for the LCA at Yucca Flat

Parameter (unit)	Radionuclide	D_0	Reference
Diffusion Coefficients in Free Water, D_0 (m^2/s)	^{14}C	1.20E-09	a
	^{99}Tc	1.48E-09	a
	Np	4.26E-10	b
	^{3}H	2.25E-09	c
	^{36}Cl	2.03E-09	a
	Pu	4.26E-10	b
	^{90}Sr	7.91E-10	d
	^{129}I	2.05E-09	d
	Eu	4.26E-10	b
	^{137}Cs	2.06E-09	e
	U	4.26E-10	e
	Ni	6.79E-10	b
Longitudinal Dispersivity (m)	Mean = 40, Standard Deviation = 10, Normal Distribution		

a = SNJV, 2007
b = Wolfsberg et al., 2002; Wolfsberg and Viswanathan, 2002
c = Li and Gregory, 1974; Lide, 2000
d = Reimus et al., 2001; Reimus et al., 2003
e = Reimus, Hershey, et al., 2006; Reimus, Murrell, et al., 2006; Reimus, Ware, et al., 2006

Table M-3
Statistics of the Sorption Parameters for the LCA at Yucca Flat
(Page 1 of 2)

Parameter (unit)	Radionuclide	Lower	Upper	Mean	Distribution	Reference
Log Fracture Sorption, K_{df} (mL/cm^2)	^{14}C	-2.2234	-1.2300	-1.4890	Log Triangular	SNJV, 2007 (Table 12-3)
	^{90}Sr	-1.5465	-1.0539	-1.4518		
	Cs	-1.3269	1.2738	0.1317		
	Np	-0.6043	-0.2702	-0.4059		
	U	-1.8024	-1.4442	-1.5874		
	Pu	-0.3328	0.4602	0.2240		

Table M-3
Statistics of the Sorption Parameters for the LCA at Yucca Flat
(Page 2 of 2)

Parameter (unit)	Radionuclide	Lower	Upper	Mean	Distribution	Reference
Log Matrix Sorption, K_{dm} (mL/g)	^{14}C	0.0000	1.3010	0.6532	Log Triangular	Zavarin, 2012a
	^{90}Sr	0.6990	1.2041	0.9494		SNJV, 2007 (Table 11-5)
	Cs	-2.6990	-0.1675	-0.4672		Zavarin, 2012a
	Eu	4.0000	5.6021	5.3118		SNJV, 2007 (Table 11-5)
	U	-1.5229	1.4771	1.1765		Rechard and Tierney, 2005 (Figure 22)
	Pu	2.9542	4.3010	4.0191		Rechard and Tierney, 2005 (Figure 22)
	Np	-2	-0.0809	-0.6383		SNJV, 2007 (Table 11-5)

M.2.5 Colloid Load

The processes and mechanisms associated with colloid attachment and detachment to and from fracture walls (filtration) are not fully understood (Wolfsberg et al., 2002; SNJV, 2007). However, efforts have been undertaken to quantify parameters associated with colloid filtration processes. In Reimus et al. (2001) and Reimus, Murrell, et al. (2006), for example, filtration parameters are fitted for multiple different natural colloid types in fractured core experiments in the laboratory.
A statistical analysis of previous investigations is presented in Table M-4.

This study assumes that colloids are aqueous species that do not diffuse out of fractures into matrix material because of their relatively large size. Aggregation, buoyancy, and other issues associated with the actual size and shape of individual colloids are not considered; however, the distribution of colloid sizes is considered with respect to estimates of available reactive surface areas. Only the concentrations of available reactive sites on colloids are considered. This approximation is warranted for this study because of the relatively low aqueous concentrations of plutonium under consideration in the BOURBON source area. The conceptual model of colloid-facilitated plutonium reactive transport in fractured rock is shown in Figure M-2, in which three competing sorption reactions of plutonium and europium are summarized as sorption onto (1) colloids, (2) matrix minerals, and

Table M-4
Statistics of the Parameters for Colloid-Facilitated Transport in the LCA at Yucca Flat

Parameter (unit)	Symbol	Mean	Standard Deviation	Distribution	Reference
Colloid Site Concentration (mol sites/mL)	C_{col}	-10.9	0.709	Lognormal	a, b
Colloid Fracture Sorption Coefficient (mL/cm^2)	K_{df}-Col	33.50	10.45	Normal	b, c
First-Order Rate Constant Pu-Col (1/hr)	k_f-PuCol	0.25	0.11	Normal	a, b
First-Order Rate Constant Plutonium (1/hr)	k_f-Pu	0.24	0.1	Normal	a, b
First-Order Rate Constant Europium (1/hr)	k_f-Eu	0.25	0.11	Normal	a, b
Log Forward Rate Constant Colloid (1/hr)	k_f-Col	7.0	1.0 (width)	Log Triangular	a, b
Log Reverse Rate Constant Colloid (1/hr)	k_r-Col	-4.2182	1.0 (width)	Log Triangular	a, b

a = Wolfsberg et al., 2002; Wolfsberg and Viswanathan, 2002
b = Reimus et al., 2001; Reimus et al., 2003
c = Reimus, Hershey, et al., 2006; Reimus, Murrell, et al., 2006; Reimus, Ware, et al., 2006

(3) fracture-coating minerals. The colloids, Pu-Col, and Eu-Col also attach to or detach from the fracture surfaces because of a combination of mechanical filtration and electrostatic charge.

Colloid Site Concentration. Assuming that the assumptions of Wolfsberg et al. (2002) are valid for this study, the concentration of colloid sites in moles per liter of groundwater in the LCA at Yucca Flat is computed as described below. As explained in Wolfsberg et al. (2002), the colloid site concentration C_{col} (mole sites per milliliter) is defined by

$$C_{col} = 4\pi r^2 n_c x_n / Av \qquad (M\text{-}4)$$

where n_c is the colloid particle concentration (particles per milliliter), r is the particle radius (nanometers per particle), x_n is the sorption sites per area (square nanometer) (2.31 sites per square nanometer was used for the calculation by Wolfsberg et al. [2002]), and Av is Avogadro's number, which equals 6.022E+23 sites per mole sites. The mean particle concentration (n_c) in LCA

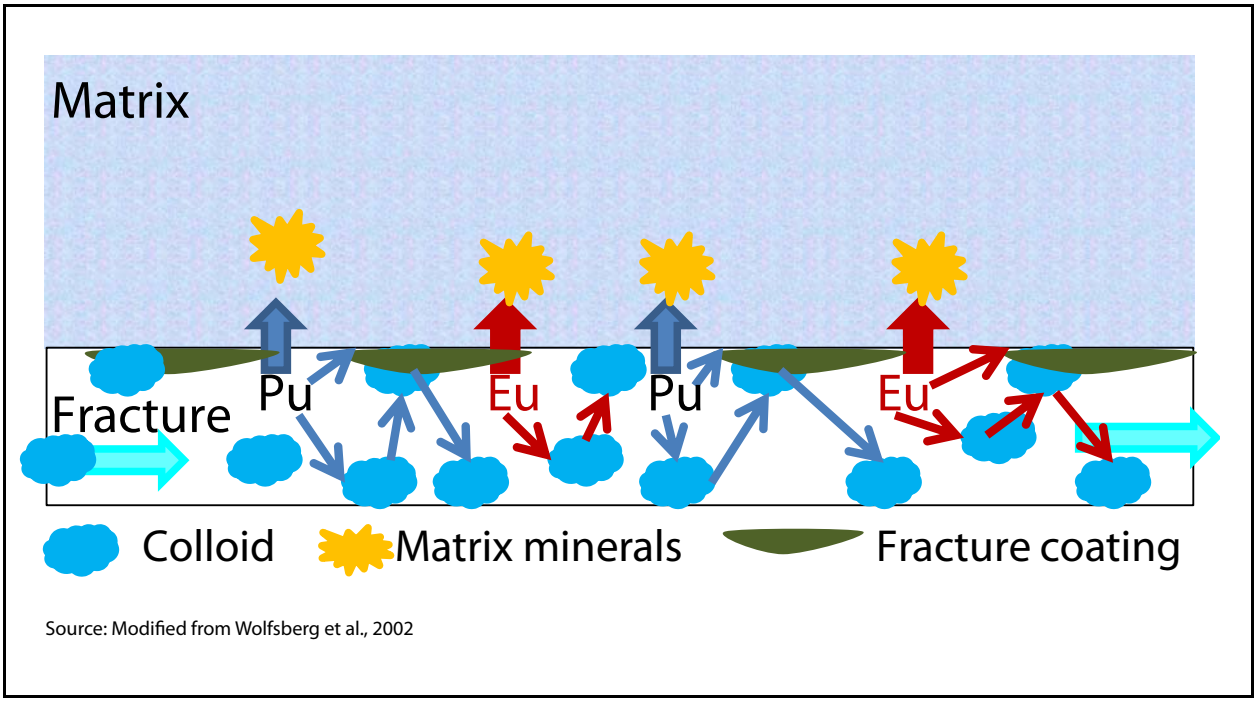

Figure M-2
Conceptual Model of Colloid-Facilitated Plutonium Reactive Transport in Fractured Rock

groundwater is calculated from data in Reimus et al. (2003) to be 7.31E+07 particles per milliliter, and the mean particle radius is 60 nanometers.

The colloid sizes and the number of colloids per milliliter of groundwater in the LCA at Yucca Flat vary from borehole to borehole. By using Equation (M-4) and the colloid measurements (size distributions of colloids sampled) in boreholes from SNJV (2007), we compute the naturally occurring colloid site concentrations in the LCA at Yucca Flat with a mean of −10.9 and a standard deviation of 0.709 on a log scale (which satisfies a lognormal distribution). This distribution takes into account the variety of sizes and respective surface areas in the measured distributions of colloids. Note that only natural colloids are considered here and that there is insufficient supporting information to address test-related colloids.

M.2.6 Rate Constants for Colloid-Facilitated Plutonium Transport

Sensitivity analyses of plutonium reactive transport processes indicate that the sorption of plutonium onto colloids, fracture surface, and matrix is kinetically controlled and is one of the most sensitive

processes for plutonium transport (Wolfsberg et al., 2002). The sorption equations take the following forms:

$$^{2xx}\text{Pu(aq)} \Leftrightarrow {}^{2xx}\text{Pu(s)} \text{ (sorption onto fracture and matrix)} \quad \textit{(M-5)}$$

$$\text{Col(aq)} \Leftrightarrow \text{Col(s)} \text{ (colloid attachment or detachment)} \quad \textit{(M-6)}$$

$$^{2xx}\text{Pu(aq)} + \text{Col(aq)} \Leftrightarrow {}^{2xx}\text{Pu-Col(aq)} \text{ (sorption onto colloids)} \quad \textit{(M-7)}$$

$$^{2xx}\text{Pu-Col(aq)} \Leftrightarrow {}^{2xx}\text{Pu-Col(s)} \text{ (sorption onto fracture surface)} \quad \textit{(M-8)}$$

where 2xx represents mass numbers 238, 239, 240, 241, and 242; (aq) denotes aqueous; (s) denotes solid; and Col stands for colloid. Equations (M-5), (M-6), and (M-8) can be simulated by the first-order kinetics with their sorption distribution coefficients (K_d) and forward rate constants (k_f) (Viswanathan, 1996, 1999). Relevant coefficients include K_{df}-Pu, K_{dm}-Pu, and k_f-Pu for Equation (M-5); K_{df}-Col and k_f-Col for Equation (M-6); and K_{df}-PuCol and k_f-PuCol for Equation (M-8). It is assumed that the sorption coefficient of colloids (K_{df}-Col) is equal to that of Pu-Col (K_{df}-PuCol) and that the forward rate constant of colloid attachment onto fracture (k_f-Col) is equal to that of Pu-Col (k_f-PuCol) because these two reactions are essentially colloid filtration.

Equation (M-7) represents the sorption reaction of plutonium onto colloids. Because the left side consists of two species, this reaction cannot be simulated as a first-order kinetic reaction but as a general kinetic reaction with forward (sorption, k_f-Col) and reverse (desorption, k_r-Col) rate constants (Zyvoloski et al., 1997). For different types of colloids, such as montmorillonite, zeolite, and silica colloids, the forward and reverse rate constants are quite different. Because the sorption of plutonium onto colloids in the LCA is very strong, the forward rate constant is relatively much larger than the reverse rate constant (Wolfsberg and Viswanathan, 2002). Based on the previous investigations by Wolfsberg and Viswanathan (2002), Reimus et al. (2001), Reimus, Hershey, et al. (2006), Reimus, Murrell, et al. (2006), and Reimus, Ware, et al. (2006), we conduct a statistical analysis of the colloid sorption coefficients and the rate constants in Equations (M-5) to (M-8). The parameters for simulating colloid-facilitated plutonium transport in the LCA are listed in Table M-4. The parameters used here were developed from laboratory experiments conducted under oxygenated conditions typical of the LCA in Yucca Flat. However, nuclear testing could locally change the redox conditions of the groundwater near the BOURBON detonation, making the applicability of these parameters less certain than assumed in the uncertainty analysis.

Recent experimental studies of the colloid-facilitated transport of Pu through slotted LCA cores have revealed the complex transport behavior of Pu, U, and Sm in groundwater in the presence of colloids and the importance of the oxidation state of individual Pu isotopes on their mobility (Zavarin et al., 2013). Reduced Pu (IV) has a greater tendency to sorb and attach to colloids than oxidized Pu (V and VI), resulting in differential breakthrough behavior for different Pu isotope species. The oxidation state of Pu in groundwater immediately following a nuclear test is not known, but overall the groundwater in the LCA of Yucca Flat is oxidizing (2.5 to 6.9 mg/L DO at wells UE-7ns and ER-6-1-2). However, as stated in Zavarin et al. (2013), "in the presence of mineral surfaces, Pu will tend to reduce to Pu(IV) over time". Thus colloid-facilitated Pu transport, as implemented in this Appendix, is consistent with the conclusions in Zavarin et al. (2013) and likely the dominant Pu transport mechanism. The sorption coefficients for the matrix, colloid and fracture minerals implemented in this Appendix span a wide range in values which are inclusive of the values reported in Zavarin et al. (2013). The experiments of Zavarin et al. (2013) also showed that Sm (and by analogy, other trivalent radionuclides such as Eu and Am) also has a strong tendency to attach to colloids. These results support the decision to also evaluate the colloid-facilitated transport of Eu in this Appendix. (Note that ^{151}Sm, ^{241}Am and ^{243}Am were not simulated in this appendix because previous screening analyses [Zavarin, 2012a] indicated their initial concentrations were orders of magnitude below their MCL, whereas initial concentrations of Eu species were near or above their MCL). Significantly, the high colloid loads used in the experiments (hundreds to tens of thousand times higher than natural colloid loads in the LCA) and the short timescales (10 days) and travel distances (4 inches) of the experiments compared with the regulatory compliance period (1,000 years) and potential contaminant transport distances (10's of kilometers) make the direct transfer of the estimated parameters from the experiments to regulatory calculations problematic. However, the models in this appendix are consistent with conclusions in Zavarin et al. (2013) regarding the essential processes surrounding colloid-faciliated radionuclide transport in the LCA.

For colloid-facilitated europium transport, we use equations similar to Equations (M-5) through (M-8):

$$^{15x}\text{Eu(aq)} \Leftrightarrow {}^{15x}\text{Eu(s)} \text{ (sorption onto fracture and matrix)} \qquad \textit{(M-9)}$$

$$\text{Col(aq)} \Leftrightarrow \text{Col(s)} \text{ (colloid attachment or detachment)} \qquad \textit{(M-10)}$$

$$^{15x}\text{Eu(aq)} + \text{Col(aq)} \Leftrightarrow {}^{15x}\text{Eu-Col(aq)} \text{ (sorption onto colloids)} \qquad \textit{(M-11)}$$

$$^{15x}\text{Eu-Col(aq)} \Leftrightarrow {}^{15x}\text{Eu-Col(s)} \text{ (sorption onto fracture surfaces)} \qquad \textit{(M-12)}$$

where 15x represents mass numbers 152 and 154. However, experiments for radionuclide sorption and desorption rates onto colloids, such as those conducted by Reimus, Hershey, et al. (2006) for plutonium, do not exist for europium. Therefore, the plutonium forward and reverse rate constants are applied for europium sorption onto colloids in Equation (M-11). The attachment and detachment rate constants of ^{15x}Eu-Col in Equation (M-12) are assumed to be equal to those of ^{2xx}Pu-Col.

M.2.7 Initial Concentrations of Radionuclides in the BOURBON Source Area

Figure M-3 illustrates the method for calculating the initial concentrations of radionuclides (C_0 in mol/L) in the BOURBON exchange volume. The random parameters related to initial concentrations and their distributions are listed in Table M-5. As was done in previous Yucca Flat investigations (e.g., Carle et al., 2008), the masses of individual radionuclides for the BOURBON detonation are estimated from the radionuclide abundances associated with the "saturated" portion of the Yucca Flat inventory (below or within 100 m above the water table) (Bowen et al., 2001) and the maximum announced yield of the BOURBON detonation (200 kt) (DOE/NV, 2000). Inventory uncertainty presented in Bowen et al. (2001) for different classes of radionuclides (^{3}H, activation products, fission products, unspent fuel/tracers) is assumed to be described with a log-triangular distribution by following the procedure of Tompson et al. (2011). It is assumed that the radionuclide sources are uniformly distributed in the fractures of the exchange volume within a radius of $f_{ev}r_c$ (in meters) and a fracture porosity of ϕ_f, where f_{ev} is the exchange volume radius factor, and r_c is the cavity radius of the BOURBON detonation (70 m) based on the maximum of the reported yield and the cavity radius relationship presented in Pawloski (1999). The initial concentration of each radionuclide also is assumed to be uniformly distributed within the exchange volume. By sampling the radionuclide uncertainty factor (f_{RST}) and the exchange volume factor (f_{ev}), along with other flow and transport parameters such as ϕ_f, the initial concentration of each radionuclide for each realization can be calculated with the equation shown in Figure M-3. It should be noted that no sorption and decay processes are applied to initial concentration calculations because these processes are assumed to occur only after the initial inventory is emplaced at time zero. Those initial concentrations are then assigned in the GDPM to the primary fracture nodes within the exchange volume (in a distance of $2f_{ev}r_c$ in meters) as shown in Figure M-3. Because the size of the sampled exchange volume varies from realization to realization, the node numbers in the fracture to which an initial concentration is assigned are also updated for each realization. Therefore, the first $2f_{ev}r_c$ (in meters) of the model domain are assigned an initial concentration of C_0 at time zero when diffusion, sorption, and

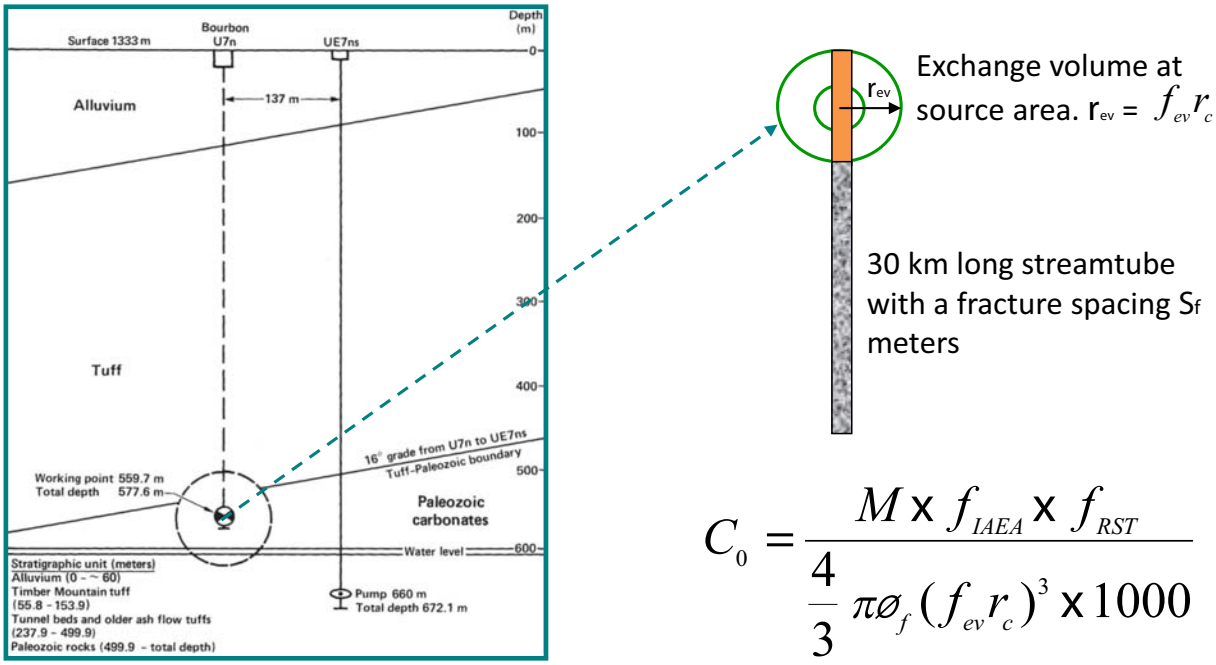

$$C_0 = \frac{M \times f_{IAEA} \times f_{RST}}{\frac{4}{3}\pi \varnothing_f (f_{ev} r_c)^3 \times 1000}$$

The initial concentrations of radionuclides (C_0 in mol/L) in the BOURBON exchange volume are calculated with the equation shown above, where M is the total mass of a radionuclide (moles), f_{IAEA} is the radionuclide partitioning data or non-melt-glass factor, and f_{RST} denotes the source uncertainty factors for the following four types of radionuclides: f_{RSTH3} for ^{3}H; f_{RST1} for activation products ^{14}C, ^{36}Cl, ^{59}Ni, ^{63}Ni, ^{152}Eu, and ^{154}Eu; f_{RST2} for fission products ^{99}Tc, ^{129}I, ^{90}Sr, and ^{137}Cs; and f_{RST3} for residual fuel/tracers ^{237}Np, U_{all}, and $^{238–242}Pu$.

Source: Modified from SNJV, 2007

Figure M-3
Calculation of Initial Concentrations of Radionuclides in the BOURBON Source Area

advective transport in the fractures begin to take place. For radionuclides that are subject to colloid-facilitated transport (plutonium and europium), competition between sorption onto colloids, facture surfaces, and rock matrix dictates the fraction of the initial radionuclide mass that eventually becomes attached to colloids. The attachment and detachment of the plutonium- or europium-bearing colloids is determined by the fracture sorption distribution coefficient of Pu-Col or Eu-Col and their forward kinetic rate constants.

Table M-5
Initial Concentration Uncertainty Parameters for the 18 Radionuclides

Radionuclide	M[a] (mol)	f_{IAEA} [b]	f_{RST} [c] (log)		f_{ev} [c] (log)		Distribution
			Minimum	Maximum	Minimum	Maximum	
^{3}H	41.700	1	-0.4772	0.4771	0.0	0.4771	Log Triangular
^{14}C	0.1160	1	-1.0	1.0	0.0	0.4771	Log Triangular
^{36}Cl	1.6700	0.5	-1.0	1.0	0.0	0.4771	Log Triangular
^{99}Tc	0.9600	0.2	-0.1549	0.1139	0.0	0.4771	Log Triangular
^{129}I	0.2050	0.5	-0.1549	0.1139	0.0	0.4771	Log Triangular
^{90}Sr	0.9607	0.6	-0.1549	0.1139	0.0	0.4771	Log Triangular
^{137}Cs	1.2152	0.75	-0.1549	0.1139	0.0	0.4771	Log Triangular
^{152}Eu	0.0859	0.05	-1.0	1.0	0.0	0.4771	Log Triangular
^{154}Eu	0.0899	0.05	-1.0	1.0	0.0	0.4771	Log Triangular
^{237}Np	0.5510	0.05	-0.0969	0.0792	0.0	0.4771	Log Triangular
U_{all}	1,744.55	0.1	-0.0969	0.0792	0.0	0.4771	Log Triangular
^{238}Pu	0.0288	0.02	-0.0969	0.0792	0.0	0.4771	Log Triangular
^{239}Pu	15.900	0.02	-0.0969	0.0792	0.0	0.4771	Log Triangular
^{240}Pu	1.1100	0.02	-0.0969	0.0792	0.0	0.4771	Log Triangular
^{241}Pu	0.0358	0.02	-0.0969	0.0792	0.0	0.4771	Log Triangular
^{242}Pu	0.0417	0.02	-0.0969	0.0792	0.0	0.4771	Log Triangular
^{59}Ni	0.07793	0.05	-1.0	1.0	0.0	0.4771	Log Triangular
^{63}Ni	0.01502	0.05	-1.0	1.0	0.0	0.4771	Log Triangular

[a] Based on yield-weighted inventory as apportioned by the "saturated" portion of the Yucca Flat inventory (Bowen et. al, 2001)

[b] As defined in Figure M-3, f_{IAEA} represents the non-melt-glass fraction of the radionuclide inventory contained in water or gas or sorbed onto rubble. The uncertainty in the factor f_{IAEA} is considered small relative to f_{RST}, and f_{IAEA} is assumed to be a known parameter as defined by IAEA (1998).

[c] As defined in Figure M-3, f_{RST} denotes the source uncertainty factors for four types of radionuclides. Both f_{RST} and f_{ev} are assumed to be log-triangular distributions from Bowen et al. (2001) and Tompson et al. (2011).

M.3.0 RADIONUCLIDE REACTIVE TRANSPORT ALONG A STREAMTUBE IN THE LCA

M.3.1 Generalized Dual-Porosity Model

The GDPM (Zyvoloski et al., 2008) is used for simulating the reactive radionuclide transport from the BOURBON source area. The reactive transport processes in the fractured LCA include radionuclide decay, equilibrium- or kinetically controlled sorption, radionuclide reactions with colloids, and colloid filtration.

The GDPM provides dual-porosity formulations for both fracture/matrix systems and porous media with heterogeneous materials of contrasting material properties (Zyvoloski et al., 2008). The term "primary porosity" (or fracture porosity) is used to represent the medium in which large-scale global flow and transport occurs, whereas "secondary porosity" (or matrix porosity) is connected locally only to the primary fracture nodes to represent the matrix storage volume, which is typically of lower permeability. The fundamental principle behind the GDPM approach is that the secondary nodes are prescribed normal to the primary nodes with user-specified high resolution near the primary nodes and gradually deceasing resolution away from the primary nodes. This enables accurate simulation of diffusive solute fronts moving out of the fracture and into the matrix. The secondary nodes of each primary node are not directly connected to those of other primary nodes, which means that only diffusive transport and sorption normal to the fracture are simulated. This leads to a highly efficient numerical scheme for simulating flow and transport in the fracture, diffusive transport into the matrix, and the full suite of reactive processes available in FEHM (Zyvoloski et al., 2008) in both the fracture and the matrix.

M.3.2 One-Dimensional Streamtube

A one-dimensional streamtube is established for radionuclide reactive transport in the LCA in Yucca Flat. The streamtube extends southward 30 km from the BOURBON detonation (Figure M-1). As mentioned earlier, the model has a fixed hydraulic gradient of 3.33E-04, which is approximately the average gradient between the northern and southern ends of Yucca Flat. The LCA has a mean conductivity of 0.16 m/day with a standard deviation of 1.34 m/day, which satisfy a lognormal

distribution (SNJV, 2006, Table 6-1). The product of the sampled conductivity and the constant hydraulic gradient determines the inflow rate through the streamtube. The inflow rate divided by the fracture porosity is the advective velocity in the absence of matrix diffusion or sorption. The streamtube model represents a spatially averaged model in which heterogeneity is ignored and groundwater flow is assumed to be at steady state.

The finite-element grid for the GDPM includes 1,001 nodes for the primary porosity in the fracture zone and 10,010 matrix nodes for the secondary porosity in the matrix zone. The matrix node resolution increases from 0.0001 m near the fracture nodes to much larger at the edge of the model (dependent on the sampled random parameter of spacing) as shown in Figure M-1. Because the fracture aperture and spacing vary in each realization, the GDPM grids are also updated with each realization, and the model is rerun to establish a new steady-state flow field before the transport simulation for that realization may begin.

M.3.3 Radionuclide Reaction Processes

To simulate radionuclide transport in the LCA at Yucca Flat without compromising reaction complexity, a GDPM was developed with the multicomponent reactive transport simulator FEHM. The processes simulated with the GDPM included radionuclide decay, equilibrium- or kinetically controlled sorption, plutonium and europium sorption onto colloids, and colloid filtration (or attachment and detachment of colloids) on the fracture walls. The radionuclides that may have potential impact on the contaminant boundary in the LCA at Yucca Flat include ^{238}Pu, ^{237}Np, U, ^{3}H, ^{14}C, ^{36}Cl, ^{63}Ni, ^{99}Tc, ^{129}I, ^{90}Sr, and ^{137}Cs (Zavarin, 2012b). Additionally, it was assumed that ^{152}Eu, ^{154}Eu, ^{59}Ni, and ^{242}Pu were of potential significance to the contaminant boundary. The reactions included in the transport simulations are summarized in Table M-6. Radioactive decay for species with very large half-lives, such as ^{59}Ni (76,000 years), ^{237}Np (2.14 million years), ^{239}Pu (24,100 years), and ^{240}Pu (6,560 years), is ignored.

Table M-6
Radionuclide Reactions in the LCA Fracture and Matrix

I: Radionuclide Sorption to Immobile Minerals	
^{2xx}Pu(aq) <=> ^{2xx} Pu(s)	(in fracture and matrix, 2xx = 238, 239, 240, 241, 242)
^{237}Np(aq) <=> ^{237}Np(s)	(in fracture)
U(aq) <=> U(s)	(in fracture and matrix)
^{14}C(aq) <=> ^{14}C(s)	(in fracture and matrix)
^{59}Ni(aq) <=> ^{59}Ni(s)	(in fracture and matrix)
^{63}Ni(aq) <=> ^{63}Ni(s)	(in fracture and matrix)
^{90}Sr(aq) <=> ^{90}Sr(s)	(in fracture and matrix)
^{137}Cs(aq) <=> ^{137}Cs(s)	(in fracture and matrix)
^{15x}Eu(aq) <=> ^{15x}Eu(s)	(in fracture and matrix, 15x = 152, 154)
II: Radionuclide Sorption onto Colloids in Fractures	
Pu(aq) + Col(aq) <=> Pu-Col(aq)	
Eu(aq) + Col(aq) <=> Eu-Col(aq)	
III: Colloid Filtration in Fractures	
Pu-Col(aq) <=> Pu-Col(s)	
Eu-Col(aq) <=> Eu-Col(s)	
Col(aq) <=> Col(s)	
IV: Radioactive Decay in Fractures and Matrix	
^{3}H(aq) => ^{3}He(aq)	($T_{1/2}$ = 12.32 years)
^{14}C(aq) => ^{14}N(aq)	($T_{1/2}$ = 5,715 years)
^{63}Ni(aq) => ^{62}Ni(aq)	($T_{1/2}$ = 100 years)
^{63}Ni(s) => ^{62}Ni(s)	($T_{1/2}$ = 100 years)
^{238}Pu(aq) => ^{234}U(aq)	($T_{1/2}$ = 87.7 years)
^{238}Pu-Col(aq) => ^{234}U(aq)	($T_{1/2}$ = 87.7 years)
^{238}Pu(s) => ^{234}U(s)	($T_{1/2}$ = 87.7 years)
^{238}Pu-Col(s) => ^{234}U(s)	($T_{1/2}$ = 87.7 years)
^{241}Pu(aq) => ^{241}Am(aq)	($T_{1/2}$ = 14.4 years)
^{241}Pu-Col(aq) => ^{241}Am-Col(aq)	($T_{1/2}$ = 14.4 years)
^{241}Pu(s) => ^{241}Am(s)	($T_{1/2}$ = 14.4 years)
^{241}Pu-Col(s) => ^{241}Am-Col(s)	($T_{1/2}$ = 14.4 years)
^{90}Sr(aq) => ^{90}Y(aq)	($T_{1/2}$ = 28.78 years)
^{152}Eu(aq) => ^{151}Eu(aq)	($T_{1/2}$ = 13.54 years)
^{137}Cs(aq) => ^{137}Ba(aq)	($T_{1/2}$ = 30.1 years)
^{154}Eu(aq) => ^{153}Eu(aq)	($T_{1/2}$ = 8.59 years)
^{152}Eu-Col(aq) => ^{151}Eu-Col(aq)	($T_{1/2}$ = 13.54 years)
^{154}Eu-Col(aq) => ^{153}Eu-Col(aq)	($T_{1/2}$ = 8.59 years)
^{152}Eu(s) => ^{151}Eu(s)	($T_{1/2}$ = 13.54 years)
^{154}Eu(s) => ^{153}Eu(s)	($T_{1/2}$ = 8.59 years)
^{152}Eu-Col(s) => ^{151}Eu-Col(s)	($T_{1/2}$ = 13.54 years)
^{154}Eu-Col(s) => ^{153}Eu-Col(s)	($T_{1/2}$ = 8.59 years)

$T_{1/2}$ = Half-life

M.4.0 PARAMETER SAMPLING AND MONTE CARLO SIMULATIONS

M.4.1 Framework of Monte Carlo Simulation

The GDPM described in Section M.3.0 is used to generate Monte Carlo realizations of reactive radionuclide transport from the BOURBON source area. The framework for conducting the Monte Carlo simulations is described as follows:

1. Establish a 30-km-long streamtube model originating from the BOURBON source area and construct a highly discretized fracture grid along the streamtube to simulate flow and reactive transport in fractured media.

2. Define the parameter uncertainties and their distributions (Tables M-1 to M-5).

3. Use the Latin hypercube sampling method within the software PSUADE (Tong, 2011) to create realizations for Monte Carlo simulations.

4. Apply appropriate relationships to calculate (1) fracture aperture based on the sampled fracture porosity and spacing of each realization (Equation [M-1]); (2) matrix diffusion coefficients based on the sampled matrix porosity; (3) inflow rate based on the sampled hydraulic conductivity, the cross-section area, and the hydraulic gradient (Equation [M-2]); and (4) initial concentrations of the selected radionuclides based on the sampled source uncertainty factor (f_{RST}), the exchange volume factor (f_{ev}), and the fracture porosity (ϕ_f) (Figure M-3).

5. Develop the matrix grids based on the sampled fracture aperture, porosity, and spacing (the coordinate of the first matrix node is equal to the sampled fracture aperture, and that of the last matrix node is equal to the sampled fracture half spacing), and connect the matrix grids with the primary fracture nodes to form the numerical grids of the GDPM for each realization.

6. Run the GDPM for water flow simulation to reach a steady state for each realization, and save the steady-state flow field as the restart file for reactive transport modeling.

7. Identify the fracture nodes in the source area within the exchange volume based on the radius of the exchange volume for the realization, and assign the initial concentration to each node for each of the 18 radionuclides.

8. Run reactive transport models with the updated flow field and flow and transport parameters.

9. Calculate the contaminant lengths at different times and percentiles (5th, 50th, and 95th) for each radionuclide and concentration profiles at 1,000 years.

10. Calculate the ratio of simulated mean plutonium concentrations (0.42 to 5 km from the source) to the mean initial concentration of the plutonium source (this ratio is called the *plutonium source reduction factor*), and develop a distribution of plutonium source reduction factors based on the Monte Carlo results at 1,000 years.

M.4.2 Parameters Sampled with Latin Hypercube Sampling

Based on the parameter uncertainty information provided in Tables M-1 to M-5, 58 input parameters were sampled with the Latin hypercube sampling method within the software PSUADE (Tong, 2011) to generate 800 realizations. The sampled results are shown in Figures M-4 to M-10c. Then, 800 Monte Carlo flow and transport simulations are run to calculate the contaminant lengths and the concentration profiles at 1,000 years for each of the 18 radionuclide species. Colloid-facilitated europium transport is treated similarly to colloid-facilitated plutonium transport in each simulation, except that the initial europium concentrations are different and that europium isotopes have shorter half-lives and stronger sorption.

A comparison of the sampled input parameter distributions shown in Figures M-4 to M-10c with the ranges of the parameters given in Tables M-1 to M-5 indicates that the sampled range of the parameters is consistent with the specified uncertainty range, except for hydraulic conductivity (Figure M-4). For saturated hydraulic conductivity, the specified mean and standard deviation resulted in hydraulic conductivity estimates of 3E-03 and 692 m/day at a 95 percent confidence level, whereas the lower and upper bounds used in the simulations were truncated at 0.1 and 100 m/day.

The initial concentration distributions shown in Figure M-10a for the individual radionuclides are almost all well above their respective maximum contaminant levels (MCLs), because the initial radionuclide mass was dissolved into the small porosity of the fracture continuum, and sorption or matrix diffusion did not decrease the concentration until after the initial radionuclide concentration was in place. Only the ^{59}Ni and ^{242}Pu distributions had a portion of their initial concentrations below their MCLs.

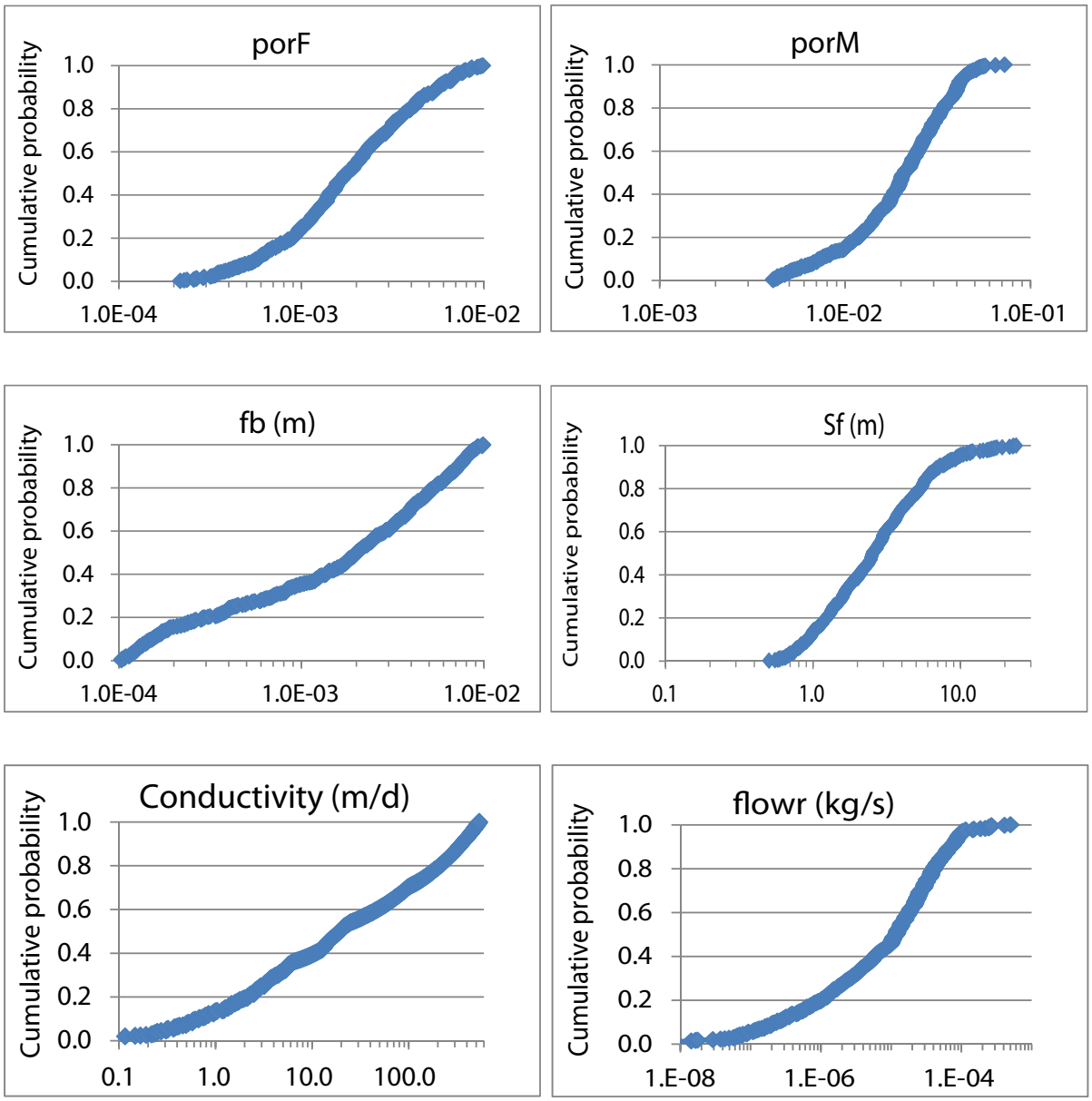

Note: The sampled hydraulic conductivity range is truncated at 0.1 and 100 m/day.

Figure M-4
Sampled Flow and Transport Parameters: Fracture Porosity (porF), Matrix Porosity (porM), Fracture Aperture (fb, m), Fracture Spacing (S_f, m), Hydraulic Conductivity (Conductivity, m/day), and Inflow Rate (flowr, kg/s)

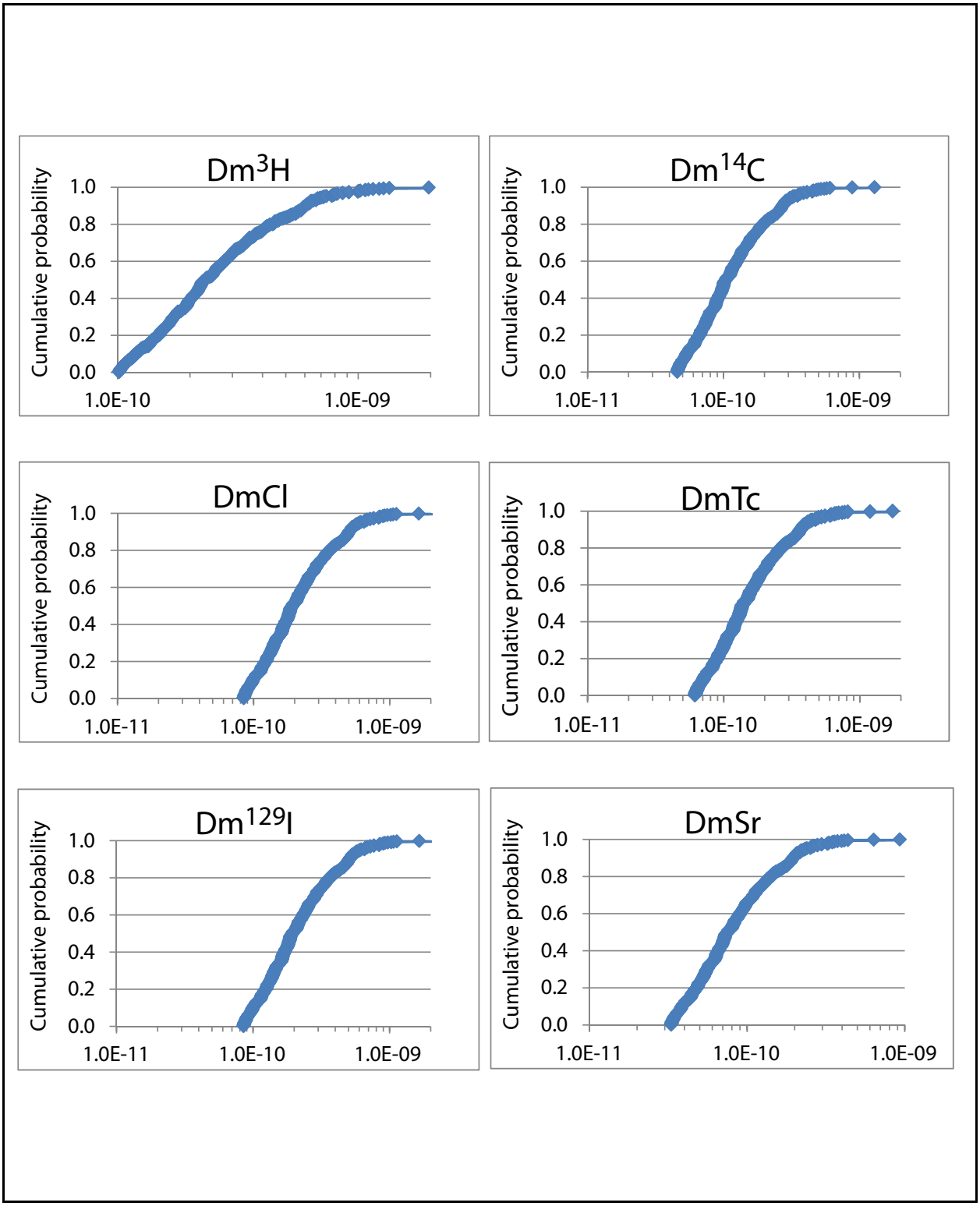

Figure M-5a
Sampled Matrix Diffusion Coefficients (D_m, m^2/s) for Different Radionuclides

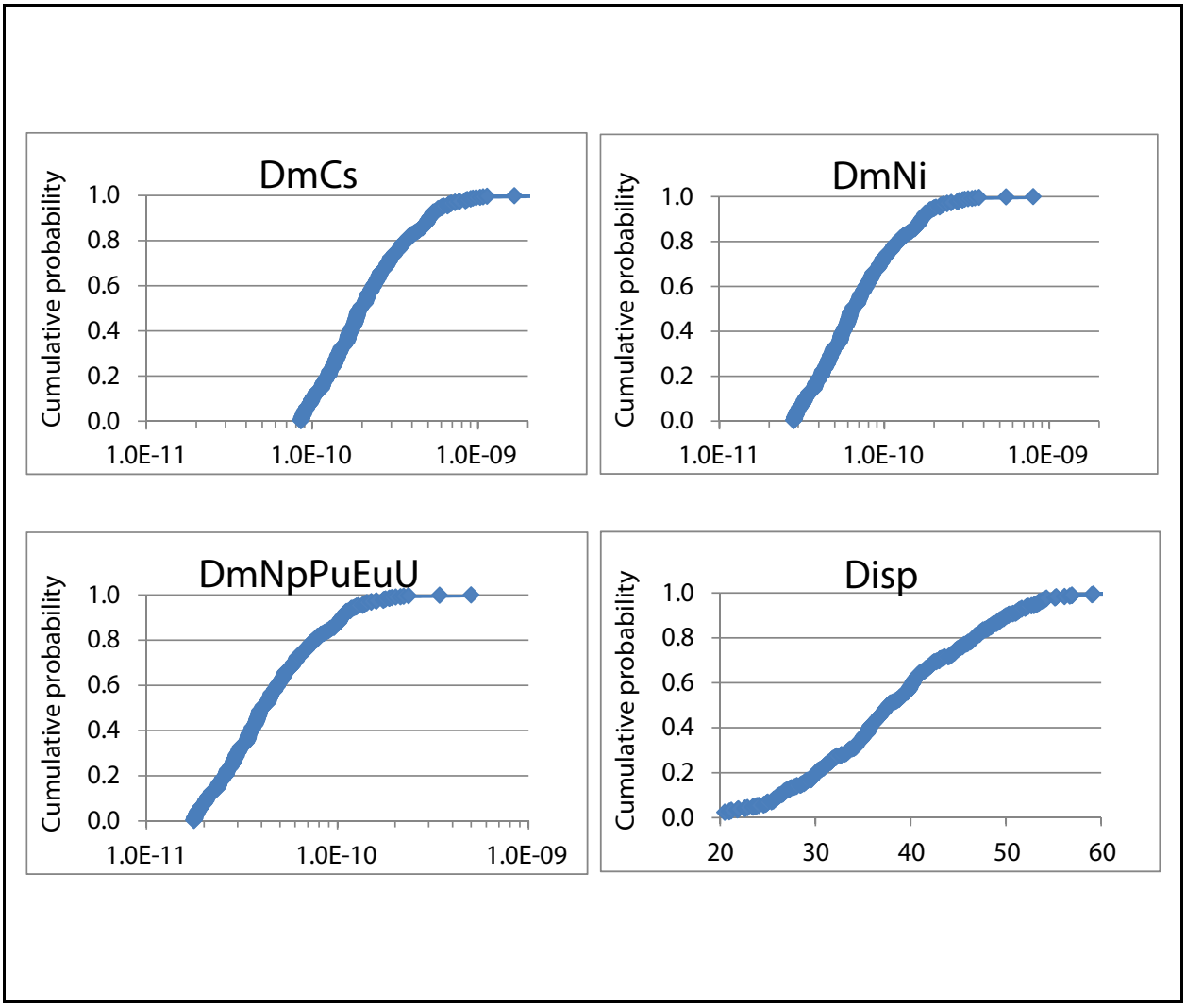

Figure M-5b
Sampled Matrix Diffusion Coefficients (D_m, m^2/s) for Different Radionuclides and Longitudinal Dispersivity (Disp, m)

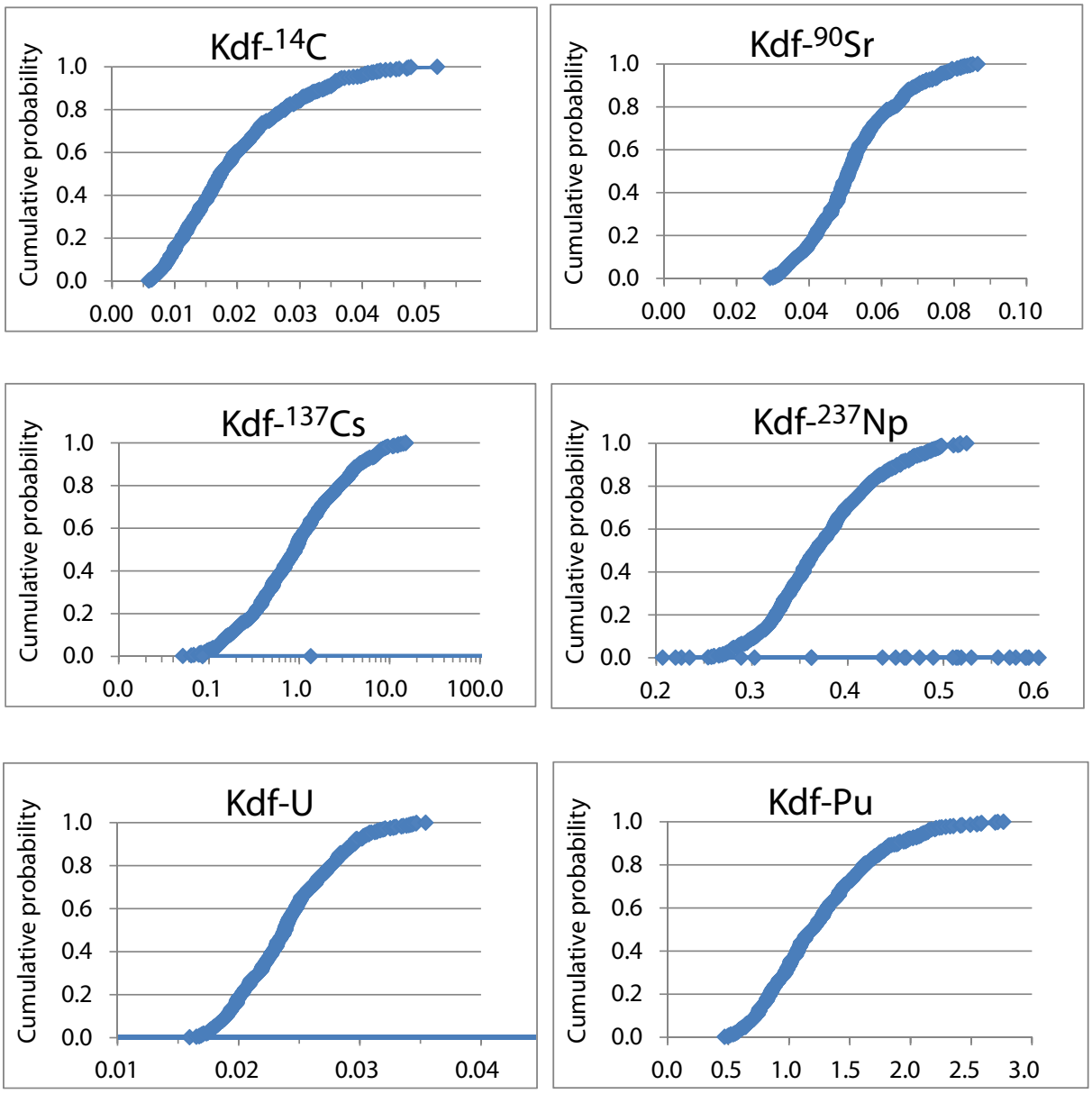

Note: The fracture sorption coefficient of Ni is assumed the same as that of ^{90}Sr (Kdf-Ni = Kdf-^{90}Sr).

Figure M-6
Sampled Fracture Sorption Coefficients
(K_{df}, mL/cm^2) for ^{14}C, ^{90}Sr, ^{137}Cs, ^{237}Np, U, and Pu

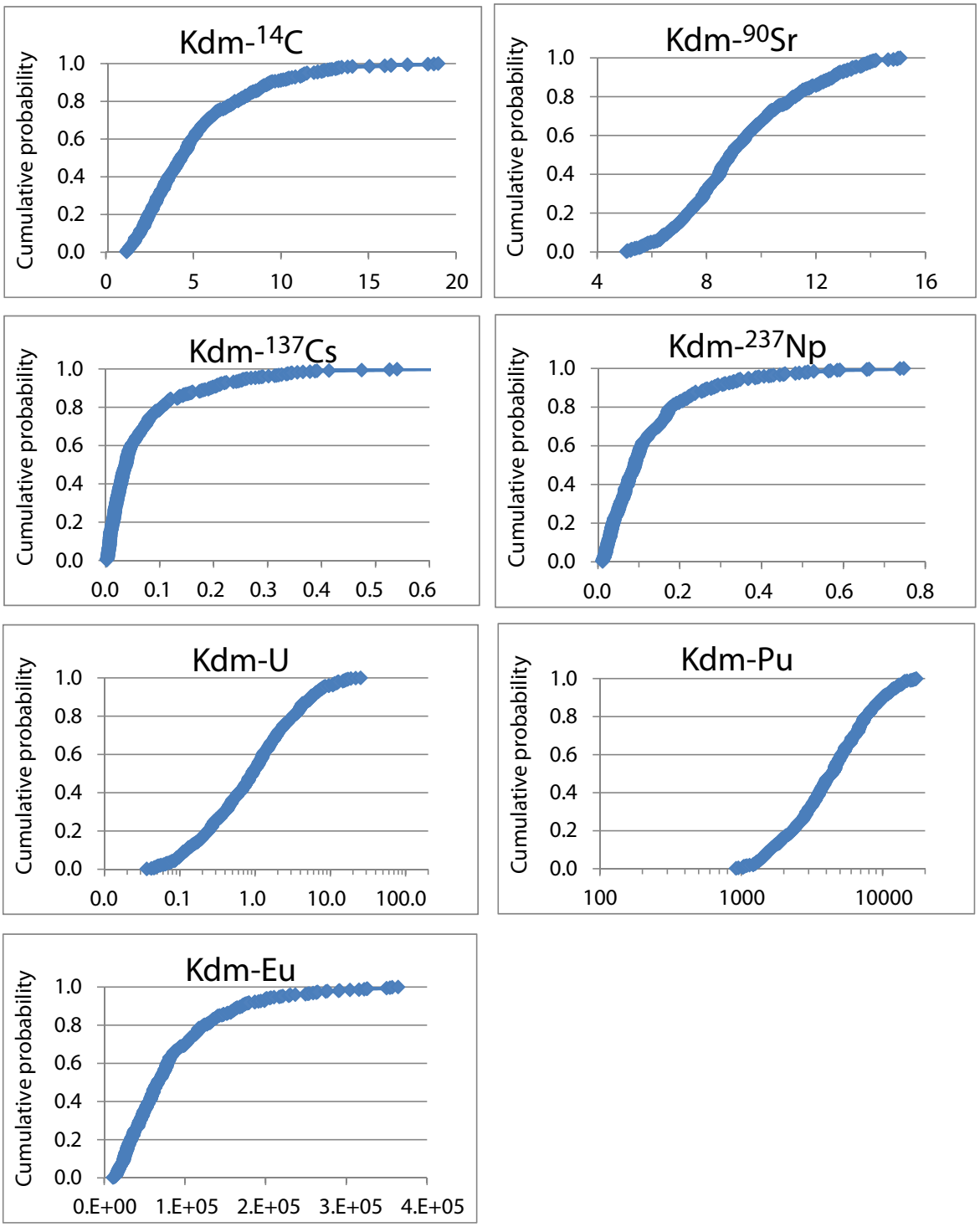

Note: The matrix sorption coefficient of Ni is assumed the same as that of ^{90}Sr (Kdm-Ni = Kdm-^{90}Sr).

Figure M-7
Sampled Matrix Sorption Coefficients (K_{dm}, mL/g) for ^{14}C, ^{90}Sr, ^{137}Cs, ^{237}Np, U, Pu, and Eu

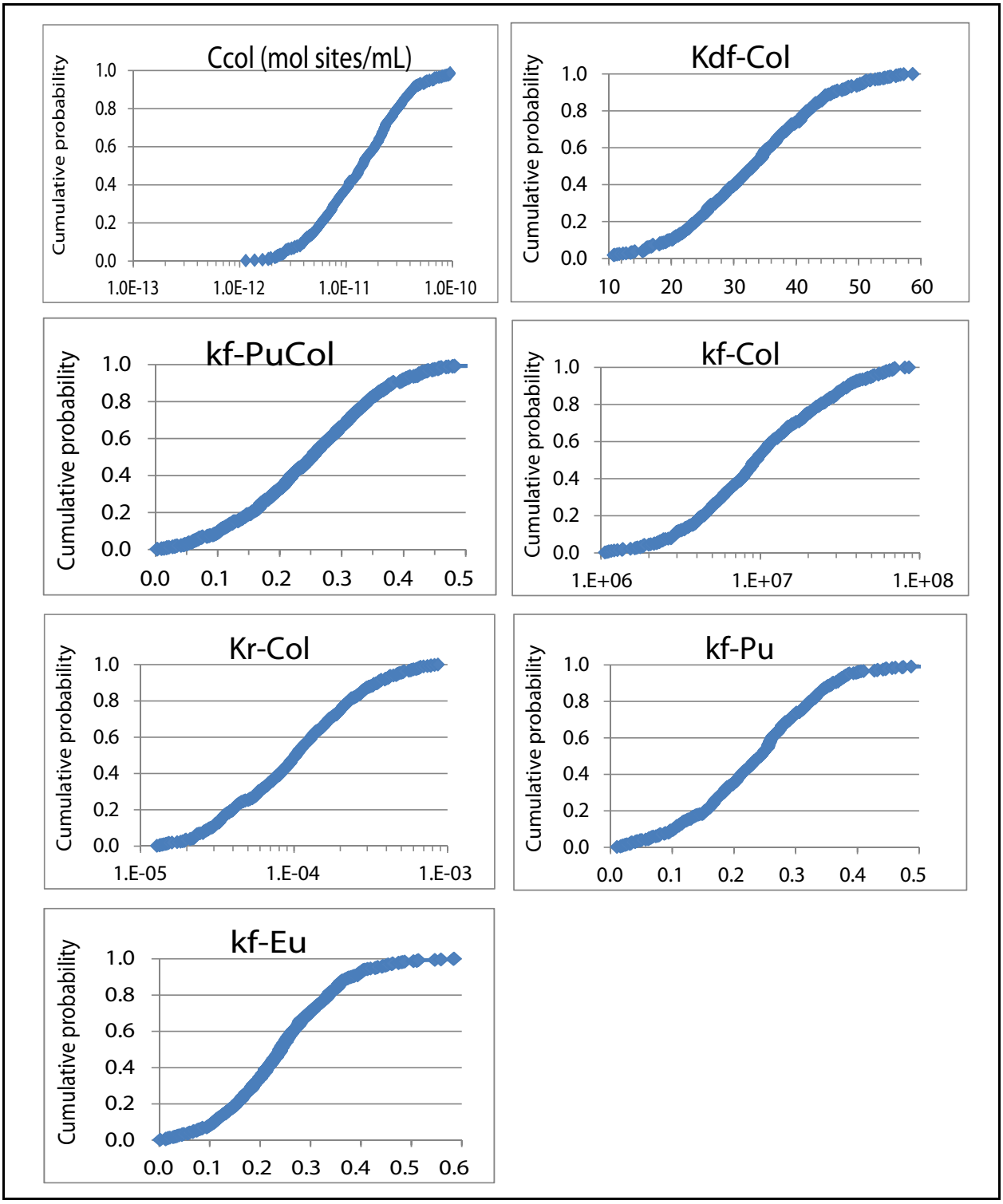

Figure M-8
Sampled Colloid Load Concentration (C_{col}, mol sites/mL), Colloid Sorption Coefficient in Fracture (K_{df}-Col, mL/cm²), Forward Rate Constant in Fracture for Pu-Col (k_f-PuCol, 1/hr), Forward and Reverse Rate Constants of Plutonium Sorption onto Colloids (k_f-Col and k_r-Col, 1/hr), and Forward Rate Constants for Plutonium and Europium Sorption onto Immobile Minerals in Matrix (k_f-Pu and k_f-Eu, 1/hr)

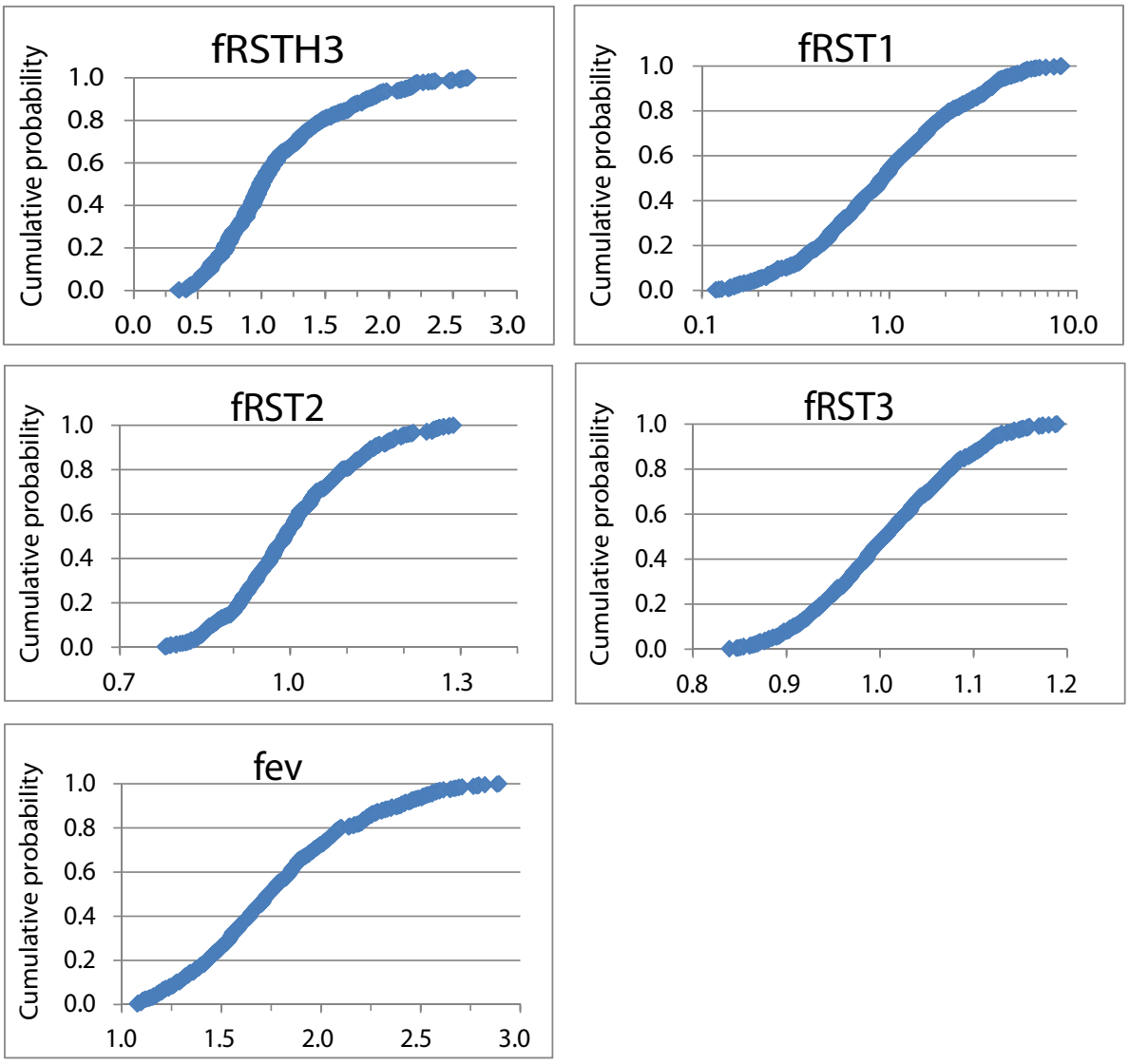

Figure M-9
Sampled Inventory Uncertainty Factors (f_{RSTH3} for ^{3}H; f_{RST1} for Activation Products ^{14}C, ^{36}Cl, ^{59}Ni, ^{63}Ni, ^{152}Eu, and ^{154}Eu; f_{RST2} for Fission Products ^{99}Tc, ^{129}I, ^{90}Sr, and ^{137}Cs; and f_{RST3} for Residual Fuel/Tracers ^{237}Np, U_{all}, and $^{238–242}Pu$) and the Exchange Volume Radius Factor (f_{ev}) (Tompson et al., 2011)

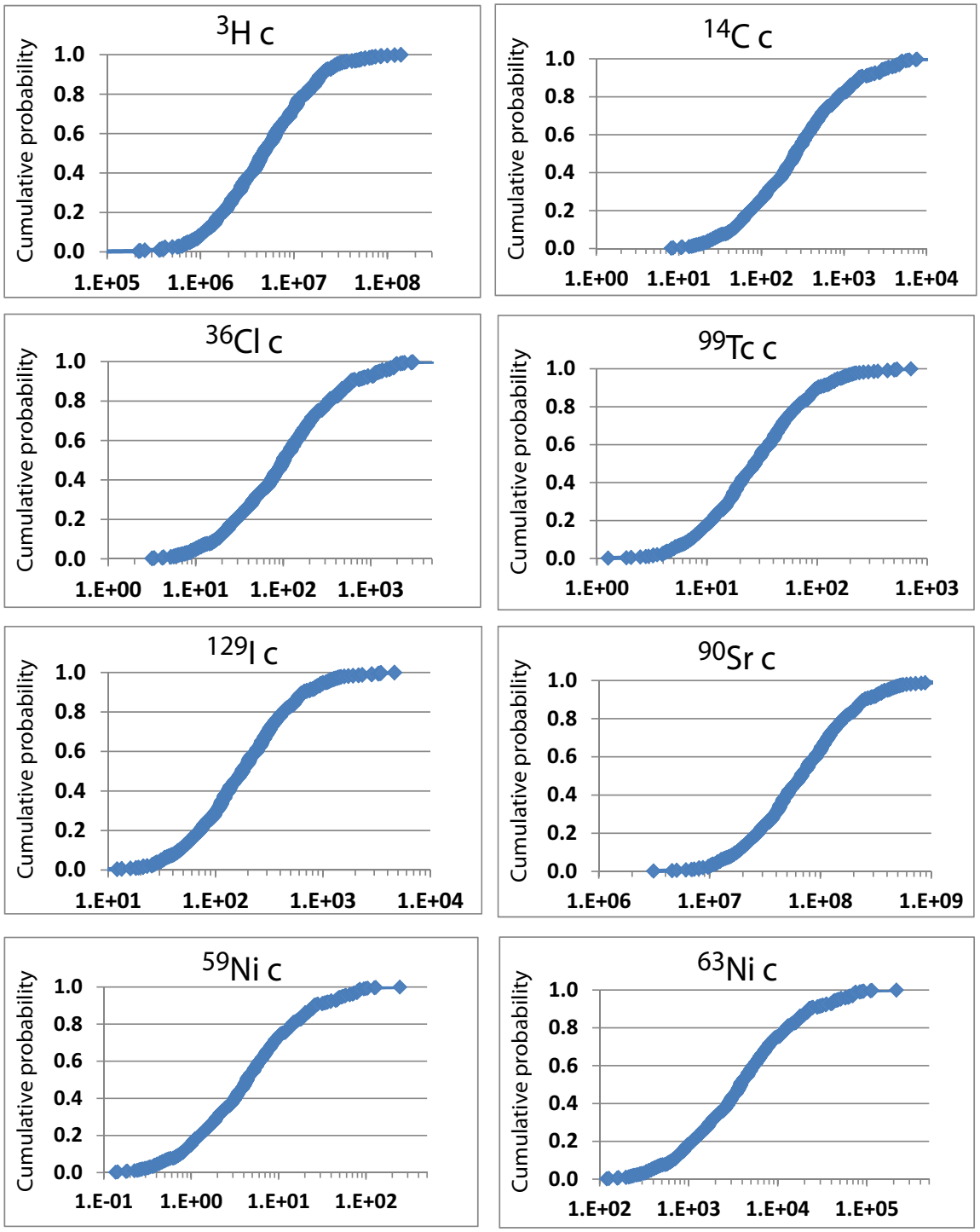

Note: Concentrations are expressed in multiples of the MCL for each individual radionuclide.

Figure M-10a
Sampled Initial Concentrations (in multiples of MCL) for ^{3}H, ^{14}C, ^{36}Cl, ^{99}Tc, ^{129}I, ^{90}Sr, ^{59}Ni, and ^{63}Ni in the Fractures of the Exchange Volume

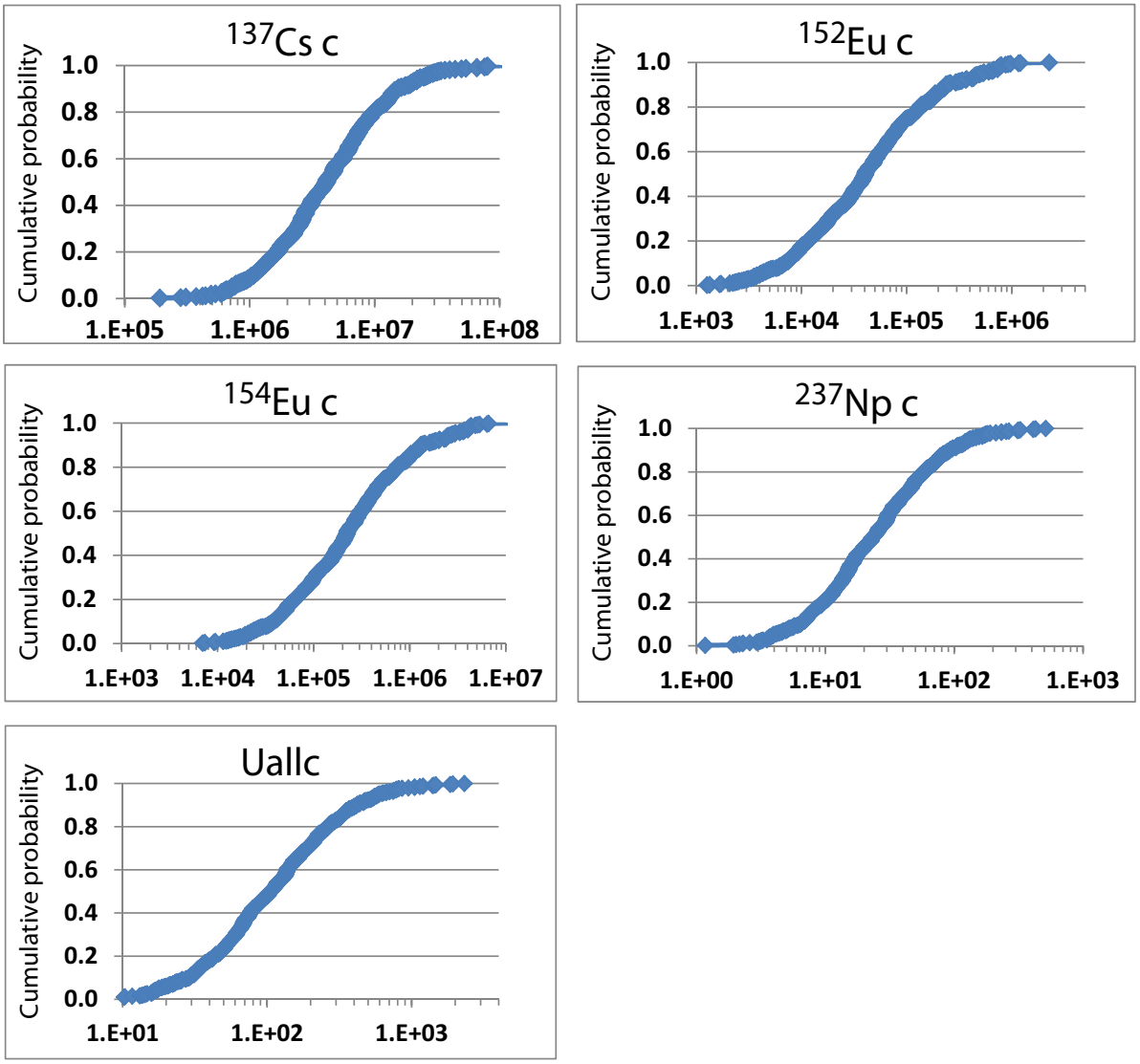

Note: Concentrations are expressed in multiples of the MCL for each individual radionuclide.

Figure M-10b
Sampled Initial Concentrations (in multiples of MCL) for ^{137}Cs, ^{152}Eu, ^{154}Eu, ^{237}Np, and U_{all} in the Fractures of the Exchange Volume

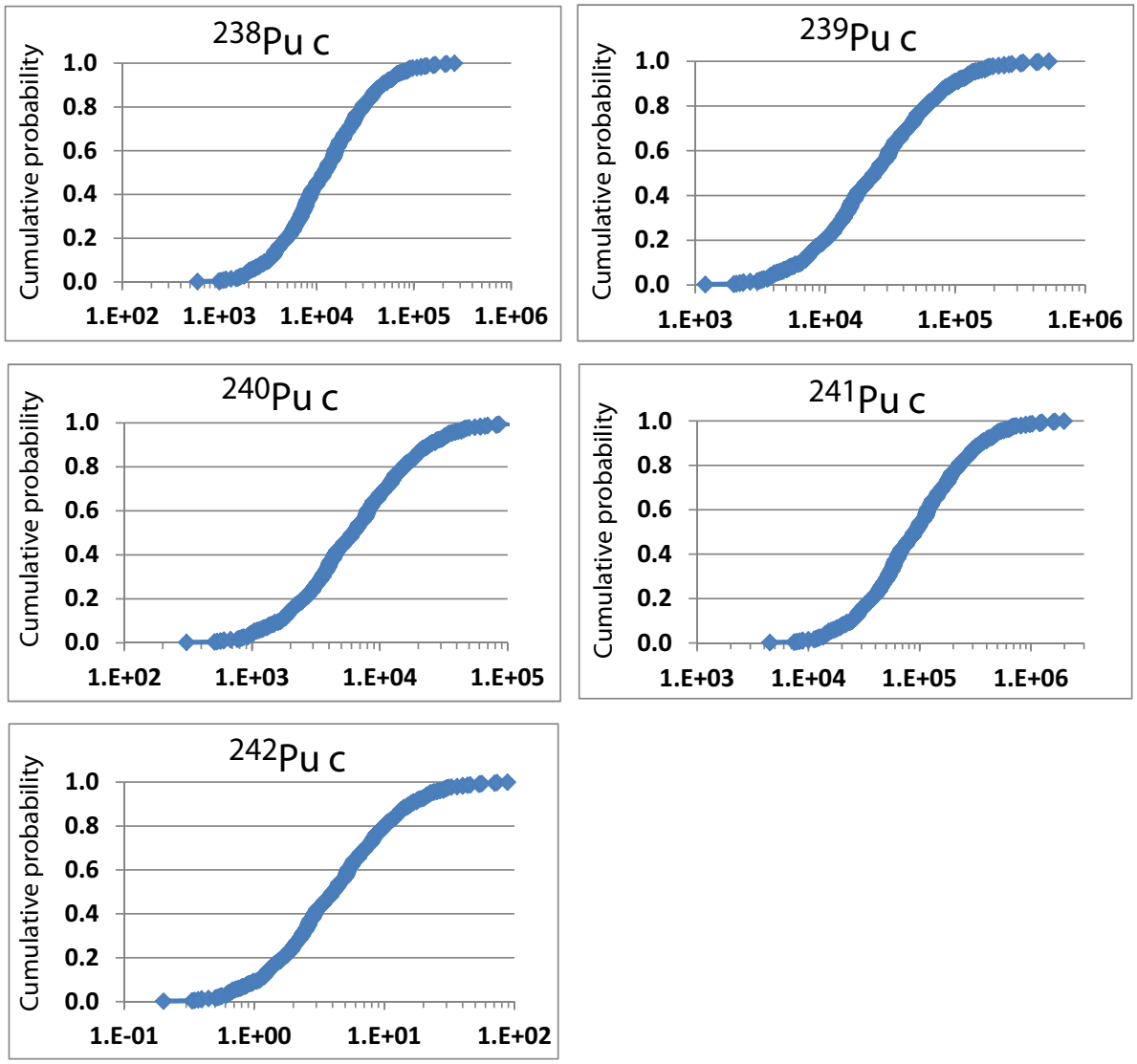

Note: Concentrations are expressed in multiples of the MCL for each individual radionuclide.

Figure M-10c
Sampled Initial Concentrations (in multiples of MCL) for Plutonium Isotopes ($^{238–242}$Pu) in the Fractures of the Exchange Volume

M.5.0 RADIONUCLIDE REACTIVE TRANSPORT SIMULATION RESULTS

Simulations of reactive, dual-porosity transport for each solute of interest are conducted by using the reactive simulator "rxn" of FEHM (Zyvoloski et al., 1997). The GDPM provides a dual-porosity representation of interacting fractures and porous media. The diffusive mass transfer between the two media (fracture and matrix) is governed by several factors including fracture and matrix porosities, fracture aperture, surface area per unit model volume, matrix diffusion coefficients, and fracture spacing, just as with classic dual-porosity analytical models (e.g., Sudicky and Frind, 1982), but the GDPM has the additional capability of taking full advantage of FEHM's "rxn" module for complex reactions in both the fracture and matrix (as shown in Table M-6). In this section, the computed contaminant lengths at different times and concentration profiles at 1,000 years are presented for each of the 18 radionuclide species.

M.5.1 Contaminant Lengths for Radionuclide Transport in the LCA

In the streamtube model, plutonium isotopes and naturally occurring colloids are included as the primary species. Radioactive decay, kinetically controlled sorption of aqueous plutonium and europium onto colloids and matrix minerals, and colloid attachment and detachment to the fracture-coating minerals are also simulated. With colloids present, the sorption of plutonium onto colloids competes with sorption of aqueous plutonium onto fracture-lining minerals and with matrix diffusion and sorption onto matrix minerals. All plutonium isotopes (^{238}Pu, ^{239}Pu, ^{240}Pu, ^{241}Pu, and ^{242}Pu) are assigned the same sorption parameters as described in the previous section, but they have different half-lives and different initial concentrations, as well as different maximum contaminant thresholds. The model includes radionuclide decay (for ^{3}H, ^{14}C, ^{63}Ni, ^{90}Sr, ^{137}Cs, ^{152}Eu, ^{154}Eu, ^{238}Pu, and ^{241}Pu). It also includes the kinetically controlled sorption for plutonium and europium onto fracture and matrix minerals, which competes with the kinetically controlled sorption onto colloids in the fractures. Other sorption reactions for ^{14}C, ^{59}Ni, ^{63}Ni, ^{90}Sr, ^{137}Cs, ^{152}Eu, ^{154}Eu, ^{237}Np, and U onto the immobile minerals are simulated as linear equilibrium sorption processes. The model treats ^{36}Cl, ^{99}Tc, and ^{129}I as conservative solutes whose transport is retarded only by matrix diffusion.

By comparing the computed radionuclide concentrations at all nodes in the streamtube model in a given realization with the MCL for that radionuclide (Table M-7), the distance from the BOURBON test over which the radionuclide concentration exceeds its MCL can be calculated at a given time. This distance, referred to as the contaminant length, varies with time and from radionuclide to radionuclide in a given realization and from realization to realization. In this Appendix, each radionuclide is tracked separately so that its importance in defining the maximum extent of contamination at different times can be determined. Analogous to the contaminant boundaries described in Section 6.0, the overall contaminant lengths for individual radionuclides are defined in a time-cumulative manner as the maximum distance over which the radionuclide exceeds its MCL at any time during the 1,000-year regulatory period. These contaminant lengths are plotted as a function of time at the 5th, 50th, and 95th percentiles in Figures M-11 to M-14. The contaminant length at a given percentile reflects the probability that contaminant lengths will be smaller than the identified distance. For example, the contaminant length at a 95th percentile indicates that 95 percent of the 800 realizations produced contaminant lengths that were smaller than this value and that only 5 percent of the realizations produced contaminant lengths that were greater.

Table M-7
The Maximum Contaminant Levels of the Selected Radionuclides
(Page 1 of 2)

Radionuclide	MCL (mol/L)
^{3}H	6.88E-13
^{14}C	3.21E-11
^{36}Cl	5.89E-10
^{59}Ni	6.38E-11
^{63}Ni	1.40E-14
^{90}Sr	6.51E-16
^{99}Tc	5.36E-10
^{129}I	4.39E-11
^{137}Cs	1.69E-14
^{152}Eu	7.55E-15
^{154}Eu	1.44E-15
$^{233–238}U$	1.26E-07
^{237}Np	8.98E-11
^{238}Pu	3.68E-15
^{239}Pu	1.01E-12

Table M-7
The Maximum Contaminant Levels of the Selected Radionuclides
(Page 2 of 2)

Radionuclide	MCL (mol/L)
^{240}Pu	2.75E-13
^{241}Pu	6.04E-16
^{242}Pu	1.58E-11

Figure M-11 shows the computed contaminant lengths of different plutonium isotopes ($^{238–242}$Pu) undergoing colloid-facilitated transport. Because of their short half-lives (Table M-6) and low initial concentrations, ^{238}Pu and ^{241}Pu have very little impact on the contaminant length of plutonium. After 500 years, both of them decrease below their MCLs throughout the model area. With a longer half-life (24,100 years) and a higher initial concentration, ^{239}Pu (mainly ^{239}Pu-Col) can migrate much longer distances, and its contaminant lengths at a 95th percentile can reach a maximum of about 4.2 km at 500 years. The maximum contaminant lengths for ^{240}Pu and ^{242}Pu reach only to 1.7 and 0.31 km, respectively, because of their much lower initial concentrations relative to their MCLs (Table M-7). At the 50th percentile, contaminant lengths are less than 1 km for all plutonium isotopes.

Figure M-12 shows the computed contaminant lengths of the species that undergo significant radioactive decay over 1,000 years (^{3}H, ^{90}Sr, ^{137}Cs, ^{152}Eu, and ^{154}Eu). The europium isotopes ^{152}Eu and ^{154}Eu, because of their very short half-lives (13.5 and 8.6 years, respectively) and low initial concentrations, decrease below their MCLs throughout the model by 100 years. They are also strongly adsorbed onto matrix minerals and do not migrate away from the source area, even though colloid-facilitated europium transport is included in the transport simulations. Because ^{3}H has a very high initial concentration relative to its MCL, but its half-life is only 12.32 years, it has a large contaminant length at the 95th percentile early in the simulation (13.5 km at about 180 years) but subsequently decreases below its MCL by 400 years. The half-lives of ^{90}Sr and ^{137}Cs are longer than that of ^{3}H (approximately 30 years), but with fracture and matrix sorption (Table M-6), ^{90}Sr and ^{137}Cs have smaller contaminant lengths compared with ^{3}H (maximums of 4.5 and 10.5 km, respectively, at 350 years) and decrease below their MCLs by 780 years. Their smaller transport mobility reflects the strength of their sorption processes. The contaminant lengths for ^{3}H, ^{90}Sr, and ^{137}Cs are under 4 km at the 50th percentile, substantially less than at the 95th percentile.

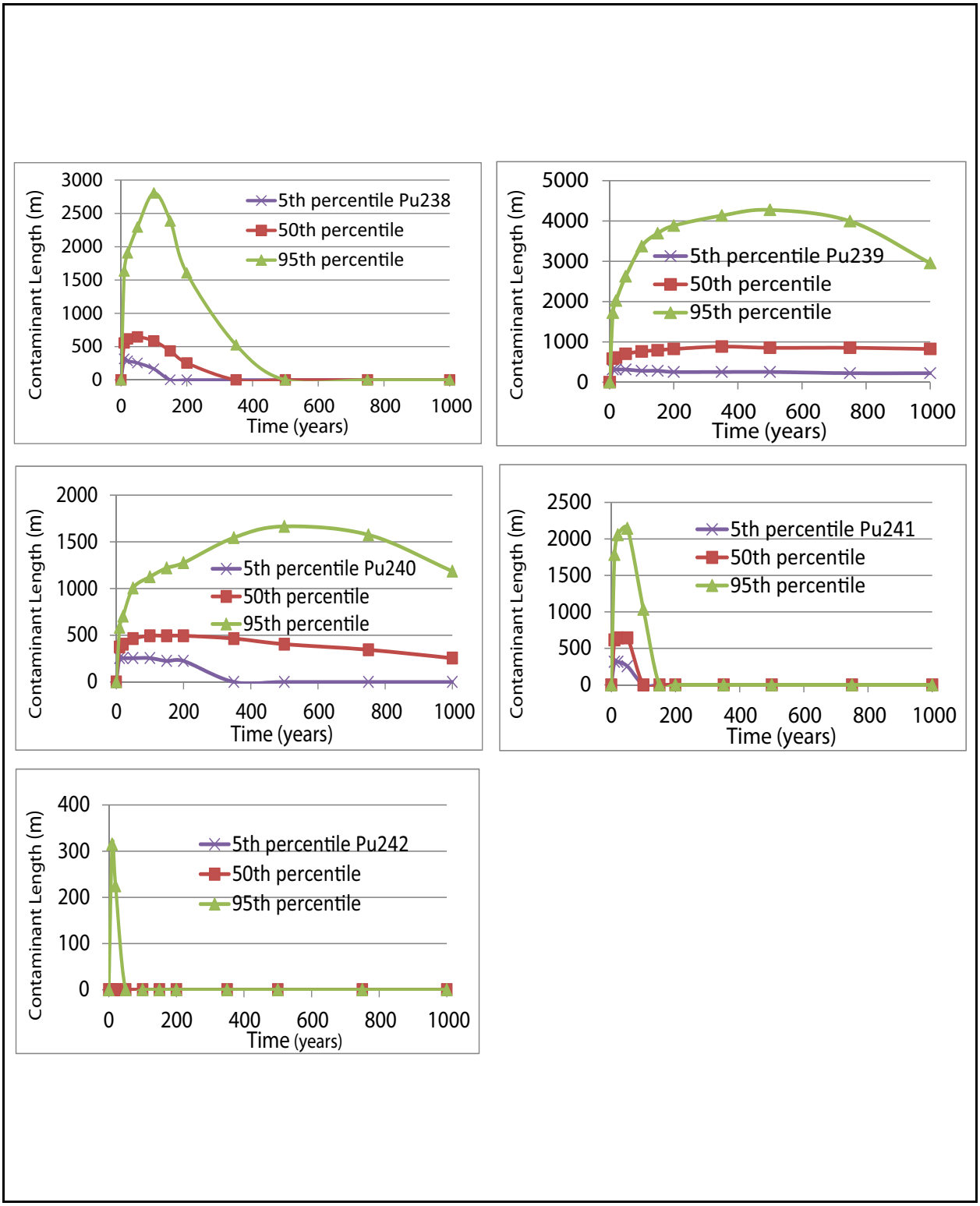

Figure M-11
Computed Plutonium Contaminant Lengths at the 5th, 50th, and 95th Percentiles from the Colloid-Facilitated Plutonium Transport Modeling

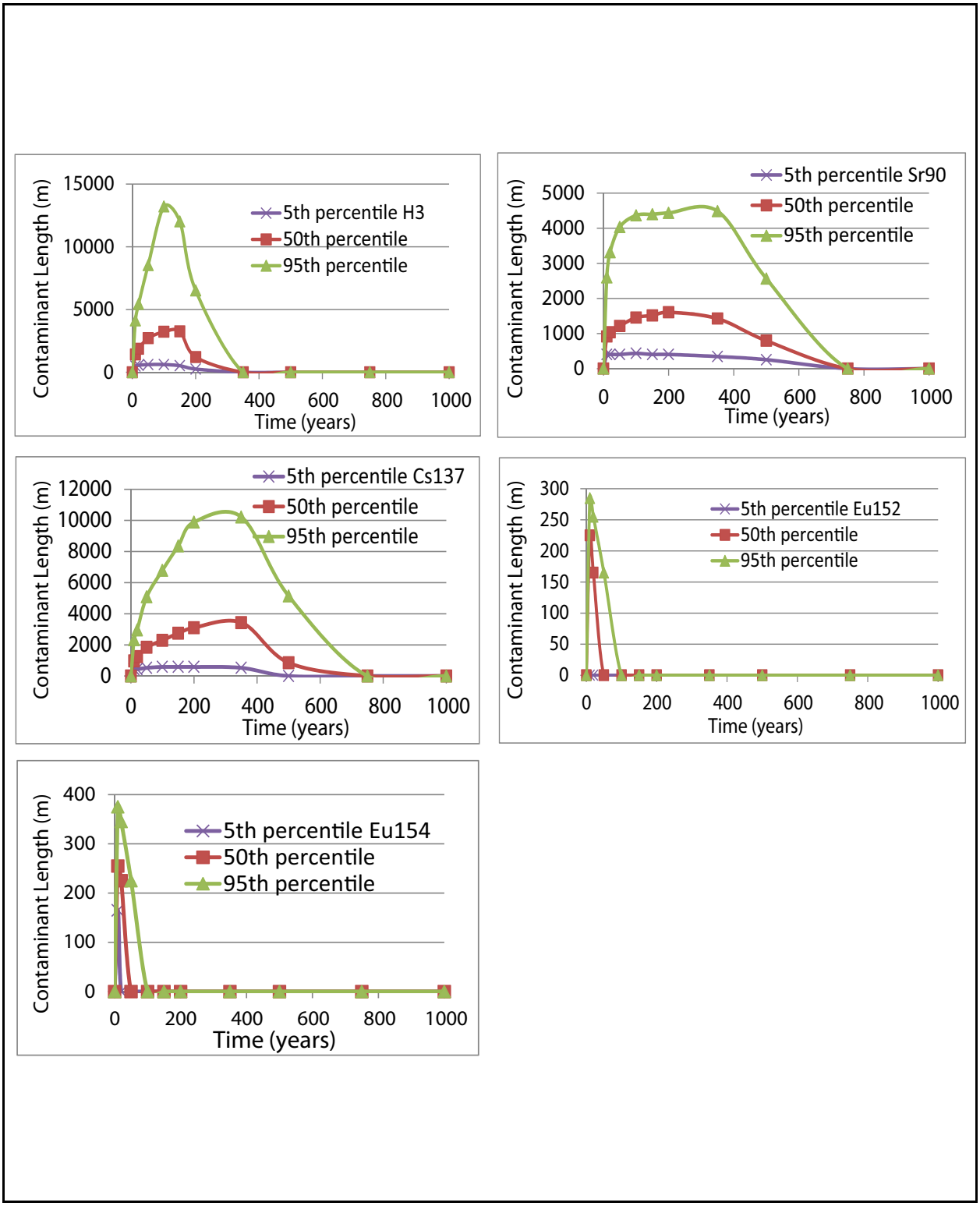

Figure M-12
Computed Contaminant Lengths at the 5th, 50th, and 95th Percentiles for Decaying Species ^{3}H, ^{90}Sr, ^{137}Cs, ^{152}Eu, and ^{154}Eu

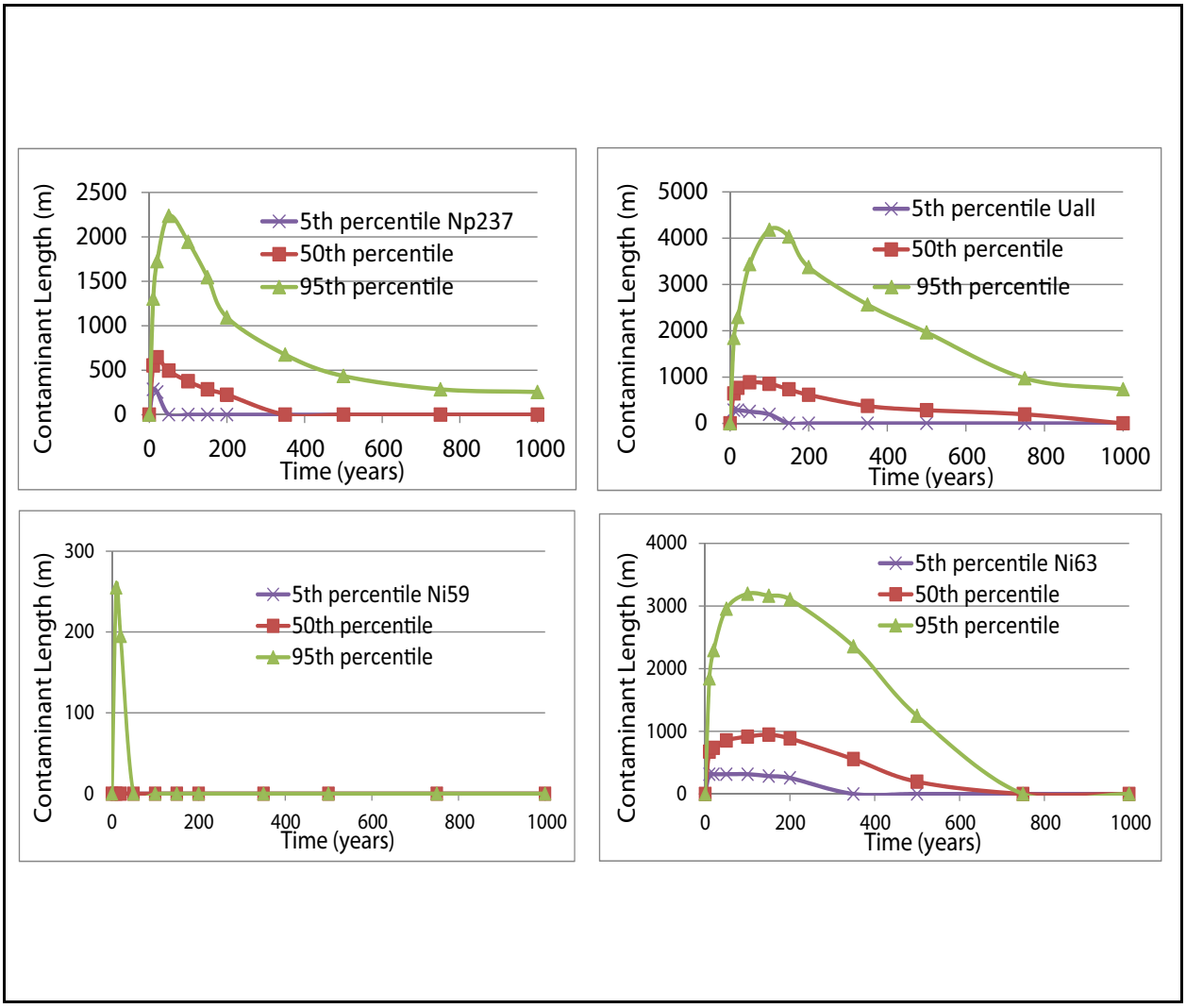

Figure M-13
Computed Contaminant Lengths at the 5th, 50th, and 95th Percentiles for the Radionuclides ^{237}Np, U_{all}, ^{59}Ni, and ^{63}Ni Sorbed onto Both Fracture Surfaces and Matrix

Figure M-13 shows the computed contaminant lengths at the 5th, 50th, and 95th percentiles for ^{237}Np, U, ^{59}Ni, and ^{63}Ni. These four species sorb to varying degrees onto the immobile minerals in the fracture and matrix. ^{237}Np has a maximum contaminant length of 2.2 km. At BOURBON as well as at other detonations, uranium mainly consists of ^{233}U, ^{234}U, ^{235}U, ^{236}U, and ^{238}U. All these isotopes have very long half-lives (greater than 1.5E+05 years) and the same MCL, so they are lumped together as one species (U_{all}), which has a maximum contaminant length of 4.1 km at the 95th percentile. Because of its very low initial concentration, ^{59}Ni does not migrate far from the source area above its MCL and has little impact on the contaminant boundary. ^{63}Ni has a much lower MCL (1.4E-14 mol/L), and its

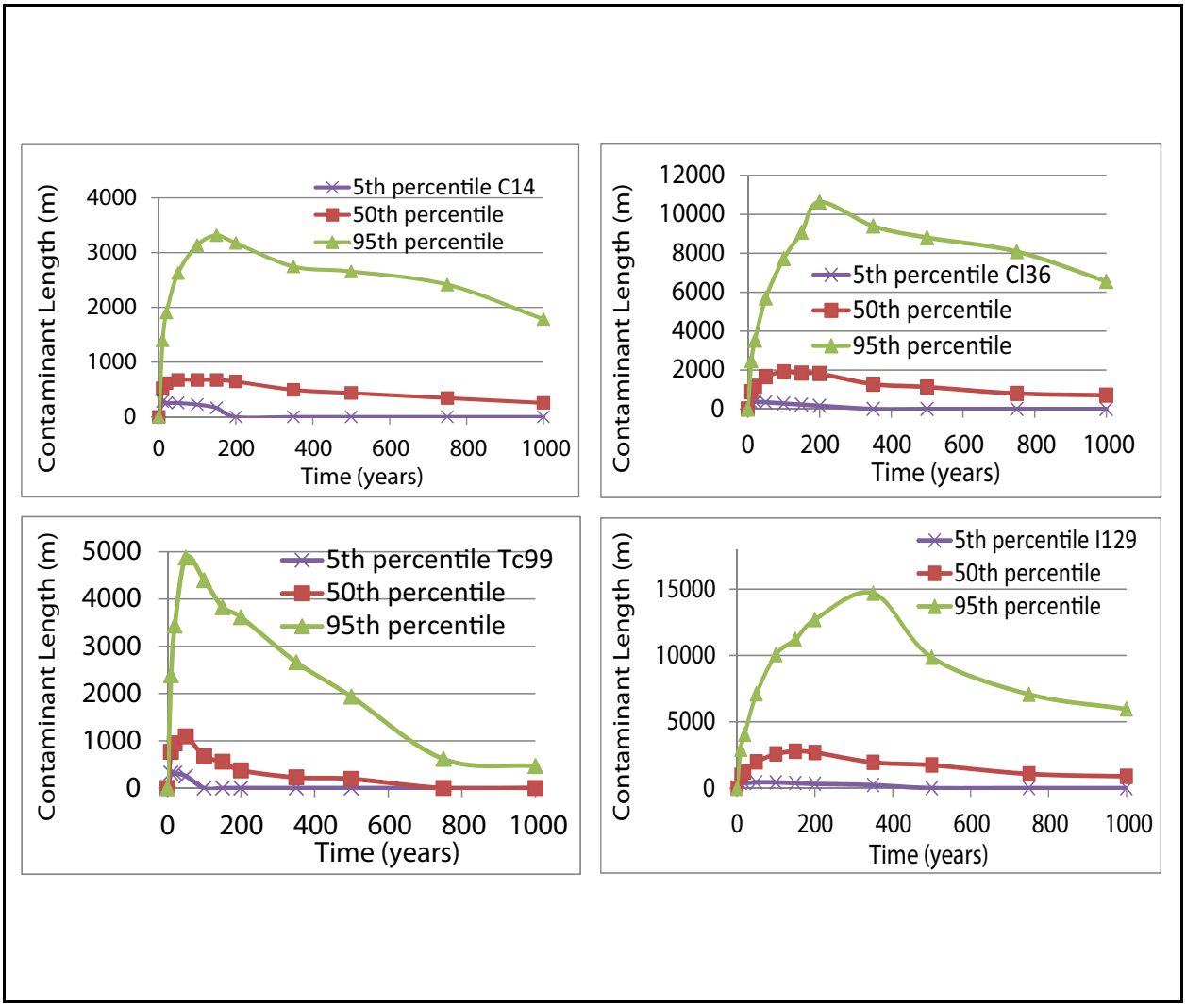

Figure M-14
Computed Contaminant Lengths at the 5th, 50th, and 95th Percentiles for the Radionuclides ^{14}C, ^{36}Cl, ^{99}Tc, and ^{129}I

contaminant length at the 95th percentile can reach 3.1 km at about 200 years, even though it has a half-life of 100 years. The 50th percentile contaminant lengths are less than 1 km for ^{237}Np, U, ^{59}Ni, and ^{63}Ni.

Figure M-14 presents contaminant lengths for ^{14}C, ^{36}Cl, ^{99}Tc, and ^{129}I as a function of time. ^{14}C is simulated as a moderately sorbing species, and its maximum contaminant length at the 95th percentile is 3.2 km. ^{36}Cl, ^{99}Tc, and ^{129}I are three non-sorbing species, and their contaminant lengths are larger than that for ^{14}C at their 95th percentiles (10.5, 5.0, and 15.0 km, respectively). At their 50th percentiles, ^{36}Cl, ^{99}Tc, and ^{129}I have contaminant lengths of only 1 to 2 km.

The contaminant lengths for each of the 18 radionuclides are listed in Table M-8 at both the 50th and 95th percentiles. The key radionuclides from the perspective of defining the maximum contaminant lengths are, in order of importance, ^{129}I, ^{3}H, ^{36}Cl, ^{137}Cs, ^{99}Tc, ^{90}Sr, ^{239}Pu, ^{14}C, and ^{63}Ni. Each of these radionuclides has a contaminant length exceeding 3 km at the 95th percentile. The remaining species have maximum contaminant lengths less than 3 km at the 95th percentile level. The dominant plutonium species ^{239}Pu has a maximum contaminant length of 4.28 km at the 95th percentile level, but six other radionuclide species have equal or greater maximum contaminant lengths, indicating that ^{239}Pu will not define the contaminant boundary. The relative contaminant lengths reflect differences in the initial radionuclide concentrations relative to their MCLs, radioactive decay rates, strength of the sorption coefficients, and diffusion constants.

Table M-8
The Statistics of the Computed Contaminant Lengths of the 18 Radionuclides

Radionuclide	At 50th Percentile			At 95th Percentile		
	Maximum Contaminant Length (km)	Time of Maximum Contaminant Length (years)	Contaminant Length at 1,000 years (km)	Maximum Contaminant Length (km)	Time of Maximum Contaminant Length (years)	Contaminant Length at 1,000 years (km)
^{3}H	3.26	150	0.0	13.2	100	0.0
^{14}C	0.68	150	0.23	3.32	150	1.79
^{36}Cl	1.91	100	0.71	10.6	200	6.56
^{59}Ni	0.0	N/A	0.0	0.26	10	0.0
^{63}Ni	0.95	150	0.0	3.2	100	0.0
^{90}Sr	1.61	200	0.0	4.49	350	0.0
^{99}Tc	1.1	50	0.0	4.88	50	0.47
^{129}I	2.78	150	0.89	14.7	350	5.96
^{137}Cs	3.44	350	0.0	10.2	350	0.0
^{152}Eu	0.23	10	0.0	0.29	10	0.0
^{154}Eu	0.26	10	0.0	0.38	10	0.0
U_{all}	0.89	50	0.0	4.19	100	0.74
^{237}Np	0.65	20	0.0	2.24	50	0.26
^{238}Pu	0.65	50	0.0	2.81	100	0.0
^{239}Pu	0.89	350	0.83	4.28	500	2.96
^{240}Pu	0.50	200	0.26	1.67	500	1.19
^{241}Pu	0.65	50	0.0	2.15	50	0.0
^{242}Pu	0.0	N/A	0.0	0.32	10	0.0

It is noteworthy that the maximum contaminant lengths usually occur within the first few hundred years and that the contaminant length at 1,000 years is usually considerably smaller than the maximum contaminant length for both the 50th and 95th percentiles. This is understandable for species with relatively short half-lives. However, it is interesting that the contaminant boundaries for even non-sorbing, long-lived species like ^{36}Cl, ^{99}Tc, and ^{129}I tend to decrease over time within 1,000 years. This is presumably due to dilution associated with longitudinal dispersion, advection, and matrix diffusion. In particular, the contraction of contaminant lengths over time could be due to the influence of fracture spacing. Large fracture spacing would provide for limited matrix diffusion and rapid advance of the contamination at early times, leading to large maximum contaminant lengths, but would continue to provide sinks for radionuclides after more closely spaced fractures had equilibrated with the rock matrix, leading to the eventual contraction of contaminant lengths. It is also noteworthy that maximum contaminant lengths at the 95th percentile are often three to four times the maximum contaminant lengths at the 50th percentile level because of the relatively large spread in some of the input parameter values.

M.5.2 Concentration Profiles for Each Radionuclide at 1,000 Years

The computed concentration profiles at the 5th, 50th, and 95th percentiles for each of the 18 radionuclides at 1,000 years are plotted in Figures M-15 to M-18. For reference, the MCL of each radionuclide is also plotted for defining the contaminant distances. Figure M-15 shows the concentration profiles and their distributions of the five isotopes of plutonium. All these isotopes are simulated with colloid-facilitated transport, but only ^{239}Pu has a significant contaminant length (3 km) after 1,000 years. Because of their short half-lives, ^{238}Pu and ^{241}Pu are not transported much beyond the initial source area, and their concentrations at 1,000 years are well below the MCLs. ^{240}Pu and ^{242}Pu migrate to a distance of less than 1.7 km because they have much lower initial concentrations relative to their MCLs; dilution due to advection, dispersion, diffusion, and sorption can readily reduce their concentrations below their MCLs (Figure M-10c).

Figure M-16 show the concentration profiles of five radionuclides with short half-lives (^{3}H, ^{90}Sr, ^{137}Cs, ^{152}Eu, and ^{154}Eu). ^{3}H, ^{152}Eu, and ^{154}Eu decay to concentrations well below their MCLs by 1,000 years because of their very short half-lives (12.3, 13.5, and 8.6 years, respectively). Colloid-facilitated transport does not move the europium isotopes away from the source area because of their strong sorption onto matrix minerals (Table M-3) and very short half-lives (Table M-6).

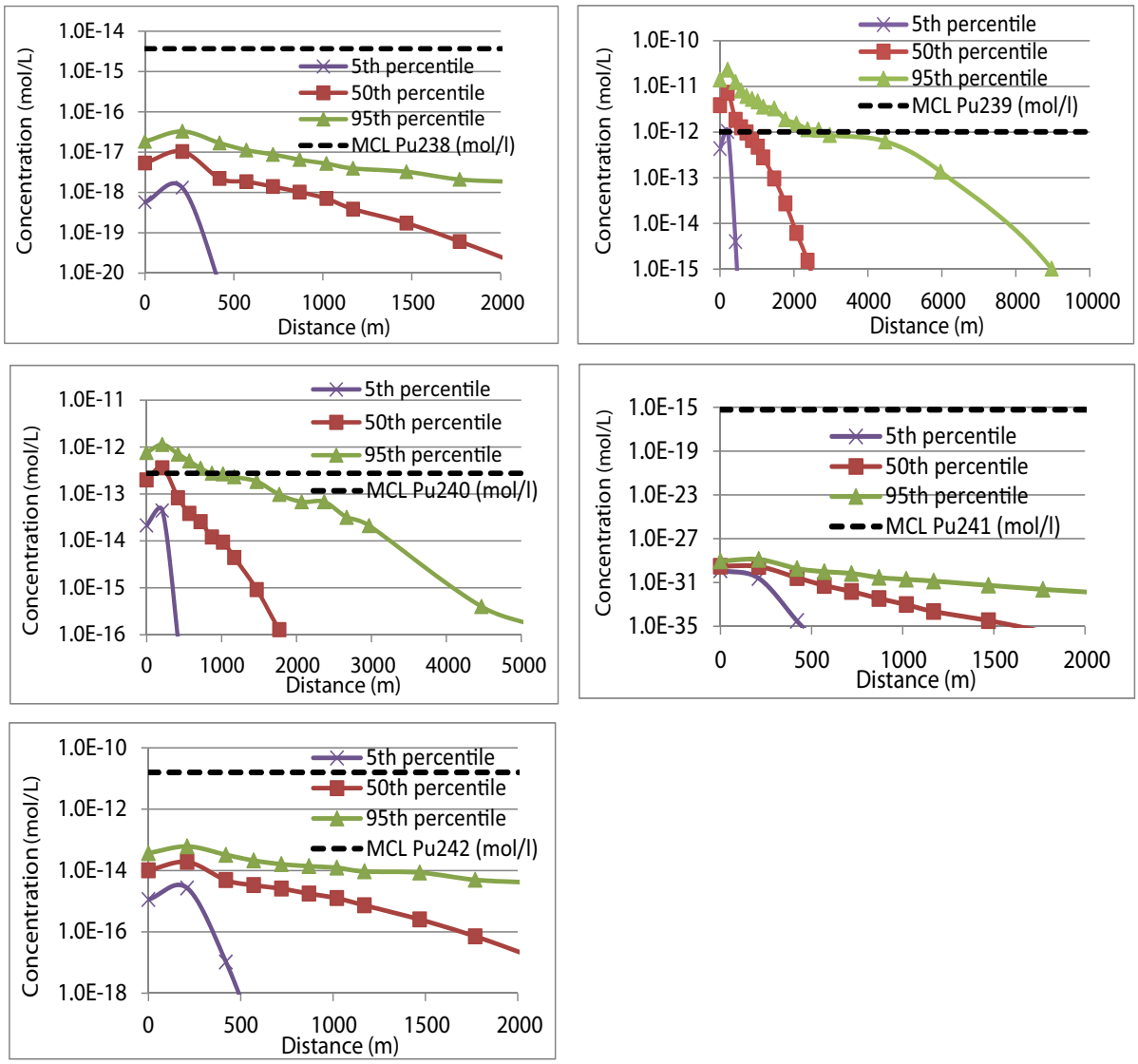

Figure M-15
Computed Concentration Profiles at the 5th, 50th, and 95th Percentiles for Plutonium Isotopes at 1,000 Years

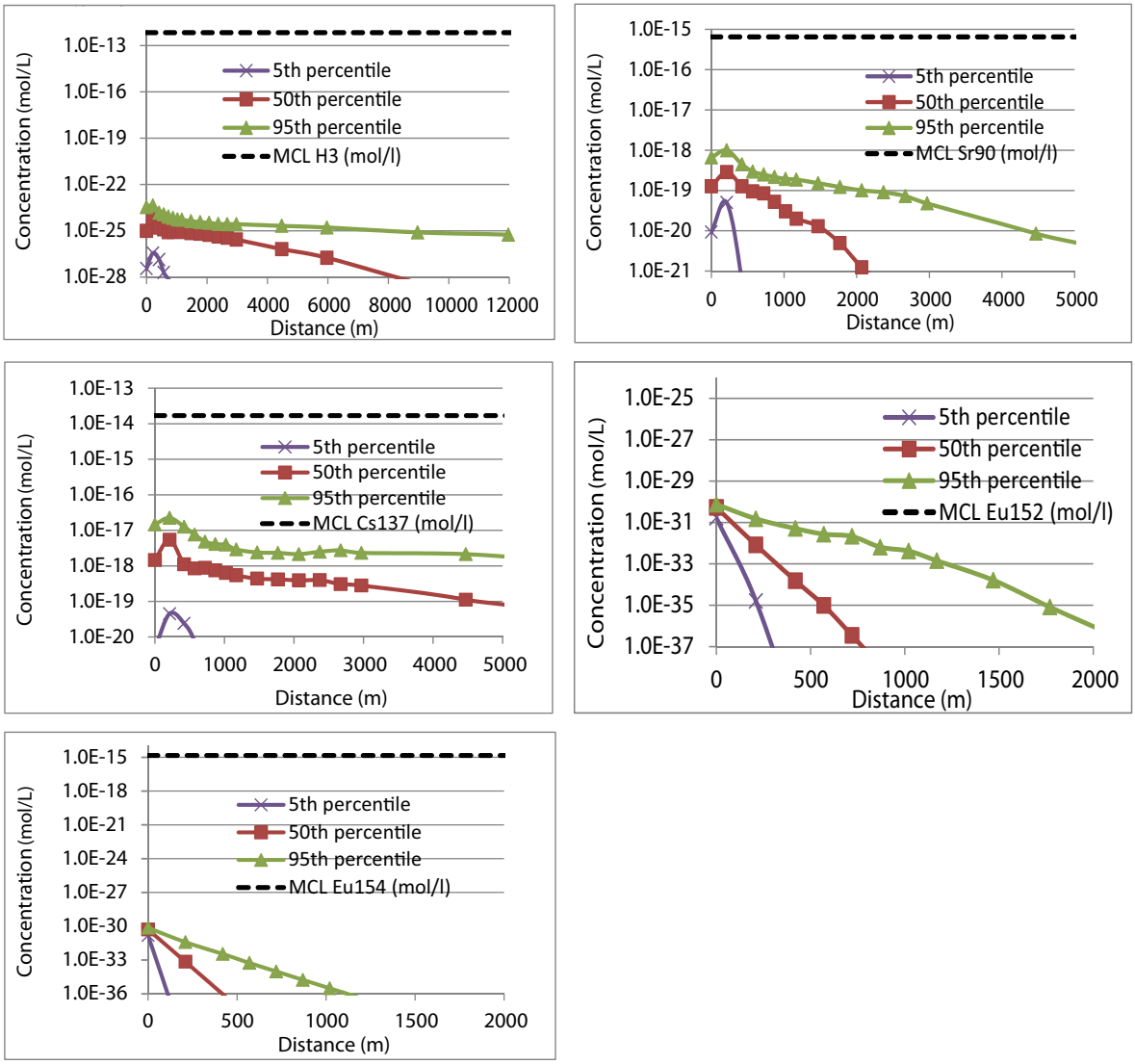

Note: The MCL for ^{152}Eu is 7.55E-15 mol/L, well above the range of computed concentrations in the ^{152}Eu plot.

Figure M-16
Computed Concentration Profiles at the 5th, 50th, and 95th Percentiles for ^{3}H, ^{90}Sr, ^{137}Cs, ^{152}Eu, and ^{154}Eu at 1,000 Years

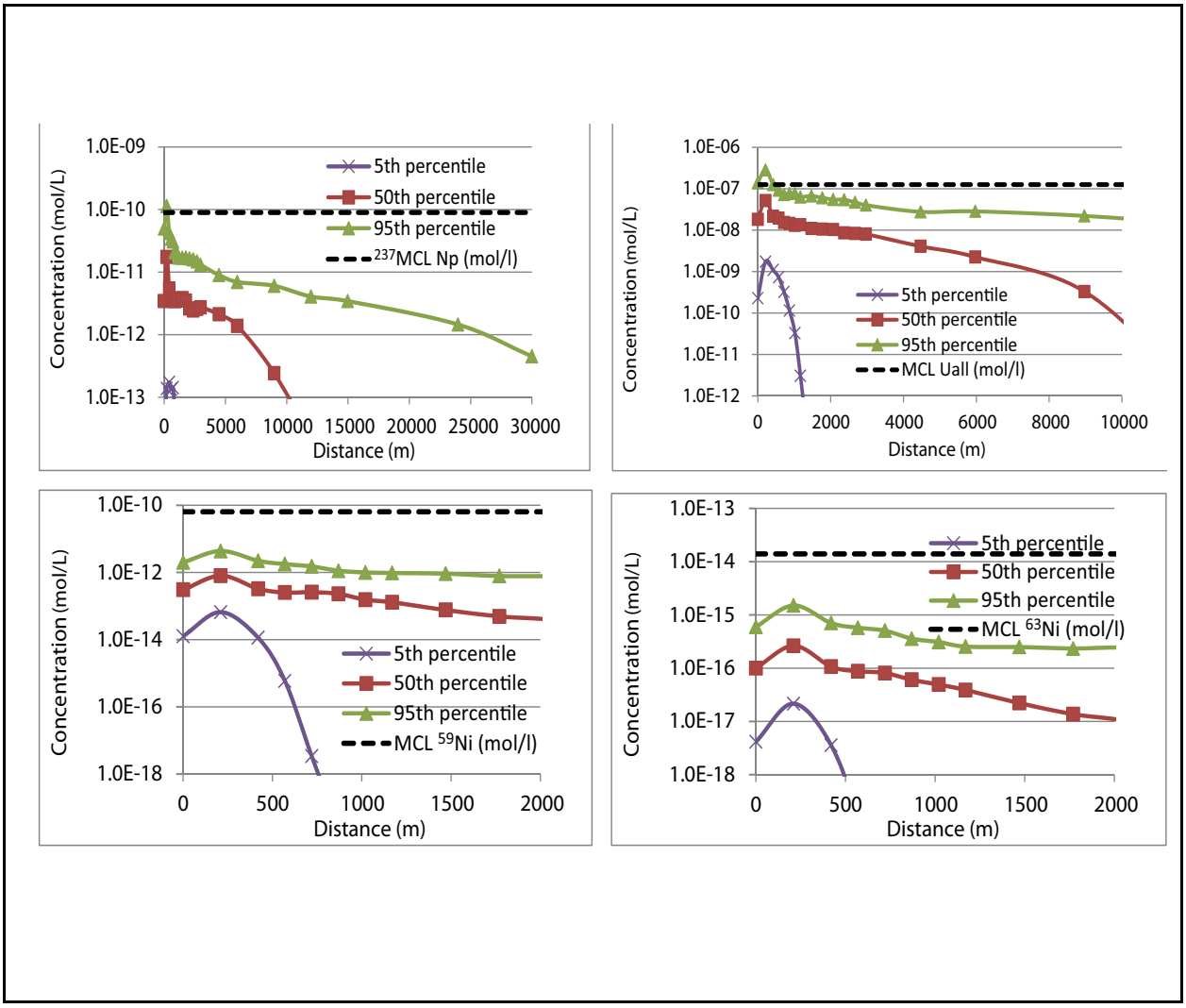

Figure M-17
Computed Concentration Profiles at the 5th, 50th, and 95th Percentiles for ^{237}Np, U_{all}, ^{59}Ni, and ^{63}Ni at 1,000 Years

Because ^{90}Sr and ^{137}Cs are both decaying and sorbing species, their concentrations are also much less than their MCLs throughout the model domain at 1,000 years.

The concentration profiles of ^{237}Np, U, ^{59}Ni, and ^{63}Ni at 1,000 years are presented in Figure M-17. With relatively small sorption coefficients in fracture and matrix but with relatively low initial concentrations relative to their MCLs (Figure M-10b), ^{237}Np and U may have concentrations above their MCLs in the source area (at their 95th percentiles) after 1,000 years, but elsewhere are below their MCLs. Likewise, the concentrations of ^{59}Ni and ^{63}Ni after 1,000 years are lower than their MCLs

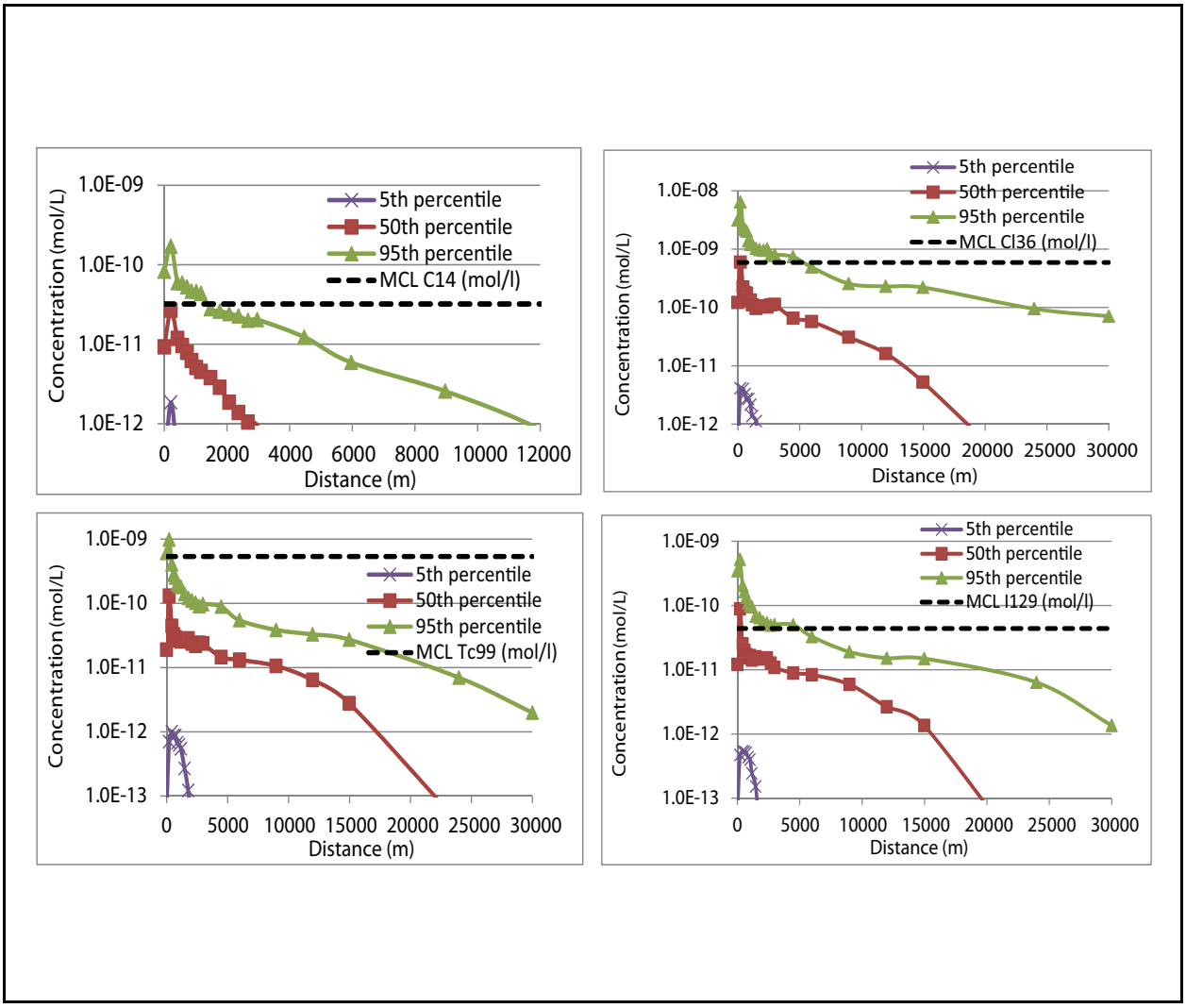

Figure M-18
Computed Concentration Profiles at the 5th, 50th, and 95th Percentiles for ^{14}C, ^{36}Cl, ^{99}Tc, and ^{129}I at 1,000 Years

throughout the model domain because of their relatively low initial concentrations and strong sorption onto fracture and matrix minerals.

Although ^{14}C, ^{36}Cl, ^{99}Tc, and ^{129}I are among the most important radionuclides for defining the contaminant boundary, Figure M-18 shows that after 1,000 years, they have contaminant lengths that have contracted significantly from their maximum values in Table M-8.

M.5.3 Plutonium Reduction Factor

Monte Carlo simulation is also used to estimate the fraction of the initial plutonium mass emplaced in the BOURBON source area that is actually mobilized by natural colloids. Before calculating the plutonium reduction factor, this subsection first presents other details of colloid-facilitated plutonium transport.

Plutonium Isotope Transport. By randomly selecting one realization from the Monte Carlo simulations, we compute the concentration distributions along the streamtube at 10, 100, 200, 500, and 1,000 years for the five isotopes of plutonium. The computed concentration distributions are shown in Figures M-19 to M-23. The MCLs of these plutonium isotopes in groundwater are also plotted in the figures as references to define the contaminant distances of this realization. Figure M-19 shows the ^{238}Pu distributions (including aqueous and colloidal ^{238}Pu) along the streamtube at different times. At about 200 years, the ^{238}Pu contaminant distance reaches its maximum length of 0.8 km. Because ^{238}Pu has a relatively short half-life of 87.7 years, its concentrations decrease with time and eventually drop below the MCL by 500 years. ^{239}Pu has a much longer half-life (24,100 years), so the decay of ^{239}Pu can be neglected. Facilitated by colloids, ^{239}Pu migrates to about 1.4 km by 1,000 years (Figure M-20). Even though it has chemical properties identical to ^{239}Pu, ^{240}Pu migrates to a distance of around 0.5 km in 1,000 years because of a much lower initial concentration relative to its MCL (Figure M-21). ^{241}Pu has a short half-life (14.4 years), and its concentration decreases very quickly by decay. ^{241}Pu reaches the maximum contaminant distance (0.6 km) in 100 years (Figure M-22) and decreases below the MCL after 200 years. With a much lower initial concentration relative to its MCL, ^{242}Pu migrates at concentrations above its MCL to a distance of only 0.2 km before decreasing below its MCL in 100 years (Figure M-23).

Figure M-24 compares the total plutonium concentration distribution with the concentration distributions of five plutonium isotopes at 1,000 years. Note that ^{239}Pu dominates the total plutonium concentration and the other isotopes contribute less than 1 percent to the total concentration. Therefore, the estimation of the plutonium source reduction factor focuses primarily on ^{239}Pu, and the other four plutonium isotopes can be ignored.

Plutonium Source Reduction Factor. The results of colloid-facilitated plutonium transport simulation summarized above indicate that away from the source area, the total concentration of Pu is essentially equal to that of ^{239}Pu. Further examination of these results indicates that the total

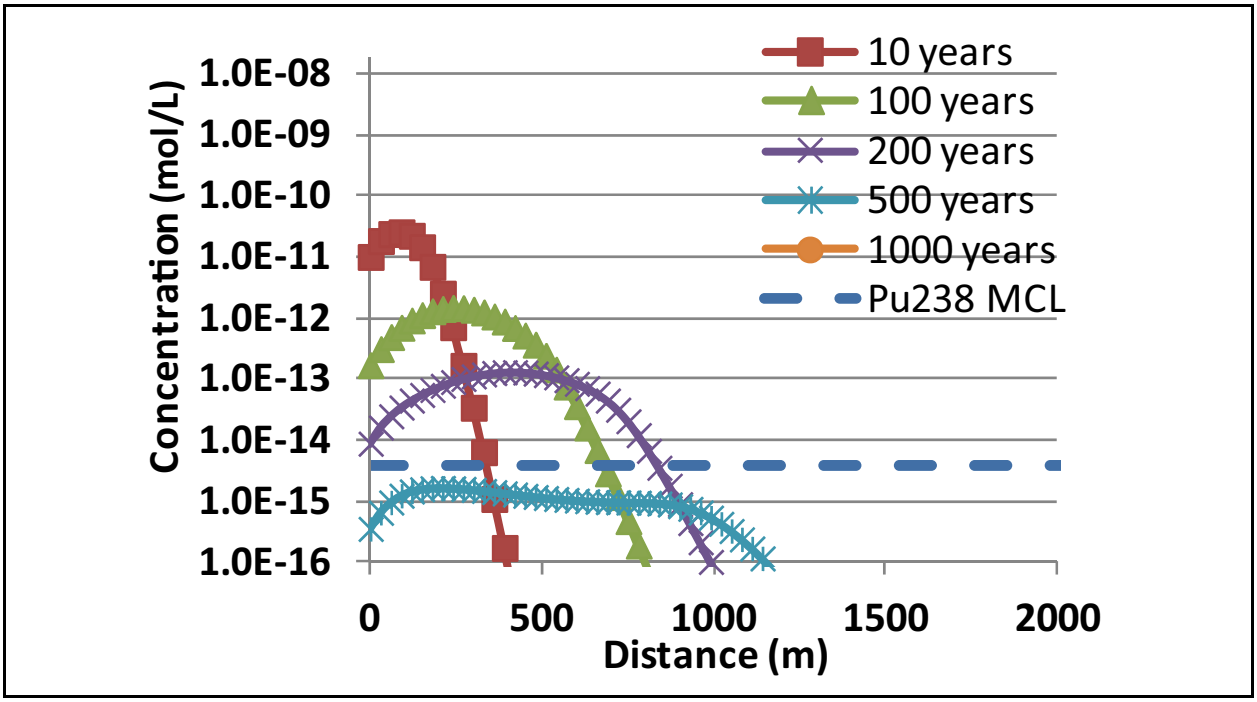

Figure M-19
^{238}Pu Concentration Distributions at Different Times

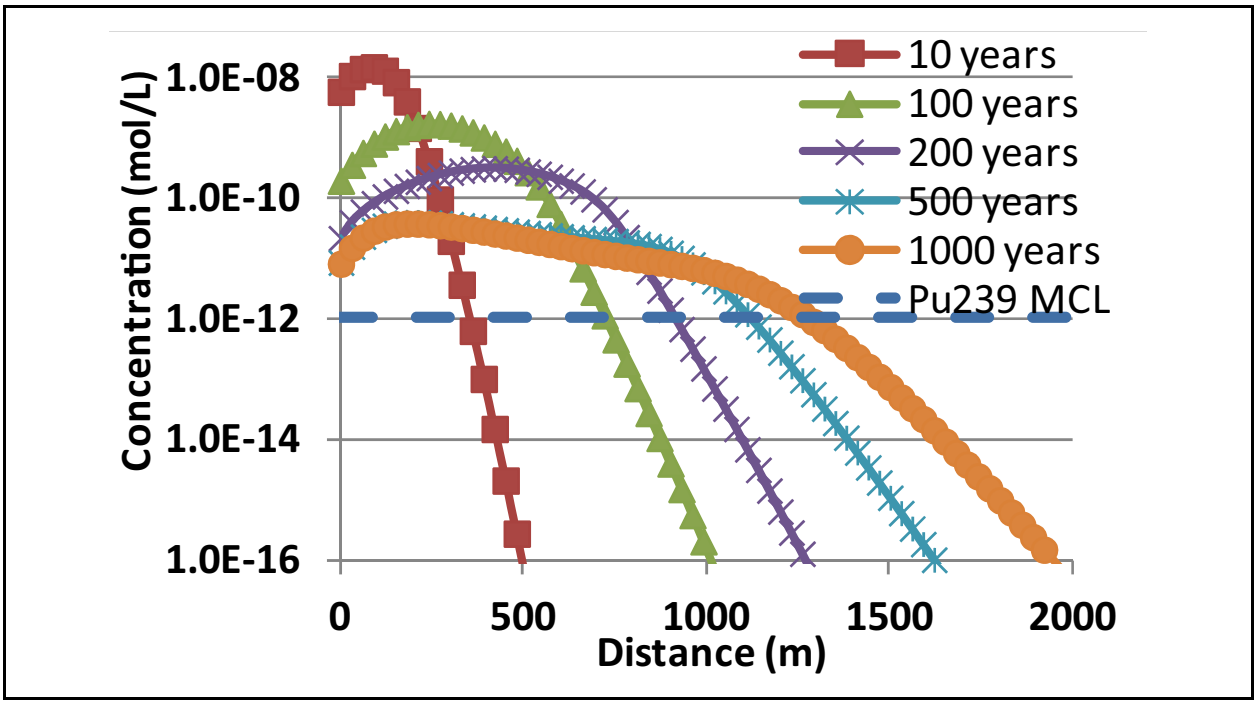

Figure M-20
^{239}Pu Concentration Distributions at Different Times

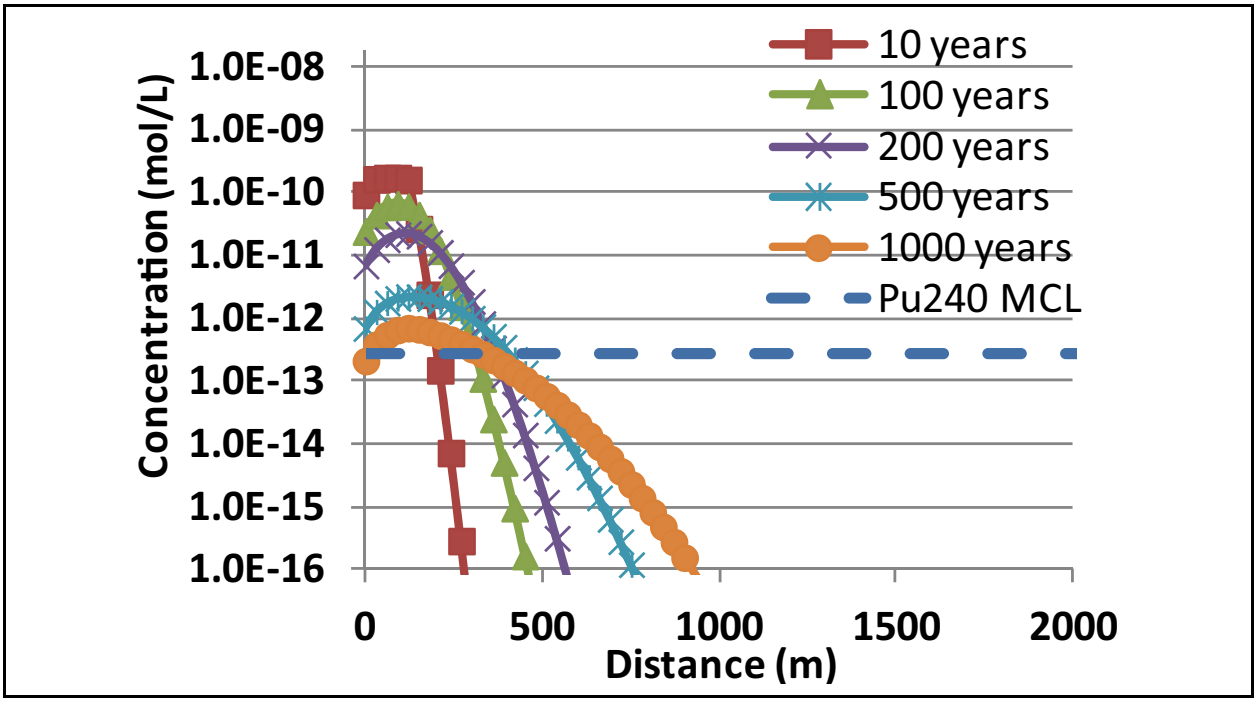

Figure M-21
^{240}Pu Concentration Distributions at Different Times

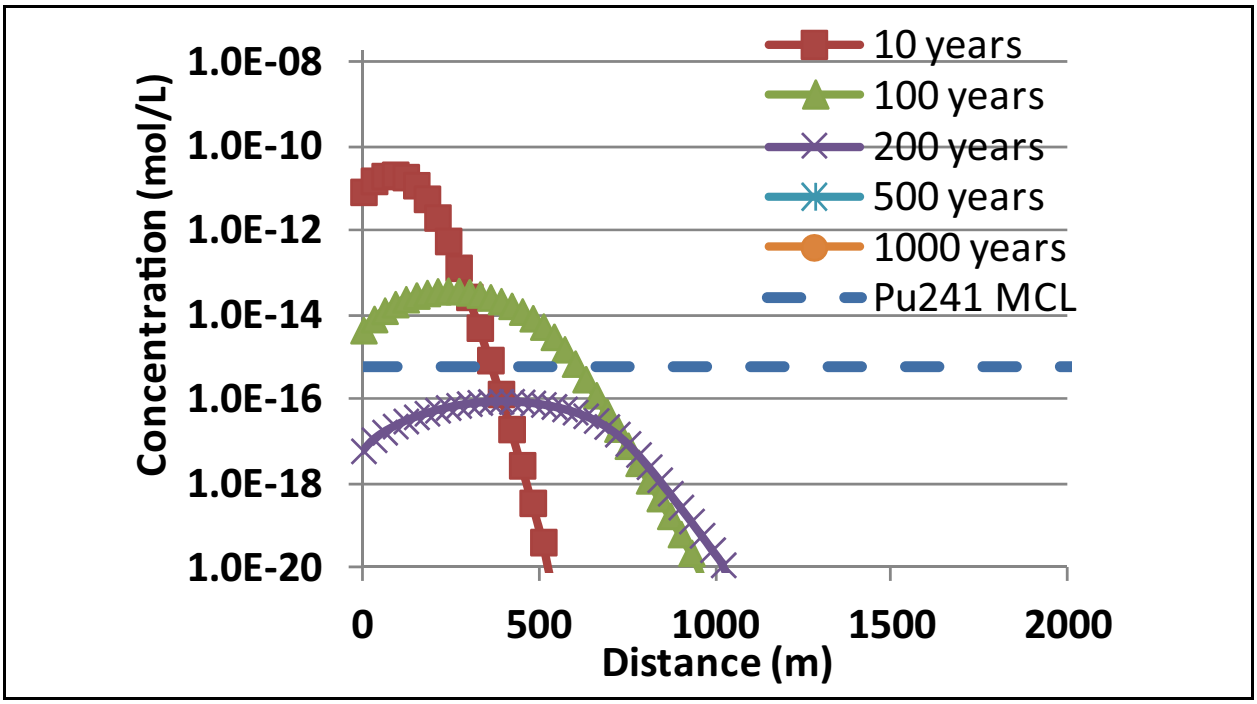

Figure M-22
^{241}Pu Concentration Distributions at Different Times

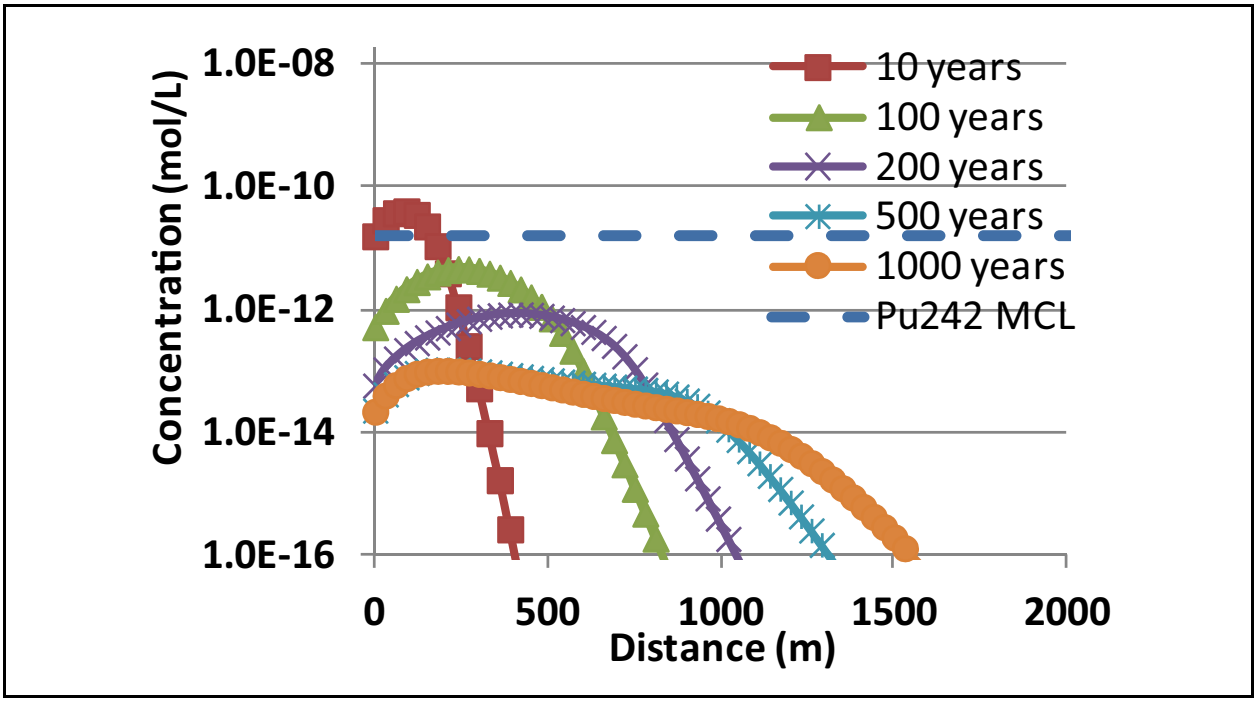

Figure M-23
^{242}Pu Concentration Distributions at Different Times

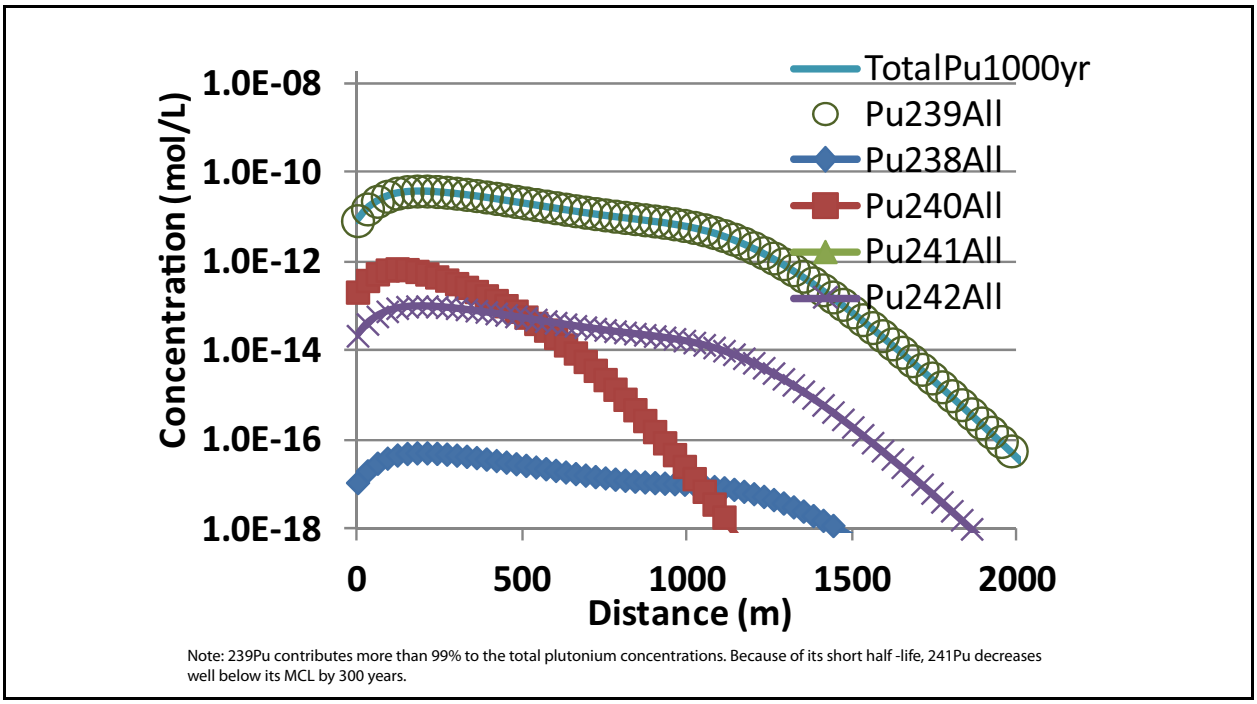

Figure M-24
The Concentration Distributions of Plutonium Isotopes and Total Plutonium at 1,000 Years

concentration of ^{239}Pu at 1,000 years is essentially equal to the concentration of ^{239}Pu-Col. This implies that only the plutonium sorbed onto colloids can migrate a substantial distance in the LCA over the long term.

Given these results, the process of colloid-facilitated transport of plutonium can be reconceptualized as one in which some fraction of the initial plutonium source is competitively sorbed onto colloids more or less permanently to produce the species Pu-Col, which moves through the fracture system without diffusing into the matrix and is slowed only by colloid attachment and detachment from the fracture wall. The attachment and detachment rates for Pu-Col are assumed to be those of the colloids themselves. The problem is therefore reduced to estimating the fraction of the initial plutonium inventory that effectively becomes permanently sorbed onto colloids during the initial competitive sorption between colloids and immobile minerals, and subsequent transport. That fraction is termed the plutonium reduction factor. As discussed earlier, this approach is compatible with the limitations of the particle-tracking algorithm used in the CAU-scale model, which can only simulate linear equilibrium sorption and cannot account for competitive, rate-dependent sorption between colloids and immobile minerals (Robinson et al., 2011).

An estimate of the range of plutonium reduction factors can be made with the mean ^{239}Pu concentrations from Monte Carlo simulations between 420 m (the maximum diameter of the BOURBON exchange volume) and 5 km (approximately the maximum contaminant length at the 95th percentile) (Figure M-25a). The mean concentrations within this range of transport distances, as calculated from 800 Monte Carlo realizations, are divided by the mean initial source concentration of ^{239}Pu (4.98E-08 mol/L) to calculate the average plutonium reduction factors over this range of transport distances (Figure M-25b). The mean plutonium reduction factor (2.83E-05) over this range can be used, along with the minimum (5.92E-06) and maximum factors (6.3E-05), to define a triangular distribution.

Once the source term of the new species ^{239}Pu-Col is generated with these reduction factors, the transport of ^{239}Pu-Col can be simulated by assuming non-diffusive transport and linear sorption on the fracture walls with the colloid attachment and detachment rates defined for colloids in Table M-4. This simplified model is verified as follows. The detailed process model of competitive plutonium sorption described earlier, along with the mean transport parameters, is used to define the “true model,” and the total plutonium concentration profiles are calculated at four time steps (200, 500,

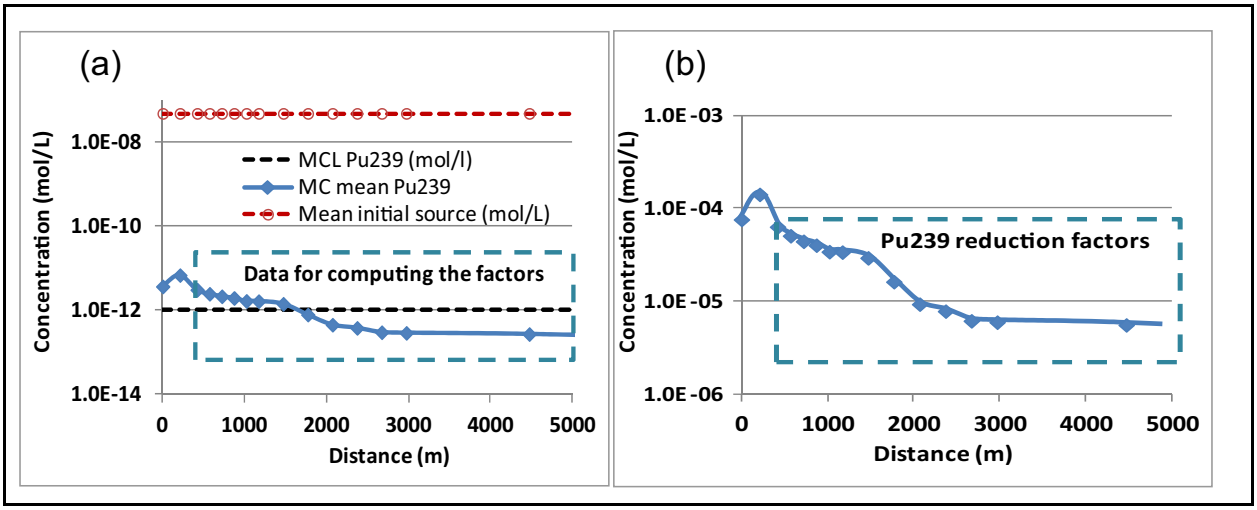

Figure M-25
The Mean ^{239}Pu Concentration Profiles at 1,000 Years Computed from (a) Monte Carlo Simulations and (b) ^{239}Pu Reduction Factors

750, and 1,000 years) and treated as "observation data." Then, a simplified transport model is run for the non-diffusing Pu-Col species that includes only linear sorption of Pu-Col onto the fracture surfaces based the mean colloid attachment and detachment rates (Table M-4). The parameter estimation code PEST is then used to find the initial Pu-Col concentration (or equivalently, the plutonium reduction factor) that allows the simplified model to best fit the "data" produced by the more detailed model. A comparison of the results of the simple and more detailed models indicates reasonably good agreement, especially at later times (Figure M-26). The estimated initial concentration of Pu-Col is 1.41E-12 mol/L, which corresponds to a plutonium reduction factor of 2.8E-05. The best-fit value agrees closely with the mean of the plutonium reduction factors calculated from the Monte Carlo simulations (2.83E-05), thereby providing support for the simplified approach as well as the plutonium reduction factors estimated from the Monte Carlo simulations.

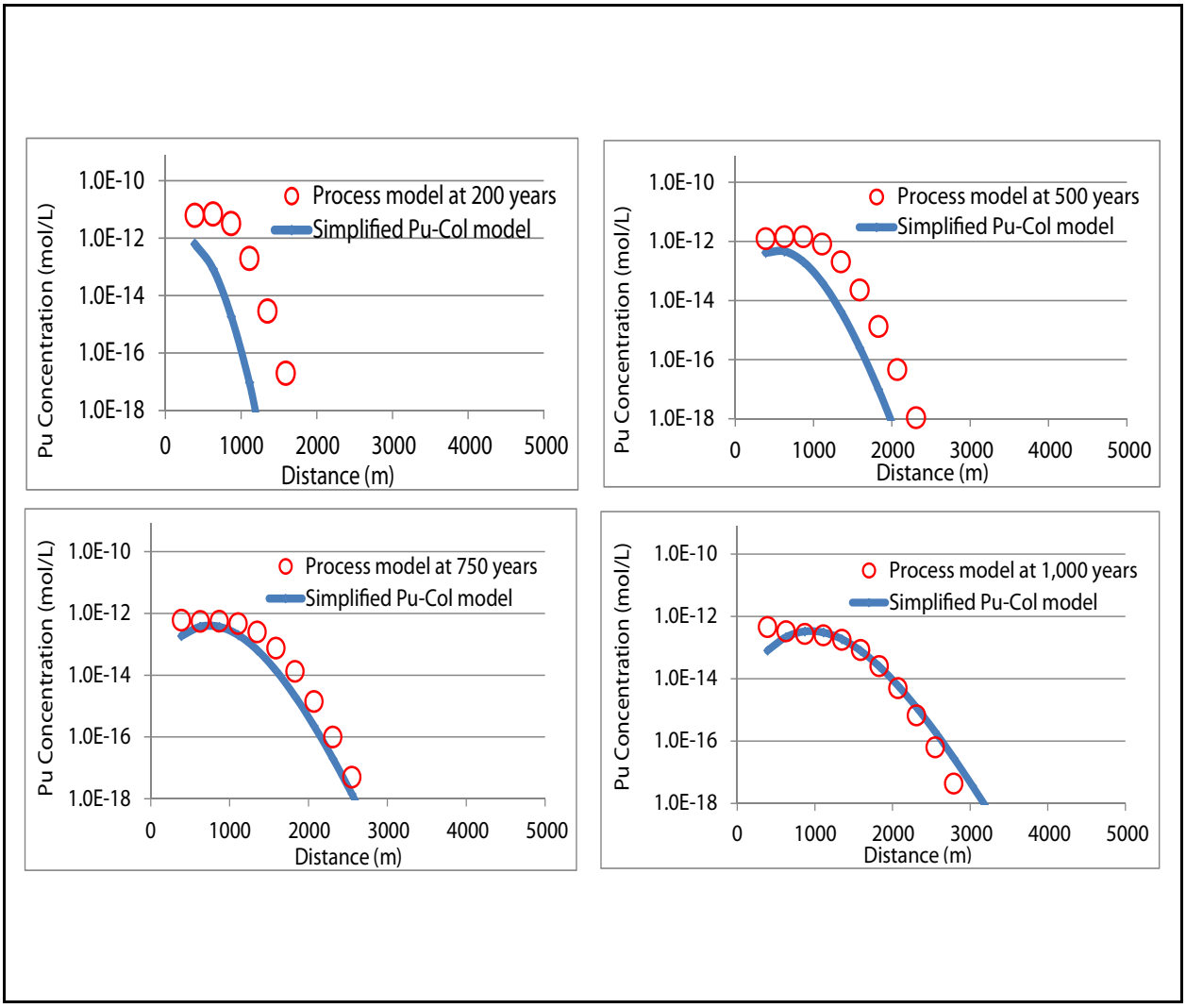

Figure M-26
The Fit Results of the Simplified Pu-Col Model against the Process Model That Includes All of Competitive Transport Processes of the Colloid-Facilitated Plutonium Transport

M.6.0 GLOBAL SENSITIVITY ANALYSIS

M.6.1 Methods for Global Sensitivity Analysis

This section discusses methods used to determine the key transport parameters driving transport behavior in the Monte Carlo simulations. Global sensitivity analysis techniques are used to investigate input-output sensitivities that are valid over the entire range of the parameter sampling. The Monte Carlo simulations provide 800 realizations of input transport parameter sets created with Latin hypercube sampling for each model. Each realization is propagated through the transport simulator that yields the output response functions represented by the contaminant length distributions to characterize transport behavior. Global sensitivity analysis entails the comparison of the contaminant length distribution to each of the input transport parameter distributions and identifies the most sensitive parameters. Two sensitivity analysis methods—the multivariate adaptive regression spline (MARS) and main effect methods (Tong, 2011)—are used to quantify the impact of uncertainty and sensitivity of the transport parameters.

The ***MARS method*** is a nonparametric technique for determining the strength of correlation between the input variables and output response. This method develops local models for each local region. To ensure continuity between adjacent regions, the method can enforce equal first or second derivatives to match on the regional boundaries. The crux of the MARS method is to automatically and adaptively choose the number and locations of the knots (points at the boundaries between regions). Once knots have been determined, basis functions are constructed for each region. The basis functions and the corresponding coefficients are examined to extract main effect information and detect interactions. Therefore, the importance of the input variables is quantified by the MARS importance ranking (Tong, 2011).

The ***main effect method*** is a variance-based main effect analysis, and it displays first-order Sobol' indices for the response surface built from the Monte Carlo simulations (Tong, 2011). The essence of this analysis is the statistical measure called variance of condition expectation. The variance-based analysis uses the following equation:

$$VCE(X_k) = \frac{100}{s}\sum_{j=1}^{s}(\overline{Y}_j - \overline{Y})^2 - \frac{1}{sr^2}\sum_{j=1}^{s}\sum_{i=1}^{r}(Y_{ij} - \overline{Y}_j)^2 \qquad (M\text{-}13)$$

where *VCE* measures the variability in the conditional expected value of Y as the input X_k takes on different values, s is the number of distinct values of each input parameter, r is the number of replications, and the product of s and r is the sample size N (Tong, 2011).

M.6.2 Normalization of Input Parameters

As discussed in Section M.4.2, there are 58 input parameters, and their values vary from 10E-12 to 10E+08. The huge difference of the input parameter values would affect the results of the global sensitivity analysis. To reduce the impact generated from different input parameters, each input parameter is normalized with the following equation:

$$X_{ki} = \frac{x_{ki} - \overline{x_k}}{\sigma_k} \qquad (M\text{-}14)$$

where X_{ki} is the ith normalized value of the parameter k, x_{ki} is the ith sample of the original parameter k; $\overline{x_k}$ is the mean of the original parameter k, and σ_k is the standard deviation of the original parameter k.

By using the Monte Carlo simulation results as the input for PSUADE (Tong, 2011), a global sensitivity analysis with the MARS and main effect methods was conducted. To compare the results from these two methods, the sensitivity indices derived from these methods are presented together in a single figure. In most cases (with a few exceptions) the results from these two methods are consistent with each other. The results are plotted in Figures M-27 to M-44 for the contaminant lengths of the 18 radionuclides, with parameters ordered according to the sensitivity as calculated with the MARS method. The contaminant lengths are most sensitive to fracture property parameters, such as fracture aperture (*fb*), porosity (porF), and spacing (*Sf*), and the lateral inflow rate (flowr). Most of the contaminant lengths are also sensitive to the matrix porosity (porM) because this

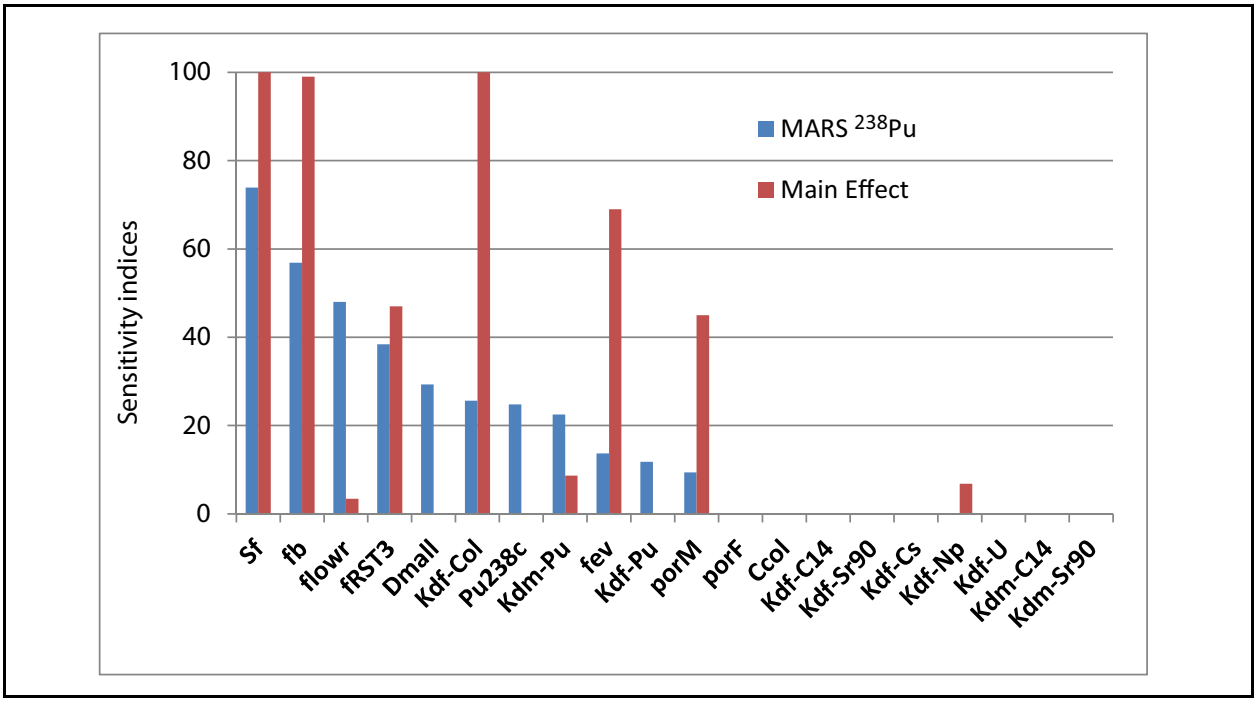

Figure M-27
Global Sensitivity Analysis of ^{238}Pu Contaminant Lengths to 58 Sampled Parameters of the Monte Carlo Simulations

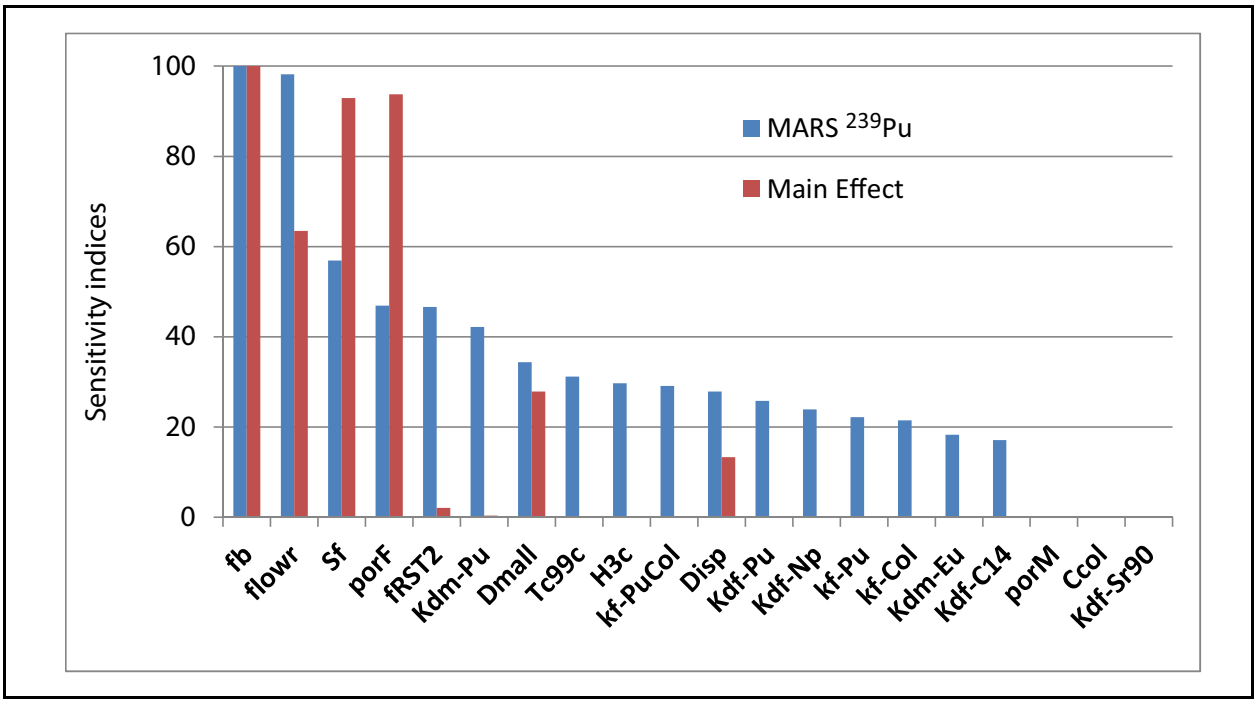

Figure M-28
Global Sensitivity Analysis of ^{239}Pu Contaminant Lengths to 58 Sampled Parameters of the Monte Carlo Simulations

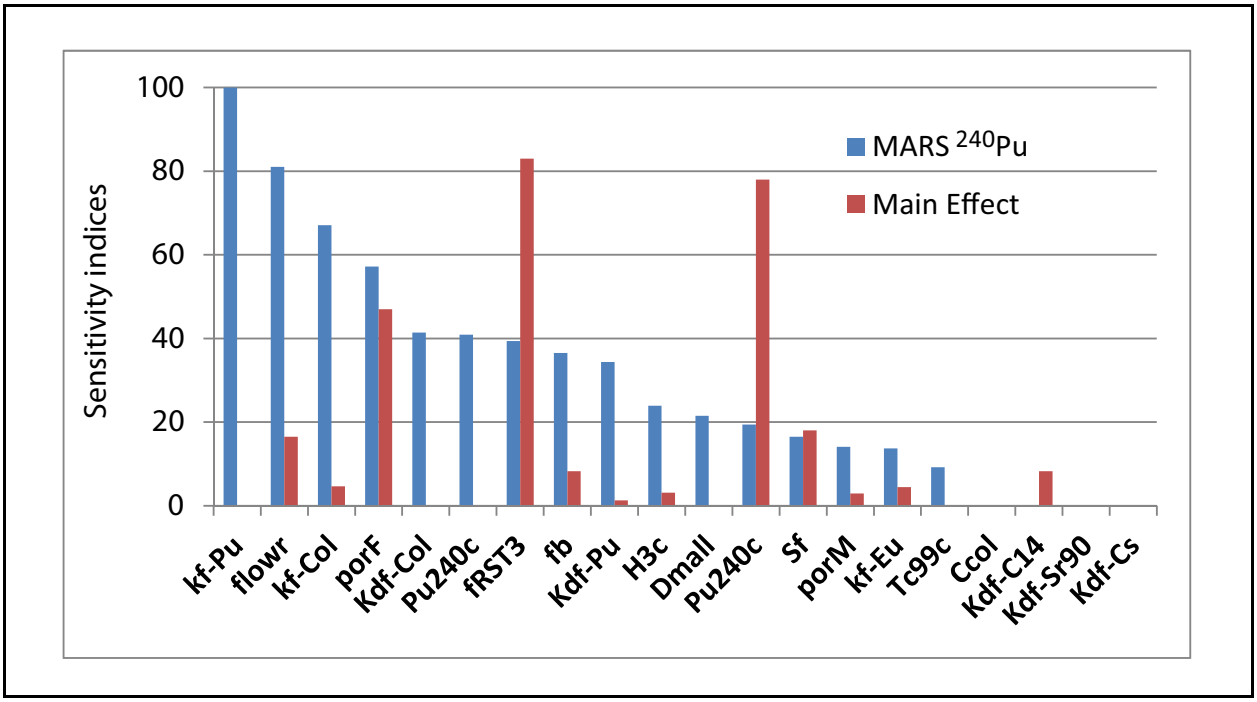

Figure M-29
Global Sensitivity Analysis of ^{240}Pu Contaminant Lengths to 58 Sampled Parameters of the Monte Carlo Simulations

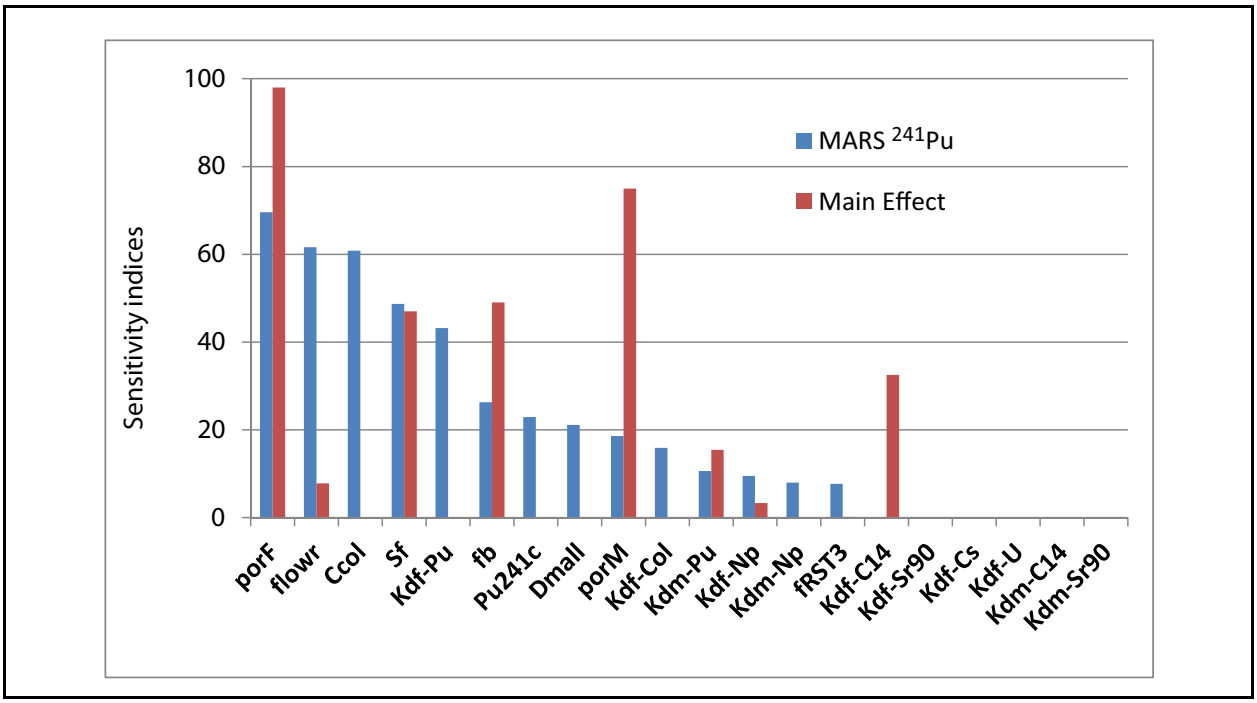

Figure M-30
Global Sensitivity Analysis of ^{241}Pu Contaminant Lengths to 58 Sampled Parameters of the Monte Carlo Simulations

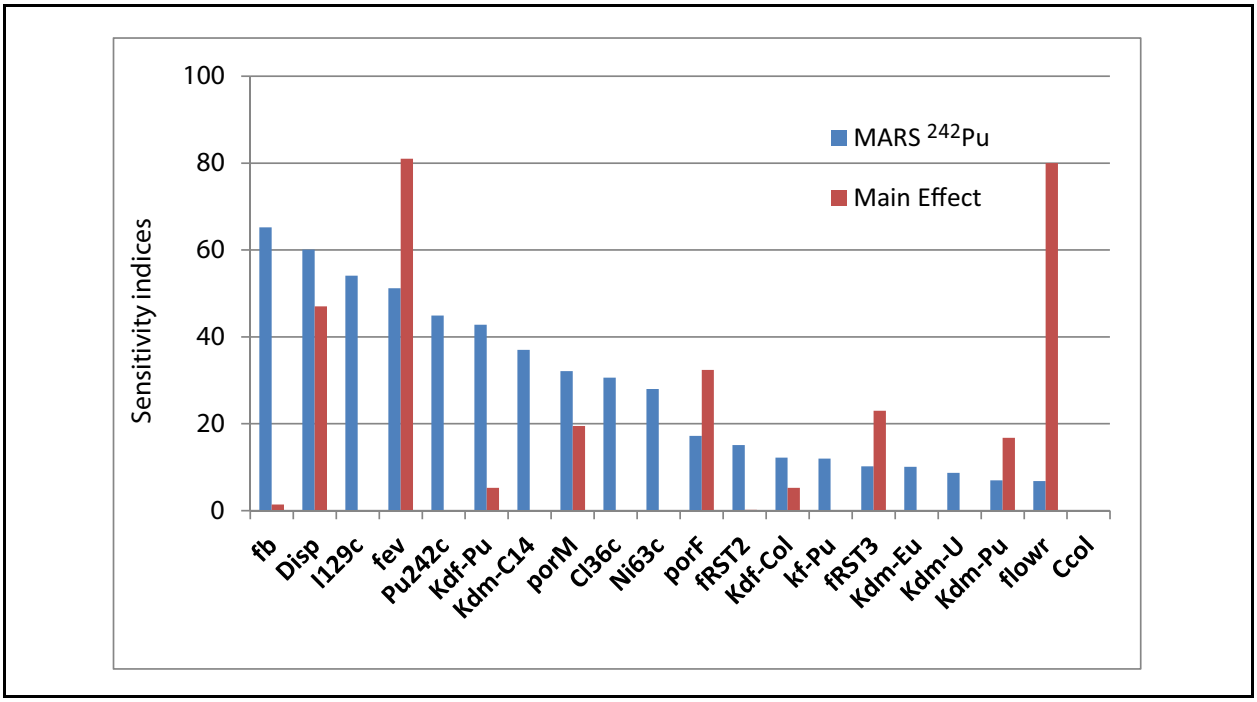

Figure M-31
Global Sensitivity Analysis of ^{242}Pu Contaminant Lengths to 58 Sampled Parameters of the Monte Carlo Simulations

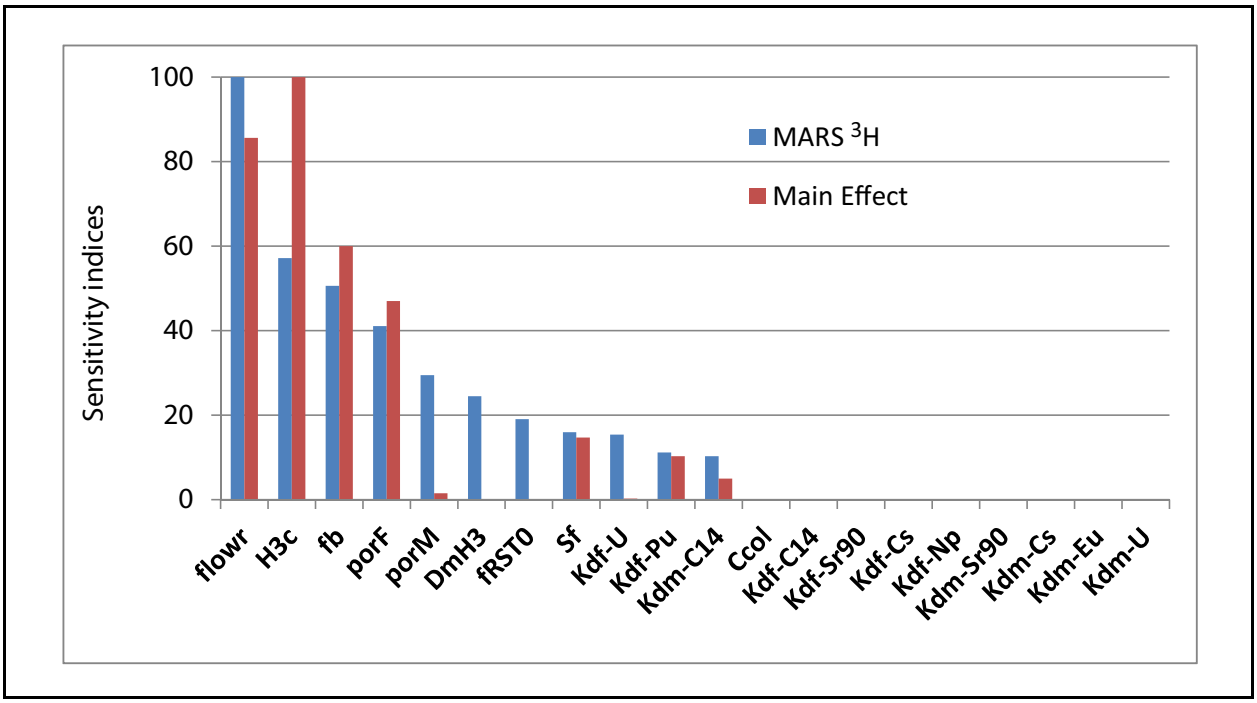

Figure M-32
Global Sensitivity Analysis of ^{3}H Contaminant Lengths to 58 Sampled Parameters of the Monte Carlo Simulations

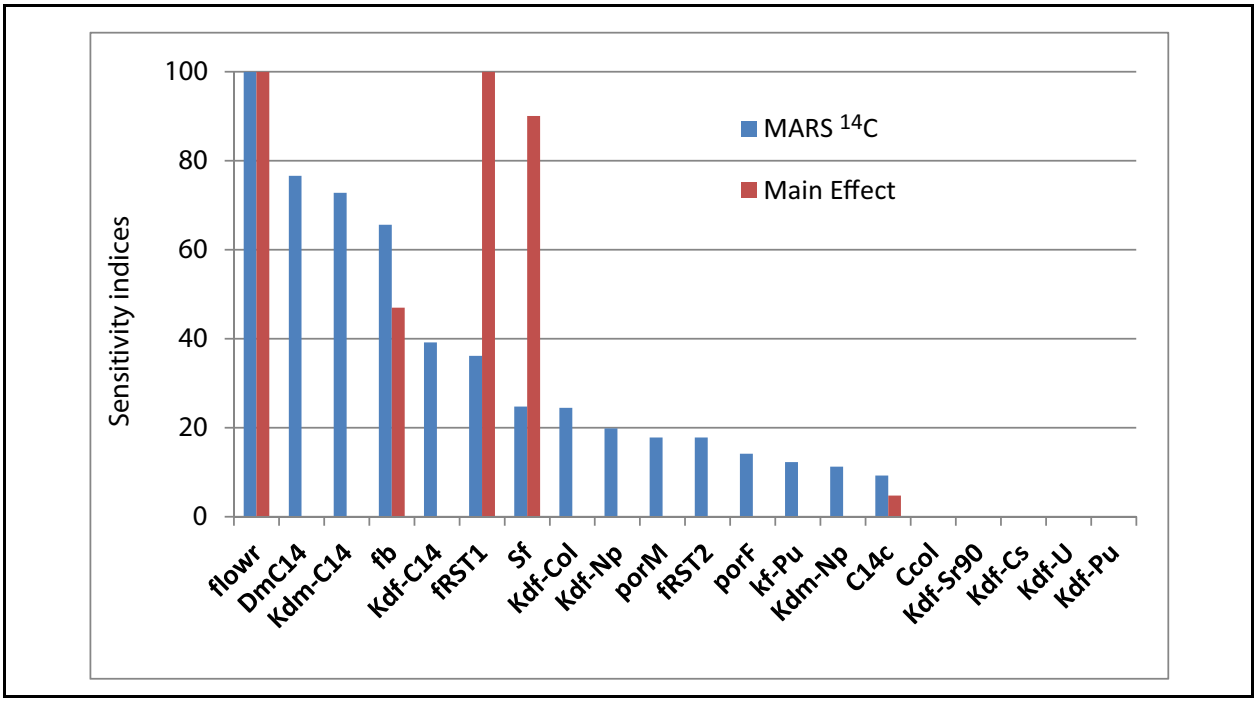

Figure M-33
Global Sensitivity Analysis of ^{14}C Contaminant Lengths to 58 Sampled Parameters of the Monte Carlo Simulations

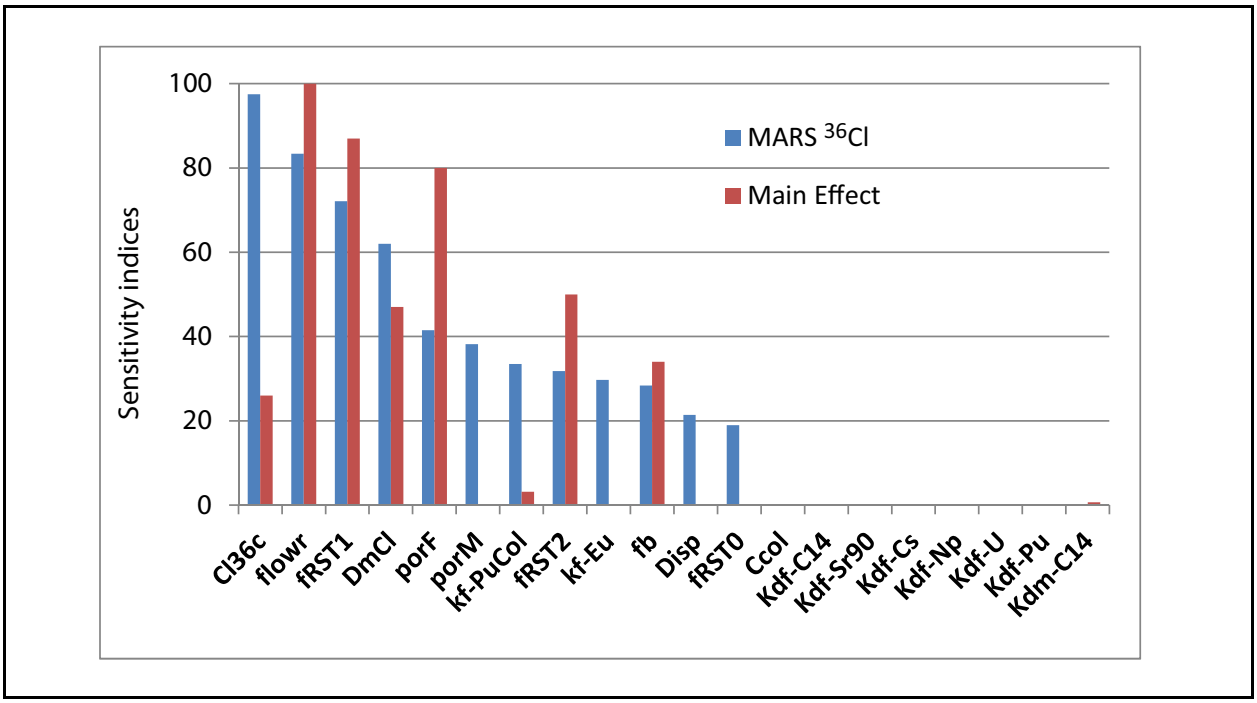

Figure M-34
Global Sensitivity Analysis of ^{36}Cl Contaminant Lengths to 58 Sampled Parameters of the Monte Carlo Simulations

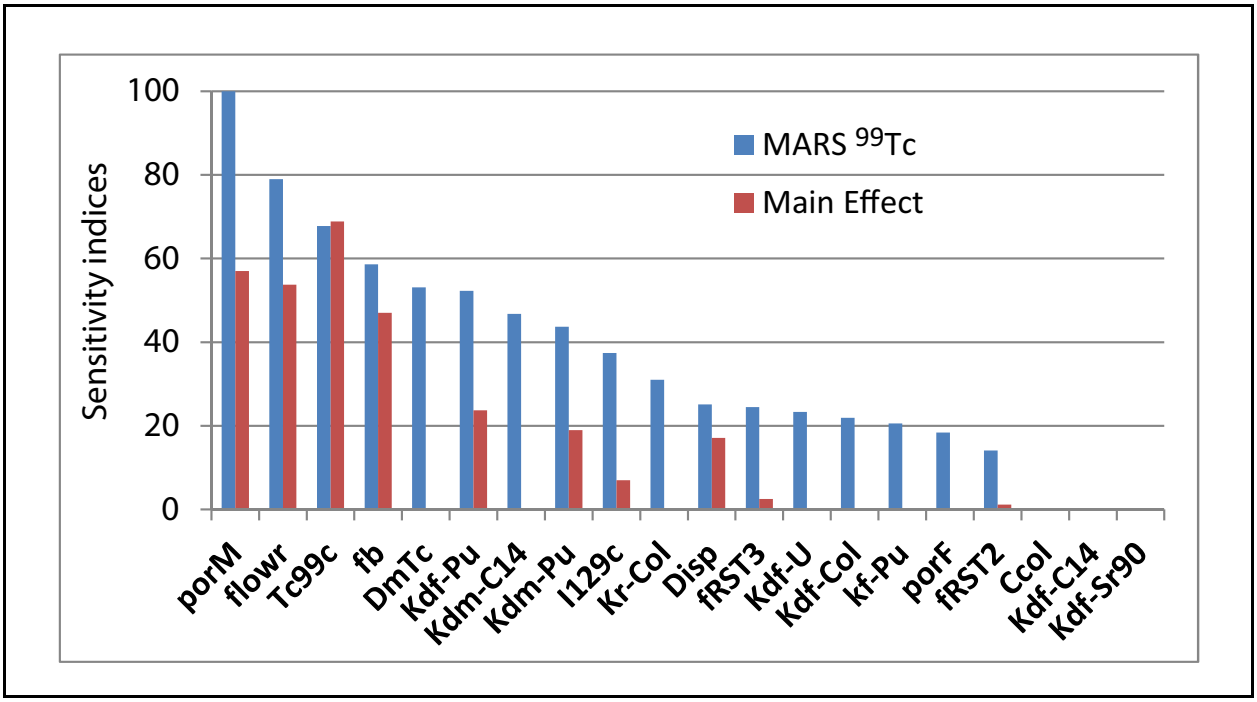

Figure M-35
Global Sensitivity Analysis of ^{99}Tc Contaminant Lengths to 58 Sampled Parameters of the Monte Carlo Simulations

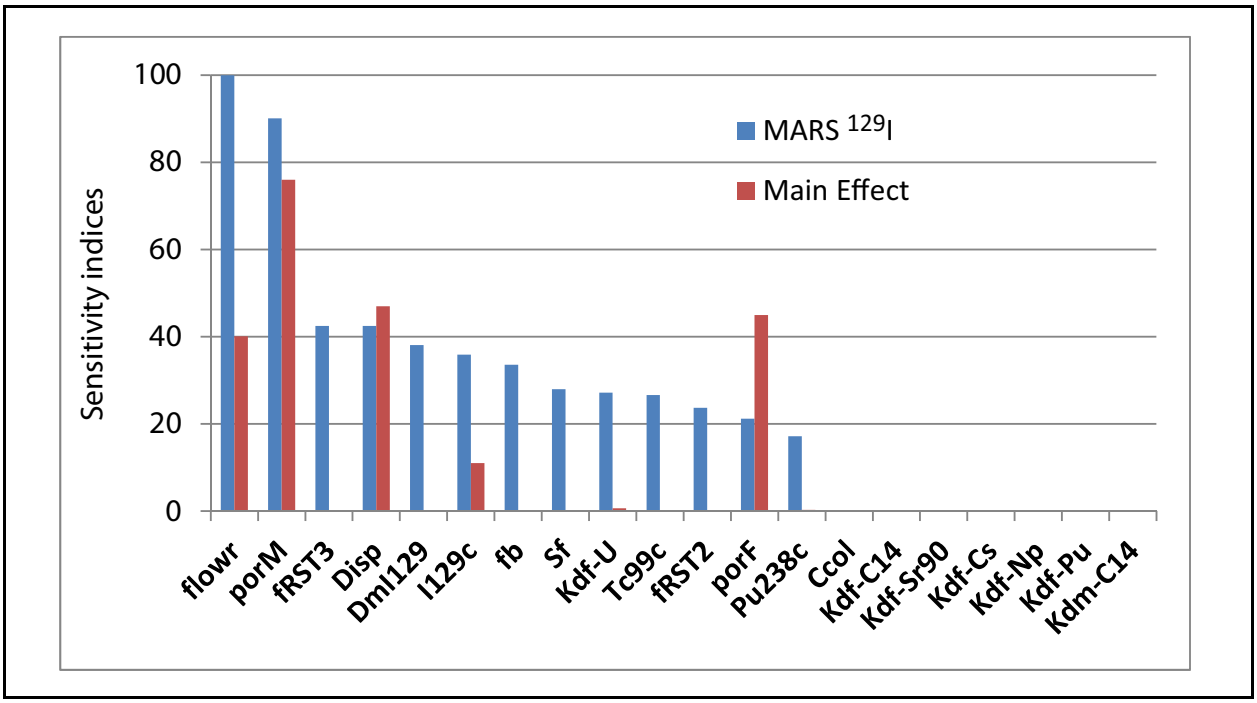

Figure M-36
Global Sensitivity Analysis of ^{129}I Contaminant Lengths to 58 Sampled Parameters of the Monte Carlo Simulations

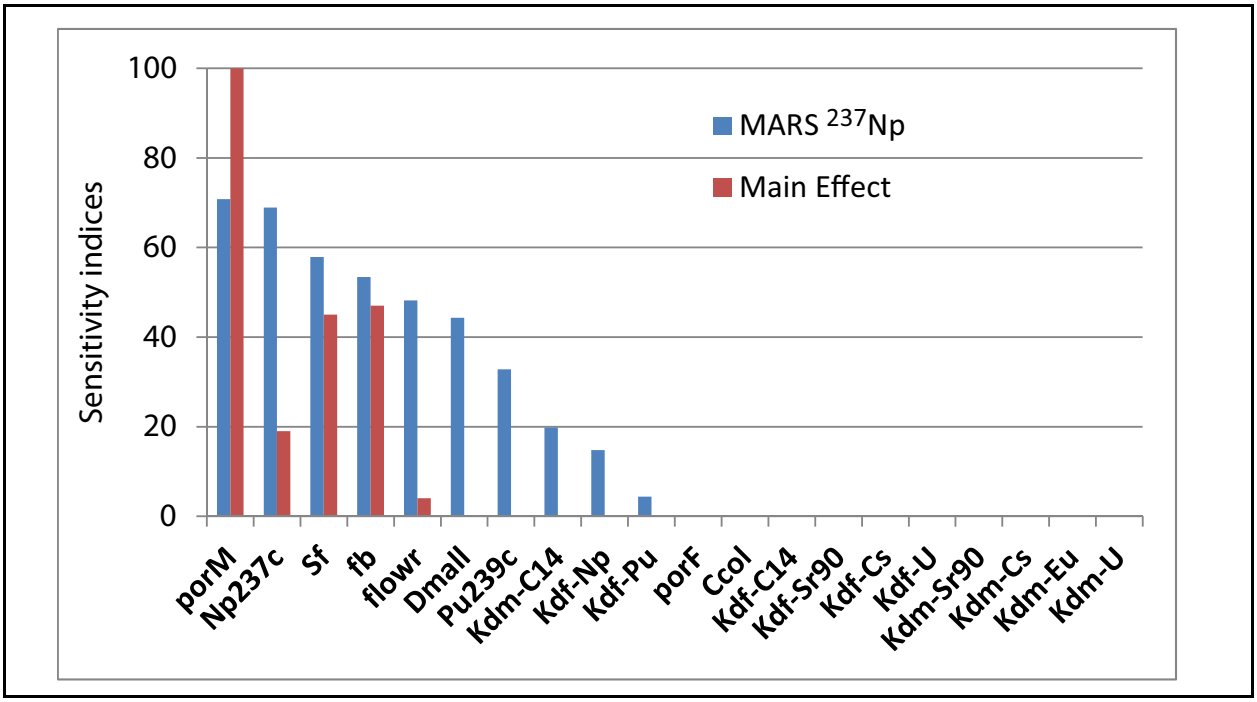

Figure M-37
Global Sensitivity Analysis of ^{237}Np Contaminant Lengths to 58 Sampled Parameters of the Monte Carlo Simulations

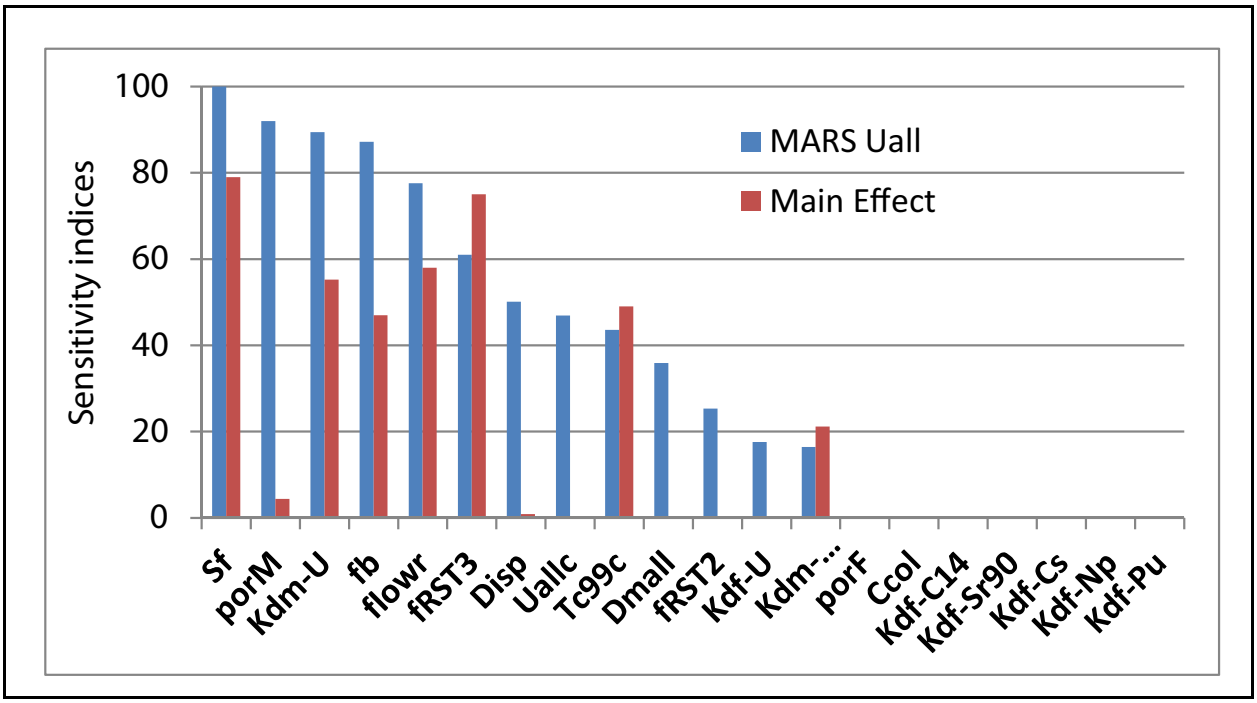

Figure M-38
Global Sensitivity Analysis of Uranium Contaminant Lengths to 58 Sampled Parameters of the Monte Carlo Simulations

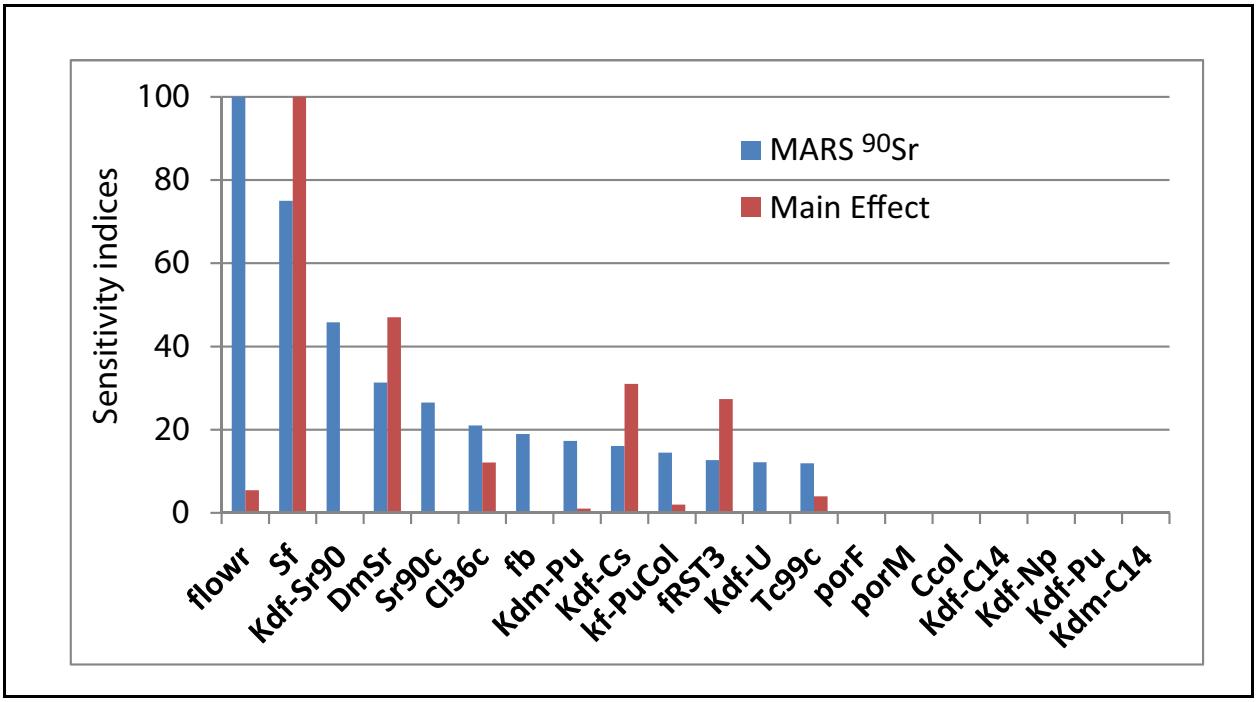

Figure M-39
Global Sensitivity Analysis of ^{90}Sr Contaminant Lengths to 58 Sampled Parameters of the Monte Carlo Simulations

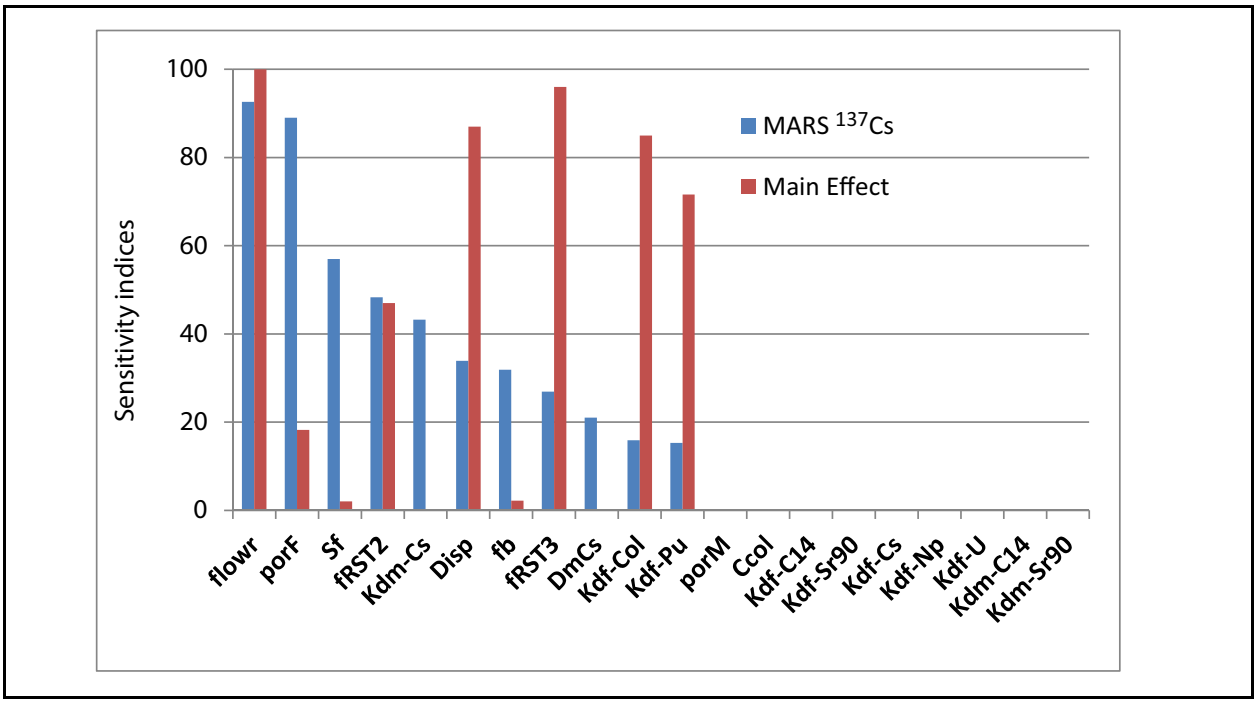

Figure M-40
Global Sensitivity Analysis of ^{137}Cs Contaminant Lengths to 58 Sampled Parameters of the Monte Carlo Simulations

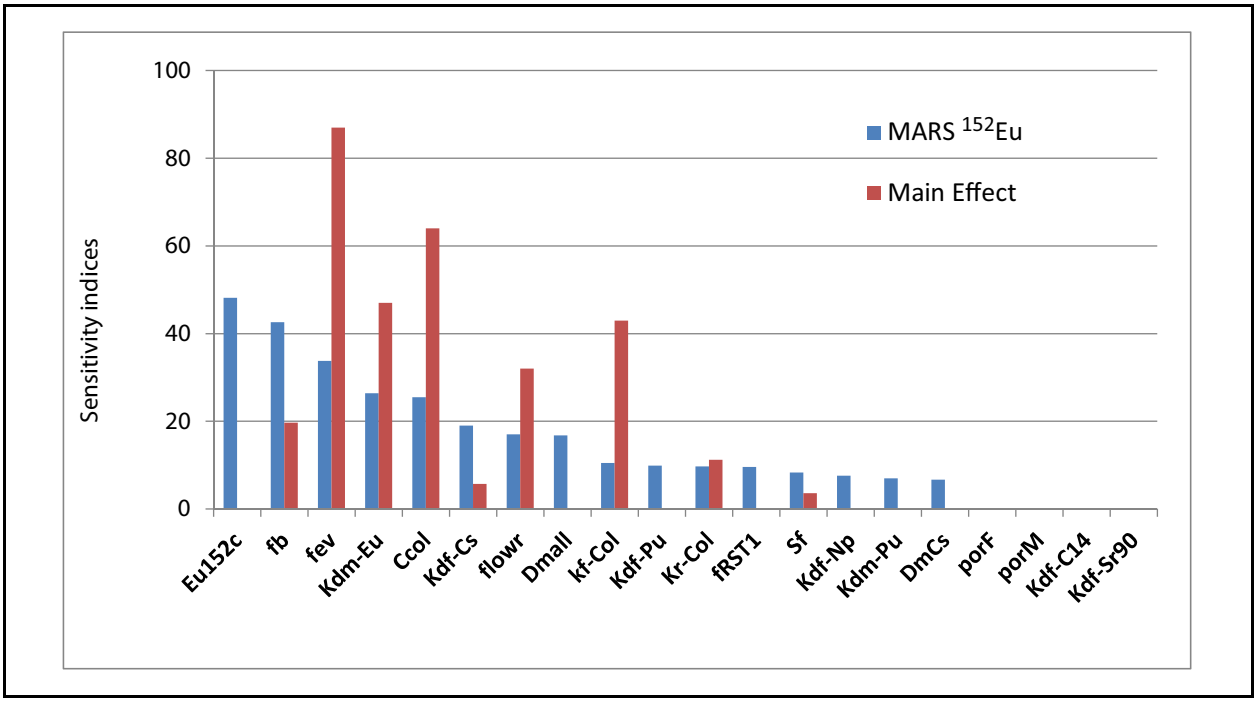

Figure M-41
Global Sensitivity Analysis of ^{152}Eu Contaminant Lengths to 58 Sampled Parameters of the Monte Carlo Simulations

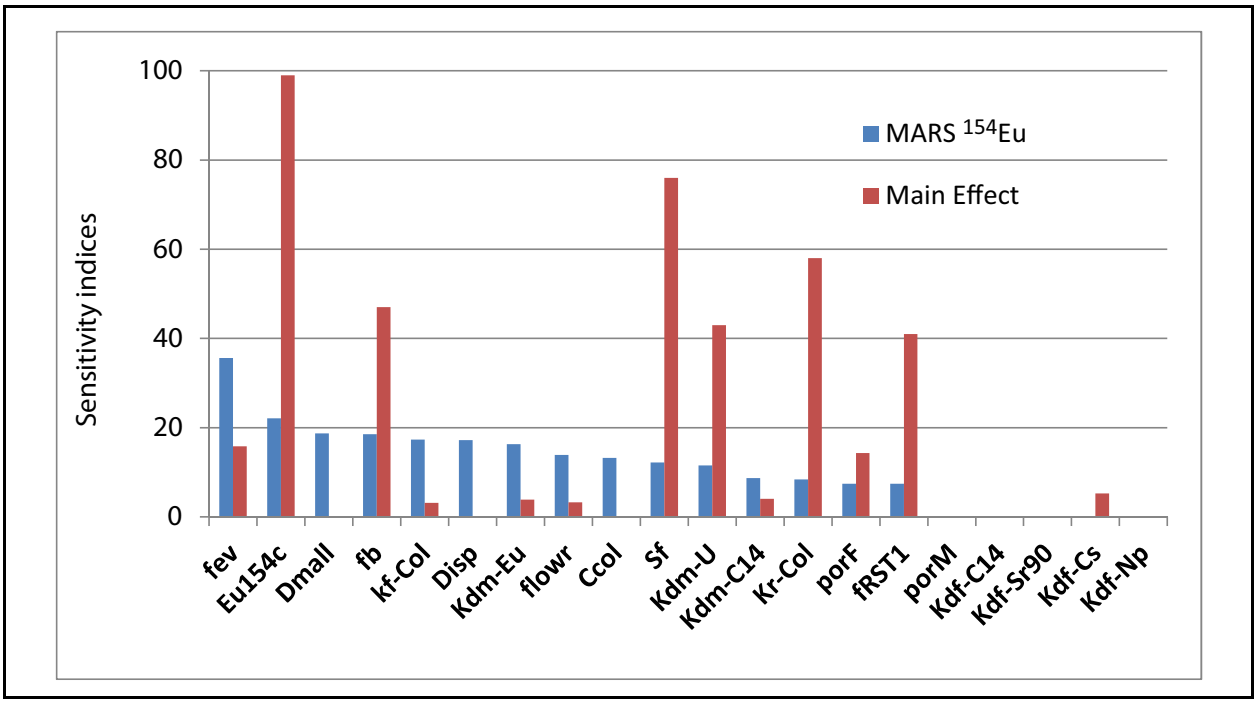

Figure M-42
Global Sensitivity Analysis of ^{154}Eu Contaminant Lengths to 58 Sampled Parameters of the Monte Carlo Simulations

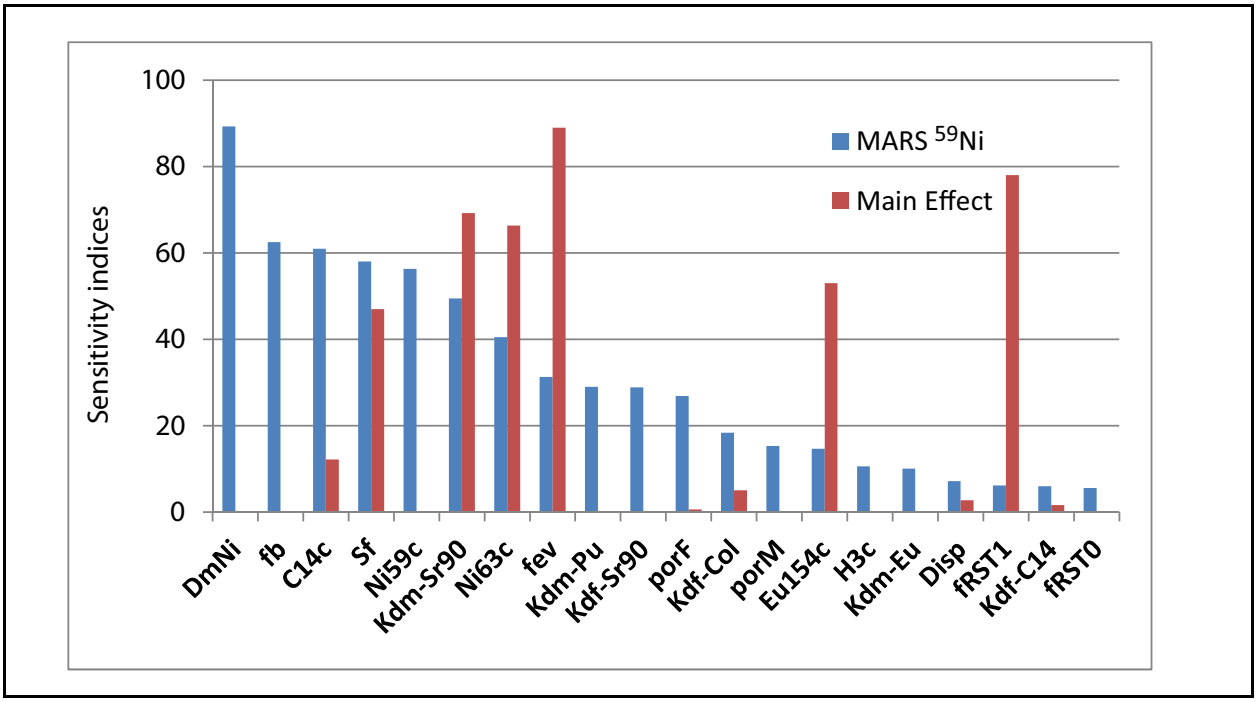

Figure M-43
Global Sensitivity Analysis of ^{59}Ni Contaminant Lengths to 58 Sampled Parameters of the Monte Carlo Simulations

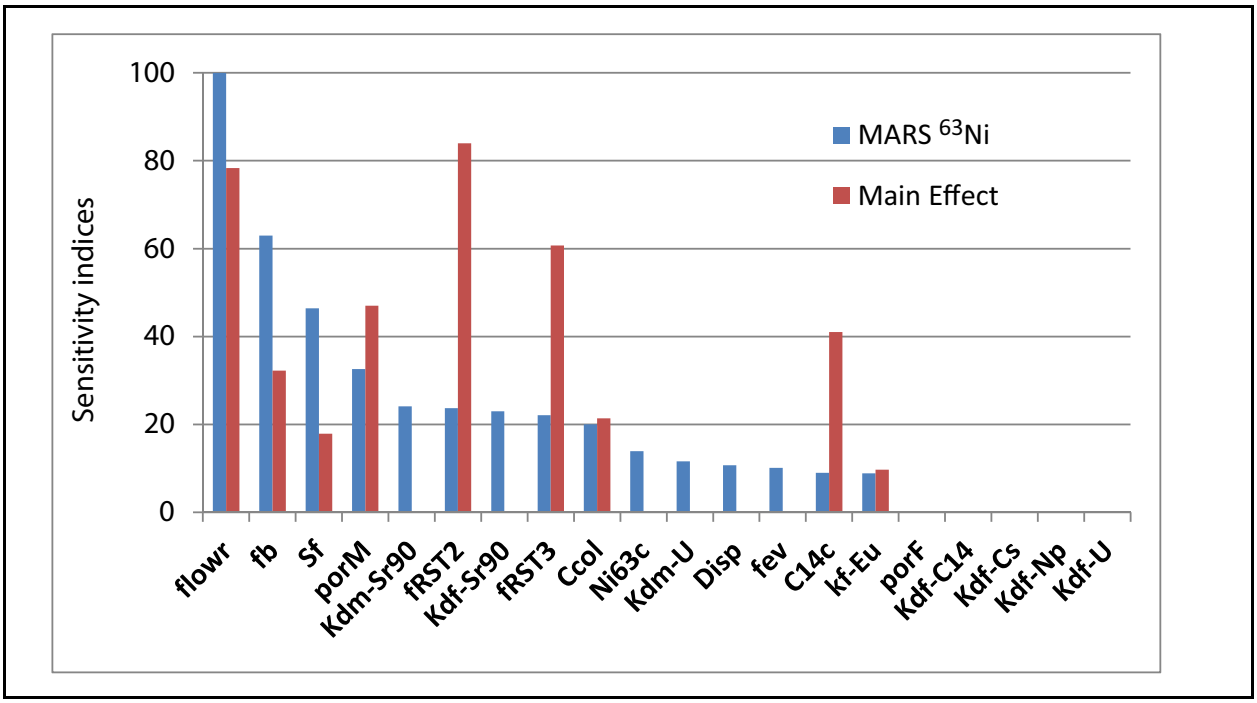

Figure M-44
Global Sensitivity Analysis of ^{63}Ni Contaminant Lengths to 58 Sampled Parameters of the Monte Carlo Simulations

parameter can directly influence the matrix diffusion and sorption onto the matrix. The contaminant lengths of some of the radionuclides are sensitive to some additional parameters. For example, Figures M-27 to M-31 show that contaminant lengths of plutonium isotopes ($^{238–241}$Pu) are also relatively sensitive to initial plutonium concentration uncertainty in the inventory (f_{RST3}), the attachment or detachment coefficient of the colloid (K_{df}-Col), and plutonium sorption coefficients in the fracture and matrix (K_{df}-Pu and K_{dm}-Pu). The results of the MARS analysis indicate very little sensitivity to the colloid load (C_{col}), except for ^{241}Pu. The contaminant lengths of most of the other radionuclides are very sensitive to the flow rate, initial concentrations, and factors that influence matrix diffusion. The contaminant lengths of the sorbing species are also sensitive to factors that affect the sorption behavior.

There is clearly a lot of statistical noise in these results, especially at lower sensitivities, as evidenced by the nonphysical nature of some of the identified sensitivities. These nonphysical sensitivities occur when some of the input parameters are correlated. For example, the matrix diffusion coefficients of different radionuclides are computed from the sampled matrix porosity with the tortuosity equation and the diffusion coefficients of radionuclides in free water. Therefore, all of the matrix diffusion coefficients of different radionuclides are highly correlated to one another. The contaminant length of one radionuclide may be sensitive (or correlated) to the matrix diffusion coefficients of other radionuclides, because the matrix diffusion coefficients have the same variation pattern as the sampled matrix porosities.

Similarly, correlations may exist among the initial concentrations of different radionuclides because the initial concentrations of the 18 radionuclides are computed from the same sampled exchange volume factors (f_{ev}), fracture porosities, and source inventory uncertainty factors (f_{RSTH3}, f_{RST1}, f_{RST2}, and f_{RST3}).

M.7.0 SUMMARY

This appendix evaluated the relative importance of colloid-facilitated transport of plutonium and europium for defining the contaminant boundary by comparing the migration distances of plutonium and europium above their MCLs with those of other radionuclides in a one-dimensional, steady-state, dual-porosity model of the LCA extending 30 km southward from the BOURBON detonation. The radionuclides considered were ^{3}H, ^{14}C, ^{36}Cl, ^{59}Ni, ^{63}Ni, ^{99}Tc, ^{129}I, ^{237}Np, U, ^{90}Sr, ^{137}Cs, ^{152}Eu, ^{154}Eu, ^{238}Pu, ^{239}Pu, ^{240}Pu, ^{241}Pu, and ^{242}Pu. The modeling was done within a Monte Carlo framework that simultaneously considered uncertainties in hydrologic and transport parameters, radionuclide inventory, and initial source distribution. The detailed process model for colloid-facilitated transport of plutonium and europium included competitive sorption between colloids and immobile minerals on the fracture walls and rock matrix, colloid attachment and detachment on the fracture walls, and matrix diffusion of the dissolved plutonium and europium.

The metric used to compare the importance of individual radionuclides was the contaminant length (the distance within which the concentrations of individual radionuclides exceed their MCLs), which is the one-dimensional equivalent of the three-dimensional contaminant boundaries considered in the main body of the report. Based on the 95th percentile of exceedance, ^{239}Pu has the seventh largest maximum contaminant length (4.3 km) after ^{129}I (14.7 km), ^{3}H (13.2 km), ^{36}Cl (10.6 km), ^{137}Cs (10.2 km), ^{99}Tc (4.9 km), and ^{90}Sr (4.5 km). Therefore, ^{239}Pu is expected to contribute little to the overall contaminant boundary. Other plutonium isotopes had shorter contaminant lengths because of smaller initial concentrations relative to their MCLs or shorter half-lives. Europium isotopes (^{152}Eu and ^{154}Eu) also were simulated as undergoing colloid-facilitated transport, but essentially were not transported much beyond the BOURBON source area because of their short half-lives and strong sorption properties. The contaminant lengths of short-lived species such as ^{3}H, ^{137}Cs, and ^{90}Sr generally reached a maximum after a few hundred years, but eventually, their concentrations dropped below their MCLs everywhere by the end of the 1,000-year regulatory period. Interestingly, the contaminant lengths of even long-lived, non-sorbing radionuclides such as ^{36}Cl, ^{99}Tc, and ^{129}I reached a maximum by 500 years, but eventually contracted over time, presumably because of dilution by advection, dispersion, and diffusion. Consequently, ^{239}Pu has the third largest contaminant length (3 km) behind ^{36}Cl (6.6 km) and ^{129}I (6.0 km) at the end of the 1,000-year

regulatory period. However, given the time progressive nature of the contaminant boundary, it is still relatively inconsequential relative to the maximum transport distances of other radionuclides.

An analysis of plutonium transport modeling results indicated that by 1,000 years, ^{239}Pu accounts for almost all of the mobile plutonium and that most of this is associated with colloids. This suggests that the detailed process model could be reconceptualized as a simpler model with a single fictitious species ^{239}Pu-Col, which is non-diffusive and slowed only by colloid attachment and detachment. Inverse modeling showed that this simple model can provide a good approximation to the more detailed competitive sorption model, provided that the fraction of the initial plutonium source that becomes more or less permanently sorbed to colloids (termed the plutonium reduction factor) can be estimated. A distribution of the plutonium reduction factors with a mean of 2.83E-05 and a range of 5.92E-06 to 6.3E-05 was estimated from the Monte Carlo transport results based on the mean ^{239}Pu concentrations between the maximum exchange volume (0.42 km) and the 95th percentile contaminant length (roughly 5 km). Alternatively, based on the results presented in this appendix, it is reasonable to ignore colloid-facilitated transport of plutonium altogether in the three-dimensional LCA models of radionuclide transport, given the fact that it is unlikely to define the contaminant boundary any time over the next 1,000 years.

Global sensitivity analysis of the contaminant lengths for individual radionuclides indicated that uncertainty in fracture parameters, such as spacing, aperture and porosity, source term concentrations, and hydraulic conductivity (or equivalently, flow rate), were among the most important factors that determine variability in contaminant lengths. Radionuclide-specific parameters such as fracture and matrix sorption coefficients also were important for sorbing radionuclides. Different three-dimensional LCA models presented in Section 6.0 estimate variable extents for the contaminant boundary depending on the assumed influx from the north, transport properties, exchange volume radii, and other factors. Some of these models predict contaminant transport extending to the southern boundary of Yucca Flat (15 km or more), consistent with the models presented in this appendix. However, Well UE-7nS, located 137 m downgradient from BOURBON, shows ^{3}H concentrations below the MCL, which differ considerably from the contaminant extents simulated with the one-dimensional model presented in this appendix. The discrepancy between the simulation results presented here and field measurements may reflect the conservatism of the assumptions used to develop the conceptual model for the source term used in the one-dimensional models, in particular that all of the radionuclide inventory from the BOURBON detonation (minus the melt-glass fraction)

is in the fractures of the saturated LCA and immediately available for transport. Nonetheless, because the primary purpose of the simplified one-dimensional model was to investigate the relative importance of the colloid-facilitated transport of plutonium relative to other radionuclide species for defining the contaminant boundary, the results of this appendix are still valuable from that perspective.

M.8.0 REFERENCES

Bear, J. 1972. *Dynamics of Fluids in Porous Media*. New York, NY: Elsevier Publishing Co.

Bowen, S.M., D.L. Finnegan, J.L. Thompson, C.M. Miller, P.L. Baca, L.F. Olivas, C.G. Geoffrion, D.K. Smith, W. Goishi, B.K. Esser, J.W. Meadows, N. Namboodiri, J.F. Wild. 2001. *Nevada Test Site Radionuclide Inventory 1951–1992*, LA-13859-MS. Los Alamos, NM: Los Alamos National Laboratory.

Carle, S.F., M. Zavarin, Y. Sun, G.A. Pawloski. 2008. *Evaluation of Hydrologic Source Term Processes for Underground Nuclear Tests in Yucca Flat, Nevada Test Site: Carbonate Tests*, LLNL-TR-403485. Livermore, CA: Lawrence Livermore National Laboratory.

DOE/NV, see U.S. Department of Energy, Nevada Operations Office.

Dai, Z., A. Wolfsberg, Z. Lu, and P. Reimus. 2007. "Upscaling Matrix Diffusion Coefficients for Heterogeneous Fractured Rocks," *Geophysical Research Letters* 34, L07408. doi:10.1029/2007GL029332.

Dai, Z., A. Wolfsberg, P. Reimus, H. Deng, E. Kwicklis, M. Ding, D. Ware, and M. Ye. 2012. "Identification of Sorption Processes and Parameters for Radionuclide Transport in Fractured Rock," *Journal of Hydrology* 414–415: 220–230. doi:10.1016/j.jhydrol.2011.10.035.

IAEA, see International Atomic Energy Agency.

International Atomic Energy Agency. 1998. *The Radiological Situation at the Atolls of Mururoa and Fangataufa, Technical Report, Volume 3: Inventory of Radionuclides Underground at the Atolls*, IAEA-MFTR-3. In *Proceedings of an IAEA Conference, Vienna, 30 June–3 July.* Vienna, Austria.

Li, Y.-H., and S. Gregory. 1974. "Diffusion of Ions in Sea Water and in Deep-Sea Sediments," *Geochimica et Cosmochimica Acta* 38 (5): 703–714.

Lide, D.R., ed. 2000. *CRC Handbook of Chemistry and Physics*, 81st Edition. Boca Raton, FL: Taylor & Francis Group/CRC Press.

Pawloski, G.A. 1999. *Development of Phenomenological Models of Underground Nuclear Tests on Pahute Mesa, Nevada Test Site—BENHAM and TYBO*, UCRL-ID-136003. Livermore, CA: Lawrence Livermore National Laboratory.

Rechard, R.P., and M.S. Tierney. 2005. "Assignment of Probability Distributions for Parameters in the 1996 Performance Assessment for the Waste Isolation Pilot Plant. Part 2. Application of Process." *Reliability Engineering and System Safety* 88 (1): 33–80. doi:10.1016/j.ress.2004.07.012.

Reimus P.W., S.D. Ware, N. Lu, A. Abdel-Fattah, K.S. Kung, and M.P. Neu. 2001. *FY 2001 Progress Report on Colloid-Facilitated Plutonium Transport in Fractured Rocks from Pahute Mesa, Nevada Test Site*, ERD.011004.0001. Los Alamos, NM: Los Alamos National Laboratory.

Reimus P., G. Pohll, T. Mihevc, J. Chapman, M. Haga, B. Lyles, S. Kosinski, R. Niswonger, P. Sanders. 2003. "Testing and Parameterizing a Conceptual Model for Solute Transport in a Fractured Granite Using Multiple Tracers in a Forced-Gradient Test," *Water Resources Research* 39 (12): 1356. doi:10.1029/2002WR001597.

Reimus, P.W., R.L. Hershey, D.L. Decker, S.D. Ware, C. Papelis, S. Earman, A. Abdel-Fattah, M. Haga, D. Counce, S. Chipera, and C. Sedlacek. 2006. *Tracer Transport Properties in the Lower Carbonate Aquifer of Yucca Flat*, LA-UR-06-0486. Los Alamos, NM: Los Alamos National Laboratory.

Reimus P.W., M. Murrell, A. Abdel-Fattah, E. Garcia, D. Norman, S. Goldstein, A. Nunn, R. Gritzo, and B. Martinez. 2006. *Colloid Characteristics and Radionuclide Associations with Colloids in Near-Field Waters at the Nevada Test Site (FY 2005 Progress Report)*, LA-UR-05-8612. Los Alamos, NM: Los Alamos National Laboratory.

Reimus, P.W., S.D. Ware, A. Abdel-Fattah, M. Ding, C. Sedlacek, M. Haga, E. Garcia, S. Chipera. 2006. *Radionuclide Sorption and Transport in Fractured Rocks of Yucca Flat, Nevada Test Site: Experimental Results and Interpretations*, Los Alamos, NM: Los Alamos National Laboratory.

Robinson, B.A. 1994. "A Strategy for Validating a Conceptual Model for Radionuclide Migration in the Saturated Zone beneath Yucca Mountain," *Radioactive Waste Management and Environmental Restoration* 19: 73–96.

Robinson, B.A., Z.V. Dash, and S.L. Painter. 2011. *User's Guide for the PLUMECALC Application with Subgridding*, LA-UR-11-02090. Los Alamos, NM: Los Alamos National Laboratory.

SNJV, see Stoller-Navarro Joint Venture.

Stoller-Navarro Joint Venture. 2006. *Phase I Hydrologic Data for the Groundwater Flow and Contaminant Transport Model of Corrective Action Unit 97: Yucca Flat/Climax Mine, Nevada Test Site, Nye County, Nevada*, Rev. 0, S-N/99205--077. Las Vegas, NV.

Stoller-Navarro Joint Venture. 2007. *Phase I Contaminant Transport Parameters for the Groundwater Flow and Contaminant Transport Model of Corrective Action Unit 97: Yucca Flat/Climax Mine, Nevada Test Site, Nye County, Nevada*. Rev. 0, S-N/99205--096. Las Vegas, NV.

Sudicky, E.A., and E.O. Frind. 1982. "Contaminant Transport in Fractured Porous Media: Analytical Solutions for a System of Parallel Fractures." *Water Resources Research* 18 (6): 1634–1642. doi:10.1029/WR018i006p01634.

Tompson, A.F.B., M. Zavarin, W.W. McNab, S.F. Carle, D.E. Shumaker, C. Lu, Y. Sun, G.A. Pawloski, Q. Hu, and S.K. Roberts. 2011. Written communication. Subject: *Hydrologic Source Term Processes and Models for Underground Nuclear Tests at Rainier Mesa and Shoshone Mountain, Nevada National Security Site*. Livermore, CA: Lawrence Livermore National Laboratory.

Tong, C. 2011. *PSUADE User's Manual (Version 1.4.0)*, LLNL-SM-407882. Livermore, CA: Lawrence Livermore National Laboratory.

U.S. Department of Energy, Nevada Operations Office. 2000. *United States Nuclear Tests, July 1945 through September 1992*, DOE/NV--209-REV 15. Las Vegas, NV.

Viswanathan, H.S. 1996. *Modification of the Finite Element Heat and Mass Transfer Code (FEHM) to Model Multicomponent Reactive Transport*, LA-13167-T. Los Alamos, NM: Los Alamos National Laboratory.

Viswanathan, H.S. 1999. *The Development and Application of Reactive Transport Modeling Techniques to Study Radionuclide Migration at Yucca Mountain, NV*, LA-13642-T. Los Alamos, NM: Los Alamos National Laboratory.

Wolfsberg, A., L. Glascoe, G. Lu, A. Olson, P. Lichtner, M. McGraw, T. Cherry, and G. Roemer. 2002. *TYBO/BENHAM: Model Analysis of Groundwater Flow and Radionuclide Migration from Underground Nuclear Tests in Southwestern Pahute Mesa, Nevada*, LA-13977. Los Alamos, NM: Los Alamos National Laboratory.

Wolfsberg, A., and H. Viswanathan. 2002. Written communication. Subject: *Reactive Transport Model Parameters for Flowing Fractures: Parameter Estimation and Comparison with Experimental Data for Colloid-Facilitated Plutonium Transport*. Los Alamos, NM: Los Alamos National Laboratory.

Zavarin, M. Lawrence Livermore National Laboratory. 2012a. Personal communication regarding LCA radionuclide sorption coefficients. 16 March. Livermore, CA.

Zavarin, M. Lawrence Livermore National Laboratory. 2012b. Personal communication regarding preliminary RST screening calculation. Livermore, CA.

Zavarin, M., S.K. Roberts, M.R. Johnson, Q. Hu, B.A. Powell, P. Zhao, A.B. Kersting, R.E. Lindvall, R.J. Pletcher, 2013. *Colloid-Facilitated Radionuclide Transport in Fractured Carbonate Rock from Yucca Flat, Nevada National Security Site*, Lawrence Livermore National Laboratory Report LLNL-TR-619352., Livermore, CA.

Zyvoloski, G.A., B.A. Robinson, Z.V. Dash, and L.L. Trease. 1997. *Summary of the Models and Methods for the FEHM Application—A Finite-Element Heat- and Mass-Transfer Code*, LA-13307-MS. Los Alamos, NM: Los Alamos National Laboratory.

Zyvoloski, G.A., B.A. Robinson, and H.S. Viswanathan. 2008. "Generalized Dual Porosity: A Numerical Method for Representing Spatially Variable Sub-grid Scale Processes," *Advances in Water Resour*ces 31 (3): 535–544. doi:10.1016/j.advwatres.2007.11.006.

Appendix N

Corroborative Software Analyses

N.1.0 INTRODUCTION

N.1.1 Purpose/Objectives Approach

Significant rigor is required to ensure software used to support environmental decisions is appropriate and adequately incorporates the features and processes relevant to the assessment and has been tested over the range of conceptual models, parameters and spatial and temporal scales used in the models of the physical system. The technical and quality basis for selecting the software used to forecast the contaminant boundary in the Yucca Flat/Climax Mine CAU is presented in Appendix K. The software selection is based in part on comparison of results generated with analytical solution as well as alternative "industry-standard" software for simple systems that mimic the spatial and temporal scales of interest to the CAU flow and transport model.

While the software testing and comparisons presented in Appendix K provide technical and quality assurance confidence that the FEHM_sptr, Walkabout and PLUMECALC software are appropriate for use in the Yucca Flat/Climax Mine transport model, given the importance of the modeling to the environmental decision, alternative "industry-standard" software have been applied to a subdomain of the LCA transport model to evaluate the potential effect difference solution schemes and algorithm might have on a scale of interest to the CAU transport model. This appendix presents the results of analyses using corroborative, industry-standard software applied to the sub domain of the Yucca Flat LCA transport model.

N.1.2 Corroborative Software

A range of alternative software meet the requisite attributes and criteria necessary to evaluate radionuclide transport given a saturated dual porosity conceptual transport model. These software include the following:

- FEHM, FEHM_sptr and PLUMECALC
- FEHM, Walkabout and PLUMECALC
- FEHM and FEHM_PTRK, or FEHM_TRAC, or FEHM_MPTR
- NUFT
- NUFT and RWHet
- MODFLOW and MT3DMS

- MODFLOW_SURFACT
- MODFLOW-USG
- ECLIPSE H20 .
- Feflow
- FRAC3DVS
- STOMP
- TOUGH2
- PORFLO
- SWIFT II.
- FracMan/MAFIC

FEHM, FEHM_sptr and PLUMECALC are used to calculate contaminant concentrations that are used as the basis for the forecast contaminant boundaries in the LCA presented in Section 6.0. MODFLOW/MT3DMS, Feflow and FracMan/MAFIC were selected as corroborative software to evaluate the representativeness of the concentrations calculated by PLUMECALC. In addition, Appendix M presents one-dimensional analyses using FEHM_TRAC that can also be compared to the PLUMECALC results. MODFLOW/MT3DMS was selected because it is a widely used software in the United States for groundwater flow and contaminant transport modeling. Feflow was selected because it is a widely used software in Europe and Asia for groundwater flow and contaminant transport modeling. FracMan/MAFIC was selected because it is a widely used software for a range of radioactive waste disposal applications. The basic attributes of each of these software relevant for the Yucca Flat LCA transport model are presented in the following sections.

N.1.2.1 MODFLOW/MT3DMS

MODFLOW is the name that has been given the USGS Modular Three-Dimensional Groundwater Flow Model (McDonald and Harbaugh, 1988). Because of its ability to simulate a wide variety of systems, its extensive publicly available documentation, and its rigorous USGS peer review, MODFLOW has become a worldwide standard groundwater flow code. MODFLOW is used to simulate systems for water supply, containment remediation and mine dewatering. MODFLOW is an industry standard software that when properly applied has been recognized and accepted by courts, regulatory agencies, universities, consultants and industry. Groundwater flow within the aquifer is simulated in MODFLOW using a block-centered finite-difference approach. Layers can be simulated as confined, unconfined, or a combination of both. Flows from external stresses such as flow to wells, areal recharge, evapotranspiration, flow to drains, and flow through riverbeds can also be simulated.

Because MODFLOW is a groundwater flow model, it must be linked to a transport code to evaluate contaminant transport. Examples of codes that MODFLOW may be linked to include: MT3D and MT3DMS among others. MT3D (Zheng, 1990) is a comprehensive three-dimensional numerical model for simulating solute transport in complex hydrogeologic settings. MT3D has a modular design that permits simulation of transport processes independently or jointly. MT3D is capable of modeling advection in complex steady-state and transient flow fields, anisotropic dispersion, first-order decay and production reactions, and linear and nonlinear sorption. The modular multispecies transport code MT3DMS includes the three major classes of transport solution techniques in a single code, i.e., the standard finite difference method; the particle-tracking-based Eulerian-Lagrangian methods; and the higher-order finite-volume total-variation-diminishing (TVD) method (Zheng and Wang, 1999). Since no single numerical technique is effective for all transport conditions, the combination of these solution techniques, each having its own strengths and limitations, provides an approach for solving the most wide-ranging transport problems with desired efficiency and accuracy.

N.1.2.2 FEFLOW

FEFLOW™ (Finite Element Subsurface FLOW system) is a computer program for simulating groundwater flow, mass transfer and heat transfer in porous media (Diersch, 2002). The program uses the finite element numerical method to solve the 3D groundwater flow equations for either saturated or unsaturated conditions as well as mass and heat transport in groundwater, including the effects of fluid density and chemical kinetics, through a single-continuum domain. The software was introduced in 1979 by Dr. Hans-Jörg G. Diersch and subsequently commercialized by the Institute for Water Resources Planning and Systems Research (WASY) in 1990. WASY was purchased by the DHI Group in 2007, which has been renamed to DHI-WASY GmbH, who currently sell, maintain, and continue to advance the FEFLOW software (www.dhi-wasy.com). An independent evaluation of the FEFLOW software and interface is provided by Trefry and Muffels (2007). Extensive white paper documentation is available for all of the software modules from DHI-WASY at: http://www.feflow.com/manuals.html.

FEFLOW provides utilities for rapidly constructing a 2D mesh of either triangular or square elements that discretize the model space but requires the sides of all individual mesh elements be vertical meaning that the vertical shape of the mesh elements must be columnar. Unique features in FEFLOW are utilities that allow for the simulation of discrete flow through 1D or 2D features designed to

simulate conduits or fracture planes and through which flow can be described with non-darcian equations. Table N-1 provides a list of the parameters and units required by FEFLOW to perform the available computations. Two methods for solving the groundwater flow equations and six methods for solving mass transport equations are available.

Flow

- The preconditioned conjugate gradient (PCG) method (Diersch, 2002, Saad, 2003), which is the default method in FEFLOW and the method used for this study.
- Stuben's algebraic multigrid (SAMG) method (Ruge and Stuben, 1987).

Transport

- The preconditioned Lanczos BiCGSTABP or Postconditioned bi-conjugate gradient stabilized method, which is the default method in FEFLOW and the method used to simulate ^{3}H and ^{129}I mass transport for this study.
- The preconditioned restarted ORTHOMIN or Orthogonalization-minimization method.
- The preconditioned restarted GMRES or Generalized minimal residual method.
- The preconditioned Lanczos CGS or Conjugate gradient square method.
- The preconditioned Lanczos BiCGSTAB or Bi-conjugate gradient stable method.
- The algebraic multigrid – SAMG method.

FEFLOW is widely used internationally. The DHI-WASY website lists 165 peer-reviewed publications where FEFLOW was used to evaluate groundwater flow and heat and mass transport problems. The software is not as widely used as MODFLOW in the United States but is used by a number of government, academic, and private organizations including:

- U.S. Geological Survey;
- U.S. Nuclear Regulatory Agency;
- U.S. Office of Surface Mining;
- Battelle;
- Lawrence Livermore National Laboratories;
- California Department of Toxic Substance Control;
- California Water Resources Control Board;
- South Florida Water Management District;
- Penn State University;
- Texas A&M University;

- Massachusetts Institute of Technology;
- University of California;
- Desert Research Institute; and
- Southwest Research Institute.

N.1.2.3 FracMan/MAFIC

FracMan (Golder, 2012) is a Discrete Fracture Network (DFN)/Equivalent Porous Media (DFN/EPM) hydrogeologic modeling code developed by Golder Associate Inc., and distributed commercially since 1989. FracMan explicitly models flow and transport in key fractures, faults, breccias, dikes and other discrete features, while supporting the EPM approximation for rock mass hydraulic properties. FracMan thus provides an alternative numerical implementation of the hydrologic conceptual model from that used in FEHM/PLUMECALC. FracMan has been used extensively by radioactive waste management programs in the UK, Sweden, Japan, Korea, and Finland, and was used by the Yucca Mountain project to model rock mechanics scenarios. FracMan is also an industry standard for DFN and hybrid DFN/EPM fractured reservoir hydrodynamic modeling, with installations at 8 of the world's 10 largest publicly traded oil companies.

In the FracMan approach, fractures are implemented as surfaces, which are modeled using triangular finite elements. Fracture flow properties are defined in terms of transmissivity, storativity, and aperture. The key to the FracMan approach is to explicitly represent the fractures that are key to flow and transport, while using an appropriate approximation for the rock matrix and less important "background" fractures. The rock matrix and background fractures can be implemented either using a rock-fracture interaction formulation, or as a hybrid discrete fracture equivalent porous medium (DFN/EPM) model in which the rock volume is discretized as tetrahedral volume elements. These volume elements are intended to provide the combined rock matrix and background fracture hydraulic and transport properties of hydraulic conductivity, specific storage, and porosity (Figure N-1).

FracMan implements flow and transport using the same Darcy flow and advection-dispersion transport conceptual model used by FEHM/PLUMECALC, but solves the equations using distinctively different numerical implementation. FracMan solves flow and transport using a head-based conjugate gradient, variable bandwidth Galerkin Finite Element approach (Pinder and Gray, 1977), random-walk based particle tracking (Prickett et al., 1981) and the Sudicky approach for multiple-immobile zone porosity fracture transport using the Laplace Transform Galerkin method

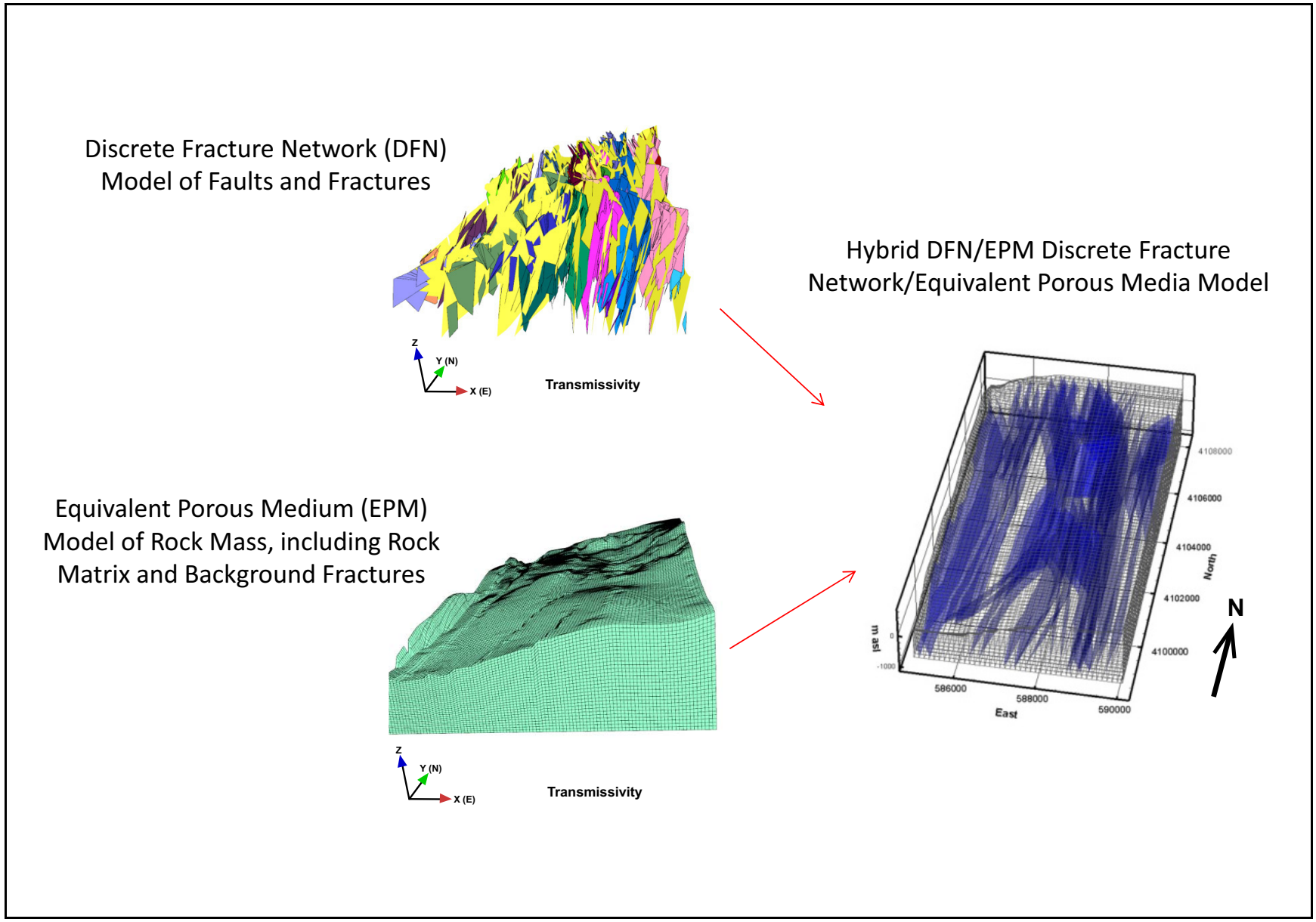

Figure N-1
FracMan Hybrid DFN/EPM Discrete Fracture Network/Equivalent Porous Media Model

(Sudicky and McLaren, 1992). The FracMan transport algorithm is able to explicitly solve transport in complex, heterogeneous rock masses considering multiple immobile zones, with diffusion, dispersion, sorption, and decay parameters appropriate for each immobile zone (Figure N-2).

N.1.3 Description of Model used for Corroborative Software Analyses

In order to have a basis for comparing the results of corroborative software applied to a CAU-relevant transport model at temporal and spatial scales of interest to determining the contaminant boundary, a subarea of the Yucca Flat LCA flow and transport models presented in Sections 5.0 and 6.0 was selected to model. The most significant contaminant sources in this subarea were included in the transport model. This section presents the extent of the subarea flow and transport model used in the corroborative software comparison, the associated flow and transport model parameters used in the comparison, the source term inputs to the subarea model and the flow and transport model results using the FEHM/FEHM_sptr and PLUMECALC software.

N.1.3.1 Model Domain

A subarea of the Yucca Flat LCA flow and transport model presented in Sections 5.0 and 6.0 was used for the corroborative software analysis. This subarea was selected to be of a sufficient spatial extent to encompass several diverse source terms and include a number of north-south trending normal faults as well as extending far enough southward, along the predominant flow direction, to capture the expected extent of contaminant migration.

The subarea model domain is illustrated in Figure N-3 and Figure N-4. The subarea chosen extends about 5 km in an east-west direction and 10 km in a north-south direction and includes a number of significant north-south faults. Although there are about 100 underground nuclear detonations with working points above the saturated LCA within this subarea, as illustrated in Figure N-4 only 5 significant sources were considered in the comparison. These five detonations are BILBY, TORRIDO, MICKEY, LAMPBLACK and BOURBON. As discussed in Section 6.0, these are 5 of the most significant sources contributing to the forecast extent of the contaminant boundary in large part because these detonations provide a significant contaminant flux to the LCA.

The subarea model upper surface is the top of the saturated LCA. In the eastern portion of the subarea model domain this corresponds to the water table surface as the water table is in the LCA in this part

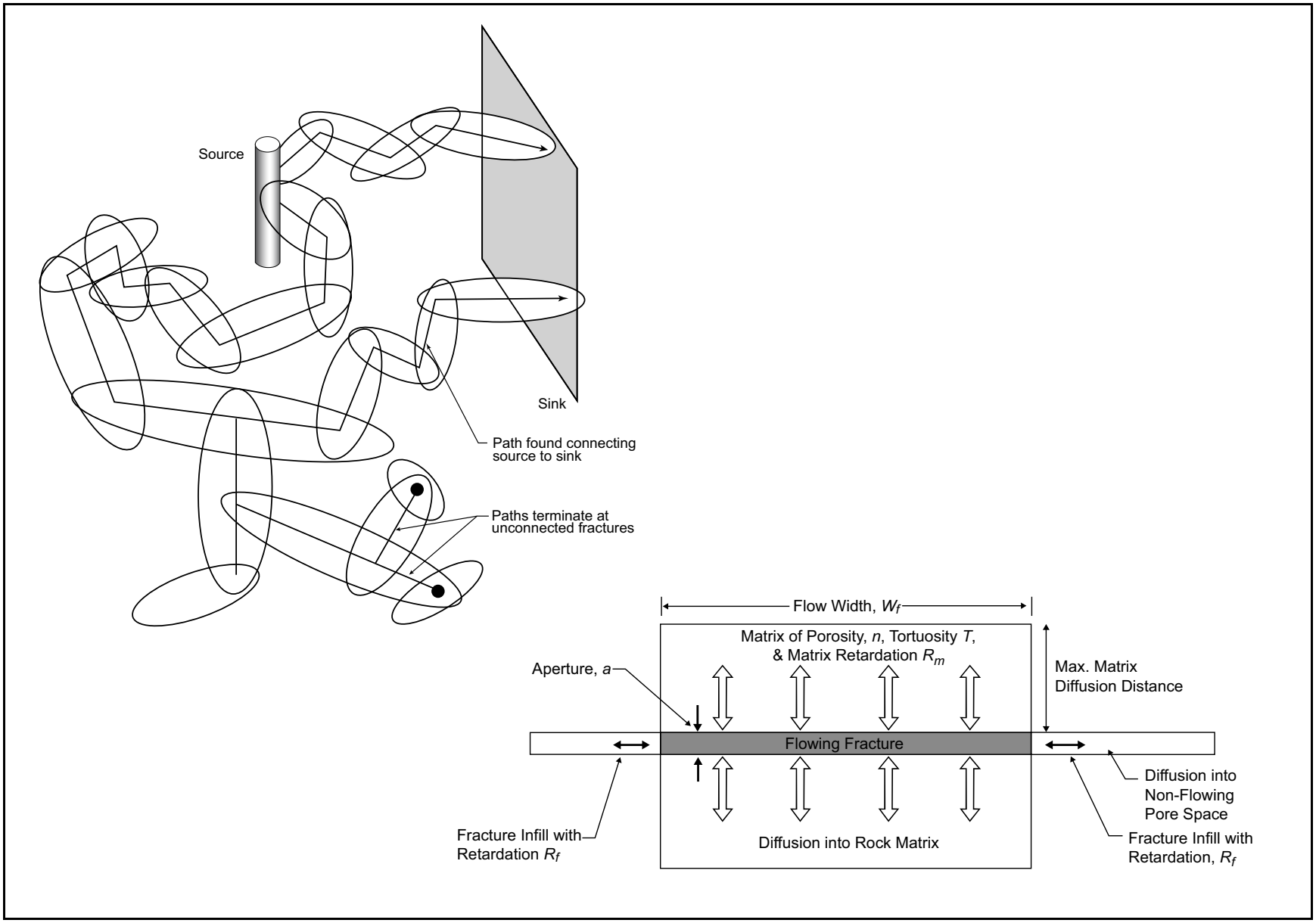

Figure N-2
FracMan Laplace Transform Galerkin Solute Transport Model – Pipe Network Pathways through Fractured Rock

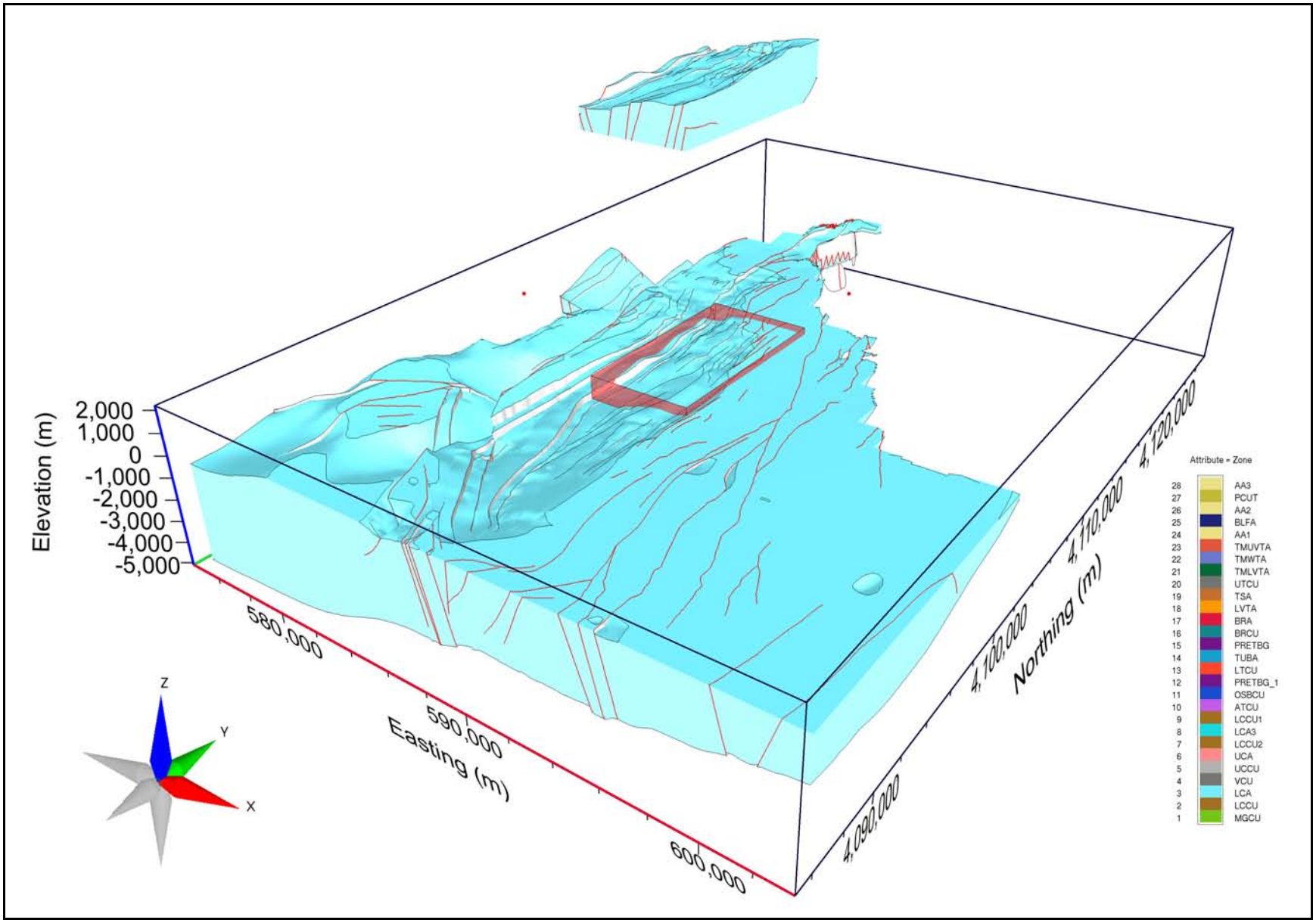

Figure N-3
Perspective Plot of Yucca Flat LCA Subarea Model Domain

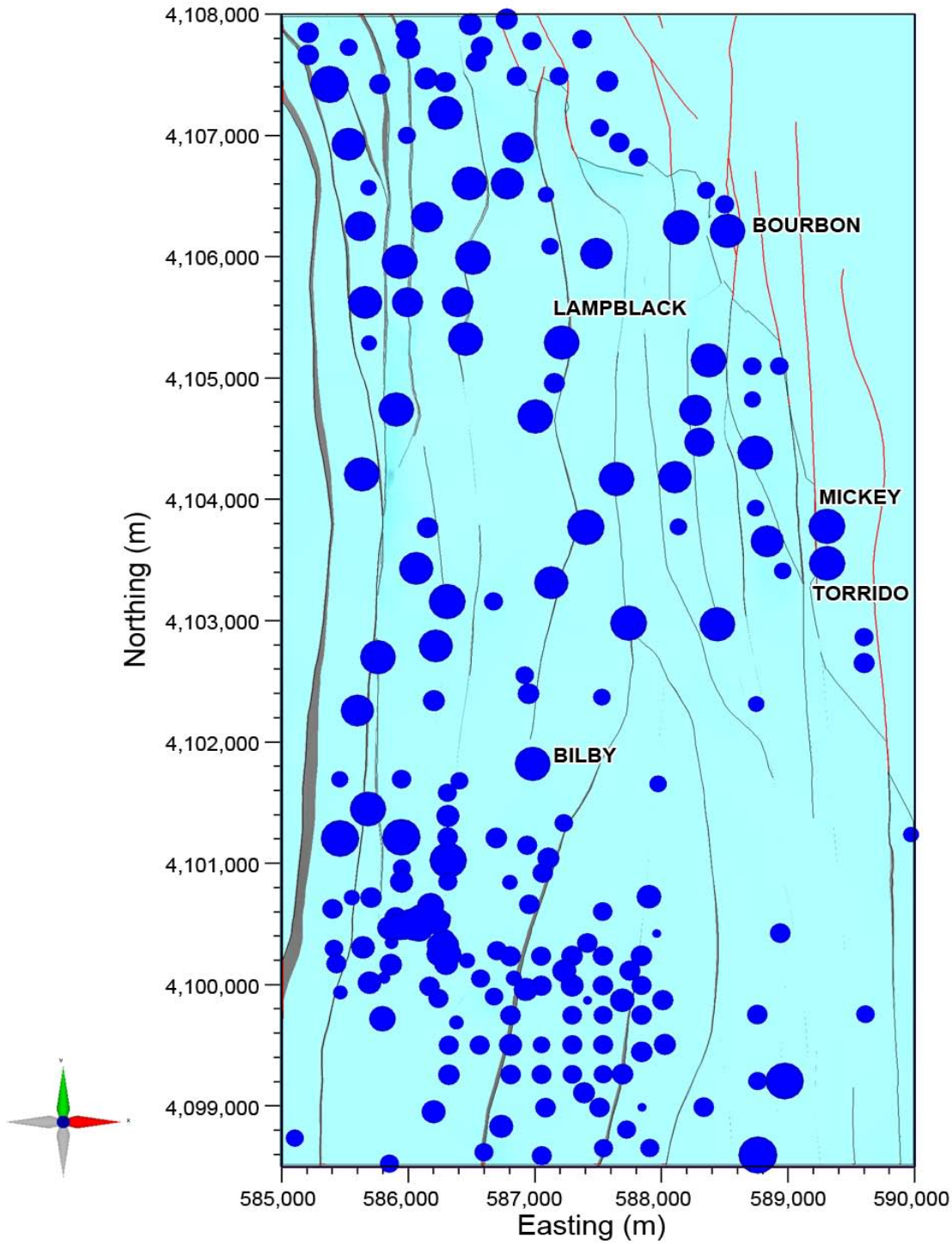

Note: Detonation size based on maximum announced yield range (DOE/NV--209).

Figure N-4
Map View of Yucca Flat LCA Subarea Model Domain with Significant HST Detonations Included in Corroborative Analysis

of Yucca Flat. The the western portion of the subarea model domain the upper surface corresponds to the structural top of the LCA which varies over the model domain due to the significant offset along the basin forming faults in central Yucca Flat.

N.1.3.2 Model Description and Inputs

The subarea model consists of LCA country rock and faults which cut the LCA. As discussed in Section 5.0, the faults consist of a higher permeability damage zone on either side of a lower permeability core. Contaminant sources to the LCA in the subarea are result of either detonations with exchange volumes that intersect the saturated LCA or overlying detonations with contaminant flux to the LCA due to the generally downward flow and transport along the faults that intersect the overlying tuff confining units.

N.1.3.2.1 Flow Model Parameters

Groundwater flow in the subarea is generally in a north-south direction and is controlled by the permeability anisotropy between the fault damage zones and country rock. The distribution of country rock, fault damage zones and fault core zones included in the FEHM flow model of the subarea is illustrated in Figure N-5. The base-case calibrated LCA flow model presented in Section 5.5 was selected for the corroborative software analyses.

N.1.3.2.2 Flow Model Boundary Conditions

Because groundwater flow in the subarea model is generally in a north-south direction, the eastern and western boundaries of the subarea model domain were considered to be no-flow boundaries. Constant heads were assigned along the northern and southern boundaries. Although the LCA flow model presented in Section 5.0 has some vertical recharge in the eastern portion of the model domain, in general the recharge is insignificant within the subarea model domain. As a result, the upper surface of the model was assumed to be a no flow boundary. These boundary conditions result in groundwater flow within the subarea model domain being generally from north to south although due to permeability heterogeneity and anisotropy it is possible to have flow that is transverse to the north-south trend locally in the subarea model domain.

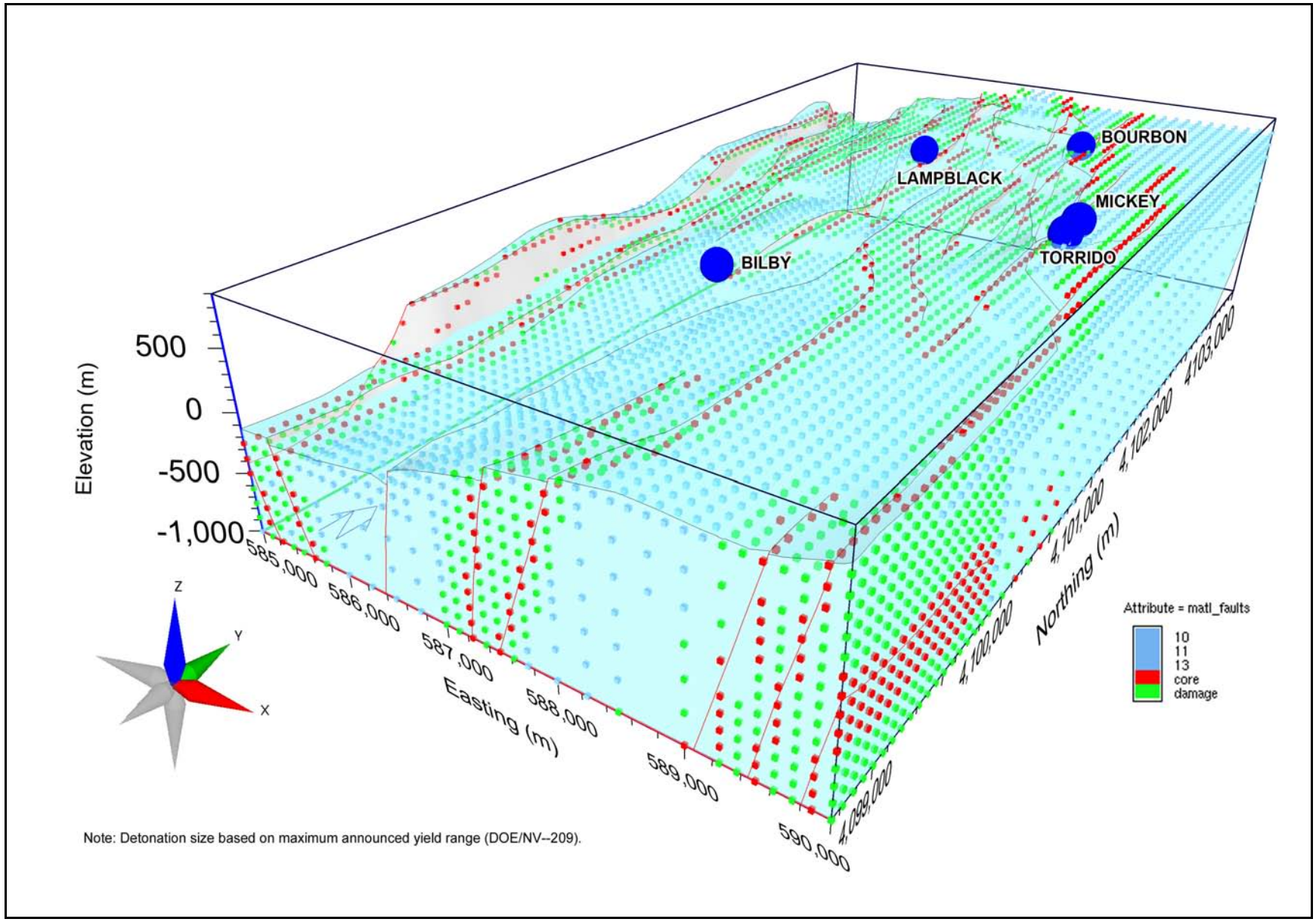

Figure N-5
LCA Permeability Zones within the Subarea Model Domain

N.1.3.2.3 Transport Model Parameters

The LCA transport model described in Section 6.1 is a dual porosity model which allows advection and dispersion of contaminants in the fractures and matrix diffusion of contaminants from the fractures into the immobile matrix. For retarded contaminants, fracture and matrix sorption are also considered. As discussed in Section 6.3, the transport model parameters used in the LCA transport model are sampled from distributions that represent the uncertainty in these values. For purposes of the corroborative software analyses, a single transport realization was selected. This single realization was based on an approximate set of transport values summarized below:

- Dispersivity – 20 m/2 m/0.2 m (longitudinal/transverse horizontal/transverse vertical)
- Fracture porosity – 0.001 (same in fault damage zone as country rock)
- Fracture spacing – 3 m (same in fault damage zone as country rock)
- Matrix porosity – 0.03 (same in fault damage zone as country rock)
- Matrix diffusion – 2×10^{-10} m^2/s (same in fault damage zone as country rock)

For purposes of the corroborative software analyses only two mobile radionuclides were considered, notably ^{3}H and ^{129}I. These radionuclides were considered because as presented in Section 6.5, these radionuclides significantly contribute to the extent of the contaminant boundary, ^{3}H at early times due to its large initial inventory and concentration in the cavity and ^{129}I because of its long half life and source flux from overlying detonations in the saturated alluvial/volcanic aquifer system. As a result, there is no need to specify fracture retardation or matrix sorption properties for the corroborative analysis.

N.1.3.2.4 Transport Model Source Inputs

Contaminant sources to the saturated LCA within the subarea model domain consist of either (a) detonations with exchange volumes that intersect the saturated LCA, (b) detonations with working points in the unsaturated zone above the saturated LCA, or (c) detonations with working points in the saturated alluvial/volcanic aquifer system above the LCA. Although there are many potential sources of contamination to the LCA within the subarea model domain, for simplicity the corroborative analysis includes only the most significant of the sources, notably:

- BOURBON – initial HST intersects saturated LCA
- BOURBON – contaminant flux to saturated LCA from portion of HST in overlying unsaturated LCA

- LAMPBLACK – initial HST intersects saturated LCA
- TORRIDO and MICKEY – initial HST intersects saturated LCA
- TORRIDO and MICKEY – contaminant flux to saturated LCA from portion of HST in overlying unsaturated tuff confining units
- BILBY – contaminant flux to saturated LCA from HST in overlying saturated tuff confining units

The initial ^{3}H and ^{129}I mass in place for the sources at these detonation locations as well as the cumulative 1,000 year mass flux from the overlying unsaturated zones and saturated alluvial/volcanic aquifer system models are indicated in Table N-1. The temporal mass flux for ^{3}H and ^{129}I to the saturated LCA from releases from the three detonation locations in the overlying units are illustrated in Figure N-6. These results are derived from a modeling case using an upper bound of net infiltration (5 mm/yr) and an upper bound of enhanced crater recharge. The run designator is 223212 for the unsaturated zone contaminant fluxes (see Section 3.0) and run 223212.5.14.5.1.2.N3.B2.s for the saturated alluvial/volcanic aquifer system model (see Section 4.0). Note that the TORRIDO and MICKEY detonations, although having separate initial mass sources in the saturated LCA are combined in the presentation of the mass flux to the saturated LCA because they are located only a few hundred meters apart.

Table N-1
Source Term Used in Corroborative Software Analyses

Detonation	^{3}H Source Term (mol)		^{129}I Source Term (mol)	
	Initial Mass in Saturated LCA	1,000 Year Mass Flux to Saturated LCA	Initial Mass in Saturated LCA	1,000 Year Mass Flux to Saturated LCA
BOURBON	1.576	0.085	3.586E-03	4.85E-03
LAMPBLACK	0.5251	0.0	0.1592E-03	0.0
TORRIDO	0.01436	0.00467	3.341E-03	0.482E-03
MICKEY	0.360		0.4933E-03	
BILBY	0.0	1.411	0.0	4.86E-03

Note: Source term mass based on yield-weighted inventory as apportioned by uniform mass based allocation method, see Section 2.0.

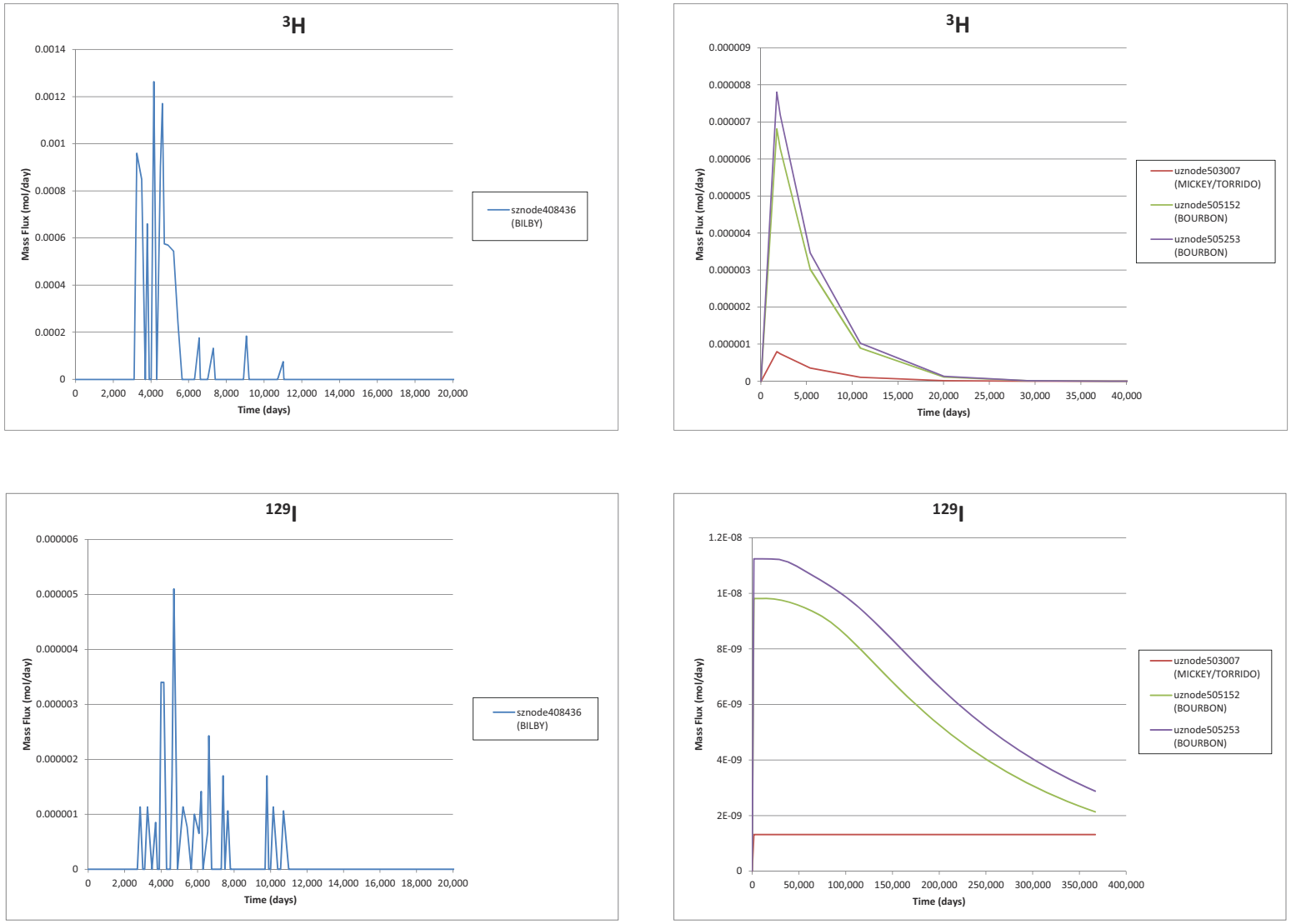

Figure N-6
Mass Flux to the Saturated LCA from the BOURBON, MICKEY/TORRIDO and BILBY Detonations

N.1.3.3 FEHM Flow Model Results

The LCA flow model results are derived from a preliminary calibrated flow field of the entire Yucca Flat model domain developed using the FEHM code. This flow field is similar to that presented in Section 5.5. Figure N-7 illustrates the particle trajectories for this flow field generated using FEHM_sptr for the source locations identified in Table N-1. As described in Section 5.5, the flow directions are generally in a southerly direction with the exception of those emanating from the BILBY source location. As described in Section 6.4, contaminant flux from the BILBY detonation to the LCA occurs at the southern terminus of a fault that terminates about four cavity radii from the BILBY working point. This fault is modeled as providing a hydraulic communication through the tuff confining units that allows for contaminants to be transported vertically into the saturated LCA. The groundwater flow in the LCA that is channeled within the damage zone along the strike of this fault has a significant flow transverse to the fault orientation at the southern end of the fault where the water (and contaminants) transition from the fault damage zone to the country rock.

N.1.3.4 PLUMECALC Transport Model Results

The groundwater flow regime described in Section N.1.3.3 developed with FEHM was used with the transport parameters presented in Section N.1.3.2.3 and the source terms presented in Section N.1.3.2.4 to calculate the concentration of ^{3}H and ^{129}I within the subarea model domain. For purposes of comparison to the corroborative software, discrete times of interest were selected, notably at 10, 50 and 100 years for ^{3}H and at 100, 300 and 1,000 years for ^{129}I. The result of calculations performed with FEHM_sptr combined with PLUMECALC are illustrated in Figures N-8 and N-9. It is worth noting that the efficiency in PLUMECALC is in part a result of the user specifying the discrete times of interest so that the solution is only at these times, as opposed to a continuum in time being simulated with alternative numerical schemes.

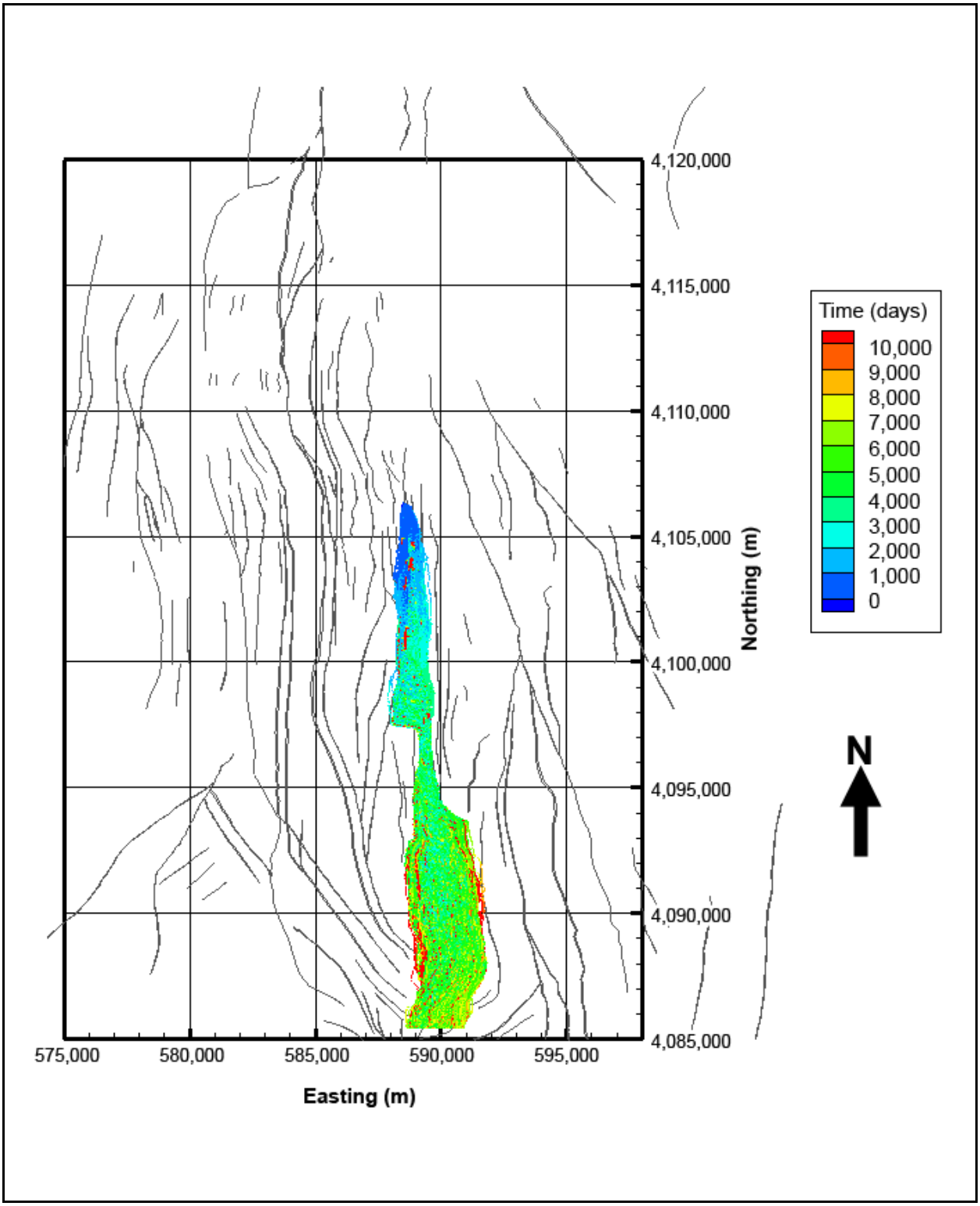

Figure N-7
Modeled LCA Groundwater Flow Paths from Sources in the Subarea Model

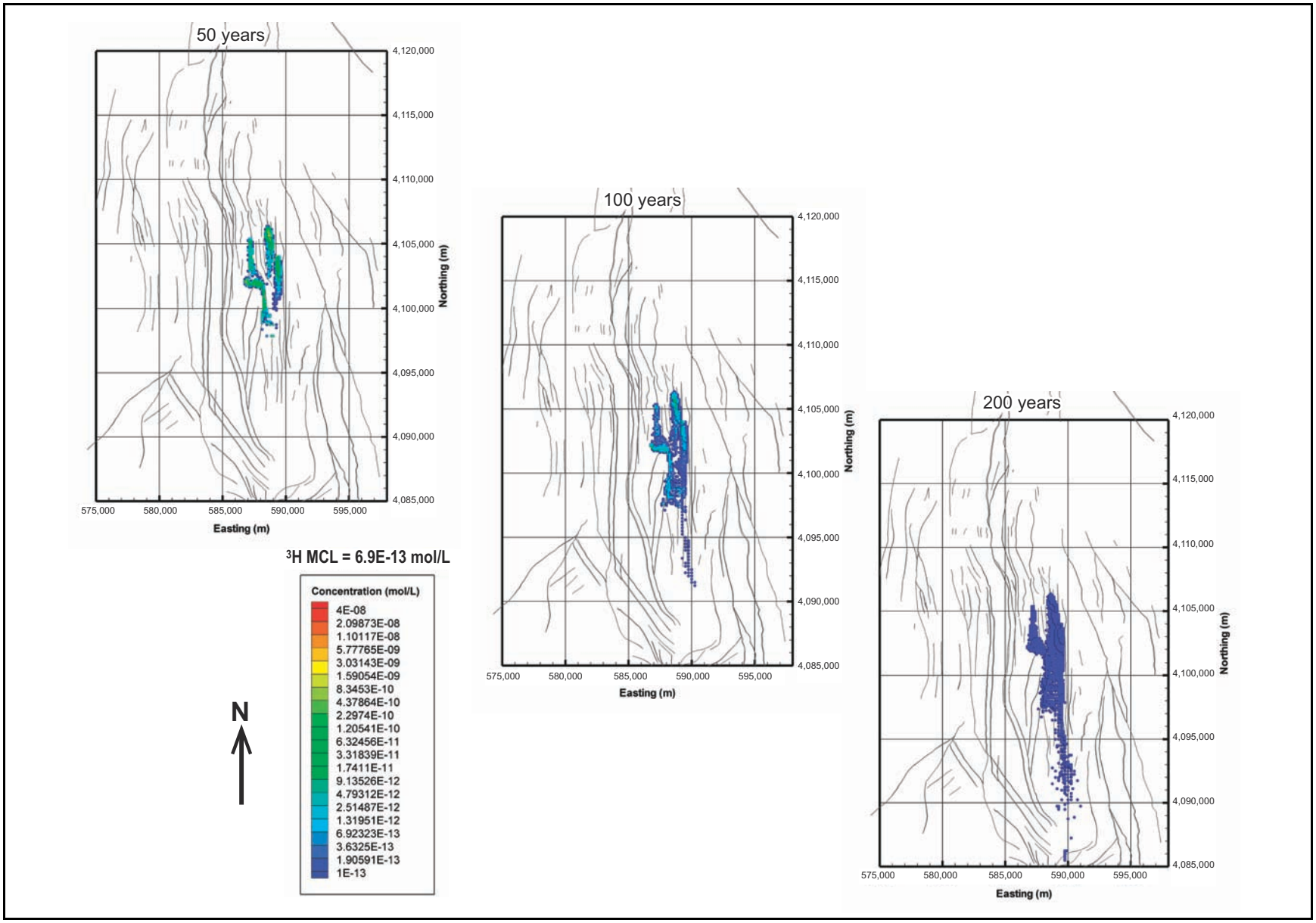

Figure N-8
^{3}H Concentrations in Subarea Model Calculated by FEHM_sptr and PLUMECALC

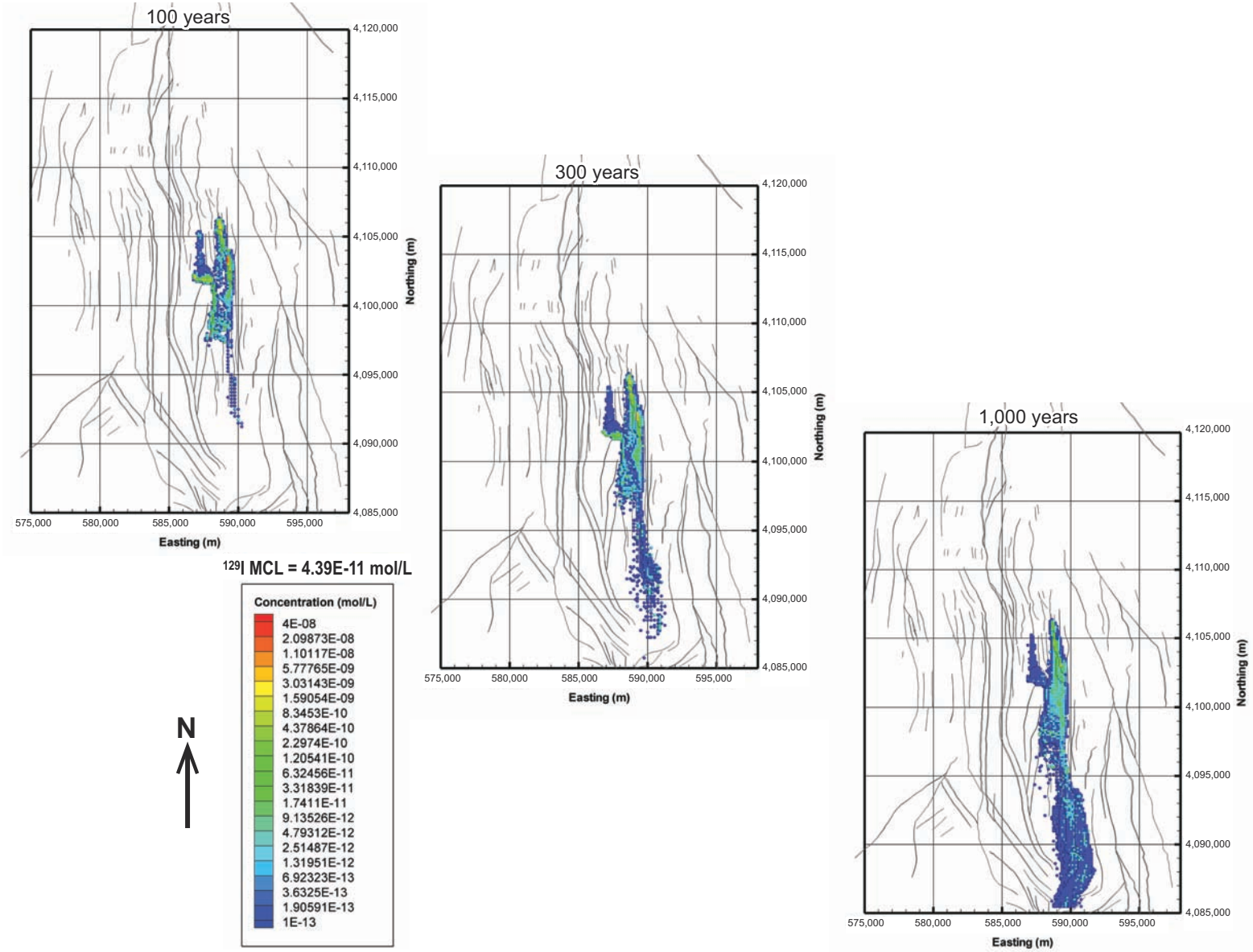

Figure N-9
^{129}I Concentrations in Subarea Model Calculated by FEHM_sptr and PLUMECALC

N.1.4 Outline of Appendix

The remainder of this appendix presents the results of applying the different corroborative software to the same subarea model domain, the same flow and transport properties and the same source terms to allow as close to an apples-to-apples comparison to the FEHM/FEHM_sptr/PLUMECALC results as possible. The organization of the appendix is as follows:

- Section N.2.0 presents the results using MODFLOW/MT3DMS
- Section N.3.0 presents the results using Feflow
- Section N.4.0 presents the results using FracMan/MAFIC
- Section N.5.0 presents a summary of the corroborative software comparisons

N.2.0 MODFLOW/MT3DMS

N.2.1 Model Description

The MODFLOW grid was designed with a grid cell spacing (62.5 m in X, Y and Z) equal to one-half of the minimum nodal spacing of the FEHM grid inside the corroborative model domain. This allowed for at least four MODFLOW grid cells per FEHM node. The top of the model was placed at the elevation of the uppermost active node in the FEHM grid inside the corroborative model domain. To avoid excessively long run times, the base of the MODFLOW model was placed at an elevation of -1,000 m, well below the active transport zone for the selected sources. Although the FEHM grid extended to a depth of -5,500 m within the corroborative model domain, PLUMECALC results show that the minimum transport elevation was about -500 m. The difference in thickness of the models may affect the flow fields, but the effect should be minimal since flow is predominately horizontal. MODFLOW grid cells that fell within inactive FEHM nodes were flagged as no-flow cells. Figure N-10 shows the MODFLOW model grid.

Hydraulic conductivity values for each grid cell in MODFLOW were assigned based on the closest FEHM node. For each grid cell, permeabilities from the nearest FEHM node were converted to hydraulic conductivities, based on isothermal conditions, and assigned to the grid cell. In a similar manner, constant head values were assigned to the boundary cells based on the head values from the calibrated FEHM run for the node closest to each boundary cell. This resulted in some unrealistic flows at the boundaries (i.e., in and out flow at adjacent boundary cells), but produced reasonable flows away from the boundaries. Fluxes into the top of the model were assigned to the uppermost MODFLOW grid cells corresponding to each FEHM node with a defined input flux. For each FEHM node, inflows were divided uniformly among the corresponding MODFLOW grid cells.

For transport, all material types were modeled in MT3DMS as dual porosity units. Table N-2 lists transport parameters. Transport parameters were assigned as homogeneous values throughout the model domain. Radionuclide sources were placed in the uppermost MODFLOW grid cells that occupy the same areas as the eight FEHM source nodes. The exact locations were moved slightly for some sources to insure that source inputs are located in fault disturbed zone material cells. Like

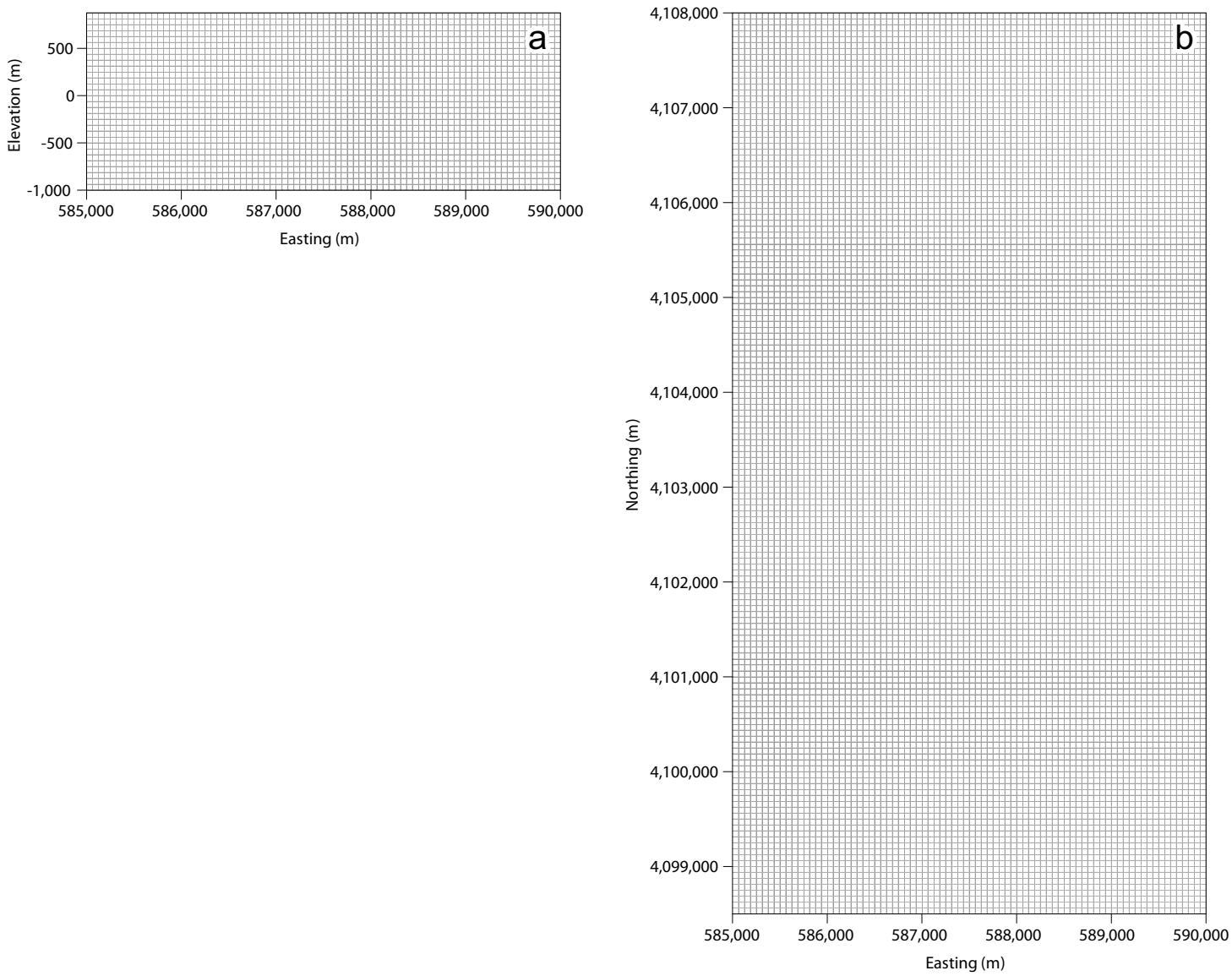

Figure N-10
MODFLOW/MT3DMS Grid: (a) XZ Cross Section and (b) XY Cross Section

Table N-2
Transport Parameters

Fracture Porosity	0.001
Matrix Porosity	0.03
Fracture Spacing	3 m
Matrix Diffusion Coefficient	2×10^{-10} m^2/s
Longitudinal Dispersivity	20 m
Transverse Horizontal Dispersivity	2 m
Transverse Vertical Dispersivity	0.2 m
Mass Transfer Coefficient	6.912×10^{-7} day^{-1}
^{3}H Half-life	12.35 years

PLUMECALC, MT3DMS allows input of time varying mass loading sources in a steady-state flow field. PLUMECALC mdot source files were converted from mol/day to kg/day for input into MT3DMS.

In MT3DMS, the exchange between the mobile and immobile domains is specified by a mass transfer coefficient. This factor was calculated assuming a fracture system of equally spaced parallel fractures (Helmke et al., 2005).

$$\alpha = \frac{a D_e n_{mat}}{l^2} \qquad (N\text{-}1)$$

where

α = the mass transfer coefficient (sec^{-1}),
a = shape factor (3 for parallel fractures),
D_e = effective matrix diffusion coefficient (m^2/s),
n_{mat} = matrix porosity, and
l = characteristic length (one half the fracture spacing for parallel fractures), (m).

N.2.2 Flow Model Results

Flow modeling for this corroborative test was performed using MODFLOW-2000 (Version 1.18.00). Steady-state results show a mass balance error of 0.01 percent. Figure N-11 compares particle tracks from the steady-state MODFLOW flow model to particle tracks from the FEHM model used to develop the MODFLOW model. The plot on the left shows particle tracks for single particles started at the center of each MODFLOW cell used as a radionuclide source location. The plot on the right shows particle tracks for a grid of particles placed every 625 m (10 grid cells) in the uppermost active cell.

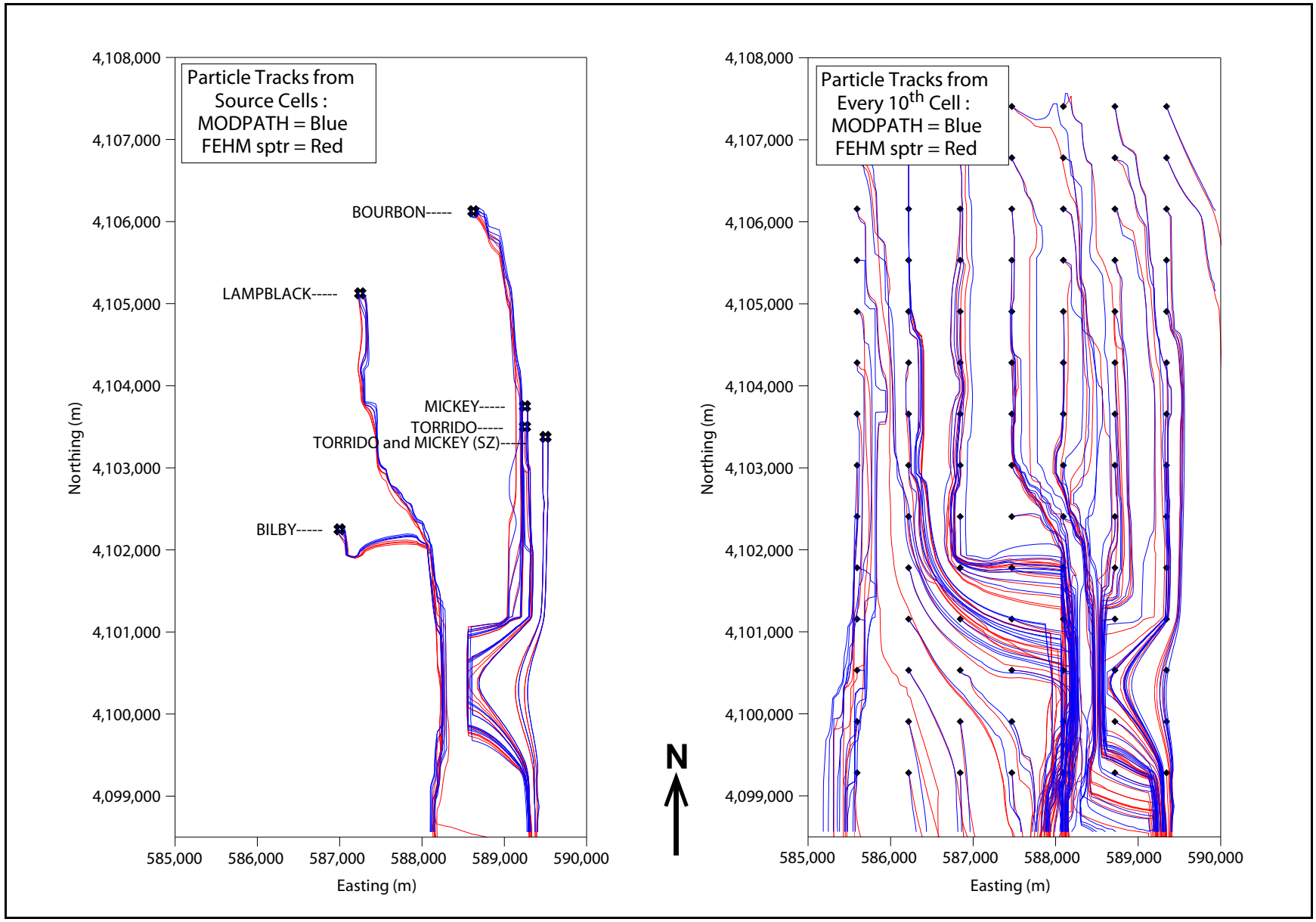

Figure N-11
Comparison of Particle Tracks for MODPATH and FEHM sptr

Particle tracks are generally similar, but show significant differences in places. Some of the differences seen may be related to the different connectivity between cells or nodes in the MODFLOW and FEHM grids. The finite element FEHM grid allows diagonal connections between nodes, unlike MODFLOW. Since the FEHM permeability values were transferred directly to the MODFLOW grid, there are likely locations where these diagonal connections were lost. The MODFLOW hydraulic conductivity values could have been modified locally to reestablish these connections, but that was beyond the scope of this analysis. The smaller grid spacing used in MODFLOW was designed to minimize this issue.

Travel times to the edge of the corroborative model domain were compared for MODFLOW/MODPATH and FEHM. On average, the MODFLOW/MODPATH travel times to the edge of the model were less than the FEHM travel times, indicating higher velocities, in general. Figure N-12 shows a cumulative distribution function for the ratio of MODFLOW/MODPATH travel times to FEHM travel times. The values appear to be normally distributed. The median value of approximately 0.75 shows the bias toward lower travel times for MODFLOW/MODPATH. These lower travel times contribute to greater distances of transport for MODFLOW/MT3DMS (used in the transport analyses presented below) compared to FEHM/PLUMECALC at selected points in time.

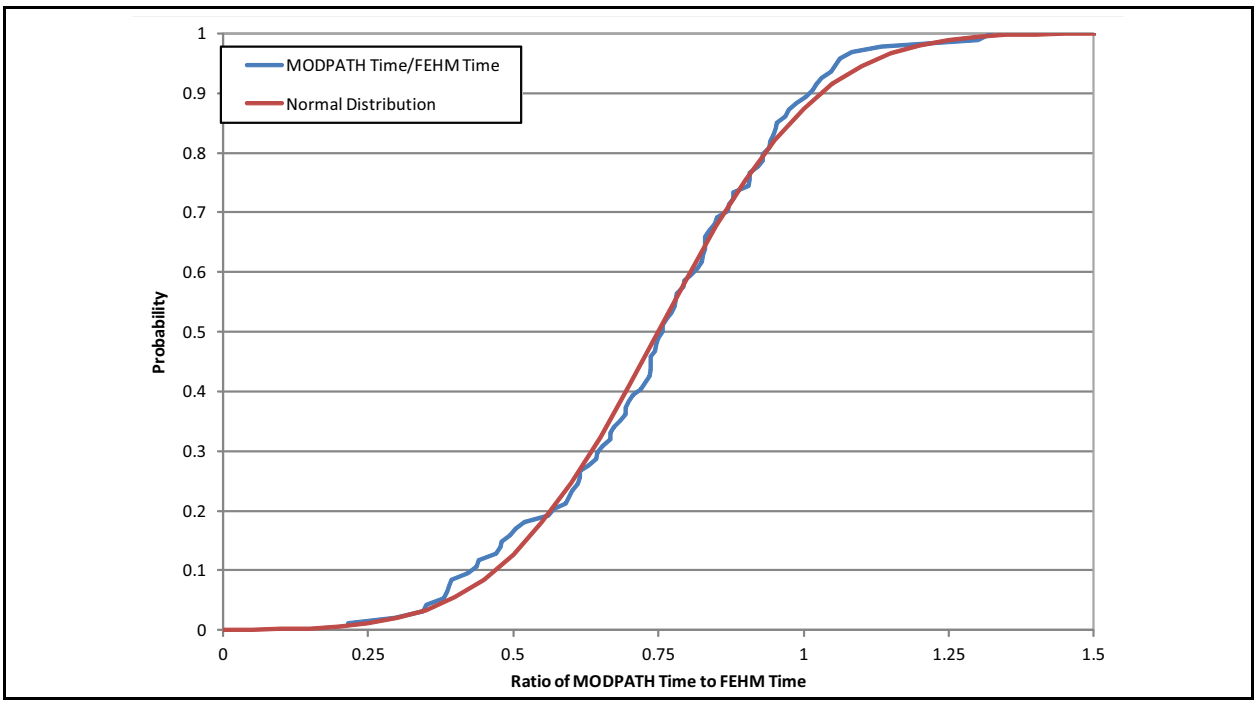

Figure N-12
CDF of Ratio of MODFLOW Travel Time to FEHM Travel Time

N.2.3 Transport Model Results

Transport modeling for this corroborative test was performed using MT3DMS Version 5.3. Transport simulations were performed for ^{3}H and ^{129}I. ^{3}H was modeled as a decaying species with a half-life of 12.35 years. Radioactive decay was not included in the ^{129}I simulation because of the extremely long half-life. For these simulations, the total-variation-diminishing (TVD) method was used for solving the advection term. The MT3DMS manual indicates that the TVD option is mass conservative and does not introduce excessive numerical dispersion and artificial oscillation. Run times for MT3DMS were considerably longer than run times for PLUMECALC (hours or days vs. minutes).

The MODFLOW-SURFACT code was also considered since it includes enhanced transport options and a faster solver. However, due to time constraints, this option was not pursued.

^{3}H concentrations were simulated for a period of 100 years, with a reported mass balance error of 0.65 percent. Figures N-13 to N-15 show ^{3}H concentrations at 10, 50 and 100 years, respectively. Plots are shown for MT3DMS and PLUMECALC concentrations in both plan (XY) and cross section (YZ) views. Cells/nodes are color coded with the color indicating the maximum concentration vertical to the viewing direction (i.e., maximum concentration at any Z for each XY location in the plan view and maximum concentration at any X for each YZ location in the cross section). The ^{3}H MCL is 6.88e-13 mol/L. The minimum plotted concentration is one tenth of the MCL.

At 10 years (Figure N-13), the MT3DMS plumes extend farther downgradient (southerly) than the PLUMECALC plumes, particularly along the eastern edge of the model. Some evidence of oscillation can be seen in the MT3DMS results, particularly upgradient of the BOURBON source and around the BILBY source. By 50 years (Figure N-14), the MT3DMS plume covers significantly more area, although most of this additional area is at concentrations below the MCL. Concentrations above the MCL show similar southerly extents but have greater width for MT3DMS. At 100 years (Figure N-15), the ^{3}H plumes are similar except at the southern edge of the model area where PLUMECALC shows higher concentrations. Also, the PLUMECALC plumes in plan view tend to be discontinuous and more noisy in comparison to the MT3DMS plumes.

The differences seen at early times may be due, in part, to the travel time or velocity difference discussed previously, the different approaches to handling dual porosity transport, and/or model differences between the MODFLOW/MT3DMS and FEHM/PLUMECALC models. The FEHM flow

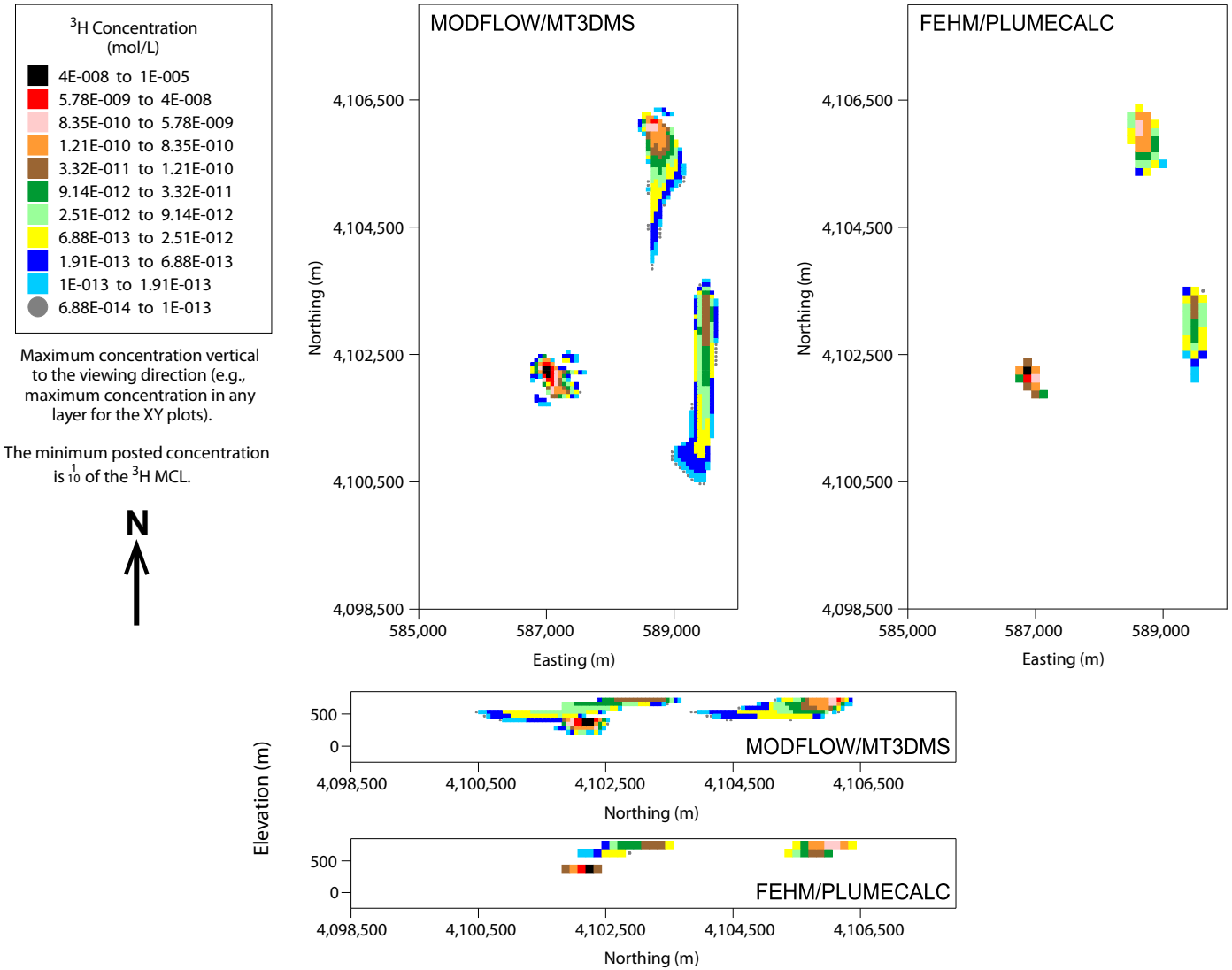

Figure N-13
Comparison of ^{3}H Concentrations (mol/L) at 10 Years (^{3}H MCL = 6.88E-13 mol/L)

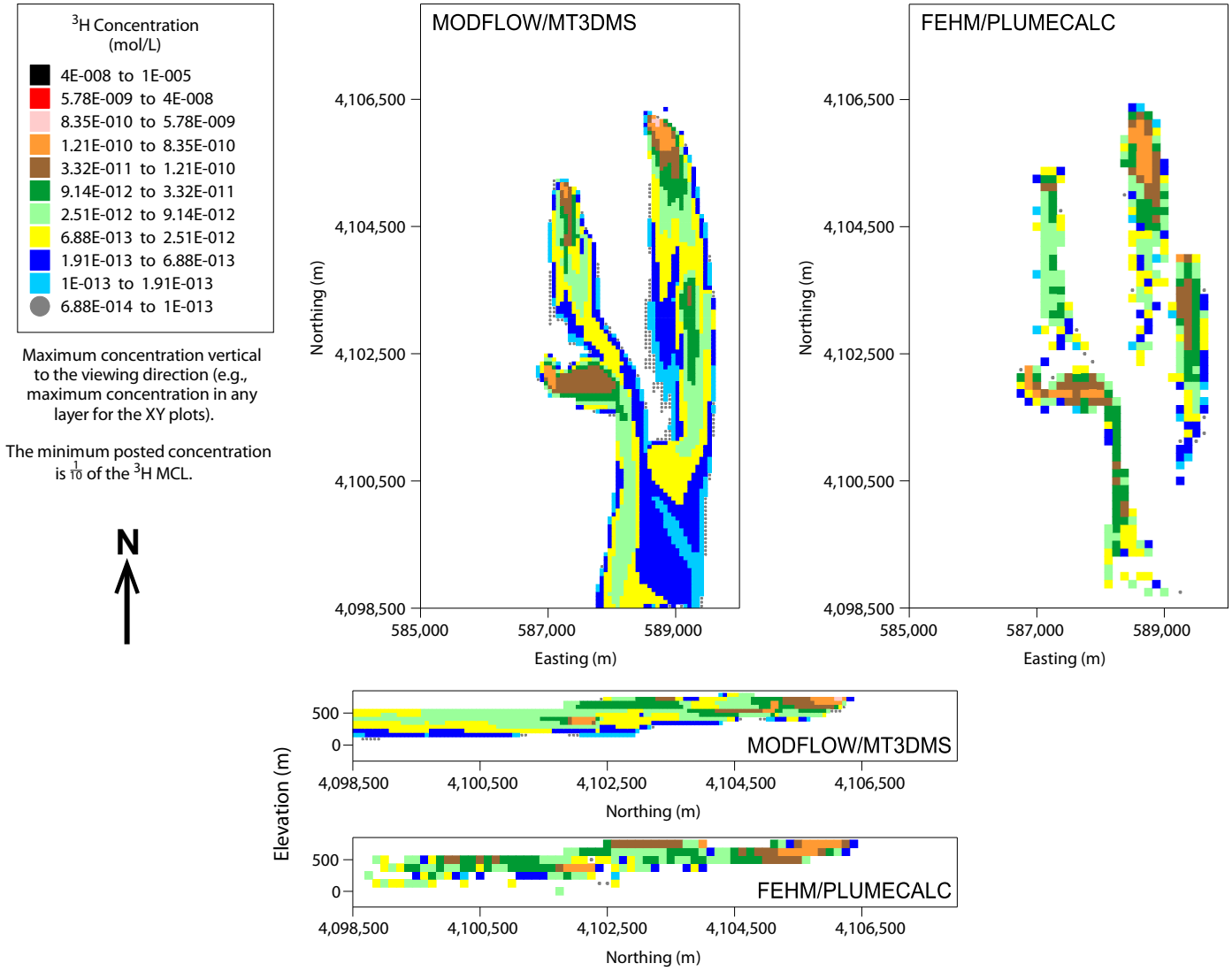

Figure N-14
Comparison of ^{3}H Concentrations (mol/L) at 50 Years (^{3}H MCL = 6.88E-13 mol/L)

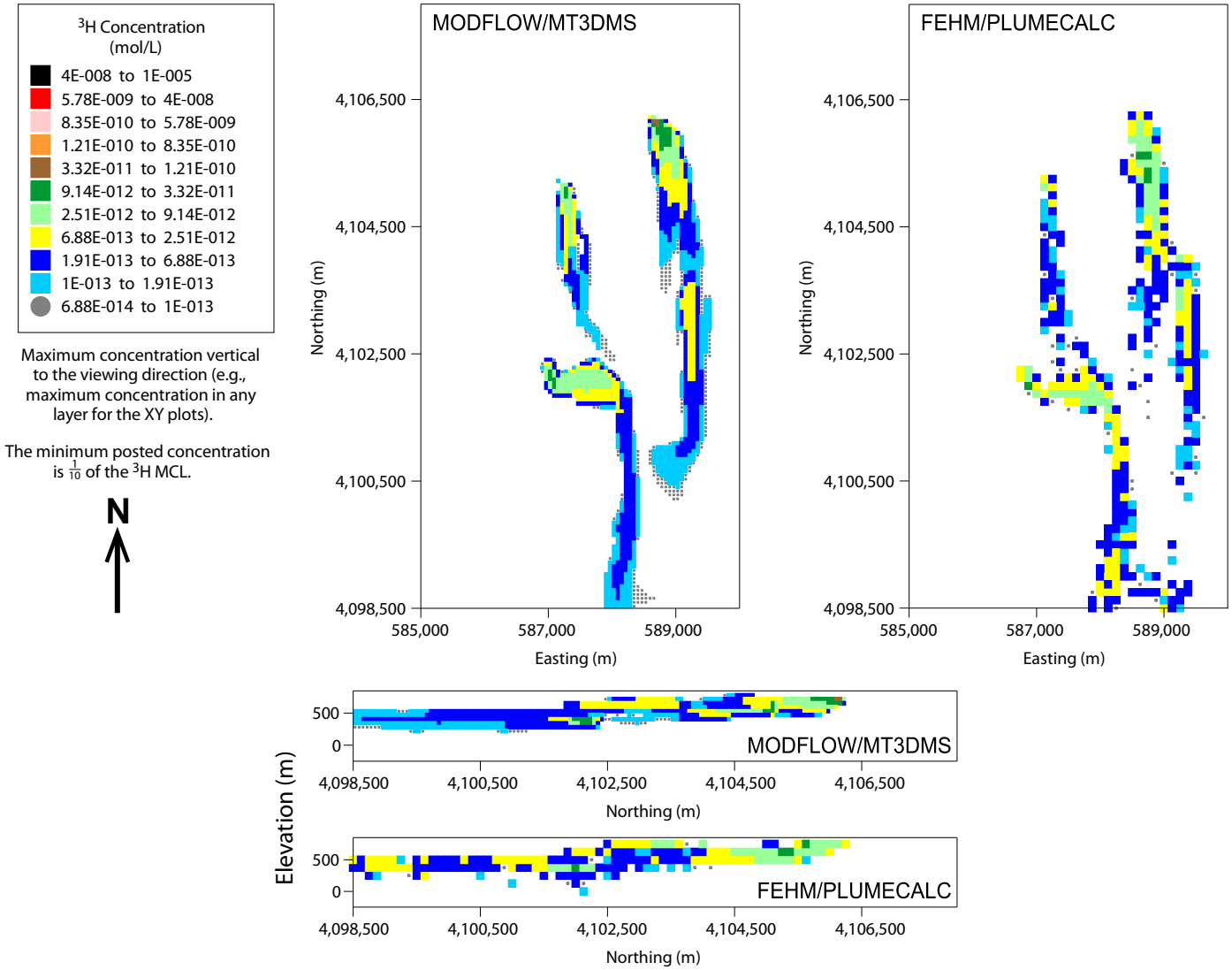

Figure N-15
Comparison of ^{3}H Concentrations (mol/L) at 100 Years (^{3}H MCL = 6.88E-13 mol/L)

model changed slightly between the time that the MODFLOW model was developed and particle tracks compared and when the FEHM/PLUMECALC transport simulations were performed. Although these minor changes are not expected to significantly affect the results, a slight difference in the trajectory of the northeastern plume (BOURBON) can be seen when the MT3DMS and PLUMECALC plumes are compared. Also, source locations and areas were not exactly the same for the MT3DMS and PLUMECALC simulations, although the differences were minor.

^{129}I concentrations were simulated for a period of 1,000 years, with a reported mass balance error of 0.005 percent. Figures N-16 to N-18 show ^{129}I concentrations at 100, 300 and 1,000 years, respectively. The ^{129}I MCL is 4.39E-11 mol/L. The minimum posted concentration is one hundredth of the MCL.

At 100 years (Figure N-16), only two cells exceed the MCL for MT3DMS (near the BOURBON source) and none for PLUMECALC. The PLUMECALC plumes extend farther downgradient to the south. By 300 years (Figure N-17), the plume extents are more similar and there are no cells/nodes above the MCL. At 1,000 years (Figure N-18), the MT3DMS plume extends farther south. As with ^{3}H, a slight difference in the trajectory of the northeastern plume (BOURBON) can be seen between the MT3DMS and PLUMECALC plumes. Overall, the ^{129}I plumes show better agreement than the ^{3}H plumes.

Figure N-19 shows a comparison of mobile mass, immobile mass and total mass for MT3DMS and PLUMECALC output within the corroborative model domain. ^{129}I mobile, immobile and total mass curves for MT3DMS and PLUMECALC are very similar. At 50 years, the mobile mass in the system is greater by a factor of about two for PLUMECALC compared to MT3DMS, but this difference reduces significantly by 100 years and is only slightly larger through 1,000 years. The slight difference in immobile and total mass is related to the amount of mass leaving the southern boundary of the corroborative model domain. The curves indicate that, at early times, more mass is passing the southern boundary in the MT3DMS simulation, probably due to the slightly higher velocities in the MODFLOW simulation as compared to the FEHM velocities.

The ^{3}H total mass curves are very similar, with a minor difference at 50 years due to the mass balance error in MT3DMS. Mobile and immobile mass are significantly different at early times (e.g., MT3DMS mobile mass is almost a factor of 3 greater than PLUMECALC mobile mass at 10 years). Differences are almost gone by 100 years. The reason for these differences between mobile

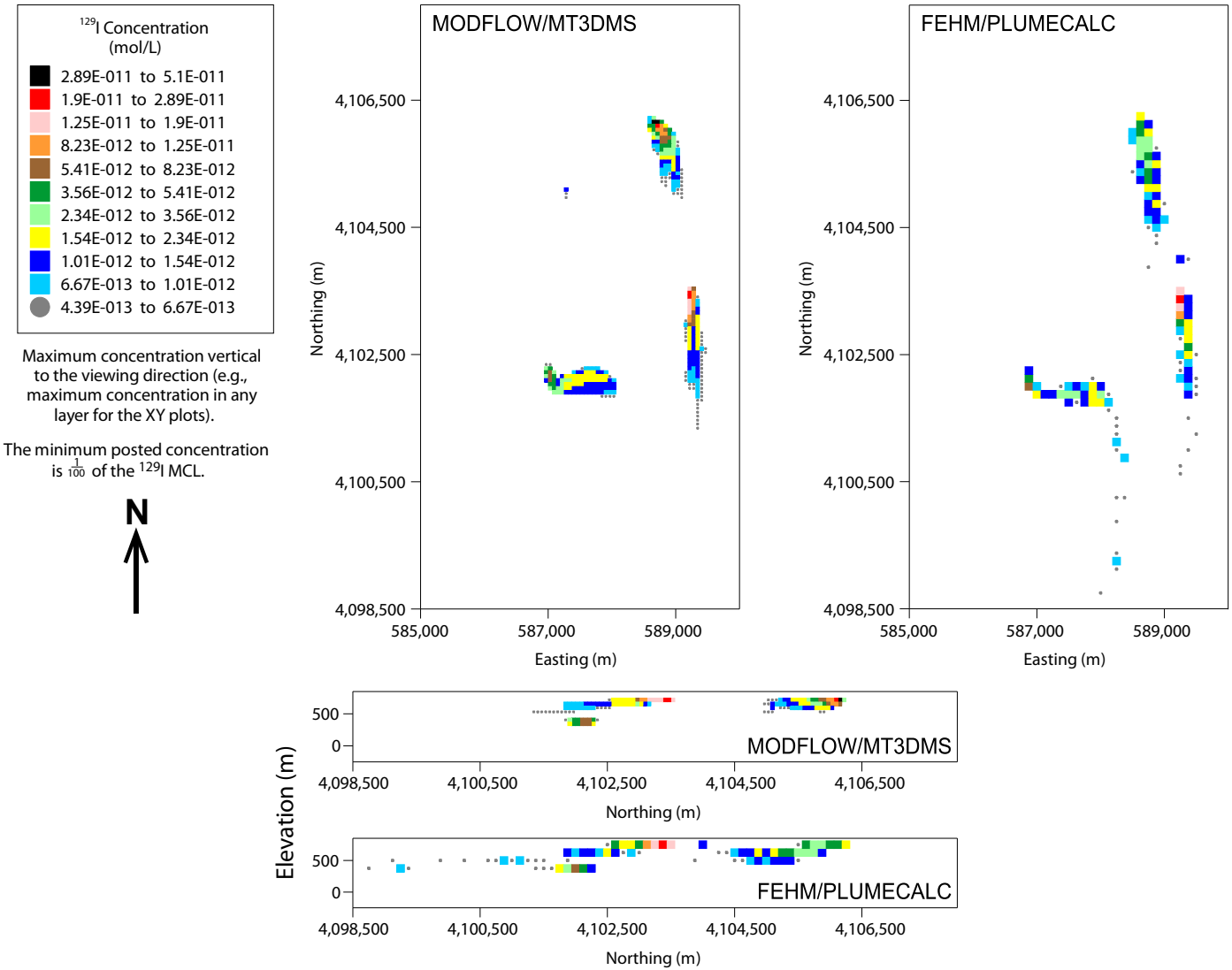

Figure N-16
Comparison of ^{129}I Concentrations (mol/L) at 100 Years (^{129}I MCL = 4.39E-11 mol/L)

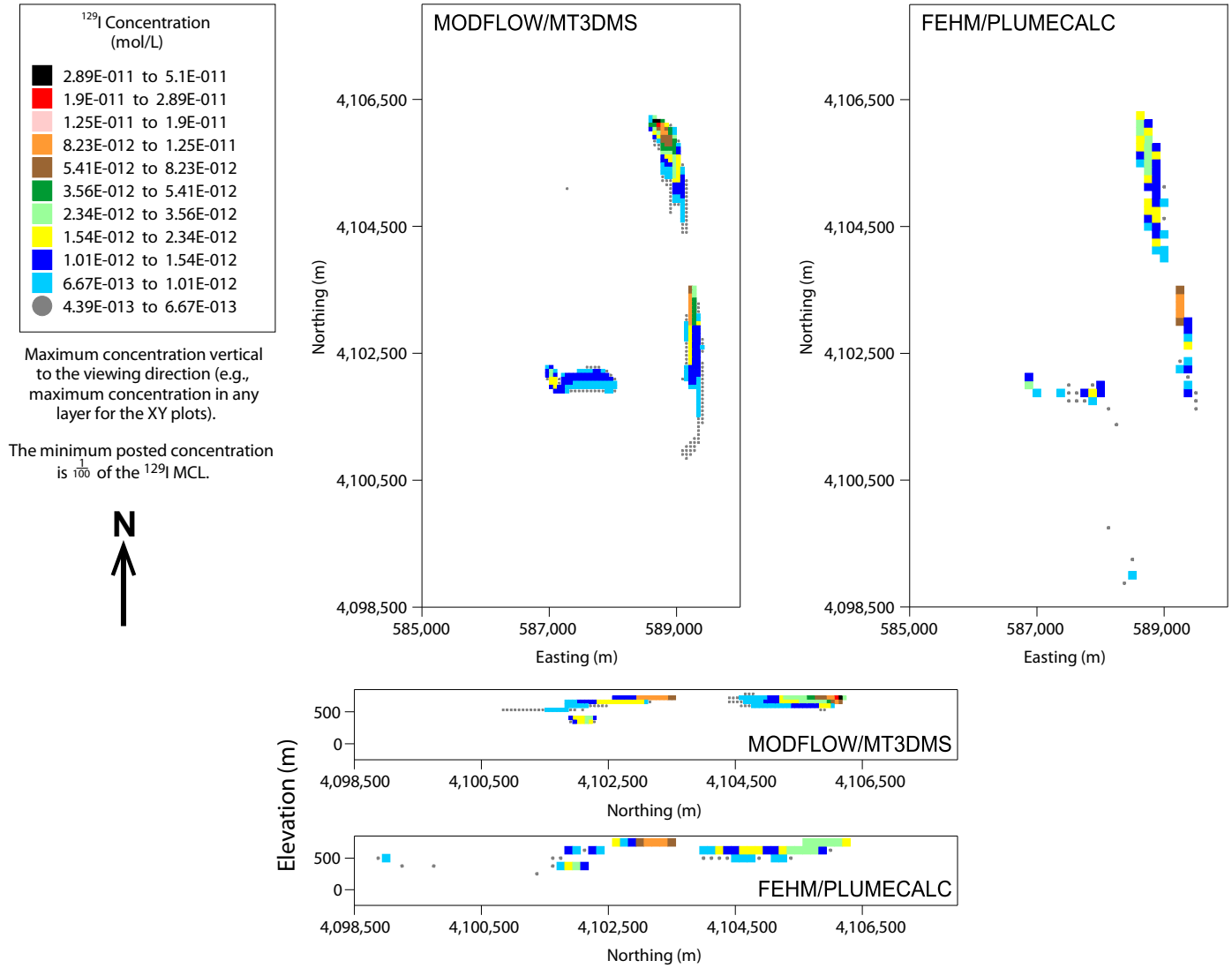

Figure N-17
Comparison of ^{129}I Concentrations (mol/L) at 300 Years (^{129}I MCL = 4.39E-11 mol/L)

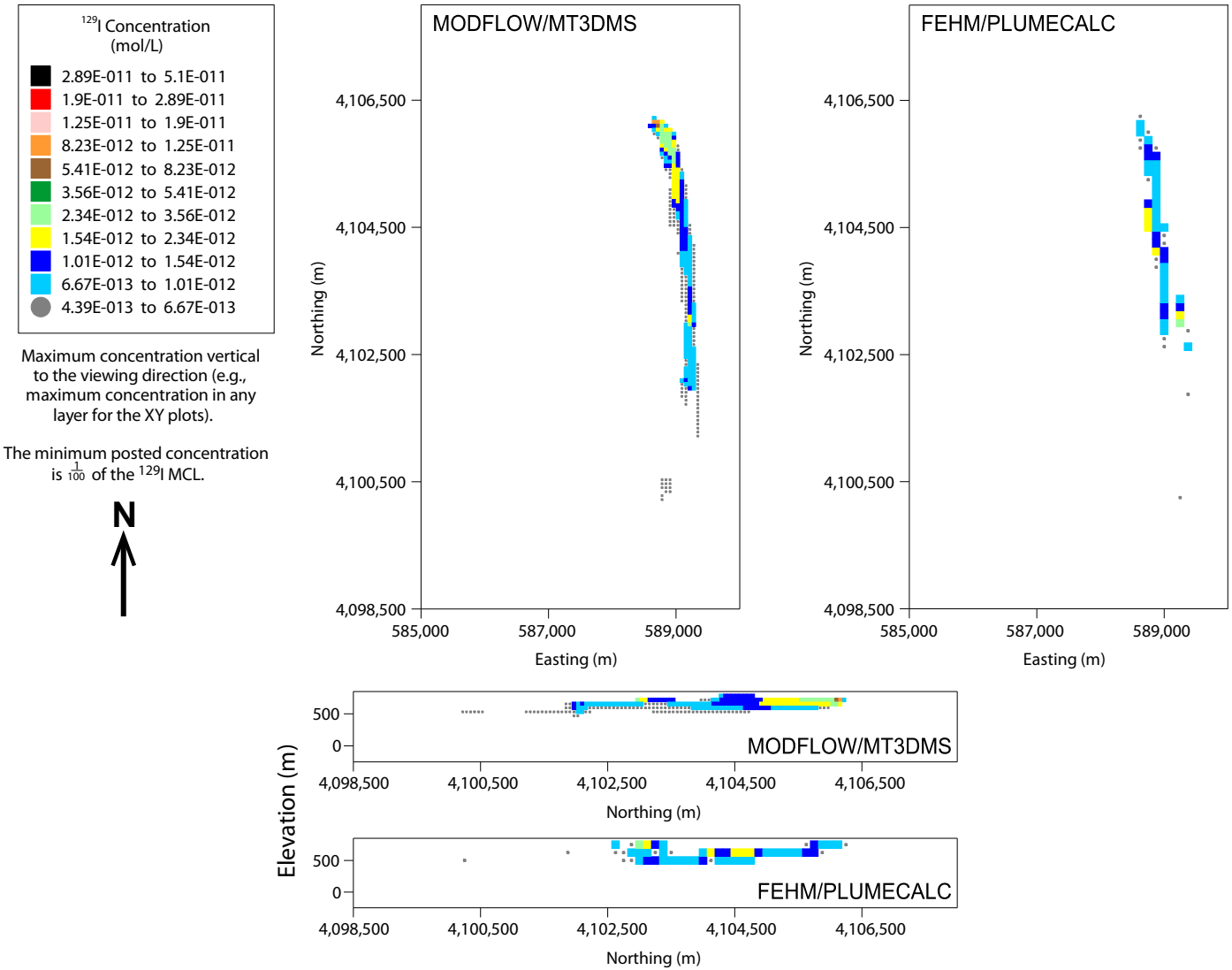

Figure N-18
Comparison of ^{129}I Concentrations (mol/L) at 1,000 Years (^{129}I MCL = 4.39E-11 mol/L)

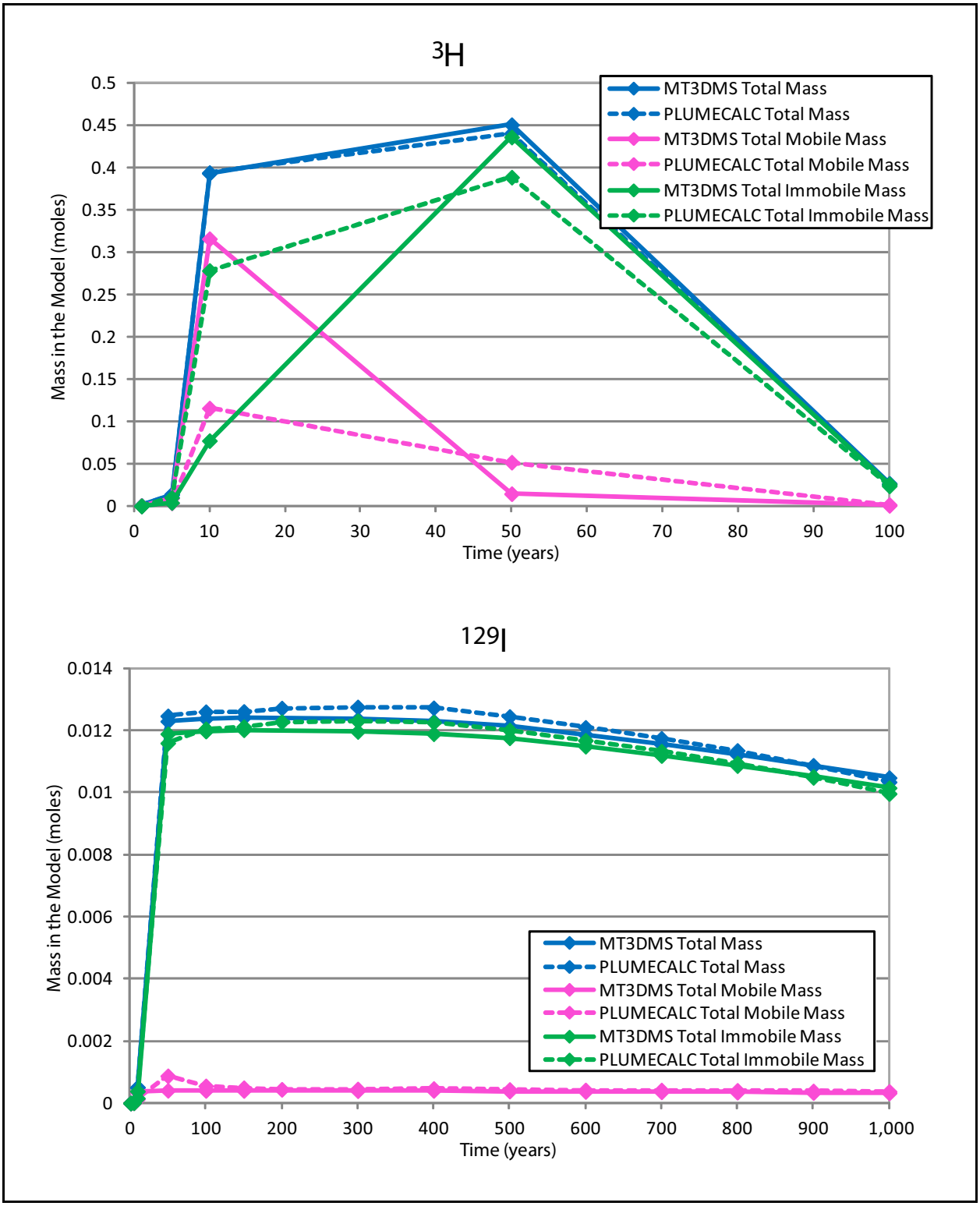

Figure N-19
Comparison of Radionuclide Mass from MT3DMS and PLUMECALC Inside the Corroborative Model Domain

and immobile mass for the two codes is unknown. The ratio of mobile to immobile mass should approach a theoretical value equal to the ratio of fracture porosity to matrix porosity. This occurred for MT3DMS but not for PLUMECALC. For PLUMECALC, the ratio of mobile to immobile mass is about double the theoretical value and growing at late time. In contrast, for the ^{129}I simulations, which did not include decay, the ratio of mobile to immobile mass for both codes compared well to the theoretical value.

N.2.4 Summary

This comparison of MODFLOW/MT3DMS to FEHM/PLUMECALC shows that results for the two models are similar, although there are significant differences. Flow directions are relatively close, but flow rates vary based on particle travel times and are somewhat biased toward shorter travel times for MODFLOW/MODPATH.

At early times (10 and 50 years), ^{3}H plumes from MT3DMS extend farther downgradient than the PLUMECALC plumes. By 100 years, the ^{3}H plumes are similar except at the southern edge of the model area where PLUMECALC shows higher concentrations and a more discontinuous and noisy plume behavior.

Overall, the ^{129}I plumes show relatively good agreement. PLUMECALC plumes extend a little farther downgradient at early time and MT3DMS plumes extend a little farther downgradient at later time.

N.3.0 FEFLOW

N.3.1 Model Description

The conceptual framework for the FEFLOW model consisted of a confined portion of the faulted Lower Carbonate aquifer (LCA) contained within a subdomain of the FEHM model consisting of three different permeability zones: country rock, fault-damage zones and fault-core zones. The upper surface of the model was the LCA surface sliced to a maximum elevation of 750 m, which is slightly higher than the maximum elevation of the potentiometric surface of the LCA within the subdomain simulated by the FEHM model. The bottom of the model was set to an arbitrary flat surface of -990 m elevation. The fault surfaces dipped according to geologic interpretations defined by NSTec. The distribution of permeability zones was defined by proximity to faults that penetrate into the LCA within the subdomain. The LCA and fault surfaces used to define the upper model surface and the distribution of permeability zones within the subdomain were exported from the EarthVision Hydrostratigraphic Framework Model (HFM) of the Yucca Flat/Climax Mine CAU. Table N-3 provides the 3D spatial boundary coordinates for the FEFLOW model. Figure N-20 provides a 3D perspective view of the LCA and fault surfaces comprising the conceptual model framework as defined by the HFM.

Table N-3
Subdomain Model Boundaries

	Minimum	Maximum	Range
	(m)		
Easting	585,000	590,000	5,000
Northing	4,098,500	4,108,000	9,500
Elevation	-990	750	1,740

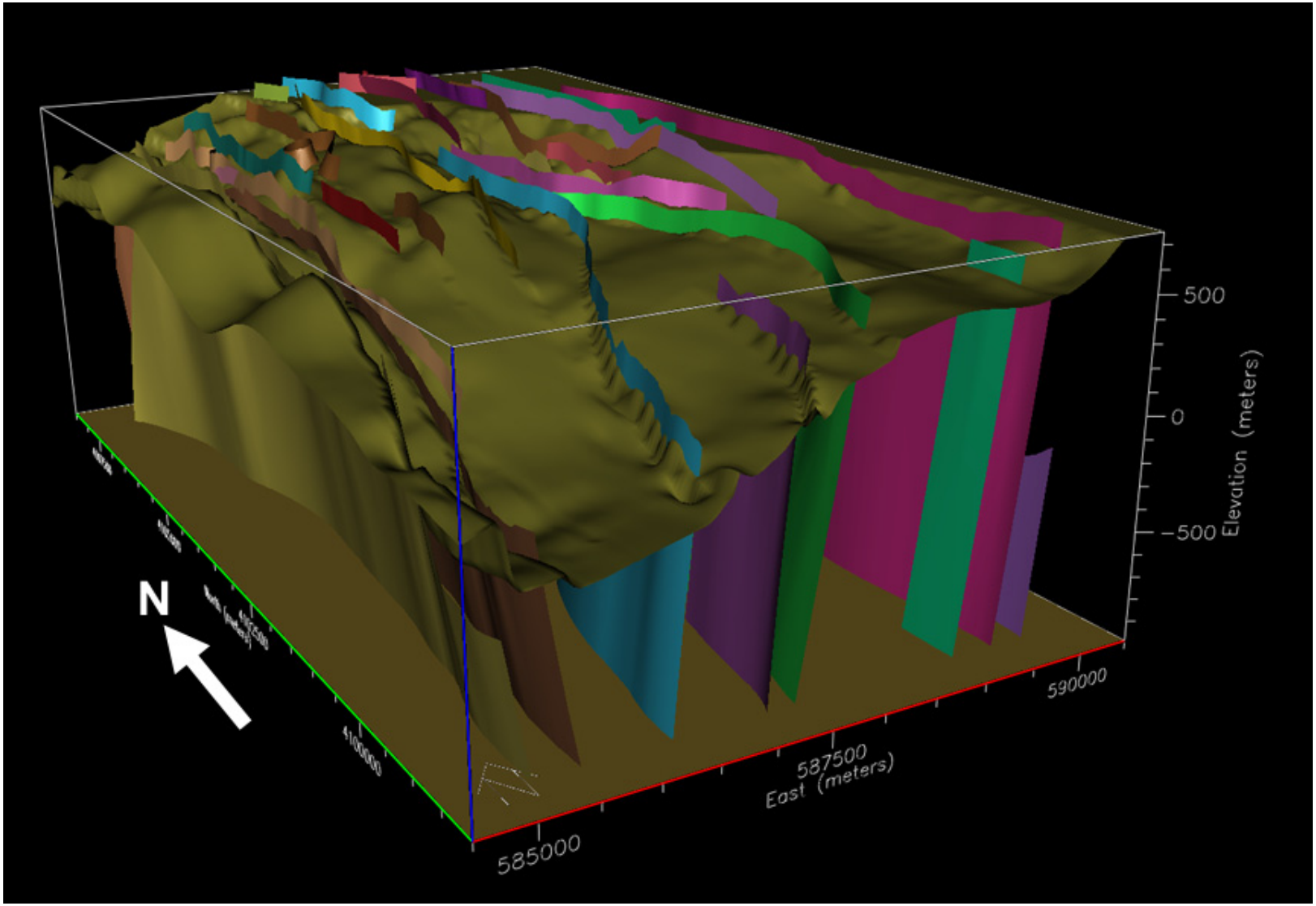

Figure N-20
3D Perspective View of the LCA and Fault Surfaces Exported from the HFM Relative to an Arbitrary Lower Surface of -990 m Elevation Surface Framed by the Subdomain Model Boundaries

A seven-step process was used to create the numerical model framework (3D mesh), define mesh element hydraulic conductivities from the FEHM intrinsic permeability values, and define the model boundary conditions.

Step-1: Mesh Construction

A flattened view of the fault surfaces bounded by the top and bottom subdomain model surfaces and the bounding coordinates of the subdomain model was exported from the HFM. A mesh of triangular elements with variable node spacing was then defined across the x-y space such that the fault intersects with the LCA surface were defined by a series of element sides. The target node spacing within the projected space of the fault planes was 30 m, which coarsened in the surrounding country-rock to minimize the number of nodes and elements. The 30-m spacing within the fault zones was chosen to ensure that at least one element would fall within a 60-m buffer zone surrounding the fault surfaces, which was specified for this exercise as the definition for the fault-core permeability zones. The resulting mesh contained 64,660 nodes and 127,856 elements. Figure N-21 depicts the flattened fault surfaces exported from the HFM relative to the FEFLOW mesh and the FEHM mesh nodes.

Step-2: Layer Construction

A sequence of slices was created replicating the mesh defined for the upper slice through the vertical component of the domain. The slices were flat with a target separation of 60 m except where the resulting slice would intersect the LCA surface in which case it was set to 4 m below the overlying slice. The 60-m maximum separation was chosen to ensure vertical continuity between fault-core mesh nodes at the minimum dip defined by the HFM for the fault surfaces. A total of 30 slices were required to cover the domain at the target spacing resulting in a total of 1,939,800 nodes and 3,707,824 elements in the 3D mesh. Figure N-22 depicts the geometry of the model layer stack.

Step-3: Hydraulic Conductivity Assignment

The center-points for all of the mesh elements were compiled into a single ASCII file. EarthVision was then used to identify the nearest fault surface at each point and the distance from each point to that surface. The ID and distance values were then used to assign a hydraulic conductivity value to the point that matched the FEHM intrinsic permeability value for the corresponding permeability zone. Each fault was defined by a unique core and damage zone hydraulic conductivity value and the

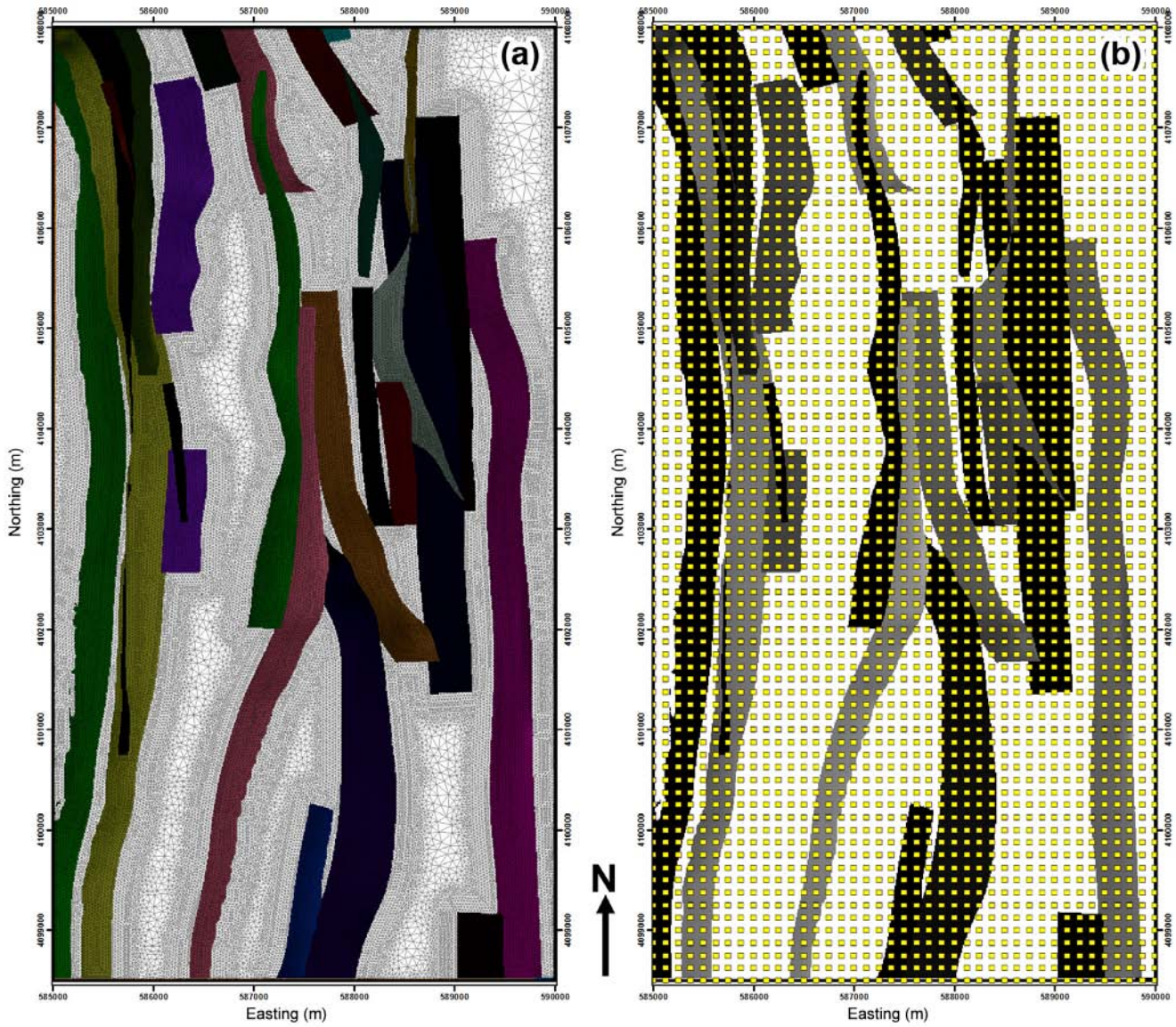

Figure N-21
Comparison of the FEFLOW Mesh (a) and the FEHM Nodes (b) Relative to a Flattened Projection of the Fault Surfaces Within the Subdomain Exported from the HFM

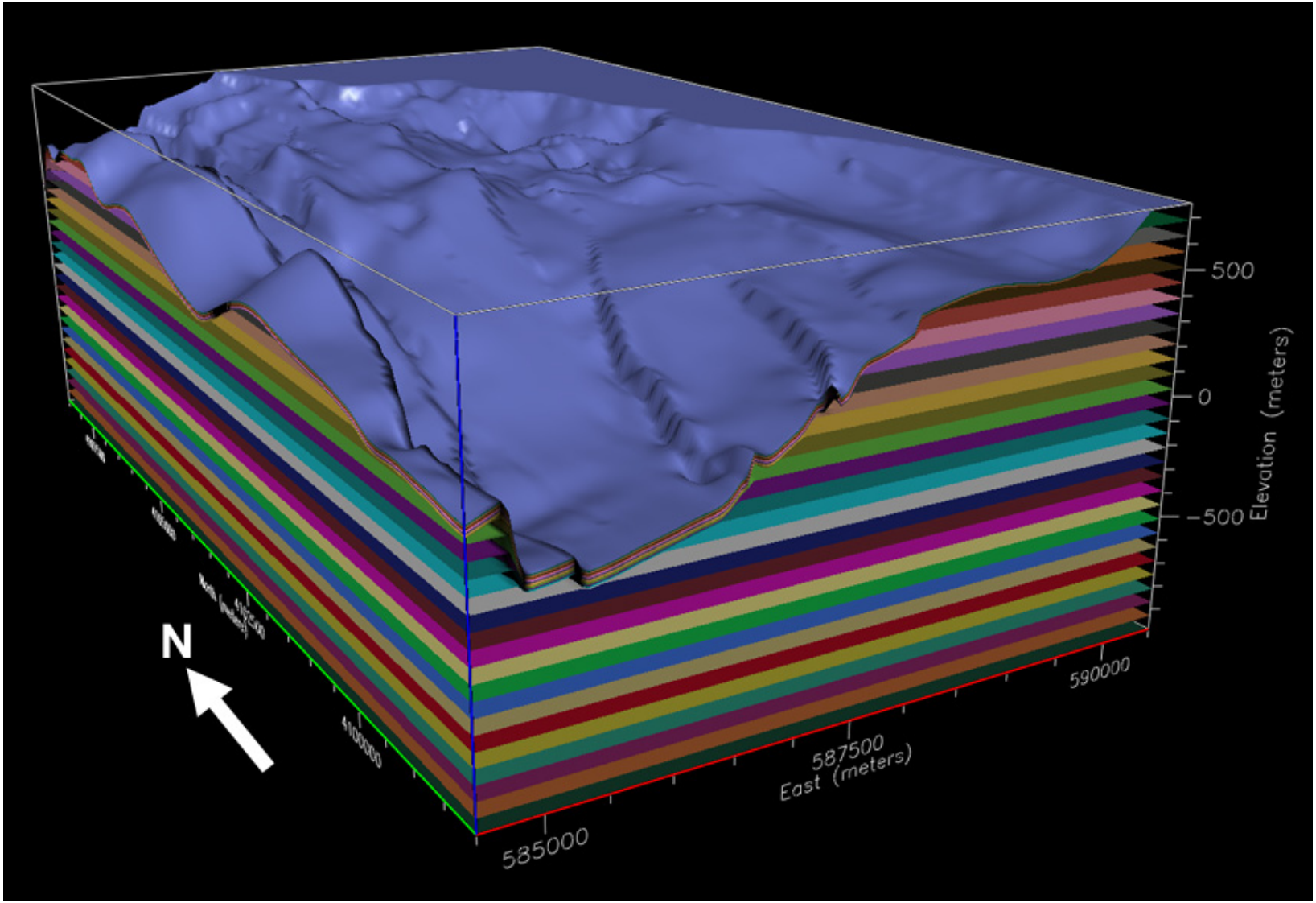

Figure N-22
3D Perspective View of the 30 Slices Used to Discretize the FEFLOW Subdomain Model

damage zones were defined by a buffer zone extending 120 m beyond the fault-core zone on both sides of the fault. FEHM intrinsic permeabilities were converted to hydraulic conductivities using the following equation.

$$K = k_i \, (\rho \, g \, / \, \mu) \qquad (N\text{-}2)$$

where

K = hydraulic conductivity,
k_i = intrinsic permeability (m^2),
ρ = density of water (993.59 kg/m^3),
g = gravitational acceleration (9.80665 m/s^2), and
μ = dynamic viscosity of water (0.00070057 kg/ms).

Figure N-23 provides a 3D perspective view of the fault surfaces and the fault-core zone and fault-damage zone mesh nodes colored by zone type, which depicts how the fault-core and fault-damage zones dip with the faults through the subdomain. Table N-4 lists the faults contained in the FEHM model and the corresponding hydraulic conductivity assignments. Note that the damage zones are anisotropic with respect to Kxx and Kyy.

Step-4: Anisotropy Assignment

The FEHM model represented the faults as orthogonal north-south oriented vertical planes whereas the fault surfaces were represented in the FEFLOW model according to the orientation and dip defined by the HFM. Accordingly, the fault-damage zones were represented in the FEHM model as orthogonal north-south oriented sets of nodes that fall within the specified distance from the faults. Those nodes were assigned with anisotropic permeabilities with respect to Kxx and Kyy. In order to accurately reflect the fault-strike anisotropies in the FEFLOW model, the anisotropy angle at each fault-damage zone node was assigned according to the strike of the corresponding fault at the point on the surface closest to the node. This was done using the ASCII file created for the mesh element center points and a series of EarthVision model queries and calculations. Figure N-23 shows the elemental Kyy hydraulic conductivity and anisotropy angle assignments for slice-1 of the FEFLOW model.

Step-5: Storativity Assignment

The FEHM model contained two specific storage values that depict two zones within the model domain, the country-rock zone and the combined fault-core and fault-damage zones. Storativity at

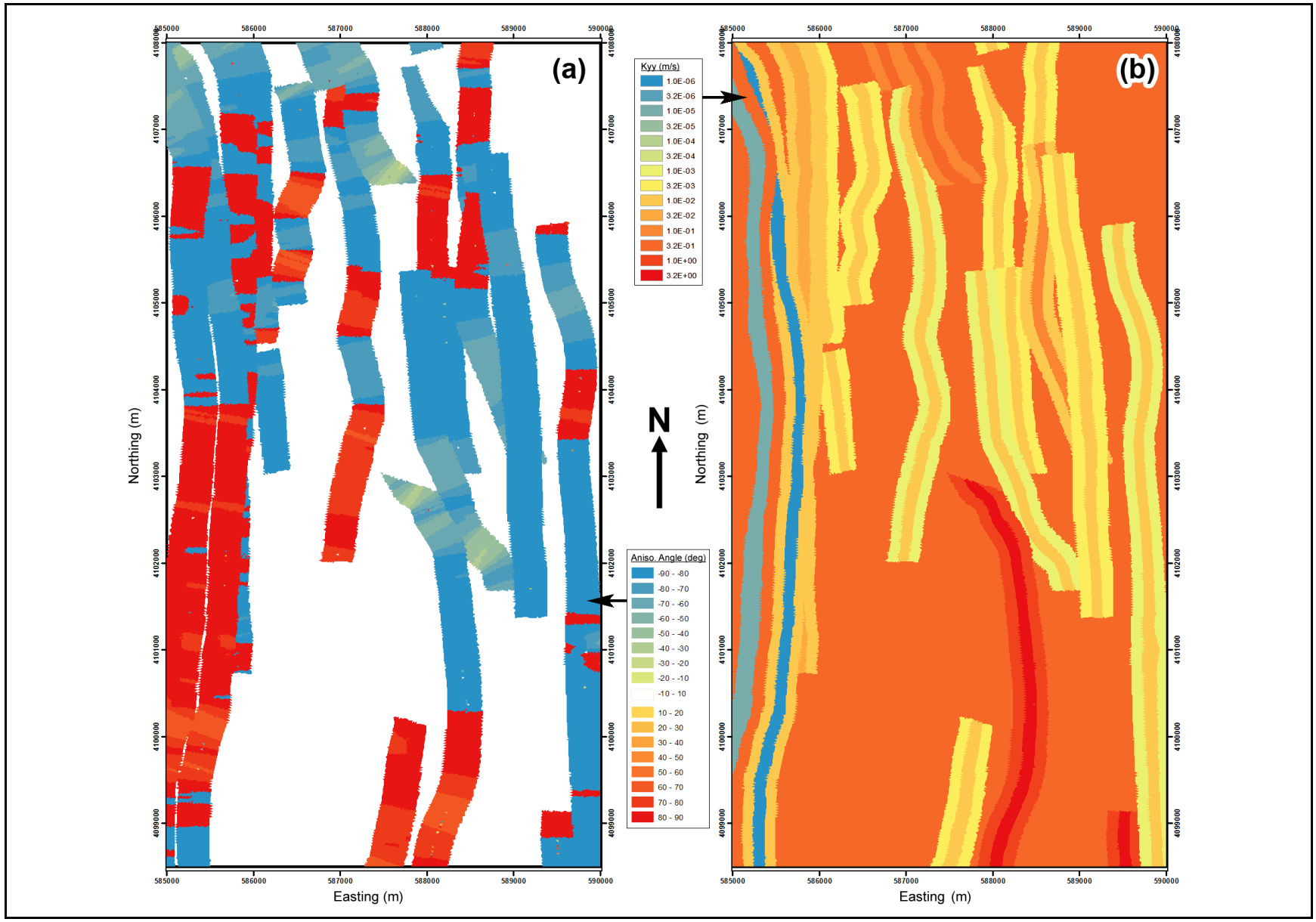

Figure N-23
Material Assignments in FEFLOW Model (a) Anisotropy Angle and (b) Kyy Hydraulic Conductivity

Table N-4
Hydraulic Conductivity Assignment by Permeability Zone

Zone	Kxx (m/s)	Kyy (m/s)	Kzz (m/s)	Kxx (m/s)	Kyy (m/s)	Kzz (m/s)
Country-Rock	3.67E-05	3.67E-05	1.86E-05	NA	NA	NA
	Core Zone			Damage Zone		
FLT-114	2.13E-06	2.13E-06	2.13E-06	4.54E-07	2.08E-05	7.04E-07
FLT-116	2.67E-06	2.67E-06	2.67E-06	5.70E-07	2.61E-05	8.84E-07
FLT-145	1.01E-09	1.01E-09	1.01E-09	4.79E-05	9.83E-04	3.37E-05
FLT-146	2.67E-06	2.67E-06	2.67E-06	5.70E-07	2.61E-05	8.84E-07
FLT-147	5.62E-04	5.62E-04	5.62E-04	1.20E-04	5.50E-03	1.86E-04
FLT-148	1.47E-10	1.47E-10	1.47E-10	1.44E-06	1.43E-04	4.77E-06
FLT-149	7.84E-05	7.84E-05	7.84E-05	1.68E-05	7.67E-04	2.60E-05
FLT-150	2.83E-06	2.83E-06	2.83E-06	6.04E-07	2.76E-05	9.36E-07
FLT-151	1.45E-06	1.45E-06	1.45E-06	3.10E-07	1.42E-05	4.81E-07
FLT-154	8.42E-06	8.42E-06	8.42E-06	1.80E-06	8.24E-05	2.79E-06
FLT-155	2.00E-06	2.00E-06	2.00E-06	4.27E-07	1.96E-05	6.63E-07
FLT-156	8.92E-05	8.92E-05	8.92E-05	1.91E-05	8.73E-04	2.96E-05
FLT-157	2.67E-06	2.67E-06	2.67E-06	5.70E-07	2.61E-05	8.84E-07
FLT-158	2.67E-06	2.67E-06	2.67E-06	5.70E-07	2.61E-05	8.84E-07
FLT-160	5.65E-04	5.65E-04	5.65E-04	1.21E-04	5.53E-03	1.87E-04
FLT-161	1.43E-06	1.43E-06	1.43E-06	3.06E-07	1.40E-05	4.74E-07
FLT-164	2.67E-06	2.67E-06	2.67E-06	5.70E-07	2.61E-05	8.84E-07
FLT-165	2.67E-06	2.67E-06	2.67E-06	5.70E-07	2.61E-05	8.84E-07
FLT-166	2.67E-06	2.67E-06	2.67E-06	5.70E-07	2.61E-05	8.84E-07
FLT-167	1.08E-05	1.08E-05	1.08E-05	2.31E-06	1.06E-04	3.58E-06
FLT-168	2.67E-06	2.67E-06	2.67E-06	5.70E-07	2.61E-05	8.84E-07
FLT-169	1.42E-06	1.42E-06	1.42E-06	3.04E-07	1.39E-05	4.71E-07
FLT-170	2.67E-06	2.67E-06	2.67E-06	5.70E-07	2.61E-05	8.84E-07
FLT-171	5.40E-06	5.40E-06	5.40E-06	1.15E-06	5.28E-05	1.79E-06
FLT-172	2.67E-06	2.67E-06	2.67E-06	5.70E-07	2.61E-05	8.84E-07
FLT-178	5.99E-09	5.99E-09	5.99E-09	6.33E-07	6.33E-05	2.18E-06
FLT-190	6.39E-09	6.39E-09	6.39E-09	7.10E-07	6.75E-05	3.07E-06

each element center point in slice-1 of the FEFLOW model was calculated as the product of FEHM-defined specific storage for the respective zone and the saturated thickness at that point, which was calculated by subtracting the FEFLOW model bottom slice elevation from the potentiometric surface of the LCA as defined by the FEHM model at the point. The resulting range in storativity values for each zone was on the order of 10^{-6}. Because the range was so small, the values were assumed to be constant within each zone. Table N-5 lists the specific storage values from the FEHM model and the corresponding calculated storativity values used in the FEFLOW model.

Table N-5
Storativity Assignments

	FEHM Specific Storage (1/m)	FEFLOW Storativity (-)
Country-Rock	4.446894E-08	1.78E-04
Fault-Core/Damage	3.717284E-07	1.48E-03

Step-6: Boundary Condition Assignment

The four vertical north-south and east-west model boundaries were assigned as constant head boundaries where the head values were set to match the FEHM model values at the respective locations. To accomplish this, head values from the FEHM model-simulated LCA potentiometric surface elevations were back-interpolated onto the boundary nodes from slice-1 using EarthVision. The nodal assignments from slice-1 were then copied down to all of the 29 lower slices. No flow was permitted across the lower model surface.

Step-7: Recharge to the LCA

Flux (recharge) through the upper surface of the LCA was assigned nodally according to nodal flux values exported from the FEHM model at the LCA surface. In order to make the assignments, the FEHM flux values were first converted from the FEHM units (kg/s) to the FEFLOW units (m^3/d) according to the following equation.

$$Q_{FEFLOW} = Q_{FEHM} \; x \; (1/\rho) \; x \; (time\ conversion) \qquad (N\text{-}3)$$

where

Q_{FEFLOW} = flux in FEFLOW units
Q_{FEHM} = flux in FEHM units
ρ = density of water (993.59 Kg/m^3).

Ideally, the nodal assignments would have been done on an individual node by node basis given a 1:1 relationship between the FEHM and FEFLOW nodes. The construction process however, which relied directly on the HFM as opposed to the FEHM mesh, precluded such a 1:1 assignment. Instead, flux from the FEHM nodes was assigned to the nearest FEFLOW node for the corresponding permeability zones. For the faults, this process equated to shifting the FEHM nodes in the x-direction such that they fell directly over the respective fault as it was defined in the FEFLOW model. In some cases, flux into a fault zone was defined by more than one FEHM node in a given model row. In these cases the flux from all FEHM nodes in the given row was summed and the total was assigned to the respective FEFLOW fault node or nodes. When the assignment involved more than 1 FEFLOW node, as was the case for most fault-damage zone nodes, the total FEHM flux was divided by the corresponding number of FEFLOW nodes and distributed equally at each node. The country-rock assignments were made by assigning the FEHM node values to the closest FEFLOW node. Figure N-24 shows the fault-core and fault-damage zone nodes as defined by the FEHM and FEFLOW models and the final flux assignments into the LCA through the upper surface of the FEFLOW model.

Mass Flux Assignments

Initial mass flux conditions for ^{3}H and ^{129}I were assigned as pumping/injection wells at specific nodes in the FEFLOW model domain that corresponded to specified locations for four detonations (MICKEY, TORRIDO, LAMPBLACK, and BOURBON) within the subdomain and one point of flux across the LCA surface. The mass flux values were assigned to match the FEHM values, which were reported in mol/day and converted to the required FEFLOW unit of g/day using the respective atomic mass values for ^{3}H (3.0160492 g/mol) and ^{129}I (128.9049877 g/mol).

Table N-6 provides the mass transport material settings, which were assigned to all elements in each layer. The area corresponding to each mass flux node in the FEHM model was calculated and used to identify the equivalent number and location of FEFLOW nodes that represented the same area and location. The mass flux assigned to the FEFLOW nodes then represented the total flux at the respective FEHM node divided by the number of FEFLOW nodes in the corresponding area. Table N-7 lists the mass flux values at each of the FEHM nodes and the corresponding FEFLOW value and number of nodes used to represent the flux.

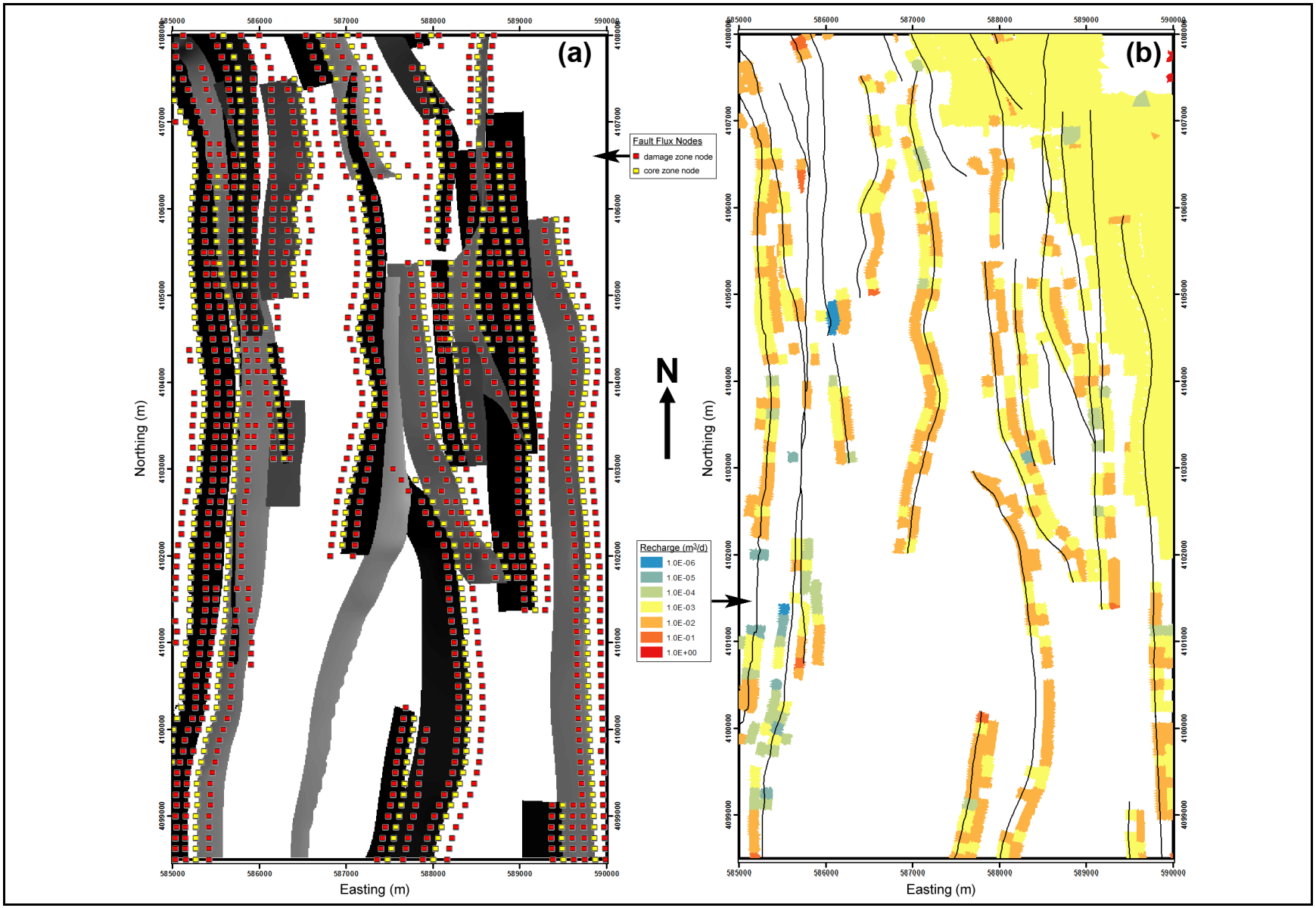

Figure N-24
Location of Fault-core and Fault-damage Zone Nodes from the FEHM Model after being Summed and Snapped to the Respective Fault Zones as Represented (a) in the FEFLOW Model and (b) Flux into the LCA Surface in the FEFLOW Model as Defined from Snapping the FEHM Nodes to the Nearest Node of the Corresponding Permeability Zone

Table N-6
Mass Transport Material Assignments

Property	Value	
Porosity	0.03	
Longitudinal dispersivity	20 m	
Transverse dispersivity	2 m	
Molecular diffusion	2.0E-10 m^2/s	
Half-life	^{3}H	^{129}I
	12.32 years	15.7 million years
1st order decay rate	^{3}H	^{129}I
	1.7828E-09 /s	1.3990E-15 /s

Table N-7
Mass Transport Initial Flux Assignments

FEHM Node	Detonation	FEHM Flux (mol/day)		FEFLOW Flux (g/day)		# FEFLOW Nodes
		^{3}H	^{129}I	^{3}H	^{129}I	
503007	MICKEY	0.36	0.0004933	1.086	0.2714	4
503007	TORRIDO	0.01436	0.003341	0.0433	0.0108	4
505253	BOURBON	1.576	0.003586	4.753	0.099	11
471756	LAMPBLACK	0.5251	1.58	0.003586	0.4321	1
408436	BILBY	0.0	0.0	0.0	0.0	12

Each of the pumping/injection well mass flux boundary nodes were assigned a set of transient concentration values based on the time-stepped FEHM exports. Time zero was assumed to be 1/1/1956. The timing of the mass flux assignments were defined as days after the start date. Single point-in-time (detonation) concentrations were assigned in the transient mass flux timeline according to the reported detonation date. Concentrations were allowed to vary linearly between the specified input dates with the exception of the concentrations on the specified detonation dates, which were held constant for a 24-hour period.

A maximum time step value of 1,000 days was used for the mass transport simulations in order to establish a Courant number of less than 1 throughout the majority of the model domain. This was done to minimize oscillations in the simulated mass concentration fields observed at very low concentrations values in runs using larger time steps.

N.3.2 Flow Model Results

The flow model ran in less than five minutes and produced a head field and particle tracks similar to those produced by the FEHM model. Figure N-25 provides a comparison of the FEFLOW and FEHM head fields. Figure N-26 shows the FEFLOW velocity field and particle track pathways emanating from the mass transfer source nodes.

N.3.3 Transport Model Results

The ^{3}H and ^{129}I transport simulations took approximately 3.5 hours each to run. Results were exported at three time steps for each of the simulations (10, 50, and 100 years for ^{3}H; and 100, 300, and 1,000 years for ^{129}I). In both sets of the transport simulations, anomalous concentrations occur near the model boundaries at very low concentrations (approximately10^{-8} mg/L). These are attributed to Courant numbers greater than 1 that occur in some mesh elements in those regions, which could be reduced using smaller time steps and/or smaller node spacings. This issue is only apparent in the first time step for each simulation when the concentration range viewed is extended down to 10^{-8} mg/L and does not impact the simulated concentrations throughout the remainder of the domain. Figures N-27 and N-28 show the results of the mass transport simulations at the specified time steps. Figure N-29 provides 3D perspective views of the transport results for ^{3}H and ^{129}I at the specified time steps.

N.3.4 Discussion

FEFLOW appears to be a viable alternative for flow and transport modeling at the NTS. Both the flow and transport results appear reliable and no insurmountable problems were encountered during the model design or setup. The primary limitation identified in this exercise was the requirement for vertical elements, which necessitated fine mesh discretization and a large number of layers in order to correctly simulate the fault surfaces as they have been defined in the HFM. This resulted in relatively large run-times, particularly for the mass transport scenarios (less than 5 minutes for flow and approximately 3.5 hours for transport).

Using the same methodologies, scaling up to the size of the full Yucca Flat/Climax Mine domain would equate to a mesh approximately 36 times larger than the subdomain model with estimated run-times of between 100 and 180 minutes for flow and as much as 5 days for transport. These estimates are based on the computational capacity that was used for the subdomain modeling, which

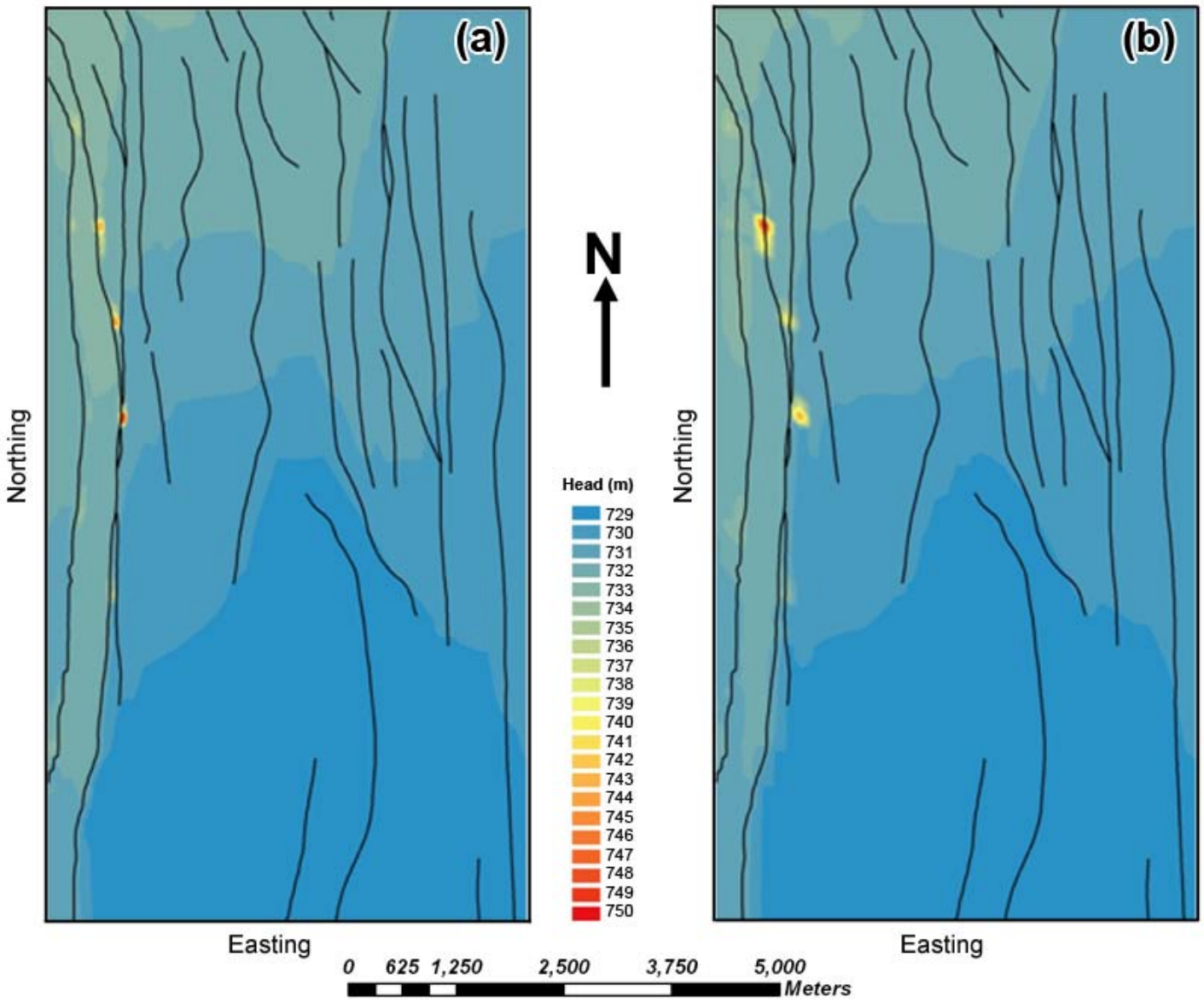

Figure N-25
Comparison of Heads at the LCA Surface Simulated by the FEFLOW (a) Subdomain Model and (b) the FEHM Model

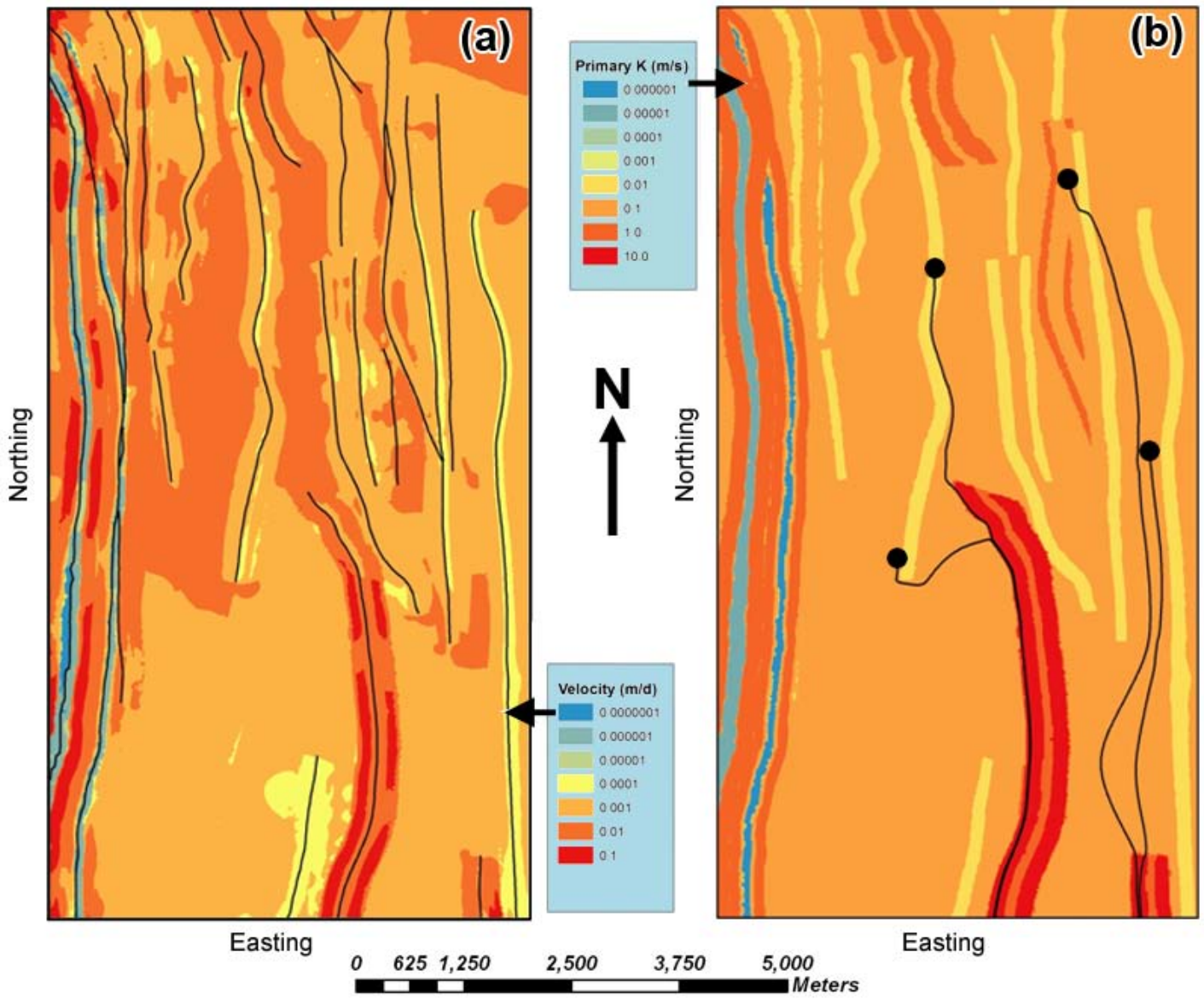

Figure N-26
Groundwater Velocities:
(a) and Particle Tracks (b) Simulated by the FEFLOW Subdomain Model at Slice-1 of the Model

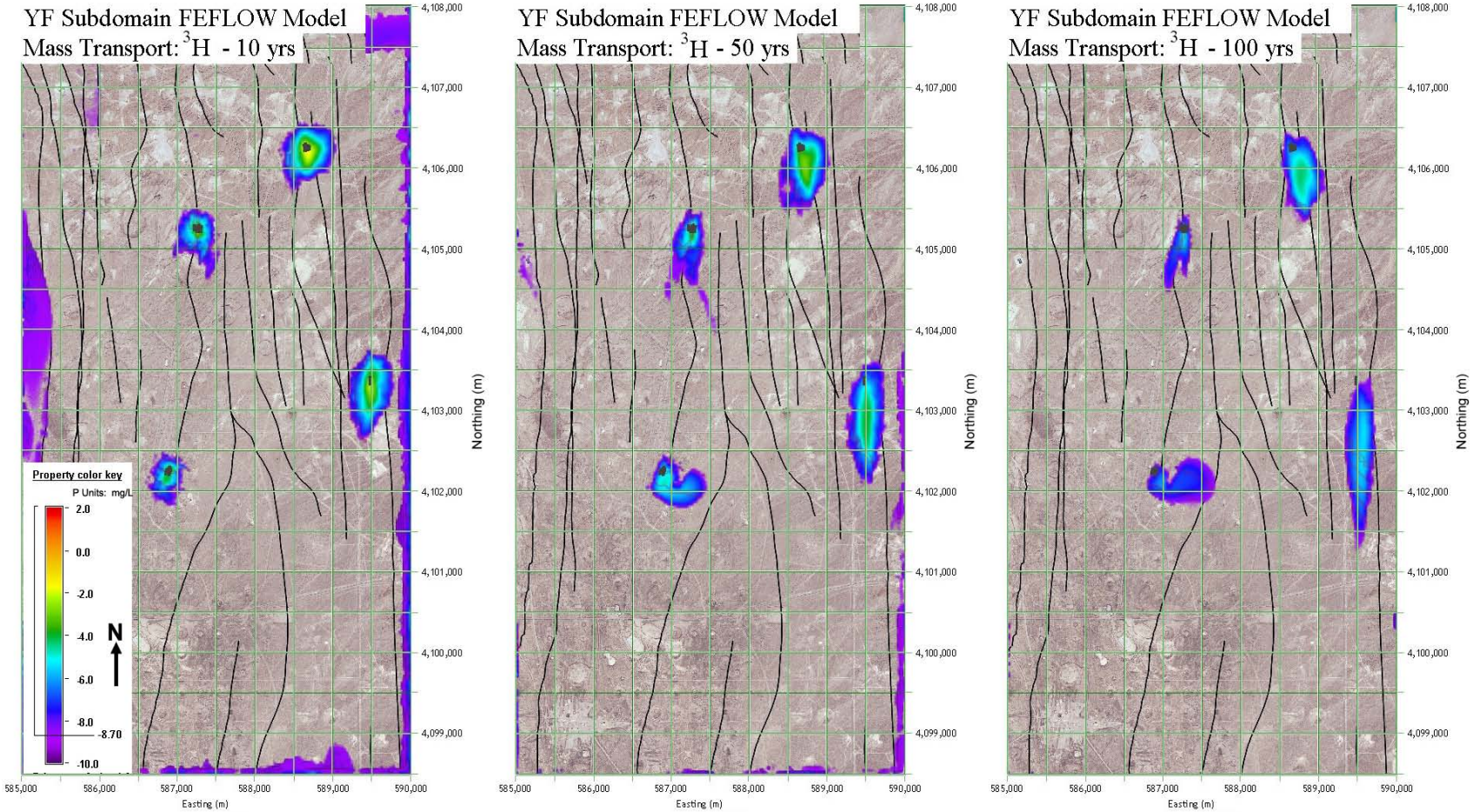

Figure N-27
Results of the FEFLOW Mass Transport Simulation at 10, 50, and 100 Years Showing the Simulated Distribution of ^{3}H > 2.1 x 10-9 mg/L

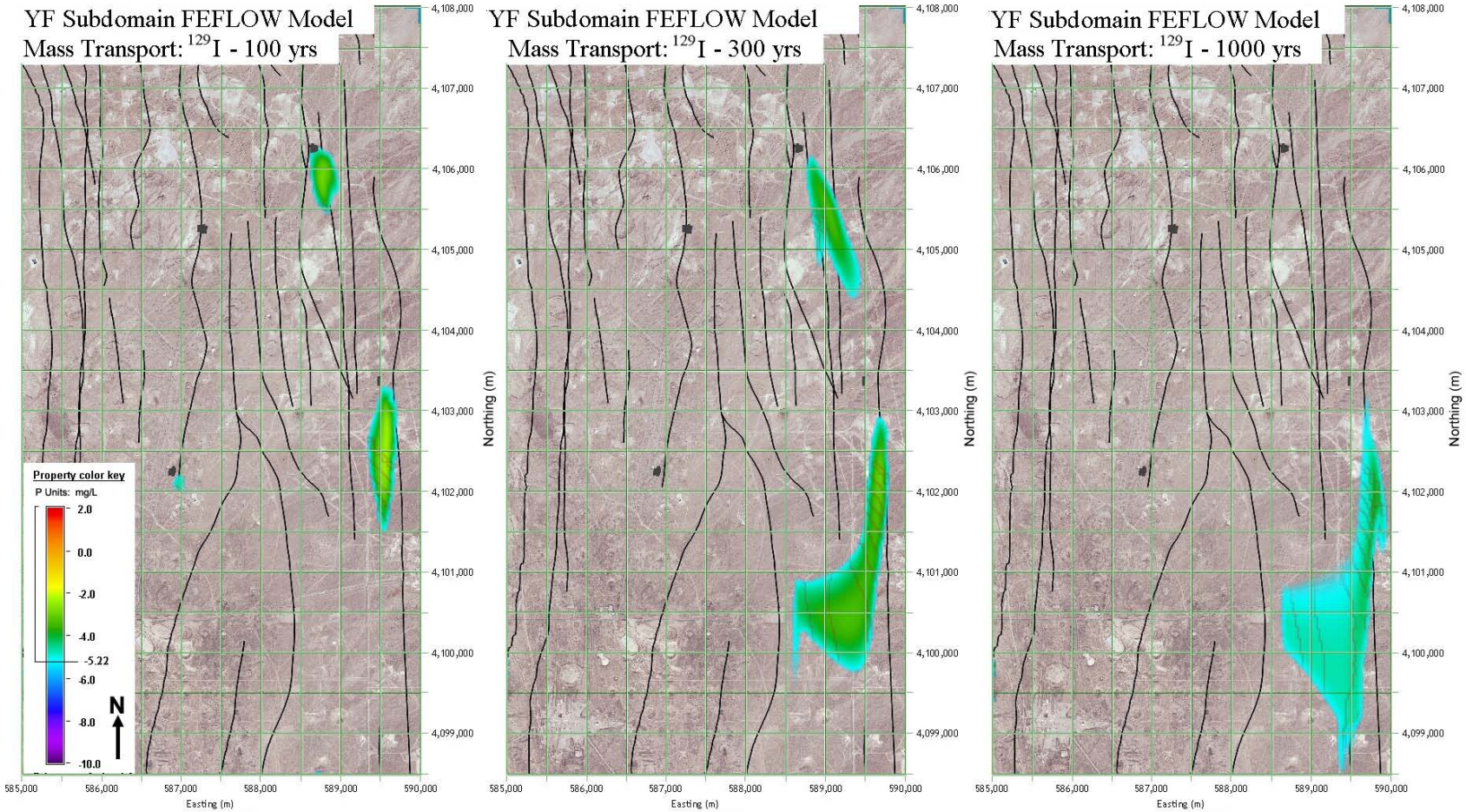

Figure N-28
Results of the FEFLOW Mass Transport Simulation at 100, 300, and 1,000 Years Showing the Simulated Distribution of ^{129}I > 5.7 x 10-6 mg/L

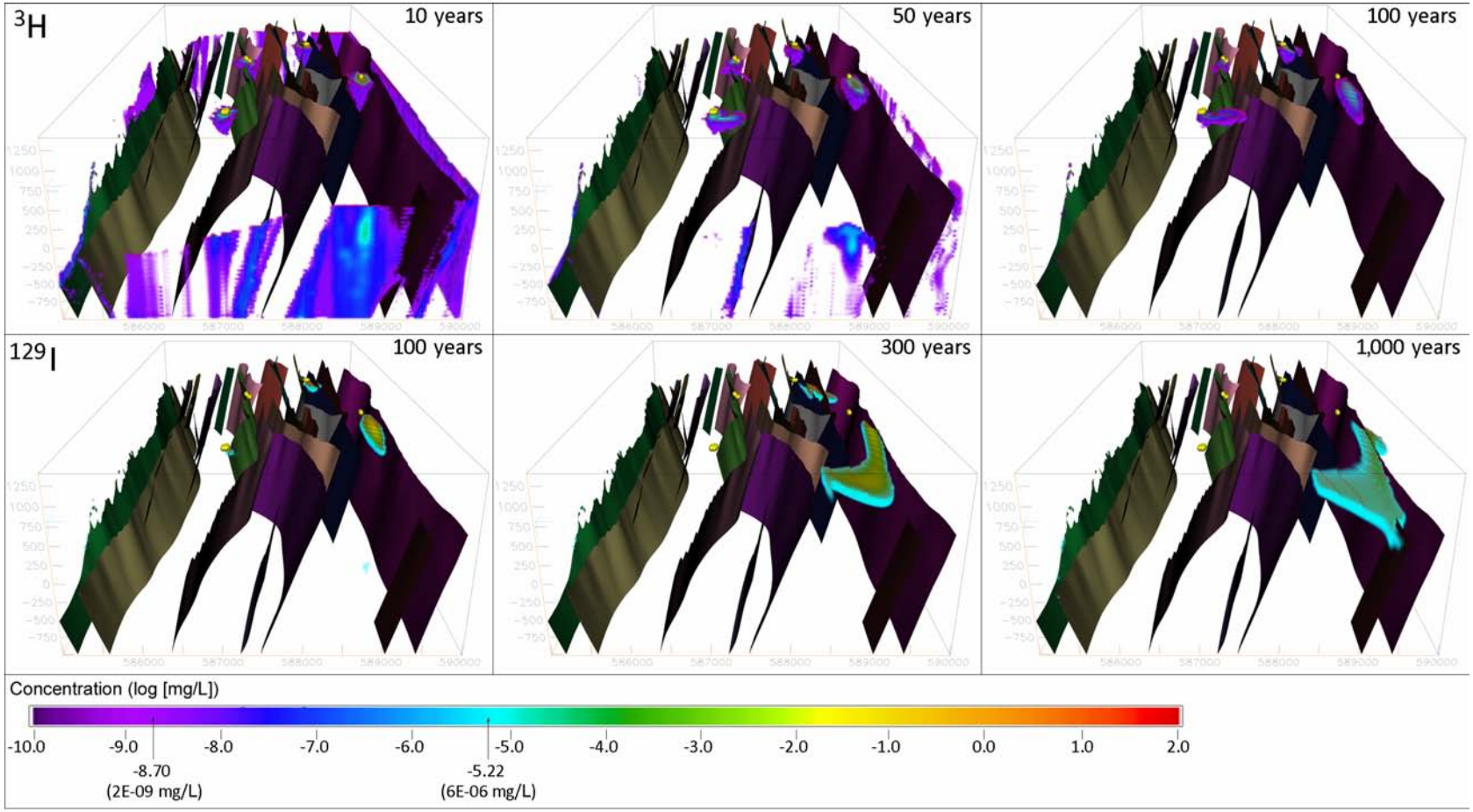

Figure N-29
Perspective View of the Results from the FEFLOW Simulation of ^{3}H and ^{129}I Mass Transport

was a quad dual-core 2.93 GHz processor set with 8 GB of RAM using 64-bit software. FEFLOW is partially parallelized, which means that the estimates for the scaled-up modeling could be substantially reduced with a larger processor set.

It is also possible that the run times could be substantially reduced by employing a different design that leverages the discrete-element features in FEFLOW to reduce the number of nodes, elements, and layers necessary to simulate the fault surfaces. Such reductions could also be achieved by assuming the faults to be vertical and revising the mesh design accordingly.

The only observed problem in the model results occurred in the transport simulations in the form of oscillations in the simulated concentrations at very low levels. These oscillations were only observed at concentration levels of 10^{-8} or less and then only in exports viewed with external software (i.e., EarthVision) because FEFLOW itself will not display or export to shape files values less than 10^{-6} mg/L. The oscillations were displayed and discussed in this report but are not considered to be impactful to the simulated distribution of mass concentrations at higher levels.

In addition to the flow model corroboration, one significant outcome of this effort was the development of processes for the rapid articulation of hydrostratigraphic and fault surfaces onto a non-uniformly spaced mesh using EarthVision and surfaces defined in a HFM. After the processes were developed, the FEFLOW model structure was built directly from the HFM surfaces in just a few man-days. This process can be scaled-up easily to a full CAU size and can be adapted to any nodally-based flow code.

Finally, another beneficial outcome was the automation of the 3D visualization of the mass transport results, which were exported from FEFLOW in ASCII x,y,z,p format. Processes were developed that automate the formatting of the output files for EarthVision input, development of 3D grids, compilation of 3D and 2D views that incorporate base maps and data files, and the export of the views to images and animations. These processes are also scalable to the full CAU scale and adaptable to any flow and transport software that will produce spatially projected ASCII output.

N.4.0 FRACMAN/MAFIC

N.4.1 Model Description

To support the Yucca Flat corroborative modeling effort, the FEHM Yucca Flat conceptual model was implemented as a FracMan hybrid Discrete Fracture Network/Equivalent Porous Medius (DFN/EPM) model. Faults are discretized explicitly as 2D (plate) finite elements (Figure N-30), and the background fracture and rock matrix permeability is modeled using volume (tetrahedral) finite elements. (Figure N-31). The volume elements represent the combined effect of the rock matrix and background fractures. Damage zones parallel to faults are the major conductive feature of the model, and are therefore modeled explicitly. Flow through these fractures introduces significant anisotropy into the conductivity field along the fault damage zones. FracMan solves for flow simultaneously in the fracture elements, and in the volume elements, such that the total flow through the rock mass is the sum of fracture and rock mass flows.

Figure N-32 presents a workflow diagram for the FracMan analysis.

- Implement fault damage zones as a DFN model mesh, parameterized according to the reference project parameters. The geometry of the fractures is defined by the geometry of the conductive fault damage zones (Figure N-30).
- Implement the rock mass as a mesh of isotropic volumetric (EPM) elements.
- The properties of these elements are mapped from the FEHM Voronoi cell hydraulic properties (Figure N-31).
- Implement hydraulic boundary conditions to the Hybrid DFN/EPM model by mapping FEHM heads to the North and South faces of the model region, and no flow conditions to all other boundaries.
- Solve the head field in the Hybrid DFN/EPM model, utilizing assigned material properties and boundary conditions on both fracture and volume elements.
- Solve for transport pathways from Yucca Flat assigned source locations through the Hybrid DFN/EPM model flow field using particle tracking.

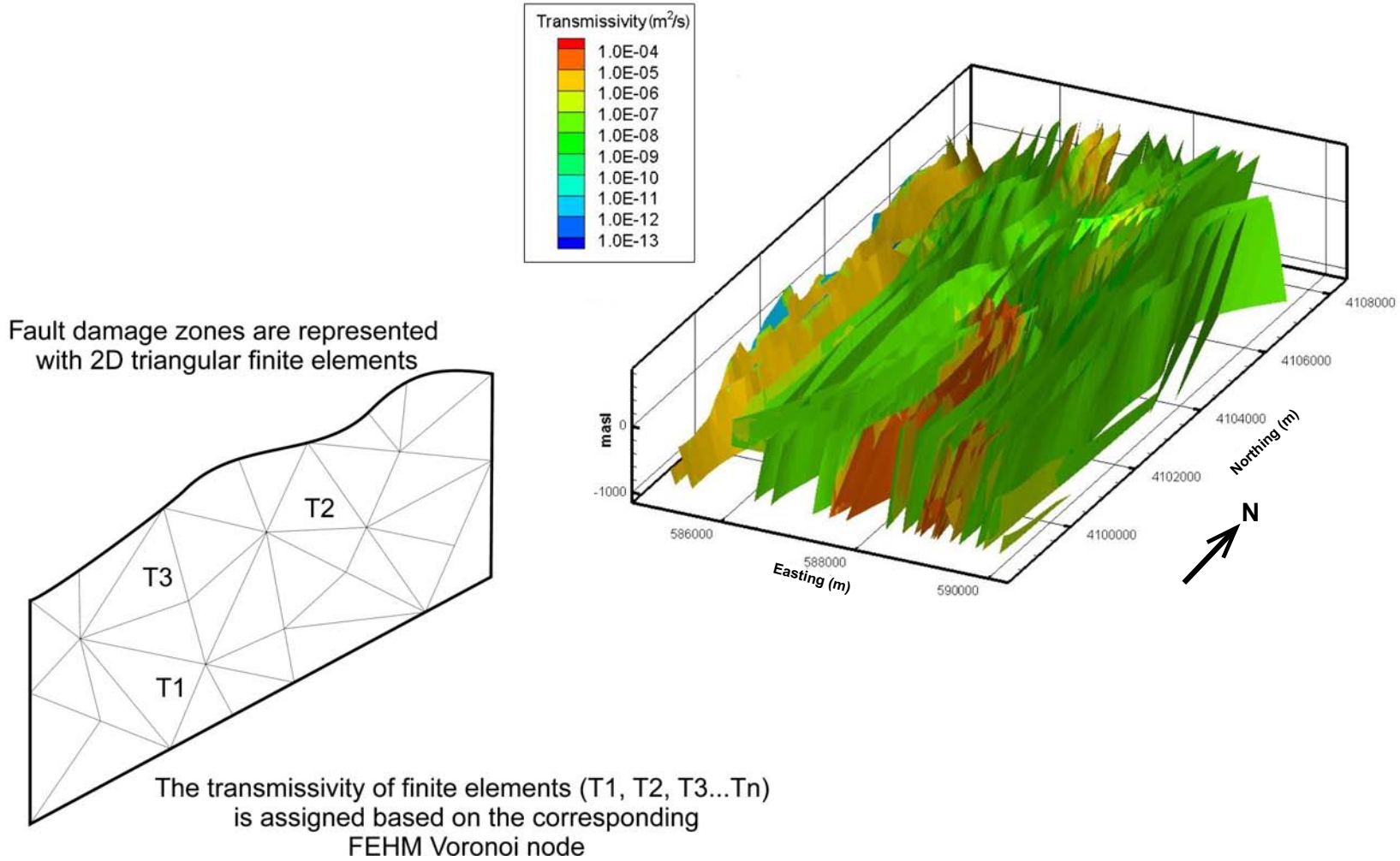

Figure N-30
FracMan DFN Model for Yucca Flat Fault Damage Zones

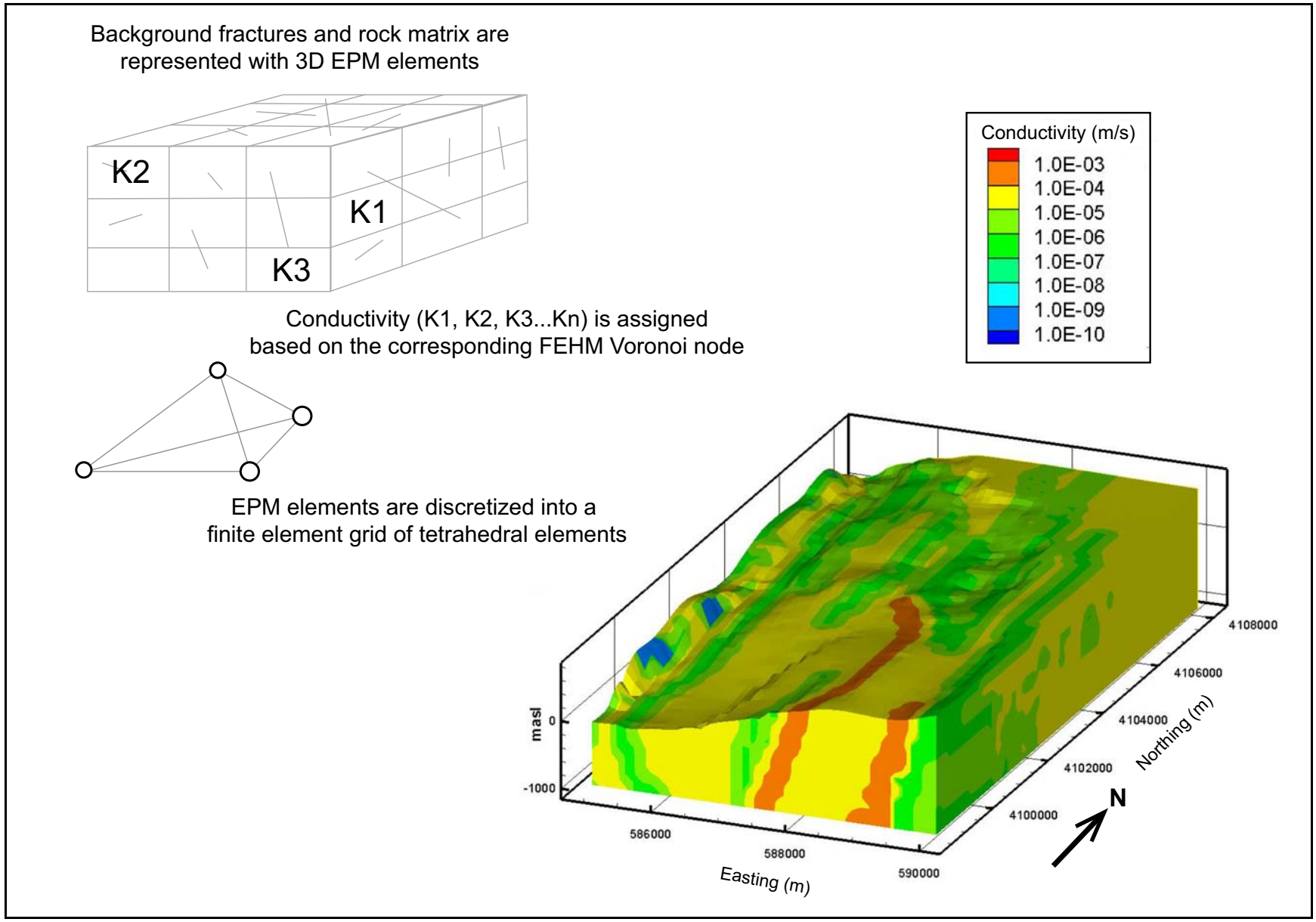

Figure N-31
FracMan EFN Model for Background Rock Mass Hydraulic Conductivity

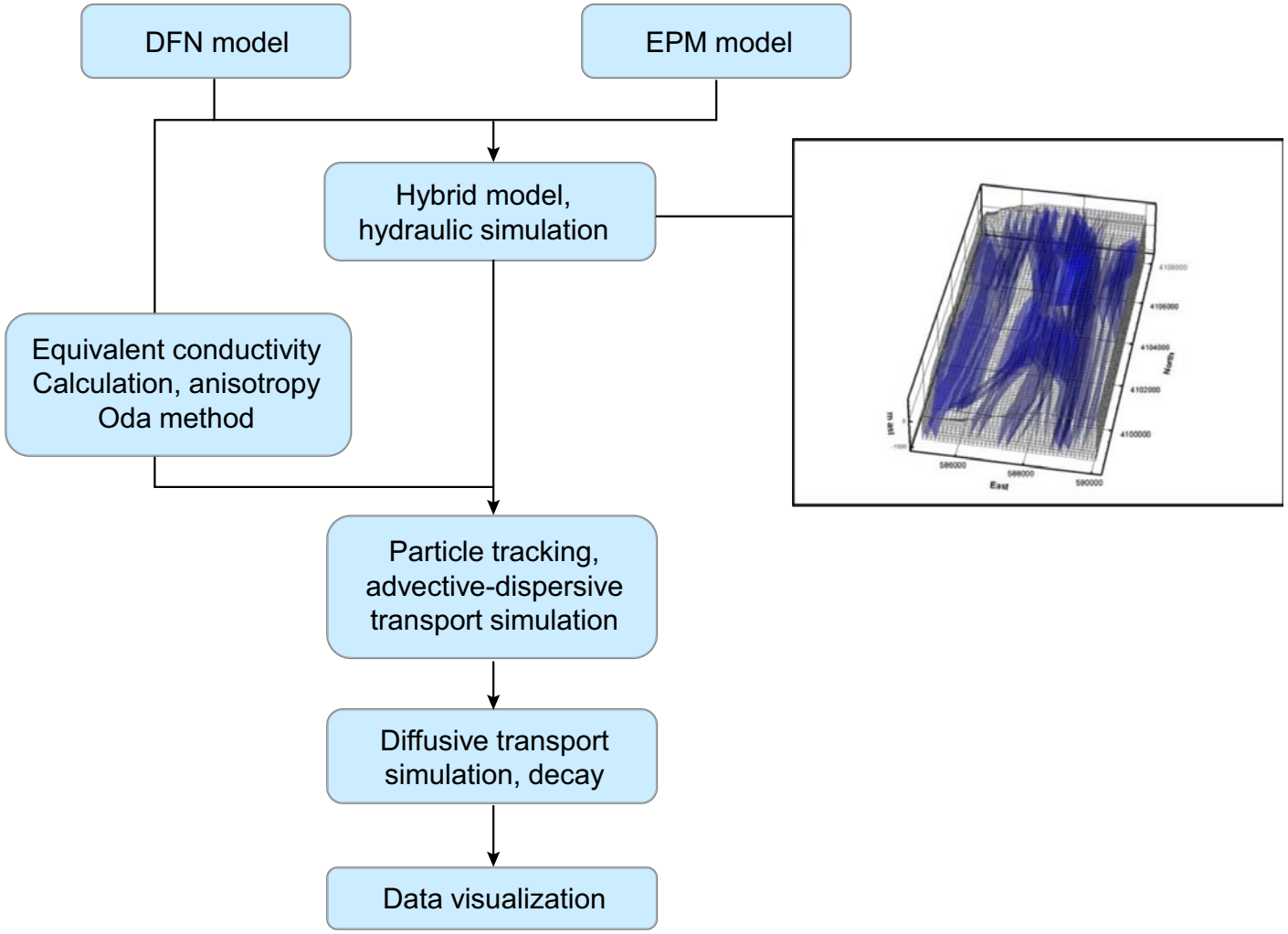

Note: Insert illustrates Hybrid DFN/EPM Model of both DFN Elements Representing Fault Damage Zones and EPM Elements Representing Rock Mass

Figure N-32
Workflow Diagram for FracMan Hybrid DFN/EPM Flow and Transport Simulation

- Solve solute transport along the particle track pathways using LTG (Laplace Transform Galerkin) mobile/immobile zone transport with advection, dispersion, matrix diffusion, and, radioactive decay.

N.4.1.1 FracMan Model Domain

The FracMan model domain was defined on X: from 584925 to 590050 and Y: from 4098550 to 4108050. The top surface of the FracMan model domain was defined by the LCA structure top surface, and the water table. The use of the water table as the top model boundary is especially important at the NE segment of the model domain. The top surface of the model is explicitly reproduced in FracMan as a smooth, continuous surface. The bottom of the model domain is defined by a horizontal surface at Z: -1062.5m

N.4.1.2 EPM (Volumetric Element Mesh) Implementation

The EPM portion of the FracMan model is based upon a mapping of FEHM model material properties at Voronoi centers to a regular grid of isotropic volumetric finite elements representing the rock matrix and background fractures. The FracMan EPM mesh was gridded to ensure that each finite element contains no more than one FEHM Voronoi center node (Figure N-33). This approach avoids smoothing of FEHM cell values on assignment to FracMan volumetric cells. In regions where the density of FEHM nodes is smaller due to the unstructured nature of FEHM mesh there are FracMan/MAFIC mesh elements containing no FEHM Voronoi center points. In these cases the Voronoi approach is used to assign hydraulic properties to FracMan cells based on the values in the single closest FEHM Voronoi center node, as described below.

The FracMan EPM grid is discretized as 15 layers. The top layers of the FracMan model is defined based on the distance between the LCA top surface and the nearest FEHM Voronoi center node. The remaining layers are fixed at a 125 m height. This layer height is approximately the distance between adjacent FEHM nodes, and was therefore selected for computational efficiency, and also to improve the mapping of properties.

For this simulation, FracMan uses isotropic properties in the volumetric (EPM) finite elements, as anisotropic behavior is introduced by the inclusion of FracMan DFN discrete features representing faults and damage zones. Since higher conductivities are accounted for by the introduction of

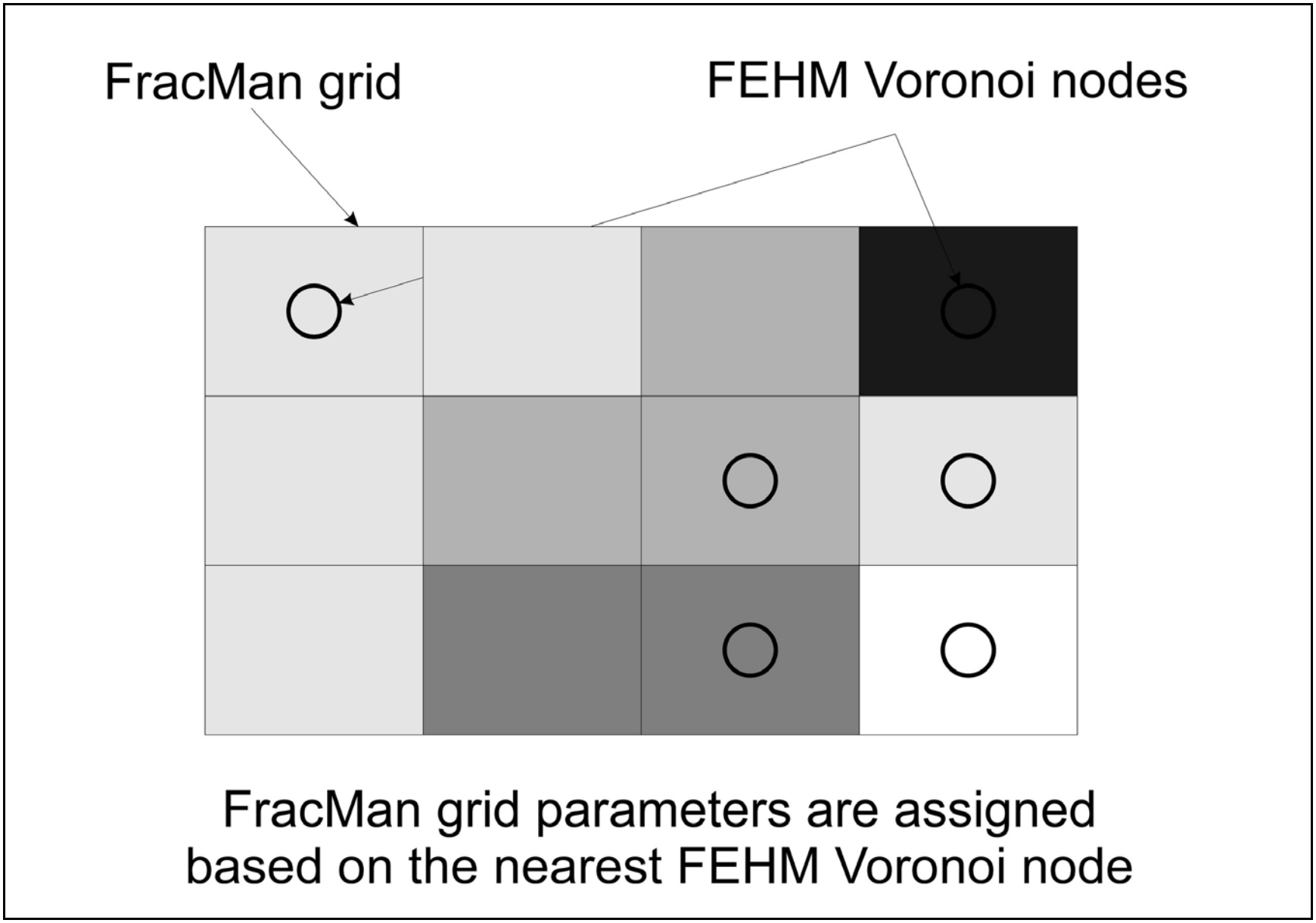

Figure N-33
Mapping from FEHM Voronoi Centers to FracMan Tetrahedral Volume Elements

Note: FracMan EPM elements are assigned values of the single closest Voronoi control volume center point.

FracMan DFN elements, the EPM volumetric elements are assigned based on the corresponding FEHM Voronoi node as,

$$K^E_x = K^E_y = K^E_z = min\ (K^f_x, K^f_y, K^f_z), \qquad (N\text{-}4)$$

where

K^E_x,K^E_y, and K^E_z=hydraulic conductivity values of the FracMan volumetric (EPM) elements, and
K^f_x, K^f_y, K^f_z=hydraulic conductivity values of the corresponding FEHM Voronoi nodes (Fig. 4).

N.4.1.3 Discrete Fracture Network (DFN) Implementation

The FracMan discrete fracture network (DFN) model has the following advantages:

- Faults and discrete conductive structures can be modeled explicitly as flowing features and as flow barriers
- The full, three dimensional (non-planar surface) geometry of faults is modeled explicitly
- Flow fields for flow and transport are directly controlled by the geometry and properties of faults and fractures.

This approach has the advantage that it has the potential to more accurately represent discrete transport pathways within the Yucca Flat HFM. Discrete flow features (faults) are defined by the Yucca Flat HFM, and have a significant effect on both flow and transport. For the FracMan model, the hydraulic properties of the faults were implemented to be consistent with the FEHM model. Fault hydraulic properties were derived by assuming that faults are defined as the central part of a complex fault structure (Caine et al., 1996). According to the Caine approach, faults are usually built up from two main elements: (1) fault core; (2) fault damage zone (Figure N-34). The relative and absolute conductivity and thickness of fault cores and fault damage zones are site-dependent. For the current project, it was assumed that fault conductivity can be represented by a 125 m thick fault damage zone, located 125 m from the specified fault centerline, based on the Yucca Flat HFM.

The Yucca Flat HFM does not specify transmissivity values of discrete faults and fractures. Therefore it was necessary to derive fault damage zone transmissivity values from the N-S equivalent hydraulic conductivity (K^f_y) of the FEHM Voronoi nodes closest to the fault damage zone locations. The parameterization of DFN elements is carried out by using the y conductivity component of FEHM because most of the faults in the model are oriented roughly North-South (y-direction). The hydraulic property of fault damage zones in FracMan is Transmissivity T_f [m^2/s], calculated as,

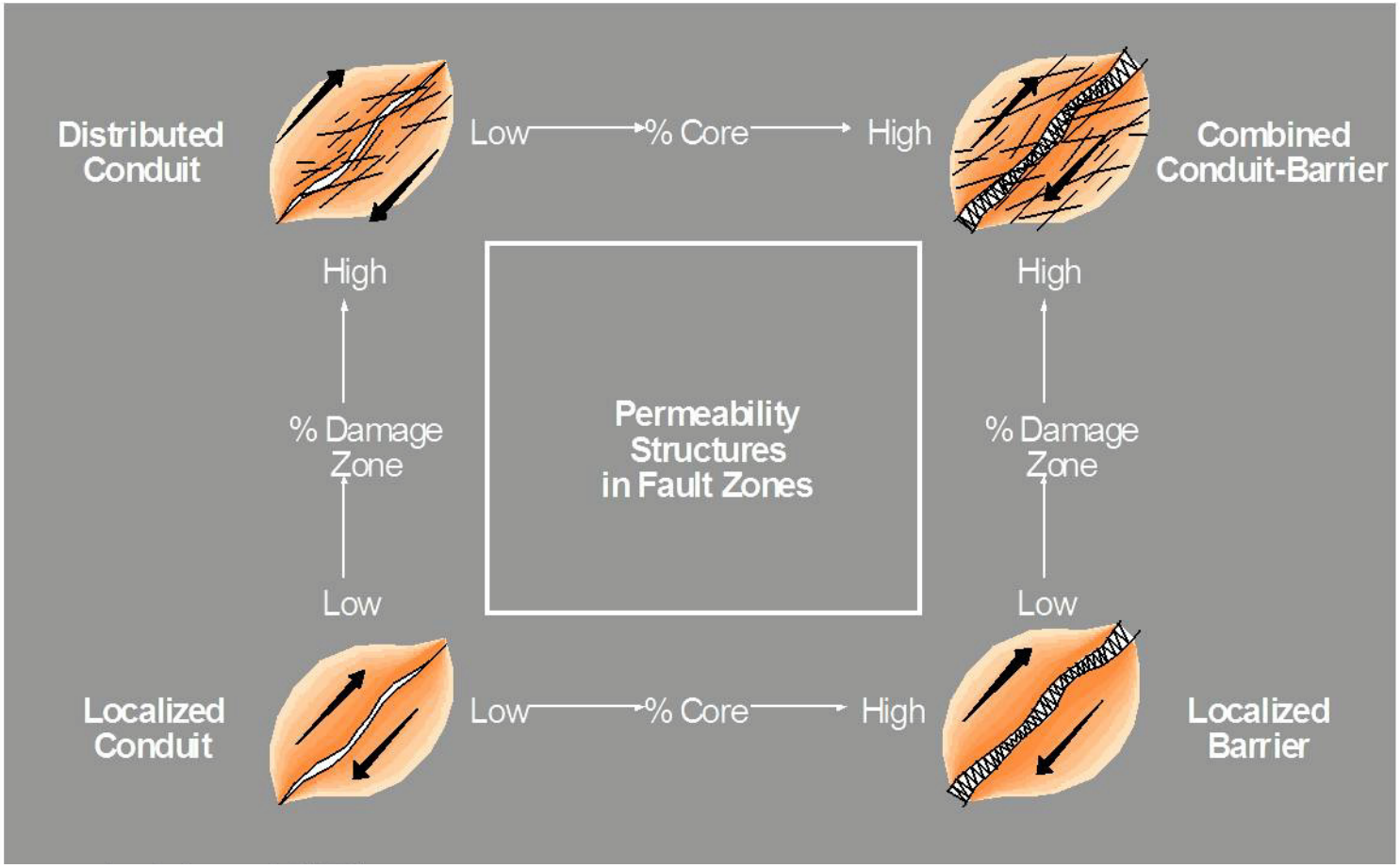

Figure N-34
Model for Fault Core and Damage Zones
Source: Caine et al., 1996

$$T_f = h_f K^f_y \,, \qquad (N\text{-}5)$$

where

h_f = fault thickness (125 m).

This approach approximates fault transmissivity by a single, isotropic number. In the FEHM model, many fault damage zones have different values for K^f_y and K^f_z . Future studies can consider the effect of anisotropy within fracture zones, and also alternative assumptions regarding the thickness of faults and fractures.

FracMan approximates fracture surfaces as triangular finite element meshes. The DFN elements in the YF Corroborative model were also discretized to a dimension of approximately 125 m, comparable to the discretization of the EPM mesh.

N.4.1.4 Boundary Conditions – Flow and Transport

The flow boundary conditions applied for the hybrid EPM/DFN FracMan model are illustrated in Figure N-35. Since this is a steady state simulation, the top of model boundary condition is approximated as a no flow surface at the top of the LCA. The model base is also assigned as a no flow boundary.

Within the model, flow is primarily from north to south and the primary faults modeled are also aligned north-south. Consequently, fixed heads were set on the north and south faces of the model volume. FracMan fixed heads are specified at the nodes defining the corners of EPM volume elements matching the north and south faces of the model region, and at the nodes defining the corners of triangular DFN elements matching the north and south faces of the model region. At each of the FracMan nodes on the north and south face boundaries, the head at the four closest FEHM nodes was interpolated to the FracMan node using the inverse distance to the node weighted to the fourth power. A comparison of FEHM and FracMan heads on the boundaries of the model is provided in Figure N-36.

Transport boundary conditions for the hybrid EPM/DFN model are illustrated in Figure N-37. This figure illustrates the source nodes in the FracMan mesh as well as an example ^{3}H mass flux input for the TORRIDO source location. Particles are released from each of the locations specified for the corroborative modeling (Table N-8). Each particle is assigned to a portion of the mass of radionuclide

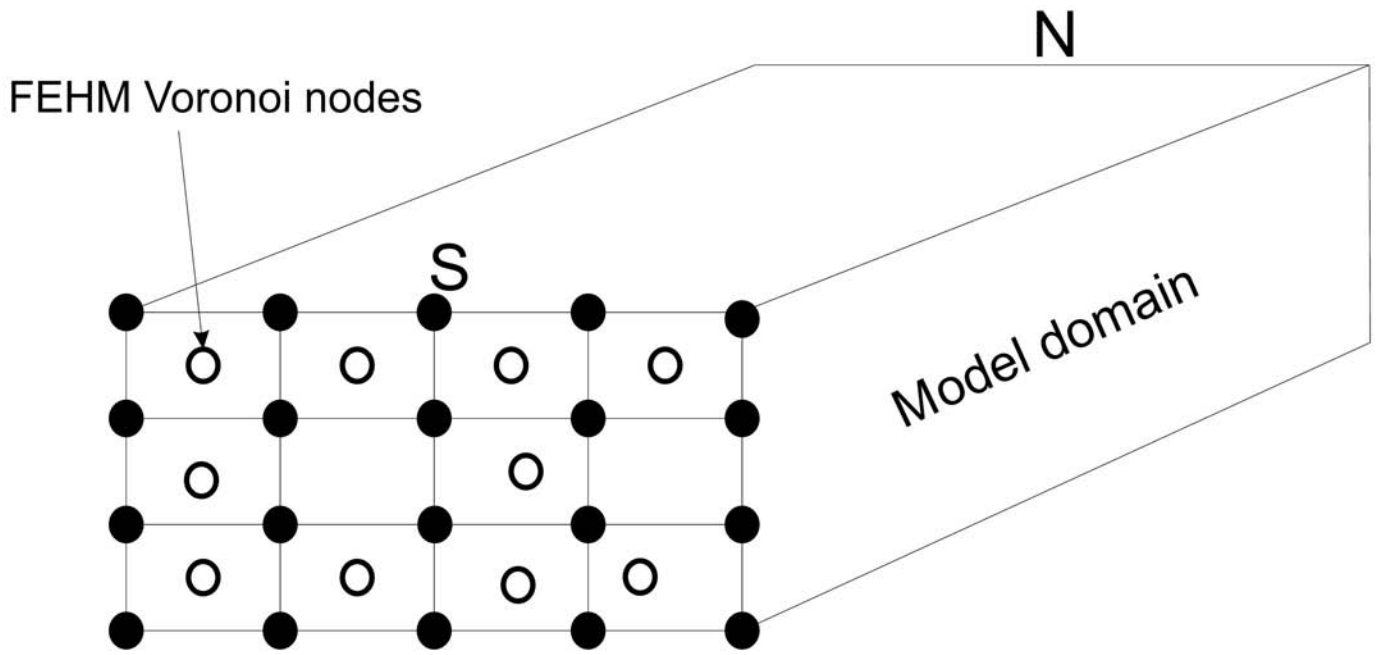

Note: Nodal head boundary conditions are assigned along the N and S faces of the model domain based on the corresponding FEHM Voronoi node.

Figure N-35
Assignment of Heads to Faces of FracMan Model Region based on FEHM Voronoi Control Volume Center Points

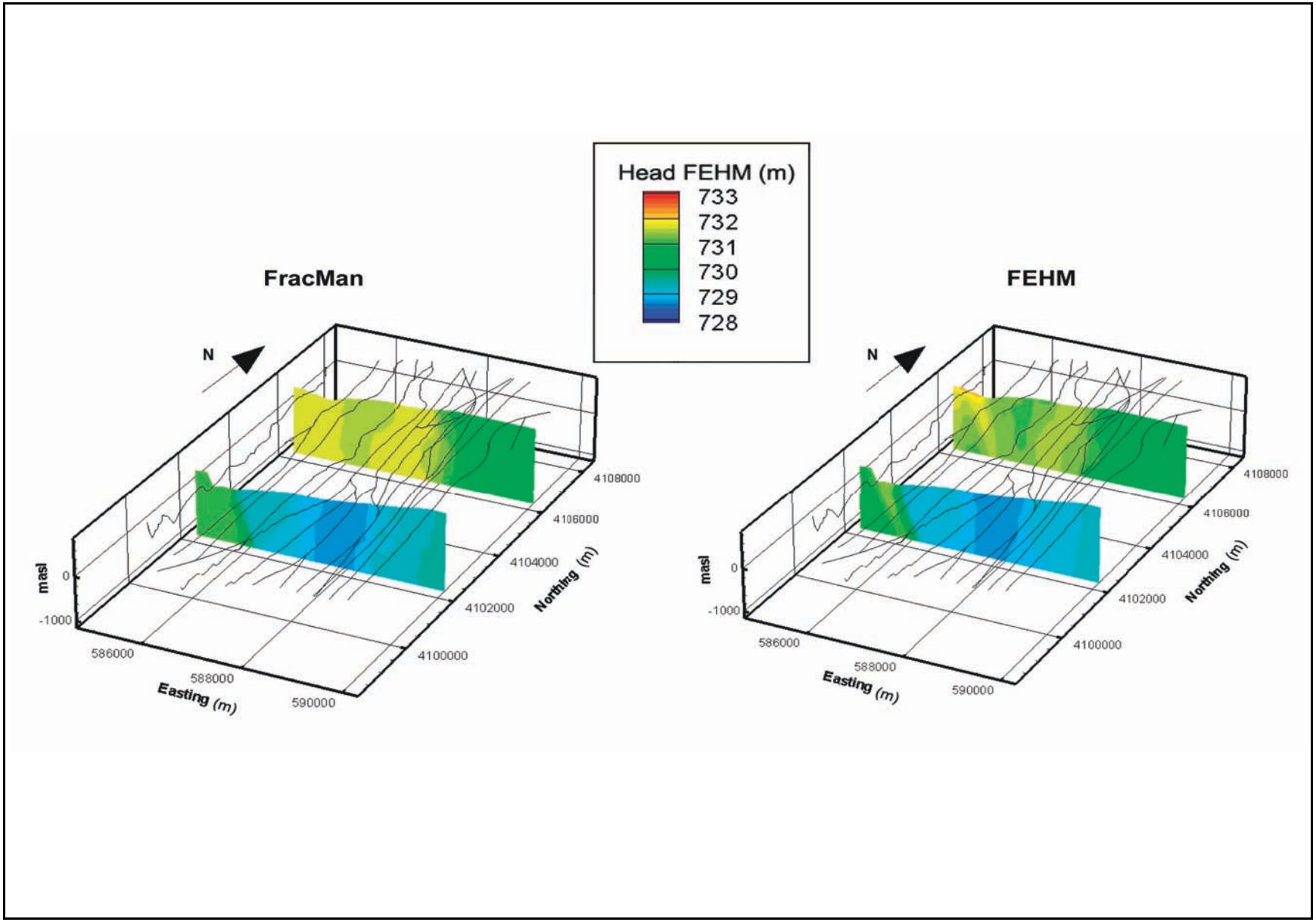

Figure N-36
Fixed Head Boundary Conditions on North and South Faces of FracMan Model Region, with Comparison to Interpolated Values from FEHM Control Volume Center Points

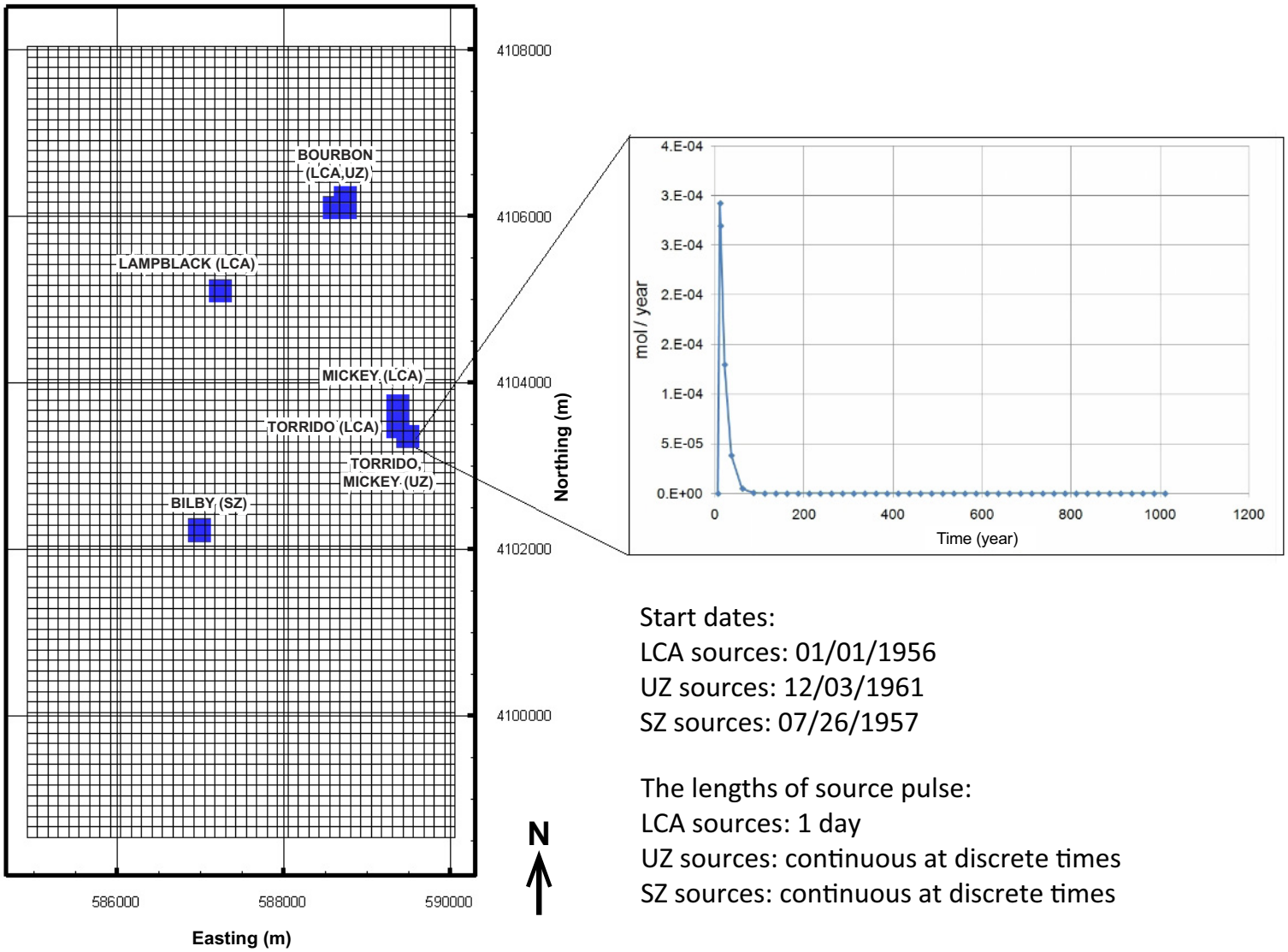

Start dates:
LCA sources: 01/01/1956
UZ sources: 12/03/1961
SZ sources: 07/26/1957

The lengths of source pulse:
LCA sources: 1 day
UZ sources: continuous at discrete times
SZ sources: continuous at discrete times

Figure N-37
Transport Boundary Conditions

Table N-8
Solute Transport Boundary Conditions

Source Name	Type of Source [a]	Coordinates (X, Y, Z)	Source Timing	Boundary Type	Mass Release Function
BILBY	S	586987.62; 4102237.50; 378.24	At discrete times after assumed time zero (07/26/1957)	Cauchy-type flux rate boundary condition	Specified
BOURBON	LCA	588612.62; 4106112.50; 625.00	On the day of detonation (calculated from a start date of 01/01/1956)	Cauchy-type flux rate boundary condition	Specified
BOURBON	U	588737.62; 4106112.50; 708.40	At discrete times after assumed time zero (12/03/1961)	Cauchy-type flux rate boundary condition	Specified
BOURBON	U	588737.62; 4106237.62; 625.00	At discrete times after assumed time zero (12/03/1961)	Cauchy-type flux rate boundary condition	Specified
LAMPBLACK	LCA	587237.62; 4105112.62; 500,00	On the day of detonation (calculated from a start date of 01/01/1956)	Cauchy-type flux rate boundary condition	Specified
MICKEY	LCA	589362.62; 4103737.50; 625.00	On the day of detonation (calculated from a start date of 01/01/1956)	Cauchy-type flux rate boundary condition	Specified
TORRIDO-MICKEY	UZ	589487.62; 4103362.50; 625.00	At discrete times after assumed time zero (12/03/1961)	Cauchy-type flux rate boundary condition	Specified
TORRIDO	LCA	589362.62; 4103487.50; 625.00	On the day of detonation (calculated from a start date of 01/01/1956)	Cauchy-type flux rate boundary condition	Specified

[a] Saturated Zone (S), Lower Carbonate Aquifer (LCA) or Unsaturated Zone source (UZ)

released according to the specified mass release function. Transport boundary conditions have been assigned by using Cauchy type mass flux.

The model calculations started at January 1, 1956, which is the zero time for LCA source locations. The timing of unsaturated sources and saturated sources has been fitted to this zero time. However, results are presented at discrete elapsed times since September 23, 1992.

N.4.1.5 Flow Field Solution

FracMan models fracture flow through a network of interconnecting DFN "plates" defined by surfaces mapped to triangular finite elements. In this hybrid DFN/EPM the rock mass (i.e., rock matrix and fractures not explicitly included in the DFN) is modeled using tetrahedral volume elements. Flow between the DFN and EPM elements is assumed to have no hydraulic resistance, such that DFN and EPM elements are in equilibrium.

The Yucca Flat corroborative model is implemented using the following features:

- Steady state, confined flow conditions
- A combination of Dirichlet (prescribed head) and Neumann (prescribed flux) boundary conditions on the six faces of the model, with the same boundary conditions assigned for fracture (DFN) and volume (EPM) elements.
- Linear basis functions for interpolation of heads at element edges
- Variable bandwidth, single matrix approach for both fracture (DFN) and volume (EPM) elements
- Pre-conditioned incomplete Cholesky conjugate gradient single, slightly compressible laminar flow solver.
- Convergence for the iterative was specified as a maximum head change between iterations of 10^{-6} (0.0001 percent).

N.4.1.6 Solute Transport Solution

Particle tracking solute transport was used in FracMan to calculate the pathways from radionuclide release locations to the down-gradient (southern) boundary. The flow field for particle tracking was provided by the flow solution of the hybrid EPM/DFN model described above. Since the hybrid DFN/EPM model was implemented with no hydraulic resistance between DFN and EPM elements, the FracMan particle tracking is generally carried out through a head field defined by the nodes at the corners of the tetrahedral volume elements. Consequently, particle tracks are not confined to DFN elements or to EPM elements, but rather follow the head field.

For the purpose of calculating particle trajectories from this head field, an equivalent EPM/DFN hydraulic conductivity tensor (K^h_x, K^h_y , K^h_z) was derived by combining the DFN fracture

transmissivity T_f of the fracture elements within each volume element with the corresponding isotropic EPM cell hydraulic conductivity K^E , using the Oda fabric tensor approach of Will et al. (2005).

Particle tracking assumes advective-dispersive transport through the hybrid DFN/EPM based head field, with longitudinal dispersion of 20 m and transverse (horizontal and vertical) dispersion of 2 m.

For each particle trajectory, solute transport was solved using the Laplace Transform Galerkin (LTG) approach of Sudicky and McLaren (1992). Solute transport was calculated assuming that each particle trajectory corresponds to a pipe pathway, as illustrated in Figure N-38. Pipe apertures were defined incorporating assumptions specified by the project. Particle trajectories provide velocities that vary along the pathway. Therefore, pipe widths were adjusted consistent with this velocity such that the volumetric flux from each pipe segment matches the volumetric flux of the subsequent segment, as shown in Figure N-39. This assumption was made specifically to be consistent with FEHM corroborative approaches. Normally, the DFN transport approach considers dilution effects due to intersecting and branching fracture networks, rather than series circuit pathways, which are come comparable to EPM streamlines.

Processes considered in FracMan solute transport solutions are:

- Advective transport
- Longitudinal and transverse dispersion
- Radionuclide decay
- Matrix diffusion from the pipe to a single matrix porosity

The FracMan LTG algorithm is designed to include multiple immobile zones and sorption processes. However, these processes were not used in corroborative modeling. Solute transport simulation parameters are summarized in Table N-9.

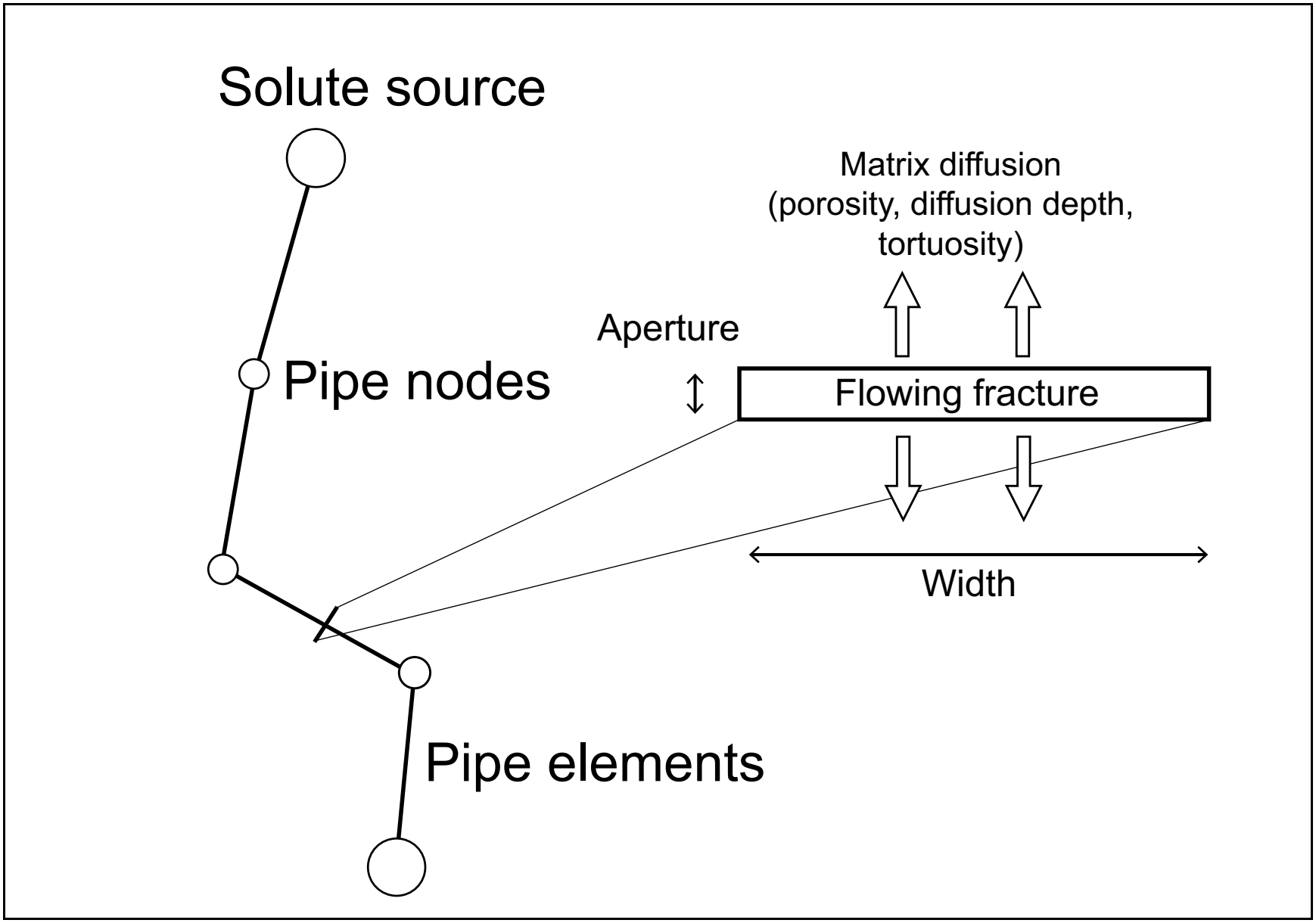

Figure N-38
Laplace Transform Galerkin Transport through Hybrid DFN/EPM Flow Field – Pathways Defined by Particle Tracking

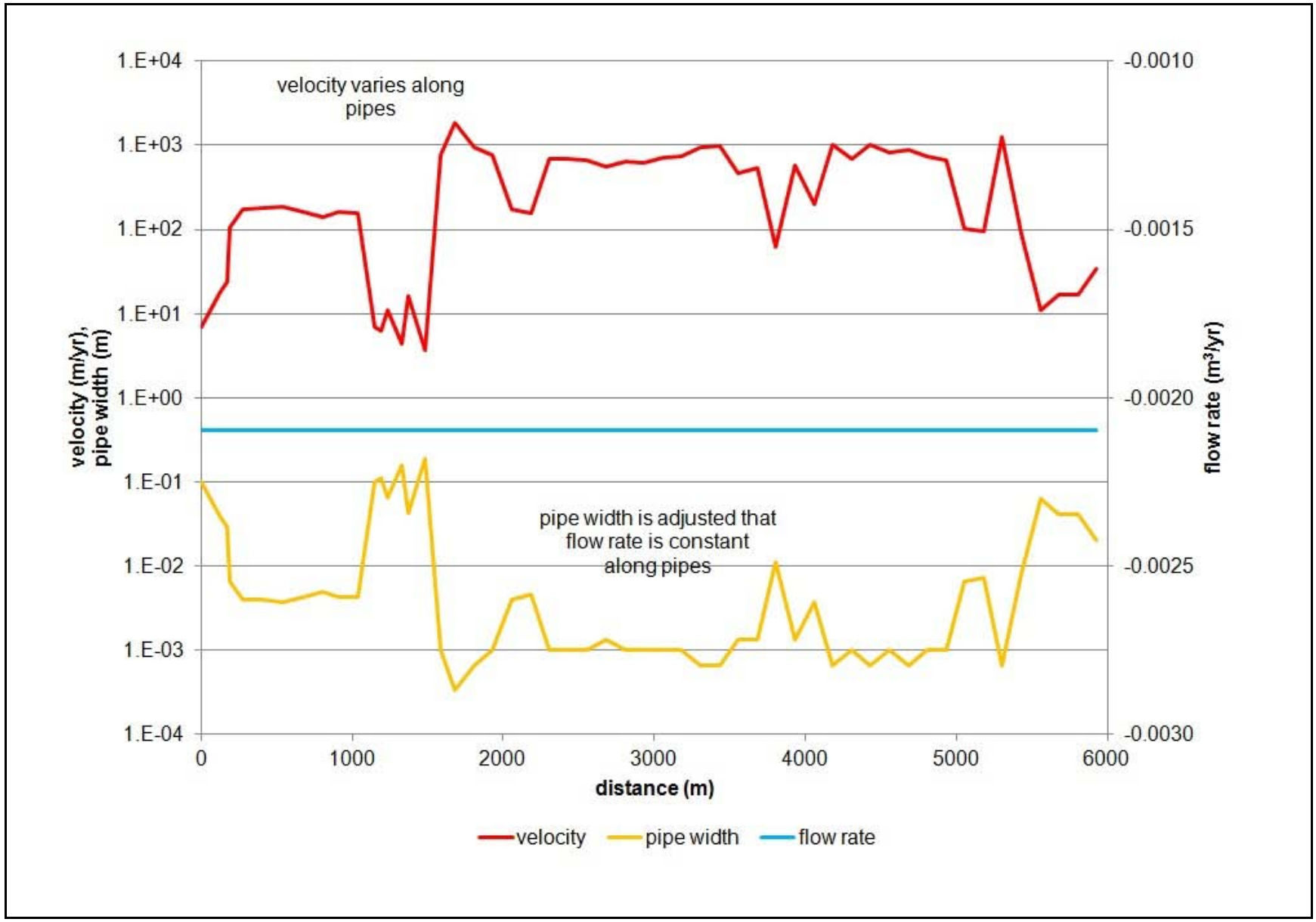

Figure N-39
Variation of Pipe Width – Series Flow Pathway Conserving Flux

Table N-9
FracMan Solute Transport Parameters

	Parameter	Value	Data Source
Pipe Parameters	Pipe velocity	Variable	Flow simulation
	Longitudinal dispersivity	20 m	Specified
	Transversal dispersivity	2 m	Specified
	Pipe aperture	0.003 m	Specified
	Pipe width	0.1 m	First pipe (See Figure N-39)
	Dispersion length	20 m	Specified
	Retardation factor	1	Specified
Matrix Parameters	Matrix porosity	3%	Specified
	Perimeter	2 × pipe width	Model assumption
	Maximum diffusion distance	1.5 m (fracture spacing / 2)	Specified
	Tortuosity	1	Assumption
	Retardation factor	1	Specified
	Diffusion coefficient in free water	6.3×10^{-3} m^2/yr	Specified
	Radionuclide decay coefficient	5.6262×10^{-2} 1/yr	^{3}H
		4.4150×10^{-8} 1/yr	^{129}I

N.4.2 FracMan Flow Simulation Results

The FracMan Hybrid DFN/EPM model solves for flow in the DFN discrete features of Figure N-30, with heads linked to those of the EPM volume element of Figure N-31. Figure N-40 provides a comparison of the three-dimensional head field produced by FracMan to that of the reference FEHM model. Figure N-41 provides a comparison of FracMan and FEHM heads on a vertical 2-D, east-west slice through the model. Considering the differences in the numerical implementations, the head distributions are similar between FracMan and FEHM. Differences are due primarily to the difference in implementation of anisotropic effects, and the use of a smoothed LCA top surface in the FracMan model.

Figure N-42 provides a comparison of velocity vectors for the FracMan and FEHM models for a horizontal slice through the model at elevation -250 m. The differences between these two flow fields are primarily due to (a) the inclusion of discrete DFN features in the FracMan model, and the (b) the difference between the anisotropic EPM elements used in FEHM and the isotropic EPM elements used in FracMan. The effect of a large sealing feature in the west of the model region is

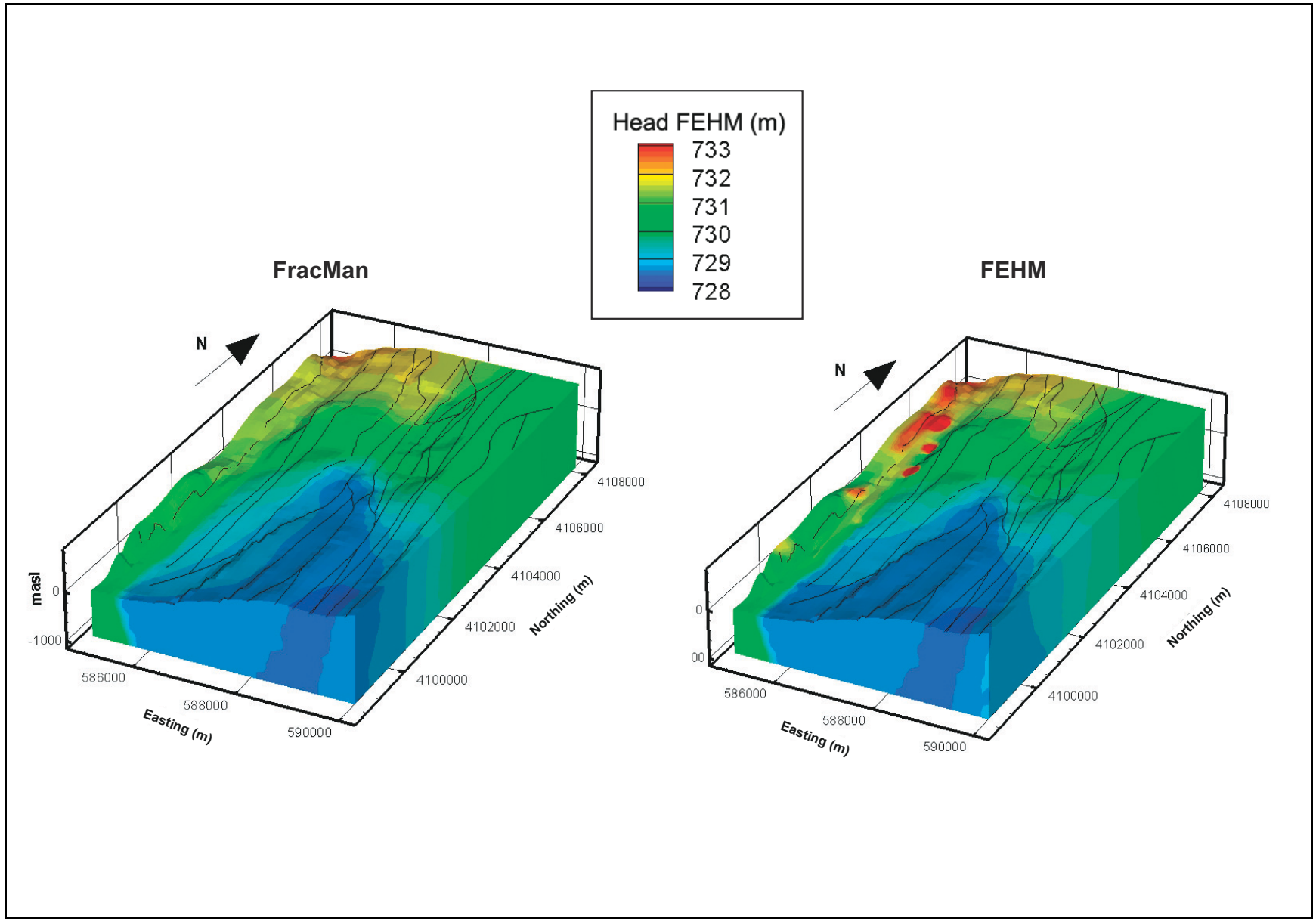

Figure N-40
Comparison of FracMan and FEHM Head Fields

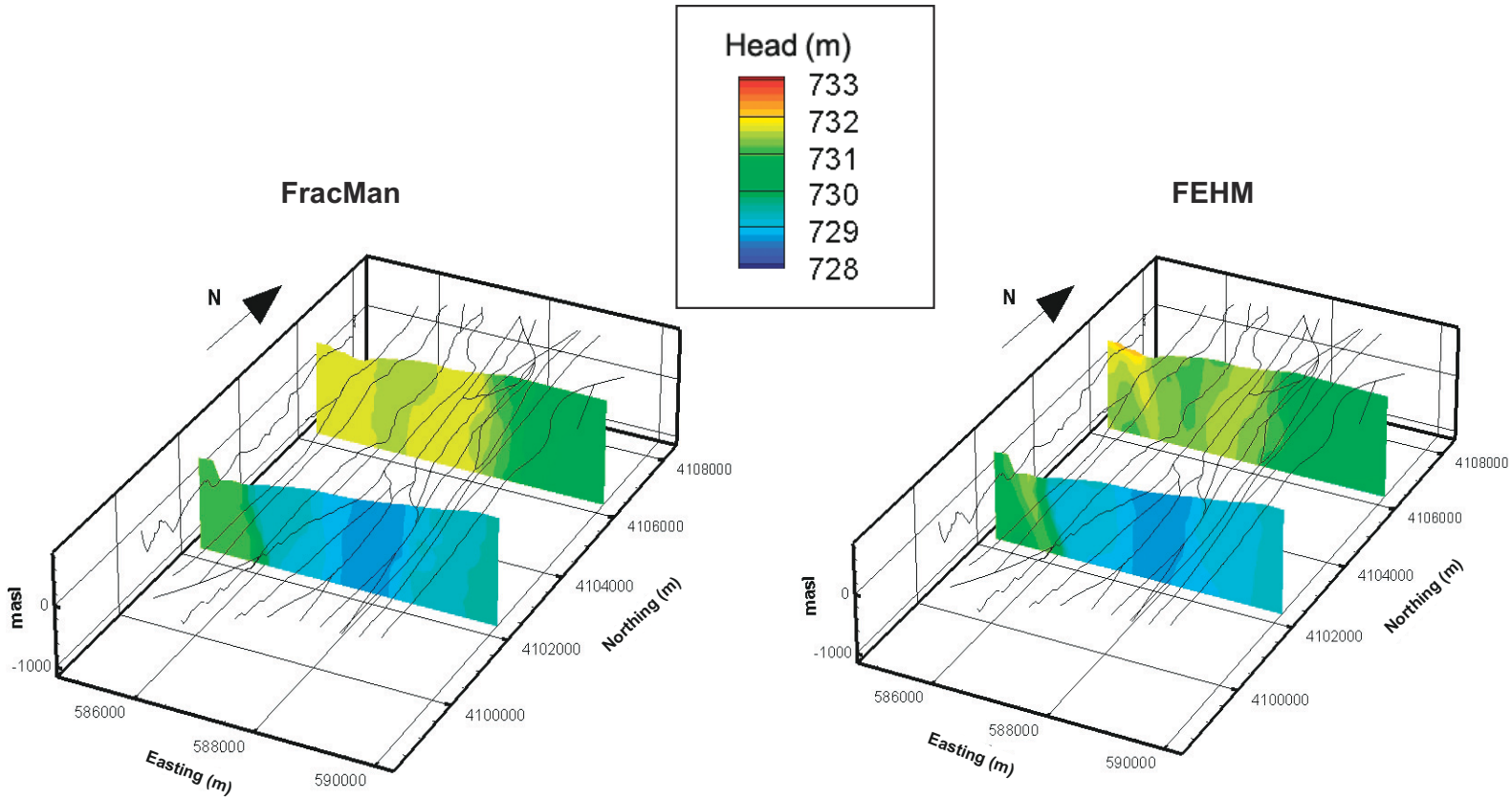

Note: Sections are located through BILBY and BOURBON detonation points.

Figure N-41
Comparison of FracMan and FEHM Head Fields – 2D Vertical Section

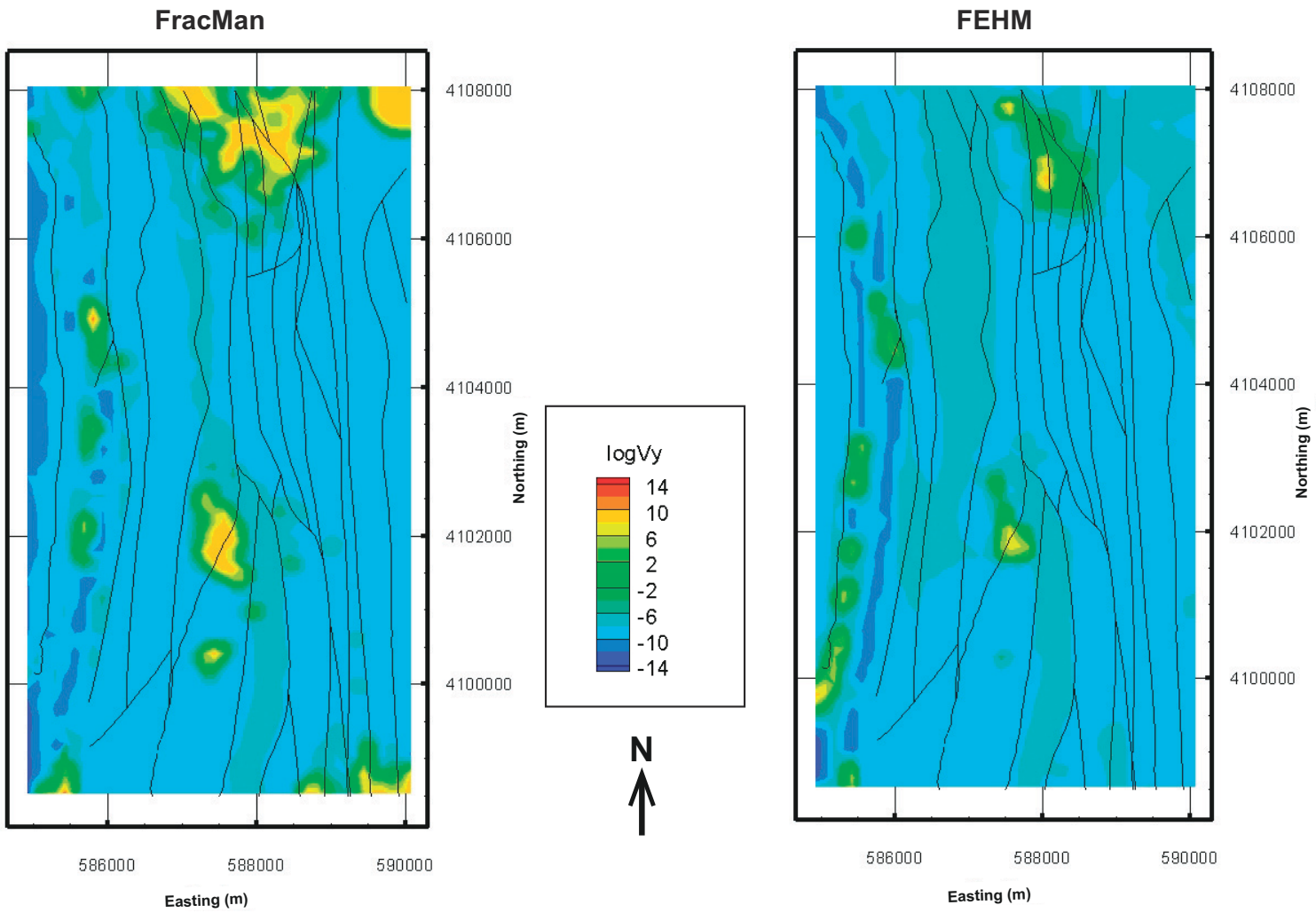

Figure N-42
Comparison of FracMan and FEHM North-South Velocity Fields ($V_{n\text{-}s}$) – 2D Horizontal Section

apparent in both FracMan and FEHM results, as is the influence of large transmissive features in the center of the model domain. Almost all of the anisotropic control volumes in the FEHM model correspond to locations of DFN fracture elements in the FracMan model (Figure N-43).

The FracMan flow solution required approximately 30 CPU minutes to solve on a Dell Latitude E6500 computer with Intel Core2 Duo, 2.8 GHz processor and 4 GB RAM.

N.4.2.1 FracMan Transport Simulation Results – Advection/Dispersion

Solute transport results from FracMan simulations are a combination of

- transport pathways defined by particle tracking through the steady state flow field, and
- diffusive, dispersive transport with decay for pipe pathways defined from the particle tracking pathways.

Figure N-44 (a) illustrates the particle trajectories through the FracMan hybrid DFN/EPM model from the sources listed in Table N-8. These trajectories can be compared visually to the FEHM particle tracks shown in Figure N-44 (b). While not identical, the pathways are very similar, particularly considering the difference in numerical implementation of the conceptual model.

The most significant pathway differences between FracMan and FEHM results are for the LAMPBLACK and BILBY sources. For the LAMPBLACK source, FracMan particle trajectories go eastward relative to the FEHM solution, which is influenced by anisotropic elements with greater North-South hydraulic conductivity. For the BILBY source, FracMan particle trajectories include a northeastward step that does not occur in the FEHM flow field. This is because the FracMan DFN damage zones provide a stronger hydraulic connection at that location.

Table N-10 provides a comparison of mean and standard deviation of advective/dispersive travel time from source points to release points at the edge of the modeled region. In general, FracMan travel times are on the average 15 percent longer than those for FEHM (SPTR) particles. However, this difference is well within the variability of travel times, and is consistent with the difference in the underlying numerical implementation of the conceptual model.

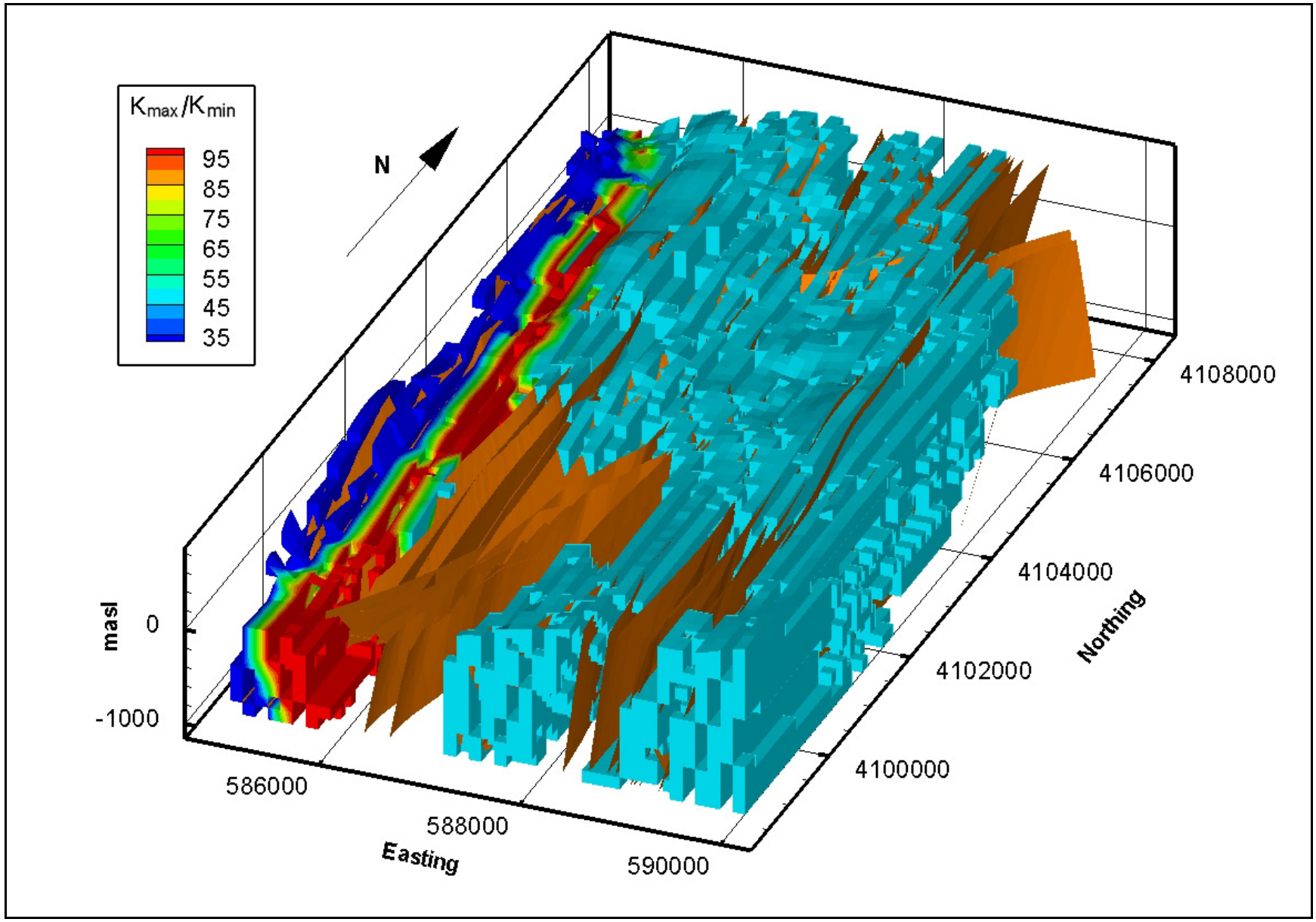

Figure N-43
Locations of Anisotropic Voronoi Volumes in FEHM Model – (K_{max}/K_{min} >2), Showing Faults from FracMan Model

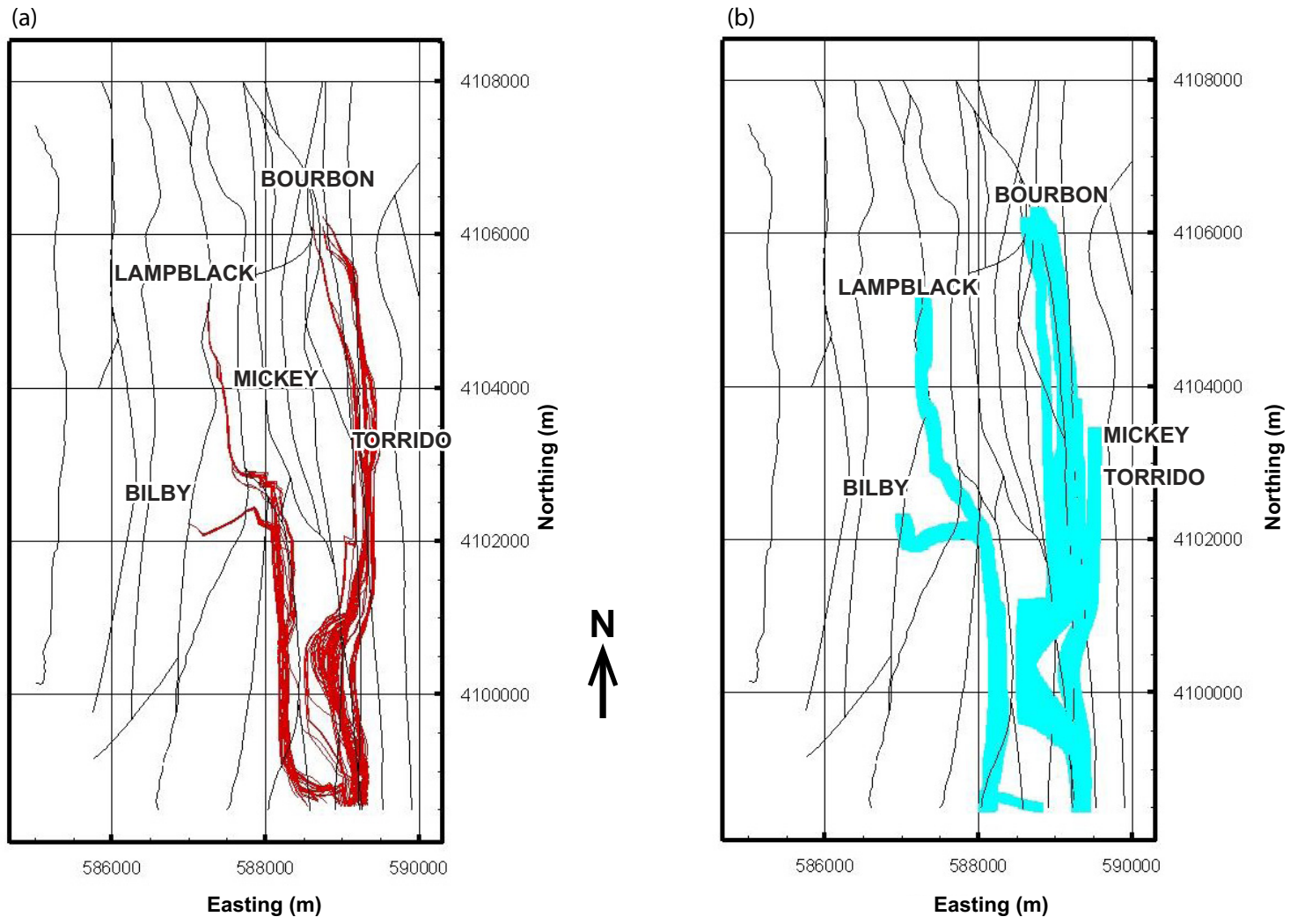

Figure N-44
Model Particle Trajectories: (a) FracMan and (b) FEHM

Table N-10
Advective/Dispersive Solute Transport in FracMan Hybrid DFN/EPM Model

Source Name	Type of Source [a]	Path Length (m) (Mean; Standard Deviation)		Travel Time (y) (Mean; Standard Deviation)	
		FEHM	FracMan	FEHM	FracMan
BILBY	S	(4952.78; 32.83)	5899.87; 346.01)	(72.75; 7.05)	(128.34; 14.20)
BOURBON	LCA	(8473.35; 142.29)	(8690.41; 384.60)	304.93; 38.19)	(373.96; 34.11)
BOURBON	U	(8532.00; 119.38)	(8976.25; 337.41)	(332.71; 70.17)	(323.99; 70.12)
BOURBON	U	(8532.00; 119.38)	(9046.76; 435.82)	(332.71; 70.17)	(326.86; 71.11)
LAMPBLACK	LCA	(7060.14; 211.97)	(7995.70; 471.53)	(163.68; 43.49)	(213.15; 45.90)
MICKEY	LCA	(5993.32; 57.41)	(6396.45; 383.73)	(131.27; 8.88)	154.16; 55.44)
TORRIDO-MICKEY	UZ	(4973.61; 43.64)	(5564.35; 436.65)	(98.18; 3.18)	(71.54; 10.31)
TORRIDO	LCA	(5629.87; 119.95)	(5949.21; 530.92)	(227.18; 60.30)	(144.54; 49.64)

[a] Saturated Zone (S), Lower Carbonate Aquifer (LCA) or Unsaturated Zone source

The FracMan particle tracking solution for a single source location required approximately 4 CPU minutes to solve on a Dell Latitude E6500 computer with Intel Core2 Duo, 2.8 GHz processor and 4 GB RAM.

N.4.2.2 FracMan Transport Simulation Results – Decay/Matrix Diffusion

FracMan solute transport results are produced for pipe-series pathways, as illustrated in Figure N-37. To compare results to PLUMECALC solutions, it is necessary to convert results from a pathway basis to a volumetric cell basis. Pipe element concentrations calculated by FracMan were converted to volumetric concentrations as follows:

1. calculate contaminant mass in FracMan pipe elements based on radionuclide concentration and fluid volume of pipes;

2. identify FracMan pipe elements corresponding to each cell of the FracMan EPM grid over the model region

3. for each EPM grid cell, calculate the total mass for each radionuclide for each time step.

4. For each EPM grid cell, calculate the radionuclide concentration as (a) the total mass of solute divided by the mobile water in volumetric cells (i.e., the volumetric flux through the cells in the FracMan flow solution, producing a volume-average concentration) and (b) the total mass of solute divided by the by mobile water in pipe elements (i.e, the concentration that would be measured were that pipe sampled discretely by a borehole).

Solute transport results for tritium are presented at 10, 50, and 100 years in Figure N-45 (Pipe based concentration) and Figure N-46 (volumetric cell based concentration). Figure N-47 provides the tritium pipe volume based concentration results reflecting the MCL. Solute transport results for iodine are presented at 100, 300, and 1,000 years in Figure N-48 (Pipe based concentration) and Figure N-49 (volumetric cell based concentration). Figure N-50 provides the iodine pipe volume based concentration results reflecting the MCL. Pipe volume based concentrations are significantly greater than volumetric cell volume based concentrations. The pipe-volume based concentrations are the values that would be measured in individual flowing fractures, while the volumetric cell volume based concentrations are lower, reflecting averaged plume concentrations. Both concentrations are important for understanding long term monitoring during closure, particularly to understand the relationship between point measurements along individual pathways and averaged plume estimates of concentration.

At 10 years four different plumes develop, corresponding to source locations: (1) BILBY; (2) LAMPBLACK; (3) BOURBON LCA and UZ sources; and (4) TORRIDO and MICKEY LCA and UZ sources. Compared to plumes at 10 years, the extent of the plumes slightly increases at 50 years, while the maximum concentration falls to 3.84×10^{-10} mol/L. At 100 years the maximum concentration further decreases (to circa 1.5×10^{-11}mol/L) and the extent of the plumes is much smaller than at earlier times. The concentration at the plume south to the TORRIDO and MICKEY LCA and UZ sources falls well below the MCL of tritium.

For iodine at 100 years the same four plumes develop consistent with the tritium plumes. The maximum iodine concentration within the model domain is 4.03×10^{-11}mol/L. This value does not significantly change throughout the simulation period: at 300 years the maximum concentration is 2.64×10^{-11} mol/L, and 1.07×10^{-11} mol/L at 1,000 years. For grid cell based concentrations the MCL of iodine (4.4×10^{-11} mol/L) is not reached.

The FracMan Laplace Transform Galerkin solute transport solution required approximately 3 CPU minutes to solve on a Dell Latitude E6500 computer with Intel Core2 Duo, 2.8 GHz processor and 4Gbt RAM.

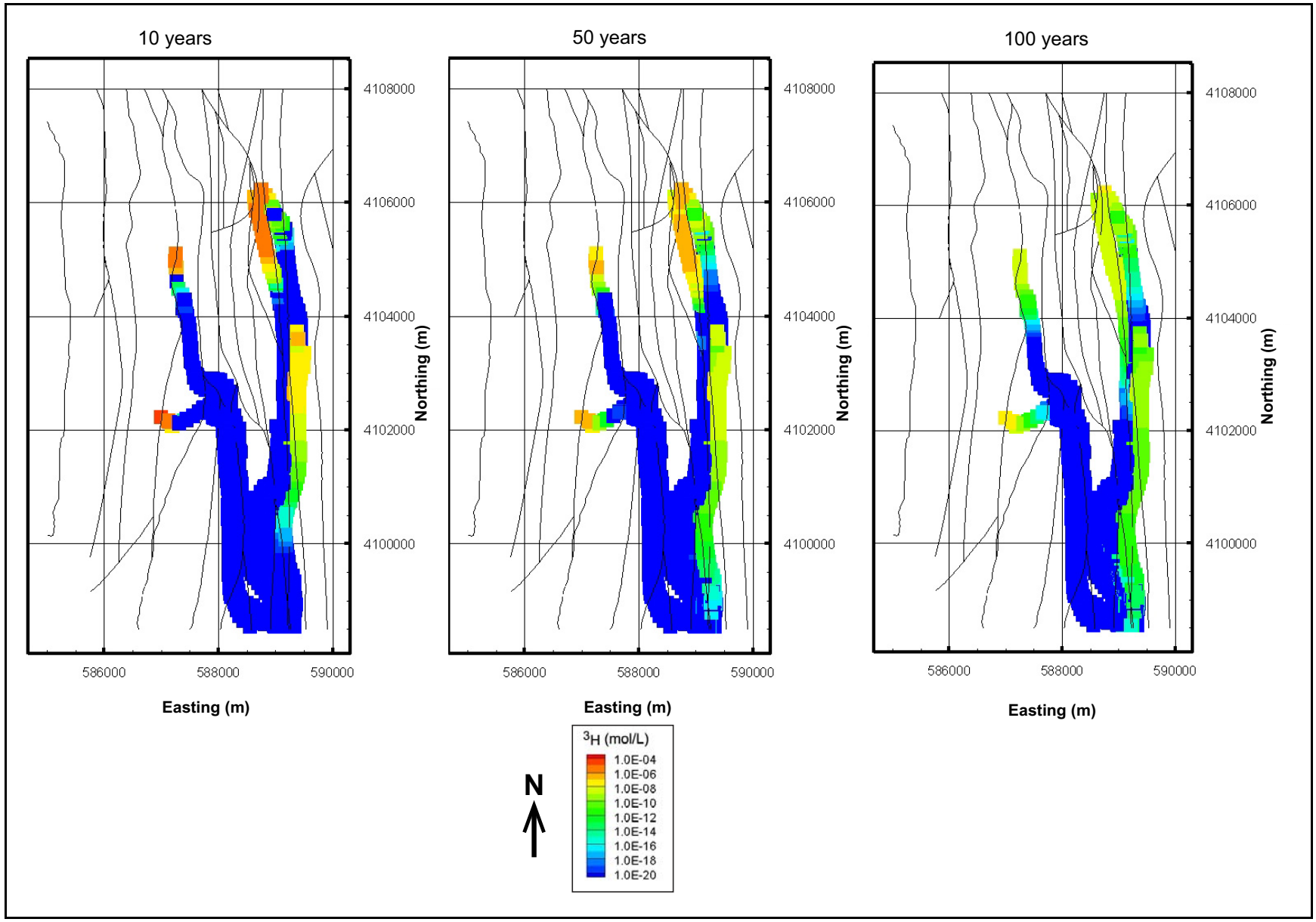

Figure N-45
Solute Transport from FracMan Simulation – ^{3}H – Concentrations based on Pipe Flow Volumes

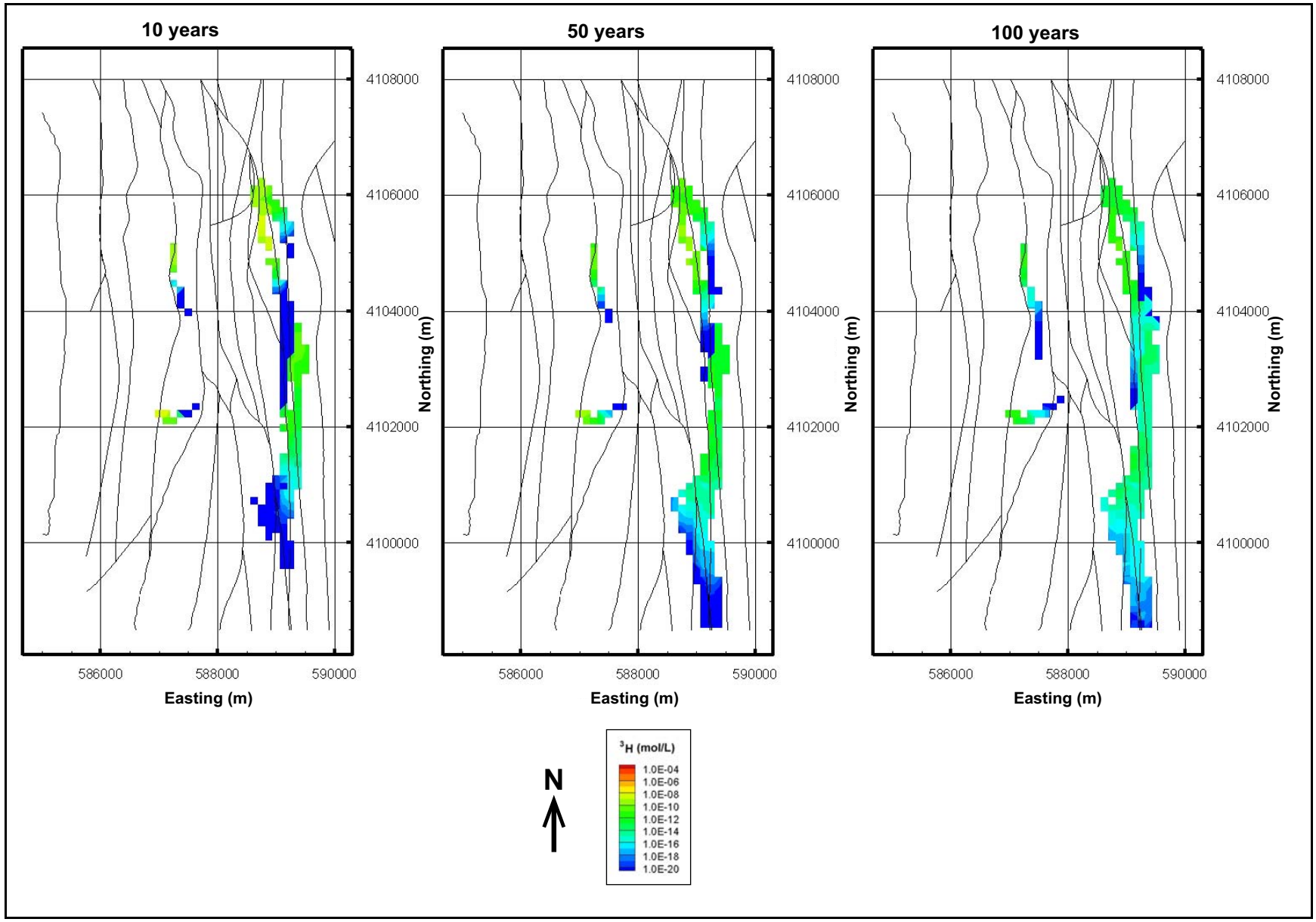

Figure N-46
Solute Transport from FracMan Simulation – ^{3}H – Concentrations based on Mobile Porosity in EPM Volumes

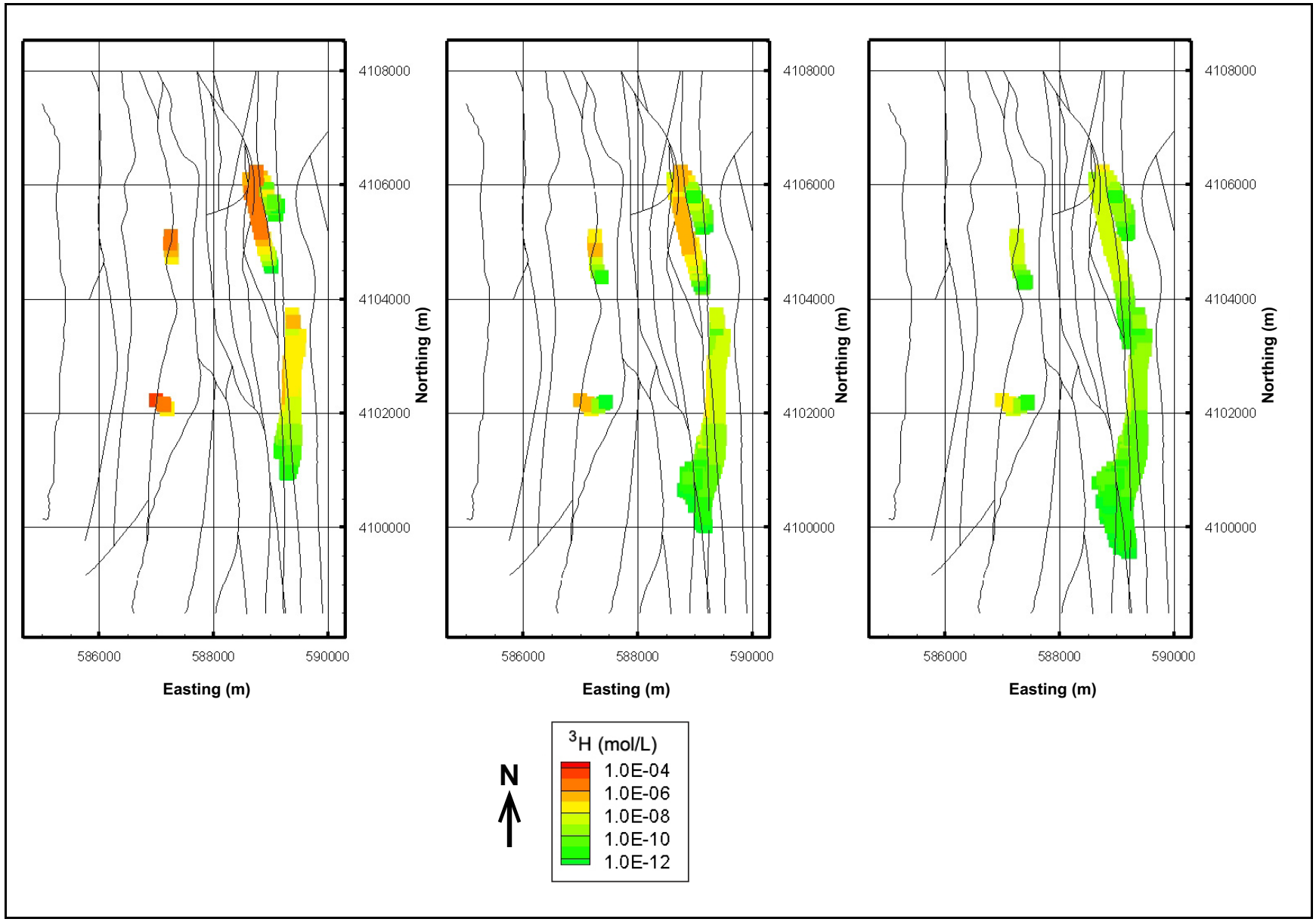

Figure N-47
Solute Transport from FracMan Simulation – ^{3}H – Concentrations based on Pipe Flow Volumes with MCL Cut-off

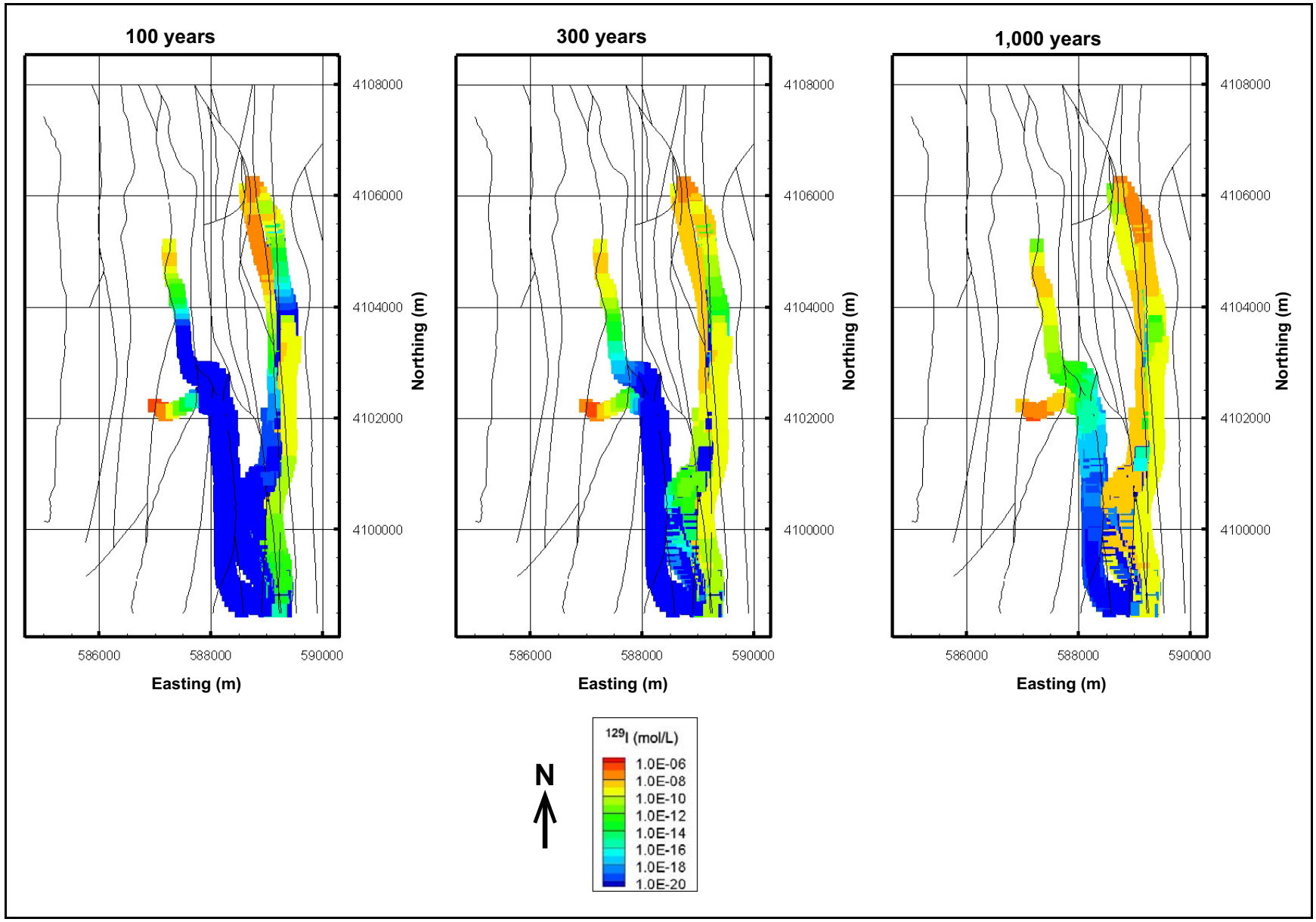

Figure N-48
Solute Transport from FracMan Simulation– ^{129}I – Concentrations based on Pipe Flow Volumes

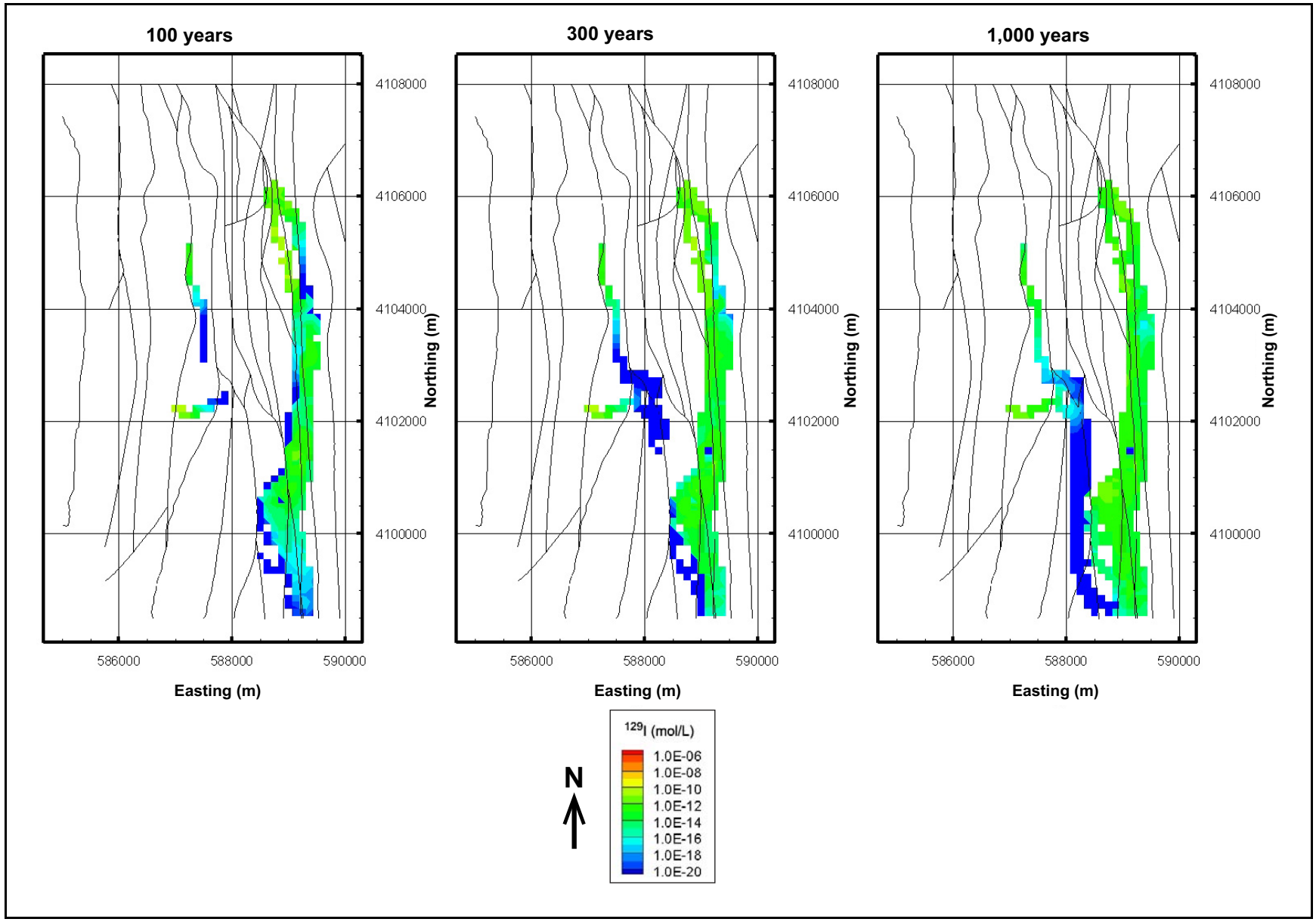

Figure N-49
Solute Transport from FracMan Simulation– ^{129}I – Concentrations based on Mobile Porosity in EPM Volumes

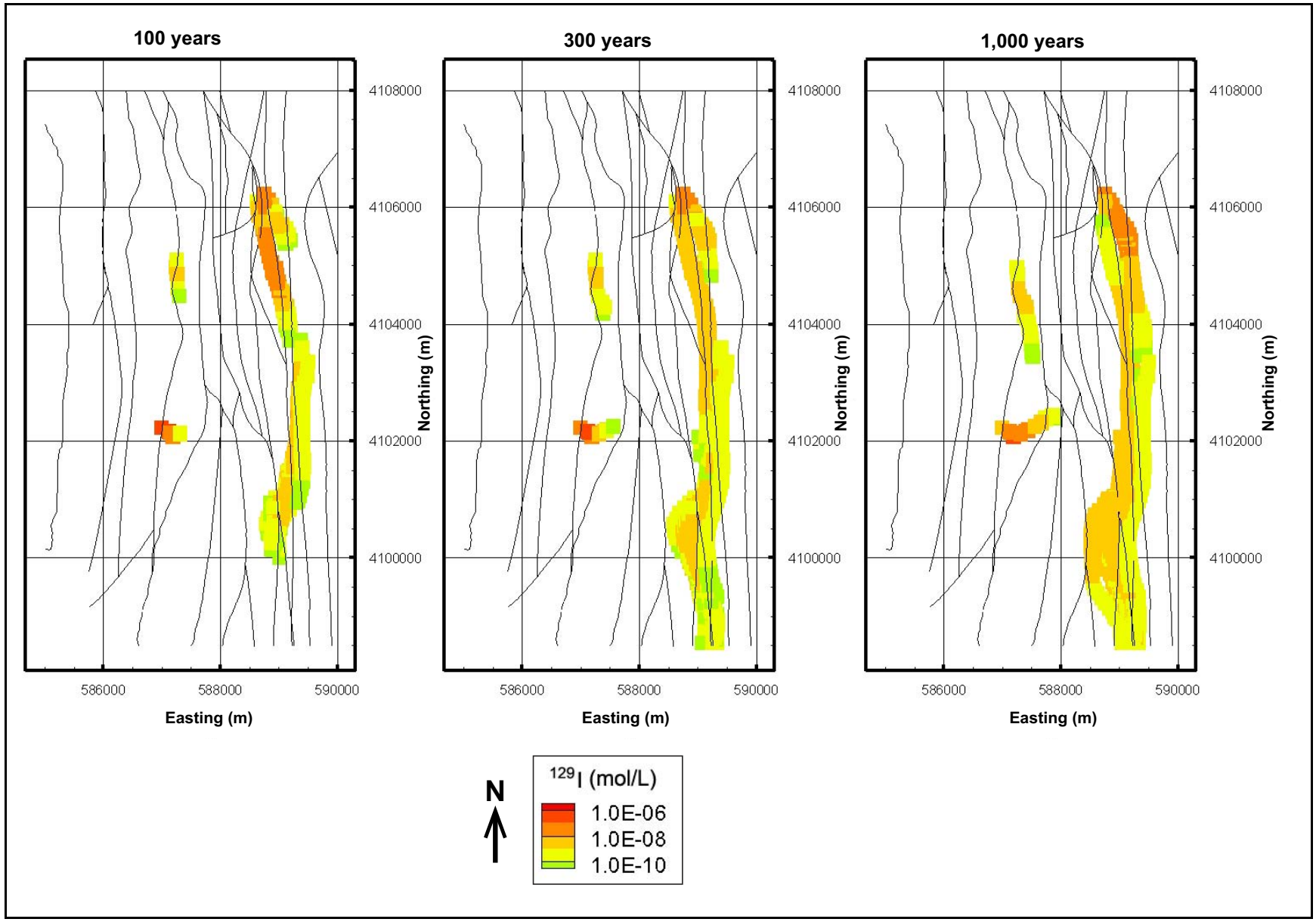

Figure N-50
Solute Transport from FracMan Simulation – ^{129}I – Concentrations based on Pipe Flow Volumes with MCL Cut-off

N.5.0 SUMMARY

The selection of software for calculating contaminant transport in the Yucca Flat/Climax Mine CAU was defined in the Yucca Flat/Climax Mine CAU CAIP. Since the time of that document, a number of advances have been made in the modeling of contaminant transport for a range of applications. Different projects in the U.S and elsewhere around the world use different software for calculating the current or future fate of radionuclide contaminants given similar processes as are relevant at Yucca Flat. The methodology for selecting appropriate groundwater transport codes is documented in ASTM Standard D6170-97(2010) *Standard Guide for Selecting a Groundwater Modeling Code*.

Although not explicitly mentioned in the guide for selecting groundwater modeling codes, a useful activity it to compare the results of alternative software on simple or more complex problems representative of the intended application. Comparisons of alternative modeling codes for simple problems have been presented in Appendix K, where the basis for selecting FEHM_SPTR (or Walkabout) for particle tracking and PLUMECALC for transport modeling is presented. In this section, corroborative analyses of contaminant transport in a complex three-dimensional sub domain of the entire Yucca Flat LCA flow and transport model have been performed using three widely used alternative software, notably MODFLOW/MT3DMS, FEFLOW and FracMan/MAFIC.

Although the goal of the analyses presented in this appendix was to use as close to the same conceptual model and parameter values as used in FEHM_SPTR and PLUMECALC for each of the three corroborative codes, slight differences in gridding techniques, boundary condition assignment and numerical method precluded the models being 100 percent consistent. As a result, there are some small differences in the models that need to be considered in addition to the code differences. One of the useful lessons from the comparisons is to recognize that it may not be possible in such a complex setting to get 100 percent consistency as it is with the simpler tests presented in Appendix K.

The results of the comparisons in this appendix confirm the appropriateness of FEHM_SPTR and PLUMECALC to be used for contaminant transport modeling of the LCA in Yucca Flat because similar trends are calculated using the different modeling software.

N.6.0 REFERENCES

ASTM, see ASTM International.

ASTM International. 1997 (reapproved 2010). Standard Guide for Selecting a Groundwater Modeling Codes, ASTM D6170 - 97(2010). West Conshohocken, PA.

Caine, J. S., J. P. Evans, and C. B. Foster. 1996. Fault Zone Architecture and Permeability Structure. Geology, Vol 24, pp 1025– 1028.Diersch, H.-J, G. 2002. Interactive, graphics-based finite-element simulation system FEFLOW for modeling groundwater flow, contaminant mass and heat transport processes. WASY Ltd., Berlin.

Golder, see Golder Associates Inc.

Golder Associates Inc. 2012. *FracMan: Discrete Fracture Network Modeling* – User Documentation. Golder Associates Inc., Redmond WA.

Helmke, M.F., W.W. Simpkins, and R. Horton. 2005. "Simulating Conservative Tracers in Fractured Till under Realistic Timescales." In *Groundwater, Vol.* 43(6): pp. 877-889.

McDonald M.D. and A.W. Harbaugh. 1988. A modular three-dimensional finite-difference flow model. *Techniques of Water Resources Investigations of the U.S. Geological Survey, Book 6*. 586 pp.

Pinder, G. F. and W. G. Gray, 1977. *Finite Elements in Simulation of Surface and Subsurface Hydrology,* Academic Press, New York.

Prickett, T. A., T. G. Naymik, and C. G. Lonnquist. 1981. A "*Random Walk*" *Solute Transport Model for Selected Groundwater Quality Evaluations*, Illinois State Water Survey Bulletin No. 65.

Ruge, J.W. and Stuben, K. 1987. "Chapter 4 – Algebraic Multigrid" *in* Frontiers in Applied Mathematics, Multigrid Methods., SIAM. ISBN 0-89871-214-9.

Saad, Yousef. 2003. "Chapter 6 – Krylov Subspace Methods, Part 1" *in* Iterative Methods for Sparse Linear Systems (2nd ed.). SIAM. ISBN 978-0-89871-534-7

Sudicky, E.A. and McLaren, R.G. 1992.*The Laplace transform Galerkin technique for large-scale simulation of mass transport in discretely fractured porous formations*, Water Resource Research, Vol 28, No. 2, pp 499-514.

Trefry, M.G., and C. Muffels. 2007. "FEFLOW: A Finite-Element Ground Water Flow and Transport Modeling Tool." In *Ground Water,* Vol. 45(5): pp. 525–528.

Will, R. R. Archer, and B. Dershowitz. 2005. Integration of Seismic Anisotropy and Reservoir-Performance Data for Characterization of Naturally Fractured Reservoirs Using Discrete-Feature-Network Models. SPE Reservoir Evaluation & Engineering Journal. Vol. 8, No. 2, pp. 132-142, April.

Zheng, C. 1990. MT3D, A Modular Three-Dimensional Transport Model for Simulation of Advection, Dispersion and Chemical Reactions of Contaminants in Groundwater Systems, Report to the U.S. Environmental Protection Agency Robert S. Kerr Environmental Research Laboratory. Ada, Oklahoma.

Zheng, C. and P.P. Wang, 1999. MT3DMS 0 A Modular Three-Dimensional Multispecies Transport Model, Report SERDP-99. U.S. Army Corp of Engineers. Washington, D.C.

Appendix O

Nevada Division of Environmental Protection Comment Responses

(41 Pages)

ndep
NEVADA DIVISION OF ENVIRONMENTAL PROTECTION
protecting the future for generations

STATE OF NEVADA
Department of Conservation & Natural Resources
DIVISION OF ENVIRONMENTAL PROTECTION

Brian Sandoval, Governor
Leo M. Drozdoff, P.E., Director
Colleen Cripps, Ph.D., Administrator

August 9, 2013

Mr. Robert F. Boehlecke
Manager
Environmental Management Operations
National Nuclear Security Administration
Nevada Field Office
P.O. Box 98518
Las Vegas, Nevada 89193-8518

RE: Submittal of Final Phase I Flow and Transport Model Document, Revision 0, For Corrective Action Unit (CAU) 97: Yucca Flat/Climax Mine, Nevada National Security Site, Nye County, Nevada, February 2013
Federal Facility Agreement and Consent Order (FFACO)

Dear Mr. Boehlecke:

The purpose of this letter is to rescind the August 6, 2013 letter from the Nevada Division of Environmental Protection, Bureau of Federal Facilities (NDEP) to the National Nuclear Security Administration Nevada Field Office (NNSA/NFO) that submitted comments on the *Final Phase I Flow and Transport Model Document, Revision 0, For Corrective Action Unit (CAU) 97: Yucca Flat/Climax Mine, Nevada National Security Site, Nye County, Nevada, February 2013* (document) and submit this letter. The August 6, 2013 letter did not include NDEP comments on Appendix G of the document. This letter also corrects the lack of header information on the August 6, 2013 letter.

The NDEP received the above-referenced document on February 28, 2013. The August 6, 2013 letter included a Notice of Completion but because that letter is being rescinded this letter now serves as a Notice of Completion for the milestone of the *Final Phase I Flow and Transport Document, Revision 0, For Corrective Action Unit (CAU) 97: Yucca Flat/Climax Mine, Nevada National Security Site, Nye County, Nevada, February 2013*, pursuant to Subpart XXV.1 of the FFACO.

The following is an all-inclusive listing of comments that the NDEP has after review of the document:

1. Page ES-6, Executive Summary, **Modeling Approach** Section, First full sentence on Page: "This philosophy has led to the decision to use models or parameters that do not underestimate the potential contaminant transport." How will this "do not underestimate" be demonstrated?

2. Page ES-9, Executive Summary, **Modeling Approach** Section, Last sentence of this Section: If the absence of significant declines in hydraulic heads in the LCA across the accommodation zone that separates Yucca Flat and Frenchman Flat indicates that the LCA is hydraulically well connected between these basins, despite their different structural styles and the termination of major basin-forming Yucca Flat faults in this area, has the flux across the southern boundary of Yucca Flat been included in the Frenchman Flat model? If no, when will this increase in flux be addressed and documented.

3. Page ES-14, Executive Summary, **Saturated LCA Flow and Transport Model** Section, First partial paragraph on Page: use of kg/s for inflows in this paragraph and throughout the document should include values in (m^3/day) for consistency with other portions in the document (e.g., page H-20, Figure H-13a, ground water flow rates m^3/day). See the bottom of Page 5-39 where both units are included.

4. Pages ES-16 and ES-17, Executive Summary, **Modeling Results and Forecast Contaminant Boundaries** Section, First full paragraph on Page, Third sentence and Figure ES-3: Additional discussion of Figure ES-3 is needed in the text because with the colors overlaying each other the continuity of the contaminant boundaries for the various models is not clear. Also, the term "Time-Cumulative" used on the Figure needs to be defined in the text.

5. Page ES-19, Executive Summary, **Modeling Results and Forecast Contaminant Boundaries** Section, First full paragraph on Page, Last Sentence: Why are the conceptual models cited in the previous sentence considered low probability models? On what information is this statement based? Where is this information documented?

6. Page ES-20, Executive Summary, **Modeling Results and Forecast Contaminant Boundaries** Section, Last sentence on top of Page: "...except for detonations in the unsaturated LCA." Either a brief explanation should be included in the Executive Summary or a reference provided to a section in the document which explains why this is an exception.

7. Page ES-20, Executive Summary, **Comparison of Model Results to In Situ Observations** Section, First Paragraph: The depth or units sampled by these wells should be indicated. A short discussion of the comparison of the sample size of the well to the estimated model contamination should be included.

8. Page ES-21, Executive Summary, **Comparison of Model Results to In Situ Observations** Section, Bullet on top of Page, First Sentence: Please give an actual range of values instead of using the phrase, "in close proximity."

9. Page 1-23, Section 1.4, First full Paragraph on Page, Second Sentence and Figures 1-10a and 1-10b: Figure 1-10a is labeled West-East Profile and Figure 1-10b is North-South

Profile. The directional descriptions are reversed in the text. Please correct the discrepancy.

10. Page 1-33, Section 1.4, First partial paragraph on Page: The phrase "except between Wells ER-3-1 and WW C-1, where the greater depth of the LCCU allows hydraulic communication between the LCA within Yucca Flat and northeast of the basin (Figure 1-7)" is not useful as Figure 1-7 covers too large of an area to prove the point attempting to be made, no wells are even shown on the Figure and the phrase leaves the reader with the question, "How does a deeper underlying unit allow hydraulic communication?" Please clarify this portion of the sentence.

11. Page 1-48, Section 1.7, First full Paragraph on the Page, Sixth Sentence: "This low probability of occurrence makes this model run unimportant from a regulatory perspective, ..." This sentence is mixing individual model assumption probabilities with the 5 percent or greater probability of exceeding the SDWA MCL for regulatory purposes. The information used to determine the model assumption probabilities needs to be presented AND de-coupled from the 5 percent or greater probability of exceeding the SDWA MCL for regulatory purposes.

12. Page 1-50, Section 1.7, Last Bullet on Page: This does not explain clearly how the assumed laterally homogeneous transport properties is a conservative assumption as indicated by the sentence above the bullets. Please add an explanation for this assumption.

13. Page 1-61, Section 1.9, Appendix L: The phrase, "... groundwater flow rates ..." have referred to volumes per time in other locations in the document. Appendix L is estimating groundwater velocity. Please check for consistent use throughout the document.

14. Page 2-4, Section 2.1, First full sentence top of Page and Figure 2-1: "... the saturated zone (green) ..." In Figure 2-1, on Page 2-3, the saturated zone is indicated by a **blue** sphere. Please correct this discrepancy

15. Page 2-49, Section 2.5, Third Paragraph, Second Sentence: "... overly conservative assessment of potential exposure should be avoided, or at a minimum, identified." This phrase doesn't make sense because the document keeps referring to the use of compounded conservatism which contradicts the "should be avoided." Please correct this sentence.

16. Page 3-4, Section 3.1, First full paragraph on Page, Last Sentence: It is stated, "... the later (more recent) detonations have transport starting years or decades before the actual event." Please add a brief discussion of the possible impact on the transport forecasts due to this simplification.

17. Page 3-5. Section 3.1.1, Second Paragraph, First Sentence: It is stated, "...the underground detonations conducted in Yucca Flat range in depth of burial from 782.4 m below ground surface and range in yield..." A lower depth of burial needs to be added to this sentence.

18. Page 3-16, Section 3.1.3.3, Second Paragraph and Page 3-17, Figure 3-6: The orange and green dots on Figure 3-6 need to be explained either in a legend on the Figure or in the text on Page 3-16.

19. Page 3-28, Section 3.2, First full paragraph on Page, Last Sentence: Based on the plot in Figure 3-8 for Area 5 Pilot Wells, there are no data presented for depths below approximately 250 m. As such, the last sentence should read "... above a depth of roughly 250 m."

20. Page 3-56, Section 3.4.3.4.1, First Paragraph, First Sentence and other locations throughout the document: "pumping-test-scale" should be "aquifer-test-scale." Please correct this in the document at all locations.

21. Page 3-56, Section 3.4.3.4.1, Table 3-4 and Page 3-58, Section 3.4.3.4.2, Table 3-5: Please indicate in the footnotes for each Table that when a count of 1 is presented in the Table, the "mean" value given is just the value of the one measurement.

22. Page 3-57, Section 3.4.3.4.1, Second Paragraph: If the UGTA Activity participants believe that the summary statistics are biased toward the high end, what is their concern about using the values in the modeling for flow and transport? Either continue the discussion and present possible impacts OR remove this paragraph.

23. Page 3-72, Section 3.6.1, First Paragraph, First Sentence: "... current infiltration rates are zero *or negative* in the upper several tens of meters ..." Remove "or negative" as there can be an upper flux of water but this is not a negative infiltration (see page 4-6, Section 4.2.2, First Paragraph, First Sentence). Please check entire document for use of negative infiltration and correct it.

24. Page 3-88., Section 3.6.3.8, First Paragraph, Last Sentence: Please add "have" between "... any perched water that may" and "been present above..."

25. Page 3-111, Section 3.6.7, First full paragraph on Page, Last Sentence: In a sensitivity analysis it is not appropriate to consider assigning a probability to any particular outcome. Therefore, please change the last sentence to read: The sensitivity analysis that was done probably spanned the range of outcomes that would have been produced with a Monte Carlo analysis.

26. Page 4-33, Section 4.4.1, Fourth Sentence on Page: Please change "closed" triangles to "solid and inverted" triangles and add "(hydrograph)" after "repeated measurements over time."

27. Page 4-50, Section 4.5.1, Second Paragraph, Last Sentence: Please explain how the values of the reduction factors were determined.

28. Page 4-51, Section 4.5.2, Last Paragraph, First Sentence: Please modify this sentence because a sensitivity study does not lead to estimates of uncertainty.

29. Page 4-59, Section 4.5.3, Last Paragraph, Third Sentence: There is no purple shading in Table 4-12. Please add the shading or indicate the relevant simulations in some other manner.

30. Page 4-63, Section 4.6.2.2, **Mass Representing Saturated-Zone Detonations**, First Paragraph, Fourth Sentence: The reference to Table 4-9 is not clear because Table 4-9 is **Parameters Used in Model Calibration**. This same comment applies to the Second Paragraph, Second Sentence on Page 4-65.

31. Page 4-66, Section 4.6.2.2, Equation (4-1): Please define $M_{f,r\,n}$.

32. Page 4-72, Section 4.6.3, First Paragraph, First Sentence: Based on the numbering to indicate the model run in the text and comparing it to the information presented in Table 4-13 on Page 4-52, there appears to be an inconsistency in the order of the numbers. Please correct this or explain how the two should be compared.

33. Page 4-88, Figure 4-35: The Figure caption needs "**(in Moles)**" added to be consistent with Figure 4-32 on Page 4-85.

34. Page 4-99, Section 4.6.5, First paragraph, First and Second Sentences: Please explain the relationship between "from 3 to 5 percent for ^{14}C, ^{36}Cl, ^{99}Tc, ^{129}I, ^{237}Np, and U, and is just under 1 percent for ^{3}H" to Table 4-31. It is not clear how the two relate.

35. Page 4-99, Section 4.6.5, Second Paragraph, Third through Ninth Sentences: Theses sentences discuss the results shown in Figure 4-38a. In the text, please indicate color of lines in the plot or the model run numbers to aid the reader. This has been done for the discussion of Figures 4-38b and 4-38c.

36. Page 4-103, Section 4.6.5, Second complete sentence on top of page: Case 9 is indicated in Table 4-34 but "base (nonthermal) case" is not indicated. Please indicate in the Table the nonthermal case.

37. Page 4-104, Section 4.6.6, Second Sentence: Please indicate in the text on Page 4-104 that the blue line on Figure 4-41 on Page 4-106 corresponds to the unaltered base case.

38. Page 4-104, Section 4.6.6, Third Sentence: Based on the results in Figure 4-41, LBB_Case 1 produces **more than** twice (bold added for emphasis of difference in

statement) as much ^{14}C breakthrough as the unaltered base case. Please modify this sentence to indicate this result.

39. Page 4-112, Section 4.6.8.2, Second Paragraph, Third Sentence: How are the masses to the LCA from the base-case model with fixed source terms (the first row of Table 4-37) shown in Figure 4-43? The 'X' in the Figure does correspond to the values in the first row of Table 4-37, however the fourth sentence indicates the masses simulated in the deterministic model are marked with 'X' in the Figure. Please clarify this discussion in the text.

40. Page 4-114, Section 4.6.8.3, Second Paragraph, Last Sentence: Please indicate in Table 4-41 on Page 4-116 which entry corresponds to the mean mass from the Monte Carlo simulations and which corresponds to the mass reported in the previous run. In addition, please indicate which previous run is being discussed.

41. Page 4-118, Figure 4-45: Please indicate what the "X" on the various plots represents.

42. Page 4-119, Section 4.6.8.3, First Sentence below Table 4-42: The $R^{(j)}$ is listed in **Table 4-41**, not Table 4-39 as stated in the text. Please correct this sentence.

43. Page 4-120, Section 4.6.8.4, Second Paragraph: Results for ^{3}H are presented in Figure 4-46 and Table 4-43; however this paragraph does not mention any conclusions concerning ^{3}H. Please include a short comment or discussion for completeness.

44. Page 4-121, Figure 4-46: Please indicate what the "X" on the various plots represents.

45. Page 5-36, Section 5.2.7, Second Full Paragraph, Second Sentence and Page 5-37, Figure 5-17: Units in the text are presented in 'm bls" while "feet bls" are used on Figure 5-17. Either a conversion should be provided in the text or consistent units should be used.

46. Page 5-53, Section 5.3.3, First Full Paragraph, Ninth Sentence and Page 5-55, Figure 5-25: The north direction should be indicated in both the text and on the Figure.

47. Page 5-61, Section 5.3.6, Second Paragraph, Third Sentence: Please define the "nominal distribution."

48. Page 5-116, Section 5.6.2, First Paragraph, Third Sentence and Page 5-117, Figure 5-56: Please describe in the text what the red line on Figure 5-56 on Page 5-117 represents. Please do the same in the text for all similar Figures in the document.

49. Page 5-164, Section 5.7.5, First Paragraph, Third and Seventh Sentences: The third sentence indicates boundary fluxes have relatively low influence on the objective function, whereas, the seventh sentence indicates the north flux is the most sensitive boundary flux. Is the key point in the third sentence the objective function? Please clarify this discussion.

50. Page 5-172, Section 5.8.3, Last Bullet on Page, Second and Third Sentences: Fenelon et al. (2010) indicated that the relative arrow widths **were** to identify tributary groundwater flow systems with "less" or "more" flow, and **NOT "may have been."** Please correct this sentence. Also, because the arrow widths are relative, these cannot be used to infer "possible flow amounts" as expressed in the third sentence. Information from this reference cannot be used in this manner. Please correct these sentences. Additionally, how does using "relative arrow widths" "in a more quantitative sense to estimate possible flow amounts." meet the UGTA QAP requirements?

51. Pages 6-26 through 6-36, Section 6.3.1.2: This section is based on the information in Table 6-4. Of the eleven (11) **Test Intervals or Pathways** used for comparison, six (6; more than half) are not in carbonates. How does this comparison meet the UGTA QAP requirements for transferability? This entire section is based on comparisons of different lithologies and locals. How are these nonparallel comparisons accounted for?

52. Page 6-50, Section 6.3.5.2, Third bullet: Please add a brief explanation as to how the LLNL guidance prescribed using the stated range of K_d values in the sensitivity analysis.

53. Page 6-75, Section 6.4.2, Second Full Paragraph, First Sentence and Pages 6-80 to 6-81, Figures 6-35 through 6-38: The Figure captions for Figures 6-35 and 6-36 indicate infiltration rate of 1 mm/yr, and the captions for Figures 6-37 and 6-38 state infiltration rates of 0.1 mm/yr. The first sentence in the second full paragraph on Page 6-75 states, "...for infiltration rates of 0.1 and 1 mm/yr (corresponding to runs 542121 and 121212, respectively) are illustrated in Figures 6-35 to 6-38." Because the run numbers are not included on the Figures did this sentence mean to imply order of infiltration rates presented on the Figures? If so, please correct or clarify the text and Figures.

54. Page 6-94, Section 6.4.3, First Paragraph, First, Third and Fourth Sentences: "(and neighboring detonations is Area 3)... (and neighboring detonations in Area 2)... (and neighboring detonations in Area 7), and several detonations conducted near the center of Area 3." While it is stated in the fourth sentence why these areas are not illustrated, the information, as written, is vague if not useless. Either name these detonations or reference a Table where they can be identified.

55. Page 6-112, Section 6.5.2, Second Full Paragraph on Page, Third Sentence: Composite contaminant boundary is described based on the combination of the ensemble of possible contaminant plumes forecasted from discrete groundwater flow **and transport** models. Please add "and transport" to the sentence. In addition, on Table 7-1 on Page 7-26, composite contaminant boundaries are defined differently that what is used throughout this document. Figure 3-4 in the Appendix VI of the FFACO is referenced in the Table as an example of composite contaminant boundaries. Please clarify the use of the composite contaminant boundaries in the text by possibly using "composite contaminant boundaries based on alternative conceptual models".

56. Page 6-131, Section 6.5.3, Second and Third Paragraphs: Two alternative LCA HSTs runs are described. In Figure 6-67, they are indicated in the caption as Preliminary $2R_c$ and Alternative Bounding HST. Please associate in the text which of the two alternatives corresponds to the appropriate descriptions.

57. Page 6-132, Section 6.5.3, Seventh Bullet on Page and Page 6-134, Figure 6-68: There are three CDFs curves presented on Figure 6-68 but the text indicates curves for the two alternative LCA source-term scenarios? Please clarify in the text.

58. Page 6-162, Section 6.5.8, Last bullet on Page: Please add a brief explanation as to why the Base-Case LCA Sources in Figures 6-89, 6-90 and 6-91 are all the same plot. In other words, please explain why the infiltration rate does not influence the probability of exceedance of MCLs.

59. Page 6-172, Section 6.5.9.3, Third Bullet: Please indicate that this discussion pertains to Figure 6-95 and based on that Figure the high and low effective porosities of the fault zones correlate to **low and high** extents of the contaminant boundary. Please check this information and correct this Bullet.

60. Page 6-172, Section 6.5.9.3, Fourth Bullet: Please indicate that this discussion pertains to both Figures 6-95 and 6-94, respectively.

61. Page 6-175, Section 6.5.9.4, Second Paragraph, First Sentence and Page 6-176, Figure 6-96: Please explain in the text the meaning of having EFFPOR_FA> in both branches of the tree in Figure 6-96 (a).

62. Page 7-12, Section 7.0, Fifth Bullet on Page: Why is the information in this bullet about saturated-zone fraction of the inventory included under the sentence: "The conclusions of the unsaturated-zone transport model presented in this document (Section 3.0) may be summarized as follows:?" Please clarify in the document.

63. Page 7-14, Section 7.0, Sixth Bullet on Page, Second Sentence: How are the "low-probability realizations" determined (on what basis)? Please add an explanation to the document.

64. Page 7-19, Section 7.0, Second Bullet: It is stated, "These calculated fluxes are insignificant in comparison to other sources of contamination in the saturated LCA transport model and are therefore appropriate for use in developing a forecast of the contaminant boundary." How can something that is insignificant be appropriate for use? Please explain.

65. Page 7-24, Table 7-1, First Column, First Row: It is stated, "Contaminant boundaries are not discrete **predictions** of the location ..." Please change predictions to forecasts.

66. Appendix E, Page E-13, Section E.3.1, **Drainage System in the Yucca Flat Basin Area,** First Sentence: The "NTNSS" should be NNSS. Please correct this.

67. Appendix F, Page F-9, Section F.1.3.1, Figure F-3(a) and (b): Units for "R" need to be included either on the Figure or in the caption.

68. Appendix F, Page F-10, Section F.1.3.1, First full Paragraph, Last Sentence: "...moderate porosity ...." Based on the information in the Figure, moderate porosity is from 0.1 to 0.4. Please change the text to "effective porosities that range from 0.1 to 0.4" rather than "moderate porosity."

69. Appendix F, Page F-14, Section F.1.3.2, Fourth Paragraph, Last Sentence: Please remove this sentence. There is no information provided to back up this expectation.

70. Appendix G, Page G-6, Section G.1.3.1, Second Full Paragraph, First Sentence: Please include an explanation or a Figure to describe the statement, "the pressurization aspects of these two models can be thought of as a single model viewed at early (Model 2) or late (Model 1) times."

71. Appendix G, Page G-7, Section G.1.3.2, Model 1: The definition of s as *dH/dr* does not make sense when compared to the definition of sH_0 as maximum distance of overpressurization. The units do not match with sH_0 being (dH/dr) (H_0), which is not distance. Please clarify these definitions.

72. Appendix G, Page G-15, Section G.1.3.2, Third Sentence below Table G-3: There is no yellow color shown in Figure G-5 to indicate no change in permeability. Please clarify this in the text.

73. Appendix G, Page G-22, Section G.1.4.2, Third full sentence on Page: Where are the results of varying boundary conditions documented? Please include this information in the text.

74. Appendix G, Page G-25, Section G.1.4.3, Second Sentence on Page: Where are the results of varying boundary conditions documented? Please include either this information or a reference in the text.

75. Appendix H, Page H-7, Section H.1.0, Second Paragraph, First Sentence: The authors need to indicate in the text how many points were measured and what type of interpolation was done in the lateral direction to produce the distributions shown in Figure 5-17.

76. Appendix I, Page I-3, Section I.2.3, First Paragraph, Third Sentence: The authors need to indicate why there appears to be several traces for the ER-7-1 Observed data presented in Figure I-1.

77. Appendix K, Page K-8, Section K.2.2, First Paragraph, Second Sentence: The information presented in Figure K-2 is not clearly explained in the text. Please correct this.

78. Appendix K, Page K-20, Section K.3.3, Second Paragraph, First and Second Sentences and Pages K-24 and K-25, Figures K-14 and K-15: In regards to Figure K-14's Z = -40 m S and Figure K-15's Z = - 40m W, why are there two red lines? Please explain in the text.
79. Appendix K, Page K-20, Section K.3.3, Third Paragraph, First and Second Sentences: The color legends for Figures K-16, K-17 and K-18 are different for the two models presented. Please correct this or point this out in the text.

80. Appendix L, Page L-21, Section L.3.0, Third Paragraph, Third Sentence and Page L-23, Figure L-10: Concerning Figure L-10, pack-rat midden data are indicated by blue **circles** on the Figure, not blue *diamonds* as indicated in the text. Please correct this in the text.

81. Appendix L, Page L-23, Section L.3.0, Figure L-10a: The legend for (a) does not need the Tuff/Alluvial symbol because this is a plot for only LCA data. Please remove this symbol for consistency with Figure L-10b.

82. Appendix L, Page L-24, Section L.3.0, First Paragraph, First full Sentence: Is Watertown 4 WW indicated by WT-4 in Figure L-10b? If so, please indicate this in the text or indicate the appropriate well notation.

83. Appendix M, Page M-11, Section M.2.6, Last Sentence on Page: There is a change bar; however, the text has not been changed from the previous version.

84. Appendix M, Page M-12, Section M.2.6, First Paragraph, Fourth Sentence: "Zavarin et al." needs to have the year added to the text for reference.

85. Appendix M, Page M-12, Section M.2.6, First Paragraph, Seventh and Eighth Sentences: The seventh sentence indicates that Eu and Am also have a strong tendency to attach to colloids. However, in the eighth sentence only Eu is considered for evaluation in the Appendix. Please explain in the text why Am is not considered.

86. Appendix M, Page M-12, Section M.2.6, First Paragraph, Ninth Sentence: This sentence needs additional explanation as to why the information evaluated in Zavarin et al. (2013) is not directly transferable to the ***types*** of calculation performed in this Appendix.

87. Appendix M, Page M-12, Section M.2.6, Last Sentence on page: There is a change bar; however, the text has not been changed from the previous version.

88. Appendix M, Page M-13, Section M.2.7, Last Sentence on page: There is a change bar; however, the text has not been changed from the previous version.

89. Appendix M, Page M-24, Section M.4.2, Figure M-6: The Figure caption includes ^{137}Cs and ^{237}Np but there are no isotope numbers on the Cs and Np in the plots. Please make this consistent.

90. Appendix M, Page M-25, Section M.4.2, Figure M-7: The Figure caption includes ^{137}Cs but there is no isotope number on the Cs in the plot. Please make this consistent. In addition, should Np on this Figure be ^{237}Np?

91. Appendix M, Page M-32, Section M.5.1, First Paragraph, First Sentence: This sentence is not clear. How can comparing the computed concentrations with the MCL lead to calculating contaminant lengths at different times for each radionuclide? Please clarify or add additional explanation.

92. Appendix M, Page M-39, Section M.5.2, First Paragraph, Last Sentence: There is no Figure M-10cc in this document. Please add the Figure or change the text.

93. Appendix M, Page M-39, Section M.5.2, Third Paragraph, Second Sentence: There is no Figure M-10cbin this document. Please add the Figure or change the text.

94. Appendix M, Page M-41, Section M.5.2, Figure M-16: The MCL line is not included on the Eu152 plot. Please add this to the plot.

95. Appendix M, Page M-48, Section M.5.3, Figure M-25: There are no (a) and (b) indications shown on the plots. Please add these.

96. Appendix M, Page M-52, Section M.6.2, Second Paragraph, Fifth Sentence: The spacing is indicated by S_f in the text, whereas in Figures M-27 to M-30, M-32 to M-33, and M-36 to M-44 it is Sf. Please make this consistent between the text and the Figures.

General Comments for the entire document:

97. Please check all Figures for North arrows.

98. Please change all use of "pump tests" to "aquifer tests" in the text and on Figures.

99. Use of phrases such as "largely successful" on Page 4-24 are unclear and should be eliminated or modified to add clarity.

100. Please make text and Figures consistent in the use of capitalization. For example, on Page 4-40, Figure 4-17 tests and units are not capitalized while in the text on Page 4-39, which describes Figure 4-17, tests and units are capitalized.

101. Please make text and Tables consistent in the use of cases and runs. For example, on Page 4-54, in the text "cases" is used, whereas in Table 4-13, "run" is used. Also, on Page

4-51, sensitivity "runs" and model "runs" are used in the third and fourth paragraphs and in the fifth paragraph "cases" is used.

102. Please make the use of the well names consistent in the text, Figures and Tables. For example, Well WW C-1 is stated in the text on Page 5-12, Section 5.2.3, Second Paragraph, Seventh Sentence but on Figure 5-4, it is listed as WW-C-1.

103. In several Figures in Section 5.6.2, the cumulative distribution is indicated by a red line, however that is not indicated in the text, such as, cumulative distribution **(red line).** Please add this to the text for completeness.

104. Please make the text consistent in the use of "nominal case" and "base case." If there is a clear distinction then it should be described fully in the text. For example, on Page 6-3, Section 6.0, First Paragraph, First full Sentence, nominal case is used, whereas, on Page 6-6, Section 6.1.2, Third Paragraph, First Sentence, base-case is used. In addition, on Page 6-110, Section 6.5.2, First Paragraph on page, First Sentence both terms are used ["...presents a nominal (or base-case) representation"]. The use of two terms can lead to confusion. Please select one term and stay consistent.

105. In several locations in the text in Chapter 6 the phrase "pumping-scale aquifer tests" is included. Please remove pumping-scale or clearly define what is meant by this term.

If you have any questions or comments regarding this matter, please contact either me or Christine Andres at (702) 486-2850, ext. 231 or 232, respectively.

Sincerely,

/s/ Tim H. Murphy

T. H. Murphy
Chief
Bureau of Federal Facilities

ec: Christine Andres, NDEP, LV
N-I Central Files, MS NSF 156, Las Vegas, NV

cc: FFACO Group, PSG, NNSA/NSO, Las Vegas, NV
J. T. Fraher, DTRA/CXTS, Kirkland AFB, NM
NSTec Correspondence Control, NLV008, Las Vegas, NV
K.K. Knapp, EMO, NNSA/NFO, Las Vegas, NV
W. R. Wilborn, ERP, NNSA/NFO, Las Vegas, NV
Bimal Mukhopadhyay, EMO, NNSA/NFSO, Las Vegas, NV
EM Records, AMEM, Las Vegas, NV

NEVADA ENVIRONMENTAL MANAGEMENT OPERATIONS ACTIVITY
DOCUMENT REVIEW SHEET

1. Document Title/Number: Final Phase I Flow and Transport Model Document, Revision 0, For Corrective Action Unit 97: Yucca Flat/Climax Mine, Nevada National Security Site, Nye County, Nevada / N-I/28091--080	2. Document Date: February 2013
3. Revision Number: Rev. 0	4. Originator/Organization: N-I / Robert Andrews (702) 295-0229
5. Responsible DOE NNSA/NFO Activity Lead: Bill Wilborn	6. Date Comments Due: August 7, 2013
7. Review Criteria: Complete Document	
8. Reviewer/Organization Phone No.: NDEP / Chris Andres (702) 486-2850 extension 232	9. Reviewer's Signature:

10. Comment Number/Location	11. Type[a]	12. Comment	13. Comment Response	14. Accept/Reject
1. Page ES-6, Executive Summary	M	**Modeling Approach** Section, First full sentence on page: "This philosophy has led to the decision to use models or parameters that do not underestimate the potential contaminant transport." How will this "do not underestimate" be demonstrated?	The "do not underestimate" has been demonstrated by comparison of model results to in-situ observations of contaminant concentrations. Changed to: "This philosophy has led to the decision to use models or parameter values that tend to overestimate the potential contaminant transport. The forecast contaminant transport overestimation is demonstrated by comparing modeled contaminant transport with discrete contaminant concentration observations downgradient from test cavities."	Accepted

[a]Comment Types: M = Mandatory, S = Suggested.
Return Document Review Sheets to NNSA/NFO Environmental Management Operations Activity, Attn: QAC, M/S NSF 505

10. Comment Number/Location	11. Type[a]	12. Comment	13. Comment Response	14. Accept/Reject
2. Page ES-9, Executive Summary	M	**Modeling Approach** Section, Last sentence of this Section: If the absence of significant declines in hydraulic heads in the LCA across the accommodation zone that separates Yucca Flat and Frenchman Flat indicates that the LCA is hydraulically well connected between these basins, despite their different structural styles and the termination of major basin-forming Yucca Flat faults in this area, has the flux across the southern boundary of Yucca Flat been included in the Frenchman Flat model? If no, when will this increase in flux be addressed and documented?	The water flux across the Yucca Flat southern boundary has been included as a boundary condition in the Frenchman Flat model. The basis for the water flux used in the Frenchman Flat model was the Death Valley Regional Flow System model. The water flux out the southern boundary of the Yucca Flat model (about 160 to 260 kg/s depending on the conceptual model) is reasonably consistent with the water flux into the Frenchman Flat model (about 300 kg/s as illustrated in Figure 5-9 of SNJV (2006c). The possible contaminant flux out of the Yucca Flat model is based on compounded conservative assumptions. If the possibility of contaminant flux out of the Yucca Flat model is still realized after completing model evaluation studies and analyses during the CADD/CAP phase of the UGTA strategy decision process, then the model may be extended to capture this unlikely scenario.	No change, see Comment Response
3. Page ES-14, Executive Summary	M	**Saturated LCA Flow and Transport Model** Section, First partial paragraph on Page: use of kg/s for inflows in this paragraph and throughout the document should include values in (m^3/day) for consistency with other portions of the document (e.g., page H-20, Figure H-13a, ground water flow rates m^3/day). See the bottom of Page 5-39 where both units are included.	The units of kg/s are commonly used to evaluate the modeled water flux because FEHM uses kg/s as an input and output parameter. Where other units are used in the literature (for example m^3/day or acre-ft/yr), the reported value is presented along with a conversion to kg/s to provide clarity. In this paragraph because only modeled results are presented, no conversion is necessary; however at other places in the document either a direct conversion is applied and both m^3/day and kg/s are presented or conversions are supplied (1 m^3/day = 0.0116 kg/s; 1 kg/s = 86.4 m^3/day)	No change, see Comment Response

[a]Comment Types: M = Mandatory, S = Suggested.
Return Document Review Sheets to NNSA/NFO Environmental Management Operations Activity, Attn: QAC, M/S NSF 505

NEVADA ENVIRONMENTAL MANAGEMENT OPERATIONS ACTIVITY
DOCUMENT REVIEW SHEET

10. Comment Number/Location	11. Type[a]	12. Comment	13. Comment Response	14. Accept/Reject
4. Pages ES-16-17, Executive Summary	M	**Modeling Results and Forecast Contaminant Boundaries** Section, First full paragraph on Page, Third sentence and Figure ES-3: Additional discussion of Figure ES-3 is needed in the text because with the colors overlaying each other the continuity of the contaminant boundaries for the various models is not clear. Also, the term "Time-Cumulative" used on the Figure needs to be defined in the text.	Added: "The figure is developed by layering the model forecasts with the bottom blue layer (Base Case (3 R_c)) having the most extensive contaminant forecast and each successive layer having a lesser contaminant forecast ending with the least contaminant forecast case in yellow. The time-cumulative forecast of contaminant migration implies that this is the maximum extent of the probability of exceeding the SDWA MCL within the 1,000-year simulation period."	Accepted
5. Page ES-19, Executive Summary	M	**Modeling Results and Forecast Contaminant Boundaries** Section, First full paragraph on Page, Last Sentence: Why are the conceptual models cited in the previous sentence considered low probability models? On what information is this statement based? Where is this information documented?	There is no direct information to support the assertion that the more conservative models are "low probability". Changed to: "However, even for these more conservative models, it is useful to note that the MCL exceedance is dominated by short-lived radionuclides . . ."	Accepted
6. Page ES-20, Executive Summary	M	**Modeling Results and Forecast Contaminant Boundaries** Section, Last sentence on top of Page: " ... except for detonations in the unsaturated LCA." Either a brief explanation should be included in the Executive Summary or a reference provided to a section in the document which explains why this is an exception.	Added: ". . .which have relatively short transport distances to the water table in the LCA."	Accepted

[a]Comment Types: M = Mandatory, S = Suggested.
Return Document Review Sheets to NNSA/NFO Environmental Management Operations Activity, Attn: QAC, M/S NSF 505

10. Comment Number/Location	11. Type[a]	12. Comment	13. Comment Response	14. Accept/Reject
7. Page ES-20, Executive Summary	M	**Comparison of Model Results to *In Situ* Observations** Section, First Paragraph: The depth or units sampled by these wells should be indicated. A short discussion of the comparison of the sample size of the well to the estimated model contamination should be included.	Added: "Each of these wells is completed in the upper portion of the LCA (or LCA3 in the case of UE-2ce) where contaminants would most likely be present, if at all. However, with the exception of Well UE-2ce, each of these wells has a limited extent of observation due to their low water production. Generally, cell volumes in the models (typically on the order of 100 m x 100 m x 50 m or 500,000 m^3 in the upper part of the LCA) are much larger than the aquifer volume interrogated by the sampling wells, so simulated concentrations are expected to be less than actual concentrations if a similar radionuclide mass was introduced to the aquifer. These relatively small aquifer volumes also mean that any nearby contamination, if it existed, may go undetected by the well, Both of these factors complicates direct comparison of measured and simulated concentration at most locations. However, at Well UE-2ce pumping conducted from 1977 to 1984 yielded about 42,000 m^3 of water and another pumping event in 2008 yielded about 150 m^3 of water. Assuming a typical fracture porosity of 0.001 for the LCA, this equates to an aquifer volume of roughly 42 x 10^6 m^3 being interrogated by the pumping well, or approximately equivalent to 80 LCA cell volumes. Therefore, Well UE-2ce provides a relatively unique opportunity to compare measured and simulated radionuclide concentrations at the top of the LCA." "	Accepted

[a]Comment Types: M = Mandatory, S = Suggested.
Return Document Review Sheets to NNSA/NFO Environmental Management Operations Activity, Attn: QAC, M/S NSF 505

10. Comment Number/Location	11. Type[a]	12. Comment	13. Comment Response	14. Accept/Reject
8. Page ES-21, Executive Summary	M	**Comparison of Model Results to *In Situ* Observations** Section, Bullet on top of Page, First Sentence: Please give an actual range of values instead of using the phrase, "in close proximity."	Added: ". . ., such as REBLOCHEN (about 250 m to the southwest of ER-2-1), CHIBERTA (about 260 m to the north of ER-2-1) and STARWORT (about 390 m to the southeast of ER-2-1)."	Accepted
9. Page 1-23, Section 1.4	M	First full Paragraph on Page, Second Sentence and Figures 1-10a and 1-10b; figure 1-10a is labeled West-East Profile and Figure 1-10b is North-South Profile. The directional descriptions are reversed in the text. Please correct the discrepancy.	Changed to: "Corresponding west-east and north-south cross sections through the HFM are illustrated in Figures 1-10a and b, respectively."	Accepted
10. Page 1-33, Section 1.4	M	First partial paragraph on Page: The phrase "except between Wells ER-3-1 and WW C-I, where the greater depth of the LCCU allows hydraulic communication between the LCA within Yucca Flat and northeast of the basin (Figure 1-7)" is not useful as Figure 1-7 covers too large of an area to prove the point attempting to be made, no wells are even shown on the Figure and the phrase leaves the reader with the question, "How does a deeper underlying unit allow hydraulic communication?" Please clarify this portion of the sentence.	To provide greater consistency with the SNJV (2006a) conclusions changed to: "in the southeastern part of the HFM area."	Accepted
11. Page 1-48, Section 1.7	M	First full Paragraph on the Page, Sixth Sentence: "This low probability of occurrence makes this model run unimportant from a regulatory perspective ..." This sentence is mixing individual model assumption probabilities with the 5 percent or greater probability of exceeding the SDWA MCL for regulatory purposes. The information used to determine the model assumption probabilities needs to be presented AND de-coupled from the 5 percent or greater probability of exceeding the SDWA MCL for regulatory purposes.	Deleted sentence.	Accepted
12. Page 1-50, Section 1.7	M	Last Bullet on Page: This does not explain clearly how the assumed laterally homogeneous transport properties is a conservative assumption as indicated by the sentence above the bullets. Please add an explanation for this assumption.	The next sentence in this bullet was meant to explain why assuming laterally homogeneous transport properties is conservative. Changed to: "Heterogeneity in transport properties would result in greater spatial averaging of these properties which would reduce averaged property variance. As a result, extreme values in the tails of the parameter distributions would exert a smaller influence on the low-probability model outcomes that define the contaminant boundary."	Accepted
13. Page 1-61, Section 1.9, and Appendix L	M	The phrase, " ... groundwater flow rates ... " have referred to volumes per time in other locations in the document. Appendix L is estimating groundwater velocity. Please check for consistent use throughout the document.	Changed "flow rates" to "velocities" Have checked the remainder of the document to ensure "flow rate" is used appropriately to mean volumetric flow rate.	Accepted

[a]Comment Types: M = Mandatory, S = Suggested.
Return Document Review Sheets to NNSA/NFO Environmental Management Operations Activity, Attn: QAC, M/S NSF 505

NEVADA ENVIRONMENTAL MANAGEMENT OPERATIONS ACTIVITY
DOCUMENT REVIEW SHEET

10. Comment Number/Location	11. Type[a]	12. Comment	13. Comment Response	14. Accept/Reject
14. Page 2-4, Section 2.1	M	First full sentence top of Page and Figure 2-1: " ... the saturated zone (green) ... " In Figure 2-1, on Page 2-3, the saturated zone is indicated by a blue sphere. Please correct this discrepancy	Changed to: "blue".	Accepted
15. Page 2-49, Section 2.5	M	Third Paragraph, Second Sentence: " ... overly conservative assessment of potential exposure should be avoided, or at a minimum, identified." This phrase doesn't make sense because the document keeps referring to the use of compounded conservatism which contradicts the "should be avoided." Please correct this sentence.	Sentence deleted. Added: "The HST conceptual models and parameter values define the boundary condition for the spatial and temporal release of contaminants to the groundwater. While the HST conceptual models and parameter values are based on available information, uncertainty remains. As a result, assumptions are necessary to address this uncertainty."	Accepted
16. Page 3-4, Section 3.1	M	First full paragraph on Page, Last Sentence: It is stated, " ... the later (more recent) detonations have transport starting years or decades before the actual event." Please add a brief discussion of the possible impact on the transport forecasts due to this simplification.	Added: “For individual detonations, this simplification can produce radionuclide arrival times at the water table that are as much as three decades earlier than would be calculated had the radionuclide mass been introduced on the actual detonation date. This is an acceptable approximation because the contaminant boundaries are calculated based on the maximum extent of contamination at any time within the 1,000-year regulatory period, and so the exact timing of the unsaturated zone inputs to the saturated-zone models are less important from that perspective.”	Accepted
17. Page 3-5. Section 3.1.1	M	Second Paragraph, First Sentence: It is stated, " ... the underground detonations conducted in Yucca Flat range in depth of burial from 782.4 m below ground surface and range in yield ... " A lower depth of burial needs to be added to this sentence.	Changed to: " ... the underground detonations conducted in Yucca Flat range in depth of burial from 114.5 m to 782.4 m below ground surface and range in yield ... "	Accepted
18. Page 3-16, Section 3.1.3.3	M	Second Paragraph and Page 3-17, Figure 3-6: The orange and green dots on Figure 3-6 need to be explained either in a legend on the Figure or in the text on Page 3-16.	Added: “Note: Green and brown bars and balls indicate faults with vertical displacement (ball on downthrown side). Green symbols are associated with the Carpetbag Fault."	Accepted
19. Page 3-28, Section 3.2	M	First full paragraph on Page, Last Sentence: Based on the plot in Figure 3-8 for Area 5 Pilot Wells, there are no data presented for depths below approximately 250 m. As such, the last sentence should read "... above a depth of roughly 250 m."	Changed to: “…above a depth of approximately 250 m.”	Accepted

[a]Comment Types: M = Mandatory, S = Suggested.
Return Document Review Sheets to NNSA/NFO Environmental Management Operations Activity, Attn: QAC, M/S NSF 505

10. Comment Number/Location	11. Type[a]	12. Comment	13. Comment Response	14. Accept/Reject
20. Page 3-56, Section 3.4.3.4.1	M	First Paragraph, First Sentence and other locations throughout the document: "pumping-test-scale" should be "aquifer-test-scale." Please correct this in the document at all locations.	Global change to: “pumping-scale test” to maintain consistency with the supporting documentation in the HDD (SNJV, 2006b). Modified sentence to “. . . core-, slug-, and pumping-scale tests for both the Yucca Flat/Climax Mine area . . .” Added: "Slug-scale tests are based on instantaneously adding or removing a volume of water from the well and observing the water-level recovery to the static condition. Pumping-scale tests are based on pumping a significant volume of water over an extended time period and observing the water-level drawdown and recovery. As summarized in SNJV (2006b, Section 6.4.1), the pumping-scale test results provide the most appropriate information for use in large-scale modeling, because they provide results representative of the greatest aquifer volume and are more likely to reflect high hydraulic conductivity structure in tested formations." See also response to Comments #98 and #105.	Accepted
21. Page 3-56, Section 3.4.3.4.1, Table 3-4, and Page 3-58, Section 3.4.3.4.2, Table 3-5:	M	Please indicate in the footnotes for each Table that when a count of 1 is presented in the Table, the "mean" value given is just the value of the one measurement.	Added: “Note: When the count is 1, the mean is the single measurement value and no standard deviation was calculated." to Tables 3-4 and 3-5	Accepted
22. Page 3-57, Section 3.4.3.4.1	M	Second Paragraph: If the UGTA Activity participants believe that the summary statistics are biased toward the high end, what is their concern about using the values in the modeling for flow and transport? Either continue the discussion and present possible impacts OR remove this paragraph.	Added: "The net effect of these measurement and reporting biases would be to provide permeability distributions that tend to overestimate groundwater fluxes and velocities that form the basis of groundwater transport models, with the result that the extent of the calculated contaminant boundaries may also be overestimated.”	Accepted

[a]Comment Types: M = Mandatory, S = Suggested.
Return Document Review Sheets to NNSA/NFO Environmental Management Operations Activity, Attn: QAC, M/S NSF 505

10. Comment Number/Location	11. Type[a]	12. Comment	13. Comment Response	14. Accept/Reject
23. Page 3-72, Section 3.6.1	M	First Paragraph, First Sentence: " ... current infiltration rates are zero or negative in the upper several tens of meters ... " Remove "or negative" as there can be an upper flux of water but this is not a negative infiltration (see page 4-6, Section 4.2.2, First Paragraph, First Sentence). Please check entire document for use of negative infiltration and correct it.	Changed to: “Despite strong evidence that current infiltration rates are zero or that water movement is upward in the upper several tens of meters of the unsaturated zone throughout much of alluvial filled parts of Yucca Flat…”	Accepted
24. Page 3-88, Section 3.6.3.8	M	First Paragraph, Last Sentence: Please add "have" between " ... any perched water that may" and "been present above ... "	Changed to: "...perched water that may have been present above the working point..."	Accepted
25. Page 3-111, Section 3.6.7	M	First full paragraph on Page, Last Sentence: In a sensitivity analysis it is not appropriate to consider assigning a probability to any particular outcome. Therefore, please change the last sentence to read: The sensitivity analysis that was done probably spanned the range of outcomes that would have been produced with a Monte Carlo analysis.	Changed to: “The sensitivity analysis probably spanned the range of outcomes that would have been produced with a Monte Carlo analysis."	Accepted
26. Page 4-33, Section 4.4.1	M	Fourth Sentence on Page: Please change "closed" triangles to "solid and inverted" triangles and add "(hydrograph)" after "repeated measurements over time."	Changed to: “Filled and inverted triangles indicate wells with repeated measurements over time (i.e., hydrographs).” Changed note on Figure 4-15 to: “Filled and inverted triangles are wells with . . .”	Accepted
27. Page 4-50, Section 4.5.1	M	Second Paragraph, Last Sentence: Please explain how the values of the reduction factors were determined.	Changed to: “All these processes are explicitly considered in simulations presented later in this section. As explained in Section 4.6.3, these processes collectively produce reduction factors ranging from 0.3 to 0.01, depending on model parameters.”	Accepted
28. Page 4-51, Section 4.5.2	M	Last Paragraph, First Sentence: Please modify this sentence because a sensitivity study does not lead to estimates of uncertainty.	Changed to: “Despite the intent to overestimate “true” uncertainty with this ensemble, the impact of these uncertainties on advective transport to the LCA shows remarkably little variation as indicated by the results of the sensitivity study.”	Accepted

[a]Comment Types: M = Mandatory, S = Suggested.
Return Document Review Sheets to NNSA/NFO Environmental Management Operations Activity, Attn: QAC, M/S NSF 505

10. Comment Number/Location	11. Type[a]	12. Comment	13. Comment Response	14. Accept/Reject
29. Page 4-59, Section 4.5.3	M	Last Paragraph, Third Sentence: There is no purple shading in Table 4-12. Please add the shading or indicate the relevant simulations in some other manner.	Added shading (dark and light gray) to Table 4-12. Changed to: "A few of the simulations significantly overestimate the amount of testing-induced water charge by slightly more than an order of magnitude (shown in dark gray shading), and some significantly underestimate the flux (light gray shading)." Changed: "Notes: Dark gray shaded cells indicate cases where simulated values are far in excess of measured values. Light gray shaded cells indicate cases with underestimate of outflow."	Accepted
30. Page 4-63, Section 4.6.2.2	M	**Mass Representing Saturated-Zone Detonations**, First Paragraph, Fourth Sentence: The reference to Table 4-9 is not clear because Table 4-9 is **Parameters Used in Model Calibration**. This same comment applies to the Second Paragraph, Second Sentence on Page 4-65.	Changed both callouts to "Table 4-13" (Sensitivity Analysis Models and Results.)	Accepted
31. Page 4-66, Section 4.6.2.2	M	Equation (4-1): Please define $M_{f,rn}$.	Changed to: "The mobile mass available for groundwater transport ($M_{f,rn}$) for each radionuclide at each detonation was computed by…"	Accepted
32. Page 4-72, Section 4.6.3	M	First Paragraph, First Sentence: Based on the numbering to indicate the model run in the text and comparing it to the information presented in Table 4-13 on Page 4-52, there appears to be an inconsistency in the order of the numbers. Please correct this or explain how the two should be compared.	Changed order of parameter values in Table 4-13 to be consistent with order of parameters presented in Table 4-11. Also modified Tables 4-4 and 4-11 for clarity and completeness in identifying different case names.	Accepted
33. Page 4-88, Figure 4-35	M	The Figure caption needs **"(in Moles)**" added to be consistent with Figure 4-32 on Page 4-85.	Changed to: "Cumulative Mass That Leaves the Model (in Moles)"	Accepted
34. Page 4-99, Section 4.6.5	M	First paragraph, First and Second Sentences: Please explain the relationship between "from 3 to 5 percent for ^{14}C, ^{36}Cl, ^{99}Tc, ^{129}I, ^{237}Np, and U, and is just under 1 percent for ^{3}H" to Table 4-31. It is not clear how the two relate.	Changed to: "For the base case (211212.s), the mass of radionuclides predicted to leave the model over 1,000 years, expressed as a fraction of total input (internal sources + mass arriving at the water table), range from 3 to 5 percent for radionuclides with long half-lives to less than 1 percent for ^{3}H which has a short half-life."	Accepted

[a]Comment Types: M = Mandatory, S = Suggested.
Return Document Review Sheets to NNSA/NFO Environmental Management Operations Activity, Attn: QAC, M/S NSF 505

10. Comment Number/Location	11. Type[a]	12. Comment	13. Comment Response	14. Accept/Reject
35. Page 4-99, Section 4.6.5	M	Second Paragraph, Third through Ninth Sentences: These sentences discuss the results shown in Figure 4-38a. In the text, please indicate color of lines in the plot or the model run numbers to aid the reader. This has been done for the discussion of Figures 4-38b and 4-38c.	Added: "In this figure, the results are bounded by the red line, representing the lowest recharge rate and an exchange volume of 2 *Rc*, and the green line representing the medium recharge rate and an exchange volume of 1 *Rc*. The other lines represent medium recharge rates and variations in vadose zone parameters (permeability anisotropy and crater infiltration rates)." after the third sentence. Deleted sentence: "The green and red lines (solid versus dashed) show very little influence of overpressurization uncertainty)." and inserted: "In this figure the line color indicates variation in recharge rates (red = low, blue/green = medium) and variations in UZ models with respect to permeability anisotropy and crater infiltration."	Accepted
36. Page 4-103, Section 4.6.5	M	Second complete sentence on top of page: Case 9 is indicated in Table 4-34 but "base (nonthermal) case" is not indicated. Please indicate in the Table the nonthermal case.	Added: "Base (non-isothermal)" in the Variation column of case 2223211.1.14.5.1.2.1.N3.B2.v.1. (second to last row of Table 4-34).	Accepted
37. Page 4-104, Section 4.6.6	M	Second Sentence: Please indicate in the text on Page 4-104 that the blue line on Figure 4-41 on Page 4-106 corresponds to the unaltered base case.	Changed to: "LBB_Case 2 and LBB_Case 3 are very similar, and produce approximately two-thirds as much ^{14}C breakthrough as the unaltered base case (blue line)."	Accepted
38. Page 4-104, Section 4.6.6	M	Third Sentence: Based on the results in Figure 4-41, LBB_Case 1 produces **more than** twice (bold added for emphasis of difference in statement) as much ^{14}C breakthrough as the unaltered base case. Please modify this sentence to indicate this result.	Changed to: "LBB_Case1 produces more than twice as much ^{14}C breakthrough as the unaltered base case, but still represents a very small fraction of the initial inventory (less than 2 percent)."	Accepted
39. Page 4-112, Section 4.6.8.2	M	Second Paragraph, Third Sentence: How are the masses to the LCA from the base-case model with fixed source terms (the first row of Table 4-37) shown in Figure 4-43? The 'X' in the Figure does correspond to the values in the first row of Table 4-37, however the fourth sentence indicates the masses simulated in the deterministic model are marked with 'X' in the Figure. Please clarify this discussion in the text.	Changed to: "This base case is simulated deterministically (i.e., inventory multiplier 1.0, melt-glass partitioning factor f_0 as listed in Table 4-40, and realization '0') and the results are marked with "X" in the figure."	Accepted

[a]Comment Types: M = Mandatory, S = Suggested.
Return Document Review Sheets to NNSA/NFO Environmental Management Operations Activity, Attn: QAC, M/S NSF 505

10. Comment Number/Location	11. Type[a]	12. Comment	13. Comment Response	14. Accept/Reject
40. Page 4-114, Section 4.6.8.3	M	Second Paragraph, Last Sentence: Please indicate in Table 4-41 on Page 4-116 which entry corresponds to the mean mass from the Monte Carlo simulations and which corresponds to the mass reported in the previous run. In addition, please indicate which previous run is being discussed.	Added: "Mean mass from Monte Carlo simulations" to first row of Table 4-41. Added: "(Base-case simulation with mean input)" to 5th row of Table 4-41. Changed 5th row of Table 4-39 to "Base-case simulation with mean input." Changed callout to Table 4-41 to: "The ratio of the mean mass from Monte Carlo simulations to the mass reported in the base-case simulation with mean input is also compared in Table 4-41."	Accepted
41. Page 4-118, Figure 4-45	M	Please indicate what the "X" on the various plots represents.	Added: "Note: "X" denotes base-case model."	Accepted
42. Page 4-119, Section 4.6.8.3	M	First Sentence below Table 4-42: The $R^{(J)}$ is listed in **Table 4-41**, not Table 4-39 as stated in the text. Please correct this sentence.	Changed to: "Table 4-42" (Statistics of Mass Into LCA Model due to Variability of Melt Glass Factors)	Accepted
43. Page 4-120, Section 4.6.8.4	M	Second Paragraph: Results for ^{3}H are presented in Figure 4-46 and Table 4-43; however this paragraph does not mention any conclusions concerning ^{3}H. Please include a short comment or discussion for completeness.	Changed to: "From this source-term and melt-glass partitioning factor uncertainty investigation, one can make the following conclusions: 1. The effect of source inventory is significant only for ^{14}C and ^{36}Cl, and not important for the other radionuclides modeled including ^{3}H."	Accepted
44. Page 4-121, Figure 4-46	M	Please indicate what the "X" on the various plots represents.	Changed to: "The mass to the LCA from these realizations is shown in Figure 4-46, where "X" in the figure represents the mass from the base-case model, and the statistics are tabulated in Table 4-43." Added: "Note: "X" denotes base-case model." To Figure 4-46	Accepted
45. Page 5-36, Section 5.2.7	M	Second Full Paragraph, Second Sentence and Page 5-37, Figure 5-17: Units in the text are presented in 'm bls" while "feet bls" are used on Figure 5-17. Either a conversion should be provided in the text or consistent units should be used.	Added: "(1,500 ft)" after 450 m to convert m to ft using two significant figures.	Accepted
46. Page 5-53, Section 5.3.3	M	First Full Paragraph, Ninth Sentence and Page 5-55, Figure 5-25: The north direction should be indicated in both the text and on the Figure.	Added: North arrow to left side of Figure 5-25.	Accepted

[a]Comment Types: M = Mandatory, S = Suggested.
Return Document Review Sheets to NNSA/NFO Environmental Management Operations Activity, Attn: QAC, M/S NSF 505

10. Comment Number/Location	11. Type[a]	12. Comment	13. Comment Response	14. Accept/Reject
47. Page 5-61, Section 5.3.6	M	Second Paragraph, Third Sentence: Please define the "nominal distribution."	Changed to: "The range of boundary fluxes is considered uncertain, with the range assumed to be constrained by the range of regional model results."	Accepted
48. Page 5-116, Section 5.6.2	M	First Paragraph, Third Sentence and Page 5-117, Figure 5-56: Please describe in the text what the red line on Figure 5-56 on Page 5-117 represents. Please do the same in the text for all similar Figures in the document.	Changed to: "For example, inflow from the north ranges between 55.7 and 402.5 kg/s as shown in the cumulative distribution (red curve) in Figure 5-56." Global change to text referencing figures with cumulative distribution curves included with histograms.	Accepted
49. Page 5-164, Section 5.7.5	M	First Paragraph, Third and Seventh Sentences: The third sentence indicates boundary fluxes have relatively low influence on the objective function, whereas, the seventh sentence indicates the north flux is the most sensitive boundary flux. Is the key point in the third sentence the objective function? Please clarify this discussion.	Changed to: "In general, with the exception of the northern boundary flux, both the boundary fluxes and hydraulic properties have relatively low influence on the objective function."	Accepted

[a]Comment Types: M = Mandatory, S = Suggested.
Return Document Review Sheets to NNSA/NFO Environmental Management Operations Activity, Attn: QAC, M/S NSF 505

10. Comment Number/Location	11. Type[a]	12. Comment	13. Comment Response	14. Accept/Reject
50. Page 5-172, Section 5.8.3	M	Last Bullet on Page, Second and Third Sentences: Fenelon et al. (2010) indicated that the relative arrow widths **were** to identify tributary groundwater flow systems with "less" or "more" flow, and **NOT "may have been."** Please correct this sentence. Also, because the arrow widths are relative, these cannot be used to infer "possible flow amounts" as expressed in the third sentence. Information from this reference cannot be used in this manner. Please correct these sentences. Additionally, how does using "relative arrow widths" "in a more quantitative sense to estimate possible flow amounts." meet the UGTA QAP requirements?	Changed to: "The modeled flux leaving the Yucca Flat LCA flow model is consistent with the relative flow rates for different flow systems that can be estimated based on the relative flow volume arrow widths indicated in Fenelon et al. (2010) illustrated in Figure 1-13. Although the intent of the arrow widths presented in Fenelon et al. (2010) was to identify tributary groundwater flow systems with "less" or "more" flow, the relative arrow widths can be used qualitatively to estimate possible flow amounts. Based on the relative arrow widths presented in Fenelon et al. (2010), it can be inferred that the LCA flow in the Yucca Flat tributary flow system is less than the flow in either the Ash Meadows flow system or the Spring Mountains tributary flow system. If the total Ash Meadows annual discharge is about 740 kg/s (19,000 acre-feet per year [acre ft/yr]) (Laczniak et al., 1999), the inferred flow rate in the Yucca Flat tributary flow system would be smaller, as is simulated in the base-case and alternative northern boundary flux model. This is also consistent with recent interpretation by Fenelon et al. (2012) who state that "the total amount of groundwater flow through Yucca Flat is relatively minor and estimated to be 1,000 acre-ft/yr or less."	Accepted

[a]Comment Types: M = Mandatory, S = Suggested.
Return Document Review Sheets to NNSA/NFO Environmental Management Operations Activity, Attn: QAC, M/S NSF 505

10. Comment Number/Location	11. Type[a]	12. Comment	13. Comment Response	14. Accept/Reject
51. Pages 6-26 through 6-36, Section 6.3.1.2	M	This section is based on the information in Table 6-4. Of the eleven (11) **Test Intervals or Pathways** used for comparison, six (6; more than half) are not in carbonates. How does this comparison meet the UGTA QAP requirements for transferability? This entire section is based on comparisons of different lithologies and locals. How are these nonparallel comparisons accounted for?	To distinguish the data that are directly relied upon from the ER-6-1 well cluster MWAT tracer test from the other sources of data used to inform the distribution used for the LCA country rock: Added: "The ER-6-1 MWAT tracer test provides a unique data set to define the tracer to hydraulic fracture aperture ratio for use in the LCA transport model. However, these data which are representative of the fault damage zone in the vicinity of ER-6-1 are not expected to be representative of the LCA country rock away from fault damage zones. To evaluate the range of tracer to hydraulic aperture ratios potentially applicable to the undamaged LCA country rock, additional in-situ and laboratory investigations were reviewed. These data are analyzed in the following paragraphs to inform the assumed distribution of this ratio. While it is recognized that these are not Yucca Flat or LCA specific data sets, they provide useful insights into the possible range of aperture ratios."	Accepted
52. Page 6-50, Section 6.3.5.2	M	Third bullet: Please add a brief explanation as to how the LLNL guidance prescribed using the stated range of Kd values in the sensitivity analysis.	Changed to: "The base-case cesium K_d of 0.0 mL/g, conservatively reflects the recommended reduced values which are close to zero." Added: ". . . to explore the parameter's potential significance." to the last sentence in this bullet.	Accepted

[a]Comment Types: M = Mandatory, S = Suggested.
Return Document Review Sheets to NNSA/NFO Environmental Management Operations Activity, Attn: QAC, M/S NSF 505

10. Comment Number/Location	11. Type[a]	12. Comment	13. Comment Response	14. Accept/Reject
53. Page 6-75, Section 6.4.2	M	Second Full Paragraph, First Sentence and Pages 6-80 to 6-81, Figures 6-35 through 6-38: The Figure captions for· Figures 6-35 and 6-36 indicate infiltration rate of 1 mm/yr, and the captions for Figures 6-37 and 6-38 state infiltration rates of 0.1 mm/yr. The first sentence in the second full paragraph on Page 6-75 states," ... for infiltration rates of 0.1 and 1 mm/yr (corresponding to runs 542121 and 121212, respectively) are illustrated in Figures 6-35 to 6-38." Because the run numbers are not included on the Figures did this sentence mean to imply order of infiltration rates presented on the Figures? If so, please correct or clarify the text and Figures.	Changed to: "The temporal distributions of contaminant flux from the unsaturated-zone transport model to the saturated LCA model for ^{3}H and ^{129}I for an infiltration rate of 1 mm/yr (corresponding to run 121212) are illustrated in Figures 6-35 and 6-36. Similar figures assuming an infiltration rate of 0.1 mm/yr (corresponding to run 542121) are illustrated in Figures 6-37 and 6-38. The time zero corresponds to the initial time used in the unsaturated-zone transport model presented in Section 3.0. These results again reinforce the significant effect that the average infiltration rate has on the timing and rate of contaminant flux to the LCA as discussed in Section 3.0."	Accepted
54. Page 6-94, Section 6.4.3	M	First Paragraph, First, Third and Fourth Sentences: "(and neighboring detonations is Area 3) ... (and neighboring detonations in Area 2) ... (and neighboring detonations in Area 7), and several detonations conducted near the center of Area 3." While it is stated in the fourth sentence why these areas are not illustrated, the information, as written, is vague if not useless. Either name these detonations or reference a Table where they can be identified.	Changed to: "The most significant source areas for saturated alluvial/volcanic aquifer system releases to the LCA are associated with the following underground detonations: BILBY (in northwest Area 3), TORTUGAS (in northwest Area 3), and LAMPBLACK (in Area 7). Temporal variations in contaminant fluxes from these source areas are illustrated in Figures 6-51 and 6-52 for ^{3}H and ^{129}I, respectively. Additional locations of significance that are not illustrated include STARWORT (in southeast Area 2), and BARREGO/BASEBALL (in southwest Area 7)."	Accepted

[a]Comment Types: M = Mandatory, S = Suggested.
Return Document Review Sheets to NNSA/NFO Environmental Management Operations Activity, Attn: QAC, M/S NSF 505

10. Comment Number/Location	11. Type[a]	12. Comment	13. Comment Response	14. Accept/Reject
55. Page 6-112, Section 6.5.2	M	Second Full Paragraph on Page, Third Sentence: Composite contaminant boundary is described based on the combination of the ensemble of possible contaminant plumes forecasted from discrete groundwater flow **and transport** models. Please add "and transport" to the sentence. In addition, on Table 7-1 on Page 7-26, composite contaminant boundaries are defined differently that what is used throughout this document. Figure 3-4 in the Appendix VI of the FFACO is referenced in the Table as an example of composite contaminant boundaries. Please clarify the use of the composite contaminant boundaries in the text by possibly using "composite contaminant boundaries based on alternative conceptual models".	Added: "and transport" Added: "This composite contaminant boundary includes contaminant boundary forecasts using alternative conceptual models." to define the intent of "composite contaminant boundaries": Added: "Contaminant boundaries are assembled using a composite of all underground detonations in the Yucca Flat/Climax Mine CAU." To Table 7-1 Figure 3-4 of Appendix VI of the FFACO relates to a "composite of underground detonations". All of the Yucca Flat LCA contaminant boundaries have included a "composite of underground detonations" because all Yucca Flat detonation source terms are included.	Accepted
56. Page 6-131, Section 6.5.3	M	Second and Third Paragraphs: Two alternative LCA HSTs runs are described. In Figure 6-67, they are indicated in the caption as Preliminary $2R_c$ and Alternative Bounding HST. Please associate in the text which of the two alternatives corresponds to the appropriate descriptions.	Added:"…(called the Preliminary $2R_c$ HST or Initial $2R_c$ HST case in subsequent figures)…" Added: "…(called the Alternative Bounding or $3R_c$ Alternative HST in subsequent figures)"	Accepted
57. Page 6-132, Section 6.5.3	M	Seventh Bullet on Page and Page 6-134, Figure 6-68: There are three CDFs curves presented on Figure 6-68 but the text indicates curves for the two alternative LCA source-term scenarios? Please clarify in the text.	Added: "The two alternative LCA source term scenarios are compared to the base-case scenario (called the 3 R_c HST on this figure)." to the bullet referencing Figure 6-68	Accepted
58. Page 6-162, Section 6.5.8	M	Last bullet on Page: Please add a brief explanation as to why the Base-Case LCA Sources in Figures 6-89, 6-90 and 6-91 are all the same plot. In other words, please explain why the infiltration rate does not influence the probability of exceedance of MCLs.	Added: "The Base-Case LCA sources plots of the time-cumulative probability of exceeding MCLs do not change for the different background infiltration rates because they use the same calibrated flow field and the same source term."	Accepted

[a]Comment Types: M = Mandatory, S = Suggested.
Return Document Review Sheets to NNSA/NFO Environmental Management Operations Activity, Attn: QAC, M/S NSF 505

10. Comment Number/Location	11. Type[a]	12. Comment	13. Comment Response	14. Accept/Reject
59. Page 6-172, Section 6.5.9.3	M	Third Bullet: Please indicate that this discussion pertains to Figure 6-95 and based on that Figure the high and low effective porosities of the fault zones correlate to **low and high** extents of the contaminant boundary. Please check this information and correct this Bullet.	Changed third bullet to: "…low and high extents of the contaminant boundary". Added: “Note that the four top ranked variables are the same for both metrics; however, the ranking between the third and fourth variables is reversed.” after the callout to Table 6-12. Added: “Note the four ranked variables presentation order in Figures 6-94 and 6-95 bubble plots is the same as presented in Table 6-12 for the two metrics.” after the callout to Figures 6-94 and 6-95.	Accepted
60. Page 6-172, Section 6.5.9.3	M	Fourth Bullet: Please indicate that this discussion pertains to both Figures 6-95 and 6-94, respectively.	Changed to: "…volume and extent of contamination (Figures 6-94 and 6-95 respectively)"	Accepted
61. Page 6-175, Section 6.5.9.4	M	Second Paragraph, First Sentence and Page 6-176, Figure 6-96: Please explain in the text the meaning of having EFFPOR_FA> in both branches of the tree in Figure 6-96 (a).	Added: “A summary of representative classification tree results for the base-case model and the base-case LCA source-term allocation is presented in Figure 6-96 for the maximum MCL exceedance volume and maximum southern extent of contaminant migration performance metrics. These results confirm the significance of the fracture porosity and fracture aperture of the fault zones in controlling the high and low exceedance volume forecasts. Classification tree plots are a visual representation of a binary regression model for a dataset. In a binary regression model, data are recursively divided based on the explanatory power of splitting the dataset across a parameter input value. The parameter chosen as the basis for the first split has the most explanatory power, with each successive split based on parameters of ever-decreasing explanatory power. So the parameter(s) at the top of the tree most explain the low and high values of the results; the maximum MCL	Accepted

[a]Comment Types: M = Mandatory, S = Suggested.
Return Document Review Sheets to NNSA/NFO Environmental Management Operations Activity, Attn: QAC, M/S NSF 505

10. Comment Number/Location	11. Type[a]	12. Comment	13. Comment Response	14. Accept/Reject
			exceedance volume (EV) and the maximum southern extent of contaminant migration in Figure 6-96(a) and (b), respectively. The parameter that most distinguish the low and high values is DM_AM_CC (the matrix diffusion coefficient) in the case of the maximum exceedance volume and EFFPOR_FA (the effective porosity of the fault damage zones) in the case of the maximum southern exceedance distance. In the case of the maximum MCL exceedance volume, values of DM_AM_CC greater than or equal to 8.48E-12 m^2/s explain 39 of the 40 lowest maximum MCL exceedance values (i.e., the left side of Figure 6-96[a]) while values of DM_AM_CC that are not greater than 8.48E-12 m^2/s explain 38 of the 40 highest values (i.e., the right side of Figure 6-96[a]). This classification is repeated with the subset that falls to each branch of the tree. For the left branch of the maximum MCL exceedance volume classification tree (Figure 6-96[a]), the second parameter that can best classify the results is EFFPOR_FA; with EFFPOR_FA values greater than or equal to 0.002121 explaining 39 of the 40 lowest values of the maximum MCL exceedance volume. For the right branch of the maximum MCL exceedance volume classification tree (Figure 6-96[a]), the second parameter than can best classify the results is also the EFFPOR_FA; with EFFPOR_FA values less than 0.0127 explaining 38 of the highest values of the maximum MCL exceedance volume. It is interesting that the same parameter is used in both the left and right branches of the maximum MCL exceedance volume classification tree, although with different values on	

[a]Comment Types: M = Mandatory, S = Suggested.
Return Document Review Sheets to NNSA/NFO Environmental Management Operations Activity, Attn: QAC, M/S NSF 505

10. Comment Number/Location	11. Type[a]	12. Comment	13. Comment Response	14. Accept/Reject
			each branch. This again illustrates the significance of this uncertain parameter in controlling both the high and low values of the forecast maximum MCL exceedance volume. Additional displays of the top and bottom 10 percent of the results are presented in partition plots illustrated in Figure 6-97. The blue squares represent the highest 40 realizations, while the red squares represent the lowest 40 realizations. These plots are analogous to the two first classification bins on the left side of the classification trees illustrated in Figure 6-96. For example, the 39 low values of the maximum MCL exceedance volume indicated by following the "yes" branches of the tree plot in Figure 6-96(a), are the 39 red squares indicated in the upper right quadrant of Figure 6-97(a), with DM_AM_CC values greater than 8.48E 12 m^2/s and EFFPOR_FA values greater than 0.002121. The propensity of the highest realizations to cluster near low fracture porosities and low matrix diffusion coefficients (which also correlate to low matrix porosities) is expected as both of these parameters lead to greater advective transport and less matrix diffusion, both of which tend to maximize the forecast MCL exceedance volume and southern extent of contamination."	
62. Page 7-12, Section 7.0	M	Fifth Bullet on Page: Why is the information in this bullet about saturated-zone fraction of the inventory included under the sentence: "The conclusions of the unsaturated-zone transport model presented in this document (Section 3.0) may be summarized as follows?" Please clarify in the document.	Deleted bullet. This conclusion is redundant with the 3rd bullet on page 7-4 under the topic of conclusions related to the source term model.	Accepted

[a]Comment Types: M = Mandatory, S = Suggested.
Return Document Review Sheets to NNSA/NFO Environmental Management Operations Activity, Attn: QAC, M/S NSF 505

10. Comment Number/Location	11. Type[a]	12. Comment	13. Comment Response	14. Accept/Reject
63. Page 7-14, Section 7.0	M	Sixth Bullet on Page, Second Sentence: How are the "low-probability realizations" determined (on what basis)? Please add an explanation to the document.	Changed bullet: "These realizations represent the low-probability (less than 10 percent) tails of the key transport parameters for the more conservative modeling cases such as the base case. Less conservative conceptual models such as the alternative northern boundary flux LCA flow model and the LCA transport models using either alternative Sr and Cs sorption coefficients, alternative fault damage zone fracture porosities, or alternative scale-dependent matrix diffusion do not result in contaminants in excess of the SDWA MCLs leaving the southern boundary of the model domain."	Accepted
64. Page 7-19, Section 7.0	M	Second Bullet: It is stated, "These calculated fluxes are insignificant in comparison to other sources of contamination in the saturated LCA transport model and are therefore appropriate for use in developing a forecast of the contaminant boundary." How can something that is insignificant be appropriate for use? Please explain.	Changed to: "…therefore do not affect the…"	Accepted
65. Page 7-24, Table 7-1	M	First Column, First Row: It is stated, "Contaminant boundaries are not discrete **predictions** of the location ... " Please change predictions to forecasts.	The first column of Table 7-1 are direct quotes from the FFACO. The statement is correct in that contaminant boundaries are not discrete predictions.	No change, see Comment Response
66. Appendix E, Page E-13, Section E.3.1	M	**Drainage System in the Yucca Flat Basin Area**, First Sentence: The "NTNSS" should be NNSS. Please correct this.	Changed to: “NNSS”	Accepted
67. Appendix F, Page F-9, Section F.1.3.1	M	Figure F-3(a) and (b): Units for "R" need to be included either on the Figure or in the caption.	Added: “Note: “R” indicates recharge rate in mm/yr.”	Accepted
68. Appendix F, Page F-10, Section F.1.3.1	M	First full Paragraph, Last Sentence: " ... moderate porosity .... " Based on the information in the Figure, moderate porosity is from 0.1 to 0.4. Please change the text to "effective porosities that range from 0.1 to 0.4" rather than "moderate porosity."	Changed to: “In general, results compatible with the transient drainage hypothesis were characterized by effective porosities that range from 0.1 to 0.4, low recharge rates, and permeabilities between 10^{-16} and 10^{-17} m^2.”	Accepted
69. Appendix F, Page F-14, Section F.1.3.2	M	Fourth Paragraph, Last Sentence: Please remove this sentence. There is no information provided to back up this expectation.	Deleted sentence	Accepted

[a]Comment Types: M = Mandatory, S = Suggested.
Return Document Review Sheets to NNSA/NFO Environmental Management Operations Activity, Attn: QAC, M/S NSF 505

10. Comment Number/Location	11. Type[a]	12. Comment	13. Comment Response	14. Accept/Reject
70. Appendix G, Page G-6, Section G.1.3.1	M	Second Full Paragraph, First Sentence: Please include an explanation or a figure to describe the statement, "the pressurization aspects of these two models can be thought of as a single model viewed at early (Model 2) or late (Model 1) times."	Changed to: "As shown in Figure G-1, overpressures will be high at early times and confined to short radial distances. At later times, pressures will dissipate and affect a broader area. Model 2 attempts to capture the overpressures at very early times, whereas Model 1 is a reasonable approximation to later times. Since the time scale of the simulations is days, not microseconds, capturing the behavior of very early times is not plausible."	Accepted
71. Appendix G, Page G-7, Section G.1.3.2	M	Model 1: The definition of *s* as *dH/dr* does not make sense when compared to the definition of sH_0 as maximum· distance of overpressurization. The units do not match with sH_0 being (*dH/dr*) (H_0), which is not distance. Please clarify these definitions.	Clarified the definition of *s* as – *dr/dH.* Note that Figure G-3 defines the slope of the *dH* vs *r* plot as equal to - 1/*s*. Because the slope in Figure G-3 is equal to *dH/dr*, *s* = - *dr/dH*. Note that at *r* = 0, $dH = H_o$ and at $r = sH_0$, *dh* = 0 as illustrated in Figure G-3.	Accepted
72. Appendix G, Page G-15, Section G.1.3.2	M	Third sentence below Table G-3: There is no yellow color shown in Figure G-5 to indicate no change in permeability. Please clarify this in the text.	Changed to: "Most of the flow domain experiences no change in permeability (green color); a moderate reduction in permeability is present in the overpressurized zone."	Accepted

[a]Comment Types: M = Mandatory, S = Suggested.
Return Document Review Sheets to NNSA/NFO Environmental Management Operations Activity, Attn: QAC, M/S NSF 505

10. Comment Number/Location	11. Type[a]	12. Comment	13. Comment Response	14. Accept/Reject
73. Appendix G, Page G-22, Section G.1.4.2	M	Third full sentence on Page: Where are the results of varying boundary conditions documented? Please include this information in the text.	Deleted the following: "By varying boundary conditions (results not shown), it was verified that the boundary that represents the LCA must be no-flow, non-specified head. The pressure pulse was entirely damped before reaching TW-7 if the lower boundary was allowed to be a sink. Likewise, the upper boundary could not be represented by a free surface, or the pressure propagation would be overly damped. This result is in agreement with the suggestion by Davis (1971) that the pressures do not move as a "water-table mound" along a free surface. Also, the hydraulic connection between the LTCU and the LCA must be low. In fact, the OSBCU separates the LTCU and the LCA at TW-7, and so perhaps stratigraphic details unaccounted for in this radial model explain this result."	Accepted
74. Appendix G, Page G-25, Section G.1.4.3	M	Second sentence on Page: Where are the results of varying boundary conditions documented? Please include either this information or a reference in the text.	Deleted the following: "Experimentation with boundary conditions on this model showed that neither unconfined conditions nor hydraulic communication with the LCA was consistent with the data. This supports the static (confined approximation) used for the upper surface of the CAU-scale model (as proposed by Davis [1971], and tends to exclude the possibility of a "moving water table mound" hypothesized by Knox et al. [1965])."	Accepted
75. Appendix H, Page H-7, Section H.1.0	M	Second Paragraph, First Sentence: The authors need to indicate in the text how many points were measured and what type of interpolation was done in the lateral direction to produce the distributions shown in Figure 5-17.	Added: "This figure was developed by using the available temperature data at the discrete depths (for example 17 data points at 450 m (1,500 ft) bls) and kriging the temperatures at these discrete locations using a north-south anisotropy." to Appendix H, Section 5.2.7	Accepted
76. Appendix I, Page I-3, Section I.2.3	M	First Paragraph, Third Sentence: The authors need to indicate why there appears to be several traces for the ER-7-1 Observed data presented in Figure I-1.	Added: "The apparent drawdown traces observed at ER-3-1 and ER-7-1 represent the effects of diurnal earth tides."	Accepted

[a]Comment Types: M = Mandatory, S = Suggested.
Return Document Review Sheets to NNSA/NFO Environmental Management Operations Activity, Attn: QAC, M/S NSF 505

10. Comment Number/Location	11. Type[a]	12. Comment	13. Comment Response	14. Accept/Reject
77. Appendix K, Page K-8, Section K.2.2	M	First Paragraph, Second Sentence: The information presented in Figure K-2 is not clearly explained in the text. Please correct this.	Added: "The left side of Figure K-2 is a top-down view illustrating the dispersion of particles in the x- and y-directions for the verification test 1a used in Figure K-1. The right side of Figure K-2 is a 3-D rendering illustrating the dispersion of particles in the x- and z-directions for this verification test." Changed figure title of Figure K-1 to "Comparison of Walkabout Particle-Tracking Results at Discrete Times with Theoretical Curves" and added the following: "Note: Results from Verification Test 1a in Painter (2011) corresponding to 3-D transport in a homogeneous and isotropic flow field with dispersivity of 1.0 m, 0.1 m and 0.01 m in the x-, y- and z-direction, respectively." Changed figure title of Figure K-2 to "Walkabout Particle-Tracking Results for Verification Test 1a of Painter (2011)" and added the following: "Note: Particle tracking results for Verification Test 1a in Painter (2011) corresponding to 3-D transport in a homogeneous and isotropic flow field with dispersivity of 1.0 m, 0.1 m and 0.01 m in the x-, y-, and z-direction, respectively.".	Accepted

[a]Comment Types: M = Mandatory, S = Suggested.
Return Document Review Sheets to NNSA/NFO Environmental Management Operations Activity, Attn: QAC, M/S NSF 505

10. Comment Number/Location	11. Type[a]	12. Comment	13. Comment Response	14. Accept/Reject
78. Appendix K, Page K-20, Section K.3.3	M	Second Paragraph, First and Second Sentences and Pages K-24 and K-25, Figures K-14 and K-15: In regards to Figure K-14's Z = -40 m S and Figure K-15's Z = - 40m W, why are there two red lines? Please explain in the text.	Added: "The code comparison test illustrated in these figures corresponds to a 20,000 m × 400 m × 400 m grid, in the x-, y- and z-directions, respectively, with nodes that are 40 m on a side. The flow field is specified along the x-direction, with no flow boundaries along the y- and z- boundaries. The permeability in all nodes is the same except for a 40-m thick high permeability layer from Z = - 20 m to Z = 20 m and X = 0 m to X = 12,000 m that has a permeability 100 times the background permeability. This layer mimics the effect of a high-permeability fault damage zone within otherwise homogeneous, less permeable country rock. The fracture porosity in all nodes is 1E-03. The x-, y-, and z-dispersivities used in the test model are 30 m, 3 m and 0.3 m, respectively which mimics a greater longitudinal dispersivity and a smaller transverse dispersivity perpendicular to the plane of the high permeability zone. The initial concentration is specified with 15,000 uniformly distributed particles at x = 1,000 m and y from -198 m to 198 m and z from -59.2 m to + 59.2 m. The simulation is run to 1,500 days to capture the leading edge of the plume. The test is performed with both FEHM_sptr/PLUMECALC and Walkabout/PLUMECALC to evaluate the effect of the different particle tracking approximations. The MODFLOW/MT3D model split Layer 5 into 4 sub-layers to better approximate the results at Z = -40 m for comparison to the particle tracking methods. As a result, two layer elevations are illustrated for MODFLOW/MT3D, one at Z = -49.34 m and the other at Z = -33.34 m, resulting in two red lines in Figures K-14 and K-15 from about X = 1,000 m to X = 12,000 m where the results converge at the end of the high permeability zone."	Accepted

[a]Comment Types: M = Mandatory, S = Suggested.
Return Document Review Sheets to NNSA/NFO Environmental Management Operations Activity, Attn: QAC, M/S NSF 505

10. Comment Number/Location	11. Type[a]	12. Comment	13. Comment Response	14. Accept/Reject
79. Appendix K, Page K-20, Section K.3.3	M	Third Paragraph, First and Second Sentences: The color legends for Figures K-16, K-17 and K-18 are different for the two models presented. Please correct this or point this out in the text.	Added: "Although these plots use the same scales, they use different color schemes for the legends. These figures again illustrate excellent agreement between the different software."	Accepted
80. Appendix L, Page L-21, Section L.3.0	M	Third Paragraph, Third Sentence and Page L-23, Figure L-10: Concerning Figure L-10, pack-rat midden data are indicated by blue **circles** on the Figure, not blue *diamonds* as indicated in the text. Please correct this in the text.	Changed to: ”blue circles”	Accepted
81. Appendix L, Page L-23, Section L.3.0	M	Figure L-10a: The legend for (a) does not need the Tuff/Alluvial symbol because this is a plot for only LCA data. Please remove this symbol for consistency with Figure L-10b.	Deleted Tuff/Alluvial symbol.	Accepted
82. Appendix L, Page L-24, Section L.3.0	M	First Paragraph, First full Sentence: Is **Watertown** 4 WW indicated by WT-4 in Figure L-10b? If so, please indicate this in the text or indicate the appropriate well notation.	Changed to: "...Watertown 4 WW (WT-4)..."	Accepted
83. Appendix M, Page M-11, Section M.2.6	M	Last Sentence on Page: There is a change bar; however, the text has not been changed from the previous version.	Deleted change bar.	Accepted
84. Appendix M, Page M-12, Section M.2.6	M	First Paragraph, Fourth Sentence: "Zavarin et al." needs to have the year added to the text for reference.	Changed to: “However, as stated in Zavarin et al. (2013), ..."	Accepted
85. Appendix M, Page M-12, Section M.2.6	M	First Paragraph, Seventh and Eighth Sentences: The seventh sentence indicates that Eu and Am also have a strong tendency to attach to colloids. However, in the eighth sentence only Eu is considered for evaluation in the Appendix. Please explain in the text why Am is not considered.	Added: "(Note that ^{151}Sm, ^{241}Am and ^{243}Am were not simulated in this appendix because previous screening analyses[Zavarin, 2012a] indicated their initial concentrations were orders of magnitude below their MCL, whereas initial concentrations of Eu species were near or above their MCL).”	Accepted

[a]Comment Types: M = Mandatory, S = Suggested.
Return Document Review Sheets to NNSA/NFO Environmental Management Operations Activity, Attn: QAC, M/S NSF 505

10. Comment Number/Location	11. Type[a]	12. Comment	13. Comment Response	14. Accept/Reject
86. Appendix M, Page M-12, Section M.2.6	M	First Paragraph, Ninth Sentence: This sentence needs additional explanation as to why the information evaluated in Zavarin et al. (2013) is not directly transferable to the ***types*** of calculation performed in this Appendix.	Changed to: "Significantly, the high colloid loads used in the experiments (hundreds to tens of thousand times higher than natural colloid loads in the LCA) and the short timescales (10 days) and travel distances (4 inches) of the experiments compared with the regulatory compliance period (1,000 years) and potential contaminant transport distances (10's of kilometers) make the direct transfer of the estimated parameters from the experiments to regulatory calculations problematic. However, the models in this appendix are consistent with conclusions in Zavarin et al. (2013) regarding the essential processes surrounding colloid-faciliated radionuclide transport in the LCA."	Accepted
87. Appendix M, Page M-12, Section M.2.6	M	Last Sentence on page: There is a change bar; however, the text has not been changed from the previous version.	Deleted change bar.	Accepted
88. Appendix M, Page M-13, Section M.2.7	M	Last Sentence on page: There is a change bar; however, the text has not been changed from the previous version.	Deleted change bar.	Accepted
89. Appendix M, Page M-24, Section M.4.2	M	Figure M-6: The Figure caption includes ^{l37}Cs and ^{237}Np but there are no isotope numbers on the Cs and Np in the plots. Please make this consistent.	Added "^{137}Cs" to plot and kept ^{137}Cs on figure caption. Added: "Note that unlike the three-dimensional transport models in Section 6.0, these one-dimensional models do not consider the ^{135}Cs transport which is estimated to have an initial concentration less than its MCL whereas the Section 6.0 models initial ^{137}Cs concentrations in the LCA are about one hundred thousand times its MCL [see Figures 2-6, 2-7, and 2-8])." after sentence starting with "The analysis, therefore, examines the factors . . ." on page M-2. Changed to: "^{237}Np" in Figure M-6 because it is the only Np species simulated.	Accepted

[a]Comment Types: M = Mandatory, S = Suggested.
Return Document Review Sheets to NNSA/NFO Environmental Management Operations Activity, Attn: QAC, M/S NSF 505

10. Comment Number/Location	11. Type[a]	12. Comment	13. Comment Response	14. Accept/Reject
90. Appendix M, Page M-25, Section M.4.2	M	Figure M-7: The Figure caption includes ^{137}Cs but there is no isotope number on the Cs in the plot. Please make this consistent. In addition, should Np on this Figure be ^{237}Np?	Added ^{137}Cs to plot and kept ^{137}Cs on figure caption. Changed to: "^{237}Np" in Figure M-7 and caption because it is the only Np species simulated.	Accepted
91. Appendix M, Page M-32, Section M.5.1	M	First Paragraph, First Sentence: This sentence is not clear. How can comparing the computed concentrations with the MCL lead to calculating contaminant lengths at different times for each radionuclide? Please clarify or add additional explanation.	Changed to: "By comparing the computed radionuclide concentrations at all nodes in the streamtube model in a given realization with the MCL for that radionuclide (Table M-7), the distance from the BOURBON test over which the radionuclide concentration exceeds its MCL can be calculated at a given time. This distance, referred to as the contaminant length, varies with time and from radionuclide to radionuclide in a given realization and from realization to realization. In this Appendix, each radionuclide is tracked separately so that its importance in defining the maximum extent of contamination at different times can be determined. Analogous to the contaminant boundaries described in Section 6.0, the overall contaminant lengths for individual radionuclides are defined in a time-cumulative manner as the maximum distance over which the radionuclide exceeds its MCL at any time during the 1,000-year regulatory period."	Accepted
92. Appendix M, Page M-39, Section M.5.2	M	First Paragraph, Last Sentence: There is no Figure M-10cc in this document. Please add the Figure or change the text.	Changed to: "Figure M-10c."	Accepted
93. Appendix M, Page M-39, Section M.5.2	M	Third Paragraph, Second Sentence: There is no Figure M-10cb in this document. Please add the Figure or change the text.	Changed reference to: "Figure M-10b."	Accepted
94. Appendix M, Page M-41, Section M.5.2	M	Figure M-16: The MCL line is not included on the Eu152 plot. Please add this to the plot.	Added: "Note: The MCL for ^{152}Eu is 7.55E-15 mol/L, well above the range of computed concentrations in the ^{152}Eu plot." to Figure M-16	Accepted

[a]Comment Types: M = Mandatory, S = Suggested.
Return Document Review Sheets to NNSA/NFO Environmental Management Operations Activity, Attn: QAC, M/S NSF 505

10. Comment Number/Location	11. Type[a]	12. Comment	13. Comment Response	14. Accept/Reject
95. Appendix M, Page M-48, Section M.5.3	M	Figure M-25: There are no (a) and (b) indications shown on the plots. Please add these.	Added: “(a)” and “(b)” to Figure M-25, respectively.	Accepted
96. Appendix M, Page M-52, Section M.6.2	M	Second Paragraph, Fifth Sentence: The spacing is indicated by S_f in the text, whereas in Figures M-27 to M-30, M-32 to M-33, and M-36 to M-44 it is Sf. Please make this consistent between the text and the Figures.	Changed to: “Sf (no subscript)”	Accepted
97. Global	M	Please check all Figures for North arrows.	Global change: either a north arrow or the Northing UTM and Easting UTM are clearly indicated.	Accepted
98. Global	M	Please change all use of "pump tests" to "aquifer tests" in the text and on Figures.	Global change to: "aquifer tests" or "pumping-scale test” depending on the use in order to maintain consistency with the supporting documentation in the HDD (SNJV, 2006b). See also response to Comments #20 and #105.	Accepted
99. Global	M	Use of phrases such as "largely successful" on Page 4-24 are unclear and should be eliminated or modified to add clarity.	Global searches on "largely successful" "largely", "successfully", "principally", "generally", "mostly" and global change to ensure the basis for the qualitative description is provided in the text or the word modified or deleted.	Accepted
100. Global	M	Please make text and Figures consistent in the use of capitalization. For example, on Page 4-40, Figure 4-17 tests and units are not capitalized while in the text on Page 4-39, which describes Figure 4-17, tests and units are capitalized.	Global change to capitalize all detonations and HSUs.	Accepted
101. Global	M	Please make text and Tables consistent in the use of cases and runs. For example, on Page 4-54, in the text "cases" is used, whereas in Table 4-13, "run" is used. Also, on Page 4-51, sensitivity "runs" and model "runs" are used in the third and fourth paragraphs and in the fifth paragraph "cases" is used.	Global change to “Case” in applicable tables and text.	Accepted
102. Global	M	Please make the use of the well names consistent in the text, Figures and Tables. For example, Well WW C-1 is stated in the text on Page 5-12, Section 5.2.3, Second Paragraph, Seventh Sentence but on Figure 5-4, it is listed as WW-C-1.	Global changes to: WW-C-1 and WW-2 Figures from legacy documents were not modified.	Accepted
103. Global	M	In several Figures in Section 5.6.2, the cumulative distribution is indicated by a red line, however that is not indicated in the text, such as, cumulative distribution (**red line**). Please add this to the text for completeness.	Added text to clarify the red lines represent the cumulative distribution for figures in Section 5.6.2.	Accepted

[a]Comment Types: M = Mandatory, S = Suggested.
Return Document Review Sheets to NNSA/NFO Environmental Management Operations Activity, Attn: QAC, M/S NSF 505

10. Comment Number/Location	11. Type[a]	12. Comment	13. Comment Response	14. Accept/Reject
104. Global	M	Please make the text consistent in the use of "nominal case" and "base case." If there is a clear distinction then it should be described fully in the text. For example, on Page 6-3, Section 6.0, First Paragraph, First full Sentence, nominal case is used, whereas, on Page 6-6, Section 6.1.2, Third Paragraph, First Sentence, base-case is used. In addition, on Page 6-110, Section 6.5.2, First Paragraph on page, First Sentence both terms are used [" ... presents a nominal (or base-case) representation"]. The use of two terms can lead to confusion. Please select one term and stay consistent.	Global change to: "base case" or removed for clarity.	Accepted
105. Global	M	In several locations in the text in Chapter 6 the phrase "pumping-scale aquifer tests" is included. Please remove pumping-scale or clearly define what is meant by this term.	The term "pumping-scale" is used to describe aquifer tests or simply tests in the HDD (SNJV, 2006b). This is noted in Sections 3.4.3.4 and 5.2.5.1. Added: "Slug-scale tests are based on instantaneously adding or removing a volume of water from the well and observing the water-level recovery to the static condition. Pumping-scale tests are based on pumping a significant volume of water over an extended period of time and observing the water-level drawdown and recovery. As summarized in SNJV (2006b, Section 6.4.1), the pumping-scale test results are considered to provide the most appropriate information for use in large-scale modeling, because they provide results representative of the greatest aquifer volume and are more likely to reflect high hydraulic conductivity structure in tested formations." in Section 3.4.3.4 See also response to Comments #20 and #98.	Accepted

[a]Comment Types: M = Mandatory, S = Suggested.
Return Document Review Sheets to NNSA/NFO Environmental Management Operations Activity, Attn: QAC, M/S NSF 505

DISTRIBUTION

	Copies
W.R. Wilborn Environmental Management Operations U.S. Department of Energy National Nuclear Security Administration Nevada Site Office P.O. Box 98518, M/S 505 Las Vegas, NV 89193-8518	1 hard copy w/electronic media
Bimal Mukhopadhyay Environmental Management Operations U.S. Department of Energy National Nuclear Security Administration Nevada Site Office P.O. Box 98518, M/S 505 Las Vegas, NV 89193-8518	UGTA website
Kathryn Knapp Environmental Management Operations Support U.S. Department of Energy National Nuclear Security Administration Nevada Site Office P.O. Box 98518, M/S 505 Las Vegas, NV 89193-8518	UGTA website
Bruce Stolte Environmental Management Operations U.S. Department of Energy National Nuclear Security Administration Nevada Site Office P.O. Box 98518, M/S 505 Las Vegas, NV 89193-8518	UGTA website
Chris Andres State of Nevada Nevada Division of Environmental Protection 2030 E. Flamingo Road, Suite 230 Las Vegas, NV 89119-0818	2 hard copies w/electronic media

	Copies
Robert Andrews Navarro-Intera, LLC P.O. Box 98952, NSF 167 Las Vegas, NV 89193-8518	UGTA website
Irene Farnham Navarro-Intera, LLC P.O. Box 98952, NSF 167 Las Vegas, NV 89193-8518	UGTA website
Gayle Pawloski Lawrence Livermore National Laboratory 7000 East Avenue, L-231 Livermore, CA 94550-9900	UGTA website
U.S. Department of Energy Office of Scientific and Technical Information P.O. Box 62 Oak Ridge, TN 37831-0062	1 electronic media
Celeste Sandoval Nye County Nuclear Waste Repository Project Office 1210 E. Basin Road, Suite #6 Pahrump, NV 89060	1 electronic media
Naomi Becker Los Alamos National Laboratory Bikini Atoll Rd., SM30, MS T003 Los Alamos, NM 87545	UGTA website
Dan Levitt Los Alamos National Laboratory Hydrology, Geochemistry, and Geology Group, EES-6 Earth and Environmental Sciences Division SM-30 Bikini Atoll Rd., MS T003 Los Alamos, NM 87545	UGTA website
Andrew Tompson Lawrence Livermore National Laboratory 7000 East Avenue, L-103 Livermore, CA 94550-9909	UGTA website

	Copies
Robert Graves U.S. Geological Survey Water Resources Division 160 North Stephanie Street Henderson, NV 89074	UGTA website
Chuck E. Russell Desert Research Institute 755 E. Flamingo Las Vegas, NV 89119	UGTA website
Ken Ortego National Security Technologies, LLC P.O. Box 98521, M/S NLV 082 Las Vegas, NV 89193-8521	UGTA website
Sam Marutzky Navarro-Intera, LLC P.O. Box 98952, NSF 167 Las Vegas, NV 89193-8518	UGTA website
Ed Kwicklis Los Alamos National Laboratory Hydrology, Geochemistry, and Geology Group, EES-6 Earth and Environmental Sciences Division SM-30 Bikini Atoll Rd., MS T003 Los Alamos, NM 87545	UGTA website
Greg Ruskauff Navarro-Intera, LLC P.O. Box 98952, NSF 167 Las Vegas, NV 89193-8518	UGTA website
Elizabeth Keating Los Alamos National Laboratory Hydrology, Geochemistry, and Geology Group, EES-6 Earth and Environmental Sciences Division SM-30 Bikini Atoll Rd., MS T003 Los Alamos, NM 87545	UGTA website

	Copies
Pete Martian Navarro-Intera, LLC P.O. Box 98952, NSF 167 Las Vegas, NV 89193-8518	UGTA website
John Pickens INTERA, Inc. 1812 Centre Creek Drive Suite 300 Austin, TX 78754	UGTA website
Mavrik Zavarin Lawrence Livermore National Laboratory 7000 East Avenue, L-231 Livermore, CA 94550-9909	UGTA website
Nicole DeNovio Senior Project Hydrogeochemist Golder Associates Inc. 18300 NE Union Hill Road, Suite 200, Redmond, Washington, 98052	UGTA website
Todd Kincaid GeoHydros, LLC 27 Keystone Avenue Reno, NV 89503	UGTA website
Sig Drellack National Security Technologies, LLC P.O. Box 98521 MS/NLV 082 Las Vegas, NV 89193	UGTA website
Lance Prothro National Security Technologies, LLC P.O. Box 98521 MS/NLV 082 Las Vegas, NV 89193	UGTA website
D. M. Reeves Desert Research Institute 2215 Raggio Parkway Reno, NV 89512	UGTA website

	Copies
K. J. Halford U. S. Geological Survey 2730 N. Deer Run Road Carson City, NV 89701	UGTA website
Southern Nevada Public Reading Facility c/o Nuclear Testing Archive P.O. Box 98521, M/S NLV 400 Las Vegas, NV 89193-8521	2 electronic media
Northern Nevada Public Reading Facility c/o Nevada State Library & Archives 100 N Stewart Street Carson City, NV 89701-4285	1 electronic media
Records: Environmental Management Records U.S. Department of Energy National Nuclear Security Administration Nevada Site Office P.O. Box 98518, M/S 505 Las Vegas, NV 89193-8518	1 hardcopy w/electronic media
Navarro-Intera, LLC Central Files P.O. Box 98952, NSF 156 Las Vegas, NV 89193-8518	1 electronic media